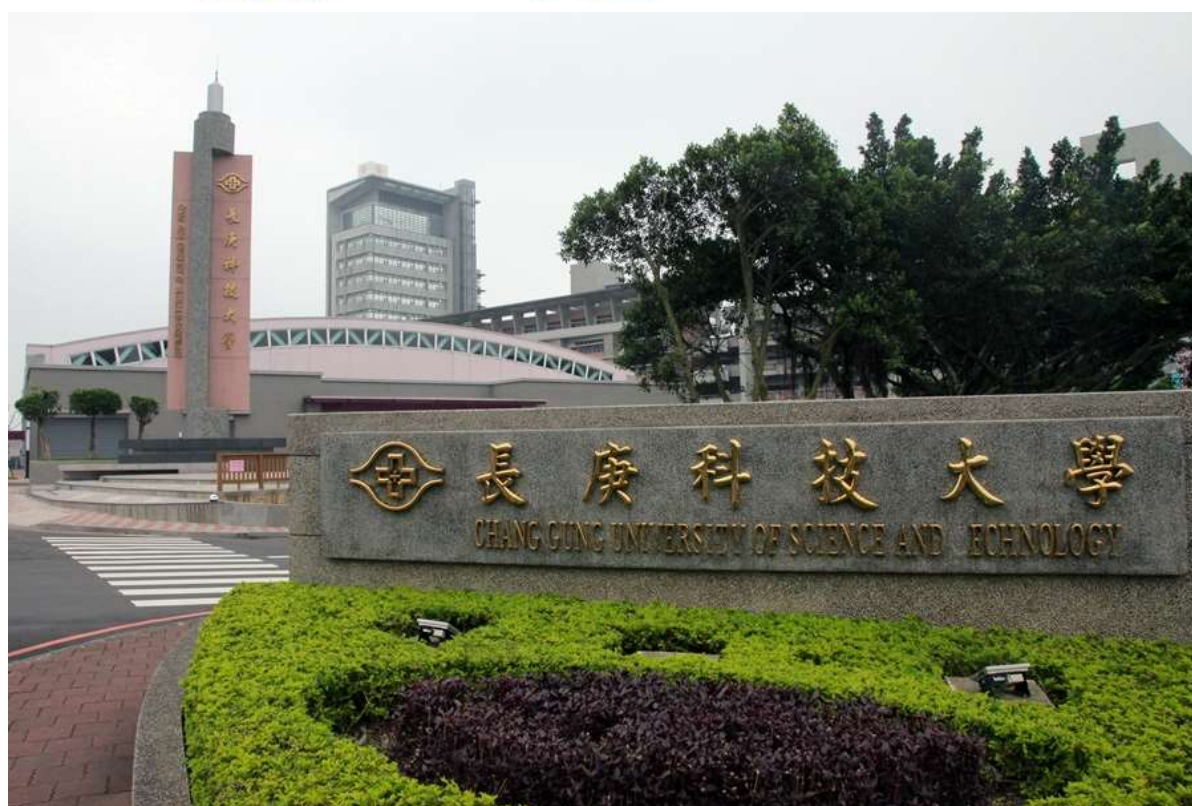
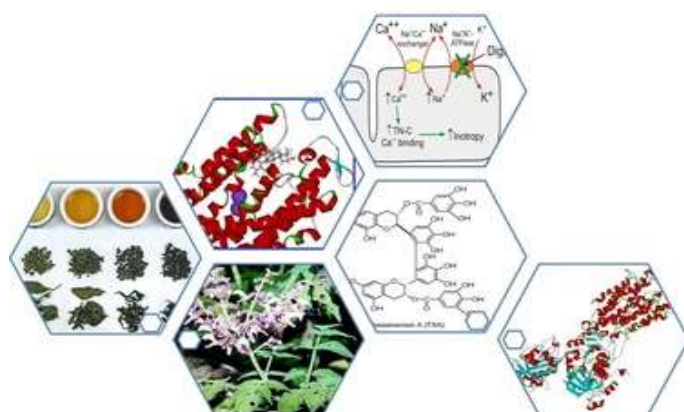


# 中草藥研究中心 論文集

2016.9.1~2017.8.31



CHANG GUNG UNIVERSITY OF SCIENCE AND TECHNOLOGY

# 長庚科技大學中草藥研究中心

## 論文集

2016.9.1~2017.8.31

## 目錄

- 一、 期刊論文出處及相關訊息.....I  
二、 論文全文

序號	論文標題	學校主要 負責教師	頁碼
01	Astrocyte as the Modulator in Brain Inflammation and Neurodegenerative Disorders	謝喜龍	1
02	Sterol regulatory element-binding protein-1c regulates inflammasome activation in gingival fibroblasts infected with high-glucose-treated Porphyromonas gingivalis	郭星君	3
03	Ilex kaushue and its bioactive component 3,5-dicaffeoylquinic acid protected mice from lipopolysaccharide-induced acute lung injury	黃聰龍、 方嘉佑、 謝佩文	15
04	Capsaicin supplementation reduces physical fatigue and improves exercise performance in mice	邱群惠	27
05	Zoanthamine-Type Alkaloids from the Zoanthid Zoanthus kuroshio Collected in Taiwan and Their Effects on Inflammation	黃聰龍	42
06	Fractional CO <sub>2</sub> laser pretreatment facilitates transdermal delivery of two vitamin C derivatives	蕭千祐	49
07	TNF- $\alpha$ -induced cPLA <sub>2</sub> expression via NADPH oxidase/reactive oxygen species-dependent NF- $\kappa$ B cascade on human pulmonary alveolar epithelial cells	楊春茂	58
08	New anti-inflammatory 9,11-secosterols with a rare tricyclo[5,2,1,1]decane ring from a Formosan gorgonian Pinnigorgia sp.	黃聰龍	73
09	Four new compounds from edible algae Cladosiphon okamuranus and Chlorella sorokiniana and their bioactivities	黃聰龍	80
10	Anti-allergic hydroxy fatty acids from Typhonium blumei explored through ChemGPS-NP	黃聰龍	84
11	Screening of Luzula species native to the Carpathian	黃聰龍	101



	Basin for anti-inflammatory activity and bioactivity-guided isolation of compounds from <i>Luzula luzuloides</i> (Lam.) Dandy & Wilmott		
12	Pinnisterols D-J, new 11-acetoxy-9,11-secosterols with a 1,4-quinone moiety from Formosan gorgonian coral <i>Pinnigorgia</i> sp. (Gorgoniidae)	黃聰龍	109
13	Bioactive new withanolides from the cultured soft coral <i>Sinularia brassica</i>	黃聰龍	120
14	Artocarpin, an isoprenyl flavonoid, induces p53-dependent or independent apoptosis via ROS-mediated MAPKs and Akt activation in non-small cell lung cancer cells	李江文	125
15	CIL-102-induced cell cycle arrest and apoptosis in colorectal cancer cells via upregulation of p21 and GADD45	郭星君	142
16	Constituents from the leaves of <i>Clausena lansium</i> and their anti-inflammatory activity	黃聰龍	159
17	Supplementation with Hualian No. 4 wild bitter gourd ( <i>Momordica charantia</i> Linn. var. <i>abbreviata</i> ser.) extract increases anti-fatigue activities and enhances exercise performance in mice	蕭千祐	168
18	Lymphoma cell isolation using multifunctional magnetic nanoparticles: Antibody conjugation and characterization	劉繼賢	178
19	Nanovesicle delivery to the liver via retinol binding protein and platelet-derived growth factor receptors: How targeting ligands affect biodistribution	方嘉佑	189
20	Changbai mountain ginseng ( <i>Panax ginseng</i> C.A. Mey) extract supplementation improves exercise performance and energy utilization and decreases fatigue-associated parameters in mice	邱群惠	204
21	Improvement of shikimic acid production in <i>Escherichia coli</i> with growth phase-dependent regulation in the biosynthetic pathway from glycerol	李明怡	218
22	Almond skin polyphenol extract inhibits inflammation and promotes lipolysis in differentiated 3T3-L1 adipocytes	黃文忠、 陳琦媛	226
23	Correlation of HAMP gene polymorphisms and expression with the susceptibility and length of hospital	郭星君	233

stays in Taiwanese children with Kawasaki disease

24	Phloretin attenuates allergic airway inflammation and oxidative stress in asthmatic mice	劉倩君、 黃文忠	243
25	Briarenols C-E, new polyoxygenated briaranes from the octocoral <i>briareum excavatum</i>	黃聰龍	256
26	Amiodarone reduces depolarization-evoked glutamate release from hippocampal synaptosomes	王素珍	265
27	New marine sterols from a gorgonian <i>Pinnigorgia</i> sp.	黃聰龍	273
28	Facile synthesis of magnetic iron oxide nanoparticles for nattokinase isolation	劉繼賢	281
29	Water extract of <i>Helminthostachys zeylanica</i> attenuates LPS-induced acute lung injury in mice by modulating NF- $\kappa$ B and MAPK pathways	劉倩君、 林傳福	289
30	Ciproxifan, a histamine H3 receptor antagonist and inverse agonist, presynaptically inhibits glutamate release in rat hippocampus	王素珍	298
31	Recent advances in oral delivery of drugs and bioactive natural products using solid lipid nanoparticles as the carriers	方嘉佑	308
32	Ugonin U stimulates NLRP3 inflammasome activation and enhances inflammasome-mediated pathogen clearance	黃聰龍	324
33	Chemical Constituents and Anti-inflammatory Principles from the Fruits of <i>Forsythia suspensa</i>	黃聰龍	336
34	Anti-inflammatory Flavan-3-ol-dihydroretrochalcones from <i>Daemonorops draco</i>	黃聰龍	346
35	Novel 11-norbetaenone isolated from an entomopathogenic fungus <i>Lecanicillium antillanum</i>	黃聰龍	353
36	Capsaicin presynaptically inhibits glutamate release through the activation of TRPV1 and calcineurin in the hippocampus of rats	王素珍	358
37	6-Hydroxy-5,7-dimethoxy-flavone suppresses the neutrophil respiratory burst via selective PDE4 inhibition to ameliorate acute lung injury	黃聰龍	368

38	Inhibition of glutamate release by cilnidipine in rat cerebrocortical nerve terminals (synaptosomes)	王素珍	382
39	Anti-melasma codrug of retinoic acid assists cutaneous absorption with attenuated skin irritation	謝佩文、 方嘉佑	388
40	Dipeptide HCH6-1 inhibits neutrophil activation and protects against acute lung injury by blocking FPR1	謝佩文、 黃聰龍	398
41	Arachidonic Acid Induces ARE/Nrf2-Dependent Heme Oxygenase-1 Transcription in Rat Brain Astrocytes	楊春茂	414
42	Exploring the structure-permeation relationship of topical tricyclic antidepressants used for skin analgesia	方嘉佑	430
43	Resveratrol inhibits BK-induced COX-2 transcription by suppressing acetylation of AP-1 and NF- $\kappa$ B in human rheumatoid arthritis synovial fibroblasts	楊春茂	442
44	Inflammation Modulatory Phorbol Esters from the Seeds of <i>Aquilaria malaccensis</i>	黃聰龍	457
45	Protein-lipid nanohybrids as emerging platforms for drug and gene delivery: Challenges and outcomes	方嘉佑	464
46	Discovery of indeno[1,2-c]quinoline derivatives as potent dual antituberculosis and anti-inflammatory agents	黃聰龍	481
47	Anti-inflammatory and neuroprotective constituents from the peels of <i>citrus grandis</i>	黃聰龍	496
48	A novel fine tuning scheme of miR-200c in modulating lung cell redox homeostasis	吳依璇、 趙崇義	507
49	Pterostilbene, a methoxylated resveratrol derivative, efficiently eradicates planktonic, biofilm, and intracellular MRSA by topical application	方嘉佑	521
50	Bioactive Triterpenoids from the Leaves and Twigs of <i>Lithocarpus litseifolius</i> and <i>L. corneus</i>	黃聰龍	535
51	Development and validation of an LC-MS/MS method for simultaneous quantification of hesperidin and hesperetin in rat plasma for pharmacokinetic studies	鮑力恒	545
52	dsRNA binding domain of PKR is proteolytically released by enterovirus A71 to facilitate viral replication	洪錦堂	554
53	Sterols from the octocoral <i>Nephthea columnaris</i>	黃聰龍	566



54	Risk of Epilepsy in Individuals with Posttraumatic Stress Disorder: A Nationwide Longitudinal Study	潘台龍	573
55	Osthole attenuates lipid accumulation, regulates the expression of inflammatory mediators, and increases antioxidants in FL83B cells	黃文忠、 吳淑如	601
56	Cross-talk between bacterial two-component systems drives stepwise regulation of flagellar biosynthesis in swarming development	賴信志	611
57	Post-traumatic Stress Disorder and Risk of Parkinson Disease: A Nationwide Longitudinal Study	潘台龍	617
58	Response of dermal fibroblasts to biochemical and physical cues in aligned polycaprolactone/silk fibroin nanofiber scaffolds for application in tendon tissue engineering	陳志平	624
59	Major achievements of evidence-based traditional Chinese medicine in treating major diseases	鮑力恒	644
60	Injectable thermosensitive hydrogel containing hyaluronic acid and chitosan as a barrier for prevention of postoperative peritoneal adhesion	陳志平	655
61	Structural characterization of an immunostimulating polysaccharide from the stems of a new medicinal Dendrobium species: Dendrobium Taiseed Tosnobile	邱群惠	666
62	Isoflavones and anti-inflammatory constituents from the fruits of <i>Psoralea corylifolia</i>	黃聰龍	675
63	The long non-coding RNA LOC441204 enhances cell growth in human glioma	林光輝	683
64	High-intensity Interval Training Improves Mitochondrial Function and Suppresses Thrombin Generation in Platelets undergoing Hypoxic Stress	王素珍	693

# 長庚科技大學中草藥研究中心

## 論文集

2016.9.1~2017.8.31

### 一、期刊論文出處及相關訊息

- 01 Hsieh, H.-L., Yang C.-M. Astrocyte as the modulator in brain inflammation and neurodegenerative disorders (2016) *Annals of Neurodegenerative Disorders*, 1(2): 1008.
- 02 Kuo, H.-C., Chang, L.-C., Chen, T.-C., Lee, K.-C., Lee, K.-F., Chen, C.-N., Yu, H.-R. Sterol regulatory element-binding protein-1c regulates inflammasome activation in gingival fibroblasts infected with high-glucose-treated *Porphyromonas gingivalis* (2016) *Frontiers in Cellular and Infection Microbiology*, 26(6):195. DOI: 10.3389/fcimb.2016.00195.
- 03 Chen, Y.-L., Hwang, T.-L., Yu, H.-P., Fang, J.-Y., Chong, K.Y., Chang, Y.-W., Chen, C.-Y., Yang, H.-W., Chang, W.-Y., Hsieh, P.-W. *Ilex kaushue* and its bioactive component 3,5-dicaffeoylquinic acid protected mice from lipopolysaccharide-induced acute lung injury (2016) *Scientific Reports*, 29(6):34243. DOI: 10.1038/srep34243.
- 04 Hsu, Y.-J., Huang, W.-C., Chiu, C.-C., Liu, Y.-L., Chiu, W.-C., Chiu, C.-H., Chiu, Y.-S., Huang, C.-C. Capsaicin supplementation reduces physical fatigue and improves exercise performance in mice (2016) *Nutrients*, 8 (10). DOI: 10.3390/nu8100648.
- 05 Hsu, Y.-M., Chang, F.-R., Lo, I.-W., Lai, K.-H., El-Shazly, M., Wu, T.-Y., Du, Y.-C., Hwang, T.-L., Cheng, Y.-B., Wu, Y.-C. Zoanthamine-Type Alkaloids from the Zoanthid *Zoanthus kuroshio* Collected in Taiwan and Their Effects on Inflammation (2016) *Journal of Natural Products*, 79 (10):2674-2680. DOI: 10.1021/acs.jnatprod.6b00625.

- 06 Hsiao, C.-Y., Sung, H.-C., Hu, S., Huang, Y.-L., Huang, C.-H. Fractional CO<sub>2</sub> laser pretreatment facilitates transdermal delivery of two vitamin C derivatives (2016) *Molecules*, 21 (11). DOI: 10.3390/molecules21111547.
- 07 Lin, C.-C., Lin, W.-N., Cho, R.-L., Wang, C.-Y., Hsiao, L.-D., Yang, C.-M. TNF- $\alpha$ -induced cPLA<sub>2</sub> expression via NADPH oxidase/reactive oxygen species-dependent NF- $\kappa$ B cascade on human pulmonary alveolar epithelial cells (2016) *Frontiers in Pharmacology*, 7 (NOV):447. DOI: 10.3389/fphar.2016.00447.
- 08 Chang, Y.-C., Hwang, T.-L., Sheu, J.-H., Wu, Y.-C., Sung, P.-J. New anti-inflammatory 9,11-secosterols with a rare tricyclo[5,2,1,1]decane ring from a Formosan gorgonian *Pinnigorgia* sp. (2016) *Marine Drugs*, 14 (12). DOI: 10.3390/md14120218.
- 09 Cheng, K.-C., Kuo, P.-C., Hung, H.-Y., Yu, K.-H., Hwang, T.-L., Shieh, P.-C., Chang, J.-S., Wu, T.-S. Four new compounds from edible algae *Cladosiphon okamuranus* and *Chlorella sorokiniana* and their bioactivities (2016) *Phytochemistry Letters*, 18:113-116. DOI: 10.1016/j.phytol.2016.09.008.
- 10 Chang, Y.-C., Hwang, T.-L., Sheu, J.-H., Wu, Y.-C., Sung, P.-J. New anti-inflammatory 9,11-secosterols with a rare tricyclo[5,2,1,1]decane ring from a formosan gorgonian *Pinnigorgia* sp. (2016) *Marine Drugs*, 14(12):218. DOI:10.3390/md14120218.
- 11 Tóth, B., Chang, F.-R., Hwang, T.-L., Szappanos, Á., Mándi, A., Hunyadi, A., Kurtán, T., Jakab, G., Hohmann, J., Vasas, A. Screening of *Luzula* species native to the Carpathian Basin for anti-inflammatory activity and bioactivity-guided isolation of compounds from *Luzula luzuloides* (Lam.) Dandy & Wilmott (2017) *Fitoterapia*, 116:131-138. DOI: 10.1016/j.fitote.2016.12.004.



- 12 Chang, Y.-C., Hwang, T.-L., Kuo, L.-M., Sung, P.-J. Pinnisterols D-J, new 11-acetoxy-9,11-secoosterols with a 1,4-quinone moiety from Formosan gorgonian coral *Pinnigorgia* sp. (Gorgoniidae) (2017) *Marine Drugs*, 15 (1). DOI: 10.3390/md15010011.
- 13 Huang, C.-Y., Ahmed, A.F., Su, J.-H., Sung, P.-J., Hwang, T.-L., Chiang, P.-L., Dai, C.-F., Liaw, C.-C., Sheu, J.-H. Bioactive new withanolides from the cultured soft coral *Sinularia brassica* (2017) *Bioorganic and Medicinal Chemistry Letters*, 27(15):3267-3271. DOI: 10.1016/j.bmcl.2017.06.029.
- 14 Tsai, M.-H., Liu, J.-F., Chiang, Y.-C., Hu, S.C., Hsu, L.-F., Lin, Y.-C., Lin, Z.-C., Lee, H.-C., Chen, M.-C., Huang, C.-L., Lee, C.-W. Artocarpin, an isoprenyl flavonoid, induces p53-dependent or independent apoptosis via ROS-mediated MAPKs and Akt activation in non-small cell lung cancer cells (2017) *Oncotarget*, 8 (17): 28342-28358. DOI: 10.18632/oncotarget.16058.
- 15 Huang, W.-S., Kuo, Y.-H., Kuo, H.-C., Hsieh, M.-C., Huang, C.-Y., Lee, K.-C., Lee, K.-F., Shen, C.-H., Tung, S.-Y., Teng, C.-C. CIL-102-induced cell cycle arrest and apoptosis in colorectal cancer cells via upregulation of p21 and GADD45 (2017) *PLoS ONE*, 12 (1). DOI: 10.1371/journal.pone.0168989.
- 16 Shen, D.-Y., Kuo, P.-C., Huang, S.-C., Hwang, T.-L., Chan, Y.-Y., Shieh, P.-C., Ngan, N.T., Thang, T.D., Wu, T.-S. Constituents from the leaves of *Clausena lansium* and their anti-inflammatory activity (2017) *Journal of Natural Medicines*, 71 (1): 96-104. DOI: 10.1007/s11418-016-1033-x.
- 17 Hsiao, C.-Y., Chen, Y.-M., Hsu, Y.-J., Huang, C.-C., Sung, H.-C., Chen, S.-S. Supplementation with Hualian No. 4 wild bitter gourd (*Momordica charantia* Linn. var. *abbreviata* ser.) extract increases anti-fatigue activities and enhances exercise performance in mice

- (2017) *Journal of Veterinary Medical Science*, 79(6): 1110–1119. DOI: 10.1292/jvms.17-0079.
- 18 Sahoo, S.L., Liu, C.-H., Wu, W.-C. Lymphoma cell isolation using multifunctional magnetic nanoparticles: Antibody conjugation and characterization (2017) *RSC Advances*, 7(36): 22468-22478. DOI:10.1039/C7RA02084H.
  - 19 Hsu, C.-Y., Chen, C.-H., Aljuffali, I.A., Dai, Y.-S., Fang, J.-Y. Nanovesicle delivery to the liver via retinol binding protein and platelet-derived growth factor receptors: How targeting ligands affect biodistribution (2017) *Nanomedicine*, 12 (4):317-331. DOI: 10.2217/nnm-2016-0319.
  - 20 Ma, G.-D., Chiu, C.-H., Hsu, Y.-J., Hou, C.-W., Chen, Y.-M., Huang, C.-C. Changbai mountain ginseng (*Panax ginseng* C.A. Mey) extract supplementation improves exercise performance and energy utilization and decreases fatigue-associated parameters in mice (2017) *Molecules*, 22 (2) .DOI: 10.3390/molecules22020237.
  - 21 Lee, M.-Y., Hung, W.-P., Tsai, S.-H. Improvement of shikimic acid production in *Escherichia coli* with growth phase-dependent regulation in the biosynthetic pathway from glycerol (2017) *World Journal of Microbiology and Biotechnology*, 33 (2). DOI: 10.1007/s11274-016-2192-3.
  - 22 Huang, W.-C., Chen, C.-Y., Wu, S.-J. Almond skin polyphenol extract inhibits inflammation and promotes lipolysis in differentiated 3T3-L1 adipocytes (2017) *Journal of Medicinal Food*, 20 (2):103-109. DOI: 10.1089/jmf.2016.3806.
  - 23 Huang, Y.-H., Yang, K.D., Hsu, Y.-W., Lu, H.-F., Wong, H.S.-C., Yu, H.-R., Kuo, H.-C., Huang, F.-C., Lo, M.-H., Hsieh, K.-S., Chen, S.-F., Chang, W.-C., Kuo, H.-C. Correlation of HAMP gene

- polymorphisms and expression with the susceptibility and length of hospital stays in Taiwanese children with Kawasaki disease (2017) *Oncotarget*, 8(31):51859-51868. DOI: 10.18632/oncotarget.17700.
- 24 Huang, W.-C., Fang, L.-W., Liou, C.-J. Phloretin attenuates allergic airway inflammation and oxidative stress in asthmatic mice (2017) *Frontiers in Immunology*, 8 (FEB):134. DOI: 10.3389/fimmu.2017.00134.
  - 25 Chen, N.-F., Su, Y.-D., Hwang, T.-L., Liao, Z.-J., Tsui, K.-H., Wen, Z.-H., Wu, Y.-C., Sung, P.-J., Schmidt, T.J. Briarenols C-E, new polyoxygenated briaranes from the octocoral *briareum excavatum* (2017) *Molecules*, 22 (3). DOI: 10.3390/molecules22030475.
  - 26 Chang, C.Y., Hung, C.F., Huang, S.K., Kuo, J.R., Wang, S.J. Amiodarone reduces depolarization-evoked glutamate release from hippocampal synaptosomes (2017) *Journal of Pharmacological Sciences*, 133 (3):168-175. DOI: 10.1016/j.jphs.2017.02.014.
  - 27 Chang, Y.-C., Hwang, T.-L., Chao, C.-H., Sung, P.-J. New marine sterols from a gorgonian *Pinnigorgia* sp. (2017) *Molecules*, 22 (3). DOI: 10.3390/molecules22030393.
  - 28 Liu, C.-H., Lai, H.-Y., Wu, W.-C. Facile synthesis of magnetic iron oxide nanoparticles for nattokinase isolation (2017) *Food and Bioproducts Processing*, 102:260-267. DOI: 10.1016/j.fbp.2017.01.006.
  - 29 Liou, C.-J., Huang, Y.-L., Huang, W.-C., Yeh, K.-W., Huang, T.-Y., Lin, C.-F. Water extract of *Helminthostachys zeylanica* attenuates LPS-induced acute lung injury in mice by modulating NF- $\kappa$ B and MAPK pathways (2017) *Journal of Ethnopharmacology*, 199:30-38. DOI: 10.1016/j.jep.2017.01.043.



- 30 Lu, C.-W., Lin, T.-Y., Chang, C.-Y., Huang, S.-K. Ciproxifan, a histamine H<sub>3</sub> receptor antagonist and inverse agonist, presynaptically inhibits glutamate release in rat hippocampus (2017) *Toxicology and Applied Pharmacology*, 319:12-21. DOI: 10.1016/j.taap.2017.01.017.
- 31 Lin, C.-H., Chen, C.-H., Lin, Z.-C., Fang, J.-Y. Recent advances in oral delivery of drugs and bioactive natural products using solid lipid nanoparticles as the carriers (2017) *Journal of Food and Drug Analysis*, 25(2): 219-234. DOI: <http://dx.doi.org/10.1016/j.jfda.2017.02.001>.
- 32 Chen, C.-Y., Yang, C.-H., Tsai, Y.-F., Liaw, C.-C., Chang, W.-Y., Hwang, T.-L. Ugonin U stimulates NLRP3 inflammasome activation and enhances inflammasome-mediated pathogen clearance (2017) *Redox Biology*, 11:263-274. DOI: 10.1016/j.redox.2016.12.018.
- 33 Kuo, P.-C., Hung, H.-Y., Nian, C.-W., Hwang, T.-L., Cheng, J.-C., Kuo, D.-H., Lee, E.-J., Tai, S.-H., Wu, T.-S. Chemical Constituents and Anti-inflammatory Principles from the Fruits of *Forsythia suspense* (2017) *Journal of Natural Products*, 80 (4):1055-1064. DOI: 10.1021/acs.jnatprod.6b01141.
- 34 Kuo, P.-C., Hung, H.-Y., Hwang, T.-L., Du, W.-K., Ku, H.-C., Lee, E.-J., Tai, S.-H., Chen, F.-A., Wu, T.-S. Anti-inflammatory Flavan-3-ol-dihydroretrochalcones from *Daemonorops draco* (2017) *Journal of Natural Products*, 80 (4):783-789. DOI: 10.1021/acs.jnatprod.7b00039.
- 35 Li, C.-Y., Lo, I.-W., Wang, S.-W., Hwang, T.-L., Chung, Y.-M., Cheng, Y.-B., Tseng, S.-P., Liu, Y.-H., Hsu, Y.-M., Chen, S.-R., Hu, H.-C., Chang, F.-R., Wu, Y.-C. Novel 11-norbetaenone isolated from an entomopathogenic fungus *Lecanicillium antillanum* (2017) *Bioorganic and Medicinal Chemistry Letters*, 27(9): 1978-1982 DOI:

10.1016/j.bmcl.2017.03.019.

- 36 Lu, C.W., Lin, T.Y., Hsie, T.Y., Huang, S.K., Wang, S.J. Capsaicin presynaptically inhibits glutamate release through the activation of TRPV1 and calcineurin in the hippocampus of rats (2017) *Food and Function*, 8(5):1859-1868. DOI: 10.1039/c7fo00011a.
- 37 Tsai, Y.-F., Chu, T.-C., Chang, W.-Y., Wu, Y.-C., Chang, F.-R., Yang, S.-C., Wu, T.-Y., Hsu, Y.-M., Chen, C.-Y., Chang, S.-H., Hwang, T.-L. 6-Hydroxy-5,7-dimethoxy-flavone suppresses the neutrophil respiratory burst via selective PDE4 inhibition to ameliorate acute lung injury (2017) *Free Radical Biology and Medicine*, 106: 379-392. DOI: 10.1016/j.freeradbiomed.2017.03.002.
- 38 Lu, C.W., Lin, T.Y., Huang, S.K., Wang, S.J. Inhibition of glutamate release by cilnidipine in rat cerebrocortical nerve terminals (synaptosomes) (2017) *NeuroReport*, 28(9):527-532 DOI: 10.1097/WNR.0000000000000795.
- 39 Hsieh, P.-W., Hung, C.-F., Lin, C.-H., Huang, C.-W., Fang, J.-Y. Anti-melasma codrug of retinoic acid assists cutaneous absorption with attenuated skin irritation (2017) *European Journal of Pharmaceutics and Biopharmaceutics*, 114:154-163 DOI: 10.1016/j.ejpb.2017.01.016.
- 40 Yang, S.-C., Chang, S.-H., Hsieh, P.-W., Huang, Y.-T., Ho, C.-M., Tsai, Y.-F., Hwang, T.-L. Dipeptide HCH6-1 inhibits neutrophil activation and protects against acute lung injury by blocking FPR1 (2017) *Free Radical Biology and Medicine*, 106: 254-269. DOI: 10.1016/j.freeradbiomed.2017.02.038.
- 41 Lin, C.-C., Yang, C.-C., Chen, Y.-W., Hsiao, L.-D., Yang, C.-M. Arachidonic Acid Induces ARE/Nrf2-Dependent Heme Oxygenase-1 Transcription in Rat Brain Astrocytes (2017) *Molecular Neurobiology*: 1-16. DOI: 10.1007/s12035-017-0590-7.

- 42 Liu, K.-S., Huang, T.-H., Aljuffali, I.A., Chen, E.-L., Wang, J.-J., Fang, J.-Y. Exploring the structure-permeation relationship of topical tricyclic antidepressants used for skin analgesia (2017) *International Journal of Pharmaceutics*, 523 (1): 386-397. DOI: 10.1016/j.ijpharm.2017.03.048.
- 43 Yang, C.-M., Chen, Y.-W., Chi, P.-L., Hsiao, L.-D. Resveratrol inhibits BK-induced COX-2 transcription by suppressing acetylation of AP-1 and NF- $\kappa$ B in human rheumatoid arthritis synovial fibroblasts (2017) *Biochemical Pharmacology*, 132: 77-91 DOI: 10.1016/j.bcp.2017.03.003.
- 44 Wagh, V.D., Korinek, M., Lo, I.-W., Hsu, Y.-M., Chen, S.-L., Hsu, H.-Y., Hwang, T.-L., Wu, Y.-C., Chen, B.-H., Cheng, Y.-B., Chang, F.-R. Inflammation Modulatory Phorbol Esters from the Seeds of *Aquilaria malaccensis* (2017) *Journal of Natural Products*, 80(5):1421-1427. DOI: 10.1021/acs.jnatprod.6b01096.
- 45 Gaber, M., Medhat, W., Hany, M., Saher, N., Fang, J.-Y., Elzoghby, A. Protein-lipid nanohybrids as emerging platforms for drug and gene delivery: Challenges and outcomes (2017) *Journal of Controlled Release*, 254:75-91. DOI: 10.1016/j.jconrel.2017.03.392.
- 46 Tseng, C.-H., Tung, C.-W., Wu, C.-H., Tzeng, C.-C., Chen, Y.-H., Hwang, T.-L., Chen, Y.-L. Discovery of indeno[1,2-c]quinoline derivatives as potent dual antituberculosis and anti-inflammatory agents (2017) *Molecules*, 22(6): 1001. DOI: 10.3390/molecules22061001.
- 47 Kuo, P.-C., Liao, Y.-R., Hung, H.-Y., Chuang, C.-W., Hwang, T.-L., Huang, S.-C., Shiao, Y.-J., Kuo, D.-H., Wu, T.-S. Anti-inflammatory and neuroprotective constituents from the peels of *Citrus grandis* (2017) *Molecules*, 22 (6): 967. DOI: 10.3390/molecules22060967.



- 48 Wu, Y.-H., Lin, H.-R., Lee, Y.-H., Huang, P.-H., Wei, H.-C., Stern, A., Chiu, D.T.-Y. A novel fine tuning scheme of miR-200c in modulating lung cell redox homeostasis (2017) *Free Radical Research*, 51(6): 591-603. DOI: 10.1080/10715762.2017.1339871.
- 49 Yang, S.-C., Tseng, C.-H., Wang, P.-W., Lu, P.-L., Weng, Y.-H., Yen, F.-L., Fang, J.-Y. Pterostilbene, a methoxylated resveratrol derivative, efficiently eradicates planktonic, biofilm, and intracellular MRSA by topical application (2017) *Frontiers in Microbiology* 8(JUN): 1103. DOI: 10.3389/fmicb.2017.01103.
- 50 Cheng, Y.-B., Liu, F.-J., Wang, C.-H., Hwang, T.-L., Tsai, Y.-F., Yen, C.-H., Wang, H.-C., Tseng, Y.-H., Chien, C.-T., Chen, Y.-M.A., Chang, F.-R., Wu, Y.-C. Bioactive Triterpenoids from the Leaves and Twigs of *Lithocarpus litseifolius* and *L. corneus* (2017) *Planta Medica*, DOI: 10.1055/s-0043-113826.
- 51 Lee, J.-T., Pao, L.-H., Hsieh, C.-D., Huang, P.-W., Hu, O.Y.-P. Development and validation of an LC-MS/MS method for simultaneous quantification of hesperidin and hesperetin in rat plasma for pharmacokinetic studies (2017) *Analytical Methods*, 9(22): 3329-3337. DOI:10.1039/C7AY00051K.
- 52 Chang, Y.-H., Lau, K.S., Kuo, R.-L., Horng, J.-T. dsRNA binding domain of PKR is proteolytically released by enterovirus A71 to facilitate viral replication (2017) *Frontiers in Cellular and Infection Microbiology*, 7(JUN): 284. DOI: 10.3389/fcimb.2017.00284.
- 53 Whuang, T.-Y., Tsai, H.-C., Su, Y.-D., Hwang, T.-L., Sung, P.-J. Sterols from the octocoral *Nephthea columnaris* (2017) *Marine Drugs*, 15(7): 212. DOI: 10.3390/md15070212.
- 54 Chen, Y.-H., Wei, H.-T., Bai, Y.-M., Hsu, J.-W., Huang, K.-L., Su,

- T.-P., Li, C.-T., Lin, W.-C., Wu, Y.-H., Pan, T.-L., Chen, T.-J., Tsai, S.-J., Chen, M.-H. Risk of Epilepsy in Individuals with Posttraumatic Stress Disorder: A Nationwide Longitudinal Study (2017) *Psychosomatic Medicine*, 79(6): 664-669. DOI: 10.1097/PSY.0000000000000463.
- 55 Huang, W.-C., Liao, P.-C., Huang, C.-H., Hu, S., Huang, S.-C., Wu, S.-J. Osthole attenuates lipid accumulation, regulates the expression of inflammatory mediators, and increases antioxidants in FL83B cell (2017) *Biomedicine and Pharmacotherapy*, 91: 78-87. DOI: 10.1016/j.biopha.2017.04.051.
- 56 Wei, C.-F., Tsai, Y.-H., Tsai, S.-H., Lin, C.-S., Chang, C.-J., Lu, C.-C., Huang, H.-C., Lai, H.-C. Cross-talk between bacterial two-component systems drives stepwise regulation of flagellar biosynthesis in swarming development (2017) *Biochemical and Biophysical Research Communications*, 489(1): 70-75. DOI: 10.1016/j.bbrc.2017.05.077.
- 57 Chan, Y.L.E., Bai, Y.-M., Hsu, J.-W., Huang, K.-L., Su, T.-P., Li, C.-T., Lin, W.-C., Pan, T.-L., Chen, T.-J., Tsai, S.-J., Chen, M.-H. Post-traumatic Stress Disorder and Risk of Parkinson Disease: A Nationwide Longitudinal Study (2017) *American Journal of Geriatric Psychiatry*, 25(8): 917-923. DOI: 10.1016/j.jagp.2017.03.012.
- 58 Chen, C.-H., Chen, S.-H., Kuo, C.-Y., Li, M.-L., Chen, J.-P. Response of dermal fibroblasts to biochemical and physical cues in aligned polycaprolactone/silk fibroin nanofiber scaffolds for application in tendon tissue engineering (2017) *Nanomaterials*, 7(8): 219. DOI: 10.3390/nano7080219.
- 59 Chao, J., Dai, Y., Verpoorte, R., Lam, W., Cheng, Y.-C., Pao, L.-H., Zhang, W., Chen, S. Major achievements of evidence-based

- traditional Chinese medicine in treating major diseases (2017) *Biochemical Pharmacology*, 139: 94-104. DOI: 10.1016/j.bcp.2017.06.123.
- 60 Chen, C.-H., Chen, S.-H., Mao, S.-H., Tsai, M.-J., Chou, P.-Y., Liao, C.-H., Chen, J.-P. Injectable thermosensitive hydrogel containing hyaluronic acid and chitosan as a barrier for prevention of postoperative peritoneal adhesion (2017) *Carbohydrate Polymers*, 173: 721-731. DOI: 10.1016/j.carbpol.2017.06.019.
  - 61 Yang, L.-C., Hsieh, C.-C., Wen, C.-L., Chiu, C.-H., Lin, W.-C. Structural characterization of an immunostimulating polysaccharide from the stems of a new medicinal *Dendrobium* species: *Dendrobium Taiseed Tosnobile* (2017) *International Journal of Biological Macromolecules*, 103: 1185-1193. DOI: 10.1016/j.ijbiomac.2017.05.185.
  - 62 Chen, C.-H., Hwang, T.-L., Chen, L.-C., Chang, T.-H., Wei, C.-S., Chen, J.-J. Isoflavones and anti-inflammatory constituents from the fruits of *Psoralea corylifolia* (2017) *Phytochemistry*, 143: 186-193. DOI: 10.1016/j.phytochem.2017.08.004.
  - 63 Lin, T.-K., Chang, C.-N., Tsai, C.-S., Huang, Y.-C., Lu, Y.-J., Chen, W.-J., Lin, Y.-H., Chung, I.-H., Lin, K.-H. The long non-coding RNA LOC441204 enhances cell growth in human glioma (2017) *Scientific Reports*, 7 (1):5603. DOI: 10.1038/s41598-017-05688-0.
  - 64 Wu, L.-H., Chang, S.-C., Fu, T.-C., Huang, C.-H., Wang, J.-S. High-intensity Interval Training Improves Mitochondrial Function and Suppresses Thrombin Generation in Platelets undergoing Hypoxic Stress (2017) *Scientific Reports*, 7(1):4191. DOI: 10.1038/s41598-017-04035-7.

## Short Note

# Astrocyte as the Modulator in Brain Inflammation and Neurodegenerative Disorders

Hsi-Lung Hsieh<sup>1,2\*</sup> and Chuen-Mao Yang<sup>3</sup>

<sup>1</sup>Department of Nursing, Division of Basic Medical Sciences, and Research Center for Industry of Human Ecology, Research Center for Chinese Herbal Medicine, and Graduate Institute of Health Industry and Technology, Chang Gung University of Science and Technology, Gui-Shan, Tao-Yuan, Taiwan

<sup>2</sup>Department of Neurology, Chang Gung Memorial Hospital, Taiwan

<sup>3</sup>Department of Physiology and Pharmacology and Health Ageing Research Center, Chang Gung University, Taiwan

## \*Corresponding author

Hsi-Lung Hsieh, Department of Nursing, Division of Basic Medical Sciences, Chang Gung University of Science and Technology, 261 Wen-Hua 1st Road, Gui-Shan, Tao-Yuan, Taiwan, Tel: (03) 2118999 EXT 5421; Fax: (03) 2118365; Email: hlhsieh@mail.cgu.edu.tw

Submitted: 20 July 2016

Accepted: 05 August 2016

Published: 07 August 2016

## Copyright

© 2016 Hsieh et al.

## OPEN ACCESS

The central nervous system (CNS) consists of neurons and neuroglial cells. Among neuroglial cells in the adult human brain, astrocytes constitute most (approximately 40 %) of cell population, and maintain homeostasis in normal CNS. Many reports indicate that astrocytes participate in various functions including guidance of the neuronal development and migration during CNS development, supporter of neuronal growth, preservation of the integrity of the blood-brain barrier (BBB), and playing a part in the immune responses to brain injury or disorders [1]. Moreover, as well as microglia, astrocytes display various receptors participated in innate immunity, including Toll-like receptors (TLRs), nucleotide-binding oligomerization domains, double-stranded RNA-dependent protein kinase, mannose receptor and components of the complement system [2]. One common feature of various neurodegenerative diseases is activation of large number of astrocytes and microglia that includes the morphological changes and expression of many inflammatory mediators. Astrogliosis is characterized by astrocytic proliferation, hypertrophy of the cell body, and functional changes, when exposed to various factors including interleukin-1 $\beta$  (IL-1 $\beta$ ), tumor necrosis factor (TNF)- $\alpha$ , and lipopolysaccharide (LPS) [3].

Accumulating studies have indicated that the cell-cell interactions between glial cells and neurons is important in the regulation of brain inflammation and neurodegeneration. Recent reports also implicate that inflammation contributes to a wide variety of brain pathologies, apparently killing of neurons via glia [1]. Thus, the activated glial cells are indicated to play a critical role in the progression and pathogenesis of neurodegeneration. Previous most reports have shown that microglial cells may be a major inflammatory cell of the brain [4]. The activated microglia produce several inflammatory mediators including cytokines or cyclooxygenase-2 (COX-2)/prostaglandins (PGs) as well as neurotoxic materials, which are indicated to be responsible for brain injury and disorders including trauma, neurodegeneration, and neural death due to the exposure of various pro-inflammatory

factors [4]. However, increasing evidence has demonstrated the characteristic changes of astrocytes in neurodegenerative diseases [5]. To date, we have demonstrated up-regulation of several inflammatory mediators by various pro-inflammatory factors such as cytokines, peptides, pathogenic structures (e.g., bacteria or virus), and per-oxidants in rat brain astrocytes [6]. Moreover, recent data also indicated that multiple factors from BK-challenged brain astrocytes may contribute to the neuronal cell apoptosis [7]. These results implicate that activated neuroglial cells, astrocytes especially, play a critical role in the brain inflammatory response leading to neurodegenerative disorders.

Inflammation is a natural protective reaction to various cell and tissue injury. The purpose of this process is to remove the detrimental agents and injured tissues, thereby benefiting tissue repair. When this helpful reaction is uncontrolled, the effect initiates extravagant cell and tissue damage that results in normal tissue destruction and chronic inflammation [8]. Moreover, the brain neurodegenerative diseases, including Alzheimer's disease (AD) and Parkinson's disease (PD), are characterized by intracellular signaling state imbalance and chronic neuroinflammation, a major cause of cell damage and death. Several of the well-known inflammatory mediators such as matrix metalloproteinases (MMPs) or COX-2/PGs system are associated with diverse signaling molecules activated by pro-inflammatory factors such as cytokines, peptides, pathogenic structures, and per-oxidants [9,10]. These intracellular signaling molecules, including various receptors, calcium (Ca<sup>2+</sup>), protein kinase Cs (PKCs), reactive oxygen species (ROS), or mitogen-activated protein kinases (MAPKs) are widely recognized as the key mediators of cell survival, proliferation, differentiation, and apoptosis [9,10]. Excessive activation of various signaling molecules by pro-inflammatory factors is usually thought to be responsible for tissue injury associated with a range of brain injury, neuroinflammation, and neurodegenerative diseases such as AD [10]. Moreover, brain cells, neuroglial cells particularly, are

susceptible to the injurious effects of various stresses. Several studies have shown that brain cells like microglia and astrocytes induce and release diverse inflammatory mediators in response to pro-inflammatory factors [1,10]. In the CNS, following the stimulation of pro-inflammatory factors, integration of various signaling molecules to trigger inflammatory responses through activation of different transcription factors, including nuclear factor- $\kappa$ B (NF- $\kappa$ B) and activator protein-1 (AP-1) [1,10]. Here, we focus on many general aspects of pro-inflammatory signaling molecular regulation, their involvement in the expression of inflammatory target proteins, and the effects of these signals on the brain neuroinflammation. Therefore, the inhibition of the expression of inflammatory target proteins (e.g., MMP-9)-mediated inflammatory pathways may provide therapeutic strategies to brain neuroinflammation and neurodegenerative diseases.

Brain glial cells maintain CNS plasticity and protect the brain for functional repair from injuries. Reactivation of glial cells may promote neuroinflammation and neurodegeneration and, ultimately, the retraction of neuronal synapses, which leads to cognitive deficits [1]. Moreover, up-regulation of these inflammatory mediators is a deleterious event in several inflammatory diseases such as AD that precedes the formation of these disease pathologies. To date, although numerous effects have been made to develop therapies based on signaling molecules or target mediators in the past years, the actual benefits to the patients have been very limited. It may be due to lack of potency, late administration and poor penetration into the brain cells [11]. Alternative strategies including searching for pro-inflammatory factors that induce inflammatory mediators via diverse signaling pathways are necessary to improve the efficacy of treatment. Hence, understanding what pro-inflammatory factors participate in these inflammatory mediators expression and the regulating mechanisms that might help to develop effectively therapeutic strategies for the CNS diseases.

First, we focus on glial cells, in particular astrocytes, and their effects on the CNS disorders. Next, we summarized the interplay between these inflammatory mediators and neuroinflammation by action of various pro-inflammatory factors contributes to neurodegeneration, thereby enhancing disease progression based on data collected from brain cells, particularly astrocytes, in *in vitro* and *in vivo* studies. Perhaps by retarding the activation of glial cells to decrease their neurotoxic properties and enhance their neuroprotective effects may offer potential targets for

therapeutic interventions in CNS degenerative disorders. Previously, pro-inflammatory factors-induced signaling transduction pathways, including  $\text{Ca}^{2+}$ -related signals, PKCs, ROS, transactivation of PDGFR, PI3K/Akt cascade, MAPKs, NF- $\kappa$ B, and AP-1 that are associated with the CNS disorders were investigated in brain astrocytes. Possible therapeutic strategies to target signaling molecules, transcription factors, or inflammatory mediators are implicated based on many updated view of pro-inflammatory factors-mediated regulation of various inflammatory mediators in brain inflammation and neurodegenerative disorders.

## REFERENCES

1. Farfara D, Lifshitz V, Frenkel D. Neuroprotective and neurotoxic properties of glial cells in the pathogenesis of Alzheimer's disease. *J Cell Mol Med.* 2008; 12: 762-780.
2. Kimelberg HK. Receptors on astrocytes--what possible functions? *Neurochem Int.* 1995; 26: 27-40.
3. Ridet JL, Malhotra SK, Privat A, Gage FH. Reactive astrocytes: cellular and molecular cues to biological function. *Trends Neurosci.* 1997; 20: 570-577.
4. Kim YS, Joh TH. Microglia, major player in the brain inflammation: their roles in the pathogenesis of Parkinson's disease. *Exp Mol Med.* 2006; 38: 333-347.
5. Mrak RE, Sheng JG, Griffin WS. Glial cytokines in Alzheimer's disease: review and pathogenic implications. *Hum Pathol.* 1995; 26: 816-823.
6. Hsieh HL, Yang CM. The role of matrix metalloproteinase-9 in pro-inflammatory factors-induced brain inflammation and neurodegenerative diseases. *Inflamm Cell Signaling.* 2014; 1:124.
7. Yang CM, Hsieh HL, Lin CC, Shih RH, Chi PL, Cheng SE, et al. Multiple factors from bradykinin-challenged astrocytes contribute to the neuronal apoptosis: involvement of astroglial ROS, MMP-9, and HO-1/CO system. *Mol Neurobiol.* 2013; 47: 1020-1033.
8. Glass CK, Saijo K, Winner B, Marchetto MC, Gage FH. Mechanisms underlying inflammation in neurodegeneration. *Cell.* 2010; 140: 918-934.
9. Chen Q, Jin M, Yang F, Zhu J, Xiao Q, Zhang L. Matrix metalloproteinases: inflammatory regulators of cell behaviors in vascular formation and remodeling. *Mediators Inflamm.* 2013; 2013:928315.
10. Hsieh HL, Yang CM. Role of redox signaling in neuroinflammation and neurodegenerative diseases. *Biomed Res Int.* 2013; 2013: 484613.
11. Shi Q, Gibson GE. Oxidative stress and transcriptional regulation in Alzheimer disease. *Alzheimer Dis Assoc Disord.* 2007; 21: 276-291.

### Cite this article

Hsieh HL, Yang CM (2016) Astrocyte as the Modulator in Brain Inflammation and Neurodegenerative Disorders. *Ann Neurodegener Dis* 1(2): 1008.



# Sterol Regulatory Element-Binding Protein-1c Regulates Inflammasome Activation in Gingival Fibroblasts Infected with High-Glucose-Treated *Porphyromonas gingivalis*

Hsing-Chun Kuo<sup>1,2,3</sup>, Li-Ching Chang<sup>4</sup>, Te-Chuan Chen<sup>5</sup>, Ko-Chao Lee<sup>6</sup>, Kam-Fai Lee<sup>7</sup>, Cheng-Nan Chen<sup>8</sup> and Hong-Ren Yu<sup>9,10\*</sup>

<sup>1</sup> Department of Nursing, Chang Gung University of Science and Technology (CGUST), Chiayi, Taiwan, <sup>2</sup> Research Center for Industry of Human Ecology and Research Center for Chinese Herbal Medicine, College of Human Ecology, Chang Gung University of Science and Technology (CGUST), Taoyuan, Taiwan, <sup>3</sup> Chronic Diseases and Health Promotion Research Center, Chang Gung University of Science and Technology (CGUST), Chiayi, Taiwan, <sup>4</sup> Department of Dentistry, Chang Gung Memorial Hospital, Chiayi, Taiwan, <sup>5</sup> Division of Nephrology Kaohsiung Chang Gung Memorial Hospital and Chang Gung University College of Medicine, Kaohsiung, Taiwan, <sup>6</sup> Division of Colorectal Surgery, Department of Surgery, Chang Gung Memorial Hospital - Kaohsiung Medical Center, Kaohsiung, Taiwan, <sup>7</sup> Department of Pathology, Chang Gung Memorial Hospital, Chiayi, Taiwan, <sup>8</sup> Department of Biochemical Science and Technology, National Chiayi University, Chiayi, Taiwan, <sup>9</sup> Department of Pediatrics, Chang Gung Memorial Hospital - Kaohsiung Medical Center, Kaohsiung, Taiwan, <sup>10</sup> Graduate Institute of Clinical Medical Science, Chang Gung University College of Medicine, Kaohsiung, Taiwan

## OPEN ACCESS

### Edited by:

Ingar Olsen,  
University of Oslo, Norway

### Reviewed by:

Ashu Sharma,  
University at Buffalo, USA  
Thomas Elliott Van Dyke,  
Forsyth Institute, USA

### \*Correspondence:

Hong-Ren Yu  
yuu2004taiwan@yahoo.com.tw

**Received:** 16 October 2016

**Accepted:** 12 December 2016

**Published:** 26 December 2016

### Citation:

Kuo H-C, Chang L-C, Chen T-C, Lee K-C, Lee K-F, Chen C-N and Yu H-R (2016) Sterol Regulatory Element-Binding Protein-1c Regulates Inflammasome Activation in Gingival Fibroblasts Infected with High-Glucose-Treated *Porphyromonas gingivalis*. *Front. Cell. Infect. Microbiol.* 6:195. doi: 10.3389/fcimb.2016.00195

**Background:** *Porphyromonas gingivalis* is a major bacterial species implicated in the progression of periodontal disease, which is recognized as a common complication of diabetes. The interleukin (IL)-1 $\beta$ , processed by the NLR family pyrin domain containing 3 (NLRP3) inflammasome, has been identified as a target for pathogenic infection of the inflammatory response. However, the effect of *P. gingivalis* in a high-glucose situation in the modulation of inflammasome activation in human gingival fibroblasts (HGFs) is not well-understood.

**Methods:** *P. gingivalis* strain CCUG25226 was used to study the mechanisms underlying the regulation of HGF NLRP3 expression by the infection of high-glucose-treated *P. gingivalis* (HGPg).

**Results:** HGF infection with HGPg increases the expression of IL-1 $\beta$  and NLRP3. We further demonstrated that the upregulation of sterol regulatory element-binding protein (SREBP)-1c by activation of the Akt and p70S6K pathways is critical for HGPg-induced NLRP3 expression. We showed that the inhibition of Janus kinase 2 (JAK2) blocks the Akt- and p70S6K-mediated SREBP-1c, NLRP3, and IL-1 $\beta$  expression. The effect of HGPg on HGF signaling and NLRP3 expression is mediated by  $\beta$ 1 integrin. In addition, gingival tissues from diabetic patients with periodontal disease exhibited higher NLRP3 and SREBP-1c expression.

**Conclusions:** Our findings identify the molecular pathways underlying HGPg-dependent NLRP3 inflammasome expression in HGFs, providing insight into the effect of *P. gingivalis* invasion in HGFs.

**Keywords:** *Porphyromonas gingivalis*, gingival fibroblasts, high glucose, NLRP3, SREBP-1c



## INTRODUCTION

Periodontal diseases, the most common chronic inflammatory diseases in adults, are characterized by bacteria-induced loss of connective tissues within the periodontium and the destruction of alveolar bone support (Hajishengallis, 2015). Infection of *Porphyromonas gingivalis*, a gram-negative oral anaerobic bacterium, has been proposed as the primary etiological pathogen associated with increased risk of periodontal breakdown and disease recurrence (Darveau, 2010; Gaddis et al., 2011; Ji et al., 2015). Moreover, it has been reported that the risk of periodontitis is significantly higher in individuals with diabetes than in normal subjects (Nibali et al., 2007). Our previous study reported that when cultured under high-glucose (HG) conditions, the invasion efficiency of HG-treated *P. gingivalis* (HGPg) into human gingival fibroblasts (HGFs) and the expression of intercellular adhesion molecule-1 was significantly increased (Chang et al., 2013). Furthermore, several reports have demonstrated that non-surgical periodontal therapies can improve the condition of patients with high blood glucose (Faria-Almeida et al., 2006; Lin et al., 2012). Periodontal treatment with antibiotics also has significantly positive effects on glycemic control in diabetic patients (Bharti et al., 2013).

Fimbriae of *P. gingivalis* play critical roles in mediating the initiation and development of periodontal disease. *P. gingivalis* can adhere to oral surfaces or mucosa predominantly by peritrichous fimbriae (Yoshimura et al., 2009). The strains with different *fimA* genotypes contribute to distinct *P. gingivalis* virulence and play a critical role in regulating the development of periodontal disease (Kato et al., 2007). Our previous study reported that the *fimA* mRNA was markedly upregulated in HGPg compared to normal glucose-treated *P. gingivalis* (NGPg), and the invasion efficiency of HGPg to HGFs was also significantly increased (Chang et al., 2013). *P. gingivalis* infection and the host inflammatory response are necessary for the progression of periodontal disease, especially in patients with diabetes. However, the precise roles and detailed mechanisms of host-mediated inflammation by HGPg infection have not been determined.

The inflammasome, a multiprotein complex that triggers the production of mature IL-1 $\beta$  in response to intracellular stress signals, plays a key role in innate immunity (Lamkanfi and Dixit, 2014). The best characterized inflammasome is the NOD-like receptor protein 3 (NLRP3) inflammasome. Upon activation, NLRP3 leads to the activation of proteinase Caspase-1, which in turn processes pro-IL-1 $\beta$  into its mature form (Jo et al., 2016). There is growing evidence of a relationship between diabetes and inflammasome activation (Lee et al., 2013). The lack of inflammasome components has provided evidence that NLRP3 activation is a key mechanism that induces systemic inflammation and the development of insulin resistance (Dixit, 2013). Although the connections between hyperglycemia and inflammation have been extensively characterized (Chen et al., 2011a; Chen T. C. et al., 2014), the molecular mechanisms responsible for NLRP3 expression after infection with *P. gingivalis* cultured under HG conditions remains unclear.

Sterol regulatory element binding protein-1c (SREBP-1c), a key lipogenic transcription factor, regulates cholesterol and fatty acid metabolism (Wang et al., 2015). SREBP-1c plays an important role in the inflammatory response; it is a critical regulator in the induction of inflammatory cytokine expression involved in lipid metabolism (Li et al., 2015). High levels of SREBP-1c expression and nuclear accumulation have been observed in diabetic mouse models (Laplane and Sabatini, 2010). Unfortunately, no studies have determined the relationship among *P. gingivalis* infection, SREBP-1c expression and inflammasome activation.

HGFs, the major cell type found in the periodontal connective tissue, can upregulate inflammatory mediators in response to pathogen-associated stimuli (Chang et al., 2013). It has been clarified that HGFs regulate inflammatory reactions in the development of periodontal disease. Furthermore, diabetes is connected with a higher risk of severe periodontal disease, and poorly controlled diabetes is a major contributor to poorer periodontal health (Preshaw et al., 2012). The mechanisms that link diabetes and periodontal disease have not been completely evaluated, but they involve an immune system response to infection and inflammation (Preshaw et al., 2012). In addition, it has been reported that the fimbriated *P. gingivalis* can activate  $\beta$  forms of integrins, leading to the manipulation of host cell function and causing disease (Hajishengallis et al., 2009; Zhang et al., 2013). These signals may lead to the activation of Janus kinase (JAK) pathways. The purpose of this study was to investigate the molecular mechanism that regulates the expression of HGF NLRP3 inflammasome by HGPg. The results demonstrated that the NLRP3 inflammasome activation induced by HGPg is mediated through the  $\beta$ 1 integrin, the intracellular signaling cascades Akt and p70S6K, and the nuclear SREBP-1c transcription factors.

## METHODS

### Materials

All culture materials were purchased from Gibco (Grand Island, NY). LY294002 (PI3K/Akt inhibitor) and rapamycin (p70S6K inhibitor) were purchased from Calbiochem (La Jolla, CA). Mouse monoclonal antibodies (mAb) against SREBP-1c, NLRP3, IL-1 $\beta$ , pro-IL-1 $\beta$ , caspase-1, pro-caspase-1, phospho-Akt, and Akt were purchased from Santa Cruz Biotechnology (Santa Cruz, CA). Rabbit polyclonal antibodies against phospho-p70S6K, p70S6K, phospho-JAK2, and JAK2 were purchased from Cell Signaling Technology (Beverly, MA). SREBP-1c, NLRP3, JAK2 siRNA and control siRNA were purchased from the National RNAi Core Facility in Academic Sinica, Taipei, Taiwan. The integrin  $\beta$ 1-siRNA were purchased from Invitrogen (Carlsbad, CA). *P. gingivalis* lipopolysaccharide (Pg-LPS) was purchased from InvivoGen (San Diego, CA). Other chemicals of reagent grade were obtained from Sigma (St. Louis, MO).

### Bacterial Strains and Growth Conditions

Periodontal pathogens *P. gingivalis* strain CCUG25226 and *Fusobacterium nucleatum* strain CCUG51781 were purchased

from the Bioresources Collection and Research Center of the Food Industry Research and Development Institute (Hsinchu, Taiwan). These bacteria were inoculated anaerobically in brain-heart infusion (BHI) broth in 37°C supplemented with 0.5% yeast extract, 5 µg/mL hemin and 1 µg/mL vitamin K3. Pathogens grown were monitored by recording the optical density at 660 nm.

For studying the effect of glucose on *P. gingivalis* and *F. nucleatum*, and the further effect of HGPg on HGF NLRP3 expression, *P. gingivalis* was cultured in BHI medium containing 5 (normal glucose, NG) or 25 (HG) mmol/L glucose. Then *P. gingivalis* was collected and defined as NGPg and HGPg. For the infection assay, the indicated multiplicity of infection (MOI) of NGPg or HGPg was added to HGFs according to different experimental treatments.

## Cell Culture

HGFs were obtained from ScienCell Research Laboratories (San Diego, CA). Cells were incubated at 37°C in DMEM medium supplemented with 10% fetal bovine serum (FBS), penicillin (100 U/mL) and streptomycin (100 µg/mL), and grown in a

humidified atmosphere containing 5% CO<sub>2</sub>. HGFs from passage levels 4–6 were used in this study.

## Invasion Assays

HGFs were infected with bacteria at 37°C with indicated MOI. After 1 h incubation, HGFs were washed with PBS and then cultured for another 2 h to kill extracellular *P. gingivalis* in medium containing gentamicin and metronidazole. Cells were then washed and lysed in 0.1% Triton X-100, and plated on blood agar plates. Bacteria present in the lysates were titrated, representing the number of bacteria intracellularly. Invasion levels were calculated as the number of *P. gingivalis* surviving divided by the total number of bacteria.

## Purification of Fimbriae from *P. gingivalis*

Fimbriae from NGPg or HGPg were purified as described previously (Chen et al., 2011b). The purified fimbriae were tested for agglutinating activity with erythrocytes. The protein content was determined and the fractions showing agglutinating activity were subjected to SDS-PAGE and western blot analysis.

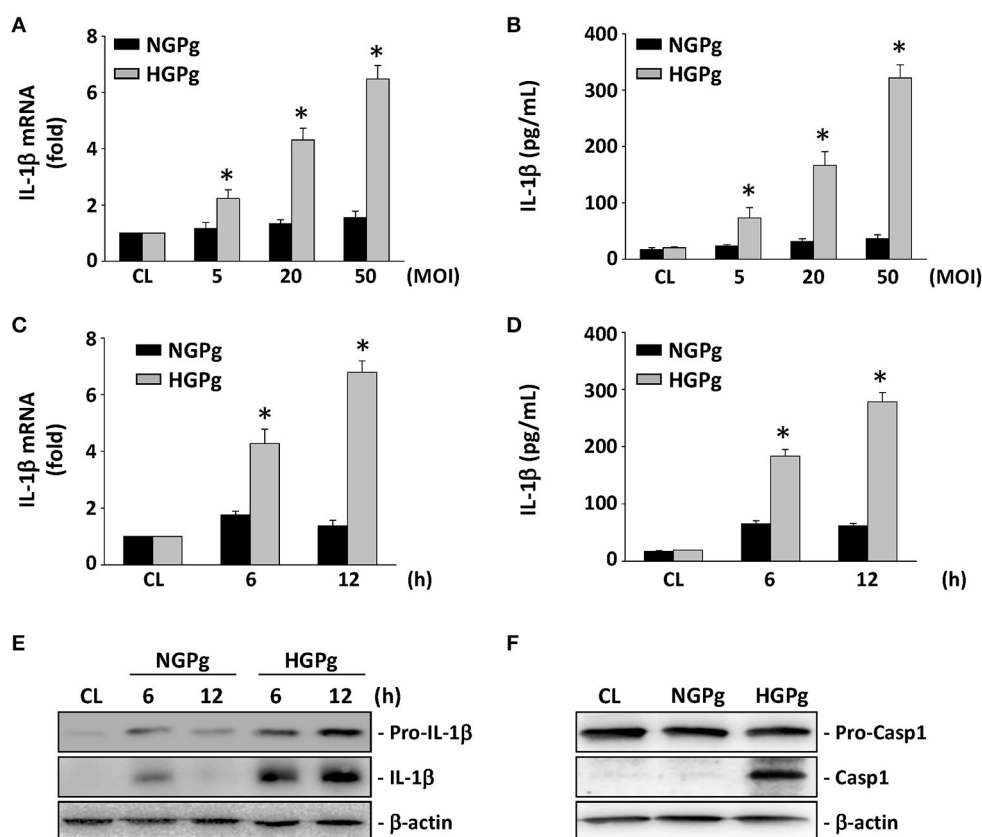


**FIGURE 1 | Induction of IL-1β expression in HGFs infected with *P. gingivalis*.** RNA samples were isolated at the indicated MOI or times. All bar graphs represent folds of control cells (CL) normalized to 18S rRNA by real-time PCR analysis (**A,C**). IL-1β secretion in medium was determined by ELISA analyses (**B,D**). (**A,B**) Cells were infected by NGPg or HGPg at various MOI for 6 h, or (**C,D**) infected with NGPg or HGPg at 20 MOI for 6 and 12 h. Data are shown as mean ± standard error of the mean (SEM). \**P* < 0.05 vs. CL HGFs or HGFs infected with NGPg. (**E,F**) The expression of pro-IL-1β and IL-1β (**E**), or pro-caspase-1 and caspase-1 (**F**) in HGF cell lysate after HGPg infection for the times indicated was determined using Western blotting.



## Real-Time Quantitative PCR

For detecting the levels of HGF mRNA expression, real-time PCR was performed, and products were detected using an ABI Prism 7900HT with the FastStart DNA SYBR Green I kit (Roche Diagnostics GmbH, Mannheim, Germany). The designed primers in this study were SREBP-1c forward primer, 5'-GTGAC ATGCA GCACC TCCTG-3'; SREBP-1c reverse primer, 5'-TCCAT GGTGA TCTCT CCTCA-3'; 18S rRNA forward primer, 5'-CGGCG ACGAC CCATT CGAAC-3'; 18S rRNA reverse primer, 5'-GAATC GAACC CTGAT TCCCC GTC-3'; NLRP3 forward primer, 5'-AAAAG ACTCA TCCGT GTGCC-3'; NLRP3 reverse primer, 5'-TTCCT GGCAT ATCAC AGTGG-3'; IL-1 $\beta$  forward primer, 5'-AAACA GATGA AGTGC TCCTT CCAGG-3'; IL-1 $\beta$  reverse primer, 5'-TGGAG AACAC CACTT GTTGC TCCA-3'. fimA forward primer, 5'-CAGCA GGAAG CCATC AAATC-3'; fimA reverse primer, 5'-CAGTC AGTTC AGTTG TCAAT-3'; 16S rRNA forward primer, 5'-TGATG ATGAC TGATG GTGAA A-3'; and 16S rRNA reverse primer, 5'-ACTGT TAGCA ACTAC CGATG T-3'. Quantification was performed using the  $2^{-\Delta\Delta C_t}$  method. All samples were measured in duplicate. The average value of both duplicates was used as the quantitative value.

## Western Blot Analysis

Cells were lysed with a buffer containing 1% NP-40, 0.5% sodium deoxycholate, 0.1% SDS, and a protease inhibitor mixture (PMSF, aprotinin, and sodium orthovanadate). The total cell lysate (50  $\mu$ g of protein) was separated by SDS-polyacrylamide gel electrophoresis (PAGE) (12% running, 4% stacking) and

analyzed using the designated antibodies and the Western-Light chemiluminescent detection system (Bio-Rad, Hercules, CA) (Huang et al., 2016).

## IL-1 $\beta$ Enzyme-Linked Immunosorbent Assay (ELISA)

The levels of IL-1 $\beta$  in the media were determined by using sandwich ELISA kit (sensitivity 18 pg/mL; R&D) according to the manufacturer's protocols (R & D Systems, Minneapolis, MN) (Tseng et al., 2016).

## siRNA Transfection

For siRNA transfection, HGFs were transfected with the specific siRNAs or control siRNA by using an RNAiMAX transfection kit (Invitrogen, Carlsbad, CA).

## Reporter Gene Construct and Luciferase Assays

SREBP-1c promoter construct contain -1470/+90 of SREBP-1c 5'-flanking DNA linked to the firefly luciferase reporter gene of plasmid pGL4 (Promega, Madison, WI). DNA plasmids at a concentration of 1 mg/ml were transfected into HGFs by using Lipofectamine (Gibco). The pSV- $\beta$ -galactosidase plasmid was cotransfected to normalize the transfection efficiency.

## Subjects and Collection of Gingival Tissue Samples

All study protocols were in accordance with the Declaration of Helsinki and were approved by the Medical Ethics Committee

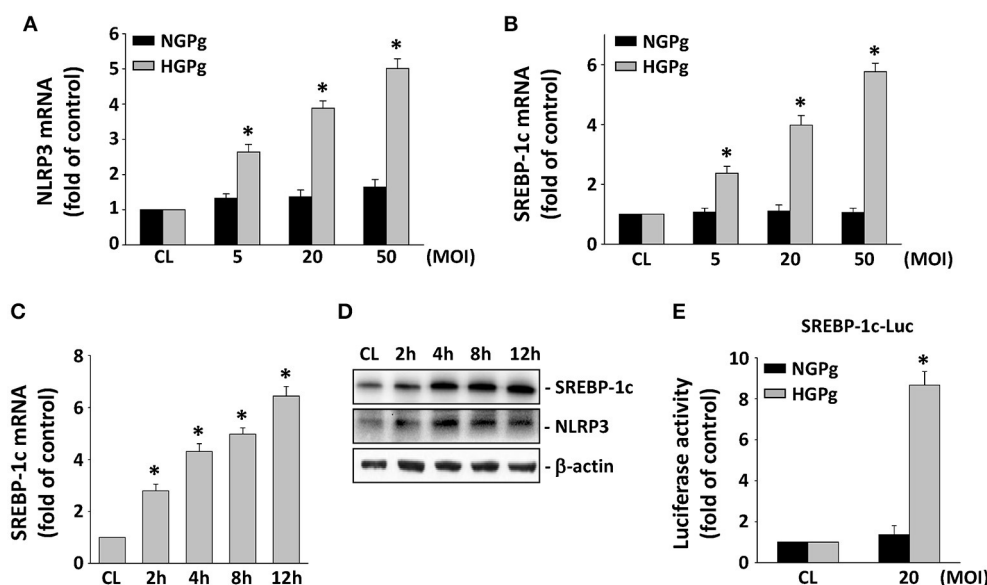


**FIGURE 2 | Induction of NLRP3 and SREBP-1c expression in HGFs infected with HGPg.** RNA samples were isolated at the indicated MOI or times. All bar graphs represent folds of control cells (CL) normalized to 18S rRNA by real-time PCR analysis (A–C). (A,B) Cells were infected by NGPp or HGPg at various MOI for 4 h, or (C) infected with HGPg at 20 MOI for times indicated. (D) The expression of mature 68 kD SREBP-1c and NLRP3 in HGF cell lysate after HGPg infection for the times indicated was determined using Western blotting. (E) HGFs were cotransfected with SREBP-1c-Luc and infected with NGPp or HGPg at 20 MOI for 4 h. SREBP-1c promoter activity was measured by luciferase assay normalized to  $\beta$ -galactosidase activity. Data are shown as mean  $\pm$  standard error of the mean (SEM). \* $P < 0.05$  vs. CL HGFs or HGFs infected with NGPp.

of Chang Gung Memorial Hospital (No. 104–1541C), and all patients provided written informed consent before enrollment. Ten patients with both periodontal disease and type 2 diabetes, and 10 control patients with periodontal disease alone were recruited in this study. The diabetic patients had a mean ( $\pm$ SEM) age of  $47.6 \pm 5.7$  years, fasting glucose of  $11.7 \pm 1.1$  mmol/L, a body mass index (BMI) of  $29.6 \pm 3.1$  kg/m<sup>2</sup>, and hemoglobin A<sub>1c</sub> (HbA<sub>1c</sub>) of  $7.4 \pm 1.3\%$ . In addition, the control subject group had a mean ( $\pm$ SEM) age of  $46.3 \pm 6.4$  years, fasting glucose of  $4.7 \pm 0.1$  mmol/L, a BMI of  $25.8 \pm 1.6$  kg/m<sup>2</sup>, and HbA<sub>1c</sub> of  $4.4 \pm 0.6\%$ . None of the control subjects had cardiac, renal, or pulmonary decompensated diseases, or other infectious or inflammatory situations. Subjects who smoked cigarettes or used alcohol, non-steroidal anti-inflammatory drugs, corticosteroids, anticoagulant drugs, or hormonal replacement therapy were excluded. Patients had not been treated for periodontitis over the previous 2 years and had taken no antibiotics in the 6 months preceding surgery. Gingival samples were obtained from subjects undergoing surgery to treat periodontitis.

### Immunohistochemical (IHC) Analysis of SREBP-1c and NLRP3 Expression

Gingival tissue samples were frozen immediately after surgery in liquid nitrogen and stored at  $-80^{\circ}\text{C}$ . Serial paraffin sections of biopsies were cut 5  $\mu\text{m}$  thick, and IHC assays was performed

using the immunoperoxidase staining. For inhibition of non-specific binding, the tissue sections were incubated with normal goat serum and non-fat dry milk. Subsequently, the sections were incubated at  $4^{\circ}\text{C}$  with primary antibodies against SREBP-1c and NLRP3, respectively. Sections stained with normal mouse IgG as primary antibody were used as a negative control (Kuo et al., 2016). Sections were then reacted with secondary antibody, followed by incubation with avidin-biotin-peroxidase complex with the addition of DAB (3,3'-diaminobenzidine tetrahydrochloride).

### Statistical Analysis

The results are expressed as mean  $\pm$  standard error of the mean (SEM). Statistical analysis was determined by using an independent Student *t*-test for two groups of data and analysis of variance (ANOVA) followed by Scheffé's test for multiple comparisons. *P*-values less than 0.05 were considered significant (Lu et al., 2016).

## RESULTS

### HGPg Infection Induced the Expression of IL-1 $\beta$ in HGFs

To demonstrate that HGPg infection upregulates the expression and secretion of IL-1 $\beta$ , the HGFs were infected with different

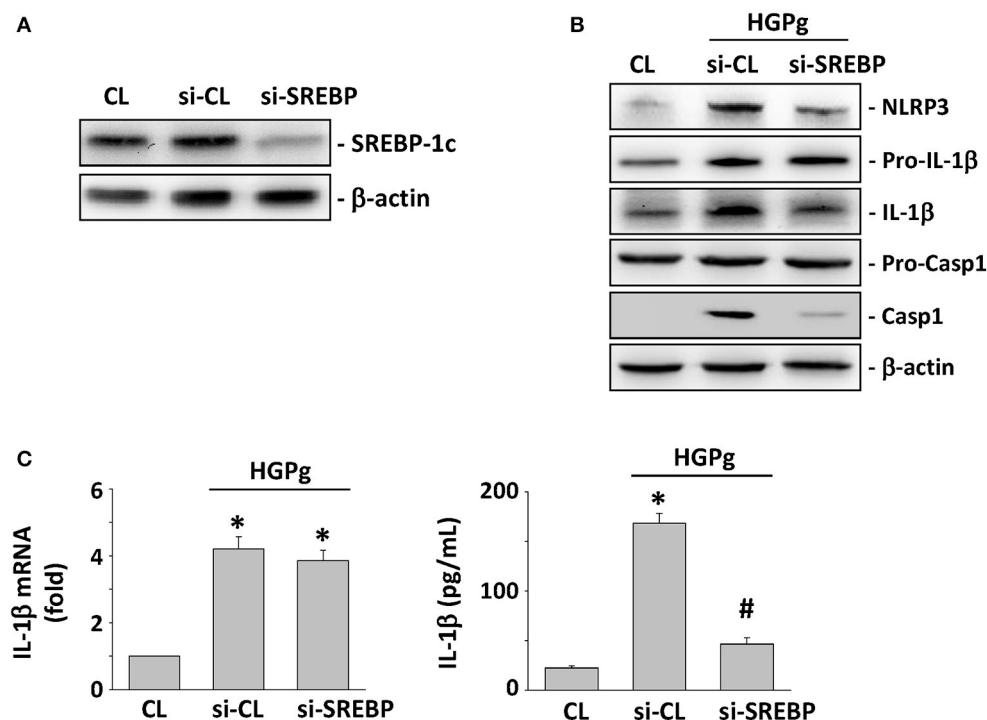


**FIGURE 3 | Effects of SREBP-1c on HGPg-induced NLRP3 and IL-1 $\beta$  expression. (A)** The gene silencing efficiency of 48 h transfection of siRNA on SREBP-1c levels of HGFs. After 48 h of transfection, protein was isolated and the SREBP-1c expression was analyzed by Western blotting. **(B,C)** HGFs were kept as CL or infected by HGPg (20 MOI). Before being kept as CL or infected by HGPg, HGFs were transfected with control siRNA (si-CL), or a specific siRNA of SREBP-1c (si-SREBP). **(B)** The expression of NLRP3, pro-IL-1 $\beta$ , IL-1 $\beta$ , pro-caspase-1, and caspase-1 in HGF cell lysate after HGPg infection was determined using Western blotting. **(C)** IL-1 $\beta$  secretion in medium was determined by ELISA analyses. \**p* < 0.05 vs. control HGFs. #*p* < 0.05 vs. si-SREBP-1c-transfected cells with HGPg infection.

MOI of HGPg (vs. NGPg) for 6 h. As shown in **Figures 1A,B**, the induction of IL-1 $\beta$  mRNA expression (**Figure 1A**) and IL-1 $\beta$  protein secretion in medium (**Figure 1B**) by HGPg infection was MOI-dependent. The time courses determined for the IL-1 $\beta$  mRNA levels revealed an increase after 6 and 12 h of HGPg infection (**Figure 1C**). HGPg also caused significant upregulation in the secretion of IL-1 $\beta$  into medium at 6 and 12 h after infection in HGFs (**Figure 1D**). In addition, the cytoplasmic pro-IL-1 $\beta$  and mature IL-1 $\beta$  protein levels were increased in HGFs infected with HGPg (**Figure 1E**). Upon inflammasome formation, pro-caspase-1 underwent autocleavage to produce caspase-1. Western blot analysis showed that active caspase-1 was observed at 6 h after HGPg infection, suggesting inflammasome activation in HGFs (**Figure 1F**).

We further investigated the invasion efficiency and IL-1 $\beta$  mRNA expression of normal or HG-cultured HGFs infected with NGPg or HGPg. HGPg infected HGFs much more readily in both normal and HG-cultured HGFs (**Figure S1A**). The IL-1 $\beta$  mRNA expression in normal or HG-culture HGFs was also significantly increased when infected with HGPg, whereas NGPg infection only had a marginal effect on IL-1 $\beta$  mRNA expression in HG-cultured HGFs (**Figure S1B**). To determine whether IL-1 $\beta$  mRNA expression was dependent on specific *P. gingivalis* carrying *fimA*, HGFs were infected with another periodontal pathogen *F. nucleatum* cultured in NG (NGFn) or HG (HGFn) conditions.

As shown in **Figure S2**, NGFn and HGFn caused a similar effect on IL-1 $\beta$  expression in HGFs. HGPg was used as a positive control.

The *fimA* mRNA expression in NGPg and HGPg was further detected by real-time PCR. As shown in **Figure S3A**, the expression levels of *fimA* mRNA were significantly higher in HGPg. To determine the protein expression levels of fimbriae in NGPg and HGPg, fimbriae were purified and detected by Western blotting. Our results revealed that FimA protein levels were also significantly increased in HGPg (**Figure S3B**). Stimulation of HGFs with purified fimbriae from HGPg, or co-stimulation of HGFs with Pg-LPS and purified fimbriae from HGPg, significantly increased IL-1 $\beta$  mRNA expression, whereas co-stimulation with Pg-LPS and purified fimbriae from NGPg had a minor effect on IL-1 $\beta$  expression in HGFs (**Figure S3C**).

## Infection of the HGFs by HGPg Induced NLRP3 and SREBP-1c Expression

The effects of HGPg infection on the mRNA expression of NLRP3 in HGFs were studied using infected cells with *P. gingivalis* grown on NG or under HG conditions. Consistent with our hypothesis, HGF infection with HGPg induced MOI-dependent NLRP3 gene expression (**Figure 2A**). NGPg infection failed to induce significant NLRP3 expression, even at a high MOI, suggesting that NGPg infection is insufficient to trigger

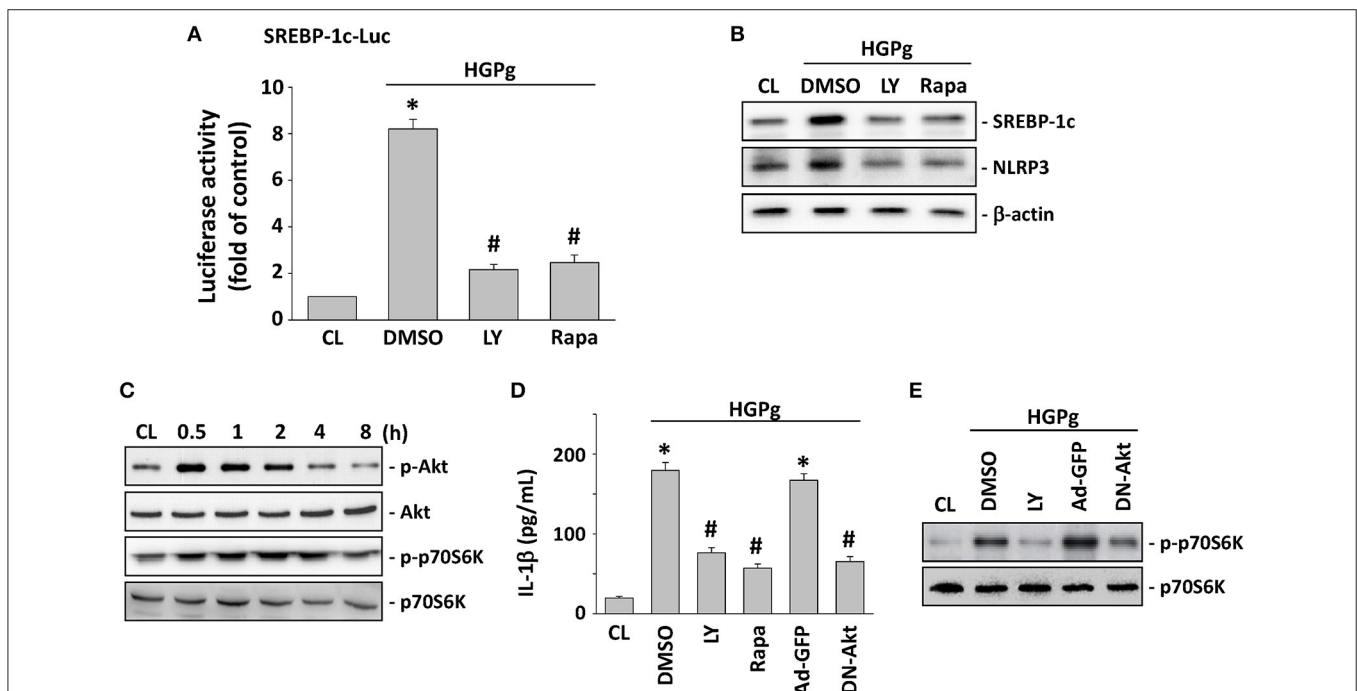


**FIGURE 4 | SREBP-1c regulates NLRP3 and IL-1 $\beta$  expression through Akt and p70S6K activation.** HGFs were kept as CL or infected by HGPg (20 MOI). Before being kept as CL or infected by HGPg, HGFs were pretreated with LY294002 (LY) or rapamycin (rapa) individually for 1 h, or infected with adenovirus expressing the GFP (ad-GFP) or dominant-negative (DN)-Akt. **(A)** SREBP-1c-Luc activity determined in HGFs pretreated with LY or rapa individually, and then infected with HGPg for 4 h. **(B)** The expression of NLRP3 and SREBP-1c in HGF cell lysate after HGPg infection was determined using Western blotting. **(C)** HGFs were kept as CL or stimulated with HGPg for the times indicated, and the phosphorylation of Akt and p70S6K was determined by Western blotting. **(D)** IL-1 $\beta$  secretion in medium was determined by ELISA analyses. The results are shown as mean  $\pm$  SEM. \* $P$  < 0.05 vs. CL. # $P$  < 0.05 vs. vehicle control (DMSO) or Ad-GFP with HGPg infection. **(E)** The phosphorylation of p70S6K in HGF cell lysate after HGPg infection was determined using Western blotting.

inflammasome activation. The infection of HGFs by HGPg also caused significant increases in the SREBP-1c gene expression in an MOI-dependent manner (**Figure 2B**). The induction of SREBP-1c mRNA expression by HGPg was time-dependent (**Figure 2C**). HGPg infection also induced an increase in NLRP3 and mature 68 kD SREBP-1c protein expression in HGFs in a time-dependent manner (**Figure 2D**). In addition, culturing of the HGFs with HGPg increased the luciferase activity 6.3-fold compared with NGPg-infected HGFs after normalization with a transfection control (**Figure 2E**).

### Effects of SREBP-1c on HGPg-Induced NLRP3 and IL-1 $\beta$ Expression

To investigate the role of SREBP-1c on HGPg-induced NLRP3 and IL-1 $\beta$  expression, HGFs were incubated with specific siRNA for SREBP-1c before infection with HGPg. The SREBP-1c-specific siRNAs (compared with the control siRNA) caused a 90% reduction in SREBP-1c protein expression (**Figure 3A**). After SREBP-1c expression was suppressed using siRNA, the expression of NLRP3, mature IL-1 $\beta$ , and active caspase-1 in the HGPg-infected HGFs was significantly decreased compared to that in the control siRNA-transfected HGFs, while pro-IL-1 $\beta$  and pro-caspase-1 were unaltered (**Figure 3B**). The IL-1 $\beta$  mRNA expression levels in the HGPg-infected HGFs did not change between the control siRNA and the SREBP-1c siRNA-treated cells (**Figure 3C**, left panel). However, the concentration of IL-1 $\beta$  in the medium was reduced due to the inhibition of SREBP-1c expression (**Figure 3C**, right panel), since pro-IL-1 $\beta$

development into mature IL-1 $\beta$  is regulated by NLRP3 activation. These results indicate that the expression of SREBP-1c in HGFs may play a critical role in regulating NLRP3 inflammasome expression infected by HGPg.

### Akt and p70S6K Activation Regulate SREBP-1c-Mediated NLRP3 and IL-1 $\beta$ Expression

The PI3K/Akt/p70S6K pathway has been shown to regulate a number of cellular processes, including gene expression and inflammation (Xie et al., 2014). To investigate the involvement of PI3K/Akt and p70S6K in the modulation of SREBP-1c and NLRP3 expression by HGPg infection, HGFs were incubated with specific inhibitors for PI3K/Akt (LY294002) and p70S6K (rapamycin) for 1 h before and during infection with HGPg. Pretreatment of the HGFs with LY294002 and rapamycin resulted in a marked inhibition of HGPg-induced SREBP-1c promoter activity (**Figure 4A**). LY294002 and rapamycin were also found to significantly inhibit the HGPg-induced protein expression of SREBP-1c and NLRP3 (**Figure 4B**). The levels of phosphorylated Akt and p70S6K in HGFs increased significantly after 30 min of HGPg infection (**Figure 4C**). To further confirm the involvement of Akt and p70S6K in the modulation of IL-1 $\beta$  secretion into medium by HGPg stimulation, we examined the effects of cells pretreated with inhibitors or adenovirus expressing the dominant-negative (DN) Akt on HGPg-induced IL-1 $\beta$  secretion. HGPg-induced IL-1 $\beta$  in medium was inhibited by cells pretreated with LY294002 and

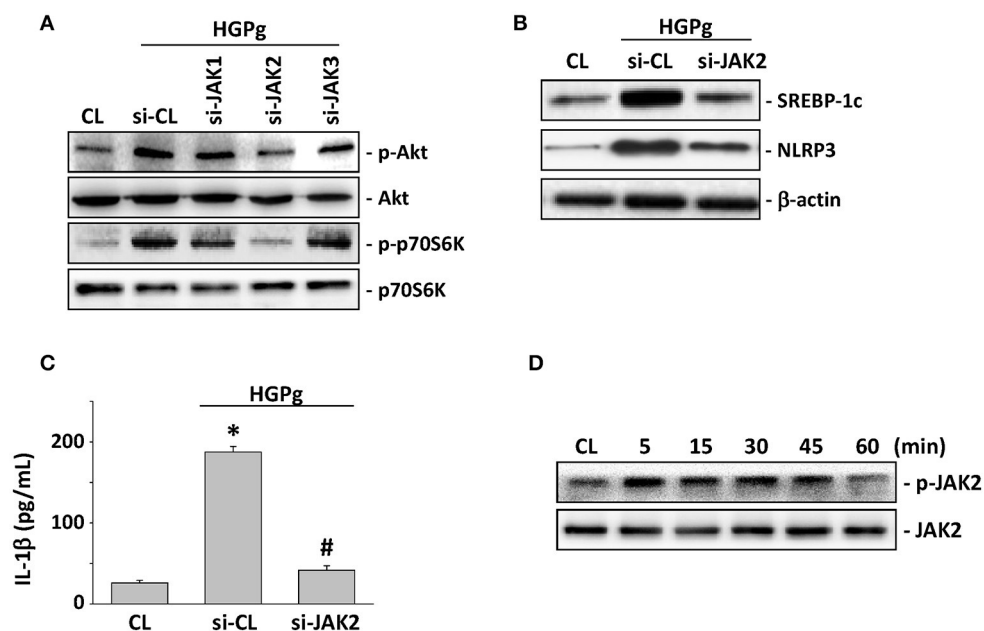


**FIGURE 5 | JAK2 is required for Akt activation and SREBP-1c-mediated NLRP3 and IL-1 $\beta$  expression.** HGFs were kept as CL or infected by HGPg (20 MOI). Before being kept as CL or infected by HGPg, HGFs were transfected with si-JAK1, 2, or 3. **(A)** The phosphorylation of Akt and p70S6K in HGF cell lysate after HGPg infection was determined using Western blotting. **(B)** The expression of NLRP3 and SREBP-1c in HGF cell lysate after HGPg infection was determined using Western blotting. **(C)** IL-1 $\beta$  secretion in medium was determined by ELISA analyses. The results are shown as mean  $\pm$  SEM. \* $P < 0.05$  vs. CL. # $P < 0.05$  vs. si-CL-transfected HGFs with HGPg infection. **(D)** The phosphorylation of JAK2 in HGF cell lysate after HGPg infection was determined using Western blotting.



rapamycin, as was infection with DN-Akt, but not by treatment with vehicle controls (Figure 4D). Furthermore, LY294002 and DN-Akt inhibited the HGPg-induced phosphorylation of p70S6K (Figure 4E). These results indicate that Akt is an upstream regulator for HGPg-induced signaling pathways in HGFs.

## JAK2 Is Required for Akt and p70S6K Phosphorylation and SREBP-1c-Mediated NLRP3 and IL-1 $\beta$ Expression

The JAK family of protein tyrosine kinases has been shown to induce Akt phosphorylation and SREBP-1 expression (Wu et al., 2013). To evaluate the role of JAK family members in HGPg-induced inflammasome activation, HGFs were transfected with JAK1, 2, or 3-siRNA and followed by infection with HGPg. The HGPg-induced Akt and p70S6K phosphorylation were significantly suppressed by the inhibition siRNA of JAK2 (Figure 5A). In addition, the HGPg-induced protein expression of SREBP-1c and NLRP3 (Figure 5B) and the secretion of IL-1 $\beta$  in medium (Figure 5C) were also markedly inhibited by specific JAK2-siRNA. Stimulation of HGFs with HGPg resulted in an increase of JAK2 Tyr1007/1008 phosphorylation in a time-dependent manner. The response peaked at 5 min and declined after 60 min of infection (Figure 5D).

## $\beta$ 1 Integrin Is Required for HGPg-Induced NLRP3 Expression

It has been reported that *P. gingivalis* fimbriae can bind and activate integrins, and further affect host cell gene expression (Zhang et al., 2013). To assess the role of  $\beta$  forms of integrins in HGPg-stimulated HGF function, we evaluated the effects of integrin  $\beta$ 1 and  $\beta$ 2-siRNA on HGF infected with HGPg. The HGPg-induced JAK2 phosphorylation was significantly reduced by integrin  $\beta$ 1-siRNA (Figure 6A). In addition, the HGPg-induced phosphorylation of Akt and p70S6K and the protein expression of SREBP-1c and NLRP3 (Figure 6B), as well as the secretion of IL-1 $\beta$  in medium (Figure 6C), were also decreased in HGFs transfected with integrin  $\beta$ 1-siRNA.

## Higher SREBP-1c and NLRP3 Expression in Human Periodontitis Tissues from Diabetes Patients

Figures 7A,B present respective images of periodontal tissue sections with SREBP-1c and NLRP3 immunostaining. These images show that the intensity and area of SREBP-1c (Figure 7A) and NLRP3 (Figure 7B) increased in diabetic patients with periodontal disease compared to patients with periodontal disease alone. We also performed real-time RT-PCR to detect FimA and NLRP3 gene expression in gingival samples from diabetic patients with periodontal disease. As shown in Figure 7C, the relative expression level of FimA was significantly associated with the expression level of NLRP3.

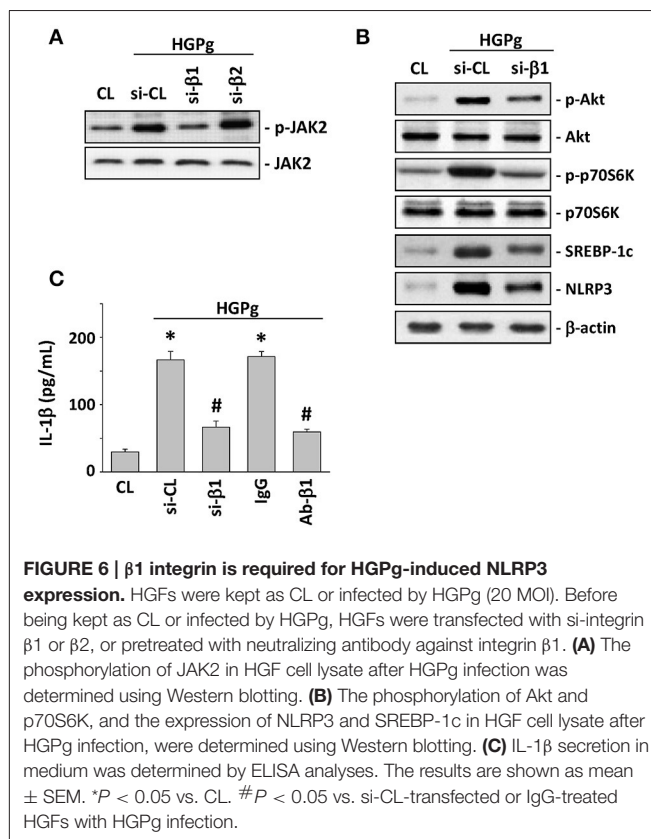


**FIGURE 6 |  $\beta$ 1 integrin is required for HGPg-induced NLRP3 expression.** HGFs were kept as CL or infected by HGPg (20 MOI). Before being kept as CL or infected by HGPg, HGFs were transfected with si-integrin  $\beta$ 1 or  $\beta$ 2, or pretreated with neutralizing antibody against integrin  $\beta$ 1. (A) The phosphorylation of JAK2 in HGF cell lysate after HGPg infection was determined using Western blotting. (B) The phosphorylation of Akt and p70S6K, and the expression of NLRP3 and SREBP-1c in HGF cell lysate after HGPg infection, were determined using Western blotting. (C) IL-1 $\beta$  secretion in medium was determined by ELISA analyses. The results are shown as mean  $\pm$  SEM. \* $P$  < 0.05 vs. CL. # $P$  < 0.05 vs. si-CL-transfected or IgG-treated HGFs with HGPg infection.

## DISCUSSION

The innate immune system is regarded as the first line of defense against pathogen infection (Mogensen, 2009). The NLRP3 inflammasome complex, a key mediator of the innate immunity system, is essential for the processing of mature IL-1 $\beta$  via activation of caspase-1 (Jo et al., 2016). Investigating the interaction between *P. gingivalis* and host cells leading to inflammasome activation and IL-1 $\beta$  release is necessary to understand the development of periodontal diseases (Bostanci et al., 2009). In addition, periodontal disease seems to be associated with higher levels of inflammatory cytokines, such as IL-1 $\beta$  in patients with diabetes (Llambés et al., 2015). Our present study aimed to link the hyperglycemic conditions and *P. gingivalis* infection to HGF inflammasome activation and IL-1 $\beta$  secretion. Our results are significant in several major respects (Figure 8): (1) HGPg infection increases the expression of IL-1 $\beta$  and NLRP3 in HGFs compared with cells infected with NGPg; (2) HGPg-induced NLRP3 expression and mature IL-1 $\beta$  release is regulated by the SREBP-1c upregulation; (3) JAK2 activation and Akt/p70S6K phosphorylation are required for SREBP-1c-mediated NLRP3 and IL-1 $\beta$  expression; and (4) integrin  $\beta$ 1 is a major upstream regulator for HGPg-induced signal transduction and inflammasome activation.

The presence of *P. gingivalis* and the host inflammatory response are necessary for periodontal disease development, especially in individuals with diabetes (Preshaw et al., 2012).

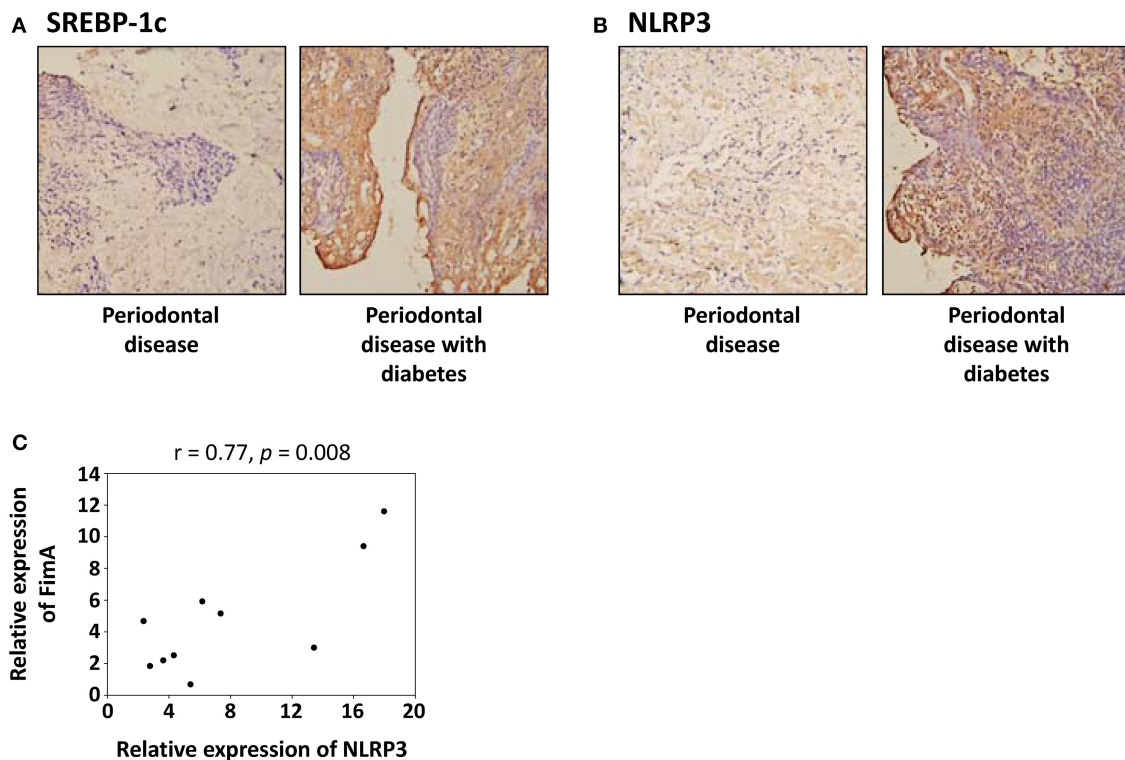
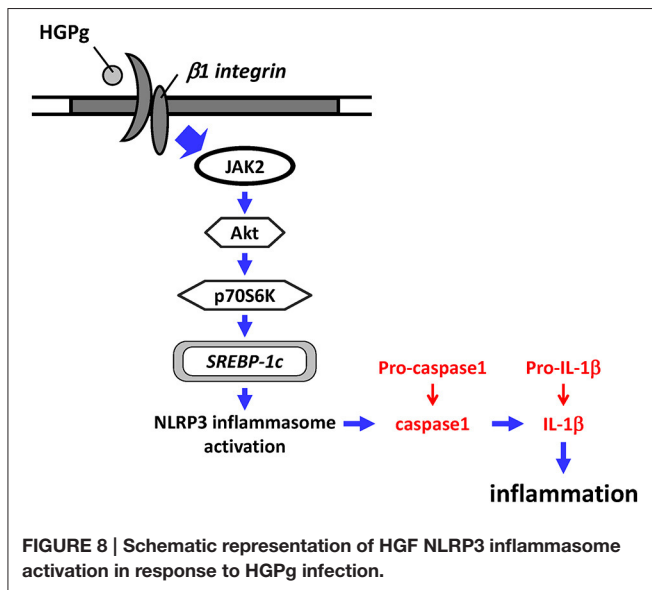


**FIGURE 7 | SREBP-1c and NLRP3 expression is increased in gingival tissues from diabetic patients with periodontal disease. (A,B)** Representative images of immunohistochemical localization of SREBP-1c **(A)** and NLRP3 **(B)** in patients with periodontal disease alone and patients with both diabetes and periodontal disease. **(C)** Correlation of the relative expression level of the FimA and the relative expression level of the NLRP3 in patients with both diabetes and periodontal disease.

Our previous findings demonstrated that when cultured under normal glucose conditions, NGPg has a lower FimA expression, whereas upregulated FimA expression under HG conditions and the invasion efficiency to HGFs are significantly increased by HGPg (Chang et al., 2013). In addition, *P. gingivalis* invasion is critical in the induction of host cell immune responses and the activation of inflammation-related signaling pathways (Lu et al., 2016). In this respect, the NLRP3 inflammasome plays an important role in IL-1 $\beta$  production in response to bacterial infection (Jo et al., 2016). The oral infection with *P. gingivalis* showed markedly increased levels of gingival NLRP3; pro-IL-1 $\beta$ , and pro-caspase-1 mRNA; and IL-1 $\beta$  protein levels compared with fimbriae-deficient mutants, suggesting that fimbriae are a virulence factor involved in NLRP3-inflammasome activation (Park et al., 2014; Yamaguchi et al., 2015). Several different cell types have been reported to express NLRP3 to process and release proinflammatory IL-1 $\beta$ ; however, little is known about the molecular mechanisms by which HG-treated *P. gingivalis* causes IL-1 $\beta$  release in HGFs. In the present study, we investigated the effect of HGPg stimulation on NLRP3 expression and IL-1 $\beta$  production in HGFs. The results of this study demonstrate that HGPg infection not only induces NLRP3 upregulation, but also enhances active caspase-1 and mature IL-1 $\beta$  expression in HGFs. These data indicate that the

NLRP3 inflammasome mediates IL-1 $\beta$  production upon HGPg infection.

SREBP-1c plays a key role in regulating the expression of genes responsible for *de novo* lipogenesis in the liver (Wang et al., 2015). In addition to examining the control of fatty acid synthesis, several studies have focused on the effect of SREBP-1c on inflammation. A previous study has shown that chronic systemic inflammation in the liver is accompanied by upregulated mRNA and protein expression of SREBP-1 *in vivo* (Zhao et al., 2015). *In vitro*, it was found that the inflammatory factors interleukin-6 and tumor necrosis factor- $\alpha$  raised the expression of SREBP-1c in hepatocytes (Jung and Choi, 2014). SREBP activity in endothelial cells has been previously shown to increase by stimulation with atherogenic factors (Chen Z. et al., 2014). Aberrant activation of SREBP-1 is also reported to correlate with vascular inflammatory response *in vivo*, as evidenced by the upregulation of NLRP3 inflammasome and IL-1 $\beta$  (Li et al., 2013). Although chronic inflammation and NLRP3 inflammasome activation have been implicated in atherosclerosis and fatty liver disease, whether SREBP-1c is involved in regulating NLRP3 and IL-1 $\beta$  expression in HGFs remains largely unknown. The results from the present study demonstrated that the upregulation of SREBP-1c in HGFs plays an important role in regulating NLRP3 inflammasome expression infected by HGPg. These



data provide evidence that the SREBP-1c-mediated NLRP3 inflammasome activation and IL-1 $\beta$  production may contribute to the progression of periodontal disease under hyperglycemic conditions.

Until now, the exact mechanisms that lead to NLRP3 inflammasome activation in periodontal cells have not been fully understood. Previous studies have shown that SREBP-1c expression can be regulated through the Akt and p70S6K pathways (Laplane and Sabatini, 2010; Jeon and Osborne, 2012). The regulation of NLRP3 inflammasome activation through the Akt-dependent pathway has also been reported (Ives et al., 2015). In addition, it has been demonstrated that activation of Akt is mediated by JAK2 (Yang et al., 2014). The JAK pathway has been implicated in the control of inflammasome activation (Benoit et al., 2012). Several lines of evidence suggest that the HGPg-induced SREBP-1c and NLRP3 expression in HGFs is mediated via JAK2 activation, and via the Akt and p70S6K pathways. First, the inhibition of Akt and p70S6K phosphorylation in HGFs through pretreatment with inhibitors, or infection with DN-Akt, abolished HGPg-induced SREBP-1c and NLRP3 expression, as well as IL-1 $\beta$  secretion. Second, the inhibition of JAK2 activation in HGFs through transfection with specific JAK2-siRNA suppressed HGPg-induced Akt and p70S6K phosphorylation, SREBP-1c and NLRP3 expression, and IL-1 $\beta$  secretion. Third, when compared to patients with periodontal disease alone, the results of IHC staining also demonstrated that SREBP-1c and NLRP3 were increased in the gingival tissues of diabetic patients with periodontal disease. Based on our results, we suggest that the augmented expression of the NLRP3 inflammasome on HGFs may be involved in HGPg-associated gingival inflammation and may contribute to periodontal pathogen-mediated gingival connective tissue injury. However, the molecular details of the SREBP-1c activation of the NLRP3 inflammasome require further investigation.

Host cells need to transduce signals from cellular receptors into the interior of the cells in response to microbial invasion. A previous report has shown that some integrins interact with bacterial cell surface components, such as fimbriae, hemagglutinin, and lipopolysaccharide, in order to induce gene expression (Mysak et al., 2014). *P. gingivalis* uses the fimbriae to bind to integrin on osteoblasts and reorganize actin microfilaments to invade osteoblasts (Lamkanfi and Dixit, 2014). These investigations demonstrate a direct involvement of the integrins in the initiation of signaling in the fimbria-induced inflammatory gene expression. The present study showed that integrin  $\beta 1$  mediates HGPg infection-induced SREBP-1c and NLRP3 expression through the activation of JAK2 and phosphorylation of Akt and p70S6K. Since there is no experimental evidence in this study to show the interaction between integrin  $\beta 1$  and JAK2 in HGFs, a more detailed investigation is therefore required to better understand their relationship.

In conclusion, the present study provides information regarding the molecular basis in HGFs by which HGPg induces SREBP-1c and NLRP3 inflammasome and IL-1 $\beta$  expression. We found that the signaling pathways activated by infection of HGFs with HGPg are mediated by integrin  $\beta 1$ . HGPg also induces the activation of the JAK2 and Akt/p70S6K signaling pathways, and ultimately enhances NLRP3 expression in HGFs. Our data indicate potential relevant clues regarding possible mechanisms for future therapeutic interventions.

## AUTHOR CONTRIBUTIONS

HK: Provision of study material, collection, and assembly of data and histopathological evaluation; LC: Design, collection, assembly of data, and manuscript writing; TC: Conception, collection, and assembly of data; KCL: Provision of study material or animals; KFL: Provision of study material or animals in pathology; CC: Provision of study material, collection, and assembly of data; HY: Conception and design, financial support, administrative support, manuscript writing, and final approval of manuscript. All authors read and approved the final manuscript.

## ACKNOWLEDGMENTS

Funding for this study was provided in part by research grants BMRPD42, CLRPG8D0112, CMRPF6C0032, CMRPF6F0031, CMRPF6E0041, CMRPF6E0021, and CMRPF6G0011. This study was supported by Chang Gung Memorial Hospital-Kaohsiung Medical Center, Chang Gung Memorial Hospital, and Chang Gung University of Science and Technology, Chia-Yi Campus, Taiwan and by the Ministry of Science and Technology, Taiwan (MOST 104-2320-B-255 -003 -MY3).

## SUPPLEMENTARY MATERIAL

The Supplementary Material for this article can be found online at: <http://journal.frontiersin.org/article/10.3389/fcimb.2016.00195/full#supplementary-material>



## REFERENCES

- Benoit, M. E., Clarke, E. V., Morgado, P., Fraser, D. A., and Tenner, A. J. (2012). Complement protein C1q directs macrophage polarization and limits inflammasome activity during the uptake of apoptotic cells. *J. Immunol.* 188, 5682–5693. doi: 10.4049/jimmunol.1103760
- Bharti, P., Katagiri, S., Nitta, H., Nagasawa, T., Kobayashi, H., Takeuchi, Y., et al. (2013). Periodontal treatment with topical antibiotics improves glycemic control in association with elevated serum adiponectin in patients with type 2 diabetes mellitus. *Obes. Res. Clin. Pract.* 7, e129–e138. doi: 10.1016/j.orcp.2011.11.005
- Bostanci, N., Emingil, G., Saygan, B., Turkoglu, O., Atilla, G., Curtis, M. A., et al. (2009). Expression and regulation of the NALP3 inflammasome complex in periodontal diseases. *Clin. Exp. Immunol.* 157, 415–422. doi: 10.1111/j.1365-2249.2009.03972.x
- Chang, L. C., Kuo, H. C., Chang, S. F., Chen, H. J., Lee, K. F., Lin, T. H., et al. (2013). Regulation of ICAM-1 expression in gingival fibroblasts infected with high-glucose-treated *P. gingivalis*. *Cell Microbiol.* 15, 1722–1734. doi: 10.1111/cmi.12146
- Chen, T. C., Chien, S. J., Kuo, H. C., Huang, W. S., Sheen, J. M., Lin, T. H., et al. (2011a). High glucose-treated macrophages augment E-selectin expression in endothelial cells. *J. Biol. Chem.* 286, 25564–25573. doi: 10.1074/jbc.M111.230540
- Chen, T. C., Sung, M. L., Kuo, H. C., Chien, S. J., Yen, C. K., and Chen, C. N. (2014). Differential regulation of human aortic smooth muscle cell proliferation by monocyte-derived macrophages from diabetic patients. *PLoS ONE* 9:e113752. doi: 10.1371/journal.pone.0113752
- Chen, T. C., Tsai, J. P., Huang, H. J., Teng, C. C., Chien, S. J., Kuo, H. C., et al. (2011b). Regulation of cyclooxygenase-2 expression in human bladder epithelial cells infected with type I fimbriated uropathogenic *E. coli*. *Cell Microbiol.* 13, 1703–1713. doi: 10.1111/j.1462-5822.2011.01650.x
- Chen, Z., Martin, M., Li, Z., and Shyy, J. Y. (2014). Endothelial dysfunction: the role of sterol regulatory element-binding protein-induced NOD-like receptor family pyrin domain-containing protein 3 inflammasome in atherosclerosis. *Curr. Opin. Lipidol.* 25, 339–349. doi: 10.1097/MOL.0000000000000107
- Darveau, R. P. (2010). Periodontitis: a polymicrobial disruption of host homeostasis. *Nat. Rev. Microbiol.* 8, 481–490. doi: 10.1038/nrmicro2337
- Dixit, V. D. (2013). Nlrp3 inflammasome activation in type 2 diabetes: is it clinically relevant? *Diabetes* 62, 22–24. doi: 10.2337/db12-1115
- Faria-Almeida, R., Navarro, A., and Bascones, A. (2006). Clinical and metabolic changes after conventional treatment of type 2 diabetic patients with chronic periodontitis. *J. Periodontol.* 77, 591–598. doi: 10.1902/jop.2006.050084
- Gaddis, D. E., Michalek, S. M., and Katz, J. (2011). TLR4 signaling via MyD88 and TRIF differentially shape the CD4<sup>+</sup> T cell response to *Porphyromonas gingivalis* hemagglutinin B. *J. Immunol.* 186, 5772–5783. doi: 10.4049/jimmunol.1003192
- Hajishengallis, G. (2015). Periodontitis: from microbial immune subversion to systemic inflammation. *Nat. Rev. Immunol.* 15, 30–44. doi: 10.1038/nri3785
- Hajishengallis, G., Wang, M., and Liang, S. (2009). Induction of distinct TLR2-mediated proinflammatory and proadhesive signaling pathways in response to *Porphyromonas gingivalis* fimbriae. *J. Immunol.* 182, 6690–6696. doi: 10.4049/jimmunol.0900524
- Huang, W. S., Hsieh, M. C., Huang, C. Y., Kuo, Y. H., Tung, S. Y., Shen, C. H., et al. (2016). The association of CXC Receptor 4 mediated signaling pathway with oxaliplatin-resistant human colorectal cancer cells. *PLoS ONE* 11:e0159927. doi: 10.1371/journal.pone.0159927
- Ives, A., Nomura, J., Martinon, F., Roger, T., LeRoy, D., Miner, J. N., et al. (2015). Xanthine oxidoreductase regulates macrophage IL1 $\beta$  secretion upon NLRP3 inflammasome activation. *Nat. Commun.* 6, 6555. doi: 10.1038/ncomms7555
- Jeon, T. I., and Osborne, T. F. (2012). SREBPs: metabolic integrators in physiology and metabolism. *Trends Endocrinol. Metab.* 23, 65–72. doi: 10.1016/j.tem.2011.10.004
- Ji, S., Choi, Y. S., and Choi, Y. (2015). Bacterial invasion and persistence: critical events in the pathogenesis of periodontitis? *J. Periodontol. Res.* 50, 570–585. doi: 10.1111/jre.12248
- Jo, E. K., Kim, J. K., Shin, D. M., and Sasakawa, C. (2016). Molecular mechanisms regulating NLRP3 inflammasome activation. *Cell Mol. Immunol.* 13, 148–159. doi: 10.1038/cmi.2015.95
- Jung, U. J., and Choi, M. S. (2014). Obesity and its metabolic complications: the role of adipokines and the relationship between obesity, inflammation, insulin resistance, dyslipidemia and nonalcoholic fatty liver disease. *Int. J. Mol. Sci.* 15, 6184–6223. doi: 10.3390/ijms15046184
- Kato, T., Kawai, S., Nakano, K., Inaba, H., Kuboniwa, M., Nakagawa, I., et al. (2007). Virulence of *Porphyromonas gingivalis* is altered by substitution of fimbria gene with different genotype. *Cell Microbiol.* 9, 753–765. doi: 10.1111/j.1462-5822.2006.00825.x
- Kuo, H. C., Lu, C. C., Shen, C. H., Tung, S. Y., Hsieh, M. C., Lee, K. C., et al. (2016). *Hericium erinaceus* mycelium and its isolated erinacine A protection from MPTP-induced neurotoxicity through the ER stress, triggering an apoptosis cascade. *J. Transl. Med.* 14:78. doi: 10.1186/s12967-016-0831-y
- Lamkanfi, M., and Dixit, V. M. (2014). Mechanisms and functions of inflammasomes. *Cell* 157, 1013–1022. doi: 10.1016/j.cell.2014.04.007
- Laplanche, M., and Sabatini, D. M. (2010). mTORC1 activates SREBP-1c and uncouples lipogenesis from gluconeogenesis. *Proc. Natl. Acad. Sci. U.S.A.* 107, 3281–3282. doi: 10.1073/pnas.1000323107
- Lee, H. M., Kim, J. J., Kim, H. J., Shong, M., Ku, B. J., and Jo, E. K. (2013). Upregulated NLRP3 inflammasome activation in patients with type 2 diabetes. *Diabetes* 62, 194–204. doi: 10.2337/db12-0420
- Li, X., Huang, W., Gu, J., Du, X., Lei, L., Yuan, X., et al. (2015). SREBP-1c overactivates ROS-mediated hepatic NF- $\kappa$ B inflammatory pathway in dairy cows with fatty liver. *Cell Signal.* 27, 2099–2109. doi: 10.1016/j.cellsig.2015.07.011
- Li, Y., Xu, S., Jiang, B., Cohen, R. A., and Zang, M. (2013). Activation of sterol regulatory element binding protein and NLRP3 inflammasome in atherosclerotic lesion development in diabetic pigs. *PLoS ONE* 8:e67532. doi: 10.1371/journal.pone.0067532
- Lin, S. J., Tu, Y. K., Tsai, S. C., Lai, S. M., and Lu, H. K. (2012). Non-surgical periodontal therapy with and without subgingival minocycline administration in patients with poorly controlled type II diabetes: a randomized controlled clinical trial. *Clin. Oral Investig.* 16, 599–609. doi: 10.1007/s00784-011-0535-x
- Llambés, F., Arias-Herrera, S., and Caffesse, R. (2015). Relationship between diabetes and periodontal infection. *World J. Diabetes* 6, 927–935. doi: 10.4239/wjd.v6.i7.927
- Lu, C. C., Huang, W. S., Lee, K. F., Lee, K. C., Hsieh, M. C., Huang, C. Y., et al. (2016). Inhibitory effect of Erinacines A on the growth of DLD-1 colorectal cancer cells is induced by generation of reactive oxygen species and activation of p70S6K and p21. *J. Funct. Foods* 21, 474–484. doi: 10.1016/j.jff.2015.12.031
- Mogensen, T. H. (2009). Pathogen recognition and inflammatory signaling in innate immune defenses. *Clin. Microbiol. Rev.* 22, 240–273. doi: 10.1128/CMR.00046-08
- Mysak, J., Podzimek, S., Sommerova, P., Lyuya-Mi, Y., Bartova, J., Janatova, T., et al. (2014). *Porphyromonas gingivalis*: major periodontopathic pathogen overview. *J. Immunol. Res.* 2014:476068. doi: 10.1155/2014/476068
- Nibali, L., D'Aiuto, F., Griffiths, G., Patel, K., Suvan, J., and Tonetti, M. S. (2007). Severe periodontitis is associated with systemic inflammation and a dysmetabolic status: a case-control study. *J. Clin. Periodontol.* 34, 931–937. doi: 10.1111/j.1600-051X.2007.01133.x
- Park, E., Na, H. S., Song, Y. R., Shin, S. Y., Kim, Y. M., and Chung, J. (2014). Activation of NLRP3 and AIM2 inflammasomes by *Porphyromonas gingivalis* infection. *Infect. Immun.* 82, 112–123. doi: 10.1128/IAI.00862-13
- Preshaw, P. M., Alba, A. L., Herrera, D., Jepsen, S., Konstantinidis, A., Makrilakis, K., et al. (2012). Periodontitis and diabetes: a two-way relationship. *Diabetologia* 55, 21–31. doi: 10.1016/j.ecl.2013.05.012
- Tseng, T. H., Lin, W. L., Chen, Z. H., Lee, Y. J., Shie, M. S., Lee, K. F., et al. (2016). Moniliformediquinone as a potential therapeutic agent, inactivation of hepatic stellate cell and inhibition of liver fibrosis *in vivo*. *J. Transl. Med.* 14:263. doi: 10.1186/s12967-016-1022-6
- Wang, Y., Viscarra, J., Kim, S. J., and Sul, H. S. (2015). Transcriptional regulation of hepatic lipogenesis. *Nat. Rev. Mol. Cell Biol.* 16, 678–689. doi: 10.1038/nrm4074
- Wu, C. F., Lin, Y. L., and Huang, Y. T. (2013). Hepatitis C virus core protein stimulates fibrogenesis in hepatic stellate cells involving the obese receptor. *J. Cell Biochem.* 114, 541–550. doi: 10.1002/jcb.24392
- Xie, S., Chen, M., Yan, B., He, X., Chen, X., and Li, D. (2014). Identification of a role for the PI3K/AKT/mTOR signaling pathway in innate immune cells. *PLoS ONE* 9:e94496. doi: 10.1371/journal.pone.0094496



- Yamaguchi, Y., Kurita-Ochiai, T., Kobayashi, R., Suzuki, T., and Ando, T. (2015). Activation of the NLRP3 inflammasome in *Porphyromonas gingivalis*-accelerated atherosclerosis. *Pathog. Dis.* 73:ftv011. doi: 10.1093/femspd/ftv011
- Yang, C. M., Lee, I. T., Chi, P. L., Cheng, S. E., Hsiao, L. D., and Hsu, C. K. (2014). TNF- $\alpha$  induces cytosolic phospholipase A2 expression via Jak2/PDGFR-dependent Elk-1/p300 activation in human lung epithelial cells. *Am. J. Physiol. Lung Cell. Mol. Physiol.* 306, L543–L551. doi: 10.1152/ajplung.00320.2013
- Yoshimura, F., Murakami, Y., Nishikawa, K., Hasegawa, Y., and Kawaminami, S. (2009). Surface components of *Porphyromonas gingivalis*. *J. Periodontol. Res.* 44, 1–12. doi: 10.1111/j.1600-0765.2008.01135.x
- Zhang, W., Ju, J., Rigney, T., and Tribble, G. (2013). Integrin  $\alpha 5 \beta 1$ -fimbriae binding and actin rearrangement are essential for *Porphyromonas gingivalis* invasion of osteoblasts and subsequent activation of the JNK pathway. *BMC Microbiol.* 13:5. doi: 10.1186/1471-2180-13-5
- Zhao, L., Zhong, S., Qu, H., Xie, Y., Cao, Z., Li, Q., et al. (2015). Chronic inflammation aggravates metabolic disorders of hepatic fatty acids in high-fat diet-induced obese mice. *Sci. Rep.* 5:10222. doi: 10.1038/srep10222

**Conflict of Interest Statement:** The authors declare that the research was conducted in the absence of any commercial or financial relationships that could be construed as a potential conflict of interest.

Copyright © 2016 Kuo, Chang, Chen, Lee, Lee, Chen and Yu. This is an open-access article distributed under the terms of the Creative Commons Attribution License (CC BY). The use, distribution or reproduction in other forums is permitted, provided the original author(s) or licensor are credited and that the original publication in this journal is cited, in accordance with accepted academic practice. No use, distribution or reproduction is permitted which does not comply with these terms.

# SCIENTIFIC REPORTS

OPEN

## *Ilex kaushue* and Its Bioactive Component 3,5-Dicaffeoylquinic Acid Protected Mice from Lipopolysaccharide-Induced Acute Lung Injury

Received: 28 January 2016  
Accepted: 09 September 2016  
Published: 29 September 2016

Yu-Li Chen<sup>1</sup>, Tsong-Long Hwang<sup>1,2,3,4,5</sup>, Huang-Ping Yu<sup>5,6</sup>, Jia-You Fang<sup>1,2,3,4,5</sup>, Kowit Yu Chong<sup>1,7,8</sup>, Yao-Wen Chang<sup>1,2</sup>, Chun-Yu Chen<sup>5</sup>, Hsuan-Wu Yang<sup>2</sup>, Wen-Yi Chang<sup>2</sup> & Pei-Wen Hsieh<sup>1,2,4,5</sup>

Acute lung injury (ALI) is a severe respiratory disease with high mortality rates worldwide. Recent reports suggest that human neutrophil elastase (HNE) plays a key role in the inflammatory response that is characteristic of ALI, which indicates that the development of HNE inhibitors could be an efficient treatment strategy. In the current study, an enzyme-based screening assay was used to identify effective HNE inhibitors from a number of traditional Chinese medicines (TCMs). Among them, a water extract of *Ilex kaushue* (IKWE) effectively inhibited HNE activity ( $IC_{50}$ ,  $11.37 \pm 1.59 \mu\text{g/mL}$ ). Using bioactivity-guided fractionation, one new compound and 23 known compounds were identified. Compound 6 (identified as 3,5-dicaffeoylquinic acid; 3,5-DCQA) exerted the most potent and selective inhibitory effect on HNE activity ( $IC_{50}$ ,  $1.86 \pm 0.06 \mu\text{M}$ ). In a cell-based assay, 3,5-DCQA not only directly reduced superoxide generation and elastase activity but also attenuated the Src family kinase (SRKs)/Vav signaling pathway in N-formyl-L-Met-L-Leu-L-Phe (fMLF)-stimulated human neutrophils. In an animal disease model, both 3,5-DCQA and standardized IKWE protected against lipopolysaccharide-induced ALI in mice, which provides support for their potential as candidates in the development of new therapeutic agents for neutrophilic inflammatory diseases.

ALI and its more severe form, acute respiratory distress syndrome (ARDS), are inflammatory diseases triggered by direct and indirect pathogenic factors, such as sepsis, pneumonia, inhalation injury and trauma<sup>1</sup>. Lipopolysaccharide (LPS) is an endotoxin that plays a pathological determinant role in sepsis-related ALI<sup>2</sup>. In the majority of cases, ALI and ARDS result in respiratory failure leading to high mortality. No effective therapeutic agents are available for ALI, and technical ventilation and supportive care constitute the primary approaches to avoid underlying complications<sup>1,3,4</sup>, highlighting the urgent requirement for novel treatment strategies and medicines.

Neutrophils form the first line of defense against pathogens in innate immunity mainly through phagocytosis. Further invasion of pathogens is prevented with the release of reactive oxygen species (ROS), serine proteases, and neutrophil extracellular traps<sup>5</sup>. In ALI pathology, circulating neutrophils are recruited and activated by chemokines and cytokines from alveolar macrophages and alveolar-type II epithelial cells, triggering neutrophil

<sup>1</sup>Graduate Institute of Biomedical Sciences, College of Medicine, Chang Gung University, Taoyuan, Taiwan. <sup>2</sup>Graduate Institute of Natural Products, College of Medicine, Chang Gung University, Taoyuan, Taiwan. <sup>3</sup>Chinese Herbal Medicine Research Team, Healthy Aging Research Center, Chang Gung University, Taoyuan, Taiwan. <sup>4</sup>Research Center for Industry of Human Ecology and Research Center for Chinese Herbal Medicine, Chang Gung University of Science and Technology, Taoyuan, Taiwan. <sup>5</sup>Department of Anesthesiology, Chang Gung Memorial Hospital, Taoyuan, Taiwan. <sup>6</sup>School Medicine, College of Medicine, Chang Gung University, Taoyuan, Taiwan. <sup>7</sup>Department of Medical Biotechnology and Laboratory Science, College of Medicine, Chang Gung University, Taoyuan, Taiwan. <sup>8</sup>Department of Thoracic Medicine, Chang Gung Memorial Hospital at Linkou, Taoyuan, Taiwan. Correspondence and requests for materials should be addressed to P.-W.H. (email: pewehs@mail.cgu.edu.tw)

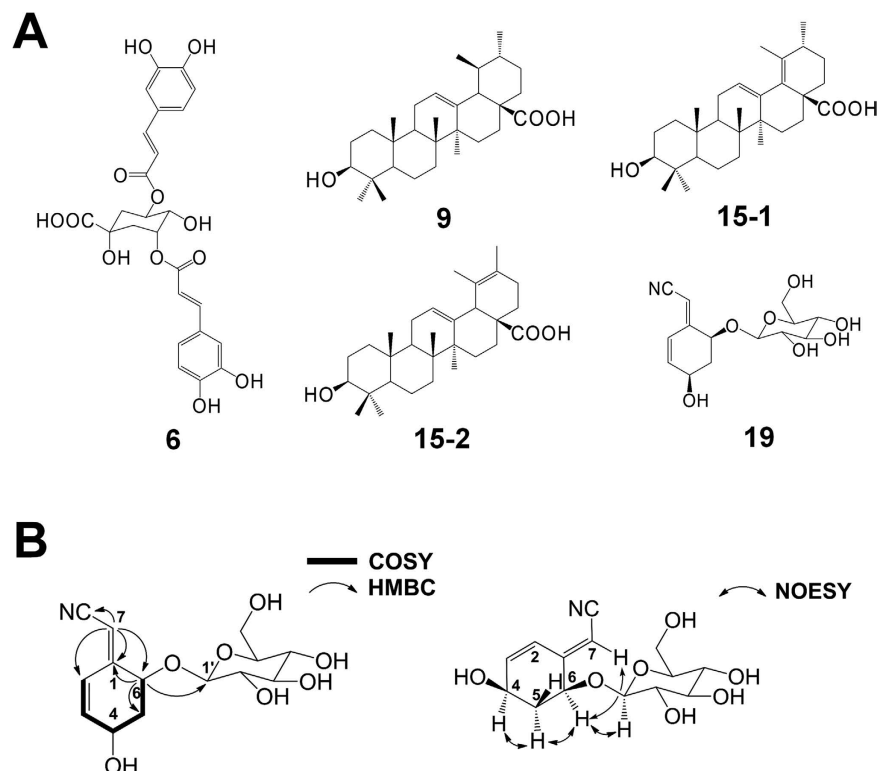


**Figure 1. Structure of selected isolates and synthetics.** (A) 3,5-DCQA (6), ursolic acid (9), randialic acid B (15-1), sanguisorbigenin (15-2), and menisdaurin F (19); (B) Selected COSY, HMBC and NOE correlation of menisdaurin F.

serine protease release, alveolar edema and impaired oxygenation. Neutrophil elastase (NE) is one of the serine proteases released from activated neutrophils that cause pulmonary damage through hydrolysis of elastin-rich connective tissue. Additionally, NE acts as an inflammatory mediator and contributes to the migration and activation of neutrophils through effects on alveolar macrophage and lung epithelial cells<sup>6</sup>.  $\alpha_1$ -Antitrypsin, an endogenous secretory elastase inhibitor abundant in the peripheral alveolar region, naturally protects lung tissue from proteolysis by elastase. Enhanced NE activity has been observed due to inactivation of  $\alpha_1$ -antitrypsin under conditions of increased oxidative stress resulted from neutrophils<sup>4,7</sup>. The development of NE inhibitors is therefore considered an effective therapeutic strategy for ALI<sup>3,4</sup>.

Botanical products and TCM are recognized as important sources of novel drugs<sup>8,9</sup>. In an attempt to identify NE inhibitors, 22 TCM extracts were prepared and their inhibitory effects on human neutrophil elastase (HNE) activity evaluated. Among these, the *I. kaushue* water extract (IKWE) inhibited HNE activity with an  $IC_{50}$  value of  $11.37 \pm 1.59 \mu\text{g/mL}$ . *I. kaushue*, syn *I. kudingcha* (also known as Kudingcha) is an evergreen tree found in China<sup>10</sup>. The leaves have been used as a daily beverage and herbal medicine in TCM for nearly two thousand years<sup>11</sup>. Triterpenoids, polyphenols, cyanoglucosides and essential oils are the major metabolites of *I. kaushue*<sup>12,13</sup>. Traditionally, the plant has beneficial physiological effects, including thirst quenching, elimination of phlegm for resuscitation, and removal of mucus from the lung<sup>14</sup>. Recent studies have additionally revealed anticancer, antidiabetes, antiobesity and antioxidant bioactivities<sup>12,13,15–17</sup>. In the current investigation, we focused on evaluating the beneficial effects of *I. kaushue* and its bioactive component on acute lung injury (ALI), both *in vitro* and *in vivo*.

## Results

**Chemical components isolated from *I. kaushue* water extracts (IKWE) via bioactivity-guided fractionation.** Using bioassay-directed fractionation, nineteen compounds, including polyphenols (1–8), triterpenoid saponins (9–15), cyanoglucosides (17–19) and phytosteroid (16) (Fig. 1A and Supplementary information Fig. S1) were isolated from IKWE. Among these, compound 19 was new, while compounds 1–8 were identified as caffeoylquinic acids (CQA) or dicaffeoylquinic acids (DCQA) based on the position and number of caffeoyl groups conjugated with quinic acid. Saccharides of 11, 14, and 15 were further hydrolyzed to generate aglycons (11-1, 11-2, 14-1, 15-1, and 15-2) for proposing structure and activity relationships (SAR). All known compounds were identified by comparing their physical and spectral data with the values provided in the literatures.

**Structural elucidation of menisdaurin F (compound 19).** Compound 19,  $[\alpha]_D^{23}$ :  $-63.6^\circ$  ( $c = 0.05$ , MeOH), was obtained as a colorless powder. The molecular formula,  $C_{14}H_{19}NO_7$ , assigned based on HRESIMS data ( $336.1048 \text{ m/z}$ ,  $[M + Na]^+$ ), implied six unsaturation degrees. The presence of a hydroxyl group was suggested based on the absorption band at  $3392 \text{ cm}^{-1}$  in the IR spectrum. The characteristic bands at 2220 and

Compounds	IC <sub>50</sub> (μM)				
	HNE	Cathepsin G	Proteinase 3	Thrombin	Chymotrypsin
1	>30	>30	>30	>30	>30
2	>30	>30	>30	>30	>30
3	>30	>30	>30	>30	>30
4	>30	>30	>30	>30	>30
6	1.86 ± 0.06	>30	>30	>30	>30
7	>30	>30	>30	>30	>30
9	11.52 ± 1.28	>30	7.33 ± 0.65	6.37 ± 0.60	6.06 ± 0.05
10	>30	>30	>30	>30	>30
11	>30	>30	>30	>30	>30
12	>30	>30	>30	>30	>30
13	>30	>30	>30	>30	>30
14	>30	>30	>30	>30	>30
15	>30	>30	>30	>30	>30
17	>30	>30	>30	>30	>30
18	>30	>30	>30	>30	>30
19	>30	>30	>30	>30	>30
11-1	>30	>30	7.62 ± 0.32	>30	8.06 ± 0.40
11-2	8.55 ± 1.77	>30	1.99 ± 0.25	2.98 ± 0.35	6.04 ± 0.29
14-1	>30	>30	>30	>30	>30
15-1	>30	>30	17.44 ± 0.16	24.94 ± 1.33	16.98 ± 0.10
15-2	24.75 ± 0.48	>30	14.77 ± 0.59	11.77 ± 2.20	11.40 ± 0.20
Elaspol <sup>a</sup>	0.03 ± 0.00	—	0.56 ± 0.06	—	—
CG inhibitor <sup>a</sup>	—	0.27 ± 0.03	—	—	—
AEBSF <sup>a</sup>	—	—	—	250.74 ± 8.78	30.96 ± 4.96

**Table 1. Serine proteases inhibition profiles of isolates and synthetics.** <sup>a</sup>Positive controls: Elaspol, CG inhibitor and AEBSF. Data were presented as mean ± S.E.M. (n ≥ 3).

1621 cm<sup>-1</sup> in the IR spectrum, <sup>13</sup>C NMR signals at δ<sub>C</sub> 93.7 (d), 117.9 (s), 124.5 (d), 143.3 (d), 159.1 (s) and <sup>1</sup>H NMR signals at δ<sub>H</sub> 5.77 (s), 6.24 (d, 10.0), 6.57 (dd, 10.0, 2.0), together with ultraviolet absorption at λ<sub>max</sub> 256 nm, signifying the presence of α, β, γ, δ-unsaturated nitrile<sup>18–20</sup>. NMR signals at δ<sub>H</sub> 3.66 (dd, 11.6, 8.0), 3.86 (d, 11.6), 4.48 (d, 8.0); δ<sub>C</sub> 62.6 (t) and 102.6 (d) suggested the presence of a glucopyranosyl group. Comparison of 1D and 2D NMR spectra revealed that compound **19** is a structural isomer of menisdaurin (**18**) (Fig. 1B, Supplementary information Figs S2–S8 and Table S1)<sup>19–21</sup>. The strong NOE (nuclear overhauser effect) correlations between H-4 and H-5a, H-5a and H-6, and H-6 and H-1' demonstrate that compound **19** shares the same orientation of H-4 and H-6 with menisdaurin. Additionally, NOE correlations between H-6 and H-7 implied an *E*-configuration of the C-1/C-7 double bond in compound **19**<sup>19,22</sup>. The downfield shift of the H-2 signal (calculated as 0.25 ppm) additionally supported the presence of the *E*-configuration<sup>19</sup>. Based on the collective data, the structure of **19** was determined as an *E*-form isomer of menisdaurin (**18**), designated menisdaurin F.

**3,5-DCQA (compound 6) showed potent and selective inhibition of HNE activity.** To identify the bioactive components and their specificities, enzyme inhibition assays involving human and bovine serine proteases were performed (Table 1). Among the isolates, 3,5-DCQA (**6**) exerted the most potent and selective inhibitory effect on HNE activity with an IC<sub>50</sub> value of 1.86 ± 0.06 μM. All triterpenoid saponins (**10–15**) were non-active, while aglycons (**11-2** and **15-2**) and ursolic acid (**9**) exerted non-selective inhibitory effects on serine proteases.

**3,5-DCQA reduced superoxide anion (O<sub>2</sub><sup>•-</sup>) production and NE activity in fMLF-activated human neutrophils.** O<sub>2</sub><sup>•-</sup> and NE from activated neutrophils cause alveolar damage in response to acute inflammatory conditions in ALI. Therefore, the effects of all isolates and semi-synthetics on O<sub>2</sub><sup>•-</sup> generation and NE release were determined using fMLF as an inducer in human neutrophils (Table 2). Our results showed that 3,5-DCQA inhibited O<sub>2</sub><sup>•-</sup> generation and NE activity with IC<sub>50</sub> values of 1.92 ± 0.54 and 12.02 ± 0.60 μM, respectively (Supplementary information Table S2). Three triterpenoids, **9**, **15-1** and **15-2**, exhibited good inhibitory effects on O<sub>2</sub><sup>•-</sup> generation and NE release as well. However, triterpenoid saponins (compounds **10–15**) showed no or weak inhibitory effects.

**3,5-DCQA attenuated the activation of SFKs and Vav in fMLF-induced neutrophils.** To investigate whether 3,5-DCQA modulated neutrophil activity through intracellular signaling pathway, the activation of SFKs, Vav, Akt and MAPKs were evaluated by Western blot. The results indicated fMLF triggered the

Compounds	IC <sub>50</sub> (μM)		Compounds	IC <sub>50</sub> (μM)	
	O <sub>2</sub> <sup>•−</sup> generation	HNE		O <sub>2</sub> <sup>•−</sup> generation	HNE
1	1.54 ± 0.29	>10	9	0.99 ± 0.26	1.07 ± 0.33
2	2.81 ± 1.00	>10	10	>10	>10
3	2.56 ± 1.06	>10	11	>10	>10
4	1.70 ± 0.28	>10	12	>10	>10
6	1.92 ± 0.54	>10	13	>10	>10
7	1.49 ± 0.38	>10	14	>10	>10
QA	>10	>10	15	>10	7.99 ± 1.18
CA	1.42 ± 0.02	>10	17	>10	>10
RA	1.29 ± 0.09	>10	18	>10	>10
THBA	1.14 ± 0.08	>10	19	>10	>10
<i>p</i> -CA	>10	>10	11-1	>10	>10
3-HCA	>10	>10	11-2	>10	>10
FA	>10	>10	14-1	4.77 ± 0.40	2.84 ± 1.02
—	—	—	15-1	0.14 ± 0.09	0.06 ± 0.01
—	—	—	15-2	0.26 ± 0.10	0.20 ± 0.02

**Table 2. Inhibitory effects on fMLF/CB-activated neutrophils of isolates and synthetics.** QA, quinic acid; CA, caffeic acid; RA, rosmarinic acid; THBA, 3,4,5-trihydroxybenzoic acid; *p*-CA, *p*-coumaric acid; 3-HCA, 3-hydroxycinnamic acid; FA, ferulic acid. Data were presented as mean ± S.E.M. (n ≥ 3).

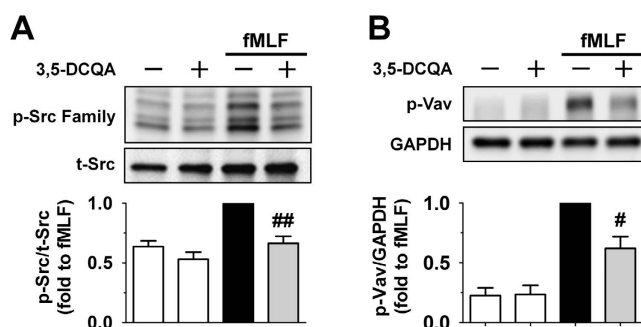


**Figure 2. 3,5-DCQA inhibited the phosphorylation of Src family kinase (Src) and Vav in fMLF-activated human neutrophils.** Human neutrophils were pre-incubated with dimethylsulfoxide (DMSO) or 3,5-DCQA (10 μM) for 5 min before stimulation with or without fMLF (0.1 μM) for another 0.5 min. All the Western blotting experiments were performed under the same condition. After transferring the blots onto nitrocellulose membranes, the targeted blots were cropped immediately according to referenced indicating markers. The targeted proteins were immunoblotted with its specific monoclonal antibody. (A) Src family kinases; (B) Vav. Targeted bands were analyzed using a densitometer and normalized to the corresponding total protein or glyceraldehyde 3-phosphate dehydrogenase (GAPDH). The densitometric data were presented as mean ± S.E.M. (n = 3–4). Compared with fMLF group: <sup>#</sup>*p* < 0.05 and <sup>##</sup>*p* < 0.01.

phosphorylation of signaling proteins, and 3,5-DCQA was able to reduce phosphorylation of SFKs and Vav, but not Akt and MAPKs (Fig. 2 and Supplementary information Fig. S9).

**Establishment of CMC (chemistry, manufacturing and controls).** CMC data are essential to maintain the quality of botanical products in manufacturing. Accordingly, SOPs (standard operating procedures) and quality control were performed for the IKWE preparation. In HPLC fingerprints, three distinct peaks were identified as 3,4-DCQA (4), 3,5-DCQA (6) and 4,5-DCQA (7), compared to the respective pure compounds (Fig. 3). We defined and quantified these DCQAs as chemical reference standards based on calibration curves (Supplementary information Fig. S10). Biological identification was additionally validated with the HNE activity assay. The yield for three batches of IKWE was generally over 35% (Supplementary information Fig. S11), and amounts of 4, 6, and 7 obtained were  $3.76 \pm 0.26\%$ ,  $4.70 \pm 0.13\%$  and  $8.85 \pm 0.15\%$ , respectively. These data indicated that 3,5-DCQA served as the main bioactive component in KSWE. Besides, batches of IKWE exerted an inhibitory effect on HNE activity with an IC<sub>50</sub> value of  $10.50 \pm 0.48 \mu\text{g/mL}$ , signifying the stable quality of bioactivity and chemical composition.

**Toxicity Evaluation of IKWE.** Safety of botanical drugs is another important concern. To evaluate the toxicity of IKWE, acute oral toxicity studies were performed at a high dose of  $10.0 \text{ g/kg}^{23}$ . All mice receiving IKWE with LD<sub>50</sub> values higher than  $10.0 \text{ g/kg}$  survived. Moreover, no significant differences were observed with regard

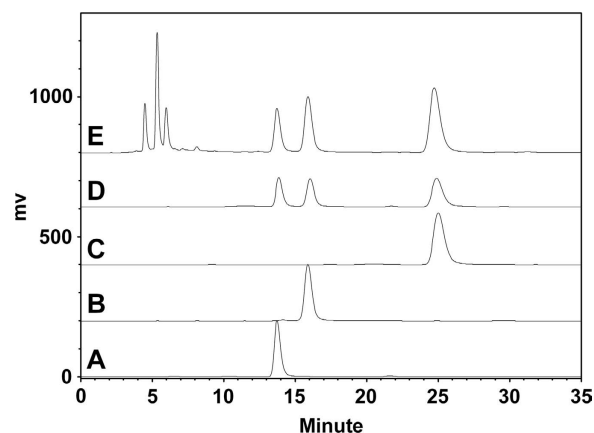


**Figure 3. HPLC fingerprint chromatography and standard references of IKWE.** (A) 3,4-DCQA, 100  $\mu\text{g/mL}$ , rt 13.5 min; (B) 3,5-DCQA, 100  $\mu\text{g/mL}$ , rt 15.9 min; (C) 4,5-DCQA, 200  $\mu\text{g/mL}$ , rt 25.0 min; (D) Combination of 3,4-DCQA, 3,5-DCQA, and 4,5-DCQA at 50, 50, 100  $\mu\text{g/mL}$  respectively; (E) IKWE, 2 mg/mL. Injection volume, 20  $\mu\text{L}$ ; Detection wavelength, 326 nm; Flow rate, 0.8 mL/min; Mobile phase, 42.5% MeOH solution with 1% formic acid.

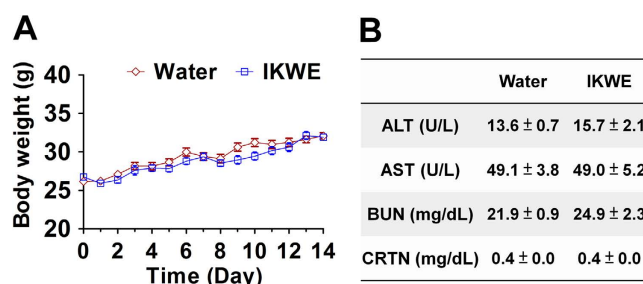


**Figure 4. Acute oral toxicity evaluation of IKWE.** IKWE were dissolved with ddH<sub>2</sub>O to give IKWE solution. Body weights of mice received vehicle or IKWE solution through gavage were observed for 14 days. Serum was obtained 24 hours after gavage for chemical parameter determination. (A) Curves of body weight growth in vehicle-received or IKWE-received mice (n = 10 for each group); (B) Examination of liver and kidney functions between vehicle and IKWE groups. ALT, alanine transaminase; AST, aspartate aminotransferase; CRTN, creatinine; BUN, blood urea nitrogen. Data were presented as mean  $\pm$  S.E.M. (n = 10).

to movement and body weight growth in mice, suggesting no adverse effects (Fig. 4A). Organ toxicity was further assessed via determination of liver and kidney function (Fig. 4B). The data collectively indicated high safety of IKWE.

**IKWE and 3,5-DCQA protected against LPS-induced ALI in mice.** In view of the finding that IKWE and its bioactive component, 3,5-DCQA, exert anti-inflammatory effects against activated neutrophils, both were prepared and their protective effects evaluated in an LPS-induced ALI disease model. Infiltrating neutrophils, thickening of the alveolar wall, lung edema and alveolar hemorrhage are pathological features of ALI<sup>1–4</sup>. Dark red color and morphological swelling of the lung in LPS-induced ALI mice suggested alveolar hemorrhage and edema (Fig. 5A). In addition to hemorrhage, histological examination revealed infiltrating neutrophils and thickening of the alveolar wall in the LPS-treated group. These pathological features were significantly improved following pretreatment with IKWE (500 mg/kg) or 3,5-DCQA (50 mg/kg). Wet/dry (W/D) weight ratio, myeloperoxidase (MPO) activity and bronchoalveolar lavage fluid (BALF) were further assessed to confirm the protective effects and determine underlying molecular mechanisms. Our results showed that IKWE and 3,5-DCQA not only improve lung edema but also suppress accumulation of neutrophils in lung tissue (Figs 5B,C and 6A–C). Reduced levels of proinflammatory cytokines (TNF- $\alpha$  and IL-6) were additionally observed (Fig. 6D,E), clearly supporting the protective effects of both IKWE and 3,5-DCQA against LPS-induced ALI in mice. Besides, the post-treatment with 3,5-DCQA was performed to further evaluate its effects against LPS-induced ALI in mice<sup>24</sup>. The results showed that pathological features of ALI were also significantly improved following treatment with 3,5-DCQA (Supplementary information Fig. S12).

## Discussion

ALI is a life-threatening disease for which no effective treatments are available. Botanical drugs are considered to be an important resource for drug development, and they require stringent testing for efficacy, safety and quality<sup>9</sup>. Because of the ability of IKWE to inhibit HNE activity, the protective effects of *I. kaushue* against ALI



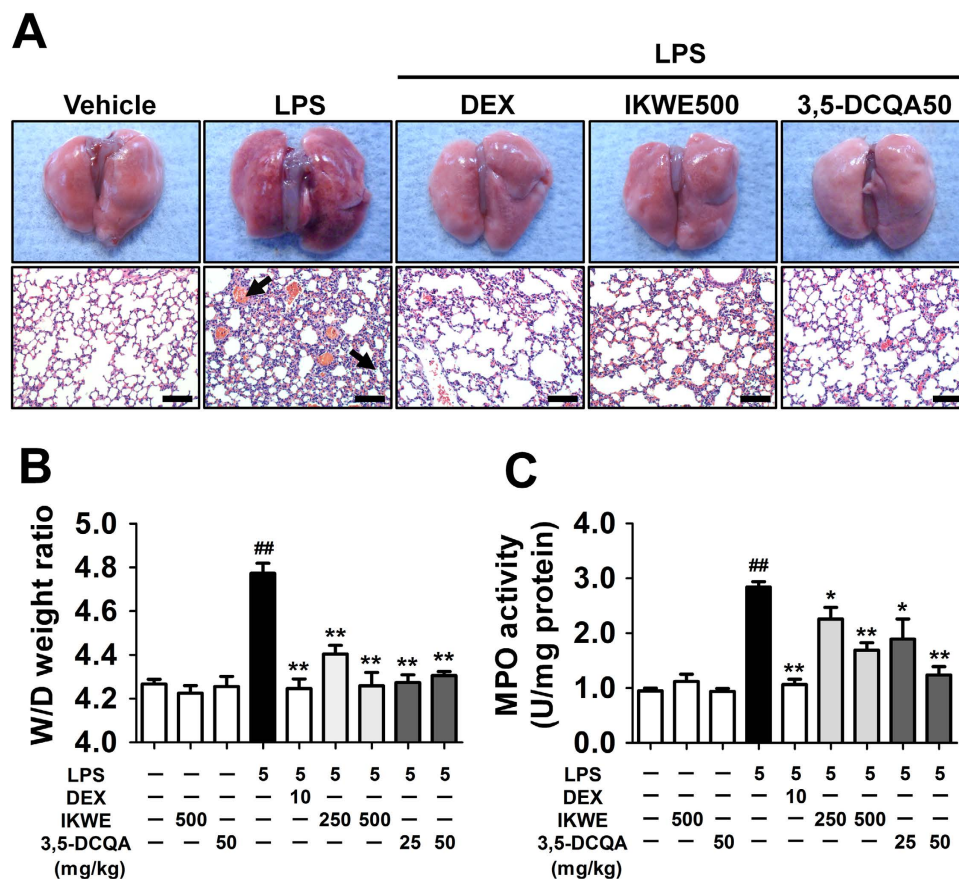


**Figure 5. IKWE and 3,5-DCQA attenuated LPS-induced ALI in mice.** Mice pretreated with vehicle or drugs intraperitoneally received intratracheal instillation of LPS. After 6 hours, mice were anesthetized and their chests were opened. Whole lungs were obtained immediately and observed for morphological changes. Left lobe was then dissected for histology or MPO activity. Right lobes were applied for W/D weight ratio. (A) Morphological observation and histological examination (arrows indicated hemorrhage and infiltrated neutrophils, scale bar = 50  $\mu$ m; (B). (C) Lung W/D weight ratio and MPO activity. Data were presented as mean  $\pm$  S.E.M. (n = 6). Compared with vehicle group: <sup>##</sup> $p < 0.01$ ; Compared with LPS group: <sup>\*</sup> $p < 0.05$  and <sup>\*\*</sup> $p < 0.01$ .

were investigated, both *in vitro* and *in vivo*. In the *in vivo* studies, dexamethasone was used as a positive control. Although the applied dosage and possible side effects of dexamethasone in clinical settings are controversial, it is still a common positive control in ALI mouse models<sup>25–27</sup>.

Although serine proteases are responsible for several physiological functions in humans, abnormal and excessive levels can cause or promote disease<sup>28,29</sup>. Recent experimental and clinical studies have shown that enhanced HNE activity is associated with the degradation of elastin-rich proteins in the pathological progression of ALI. Consequently, HNE is considered to be a promising therapeutic target for treating ALI<sup>4,28,30</sup>. In our experiments, 3,5-DCQA exhibited high selectivity for HNE among the five serine proteases that were examined. Further exploration of the SAR of the caffeic acid analogues showed that the inhibitory effects on HNE activity of the compounds did not depend on the caffeic acid moiety, but were correlated with the regioselectivity of caffeic acids conjugated to quinic acid (Supplementary information Table S3).

In addition to serine proteases, enhanced oxidative stress also contributes to the pathogenesis of inflammatory diseases<sup>1,4,30</sup>. The production of superoxide anions from human neutrophils can be reduced through intracellular mechanisms or ROS scavenging agents<sup>4,30</sup>. 3,5-DCQA was previously reported to be a ROS-scavenger and to exert anti-oxidant effects<sup>31</sup>. The *ortho*-dihydroxyphenyl moiety significantly promotes ROS scavenging activity via a highly favorable electron acceptance and resonance system<sup>32,33</sup>. Our results showed that all caffeoylquinic acid derivatives, together with CA, RA and THBA, potently inhibit  $O_2^{\cdot -}$  generation in neutrophils (Table 2). In contrast, compounds *p*-CA, 3-HCA and FA were non-active because the *ortho*-dihydroxyphenyl group was absent. Interestingly, the HNE inhibitory effects of 3,5-DCQA decreased in fMLF-induced neutrophils, which was demonstrated by comparing the results of an enzyme inhibition assay. To eliminate the influence of  $O_2^{\cdot -}$  generation, leukotriene B<sub>4</sub> (LTB<sub>4</sub>) was used as an inducer in human neutrophils (Supplementary information Table S2), which led to the recovery of 3,5-DCQA-induced HNE inhibition<sup>34</sup>. These data confirmed that 3,5-DCQA at a high dose (100  $\mu$ M) was able to inhibit elastase release, myeloperoxidase activity and superoxide production in human neutrophils<sup>35</sup>.

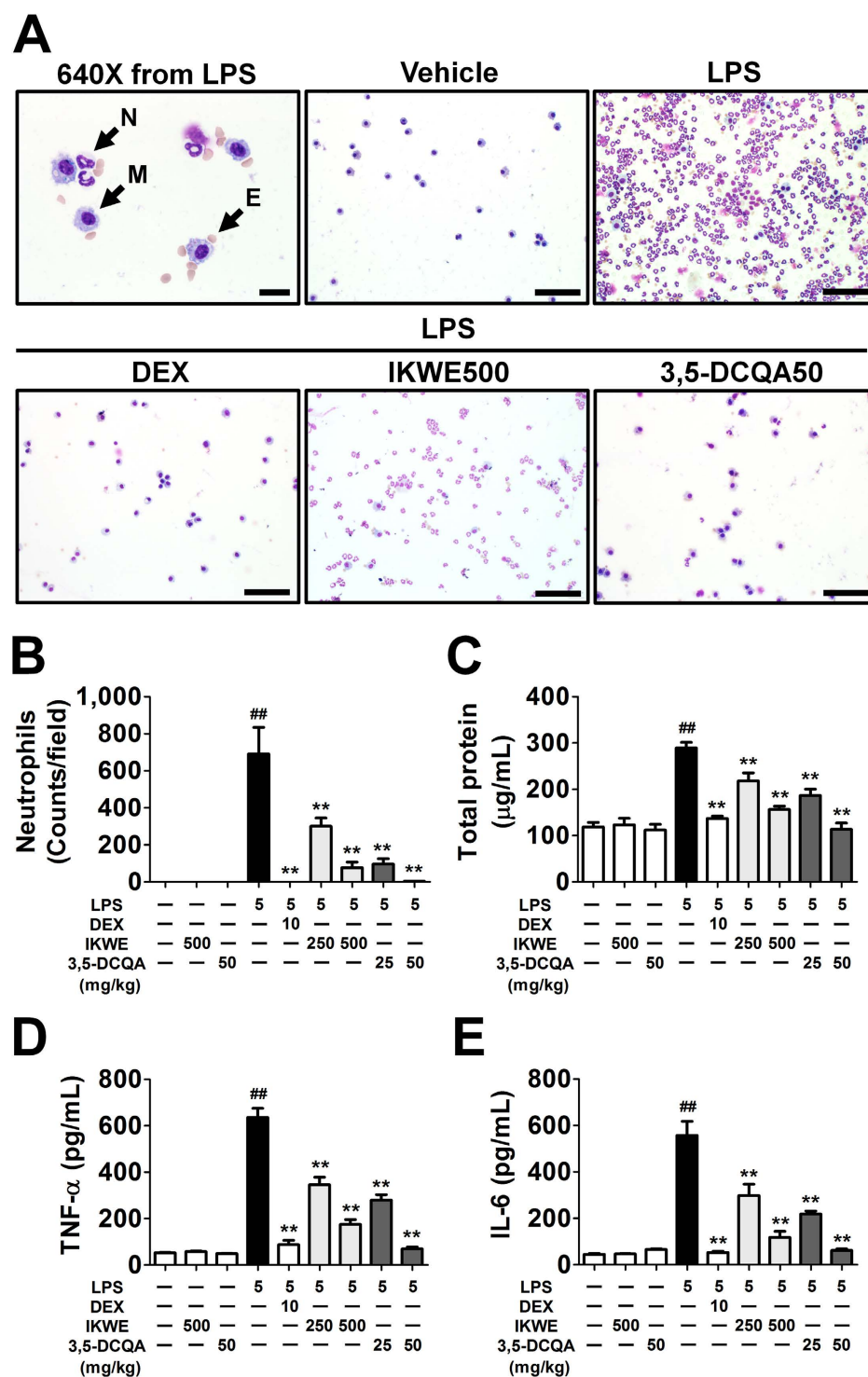


**Figure 6. Content analysis of BALF.** Mice were anesthetized and inserted with a plastic cannula into the trachea. After clamping the hilum of left lobe, PBS was injected and recovered to give BALF. Supernatant from centrifuged BALF were applied for total proteins, TNF-α and IL-6 measurement. Cell pellets were resuspended and cytopun for population analysis. (A) Examination of cell populations, N: neutrophils, M: macrophages, E: erythrocytes (scale bar = 50 μm in ×200 magnification or 10 μm in ×640 magnification); (B) Counts of BALF neutrophils; (C) Levels of total proteins; (D) Levels of TNF-α; (E) Levels of IL-6. Data were presented as mean ± S.E.M. (n = 6). Compared with vehicle group: <sup>##</sup>*p* < 0.01; compared with LPS group: <sup>\*\*</sup>*p* < 0.01.

SFKs belong to the family of tyrosine kinases and play important roles in neutrophil activation<sup>36,37</sup>. Previous reports have shown that SFKs are responsible for O<sub>2</sub><sup>•−</sup> generation and cell migration in fMLF-stimulated neutrophils<sup>36</sup>. In addition, SFKs have been shown to cause elevated expression of TNF-α and chemokines in



LPS-induced neutrophils<sup>37</sup>. These effects have been inhibited effectively by PP2, a highly selective SFK inhibitor<sup>36,37</sup>. Vav, a member of the guanine nucleotide exchange factors (GEFs) family, causes activation of NADPH oxidase by activating Rac<sup>38</sup>. A previous study revealed that SFKs were able to enhance Vav phosphorylation and activity<sup>39</sup>. Our immunoblotting assay showed that 3,5-DCQA inhibited SFKs and Vav phosphorylation in fMLF-induced neutrophils, which suggests that 3,5-DCQA might attenuate  $O_2^{\cdot-}$  generation, cell migration and TNF- $\alpha$  and chemokine expression in stimulated neutrophils through the SFKs/Vav signaling pathway. Other signaling proteins such as ERK, p38 and Akt are also important in neutrophil activation<sup>36</sup>. However, 3,5-DCQA does not reduce the levels of phosphorylated ERK, p38, and Akt. Based on enzyme-based and cell-based data, we proposed that 3,5-DCQA modulates neutrophil function through intercellular and intracellular mechanisms simultaneously.

Ursolic acid (**9**) was previously reported to inhibit  $O_2^{\cdot-}$  production and NE release from neutrophils through an intracellular mechanism<sup>40</sup>. The findings of the effects of ursolic acid on neutrophils were supported by our enzyme-based and cell-based data. In addition, randialic acid B (**15-1**) and sanguisorbigenin (**15-2**) exhibited 5-fold greater efficacy than ursolic acid. SARs analysis of triterpenoid saponins (**10-15**) and aglycons indicated that their efficacy in fMLF-induced neutrophils was affected by sugar moiety and structural modifications at the E-ring. For example, triterpenoid saponins showed weak or no inhibitory effects on  $O_2^{\cdot-}$  generation and NE release, indicating that saccharides in saponins are unfavorable for bioactivity in human neutrophils. Further, when the carboxylic acid at C-15 was cyclized with a hydroxyl group at C-20 to form a  $\delta$ -lactone ring (**11-1** and **11-2**), bioactivity vanished, suggesting that carboxylic acid is necessary for this activity. Conversely, the presence of a double bond at C-18/C-19 or C-19/C-20 (**15-1** and **15-2**) enhanced human neutrophil activity.

Increased oxidative stress has also been reported to enhance elastase activity by inactivating  $\alpha_1$ -antitrypsin<sup>4,7</sup>. Therefore, a combination of HNE inhibitors and free radical scavengers is considered to be an effective strategy for treating ALI. A previous study reported that better therapeutic effects could be achieved with a combined treatment of sivelestat sodium and edaravone in LPS-induced ALI in rats<sup>41</sup>. In our current experiments, enhanced protective effects were observed following treatment with IKWE (500 mg/kg) compared to treatment with 3,5-DCQA (25 mg/kg) alone. The amount of 3,5-DCQA in IKWE at a 500 mg/kg dose is ~25 mg/kg. Because caffeoylquinic acid derivatives may improve  $\alpha_1$ -antitrypsin activity via their ROS scavenging ability, our results suggest that there are synergistic ROS-scavenging effects and a protease-antiprotease balance of other caffeoylquinic acid derivatives in the extract.

Neutrophil recruitment into inflammatory tissue by chemokines is a key event in ALI. Neutrophil locomotion includes adhesion and migration through endothelial cells. L-selectin,  $\beta_2$ -integrin and platelet-endothelial cell adhesion molecule-1 (PECAM-1) are important adhesion proteins and are quickly expressed in activated neutrophils. These adhesion proteins promote neutrophil attachment to endothelial cells and firm their migration<sup>30</sup>. Chlorogenic acid (**3**) is another major chemical component in *I. Kaushue*<sup>12</sup>, and it was able to attenuate the adhesive ability of neutrophils by inhibiting L-selectin cleavage and reducing  $\beta_2$  integrin levels, as well as suppressing the expression of PECAM-1 that is induced by LPS in neutrophils<sup>42</sup>. In the same study, chlorogenic acid also exhibited inhibitory effects on fMLF-induced neutrophil migration. In our experiments, both a BALF analysis and histological data showed that neutrophil infiltration in ALI mice was significantly reduced following treatment with IKWE or 3,5-DCQA. However, no difference was found between the IKWE (500 mg/kg) and 3,5-DCQA (25 mg/kg) groups. These findings suggest that the effects of chlorogenic acid on reducing neutrophil recruitment were not apparent in our *in vivo* experiments. Because the effects of 3,5-DCQA on neutrophil recruitment, adhesion and migration are unclear, further evaluation of the effects of 3,5-DCQA is necessary.

Macrophages are also important in inflammatory diseases. In ALI, there is an increased release of inflammatory cytokines from stimulated macrophages<sup>43</sup>. Neutrophil elastase has been shown to stimulate TNF- $\alpha$  and IL-6 expression in macrophages<sup>44</sup>. A previous study demonstrated that 3,5-DCQA was able to reduce TNF- $\alpha$  and IL-6 expression in LPS-stimulated RAW 264.7 cells<sup>45</sup>. In the current study, 3,5-DCQA inhibited neutrophil elastase and reduced BALF inflammatory cytokines *in vitro* and *in vivo*. These suggested that 3,5-DCQA might be able to modulate macrophage function by inhibiting elastase and intracellular mechanisms simultaneously<sup>44</sup>.

Pharmacokinetic properties are important in drug development. Previous studies have reported that although caffeoylquinic acids derivatives have similar chemical properties, their pharmacokinetic parameters are different<sup>46-49</sup>. Specifically, the terminal elimination half-life ( $T_{1/2\alpha}$ ) and the mean residence time (MRT) of 3,5-DCQA were 227~292 min and 227~438 min, respectively, after oral administration, and 3,5-DCQA was detectable in the plasma for 4 hours after intravenous administration<sup>46,47,49</sup>. In addition, chlorogenic acid was distributed in lung tissue more than 1.5 hours after oral administration<sup>48</sup>. These studies may be able to illustrate the efficacy of 3,5-DCQA and its possible metabolites *in vivo*; however, further investigation of the bio-distribution of 3,5-DCQA and its possible metabolites in lung tissue is necessary.

CMC data are critical to determine and maintain the quality of botanical products. Original identification, HPLC fingerprints, chemical and biological references and standardized manufacturing procedures are required for CMC. The internal transcribed spacer (ITS) sequence is the determining factor in genomic identification. However, no ITS information is available for *I. kaushue*, excepting a review article published in 2010<sup>50</sup>. To identify the origin of *I. kaushue* from commercial, two gene sequences, *trnS-trnG* and *trnH-psbA*, were analyzed and compared using the genomic identification database. The results confirmed 100% and 99% sequence identity to *I. kaushue*, respectively. Subsequently, three batches of IKWE (IKWE-1-3) and water extracts from other two commercial Kudingcha materials (KUD-1 and NKUD-1) were prepared using a standardized manufacturing protocol, followed by determination of HPLC fingerprints, extraction yield, amounts of chemical references and biological activity of each extract. The results indicate good quality of each extract with high reproducibility and consistency (Supplementary information Fig. S11).

In addition to anti-oxidative capacity, 3,5-DCQAs and other DCQAs display diverse bioactivities, including hepatoprotection, anti-hyperlipidemia and anti-thrombosis<sup>51-53</sup>. Anti-viral activities against HIV, RSV, H1N1

and HBV have additionally been demonstrated<sup>54–57</sup>. Here, we identified three abundant DCQAs in IKWE, supporting the possibility of different biological applications. For example, Shuang-Huang-Lian, a TCM preparation composed of *Flos lonicerae* and other two herbs, is applied to treat various acute respiratory infections, such as influenza virus A-induced pneumonia in China<sup>46,47</sup>. Chlorogenic acid is the main bioactive component in *F. lonicerae*. A pharmacokinetic study reported that the amount of chlorogenic acid is 50-fold higher than that of 3,4-DCQA and 200-fold higher than that of 3,5-DCQA in rat blood plasma<sup>45</sup>. The CQA amount is comparable to that of DCQA in *I. kaushue*<sup>12</sup>. Considering the anti-inflammatory and broad anti-viral effects of DCQAs, further evaluation of the effects of IKWE on influenza virus A-induced pneumonia is warranted.

In conclusion, we have developed a standard protocol to prepare a water extract of *I. kaushue* with good reproducibility, consistency, and safety. 3,5-DCQA, the bioactive component in *I. kaushue*, modulated neutrophil function not only by directly targeting HNE and ROS but also by inhibiting the SRKs/Vav signaling pathway. Both IKWE and 3,5-DCQA exhibited protective effects against LPS-induced ALI in mice. These data provide support for both IKWE and 3,5-DCQA as candidates in the development of new lead agents to treat ALI.

## Methods

**Genomic identification of *I. kaushue*.** Three raw materials of Kudingcha were purchased from two retailers. Two (IK and KUD) were from Huang-De-An (New Taipei, Taiwan) on 2013/11/20. The third (NKUD) was from Da-Ye (Nantou, Taiwan) on 2015/06/01. Samples from IK were prepared for genomic analysis by Bioproduction Engineering Technology Department, Biomedical Technology and Device Research Laboratories, ITR (Hsinchu, Taiwan). Briefly, genomic DNA was obtained and two genes, *trnS-trnG* and *trnH-psbA*, subsequently sequenced. Sequence identities to *I. Kaushue* were determined as 100% and 99%, respectively, according to the NCBI genome database.

**Preparation and quality control of water extracts.** Each raw material sample (20 g) was refluxed twice with 200 mL ddH<sub>2</sub>O for 2 h. The solutions were filtered and concentrated under vacuum to generate crude extracts (IKWE-1~3, KUD-1, and NKUD-1). The specifications of quality control included extraction yield, HPLC fingerprint chromatography, as well as determination of chemical and biological references. To establish HPLC chromatographic fingerprints, each extract (2.0 mg/mL) was dissolved in mobile phase solution (1% formic acid in 42.5% MeOH aqueous solution), filtered through a 0.45 µm membrane filter, and passed through an HPLC system. The Develosil™ C30-UG-5 column (4.6 × 250 mm, 5 µm) (Nomura, Japan) was eluted with a mobile phase consisting of 1% formic acid in 42.5% MeOH aqueous solution at a flow rate of 0.8 mL/min. The detector wavelength and injection volume were set at 326 nm and 20 µL, respectively. Chemical reference levels were determined from calibration curves generated at a concentration range of 40 to 120 µg/mL for 3,4-DCQA and 3,5-DCQA or 80 to 240 µg/mL for 4,5-DCQA. The HNE activity assay was further performed for biological validation.

**Bioactivity-guided fractionation.** The isolation procedures and 1D/2D NMR and physical properties of isolates and semi-synthetics are described in Supplementary information S1.

**Menisdaurin F** (Supplementary information Figs S2–S8).

Colorless plate;  $[\alpha]_D^{25}$ : −63.6° ( $c = 0.05$ , MeOH); UV  $\lambda_{max}$  (MeOH) nm (log  $\epsilon$ ): 256 (4.37); IR  $\nu_{max}$  (KBr) cm<sup>−1</sup>: 3392, 2924, 2220, 1621, 1018; Mp: 176–177°; ESIMS:  $m/z$  336.2 [M + Na]<sup>+</sup>; HRESIMS:  $m/z$  336.1048 [M + Na]<sup>+</sup> (calcd. for C<sub>14</sub>H<sub>9</sub>NO<sub>7</sub>Na, 336.1054); <sup>1</sup>H NMR (CD<sub>3</sub>OD, 400 MHz)  $\delta$ : 6.57 (1H, dd,  $J = 10.0, 2.0$  Hz, H-2), 6.24 (1H, d,  $J = 10.0$  Hz, H-3), 5.77 (1H, s, H-7), 4.62 (1H, m, H-6), 4.49 (1H, m, H-4), 4.48 (1H, d,  $J = 8.0$  Hz, H-1'), 3.86 (1H, d,  $J = 11.6$  Hz, H-6'a), 3.66 (1H, dd,  $J = 11.6, 5.2$  Hz, H-6'b), 3.22–3.40 (4H, m, H-2'~H-5'), 2.56 (1H, m, H-5a), 1.66 (1H, m, H-5b); <sup>13</sup>C NMR (CD<sub>3</sub>OD, 100 MHz)  $\delta$ : 159.1 (s, C-1), 143.3 (d, C-3), 124.5 (d, C-2), 117.9 (s, C-8), 102.6 (d, C-1'), 93.7 (d, C-7), 78.2 (d, C-5'), 78.0 (d, C-3'), 74.8 (d, C-6), 74.7 (d, C-2'), 71.5 (d, C-4'), 67.6 (d, C-4), 62.6 (t, C-6'), 36.4 (t, C-5).

**Serine protease inhibition.** Enzyme inhibition assays are described in Supplementary information S2.

**Determination of O<sub>2</sub><sup>•−</sup> generation and elastase release from neutrophils.** All assays were performed as described previously<sup>58,59</sup>. Neutrophils isolated from the blood of healthy volunteers (20–30 years old) were resuspended in a Ca<sup>2+</sup>-free HBSS buffer (pH 7.4) at 4 °C before use. O<sub>2</sub><sup>•−</sup> generation was measured based on reduction of ferricytochrome *c*. In brief, after supplementation with 0.5 mg/ml ferricytochrome *c* and 1 mM Ca<sup>2+</sup>, neutrophils were equilibrated at 37 °C for 2 min and incubated with the specified drugs for 5 min. Neutrophils were activated using 30 nM fMLF or 100 nM LTB<sub>4</sub> for 10 min after addition of cytochalasin B (CB, 1 µg/mL) for 3 min. Changes in absorbance concomitant with reduction of ferricytochrome *c* at 550 nm were continuously monitored. For elastase release, neutrophils (6 × 10<sup>5</sup> cells/mL) were mixed with methoxysuccinyl-Ala-Ala-Pro-Val-pNA (100 µM) substrate at 37 °C for 5 min. After incubation with DMSO or test agents, neutrophils were activated as described previously, and changes in absorbance at 405 nm continuously monitored to assay elastase release. Inhibition of superoxide generation and elastase release were calculated in keeping with previous reports.

**Immunoblotting assay.** Neutrophils were pretreated with DMSO or 3,5-DCQA (10 µM) for 5 min before fMLF stimulation for 0.5 min at 37 °C. Cells were lysed with lysis buffer consisting of 50 mM HEPES (pH 7.4), 100 mM NaCl, 1 mM Ca<sup>2+</sup>, 2 mM Na<sub>2</sub>VO<sub>4</sub>, 1 mM phenylmethanesulfonyl fluoride, 5% b-mercaptoethanol, 10 mM p-nitrophenyl phosphate, 1% protease inhibitor cocktail (Sigma-Aldrich), and 1% Triton X-100. Cell lysates were collected by centrifugation at 14,000 rpm for 20 min at 4 °C. After gel electrophoresis and transferring to membranes, samples were blocked with 5% nonfat milk in a mixture of Tris-buffer saline and Tween 20. Target protein was identified by the corresponding primary antibody overnight at 4 °C. Membranes were incubated with horseradish peroxidase-conjugated, secondary anti-rabbit or anti-mouse antibodies at room temperature

for 1 h. After washing, enhanced chemiluminescence solution was used and protein expression was analyzed by the BioSpectrum Imaging System (UVP, Upland, CA). The quantitative ratio of target protein was normalized to total protein or GAPDH.

**Animals.** All animal experiments were performed in accordance with the guidelines of the Animal Welfare Act and The Guide for Care and Use of Laboratory Animals from the National Institutes of Health. The animal protocols were approved by the Institutional Animal Care and Use Committee of Chang Gung University (Taoyuan, Taiwan, IACUC Approval no.: CGU12-011, period of protocol valid from June 01, 2012 to May 31, 2015). Male ICR mice (5–6 weeks; 25–30 g) were purchased from BioLasco (Ilan, Taiwan). Mice were housed under standard laboratory conditions, and fed a standard laboratory diet and water *ad libitum*. Animals were allowed to adapt to the environment for at least one week before experiments.

**Acute oral toxicity.** IKWE powder was dissolved in 600  $\mu$ L ddH<sub>2</sub>O to generate a solution at a dose equivalent to 10.0 g/kg. Mice were administered IKWE solution (300  $\mu$ L) or ddH<sub>2</sub>O via gavage at intervals of 4 h. After 24 h, blood (ca. 1.0 mL) was collected through cardiac puncture under anesthesia with intraperitoneal injection of Zoletil 50 (50 mg/kg) and Xylazine (10 mg/kg). Blood samples were immediately mixed with 100  $\mu$ L acid citrate dextrose solution (BD Vacutainer, 364606), centrifuged at 1,000 rpm for 15 min and stored at  $-20^{\circ}\text{C}$ . Supernatant fractions were further analyzed to determine the AST, ALT, CRTN and BUN levels using FUJI DRI-CHEM 3000 and four FUJI DRI-CHEM SLIDE products ( $n = 10$ ). LD<sub>50</sub> and body weight growth were additionally determined for 14 days ( $n = 10$ )<sup>23</sup>. Data were presented as mean  $\pm$  S.E.M.

**LPS-induced ALI in mice.** Mice were randomly divided into nine groups ( $n = 6$  per group): (1) Vehicle, (2) IKWE (500 mg/kg), (3) 3,5-DCQA (50 mg/kg), (4) LPS, (5) LPS + DEX (10 mg/kg), (6) LPS + IKWE (250 mg/kg), (7) LPS + IKWE (500 mg/kg), (8) LPS + 3,5-DCQA (25 mg/kg), and (9) LPS + 3,5-DCQA (50 mg/kg). Agents were dissolved in vehicle solution (PBS containing 10% Tween-80). All animals were pretreated intraperitoneally with 100  $\mu$ L vehicle solution or agents, respectively, 1 h before PBS or LPS (Sigma, *Escherichia coli* 055:B5) intratracheal injection (5 mg/kg in 50  $\mu$ L of PBS)<sup>26,27</sup>. Mice were sacrificed at 6 h post-dosage, and the left lung collected for histological examination or MPO activity measurement. Lung tissue was fixed with 10% formalin before embedding with paraffin wax and routine H&E staining. MPO activity was measured as described earlier<sup>59</sup>. The right lobes were prepared for W/D weight ratio determination or BALF analysis. To obtain the W/D weight ratio, wet tissues were weighed immediately after collection, dried in the oven at  $80^{\circ}\text{C}$  for 48 h, and re-weighed. For post-treatment experiments, mice treated with vehicle or 3,5-DCQA (50 mg/kg) intraperitoneally 1 h after LPS treatment<sup>24</sup>.

**Bronchoalveolar lavage fluid preparation and analysis.** Mice were sacrificed and hilum of the left lung sealed. BALF was collected following injection with 0.2, 0.2, 0.3, 0.3 or 0.5 mL PBS. BALF samples were combined and centrifuged at 1,000 rpm for 15 min at  $4^{\circ}\text{C}$ . Total proteins in the supernatant fraction were determined using the protein assay dye (BIO-RAD, 500-0006) with BSA as the reference, and TNF- $\alpha$  and IL-6 levels measured with ELISA kits (eBioscience, 88-7324-88 and 88-7064-88). Cell pellets from BALF were resuspended in 100  $\mu$ L PBS and cytopun (200 g, 3 min) onto a glass microscope slide, followed by staining with Liu's stain. Neutrophils were counted under a light microscope in five randomly selected fields ( $\times 200$  magnification)<sup>60</sup>.

**Statistical analysis.** All data were expressed as mean  $\pm$  S.E.M. and analyzed with two-tailed indirect Student tests or one-way ANOVA followed by Dunnet's multiple comparison test. GraphPad Prism 5.01 was applied for statistical analysis (GraphPad Software, Inc., USA).

## References

- Modrykamien, A. M. & Gupta, P. The acute respiratory distress syndrome. *Proc. (Bayl. Univ. Med. Cent.)* **28**, 163–171 (2015).
- Rojas, M., Woods, C. R., Mora, A. L., Xu, J. & Brigham, K. L. Endotoxin-induced lung injury in mice: structural, functional, and biochemical responses. *Am. J. Physiol. Lung. Mol. Physiol.* **288**, L333–L341 (2005).
- Standford, T. J. & Ward, P. A. Therapeutic targeting of acute lung injury and acute respiratory distress syndrome. *Transl. Res.* **167**, 183–191 (2016).
- Aikawa, N. & Kawasaki, Y. Clinical utility of the neutrophil elastase inhibitor sivelestat for the treatment of acute respiratory distress syndrome. *Ther. Clin. Risk Manag.* **10**, 621–629 (2014).
- Mantovani, A., Cassatella, M. A., Costantini, C. & Jaillon, S. Neutrophils in the activation and regulation of innate and adaptive immunity. *Nat. Rev. Immunol.* **11**, 519–531 (2011).
- Williams, A. E. & Chambers, R. C. The mercurial nature of neutrophils: still an enigma in ARDS? *Am. J. Physiol. Lung Cell. Mol. Physiol.* **306**, L217–L230 (2014).
- Sandhaus, R. A. & Turino, G. Neutrophil elastase-mediated lung disease. *COPD* **10**, 60–63 (2013).
- Newman, D. J. & Cragg, G. M. Natural products as sources of new drugs over the 30 years from 1981 to 2010. *J. Nat. Prod.* **75**, 311–335 (2012).
- Tang, T. Y., Li, F. Z. & Afseth, J. Review of the regulations for clinical research in herbal medicines in USA. *Chin. J. Integr. Med.* **20**, 883–893 (2014).
- Flora Reipublicae Popularis Sinicae*, Vol. 45(2) (eds Wu, C. Y. *et al.*) 105–107 (Science, 1999).
- Qin, L. F., Qu, X. C., Hu, G., Huang, Y. F. & Zhang, Q. W. Development of microsatellite markers in *Ilex kaushue* (Aquifoliaceae), a medicinal plant species. *Appl. Plant Sci.* **3**, 1500040 (2015).
- Li, L. *et al.* The large-leaved kudingcha (*Ilex latifolia* Thunb and *Ilex kudingcha* C. J. Tseng): a traditional Chinese tea with plentiful secondary metabolites and potential biological activities. *J. Nat. Med.* **67**, 425–437 (2013).
- Hao, D. *et al.* Research progress in the phytochemistry and biology of *Ilex* pharmaceutical resources. *Acta Pharm. Sin.* **B 3**, 8–19 (2013).
- Zhongyaodacidian* 2nd edn, Vol. 1 (eds Nanjing University of Chinese Medicine) 1763–1765 (Shanghai Scientific & Technical Publisher, 2006).

15. Xu, d. *et al.* Inhibitory activities of caffeoylquinic acid derivatives from *Ilex kudingcha* C. J. Tseng on  $\alpha$ -glucosidase from *Saccharomyces*. *J. Agric. Food Chem.* **63**, 3694–3703 (2015).
16. Zhu, K., Li, G., Sun, P., Wang, R., Qian, Y. & Zhao, X. *In vitro* and *in vivo* anti-cancer activities of Kuding tea (*Ilex kudingcha* C. J. Tseng) against oral cancer. *Exp. Ther. Med.* **7**, 709–715 (2014).
17. Song, J. L., Qian, Y., Li, G. J. & Zhao, X. Anti-inflammatory effects of kudingcha methanol extract (*Ilex kudingcha* C. J. Tseng) in dextran sulfate sodium-induced ulcerative colitis. *Mol. Med. Rep.* **8**, 1256–1262 (2013).
18. Takahashi, K., Matsuzawa, S. & Takani, M. The constituent of the vines of *Menispermum dauricum* DC. *Chem. Pharm. Bull.* **26**, 1677–1681 (1978).
19. Yogo, M., Ishiguro, S., Murata, H. & Furukawa, H. Coclauril, a nonglucosidic 2-cyclohexen-1-ylideneacetonitrile, from *Cocculus laurifolium* DC. *Chem. Pharm. Bull.* **38**, 225–226 (1990).
20. Ueda, K., Yasutomi, K. & Mori, I. Structure of a new cyanoglucoside from *Ilex warburgii* Loesn. *Chem. Lett.* **12**, 149–150 (1983).
21. Seigler, D. S. *et al.* Cyanogenic glycosides and menisdaurins from *Guazuma ulmifolia*, *Ostrya virginiana*, *Tiquilia plicata*, and *Tiquilia canescens*. *Phytochemistry* **66**, 1567–1580 (2005).
22. Nahrstedt, A. & Wray, V. Structural revision of a putative cyanogenic glucoside from *Ilex aquifolium*. *Phytochemistry* **29**, 3934–3936 (1990).
23. Lee, Y. J. *et al.* Toxicity of fermented soybean product (cheonggukjang) manufactured by mixed culture of *Bacillus subtilis* MC31 and *Lactobacillus sakei* 383 on liver and kidney of ICR mice. *Lab. Anim. Res.* **30**, 54–63 (2014).
24. Zhang, J. L., Huang, W. M. & Zeng, Q. Y. Atractylenolide I protects mice from lipopolysaccharide-induced acute lung injury. *Eur. J. Pharmacol.* **765**, 94–99 (2015).
25. Horita, N. *et al.* Impact of corticosteroids on mortality in patients with acute respiratory distress syndrome: a systematic review and meta-analysis. *Intern. Med.* **54**, 1473–1479 (2015).
26. Ma, C. *et al.* Anti-inflammatory effects of water extract of *Taraxacum mongolicum* hand.-Mazz on lipopolysaccharide-induced inflammation in acute lung injury by suppressing PI3K/AKT/mTOR signaling pathway. *J. Ethnopharmacol.* **168**, 349–355 (2015).
27. Huang, G. J. *et al.* Methanol extract of *Antrodia camphorata* protects against lipopolysaccharide-induced acute lung injury by suppressing NF- $\kappa$ B and MAPK pathways in mice. *J. Agric. Food Chem.* **62**, 5321–5329 (2014).
28. Korkmaz, B., Horwitz, M. S., Jenne, D. E. & Gauthier, F. Neutrophil elastase, proteinase 3, and cathepsin G as therapeutic targets in human diseases. *Pharmacol. Rev.* **62**, 726–759 (2010).
29. Chen, D. *et al.* Design, synthesis and antithrombotic evaluation of novel dabigatran etexilate analogs, a new series of non-peptides thrombin inhibitors. *Bioorg. Med. Chem.* **23**, 7405–7416 (2015).
30. Grommes, J. & Soehnlein, O. Contribution of neutrophils to acute lung injury. *Mol. Med.* **17**, 293–307 (2011).
31. Iwai, K., Kishimoto, N., Kakino, Y., Mochida, K. & Fujita, T. *In vitro* antioxidative effects and tyrosinase inhibitory activities of seven hydroxycinnamoyl derivatives in green coffee beans. *J. Agric. Food Chem.* **52**, 4893–4898 (2004).
32. Greunke, C. *et al.* A systematic study on the influence of the main ingredients of an ivy leaves dry extract on the  $\beta_2$ -adrenergic responsiveness of human airway smooth muscle cells. *Pulm. Pharmacol. Ther.* **31**, 92–98 (2015).
33. Bors, W., Michel, C., Stettmaier, K., Lu, Y. & Foo, L. Y. Antioxidant mechanisms of polyphenolic caffeic acid oligomers, constituents of *Salvia officinalis*. *Biol. Res.* **37**, 301–311 (2004).
34. Omann, G. M., Traynor, A. E., Harris, A. L. & Sklar, L. A. LTB<sub>4</sub> induced activation signals and responses in neutrophils are short-lived compared to formylpeptide. *J. Immunol.* **138**, 2626–2632 (1987).
35. Góngora, L. *et al.* Effects of caffeoyl conjugates of isorenol-3-hydroquinone glucoside and quinic acid on leukocyte function. *Life Sci.* **71**, 2995–3004 (2002).
36. Fumagalli, L., Zhang, H., Baruzzi, A., Lowell, C. A. & Berton, G. The Src family kinases Hck and Fgr regulate neutrophil responses to N-formyl-methionyl-leucyl-phenylalanine. *J. Immunol.* **178**, 3874–3885 (2007).
37. Mazzi, P., Cavegion, E., Lapinet-Vera, J. A., Lowell, C. A. & Berton, G. The src-family kinases Hck and Fgr regulate early lipopolysaccharide-induced myeloid cell recruitment into the lung and their ability to secrete chemokines. *J. Immunol.* **195**, 2383–2395 (2015).
38. Roepstorff, K. *et al.* Stimulus-dependent regulation of the phagocyte NADPH oxidase by a VAV1, Rac1, and PAK1 signaling axis. *J. Biol. Chem.* **283**, 7983–7993 (2008).
39. Turner, M. & Billadeau, D. D. VAV proteins as signal integrators for multi-subunit immune-recognition receptors. *Nat. Rev. Immunol.* **2**, 476–486 (2002).
40. Hwang, T. L. *et al.* Ursolic acid inhibits superoxide production in activated neutrophils and attenuates trauma-hemorrhage shock-induced organ injury in rats. *PLoS One* **9**, e111365 (2014).
41. Yang, T. *et al.* Combined effects of a neutrophil elastase inhibitor (sivelestat sodium) and a free radical scavenger (edaravone) on lipopolysaccharide-induced acute lung injury in rats. *Inflamm. Res.* **61**, 563–569 (2012).
42. Hebeda, C. B. *et al.* Effects of chlorogenic acid on neutrophil locomotion functions in response to inflammatory stimulus. *J. Ethnopharmacol.* **135**, 261–269 (2011).
43. Tushima, K. *et al.* Acute lung injury review. *Intern. Med.* **48**, 621–630 (2009).
44. Benabid, R. *et al.* Neutrophil elastase modulates cytokine expression: contribution to host defense against *Pseudomonas aeruginosa*-induced pneumonia. *J. Biol. Chem.* **287**, 34883–34893 (2012).
45. Chen, X. *et al.* The anti-inflammatory activities of *Ainsliaea fragrans* Champ. extract and its components in lipopolysaccharide-stimulated RAW264.7 macrophages through inhibition of NF- $\kappa$ B pathway. *J. Ethnopharmacol.* **170**, 72–80 (2015).
46. Zhou, W. *et al.* Simultaneous determination of caffeic acid derivatives by UPLC-MS/MS in rat plasma and its application in pharmacokinetic study after oral administration of *Flos lonicerae*-*Fructus forsythiae* herb combination. *J. Chromatogr. B* **949–950**, 7–15 (2014).
47. Zhou, W. *et al.* Study on the main components interaction from *Flos lonicerae* and *Fructus forsythiae* and their dissolution *in vitro* and intestinal absorption in rats. *PLoS One* **9**, e109619 (2014).
48. Zhou, Y., Zhou, T., Pei, Q., Liu, S. & Yuan, H. Pharmacokinetics and tissue distribution study of chlorogenic acid from *Lonicerae japonicae* flos following oral administrations in rats. *Evid. Based Complement. Alternat. Med.* **2014**, 979414 (2014).
49. Wang, W. *et al.* Simultaneous quantitation of dicaffeoylquinic acids in rat plasma after an intravenous administration of mailuoning injection using liquid chromatography-mass spectrometry. *J. Chromatogr. Sci.* **47**, 216–222 (2009).
50. Manen, J. F., Barriera, G., Loizeau, P. A. & Naciri, Y. The history of extant *Ilex* species (Aquifoliaceae): Evidence of hybridization within a Miocene radiation. *Mol. Phylogenet. Evol.* **57**, 961–977 (2010).
51. Basnet, P., Matsushige, K., Hase, K., Kadota, S. & Namba, T. Four di-O-caffeoyl quinic acid derivatives from propolis. Potent Hepatoprotective activity in experimental liver injury models. *Biol. Pharm. Bull.* **19**, 1479–1484 (1996).
52. Zhang, X. *et al.* Anti-hyperlipidemic effects and potential mechanisms of action of the caffeoylquinic acid-rich *Pandanus tectorius* fruit extract in hamsters fed a high fat-diet. *PLoS One* **8**, e61922 (2013).
53. Satake, T., Kamiya, K., An, Y., Oishi, T. & Yamamoto, J. The anti-thrombotic active constituents from *Centella asiatica*. *Biol. Pharm. Bull.* **30**, 935–940 (2007).
54. Hu, Z., Chen, D., Dong, L. & Southerland, W. M. Prediction of the interaction of HIV-1 integrase and its dicaffeoylquinic acid inhibitor through molecular modeling approach. *Ethn. Dis.* **20**, 45–49 (2010).
55. Ojwang, J. O. *et al.* A novel inhibitor of respiratory syncytial virus isolated from ethnobotanicals. *Antiviral Res.* **68**, 163–172 (2005).



56. Takemura, T. *et al.* 3,4-Dicaffeoylquinic acid, a major constituent of Brazilian propolis, increases TRAIL expression and extends the lifetimes of mice infected with the influenza A virus. *Evid. Based Complement. Alternat. Med.* doi: 10.1155/2012/946867 (2012).
57. Zhao, Y. *et al.* UFLC/MS-IT-TOF guided isolation of anti-HBV active chlorogenic acid analogues from *Artemisia capillaris* as a traditional Chinese herb for the treatment of hepatitis. *J. Ethnopharmacol.* **156**, 147–154 (2014).
58. Hwang, T. L., Wang, W. H., Wang, T. Y., Yu, H. P. & Hsieh, P. W. Synthesis and pharmacological characterization of 2-aminobenzaldehyde oxime analogs as dual inhibitors of neutrophil elastase and proteinase 3. *Bioorg. Med. Chem.* **23**, 1123–1134 (2015).
59. Tsai, Y. F. *et al.* Sirtinol inhibits neutrophil elastase activity and attenuates lipopolysaccharide-mediated acute lung injury in mice. *Sci. Rep.* **5**, 8347 (2015).
60. McKenzie, C. G. *et al.* Peripheral blood monocyte-derived chemokine blockage prevents murine transfusion-related acute lung injury (TRALI). *Blood* **123**, 3496–3503 (2014).

## Acknowledgements

We appreciated Mr. Jui-Hung Yen (Bioproduction Engineering Technology Department, Biomedical Technology and Device Research Laboratories, ITR) for performing genomic analysis of plant material. This work was supported by a grant from the Ministry of Science and Technology (MOST102-2320-B-182-008-MY3) and Chang Gung Memorial Hospital and Chang Gung University (CMRPD1F0241~3 and BMRPB23 to P.-W.H. and CMRPD1B0332, CMRPF1F0061~3 and EMRPD1D1F0311 to T.-L.H.). The funders had no role in the study design, the data collection and analysis, the decision to publish, or the preparation of the manuscript.

## Author Contributions

Y.-L.C. and P.-W.H. participated in the study designs. Y.-L.C. performed the preparation of herbal constituents and extracts, enzyme inhibition assays and *in vivo* studies. T.-L.H., W.-Y.C. and H.-W.Y. carried out human neutrophil assays. W.-Y.C. performed Western blotting assays. Y.-L.C., H.-P.Y., J.-Y.F., K.-Y.C., Y.-W.C. and C.-Y.C. carried out BALF or MPO analysis in animal tests. Y.-L.C. wrote the manuscript. P.-W.H. was in charge of the whole experimental conduction and proofread manuscript.

## Additional Information

**Supplementary information** accompanies this paper at <http://www.nature.com/srep>

**Competing financial interests:** The authors declare no competing financial interests.

**How to cite this article:** Chen, Y.-L. *et al.* *Ilex kaushue* and Its Bioactive Component 3,5-Dicaffeoylquinic Acid Protected Mice from Lipopolysaccharide-Induced Acute Lung Injury. *Sci. Rep.* **6**, 34243; doi: 10.1038/srep34243 (2016).



This work is licensed under a Creative Commons Attribution 4.0 International License. The images or other third party material in this article are included in the article's Creative Commons license, unless indicated otherwise in the credit line; if the material is not included under the Creative Commons license, users will need to obtain permission from the license holder to reproduce the material. To view a copy of this license, visit <http://creativecommons.org/licenses/by/4.0/>

© The Author(s) 2016

## Article

# Capsaicin Supplementation Reduces Physical Fatigue and Improves Exercise Performance in Mice

Yi-Ju Hsu <sup>1,†</sup>, Wen-Ching Huang <sup>1,†</sup>, Chien-Chao Chiu <sup>1</sup>, Yan-Lin Liu <sup>1</sup>, Wan-Chun Chiu <sup>2</sup>, Chun-Hui Chiu <sup>3</sup>, Yen-Shuo Chiu <sup>1,2,4,\*</sup> and Chi-Chang Huang <sup>1,\*</sup>

<sup>1</sup> Graduate Institute of Sports Science, National Taiwan Sport University, Taoyuan 33301, Taiwan; 1041302@ntsue.edu.tw (Y.-J.H.); 1010503@ntsue.edu.tw (W.-C.H.); chiu2295@yahoo.com.tw (C.-C.C.); 1040204@ntsue.edu.tw (Y.-L.L.)

<sup>2</sup> School of Nutrition and Health Sciences, Taipei Medical University, Taipei 11031, Taiwan; wanchun@tmu.edu.tw

<sup>3</sup> Graduate Institute of Health Industry Technology, Research Center for Industry of Human Ecology and Research Center for Chinese Herbal Medicine, College of Human Ecology, Chang Gung University of Science and Technology, Taoyuan 33303, Taiwan; chchiu@mail.cgu.edu.tw

<sup>4</sup> Department of Orthopedic Surgery, Taipei Medical University Shuang Ho Hospital, New Taipei City 23561, Taiwan

\* Correspondence: 1021301@ntsue.edu.tw (Y.-S.C.); john5523@ntsue.edu.tw (C.-C.H.); Tel.: +886-3-328-3201 (ext. 2619) (Y.-S.C. & C.-C.H.)

† These authors contributed equally to this work.

Received: 23 August 2016; Accepted: 13 October 2016; Published: 20 October 2016

**Abstract:** Chili pepper is used as a food, seasoning and has been revered for its medicinal and health claims. It is very popular and is the most common spice worldwide. Capsaicin (CAP) is a major pungent and bioactive phytochemical in chili peppers. CAP has been shown to improve mitochondrial biogenesis and adenosine triphosphate (ATP) production. However, there is limited evidence around the effects of CAP on physical fatigue and exercise performance. The purpose of this study was to evaluate the potential beneficial effects of CAP on anti-fatigue and ergogenic functions following physiological challenge. Female Institute of Cancer Research (ICR) mice from four groups ( $n = 8$  per group) were orally administered CAP for 4 weeks at 0, 205, 410, and 1025 mg/kg/day, which were respectively designated the vehicle, CAP-1X, CAP-2X, and CAP-5X groups. The anti-fatigue activity and exercise performance was evaluated using forelimb grip strength, exhaustive swimming time, and levels of serum lactate, ammonia, glucose, BUN (blood urea nitrogen) and creatine kinase (CK) after a 15-min swimming exercise. The grip strength and exhaustive swimming time of the CAP-5X group were significantly higher than other groups. CAP supplementation dose-dependently reduced serum lactate, ammonia, BUN and CK levels, and increased glucose concentration after the 15-min swimming test. In addition, CAP also increased hepatic glycogen content, an important energy source for exercise. The possible mechanism was relevant to energy homeostasis and the physiological modulations by CAP supplementation. Therefore, our results suggest that CAP supplementation may have a wide spectrum of bioactivities for promoting health, performance improvement and fatigue amelioration.

**Keywords:** capsaicin; anti-fatigue; exercise performance; forelimb grip strength; glycogen

## 1. Introduction

Capsaicin (CAP, trans-8-methyl-N-vanillyl-6-nonenamide) is, a plant with origins in the Americas. It is a naturally occurring phytochemical and is one of the active ingredients of red and chili peppers [1,2]. Peppers have become a popular culinary spice for food throughout the world. Pepper plants are shallow-rooted and lack a taproot, which are notorious for their sensitivity to moisture stress at

flowering and fruit setting. CAP is an odorless white crystal with severe burning pungency [3]. On the other hand, pungency is influenced by the weather conditions such as heat waves and moisture and increases with the growth of the maturity of fruit [4,5]. The gland on the placenta of the fruit produces CAP, mostly located in vesicles or vacuole like sub-cellular organelles of epidermal cells of placenta in the pod [6]. The highest concentrations of CAP are found in the ovary and in the lower flesh (tip) and the lowest content in the plant seeds [7].

Capsaicin has been widely investigated, and is an important molecule in the area of research in medicinal field. Numerous studies have demonstrated that CAP has extensive bioactivities, such as analgesic [8], antioxidant [9], anti-inflammatory, anti-cancer [10], and anti-obesity properties [11,12]. In addition, the CAP is known to increase energy metabolism by proposed mitochondrial function via activation of the TRPV1 (transient receptor potential vanilloid 1) [12]. TRPV1 activation by dietary capsaicin activates mitochondrial respiration, promotes mitochondrial biogenesis, and improves energy metabolism and exercise endurance by upregulating PGC-1 $\alpha$  (peroxisome proliferator-activated receptor- $\gamma$  coactivator-1 $\alpha$ ) in skeletal muscles [13,14]. TRPV1 channels may also participate in some chronic adaptations induced by regular physical exercise or training programs, including muscular hypertrophy and ATP production in muscle [15].

However, relatively few studies directly address the possible anti-fatigue function of CAP. Fatigue is defined as an exercise-induced inability to perform the expected or desired work output. Physiological fatigue results from excessive physical loading, inadequate rest, or mental strain/pressure and is further classified as central and peripheral fatigue [16]. Physical fatigue can be accompanied by deterioration in functional performance [17]. Exhaustion theory suggests that energy source depletion and excess metabolite accumulation can lead to fatigue [18]. A previous article reviewed the physiological effects on energy metabolism and utilization via TRPV1 activation [15]. Therefore, we conducted this study to evaluate the potential ergogenic and anti-fatigue effects of CAP using our previously established in vivo platform [19,20].

## 2. Materials and Methods

### 2.1. High-Performance Liquid Chromatography (HPLC) Analysis

The CAP used for supplementation in the study was purchased from Nowfoods LLC (Taichung City, Taiwan). The total capsaicin content of CAP product was determined by a high-performance liquid chromatography (HPLC) method. Reversed-phase HPLC was performed using a Hitachi Primaide 1110 HPLC pump system equipped with a Primaide 1430 diode array detector, and a Primaide 1210 autosampler was used to analyze capsaicin on a Phenomenex Luna C18 column (I.D. 4.6  $\times$  250 mm) at 280 nm. A mixture of 5% methanol in 0.1% phosphoric acid was used as the mobile phase at a flow rate of 1 mL/min and an injection volume of 20  $\mu$ L.

### 2.2. Animals and Experiment Design

Thirty-two 8-week-old female ICR mice in a specific pathogen-free condition were obtained from the BioLASCO (Yi-Lan, Taiwan). The mice were housed in an animal room at a constant temperature ( $22 \pm 1$  °C) and humidity (50%–60%) under a 12:12 h light-dark cycle with standard laboratory diet (No. 5001; PMI Nutrition International, Brentwood, MO, USA). The distilled water was provided ad libitum. A total of eight cages housing ICR female mice ( $n = 4$  animals per cage) were administrated in the current study. All animal experiments were reviewed and approved by the Animal Care and Use Committee (IACUC) on the ethics of animal experiments at the University of National Taiwan Sport, and this study conformed to guidelines of protocol IACUC-10508 for animal welfare.

After one week of acclimation, the animals were randomly divided into the four groups ( $n = 8$  per group in each test) for oral gavage treatment with CAP once a day for 28 consecutive days: (1) vehicle control; (2) 205 mg/kg CAP (CAP-1X); (3) 410 mg/kg CAP (CAP-2X); and (4) 1025 mg/kg CAP (CAP-5X). Vehicle or CAP was administrated by oral gavage. The control group received the

vehicle at the same dosage volume of solution equivalent to body weight (BW). The food intake and water consumption were monitored daily, and BW was recorded weekly.

### 2.3. CAP Preparation and Supplementation

CAP extracts was prepared using good manufacturing practices (GMP) and stored at 4 °C for following experiments. The administration dose of CAP was 16.7 mg/kg for human daily recommended intake. The mouse dosage was converted from a human equivalent dose (HED) based on body surface area by the following formula from the US Food and Drug Administration: assuming a human weight of 60 kg, the HED for 1000 (mg)/60 (kg) = 16.67 × 12.3 = a mouse dose of 205 mg/kg; the conversion coefficient 12.3 was used to account for differences in body surface area between mice and humans as we described previously [21].

### 2.4. Sample Collection

All animals were euthanized by 95% CO<sub>2</sub> after the last treatment, and blood was immediately collected. Blood collected by cardiac puncture was centrifuged at 1500× g for 10 min at 4 °C and then sera was collected for −80 °C storage. The liver, skeletal muscle (including gastrocnemius and soleus muscles in the back part of the lower legs), kidney, heart, lung, uterine fat pad (UFP), and brown adipose tissue (BAT) were excised and weighed. The liver and gastrocnemius muscle were collected immediately after saline cleaning. Those samples were maintained at −80 °C until analysis of glycogen content.

### 2.5. Forelimb Grip Strength Test

A low-force testing system (Model-RX-5, Aikoh Engineering, Nagoya, Japan) was used to measure the forelimb grip strength of mice undergoing vehicle or CAP treatments. The amount of tensile force exerted by each mouse was measured using a force transducer equipped with a metal bar (2 mm in diameter and 7.5 cm in length). The mice were allowed to grip the pull bar on the grip wire with only their front paws was steadily pulled back until they lost their grip with the metal bar. The detailed procedures have been described in our previous reports [21,22]. The test of forelimb grip strength was performed after administration of the indicated CAP supplementation for 4 weeks. Grip strength was measured 10 times and the peak tension during each trial was recorded with the attached force gauge. The maximal force (in grams) recorded using this low-force system was used as the grip strength.

### 2.6. Swimming Exercise Performance Test

The swimming exercise performance test was performed as previously described [20]. After 4 weeks of CAP supplementation, a lead sheet (5% equivalent to individual body weight) was attached to the tail of mice for exhaustive swimming challenge. Swimming was performed in plastic containers (65 cm tall and radius 20 cm), filled with water to 40 cm water depth and a temperature of 27 ± 1 °C was maintained. The mice were considered exhausted when they failed to rise to the surface of the water to breathe after 7 s. Swim time to exhaustion was evaluated as the index of exercise performance.

### 2.7. Determination of Fatigue-Associated Biochemical Variables

The effect of CAP supplementation on levels of serum lactate, ammonia, glucose, blood urea nitrogen (BUN), and creatinine kinase (CK) was assessed immediately after exercise. One hour after the last treatment, mice underwent a 15-min swimming test without weight loading. After the swimming exercise, blood samples were immediately collected from the submandibular duct of mice and centrifuged at 1500× g and 4 °C for 10 min for serum preparation. The serum was determined by use of an autoanalyzer (Hitachi 7060, Hitachi, Tokyo, Japan) on the same day.



## 2.8. Clinical Biochemical Profiles

At the end of the experimental period, all mice were euthanized by 95% CO<sub>2</sub> and blood was immediately collected at rest status. Serum was collected by centrifugation and the clinical biochemical variables including AST (aspartate transaminase), ALT (alanine transaminase), albumin, TP (total protein), BUN (blood urea nitrogen), creatinine, CK (creatinase), UA (uric acid), total cholesterol (TC), TG (triglycerides) and glucose were measured using an auto analyzer (Hitachi 7060, Hitachi, Tokyo, Japan).

## 2.9. Tissue Glycogen Determination

Since liver and skeletal muscles are the two major tissues for glycogen deposition, we investigated whether glycogen contents of these two target tissues could be elevated by CAP administration. Liver and muscle tissues were excised and stored in −80 °C for glycogen content analysis as we described previously [22]. The weights of related visceral organs were also recorded for body compositions.

## 2.10. Histological Staining of Tissue

Liver, skeletal muscle, heart, kidney and uterine fat pad tissue were removed from the vehicle and experimental groups at the end of experiment, fixed in 10% phosphate-buffered formalin and then embedded in paraffin. Tissues were embedded in paraffin, cut into 4-μm-thick transverse sections, and stained with hematoxylin-eosin for blinded histopathological assessment and examined by light microscopy with a charge-coupled device (CCD) camera (BX-51; Olympus, Tokyo, Japan) by a clinical pathologist.

## 2.11. Statistical Analysis

Data are presented as mean ± standard error of mean (SEM). Statistical differences among groups were analyzed using one-way ANOVA and the Cochran–Armitage test for dose-effect trend analysis with SAS 9.0 (SAS Inst., Cary, NC, USA). The level of statistical significance was set at  $p < 0.05$ .

# 3. Results

## 3.1. Content of Capsaicin in CAP

The total capsaicin content of CAP extracts was determined by a high-performance liquid chromatography (HPLC) method. A Hitachi Primaide 1110 HPLC pump system equipped with a Primaide 1430 diode array detector and Primaide 1210 autosampler was used to analyze capsaicin on an Phenomenex Luna C18 column (i.d. 4.6 × 250 mm) at 280 nm. A mixture of 5% methanol in 0.1% phosphoric acid was used as the mobile phase at a flow rate of 1 mL/min and an injection volume of 20 μL. The retention time of CAP was 21.9 min (Figure 1). The content of capsaicin was 85% based on a calibration curve from an absolute standard.

## 3.2. Effect of CAP Supplementation on Body Weight and Organ Weights

The initial and final body weights did not significantly differ among the vehicle, CAP-1X, CAP-2X, and CAP-5X groups (Figure 2). The body weight, food consumption, and body compositions are summarized in Table 1. Significantly, the food and water intake of the CAP-2X group was 7.2% ( $p = 0.0439$ ) and 8.0% ( $p = 0.0226$ ) lower, respectively, as compared with vehicle group. There were no significant differences in food and water intake among the vehicle, CAP-1X and CAP-5X groups.

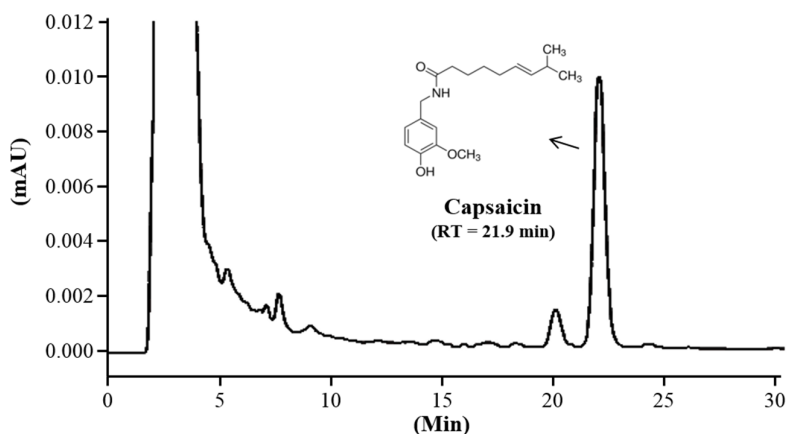


**Figure 1.** High-performance liquid chromatography (HPLC) chromatogram of capsaicin (CAP) in the supplement sample (mAU: milli absorbance units; Rt: Retention time).

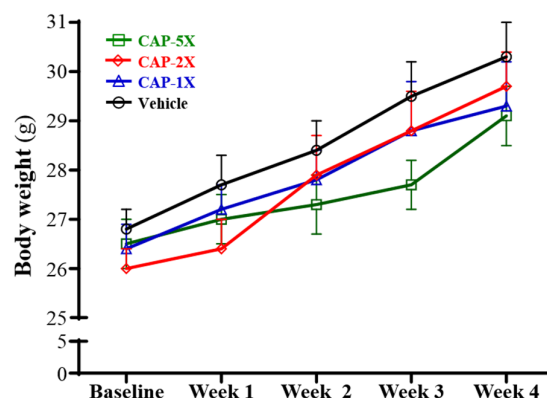


**Figure 2.** The effect of CAP supplementation on growth curve. Data are mean  $\pm$  SEM for  $n = 8$  mice per group.

**Table 1.** General characteristics of the experimental groups with capsaicin supplementation.

Characteristic	Vehicle	CAP-1X	CAP-2X	CAP-5X	Trend Analysis
Initial BW (g)	26.8 $\pm$ 0.4	26.4 $\pm$ 0.5	26.0 $\pm$ 0.4	26.5 $\pm$ 0.5	0.1161
Final BW (g)	30.3 $\pm$ 0.7	29.3 $\pm$ 0.9	29.7 $\pm$ 0.7	29.1 $\pm$ 0.6	0.3282
Food intake (g/day)	5.57 $\pm$ 0.02 <sup>b</sup>	5.52 $\pm$ 0.26 <sup>a,b</sup>	5.17 $\pm$ 0.00 <sup>a</sup>	5.34 $\pm$ 0.03 <sup>a,b</sup>	0.6056
Water intake (mL/day)	6.37 $\pm$ 0.08 <sup>b</sup>	6.14 $\pm$ 0.22 <sup>a,b</sup>	5.86 $\pm$ 0.03 <sup>a</sup>	6.14 $\pm$ 0.20 <sup>a,b</sup>	0.0875
Liver (g)	1.41 $\pm$ 0.04	1.37 $\pm$ 0.04	1.37 $\pm$ 0.04	1.46 $\pm$ 0.02	0.2536
Muscle (g)	0.30 $\pm$ 0.01	0.30 $\pm$ 0.00	0.30 $\pm$ 0.01	0.30 $\pm$ 0.00	0.6938
Kidney (g)	0.38 $\pm$ 0.01	0.38 $\pm$ 0.00	0.38 $\pm$ 0.01	0.38 $\pm$ 0.01	0.9420
Heart (g)	0.18 $\pm$ 0.01	0.16 $\pm$ 0.01	0.15 $\pm$ 0.00	0.16 $\pm$ 0.00	0.7942
UFP (g)	0.20 $\pm$ 0.01	0.19 $\pm$ 0.02	0.20 $\pm$ 0.02	0.20 $\pm$ 0.01	0.7942
BAT (g)	0.08 $\pm$ 0.003	0.09 $\pm$ 0.002	0.08 $\pm$ 0.004	0.09 $\pm$ 0.003	0.9519
Relative liver weight (%)	4.73 $\pm$ 0.18	4.92 $\pm$ 0.10	4.73 $\pm$ 0.18	5.03 $\pm$ 0.14	0.3336
Relative muscle weight (%)	1.00 $\pm$ 0.01	1.02 $\pm$ 0.02	1.03 $\pm$ 0.03	1.04 $\pm$ 0.02	0.3257
Relative kidney weight (%)	1.28 $\pm$ 0.05	1.28 $\pm$ 0.03	1.31 $\pm$ 0.03	1.30 $\pm$ 0.05	0.9771
Relative heart weight (%)	0.59 $\pm$ 0.03 <sup>b</sup>	0.54 $\pm$ 0.03 <sup>a,b</sup>	0.51 $\pm$ 0.02 <sup>a</sup>	0.56 $\pm$ 0.02 <sup>a,b</sup>	0.6981
Relative UFP weight (%)	0.68 $\pm$ 0.03	0.66 $\pm$ 0.08	0.69 $\pm$ 0.08	0.67 $\pm$ 0.05	0.9121
Relative BAT weight (%)	0.28 $\pm$ 0.01	0.30 $\pm$ 0.01	0.29 $\pm$ 0.02	0.30 $\pm$ 0.01	0.5119

Data are the mean  $\pm$  SEM for  $n = 8$  mice in each group. Values in the same row with different superscript letters (a, b) differ significantly,  $p < 0.05$ , by one-way ANOVA; Muscle mass includes both gastrocnemius and soleus muscles in the back part of the lower legs. BW: Body weight; UFP: Uterine fat pads; BAT: Brown adipose tissue. Low-dose (CAP-1X), medium-dose (CAP-2X) and high-dose (CAP-5X) CAP at 250, 410 and 1025 mg/kg/day, respectively.

### 3.3. Effect of CAP on Forelimb Grip Strength

The grip strength test is a test designed to assess changes in neuromuscular coordination, muscle strength and overall functional capacity [23]. As shown in Figure 3A, the forelimb grip strength values in the vehicle, CAP-1X, CAP-2X and CAP-5X groups were 118, 117, 125 and 131 g, respectively. The values of the CAP-5X group were significantly 1.10- ( $p = 0.0082$ ) and 1.12-fold ( $p = 0.004$ ) higher than those of the vehicle and CAP-1X groups, respectively. However, there were no significant differences in forelimb grip strength among the vehicle, CAP-1X, and CAP-2X groups. In the trend analysis, absolute forelimb grip strength dose-dependently increased as the CAP dose ( $p = 0.0003$ ) increased. Therefore, grip strength was calibrated by individual body weight to obtain relative grip strength (%) and was still higher with CAP treatment (Figure 3B) than the vehicle group, with significant trend findings ( $p < 0.0001$ ).

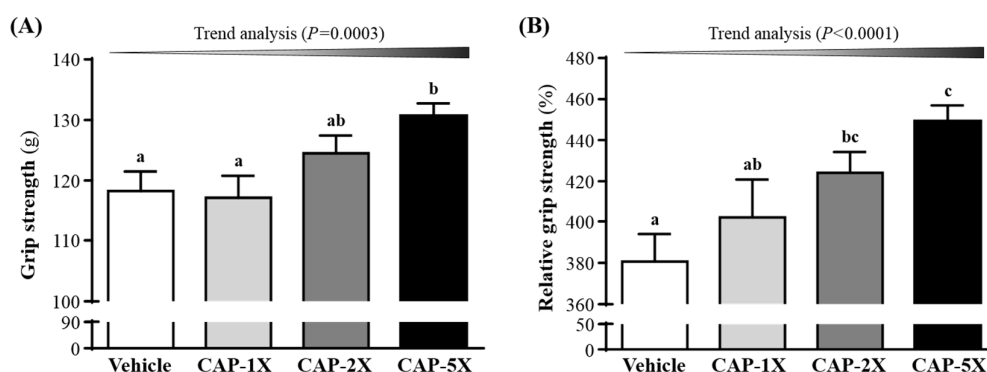


**Figure 3.** Effect of CAP supplementation on forelimb grip strength. (A) Grip strength; (B) Relative grip strength. Data are mean  $\pm$  SEM for  $n = 8$  mice in each group. Different letters indicate significant difference at  $p < 0.05$  by one-way ANOVA. Low-dose (CAP-1X), medium-dose (CAP-2X) and high-dose (CAP-5X) CAP at 205, 410 and 1025 mg/kg/day, respectively.

### 3.4. Effect of CAP Supplementation on Exhaustive Swimming Test

The exercise endurance in mice administered the vehicle, CAP-1X, CAP-2X, and CAP-5X were 9.30, 11.06, 11.28, and 46.99 min, respectively, as shown in Figure 4. The swimming time of the CAP-5X group was significantly higher, 5.06-, 4.25- and 4.17-fold (all  $p < 0.0001$ ) with regard to those of the vehicle, CAP-1X and CAP-2X groups, respectively. In the trend analysis, maximal swimming time was increased dose-dependently with the CAP doses ( $p = 0.0122$ ).

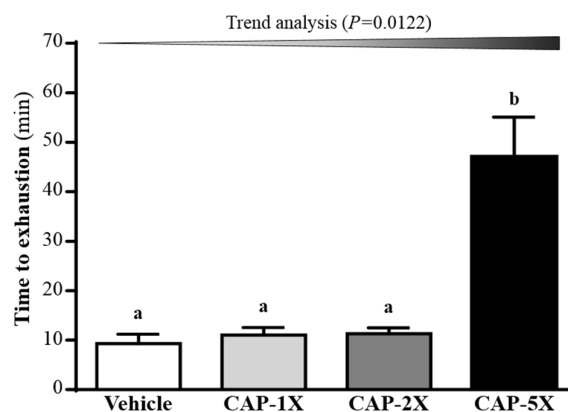


**Figure 4.** Effect of CAP supplementation on exhaustive swimming test. Data are mean  $\pm$  SEM for  $n = 8$  mice in each group. Different letters indicate significant difference at  $p < 0.05$  by one-way ANOVA.

### 3.5. Effect of CAP Supplementation on Exercise Fatigue-Related Indicators after Acute Exercise

The status of peripheral fatigue can be evaluated by important biochemical indicators, including lactate, ammonia, glucose, BUN and CK, after exercise [19,20]. Compared to vehicle treatment, serum lactate concentrations were lower for CAP-1X, CAP-2X, and CAP-5X treatment, by 32.3%, 35.8% and 37.3% (all  $p < 0.0001$ ), respectively, as compared to vehicle group (Figure 5A). Ammonia is a ubiquitous metabolic product which has multiple effects on physiological and biochemical systems [24]. As shown in the Figure 5B, serum ammonia levels of CAP-1X, CAP-2X, and CAP-5X groups were significantly lower, by 33.5%, 39.3% and 41.3% (all  $p < 0.0001$ ), respectively, as compared with vehicle group. Figure 5C shows that respective levels of serum glucose were significantly higher, by 19.0%, 26.0% and 28.1% (all  $p < 0.0001$ ), for CAP-1X, CAP-2X, and CAP-5X groups, when compared to the vehicle group. BUN level was lower with CAP treatments than vehicle treatment after exercise (Figure 5D) and significantly differed among CAP treatments. BUN level after exercise decreased by 9.4% ( $p = 0.0194$ ), 13.0% ( $p = 0.0012$ ) and 19.2% ( $p < 0.0001$ ) for CAP-1X, CAP-2X, and CAP-5X groups, respectively, as compared to the vehicle group. CK level significantly differed among CAP treatments (Figure 5E) and was lower, by 35.2%, 39.5% and 41.5% (all  $p < 0.001$ ), for CAP-1X, CAP-2X, and CAP-5X treatments, respectively, in comparison to vehicle treatment. The trend analysis evaluates whether CAP treatment had a significant dose-dependent effect. The statistics results show the increase of dosage-dependence on blood glucose content ( $p < 0.0001$ ) and the decrease of dosage-dependence on serum lactate, ammonia, BUN and CK levels (all  $p < 0.0001$ ).

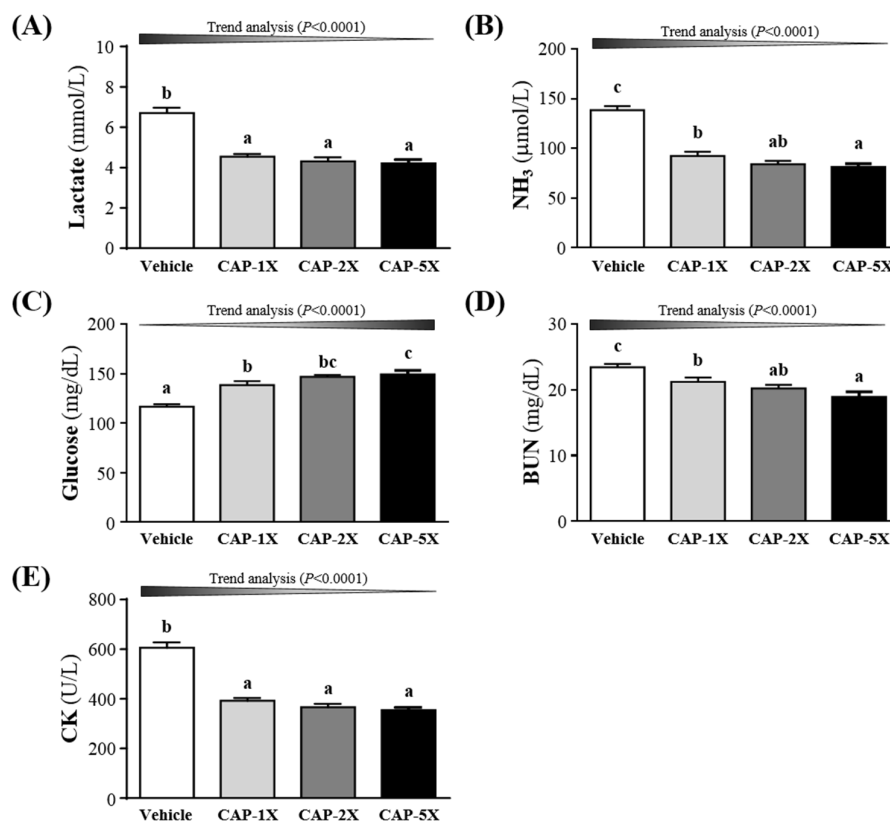


**Figure 5.** Effect of CAP supplementation on serum (A) lactate; (B) ammonia; (C) glucose; (D) blood urea nitrogen (BUN); and (E) creatine kinase (CK) levels after acute exercise challenge. Data are mean  $\pm$  SEM for  $n = 8$  mice in each group. Different letters indicate significant difference at  $p < 0.05$  by one-way ANOVA.

### 3.6. Effect of CAP Supplementation on Hepatic and Muscular Glycogen Level

Glycogen is an important source of energy during exercise, and the increase in glycogen stored in liver is beneficial for enhancing physical endurance [25]. Glycogen content is an integral determining factor in fatigue. In Figure 6A, CAP-2X and CAP-5X groups showed significantly elevated glycogen stores in liver, increased 1.34- ( $p = 0.0191$ ) and 1.34-fold ( $p = 0.0193$ ), respectively, as compared with vehicle group. There were no significant differences between the vehicle and CAP-1X group. In the trend analysis, absolute liver glycogen showed significantly dose-dependent increase ( $p = 0.0039$ ). However, muscle glycogen level did not differ among CAP treatments (Figure 6B).

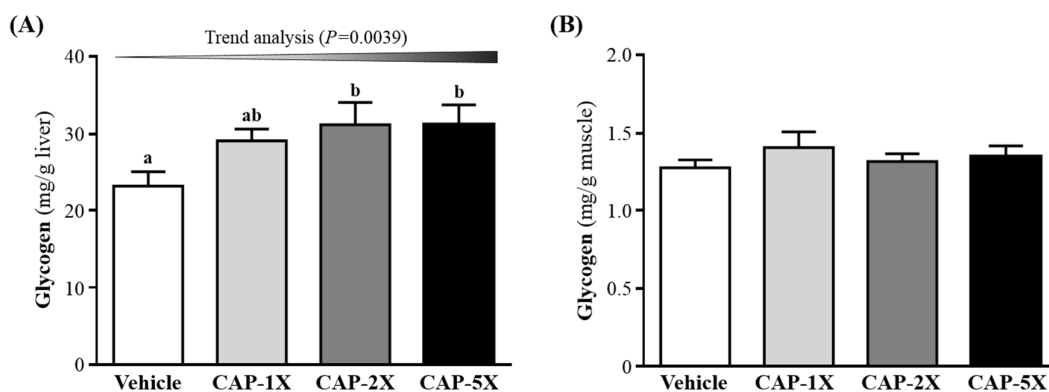


**Figure 6.** Effect of CAP supplementation on glycogen content in (A) liver and (B) muscle. Data are mean  $\pm$  SEM for  $n = 8$  mice in each group. Different letters indicate significant difference at  $p < 0.05$  by one-way ANOVA.

### 3.7. Effect of CAP Supplementation on Biochemical Analyses at the End of the Experiment

In the present study, we observed beneficial effects of CAP on the grip strength, exhaustive exercise challenge and other physiological effects with 4 weeks of CAP supplementation. We further investigated whether CAP treatments for 4 weeks could cause any negative effects on other biochemical markers of healthy mice. Therefore, we examined the related biochemical parameters to these CAP-treated mice (Table 2).

Levels of biochemical indices, including albumin, TP, TC, and glucose, did not differ among groups ( $p > 0.05$ , Table 2). Moreover, AST levels were significantly lower, by 16.1% ( $p = 0.0037$ ), 16.1% ( $p = 0.0037$ ), and 19.6% ( $p = 0.0006$ ) for CAP-1X, CAP-2X, and CAP-5X, respectively, when compared to vehicle treatment. In the trend analysis, AST levels were decreased dose-dependently with the CAP doses ( $p = 0.0003$ ). Levels of ALT were significantly lower, by 18.0% ( $p = 0.0051$ ), 30.9% ( $p < 0.0001$ ), and 31.7% ( $p < 0.0001$ ) for CAP-1X, CAP-2X, and CAP-5X, respectively, when compared to vehicle treatment. Serum levels of BUN in the CAP-1X, CAP-2X, and CAP-5X groups were 15.6%, 19.6%, and 25.5% (all  $p < 0.0001$ ), respectively; significantly lower than in the vehicle group. Levels of creatinine in the CAP-1X, CAP-2X, and CAP-5X groups were significantly lower by 13.0% ( $p = 0.0015$ ), 18.6% ( $p < 0.0001$ ), and 29.4% ( $p < 0.0001$ ), respectively, than in the vehicle group. UA levels were significantly lower, by 42.1%, 48.6%, and 55.0% (all  $p < 0.0001$ ) for CAP-1X, CAP-2X, and CAP-5X, respectively, when compared to vehicle treatment. CK levels were significantly lower, by 33.2% ( $p = 0.0003$ ), 51.4% ( $p < 0.0001$ ), and 61.0% ( $p < 0.0001$ ) for CAP-1X, CAP-2X, and CAP-5X, respectively, when compared to vehicle treatment. In the trend analysis, ALT, BUN, creatinine, CK and UA levels decreased dose-dependently with the CAP doses (all  $p < 0.0001$ ). Serum TG levels of CAP-2X, and CAP-5X groups were significantly lower, by 9.4% ( $p = 0.0284$ ) and 12.3% ( $p = 0.0051$ ), respectively, when compared with vehicle group. In the trend analysis, TG level was decreased dose-dependently with the CAP doses ( $p = 0.0014$ ).



**Table 2.** Biochemical analysis at the end of treatment.

Parameter	Vehicle	CAP-1X	CAP-2X	CAP-5X	Trend Analysis
AST (U/L)	95 ± 5 <sup>b</sup>	80 ± 2 <sup>a</sup>	80 ± 3 <sup>a</sup>	77 ± 3 <sup>a</sup>	0.0003
ALT (U/L)	45 ± 3 <sup>d</sup>	37 ± 2 <sup>c</sup>	31 ± 1 <sup>a,b</sup>	30 ± 2 <sup>a</sup>	<0.0001
Albumin (g/dL)	3.26 ± 0.04	3.28 ± 0.04	3.26 ± 0.04	3.28 ± 0.03	0.8838
TP (g/dL)	5.04 ± 0.06	4.98 ± 0.07	5.04 ± 0.05	5.05 ± 0.02	0.5837
BUN (mg/dL)	22.3 ± 0.6 <sup>c</sup>	18.8 ± 0.3 <sup>b</sup>	17.9 ± 0.2 <sup>b</sup>	16.6 ± 0.5 <sup>a</sup>	<0.0001
Creatinine (mg/dL)	0.29 ± 0.01 <sup>c</sup>	0.25 ± 0.01 <sup>b</sup>	0.24 ± 0.01 <sup>b</sup>	0.20 ± 0.01 <sup>a</sup>	<0.0001
UA (mg/dL)	1.75 ± 0.11 <sup>b</sup>	1.01 ± 0.09 <sup>a</sup>	0.90 ± 0.07 <sup>a</sup>	0.79 ± 0.04 <sup>a</sup>	<0.0001
CK (U/L)	259 ± 24 <sup>d</sup>	173 ± 12 <sup>c</sup>	126 ± 10 <sup>a,b</sup>	101 ± 7 <sup>a</sup>	<0.0001
TC (mg/dL)	111 ± 3	103 ± 4	104 ± 5	102 ± 5	0.1701
TG (mg/dL)	152 ± 5 <sup>b</sup>	147 ± 4 <sup>b,c</sup>	138 ± 6 <sup>a,c</sup>	134 ± 3 <sup>a</sup>	0.0014
Glucose (mg/dL)	154 ± 3	153 ± 4	158 ± 2	158 ± 3	0.5448

Data are the mean ± SEM for  $n = 8$  mice in each group. Values in the same row with different superscript letters (a, b, c) differ significantly,  $p < 0.05$ , by one-way ANOVA; Muscle mass includes both gastrocnemius and soleus muscles in the back part of the lower legs. AST: Aspartate aminotransferase; ALT: Alanine aminotransferase; TP: Total protein; BUN: Blood urea nitrogen; CK: Creatine kinase; UA: Uric acid; TC: Total cholesterol; TG: Triacylglycerol.

### 3.8. Effect of CAP Supplementation on Histological Examinations at the End of the Experiment

On morphological observation, the arrangement of sinusoid and hepatic cords in liver showed no changes with CAP treatment (Figure 7). Hypertrophy and hyperplasia were not observed in heart cardiomyocytes or skeletal muscles. The structure of renal tubules and glomerulus did not differ among treatments. In addition, the morphology of adipose tissue and fat cell size did not show differences between groups.

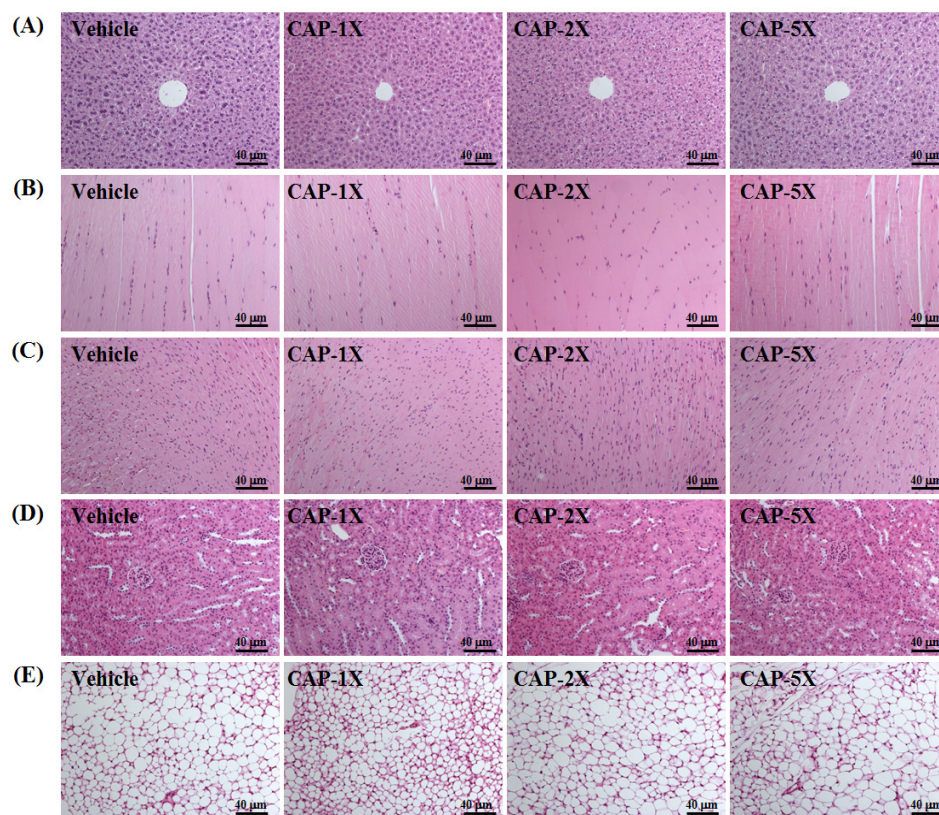


**Figure 7.** Effect of CAP supplementation on morphology of (A) liver; (B) skeletal muscle; (C) heart; (D) kidney; and (E) uterine fat pad in mice. Specimens were photographed by light microscopy. (H&E stain, magnification:  $\times 200$ ; Scale bar, 40  $\mu\text{m}$ ).



#### 4. Discussion

Previous studies have reported that optimized dose of CAP may significantly affect fat oxidation and energy expenditure [12,26]. Thus, we found the CAP-2X groups showed a significant decrease in food consumption, but not in other CAP groups, which was consistent with previous study. Organ weights of experimental animals could provide information about the health status of test mice and possible effects to the test article. The weight differences of the liver, muscle, kidney, heart, uterine fat pads (UFP) and brown adipose tissue (BAT) were not observed among the four groups. The relative liver, muscle, kidney, UFP and BAT weight (%) also did not show significant differences between groups. The no-observed-adverse-effect level (NOAEL) of CAP could provide optimized dosages for its physiological benefits without health risk. The results suggested that the supplementation with CAP treatments should be safe for all test animals.

Forelimb grip strength is a routine physical examination test. Our previous study had found that muscle strength was positively correlated with forelimb grip strength [19]. In this study, we found the grip of CAP-5X group was greater than other groups. Therefore, the results indicated that long-term CAP supplementation could benefit grip strength when no training protocol is implemented. Our previous reports have shown that long-term phytochemical supplementation, such as resveratrol and curcumin, also improves the grip strength of untrained animals [19,20]. CAP also demonstrated the improvement of mechanical performance and bioenergetic efficiency in contracting mouse skeletal muscle [27], which is consistent with our grip results. Our experimental results (Figure 4) indicated that physical fatigue could be ameliorated according to swimming time extension with 4 weeks CAP administration. TRPV1 activation by dietary capsaicin supplementation had revealed one of its roles in skeletal muscle function [14]. The TRPV1 activation promoted mitochondrial biogenesis and ATP production through PGC-1 $\alpha$  regulation in skeletal muscle. A previous study has shown that TRPV1, activated by CAP administration, could improve endurance capacity and energy metabolism in mice [13]. CAP was able to significantly extend the endurance time to exhaustion, so it had anti-fatigue activity due to endurance enhancement. Swimming test to exhaustion is an experimental exercise model to evaluate physical fatigue. It is one of the most commonly used animal models that works well for evaluating the physical endurance capacity [18,28]. In short-term intensive exercise, blood lactate is the glycolysis product of carbohydrate under an anaerobic condition and glycolysis is the main energy source [29]. The increased lactate levels further reduce pH, which could induce various biochemical and physiological side effects, including glycolysis, as well as phosphofructokinase and calcium ion release, through muscular contraction [30]. Therefore, lactate metabolism is beneficial to relieve fatigue. We found that CAP supplementation prolonged the period to exhaustion and suppressed the increase in the blood lactate level during swimming (Figure 5A). Another study also demonstrated that CAP administration could also modulate serum lactic acid levels after 30 min of swimming via stimulation of their vanilloid receptors [31].

High-intensive and prolonged exercise significantly enhances the blood ammonia concentration, a metabolite with toxic effects on the central and peripheral fatigue [32]. During exercise, ammonia is produced and accumulates in skeletal muscle when AMP is deaminated to IMP by AMP deaminase (AMPD) during resynthesis of ATP. Ammonia is very toxic and has deleterious influences on the physiology, including activation of phosphofructokinase (PFK), which is the rate-limiting enzyme in glycolysis, and inhibition of pyruvate oxidation to acetyl-CoA [33]. Our previous reports have also shown that long-term phytochemical supplementation, such as resveratrol and curcumin, could reduce the concentration of ammonia after exercise [19,20]. Higher concentrations of ammonia content could bring negative effects on the productivity pathway. Thus, it is suggested that when CAP supplementation for 4 weeks, the ammonia level could be significantly modulated after the exercise test (Figure 5B).

Glucose, a breakdown product of tissue glycogen, is released as a circulating substrate for energy utilization after intense exercise [34]. During exercise, energy demand expedite muscular glucose utilization and, consequently, increases blood glucose disposal [35]. Blood glucose is an important

fuel for increased ATP production within contracting skeletal muscle during exercise [36]. Previous reports showed that the plasma glucose of CAP-treated rats at a dose of 15 mg/kg was significantly higher than the non-CAP-treated control group after immediate exhaustion [37]. The other studies also demonstrated that CAP increased glucose uptake directly by activating AMP-activated protein kinase (AMPK) [38], improved oxidative metabolism in exercising muscle, and promoted muscular mass gain with chronic administration [39]. Therefore, continuous 4 weeks CAP supplementation could increase energy utilization and improve exercise performance in current results (Figure 4).

Serum BUN (blood urea nitrogen), creatinine, and urine output were closely monitored to measure renal function. Many factors other than renal disease can cause BUN alteration [40]. Urea is formed by the liver and carried by the blood to the kidneys, and urea is an important index correlation with protein breakdown, dehydration, stress and fatigue [40]. CAP is also reported to mitigate the cisplatin-induced renal dysfunction, by assessing the levels of serum creatinine and BUN, through induction of HO-1 as well as inhibition oxidative stress and inflammation [41].

The appearance of creatine kinase (CK) in blood has been generally considered to be an indirect marker of muscle damage, particularly for diagnosis of medical conditions such as myocardial infarction, muscular dystrophy, and cerebral diseases [42]. Therefore, serum CK activity has been considered to be useful as a marker in exercise physiology and sports medicine for the detection of muscle injury and overwork [43]. Thus, CAP supplementation should ameliorate skeletal muscle injury induced by acute exercise challenge.

Energy storage and supply is another important factor related to exercise performance. Glycogen is the predominant source of glycolysis for ATP production. High pre-exercise muscle and liver glycogen concentrations are believed to be essential for exercise performance [44]. In a previous study, the oral administration of CAP (15 mg/kg) could substantially improve the endurance performance by stimulating lipolysis and sparing tissue glycogen [45]. The non-esterified fatty acids could be utilized prior to glycogen due to CAP-increased adrenal catecholamine levels [37,45]. Administration of CAP or its analog, capsiate, promotes hepatic insulin sensitivity and increases the glycogen storage via pAkt, PEPCK and pAMPK signaling pathways [46]. CAP increases liver insulin sensitivity, but not muscular insulin sensitivity responsiveness, thereby creating a metabolism milieu that favors in vivo insulin sensitivity with respect to glucose uptake or production, glycogenesis and lipogenesis [47]. Exercise expedites the gluconeogenesis and glucose utilization to meet the body's energy demands. In the acute phase of exercise, liver glycogen may break down to glucose as an alternative energy source, and then blood flow carries nutrients, including glucose, to working muscles supporting exercise [21]. Our data also showed similar result; breakdown of glycogen resulted in elevated blood glucose for sufficient energy during exercise. This may help to explain that the elevated blood glucose levels in the CAP-treated groups after a 15-min exercise challenge were all significantly higher as compared to the vehicle control group (Figure 5C). We found that CAP supplementation could increase glycogen content in liver. These results suggest that the glycogen deposit could become an available energy source for the following phases of exercise, which increase endurance capacity and delays onset of fatigue.

Liver function could be evaluated by measuring plasma levels of aminotransferase such as AST and ALT. In a previous study, CAP treatment showed significant improvement in the anti-oxidation and anti-apoptosis against carbon tetrachloride-induced hepatotoxicity in rats [48]. In the current study, it was also demonstrated CAP supplementation could be beneficial to the liver function. The kidney-related indexes including BUN, creatinine, and UA were all improved by CAP supplementation. During renal ischemia-reperfusion (I/R) injury, the burst of reactive oxygen species (ROS), mainly produced by xanthine oxidase, can trigger inflammation and tubular cell injury and subsequent generation of UA [49]. Therefore, CAP may have potential for renal protection due to its antioxidant activity.

Blood CK activity is a marker of exercise-induced skeletal muscle damage [42]. The CAP showed improvement of cardiac function recovery and CK amelioration in heart reperfusion injury,

possibly related to stimulation of calcitonin gene-related peptide (CGRP) release [50]. Therefore, CAP supplementation should mitigate the muscular injury induced by acute exercise or ischemia. A previous study also showed that dietary capsaicin significantly decreased triglyceride levels in the plasma and/or liver, as well as the expression of inflammatory adipocytokine genes (e.g., monocyte chemoattractant protein-1 and interleukin-6) and macrophage infiltration [11]. The capsaicin-induced TRPV1 activation promoted lipolysis of visceral fat, and reduced triglyceride level via upregulation of hepatic uncoupling protein 2 (UCP2) [51].

Histological data related to the pathological effects of CAP is quite limited, especially with respect to the indicated bioactivity doses. We found no changes in arrangement of sinusoid and hepatic cords with CAP treatment in mice and no hypertrophy or hyperplasia response in heart cardiomyocytes and rhabdomyocytes of gastrocnemius muscles. We found no significant difference in structure of renal tubules and glomerulus with CAP treatment and no significant alteration in the alveolar, bronchial and interstitial space. The morphology of adipose tissue morphology and fat cell size were not shown to be different between groups. Histological examination of organs showed no apparent damage in any mice.

## 5. Conclusions

In this study, we found that CAP supplementation could improve physical activities, including grip strength and endurance performance, by increasing liver glycogen content. In addition, exercise-induced fatigue-related parameters, including lactate, ammonia, glucose, BUN and CK, were positively modulated by CAP supplementation in a dosage-dependent manner (trend analysis,  $p < 0.0001$ ). We suggest that CAP could be a potential ergogenic phytochemical for supplementation, with fatigue mitigation and exercise performance enhancement.

**Acknowledgments:** This study was not supported by any grant, outside sources of funding or industry sponsorship. The authors are grateful to Yi-Ming Chen and Chien-Chun Chang and Mon-Chien Lee for technical assistance in animal experiments. The authors thank Chien-Chao Chiu for conducting histological examination. The HPLC analysis was performed by Research Center for Industry of Human Ecology and Food Safety Testing Laboratory, College of Human Ecology, Chang Gung University of Science and Technology.

**Author Contributions:** Chi-Chang Huang and Yen-Shuo Chiu designed the experiments. Yi-Ju Hsu, Chien-Chao Chiu, Yan-Lin Liu and Chun-Hui Chiu carried out the laboratory experiments. Yi-Ju Hsu, Wen-Ching Huang, Wan-Chun Chiu, and Chi-Chang Huang analyzed the data, interpreted the results, prepared figures, and wrote the manuscript. Yi-Ju Hsu, Wen-Ching Huang and Chi-Chang Huang revised the manuscript. Yen-Shuo Chiu and Chi-Chang Huang contributed the reagents, materials and analysis platforms.

**Conflicts of Interest:** The authors declare no conflict of interest.

## References

1. Naj, A. *Peppers: A Story of Hot Pursuits*; Knopf: New York, NY, USA, 1992.
2. Qiu, J.; Niu, X.; Wang, J.; Xing, Y.; Leng, B.; Dong, J.; Li, H.; Luo, M.; Zhang, Y.; Dai, X.; et al. Capsaicin protects mice from community-associated methicillin-resistant *Staphylococcus aureus* pneumonia. *PLoS ONE* **2012**, *7*, e33032. [[CrossRef](#)] [[PubMed](#)]
3. Arora, R.; Gill, N.S.; Chauhan, G.; Rana, A.C. An overview about versatile molecule capsaicin. *Int. J. Pharm. Sci. Drug Res.* **2011**, *4*, 280–286.
4. Purseglove, J.W.; Brown, E.G.; Green, C.L.; Robbins, S.R.J. Spices. *Longman* **1981**, *2*, 10–99.
5. Sung, Y.; Chang, Y.Y.; Ting, N.L. Capsaicin biosynthesis in water-stressed hot pepper fruits. *Bot. Bull. Acad. Sin.* **2005**, *46*, 35–42.
6. Cheema, S.K.; Pant, M.R. Estimation of capsaicin in seven cultivated varieties of *Capsicum Annuum* L. *Res. J. Pharm. Biol. Chem. Sci.* **2011**, *2*, 701–706.
7. Supalkova, V.; Stavelikova, H.; Krizkova, S.; Adam, V.; Horna, A.; Havel, L.; Ryant, P.; Babula, B.; Kizek, R. Study of capsaicin content in various parts of pepper fruit by liquid chromatography with electrochemical detection. *Acta Chim. Slov.* **2007**, *54*, 55–59.

8. Derry, S.; Sven-Rice, A.; Cole, P.; Tan, T.; Moore, R.A. Topical capsaicin (high concentration) for chronic neuropathic pain in adults. *Cochrane Database Syst. Rev.* **2013**, *28*, Cd007393.
9. Chen, K.S.; Chen, P.N.; Hsieh, Y.S.; Lin, C.Y.; Lee, Y.H.; Chu, S.C. Capsaicin protects endothelial cells and macrophage against oxidized low-density lipoprotein-induced injury by direct antioxidant action. *Chem. Biol. Interact.* **2015**, *228*, 35–45. [[CrossRef](#)] [[PubMed](#)]
10. Clark, R.; Lee, S.H. Anticancer Properties of Capsaicin against Human Cancer. *Anticancer Res.* **2016**, *36*, 837–843. [[PubMed](#)]
11. Kang, J.H.; Tsuyoshi, G.; Le Ngoc, H.; Kim, H.M.; Tu, T.H.; Noh, H.J.; Kim, C.S.; Choe, S.Y.; Kawada, T.; Yoo, H.; et al. Dietary capsaicin attenuates metabolic dysregulation in genetically obese diabetic mice. *J. Med. Food* **2011**, *14*, 310–315. [[CrossRef](#)] [[PubMed](#)]
12. Janssens, P.L.; Hursel, R.; Martens, E.A.; Westerterp-Plantenga, M.S. Acute effects of capsaicin on energy expenditure and fat oxidation in negative energy balance. *PLoS ONE* **2013**, *8*, e67786. [[CrossRef](#)] [[PubMed](#)]
13. Luo, Z.; Ma, L.; Zhao, Z.; He, H.; Yang, D.; Feng, X.; Ma, S.; Chen, X.; Zhu, T.; Cao, T.; et al. TRPV1 activation improves exercise endurance and energy metabolism through PGC-1alpha upregulation in mice. *Cell Res.* **2012**, *22*, 551–564. [[CrossRef](#)] [[PubMed](#)]
14. Lotteau, S.; Ducreux, S.; Romestaing, C.; Legrand, C.; Van Coppenolle, F. Characterization of functional TRPV1 channels in the sarcoplasmic reticulum of mouse skeletal muscle. *PLoS ONE* **2013**, *8*, e58673. [[CrossRef](#)] [[PubMed](#)]
15. Hudson, A.S.; Kunstetter, A.C.; Damasceno, W.C.; Wanner, S.P. Involvement of the TRPV1 channel in the modulation of spontaneous locomotor activity, physical performance and physical exercise-induced physiological responses. *Braz. J. Med. Biol. Res.* **2016**, *49*, e5183. [[CrossRef](#)] [[PubMed](#)]
16. Yamamoto, T.; Azechi, H.; Board, M. Essential role of excessive tryptophan and its neurometabolites in fatigue. *Can. J. Neurol. Sci.* **2012**, *39*, 40–47. [[CrossRef](#)] [[PubMed](#)]
17. Fitts, R.H. Cellular mechanisms of muscle fatigue. *Physiol. Rev.* **1994**, *74*, 49–94. [[PubMed](#)]
18. You, L.; Zhao, M.; Regenstein, J.M.; Ren, J. In vitro antioxidant activity and in vivo anti-fatigue effect of loach (*Misgurnus anguillicaudatus*) peptides prepared by papain digestion. *Food Chem.* **2011**, *124*, 188–194. [[CrossRef](#)]
19. Wu, R.E.; Huang, W.C.; Liao, C.C.; Chang, Y.K.; Kan, N.W.; Huang, C.C. Resveratrol protects against physical fatigue and improves exercise performance in mice. *Molecules* **2013**, *18*, 4689–4702. [[CrossRef](#)] [[PubMed](#)]
20. Huang, W.C.; Chiu, W.C.; Chuang, H.L.; Tang, D.W.; Lee, Z.M.; Wei, L.; Chen, F.A.; Huang, C.C. Effect of curcumin supplementation on physiological fatigue and physical performance in mice. *Nutrients* **2015**, *7*, 905–921. [[CrossRef](#)] [[PubMed](#)]
21. Chen, W.C.; Huang, W.C.; Chiu, C.C.; Chang, Y.K.; Huang, C.C. Whey protein improves exercise performance and biochemical profiles in trained mice. *Med. Sci. Sports Exerc.* **2014**, *46*, 1517–1524. [[CrossRef](#)] [[PubMed](#)]
22. Wang, S.Y.; Huang, W.C.; Liu, C.C.; Wang, M.F.; Ho, C.S.; Huang, W.P.; Hou, C.C.; Chuang, H.L.; Huang, C.C. Pumpkin (*Cucurbita moschata*) fruit extract improves physical fatigue and exercise performance in mice. *Molecules* **2012**, *17*, 11864–11876. [[CrossRef](#)] [[PubMed](#)]
23. Radley, H.G.; de Luca, A.; Lynch, G.S.; Grounds, M.D. Duchenne muscular dystrophy: Focus on pharmaceutical and nutritional interventions. *Int. J. Biochem. Cell Biol.* **2007**, *39*, 469–477. [[CrossRef](#)] [[PubMed](#)]
24. Katunuma, N.; Okada, M.; Nishii, Y. Regulation of the urea cycle and TCA cycle by ammonia. *Adv. Enzyme Regul.* **1996**, *4*, 317–336. [[CrossRef](#)]
25. Young, A.J.; Castellani, J.W. Exertion-induced fatigue and thermoregulation in the cold. *Comp. Biochem. Physiol. A Mol. Integr. Physiol.* **2001**, *128*, 769–776. [[CrossRef](#)]
26. Mun, J.M.; Ok, H.M.; Kwon, O. Corn gluten hydrolysate and capsaicin have complimentary actions on body weight reduction and lipid-related genes in diet-induced obese rats. *Nutr Res.* **2014**, *34*, 458–465. [[CrossRef](#)] [[PubMed](#)]
27. Kazuya, Y.; Tonson, A.; Pecchi, E.; Dalmaso, C.; Vilmen, C.; Fur, Y.L.; Bernard, M.; Bendahan, D.; Giannesini, B. A single intake of capsaicin improves mechanical performance and bioenergetics efficiency in contracting mouse skeletal muscle. *Am. J. Physiol. Endocrinol. Metab.* **2014**, *15*, E1110–E1119. [[CrossRef](#)] [[PubMed](#)]

28. Kumar, G.P.; Anand, T.; Singsit, D.; Khanum, F.; Anilakumar, K.R. Evaluation of antioxidant and anti-fatigue properties of *Trigonella foenum-graecum* L. in rats subjected to weight loaded forced swim test. *Pharmacogn. J.* **2013**, *5*, 66–71. [[CrossRef](#)]
29. Yue, Z.; Xiuhong, Z.; Shuyan, Y.; Zhonghua, Z. Effect of *Inonotus Obliquus* Polysaccharides on physical fatigue in mice. *J. Tradit. Chin. Med.* **2015**, *35*, 468–472. [[PubMed](#)]
30. Cairns, S.P. Lactic acid and exercise performance: Culprit or friend? *Sports Med.* **2006**, *36*, 279–291. [[CrossRef](#)] [[PubMed](#)]
31. Haramizu, S.; Mizunoya, W.; Masuda, Y.; Ohnuki, K.; Watanabe, T.; Yazawa, S.; Fushiki, T. Capsiate, a nonpungent capsaicin analog, increases endurance swimming capacity of mice by stimulation of vanilloid receptors. *Biosci. Biotechnol. Biochem.* **2006**, *70*, 774–781. [[CrossRef](#)] [[PubMed](#)]
32. Bassini-Cameron, A.; Monteiro, A.; Gomes, A.; Werneck-de-Castro, J.P.; Cameron, L. Glutamine protects against increases in blood ammonia in football players in an exercise intensity-dependent way. *Br. J. Sports Med.* **2008**, *42*, 260–266. [[CrossRef](#)] [[PubMed](#)]
33. Verlander, J.W.; Chu, D.; Lee, H.W.; Handlogten, M.E.; Weiner, I.D. Expression of glutamine synthetase in the mouse kidney: Localization in multiple epithelial cell types and differential regulation by hypokalemia. *Am. J. Physiol.-Ren. Physiol.* **2013**, *305*, F701–F713. [[CrossRef](#)] [[PubMed](#)]
34. Suh, S.H.; Paik, I.Y.; Jacobs, K. Regulation of blood glucose homeostasis during prolonged. *Mol. Cells* **2007**, *23*, 272–279. [[PubMed](#)]
35. Emhoff, C.A.; Messonnier, L.A.; Horning, M.A.; Fattor, J.A.; Carlson, T.J.; Brooks, G.A. Gluconeogenesis and hepatic glycogenolysis during exercise at the lactate threshold. *J. Appl. Physiol.* **2013**, *114*, 297–306. [[CrossRef](#)] [[PubMed](#)]
36. Hargreaves, M. Exercise, muscle, and CHO metabolism. *Scand. J. Med. Sci. Sports* **2015**, *25*, 29–33. [[CrossRef](#)] [[PubMed](#)]
37. Oh, T.W.; Ohta, F. Dose-dependent effect of capsaicin on endurance capacity in rats. *Br. J. Nutr.* **2003**, *90*, 515–520. [[CrossRef](#)] [[PubMed](#)]
38. Kim, S.H.; Hwang, J.T.; Park, H.S.; Kwon, D.Y.; Kim, M.S. Capsaicin stimulates glucose uptake in C2C12 muscle cells via the reactive oxygen species (ROS)/AMPK/p38 MAPK pathway. *Biochem. Biophys. Res. Commun.* **2013**, *43*, 66–70. [[CrossRef](#)] [[PubMed](#)]
39. Yashiro, K.; Tonson, A.; Pecchi, É.; Vilmen, C.; le Fur, Y.; Bernard, M.; Bendahan, D.; Giannesini, B. Capsiate supplementation reduces oxidative cost of contraction in exercising mouse skeletal muscle in vivo. *PLoS ONE* **2015**, *1*, e0128016. [[CrossRef](#)] [[PubMed](#)]
40. Langenberg, C.; Wan, L.; Egi, M.; May, C.N.; Bellomo, R. Renal blood flow in experimental septic acute renal failure. *Kidney Int.* **2006**, *69*, 1996–2002. [[CrossRef](#)] [[PubMed](#)]
41. Jung, S.H.; Kim, H.J.; Oh, G.S.; Shen, A.; Lee, S.; Choe, S.K.; Park, R.; So, H.S. Capsaicin ameliorates cisplatin-induced renal injury through induction of heme oxygenase-1. *Mol. Cells* **2014**, *37*, 234–240. [[CrossRef](#)] [[PubMed](#)]
42. Baird, M.F.; Graham, S.M.; Baker, J.S.; Bickerstaff, G.F. Creatine-kinase- and exercise-related muscle damage implications for muscle performance and recovery. *J. Nutr. Metab.* **2012**, *2012*, 960363. [[CrossRef](#)] [[PubMed](#)]
43. Houmard, J.A.; Costill, D.L.; Mitchell, J.B.; Park, S.H.; Fink, W.J.; Burns, J.M. Testosterone, cortisol, and creatine kinase levels in male distance runners during reduced training. *Int. J. Sports Med.* **1990**, *11*, 41–45. [[CrossRef](#)] [[PubMed](#)]
44. Hargreaves, M. Skeletal muscle metabolism during exercise in humans. *Clin. Exp. Pharmacol. Physiol.* **2000**, *27*, 225–228. [[CrossRef](#)] [[PubMed](#)]
45. Kim, K.M.; Kawada, T.; Ishihara, K.; Inoue, K.; Fushiki, T. Increase in swimming endurance capacity of mice by capsaicin-induced adrenal catecholamine secretion. *Biosci. Biotechnol. Biochem.* **1997**, *61*, 1718–1723. [[CrossRef](#)] [[PubMed](#)]
46. Kwon, D.Y.; Kim, Y.S.; Ryu, S.Y.; Cha, M.R.; Yon, G.H.; Yang, H.J.; Kim, M.J.; Kang, S.; Park, S. Capsiate improves glucose metabolism by improving insulin sensitivity better than capsaicin in diabetic rats. *J. Nutr. Biochem.* **2013**, *24*, 1078–1085. [[CrossRef](#)] [[PubMed](#)]
47. Koopmans, S.J.; Leighton, B.; DeFronzo, R.A. Neonatal de-afferentation of capsaicin-sensitive sensory nerves increases in vivo insulin sensitivity in conscious adult rats. *Diabetologia* **1998**, *41*, 813–820. [[CrossRef](#)] [[PubMed](#)]



48. Hassan, M.H.; Edfawy, M.; Mansour, A.; Hamed, A.A. Antioxidant and antiapoptotic effects of capsaicin against carbon tetrachloride-induced hepatotoxicity in rats. *Toxicol. Ind. Health* **2012**, *28*, 428–438. [[CrossRef](#)] [[PubMed](#)]
49. Tsuda, H.; Kawada, N.; Kaimori, J.Y.; Kitamura, H.; Moriyama, T.; Rakugi, H.; Takahara, S.; Isaka, Y. Febuxostat suppressed renal ischemia-reperfusion injury via educed oxidative stress. *Biochem. Biophys. Res. Commun.* **2012**, *427*, 266–272. [[CrossRef](#)] [[PubMed](#)]
50. Zhou, F.W.; Li, Y.J.; Deng, H.W. Early and delayed protection by capsaicin against reperfusion injury in rat hearts. *Eur. PMC* **1999**, *20*, 912–916.
51. Li, L.; Chen, J.; Ni, Y.; Feng, X.; Zhao, Z.; Wang, P.; Sun, J.; Yu, H.; Yan, Z.; Liu, D.; et al. TRPV1 activation prevents nonalcoholic fatty liver through UCP2 upregulation in mice. *Pflugers Arch.* **2012**, *463*, 727–732. [[CrossRef](#)] [[PubMed](#)]



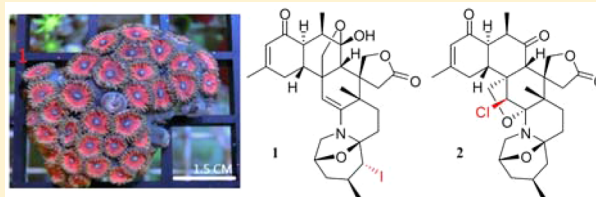
© 2016 by the authors; licensee MDPI, Basel, Switzerland. This article is an open access article distributed under the terms and conditions of the Creative Commons Attribution (CC-BY) license (<http://creativecommons.org/licenses/by/4.0/>).



Zoanthamine-Type Alkaloids from the Zoanthid *Zoanthus kuroshio* Collected in Taiwan and Their Effects on InflammationYu-Ming Hsu,<sup>†,‡</sup> Fang-Rong Chang,<sup>†,‡,||,§,⊥,‡</sup> I-Wen Lo,<sup>†</sup> Kuei-Hung Lai,<sup>†,▽</sup> Mohamed El-Shazly,<sup>○</sup> Tung-Ying Wu,<sup>□</sup> Ying-Chi Du,<sup>†</sup> Tsong-Long Hwang,<sup>△,○,¶</sup> Yuan-Bin Cheng,<sup>\*,†,‡,■</sup> and Yang-Chang Wu<sup>\*,†,□,▽,●,▲</sup><sup>†</sup>Graduate Institute of Natural Products, College of Pharmacy, <sup>‡</sup>Center for Infectious Disease and Cancer Research, <sup>||</sup>Research Center for Environmental Medicine, and <sup>■</sup>Research Center for Natural Products & Drug Development, Kaohsiung Medical University, Kaohsiung 80708, Taiwan<sup>§</sup>Department of Marine Biotechnology and Resources, National Sun Yat-sen University, Kaohsiung 80424, Taiwan<sup>⊥</sup>Cancer Center, Kaohsiung Medical University Hospital, Kaohsiung 80708, Taiwan<sup>▽</sup>Division of Pharmacognosy, Department of Medicinal Chemistry, Uppsala University, 75105 Uppsala, Sweden<sup>○</sup>Department of Pharmacognosy and Natural Products Chemistry, Faculty of Pharmacy, Ain-Shams University, Cairo 11566, Egypt<sup>□</sup>Chinese Medicine Research and Development Center and <sup>▼</sup>Center for Molecular Medicine, China Medical University Hospital, Taichung 40402, Taiwan<sup>△</sup>Graduate Institute of Natural Products, College of Medicine, Chang Gung University, Taoyuan 33302, Taiwan<sup>○</sup>Research Center for Industry of Human Ecology, Research Center for Chinese Herbal Medicine, and Graduate Institute of Health Industry Technology, Chang Gung University of Science and Technology, Taoyuan 33302, Taiwan<sup>¶</sup>Department of Anesthesiology, Chang Gung Memorial Hospital, Taoyuan 33302, Taiwan<sup>●</sup>School of Pharmacy, College of Pharmacy, and <sup>▲</sup>Research Center for Chinese Herbal Medicine, China Medical University, Taichung 40402, Taiwan

## S Supporting Information

**ABSTRACT:** *Zoanthus kuroshio* is a colorful zoanthid with a fluorescent pink oral disc and brown tentacles, which dominates certain parts of the Taiwanese and Japanese coasts. This sea anemone is a rich source of biologically active alkaloids. In the current investigation, two novel halogenated zoanthamines [5*α*-iodozoanthamine (1) and 11*β*-chloro-11-deoxykuroshine A (2)], along with four new zoanthamines [18-*epi*-kuroshine A (3), 7*α*-hydroxykuroshine E (4), 5*α*-methoxykuroshine E (5), and 18-*epi*-kuroshine E (6)], and six known compounds were isolated from *Z. kuroshio*. Compounds 1 and 2 are the first examples of halogenated zoanthamine-type alkaloids isolated from nature. Compounds 3 and 6 are the first zoanthamine stereoisomers with a *cis*-junction of the A/B rings. All isolated compounds were evaluated for their anti-inflammatory activities by measuring their effects on superoxide anion generation and elastase release by human neutrophils in response to fMLP.



Zoanthamine-type alkaloids, isolated from *Zoanthus* sea anemone species, belong to a specific family of marine alkaloids.<sup>1</sup> The framework of zoanthamine-type alkaloids is recognized by its densely functionalized fragments, an 8-oxa-6-azabicyclo[3.2.1] ring and a  $\beta$ -methyl enone functionality, within the octacyclic ring system. These zoanthamines are divided into two structural groups depending on the presence of a methyl group at C-19 (type I) or not (type II).<sup>2</sup> Type I structures are further categorized into two subgroups, a group with a six-membered lactone ring constructed by the connection of C<sub>9</sub>–C<sub>10</sub>–C<sub>22</sub>–C<sub>23</sub>–C<sub>24</sub> (Ia) and another group with a five-membered lactone ring formed by the connection of C<sub>22</sub>–C<sub>23</sub>–C<sub>24</sub>–C<sub>25</sub> (Ib). So far, only 28 zoanthamines have been reported since the first isolate was identified.<sup>3</sup> The densely functionalized structures of the zoanthamines along with their

multiple stereogenic centers hindered their synthesis for almost 20 years after their first isolation.<sup>4</sup>

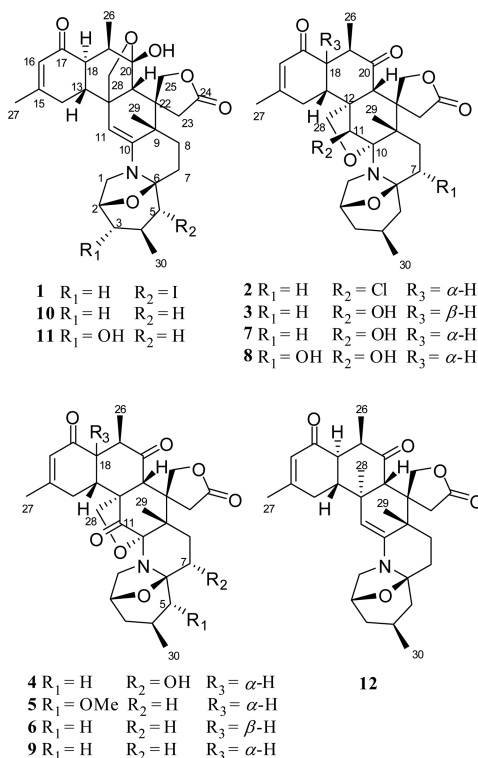
The main attractiveness of zoanthamine-type alkaloids is not only the unique skeleton but also their potential pharmacological properties. The pharmacological activities of zoanthamines have been studied extensively, demonstrating antiplatelet aggregation,<sup>5</sup> antiosteoporotic,<sup>6,7</sup> anti-inflammatory,<sup>8</sup> antibacterial,<sup>9</sup> and cytotoxic activities.<sup>10</sup> However, the mechanisms of action for most zoanthamines remain undefined except for norzoanthamine, a promising antiosteoporotic agent,

Received: July 7, 2016

Published: October 19, 2016

which suppressed the loss of bone weight through the inhibition of IL-6 secretion.<sup>6</sup>

In previous studies, most of the isolated zoanthamine-type alkaloids were found to belong to a type Ia or type II skeleton.<sup>2</sup> However, all of the nine zoanthamine-type alkaloids (kuroshines A–G, 3 $\beta$ -hydroxyzoanthenamide, and 7 $\alpha$ -hydroxyzoanthenamide) isolated from *Zoanthus kuroshio* by our group possessed the less common Ib-type skeleton.<sup>11,12</sup> This unique structural feature encouraged us to continue investigating other zoanthamine-type alkaloids from *Z. kuroshio*. In the current study, we isolated 12 zoanthamines, including six new alkaloids [5 $\alpha$ -iodozoanthenamine (1), 11 $\beta$ -chloro-11-deoxykuroshine A (2), 18-*epi*-kuroshine A (3), 7 $\alpha$ -hydroxykuroshine E (4), 5 $\alpha$ -methoxykuroshine E (5), and 18-*epi*-kuroshine E (6)] and six known components [kuroshines A, D, and E (7, 8, and 9),<sup>11,12</sup> zoanthenamine (10),<sup>8</sup> 3 $\beta$ -hydroxyzoanthenamide (11),<sup>12</sup> and 28-deoxyzoanthenamide (12)<sup>5</sup>]. Among those isolates, 5 $\alpha$ -iodozoanthenamine (1) and 11 $\beta$ -chloro-11-deoxykuroshine A (2) are the first halogenated examples of zoanthamines isolated from nature. In addition, 18-*epi*-kuroshine A (3) and 18-*epi*-kuroshine E (6) are two 18-epimeric zoanthamines with a *cis*-junction of the A/B rings, which are also reported for the first time. In the current study, the isolation, purification, structure elucidation, and anti-inflammatory activities of zoanthamine-type alkaloids from *Z. kuroshio* were carried out.



## RESULTS AND DISCUSSION

The ethanolic extracts of the freeze-dried zoanthid materials (*Z. kuroshio*) collected in Kaohsiung City (batch 1) and Taitung County (batch 2) were analyzed by NMR to identify if their major secondary metabolites belong to the rare Ib-type skeleton. The results showed similar NMR fingerprints, with the characteristic signals of the five-membered lactone ring of type Ib at  $\delta_{\text{H}}$  4.00–5.00 ppm (Figures S1 and S2). The small quantity obtained in each collection along with the similar

NMR fingerprints encouraged us to combine the extracts of batches 1 and 2, hoping to isolate more zoanthamine-type alkaloids with the Ib-type skeleton. Thus, the combined extracts were partitioned between EtOAc and H<sub>2</sub>O to yield two layers. The organic layer was further partitioned between *n*-hexane and 80% aqueous MeOH. The aqueous methanolic extract was subjected to column chromatography using Sephadex LH-20 and Si-60 silica gel, as well as reversed-phase HPLC, to yield six new (1–6) and six known (7–12) zoanthamines.

Compound 1 was obtained as a white, amorphous powder, and its molecular formula (C<sub>30</sub>H<sub>38</sub>INO<sub>6</sub>) was confirmed by the analysis of its <sup>13</sup>C NMR and HRESIMS data ( $m/z$  658.1637 [M + Na]<sup>+</sup>). The IR spectrum showed hydroxy (3419 cm<sup>−1</sup>),  $\gamma$ -lactone (1769 cm<sup>−1</sup>), and  $\alpha,\beta$ -unsaturated ketone (1714 cm<sup>−1</sup>) vibration bands. Together with the maximum UV absorption at 237 nm, compound 1 was suggested to be a zoanthamine-type alkaloid.<sup>3</sup> Furthermore, the detailed analysis of the characteristic NMR signals indicated that 1 was a derivative of zoanthenamine (10) (Tables 1 and 2).<sup>8</sup> The only differences were the methylene signal of 10 at C-5 was replaced by a methine and the carbon signal was deshielded from  $\delta_{\text{C}}$  44.5 to 54.1. Regarding the molecular formula, a fragment peak at  $m/z$  509 [M − I + H]<sup>+</sup> was observed in the ESIMS spectra, suggesting the presence of an iodine atom. The connection of the iodine atom to C-5 was suggested by the correlations between H-1/H-2/H-3 in the COSY spectrum and H-5/C-30 and H<sub>3</sub>-30/C-3, C-4, and C-5 in the HMBC spectrum. The remaining planar structure of 1 was confirmed by the key COSY and HMBC correlations (Figure 1).

The relative configuration of 1 was assigned on the basis of a NOESY experiment, and the NOESY correlations (Figure 1) were compared to those of 3 $\beta$ -hydroxyzoanthenamide (11).<sup>12</sup> The same NOESY correlations between H-21/H-13, H-25a, H<sub>3</sub>-26, and H<sub>3</sub>-29 in 1 and 11 indicated that they were located on the  $\beta$ -face. Simultaneously, the cross-peaks between H-18/H-19 and H-28b supported the  $\alpha$ -orientation of these protons. In addition, the strong NOESY correlations between H<sub>3</sub>-29/H-7b and H-5/H-7a and H<sub>3</sub>-30 as well as the coupling constant between H-4 and H-5 (7.2 Hz) suggested a diaxial arrangement of these hydrogens, which revealed the orientation of the iodine atom at C-5 as  $\alpha$ . Thus, the structure of 1 was elucidated and named 5 $\alpha$ -iodozoanthenamine.

Compound 2 was purified as a white, amorphous powder. It was found to possess a chloride atom as inferred from the ESIMS protonated molecule peaks [M + H]<sup>+</sup> at  $m/z$  543 and 545 in a 3:1 ratio, which are characteristic peaks of a monochlorinated compound. The exact masses of [M + Na]<sup>+</sup> at  $m/z$  566.2278 and 568.2249 matched the molecular formulas of C<sub>30</sub>H<sub>38</sub><sup>35</sup>ClNO<sub>6</sub>Na and C<sub>30</sub>H<sub>38</sub><sup>37</sup>ClNO<sub>6</sub>Na, respectively, which were confirmed with the <sup>13</sup>C NMR data. The absorption bands of the IR spectrum, maximum UV absorption, and the characteristic NMR signals indicated that 2 was a chlorinated derivative of kuroshine A (7) (Tables 1 and 2).<sup>11</sup> However, the shielded signal of C-11 from  $\delta_{\text{C}}$  73.1 to 62.2 and the HMBC correlations between H-11/C-10, C-12, C-21, and C-28, H-21/C-12 and C-22, and H-29/C-9 and C-10 revealed that the hydroxy group at C-11 was replaced by a chlorine atom (Figure 2). The NOE correlations between H-18/H-28a and H-28b, H-11/H-1a, H-1b, H-14eq, and H-28b, and H-13/H-14eq suggested the  $\beta$ -orientation of the chloride substitution at C-11. The other stereochemical details were confirmed by similar cross-peaks shown in the NOESY spectra of 2 and 7 (Figure 2). The absolute configuration of 2 was established as 2R, 4S, 6S,

Table 1.  $^1\text{H}$  NMR Data of Compounds 1–6 in  $\text{C}_5\text{D}_5\text{N}^a$ 

no.	1	2	3	4	5	6
1a	3.15, t (5.6)	3.11, d (6.4)	3.32, d (6.8)	2.86, dd (4.8, 0.4)	2.73, d (6.6)	2.76, d (7.2)
1b	3.43, d (5.6)	3.39, t (6.4)	3.65, t (6.8)	3.80, t (4.8)	3.96, t (6.6)	3.73, t (7.2)
2	4.55, m	4.52, m	4.51, m	4.57, m	4.49, m	4.78, m
3a	1.53, m	1.38, m	1.46, m	1.47, m	1.49, m	1.37, m
3b	1.59, m					
4	1.33, m	2.13, m	2.21, m	2.35, m	2.21, m	2.12, m
5a	3.93, d (7.2)	1.09, t (12.0)	1.13, t (11.6)	2.10, t (9.2)	2.89, d (10.2)	1.10, d (6.0)
5b		2.24, dd (12.0, 5.2)	2.31, m	2.21, dd (9.2, 3.2)		2.16, t (6.0)
7a	2.35, t (7.6)	1.66, dt (12.0, 3.2)	1.70, dt (12.0, 3.2)	4.27, d (8.0)	1.83, m	1.68, dt (12.6, 3.6)
7b	2.46, d (8.8)	1.87, td (13.2, 3.2)	1.96, td (13.2, 3.2)		2.01, dt (11.2, 3.6)	1.80, td (12.0, 3.6)
8a	1.64, m	1.24, m	1.23, dt (12.8, 3.2)	2.02, dd (12.6, 4.8)	1.46, m	1.36, m
8b	2.92, td (10.0, 4.0)	2.28, td (13.4, 3.2)	2.29, m	2.67, t (13.2)	2.97, td (12.9, 3.6)	2.25, td (16.2, 4.2)
11	4.41, s	4.63, s	4.47, d (4.8)			
13	2.23, s	3.02, m	2.68, m	3.28, ddd (14.1, 11.7, 4.8)	3.24, ddd (14.1, 11.7, 4.8)	3.53, m
14a	2.06, ddd (14.8, 4.8, 1.8)	2.61, m	2.11, m	2.53, dd (18.0, 12.9)	2.47, m	2.30, dd (19.8, 4.8)
14b	2.25, ddd (24.0, 12.0, 6.0)			2.71, dd (18.0, 4.2)	2.71, dd (18.0, 4.8)	2.64, dd (14.4, 4.8)
16	6.04, s	6.07, s	5.91, s	6.02, s	6.01, s	6.00, s
18	2.83, dd (8.8, 3.6)	2.64, d (9.6)	2.59, d (13.6)	2.66, dd (14.4, 4.8)	2.60, dd (13.2, 4.2)	2.94, t (4.2)
19	2.65, t (4.8)	3.52, m	3.31, m	3.47, dd (7.8, 4.8)	3.44, dd (7.2, 4.2)	3.40, dd (7.8, 4.2)
21	2.46, s	3.43, d (1.2)	4.01, s	3.63, d (0.8)	3.60, d (1.2)	3.52, s
23a	3.27, d (12.0)	3.58, s	3.54, d (18.4)	3.83, d (12.8)	3.87, d (19.2)	3.64, d (3.0)
23b	4.22, d (12.0)		3.98, d (18.4)	3.92, d (12.8)	4.09, d (19.2)	
25a	4.46, d (6.4)	4.43, d (9.6)	4.17, d (10.0)	4.26, d (6.8)	4.28, d (10.2)	4.13, d (10.2)
25b	5.51, d (6.4)	4.51, d (9.6)	4.56, d (10.0)	4.52, d (6.8)	4.42, d (10.2)	4.38, d (10.2)
26	1.42, d (4.8)	1.21, d (7.2)	1.30, d (7.6)	1.24, d (4.8)	1.23, d (7.2)	1.27, d (7.8)
27	1.92, s	1.92, s	1.78, s	1.89, s	1.87, s	1.75, s
28a	3.74, d (5.6)	4.12, d (8.8)	3.83, q (9.2)	4.51, d (6.0)	4.39, d (9.6)	4.03, d (14.0)
28b	4.14, d (5.6)	4.27, d (8.8)		4.64, d (6.0)	4.60, dd (9.6, 1.2)	4.05, d (14.0)
29	1.25, s	1.34, s	1.50, s	1.20, s	1.09, s	1.07, s
30	1.02, d (4.4)	0.84, d (6.4)	0.90, d (3.2)	0.89, d (4.4)	0.96, d (6.6)	0.81, d (6.0)
$\text{OCH}_3$					3.42, s	

<sup>a</sup>1, 4, 5, and 6 were measured at 600 MHz NMR; 2 and 3 were measured at 400 MHz NMR.

9S, 10S, 11R, 12S, 13R, 15Z, 18R, 19R, 21R, 22R by comparing the specific rotation data of 2 with those of 7, the absolute configuration of which was determined by X-ray single-crystallographic analysis using Cu K $\alpha$  radiation in our previous study.<sup>11</sup> Therefore, the structure of 2 was determined, and the trivial name 11 $\beta$ -chloro-11-deoxykuroshine A was given.

Compound 3 was also obtained as a white, amorphous powder. The molecular formula ( $\text{C}_{30}\text{H}_{39}\text{NO}_7$ ) was deduced from HRESIMS and  $^{13}\text{C}$  NMR data, indicating that 3 possessed the same molecular formula as 7.<sup>11</sup> Furthermore, similar signals in the 1D NMR spectra (Tables 1 and 2) and close correlations in the COSY and HMBC experiments between 3 and 7 (Figure 2) indicated that they both possessed the same planar structure. Originally, we assumed that 3 and 7 are one compound; however, they were separated into two peaks in the HPLC chromatogram. Through comparing the NOESY spectra of 3 and 7, we found that the only difference between these compounds was the orientation of H-18. Significant NOESY correlations between H-18/H-13 and H<sub>3</sub>-26 and H-21/H-25a, H<sub>3</sub>-26, and H<sub>3</sub>-29 were observed in 3, which were different from those in 7 (correlations between H-21/H-13, H-25, H<sub>3</sub>-26, and H<sub>3</sub>-29 and H-18/H-19), indicating a *cis*-junction of the A/B rings in 3 (Figure 2). Therefore, the orientation of H-18 in 3 was assigned as  $\beta$  rather than  $\alpha$  as in 7. On the basis of the above-mentioned NOESY correlations and by comparing the specific rotation data with those of 7, the absolute configuration of 3 was determined as 2R, 4S, 6S, 9S, 10S, 11R, 12S, 13R, 15Z,

18S, 19R, 21R, 22R. Thus, compound 3 was identified as an epimer of 7 and named 18-*epi*-kuroshine A.

Compound 4 was isolated as a white, amorphous powder, and its molecular formula ( $\text{C}_{30}\text{H}_{37}\text{NO}_8$ ) was confirmed by the analysis of its  $^{13}\text{C}$  NMR, DEPT, and HRESIMS data. Compound 4 was proposed to be a hydroxylated derivative of kuroshine E (9) by the closely similar NMR signals (Tables 1 and 2) and the replacement of a methylene group ( $\delta_{\text{H}}$  1.71;  $\delta_{\text{C}}$  30.0) in 9 by an oxymethine ( $\delta_{\text{H}}$  4.27;  $\delta_{\text{C}}$  69.0) in 4, which showed 16 mass units more than 9 in the HRESIMS spectrum.<sup>12</sup> The hydroxy group at C-7 in 4 was confirmed by the COSY correlations between H-7/H<sub>2</sub>-8 and the HMBC correlations between H-7/C-6, H<sub>2</sub>-8/C-7 and C-9, and H<sub>3</sub>-29/C-8 (Figure 3). The orientation of OH-7 was assigned as  $\alpha$  based on the NOESY correlations between the  $\beta$ -oriented H-8a/H-7, H-25b, and H<sub>3</sub>-29 and H-8b/H-23b (Figure 3). Thus, 4 was assigned as 7 $\alpha$ -hydroxykuroshine E.

Compound 5 was suggested to be another analogue of 9 based on the spectroscopic data. HRESIMS and  $^{13}\text{C}$  NMR data of 5 suggested the molecular formula  $\text{C}_{31}\text{H}_{39}\text{NO}_8\text{Na}$ . The assignments of the  $^1\text{H}$  and  $^{13}\text{C}$  NMR signals, which were assisted by extended 2D NMR methods, indicated that 5 is an analogue of kuroshine E (9)<sup>12</sup> bearing one secondary methoxy group ( $\delta_{\text{H}}$  3.42;  $\delta_{\text{C}}$  61.3) (Tables 1 and 2). The methoxy group was confirmed at C-5 by the key COSY [H-3/H-4/H-5 and H<sub>3</sub>-30/H-4] and HMBC [ $\text{OCH}_3$ /C-5] correlations, and the  $\alpha$ -orientation was supported by the NOESY correlations between H<sub>3</sub>-29/H-21 and H-7a and between H-5/H-7b and H<sub>3</sub>-30

Table 2.  $^{13}\text{C}$  NMR Data of Compounds 1–6 in  $\text{C}_5\text{D}_5\text{N}^a$ 

no.	1	2	3	4	5	6
1	58.1, $\text{CH}_2$	46.3, $\text{CH}_2$	47.0, $\text{CH}_2$	47.2, $\text{CH}_2$	47.2, $\text{CH}_2$	46.8, $\text{CH}$
2	73.4, $\text{CH}$	73.7, $\text{CH}$	73.9, $\text{CH}$	74.5, $\text{CH}$	73.9, $\text{CH}$	74.2, $\text{CH}$
3	39.2, $\text{CH}_2$	39.1, $\text{CH}_2$	39.5, $\text{CH}_2$	39.2, $\text{CH}_2$	39.3, $\text{CH}_2$	39.0, $\text{CH}_2$
4	35.7, $\text{CH}$	23.3, $\text{CH}$	23.5, $\text{CH}$	23.0, $\text{CH}$	31.2, $\text{CH}$	23.2, $\text{CH}$
5	54.1, $\text{CH}$	44.4, $\text{CH}_2$	44.8, $\text{CH}_2$	37.4, $\text{CH}_2$	94.3, $\text{CH}$	43.6, $\text{CH}_2$
6	89.7, $\text{C}$	90.5, $\text{C}$	90.6, $\text{C}$	94.4, $\text{C}$	90.3, $\text{C}$	90.0, $\text{C}$
7	32.6, $\text{CH}_2$	30.0, $\text{CH}_2$	30.5, $\text{CH}_2$	69.0, $\text{CH}$	28.9, $\text{CH}_2$	30.0, $\text{CH}_2$
8	26.7, $\text{CH}_2$	28.8, $\text{CH}_2$	28.0, $\text{CH}_2$	35.8, $\text{CH}_2$	26.8, $\text{CH}_2$	26.4, $\text{CH}_2$
9	45.5, $\text{C}$	44.7, $\text{C}$	46.8, $\text{C}$	47.4, $\text{C}$	47.4, $\text{C}$	46.8, $\text{C}$
10	148.5, $\text{C}$	96.8, $\text{C}$	96.4, $\text{C}$	94.6, $\text{C}$	94.3, $\text{C}$	94.6, $\text{C}$
11	96.2, $\text{CH}$	62.2, $\text{CH}$	81.1, $\text{CH}$	206.1, $\text{C}$	206.6, $\text{C}$	206.1, $\text{C}$
12	30.0, $\text{C}$	52.0, $\text{C}$	50.4, $\text{C}$	56.1, $\text{C}$	56.2, $\text{C}$	56.1, $\text{C}$
13	45.0, $\text{CH}$	32.9, $\text{CH}$	39.1, $\text{CH}$	32.1, $\text{CH}$	32.2, $\text{CH}$	31.4, $\text{CH}$
14	31.0, $\text{CH}_2$	28.9, $\text{CH}_2$	30.2, $\text{CH}_2$	30.9, $\text{CH}_2$	30.8, $\text{CH}_2$	31.9, $\text{CH}_2$
15	159.9, $\text{C}$	161.5, $\text{C}$	161.5, $\text{C}$	162.0, $\text{C}$	162.0, $\text{C}$	160.6, $\text{C}$
16	127.2, $\text{CH}$	126.9, $\text{CH}$	124.9, $\text{CH}$	126.7, $\text{CH}$	126.7, $\text{CH}$	126.4, $\text{CH}$
17	199.8, $\text{C}$	196.5, $\text{C}$	197.5, $\text{C}$	196.2, $\text{C}$	196.3, $\text{C}$	196.7, $\text{C}$
18	48.7, $\text{CH}$	45.8, $\text{CH}$	44.5, $\text{CH}$	47.0, $\text{CH}$	46.9, $\text{CH}$	49.6, $\text{CH}$
19	44.4, $\text{CH}$	46.3, $\text{CH}$	50.3, $\text{CH}$	45.8, $\text{CH}$	45.8, $\text{CH}$	43.3, $\text{CH}$
20	112.1, $\text{C}$	212.4, $\text{C}$	215.6, $\text{C}$	210.2, $\text{C}$	210.3, $\text{C}$	210.3, $\text{C}$
21	44.2, $\text{CH}$	49.6, $\text{CH}$	45.3, $\text{CH}$	57.5, $\text{CH}$	57.2, $\text{CH}$	56.3, $\text{CH}$
22	41.3, $\text{C}$	47.6, $\text{C}$	44.8, $\text{C}$	51.6, $\text{C}$	48.9, $\text{C}$	49.9, $\text{C}$
23	34.8, $\text{CH}_2$	35.2, $\text{CH}_2$	34.5, $\text{CH}_2$	34.8, $\text{CH}_2$	34.3, $\text{CH}_2$	34.4, $\text{CH}_2$
24	178.5, $\text{C}$	178.6, $\text{C}$	178.9, $\text{C}$	178.1, $\text{C}$	178.7, $\text{C}$	178.0, $\text{C}$
25	72.3, $\text{CH}_2$	74.4, $\text{CH}_2$	74.0, $\text{CH}_3$	74.0, $\text{CH}_2$	73.7, $\text{CH}_2$	73.8, $\text{CH}_2$
26	13.3, $\text{CH}_3$	13.4, $\text{CH}_3$	16.4, $\text{CH}_3$	13.5, $\text{CH}_3$	13.5, $\text{CH}_3$	17.0, $\text{CH}_3$
27	24.1, $\text{CH}_3$	24.4, $\text{CH}_3$	23.8, $\text{CH}_3$	24.3, $\text{CH}_3$	24.2, $\text{CH}_3$	23.5, $\text{CH}_3$
28	73.2, $\text{CH}_2$	66.0, $\text{CH}_2$	66.6, $\text{CH}_3$	65.7, $\text{CH}_2$	65.2, $\text{CH}_2$	66.7, $\text{CH}_2$
29	24.2, $\text{CH}_3$	25.8, $\text{CH}_3$	23.9, $\text{CH}_3$	22.2, $\text{CH}_3$	21.5, $\text{CH}_3$	20.6, $\text{CH}_3$
30	22.4, $\text{CH}_3$	24.4, $\text{CH}_3$	22.2, $\text{CH}_3$	22.5, $\text{CH}_3$	18.3, $\text{CH}_3$	22.1, $\text{CH}_3$
$\text{OCH}_3$					61.3, $\text{CH}_3$	

<sup>a</sup>1, 4, 5, and 6 were measured at 150 MHz NMR; 2 and 3 were measured at 100 MHz NMR.

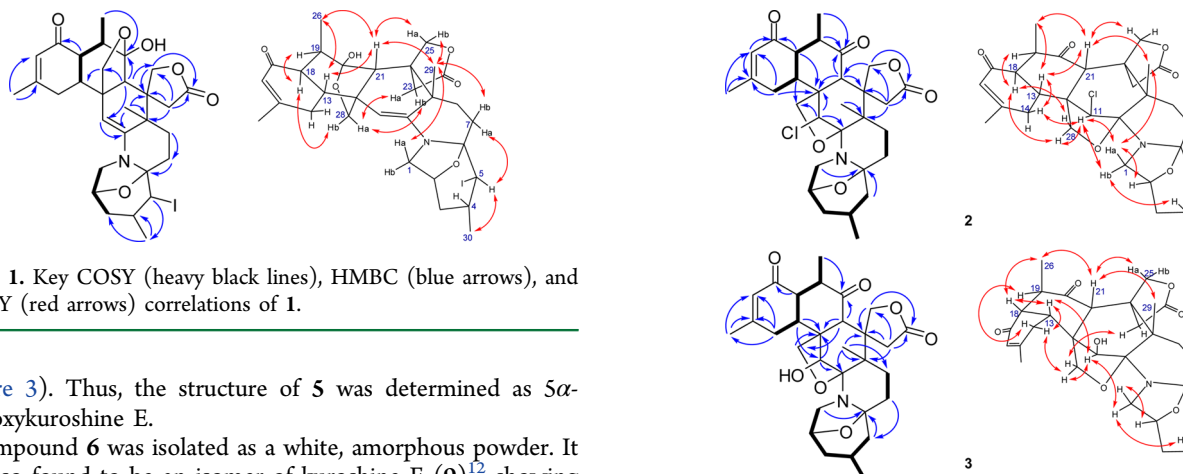


**Figure 1.** Key COSY (heavy black lines), HMBC (blue arrows), and NOESY (red arrows) correlations of 1.

(Figure 3). Thus, the structure of 5 was determined as 5 $\alpha$ -methoxykuroshine E.

Compound 6 was isolated as a white, amorphous powder. It was also found to be an isomer of kuroshine E (9)<sup>12</sup> showing the same molecular formula of  $\text{C}_{30}\text{H}_{37}\text{NO}_7$  from HRESIMS and  $^{13}\text{C}$  NMR data. Through comparing the COSY and HMBC correlations in 6 and 9, it was found that both compounds possessed the same planar structure (Figure 3). The stereo-configuration of 6 was almost the same as that of 9 except at C-18. The NOESY correlations between H-13/H-18 and H<sub>3</sub>-26 and between H-21/H-25a, H<sub>3</sub>-26, and H<sub>3</sub>-29 indicated that H-18 in 6 was  $\beta$ -oriented (Figure 3). The structure of 6 was determined as 18-*epi*-kuroshine E.

In our previous study on zoanthamine-type alkaloids, kuroshine A (7) was the only compound to be studied by X-

**Figure 2.** Key COSY (heavy black lines), HMBC (blue arrows), and NOESY (red arrows) correlations of 2 and 3.

ray single-crystallographic analysis using Cu K $\alpha$  radiation, and its absolute configuration was established based on this analysis.<sup>11</sup> In the current study, the isolated zoanthamine-type alkaloids possessed very similar structures and were isolated from the same organism, and thus it was proposed to share a similar biogenetic pathway. On the basis of this proposal, compounds 4–6 were suggested to possess the same absolute



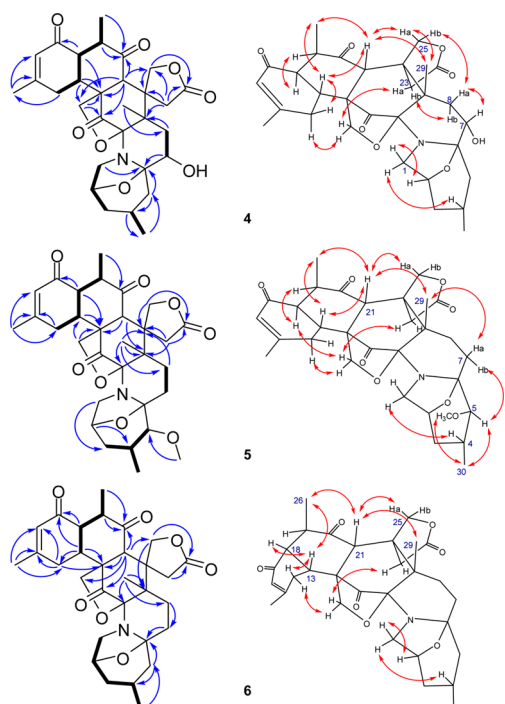


**Figure 3.** Key COSY (heavy black lines), HMBC (blue arrows), and NOESY (red arrows) correlations of 4–6.

configuration as 7. Thus, the absolute configurations for the main skeleton of compounds 4 and 5 were proposed as 2*R*, 4*S*, 6*S*, 9*S*, 10*S*, 12*S*, 13*R*, 15*Z*, 18*R*, 19*R*, 21*R*, 22*R*, and those at C-7 of 4 and C-5 of 5 were deduced as *S* and *R*, respectively. Furthermore, the absolute configuration of 6, the 18-epimer of 7, was suggested as 2*R*, 4*S*, 6*S*, 9*S*, 10*S*, 12*S*, 13*R*, 15*Z*, 18*S*, 19*R*, 21*R*, 22*R*.

**Anti-inflammatory Effects of Zoanthamines 1–12 on Superoxide Anion and Elastase Release Assays.** All isolated compounds in this study were evaluated for their anti-inflammatory activities by measuring their effects on superoxide anion generation and elastase release by human neutrophils in response to fMLP (Table 3). LY294002, a phosphatidylinositol-3-kinase inhibitor, was used as a positive control. Among the tested compounds, 1 showed the most potent inhibitory activity on both superoxide anion generation ( $24 \pm 6\%$ ) and elastase release ( $43 \pm 2\%$ ). In addition, most of the tested zoanthamines, except for 2, 3, 4, 7, and 10, showed greater inhibition of elastase release. Interestingly, compound 1, the 5-iodo-substituted derivatives of 10, showed more potent inhibitory activity on elastase release than 10. Also, the inhibitory activity on elastase release of 2, the chloro-substituted derivatives of 7, was 3-fold more than 7. According to literature reviews, halogenated derivatives of marine natural products usually possess more potent effects on different bioassays compared with the nonhalogenated analogues.<sup>13</sup> A similar phenomenon was also observed in our anti-inflammatory screening assay. Thus, the role of halogen atoms in promoting the anti-inflammatory activity of the zoanthamines is worthy of further detailed investigation. Several factors should be considered upon studying the effect of the halogen atoms on the activity of zoanthamines such as halogen position and orientation and electrostatic, steric, and lipophilic effects.

In this study, six new zoanthamine-type alkaloids were isolated from the Taiwanese zoanthid *Z. kuroshio*, together with

**Table 3.** Inhibitory Effects of *Z. kuroshio* Isolates on Superoxide Anion Generation and Elastase Release in FMLP/CB-Induced Human Neutrophils

compound	percentage of inhibition (Inh%) <sup>a</sup>	
	superoxide anion	elastase release
5 <i>α</i> -iodozoanthamine (1)	$24 \pm 6^{**}$	$43 \pm 2^{***}$
11 <i>β</i> -chloro-11-deoxykuroshine A (2)	$23 \pm 6^*$	$25 \pm 3^{**}$
18- <i>epi</i> -kuroshine A (3)	$15 \pm 6$	$13 \pm 7$
7 <i>α</i> -hydroxykuroshine E (4)	$13 \pm 3^*$	$15 \pm 4^*$
5 <i>α</i> -methoxykuroshine E (5)	$20 \pm 5^*$	$33 \pm 7^{**}$
18- <i>epi</i> -kuroshine E (6)	$14 \pm 5^*$	$23 \pm 6^{**}$
kuroshine A (7)	$9 \pm 4$	$6 \pm 2^*$
kuroshine D (8)	$11 \pm 3^*$	$27 \pm 5^{**}$
kuroshine E (9)	$7 \pm 3$	$27 \pm 7^*$
zoanthamine (10)	$17 \pm 4^*$	$17 \pm 5^*$
3 <i>β</i> -hydroxyzoanthamine (11)	$14 \pm 5^*$	$25 \pm 6^*$
28-deoxyzoanthamine (12)	$18 \pm 6^*$	$30 \pm 6^{**}$
LY294002 <sup>b</sup>	$99 \pm 1^{***}$	$73 \pm 1^{***}$

<sup>a</sup>Percentage of inhibition (Inh%) at 10  $\mu$ M concentration. Results are presented as mean  $\pm$  SEM ( $n = 3, 4$ ). <sup>\*</sup> $P < 0.05$ , <sup>\*\*</sup> $P < 0.01$ , <sup>\*\*\*</sup> $P < 0.001$  compared with the control value. <sup>b</sup>LY294002 was used as the positive control.

six known zoanthamines. The halogenated zoanthamines (1 and 2) and 18-*epi*-zoanthamines (3 and 6) were isolated for the first time from natural sources. The anti-inflammatory activities of 1–12 were evaluated by superoxide anion and elastase release assays. Among the tested compounds, the iodinated zoanthamine 1 showed the most significant anti-inflammatory effect on inhibiting superoxide anion generation and elastase release at 10  $\mu$ M ( $24 \pm 6\%$  and  $43 \pm 2\%$ , respectively).

## EXPERIMENTAL SECTION

**General Experimental Procedures.** Optical rotations were measured with a JASCO P-2000 polarimeter, whereas IR spectra were obtained on a JASCO FT/IR-4600 spectrometer. <sup>1</sup>H and <sup>13</sup>C NMR spectra were recorded on Varian VNMR-600 instruments (600 and 150 MHz for <sup>1</sup>H and <sup>13</sup>C, respectively) and Varian INOVA 400 spectrometers (400 and 100 MHz for <sup>1</sup>H and <sup>13</sup>C, respectively). All NMR experiments were performed at room temperature, using C<sub>3</sub>D<sub>8</sub>N or CDCl<sub>3</sub> as the solvent. Chemical shifts were referenced to residual solvent signals for C<sub>3</sub>D<sub>8</sub>N ( $\delta_H$  7.21 and  $\delta_C$  123.5) and CDCl<sub>3</sub> ( $\delta_H$  7.26 and  $\delta_C$  77.0 ppm). LRESIMS were measured on a VG Biotech Quattro 5022 mass spectrometer. HRESIMS data were collected using a Bruker Daltonics APEX II mass spectrometer. Silica gel 60 (Merck, 70–230 and 230–400 mesh) and Sephadex LH-20 were used for column chromatography (CC), while TLC analyses were carried out on silica gel F<sub>254</sub> and RP-18 F<sub>254s</sub> precoated plates, and the spots were detected using 50%<sub>(aq)</sub> H<sub>2</sub>SO<sub>4</sub> and Dragendorff's reagent followed by heating on a hot plate. HPLC analyses were performed with Shimadzu SPD-M10A DAD and Shimadzu SPD-20A UV instruments.

**Animal Material.** Specimens of *Zoanthus kuroshio* were collected in Kaohsiung City (September 2012) and Taitung County (July 2014), Taiwan. The animal material was identified by Dr. Wei-Chun Liu. A voucher specimen (code no. KMU-Z7-1) was deposited in the Graduate Institute of Natural Products, College of Pharmacy, Kaohsiung Medical University, Kaohsiung, Taiwan.

**Separation and Isolation of Compounds 1–12.** The freeze-dried animal materials of *Z. kuroshio* were extracted with 95% EtOH at room temperature three times. The collected extracts were combined and concentrated under reduced pressure to obtain the ethanolic extracts. The concentrated EtOH extract (23.9 g) was partitioned between EtOAc and H<sub>2</sub>O to yield two layers. The EtOAc layer was then partitioned between *n*-hexane and MeOH/H<sub>2</sub>O (8:2) layers. The MeOH/H<sub>2</sub>O extract (3.4 g) was subjected to Sephadex LH-20 CC,

eluting with MeOH, to yield five subfractions (Fr. S1 to S5). After checking with Dragendorff's reagent, fraction S2 (1.5 g), the alkaloid-rich fraction, was further chromatographed on Si-60 silica gel using CH<sub>2</sub>Cl<sub>2</sub>/MeOH (30:1) to obtain six fractions (Fr. S2-1 to S2-6).

Fraction S2-1 (75.6 mg) was purified by reversed-phase HPLC (Phenomenex C18, 10 mm × 250 mm, flow rate = 2 mL/min, 75% MeOH/H<sub>2</sub>O, isocratic elution), and four subfractions were collected (Fr. S2-1-H1 to S2-1-H4). Compound 9 (48.2 mg) was obtained from the subfraction S2-1-H1. Subfraction S2-1-H4 (3.4 mg) was further purified by reversed-phase HPLC (Phenomenex C18, 10 mm × 250 mm, flow rate = 2 mL/min, 70% MeOH/H<sub>2</sub>O, isocratic elution) to afford 2 (2.1 mg).

Compound 9 (105.5 mg) also precipitated from Fr. S2-2 (575.9 mg). The rest of Fr. S2-2 was subjected to SPE, eluting with a stepped gradient of MeOH/H<sub>2</sub>O (30:70, 40:60, 50:50, 60:40, 70:30, 80:20, 90:10, 100:0; 3 × 100 mL fractions were collected for each solvent system), and six subfractions were obtained (Fr. S2-2-E1 to S2-2-E2). Fraction S2-2-E1 (83.7 mg) was purified by reversed-phase HPLC (Phenomenex C18, 10 mm × 250 mm, flow rate = 2 mL/min, 50% CH<sub>3</sub>CN/H<sub>2</sub>O, isocratic elution) to afford 5 (2.6 mg) and 6 (2.8 mg).

Fraction S2-3 (424.6 mg) was purified by reversed-phase HPLC (Phenomenex phenyl-hexyl, 10 mm × 250 mm, flow rate = 2 mL/min, 80% MeOH/H<sub>2</sub>O, with 0.05% NH<sub>4</sub>OH, isocratic elution), and five fractions (Fr. S2-3-H1 to S2-3-H5) were obtained. From Fr. S2-3-H2, S2-3-H3, and S2-3-H4, compounds 10 (227.1 mg), 12 (3.0 mg), and 1 (3.4 mg) were purified, respectively. Fraction S2-3-H1 (79.3 mg) was further purified by reversed-phase HPLC (Phenomenex C18, 10 mm × 250 mm, flow rate = 2 mL/min, 60% MeOH/H<sub>2</sub>O, isocratic elution), and compounds 3 (11.6 mg) and 7 (36.4 mg) were obtained.

Fraction S2-4 (275.2 mg) was subjected to SPE, eluting with a stepped gradient of CH<sub>3</sub>CN/H<sub>2</sub>O (10:90, 20:80, 30:70, 40:60, 50:50, 60:40, 70:30, 80:20, 90:10, 100:0; 3 × 100 mL fractions were collected for each solvent system), to afford six subfractions (Fr. S2-4-E1 to S2-4-E6). Fraction S2-4-E3 (64.4 mg) was then purified by reversed-phase HPLC (Phenomenex phenyl-hexyl, 10 mm × 250 mm, flow rate = 2 mL/min, 33% CH<sub>3</sub>CN/H<sub>2</sub>O with 0.05% NH<sub>4</sub>OH, isocratic elution), and 10 fractions (Fr. S2-4-E3-H1 to S2-4-E3-H10) were obtained. Among these fractions, S2-4-E3-H3 and S2-4-E3-H6 were pure compounds 6 (1.9 mg) and 11 (1.4 mg), respectively. Fraction S2-4-E3-H9 (6.2 mg) was further purified by reversed-phase HPLC (Phenomenex C18, 10 mm × 250 mm, flow rate = 2 mL/min, 40% CH<sub>3</sub>CN/H<sub>2</sub>O, isocratic elution) to provide 4 (2.6 mg).

**5*α*-Iodozoanthenaminate (1):** amorphous white powder; [ $\alpha$ ]<sub>D</sub><sup>25</sup> −78 (c 0.01, MeOH); UV (MeOH)  $\lambda_{\max}$  (log  $\epsilon$ ) 237 (4.3) nm; IR (neat)  $\nu_{\max}$  3419, 2925, 2853, 1769, 1714, 1696, 1658, 1590, 1457, 1394 cm<sup>−1</sup>; <sup>1</sup>H NMR (C<sub>5</sub>D<sub>5</sub>N, 600 MHz) and <sup>13</sup>C NMR (C<sub>5</sub>D<sub>5</sub>N, 150 MHz) data, Tables 1 and 2; ESIMS  $m/z$  636 [M + H]<sup>+</sup>; HRESIMS  $m/z$  658.1637 [M + Na]<sup>+</sup> (calcd for C<sub>30</sub>H<sub>38</sub>INO<sub>6</sub>Na, 658.2280).

**11*β*-Chloro-11-deoxykuroshine A (2):** amorphous, white powder; [ $\alpha$ ]<sub>D</sub><sup>25</sup> −150 (c 0.01, MeOH); UV (MeOH)  $\lambda_{\max}$  (log  $\epsilon$ ) 238 (4.0) nm; IR (neat)  $\nu_{\max}$  3418, 2893, 1771, 1706, 1658, 1588, 1382, 1268, 1206 cm<sup>−1</sup>; <sup>1</sup>H NMR (C<sub>5</sub>D<sub>5</sub>N, 400 MHz) and <sup>13</sup>C NMR (C<sub>5</sub>D<sub>5</sub>N, 100 MHz) data, Tables 1 and 2; ESIMS  $m/z$  544 [M + H]<sup>+</sup>; HRESIMS  $m/z$  566.2278 [M + Na]<sup>+</sup> (calcd for C<sub>30</sub>H<sub>38</sub><sup>35</sup>ClNO<sub>6</sub>Na, 566.2280).

**18-*epi*-Kuroshine A (3):** amorphous, white powder; [ $\alpha$ ]<sub>D</sub><sup>25</sup> −110 (c 0.01, MeOH); UV (MeOH)  $\lambda_{\max}$  (log  $\epsilon$ ) 239 (3.8) nm; IR (neat)  $\nu_{\max}$  3430, 2926, 1756, 1698, 1658, 1592, 1430, 1369, 1263, 1206, 1149 cm<sup>−1</sup>; <sup>1</sup>H NMR (C<sub>5</sub>D<sub>5</sub>N, 400 MHz) and <sup>13</sup>C NMR (C<sub>5</sub>D<sub>5</sub>N, 100 MHz) data, Tables 1 and 2; ESIMS  $m/z$  526 [M + H]<sup>+</sup>; HRESIMS  $m/z$  548.2618 [M + Na]<sup>+</sup> (calcd for C<sub>30</sub>H<sub>39</sub>NO<sub>7</sub>Na, 548.2619).

**7*α*-Hydroxykuroshine E (4):** amorphous, white powder; [ $\alpha$ ]<sub>D</sub><sup>25</sup> −8.4 (c 0.01, MeOH); UV (MeOH)  $\lambda_{\max}$  (log  $\epsilon$ ) 236 (3.8) nm; IR (neat)  $\nu_{\max}$  3431, 2954, 1766, 1714, 1655, 1588, 1382, 1347, 1317, 1258, 1181 cm<sup>−1</sup>; <sup>1</sup>H NMR (C<sub>5</sub>D<sub>5</sub>N, 600 MHz) and <sup>13</sup>C NMR (C<sub>5</sub>D<sub>5</sub>N, 150 MHz) data, Tables 1 and 2; ESIMS  $m/z$  540 [M + H]<sup>+</sup>; HRESIMS  $m/z$  562.2410 [M + Na]<sup>+</sup> (calcd for C<sub>30</sub>H<sub>37</sub>NO<sub>8</sub>Na, 562.2411).

**5*α*-Methoxykuroshine E (5):** amorphous, white powder; [ $\alpha$ ]<sub>D</sub><sup>25</sup> −110 (c 0.01, MeOH); UV (MeOH)  $\lambda_{\max}$  (log  $\epsilon$ ) 237 (4.1) nm; IR (neat)  $\nu_{\max}$  3432, 2942, 1766, 1712, 1656, 1594, 1380, 1314, 1258, 1186, 1094 cm<sup>−1</sup>; <sup>1</sup>H NMR (C<sub>5</sub>D<sub>5</sub>N, 600 MHz) and <sup>13</sup>C NMR

(C<sub>5</sub>D<sub>5</sub>N, 150 MHz) data, Tables 1 and 2; ESIMS  $m/z$  554 [M + H]<sup>+</sup>; HRESIMS  $m/z$  576.2566 [M + Na]<sup>+</sup> (calcd for C<sub>31</sub>H<sub>39</sub>NO<sub>8</sub>Na, 576.2568).

**18-*epi*-Kuroshine E (6):** amorphous, white powder; [ $\alpha$ ]<sub>D</sub><sup>25</sup> −120 (c 0.01, MeOH); UV (MeOH)  $\lambda_{\max}$  (log  $\epsilon$ ) 237 (4.1) nm; IR (neat)  $\nu_{\max}$  3397, 2954, 1768, 1712, 1658, 1429, 1373, 1319, 1268, 1211, 1144, 1101 cm<sup>−1</sup>; <sup>1</sup>H NMR (C<sub>5</sub>D<sub>5</sub>N, 600 MHz) and <sup>13</sup>C NMR (C<sub>5</sub>D<sub>5</sub>N, 150 MHz) data, Tables 1 and 2; ESIMS  $m/z$  524 [M + H]<sup>+</sup>; HRESIMS  $m/z$  546.2462 [M + Na]<sup>+</sup> (calcd for C<sub>30</sub>H<sub>37</sub>NO<sub>7</sub>Na, 546.2462).

**Kuroshine A (7):** [ $\alpha$ ]<sub>D</sub><sup>25</sup> −40 (c 0.3, MeOH), which was reported in our previous study as [ $\alpha$ ]<sub>D</sub><sup>25</sup> −35 (c 0.5, MeOH).<sup>11</sup>

**Superoxide Anion and Elastase Release Assays.** Human neutrophils were prepared from healthy human donors (20–35 years old) by venipuncture, using a protocol approved by the institutional review board at Chang Gung Memorial Hospital (102-1595A3). Neutrophils were isolated using a standard method as previously described.<sup>14</sup>

**Measurement of Superoxide Generation.** Inhibition ratio (%) of superoxide dismutase (SOD) was measured by the reduction of ferricytochrome *c* as previously described.<sup>14</sup> Neutrophils were equilibrated in 0.5 mg/mL ferricytochrome *c* and 1 mM Ca<sup>2+</sup> ion solution at 37 °C for 2 min and then incubated with the test compounds for 5 min. Cells were activated with formyl-methionyl-leucyl-phenylalanine (fMLP, 100 nM)/cytochalasin B (CB, 1  $\mu$ g/mL) for 10 min. The absorbance was continuously monitored at 550 nm using a Hitachi U-3010 double-beam six-cell positioned spectrophotometer with constant stirring. Calculations were based on the differences in absorbance with and without SOD (100 U/mL), and the extinction coefficient for reduction of ferricytochrome *c* to ferrocyclochrome *c* ( $\epsilon$  = 21.1/mM/10 mm) was used.

**Measurement of Elastase Release.** Elastase release was measured by the degranulation of azurophilic granules.<sup>14</sup> Neutrophils were equilibrated in MeO-Suc-Ala-Ala-Pro-Val-*p*-nitroanilide (100  $\mu$ M), an elastase substrate, at 37 °C for 2 min and then incubated with the test compounds for 5 min. Cells were activated by 100 nM fMLP and 0.5  $\mu$ g/mL CB, and changes in the absorbance at 405 nm were continuously monitored to detect the elastase release. The results are expressed as the percent of the initial rate of elastase release in the fMLP/CB-activated, drug-free control system.

## ■ ASSOCIATED CONTENT

### § Supporting Information

The Supporting Information is available free of charge on the ACS Publications website at DOI: 10.1021/acs.jnatprod.6b00625.

<sup>1</sup>H NMR spectra for the extracts of batches 1 and 2; 1D and 2D NMR and HRESIMS spectra of compounds 1–6 (PDF)

## ■ AUTHOR INFORMATION

### Corresponding Authors

\*Tel: +886-7-3121101, ext. 2162. Fax: +886-7-3114773. E-mail: jmb@kmu.edu.tw (Y.-B. Cheng).

\*Tel: +886-4-22057153. Fax: +886-4-22060248. E-mail: yachwu@mail.cmu.edu.tw (Y.-C. Wu).

### Author Contributions

#Y.-M. Hsu and F.-R. Chang contributed equally to this work.

### Notes

The authors declare no competing financial interest.

## ■ ACKNOWLEDGMENTS

We gratefully acknowledge the financial support for the projects from the Ministry of Science and Technology of Taiwan (NSC 102-2628-B-037-003-MY3, MOST 103-2320-B-037-005-MY2, awarded to F.-R.C., MOST103-2628-B-037-001-MY3 award to



Y.-B.C., and MOST 105-2911-I-002-302, 103-2911-I-002-303, 103-2325-B-039-008, 103-2325-B-039-007-CC1, and 102-2320-B-037-012-MY2, awarded to Y.-C.W.). This study is also partially supported by Kaohsiung Medical University (Aim for the Top Universities Grant, grant no. KMU-TP104E39, KMU-TP104A26), Ministry of Health and Welfare of Taiwan (MOHW105-TDU-B-212-134007), and Health and Welfare Surcharge of Tobacco Products. This work was also in-kind supported by grants from the National Health Research Institutes (NHRI-EX103-10241BI) and a grant from the Chinese Medicine Research Center, China Medical University (Ministry of Education, Aim for the Top University Plan). HRESIMS was supported by the Joint Center for High Valued Instrument, National Sun Yat-sen University; 400 and 600 MHz NMR as well as ESIMS were supported by Center for Research Resources and Development, Kaohsiung Medical University.

## ■ REFERENCES

- (1) Cen-Pacheco, F.; Norte, M.; Fernández, J. J.; Daranas, A. H. *Org. Lett.* **2014**, *16*, 2880–2883.
- (2) Behenna, D. C.; Stockdill, J. L.; Stoltz, B. M. *Angew. Chem., Int. Ed.* **2008**, *47*, 2365–2386.
- (3) Rao, C. B.; Anjaneyula, A. S. R.; Sarma, N. S.; Venkateswarlu, Y. *J. Am. Chem. Soc.* **1984**, *106*, 7983–7984.
- (4) Miyashita, M.; Sasaki, M.; Hattori, I.; Sakai, M.; Tanino, K. *Science* **2004**, *305*, 495–499.
- (5) Villar, R. M.; JoseGil-Longo; Daranas, A. H.; Souto, M. L.; Fernandez, J. J.; Peixinho, S.; Barral, M. A.; Santafe, G.; Rodriguez, J.; Jimenez, C. *Bioorg. Med. Chem.* **2003**, *11*, 2301–2306.
- (6) Kuramoto, M.; Hayashi, K.; Yamaguchi, K.; Yada, M.; Tsuji, T.; Uemura, D. *Bull. Chem. Soc. Jpn.* **1998**, *71*, 771–779.
- (7) Yamaguchi, K.; Yada, M.; Tsuji, T.; Kuramoto, M.; Uemura, D. *Biol. Pharm. Bull.* **1999**, *22*, 920–924.
- (8) Rao, C. B.; Anjaneyulu, A. S. R.; Sarma, N. S.; Venkateswarlu, Y.; Rosser, R. M.; Faulkner, D. J. *J. Org. Chem.* **1985**, *50*, 3757–3760.
- (9) Venkateswarlu, Y.; Srinivasa Reddy, N.; Ramesh, P.; Srinivasa Reddy, P.; Jamil, K. *Heterocycl. Commun.* **1998**, *4*, 575–580.
- (10) Hirai, G.; Oguri, H.; Hayashi, M.; Koyama, K.; Koizumi, Y.; Moharram, S. M.; Hiram, M. *Bioorg. Med. Chem. Lett.* **2004**, *14*, 2647–2651.
- (11) Cheng, Y.-B.; Lan, C.-C.; Liu, W.-C.; Lai, W.-C.; Tsai, Y.-C.; Chiang, M. Y.; Wu, Y.-C.; Chang, F.-R. *Tetrahedron Lett.* **2014**, *55*, 5369–5372.
- (12) Cheng, Y.-B.; Lo, I.-W.; Shyur, L.-F.; Yang, C.-C.; Hsu, Y.-M.; Su, J.-H.; Lu, M.-C.; Chiou, S.-F.; Lan, C.-C.; Wu, Y.-C.; Chang, F.-R. *Tetrahedron* **2015**, *71*, 8601–8606.
- (13) Blunt, J. W.; Copp, B. R.; Keyzers, R. A.; Munro, M. H. G.; Prinsep, M. R. *Nat. Prod. Rep.* **2016**, *33*, 382–431.
- (14) Yang, S.-C.; Chung, P.-J.; Ho, C.-M.; Kuo, C.-Y.; Hung, M.-F.; Huang, Y.-T.; Chang, W.-Y.; Chang, Y.-W.; Chan, K.-H.; Hwang, T.-L. *J. Immunol.* **2013**, *190*, 6511–6519.

## Article

# Fractional CO<sub>2</sub> Laser Pretreatment Facilitates Transdermal Delivery of Two Vitamin C Derivatives

Chien-Yu Hsiao <sup>1,2,3</sup>, Hsin-Ching Sung <sup>3,4</sup>, Sindy Hu <sup>3,5,6</sup>, Yau-Li Huang <sup>3,5,6</sup> and Chun-Hsun Huang <sup>2,3,6,\*</sup>

<sup>1</sup> Department of Nutrition and Health Sciences, Chang Gung University of Science and Technology, Taoyuan 333, Taiwan; chienyuhhsiao@sina.com

<sup>2</sup> Research Center for Industry of Human Ecology and Research Center for Chinese Herbal Medicine, College of Human Ecology, Chang Gung University of Science and Technology, Taoyuan 33301, Taiwan

<sup>3</sup> Aesthetic Medical Center, Department of Dermatology, Chang Gung Memorial Hospital, Taoyuan 333, Taiwan; hsinchingsungs@sina.com (H.-C.S.); sindyhuh@sina.com (S.H.); yaulihuangh@sina.com, (Y.-L.H.)

<sup>4</sup> Department of Anatomy, College of Medicine, Chang Gung University, Taoyuan 333, Taiwan

<sup>5</sup> College of Medicine, Chang Gung University, Taoyuan 333, Taiwan

<sup>6</sup> Department of Cosmetic Science, Chang Gung University of Science and Technology, Taoyuan 333, Taiwan

\* Correspondence: chuang@gw.cgust.edu.tw; Tel.: +886-3-2118999 (ext. 5848); Fax: +886-3-2118768

Academic Editor: Yogeshvar N. Kalia

Received: 19 July 2016; Accepted: 10 November 2016; Published: 16 November 2016

**Abstract:** Background: Topical vitamin C derivatives have been used to treat melasma and used as a skin whitener. The aim of this study was to compare skin histology and permeation of L-ascorbic acid 2-phosphate sesquimagnesium salt (MAP-1) and magnesium L-ascorbic acid-2-phosphate (MAP-2) after fractional CO<sub>2</sub> laser pretreatment. Methods: The effect of fractional laser treatment on porcine skin was examined by scanning electron microscopy and confocal laser scanning electron microscopy. The effect of fractional CO<sub>2</sub> laser treatment of different fluencies and pass numbers on transdermal flux of the two vitamin C derivatives through porcine skin was examined in vitro using a Franz diffusion chamber. Results: Fluxes of MAP-1 and MAP-2 across fractional CO<sub>2</sub> laser-treated (5 W) skin were eight- to 13-fold, and 20- to 22-fold higher, respectively, than the fluxes of these compounds across intact skin. Fluxes of MAP-1 and MAP-2 across fractional CO<sub>2</sub> laser-treated (9 W) skin were 14- to 19-fold, and 30- to 42-fold higher, respectively, than their fluxes across intact skin. Conclusion: Fractional CO<sub>2</sub> laser treatment is an effective way of delivering vitamin C derivatives into the skin.

**Keywords:** vitamin C derivatives; fractional CO<sub>2</sub> laser; transdermal delivery

## 1. Introduction

Vitamin C inhibits melanogenesis, promotes collagen synthesis, and has antioxidant properties [1–6]. Due to these actions, it has been used topically to restore aged skin and as a skin whitener [4,7,8]. Vitamin C itself undergoes rapid breakdown, which makes the use of stable derivatives more practical. To reach its site of action, vitamin C and its derivatives must penetrate through the stratum corneum into the skin layers underneath. The stratum corneum is composed of a layer of cornified cells and an intracellular, lipid-rich area [9,10]. Hydrophilic compounds, like vitamin C and its derivatives, can enter the hydrophilic interior of the cells in the stratum corneum, but, unlike lipophilic compounds [11,12], cannot cross the lipid-containing region underneath and, therefore, penetrate through the outer layer of the stratum corneum very poorly after topical treatment. Laser treatment can remove the stratum corneum with little damage to the skin layers underneath [13]. Therefore, laser treatment is one way to increase permeability to hydrophilic compounds [14]. However, conventional laser treatment causes the ablation of the entire skin surface, and a period of several days is required for the skin surface to recover fully [15]. Fractional laser treatment is a non-invasive treatment that uses a device to deliver a

laser beam divided into thousands of microscopic treatment zones (“micropores”) that target a fraction of the skin at a time. Fractional laser treatment has been used to increase topical absorption of a number of compounds, including vitamin C derivatives [11,14–17].

CO<sub>2</sub> and Er:YAG lasers have both been used to increase skin permeability. Both lasers ablate the stratum corneum, but the CO<sub>2</sub> laser also produces thermal effects below the stratum corneum that can enhance transdermal delivery [18–22]. Our early comparison between the effects of conventional Er:YAG and CO<sub>2</sub> laser pre-treatment on transdermal delivery of two vitamin C derivatives, 2-O-ethyl ascorbic acid and ascorbic acid 2-glucoside, showed that the two derivatives differed in their responsiveness to laser pre-treatment, and that the CO<sub>2</sub> laser was more effective than the Er:YAG laser on both compounds [16]. An optimal fluency for the CO<sub>2</sub> laser was not determined in this study. A later comparison of the effects of Er:YAG and CO<sub>2</sub> laser pre-treatment on transdermal permeability of three additional vitamin C derivatives, 2-phospho-L-ascorbic acid trisodium salt, L-ascorbic acid 2-phosphate sesquimagnesium salt (MAP-1), and magnesium L-ascorbic acid-2-phosphate (MAP-2), showed that these also differed in their responsiveness to laser pre-treatment, that CO<sub>2</sub> laser pre-treatment was more effective than Er:YAG laser pre-treatment, and that optimal fluency was the same (5 W) for all three derivatives [15].

Having demonstrated that conventional CO<sub>2</sub> laser treatment was more effective than the conventional Er:YAG laser in increasing permeability for the five vitamin C derivatives examined, we then investigated whether fractional CO<sub>2</sub> laser pre-treatment, which causes less skin damage, could equal conventional CO<sub>2</sub> laser treatment in increasing transdermal permeability. In these studies, we found that four passes of the fractional CO<sub>2</sub> laser caused similar permeability but less skin disruption than conventional CO<sub>2</sub> laser treatment for two skin whiteners (the vitamin C derivative ascorbic acid 2-glucoside and a chemically-unrelated skin whitener, tranexamic acid) and that as fluency increased, the number of passes needed to produce results similar to those of conventional CO<sub>2</sub> laser pretreatment decreased [13,17].

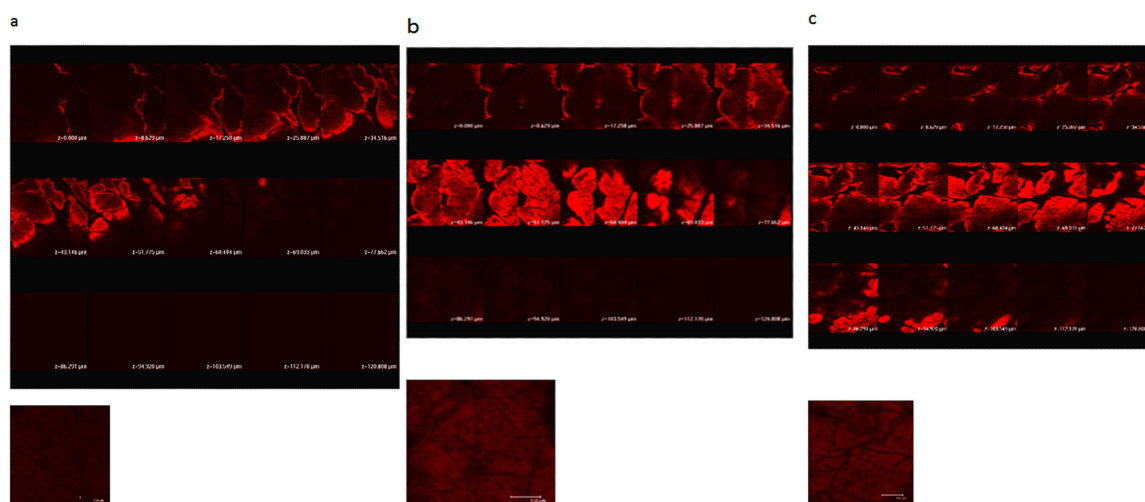
Comparisons between CO<sub>2</sub> laser treatment-induced permeabilities of different vitamin C derivatives are incomplete. The normalized flux of the 2-phospho-L-ascorbic acid trisodium salt through CO<sub>2</sub> laser pretreated porcine skin at fluencies of 5 W and 9 W has been reported to be higher than that for the magnesium derivatives MAP-1 and MAP-2, but no studies of the effect of fractional laser pretreatment on this vitamin C derivative have been done [13], and CO<sub>2</sub> laser pretreatment of nude mouse skin has reported O-ethyl ascorbic acid to have higher fluency at 5 W and 7 W than ascorbic acid 2-glucoside, but no comparable studies have been performed on porcine skin [16].

There is no standard pretreatment fractional CO<sub>2</sub> laser procedure for MAP-1 and MAP-2 delivery. In the present study, we examined permeation of these two vitamin C derivatives through porcine skin at different fluencies and pass numbers of fractional CO<sub>2</sub> laser pretreatment in order to help the clinician determine the fluency and number of passes that will result in a combination of optimal permeation and minimal skin damage.

## 2. Results

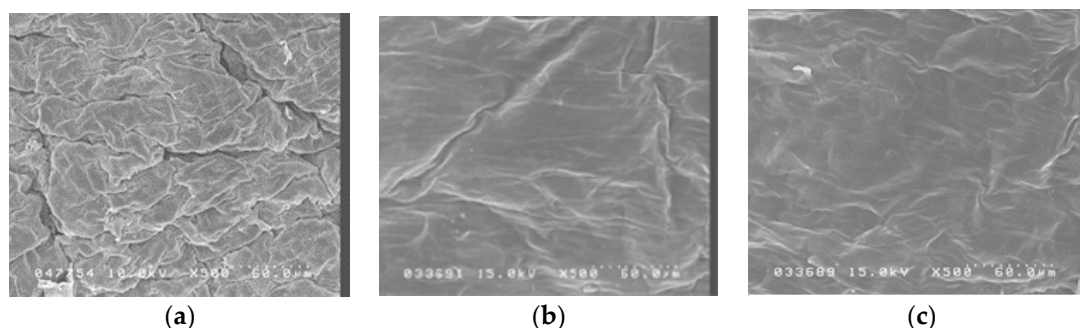
### 2.1. Ultrastructure of Fractional Laser Treatment of Porcine Skin

Figure 1 shows confocal scanning electron microscopy of porcine skin after 5 W and 9 W fractional CO<sub>2</sub> laser treatment. Untreated skin shows low permeation of the test compound used, rhodamine B, a compound with a molecular weight similar to MAP-1 and MAP-2. Fractional laser treatment causes permeation of rhodamine B, and permeation is deeper when the higher fluency is used.



**Figure 1.** Confocal laser scanning microscopic (CLSM) micrographs of porcine skin after in vitro topical administration of rhodamine B via the skin by laser pretreatment: (a) Non-treatment group; (b) Fractional CO<sub>2</sub> laser treatment at 12 mm, 5 W; (c) Fractional CO<sub>2</sub> laser treatment at 12 mm, 9 W (original magnification, 20 $\times$ ). The skin specimen was viewed by CLSM at 8- $\mu$ m increments through the Z-axis. The images below the photographs of the 15 fragments are the sum of all fragments.

Figure 2 shows scanning electron micrographs of porcine skin after 5 W and 9 W fractional CO<sub>2</sub> laser treatment. Untreated skin (Figure 1a) shows intact, regularly arranged, overlapping corneocytes. Fractional laser treatment at 5 W and 9 W shows some irregularity, but no disruption, of the skin surface.



**Figure 2.** Scanning electron microscopy (SEM) observations (magnification 500 $\times$ ) of porcine skin. (a) Without any treatment; (b) Fractional CO<sub>2</sub> laser treatment at 12 mm, 5 W; (c) Fractional CO<sub>2</sub> laser treatment at 12 mm, 9 W.

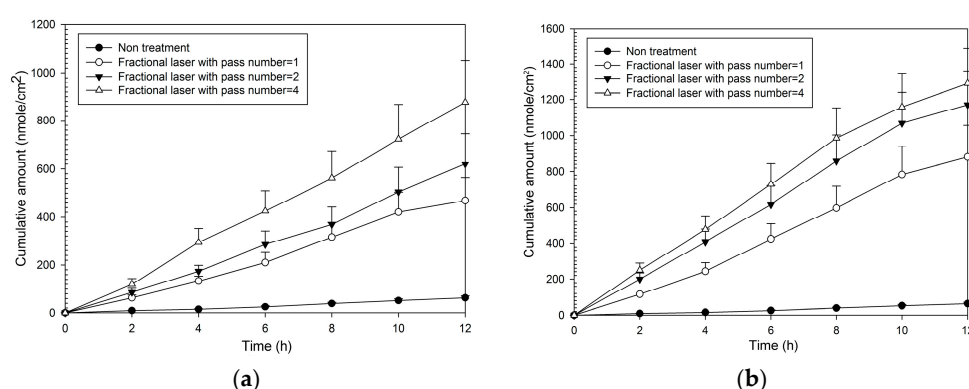
## 2.2. Normalized Fluxes of MAP-1 Across Porcine Skin after Fractional CO<sub>2</sub> Laser Pretreatment

Fluxes and enhancement ratios for MAP-1 were significantly increased compared to no treatment at each pass number at both fluencies (Table 1). Enhancement ratios for MAP-2 ranged from 8–13 at 5 W and from 14–19 at 9 W. The cumulative amount with time (Figure 3) was also increased at both fluencies compared to no laser pretreatment, and increased as fluency and pass number increased. It was only necessary to produce a small number of microscopic pores with fractional treatment to cause a large relative increase in flux, for one pass at 5 W (that is, covering only 2% of the treatment area with the microscopic pores, caused an eight-fold increase in flux compared to no treatment).

**Table 1.** MAP-1 normalized fluxes across porcine skin after pretreatment with a fractional CO<sub>2</sub> laser (*n* = 8 for each fluency condition).

Fluence (W)	Pass Number	Flux ‡ (nmol/cm <sup>2</sup> /h)	Enhancement Ratio † (ER)
0 (no treatment)	0	5.62 ± 0.89 <sup>a</sup>	1
5	1	43.09 ± 5.89 <sup>b</sup>	8
	2	55.65 ± 6.92 <sup>b</sup>	10
	4	74.40 ± 8.16 <sup>c</sup>	13
9	1	80.28 ± 11.02 <sup>c</sup>	14
	2	101.15 ± 16.58 <sup>c</sup>	18
	4	107.83 ± 15.22 <sup>c</sup>	19

Each value is represented as mean ± SD (*n* = 8). † Enhancement ratio (ER) is the flux of the laser-pretreated group/flux of the no-treatment group, that is, fluence = 0 W and pass number = 0. NA: Not assessed. ‡ *p* < 0.05 through one-way ANOVA test with a post-hoc Duncan test *a* < *b* < *c*.

**Figure 3.** Cumulative amount of time profiles of in vitro transdermal permeation through porcine skin of MAP-1, after fractional CO<sub>2</sub> laser pre-treatment with a 12 mm spot size and different pass numbers at (a) 5 W and (b) 9 W fluence.

### 2.3. Normalized Fluxes of MAP-2 Across Porcine Skin after Pretreatment with a Fractional Laser

As with MAP-1, all combinations of fractional laser pass number and fluency caused significantly greater flux than that seen with no fractional laser pre-treatment (Table 2). Enhancement ratios were greater than those seen with MAP-1 and ranged from 20–22 at 5 W and from 30–42 at 9 W. The pattern of the cumulative amount-time profile of MAP-2 (Figure 4) was similar with that of MAP-1. However, MAP-1 had a flux rate through untreated skin that was three times that seen with MAP-2, so although enhancement ratios were higher with MAP-2, the actual flux rate through fractional laser-treated skin was higher with MAP-1.

**Table 2.** MAP-2 normalized fluxes across porcine skin after pretreatment with a fractional CO<sub>2</sub> laser (*n* = 8 for each fluency condition).

Fluence (W)	Pass Number	Flux ‡ (nmol/cm <sup>2</sup> /h)	Enhancement Ratio † (ER)
0 (No treatment)	0	1.86 ± 0.43 <sup>a</sup>	1
5	1	37.06 ± 4.22 <sup>b</sup>	20
	2	40.15 ± 5.85 <sup>b</sup>	22
	4	41.72 ± 6.05 <sup>b</sup>	22
9	1	56.06 ± 7.22 <sup>c</sup>	30
	2	73.28 ± 8.02 <sup>d</sup>	39
	4	77.71 ± 8.14 <sup>d</sup>	42

Each value is represented as mean ± SD (*n* = 8). † Enhancement ratio (ER) is the flux of laser-pretreated group/flux of no-treatment group, that is, fluence = 0 W and pass number = 0. NA: Not assessed. ‡ *p* < 0.05 through one-way ANOVA test with a post-hoc Duncan test *a* < *b* < *c* < *d*.

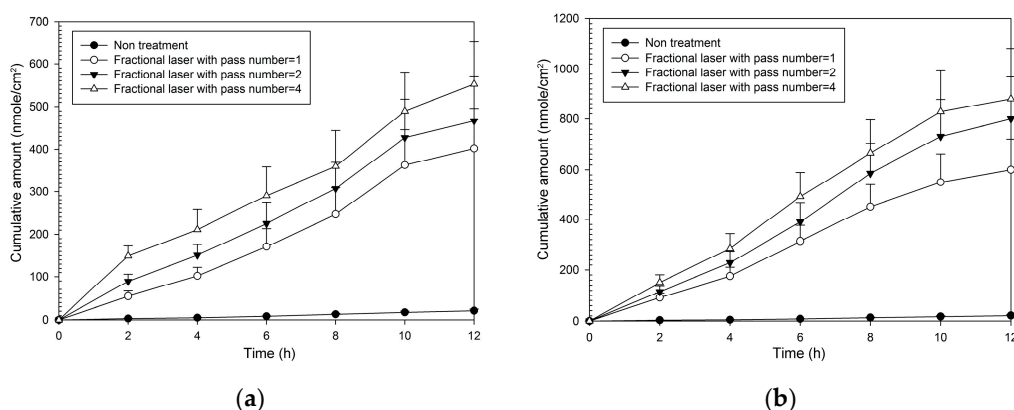


**Figure 4.** Cumulative amount of time profiles of in vitro transdermal permeation through porcine skin of MAP-2, after fractional CO<sub>2</sub> laser pre-treatment with a 12 mm spot size and different pass number at (a) 5 W and (b) 9 W fluence.

### 3. Discussion

Fractional CO<sub>2</sub> laser treatment increased the flux through porcine skin of both MAP-1 and MAP-2, increasing as the pass number increased, and being higher at 9 W than at 5 W. The enhancement ratios seen with MAP-2 were higher than those seen with MAP-1, but the actual flux was greater with MAP-1.

This study is a continuation of our efforts to find optimal conditions to increase transdermal permeation of skin whiteners using laser pretreatment. The current results for MAP-1 and MAP-2 combined with previous results for other compounds show that fractional CO<sub>2</sub> laser pretreatment at appropriate fluencies and pass numbers can produce increases in permeability equivalent to conventional pretreatment. However, they also show that the increase in permeation using fractional laser pre-treatment is very dependent of the specific compound being used, and that some puzzles remain to be investigated. Our results demonstrate such a puzzle. MAP-1 flux is slightly higher than MAP-2 flux in both fractional and conventional [13] laser-treated skin. However, when the normalized flux after conventional and fractional laser pre-treatment are compared, conventional pretreatment produces about twice the normalized flux as fractional pretreatment for MAP-1 and about four times the normalized flux as fractional pre-treatment for MAP-2 (MAP-1, approximately 185 vs. 43–70 nmol/cm<sup>2</sup>/h at 5 W and approximately 230 vs. 80–108 nmol/cm<sup>2</sup>/h at 9 W; MAP-2 approximately 210 vs. 37–42 nmol/cm<sup>2</sup>/h at 5 W and approximately 325 vs. 56–78 nmol/cm<sup>2</sup>/h at 9 W). The physical and chemical barriers in the skin that need to be crossed are the same in fractional and conventional laser pretreatment. The reasons why fractional laser treatment is less effective compared to conventional laser treatment for MAP-2 than for MAP-1 are unknown. Nor is it known why, unlike MAP-1 and MAP-2, another vitamin C derivative, ascorbic acid 2-glucoside, has a normalized flux with fractional treatment that is virtually equal (95%–100%) to that seen with conventional laser treatment [15].

A question which cannot be answered in this study because it was not performed in vivo is whether fractional CO<sub>2</sub> laser treatment caused inflammation or other reactive effects. Fractional laser treatment leaves the majority of skin tissue intact and the corneocytes that remain serve as a reservoir for healing. In other studies, complete reepithelization of the SC after fractional laser treatment has been reported to be complete within one day after treatment [23–26].

The CO<sub>2</sub> laser is thought to enhance the permeation of drugs in the following way. It ablates part of the SC, as can be seen in histopathological observations, an action that increases permeability by reducing the barrier function of this skin layer. It also disrupts the remnant SC structures by photomechanical waves. However coverage of the complete skin surface with conventional CO<sub>2</sub> laser treatment can have undesirable thermal effects. Fractional CO<sub>2</sub> laser treatment, instead of acting



over the entire skin surface, uses SC ablation and photomechanical waves to introduce microscopic channels into the skin to deliver drugs into deeper skin strata in a manner similar to the microneedle technique [27].

Lasers at low fluency can promote drug delivery through precise control of SC removal. They have the advantage of not touching the skin, thus avoiding the risk of contamination, and of having a very short treatment time. Fractional laser treatment is a relatively new procedure accomplished by the placement of numerous microscopic zones of damage in the skin without injuring the surrounding skin. This laser system resurfaces only 5%–20% of the skin at one time and does not cause full epidermal wounds, so healing time is minimized. A disadvantage of laser therapy is that it takes time to determine the laser energy and drug concentration needed to deliver each specific drug through the skin.

We have previously reported on various aspects of laser-induced increases in transdermal permeability for five vitamin C derivatives, but the laser preparations, skin preparations, and objectives vary. In the current study, our goal was to find optimum fractional laser fluency and number of pass information for use in guiding clinical practice. A future useful goal might be to use the available vitamin C derivatives in identical CO<sub>2</sub> laser conditions to study the influence of the specific chemical and physical characteristics of these compounds (such as molecular weight, size, polarity, pH, log partition coefficient) on permeability of porcine skin with no laser treatment, conventional laser treatment, and fractional laser treatment. The information gained would lead to a deeper understanding of the forces determining skin permeation and serve as a guide for future drug design.

#### 4. Materials and Methods

##### 4.1. Ascorbic Acid Derivatives

L-ascorbic acid 2-phosphate sesquimagnesium salt (MAP-1, 289.54) was obtained from Sigma-Aldrich (St. Louis, MO, USA). Magnesium L-ascorbic acid-2-phosphate (MAP-2, 759.22) was obtained from Showa Denko K.K. Company (Tokyo, Japan).

##### 4.2. Laser Assembly and Experimental Protocol

The fractional CO<sub>2</sub> laser used (150XJ, Sharplan Laser Inc., Yokneam, Japan) has an articulated arm and a wavelength of 10,600 nm. Its handpiece created microscopic columns of ablated skin (irradiation dots) that typically have a diameter of 150  $\mu$ m (that is, an area of about 0.018 mm<sup>2</sup>). The treatment area of the handpiece is 12  $\times$  12 mm and contains 160 (13  $\times$  13) irradiation dots, covering 2% of the total treatment area when one pulse of the laser is used. The distance between the laser and the skin was 10 mm, and the duration of the laser treatment was 1–3 s. Skin temperature was not determined after laser treatment, but as can be seen in Figure 2, and experimental skin showed little damage after laser treatment.

One to four passes at fluencies of 5 W and 9 W were used in the current study. The handpiece was rotated when more than one pass was used, so that the irradiation areas did not overlap.

##### 4.3. Porcine Skin Samples

Skin from eight one-week-old, pathogen-free pigs was supplied by the Animal Technology Institute Taiwan (Miaoli, Taiwan). The supplier harvested the dorsal skin after euthanizing the piglets by electrocution, cut the skin to appropriate size, and shipped it directly to the author's laboratory. For these studies, ten 2  $\times$  2 cm<sup>2</sup> portions of dorsal skin were removed from each pig (one for each laser condition), and were further divided as needed. The skin samples were then used for scanning electron microscopy (SEM, Hitachi S-5000, Tokyo, Japan), confocal scanning electron microscopy (CLSM, Leica Microsystems, Mannheim, Germany), and in vitro permeation studies of the two vitamin C derivatives. TEM, SEM, and diffusion assays were all performed on skin from the same pig. Eight pigs were used in all. Due to the many combinations and evaluations conducted in the present study, we needed at

least 200 individual pieces of skin. The skin from one pig can be cut into 20–25 pieces. So eight pigs was a number to use for the study.

#### 4.4. Ultrastructure Examination by Scanning Electron Microscopy

Porcine skin samples either with or without laser treatment were cut into appropriate-sized cubes, immediately fixed in 3% paraformaldehyde and 2% glutaraldehyde in 0.1 M cacodylate buffer (pH 7.4) at 4 °C overnight, then washed with 0.1 M cacodylate and 7% sucrose buffer three times for 15 min, post-fixed with 2% osmium tetroxide for 1 h, washed three times as before, and immersed for 30 min in 0.5% aqueous uranyl acetate. Specimens were then dehydrated in graded concentrations of ethanol, transferred to isoamyl acetate, and critical-point dried using liquid CO<sub>2</sub>. After drying, specimens were affixed with gold-palladium in an ion coater and examined with a scanning electron microscope (Hitachi S-5000, Tokyo, Japan).

#### 4.5. In Vitro Permeation of Vitamin C Derivatives

To study the ability of the vitamin C derivatives to permeate skin, a section of porcine dorsal skin was mounted in a Franz side-by-side diffusion cell with the stratum corneum facing the donor compartment. The stratum corneum was then given laser treatment at specified fluencies and pass numbers, after which its surface was wiped several times with a cotton wool swab. The receptor compartment (5.5 mL) was filled with citrate-phosphate buffer (pH 7.4). The donor compartment (0.5 mL) contained 13 mM MAP-1 or MAP-2, also in a citrate-phosphate buffer (pH 7.4). The receptor compartment was maintained at 37% and its contents stirred with a magnetic bar at 600 rpm. At appropriate intervals, 300 µL aliquots were withdrawn from the receptor compartment and immediately replaced with an equal volume of fresh receptor solution. Sampling was performed for a 12 h period, and the amount of drug in the receptor medium was determined by high-performance liquid chromatography (HPLC) (Thermo Ultimate 3000LC, Thermo Fisher Scientific, Sunnyvale, CA, USA). We did not analyze the amount of MAP-1 or MAP-2 deposited on skin during these experiments. However, these vitamin C derivatives are similar in physical properties and were not expected to differ in the amount deposited.

#### 4.6. HPLC Analysis of MAP-1 and MAP-2

The amount of MAP-1 or MAP-2 in the samples was analyzed using a 15-cm-long, 4.6 mm-inner diameter Inertsil ODS-4V column (GL Science, Tokyo, Japan), a UltiMate 3000 pump (Thermo Fisher Scientific), a UltiMate 3000 autosampler, and a UltiMate 3000 UV detector. The mobile phase was set at a flow rate of 1 mL/min, and the UV detector set at a wavelength of 254 nm.

#### 4.7. Rhodamine B Permeation of Laser-Treated Porcine Skin

Sections of dorsal skin were exposed to fractional CO<sub>2</sub> laser pretreatment. The skin samples were glued into a glass cylinder with an available area of 0.7854 cm<sup>2</sup> that was filled with 0.2 mL of 0.1% rhodamine B buffer (pH 7.4) and incubated for one hour. To examine rhodamine B fluorescence, the skin thickness was optically scanned at approximately 8 µm increments through the Z-axis of a Leica TCS SP2 confocal microscope (Manheim, Germany). Optical excitation was done with a 514-nm argon laser beam and fluorescence emission was detected at 590 nm–635 nm.

#### 4.8. Data

To analyze permeation, the total amount of vitamin C derivative permeating across a unit skin surface was calculated and plotted as a function of time. Flux (nmole/cm<sup>2</sup>/h) was calculated from the slope of the linear portion of this curve. Normalized flux was calculated by extrapolating the recorded laser-induced permeation to 100% of the area available in the no-treatment condition.

#### 4.9. Statistical Analysis

Data were graphed and analyzed using SigmaPlot software (version 12, Systat Software Inc., Chicago, IL, USA). The Kolmogorov-Smirnov test was used to examine the normality of the data in each group. The results showed the data of each group to be normally distributed. Cumulative amount-time profiles of in vitro transdermal permeation were graphed as a line plot with mean and standard deviation (SD) for each condition. Results of flux across porcine skin were summarized as mean  $\pm$  SD for each condition, and these results were compared using one-way analysis of variance with a post hoc Duncan test. For the sample test in a one-way ANOVA method, a sample size of eight in each group achieved 100% power to detect differences among means versus the alternative methods of testing equal means using an F test with a  $p < 0.05$  significance level. Statistical assessments were considered significant at  $p < 0.05$ .

In conclusion, fractional CO<sub>2</sub> laser pretreatment is an effective way of improving transdermal delivery of MAP-1 and MAP-2, and may have future clinical usefulness.

**Acknowledgments:** This work was supported by Chang Gung Memorial Hospital Grants (CMRPF1D0091, CMRPF1D0092, CMRPF1D0093).

**Author Contributions:** Chien-Yu Hsiao: Conception and design, Acquisition of data, Analysis and interpretation of data, Drafting of the manuscript, Critical revision of the manuscript, Final approval of the manuscript, Literature research, clinical studies, experimental studies, Obtaining funding; Hsin-Ching Sung: Acquisition of data, Critical revision of the manuscript, Final approval of the manuscript, Statistical analysis, Administrative, technical or material support; Sindy Hu: Critical revision of the manuscript, Final approval of the manuscript, Literature research, clinical studies, Administrative, technical or material support; Yau-Li Huang: Literature research, clinical studies, Administrative, technical or material support; Chun-Hsun Huang: Conception and design, Critical revision of the manuscript, Final approval of the manuscript, guarantor of integrity of the entire study, Supervision; All authors read and approved the study.

**Conflicts of Interest:** The authors declare that there is no conflict of interest.

#### References

1. Wu, S.; Shi, H.; Wu, H.; Yan, S.; Guo, J.; Sun, Y.; Pan, L. Treatment of melasma with oral administration of tranexamic acid. *Aesthet. Plast. Surg.* **2012**, *36*, 964–970. [[CrossRef](#)] [[PubMed](#)]
2. Na, J.; Choi, S.Y.; Yang, S.H.; Choi, H.R.; Kang, H.Y.; Park, K.C. Effect of tranexamic acid on melasma: a clinical trial with histological evaluation. *J. Eur. Acad. Dermatol. Venereol.* **2013**, *27*, 1035–1039. [[CrossRef](#)] [[PubMed](#)]
3. Reszko, A.E.; Bereson, D.; Lupo, M.P. Cosmeceuticals: Practical applications. *Dermatol. Clin.* **2009**, *27*, 401–416. [[CrossRef](#)] [[PubMed](#)]
4. Humbert, P.G.; Haftek, M.; Creidi, P.; Apiere, C.; Nusgens, B.; Richard, A.; Schmidt, D.; Zahouani, H. Topical ascorbic acid on photoaged skin. Clinical topographical and ultrastructural evaluation: Double-blind study vs. placebo. *Exp. Dermatol.* **2003**, *12*, 237–244. [[CrossRef](#)] [[PubMed](#)]
5. Dumas, M.; Chaudagne, C.; Bonte, F.; Mybeck, A. Age-related response of human dermal fibroblasts to 1-ascorbic acid. Study of type I and type II collagen synthesis. *C. R. Acad. Sci. Ser. III* **1996**, *319*, 1129–1132.
6. Darr, D.; Dunstan, S.; Faust, H.; Pinnell, S. Effectiveness of antioxidants (vitamin C and E) with and without sunscreens as topical photoprotectants. *Acta Derm. Venereol.* **1996**, *76*, 264–268. [[PubMed](#)]
7. Fitzpatrick, R.E.; Rostan, E.F. Double-blind, half-face study comparing topical vitamin C and vehicle for rejuvenation of photodamage. *Dermatol. Surg.* **2002**, *28*, 231–236. [[PubMed](#)]
8. Espinal-Perez, L.E.; Moncada, B.; Castanedo-Cazares, J.P. A double-blind randomized trial of 5% ascorbic acid vs. 4% hydroquinone in melasma. *Int. J. Dermatol.* **2004**, *43*, 604–607. [[CrossRef](#)] [[PubMed](#)]
9. Lee, W.R.; Shen, S.C.; Wang, K.H.; Fang, J.Y. Lasers and microdermabrasion enhance and control topical delivery of vitamin C. *J. Investig. Dermatol.* **2003**, *121*, 1118–1125. [[CrossRef](#)] [[PubMed](#)]
10. Lee, W.R.; Shen, S.C.; Wang, K.H.; Hu, C.H.; Fang, J.Y. The effect of laser treatment on skin to enhance and control transdermal delivery of 5-fluorouracil. *Lasers Med. Sci.* **2003**, *28*, 807–814.
11. Lee, W.R.; Shen, S.C.; Al-Suwayeh, S.A.; Yang, H.H.; Yuan, C.Y.; Fang, J.Y. Laser-assisted topical drug delivery by using a low-fluence fractional laser: Imiquimod and macromolecules. *J. Control. Release* **2011**, *153*, 240–248. [[CrossRef](#)] [[PubMed](#)]

12. Lee, W.R.; Shen, S.C.; Lai, H.H.; Hu, C.H.; Fang, J.Y. Transdermal delivery enhanced and controlled by erbium:YAG laser: A comparative study of lipophilic and hydrophilic drugs. *J. Control. Release* **2001**, *75*, 155–166. [[CrossRef](#)]
13. Huang, C.H.; Sung, H.C.; Hsiao, C.Y.; Hu, S.; Ko, Y.S. Transdermal delivery of three vitamin C derivatives by Er:YAG and carbon dioxide laser pretreatment. *Lasers Med. Sci.* **2013**, *28*, 807–814. [[CrossRef](#)] [[PubMed](#)]
14. Alexiades-Armenakas, M.R.; Dover, J.S.; Arndt, K.A. The spectrum of laser skin resurfacing: Nonablative, fractional, and ablative resurfacing. *J. Investig. Dermatol.* **2008**, *121*, 1118–1125. [[CrossRef](#)] [[PubMed](#)]
15. Hsiao, C.Y.; Huang, C.H.; Hu, S.; Ko, Y.S.; Sung, H.C.; Chen, C.C.; Huang, S.Y. Fractional carbon dioxide laser treatment to enhance skin permeation of ascorbic acid 2-glucoside with minimal skin disruption. *Dermatol. Surg.* **2012**, *38*, 1284–1293. [[CrossRef](#)] [[PubMed](#)]
16. Hsiao, C.Y.; Huang, C.H.; Hu, S.; Ko, Y.S.; Sung, H.C.; Huang, S.Y. Skin pretreatment with lasers promotes the transdermal delivery of vitamin C derivatives. *Lasers Med. Sci.* **2011**, *26*, 369–376. [[CrossRef](#)] [[PubMed](#)]
17. Hsiao, C.Y.; Sung, H.C.; Hu, S.; Huang, C.H. Fractional laser treatment to enhance skin permeation of tranexamic acid with minimal skin disruption. *Dermatology* **2015**, *230*, 269–275. [[CrossRef](#)] [[PubMed](#)]
18. Laubach, H.J.; Tannous, Z.; Anderson, R.R.; Manstein, D. Skin responses to fractional photothermolysis. *Lasers Surg. Med.* **2006**, *38*, 142–149. [[CrossRef](#)] [[PubMed](#)]
19. Tannous, Z. Fractional resurfacing. *Clin. Dermatol.* **2007**, *25*, 480–486. [[CrossRef](#)] [[PubMed](#)]
20. Hantash, B.M.; Vikramaditya, P.B.; Chan, K.F.; Zachary, C.B. Ex vivo histological characterization of a novel ablative fractional resurfacing device. *Lasers Surg. Med.* **2007**, *39*, 87–95. [[CrossRef](#)] [[PubMed](#)]
21. Hantash, B.M.; Vikramaditya, P.B.; Kapadia, B.; Rahman, Z.; Jiang, K.; Tanner, H.; Chan, K.F.; Zachary, C.B. In vivo histological evaluation of a novel ablative fractional resurfacing device. *Lasers Surg. Med.* **2007**, *39*, 96–107. [[CrossRef](#)] [[PubMed](#)]
22. Chapas, A.M.; Brightman, L.; Sukal, S.; Hale, E.; Daniel, D.; Bernstein, J.L.; Geronemus, R.G. Successful treatment of acneiform scarring with CO<sub>2</sub> ablative fractional resurfacing. *Lasers Surg. Med.* **2008**, *40*, 381–386. [[CrossRef](#)] [[PubMed](#)]
23. Levin, J.; Maibach, H.I. The correlation between transepidermal water loss and percutaneous absorption: An overview. *J. Control. Release* **2005**, *103*, 291–299. [[CrossRef](#)] [[PubMed](#)]
24. Rokhsar, C.K.; Fitzpatrick, R.E. The treatment of melasma with fractional photothermolysis: A pilot study. *Dermatol. Surg.* **2005**, *31*, 1645–1650. [[CrossRef](#)] [[PubMed](#)]
25. Manstein, D.; Herron, G.S.; Sink, R.K.; Tanner, H.; Anderson, R.R. Fractional photothermolysis: A new concept for cutaneous remodeling using microscopic patterns of thermal injury. *Lasers Surg. Med.* **2004**, *34*, 426–438. [[CrossRef](#)] [[PubMed](#)]
26. Chan, H.H.L.; Manstein, D.; Yu, C.S.; Shek, S.; Kono, T.; Wei, W.I. The prevalence and risk factors of post-inflammatory hyperpigmentation after fractional resurfacing in Asians. *Lasers Surg. Med.* **2007**, *38*, 381–385. [[CrossRef](#)] [[PubMed](#)]
27. Lee, W.-R.; Chen, S.-C.; Al-Suwayeh, S.A.; Yang, H.-H.; Li, Y.-C.; Fang, J.-Y. Skin permeation of small-molecule drugs, macromolecules, and nanoparticles mediated by a fractional carbon dioxide laser: The role of hair follicles. *Pharm. Res.* **2013**, *30*, 792–802. [[CrossRef](#)] [[PubMed](#)]

**Sample Availability:** Samples of the compounds are not available from the authors.



© 2016 by the authors; licensee MDPI, Basel, Switzerland. This article is an open access article distributed under the terms and conditions of the Creative Commons Attribution (CC-BY) license (<http://creativecommons.org/licenses/by/4.0/>).



# TNF- $\alpha$ -Induced cPLA<sub>2</sub> Expression via NADPH Oxidase/Reactive Oxygen Species-Dependent NF- $\kappa$ B Cascade on Human Pulmonary Alveolar Epithelial Cells

Chih-Chung Lin<sup>1†</sup>, Wei-Ning Lin<sup>2†</sup>, Rou-Ling Cho<sup>3</sup>, Chen-yu Wang<sup>3</sup>, Li-Der Hsiao<sup>1</sup> and Chuen-Mao Yang<sup>1,3,4\*</sup>

<sup>1</sup> Department of Anesthetics, Chang Gung Memorial Hospital at Linkou and College of Medicine, Chang Gung University, Tao-Yuan, Taiwan, <sup>2</sup> Graduate Institute of Basic Medicine, Fu Jen Catholic University, New Taipei City, Taiwan, <sup>3</sup> Department of Physiology and Pharmacology and Health Aging Research Center, College of Medicine, Chang Gung University, Tao-Yuan, Taiwan, <sup>4</sup> Research Center for Industry of Human Ecology, Research Center for Chinese Herbal Medicine, and Graduate Institute of Health Industry Technology, Chang Gung University of Science and Technology, Tao-Yuan, Taiwan

## OPEN ACCESS

### Edited by:

Wenliang Song,  
Vanderbilt University Medical Center,  
USA

### Reviewed by:

Aida Habib,  
American University of Beirut,  
Lebanon  
Hui Huang,  
Vanderbilt University, USA

### \*Correspondence:

Chuen-Mao Yang  
chuenmao@mail.cgu.edu.tw

<sup>†</sup>These authors have contributed  
equally to this work.

### Specialty section:

This article was submitted to  
Inflammation Pharmacology,  
a section of the journal  
Frontiers in Pharmacology

Received: 28 July 2016

Accepted: 08 November 2016

Published: 25 November 2016

### Citation:

Lin C-C, Lin W-N, Cho R-L,  
Wang C-y, Hsiao L-D and Yang C-M  
(2016) TNF- $\alpha$ -Induced cPLA<sub>2</sub>  
Expression via NADPH  
Oxidase/Reactive Oxygen  
Species-Dependent NF- $\kappa$ B Cascade  
on Human Pulmonary Alveolar  
Epithelial Cells.  
Front. Pharmacol. 7:447.  
doi: 10.3389/fphar.2016.00447

Tumor necrosis factor- $\alpha$  (TNF- $\alpha$ ) triggers activation of cytosolic phospholipase A<sub>2</sub> (cPLA<sub>2</sub>) and then enhancing the synthesis of prostaglandin (PG) in inflammatory diseases. However, the detailed mechanisms of TNF- $\alpha$  induced cPLA<sub>2</sub> expression were not fully defined in human pulmonary alveolar epithelial cells (HPAEPiCs). We found that TNF- $\alpha$ -stimulated increases in cPLA<sub>2</sub> mRNA (5.2 folds) and protein (3.9 folds) expression, promoter activity (4.3 folds), and PGE<sub>2</sub> secretion (4.7 folds) in HPAEPiCs, determined by Western blot, real-time PCR, promoter activity assay and PGE<sub>2</sub> ELISA kit. These TNF- $\alpha$ -mediated responses were abrogated by the inhibitors of NADPH oxidase [apocynin (APO) and diphenyleneiodonium chloride (DPI)], ROS [N-acetyl cysteine, (NAC)], NF- $\kappa$ B (Bay11-7082) and transfection with siRNA of ASK1, p47<sup>phox</sup>, TRAF2, NIK, IKK $\alpha$ , IKK $\beta$ , or p65. TNF- $\alpha$  markedly stimulated NADPH oxidase activation and ROS including superoxide and hydrogen peroxide production which were inhibited by pretreatment with a TNFR1 neutralizing antibody, APO, DPI or transfection with siRNA of TRAF2, ASK1, or p47<sup>phox</sup>. In addition, TNF- $\alpha$  also stimulated p47<sup>phox</sup> phosphorylation and translocation in a time-dependent manner. On the other hand, TNF- $\alpha$  induced TNFR1, TRAF2, ASK1, and p47<sup>phox</sup> complex formation in HPAEPiCs, which were attenuated by a TNF- $\alpha$  neutralizing antibody. We found that pretreatment with NAC, DPI, or APO also attenuated the TNF- $\alpha$ -stimulated IKK $\alpha$ / $\beta$  and NF- $\kappa$ B p65 phosphorylation, NF- $\kappa$ B (p65) translocation, and NF- $\kappa$ B promoter activity in HPAEPiCs. Finally, we observed that TNF- $\alpha$ -stimulated NADPH oxidase activation and ROS generation activates NF- $\kappa$ B through the NIK/IKK $\alpha$ / $\beta$  pathway. Taken together, our results demonstrated that in HPAEPiCs, up-regulation of cPLA<sub>2</sub> by TNF- $\alpha$  is, at least in part, mediated through the cooperation of TNFR1, TRAF2, ASK1, and NADPH oxidase leading to ROS generation and ultimately activates NF- $\kappa$ B pathway.

**Keywords:** ASK1, cytokines, cytosolic phospholipase A<sub>2</sub>, lung inflammation, signaling transduction



## INTRODUCTION

The occurrence and exacerbation of lung diseases, including chronic obstructive pulmonary disease (COPD) and asthma, is dependent on the severity of lung inflammation (Lee and Yang, 2012). Eicosanoids, one of lipid mediators generating from conversion of arachidonic acid (AA), have been found *in situ* in airway secretion of asthmatics (Barnes, 1989; Henderson et al., 2002). Phospholipase A<sub>2</sub> (PLA<sub>2</sub>) enzymes catalyze the hydrolysis of membrane phospholipids resulting in the release of AA (Borsch-Haubold et al., 1998). The constitutive enzyme cyclooxygenase (COX)-1 or the inducible COX-2 then converts AA to prostaglandins (PGs), such as PGE<sub>2</sub> (Yang et al., 2002; Hsieh et al., 2006). Three PLA<sub>2</sub> have been identified including secretory PLA<sub>2</sub>, the 85 kDa cytosolic group IV PLA<sub>2</sub> (cPLA<sub>2</sub>), and a calcium-independent group VI PLA<sub>2</sub> in mammalian cells (Six and Dennis, 2000). cPLA<sub>2</sub> plays a major role in agonist-induced AA release and eicosanoid production (Leslie, 1997). Involvement of cPLA<sub>2</sub> in sepsis-related acute lung injury (Nagase et al., 2000) and anaphylaxis-associated bronchial reactivity has been proved (Uozumi et al., 1997). Furthermore, PGE<sub>2</sub> synthesis increases are dependent on upregulation of cPLA<sub>2</sub> activity in various cell types (Dieter et al., 2002; Gilroy et al., 2004). Elevated levels of TNF- $\alpha$  have been detected in the bronchoalveolar lavage fluid of asthmatic patients. TNF- $\alpha$  could exaggerate inflammatory responses through up-regulation of inflammatory genes, such as cPLA<sub>2</sub> (Hulkower et al., 1994; Van Putten et al., 2001). Up-regulation of cPLA<sub>2</sub> further catalyzes the hydrolysis of membrane phospholipids and releases AA served as a substrate for PGs synthesis (i.e., PGE<sub>2</sub>) that augments lung inflammation. Moreover, our previous findings also provided insights into the correlation between COX-2 and cPLA<sub>2</sub> expression in ATP $\gamma$ S-stimulated vascular smooth muscle cells (VSMCs) with similar molecular mechanisms and functional coupling to amplify the occurrence of vascular inflammation (Lin et al., 2009). Therefore, the synthesis of PGE<sub>2</sub> could be a good index of AA release that is more sensitive than [<sup>3</sup>H]AA mobilization (Berenbaum et al., 2003). In this study, although the effect of TNF- $\alpha$  on COX-2 expression was not investigated, we tested the effect of TNF- $\alpha$  on PGE<sub>2</sub> synthesis as a parameter of cPLA<sub>2</sub> activity in human pulmonary alveolar epithelial cells (HPAECs). Therefore, up-regulation of cPLA<sub>2</sub> may play a key role in local and systemic inflammation in airway diseases. However, the molecular mechanisms by which TNF- $\alpha$  induces cPLA<sub>2</sub> expression and PGE<sub>2</sub> synthesis in HPAECs are not completely understood.

Previous report indicates that TNF- $\alpha$  binds to distinct receptors, TNFR1 and TNFR2, and triggers various inflammatory responses (Lee et al., 2009). The association of TNF- $\alpha$  and TNFR1 modulates the severity of tissue injury via activation of proinflammatory or programmed cell death pathway (van Vliet et al., 2005; Lee et al., 2009). TNF receptor associated factor 2 (TRAF2) plays an important role in innate immune and inflammatory responses. However, the interaction among TNF- $\alpha$ , TNFR1, TRAF2 and downstream components leading to cPLA<sub>2</sub> expression is still unknown in HPAECs.

Reactive oxygen species (ROS) are products of normal cellular metabolism acting as second messengers (Lee and Yang, 2012). However, either reduced nicotinamide adenine dinucleotide phosphate (NADPH) by pro-inflammatory cytokines such as TNF- $\alpha$  or the mitochondrial electron transport chain and xanthine oxidase leads to increased production of ROS and unbalance of cellular oxidative stress, which are causes of airway/lung damages and subsequently respiratory inflammatory diseases/injuries (Lee and Yang, 2012). Apoptosis signal-regulating kinase 1 (ASK1), a mitogen-activated protein kinase kinase kinase, participates in regulating stress and immune responses. ASK1 is activated by cytokines and various environmental and cellular stresses. Hsu et al. indicated that peptidoglycan (PGN) induced COX-2 expression via an ASK1 signaling in A549 cells (Hsu et al., 2010). Therefore, we explored whether TNFR1, TRAF2, ASK1, and NADPH oxidase/ROS are involved in TNF- $\alpha$ -induced cPLA<sub>2</sub> expression and PGE<sub>2</sub> release.

NF- $\kappa$ B plays major roles not only in the evolution but also in the resolution of inflammatory responses. A wide spectrum of biological effects including immune and stress-induced responses, proliferation, differentiation, tumorigenesis, apoptosis, and tissue remodeling are all controlled by activated NF- $\kappa$ B (Lee and Yang, 2012). The activation of NF- $\kappa$ B can be regulated by various extracellular stimuli, including cytokines and oxidative stress (Lee and Yang, 2012). We noticed that ROS generation can impact NF- $\kappa$ B signaling pathways (Morgan and Liu, 2011). In addition, NF- $\kappa$ B modulates cPLA<sub>2</sub> gene activity in various cell types (Luo et al., 2006; Huwiler et al., 2012; Chi et al., 2014). Therefore, we examined whether TNF- $\alpha$  regulates cPLA<sub>2</sub> expression via ROS-dependent NF- $\kappa$ B activation in HPAECs.

In addressing these questions, the experiments were performed to investigate the mechanisms underlying TNF- $\alpha$ -induced cPLA<sub>2</sub> expression and PGE<sub>2</sub> synthesis in HPAECs. These findings suggested that TNF- $\alpha$ -induced cPLA<sub>2</sub>-expression associated PGE<sub>2</sub> release is, at least in part, mediated through a TNFR1/TRAF2/ASK1/p47<sup>phox</sup>/NADPH oxidase/ROS/NIK/IKK $\alpha$ / $\beta$ /NF- $\kappa$ B pathway in these cells.

## MATERIALS AND METHODS

### Materials

Recombinant human TNF- $\alpha$  was from R&D System (Minneapolis, MN, USA). Anti-cPLA<sub>2</sub> (sc-454), anti-p47<sup>phox</sup> (sc-14015), anti-G $\alpha$ s (sc-823), anti-TRAF2 (sc-7346), anti-ASK1 (sc-5294), anti-TNFR1 (sc-52739), anti-NIK (sc7211), anti-IKK $\alpha$  (sc7218), anti-IKK $\beta$  (sc8014), anti-p65 (sc-7151) and anti-phospho-serine (sc-81515) antibodies were from Santa Cruz (Santa Cruz, CA). An anti-GAPDH antibody (#MCA-1D4) was from Encor (Gainesville, FL, USA). Human TNF- $\alpha$  neutralizing antibody (#7321), anti-phospho-tyrosine (#9411), anti-phospho-ASK1 (#3765), anti-phospho-p65 (#3031), and anti-phospho-IKK $\alpha$ / $\beta$  (#2697) antibodies were from Cell Signaling (Danvers, MA, USA). N-Acetyl cysteine (NAC), diphenyleneiodonium chloride (DPI), apocynin (APO), and Bay11-7082 were from Biomol (Plymouth



Meeting, PA, USA). Dihydroethidium (DHE) and 5-(and-6)-chloromethyl-2',7'-dichlorodihydrofluorescein diacetate, acetyl ester (CM-H<sub>2</sub>DCFDA) were from Molecular Probes (Eugene, OR, USA). SDS-PAGE supplies were from MDBio Inc (Taipei, Taiwan). All other reagents were from Sigma (St. Louis, MO, USA).

## Cell Culture and Treatment

Human pulmonary alveolar epithelial cells (HPAECs) were ordered from ScienCell Research Lab (San Diego, CA, USA). The passages 4–7 were used throughout this study. HPAECs were cultured in DMEM/F12 medium containing 10% FBS, as previously described Lee et al. (2008). The growth medium was changed after 48 h and then every 3 days. The viability of HPAECs after treatment with DMSO or the pharmacological inhibitors alone was determined by an XTT [2,3-bis-(2-methoxy-4-nitro-5-sulphophenyl)-2H-tetrazolium-5-carboxanilide] assay, which showed no significant differences (data not shown).

## Western Blot Analysis

Serum-starved HPAECs were incubated with TNF- $\alpha$  at 37°C for the various time points. At the end of treatment, the cells were harvested and centrifuged at 45000  $\times$  g at 4°C for 1 h to prepare the whole cell lysate, as previously described (Chi et al., 2012). The denatured samples were analyzed by 10% SDS-PAGE gels and transferred to nitrocellulose membrane. The Western blot was performed by incubation membrane with an anti-cPLA<sub>2</sub>, anti-p47<sup>phox</sup>, anti-Gas, anti-TRAF2, anti-ASK1, anti-TNFR1, anti-NIK, anti-IKK $\alpha$ , anti-IKK $\beta$ , anti-p65, anti-phospho-serine or anti-GAPDH (1:1000) antibody for 24 h, and then incubated with an anti-mouse horseradish peroxidase antibody (1:2000) for 1 h. ECL reagents and UVP BioSpectrum 500 Imaging System (Upland, CA, USA) were used to detect and capture the immunoreactive bands. The image densitometry of each immunoreactive band was analyzed and quantified by the UN-SCAN-IT gel software (Orem, UT, USA).

## Real-Time PCR Analysis

Total RNA of HPAECs was extracted using TRIzol reagent and reverse-transcribed into cDNA. Real-time PCR using SYBR Green PCR reagents (Applied Biosystems, Branchburg, NJ, USA) and primers specific for cPLA<sub>2</sub> and GAPDH genes were used, as previously described (Chi et al., 2012). The real-time primers were as follows: cPLA<sub>2</sub> $\alpha$ , forward primer: 5'-ATGATAGCTCGGACAGTGATGATGA-3'; reverse primer: 5'-CATACGATGAATCCAACCTGCTTGA-3' and GAPDH, forward primer: 5'-CTCTGCTCCTCCTGTTTCGAC-3'; reverse primer: 5'-TTAAAAGCAGCCCTGGTGAC-3'. The expression of cPLA<sub>2</sub> was quantified by normalization to the GAPDH expression.

## Measurement of Intracellular ROS Accumulation

The intracellular H<sub>2</sub>O<sub>2</sub> levels were determined by measuring fluorescence of 2',7'-dichloro fluorescein diacetate (DCF-DA) and the O<sub>2</sub><sup>•-</sup> levels were determined by measuring the level

of dihydroethidium (DHE), as previously described Hsu et al. (2014). The fluorescence for DCF and DHE staining was detected at 495/529 and 518/605 nm, respectively, using a fluorescence microscope (Zeiss, Axiovert 200M). For the purpose of these experiments, HPAECs were washed with warm HBSS and incubated in HBSS or cell medium containing 10  $\mu$ M DCFH-DA or DHE at 37°C for 45 min. Subsequently, HBSS or medium containing DCFH-DA or DHE was removed and replaced with fresh medium. HPAECs were then incubated with TNF- $\alpha$ . Cells were washed twice with PBS and detached with trypsin/EDTA, and the fluorescence intensity of the cells was analyzed using a multi-technology reader (Thermo, Appliskan) at Ex/Em: 485/530 nm.

## Determination of NADPH Oxidase Activity by Chemiluminescence Assay

HPAECs (2  $\times$  10<sup>6</sup> cells/ml) were cultured in 6-well plates and then incubated with TNF- $\alpha$  after growth to confluence and serum-starved. At the end of incubation, cells were harvested and centrifuged at 400  $\times$  g for 10 min at 4°C. The cell pellet was kept on ice after re-suspended by 35  $\mu$ l/per well of ice-cold RPMI-1640 medium. The complex including NADPH (1  $\mu$ M) or lucigenin (20  $\mu$ M), 5  $\mu$ l of cell suspension (0.2  $\times$  10<sup>5</sup> cells) and a final 200  $\mu$ l volume of pre-warmed (37°C) RPMI-1640 medium were prepared and the chemiluminescence was immediate recorded with an Appliskan luminometer (Thermo®) in out-of-coincidence mode. Appropriate blanks and controls were used. There was no background chemiluminescence of lucigenin in NADPH or NADH alone group (30–40 counts per min), as previously described Hsu et al. (2014). The signals of chemiluminescence were continuously measured for 12 min, and the activity of NADPH oxidase was expressed as counts per million cells.

## Measurement of cPLA<sub>2</sub> Luciferase Activity

Human cPLA<sub>2</sub> promoter spanning – 2375 to +75 bp as cloned into pGL3-basic vector (Promega, Madison, WI, USA) as cPLA<sub>2</sub>-luc plasmid. The activity of cPLA<sub>2</sub>-luc was detected using a luciferase assay system (Promega, Madison, WI, USA), as previously described Chi et al. (2012). The detected luciferase activities were standardized with the activity of  $\beta$ -gal.

## Measurement of PGE<sub>2</sub> Generation

The serum-starved cells were treated with TNF- $\alpha$  for the different time points. At the end of treatment, culture media were collected and stored at –80°C. The concentrations of PGE<sub>2</sub> were detected by a PGE<sub>2</sub> enzyme immunoassay kit (Cayman) according to the manufacturer's instructions, as previously described Lee et al. (2008).

## Transient Transfection with siRNAs

All human ASK1, p47<sup>phox</sup>, TRAF2, NIK, IKK $\alpha$ , IKK $\beta$ , and p65 siRNA together with scramble siRNA were purchased from Sigma (St. Louis, MO, USA). Lipofectamine<sup>TM</sup> RNAiMAX reagents were used to prepare siRNA liposome complexes (100 nM

of siRNAs) according to the manufacturer's instructions, as previously described Lee et al. (2008).

## Co-immunoprecipitation Assay

Cell lysates containing 1 mg of protein were incubated with 2  $\mu$ g of an anti-p47<sup>phox</sup>, anti-TNFR1, anti-TRAF2, or anti-ASK1 antibody at 4°C for 24 h, and then 10  $\mu$ l of 50% protein A-agarose beads was added and mixed at 4°C for 24 h. The immunoprecipitates were collected and washed thrice with a lysis buffer without Triton X-100. 5x Laemmli buffer was added and subjected to electrophoresis on SDS-PAGE, and then blotted using an anti-phospho-tyrosine, anti-phospho-serine, anti-p47<sup>phox</sup>, anti-TRAF2, anti-TNFR1, or anti-ASK1 antibody, as previously described (Yang et al., 2014).

## Immunofluorescence Staining

Growth-arrested HPAEpiCs were incubated with TNF- $\alpha$  for the indicated time intervals. After washing twice with ice-cold PBS, cells were fixed, permeabilized and stained using an anti-p65 antibody, as previously described (Chi et al., 2011). A fluorescence microscope (Zeiss, Axiovert 200M) were used to observe images.

## Cell Fractions Isolation

The cell lysates were sonicated for 5 s at output 1.5 using a sonicator (Misonix, Farmingdale, NY, USA) and then centrifuged at 6800  $\times$  g for 15 min at 4°C, as previously described Lee et al. (2008). The pellet was collected as the nuclear fraction. The supernatant was further centrifuged at 20,000  $\times$  g at 4°C for 60 min to yield the pellet (membrane fraction) and the supernatant (cytosolic fraction).

## Statistical Analysis of Data

Data were showed as the mean or mean  $\pm$  SEM of five individual experiments and estimated using GraphPad Prism Program (GraphPad, San Diego, CA, USA). All the data were analyzed by paired two-tailed Student's *t*-test or by one-way analysis of variance (ANOVA) followed with Tukey's *post hoc* test at *p* < 0.05 level of significance.

# RESULTS

## TNF- $\alpha$ Induces cPLA<sub>2</sub> Expression via NADPH Oxidase and ROS

Reactive oxygen species play both deleterious and beneficial roles. Accumulation of ROS and cellular oxidative stress trigger expression of inflammatory genes and result in tissue damages and various diseases (Lee and Yang, 2012). Thus, we attempted to investigate the roles of NADPH Oxidase and ROS in cPLA<sub>2</sub> expression. Here we reported that TNF- $\alpha$ -induced cPLA<sub>2</sub> protein levels were significantly reduced by pretreatment with a ROS scavenger (NAC) or the inhibitors of NADPH oxidase (APO and DPI) (Figure 1A). In addition, pretreatment with NAC, DPI, or APO also attenuated the TNF- $\alpha$ -stimulated cPLA<sub>2</sub> mRNA expression and promoter

activity (Figure 1B). The p47<sup>phox</sup> protein, one of cytosolic subunits of NADPH oxidase, contributed to acute NADPH oxidase activation via being phosphorylated and binding to p22<sup>phox</sup> (Lee et al., 2009). Thus, we confirmed the role of p47<sup>phox</sup> in cPLA<sub>2</sub> expression by transfection with p47<sup>phox</sup> siRNA which knocked down protein expression of p47<sup>phox</sup> and then markedly inhibited TNF- $\alpha$ -induced cPLA<sub>2</sub> protein expression in these cells (Figure 1C). To confirm this cPLA<sub>2</sub> expression is mediated through TNF- $\alpha$ -dependent induction, HPAEpiCs were pretreated with a human TNF- $\alpha$  neutralizing antibody followed by TNF- $\alpha$  treatment. We found that TNF- $\alpha$  neutralizing antibody significantly blocked the cPLA<sub>2</sub> induction in a dose-dependent manner (Figure 1D). These results indicated that TNF- $\alpha$  induces cPLA<sub>2</sub> expression via NADPH oxidase and ROS in HPAEpiCs.

## TNF- $\alpha$ Induces NADPH Oxidase-Dependent Superoxide and Hydrogen Peroxide Production

TNF- $\alpha$  may stimulate ROS production by several sources, such as mitochondria, but recent studies have strongly suggested that a major source of ROS is a phagocyte-type NADPH oxidase. Several reports also demonstrate that TNF- $\alpha$  triggers several signal transduction pathways to activate the NOX activity and enhances intracellular ROS generation leading to expression of inflammatory genes (Rahman et al., 1998; Hashimoto et al., 2001; Li et al., 2005; Lee et al., 2013; Yang et al., 2014). Therefore, we investigated whether TNF- $\alpha$ -induced cPLA<sub>2</sub> expression is due to activation of NADPH oxidase and ROS generation. Here, we found that TNF- $\alpha$  markedly induced superoxide and hydrogen peroxide production, determined by using DHE or DCF under a fluorescence microscope (Figure 2A). On the other hand, we also observed that TNF- $\alpha$  time-dependently induces NADPH oxidase activation (Figure 2B), which was reduced by TNFR1 neutralizing antibody, APO, or DPI (Figure 2C). These results suggested that TNF- $\alpha$  induced ROS generation via NADPH oxidase activation. The p47<sup>phox</sup> is phosphorylated on several serine residues within the polybasic region of the protein, and these multiple phosphorylation events induce conformational changes that permit p47<sup>phox</sup> to interact with the cytoplasmic tail of p22<sup>phox</sup> and to initiate the formation of the active NADPH oxidase complex (Dang et al., 2006). Previous report also indicates that Src modulates tyrosine phosphorylation of p47<sup>phox</sup> in hyperoxia-induced activation of NADPH oxidase and generation of ROS in lung endothelial cells (Chowdhury et al., 2005). Thus, we investigated whether TNF- $\alpha$  stimulates the phosphorylation of tyrosine or serine on p47<sup>phox</sup>. As shown in Figure 2D, TNF- $\alpha$  increased tyrosine and serine phosphorylation of p47<sup>phox</sup> in a time-dependent manner. Moreover, p47<sup>phox</sup> was translocated from the cytosol to the membrane fractions in TNF- $\alpha$ -stimulated cells (Figure 2E). Finally, we investigated whether TNF- $\alpha$ -induced superoxide and hydrogen peroxide production are mediated through NADPH oxidase activation. Here, we observed that TNF- $\alpha$ -induced superoxide and hydrogen peroxide production were inhibited by TNFR1 neutralizing antibody, APO, DPI and NAC (Figure 2F). These results suggested that

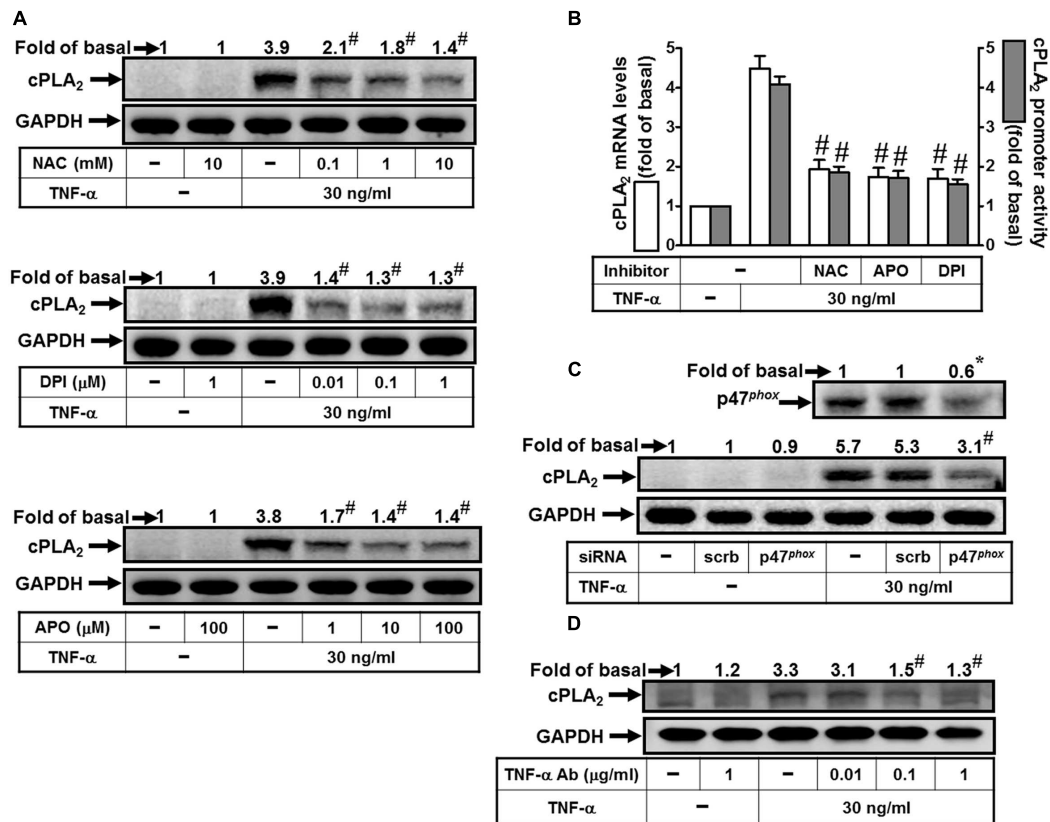


**FIGURE 1 | TNF- $\alpha$  induces NADPH oxidase- and ROS-dependent cPLA<sub>2</sub> expression.** (A) HPAEpiCs were pretreated with NAC, DPI, or APO for 1 h, and then incubated with TNF- $\alpha$  for 24 h. (B) Cells were pretreated with NAC (10 mM), DPI (1  $\mu$ M), or APO (100  $\mu$ M) for 1 h, and then incubated with TNF- $\alpha$  for 6 h. cPLA<sub>2</sub> mRNA levels and promoter activity were determined. (C) Cells were transfected with scrambled or p47<sup>phox</sup> siRNA, and then incubated with TNF- $\alpha$  for 24 h. (D) HPAEpiCs were pretreated with human TNF- $\alpha$  neutralizing antibody (TNF- $\alpha$  nAb: 0.01, 0.1 and 1  $\mu$ g/ml) for 1 h, and then incubated with TNF- $\alpha$  for 24 h. (A,C,D) The protein levels of cPLA<sub>2</sub> and p47<sup>phox</sup> were determined by Western blot. Data are expressed as mean  $\pm$  SEM of three independent experiments. \* $P$  < 0.05, # $P$  < 0.01 as compared with the cells exposed to TNF- $\alpha$  alone.

TNF- $\alpha$  induces ROS generation via p47<sup>phox</sup> translocation and NADPH oxidase activation in HPAEpiCs.

## TNF- $\alpha$ Induces TNFR1, TRAF2, ASK1, and p47<sup>phox</sup> Complex Formation

Both tissue injury-related proinflammatory and programmed cell death pathways are activated by TNF- $\alpha$  via binding to TNFR1 (van Vliet et al., 2005; Lee et al., 2009). TRAF2 plays an important role in innate immune and inflammatory responses. Thus, we determine whether TRAF2 is a downstream component of TNF- $\alpha$ /TNFR1 complex in cPLA<sub>2</sub> expression. Here, we demonstrated that TNF- $\alpha$  induced cPLA<sub>2</sub> expression via TRAF2 by transfection with TRAF2 siRNA (Figure 3A). We found that transfection with TRAF2 siRNA reduced TRAF2 protein expression by about 50% and significantly attenuated the TNF- $\alpha$ -induced cPLA<sub>2</sub> expression from 5.4-fold to 2.2-fold. In addition, we also showed that TNF- $\alpha$  stimulated TRAF2 and TNFR1 complex formation and its downstream components (Figure 3B). Therefore, we further studied whether TNF- $\alpha$  promoted the association of TNFR1, TRAF2, ASK1, and p47<sup>phox</sup> in HPAEpiCs. Data in Figure 3B

showed that TNF- $\alpha$  time-dependently induced TNFR1, TRAF2, ASK1, and p47<sup>phox</sup> complex formation. Importantly, this interaction was blocked by pretreatment with TNF- $\alpha$  neutralizing antibody.

Various cell stresses, including ROS, TNF- $\alpha$ , lipopolysaccharide (LPS), and ER stress, activate ASK1 and resulting in apoptosis, differentiation and inflammation (Soga et al., 2012). However, whether ASK1 involved in TNF- $\alpha$ -mediated responses was still unknown in HPAEpiCs. Here, we found that transfection with ASK1 siRNA knocked down ASK1 protein level by about 50% and then significantly attenuated the TNF- $\alpha$ -induced cPLA<sub>2</sub> expression from 4.9-fold to 1.9-fold (Figure 3C). ASK1 plays a pivotal role in ROS generation. In resting cells, endogenous ASK1 constitutively associated with thioredoxin (Trx) forming an inactive high-molecular-mass complex, known as ASK1 signalosome. Once cellular ROS increased, Trx dissociated from ASK1 signalosome and resulted in full activation of higher-molecular-mass complex by the recruitment of TRAF2 and TRAF6 (Fujino et al., 2007). Thus, we further investigated whether p47<sup>phox</sup> was recruited to the complex of TNF- $\alpha$ /TNFR1/TRAF2/ASK1. We observed that

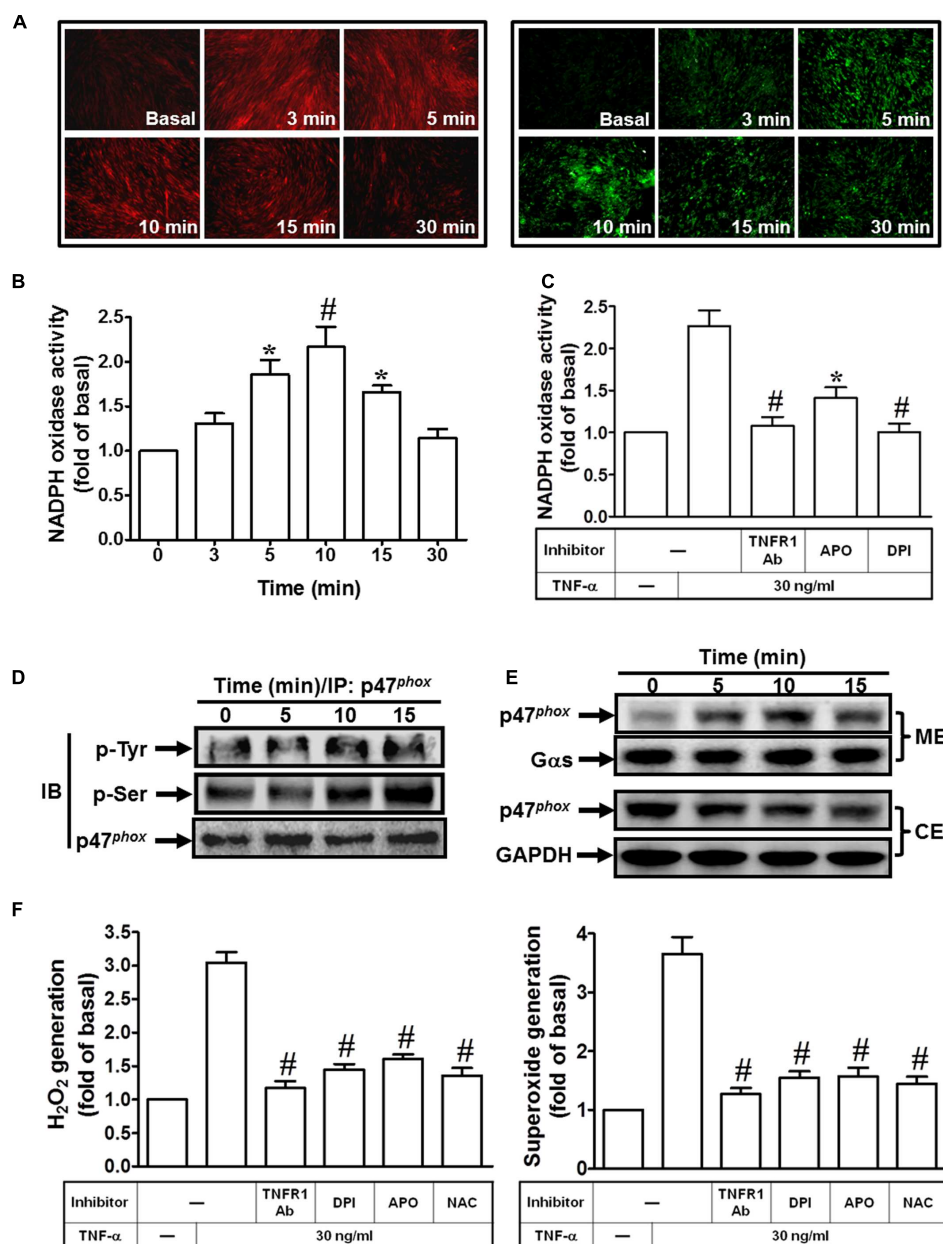


**FIGURE 2 | TNF- $\alpha$  induces NADPH oxidase-dependent ROS generation. (A)** HPAEpiCs were treated with TNF- $\alpha$  for the indicated time intervals. DHE (red) or DCF (green) fluorescence image was observed. Images shown are representative of five independent experiments with similar results. Cells were **(B)** treated with TNF- $\alpha$  for the indicated time intervals or **(C)** pretreated with TNFR1 neutralizing antibody (10  $\mu$ g/ml), APO (100  $\mu$ M), or DPI (1  $\mu$ M) for 1 h, and then treated with TNF- $\alpha$  for 10 min. NADPH oxidase activity was measured. **(D)** Cells were treated with TNF- $\alpha$  for the indicated time intervals. The cell lysates were subjected to immunoprecipitation using an anti-p47<sup>phox</sup> antibody, and then the immunoprecipitates were analyzed by Western blot using an anti-phospho-tyrosine, anti-phospho-serine, or anti-p47<sup>phox</sup> antibody. **(E)** Cells were treated with TNF- $\alpha$  for the indicated time intervals. The cytosolic and membrane fractions were prepared and analyzed by Western blot using an anti-p47<sup>phox</sup>, anti-G $\alpha$ s, or anti-GAPDH antibody. GAPDH and G $\alpha$ s were used as a marker protein for cytosolic and membrane fractions, respectively. **(F)** Cells were pretreated with TNFR1 neutralizing antibody, NAC, APO, or DPI for 1 h, and then incubated with TNF- $\alpha$  for 10 min. H<sub>2</sub>O<sub>2</sub> and superoxide generation were measured. Data are expressed as mean  $\pm$  SEM of three independent experiments. \* $P$  < 0.05, # $P$  < 0.01 as compared with the cells exposed to vesicle alone **(B)** or TNF- $\alpha$  alone **(C,F)**.

TNF- $\alpha$  time-dependently induced TNFR1, TRAF2, ASK1, and p47<sup>phox</sup> complex formation determined by immunoprecipitation (Figure 3B). Consistently, this interaction was also blocked by pretreatment with a TNF- $\alpha$  neutralizing antibody. To confirm

whether ASK1 phosphorylation is necessary for TNF- $\alpha$ -induced cPLA<sub>2</sub> expression, activation of the ASK1 was assayed by Western blot using an antibody specific for the phosphorylated form of ASK1. We found that TNF- $\alpha$  significantly stimulated



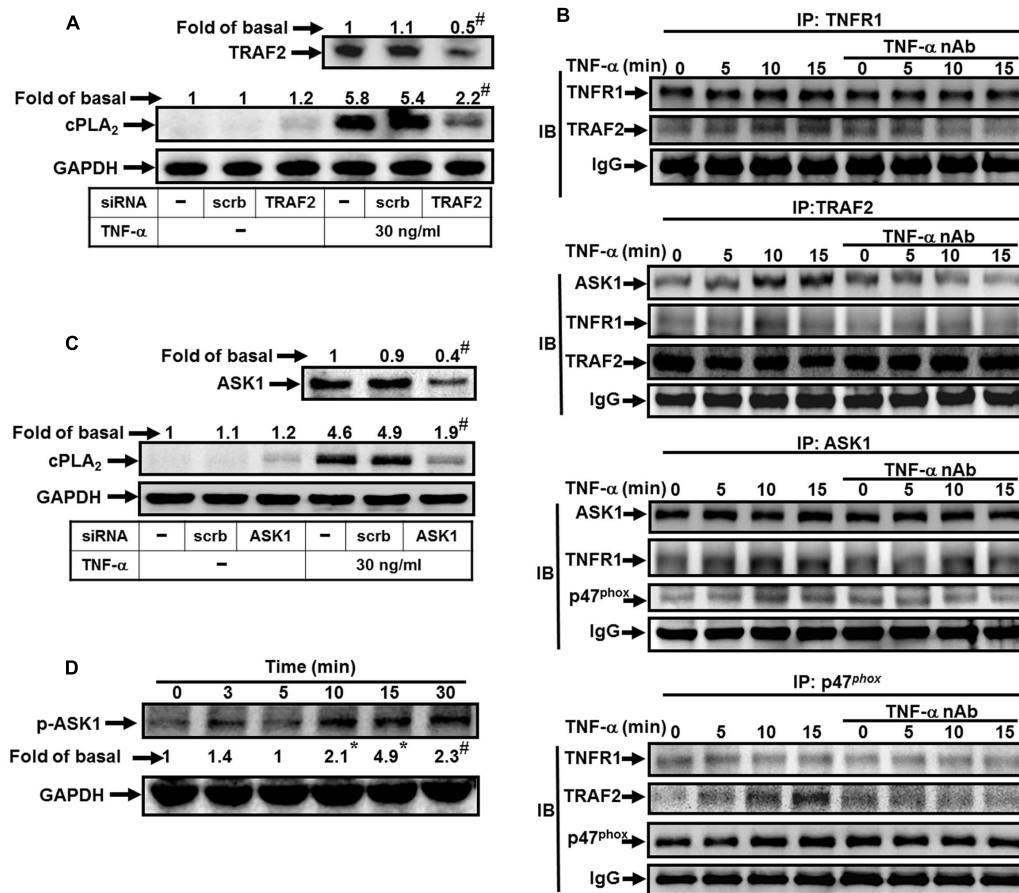


**FIGURE 3 | TNF- $\alpha$  induces TNFR1/TRAF2/ASK1/p47<sup>phox</sup> complex formation.** (A) HPAEpiCs were transfected with scrambled or TRAF2 siRNA, and then incubated with TNF- $\alpha$  for 24 h. The protein levels of TRAF2 and cPLA<sub>2</sub> were determined. (B) Cells were pretreated without or with human TNF- $\alpha$  neutralizing antibody (TNF- $\alpha$  nAb: 1  $\mu$ g/ml) for 1 h and then incubated with TNF- $\alpha$  for the indicated time intervals. The cell lysates were subjected to immunoprecipitation using an anti-TNFR1, anti-TRAF2, anti-ASK1, or anti-p47<sup>phox</sup> antibody, and then the immunoprecipitates were analyzed by Western blot by using an anti-TNFR1, anti-TRAF2, anti-ASK1, anti-p47<sup>phox</sup> or anti-IgG antibody. The results of IgG were used to be the loading control. (C) Cells were transfected with scrambled or ASK1 siRNA, and then incubated with TNF- $\alpha$  for 24 h. The protein levels of ASK1 and cPLA<sub>2</sub> were determined. (D) Cells were treated with TNF- $\alpha$  for the indicated time intervals. The levels of phospho-ASK1 were determined by Western blot. Data are representative of three independent experiments with similar results. \* $P$  < 0.05, # $P$  < 0.01 as compared with the basal group.

ASK1 phosphorylation in a time-dependent manner (Figure 3D). These results suggested that TNF- $\alpha$  stimulates TNFR1, TRAF2, ASK1, and p47<sup>phox</sup> complex formation leading to NADPH oxidase activation and ROS generation in HPAEpiCs.

### TNF- $\alpha$ Induces NADPH Oxidase/ROS Generation and PGE<sub>2</sub> Release via TRAF2, ASK1, and p47<sup>phox</sup>

Next, we investigated whether TRAF2, ASK1 and p47<sup>phox</sup> are involved in TNF- $\alpha$ -induced ROS generation. As shown in Figure 4A, transfection with TRAF2, ASK1, or p47<sup>phox</sup> siRNA markedly inhibited TNF- $\alpha$ -induced superoxide and hydrogen peroxide production. In addition, these siRNAs also inhibited the TNF- $\alpha$ -induced NADPH oxidase activation (Figure 4B). Moreover, our previous findings also provided the correlation between COX-2 and cPLA<sub>2</sub> expression in ATP $\gamma$ S-stimulated

VSMCs with similar molecular mechanisms and functional coupling to amplify the occurrence of vascular inflammation (Lin et al., 2009). Therefore, the synthesis of PGE<sub>2</sub> could be a good index of AA release that is more sensitive than [<sup>3</sup>H]AA mobilization (Berenbaum et al., 2003). In this study, we tested the effect of TNF- $\alpha$  on PGE<sub>2</sub> synthesis as a parameter of cPLA<sub>2</sub> activity in HPAEpiCs. Here, we observed that TNF- $\alpha$ -induced PGE<sub>2</sub> release was reduced by transfection with TRAF2, ASK1, or p47<sup>phox</sup> siRNA (Figure 4C). These results suggested that TNF- $\alpha$  induces ROS generation and PGE<sub>2</sub> release via TRAF2, ASK1, and p47<sup>phox</sup> in HPAEpiCs.

### TNF- $\alpha$ Induces cPLA<sub>2</sub> Expression via NIK, IKK $\alpha$ / $\beta$ , and NF- $\kappa$ B

NF- $\kappa$ B is mainly involved in stress-induced immune and inflammatory responses. Activities of NF- $\kappa$ B are regulated by various inflammatory cytokines such as TNF- $\alpha$  (Lee et al., 2007).



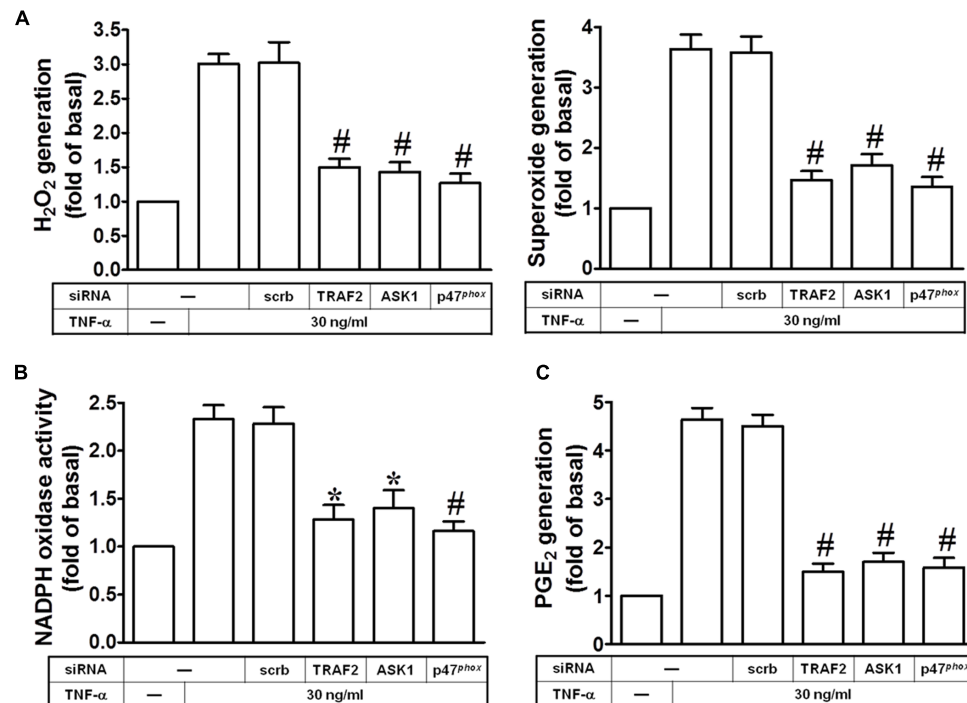


**FIGURE 4 | TNF- $\alpha$  induces NADPH oxidase/ROS generation and PGE<sub>2</sub> release via TRAF2, ASK1, and p47<sup>phox</sup>.** HPAEpiCs were transfected with scrambled, ASK1, p47<sup>phox</sup>, or TRAF2 siRNA, and then incubated with TNF- $\alpha$  for (A,B) 10 min or (C) 24 h. (A) H<sub>2</sub>O<sub>2</sub> and superoxide generation were measured. (B) NADPH oxidase activity was measured. (C) PGE<sub>2</sub> generation was measured. Data are expressed as mean  $\pm$  SEM of three independent experiments. \* $P$  < 0.05, # $P$  < 0.01 as compared with the cells exposed to TNF- $\alpha$  + scrambled siRNA.

The signaling mechanisms mediated activation of NF- $\kappa$ B includes canonical and non-canonical pathways (Tak and Firestein, 2001). The canonical pathway has been well documented to regulate the pathophysiological functions; however, the non-canonical NF- $\kappa$ B-inducing kinase (NIK) pathway is not well understood in the expression of inflammatory genes (Uno et al., 2014). NIK plays central roles in the activation of non-canonical NF- $\kappa$ B pathway (Tak and Firestein, 2001; Uno et al., 2014). NIK was first identified as a TRAF2 interacting protein. In addition, I $\kappa$ Bs associate with NF- $\kappa$ B being inactive forms. I $\kappa$ Bs are phosphorylated by IKK $\alpha$  and IKK $\beta$  then degradation via ubiquitination to release NF- $\kappa$ B and nuclear translocation (Sun, 2011). Therefore, we investigated whether TNF- $\alpha$  induced cPLA<sub>2</sub> expression via NIK, IKK $\alpha$ , and IKK $\beta$  by transfection with respective siRNAs. Transfection with NIK, IKK $\alpha$ , or IKK $\beta$  siRNAs knocked down their own protein levels and subsequently attenuated the TNF- $\alpha$ -induced cPLA<sub>2</sub> expression (Figure 5A). To ascertain whether NF- $\kappa$ B participated in TNF- $\alpha$ -induced cPLA<sub>2</sub> expression, a selective pharmacological inhibitor of NF- $\kappa$ B, Bay11-7082, was used for this purpose. Pretreatment with Bay11-7082 significantly reduced the TNF- $\alpha$ -induced cPLA<sub>2</sub> protein, mRNA, and promoter activity (Figures 5B,C). Moreover, p65 siRNA was used to confirm the role of NF- $\kappa$ B in TNF- $\alpha$ -mediated effects. In addition, transfection with p65 siRNA also reduced TNF- $\alpha$ -induced cPLA<sub>2</sub> expression (Figure 5D) and PGE<sub>2</sub> secretion (Figure 5E) in these cells. The non-canonical NF- $\kappa$ B pathway

is activated through particular TNF- $\alpha$  receptors that bind to the TRAF2 which leads to translocation of NF- $\kappa$ B into nucleus and induction of target gene expression (Tak and Firestein, 2001). Therefore, the translocation of NF- $\kappa$ B p65 was observed by an immunofluorescence microscope. Our findings showed that TNF- $\alpha$  time-dependently stimulated NF- $\kappa$ B p65 translocation from the cytosol into the nucleus fractions (Figure 5F) together with enhancing NF- $\kappa$ B promoter activity (Figure 5G). These results suggested that TNF- $\alpha$ -induced cPLA<sub>2</sub> expression is mediated through NIK, IKK $\alpha$ / $\beta$ , and NF- $\kappa$ B in these cells.

### TNF- $\alpha$ Induces NIK/IKK $\alpha$ / $\beta$ -Dependent NF- $\kappa$ B Activation

In this study, we investigated whether TNF- $\alpha$  stimulates NF- $\kappa$ B p65 activation via an NADPH oxidase/ROS-dependent pathway. As shown in Figure 6A, TNF- $\alpha$  markedly stimulated NF- $\kappa$ B p65 phosphorylation which was inhibited by NAC, DPI, APO or Bay11-7082. In addition, pretreatment with NAC, DPI, or APO also inhibited TNF- $\alpha$ -induced NF- $\kappa$ B promoter activity and NF- $\kappa$ B p65 translocation in HPAEpiCs (Figures 6B,C). On the other hand, we also observed that TNF- $\alpha$  significantly stimulated IKK $\alpha$ / $\beta$  phosphorylation in a time-dependent manner, which was reduced by NAC, DPI or APO (Figure 6D). Finally, we investigated whether TNF- $\alpha$  stimulates NF- $\kappa$ B p65 phosphorylation via an NIK/IKK $\alpha$ / $\beta$  pathway. As shown

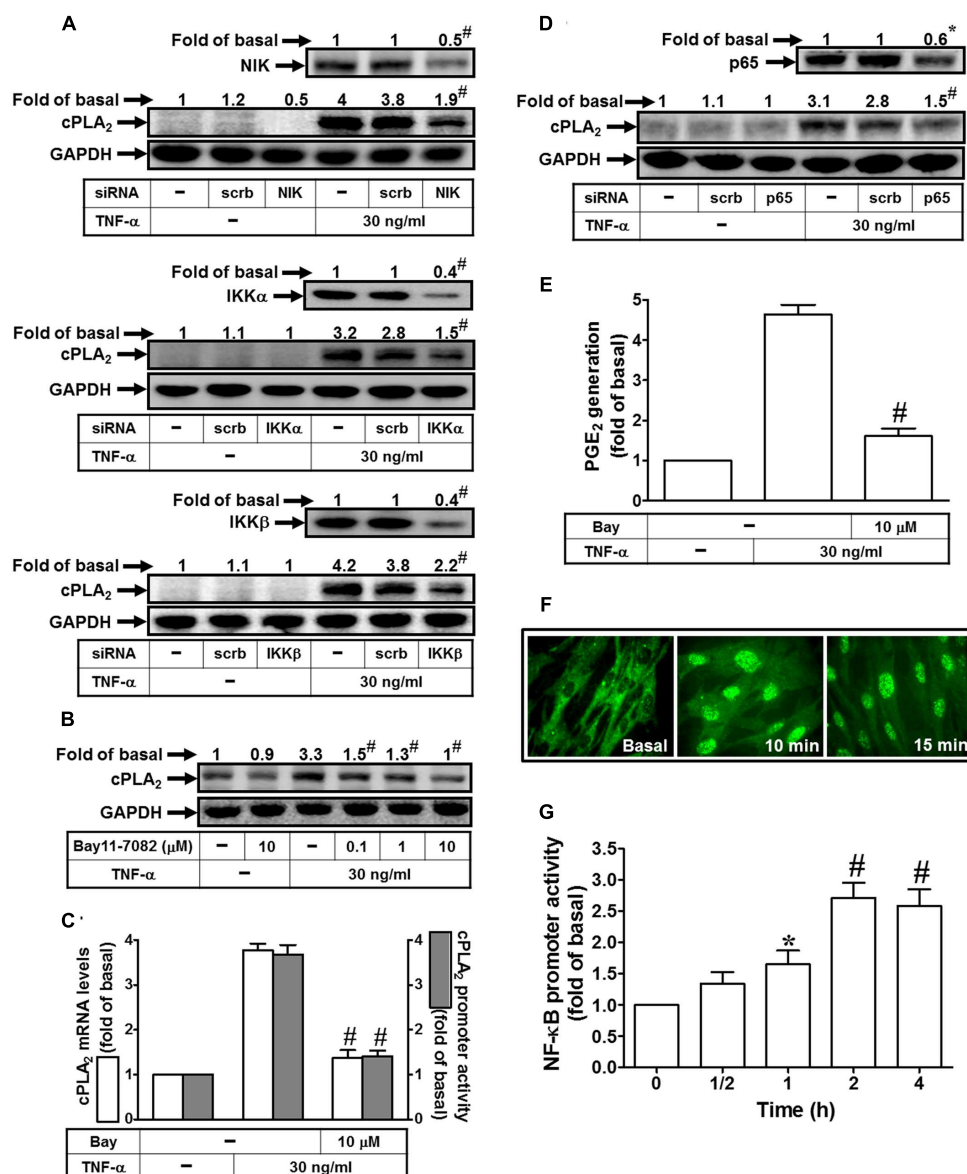


**FIGURE 5 | TNF- $\alpha$  induces cPLA<sub>2</sub> expression via NIK, IKK $\alpha$ / $\beta$ , and NF- $\kappa$ B. (A)** HPAEpiCs were transfected with scrambled, NIK, IKK $\alpha$ , or IKK $\beta$  siRNA, and then incubated with TNF- $\alpha$  for 24 h. The protein levels of NIK, IKK $\alpha$ , IKK $\beta$ , and cPLA<sub>2</sub> were determined by Western blot. **(B)** Cells were pretreated with Bay11-7082 for 1 h, and then incubated with TNF- $\alpha$  for 24 h. The protein levels of cPLA<sub>2</sub> were determined by Western blot. **(C)** Cells were pretreated with Bay11-7082 for 1 h, and then incubated with TNF- $\alpha$  for 6 h. cPLA<sub>2</sub> mRNA levels and promoter activity were determined. **(D)** Cells were transfected with scrambled or p65 siRNA, and then incubated with TNF- $\alpha$  for 24 h. The protein levels of p65 and cPLA<sub>2</sub> were determined. **(E)** Cells were pretreated with Bay11-7082 for 1 h, and then incubated with TNF- $\alpha$  for 24 h. PGE<sub>2</sub> generation was measured. **(F)** Cells were incubated with TNF- $\alpha$  for the indicated time intervals. Cells were fixed, labeled with an anti-p65 antibody, and then FITC-conjugated secondary antibody. Individual cells were imaged. **(G)** Cells were incubated with TNF- $\alpha$  for the indicated time intervals. NF- $\kappa$ B promoter activity was determined. Data are expressed as mean  $\pm$  SEM of three independent experiments. \* $P$  < 0.05, # $P$  < 0.01 as compared with the cells exposed to TNF- $\alpha$  alone **(C,E)** or vesicle alone **(G)**.

in **Figure 6E**, transfection with NIK siRNA attenuated the TNF- $\alpha$ -induced IKK $\alpha$ / $\beta$  and NF- $\kappa$ B p65 activation. In addition, transfection with siRNA of IKK $\alpha$  or IKK $\beta$  markedly inhibited TNF- $\alpha$ -induced NF- $\kappa$ B p65 phosphorylation (**Figure 6E**). These results suggested that TNF- $\alpha$  stimulates NF- $\kappa$ B p65 activation through an NIK/IKK $\alpha$ / $\beta$ -dependent cascade in HPAEpiCs.

## DISCUSSION

Various degrees of inflammation and tissue remodeling are characteristics of different pulmonary disorders including asthma and COPD. Expression of cPLA<sub>2</sub> by mesenchymal cells in several extra-pulmonary sites contributes to the production of PGE<sub>2</sub> which functions as biologically active lipid mediators in

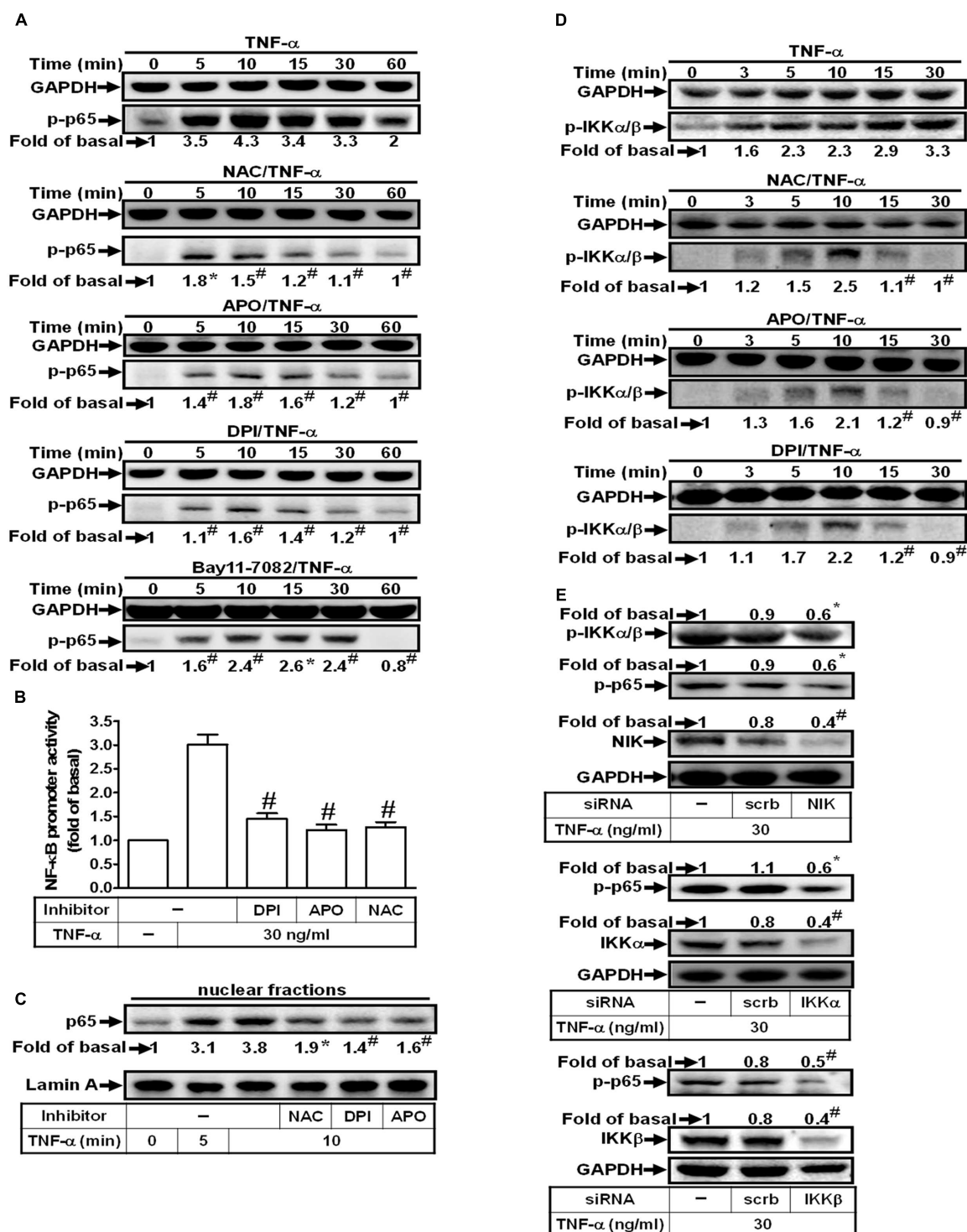


**FIGURE 6 | TNF- $\alpha$  induces NIK/IKK $\alpha/\beta$ -dependent NF- $\kappa$ B activation. (A)** HPAEpiCs were pretreated with NAC (10 mM), DPI (1  $\mu$ M), APO (100  $\mu$ M) or Bay11-7082 (10  $\mu$ M) for 1 h, and then treated with TNF- $\alpha$  for the indicated time intervals. The levels of p65 phosphorylation were determined by Western blot. The raw data of the GAPDH of (A) were provided with a supplementary data (Supplementary Figure S2). **(B)** Cells were pretreated with NAC, DPI, or APO for 1 h, and then treated with TNF- $\alpha$  for 2 h. NF- $\kappa$ B promoter activity was determined. **(C)** Cells were pretreated with NAC, DPI, or APO for 1 h, and then treated with TNF- $\alpha$  for the indicated time intervals. The nuclear fractions were prepared and analyzed by Western blot using an anti-p65 antibody. Lamin A was used as a marker protein for nuclear fractions. **(D)** Cells were pretreated with NAC, APO, or DPI for 1 h, and then treated with TNF- $\alpha$  for the indicated time intervals. The levels of IKK $\alpha/\beta$  phosphorylation were determined by Western blot. **(E)** Cells were transfected with scrambled, NIK, IKK $\alpha$ , or IKK $\beta$  siRNA, and then incubated with TNF- $\alpha$  for 10 min. The protein levels of phospho-IKK $\alpha/\beta$ , phospho-p65, NIK, IKK $\alpha$ , and IKK $\beta$  were determined. Data are expressed as mean  $\pm$  SEM of three independent experiments. \* $P$  < 0.05, # $P$  < 0.01 as compared with the cells exposed to TNF- $\alpha$  alone.

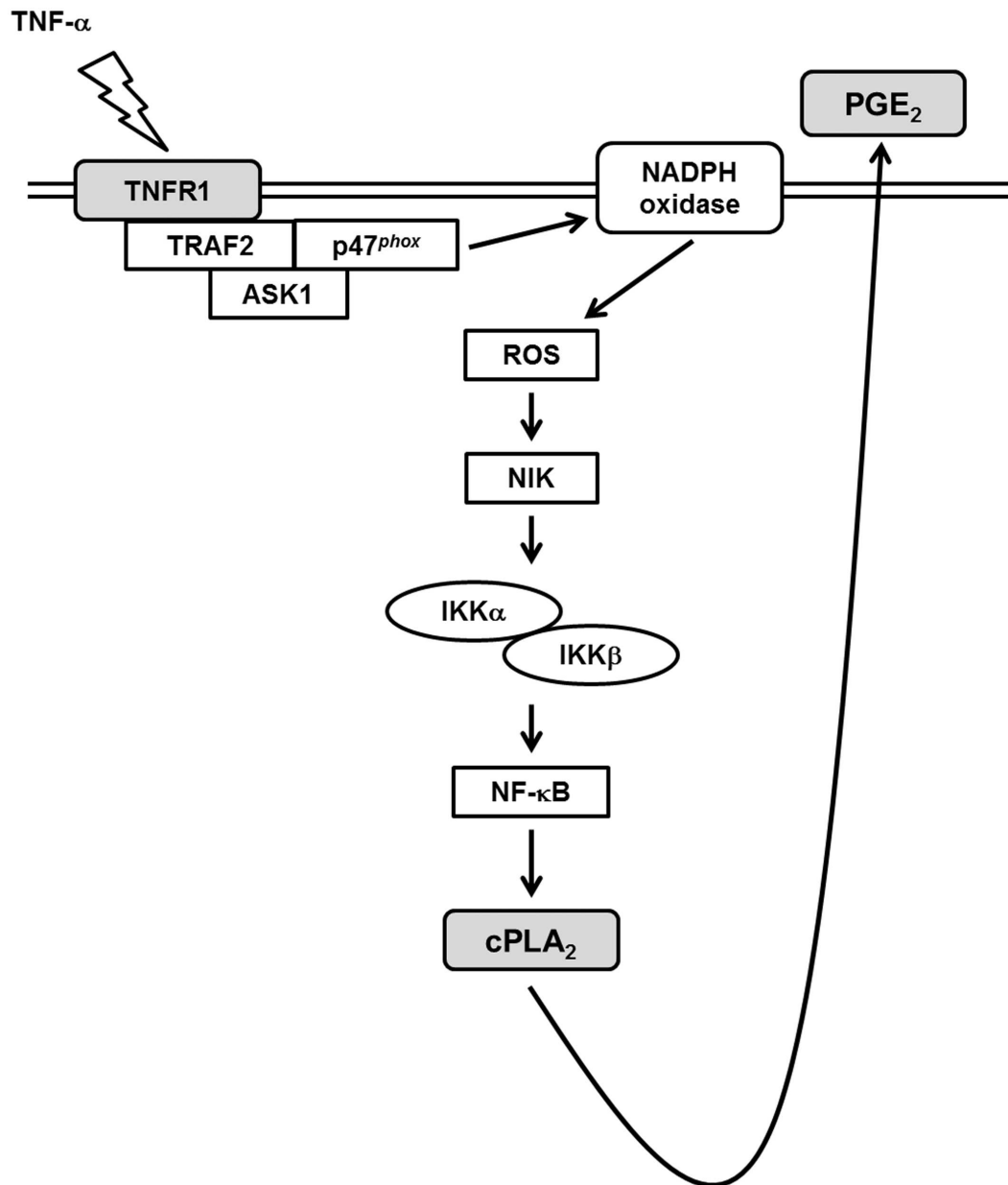


**FIGURE 7 | Schematic representation of the signaling pathways involved in the TNF- $\alpha$ -induced cPLA<sub>2</sub> expression in HPAEpiCs.** The mechanisms underlying TNF- $\alpha$ -mediated activation of TNFR1/TRAF2/ASK1/p47<sup>phox</sup>-dependent NADPH oxidase is required for the expression of cPLA<sub>2</sub> in HPAEpiCs. Finally, the activation of ROS/NIK/IKK $\alpha$ / $\beta$ /NF- $\kappa$ B pathway led to cPLA<sub>2</sub> gene transcription and PGE<sub>2</sub> release.

inflammatory responses (Khanapure et al., 2007). TNF- $\alpha$  has been shown to activate cPLA<sub>2</sub> gene and involves in the late-phase airway hyperresponsiveness and inflammation (Choi et al., 2005), but few studies address the intracellular signaling pathways leading to its expression. It is showed that TNF- $\alpha$  activates ASK1, NADPH oxidase/ROS, IKK $\alpha$ / $\beta$ , and NF- $\kappa$ B pathways in several cell types (Lee et al., 2009, 2011; Byeon et al., 2012). However, whether these signaling molecules participated in cPLA<sub>2</sub> expression in TNF- $\alpha$ -treated HPAEpiCs was not completely defined. In this study, **Figure 7** addressed that pretreatment with

the inhibitors of NADPH oxidase (APO and DPI), ROS (NAC), or NF- $\kappa$ B (Bay11-7082) or transfection with siRNA of ASK1, TRAF2, p47<sup>phox</sup>, NIK, IKK $\alpha$ , IKK $\beta$ , or p65 attenuated TNF- $\alpha$ -induced cPLA<sub>2</sub> expression and PGE<sub>2</sub> production in HPAEpiCs. Our studies confirmed that activation of NADPH oxidase, ROS, NIK, IKK $\alpha$ / $\beta$ , and NF- $\kappa$ B via association of TNFR1, TRAF2, ASK1, and p47<sup>phox</sup> may be essential for cPLA<sub>2</sub> expression in TNF- $\alpha$ -stimulated HPAEpiCs. cPLA<sub>2</sub> induction and TNF- $\alpha$ -induced complex formation of TNFR1, TRAF2, ASK1, and p47<sup>phox</sup> were blocked by pretreatment with TNF- $\alpha$  neutralizing antibody.

These results suggested that up-regulation of cPLA<sub>2</sub> by TNF- $\alpha$  is, at least in part, mediated through the cooperation of TNFR1, TRAF2, ASK1, and NADPH oxidase leading to ROS generation and ultimately activates NF- $\kappa$ B pathway.

Several reports indicate that TNF- $\alpha$  may regulate inflammatory protein expression via activating various downstream protein kinases (Lin et al., 2004; Lee et al., 2009). Effects of TNF- $\alpha$  are achieved by binding to one of two distinct receptors, known as TNFR1 and TNFR2 (Lee et al., 2009). However, it is reported that TNF- $\alpha$  activates the proinflammatory or the programmed cell death pathways leading to tissue injury via binding to TNFR1 (van Vliet et al., 2005; Lee et al., 2009). In contrast, TNFR2 is involved in promoting tissue repair and angiogenesis (Bradley, 2008). Indeed, transfection with TNFR1 siRNA attenuated NADPH oxidase and ROS generation, revealing that TNFR1 plays a key role in modulating inflammatory responses in TNF- $\alpha$ -stimulated HPAEpiCs.

Reactive oxygen species are generated by various enzymatic reactions and chemical processes or can directly be inhaled from environment (Lee and Yang, 2012). Formation of ROS takes place constantly in every cell during normal metabolic processes. Activated phagocytic cells could produce large amounts of ROS induced by inhaled particles, microorganisms, or other mediators leading to the activation of the membrane-bound NADPH oxidase complex and the generation of superoxide anion (Lee and Yang, 2012). NADPH oxidase is recognized to be a key player in the generation of ROS when the cells or tissues exposed to various insults. Upon activation of NADPH oxidase by various stimuli, the complex of catalytic subunit (gp91<sup>phox</sup>) and p22<sup>phox</sup> is anchored in plasma membrane which assembles with the regulatory subunits (p47<sup>phox</sup>, p40<sup>phox</sup>, p67<sup>phox</sup>, and small GTPase Rac) distributed in cytoplasm and leading to ROS generation (El-Benna et al., 2008). The initiation of the assembly NADPH oxidase is first dependent on the phosphorylation of p47<sup>phox</sup> triggered by various activated protein kinases. Thus, p47<sup>phox</sup> plays a role in the membrane translocation and ROS generation. Indeed, our results confirmed that blockage ROS accumulation either by a ROS scavenger (NAC), the inhibitors of NADPH oxidase (DPI and APO) or transfection with p47<sup>phox</sup> siRNA significantly attenuated TNF- $\alpha$ -induced cPLA<sub>2</sub> expression and PGE<sub>2</sub> synthesis. DPI or APO pretreatment reduced TNF- $\alpha$ -stimulated ROS generation. These results revealed that TNF- $\alpha$  increased cPLA<sub>2</sub>/PGE<sub>2</sub> expression via NADPH oxidase-dependent ROS generation. p47<sup>phox</sup> is phosphorylated on several serine residues within the polybasic region of the protein, and these multiple phosphorylation events induce conformational changes that permit p47<sup>phox</sup> to interact with the cytoplasmic tail of p22<sup>phox</sup> and to initiate the formation of the active oxidase (Dang et al., 2006). In lung endothelial cells, Src regulates tyrosine phosphorylation of p47<sup>phox</sup> in hyperoxia-induced activation of NADPH oxidase and generation of ROS (Chowdhury et al., 2005). Moreover, in HPAEpiCs, we found that TNF- $\alpha$  could stimulate both serine and tyrosine phosphorylation of p47<sup>phox</sup>, and then promotes p47<sup>phox</sup> translocation from the cytosol to the membrane.

TRAF2 plays a central role in the cellular responses to stress and cytokines via their regulation of stress kinases, resulting in the activation of key transcription factors, including NF- $\kappa$ B, c-Jun, and ATF2. Upon exposure to TNF- $\alpha$ , TRAF2 is recruited directly to TNFR2 or via TRADD to TNFR1, which results in the activation of JNK1/2, p38 MAPK and NF- $\kappa$ B (Cabal-Hierro and Lazo, 2012). However, our previous report indicated that Jak2 also mediates the TNF- $\alpha$ -induced cPLA<sub>2</sub> expression (Yang et al., 2014). To evaluate the relationship between Jak2 and MAPKs pathways, we have performed some more experiments to determine whether there is any connection between MAPKs and Jak2 using pharmacological inhibitors (AG490, SB202190, SP600125 and U0126). We found that pretreatment with AG490 had no effect on TNF- $\alpha$ -stimulated MAPKs phosphorylation, or with MAPK inhibitors (SB202190, SP600125 and U0126) failed to inhibit Jak2 phosphorylation (Supplementary Figure S1). These results suggested that Jak2 and MAPKs are independent pathways to mediate the TNF- $\alpha$ -induced cPLA<sub>2</sub> expression. Here, we also found that TNF- $\alpha$ -induced cPLA<sub>2</sub> expression and PGE<sub>2</sub> release were markedly inhibited by blockage TRAF2. In addition, we also observed that TNF- $\alpha$  induced TNFR1 and TRAF2 complex formation. Previous study indicated that TNF- $\alpha$  stimulated the formation of a TNFR1/c-Src/p47<sup>phox</sup> complex in human airway smooth muscle cells (Lee et al., 2009). Here, we demonstrated that TNF- $\alpha$  induced TNFR1, TRAF2, and p47<sup>phox</sup> complex formation which was blocked by pretreatment with TNF- $\alpha$  neutralizing antibody, and leading to cPLA<sub>2</sub> expression in HPAEpiCs.

ASK1, a member of the MAP3K family, regulates the activation of MAPK kinase 4 (MKK4)/MKK7-JNK and MKK3/6-p38 pathways. ASK1 can be activated by various types of stresses, such as ROS, TNF- $\alpha$ , and ER stress, and exerts pivotal roles in regulating cell apoptosis, differentiation, and inflammation (Fujino et al., 2007). Therefore, unregulated ASK1 activation is tightly related to various diseases. Moreover, we found that inhibition of ASK1 markedly reduced TNF- $\alpha$ -induced cPLA<sub>2</sub> expression and PGE<sub>2</sub> release. TNF- $\alpha$  also stimulated ASK1 phosphorylation in these cells. Upon exposure to ROS, Trx dissociated from the N-terminal of ASK1, which then became fully activated by recruitment of TRAF2 and TRAF6 (Fujino et al., 2007). Indeed, we found consistent results that TNF- $\alpha$  induces TRAF2 and ASK1 complex formation which is also blocked by pretreatment with TNF- $\alpha$  neutralizing antibody. In this study, we are the first to show a novel role of TNFR1/TRAF2/ASK1/p47<sup>phox</sup> complex formation in TNF- $\alpha$ -induced NADPH oxidase activation and ROS production in HPAEpiCs. In the future, we will further determine which domains of TNFR1, TRAF2, ASK1, and p47<sup>phox</sup> are involved in protein-protein interactions caused by TNF- $\alpha$ . Although ROS have been shown to regulate ASK1 activation (Fujino et al., 2007), in this study, we emphasized the critical role of ASK1 in TNF- $\alpha$ -induced ROS generation. Thus, in addition to the role of ROS in ASK1 activation, our results supported that the opposite hierarchical relationship exists between ROS and ASK1. Therefore, NADPH oxidase/ROS may act both as upstream regulators and downstream effectors of ASK1 in various cell types.



The NF- $\kappa$ B/Rel family complex, a redox-sensitive transcription factor, participates in controlling expression of many inflammatory genes (Sun, 2011). NF- $\kappa$ B usually forms heterodimer by p50 and p65/RelA subunits. In resting cells, nuclear translocation signal of NF- $\kappa$ B is masked by binding with an inhibitor protein called inhibitory  $\kappa$ B (I $\kappa$ B) as an inactive non-DNA-binding form. Upon the stimulation by various NF- $\kappa$ B inducers, two serine residues of I $\kappa$ B $\alpha$  is phosphorylated, which then being ubiquitinated by E3 ubiquitin-ligases (E3RSI $\kappa$ B) and subsequently degraded by the 26S proteasome (Sun, 2011). The released NF- $\kappa$ B dimers can then translocate into the nucleus and bind to the  $\kappa$ B elements on the promoter of target genes. NIK was first identified as a TRAF2 interacting protein (Tak and Firestein, 2001). In inactive form, NF- $\kappa$ B transcription factors binds with the inhibitory proteins I $\kappa$ Bs. IKK $\alpha$  and IKK $\beta$  regulates the phosphorylation of I $\kappa$ B proteins, which then being ubiquitination and degradation leading to nuclear localization of NF- $\kappa$ B transcription factors (Sun, 2011). In this study, inhibition of NIK, IKK $\alpha$ , IKK $\beta$ , and NF- $\kappa$ B markedly inhibited TNF- $\alpha$ -induced cPLA<sub>2</sub> expression. Various extracellular stimuli such as TNF- $\alpha$  and IL-1 $\beta$ , viruses and environmental particulates (PM10s), and oxidative stress regulate the activation of NF- $\kappa$ B (Sun, 2011). Here, we reported that TNF- $\alpha$  time-dependently induced phosphorylation and translocation of NF- $\kappa$ B p65 and NF- $\kappa$ B promoter activity via an NADPH oxidase/ROS pathway. Otherwise, we also proved that TNF- $\alpha$  significantly induced IKK $\alpha$ /IKK $\beta$  phosphorylation via an NIK-dependent signaling, and then promoted NF- $\kappa$ B activation. Thus, we recognized that TNF- $\alpha$ -induced ROS generation may promote activation of the NIK/IKK $\alpha$ /IKK $\beta$ /NF- $\kappa$ B pathway in HPAEpiCs.

COX-2 and cPLA<sub>2</sub> are tightly regulated by various mediators in several species (Beasley, 1999; Ali et al., 2008; Pavicevic et al., 2008). cPLA<sub>2</sub> hydrolyzes the membrane phospholipids, resulting in the release of AA, which is further converted by the constitutive enzyme COX-1 or by the inducible COX-2, and PG synthases to biologically active PGs (DeWitt, 1999). On the other hand, several reports indicated that the levels of PGE<sub>2</sub> are also degraded by an important enzyme, 15-hydroxyprostaglandin dehydrogenase (15-PGDH) to regulate the levels of PGEs (Pomini et al., 1999; Otani et al., 2006; Thiel et al., 2009). In our previous study, up-regulation of COX-2 in TSMCs has been shown to enhance PGE<sub>2</sub> synthesis induced by LPS (Luo et al., 2003). Moreover, we also provided insights into the correlation between COX-2 and cPLA<sub>2</sub> expression in ATP $\gamma$ S-stimulated VSMCs with similar molecular mechanisms and functional coupling to amplify the occurrence of vascular inflammation (Lin et al., 2009). PGE<sub>2</sub> treatment also induced cPLA<sub>2</sub> expression in VSMCs, which exerted as a positive feedback regulator in this response (Lin et al., 2009). Therefore, the synthesis of PGE<sub>2</sub> could be a good index of AA release that is more sensitive than [<sup>3</sup>H]AA mobilization (Berenbaum et al., 2003) and PGE<sub>2</sub> may further induce cPLA<sub>2</sub> expression to amplify the occurrence of pulmonary inflammation. In this study, although the effect of PGE<sub>2</sub> on COX-2 expression was not investigated, we tested the effect of TNF- $\alpha$  on PGE<sub>2</sub> synthesis as a parameter of cPLA<sub>2</sub> activity which may be an important issue for further study in HPAEpiCs.

## CONCLUSION

According to the literature reports and our results, **Figure 7** addresses a model for the molecular mechanisms of TNF- $\alpha$ -stimulated cPLA<sub>2</sub> expression and PGE<sub>2</sub> release in HPAEpiCs. To our knowledge, this is the first study to indicate that in HPAEpiCs, TNF- $\alpha$ -regulated activation of TNFR1/TRAF2/ASK1/p47<sup>phox</sup>-dependent NADPH oxidase is required for the expression of cPLA<sub>2</sub>. Finally, activation of the ROS/NIK/IKK $\alpha$ /IKK $\beta$ /NF- $\kappa$ B pathway leads to cPLA<sub>2</sub> gene activation and expression. It is an important link for TNF- $\alpha$ -regulated cPLA<sub>2</sub> expression in the pathogenesis of lung inflammatory diseases. Therefore, uncovering the signaling components in TNF- $\alpha$ -mediated cPLA<sub>2</sub> expression in HPAEpiCs is important to develop new therapeutic strategies in pulmonary diseases.

## AUTHOR CONTRIBUTIONS

C-CL, W-NL, R-LC, C-yW, L-DH, and C-MY substantially contributed to the conception or design of the work, the acquisition, analysis, and interpretation of data for the work. C-CL, W-NL, R-LC, C-yW, L-DH, and C-MY drafted the work and revised it critically for important intellectual content. C-CL, W-NL, R-LC, C-yW, L-DH, and C-MY finally approved the version to be published. C-CL, W-NL, R-LC, C-yW, L-DH, and C-MY agreed to be accountable for all aspects of the work in ensuring that questions related to the accuracy or integrity of any part of the work are appropriately investigated and resolved.

## FUNDING

This work was supported by the Ministry of Education, Taiwan, Grant number: EMRPD1E1641; the Ministry of Science and Technology, Taiwan, Grant number: MOST104-2320-B-182A-003-MY3, MOST104-2320-B-182-010 and MOST105-2320-B-182-005-MY3; Chang Gung Medical Research Foundation, Grant number: CMRPD1C0103, CMRPD1C0563, CMRPD1B0332, CMRPD1F0021, CMRPG3B1093, CMRPG3C1303, CMRPG3A0051, and CMRPG3E2231; and Fu Jen Catholic University Research Foundation, Grant number: 9991A01.

## ACKNOWLEDGMENTS

We thank Ms. Yu-Wen Chen for her technical assistance.

## SUPPLEMENTARY MATERIAL

The Supplementary Material for this article can be found online at: <http://journal.frontiersin.org/article/10.3389/fphar.2016.00447/full#supplementary-material>

## REFERENCES

- Ali, K., Lund-Katz, S., Lawson, J., Phillips, M. C., and Rader, D. J. (2008). Structure function properties of the apoE-dependent COX-2 pathway in vascular smooth muscle cells. *Atherosclerosis* 196, 201–209. doi: 10.1016/j.atherosclerosis.2007.03.038
- Barnes, P. J. (1989). New concepts in the pathogenesis of bronchial hyperresponsiveness and asthma. *J. Allergy Clin. Immunol.* 83, 1013–1026. doi: 10.1016/0091-6749(89)90441-7
- Beasley, D. (1999). COX-2 and cytosolic PLA2 mediate IL-1 $\beta$ -induced cAMP production in human vascular smooth muscle cells. *Am. J. Physiol.* 276, H1369–H1378.
- Berenbaum, F., Humber, L., Berezat, G., and Thirion, S. (2003). Concomitant recruitment of ERK1/2 and p38 MAPK signalling pathway is required for activation of cytoplasmic phospholipase A2 via ATP in articular chondrocytes. *J. Biol. Chem.* 278, 13680–13687. doi: 10.1074/jbc.M211570200
- Borsch-Haubold, A. G., Bartoli, F., Asselin, J., Dudler, T., Kramer, R. M., Apitz-Castro, R., et al. (1998). Identification of the phosphorylation sites of cytosolic phospholipase A2 in agonist-stimulated human platelets and HeLa cells. *J. Biol. Chem.* 273, 4449–4458. doi: 10.1074/jbc.273.8.4449
- Bradley, J. R. (2008). TNF-mediated inflammatory disease. *J. Pathol.* 214, 149–160. doi: 10.1002/path.2287
- Byeon, H. E., Um, S. H., Yim, J. H., Lee, H. K., and Pyo, S. (2012). Ohioensin F suppresses TNF- $\alpha$ -induced adhesion molecule expression by inactivation of the MAPK, Akt and NF- $\kappa$ B pathways in vascular smooth muscle cells. *Life Sci.* 90, 396–406. doi: 10.1016/j.lfs.2011.12.017
- Cabal-Hierro, L., and Lazo, P. S. (2012). Signal transduction by tumor necrosis factor receptors. *Cell. Signal.* 24, 1297–1305. doi: 10.1016/j.cellsig.2012.02.006
- Chi, P. L., Chen, Y. W., Hsiao, L. D., Chen, Y. L., and Yang, C. M. (2012). Heme oxygenase-1 attenuates IL-1 $\beta$ -induced cPLA2 expression via a decrease in NADPH oxidase/ROS/AP-1 activation in human rheumatoid arthritis synovial fibroblasts. *Arthritis Rheum.* 64, 2114–2125. doi: 10.1002/art.34371
- Chi, P. L., Liu, C. J., Lee, I. T., Chen, Y. W., Hsiao, L. D., and Yang, C. M. (2014). HO-1 induction by CO-RM2 attenuates TNF- $\alpha$ -induced cytosolic phospholipase A2 expression via inhibition of PKC $\alpha$ -dependent NADPH oxidase/ROS and NF- $\kappa$ B. *Mediators Inflamm.* 2014:279171. doi: 10.1155/2014/279171
- Chi, P. L., Luo, S. F., Hsieh, H. L., Lee, I. T., Hsiao, L. D., Chen, Y. L., et al. (2011). cPLA2 induction and PGE2 release by IL-1 $\beta$  via the MyD88-dependent and cooperation of p300, Akt, and NF- $\kappa$ B pathway in human rheumatoid arthritis synovial fibroblasts. *Arthritis Rheum.* 63, 2905–2917. doi: 10.1002/art.30504
- Choi, I. W., Sun, K., Kim, Y. S., Ko, H. M., Im, S. Y., Kim, J. H., et al. (2005). TNF- $\alpha$  induces the late-phase airway hyperresponsiveness and airway inflammation through cytosolic phospholipase A2 activation. *J. Allergy Clin. Immunol.* 116, 537–543. doi: 10.1016/j.jaci.2005.05.034
- Chowdhury, A. K., Watkins, T., Parinandi, N. L., Saatian, B., Kleinberg, M. E., Usatyuk, V., et al. (2005). Src-mediated tyrosine phosphorylation of p47phox in hyperoxia-induced activation of NADPH oxidase and generation of reactive oxygen species in lung endothelial cells. *J. Biol. Chem.* 280, 20700–20711. doi: 10.1074/jbc.M411722200
- Dang, P. M., Elbim, C., Marie, J. C., Chianotto, M., Gougerot-Pocidallo, M. A., and El-Benna, J. (2006). Anti-inflammatory effect of interleukin-10 on human neutrophil respiratory burst involves inhibition of GM-CSF-induced p47phox phosphorylation through a decrease in ERK1/2 activity. *FASEB J.* 20, 1504–1506. doi: 10.1096/fj.05-5395fje
- DeWitt, D. L. (1999). Cox-2-selective inhibitors: the new super aspirins. *Mol. Pharmacol.* 55, 625–631.
- Dieter, P., Kolada, A., Kamionka, S., Schadow, A., and Kaszkin, M. (2002). Lipopolysaccharide-induced release of arachidonic acid and prostaglandins in liver macrophages: regulation by Group IV cytosolic phospholipase A2, but not by Group V and Group IIA secretory phospholipase A2. *Cell. Signal.* 14, 199–204. doi: 10.1016/S0898-6568(01)00243-1
- El-Benna, J., Dang, P. M. C., and Gougerot-Pocidallo, M. A. (2008). Priming of the neutrophil NADPH oxidase activation: role of p47phox phosphorylation and NOX2 mobilization to the plasma membrane. *Semin. Immunopathol.* 30, 279–289. doi: 10.1007/s00281-008-0118-3
- Fujino, G., Noguchi, T., Matsuzawa, A., Yamauchi, S., Saitoh, M., Takeda, K., et al. (2007). Thioredoxin and TRAF family proteins regulate reactive oxygen species-dependent activation of ASK1 through reciprocal modulation of the N-terminal homophilic interaction of ASK1. *Mol. Cell. Biol.* 27, 8152–8163. doi: 10.1128/MCB.00227-07
- Gilroy, D. W., Newson, J., Sawmynaden, P., Willoughby, D. A., and Croxtall, J. D. (2004). A novel role for phospholipase A2 isoforms in the checkpoint control of acute inflammation. *FASEB J.* 18, 489–498. doi: 10.1096/fj.03-0837com
- Hashimoto, S., Gon, Y., Matsumoto, K., Takeshita, I., and Horie, T. (2001). N-acetylcysteine attenuates TNF- $\alpha$ -induced p38 MAP kinase activation and p38 MAP kinase-mediated IL-8 production by human pulmonary vascular endothelial cells. *Br. J. Pharmacol.* 132, 270–276. doi: 10.1038/sj.bjp.0703787
- Henderson, W. R. Jr., Tang, L. O., Chu, S. J., Tsao, S. M., Chiang, G. K., Jones, F., et al. (2002). A role for cysteinyl leukotrienes in airway remodeling in a mouse asthma model. *Am. J. Respir. Crit. Care Med.* 165, 108–116. doi: 10.1164/ajrccm.165.1.2105051
- Hsieh, H. L., Wu, C. Y., Hwang, T. L., Yen, M. H., Parker, P., and Yang, C. M. (2006). BK-induced cytosolic phospholipase A2 expression via sequential PKC- $\alpha$ , p42/p44 MAPK, and NF- $\kappa$ B activation in rat brain astrocytes. *J. Cell. Physiol.* 206, 246–254. doi: 10.1002/jcp.20457
- Hsu, C. K., Lee, I. T., Lin, C. C., Hsiao, L. D., and Yang, C. M. (2014). Nox2/ROS-dependent human antigen R translocation contributes to TNF- $\alpha$ -induced SOCS-3 expression in human tracheal smooth muscle cells. *Am. J. Physiol. Lung Mol. Cell. Biol.* 306, L521–L533. doi: 10.1152/ajplung.00274.2013
- Hsu, M. J., Chang, C. K., Chen, M. C., Chen, B. C., Ma, H. P., Hong, C. Y., et al. (2010). Apoptosis signal-regulating kinase 1 in peptidoglycan-induced COX-2 expression in macrophages. *J. Leukoc. Biol.* 87, 1069–1082. doi: 10.1189/jlb.1009668
- Hulkower, K. I., Wertheimer, S. J., Levin, W., Coffey, J. W., Anderson, C. M., Chen, T., et al. (1994). Interleukin-1 $\beta$  induces cytosolic phospholipase A2 and prostaglandin H synthase in rheumatoid synovial fibroblasts. Evidence for their roles in the production of prostaglandin E2. *Arthritis Rheum.* 37, 653–661. doi: 10.1002/art.1780370508
- Huwiler, A., Feuerherm, A. J., Sakem, B., Pastukhov, O., Filipenko, I., Nguyen, T., et al. (2012). The omega3-polyunsaturated fatty acid derivatives AVX001 and AVX002 directly inhibit cytosolic phospholipase A2 and suppress PGE2 formation in mesangial cells. *Br. J. Pharmacol.* 167, 1691–1701. doi: 10.1111/j.1476-5381.2012.02114.x
- Khanapure, S. P., Garvey, D. S., Janero, D. R., and Letts, L. G. (2007). Eicosanoids in inflammation: biosynthesis, pharmacology, and therapeutic frontiers. *Curr. Top. Med. Chem.* 7, 311–340. doi: 10.2174/15680260779941314
- Lee, C. W., Lin, C. C., Lee, I. T., Lee, H. C., and Yang, C. M. (2011). Activation and induction of cytosolic phospholipase A2 by TNF- $\alpha$  mediated through Nox2, MAPKs, NF- $\kappa$ B, and p300 in human tracheal smooth muscle cells. *J. Cell. Physiol.* 226, 2103–2114. doi: 10.1002/jcp.22537
- Lee, C. W., Lin, C. C., Lin, W. N., Liang, K. C., Luo, S. F., Wu, C. B., et al. (2007). TNF- $\alpha$  induces MMP-9 expression via activation of Src/EGFR, PDGFR/PI3K/Akt cascade and promotion of NF- $\kappa$ B/p300 binding in human tracheal smooth muscle cells. *Am. J. Physiol. Lung Cell. Mol. Physiol.* 292, L799–L812. doi: 10.1152/ajplung.00311.2006
- Lee, I. T., Lin, C. C., Lee, C. Y., Hsieh, P. W., and Yang, C. M. (2013). Protective effects of (-)-epigallocatechin-3-gallate against TNF- $\alpha$ -induced lung inflammation via ROS-dependent ICAM-1 inhibition. *J. Nutr. Biochem.* 24, 124–136. doi: 10.1016/j.jnutbio.2012.03.009
- Lee, I. T., Luo, S. F., Lee, C. W., Wang, S. W., Lin, C. C., Chang, C. C., et al. (2009). Overexpression of HO-1 protects against TNF- $\alpha$ -mediated airway inflammation by down-regulation of TNFR1-dependent oxidative stress. *Am. J. Pathol.* 175, 519–532. doi: 10.2353/ajpath.2009.090016
- Lee, I. T., Wang, S. W., Lee, C. W., Chang, C. C., Lin, C. C., Luo, S. F., et al. (2008). Lipoteichoic acid induces HO-1 expression via the TLR2/MyD88/c-Src/NADPH oxidase pathway and Nrf2 in human tracheal smooth muscle cells. *J. Immunol.* 181, 5098–5110. doi: 10.4049/jimmunol.181.7.5098
- Lee, I. T., and Yang, C. M. (2012). Role of NADPH oxidase/ROS in pro-inflammatory mediators-induced airway and pulmonary diseases. *Biochem. Pharmacol.* 84, 581–590. doi: 10.1016/j.bcp.2012.05.005
- Leslie, C. C. (1997). Properties and regulation of cytosolic phospholipase A2. *J. Biol. Chem.* 272, 16709–16712. doi: 10.1074/jbc.272.27.16709
- Li, J. M., Fan, L. M., Christie, M. R., and Shah, A. M. (2005). Acute tumor necrosis factor  $\alpha$  signaling via NADPH oxidase in microvascular endothelial cells:

- role of p47phox phosphorylation and binding to TRAF4. *Mol. Cell. Biol.* 25, 2320–2330. doi: 10.1128/MCB.25.6.2320-2330.2005
- Lin, C. C., Hsiao, L. D., Chien, C. S., Lee, C. W., Hsieh, J. T., and Yang, C. M. (2004). Tumor necrosis factor- $\alpha$ -induced cyclooxygenase-2 expression in human tracheal smooth muscle cells: involvement of p42/p44 and p38 mitogen-activated protein kinases and nuclear factor- $\kappa$ B. *Cell. Signal.* 16, 597–607. doi: 10.1016/j.cellsig.2003.10.002
- Lin, C. C., Lin, W. N., Wang, W. J., Sun, C. C., Tung, W. H., Wang, H. H., et al. (2009). Functional coupling expression of COX-2 and cPLA2 induced by ATP in rat vascular smooth muscle cells: role of ERK1/2, p38 MAPK, and NF- $\kappa$ B. *Cardiovasc. Res.* 82, 522–531. doi: 10.1093/cvr/cvp069
- Luo, S. F., Lin, W. N., Yang, C. M., Lee, C. W., Liao, C. H., Leu, Y. L., et al. (2006). Induction of cytosolic phospholipase A2 by lipopolysaccharide in canine tracheal smooth muscle cells: involvement of MAPKs and NF- $\kappa$ B pathways. *Cell. Signal.* 18, 1201–1211. doi: 10.1016/j.cellsig.2005.09.011
- Luo, S. F., Wang, C. C., Chien, C. S., Hsiao, L. D., and Yang, C. M. (2003). Induction of cyclooxygenase-2 by lipopolysaccharide in canine tracheal smooth muscle cells: involvement of p42/p44 and p38 mitogen-activated protein kinases and nuclear factor- $\kappa$ B pathways. *Cell. Signal.* 15, 497–509. doi: 10.1016/S0898-6568(02)00135-3
- Morgan, M. J., and Liu, Z. G. (2011). Crosstalk of reactive oxygen species and NF- $\kappa$ B signaling. *Cell Res.* 21, 103–115. doi: 10.1038/cr.2010.178
- Nagase, T., Uozumi, N., Ishii, S., Kume, K., Izumi, T., Ouchi, Y., et al. (2000). Acute lung injury by sepsis and acid aspiration: a key role for cytosolic phospholipase A2. *Nat. Immunol.* 1, 42–46. doi: 10.1038/76897
- Otani, T., Yamaguchi, K., Scherl, E., Du, B., Tai, H. H., Greifer, M., et al. (2006). Levels of NAD<sup>+</sup>-dependent 15-hydroxyprostaglandin dehydrogenase are reduced in inflammatory bowel disease: evidence for involvement of TNF- $\alpha$ . *Am. J. Physiol. Gastrointest. Liver Physiol.* 290, G361–G368. doi: 10.1152/ajpgi.00348.2005
- Pavicevic, Z., Leslie, C. C., and Malik, K. U. (2008). cPLA2 phosphorylation at S515 and S505 is required for arachidonic acid release in vascular smooth muscle cell. *J. Lipid Res.* 49, 724–737. doi: 10.1194/jlr.M700419-JLR200
- Pomini, F., Caruso, A., and Challis, J. R. G. (1999). Interleukin-10 modifies the effects of interleukin-1 $\beta$  and tumor necrosis factor- $\alpha$  on the activity and expression of prostaglandin H synthase-2 and the NAD<sup>+</sup>-dependent 15-hydroxyprostaglandin dehydrogenase in cultured term human villous trophoblast and chorion trophoblast cells. *J. Clin. Endocrinol. Metab.* 84, 4645–4651.
- Rahman, A., Kefer, J., Bando, M., Niles, W. D., and Malik, A. B. (1998). E-selectin expression in human endothelial cells by TNF- $\alpha$ -induced oxidant generation and NF- $\kappa$ B activation. *Am. J. Physiol.* 275, L533–L544.
- Six, D. A., and Dennis, E. A. (2000). The expanding superfamily of phospholipase A2 enzymes: classification and characterization. *Biochim. Biophys. Acta* 1488, 1–19. doi: 10.1016/S1388-1981(00)00105-0
- Soga, M., Matsuzawa, A., and Ichijo, H. (2012). Oxidative stress-induced diseases via the ASK1 signaling pathway. *Int. J. Cell Biol.* 2012:439587. doi: 10.1155/2012/439587
- Sun, S. C. (2011). Non-canonical NF- $\kappa$ B signaling pathway. *Cell Res.* 21, 71–85. doi: 10.1038/cr.2010.177
- Tak, P. P., and Firestein, G. S. (2001). NF- $\kappa$ B: a key role in inflammatory diseases. *J. Clin. Invest.* 107, 7–11. doi: 10.1172/JCI11830
- Thiel, A., Ganesan, A., Mrena, J., Junnila, S., Nykänen, A., Hemmes, A., et al. (2009). 15-hydroxyprostaglandin dehydrogenase is down-regulated in gastric cancer. *Clin. Cancer Res.* 15, 4572–4580. doi: 10.1158/1078-0432.CCR-08-2518
- Uno, M., Saitoh, Y., Mochida, K., Tsuruyama, E., Kiyono, T., Imoto, I., et al. (2014). NF- $\kappa$ B inducing kinase, a central signaling component of the non-canonical pathway of NF- $\kappa$ B, contributes to ovarian cancer progression. *PLoS ONE* 9:e88347. doi: 10.1371/journal.pone.0088347
- Uozumi, N., Kume, K., Nagase, T., Nakatani, N., Ishii, S., Tashiro, F., et al. (1997). Role of cytosolic phospholipase A2 in allergic response and parturition. *Nature* 390, 618–622. doi: 10.1038/37622
- Van Putten, V., Refaat, Z., Dessev, C., Blaine, S., Wick, M., Butterfield, L., et al. (2001). Induction of cytosolic phospholipase A2 by oncogenic Ras is mediated through the JNK and ERK pathways in rat epithelial cells. *J. Biol. Chem.* 276, 1226–1232. doi: 10.1074/jbc.M003581200
- van Vliet, C., Bukczynska, P. E., Puryer, M. A., Sadek, C. M., Shields, B. J., Tremblay, M. L., et al. (2005). Selective regulation of tumor necrosis factor-induced Erk signaling by Src family kinases and the T cell protein tyrosine phosphatase. *Nat. Immunol.* 6, 253–260. doi: 10.1038/ni1169
- Yang, C. M., Chien, C. S., Hsiao, L. D., Luo, S. F., and Wang, C. C. (2002). Interleukin-1 $\beta$ -induced cyclooxygenase-2 expression is mediated through activation of p42/44 and p38 MAPKs, and NF- $\kappa$ B pathways in canine tracheal smooth muscle cells. *Cell. Signal.* 14, 899–911. doi: 10.1016/S0898-6568(02)00037-2
- Yang, C. M., Lee, I. T., Chi, P. L., Cheng, S. E., Hsiao, L. D., and Hsu, C. K. (2014). TNF- $\alpha$  induces cytosolic phospholipase A2 expression via Jak2/PDGFR-dependent Elk-1/p300 activation in human lung epithelial cells. *Am. J. Physiol. Lung Cell. Mol. Biol.* 306, L543–L551. doi: 10.1152/ajplung.00320.2013

**Conflict of Interest Statement:** The authors declare that the research was conducted in the absence of any commercial or financial relationships that could be construed as a potential conflict of interest.

The reviewer HH and handling Editor declared their shared affiliation, and the handling Editor states that the process nevertheless met the standards of a fair and objective review.

Copyright © 2016 Lin, Lin, Cho, Wang, Hsiao and Yang. This is an open-access article distributed under the terms of the Creative Commons Attribution License (CC BY). The use, distribution or reproduction in other forums is permitted, provided the original author(s) or licensor are credited and that the original publication in this journal is cited, in accordance with accepted academic practice. No use, distribution or reproduction is permitted which does not comply with these terms.

## Article

# New Anti-Inflammatory 9,11-Secosterols with a Rare Tricyclo[5,2,1,1]decane Ring from a Formosan Gorgonian *Pinnigorgia* sp.

Yu-Chia Chang <sup>1</sup>, Tsong-Long Hwang <sup>2,3,4</sup>, Jyh-Horng Sheu <sup>5,\*</sup>, Yang-Chang Wu <sup>6,7,8,9,\*</sup> and Ping-Jyun Sung <sup>1,5,7,9,10,\*</sup>

<sup>1</sup> National Museum of Marine Biology and Aquarium, Pingtung 944, Taiwan; jay0404@gmail.com

<sup>2</sup> Graduate Institute of Natural Products, College of Medicine, Chang Gung University, Taoyuan 333, Taiwan; htl@mail.cgu.edu.tw

<sup>3</sup> Research Center for Industry of Human Ecology, Research Center for Chinese Herbal Medicine and Graduate Institute of Healthy Industry Technology, College of Human Ecology, Chang Gung University of Science and Technology, Taoyuan 333, Taiwan

<sup>4</sup> Department of Anesthesiology, Chang Gung Memorial Hospital, Taoyuan 333, Taiwan

<sup>5</sup> Department of Marine Biotechnology and Resources, National Sun Yat-sen University, Kaohsiung 804, Taiwan

<sup>6</sup> School of Pharmacy, College of Pharmacy, China Medical University, Taichung 404, Taiwan

<sup>7</sup> Chinese Medicine Research and Development Center, China Medical University Hospital, Taichung 404, Taiwan

<sup>8</sup> Center for Molecular Medicine, China Medical University Hospital, Taichung 404, Taiwan

<sup>9</sup> Graduate Institute of Natural Products, Kaohsiung Medical University, Kaohsiung 807, Taiwan

<sup>10</sup> Graduate Institute of Marine Biology, National Dong Hwa University, Pingtung 944, Taiwan

\* Correspondence: sheu@mail.nsysu.edu.tw (J.-H.S.); yachwu@mail.cmu.edu.tw (Y.-C.W.); pjsung@nmmba.gov.tw (P.-J.S.); Tel.: +886-7-525-2000 (ext. 5030) (J.-H.S.); +886-4-2205-7513 (Y.-C.W.); +886-8-882-5037 (P.-J.S.); Fax: +886-7-525-5020 (J.-H.S.); +886-4-2206-0248 (Y.-C.W.); +886-8-882-5087 (P.-J.S.)

Academic Editor: Vassilios Roussis

Received: 24 October 2016; Accepted: 16 November 2016; Published: 26 November 2016

**Abstract:** Pinnigorgiols D (1) and E (2), two new 9,11-secosterols with a rearranged carbon skeleton, were isolated from a Taiwan gorgonian *Pinnigorgia* sp. The structures of these two compounds were elucidated on the basis of spectroscopic methods and were proven to possess a tricyclo[5,2,1,1]decane ring. The new secosterols 1 and 2 displayed significant inhibitory effects on the generation of superoxide anions and the release of elastase by human neutrophils.

**Keywords:** 9,11-secosterol; gorgonian; *Pinnigorgia*; anti-inflammatory; superoxide anion; elastase

## 1. Introduction

Gorgonian corals belonging to the genus *Pinnigorgia* (Family Gorgoniidae), have proven to be rich sources of bioactive sterols [1–4]. Previous bioassay results of these sterol analogues have demonstrated cytotoxic and anti-inflammatory activities. Following the above investigations, with the aim of discovering bioactive substances for new drug development in the future, we continue here to carry out an investigation on a Taiwan gorgonian *Pinnigorgia* sp., and two novel 9,11-secosterols, pinnigorgiols D (1) and E (2), with a rare carbon skeleton arrangement, were discovered (Figure 1). The ability of these two compounds to inhibit the generation of superoxide anions and the release of elastase in *N*-formyl methionyl leucylphenylalanine/cytochalasin B (fMLP/CB)-induced neutrophils were also evaluated.



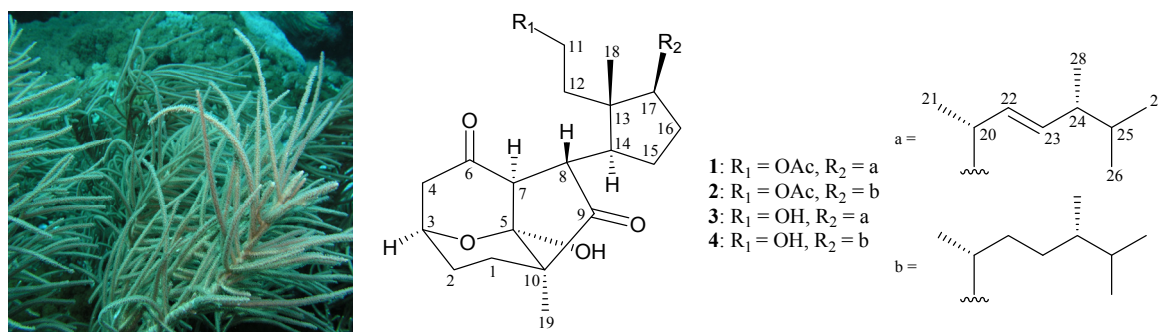


**Figure 1.** Gorgonian coral *Pinnigorgia* sp. and the structures of pinnigorgiols D (1), E (2), A (3), and B (4).

## 2. Results and Discussion

Pinnigorgiol D (1) was obtained as an oil and had the molecular formula C<sub>30</sub>H<sub>46</sub>O<sub>6</sub> as determined by high-resolution electrospray ionization mass spectrum (HRESIMS) at  $m/z$  525.31883 (calcd. for C<sub>30</sub>H<sub>46</sub>O<sub>6</sub> + Na, 525.31866), requiring eight degrees of unsaturation. The IR absorptions of **1** showed the presence of hydroxy ( $\nu_{\max}$  3446 cm<sup>−1</sup>), ester ( $\nu_{\max}$  1739 cm<sup>−1</sup>), and ketonic carbonyl ( $\nu_{\max}$  1717 cm<sup>−1</sup>) groups. The <sup>13</sup>C NMR and distortionless enhancement of polarization transfer (DEPT) data of **1** (Table 1) indicated the presence of 30 carbons, including seven methyls, seven sp<sup>3</sup> methylenes, eight sp<sup>3</sup> methines, a disubstituted double bond, and six quaternary carbons. The <sup>1</sup>H NMR spectrum (Table 1) exhibited seven methyl signals at  $\delta_H$  2.06 (3H, s, acetate methyl), 1.12 (3H, s), 1.04 (3H, d,  $J$  = 7.2 Hz), 0.91 (3H, d,  $J$  = 6.8 Hz), 0.90 (3H, s), 0.83 (3H, d,  $J$  = 6.8 Hz), and 0.81 (3H, d,  $J$  = 6.8 Hz). The signal at  $\delta_H$  4.54 (1H, ddd,  $J$  = 11.6, 11.6, 4.4 Hz) and 3.86 (1H, ddd,  $J$  = 11.6, 11.6, 6.0 Hz) were assumed to be an oxymethylene group. It was found that the NMR signals of **1** were similar to those of a known 9,11-secosterol analogue, pinnigorgiol A (3) (Figure 1) [1], except that the signals corresponding to the 11-hydroxy group in **3** were replaced by signals for an acetoxymethylene group in **1** (Table 2). The correlations from a nuclear Overhauser effect spectroscopy (NOESY) experiment of **1** also revealed that the stereochemistry of this metabolite was identical to that of **3**. Thus, pinnigorgiol D (1) was found to be the 11-O-acetyl derivative of **3**.

**Table 1.** <sup>1</sup>H (400 MHz, CDCl<sub>3</sub>) and <sup>13</sup>C (100 MHz, CDCl<sub>3</sub>) NMR data for secosterols **1** and **2**.

Position	1		2	
	$\delta_H$ ( $J$ in Hz)	$\delta_C$ , Multiple	$\delta_H$ ( $J$ in Hz)	$\delta_C$ , Multiple
1	1.38 m; 1.25 m	26.5, CH <sub>2</sub>	1.38 m; 1.25 m	26.6, CH <sub>2</sub>
2	2.02 m; 1.59 m	23.8, CH <sub>2</sub>	2.03 m; 1.59 m	24.1, CH <sub>2</sub>
3	4.65 br s	70.2, CH	4.65 dd (6.0, 5.2)	70.2, CH
4	2.91 dd (16.4, 6.8); 2.39 d (16.4)	44.1, CH <sub>2</sub>	2.91 dd (16.4, 6.8); 2.39 d (16.4)	44.0, CH <sub>2</sub>
5		101.4, C		101.4, C
6		207.7, C		207.7, C
7	3.04 s	59.6, CH	3.05 s	59.9, CH
8	3.18 dd (10.0, 2.0)	48.2, CH	3.19 dd (10.0, 2.0)	48.0, CH
9		216.6, C		216.6, C
10		49.4, C		49.5, C
11	4.54 ddd (11.6, 11.6, 4.4) 3.86 ddd (11.6, 11.6, 6.0)	61.2, CH <sub>2</sub>	4.52 ddd (11.6, 11.6, 4.8) 3.87 ddd (11.6, 11.6, 6.0)	61.3, CH <sub>2</sub>
12	1.89 m; 1.67 m	36.1, CH <sub>2</sub>	1.89 m; 1.61 m	36.1, CH <sub>2</sub>
13		46.7, C		46.8, C
14	2.04 m	45.8, CH	2.04 m	46.1, CH
15	1.94 m; 1.77 m	27.3, CH <sub>2</sub>	1.92 m; 1.80 m	27.0, CH <sub>2</sub>
16	1.98 m; 1.45 m	24.0, CH <sub>2</sub>	2.02 m; 1.42 m	24.2, CH <sub>2</sub>
17	1.43 m	50.0, CH	1.42 m	49.8, CH



Table 1. Cont.

Position	1		2	
	$\delta_H$ (J in Hz)	$\delta_C$ , Multiple	$\delta_H$ (J in Hz)	$\delta_C$ , Multiple
18	0.90 s	17.0, CH <sub>3</sub>	0.90 s	16.8, CH <sub>3</sub>
19	1.12 s	12.1, CH <sub>3</sub>	1.12 s	12.1, CH <sub>3</sub>
20	2.27 m	36.8, CH	1.45 m	33.3, CH
21	1.04 d (7.2)	22.6, CH <sub>3</sub>	1.04 d (7.2)	20.4, CH <sub>3</sub>
22	5.26 dd (15.6, 7.6)	133.7, CH	1.45 m; 0.90 m	32.6, CH <sub>2</sub>
23	5.23 dd (15.6, 7.6)	133.3, CH	1.37 m; 0.90 m	31.8, CH <sub>2</sub>
24	1.89 m	43.1, CH	1.21 m	39.0, CH
25	1.48 m	33.1, CH	1.56 m	31.5, CH
26	0.83 d (6.8)	20.0, CH <sub>3</sub>	0.78 d (6.8)	17.6, CH <sub>3</sub>
27	0.81 d (6.8)	19.7, CH <sub>3</sub>	0.85 d (6.8)	20.4, CH <sub>3</sub>
28	0.91 d (6.8)	17.5, CH <sub>3</sub>	0.77 d (6.8)	15.5, CH <sub>3</sub>
11-OAc		172.5, C		172.4, C
	2.06 s	21.2, CH <sub>3</sub>	2.05 s	21.2, CH <sub>3</sub>

Table 2. NMR data for the 11-acetoxy component in pinnigorgiol D (1), and the 11-hydroxy component in pinnigorgiol A (3).

Position	1		3 <sup>a</sup>	
	$\delta_H$ (J in Hz)	$\delta_C$ , Multiple	$\delta_H$ (J in Hz)	$\delta_C$ , Multiple
11	4.54 ddd (11.6, 11.6, 4.4) 3.86 ddd (11.6, 11.6, 6.0)	61.2, CH <sub>2</sub>	3.83 m	59.0, CH <sub>2</sub>
12	1.89 m; 1.67 m	36.1, CH <sub>2</sub>	1.89 dt (15.5, 5.5); 1.74 m	39.5, CH <sub>2</sub>
13		46.7, C		46.6, C
11-OAc		172.5, C		
	2.06 s	21.2, CH <sub>3</sub>		

<sup>a</sup> Data was reported by Chang et al. [1].

Pinnigorgiol E (2) was obtained as an oil and had the molecular formula C<sub>30</sub>H<sub>48</sub>O<sub>6</sub> as determined by HRESIMS at *m/z* 527.33444 (calcd. for C<sub>30</sub>H<sub>48</sub>O<sub>6</sub> + Na, 527.33431) and by analysis of NMR spectral data, requiring seven degrees of unsaturation. Initial analyses of the <sup>1</sup>H and <sup>13</sup>C NMR spectral data of 2 illustrated features very similar to those of 1 (Table 1) and a known secosterol, pinnigorgiol B (4) (Figure 1) [1], except that the signals corresponding to the 11-hydroxy group in 4 were replaced by signals for an acetoxy group in 2 (Table 3). Based on the above observations, pinnigorgiol E (2) was assigned as the 11-O-acetyl derivative of pinnigorgiol B (4).

Table 3. NMR data for the 11-acetoxy component in pinnigorgiol E (2), and the 11-hydroxy component in pinnigorgiol B (4).

Position	2		4 <sup>a</sup>	
	$\delta_H$ (J in Hz)	$\delta_C$ , Multiple	$\delta_H$ (J in Hz)	$\delta_C$ , Multiple
11	4.52 ddd (11.6, 11.6, 4.8) 3.87 ddd (11.6, 11.6, 6.0)	61.3, CH <sub>2</sub>	3.81 m	59.1, CH <sub>2</sub>
12	1.89 m; 1.61 m	36.1, CH <sub>2</sub>	1.89 ddd (16.0, 6.0, 5.2); 1.69 m	39.7, CH <sub>2</sub>
13		46.8, C		46.6, C
11-OAc		172.4, C		
	2.05 s	21.2, CH <sub>3</sub>		

<sup>a</sup> Data was reported by Chang et al. [1].

The CD spectra of pinnigorgiols D (1), E (2), A (3), and B (4) in methanol displayed positive Cotton effects at 216 nm ( $\Delta\epsilon = +4.0$ ), 214 nm ( $\Delta\epsilon = +4.6$ ), 216 nm ( $\Delta\epsilon = +4.6$ ), and 218 nm ( $\Delta\epsilon = +2.7$ ), respectively, [1] (Figure 2). These highlights confirmed that secosterols 1–4 possess the same configurations.

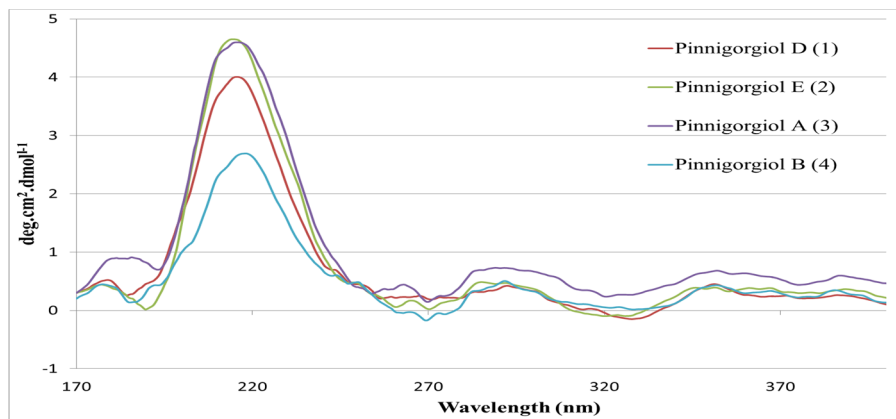


Figure 2. CD spectra of pinnigorgiols D (1), E (2), A (3), and B (4) [1].

The hepatic stellate cell is the major cell type involved in liver fibrosis, which is the formation of scar tissue in response to liver damage. Secosterols 1 and 2 were tested against the HSC-T6 rat hepatic stellate cell line. Compounds 1 and 2 decreased the viability of HSC-T6 cells to 31.9% and 51.7%, respectively, at a concentration of 10  $\mu$ M (Figure 3).

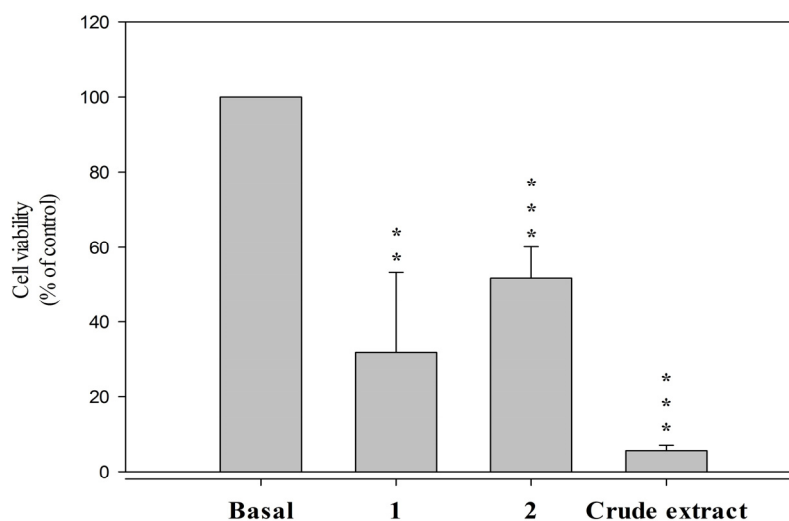


Figure 3. Secosterols 1 and 2 decreased viability of HSC-T6 in 10  $\mu$ M for 24 h. Cells were treated with DMSO (control) and coral crude extract in 6  $\mu$ g/mL. Cytotoxicity assay was monitored spectrophotometrically at 450 nm. Quantitative data are expressed as the mean  $\pm$  S.E.M. ( $n = 3$ –4). \*\*  $p < 0.01$ , \*\*\*  $p < 0.001$  compared to basal.

In a previous study, pinnigorgiols A (3) and B (4) were reported to significantly decrease the cell viability of HSC-T6 cells to 13.0% and 20.8%, respectively, at a concentration of 10  $\mu$ M (Table 4) [1]. It seemed that the C-11 hydroxy group and the double bond between C-22/23 are critical for the cytotoxic activity of secosterols 1–4.

**Table 4.** Secosterols 1–4 decreased viability of HSC-T6 in 10  $\mu$ M for 24 h.

Compound	1	2	3 <sup>a</sup>	4 <sup>a</sup>
Inhibition rate (% of basal)	31.9	51.7	13.0	20.8

<sup>a</sup> Data was reported by Chang et al. [1].

The in vitro anti-inflammatory effects of secosterols **1** and **2** were tested. Pinnigorgiols D (**1**) and E (**2**) were found to exhibit inhibitory effects on the generation of superoxide anions ( $IC_{50}$  = 3.5 and 3.9  $\mu$ M, respectively) and the release of elastase ( $IC_{50}$  = 2.1 and 1.6  $\mu$ M, respectively) by human neutrophils (Table 5). Pinnigorgiols A (**3**) and B (**4**) were also found to display inhibitory effects on the generation of superoxide anions ( $IC_{50}$  = 4.0 and 2.5  $\mu$ M, respectively) and the release of elastase ( $IC_{50}$  = 5.3 and 3.1  $\mu$ M, respectively) [1]. Secosterol **2** show stronger activity in the inhibitory effect on the release of elastase, which indicated that an acetoxy substituent at C-11 and the absence of C-22/23 double bond would enhance the activity by comparison with the structure and anti-inflammatory data of **2** with those of **1**, **3**, and **4**.

**Table 5.** Inhibitory effects of secosterols 1–4 on the generation of superoxide anions and the release of elastase by human neutrophils in response to fMet-Leu-Phe/cytochalasin B (fMLP/CB).

Compound	Superoxide Anion	Elastase Release
	$IC_{50}$ ( $\mu$ M)	$IC_{50}$ ( $\mu$ M)
<b>1</b>	3.5	2.1
<b>2</b>	3.9	1.6
<b>3<sup>a</sup></b>	4.0	5.3
<b>4<sup>a</sup></b>	2.5	3.1

<sup>a</sup> Data was reported by Chang et al. [1].

### 3. Experimental Section

#### 3.1. General Experimental Procedures

Optical rotations were measured on a Jasco P-1010 digital polarimeter (Japan Spectroscopic Corporation, Tokyo, Japan). CD spectra were recorded on a Jasco J-810 circular dichroism spectropolarimeter (Japan Spectroscopic Corporation, Tokyo, Japan). Infrared spectra were recorded on a Jasco FT/IR-4100 spectrometer (Japan Spectroscopic Corporation, Tokyo, Japan); peaks are reported in  $cm^{-1}$ . The NMR spectra were recorded on a Varian Mercury Plus 400 spectrometer, using the residual  $CHCl_3$  signal ( $\delta_H$  7.26 ppm) as an internal standard for  $^1H$  NMR and  $CDCl_3$  ( $\delta_C$  77.1 ppm) for  $^{13}C$  NMR; coupling constants (J) are given in Hz. ESIMS and HRESIMS were recorded using a Bruker 7 Tesla solariX FTMS system (Bruker, Bremen, Germany). Column chromatography was performed on silica gel (230–400 mesh, Merck, Darmstadt, Germany). TLC was carried out on precoated Kieselgel 60 F<sub>254</sub> (0.25 mm, Merck, Darmstadt, Germany); spots were visualized by spraying with 10%  $H_2SO_4$  solution followed by heating. Normal-phase HPLC (NP-HPLC) was performed using a system comprised of a Hitachi L-7110 pump (Hitachi Ltd., Tokyo, Japan) and a Rheodyne 7725 injection port (Rheodyne LLC, Rohnert Park, CA, USA). A semi-preparative normal-phase column (Supelco Ascentis Si Cat #:581515-U, 25 cm  $\times$  21.2 mm, 5  $\mu$ m, Sigma-Aldrich, St. Louis, MO, USA) was used for NP-HPLC. Reversed-phase HPLC (RP-HPLC) was performed using a system comprised of a Hitachi L-2130 pump (Hitachi Ltd., Tokyo, Japan), a Hitachi L-2455 photodiode array detector (Hitachi Ltd., Tokyo, Japan), and a Rheodyne 7725 injection port (Rheodyne LLC, Rohnert Park, CA, USA). A reverse phase column (Luna<sup>®</sup> 5  $\mu$ m C18(2) 100 Å, AXIA Packed, 25 cm  $\times$  21.2 mm, Phenomenex Inc., Torrance, CA, USA) was used for RP-HPLC.

### 3.2. Animal Material

Specimens of the gorgonian corals *Pinnigorgia* sp. were collected by hand via scuba off the coast of Green Island, Taiwan, in August 2012 and stored in a freezer until extraction. A voucher specimen (NMMBA-TW-GC-2012-130) was deposited in the National Museum of Marine Biology & Aquarium, Taiwan. This organism was identified by a comparison with previous descriptions [5].

### 3.3. Extraction and Separation

Sliced bodies of *Pinnigorgia* sp. (wet weight 1.98 kg; dry weight 0.86 kg) were extracted with ethyl acetate (EtOAc) at room temperature. The EtOAc extract (84.9 g) was partitioned between methanol (MeOH) and *n*-hexane. The MeOH layer (12.6 g) was separated on Sephadex LH-20 and eluted using a mixture of dichloromethane (DCM) and MeOH (1:1) to yield 7 subfractions A–F. Fraction F was separated by silica gel column chromatography and eluted using *n*-hexane/acetone (stepwise, 1:1–pure acetone) to afford eight subfractions F1–F8. Fraction F2 was purified by silica gel column chromatography and eluted using *n*-hexane/acetone (stepwise, 9:1–pure acetone) to yield 13 subfractions F2A–F2M. Fraction F2D was purified by NP-HPLC using a mixture of *n*-hexane/EtOAc (3:1) to yield 17 subfractions F2D1–F2D17. Fraction F2D15 was purified by RP-HPLC, using a mixture of MeOH/H<sub>2</sub>O (95:5) to yield **1** (6.5 mg) and **2** (8.7 mg), respectively.

Pinnigorgiol D (**1**): colorless oil;  $[\alpha]_D^{25} -6$  (c 0.44, CHCl<sub>3</sub>); IR (neat)  $\nu_{\max}$  3446, 1739, 1717 cm<sup>−1</sup>; <sup>1</sup>H and <sup>13</sup>C NMR data, see Table 1; ESIMS  $m/z$  525 [M + Na]<sup>+</sup>; HRESIMS  $m/z$  525.31883 (calcd. for C<sub>30</sub>H<sub>46</sub>O<sub>6</sub> + Na, 525.31866).

Pinnigorgiol E (**2**): colorless oil;  $[\alpha]_D^{25} -4$  (c 0.33, CHCl<sub>3</sub>); IR (neat)  $\nu_{\max}$  3446, 1734, 1717 cm<sup>−1</sup>; <sup>1</sup>H and <sup>13</sup>C NMR data, see Table 1; ESIMS  $m/z$  527 [M + Na]<sup>+</sup>; HRESIMS  $m/z$  527.33444 (calcd. for C<sub>30</sub>H<sub>48</sub>O<sub>6</sub> + Na, 527.33431).

### 3.4. Anti-Hepatofibrotic Assay

The anti-hepatofibrotic effects of tested secosterols **1** and **2** were assayed using a WST-1 assay method. Anti-hepatofibrotic assays were carried out according to procedures described previously [6].

### 3.5. Generation of Superoxide Anions and Release of Elastase by Human Neutrophils

Human neutrophils were obtained by means of dextran sedimentation and Ficoll centrifugation. Measurements of superoxide anion generation and elastase release were carried out according to previously described procedures [7,8]. Briefly, superoxide anion production was assayed by monitoring the superoxide dismutase-inhibitable reduction of ferricytochrome *c*. Elastase release experiments were performed using MeO–Suc–Ala–Ala–Pro–Valp–nitroanilide as the elastase substrate.

## 4. Conclusions

Pinnigorgiols D (**1**) and E (**2**) are rare sterols containing a tricyclo[5,2,1,1]decane ring in their structures. Prior to this study, only four compounds of this type had been isolated from sea hare *Aplysia kurodai* [9] and gorgonian coral *Pinnigorgia* sp. [1]. In an anti-inflammatory activity test, secosterol **2** displayed significantly inhibitory effects on the release of elastase by human neutrophils and may become lead compounds in future marine anti-inflammatory drug development [10,11]. The gorgonian coral *Pinnigorgia* sp. will be transplanted to culturing tanks located in the National Museum of Marine Biology & Aquarium, Taiwan, for the extraction of additional natural products to establish a stable supply of bioactive material.

**Acknowledgments:** This research was supported by grants from the National Museum of Marine Biology and Aquarium; the National Dong Hwa University; the National Sun Yat-sen University; the National Research Program for Biopharmaceuticals, Ministry of Science and Technology (Grant Nos. MOST 105-2325-B-291-001, 105-2811-B-291-003, 104-2320-B-291-001-MY3 and 104-2325-B-291-001); the National Health Research Institutes (NHRI-EX103-10241BI); and in part by a grant from the Chinese Medicine Research Center, China Medical

University (Ministry of Education, Aim for the Top University Plan), Taiwan, awarded to Jyh-Horng Sheu, Yang-Chang Wu, and Ping-Jyun Sung.

**Author Contributions:** Jyh-Horng Sheu, Yang-Chang Wu and Ping-Jyun Sung designed the whole experiment and contributed to manuscript preparation. Yu-Chia Chang researched data. Tsong-Long Hwang analyzed the data and performed data acquisition.

**Conflicts of Interest:** The authors declare no conflicts of interest.

## References

1. Chang, Y.-C.; Kuo, L.-M.; Su, J.-H.; Hwang, T.-L.; Kuo, Y.-H.; Lin, C.-S.; Wu, Y.-C.; Sheu, J.-H.; Sung, P.-J. Pinnigorgiols A–C, 9,11-secoosterols with a rare ring arrangement from a gorgonian coral *Pinnigorgia* sp. *Tetrahedron* **2016**, *72*, 999–1004. [[CrossRef](#)]
2. Chang, Y.-C.; Kuo, L.-M.; Hwang, T.-L.; Yeh, J.; Wen, Z.-H.; Fang, L.-S.; Wu, Y.-C.; Lin, C.-S.; Sheu, J.-H.; Sung, P.-J. Pinnisterols A–C, new 9,11-secoosterols from a gorgonian *Pinnigorgia* sp. *Mar. Drugs* **2016**, *14*, 12. [[CrossRef](#)] [[PubMed](#)]
3. Su, Y.-D.; Cheng, C.-H.; Wen, Z.-H.; Wu, Y.-C.; Sung, P.-J. New anti-inflammatory sterols from a gorgonian *Pinnigorgia* sp. *Bioorg. Med. Chem. Lett.* **2016**, *26*, 3060–3063. [[CrossRef](#)] [[PubMed](#)]
4. Chang, Y.-C.; Chen, N.-F.; Hwang, T.-L.; Tseng, C.-C.; Wu, T.-Y.; Peng, B.-R.; Wen, Z.-H.; Fang, L.-S.; Wu, Y.-C.; Sheu, J.-H.; et al. New marine sterols from an algal-bearing gorgonian coral *Pinnigorgia* sp. *Steroids* **2016**, *115*, 123–129. [[CrossRef](#)] [[PubMed](#)]
5. Fabricius, K.; Alderslade, P. *Soft Corals and Sea Fans—A Comprehensive Guide to the Tropical Shallow-Water Genera of the Central-West Pacific, the Indian Ocean and the Red Sea*, 1st ed.; Australian Institute of Marine Science: Townsville, Australia, 2001; pp. 218–219.
6. Kuo, L.-M.; Kuo, C.-Y.; Lin, C.-Y.; Hung, M.-F.; Shen, J.-J.; Hwang, T.-L. Intracellular glutathione depletion by oridonin leads to apoptosis in hepatic stellate cells. *Molecules* **2014**, *19*, 3327–3344. [[CrossRef](#)] [[PubMed](#)]
7. Yu, H.-P.; Yang, S.-C.; Chung, P.-J.; Ho, C.-M.; Kuo, C.-Y.; Hung, M.-F.; Huang, Y.-T.; Chang, W.-Y.; Chang, Y.-W.; et al. Propofol inhibits superoxide production, elastase release, and chemotaxis in formyl peptide-activated human neutrophils by blocking formyl peptide receptor 1. *J. Immunol.* **2013**, *190*, 6511–6519.
8. Yu, H.-P.; Hsieh, P.-W.; Chang, Y.-J.; Chung, P.-J.; Kuo, L.-M.; Hwang, T.-L. 2-(2-Fluorobenzamido) benzoate ethyl ester (EFB-1) inhibits superoxide production by human neutrophils and attenuates hemorrhagic shock-induced organ dysfunction in rats. *Free Radic. Biol. Med.* **2011**, *50*, 1737–1748. [[CrossRef](#)] [[PubMed](#)]
9. Kawamura, A.; Kita, M.; Kigoshi, H. Aplysiasecoesterol A: A 9,11-seco steroid with an unprecedented tricyclic  $\gamma$ -diketone structure from the sea hare *Aplysia kurodai*. *Angew. Chem. Int. Ed.* **2015**, *54*, 7073–7076. [[CrossRef](#)] [[PubMed](#)]
10. Wei, W.-C.; Sung, P.-J.; Duh, C.-Y.; Chen, B.-W.; Sheu, J.-H.; Yang, N.-S. Anti-inflammatory activities of natural products isolated from soft corals of Taiwan between 2008 and 2012. *Mar. Drugs* **2013**, *11*, 4083–4126. [[CrossRef](#)] [[PubMed](#)]
11. Senthilkumar, K.; Kim, S.-K. Marine invertebrate natural products for anti-inflammatory and chronic diseases. *Evid.-Based Complement. Altern. Med.* **2013**, 2013. [[CrossRef](#)] [[PubMed](#)]



© 2016 by the authors; licensee MDPI, Basel, Switzerland. This article is an open access article distributed under the terms and conditions of the Creative Commons Attribution (CC-BY) license (<http://creativecommons.org/licenses/by/4.0/>).





## Short communication

Four new compounds from edible algae *Cladosiphon okamuranus* and *Chlorella sorokiniana* and their bioactivities

Kun-Ching Cheng<sup>a,b,1</sup>, Ping-Chung Kuo<sup>c,1</sup>, Hsin-Yi Hung<sup>c,1</sup>, Ko-Hua Yu<sup>c</sup>,  
Tsong-Long Hwang<sup>d,e,f</sup>, Po-Chuen Shieh<sup>g</sup>, Jo-Shu Chang<sup>h</sup>, Tian-Shung Wu<sup>c,g,\*</sup>

<sup>a</sup> Taiwan Sugar Research Institute, Tainan 70176, Taiwan, ROC

<sup>b</sup> Department of Chemistry, National Cheng Kung University, Tainan 701, Taiwan, ROC

<sup>c</sup> School of Pharmacy, National Cheng Kung University Hospital, College of Medicine, National Cheng Kung University, Tainan 701, Taiwan, ROC

<sup>d</sup> Graduate Institute of Natural Products, College of Medicine, Chang Gung University, Taoyuan 333, Taiwan, ROC

<sup>e</sup> Research Center for Industry of Human Ecology, Research Center for Chinese Herbal Medicine, and Graduate Institute of Health Industry Technology, College of Human Ecology, Chang Gung University of Science and Technology, Taoyuan 333, Taiwan, ROC

<sup>f</sup> Department of Anesthesiology, Chang Gung Memorial Hospital, Taoyuan 333, Taiwan, ROC

<sup>g</sup> Department of Pharmacy, Tajen University, Pingtung 90741, Taiwan, ROC

<sup>h</sup> Department of Chemical Engineering, National Cheng Kung University, Tainan 701, Taiwan, ROC

## ARTICLE INFO

## Article history:

Received 14 July 2016

Received in revised form 8 September 2016

Accepted 20 September 2016

Available online 29 September 2016

## Keywords:

Alga

Fucoidan

Anti-inflammatory

Lutein

Quantitative analysis

## ABSTRACT

In the present work, two new compounds, known as mozukulins A (**1**) and B (**2**), together with three known compounds, including eicosapentaenoic acid (EPA), heneicosahexaene and phytol, were characterized from edible brown alga *Cladosiphon okamuranus*. The anti-inflammatory activity results demonstrated that eicosapentaenoic acid (EPA) displayed significant bioactivity. We did not observe significant bioactivity for the two new compounds (**1** and **2**), which indicates the need for further studies in the future. In addition, the constituent analysis of *Chlorella sorokiniana* from Taiwan produced chlorellatins A (**3**) and B (**4**) that are reported from the natural sources for the first time, as well as eight other known compounds. Moreover, the lutein content was as high as 4.54% in the fraction of extracts.

© 2016 Phytochemical Society of Europe. Published by Elsevier Ltd. All rights reserved.

## 1. Introduction

Various phytochemicals characterized from natural dietary plants, including epigallocatechin gallate, curcumin, and isoflavonoids, have previously been identified as potential bioactive candidates (Newman et al., 2000; Bar-Sela et al., 2010; Shu et al., 2010). Population growth worldwide and insufficient supplies of foods have resulted in the nutrition deficiencies among the habitants in the developing countries. Thus, the discovery of new food sources possessing myriad bioactive natural chemicals has been claimed by various research groups.

*Cladosiphon okamuranus* (Chordariaceae), commonly known as “mozuku”, is a type of edible seaweed that is classified as brown algae. Fucoidan, the most famous compound reported from mozuku, is used in the treatment of cancer and as an ingredient

in certain dietary supplement products (Aguilar-Briseño et al., 2015). In addition, fucoidan is reported to exhibit various bioactivities (Matsumoto et al., 2004; Elizondo-Gonzalez et al., 2012; Takeda et al., 2012). However, the chemical constituents of *C. okamuranus*, excluding sulfonated polysaccharides, such as fucoidan, have been studied less frequently. Therefore, in the present study, the isolation and structural elucidation of compounds from *C. okamuranus* were performed. In addition, the isolated compounds were examined for their anti-inflammatory potential.

*Chlorella* genus (Chlorellaceae) is a single-cell green microalga. Within this genus, *C. sorokiniana* is characterized by green color and pleasant grass odor. In preliminary examinations, the microalga *C. sorokiniana* originating from Taiwan was found to contain 1% lutein in dry materials. Lutein is a yellow xanthophyll in the macular region of the retina, which exhibits a variety of biological activities (Demmig-Adams and Adams, 2002; Heber and Lu, 2002). However, low contents of lutein are usually extracted from plants for nutritional supplements. The aim of the present study was to conduct the constituent purification and lutein content analysis of the microalga *C. sorokiniana*.

\* Corresponding author at: School of Pharmacy, National Cheng Kung University Hospital, College of Medicine, National Cheng Kung University, Tainan 701, Taiwan, ROC.

E-mail address: [tswu@mail.ncku.edu.tw](mailto:tswu@mail.ncku.edu.tw) (T.-S. Wu).

<sup>1</sup> These authors contributed equally to this work.

## 2. Results and discussion

The fresh brown algae *C. okamuranus* were purified by column chromatography (See Supplementary data) to yield four known compounds and two new compounds, mozukulins A (**1**) and B (**2**). The known compounds, i.e., *cis*-5,8,11,14, 17-eicosapentaenoic acid (EPA), (6Z,9Z,12Z,15Z,18Z)-1,6,9,12,15, 18-henicosahexaene, and phytol, were identified by comparison of their physical and spectroscopic data with those reported (See Supplementary data). The molecular formula of **1** was reported as  $C_{29}H_{42}O_2$  according to the HR-ESI-MS spectrometric data. In the  $^1H$  NMR spectrum, there were proton signals represented for the six methyl groups at  $\delta$  0.87, 0.88, 1.01, 1.09, 1.88, and 2.15; and two upfield mutually coupled doublets at  $\delta$  1.22 and 0.50 indicated the presence of cyclopropane ring connected between C-9 and -19, which were the spectral characteristic of the cycloartane basic triterpenoid skeleton (Long et al., 2012). In the downfield region, another two mutually coupled doublets at  $\delta$  6.87 and 6.00 were assigned to be H-1 and H-2, respectively, which was supported by the  $^3J$ -HMBC correlations (Fig. 1) from H-1 to C-3 and C-19 and from H-2 to C-4. The locations of diketo functions at C-3 and C-25 were determined with the assistance of HMBC spectroscopy in which  $^2J$ ,  $^3J$ -correlations of  $CH_3$ -18/C-3, H-24/C-25, and H-26/C-25 could be observed. These HMBC correlations also supported the presence of olefin function at C-26/C-27. The NOESY spectral analytical results further evidenced the stereochemistry of this compound was similar with those reported from *Neoboutonia melleri* (Long et al., 2012). Conclusively, these spectral findings established the stereochemical structure of **1** as shown (Fig. 1). The compound was trivially named as mozukulin A.

Mozukulin B (**2**) appeared as a colorless syrup with a negative specific rotation. The pseudo-molecular formula  $C_{29}H_{44}NaO_2$  was revealed from the HR-ESI-MS analysis, which suggested **2** to be the

reduced form of **1** (See Supplementary data). The corresponding UV, IR, and NMR spectral data were very similar to those of **1**. Minor differences between **2** and **1** were observed, such as the loss of olefinic singlet in the  $^1H$  NMR spectrum of **2**, one vinyl group in **1** [ $\delta$  154.8 (C-27) and 124.4 (C-26)] being replaced by two  $sp^3$  carbons in **2** [ $\delta$  52.6 (C-26) and 24.5 (C-27)]. To confirm the structure of **2**, 2D NMR experiments were conducted. Correlation spectroscopic data revealed the stereochemical structure of **2** was nearly identical to **1**, and the only change in **2** was the saturation of C-26/C-27. The chemical structure of **2** was then constructed (Fig. 1).

All purified compounds from *C. okamuranus* were examined for any associated inhibitory effects on superoxide anion generation and elastase release by human neutrophils in response to fMLP/CB (Table 1). Among the examined compounds, only eicosapentaenoic acid (EPA) displayed significant inhibition of fMLP/CB induced superoxide anion generation with  $IC_{50}$  values of  $2.89 \pm 0.36$  and  $1.26 \pm 0.18$   $\mu g/ml$ , respectively. These  $IC_{50}$  values were comparable

**Table 1**

Inhibitory effects of isolated compounds from *C. okamuranus* on superoxide anion generation and elastase release by human neutrophils in response to fMLP/CB.

Compounds	$IC_{50}$ ( $\mu g/ml$ ) <sup>a</sup>	
	Superoxide Anion Generation	Elastase Release
<b>1</b>	>10	>10
<b>2</b>	>10	>10
EPA	$2.89 \pm 0.36$	$1.26 \pm 0.18$
Henicosahexaene	>10	>10
Phytol	>10	>10
LY294002 <sup>b</sup>	$0.4 \pm 0.02^{***}$	$1.5 \pm 0.3^{***}$

<sup>a</sup> Concentration necessary for 50% inhibition; Results are presented as the mean  $\pm$  S.D. (n = 3–4).

<sup>b</sup> A phosphatidylinositol-3-kinase inhibitor was used as a positive control for superoxide anion generation and elastase release.

<sup>\*\*\*</sup>  $p < 0.001$  compared with the control value.

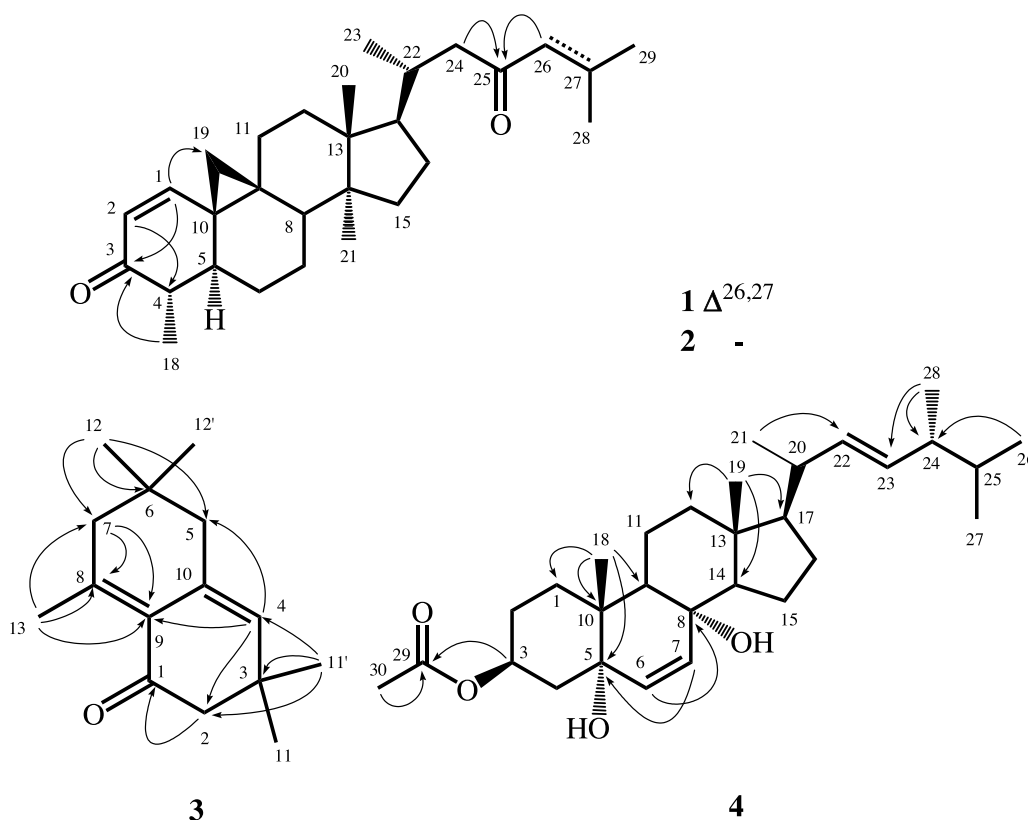


**Fig. 1.** Structures and significant HMBC (H  $\rightarrow$  C) correlations of compounds mozukulins A (**1**), B (**2**), chlorellatins A (**3**), and B (**4**).

to other reports of EPA superoxide anion inhibition (Jaswir and Monsur, 2011; Kim, 2013; Barbosa et al., 2014). These results demonstrated that the anti-inflammatory activity of the two new compounds (mozukulins A and B) were considerably lower than the known compound of this algae, EPA, highlighting the need for deeper investigation in future studies.

In addition, dried materials of microalga *C. sorokiniana* were extracted with acetone in at ambient temperature and purified by column chromatography (See Supplementary data), resulting in eight known compounds and two new naturally-occurring compounds, chlorellatins A (**3**) and B (**4**). The known compounds, i.e., the mixture of (1Z)- and (1E)-2-propanone 1-(3,5,5-trimethyl-2-cyclohexen-1-ylidene), 2,2,8,8-tetramethyl-spiro[5.5]undecan-4,10-dione, ergosta-7,9,22-trien-3 $\beta$ -ol, ergosta-6,22-dien-3 $\beta$ ,5 $\alpha$ ,8 $\alpha$ -triol, ergosta-7-en-3 $\beta$ -ol, and the mixture of  $\beta$ -sitosterol and stigmasterol, respectively, were identified by comparison of their physical and spectroscopic data with the reported values in the literature (See Supplementary data).

Chlorellatin A (**3**) was obtained as colorless crystals. The molecular formula of **3** was determined to be C<sub>15</sub>H<sub>22</sub>O according to its HRESIMS data. Elucidation of the <sup>1</sup>H-, <sup>13</sup>C NMR, and HSQC spectra revealed five methyl groups at  $\delta$  2.13, 1.05, and 0.88; three methylene groups at  $\delta$  2.38, 2.07, and 2.02; one olefinic proton at  $\delta$  5.38; one conjugated carbonyl carbon at  $\delta$  201.7; two sets of C=C double bond at  $\delta$  146.1 (C-8), 132.5 (C-4), 132.0 (C-10), and 126.7 (C-9), including three quaternary carbons; and two *sp*<sup>3</sup> quaternary carbons at  $\delta$  35.1 (C-3) and 29.5 (C-6), respectively. The <sup>1</sup>H and <sup>13</sup>C NMR spectra data of **3** correlated well with those of a known synthetic compound called 3,3,6,6,8-pentamethyl-2,3,6,7-tetrahydronaphthalen-1(5H)-one (Bueschken and Rindtorff, 1988). This characterization was further confirmed by the HMBC correlations (Fig. 1) from H-2 to C-1; from H-4 to C-2, C-5, C-9; from CH<sub>3</sub>-11 to C-2, C-3, C-4; from CH<sub>3</sub>-12 to C-5, C-6, C-7; and from CH<sub>3</sub>-13 to C-7, C-8, C-9, respectively. Therefore, the chemical structure of **3** was determined (Fig. 1).

The molecular formula of **4** was established by the HRESIMS spectrometric analysis as C<sub>30</sub>H<sub>48</sub>O<sub>4</sub>, in which seven indices of hydrogen deficiency (IHD) were shown. In the <sup>1</sup>H NMR spectrum, there were proton signals characteristic of the ergosterol basic skeleton for the six methyl groups at  $\delta$  2.01, 0.99, 0.90, 0.89, 0.83, 0.81, and 0.81, (Huang et al., 2010; Ma and Shi, 2011; Shirane et al., 1996). In addition, one mutually coupled doublet at  $\delta$  6.51 and 6.22 was observed. Another doublet of doublet at  $\delta$  5.22 and 5.14 indicated the presence of two sets of olefinic double bonds in the structure. In the downfield region, one oxygenated proton at  $\delta$  4.99 was assigned at C-3, which was supported by the <sup>3</sup>J-HMBC correlation (Fig. 1) from  $\delta$  4.99 (H-3) to  $\delta$  170.1 (C-29). The presence of acetoxy group at C-3 was also evidenced by an acetyl methyl group at  $\delta$  2.01 and the <sup>2</sup>J-HMBC correlation (Fig. 1) between CH<sub>3</sub>-30 and C-29. The configuration of C-3 acetoxy group was established as  $\beta$  according to the coupling pattern of H-3 and NOESY spectral analysis. In the <sup>13</sup>C NMR spectrum, in addition to one acetyl group at  $\delta$  170.1 (C-29) and 21.3 (C-30), two sets of double bonds at  $\delta$  135.3 (C-7), 135.2 (C-23), 132.3 (C-22), and 130.9 (C-6) were observed. One oxygenated methine at  $\delta$  69.5 (C-3) and two oxygenated quaternary carbons at  $\delta$  81.7 (C-8) and 79.4 (C-5) were also recorded. The <sup>2</sup>J, <sup>3</sup>J-HMBC correlations (Fig. 1) from H-7 to C-5 and C-8, from H-6 to C-5 and C-8, from CH<sub>3</sub>-21 to C-22, and from CH<sub>3</sub>-28 to C-23, established the partial structures of 6,22-dien-5,8-diol as occurred in the literature (Ma and Shi, 2011). The stereochemistry of OH-5 and OH-8 could be further determined as  $\alpha$  and  $\alpha$  by NOESY spectral analysis and comparison of its <sup>1</sup>H NMR spectrum with that in the literature. Given the spectral evidence described above, the structure of **4** was the same as ergosta-3 $\beta$ -acetoxy-6,22-dien-5 $\alpha$ ,8 $\alpha$ -diol, which is a known synthetic compound (Achtermann, 1933; Bladon, 1954). Accordingly, the

stereochemical structure of **4** was constructed (Fig. 1). The compound was trivially named as chlorellatin B.

In addition, the lutein content in microalga *C. sorokiniana* was analyzed by HPLC. In the development of the HPLC method for the quantitative determination of lutein, several solvent systems and separation columns were compared and evaluated. The selected wavelength of detection was also optimized in this work. The maximum number of peaks and the associated heights were determined, and the chromatogram baseline was stable. The reproducibility of the developed analytical method was examined, and the data showed satisfactory RSD values. The precision and recovery experimental results also indicated that the established HPLC chromatographic method was valid for the quantitative determination of lutein. The present method was a convenient and feasible tool for species authentication and quality assessment of the fungal or herbal raw materials in the future. Fractions 5–8 were quantitatively analyzed for their lutein contents (See Supplementary data). Under the optimized HPLC condition, the lutein contents were in the range of 0.56% and 4.54% in the partial purified fractions of microalga. It evidenced the microalga to be an important source for lutein supplement. These data provide support of *C. sorokiniana* as an inexpensive source for new healthy foods.

### 3. Materials and methods

#### 3.1. General

Optical rotations were measured using a JASCO DIP-370 polarimeter. The UV spectra were obtained on a Hitachi UV-3210 spectrophotometer. IR spectra were recorded on a Shimadzu FTIR-8501 spectrophotometer. <sup>1</sup>H- and <sup>13</sup>C NMR, COSY, NOESY, HMQC, and HMBC spectra were obtained on the Bruker Avance III-400 and Avance 300 NMR spectrometers, with tetramethylsilane (TMS) as internal standard and the chemical shifts were reported in  $\delta$  values (ppm). The ESIMS and HRESIMS were taken on a Bruker Daltonics APEX II 30e spectrometer. Column chromatography (CC) was performed on silica gel (Kieselgel 60, 70–230 mesh and 230–400 mesh, E. Merck). Thin layer chromatography (TLC) was conducted on precoated Kieselgel 60 F 254 plates (Merck) and the compounds were visualized by spraying with 10% (v/v) H<sub>2</sub>SO<sub>4</sub> followed by heating at 110 °C for 10 min. HPLC was performed on a Shimadzu LC-20AT series pumping system equipped with a Shimadzu SPD-20A UV-vis detector and an Inertsil ODS column (4.6 mm  $\times$  250 mm, 5  $\mu$ m) at ambient temperature.

#### 3.2. Materials

Fresh brown algae *C. okamuranus* (TSWu 201501001) were kindly provided as a gift from Heruen International Enterprise Company Limited. The dried materials of microalga *C. sorokiniana* (TSWu 201501002) were provided by Prof. Jo-Shu Chang, Department of Chemical Engineering, National Cheng Kung University. These specimens were deposited at the herbarium of the School of Pharmacy, National Cheng Kung University.

#### 3.3. Extraction and isolation

Fresh brown algae *C. okamuranus* (1.0 kg) were soaked in methanol (1 L  $\times$  5), and the combined extracts were concentrated under reduced pressure to give a deep brown syrup (10 g). The syrup was suspended in 100 mL water and extracted with ethyl acetate (4  $\times$  100 mL) to yield an ethyl acetate extract (1 g). The syrup was further subjected to column chromatography on silica gel, eluted with dichloromethane-EtOAc step gradient system

(20:1, 10:1, 5:1, 2:1, and 1:1, respectively) (5:1) and monitored by TLC to yield five fractions (Fr 1–5). Frs 4 and 5 did not display significant spots based on TLC profile, as such it was not further purified or analyzed. Fr 1 was purified by SiO<sub>2</sub> CC with a mixed eluent of *n*-hexane/dichloromethane (5:1) and step gradient with dichloromethane to yield 5 subfractions. The first subfraction (Fr 1.1) was subjected to SiO<sub>2</sub> CC eluting with a mixture of *n*-hexane and benzene (20:1, 10:1, 5:1, 2:1, 1:1, respectively) and further conducted on preparative TLC (pTLC) to yield *cis*-5,8,11,14,17-EPA (5.0 mg), and (6Z,9Z,12Z,15Z,18Z)-1,6,9,12,15,18-henicosahexaene (3.2 mg), respectively. The third subfraction (Fr 1.3) was purified by SiO<sub>2</sub> CC with a mixed eluent of benzene/ethyl acetate (30:1) and step gradient with ethyl acetate and further conducted on pTLC to yield phytol (2.8 mg), **1** (1.5 mg), and **2** (3.3 mg), respectively.

The dried and powdered microalga materials of *C. sorokiniana* (720 g) were soaked with acetone (10 L × 3), and the combined extracts were concentrated under reduced pressure to give deep brown syrup (45 g). The extracts were subjected to silica gel CC eluted with *n*-hexane and ethyl acetate step gradient system (100:0, 20:1, 10:1, 5:1, 2:1, and 1:1, respectively) to yield minor fractions. These fractions were monitored by TLC to combine into nine fractions. Fractions 1 and 9 did not display significant spots based on TLC profile and were not further purified or analyzed. Fraction 2 was purified by SiO<sub>2</sub> CC with a mixed eluent of benzene/chloroform (20:1) and step gradient with chloroform to yield 5 subfractions; the third subfraction (Fr 2.3) of which was further recrystallized with chloroform-methanol to yield the mixture of (1Z)- and (1E)-2-propanone 1-(3,5,5-trimethyl-2-cyclohexen-1-ylidene) (144 mg). Fraction 3 was subjected to SiO<sub>2</sub> CC eluting with a mixture of *n*-hexane and diisopropyl ether (20:1, 10:1, 5:1, 2:1, 1:1, successively) to afford four subfractions (F3-1–F3-4). Subfractions Fr 3.2 and 3.3 were major fractions and displayed significant spots on TLC. Fr 3.2 was conducted on preparative TLC (pTLC) to yield compound **3** (4 mg). Fr 3.3 was repeatedly purified by SiO<sub>2</sub> CC and pTLC to yield 2,2,8,8-tetramethyl-spiro <5.5> undecan-4,10-dione (90 mg). Fraction 4 was purified by SiO<sub>2</sub> CC with *n*-hexane and ethyl acetate step gradient system (20:1, 10:1, 5:1, 2:1, and 1:1, respectively) to yield 5 subfractions; the fifth subfraction (Fr 4.5) was further recrystallized with chloroform-methanol to yield the mixture of β-sitosterol and stigmasterol (100 mg). In addition, subfractions Fr 4.2 and 4.3 were major fractions and displayed significant spots on TLC. Fr 4.2 was repeatedly purified by SiO<sub>2</sub> CC and pTLC to afford **4** (1 mg) and ergosta-7,9,22-trien-3β-ol (46 mg), respectively. Fr 4.3 was conducted on SiO<sub>2</sub> CC repeatedly and further purified by pTLC to yield ergosta-6,22-dien-3β,5α,8α-triol (26 mg) and ergosta-7-en-3β-ol (7 mg), respectively. Fractions 5 (0.66 g), 6 (1.22 g), 7 (1.54 g), and 8 (2.27 g) were subjected to the HPLC analysis of their lutein contents.

### 3.4. Determination of anti-inflammatory bioactivity

The assay for measurement of superoxide anion generation was based on the SOD-inhibitable reduction of ferricytochrome c. Degranulation of azurophilic granules was determined by measuring elastase release as described previously (Yu et al., 2011; Yang et al., 2013).

### 3.5. HPLC analysis of lutein content

Fractions 5–8 were conducted the HPLC analysis, and the samples were dissolved in methanol at ambient temperature. The analysis details were provided in the Supporting information.

### Conflicts of interest

The authors declare no conflict of interest.

### Acknowledgments

This study was sponsored by the Ministry of Science and Technology, Taiwan, ROC granted to T.-S. Wu, and supported in part by Ministry of Education, Taiwan, ROC under the Aim for the Top University Project to NCKU (also known as the “5-Years-50-Billion” Grants). Authors are also grateful for the financial support partly provided by Heruen International Enterprise Company Limited.

### Appendix A. Supplementary data

Supplementary data associated with this article can be found, in the online version, at <http://dx.doi.org/10.1016/j.phytol.2016.09.008>.

### References

- Achtermann, Th., 1933. Zur kenntnis der ergostadien-triole. Hoppe-Seyler's Zeitschrift für physiologische Chemie 217, 281–284.
- Aguilar-Briseño, J.A., Cruz-Suarez, L.E., Sassi, J.F., Ricque-Marie, D., Zapata-Benavides, P., Mendoza-Gamboa, E., Rodríguez-Padilla, C., Trejo-Avila, L.M., 2015. Sulphated polysaccharides from *Ulva clathrata* and *Cladosiphon okamuranus* seaweeds both inhibit viral attachment/entry and cell–cell fusion, in NDV infection. Mar. Drugs 13, 697–712.
- Bar-Sela, G., Epelbaum, R., Schaffer, M., 2010. Curcumin as an anti-cancer agent: review of the gap between basic and clinical applications. Curr. Med. Chem. 17, 190–197.
- Barbosa, M., Valentão, P., Andrade, P.B., 2014. Bioactive compounds from macroalgae in the new millennium: implications for neurodegenerative diseases. Mar. Drugs 12, 4934–4972.
- Bladon, P., 1954. Steroid group. LXVI. Formation of 14-ergostene-3β,5α-diol and related compounds. J. Chem. Soc. 736–738.
- Bueschken, W., Rindtorff, K., 1988. Preparation of 4,4,8,8,10-pentamethyl-10-cyano-bicyclo[4.4.0]dec-1(6)-en-2-one. German Patent, Ger Offen DE 3640306 A1.
- Demmig-Adams, B., Adams, W.W., 2002. Antioxidants in photosynthesis and human nutrition. Science 298, 2149–2153.
- Elizondo-Gonzalez, R., Cruz-Suarez, L.E., Ricque-Marie, D., Mendoza-Gamboa, E., Rodríguez-Padilla, C., Trejo-Avila, L.M., 2012. In vitro characterization of the antiviral activity of fucoidan from *Cladosiphon okamuranus* against Newcastle Disease Virus. Virol. J. 9, 307.
- Heber, D., Lu, Q.Y., 2002. Overview of mechanisms of action of lycopene. Exp. Biol. Med. 227, 920–923.
- Huang, G.J., Huang, S.S., Lin, S.S., Shao, Y.Y., Chen, C.C., Hou, W.C., Kuo, Y.H., 2010. Analgesic effects and the mechanisms of anti-inflammation of ergostatrien-3β-ol from *Antrodia camphorata* submerged whole broth in mice. J. Agric. Food Chem. 58, 7445–7452.
- Jaswir, I., Monsur, H.A., 2011. Anti-inflammatory compounds of macro algae origin: a review. J. Med. Plants Res. 5, 7146–7154.
- Kim, S.K., 2013. Marine Microbiology: Bioactive Compounds and Biotechnological Applications. Wiley-VCH, Germany.
- Long, C., Beck, J., Cantagrel, F., Marcourt, L., Vendier, L., David, B., Plisson, F., Derguini, F., Vandenbergh, I., Aussagues, Y., Ausseil, F., Lavaud, C., Sautel, F., Massiot, G., 2012. Proteasome inhibitors from *Neoboutonia melleri*. J. Nat. Prod. 75, 34–47.
- Ma, X.M., Shi, Y.P., 2011. Chemical constituents of *Ligularia nanchuanica*. Chem. Nat. Compd. 46, 997–1000.
- Matsumoto, S., Nagaoka, M., Hara, T., Kimura-Takagi, I., Mistuyama, K., Ueyama, S., 2004. Fucoidan derived from *Cladosiphon okamuranus* Tokida ameliorates murine chronic colitis through the down-regulation of interleukin-6 production on colonic epithelial cells. Clin. Exp. Immunol. 136, 432–439.
- Newman, D.J., Cragg, G.M., Snader, K.M., 2000. The influence of natural products upon drug discovery. Nat. Prod. Rep. 17, 215–234.
- Shirane, N., Takenaka, H., Ueda, K., Hashimoto, Y., Katoh, K., Ishii, H., 1996. Sterol analysis of DMI-resistant and -sensitive strains of *Venturia inaequalis*. Phytochemistry 41, 1301–1308.
- Shu, L., Cheung, K.L., Khor, T.O., Chen, C., Kong, A.N., 2010. Phytochemicals: cancer chemoprevention and suppression of tumor onset and metastasis. Cancer Metast. Rev. 29, 483–502.
- Takeda, K., Tomimori, K., Kimura, R., Ishikawa, C., Nowling, T.K., Mori, N., 2012. Anti-tumor activity of fucoidan is mediated by nitric oxide released from macrophages. Int. J. Oncol. 40, 251–260.
- Yang, S.C., Chung, P.J., Ho, C.M., Kuo, C.Y., Hung, M.F., Huang, Y.T., Chang, W.Y., Chang, Y.W., Chan, K.H., Hwang, T.L., 2013. Propofol inhibits superoxide production, elastase release, and chemotaxis in formyl peptide-activated human neutrophils by blocking formyl peptide receptor 1. J. Immunol. 190, 6511–6519.
- Yu, H.P., Hsieh, P.W., Chang, Y.J., Chung, P.J., Kuo, L.M., Hwang, T.L., 2011. 2-(2-Fluorobenzamido)benzoate ethyl ester (EFB-1) inhibits superoxide production by human neutrophils and attenuates hemorrhagic shock-induced organ dysfunction in rats. Free Radic. Biol. Med. 50, 1737–1748.





# Anti-allergic Hydroxy Fatty Acids from *Typhonium blumei* Explored through ChemGPS-NP

Michal Korinek<sup>1,2</sup>, Yi-Hong Tsai<sup>1</sup>, Mohamed El-Shazly<sup>1,3</sup>, Kuei-Hung Lai<sup>1,4</sup>, Anders Backlund<sup>4</sup>, Shou-Fang Wu<sup>1,5</sup>, Wan-Chun Lai<sup>1</sup>, Tung-Ying Wu<sup>1</sup>, Shu-Li Chen<sup>1</sup>, Yang-Chang Wu<sup>1,6,7</sup>, Yuan-Bin Cheng<sup>1,6,8</sup>, Tsong-Long Hwang<sup>9,10,11\*</sup>, Bing-Hung Chen<sup>2,7,12\*</sup> and Fang-Rong Chang<sup>1,8,13,14,15\*</sup>

<sup>1</sup> Graduate Institute of Natural Products, College of Pharmacy, Kaohsiung Medical University, Kaohsiung, Taiwan, <sup>2</sup> Department of Biotechnology, College of Life Science, Kaohsiung Medical University, Kaohsiung, Taiwan, <sup>3</sup> Department of Pharmacognosy, Faculty of Pharmacy, Ain-Shams University, Cairo, Egypt, <sup>4</sup> Division of Pharmacognosy, Department of Medicinal Chemistry, Uppsala University, Uppsala, Sweden, <sup>5</sup> Natural Resource Development Institute of Pharmaceuticals, Development Center for Biotechnology, New Taipei City, Taiwan, <sup>6</sup> Research Center for Natural Products and Drug Development, Kaohsiung Medical University, Kaohsiung, Taiwan, <sup>7</sup> Department of Medical Research, Kaohsiung Medical University Hospital, Kaohsiung, Taiwan, <sup>8</sup> Center for Infectious Disease and Cancer Research, Kaohsiung Medical University, Kaohsiung, Taiwan, <sup>9</sup> Graduate Institute of Natural Products, College of Medicine, Chang Gung University, Taoyuan, Taiwan, <sup>10</sup> Research Center for Chinese Herbal Medicine, Research Center for Food and Cosmetic Safety, and Graduate Institute of Health Industry Technology, College of Human Ecology, Chang Gung University of Science and Technology, Taoyuan, Taiwan, <sup>11</sup> Department of Anesthesiology, Chang Gung Memorial Hospital, Taoyuan, Taiwan, <sup>12</sup> The Institute of Biomedical Sciences, National Sun Yat-sen University, Kaohsiung, Taiwan, <sup>13</sup> Department of Marine Biotechnology and Resources, National Sun Yat-sen University, Kaohsiung, Taiwan, <sup>14</sup> Research Center for Environmental Medicine, Kaohsiung Medical University, Kaohsiung, Taiwan, <sup>15</sup> Cancer Center, Kaohsiung Medical University Hospital, Kaohsiung, Taiwan

## OPEN ACCESS

### Edited by:

Anna Karolina Kiss,  
Medical University of Warsaw, Poland

### Reviewed by:

Antonio Ferrante,  
South Australia Pathology, Australia  
Souaibou Yaouba,  
University of Nairobi, Kenya

### \*Correspondence:

Tsong-Long Hwang  
htl@mail.cgu.edu.tw  
Bing-Hung Chen  
bhchen@kmu.edu.tw  
Fang-Rong Chang  
aaronfrc@kmu.edu.tw

### Specialty section:

This article was submitted to  
Ethnopharmacology,  
a section of the journal  
Frontiers in Pharmacology

Received: 24 March 2017

Accepted: 24 May 2017

Published: 19 June 2017

### Citation:

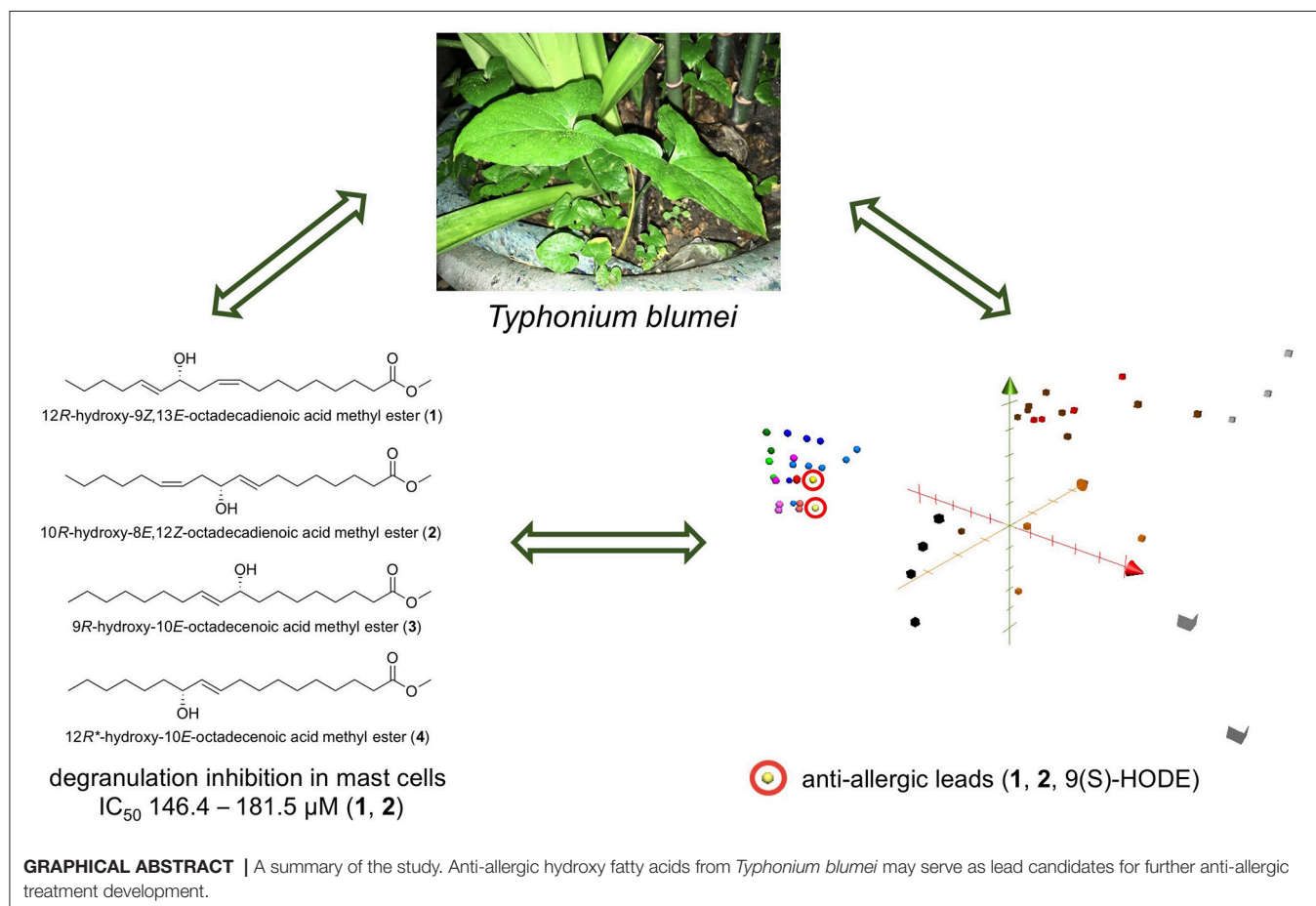
Korinek M, Tsai Y-H, El-Shazly M,  
Lai K-H, Backlund A, Wu S-F,  
Lai W-C, Wu T-Y, Chen S-L, Wu Y-C,  
Cheng Y-B, Hwang T-L, Chen B-H  
and Chang F-R (2017) Anti-allergic  
Hydroxy Fatty Acids from *Typhonium  
blumei* Explored through  
ChemGPS-NP.  
Front. Pharmacol. 8:356.  
doi: 10.3389/fphar.2017.00356

Increasing prevalence of allergic diseases with an inadequate variety of treatment drives forward search for new alternative drugs. Fatty acids, abundant in nature, are regarded as important bioactive compounds and powerful nutrients playing an important role in lipid homeostasis and inflammation. Phytochemical study on *Typhonium blumei* Nicolson and Sivadasan (Araceae), a folk anti-cancer and anti-inflammatory medicine, yielded four oxygenated fatty acids, 12*R*-hydroxyoctadec-9*Z*,13*E*-dienoic acid methyl ester (**1**) and 10*R*-hydroxyoctadec-8*E*,12*Z*-dienoic acid methyl ester (**2**), 9*R*-hydroxy-10*E*-octadecenoic acid methyl ester (**3**), and 12*R*\*-hydroxy-10*E*-octadecenoic acid methyl ester (**4**). Isolated compounds were identified by spectroscopic methods along with GC-MS analysis. Isolated fatty acids together with a series of saturated, unsaturated and oxygenated fatty acids were evaluated for their anti-inflammatory and anti-allergic activities *in vitro*. Unsaturated (including docosahexaenoic and eicosapentaenoic acids) as well as hydroxylated unsaturated fatty acids exerted strong anti-inflammatory activity in superoxide anion generation (IC<sub>50</sub> 2.14–3.73 μM) and elastase release (IC<sub>50</sub> 1.26–4.57 μM) assays. On the other hand, in the anti-allergic assays, the unsaturated fatty acids were inactive, while hydroxylated fatty acids showed promising inhibitory activity in A23187- and antigen-induced degranulation assays (e.g., 9*S*-hydroxy-10*E*,12*Z*-octadecadienoic acid, IC<sub>50</sub> 92.4 and 49.7 μM, respectively). According to our results, the presence of a



hydroxy group in the long chain did not influence the potent anti-inflammatory activity of free unsaturated acids. Nevertheless, hydroxylation of fatty acids (or their methyl esters) seems to be a key factor for the anti-allergic activity observed in the current study. Moreover, ChemGPS-NP was explored to predict the structure-activity relationship of fatty acids. The anti-allergic fatty acids formed different cluster distant from clinically used drugs. The bioactivity of *T. blumei*, which is historically utilized in folk medicine, might be related to the content of fatty acids and their metabolites.

**Keywords:** *Typhonium blumei*, hydroxy fatty acids, polyunsaturated fatty acids (PUFA), anti-allergic, anti-inflammatory, cytotoxic, ChemGPS-NP



## INTRODUCTION

Inflammation is a crucial part of an organism immunologic response to defend itself from invading pathogens and maintain homeostasis. However, pathological inflammatory responses or

allergic reactions can cause a substantial burden to human health. For instance, prolonged inflammation plays an important role in various diseases including allergy, cardiovascular diseases and carcinogenesis (Shacter and Weitzman, 2002; Grivennikov et al., 2010). Neutrophils play an essential role in the non-specific (innate) immune system against invading pathogens and are usually the first cells recruited to inflammatory sites. Uncontrolled activation of neutrophils will trigger pathological degranulation and respiratory burst, leading to tissue damage, a hallmark associated with many inflammatory diseases (Korkmaz et al., 2010). Therefore, elastase levels, as well as the production of superoxide, serve as important markers of inflammation in human neutrophils (Tsai et al., 2015).

**Abbreviations:** TB, *Typhonium blumei*; DHA, cis-4,7,10,13,16,19-docosahexaenoic acid; EPA, cis-5,8,11,14,17-eicosapentaenoic acid; 9(S)-HODE, 9S-hydroxy-10E,12Z-octadecadienoic acid; 2OHOA, 2-hydroxy-9Z-octadecenoic acid; RBL, rat basophilic leukemia; fMLF/CB, formyl-methionyl-leucyl-phenylalanine/cytochalasin B; 12/15-LOX, 12/15-lipoxygenase; 15-HPETE, 15S-hydroperoxy-5Z,8Z,11Z,13E-eicosatetraenoic acid; 15(S)-HETE, 15S-hydroxy-5Z,8Z,11Z,13E-eicosatetraenoic acid.

Allergic disorders, such as allergic rhinitis, allergic conjunctivitis, asthma, atopic eczema, or food allergies, are caused by pathological hypersensitivity reactions initiated by immunologic mechanisms (Johansson et al., 2001). Mast cells play a crucial role in triggering allergic response via IgE-mediated degranulation. The *in vitro* model, detecting the release of  $\beta$ -hexosaminidase or histamine by RBL-2H3 cells, has been regarded as a useful indicator to evaluate the activation of mast cells in various acute allergic and inflammatory responses (Chen et al., 2009). Over the last century, several classes of anti-allergic and anti-inflammatory agents were developed. Natural compounds proved effective as drug leads fighting inflammatory reactions, however, they did not show such effect against allergic conditions (Newman and Cragg, 2016). The untapped potential of natural products as an inexhaustible mine of biologically active compounds along with their excellent safety profile encouraged us to investigate the potential of separating natural products with promising anti-allergic activity.

*Typhonium* is a genus of tropical plants, which belongs to family Araceae and comprises about 40 species. Several *Typhonium* species are often confused, four of them, namely *Typhonium blumei* (= *Typhonium divaricatum*), *Typhonium roxburghii*, *Typhonium flagelliforme*, and *Typhonium trilobatum*, were critically revised by Nicolson and Sivadasan (1981). *Typhonium* species are widely used as traditional and folk medicines to treat a myriad of ailments. For example, *T. giganteum* is a traditional Chinese medicine (TCM) used as a part of various formulas to treat respiratory diseases, stroke, epilepsy and nowadays applied in cancer treatment (Chang, 1992). Another species common in Malaysia, *T. flagelliforme*, has been extensively studied for its anticancer activity based on its folk medicinal use (Lai et al., 2008). Additionally, *T. flagelliforme* extracts were reported to exhibit anti-asthmatic, anti-inflammatory and analgesic effects (Zhong et al., 2001).

*Typhonium blumei* Nicolson and Sivadasan (= *T. divaricatum*, in Chinese Tu-Ban-Xia), is a widely growing weed native to South and Southeast Asia, and naturalized in Australia and Africa (Wang and Yang, 1996; Huang, 2000). In Taiwan, *T. blumei* is consumed in order to treat cancer such as leukemia or liver cancer, cough, swelling, and snake bites, and it is used topically to treat bruises and skin cancer (Li, 2006). Phytochemical and biological studies on *T. blumei* are scanty. Antiviral mannose-binding lectin has been isolated from this plant (Kong et al., 2006; Luo et al., 2007). A cytotoxic study on *T. blumei* crude extract revealed the presence of lipids and steroids using GC-MS analysis (Hsu et al., 2011). Recently, we showed that the nonpolar extracts of *T. blumei* and *T. roxburghii* exhibited potent anti-allergic activity through affecting the calcium signaling pathway (Korinek et al., 2016a). Our results suggested that the saturated and unsaturated fatty acid content of the nonpolar extracts is responsible for such activity. However, the specific components of *T. blumei* nonpolar extracts responsible for the anti-allergic activity have never been revealed.

Fatty acids, particularly unsaturated essential fatty acids with proper ratio of n-6 to n-3, represent interesting bioactive compounds and powerful nutrients that play an important role in lipid homeostasis and in the prevention of cardiovascular diseases (Rajaram, 2014; Maehre et al., 2015; Vangaveti et al.,

2016; Xu et al., 2016). An imbalance caused by excessive intake of n-6 fatty acids from the modern Western diet may contribute to several chronic diseases (Lopez-Vicario et al., 2016). Therefore, higher intake of n-3 fatty acids is recommended (Calder, 2008; Beermann et al., 2016; Michalak et al., 2016). The biological properties of n-3 fatty acids have been extensively studied and their beneficial effects may be due, in part, to their suppressive activity on inflammatory processes (Hwang et al., 2009; Calder, 2015). Recently, it was found that the metabolism of n-3 fatty acids (such as docosahexaenoic, DHA, and eicosapentaenoic, EPA) gives rise to oxygenated mediators (i.e., oxygenated fatty acid derivatives), called resolvins, protectins, and maresins, which possess considerable inflammation resolving properties (Lundstrom et al., 2013). Several mechanisms underlying the anti-inflammatory effect of n-3 fatty acids and their oxidative metabolites were reported. Those mechanisms include the alteration of the fatty acid composition of cell membrane phospholipids, disruption of lipid rafts and modulation of T-cell function. Modulation of the expression of some inflammation-related genes is also involved through the alteration of transcription factors activity, such as nuclear factor kappa B (NF- $\kappa$ B), and peroxisome proliferator-activated receptor (PPAR $\gamma$ ) (Calder, 2015).

The growing evidence on allergy preventive (Willemsen, 2016), anti-inflammatory (Calder, 2015; Michalak et al., 2016), and cytotoxic (Jing et al., 2013) effects of fatty acids, led us to conduct a study aiming to understand the structural requirements of these activities, using *in vitro* cell line models. We performed a biological and phytochemical study on *T. blumei* and discussed the isolation of four hydroxylated fatty acids. We also evaluated the cytotoxic, anti-inflammatory and anti-allergic activities of a series of saturated, unsaturated and hydroxylated fatty acids.

## MATERIALS AND METHODS

### Chemicals and Reagents

Optical rotations were achieved by a JASCO P-2000 digital polarimeter (JASCO Inc., Tokyo, Japan). JASCO V-570 UV/vis/NIR spectrophotometer (JASCO Inc., Tokyo, Japan) was used to measure UV spectra. CD spectra were measured on a JASCO J-810 spectropolarimeter (JASCO Inc., Tokyo, Japan). IR spectra were obtained on an FT/IR-4600 JASCO spectrophotometer (JASCO Inc., Tokyo, Japan). NMR spectra were obtained by Varian-Mercury-plus 400 MHz FT-NMR (Varian Inc., Palo Alto, CA, USA) and JEOL JNM-ECS 400 MHz NMR spectrometer (JEOL Ltd., Tokyo, Japan). Sephadex LH-20 (Merck KGaA, Darmstadt, Germany) and silica gel (Kieselgel 60, 70–230 and 230–400 mesh, Merck KGaA, Darmstadt, Germany) were used for column chromatography. TLC analyses were carried out on silica gel pre-coated (Kieselgel 60 F<sub>254</sub> and RP-18 F<sub>254s</sub>, Merck KGaA, Darmstadt, Germany). Spots on TLC plates were detected using 50%<sub>(aq)</sub> H<sub>2</sub>SO<sub>4</sub> followed by heating on a hot plate. Gas chromatography-mass spectrometry analyses were performed on DSQ II Single Quadrupole GC/MS (Thermo Fisher Scientific Inc., Waltham, MA, USA) using DB-5MS and HP-5MS capillary columns (30 m  $\times$  0.25 mm, with 0.25  $\mu$ m coating, Agilent, J & W

Scientific, Santa Clara, CA, USA). The RP-HPLC analysis was performed using Shimadzu LC-10AT instrument equipped with Shimadzu RIP-10A refractive index detector (Shimadzu Inc., Kyoto, Japan) using C-18 column (20 × 250 mm, Cosmosil). Dulbecco's modified Eagle's medium (high glucose) powder (DMEM), 3-(4,5-dimethylthiazol-2-yl)-2,5-diphenyltetrazolium bromide (MTT), *p*-nitrophenyl-*N*-acetyl-*D*-glucosaminide (*p*-NAG), penicillin and streptomycin, genistein, dexamethasone, doxorubicin hydrochloride, calcium ionophore A23187, and dimethyl sulfoxide (DMSO) were purchased from Sigma-Aldrich (St. Louis, MO, USA). Fetal bovine serum (FBS) was obtained from Hyclone (Logan, UT, USA). Mouse anti-DNP IgE (mIgE-DNP) antibody was a generous gift from Dr. Daniel H. Conrad (Virginia Commonwealth University, Richmond, VA, USA). Dinitrophenyl-conjugated bovine serum albumin (DNP-BSA) was purchased from Pierce (Rockford, IL, USA). Stearic acid, stearic acid methyl ester, palmitic acid, palmitic acid methyl ester, oleic acid, oleic acid methyl ester, *cis*-vaccenic acid methyl ester, petroselinic acid methyl ester, and  $\gamma$ -linolenic acid were obtained from TCI (Tokyo Chemical Industry Co., Ltd., Japan); undecylenic acid, undecylenic acid methyl ester, *cis*-vaccenic acid, petroselinic acid, conjugated (9*Z*,11*E*)-linoleic acid, *cis*-5,8,11,14,17-eicosapentaenoic acid (EPA), *cis*-4,7,10,13,16,19-docosahexaenoic acid (DHA), 2-hydroxystearic acid, 12-hydroxystearic acid methyl ester, 12-oxostearic acid methyl ester, 2-hydroxy-9*Z*-octadecenoic acid (2OHOA), ricinoleic acid, ricinoleic acid methyl ester, ricinelaidic acid, 9*S*-hydroxy-10*E*,12*Z*-octadecadienoic acid (9*S*)-HODE) from Sigma-Aldrich; linoleic acid,  $\alpha$ -linolenic acid,  $\alpha$ -linolenic acid methyl ester from Acros Organics (Thermo Fisher Scientific Inc., Geel, Belgium); linoleic acid methyl ester, 12-hydroxystearic acid from Alfa Aesar (Thermo Fisher Scientific Inc., Heysham, Lancashire, United Kingdom). All other chemicals and reagents were purchased at the highest purity and quality possible.

## Plant Materials

*Typhonium blumei* was collected from Nantou county, Taiwan, in September 2009. Botanical identification of the plant was made by Professor Ming-Hong Yen of Kaohsiung Medical University, Taiwan. Voucher specimen no. KMU-TB1 was deposited at Kaohsiung Medical University, Taiwan.

## Extraction and Isolation

*Typhonium blumei* plant material was washed by tap water and separated into leaves (aerial) and rhizomes (underground part). Leaves were cut and extracted with methanol (2 l × 3, 24 h). Extracts were filtrated and evaporated to dryness under reduced pressure using rotary evaporator and vacuum drying oven. The methanol extract of the leaves was partitioned between dichloromethane and water. *Typhonium blumei* rhizomes (423 g) were chipped, air-dried, and extracted repeatedly with methanol (2 l × 3, 24 h) at room temperature. The combined methanol extracts were then evaporated. The methanol extract (14.4 g) was partitioned between ethyl acetate and water. The sample of non-polar fractions, dichloromethane for leaves (100 mg) and ethyl acetate for rhizomes (100 mg) were further partitioned

using *n*-hexane and methanol. The corresponding partition fractions were collected, filtered and evaporated to dryness. Filtered ethyl acetate layer (1.32 g) was subjected to a silica gel column chromatography (95 g, 70–230 mesh) eluted with *n*-hexane/dichloromethane (4:1) gradually changed to dichloromethane/methanol (5:1) and separated into 13 fractions according to TLC analysis. A mixture C (stigmasterol and  $\beta$ -sitosterol, 9 mg) was precipitated from fraction 5 using *n*-hexane. Fr. 5 (47 mg) was subjected to silica gel column chromatography eluted with solvent system *n*-hexane/ethyl acetate (10:1) gradually changed to ethyl acetate/methanol (4:1) furnishing 13 fractions. Fr. 5-6 was identified as a mixture A (palmitic acid methyl ester, stearic acid methyl ester, oleic acid methyl ester, margaric acid methyl ester, pentadecanoic acid methyl ester, 8 mg, GC-MS). Fr. 5-10 was purified using preparative TLC eluted with dichloromethane/*n*-hexane (100:1) and yielded a mixture B ( $\beta$ -sitost-4-en-3-one, stigmasta-4,22-dien-3-one, campest-4-en-3-one, 2.5 mg, GC-MS). Fraction 7 (128 mg) was eluted with dichloromethane/methanol (1:1) on Sephadex LH-20 column. Fraction 7-2 was subjected to NP-SPE eluted with *n*-hexane/ethyl acetate (15:1 yielding fr.1, 10:1 fr.2, 7:1 fr.3, 3:1 fr.4) and washed with methanol (fr.5). Fractions 7-2-2 and 7-2-3 were subsequently subjected to RP-HPLC chromatography (Shimadzu RID-10A, 20 × 250, 5 ml/min) eluted by acetonitrile/water (72:28) yielding compound 1 (12*R*-hydroxy-9*Z*,13*E*-octadecadienoic acid methyl ester, 2.4 mg), compound 2 (10*R*-hydroxy-8*E*,12*Z*-octadecadienoic acid methyl ester, 3.5 mg), compound 3 (9*R*-hydroxy-10*E*-octadecenoic acid methyl ester, 1 mg) and compound 4 (12*R*\*-hydroxy-10*E*-octadecenoic acid methyl ester, 0.6 mg). Precipitation of fraction 9 yielded a mixture D (stigmasterol-3-*O*- $\beta$ -*D*-glucoside,  $\beta$ -sitosterol-3-*O*- $\beta$ -*D*-glucoside, 1 mg). The isolated compounds were identified by spectroscopic data and GC-MS analyses, comparing the mass spectra with data from Wiley/NBS Registry of Mass Spectral Data (version 5.0)/ National Institute of Standards and Technology (NIST) Library MS Search (version 2.0) or literature.

## Experimental

### 12*R*-Hydroxy-9*Z*,13*E*-Octadecadienoic Acid Methyl Ester (1, 2.4 mg)

$[\alpha]_D^{25}$  −257 (*c* 0.06, EtOH); UV (EtOH)  $\lambda_{\max}$  (log  $\epsilon$ ) 226 (3.15), 236 (3.15), 275 (2.77) nm; CD (*c* 5 mM, EtOH)  $\lambda_{\max}$  ( $\Delta\epsilon_{\max}$ ) 203 (0.05), 246.5 (−0.07) nm; IR (neat)  $\nu_{\max}$  3428 (OH), 2925, 2855, 1737 (C=O), 1462 (C=C), 1285, 1038, 805  $\text{cm}^{-1}$ ;  $^1\text{H}$  NMR ( $\text{CD}_3\text{OD}$ , 400 MHz) and  $^{13}\text{C}$  NMR ( $\text{CD}_3\text{OD}$ , 100 MHz): see Table 1, GC-EIMS (Figure S7) *m/z* (rel. intensity); 292 [ $\text{M}^+ - \text{H}_2\text{O}$ ] (2), 198 (2), 166 (10), 124 (11), 113 (73), 95 (59), 81 (17), 69 (24), 67 (26), 57 (100). Mosher's esterification reaction (MTPA chloride, DCM, crystal of DMAP, 40°C, overnight) led to decomposition yielding decarboxylated product.

### 10*R*-Hydroxy-8*E*,12*Z*-Octadecadienoic Acid Methyl Ester (2, 3.5 mg)

$[\alpha]_D^{25}$  −266 (*c* 0.06, EtOH); UV (EtOH)  $\lambda_{\max}$  (log  $\epsilon$ ) 226 (3.17), 278 (2.92) nm; CD (*c* 5 mM, EtOH)  $\lambda_{\max}$  ( $\Delta\epsilon_{\max}$ ) 190.5 (+0.01), 236 (−0.08) nm; IR (neat)  $\nu_{\max}$  3415 (OH), 2925, 2855, 1734

**TABLE 1** |  $^1\text{H}$  NMR (400 MHz) and  $^{13}\text{C}$  NMR (100 MHz) data of isolated compounds.

Position	1 <sup>a</sup> $\delta_{\text{H}}$ ppm (mult., J in Hz)	2 <sup>a</sup> $\delta_{\text{H}}$ ppm (mult., J in Hz)	3 <sup>b</sup> $\delta_{\text{H}}$ ppm (mult., J in Hz)	4 <sup>b</sup> $\delta_{\text{H}}$ ppm (mult., J in Hz)	1 <sup>a</sup> $\delta_{\text{C}}$ ppm	2 <sup>a</sup> $\delta_{\text{C}}$ ppm
1					176.0 C	176.0 C
2	2.32, t (7.2)	2.31, t (7.2)	2.30, t (7.6)	2.30, t (7.6)	34.8 CH <sub>2</sub>	34.8 CH <sub>2</sub>
3	1.60, m	1.60, m	1.60, m	1.58, m	26.0 CH <sub>2</sub>	26.0 CH <sub>2</sub>
4	1.32, m	1.32, m	1.32, m	1.32, m	30.2 CH <sub>2</sub>	29.8 CH <sub>2</sub>
5	1.32, m	1.32, m	1.32, m	1.32, m	30.2 CH <sub>2</sub>	30.0 CH <sub>2</sub>
6	1.32, m	1.32, m	1.32, m	1.32, m	30.3 CH <sub>2</sub>	32.7 CH <sub>2</sub>
7	1.32, m	2.04, m	1.32, m	1.32, m	30.6 CH <sub>2</sub>	33.2 CH <sub>2</sub>
8	2.04, q (6.4)	5.62, dt (15.2, 6.8)	1.47, m	1.32, m	28.4 CH <sub>2</sub>	132.7 CH
9	5.44, m	5.44, m	4.03, q (6.4)	2.02, q (6.8)	132.6 CH	134.0 CH
10	5.44, m	3.99, q (6.8)	5.44, dd (15.2, 6.8)	5.62, dtd (15.2, 6.8, 3.2)	126.4 CH	73.7 CH
11a	2.27, t (6.4)	2.27, t (6.4)	5.62, dtd (15.2, 6.8, 4.4)	5.44, dd (15.2, 7.2)	36.5 CH <sub>2</sub>	36.4 CH <sub>2</sub>
11b	2.20, m	2.20, m				
12	3.99, q (6.8)	5.44, m	2.02, q (6.8)	4.03, q (6.4)	73.7 CH	126.4 CH
13	5.44, m	5.44, m	1.32, m	1.47, m <sup>c</sup>	133.9 CH	132.4 CH
14	5.62, dt (15.2, 6.4)	2.05, m	1.32, m	1.32, m	132.6 CH	28.4 CH <sub>2</sub>
15	2.05, q (6.4)	1.32, m	1.32, m	1.32, m	33.0 CH <sub>2</sub>	30.4 CH <sub>2</sub>
16	1.32, m	1.32, m	1.32, m	1.32, m	32.6 CH <sub>2</sub>	30.2 CH <sub>2</sub>
17	1.32, m	1.32, m	1.32, m	1.32, m	23.2 CH <sub>2</sub>	23.6 CH <sub>2</sub>
18	0.91, t (7.2)	0.91, t (6.8)	0.88, t (6.4)	0.88, t (6.4)	14.3 CH <sub>2</sub>	14.4 CH <sub>2</sub>
–OCH <sub>3</sub>	3.65, s	3.65, s	3.66, s	3.66, s	52.0 CH <sub>3</sub>	52.0 CH <sub>3</sub>

<sup>a</sup>Compounds **1** and **2** were dissolved in CD<sub>3</sub>OD.<sup>b</sup>Compounds **3** and **4** in CDCl<sub>3</sub>.<sup>c</sup>The signal is overlapping with H<sub>2</sub>O.

(C=O), 1437 (C=C), 1262, 1014, 736 cm<sup>−1</sup>;  $^1\text{H}$  NMR (CD<sub>3</sub>OD, 400 MHz) and  $^{13}\text{C}$  NMR (CD<sub>3</sub>OD, 100 MHz): see **Table 1**; GC-EIMS (Figure S14)  $m/z$  (rel. intensity); 292 [ $\text{M}^+ - \text{H}_2\text{O}$ ] (1), 199 (27), 181 (6), 167 (100), 149 (28), 139 (40), 121 (75), 83 (37), 69 (20), 67 (16), 57 (32).

### 9R-Hydroxy-10E-Octadecenoic Acid Methyl Ester (**3**, 1.0 mg)

$[\alpha]_{\text{D}}^{25} -386$  ( $c$  0.01, EtOH); UV (EtOH)  $\lambda_{\text{max}}$  (log  $\epsilon$ ) 244 (2.84), 273 (2.75) nm; IR (neat)  $\nu_{\text{max}}$  3452 (OH), 2925, 2855, 1742 (C=O), 1460 (C=C), 1261, 1036, 806 cm<sup>−1</sup>;  $^1\text{H}$  NMR (CDCl<sub>3</sub>, 400 MHz): see **Table 1**; GC-EIMS (Figure S15)  $m/z$  (rel. intensity); 294 [ $\text{M}^+ - \text{H}_2\text{O}$ ] (10), 213 (4), 181 (8), 155 (34), 121 (20), 95 (48), 81 (82), 67 (84), 55 (93), 43 (100).

### 12R\*-Hydroxy-10E-Octadecenoic Acid Methyl Ester (**4**, 0.6 mg)

$[\alpha]_{\text{D}}^{25} -80$  ( $c$  0.015, EtOH); UV (EtOH)  $\lambda_{\text{max}}$  (log  $\epsilon$ ) 244 (2.84), 273 (2.75) nm; IR (neat)  $\nu_{\text{max}}$  3404 (OH), 2922, 2852, 1680 (C=O), 1463 (C=C), 1260, 1028, 798 cm<sup>−1</sup>;  $^1\text{H}$  NMR (CDCl<sub>3</sub>, 400 MHz): see **Table 1**; GC-EIMS (Figure S16)  $m/z$  (rel. intensity); 294 [ $\text{M}^+ - \text{H}_2\text{O}$ ] (2), 227 (10), 195 (36), 149 (20), 127 (34), 109 (46), 81 (68), 67 (80), 55 (100).

### Mixture A (9 mg)

GC-MS analysis (palmitic acid methyl ester 64.2%, stearic acid methyl ester 18.0%, oleic acid methyl ester 12.3%, margaric acid

methyl ester 3.6%, pentadecanoic acid methyl ester 1.9%; see Supporting Information, Figure S17).

### Mixture B (2.5 mg)

GC-MS analysis ( $\beta$ -sitost-4-en-3-one 51.2%, stigmasta-4,22-dien-3-one 26.0%, campest-4-en-3-one 22.8%; see Supporting Information, Figure S18).

### Cell Culture

The mucosal mast cell-derived rat basophilic leukemia (RBL-2H3) cell line was purchased from Bioresource Collection and Research Center (Hsin-Chu, Taiwan). Cells were grown in DMEM supplemented with 10% FBS and 100 U/ml penicillin plus 100  $\mu\text{g}/\text{ml}$  streptomycin. Cells were cultured in 10 cm cell culture dishes (Cellstar) at 37°C in a humidified chamber with 5% CO<sub>2</sub> in the air. Cells were subcultured using trypsin at 80% confluency and were plated at  $2 \times 10^5$  cells/ml in culture plates for the secretion assays.

### Cell Viability Assay

A methyl thiazolyl tetrazolium (MTT) assay was used to measure potential toxic effects of samples on RBL-2H3 cells (Korinek et al., 2016b). The method is based on the cleavage of the tetrazolium rings of pale yellow MTT by mitochondrial dehydrogenase enzyme from viable cells forming crystals of dark blue formazan accumulated in healthy cells. Briefly, RBL-2H3 cells at a concentration of  $2 \times 10^4$  cells/well were seeded in 96 wells plate overnight. Cells were washed with PBS (phosphate



buffer saline) and treated with various concentrations of samples (dissolved in DMSO) or untreated control (0.5% DMSO in medium). After 24 h of incubation at 37°C in 5% CO<sub>2</sub>, the medium was removed from each well. A stock MTT solution (5 mg/ml) was diluted 1:10 in culture medium and was added to wells (100 µl per well). Cells were incubated at 37°C in 5% CO<sub>2</sub> for 1 h. The medium was removed and formed formazan crystals were dissolved in DMSO (100 µl). The plate was gently shaken and the absorbance at 550 nm was measured using microplate reader. The degree of cell viability of each sample was calculated as the percentage of control value (untreated cells). Maximal tolerated dose of DMSO was 0.5%. It served as a positive control not affecting RBL-2H3 cells growth. Triton X-100 (0.5% solution) was used as positive control causing the death of all cells in a well.

### Degranulation $\beta$ -Hexosaminidase Assay Induced by A23187 or Antigen

The degree of A23187-induced and antigen-induced degranulation in RBL-2H3 cells was determined by a  $\beta$ -hexosaminidase activity assay as previously described (Korinek et al., 2016b) with some modifications. Briefly, RBL-2H3 cells were dispensed into the 96-wells plate at a density of  $2 \times 10^4$  cells/well. Cells were incubated at 37°C in 5% CO<sub>2</sub> for at least 5 h to allow cells complete adherence to the bottom of the wells. Cells were washed with PBS and various concentrations of samples (dissolved in DMSO) or medium (0.5% DMSO, untreated control) were added to each well (100 µl), followed by 20 h of incubation at 37°C in 5% CO<sub>2</sub>. Then the cells were washed twice by pre-warmed Tyrode's buffer (135 mM NaCl, 5 mM KCl, 1.8 mM CaCl<sub>2</sub>, 1.0 mM MgCl<sub>2</sub>, 5.6 mM glucose, 20 mM HEPES, and 1 mg/ml BSA at pH 7.4). The cells for the antigen-induced experiment were first sensitized with anti-DNP IgE (2 µg/ml) for at least 2 h, followed by thorough washing by pre-warmed Tyrode's buffer. The cells were stimulated by calcium ionophore A23187 (1 µM, A23187-induced) or with the cross-linking antigen DNP-BSA (100 ng/ml, antigen-induced). The cells were incubated at 37°C in 5% CO<sub>2</sub> for 1 h. Unstimulated cells were either lysed with 0.5% Triton X-100 solution for the total amount of  $\beta$ -hexosaminidase release or left untreated for spontaneous release of  $\beta$ -hexosaminidase. Stimulated but untreated cells served as control. Then aliquots of supernatants (50 µl) collected from the control and experimental wells were incubated with an equal volume (50 µl) of 1 µM of *p*-NAG prepared in 0.1 M citrate buffer (pH 4.5) serving as a substrate for released  $\beta$ -hexosaminidase. After 1 h of incubation at 37°C, the reaction was quenched by the addition of 100 µl of stop buffer (0.1 M Na<sub>2</sub>/NaHCO<sub>3</sub>, pH 10.0). Absorbance was measured at 405 nm on a microplate reader. The inhibition percentage of  $\beta$ -hexosaminidase release from RBL-2H3 cells was calculated as the percentage of control value (untreated stimulated cells). Dexamethasone was used as a positive control.

### Measurement of Platelet Aggregation

Human blood was obtained from healthy human volunteers and the coagulation was prevented by addition of acid citrate dextrose. The platelet suspension was washed and further processed as previously described (Wei et al., 2015). Platelets were then suspended in Tyrode's solution (containing

2 mM Ca<sup>2+</sup>, 11.1 mM glucose and 3.5 mg/ml bovine serum albumin) at a concentration of  $3 \times 10^8$  platelets/ml. Platelet aggregation was measured turbidimetrically using light-transmission aggregometer (Chrono-Log, Havertown, PA, USA; Wu et al., 2004). Briefly, the platelet suspension was incubated with samples or with dimethyl sulfoxide (DMSO, vehicle) for 3 min while stirring at 1,200 rpm, followed by the addition of platelet aggregation inducers (collagen at 10 µg/ml or thrombin 0.05 U/ml). The level of platelet aggregation was represented by the maximal increase of light transmission within 5 min after the addition of inducer.

### Preparation of Human Neutrophils

Human neutrophils were obtained from venous blood of healthy, adult volunteers (20–30 years old) using a protocol approved by the Institutional Review Board at Chang Gung Memorial Hospital (protocol number 102-1595A3). Human neutrophils were isolated using a standard method of dextran sedimentation prior to centrifugation in a Ficoll-Hypaque gradient and hypotonic lysis of erythrocytes (Boyum, 1968). Purified neutrophils containing >98% viable cells, as determined by the trypan-blue exclusion method (Jauregui et al., 1981), were resuspended in a Ca<sup>2+</sup>-free Hank's buffered salt solution (HBSS) at pH 7.4 and were maintained at 4°C prior to use.

### Superoxide Anion Generation Assay

Neutrophil superoxide anion generation was based on the superoxide dismutase (SOD)-inhibitable reduction of ferricytochrome *c* according to described procedures (Hwang et al., 2006; Yang et al., 2013). Briefly, after supplementation with 0.5 mg/ml ferricytochrome *c* and 1 mM Ca<sup>2+</sup>, neutrophils ( $6 \times 10^5$ /ml) were equilibrated at 37°C for 2 min and incubated with different concentrations of fractions or DMSO (as control) for 5 min. Cells were incubated with cytochalasin B (CB; 1 µg/ml) for 3 min prior to the activation with formyl-methionyl-leucyl-phenylalanine (fMLF; 100 nM) for 10 min. Changes in absorbance with the reduction of ferricytochrome *c* at 550 nm were continuously monitored in a double-beam, six-cell positioner spectrophotometer with constant stirring (Hitachi U-3010, Tokyo, Japan). Calculations were based on the differences in the reactions with and without SOD (100 U/ml) divided by the extinction coefficient for the reduction of ferricytochrome *c* (21.1 mM<sup>-1</sup> cm<sup>-1</sup>). Genistein was used as the positive control.

### Elastase Release Inhibition Assay

Degranulation of azurophilic granules was determined by measuring the elastase release as described previously (Yang et al., 2013). Experiments were performed using MeOSuc-Ala-Ala-Pro-Val-*p*-nitroanilide as the elastase substrate. After supplementation with MeOSuc-Ala-Ala-Pro-Val-*p*-nitroanilide (100 µM), neutrophils ( $6 \times 10^5$ /ml) were equilibrated at 37°C for 2 min and incubated with fractions for 5 min. Cells were stimulated with fMLF (100 nM)/CB (0.5 µg/ml), and changes in the absorbance at 405 nm were monitored continuously in order to measure the elastase release. The results were expressed as the percent of elastase release in the fMLF/CB-activated, drug-free control system. Genistein was used as the positive control.



## Cytotoxicity Assay

MTT viability assay was used according to a previously described method (Lai et al., 2013). HepG2 ( $1 \times 10^4$  cells), A549 ( $5 \times 10^3$  cells), and MDA-MB-231 ( $1 \times 10^4$  cells) were seeded into 96-well plates. The cells were treated with the test compounds for 72 h. The medium was removed from wells and 100  $\mu$ l of MTT solution (0.5 mg/ml) were added. The plates were incubated at 37°C for 1 h to form formazan crystals. The crystals were dissolved in DMSO (100  $\mu$ l) and plates were gently shaken. Absorbance at 550 nm was measured using microplate reader. The degree of cell viability of each sample was calculated as the percentage of control value (untreated cells). Doxorubicin hydrochloride was used as a positive control.

## GC-MS Analysis

The samples were filtered through 0.22  $\mu$ m filter and subjected to GC-MS (gas chromatography-mass spectrometry) analysis using DSQ II Single Quadrupole GC/MS (Thermo Fisher Scientific, USA). The samples were vaporized at 250°C in standard split mode (1:50) and separated on DB-5MS and HP-5MS capillary columns (30 m  $\times$  0.25 mm, with 0.25  $\mu$ m coating, Agilent, J & W Scientific, Santa Clara, CA, USA). The column oven temperature program for compound 1 was set as follows, initial 200°C, held for 10 min, increased to 300°C at 10°C/min, held for 5 min. For compound 2, initial 100°C was held for 5 min, increased to 200°C at 50°C/min, held for 5 min, then increased to 300°C at 50°C/min and held for 5 min. For compounds 3 and 4, the column oven temperature was maintained at 70°C, held for 3 min, then increased to 180°C at 20°C/min, held for 5 min, then increased to 280°C at 5°C/min and held for 5 min. For mixtures A and B, the initial temperature was 100°C, held for 10 min, then increased to 300°C by 20°C/min and held for 10 min. Helium gas carrier flow was set to 1 ml/min. The interface and ion source temperature were adjusted to 250°C. Electron impact ionization of 70 eV was utilized. Injection volume was 1  $\mu$ l and the mass range was  $m/z$  45–800. Identification of the compounds was based on a comparison of the mass spectra with data from Wiley/NBS Registry of Mass Spectral Data (version 5.0)/National Institute of Standards and Technology (NIST) MS Search (version 2.0). The relative percentage of each compound in mixtures A and B was quantified based on the peak area integrated by the analysis program.

## ChemGPS-NP Analysis

ChemGPS-NP (<http://chemgps.bmc.uu.se>) is principal component analysis (PCA)-based model that serves as a tool for navigation in biologically relevant chemical space. It is composed of eight principal components (PCs) based on 35 chemical descriptors, which represent physico-chemical properties such as size, shape, flexibility, rigidity, polarizability, lipophilicity, polarity, and hydrogen bond capacity. PC1 represents size, shape, and polarizability (red axis), PC2 aromatic- and conjugation-related properties (orange axis), and PC3 lipophilicity, polarity, and H-bond capacity (green axis). ChemGPS-NP<sub>Web</sub> (Rosen et al., 2009) (<http://chemgps.bmc.uu.se>) online tool was used to calculate the prediction scores based on the structural information of fatty acids derived from SMILES using the

ChemBioDraw software. The following clinically used anti-allergic drugs were plotted into chemical space: glucocorticoids (black squares; dexamethasone, triamcinolone, budesonide, fluticasone), immunosuppressants (white squares; pimecrolimus, tacrolimus), leukotriene inhibitors (gray squares; pranlukast, zafirlukast, montelukast), mast cell stabilizers (orange squares; lodoxamide, nedocromil, cromolyn), antihistaminics (brown squares; chlorpheniramine, diphenhydramine, dimetindene, clemastine, loratadine, cetirizine, bilastine, fexofenadine) and “dual antihistaminics” known to inhibit mast cell degranulation (red squares; ketotifen, azelastine, rupatadine). The drugs are listed by increasing value of PC1 (red axis) within each group. All compounds were then plotted into ChemGPS-NP chemical property space using the software Grapher 2.5 (Mac OS).

## Statistics

The results were expressed as mean  $\pm$  SD value of three independent determinations unless otherwise specified. The IC<sub>50</sub> values were calculated using the Microsoft Office (linear function). Statistical significance was calculated by one-way analysis of variance (ANOVA), followed by Dunnett's test (SigmaPlot, Systat Software Inc., San Jose, CA, USA). Values with \* $p < 0.05$ , \*\* $p < 0.001$  were considered statistically significant.

## RESULTS

### Bioactivity Screening of *Typhonium blumei* (TB)

TB plant was separated into leaves (aerial) and rhizomes (underground) and extracted with methanol. The crude extracts and partition fractions were screened for anti-platelet, cytotoxic, anti-inflammatory, and anti-allergic activities. The results showed that the polar butanol layer of TB leaves exhibited 100% inhibitory activity on aggregation induced by either collagen or thrombin at 50  $\mu$ g/ml (Table S2). On the other hand, the nonpolar dichloromethane (TB leaves) or ethyl acetate (TB rhizomes) layers inhibited specifically collagen-induced aggregation by 93.6 and 42.9%, respectively (Table S2). Cytotoxicity screening on six cancer cell lines showed the cytotoxic effect of the nonpolar dichloromethane (TB leaves) and ethyl acetate (TB rhizomes) layers against hepatocellular carcinoma cells, HepG2 (49.6 and 51.7% at 20  $\mu$ g/ml, respectively, Table S3). Partition fractions, except for the polar water layers, exhibited significant anti-inflammatory activity by inhibiting superoxide anion generation and elastase release in human neutrophils reaching up to 100% inhibition at 10  $\mu$ g/ml (Table S4). The ethyl acetate layer (TB rhizomes) was shown to exert anti-allergic activities inhibiting A23187-induced  $\beta$ -hexosaminidase release with IC<sub>50</sub> 94.5  $\mu$ g/ml (Korinek et al., 2016a). The active nonpolar ethyl acetate layer of TB rhizomes was further separated using silica gel column chromatography to yield 13 fractions, TB-1 to TB-13. Among these fractions, fractions TB-7 and TB-9 demonstrated cytotoxic activity toward HepG2 cells with 33.5 and 56.8% inhibition, respectively (Table S5). Certain fractions showed anti-inflammatory activity including TB-2, TB-8 to TB-11, and TB-13 that inhibited superoxide anion generation (IC<sub>50</sub> values 1.45–6.5  $\mu$ g/ml) and TB-1, TB-2 and TB-7 to TB-13 that inhibited elastase release

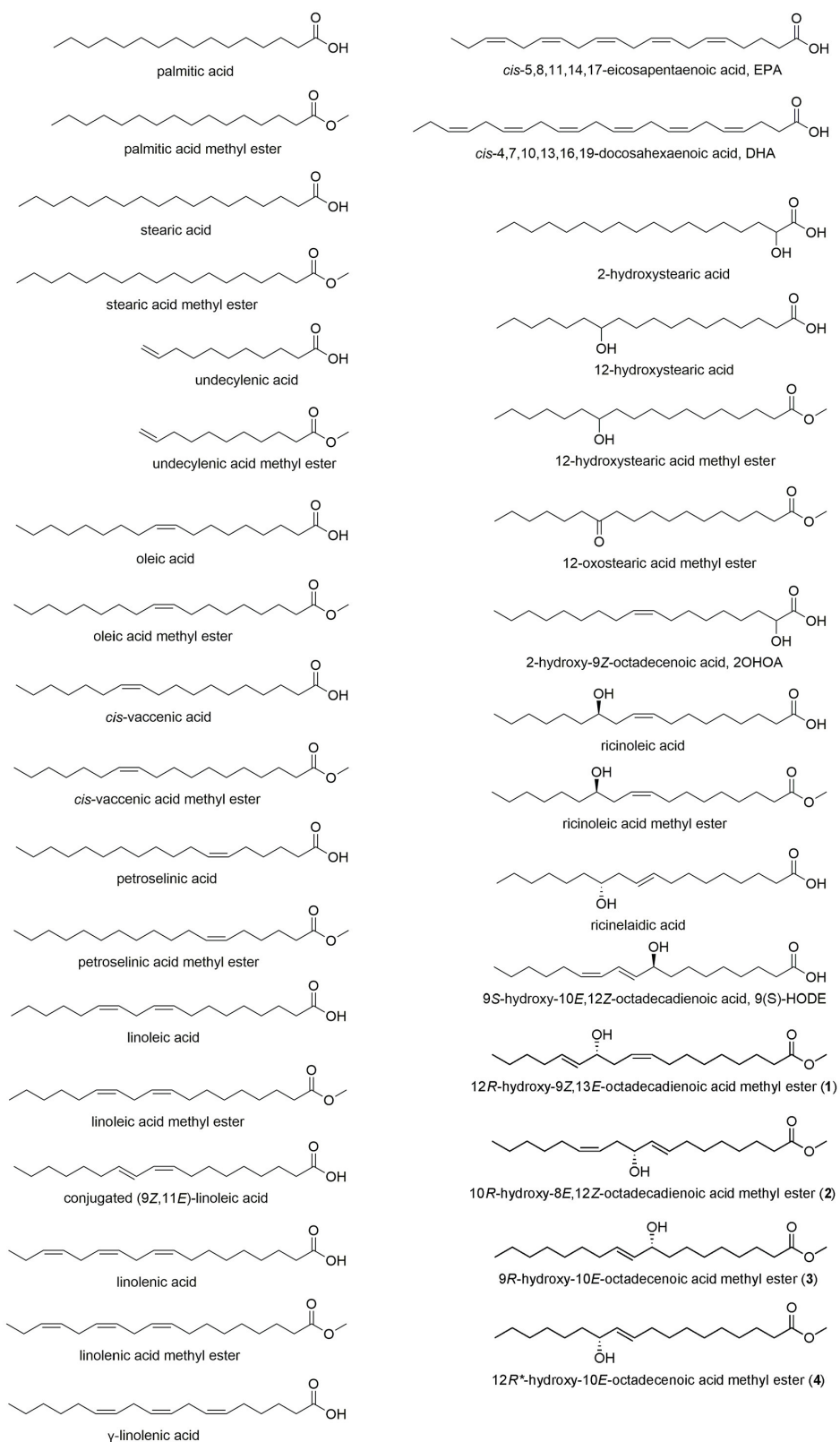


**FIGURE 1 |** Structures of fatty acids, including the hydroxy fatty acids **1–4** isolated from *Typhonium blumei*.

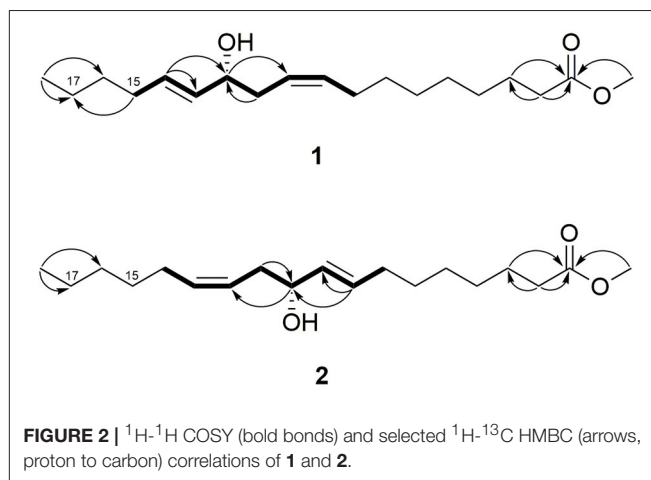
(IC<sub>50</sub> 1.31–6.42 µg/ml) in human neutrophils (Table S6). Also, several fractions showed anti-allergic activity including TB-2, TB-4, TB-7, and TB-11 that inhibited A23187-induced degranulation of mast cells (25.7–41.0% at 100 µg/ml), while TB-9 and TB-10 showed 42.7 and 42.0% inhibition of degranulation at nontoxic concentration of 50 µg/ml in RBL-2H3 cells (Table S7). The purification of TB-7 led to the isolation of four hydroxylated fatty acids (Figure 1).

## Structure Elucidation

Compound **1** was isolated as a colorless oil. The NMR data (<sup>1</sup>H, <sup>13</sup>C, and HMQC, Table 1, Figures S1–S6) revealed the presence of two olefinic double bonds (δ<sub>H</sub> 5.44, m, 3H, δ<sub>C</sub> 132.6, 126.4, 133.9; δ<sub>H</sub> 5.62, dt, *J* = 15.2, 6.4, δ<sub>C</sub> 132.6) and an allylic hydroxy group (δ<sub>H</sub> 3.99, q, *J* = 6.8 Hz) together with carbonyl group (δ<sub>C</sub> 176.0), and a methoxy group (δ<sub>H</sub> 3.65, s). The COSY between C-8 and C-15 together with the HMBC correlations established the 1,5-dien-4-hydroxy moiety in the long chain structure. The HMBC correlation between H-15 (δ<sub>H</sub> 2.05) and C-17 (δ<sub>C</sub> 23.2) suggested the position of the 1,5-dien-4-hydroxy moiety (Figure 2), which was further confirmed by GC-EIMS analysis, showing a typical fragment of *m/z* = 113 (C<sub>7</sub>H<sub>13</sub>O). The <sup>1</sup>H NMR and GC-EIMS data were in agreement with the previously reported data of 12-hydroxy-9Z,13E-octadecadienoic acid methyl ester (Koshino et al., 1987). The stereochemistry of the hydroxy group was determined by measuring the optical rotation ([α]<sub>D</sub><sup>25</sup> = −257, *c* 0.06, EtOH), and comparing the result with the previously reported value ([α]<sub>D</sub><sup>25</sup> = −6.25, *c* 0.32, EtOH) (Koshino et al., 1987). Compound **1** was identified as 12R-hydroxy-9Z,13E-octadecadienoic acid methyl ester.

Compound **2** was also isolated as a colorless oil. The NMR data (<sup>1</sup>H, <sup>13</sup>C and HMQC, Table 1, Figures S8–S13) were similar to compound **1**, indicating the presence of two olefinic double bonds (δ<sub>H</sub> 5.44, m, 3H, δ<sub>C</sub> 132.4, 126.4, 134.0; δ<sub>H</sub> 5.62, dt, *J* = 15.2, 6.8, δ<sub>C</sub> 132.7) and an allylic hydroxy group (δ<sub>H</sub> 3.99, q, *J* = 6.8 Hz) in the long chain of the methylated fatty acid (δ<sub>H</sub> 3.65, s). Similar COSY correlations to compound **1**, indicated the presence of similar 1,5-dien-4-hydroxy moiety. However, the absence of HMBC correlation between H-15 and C-17 indicated different position of the 1,5-dien-4-hydroxy moiety (Figure 2). The reverse position of the moiety was further elaborated based on the GC-EIMS analysis, revealing a fragment of *m/z* = 167. The spectroscopic data were in agreement with the reported data of previously isolated fatty acid (Koshino et al., 1987). The relative configuration of the hydroxy group was assigned as *R* by means of optical rotation ([α]<sub>D</sub><sup>25</sup> = −266, *c* 0.06, EtOH) compared with the reported value ([α]<sub>D</sub><sup>25</sup> = −6.20, *c* 1.0, EtOH) (Kashihara et al., 1989). Therefore, compound **2** was identified as 10R-hydroxy-8E,12Z-octadecadienoic acid methyl ester.

Compound **3** was obtained as a colorless oil. The <sup>1</sup>H NMR data (Table 1) revealed the presence of a trans double bond (δ<sub>H</sub> 5.44, dd, *J* = 15.2, 6.8; δ<sub>H</sub> 5.62, dtd, *J* = 15.2, 6.8, 4.4 Hz) and hydroxy group (δ<sub>H</sub> 4.03, q, *J* = 6.4 Hz) in long-chain fatty acid, which was methylated (δ<sub>H</sub> 3.66, s). The position of the double bond and hydroxy group was assigned by GC-EIMS, which showed a strong peak at *m/z* 155 (C<sub>10</sub>H<sub>19</sub>O) and was identical to the reported spectroscopic data (Frankel et al., 1984;



Koshino et al., 1987). The comparison of the optical rotation ([α]<sub>D</sub><sup>25</sup> = −386, *c* 0.01, EtOH) with the reference data ([α]<sub>D</sub><sup>25</sup> = −2.14, *c* 0.28, EtOH) indicated *R* configuration of the hydroxy group (Koshino et al., 1987). Thus, compound **3** was assigned as 9R-hydroxy-10E-octadecenoic acid methyl ester.

Compound **4** was isolated as another colorless oil. The <sup>1</sup>H NMR data (Table 1) were similar to that of compound **3**, indicating the presence of a trans double bond (δ<sub>H</sub> 5.44, dd, *J* = 15.2, 7.2; δ<sub>H</sub> 5.63, dtd, *J* = 15.2, 6.8, 3.2 Hz) and hydroxy group (δ<sub>H</sub> 4.03, q, *J* = 6.4 Hz) in the long chain of the methylated fatty acid (δ<sub>H</sub> 3.66, s). The position of the double bond at C-10 and the hydroxy group at C-12 was assigned by means of GC-EIMS (*m/z* 227 and 195) (Frankel et al., 1984). The relative configuration of the hydroxy group was determined as *R* by means of optical rotation ([α]<sub>D</sub><sup>25</sup> = −80, *c* 0.015, EtOH), in correlation with the negative optical rotation of other isolated compounds. The structure of compound **4** was assigned as 12R\*-hydroxy-10E-octadecenoic acid methyl ester.

Moreover, a mixture of lipids (A: palmitic acid methyl ester, stearic acid methyl ester, oleic acid methyl ester, margaric acid methyl ester, pentadecanoic acid methyl ester) and mixtures of steroids (B: β-sitost-4-en-3-one, stigmasta-4,22-dien-3-one, campest-4-en-3-one; C: β-sitosterol, stigmasterol; D: stigmasterol-3-O-β-D-glucoside, β-sitosterol-3-O-β-D-glucoside) were extracted from the rhizomes EtOAc fraction by column chromatography and identified by <sup>1</sup>H NMR and GC-MS analyses (mixture A, see Figure S17; mixture B, see Figure S18). These mixtures were inactive in the cytotoxic (at 200 µg/ml), anti-inflammatory (at 10 µg/ml) or anti-allergic (up to 200 µg/ml) assays (data not shown).

The isolated hydroxylated fatty acids were obtained from *Typhonium* sp. for the first time. Moreover, <sup>13</sup>C NMR data, as well as 2D NMR data of **1** and **2**, were never reported before. These fatty acids might be biosynthesized by photooxidation or enzymatic oxidation (possibly via endophytic symbiosis) of the essential unsaturated fatty acid, linoleic acid (Koshino et al., 1987), which was previously identified as one of the major components of *T. blumei* (Korinek et al., 2016a).

## Bioactivity of Isolated Compounds

We evaluated the anti-inflammatory and anti-allergic activities of the isolated compounds (Tables 3, 4). As reported before, the methylation of fatty acids decreased their anti-inflammatory activity (Hwang et al., 2009). Compound 1, the methyl ester of a hydroxylated fatty acid, did not exhibit anti-inflammatory activity in superoxide anion generation or elastase release assays ( $IC_{50} > 10 \mu M$ ) (Table 3). Both compounds 1 and 2, the methyl esters of hydroxylated fatty acids possessing two double bonds, showed anti-allergic inhibitory activity on A23187- and antigen-induced degranulation in RBL-2H3 cells with  $IC_{50}$  values 146.4–181.5  $\mu M$  (Table 4). Compounds 1–3 were previously reported to exert fungitoxic activity against *Cladosporium herbarum*. They were related to the resistant mechanism of infected timothy plants (*Phleum pratense*) by phytopathogenic fungi (Koshino et al., 1987). Several oxygenated unsaturated fatty acids were previously described in rice plants as self-defensive substances against rice blast fungal disease (Kato et al., 1984). Thus, the isolated oxidation products of linoleic acid, compounds 1 and 2, may contribute to the self-defensive function and bioactivity of *T. blumei*.

## In Vitro Cytotoxic, Anti-inflammatory and Anti-allergic Activities of Fatty Acids and their Structure-Activity Relationship (SAR)

The high content of saturated and unsaturated fatty acids in *T. blumei* (Korinek et al., 2016a) together with the isolation of hydroxylated fatty acids (1–4) motivated us to further study the bioactivity of a series of saturated, unsaturated and hydroxylated fatty acids. Although several fatty acids were reported to exert anti-allergic (Willemsen, 2016), anti-inflammatory (Hwang et al., 2009; Calder, 2015), and cytotoxic effects (Jing et al., 2013; Vangaveti et al., 2016), complex bioactivity data describing the structural requirements of fatty acids for the bioactivities are lacking. Moreover, very few reports examined the bioactivity of hydroxylated fatty acids (Hou, 2009).

We obtained a series of saturated, unsaturated and hydroxylated fatty acids (Figure 1) and evaluated their *in vitro* cytotoxic, anti-inflammatory and anti-allergic activities with the aim to elucidate the possible correlation between the activity and certain structural features, including level and position of unsaturation, hydroxylation, position of the hydroxy group or acid methylated derivatives.

### Cytotoxicity

Cytotoxic activity against hepatoma (HepG2), breast (MDA-MB-231) or lung (A549) cancer cell lines was exerted by  $\gamma$ -linolenic acid (C18:3n-6), DHA (C22:6n-3), 12-hydroxystearic acid (C18:0, 12-OH), and ricinoleic acid (C18:1n-9, cis, 12-OH) without any selective toxicity to a specific cell line (Table 2). 12-Hydroxystearic acid exerted the most potent cytotoxic activity among the tested compounds ( $IC_{50}$  86.3–119.0  $\mu M$  for three cell lines). Previous literature demonstrated *in vitro* cytotoxic effects of fatty acids (such as DHA) and lipids on several cancer cell lines, inducing apoptosis by modulation of various signaling molecules and pathways (Fauser et al., 2011; Hsu et al., 2011).

### Anti-inflammatory Activity

Following up on the potent anti-inflammatory activity of a series of saturated and unsaturated fatty acids previously reported by our group (Hwang et al., 2009), we aimed to further extend the list of the tested fatty acids, particularly focusing on those containing a hydroxy group. In agreement with previous data, all tested methyl esters were inactive (Table 3). Similarly, free acidic group and unsaturation were the structural requirements for the anti-inflammatory activity of the tested fatty acids. Petroselinic acid (C18:1n-12), conjugated linoleic acid (C18:2n-7), DHA (C22:6n-3), and EPA (C20:5n-3) exerted significant anti-inflammatory activity by inhibiting superoxide anion generation ( $IC_{50}$  2.08–3.73  $\mu M$ ) and elastase release ( $IC_{50}$  1.26–2.54  $\mu M$ ), which were comparable to the previously reported data for oleic, *cis*-vaccinic, linoleic, and  $\alpha$ -linolenic acids (Hwang et al., 2009). Interestingly, the lack of activity of undecylenic acid (C11:1n-1) indicated that short chain FA did not exert activity. In agreement with our previous results (Hwang et al., 2009), plain saturated fatty acids (palmitic acid, C16:0, and stearic acid, C18:0) were inactive, and similarly, 2-OH or 12-OH saturated fatty acids did not show anti-inflammatory activity. On the other hand, the hydroxylated monounsaturated fatty acids, 2-hydroxy-9Z-octadecenoic acid (2OHOA, C18:1n-9, *cis*, 2-OH), and ricinelaidic acid (C18:1n-9, *trans*, 12-OH) exerted significant inhibitory activity on both superoxide anion generation ( $IC_{50}$  2.40 and 2.32  $\mu M$ , respectively) and elastase release ( $IC_{50}$  2.02 and 1.63  $\mu M$ , respectively) by human neutrophils. The comparison of the superoxide generation and elastase release inhibitory activities of the hydroxylated monounsaturated fatty acids with the monounsaturated fatty acids without a hydroxy group (oleic acid  $IC_{50}$  2.56 and 1.40  $\mu M$ , respectively (Hwang et al., 2009), and petroselinic acid  $IC_{50}$  2.14 and 1.39  $\mu M$ , respectively), showed that the addition of a hydroxy group yielded similar activity.

### Anti-allergic Activity

A23187- and antigen-induced degranulation assays by mast cells (RBL-2H3) were utilized to evaluate the anti-allergic activity of all fatty acids (Table 4). The high doses used of fatty acids in the assay may be justified by the fact that human beings consume large amounts of these compounds on regular basis (Sun et al., 2015). Potential cytotoxic effect toward RBL-2H3 cells was measured by MTT viability assay and only non-toxic concentrations (viability over 85%, Table S1) were further used in the degranulation assay. Among the tested compounds, none of the unsaturated fatty acids, regardless of the double bond position, showed inhibitory activity on A23187- or antigen-induced degranulation by mast cells. Interestingly, at 1,000  $\mu M$  the plain saturated palmitic (C16:0) and stearic (C18:0) fatty acids, common in plants, particularly in seeds and oils, exerted significant inhibition on A23187-induced ( $29.7 \pm 4.7$  and  $35.3 \pm 2.3\%$ , respectively) and antigen-induced ( $40.7 \pm 3.8$  and  $45.3 \pm 1.2\%$ , respectively) degranulation. This finding may be of interest to companies focusing on the preparation of oils and food supplements. Also, the hydroxylated saturated fatty acids exerted anti-allergic activity, as 12-hydroxystearic acid



**TABLE 2 |** Cytotoxic data of fatty acids.

Name	Abbreviation	Mol. weight	Cytotoxicity assay <sup>a</sup>		
			HepG2 <sup>b</sup> IC <sub>50</sub> (μM) <sup>c</sup>	MDA-MB-231 <sup>b</sup> IC <sub>50</sub> (μM) <sup>c</sup>	A549 <sup>b</sup> IC <sub>50</sub> (μM) <sup>c</sup>
Palmitic acid	C16:0	256.4	NS	NS	NS
Palmitic acid methyl ester	C16:0, me	270.5	NS	NS	NS
Stearic acid	C18:0	284.5	NS	NS	NS
Stearic acid methyl ester	C18:0, me	298.5	NS	NS	NS
Undecylenic acid	C11:1n-1	184.3	NS	NS	NS
Undecylenic acid methyl ester	C11:1n-1, me	198.3	NS	NS	NS
<i>cis</i> -Vaccenic acid	C18:1n-7	282.5	NS	NS	NS
<i>cis</i> -Vaccenic acid methyl ester	C18:1n-7, me	296.5	NS	NS	NS
Oleic acid	C18:1n-9	282.5	NS	NS	NS
Oleic acid methyl ester	C18:1n-9, me	296.5	NS	NS	NS
Petroselinic acid	C18:1n-12	282.5	NS	NS	NS
Petroselinic acid methyl ester	C18:1n-12, me	296.5	NS	NS	NS
Linoleic acid	C18:2n-6	280.5	NS	NS	NS
Linoleic acid methyl ester	C18:2n-6, me	294.5	NS	NS	NS
Conjugated (9Z,11E)-linoleic acid	C18:2n-7	280.5	NS	NS	NS
α-Linolenic acid	C18:3n-3	278.4	NS	NS	NS
α-Linolenic acid methyl ester	C18:3n-3, me	292.5	NS	NS	NS
γ-Linolenic acid	C18:3n-6	278.4	>200 <sup>d</sup>	192.7	190.9
<i>cis</i> -5,8,11,14,17-Eicosapentaenoic acid (EPA)	C20:5n-3	302.5	>200 <sup>d</sup>	>200 <sup>d</sup>	NS
<i>cis</i> -4,7,10,13,16,19-Docosahexaenoic acid (DHA)	C22:6n-3	328.5	146.9	140.0	>200 <sup>d</sup>
2-Hydroxystearic acid	C18:0, 2-OH	300.5	NS	NS	NS
12-Hydroxystearic acid	C18:0, 12-OH	300.5	119.0	105.0	86.3
12-Hydroxystearic acid methyl ester	C18:0, 12-OH, me	314.5	NS	NS	NS
12-Oxostearic acid methyl ester	C18:0, 12-oxo, me	312.5	NS	NS	NS
2-Hydroxy-9Z-octadecenoic acid (minerval, 2OHOA)	C18:1n-9, <i>cis</i> , 2-OH	298.5	NS	NS	NS
12R-Hydroxy-9Z-octadecenoic acid (ricinoleic acid)	C18:1n-9, <i>cis</i> , 12-OH	298.5	174.8	NS	154.8
12R-Hydroxy-9Z-octadecenoic acid (ricinoleic acid) methyl ester	C18:1n-9, <i>cis</i> , 12-OH, me	312.5	NS	NS	NS
12R-Hydroxy-9E-octadecenoic acid (ricinelaidic acid)	C18:1n-9, <i>trans</i> , 12-OH	298.5	NS	NS	NS
Doxorubicin			0.62	0.67	0.90

<sup>a</sup> The cytotoxicity was evaluated using MTT viability assay; IC<sub>50</sub> values; results are presented as mean (n = 3); NS, not significant at 200 μM (n = 1).

<sup>b</sup> Hep-G2, Human hepatocellular carcinoma cells; MDA-MB-231, human breast adenocarcinoma cells; A549, human lung adenocarcinoma cells.

<sup>c</sup> IC<sub>50</sub> values express the concentration of the sample required to inhibit cancer cell growth by 50%.

<sup>d</sup> >200 μM means that the sample inhibited the growth of the cells, but didn't reach IC<sub>50</sub> (n = 3).

(C18:0, 12-OH, IC<sub>50</sub> 162.9 μM) and 12-hydroxystearic acid methyl ester (C18:0, 12-OH, me, IC<sub>50</sub> 491.2 μM) in A23187-induced degranulation assay. Monounsaturated hydroxylated fatty acids (2OHOA, C18:1n-9, *cis*, 2-OH and ricinoleic acid methyl ester C18:1n-9, *cis*, 12-OH, me) at 1000 μM showed significant inhibitory effect on A23187-induced (20.0 ± 4.4 and 43.0 ± 2.6%, respectively) and antigen-induced (20.3 ± 3.1, and 58.0 ± 2.6%, respectively) degranulation. Among the tested hydroxylated unsaturated fatty acids, the hydroxylated diunsaturated 9S-hydroxy-10E,12Z-octadecadienoic acid (9(S)-HODE, C18:2n-6, 9-OH, IC<sub>50</sub> 92.4 and 49.7 μM in A23187- and antigen-induced degranulation assay, respectively) showed a more potent anti-allergic effect in comparison with the monounsaturated hydroxylated fatty acids. In correlation with this result, the isolated hydroxylated diunsaturated compounds

**1** and **2** also exerted significant anti-allergic activities, with IC<sub>50</sub> values 146.4–181.5 μM.

In comparison with a series of unsaturated fatty acids (including oleic acid, linoleic acid, linolenic acid, DHA, and EPA), only hydroxylated fatty acids exerted anti-allergic activity. Based on our results, in contrast with the anti-inflammatory effect, a free acid is not a requirement for the anti-allergic activity of fatty acids but may influence their cytotoxicity (as demonstrated by ricinoleic acid vs. its methyl ester), and the level of inhibition of degranulation (palmitic acid vs. its methyl ester). Furthermore, the substitution of the hydroxy group with a keto group resulted in weaker anti-allergic activities. 12-Hydroxystearic acid (C18:0, 12-OH) or its methyl ester (C18:0, 12-OH, me) exhibited more potent anti-allergic activity compared with 12-oxostearic acid methyl ester (C18:0, 12-oxo, me).



**TABLE 3 |** Anti-inflammatory data of fatty acids.

Name	Abbreviation	Anti-inflammatory assay <sup>a</sup>	
		Superoxide anion	Elastase release
		IC <sub>50</sub> (μM) <sup>b</sup>	IC <sub>50</sub> (μM) <sup>b</sup>
Palmitic acid	C16:0	>10	>10
Palmitic acid methyl ester	C16:0, me	>10	>10
Stearic acid	C18:0	>10 <sup>c</sup>	>10 <sup>c</sup>
Stearic acid methyl ester	C18:0, me	>10	>10
Undecylenic acid	C11:1n-1	>10	>10
Undecylenic acid methyl ester	C11:1n-1, me	>10	>10
<i>cis</i> -Vaccenic acid	C18:1n-7	2.31 ± 0.20 <sup>c</sup>	1.36 ± 0.07 <sup>c</sup>
<i>cis</i> -Vaccenic acid methyl ester	C18:1n-7, me	>10	>10
Oleic acid	C18:1n-9	2.56 ± 0.13 <sup>c</sup>	1.40 ± 0.07 <sup>c</sup>
Oleic acid methyl ester	C18:1n-9, me	>10 <sup>c</sup>	>10 <sup>c</sup>
Petroselinic acid	C18:1n-12	2.14 ± 0.47	1.39 ± 0.07
Petroselinic acid methyl ester	C18:1n-12, me	>10	>10
Linoleic acid	C18:2n-6	2.64 ± 0.17 <sup>c</sup>	1.80 ± 0.12 <sup>c</sup>
Linoleic acid methyl ester	C18:2n-6, me	>10	>10
Conjugated (9Z,11E)-linoleic acid	C18:2n-7	2.08 ± 0.50	1.26 ± 0.15
α-Linolenic acid	C18:3n-3	3.49 ± 0.22	4.57 ± 0.08
α-Linolenic acid methyl ester	C18:3n-3, me	>10	>10
γ-Linolenic acid	C18:3n-6	4.57 ± 0.25 <sup>c</sup>	3.17 ± 0.18 <sup>c</sup>
<i>cis</i> -5,8,11,14,17-Eicosapentaenoic acid (EPA)	C20:5n-3	3.73 ± 0.91	1.52 ± 0.14
<i>cis</i> -4,7,10,13,16,19-Docosahexaenoic acid (DHA)	C22:6n-3	2.82 ± 0.44	2.54 ± 0.13
2-Hydroxystearic acid	C18:0, 2-OH	>10	>10
12-Hydroxystearic acid	C18:0, 12-OH	>10	>10
12-Hydroxystearic acid methyl ester	C18:0, 12-OH, me	>10	>10
12-Oxostearic acid methyl ester	C18:0, 12-oxo, me	>10	>10
2-Hydroxy-9Z-octadecenoic acid (minerval, 2OHOA)	C18:1n-9, <i>cis</i> , 2-OH	2.40 ± 0.69	2.02 ± 0.70
12R-Hydroxy-9Z-octadecenoic acid (ricinoleic acid)	C18:1n-9, <i>cis</i> , 12-OH	>10 <sup>d</sup>	>10 <sup>d</sup>
12R-Hydroxy-9Z-octadecenoic acid (ricinoleic acid) methyl ester	C18:1n-9, <i>cis</i> , 12-OH, me	>10	Enhancing effect <sup>e</sup>
12R-Hydroxy-9E-octadecenoic acid (ricinelaidic acid)	C18:1n-9, <i>trans</i> , 12-OH	2.32 ± 0.59	1.63 ± 0.16
12R-Hydroxy-9Z,13E-octadecadienoic acid methyl ester ( <b>1</b> )	C18:2n-5, 12-OH, me	>10	>10
Genistein		1.37 ± 0.53	40.0 ± 8.9

<sup>a</sup>Anti-inflammatory capacity was evaluated by superoxide anion generation and elastase release assays in human neutrophils using fMLF/CB as an inducer. IC<sub>50</sub> values; results are presented as mean ± SEM (n = 3–4); compared with the control value (fMLF/CB).

<sup>b</sup>IC<sub>50</sub> values express the concentration of the sample required to inhibit superoxide anion generation or elastase release by 50%.

<sup>c</sup>The samples were tested in Hwang et al. (2009).

<sup>d</sup>Ricinoleic acid exerted significant inhibitory activity in superoxide anion generation (39.9 ± 5.6%) and elastase release (39.9 ± 4.1%) assay at 10 μM.

<sup>e</sup>The compound showed enhancing effects on elastase release at 10 μM (42.8 ± 6.5%) in the presence of CB. Compared with fMLF/CB (as 100%).

DHA and EPA (n-3) fatty acids at 100 μM were previously reported to exert anti-allergic effects in phorbol 12-myristate 13-acetate- and ionomycin-activated RBL-2H3 mast cells (Jin et al., 2014; Willemsen, 2016). However, in our experimental model using A23187 or antigen as inducers, DHA and EPA did not show significant inhibitory activity on degranulation in mast cells at a non-toxic concentration of 200 μM.

## ChemGPS, Physico-Chemical Properties of Fatty Acids

ChemGPS-NP (chemical global positioning system for natural products) was developed as a computational model based on the principal component analysis (PCA) of physico-chemical

properties of nature-derived compounds. Compounds are placed into a chemical space based on their properties, which can be calculated from simplified molecular input line entry specification (SMILES) structure data, followed by execution of score prediction in ChemGPS-NP. The system provides a bioinformatics tool for plotting and navigating biologically relevant chemical spaces (Larsson et al., 2007; Lai et al., 2016). It can further serve as a tool for discussing the structure-activity relationships as well as to predict possible bioactivities for specific groups of compounds. We plotted the long-chain fatty acids into ChemGPS-NP (<http://chemgps.bmc.uu.se>) with the aim to observe a possible correlation between oxygenation and bioactivity in relevant chemical space (**Figure 3**). Anti-allergic

**TABLE 4 |** Anti-allergic data of fatty acids.

Name	Abbreviation	Anti-allergic assay <sup>a</sup>	
		A23187-induced IC <sub>50</sub> (μM) <sup>b</sup>	Antigen-induced IC <sub>50</sub> (μM) <sup>b</sup>
Palmitic acid	C16:0	>1,000 <sup>c</sup>	>1,000 <sup>c</sup>
Palmitic acid methyl ester	C16:0, me	>1,000	>1,000
Stearic acid	C18:0	>1,000 <sup>d</sup>	>1,000 <sup>d</sup>
Stearic acid methyl ester	C18:0, me	>1,000	>1,000
Undecylenic acid	C11:1n-1	>500 <sup>e</sup>	>500 <sup>e</sup>
Undecylenic acid methyl ester	C11:1n-1, me	>1,000	>1,000
<i>cis</i> -Vaccenic acid	C18:1n-7	>500 <sup>e</sup>	>500 <sup>e</sup>
<i>cis</i> -Vaccenic acid methyl ester	C18:1n-7, me	>1,000	>1,000
Oleic acid	C18:1n-9	>500 <sup>e</sup>	>500 <sup>e</sup>
Oleic acid methyl ester	C18:1n-9, me	>1,000	>1,000
Petroselinic acid	C18:1n-12	>500 <sup>e</sup>	>500 <sup>e</sup>
Petroselinic acid methyl ester	C18:1n-12, me	>1,000	>1,000
Linoleic acid	C18:2n-6	>500 <sup>e</sup>	>500 <sup>e</sup>
Linoleic acid methyl ester	C18:2n-6, me	>500 <sup>e</sup>	>500 <sup>e</sup>
Conjugated (9Z,11E)-linoleic acid	C18:2n-7	>200 <sup>f</sup>	>200 <sup>f</sup>
α-Linolenic acid	C18:3n-3	>200 <sup>f</sup>	>200 <sup>f</sup>
α-Linolenic acid methyl ester	C18:3n-3, me	>500 <sup>e</sup>	>500 <sup>e</sup>
γ-Linolenic acid	C18:3n-6	>200 <sup>f</sup>	>200 <sup>f</sup>
<i>cis</i> -5,8,11,14,17-Eicosapentaenoic acid (EPA)	C20:5n-3	>200 <sup>f</sup>	>200 <sup>f</sup>
<i>cis</i> -4,7,10,13,16,19-Docosahexaenoic acid (DHA)	C22:6n-3	>200 <sup>f</sup>	>200 <sup>f</sup>
2-Hydroxystearic acid	C18:0, 2-OH	>200 <sup>g</sup>	>200 <sup>g</sup>
12-Hydroxystearic acid	C18:0, 12-OH	162.9 <sup>g</sup>	>200 <sup>g</sup>
12-Hydroxystearic acid methyl ester	C18:0, 12-OH, me	491.2	>1,000
12-Oxostearic acid methyl ester	C18:0, 12-oxo, me	>1,000 <sup>h</sup>	>1,000 <sup>h</sup>
2-Hydroxy-9Z-octadecenoic acid (minerval, 2OHOA)	C18:1n-9, <i>cis</i> , 2-OH	>1,000 <sup>i</sup>	>1,000 <sup>i</sup>
12R-Hydroxy-9Z-octadecenoic acid (ricinoleic acid)	C18:1n-9, <i>cis</i> , 12-OH	>200 <sup>f</sup>	>200 <sup>f</sup>
12R-Hydroxy-9Z-octadecenoic acid (ricinoleic acid) methyl ester	C18:1n-9, <i>cis</i> , 12-OH, me	>1,000 <sup>j</sup>	913.0
12R-Hydroxy-9E-octadecenoic acid (ricinelaidic acid)	C18:1n-9, <i>trans</i> , 12-OH	>500 <sup>e</sup>	>500 <sup>e</sup>
12R-Hydroxy-9Z,13E-octadecadienoic acid methyl ester (1)	C18:2n-5, 12-OH, me	146.4 <sup>f</sup>	153.0 <sup>f</sup>
9S-Hydroxy-10E,12Z-octadecadienoic acid (9(S)-HODE)	C18:2n-6, 9-OH	92.4 <sup>k</sup>	49.7 <sup>k</sup>
10R-Hydroxy-8E,12Z-octadecadienoic acid methyl ester (2)	C18:2n-6, 10-OH, me	181.5 <sup>f</sup>	154.1 <sup>f</sup>
Dexamethasone		80% at 10 nM	62% at 10 nM

<sup>a</sup>The inhibition of degranulation was assessed by A23187- or antigen-induced β-hexosaminidase release assays in RBL-2H3 cells; IC<sub>50</sub> values; results are presented as mean (n = 3); compared with the control value (A23187 or antigen). For detail information about cytotoxicity toward RBL-2H3 cells and degranulation inhibitory data (1 μM–1,000 μM) please refer to Table S1 in Supporting information.

<sup>b</sup>IC<sub>50</sub> values express the concentration of the sample required to inhibit degranulation by 50%.

<sup>c</sup>Palmitic acid exerted significant inhibitory activity in both A23187- (29.7 ± 4.7%) and antigen-induced (40.7 ± 3.8%) degranulation assay at 1,000 μM.

<sup>d</sup>Stearic acid exerted significant inhibitory activity in both A23187- (35.3 ± 2.3%) and antigen-induced (45.3 ± 1.2%) degranulation assay at 1,000 μM.

<sup>e</sup>Sample exerted cytotoxic effects (viability <80%) toward RBL-2H3 cells at concentrations higher than 500 μM.

<sup>f</sup>Sample exerted cytotoxic effects (viability <80%) toward RBL-2H3 cells at concentrations higher than 200 μM.

<sup>g</sup>Micelles were formed upon addition into the medium at concentrations above 200 μM, therefore the results at these concentrations couldn't be justified.

<sup>h</sup>12-Oxostearic acid methyl ester exerted significant inhibitory activity in both A23187- (40.3 ± 3.5%) and antigen-induced (23.7 ± 3.1%) degranulation assay at 1,000 μM.

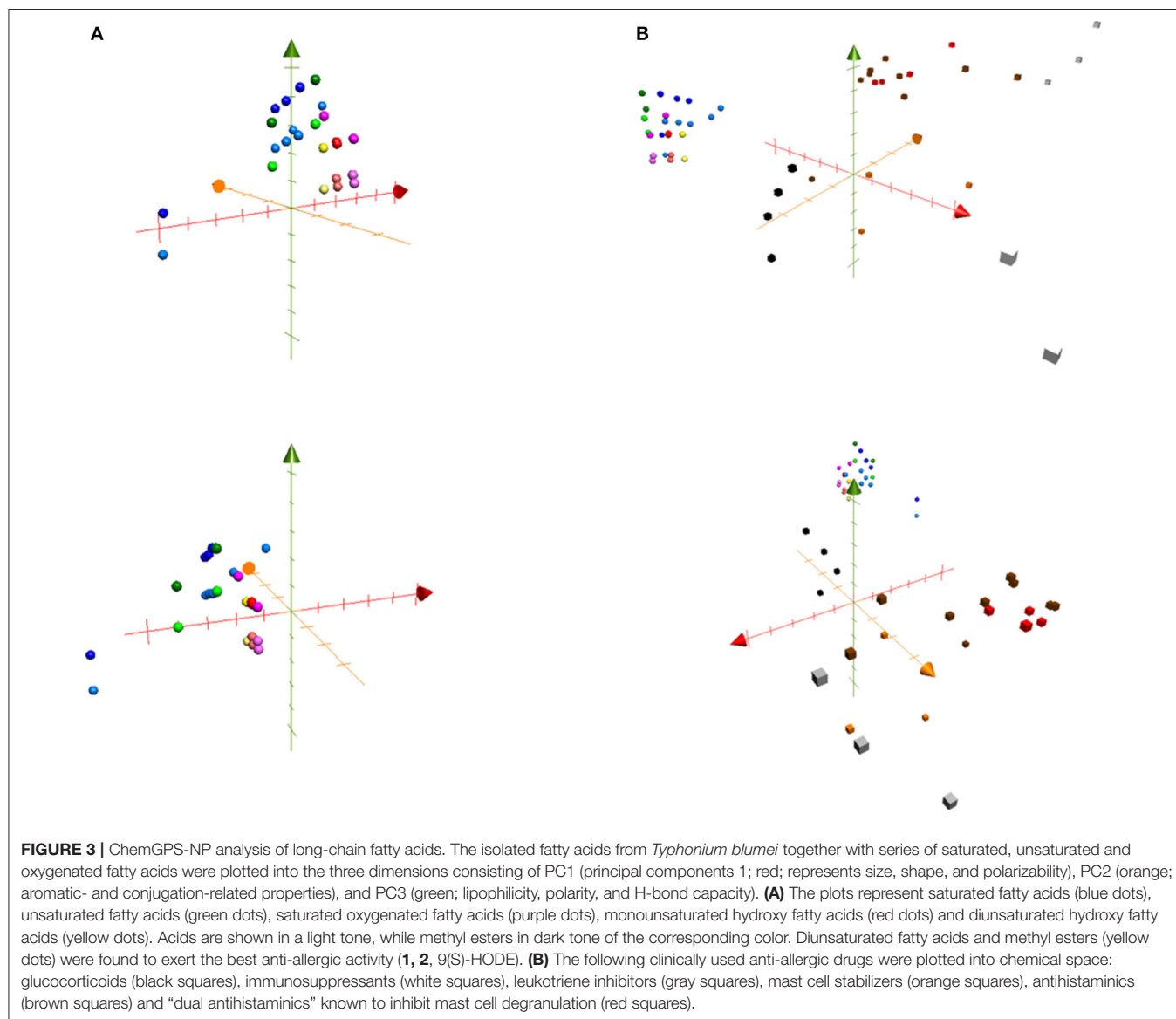
<sup>i</sup>Minerval (2OHOA) exerted significant inhibitory activity in both A23187- (20.0 ± 4.4%) and antigen-induced (20.3 ± 3.1%) degranulation assay at 1,000 μM.

<sup>j</sup>Ricinoleic acid methyl ester exerted significant inhibitory activity in A23187-induced (43.0 ± 2.6%) degranulation assay at 1,000 μM.

<sup>k</sup>The highest tested concentration of 9(S)HODE was 100 μM.

hydroxylated fatty acids and their methyl esters (purple, red and yellow dots), explored particularly by the first dimension (PC1, red axis, representing size, shape, and polarizability), formed a cluster in the analyzing graphic (**Figure 3A**). Thus, fatty acids possessing hydroxy groups which would be plotted in the space toward an increase in size, shape, and polarizability (PC1, red axis) may yield better anti-allergic activity.

Furthermore, we plotted clinical anti-allergic drugs, namely glucocorticoids (black squares), immunosuppressants (white squares), leukotriene inhibitors (gray squares), mast cells stabilizers (orange squares), and antihistaminics (brown and red squares), into the chemical space (PC1, PC2, PC3). Antihistaminics analyzed, including antihistaminics of 1st and 2nd generation, were further divided into two groups:



antihistaminics with regular histamine receptor antagonizing capacity (brown squares) and antihistaminics with a dual mode of action that are known to additionally inhibit mast cell degranulation (“dual antihistaminics,” red squares). The drugs formed different clusters distant from fatty acids group (**Figure 3B**). Among the different groups, the antihistaminics (brown squares) and “dual antihistaminics” known to inhibit mast cell degranulation (red squares), shared chemical properties regarding the first dimension (PC1, red axis, representing size, shape, and polarizability) and the third dimension (PC3, green axis, representing lipophilicity, polarity, and H-bond capacity) compared with the fatty acids group. Taken together, the anti-allergic fatty acids group represents a new cluster regarding the anti-allergic activity, showing a new pattern of chemical properties that could be of use for the future development of anti-allergic drugs.

## DISCUSSION

12/15-Lipoxygenase (12/15-LOX) catalyzes the oxidation of free and esterified fatty acids, thus forming a variety of bioactive lipid mediators. 12/15-LOX plays a key role in the regulation of different homeostatic processes as well as in the pathogenesis of several diseases (Uderhardt and Kronke, 2012; Lopez-Vicario et al., 2016). Oxygenated products of unsaturated fatty acids possess immune modulatory properties that effect inflammatory responses (Duvall and Levy, 2016; Whelan et al., 2016). Several studies investigated the properties and function of fatty acid derivatives, particularly arachidonic acid (AA, C20:4n-6) and DHA (C22:6n-3) and their related metabolic pathways (Lopez-Vicario et al., 2016). Elegant reviews described the pro-inflammatory as well as the inflammatory-resolving functions of various 12/15-LOX products (Kuhn and O'Donnell,

2006; Ackermann et al., 2017). For example, 15S-hydroxy-5Z,8Z,11Z,13E-eicosatetraenoic acid (15(S)-HETE), but not its methyl ester, was reported to serve as a mediator limiting and/or reversing acute inflammation by exhibiting counterbalancing effects on neutrophil trafficking across endothelium. 15(S)-HETE was found to inhibit respiratory burst and degranulation of neutrophils activated with receptor-specific agonists, such as fMLF, platelet-activating factor, and leukotriene B<sub>4</sub> (Smith et al., 1993; Takata et al., 1994). In agreement with the anti-inflammatory effect of 15(S)-HETE, our findings revealed that unsaturated hydroxylated free fatty acids (2-hydroxy-9Z-octadecenoic acid, 12R-hydroxy-9E-octadecenoic acid) inhibited fMLF/CB-induced superoxide generation and elastase release in human neutrophils (Table 3). The introduction of either hydroperoxy or hydroxyl groups into arachidonic acid (AA, 20:4n-6) abolished its neutrophil adherence stimulating ability and decreased its capacity to stimulate the release of both specific and azurophilic granules (Bates et al., 1995). It was found that the conversion of AA to 15S-hydroperoxy-5Z,8Z,11Z,13E-eicosatetraenoic acid (15-HPETE) led to the loss of the compound ability to activate the neutrophil responses of superoxide production, degranulation, and adherence (Huang et al., 1997; Ferrante and Ferrante, 2005). Moreover, 15-HPETE suppressed the lipopolysaccharide (LPS)-induced production and mRNA expression of tumor necrosis factor alpha (TNF- $\alpha$ ), and significantly reduced the LPS-induced translocation of protein kinase C (PKC) (Ferrante et al., 1997). Oxidative products of 12/15-LOX were, moreover, reported as coactivators of anti-inflammatory peroxisome proliferator-activated receptor (PPAR $\gamma$ ) (Huang et al., 1999), regulators of cytokine generation, and modulators of gene expression related to inflammation resolution (Kuhn and O'Donnell, 2006).

During the innate and adaptive immune response, 12/15-LOX and its products exert both pro- and anti-inflammatory effects (Ackermann et al., 2017). Recently, some of the oxygenated fatty acid metabolites of n-3 unsaturated fatty acids, such as 17,18-epoxy-5Z,8Z,11Z,14Z-eicosatetraenoic and 17,18-dihydroxy-5Z,8Z,11Z,14Z-eicosatetraenoic acid, demonstrated the anti-allergic effect *in vivo* due to impairment of mast cells degranulation (Kunisawa et al., 2015). Similarly, according to our current findings, oxygenated fatty acids (1, 2, 9(S)-HODE) formed upon the oxidation of linoleic acid exerted suppressive effects on the mast cells degranulation (Table 4). It has been reported that the high intake of unsaturated fatty acids in pregnancy or early childhood may prevent the development of allergic diseases, particularly asthma and atopic eczema (Lumia et al., 2011; Willemsen, 2016). In correlation with our findings, the elucidation of whether such effects might be a consequence of oxidative metabolism of the consumed fatty acids would be warranted.

## CONCLUSION

According to our results, the presence of a hydroxy group in the long chain did not influence the potent anti-inflammatory activity of free unsaturated acids. Nevertheless, hydroxylation

of fatty acids (or their methyl esters) seems to be a key factor for the anti-allergic activity observed in the current study (Graphical Abstract). Considering the high content in plants and high daily intake of fatty acids from food and oils, the presented results may shed light on the utilization of fatty acids and their hydroxylated products in the treatment of inflammatory and allergic diseases. Thus, the bioactivity of *T. blumei*, which is historically utilized in folk medicine, might be related to the content of fatty acids and their metabolites.

## AUTHOR CONTRIBUTIONS

TH, BC, and FC conceived and designed the experiments and contributed to the manuscript preparation. MK executed the phytochemical and anti-allergic experiments, analyzed the data and wrote the manuscript. SC performed cytotoxicity experiments. TH completed anti-inflammatory *in vitro* study. YT performed GC-MS experiments. KL and AB assisted with utilizing ChemGPS-NP in the study. SW, WL, and TW assisted with the phytochemical experiments. MK, ME, YC, and YW revised the manuscript. All the authors approved the final version of the manuscript.

## FUNDING

This work was supported by the grants from Ministry of Science and Technology, Taiwan (NSC 102-2628-B-037-003-MY3, MOST 103-2320-B-037-005-MY2, awarded to FC., MOST 103-2628-B-037-001-MY3 awarded to YC, MOST 104-2320-B-255-004-MY3 awarded to TH). This study was also supported by Kaohsiung Medical University, Taiwan (Aim for the Top Universities Grant, grant No. KMU-TP105E31, KMU-TP105E32, KMU-TP104A26, KMU-M106009), National Sun Yat-sen University-KMU Joint Research Project (NSYSUKMU106-P015), Kaohsiung Medical University Research Foundation (105KMUOR02), Chang Gung Memorial Hospital, Taiwan (CMRPD1B0281~3, CMRPF1D0442~3, CMRPF1F0011~3, CMRPF1F0061~3, and BMRP450) and Ministry of Health and Welfare, Taiwan (MOHW106-TDU-B-212-144007, Health and Welfare Surcharge of Tobacco Products).

## ACKNOWLEDGMENTS

We thank the Center for Research Resources and Development at Kaohsiung Medical University for providing instrumentation support. We are grateful to Prof. Ming-Hong Yen for plant identification, Yu-Ming Hsu, Ying-Chi Du, Shih-Wei Jheng, Wan-Hui Huang for assistance with the experiments. Special thanks to Joel Stocker and Laura Fasi for English editing.

## SUPPLEMENTARY MATERIAL

The Supplementary Material for this article can be found online at: <http://journal.frontiersin.org/article/10.3389/fphar.2017.00356/full#supplementary-material>

## REFERENCES

- Ackermann, J. A., Hofheinz, K., Zaiss, M. M., and Kronke, G. (2017). The double-edged role of 12/15-lipoxygenase during inflammation and immunity. *Biochim. Biophys. Acta* 1862, 371–381. doi: 10.1016/j.bbaliip.2016.07.014
- Bates, E. J., Ferrante, A., Smithers, L., Poulos, A., and Robinson, B. S. (1995). Effect of fatty acid structure on neutrophil adhesion, degranulation and damage to endothelial cells. *Atherosclerosis* 116, 247–259. doi: 10.1016/0021-9150(95)05553-9
- Beermann, C., Neumann, S., Fussbroich, D., Zielen, S., and Schubert, R. (2016). Combinations of distinct long-chain polyunsaturated fatty acid species for improved dietary treatment against allergic bronchial asthma. *Nutrition* 32, 1165–1170. doi: 10.1016/j.nut.2016.04.004
- Boyum, A. (1968). Isolation of mononuclear cells and granulocytes from human blood. Isolation of mononuclear cells by one centrifugation, and of granulocytes by combining centrifugation and sedimentation at 1 g. *Scand. J. Clin. Lab. Invest. Suppl.* 97, 77–89.
- Calder, P. C. (2008). Polyunsaturated fatty acids, inflammatory processes and inflammatory bowel diseases. *Mol. Nutr. Food Res.* 52, 885–897. doi: 10.1002/mnfr.200700289
- Calder, P. C. (2015). Marine omega-3 fatty acids and inflammatory processes: effects, mechanisms and clinical relevance. *Biochim. Biophys. Acta* 1851, 469–484. doi: 10.1016/j.bbaliip.2014.08.010
- Chang, M. Y. (1992). *Anticancer Medicinal Herbs*. Changsha: Hunan Science & Technology Press.
- Chen, B. H., Wu, P. Y., Chen, K. M., Fu, T. F., Wang, H. M., and Chen, C. Y. (2009). Antiallergic potential on RBL-2H3 cells of some phenolic constituents of *Zingiber officinale* (ginger). *J. Nat. Prod.* 72, 950–953. doi: 10.1021/np800555y
- Duvall, M. G., and Levy, B. D. (2016). DHA- and EPA-derived resolvins, protectins, and maresins in airway inflammation. *Eur. J. Pharmacol.* 785, 144–155. doi: 10.1016/j.ejphar.2015.11.001
- Fausser, J. K., Prisciandaro, L. D., Cummins, A. G., and Howarth, G. S. (2011). Fatty acids as potential adjunctive colorectal chemotherapeutic agents. *Cancer Biol. Ther.* 11, 724–731. doi: 10.4161/cbt.11.8.15281
- Ferrante, J. V., and Ferrante, A. (2005). Cutting edge: novel role of lipoxygenases in the inflammatory response: promotion of TNF mRNA decay by 15-hydroperoxyeicosatetraenoic acid in a monocytic cell line. *J. Immunol.* 174, 3169–3172. doi: 10.4049/jimmunol.174.6.3169
- Ferrante, J. V., Huang, Z. H., Nandoskar, M., Hii, C. S., Robinson, B. S., Rathjen, D. A., et al. (1997). Altered responses of human macrophages to lipopolysaccharide by hydroperoxy eicosatetraenoic acid, hydroxy eicosatetraenoic acid, and arachidonic acid. Inhibition of tumor necrosis factor production. *J. Clin. Invest.* 99, 1445–1452. doi: 10.1172/JCI119303
- Frankel, E. N., Garwood, R. F., Khambay, B. P. S., Moss, G. P., and Weedon, B. C. L. (1984). Stereochemistry of olefin and fatty acid oxidation. Part 3. The allylic hydroperoxides from the autooxidation of methyl oleate. *J. Chem. Soc. Perkin 1*, 2233–2240. doi: 10.1039/p19840002233
- Grivennikov, S. I., Greten, F. R., and Karin, M. (2010). Immunity, inflammation, and cancer. *Cell* 140, 883–899. doi: 10.1016/j.cell.2010.01.025
- Hou, C. T. (2009). Biotechnology for fats and oils: new oxygenated fatty acids. *N. Biotechnol.* 26, 2–10. doi: 10.1016/j.nbt.2009.05.001
- Hsu, H. F., Huang, K. H., Lu, K. J., Chiou, S. J., Yen, J. H., Chang, C. C., et al. (2011). *Typhonium blumei* extract inhibits proliferation of human lung adenocarcinoma A549 cells via induction of cell cycle arrest and apoptosis. *J. Ethnopharmacol.* 135, 492–500. doi: 10.1016/j.jep.2011.03.048
- Huang, J. T., Welch, J. S., Ricote, M., Binder, C. J., Willson, T. M., Kelly, C., et al. (1999). Interleukin-4-dependent production of PPAR- $\gamma$  ligands in macrophages by 12/15-lipoxygenase. *Nature* 400, 378–382. doi: 10.1038/22572
- Huang, T. C. (2000). *Flora of Taiwan*. Taipei: Epoch Publishing Co. Ltd.
- Huang, Z. H., Bates, E. J., Ferrante, J. V., Hii, C. S., Poulos, A., Robinson, B. S., et al. (1997). Inhibition of stimulus-induced endothelial cell intercellular adhesion molecule-1, E-selectin, and vascular cellular adhesion molecule-1 expression by arachidonic acid and its hydroxy and hydroperoxy derivatives. *Circ. Res.* 80, 149–158. doi: 10.1161/01.RES.80.2.149
- Hwang, T. L., Leu, Y. L., Kao, S. H., Tang, M. C., and Chang, H. L. (2006). Viscolin, a new chalcone from *Viscum coloratum*, inhibits human neutrophil superoxide anion and elastase release via a cAMP-dependent pathway. *Free Radic. Biol. Med.* 41, 1433–1441. doi: 10.1016/j.freeradbiomed.2006.08.001
- Hwang, T. L., Su, Y. C., Chang, H. L., Leu, Y. L., Chung, P. J., Kuo, L. M., et al. (2009). Suppression of superoxide anion and elastase release by C<sub>18</sub> unsaturated fatty acids in human neutrophils. *J. Lipid Res.* 50, 1395–1408. doi: 10.1194/jlr.M800574-JLR200
- Jauregui, H. O., Hayner, N. T., Driscoll, J. L., Williams-Holland, R., Lipsky, M. H., and Galletti, P. M. (1981). Trypan blue dye uptake and lactate dehydrogenase in adult rat hepatocytes—freshly isolated cells, cell suspensions, and primary monolayer cultures. *In vitro* 17, 1100–1110. doi: 10.1007/BF02618612
- Jin, M., Park, S., Park, B. K., Choi, J. J., Yoon, S. J., Yang, M., et al. (2014). Eicosapentaenoic acid and docosahexaenoic acid suppress Th2 cytokine expression in RBL-2H3 basophilic leukemia cells. *J. Med. Food* 17, 198–205. doi: 10.1089/jmf.2013.2935
- Jing, K., Wu, T., and Lim, K. (2013). Omega-3 polyunsaturated fatty acids and cancer. *Anticancer Agents Med. Chem.* 13, 1162–1177. doi: 10.2174/18715206113139990319
- Johansson, S. G., Hourihane, J. O., Bousquet, J., Brujnzeel-Koomen, C., Dreborg, S., Haahtela, T., et al. (2001). A revised nomenclature for allergy. An EAACI position statement from the EAACI nomenclature task force. *Allergy* 56, 813–824. doi: 10.1034/j.1398-9995.2001.t011-1-00001.x
- Kashihara, H., Suemune, H., Fujimoto, K., and Sakai, K. (1989). A new synthetic route to optically active  $\alpha$ ,  $\beta$ - and  $\beta'$ ,  $\gamma'$ -unsaturated alcohols, and its application to the synthesis of a fungitoxic C-18 hydroxy unsaturated fatty acid. *Chem. Pharm. Bull.* 37, 2610–2614. doi: 10.1248/cpb.37.2610
- Kato, T., Yamaguchi, Y., Hirano, T., Yokoyama, T., Uyehara, T., Namai, T., et al. (1984). Unsaturated hydroxy fatty acids, the self defensive substances in rice plant against rice blast disease. *Chem. Lett.* 13, 409–412. doi: 10.1246/cl.1984.409
- Kong, W. W., Deng, Z. X., Fei, J., Wang, Q., Sun, X. F., and Tang, K. X. (2006). Characterization of a mannose-binding lectin gene from *Typhonium divaricatum* (L.) Decne. *Afr. J. Biotechnol.* 5, 793–799. doi: 10.5897/AJB06.175
- Korinek, M., Chen, K. M., Jiang, Y. H., El-Shazly, M., Stocker, J., Chou, C. K., et al. (2016a). Anti-allergic potential of *Typhonium blumei*: inhibition of degranulation via suppression of PI3K/PLC $\gamma$ 2 phosphorylation and calcium influx. *Phytomedicine* 23, 1706–1715. doi: 10.1016/j.phymed.2016.10.011
- Korinek, M., Wagh, V. D., Lo, I. W., Hsu, Y. M., Hsu, H. Y., Hwang, T. L., et al. (2016b). Antiallergic phorbol ester from the seeds of *Aquilaria malaccensis*. *Int. J. Mol. Sci.* 17:398. doi: 10.3390/ijms17030398
- Korkmaz, B., Horwitz, M. S., Jenne, D. E., and Gauthier, F. (2010). Neutrophil elastase, proteinase 3, and cathepsin G as therapeutic targets in human diseases. *Pharmacol. Rev.* 62, 726–759. doi: 10.1124/pr.110.002733
- Koshino, H., Togiya, S., Yoshihara, T., and Sakamura, S. (1987). Four fungitoxic C-18 hydroxy unsaturated fatty acids from stromata of *Epichloe typhina*. *Tetrahedron Lett.* 28, 73–76. doi: 10.1016/S0040-4039(00)95652-1
- Kuhn, H., and O'Donnell, V. B. (2006). Inflammation and immune regulation by 12/15-lipoxygenases. *Prog. Lipid Res.* 45, 334–356. doi: 10.1016/j.plipres.2006.02.003
- Kunisawa, J., Arita, M., Hayasaka, T., Harada, T., Iwamoto, R., Nagasawa, R., et al. (2015). Dietary  $\omega$ 3 fatty acid exerts anti-allergic effect through the conversion to 17,18-epoxyeicosatetraenoic acid in the gut. *Sci. Rep.* 5:9750. doi: 10.1038/srep09750
- Lai, C. S., Mas, R. H., Nair, N. K., Majid, M. I., Mansor, S. M., and Navaratnam, V. (2008). *Typhonium flagelliforme* inhibits cancer cell growth *in vitro* and induces apoptosis: an evaluation by the bioactivity guided approach. *J. Ethnopharmacol.* 118, 14–20. doi: 10.1016/j.jep.2008.02.034
- Lai, K. H., Lu, M. C., Du, Y. C., El-Shazly, M., Wu, T. Y., Hsu, Y. M., et al. (2016). Cytotoxic lanostanoids from *Poria cocos*. *J. Nat. Prod.* 79, 2805–2813. doi: 10.1021/acs.jnatprod.6b00575
- Lai, W. C., Tsui, Y. T., Singab, A. N., El-Shazly, M., Du, Y. C., Hwang, T. L., et al. (2013). Phyto-SERM constitutes from *Flemingia macrophylla*. *Int. J. Mol. Sci.* 14, 15578–15594. doi: 10.3390/ijms140815578
- Larsson, J., Gottfries, J., Muresan, S., and Backlund, A. (2007). ChemGPS-NP: tuned for navigation in biologically relevant chemical space. *J. Nat. Prod.* 70, 789–794. doi: 10.1021/np070002y
- Li, T. S. C. (2006). *Taiwanese Native Medicinal Plants: Phytopharmacology and Therapeutic Values*. Boca Raton, FL: CRC press/Taylor & Francis Group.
- Lopez-Vicario, C., Rius, B., Alcaraz-Quiles, J., Garcia-Alonso, V., Lopategi, A., Titos, E., et al. (2016). Pro-resolving mediators produced from EPA and DHA: overview of the pathways involved and their mechanisms in



- metabolic syndrome and related liver diseases. *Eur. J. Pharmacol.* 785, 133–143. doi: 10.1016/j.ejphar.2015.03.092
- Lumia, M., Luukkainen, P., Tapanainen, H., Kaila, M., Erkkola, M., Uusitalo, L., et al. (2011). Dietary fatty acid composition during pregnancy and the risk of asthma in the offspring. *Pediatr. Allergy Immunol.* 22, 827–835. doi: 10.1111/j.1399-3038.2011.01202.x
- Lundstrom, S. L., Yang, J., Brannan, J. D., Haeggstrom, J. Z., Hammock, B. D., Nair, P., et al. (2013). Lipid mediator serum profiles in asthmatics significantly shift following dietary supplementation with omega-3 fatty acids. *Mol. Nutr. Food Res.* 57, 1378–1389. doi: 10.1002/mnfr.201200827
- Luo, Y., Xu, X., Liu, J., Li, J., Sun, Y., Liu, Z., et al. (2007). A novel mannose-binding tuber lectin from *Typhonium divaricatum* (L.) Decne (family Araceae) with antiviral activity against HSV-II and anti-proliferative effect on human cancer cell lines. *J. Biochem. Mol. Biol.* 40, 358–367. doi: 10.5483/bmbrep.2007.40.3.358
- Maehre, H. K., Jensen, I. J., Elvevoll, E. O., and Eilertsen, K. E. (2015). Omega-3 fatty acids and cardiovascular diseases: effects, mechanisms and dietary relevance. *Int. J. Mol. Sci.* 16, 22636–22661. doi: 10.3390/ijms160922636
- Michalak, A., Mosinska, P., and Fichna, J. (2016). Polyunsaturated fatty acids and their derivatives: therapeutic value for inflammatory, functional gastrointestinal disorders, and colorectal cancer. *Front. Pharmacol.* 7:459. doi: 10.3389/fphar.2016.00459
- Newman, D. J., and Cragg, G. M. (2016). Natural products as sources of new drugs from 1981 to 2014. *J. Nat. Prod.* 79, 629–661. doi: 10.1021/acs.jnatprod.5b01055
- Nicolson, D. H., and Sivadasan, M. (1981). Four frequently confused species of *Typhonium* Schott (Araceae). *Blumea* 27, 483–497.
- Rajaram, S. (2014). Health benefits of plant-derived alpha-linolenic acid. *Am. J. Clin. Nutr.* 100(Suppl. 1), 443S–448S. doi: 10.3945/ajcn.113.071514
- Rosen, J., Lovgren, A., Kogej, T., Muresan, S., Gottfries, J., and Backlund, A. (2009). ChemGPS-NP(Web): chemical space navigation online. *J. Comput. Aided Mol. Des.* 23, 253–259. doi: 10.1007/s10822-008-9255-y
- Shacter, E., and Weitzman, S. A. (2002). Chronic inflammation and cancer. *Oncology* 16, 217–226, discussion 230–212.
- Smith, R. J., Justen, J. M., Nidy, E. G., Sam, L. M., and Bleasdale, J. E. (1993). Transmembrane signaling in human polymorphonuclear neutrophils: 15(S)-hydroxy-(5Z,8Z,11Z,13E)-eicosatetraenoic acid modulates receptor agonist-triggered cell activation. *Proc. Natl. Acad. Sci. U.S.A.* 90, 7270–7274. doi: 10.1073/pnas.90.15.7270
- Sun, Y., Neelakantan, N., Wu, Y., Lote-Oke, R., Pan, A., and van Dam, R. M. (2015). Palm oil consumption increases LDL cholesterol compared with vegetable oils low in saturated fat in a meta-analysis of clinical trials. *J. Nutr.* 145, 1549–1558. doi: 10.3945/jn.115.210575
- Takata, S., Matsubara, M., Allen, P. G., Janmey, P. A., Serhan, C. N., and Brady, H. R. (1994). Remodeling of neutrophil phospholipids with 15(S)-hydroxyeicosatetraenoic acid inhibits leukotriene B<sub>4</sub>-induced neutrophil migration across endothelium. *J. Clin. Invest.* 93, 499–508. doi: 10.1172/JCI116999
- Tsai, Y. F., Yu, H. P., Chang, W. Y., Liu, F. C., Huang, Z. C., and Hwang, T. L. (2015). Sirtinol inhibits neutrophil elastase activity and attenuates lipopolysaccharide-mediated acute lung injury in mice. *Sci. Rep.* 5:8347. doi: 10.1038/srep08347
- Uderhardt, S., and Kronke, G. (2012). 12/15-lipoxygenase during the regulation of inflammation, immunity, and self-tolerance. *J. Mol. Med.* 90, 1247–1256. doi: 10.1007/s00109-012-0954-4
- Vangaveti, V. N., Jansen, H., Kennedy, R. L., and Malabu, U. H. (2016). Hydroxyoctadecadienoic acids: oxidised derivatives of linoleic acid and their role in inflammation associated with metabolic syndrome and cancer. *Eur. J. Pharmacol.* 785, 70–76. doi: 10.1016/j.ejphar.2015.03.096
- Wang, J. C., and Yang, K. C. (1996). The genus *Typhonium* (Araceae) in Taiwan. *Bot. Bull. Acad. Sin.* 37, 159–163.
- Wei, C. K., Chang, F. R., Hsieh, P. W., and Wu, C. C. (2015). Inhibition of the interactions between metastatic human breast cancer cells and platelets by  $\beta$ -nitrostyrene derivatives. *Life Sci.* 143, 147–155. doi: 10.1016/j.lfs.2015.11.003
- Whelan, J., Gowdy, K. M., and Shaikh, S. R. (2016). N-3 polyunsaturated fatty acids modulate B cell activity in pre-clinical models: implications for the immune response to infections. *Eur. J. Pharmacol.* 785, 10–17. doi: 10.1016/j.ejphar.2015.03.100
- Willemssen, L. E. (2016). Dietary n-3 long chain polyunsaturated fatty acids in allergy prevention and asthma treatment. *Eur. J. Pharmacol.* 785, 174–186. doi: 10.1016/j.ejphar.2016.03.062
- Wu, C. C., Wang, W. Y., Kuo, R. Y., Chang, F. R., and Wu, Y. C. (2004). Antiplatelet effects of KW-7, a new inhibitor of cyclic nucleotide phosphodiesterases. *Eur. J. Pharmacol.* 483, 187–194. doi: 10.1016/j.ejphar.2003.10.046
- Xu, T., Sun, Y., Sun, W., Yao, L., Sun, L., Liu, L., et al. (2016). Effect of omega-3 fatty acid supplementation on serum lipids and vascular inflammation in patients with end-stage renal disease: a meta-analysis. *Sci. Rep.* 6:39346. doi: 10.1038/srep39346
- Yang, S. C., Chung, P. J., Ho, C. M., Kuo, C. Y., Hung, M. F., Huang, Y. T., et al. (2013). Propofol inhibits superoxide production, elastase release, and chemotaxis in formyl peptide-activated human neutrophils by blocking formyl peptide receptor 1. *J. Immunol.* 190, 6511–6519. doi: 10.4049/jimmunol.1202215
- Zhong, Z., Zhou, G., Chen, X., and Huang, P. (2001). [Pharmacological study on the extracts from *Typhonium flagelliforme* Blume]. *Zhong Yao Cai* 24, 735–738.

**Conflict of Interest Statement:** The authors declare that the research was conducted in the absence of any commercial or financial relationships that could be construed as a potential conflict of interest.

Copyright © 2017 Korinek, Tsai, El-Shazly, Lai, Backlund, Wu, Lai, Wu, Chen, Wu, Cheng, Hwang, Chen and Chang. This is an open-access article distributed under the terms of the Creative Commons Attribution License (CC BY). The use, distribution or reproduction in other forums is permitted, provided the original author(s) or licensor are credited and that the original publication in this journal is cited, in accordance with accepted academic practice. No use, distribution or reproduction is permitted which does not comply with these terms.



# Screening of *Luzula* species native to the Carpathian Basin for anti-inflammatory activity and bioactivity-guided isolation of compounds from *Luzula luzuloides* (Lam.) Dandy & Wilmott

Barbara Tóth<sup>a</sup>, Fang-Rong Chang<sup>b,c,d</sup>, Tsong-Long Hwang<sup>e,f,g,k,l</sup>, Ádám Szappanos<sup>h</sup>, Attila Mándi<sup>h</sup>, Attila Hunyadi<sup>a</sup>, Tibor Kurtán<sup>h</sup>, Gusztáv Jakab<sup>i</sup>, Judit Hohmann<sup>a,j</sup>, Andrea Vasas<sup>a,\*</sup>

<sup>a</sup> Department of Pharmacognosy, University of Szeged, 6720 Szeged, Hungary

<sup>b</sup> Graduate Institute of Natural Products, Kaohsiung Medical University, 807 Kaohsiung, Taiwan

<sup>c</sup> Research Center for Environmental Medicine, Kaohsiung Medical University, 807 Kaohsiung, Taiwan

<sup>d</sup> Department of Marine Biotechnology and Resources, National Sun Yat-sen University, 804 Kaohsiung, Taiwan

<sup>e</sup> Graduate Institute of Natural Products, Chang Gung University, 333 Taoyuan, Taiwan

<sup>f</sup> Research Center for Industry of Human Ecology, Chang Gung University of Science and Technology, 333 Taoyuan, Taiwan

<sup>g</sup> Department of Anesthesiology, Chang Gung Memorial Hospital, 333 Taoyuan, Taiwan

<sup>h</sup> Department of Organic Chemistry, University of Debrecen, 4032 Debrecen, Hungary

<sup>i</sup> Institute of Environmental Sciences, Faculty of Water and Environmental Management, Szent István University, 5540 Szarvas, Hungary

<sup>j</sup> Interdisciplinary Centre of Natural Products, University of Szeged, 6720 Szeged, Hungary

<sup>k</sup> Research Center for Chinese Herbal Medicine, Chang Gung University of Science and Technology, 333 Taoyuan, Taiwan

<sup>l</sup> Graduate Institute of Health Industry Technology, Chang Gung University of Science and Technology, 333 Taoyuan, Taiwan

## ARTICLE INFO

### Article history:

Received 28 October 2016

Received in revised form 1 December 2016

Accepted 3 December 2016

Available online 7 December 2016

### Keywords:

Juncaceae

*Luzula luzuloides*

Phenanthrenes

Flavonoids

Anti-inflammatory activity

Electronic circular dichroism

## ABSTRACT

The present study focused on the anti-inflammatory screening of *Luzula* species native to the Carpathian Basin and bioactivity-guided isolation of compounds of *Luzula luzuloides* (Lam.) Dandy & Wilmott. The anti-inflammatory properties of extracts with different polarity prepared from *Luzula* species were determined. Among them, the CH<sub>2</sub>Cl<sub>2</sub>-soluble fraction of *L. luzuloides* possessed strong inhibitory effects on superoxide anion generation ( $99.39 \pm 0.37\%$ ) and elastase release ( $114.22 \pm 3.13\%$ ) in fMLP/CB-induced human neutrophils at concentration of 10 µg/mL. From this fraction, six compounds (**1–6**) were isolated by the combination of different chromatographic methods. The structures of the compounds were determined by means of MS, 1D and 2D NMR spectroscopy. The results allowed the identification of the new 1,6-dihydroxy-2-keto-1,7-dimethyl-8-vinyl-1,2-dihydrophenanthrene (**1**) from the plant, named luzulin A. Chiral HPLC and HPLC-ECD analysis revealed that **1** possesses low enantiomeric excess and TDDFT-ECD calculations afforded the configurational assignment of the separated enantiomers. Three known phenanthrenes [juncuenin B (**2**), dehydrojuncuenin B (**3**) and juncusol (**4**)] and two flavonoids [apigenin (**5**) and luteolin (**6**)] were also isolated. The anti-inflammatory activity of the isolated compounds was tested and IC<sub>50</sub> values were determined. This was the first time that phenanthrenes were detected in a *Luzula* species. The oxidative transformation of juncuenin B (**3**) led to the isolation of its possible biometabolites, namely luzulin A (**1**), dehydrojuncuenin B (**4**), and juncuenin D (**7**). The isolated compounds (**1–4**) confirm that besides flavonoids, phenanthrenes could also serve as chemotaxonomic markers for *Luzula* species and prove the close relationship of *Juncus* and *Luzula* genus.

© 2016 Elsevier B.V. All rights reserved.

## 1. Introduction

The family Juncaceae includes >500 species, which are distributed worldwide. *Juncus* and *Luzula* are the two largest genera of the family Juncaceae, comprising approximately 340 and 115 species, respectively [1,2]. Among them up to 45 species are native to the Carpathian Basin. Although traditional use of plants belonging to the genus *Luzula* has

not been reported yet, several *Juncus* species (e.g. *J. effusus* and *J. acutus*) are used in oriental folk medicine for the treatment of cold, fever, anxiety or insomnia [3–5].

Despite of the comprehensive research focused on Juncaceae family, until now only species belonging to the genus *Juncus* were investigated extensively [6–9]. There is a significant lack of information with regards to chemical constituents of the plants belonging to the genus *Luzula*. Hitherto only the flavonoid components of *Luzula* species were studied. Luteolin and lutenolin-7-O-glucoside were isolated by the use of preparative paper chromatography from *L. sylvatica* [10]. Williams et al.

\* Corresponding author.

E-mail address: [vasasa@pharmacognosy.hu](mailto:vasasa@pharmacognosy.hu) (A. Vasas).

identified several flavonoids by using TLC, comparing their  $R_f$  values and colors with standards, and luteolin and luteolin 7-O-glucoside were detected from all of the investigated *Luzula* samples (*L. arcuata*, *L. campestris*, *L. confusa*, *L. forsteri*, *L. lactea*, *L. multiflora*, *L. nivea*, *L. nodulosa*, *L. nutans*, *L. pilosa*, *L. spicata* and *L. sylvatica*) [11]. Quercetin, procyanidin and other luteolin derivatives (luteolin 5-methyl ether, luteolin 5-methyl ether 7-O-glucoside) were also identified in some species [11]. Therefore, flavonoids are considered to be the main secondary metabolites, and one of the most characteristic components of *Luzula* species.

Previously benzocoumarins, diterpenoids, cycloartane triterpenes, carotenoids, phenanthrenes, flavonoids, and other phenolic compounds were isolated from *Juncus* species [12–16]. Apart from flavonoids, phenanthrenes and 9,10-dihydrophenanthrenes are the most specific chemical constituents of the family. To date >90 novel monomeric and 8 dimeric phenanthrenes have been identified from Juncaceae species [6–9]. Phenanthrenes are considered to be important taxonomic markers, because of their limited occurrence. Moreover, vinylated phenanthrenes have been reported only from species of the family Juncaceae [6–9]. Phenanthrenes occurring in plants have drawn considerable interest from the aspect of natural product drug discovery because of the wide range of their potentially valuable biological activities, e.g. cytotoxic, antimicrobial and anti-inflammatory activities [6–9].

*Juncus effusus* has been used in the traditional oriental medicine as a remedy for inflammation, therefore, isolated phenanthrenes from the plant were also tested for their anti-inflammatory activity by the inhibition of LPS-induced NO production on RAW 264.7 cells and compounds showed promising effect [17–20]. By the use of this assay a strong anti-inflammatory activity was detected in case of effusin B ( $IC_{50} = 7.42 \pm 0.50 \mu M$ ), compared to the positive control quercetin ( $IC_{50} = 6.63 \pm 0.28 \mu M$ ) [17]. 8-Hydroxymethyl-2-hydroxy-1-methyl-5-vinyl-9,10-dihydrophenanthrene ( $IC_{50} = 14.42 \pm 2.82 \mu M$ ), 5-(1-methoxyethyl)-1-methylphenanthrene-2,7-diol ( $IC_{50} = 11.10 \pm 1.67 \mu M$ ), effusol ( $IC_{50} = 15.13 \pm 0.54 \mu M$ ), dehydroeffusol ( $IC_{50} = 12.69 \pm 1.68 \mu M$ ), dehydroeffusol ( $IC_{50} = 10.50 \pm 0.90 \mu M$ ), 2,7-dihydroxy-5-hydroxymethyl-1-methyl-9,10-dihydrophenanthrene ( $IC_{50} = 16.06 \pm 1.18 \mu M$ ), 5-hydroxymethyl-1-methylphenanthrene-2,7-diol ( $IC_{50} = 16.30 \pm 2.41 \mu M$ ), dehydrojuncusol ( $IC_{50} = 15.57 \pm 1.08 \mu M$ ), and the mixture of 2,7-dihydroxy-1,8-dimethyl-5-vinyl-9,10-dihydrophenanthrene and juncusol ( $IC_{50} = 13.65 \pm 1.40 \mu M$ ) also had remarkable activities in comparison with the positive control quercetin [18].

Juncutol displayed noteworthy anti-inflammatory activity by the inhibition of the iNOS protein expression in LPS-stimulated RAW 264.7 cells. The iNOS level was reduced to  $11.2 \pm 13.1\%$  from 100% after treating with  $10 \mu M$  juncutol [19]. Dehydrojuncusol and its dimer, 8,8'-bidehydrojuncusol were also assayed by the abovementioned method. According to the immunoblot analysis, the effect of dehydrojuncusol on the iNOS protein ( $41.0 \pm 8.0\%$  inhibition at  $10 \mu M$ ) decreased dramatically after dimerization ( $<12.0\%$  inhibition at  $10 \mu M$ ) [20].

The anti-inflammatory activity of flavonoids is well-studied, but in some cases the mechanism of action of these compounds is not completely established [21,22]. Apigenin and luteolin inhibited the LPS induced NO-production on RAW 264.7 macrophages with  $IC_{50}$  values of  $23 \mu M$  and  $27 \mu M$ , respectively. While luteolin reduced the iNOS expression and interestingly increased the enzyme activity in a dose-dependent manner, apigenin inhibited the iNOS and COX-2 expression in LPS-activated RAW264.7 cells, but had no effect on the iNOS enzyme activity [23,24]. Both apigenin and luteolin inhibited significantly the TNF  $\alpha$ -induced NF- $\kappa$ B activation on KF 8 cells. Moreover, their anti-inflammatory activity was confirmed *in vivo* by the inhibition of carrageenan-induced paw inflammation on mice [25].

The purposes of the present study were to investigate the anti-inflammatory properties of *Luzula* species, and to perform an activity-guided fractionation of *Luzula luzuloides* in order to isolate the compounds responsible for this effect.

## 2. Experimental

### 2.1. General

Normal phase vacuum liquid chromatography (VLC) was carried out on silica gel (Kieselgel GF<sub>254</sub>, 15  $\mu m$ , Merck). LiChroprep RP-18 (40–63  $\mu m$ , Merck) stationary phase was used for reversed-phase VLC. Column chromatography (CC) was performed on polyamide (MP Biomedicals). Sephadex LH-20 (25–100  $\mu m$ , Pharmacia Fine Chemicals) was used for gel filtration. Preparative thin-layer chromatography (preparative TLC) was carried out on silica gel 60 F<sub>254</sub> plates (Merck).

NMR spectra were recorded in CD<sub>3</sub>OD and DMSO-*d*<sub>6</sub> on a Bruker Avance DRX 500 spectrometer at 500 MHz (<sup>1</sup>H) and 125 MHz (<sup>13</sup>C). The signals of the deuterated solvents were taken as reference. Two-dimensional (2D) experiments were performed with a standard Bruker software. In the COSY, HSQC and HMBC experiments, gradient-enhanced versions were applied. The high resolution MS spectra were acquired on a Thermo Scientific Q-Exactive Plus orbitrap mass spectrometer equipped with ESI ion source in positive ionization mode. The resolution was over 1 ppm. The data were acquired and processed with the MassLynx software. ECD spectra was recorded on a J-810 spectropolarimeter.

HPLC-ECD analysis: chiral HPLC separation was performed with a JASCO HPLC system using Chiralpak IA column with 250 mm  $\times$  4.6 mm i.d., 5  $\mu m$  (Daicel, Chemical Industries, Ltd.), and *n*-hexane–propan-2-ol eluent at a flow rate of 1.0 mL/min was used. HPLC-UV and OR chromatograms were recorded with JASCO MD-910 multiwavelength and OR-2090 Plus chiral detector, respectively. The on-line ECD and UV spectra were measured simultaneously by stopping the flow at the UV absorption maximum of each peak. The values of the ECD ellipticity ( $\phi$ ) were not corrected for the concentration. Three consecutive scans were recorded and averaged for an HPLC-ECD spectrum with standard sensitivity, 2 nm bandwidth and 1 s response. The background HPLC-ECD spectrum of the eluent was recorded in the same way.

### 2.2. Plant material

Plants (*Luzula campestris* (L.) DC., *L. forsteri* (Sm.) DC., *L. luzuloides* (Lam.) Dandy & Wilmott, *L. sudetica* (Willd.) Schult., *L. sylvatica* (Huds.) Gaudin) were collected during the flowering period between June and September 2014, in several regions of the Carpathian Basin (Hungary, Croatia and Romania). Botanical identification of the plant material was performed by Gusztáv Jakab (Institute of Environmental Sciences, Szent István University, Szarvas, Hungary) and voucher specimens (No. 869–873) have been deposited at the Department of Pharmacognosy, University of Szeged, Szeged, Hungary.

### 2.3. Preparation of plant samples

For the anti-inflammatory screening assay, extracts were prepared from 20 g of air-dried plant materials (whole plant, roots and aerial parts) with  $5 \times 100$  mL of MeOH with the use of ultrasonic bath ( $5 \times 15$  min). After filtration, the solutions were evaporated to dryness under reduced pressure. The residues were dissolved in 50 mL of 50% aqueous MeOH and subjected to solvent–solvent partition between *n*-hexane ( $3 \times 100$  mL) (extracts A), dichloromethane ( $3 \times 100$  mL) (extracts B), and EtOAc ( $3 \times 100$  mL) (extracts C), and the remaining H<sub>2</sub>O extracts gave extracts D.

### 2.4. Extraction and isolation

The air-dried whole plant of *L. luzuloides* (480 g) was percolated with MeOH (20 L) at room temperature. The crude methanol extract was concentrated under reduced pressure (76 g) and subjected to solvent–solvent partitioning with CH<sub>2</sub>Cl<sub>2</sub> (2.5 L). After evaporation, the

CH<sub>2</sub>Cl<sub>2</sub> fraction (4.95 g) was chromatographed on a polyamide column with mixtures of MeOH and H<sub>2</sub>O [1:1, 4:1 (1 L and 4 L, respectively); each eluent was collected as a fraction]. The fraction obtained from the polyamide column with methanol–water 4:1 (1.10 g) was further chromatographed by VLC on silica gel with a gradient system of cyclohexane–EtOAc–EtOH [from 9:1:0 to 5:5:1 (300 mL/eluent), and finally with EtOH (200 mL); volume of collected fractions was 20 mL] to yield twelve major fractions (1–12).

From fraction 1 (9.2 mg) compound **2** (5.2 mg) was crystallized. Fraction 4 (31.3 mg) was purified by Sephadex LH-20 gel chromatography using MeOH as eluent [(100 mL); volume of collected fractions was 2 mL] to afford four subfractions (4/1–4). Compound **1** (3.0 mg) was purified from subfraction 4/1 by preparative TLC using *n*-hexane–EtOAc (7:3) as solvent system. Subfraction 4/3 (14.1 mg) was also purified by preparative TLC on silica gel, with cyclohexane–EtOAc–MeOH (20:10:1) as solvent system to afford compound **3** (5.1 mg). Compound **4** (3.2 mg) was crystallized from subfraction 4/4. Fraction 6 (25.1 mg) was separated by RP-VLC, with a gradient system of MeOH–H<sub>2</sub>O [from 4:6 to 9:1 (150 mL/eluent), and finally with MeOH (100 mL); volume of collected fractions was 10 mL] to yield five subfractions (6/1–5). Compound **5** (9.0 mg) was crystallized from subfraction 6/2. Furthermore, compound **6** (7.1 mg) was crystallized from fraction 7.

#### 2.4.1. Luzulin A (**1**)

Amorphous solid; [ $\alpha$ ]<sub>D</sub><sup>26</sup> 0 (c 0.1, MeOH); <sup>1</sup>H and <sup>13</sup>C NMR data, see Table 2; (+)-HRESIMS *m/z* 281.1175 [M + H]<sup>+</sup> (calcd for C<sub>18</sub>H<sub>17</sub>O<sub>3</sub>, 281.1177). 25% ee with an excess of (S)-**1**.

(R)-**1**: *t*<sub>R</sub> = 4.88 min on Chiralpak IA column (*n*-hexane–propan-2-ol, 8:2); HPLC-ECD {*n*-hexane–propan-2-ol, 8:2,  $\lambda$  [nm] ( $\phi$ ): 424 (2.30), 376 (–4.49), 312 (–3.51), 287 (0.10), 266 (–2.52), 244sh (3.92), 229 (5.17), 204 (–7.81)}.

(S)-**1**: *t*<sub>R</sub> = 5.41 min on Chiralpak IA column (*n*-hexane–propan-2-ol, 8:2); HPLC-ECD {*n*-hexane–propan-2-ol, 9:1,  $\lambda$  [nm] ( $\phi$ ): 424 (–2.96), 374 (4.26), 312 (2.68), 287 (–1.23), 268 (1.53), 244sh (–7.57), 227 (–8.36), 204 (5.46)}.

#### 2.5. Oxidation of juncuenin B

50.0 mg of juncuenin B (**3**) was dissolved in CH<sub>3</sub>CN–H<sub>2</sub>O (9:1, 50 mL). 2 eq. [bis(trifluoroacetoxy)iodo]benzene (PIFA) (106.1 mg) was added to the solution in a careful manner to prevent sudden boiling. The reaction was monitored by TLC using cyclohexane–EtOAc–EtOH (20:10:1) as solvent system. After 30 min of stirring at room temperature, all of the starting material, juncuenin B (**3**) was converted. The mixture was cooled down in an ice bath, and evaporated at room temperature.

#### 2.6. Separation of the oxidative products of juncuenin B

The concentrated mixture was chromatographed by VLC on silica gel (25 mm × 100 mm) with a gradient system of CH<sub>2</sub>Cl<sub>2</sub>–acetone [from 99:1 to 7:3 (200 mL/eluent), and finally with MeOH (150 mL); volume of collected fractions was 20 mL] to yield seven major fractions (1–7). Dehydrojuncuenin B (**4**) (8.9 mg) was purified from fraction 2 after gel filtration on Sephadex LH-20 using MeOH–CH<sub>2</sub>Cl<sub>2</sub> (3:1) as eluent [(60 mL); volume of collected fractions was 3 mL]. Fraction 4 was further separated by gel filtration on Sephadex LH-20 using MeOH as eluent [(50 mL); volume of collected fractions was 2 mL] to afford three subfractions (4/1–3). From subfraction 4/2 luzulin A (**1**) (8.1 mg) was obtained by the use of preparative TLC using toluene–acetone (8:2) as solvent system. Juncuenin D (**7**) (11.2 mg) was isolated from fraction 6 after gel filtration on Sephadex LH-20 using MeOH–CH<sub>2</sub>Cl<sub>2</sub> (3:1) as eluent [(50 mL); volume of collected fractions was 2 mL]. The compounds were identified according to their TLC patterns and the comparison of their <sup>1</sup>H NMR spectrum with literature data [5].

#### 2.7. Preparation of human neutrophils

Blood was taken from healthy human donors (20–30 years old) by venipuncture using a protocol approved by the Institutional Review Board at Chang Gung Memorial Hospital. Neutrophils were isolated using a standard method as previously described [26,27]. The cells were obtained from peripheral blood according to the standard method of dextran sedimentation, followed by centrifugation in a Ficoll-Hypaque gradient and the hypotonic lysis of the erythrocytes. The purified neutrophils contained >98% of viable cells, as determined by Trypan blue exclusion, and were suspended in calcium-free HBSS at 4 °C before used.

#### 2.8. Measurement of superoxide generation

SOD inhibition was measured by reduction of ferricytochrome *c* [26, 27]. Neutrophils (6 × 10<sup>5</sup> cells/mL) in 0.5 mg/mL ferricytochrome *c* and 1 mM Ca<sup>2+</sup> were equilibrated at 37 °C for 2 min and then incubated with drugs for 5 min. The cells were activated using formyl-methionyl-leucyl-phenylalanine (fMLP, 100 nM)/cytochalasin B (CB, 1 µg/mL) for 10 min. The absorbance was continuously monitored at 550 nm using a double-beam, six-cell positioned spectrophotometer with constant stirring (Hitachi U-3010, Tokyo, Japan). Calculations were based on the differences in absorbance with and without SOD (100 µg/mL) divided by the extinction coefficient for the reduction of ferricytochrome *c* ( $\epsilon$  = 21.1/mM/10 mm).

#### 2.9. Measurement of elastase release

The degranulation of azurophilic granules was determined by elastase release as described previously [26,27]. Neutrophils (6 × 10<sup>5</sup>/mL) were equilibrated in MeO–Suc–Ala–Ala–Pro–Val–*p*-nitroanilide (100 µM), an elastase substrate, at 37 °C for 2 min and then incubated with drugs for 5 min. The cells were activated using fMLP (100 nM) in the presence of CB (0.5 µg/mL), and changes in the absorbance at 405 nm were continuously measured to monitor elastase release. The results are expressed as a percentage of elastase release in the fMLP/CB-activated, drug-free control system.

#### 2.10. Statistical methods

Results of the anti-inflammatory assays were expressed as means ± S.E.M. Statistical analysis using Student's *t*-test was performed with SigmaPlot (Systat Software, San Jose, CA, USA). A value of *P* < 0.05 was considered statistically significant.

#### 2.11. Computational section

Mixed torsional/low-frequency mode conformational searches were carried out by means of the MacroModel 9.9.223 software using the Merck Molecular Force Field (MMFF) with an implicit solvent model for CHCl<sub>3</sub> [28]. Geometry reoptimizations were carried out at the B3LYP/6-31G(d) level in vacuo, the B97D/TZVP [29,30] and the CAM-B3LYP/TZVP [31,32] levels with the PCM solvent model for CHCl<sub>3</sub>. TDDFT ECD calculations were run with various functionals (B3LYP, BH&HLYP, CAM-B3LYP, PBE0) and the TZVP basis set as implemented in the Gaussian 09 package with the same or no solvent model as in the preceding DFT optimization step [33]. ECD spectra were generated as sums of Gaussians with 3000 cm<sup>–1</sup> widths at half-height (corresponding to ca. 41 nm at 370 nm), using dipole-velocity-computed rotational strength values [34]. Boltzmann distributions were estimated from the ZPVE-corrected B3LYP/6-31G(d) energies in the gas-phase calculations and from the B97D/TZVP and CAM-B3LYP/TZVP energies in the solvated ones. The MOLEKEL software package was used for visualization of the results [35–37].



### 3. Results and discussion

In the course of our screening study, the anti-inflammatory activities of 5 species of the *Luzula* genus native to the Carpathian Basin were evaluated. The results of the assays are listed in Table 1. Extracts were prepared with methanol from whole plants of *L. campestris*, *L. forsteri*, *L. luzuloides* and *L. sudetica*. The plant material allowed the separation of *L. sylvatica* into aerial and root parts, therefore methanol extracts were prepared from selected plant organs in case of *L. sylvatica*. The crude extracts were concentrated and suspended in 50% MeOH, and then solvent–solvent partitions were made with *n*-hexane (A), CH<sub>2</sub>Cl<sub>2</sub> (B), and EtOAc (C). The remaining H<sub>2</sub>O fractions were signed as D (altogether 24 extracts). The apolar, *n*-hexane-soluble fractions of *L. forsteri*, *L. luzuloides*, *L. sudetica* and *L. sylvatica* showed >70% inhibition at the tested concentration (10 µg/mL) in both anti-inflammatory assays. The fraction A of *L. campestris* exerted the most selective elastase release inhibition. Among the fractions with different polarities, fractions B (containing CH<sub>2</sub>Cl<sub>2</sub>-soluble lipophilic constituents) had the most remarkable activities (>93% inhibition) at concentration of 10 µg/mL. All of the CH<sub>2</sub>Cl<sub>2</sub>-soluble fractions displayed significant activities on the inhibition of elastase release, and proved to be slightly less active on superoxide generation. The EtOAc-soluble fractions of *L. campestris*, *L. luzuloides*, *L. sudetica*, *L. sylvatica* (aerial part) possessed noteworthy (>65%) inhibitory activities at concentration of 10 µg/mL. The remaining H<sub>2</sub>O fraction of *L. luzuloides* also showed notable anti-inflammatory activities (>65%) in both methods. On the basis of these preliminary results, *L. luzuloides* has been chosen for further investigation.

Dried whole plant material of *L. luzuloides* (480 g) was powdered and extracted with methanol at room temperature. After concentration, the extract was dissolved in 50% aqueous MeOH, and solvent–solvent partition was performed with *n*-hexane, CH<sub>2</sub>Cl<sub>2</sub>, and EtOAc. The CH<sub>2</sub>Cl<sub>2</sub> fraction was separated and purified with the combination of different chromatographic methods (CC, VLC, Sephadex LH-20 gel chromatography, prep TLC) to afford 6 compounds (**1–6**, Fig. 1).

The structure determination was carried out by extensive spectroscopic analysis, using one- and two-dimensional NMR (<sup>1</sup>H–<sup>1</sup>H COSY, HSQC, HMBC) spectroscopy, HRESIMS and HPLC-ECD experiments and comparison of the spectral data with literature data.

Compound **1** was obtained as an amorphous solid with [α]<sub>D</sub><sup>26</sup> 0 (c 0.1, MeOH). Its HRESIMS provided the molecular formula C<sub>18</sub>H<sub>16</sub>O<sub>3</sub> through the presence of a peak at *m/z* 281.1175 [M + H]<sup>+</sup> (calcd for C<sub>18</sub>H<sub>17</sub>O<sub>3</sub>, 281.1172). The <sup>1</sup>H NMR spectrum (Table 2) displayed signals of two pairs of *ortho*-coupled aromatic protons (δ<sub>H</sub> 6.25 d/8.35 d and δ<sub>H</sub> 8.12 d/7.63 d), and one aromatic proton as a singlet (δ<sub>H</sub> 7.52), two methyl singlets at δ<sub>H</sub> 1.53 and δ<sub>H</sub> 2.35, and a vinylic system at δ<sub>H</sub> 5.81, 5.35 and 7.05 (C-14, C-13). In the JMOD spectrum, the presence of 18 carbon signals was detected (Table 2). In the <sup>1</sup>H NMR spectrum the presence of *ortho*-coupled aromatic protons at δ<sub>H</sub> 8.12 d and 7.63 d could be assigned to the H-9 and H-10 protons of a phenanthrene derivative. In the <sup>1</sup>H–<sup>1</sup>H COSY spectrum four correlations were observed between δ<sub>H</sub> 8.12 d and 7.63 d (H-9/H-10), between δ<sub>H</sub> 6.25 d and 8.35 d (H-3/H-4), between δ<sub>H</sub> 7.05 dd and 5.81 d (H-13/H-14a), and between δ<sub>H</sub> 7.05 dd and 5.35 d (H-13/H-14b). The two *ortho*-coupled doublets at δ<sub>H</sub> 6.25 and 8.35 were assigned to the H-3 and H-4 protons. According to the <sup>13</sup>C NMR signals at δ<sub>C</sub> 207.1 one carbonyl group was identified, which was placed to C-2 as confirmed by HMBC correlations of the CH<sub>3</sub>-11 (δ<sub>H</sub> 1.53) and H-4 (δ<sub>H</sub> 8.35 d) with C-2 (δ<sub>C</sub> 207.1) (Table 2, Fig. 2). The location of one of the methyl groups (δ<sub>H</sub> 1.53 s) was confirmed at C-1 on the basis of its HMBC correlation with the quaternary carbons δ<sub>C</sub> 146.6 (C-1a), 78.1 (C-1) and 207.1 (C-2). The linkage of hydroxy groups to C-1 and C-6 was confirmed by the chemical shifts of the quaternary carbons at δ<sub>C-1</sub> 78.1 and δ<sub>C-6</sub> 157.0, respectively. In the HMBC spectrum another methyl group was assigned at C-7 by the correlation of H-12/C-7. The vinyl substitution at C-8 was indicated by the HMBC cross-peaks between H-14a/C-8 and H-14b/C-8.

The NOESY correlations further confirmed the structure of compound **1**. Overhauser effects were detected between H-3/H-4, H-4/H-5, H-9/H-10, H-9/H-13, H-9/H-14b, H-13/CH<sub>3</sub>-12, H-14b/CH<sub>3</sub>-12. All of the above evidence confirmed the planar structure of **1** named as luzulin A (Fig. 1).

Luzulin A (**1**) is a chiral natural product but it had a very weak ECD spectrum in acetonitrile and zero specific rotation, which suggested that it had low enantiomeric excess. Thus chiral HPLC analysis of **1** was carried out, which resulted in the separation of the two enantiomers on a Chiralpak IA column and determined the enantiomeric excess as 25%. The quaternary stereogenic center does not enable inversion of the absolute configuration during the isolation and hence the low

**Table 1**  
Inhibitory effects of extracts with different polarity from *Luzula* species on superoxide anion generation and elastase release by human neutrophils in response to fMLP/CB at concentration 10 µg/mL.

Species	Fraction	Yield (w/w %)	Superoxide anion inhibition (%)	Elastase inhibition (%)
<i>Luzula campestris</i> (L.) DC.	A	8.06	50.04 ± 5.08***	106.98 ± 6.35***
	B	3.55	96.06 ± 0.91***	112.19 ± 6.16***
	C	7.42	77.45 ± 6.44***	84.22 ± 4.09***
	D	54.84	32.52 ± 5.43***	45.18 ± 6.47***
<i>L. forsteri</i> (Sm.) DC.	A	10.54	71.53 ± 7.75***	71.88 ± 7.07***
	B	6.67	93.14 ± 6.14***	113.51 ± 1.07***
	C	46.67	35.24 ± 1.43***	37.95 ± 6.88**
	D	22.67	32.80 ± 3.40***	54.52 ± 0.99***
<i>L. luzuloides</i> (Lam.) Dandy & Wilmott	A	23.44	70.65 ± 6.65***	92.50 ± 3.58***
	B	4.69	99.39 ± 0.37***	114.22 ± 3.13***
	C	49.89	62.84 ± 3.50***	68.39 ± 5.74***
	D	11.18	68.80 ± 5.92***	77.71 ± 4.99***
<i>L. sudetica</i> (Willd.) Schult.	A	17.86	72.85 ± 6.35***	76.08 ± 5.45***
	B	7.14	109.25 ± 6.01***	115.21 ± 4.14***
	C	17.86	77.95 ± 0.22***	91.41 ± 1.84***
	D	47.62	37.92 ± 5.39**	8.59 ± 3.19
<i>L. sylvatica</i> (Huds.) Gaudin (aerial part)	A	8.57	85.27 ± 4.20***	89.10 ± 6.41***
	B	5.71	96.09 ± 1.92***	111.90 ± 2.99***
	C	18.10	73.32 ± 2.91***	54.82 ± 4.11***
	D	43.81	26.90 ± 7.01**	48.83 ± 6.51**
<i>L. sylvatica</i> (root part)	A	7.96	89.18 ± 6.58***	107.88 ± 3.96***
	B	4.69	95.28 ± 2.48***	104.23 ± 5.67***
	C	46.12	53.62 ± 7.13***	54.13 ± 3.03***
	D	12.65	41.60 ± 6.19***	43.02 ± 2.96***

A = *n*-hexane fraction, B = CH<sub>2</sub>Cl<sub>2</sub> fraction, C = EtOAc fraction, D = remaining H<sub>2</sub>O fraction.

Results are presented as mean ± S.E.M. (*n* = 3–5). \*\**P* < 0.01, \*\*\**P* < 0.001 compared with the control value (DMSO).



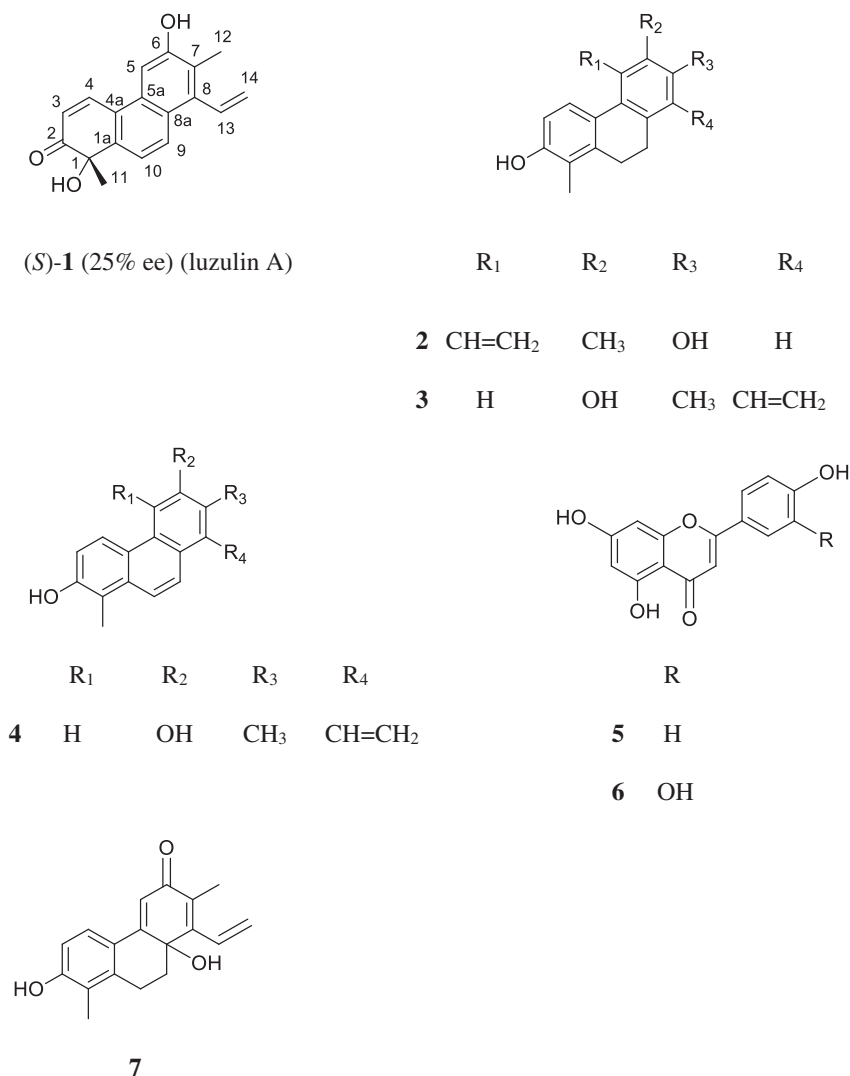


Fig. 1. Structures of compounds 1–7.

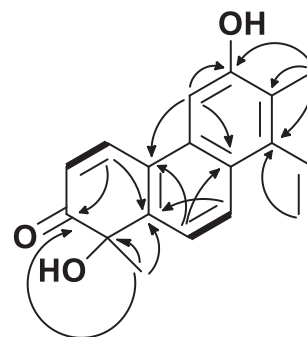
enantiomeric excess can be attributed to the low enantioselectivity of the biosynthetic step, which has been observed for other natural phenanthrenes as well [38].

Table 2

NMR spectroscopic data for luzulin A (**1**) (500 MHz, CD<sub>3</sub>OD).

Position	<b>1</b> δ <sub>H</sub> (J in Hz)	δ <sub>C</sub> , type	HMBC (H → C)
1		78.1, C	
1a		146.6, C	
2		207.1, C	
3	6.25, d (10.2)	123.1, CH	1, 4a
4	8.35, d (10.1)	141.9, CH	1a, 2
4a		122.6, C	
5	7.52, s	103.3, CH	4a, 6, 8a
5a		132.2, C	
6		157.0, C	
7		126.3, C	
8		138.3, C	
8a		127.7, C	
9	8.12, d (8.5)	129.8, CH	1a, 5a
10	7.63, d (8.7)	121.0, CH	4a, 8a
11	1.53, s	32.1, CH <sub>3</sub>	1, 1a, 2
12	2.35, s	13.4, CH <sub>3</sub>	6, 7, 8
13	7.05, dd (17.9, 11.5)	135.7, CH	
14a	5.81, d (11.5)	122.2, CH <sub>2</sub>	8
14b	5.35, d (18.0)		8

In order to elucidate the absolute configuration of the enantiomers and identify the major enantiomer, HPLC-ECD spectra of the separated enantiomers were recorded and the solution TDDFT-ECD protocol was applied on the arbitrarily chosen (*R*) enantiomer (Fig. 3) [36]. The initial Merck Molecular Force Field (MMFF) conformational search resulted in 5 conformers in a 21 kJ/mol energy window, which were reoptimized at various DFT levels [B3LYP/6-31G(d) in vacuo, B97D/TZVP PCM/CHCl<sub>3</sub> and CAM-B3LYP/TZVP PCM/CHCl<sub>3</sub>] and ECD spectra were computed with B3LYP, BH&HLYP, CAM-B3LYP and PBE0 functionals and TZVP

Fig. 2. Diagnostic COSY (→) and HMBC correlations (→) for **1**.

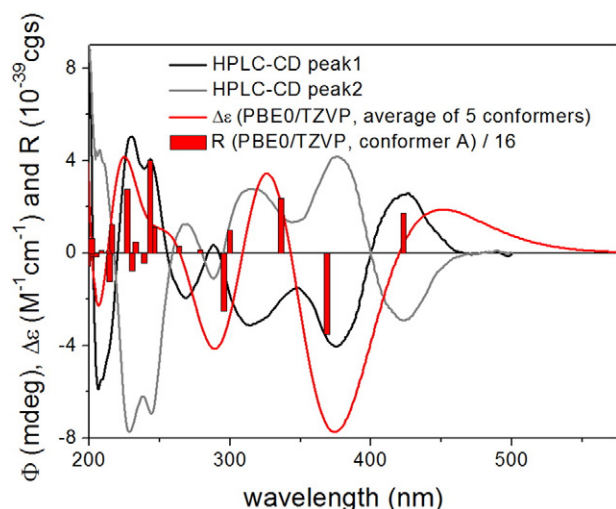


**Fig. 3.** Experimental HPLC-ECD spectra of **1** (black: first eluting enantiomer; grey: second eluting enantiomer) compared with the Boltzmann-weighted PBE0/TZVP (PCM/CHCl<sub>3</sub>) ECD spectrum of (*R*)-**1** computed for the B97D/TZVP PCM/CHCl<sub>3</sub> conformers. Bars represent the rotational strength of the lowest-energy conformer.

basis set. The computed conformers differed in the orientation of the OH-6 proton and the C-8 vinyl group, the latter of which influenced the ECD spectra as well. The OH-1 group adopted equatorial position in all the computed conformers (Fig. 4). All the applied combinations for all conformers reproduced the first two transitions at ca. 422 and 375 nm and Boltzmann-weighted spectra acquired at all applied levels resembled also the high-energy transitions at ca. 227 and 206 nm allowing the elucidation of the absolute configuration as (*R*) for the first-eluting enantiomer (minor component) and (*S*) for the second-eluting enantiomer (major component). Interestingly, the 312 nm Cotton effect (CE) could not be reproduced by any applied combination of theoretical levels, which can be attributed to difficulties in estimating the proper orientation of the conjugating quite freely rotating vinyl chromophore and the overlapping transitions of this region [37].

Besides the new compound, luzulin A (**1**), two dihydrophenanthrenes [juncusol (**2**) and juncuenin B (**3**)], one phenanthrene [dehydrojuncuenin B (**4**)] and two flavonoids [apigenin (**5**) and luteolin (**6**)] were also isolated from *L. luzuloides*. Their structures were determined by analyses of MS, 1D and 2D NMR data, and by comparison with literature data [38–40].

All compounds were isolated for the first time from *L. luzuloides*. The methyl group at C-1, a hydroxyl group at C-2 and vinyl, methyl and hydroxyl substitution on ring B are characteristic features of the isolated phenanthrenes. In compound **1**, a carbonyl group can also be found in the molecule. The absolute configuration of luzulin A (**1**) was determined by HPLC-ECD measurements and TDDFT-ECD calculations.

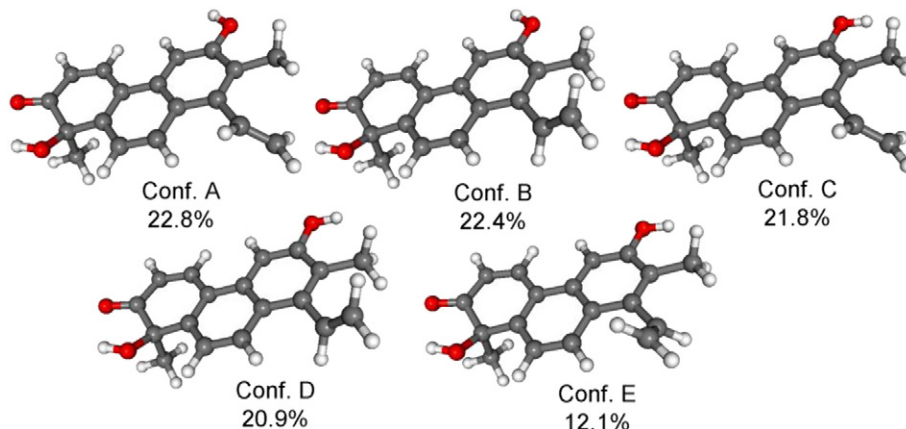


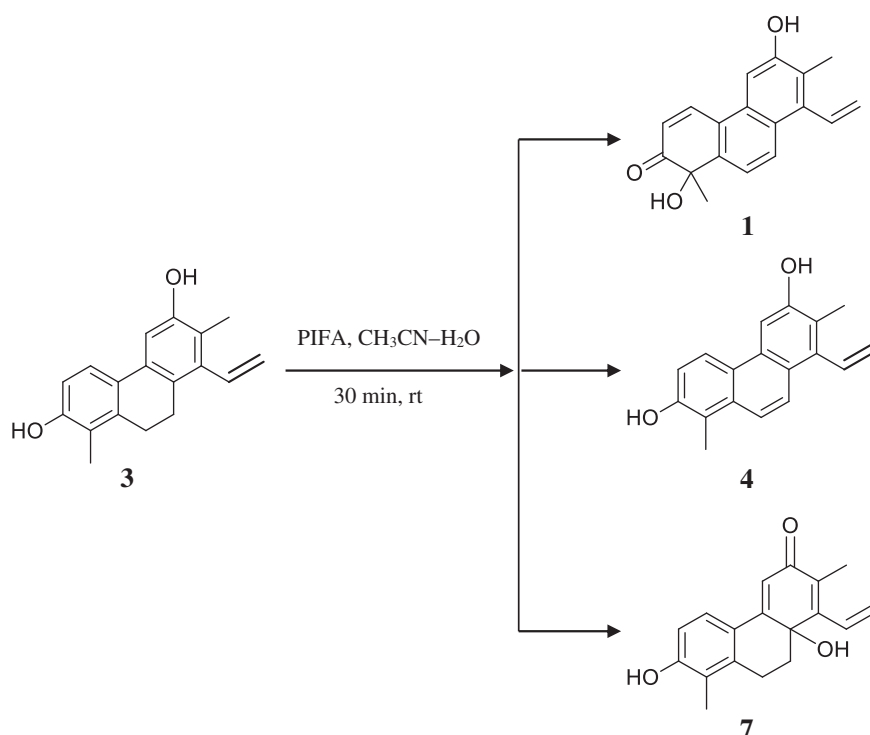
**Fig. 4.** Structures and populations of the B97D/TZVP PCM/CHCl<sub>3</sub> conformers of (*R*)-**1**.

So far >90 novel phenanthrenes have been reported from 6 *Juncus* species (*J. acutus*, *J. effusus*, *J. inflexus*, *J. roemerianus*, *J. setchuensis* and *J. subulatus*) [5–7,38]. The first example of nitrogen-free alkylated phenanthrenes was juncusol (**2**) isolated from *J. roemerianus* [41]. Until now phenanthrenes have not been isolated from the genus *Luzula*. This was the first time when extensive phytochemical and pharmacological investigations were performed with the genus *Luzula* and with *L. luzuloides*. Our results allowed the identification of four phenanthrenes (**1–4**) substituted with vinyl, hydroxyl, methyl and methoxy groups, one of them (**1**) is new natural product. The other phenanthrenes (**2–4**) were isolated previously only from other Juncaceae species. All of the compounds were isolated for the first time from *L. luzuloides*.

In the course of our previous investigations considerable amount of juncuenin B (**3**) (850 mg) and its unsaturated form, dehydrojuncuenin B (**4**) have been isolated from *J. inflexus* [38]. Luzulin A (**1**) from *L. luzuloides* and juncuenin D (**7**) from *J. inflexus* have obvious structure similarity with the abovementioned two phenanthrenes [juncuenin B (**3**) and dehydrojuncuenin B (**4**)], suggesting that both phenanthrenequinones are possibly derived from the oxidation of juncuenin B (**3**). In the case of luzulin A (**1**), ring A is oxidized, and in the case of juncuenin D (**7**) ring C has changed. In order to confirm their possible biosynthetic connection, juncuenin B (**3**) was subjected to an oxidative reaction by the use of hypervalent iodine reagent (PIFA). 50 mg juncuenin B (**3**) was dissolved in CH<sub>3</sub>CN–H<sub>2</sub>O (9:1, 1 mg/mL), and a reaction with 2 eq. of PIFA was performed at room temperature for 30 min (Scheme 1). After purification by NP-VLC, Sephadex LH-20 gel filtration and preparative TLC, three major compounds were isolated from the mixture. The compounds were identified as juncuenin D (**7**, 22%), dehydrojuncuenin B (**4**, 18%) and luzulin A (**1**, 16%) by comparison of their <sup>1</sup>H NMR spectrum with literature data [5]. These findings confirm that luzulin A (**1**), dehydrojuncuenin B (**4**), and juncuenin D (**7**) can form by oxidation of juncuenin B (**3**), and most probably similar process may be performing during their biosynthesis.

Although, several phenanthrenes and flavonoids have been reported to exhibit remarkable anti-inflammatory activity, there were no previous data for the anti-inflammatory effects of metabolites from the genus *Luzula*. In the performed assay, effects against superoxide anion production and elastase release by human neutrophils in response to fMLP/CB were measured according to previously published methods [26,27]. Among the isolated compounds, noteworthy anti-inflammatory activities were measured for juncusol (**2**), juncuenin B (**3**), dehydrojuncuenin B (**4**), apigenin (**5**) and luteolin (**6**) (Table 3). Although great deals of phenanthrenes were assayed for their anti-inflammatory properties, this was the first time when the anti-inflammatory activity of the isolated phenanthrenes (**1–4**, **7**) was evaluated [5,6].

In the superoxide anion generation assay, significant inhibitory activities were recorded for juncusol (**2**) (IC<sub>50</sub> = 3.11 μM), juncuenin B



**Scheme 1.** Oxidation of juncuenin B (3).

(3) ( $\text{IC}_{50} = 4.92 \mu\text{M}$ ), dehydrojuncuenin B (4) ( $\text{IC}_{50} = 3.17 \mu\text{M}$ ), apigenin (5) ( $\text{IC}_{50} = 6.12 \mu\text{M}$ ), and luteolin (6) ( $\text{IC}_{50} = 4.73 \mu\text{M}$ ). Furthermore, juncuenin B (3) and luteolin (6) inhibited effectively the elastase release with  $\text{IC}_{50}$ s  $5.47 \mu\text{M}$  and  $6.91 \mu\text{M}$ , respectively, comparable to that of LY294002 ( $\text{IC}_{50} = 4.79 \mu\text{M}$ ). These results suggest that compounds 2–6 display promising anti-inflammatory activity, juncusol (2), dehydrojuncuenin B (4) and apigenin (5) were considered to be active only in case of inhibition of superoxide generation, while luzulin A (1) and juncuenin D (7) were proved to be inactive in both assays. With its unsaturation at ring B, juncuenin B (3) lost its effect on the elastase release, but dehydrojuncuenin B (4) inhibited the superoxide generation more effectively than juncuenin B (3). The two phenanthrenequinones, luzulin A (1) and juncuenin D (7), presumably derived from juncuenin B (3) showed significantly lower anti-inflammatory activities compared to their possible biosynthetic precursor.

In conclusion, phenanthrenes are the most characteristic compounds of Juncaceae species. Although phenanthrenes have been identified from taxonomically distant families [6], vinyl substituted derivatives can be considered as chemotaxonomic markers for plants belonging to Juncaceae family, since these specifically substituted

phenanthrenes were only reported from *Juncus* species, and this was the first time when they were isolated from the genus *Luzula*. The chemical characterization of *L. luzuloides*, and the presence of vinylated phenanthrenes in the plant further confirm the close botanical relationship between the genera *Luzula* and *Juncus*.

This was the first time when the anti-inflammatory activity of species belonging to the genus *Luzula* was evaluated. Along with the extracts prepared from different species of the genus, several isolated compounds showed promising anti-inflammatory activities. The present study highlights that phytochemical and pharmacological studies of the previously uninvestigated genus *Luzula* are very promising.

### Conflict of interest

The authors declare no competing financial interest.

### Acknowledgements

Financial support from the Hungarian Scientific Research Fund (OTKA K109846) is gratefully acknowledged. A.V. acknowledges the award of a János Bolyai scholarship of the Hungarian Academy of Sciences. A.S., A.M. and T.K. thank the National Research, Development and Innovation Office (NKFI K 120181 and PD 121020) for financial support and the National Information Infrastructure Development Institute (NIIFI 10038) for CPU time. T.L.H. thanks the Chang Gung Memorial Hospital (CMRPD1B0281~3, CMRPF1D0442~3, CMRPF 1F0011~3, CMRPF1F0061~3 and BMRP450) for financial support. The authors would like to thank to Attila Csorba (Department of Pharmacognosy, University of Szeged) for the HRMS measurements.

### Appendix A. Supplementary data

1D and 2D NMR and ECD spectra of compound 1 are available in the Supplementary data. Supplementary data associated with this article can be found in the online version, at <http://dx.doi.org/10.1016/j.fitote.2016.12.004>.

**Table 3**

Inhibitory effects of compounds 1–7 on superoxide anion generation and elastase release by human neutrophils in response to fMLP/CB.

Compound	Superoxide anion		Elastase release	
	$\text{IC}_{50}$ ( $\mu\text{M}$ )	Inhibition (%)	$\text{IC}_{50}$ ( $\mu\text{M}$ )	Inhibition (%)
1	>10	$12.26 \pm 3.76^*$	>10	$40.5 \pm 5.57^{**}$
2	$3.11 \pm 0.25$	$93.07 \pm 0.48^{***}$	>10	$2.05 \pm 2.07$
3	$4.92 \pm 0.27$	$81.54 \pm 3.5^{***}$	$5.47 \pm 1.11$	$80.57 \pm 4.15^{***}$
4	$3.17 \pm 1.19$	$82.90 \pm 7.65^{***}$	>10	$25.58 \pm 2.83^{**}$
5	$6.12 \pm 0.72$	$73.92 \pm 4.11^{***}$	>10	$46.14 \pm 6.03^{**}$
6	$4.73 \pm 0.49$	$79.77 \pm 4.37^{***}$	$6.91 \pm 2.25$	$54.16 \pm 4.66^{***}$
7	>10	$43.29 \pm 5.77^{***}$	>10	$32.75 \pm 6.98^{**}$
LY294002	$1.29 \pm 0.05$	–	$4.97 \pm 0.80$	–

Percentage of inhibition (inhibition %) at  $10 \mu\text{M}$  concentration. Results are presented as mean  $\pm$  S.E.M. ( $n = 3-5$ ).  $^*P < 0.05$ ,  $^{**}P < 0.01$ ,  $^{***}P < 0.001$  compared with the control value. LY294002, a PI3K inhibitor, was used as positive control.

## References

- [1] The plant list, <http://www.theplantlist.org/browse/A/Juncaceae/> (accessed 16.08.15).
- [2] L. Drábková, J. Kirschner, O. Seberg, G. Petersen, C. Vlecek, Phylogeny of the Juncaceae based on rbcL sequences, with special emphasis on *Luzula* DC. and *Juncus* L. Plant Syst. Evol. 240 (2003) 133–147.
- [3] Y.G. Wang, Y.L. Wang, H.F. Zhai, Y.J. Liao, B. Zhang, J.M. Huang, Phenanthrenes from *Juncus effusus* with anxiolytic and sedative activities, Nat. Prod. Res. 26 (2012) 1234–1239.
- [4] K. Shima, M. Toyota, Y. Asakawa, Phenanthrene derivatives from the medullae of *Juncus effusus*, Phytochemistry 30 (1991) 3149–3151.
- [5] X.Y. Wang, C.Q. Ke, C.P. Tang, D. Yuan, Y. Ye, 9,10-dihydrophenanthrenes and phenanthrenes from *Juncus setchuensis*, J. Nat. Prod. 72 (2009) 1209–1212.
- [6] A. Kovács, A. Vasas, J. Hohmann, Natural phenanthrenes and their biological activity, Phytochemistry 69 (2008) 1084–1110.
- [7] A.F. Abdel-Razik, A.-S.I. Elshamy, M.I. Nassar, S.M. El-Kousy, H. Hamdy, Chemical constituents and hepatoprotective activity of *Juncus subulatus*, Rev. Latinoam. Quim. 37 (2009) 70–84.
- [8] X.H. Su, Z.P. Yuan, C.Y. Li, Y.J. Zhong, H.J. Du, Y.Y. Wen, Y.F. Li, B. Liang, Phenanthrenes from *Juncus effusus*, Planta Med. 79 (2013) 1447–1452.
- [9] K. Ishiuchi, Y. Kosuge, H. Hamagami, M. Ozaki, K. Ishige, Y. Ito, S. Kitanaka, Chemical constituents isolated from *Juncus effusus* induce cytotoxicity in HT22 cells, J. Nat. Med. 69 (2015) 421–426.
- [10] A. Stabursvik, Luteolin-7-glucoside as a characteristic component of the plant genera *Juncus* and *Luzula* (family Juncaceae), Acta Chem. Scand. 22 (1968) 2371–2373.
- [11] C.A. Williams, J.B. Harborne, Luteolin and daphnetin derivatives in the Juncaceae and their systematic significance, Biochem. Syst. Ecol. 3 (1975) 181–190.
- [12] M. Della Greca, A. Fiorentino, M. Isidori, L. Previtera, F. Temussi, A. Zarrelli, Benzocoumarins from the rhizomes of *Juncus acutus*, Tetrahedron 59 (2003) 4821–4825.
- [13] G.Z. Yang, H.X. Li, F.J. Song, Y. Chen, Diterpenoid and phenolic compounds from *Juncus effusus* L. Helv. Chim. Acta 90 (2007) 1289–1295.
- [14] A. Stabursvik, The carotenoids of two *Juncus* spp. (family Juncaceae) and one *Scirpus* sp. (family Cyperaceae), Acta Chem. Scand. 22 (1968) 2056–2057.
- [15] M. Della Greca, A. Fiorentino, P. Monaco, L. Previtera, Cycloartane triterpenes from *Juncus effusus*, Phytochemistry 35 (1994) 1017–1022.
- [16] S. Park, S. Yang, D. Ahn, J.H. Yang, D.K. Kim, Antioxidative phenolic compounds from the whole plant of *Juncus diastrophanthus*, J. Korean Soc. Appl. Biol. Chem. 54 (2011) 685–692.
- [17] W. Ma, F. Liu, Y.Y. Ding, Y. Zhang, N. Li, Four new phenanthrenoid dimers from *Juncus effusus* L. with cytotoxic and anti-inflammatory activities, Fitoterapia 105 (2015) 83–88.
- [18] W. Ma, Y. Zhang, Y.-Y. Ding, F. Liu, N. Li, Cytotoxic and anti-inflammatory activities of phenanthrenes from the medullae of *Juncus effusus* L. Arch. Pharm. Res. 39 (2015) 154–160.
- [19] F.A.A. Beheri, Z.E.M. Naeem, G.T. Maatooq, M.M.A. Amer, Z.H. Wen, J.-H. Sheu, A.F. Ahmed, Phenanthrenoids from *Juncus acutus* L., new natural lipopolysaccharide-inducible nitric oxide synthase inhibitors, Chem. Pharm. Bull. 55 (2007) 1264–1266.
- [20] F.A.A. Beheri, Z.E.M. Naeem, G.T. Maatooq, M.M.A. Amer, A.F. Ahmed, A novel anti-oxidant phenanthrenoid dimer from *Juncus acutus* L. Nat. Prod. Res. 27 (2013) 155–163.
- [21] O. Benavente-García, J. Castillo, Update on uses and properties of citrus flavonoids: new findings in anticancer, cardiovascular, and anti-inflammatory activity, J. Agric. Food Chem. 56 (2008) 6185–6205.
- [22] M. Serafini, I. Peluso, A. Raguzzini, 3rd international immunonutrition workshop. Session 1: antioxidants and the immune system, flavonoids as anti-inflammatory agents, Proc. Nutr. Soc. 69 (2010) 273–278.
- [23] H.K. Kim, B.S. Cheon, Y.H. Kim, S.Y. Kim, H.P. Kim, Effects of naturally occurring flavonoids on nitric oxide production in the macrophage cell line RAW 264.7 and their structure-activity relationships, Biochem. Pharmacol. 58 (1999) 759–765.
- [24] Y.C. Liang, Y.T. Huang, S.H. Tsai, S.Y. Lin-Shiau, C.F. Chen, J.K. Lin, Suppression of inducible cyclooxygenase and inducible nitric oxide synthase by apigenin and related flavonoids in mouse macrophages, Carcinogenesis 20 (1999) 1945–1952.
- [25] M. Funakoshi-Tago, K. Nakamura, K. Tago, T. Mashino, T. Kasahara, Anti-inflammatory activity of structurally related flavonoids, apigenin, luteolin and fisetin, Int. Immunopharmacol. 11 (2011) 1150–1159.
- [26] T.L. Hwang, G.L. Li, Y.H. Lan, Y.C. Chia, P.W. Hsieh, Y.H. Wu, Y.C. Wu, Potent inhibition of superoxide anion production in activated human neutrophils by isopedicin, a bioactive component of the Chinese medicinal herb *Fissistigma oldhamii*, Free Radic. Biol. Med. 46 (2009) 520–528.
- [27] S.C. Yang, P.J. Chung, C.M. Ho, C.Y. Kuo, M.F. Hung, Y.T. Huang, W.Y. Chang, Y.W. Chang, K.H. Chan, T.L. Hwang, Propofol inhibits superoxide production, elastase release, and chemotaxis in formyl peptide-activated human neutrophils by blocking formyl peptide receptor 1, J. Immunol. 190 (2013) 6511–6519.
- [28] MacroModel, L.L.C. Schrödinger, <http://www.schrodinger.com/MacroModel2012> (accessed 16.08.15).
- [29] S. Grimme, Semiempirical GGA-type density functional constructed with a long-range dispersion correction, J. Comput. Chem. 27 (2006) 1787–1799.
- [30] P. Sun, D.X. Xu, A. Mándi, T. Kurtán, T.J. Li, B. Schulz, W. Zhang, Structure, absolute configuration, and conformational study of 12-membered macrolides from the fungus *Dendrodochium* sp. associated with the sea cucumber *Holothuria nobilis* Selenka, J. Org. Chem. 78 (2013) 7030–7047.
- [31] T. Yanai, D. Tew, N. Handy, A new hybrid exchange-correlation functional using the coulomb-attenuating method (CAM-B3LYP), Chem. Phys. Lett. 393 (2004) 51–57.
- [32] G. Pescitelli, L. Di Bari, N. Berova, Conformational aspects in the studies of organic compounds by electronic circular dichroism, Chem. Soc. Rev. 40 (2011) 4603–4625.
- [33] M.J. Frisch, G.W. Trucks, H.B. Schlegel, G.E. Scuseria, M.A. Robb, J.R. Cheeseman, G. Scalmani, V. Barone, B. Mennucci, G.A. Petersson, H. Nakatsuji, M. Caricato, X. Li, H.P. Hratchian, A.F. Izmaylov, J. Bloino, G. Zheng, J.L. Sonnenberg, M. Hada, M. Ehara, K. Toyota, R. Fukuda, J. Hasegawa, M. Ishida, T. Nakajima, Y. Honda, O. Kitao, H. Nakai, T. Vreven, J.A. Montgomery Jr., J.E. Peralta, F. Ogliaro, M. Bearpark, J.J. Heyd, E. Brothers, K.N. Kudin, V.N. Staroverov, R. Kobayashi, J. Normand, K. Raghavachari, A. Rendell, J.C. Burant, S.S. Iyengar, J. Tomasi, M. Cossi, N. Rega, J.M. Millam, M. Klene, J.E. Knox, J.B. Cross, V. Bakken, C. Adamo, J. Jaramillo, R. Gomperts, R.E. Stratmann, O. Yazyev, A.J. Austin, R. Cammi, C. Pomelli, J.W. Ochterski, R.L. Martin, K. Morokuma, V.G. Zakrzewski, G.A. Voth, P. Salvador, J.J. Dannenberg, S. Dapprich, A.D. Daniels, O. Farkas, J.B. Foresman, J.V. Ortiz, J. Cioslowski, D.J. Fox, Gaussian 09, Revision B.01, Gaussian, Inc., Wallingford, CT, 2010.
- [34] P.J. Stephens, N. Harada, ECD cotton effect approximated by the Gaussian curve and other methods, Chirality 22 (2010) 229–233.
- [35] U. Varetto, MOLEKEL, v. 5.4, Swiss National Supercomputing Centre, Manno, Switzerland, 2009.
- [36] A. Mándi, I.W. Mudianta, T. Kurtán, M.J. Garson, Absolute configuration and conformational study of psammaphysins A and B from the Balinese marine sponge *Aplysina strongylata*, J. Nat. Prod. 78 (2015) 2051–2056.
- [37] A. Mándi, M.M.M. Swamy, T. Taniguchi, M. Anetai, K. Monde, Reducing molecular flexibility by cyclization for elucidation of absolute configuration by CD calculations: daurichromenic acid, Chirality 28 (2016) 453–459.
- [38] B. Tóth, E. Liktör-Busa, N. Kúsz, Á. Szappanos, A. Mándi, T. Kurtán, E. Urbán, J. Hohmann, F.R. Chang, A. Vasas, Phenanthrenes from *Juncus inflexus* with antimicrobial activity against methicillin-resistant *Staphylococcus aureus*, J. Nat. Prod. 79 (2016) 2814–2823.
- [39] C.C. Shen, Y.S. Chang, L.K. Ho, Nuclear magnetic resonance studies of 5,7-dihydroxyflavonoids, Phytochemistry 34 (1993) 843–845.
- [40] L.C. Lin, Y.F. Pai, T.H. Tsai, Isolation of luteolin and luteolin-7-O-glucoside from *Dendranthema morifolium* Ramat Tzvel and their pharmacokinetics in rats, J. Agric. Food Chem. 63 (2015) 7700–7706.
- [41] D.H. Miles, J. Bhattacharyya, N.V. Mody, J.L. Atwood, S. Black, P.A. Hedin, The structure of juncusol. A novel cytotoxic dihydrophenanthrene from the estuarine marsh plant *Juncus roemerianus*, J. Am. Chem. Soc. 99 (1977) 618–620.

## Article

# Pinnisterols D–J, New 11-Acetoxy-9,11-secosterols with a 1,4-Quinone Moiety from Formosan Gorgonian Coral *Pinnigorgia* sp. (Gorgoniidae)

Yu-Chia Chang <sup>1,2,†</sup>, Tsong-Long Hwang <sup>3,4,5,†</sup>, Liang-Mou Kuo <sup>6,7</sup> and Ping-Jyun Sung <sup>1,8,9,10,11,\*</sup><sup>1</sup> National Museum of Marine Biology & Aquarium, Pingtung 944, Taiwan; jay0404@gmail.com<sup>2</sup> Doctoral Degree Program in Marine Biotechnology, National Sun Yat-sen University and Academia Sinica, Kaohsiung 804, Taiwan<sup>3</sup> Graduate Institute of Natural Products, College of Medicine, Chang Gung University, Taoyuan 333, Taiwan; htl@mail.cgu.edu.tw<sup>4</sup> Research Center for Industry of Human Ecology, Research Center for Chinese Herbal Medicine, and Graduate Institute of Healthy Industry Technology, College of Human Ecology, Chang Gung University of Science and Technology, Taoyuan 333, Taiwan<sup>5</sup> Department of Anesthesiology, Chang Gung Memorial Hospital, Taoyuan 333, Taiwan<sup>6</sup> Graduate Institute of Clinical Medical Sciences, College of Medicine, Chang Gung University, Taoyuan 333, Taiwan; kuo33410@yahoo.com.tw<sup>7</sup> Division of General Surgery, Department of Surgery, Chang Gung Memorial Hospital, Chiayi 613, Taiwan<sup>8</sup> Graduate Institute of Marine Biology, National Dong Hwa University, Pingtung 944, Taiwan<sup>9</sup> Chinese Medicine Research and Development Center, China Medical University Hospital, Taichung 404, Taiwan<sup>10</sup> Department of Marine Biotechnology and Resources, National Sun Yat-sen University, Kaohsiung 804, Taiwan<sup>11</sup> Graduate Institute of Natural Products, Kaohsiung Medical University, Kaohsiung 807, Taiwan

\* Correspondence: pjsung@nmmba.gov.tw; Tel.: +886-8-882-5037; Fax: +886-8-882-5087

† These authors contributed equally to this work.

Academic Editor: Orazio Tagliatela-Scafati

Received: 20 November 2016; Accepted: 28 December 2016; Published: 6 January 2017

**Abstract:** Seven new marine 11-acetoxy-9,11-secosterols, pinnisterols D–J (1–7), with a 1,4-quinone moiety, were discovered from the gorgonian coral *Pinnigorgia* sp. In this study, the structures of secosterols 1–7 were revealed by spectroscopic analysis. Bioactivity study showed that secosterol 1 treatment inhibited cell viability in a hepatic stellate cell line, HSC-T6, with an IC<sub>50</sub> value of 3.93 μM; and secosterols 2, 5, and 7 reduced elastase enzyme release, and 3, 5, and 7 decreased the production of superoxide anions from human neutrophils.

**Keywords:** 9,11-secosterol; gorgonian; *Pinnigorgia*; cytotoxicity; hepatic stellate cell line (HSC-T6); anti-inflammatory; superoxide anion; elastase

## 1. Introduction

Since the isolation in 1972 of the first marine 9,11-secosteroid, 9-oxo-9,11-secogorgost-5-ene-3β, 11-diol 11-acetate, from the gorgonian coral *Pseudopterogorgia americana* [1], a series of compounds of this group has been prepared from various marine invertebrates, particularly sponges and octocorals, with complex structures and interesting bioactivities [2]. Our continued investigations of gorgonian coral *Pinnigorgia* sp. (phylum Cnidaria, class Anthozoa, subclass Octocorallia, order Alcyonacea, family Gorgoniidae) have yielded various interesting secondary metabolites [3–8], including 9,11-secosterols [3–5], some of which have been shown to possess bioactivity, such as anti-inflammatory and cytotoxic properties [3–8]. With the aim of discovering bioactive marine



metabolites for new drug development in the future, we carried out an investigation of the chemical composition of the gorgonian coral *Pinnigorgia* sp. In this study, we performed compound preparation and structure determination, and investigated the cytotoxicity and anti-inflammatory activities of seven new 9,11-secosterols, pinnisterols D–J (1–7), following further study of *Pinnigorgia* sp. (Figure 1).

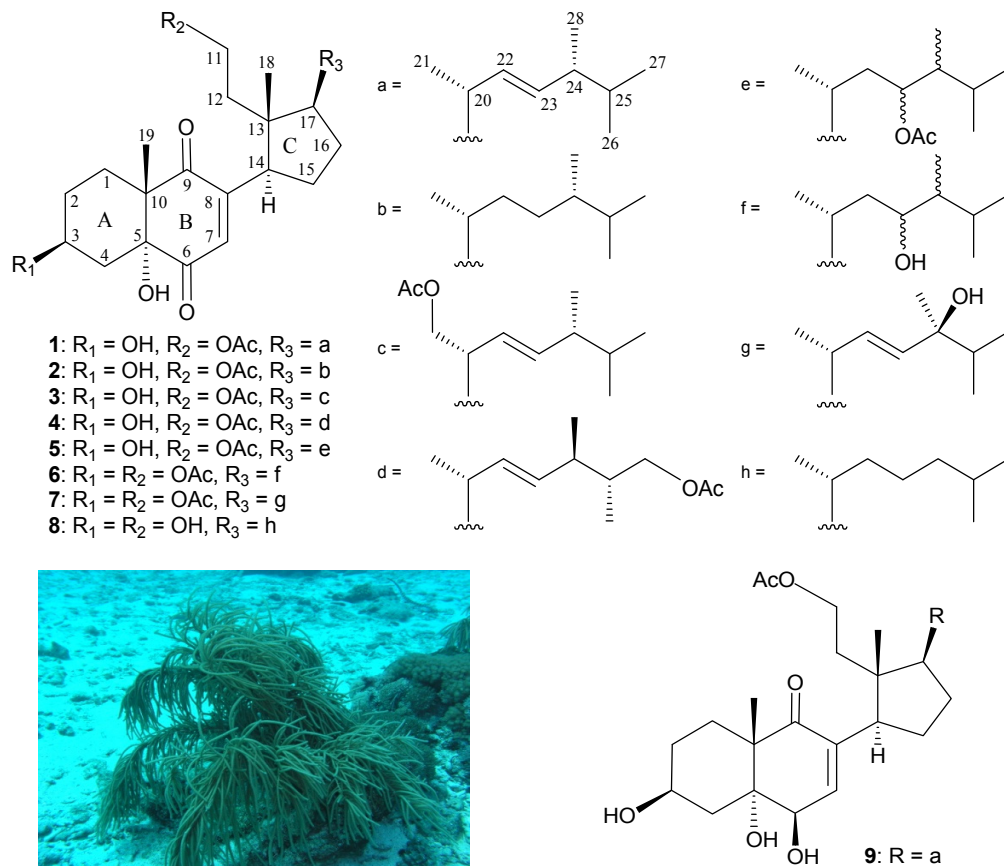


**Figure 1.** Chemical structures of pinnisterols D–J (1–7), sterol 8, and pinnisterol A (9), and an image of gorgonian coral *Pinnigorgia* sp.

## 2. Results and Discussion

A new metabolite was isolated as a colorless oil, and was named pinnisterol D (1). The high-resolution electrospray ionization mass spectrum (HRESIMS) showed a signal at  $m/z$  525.31853 (calcd. for  $C_{30}H_{46}O_6 + Na$ , 525.31921), and therefore the molecular formula of 1 was determined to be  $C_{30}H_{46}O_6$  (8° of unsaturation).  $^{13}C$  and distortionless enhancement polarization transfer (DEPT) experimental data indicated that 1 had 30 carbons, including seven methyls, seven  $sp^3$  methylenes (including one oxymethylene), six  $sp^3$  methines (including one oxymethine), two  $sp^3$  quaternary carbons, one  $sp^3$  tertiary alcohol, three  $sp^2$  methines, one  $sp^2$  tertiary carbon, two ketonic carbonyls, and one ester carbonyl (Table 1). In addition, IR spectroscopy demonstrated that the compound contained hydroxy ( $\nu_{max}$  3446  $cm^{-1}$ ), ester ( $\nu_{max}$  1741  $cm^{-1}$ ), and  $\alpha,\beta$ -unsaturated ketonic carbonyl ( $\nu_{max}$  1685  $cm^{-1}$ ) groups. The latter structural feature of 1 was further proven by the presence of signals at  $\delta_C$  197.5 (C-6), 134.1 (CH-7), 152.0 (C-8), and 201.6 (C-9) in the  $^{13}C$  NMR spectrum. Signals of carbons at  $\delta_C$  133.8 (CH-22) and 133.5 (CH-23) suggested the existence of a disubstituted olefin, and this was confirmed by two olefin proton signals at  $\delta_H$  5.26 (1H, dd,  $J = 14.8, 6.8$  Hz, H-23) and 5.23 (1H, dd,  $J = 14.8, 6.8$  Hz, H-22) (Table 1). The presence of Me-21, Me-28, Me-26, and Me-27 groups resulted in four doublets located at  $\delta_H$  1.05 (3H,  $J = 6.8$  Hz), 0.91 (3H,  $J = 6.8$  Hz), 0.84 (3H,  $J = 7.2$  Hz), and 0.82 (3H,  $J = 7.2$  Hz), respectively, and the existence of H<sub>3</sub>-18 and H<sub>3</sub>-19 resulted in two

sharp singlets at  $\delta_H$  0.73 and  $\delta_H$  1.21, respectively. In the  $^1H$  NMR spectrum, one acetyl methyl signal ( $\delta_H$  2.02, 3H, s) was observed. Based on the aforementioned findings, metabolite **1** was determined to be a tricyclic compound.

From the  $^1H$  NMR spectrum and  $^1H$ - $^1H$  correlation spectroscopy (COSY) of **1** (Table 1), the following correlations were revealed: H<sub>2</sub>-1/H<sub>2</sub>-2/H-3/H<sub>2</sub>-4, H<sub>2</sub>-11/H<sub>2</sub>-12, H-14/H<sub>2</sub>-15/H<sub>2</sub>-16/H-17/H-20/H-22/H-23/H-24/H-25/H<sub>3</sub>-26, H-20/H<sub>3</sub>-21, H-24/H<sub>3</sub>-28, and H-25/H<sub>3</sub>-27. Together with data of key heteronuclear multiple bond coherence (HMBC) correlations between H<sub>2</sub>-4, H-7, H<sub>3</sub>-19/C-5; H<sub>2</sub>-4/C-6; H-7, H-14/C-8; H-7, H-14, H<sub>3</sub>-19/C-9; H<sub>2</sub>-1, H<sub>2</sub>-4, H<sub>3</sub>-19/C-10; and H<sub>2</sub>-11, H<sub>2</sub>-12, H-14, and H<sub>3</sub>-18/C-13, all the information allowed determination of the main carbon skeleton of **1** (Table 1).

**Table 1.** Results of  $^1H$  (400 MHz,  $CDCl_3$ ) and  $^{13}C$  (100 MHz,  $CDCl_3$ ) NMR experiments and  $^1H$ - $^1H$  COSY and HMBC correlations for secoosterol **1**.

Position	$\delta_H$ (J in Hz)	$\delta_C$ , Multiple	$^1H$ - $^1H$ COSY	HMBC
1	2.21 m; 1.78 m	25.9, CH <sub>2</sub>	H <sub>2</sub> -2	C-2, -10
2	2.00 m; 1.49 m	29.9, CH <sub>2</sub>	H <sub>2</sub> -1, H-3	n. o. <sup>a</sup>
3	4.03 m	66.7, CH	H <sub>2</sub> -2, H <sub>2</sub> -4	n. o.
4	2.17 m; 1.79 m	35.7, CH <sub>2</sub>	H-3	C-2, -3, -5, -6, -10
5		80.6, C		
6		197.5, C		
7	6.45 s	134.1, CH		C-5, -8, -9, -14
8		152.0, C		
9		201.6, C		
10		52.0, C		
11	4.18 m	61.0, CH <sub>2</sub>	H <sub>2</sub> -12	C-12, -13, acetate carbonyl
12	1.68 m; 1.26 ddd (14.8, 9.2, 5.6)	37.1, CH <sub>2</sub>	H <sub>2</sub> -11	C-11, -13, -14, -17, -18
13		47.4, C		
14	3.37 dd (10.8, 8.0)	43.9, CH	H <sub>2</sub> -15	C-7, -8, -9, -13, -15, -18
15	1.75 m; 1.66 m	27.1, CH <sub>2</sub>	H-14, H <sub>2</sub> -16	C-16
16	1.78 m; 1.57 m	25.6, CH <sub>2</sub>	H <sub>2</sub> -15, H-17	C-15
17	1.81 m	51.0, CH	H <sub>2</sub> -16, H-20	C-15, -16, -18, -21
18	0.73 s	18.0, CH <sub>3</sub>		C-12, -13, -14, -17
19	1.21 s	20.5, CH <sub>3</sub>		C-1, -5, -9, -10
20	2.24 m	38.3, CH	H-17, H <sub>3</sub> -21, H-22	C-16, -17, -22, -23
21	1.05 d (6.8)	21.8, CH <sub>3</sub>	H-20	C-17, -20, -22
22	5.23 dd (14.8, 6.8)	133.8, CH	H-20, H-23	C-20, -24
23	5.26 dd (14.8, 6.8)	133.5, CH	H-22, H-24	C-20, -24
24	1.86 m	43.0, CH	H-23, H-25, H <sub>3</sub> -28	C-22, -23, -25, -26, -27, -28
25	1.46 m	33.1, CH	H-24, H <sub>3</sub> -26, H <sub>3</sub> -27	C-23, -24, -26, -27, -28
26	0.84 d (7.2)	20.0, CH <sub>3</sub>	H-25	C-24, -25, -27
27	0.82 d (7.2)	19.7, CH <sub>3</sub>	H-25	C-24, -25, -26
28	0.91 d (6.8)	17.5, CH <sub>3</sub>	H-24	C-23, -24, -25
11-OAc		171.1, C		
	2.02 s	21.1, CH <sub>3</sub>		Acetate carbonyl

<sup>a</sup> n. o. = not observed.

The correlations identified using nuclear Overhauser effect spectroscopy (NOESY) in addition to comparison of NMR data with those of known 9,11-secoosterol **8**, isolated from Korean marine sponge *Ircinia* sp. [9], and pinnisterol A (**9**) [4], enabled clarification of the configuration of **1** (Figure 1). The stereochemistries of stereogenic centers C-3, C-5, C-10, C-13, C-14, and C-17 in **1** were the same as those of **8**. In addition, the main NOE correlations for **1** were interactions between H-3/H-2 $\alpha$  ( $\delta_H$  2.00), H-2 $\beta$  ( $\delta_H$  1.49)/H<sub>3</sub>-19, H-3/H-4 $\alpha$  ( $\delta_H$  2.17), H-4 $\beta$  ( $\delta_H$  1.79)/H<sub>3</sub>-19; thus, H-3 and the 5-hydroxy group in **1** should be positioned on the  $\alpha$ -face (Figure 2).

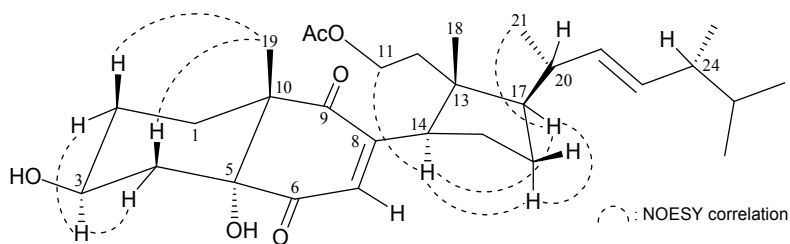


Figure 2. Selected NOESY correlations observed for **1**.

There was a greater coupling constant between H-22 and H-23 ( $J = 14.8$  Hz), which supported a *trans* relationship between H-22 and H-23. This implied that the configuration of C-24 should be *R* according to the  $^{13}\text{C}$  NMR chemical shift of C-28 ( $\delta_{\text{C}}$  17.5). A previous study showed that, for a known sterol, (22*E*,24*R*)-24-methylcholesta-5,22-dien-3 $\beta$ -ol, with an identical chain, and the 24*S* epimer, (22*E*,24*S*)-24-methylcholesta-5,22-dien-3 $\beta$ -ol, the  $^{13}\text{C}$  NMR value of C-28 resonates at  $\delta_{\text{C}}$  17.68 ppm in the 24*R* epimer, with a relative 0.4 ppm downfield chemical shift (Figure 3) [10].

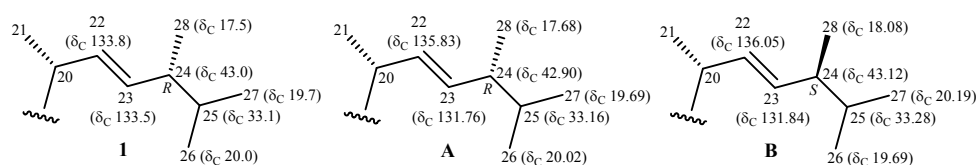


Figure 3. Schematic diagrams of  $^{13}\text{C}$  NMR chemical shift data of the side-chain of pinnisterol D (**1**), (22*E*,24*R*)-24-methylcholesta-5,22-dien-3 $\beta$ -ol (**A**), and (22*E*,24*S*)-24-methylcholesta-5,22-dien-3 $\beta$ -ol (**B**) [10].

Pinnisterol E (**2**) was present as a colorless oil. From HRESIMS analysis, the signal at  $m/z$  527.33410 (calcd. for  $\text{C}_{30}\text{H}_{48}\text{O}_6 + \text{Na}$ , 527.33486) suggested the molecular formula of **2** to be  $\text{C}_{30}\text{H}_{48}\text{O}_6$  (7° of unsaturation), and the IR spectrum demonstrated the existence of hydroxy ( $\nu_{\text{max}}$  3381  $\text{cm}^{-1}$ ), ester ( $\nu_{\text{max}}$  1740  $\text{cm}^{-1}$ ), and  $\alpha,\beta$ -unsaturated ketonic carbonyl ( $\nu_{\text{max}}$  1686  $\text{cm}^{-1}$ ) groups. The whole series of spectroscopic data demonstrated that secosterols **2** and **1** had an identical core structure, the difference being limited to the absence in **2** of the carbon-carbon double bond between C-22/23. The complete assignments of  $^1\text{H}$  and  $^{13}\text{C}$  NMR of **2** (Tables 2 and 3) were compared with the values of **1**, and secosterol **2** was assigned as having structure **2**, with the same configurations of the core rings A–C. In addition, both compounds had identical stereogenic centers at C-3, C-5, C-10, C-13, C-14, and C-17, and their  $^1\text{H}$  and  $^{13}\text{C}$  NMR chemical shifts and proton coupling constants were in concurrence also. Based on the  $^{13}\text{C}$  NMR chemical shifts of C-25 ( $\delta_{\text{C}}$  31.5), C-26 ( $\delta_{\text{C}}$  17.6), and C-27 ( $\delta_{\text{C}}$  20.5), the configuration of the stereogenic center at C-24 was assigned as *S*. Previous study also showed that the  $^{13}\text{C}$  NMR values of C-25, C-26, and C-27 resonates at  $\delta_{\text{C}}$  31.54, 17.68, and 20.56 ppm in a 24*S* epimer of a known sterol, (24*S*)-24-methylcholest-5-en-3 $\beta$ -ol, with an identical side chain, and the  $^{13}\text{C}$  NMR values of C-25, C-26, and C-27 in a 24*R* epimer, (24*R*)-24-methylcholest-5-en-3 $\beta$ -ol, were observed at  $\delta_{\text{C}}$  32.49, 20.26, and 18.32 ppm, respectively (Figure 4) [10].

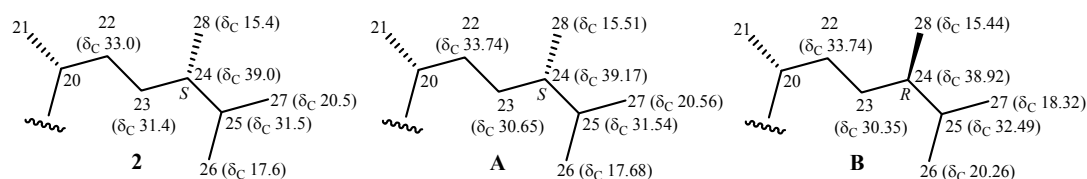


Figure 4. Schematic diagrams of  $^{13}\text{C}$  NMR chemical shift data of the side-chain of pinnisterol E (**2**), (24*S*)-24-methylcholest-5-en-3 $\beta$ -ol (**A**), and (24*R*)-24-methylcholest-5-en-3 $\beta$ -ol (**B**) [9].

Pinnisterol F (**3**) was present as a colorless oil. From HRESIMS analysis, the signal at  $m/z$  583.32406 (calcd. for  $C_{32}H_{48}O_8 + Na$ , 583.32469) suggested the molecular formula of **3** to be  $C_{32}H_{48}O_8$  (9° of unsaturation). The NMR signals of **3** (Tables 2 and 3) were similar to those of **1**, except that the signals related to the C-21 methyl in **1** were substituted by signals for an acetoxymethylene group in **3**. From the HMBC spectrum of **3**, it was revealed that an ester carbonyl carbon at  $\delta_C$  171.1 correlated with a methyl signal at  $\delta_H$  2.04 and a pair of oxygenated methylene protons at  $\delta_H$  4.01 (1H, dd,  $J = 10.5$ , 7.0 Hz) and 3.96 (1H, dd,  $J = 10.5$ , 7.0 Hz), which revealed that an acetoxy group was at the position C-21 in the side chain of **3**. Thus, pinnisterol F (**3**) was found to be the 21-acetoxy derivative of **1**.

Pinnisterol G (**4**) had a molecular formula identical to that of **3**,  $C_{32}H_{48}O_8$ , with a HRESIMS signal located at  $m/z$  583.32432 (calcd. for  $C_{32}H_{48}O_8 + Na$ , 583.32469) with nine degrees of unsaturation, indicating that secosterols **3** and **4** were isomers. Comparison of the NMR data of **4** with those of **3** (Tables 2 and 3) showed that both compounds possessed the same sterol nucleus and a similar side chain, but differed in terms of the location of one acetoxy group. From an HMBC experiment, it was revealed that one ester carbonyl carbon at  $\delta_C$  171.3 correlated with one methyl signal at  $\delta_H$  2.07 and a pair of oxymethylene protons signals at  $\delta_H$  3.98 (dd,  $J = 10.5$ , 6.3 Hz) and 3.85 (dd,  $J = 10.5$ , 6.3 Hz), which indicated that an acetoxy group was located at C-27 in the side chain. The configurations at C-24 and C-25 were therefore designated as *S*- and *R*-forms, respectively, on the basis of the  $^{13}C$  NMR chemical shifts of C-24 ( $\delta_C$  38.2), C-25 ( $\delta_C$  37.4), C-26 ( $\delta_C$  13.1), C-27 ( $\delta_C$  67.9), and C-28 ( $\delta_C$  18.3). It was reported that the  $^{13}C$  NMR values of C-24, C-25, C-26, C-27, and C-28 resonate at  $\delta_C$  38.2, 37.6, 13.0, 68.1, and 18.6 ppm in a 24*S* and a 25*R* epimer of a known sterol, echresteroid C, with the same side chain, and the  $^{13}C$  NMR values of C-24, C-25, C-26, C-27, and C-28 in a 24*S* and 25*S* epimer, echresteroid B, appeared at  $\delta_C$  38.8, 37.5, 14.1, 67.9, and 17.1 ppm (Figure 5) [11].

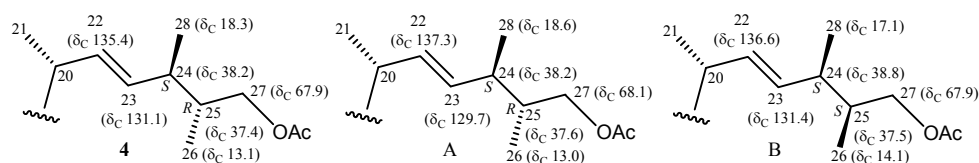
Table 2.  $^1H$  NMR data for secosterols 2–4.

$\delta_H$	2 <sup>a</sup>	3 <sup>b</sup>	4 <sup>b</sup>
1	2.21 m; 1.76 m	2.21 m; 1.74 m	2.20 m; 1.72 m
2	2.00 m; 1.47 m	2.00 m; 1.47 m	2.00 m; 1.49 m
3	4.04 m	4.04 m	4.04 m
4	2.15 ddd (14.4, 5.2, 2.0) <sup>c</sup> ; 1.79 m	2.14 m; 1.77 m	2.13 m; 1.79 m
7	6.47 s	6.46 s	6.46 s
11	4.16 m	4.17 t (6.3)	4.18 m
12	1.73 m; 1.23 m	1.59 m; 1.30 m	1.69 m; 1.25 m
14	3.39 dd (10.8, 8.4)	3.37 t (9.8)	3.38 dd (11.2, 8.4)
15	1.76 m; 1.68 m	1.77 m; 1.69 m	1.76 m; 1.65 m
16	1.89 m; 1.53 m	1.75 m; 1.49 m	1.76 m; 1.55 m
17	1.76 m	1.97 m	1.77 m
18	0.74 s	0.73 s	0.73 s
19	1.22 s	1.21 s	1.22 s
20	1.42 m	1.46 m	2.23 m
21	0.99 d (6.8)	4.01 dd (10.5, 7.0); 3.96 dd (10.5, 7.0)	1.06 d (7.0)
22	1.44 m; 0.95 m	5.36 dd (15.4, 8.4)	5.24 dd (15.4, 8.4)
23	1.40 m; 0.96 m	5.22 dd (15.4, 8.4)	5.30 dd (15.4, 8.4)
24	1.20 m	1.90 m	2.19 m
25	1.61 m	1.45 m	1.71 m
26	0.79 d (6.8)	0.84 d (7.0)	0.85 d (7.0)
27	0.86 d (6.8)	0.82 d (7.0)	3.98 dd (10.5, 6.3); 3.85 dd (10.5, 6.3)
28	0.78 d (6.8)	0.93 d (7.0)	0.98 d (7.0)
11-OAc	2.02 s	2.02 s	2.03 s
21-OAc		2.04 s	
27-OAc			2.07 s

<sup>a</sup> Spectra recorded at 400 MHz in  $CDCl_3$ ; <sup>b</sup> Spectra recorded at 700 MHz in  $CDCl_3$ ; <sup>c</sup>  $J$  values (in Hz) in parentheses.

**Table 3.**  $^{13}\text{C}$  NMR data for secosterols 2–7.

$\delta_{\text{C}}$	2 <sup>a</sup>	3 <sup>b</sup>	4 <sup>b</sup>	5 <sup>a</sup>	6 <sup>a</sup>	7 <sup>a</sup>
1	25.9, CH <sub>2</sub>	25.8, CH <sub>2</sub>	25.9, CH <sub>2</sub>	25.9, CH <sub>2</sub>	25.7, CH <sub>2</sub>	25.7, CH <sub>2</sub>
2	29.9, CH <sub>2</sub>	29.9, CH <sub>2</sub>	29.9, CH <sub>2</sub>	29.9, CH <sub>2</sub>	25.9, CH <sub>2</sub>	25.9, CH <sub>2</sub>
3	66.7, CH	66.7, CH	66.7, CH	66.7, CH	69.7, CH	69.8, CH
4	35.8, CH <sub>2</sub>	35.7, CH <sub>2</sub>	35.7, CH <sub>2</sub>	35.6, CH <sub>2</sub>	32.0, CH <sub>2</sub>	31.9, CH <sub>2</sub>
5	80.6, C	80.6, C	80.6, C	80.5, C	80.1, C	80.0, C
6	197.4, C	197.4, C	197.5, C	197.5, C	197.3, C	197.5, C
7	134.1, CH	134.1, CH	134.1, CH	134.2, CH	134.2, CH	134.2, CH
8	152.1, C	151.6, C	151.8, C	151.7, C	151.8, C	151.6, C
9	201.5, C	201.6, C	201.6, C	201.6, C	201.2, C	201.3, C
10	52.0, C	52.0, C	52.0, C	52.0, C	51.9, C	51.9, C
11	61.0, CH <sub>2</sub>	60.8, CH <sub>2</sub>	61.0, CH <sub>2</sub>	60.9, CH <sub>2</sub>	61.0, CH <sub>2</sub>	61.0, CH <sub>2</sub>
12	37.2, CH <sub>2</sub>	36.7, CH <sub>2</sub>	37.0, CH <sub>2</sub>	37.0, CH <sub>2</sub>	37.2, CH <sub>2</sub>	37.2, CH <sub>2</sub>
13	47.5, C	47.5, C	47.3, C	47.4, C	47.4, C	47.4, C
14	43.7, CH	43.5, CH	43.8, CH	43.7, CH	43.7, CH	43.8, CH
15	27.2, CH <sub>2</sub>	27.1, CH <sub>2</sub>	26.9, CH <sub>2</sub>	27.0, CH <sub>2</sub>	27.1, CH <sub>2</sub>	27.1, CH <sub>2</sub>
16	26.2, CH <sub>2</sub>	25.8, CH <sub>2</sub>	25.7, CH <sub>2</sub>	26.2, CH <sub>2</sub>	26.4, CH <sub>2</sub>	25.8, CH <sub>2</sub>
17	50.7, CH	46.3, CH	50.7, CH	51.4, CH	51.6, CH	50.9, CH
18	17.6, CH <sub>3</sub>	18.5, CH <sub>3</sub>	18.0, CH <sub>3</sub>	17.6, CH <sub>3</sub>	17.8, CH <sub>3</sub>	18.0, CH <sub>3</sub>
19	20.5, CH <sub>3</sub>	20.4, CH <sub>3</sub>	20.5, CH <sub>3</sub>	20.4, CH <sub>3</sub>	20.3, CH <sub>3</sub>	20.2, CH <sub>3</sub>
20	34.9, CH	42.2, CH	38.4, CH	33.2, CH	33.9, CH	38.2, CH
21	19.2, CH <sub>3</sub>	67.2, CH <sub>2</sub>	21.7, CH <sub>3</sub>	20.4, CH <sub>3</sub>	21.1, CH <sub>3</sub>	21.6, CH <sub>3</sub>
22	33.0, CH <sub>2</sub>	127.5, CH	135.4, CH	35.4, CH <sub>2</sub>	39.4, CH <sub>2</sub>	132.9, CH
23	21.4, CH <sub>2</sub>	138.1, CH	131.1, CH	76.7, CH	74.6, CH	134.5, CH
24	39.0, CH	43.4, CH	38.2, CH	42.7, CH	45.5, CH	75.0, C
25	31.5, CH	32.9, CH	37.4, CH	28.5, CH	27.7, CH	38.1, CH
26	17.6, CH <sub>3</sub>	20.0, CH <sub>3</sub>	13.1, CH <sub>3</sub>	21.6, CH <sub>3</sub>	21.7, CH <sub>3</sub>	17.5, CH <sub>3</sub>
27	20.5, CH <sub>3</sub>	19.7, CH <sub>3</sub>	67.9, CH <sub>2</sub>	18.6, CH <sub>3</sub>	17.6, CH <sub>3</sub>	17.1, CH <sub>3</sub>
28	15.4, CH <sub>3</sub>	17.5, CH <sub>3</sub>	18.3, CH <sub>3</sub>	11.0, CH <sub>3</sub>	10.5, CH <sub>3</sub>	25.2, CH <sub>3</sub>
3-OAc					170.8, C	170.9, C
11-OAc	171.1, C	171.1, C	171.1, C	171.1, C	21.3, CH <sub>3</sub>	21.1, CH <sub>3</sub>
	21.1, CH <sub>3</sub>	21.1, CH <sub>3</sub>	21.1, CH <sub>3</sub>	21.1, CH <sub>3</sub>	171.0, C	170.9, C
21-OAc		171.1, C			21.1, CH <sub>3</sub>	21.1, CH <sub>3</sub>
		21.0, CH <sub>3</sub>				
23-OAc				170.7, C		
				21.4, CH <sub>3</sub>		
27-OAc			171.3, C			
			21.1, CH <sub>3</sub>			

<sup>a</sup> Spectra recorded at 100 MHz in CDCl<sub>3</sub>; <sup>b</sup> Spectra recorded at 175 MHz in CDCl<sub>3</sub>.**Figure 5.** Schematic diagrams of  $^{13}\text{C}$  NMR chemical shift data of the side-chain of pinnisterol G (4), echresteroid C (A), and echresteroid B (B) [11].

Pinnisterol H (5) was isolated as a colorless oil. Based on the HRESIMS signal located at  $m/z$  585.33988 (calcd. for  $\text{C}_{32}\text{H}_{50}\text{O}_8 + \text{Na}$ , 585.34034), it was concluded that the molecular formula of 5 was  $\text{C}_{32}\text{H}_{50}\text{O}_8$  (8° of unsaturation). The IR spectrum of 5 indicated the presence of hydroxy ( $\nu_{\text{max}}$  3448  $\text{cm}^{-1}$ ), ester ( $\nu_{\text{max}}$  1736  $\text{cm}^{-1}$ ) and  $\alpha,\beta$ -unsaturated ketonic carbonyl ( $\nu_{\text{max}}$  1686  $\text{cm}^{-1}$ ) groups. The whole series of spectroscopic data showed that secosterol 5 and secosterol 1 shared the same core structure, with the exception of the addition of an acetoxy group to substitute the alkene at C-23 in 5. The complete assignments of the  $^{13}\text{C}$  and  $^1\text{H}$  NMR of pinnisterol H (5) (Tables 3 and 4) were compared with the values of 1, and the HMBC correlations fully supported the positions of the functional groups



of **5**, indicating that it had a structure of the same configuration as secosterols **1–4** in the core rings A–C. The proton coupling constants and NMR chemical shift data also further supported this finding, though the configurations of C-23 and C-24 were not determined at this stage.

Pinnisterol I (**6**) was obtained as a colorless oil. The HRESIMS signal at  $m/z$  585.33988 (calcd. for  $C_{32}H_{50}O_8 + Na$ , 585.34034) suggested the molecular formula of **6** to be  $C_{32}H_{50}O_8$  (8° of unsaturation). The NMR signals of **6** (Tables 3 and 4) were very similar to those of **5**, with the exception that **5** had signals corresponding to 3-hydroxy and 23-acetoxy groups, which were substituted by signals for acetoxy and hydroxy groups, respectively, in **6**. From a NOESY experiment, the correlations of data of **5** and **6** demonstrated that the configurations of the stereogenic centers in the core rings A–C were identical to those of **1**. The configurations of stereogenic centers C-23 and C-24 of **6** were also not determined at this stage.

**Table 4.**  $^1H$  NMR (400 MHz,  $CDCl_3$ ) data for secosterols **5–7**.

$\delta_H$	<b>5</b>	<b>6</b>	<b>7</b>
1	2.22 m; 1.76 m	2.27 m; 1.78 m	2.28 m; 1.76 m
2	1.97 m; 1.48 m	1.98 m; 1.60 m	1.96 m; 1.61 m
3	4.02 m	5.05 m	5.05 m
4	2.12 m; 1.78 m	2.24 m; 1.81 m	2.24 m; 1.79 m
7	6.45 s	6.46 s	6.45 s
11	4.14 m	4.18 m	4.17 m
12	1.63 m; 1.23 m	1.70 m; 1.27 m	1.67 m; 1.26 m
14	3.36 dd (11.2, 8.4) <sup>a</sup>	3.39 dd (10.8, 8.0)	3.39 dd (10.4, 8.0)
15	1.76 m; 1.65 m	1.80 m; 1.69 m	1.76 m; 1.69 m
16	1.91 m; 1.52 m	1.93 m; 1.53 m	1.99 m; 1.53 m
17	1.69 m	1.81 m	1.81 m
18	0.73 s	0.74 s	0.73 s
19	1.20 s	1.22 s	1.21 s
20	1.54 m	1.63 m	2.28 m
21	1.02 d (6.8)	1.13 d (6.8)	1.08 d (6.8)
22	1.67 m; 1.24 m	1.72 m; 1.07 m	5.53 dd (15.6, 8.4)
23	5.01 m	3.59 m	5.48 (15.6)
24	1.47 m	1.32 m	
25	1.57 m	1.84 m	1.67 m
26	0.93 d (6.8)	0.94 d (7.2)	0.89 d (6.8)
27	0.83 d (6.8)	0.84 d (7.2)	0.88 d (6.8)
28	0.81 d (6.8)	0.79 d (7.2)	1.21 s
3-OAc		2.04 s	2.04 s
11-OAc	2.02 s	2.02 s	2.02 s
23-OAc	2.03 s		

<sup>a</sup>  $J$  values (in Hz) in parentheses.

Pinnisterol J (**7**) was obtained as a colorless oil and had the molecular formula  $C_{32}H_{48}O_8$ , as determined by the HRESIMS signal at  $m/z$  583.32433 (calcd. for  $C_{32}H_{48}O_8 + Na$ , 583.32469) (9° of unsaturation). According to the NMR spectroscopic data (Tables 3 and 4), compound **7** showed the same nuclear structure as that of compound **6**. In the  $^{13}C$  NMR data of **7**, one additional disubstituted olefin was identified from signals of carbons at  $\delta_C$  132.9 (CH-22) and 134.5 (CH-23). The presence of a 24-hydroxy group was evidenced by HMBC correlations between H-22, H-23, H-25, H<sub>3</sub>-26, H<sub>3</sub>-27, and H<sub>3</sub>-28/C-24 ( $\delta_C$  75.0), a methyl-containing oxygenated tertiary carbon. There was a greater coupling constant between H-22 and H-23 ( $J$  = 15.6 Hz), suggesting that a *trans* relationship existed between H-22 and H-23. The configuration of the C-24 stereogenic center was assigned as *S* on the basis of the  $^{13}C$  NMR chemical shifts of C-24 ( $\delta_C$  75.0), C-25 ( $\delta_C$  38.1), C-26 ( $\delta_C$  17.5), C-27 ( $\delta_C$  17.1), and C-28 ( $\delta_C$  25.2). It was reported that the  $^{13}C$  NMR values of C-24, C-25, C-26, C-27, and C-28 resonates at  $\delta_C$  75.1, 38.3, 17.7, 17.4, and 25.2 ppm in a 24*S* epimer of a known synthetic product, 24(*S*)-hydroxyvitamin D<sub>2</sub>, with the same side chain (Figure 6) [12].

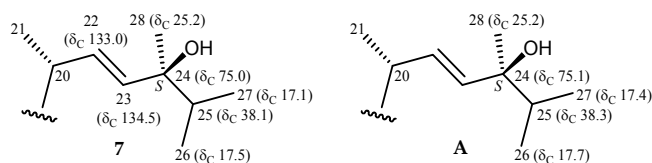


**Figure 6.** Schematic diagrams of <sup>13</sup>C NMR chemical shift data of the side-chain of pinnisterol J (7) and 24(S)-hydroxyvitamin D<sub>2</sub> (A) [12].

The hepatic stellate cell, a major cell type involved in liver fibrosis, is also responsible for liver damage by increasing proliferation and protein secretion associated with the formation of scar tissue. In cytotoxicity testing, secosterols 1–7 were examined in terms of their cytotoxic effects on HSC-T6, an immortalized rat hepatic stellate cell lines. At a concentration of 10 μM, secosterols 1, 3, and 5 significantly decreased the viability of HSC-T6 cells to 16.8 (IC<sub>50</sub> = 3.93 μM), 56.9 and 37.1%, respectively (Figure 7). These results implied that the functional groups in the side chain of secosterols 1–7 play important roles in determining the activity of the compounds.

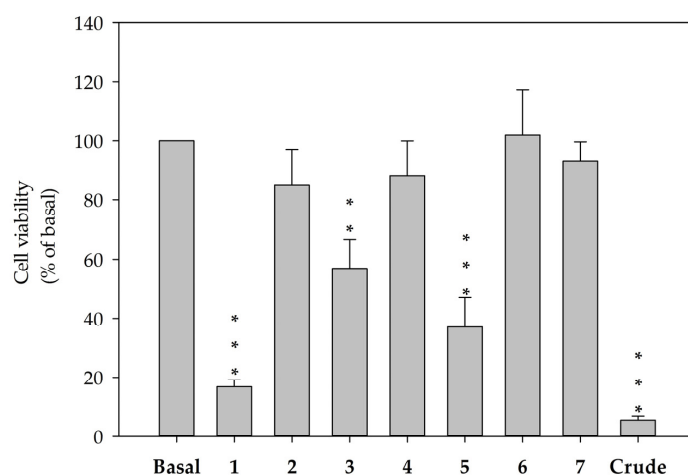


**Figure 7.** Decreased cell viability in HSC-T6 cells treated with secosterols 1–7 for 24 h at a concentration of 10 μM. Cells were treated with secosterols, DMSO (control) or coral crude extract at 6 μg/mL. Cytotoxicity was monitored spectrophotometrically at OD 450 nm. Quantitative data are expressed as the mean ± S.E.M. (n = 3–4). \*\* p < 0.01, \*\*\* p < 0.001 compared to basal.

In anti-inflammatory testing, secosterols 2, 5, and 7 displayed inhibitory effects on the release of elastase (IC<sub>50</sub> = 2.33, 2.59 and 3.89 μM, respectively), and secosterols 3, 5, and 7 showed inhibitory effects on human neutrophils in terms of the generation of superoxide anions (IC<sub>50</sub> = 5.52, 3.26, and 3.71 μM, respectively) (Table 5).

**Table 5.** Inhibitory effects of secosterols 2–7 on elastase release and superoxide anion generation by human neutrophils in response to fMet-Leu-Phe/Cytochalasin B.

Compound	Elastase Release	Superoxide Anions
	IC <sub>50</sub> (μM)	IC <sub>50</sub> (μM)
2	2.33 ± 0.27	>10
3	>10	5.52 ± 1.06
4	>10	>10
5	2.59 ± 0.29	3.26 ± 0.33
6	>10	>10
7	3.89 ± 1.16	3.71 ± 0.51

### 3. Experimental Section

#### 3.1. General Experimental Procedures

Optical rotations were measured with a digital polarimeter (P-1010; Japan Spectroscopic Corporation, Tokyo, Japan); and infrared spectra were recorded on a spectrometer (FT/IR-4100; Japan Spectroscopic Corporation); peaks are reported in  $\text{cm}^{-1}$ . NMR spectra were obtained on a 400 MHz NMR spectrometer (Mercury Plus; Varian, Palo Alto, CA, USA) and a 700 MHz NMR spectrometer (AVIIIHD700X; Bruker, Bremen, Germany), using the residual  $\text{CHCl}_3$  signal ( $\delta_{\text{H}}$  7.26 ppm) and  $\text{CDCl}_3$  ( $\delta_{\text{C}}$  77.1 ppm) as internal standards for  $^1\text{H}$  NMR and  $^{13}\text{C}$  NMR, respectively. Coupling constant values ( $J$ ) are given in Hz. ESIMS and HRESIMS were performed using mass spectrometry (Tesla solariX FTMS system, Bruker). TLC was carried out on Kieselgel 60  $\text{F}_{254}$  precoated plates (0.25 mm, Merck, Darmstadt, Germany), and spots were visualized by the standard method. Column chromatography was performed on silica gel at a size of 230–400 mesh (Merck). HPLC experiments were performed using the following systems: normal-phase HPLC (NP-HPLC) injection port, 7725 (Rheodyne, Rohnert Park, CA, USA); pump, L-7110 (Hitachi, Tokyo, Japan); and semi-preparative normal-phase column (Supelco Ascentis Si Cat #:581515-U, 25 cm  $\times$  21.2 mm, 5  $\mu\text{m}$ , Sigma-Aldrich, St. Louis, MO, USA). Reverse-phase HPLC (RP-HPLC) injection port (7725; Rheodyne); pump, L-2130 (Hitachi); photodiode array detector (L-2455; Hitachi); and reverse-phase column (25 cm  $\times$  21.2 mm, Luna 5  $\mu\text{m}$  C18(2) 100 Å, AXIA Packed; Phenomenex, Torrance, CA, USA).

#### 3.2. Animal Material

Specimens of gorgonian coral *Pinnigorgia* sp. were collected in August 2012 by hand while scuba diving off the coast of Green Island located near the southeast of Taiwan. The samples were then stored in a freezer until extraction. A voucher specimen was deposited in the National Museum of Marine Biology & Aquarium, Taiwan (specimen No.: NMMBA-TW-GC-2012-130). Identification of the species of this organism was done by comparison as described in the previous publication [13].

#### 3.3. Extraction and Separation

Extraction of compounds was performed at room temperature unless otherwise specified. *Pinnigorgia* sp. (wet weight 1.98 kg; dry weight 0.86 kg) was sliced, and the sliced bodies were then extracted with ethyl acetate (EtOAc). The EtOAc extract (84.9 g) was partitioned with *n*-hexane and methanol (MeOH). The MeOH layer (12.6 g) was separated on a Sephadex LH-20 column and elution was performed using a solvent mixture dichloromethane (DCM):MeOH (1:1); the separation yielded 7 subfractions A–G. Fraction F was separated by silica gel column chromatography and then eluted with *n*-hexane/acetone (stepwise, 50/50 %v/v to 100% acetone) to afford eight subfractions F1–F8. Fraction F2 was purified by silica gel column chromatography and then eluted with *n*-hexane/acetone (stepwise, 90/10 %v/v to 100% acetone) to yield 13 subfractions F2A–F2M. Fraction F2F was purified by NP-HPLC using a mixture of *n*-hexane/EtOAc (5:2) to afford 14 subfractions F2F1–F2F14. Fractions F2F5 and F2F6 were repurified by RP-HPLC using a mixture of MeOH/ $\text{H}_2\text{O}$  (90/10 %v/v at 5.0 mL/min flow rate) to yield **6** (1.8 mg) and **7** (4.8 mg), respectively. Fraction F2H was purified by NP-HPLC using a mixture of *n*-hexane/EtOAc (50/50 %v/v) to yield 14 subfractions F2H1–F2H14. Fractions F2H9 and F2H10 were repurified by RP-HPLC using a mixture of MeOH/ $\text{H}_2\text{O}$  (90/10 %v/v at 5.0 mL/min flow rate) to yield **1** (3.8 mg) and **2** (1.5 mg), respectively. Fraction F2I was repurified by NP-HPLC using a mixture of *n*-hexane/EtOAc (50/50 %v/v at 3.0 mL/min flow rate) to afford 15 subfractions F2I1–F2I15, including compound **5** (F2I9, 6.4 mg). Fraction F2I10 was purified by RP-HPLC using a mixture of MeOH/ $\text{H}_2\text{O}$  (85/15 %v/v at 5.0 mL/min, flow rate) to afford **3** (1.0 mg) and **4** (1.0 mg), respectively.

Pinnisterol D (**1**): colorless oil;  $[\alpha]_{\text{D}}^{25} +44$  ( $c$  1.3,  $\text{CHCl}_3$ ); IR (neat)  $\nu_{\text{max}}$  3446, 1741, 1685  $\text{cm}^{-1}$ ;  $^1\text{H}$  (400 MHz,  $\text{CDCl}_3$ ) and  $^{13}\text{C}$  (100 MHz,  $\text{CDCl}_3$ ) NMR data (see Table 1); ESIMS  $m/z$  525  $[\text{M} + \text{Na}]^+$ ; HRESIMS  $m/z$  525.31853 (calcd. for  $\text{C}_{30}\text{H}_{46}\text{O}_6 + \text{Na}$ , 525.31921).

Pinnisterol E (2): colorless oil;  $[\alpha]_D^{25}$   $-35$  (c 0.5,  $\text{CHCl}_3$ ); IR (neat)  $\nu_{\text{max}}$  3381, 1740, 1686  $\text{cm}^{-1}$ ;  $^1\text{H}$  (400 MHz,  $\text{CDCl}_3$ ) and  $^{13}\text{C}$  (100 MHz,  $\text{CDCl}_3$ ) NMR data (see Tables 2 and 3); ESIMS  $m/z$  527  $[\text{M} + \text{Na}]^+$ ; HRESIMS  $m/z$  527.33410 (calcd. for  $\text{C}_{30}\text{H}_{48}\text{O}_6 + \text{Na}$ , 527.33486).

Pinnisterol F (3): colorless oil;  $[\alpha]_D^{27}$   $-152$  (c 0.3,  $\text{CHCl}_3$ ); IR (neat)  $\nu_{\text{max}}$  3446, 1736, 1686  $\text{cm}^{-1}$ ;  $^1\text{H}$  (700 MHz,  $\text{CDCl}_3$ ) and  $^{13}\text{C}$  (175 MHz,  $\text{CDCl}_3$ ) NMR data (see Tables 2 and 3); ESIMS  $m/z$  583  $[\text{M} + \text{Na}]^+$ ; HRESIMS  $m/z$  583.32406 (calcd. for  $\text{C}_{32}\text{H}_{48}\text{O}_8 + \text{Na}$ , 583.32469).

Pinnisterol G (4): colorless oil;  $[\alpha]_D^{27}$   $-176$  (c 0.3,  $\text{CHCl}_3$ ); IR (neat)  $\nu_{\text{max}}$  3447, 1739, 1686  $\text{cm}^{-1}$ ;  $^1\text{H}$  (700 MHz,  $\text{CDCl}_3$ ) and  $^{13}\text{C}$  (175 MHz,  $\text{CDCl}_3$ ) NMR data (see Tables 2 and 3); ESIMS  $m/z$  583  $[\text{M} + \text{Na}]^+$ ; HRESIMS  $m/z$  583.32432 (calcd. for  $\text{C}_{32}\text{H}_{48}\text{O}_8 + \text{Na}$ , 583.32469).

Pinnisterol H (5): colorless oil;  $[\alpha]_D^{25}$   $-20$  (c 0.3,  $\text{CHCl}_3$ ); IR (neat)  $\nu_{\text{max}}$  3448, 1736, 1686  $\text{cm}^{-1}$ ;  $^1\text{H}$  (400 MHz,  $\text{CDCl}_3$ ) and  $^{13}\text{C}$  (100 MHz,  $\text{CDCl}_3$ ) NMR data (see Tables 3 and 4); ESIMS  $m/z$  585  $[\text{M} + \text{Na}]^+$ ; HRESIMS  $m/z$  585.33988 (calcd. for  $\text{C}_{32}\text{H}_{50}\text{O}_8 + \text{Na}$ , 585.34034).

Pinnisterol I (6): colorless oil;  $[\alpha]_D^{25}$   $-129$  (c 0.5,  $\text{CHCl}_3$ ); IR (neat)  $\nu_{\text{max}}$  3446, 1736, 1685  $\text{cm}^{-1}$ ;  $^1\text{H}$  (400 MHz,  $\text{CDCl}_3$ ) and  $^{13}\text{C}$  (100 MHz,  $\text{CDCl}_3$ ) NMR data (see Tables 3 and 4); ESIMS  $m/z$  585  $[\text{M} + \text{Na}]^+$ ; HRESIMS  $m/z$  585.33988 (calcd. for  $\text{C}_{32}\text{H}_{50}\text{O}_8 + \text{Na}$ , 585.34034).

Pinnisterol J (7): colorless oil;  $[\alpha]_D^{25}$   $-5$  (c 0.2,  $\text{CHCl}_3$ ); IR (neat)  $\nu_{\text{max}}$  3455, 1736, 1687  $\text{cm}^{-1}$ ;  $^1\text{H}$  (400 MHz,  $\text{CDCl}_3$ ) and  $^{13}\text{C}$  (100 MHz,  $\text{CDCl}_3$ ) NMR data (see Tables 3 and 4); ESIMS  $m/z$  583  $[\text{M} + \text{Na}]^+$ ; HRESIMS  $m/z$  583.32433 (calcd. for  $\text{C}_{32}\text{H}_{48}\text{O}_8 + \text{Na}$ , 583.32469).

### 3.4. Anti-Hepatofibrotic Assay

The anti-hepatofibrotic effects of secosterols 1–7, at a concentration of 10  $\mu\text{M}$ , were analyzed using a colorimetric assay (WST-1-based method). The steps of the assay were performed according to a previously-published method [14].

### 3.5. Generation of Superoxide Anions and Release of Elastase by Human Neutrophils

Human neutrophils were prepared by Ficoll centrifugation followed by dextran sedimentation. Measurements of superoxide anion generation and elastase release from neutrophils were performed based on published procedures [15,16]. Briefly, MeO-Suc-Ala-Ala-Pro-Valp-nitroanilide was used as the elastase substrate for the elastase release assay, and the method using superoxide dismutase-inhibitable reduction of ferricytochrome *c* was employed to measure superoxide anion production.

## 4. Conclusions

Our ongoing investigations of coral metabolites showed that gorgonian corals belonging to the genus *Pinnigorgia* are rich in 9,11-secosterols. In cytotoxicity tests, secosterol 1 showed significant cytotoxicity against HSC-T6 cells. In anti-inflammatory activity tests on human neutrophils, secosterols 2, 5, and 7 displayed inhibitory effects on elastase release, and 3, 5, and 7 showed inhibitory effects on the generation of superoxide anions. Our findings suggested that these new 9,11-secosterols could be developed as promising bioactive agents, and further biomedical study is necessary in order to identify their potential applications in the treatment of disease.

**Supplementary Materials:** HRESIMS,  $^1\text{H}$  and  $^{13}\text{C}$  spectra of new compounds 1–7 and 2D NMR data (HSQC,  $^1\text{H}$ – $^1\text{H}$  COSY, HMBC and NOESY spectra) of new compound 1 are available online at [www.mdpi.com/1660-3397/15/1/11/s1](http://www.mdpi.com/1660-3397/15/1/11/s1).

**Acknowledgments:** This research was supported by grants from several institutions, including the National Museum of Marine Biology & Aquarium; the National Dong Hwa University; the National Sun Yat-sen University; and the National Research Program for Biopharmaceuticals, Ministry of Science and Technology (Grant No. MOST 105-2325-B-291-001, 105-2811-B-291-003, 104-2325-B-291-001, 103-2325-B-291-001 and 104-2320-B-291-001-MY3) awarded to P.-J.S.

**Author Contributions:** P.-J.S. designed the whole experiment and contributed to manuscript preparation. Y.-C.C. and T.-L.H. researched data. L.-M.K. analyzed the data and performed data acquisition.

**Conflicts of Interest:** The authors declare no conflicts of interest.

## References

1. Enwall, E.L.; van der Helm, D.; Hsu, I.N.; Pattabhiraman, T.; Schmitz, F.J.; Spraggins, R.L.; Weinheimer, A.J. Crystal structure and absolute configuration of two cyclopropane containing marine steroids. *J. Chem. Soc. Chem. Commun.* **1972**, 215–216. [[CrossRef](#)]
2. Sica, D.; Musumeci, D. Secosteroids of marine origin. *Steroids* **2004**, *69*, 743–756. [[CrossRef](#)] [[PubMed](#)]
3. Chang, Y.-C.; Kuo, L.-M.; Su, J.-H.; Hwang, T.-L.; Kuo, Y.-H.; Lin, C.-S.; Wu, Y.-C.; Sheu, J.-H.; Sung, P.-J. Pinnigorgiols A–C, 9,11-secosterols with a rare ring arrangement from a gorgonian coral *Pinnigorgia* sp. *Tetrahedron* **2016**, *72*, 999–1004. [[CrossRef](#)]
4. Chang, Y.-C.; Kuo, L.-M.; Hwang, T.-L.; Yeh, J.; Wen, Z.-H.; Fang, L.-S.; Wu, Y.-C.; Lin, C.-S.; Sheu, J.-H.; Sung, P.-J. Pinnisterols A–C, new 9,11-secosterols from a gorgonian *Pinnigorgia* sp. *Mar. Drugs* **2016**, *14*, 12. [[CrossRef](#)] [[PubMed](#)]
5. Su, Y.-D.; Cheng, C.-H.; Wen, Z.-H.; Wu, Y.-C.; Sung, P.-J. New anti-inflammatory sterols from a gorgonian *Pinnigorgia* sp. *Bioorg. Med. Chem. Lett.* **2016**, *26*, 3060–3063. [[CrossRef](#)] [[PubMed](#)]
6. Chang, Y.-C.; Chen, N.-F.; Hwang, T.-L.; Tseng, C.-C.; Wu, T.-Y.; Peng, B.-R.; Wen, Z.-H.; Fang, L.-S.; Wu, Y.-C.; Sheu, J.-H.; et al. New marine sterols from an algal-bearing gorgonian coral *Pinnigorgia* sp. *Steroids* **2016**, *115*, 123–129. [[CrossRef](#)] [[PubMed](#)]
7. Chang, H.-H.; Chang, Y.-C.; Chen, W.-F.; Hwang, T.-L.; Fang, L.-S.; Wen, Z.-H.; Chen, Y.-H.; Wu, Y.-C.; Sung, P.-J. Pubinernoid A and apo-9'-fucoxanthinone, secondary metabolites from a gorgonian coral *Pinnigorgia* sp. *Nat. Prod. Commun.* **2016**, *11*, 707–708. [[PubMed](#)]
8. Chang, Y.-C.; Hwang, T.-L.; Sheu, J.-H.; Wu, Y.-C.; Sung, P.-J. New anti-inflammatory 9,11-secosterols with a rare tricyclo[5,2,1,1]decane ring from a Formosan gorgonian *Pinnigorgia* sp. *Mar. Drugs* **2016**, *14*, 218. [[CrossRef](#)] [[PubMed](#)]
9. Yang, I.; Choi, H.; Won, D.H.; Nam, S.-J.; Kang, H. An antibacterial 9,11-secosterol from a marine sponge *Ircinia* sp. *Bull. Korean Chem. Soc.* **2014**, *35*, 3360–3362. [[CrossRef](#)]
10. Wright, J.L.C.; McInnes, A.G.; Shimizu, S.; Smith, D.G.; Walter, J.A.; Idler, D.; Khalil, W. Identification of C-24 alkyl epimers of marine sterols by <sup>13</sup>C nuclear magnetic resonances spectroscopy. *Can. J. Chem.* **1978**, *56*, 1898–1903.
11. Cao, F.; Shao, C.-L.; Chen, M.; Zhang, M.-Q.; Xu, K.-X.; Meng, H.; Wang, C.-Y. Antiviral C-25 epimers of 26-acetoxy steroids from the South China Sea gorgonian *Echinogorgia rebekka*. *J. Nat. Prod.* **2014**, *77*, 1488–1493. [[CrossRef](#)] [[PubMed](#)]
12. Coutts, L.D.; Geiss, W.B.; Gregg, B.T.; Helle, M.A.; King, C.-H.R.; Itov, Z.; Mateo, M.E.; Meckler, H.; Zettler, M.W.; Knutson, J.C. A stereospecific synthesis of 24(S)-hydroxyvitamin D<sub>2</sub>, a prodrug for 1 $\alpha$ ,24(S)-dihydroxyvitamin D<sub>2</sub>. *Org. Process Res. Dev.* **2002**, *6*, 246–255. [[CrossRef](#)]
13. Fabricius, K.; Alderslade, P. *Soft Corals and Sea Fans—A Comprehensive Guide to the Tropical Shallow-Water Genera of the Central-West Pacific, the Indian Ocean and the Red Sea*, 1st ed.; Australian Institute of Marine Science: Townsville, Australia, 2001; pp. 218–219.
14. Kuo, L.-M.; Kuo, C.-Y.; Lin, C.-Y.; Hung, M.-F.; Shen, J.-J.; Hwang, T.-L. Intracellular glutathione depletion by oridonin leads to apoptosis in hepatic stellate cells. *Molecules* **2014**, *19*, 3327–3344. [[CrossRef](#)] [[PubMed](#)]
15. Yang, S.-C.; Chung, P.-J.; Ho, C.-M.; Kuo, C.-Y.; Hung, M.-F.; Huang, Y.-T.; Chang, W.-Y.; Chang, Y.-W.; Chan, K.-H.; Hwang, T.-L. Propofol inhibits superoxide production, elastase release, and chemotaxis in formyl peptide-activated human neutrophils by blocking formyl peptide receptor 1. *J. Immunol.* **2013**, *190*, 6511–6519. [[CrossRef](#)] [[PubMed](#)]
16. Yu, H.-P.; Hsieh, P.-W.; Chang, Y.-J.; Chung, P.-J.; Kuo, L.-M.; Hwang, T.-L. 2-(2-Fluorobenzamido) benzoate ethyl ester (EFB-1) inhibits superoxide production by human neutrophils and attenuates hemorrhagic shock-induced organ dysfunction in rats. *Free Radic. Biol. Med.* **2011**, *50*, 1737–1748. [[CrossRef](#)] [[PubMed](#)]



© 2017 by the authors; licensee MDPI, Basel, Switzerland. This article is an open access article distributed under the terms and conditions of the Creative Commons Attribution (CC-BY) license (<http://creativecommons.org/licenses/by/4.0/>).





Contents lists available at ScienceDirect

# Bioorganic & Medicinal Chemistry Letters

journal homepage: [www.elsevier.com/locate/bmcl](http://www.elsevier.com/locate/bmcl)

## Bioactive new withanolides from the cultured soft coral *Sinularia brassica*



Chiung-Yao Huang<sup>a</sup>, Atallah F. Ahmed<sup>b</sup>, Jui-Hsin Su<sup>c,d</sup>, Ping-Jyun Sung<sup>a,c</sup>, Tsong-Long Hwang<sup>e,f,g</sup>,  
Pei-Lun Chiang<sup>h</sup>, Chang-Feng Dai<sup>i</sup>, Chih-Chuang Liaw<sup>a</sup>, Jyh-Horng Sheu<sup>a,j,k,l,\*</sup>

<sup>a</sup> Department of Marine Biotechnology and Resources, National Sun Yat-sen University, Kaohsiung 804, Taiwan<sup>b</sup> Department of Pharmacognosy, College of Pharmacy, King Saud University, Riyadh 11451, Saudi Arabia<sup>c</sup> National Museum of Marine Biology & Aquarium, Pingtung 944, Taiwan<sup>d</sup> Institute of Marine Biotechnology, National Dong Hwa University, Pingtung 944, Taiwan<sup>e</sup> Graduate Institute of Natural Products, College of Medicine, Chang Gung University, Taoyuan 333, Taiwan<sup>f</sup> Research Center for Chinese Herbal Medicine, Research Center for Food and Cosmetic Safety, and Graduate Institute of Health Industry Technology, College of Human Ecology, Chang Gung University of Science and Technology, Taoyuan 333, Taiwan<sup>g</sup> Department of Anesthesiology, Chang Gung Memorial Hospital, Taoyuan 333, Taiwan<sup>h</sup> Department of Biochemistry, University of Toronto, Toronto M5G2R3, Canada<sup>i</sup> Institute of Oceanography, National Taiwan University, Taipei 112, Taiwan<sup>j</sup> Department of Medical Research, China Medical University Hospital, China Medical University, Taichung 404, Taiwan<sup>k</sup> Graduate Institute of Natural Products, Kaohsiung Medical University, Kaohsiung 807, Taiwan<sup>l</sup> Frontier Center for Ocean Science and Technology, National Sun Yat-sen University, Kaohsiung 804, Taiwan

### ARTICLE INFO

#### Article history:

Received 4 May 2017

Revised 9 June 2017

Accepted 9 June 2017

Available online 10 June 2017

#### Keywords:

Soft coral

*Sinularia brassica*

Withanolide

Cytotoxicity

Anti-inflammatory activity

### ABSTRACT

Continuing study of the ethyl acetate (EtOAc) extract of the cultured soft coral *Sinularia brassica* afforded five new withanolides, sinubrasolides H–L (**1–5**). The structures of the new compounds were elucidated on the basis of spectroscopic analysis. The cytotoxicities of new compounds **1–5** and a known compound sinubrasolide A (**6**) against the proliferation of a limited panel of cancer cell lines were assayed. The anti-inflammatory activities of compounds **1–6** were evaluated by measuring their ability to suppress *N*-formyl-methionyl-leucyl-phenyl-alanine/cytochalasin B (fMLP/CB)-induced superoxide anion generation and elastase release in human neutrophils.

© 2017 Elsevier Ltd. All rights reserved.

Withanolides are a group of C<sub>28</sub> steroidal lactones possessing mostly a C-22/C-26 δ-lactone or in some cases a C-23/C-26 γ-lactone in the side chain.<sup>1–9</sup> Many withanolides were discovered from terrestrial plants and they have been shown to display attracting bioactivities such as antitumor,<sup>2,3,10</sup> anti-inflammatory<sup>8,11–13</sup> and chemopreventive<sup>9,14</sup> activities. Literature study showed that only a few withanolides of marine origin have been discovered from two wild-type soft corals, *Paraminabea acronocephala*<sup>8</sup> and *Minabea* sp.<sup>15</sup> and some of which also displayed cytotoxic and anti-inflammatory activities. Our group further isolated seven cytotoxic withanolides sinubrasolides A–G from the organic extract of a cultured soft coral *Sinularia brassica*.<sup>16</sup> Our continuing chemical investigation of the same collection of this cultured soft coral, with the aim for discovery of new bioactive compounds, was carried out and resulted in the isolation of five new withanolides, sinubra-

solides H–L (**1–5**) (Fig. 1). The structures of **1–5** were established by extensive spectroscopic analysis, including 2D NMR (COSY, HSQC, HMBC, and NOESY) spectroscopy. The *in vitro* cytotoxicities of new compounds **1–5** and a known compound sinubrasolide A (**6**)<sup>16</sup> against four cancer cell lines, murine leukemia (P388), human T-lymphoid (MOLT-4), human erythroleukemia (K-562), and human colon carcinoma (HT-29), were measured. The abilities of compounds **1–6** to inhibit superoxide anion generation and elastase release in *N*-formyl-methionyl-leucyl-phenyl-alanine/cytochalasin B (fMLP/CB)-induced human neutrophils were also assayed.

Specimens of the cultured soft coral *Sinularia brassica* were collected by hand from a cultivation pool located at the National Museum of Marine Biology and Aquarium, Taiwan, in January 2010, and stored in a freezer until extraction. The frozen bodies were minced and extracted with CH<sub>2</sub>Cl<sub>2</sub>–MeOH solvent mixture and then partitioned between EtOAc and H<sub>2</sub>O to yield 24 fractions, as reported previously.<sup>16</sup> Fractions 13–15, which contained withanolide-type steroids, as revealed by <sup>1</sup>H NMR spectra, were further

\* Corresponding author at: Department of Marine Biotechnology and Resources, National Sun Yat-sen University, Kaohsiung 804, Taiwan.

E-mail address: [sheu@mail.nsysu.edu.tw](mailto:sheu@mail.nsysu.edu.tw) (J.-H. Sheu).

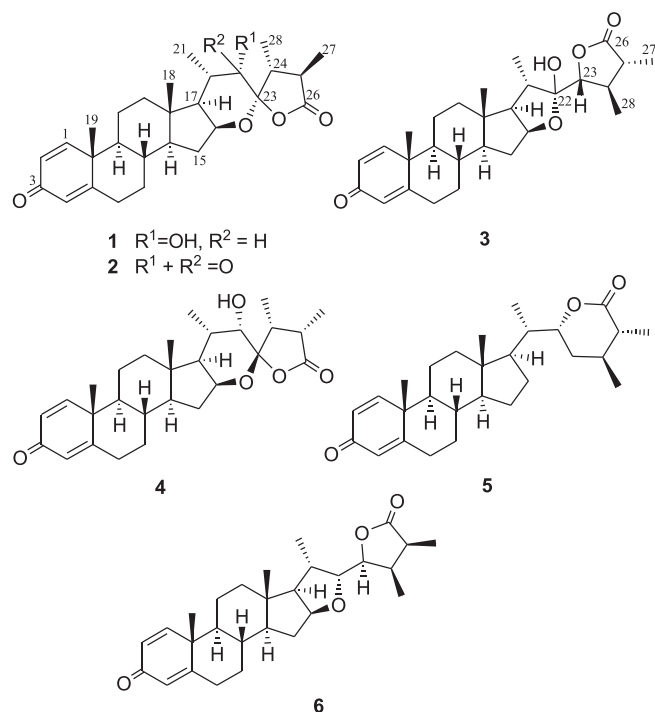


Fig. 1. Structures of metabolites 1–6.

purified by open column chromatography and reversed-phase HPLC to afford 1–5.<sup>17</sup>

Sinubrasolide H (**1**) was isolated as an amorphous solid. The HRESIMS spectrum of **1** exhibited a  $[M+H]^+$  peak at  $m/z$  455.2795, indicating the molecular formula  $C_{28}H_{38}O_5$ , requiring 10 degrees of unsaturation. The IR spectrum revealed the presence of a hydroxy group ( $3453\text{ cm}^{-1}$ ) and a  $\gamma$ -lactone ( $1767\text{ cm}^{-1}$ ) group. The  $^{13}\text{C}$  NMR spectroscopic data of **1** exhibited 28 carbon signals (Table 1), which were assigned by the assistance of DEPT spectra to five methyls, five  $\text{sp}^3$  methylenes, nine  $\text{sp}^3$  methines (including two oxymethines), three  $\text{sp}^2$  methines, and three  $\text{sp}^2$  non-protonated carbons (including an ester carbonyl, a ketone, and a dioxygenated carbon). Proton signals (Table 1) resonating at  $\delta_{\text{H}}$  7.04 (1H, d,  $J = 10.0\text{ Hz}$ ), 6.23 (1H, d,  $J = 10.0\text{ Hz}$ ), and 6.08 (1H, s), as well as carbon signals appearing at  $\delta_{\text{C}}$  186.3 (C), 155.5 (CH), 127.6 (CH), 124.0 (CH), and 168.7 (C), indicated the presence of a 1,4-dien-3-one structural unit in ring A of the steroids.<sup>8,16,18</sup> The molecular framework of **1** was further established by COSY and HMBC correlations (Fig. 2). Furthermore, the NOESY spectrum of **1** showed NOE correlations of H-22 with H-20 and H<sub>3</sub>-21, but not with H-17, revealed the  $\beta$ -orientation of H-22. Therefore, correlations of H<sub>3</sub>-28 with H-22 and H-25, and H<sub>3</sub>-27 with H-24, revealed the (20S,22S,23S,24R,25R)-configuration of **1**, as shown in Fig. 3. Compound **1** was thus found to be the C-25 epimer of sinubrasolide E.<sup>16</sup>

HRESIMS analysis and  $^{13}\text{C}$  NMR of sinubrasolide I (**2**) provided the molecular formula of  $C_{28}H_{36}O_5$ . The IR absorption spectrum showed the presence of a  $\gamma$ -lactone ( $1784\text{ cm}^{-1}$ ). Compounds **1**

**Table 1**  
 $^1\text{H}$  and  $^{13}\text{C}$  NMR spectroscopic data of compounds 1–3.

Position	1		2		3	
	$\delta_{\text{C}}^{\text{a}}$ , type <sup>b</sup>	$\delta_{\text{H}}^{\text{c}}$ , mult ( $J$ in Hz)	$\delta_{\text{C}}^{\text{a}}$ , type	$\delta_{\text{H}}^{\text{c}}$ , mult ( $J$ in Hz)	$\delta_{\text{C}}^{\text{d}}$ , type	$\delta_{\text{H}}^{\text{e}}$ , mult ( $J$ in Hz)
1	155.5, CH	7.04 d (10.0)	155.2, CH	7.03 d (10.0)	155.5, CH	7.04 d (10.0)
2	127.6, CH	6.23 d (10.0)	127.7, CH	6.24 d (10.0)	127.6, CH	6.24 d (10.0)
3	186.3, C		186.2, C		186.3, C	
4	124.0, CH	6.08 s	124.1, CH	6.09 s	124.0, CH	6.08 s
5	168.7, C		168.3, C		168.7, C	
6	32.7, CH <sub>2</sub>	2.49 ddd (13.0, 13.0, 4.0) 2.38 br d (13.0)	32.6, CH <sub>2</sub>	2.50 m 2.40 ddd (12.0, 2.5, 2.5)	32.7, CH <sub>2</sub>	2.46 ddd (13.6, 13.6, 4.8) 2.37 ddd (13.6, 3.6, 2.4)
7	33.6, CH <sub>2</sub>	1.97 br d (12.5) 1.07 m	33.6, CH <sub>2</sub>	1.95 m 1.11 m	33.6, CH <sub>2</sub>	1.96 m 1.04 m
8	35.0, CH	1.75 m	35.2, CH	1.84 dddd (11.0, 11.0, 11.0, 3.0)	35.2, CH	1.82 m
9	52.3, CH	1.09 m	52.0, CH	1.10 m	52.2, CH	1.07 m
10	43.5, C		43.3, C		43.5, C	
11	22.6, CH <sub>2</sub>	1.71 m	22.6, CH <sub>2</sub>	1.74 m	22.6, CH <sub>2</sub>	1.71 m
12	39.4, CH <sub>2</sub>	1.88 ddd (12.5, 3.0, 3.0) 1.22 m	39.2, CH <sub>2</sub>	1.92 m 1.23 m	39.1, CH <sub>2</sub>	1.79 m 1.19 m
13	41.6, C		43.0, C		41.2, C	
14	51.8, CH	0.94 m	52.0, CH	0.99 m	55.2, CH	1.12 m
15	33.3, CH <sub>2</sub>	2.17 m 1.27 m	32.9, CH <sub>2</sub>	2.24 m 1.47 ddd (13.5, 13.5, 6.0)	32.0, CH <sub>2</sub>	2.04 ddd (12.8, 7.6, 6.0) 1.36 ddd (12.8, 12.8, 6.0)
16	74.6, CH	4.49 ddd (7.5, 7.5, 5.5)	74.9, CH	4.46 dd (8.0, 8.0, 6.0)	82.3, CH	4.67 ddd (7.6, 7.6, 5.6)
17	52.7, CH	1.37 dd (8.0, 8.0)	56.6, CH	1.39 dd (8.0, 8.0)	62.7, CH	1.80 m
18	14.9, CH <sub>3</sub>	0.89 s	14.8, CH <sub>3</sub>	1.09 s	16.3, CH <sub>3</sub>	0.89 s
19	18.7, CH <sub>3</sub>	1.25 s	18.7, CH <sub>3</sub>	1.27 s	18.7, CH <sub>3</sub>	1.25 s
20	29.7, CH	1.77 m	41.0, CH	2.75 dq (8.0, 6.5)	39.9, CH	2.24 m
21	17.4, CH <sub>3</sub>	1.18 d (6.5)	12.6, CH <sub>3</sub>	1.13 d (6.5)	15.6, CH <sub>3</sub>	1.12 d (7.2)
22	69.8, CH	3.81 s	209.3, C		107.6, C	
23	108.7, C		106.7, C		87.0, CH	3.98 d (8.0)
24	47.5, CH	2.15 m	46.9, CH	2.15 m	38.3, CH	2.22 m
25	41.9, CH	2.32 m	41.1, CH	2.52 m	43.0, CH	2.23 m
26	176.0, C		176.0, C		178.4, C	
27	13.2, CH <sub>3</sub>	1.26 d (7.0)	13.3, CH <sub>3</sub>	1.21 d (7.5)	13.6, CH <sub>3</sub>	1.25 d (6.8)
28	12.2, CH <sub>3</sub>	1.12 d (7.0)	12.6, CH <sub>3</sub>	1.05 d (7.0)	17.8, CH <sub>3</sub>	1.25 d (6.8)

<sup>a</sup> Spectrum recorded at 125 MHz in  $\text{CDCl}_3$ .

<sup>b</sup> Attached protons were deduced by DEPT experiment.

<sup>c</sup> Spectrum recorded at 500 MHz in  $\text{CDCl}_3$ .

<sup>d</sup> Spectrum recorded at 100 MHz in  $\text{CDCl}_3$ .

<sup>e</sup> Spectrum recorded at 400 MHz in  $\text{CDCl}_3$ .

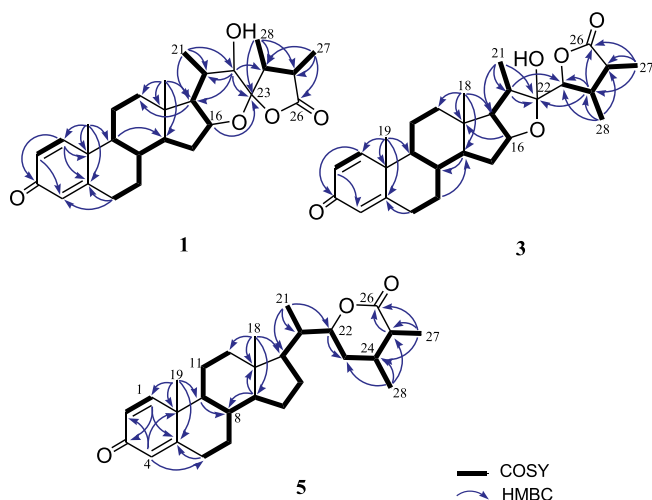


Fig. 2. Selected COSY and HMBC correlations of **1**, **3** and **5**.

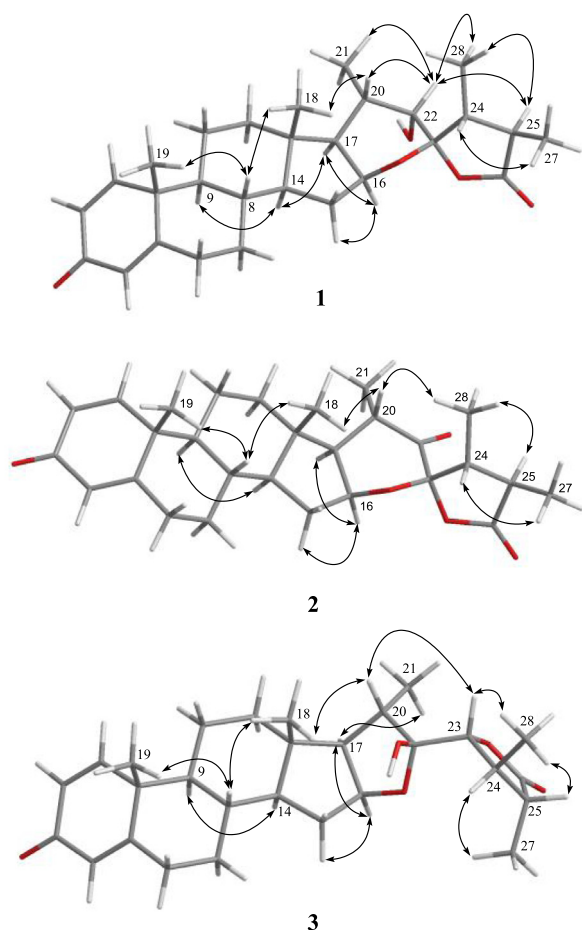


Fig. 3. Key NOESY correlations of **1–3**.

and **2** were found to have very similar structures, with the only difference that the hydroxylated carbon C-22 in **1** ( $\delta_C$  69.8) was oxidized to a carbonyl group in **2** ( $\delta_C$  209.3). These results and other NMR data including NOE correlations (Fig. 3), showed that **2** is the 22-keto derivative of **1**.

Sinubrasolide J (**3**) was isolated as an amorphous solid. The IR absorption bands showed the presence of a hydroxy group ( $3443\text{ cm}^{-1}$ ) and a  $\gamma$ -lactone ( $1774\text{ cm}^{-1}$ ). The  $\gamma$ -lactone unit was

confirmed by the carbon resonances at  $\delta_C$  87.0 (C-23, CH) and 178.4 (C-26, C)<sup>16</sup> (Table 1). It was further found to possess the same molecular formula ( $\text{C}_{28}\text{H}_{38}\text{O}_5$ ) as **1** as revealed by HRESIMS. Furthermore, it was found that the NMR spectroscopic data of **3** were very similar to those of sinubrasolide C,<sup>16</sup> except for the significant downfield shifts observed at C-24 ( $\Delta\delta_C +4.7\text{ ppm}$ ) and C-25 ( $\Delta\delta_C +5.6\text{ ppm}$ ) relative to those of sinubrasolide C, and the larger  $J$  value of 8.0 Hz at H-23 of **3** relative to that of sinubrasolide C (8.0 Hz). The above data suggested that **3** could be an epimer of sinubrasolide C at the lactone ring. By 2D NMR (COSY, HSQC, and HMBC), compound **3** was found to possess the same molecular framework as sinubrasolide C, while the configurations, in particular at C-22, C-23 and C-25, were resolved by NOESY experiment measured in  $\text{C}_6\text{D}_6$ . It was found that H-20 ( $\delta_H$  2.25, m) exhibited an NOE interaction with H-23 ( $\delta_H$  3.74, d,  $J = 8.0\text{ Hz}$ ) but not with H<sub>3</sub>-21, and H<sub>3</sub>-28 ( $\delta_H$  0.99, d,  $J = 7.2\text{ Hz}$ ) exhibited interactions with H-23 and H-25 ( $\delta_H$  1.80, m), revealing the  $\beta$ -orientations of H-23, H-25 and H<sub>3</sub>-28 and the  $\alpha$ -orientation of the hydroxy group at C-22. Finally, H-24 ( $\delta_H$  2.20, m) showed interaction with H<sub>3</sub>-27 ( $\delta_H$  1.20, d,  $J = 7.2\text{ Hz}$ ), but not with H-25, revealing the  $\alpha$ -orientations of H-24 and H<sub>3</sub>-27 (Fig. 3).

Analysis of the  $^{13}\text{C}$  NMR and HRESIMS spectral data of **4** revealed it to have the same molecular formula as **1**. The presence of a  $\gamma$ -lactone ring also was evidenced by an IR absorption at  $1773\text{ cm}^{-1}$ . The  $^{13}\text{C}$  and  $^1\text{H}$  NMR data of **4** (Table 2) were found to be similar to those of **1** (Table 1), except for C-22, C-24, C-27 and C-28 resonating at  $\delta_C$  69.8 (CH), 47.5 (CH), 13.2 ( $\text{CH}_3$ ) and 12.2 ( $\text{CH}_3$ ) in **1** and at  $\delta_C$  77.0 (CH), 39.9 (CH), 12.7 ( $\text{CH}_3$ ) and 9.9 ( $\text{CH}_3$ ), respectively, in **4**; and the H-22, H-24 and H-25 protons resonating at  $\delta_H$  3.81 (s), 2.15 (m) and 2.32 (m) in **1** and at  $\delta_H$  3.68 (d,  $J = 3.0\text{ Hz}$ ), 2.74 (dq,  $J = 7.5, 7.5\text{ Hz}$ ) and 2.65 (dq,  $J = 7.5, 7.5\text{ Hz}$ ), respectively, in **4**, suggesting that **4** was the configurational isomer of **1**. On the basis of the above findings, and according to NOE correlations of H<sub>3</sub>-18 with H-20, H-20 with H-22, H-24 with H-22 and H-25, and H<sub>3</sub>-28 with H-16, the configuration of 20S,22S,23R,24R,25S was determined for **4** (Fig. 4).

HRESIMS of sinubrasolide L (**5**) displayed a quasi-molecular ion peak at  $m/z$  425.3062  $[\text{M}+\text{H}]^+$ , indicative of the molecular formula  $\text{C}_{28}\text{H}_{40}\text{O}_3$ , suggesting nine degrees of unsaturation. The  $^{13}\text{C}$  NMR and DEPT spectra showed signals of five methyls, seven methylenes, 11 methines (including an oxymethine), and five non-protonated carbons (including an ester carbonyl and a cross-conjugated dienone). Except for the oxidation at C-16, compounds **1–5** were found to have the same A–D rings by comparison of their 1D and 2D NMR spectroscopic data. This was further confirmed by detailed analysis of COSY and HMBC correlations (Fig. 2). In consideration of the degrees of unsaturation and molecular formula, an ether linkage was placed between C-22 and C-26. This was further confirmed by the IR absorption band at  $1738\text{ cm}^{-1}$ , which revealed the presence of a six-membered lactone ring in **5** rather than a five-membered lactone ring. On the basis of the above analysis, the gross structure of **5** was established.

An NOE experiment allowed the relative configuration of **5** to be defined. As shown in Fig. 4, the NOE correlations of H-20 ( $\delta_H$  2.00, m) with H<sub>3</sub>-18 ( $\delta_H$  0.77, s) and H-22 ( $\delta_H$  4.33, ddd,  $J = 11.6, 3.2, 3.2\text{ Hz}$ ), H-22 with H-23 $\beta$  ( $\delta_H$  1.31, ddd,  $J = 14.0, 3.2, 3.2\text{ Hz}$ ) and H-25 ( $\delta_H$  2.15, dq,  $J = 12.4, 6.8\text{ Hz}$ ), and H-23 $\beta$  with H<sub>3</sub>-28 were observed, while H-24 ( $\delta_H$  1.70, m) was correlated with H<sub>3</sub>-27 ( $\delta_H$  1.22, d,  $J = 6.8\text{ Hz}$ ), suggesting  $\beta$ -orientations of H-22, H-25 and H<sub>3</sub>-28, and  $\alpha$ -orientations of H-24 and H<sub>3</sub>-27. On the basis of the above findings, the relative structure of **5** was determined as illustrated in Fig. 4.

Compounds **1–5** were evaluated in terms of their cytotoxic activities against murine leukemia (P388), human T-lymphoid (MOLT-4), human erythroleukemia (K-562), and human colon carcinoma (HT-29) cell lines using the Alamar Blue assay. The results

**Table 2**  
<sup>1</sup>H and <sup>13</sup>C NMR spectroscopic data of compounds **4** and **5**.

Position	<b>4</b>		<b>5</b>	
	$\delta_c^a$ , type <sup>b</sup>	$\delta_H^c$ , mult (J in Hz)	$\delta_c^d$ , type	$\delta_H^e$ , mult (J in Hz)
1	155.8, CH	7.05 d (10.0)	155.8, CH	7.05 d (10.0)
2	127.5, CH	6.23 d (10.0)	127.5, CH	6.23 d (10.0)
3	186.4, C		186.4, C	
4	123.9, CH	6.07 s	123.9, CH	6.07 s
5	169.0, C		169.1, C	
6	32.8, CH <sub>2</sub>	2.48 ddd (13.5, 13.5, 5.5) 2.37 m	32.8, CH <sub>2</sub>	2.47 ddd (13.6, 13.6, 5.2) 2.36 br d (13.6)
7	33.7, CH <sub>2</sub>	1.97 m 1.07 m	33.6, CH <sub>2</sub>	1.98 m 1.02 m
8	35.1, CH	1.78 m	35.5, CH	1.62 m
9	52.5, CH	1.06 m	52.4, CH	1.04 m
10	43.6, C		43.5, C	
11	22.6, CH <sub>2</sub>	1.72 m	22.8, CH <sub>2</sub>	1.68 m
12	39.6, CH <sub>2</sub>	1.87 m 1.19 m	39.4, CH <sub>2</sub>	2.03 m 1.16 m
13	41.8, C		43.1, C	
14	51.8, CH	0.88 m	55.1, CH	1.00 m
15	33.9, CH <sub>2</sub>	2.15 m 1.32 m	24.4, CH <sub>2</sub>	1.62 m 1.17 m
16	74.2, CH	4.36 ddd (7.5, 7.5, 6.0)	27.2, CH <sub>2</sub>	1.72 m; 1.38 m
17	53.8, CH	1.17 m	52.1, CH	1.00 m
18	15.2, CH <sub>3</sub>	0.94 s	12.0, CH <sub>3</sub>	0.77 s
19	18.7, CH <sub>3</sub>	1.26 s	18.7, CH <sub>3</sub>	1.24 s
20	28.1, CH	2.18 m	38.7, CH	2.00 m
21	17.6, CH <sub>3</sub>	1.08 d (7.0)	12.7, CH <sub>3</sub>	0.96 d (6.8)
22	77.0, CH	3.68 d (3.0)	77.0, CH	4.33 ddd (11.6, 3.2, 3.2)
23	108.8, C		28.8, CH <sub>2</sub>	1.84 ddd (14.0, 11.6, 8.8) 1.31 ddd (14.0, 3.2, 3.2)
24	39.9, CH	2.74 dq (7.5, 7.5)	31.1, CH	1.70 m
25	39.3, CH	2.65 dq (7.5, 7.5)	40.6, CH	2.15 dq (12.4, 6.8)
26	178.9, C		176.4, C	
27	12.7, CH <sub>3</sub>	1.28 d (7.5)	14.4, CH <sub>3</sub>	1.22, d (6.8)
28	9.9, CH <sub>3</sub>	1.16 d (7.5)	21.4, CH <sub>3</sub>	1.12, d (6.4)

<sup>a</sup> Spectrum recorded at 125 MHz in CDCl<sub>3</sub>.

<sup>b</sup> Attached protons were deduced by DEPT experiment.

<sup>c</sup> Spectrum recorded at 500 MHz in CDCl<sub>3</sub>.

<sup>d</sup> Spectrum recorded at 100 MHz in CDCl<sub>3</sub>.

<sup>e</sup> Spectrum recorded at 400 MHz in CDCl<sub>3</sub>.

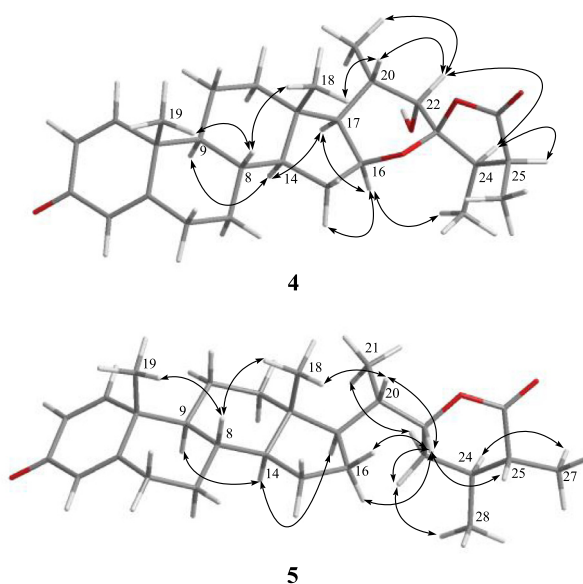


**Fig. 4.** Key NOESY correlations of **4** and **5**.

showed compounds with a hydroxy group at C-22 (**1**, **3** and **4**) exhibited cytotoxic activity against the four cell lines, whereas **2** and **5** showed no activity towards all of the above cell lines. Moreover, sinubrasolide A (**6**) which was isolated from the same organism and was shown to exhibit significant cytotoxicity towards K-562 cells previously,<sup>16</sup> also displayed activity against the growth of P388, MOLT-4 and HT-29 cells (Table 3).

The anti-inflammatory activities of compounds **1–6** on neutrophil pro-inflammatory responses were evaluated by measuring their ability to suppress fMLP/CB-induced superoxide anion (O<sub>2</sub><sup>•−</sup>) generation and elastase release in human neutrophils, and the results are shown in Table 4. From the results, **6** showed potent inhibitory effects against superoxide anion generation and elastase release in fMLP/CB-stimulated cells (87.7 ± 5.9 and 113.9 ± 1.8%, respectively). The IC<sub>50</sub> values of compound **6** for the superoxide anion generation and elastase release were found to be lower than 5 μM. Further, compounds **3–5** also exhibited moderate inhibitory activities against superoxide anion generation, with inhibition percentages of 32.1 ± 5.3, 34.3 ± 6.6% and 26.3 ± 0.7%. Compounds **1** and **5** also could exhibit moderate inhibitory activities against elastase release (32.4 ± 5.6 and 25.0 ± 1.3%).

Our continuing investigations demonstrated that the cultured octocoral *Sinularia brassica* is a good source of bioactive withano-



**Table 3**

Cytotoxicity data of compounds 1–6.

Compound	Cell lines IC <sub>50</sub> (μM)			
	P388	MOLT-4	K-562	HT-29
<b>1</b>	39.8 ± 7.7	28.6 ± 5.9	29.7 ± 8.6	24.4 ± 6.2
<b>2</b>	– <sup>a</sup>	–	–	–
<b>3</b>	18.7 ± 3.1	17.2 ± 1.5	12.6 ± 3.1	11.2 ± 1.1
<b>4</b>	18.3 ± 2.6	13.7 ± 3.3	17.4 ± 3.3	20.5 ± 3.7
<b>5</b>	–	–	–	–
<b>6</b>	29.9 ± 3.0	12.1 ± 1.1	8.7 ± 1.4 <sup>b</sup>	18.7 ± 2.5
5-Fluorouracil	5.8 ± 0.6	6.2 ± 1.0	30.5 ± 6.3	7.2 ± 0.7

<sup>a</sup> IC<sub>50</sub> >40 μM. Results presented as mean ± S.E.M. (n = 3–4).<sup>b</sup> Cytotoxicity reported previously as in Ref. 16.**Table 4**

Inhibitory effects of compounds 1–6 on superoxide anion generation and elastase release in fMLP/CB-induced human neutrophils.

Compounds	Superoxide anion		Elastase release	
	IC <sub>50</sub> (μM) <sup>a</sup>	Inh% <sup>b</sup>	IC <sub>50</sub> (μM) <sup>a</sup>	Inh% <sup>b</sup>
<b>1</b>	>10	14.4 ± 3.1 <sup>*</sup>	>10	32.4 ± 5.6 <sup>**</sup>
<b>2</b>	>10	17.3 ± 5.5 <sup>*</sup>	>10	12.5 ± 6.1
<b>3</b>	>10	32.1 ± 5.3 <sup>**</sup>	>10	9.5 ± 5.2
<b>4</b>	>10	34.3 ± 6.6 <sup>**</sup>	>10	11.4 ± 3.2 <sup>*</sup>
<b>5</b>	>10	26.3 ± 0.7 <sup>***</sup>	>10	25.0 ± 1.3 <sup>***</sup>
<b>6</b>	3.5 ± 0.9	87.7 ± 5.9 <sup>***</sup>	1.4 ± 0.1	113.9 ± 1.8 <sup>***</sup>
Idelalisib	0.07 ± 0.01	102.8 ± 2.2 <sup>***</sup>	0.3 ± 0.1	99.6 ± 4.2 <sup>***</sup>

<sup>a</sup> Concentration necessary for 50% inhibition (IC<sub>50</sub>).<sup>b</sup> Percentage of inhibition (Inh %) at 10 μM concentration. Results are presented as mean ± S.E.M. (n = 3–4).<sup>\*</sup> P < 0.05.<sup>\*\*</sup> P < 0.01.<sup>\*\*\*</sup> P < 0.001 compared with the control value.

lides and steroids. Several of the isolated compounds, in particular **6**, can be considered as potential anti-inflammatory agents. Moreover, it is worthwhile to note here that **1**, **2** and **4** were found to be novel withanolides with a 16,23-oxa-bridged tetrahydropyran. Compounds **1**, **3**, **4** and **6** exhibited significant cytotoxicity toward a limited panel of cancer cell lines. Owing to these attractive biological activities, the active compounds might be useful in the development of new chemotherapeutic and anti-inflammatory drugs.

## Acknowledgments

This work was supported by grants from Ministry of Science and Technology of Taiwan (MOST 102-2628-B-110-002-MY2, 104-2320-B-110-001-MY2, and 104-2113-M-110-006-) and NSYSU-KMU Joint Research Project (NSYSUKMU105-I008) awarded to J.-H. S.

## A. Supplementary data

Supplementary data (experiment details and NMR spectra of **1**–**5**) associated with this article can be found, in the online version, at <http://dx.doi.org/10.1016/j.bmcl.2017.06.029>.

## References

- Habtemariam S. *Planta Med.* 1997;63:15–17.
- Das H, Dutta SK, Bhattacharya B, Chakraborti SK. *Indian J Cancer Chemother.* 1985;7:59–65.
- Gunasekera SP, Cordell GA, Farnsworth NR. *Planta Med.* 1981;43:389–391.
- Luis JG, Echeverri F, Garcia F, Rojas M. *Planta Med.* 1994;60:348–350.
- Shohat B, Kirson I, Lavie D. *Biomedicine.* 1978;28:18–24.
- Jamal SA, Qureshi S, Ali SN, Choudhary M. *Khim Geterotsikl Soedin.* 1995;9:1200–1213.
- Su B-N, Misico R, Park EJ, et al. *Tetrahedron.* 2002;58:3453–3466.
- Chao C-H, Chou K-J, Wen Z-H, et al. *J Nat Prod.* 2011;74:1132–1141.
- Su B-N, Park EJ, Nikolic D, et al. *J Org Chem.* 2003;68:2350–2361.
- Antony ML, Lee J, Hahm ER, et al. *J Biol Chem.* 2014;289:1852–1865.
- Kaileh M, Vanden Berghe W, Heyerick A, et al. *J Biol Chem.* 2007;282:4253–4264.
- Takimoto T, Kanbayashi Y, Toyoda T, et al. *Int J Obesity.* 2014;38:1432–1439.
- Chen B-W, Chen Y-Y, Lin Y-C, et al. *RSC Adv.* 2015;5:88841–88847.
- Su B-N, Park EJ, Nikolic D, et al. *J Nat Prod.* 2003;66:1089–1093.
- Ksebati MB, Schmitz FJ. *J Org Chem.* 1988;53:3926–3929.
- Huang C-Y, Liaw C-C, Chen B-W, et al. *J Nat Prod.* 2013;76:1902–1908.
- The frozen bodies of *S. brassica* (0.4 kg, wet weight) were minced and extracted exhaustively with CH<sub>2</sub>Cl<sub>2</sub> and MeOH (1:1, 0.5 L × 6). The extract was partitioned between EtOAc and H<sub>2</sub>O to afford the EtOAc soluble fraction. The EtOAc extract (3.7 g) was chromatographed over silica gel by column chromatography and eluted with EtOAc in *n*-hexane (0–100%, stepwise), and then with MeOH in EtOAc (5–50%, stepwise) to yield 24 fractions. Fraction 13, eluting with *n*-hexane–EtOAc (8:1), was further purified over silica gel using *n*-hexane–acetone (7:1) to afford five subfractions (13A–13E). Subfraction 13A was separated by reversed-phase HPLC using MeOH–H<sub>2</sub>O (3:1) to afford **5** (0.9 mg). Fraction 14, eluting with *n*-hexane–EtOAc (7:1), was further purified over silica gel using *n*-hexane–acetone (6:1) to afford five subfractions (14A–14E). Subfraction 14C was separated by reversed-phase HPLC using MeOH–H<sub>2</sub>O (2:1) to afford **2** (0.9 mg) and **3** (2.1 mg). Fraction 15, eluting with *n*-hexane–EtOAc (6:1), was further purified by reversed-phase HPLC using MeOH–H<sub>2</sub>O (2:1) to afford **1** (3.0 mg) and **4** (0.7 mg). Sinubrasolide H (**1**): amorphous solid; [α]<sub>D</sub><sup>25</sup> –165 (c 0.26, CHCl<sub>3</sub>); UV (MeOH) λ<sub>max</sub> (log ε) 245 (4.2); IR (neat) ν<sub>max</sub> 3453, 2966, 2934, 1767 and 1660 cm<sup>–1</sup>; <sup>13</sup>C and <sup>1</sup>H NMR data, see Table 1; ESIMS *m/z* 455 [M + H]<sup>+</sup>; HRESIMS *m/z* 455.2795 [M + H]<sup>+</sup> (calcd for C<sub>28</sub>H<sub>39</sub>O<sub>5</sub>, 455.2792). Sinubrasolide I (**2**): amorphous solid; [α]<sub>D</sub><sup>24</sup> –187 (c 0.009, CHCl<sub>3</sub>); UV (MeOH) λ<sub>max</sub> (log ε) 244 (4.2); IR (neat) ν<sub>max</sub> 2971, 2935, 1784, 1737 and 1661 cm<sup>–1</sup>; <sup>13</sup>C and <sup>1</sup>H NMR data, see Table 1; ESIMS *m/z* 475 [M+Na]<sup>+</sup>; HRESIMS *m/z* 475.2458 [M+Na]<sup>+</sup> (calcd for C<sub>28</sub>H<sub>36</sub>O<sub>5</sub>Na, 475.2460). Sinubrasolide J (**3**): amorphous solid; [α]<sub>D</sub><sup>25</sup> –170 (c 0.06, CHCl<sub>3</sub>); UV (MeOH) λ<sub>max</sub> (log ε) 245 (4.3); IR (neat) ν<sub>max</sub> 3443, 2935, 2852, 1774 and 1659 cm<sup>–1</sup>; <sup>13</sup>C and <sup>1</sup>H NMR data, see Table 1; <sup>1</sup>H NMR (C<sub>6</sub>D<sub>6</sub>, 400 MHz): δ<sub>H</sub> 6.53 (1H, d, *J* = 10.0 Hz, H-1), 6.45 (1H, d, *J* = 10.0 Hz, H-2), 6.31 (1H, s, H-4), 4.66 (1H, ddd, *J* = 7.6, 7.6, 5.6 Hz, H-16), 3.74 (1H, d, *J* = 8.0 Hz, H-23), 2.25 (1H, m, H-20), 2.20 (1H, m, H-24), 2.00 (1H, ddd, *J* = 13.6, 13.6, 4.8 Hz, H-6a), 1.94 (1H, ddd, *J* = 13.6, 3.6, 2.4 Hz, H-6b), 1.83 (1H, m, H-15a), 1.80 (1H, m, H-25), 1.62 (1H, m, H-17), 1.56 (1H, m, H-12a), 1.46 (1H, m, H-7a), 1.36 (1H, m, H-8), 1.29 (2H, m, H<sub>2</sub>-11), 1.25 (1H, m, H-15b), 1.22 (3H, d, *J* = 7.2 Hz, H<sub>3</sub>-21), 1.20 (3H, d, *J* = 7.2 Hz, H<sub>3</sub>-27), 0.99 (3H, d, *J* = 7.2 Hz, H<sub>3</sub>-28), 0.86 (3H, s, H<sub>3</sub>-19), 0.86 (1H, m, H-12b), 0.77 (3H, s, H<sub>3</sub>-18), 0.72 (1H, m, H-14), 0.70 (1H, m, H-9), 0.62 (1H, m, H-7b); <sup>13</sup>C NMR (C<sub>6</sub>D<sub>6</sub>, 100 MHz): δ<sub>C</sub> 185.1 (C, C-3), 177.1 (C, C-26), 166.7 (C, C-5), 154.0 (CH, C-1), 127.3 (CH, C-2), 124.6 (CH, C-4), 108.0 (C, C-22), 86.6 (CH, C-23), 82.2 (CH, C-16), 63.1 (CH, C-17), 55.0 (CH, C-14), 51.9 (CH, C-9), 42.9 (C, C-10), 42.8 (CH, C-25), 41.0 (C, C-13), 40.2 (CH, C-20), 39.2 (CH<sub>2</sub>, C-12), 38.5 (CH, C-24), 34.9 (CH, C-8), 33.4 (CH<sub>2</sub>, C-7), 32.4 (CH<sub>2</sub>, C-6), 32.0 (CH<sub>2</sub>, C-15), 22.4 (CH<sub>2</sub>, C-11), 18.5 (CH<sub>3</sub>, C-19), 17.4 (CH<sub>3</sub>, C-28), 16.3 (CH, C-18), 15.9 (CH<sub>3</sub>, C-21), 13.7 (CH<sub>3</sub>, C-27); ESIMS *m/z* 455 [M+H]<sup>+</sup>; HRESIMS *m/z* 455.2796 [M+H]<sup>+</sup> (calcd for C<sub>28</sub>H<sub>39</sub>O<sub>5</sub>, 455.2792). Sinubrasolide K (**4**): amorphous solid; [α]<sub>D</sub><sup>24</sup> –175 (c 0.002, CHCl<sub>3</sub>); UV (MeOH) λ<sub>max</sub> (log ε) 245 (4.1); IR (neat) ν<sub>max</sub> 3443, 2936, 1773 and 1658 cm<sup>–1</sup>; <sup>13</sup>C and <sup>1</sup>H NMR data, see Table 2; ESIMS *m/z* 477 [M+Na]<sup>+</sup>; HRESIMS *m/z* 477.2612 [M+Na]<sup>+</sup> (calcd for C<sub>28</sub>H<sub>38</sub>O<sub>5</sub>Na, 477.2611). Sinubrasolide L (**5**): amorphous solid; [α]<sub>D</sub><sup>25</sup> –26 (c 0.25, CHCl<sub>3</sub>); UV (MeOH) λ<sub>max</sub> (log ε) 245 (4.3); IR (neat) ν<sub>max</sub> 2939, 1738 and 1661 cm<sup>–1</sup>; <sup>13</sup>C and <sup>1</sup>H NMR data, see Table 2; ESIMS *m/z* 425 [M+H]<sup>+</sup>; HRESIMS *m/z* 425.3062 [M+H]<sup>+</sup> (calcd for C<sub>28</sub>H<sub>41</sub>O<sub>3</sub>, 425.3050).
- Huang C-Y, Chang C-W, Tseng Y-J, et al. *Mar Drugs.* 2016;14:180.



## Research Paper

# Artocarpin, an isoprenyl flavonoid, induces p53-dependent or independent apoptosis via ROS-mediated MAPKs and Akt activation in non-small cell lung cancer cells

Ming-Horng Tsai<sup>1,\*</sup>, Ju-Fang Liu<sup>2,\*</sup>, Yao-Chang Chiang<sup>3,4</sup>, Stephen Chu-Sung Hu<sup>5,6</sup>, Lee-Fen Hsu<sup>7</sup>, Yu-Ching Lin<sup>7,8,9</sup>, Zih-Chan Lin<sup>10</sup>, Hui-Chun Lee<sup>1</sup>, Mei-Chuan Chen<sup>11</sup>, Chieh-Liang Huang<sup>3</sup>, Chiang-Wen Lee<sup>4,12,13</sup>

<sup>1</sup>Department of Pediatrics, Division of Neonatology and Pediatric Hematology/Oncology, Chang Gung Memorial Hospital, Yunlin, Taiwan

<sup>2</sup>Central Laboratory, Shin-Kong Wu Ho-Su Memorial Hospital, Taipei, Taiwan

<sup>3</sup>Center for Drug Abuse and Addiction, China Medical University Hospital, China Medical University, Taichung, Taiwan

<sup>4</sup>Department of Nursing, Division of Basic Medical Sciences, Chang Gung University of Science and Technology, Chia-Yi, Taiwan

<sup>5</sup>Department of Dermatology, College of Medicine, Kaohsiung Medical University, Kaohsiung, Taiwan

<sup>6</sup>Department of Dermatology, Kaohsiung Medical University Hospital, Kaohsiung, Taiwan

<sup>7</sup>Department of Respiratory Care, Chang Gung University of Science and Technology, Chiayi Campus, Chiayi, Taiwan

<sup>8</sup>Division of Pulmonary and Critical Care Medicine, Chang Gung Memorial Hospital, Chiayi, Taiwan

<sup>9</sup>Department of Respiratory Care, Chang Gung University, Taoyuan, Taiwan

<sup>10</sup>Graduate Institute of Biomedical Sciences, Chang Gung University, Taoyuan, Taiwan

<sup>11</sup>Program for the Clinical Drug Discovery from Botanical Herbs, College of Pharmacy, Taipei Medical University, Taipei, Taiwan

<sup>12</sup>Chronic Diseases and Health Promotion Research Center, Chang Gung University of Science and Technology, Chia-Yi, Taiwan

<sup>13</sup>Research Center for Industry of Human Ecology and Research Center for Chinese Herbal Medicine, College of Human Ecology, Chang Gung University of Science and Technology, Taoyuan, Taiwan

\*These authors contributed equally to this work

**Correspondence to:** Chiang-Wen Lee, email: cwlee@mail.cgust.edu.tw

**Keywords:** artocarpin, pro-oxidation, lung cancer, p53, apoptosis

**Received:** June 15, 2016

**Accepted:** February 27, 2017

**Published:** March 09, 2017

Copyright: Tsai et al. This is an open-access article distributed under the terms of the Creative Commons Attribution License (CC-BY), which permits unrestricted use, distribution, and reproduction in any medium, provided the original author and source are credited.

## ABSTRACT

Artocarpin has been shown to exhibit cytotoxic effects on different cancer cells, including non-small cell lung carcinoma (NSCLC, A549). However, the underlying mechanisms remain unclear. Here, we explore both p53-dependent and independent apoptosis pathways in artocarpin-treated NSCLC cells. Our results showed that artocarpin rapidly induced activation of cellular protein kinases including Erk1/2, p38 and Akt<sup>S473</sup>. Inhibition of these protein kinases prevented artocarpin-induced cell death. Moreover, artocarpin-induced phosphorylation of these protein kinases and apoptosis were mediated by induction of reactive oxygen species (ROS), as pretreatment with NAC (a ROS scavenger) and Apocynin (a Nox-2 inhibitor) blocked these events. Similarly, transient transfection of p47<sup>Phox</sup> or p91<sup>Phox</sup> siRNA attenuated artocarpin-induced NADPH oxidase activity and cell death. In addition, p53 dependent apoptotic proteins including PUMA, cytochrome c, Apaf-1 and caspase 3 were activated by artocarpin, and these effects can be abolished by antioxidants, MAPK inhibitors (U0126 and SB202190), but not by PI3K inhibitor (LY294002). Furthermore, we found that artocarpin-induced Akt phosphorylation led to increased NF-κB activity, which may act as an upstream regulator in the c-Myc and Noxa pathway. Therefore, we propose that enhancement of both ERK/ p38/ p53-dependent or independent Akt<sup>S473</sup>/NF-κB/c-Myc/Noxa cascade by Nox-derived ROS generation plays an important role in artocarpin-induced apoptosis in NSCLC cells.

## INTRODUCTION

Lung cancer, which causes about 1.59 million deaths a year, is a very common cancer and a major cause of death worldwide [1]. Apoptosis, a form of programmed cell death, plays an important biological role in homeostasis. Insufficient apoptosis may result in uncontrolled cell proliferation and has been shown to be involved in various diseases, such as cancer [2–4]. Chemotherapy and  $\gamma$ -irradiation are major therapeutic modalities to decrease cancer cell proliferation in clinical medicine, but these therapies may also kill normal cells and lead to many side effects in human body, such as loss of immunity. Erridge et al. revealed that the five-year survival rate in lung cancer cases is less than 15% due to patient resistance to  $\gamma$ -radiation, chemotherapy and surgical intervention [5, 6]. Therefore, many researchers and pharmaceutical industries have been enthusiastically developing novel anticancer agents to increase the survival rate and improve life quality of lung cancer patients [7–9].

To the best of our knowledge, reactive oxygen species (ROS) plays a double-edged role in free radical biology and medicine [10–12]. On one hand, under normal physiologic conditions, the generation of ROS have important roles in phagocytosis, cell signaling and homeostasis, and ROS are subsequently eliminated by the scavenging system in normal cells [13]. On the other hand, under oxidative stress conditions, greater ROS amounts may oxidize the cellular lipids, proteins and DNA, leading to the aggravation of many clinical diseases, including inflammation, aging, cancer, neurodegenerative and cardiovascular diseases [14–16]. During the last decade, some anticancer drugs in clinical practice, such as platinum [17], paclitaxel [18], resveratrol [19], EGCG [20] and curcumin [21], have been shown to increase the level of NADPH oxidase (Nox)-derived ROS production to suppress cancer cell growth through mediating p53-independent apoptotic signaling components, including MAPKs (p38, ERK1/2 and JNK), PI3K/Akt, BAX/Bcl2 ratio, cytochrome c, Apaf-1, caspase cascade (caspase 3, 8 and 9) and PARP activation. Increasing evidence has also demonstrated that the mitogen activated protein kinase (MAPK) family is involved in p53-independent apoptosis [20–23]. In addition, Wartenber et al. indicated that overexpressing Nox-1 can increase ROS production and diminish the function of P-glycoprotein (an ABC cassette transporter which is involved in chemotherapeutic resistance), and finally overcome cancer drug resistance [24]. According to these viewpoints, a novel anticancer drug functioning as a Nox-derived ROS activator may have therapeutic effects in various types of cancer [25–27].

Artocarpus species are mainly grown in Southeast Asia and also extensively used in food, traditional medicine, agriculture and industry. Artocarpin, an isoprenyl flavonoid, is abundantly found in Artocarpus species, such as *Artocarpus altilis* and *Artocarpus heterophylli*,

and has been reported to possess many pharmacological activities, including antityrosinase [28], antibacterial [28], 5 $\alpha$ -reductase inhibitor [29], photoprotective [30], and anticancer properties [31]. In particular, Wang et al. [32] reported that artocarpin has a powerful cytotoxic effect on various human cancer cells, including non-small cell lung carcinoma (NSCLC, A549), breast adenocarcinoma (MCF-7), ovarian carcinoma (1A9), glioblastoma (U87-MG) and epidermoid carcinoma of the nasopharynx (KB). Until now, however, the molecular biological mechanisms by which artocarpin induce cancer cell apoptosis has not been clearly clarified.

This is the first study to evaluate the anticancer mechanisms of artocarpin on human non-small cell lung carcinoma cells. Here, we hypothesized that artocarpin induces apoptosis of non-small cell lung carcinoma cells via Nox-derived ROS generation. Furthermore, the ROS-mediated signaling contributes to activation of p38 MAPK, ERK1/2 or PI3K/Akt/NF- $\kappa$ B, which regulates p53-dependent or independent cell apoptosis.

## RESULTS

### Effects of artocarpin on cell proliferation and survival *in vitro*

We first determined the anti-proliferative activities of artocarpin (Figure 1A) in the human NSCLC cell lines A549, H226 and H1299 using the sulforhodamine B (SRB) assay. Artocarpin inhibited cell proliferation in a concentration-dependent fashion, with IC<sub>50</sub> values as shown in Figure 1B. Cytotoxicity was determined by the MTT assay after 24 or 48 h of treatment with artocarpin. When incubated with artocarpin (1–10  $\mu$ M), the growth of A549, H226 and H1299 cells was markedly inhibited in a concentration-dependent manner (Figure 1C). To confirm the selectivity of the cytotoxic effect, nontumorous cells, such as human pulmonary epithelial cells (HPA-EpiCs), were also evaluated. However, artocarpin showed much less activity against human pulmonary epithelial cells (Figure 1D and 1E). These data indicate that A549, H226 and H1299 cells were much more sensitive to the cytotoxic effects of artocarpin, in comparison with normal cells. In addition, cell death detection ELISA<sup>PLUS</sup> assay revealed that artocarpin induced DNA fragmentation in A549 cells. Moreover, increased proportion of cells in subG1 phase was observed in the artocarpin-treated cells (Figure 1F). In H1299 cells, the artocarpin-induced increase in subG1 phase cells was suppressed by pretreatment with the inhibitors NAC, APO, LY294002, Akti, and Bay117082. Cell morphology was captured by phase-contrast images after treatment with 10 and 20  $\mu$ M of artocarpin for 24 h or 48 h. The morphological analysis revealed prominent cytotoxicity in artocarpin-treated A549 cells (Figure 1G). Moreover, the Annexin-V-FITC/PI assay showed induction of apoptosis following artocarpin

exposure in A549 and H1299 cells. Representative results of Annexin-V-FITC/PI assay are presented in Figure 1H. Under control conditions, the majority of cells were viable cells (Annexin-V-negative/PI-negative). Following treatment with various concentrations of artocarpin for 24 h, the proportion of viable cells was decreased, while the proportions of cells in early apoptosis (Annexin-V-positive /PI-negative) and late apoptosis (Annexin-V-positive /PI-positive) were increased. All tested concentrations of artocarpin could induce early apoptosis, while only 15 and 20  $\mu$ M could significantly induce late apoptosis. The results demonstrated that artocarpin induced apoptosis of A549 and H1299 cells in a concentration-dependent manner, particularly early apoptosis (Figure 1).

### Artocarpin-induced apoptosis is associated with generation of ROS

Accumulating studies have reported that various natural products exhibited powerful anti-tumor effects by generation of reactive oxygen species (ROS) with their pro-oxidative activities [25]. ROS are known to induce oxidative stress and DNA damage, and may act as a mediator of apoptosis. It is not known whether this form of pro-oxidative action of artocarpin occurs in A549 and H1299 cells. The intracellular levels of ROS induced by stimulation of A549 and H1299 cells with 10  $\mu$ M artocarpin were measured using a fluorescent probe, dichlorofluorescein diacetate (DCF-DA). Cells were first stained with DCF-DA, incubated with artocarpin for the indicated times, and then the fluorescence emission intensity at 530 nm was determined following excitation at 485 nm. The fluorescence was evaluated via flow cytometer, ELISA reader or confocal microscope. In addition, the Nox activity in lung cancer cells was evaluated by lucigenin chemiluminescence and measured using a luminometer. As illustrated in Figure 2A, artocarpin induced ROS production in A549 and H1299 cells in a time and dose-dependent manner, however, the formation of ROS was not seen upon artocarpin stimulation of HPAEpiCs. Pretreatment with APO (a Nox2 inhibitor), DPI (a Nox inhibitor) or NAC (a ROS scavenger) significantly decreased artocarpin-induced ROS generation in A549 and H1299 cells (Figure 2B), and similar findings were shown from the confocal microscope (Figure 2C). Image fluorescence from mitochondrial membrane potential dye (TMRM, Figure 2C) showed that mitochondrial membrane potential was not changed after 2h of artocarpin exposure, suggesting that ROS generation may not be directly related to the mitochondria at this time point. We further found that in A549 and H1299 cells, treatment with artocarpin resulted in increased mitochondrial superoxide level at the 24 hour time point, which was partially suppressed by pretreatment with MitoTEMPO (a specific scavenger for mitochondrial superoxide anions) (Supplementary Figure 1). In addition,

artocarpin-induced apoptosis in A549 and H1299 cells can be attenuated by pre-treatment with MitoTEMPO (Supplementary Figure 2). Moreover, pretreatment with APO or NAC markedly inhibited artocarpin-induced apoptosis as observed with the MTT, DNA fragmentation, real-time cytotoxicity and Annexin-V-FITC/PI assays (Figure 2D–2F). These data indicated that Nox2-mediated ROS generation may participate in artocarpin-induced oxidative damage to DNA and apoptosis in A549 and H1299 cells. Furthermore, previous studies have shown that during the process of Nox2 activation, the p47<sup>phox</sup> cytosolic subunit is phosphorylated and translocates with the p67<sup>phox</sup> subunit to the cell membrane, and combine with the gp91<sup>phox</sup> (Nox2) subunit to form an active enzyme complex [33]. Therefore, we found that artocarpin induced phosphorylation of p47<sup>phox</sup> in a time dependent manner (Figure 2G), and promoted p47<sup>phox</sup> translocation from the cytoplasm to the cell membrane in 30 min. Additionally, transfection with siRNAs for Nox2 (gp91<sup>phox</sup>) and p47<sup>phox</sup> effectively attenuated artocarpin-induced ROS formation and Nox activity (Figure 2H), which in turn inhibited apoptosis of A549 cells (Figure 2I). These results indicated that artocarpin-induced DNA damage and cell apoptosis are mediated via Nox2/ p47<sup>phox</sup> dependent ROS production in A549 cells.

### Involvement of ROS-dependent MAP kinases and PI3K/Akt pathways in apoptosis induction in A549 and H1299 cells by artocarpin

Previous studies have shown that ROS formation can elicit changes in the phosphorylation of MAPKs or Akt [21, 34], and that MAPKs or Akt regulate apoptosis [21, 22, 34, 35]. Therefore, we first examined whether MAPKs and Akt are also involved in artocarpin-induced apoptosis in A549 and H1299 cells. The effects of artocarpin on the phosphorylation of MAPKs and Akt<sup>S473</sup> were evaluated by Western blot analysis. As shown in Figure 3A, artocarpin induced phosphorylation of p38 MAPK, ERK1/2 and Akt<sup>S473</sup>, but not JNK1/2 (data not shown) in a time dependent manner, and these effects were significantly attenuated by their specific inhibitors as well as APO and NAC. We also used specific inhibitors to further evaluate the role of these pathways and the inter-relationship between them. As shown in Figure 3B, phosphorylation of p38 MAPK, ERK1/2 and Akt<sup>S473</sup> stimulated by artocarpin for 4 hours was suppressed by pretreatment with the specific inhibitors U0126, SB202190 and LY294002, respectively. Moreover, inhibition of one signaling kinase did not affect the other kinases, indicating that phosphorylation of p38 MAPK, ERK1/2 and Akt<sup>S473</sup> by artocarpin occurred in parallel. As shown in Figure 3C, artocarpin-induced phosphorylation of ERK, p38 and Akt was significantly suppressed by transfection with p47<sup>phox</sup> siRNA but not scrambled siRNA. This indicates that artocarpin-induced phosphorylation of ERK, p38



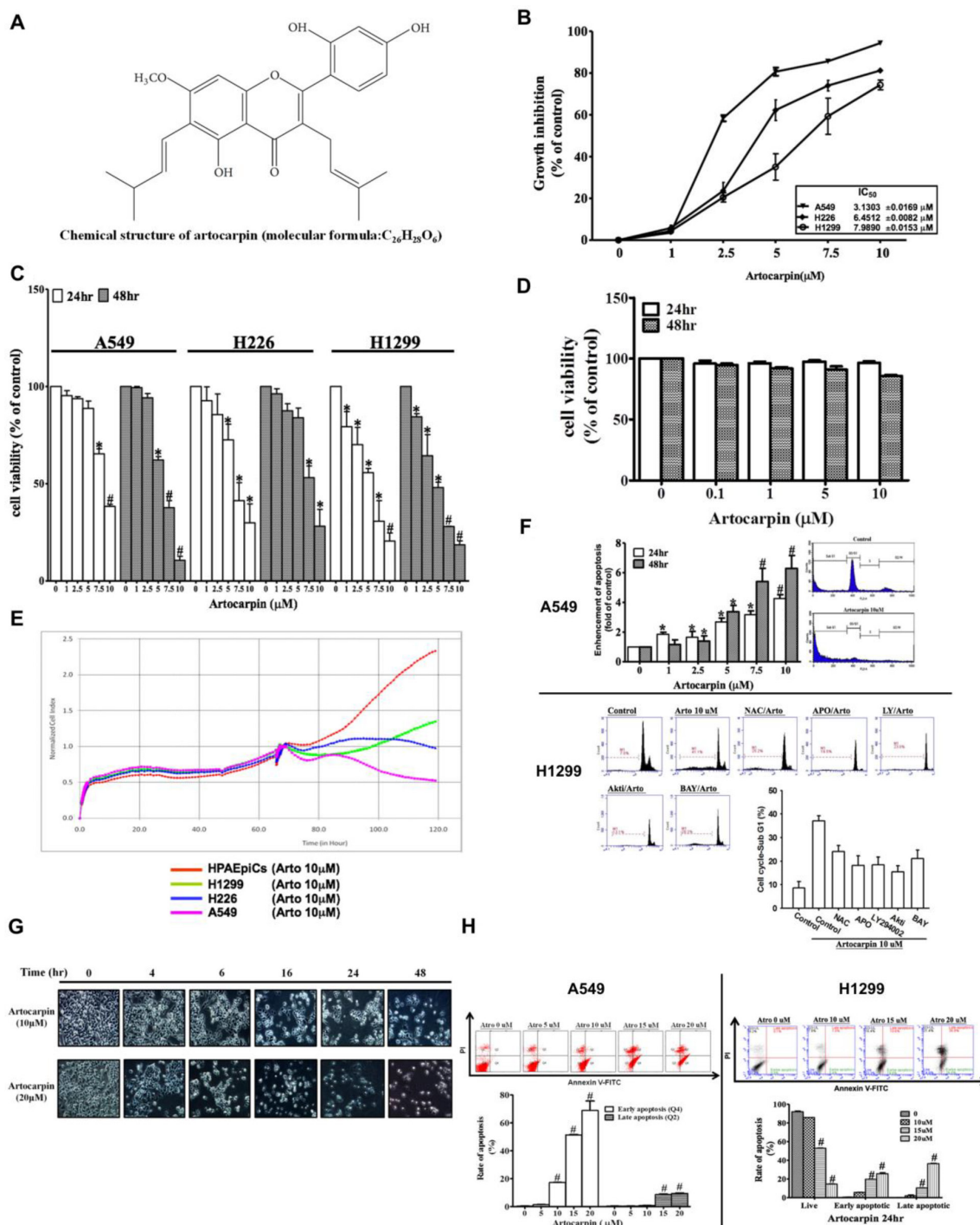


**Figure 1: Growth inhibition of NSCLC cell lines by artocarpin.** (A) Chemical structure of artocarpin. (B) A549, H226 and H1299 cells were treated with different concentrations of artocarpin for 24 h. Inhibition of cell growth was evaluated using the SRB assay. (C) A549, H226, H1299 cells and (D) HPAEpiCs were treated with the indicated concentrations of artocarpin for 24 and 48 h. Cytotoxicity was evaluated using the MTT assay. Data shown are means  $\pm$  SEM of at least three independent experiments.  $*P < 0.05$ ,  $^{#}P < 0.01$  compared with the control group. (E) Real-time cytotoxicity assay to assess the time-dependent effect of artocarpin on cell viability in HPAEpiCs, H1299, H226 and A549 cells. Artocarpin was added at the 65 hour time point. (F) Following treatment with different concentrations of artocarpin for 24 h, apoptosis induction in A549 cells was evaluated by measuring the amounts of oligonucleosomal DNA fragmentation using the Cell Death ELISA<sup>PLUS</sup> kit. In addition, cell cycle analysis was performed in A549 and H1299 cells using flow cytometry. H1299 cells were also pretreated with the inhibitors NAC, APO, LY294002, Akti, and Bay117082. Data shown are means  $\pm$  SEM.  $*P < 0.05$ ,  $^{#}P < 0.01$ , compared with the control group. (G) Morphological changes in A549 cells were observed by light microscopy. (H) After incubation with 0–20  $\mu$ M artocarpin for 24 h, A549 and H1299 cells were stained with Annexin-V-FITC and PI for 15 min, and then evaluated by flow cytometry. Each bar represents the mean  $\pm$  SD ( $n = 3$ ).  $*P < 0.05$ ,  $^{#}P < 0.01$  compared with the control group.

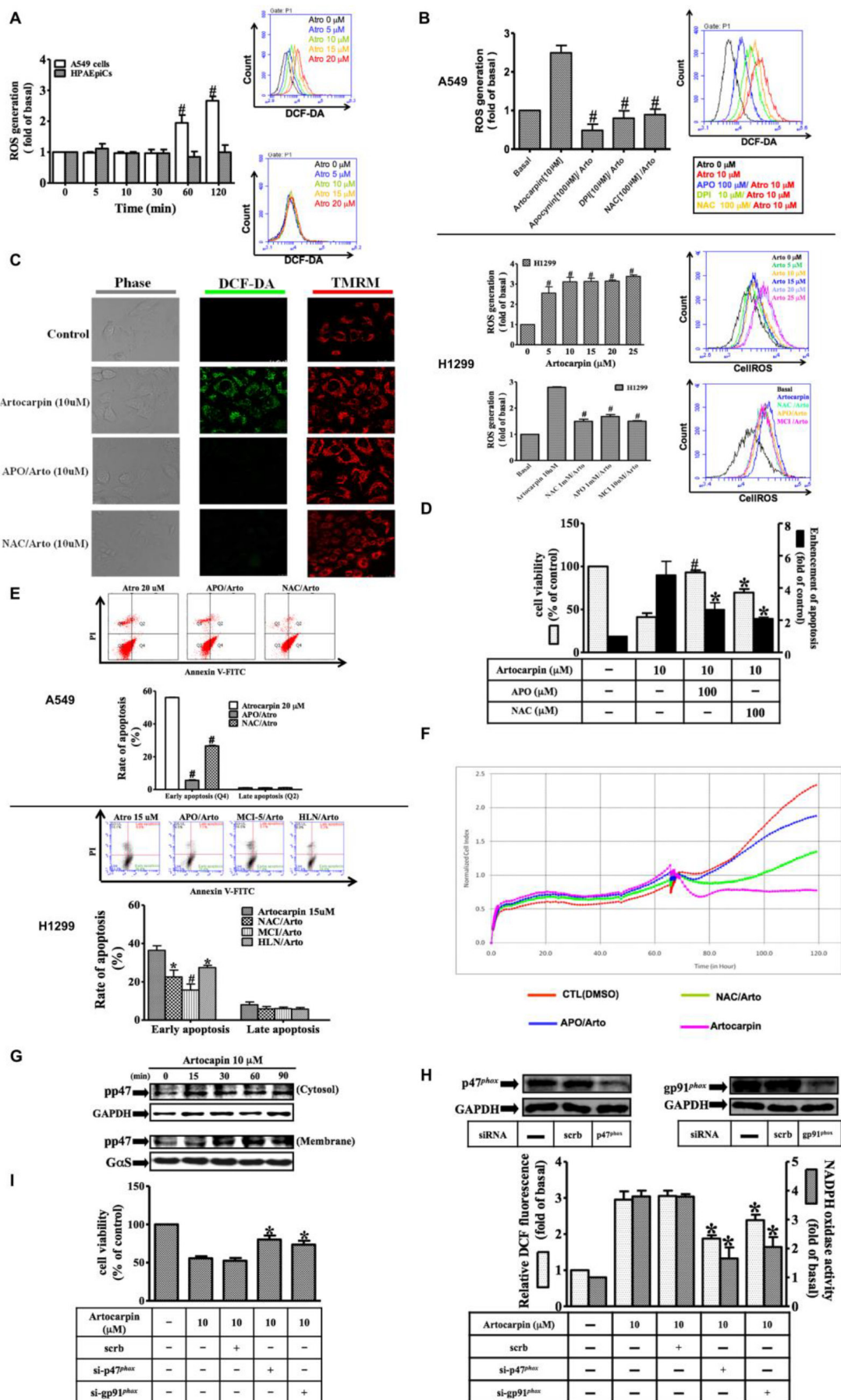




**Figure 2: Artocarpin-induced activation of NADPH oxidase and generation of ROS triggers apoptosis in tumor cells.**

Time dependence of artocarpin-induced ROS generation and p47<sup>phox</sup> activation are shown. (A) A549 cells and HPAEpiCs were stained with DCF-DA (10  $\mu$ M) and treated with artocarpin for different periods of time. The fluorescence intensity was then determined. (B) A549 and H1299 cells were pretreated with DPI (10  $\mu$ M), APO (100  $\mu$ M), or NAC (100  $\mu$ M) for 1 h and then stimulated with 10  $\mu$ M artocarpin for 120 min. ROS generation was determined via fluorescent plate reader and flow cytometry. (C) Cells were stained with DCF-DA (10  $\mu$ M) and TMRM (10  $\mu$ M) and then pretreated with APO or NAC for 1 h before artocarpin administration. The ROS generation (green color) and mitochondrial membrane potential (red color) were detected via confocal microscope. (D–F) A549 cells were pretreated with APO or NAC for 1 h, and then incubated with 10  $\mu$ M artocarpin for 24 h. Cytotoxicity was determined using MTT assay, flow cytometry (cells stained with Annexin-V and PI) and real-time cytotoxicity assay. (G) The membrane (ME) and cytosolic (CE) fractions were collected and subjected to Western blot analysis with an anti-phospho-p47<sup>phox</sup> antibody. (H) A549 cells were transfected with siRNAs for scrambled, Nox2 (gp91<sup>phox</sup>) or p47<sup>phox</sup>, and then treated with 10  $\mu$ M artocarpin for 120 min. ROS generation (open bars) and Nox activity (shaded bars) were determined via ELISA reader. (I) A549 cells were transfected with siRNAs of Nox2 (gp91<sup>phox</sup>) or p47<sup>phox</sup>, and then treated with 10  $\mu$ M artocarpin for 24 hr. Cytotoxicity was determined using MTT assay. (A–I) are means  $\pm$  SEM. \* $P$  < 0.05, # $P$  < 0.01, compared with the control group.

and Akt was mediated through the p47<sup>phox</sup> pathway. Additionally, pretreatment with U0126 and SB202190 for 1 hour markedly inhibited artocarpin-induced cytotoxicity (Figure 3D), early apoptosis (Figure 3E) and real-time cytotoxicity (Figure 3F), and such effects were also partially significantly reduced by pretreatment with LY294002 and Wortmannin (inhibitors of PI3K). These results suggest that ROS plays a critical role in artocarpin-induced p38 MAPK, ERK1/2 and Akt<sup>S473</sup> phosphorylation, leading to the induction of cytotoxicity and apoptosis in A549 and H1299 cells.

**ROS mediated MAPKs activation contributes to artocarpin-elicited p53 activation, PUMA and Cytochrome C expression, and apoptosis induction**

MAPKs have been shown to activate p53 in response to different stressful stimuli, and the phosphorylation of p53 may lead to cell cycle arrest and apoptosis [36, 37]. To examine whether MAPKs activation plays a role in artocarpin-induced p53 phosphorylation and downstream apoptotic events, A549 cells were pretreated with antioxidants, MAPK inhibitors (U0126, SB202190) and PI3K inhibitor (LY294002) for 1 h prior to artocarpin incubation. The levels of p53, PUMA, Cytochrome C, Apaf-1 and cleaved-caspase 3 were evaluated by Western blotting. As shown in Figure 4, artocarpin promoted phosphorylation of p53 and expression of PUMA, Cytochrome C, Apaf-1 and cleaved-caspase 3 in a time dependent manner, and these effects can be decreased by pretreatment with antioxidants, SB202190 and U0126, but not by LY294002. We also performed experiments to show that treatment of A549 cells with artocarpin resulted in increased caspase-3, caspase-7 and caspase-9 activity, which were attenuated by pre-treatment with APO, NAC, MCI, U0126 and SB202190 (Supplementary Figure 3). These data indicate that artocarpin induction of ROS leads to activation of p38 and ERK1/2 pathways and partial activation of PI3K/ Akt<sup>S473</sup>, thereby leading to p53-dependent or independent apoptosis of tumor cells.

**PI3K/Akt-dependent activation of NF- $\kappa$ B and expression of c-Myc/Noxa are required for artocarpin-induced apoptosis of A549 and H1299 cells**

To elucidate the pathways involved in regulation of artocarpin-induced apoptosis by PI3K/Akt pathway, we evaluated the activation status of NF- $\kappa$ B, which regulates the transcription of DNA and is delicately susceptible to cellular oxidative stress [38]. NF- $\kappa$ B activation by artocarpin was investigated by Gel-shift assay, promoter assay and P65 nuclear translocation assay (fluorescence immunocytochemistry). As shown in Figure 5A–5C, NF- $\kappa$ B binding activity, promoter activity and P65 nuclear translocation were low in untreated controls but were significantly increased following treatment with artocarpin in A549 cells. Pretreatment with APO, NAC, LY294002, SH-5, Bay117082, U0126 and SB202190 blocked the artocarpin-stimulated increase in NF- $\kappa$ B activity. Furthermore, the nuclear fraction was prepared to determine whether artocarpin increased nuclear translocation of the NF- $\kappa$ B p65 subunit. As shown in Figure 5D, artocarpin stimulated rapid phosphorylation and translocation of p65 in A549 and H1299 cells, which was significantly suppressed by pretreatment with APO, LY294002 and Bay117082. Finally, we confirmed that accumulation of c-Myc (a transcription target of NF- $\kappa$ B) and Noxa (a transcription target of c-Myc) proteins was due to NF- $\kappa$ B activation. As expected, artocarpin induced expression of c-Myc and Noxa in a time dependent manner, and these effects were significantly suppressed by APO, LY294002 and Bay117082 (Figure 5D). These results demonstrated that NF- $\kappa$ B/c-Myc/Noxa was involved in cell apoptosis mediated through Nox/ROS generation following the activation of PI3K/Akt in A549 and H1299 cells.

**Artocarpin suppressed lung cancer growth in the mouse xenograft model**

To evaluate whether artocarpin shows anticancer properties *in vivo*, we implanted xenografts of A549 and

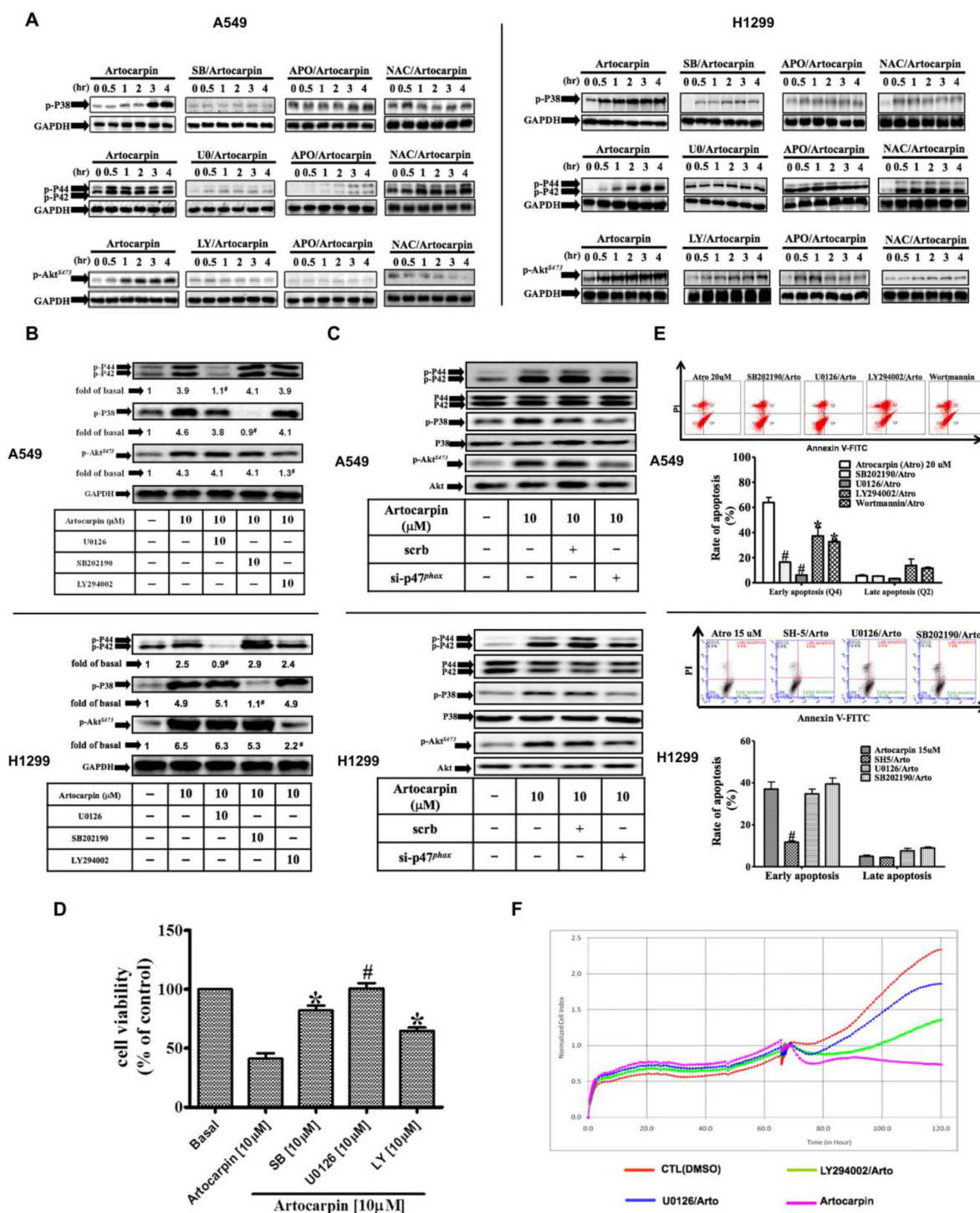


**Figure 3: ROS-dependent MAPKs activation is involved in artocarpin-induced apoptosis in A549 and H1299 cells.** Cells were treated with 10 μM artocarpin for different periods of time, followed by Western blot analysis using antibodies against phospho-p38 MAPK, phospho-ERK1/2 or phospho-Akt. (A) Western blot analysis showing the effects of 10 μM SB202190 (p38 inhibitor), 10 μM U0126 (ERK1/2 inhibitor), 10 μM LY294002 (PI3K inhibitor), APO (100 μM) or NAC (100 μM) on the phosphorylation of p38 MAPK, ERK1/2 or Akt in artocarpin-treated A549 and H1299 cells. The blots were probed for GAPDH as a loading control. (B) Cross talk between MAPKs and Akt phosphorylation in artocarpin-treated A549 and H1299 cells. Cells were pretreated with 10 μM SB202190, 10 μM U0126 or 10 μM LY294002 for 1 hr and then treated with 10 μM artocarpin for 4 hr. (C) Relationship between MAPKs, Akt and p47<sup>phox</sup> in artocarpin-treated A549 and H1299 cells. Cells were transfected with either scrambled siRNA or p47<sup>phox</sup> siRNA and then treated with 10 μM artocarpin for 4 hr. (D, E) Cells were pretreated with 10 μM SB202190, 10 μM U0126 or 10 μM LY294002 for 1 h, and then treated with 10 μM artocarpin for 24 hr. Cytotoxicity was determined using MTT assay and stained with Annexin-V and PI as previously described in Figure 1. Data shown are means ± SEM. \**P* < 0.05, #*P* < 0.01, compared to artocarpin treatment alone. (F) Real-time cytotoxicity assay to assess the effect of U0126 and LY294002 on artocarpin-induced cell cytotoxicity in A549 cells. Artocarpin was added at the 65 hour time point.

H1299 cells into SCID mice. When the xenograft tumors grew to 100 mm<sup>3</sup> in size, the mice were allocated into two groups, the first group treated with vehicle and the second group treated with artocarpin (1 mg/kg/day). Artocarpin significantly inhibited tumor growth (Figure 6B). The mean tumor volume in artocarpin-treated mice was significantly reduced compared with vehicle-treated control mice (Figure 6A). Western blot analysis of excised tumor tissues *ex vivo* revealed significant increases in ERK, p53, PUMA, Cytochrome C, Apaf-1, caspase 3, Akt<sup>S473</sup>, p65, c-Myc and Noxa expression in the artocarpin treated group compared with tumors from the control group (Figure 6D). These findings indicate that artocarpin suppressed tumor growth by promoting apoptosis of A549 and H1299 cells *in vivo*.

## DISCUSSION

In this study, we clearly demonstrate that artocarpin dose-dependently suppressed the proliferation of non-small cell lung cancer (NSCLC) cell lines, but showed much less activity in normal human pulmonary epithelial cells (HPAEPiCs). We also found that artocarpin induced formation of ROS and promoted apoptosis only in NSCLC cell lines, but showed no significant effects in normal cells. These results are consistent with findings in other

bioactive compounds and plant secondary metabolites, such as curcumin [21], EGCG [39] and resveratrol [19]. To our knowledge, this is the first study to show that artocarpin induces ROS generation and consequently causes DNA oxidative damage in tumor cells.

Artocarpus species (Moraceae) are evergreen trees distributed over tropical regions of Asia and are extensively used in food, traditional folk medicines, agriculture and industry. Artocarpin is a prenylated flavonoid derived from Artocarpus species. The chemical structure of artocarpin contains lipophilic isoprenoid groups, which increases its affinity to biological membranes [40]. Previously, artocarpin has been shown to exhibit cytotoxic activity against cancer cells. The results of the present study revealed that the IC<sub>50</sub> of artocarpin in three NSCLC cell lines at 24 h was 3 to 8 μM, which was much lower than that of many natural anticancer compounds, such as curcumin (about 78 μM), resveratrol (about 33 μM) and EGCG (about 68 μM) [41–43]. How artocarpin exerts its powerful anticancer activities on A549 and H1299 cells have not been reported. It is important to elucidate the mechanisms involved in artocarpin-induced cell death.

Accumulating investigations have demonstrated that ROS acts as a mediator of apoptosis. ROS species, including free radicals such as superoxide and hydroxyl

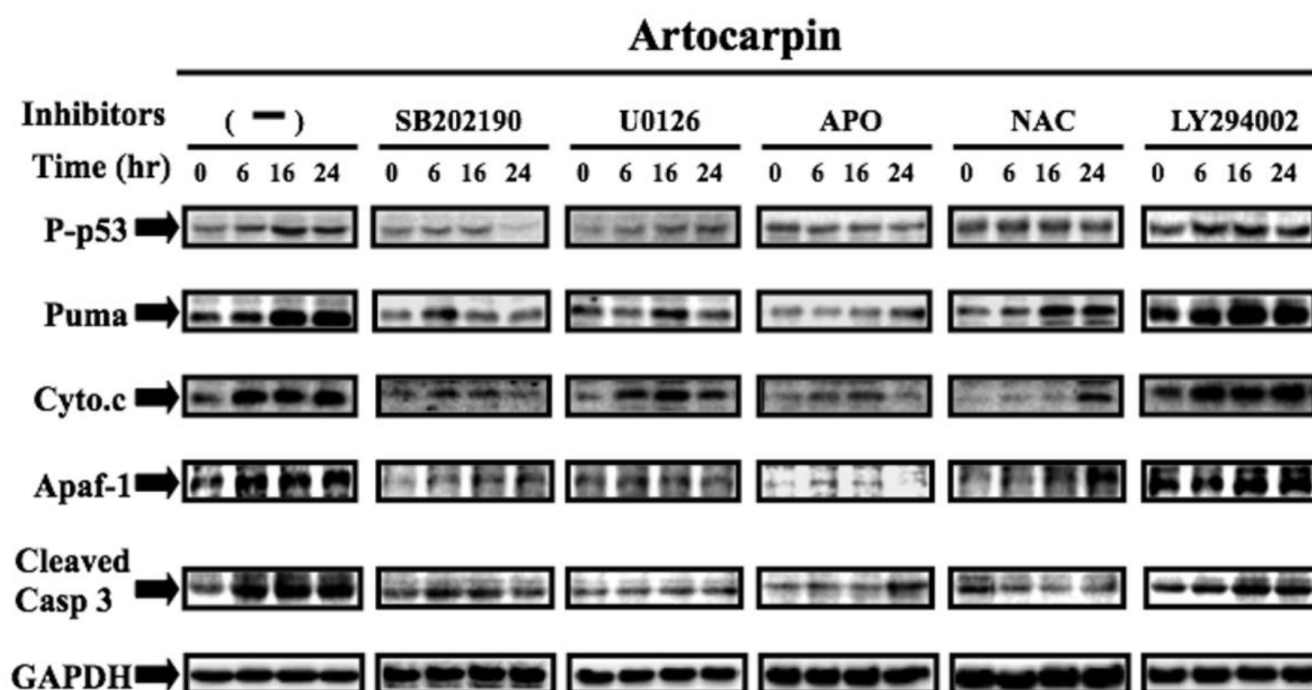


**Figure 4: Artocarpin up-regulated the expression of p53-dependent apoptotic proteins via p38 MAPK and ERK1/2 pathway, but not by Akt pathway.** A549 cells were treated with 10 μM artocarpin for various periods of time, followed by Western blot analysis using antibodies against phospho-p53, PUMA, Cytochrome C, Apaf-1 and caspase-3. Western blot analysis also demonstrating the effects of 10 μM SB202190, 10 μM U0126, 10 μM LY294002, APO (100 μM) or NAC (100 μM) treatment on the up-regulation of phospho-p53, PUMA, Cytochrome C, Apaf-1 and caspase-3 in artocarpin-treated A549 cells. The blots were probed for GAPDH as a loading control. Each blot is representative of three independent experiments, all of which had similar results.



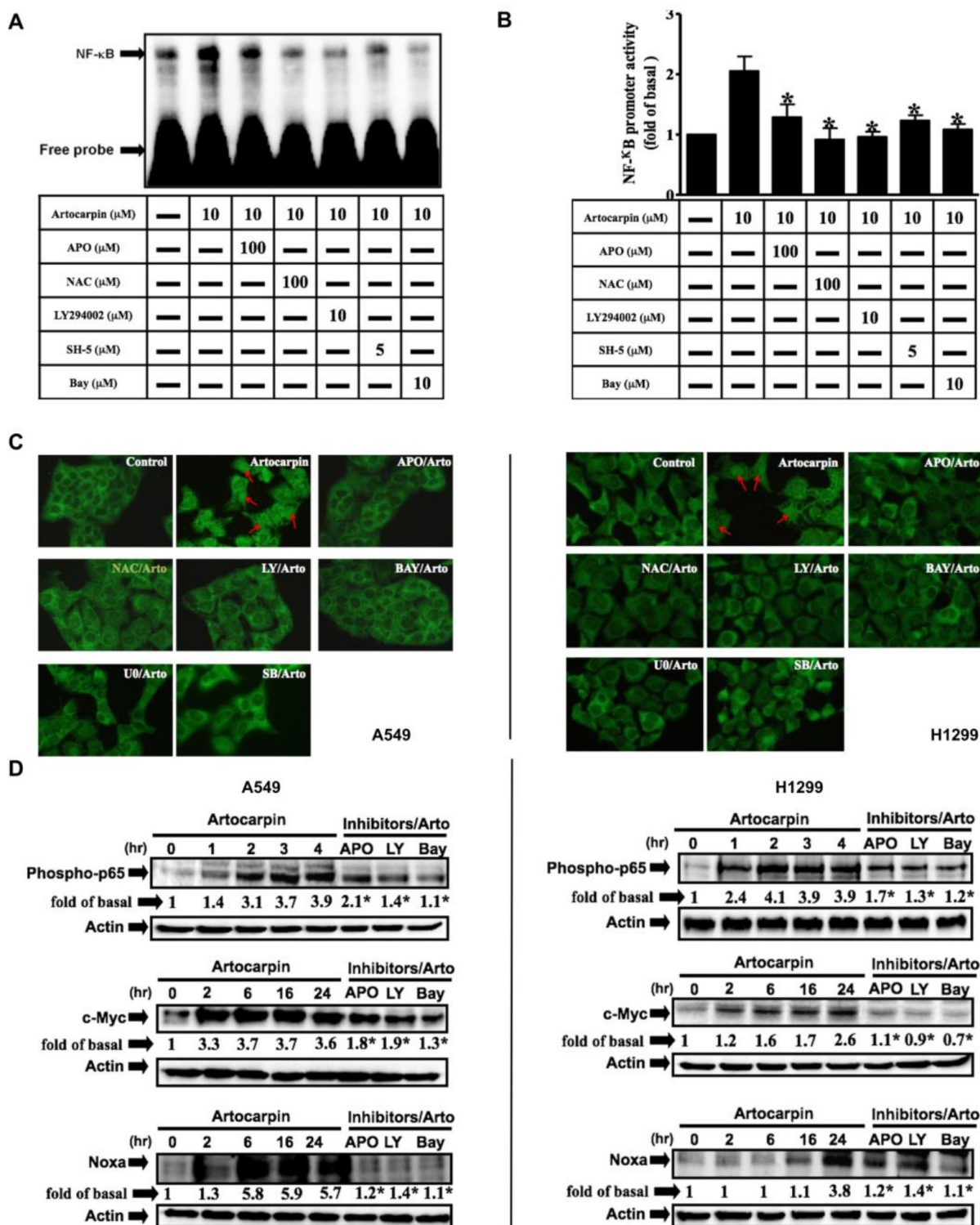


**Figure 5: Artocarpin induced activation of NF-κB and expression of c-Myc/Noxa via Akt pathway.** (A) Nuclear extracts from untreated cells or cells pretreated with APO, LY294002 or BAY117082 for 1hr followed by incubation with 10 μM artocarpin for 4 h were tested for NF-κB DNA binding activity by EMSA. (B) A549 cells were pretreated with APO, LY294002 or BAY117082 for 1hr, then treated with 10 μM artocarpin for 4 h were tested for NF-κB transcription activity by reporter gene assay. \**P* < 0.05 compared to artocarpin treatment alone. (C) Fluorescence immunocytochemistry to assess P65 nuclear translocation. A549 and H1299 cells were pretreated with APO, NAC, LY294002, BAY117082, U0126 or SB202190 for 1 h, and then treated with 10 μM artocarpin. (D) A549 and H1299 cells were pretreated with APO, LY294002 or BAY117082 for 1 h, and then treated with 10 μM artocarpin for the indicated times. The nuclear extract levels of phospho-p65, c-Myc and Noxa proteins were evaluated by Western blotting. (A–D) Each blot is representative of three independent experiments, all of which had similar results.

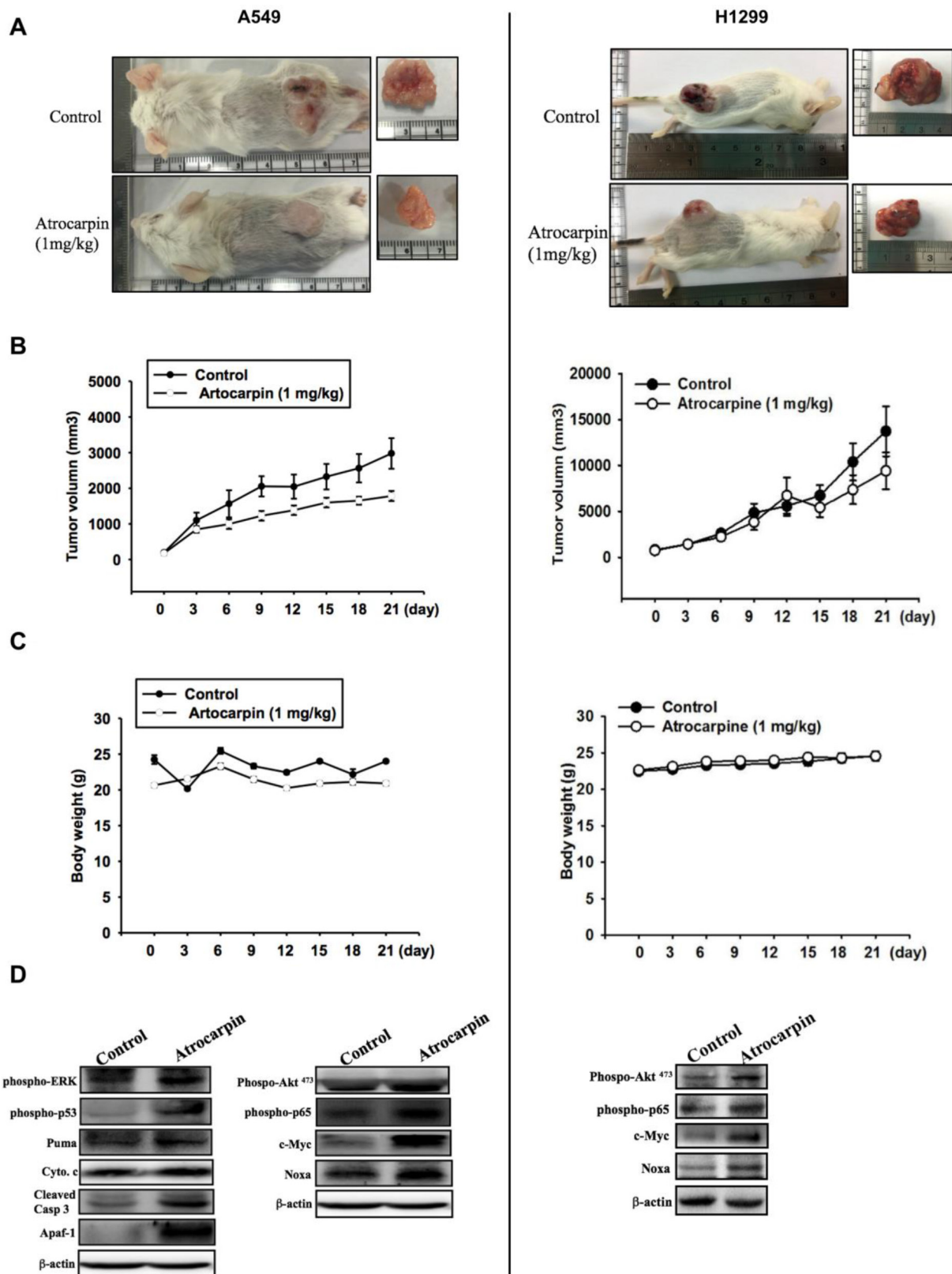


**Figure 6: Artocarpin inhibits xenograft tumor growth in SCID mice.** (A, B) Mice were subcutaneously injected with A549 or H1299 cells. When the tumors grew to 100 mm<sup>3</sup> in size, the mice were administered artocarpin (1 mg/kg) or vehicle once a day for 3 weeks. Tumor volume was determined at various times following tumor implantation ( $n = 8-10$ ). (C) Mice body weight was evaluated at various times after tumor implantation. (D) Western blot analysis for levels of ERK, p53, PUMA, Cytochrome C, Apaf-1, caspase 3, Akt<sup>S473</sup>, p65, c-Myc and Noxa in tumors with and without artocarpin treatment.



radicals, are produced by multiple cellular sources, such as the mitochondria and NADPH oxidases, lipoxygenases and cyclooxygenases. In our study, we have established that after artocarpin treatment of A549 and H1299 cells, both Nox activity (Figure 2G) and ROS generation (Figure 2A–C and 2G) were significantly increased, and these effects were suppressed by pretreatment with inhibitors including APO (a Nox2 inhibitor) and NAC (a ROS scavenger) or by transfection with siRNAs for Nox2 (gp91<sup>phox</sup>) and p47<sup>phox</sup>. In fact, our data also provide evidence that tetramethyl rhodamine methyl ester (TMRM) is suitable for determining mitochondrial membrane permeability transition, which was not changed in response to artocarpin at the two hour time point (Figure 2B). These data indicated that the major source of ROS is NADPH oxidases and not the mitochondria. However, excessive amounts of ROS can induce oxidative damage to DNA, proteins, and lipids leading to cell death. We found that pre-incubation with antioxidants or siRNAs for Nox2 (gp91<sup>phox</sup>) and p47<sup>phox</sup> significantly attenuated artocarpin-induced DNA oxidative damage and cell apoptosis, as determined by MTT assay, Annexin-V-FITC/PI staining, DNA fragmentation and real-time cytotoxicity assay. Therefore, the findings of the present study indicate that artocarpin exerted powerful anti-tumor effects by targeting NADPH oxidases and generation of ROS with their pro-oxidative activities.

Previous studies have revealed that MAPKs or PI3K/Akt regulate cell growth, apoptosis, and inflammation, and may be activated following oxidative stress [25, 44]. Thus, we further investigated whether artocarpin-induced apoptosis is mediated by activation of MAPKs or PI3K/Akt pathways. In this study, we showed that artocarpin-induced phosphorylation of ERK1/2, p38 MAPK and Akt473 are due to the induction of Nox2-derived ROS which were confirmed using APO and NAC. Next, we established that phosphorylation of ERK1/2, p38 MAPK and Akt473 by artocarpin occurred in parallel. These findings are consistent with previous studies showing that distinct members of the MAPK family are activated in a ROS-dependent manner [45]. Interestingly, most studies have shown that Akt serves as a proliferation and anti-apoptotic signal. In our study, pretreatment of cells with specific inhibitors of ERK1/2, p38 and Akt473 significantly suppressed the growth of A549 and H1299 cells, indicating that ERK1/2, p38 and Akt473 are required for artocarpin-induced apoptosis. Phosphorylated Akt at S473 is the main active form Akt, and similar findings were also reported by Wang et al. [46].

The tumor suppressor gene p53 often shows somatic mutations or deletions in various human NSCLC cells. Previous studies have shown that two of the most important signaling pathways involved in cancer are the MAPKs and PI3K/Akt pathways, which may contribute to both p53-dependent and p53-independent apoptosis [21, 46–49]. In this study, we noticed that artocarpin is able to induce

apoptosis in not only p53-wild type tumor cells (A549), but also p53-mutant tumor cells (H1299 and H226) (Figure 1A and 1B). Moreover, we found that activation of p53 by artocarpin subsequently regulated downstream apoptotic proteins, including PUMA, Cytochrome C, Apaf-1 and caspase 3, and such effects were ameliorated by reduction of ROS and inhibition of ERK1/2 or p38 MAPK. However, blocking of PI3K/Akt pathway by LY294002 showed less effect on p53-dependent apoptotic pathway. Thus we consider that, although ERK1/2 or p38 MAPK play a major role in artocarpin-induced p53-dependent apoptosis, artocarpin may also induce PI3K/Akt signaling via a p53-independent pathway.

The transcription factor NF- $\kappa$ B is a major PI3K/Akt downstream effector, and plays a dual role as an attenuator or promoter of apoptosis. It regulates the transcription of DNA, and mediates apoptosis in response to oxidative stress [38]. Recent studies have demonstrated that ROS-dependent NF- $\kappa$ B activation induced the protein expression of c-Myc and Noxa in p53-independent human NSCLC cell death [50]. On the contrary, NF- $\kappa$ B activation was involved in resistance to oxidative stress and p53-mediated programmed cell death [51–53]. Therefore, we investigated whether this transcription factor may play a role in artocarpin-induced apoptosis. In the current study, we observed that artocarpin induced the activation of NF- $\kappa$ B via a Nox2/ROS/PI3K/Akt dependent signaling pathway. Correspondingly, amelioration of Nox2/ROS/PI3K/Akt pathway significantly attenuated artocarpin-induced translocation of NF- $\kappa$ B and up-regulation of c-Myc and Noxa proteins. These results demonstrated that activation of the p53-independent ROS/NF- $\kappa$ B/c-Myc/Noxa signaling pathway by artocarpin plays a critical role in inducing apoptosis in A549 and H1299 cells.

In conclusion, our results demonstrated that whereas artocarpin induces cytotoxic effects in human NSCLC cells, it may exert protective effects in normal HPAEpiCs. In addition, artocarpin may serve as a pro-oxidant only in human NSCLC cells, but not in normal HPAEpiCs. Previously, various flavonoids (including flavone acetic acid, quercetin, and flavopiridol) have entered human clinical trials, and have shown promising anticancer effects clinically [54]. We propose that cell apoptosis caused by artocarpin-induced oxidative stress and ROS generation can be an important mechanism for cancer prevention and therapy. Additionally, this study is the first to demonstrate that artocarpin-induced apoptosis is mediated through activation of the Nox2/p47<sup>phox</sup> pathway leading to enhanced ROS production, which then induces the activation of two distinct signaling cascades, including ERK MAPK/ p38 MAPK/p53-dependent activation of PUMA/Cytochrome C/ Apaf-1/ caspase 3 pathway in A549 cells and PI3K/ Akt<sup>s473</sup>/ p53-independent activation of NF- $\kappa$ B/ c-Myc/Noxa pathway in both A549 and H1299 cells, as shown in the composite scheme in Figure 7.

## MATERIALS AND METHODS

### Reagents and chemicals

DMEM/F-12 medium, FBS, and Lipofectamine 2000 were obtained from Invitrogen (Carlsbad, CA, USA). Western blotting materials (Hybond C membrane, enhanced chemiluminescence (ECL) system and Hyperfilms) were purchased from GE Healthcare Biosciences (Buckinghamshire, UK). The monoclonal antibodies cytochrome C, Apaf-1, caspase 3 and anti-phospho p65 were obtained from Santa Cruz Biotechnology (Santa Cruz, CA, USA). PhosphoPlus p53, ERK1/2, p38 and Akt antibodies were obtained from Cell Signaling Technology (Danvers, MA, USA), and phosphoPlus p47<sup>phox</sup> antibody was purchased from Assay Biotechnology (Sunnyvale, CA, USA). GAPDH antibody was obtained from Biogenesis (Boumemouth, UK). c-Myc and Noxa were purchased from Calbiochem, San Diego, CA, USA. N-acetylcysteine (NAC), apocynin (APO), Bay117082, U0126, SB202190, SH-5, LY294002

and wortmannin were from Biomol (Plymouth Meeting, PA, USA). Artocarpin (purity > 98% by high performance liquid chromatography analysis) was obtained from Pulin Biotech Company Limited (Taipei, Taiwan).

### Cell cultures

A549 cells (p53 wild-type) were obtained from the Food Industry Research and Development Institute (Taiwan) in the year 2012. p53 null H1299 and p53 mutant H226 cells were generously provided by Professor Mei-Chuan Chen (Program for the Clinical Drug Discovery from Botanical Herbs, College of Pharmacy, Taipei Medical University, Taiwan). HPAEpiCs were purchased from Cell Applications, Inc (San Diego, CA) in the year 2012. All cells were cultured in DMEM/F-12 with 10% fetal bovine serum (FBS) and antibiotics (100 U/ml penicillin G, 100 mg/ml streptomycin, and 250 ng/ml fungizone), and kept in an incubator with 5% CO<sub>2</sub> at 37°C. For evaluation of protein expression and cell cytotoxicity, cells were seeded onto 12-

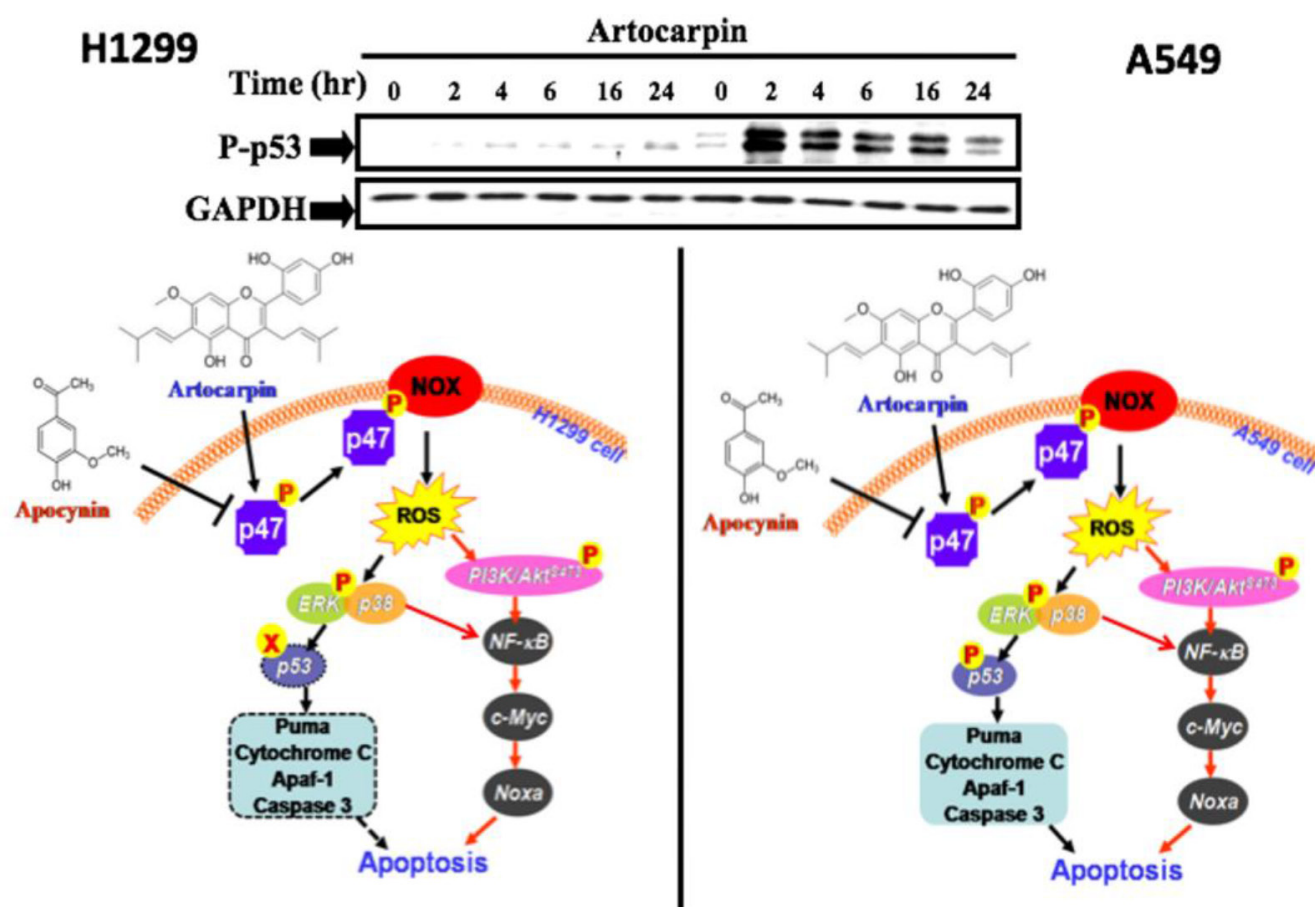


**Figure 7: Schematic diagram showing the proposed signaling pathways involved in artocarpin-induced apoptosis in A549 and H1299 cells.** Artocarpin-induced apoptosis is mediated by activation of the Nox2/p47<sup>phox</sup> pathway leading to enhanced ROS production, which then induces the activation of two distinct signaling cascades, including ERK MAPK/ p38 MAPK/p53-dependent activation of PUMA/Cytochrome C/ Apaf-1/ caspase 3 pathway in A549 cells and PI3K/ Akt<sup>473</sup>/ p53-independent activation of NF-κB/ c-Myc/Noxa pathway in both A549 and H1299 cells.

well culture plates and 96-cm culture dishes, respectively. Cells from passages 5 to 20 were used in this study.

### Cell proliferation assay

Cell proliferation was evaluated using the sulforhodamine B (SRB) assay as described previously [55]. Following treatment with artocarpin with or without various inhibitors, viable cells were fixed with 10% trichloroacetic acid (TCA) and stained with 0.4% sulforhodamine B (SRB). After washing with 1% acetic acid, the cell-bound dye was dissolved with 10 mM Tris-base. The absorbance was then measured by a microplate reader at 515 nm.

### Cell viability assay

The MTT assay was used for evaluation of cell viability. Lung cancer cells were seeded onto 96-well plates overnight. After treatment with different concentrations of artocarpin for 24 h or 48 h, MTT solution was added. Following incubation for one hour at 37°C, the plates were read using a microplate spectrophotometer at a wavelength of 550 nm.

### Cell apoptosis assay

The Cell Death Detection ELISA<sup>PLUS</sup> kit (Roche Diagnostics, Basel, Switzerland) was employed to evaluate artocarpin-induced apoptosis in accordance with the manufacturer's protocols. After artocarpin treatment for 24 h or 48 h, the amount of apoptotic oligonucleosomal DNA fragments was detected using an ELISA reader (absorption wavelength 405 nm, reference wavelength 490 nm).

### Real-time cytotoxicity assay

To determine the time-dependent cytotoxic effect of artocarpin on lung cancer cells, the xCELLigence Real-Time Cell Analyzer (ACEA Biosciences, San Diego, CA, USA) was also used [56]. Cell viability was measured over a 48 hour period following treatment with 10  $\mu$ M artocarpin with or without inhibitors.

### Flow cytometric analysis

Evaluation of apoptosis was performed using an Annexin-V-FITC/propidium iodide (PI) apoptosis kit as described previously [51]. Following treatment with artocarpin with or without inhibitors, cells were labeled with Annexin-V and PI, and then evaluated by a flow cytometer.

### Cell transfection of siRNAs

The human p47<sup>phox</sup> siRNA (SC-29422), Nox2 siRNA (gp91<sup>phox</sup>, SC35503) and scrambled siRNA (SC-

37007) were purchased from Santa Cruz Biotechnology (CA, USA). Transient transfections with various siRNAs (100 nM) were performed using Lipofectamine transfection reagent in accordance with the manufacturer's protocols. The siRNA used in this study were labeled with EGFP. The transfection efficiency was evaluated by transfection with EGFP, and was determined to be approximately 60%.

### Western blotting

Cells were seeded onto 12-well plates and serum starved for 24 h. Following treatment with artocarpin (10  $\mu$ M) with or without inhibitors or siRNAs for different periods of time, cells were collected and lysed in lysis buffer. The protein concentration was measured by the BCA kit. Proteins were separated using sodium dodecyl sulfate polyacrylamide gel electrophoresis (SDS-PAGE). Following transfer onto nitrocellulose membranes, the proteins were incubated with various antibodies overnight at 4°C, including phospho-p65, cytochrome c, p-ERK1/2, p-p38, p-AKT, caspase-3, phospho-p53 (Ser15), PUMA, Apaf-1, c-Myc and Noxa. Secondary anti-goat or anti-mouse horseradish peroxidase antibodies (1:2000 dilution) were then added for 1 h, and the bands were visualized using ECL reagents and developed by Hyperfilm-ECL.

### Nuclear protein extraction

Extraction of nuclear proteins was performed as described previously [55]. After artocarpin treatment, cells were collected, centrifuged at 400  $\times$  g for 5 min at 4°C. The supernatant representing the cytoplasmic protein fraction was discarded, and the pellet was centrifuged at 11000  $\times$  g for 10 min at 4°C. The final supernatant representing the nuclear protein fraction was stored at -20°C. Western blotting with p65, Noxa or c-Myc monoclonal antibodies were performed on the nuclear fractions.

### Isolation of cell fraction

The cytosolic and plasma membrane fractions were isolated as previously described [33]. Cells were lysed in lysis buffer, and then centrifuged at 16,000 g for 20 min at 4°C. The supernatant which represented the cytosolic fraction was collected. Following centrifugation, the pellet (representing the plasma membrane fraction) was collected. Western blotting with p47<sup>phox</sup> monoclonal mouse antibody was carried out on the plasma membrane fractions.

### Measurement of NF- $\kappa$ B luciferase activity

The NF- $\kappa$ B promoter activity was evaluated using the luciferase assay kit (Promega, Madison, WI, USA) as described previously [57]. Cells were transfected with the pNF- $\kappa$ B-Luc plasmid (Clontech). Following treatment, luciferase assay solution was added, and the luminescence



was determined using a luminometer. The promoter luciferase activities were standardized to  $\beta$ -galactosidase.

### Measurement of NADPH oxidase activity

The NADPH oxidase (Nox) activity in lung cancer cells was evaluated by the lucigenin chemiluminescence assay as described previously [58, 59]. Following treatment, the cell membrane fraction was collected, NADPH (Sigma) (1  $\mu$ M) and lucigenin (Sigma) (20  $\mu$ M) were added, and chemiluminescence was determined using a Fluoroskan Ascent FL (Thermo®) in an out-of-coincidence mode.

### Determination of intracellular ROS generation

The  $H_2O_2$  levels were evaluated using the dichlorofluorescein diacetate (DCFH-DA) method. Following treatment, 10  $\mu$ M DCFH-DA was added to cells for 45 min at 37°C. The cells were then harvested and the fluorescence was determined using a Fluoroskan Ascent FL plate reader with wavelengths of 485 nm (excitation) and 530 nm (emission).

### Chemicals and fluorescent probes for studying ROS generation

The fluorescent dyes were obtained from Molecular Probes (Eugene, Oreg., USA). With regards to loading conditions for the fluorescent probes, the mitochondrial membrane potential dye Tetramethyl rhodamine ethyl ester (TMRM) was used at 100 nM, while the ROS probe 6-carboxy-2',7'-dichlorodihydrofluorescein diacetate (DCF) was used at 500 nM. Cells were incubated with the fluorescent probes for 20–30 min at room temperature, and then rinsed with PBS-buffered saline solution. Subsequently, cells were mounted on a cell chamber, and visualized using a Leica confocal microscope (model TCSNT) with filters specific for DCF (excitation 450–490 nm, emission 515–565 nm) and TMRM (excitation 540–550 nm, emission 590–600 nm).

### Electrophoretic mobility-shift assay (EMSA)

The procedures for EMSA has been described previously [33, 58, 60]. Nuclear proteins were isolated with NE-PER reagent (Pierce, Rockford, IL, USA) in accordance with the manufacturer's instructions. The Light Shift chemiluminescence EMSA kit (Pierce) was used to determine the NF- $\kappa$ B binding activity of nuclear proteins. The sequences of the double-stranded EMSA probes were 5'-AGTTGAGGGGACTTTCCAGGC-3' and 3'-TCAACTCCCCTGAAAGGGT CCG-5' for NF- $\kappa$ B.

### Immunofluorescence staining

Growth-arrested A549 and H1299 cells were pretreated with or without inhibitors for 1 h, and then

treated with 10  $\mu$ M artocarpin. Cells were washed twice with ice-cold PBS, then fixed and incubated with an anti-p65 antibody [61]. Images were visualized by fluorescence microscopy (Zeiss, Axiovert 200 M).

### Mice tumor xenograft study

Six weeks old male SCID mice [BALB/cA-nu (nu/nu)] were obtained from the National Science Council Animal Center (Taipei, Taiwan) and kept in a pathogen-free environment. A549 or H1299 cells ( $1 \times 10^6$  cells in 200  $\mu$ l normal saline) were injected subcutaneously into the flanks of mice, and tumors were allowed to grow for 14 days, reaching approximately 100 mm<sup>3</sup> in size. The mice (10 mice/group) were then treated with vehicle or 1 mg/kg artocarpin daily for 21 days. The tumor volume was determined twice a week using a caliper, according to the formula  $V = (LW^2) \pi/6$ : where  $V$  = volume (mm<sup>3</sup>),  $L$  = biggest diameter (mm),  $W$  = smallest diameter (mm). Animal studies adhered to institutional guidelines and were approved by the Animal Care Committee of Shin-Kong Wu Ho-Su Memorial Hospital.

### ACKNOWLEDGMENTS

We are grateful for financial support from the Chang Gung Medical Research Program Foundation (grants CMRPGMC0011, CMRPGMC0012, CMRPF6F0011), the Ministry of Science and Technology of Taiwan (MOST 105-2320-B-255-002) and China Medical University Hospital (DMR-105-074, DMR-106-038, DMR-102-069).

### CONFLICTS OF INTEREST

All of the authors declare no conflicts of interest.

### Authors' contributions

MHT and JFL performed the experiments and wrote the manuscript. JFL, ZCL, YCC, YCL, HCL, MCC and LFH supervised the Western blotting, qPCR, luciferase reporter assay and ELISA assay and oversaw analysis of the results. CWL and MHT helped in writing of the manuscript. YCC and JFL designed the animal experiments. MHT and CWL designed the experimental protocols, supervised all experiments, interpreted the results and contributed to writing the paper. All authors have read and approved the final manuscript.

### REFERENCES

1. Bray F, Jemal A, Grey N, Ferlay J, Forman D. Global cancer transitions according to the Human Development Index (2008–2030): a population-based study. *Lancet Oncol.* 2012; 13:790–801.

2. Khan HY, Zubair H, Ullah MF, Ahmad A, Hadi SM. A prooxidant mechanism for the anticancer and chemopreventive properties of plant polyphenols. *Curr Drug Targets*. 2012; 13:1738–1749.
3. Sui X, Kong N, Ye L, Han W, Zhou J, Zhang Q, He C, Pan H. p38 and JNK MAPK pathways control the balance of apoptosis and autophagy in response to chemotherapeutic agents. *Cancer Lett*. 2014; 344:174–179.
4. Ivanova D, Bakalova R, Lazarova D, Gadjeva V, Zhelev Z. The impact of reactive oxygen species on anticancer therapeutic strategies. *Adv Clin Exp Med*. 2013; 22:899–908.
5. Fulda S, Debatin KM. Apoptosis signaling in tumor therapy. *Ann N Y Acad Sci*. 2004; 1028:150–156.
6. Fulda S, Debatin KM. Extrinsic versus intrinsic apoptosis pathways in anticancer chemotherapy. *Oncogene*. 2006; 25:4798–4811.
7. Petrelli R, Vita P, Torquati I, Felczak K, Wilson DJ, Franchetti P, Cappellacci L. Novel inhibitors of inosine monophosphate dehydrogenase in patent literature of the last decade. *Recent Pat Anticancer Drug Discov*. 2013; 8:103–125.
8. Shen C, Chien CR, Geynisman DM, Smieliauskas F, Shih YC. A review of economic impact of targeted oral anticancer medications. *Expert Rev Pharmacoecon Outcomes Res*. 2014; 14:45–69.
9. Vera-Badillo FE, Al-Mubarak M, Templeton AJ, Amir E. Benefit and harms of new anti-cancer drugs. *Curr Oncol Rep*. 2013; 15:270–275.
10. Brandes RP, Weissmann N, Schroder K. Nox family NADPH oxidases: Molecular mechanisms of activation. *Free Radic Biol Med*. 2014; 76:208–226.
11. Day BJ. Antioxidant therapeutics: Pandora's box. *Free Radic Biol Med*. 2014; 66:58–64.
12. Singh S, Brocker C, Koppaka V, Chen Y, Jackson BC, Matsumoto A, Thompson DC, Vasiliou V. Aldehyde dehydrogenases in cellular responses to oxidative/electrophilic stress. *Free Radic Biol Med*. 2013; 56:89–101.
13. Devasagayam TP, Tilak JC, Boloor KK, Sane KS, Ghaskadbi SS, Lele RD. Free radicals and antioxidants in human health: current status and future prospects. *J Assoc Physicians India*. 2004; 52:794–804.
14. Farmer EE, Mueller MJ. ROS-mediated lipid peroxidation and RES-activated signaling. *Annu Rev Plant Biol*. 2013; 64:429–450.
15. Radak Z, Zhao Z, Goto S, Koltai E. Age-associated neurodegeneration and oxidative damage to lipids, proteins and DNA. *Mol Aspects Med*. 2011; 32:305–315.
16. Zhang W, Xiao S, Ahn DU. Protein oxidation: basic principles and implications for meat quality. *Crit Rev Food Sci Nutr*. 2013; 53:1191–1201.
17. Witte AB, Anestel K, Jerremalm E, Ehrsson H, Arner ES. Inhibition of thioredoxin reductase but not of glutathione reductase by the major classes of alkylating and platinum-containing anticancer compounds. *Free Radic Biol Med*. 2005; 39:696–703.
18. Alexandre J, Hu Y, Lu W, Pelicano H, Huang P. Novel action of paclitaxel against cancer cells: bystander effect mediated by reactive oxygen species. *Cancer Res*. 2007; 67:3512–3517.
19. Colin DJ, Limagne E, Ragot K, Lizard G, Ghiringhelli F, Solary E, Chauffert B, Latruffe N, Delmas D. The role of reactive oxygen species and subsequent DNA-damage response in the emergence of resistance towards resveratrol in colon cancer models. *Cell Death Dis*. 2014; 5:e1533.
20. Li GX, Chen YK, Hou Z, Xiao H, Jin H, Lu G, Lee MJ, Liu B, Guan F, Yang Z, Yu A, Yang CS. Pro-oxidative activities and dose-response relationship of (-)-epigallocatechin-3-gallate in the inhibition of lung cancer cell growth: a comparative study *in vivo* and *in vitro*. *Carcinogenesis*. 2010; 31:902–910.
21. Han X, Xu B, Beevers CS, Odaka Y, Chen L, Liu L, Luo Y, Zhou H, Chen W, Shen T, Huang S. Curcumin inhibits protein phosphatases 2A and 5, leading to activation of mitogen-activated protein kinases and death in tumor cells. *Carcinogenesis*. 2012; 33:868–875.
22. Changchien JJ, Chen YJ, Huang CH, Cheng TL, Lin SR, Chang LS. Quinacrine induces apoptosis in human leukemia K562 cells via p38 MAPK-elicited BCL2 down-regulation and suppression of ERK/c-Jun-mediated BCL2L1 expression. *Toxicol Appl Pharmacol*. 2015; 284:33–41.
23. Lee WJ, Hsiao M, Chang JL, Yang SF, Tseng TH, Cheng CW, Chow JM, Lin KH, Lin YW, Liu CC, Lee LM, Chien MH. Quercetin induces mitochondrial-derived apoptosis via reactive oxygen species-mediated ERK activation in HL-60 leukemia cells and xenograft. *Arch Toxicol*. 2014; 89:1103–17.
24. Wartenberg M, Hoffmann E, Schwindt H, Grunheck F, Petros J, Arnold JR, Hescheler J, Sauer H. Reactive oxygen species-linked regulation of the multidrug resistance transporter P-glycoprotein in Nox-1 overexpressing prostate tumor spheroids. *FEBS Lett*. 2005; 579:4541–4549.
25. Li-Weber M. Targeting apoptosis pathways in cancer by Chinese medicine. *Cancer Lett*. 2013; 332:304–312.
26. Macip S, Igarashi M, Berggren P, Yu J, Lee SW, Aaronson SA. Influence of induced reactive oxygen species in p53-mediated cell fate decisions. *Mol Cell Biol*. 2003; 23:8576–8585.
27. Paletta-Silva R, Rocco-Machado N, Meyer -Fernandes JR. NADPH oxidase biology and the regulation of tyrosine kinase receptor signaling and cancer drug cytotoxicity. *Int J Mol Sci*. 2013; 14:3683–3704.
28. Dej-Adisai S, Meechai I, Puripattanavong J, Kummee S. Antityrosinase and antimicrobial activities from Thai medicinal plants. *Arch Pharm Res*. 2014; 37:473–483.
29. Pitaksuteepong T, Somsiri A, Waranuch N. Targeted transfollicular delivery of artocarpin extract from *Artocarpus incisos* by means of microparticles. *Eur J Pharm Biopharm*. 2007; 67:639–645.
30. Lee CW, Ko HH, Lin CC, Chai CY, Chen WT, Yen FL. Artocarpin attenuates ultraviolet B-induced skin damage in



- hairless mice by antioxidant and anti-inflammatory effect. *Food Chem Toxicol.* 2013; 60:123–129.
31. Arung ET, Wicaksono BD, Handoko YA, Kusuma IW, Shimizu K, Yulia D, Sandra F. Cytotoxic effect of artocarpin on T47D cells. *J Nat Med.* 2010; 64:423–429.
  32. Wang YH, Hou AJ, Chen L, Chen DF, Sun HD, Zhao QS, Bastow KF, Nakanish Y, Wang XH, Lee KH. New isoprenylated flavones, artochamins A–E, and cytotoxic principles from *Artocarpus chama*. *J Nat Prod.* 2004; 67:757–761.
  33. Tsai MH, Lin ZC, Liang CJ, Yen FL, Chiang YC, Lee CW. Eupafolin inhibits PGE2 production and COX2 expression in LPS-stimulated human dermal fibroblasts by blocking JNK/AP-1 and Nox2/p47(phox) pathway. *Toxicol Appl Pharmacol.* 2014; 279:240–251.
  34. Hao W, Yuan X, Yu L, Gao C, Sun X, Wang D, Zheng Q. Licochalcone A-induced human gastric cancer BGC-823 cells apoptosis by regulating ROS-mediated MAPKs and PI3K/AKT signaling pathways. *Sci Rep.* 2015; 5:10336.
  35. Kim MS, Blake M, Baek JH, Kohlhagen G, Pommier Y, Carrier F. Inhibition of histone deacetylase increases cytotoxicity to anticancer drugs targeting DNA. *Cancer Res.* 2003; 63:7291–7300.
  36. Tanel A, Averill -Bates DA. P38 and ERK mitogen-activated protein kinases mediate acrolein-induced apoptosis in Chinese hamster ovary cells. *Cell Signal.* 2007; 19:968–977.
  37. Wu GS. The functional interactions between the p53 and MAPK signaling pathways. *Cancer Biol Ther.* 2004; 3:156–161.
  38. Pal PB, Sinha K, Sil PC. Mangiferin, a natural xanthone, protects murine liver in Pb(II) induced hepatic damage and cell death via MAP kinase, NF-kappaB and mitochondria dependent pathways. *PLoS One.* 2013; 8:e56894.
  39. Tao L, Forester SC, Lambert JD. The role of the mitochondrial oxidative stress in the cytotoxic effects of the green tea catechin, (-)-epigallocatechin-3-gallate, in oral cells. *Mol Nutr Food Res.* 2014; 58:665–676.
  40. Botta B, Vitali A, Menendez P, Misiti D, Delle Monache G. Prenylated flavonoids: pharmacology and biotechnology. *Curr Med Chem.* 2005; 12:717–739.
  41. Chen Z, Jin K, Gao L, Lou G, Jin Y, Yu Y, Lou Y. Anti-tumor effects of bakuchiol, an analogue of resveratrol, on human lung adenocarcinoma A549 cell line. *Eur J Pharmacol.* 2010; 643:170–179.
  42. Sonoda JI, Ikeda R, Baba Y, Narumi K, Kawachi A, Tomishige E, Nishihara K, Takeda Y, Yamada K, Sato K, Motoya T. Green tea catechin, epigallocatechin-3-gallate, attenuates the cell viability of human non-small-cell lung cancer A549 cells via reducing Bcl-xL expression. *Exp Ther Med.* 2014; 8:59–63.
  43. Wang P, Zhang L, Peng H, Li Y, Xiong J, Xu Z. The formulation and delivery of curcumin with solid lipid nanoparticles for the treatment of on non-small cell lung cancer both *in vitro* and *in vivo*. *Mater Sci Eng C Mater Biol Appl.* 2013; 33:4802–4808.
  44. Thannickal VJ, Fanburg BL. Reactive oxygen species in cell signaling. *Am J Physiol Lung Cell Mol Physiol.* 2000; 279:L1005–1028.
  45. Hsieh HL, Wang HH, Wu CY, Yang CM. Reactive Oxygen Species-Dependent c-Fos/Activator Protein 1 Induction Upregulates Heme Oxygenase-1 Expression by Bradykinin in Brain Astrocytes. *Antioxid Redox Signal.* 2010; 13:1829–1844.
  46. Wang JP, Yu YC, Chen SP, Liang HC, Lin CW, Fang K. The collective nuclear migration of p53 and phosphorylated S473 of Akt during ellipticine-mediated apoptosis in human lung epithelial cancer cells. *Mol Cell Biochem.* 2015; 407:123–33.
  47. Taylor CA, Zheng Q, Liu Z, Thompson JE. Role of p38 and JNK MAPK signaling pathways and tumor suppressor p53 on induction of apoptosis in response to Ad-elf5A1 in A549 lung cancer cells. *Mol Cancer.* 2013; 12:35.
  48. Allen WL, Turkington RC, Stevenson L, Carson G, Coyle VM, Hector S, Dunne P, Van Schaeybroeck S, Longley DB, Johnston PG. Pharmacogenomic profiling and pathway analyses identify MAPK-dependent migration as an acute response to SN38 in p53 null and p53-mutant colorectal cancer cells. *Mol Cancer Ther.* 2012; 11:1724–1734.
  49. Jeong SJ, Dasgupta A, Jung KJ, Um JH, Burke A, Park HU, Brady JN. PI3K/AKT inhibition induces caspase-dependent apoptosis in HTLV-1-transformed cells. *Virology.* 2008; 370:264–272.
  50. Yun HS, Baek JH, Yim JH, Lee SJ, Lee CW, Song JY, Um HD, Park JK, Park IC, Hwang SG. Knockdown of hepatoma-derived growth factor-related protein-3 induces apoptosis of H1299 cells via ROS-dependent and p53-independent NF-kappaB activation. *Biochem Biophys Res Commun.* 2014; 449:471–476.
  51. Qing Y, Liang Y, Du Q, Fan P, Xu H, Xu Y, Shi N. Apoptosis induced by trimethyltin chloride in human neuroblastoma cells SY5Y is regulated by a balance and cross-talk between NF-kappaB and MAPKs signaling pathways. *Arch Toxicol.* 2013; 87:1273–1285.
  52. Wang LH, Li Y, Yang SN, Wang FY, Hou Y, Cui W, Chen K, Cao Q, Wang S, Zhang TY, Wang ZZ, Xiao W, Yang JY, et al. Gambogic acid synergistically potentiates cisplatin-induced apoptosis in non-small-cell lung cancer through suppressing NF-kappaB and MAPK/HO-1 signalling. *Br J Cancer.* 2014; 110:341–352.
  53. Meylan E, Dooley AL, Feldser DM, Shen L, Turk E, Ouyang C, Jacks T. Requirement for NF-kappaB signalling in a mouse model of lung adenocarcinoma. *Nature.* 2009; 462:104–107.
  54. Ren W, Qiao Z, Wang H, Zhu L, Zhang L. Flavonoids: promising anticancer agents. *Med Res Rev.* 2003; 23:519–534.
  55. Tsai AC, Pai HC, Wang CY, Liou JP, Teng CM, Wang JC, Pan SL. *In vitro* and *in vivo* anti-tumour effects of MPT0B014, a novel derivative aroylquinoline, and in combination with erlotinib in human non-small-cell lung cancer cells. *Br J Pharmacol.* 2014; 171:122–133.

56. Lin ZC, Lee CW, Tsai MH, Ko HH, Fang JY, Chiang YC, Liang CJ, Hsu LF, Hu SC, Yen FL. Eupafolin nanoparticles protect HaCaT keratinocytes from particulate matter-induced inflammation and oxidative stress. *Int J Nanomedicine*. 2016; 11:3907–3926.
57. Obara H, Takayanagi A, Hirahashi J, Tanaka K, Wakabayashi G, Matsumoto K, Shimazu M, Shimizu N, Kitajima M. Overexpression of truncated IkappaBalpha induces TNF-alpha-dependent apoptosis in human vascular smooth muscle cells. *Arterioscler Thromb Vasc Biol*. 2000; 20:2198–2204.
58. Yen FL, Tsai MH, Yang CM, Liang CJ, Lin CC, Chiang YC, Lee HC, Ko HH, Lee CW. Curcumin nanoparticles ameliorate ICAM-1 expression in TNF-alpha-treated lung epithelial cells through p47 (phox) and MAPKs/AP-1 pathways. *PLoS One*. 2013; 8:e63845.
59. Hsieh HL, Yang SH, Lee TH, Fang JY, Lin CF. Evaluation of Anti-Inflammatory Effects of *Helminthostachys zeylanica* Extracts via Inhibiting Bradykinin-Induced MMP-9 Expression in Brain Astrocytes. *Mol Neurobiol*. 2016; 53:5995–6005.
60. Lee CW, Lin ZC, Hu SC, Chiang YC, Hsu LF, Lin YC, Lee IT, Tsai MH, Fang JY. Urban particulate matter down-regulates filaggrin via COX2 expression/PGE2 production leading to skin barrier dysfunction. *Sci Rep*. 2016; 6:27995.
61. Lee IT, Lee CW, Tung WH, Wang SW, Lin CC, Shu JC, Yang CM. Cooperation of TLR2 with MyD88, PI3K, and Rac1 in lipoteichoic acid-induced cPLA2/COX-2-dependent airway inflammatory responses. *Am J Pathol*. 2010; 176:1671–1684.

RESEARCH ARTICLE

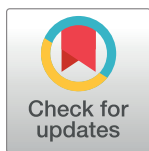
# CIL-102-Induced Cell Cycle Arrest and Apoptosis in Colorectal Cancer Cells via Upregulation of p21 and GADD45

Wen-Shih Huang<sup>1,2‡</sup>, Yi-Hung Kuo<sup>1,3‡</sup>, Hsing-Chun Kuo<sup>4,5,6</sup>, Meng-Chiao Hsieh<sup>1,3</sup>, Cheng-Yi Huang<sup>1</sup>, Ko-Chao Lee<sup>7</sup>, Kam-Fai Lee<sup>8</sup>, Chien-Heng Shen<sup>3,9</sup>, Shui-Yi Tung<sup>2,9</sup>, Chih-Chuan Teng<sup>4,6\*</sup>

**1** Division of Colon and Rectal Surgery, Department of Surgery, Chang Gung Memorial Hospital, Chiayi, Taiwan, **2** Chang Gung University College of Medicine, Taoyuan, Taiwan, **3** Graduate Institute of Clinical Medical Sciences, College of Medicine, Chang Gung University, Chiayi, Taiwan, **4** Department of Nursing, Chang Gung University of Science and Technology, Chiayi, Taiwan, **5** Research Center for Industry of Human Ecology and Research Center for Chinese Herbal Medicine, College of Human Ecology, Chang Gung University of Science and Technology, Taoyuan, Taiwan, **6** Chronic Diseases and Health Promotion Research Center, CGUST, Chiayi, Taiwan, **7** Division of Colorectal Surgery, Department of Surgery, Chang Gung Memorial Hospital, Kaohsiung Medical Center, Chang Gung University College of Medicine, Kaohsiung, Taiwan, **8** Department of Pathology, Chang Gung Memorial Hospital at Chiayi, Taiwan, **9** Department of Hepato-Gastroenterology, Chang Gung Memorial Hospital, Chiayi, Taiwan

‡ These authors contributed equally as first author on this work.

\* [ccteng@gw.cgust.edu.tw](mailto:ccteng@gw.cgust.edu.tw)



## OPEN ACCESS

**Citation:** Huang W-S, Kuo Y-H, Kuo H-C, Hsieh M-C, Huang C-Y, Lee K-C, et al. (2017) CIL-102-Induced Cell Cycle Arrest and Apoptosis in Colorectal Cancer Cells via Upregulation of p21 and GADD45. PLoS ONE 12(1): e0168989. doi:10.1371/journal.pone.0168989

**Editor:** Aamir Ahmad, University of South Alabama Mitchell Cancer Institute, UNITED STATES

**Received:** November 12, 2016

**Accepted:** December 9, 2016

**Published:** January 9, 2017

**Copyright:** © 2017 Huang et al. This is an open access article distributed under the terms of the [Creative Commons Attribution License](https://creativecommons.org/licenses/by/4.0/), which permits unrestricted use, distribution, and reproduction in any medium, provided the original author and source are credited.

**Data Availability Statement:** All relevant data are within the paper.

**Funding:** This work was supported by Chang Gung Memorial Hospital, Linkou CMRPF6D0071, CMRPF6D0072, CMRPF6D0073 (Dr Chih-Chuan Teng); Chang Gung Memorial Hospital, Linkou, CMRPG6E0192 (Dr Cheng-Yi Huang); Chang Gung Memorial Hospital, Linkou, CMRPG6F0251 (Dr Wen-Shih Huang); and Chang Gung Memorial Hospital, Linkou, CMRPG690171, CMRPG690172

## Abstract

CIL-102 (1-[4-(furo[2,3-b]quinolin-4-ylamino)phenyl]ethanone) is a well-known, major active agent of the alkaloid derivative of *Camptotheca acuminata* with valuable biological properties, including anti-tumorigenic activity. In this study, we investigated the molecular mechanisms by which CIL-102 mediated the induction of cell death, and we performed cell cycle G2/M arrest to clarify molecular changes in colorectal cancer cells (CRC). Treatment of DLD-1 cells with CIL-102 resulted in triggering the extrinsic apoptosis pathway through the activation of Fas-L, caspase-8 and the induction of Bid cleavage and cytochrome c release in a time-dependent manner. In addition, CIL-102 mediated apoptosis and G2/M arrest by phosphorylation of the Jun N-terminus kinase (JNK1/2) signaling pathway. This resulted in the expression of NFκB p50, p300 and CREB-binding protein (CBP) levels, and in the induction of p21 and GADD45 as well as the decreased association of cdc2/cyclin B. Furthermore, treatment with the JNK1/2 (SP600125), NFκB (PDTI) or the p300/CBP (C646) inhibitors abolished CIL-102-induced cell cycle G2/M arrest and reversed the association of cdc2 with cyclin B. Therefore, we demonstrated that there was an increase in the cellular levels of p21 and GADD45 by CIL-102 reduction in cell viability and cell cycle arrest via the activation of the JNK1/2, NFκB p50, p300 and CBP signaling modules. Collectively, our results demonstrated that CIL-102 induced cell cycle arrest and apoptosis of colon cancer cells by upregulating p21 and GADD45 expression and by activating JNK1/2, NFκB p50 and p300 to provide a new mechanism for CIL-102 treatment.

(Dr Yi-Hung Kuo). There is no financial/commercial conflict of interest.

**Competing Interests:** The authors have declared that no competing interests exist.

## Introduction

Colorectal cancer (CRC), an aggressive malignant disease with a poor prognosis, is the fourth leading cause of cancer-related death in the industrialized world [1]. A large body of evidence indicates CRC cells' self-sufficiency in growth signals, their ability to escape from apoptosis, and their tendency toward tissue invasion and metastasis [2]. Moreover, chemotherapy treatments for CRC are often ineffective because of the intrinsic chemoresistance of these tumors [3]. Therefore, it is imperative to develop more effective drugs. Apoptosis is a morphologically and biochemically driven process, while impaired apoptosis and defects in the regulation of the cell cycle are hallmarks that contribute to cancer growth and aggressiveness [4]. Recent studies have suggested that phenolic phytochemicals having antioxidant activity should short-circuit the signaling events and eventually inhibit CRC cell proliferation [5]. Previous study has shown that Camptothecin (CPT) is an alkaloid originally isolated from the bark and stem of *Camptotheca acuminata*, a tree native to China [6]. As described in detail previously that CPT induces cancer cells apoptosis, interacts with DNA to form a complex, and reduces DNA, RNA, and protein synthesis [7]. A number of furo[2,3-b]quinoline derivatives, such as CIL-102, have also been synthesized and have been found to exhibit antitumor effects [8]. The survival curve showed that CIL-102 may possess antitumor activity against cancer cells of the prostate and breast, as well as those found in leukemia and cervical carcinoma [9]. This is studied by the inhibition of tubulin polymerization followed by apoptosis processed via the caspase and non-caspase pathways [10]. However, little is known about the anti-colorectal cancer mechanism. Similarly, the mechanism by which CIL-102 initiates cell death and cell cycle arrest and by which the signaling cascades become activated remains poorly understood.

Chemopreventive compounds may induce cell apoptosis through the regulation of the MAPK pathways [11]. The mitogen-activated protein kinases (MAPKs) are a family of protein kinases that transfer signals of stimuli from the cell membrane to the nucleus [12]. Intracellular signaling pathways for apoptosis have mainly focused on two cascades, the extrinsic and intrinsic pathways, which both lead to the kinase cascade [13]. The extrinsic pathway is triggered at the plasma membrane by the activation of TNFR1/Fas. This results in the cleavage of cytosolic BID to truncated tBID by caspase-8, which translocates to the mitochondria [14]. The kinase-signaling cascade, the intrinsic pathway, was originally identified as an important pathway in the transduction of apoptotic signals initiated by stress or anticancer drug stimuli [15]. The release of cytochrome c from the mitochondria represents a critical event in initiating the activation of caspase 9 and caspase 3 [16]. Herein, the effect of CIL-102-mediated apoptosis and the triggering mechanism of the signaling pathways on human CRC remain unclear.

Proliferation of CRC cells usually fails to control checkpoints, one of which is the G2/M phase checkpoint [17]. The inhibitors of the cell cycle progression stimulatory signaling pathway have been shown to target cdc2, cyclin B1 and cyclin A, which are required for mitotic entry in mammalian cells, thereby suppressing cdc2 activity by inhibiting the accumulation of cyclin B1 mRNA and protein [18]. DNA damage also correlates with the inhibition of cdc2-cyclin B kinase activity through clinical treatment with anti-microtubule drugs to inhibit colorectal cells' proliferation and induce cell growth arrest [10, 17]. A cyclin-dependent kinase inhibitor called p21/WAF1 plays an important role as a tumor suppressor [19]. With respect to cell-cycle regulation, p21 has been reported to induce G2/M arrest by blocking CDK1 activity. It was suggested that p21/WAF1 and Gadd45 may participate in a coordinated manner in a DNA damage response [20]. Evidence has emerged that GADD45, a cell cycle regulated nuclear protein, disrupts the interactions of Cdc2 with cyclin B1 and that GADD45 may thus induce G2/M arrest. Therefore, it is imperative to investigate how diet prevents the malignance

and progression of CRC [21]. In addition to previous strategies that can reduce CRC risk, dietary phytochemicals are emerging as a promising chemoprevention approach. The cell cycle regulation and the *in vivo* anti-tumor effect of the 9-anilinofuroquinoline derivative, CIL-102, are not clearly known in CRC. GADD45 and p21, therefore, may represent a unique target for drugs that induce cell cycle arrest, apoptosis, and differentiation such as CIL-102.

The 9-anilinofuroquinoline derivative, CIL-102, has been used clinically as an antiseptic drug, which was not a natural product and, is impossible to be found in the bark and stem of *Camptotheca acuminata* [22]. Numerous studies have suggested that it possesses anticancer and chemopreventive properties and inhibits the proliferation of tumor cells [23, 24]. Our recent study showed that CIL-102 inhibited the proliferation and the invasiveness property in glioma cells and altered the expression of genes related to cell cycle regulation by activating the ERK1/2 and Cdc25cSer<sup>216</sup> cell-cycle-related proteins and inducing ROS generation [23]. However, the mechanism by which CIL-102 induces apoptosis remains poorly understood. In our study, we first investigated whether CIL-102 had a dose-dependent effect on the cytotoxicity of CRC. It was found to cause apoptosis, which was preceded by the sustained activation of JNK, activated caspase-8 and cleaved Bid protein to its truncated form, t-Bid, and caused the release of cytochrome c. It then directly activated the downstream effector caspases such as caspase-3 and caspase-9. Our results strongly suggested an essential role for the JNK1/2/NFκB p50/p300/CBP as well as the p21 and GADD45 pathways during the execution of cell cycle G2/M arrest, which might be controlled by inhibiting CRC cell proliferation and which seems to play a role in CIL-102-induced apoptosis.

## Materials and Methods

### Chemical reagents and antibodies

All culture materials were purchased from Gibco (Grand Island, NY, USA). 1-[4-(Furo[2,3-b]quinolin-4-ylamino)phenyl]ethanone (CIL-102), 3-(4,5-dimethylthiazol-2-yl)-2,5-diphenyltetrazolium bromide (MTT), ROS scavenger (*N*-acetyl cysteine [NAC]), 2,7-dichlorodihydrofluorescein diacetate (H<sub>2</sub>DCFDA), dihydroethidium (DHE), ERK inhibitor (PD98059), c-Jun N-terminal kinase (JNK1/2) inhibitor (SP600125), p38 inhibitor (SB203580), and mTOR inhibitor (rapamycin) were purchased from Sigma (St. Louis, MO, USA). Mouse monoclonal antibodies against cyclin A, cyclin D1, cyclin E, cyclin B1, acetylation of H3 (Ac-Histone H3) at Lys 9 and Lys 14, cytochrome c, caspase-3, -8, -9 and β-actin were purchased from Santa Cruz Biotechnology (Santa Cruz, CA, USA). Rabbit polyclonal antibodies against cdk2, ERK1/2Thr<sup>202</sup>Tyr<sup>204</sup>, p38 Thr<sup>180</sup>Tyr<sup>182</sup>, and JNK1/2 Thr<sup>183</sup>Tyr<sup>185</sup> mouse monoclonal cdc2, t-BID, p300, CBP, p21, GADD45, and Fas-L antibodies were purchased from Cell Signaling Technology (Beverly, MA, USA). SDS, NP-40, sodium deoxycholate, protease inhibitor cocktails were purchased from Sigma (St Louis, MO, USA).

### Cell culture

Human colon cancer cell line DLD-1 (CCL-221) and human colorectal carcinoma cell line HCT-116 (CCL-247) were purchased from American Type Culture Collection (ATCC). DLD-1 cells were cultured in RPMI 1640 medium composed of 10% fetal calf serum (FCS) (S0113; Biochrom KG, Berlin, Germany) and 1% antibiotics (100 units/mL of penicillin and 100 µg/mL of streptomycin) (Sigma Chemicals, St. Louis, MO, USA) and incubated at 37°C with 5% CO<sub>2</sub>. We purchased passage number 1 of human normal astrocytes (HNA) from ScienCell Research Laboratories (Carlsbad, CA) and cells were grown. Adhered cells were washed twice with PBS. HCT-116 was cultured in DMEM supplemented with 10% heat-inactivated newborn calf serum at 37°C in a humidified 5% CO<sub>2</sub> incubator [25].



## Cell growth and proliferation assay

The previously reported MTT quantitative colorimetric assay was previously described [23,26]. Cells were seeded and incubated with the various agents. Thereafter, the medium was changed, and cells were incubated with MTT (0.5 mg/mL) for 4 h. The viable cell number was directly proportional to the production of formazan, which was measured spectrophotometrically ( $\lambda = 563$  nm) after solubilization with isopropanol. Cell growth was determined by counting the cells at the indicated time points with a Coulter counter, combined with a trypan blue (0.2%) exclusion assay [27].

## Apoptosis assay and cell cycle distribution analysis

Changes in cell morphological characteristics during apoptosis were examined using fluorescence microscopy of 4',6-diamidino-2-phenylindole (DAPI)-stained cells, as described in detail previously [23,27]. The monolayer of cells was fixed with 4% paraformaldehyde for 30 min at room temperature. The fixed cells were permeabilized with 3 treatments in 0.2% Triton X-100 in phosphate-buffered saline, followed by incubation with 1  $\mu$ g/mL of DAPI for 30 min. The apoptotic nuclei were detected under 200 $\times$  magnification using a fluorescent microscope with a 340/380 nm excitation filter and were scored according to the percentage of apoptotic nuclei found in samples containing 200 to 300 cells.

Cell viability, as previously reported by Annexin V-FITC/ propidium iodide (Biosource International, USA), used to quantify the percentage of cells undergoing apoptosis, and the cells were washed prior to FACS analysis and Cell Quest software was used (Becton Dickinson). The results were presented as a percentage of the fluorescent intensity compared with the control sample. Data were analyzed with CellQuest and WinMDI software. The apoptotic cells (V+/PI-) were measured by the fluorescence-activated cell sorter analysis in a FACS analyzer (Becton Dickinson). The data represented three independent experiments [26].

Cell-cycle distribution was analyzed using flow cytometry. Cells stained with propidium iodide were analyzed with a FACScalibur™ (Becton Dickinson), and the data were analyzed using a mod-fit cell cycle analysis program [26].

## Preparation of total cell extracts and immunoblot analyses

Cells were lysed with a buffer containing 1% NP-40, 0.5% sodium deoxycholate, 0.1% sodium dodecyl sulfate (SDS), and a protease inhibitor mixture (phenylmethylsulfonyl fluoride, aprotinin, and sodium orthovanadate). The total cell lysate (50  $\mu$ g of protein) was separated by SDS-polyacrylamide gel electrophoresis (PAGE) (12% running, 4% stacking) and analyzed by using the designated antibodies and the Western-Light chemiluminescent detection system (Bio-Rad, Hercules, CA), as previously described [23,28].

## Statistical analysis

The experiments were performed in triplicate and data were reported as the mean  $\pm$  standard deviation from 3 independent experiments and evaluated by one-way ANOVA. Significant differences were established at  $P < 0.05$  [28].

## Results

### Effects of CIL-102 on the viability of human CRC cells

By evaluating the apoptosis and anti-invasion potential involving the signaling pathway, we assayed whether CIL-102 provides substantial therapeutic advantages. To determine whether CIL-102 is cytotoxic to human CRC cells, we evaluated the apoptosis and anti-tumor

proliferation potential involving the signaling pathway. We treated DLD-1, HCT-116 and normal human colonic epithelial cells (HCoEpiC) with a range of CIL-102 doses for 24 h and examined them by MTT assays. CIL-102 treatment resulted in a dose-dependent loss of cell viability, as shown in Fig 1A. After treatment with 1  $\mu$ M CIL-102 for 24 h, 55% and 50% of DLD-1 and HCT-116 cells ( $P < 0.01$ ), respectively, survived in culture (Fig 1A). However, CIL-102 did not significantly show cytotoxic effects in HCoEpiC cells. In addition, to verify CIL-102-induced cell toxicity, we examined the changes in cell morphology after CIL-102 exposure. Fig 1B shows that exposure to erinacine A for 24 h caused DLD-1 cells to morphologically display features of cell shrinking, with the growths to which they belong becoming smaller.

### CIL-102 induces apoptosis and cell cycle G2/M arrest in DLD-1 CRC cells

The addition of Annexin-V stain has led to similar findings (Fig 2). The extent of apoptosis of CIL-102 induction was quantified as a percentage of annexin V-positive cells and was shown as  $12 \pm 4$  (6 h),  $13 \pm 2$  (12 h), and  $26 \pm 3\%$  (24 h), respectively. Both experiments proved that CIL-102 elicits apoptosis. Cell cycle distribution analysis showed that CIL-102 induces cell cycle G2/M arrest in DLD-1 cells. As demonstrated in Fig 3, following a 24 h treatment with 1  $\mu$ M CIL-102, the percentages of G2/M phase cells increased to  $22 \pm 2$  (6 h),  $35 \pm 2$  (12 h), and  $52 \pm 2\%$  (24 h), respectively. These results suggest that CIL-102 induces G2/M arrest in a time-dependent manner.

### Activation of apoptosis pathway by CIL-102 in DLD-1 cells

Recent theories pertain to the persistent extrinsic apoptosis pathway involved in the binding of a ligand to one of the tumor necrosis factor families of death receptors, followed by the activation of caspase-8 by phytochemicals. It was concluded that the intrinsic pathways are linked through the ability of caspase-8 to cleave Bid, which in turn leads to the release of cytochrome c from the mitochondria pathways. To elucidate the events of CIL-102-stimulated DLD-1 cell death, we examined kinetic studies to evaluate Fas-L, caspase 8 and t-BID expression as well as caspase 3 and caspase 9 during a 24 h period. As shown in Fig 4, CIL-102 was shown to cause detectable and increased levels of Fas-L and cytochrome c in the cytosol and a time-dependent cleavage of Bid for 24 h. Treatment with CIL-102 resulted in proteolytic processing of the caspase 3 and caspase 9 (36 kDa) into two smaller subunits.

### Expression of p21 and GADD45 as well as NF $\kappa$ B p50/p300/CBP signaling pathways by CIL-102 in DLD-1 cells

Numerous investigations have shown the among proteins known to the transcriptional co-activator p300/CBP deserves DNA damage that control G2/M regulation and delayed entry into mitosis correlation with cdc2/cyclin B1 association [29]. To demonstrate the effect of CIL-102 on the cell-cycle-related proteins and the kinase-signaling pathway, we assessed whole-cell lysates from erinacine A-treated DLD-1 cells by Western blot analysis using antibodies against the expressed forms of p21 and GADD45 as well as NF $\kappa$ B p50/p300/CBP. As shown in Fig 5, treatment of DLD-1 cells with CIL-102 resulted in the marked expression of p21 and GADD45 as well as NF $\kappa$ B p50/p300/CBP compared with the control for a period of time points. In addition, the analysis showed a marked downregulation of cdc2/cyclin B1 association after CIL-102 treatment of DLD-1 cells in a time-dependent manner.

**Fig. 1A**

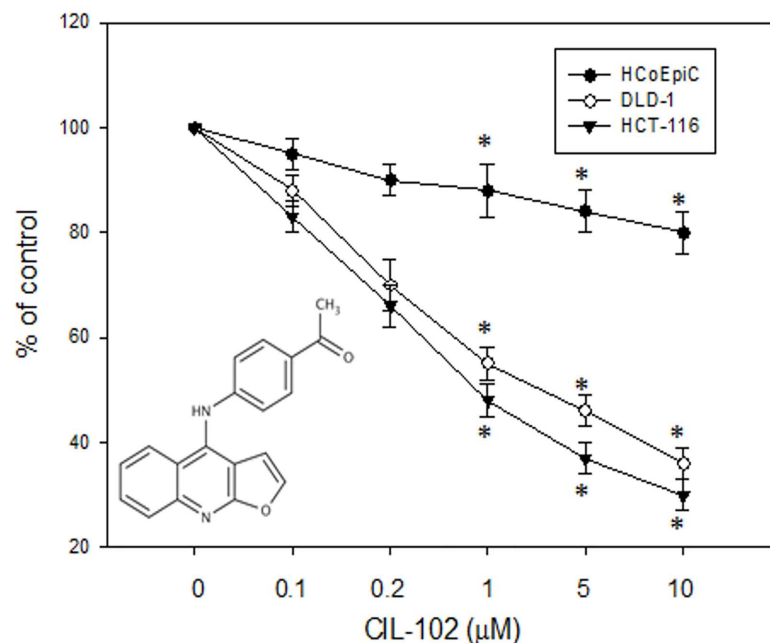


**Fig. 1B**

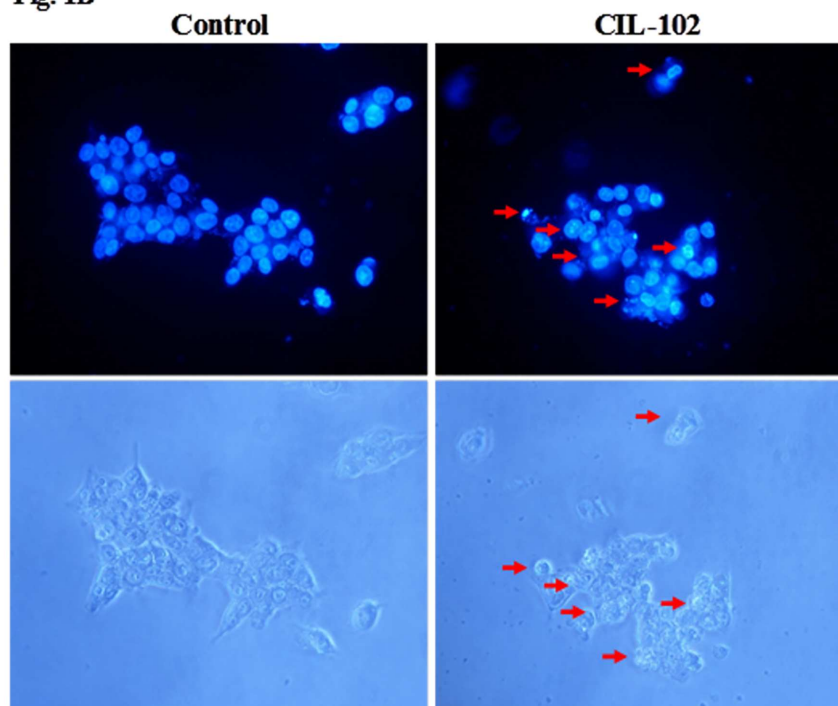


**Fig 1. Effect of CIL-102 on cell viability and morphological characteristics of human colorectal cancer DLD-1 cells, and its role in assessing cell death.** (A) DLD-1, HAT-116 and HCoEpiC cell were treated with either 0.1% DMSO (as control) or CIL-102 (0.1–10 mM) for 24 h and the proportion of surviving cells was measured by the MTT assay. (B) Changes in nuclei by DAPI staining. DLD-1 cells were treated with vehicle or 1 mM CIL-102 for 24 h, and stained with DAPI. Apoptotic cells were measured under fluorescence microscopy. The data were presented as the mean of three repeats from one independent experiment. Other

data in this figure is presented as mean  $\pm$  SD of three independent experiments. \* indicate means that are significantly different when compared to the control group of DLD-1 with  $P < 0.05$ .

doi:10.1371/journal.pone.0168989.g001

## JNK1/2 MAPK and p50/p300 pathways are involved in the regulation of CIL-102-induced cell death and cell cycle G2/M arrest in DLD-1 cells

Western blot analysis was used to determine whether CIL-102 induces apoptosis and cell cycle arrest by modulating the level of cell-cycle-related proteins, as shown in Fig 6A. The analysis showed a marked expression, with the treatment of DLD-1 cells with CIL-102 resulting in a time-dependent phosphorylation of JNK1/2 Thr<sup>183</sup>/Tyr<sup>185</sup> at both 3 h and 6 h. Activation

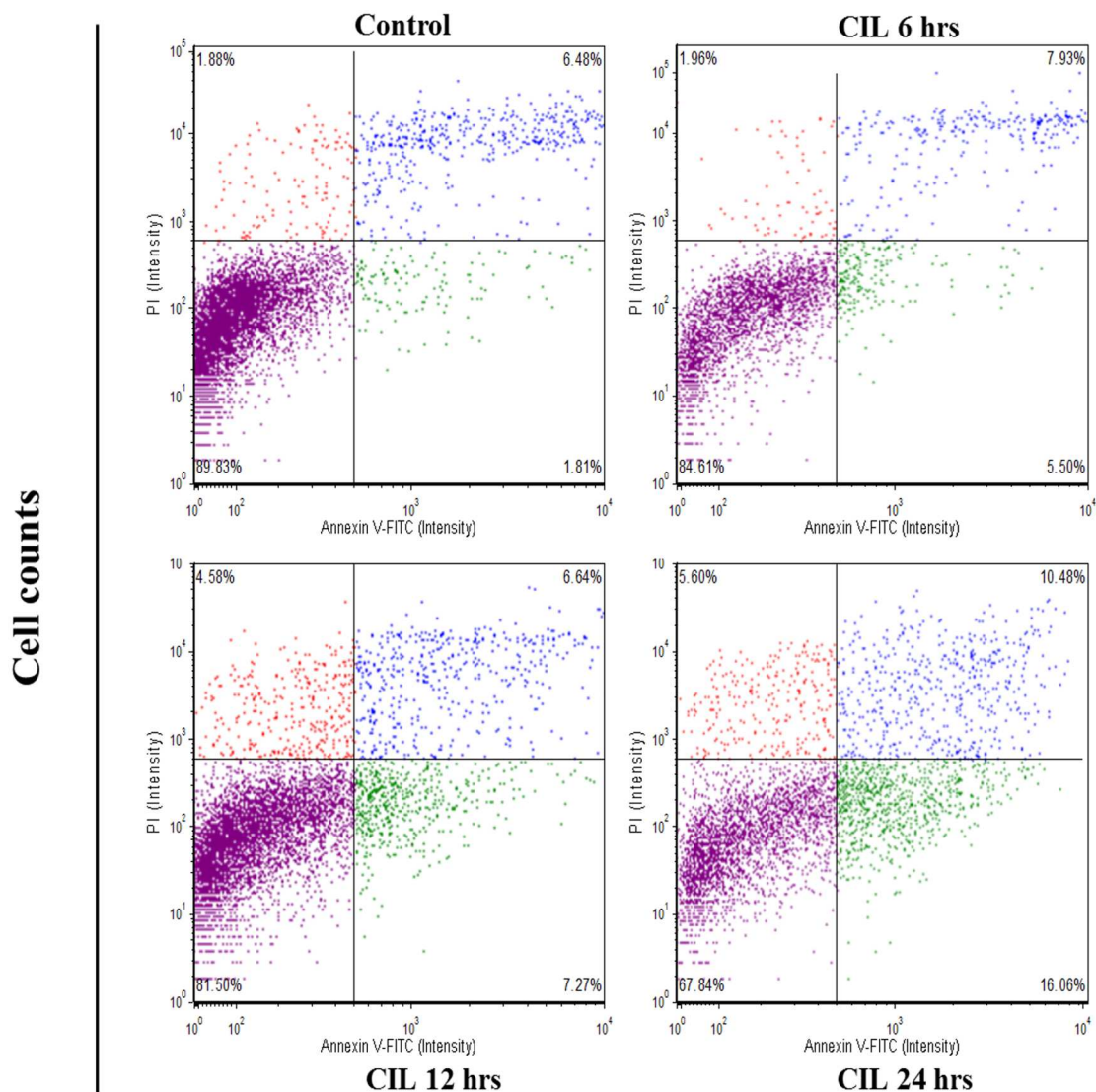


**Fig 2.** After an indicated treatment for 24 h, the DLD-1 cells were stained with FITC-conjugated Annexin-V and PI for flow cytometry analysis as described in Materials and methods. The percentages presented in each frame depicted the apoptotic cells. \* $P < 0.01$ , compared with the control group (0.2% DMSO).

doi:10.1371/journal.pone.0168989.g002

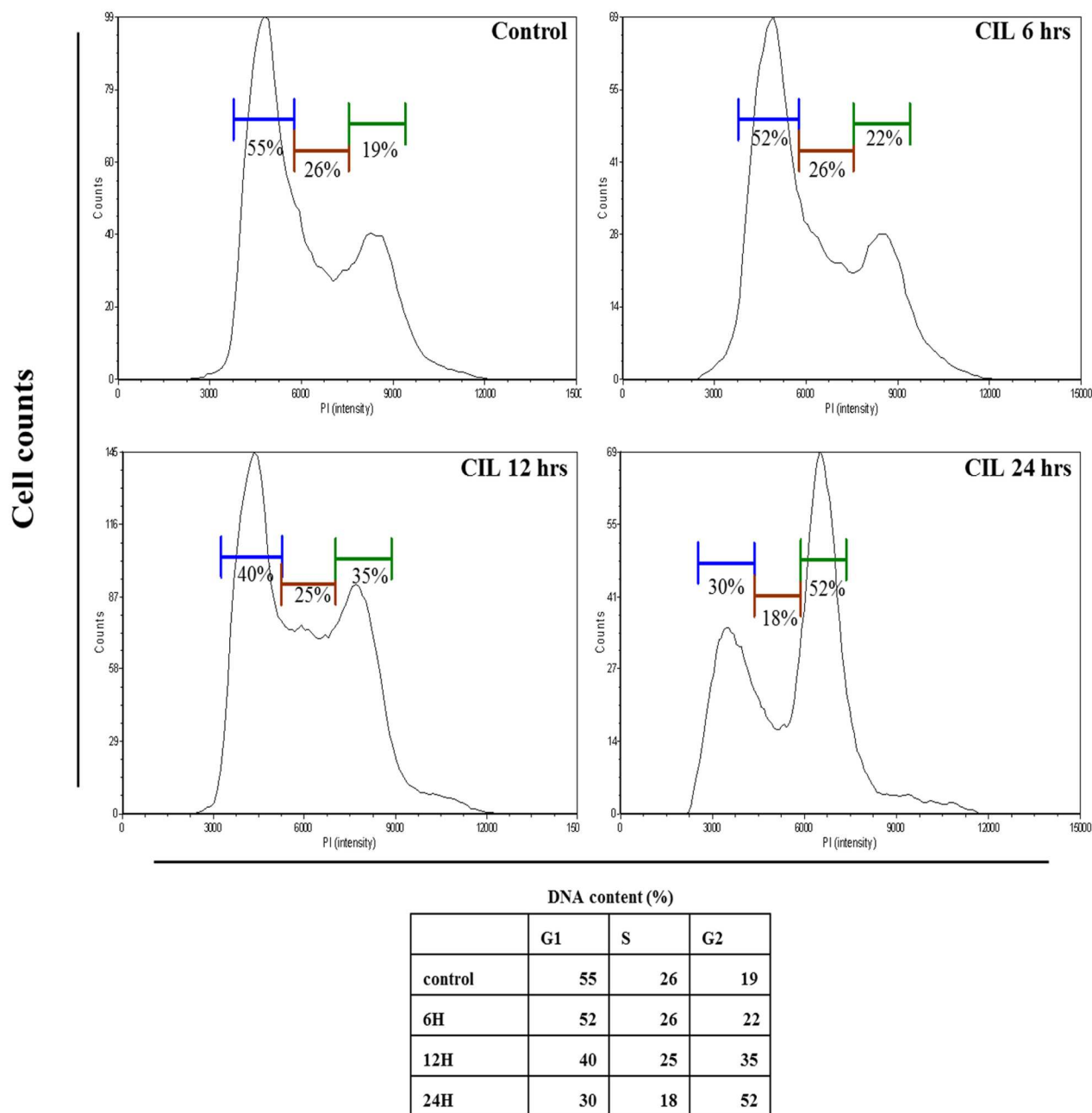


**Fig 3. Effect of CIL-102 on cell cycle distribution in DLD-1 cells.** (A) After treatment with Erinacine A (1 mM) for 24 h, the cells were fixed and stained with propidium iodide, and the DNA content was analyzed by flow cytometry (FACS). The cell number percentage in each phase (G1, S, and G2/M) of cell cycle was calculated and expressed.

doi:10.1371/journal.pone.0168989.g003

of both kinases was observed after treatment with CIL-102 and was markedly sustained for at least 6 h. ERK1/2Thr<sup>202</sup>/Tyr<sup>204</sup> was found to be not constitutively activated, but it exhibited no changes after CIL-102 treatment. To investigate the roles of the JNK1/2 signaling pathway and the NFκB p50/p300 pathways in CIL-102-induced apoptosis and cell cycle retardation, we exposed DLD-1 cells to CIL-102 and then co-treated them with the specific JNK inhibitor



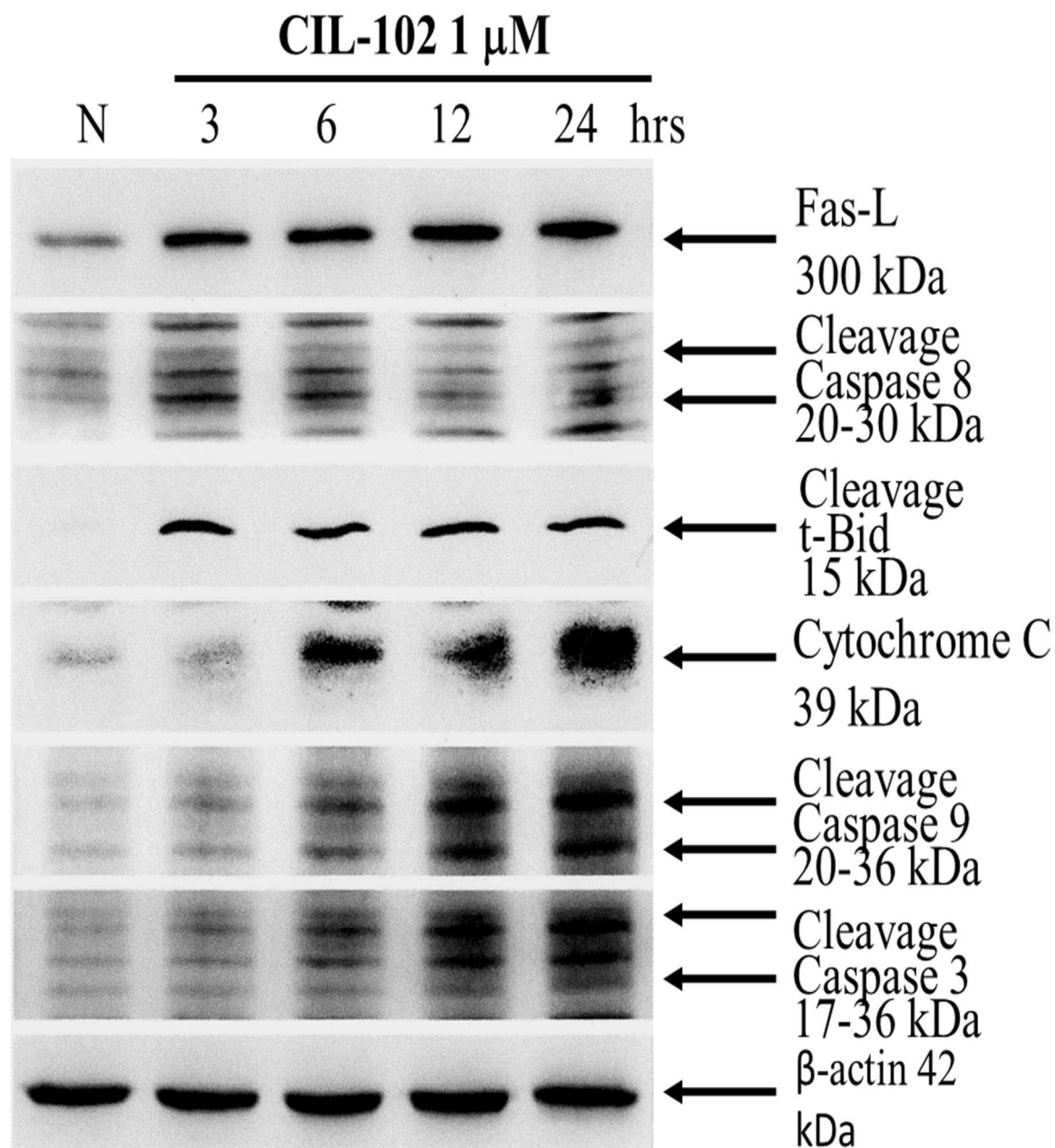


**Fig 4. Effect of CIL-102 on Fas-L, caspase 8, t-Bid, cytochrome c, caspase 3 and caspase 9.** Cells were treated with CIL-102 for 0–24 hr, and were separated by a 15% SDS–PAGE, and, subsequently, immunoblotted with antibodies against Fas-L, cleavage caspase 8, cleavage t-Bid, cytochrome c, cleavage caspase 3 and cleavage caspase 9, or b-actin which served as internal control. CIL-102 induced translocation of cytochrome c. Equal amounts of protein from cytosolic fraction of DLD-1 cells which has been treated with 1 mM of CIL-102.

doi:10.1371/journal.pone.0168989.g004

SP600125, NF- $\kappa$ B p50 inhibitor (PDTC), or the p300/CBP inhibitor C646. The effects of those inhibitors in blocking CIL-102-induced cell death were assessed, and the cell cycle G2M distribution (%) was determined. As shown in Table 1, JNK inhibitor SP600125, NF- $\kappa$ B p50 inhibitor (PDTC), and p300/CBP inhibitor C646 almost blocked CIL-induced cell death and cell

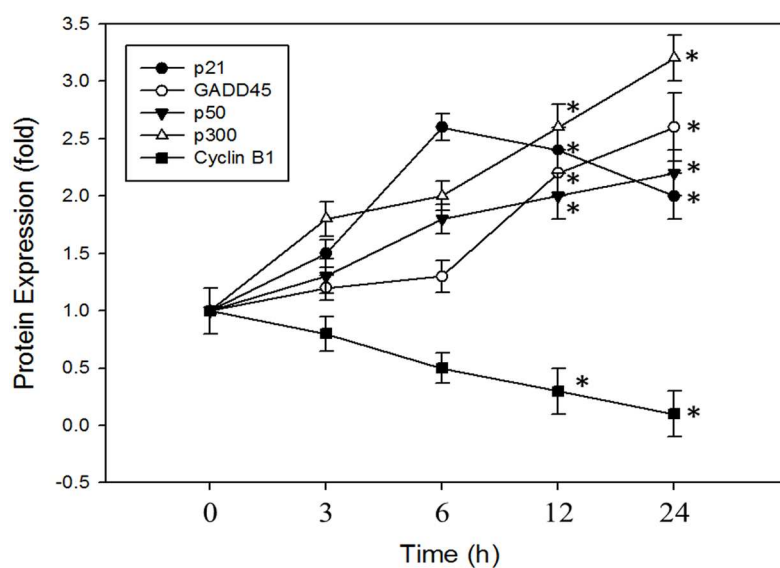
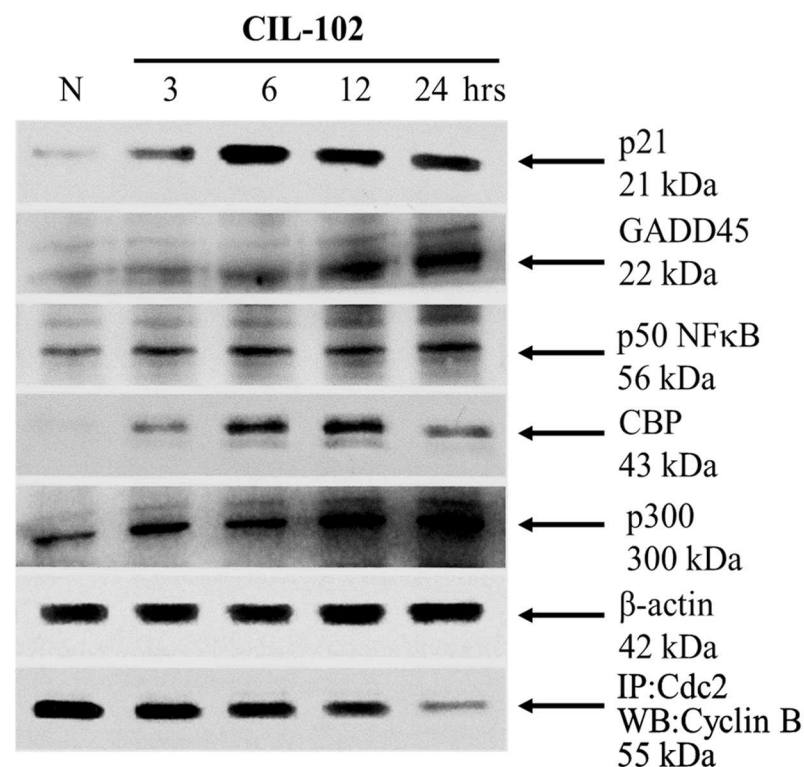


**Fig 5. Effect of CIL-102 on the p21, GADD45, p50 NFκB, p300/CBP, CREB as well as expression of cell cycle associated proteins.** DLD-1 cells were pretreated with CIL-102 for indicated time points. Whole cell lysate proteins were prepared and analyzed by western blot, with β-actin serving as loading control. CIL-102 for the indicated times were analyzed by 10% SDS-PAGE and subsequently treated with antibodies against p21, GADD45, p50 NFκB, p300/CBP and CREB. The association of cdc2 with Cyclin B were determined by immunoprecipitation followed by western blot with antibody.

doi:10.1371/journal.pone.0168989.g005

Fig. 6A

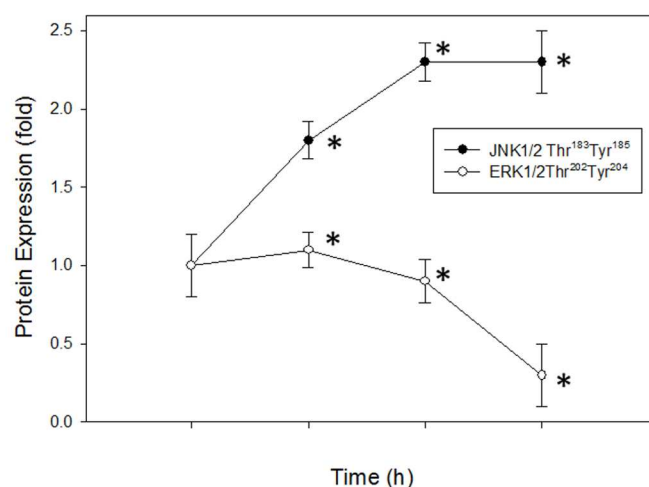
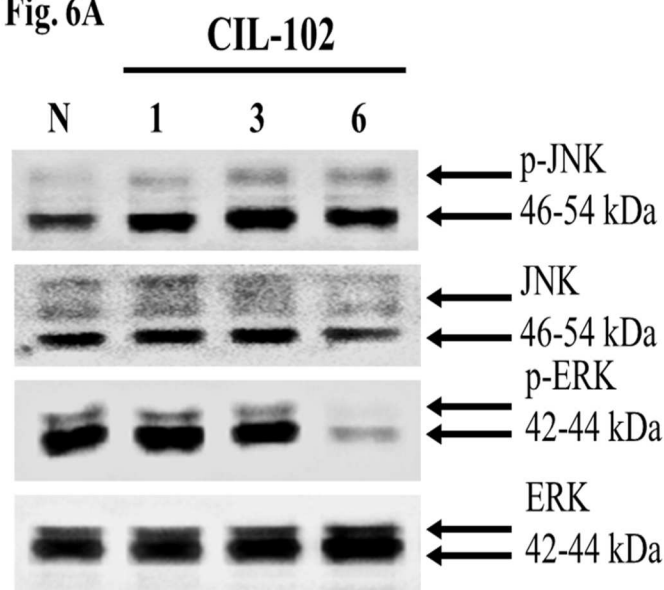
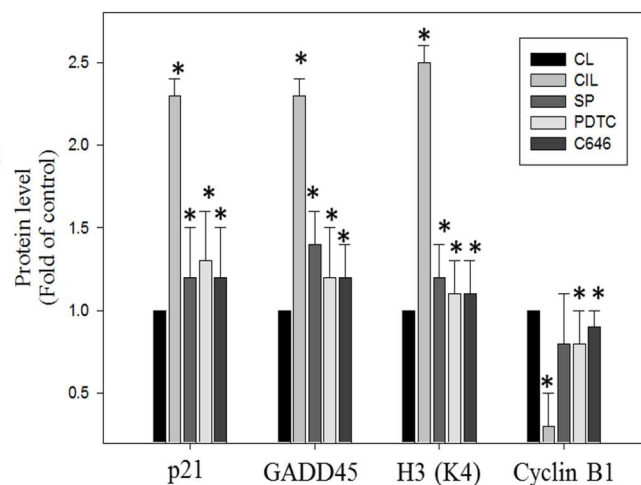
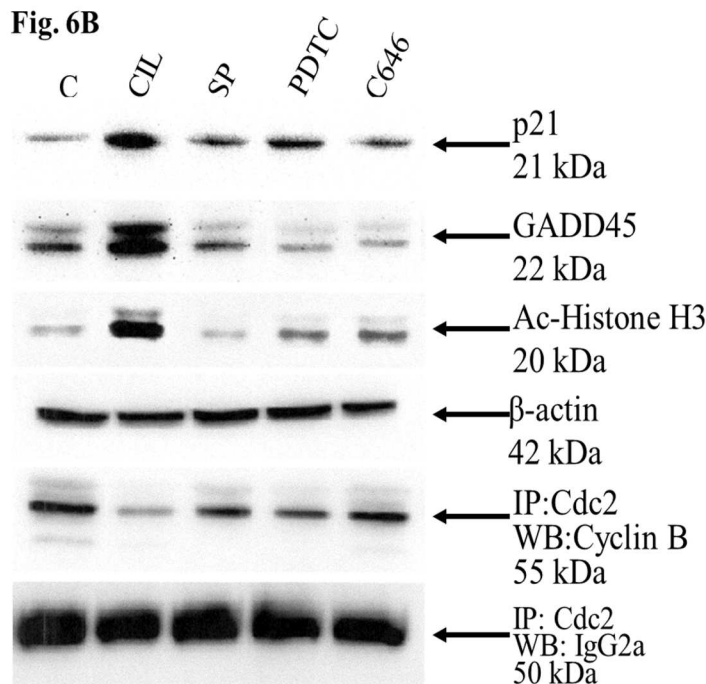


Fig. 6B



**Fig 6. Effect of the kinase inhibitors in blocking CIL-102-induced cell cycle G2/M arrest and apoptosis-related protein.** (A) The expression levels of phosphorylation and protein levels of JNK and ERK, after treatment with CIL-102. DLD-1 cells were treated with CIL-102 for the indicated time points. Total cell lysates were analyzed by SDS-PAGE and subsequently immunoblotted with antisera. (B) DLD-1 were incubated with various concentrations of the specific JNK1/2 inhibitor SP600125, NF $\kappa$ B inhibitor PDTC or the p300/CREB-Binding Protein inhibitor C646 for 1 h. Next, the cells were treated with CIL-102 for 12 h. Total cell lysates of cells treated with or without CIL-102 for the indicated time were extracted, and the expression of p21, GADD45, p50 NF $\kappa$ B, Histone H3 (K4) as well as The association of cdc2 with Cyclin B were determined, as described in "Materials and methods". Protein levels were quantified by densitometric analysis with the ratio of untreated control being set 1 fold. The quantitative data were presented as the mean of three repeats from one independent experiment. The data were presented as mean  $\pm$  SD of three independent experiments. \* $P$ <0.05, compared to the control group.

doi:10.1371/journal.pone.0168989.g006

**Table 1. Effects of the kinase inhibitor on the CIL-102 treatment associated with apoptosis and cell cycle distribution in DLD-1 cells.**

	% of cell death	Cell cycle G2M arrest (%)
<b>Control</b>	<b>6</b>	<b>18</b>
<b>CIL-102</b>	<b>28</b>	<b>54</b>
<b>CIL-102+SP</b>	<b>14</b>	<b>34</b>
<b>CIL-102+PDTC</b>	<b>13</b>	<b>30</b>
<b>CIL-102+C646</b>	<b>12</b>	<b>26</b>

doi:10.1371/journal.pone.0168989.t001

cycle G2/M arrest in DLD-1 cells. Furthermore, it was found that the expression of these proteins, p21 and GADD45, and the acetylation of H3 (Ac-Histone H3) at Lys 9 and Lys 14 clearly increased with the use of CIL-102, compared with the control. This data significantly demonstrated that CIL-102 inhibited cell growth and decreased the association of cdc2 with cyclin B (Fig 6B). We then examined the regulation of the JNK1/2 MAPK and p50/p300 pathways in CIL-102-mediated DLD-1 cell cycle arrest, while cells were incubated for 2 h with the specific inhibitors JNK inhibitor SP600125, NF- $\kappa$ B p50 inhibitor (PDTC) and p300/CBP inhibitor C646, and were then treated with CIL-102. The expressions of p21, GADD45, and Ac-Histone H3, as well as the association of cdc2/cyclin B, were analyzed. SP600125, PDTC and C646 significantly reversed the CIL-102-induced expression of p21, GADD45, Ac-Histone H3 and the reduced association of cdc2/cyclin B. Taken together, these results show that CIL-102 induces sustained activation of the JNK1/2 and p50/p300 pathway, GADD45 and p21, and that the apoptotic pathway is required for CIL-102 inhibition of DLD-1 cell growth (Fig 6B).

## Discussion

The development of colorectal cancer (CRC) is a sequential multistage process consisting of tumor initiation, tumor promotion, and tumor metastasis [30]. Despite intense efforts to develop treatments, effective agents have not yet been found. Medicinal herbs or foods are a potential source of chemopreventive compounds for antitumor activities that target the apoptosis pathways in cancer cells that damage DNA and activate the signaling pathways, and for the expression of proteins involved in the growth arrest of cancer cells [5, 11]. Previous studies have shown that anticancer drugs, including Cisplatin, Camptothecin, Etoposide and Doxorubicin, act by inflicting DNA damage. Most of these bioactive compounds are plant secondary metabolites such as terpenoids, flavonoids and alkaloids, all of which kill tumor cells by apoptosis induction [31]. Our *in vitro* data demonstrated that furo[2,3-b]quinoline derivatives, such as CIL-102, and treatment above a concentration of 1  $\mu$ M resulted in a significant anti-proliferative effect against human colorectal cancer cells but not for normal HCoEpiC cells (Fig 1). Here, CIL-102 treatment at the concentration of 10  $\mu$ M for 24 h resulted in an induction of DLD-1 cell apoptosis (Fig 2). We also found that CIL-102 induced DLD-1 cell accumulation in the G2/M phase (Fig 3), the same as the effect on other HCT-116 cells (unpublished data). CIL-102 was studied for the mechanism of its action in the apoptotic pathway in the human colonic carcinoma cell. Treatment of CIL-102 resulted in the activation of the caspase 8, caspase 9 and caspase 3, and the release of cytochrome c in the time-dependent induction of apoptosis (Fig 4). In addition, there was an increase in the cellular levels of phospho JNK1/2, Fas-L and t-BID in the CIL-102-induced apoptosis via the activation of JNK (Figs 4 and 6A). The induction of apoptosis was alleviated by inhibitors for JNK1/2MAPK (Table 1). Furthermore, our study demonstrated that the cytotoxic effect of CIL-102 on the DLD-1 appeared to



be through G2/M phase arrest with GADD45 and p21 expression, as well as activation of the p50/p300/CBP pathway, and that it caused a decrease in cdc2/cyclin B1 activity (Fig 5). Additionally, the JNK1/2 and p50/p300 pathways were directly involved in activating GADD45 and p21 during the mitosis transition (Table 1). CIL-102 activated JNK1/2 and p50/p300 as well as the expression of GADD45 and p21 on DLD-1 following the DNA damage response, suggesting this as a target with CIL-102 (Fig 6B).

Studies have shown that the potential antitumor activity of CIL-102 may be mediated mitotic arrest and apoptosis in human prostate cancer cells via binding to tubulin and disrupting microtubule organization with a variety of signaling pathways [10]. Our previous study demonstrated that CIL-102 inhibited proliferation in human astrocytoma cells by activating the ERK1/2 and Cdc25cSer<sup>216</sup> cell-cycle-related proteins and inducing ROS production, leading to oxidative stress [23, 24]. Therefore, based on this study, by evaluating the apoptosis and mitotic phase arrest involving the signaling pathway, we assayed whether CIL-102 related to growth inhibition and activation of the signaling pathway in human CRC cells provides substantial therapeutic advantages. Recent findings have demonstrated that the overexpression of Gadd45 in human normal fibroblasts causes cells to arrest in the mitotic phase. Cancer cells show abnormality of the cell cycle G2/M checkpoint following exposure to certain DNA-damaging agents [32]. Gadd45 has been shown to interact with cdc2 kinase, which is required for the G2-M transition. The interaction between GADD45 and p21 results in the inhibition of cdc2-cyclin B1 kinase activity [20, 32]. Our results determined that the upregulation of GADD45 and p21 protein affected the G2/M cell cycle arrest of DLD-1 cells with a decrease in the association of the cdc2/cyclin B1 complexes, which was preceded by the JNK1/2MAPK/NF-κBp50/p300/CBP pathway (Fig 6).

Many studies have shown that cellular mechanisms contribute to the overall cancer-prevention effects of these dietary phytochemicals [33]. Natural phytochemicals from certain plants have the capability to affect the epigenome and can also trigger sustained DNA damage and apoptosis induction. Additionally, they can disrupt the G2/M cell cycle in cancer cells exposed to dietary phytochemicals such as histone deacetylase inhibitors (HDAC) [34]. Inhibition of HDAC activity may occur in human colon cancer lines, with an increase in histone H3 acetylation in global or local histone modification status, such as induction of TRAIL, DR4 and Fas-L, p21 genes, via histone acetyltransferase (HAT) p300/CBP [35, 36]. Furthermore, the current *in vitro* study demonstrated that CIL-102 treatment significantly upregulated the expression of p300/CBP and acetylation of H3 (Ac-Histone H3) in DLD-1 cells (Figs 5 and 6B). Thus, CIL-102, as an individual dietary phytochemical, represents a novel chemotherapeutic agent worth continued investigation in the treatment of CRC. Additional studies are still needed to elucidate the CIL-102 effects on the HAT and HDAC between different molecular cellular signaling pathways and epigenetic machinery as well as to determine *in vivo* CRC cells' xenograft and CIL-102 dose treatment.

In this study, we evaluated CIL-102-induced apoptosis and the cell cycle arrest G2/M phase in human DLD-1 cancer cells as a result of the expression of p21 and GADD45 and cdc2/cyclin B inactivation by the activation of the JNK1/2 signaling pathway and the p50NF-κB/p300/CBP pathway. These results lead us to speculate that CIL-102 may play a role in an apoptotic cascade in DLD-1 cells via Fas-L, t-BID expression and cytochrome c release, and caspase-8, 3, and 9 activation (Fig 7). This study is potentially interesting with regard to the antitumor effect of CIL-102 as it relates to the development of novel chemotherapeutic approaches in the treatment of malignant CRC. Further study is required.



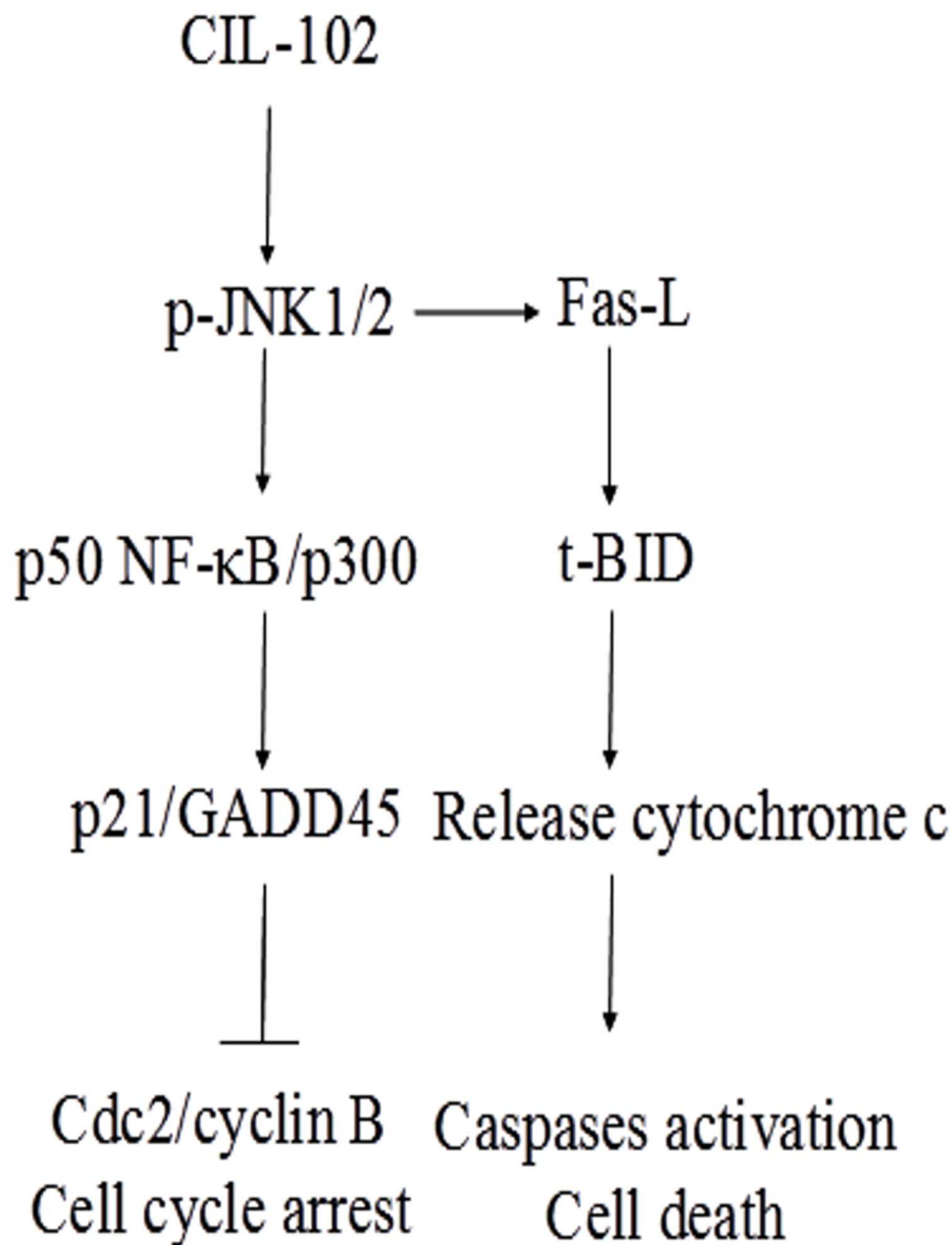


**Fig 7. Schematic presentation of the signaling pathways involved in CIL-102 induced cell cycle arrest G2/M phase and apoptosis in human DLD-1 cancer cells.** The effect of CIL-102 on the activation JNK1/2, and p50 NF-κB/p300 pathways, which leads to p21 and GADD45 expression and cdc2/cyclin B inactivation and increases cell cycle arrest in human DLD-1. CIL-102 triggered the extrinsic apoptosis pathway through activation of Fas-L and induction of Bid cleavage, cytochrome c release and caspase-8, -3, -9 activation.

doi:10.1371/journal.pone.0168989.g007

## Author Contributions

**Conceptualization:** W-SH Y-HK C-CT.

**Funding acquisition:** H-CK C-CT.

**Investigation:** H-CK C-CT.

**Methodology:** H-CK C-CT.

**Project administration:** H-CK C-CT.

**Resources:** K-FL C-HS M-CH.

**Software:** C-YH K-CL.

**Supervision:** S-YT H-CK C-CT.

**Validation:** K-FL C-HS M-CH.

**Visualization:** C-YH K-CL.

**Writing – original draft:** S-YT H-CK C-CT.

**Writing – review & editing:** S-YT H-CK C-CT.

## References

1. Haggard FA, Boushey RP. Colorectal cancer epidemiology: incidence, mortality, survival, and risk factors. *Clin Colon Rectal Surg.* 2009; 22:191–7. doi: [10.1055/s-0029-1242458](https://doi.org/10.1055/s-0029-1242458) PMID: [21037809](https://pubmed.ncbi.nlm.nih.gov/21037809/)
2. Sillars-Hardebol AH, Carvalho B, de Wit M, Postma C, Delis-van Diemen PM, Mongera S et al. Identification of key genes for carcinogenic pathways associated with colorectal adenoma-to-carcinoma progression. *Tumour Biol.* 2010; 31:89–96. doi: [10.1007/s13277-009-0012-1](https://doi.org/10.1007/s13277-009-0012-1) PMID: [20358421](https://pubmed.ncbi.nlm.nih.gov/20358421/)
3. Chan SK, Griffith OL, Tai IT, Jones SJ. Meta-analysis of colorectal cancer gene expression profiling studies identifies consistently reported candidate biomarkers. *Cancer Epidemiol Biomarkers Prev.* 2008; 17:543–52. doi: [10.1158/1055-9965.EPI-07-2615](https://doi.org/10.1158/1055-9965.EPI-07-2615) PMID: [18349271](https://pubmed.ncbi.nlm.nih.gov/18349271/)
4. Hanahan D, Weinberg RA. The hallmarks of cancer. *Cell.* 2000; 100:57–70. PMID: [10647931](https://pubmed.ncbi.nlm.nih.gov/10647931/)
5. Li-Weber M. Targeting apoptosis pathways in cancer by Chinese medicine. *Cancer Lett.* 2013; 332:304–12. doi: [10.1016/j.canlet.2010.07.015](https://doi.org/10.1016/j.canlet.2010.07.015) PMID: [20685036](https://pubmed.ncbi.nlm.nih.gov/20685036/)
6. Chen IL, Chen YL, Tzeng CC, Tzeng CC, Chen IS. Synthesis and cytotoxic evaluation of some 4-anilino-furo[2,3-b]quinoline derivatives. *Helv Chim Acta* 2002; 85:2214–21.
7. Chen IL, Chen YL, Tzeng CC. An efficient synthesis of antitumor 4-anilino-furo[2,3-b]quinoline derivatives. *Chin Pharm J.* 2003; 55:49–53.
8. Zhao YL, Chen YL, Tzeng CC, Chen IL, Wang TC, Han CH. Synthesis and cytotoxic evaluation of certain 4-(phenylamino)furo[2,3-b]quinoline and 2-(furan-2-yl)-4-(phenylamino)quinoline derivatives. *Chem Biodivers.* 2005; 2:205–14. doi: [10.1002/cbdv.200590003](https://doi.org/10.1002/cbdv.200590003) PMID: [17191973](https://pubmed.ncbi.nlm.nih.gov/17191973/)
9. Chen YL, Chen IL, Wang TC, Han CH, Tzeng CC. Synthesis and anticancer evaluation of certain 4-anilino-furo[2,3-b]quinoline and 4-anilino-furo[3,2-c]quinolone derivatives. *Eur J Med Chem.* 2005; 40:928–34. doi: [10.1016/j.ejmech.2005.04.003](https://doi.org/10.1016/j.ejmech.2005.04.003) PMID: [15913847](https://pubmed.ncbi.nlm.nih.gov/15913847/)
10. Huang YT, Huang DM, Guh JH, Chen IL, Tzeng CC, Teng CM. CIL-102 interacts with microtubule polymerization and causes mitotic arrest following apoptosis in the human prostate cancer PC-3 cell line. *J Biol Chem.* 2005; 280:2771–9. doi: [10.1074/jbc.M408850200](https://doi.org/10.1074/jbc.M408850200) PMID: [15536083](https://pubmed.ncbi.nlm.nih.gov/15536083/)
11. Li-Weber M. New therapeutic aspects of flavones: The anticancer properties of Scutellaria and its main active constituents Wogonin, Baicalein and Baicalin. *Cancer Treat Rev.* 2009; 35:57–68. doi: [10.1016/j.ctrv.2008.09.005](https://doi.org/10.1016/j.ctrv.2008.09.005) PMID: [19004559](https://pubmed.ncbi.nlm.nih.gov/19004559/)
12. Thomas GM, Huganir RL. MAPK cascade signalling and synaptic plasticity. *Nat Rev Neurosci.* 2004; 5:173–83. doi: [10.1038/nrn1346](https://doi.org/10.1038/nrn1346) PMID: [14976517](https://pubmed.ncbi.nlm.nih.gov/14976517/)
13. Raman M, Chen W, Cobb MH. Differential regulation and properties of MAPKs. *Oncogene.* 2007; 26:3100–12. doi: [10.1038/sj.onc.1210392](https://doi.org/10.1038/sj.onc.1210392) PMID: [17496909](https://pubmed.ncbi.nlm.nih.gov/17496909/)
14. Desagher S, Osen-Sand A, Nichols A, Eskes R, Montessuit S, Lauper S, et al. Bid-induced conformational change of Bax is responsible for mitochondrial cytochrome c release during apoptosis. *J Cell Biol.* 1999; 144:891–901. PMID: [10085289](https://pubmed.ncbi.nlm.nih.gov/10085289/)
15. Luo X, Budiardjo I, Zou H, Slaughter C, Wang X. Bid, a Bcl2 interacting protein, mediates cytochrome c release from mitochondria in response to activation of cell surface death receptors. *Cell.* 1998; 94:481–90. PMID: [9727491](https://pubmed.ncbi.nlm.nih.gov/9727491/)

16. Wei MC, Lindsten T, Mootha VK, Weiler S, Gross A, Ashiya M, et al. tBID, a membrane-targeted death ligand, oligomerizes BAK to release cytochrome c. *Genes Dev.* 2000; 14:2060–71. PMID: [10950869](#)
17. Rowinsky EK. The development and clinical utility of the taxane class of antimicrotubule chemotherapy agents. *Annu Rev Med.* 1997; 48:353–74. doi: [10.1146/annurev.med.48.1.353](#) PMID: [9046968](#)
18. Zhan Q, Antinore MJ, Wang XW, Carrier F, Smith ML, Harris CC, et al. Association with Cdc2 and inhibition of Cdc2/Cyclin B1 kinase activity by the p53-regulated protein Gadd45. *Oncogene.* 1999; 18:2892–900. doi: [10.1038/sj.onc.1202667](#) PMID: [10362260](#)
19. Cazzalini O, Perucca P, Savio M, Necchi D, Bianchi L, Stivala LA, Interaction of p21(CDKN1A) with PCNA regulates the histone acetyltransferase activity of p300 in nucleotide excision repair. *Nucleic Acids Res.* 2008; 36:1713–22. doi: [10.1093/nar/gkn014](#) PMID: [18263614](#)
20. Jin S, Tong T, Fan W, Fan F, Antinore MJ, Zhu X, et al. GADD45-induced cell cycle G2-M arrest associates with altered subcellular distribution of cyclin B1 and is independent of p38 kinase activity. *Oncogene.* 2002; 21:8696–704. doi: [10.1038/sj.onc.1206034](#) PMID: [12483522](#)
21. Lu CC, Huang WS, Lee KF, Lee KC, Hsieh MC, Huang CY et al. Inhibitory effect of Erinacines A on the growth of DLD-1 colorectal cancer cells is induced by generation of reactive oxygen species and activation of p70S6K and p21. *J Funct Foods.* 2016; 21:474–84.
22. Liu WH, Chen YL, Chang LS. CIL-102 induces matrix metalloproteinase-2 (MMP-2)/MMP-9 down-regulation via simultaneous suppression of genetic transcription and mRNA stability. *Int J Biochem Cell Biol.* 2012; 44:2212–22. doi: [10.1016/j.biocel.2012.08.021](#) PMID: [22964005](#)
23. Teng CC, Kuo HC, Cheng HC, Wang TC, Sze CI. The inhibitory effect of CIL-102 on the growth of human astrocytoma cells is mediated by the generation of reactive oxygen species and induction of ERK1/2 MAPK. *Toxicol Appl Pharmacol.* 2012; 263:73–80. doi: [10.1016/j.taap.2012.05.025](#) PMID: [22683510](#)
24. Teng CC, Kuo HC, Sze CI. Quantitative proteomic analysis of the inhibitory effects of CIL-102 on viability and invasiveness in human glioma cells. *Toxicol Appl Pharmacol.* 2013; 272:579–90. doi: [10.1016/j.taap.2013.07.009](#) PMID: [23891858](#)
25. Huang WS, Chin CC, Chen CN, Kuo YH, Chen TC, Yu HR et al. Stromal cell-derived factor-1/CXC receptor 4 and  $\beta$ 1 integrin interaction regulates urokinase-type plasminogen activator expression in human colorectal cancer cells. *J Cell Physiol.* 2012; 227:1114–22. doi: [10.1002/jcp.22831](#) PMID: [21567400](#)
26. Chiu YW, Lin TH, Huang WS, Teng CY, Liou YS, Kuo WH et al. Baicalein inhibits the migration and invasive properties of human hepatoma cells. *Toxicol Appl Pharmacol.* 2011; 255:316–26. doi: [10.1016/j.taap.2011.07.008](#) PMID: [21803068](#)
27. Huang WS, Kuo YH, Chin CC, Wang JY, Yu HR, Sheen JM, et al. Proteomic analysis of the effects of baicalein on colorectal cancer cells. *Proteomics.* 2012; 12:810–9. doi: [10.1002/pmic.201100270](#) PMID: [22539432](#)
28. Kuo HC, Lu CC, Shen CH, Tung SY, Hsieh MC, Lee KC et al. Hericium erinaceus mycelium and its isolated erinacine A protection from MPTP-induced neurotoxicity through the ER stress, triggering an apoptosis cascade. *J Transl Med.* 2016; 14:78. doi: [10.1186/s12967-016-0831-y](#) PMID: [26988860](#)
29. Stauffer D, Chang B, Huang J, Dunn A, Thayer M. p300/CREB-binding protein interacts with ATR and is required for the DNA replication checkpoint. *J Biol Chem.* 2007; 282:9678–87. doi: [10.1074/jbc.M609261200](#) PMID: [17272271](#)
30. Sarsour EH, Kumar MG, Chaudhuri L, Kalen AL, Goswami PC. Redox control of the cell cycle in health and disease. *Antioxid Redox Signal.* 2009; 11:2985–3011. doi: [10.1089/ARS.2009.2513](#) PMID: [19505186](#)
31. Weng CJ, Yen GC. Chemopreventive effects of dietary phytochemicals against cancer invasion and metastasis: phenolic acids, monophenol, polyphenol, and their derivatives. *Cancer Treat Rev.* 2012; 38:76–87. doi: [10.1016/j.ctrv.2011.03.001](#) PMID: [21481535](#)
32. Jin S, Antinore MJ, Lung FD, Dong X, Zhao H, Fan F et al. The GADD45 inhibition of Cdc2 kinase correlates with GADD45-mediated growth suppression. *J Biol Chem.* 2000; 275:16602–8. doi: [10.1074/jbc.M000284200](#) PMID: [10747892](#)
33. Hun Lee J, Shu L, Fuentes F, Su ZY, Tony Kong AN. Cancer chemoprevention by traditional chinese herbal medicine and dietary phytochemicals: targeting nrf2-mediated oxidative stress/anti-inflammatory responses, epigenetics, and cancer stem cells. *J Tradit Complement Med.* 2013; 3:69–79. doi: [10.4103/2225-4110.107700](#) PMID: [24716158](#)
34. Dashwood RH, Ho E. Dietary histone deacetylase inhibitors: from cells to mice to man. *Semin Cancer Biol.* 2007; 17:363–9. doi: [10.1016/j.semcancer.2007.04.001](#) PMID: [17555985](#)

35. Myzak MC, Karplus PA, Chung FL, Dashwood RH. A novel mechanism of chemoprotection by sulforaphane: inhibition of histone deacetylase. *Cancer Res.* 2004; 64:5767–74. doi: [10.1158/0008-5472.CAN-04-1326](https://doi.org/10.1158/0008-5472.CAN-04-1326) PMID: [15313918](https://pubmed.ncbi.nlm.nih.gov/15313918/)
36. Rajendran P, Ho E, Williams DE, Dashwood RH. Dietary phytochemicals, HDAC inhibition, and DNA damage/repair defects in cancer cells. *Clin Epigenetics.* 2011; 3:4. doi: [10.1186/1868-7083-3-4](https://doi.org/10.1186/1868-7083-3-4) PMID: [22247744](https://pubmed.ncbi.nlm.nih.gov/22247744/)



# Constituents from the leaves of *Clausena lansium* and their anti-inflammatory activity

De-Yang Shen<sup>1</sup> · Ping-Chung Kuo<sup>1</sup> · Shiow-Chyn Huang<sup>2</sup> · Tsong-Long Hwang<sup>3,4,5</sup> · Yu-Yi Chan<sup>6</sup> · Po-Chuen Shieh<sup>7</sup> · Nguyen Thi Ngan<sup>8</sup> · Tran Dinh Thang<sup>8</sup> · Tian-Shung Wu<sup>1,7</sup>

Received: 4 July 2016 / Accepted: 7 August 2016  
© The Japanese Society of Pharmacognosy and Springer Japan 2016

**Abstract** Five new acyclic amides, clausenalansamides C-G (**1–5**), clausenaline G (**6**) and (±)-5-(4-methylphenyl)-γ-valerolactone (**7**) reported from the natural source for the first time, were characterized from the leaves of *Clausena lansium*. Their structures were established by spectroscopic and spectrometric methods, and the absolute configurations of new compounds **1–5** were determined by electronic circular dichroism and single-crystal X-ray diffraction analyses. Eighteen compounds were evaluated for their anti-inflammatory activity and only imperatorin (**11**) and wampetin (**12**) displayed significant inhibition of fMLP/CB-induced superoxide anion generation with IC<sub>50</sub> values of 1.7 ± 0.3 and 6.8 ± 1.1 μM, respectively.

**Keywords** Clausenalansamide · Electronic circular dichroism · Single-crystal X-ray diffraction analysis · Anti-inflammatory · Superoxide anion generation

## Introduction

Various parts of *Clausena lansium* Skeels (Rutaceae) have been traditionally used as folk medicines for a long time. This species was commonly cultivated in southern mainland China, Southeast Asia and North America due to its widespread biological activities [1]. The roots, stems, and leaves of *Clausena* species were extensively investigated for their phytochemical compositions and therefore a number of physiologically active compounds, including amides, flavonoids, coumarins, and carbazole alkaloids [2–8] were reported in the previous literature. The leaves of *C. lansium* have been used for the treatment of coughs, bronchial asthma, gastrointestinal inflammation, and abscesses [9]. In recent studies performed by our group, phenyl glycosides,

D.-Y. Shen and P.-C. Kuo contributed equally to this work.

**Electronic supplementary material** The online version of this article (doi:10.1007/s11418-016-1033-x) contains supplementary material, which is available to authorized users.

✉ Tian-Shung Wu  
tswu@mail.ncku.edu.tw

- <sup>1</sup> School of Pharmacy, National Cheng Kung University Hospital, College of Medicine, National Cheng Kung University, Tainan 701, Taiwan, ROC
- <sup>2</sup> Department of Pharmacy, Chia-Nan University of Pharmacy and Science, Tainan 71710, Taiwan, ROC
- <sup>3</sup> Graduate Institute of Natural Products, College of Medicine, Chang Gung University, Taoyuan 333, Taiwan, ROC
- <sup>4</sup> Research Center for Industry of Human Ecology, Research Center for Chinese Herbal Medicine, and Graduate Institute of Health Industry Technology, College of Human Ecology, Chang Gung University of Science and Technology, Taoyuan 333, Taiwan, ROC

- <sup>5</sup> Department of Anesthesiology, Chang Gung Memorial Hospital, Taoyuan 333, Taiwan, ROC
- <sup>6</sup> Department of Biotechnology, Southern Taiwan University of Science and Technology, Tainan 71005, Taiwan
- <sup>7</sup> Department of Pharmacy, Tajen University, Pingtung 90741, Taiwan, ROC
- <sup>8</sup> Department of Chemistry, Vinh University, Vinh City, Vietnam



carbazole alkaloids, coumarins, and lactams were characterized from the stems, roots, and leaves of *C. lانسium* [10–12] and the anti-inflammatory activities of several compounds were reported. In our long-term program to discover anti-inflammatory lead drugs from natural sources, the chemical composition of the ethanol extract of the leaves from *C. lانسium* was thoroughly investigated to search for the bioactive constituents. Here, we describe the isolation and structural elucidation of the new compounds and determination of their absolute configurations through spectroscopic analysis, electronic circular dichroism (ECD) experiments, and single-crystal X-ray diffraction analyses. Furthermore, the purified constituents were examined for inhibition of superoxide anion generation and elastase release to evaluate their anti-inflammatory potential.

## Materials and methods

### General

Melting points were determined using Yanagimoto MP-S3 apparatus without corrections. Optical rotations were measured with a JASCO P-2000 digital polarimeter in a 0.5 dm cell. UV spectra were obtained with a Hitachi UV-3210 spectrophotometer, and IR spectra were measured with a Shimadzu FTIR Prestige-21 spectrometer. The ECD spectrum was recorded in a JASCO J-720 spectrometer. The  $^1\text{H}$  and  $^{13}\text{C}$  NMR spectra were measured using Bruker AMX-400 spectrometers with TMS as the internal reference, and chemical shifts are expressed in  $\delta$  (ppm). The ESIMS and HRESIMS were taken on a Bruker Daltonics APEX II 30e spectrometer. Silica gel (70–230 and 230–400 mesh; Merck), Diaion HP-20 resin (Mitsubishi, Chemical, Tokyo, Japan), and silica gel 60 F<sub>254</sub> (Merck) were used for preparative TLC and TLC, respectively. HPLC was performed on a Shimadzu LC-10AT<sub>VP</sub> (Japan) system equipped with a Shimadzu SPD-M20A diode array detector at 250 nm, a Purospher STAR RP-8e column (5  $\mu\text{m}$ , 250  $\times$  4.6 mm) and Cosmosil 5C<sub>18</sub> ARII (250  $\times$  4.6 mm i.d. Nacalai Tesque Inc.). The X-ray diffraction experiments were carried out on a Bruker D8 VENTURE with PHOTON 100 CMOS detector system equipped with a Cu Incoatec I $\mu$ S Microfocus Source ( $\lambda = 1.54178 \text{ \AA}$ ).

### Materials

The leaves of *C. lانسium* were collected from Quynh district, Nghean province, Vietnam (N19°19' 32.69", E 105° 11' 36.57") in July 2011. The plant material was identified and authenticated by Prof. Dr. Tran Huy Thai, Institute of Ecology and Biological Resources, Vietnamese Academy of Science and Technology. A voucher specimen

(Viet-TSWu- 20110703) was deposited in the Herbarium of the Faculty of Biology, Vinh University, Vietnam.

### Extraction and isolation

Dried leaves of *C. lانسium* (12 kg) were extracted with 95 % EtOH (6  $\times$  20 L) under reflux for 8 h and concentrated to yield a dark brown residue (510 g). The syrup was suspended in 3 L water and then extracted successively with CHCl<sub>3</sub> (4  $\times$  3 L). After concentration, the CHCl<sub>3</sub> extract (310 g) was first subjected to column chromatography on silica gel, and then eluted with *n*-hexane–EtOAc (3:1) to afford six fractions. Fraction 3 was chromatographed on silica gel with *n*-hexane–diisopropyl ether (3:1) to give six subfractions (Subfr. 3.1–3.6). Subfr. 3.3 was chromatographed on silica gel *n*-hexane–diisopropyl ether (5:1) to obtain phytene-1,2-diol (6.3 mg). Subfr. 3.4 was chromatographed on silica gel with *n*-hexane–EtOAc (9:1) to give  $\beta$ -sitosterol (25 mg). Subfr. 3.5 was chromatographed on silica gel with CHCl<sub>3</sub>–acetone (59:1) to yield **6** (5.3 mg), **9** (3.1 mg), madolin A (3.3 mg), **12** (7.6 mg), (2-hydroxy-phenyl)-acetic acid methyl ester (2.6 mg), 1-methyl-3-(methoxycarbonyl)carbazole (3.9 mg), heneicosa-5,8,11,14-tetraenoic acid (5.5 mg), and 4-hydroxybenzaldehyde (1.2 mg). Fraction 4 was chromatographed on silica gel using CHCl<sub>3</sub>–acetone (14:1) to yield six subfractions (Subfr. 4.1–4.6). Subfr. 4.2 was chromatographed on silica gel with CHCl<sub>3</sub>–acetone (19:1) to give **2** (5.4 mg), **3** (6.3 mg), **10** (2.0 mg), **11** (9.3 mg), 3-formyl-2-methoxy-9*H*-carbazole (3.6 mg), clausine G (2.3 mg), methyl pheophorbide *a* (1.1 mg), methyl (10*S*)-hydroxypheophorbide *a* (0.6 mg), phytene 1,2-diol (45.2 mg), and 3-formyl-6-methoxycarbazole (1.3 mg). Subfr. 4.4 was chromatographed on silica gel with *n*-hexane–acetone (2:1) to yield xanthotoxol (3.8 mg) and benzoic acid (2.6 mg). Subfr. 4.6 was chromatographed on silica gel with *n*-hexane–acetone (2:1) to afford **1** (43.2 mg). Fraction 5 was subjected to column chromatography on silica gel using CHCl<sub>3</sub>–acetone (19:1) to give five subfractions (Subfr. 5.1–5.5). Subfr. 5.2 was chromatographed on silica gel with *n*-hexane–EtOAc (2:1) to give **2** (5.6 mg), **5** (5.5 mg), **8** (6.3 mg), **12** (6.3 mg), and (3*R*, 6*R*, 7*E*)-3-hydroxy-4,7-megastigma-dien-9-one (1.2 mg). Subfr. 5.5 was chromatographed on silica gel with diisopropyl ether–acetone (7:1) to give **1** (3.1 mg), **3** (2.6 mg), clausenalansamide B (5.1 mg), loliolide (2.2 mg), dehydrolololide (2.4 mg), (6*R*, 7*E*)-4,7-megastigma-dien-3,9-dione (3.3 mg), dehydromifolol (1.9 mg), umberliferone (1.0 mg), and (2*S*, 3*S*)-2,3-dihydroxy-3-phenylpropanoic acid methyl ester (3.2 mg). Fraction 6 was subjected to column chromatography on silica gel using CHCl<sub>3</sub>–MeOH (9:1) to give six subfractions (Subfr. 6.1–6.6). Subfr. 6.2 was chromatographed on silica gel with diisopropyl ether–MeOH (14:1) to yield **4** (5.5 mg) and 2,3-dihydroxy-*N*-methyl-3-

phenyl-*N*-(2-phenylethyl)-propionic acid amide (69.3 mg). Subfr. 6.3 was chromatographed on silica gel with diisopropyl ether–MeOH (9:1) to give  $\beta$ -sitosteryl-3-*O*- $\beta$ -glucopyranoside (13.2 mg). The H<sub>2</sub>O-soluble layer (390 g) was directly subjected to Diaion HP-20 column chromatography using H<sub>2</sub>O containing increasing proportions of MeOH to give six fractions. Fraction 5 was subjected to column chromatography on silica gel using EtOAc–MeOH (5:1) to give subfractions (Subfr. 5.1–5.6). Subfr. 5.2 was chromatographed on silica gel using EtOAc–MeOH (9:1) to give 4-hydroxycinnamic acid (2.9 mg). Subfr. 5.4 was chromatographed on silica gel with diisopropyl ether–MeOH (7:1) to give rutin (6.7 mg). Fraction 6 was chromatographed on silica gel using CHCl<sub>3</sub>–MeOH (6:1) to give subfractions (Subfr. 6.1–6.6). Subfr. 6.2 was chromatographed on silica gel with CHCl<sub>3</sub>–MeOH (9:1) to give methyl (*E*)-3-(4-hydroxy-3-methoxyphenyl)prop-2-enoate (2.9 mg) and methyl *trans*-4-hydroxy-cinnamate (1.3 mg).

**Clausenalanamide C (1)** Colorless crystals (MeOH), mp 88–90 °C;  $[\alpha]_D^{24} +172$  (*c* 0.3, MeOH); UV (MeOH)  $\lambda_{\max}$  (log  $\epsilon$ ) 209 (3.55), 262 (3.32) nm; IR (KBr)  $\nu_{\max}$  3386, 2927, 1660, 1630, 1448, 1105, 1073 cm<sup>−1</sup>; <sup>1</sup>H and <sup>13</sup>C NMR data, see Table 1; ECD (MeOH) 228 ( $\Delta\epsilon +2.89$ ), 260 ( $\Delta\epsilon -0.63$ ) nm; ESIMS *m/z* 334 [M+Na]<sup>+</sup>; HRESIMS *m/z* 334.1410 (calcd for C<sub>19</sub>H<sub>21</sub>NO<sub>3</sub>Na, 334.1413).

**Clausenalanamide D (2)** Colorless crystals (MeOH), mp 68–70 °C;  $[\alpha]_D^{24} -90$  (*c* 1.0, MeOH); UV (MeOH)  $\lambda_{\max}$  (log

$\epsilon$ ) 207 (3.35), 261 (3.14) nm; IR (KBr)  $\nu_{\max}$  3435, 2893, 1663, 1560, 1446, 1398, 1176 cm<sup>−1</sup>; <sup>1</sup>H and <sup>13</sup>C NMR data, see Table 1; ECD (MeOH) 207 ( $\Delta\epsilon -1.36$ ), 228 ( $\Delta\epsilon -4.15$ ), 273 ( $\Delta\epsilon -2.55$ ) nm; ESIMS *m/z* 338 [M+Na]<sup>+</sup>; HRESIMS *m/z* 338.0922 (calcd for C<sub>18</sub>H<sub>18</sub>ClNO<sub>2</sub>Na, 338.0924).

**Clausenalanamide E (3)** Colorless crystals (MeOH), mp 108–110 °C;  $[\alpha]_D^{24} +118.5$  (*c* 0.5, MeOH); UV (MeOH)  $\lambda_{\max}$  (log  $\epsilon$ ) 212 (3.21), 262 (2.87) nm; IR (KBr)  $\nu_{\max}$  3387, 1660, 1633, 1543, 1493, 1453, 1113, 1074 cm<sup>−1</sup>; <sup>1</sup>H and <sup>13</sup>C NMR data, see Table 1; ECD (MeOH) 217 ( $\Delta\epsilon +1.80$ ), 229 ( $\Delta\epsilon +4.53$ ), 244 ( $\Delta\epsilon -0.72$ ), 275 ( $\Delta\epsilon +4.09$ ) nm; ESIMS *m/z* 338 [M+Na]<sup>+</sup>; HRESIMS *m/z* 338.0920 (calcd for C<sub>18</sub>H<sub>18</sub>ClNO<sub>2</sub>Na, 338.0924).

**Clausenalanamide F (4)** Colorless crystals (MeOH), mp 164–166 °C;  $[\alpha]_D^{24} +46.5$  (*c* 0.6, MeOH); UV (MeOH)  $\lambda_{\max}$  (log  $\epsilon$ ) 209 (2.57), 265 (2.36) nm; IR (KBr)  $\nu_{\max}$  3437, 2920, 1666, 1640, 1553, 1302, 1122, 1076 cm<sup>−1</sup>; <sup>1</sup>H and <sup>13</sup>C NMR data, see Table 1; ECD (MeOH) 205 ( $\Delta\epsilon -0.83$ ), 226 ( $\Delta\epsilon +5.63$ ), 248 ( $\Delta\epsilon -1.95$ ), 276 ( $\Delta\epsilon +2.78$ ) nm; ESIMS *m/z* 382 [M+Na]<sup>+</sup>; HRESIMS *m/z* 382.1082 (calcd for C<sub>19</sub>H<sub>21</sub>NO<sub>4</sub>Na, 382.1083).

**Clausenalanamide G (5)** White powder (MeOH);  $[\alpha]_D^{24} -11$  (*c* 0.2, MeOH); UV (MeOH)  $\lambda_{\max}$  (log  $\epsilon$ ) 209 (2.46) nm; IR (KBr)  $\nu_{\max}$  3403, 2920, 2866, 1730, 1703, 1650, 1544, 1460, 1366, 1110 cm<sup>−1</sup>; <sup>1</sup>H NMR (CD<sub>3</sub>OD, 400 MHz)  $\delta_H$  7.35 (2H, d, *J* = 8.0 Hz, H-2', 6'), 7.25 (3H,

**Table 1** <sup>1</sup>H and <sup>13</sup>C NMR [ $\delta$ , mult, (*J* in Hz)] data for compounds 1–4 (<sup>1</sup>H NMR data measured at 400 MHz and <sup>13</sup>C NMR data measured at 100 MHz in CDCl<sub>3</sub>)

No.	1		2		3		4	
	$\delta_H$	$\delta_C$	$\delta_H$	$\delta_C$	$\delta_H$	$\delta_C$	$\delta_H$	$\delta_C$
2		173.0		169.0		171.3		170.9
3	4.62 dd (9.6, 6.9)	71.9	4.64 d (6.4)	55.6	4.86 dd (8.8, 6.8)	72.6	5.40 dd (5.2, 2.8)	68.7
4	4.27 d (6.9)	85.8	5.08 dd (6.4, 6.4)	75.1	5.04 d (6.8)	62.5	4.43 d (2.8)	70.9
5	6.38 d (9.0)	127.9	6.31 d (8.4)	127.1	6.40 d (8.8)	127.2	6.47 d (8.8)	125.9
6	6.16 d (9.0)	124.7	6.23 d (8.4)	127.4	6.30 d (8.8)	126.6	6.35 d (8.8)	126.7
N-CH <sub>3</sub>	3.00 s	34.9	2.92 s	34.6	3.04 s	35.0	2.92 s	35.8
OCH <sub>3</sub>	3.19 s	56.8						
OH	3.10 d (9.6)		4.42 d (6.4)		3.09 d (8.8)		4.29 d (5.2)	
SOOCH <sub>3</sub>							2.86 s	39.3
1'		137.7		139.3		136.9		129.1
2',6'	7.24–7.40	127.5–128.7	7.24–7.40	126.7–128.7	7.29–7.39	128.2–128.9	7.48 d (8.0)	128.7–130.7
3',4',5'	7.24–7.40	127.5–128.7	7.24–7.40	126.7–128.7	7.29–7.39	128.2–128.9	7.34–7.40 m	128.7–130.7
1''		134.0		133.3		133.5		133.1
2'',6''	7.24–7.40	127.5–128.7	7.24–7.40	126.7–128.7	7.29–7.39	128.2–128.9	7.14 dd (8.0, 2.0)	128.7–130.7
3'',4'',5''	7.24–7.40	127.5–128.7	7.24–7.40	126.7–128.7	7.29–7.39	128.2–128.9	7.29 m	128.7–130.7

*d* doublet, *dd* doublet of doublet, *s* singlet, *m* multiplet

m, H-3', 4', 5'), 7.20 (3H, m, H-3'', 4'', 5''), 7.03 (2H, d,  $J = 8.0$  Hz, H-2'', 6''), 5.14 (1H, d,  $J = 3.2$  Hz, H-4), 4.58 (1H, d,  $J = 7.6$  Hz, H-1'''), 4.54 (1H, d,  $J = 3.2$  Hz, H-3), 3.76 (1H, dd,  $J = 12.0, 2.0$  Hz, H-6'''a), 3.61 (1H, dd,  $J = 12.0, 4.8$  Hz, H-6'''b), 3.39 (1H, m, H-3'''), 3.35 (1H, ddd,  $J = 13.2, 8.8, 6.0$  Hz, H-6a), 3.30 (1H, m, H-2'''), 3.28 (1H, m, H-4'''), 3.26 (1H, m, H-5'''), 3.17 (1H, ddd,  $J = 13.2, 8.4, 7.2$  Hz, H-6b), 2.60 (1H, ddd,  $J = 13.6, 8.8, 6.0$  Hz, H-5a), 2.45 (1H, ddd,  $J = 13.6, 8.4, 7.2$  Hz, H-5b);  $^{13}\text{C}$  NMR ( $\text{CD}_3\text{OD}$ , 100 MHz)  $\delta_{\text{C}}$  173.4 (C-2), 140.2 (C-1''), 138.6 (C-1'), 127.3–129.7 (C-2'–6', 2''–6''), 102.9 (C-1'''), 82.4 (C-4), 78.0 (C-3'', 5'''), 75.3 (C-2'''), 74.4 (C-3), 71.3 (C-4'''), 62.4 (C-6'''), 41.3 (C-5), 36.4 (C-6); ECD (MeOH) 205 ( $\Delta\epsilon +1.01$ ), 211 ( $\Delta\epsilon -0.64$ ), 215 ( $\Delta\epsilon +0.37$ ), 227 ( $\Delta\epsilon -1.67$ ) nm; ESIMS  $m/z$  470  $[\text{M}+\text{Na}]^+$ ; HRESIMS  $m/z$  470.1788 (calcd for  $\text{C}_{23}\text{H}_{29}\text{NO}_8\text{Na}$ , 470.1791).

**Clausenaline G (6)** Pale yellow powder; UV (MeOH)  $\lambda_{\text{max}}$  (log  $\epsilon$ ) 212 (3.12), 233 (3.37), 275 (3.24), 311 (2.68) nm; IR (KBr)  $\nu_{\text{max}}$  2926, 2853, 1700, 1580, 1436, 1323, 1240, 1113  $\text{cm}^{-1}$ ;  $^1\text{H}$  NMR ( $\text{CDCl}_3$ , 400 MHz)  $\delta_{\text{H}}$  8.79 (1H, d,  $J = 2.0$  Hz, H-4), 8.47 (1H, br s, N–H), 8.12 (1H, dd,  $J = 8.8, 2.0$  Hz, H-2), 7.72 (1H, d,  $J = 8.0$  Hz, H-5), 7.45 (1H, d,  $J = 8.8$  Hz, H-1), 7.21 (1H, dd,  $J = 8.0, 8.0$  Hz, H-6), 6.94 (1H, d,  $J = 8.0$  Hz, H-7), 4.02 (3H, s,  $\text{OCH}_3$ -8), 3.97 (3H, s,  $\text{COOCH}_3$ );  $^{13}\text{C}$  NMR ( $\text{CDCl}_3$ , 100 MHz)  $\delta_{\text{C}}$  167.8 (C=O), 145.7 (C-8), 141.8 (C-1a), 130.2 (C-8a), 127.3 (C-2), 124.3 (C-5a), 123.4 (C-4a), 123.2 (C-4), 121.4 (C-3), 120.7 (C-6), 113.0 (C-5), 110.4 (C-1), 106.6 (C-7), 55.6 ( $\text{OCH}_3$ -8), 51.9 ( $\text{COOCH}_3$ ); ESIMS  $m/z$  278  $[\text{M}+\text{Na}]^+$ ; HRESIMS  $m/z$  278.0795 (calcd for  $\text{C}_{15}\text{H}_{13}\text{NO}_3\text{Na}$ , 278.0793).

(±)-5-(4-methylphenyl)- $\gamma$ -valerolactone (7) White amorphous powder; UV (MeOH)  $\lambda_{\text{max}}$  (log  $\epsilon$ ) 211 (2.36), 263 (1.83) nm; IR (KBr)  $\nu_{\text{max}}$  2980, 2927, 1773, 1620, 1513, 1453, 1133  $\text{cm}^{-1}$ ;  $^1\text{H}$  NMR ( $\text{CDCl}_3$ , 300 MHz)  $\delta_{\text{H}}$  7.26 (2H, d,  $J = 6.8$  Hz, H-6, 10), 7.18 (2H, d,  $J = 6.8$  Hz, H-7, 9), 2.59 (1H, m, H-2a), 2.48 (1H, m, H-2b), 2.46 (1H, m, H-3a), 2.38 (1H, m, H-3b), 2.34 (3H, s, H-11), 1.70 (3H, s, H-12);  $^{13}\text{C}$  NMR ( $\text{CDCl}_3$ , 75 MHz)  $\delta_{\text{C}}$  176.5 (C-1), 141.2 (C-5), 137.3 (C-8), 129.2 (C-7, 9), 124.0 (C-6, 10), 87.0 (C-4), 36.1 (C-3), 29.4 (C-11), 28.9 (C-2), 20.9 (C-12); ESIMS  $m/z$  213  $[\text{M}+\text{Na}]^+$ ; HRESIMS  $m/z$  213.0892 (calcd for  $\text{C}_{12}\text{H}_{14}\text{O}_2\text{Na}$ , 213.0891).

#### Single-crystal X-ray diffraction analysis and crystallographic data of compounds 2–4, and 9

The diffraction intensity data for compounds 2–4, and 9 were acquired on a Bruker D8 VENTURE with PHOTON 100 CMOS detector system equipped with a Cu Incoatec  $\mu\text{S}$  Microfocus Source ( $\lambda = 1.54178$  Å). The data were collected by Bruker APEX2 software. Data reductions

were conducted with Bruker SAINT. Structure solutions and refinements were performed with the SHELXTL program package. The crystal structures of selected compounds 2–4, and 9 were drawn by ORTEP and shown in Fig. 4.

**Crystallographic data of 2:**  $\text{C}_{18}\text{H}_{20}\text{ClNO}_3$ , formula weight 333.80, crystal size  $0.30 \times 0.25 \times 0.20$  mm<sup>3</sup>, crystal system monoclinic, space group  $P1_21_1$ ,  $a = 8.3756(2)$  Å,  $b = 6.2938(2)$  Å,  $c = 16.0127(5)$  Å,  $\alpha = \gamma = 90^\circ$ ,  $\beta = 96.4540(10)^\circ$ ,  $V = 838.75(4)$  Å<sup>3</sup>,  $Z = 2$ ,  $D_{\text{calcd}} = 1.322$  Mg/m<sup>3</sup>,  $\mu(\text{CuK}\alpha) = 2.136$  mm<sup>−1</sup>,  $F(000) = 352$ ; total 5754 reflections, 2516 independent reflections [ $R(\text{int}) = 0.0183$ ]; final  $R$  indices [ $I > 2\sigma(I)$ ]  $R_1 = 0.0236$ ,  $wR_2 = 0.0615$ ;  $R$  indices (all data)  $R_1 = 0.0237$ ,  $wR_2 = 0.0616$ ; Flack parameter 0.062(11).

**Crystallographic data of 3:**  $\text{C}_{18}\text{H}_{18}\text{ClNO}_2$ , formula weight 315.79, crystal size  $0.47 \times 0.26 \times 0.24$  mm<sup>3</sup>, crystal system monoclinic, space group  $P2_1$ ,  $a = 8.6584(7)$  Å,  $b = 5.9697(5)$  Å,  $c = 17.0605(13)$  Å,  $\alpha = \gamma = 90^\circ$ ,  $\beta = 98.943(4)^\circ$ ,  $V = 871.10(12)$  Å<sup>3</sup>,  $Z = 2$ ,  $D_{\text{calcd}} = 1.273$  Mg/m<sup>3</sup>,  $\mu(\text{CuK}\alpha) = 2.056$  mm<sup>−1</sup>,  $F(000) = 352$ ; total 7196 reflections, 2602 independent reflections [ $R(\text{int}) = 0.0436$ ]; final  $R$  indices [ $I > 2\sigma(I)$ ]  $R_1 = 0.0828$ ,  $wR_2 = 0.2544$ ;  $R$  indices (all data)  $R_1 = 0.0853$ ,  $wR_2 = 0.2573$ ; Flack parameter 0.12(5).

**Crystallographic data of 4:**  $\text{C}_{19}\text{H}_{21}\text{SNO}_4$ , formula weight 359.43, crystal size  $0.62 \times 0.32 \times 0.12$  mm<sup>3</sup>, crystal system triclinic, space group  $P1$ ,  $a = 6.2738(7)$  Å,  $b = 8.6837(7)$  Å,  $c = 9.2660(8)$  Å,  $\alpha = 69.457(8)^\circ$ ,  $\beta = 79.789(8)^\circ$ ,  $\gamma = 76.575(8)^\circ$ ,  $V = 457.24(7)$  Å<sup>3</sup>,  $Z = 1$ ,  $D_{\text{calcd}} = 1.305$  Mg/m<sup>3</sup>,  $\mu(\text{CuK}\alpha) = 1.767$  mm<sup>−1</sup>,  $F(000) = 190$ ; total 6197 reflections, 3154 independent reflections [ $R(\text{int}) = 0.0329$ ]; final  $R$  indices [ $I > 2\sigma(I)$ ]  $R_1 = 0.0550$ ,  $wR_2 = 0.1424$ ;  $R$  indices (all data)  $R_1 = 0.0609$ ,  $wR_2 = 0.1510$ ; Flack parameter 0.00(2).

**Crystallographic data of 9:**  $\text{C}_{18}\text{H}_{19}\text{NO}_3$ , formula weight 297.34, crystal size  $0.56 \times 0.38 \times 0.20$  mm<sup>3</sup>, crystal system monoclinic, space group  $P2_1$ ,  $a = 11.1150(6)$  Å,  $b = 5.2680(4)$  Å,  $c = 13.1802(6)$  Å,  $\alpha = \gamma = 90^\circ$ ,  $\beta = 93.185(5)^\circ$ ,  $V = 770.56(8)$  Å<sup>3</sup>,  $Z = 2$ ,  $D_{\text{calcd}} = 1.282$  Mg/m<sup>3</sup>,  $\mu(\text{CuK}\alpha) = 0.705$  mm<sup>−1</sup>,  $F(000) = 316$ ; total 5992 reflections, 2688 independent reflections [ $R(\text{int}) = 0.0264$ ]; final  $R$  indices [ $I > 2\sigma(I)$ ]  $R_1 = 0.0366$ ,  $wR_2 = 0.1009$ ;  $R$  indices (all data)  $R_1 = 0.0383$ ,  $wR_2 = 0.1028$ ; Flack parameter  $-0.3(2)$ .

The crystallographic data for the structures of compounds 2–4, and 9 reported in this paper have been deposited with the Cambridge Crystallographic Data Centre (deposit numbers CCDC 991727–991730, respectively). Copies of these data can be obtained, free of charge, on application to Director, CCDC, 12 Union Road, Cambridge CB2 1EZ, UK (fax: +44-(0)1223-336033 or e-mail: deposit@ccdc.cam.ac.uk).

## Determination of aldose configuration

Compound **5** (0.5 mg) was hydrolyzed with 0.5 M HCl (0.4 mL) in a screw-capped vial at 60 °C for 1 h. The reaction mixture was neutralized with Amberlite IRA400 and filtered. The filtrate was dried in vacuo, then dissolved in 0.1 mL of pyridine containing L-cysteine methyl ester (0.5 mg), and reacted at 60 °C for 1 h. To the mixture was added a solution of *o*-tolylisothiocyanate in pyridine (5 mg/1 mL) at room temperature for 1 h. This reaction mixture was directly analyzed by HPLC [Cosmosil 5C<sub>18</sub> ARII (250 × 4.6 mm i.d. Nacalai Tesque Inc.); 20 % CH<sub>3</sub>CN in 50 mM acetate; flow rate 0.8 mL/min; detection, 250 nm] as reported [2]. D-glucose (*t<sub>R</sub>* 40.3 min) was identified as the sugar moiety of **5** based on comparisons with authentic sample of D-glucose (*t<sub>R</sub>* 40.3 min).

## Preparation of human neutrophils

The study of human neutrophils was approved by the Institutional Review Board at Chang Gung Memorial Hospital, Taoyuan, Taiwan. Written informed consent was obtained from every volunteer. Neutrophils were isolated using a standard dextran sedimentation method prior to centrifugation on a Ficoll Hypaque gradient and hypotonic lysis of erythrocytes. Blood was drawn from healthy human donors (aged 20–30 years) by venipuncture into heparin-coated vacutainer tubes using a protocol approved by the Institutional Review Board at Chang Gung Memorial Hospital. Purified neutrophils were pelleted and then resuspended in calcium (Ca<sup>2+</sup>)-free Hank's balanced salt solution (HBSS) buffer at pH 7.4 and were maintained at 4 °C before use.

## Measurements of superoxide anion generation and elastase release

The assay for measurement of superoxide anion generation was based on the SOD-inhibitable reduction of ferricytochrome *c* [13, 14]. Degranulation of azurophilic granules was determined by measuring elastase release as described previously [13, 14].

## Results and discussion

The ethanol extracts of the dried leaves from *C. lansium* were partitioned between chloroform and water to afford chloroform and water soluble fractions, respectively. Purification of the chloroform and water soluble fractions by a conventional combination of column chromatographic methods totally afforded five new acyclic amides **1–5** (Fig. 1), two compounds **6–7** first reported from the natural

sources, and thirty-seven other known compounds. The known compounds were identified by comparison of their physical and spectroscopic data with the reported values.

Clausenalansamide **1** was obtained as colorless crystals. The molecular formula of **1** was determined as C<sub>19</sub>H<sub>21</sub>NO<sub>3</sub> by its HRESIMS data, which showed the sodium adduct ion at *m/z* 334.1410 ([M+Na]<sup>+</sup>, calcd for C<sub>19</sub>H<sub>21</sub>NO<sub>3</sub>Na, 334.1413). The UV spectrum displayed two absorption maximum peaks ( $\lambda_{\text{max}}$ ) at 262 and 209 nm, indicating the presence of a conjugated benzene chromophore [15]. The IR absorption bands at 3386 and 1630 cm<sup>-1</sup> coincided well with the hydroxy and amide carbonyl groups, respectively. Analysis of the <sup>1</sup>H-, <sup>13</sup>C-NMR (Table 1), and HSQC spectra revealed two oxymethine protons [( $\delta_{\text{H}}$  4.62;  $\delta_{\text{C}}$  71.9, C-3) and ( $\delta_{\text{H}}$  4.27;  $\delta_{\text{C}}$  85.8, C-4)], two *cis*-olefinic protons [( $\delta_{\text{H}}$  6.38, *d*, *J* = 9.0 Hz;  $\delta_{\text{C}}$  127.9, C-5) and ( $\delta_{\text{H}}$  6.16, *d*, *J* = 9.0 Hz;  $\delta_{\text{C}}$  124.7, C-6)], one amide carbonyl carbon ( $\delta_{\text{C}}$  173.0, C-2), two quaternary carbons ( $\delta_{\text{C}}$  137.7, C-1';  $\delta_{\text{C}}$  134.0, C-1''), and two monosubstituted phenyl rings. The <sup>1</sup>H and <sup>13</sup>C NMR spectra data of **1** were similar to those of the co-occurring known compound clausenalansamide **9** [16], except that the C-4 hydroxy group in **9** was replaced by a methoxy group in **1**. Thus, compound **1** is the 4-*O*-methyl derivative of **9**. This assignment was further confirmed by the HMBC correlation (Fig. 2) between OCH<sub>3</sub>-4 ( $\delta_{\text{H}}$  3.19, *s*) and C-4 ( $\delta_{\text{C}}$  85.8). The 3*R*, 4*R* absolute configurations of **1** were established by ECD analysis (Fig. 3), in which an excellent fit was found between **1** and **9** [17]. Therefore, the stereochemical structure of **1** was determined as shown and its trivial name was given according to the previous convention.

The molecular formula of **2** and **3** were both established as C<sub>18</sub>H<sub>18</sub>ClNO<sub>2</sub>, according to their HRESIMS analytical data. Their <sup>1</sup>H-, <sup>13</sup>C-NMR (Table 1), and HSQC spectra also displayed the similar characteristics of two methine protons, two *cis*-olefinic protons, one amide carbonyl carbon, two quaternary carbons, and two monosubstituted phenyl rings, as those of **1**. Comparison of their NMR and mass spectral data with compounds **1**, **9**, and **10** [18] inferred that **2** and **3** should be 3-chloro-4-hydroxy or 3-hydroxy-4-chloro derivatives resulting from the epoxide ring-opening of **10**. The substitution patterns of **2** and **3** were confirmed by HMBC correlations (Fig. 2) of H-3/C-1' in **2** and H-4/C-2 in **3**, respectively. The relative configurations were determined by single-crystal X-ray diffraction analysis (Fig. 4) and the absolute configurations of C-3 and C-4 were further confirmed by ECD spectra (Fig. 3). In their ECD spectra (Fig. 3), a negative Cotton effect at 228 nm in **2** and a positive Cotton effect at 229 nm in **3**, compared with the positive Cotton effect at 228 nm in **1**, suggested the orientations of C-3 substituents of **2** and **3** to be  $\beta$  and  $\alpha$ . Moreover, according to the ORTEP drawing

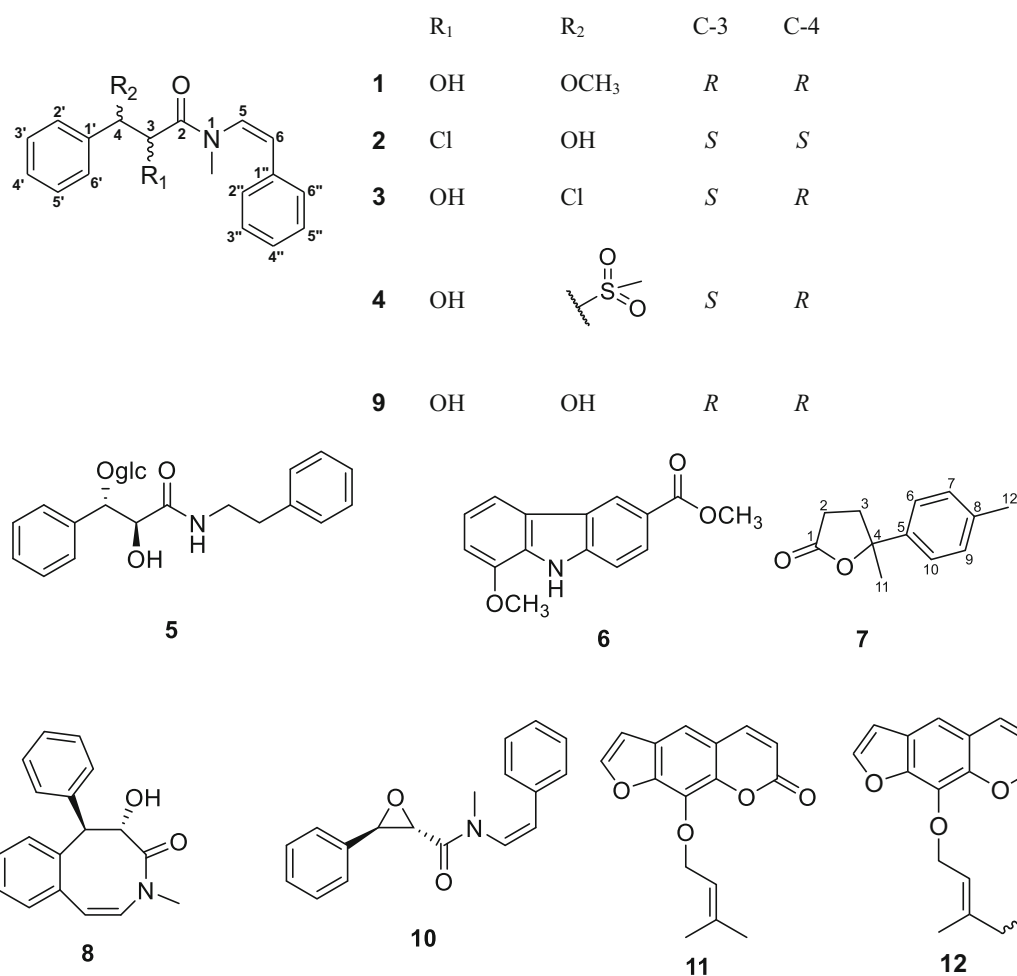
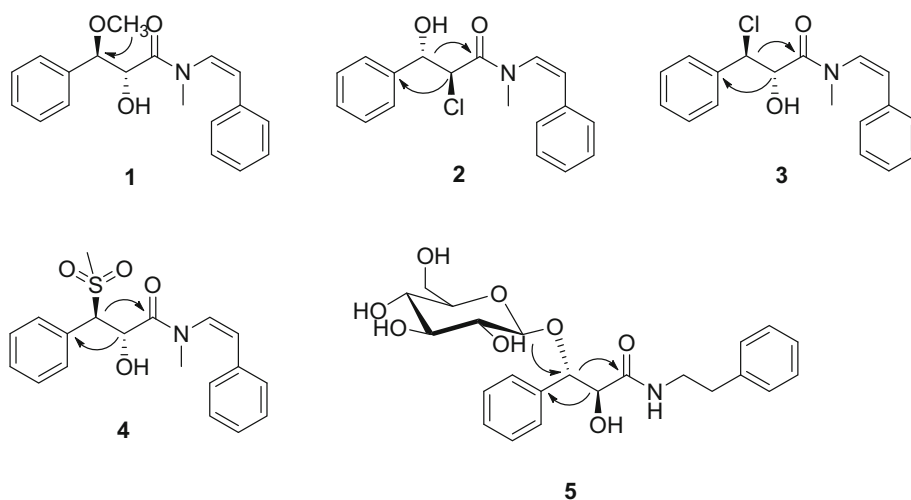


**Fig. 1** Chemical structures of compounds 1–12

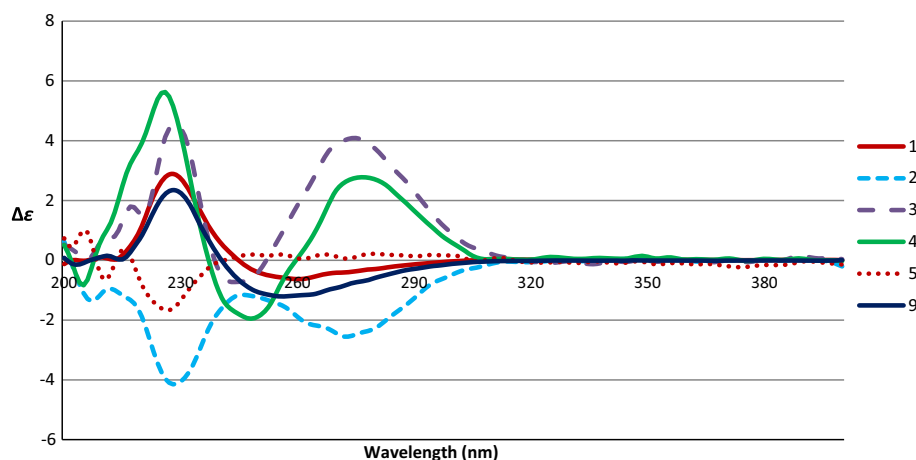
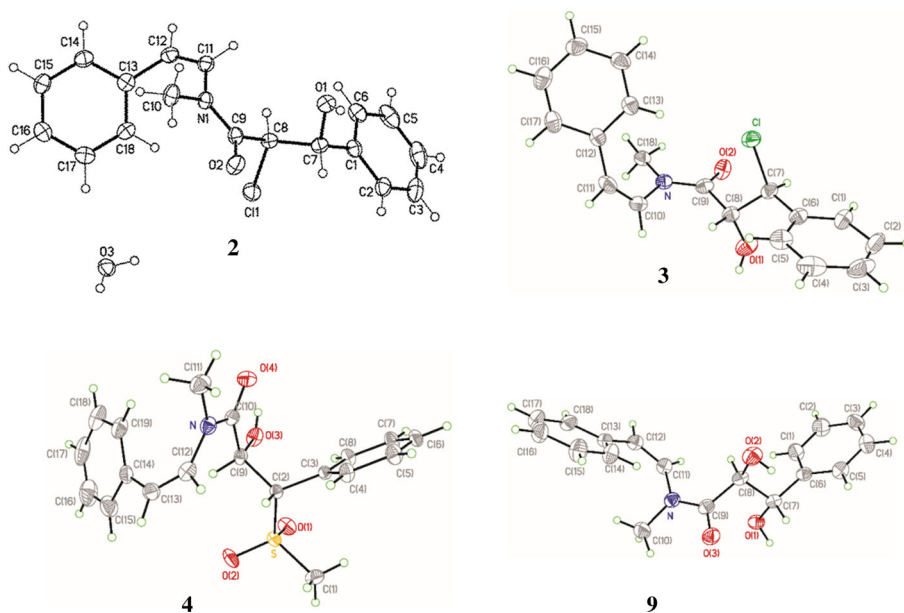
**Fig. 2** Key HMBC ( $H \rightarrow C$ ) correlations of 1–5



and Cahn–Ingold–Prelog priority rules (CIP rules), the absolute configurations of **2** and **3** were assigned as 3*S*, 4*S*, and 3*S*, 4*R*, respectively, and named trivially as clausealansamides D (**2**) and E (**3**) (Fig. 1).

Compound **4** had a molecular formula of C<sub>19</sub>H<sub>21</sub>NO<sub>4</sub>S according to HRESIMS analysis. The IR spectrum exhibited strong absorption bands at 1302 and 1122 cm<sup>−1</sup>, which were typical signals of a sulfone group [19]. Its <sup>1</sup>H-, <sup>13</sup>C-



**Fig. 3** ECD spectra of compounds **1–5** and **9****Fig. 4** ORTEP drawings of compounds **2–4** and **9**

NMR (Table 1), and HSQC spectra indicated the characteristic proton and carbon signals as those of **1**, including two methine protons, two *cis*-olefinic protons, one amide carbonyl carbon, two quaternary carbons, and two mono-substituted phenyl rings. Since the UV, IR, and NMR spectra of **4** were very similar to those of **1**, suggesting that **4** had the same acyclic amide skeleton as **1**. The observed  $^1\text{H}$ -NMR spectral difference between **1** and **4** was that one more methyl group ( $\delta_{\text{H}}$  2.86, s) in **4** could be found, which also supports the presence of sulfone substituent. Its two-dimensional chemical structure and absolute configurations (3*S*, 4*R*) were also confirmed by HMBC correlations (Fig. 2), ECD spectrum (Fig. 3), and single-crystal X-ray diffraction analysis (Fig. 4). On the basis of the above spectral evidence, the structure of **4** was assigned as shown and named trivially as clausenalansamide F.

Clausenalansamide G (**5**) was afforded as white powder, possessing the molecular formula of  $\text{C}_{23}\text{H}_{29}\text{NO}_8$

determined from HRESIMS analytical data which showed a pseudomolecular ion peak at  $m/z$  470.1788 ( $[\text{M}+\text{Na}]^+$ , calcd for  $\text{C}_{23}\text{H}_{29}\text{NO}_8\text{Na}$ , 470.1791). The  $^1\text{H}$ - and  $^{13}\text{C}$ -NMR data of **5** suggested that it was an acyclic amide glycoside similar to secoclausenamamide [20]. Acid hydrolysis of **5**, preparation of the *o*-tolylthiocarbamate derivative successively, and further HPLC analysis of the sugar derivative with an authentic sample, identified the sugar moiety as D-glucose according to our previously published method [10]. The coupling constant (7.6 Hz) of the anomeric proton (H-1'') established the sugar unit as  $\beta$ -D-glucopyranosyl moiety. In the HMBC spectrum (Fig. 2) of **5**, the correlations between H-1'' ( $\delta_{\text{H}}$  4.58, d,  $J = 7.6$  Hz) and C-4 ( $\delta_{\text{C}}$  82.4) evidenced the location of the  $\beta$ -D-glucopyranosyl moiety attached to C-4 of the aglycone. The ECD spectrum (Fig. 3) of **5** showed a negative Cotton effect at 227 nm, which was similar to that of **2**, indicating the 3*S*, 4*S* configurations. Conclusively, the structure of **5** was

characterized as shown in Fig. 1. The occurrence of acyclic amides **1–5** may derive from the same biogenetic origin, compound **10**, through the epoxide ring opening which resulted from the addition of small molecules, such as water or solvent.

In addition, clausenaline G (**6**) and ( $\pm$ )-5-(4-methyl-phenyl)- $\gamma$ -valerolactone (**7**) were also purified and their structures were characterized as shown (Fig. 1) with the aid of spectroscopic and mass analysis. Although the chemical synthesis of **6** and **7** had already been reported previously [21, 22], these compounds were isolated from the natural sources for the first time. The other thirty-seven isolated known compounds were identified as (–)- $\zeta$ -clausenamide (**8**) [23], clausenalansamide A (**9**) [17], (+)-SB204900 (**10**) [24], imperatorin (**11**) [10], wampetin (**12**) [10], phytene-1,2-diol [25], *N*-phenethylcinnaamide [10], lansiumamide B [26], lansamide I [26], loliolide [25], (+)-(*S*)-dehydrovomifoliol [25], 7-hydroxycoumarin [27], xanthotoxol [10], 8-geranyloxypsolarin [10],  $\beta$ -sitosteryl-3-*O*-glucopyranoside [25], quercetin-3-*O*-rutinoside [28],  $\beta$ -sitosterol [10], madolin A [29], (2-hydroxyphenyl)acetic acid methyl ester [30], mukonine [31], heneicos-5,8,11,14-tetraenoic acid [32], 4-hydroxybenzaldehyde [33], *O*-methylmukonal [10], clausine G [34], methyl pheophorbide a [35], (10*S*)-hydroxypheophorbide a [36], 3-formyl-6-methoxy-carbazole [10], benzoic acid [37], (3*R*,6*R*,7*E*)-3-hydroxy-4,7-megastigmadien-9-one [38], clausenalansamide B [16], dehydrolololide [39], (6*R*,7*E*)-4,7-megastigmadien-3,9-dione [38], (2*S*,3*S*)-2,3-dihydroxy-3-phenylpropanoic acid methyl ester [40], 2,3-dihydroxy-*N*-methyl-3-phenyl-*N*-(2-phenylethyl)propionic acid amide [41], 4-hydroxycinnamic acid [10], (*E*)-3-(4-hydroxy-3-methoxyphenyl)prop-2-enoate [25], and methyl *trans*-4-hydroxycinnamate [25], based on their spectroscopic and spectrometric profiles (NMR, UV, IR, and MS).

A cellular model in isolated human neutrophils was used to evaluate the anti-inflammatory activity of the isolated compounds from the leaves of *C. lansium*. Eighteen

isolated compounds were examined for their inhibitory effects on superoxide anion generation and elastase release by human neutrophils in response to formyl-L-methionyl-L-leucyl-L-phenylalanine/cytochalasin B (fMLP/CB) [13, 14], and only imperatorin (**11**) and wampetin (**12**) displayed the most significant inhibition of fMLP/CB-induced superoxide anion generation with IC<sub>50</sub> values of  $1.7 \pm 0.3$  and  $6.8 \pm 1.1$   $\mu$ M, respectively (Table 2). Other compounds did not show significant anti-inflammatory activity with IC<sub>50</sub> values >10  $\mu$ M.

## Conclusion

In the present study, a series of amides including acyclic amides and lactams were characterized from the leaves of *C. lansium*, and fewer carbazoles and coumarins were purified as compared with other reports of the stems and roots of the same plants. In addition, among the examined natural compounds, only coumarins **11** and **12** displayed inhibition of fMLP/CB-induced superoxide anion generation. This finding encouraged us to pay more attentions to coumarins in *Clausena* species and their structure–activity relationships in the future work of searching for new anti-inflammatory lead compounds.

**Acknowledgments** This study was sponsored by the Ministry of Science and Technology, Taiwan, ROC granted to T.-S. Wu, and supported in part by the Vietnam National Foundation for Science and Technology Development (Nr. 104.01-2010.27), and Chang Gung Memorial Hospital (CMRPD1B0481~3, CMRPD1D0281~3, and BMRP450 to H.-L. Hwang). We also thank Associate Prof. Dr. Tran Huy Thai (Institute of Ecology and Biological Resources, Vietnamese Academy of Science and Technology, Vietnam) for the identification of the plant materials.

## Compliance with ethical standards

**Conflict of interest** The authors declare no conflict of interest.

## References

- Huang CC (1959) Preliminary Study on Chinese Rutaceae (3). Acta Phytotax Sin 8:69–124
- Yang MH, Cao YH, Li WX, Yang YQ, Cheng YY, Huang L (1987) Isolation and structural elucidation of clausenamide from the leaves of *Clausena lansium* (Lour.) Skeels. Acta Pharm Sin B 22:33–40
- Yang MH, Chen YY, Huang L (1987) Studies on the chemical constituents of *Clausena lansium* (Lour.) Skeels II: The isolation and structural elucidation of neoclausenamide and cycloclausenamide. Acta Chin Sin 45:1170–1174
- Yang MH, Chen YY, Huang L (1988) Three novel cyclic amides from *Clausena lansium*. Phytochemistry 27:445–450
- Lakshmi V, Raj K, Kapil RS (1998) Chemical constituents of *Clausena lansium*: Part III. Structure of lansamide-3 and 4. Indian J Chem Sect B Org Chem Incl Med Chem 37B:422–424

**Table 2** Inhibitory effects of compounds **11** and **12** from the leaves of *C. lansium* on superoxide anion generation and elastase release by human neutrophils in response to fMLP/CB

Compounds	IC <sub>50</sub> ( $\mu$ M) <sup>a</sup>	
	Superoxide anion generation	Elastase release
<b>11</b>	$1.7 \pm 0.3^{**}$	>10
<b>12</b>	$6.8 \pm 1.1^{***}$	>10
<b>LY294002<sup>b</sup></b>	$0.4 \pm 0.02^{***}$	$1.5 \pm 0.3^{***}$

<sup>a</sup> Concentration necessary for 50 % inhibition; results are presented as mean  $\pm$  SD ( $n = 3$ –4)

<sup>b</sup> A phosphatidylinositol-3-kinase inhibitor was used as a positive control for superoxide anion generation and elastase release

\*\*\*  $p < 0.001$  and \*\*  $p < 0.01$  compared with the control value

6. Ji X, van der Helm D, Lakshmi V, Agarwal SK, Kapil RS (1992) Structure of lansimide 2, a product from *Clausena lansium*. Acta Crystallogr Sect C Cryst Struct Commun 48:1082–1085
7. Chokeyprasert P, Charles AL, Sue KH, Huang TC (2007) Volatile components of the leaves, fruits and seeds of wampee [*Clausena lansium* (Lour.) Skeels]. J Food Compos Anal 20:52–56
8. Wong KC, Wong SN, Sam TW, Chee SG (1998) Volatile constituents of *Clausena lansium* (Lour.) Skeels fruit. J Essent Oil Res 10:700–702
9. Adebajo AC, Iwalewa EO, Obuotor EM, Ibikunle GF, Omisore NO, Adewunmi CO, Obaparusi OO, Klaes M, Adetogun GE, Schmidt TJ, Verspohl EJ (2009) Pharmacological properties of the extract and some isolated compounds of *Clausena lansium* stem bark: anti-trichomonal, antidiabetic, anti-inflammatory, hepatoprotective and antioxidant effects. J Ethnopharmacol 122:10–19
10. Shen DY, Chao CH, Chan HH, Huang GJ, Hwang TL, Lai CY, Lee KH, Thang TD, Wu TS (2012) Bioactive constituents of *Clausena lansium* and a method for discrimination of aldose enantiomers. Phytochemistry 82:110–117
11. Shen DY, Chan YY, Hwang TL, Juang SH, Huang SC, Kuo PC, Thang TD, Lee EJ, Damu AG, Wu TS (2014) Constituents of the roots of *Clausena lansium* and their potential anti-inflammatory activity. J Nat Prod 77:1215–1223
12. Shen DY, Nguyen TN, Wu SJ, Shiao YJ, Hung HY, Kuo PC, Kuo DH, Thang TD, Wu TS (2014)  $\gamma$ - and  $\delta$ -Lactams from the leaves of *Clausena lansium*. J Nat Prod 78:2521–2530
13. Yang SC, Chung PJ, Ho CM, Kuo CY, Hung MF, Huang YT, Chang WY, Chang YW, Chan KH, Hwang TL (2013) Propofol inhibits superoxide production, elastase release, and chemotaxis in formyl peptide-activated human neutrophils by blocking formyl peptide receptor 1. J Immunol 190:6511–6519
14. Yu HP, Hsieh PW, Chang YJ, Chung PJ, Kuo LM, Hwang TL (2011) 2-(2-Fluorobenzamido)benzoate ethyl ester (EFB-1) inhibits superoxide production by human neutrophils and attenuates hemorrhagic shock-induced organ dysfunction in rats. Free Radic Biol Med 50:1737–1748
15. Scott AI (1964) Interpretation ultraviolet spectra of natural products, 2nd edn. Pergamon Press, New York
16. Maneerat W, Tha-in S, Cheenpracha S, Prawat U, Laphookhieo S (2011) New amides from the seeds of *Clausana lansium*. J Med Plant Res 5:2812–2815
17. Song WW, Zeng GZ, Peng WW, Chen KX, Tan NH (2014) Cytotoxic amides and quinolones from *Clausena lansium*. Helv Chim Acta 97:298–305
18. Milner PH, Coates NJ, Gilpin ML, Spear SR, Eggleston DS (1996) SB-204900, a novel oxirane carboxamide from *Clausena lansium*. J Nat Prod 59:400–402
19. Teshima KI, Kaneko T, Ohtani K, Kasai R, Lhieochaiphant S, Picheansoonthon C, Yamasak K (1998) Sulfur-containing glucosides from *Clinacanthus nutans*. Phytochemistry 48:831–835
20. Liu GT, Li WX, Chen YY, Wei HL (1996) Hepatoprotective action of nine constituents isolated from the leaves of *Clausena lansium* in mice. Drug Dev Res 39:174–178
21. Sowmithran D, Prasad KJR (1986) Heterocycles 2: synthesis of 1-hydroxycarbazoles and mukonine isomers. Heterocycles 24:711–717
22. Wang B, Shen YM, Shi Y (2006) Enantioselective synthesis of  $\gamma$ -aryl- $\gamma$ -butyrolactones by sequential asymmetric epoxidation, ring expansion, and Baeyer–Villiger oxidation. J Org Chem 71:9519–9521
23. Yang MH, Chen YY, Huang L (1991) Studies on the chemical constituents of *Clausena lansium* (Lour.) Skeels. III. The structural elucidation of homo- and  $\zeta$ -clausenamide. Chin Chem Lett 2:291–292
24. Yang L, Deng G, Wang DX, Huang ZT, Zhu JP, Wang MX (2007) Highly efficient and stereoselective *N*-vinylation of oxiranecarboxamides and unprecedented 8-endo-epoxy-arene cyclization: expedient and biomimetic synthesis of some *Clausena* alkaloids. Org Lett 9:1387–1390
25. Shen DY, Juang SH, Kuo PC, Huang GJ, Chan YY, Damu AG, Wu TS (2013) Chemical constituents from *Andrographis echinoides* and their anti-inflammatory activity. Int J Mol Sci 14:496–514
26. Lin J (1989) Cinnamamide derivatives from *Clausena lansium*. Phytochemistry 28:621–622
27. Maneerat W, Ritthiwigrom T, Cheenpracha S, Laphookhieo S (2012) Carbazole alkaloids and coumarins from *Clausena lansium* roots. Phytochem Lett 5:26–28
28. Kofinas C, Chinou I, Loukis A, Harvala C, Maillard M, Hostettmann K (1998) Flavonoids and bioactive coumarins of *Tordilium apulum*. Phytochemistry 48:637–641
29. Wu TS, Chan YY, Leu YL (1998) Sesquiterpenes from the root and stem of *Aristolochia cucurbitifolia*. J Nat Prod 61:511–514
30. Ariza MR, Larsen TO, Petersen BO, Duus JØ, Barrero AF (2002) *Penicillium digitatum* metabolites on synthetic media and *Citrus* fruits. J Agric Food Chem 50:6361–6365
31. Wu TS, Huang SC, Wu PL, Teng CM (1996) Carbazole alkaloids from *Clausena excavata* and their biological activity. Phytochemistry 43:133–140
32. Vasskog T, Andersen JH, Hansen E, Svenson J (2012) Characterization and cytotoxicity studies of the rare 21:4 n-7 acid and other polyunsaturated fatty acids from the marine opisthobranch *Scaphander lignarius*, isolated using bioassay guided fractionation. Mar Drugs 10:2676–2690
33. Kuo PC, Yang ML, Hwang TL, Lai YY, Li YC, Thang TD, Wu TS (2013) Anti-inflammatory diterpenoids from *Croton tonkinensis*. J Nat Prod 76:230–236
34. Wu TS, Huang SC, Wu PL (1996) Carbazole alkaloids from stem bark of *Clausena excavata*. Phytochemistry 43:1427–1429
35. Hargus JA, Fronczek FR, Vicente MGH, Smith KM (2007) Mono-(L)-aspartylchlorine-6. Photochem Photobiol 83:1006–1015
36. Cheng HH, Wang HK, Ito J, Bastow KF, Tachibana Y, Nakanishi Y, Xu Z, Luo TY, Lee KH (2001) Cytotoxic pheophorbide-related compounds from *Clerodendrum calamitosum* and *C. cyrtophyllum*. J Nat Prod 64:915–919
37. Wu PL, Lin FW, Wu TS, Kuoh CS, Lee KH, Lee SJ (2004) Cytotoxic and anti-HIV principles from the rhizomes of *Begonia nantoensis*. Chem Pharm Bull 52:345–349
38. Machida K, Kikuchi M (1996) Norisoprenoids from *Viburnum dilatatum*. Phytochemistry 41:1333–1336
39. Macías FA, Lacret R, Varela RM, Nogueiras C, Molinillo JMG (2008) Bioactive apocarotenoids from *Tectona grandis*. Phytochemistry 69:2708–2715
40. Adam W, Zhang A (2004) High  $\pi$ -facial selectivity through chelation of magnesium ions in the DMD epoxidation of  $\alpha$ ,  $\beta$ -unsaturated imides with chiral pyrrolidinone auxiliaries. Eur J Org Chem 2004:147–152
41. Chen YR, Yang MH, Liu GT, Huang L (1989) 2,3-Dihydroxy-3-phenyl-*N*-(2-phenylethyl)-propionic acid amides derivatives thereof. US Patent 04826873



FULL PAPER

Physiology

# Supplementation with Hualian No. 4 wild bitter gourd (*Momordica charantia* Linn. var. *abbreviata* ser.) extract increases anti-fatigue activities and enhances exercise performance in mice

Chien-Yu HSIAO<sup>1,2)</sup>, Yi-Ming CHEN<sup>3)</sup>, Yi-Ju HSU<sup>3)</sup>, Chi-Chang HUANG<sup>3)</sup>,  
Hsin-Ching SUNG<sup>4)</sup>\* and Sheng-Shih CHEN<sup>5)</sup>\*

<sup>1)</sup>Department of Nutrition and Health Sciences, Chang Gung University of Science and Technology, Taoyuan 33301, Taiwan

<sup>2)</sup>Research Center for Food and Cosmetic Safety, and Research Center for Chinese Herbal Medicine, College of Human Ecology, Chang Gung University of Science and Technology, Taoyuan 33301, Taiwan

<sup>3)</sup>Graduate Institute of Sports Science, National Taiwan Sport University, Taoyuan 33301, Taiwan

<sup>4)</sup>Department of Anatomy, College of Medicine, Chang Gung University, Taoyuan 33301, Taiwan

<sup>5)</sup>Department of General Surgery, Kaohsiung Veterans General Hospital, Kaohsiung 81362, Taiwan

**ABSTRACT.** Hualian No. 4 wild bitter gourd (WBG) is a specific vegetable cultivated by the Hualien District Agricultural Research and Extension Station in Taiwan. WBG is commonly consumed as a vegetable and used as a popular folk medicine. However, few studies have demonstrated the effects of WBG supplementation on exercise performance, physical fatigue and the biochemical profile. The purpose of this study was to evaluate the potential beneficial effects of WBG extract on fatigue and ergogenic functions following physiological challenge. Three groups of male ICR mice (n=8 per group) were orally administered 0, 1 or 2.5 g/kg/day of WBG for 4 weeks. They were respectively designated the vehicle, WBG-1X and WBG-2.5X groups. WBG significantly decreased body weight (BW) and epididymal fat pad (EFP) weight. Concerning physical performance, WBG supplementation dose-dependently increased grip strength and endurance swimming time. Concerning anti-fatigue activity, WBG decreased levels of serum lactate, ammonia, creatine kinase and blood urea nitrogen, and economized glucose metabolism after acute exercise challenge. Glycogen in the liver and gastrocnemius muscle dose-dependently increased with WBG treatment. Concerning the biochemical profile, WBG treatment significantly decreased alanine aminotransferase (ALT), blood urea nitrogen (BUN) and urea acid (UA), and increased total protein (TP). Therefore, 4-week supplementation with WBG may decrease white adipose weight, enhance energy economy, increase glycogen storage to enhance exercise performance and reduce fatigue.

**KEY WORDS:** anti-fatigue, exercise performance, glycogen storage, wild bitter gourd

J. Vet. Med. Sci.

79(6): 1110–1119, 2017

doi: 10.1292/jvms.17-0079

Received: 2 March 2017

Accepted: 19 April 2017

Published online in J-STAGE:

1 May 2017

Hualian No. 4 wild bitter gourd (*Momordica charantia* L. var. *abbreviata* Seringe, WBG) is a wild variety of *M. charantia* that is cultivated by Hualien District Agricultural Research and Extension Station (HDARES) in Taiwan. WBG, which is normally smaller than domesticated bitter gourd (*M. charantia* L.), belongs to the family Cucurbitaceae. The fresh fruits of WBG are frequently eaten as a vegetable in soup, fried dishes and other dishes. The inheritance similarity of WBG to bitter gourd is 80–98%. The HDARES, capitalizing on the continuous female flower initiation and high fruit bearing ability of bitter gourd, bred the new cultivars Hualien Nos.1–4, which are high in Vitamin C, anti-oxidants and charantin. Recent publications have reported many pharmacological activities of WBG, such as improving metabolic syndrome [37], countering alcoholic fatty liver [28] and reducing inflammation [18]. The nutritional analysis of bitter gourd fruits shows that it is rich in carbohydrates, proteins, vitamins, fiber and minerals, holds the highest nutritive value among all cucurbits [21]. In general, the main phytoconstituents present in *M. charantia*

\*Correspondence to: Sung, H.-C., Department of Anatomy, College of Medicine, Chang Gung University, Taoyuan 33301, Taiwan.

e-mail: hcs@mail.cgu.edu.tw

Chen, S. S., Department of General Surgery, Kaohsiung Veterans General Hospital, Kaohsiung 81362, Taiwan. e-mail: sschen@vghks.gov.tw

©2017 The Japanese Society of Veterinary Science



This is an open-access article distributed under the terms of the Creative Commons Attribution Non-Commercial No Derivatives (by-nc-nd) License. (CC-BY-NC-ND 4.0: <https://creativecommons.org/licenses/by-nc-nd/4.0/>)

are charantin, momordicin, momordin, stigmasta-5, 25-dien-3- $\beta$ -O-glucoside,  $\beta$ -sitosterol- $\beta$ -D-glucoside, momordicoside G, momordicoside F1, momordicoside F2, momordicoside I, momordicoside K and momordicoside L [13, 42]. Of these, charantin is the main active constituent of *M. charantia* fruits, and its potential hypoglycemic activity has been reported [29, 38, 44]. Moreover, several studies have been conducted to establish the therapeutic activities of bitter melon for various disorders, and it appears to have the ability to target several cancers [19, 27, 31, 39].

WBG is known to increase glycogen storage by potentiating mitochondrial function via activation of the PPAR $\alpha$  and PPAR $\gamma$  signaling pathways. However, relatively few studies have directly addressed the possible anti-fatigue function of WBG and its effects on exercise performance. Exercise performance can be defined for both humans and animals as performance in athletic events. Research focusing on exercise performance can provide important insights on oxygen transport, muscle performance, metabolism, cardiovascular control and the operations of various components of the nervous system [23]. Physical fatigue is often accompanied by deterioration in functional performance [15]. The occurrence of physical fatigue can be explained by at least two mechanisms: oxidative stress and energy exhaustion [11]. Exhaustive or intensive exercise can lead to the accumulation of excess reactive free radicals that cause tissue damage. Exhaustion theory suggests that energy source depletion and excess metabolite accumulation can lead to fatigue [43]. A previous article reviewed the physiological effects of WBG on energy metabolism and utilization via the AMPK pathway, peroxisome proliferator-activated  $\alpha$  (PPAR $\alpha$ ) and PPAR $\gamma$  activation [6, 36]. In this study, we evaluated the potential ergogenic, anti-fatigue and health promotion effects of WBG supplementation in mice using our established *in vivo* platform [9].

## MATERIALS AND METHODS

### *Materials, animals and experiment design*

Hualian No. 4 Wild Bitter Melon (WBG) extract was provided by Aquavan Technology Co., Ltd. (Taipei, Taiwan). Male ICR mice (8 weeks old) grown under specific pathogen-free conditions were purchased from BioLASCO (Yi-Lan, Taiwan). All mice were provided a standard laboratory diet (No. 5001; PMI Nutrition International, Brentwood, MO, U.S.A.) and distilled water *ad libitum*, and housed in a 12-hr light/12-hr dark cycle at room temperature ( $22 \pm 1^\circ\text{C}$ ) and 50–60% humidity. The Institutional Animal Care and Use Committee (IACUC) of National Taiwan Sport University (NTSU) inspected all animal experiments, and this study conformed to the guidelines of protocol IACUC-10501 approved by the IACUC ethics committee. In this study, the dose of WBG designed for humans was 4.8 g per day (WBG extract). The mouse dose (1 g/kg) we used in this study was converted from a human-equivalent dose (HED) based on body surface area by the following formula from the US Food and Drug Administration: Assuming a human weight of 60 kg, the HED for 4.8 (g)/60 (kg) =  $0.08 \times 12.3 = 1$  g/kg; the conversion coefficient 12.3 was used to account for differences in body surface area between mice and humans as we recently described [24]. In total, 24 mice were randomly assigned to 3 groups (8 mice/group) for daily oral WBG treatment for 4 weeks. The three groups were the vehicle group; the WBG-1X group, receiving 1 g/kg; and the WBG-2.5X group, receiving 2.5 g/kg. The vehicle group received the same volume of solution equivalent to individual body weight (BW). The mice were randomly housed in groups of 4 per cage.

### *Determination of charantin with high performance liquid chromatography (HPLC) equipment and conditions*

The WBG extract was dissolved in 25 mg/ml methanol and filtered through a 0.45  $\mu\text{l}$  membrane filter for HPLC analysis. The HPLC system was a Dionex UltiMate 3000 HPLC system, which consisted of an UltiMate 3000 RS pump, an UltiMate 3000 RS autosampler, an UltiMate 3000 RS column compartment, a variable wavelength detector (Dionex, Olten, Switzerland) and a reversed-phase column (Inertsil ODS-3V, 4.6  $\text{\AA}$ , 150 mm, GL Science, Inc., Tokyo, Japan). Each charantin standard and all samples were prepared in injection volumes of 20  $\mu\text{l}$  with detection at a wavelength of 204 nm and a column flow rate of 1 ml, and the mobile phase was methanol-water 100:2 (V/V). Data were collected and stored in the Chromelion software from Dionex Corporation (Sunnyvale, CA, U.S.A.).

### *Forelimb grip strength test*

A low-force testing system (Model-RX-5, Aikoh Engineering, Nagoya, Japan) was used to measure the forelimb grip strength of treated mice as we previously described [8].

### *Swimming exercise performance test*

The swim-to-exhaustion test involved loads corresponding to 5% of the mouse BW attached to the tail to evaluate endurance time as we previously described [8]. The swimming endurance time of each mouse was recorded from beginning to exhaustion, determined by observing loss of coordinated movements and failure to return to the surface within 7 sec.

### *Determination of fatigue-associated biochemical variables*

The effect of WBG supplementation on fatigue-associated biochemical indices was evaluated after exercise as we previously described [8, 10]. At 1 hr after WBG supplementation, all mice underwent a 15-min swim test without weight loading. Immediately after the swim test, blood samples were collected from the submandibular duct of mice and centrifuged at  $1,500 \times g$  and  $4^\circ\text{C}$  for 10 min for serum separation. Serum lactate, ammonia, glucose, creatine kinase (CK) and blood urea nitrogen (BUN) levels were determined with an autoanalyzer (Hitachi 7060, Hitachi, Tokyo, Japan).



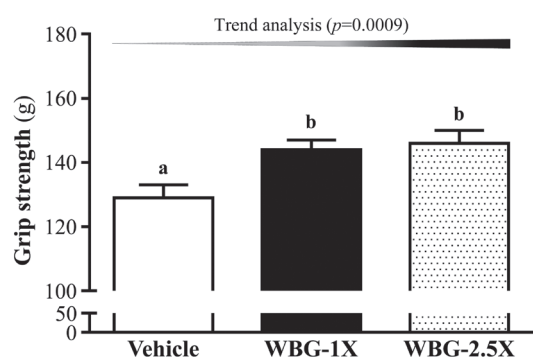


**Fig. 1.** Effect of WBG (Hualian No. 4 Wild Bitter Gourd) supplementation for 4 weeks on forelimb grip strength. Mice were pretreated with vehicle, WBG-1X or WBG-2.5X for 4 weeks before forelimb grip strength was tested. Data are mean  $\pm$  SEM, 8 mice/group, by one-way ANOVA. Different letters (a, b) indicate a significant difference at  $P < 0.05$ .

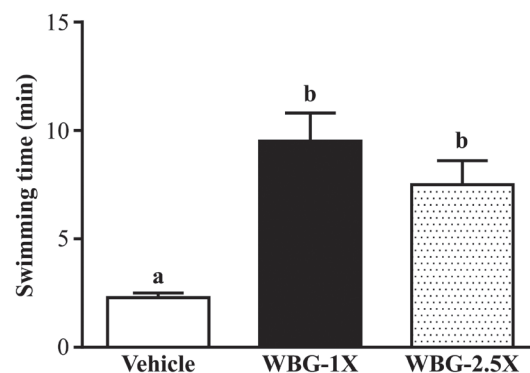


**Fig. 2.** Effect of WBG supplementation on swimming exercise performance. Mice were pretreated with vehicle, WBG-1X or WBG-2.5X for 4 weeks and then 1 hr later performed an exhaustive swimming exercise with a load equivalent to 5% of body weight attached to the tail. Data are mean  $\pm$  SEM,  $n = 8$  mice/group, by one-way ANOVA. Different letters (a, b) indicate a significant difference at  $P < 0.05$ .

### Clinical biochemical profiles

Two days after the 15-min swimming test, all mice were sacrificed with 95% CO<sub>2</sub> asphyxiation, and blood was immediately collected. Serum was separated by centrifugation and the levels of the clinical biochemical variables, aspartate aminotransferase (AST), alanine aminotransferase (ALT), creatine kinase (CK), total protein (TP), albumin, blood urea nitrogen (BUN), creatinine, uric acid (UA), total cholesterol (TC), triacylglycerol (TG) and glucose, were measured with an autoanalyzer (Hitachi 7060).

### Tissue glycogen determination and visceral organ weight

The stored form of glucose is glycogen, which exists mostly in liver and muscle tissue. Liver and muscle tissues were excised after the mice were sacrificed and weighed for glycogen content analysis as we described previously [20]. The weights of the related visceral organs were recorded.

### Histology of tissues

All tissues were carefully removed, minced and fixed in 10% formalin. Samples were embedded in paraffin and cut into 4- $\mu$ m thick slices for morphological and pathological evaluations. Tissue was stained with hematoxylin and eosin (H&E) and examined under an optical microscope equipped with a CCD camera (BX-51, Olympus, Tokyo, Japan) by a veterinary pathologist.

### Statistical analysis

All data are expressed as mean  $\pm$  SEM,  $n = 8$  mice/group. Statistical differences among groups were analyzed by a one-way analysis of variance (ANOVA) and the Cochran-Armitage test for dose-effect trend analysis with SAS 9.0 (SAS Inst., Cary, NC, U.S.A.).  $P < 0.05$  was considered statistically significant. Differences between groups were analyzed by one-way analysis of variance (ANOVA) using Duncan's *post-hoc* test, and  $P$  values  $< 0.05$  were considered significant.

## RESULTS

### Charantin content of WBG extract

We measured the charantin content in Hualian No. 4 Wild Bitter Gourd extract (WBG) by HPLC analysis. The retention time of charantin was approximately 13 min, and the content of charantin in WBG extract was 0.45 mg/g.

### Effects of WBG on forelimb grip strength

After supplementation with WBG for 4 weeks, the forelimb grip strengths in the vehicle, WBG-1X and WBG-2.5X groups were  $129 \pm 4$ ,  $144 \pm 3$  and  $146 \pm 4$  g, respectively (Fig. 1). Forelimb grip strength was significantly higher in the WBG-1X and WBG-2.5X groups (by 1.14-fold;  $P = 0.0090$  and  $P = 0.0035$ , respectively) than in the vehicle group. Trend analysis indicated that absolute forelimb grip strength dose-dependently increased with increasing WBG dose ( $P = 0.0009$ ).

### Effect of WBG on exercise performance in a weight-loaded swimming test

Endurance swimming times were  $2.3 \pm 0.2$ ,  $9.5 \pm 1.3$  and  $7.5 \pm 1.1$  min in the vehicle, WBG-1X and WBG-2.5X groups, respectively (Fig. 2). The exhaustive swimming times were longer in the WBG-1X and WBG-2.5X groups (by 4.10- and 3.23-fold;  $P < 0.0001$  and  $P = 0.0013$ , respectively) than in the vehicle group.

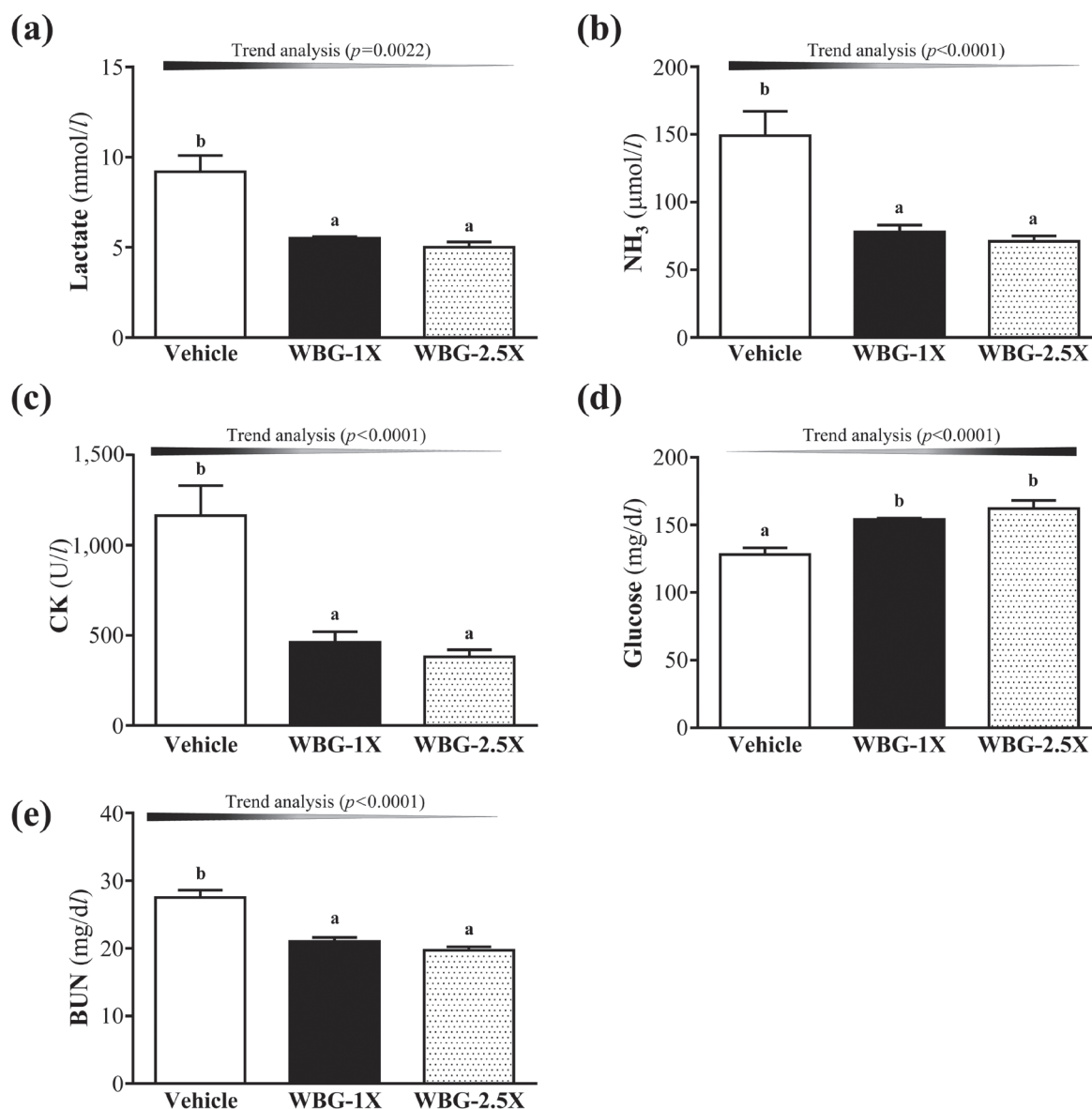


**Fig. 3.** Effect of WBG supplementation on serum levels of lactate (a); ammonia (b); creatine kinase (CK) (c); glucose (d) and blood urea nitrogen (BUN) (e) after acute exercise challenge. Data are mean  $\pm$  SEM,  $n=8$  mice/group, by one-way ANOVA. Different letters (a, b) indicate a significant difference at  $P<0.05$ .

### Effect of WBG supplementation on serum lactate, ammonia, glucose, CK and BUN levels after acute exercise challenge

The lactate levels in the vehicle, WBG-1X and WBG-2.5X groups were  $9.2 \pm 0.9$ ,  $5.5 \pm 0.1$  and  $5.0 \pm 0.3$  mmol/l, respectively (Fig. 3a). The lactate levels were significantly lower in the WBG-1X and WBG-2.5X groups (40.16% and 45.45%;  $P=0.0005$  and  $P<0.0001$ , respectively) than in the vehicle treatment group. Trend analysis indicated that serum lactate level dose-dependently decreased with increasing WBG dose ( $P<0.0001$ ). Therefore, WBG supplementation may have the potential for clearance or utilization of blood lactate during exercise.

Ammonia is an important metabolite during energy metabolism for exercise. Serum ammonia is a useful marker of exercise-related metabolic responses in endurance-trained competitive athletes. The serum ammonia levels of the vehicle, WBG-1X and WBG-2.5X groups were  $149 \pm 18$ ,  $78 \pm 5$  and  $71 \pm 4$   $\mu$ mol/l, respectively (Fig. 3b). The ammonia levels were significantly lower in the WBG-1X and WBG-2.5X groups (40.16% and 45.45% lower;  $P=0.0005$  and  $P=0.0002$ , respectively) than in the vehicle group. Trend analysis indicated that serum ammonia level dose-dependently decreased with increasing WBG dose ( $P<0.0001$ ). Thus, continuous supplementation with WBG for 4 weeks could decrease ammonia levels during exercise.

Serum CK level is an important clinical biomarker of muscle damage and may represent recovery capacity from exercise-induced muscle damage. The serum CK levels of the vehicle, WBG-1X and WBG-2.5X groups were  $1,164 \pm 167$ ,  $462 \pm 58$  and  $382 \pm 39$  mg/dl, respectively (Fig. 3c). CK levels were respectively 60.34% ( $P=0.0004$ ) and 67.22% ( $P=0.0001$ ) lower in the

WBG-1X and WBG-2.5X groups than in the vehicle treatment group. Therefore, WBG supplementation could ameliorate skeletal muscle injury induced by acute exercise challenge. Trend analysis showed that WBG treatment had a significant dose-dependent effect on CK level ( $P=0.0002$ ).

Blood glucose level is an important index for performance maintenance during exercise. The serum glucose levels in the vehicle, WBG-1X and WBG-2.5X groups were  $128 \pm 5$ ,  $154 \pm 1$  and  $162 \pm 6$  mg/dl, respectively (Fig. 3d). The glucose levels were significantly higher in the WBG-1X and WBG-2.5X groups (by 1.21- and 1.27-fold;  $P=0.0011$  and  $P<0.0001$ , respectively) than in the vehicle group. Trend analysis showed that serum glucose levels dose-dependently increased with WBG supplementation dose ( $P=0.0022$ ). Therefore, continuous supplementation with WBG for 4 weeks could increase serum glucose levels and glucose uptake capacity to improve anti-fatigue activity.

BUN is an important biochemical parameter related to fatigue. The BUN level is used to measure the amount of nitrogen in blood from the waste product of urea. Urea serves an important role in the metabolism of nitrogen-containing compounds. The serum BUN levels of the vehicle, WBG-1X and WBG-2.5X groups were  $27.5 \pm 1.1$ ,  $21.0 \pm 0.6$  and  $19.7 \pm 0.5$ , respectively (Fig. 3e). The BUN levels in the WBG-1X and WBG-2.5X groups were respectively 23.41% ( $P<0.0001$ ) and 28.14% ( $P<0.0001$ ) lower than in the vehicle group. Trend analysis revealed that WBG treatment had a significantly dose-dependent effect on BUN level ( $P<0.0001$ ). Above all, WBG may have potential as an ergogenic supplement for improving the removal of the metabolic waste during exercise.

#### *Effect of WBG supplementation for 4 weeks on hepatic and muscle glycogen levels*

We also measured the glycogen contents of the liver and muscle tissues (Fig. 4). The liver glycogen levels in the vehicle, WBG-1X and WBG-2.5X groups were  $26.01 \pm 2.11$ ,  $34.56 \pm 5.55$  and  $59.68 \pm 15.07$  mg/g liver, respectively. The liver glycogen level was significantly higher in the WBG-2.5X group (by 2.29-fold;  $P=0.0122$ ) than in the vehicle group. The muscle glycogen levels in the vehicle, WBG-1X and WBG-2.5X groups were  $0.36 \pm 0.01$ ,  $0.47 \pm 0.03$  and  $0.49 \pm 0.03$  mg/g muscle. The muscle glycogen content was significantly higher in the WBG-1X and WBG-2.5X groups (by 1.31- and 1.36-fold;  $P=0.0018$  and  $P=0.0002$ , respectively) than in the vehicle group. Thus, WBG slightly increased the liver and muscle glycogen storage. Trend analysis indicated that liver glycogen and muscle glycogen increased with WBG dose ( $P=0.0039$  and  $P<0.0001$ ). After 4 weeks of WBG supplementation, both liver and muscle glycogen increased as exercise fuels to enhance exercise performance.

#### *General characteristics of mice with WBG supplementation for 4 weeks*

Initial BW did not differ among the vehicle, WBG-1X and WBG-2.5X groups (Table 1). After 4-week supplementation with WBG, the final BWs were significantly lower in the WBG-1X and WBG-2.5X groups (9.45% and 9.91%;  $P=0.0035$  and  $P=0.0024$ , respectively) than in the vehicle group. In addition, daily intake of diet and water did not differ in the vehicle and WBG supplementation groups. Trend analysis showed that final BW dose-dependently decreased with WBG supplementation ( $P=0.0019$ ). Thus, the 4-week WBG supplementation reduced the final BW. In addition, the epididymal fat pad (EFP) weight of the WBG-2.5X group was 26.55% ( $P=0.0164$ ) lower than that of the vehicle treatment group. The brown adipose tissue (BAT) weight was higher in the WBG-1X and WBG-2.5X groups (by 1.19- and 1.17-fold;  $P=0.0013$  and  $P=0.0051$ , respectively) than in the vehicle treatment group. Trend analysis indicated that the absolute EFP ( $P=0.0004$ ) and BAT ( $P=0.0396$ ) weights varied dose-dependently with WBG treatment. We also measured the effect of WBG on the relative tissue weight (different tissue weights adjusted for individual BW%). The relative EFP weight was 18.72% ( $P=0.0164$ ) lower in the WBG-2.5X group than in the vehicle treatment group. The relative BAT weights were significantly higher in the WBG-1X and WBG-2.5X groups (by 1.35- and 1.30-fold;  $P=0.0067$  and  $P=0.0314$ , respectively) than in the vehicle group. Trend analysis also showed that BAT weight dose-dependently increased with WBG supplementation ( $P=0.0048$ ).

#### *Effect of WBG supplementation on biochemical variables at the end of the experiment*

We observed beneficial effects of WBG on grip strength, exhaustive exercise challenge and body composition after 4-week WBG supplementation. We further investigated whether 4-week WBG treatment affected other biochemical markers in healthy mice. We examined tissue- and health status-related biochemical variables and major organs, including skeletal muscle, heart, kidney and lung (Table 2). The levels of the biochemical indices, AST, CK, creatinine, TC, TG and glucose did not differ among

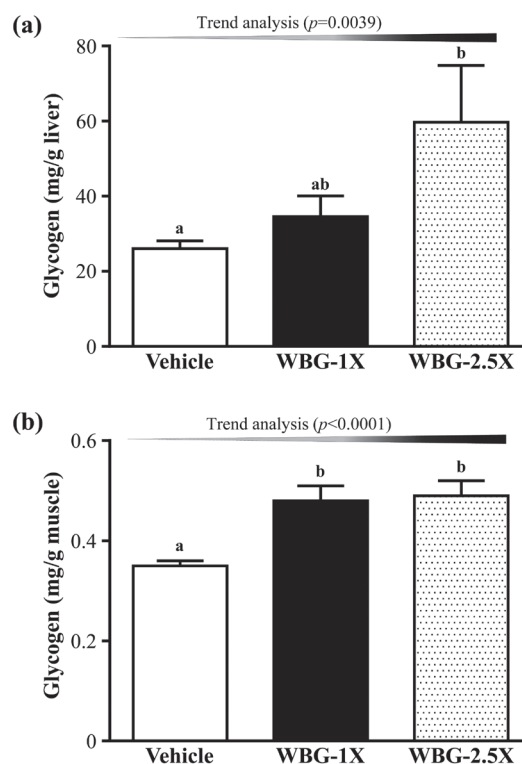


**Fig. 4.** Effect of WBG supplementation on glycogen levels in liver (a) and muscle (b). Data are mean  $\pm$  SEM,  $n=8$  mice/group, by one-way ANOVA. Different letters (a, b) indicate a significant difference at  $P<0.05$ .

**Table 1.** General characteristics of mice with Hualian No. 4 wild bitter gourd (WBG) supplementation

Characteristic	Vehicle	WBG-1X	WBG-2.5X	Trend analysis
Initial BW (g)	34.4 ± 0.4	34.1 ± 0.4	34.8 ± 0.4	0.9791
Final BW (g)	38.2 ± 0.8 <sup>b</sup>	34.6 ± 0.6 <sup>a</sup>	34.5 ± 0.8 <sup>a</sup>	0.0019
Food intake (g/day)	5.8 ± 0.3	5.7 ± 0.1	5.5 ± 0.1	0.0055
Water intake (ml/day)	6.9 ± 0.1	6.8 ± 0.1	6.9 ± 0.1	0.4671
Liver (g)	1.71 ± 0.05	1.52 ± 0.03	1.59 ± 0.08	0.1527
Kidney (g)	0.51 ± 0.02	0.50 ± 0.01	0.50 ± 0.01	0.8691
Heart (g)	0.23 ± 0.01	0.23 ± 0.01	0.22 ± 0.01	0.7113
Lung (g)	0.22 ± 0.01	0.22 ± 0.00	0.22 ± 0.01	0.9714
Muscle (g)	0.37 ± 0.01	0.36 ± 0.01	0.36 ± 0.01	0.0590
EFP (g)	0.34 ± 0.04 <sup>b</sup>	0.28 ± 0.02 <sup>a,b</sup>	0.25 ± 0.01 <sup>a</sup>	0.0004 (↓)
BAT (g)	0.08 ± 0.00 <sup>a</sup>	0.10 ± 0.00 <sup>b</sup>	0.09 ± 0.01 <sup>b</sup>	0.0396 (↑)
Relative Liver weight (%)	4.48 ± 0.18	4.40 ± 0.12	4.63 ± 0.26	0.8880
Relative Kidney weight (%)	1.33 ± 0.07	1.42 ± 0.04	1.47 ± 0.06	0.1493
Relative Heart weight (%)	0.59 ± 0.03	0.65 ± 0.02	0.65 ± 0.02	0.1596
Relative Lung weight (%)	0.57 ± 0.02	0.62 ± 0.04	0.63 ± 0.02	0.0141 (↑)
Relative Muscle weight (%)	0.98 ± 0.02	1.05 ± 0.03	1.05 ± 0.05	0.1435
Relative EFP weight (%)	0.91 ± 0.11 <sup>b</sup>	0.92 ± 0.07 <sup>a,b</sup>	0.74 ± 0.04 <sup>a</sup>	0.0835
Relative BAT weight (%)	0.21 ± 0.01 <sup>a</sup>	0.29 ± 0.01 <sup>b</sup>	0.28 ± 0.02 <sup>b</sup>	0.0048 (↑)

Data are mean ± SEM, n=8 mice/group. Different letters (a, b) in the same row indicate a significant difference at  $P<0.05$ . Food efficiency ratio: body weight (BW) gain (g/day)/food intake (g/day). Muscle mass includes both gastrocnemius and soleus muscles in the back part of the lower legs. BAT: brown adipose tissue; EFP: epididymal fat pad. Mice were pretreated with vehicle, WBG-1X or WBG-2.5X for 4 weeks. The arrows up and down mean dose-dependently increased and decreased by WBG supplementation.

**Table 2.** Biochemical analysis after WBG supplementation, at the end of the experiment

Parameter	Vehicle	WBG-1X	WBG-2.5X	Trend analysis
AST (U/l)	90 ± 5	83 ± 3	80 ± 4	0.2419
ALT (U/l)	48 ± 4 <sup>b</sup>	38 ± 2 <sup>a</sup>	38 ± 1 <sup>a</sup>	0.0483 (↓)
CK (U/l)	255 ± 33	253 ± 17	242 ± 21	0.9089
TP (g/dl)	4.7 ± 0.1 <sup>a</sup>	5.1 ± 0.1 <sup>b</sup>	5.2 ± 0.1 <sup>b</sup>	<0.0001 (↑)
Albumin (g/dl)	2.8 ± 0.0 <sup>a</sup>	3.1 ± 0.0 <sup>b</sup>	3.0 ± 0.0 <sup>b</sup>	0.0222 (↑)
BUN (mg/dl)	25.3 ± 1.4 <sup>c</sup>	20.6 ± 0.5 <sup>b</sup>	16.3 ± 0.6 <sup>a</sup>	<0.0001 (↓)
Creatinine (mg/dl)	0.28 ± 0.01	0.27 ± 0.02	0.27 ± 0.01	0.1770
UA (mg/dl)	2.9 ± 0.3 <sup>b</sup>	1.2 ± 0.1 <sup>a</sup>	1.2 ± 0.1 <sup>a</sup>	<0.0001 (↓)
TC (mg/dl)	136 ± 6	138 ± 4	138 ± 4	0.7146
TG (mg/dl)	153 ± 3	148 ± 3	141 ± 7	0.2868
Glucose (mg/dl)	142 ± 3	151 ± 3	140 ± 5	1.0000

Data are the mean ± SEM for n=8 mice in each group. Values in the same row with different superscript letters (a, b, c) differ significantly,  $P<0.05$ , by one-way ANOVA. Muscle mass includes both gastrocnemius and soleus muscles in the back part of the lower legs. The arrows up and down mean dose-dependently increased and decreased by WBG supplementation. AST, aspartate aminotransferase; ALT, alanine aminotransferase; TP, total protein; BUN, blood urea nitrogen; CK, creatine kinase; UA, uric acid; TC, total cholesterol; TG, triacylglycerol.

groups ( $P>0.05$ , Table 2). Serum ALT levels were lower in the WBG-1X and WBG-2.5X groups (20.83 and 21.09%;  $P=0.0323$  and  $P=0.0304$ , respectively) than in the vehicle treatment group. Serum BUN levels were significantly lower in the WBG-1X and WBG-2.5X groups (18.54 and 35.44%;  $P=0.0049$  and  $P<0.0001$ , respectively) than in the vehicle treatment group. Serum UA levels were significantly lower in the WBG-1X and WBG-2.5X groups (59.05 and 57.76%;  $P<0.0001$  and  $P<0.0001$ , respectively) than in the vehicle group. Serum TP was higher in the WBG-1X and WBG-2.5X groups (by 1.08- and 1.09-fold;  $P=0.0035$  and  $P=0.001$ , respectively) than in the vehicle treatment group. The trend analysis revealed that WBG treatment had significant dose-dependent effects on ALT ( $P=0.0483$ ), TP ( $P<0.0001$ ), BUN ( $P<0.0001$ ) and UA levels ( $P<0.0001$ ). In addition, serum albumin was slightly increased by WBG supplementation, but remained within the normal range. Therefore, long-term daily supplementation with WBG may have the potential for tissue protection by enhancing nutrient absorption with increases in serum TP.

#### *Effect of WBG supplementation on histological examinations at the end of the experiment*

We also examined tissue morphology. WBG supplementation for 4 weeks had no adverse effects on the liver, skeletal muscle, heart, kidneys, lungs or EFP. Therefore, the dose of WBG supplementation used in this study was safe (Fig. 5).



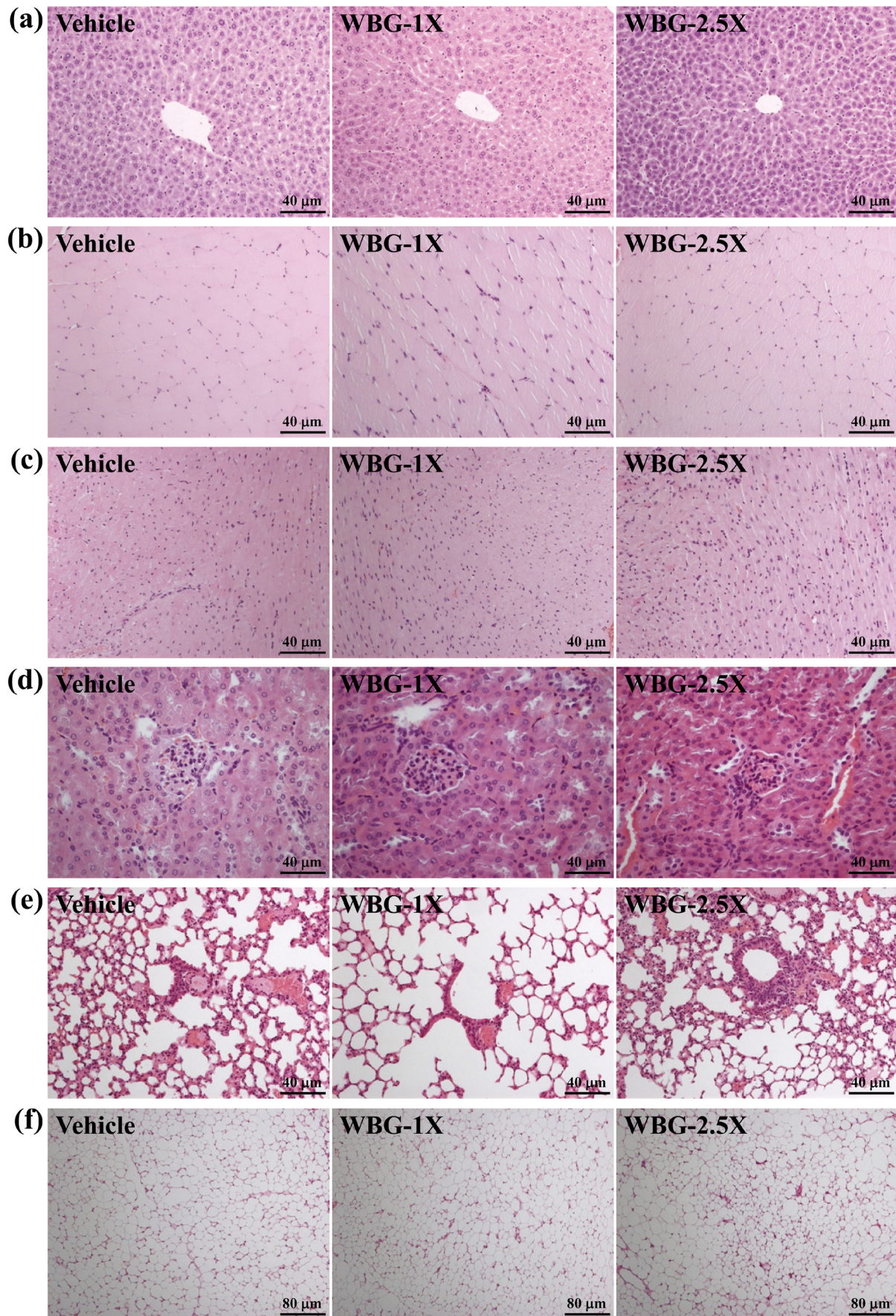


**Fig. 5.** Effects of WBG supplementation on morphology of liver (a); skeletal muscle (b); heart (c); kidney (d); lungs (e) and EFP (f). Specimens were photographed by light microscopy. H&E stain, magnification:  $\times 200$  (a–e) and  $\times 100$  (f). EFP: epididymal fat pad.



## DISCUSSION

Charantin, the main active constituent of *M. charantia*, is an insulin-like compound that makes it useful for moderating blood glucose. Previous studies have demonstrated that WBG extract contains charantin and alkaloids for increasing blood glucose uptake [12, 17]. One of the best-known food factors, resveratrol, is under consideration as an additional phytochemical for treatment of metabolic diseases. In a previous study, we found that resveratrol reduces fatigue by increasing utilization of important fuel sources [41]. Thus, WBG could be a potential agent with an anti-fatigue pharmacological effect.

In general, programmed exercise training is required to increase grip strength [7]; however, we found that WBG supplementation increased grip strength, even though the test animals did not undergo a training intervention. Multiple pathways mediate the benefits of exercise in terms of muscle biology, growth and metabolism. Among them, peroxisome proliferator-activated receptor (PPAR) is a coactivator essential to various cellular processes, including mitochondrial biogenesis, oxidative metabolism and energy homeostasis. PPAR $\alpha$  and PPAR $\gamma$ , in the PPAR sub-family, may be activated by WBG supplementation [6, 36]. PPAR $\alpha$  and PPAR $\gamma$  can reflect athletic performance and activation by exercise training [1, 7]. They are induced in the adipose tissue and skeletal muscle [14, 30] of type 2 diabetes patients following a prescription of exercise [34]. PPAR $\gamma$  is activated in adipose tissue. Thus, WBG supplementation could activate PPAR pathways to improve exercise performance [4].

Exercise-induced muscle fatigue can be evaluated by biochemical indicators including lactate, ammonia, glucose, CK and BUN levels [22, 35]. The clearance of lactate is believed to reduce peripheral neuromuscular fatigue and has positive effects on muscle function [40]. After acute exercise, lactate accumulates in the muscles, and approximately 75% of the total amount of lactate produced is used for oxidative production of energy in the exercising body [2]. A previous study reported that ammonia levels are more intensity-sensitive than blood lactate levels across the whole intensity range during incremental exercise [25]. The reason is that peripheral and central fatigue levels are related to increased ammonia during exercise [5]. As exercise continues, glucose uptake increases and intramuscular glucose concentration decreases as hexokinase inhibition is relieved by a lower glucose 6-phosphate (G-6-P) concentration [26]. This mechanism contributes to the explanation of the temporal relationship between the decrease in muscle glycogen and the progressive increase in glucose uptake during moderate intensity exercise [32]. In our present data, WBG showed a great capacity to remove lactate and decrease levels of ammonia, CK and BUN after exercise and also to economize glucose utilization during exercise.

We focused on glycogen storage in the liver and muscle after 4-week WBG supplementation. WBG supplementation increased energy storage, thereby improving exercise performance. Utilization of carbohydrate in the form of intramuscular glycogen stores and glucose delivered from plasma becomes a crucial energy substrate to the exercise muscle [33]. Charantin and its derivatives may in part be responsible for the observed up-regulatory activities of high glycogen storage, glucose uptake and increased levels of the glucose transporter Glucose transporter type 4 (GLUT4), in bitter melon extracts [16].

We also evaluated the body compositions of the mice after 4-week WBG supplementation. Data showed that WBG supplementation could increase BAT. Previous research has shown that both aerobic exercise training and AMPK/PPAR agonists accelerate the oxidative metabolism. An expected result would be reduction of the amount of fat in the body [3]. Thus, supplementation with WBG for 4 weeks could increase the BAT weight and decrease the EFP weight via AMPK/PPAR activation, which would stimulate lipid utilization and reduce adipose accumulation.

In summary, WBG is a specific tropical vegetable cultivated in Taiwan. We found that 4-week supplementation with WBG extract significantly improved the forelimb grip strength and swimming time to exhaustion of test mice. WBG reduces fatigue by decreasing plasma lactate, ammonia, CK and BUN levels, and increasing serum glucose levels after acute exercise in mice. Exercise-induced fatigue-related parameters, including lactate, ammonia, CK, glucose and BUN levels, were positively modulated by WBG supplementation in a dose-dependent manner, as confirmed by trend analysis. WBG also had positive effects on liver and kidney protection and enhanced nutrient absorption by decreasing ALT, BUN, albumin and UA levels, and increasing TP levels. Concerning body composition, our data showed that BW decreased after 4-week WBG supplementation; white adipose tissue weight was decreased by WBG-2.5X supplementation. On the other hand, BAT weight and relative weight increased dose-dependently with WBG supplementation. In conclusion, we provide evidence that 4-week WBG supplementation affected biochemical assessments, enhanced exercise performance, had anti-fatigue activity and reduced white adipose tissue. Therefore, we suggest that WBG may be considered for use as a nutrient supplement to improve health, reduce adipose generation and enhance energy storage.

**CONFLICTS OF INTEREST.** The authors declare no conflict of interest.

**ACKNOWLEDGMENTS.** This study was not supported by any grant, outside sources of funding or industry sponsorship. The authors are grateful to Ms. Sin-Jie Lin for technical assistance in animal experiments. The authors thank Mr. John Ring (National Taiwan University, Taipei City, Taiwan) for his careful editing of the manuscript and Dr. Chien-Chao Chiu for conducting histological examination. The HPLC analysis was performed by Research Center for Industry of Human Ecology and Food Safety Testing Laboratory, College of Human Ecology, Chang Gung University of Science and Technology.

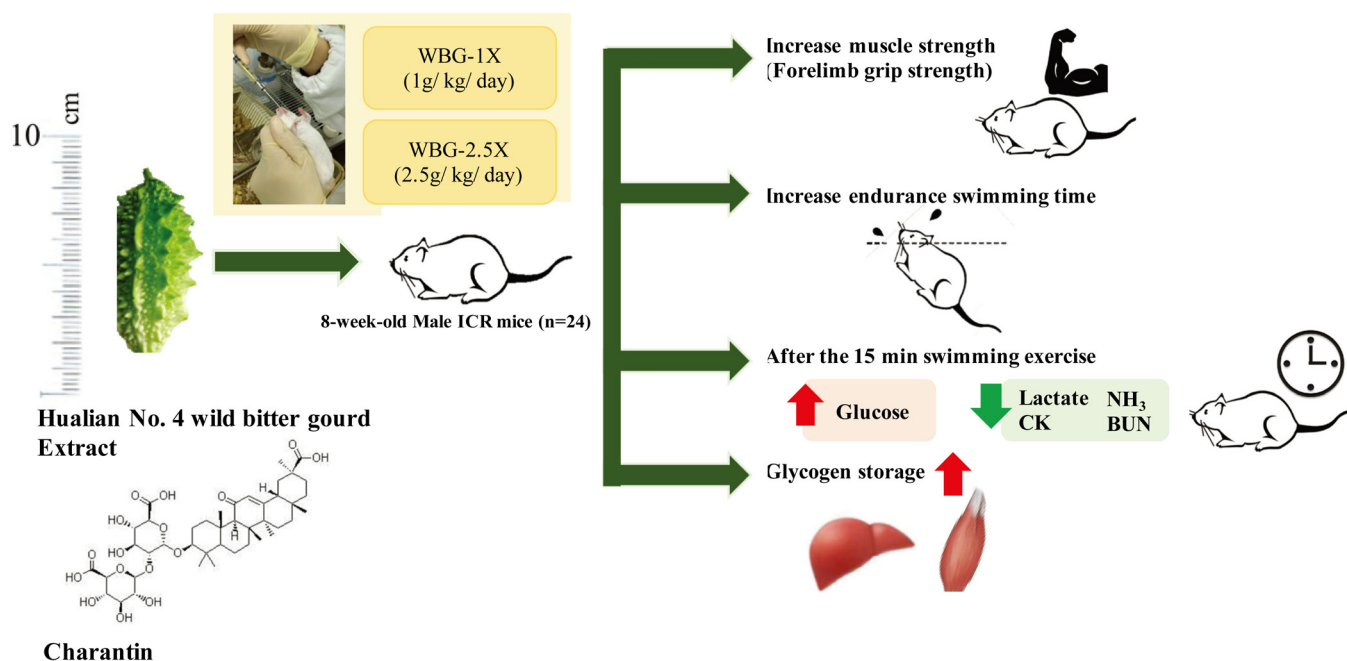
## REFERENCES

1. Ahmetov, I. I., Mozhayskaya, I. A., Flavell, D. M., Astratenkova, I. V., Komkova, A. I., Lyubaeva, E. V., Tarakin, P. P., Shenkman, B. S., Vdovina,

- A. B., Netreba, A. I., Popov, D. V., Vinogradova, O. L., Montgomery, H. E. and Rogozkin, V. A. 2006. PPARalpha gene variation and physical performance in Russian athletes. *Eur. J. Appl. Physiol.* **97**: 103–108. [Medline] [CrossRef]
2. Brooks, S. P. and Storey, K. B. 1991. A quantitative evaluation of the effect of enzyme complexes on the glycolytic rate in vivo: mathematical modeling of the glycolytic complex. *J. Theor. Biol.* **149**: 361–375. [Medline] [CrossRef]
3. Bueno Júnior, C. R., Pantaleão, L. C., Voltarelli, V. A., Bozi, L. H., Brum, P. C. and Zatz, M. 2012. Combined effect of AMPK/PPAR agonists and exercise training in mdx mice functional performance. *PLoS ONE* **7**: e45699. [Medline] [CrossRef]
4. Calvo, J. A., Daniels, T. G., Wang, X., Paul, A., Lin, J., Spiegelman, B. M., Stevenson, S. C. and Rangwala, S. M. 2008. Muscle-specific expression of PPARgamma coactivator-1 $\alpha$  improves exercise performance and increases peak oxygen uptake. *J. Appl. Physiol.* **104**: 1304–1312. [Medline] [CrossRef]
5. Carvalho-Peixoto, J., Alves, R. C. and Cameron, L. C. 2007. Glutamine and carbohydrate supplements reduce ammonemia increase during endurance field exercise. *Appl. Physiol. Nutr. Metab.* **32**: 1186–1190. [Medline] [CrossRef]
6. Chao, C. Y., Yin, M. C. and Huang, C. J. 2011. Wild bitter gourd extract up-regulates mRNA expression of PPAR $\alpha$ , PPAR $\gamma$  and their target genes in C57BL/6J mice. *J. Ethnopharmacol.* **135**: 156–161. [Medline] [CrossRef]
7. Chen, W. C., Huang, W. C., Chiu, C. C., Chang, Y. K. and Huang, C. C. 2014. Whey protein improves exercise performance and biochemical profiles in trained mice. *Med. Sci. Sports Exerc.* **46**: 1517–1524. [Medline] [CrossRef]
8. Chen, Y. M., Lin, C. L., Wei, L., Hsu, Y. J., Chen, K. N., Huang, C. C. and Kao, C. H. 2016. Sake protein supplementation affects exercise performance and biochemical profiles in power-exercise-trained mice. *Nutrients* **8**: 106. [Medline] [CrossRef]
9. Chen, Y. M., Tsai, Y. H., Tsai, T. Y., Chiu, Y. S., Wei, L., Chen, W. C. and Huang, C. C. 2014. Fucoidan supplementation improves exercise performance and exhibits anti-fatigue action in mice. *Nutrients* **7**: 239–252. [Medline] [CrossRef]
10. Chen, Y. M., Wei, L., Chiu, Y. S., Hsu, Y. J., Tsai, T. Y., Wang, M. F. and Huang, C. C. 2016. *Lactobacillus plantarum* TWK10 Supplementation Improves Exercise Performance and Increases Muscle Mass in Mice. *Nutrients* **8**: 205. [Medline] [CrossRef]
11. Coombes, J. S., Rowell, B., Dodd, S. L., Demirel, H. A., Naito, H., Shanely, R. A. and Powers, S. K. 2002. Effects of vitamin E deficiency on fatigue and muscle contractile properties. *Eur. J. Appl. Physiol.* **87**: 272–277. [Medline] [CrossRef]
12. Das, D. R., Sachan, A. K., Imtiyaz, M. and Shuaib, M. 2015. *Momordica charantia* as a Potential Medicinal Herb: An Overview. *J. Med. Plants Stud.* **3**: 23–26.
13. Desai, S. and Tatke, P. 2015. Charantin: An important lead compound from *Momordica charantia* for the treatment of diabetes. *J. Pharmacogn. Phytochem.* **3**: 163–166.
14. Fatone, C., Guescini, M., Balducci, S., Battistoni, S., Settequattrini, A., Pippi, R., Stocchi, L., Mantuano, M., Stocchi, V. and De Feo, P. 2010. Two weekly sessions of combined aerobic and resistance exercise are sufficient to provide beneficial effects in subjects with Type 2 diabetes mellitus and metabolic syndrome. *J. Endocrinol. Invest.* **33**: 489–495. [Medline] [CrossRef]
15. Fitts, R. H. 1994. Cellular mechanisms of muscle fatigue. *Physiol. Rev.* **74**: 49–94. [Medline]
16. Hanhineva, K., Törrönen, R., Bondia-Pons, I., Pekkinen, J., Kolehmainen, M., Mykkänen, H. and Poutanen, K. 2010. Impact of dietary polyphenols on carbohydrate metabolism. *Int. J. Mol. Sci.* **11**: 1365–1402. [Medline] [CrossRef]
17. Hazarika, R., Parida, P., Neog, B. and Yadav, R. N. 2012. Binding energy calculation of GSK-3 protein of human against some anti-diabetic compounds of *Momordica charantia* linn (Bitter melon). *Bioinformation* **8**: 251–254. [Medline] [CrossRef]
18. Hsu, C., Tsai, T. H., Li, Y. Y., Wu, W. H., Huang, C. J. and Tsai, P. J. 2012. Wild bitter melon (*Momordica charantia* Linn. var. *abbreviata* Ser.) extract and its bioactive components suppress *Propionibacterium acnes*-induced inflammation. *Food Chem.* **135**: 976–984. [Medline] [CrossRef]
19. Hsu, H. Y., Lin, J. H., Li, C. J., Tsang, S. F., Tsai, C. H., Chyuan, J. H. and Chuang, S. E. 2012. Antimigratory effects of the methanol extract from *Momordica charantia* on human lung adenocarcinoma CL1 cells. *Evid-Based Compl. Alt.* **2012**: 819632.
20. Huang, C. C., Hsu, M. C., Huang, W. C., Yang, H. R. and Hou, C. C. 2012. Triterpenoid-rich extract from *Antrodia camphorata* improves physical fatigue and exercise performance in mice. *Evid-Based Compl. Alt.* **2012**: 364741.
21. Huang, S., Li, R., Zhang, Z., Li, L., Gu, X., Fan, W., Lucas, W. J., Wang, X., Xie, B., Ni, P., Ren, Y., Zhu, H., Li, J., Lin, K., Jin, W., Fei, Z., Li, G., Staub, J., Kilian, A., van der Vossen, E. A., Wu, Y., Guo, J., He, J., Jia, Z., Ren, Y., Tian, G., Lu, Y., Ruan, J., Qian, W., Wang, M., Huang, Q., Li, B., Xuan, Z., Cao, J., Asan, W., Zhang, J., Cai, Q., Bai, Y., Zhao, B., Han, Y., Li, Y., Li, X., Wang, S., Shi, Q., Liu, S., Cho, W. K., Kim, J. Y., Xu, Y., Heller-Uszynska, K., Miao, H., Cheng, Z., Zhang, S., Wu, J., Yang, Y., Kang, H., Li, M., Liang, H., Ren, X., Shi, Z., Wen, M., Jian, M., Yang, H., Zhang, G., Yang, Z., Chen, R., Liu, S., Li, J., Ma, L., Liu, H., Zhou, Y., Zhao, J., Fang, X., Li, G., Fang, L., Li, Y., Liu, D., Zheng, H., Zhang, Y., Qin, N., Li, Z., Yang, G., Yang, S., Bolund, L., Kristiansen, K., Zheng, H., Li, S., Zhang, X., Yang, H., Wang, J., Sun, R., Zhang, B., Jiang, S., Wang, J., Du, Y. and Li, S. 2009. The genome of the cucumber, *Cucumis sativus* L. *Nat. Genet.* **41**: 1275–1281. [Medline] [CrossRef]
22. Izquierdo, M., González-Izal, M., Navarro-Amezqueta, I., Calbet, J. A., Ibañez, J., Malanda, A., Mallor, F., Häkkinen, K., Kraemer, W. J. and Gorostiaga, E. M. 2011. Effects of strength training on muscle fatigue mapping from surface EMG and blood metabolites. *Med. Sci. Sports Exerc.* **43**: 303–311. [Medline] [CrossRef]
23. Joyner, M. J. and Coyle, E. F. 2008. Endurance exercise performance: the physiology of champions. *J. Physiol.* **586**: 35–44. [Medline] [CrossRef]
24. Kan, N. W., Ho, C. S., Chiu, Y. S., Huang, W. C., Chen, P. Y., Tung, Y. T. and Huang, C. C. 2016. Effects of resveratrol supplementation and exercise training on exercise performance in middle-aged mice. *Molecules* **21**: 661. [Medline] [CrossRef]
25. Kantanista, A., Kusy, K., Zarębska, E., Włodarczyk, M., Ciekot-Sołtysiak, M. and Zieliński, J. 2016. Blood ammonia and lactate responses to incremental exercise in highly-trained male sprinters and triathletes. *Biomed. Hum. Kinetic.* **8**: 32–38. [CrossRef]
26. Kawanaka, K., Nolte, L. A., Han, D. H., Hansen, P. A. and Holloszy, J. O. 2000. Mechanisms underlying impaired GLUT-4 translocation in glycogen-supercompensated muscles of exercised rats. *Am. J. Physiol. Endocrinol. Metab.* **279**: E1311–E1318. [Medline]
27. Konishi, T., Satsu, H., Hatsugai, Y., Aizawa, K., Inakuma, T., Nagata, S., Sakuda, S. H., Nagasawa, H. and Shimizu, M. 2004. A bitter melon extract inhibits the P-glycoprotein activity in intestinal Caco-2 cells: monoglyceride as an active compound. *Biofactors* **22**: 71–74. [Medline] [CrossRef]
28. Lu, K. H., Tseng, H. C., Liu, C. T., Huang, C. J., Chyuan, J. H. and Sheen, L. Y. 2014. Wild bitter gourd protects against alcoholic fatty liver in mice by attenuating oxidative stress and inflammatory responses. *Food Funct.* **5**: 1027–1037. [Medline] [CrossRef]
29. Miura, T., Itoh, C., Iwamoto, N., Kato, M., Kawai, M., Park, S. R. and Suzuki, I. 2001. Hypoglycemic activity of the fruit of the *Momordica charantia* in type 2 diabetic mice. *J. Nutr. Sci. Vitaminol. (Tokyo)* **47**: 340–344. [Medline] [CrossRef]
30. Petridou, A., Tsalouhidou, S., Tsalis, G., Schulz, T., Michna, H. and Mougios, V. 2007. Long-term exercise increases the DNA binding activity of peroxisome proliferator-activated receptor  $\gamma$  in rat adipose tissue. *Metabolism* **56**: 1029–1036. [Medline] [CrossRef]
31. Rajamoorthy, A., Shrivastava, S., Steele, R., Nerurkar, P., Gonzalez, J. G., Crawford, S., Varvares, M. and Ray, R. B. 2013. Bitter melon reduces head and neck squamous cell carcinoma growth by targeting c-Met signaling. *PLoS ONE* **8**: e78006. [Medline] [CrossRef]
32. Richter, E. A. and Hargreaves, M. 2013. Exercise, GLUT4, and skeletal muscle glucose uptake. *Physiol. Rev.* **93**: 993–1017. [Medline] [CrossRef]
33. Rodriguez, N. R., Di Marco, N. M., Langley S., American Dietetic Association Dietitians of Canada American College of Sports Medicine 2009.

- American College of Sports Medicine position stand. Nutrition and athletic performance. *Med. Sci. Sports Exerc.* **41**: 709–731. [Medline]
34. Sixt, S., Beer, S., Blüher, M., Korff, N., Peschel, T., Sonnabend, M., Teupser, D., Thiery, J., Adams, V., Schuler, G. and Niebauer, J. 2010. Long- but not short-term multifactorial intervention with focus on exercise training improves coronary endothelial dysfunction in diabetes mellitus type 2 and coronary artery disease. *Eur. Heart J.* **31**: 112–119. [Medline] [CrossRef]
35. Strojnik, V. and Komi, P. V. 2000. Fatigue after submaximal intensive stretch-shortening cycle exercise. *Med. Sci. Sports Exerc.* **32**: 1314–1319. [Medline] [CrossRef]
36. Tan, M. J., Ye, J. M., Turner, N., Hohnen-Behrens, C., Ke, C. Q., Tang, C. P., Chen, T., Weiss, H. C., Gesing, E. R., Rowland, A., James, D. E. and Ye, Y. 2008. Antidiabetic activities of triterpenoids isolated from bitter melon associated with activation of the AMPK pathway. *Chem. Biol.* **15**: 263–273. [Medline] [CrossRef]
37. Tsai, C. H., Chen, E. C., Tsay, H. S. and Huang, C. J. 2012. Wild bitter gourd improves metabolic syndrome: a preliminary dietary supplementation trial. *Nutr. J.* **11**: 4. [Medline] [CrossRef]
38. Wang, H. Y., Kan, W. C., Cheng, T. J., Yu, S. H., Chang, L. H. and Chuu, J. J. 2014. Differential anti-diabetic effects and mechanism of action of charantin-rich extract of Taiwanese *Momordica charantia* between type 1 and type 2 diabetic mice. *Food Chem. Toxicol.* **69**: 347–356. [Medline] [CrossRef]
39. Weng, J. R., Bai, L. Y., Chiu, C. F., Hu, J. L., Chiu, S. J. and Wu, C. Y. 2013. Cucurbitane triterpenoid from *Momordica charantia* induces apoptosis and autophagy in breast cancer cells, in part, through peroxisome proliferator-activated receptor  $\gamma$  activation. *Evid-Based Compl. Evid. Based Complement. Alternat. Med.* **2013**: 935675. [Medline] [CrossRef]
40. White, G. E. and Wells, G. D. 2015. The effect of on-hill active recovery performed between runs on blood lactate concentration and fatigue in alpine ski racers. *J. Strength Cond. Res.* **29**: 800–806. [Medline] [CrossRef]
41. Wu, R. E., Huang, W. C., Liao, C. C., Chang, Y. K., Kan, N. W. and Huang, C. C. 2013. Resveratrol protects against physical fatigue and improves exercise performance in mice. *Molecules* **18**: 4689–4702. [Medline] [CrossRef]
42. Wu, S. J. and Ng, L. T. 2008. Antioxidant and free radical scavenging activities of wild bitter melon (*Momordica charantia* Linn. var. *abbreviata* Ser.) in Taiwan. *LWT-Food. Sci. Tech. (Paris)* **41**: 323–330.
43. You, L., Zhao, M., Regenstein, J. M. and Ren, J. 2011. *In vitro* antioxidant activity and *in vivo* anti-fatigue effect of loach (*Misgurnus anguillicaudatus*) peptides prepared by papain digestion. *Food Chem.* **124**: 188–194. [CrossRef]
44. Yu, S. H., Chen, S. Y., Li, W. S., Dubey, N. K., Chen, W. H., Chuu, J. J., Leu, S. J. and Deng, W. P. 2015. Hypoglycemic activity through a novel combination of fruiting body and mycelia of *Cordyceps Militaris* in high-fat diet-induced type 2 diabetes mellitus mice. *J. Diabetes Res.* **2015**: 723190. [Medline] [CrossRef]

## Appendix.



**Appendix Fig.** The bioactivities of hualian no. 4 wild bitter gourd (WBG) extract on anti-fatigue *in vivo*.


Cite this: *RSC Adv.*, 2017, 7, 22468

# Lymphoma cell isolation using multifunctional magnetic nanoparticles: antibody conjugation and characterization†

Soubhagya Laxmi Sahoo,<sup>a</sup> Chi-Hsien Liu  <sup>\*abcd</sup> and Wei-Chi Wu<sup>de</sup>

The early detection of B-cell lymphoma and non-Hodgkin's lymphoma has a wide impact on the diagnosis and therapy of lymphoma patients. Capturing and sorting tumour cells with magnetic nanoparticles (MNPs) has received considerable attention in recent years. Despite these successes, the efficient isolation of circulating tumour cells from complex biological fluids is still under development for the early diagnosis of lymphoma. In this study, MNPs are functionalized with anti-CD20 antibodies using an avidin-biotin linkage, with the aim of achieving specific cancer cell detection and efficient isolation. Anti-CD20 antibody-conjugated MNPs (Ab MNPs) could specifically target CD20-expressing lymphoma cells. The capture efficiency of the Ab MNPs in the lymphoma cell line was >95% with regard to the mixture of two cell lines, as confirmed by flow cytometry and confocal microscopy. Transmission electron microscopy confirmed that the conjugation of an antibody with the MNPs increased the size from 12 to 47 nm. The surface charge of the Ab MNPs was examined by using zeta potential measurements. Furthermore, Prussian blue staining was performed to confirm the interaction of Ab MNPs with the targeted lymphoma cells. Our results indicated that the receptor recognition ability of the antibody was fully retained after conjugation with MNPs. In conclusion, anti-CD20 MNPs can be used for very sensitive detection and quick isolation of CD20-positive lymphoma cells among mixed cells by using only a permanent magnet.

Received 20th February 2017  
Accepted 13th April 2017

DOI: 10.1039/c7ra02084h

rsc.li/rsc-advances

## Introduction

Cancers are among the most serious diseases that can ultimately lead to death. Sensitive and rapid isolation of cancer cells from complex bio-fluids is of critical importance for cancer research, prevention and therapy.<sup>1</sup> Cell sorting is often used to enrich rare cells for further well-defined culture conditions and to enhance the cell population. The current capture techniques for cancer cells include flow cytometry, magnetic-based sorting devices and microfluidic chips, using for example fluorescence signals, magnetic forces and physical principles.<sup>2</sup> Flow cytometry provides precise isolation; however, it involves a sophisticated instrument and needs expensive fluorescent probes for

cell labelling. A robust sorting platform is needed to isolate tumour cells for further diagnosis and expansion. Among these techniques, magnetic sorting utilizes targeting magnetic nanoparticles (MNPs), which are biodegradable and have low toxicity.<sup>3,4</sup> The MNP-based technology has several advantages, such as a high surface-to-volume ratio, high-binding capacity and specific interactions between nanoparticles.<sup>5</sup> Moreover, the diffusion limitation within the micron-sized particles leads to a decrease in their binding efficacy on the targeted cells in biological fluids, such as blood.<sup>6</sup> Therefore, the nano-scaled MNPs provide several advantages for capture applications, including a low diffusion barrier, high surface area, stability and specificity.

Specific targeting is a key step in realizing the full potential of MNPs in tumour-associated diagnosis and the capture of tumour cells. Researchers have devoted a tremendous amount of time to develop MNPs-based models for the capture and early detection of cancer cells that simultaneously conjugate MNPs to active targeting moieties, such as ligands and monoclonal antibodies. Antibodies are promising moieties for targeting cancer cells, using high affinity and ligand-receptor specificity for the surface antigen on the tumour.<sup>7</sup> For example, the anti-CD20 antibody (rituximab) has been applied to the treatment of non-Hodgkin's lymphoma and inflammatory diseases, such as rheumatoid arthritis and myositis.<sup>8</sup> The CD20 is a non-glycosylated antigen expressed on B-cell non-Hodgkin's

<sup>a</sup>Graduate Institute of Biochemical and Biomedical Engineering, Chang Gung University, 259, Wen-Hwa First Road, Kwei-Shan, Tao-Yuan 333, Taiwan

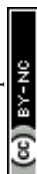
<sup>b</sup>Research Center for Chinese Herbal Medicine, Research Center for Food and Cosmetic Safety, College of Human Ecology, Chang Gung University of Science and Technology, 261, Wen-Hwa First Road, Taoyuan, Taiwan

<sup>c</sup>Department of Chemical Engineering, Ming Chi University of Technology, 84, Gung-Juan Road, New Taipei City, Taiwan

<sup>d</sup>Department of Ophthalmology, Chang Gung Memorial Hospital, 5, Fu-Hsing Street, Taoyuan, Taiwan

<sup>e</sup>College of Medicine, Chang Gung University, 259, Wen-Hwa First Road, Taoyuan, Taiwan. E-mail: CHL@mail.cgu.edu.tw

† Electronic supplementary information (ESI) available. See DOI: 10.1039/c7ra02084h





lymphomas,<sup>9</sup> and cannot be found on stem cells, pro-B cells, normal plasma cells or other normal tissues.<sup>10</sup> In addition, the CD20 on the cell membrane, which is not internalized in response to antibody binding, is a good candidate as a target for cell isolation.

Cancer cells have been successfully detected and isolated by using MNPs based on antibody and antigen interactions.<sup>11,12</sup> Cirstoiu-Hapca *et al.* (2007) and Xu *et al.* (2014) have used anti-HER2 and anti-GD2 antibodies conjugated with nanoparticles to specifically isolate the tumour cells bearing the surface antigens.<sup>6,13</sup> However, only one type of cancer cell was isolated in their targeting studies. In contrast, Song *et al.* (2011) analyzed the capture efficiencies of tumour cells by using fluorescent MNPs to isolate a small number of spiked tumour cells in a large population of normal cells.<sup>14</sup> Magnetic particles labelled with a fluorescent dye for optical detection and conjugated with a monoclonal antibody against the neu receptor have been demonstrated to significantly identify primary and metastatic breast tumours.<sup>15</sup> The anti-EGFR antibody-conjugated nanoparticles can be used to capture circulating tumour cells expressing EGFR and in the subsequent diagnostic analysis.<sup>16</sup> Wu *et al.* have successfully developed multifunctional magnetic particles conjugated with anti-EpCAM antibody that could detect endogenous metabolites and isolate rare tumour cell isolation.<sup>17</sup> These antibody-conjugated nanoparticles have been proven useful for sensitive detection and rapid isolation of cancer cells in early diagnoses.

Our objectives are to synthesize and characterize the antibody-conjugated MNPs (Ab MNPs) and to assay their biocompatibility and separation efficacy. The anti-CD20 Ab MNPs were synthesized to detect and isolate lymphoma cells from two kinds of mixed cells *via* a process based on the high affinity between antigens and antibodies. Specifically, the carboxylic group of MNPs was activated using the EDC/NHS linker, and then avidin was conjugated onto MNPs to form avidin MNPs. Biotin maleimide was conjugated with an anti-CD20 antibody, and in the final step, a biotinylated antibody was added to interact with the avidin MNPs to form Ab MNPs. The morphology and surface charge of the Ab MNPs were examined with a transmission electron microscope and using zeta potential measurements. The use of Ab MNPs to specifically isolate the cancer cells was evaluated by flow cytometry analysis, confocal image and Prussian blue staining.

## Experimental section

### Materials

All the chemical reagents were commercially purchased and used without further purification. The materials include avidin, biotin maleimide, ethylenediaminetetraacetic acid (EDTA), Hoechst 33342, neutral red, *N*-(3-dimethylaminopropyl)-ethyl carbodiimide (EDC), hydroxy succinimide (NHS), and Trypan blue solution were purchased from Sigma-Aldrich (MO, USA). Rhodamine B was purchased from Acros Organics (NJ, USA). Potassium thiocyanate and hydrochloric acid were purchased from J.T Baker (PA, USA). Fetal bovine serum (FBS) was purchased from Biological Industries (Haemek, Israel). Paramagnetic iron oxide

nanoparticles (COOH-surface modified) were purchased from Taiwan Advance Nanotech (Taoyuan, Taiwan).

### Functionalization of Ab MNPs

For the targeting approach, the carboxylic group of magnetic nanoparticles (1 mg mL<sup>-1</sup>) were activated using EDC/NHS linker (0.64 and 1.2 mg mL<sup>-1</sup>, respectively) at a constant vortex rate for 2 hours at room temperature. Next, avidin (0.2 mg mL<sup>-1</sup>) was conjugated onto magnetic nanoparticles for 1 hour at room temperature to form avidin MNPs. The unconjugated avidin was removed by washing three times with deionized water using magnetic separation system (Millipore). The anti-CD20 antibodies were purified from the spent media of BCRC 60427 hybridoma cell line by using liquid chromatography and protein A sepharose column (GE). Separately, the biotinylated Ab was prepared as follows. Anti-CD20 antibody (1 mg mL<sup>-1</sup>) was mixed with biotin maleimide (0.25 mg mL<sup>-1</sup>) in phosphate buffer (pH 7.2) and reacted for 2 hours at room temperature. The detailed methods are referred to the chemical conjugation textbook.<sup>18</sup> In the final step, the biotinylated Ab was mixed with avidin MNPs to form the Ab MNPs for 30 minutes. The Ab MNPs was washed three times to remove unreacted biotinylated Ab and then stored at 4 °C. For the dose effect of MNP isolation, high Ab conjugated MNPs (15.86 µg Ab per mg MNPs) and low Ab conjugated MNPs (8.07 µg Ab per mg MNPs) were prepared by adjusting the amount of biotinylated antibody in the conjugation procedure.

### Cell culture

The hybridoma cells (BCRC 60427) secreting the immunoglobulin IgG2a, which recognizes the human CD20 antigen, Chinese hamster ovary cell line (CHO, BCRC 60185), and CD20-expressing Ramos lymphoma (BCRC 60252) were obtained from the Bioresource Collection and Research Center (BCRC, Hsinchu, Taiwan). BCRC 60252 was maintained in RPMI-1640 medium supplemented with 10% heat inactivated fetal bovine serum (FBS). BCRC 60427 was maintained in CD hybridoma medium (Thermo Fisher Scientific, Sugar Land, USA). The CD20 free cell line such as CHO BCRC 60185 was maintained in Excel medium. HaCat cells are kindly donated by Prof. Sheu, Hamm-Ming (NCKU, Taiwan) and maintained in DMEM with 10% serum. All cells were incubated at 37 °C under a humidified atmosphere with 5% CO<sub>2</sub>. The cell morphology and growth were monitored daily using a light microscope. Cell passage was performed every four days to maintain an exponential growth phase. The cell density and viability were determined using a Beckman Coulter counter (MS3 model) and hemocytometer, respectively, prior to all experiments.

### Characterization

The size and surface property of MNPs were characterized by transmission electron microscopy (TEM). A drop of diluted sample was dispersed onto a 100-mesh copper grid (CF200-Cu, Electron Microscopy Science) and the excess drop was removed with filter paper. The sample containing copper grid was dried for 2 hours at 55 °C prior to TEM analysis. The morphology of the COOH MNPs and Ab MNPs were observed by TEM (JM-1011,





JEOL, and Tokyo, Japan). The zeta potential was characterized using a Zetasizer Nano ZS 90 (Malvern, Worcestershire, U.K.) at 32 °C. The tested MNPs under different pH conditions were 1  $\mu\text{g mL}^{-1}$ . The different pH (pH 3, 5, 7, 9, and 11) were obtained by adjusting the amount of HCL (0.1%) and NaOH (0.1%). Fourier transform infrared spectroscopy (Alpha, Bruker, Germany) was used to characterize the presence of specific chemical groups in the modified magnetic nanoparticles. Dried samples (0.8 mg) were mixed with KBr (IR grade, Sigma) powder (80 mg) and compressed into a thin membrane using a desktop pellet press (ICL, Garfield, NJ). The spectra of the samples were then processed by Bruker OPUS software. The loading antibody on the MNPs was determined by Nanodrop spectrophotometer (Thermo, Wilmington, DE).

### Detection and isolation of CD20 positive lymphocyte cells by Ab MNPs

To demonstrate the abilities of Ab MNPs for detection and isolation of cancer cell, Ramos lymphoma cells were used as target cells. The CD20 free cells including hybridoma cells, HaCaT and CHO cells were used as control. The CD20 positive cells stained with Hoechst 33342 nucleic acid dye with a final concentration of 1 ppm and the control cells were stained with Rhodamine B (with a final concentration of 10 ppm) were mixed with Ab MNPs or COOH MNPs and incubated for 20 minutes at 4 °C to prevent the endocytosis. The target cells bound by their prospective MNPs were washed three times with PBS using a magnet and then imaged with the aid of a confocal microscope and flow cytometry. To demonstrate the Ab MNPs selectivity towards the target cells, we carried out a control experiment with target cancer cells and non-target normal cells. We mixed Ab MNPs with a sample containing  $1 \times 10^6$  CD20 positive lymphoma cells and CD20 negative cells and incubated for 20 minutes at 4 °C. After magnetic separation, the precipitate was imaged under a confocal microscope and flow cytometry. The number of cells before and after isolation with Ab MNPs was imaged with the confocal microscope to know the efficiency of the Ab MNPs to capture the target cancer cells.

### Targeting efficiency of Ab MNPs to lymphocyte cells

Magnetic separation was performed by adding Ab MNPs to each 1 mL of sample ( $1 \times 10^6$  cells) as describe in the above procedure. The different concentration (10, 30, 50  $\mu\text{g mL}^{-1}$ ) of high Ab conjugated MNPs (15.86  $\mu\text{g Ab per mg MNPs}$ ), and low Ab conjugated MNPs (8.07  $\mu\text{g Ab per mg MNPs}$ ) were incubated with the cell samples for 20 minutes at 4 °C. Then, a magnet was introduced to the sample tubes, and after 3 minutes the target cells were attached to the tube wall while the supernatant was collected carefully using a pipet. After magnetic separation, the number of isolated cells by Ab MNPs was determined with flow cytometry to know the efficiency of the Ab MNPs to capture the target lymphocyte cells.

The specificity of Ab MNPs towards CD20 positive lymphocytes was evaluated by mixing target cells with CD20 free cells in different ratios. The Hoechst 33342 stained lymphocytes were varied from  $5 \times 10^4$  to  $1 \times 10^6$  and n CD20

free cells by stained Rhodamine B were fixed at  $1 \times 10^6$ . The mixed cells were incubated with the Ab MNPs (30  $\mu\text{g mL}^{-1}$ ) for 20 minutes. The isolation was performed using a magnet and the isolated cells were analyzed by flow cytometry. The isolation efficiency of the Ab MNPs was calculated as follows.

$$\text{Isolation efficiency (\%)} = \frac{\text{isolated CD20 positive cells}}{\text{initial CD20 positive cells}} \times 100$$

### Biocompatibility studies

The CD20-expressing cells and CHO cells were employed for cytotoxicity evaluation. Cells treated with Ab MNPs at different concentrations were examined with Coulter counter, MTT, and Trypan blue assay to measure cell viability. For MTT assay, cells were seeded into 96-well plates ( $2 \times 10^4$  cells per well) with 100  $\mu\text{L}$  medium and incubated overnight. Subsequently, Ab MNPs at different concentrations (10, 30, 50  $\mu\text{g mL}^{-1}$ ) were added to the well and incubated for 24 hours at 37 °C. The control group was incubated with only sterile PBS. Add 200  $\mu\text{L}$  of 0.5  $\text{mg mL}^{-1}$  MTT reagent into each well and incubated for additional 4 hours. After incubation, the supernatants were removed carefully and 200  $\mu\text{L}$  of DMSO was added to each well. Next, plates were shaken on an orbital incubator for 10 minutes in order to dissolve the formazan crystals. Finally, the absorbance of each well was measured by a spectrophotometer. Also, coulter counter and Trypan blue assay was performed to count the cell number and to evaluate the toxicity effect. The cells ( $2 \times 10^5$  cells per well) were cultured in a 6 well plate. The control group were incubated with sterile PBS, whereas different concentrations (10, 30, 50  $\mu\text{g mL}^{-1}$ ) of Ab MNPs were added to cells. At each hour, 100  $\mu\text{L}$  of the cell suspension was transferred to an Eppendorf, and the cell number was evaluated by using Beckman Coulter counter (MS3 model) and femocytometer. For all the experiments, measurements were carried out in triplicate. The viability of the cells in the treated groups was calculated according to the following equation.

$$\text{Viability (\%)} = \frac{\text{final cell population of treated group}}{\text{final cell population of control group}} \times 100$$

### Localization of nanoparticles in the lymphoma cell line

Prussian blue staining and potassium thiocyanate method were used to study iron uptake in cells. Equal volumes of 10% potassium ferrocyanide solution and 20% hydrochloric acid solution were freshly mixed to prepare the Prussian blue solution. Ramos lymphoma cells ( $1 \times 10^6$ ) were incubated with 30  $\mu\text{g mL}^{-1}$  Ab MNPs or COOH MNPs for one hour at room temperature. Then, washed three times with PBS and incubated 5 minutes with 150  $\mu\text{L}$  ice-cold ethanol (95%). After five minutes, cells were centrifuged to remove ethanol and washed three times with deionized water. Then, the cells were incubated with 150  $\mu\text{L}$  of Prussian blue solution for 20 minutes in the dark. After washing three times in PBS, the cells were counterstained with neutral red (1 ppm) for 2 minutes and imaged under the microscope for Prussian blue staining.



For potassium thiocyanate method,  $1 \times 10^6$  cells from Ramos lymphoma cell line, hybridoma or CHO cells were incubated with  $30 \mu\text{g mL}^{-1}$  MNPs at  $37^\circ\text{C}$  for 2 hours. The excess iron was removed by washing with PBS, and the iron concentration in  $1 \times 10^6$  cells was determined using the following thiocyanate-based spectrophotometric assay. The cell samples were mixed with  $100 \mu\text{L}$  of  $12 \text{ N HCl}$  for 4 hours at room temperature. Then,  $400 \mu\text{L}$  of 5% (w/v) potassium thiocyanate was added to the solution and incubated for 15 minutes. Samples were centrifuged at  $12\,000 \times g$  for 10 min and  $100 \mu\text{L}$  of the supernatant was added to a 96 well microtiter plate. The absorbance at 480 nm was measured using a microplate reader (Synergy HT, BioTek, Hong Kong). Two calibration curves of MNPs were prepared by using Ab MNPs and COOH MNPs (antibody free). The detailed procedure of potassium thiocyanate method was referred to previous papers.<sup>19,20</sup>

## Results and discussion

### Functionalization of antibody magnetic nanoparticles (Ab MNPs)

We firstly chose biotin maleimide to conjugate the biotins to antibodies. The maleimide-containing biotins efficiently react to

the thiol groups on the antibody and form a thio-succinimide linkage that can maintain the antibody's targeting ability. The disulfide bonds of antibodies as conjugation sites provide advantages over other reactive groups, such as amines and carboxylates. Avidin is conjugated with COOH MNPs through the EDC/NHS linker, and the biotinylated antibody is eventually bound with COOH MNPs through a biotin-avidin non-covalent interaction to form Ab MNPs. The strong binding affinity of biotin towards avidin is stable during proteolysis and within a wide range of pH and temperature levels and with a variety of denaturing agents.<sup>14,21–23</sup> The EDC/NHS linker directly connects carboxylic and amino groups, for conjugating molecules with multiple carboxylic and amino groups. The functionalization procedure of Ab MNPs is shown in the schematic diagram (Fig. 1). The conjugation strategy allows the functional and directional conjugation of the Fc portion of an antibody to MNPs and is directed outward from the surfaces of Ab MNPs, while the Fab (capture site) is largely available for efficient targeting. Conjugating MNPs specifically to the Fc portion decreases the opsonin role of the antibody molecules that are used for targeting the cell surface antigen.<sup>24</sup> While conjugating the Fc-directed method, the opsonin activity of the antibody is concealed and reduces the

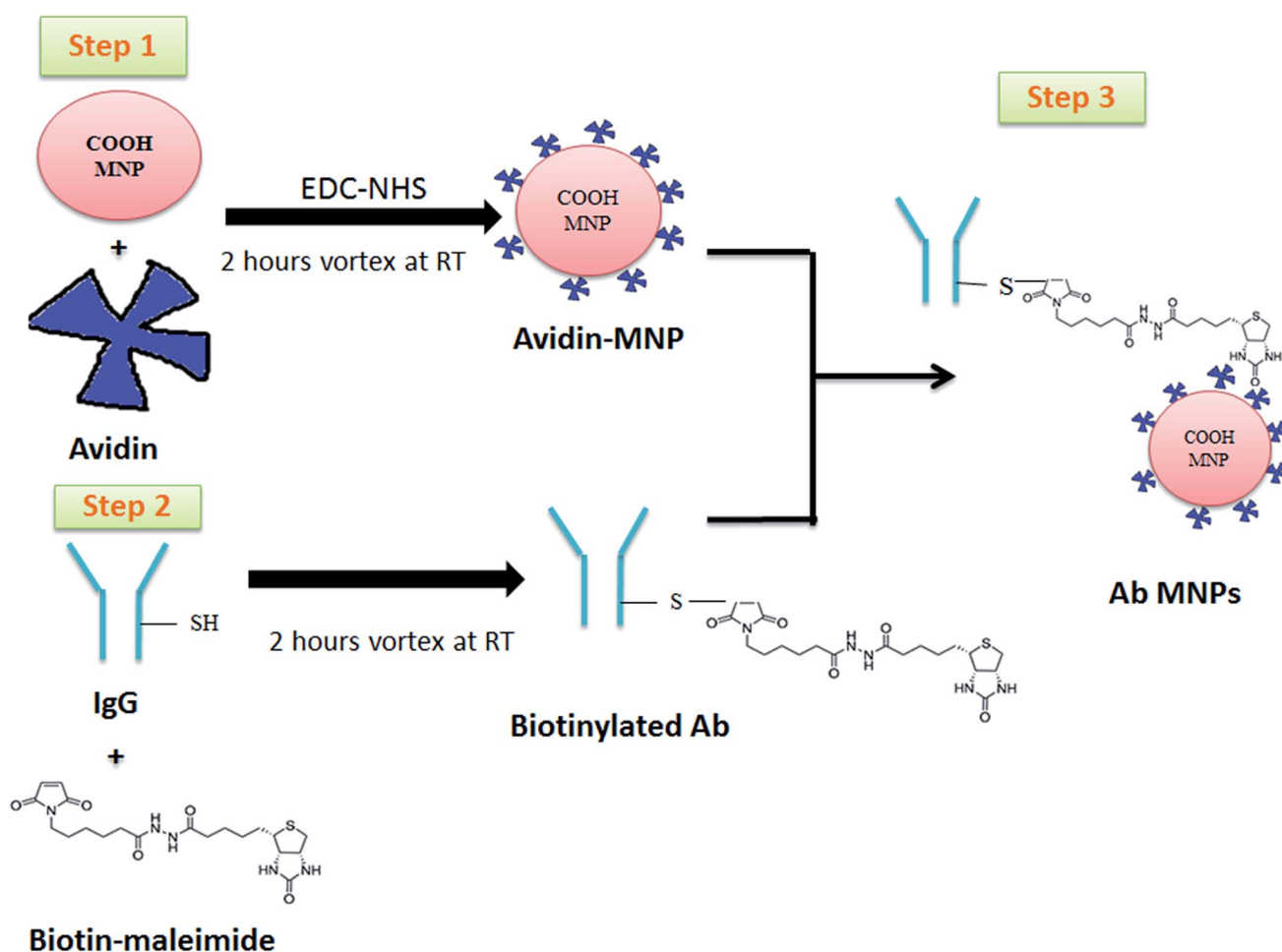


**Fig. 1** Schematic representation of antibody and MNPs conjugation. step 1. Avidin is conjugated with COOH MNPs in presence of EDC/NHS linker, step 2. Biotin is conjugated with the anti-CD20 antibody to obtain biotinylated antibody, step 3. Finally, biotinylated antibody is eventually bound with avidin modified COOH MNPs through a biotin-avidin non-covalent interaction to form antibody MNPs (Ab MNPs).



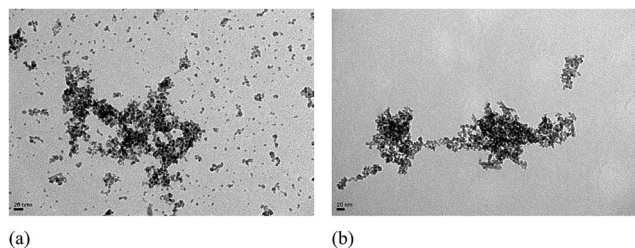


Fig. 2 TEM image for COOH MNPs (bare MNPs) and Ab MNPs (conjugated with Ab). (a) COOH MNPs (b) modified Ab MNPs. The average sizes for COOH MNPs and Ab MNPs were 12 nm and 47 nm respectively by using image J.

endocytosis of MNPs. Finally, modified MNPs with fewer cytotoxic effects are expected. The target efficiency of the anti-CD20 antibody in relation to the CD20 antigen result in functionalized Ab MNPs. The modified MNPs are characterized and investigated in terms of the isolation of lymphoma cells in the following sections.

### Characterization of Ab MNPs

Physical properties were measured using TEM, zeta potential, and Prussian blue staining to confirm the quality of the Ab MNPs. The size and morphology of the Ab MNPs were investigated by TEM (Fig. 2). The particle size was calculated with at least 50 particles chosen at random in both the prepared samples through an image J analysis program. From Fig. 2(a and b), it is clear that the size of the MNPs increased from 12 nm to 47 nm after conjugation with Ab. The properties of the coating materials have a major effect on the diameter, and the diameters of Ab MNPs were shown to be larger than the bare MNPs. Further, the thickness of the coating layer around the surface of the particle increased due to the decrease of water molecules in the magnetic core, which proves the successful conjugation of MNPs with Ab. The smaller size of the MNPs might improve their ability to enter the target site and to avoid endocytosis. Here, we have obtained Ab MNPs of about 47 nm; in a previous study, the sizes of antibody-modified nanoparticles were 340 to 410 nm.<sup>25</sup> The TEM images of the antibody-conjugated MNPs revealed a uniform size distribution and no significant change in their morphology, even after the conjugation reaction.

Fig. 3 illustrates the zeta-potential of COOH MNPs (unconjugated Ab) and Ab MNPs (conjugated with Ab) as a function of pH, which has been shown to confirm the presence of functional groups on the surface of MNPs. The zeta potential values for COOH MNPs and Ab MNPs were 3 and 5 mV, respectively, at pH 3. The zeta potential of COOH MNPs was observed at around −21 mV. However, the zeta potential of the Ab MNPs shifted from −21 mV to −10 mV at pH 11 (Fig. 3), confirming the successful conjugation of Ab to the surface of the MNPs. The positive zeta potential values started to decrease for both the MNPs as the pH was raised towards 11. The negative zeta values started to increase with the increase in pH, which indicated that the surface charges of both conjugates had increased slightly. The fact that the isoelectric points of COOH MNPs and Ab MNPs

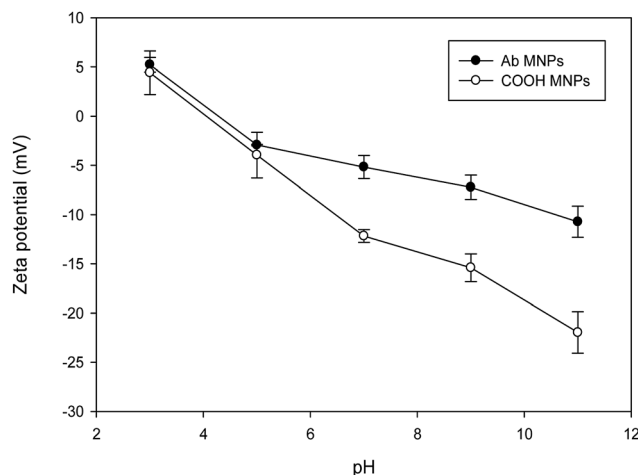


Fig. 3 Zeta potentials of COOH MNPs (unconjugated Ab) and Ab MNPs (conjugated with Ab) under different pH conditions. MNPs were dispersed in water ranged from pH 3 to pH 11.

were 3.6 and 4.4, respectively, was attributed to the presence of carboxylic groups in the MNPs. The IR spectra of COOH MNPs and Ab MNPs were presented in Fig. S1† A prominent absorption band at  $1717\text{ cm}^{-1}$  in COOH group (Fig. S1A†) which was due to C=O stretch of carboxylic group. On the other hand, in Ab MNPs (Fig. S1B†), bands related to the presence of protein show up, the amide I and amide II bands at  $1646$  and  $1533\text{ cm}^{-1}$ , respectively. These results confirmed that the MNPs were successfully conjugated with antibodies.

### The capture and isolation of CD20-positive lymphocyte cells by Ab MNPs

We developed a system in which the constituents are avidin-labelled MNPs, conjugated to a biotin-labelled anti-CD20 antibody (Ab MNPs) (Fig. 1). To demonstrate the specific capturing efficiency of Ab MNPs in targeting CD20-positive lymphocyte cells, we analyzed the MNP-targeted cells using confocal microscopy and flow cytometry. To examine the specific or nonspecific binding effect of MNPs, a magnetic isolation experiment was conducted, as described in the Experimental section. The 106 cells treated by  $30\text{ }\mu\text{g}$  of MNPs per mL were used for the cell capture assay. To test the capture efficiency, two kinds of cells (lymphoma and hybridoma cells) were mixed and incubated for 20 minutes with MNPs followed by isolation using a magnet. After magnetic isolation, the flow cytometry analysis indicated that COOH MNPs did not show specificity towards any cell lines. Sequentially, an equal number of mixed cells, that is, 48% of the hybridoma cells (CD20 negative cells) and 50% of the lymphocyte cells (CD20-positive cells) were obtained by COOH MNPs. In contrast, Ab MNPs separated 98% of lymphocyte cells and a negligible percentage (only 2%) of hybridoma cells (Fig. 4b). The fact that COOH MNPs could nonspecifically capture both cell types (Fig. S3†) from mixed cells indicated that COOH MNPs need further modification to enhance the selectivity.<sup>26</sup> It also implies that the Ab MNPs display higher binding sensitivity than that of bare MNPs (COOH MNPs). More importantly, our conjugation strategy allows the quick and



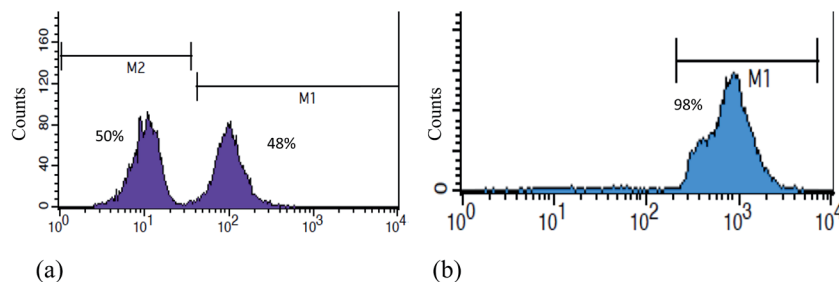


**Fig. 4** Representative specific cell isolation using Ab MNPs or COOH MNPs. (a) Cell sorting by COOH MNPs and (b) cell sorting by Ab MNPs. Two kinds of cells (BCRC 60427 and Ramos lymphoma) were incubated with (a) COOH MNPs (50  $\mu$ L) or (b) Ab MNPs (50  $\mu$ L). The targeted cells were isolated with a magnet and washed three times. The results are expressed as the mean and standard deviation from two experiments, (a)  $52\% \pm 2.8$  lymphoma cells and  $46.3\% \pm 2.3$  hybridoma cells were isolated by COOH MNPs. (b)  $97.5\% \pm 0.7$  lymphoma cells were isolated by Ab MNPs.

efficient capture of CD20-positive cells using a low dose of Ab MNPs. In a previous approach, more than an hour of incubation was required for the isolation of the cells.<sup>6</sup> The specific binding capacity of Ab MNPs was made possible by targeting the anti-CD20 Ab at the CD20 antigen on lymphocyte cells. These results suggested that the conjugation of anti-CD20 with MNPs can effectively enhance the specific binding of nanoparticles to the cells.

The ability of Ab MNPs to recognize the target cells was evaluated in the following experiments. The Ab MNPs were incubated with mixed cells (Fig. 4b), as mentioned in the Experimental section. For the specific isolation, the hybridoma cells (BCRC 60427) and HaCaT cells (skin cells) were used as the negative control and lymphocyte cells expressing CD20 were the target cells. Because the control cells had been stained with Rhodamine B and the target cancer cells with Hoechst dyes, they could be visualized by their different fluorescent qualities when excited under various levels of excitation. If blue fluorescence from the target cell nucleus and red fluorescence on the surface of the cells appeared, we could conclude that the respective cells were detected by the Ab MNPs. The cell mixtures were incubated with Ab MNPs for 20 minutes and isolated by a magnet. Confocal microscopic images of the precipitates were then taken. Fig. S3† shows the experimental results in which the Ab MNPs isolated only CD20-positive lymphoma cells stained with blue fluorescence (from Hoechst 33342), while CD20-free

cells stained with red fluorescence (Rhodamine B) were found in the supernatant (as presented in Fig. S4 in the ESI† section). Ab MNPs binding to CD20-negative cells (such as BCRC 60427 cells or HaCaT cells) was negligible, indicating the ability to recognize CD20 antigens with high specificity. The binding of Ab MNPs to CD20-positive cells was confirmed in the confocal images (Fig. S3†). For the recognition and isolation of markers on the cell surface, MNPs are advantageous because the high volume ratio offers a greater surface area for attaching specific ligands and for capturing markers. Most importantly, the size of the MNPs is smaller by orders of magnitude (approximately) than that of a cell, which allows multiple MNPs to be attached to a cell to facilitate magnetic isolation. Hence, the advantages of using the surface-modified MNPs with a target ligand for targeting and isolating cells are that they require only a short incubation time (20 minutes) and a simple washing process with a PBS buffer. The above experiments suggested that the mechanism of interaction between CD20-expressing cells and Ab MNPs is cell surface clustering.<sup>27</sup> The high target specificity makes these MNPs ideal as isolation tools for recognizing and sorting cells.

After showing the expected binding, we tested the feasibility of Ab MNPs to isolate target cells from cell mixtures by first preparing mixed samples of CD20-positive cells (lymphoma) and CD20 negative cells, such as hybridoma cells (BCRC 60427), CHO (Chinese hamster ovary cells) and HaCaT cells. The

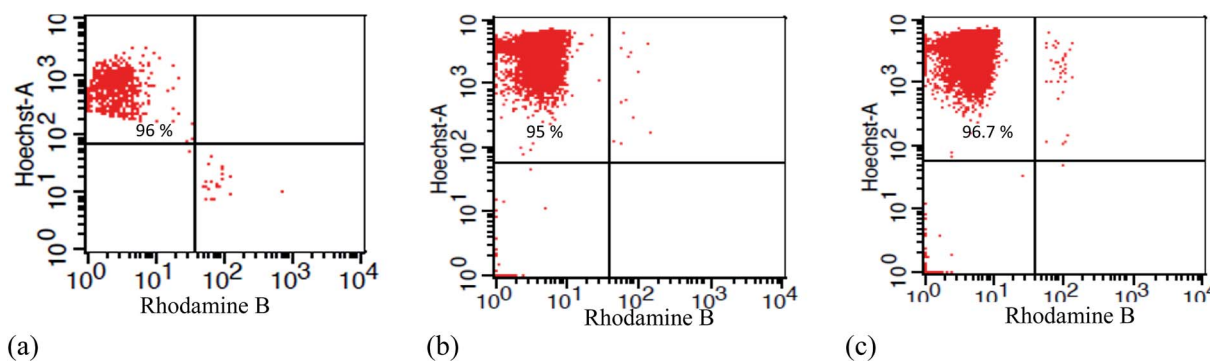


**Fig. 5** Flow cytometric analysis for cell separation efficacy using Ab MNPs in different cell mixtures. (a) Lymphoma and hybridoma, (b) lymphoma and CHO cells and (c) lymphoma and HaCaT.  $30 \mu\text{g mL}^{-1}$  Ab MNPs were added to each cell samples and incubated for 20 minutes at  $4^\circ\text{C}$ . The results are obtained as the mean and standard deviation of two determinations,  $96.5\% \pm 0.7$  (a)  $94.5\% \pm 0.7$  (b) and  $94.8 \pm 2.6$  (c).





sample was prepared by mixing approximately  $1 \times 10^6$  target cells and  $1 \times 10^6$  of other kinds of cells, such as hybridoma, CHO or HaCaT cells, and then incubated with  $30 \mu\text{g mL}^{-1}$  of Ab MNPs. The lymphoma cells were stained with Hoechst and BCRC 60427, and CHO or HaCaT cells were stained with Rhodamine B to distinguish the target and non-target cells. After incubation and magnetic separation, the magnetically isolated cells were analyzed by flow cytometry. When lymphoma cells mixed with CD20-negative hybridoma cells, the isolated cells contained 96% of CD20-positive cells, as shown in Fig. 5. Similarly, when mixed with either CHO or HaCaT cells, 95% of CD20 positive cells could be isolated by using the Ab MNPs. We also examined the cells that remained in the supernatant, and most of these cells were CD20 negative, as shown in Fig. S4.†

### Dose effect of Ab MNPs on the isolation of target lymphoma cells

To evaluate the effects of different concentrations, different doses of antibody were conjugated with MNPs to isolate CD20-positive cells and quantified by flow cytometry. A comparison of the high Ab-loaded MNPs ( $15.86 \mu\text{g Ab per mg MNPs}$ ) and the low Ab-loaded MNPs ( $8.07 \mu\text{g Ab per mg MNPs}$ ) was evaluated with mixed cells having both CD20-positive cells and CD20-negative cells. Different amounts ( $10, 30$ , and  $50 \mu\text{g mL}^{-1}$ ) of both high and low Ab-loaded MNPs were incubated with lymphoma (CD20 positive) and CD20-negative cells for 20

minutes and isolated by 3 minutes of magnetic separation. The CD20-positive cell binding increased with increasing concentrations of Ab MNPs. Both the high and low Ab-loaded MNPs showed good separation ability (Fig. 6a–f). The high Ab-loaded MNPs ( $10 \mu\text{g mL}^{-1}$ ) could efficiently isolate 95% of the CD20-positive cells from CD20-negative hybridoma cells. Furthermore,  $30 \mu\text{g}$  and  $50 \mu\text{g mL}^{-1}$  of Ab MNPs separated 96% and 98% of CD20-positive cells, respectively. In contrast, the low Ab-loaded MNPs showed that  $10 \mu\text{g mL}^{-1}$  of MNPs separated 88% of CD20-positive cells (Fig. 6d). The cell-capture rate of high concentrations of Ab MNPs had higher separation efficacy even at a low concentration ( $10 \mu\text{g mL}^{-1}$ ) of Ab MNP treatment of cells. Whereas, with a low concentration of Ab MNPs, at  $10 \mu\text{g}$ ,  $30 \mu\text{g}$  and  $50 \mu\text{g mL}^{-1}$ , separated 88%, 90% and 95% of CD20-positive cells, respectively, and resulted in a few more CD20 negative cells compared with the high Ab MNPs (Fig. 6a–f). This proves the successful Ab conjugation on MNPs since lower concentrations of Ab MNPs can specifically bind to CD20-positive cells. The isolation of the CD20 cells demonstrated some differences in binding, further indicating the Ab effect on MNPs. However, in the studied concentration range, Ab MNPs with high Ab conjugation exhibited more specific isolation of lymphocyte cells than those with low Ab modification on MNPs. A similar result was obtained when CD20-positive cells were mixed with CD20-negative CHO cells, as indicated in Fig. S7.† In a previous report, it was suggested that an optimal

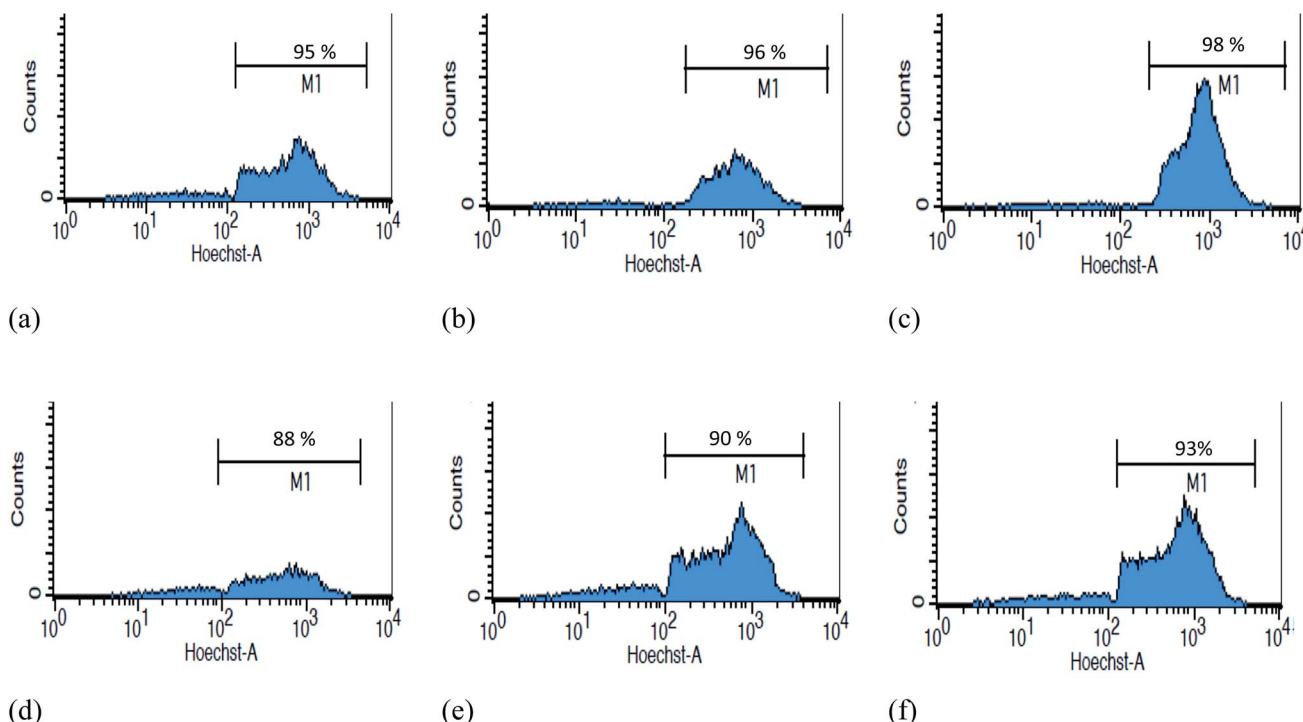


**Fig. 6** Representative dose-dependent capture efficacy by two kinds of Ab MNPs. CD20 positive cells (BCRC 60252) and CD20 negative cells (BCRC 60427) were isolated by using high Ab conjugated or low Ab conjugated MNPs at different concentrations. Panel (a–c): high Ab conjugated MNPs ( $15.86 \mu\text{g Ab per mg MNPs}$ ). Panel (d–f): low Ab conjugated MNPs ( $8.07 \mu\text{g Ab per mg MNPs}$ ) at  $10, 30, 50 \mu\text{g mL}^{-1}$  MNPs. The flow cytometry data are reported as the mean and standard deviations ( $n = 2$ ). The separation efficacy was  $94.2 \pm 1.3\%$  (a)  $96 \pm 0.92\%$  (b) or  $98 \pm 0.68\%$  (c) for high Ab conjugated MNPs. The separation efficacy was  $86.5 \pm 2.1\%$  (d)  $94.47 \pm 5.5\%$  (e) or  $93.6 \pm 1.0\%$  (f) for low Ab conjugated MNPs.





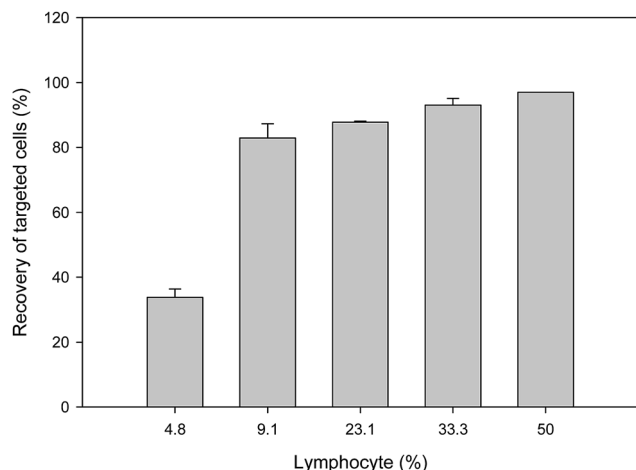


Fig. 7 The isolation efficacy of targeted lymphoma cells from a higher population of hybridoma (CD20 negative) cells by using Ab MNPs. A small number of spiked lymphoma cells ranged from  $5 \times 10^4$  to  $1 \times 10^6$  were mixed with hybridoma cells fixed at  $1 \times 10^6$  cells. Each bar represents the standard deviation ( $n = 2$ ).

concentration of Ab would be necessary to achieve efficient cellular targeting of MNPs.<sup>25</sup> The above studies showed that both Ab concentrations (high and low) showed specificity towards the target cells.

Generally, in the early stage of cancer, very few cancer cells are present within a large number of normal cells in the blood. To determine the specificity of Ab MNPs towards less CD20-positive lymphocyte cells, the target cells were mixed with non-target cells in different ratios (Fig. 7); stained (Hoechst 33342) target cells ratio were varied ( $5 \times 10^4$ – $1 \times 10^6$ ), and stained (Rhodamine B) non-target cells ratio were fixed ( $1 \times 10^6$ ). The mixed cells were incubated with fixed concentrations ( $30 \mu\text{g mL}^{-1}$ ) of Ab MNPs for 20 minutes and then isolated using a magnet and analyzed by flow cytometry. The results showed that even if we used low concentrations of target cells, the Ab MNPs could recognize the specific target cells against the large population of normal cells. When the target cells were very rare

(i.e. only  $5 \times 10^4$  target lymphocyte cells mixed with  $10^6$  non-target cells), only 31% of target cells were isolated.

### Biocompatibility studies

Factors such as surface conjugation, charges and sizes of MNPs are key aspects in understanding the biocompatibility of the functionalized MNPs. A high concentration of MNPs has been reported to be toxic to *in vitro* cells due to the generation of reactive oxygen species.<sup>28</sup> On the contrary, trivial effects on the viability of various cell lines have been reported for these MNPs by other authors.<sup>29,30</sup> Herein, we evaluated the biocompatibility of modified Ab MNPs using several complementary approaches, such as Trypan blue, cell counting and MTT assay for CD20-positive lymphocyte cells. The results of Trypan blue assay and cell counting (Fig. 8a and b) confirmed the biocompatibility of Ab MNPs. The cell viability was above 90% after 8 hours of incubation. Trypan blue test has been proposed as the standard method to validate cell viability after MNP incubation. The results of cell counting showed that cell density remained the same after 8 hours of incubation with Ab MNPs. The MTT assay (Fig. 8) showed that cell activity was not significantly affected by the presence of Ab MNPs at 24 hours of treatment (>80% viability in relation to the control sample), even at the highest concentration ( $50 \mu\text{g mL}^{-1}$ ). Moreover, Ab MNPs toxicity effect was also evaluated with normal cell (CHO cells) and presented in Fig. S8.† Higher viability has been observed for the two cell types when compared to the control conditions. MTT assay shows that Ab MNPs do not exert acute adverse effect on CHO cells and lymphoma cells even at high dosage, suggesting that it can be applicable *in vivo* applications. The MTT assay is based on the reduction of soluble yellow tetrazolium into insoluble purple formazan crystals by mitochondrial succinate dehydrogenase of the viable cell. Thus, the rate of formazan crystal formation is directly proportional to the total number of viable cells, which is measured in terms of absorbance.<sup>31</sup> A modified MTT assay has been adopted here to avoid the influence of MNPs on the colorimetric assay.<sup>32</sup> Fig. 8c, shows that the viability of cells exhibited a slightly decreasing trend from 1

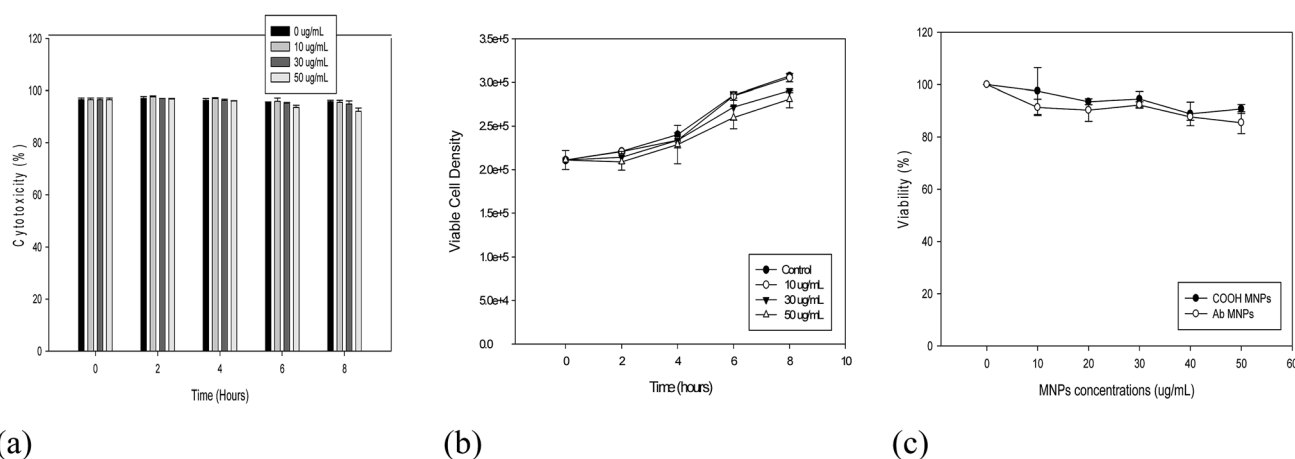


Fig. 8 Biocompatibility of Ab MNPs in lymphoma cell line evaluated by hemocytometer (a) cell counting (b) and MTT assay (c) with different Ab MNPs concentrations ranging from 10–50  $\mu\text{g mL}^{-1}$  for 8 hours. In the MTT assay, cells with Ab MNPs or COOH MNPs were incubated for 24 hours. The coefficient of variation (SD/mean) is around 4%.



hour to 24 hours of co-culture for both bare and Ab MNPs in a similar manner to that of the control sample (without MNPs), and the viability remained more than 80%. All the Trypan blue dye, MTT assay, and cell counting results confirmed the compatibility of the Ab MNPs developed in this study. Cell viability could be maintained within the 24 h incubation using  $50 \mu\text{g mL}^{-1}$  of MNPs.

### Localization of nanoparticles in the lymphoma cell line

The Prussian blue staining test was employed to detect the localization of the nanoparticles with antibody-conjugated and unconjugated MNPs on CD20-positive lymphocyte cells (Fig. S9†). This method detects iron within the treated cells through the reduction of ferric ions into the ferrous state, which is shown as a blue colour.<sup>33</sup> The cells treated with COOH MNPs (antibody free) showed occasional blue spots outside of the cells (Fig. S9a†), whereas the cells treated with antibody-conjugated nanoparticles showed clear blue shells around the cells, confirming the presence of Ab MNPs around the cell membranes (Fig. S9b†). There is abundant literature on MNPs conjugation efficiency; however, the results are difficult to compare due to the different experimental protocols, such as size, incubation time, surface coating, longer incubation time and higher concentration. Moreover, longer incubation time and higher concentrations of MNPs enable high interactions with the cell surface and increase the detection efficiency.<sup>34</sup> High concentrations of MNPs for an extended incubation may reduce viability and enhance cell aggregation.<sup>35</sup> Therefore, the required quantity of MNPs for cellular uptake must be balanced with their biocompatibility for efficient diagnosis or treatment.<sup>29</sup> To evaluate the selectivity of Ab MNPs, the iron concentration was also obtained by the potassium thiocyanate method (Fig. 9). In brief, the iron content of different cells ( $1 \times 10^6$ ) was measured after 2 hours of incubation with  $30 \mu\text{g}$  of Ab MNPs or COOH MNPs at  $37^\circ\text{C}$ . The results showed that a small difference in the amount of accumulated iron in the two cell lines used as controls could be due to either different MNP sizes or the type of cell line. Our potassium thiocyanate data indicated that Ab MNPs bound effectively at the level of  $16.8 \mu\text{g}$  per  $10^6$  cells on the cell surface of lymphocytes. In contrast, half the quantity of Ab MNPs was deposited on CD20-free hybridoma and CHO cells at the level of  $7.9$  and  $8.8 \mu\text{g}$  per  $10^6$  cells, respectively. Nonspecific iron binding ( $13\text{--}20 \mu\text{g}$  per  $10^6$  cells) was observed in the three cell lines when isolation was performed by using COOH MNPs. This result confirmed the nonspecific binding of COOH MNPs to cells. Recently, the location of functionalized MNPs in MCF-7 cells after 24 h incubation has been observed by optical microscopy and TEM. Most of the MNPs were distributed in the periplasmic area.<sup>30</sup> In addition, their results for Prussian blue staining and ferrozine-based assay also indicated that MNPs ( $21 \mu\text{g}$  per  $10^6$  cells) can be internalized effectively ( $21 \mu\text{g}$  per  $10^6$  cells) by MCF-7 cells. In contrast, the major location of our Ab MNPs or COOH MNPs was on the surface of cellular membranes in the lymphoma cells, as indicated in Fig. S9b.† It is important to point out the dose of our MNPs was 13-fold lower than in Calero's paper, which might have resulted in the difference.<sup>30</sup>

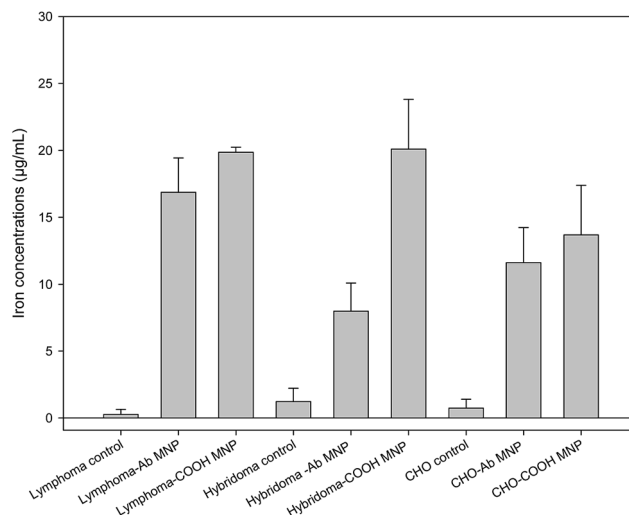


Fig. 9 Quantification of intracellular iron content. Thiocyanate-based iron uptake among the cell lines. The three cell lines were incubated with  $30 \mu\text{g mL}^{-1}$  of Ab MNPs or COOH MNPs at  $37^\circ\text{C}$  for 2 hours. The excess iron was washed with PBS, and the iron concentration in  $1 \times 10^6$  cells from each cell line was determined using a thiocyanate-based spectrophotometric assay. The error bars in the figure represent the mean and standard deviation (SD) of four repeats.

## Conclusion

In this study, we demonstrated a simple and robust conjugation method by using antibodies and MNPs. The specificity for targeting the thiols of the Fc fragment in an antibody can be improved by using maleimide conjugation. The synthetic platform described herein was efficient. It has the potential for further optimization for antibody conjugation on different nanoparticles. In addition, the lymphocytes cells were successfully detected and isolated from mixed samples containing other cells and target lymphocytes cells. The Ab MNPs fully retained their antibody binding capacity and could detect and isolate the CD20-positive cells from the mixed cells. The capture efficiency of Ab MNPs for lymphoma cells was above 95% under our experimental conditions. The capture efficiency was confirmed by complementary techniques, such as flow cytometry and confocal microscopy. Based on this simple antibody conjugation on MNPs, this platform enables robust cell sorting by using only a permanent magnet. The present approach demonstrated a facile, time saving and economical synthesis of Ab MNPs that can be used as an efficient capture platform for tumour cells.

## Conflict of interest

The authors would like to declare that no potential conflicts of interest exist.

## Acknowledgements

We express gratitude to Ministry of Science and Technology (MOST 105-2221-E-182-070), Chang Gung University (BMRP



758) and Chang Gung Memorial Hospital (CMRPD 1E0352) for funding and supporting this research.

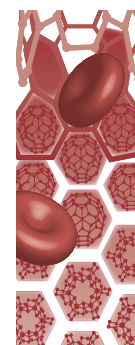
## References

- 1 M. Yu, S. Stott, M. Toner, S. Maheswaran and D. A. Haber, Circulating tumor cells: approaches to isolation and characterization, *J. Cell Biol.*, 2011, **192**, 373–382.
- 2 C. Wyatt Shields IV, C. D. Reyes and G. P. López, Microfluidic cell sorting: a review of the advances in the separation of cells from debulking to rare cell isolation, *Lab Chip*, 2015, **15**, 1230–1249.
- 3 Z. Bakhtiary, A. A. Saei, M. J. Hajipour, M. Raoufi, O. Vermesh and M. Mahmoudi, Targeted superparamagnetic iron oxide nanoparticles for early detection of cancer: possibilities and challenges, *Nanomedicine: Nanotechnology, Biology and Medicine*, 2016, **12**, 287–307.
- 4 D. Guldner, J. K. Hwang, M. C. D. Cardieri, M. Eren, P. Ziaei, M. G. Norton, *et al.*, In vitro evaluation of the biological responses of canine macrophages challenged with PLGA nanoparticles containing monophosphoryl lipid A, *PLoS One*, 2016, **11**(11), e0165477.
- 5 S. H. Huang and R. S. Juang, Biochemical and biomedical applications of multifunctional magnetic nanoparticles: a review, *J. Nanopart. Res.*, 2011, **13**, 4411–4430.
- 6 H. Xu, Z. P. Aguilar, L. Yang, M. Kuang, H. Duan, Y. Xiong, *et al.*, Antibody conjugated magnetic iron oxide nanoparticles for cancer cell separation in fresh whole blood, *Biomaterials*, 2011, **32**, 9758–9765.
- 7 M. A. Firer and G. Gellerman, Targeted drug delivery for cancer therapy: the other side of antibodies, *J. Hematol. Oncol.*, 2012, **5**, 1–16.
- 8 S. H. Lim, S. A. Beers, R. R. French, P. W. M. Johnson, M. J. Glennie and M. S. Cragg, Anti-CD20 monoclonal antibodies: historical and future perspectives, *Haematologica*, 2010, **95**, 135–143.
- 9 L. Al-Zoobi, S. Salti, A. Colavecchio, M. Jundi, A. Nadiri, G. S. Hassan, *et al.*, Enhancement of rituximab-induced cell death by the physical association of CD20 with CD40 molecules on the cell surface, *Int. Immunol.*, 2014, **26**, 451–465.
- 10 P. Jain and S. O'Brien, Anti-CD20 monoclonal antibodies in chronic lymphocytic leukemia, *Expert Opin. Biol. Ther.*, 2013, **13**, 169–182.
- 11 F. M. Kievit, Z. R. Stephen, O. Veiseh, H. Arami, T. Wang, V. P. Lai, *et al.*, Targeting of primary breast cancers and metastases in a transgenic mouse model using rationally designed multifunctional SPIONs, *ACS Nano*, 2012, **6**, 2591–2601.
- 12 H. J. Hathaway, K. S. Butler, N. L. Adolphi, D. M. Lovato, R. Belfon, D. Fegan, *et al.*, Detection of breast cancer cells using targeted magnetic nanoparticles and ultra-sensitive magnetic field sensors, *Breast Cancer Res.*, 2011, **13**, R108.
- 13 A. Cirstoiu-Hapca, L. Bossy-Nobs, F. Buchegger, R. Gurny and F. Delie, Differential tumor cell targeting of anti-HER2 (Herceptin®) and anti-CD20 (Mabthera®) coupled nanoparticles, *Int. J. Pharm.*, 2007, **331**, 190–196.
- 14 E. Q. Song, J. Hu, C. Y. Wen, Z. Q. Tian, X. Yu, Z. L. Zhang, *et al.*, Fluorescent-magnetic-biotargeting multifunctional nanobioprobes for detecting and isolating multiple types of tumor cells, *ACS Nano*, 2011, **5**, 761–770.
- 15 F. M. Kievit, Z. R. Stephen, O. Veiseh, H. Arami, T. Wang, V. P. Lai, *et al.*, Targeting of primary breast cancers and metastases in a transgenic mouse model using rationally designed multifunctional SPIONs, *ACS Nano*, 2012, **6**, 2591–2601.
- 16 S.-M. Jo, S.-H. Noh, Z. Jin, Y. Lim, J. Cheon and H.-S. Kim, Simple and efficient capture of EGFR-expressing tumor cells using magnetic nanoparticles, *Sens. Actuators, B*, 2014, **201**, 144–152.
- 17 J. Wu, X. Wei, J. Gan, L. Huang, T. Shen, J. Lou, *et al.*, Multifunctional Magnetic Particles for Combined Circulating Tumor Cells Isolation and Cellular Metabolism Detection, *Adv. Funct. Mater.*, 2016, **26**, 4016–4025.
- 18 G. T. Hermanson, *8-Tags and Probes. Bioconjugate Techniques*, Academic Press, San Diego, 1996, pp. 297–416.
- 19 S. H. Tseng, M. Y. Chou and I. M. Chu, Cetuximab-conjugated iron oxide nanoparticles for cancer imaging and therapy, *Int. J. Nanomed.*, 2015, **10**, 3663–3685.
- 20 Y.-C. Lu, P.-C. Luo, C.-W. Huang, Y.-L. Leu, T.-H. Wang, K.-C. Wei, *et al.*, Augmented cellular uptake of nanoparticles using tea catechins: effect of surface modification on nanoparticle-cell interaction, *Nanoscale*, 2014, **6**, 10297–10306.
- 21 F. Rusmini, Z. Zhong and J. Feijen, Protein immobilization strategies for protein biochips, *Biomacromolecules*, 2007, **8**, 1775–1789.
- 22 M. Wilchek, E. A. Bayer and O. Livnah, Essentials of biorecognition: the (strept)avidin-biotin system as a model for protein-protein and protein-ligand interaction, *Immunol. Lett.*, 2006, **103**, 27–32.
- 23 S. Sun, M. Ma, N. Qiu, X. Huang, Z. Cai, Q. Huang, *et al.*, Affinity adsorption and separation behaviors of avidin on biofunctional magnetic nanoparticles binding to iminobiotin, *Colloids Surf., B*, 2011, **88**, 246–253.
- 24 R. Rezaeiipoor, R. John, S. G. Adie, E. J. Chaney, M. Marjanovic, A. L. Oldenburg, *et al.*, Fc-directed antibody conjugation of magnetic nanoparticles for enhanced molecular targeting, *J. Innovative Opt. Health Sci.*, 2009, **2**, 387–396.
- 25 L. Nobs, F. Buchegger, R. Gurny and E. Allémann, Biodegradable nanoparticles for direct or two-step tumor immunotargeting, *Bioconjugate Chem.*, 2006, **17**, 139–145.
- 26 K. Yan, P. Li, H. Zhu, Y. Zhou, J. Ding, J. Shen, *et al.*, Recent advances in multifunctional magnetic nanoparticles and applications to biomedical diagnosis and treatment, *RSC Adv.*, 2013, **3**, 10598–10618.
- 27 A. Cirstoiu-Hapca, L. Bossy-Nobs, F. Buchegger, R. Gurny and F. Delie, Differential tumor cell targeting of anti-HER2 (Herceptin) and anti-CD20 (Mabthera) coupled nanoparticles, *Int. J. Pharm.*, 2007, **331**, 190–196.
- 28 A. Hanini, A. Schmitt, K. Kacem, F. Chau, S. Ammar and J. Gavard, Evaluation of iron oxide nanoparticle biocompatibility, *Int. J. Nanomed.*, 2011, **6**, 787–794.



- 29 M. Calero, L. Gutiérrez, G. Salas, Y. Luengo, A. Lázaro, P. Acedo, *et al.*, Efficient and safe internalization of magnetic iron oxide nanoparticles: two fundamental requirements for biomedical applications, *Nanomedicine: Nanotechnology, Biology and Medicine*, 2014, **10**, 733–743.
- 30 M. Calero, M. Chiappi, A. Lazaro-Carrillo, M. J. Rodriguez, F. J. Chichon, K. Crosbie-Staunton, *et al.*, Characterization of interaction of magnetic nanoparticles with breast cancer cells, *J. Nanobiotechnol.*, 2015, **13**, 16.
- 31 S. Shukla, A. Jadaun, V. Arora, R. K. Sinha, N. Biyani and V. K. Jain, *In vitro* toxicity assessment of chitosan oligosaccharide coated iron oxide nanoparticles, *Toxicol. Rep.*, 2015, **2**, 27–39.
- 32 S. Laurent, C. Burtea, C. Thirifays, U. O. Häfeli and M. Mahmoudi, Crucial ignored parameters on nanotoxicology: the importance of toxicity assay modifications and “cell vision”, *PLoS One*, 2012, **7**, e29997.
- 33 M. Neri, C. Maderna, C. Cavazzin, V. Deidda-Vigoriti, L. S. Politi, G. Scotti, *et al.*, Efficient *in vitro* labeling of human neural precursor cells with superparamagnetic iron oxide particles: relevance for *in vivo* cell tracking, *Stem Cells*, 2008, **26**, 505–516.
- 34 T. Schlörf, M. Meincke, E. Kossel, C. C. Gluer, O. Jansen and R. Mentlein, Biological properties of iron oxide nanoparticles for cellular and molecular magnetic resonance imaging, *Int. J. Mol. Sci.*, 2010, **12**, 12–23.
- 35 S. Naqvi, M. Samim, M. Abidin, F. J. Ahmed, A. Maitra, C. Prashant, *et al.*, Concentration-dependent toxicity of iron oxide nanoparticles mediated by increased oxidative stress, *Int. J. Nanomed.*, 2010, **5**, 983–989.





# Nanovesicle delivery to the liver via retinol binding protein and platelet-derived growth factor receptors: how targeting ligands affect biodistribution

**Aim:** Nanovesicles (NVs) conjugating ligands can deliver to the specific nidus. We designed a nanosystem targeting the injectable niosomes to liver for examining biodistribution. **Methodology:** Vitamin A and antiplatelet-derived growth factor receptor antibody were employed as the ligands to be taken by hepatic stellate cells. The biodistribution in rats was visualized by bioimaging. **Results:** A significant liver accumulation was detected for antibody-embedded NVs at 2 h after dosing. The vitamin A embedded NVs exhibited a delayed targeting to the liver (5 h). The spleen, intestine and kidneys were the nontargeted organs where the vitamin A loaded niosomes largely accumulated. The antibody-loaded NVs could deliver to the spleen, kidneys and lungs. The antibody-loaded nanocarriers increased silibinin uptake to lungs by fourfold than the plain NVs. **Conclusion:** The results have practical application for better designing of active targeting nanocarriers.

First draft submitted: 30 August 2016; Accepted for publication: 5 December 2016; Published online: 12 January 2017

**Keywords:** antibody • biodistribution • liver • nanovesicle • niosome • vitamin A

Nanoparticulate drug delivery is now gaining attention due to its ability to improve pharmacokinetics, biodistribution and the therapeutic effect as compared with free drugs. Nanocarriers with a size of <200 nm can be administered by intravenous injection to reach multiple organs for medical use [1]. The nanoparticle-encapsulated drugs reduce the applied dose and minimize the adverse effects with the utilization of targeting ligands since the conjugation of receptor-binding molecules to nanoparticles can specifically adhere to the target cells. The active targeting involves the coupling of ligands, such as peptides, proteins, carbohydrates, vitamins and antibodies [2]. For instance, nanomedicine is a potential tool for drug-delivery development to manage liver fibrosis [3]. Hepatic fibrosis resulting from toxins, viruses, alcohol abuse and metabolic diseases is the most common cause of non-neoplastic death associated with digestive disorders [4].

The target cells for liver fibrosis therapy are the hepatic stellate cells (HSCs), which play a critical role in fibrogenesis [5]. Receptors for retinol binding protein and platelet-derived growth factor (PDGF) are upregulated during liver injury [6]. Both receptors can act as the targeting sites for drug nanocarriers to achieve valid therapy [7,8].

The original intention to design the targeting ligands focuses on the cellular level. The ligands in nanocarriers certify the promoted drug delivery to target cells rather than target organs [9]. It is possible that the ligand-conjugated nanocarriers produce compromised targeting, nonspecific plasma protein binding and rapid clearance from the circulation. In addition to the influence of the ligands, the biodistribution of the nanoparticles is governed by size, surface charge and morphology [10]. Some investigations involved in the relationship between biodistribution and physicochemical characters of ligand-

Ching-Yun Hsu<sup>1,2</sup>, Chun-Han Chen<sup>3,4</sup>, Ibrahim A Aljuffali<sup>5</sup>, You-Shan Dai<sup>6</sup> & Jia-You Fang<sup>\*,2,6,7,8</sup>

<sup>1</sup>Department of Nutrition & Health Sciences, Chang Gung University of Science & Technology, Kweishan, Taoyuan, Taiwan

<sup>2</sup>Research Center for Chinese Herbal Medicine & Research Center for Food and Cosmetic Safety, Chang Gung University of Science & Technology, Kweishan, Taoyuan, Taiwan

<sup>3</sup>Graduate Institute of Clinical Medical Sciences, College of Medicine, Chang Gung University, Kweishan, Taoyuan, Taiwan

<sup>4</sup>Division of General Surgery, Department of Surgery, Chang Gung Memorial Hospital, Chiayi, Taiwan

<sup>5</sup>Department of Pharmaceutics, College of Pharmacy, King Saud University, Riyadh, Saudi Arabia

<sup>6</sup>Pharmaceutics Laboratory, Graduate Institute of Natural Products, Chang Gung University, Kweishan, Taoyuan, Taiwan

<sup>7</sup>Chinese Herbal Medicine Research Team, Healthy Aging Research Center, Chang Gung University, Kweishan, Taoyuan, Taiwan

<sup>8</sup>Department of Anesthesiology, Chang Gung Memorial Hospital, Kweishan, Taoyuan, Taiwan

\*Author for correspondence:

Tel.: +886 3 2118800

Fax: +886 3 2118236

[fajy@mail.cgu.edu.tw](mailto:fajy@mail.cgu.edu.tw)

Future  
Medicine

part of  
fsg



embedded nanosystems are reported [11–14]. The aim of this study was to investigate how the ligands in nanocarriers affected targeting efficiency and biofate at the organ level. To this end, we employed vitamin A and anti-PDGF receptor antibody as the ligands to be adsorbed onto the nanoparticulate surface for HSC targeting in the liver. Niosomes were used in this work as the model nanovesicles (NVs) due to their successful application in liver-targeting drug delivery [15]. Niosomes are formed by nonionic amphiphiles and cholesterol in aqueous solution, resulting in concentric bilayers, the same as liposomal conformation. The niosomes are generally nontoxic, less costly and more stable as compared with liposomes [16]. The NVs made of nonionic surfactants represent a promising alternative to liposomes due to greater stability in serum, adaptable handling and potential cell membrane interaction [17,18].

Silibinin was incorporated into niosomes in order to examine the biodistribution in different organs. It is a natural active compound derived from milk thistle. The antioxidant and hepatoprotective effects of silibinin have led to the capability to reverse liver fibrosis [19]. The NVs were characterized in terms of size,  $\zeta$  potential, mobilization, morphology, crystallinity and polarity. We evaluated silibinin entrapment and release *in vitro*. Furthermore, the biodistribution of various NV formulations was compared by *ex vivo* and *in vivo* bioimaging techniques. Finally, we demonstrated silibinin accumulation in organs by the intravenous route. The definitive scope of this study was to understand how the niosome biodistribution was controlled by the ligands and physicochemical properties.

## Methods

### Preparation of the NVs

A thin-film method was employed to fabricate the NVs. Span 60 (30 mg, 0.070 mmol), cholesterol (30 mg, 0.076 mmol) and soy phosphatidylcholine (Phospholipon® 80H, 80% phosphatidylcholine, 20 mg, American Lecithin Co., CT, USA) were dissolved in chloroform:ethanol (2:1) solvent for preparing anionic NVs. Additional soyaethyl morpholinium ethosulfate (SME; 60 mg, 0.164 mmol) was added in the dispersion to produce cationic NVs. For producing vitamin A loaded NVs, vitamin A (4 mg, 0.014 mmol) was further incorporated in the cationic NVs. Silibinin (10 mg), iFluor® 790 acid (AAT Bioquest, CA, USA) or 1,1'-dioctadecyl-3,3,3',3'-tetramethyl indotricarbocyanine iodide (DiR, 5 mg) was added in the dispersion as the model drug or near-IR (NIR) dye if necessary. The solvent was evaporated in a rotary evaporator at 65°C. The solvent trace was removed

under a vacuum. The double-distilled water was added to hydrate the film by a homogenizer (12,000 rpm) and a probe-type sonicator (35 W) for 10 min at 85°C, respectively. The anti-PDGF receptor antibody (8 mg) was added into the aqueous dispersion after cooling to room temperature for preparing antibody-embedded niosomes. The total volume of the final products was 10 ml. All materials were purchased from Sigma-Aldrich (MO, USA). The antibody was obtained from Abcam (MA, USA).

### Vesicle size & $\zeta$ potential

The vesicle diameter and  $\zeta$  potential of the prepared niosomes were detected using a laser-scattering technique (Nano ZS90, Malvern, Worcestershire, UK). The detection was performed at the vesicle concentration after a 100-fold dilution with water. The stability of the NVs was monitored for 28 days. The NV dispersions were stored in an incubator. The setup of temperature (40°C) and relative humidity (75%) was based on the stability test guidelines of International Council for Harmonization. The mean diameter and  $\zeta$  potential were analyzed to evaluate the storage stability.

### Mobilization of Span 60 in the NVs

The mobilization of Span 60 in the vesicles was quantified by NMR. The nanodispersions were threefold diluted with deuterium oxide. The aliquots were placed in an NMR tube. <sup>2</sup>H-NMR spectra were recorded by an Avance 400 spectrometer (Bruker, MA, USA). The line width at half amplitude (Hz) of the methyl group of Span signal was measured as the indicator of mobilization in NVs.

### Morphology of the NVs

The NV morphology was visualized by transmission electron microscopy (TEM). A drop of the nanodispersions was positioned on a carbon-coated grid. The excess dispersion was withdrawn by filter paper. The sample was dried and stained using 2% phosphotungstic acid. The prepared sample was observed under a JEOL JEM-1200Ex microscope.

### Differential scanning calorimetry

Differential scanning calorimetry (DSC) analysis was carried out using a Q2000 calorimeter (TA Instruments, DE, USA), and an empty standard aluminum pan was used as reference. The NVs were lyophilized to obtain a powder form before the determination. The heating curve was recorded from 0°C to 90°C at a scan rate of 10°C/min under nitrogen. Span 60 was used as the bulk material. Data were evaluated from the peak areas using the Q2000 software.

### Polarity of the NVs

The polarity (molecular environment) of the nanovesicles was detected by fluorescence spectrophotometry (F2500, Hitachi, Tokyo, Japan) based on the solvatochromism of Nile red (1 ppm) in the nanosystems. The emission fluorescence spectra of the Nile red loaded NVs were scanned from 550 to 700 nm. The excitation wavelength was set to 546 nm.

### Silibinin entrapment percentage

The nanosystems were centrifuged at  $48,000 \times g$  and  $4^\circ\text{C}$  for 30 min. The supernatant was withdrawn and filtered with polyvinylidene fluoride membrane with a pore diameter of  $0.45 \mu\text{m}$ . The precipitate was dissolved by Triton X-100 to solubilize the vesicles. Both the supernatant and precipitate were analyzed by HPLC. The HPLC setup was the same as in our previous work [20]. In brief, a 25 cm long, 4 mm inner diameter C18 column (Merck) was used in a Hitachi HPLC system. The mobile phase was acetonitrile and pH 4.7 water adjusted by phosphoric acid (40:60) at a flow rate of 1 ml/min. The wavelength of the ultraviolet detector was set at 288 nm.

### Silibinin release from the NVs

The Franz diffusion cell was used to assess silibinin release from NVs. The cellulose membrane with an MW cutoff of 6000–8000 g/mol was mounted between the donor and receptor. The donor medium consisted of 0.5 ml of NVs with silibinin (0.1%). The receptor medium consisted of 5.5 ml of 30% ethanol/pH 7.4 buffer. The available region for silibinin release was  $0.785 \text{ cm}^2$ . The stirring rate and temperature of the receptor were maintained at 600 rpm and  $37^\circ\text{C}$ , respectively. At determined time points, the receptor medium (0.3 ml) was taken and immediately replaced with fresh medium. The released percentage of silibinin was calculated after HPLC analysis.

### Animals

All animal studies were approved by the Institutional Animal Care and Use Committee of Chang Gung University. Male Sprague–Dawley rats (9 weeks old) were employed to investigate the *ex vivo* and *in vivo* biodistribution of NVs by optical imaging and silibinin accumulation.

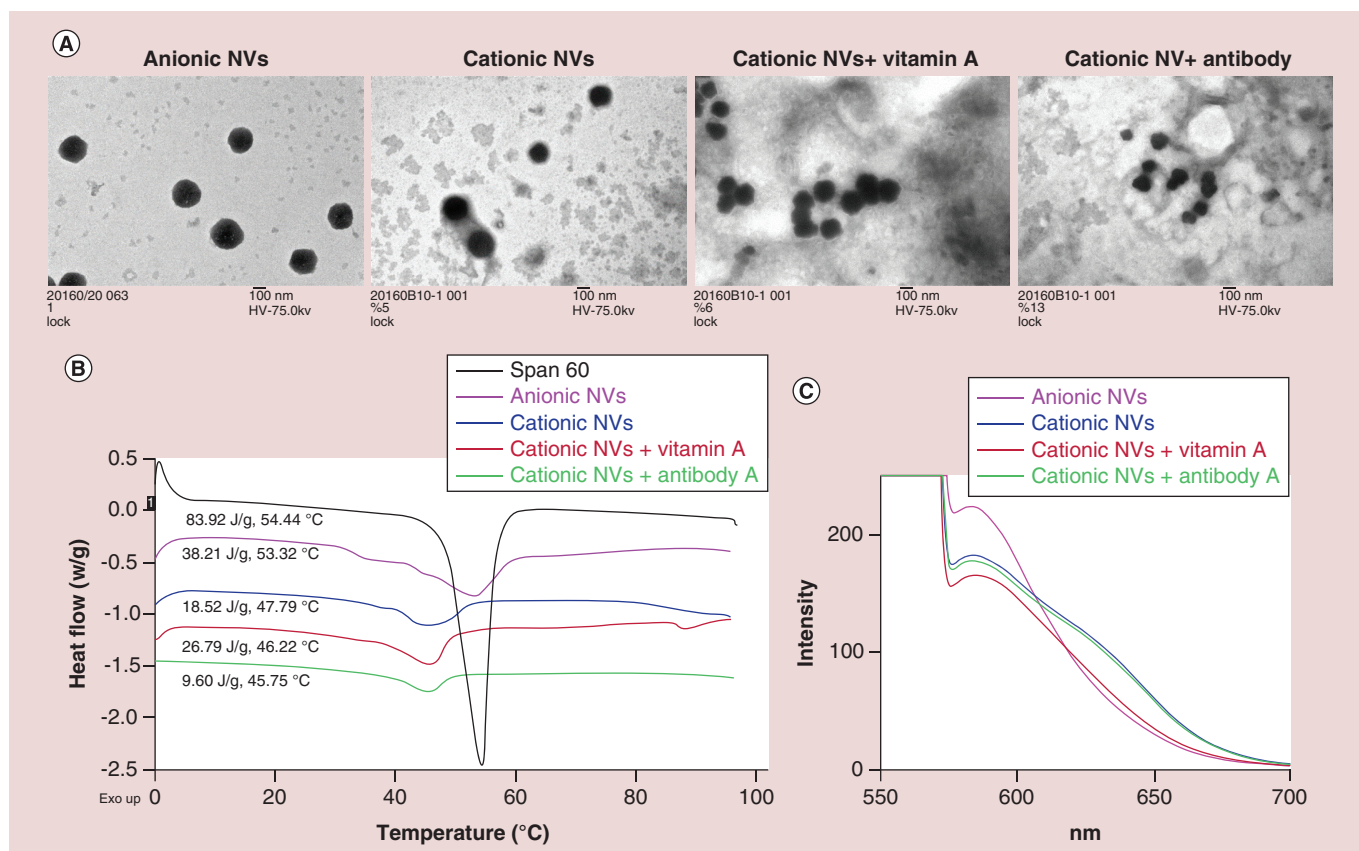


**Figure 1. Comparison of physicochemical properties of various nanovesicles: (A) Transmission electron microscopy images of NVs (magnification: 100,000 $\times$ ), (B) differential scanning calorimetry profiles of the melting process of bulk Span 60 and NVs after freeze-drying and (C) fluorescence emission profiles of Nile red in NVs.**  
NV: Nanovesicle.

Ex vivo & in vivo bioimaging

The liver-targeting ability and biodistribution of NVs were assessed by *ex vivo* and *in vivo* bioimaging. To monitor the *ex vivo* distribution, an NIR dye, iFluor 790 acid, was doped into NVs at a concentration of 0.08% (w/v). The free control solution was the NIR dye in DMSO/Tween 80/normal saline (2:1:2). The rats were divided randomly into five groups with six animals in each. Group 1 received intravenous free iFluor 790 via the femoral vein at a dose of 0.64 mg/kg. Groups 2–5 received the same dose in the form of anionic NVs, cationic NVs, cationic NVs with vitamin A and cationic NVs with anti-PDGF antibody. The rats were anesthetized with Zoletil® 50 (tiletamine and zolazepam at a dose of 30 mg/kg of each, Virbac, Carros, France). The anesthetized status was maintained by isoflurane/oxygen. The rats were sacrificed by CO<sub>2</sub> gas at 2- and 5-h postadministration. The organs, including the brain, heart, lungs, spleen, liver, gastrointestinal (GI) tract and kidneys, were excised and washed with normal saline. The NIR signal in the organs was observed using Pearl® Impulse (Li-Cor, NE, USA).

In order to obtain a clear visualization of the vascular structures, DiR was used as the NIR dye to detect the real-time imaging (Pearl Impulse). DiR was approved as an angiography contrast agent for observing clear vascular structures [21]. The animals were divided into groups the same as for *ex vivo* organ imaging. The real-time image of rat circulation was monitored during a 5-h period after intravenous injection.

Silibinin biodistribution

The rats received an intravenous injection of the control solution or NVs via the femoral vein at a silibinin dose of 0.8 mg/kg. The blood was withdrawn from the tail vein 5-h postinjection. Subsequently, the animals were sacrificed, and the organs were harvested and weighed. The organs were suspended in methanol for homogenization by MagNA Lyser (Roche, IN, USA). The homogenates

were centrifuged at 10,000xg for 10 min. The silibinin amount in supernatant was quantified by HPLC.

Statistical analysis

The statistical difference between the experimental groups was determined using the unpaired *t*-test and ANOVA test. The *post hoc* Newman–Keuls test was used to check the individual differences between the groups. The *p*-value < 0.05 was considered significant. All data were expressed as mean ± SD.

Results

Physicochemical properties of the NVs

We had designed NVs to prepare uniform and stable nano-sized carriers to examine liver targeting and biodistribution. Two regular nanosystems were prepared: anionic and cationic NVs. The positive surface charge of cationic nanocarriers can help to enhance interaction with the cell membrane and then facilitate cellular internalization. We further developed cationic NVs made up of vitamin A and antibody capable of targeting HSCs in order to treat hepatic fibrosis. As seen in Table 1, the anionic NVs showed a narrow size distribution with an average diameter of 211 nm, exhibiting a negative ζ potential. SME incorporation (cationic NVs) rendered to a positive ζ potential and a smaller size of 121 nm. The size and polydispersity index were slightly but significantly increased (*p* < 0.05) by vitamin A incorporation with a veil of surface charge. The size and ζ potential remained unchanged with antibody loading (*p* > 0.05). The mobility of Span 60 in the NVs was detected by proton NMR. The neat Span 60 showed the NMR line width of 3.47 Hz. The width was increased as Span 60 embedded into the NVs as shown in Table 1, indicating a restricted mobility in the NV structure. The immobility or interaction of Span 60 in plain cationic NVs was higher than that of anionic NVs. This may have demonstrated a loosening structure of anionic NVs, resulting in the

Table 1. The characterization of nanovesicles by vesicle size, polydispersity index, ζ potential, mobilization and silibinin encapsulation efficiency.

Formulation	Size (nm)	PDI	ζ potential (mV)	Immobilization (line width at half-amplitude, Hz)	Silibinin encapsulation (%)
Anionic NVs	211.2 ± 3.0	0.19 ± 0.08	-34.1 ± 1.7	4.43	99.87 ± 0.06
Cationic NVs	120.5 ± 1.3	0.27 ± 0.02	48.5 ± 0.6	5.36	98.44 ± 0.01
Cationic NVs + vitamin A	136.9 ± 6.2	0.32 ± 0.01	40.3 ± 3.3	5.84	99.89 ± 0.02
Cationic NVs + antibody	120.9 ± 2.9	0.25 ± 0.01	45.1 ± 1.8	4.72	97.92 ± 0.05

Each value represents the mean ± SD (n = 3).  
NV: Nanovesicle; PDI: Polydispersity index.

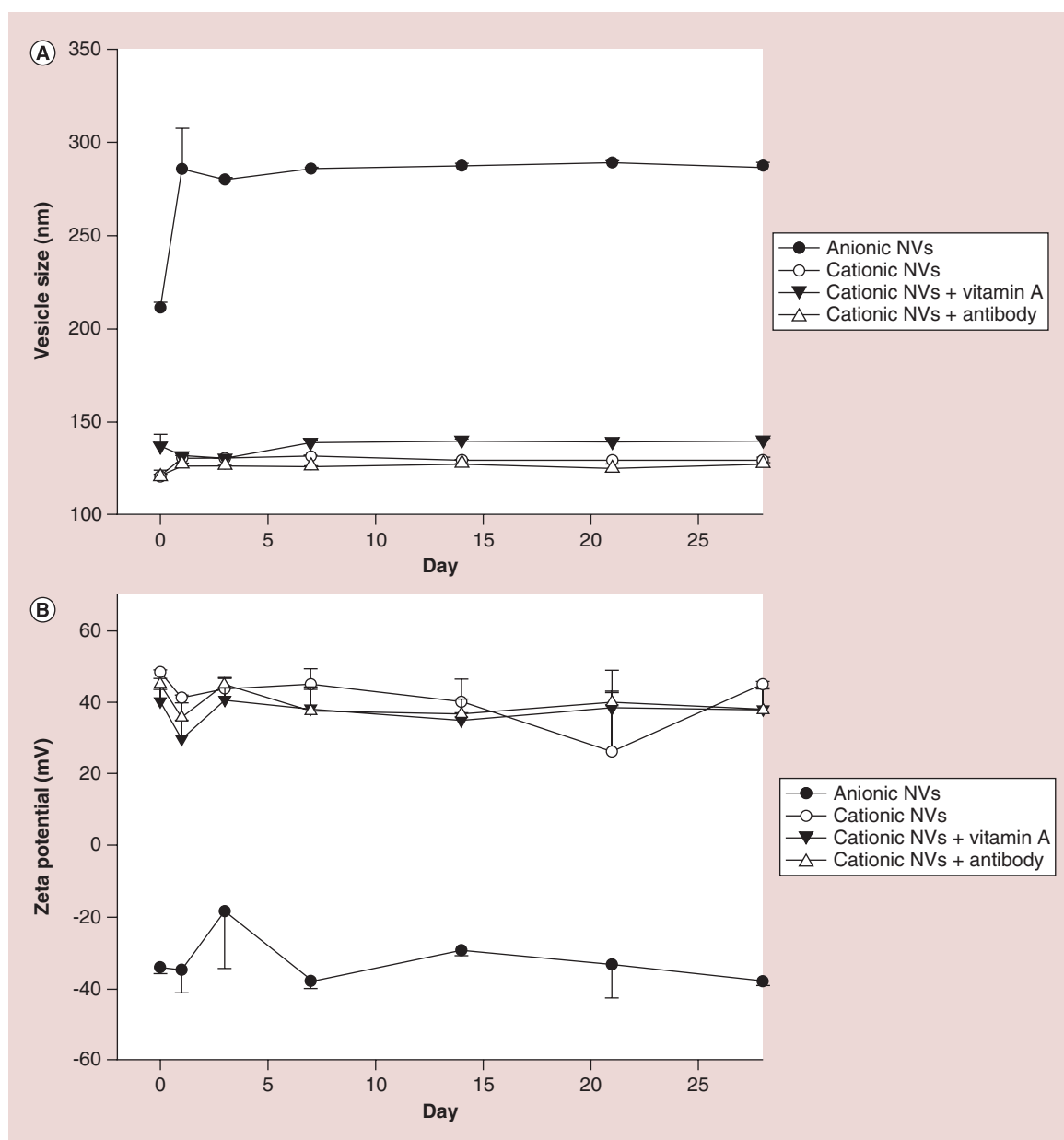


**Figure 2. The storage stability of nanovesicles determined by (A) vesicle size and (B)  $\zeta$  potential at 40°C and 75% relative humidity for 28 days.** Each value represents the mean  $\pm$  SD ( $n = 4$ ).

NV: Nanovesicle.

larger vesicle size ( $p < 0.05$ ) and a greater tendency for aggregation compared with cationic NVs. The vitamin A loaded NVs revealed the highest width, suggesting a stronger interaction with the vesicles after vitamin A inclusion. A contrary result was observed for antibody-loaded NVs. Silibinin is a lipophilic compound. The encapsulation of silibinin into the bilayers of NVs resulted in an entrapment percentage of  $>97\%$  for all formulations (Table 1).

The geometries of NVs were analyzed using TEM. The vesicle morphology was spherical or nearly spherical with a smooth surface as illustrated in Figure 1A.

The anionic NVs were well dispersed with a mean size of 230 nm, approximating the results of hydrodynamic size. A size reduction was observed by adding SME into the NVs, with the antibody NVs having the smallest size. This result was somewhat different from the result of laser scattering. The vesicle diameter of plain cationic NVs observed in TEM was larger than that measured by laser scattering. It could be the artificial preparation process for TEM visualization. TEM was imaged in the condition of dry environment, whereas the niosomes were dispersed in water for determining the size by dynamic light scattering.

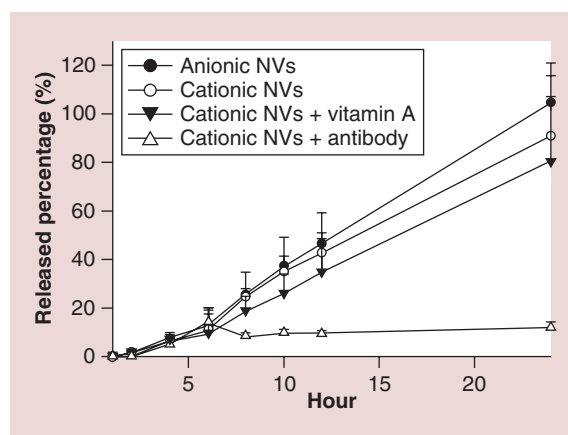


**Figure 3.** *In vitro* released percentage (%) of silibinin across a cellulose membrane from the free control solution and nanovesicles during 24 h. Each value represents the mean  $\pm$  SD ( $n = 4$ ). NV: Nanovesicle.

The crystalline states of NVs were assessed using DSC. As shown in **Figure 1B**, neat Span 60 had an endothermic peak at 54.4°C. Span 60 in NVs contributed to the left shift of the endothermic melting peak and reduction of enthalpy. The regular cationic NVs showed a greater shift (47.8°C) compared with anionic NVs (53.3°C), indicating a less-crystalline condition of cationic vesicles. The addition of ligands slightly changed the peak temperature. The Span 60 melting peak practically disappeared in the thermogram of antibody-loaded NVs, demonstrating the existence of an amorphous state.

The polarity of the nanodispersions was determined by incorporating Nile red into NVs to analyze fluorometric spectra. The fluorescence of Nile red was quenched in a hydrophilic environment. **Figure 1C** demonstrates that the addition of SME significantly quenched fluorescence. This indicated the higher hydrophilicity of cationic vesicles compared with anionic vesicles. Ligand conjugation further increased the hydrophilicity, with vitamin A loaded NVs showing the highest polarity.

### Stability of the NVs

The storage stability of the nanosystems was evaluated by determining the size and  $\zeta$  potential prior to evaluating *in vivo* biodistribution. As shown in **Figure 2A**, anionic NVs exhibited a substantial increase ( $p < 0.05$ ) in size over the first day and then remained unchanged. The vesicle diameter increased from 211 to 286 nm ( $p < 0.05$ ) after storage at 40°C for 1 day. All three cationic NVs showed no aggregation for 28 days, indicating good physical stability and adaptability for the standard of injectable pharmaceuticals. Good stability was also achieved by examining  $\zeta$  potential as depicted

in **Figure 2B**. The surface charge of all formulations remained stable for at least 28 days.

### Silibinin release from the NVs

*In vitro* silibinin release was measured to assess whether silibinin was readily released from the nanocarriers. **Figure 3** shows the release percentage at the determined times. The order of release was found to be anionic NVs > cationic NVs > vitamin A NVs > antibody NVs. Anionic NVs revealed a complete silibinin release within 24 h. The formulations, with the exception of antibody-loaded NVs, demonstrated a monophasic release pattern without burst effect which fitted zero-order fashion ( $r = 0.9955$  for anionic NVs,  $r = 0.9954$  for cationic NVs,  $r = 0.9938$  for vitamin A NVs). The release constant (slope) estimated from release-time profiles was 4.68, 4.12 and 3.54 for anionic, cationic and vitamin A formulations, respectively. This suggests a controlled and sustained silibinin release. Silibinin encapsulation by antibody-embedded NVs greatly lowered the release, with only 12% silibinin released after a 24-h incubation.

### Ex vivo bioimaging

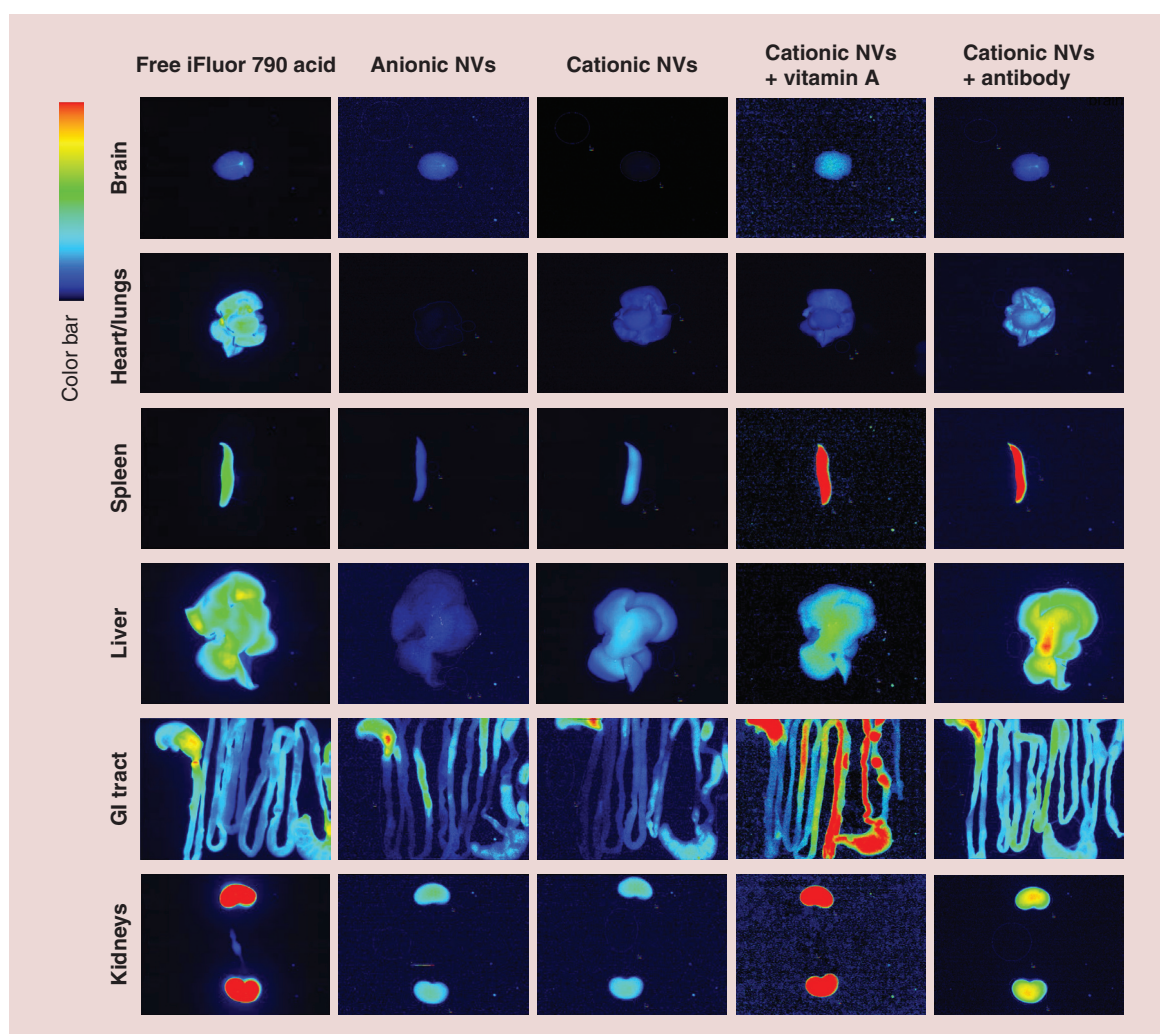
The biodistribution of niosomes was investigated after intravenous injection in rats. The NIR dye of iFluor 790 was employed as the probe entrapped in NVs to trace the nanocarriers. At 2 and 5 h, the organs were removed and visualized by *ex vivo* imaging as shown in **Figures 4 & 5**, respectively. Since the NIR intensity of the dye-stained NVs was different due to the different optical properties, the scale of bioimaging was normalized by the intensity of the formulations for impartial comparison. Note that, because of this calibration for the comparison of biodistribution, some images in **Figures 4 & 5** display a bright background. Two hours after administration, the free iFluor 790 accumulated significantly in the kidneys, reflecting the renal clearance (**Figure 4**). A moderate portion of free dye also accumulated in the heart/lungs, spleen, liver and GI tract. In contrast, there was a negligible NIR signal in the brain. Dye entrapment in anionic NVs showed a significantly reduced uptake compared with free control in the heart/lungs and kidneys after a 2-h administration. The NIR intensity in the reticuloendothelial system (RES), including the spleen and liver, was also decreased by anionic vesicle encapsulation compared with free dye. SME addition (cationic NVs) enhanced the signal in the heart/lungs and RES compared with anionic NVs with no influence on the GI tract and kidneys. The signal in the brain was absent in cationic NV-treated rats. The organs from the rats treated by NVs with ligands generally represented stronger NIR intensity than those treated by



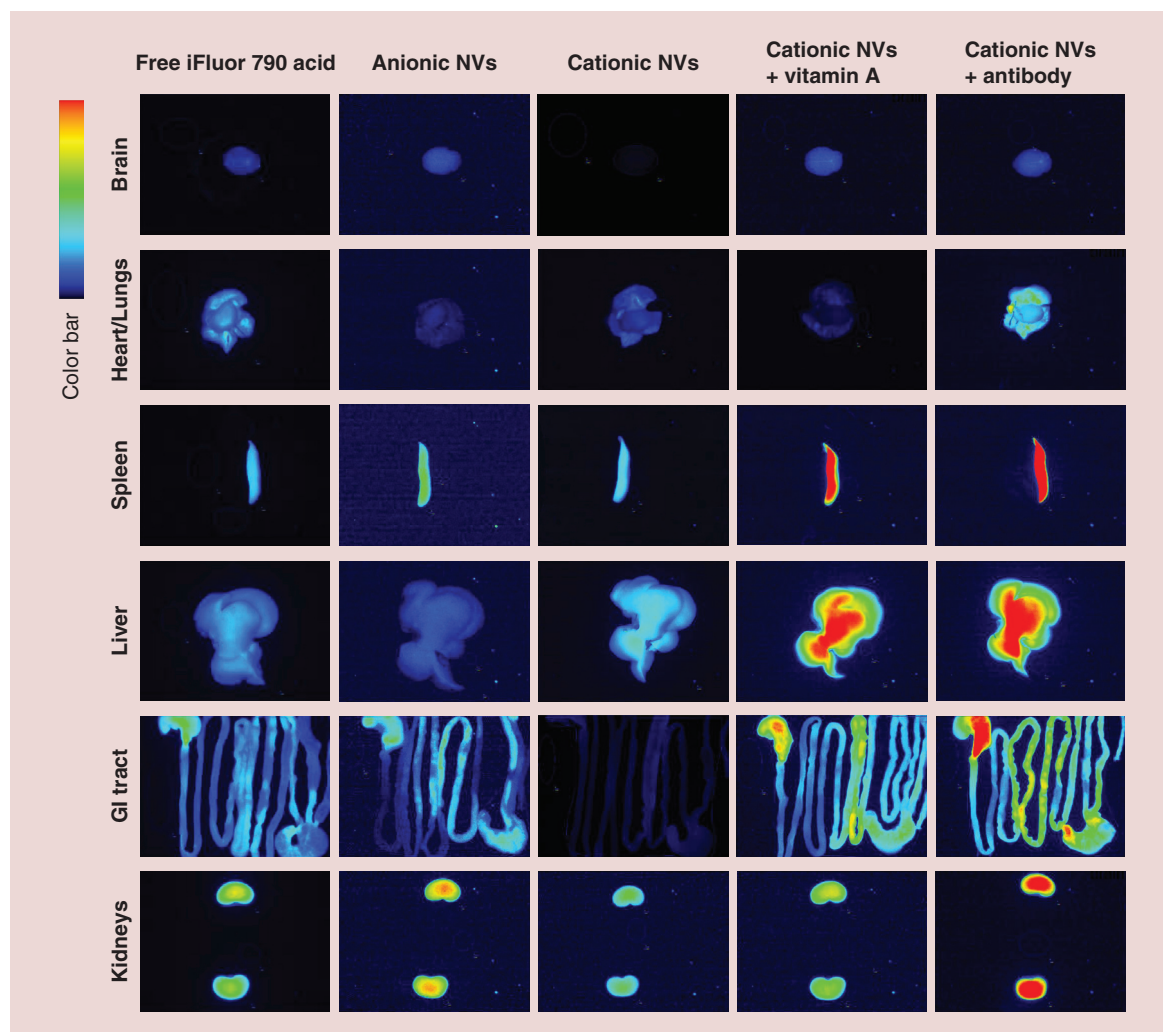
the other formulations. This suggests a stronger tendency from the circulation to the peripheral organs by adding the ligands to the niosomes. The *ex vivo* imaging revealed that vitamin A loaded vesicles preferentially accumulated in the spleen, GI and kidneys at 2-h postinjection (Figure 4). The signal was also visualized in the liver but not in the brain and heart/lungs. In the group of antibody-loaded NVs, NIR in the spleen was much higher than in the other organs, followed by the liver and kidneys. Table 2 shows the percentage of NIR signal intensity in six main organs by each nanosystem injection.

Figure 5 summarizes the *ex vivo* organ imaging at 5-h postinjection. The NIR intensity of the free dye group at 5 h was less than that at 2 h, indicating a possible metabolism or excretion of iFluor 790. A similar trend of accumulation was observed for the rats receiving

anionic NVs. A stronger signal was present in the kidneys after treatment at 5 h as compared with 2 h. There was no significant change in the NIR percentage in the brain, heart/lungs and RES of cationic NVs between the 2- and 5-h incubations (Table 2). Inspection of the organs from the NVs containing vitamin A revealed a significant uptake in the spleen and liver compared with regular cationic NVs. The NIR signal percentage of the liver treated using the vitamin A loaded nanosystem increased by threefold from 2 to 5 h (Table 2,  $p < 0.05$ ), demonstrating a relatively slow liver targeting compared with the NVs conjugated with antibody. The vitamin A loaded NVs mediated a lower level of kidney accumulation at 5 h than that at 2 h. We observed a preferential uptake of antibody-loaded NVs in the RES and kidneys. As shown in Table 2, the NIR percentage of the spleen, liver and kidneys at 5 h was



**Figure 4.** *Ex vivo* bioimaging of six main organs from representative animals at 2 h following an intravenous injection of iFluor® 790 loaded in a control solution and in nanovesicles. The scale of bioimaging was calibrated by the intensity of the formulations for impartial comparison. GI: Gastrointestinal; NV: Nanovesicle.



**Figure 5.** *Ex vivo* bioimaging of six main organs from representative animals at 5 h following an intravenous injection of iFluor® 790 loaded in a control solution and in nanovesicles. The scale of bioimaging was calibrated by the intensity of the formulations for impartial comparison. GI: Gastrointestinal; NV: Nanovesicle.

comparable ( $p < 0.05$ ) in the antibody-treated group. Contrary to the vitamin A group, antibody-loaded niosome accumulation in the kidneys was extended following the increase in time. Collectively, the hepatic targeting characteristic of ligand-containing NVs was verified here.

#### *In vivo* real-time bioimaging

The circulation residence of NVs was evaluated by noninvasive ventral imaging using DiR as the NIR probe. Figure 6 presents the DiR signal as a function of time for free DiR and niosomes administered intravenously. We detected no NIR signal in the vessels and tissues before intravenous injection. Rapid distribution of DiR throughout the body was visualized within 1 min for all formulations tested. It was found that free DiR could remain in circulation for at least 2 h.

The NIR signal became significant in the liver region after free DiR injection for 3 h (arrows in Figure 6). A strong signal was also observed by the rats treated with anionic NVs. The vessels were still visible after a 1-h administration. The signal in circulation was quickly cleared at 15 min postadministration of plain cationic NVs. The cationic niosomes significantly entered the liver area (arrows in Figure 6). Incorporation of vitamin A could prolong vesicle retention in the circulatory system. However, this extension did not surpass the level of free DiR and anionic nanocarriers.

#### Silibinin biodistribution

Figure 7 depicts the silibinin concentration in the organs at 5 h after intravenous injection of free and NV-encapsulated silibinin. The amount of silibinin in the blood, brain, heart and kidneys was under the

**Table 2.** The percentage of near-IR signal in different organs of rats by intravenous injection of nanovesicles containing iFluor® 790 acid.

Time (h)	Organ	Anionic NVs	Cationic NVs	Cationic NVs + vitamin A	Cationic NVs + antibody
2	Brain	14.55 ± 3.16	3.96 ± 1.26	6.08 ± 0.42	3.75 ± 0.18
	Heart/lungs	2.52 ± 1.16	12.37 ± 2.29	3.59 ± 0.41	10.98 ± 0.96
	Spleen	18.55 ± 1.61	20.52 ± 7.66	29.32 ± 1.81	29.72 ± 1.17
	Liver	8.79 ± 3.29	18.66 ± 2.70	9.67 ± 1.04	20.99 ± 1.08
	GI tract	22.39 ± 1.97	23.28 ± 6.85	11.10 ± 1.29	12.47 ± 1.42
	Kidneys	33.20 ± 4.56	21.21 ± 9.63	40.24 ± 0.91	22.09 ± 0.21
5	Brain	18.42 ± 19.5	2.91 ± 0.58	6.90 ± 0.52	3.20 ± 0.67
	Heart/lungs	2.38 ± 0.43	9.76 ± 1.80	3.11 ± 0.26	8.44 ± 0.85
	Spleen	19.06 ± 4.19	25.88 ± 7.55	32.97 ± 5.29	28.00 ± 6.63
	Liver	6.97 ± 0.30	17.62 ± 2.09	32.33 ± 8.28	24.31 ± 5.47
	GI tract	10.18 ± 3.50	9.47 ± 0.96	12.06 ± 0.76	9.62 ± 2.81
	Kidneys	42.99 ± 12.31	34.36 ± 7.86	12.64 ± 4.39	26.43 ± 2.58

Each value represents the mean ± SD (n = 6).

GI: Gastrointestinal; NV: Nanovesicle.

detection limit by HPLC analysis. Distribution of free silibinin (control) was in the following order: lungs > spleen > liver. The hepatic silibinin concentration was 3.5 ng/mg. A similar trend was detected for anionic NVs, with no significant difference ( $p > 0.05$ ) in the silibinin amount compared with the free control. The exposure in the liver following cationic NV administration was fourfold greater ( $p < 0.05$ ) than that for the control solution. The NVs with vitamin A and anti-PDGF receptor antibody further ameliorated the silibinin concentration in the liver to seven- and six-times higher than that in the control. However, no significant difference ( $p > 0.05$ ) was calculated between the hepatic uptake of plain and antibody niosomes. The silibinin concentration in the spleen for the NVs containing active ligands was about twofold higher ( $p < 0.05$ ) than that of plain cationic NVs, suggesting a greater uptake into the RES. A substantial silibinin delivery to the lungs was detected in the case of antibody-decorated NVs. This result coincided with the *ex vivo* bioimaging. Contrary to this result, the vitamin A loaded niosomes showed the least silibinin exposure in the lungs.

## Discussion

The exploration of therapeutic strategies by nanoparticle targeting has been an active research field over the past two decades. The drug uptake in targeted or nontargeted organs differs depending on the targeting ligands and physicochemical properties of the nanoparticles and their interaction with the living system [22]. Seeing how the biodistribution is affected

by the nanocarriers can be beneficial when trying to design nanoparticulate drug delivery systems. In this study, we fabricated NVs that differed in the surface charge and ligands in order to compare the targeting capability and biofate after intravenous application. Span 60 was the main ingredient to form NVs in the present work due to its ability to support a stable nano-system [23]. Phosphatidylcholine was also added in NVs to promote the interfacial rigidity and biocompatibility [24]. SME was the cationic surfactant offering a positive charge on the vesicle surface. SME is less toxic than stearylamine and cetyltrimethylammonium bromide, which are commonly used in preparing cationic nanoparticles [25]. It was demonstrated that the NVs developed in this study were promising drug delivery platforms with a relatively uniform size, complete encapsulation efficiency and physical stability.

The mobility of the materials in nanoparticles is related to the line width at half-amplitude of the signals in NMR. Narrow signals and large amplitudes are characteristics of molecules with less-restricted mobility and weak interaction [26,27]. It was found that the NMR line width of Span 60 in anionic NVs was smaller than that of the NVs with a positive charge. This result was confirmed by DSC profiles since Span 60 maintained the melting temperature after loading into anionic NVs, showing less interaction of Span 60 in NVs. The melting peak reduction in DSC means bilayer disruption of NVs. This can lead to NV structure deformability [28]. The DSC analysis indicated the deformable and less-crystalline characters of positively charged NVs, especially the antibody-embedded for-



mulations. A  $\zeta$  potential of  $>|30|$  mV is considered sufficient to show a storage stability of niosomes because of the electrical repulsion [29]. Although the anionic NVs fulfilled this criterion, the vesicle was fused within 1 day after preparation. Since the  $\zeta$  potential of anionic NVs remained constant during storage, the lack of steric stabilization could have been the reason for the size instability. The incorporation of SME and ligands could have prevented the aggregation, demonstrating the possibility of steric repulsion by these additives. Another explanation is the lower absolute value of  $\zeta$  potential of anionic NVs (34 mV) than all cationic NVs (40–49 mV). The less electrical repulsion between the anionic NVs than cationic ones may contribute to the aggregation.

As the nanocarriers extravasate into the target tissue, the pharmacological response is exerted either by extracellular drug release or by intracellular drug release after cellular endocytosis. The fluidity and hydrophilicity of niosomes are recognized as the critical factors predominating drug release, with the greater fluidity and hydrophilicity showing a faster drug release [30]. This was not the case in our study since the flexible and hydrophilic antibody-loaded NVs exhibited the least release. The antibody intercalation on the vesicle shell may have downgraded the bilayer permeability, hindering silibinin diffusion across the bilayers. Our inference is that the antibody with large molecular size may form an extra steric barrier on NV shell for retarding drug release. The other NVs showed a zero-order release kinetic. The sustained release is advantageous in controlling the rate of metabolism *in vivo* [31]. Although the antibody-loaded NVs displayed a retarded *in vitro* silibinin release, it is important to note that the vesicles may release the active in the interstitial enzyme-rich environment or in the lysosomal compartments after cellular uptake.

In the *in vivo* biodistribution experiment, NVs containing active ligands revealed a liver-targeting capability relative to nontargeted NVs when the NIR signal was normalized by the signal intensity of the prepared formulations. The NIR signal percentage in the organs indicated that the nanocarriers were primarily taken up by RES, followed by the kidneys and the GI tract. The use of polyethylene glycol (PEG) in the nanoparticles can help to prohibit protein binding and RES uptake [32]. Our previous study [24] suggested that intravenous PEGylated niosomes could passively target the lungs. The stealth nanocarriers were excluded in the present study since the liver was the main delivery site of NVs. PEG moieties also hindered the nanoparticle interaction with the target cells, leading to decreased bioactivity. Following systemic administration, the nanoparticles without stealth property were

easily opsonized by plasma proteins and captured by resident macrophages in RES [33]. The liver sinusoids had fenestration of 100–150 nm [34]. All cationic formulations were expected to enter into the fenestration. The anionic NVs with a size of 211 nm exemplified a limited uptake in RES because of the large vesicle dimension. The deformability of NVs demonstrated a great impact on extravasating through the sinusoid endothelial fenestration [35]. The ligand-loaded NVs were more flexible than plain NVs according to the data of NMR and DSC. It was evident that the ligand-loaded NVs entered RES with ease compared with the regular NVs, although the vitamin A embedded NVs displayed a slower liver targeting than the antibody-embedded NVs.

The prime target cells for vitamin A- and anti-PDGF receptor antibody-embedded NVs are HSCs. These cells constitute only 15% of the total resident cells in hepatic tissue [36]. The organ imaging manifested a broad NIR signal throughout the whole liver after administration of active ligand nanocarriers. This implied that not only HSCs but also the other cells in the liver are involved in the vesicle delivery. These may include Kupffer cells, endothelial cells and hepatocytes. Kupffer cells or macrophages are predominantly responsible for the uptake of most of the xenobiotic nanoparticles in the liver [37]. The macrophage uptake can be more apparent in the fibrotic liver, owing to the abundant macrophage accumulation and abnormal neovascular structure in the diseased liver. Sato *et al.* [7] also suggested a nonspecific engulfment of vitamin A-coupled liposomes into hepatic macrophages. In addition, vitamin A is taken up by hepatocytes [38]. Beljaars *et al.* [39] demonstrated that PDGF receptor-recognizing albumin can be localized in both hepatocytes and nonparenchymal cells in the liver.

Although the target site of the NVs was the liver, the proportion of the total organ distribution of the ligand-loaded vesicles in the spleen still exceeded or was comparable to the proportion in the liver. The nonionic surfactant vesicles were confirmed to be efficiently taken by the spleen [24,40]. Many immune cells reside in the spleen, including macrophages, lymphocytes and dendritic cells, and these were responsive to mediating NV uptake. A prolonged circulation permits greater exposure to the phagocytic cells in the spleen [41]. The real-time imaging showed a longer retention of vitamin A NVs in the vessels compared with plain cationic NVs. The hydrophilic nature of NVs is responsible for the longevity in the circulation [42,43]. The addition of ligands increased the NV hydrophilicity based on Nile red solvatochromism. This could contribute to a significant distribution in the spleen. Previous studies [10,44] suggest the vital role of nanoparticulate deformability

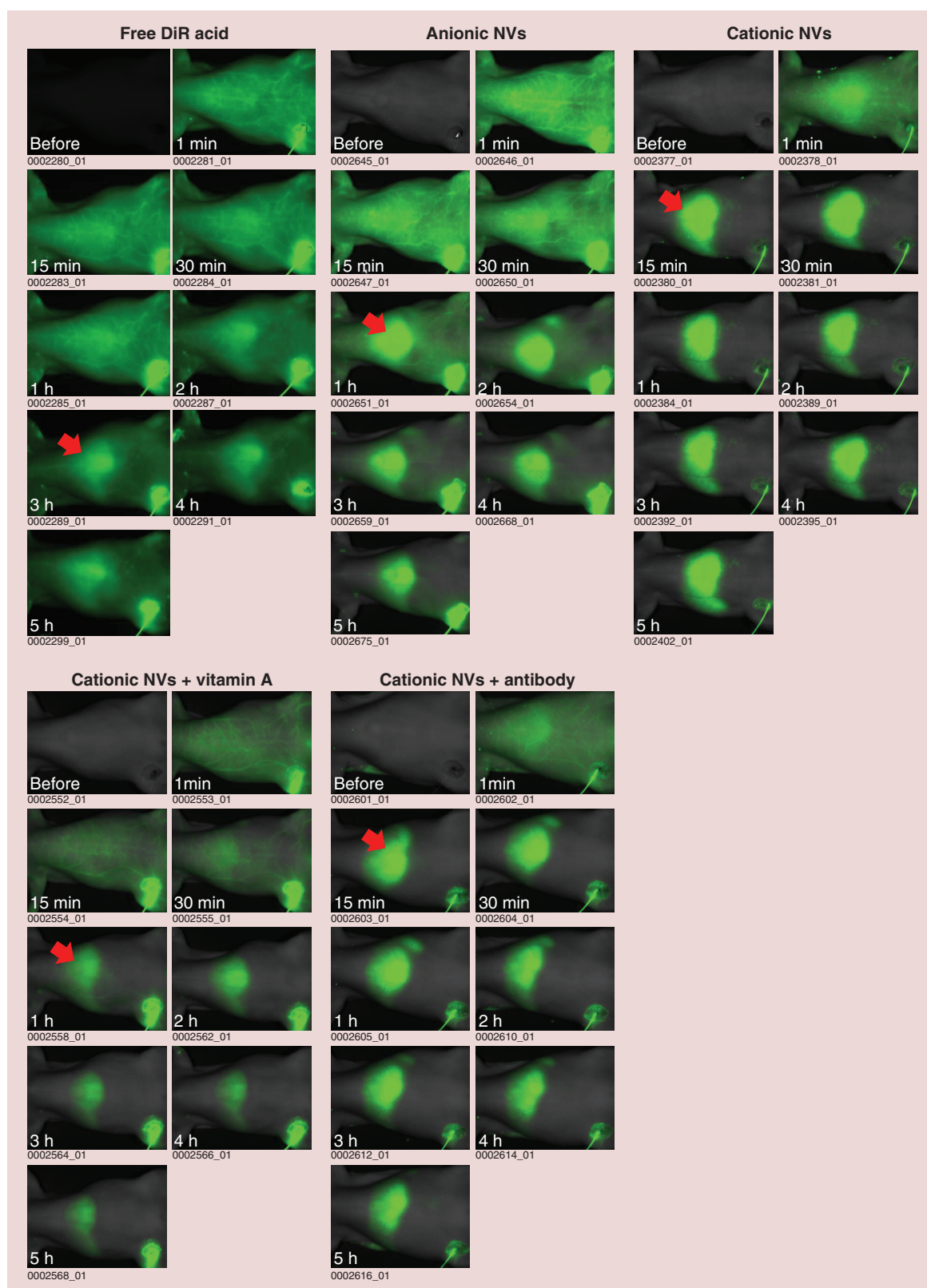


**Figure 6.** *In vivo* real-time bioimaging of representative animals at different time points from 0 to 5 h following an intravenous injection of 1,1'-diiodo-3,3',3',3'-tetramethyl indotricarbocyanine iodide loaded in a control solution and in nanovesicles.

DiR: 1,1'-diiodo-3,3',3',3'-tetramethyl indotricarbocyanine iodide; NV: Nanovesicle.



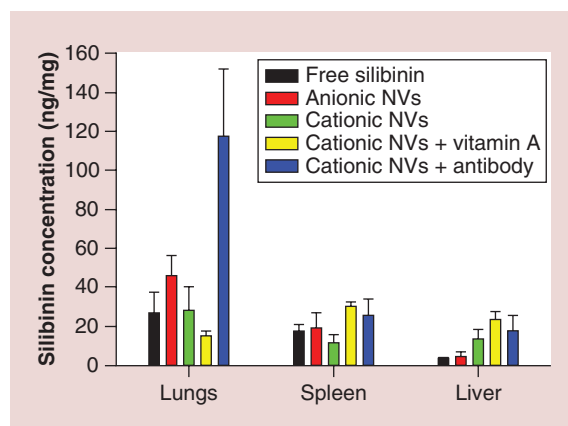


**Figure 7. In vivo biodistribution of silibinin in lungs, spleen and liver after intravenous injection of silibinin (0.8 mg/kg) in control solution and nanovesicles.** Each value represents the mean  $\pm$  SD ( $n = 6$ ). NV: Nanovesicle.

on an extended circulation duration. The present work confirmed this inference. The anionic NVs caused a longer circulation period compared with the cationic formulations. This could explain the lower NIR intensity in peripheral organs treated by anionic NVs rather than cationic nanocarriers as observed in the *ex vivo* optical imaging, though the spleen accumulation of the anionic vesicles was also low. The NIR signal in the vessels disappeared within 1 h for all intravenous NVs. The short duration in circulation could be attributed to the lack of stealth effect.

The NVs with antibody exhibited a 10% accumulation in the heart/lungs. Previous study [39] indicated that the peptide-modified albumin having the ability to bind to the PDGF receptor can accumulate in the cardiac region. It is an important concept that the active ligands on the nanoparticulate surface can bind to the cells in the nontargeted organs apart from the cells in the target organs. We cannot expect a thorough delivery of the active-targeting nanocarriers to the target nidus and a minimized distribution in the other organs or tissues. For example, the upregulation of PDGF receptors was detected in the mesangial cells and interstitial fibroblasts in the kidneys in addition to the HSCs in the liver [39,45]. The receptors for retinol binding protein were abundant in the liver, spleen, intestine and kidneys [46,47]. A remarkable accumulation of vesicles in these organs for the active targeted NVs was seen. vitamin A embedded NVs showed a significant uptake in the spleen, GI tract, and kidneys after a 2-h administration. Antibody-embedded NVs represented a different biodistribution behavior, with an increased NIR intensity in the kidneys from 2 to 5 h. The accumulation of ligand-containing NVs in the kidneys was unlikely to be related to the urine excretion since only the nanoparticles of  $<5$  nm can be filtered

by the glomerular capillary membrane [48]. Besides the binding to specific receptors of the cells, the NIR probe in the NVs may have been released from the nanocarriers as the vesicles started to dissolve in the body and subsequently accumulated in the kidneys. The effortless delivery of free dye into the kidneys was proved in the *ex vivo* imaging.

The liver is a major route for both metabolism and excretion of nanoparticles [22]. The excretion mainly occurs through the biliary clearance. In rats, the bile passes directly from the liver to the GI system because rats have no gall bladder. Based on the apparent and nonhomogeneous NIR signal in the gut, the NVs containing ligands were excreted by the bile. The nonhomogeneous distribution in the GI tract is attributed to the intermittent secretion of bile into the intestine [31]. The percentage of free iFluor in the brain achieved approximately 15% of the total organ distribution. This demonstrated the small molecules' ease of penetrating across the blood–brain barrier. Almost no NIR signal was discovered in the brain after the administration of the plain cationic NVs. Ligand incorporation increased the brain distribution although this increment was small. The NVs with ligands possessed a softer characteristic compared with the regular NVs. They could be deformable enough to extrude and diffuse across the blood–brain barrier and bypass the interendothelial cell slits [49,50].

The silibinin biodistribution profiles were basically consistent with the results of bioimaging. Silibinin entrapment into ligand-loaded NVs largely increased the opportunity of the RES entrance. The antibody-loaded NVs did not further improve the hepatic silibinin delivery as compared with the plain NVs. This result was quite different from the *ex vivo* bioimaging. The photonic imaging reflected the distribution of NIR dye but not the drug. Moreover, the drug encapsulation procedure may highly influence the physicochemical properties of the nanoparticles and change the *in vivo* biodistribution. It is supposed that the same nanoparticle platforms for encapsulating different drugs or diagnostics can result in the diverse distribution in the body. Caution should be taken when designing the nanoparticulate formulations for a specific drug by directly employing the dosage forms for other drugs.

## Conclusion

We developed the cationic niosomes conjugating vitamin A or anti-PDGF antibody, which were suitable for targeting to HSCs in the liver. Niosome entrapment would offer parenteral administration of silibinin, enhancing the liver delivery and reducing the adverse effects for treating hepatic fibrosis. The biodistribu-

tion study demonstrated that the ligand-loaded NVs were preferentially accumulated in the liver. The broad signal of NIR dye in the liver had suggested that the vesicles not only resided in HSCs but also possibly in the other cells, such as Kupffer cells, endothelial cells and hepatocytes. vitamin A loaded NVs also delivered to the spleen, GI tract and kidneys as well as to the liver. A significant uptake of antibody-loaded NVs was observed in the spleen, kidneys and lungs. The NV distribution in these organs could result from the phagocyte uptake and the binding to the target receptors existing in the cells of nontargeted organs. The biodistribution of the NVs was greatly influenced by the physicochemical characteristics, such as size, surface charge, flexibility and polarity. The prolonged circulation residence of the vesicles might lead to less vesicle accumulation to the peripheral organs according to *ex vivo* bioimaging and real-time monitoring. The biodistribution behavior of silibinin in the NVs was somewhat different from that in the dye-loaded NVs. This indicates that the loading drugs or diagnostics could affect the biodistribution of the nanocarriers. It is concluded that in addition to the target

organs, the delivery capability of the nanosystems containing the active targeting ligands to the other organs cannot be ignored. For instance, the toxicity associated with the nanoparticles in the healthy organs should be considered.

### Financial & competing interests disclosure

The authors are grateful to the financial support by Chang Gung Memorial Hospital (BMRP428 and CMRPD1F0331-3). The authors have no other relevant affiliations or financial involvement with any organization or entity with a financial interest in or financial conflict with the subject matter or materials discussed in the manuscript apart from those disclosed.

No writing assistance was utilized in the production of this manuscript.

### Ethical conduct of research

The authors state that they have obtained appropriate institutional review board approval or have followed the principles outlined in the Declaration of Helsinki for all human or animal experimental investigations. In addition, for investigations involving human subjects, informed consent has been obtained from the participants involved.

### Executive summary

- This study endeavored to develop nanovesicles (NVs) that can target to hepatic stellate cells via retinol binding protein and platelet-derived growth factor receptors.
- The biodistribution was examined in a rat model by intravenous administration.
- A significant liver accumulation was detected for antibody-embedded NVs as early as 2 h after dosing, whereas the targeting efficiency for vitamin A embedded NVs was delayed (5 h).
- Reticuloendothelial system, intestine and kidneys are the nontargeted organs where the vitamin A loaded niosomes largely accumulated, whereas the antibody-loaded NVs could significantly deliver to reticuloendothelial system, kidneys and lungs.

### References

Papers of special note have been highlighted as: • of interest; •• of considerable interest

- 1 Lundy DJ, Chen KH, Toh EKW, Hsieh PCH. Distribution of systemically administered nanoparticles reveals a size-dependent effect immediately following cardiac ischaemia-reperfusion injury. *Sci. Rep.* 6, 25613 (2016).
- 2 Noble GT, Stefanick JF, Ashley JD, Kiziltepe T, Bilgic B. Ligand-targeted liposome design: challenges and fundamental considerations. *Trends Biotechnol.* 32, 32–45 (2014).
- Introduces the nanovesicle design with active target ligands.
- 3 Taymouri S, Taheri A. Use of nanotechnology in diagnosis and treatment of hepatic fibrosis: a review. *Curr. Drug Deliv.* 13, 662–672 (2016).
- Introduces the application of nanoparticles for liver fibrosis treatment.
- 4 Poelstra K. Liver fibrosis in 2015: crucial steps towards an effective treatment. *Nat. Rev. Gastroenterol. Hepatol.* 13, 67–68 (2016).
- 5 Kitano M, Bloomston PM. Hepatic stellate cells and microRNAs in pathogenesis of liver fibrosis. *J. Clin. Med.* 5, 38 (2016).
- 6 Li L, Wang H, Ong ZY *et al.* Polymer- and lipid-based nanoparticle therapeutics for the treatment of liver diseases. *Nano Today* 5, 296–312 (2010).
- 7 Sato Y, Murase K, Kato J *et al.* Resolution of liver cirrhosis using vitamin A-coupled liposomes to deliver siRNA against a collagen-specific chaperone. *Nat. Biotechnol.* 26, 431–442 (2008).
- Previous work investigating the liver delivery of vitamin A-coupled nanovesicles.
- 8 Hagens WI, Mattos R, Greupink R *et al.* Targeting 15d-prostaglandin J<sub>2</sub> to hepatic stellate cells: two options evaluated. *Pharm. Res.* 24, 556–574 (2007).
- 9 Ernsting MJ, Murakami M, Roy A, Li SD. Factors controlling the pharmacokinetics, biodistribution and intratumoral penetration of nanoparticles. *J. Control. Release* 172, 782–794 (2013).
- 10 Phillips MA, Gran ML, Peppas NA. Targeted nanodelivery of drugs and diagnostics. *Nano Today* 5, 143–159 (2010).

- 11 Drummond DC, Noble CO, Hayes ME, Park JW, Kirpotin DB. Pharmacokinetics and *in vivo* drug release rates in liposomal nanocarrier development. *J. Pharm. Sci.* 97, 4696–4740 (2008).
- 12 Mane V, Muro S. Biodistribution and endocytosis of ICAM-1-targeting antibodies versus nanocarriers in the gastrointestinal tract in mice. *Int. J. Nanomed.* 7, 4223–4237 (2012).
- 13 David S, Passirani C, Carmoy N *et al.* DNA nanocarriers for systemic administration: characterization and *in vivo* bioimaging in healthy mice. *Mol. Ther. Nucleic Acids* 2, e64 (2013).
- 14 Papademetriou IT, Garnacho C, Schuchman EH, Muro S. *In vivo* performance of polymer nanocarriers dually-targeted to epitopes of the same or different receptors. *Biomaterials* 34, 3459–3466 (2013).
- 15 Rohilla R, Garg T, Goyal AK, Rath G. Herbal and polymeric approaches for liver-targeting drug delivery: novel strategies and their significance. *Drug Deliv.* 23, 1645–1661 (2016).
- 16 Marianecci C, Di Marzio L, Rinaldi F *et al.* Niosomes from 80s to present: the state of the art. *Adv. Colloid Interf. Sci.* 205, 187–206 (2014).
- Describes the niosome application in drug delivery.
- 17 Di Marzio L, Esposito S, Rinaldi F, Marianecci C, Carafa M. Polysorbate 20 vesicles as oral delivery system: *in vitro* characterization. *Colloids Surf. B* 104, 200–206 (2013).
- 18 Marianecci C, Rinaldi F, Di Marzio L *et al.* Interaction of pH-sensitive non-phospholipid liposomes with cellular mimetic membranes. *Biomed. Microdevices* 15, 299–309 (2013).
- 19 Vargas-Mendoza N, Madrigal-Santillán E, Morales-González Á *et al.* Hepatoprotective effect of silymarin. *World J. Hepatol.* 6, 144–149 (2014).
- 20 Chen CH, Chang CC, Shih TH, Aljuffali IA, Yeh TS, Fang JY. Self-nanoemulsifying drug delivery systems ameliorate the oral delivery of silymarin in rats with Roux-en-Y gastric bypass surgery. *Int. J. Nanomed.* 10, 2403–2416 (2015).
- 21 Pan TL, Wang PW, Hung CF, Aljuffali IA, Dai YS, Fang JY. The impact of retinol loading and surface charge on the hepatic delivery of lipid nanoparticles. *Colloids Surf. B* 141, 584–594 (2016).
- 22 Li M, Al-Jamal KT, Kostarelos K, Reineke J. Physiologically based pharmacokinetic modeling of nanoparticles. *ACS Nano* 4, 6303–6317 (2010).
- 23 Shi B, Fang C, Pei Y. Stealth PEG-PHDCA niosomes: effects of chain length of PEG and particle size on niosomes surface properties, *in vitro* drug release, phagocytic uptake, *in vivo* pharmacokinetics and antitumor activity. *J. Pharm. Sci.* 95, 1873–1887 (2006).
- 24 Fang CL, Wen CJ, Aljuffali IA, Sung CT, Huang CL, Fang JY. Passive targeting of phosphatiosomes increases rolipram delivery to the lungs for treatment of acute lung injury: an animal study. *J. Control. Release* 213, 69–78 (2015).
- 25 Hwang TL, Aljuffali IA, Lin CF, Chang YT, Fang JY. Cationic additives in nanosystems interact with human neutrophils to activate cytotoxicity and inflammatory response: lipid nanoparticles versus polymeric nanoparticles. *Int. J. Nanomed.* 10, 371–385 (2015).
- 26 Schubert MA, Harms M, Müller-Goymann CC. Structural investigations on lipid nanoparticles containing high amounts of lecithin. *Eur. J. Pharm. Sci.* 27, 226–236 (2006).
- 27 Hsu SH, Wen CJ, Al-Suwayeh SA, Chang HW, Yen TC, Fang JY. Physicochemical characterization and *in vivo* bioluminescence imaging of nanostructured lipid carriers (NLCs) for targeting the brain: apomorphine as a model drug. *Nanotechnology* 21, 405101 (2010).
- 28 Chirio D, Cavalli R, Trotta F, Carlotti ME, Trotta M. Deformable liposomes containing alkylcarbonates of  $\gamma$ -cyclodextrins for dermal applications. *J. Incl. Phenom. Macrocycl. Chem.* 57, 645–649 (2007).
- 29 Juyaprasert VB, Teeranachaideekul V, Supaperm T. Effect of charged and non-ionic membrane additives on physicochemical properties and stability of niosomes. *AAPS PharmSciTech* 9, 851–859 (2008).
- 30 Waddad AY, Abbas S, Yu F *et al.* Formulation, characterization and pharmacokinetics of morin hydrate niosomes prepared from various non-ionic surfactants. *Int. J. Pharm.* 456, 446–458 (2013).
- 31 Hsieh PW, Wen CJ, Yu HP, Aljuffali IA, Huang YH, Fang JY. Nanostructured lipid carriers containing a high percentage of a Pluronic copolymer increase the biodistribution of novel PDE4 inhibitors for the treatment of traumatic hemorrhage. *J. Biomed. Nanotechnol.* 10, 1520–1535 (2014).
- 32 Dobrovolskaia MA, Aggarwal P, Hall JB, McNeil SE. Preclinical studies to understand nanoparticle interaction with the immune system and its potential effects on nanoparticle biodistribution. *Mol. Pharm.* 5, 487–495 (2008).
- Introducing the interaction of nanoparticles with immune system and the subsequent influence on biodistribution.
- 33 Giannitrapani L, Soresi M, Bondi ML, Montalto G, Cervello M. Nanotechnology applications for the therapy of liver fibrosis. *World J. Gastroenterol.* 20, 7242–7251 (2014).
- 34 Mishra N, Yadav NP, Rai VK *et al.* Efficient hepatic delivery of drugs: novel strategies and their significance. *BioMed. Res. Int.* 2013, 382184 (2013).
- 35 Romero EL, Morilla MJ, Regts J, Koning GA, Scherphof GL. On the mechanism of hepatic transendothelial passage of large liposomes. *FEBS Lett.* 448, 193–196 (1999).
- 36 Li D, He L, Guo H, Chen H, Shan H. Targeting activated hepatic stellate cells (aHSCs) for liver fibrosis imaging. *EJNMMI Res.* 5, 71 (2015).
- 37 Shah NB, Vercellotti GM, White JG, Fegan A, Wagner CR, Bischof JC. Blood-nanoparticle interactions and *in vivo* biodistribution: impact of surface PEG and ligand properties. *Mol. Pharm.* 9, 2146–2155 (2012).
- Possible nanoparticle interaction with blood components via surface modification.
- 38 Jiménez Calvente C, Sehgal A, Popov Y *et al.* Specific hepatic delivery of procollagen  $\alpha 1(I)$  small interfering RNA in lipid-like nanoparticles resolves liver fibrosis. *Hepatology* 62, 1285–1297 (2015).
- 39 Beljaars L, Weert B, Geerts A, Meijer DKF, Poelstra K. The preferential homing of a platelet derived growth

- factor receptor-recognizing macromolecule to fibroblast-like cells in fibrotic tissue. *Biochem. Pharmacol.* 66, 1307–1317 (2003).
- 40 Ruckmani K, Sankar V, Sivakumar M. Tissue distribution, pharmacokinetics and stability studies of zidovudine delivered by niosomes and proniosomes. *J. Biomed. Nanotechnol.* 6, 43–51 (2010).
  - 41 Jia L, Zhang D, Li Z *et al.* Nanostructured lipid carriers for parenteral delivery of silybin: biodistribution and pharmacokinetic studies. *Colloids Surf. B Biointerfaces* 80, 213–218 (2010).
  - 42 Belouqui A, Solinís MA, Delgado A, Évora C, del Pozo-Rodríguez A, Rodríguez-Gascón A. Biodistribution of nanostructured lipid carriers (NLCs) after intravenous administration to rats: influence of technological factors. *Eur. J. Pharm. Biopharm.* 84, 309–314 (2013).
  - 43 Pawar S, Shevalkar G, Vavia P. Glucosamine-anchored doxorubicin-loaded targeted nano-niosomes: pharmacokinetic, toxicity and pharmacodynamic evaluation. *J. Drug Target.* 24, 730–743 (2016).
  - 44 Phillips MA, Gran ML, Peppas NA. Targeted nanodelivery of drugs and diagnostics. *Nano Today* 5, 143–159 (2010).
  - 45 Hagens WI, Mattos A, Greupink R *et al.* Targeting 15d-prostaglandin J<sub>2</sub> to hepatic stellate cells: two options evaluated. *Pharm. Res.* 24, 566–574 (2007).
  - 46 Smeland S, Bjerknes T, Malaba L, Eskild W, Norum KR, Blomhoff R. Tissue distribution of the receptor for plasma retinol-binding protein. *Biochem. J.* 305, 419–424 (1995).
  - 47 Alapatt P, Guo F, Komanetsky SM *et al.* Liver retinol transporter and receptor for serum retinol-binding protein (RBP4). *J. Biol. Chem.* 288, 1250–1265 (2013).
  - 48 Petros RA, DeSimone JM. Strategies in the design of nanoparticles for therapeutic applications. *Nat. Rev. Drug Discov.* 9, 615–627 (2010).
  - Describes the design approach of nanocarriers for drug therapy.
  - 49 Kaur IP, Bhandari R, Bhandari S, Kakkar V. Potential of solid lipid nanoparticles in brain targeting. *J. Control. Release* 127, 97–109 (2008).
  - 50 Wen CJ, Yen TC, Al-Suwayeh SA, Chang HW, Fang JY. *In vivo* real-time fluorescence visualization and brain-targeting mechanisms of lipid nanocarriers with different fatty ester:oil ratios. *Nanomedicine* 6, 1545–1559 (2011).

## Article

# Changbai Mountain Ginseng (*Panax ginseng* C.A. Mey) Extract Supplementation Improves Exercise Performance and Energy Utilization and Decreases Fatigue-Associated Parameters in Mice

Guo-Dong Ma <sup>1</sup>, Chun-Hui Chiu <sup>2,†</sup>, Yi-Ju Hsu <sup>3,†</sup>, Chien-Wen Hou <sup>4</sup>, Yi-Ming Chen <sup>3,\*</sup> and Chi-Chang Huang <sup>3,\*</sup>

<sup>1</sup> Sport Science College, Jilin Sport University, Changchun 130022, Jilin, China; magd2008@126.com

<sup>2</sup> Graduate Institute of Health Industry Technology, Research Center for Industry of Human Ecology and Research Center for Chinese Herbal Medicine, College of Human Ecology, Chang Gung University of Science and Technology, Taoyuan 33303, Taiwan; chchiu@mail.cgust.edu.tw

<sup>3</sup> Graduate Institute of Sports Science, National Taiwan Sport University, Taoyuan 33301, Taiwan; 1041302@ntsus.edu.tw

<sup>4</sup> Laboratory of Exercise Biochemistry, Department of Sports Sciences, University of Taipei, Taipei 11153, Taiwan; om65726@yahoo.com.tw

\* Correspondence: 1021302@ntsus.edu.tw (Y.-M.C.); john5523@ntsus.edu.tw or d301090007@gmail.com (C.-C.H.); Tel.: +886-3-328-3201 (ext. 2409) (Y.-M.C. & C.-C.H.)

† These authors contributed equally to this work.

Academic Editors: Anusha Chaparala, Lorne Hofseth and Woo-Sik Jeong

Received: 11 December 2016; Accepted: 3 February 2017; Published: 5 February 2017

**Abstract:** Changbai Mountain Ginseng (CMG, *Panax ginseng* C.A. Mey) is a traditional medicine commonly found in Northeast China and grows at elevations of 2000 m or higher in the Changbai Mountain Range. CMG, considered to be a “buried treasure medicine”, is priced higher than other types of ginseng. However, few studies have demonstrated the effects of CMG supplementation on exercise performance, physical fatigue, and the biochemical profile. The major compound of CMG extract was characterized by electrospray ionization tandem mass spectrometry (HPLC-ESI-MS/MS). Male ICR mice were divided into 3 groups, the vehicle, CMG-1X and CMG-5X groups ( $n = 8$  per group), and respectively administered 0, 5, or 25 mg/kg/day of CMG extract orally for four weeks. HPLC-ESI-MS/MS results showed that the major compound in CMG extract is ginsenoside Ro. CMG extract significantly increased muscle weight and relative muscle weight (%). CMG extract supplementation dose-dependently increased grip strength ( $p < 0.0001$ ) and endurance swimming time, decreased levels of serum lactate ( $p < 0.0001$ ), ammonia ( $p < 0.0001$ ), creatine kinase (CK,  $p = 0.0002$ ), and blood urea nitrogen ( $p < 0.0001$ ), and economized glucose levels ( $p < 0.0001$ ) after acute exercise challenge. The glycogen in the gastrocnemius muscle was significantly increased with CMG extract treatment. Biochemical profile results showed that creatinine and triacylglycerol significantly decreased and total protein and glucose increased with CMG treatment. This is the first report that CMG extract supplementation increases muscle mass, improves exercise performance and energy utilization, and decreases fatigue-associated parameters in vivo. The major component of CMG extract is ginsenoside Ro, which could be a potential bioactive compound for use as an ergogenic aid ingredient by the food industry.

**Keywords:** ginsenoside; Ro; exercise performance; anti-fatigue; muscle mass



## 1. Introduction

Changbai Mountain ginseng (*Panax ginseng* C.A. Mey, CMG) is a wild ginseng that grows in the Changbai Mountain Range in Jilin Province, the highest mountains (2750 m) in Northeastern China. CMG is harvested from the local forests and has been used as a traditional Chinese medicine (TCM) for more than a century. Recently, the Chinese government has developed large wild ginseng growing bases, where traditional Chinese herbs are produced, to meet the Good Agricultural Practices (GAP) standards and encourage the development of the pharmaceutical industry in Northern China [1]. In general, the two major species of ginseng are Asian (*Panax ginseng*) and American (*Panax quinquefolius*) [2]. In previous reports, a common mixture of active ingredients was demonstrated to be ginsenosides [3–5]. The benefits of ginseng are attributed to bioactive compounds, such as ginsenosides, volatile oils, polyphenols, flavonoids, polysaccharides, and vitamins [6–10]. In previous reports on physiological functions, ginseng exhibited anti-cancer [11], immunomodulatory [12], and antidiabetic [13] effects, and cardiovascular improvement [14] in delivering ginseng ginsenosides. Ginseng roots vary from different regions, and differences in environmental factors could influence the genotypes [15]. Thus, CMG could be more bioactive than ginseng grown in other locations. The aim of the current study was to evaluate the anti-fatigue activities of ginseng polysaccharides, as well as the neutral, acidic portions and ginseng polysaccharides of CMG [16]. However, there is a lack of research to support the anti-fatigue effects of the major compounds of CMG, which could improve exercise performance. In this study, we identified the major compound of CMG extract and evaluated the ergogenic, anti-fatigue, and health promotion effects of CMG supplementation using our previously established in vivo platform [17,18].

## 2. Results

### 2.1. Characterized the Major Compound of CMG Extract by HPLC-ESI-MS/MS

CMG was systematically characterized by electrospray ionization tandem mass spectrometry (HPLC-ESI-MS/MSn). Figure 1a shows the ginsenoside standard chromatogram (Rc, Rb2, Rd, Rg2, Rb1, Rf, Re, Rg1); no ginsenoside Rc, Rb2, Rd, Rg2, Rb1, Rf, Re, Rg1 were found in the CMG extract (Figure 1b). The major compound was found at a 44.2 min retention time. The major parent ion was detected and processed for multiple fragment analysis. As shown in Figure 2a, the MS1 parent ions were identified as 955  $m/z$   $[M - H]^-$ , the MS2 secondary ions were 793  $m/z$   $[M - H - \text{glc}]^-$ , the MS3 ions were 613  $m/z$   $[M - H - 2\text{glc} - \text{H}_2\text{O}]^-$ , and the MS4 ions were 455  $m/z$   $[M - H - 2\text{glc} - \text{glcA}]^-$ , which were oleanolic acid aglycone. Above all, the major compound in CMG was ginsenoside Ro, which is consistent with a previous study [19]. The structure of that compound is shown in Figure 2b.

### 2.2. Effects of CMG on Forelimb Grip Strength

After four weeks of CMG supplementation, the forelimb grip strength (Table 1, Figure 3) was 1.27-fold higher in the CMG-5X mice than in the vehicle treatment mice ( $p < 0.0001$ ). In the trend analysis, absolute forelimb grip strength dose-dependently increased with increasing CMG dose ( $p < 0.0001$ ).

**Table 1.** Effect of CMG (Changbai Mountain Ginseng) supplementation for four weeks on exercise performance.

Exercise Performance	Vehicle	CMG-1X	CMG-5X	Trend Analysis
Forelimb grip strength (g)	114 ± 13 <sup>a</sup>	125 ± 10 <sup>a</sup>	145 ± 14 <sup>b</sup>	<0.0001 (↑)
Weight-loaded Swimming time (min)	2.5 ± 0.4 <sup>a</sup>	4.1 ± 1.4 <sup>b</sup>	4.0 ± 1.1 <sup>b</sup>	0.0017 (↑)

All mice were sacrificed at the end of the experiment and examined for serum levels of clinical biochemistry. Values are mean ± SD for  $n = 8$  mice per group. Values in the same line with different superscripts letters (a and b) differ significantly,  $p < 0.05$  by one-way ANOVA. The arrows up mean dose-dependently increase by CMG supplementation.

### 2.3. Effect of CMG on Exercise Performance in a Weight-Loaded Swimming Test

Energy metabolism during muscular activity determines the level of physiological fatigue, and exercise endurance is an important index for evaluating anti-fatigue treatment. Endurance swimming times were  $2.5 \pm 0.4$ ,  $4.1 \pm 1.4$ , and  $4.0 \pm 1.1$  min with the vehicle, CMG-1X, and CMG-5X treatments, respectively (Table 1, Figure 3). The endurance swimming times were respectively 1.67- and 1.60-fold longer in the CMG-1X and CMG-5X groups than in the vehicle treatment group ( $p = 0.0055$  and  $p = 0.0196$ , respectively).

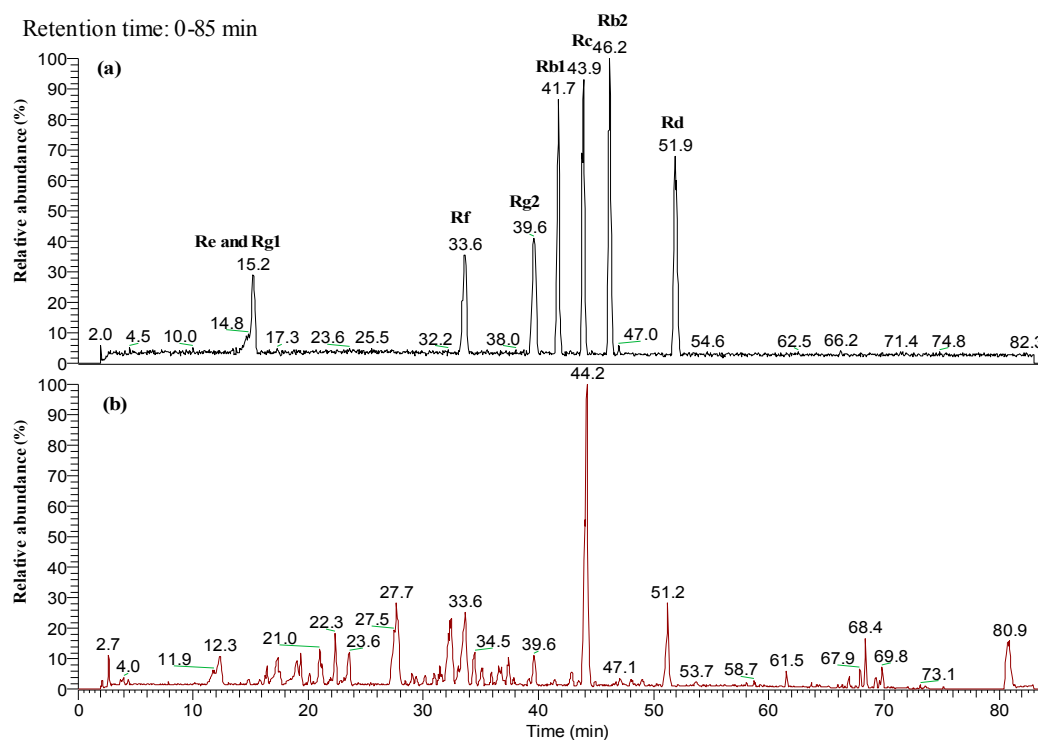


**Figure 1.** Base peak HPLC-ESI-MS chromatogram of ginsenosides in CMG extract. Ginseng ginsenoside mix standard (a, upper panel); CMG extract (b, bottom panel).

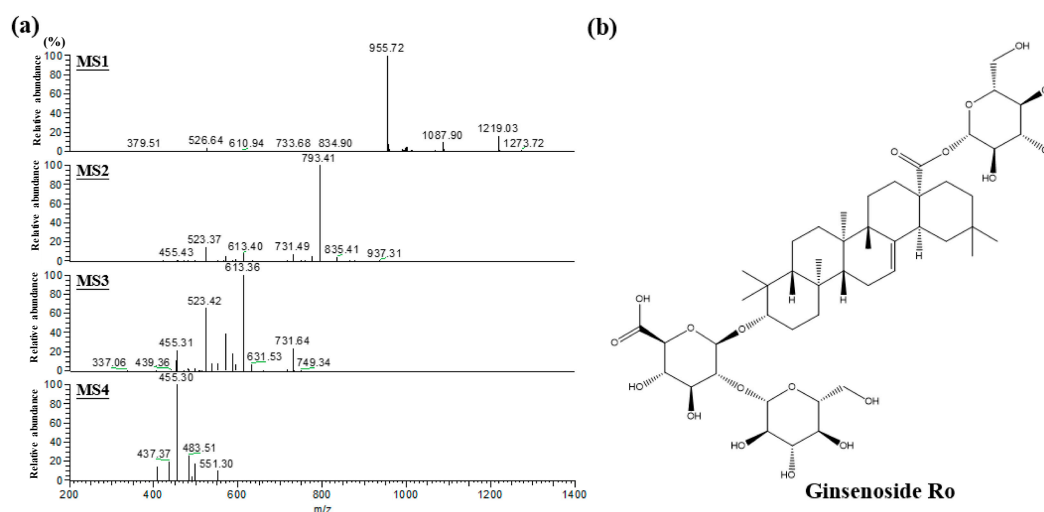


**Figure 2.** Characterized CMG extract by HPLC-ESI-MS/MSn. HPLC-ESI-MS/MSn chromatogram of major ginsenoside in CMG extract (a); and the chemical structure of the major compound in CMG extract (b).

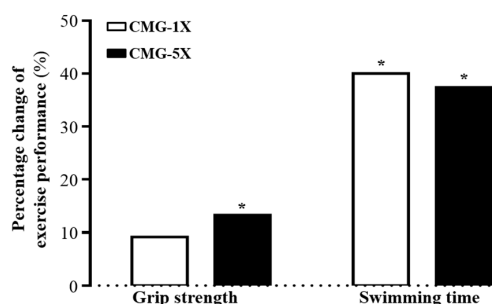


**Figure 3.** Percentage change with vehicle treatment of CMG (Changbai Mountain Ginseng) supplementation for four weeks on forelimb grip strength and swimming time. Mice were pretreated with vehicle, CMG-1X, or CMG-5X for four weeks before forelimb grip strength was tested. Asterisk (\*), significant difference ( $p < 0.05$ ) from vehicle group.

#### 2.4. Effect of CMG Supplementation on Serum Lactate, Ammonia, Glucose, CK, and BUN Levels after Acute Exercise Challenge

In the present study, we determined anti-fatigue related serum levels after 15 min swimming (Table 2, Figure 4). Lactate levels were significantly lower in the CMG-1X and CMG-5X supplementation groups (36.2%,  $p < 0.0001$  and 37.0%,  $p < 0.005$ , respectively) than in the vehicle treatment group, indicating that CMG supplementation was a factor in the removal and utilization of blood lactate after exercise. Serum ammonia levels were respectively 34.9% ( $p = 0.0123$ ) and 45.9% ( $p = 0.0017$ ) lower in the CMG-1X and CMG-5X groups than in the vehicle treatment group. The trend analysis revealed that lactate and serum ammonia level dose-dependently decreased with increasing CMG dose ( $p < 0.0001$ ). Thus, continuous supplementation with CMG for four weeks decreased lactate and ammonia levels during exercise. Serum CK level is an important clinical biomarker of muscle damage. Therefore, reduced serum CK levels could represent increased recovery capacity from exercise-induced muscle damage. CK levels were respectively 55.9% and 56.3% ( $p < 0.0001$ ) lower in the CMG-1X and CMG-5X groups than in the vehicle group, indicating that CMG supplementation may ameliorate skeletal muscle injury induced by acute exercise challenge.

Blood glucose level is an important index for performance maintenance during exercise. The glucose level was 1.4-fold higher ( $p = 0.0001$ ) in the CMG-5X group than in the vehicle group (Figure 4). The trend analysis showed that serum glucose levels dose-dependently increased with CMG supplementation dose ( $p < 0.0001$ ). BUN is an important biochemical parameter related to fatigue. The BUN level is a measure of the amount of nitrogen in blood from the waste product of urea. Urea serves an important role in the metabolism of nitrogen-containing compounds. Serum BUN levels were respectively 21.4% and 25.0% ( $p < 0.0001$ ) lower in the CMG-1X and CMG-5X groups than in the vehicle group. Trend analysis showed that absolute BUN level decreased dose-dependently with increases in CMG dose ( $p < 0.0001$ ). Therefore, CMG may be considered as an ergogenic supplement that facilitates the removal of metabolic waste during exercise.

**Table 2.** Effect of CMG supplementation on serum levels after acute exercise challenge.

Serum Levels after 15 min Swimming	Vehicle	CMG-1X	CMG-5X	Trend Analysis
Lactate(mmol/L)	7.3 ± 0.7 <sup>a</sup>	4.7 ± 0.8 <sup>b</sup>	4.6 ± 0.4 <sup>b</sup>	<0.0001 (↓)
NH <sub>3</sub> (μmol/L)	223 ± 95 <sup>a</sup>	145 ± 15 <sup>b</sup>	121 ± 20 <sup>b</sup>	<0.0001 (↓)
CK (U/L)	907 ± 328 <sup>a</sup>	400 ± 75 <sup>b</sup>	397 ± 37 <sup>b</sup>	0.0002 (↓)
Glucose (mg/dL)	125 ± 22 <sup>a</sup>	143 ± 19 <sup>b</sup>	177 ± 25 <sup>b</sup>	<0.0001 (↑)
BUN (mg/dL)	34.6 ± 4.5 <sup>a</sup>	27.2 ± 1.6 <sup>b</sup>	25.9 ± 2.2 <sup>b</sup>	<0.0001 (↓)

All mice were sacrificed at the end of experiment and examined for serum levels of clinical biochemistry. Values are mean ± SD for  $n = 8$  mice per group. Values in the same line with different superscripts letters (a and b) differ significantly,  $p < 0.05$  by one-way ANOVA. CK, creatine kinase; BUN, blood urea nitrogen. The arrows up (down) mean dose-dependently increase (decrease) by CMG supplementation.

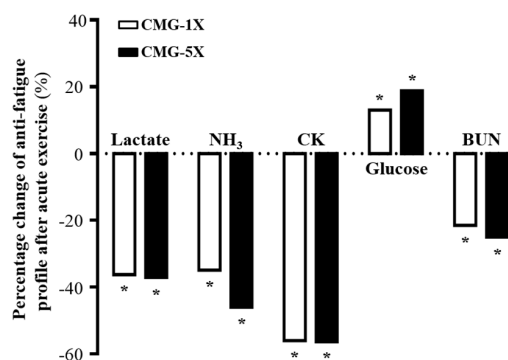


**Figure 4.** Percentage change with vehicle treatment of CMG supplementation on serum levels of lactate, ammonia, creatine kinase (CK), glucose, and blood urea nitrogen (BUN) after acute exercise challenge. Asterisk (\*), significant difference ( $p < 0.05$ ) from vehicle group.

### 2.5. Effect of CMG Supplementation for 4 Weeks on Hepatic and Muscle Glycogen Levels

Glycogen storage directly affects exercise ability, so we measured the glycogen contents of liver and muscle tissues (Table 3). The liver glycogen content suggested no significant differences with all treatments (Figure 5); however, the liver glycogen was slightly higher in the supplementation groups than in the vehicle group. On the other hand, the muscle glycogen content was 1.38-fold ( $p = 0.0073$ ) higher in the CMG-1X group than in the vehicle group. Thus, CMG-1X slightly increased liver and muscle glycogen storage.

**Table 3.** Effects of CMG supplementation on glycogen levels in liver and muscle.

Glycogen Contents	Vehicle	CMG-1X	CMG-5X	Trend Analysis
Liver ( $\mu\text{g/g}$ )	$8.0 \pm 4.0$	$11.3 \pm 6.1$	$9.2 \pm 2.0$	0.3564
Muscle ( $\mu\text{g/g}$ )	$0.16 \pm 0.03$ <sup>a</sup>	$0.23 \pm 0.06$ <sup>b</sup>	$0.15 \pm 0.03$ <sup>a</sup>	0.4625

All mice were sacrificed at the end of experiment and examined for serum levels of clinical biochemistry. Values are mean  $\pm$  SD for  $n = 8$  mice per group. Values in the same line with different superscripts letters (a, b) differ significantly,  $p < 0.05$  by one-way ANOVA.

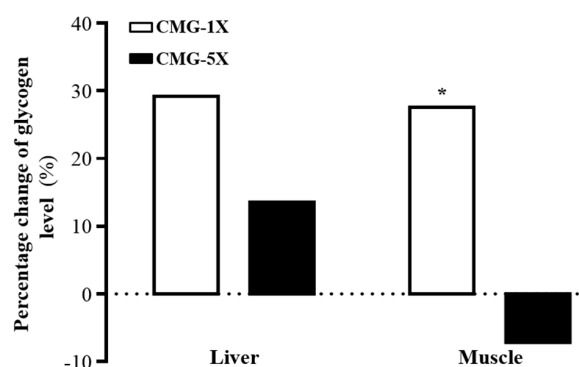


**Figure 5.** Percentage change with vehicle treatment of CMG supplementation on glycogen levels in liver and muscle. Asterisk (\*), significant difference ( $p < 0.05$ ) from vehicle group.

### 2.6. General Characteristics of Mice with CMG Supplementation for Four Weeks

Initial BW did not differ among the vehicle, CMG-1X, and CMG-5X groups (Table 4). After four-week supplementation with CMG, the final BW was not different in each group. Daily intake of diet and water was not different in the vehicle and CMG supplementation groups, either. Thus, four-week supplementation with CMG affected neither BW nor water and diet intake. We also

measured the effect of CMG on muscle mass and relative muscle weight (different tissue weights adjusted for individual BW %). The muscle weights (gastrocnemius and soleus muscles) were, respectively, 1.08- ( $p = 0.0021$ ) and 1.09-fold ( $p = 0.0005$ ) higher in the CMG-1X and CMG-5X groups than in the vehicle group. Trend analysis showed that muscle weight dose-dependently increased with CMG supplementation ( $p < 0.0001$ ). The relative muscle weights (%) were, respectively, 1.17- ( $p = 0.021$ ) and 1.23-fold ( $p = 0.0032$ ) greater in the CMG-1X and CMG-5X groups than in the vehicle group. Trend analysis also showed significant dose-dependent increases in muscle weight ( $p < 0.0001$ ) and relative muscle weight ( $p = 0.0004$ ) with CMG supplementation. In addition, the BAT weights were, respectively, 1.18- ( $p = 0.006$ ) and 1.24-fold ( $p = 0.0006$ ) higher in the CMG-1X and CMG-5X groups than in the vehicle group. Trend analysis revealed that BAT weight and relative BAT weight (both  $p < 0.0001$ ) had significant dose-dependent effects with CMG supplementation. Thus, supplementation with CMG for four weeks could be beneficial to muscle mass and BAT weight. According to this data, we found no gross abnormalities attributed to CMG when weighing organs.

**Table 4.** General characteristics of mice with Changbai Mountain Ginseng (CMG) supplementation.

Characteristic	Vehicle	CMG-1X	CMG-5X	Trend Analysis
Initial BW (g)	37.26 ± 1.0	37.3 ± 1.3	37.8 ± 1.7	0.2231
Final BW (g)	38.5 ± 1.5	38.9 ± 0.9	38.6 ± 1.3	0.7732
Food intake (g/day)	7.3 ± 0.6	7.2 ± 0.7	7.2 ± 0.3	0.8104
Water intake (mL/day)	8.5 ± 0.6	8.6 ± 0.5	8.3 ± 0.3	0.1808
Liver (g)	2.09 ± 0.16	2.10 ± 0.10	2.08 ± 0.14	0.8814
Kidney (g)	0.60 ± 0.05	0.60 ± 0.03	0.61 ± 0.05	0.7797
Heart (g)	0.26 ± 0.04	0.27 ± 0.03	0.27 ± 0.04	0.4513
Lung (g)	0.22 ± 0.02	0.22 ± 0.01	0.22 ± 0.02	0.9438
Muscle (g)	0.37 ± 0.02 <sup>a</sup>	0.39 ± 0.01 <sup>b</sup>	0.40 ± 0.01 <sup>b</sup>	<0.0001 (↑)
EFP (g)	0.33 ± 0.15	0.31 ± 0.01	0.29 ± 0.01	0.8270
BAT (g)	0.076 ± 0.011 <sup>a</sup>	0.090 ± 0.006 <sup>b</sup>	0.095 ± 0.009 <sup>b</sup>	<0.0001 (↑)
Relative liver weight (%)	5.43 ± 0.32	5.40 ± 0.30	5.38 ± 0.22	0.8766
Relative kidney weight (%)	1.56 ± 0.11	1.55 ± 0.08	1.57 ± 0.13	0.9078
Relative Heart weight (%)	0.67 ± 0.10	0.70 ± 0.08	0.69 ± 0.10	0.4836
Relative Lung weight (%)	0.58 ± 0.05	0.56 ± 0.03	0.58 ± 0.05	1.0000
Relative Muscle weight (%)	0.95 ± 0.05 <sup>a</sup>	1.01 ± 0.03 <sup>b</sup>	1.03 ± 0.05 <sup>b</sup>	0.0004 (↑)
Relative EFP weight (%)	0.85 ± 0.37	0.79 ± 0.18	0.76 ± 0.20	0.8081
Relative BAT weight (%)	0.20 ± 0.03 <sup>a</sup>	0.23 ± 0.02 <sup>b</sup>	0.25 ± 0.03 <sup>b</sup>	<0.0001 (↑)

Data are mean ± SD,  $n = 8$  mice/group. Values in the same line with different superscripts letters (a, b) differ significantly,  $p < 0.05$  by one-way ANOVA. Food efficiency ratio: body weight (BW) gain (g/day)/food intake (g/day). Muscle mass includes both gastrocnemius and soleus muscles in the lower legs. BAT: brown adipose tissue; EFP: epididymal fat pad. Mice were pretreated with vehicle, CMG-1X, or CMG-5X for 4 weeks. The arrows up mean dose-dependently increase by CMG supplementation.

## 2.7. Effect of CMG Supplementation on Biochemical Variables at the End of the Experiment

We observed beneficial effects of CMG on grip strength, exhaustive exercise challenge, and body composition with four-week CMG supplementation. We further investigated whether four-week CMG treatment affected other biochemical markers in healthy mice (Table 5).

Levels of biochemical indices, including aspartate aminotransferase (AST), alanine aminotransferase (ALT), lactate dehydrogenase (LDH), blood urea nitrogen (BUN), creatinine, uric acid (UA), and total cholesterol (TC), were the same among groups ( $p > 0.05$ , Table 2). Serum CK levels were 26.63% ( $p = 0.0455$ ) lower with CMG-5X than with vehicle treatment. Serum TP and glucose levels were respectively 1.06- ( $p = 0.0268$ ) and 1.14-fold ( $p = 0.0145$ ) higher with CMG-5X than with vehicle treatment. Serum TG levels were significantly lower with CMG-1X ( $p = 0.0025$ ) and CMG-5X ( $p = 0.0022$ ) than with vehicle treatment. Trend analysis showed that serum CK ( $p = 0.0045$ ) and TG ( $p < 0.0001$ ) levels dose-dependently decreased with CMG extract supplementation; serum TP ( $p = 0.0017$ ) and glucose ( $p = 0.0030$ ) dose-dependently increased with CMG extract supplementation.



In addition, serum albumin slightly increased with CMG-5X treatment, while the albumin levels were still within the normal range. Therefore, long-term daily supplementation with CMG extract may have the potential to protect tissue and enhance nutrient absorption, with increases in serum TP and glucose level. We also examined the tissue morphology. CMG supplementation for four weeks had no adverse effects on major organs such as the liver, skeletal muscle, heart, kidney, lung, and epididymal fat pad (EFP). Therefore, the dose of CMG extract supplementation used in this study was safe (Figure 6).

**Table 5.** Biochemical analysis with CMG supplementation at the end of the experiment.

Variables	Vehicle	CMG-1X	CMG-5X	Trend Analysis
AST (U/L)	102 ± 14	102 ± 11	101 ± 11	0.5837
ALT (U/L)	61 ± 16	59 ± 19	60 ± 22	0.7688
LDH (U/L)	534 ± 60	528 ± 82	537 ± 76	0.9100
CK (U/L)	560 ± 140 <sup>b</sup>	507 ± 148 <sup>ab</sup>	413 ± 124 <sup>a</sup>	0.0045 (↓)
TP (g/dL)	4.9 ± 0.2 <sup>a</sup>	5.0 ± 0.4 <sup>ab</sup>	5.2 ± 0.2 <sup>b</sup>	0.0017 (↑)
Albumin (g/dL)	3.0 ± 0.1 <sup>a</sup>	3.0 ± 0.1 <sup>a</sup>	3.2 ± 0.1 <sup>b</sup>	<0.0001 (↑)
BUN (mg/dL)	23.6 ± 1.8	23.9 ± 1.6	22.5 ± 1.7	0.4280
Creatinine (mg/dL)	0.30 ± 0.03	0.31 ± 0.04	0.30 ± 0.02	0.8319
UA (mg/dL)	1.9 ± 0.6	1.7 ± 0.3	1.7 ± 0.3	0.5904
TC (mg/dL)	137 ± 13	133 ± 8	131 ± 8	0.3105
TG (mg/dL)	153 ± 15 <sup>b</sup>	124 ± 22 <sup>a</sup>	124 ± 11 <sup>a</sup>	<0.0001 (↓)
Glucose (mg/dL)	148 ± 18 <sup>a</sup>	155 ± 16 <sup>ab</sup>	168 ± 10 <sup>b</sup>	0.0030 (↑)

Data are mean ± SD, *n* = 8 mice/group. Values in the same line with different superscripts letters (a, b) differ significantly, *p* < 0.05 by one-way ANOVA. AST, aspartate aminotransferase; ALT, alanine aminotransferase; LDH, lactate dehydrogenase; CK, creatine kinase; TP, total protein; BUN, blood urea nitrogen; UA, uric acid; TC, total cholesterol; TG, triacylglycerols. The arrows up (down) mean dose-dependently increase (decrease) by CMG supplementation.

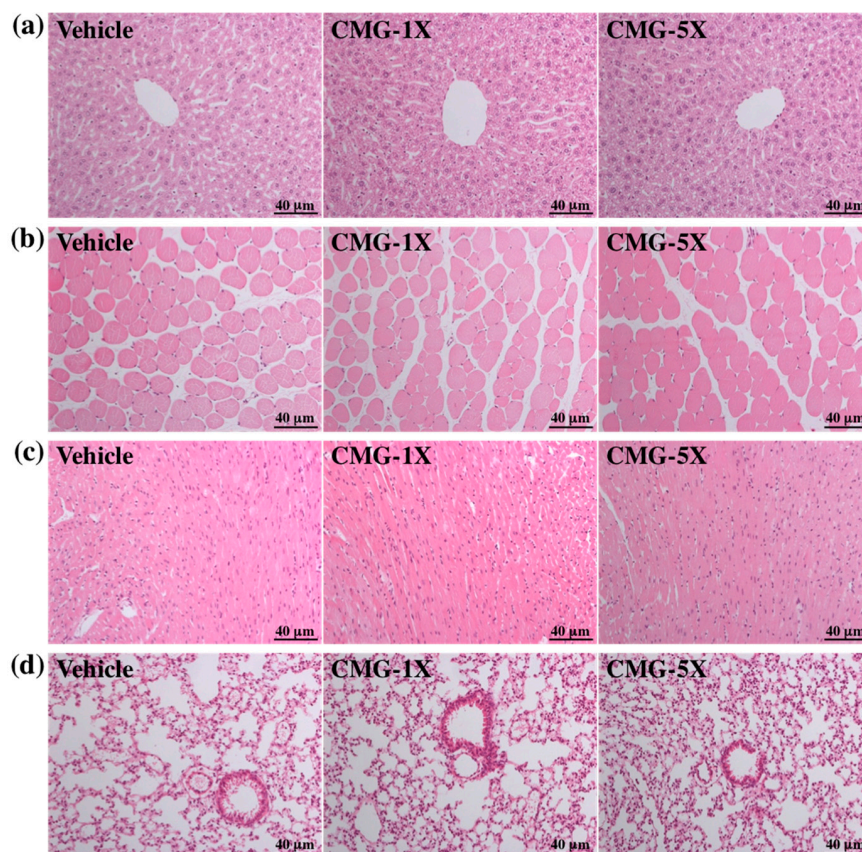


**Figure 6.** Cont.

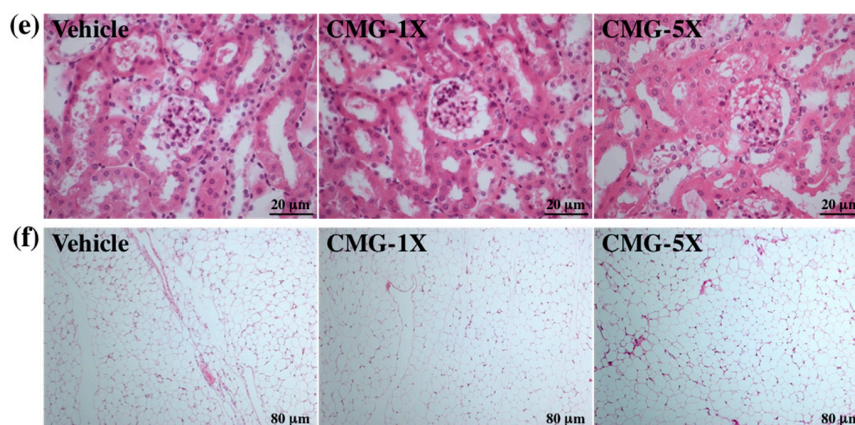


**Figure 6.** Effect of CMG supplementation on morphology of liver (a); skeletal muscle (b); heart (c); lungs (d); kidney (e); and epididymal fat pad (f). Specimens were photographed by light microscopy. (H and E stain, magnification: (a–d), 200×, Scale bar, 40 µm; (e), 400×, Scale bar, 20 µm; (f), 100×, Scale bar, 80 µm).

### 3. Discussion

The beneficial effects of ginsenoside species have been well demonstrated in many studies. However, the function of ginsenoside Ro, an oleanane-type saponin, has not been sufficiently investigated. The place of origin and weather could influence ginseng trace elements and secondary metabolites, which could explain why CMG differs from other types of ginseng and has a high content of ginsenoside Ro. In general, programmed exercise training is required to increase grip strength [20]; however, we found that ginsenoside Ro supplementation benefited grip strength even though the test animals underwent no training intervention. Thus, long-term ginsenoside Ro supplementation could benefit the muscle explosive force under non-training conditions. However, few studies have investigated the use of ginseng supplementation to improve muscle strength. According to a previous study, dammarane steroid, a ginseng steroid that is present in many ginseng species, has anti-inflammatory effects on skeletal muscle following a bout of muscle-damaging exercise [21]. Thus, ginsenoside Ro may have an anti-inflammation effect and enhance skeletal muscle performance. Ginseng has a wide range of benefits that could promote physical performance and recovery capacity from interval exercise [22]. We suggest that ginsenoside Ro may improve endurance performance in the absence of training. Further investigation is required to clarify which types of saponins could benefit exercise training for endurance and explosive force performance. In a previous report, 20(R)-ginsenoside Rg3 was demonstrated to increase weight-loaded swimming time [23]. Moreover, ginsenoside Ro may act as a potential ergogenic aid for exercise supplementation.

Exercise-induced muscle fatigue can be evaluated with biochemical indicators, including lactate, ammonia, glucose, CK, and BUN levels [24,25]. The clearance of lactate is thought to reduce peripheral neuromuscular fatigue and have positive effects on muscle function [26]. After acute exercise, relaxation is significantly affected by the blood lactate clearance rate. Approximately 75% of the total amount of lactate produced is used for oxidative production of energy in the exercising body, and lactate could be utilized for the de novo synthesis of glucose in the liver [27]. During exercise, muscle utilizes glucose from glycogen by intramuscular glycogenolysis and by increased glucose uptake. Regardless, aerobic and resistance exercises increase glucose transporter type 4 (GLUT4) abundance and translocation, thereby increasing serum glucose uptake by a pathway that is not dependent on insulin [28,29]. Ammonia, an important metabolite during energy metabolism for exercise, is generated by different sources. Accumulation of ammonia in the blood and brain during exercise can negatively affect the central nervous system and cause fatigue. The present data suggest that continuous supplementation with CMG extract for four weeks could decrease lactate, ammonia, and BUN accumulation, economize serum glucose levels and, thus, CMG extract could

have anti-fatigue activity. The effect on CK serum response appears to be related to the magnitude of eccentric contractions involved in the activity and the subsequent extent of muscle disruption [30]. High-intensity exercise challenge can physically or chemically cause tissue damage and muscular cell necrosis [31]. Thus, ginsenoside Ro could reduce muscle damage after exercise.

Concerning glycogen, in our present study, ginsenoside Ro may have influenced hepatic and muscle glycogen metabolism. Previously, it has been reported that ginsenoside suppresses hepatic glucose production through inhibiting the small heterodimer partner (SHP) gene expression [32] or increasing hepatic glycogen storage [33]. Ginseng, or ginsenosides associated with acetyl CoA carboxylase kinase (AMPK) activation, switches off anabolic pathways, including glycolysis, lipolysis, glycogen synthesis, and protein synthesis in the liver [34]. There are at least three mechanisms to regulate the glucose uptake of skeletal muscle. To begin with, glucose delivery to the skeletal muscle cells; then, glucose transport through the cell surface membrane; and, finally, flux through intracellular metabolism [35]. During short-term exercise, the muscle glycogen is the preferred carbohydrate fuel for both aerobic and anaerobic metabolism. When exercise is prolonged, glycogen stores in muscle and liver are depleted during exercise, and blood glucose utilization becomes the main carbohydrate fuel during exercise [36]. Therefore, we suggested that CMG-1X supplementation was the proper dose for recommendation as an ergogenic aid. Our present data also showed that CMG-5X could increase the serum glucose levels by decreasing glycogen storage. We suggested that the ginsenosides may increase glycolysis [37]. During exercise, both serum glucose and muscle glycogen are important fuels. The increase of muscle glucose uptake during exercise depends upon the delivery of glucose (capillary perfusion and plasma glucose concentration) and the permeability of the muscle membrane to glucose [35]. In addition to muscle glycogen content, serum glucose level is the other energy utilization index. Therefore, CMG could modulate the muscle glycogen storage and ginsenoside Ro could be as an ergogenic supplement. It had been reported that ginseng saponin decreases plasma triglyceride levels and inhibits atheroma formation in animals with hypercholesterolemia [38]. The reason why enhanced nutrition absorption with TP was increased by CMG extract supplementation could be that the ginsenosides were biotransformed by intestinal bacteria, which further improved intestinal absorption and bioactivity and diminished the toxicity of the metabolite [39,40].

However, there were still some imitations of this study. The major limitation of the study is that we cannot extrapolate our results to the human because only animal blood of tissue samples were included in this study. Another limitation of the study is the lack of information on the major compound of ginsenoside profiling data from fresh or dried material or during growth of Changbai Mountain Ginseng in different seasons.

#### 4. Materials and Methods

##### 4.1. Preparation of Changbai Mountain Ginseng (CMG) Extract

CMG specimens were cut into small pieces and soaked in ethanol at ambient temperature for seven days. The extracts were decanted and filtered through Whatman No. 2 filter paper (Sigma, St. Louis, MO, USA), and the filtrates were concentrated in a rotary evaporator before being lyophilized. The yield of CMG was 0.4% ( $1.96 \text{ g}/470.5 \text{ g} \times 100$ ).

##### 4.2. Liquid Chromatographic-Mass Spectrometry (LC-MS) Analysis of CMG Extract

One hundred microliters of CMG extract powder (670 mg/mL) were dissolved in milli-Q water. Before being loaded into SPE (polymeric reversed-phase solid-phase-extraction cartridges; 200 mg/3 mL; StrataX, Phenomenex, Denver, CO, USA), the CMG extract liquid was added into 600  $\mu\text{L}$  methanol and then eluted out with 10%–100% of acetonitrile. The system included an HPLC equipped with a Thermo Finnigan model LXQ linear ion trap mass spectrometer (San Jose, CA, USA) operated in negative ion electrospray mode. A YMC Hydrosphere C18 analytical column ( $2.0 \times 150 \text{ mm}$ , 5  $\mu\text{m}$ , YMC, Kyoto, Japan) was maintained at room temperature, and a flow-rate of 0.2 mL/min was used.



The mobile phase consisted of water with 0.1% formic acid (solvent A) and acetonitrile with 0.1% formic acid (solvent B). Gradients were programmed as follows: 21% B for 0–5 min, 21%–34% B for 5–40 min, holding at 34% B for 40–60 min, 34%–38% B for 60–70 min, 38%–100% B for 70–80 min, and holding at 100% B for 80–85 min. A ginseng ginsenosides standard kit (Sigma, G-015, St. Louis, MO, USA) was prepared for injection volumes of 10  $\mu$ L.

#### 4.3. Animals and Experiment Design

Male ICR mice (nine weeks old) grown under specific pathogen-free conditions were purchased from BioLASCO (Yi-Lan, Taiwan). All mice were provided a standard laboratory diet (No. 5001; PMI Nutrition International, Brentwood, MO, USA) and distilled water ad libitum, and they were housed with a 12-h light/12-h dark cycle at room temperature ( $22 \pm 1$  °C) and 50%–60% humidity. The Institutional Animal Care and Use Committee (IACUC) of National Taiwan Sport University (NTSU) inspected all animal experiments, and this study conformed to the guidelines of protocol IACUC-105,020 approved by the IACUC ethics committee. In this study, the dose of CMG for humans was 24.4 mg per day (CMG extract). The mice dose (5 mg/kg) we used was converted from a human-equivalent dose (HED) based on body surface area by the following formula from the US Food and Drug Administration: assuming a human weight of 60 kg, the HED for 24.4 (mg)/60 (kg) =  $0.406 \times 12.3 = 5$  mg/kg; the conversion coefficient 12.3 was used to account for differences in body surface area between mice and humans as recently described [41]. In total, 24 mice were randomly assigned to three groups (eight mice/group) for daily oral CMG treatment for 4 weeks. The groups and treatment courses were as follows: vehicle; 5 mg/kg (CMG-1X); and 25 mg/kg (CMG-5X). The vehicle group received the same volume of solution equivalent to individual body weight (BW). Mice were randomly housed in groups of four per cage.

#### 4.4. Forelimb Grip Strength Test

A low-force testing system (Model-RX-5, Aikoh Engineering, Nagoya, Japan) was used to measure the forelimb grip strength of treated mice as previously described [42]. Forelimb grip strength was tested one hour after administration of the indicated CMG supplementation for four weeks. The forelimb grip strengths of all mice were measured on the same day.

#### 4.5. Swimming Exercise Performance Test

The swimming endurance test was conducted after the forearm grip strength test for all mice. For the swim-to-exhaustion test, loads corresponding to 5% of the mouse BW were attached to the tail to evaluate endurance time [43]. The swimming endurance time of each mouse was recorded from the beginning to exhaustion, determined by observing loss of coordinated movements and failure to return to the surface within 7 s. The test of swimming endurance time was performed one hour after administration of the indicated CMG supplementation for 28 days. The swimming exercise performance tests of all mice were performed on the same day as the forelimb grip strength measurement.

#### 4.6. Determination of Fatigue-Associated Biochemical Variables

The effect of CMG supplementation on fatigue-associated biochemical indices was evaluated after exercise as previously described [43]. The 15-min swimming test was performed one day after the forelimb grip strength and the swimming exercise performance test. After CMG supplementation for one hour, all mice underwent a 15-min swimming test without weight loading. Immediately after the 15-min test, blood samples were immediately collected from the submandibular duct of mice and centrifuged at  $1500 \times g$  and 4 °C for 10 min for serum preparation. Serum lactate, ammonia, glucose, creatine kinase (CK), and blood urea nitrogen (BUN) levels were determined with an autoanalyzer (Hitachi 7060, Hitachi, Tokyo, Japan).

#### 4.7. Clinical Biochemical Profiles

Two days after the 15-min swimming test, all mice were sacrificed with 95% CO<sub>2</sub> asphyxiation, and their blood was immediately collected. Blood collected by cardiac puncture was centrifuged at 1500× *g* for 10 min at 4 °C. Serum was separated by centrifugation and the levels of clinical biochemical variables (CK, albumin, total protein (TP), BUN, creatinine, uric acid (UA), total cholesterol (TC), triacylglycerols (TG), and glucose) were measured with an autoanalyzer (Hitachi 7060, Hitachi, Tokyo, Japan).

#### 4.8. Histology of Tissues

Liver, skeletal muscle, heart, lung, kidney, and epididymal fat pad (EFP) tissues were carefully removed, minced, and fixed in 10% formalin. Samples were embedded in paraffin and cut into 4-μm thick slices for morphological and pathological evaluations. Tissues were stained with hematoxylin and eosin (H and E) and examined under a light microscope equipped with a CCD camera (BX-51, Olympus, Tokyo) by a veterinary pathologist.

#### 4.9. Tissue Glycogen Determination and Visceral Organ Weight

The stored form of glucose is glycogen, which mostly exists in liver and muscle tissue. Liver and muscle tissues were excised after the mice were sacrificed and weighed for glycogen content analysis as described previously [44]. The weights of the liver, skeletal muscle, heart, lung, kidney, epididymal fat pad (EFP), and brown adipose tissue (BAT) related to visceral organs were recorded.

#### 4.10. Statistical Analysis

All data are expressed as mean ± SD, *n* = 8 mice per group. Statistical differences among groups were analyzed with one-way analysis of variance (ANOVA and the Cochran-Armitage test for dose-effect trend analysis with SAS 9.0 (SAS Inst., Cary, NC, USA). *p* < 0.05 was considered statistically significant. Differences between groups were analyzed by one-way analysis of variance (ANOVA) using Duncan's post-hoc test, and *p* values < 0.05 were considered significant.

### 5. Conclusions

We demonstrated that the major compound of CMG is ginsenoside Ro. CMG supplementation for four weeks significantly improved forelimb grip strength and swimming time to exhaustion in test animals (Figure A1). CMG has anti-fatigue activity; it decreased plasma lactate, ammonia, and CK and increased serum glucose levels, thereby enhancing exercise performance in mice. Exercise-induced fatigue-related parameters including lactate, ammonia, CK, and glucose levels were dose-dependently modulated by CMG supplementation. CMG also has positive effects on the lipid profile, tissue protection, and nutritional status in vivo. In this study, we found that CMG supplementation could increase exercise performance, and increase muscle mass. These findings suggest potential biological mechanisms by which ginsenoside Ro may increase energy utilization via glycolysis and thereby increase serum glucose levels or decrease physical fatigue during exercise. Ginsenoside Ro may be associated with AMPK activation, which regulates metabolic processes, including glycolysis or glycogen synthesis. Previous studies have been demonstrated that ginsenoside has an anti-fatigue effect which related to improve energy metabolism and decrease the oxidative stress of skeletal muscle [45,46]. The underlying mechanism might be associated with an increase in the content of adenosine triphosphate (ATP) and an enhancement in the activity of energy metabolic enzymes, but the feasibility of other mechanisms still warrants further study. To our best knowledge, this is the first study to investigate that the ginsenoside Ro-rich CMG exhibits anti-fatigue function. Although we have evidence that reveals CMG could improve exercise performance, there is a lack of studies of ginsenoside-Ro in humans. Therefore, these results should be conducted to verify the biological effectiveness in human studies.



**Acknowledgments:** This study was not supported by any grant, outside sources of funding, or industry sponsorship. The authors are grateful to Mon-Chien Lee and Chien-Chao Chiu and Yu-Tang Tung for technical assistance in animal experiments and preparation of the CMG extract. The HPLC analysis was performed by the Research Center for Industry of Human Ecology and the Food Safety Testing Laboratory, College of Human Ecology, Chang Gung University of Science and Technology. We also thank Yu-Ping Liao (Centre for International Affairs, National Taiwan Sport University, Taoyuan City, Taiwan) and John P. Ring (Academic Writing Education Center, National Taiwan University, Taipei City, Taiwan) for their careful reading of the manuscript.

**Author Contributions:** Chi-Chang Huang and Guo-Dong Ma conceived and designed the experiments; Yi-Ming Chen, Chun-Hui Chiu, Yi-Ju Hsu, Chien-Wen Hou performed the experiments; Yi-Ming Chen, Yi-Ju Hsu, Chun-Hui Chiu and Chi-Chang Huang analyzed the data; Guo-Dong Ma and Chien-Wen Hou contributed reagents and materials; Yi-Ming Chen and Chi-Chang Huang wrote and revised the paper.

**Conflicts of Interest:** The authors declare no conflict of interest.

## Appendix A

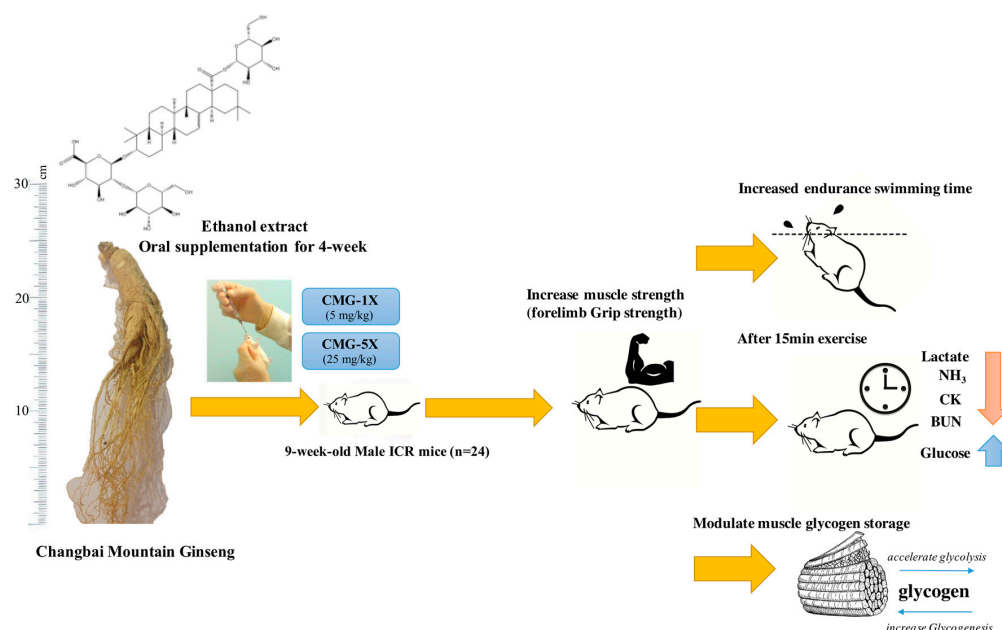


**Figure A1.** The Bioactivities of Changbai Mountain Ginseng (CMG) Extract on Anti-Fatigue In Vivo.

## References

- Shuna, L.; Zhaohuai, J. Development Models of Resource-dependent Cities' Transformations and Its Experience and Lessons-Take Baishan City's Development of Transformations as an Example. *Energy Procedia* **2011**, *5*, 1626–1630. [[CrossRef](#)]
- Attele, A.S.; Wu, J.A.; Yuan, C.S. Ginseng pharmacology: Multiple constituents and multiple actions. *Biochem. Pharmacol.* **1999**, *58*, 1685–1693. [[CrossRef](#)]
- Cui, J. Identification and quantification of ginsenosides in various commercial ginseng preparations. *Eur. J. Pharm. Sci.* **1995**, *3*, 77–85. [[CrossRef](#)]
- Tadano, T.; Nakagawasai, O.; Nijima, F. The effects of traditional tonics on fatigue in mice differ from those of the antidepressant imipramine: A pharmacological and behavioral study. *Am. J. Chin. Med.* **2000**, *28*, 97–104. [[CrossRef](#)] [[PubMed](#)]
- Barton, D.L.; Liu, H.; Dakhil, S.R.; Linquist, B.; Sloan, J.A.; Nichols, C.R.; Loprinzi, C.L. Wisconsin Ginseng (*Panax quinquefolius*) to improve cancer-related fatigue: A randomized, double-blind trial. *J. Natl. Cancer Inst.* **2013**, *105*, 1230–1238. [[CrossRef](#)] [[PubMed](#)]
- Bae, H.J.; Chung, S.I.; Lee, S.C.; Kang, M.Y. Influence of Aging Process on the Bioactive Components and Antioxidant Activity of Ginseng (*Panax ginseng* L.). *J. Food Sci.* **2014**, *79*, H2127–H2131. [[CrossRef](#)] [[PubMed](#)]
- Hou, Y.L.; Tsai, Y.H.; Lin, Y.H.; Chao, J.C. Ginseng extract and ginsenoside Rb1 attenuate carbon tetrachloride-induced liver fibrosis in rats. *BMC Complement. Altern. Med.* **2014**, *14*, 415. [[CrossRef](#)] [[PubMed](#)]

8. Lee, S.H.; Oh, M.; Park, J.; Jang, S.Y.; Cheong, S.H.; Lee, H.; Moon, S.H. Antioxidant and anti-inflammatory activities of the ethanolic extract of fermented red ginseng marc. *Food Sci. Biotechnol.* **2015**, *24*, 651–657. [[CrossRef](#)]
9. Wang, J.R.; Yau, L.F.; Tong, T.T.; Feng, Q.T.; Bai, L.P.; Ma, J.; Jiang, Z.H. Characterization of Oxygenated Metabolites of Ginsenoside Rb1 in Plasma and Urine of Rat. *J. Agric. Food Chem.* **2015**, *63*, 2689–2700. [[CrossRef](#)] [[PubMed](#)]
10. Zhou, Y.; Li, H.Q.; Lu, L.; Fu, D.L.; Liu, A.J.; Li, J.H.; Zheng, G.Q. Ginsenoside Rg1 provides neuroprotection against blood brain barrier disruption and neurological injury in a rat model of cerebral ischemia/reperfusion through downregulation of aquaporin 4 expression. *Phytomedicine* **2014**, *21*, 998–1003. [[CrossRef](#)] [[PubMed](#)]
11. Sun, S.; Qi, L.W.; Du, G.J.; Mehendale, S.R.; Wang, C.Z.; Yuan, C.S. Red notoginseng: Higher ginsenoside content and stronger anticancer potential than Asian and American ginseng. *Food Chem.* **2011**, *125*, 1299–1305. [[CrossRef](#)] [[PubMed](#)]
12. Wang, Y.; Liu, Y.; Zhang, X.Y.; Xu, L.H.; Ouyang, D.Y.; Liu, K.P.; He, X.H. Ginsenoside Rg1 regulates innate immune responses in macrophages through differentially modulating the NF- $\kappa$ B and PI3K/Akt/mTOR pathways. *Int. Immunopharmacol.* **2014**, *23*, 77–84. [[CrossRef](#)] [[PubMed](#)]
13. Liu, Z.; Li, W.; Li, X.; Zhang, M.; Chen, L.; Zheng, Y.N.; Ruan, C.C. Antidiabetic effects of malonyl ginsenosides from *Panax ginseng* on type 2 diabetic rats induced by high-fat diet and streptozotocin. *J. Ethnopharmacol.* **2013**, *145*, 233–240. [[CrossRef](#)] [[PubMed](#)]
14. Lee, C.H.; Kim, J.H. A review on the medicinal potentials of ginseng and ginsenosides on cardiovascular diseases. *J. Ginseng Res.* **2014**, *38*, 161–166. [[CrossRef](#)] [[PubMed](#)]
15. Lim, W.; Mudge, K.W.; Vermeylen, F. Effects of population, age, and cultivation methods on ginsenoside content of wild American ginseng (*Panax quinquefolium*). *J. Agric. Food Chem.* **2005**, *53*, 8498–8505. [[CrossRef](#)] [[PubMed](#)]
16. Wang, J.; Li, S.; Fan, Y.; Chen, Y.; Liu, D.; Cheng, H.; Zhou, Y. Anti-fatigue activity of the water-soluble polysaccharides isolated from *Panax ginseng* C.A. Meyer. *J. Ethnopharmacol.* **2010**, *130*, 421–423. [[CrossRef](#)] [[PubMed](#)]
17. Wu, R.E.; Huang, W.C.; Liao, C.C.; Chang, Y.K.; Kan, N.W.; Huang, C.C. Resveratrol protects against physical fatigue and improves exercise performance in mice. *Molecules* **2013**, *18*, 4689–4702. [[CrossRef](#)] [[PubMed](#)]
18. Hsu, Y.J.; Chiu, C.C.; Li, Y.P.; Huang, W.C.; Huang, Y.T.; Huang, C.C.; Chuang, H.L. Effect of intestinal microbiota on exercise performance in mice. *J. Strength Cond. Res.* **2015**, *29*, 552–558. [[CrossRef](#)] [[PubMed](#)]
19. Wang, H.P.; Zhang, Y.B.; Yang, X.W.; Yang, X.B.; Xu, W.; Xu, F.; Zhang, L.X. High-Performance Liquid Chromatography with Diode Array Detector and Electrospray Ionization Ion Trap Time-of-Flight Tandem Mass Spectrometry to Evaluate Ginseng Roots and Rhizomes from Different Regions. *Molecules* **2016**, *21*, 603. [[CrossRef](#)] [[PubMed](#)]
20. Chen, W.C.; Huang, W.C.; Chiu, C.C.; Chang, Y.K.; Huang, C.C. Whey protein improves exercise performance and biochemical profiles in trained mice. *Med. Sci. Sports Exerc.* **2014**, *46*, 1517–1524. [[CrossRef](#)] [[PubMed](#)]
21. Yu, S.H.; Huang, C.Y.; Lee, S.D.; Hsu, M.F.; Wang, R.Y.; Kao, C.L.; Kuo, C.H. Decreased eccentric exercise-induced macrophage infiltration in skeletal muscle after supplementation with a class of ginseng-derived steroids. *PLoS ONE* **2014**, *9*, e114649. [[CrossRef](#)] [[PubMed](#)]
22. Engels, H.J.; Fahlman, M.M.; Wirth, J.C. Effects of ginseng on secretory IgA, performance, and recovery from interval exercise. *Med. Sci. Sports Exerc.* **2003**, *35*, 690–696. [[CrossRef](#)] [[PubMed](#)]
23. Tang, W.; Zhang, Y.; Gao, J.; Ding, X.; Gao, S. The anti-fatigue effect of 20(R)-ginsenoside Rg3 in mice by intranasally administration. *Biol. Pharm. Bull.* **2008**, *31*, 2024–2027. [[CrossRef](#)] [[PubMed](#)]
24. Strojnik, V.; Komi, P.V. Fatigue after submaximal intensive stretch-shortening cycle exercise. *Med. Sci. Sports Exerc.* **2000**, *32*, 1314–1319. [[CrossRef](#)] [[PubMed](#)]
25. Izquierdo, M.; González-Izal, M.; Navarro-Amezqueta, I.; Calbet, J.A.; Ibañez, J.; Malanda, A.; Mallor, F.; Häkkinen, K.; Kraemer, W.J.; Gorostiaga, E.M. Effects of strength training on muscle fatigue mapping from surface EMG and blood metabolites. *Med. Sci. Sports Exerc.* **2011**, *43*, 303–311. [[CrossRef](#)] [[PubMed](#)]
26. White, G.E.; Wells, G.D. The effect of on-hill active recovery performed between runs on blood lactate concentration and fatigue in alpine ski racers. *J. Strength Cond. Res.* **2015**, *29*, 800–806. [[CrossRef](#)] [[PubMed](#)]
27. Brooks, S.P.; Storey, K.B. A quantitative evaluation of the effect of enzyme complexes on the glycolytic rate in vivo: Mathematical modeling of the glycolytic complex. *J. Theor. Biol.* **1991**, *149*, 361–375. [[CrossRef](#)]

28. Colberg, S.R.; Sigal, R.J.; Fernhall, B.; Regensteiner, J.G.; Blissmer, B.J.; Rubin, R.R.; Braun, B. Exercise and type 2 diabetes the American College of Sports Medicine and the American Diabetes Association: Joint position statement executive summary. *Diabetes Care* **2010**, *33*, 2692–2696. [[CrossRef](#)] [[PubMed](#)]
29. Adams, O.P. The impact of brief high-intensity exercise on blood glucose levels. *Diabetes Metab. Syndr. Obes.* **2013**, *6*, 113–122. [[CrossRef](#)] [[PubMed](#)]
30. Baird, M.F.; Graham, S.M.; Baker, J.S.; Bickerstaff, G.F. Creatine-kinase-and exercise-related muscle damage implications for muscle performance and recovery. *J. Nutr. Metab.* **2012**, *2012*, 960363. [[CrossRef](#)] [[PubMed](#)]
31. Coyle, E.F.; Hagberg, J.M.; Hurley, B.F.; Martin, W.H.; Ehsani, A.A.; Holloszy, J.O. Carbohydrate feeding during prolonged strenuous exercise can delay fatigue. *J. Appl. Physiol. Respir. Environ. Exerc. Physiol.* **1983**, *55*, 230–235. [[PubMed](#)]
32. Yuan, H.D.; Quan, H.Y.; Kim, S.J.; Jung, M.S.; Chung, S.H. Ginsenoside Rg2 induces orphan nuclear receptor SHP gene expression and inactivates GSK3 $\beta$  via AMP-activated protein kinase to inhibit hepatic glucose production in HepG2 cells. *Chem. Biol. Interact.* **2012**, *195*, 35–42. [[CrossRef](#)] [[PubMed](#)]
33. Jeong, K.J.; Kim, G.W.; Chung, S.H. AMP-activated protein kinase: An emerging target for ginseng. *J. Ginseng Res.* **2014**, *38*, 83–88. [[CrossRef](#)] [[PubMed](#)]
34. Im Chung, S.; Nam, S.J.; Xu, M.; Kang, M.Y.; Lee, S.C. Aged ginseng (*Panax ginseng* Meyer) reduces blood glucose levels and improves lipid metabolism in high fat diet-fed mice. *Food Sci. Biotechnol.* **2016**, *25*, 267–273. [[CrossRef](#)]
35. Jensen, T.E.; Richter, E.A. Regulation of glucose and glycogen metabolism during and after exercise. *J. Physiol.* **2012**, *590*, 1069–1076. [[CrossRef](#)] [[PubMed](#)]
36. Coggan, A.R.; Coyle, E.F. Carbohydrate Ingestion during Prolonged Exercise: Effects on Metabolism and Performance. *Exerc. Sport Sci. Rev.* **1991**, *19*, 1–40. [[CrossRef](#)] [[PubMed](#)]
37. Radad, K.; Gille, G.; Moldzio, R.; Saito, H.; Rausch, W.D. Ginsenosides Rb1 and Rg1 effects on mesencephalic dopaminergic cells stressed with glutamate. *Brain Res.* **2004**, *1021*, 41–53. [[CrossRef](#)] [[PubMed](#)]
38. Lee, L.S.; Cho, C.W.; Hong, H.D.; Lee, Y.C.; Choi, U.K.; Kim, Y.C. Hypolipidemic and antioxidant properties of phenolic compound-rich extracts from white ginseng (*Panax ginseng*) in cholesterol-fed rabbits. *Molecules* **2013**, *18*, 12548–12560. [[CrossRef](#)] [[PubMed](#)]
39. Li, H.; Zhou, M.; Zhao, A.; Jia, W. Traditional Chinese medicine: Balancing the gut ecosystem. *Phytother. Res.* **2009**, *23*, 1332–1335. [[CrossRef](#)] [[PubMed](#)]
40. Wang, H.Y.; Qi, L.W.; Wang, C.Z.; Li, P. Bioactivity enhancement of herbal supplements by intestinal microbiota focusing on ginsenosides. *Am. J. Chin. Med.* **2011**, *39*, 1103–1115. [[CrossRef](#)] [[PubMed](#)]
41. Chen, Y.M.; Lin, C.L.; Wei, L.; Hsu, Y.J.; Chen, K.N.; Huang, C.C.; Kao, C.H. Sake Protein Supplementation Affects Exercise Performance and Biochemical Profiles in Power-Exercise-Trained Mice. *Nutrients* **2016**, *8*, 106. [[CrossRef](#)] [[PubMed](#)]
42. Chen, Y.M.; Tsai, Y.H.; Tsai, T.Y.; Chiu, Y.S.; Wei, L.; Chen, W.C.; Huang, C.C. Fucoidan supplementation improves exercise performance and exhibits anti-fatigue action in mice. *Nutrients* **2014**, *7*, 239–252. [[CrossRef](#)] [[PubMed](#)]
43. Huang, W.C.; Chiu, W.C.; Chuang, H.L.; Tang, D.W.; Lee, Z.M.; Wei, L.; Huang, C.C. Effect of curcumin supplementation on physiological fatigue and physical performance in mice. *Nutrients* **2015**, *7*, 905–921. [[CrossRef](#)] [[PubMed](#)]
44. Huang, W.C.; Lin, C.I.; Chiu, C.C.; Lin, Y.T.; Huang, W.K.; Huang, H.Y.; Huang, C.C. Chicken essence improves exercise performance and ameliorates physical fatigue. *Nutrients* **2014**, *6*, 2681–2696. [[CrossRef](#)] [[PubMed](#)]
45. Tan, S.J.; Li, N.; Zhou, F.; Dong, Q.T.; Zhang, X.D.; Chen, B.C.; Yu, Z. Ginsenoside Rb1 improves energy metabolism in the skeletal muscle of an animal model of postoperative fatigue syndrome. *J. Surg. Res.* **2014**, *191*, 344–349. [[CrossRef](#)] [[PubMed](#)]
46. Zhuang, C.L.; Mao, X.Y.; Liu, S.; Chen, W.Z.; Huang, D.D.; Zhang, C.J.; Yu, Z. Ginsenoside Rb1 improves postoperative fatigue syndrome by reducing skeletal muscle oxidative stress through activation of the PI3K/Akt/Nrf2 pathway in aged rats. *Eur. J. Pharmacol.* **2014**, *740*, 480–487. [[CrossRef](#)] [[PubMed](#)]

**Sample Availability:** Not available.



© 2017 by the authors; licensee MDPI, Basel, Switzerland. This article is an open access article distributed under the terms and conditions of the Creative Commons Attribution (CC BY) license (<http://creativecommons.org/licenses/by/4.0/>).

# Improvement of shikimic acid production in *Escherichia coli* with growth phase-dependent regulation in the biosynthetic pathway from glycerol

Ming-Yi Lee<sup>1</sup> · Wen-Pin Hung<sup>2</sup> · Shu-Hsien Tsai<sup>2</sup>

Received: 31 October 2016 / Accepted: 19 December 2016 / Published online: 2 January 2017  
© Springer Science+Business Media Dordrecht 2016

**Abstract** Shikimic acid is an important metabolic intermediate with various applications. This paper presents a novel control strategy for the construction of shikimic acid producing strains, without completely blocking the aromatic amino acid biosynthesis pathways. Growth phase-dependent expression and gene deletion was performed to regulate the *aroK* gene expression in the shikimic acid producing *Escherichia coli* strain, SK4/rpsM. In this strain, the *aroL* and *aroK* genes were deleted, and the *aroB*, *aroG*\*, *ppsA*, and *tktA* genes were overexpressed. The relative amount of shikimic acid that accumulated in SK4/rpsM was 1.28-fold higher than that in SK4/pLac. Furthermore, a novel shikimic acid production pathway, combining the expression of the dehydroquinate dehydratase-shikimate dehydrogenase (DHQ-SDH) enzyme from woody plants, was constructed in *E. coli* strains. The results demonstrated that a growth phase-dependent control of the *aroK* gene leads to higher SA accumulation (5.33 g/L) in SK5/pSK6. This novel design can achieve higher shikimic acid production by using the same amount of medium used by the current methods and can also be widely used for modifying other metabolic pathways.

**Keywords** *AroK* gene · Biosynthetic pathway · *Escherichia coli* · Metabolic engineering · Shikimic acid

## Introduction

Shikimic acid (3,4,5-trihydroxy cyclohexene carboxylic acid; SA) is an industrially important compound that acts as a precursor in the synthesis of many chemical substances like oseltamivir phosphate (Tamiflu) (Kancharla et al. 2009). SA is a key metabolic intermediate of the aromatic amino acid biosynthesis pathway, found in microbes and plants (Sprenger 2006). In the present decade, in addition to its industrial and biotechnological applications, SA research has attracted much attention due to concerns over outbreak of swine/avian flu, which has raised the demand of this important biomolecule (Ghosh et al. 2012). Furthermore, it finds many applications in the formulation of a variety of industrially important chemical products such as aromatic amino acids, indole and its derivatives, alkaloids, and many other aromatic metabolites (Bochkova et al. 2011). Recently, it has also been reported that SA has several innovative and multifunctional roles in dermo-cosmetic preparations, anti-enzymatic activity, and as an exfoliating agent for stratum corneum (Guglielmini 2010).

Majority of the commercially synthesized SA is from the Chinese plant star anise; however, it is expensive and has many drawbacks. To achieve large-scale production, fermentation has been proved as a more efficient and viable alternative (Ghosh et al. 2012). Several metabolic and genetic manipulations have been conducted on different microorganisms, particularly *Escherichia coli*, to obtain SA. Enhancements in carbon channeling towards SA by overexpression of DHQ synthase enzymes, feedback-resistant DAHP synthases, and transketolase (coded by *aroB*, *aroG*\*, and *tktA*, respectively). In an attempt to further increase the intracellular availability of PEP, strains overexpressing PEP synthase (coded by *ppsA*), have also been evaluated. Furthermore, the side reactions catalyzed by

✉ Shu-Hsien Tsai  
d92b47401@ntu.edu.tw

<sup>1</sup> Department of Nutrition and Health Sciences, Research Center for Food and Cosmetic Safety, and Research Center for Chinese Herbal Medicine, College of Human Ecology, Chang Gung University of Science and Technology, Kweishan, Taoyuan, Taiwan

<sup>2</sup> Material and Chemical Research Laboratories, Industrial Technology Research Institute, Hsinchu, Taiwan

quininate/shikimate dehydrogenase (coded by *ydiB*), phosphoenolpyruvate carboxylase (coded by *ppc*), and lactate dehydrogenase (coded by *ldhA*) was also reported as limiting in the development of shikimic acid production strains (Rodriguez et al. 2014). Although the implementation of these modifications, along with metabolic engineering strategies, has led to diverse *E. coli* strains capable of accumulating SA, the yields (approximately 40%) obtained till date are far from the maximum theoretical yield. (Chandran et al. 2003; Escalante et al. 2010; Ahn et al. 2008; Ghosh et al. 2012; Cui et al. 2014; Gu et al. 2016). The best producing strain accumulated up to 6.1 g/L of SA in 56 h with 250 mL flask. (Rodriguez et al. 2013). This can be partially attributed to the fact that most of the expression systems used, involve genes controlled by a mixture of inducible and native promoters of variable strengths. Therefore, optimized DNA expression systems and genetic backgrounds are required for promoting a more efficient carbon channeling towards SA formation.

Deletion of both the *aroL* and *aroK* genes, which can block the biosynthesis of aromatic amino acids, may negatively affect the growth of the recombinant strains, resulting in decreased overall SA accumulation. As a result, when culturing this auxotroph in minimal salts medium, it would be necessary to supply L-phenylalanine, L-tyrosine, L-tryptophan, *p*-aminobenzoic acid, *p*-hydroxybenzoic acid, 2,3-dihydroxybenzoic acid, or SA, for cell growth and enzyme synthesis. Accordingly, Zou et al. maintained the *aroK* gene; however, the SA accumulation of this strain was only 392 mg/L in shake flask cultures (Zou et al. 2011), and this level is considered unsuitable for industrial use. To obtain higher SA accumulation, antisense RNA interference (RNAi) was first employed to inactivate the *aroK* gene expression in *E. coli*, because it is genome friendly and can be easily controlled. However, the data obtained indicated that knocking down the expression of the *aroK* gene by antisense RNAi enhanced the accumulation of SA, whereas deletion of the *aroK* gene increased SA accumulation even

further (Chen et al. 2012). Lemke et al. (2011) reported that the promoters for many of the *Escherichia coli* ribosomal protein operons are regulated directly by two transcription factors, the small RNA polymerase-binding protein DksA and the nutritional stress-induced nucleotide ppGpp. Of the promoters examined, *rpsM*, and *rpsJ* were inhibited strongly by ppGpp/DksA, almost as much as the rRNA promoter *rrnB* P1. In this study, it was successfully established that a growth phase-dependent regulation of *aroK* expression allows a small conduit in the SA pathway, past SA, thereby making the addition of aromatic amino acids potentially unnecessary.

## Materials and methods

### Synthesis and construction of *E. coli* derivatives and plasmids

In this study, the laboratory-evolved SK4 strain of *E. coli* K12, BW25113, was genetically modified. The bacterial strains and plasmids used in this study are listed in Table 1. The inactivated *aroK* gene was transduced to SK4 *aroL*<sup>-</sup> using a P1 phage lysate, obtained from the strain JW5947 (*aroK*::km) (Thomason et al. 2007). In all cases, plasmid pCP20 allowed removal of the kanamycin resistance cassette after each event. Every step was verified by polymerase chain reaction (PCR), identifying the clones that presented the expected amplicon sizes when using different sets of oligonucleotides and chromosomal DNA as a template. According to the amino acid sequence of dehydroquininate dehydratase-shikimate dehydrogenase (DHQ-SDH) from *Populus trichocarpa* (Fig. 1a) (Tuskan et al. 2006), the DNA sequence of the *DHQ-SDH* gene (Fig. 1b) was chemically synthesized (GenScript Corp., Piscataway, NJ). The construction of all expression vectors was also accomplished by GenScript's gene synthesis services. For improved *E. coli* expression, the choice of

**Table 1** Strains and plasmids

Strains or plasmids	Relevant characteristics	Source
<b>Strains</b>		
<i>E. coli</i> K-12 BW25113	<i>lacI</i> <sup>f</sup> <i>rrnB</i> <sub>T14</sub> <i>ΔlacZ</i> <sub>WJ16</sub> <i>hsdR514</i> <i>ΔaraBAD</i> <sub>AH33</sub> <i>ΔrhaBAD</i> <sub>LD78</sub>	(Datsenko and Wanner 2000)
SK4	<i>E. coli</i> K12 BW25113 derivative, <i>aroB</i> , <i>aroG</i> <sup>*</sup> , <i>ppsA</i> , <i>tktA</i> , <i>ΔaroL</i> , <i>ΔaroK</i>	This study
SK5	<i>E. coli</i> K12 BW25113 derivative, <i>ΔaroL</i> , <i>ΔaroK</i> , <i>ΔydiB</i> , <i>Δppc</i> , <i>ΔldhA</i>	This study
<b>Plasmids</b>		
pSA40	ColE1 ori, Amp <sup>r</sup> , PLlacO1::MCS	Atsumi et al. (2008)
pLac	ColE1 ori, km <sup>r</sup> , PLlacO1, <i>aroK</i>	This study
prnBP1	ColE1 ori, km <sup>r</sup> , <i>rrnBP1</i> (C), <i>aroK</i>	This study
prpsM	ColE1 ori, km <sup>r</sup> , <i>rpsM</i> , <i>aroK</i>	This study
pSK5	ColE1 ori, <i>aroB</i> , <i>tktA</i> , <i>aroG</i> <sup>*</sup> , DHQ/SDH, Spe <sup>r</sup>	This study
pSK6	ColE1 ori, <i>aroB</i> , <i>tktA</i> , <i>aroG</i> <sup>*</sup> , DHQ/SDH, <i>rpsM</i> , <i>aroK</i> , Spe <sup>r</sup>	This study



codons was made according to the *E. coli* codon usage. The primers 5'-GCTGGATCCAAGTGGGAAGGTTTTTC-3' and 5'-GAGAGCTCACTATTACAAAGCCTTAG-3' were used to obtain *Bam*HI and *Sac* I restriction sites for subcloning. The synthesized fragments were amplified by PCR and inserted into a pUC18 vector, following which it was subcloned into the expression vector pET23 for DHQ-SDH protein expression, or pSA40 under the control of a growth phase-dependent promoter for strain improvement. We created multiple knockout strains via successive P1 transductions. These new constructs were named pLac, prnBP1, prpsM, pSK5, and pSK6 (Table 1). All the enzymes and reagents used in the molecular biology procedures were purchased from New England Biolabs (USA). When required, kits for the purification of PCR, plasmid, and agarose-embedded DNA were utilized (Invitrogen, USA). *E. coli* DH5 $\alpha$  cells (Invitrogen, USA) were used as a host for screening of DNA ligations during intermediate steps in vector construction.

### Expression and purification of the DHQ-SDH enzyme

Expression and purification of the DHQ-SDH protein were accomplished as follows: DHQ-SDH was expressed in the *E. coli* strain BL21 (DE3), in 1 L of Luria–Bertani medium supplemented with kanamycin (50  $\mu$ g/mL) and incubated at 37 °C with shaking (200 rpm), until the cultures reached an OD<sub>600</sub> of 0.6–0.8. The cultures were induced with 0.4 mM isopropyl- $\alpha$ -D-thiogalactopyranoside for 3 h at 37 °C. Cells were harvested by centrifugation and disrupted by sonication, and the insoluble cellular material was removed by centrifugation. The recombinant proteins were purified from the other contaminating proteins using Ni–NTA affinity chromatography. Protein samples for kinetic studies were dialyzed and stored in 10 mM Tris–HCl (pH 7.5), 500 mM NaCl, and 5% glycerol. The purified proteins were dialyzed and stored in a buffer containing 10 mM HEPES

(pH 7.5) and 500 mM NaCl. All purified proteins were quantified at 280 nm using an extinction coefficient of 40,470 M<sup>-1</sup> cm<sup>-1</sup>.

### SDS/PAGE analysis

Total cellular proteins and the progress of the enzyme purification, were analyzed by Tricine-SDS-PAGE (12.5% gel). All gels were run using a Hoefer system (Hoefer Scientific Instruments, San Francisco, CA) according to the manufacturer's recommendations. Protein visualization was accomplished by staining the gels with Coomassie blue.

### Enzymatic activity assay and apparent kinetic parameters

The SDH domain (SD) of DHQ-SDH catalyzes the NADPH-dependent reduction of 3-dehydroshikimate (DHS) to form shikimate and NADP<sup>+</sup>. SDH activity was either based on the decreasing concentration of NADPH, upon DHS reduction, or on the increasing concentration of NADPH, upon shikimate oxidation. The enzymatic activity was measured by monitoring the reduction of NADP<sup>+</sup> (6220 M<sup>-1</sup> cm<sup>-1</sup>) at 340 nm and 22 °C, in the presence of shikimate (Chaudhuri et al. 1987). Determination of the apparent steady-state kinetics parameters,  $V_{\max}$  and  $K_m$ , for DHS and NADPH, in the forward reaction, was carried out by varying the concentration of one substrate (5, 10, 20, 30, 50, 100, and 200  $\mu$ M) and maintaining the other substrate at a constant saturation level. The reverse reaction was performed under the same conditions of pH (100 mM Tris–HCl buffer, pH 7.0), temperature (25 °C), and substrate concentrations. The reaction was initiated with addition of 6 pmol of homogeneous SD enzyme and was monitored for 1 min. The kinetic data were analyzed with double reciprocal plots.

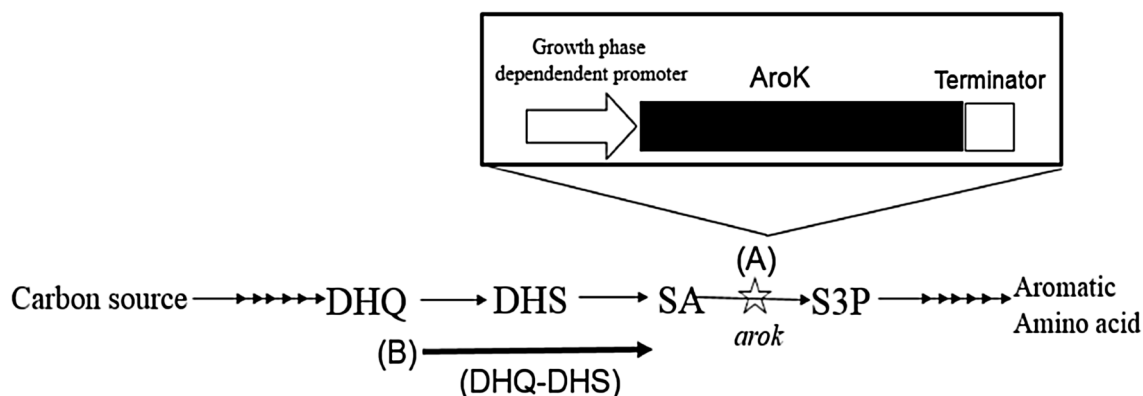


**Fig. 1** Shikimic acid metabolic engineering by **a** growth phase dependent promoter control on *aroK* expression, and **b** DHQ-SDH protein with *E. coli* codon usage from *Populus trichocarpa*

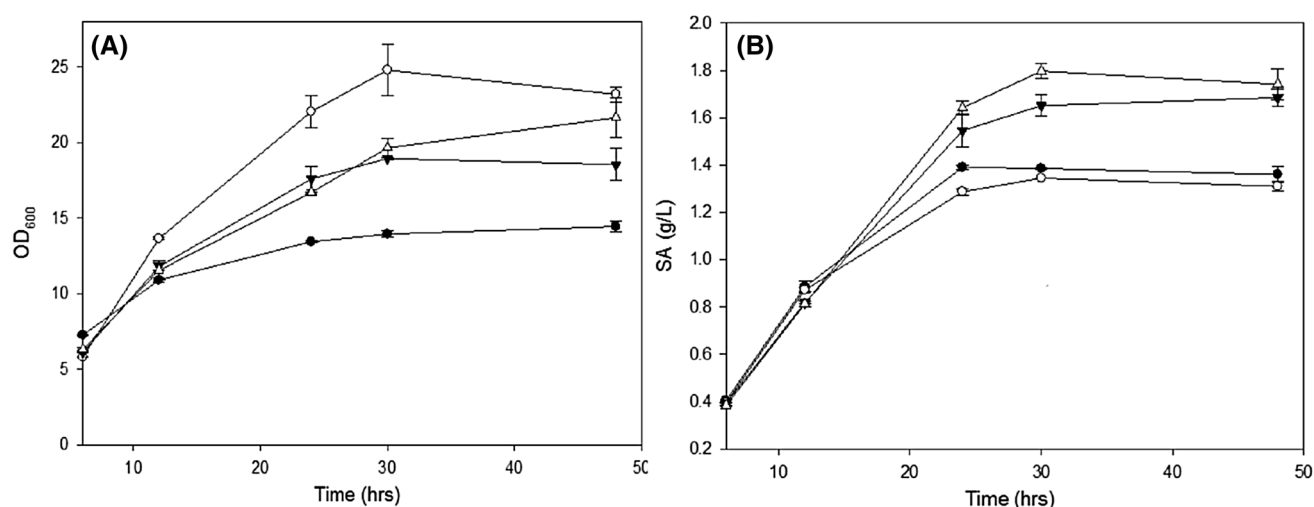


**Fig. 2** Flask cultures of SK4 derivative strains for the accumulation of shikimic acid. **a** Growth curves, and **b** shikimic acid accumulation (filled circle) SK4 (parental strain); (open circle) SK4/Lac; (filled tri-

angle) SK4/rnBP1; (open triangle) SK4/rpsM. The graphs show the mean results from triplicate experiments

### Cultivation media and growth conditions

Luria–Bertani and M9 minimal media were prepared and used as previously described (Sambrook and Russell 2001). The SA production medium contained (per liter):  $K_2HPO_4$  (7.5 g),  $KH_2PO_4$  (7.5 g), citric acid monohydrate (2.1 g), ammonium iron(III) citrate (0.3 g), concentrated  $H_2SO_4$  (1.2 mL),  $MgSO_4$  (0.64 g),  $CaCl_2$  (0.06 g),  $(NH_4)_6(Mo_7O_{24})$  (0.0037 g),  $ZnSO_4$  (0.0029 g),  $H_3BO_3$  (0.0247 g),  $CuSO_4$  (0.0025 g),  $MnCl_2$  (0.0158 g), and  $CoCl_2$  (0.00129 g). When required, kanamycin (25  $\mu$ g/mL) and spectinomycin (25  $\mu$ g/mL) were added to the culture inoculum, for the maintenance of plasmids. Glycerol (filter-sterilized) and yeast extract (added before autoclaving) were supplied at the concentrations indicated for each experiment. The glycerol was purchased from JT Baker (USA), and the autolyzed yeast extract from Sigma (USA).

### Shake flask cultures

The inoculum for the shake flask cultures was prepared by adding 1 mL frozen aliquots to 250 mL shake flasks containing 25 mL of SA production medium, supplemented with glycerol (25 g/L) and yeast extract (15 g/L). The inoculum was grown at 37 °C under shaking (200 rpm) to mid-exponential phase. Approximately 5% of the final volume was then transferred to the test shake flasks and incubated under the same controlled conditions, with media containing glycerol (25 g/L) and yeast extract (15 g/L). Cell growth was monitored by measuring the optical density of the culture at 600 nm ( $OD_{600}$ ) using a BioPhotometer spectrophotometer (Eppendorf, USA). Samples were taken periodically and centrifuged, and the supernatant was stored at

–20 °C for metabolite analysis. All cultures started approximately at an  $OD_{600}$  of 0.3.

### Data analysis

Metabolite concentrations were determined using an Agilent 1200 HPLC system (Waldbronn, Germany). For the determination of D-glycerol, DHS, shikimate, and acetic acid, an Aminex HPX-87H column (300  $\times$  7.8 mm) (Bio-Rad, Hercules, CA) was used. Column temperature was maintained at 50 °C. The mobile phase was 5 mM  $H_2SO_4$  at a flow rate of 0.5 mL/min. Under these conditions, distinct peaks of glycerol were detected by refraction index. All experiments were performed in triplicates and data were averaged and presented as the mean  $\pm$  standard deviation. Significant differences were determined by one-way analysis of variance and Tukey post-hoc tests, using the SPSS (version 11) software. A p value of less than 0.05 was considered statistically significant.

## Results

### Improvement of SA production in *E. coli* with different growth phase-dependent regulation

The capacity of the SK4 derivative strains to accumulate SA was evaluated in flask cultures. In order to increase the growth rate of microbial auxotrophic strains, and save medium cost (supplementation of cultures with aromatic amino acids), a growth phase-dependent control (rnBP1 or rpsM) of the *aroK* gene was developed, instead of a general knockout or knockdown, as shown in Fig. 1. Figure 2

**Fig. 3** **a** DHQ-SDH protein sequence from *Populus trichocarpa*, and **b** DHQ-SDH gene sequence was codon optimized with *E. coli* codon usage

### (A) Protein Sequence

MDSASNVLLASSPSAAAAVGMGSGGVRRNPTLICTPIMADSVDKMAILMAEAKSVGADLVEI  
RLDSLKDFNPNSDIKTLILHSPLPTLFTYRPMWEGGQYNGDEKPRLDALRLAMELGADYIDVE  
LKVAHEFNELLRGKPKGCKLIVSSHNYENTPSVEELGNLVARIQAAGADIVKIATTALDISDV  
ARIFQITVHSQVPIIGLVMGERGLISRLCAKFGGYLTFTGTLESGVVSAPGQPTIKDLLDLNFR  
IGPDTKVFGIIGKPVGHKSPVLFNEAFKSVGNGVYVHLLVDDIARFLQYSSSTDFAGFSCTIPH  
KEDAAKCCDEVHPVAKSIGAVNCIIRRNQNDGKLFYNTDYVGAISAIEEGLRASQNVSNVTGS  
PLAGKLFVVIGAGGAGKALAYGAKEKGARVVIANRTYERAKVLADIIGGDAITLADLENFHP  
DGMILANTTSIGMQPKVDETPVSKNALRSYSLVFDVYTPKITRLLREAEESGAKIVTGLEMFI  
GQAYEQFERFTELPAPKELFQKIMSKY\*

### (B) Nucleotide Sequence

ATGGATTCGGCGTCAAATGTCCTGCTGGCGTCGTCTCCGTCGGCGGCTGCTGCTGTCGGTA  
TGGGCTCGGGCGGTGTTCTGTCGTAATCCGACCCTGATTGCACGCCGATCATGGCTGATTC  
AGTGGACAAAATGGCGATTCTGATGGCGGAAGCCAAGTCGGTGGGTGCCGATCTGGTTGA  
AATCCGCTCTGGATAGCCTGAAAGACTTTAACCCTGAATTCTGATATTAAGACCCTGATCCTG  
CATAGTCCGCTGCCGACCCTGTTACGTATCGCCGATGTGGGAAGGCGGTCAATACAAC  
GGTGATGAAAAACCGCTCTGGACGCACTGCGCCTGGCTATGGAAGTGGGCGCTGATTAT  
ATTGACGTTGAAGTGAAGTCGCGCATGAATTTAACGAAGTCTGCGTGGCAATAAGCCG  
GGTAAATGCAAGCTGATTGTGAGCTCTCACAACACGAAAATACCCGTCAGTTGAAGAA  
CTGGGTAATCTGGTCGCACGTATTCAGGCAGCAGGTGCAGATATTGTTAAATCGCGACC  
ACGGCCCTGGATATCAGTGACGTCGCCCCGATTTTCAGATCACCGTGCACCTCCCAAGTTC  
CGATTATCGGTCTGGTGATGGGCGAACGTGGTCTGATTCTCGCATCCTGTGTGCGAAATT  
TGGCGGTTATCTGACCTTCGGCACGCTGGAAGTGGTGTGGTTTCCGACCGGGTCAGCCG  
ACCATTAAGATCTGCTGGACCTGTACAACCTTCGTCTGATCGGTCCGGATACGAAAGTTT  
TCGGCATTATCGGTAAACCGGTGGGCCATTCAAAGTCGCCGTTCTGTTTAAACGAAGCGTT  
CAAAAGCGTCGGCATTAAATGGTGTGTATGTTTCATCTGCTGGTTGATGACATCGCTCGCTTT  
CTGCAAACCTACAGTTCACGGATTTTTCGGGTTTCTCATGCACCATTCGCGATAAAGAAG  
ATGCCGCTAAGTGCTGTGACGAAGTCCACCCGGTGGCGAAATCGATCGGCGCCGTGAAGT  
GTATTATCCGTCGCCAGAATGATGGCAAACGTGTTTGGTTATAATACCGACTACGTTGGTGC  
AATTAGTGCTATCGAAGAAGGCCTGCGTGCCTCAGAAACGTCTCGAATACGGTGGGCTC  
CCCGCTGGCAGGTAAACTGTTCTGTCGTGATTGGTGGCGGCGGTGCCGGAAGGCACTGGC  
TTATGGCGCAAAAGAAAAGGGTGCTCGCGTTGTCATTGCGAACCCTACCTACGAACGCGC  
GAAAGTGCTGGCCGATATTATCGGCGGTGACGCAATCACGCTGGCTGATCTGGAACACTT  
TCATCCGGAAGACGGTATGATTCTGGCAAATACCACGAGCATCGGCATGCAGCCGAAAGT  
CGATGAAACCCCGGTGTCTAAGAATGCCCTGCGCAGCTATTCTCTGGTTTTTCATGACGTC  
TACACCCGAAAATTACGCGTCTGCTGCGCGAAGCCGAAGAAAGCGGCGCAAGATTGTT  
ACCGGTCTGGAATGTTTATCGGCCAGGCGTATGAACAATTCGAACGTTTACCCGAAGTGC  
CGGCCCCGAAGGAAGTGTTCAAAAGATTATGAGCAAATACTGA

compares the growth rate and SA accumulation of the SK4 derivative strains. It was observed that cultures of the SK4 parental strains reached an OD<sub>600</sub> of 14.5 after 48 h of fermentation. The most significant increase in OD<sub>600</sub> was observed in the SK4/rpsM strain (OD<sub>600</sub> of 21.7). Cultures of the SK4/Lac strain also showed a similar increase (OD<sub>600</sub> of 18.9), as shown in Fig. 2a. However, SA accumulation in the SK4/Lac strain (lactose-induce promoter) was only 1.31 g/L after 48 h of cultivation, whereas the SA accumulation in SK4/rpnBP1 and SK4/rpsM (growth phase-regulated promoter) were 1.69 and 1.74 g/L, respectively, which was 1.33-fold higher (Fig. 2b). A comparison of the SA accumulation in the two *E. coli* strains, SK4/Lac and SK4/rpsM, indicated that a growth phase-dependent

control of the *aroK* gene achieved greater SA accumulation than the lactose-inducible promoter control (Fig. 2b).

### Identification, purification and kinetic analysis of the DHQ-SDH enzyme

To obtain a stable and active DHQ-SDH enzyme, in addition to the full-length protein, the DNA sequence of the *DHQ-SDH* gene (Fig. 3b) was chemically synthesized, based on the its amino acid sequence from *P. trichocarpa* (Fig. 3a). For improved *E. coli* expression, the choice of codons was made according to the *E. coli* codon usage. Enzymatic assay of the DHQ-SDH demonstrated that this construct produced an active SDH, which was used for all

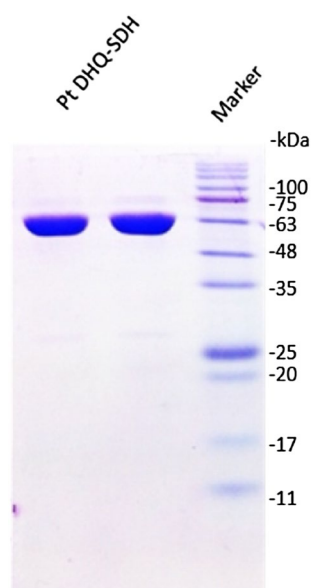


**Fig. 4** SDS–PAGE (12.5%) analysis of pooled fractions from purified DHQ-SDH. Lane 1 and 2, affinity purification by Ni column of DHQ-SDH, marker, The blueye prestained protein ladder (Genedirex)

subsequent functional studies. The DHQ-SDH was purified as described previously in this paper (Fig. 4). The samples of each chromatographic step were analyzed by SDS–PAGE using Coomassie blue staining, and assayed for enzyme activity in the reverse direction, following the increase in absorbance at 340 nm due to the NADP<sup>+</sup> dependent oxidation of D-shikimate to form NADPH and DHS (Table 2). The  $K_m$  and  $V_{max}$  values for DHS were found to be 57.9  $\mu\text{M}$  and 250 U/mg, respectively and those for NADPH were 29.7  $\mu\text{M}$  and 179.5 U/mg, respectively. The  $k_{cat}$  for DHS at saturating NADPH was 347 s<sup>−1</sup> yielding a  $k_{cat}/K_m$  of  $6 \times 10^6 \text{ M}^{-1} \text{ s}^{-1}$ . For the reverse reaction, the  $K_m$  and  $V_{max}$  values for SA were found to be 81.8  $\mu\text{M}$  and 16.4 U/mg, respectively and those for NADP<sup>+</sup> were 27.8  $\mu\text{M}$  and 20.1 U/mg, respectively. The  $k_{cat}$  for SA at saturating NADP<sup>+</sup> was 22.8 s<sup>−1</sup> yielding a  $k_{cat}/K_m$  of  $2.8 \times 10^5 \text{ M}^{-1} \text{ s}^{-1}$ .

**Table 2** Apparent kinetic parameters for shikimate dehydrogenase

Substrates	Vmax (U/mg)	Km ( $\mu\text{M}$ )	kcat (s <sup>−1</sup> )	kcat/Km (M <sup>−1</sup> s <sup>−1</sup> )
DHS	250 ± 43.7	57.9 ± 5.9	347 ± 61	$6.0 (\pm 0.5) \times 10^6$
NADPH	179.5 ± 2.2	29.7 ± 11.5	249 ± 3	$8.4 (\pm 5.2) \times 10^6$
SA	16.4 ± 1	81.8 ± 4.9	22.8 ± 1.4	$2.8 (\pm 0.1) \times 10^5$
NADP <sup>+</sup>	20.1 ± 6.4	27.8 ± 3.4	27.9 ± 8.9	$1.0 (\pm 0.4) \times 10^6$

All constants were measured in Tris–HCl 100 mM (pH 7.0) at 25 °C

## Improvement of SA production in *E. coli* with the DHQ-SDH enzyme expression under growth phase-dependent regulation

To test the possibility that metabolite channeling in DHQ-SDH increases accumulation of SA, a shikimate-synthesizing *E. coli* construct expressing *P. trichocarpa* DHQ-SDH was needed. The *E. coli* SK5 strain was selected as the starting point for the construction of the host strain (Table 1). The capacity of the SK5 derivative strains to accumulate SA was evaluated in flask cultures. As shown in Fig. 5, the growth rate and SA accumulation were measured after 24 h of incubation. It was observed that cultures of the SK5 parental strains reached an OD<sub>600</sub> of 5.9 after 24 h of incubation. The SK5/pSK5 strain, cultivated in the presence of methyl- $\alpha$ -D-glucopyranoside, and supplemented with 5 g/L yeast extract, showed a significant increase in OD<sub>600</sub> (OD<sub>600</sub> = 13.4). The SK5/pSK6 strain was cultivated in the absence of methyl- $\alpha$ -D-glucopyranoside, and supplemented with yeast extract (ranging from 1 to 5 g/L), under growth phase-dependent regulation. With increasing yeast extract concentration, the growth rate of the SK5/pSK6 strain was also increased (Fig. 5a). SA accumulation in the SK5/pSK5 strain (lactose-induce promoter) was only 3.16 g/L after 24 h of cultivation, whereas that in the SK5/pSK6 strain (growth phase-regulated promoter) was 5.33 g/L, which was 1.69-fold higher (Fig. 5b). A comparison between the two *E. coli* strains, SK5/pSK5 (growth phase-dependent promoter control) and SK5/pSK6 (lactose-inducible promoter control), indicated that a growth phase-dependent control of the *aroK* gene can achieve higher SA production by using the same amount of medium used by the current methods.

## Discussion

In DeFeyter and Pittard 1986, studied the affinity of the shikimate kinase isoenzymes. They revealed that the  $K_m$  of shikimate kinase I (encoded by the *aroK* gene) was higher than that of shikimate kinase II (encoded by the *aroL* gene). Supplementation of cultures with aromatic amino acids and yeast extract is also less cost-effective. Chen et al. (2012) indicated that knocking down the expression of the *aroK* gene by antisense RNAi enhanced the accumulation of SA, while deletion of the *aroK* gene increased SA accumulation even further. According to the data obtained in the present study (Fig. 2), there was a noticeable increase in OD<sub>600</sub> in the flask cultures. The amount of SA accumulation in SK4/rrnBP1 and SK4/rpsM was 1.24-fold and 1.28-fold higher than that in SK4/pLac, respectively. This suggested that a growth phase-dependent control of *aroK* expression contributes to the accumulation of SA. Furthermore,

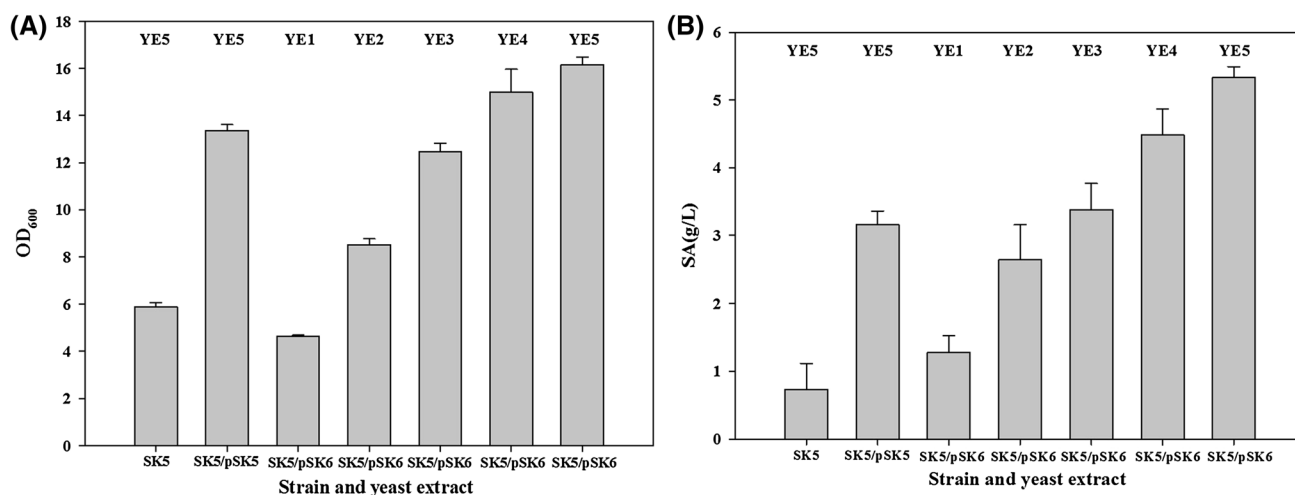


**Fig. 5** Flask cultures of shikimic acid producing strains for the accumulation of shikimic acid. **a** Cell concentration, and **b** shikimic acid accumulation with different concentration of yeast extract supplement

we created *ydiB*, *ppc* and *ldhA* knockout SK5 strains via successive P1 transductions to block the side reactions catalyzed by quinate/shikimate dehydrogenase, phosphoenolpyruvate carboxylase, and lactate dehydrogenase.

In Table 2, the DHQ/SDH V<sub>max</sub> for DHS was the highest among the four substrates, but the corresponding K<sub>m</sub> for DHS was not the lowest. Kinetic analysis of the SD indicated that it belongs to the AroE class of SDH, and is similar to previously reported values for the AroE enzymes from other plant species (Schmidt et al. 1991; Singh and Christendat 2006), or *Mycobacterium tuberculosis* (Fonseca et al. 2006). In plants, DHQ and SDH are two activities of a single, bifunctional enzyme. The bifunctional enzyme DHQ-SDH plays an important role in regulating the partitioning of metabolites to the quinate biosynthetic pathway, by channeling the substrate (DHS) from the DHQ to the SDH active site (Moore 2004). DHQ-SDH is the only bifunctional shikimate pathway enzyme in plants. It catalyzes the dehydration of dehydroquininate to DHS, and the reduction of DHS to shikimate in the shikimate pathway. DHQ-SDH plays an important role at the branch point for quinate biosynthesis. Substrate channeling from the DHQ to the DHS site ensures a constant flux through the shikimate pathway for chorismate biosynthesis (Singh and Christendat 2006). We report the first successfully developed *E. coli* construct from a woody plant, expressing DHQ-SDH, and resulting in increased SA production.

Inactivation of both the *aroL* and *aroK* genes can completely block the aromatic amino acid pathway downstream of SA. However, the total blockage of this pathway can lead to a deficiency in the necessary vitamins and aromatic amino acids, and may negatively affect growth. In this

study, a novel control strategy for the construction for SA-producing strains, without completely blocking the pathway, was developed. It can be widely used in other metabolic pathways as well. Furthermore, this is the first report describing the microbial synthesis of SA, along with the heterologous expression of DHQ-SDH from a woody plant, in *E. coli* strains.

## References

- Ahn JO, Lee HW, Saha R, Park MS, Jung JK, Lee DY (2008) Exploring the effects of carbon sources on the metabolic capacity for shikimic acid production in *Escherichia coli* using in silico metabolic predictions. *J Microbiol Biotechnol* 18:1773–1784
- Atsumi S, Hanai T, Liao JC (2008) Non-fermentative pathways for synthesis of branched-chain higher alcohols as biofuels. *Nature* 451:86–89
- Bochkova DV, Sysolyatin SV, Kalashnikov AI, Surmachena IA (2011) Shikimic acid: review of its analytical, isolation and purification techniques from plant and microbial sources. *J Chem Bio* 15:5–17
- Chandran SS, Yi J, Draths KM, Von Daeniken R, Weber W, Frost JW (2003) Phosphoenolpyruvate availability and the biosynthesis of shikimic acid. *Biotechnol Prog* 19:808–814
- Chaudhuri S, Anton IA, Coggins JR (1987) Shikimate dehydrogenase from *Escherichia coli*. *Methods Enzymol* 142:315–320
- Chen K, Dou J, Tang S, Yang Y, Wang H, Fang H, Zhou C (2012) Deletion of the *aroK* gene is essential for high shikimic acid accumulation through the shikimate pathway in *E. coli*. *Biore-sour Technol* 119:141–147
- Cui YY, Ling C, Zhang Y, Huang J, Liu JZ (2014) Production of shikimic acid from *Escherichia coli* through chemically inducible chromosomal evolution and cofactor metabolic engineering. *Microb Cell Fact* 13:21–31
- Datsenko KA, Wanner BL (2000) One-step inactivation of chromosomal genes in *Escherichia coli* K-12 using PCR products. *PNAS* 12:6640–6645



- Defeyer RC, Pittard J (1986) Genetic and molecular analysis of *aroL*, the gene for shikimate kinase II in *Escherichia coli* K12. *J Bacteriol* 165:226–232
- Escalante A, Calderón R, Valdivia A, De Anda R, Hernández G, Ramírez OT, Gosset G, Bolívar F (2010) Metabolic engineering for the production of shikimic acid in an evolved *Escherichia coli* strain lacking the phosphoenolpyruvate: carbohydrate phosphotransferase system. *Microb Cell Fact* 9:21–32
- Fonseca IO, Magalhaes MLB, Oliveira JS, Silva RG, Mendes MA, Palma MS, Santos DS, Basso LA (2006) Functional shikimate dehydrogenase from *Mycobacterium tuberculosis* H37Rv: purification and characterization. *Protein Express Purif* 46:429–437
- Ghosh S, Chisti Y, Banerjee UC (2012) Production of shikimic acid. *Biotechnol Adv* 30:1425–1431
- Gu P, Su T, Wang Q, Liang Q, Qi Q (2016) Tunable switch mediated shikimate biosynthesis in an engineered nonauxotrophic *Escherichia coli*. *Sci Rep* 6:29745–29754
- Guglielmini G (2010) Shikimic acid: an innovative ingredient formulate cosmetic uses. Available from <http://www.specchemonline.com/articles/view/an-ingredient-for-multiple-cosmetic-uses>
- Kancharla PK, Doddi VR, Kokatla H, Vankar TD (2009) A concise route to (–) shikimic acid and (–)-5-epi-shikimic acid, and their enantiomer via Barbier reaction and ring closing metathesis. *Tetrahedron Lett* 50:6951–6954
- Lemke JJ, Sanchez-Vazquez P, Burgos HL, Hedberg G, Ross W, Gourse RL (2011) Direct regulation of *Escherichia coli* ribosomal protein promoters by the transcription factors ppGpp and DksA. *PNAS* 108:5712–5717
- Moore B (2004) Bifunctional and moonlighting enzymes: lighting the way to regulatory control. *Trends Plant Sci* 9:221–228
- Rodríguez A, Martínez JA, Báez-Viveros JL, Flores N, Hernández-Chávez G, Ramírez OT, Gosset G, Bolívar F (2013) Constitutive expression of selected genes from the pentose phosphate and aromatic pathways increases the shikimic acid yield in high-glucose batch cultures of an *Escherichia coli* strain lacking PTS and *pykF*. *Microb Cell Fact* 12:86–101
- Rodríguez A, Martínez JA, Flores N, Escalante A, Gosset G, Bolívar F (2014) Engineering *Escherichia coli* to overproduce aromatic amino acids and derived compounds. *Microb Cell Fact* 13:126–140
- Sambrook J, Russell DW (2001) Molecular cloning: a laboratory manual. Cold Spring Harbor Laboratory, Cold Spring Harbor
- Schmidt C, Grundemann D, Groth G, Muller B, Henning H, Schultz G (1991) Shikimate pathway in non-photosynthetic tissues. Identification of common enzymes and partial purification of dehydroquinate hydrolyase-shikimate oxidoreductase and chorismate mutase from roots. *J Plant Physiol* 138:51–56
- Singh SA, Christendat D (2006) Structure of Arabidopsis dehydroquinate dehydratase-shikimate dehydrogenase and implications for metabolic channeling in the shikimate pathway. *Biochemistry* 45:7787–7796
- Sprenger A (2006) Aromatic amino acids. *Microbiol Monogr* 5:93–127
- Thomason LC, Costantino N, Court DL (2007) *E. coli* genome manipulation by P1 transduction. *Curr Protoc Mol Biol* 1.17:1–8
- Tuskan GA et al (2006) The genome of black cottonwood, *Populus trichocarpa* (Torr. & Gray). *Science* 313:1596–1604
- Zou YK, Zhou JZ, Sun X, Cai YF, Dai HM, Li SL, Zhou CL, Fang HQ (2011) Construction of shikimic acid-producing engineered *Escherichia coli* strains based on ptsHICrr mutants. *Microbiol China* 38:1186–1192

## Almond Skin Polyphenol Extract Inhibits Inflammation and Promotes Lipolysis in Differentiated 3T3-L1 Adipocytes

Wen-Chung Huang,<sup>1,\*</sup> Chi-Yuan Chen,<sup>1,\*</sup> and Shu-Ju Wu<sup>2,3</sup>

<sup>1</sup>*Graduate Institute of Health Industry Technology and* <sup>2</sup>*Department of Nutrition and Health Sciences, Research Center for Industry of Human Ecology, Research Center for Chinese Herbal Medicine, College of Human Ecology, Chang Gung University of Science and Technology, Taoyuan City, Taiwan.*  
<sup>3</sup>*Department of Dermatology, Aesthetic Medical Center, Chang Gung Memorial Hospital, Taoyuan City, Taiwan.*

**ABSTRACT** Studies have shown that polyphenols reduce the risk of inflammation-related diseases and upregulates energy expenditure in adipose tissue. Here, we investigated the mechanism of the anti-inflammatory and antiobesity effects of almond skin polyphenol extract (ASP) in differentiated 3T3-L1 adipocytes. The antioxidant effects of ASP were measured based on DPPH radical scavenging activity, Trolox equivalent antioxidant capacity, and total phenolic content. Differentiated 3T3-L1 cells were treated with ASP. Subsequently, lipolysis proteins and transcription factors of adipogenesis were measured. The proinflammatory mediators monocyte chemoattractant protein-1 (MCP-1) and chemokine ligand 5 (CCL-5) were determined by enzyme-linked immunosorbent assay. We found that ASP significantly promoted phosphorylation of AMP-activated protein kinase (AMPK), increased activity of adipose triglyceride lipase and hormone-sensitive lipase, and inhibited adipogenesis-related transcription factors. In addition, ASP inhibited the tumor necrosis factor- $\alpha$  (TNF- $\alpha$ )-induced cell inflammatory response via downregulation of MCP-1 and CCL-5 secretion. This study suggests that ASP regulates lipolysis through activation of AMPK, reduced adipogenesis, and suppresses proinflammatory cytokines in adipocytes.

**KEYWORDS:** • 3T3-L1 adipocyte • adipogenesis • almond skin polyphenol extract • lipolysis • proinflammatory mediators

### INTRODUCTION

PREVIOUS STUDIES HAVE SHOWN that obesity results in chronic low-grade inflammation, which increases the risk of chronic diseases such as cardiovascular disease, insulin resistance, nonalcoholic fatty liver disease, and various cancers in both humans and laboratory animals.<sup>1–3</sup> Obesity can be defined as excess accumulation of body fat from an energy imbalance resulting from excessive energy consumption and insufficient energy expenditure. Two types of adipose tissue, brown adipose tissue and white adipose tissue (WAT), are present in mammals. WAT is a producer of bioactive substances called adipokines. Some adipokines have inflammatory functions and induce reactive oxygen species (ROS), and excessive adipose tissue is considered to result in oxidative stress (OS).<sup>4</sup> There is considerable evidence for the pathophysiological role of macrophage- and/or hypertrophic adipocyte-derived chemotactic MCP-1 (monocyte chemoattractant protein-1)/ chemokine receptor 2

pathways in the regulation of monocyte accumulation in obese adipose tissue.<sup>5,6</sup> Chemokine ligand 5 (CCL-5) could participate in the inflammation of WAT in the obese by recruiting blood monocytes and exerting antiapoptotic properties on WAT macrophages.<sup>7</sup> Therefore, excessive fat accumulation suggests the presence of inflammation and OS in the development and progression of chronic diseases.

In addition, adipose tissue can be considered a highly active metabolic and endocrine organ. The major transcriptional factors involved in the adipogenic process include peroxisome proliferator-activated receptor  $\gamma$  (PPAR $\gamma$ ), CCAAT/enhancer binding proteins  $\alpha$  (C/EBP $\alpha$ ), and sterol regulatory element binding proteins (SREBPs).<sup>8–10</sup> The primary function of SREBP-1c is to regulate transcription of genes involved in lipogenesis, including acetyl-CoA carboxylase (ACC), fatty acid synthase (FAS), and 3-hydroxy-3-methylglutaryl CoA (HMG-CoA) reductase.<sup>11</sup> PPAR $\gamma$  is one of the master regulators of adipocyte differentiation, and studies have provided evidence that SREBP-1c can upregulate PPAR $\gamma$  mRNA expression.<sup>10</sup> AMP-activated protein kinase (AMPK) is an energy sensor activated by increased intracellular stress, including glucose deficiency, and by oxidant stress or hypoxia.<sup>12</sup> Lipolysis in WAT is responsible for the release of free fatty acids from triacylglycerol decomposition by adipose triglyceride lipase (ATGL), and hormone-sensitive lipases (HSLs) are key enzymes involved in intracellular degradation of triacylglycerols.<sup>13</sup>

Manuscript received 26 July 2016. Revision accepted 18 December 2016.

\*These authors contributed equally to this article.

Address correspondence to: Shu-Ju Wu, PhD, Department of Nutrition and Health Sciences, Research Center for Industry of Human Ecology, Research Center for Chinese Herbal Medicine, College of Human Ecology, Chang Gung University of Science and Technology, 261 Wen-Hua 1st Road, Kwei-Shan, Taoyuan City 333, Taiwan, E-mail: sjwu@gw.cgust.edu.tw

Diet therapy and exercise are two approaches to decreasing adipose tissue, and food supplements may assist and enhance weight loss and reduce inflammation. Previous studies have shown that dietary polyphenols have anti-inflammatory, antioxidant, and anticancer effects and can be active in the prevention of obesity and obesity-related chronic diseases.<sup>14</sup> Polyphenols, chemicals derived from plants and also known as “phytochemicals,” have gained the interest of the public and scientific communities for their role in maintaining health and preventing disease.<sup>13,14</sup> Many epidemiological studies have demonstrated beneficial effects of peanut and nut consumption, including consumption of almonds, effects that include a reduced incidence of coronary heart disease.<sup>15,16</sup> Almonds (*Prunus amygdalus* Batsch; members of the Rosaceae family, which also includes apples, pears, prunes, and raspberries) are one of the most popular tree nuts worldwide.<sup>17</sup> Almonds are a rich source of bioactive compounds and antioxidants and contain various nutrients and phytochemicals, including monounsaturated fatty acids, polyunsaturated fatty acids,  $\alpha$ -tocopherol, arginine, and potassium, which could be responsible for modifying coronary artery disease risk factors.<sup>18–20</sup> The health-promoting phytochemicals in almond skins are polyphenols, including catechins, flavonols, and flavanones in their aglycone and glycoside forms. Some compelling evidence suggests that polyphenols have cardioprotective effects.<sup>21,22</sup> Previous work has shown that flavonoids from almond skins enhance hamster and human LDL resistance to oxidation.<sup>23</sup> *In vitro* study results indicate that polyphenols from almond skins are effective against *Helicobacter pylori* and could be used in combination with antibiotics as a novel strategy for antibiotic resistance.<sup>24</sup> Almond skin polyphenol extracts (ASPs) protect hepatocytes against hydrogen peroxide-induced hepatocyte OS.<sup>25</sup>

The world is witnessing a major shift in human disease due to the unprecedented obesity epidemic,<sup>26</sup> and identification of food compounds that might address some aspects of obesity and related effects is becoming increasingly important. The present study tested the hypothesis that ASP can influence lipolysis via AMPK activation and fatty acid metabolism in 3T3-L1 cells, as well as by the signaling pathway involved in PPAR $\gamma$  molecular activation, and can exert antioxidant activity to decrease adipose tissue inflammatory responses.

## MATERIALS AND METHODS

### *Preparation of the almond skin extract*

Natural almonds (*Amygdalus communis*) were bought from local markets and stored in the dark. Natural almond skins were blanched in boiling water for about 2 sec for easier removal and then rapidly skinned. The almond skin was dried overnight in an oven, followed by extraction in 75% ethanol (20 g in 200 mL). The microwave (Milestone, Copenhagen, Denmark) settings were 400 W, 15 min, and 88°C, applied three times. Vacuum filtering and concentration were achieved by repeated steps in a concentrator

until ethanol evaporation. Almond skin extract was dissolved in dimethyl sulfoxide (DMSO) to obtain a 100 mM stock solution and stored at –20°C. The final concentration of DMSO in the culture was  $\leq 0.1\%$ .

### *Chemicals*

Almond skin total phenolic content was determined using the Folin–Ciocalteu phenol reagent, and antioxidant capacity was determined based on the DPPH free radical scavenging activity and Trolox equivalent antioxidant capacity (TEAC). The stable free radical 1,1-diphenyl-2-picryl-hydrazyl (DPPH $\bullet$ ), 2,2'-Azino-bis (3-ethylbenzothiazoline-6-sulfonic acid) (ABTS), 30% hydrogen peroxide, peroxidase, 6-hydroxy-2,5,7,8-tetramethylchroman-2-carboxylic acid (Trolox), ascorbic acid, butylated hydroxytoluene, gallic acid, Folin–Ciocalteu phenol reagent, and sodium carbonate (Na<sub>2</sub>CO<sub>3</sub>) were obtained from Sigma (Sigma-Aldrich GmbH, Steinheim, Germany). All other chemicals used were of analytical grade.

### *Determination of total phenolic content*

The total phenolic content of the almond skin extracts was determined colorimetrically using the Folin–Ciocalteu reagent and modified as previously described.<sup>27</sup> Gallic acid was used as the reference compound. Each determination was performed in triplicate and repeated at least three times. Total phenolic content was expressed as milligrams of gallic acid equivalents (GAEs) per gram of almond skin extracts. The results were calculated using a standard calibration curve constructed with different concentrations of gallic acid.<sup>28</sup>

### *Assays for antioxidant activity:*

#### *DPPH radical scavenging activity*

The antiradical activity of ASP was determined based on the principle of scavenging. The DPPH $\bullet$  radical was added to the solutions prepared with ASP and standard antioxidant substances and stirred. Each mixture was kept in the dark for 30 min, and the absorbance was measured at 517 nm, following modified protocols as previously described.<sup>29</sup> The DPPH $\bullet$  concentration in the reaction medium was calculated from a calibration curve analyzed by linear regression. Each determination was carried out in triplicate and repeated at least three times. Absorbance was recorded at 517 nm with a spectrophotometer, and the percentage of scavenged DPPH was calculated using the following equation:

$$\text{DDPH scavenging activity} = \frac{[\text{Absorbance}_{\text{control}} - \text{Absorbance}_{\text{sample}}]}{[\text{Absorbance}_{\text{control}}]} \times 100$$

The extract concentration inducing 50% inhibition (IC<sub>50</sub>) was calculated from the graph of radical scavenging activity % versus sample extract.

### Assays for antioxidant activity: TEAC

The TEAC assay is based on the scavenging of the long-lived radical anion ABTS and radical (ABTS<sup>+</sup>), converting them into a colorless product. The ABTS<sup>+</sup> is decolorized by antioxidants in the test sample when ABTS is incubated with peroxidase and H<sub>2</sub>O<sub>2</sub> according to their concentrations, and antioxidant capacities can be detected spectrophotometrically at 410 nm by comparison with that of Trolox, a water-soluble vitamin E analogue. Each determination was carried out in triplicate and repeated at least three times. The results were expressed as micrograms of Trolox equivalents per gram of food extract.

### Cell line and culture conditions

3T3-L1 murine preadipocyte cell lines were purchased from the Bioresource Collection and Research Center (Taiwan). The 3T3-L1 preadipocyte cells were cultured in Dulbecco's modified Eagle's medium (DMEM) supplemented with 10% fetal calf serum until adipocyte differentiation. The cells were incubated at 37°C in 5% CO<sub>2</sub> humidified air and subcultured twice each week.

### Adipocyte differentiation

For differentiation induction, the 3T3-L1 preadipocytes were stimulated with 10 µg/mL insulin (Sigma-Aldrich), 0.5 mM 1-isobutyl-3-methylxanthine (Sigma-Aldrich), and 1 µM dexamethasone (Sigma-Aldrich) in DMEM culture medium containing 10% fetal bovine serum for 2 days. Next, the culture medium was replaced with DMEM containing 10 µg/mL insulin for 2 days, and the medium was replaced with DMEM every 2 days until day 8.<sup>30</sup> On day 8, the cells were treated with a range of concentrations of ASP (25–100 µM) and were treated on day 9 with tumor necrosis factor-α (TNF-α) (5 µg/mL).

### Measurement of MCP-1 and CCL-5

The levels of MCP-1 and CCL-5 were measured by enzyme-linked immunosorbent assay (ELISA) as previously described.<sup>30,31</sup> The 3T3-L1 cells were cultured and treated with different ASP concentrations (25–100 µg/mL) on day 8, then TNF-α (5 µg/mL) was added and cells were cultured for 24 h. The supernatants were harvested using specific ELISA kits for MCP-1 and CCL-5 (R&D Systems, Minneapolis, MN, USA) and read at 450 nm in a microplate reader (Multiskan FC; Thermo).

### Preparation of total protein

For the total protein assay, 3T3-L1 cells were treated with different concentrations of ASP (25–100 µg/mL) in six-well plates. After incubation, the cells were washed with ice-cold phosphate-buffered saline and harvested with 300 µL protein lysis buffer (0.5 mM Tris-HCl, pH 7.4, 150 mM NaCl, 1 mM EDTA, 0.5% NP40, 0.1% sodium dodecyl sulfate [SDS], 1 mM DTT) containing protease inhibitor cocktail (Sigma). The lysate was centrifuged at 21,500 × g (Tabletop Centrifuge

himac CT15E/RE [Hitachi]) for 5 min, and supernatant was stored for subsequent analysis. Total protein was determined using the BCA protein assay kit (Pierce).

### Western blot analysis

Western blotting was performed as described previously.<sup>30,32</sup> A sample (10 or 20 µg) of protein was mixed with loading dye and separated on 10% SDS polyacrylamide gels. The protein on the gel was transferred to polyvinylidene fluoride membranes (Millipore, Billerica, MA, USA) as previously described.<sup>30</sup> The membranes were incubated with primary antibodies, including C/EBPα, C/EBPβ, phosphorylated AMPKα, PPARγ, ATGL, phosphorylated HSL (Ser853), and phosphorylated ACC (Epitomics, Burlingame, CA, USA) and β-actin (Sigma), overnight at 4°C. The membranes were washed three times with Tris-buffered saline Tween 20 (TBST) buffer (150 mM NaCl, 10 mM Tris pH 8.0, 0.1% Tween 20) for 10 min each. Then, the membranes were incubated with horseradish peroxidase-conjugated secondary antibodies for 1 h at room temperature. Finally, the membranes were washed with TBST and incubated with Luminol/Enhancer Solution (Millipore) to detect and quantify the specific protein using the BioSpectrum 600 system (UVP, Upland, CA, USA).<sup>30,31</sup>

### Statistical analysis

Data are presented as mean ± standard deviation and were assessed by one-way analysis of variance (ANOVA) and Dunnett's *post hoc* test. A *P* < .05 was considered statistically significant. The free radical scavenging activity and total phenolic content were examined using ANOVA and *t*-tests.

## RESULTS

### Total phenolic content and antioxidant capacity of ASP

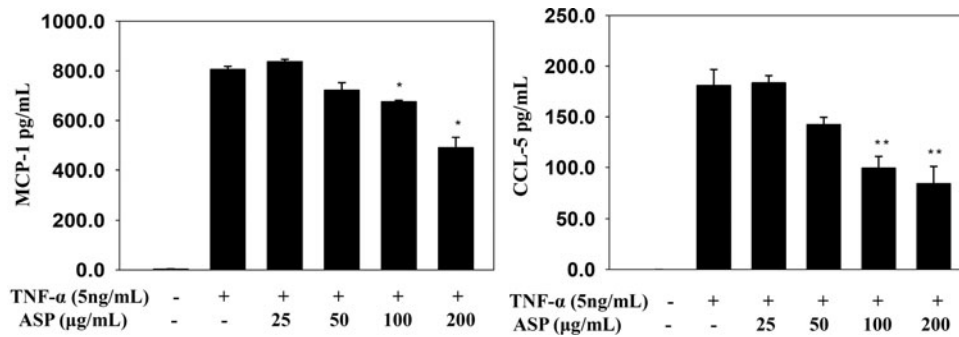
In this study, total phenolic contents in the extracts were determined using the standard curve calculation for GAE. An ASP concentration of 10 mg/mL was equal to 0.35 GAE mg/g. DPPH free radical scavenging activity was 91.88% with an IC<sub>50</sub> = 4 mg/mL. TEAC which is based on the ABTS<sup>+</sup> radical inhibition activity was 96.96 ± 1.11 µg Trolox/g. Thus, ASP contains high amounts of phenolic substances

TABLE 1. TOTAL PHENOLIC CONTENT AND ANTIOXIDANT CAPACITY OF ALMOND SKIN EXTRACTS *IN VITRO*

Concentration of total phenolic (GAE mg/g extracts)	Antioxidant activity	
0.35 GAE mg/g	DPPH free radical scavenging activity	IC <sub>50</sub> = 4 mg/mL
	Trolox equivalent antioxidant capacity (TEAC = µg Trolox/g)	96.96 ± 1.11

The results are expressed as the mean ± standard deviation of triplicate measurements.

DPPH, 1,1-diphenyl-2-picryl-hydrazyl; GAE, gallic acid equivalent.



**FIG. 1.** Effects of ASP on chemokine concentrations in TNF- $\alpha$ -induced 3T3-L1 adipocytes. MCP-1 and CCL-5 concentrations were assayed in differentiated 3T3-L1 adipocytes treated with various ASP concentrations (25–200  $\mu$ M) for 24 h. Data are presented as mean  $\pm$  SD,  $n=6$ . \* $P<.05$ , \*\* $P<.01$ , compared with the TNF- $\alpha$  alone. ASP, almond skin polyphenol extract; CCL-5, chemokine ligand 5; MCP-1, monocyte chemotactic protein-1; SD, standard deviation; TNF- $\alpha$ , tumor necrosis factor- $\alpha$ .

with strong DPPH radical scavenging activity and ABTS<sup>+</sup> radical inhibiting activity (Table 1).

#### Effects of ASP on chemokine concentrations in TNF- $\alpha$ -induced 3T3-L1 cells

ELISA was used to evaluate the effects of ASPs on the levels of proinflammatory chemokines. Because TNF- $\alpha$ -induced 3T3-L1 adipocytes convert as insulin-resistant cells and release MCP-1 and CCL-5,<sup>33,34</sup> we hypothesized that ASP could suppress chemokine concentrations following TNF- $\alpha$  treatment of 3T3-L1 adipocytes. The results showed that TNF- $\alpha$  significantly increased MCP-1 and CCL-5 concentrations in 3T3-L1 adipocytes (Fig. 1). An ASP concentration  $\geq 100$   $\mu$ g/mL significantly suppressed MCP-1 and CCL-5 levels compared with TNF- $\alpha$  treatment of 3T3-L1 adipocytes.

#### The effect of ASP on transcription factors of adipogenesis

Because C/EBP $\alpha$ , C/EBP $\beta$ , and PPAR $\gamma$  are adipogenesis-related transcription factors expressed in differentiated adipocytes,<sup>30</sup> we investigated whether ASP suppresses adipogenesis-related transcription factor expression. We found that treatment with ASP significantly decreased C/EBP $\alpha$ , C/EBP $\beta$ , and PPAR $\gamma$  expression compared with the TNF- $\alpha$ -treated group (Fig. 2). ASP suppressed C/EBP $\alpha$  and C/EBP $\beta$  protein expression at concentrations  $\geq 100$   $\mu$ g/mL and  $\geq 50$   $\mu$ g/mL, respectively. ASP concentrations  $\geq 25$   $\mu$ g/mL inhibited PPAR $\gamma$  expression. Thus, ASPs inhibit adipogenesis-related transcription factors.

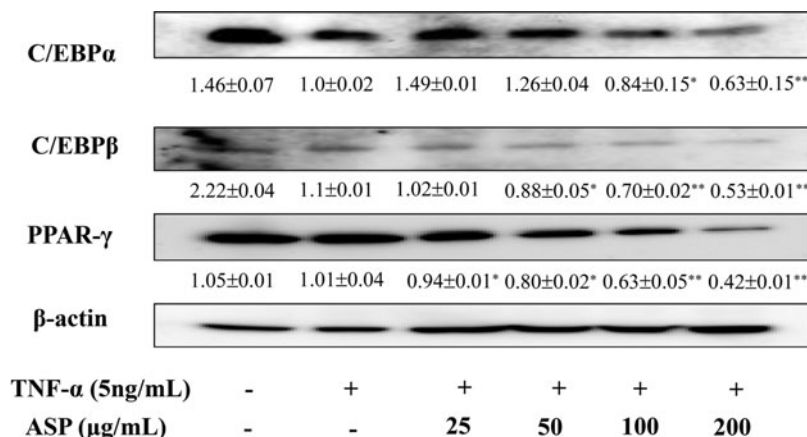


**FIG. 2.** Effects of ASP on transcription factors of adipogenesis in differentiated 3T3-L1 adipocytes. The 3T3-L1 cells ( $10^6$  cells/mL) were treated with various ASP concentrations (25–200  $\mu$ M) for 24 h. C/EBP $\alpha$ , C/EBP $\beta$ , and PPAR $\gamma$  proteins in ASP-treated cells were detected by Western blot ( $n=3$  per group).  $\beta$ -Actin expression was used as an internal control. The densitometry values of three independent experiments were analyzed and expressed as the mean  $\pm$  SD; \* $P<.05$ , \*\* $P<.01$ , compared with the TNF- $\alpha$  alone. C/EBP, CCAAT/enhancer binding protein; PPAR $\gamma$ , peroxisome proliferator-activated receptor  $\gamma$ .

#### The effect of ASP on the expression of proteins involved in lipolysis in 3T3-L1 cells

Key enzymes for lipolysis in WAT are ATGL and HSL,<sup>13</sup> and we thus analyzed expression of these proteins. Based on our results, treatment with ASPs at concentrations  $\geq 50$   $\mu$ g/mL significantly enhanced expression of ATGL, and ASP concentration = 100  $\mu$ g/mL enhanced phosphorylated HSL compared with the TNF- $\alpha$ -treated group in differentiated adipocytes (Fig. 3). Hence, ASP promoted lipolysis in 3T3-L1 cells.

#### The effect of ASP on the AMPK pathway

AMPK plays an important role in glucose and lipid metabolism, enhancing HSL phosphorylation and ATGL accelerated lipolysis.<sup>35,36</sup> Based on our results above, ASP can significantly enhance expression of ATGL and phosphorylated HSL. Thus, we evaluated whether the AMPK pathway was regulated by ASP in 3T3-L1 cells. ASP  $\geq 50$   $\mu$ g/mL significantly increased AMPK $\alpha$  phosphorylation, while ASP  $\geq 100$   $\mu$ g/mL significantly decreased phosphorylation of the substrate ACC-1 compared with the TNF- $\alpha$  treatment group (Fig. 4).

## DISCUSSION

Total phenolic content of almond skin is reflected in the amount of phenols (expressed as  $\mu$ g GAE) present in skin extract and in their antioxidant activity. ASP had excellent



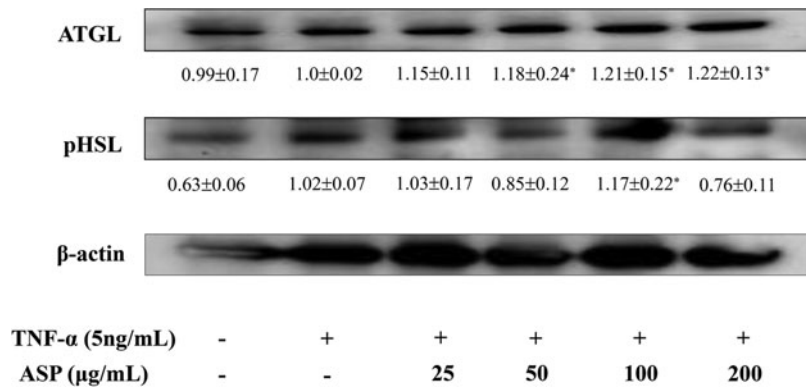


**FIG. 3.** Effects of ASP on lipolysis protein expression in differentiated 3T3-L1 adipocytes. The 3T3-L1 cells ( $10^6$  cells/mL) were treated with various ASP concentrations (25–200  $\mu$ M) for 24 h. ATGL and phosphorylated HSL proteins were detected by Western blots ( $n=3$  per group) in ASP-treated cells.  $\beta$ -Actin expression was used as an internal control. The densitometry values of three independent experiments were analyzed and expressed as the mean  $\pm$  SD; \* $P<.05$ , compared with the TNF- $\alpha$  alone. ATGL, adipose triglyceride lipase; HSL, hormone-sensitive lipase.

radical scavenging activity in the DPPH $^{\bullet}$  assay and good ABTS $^+$  radical inhibition activity. Previous studies have shown that almond skin contains significant amounts of phenolics and flavonoids that are potentially bioavailable for absorption in the gastrointestinal tract.<sup>37</sup> Research indicates that flavonoids and polyphenols exert potent antioxidant/radical scavenging properties in disease prevention. Many studies have shown that flavonoids and polyphenols have anti-inflammatory activity and potential therapeutic applications in inflammation-related diseases, such as arthritis, asthma, encephalomyelitis, and atherosclerosis.<sup>38</sup>

Obesity involves excessive accumulation of triglycerides in adipocytes, which is associated with low-grade chronic inflammation and might cause diabetes, cardiovascular disease, hypercholesterolemia, hypertension, arthritis, and asthma and increase risk of cancers.<sup>34</sup> Obesity leads to functional and morphological damage to remote tissues via circulating factors. White adipocytes function as an important endocrine organ and secrete a multiplicity of inflammation-related adipokines. The adipokines include cytokines (*e.g.*, TNF- $\alpha$ , interleukin-6 [IL-6]), chemokines (*e.g.*, MCP-1, CCL-5), and proteins (*e.g.*, adiponin).<sup>39</sup> Studies indicate that adipocytes secrete the chemokines MCP-1 and CCL-5 to attract macrophage infiltration to adipose tissue.<sup>8</sup> MCP-1 and CCL-5 are crucial for the attraction of mononuclear cells from the circulation into adipose tissue. The inflammatory changes lead to the generation of ROS and insulin resistance in adipose tissue, and adipocyte-derived free fatty acids and MCP-1 and macrophage-derived TNF- $\alpha$  establish a vicious cycle that

aggravates the inflammatory changes and insulin resistance in adipose tissue.<sup>4</sup> Hence, it is important to maintain a healthy weight and normal physiological functions in adipocytes.

The effect of dietary ASP on obesity-related chronic inflammation has not yet been reported. Therefore, in this initial study, we investigated whether ASP could be anti-inflammatory in 3T3-L1 cells induced by TNF- $\alpha$ . TNF- $\alpha$  significantly enhanced the production of MCP-1 and CCL-5, and ASP significantly suppressed the inflammatory factor production at concentrations  $\geq 100$   $\mu$ g/mL. There is evidence that accumulated excess triglycerides lead mature adipocytes to secrete TNF- $\alpha$ , leading to pro-inflammatory cytokines IL-6, MCP-1 and IL-1 $\beta$  production. Studies have reported that activation of AMPK is anti-inflammatory and can inhibit the synthesis of proinflammatory cytokines such as IL-6 and IL-8 in adipocytes.<sup>40</sup> Our results found that ASP significantly promoted AMPK activation. Therefore, we suggested that ASP possesses anti-inflammatory activity due to activation of AMPK and then downregulates MCP-1 and CCL-5 secretion. This result suggests that ASP can suppress TNF- $\alpha$ -induced inflammation in 3T3-L1 adipocytes and may reduce the infiltration of immune cells into adipose tissue; therefore, ASP may suppress the propagation of adipose tissue inflammation in obesity.

In adipose tissue, triglyceride hydrolyzes to fatty acids and glycerol requires three enzymes: ATGL hydrolyzes triglycerides into diacylglycerols and free fatty acids; HSL is phosphorylated by protein kinase A and hydrolyzes diacylglycerols into monoacylglycerols and fatty acids; and

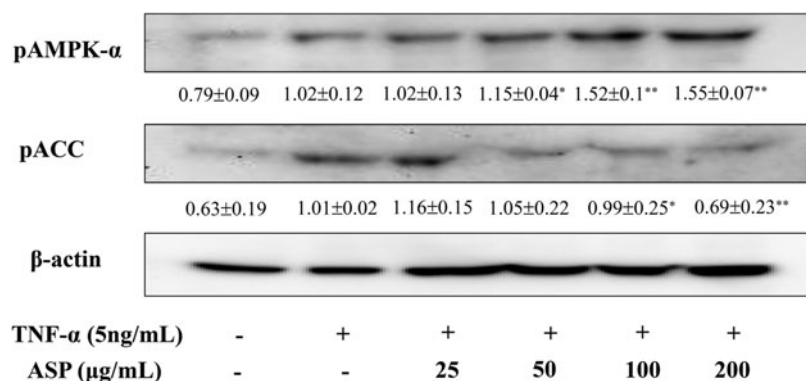


**FIG. 4.** Effects of ASP on the AMPK pathway in differentiated 3T3-L1 adipocytes. The 3T3-L1 cells ( $10^6$  cells/mL) were treated with various ASP concentrations (25–200  $\mu$ M) for 24 h. Phosphorylation of ACC and AMPK $\alpha$  in ASP-treated cells was detected by Western blots ( $n=3$  per group).  $\beta$ -actin or AMPK $\alpha$  expression was used as an internal control. The densitometry values of three independent experiments were analyzed and expressed as the mean  $\pm$  SD; \* $P<.05$ , \*\* $P<.01$ , compared with the TNF- $\alpha$  alone. ACC, acetyl-CoA carboxylase; AMPK, AMP-activated protein kinase.

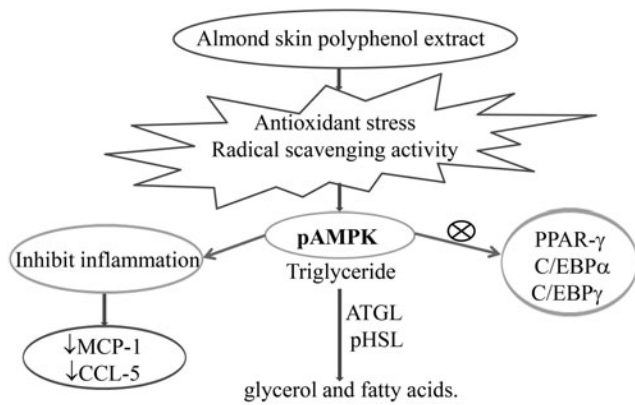


**FIG. 5.** Model explaining the mechanism for the antiobesity effects of ASP in 3T3-L1 cells. Treating differentiated adipocytes with ASP prevents expression of transcription factors of adipogenesis, including PPAR $\gamma$ , C/EBP $\alpha$ , and C/EBP $\beta$ . In addition, ASP through AMPK promotes activity of ATGL and HSL phosphorylation. ASP also exerts antioxidant activity to suppress inflammation and decrease MCP-1 and CCL-5 secretion.

monoacylglycerol lipase hydrolyzes monoacylglycerols to produce glycerol and fatty acids. ATGL and HSL are responsible for more than 90% of triglyceride hydrolysis.<sup>41</sup> Reports indicate that TNF- $\alpha$  reduces ATGL and HSL mRNA levels in adipocytes.<sup>42</sup> Hence, it is important to evaluate the expression of lipolytic enzymes that hydrolyze triglycerides in adipocytes. Furthermore, in this study, we investigated whether ASP could also act as anti-inflammatory and anti-obesity factors. The results demonstrated that ASP significantly promotes HSL phosphorylation and ATGL expression to increase lipolysis and indicate that ASP may produce an antiobesity effect by promoting lipolysis.

In addition, our results found that ASP promotes AMPK activation and increases HSL phosphorylation and ATGL protein expression. Previous results showed that ginkgolide C is a flavone that enhanced ATGL and pHSL production for increasing lipolysis in adipocytes through the activated AMPK pathway.<sup>43</sup> Taken together, these findings suggest that AMPK may via ATGL and phosphorylate HSL stimulate lipolysis. Indeed, enhancing AMPK activity to increase lipolysis can improve the excessive accumulation of triglycerides in adipocytes. Of interest, reports have shown that flavonoids inhibit adipogenesis, which was associated with suppressed C/EBP $\alpha$ , PPAR $\gamma$ , and SREBP-1 expression in the 3T3-L1 preadipocytes.<sup>44</sup> Our results found that ASP significantly suppressed adipogenesis-related transcription factor expression, including PPAR $\gamma$ , C/EBP $\alpha$ , and C/EBP $\beta$ . Previous results confirmed that activation of AMPK reduced protein expression of C/EBP $\beta$ , PPAR $\gamma$  and SREBP-1c in adipocytes.<sup>45</sup> AMPK plays a role in glucose and lipid metabolism and is a central regulator of adipogenesis and lipid storage in adipocytes.<sup>46</sup> The results of the present study indicate that ASP can beneficially regulate adipocyte lipolysis and adipogenesis transcription factors through the AMPK pathway, and reduce the inflammation in TNF- $\alpha$ -induced adipocytes.

In conclusion, based on our results, we suggest that almond skin extract is polyphenol rich, exerting antioxidant activity. ASP significantly inhibits the release of MCP-1 and CCL-5 in 3T3-L1 cells stimulated by TNF- $\alpha$ . ASP promotes AMPK activity to induce lipolysis via HSL phosphorylation and ATGL activity. In addition, ASP suppresses adipogenesis transcription factors PPAR $\gamma$ , C/EBP $\alpha$ , and C/EBP $\beta$  protein expression. Hence, ASP may through AMPK activity diminish obesity and attenuate obesity-related inflammation (Fig. 5).

## ACKNOWLEDGMENTS

This study was supported, in part, by grants from the Chang Gung Memorial Hospital (CMRPF1C0033) and from the Chang Gung University of Science and Technology (EZRP3E0241 and EZRP3F0131 ~ 140).

## AUTHOR DISCLOSURE STATEMENT

No competing financial interests exist.

## REFERENCES

1. Festa A, D'Agostino JR, Howard G, Mykkanen L, Tracy RP, Haffner SM: Chronic subclinical inflammation as part of the insulin resistance syndrome: The Insulin Resistance Atherosclerosis Study (IRAS). *Circulation* 2000;102:42–47.
2. Dandona P, Aljada A, Bandyopadhyay A: Inflammation the link between insulin resistance, obesity and diabetes. *Trends Immunol* 2004;25:4–7.
3. Achike FI, To NH, Wang H, Kwan CY: Obesity, metabolic syndrome, adipocytes and vascular function a holistic viewpoint. *Clin Exp Pharmacol Physiol* 2011;38:1–10.
4. Alba FS, Eduardo MS, Mirandeli B, et al.: Inflammation, oxidative stress, and obesity. *Int J Mol Sci* 2011;12:3117–3132.
5. Kanda H, Tateya S, Tamori Y, et al.: MCP-1 contributes to macrophage infiltration into adipose tissue, insulin resistance, and hepatic steatosis in obesity. *J Clin Invest* 2006;116:1494–1505.
6. Weisberg SP, Hunter D, Huber R, et al.: CCR2 modulates inflammatory and metabolic effects of high-fat feeding. *J Clin Invest* 2006;116:115–124.
7. Keophiphath M, Rouault C, Divoux A, et al.: CCL5 promotes macrophage recruitment and survival in human adipose tissue. *Arterioscler Thromb Vasc Biol* 2010;30:39–45.
8. Smith MM, Minson CT: Obesity and adipokines: Effects on sympathetic over activity. *J Physiol* 2012;590:1787–1801.
9. Sun K, Kusminski CM, Scherer PE: Adipose tissue remodeling and obesity. *J Clin Invest* 2011;121:2094–2101.
10. Koppen A, Kalkhoven E: Brown vs white adipocytes: The PPARgamma coregulator story. *FEBS Lett* 2010;584:3250–3259.
11. Horton JD, Goldstein JL, Brown MS: SREBPs: Activators of the complete program of cholesterol and fatty acid synthesis in the liver. *J Clin Invest* 2002;109:1125–1131.
12. Mungai PT, Waypa GB, Jairaman A, et al.: Hypoxia triggers AMPK activation through reactive oxygen species-mediated activation of calcium release-activated calcium channels. *Mol Cell Biol* 2011;31:3531–3545.
13. Morak M, Schmidinger H, Riesenhuber G, et al.: Adipose triglyceride lipase (ATGL) and hormone-sensitive lipase (HSL) deficiencies affect expression of lipolytic activities in mouse adipose tissues. *Mol Cell Proteomics* 2012;11:1777–1789.

14. Wanga S, Moustaid-Moussaa N, Chenb L, *et al.*: Novel insights of dietary polyphenols and obesity. *J Nutr Biochem* 2014;25:1–18.
15. Kris-Etherton PM, Zhao G, Binkoski AE, Coval SM, *et al.*: The effect of nuts on coronary heart disease risk. *Nutr Rev* 2001;59:103–111.
16. Kelly JH Jr., Sabaté J: Nuts and coronary heart disease: An epidemiological perspective. *Br J Nutr* 2006;96:S61–S67.
17. Weiss EC, Galuska DA, Khan KL, *et al.*: Weight regain in U.S. adults who experienced substantial weight loss, 1999–2002. *Am J Prev Med* 2007;33:34–40.
18. Lin JK, Lin-Shiau SY: Mechanisms of hypolipidemic and anti-obesity effects of tea and tea polyphenols. *Mol Nutr Food Res* 2006;50:211–217.
19. Lin J, Della-Fera MA, Baile CA: Green tea polyphenol epigallocatechin gallate inhibits adipogenesis and induces apoptosis in 3T3-L1 adipocytes. *Obes Res* 2005;13:982–990.
20. Kris-Etherton PM, Yu-Poth S, Sabate J, Ratcliffe HE: Nuts and their bioactive constituents: Effects on serum lipids and other factors that affect disease risk. *Am J Clin Nutr* 1999;70:504S–511S.
21. Sang S, Lapsley K, Jeong WS, *et al.*: Antioxidative phenolic compounds isolated from almond skins (*Prunus amygdalus* Batsch). *J Agric Food Chem* 2001;50:2459–2463.
22. Frison-Norrie S, Sporns P: Identification and quantification of flavonol glycosides in almond seedcoats using MALDI-TOF MS. *J Agric Food Chem* 2001;50:2782–2787.
23. Chen CY, Milbury PE, Lapsley K, Blumberg JB: Flavonoids from almond skins are bioavailable and act synergistically with vitamins C and E to enhance hamster and human LDL resistance to oxidation. *J Nutr* 2005;135:1366–1373.
24. Bisignano C, Filocamo A, La Camera E, *et al.*: Antibacterial activities of almond skins on cagA-positive and-negative clinical isolates of *Helicobacter pylori*. *BMC Microbiol* 2013;13:103.
25. Dong Q, Banaich MS, O'Brien PJ: Cytoprotection by almond skin extracts or catechins of hepatocyte cytotoxicity induced by hydroperoxide (oxidative stress model) versus glyoxal or methylglyoxal (carbonylation model). *Chem Biol Interact* 2010;185:101–109.
26. Dixon AE: Obesity: Changing asthma in the 21st century. *Am J Respir Crit Care Med* 2012;186:395–396.
27. Kujala TS, Loponen JM, Klika KD, Pihlaja K: Phenolics and betacyanins in red beetroot (*Beta vulgaris*) root: Distribution and effect of phenolics and three individual compounds. *J Agric Food Chem* 2000;48:5338–5342.
28. Aksoy L, Kolay E, Ağılönü Y, *et al.*: Free radical scavenging activity, total phenolic content, total antioxidant status, and total oxidant status of endemic *Thermopsis turcica*. *Saudi J Biol Sci* 2013;20:235–239.
29. Shimada K, Fujikawa K, Yahara K, Nakamura T: Antioxidative properties of xanthan on the autoxidation of soybean oil in cyclodextrin emulsion. *J Agric Food Chem* 1992;40:945–948.
30. Huang WC, Chang WT, Wu SJ, *et al.*: Phloretin and phlorizin promote lipolysis and inhibit inflammation in mouse 3T3-L1 cells and in macrophage-adipocyte co-cultures. *Mol Nutr Food Res* 2013;57:1803–1813.
31. Wun ZY, Lin CF, Huang WC, *et al.*: Anti-inflammatory effect of sophoraflavanone G isolated from *Sophora flavescens* in lipopolysaccharide-stimulated mouse macrophages. *Food Chem Toxicol* 2013;62:255–261.
32. Takahashi N, Kawada T, Yamamoto T, *et al.*: Overexpression and ribozyme-mediated targeting of transcriptional coactivators CREB-binding protein and p300 revealed their indispensable roles in adipocyte differentiation through the regulation of peroxisome proliferator-activated receptor gamma. *J Biol Chem* 2002;277:16906–16912.
33. Velioglu YS, Mazza G, Gao L, Oomah BD: Antioxidant activity and total phenolics in selected fruits, vegetables, and grain products. *J Agric Food Chem* 1998;46:4113–4117.
34. Lumeng CN, Saltiel AR: Inflammatory links between obesity and metabolic disease. *J Clin Invest* 2011;121:2111–2117.
35. Lasa A, Schweiger M, Kotzbeck P, *et al.*: Resveratrol regulates lipolysis via adipose triglyceride lipase. *J Nutr Biochem* 2012;23:379–384.
36. Hwang YP, Choi JH, Kim HG, *et al.*: Saponins from *Platycodon grandiflorum* inhibit hepatic lipogenesis through induction of SIRT1 and activation of AMP-activated protein kinase in high-glucose-induced HepG2 cells. *Food Chem* 2013;140:115–123.
37. Mandalari G, Bisignano C, Arrigo MD, *et al.*: Antimicrobial potential of polyphenols extracted from almond skins. *Lett Appl Microbiol* 2012;51:83–89.
38. González R, Ballester I, López-Posadas R, *et al.*: Effects of flavonoids and other polyphenols on inflammation. *Crit Rev Food Sci Nutr* 2011;51:331–362.
39. Trayhurn P, Bing C, Wood IS: Adipose tissue and adipokines—Energy regulation from the human perspective. *J Nutr* 2006;136:1935S–1939S.
40. Bijland S, Mancini SJ, Salt IP: Role of AMP-activated protein kinase in adipose tissue metabolism and inflammation. *Clin Sci* 2013;124:491–507.
41. Schweiger M, Schreiber R, Haemmerle G, *et al.*: Adipose triglyceride lipase and hormone-sensitive lipase are the major enzymes in adipose tissue triacylglycerol catabolism. *J Biol Chem* 2006;281:40236–40241.
42. Kralisch S, Klein J, Lossner U, *et al.*: Isoproterenol, TNFalpha, and insulin downregulate adipose triglyceride lipase in 3T3-L1 adipocytes. *Mol Cell Endocrinol* 2005;240:43–49.
43. Liou CJ, Lai XY, Chen YL, *et al.*: Ginkgolide C suppresses adipogenesis in 3T3-L1 adipocytes via the AMPK signaling pathway. *Evid Based Complement Alternat Med* 2015;2015:298635.
44. Chien PJ, Chen YC, Lu SC, *et al.*: Dietary flavonoids suppress adipogenesis in 3T3-L1 preadipocytes. *J Food Drug Anal* 2005;13:168–175.
45. Kim EJ, Lee DH, Kim HJ, *et al.*: Thiacremonone, a sulfur compound isolated from garlic, attenuates lipid accumulation partially mediated via AMPK activation in 3T3-L1 adipocytes. *J Nutr Biochem* 2012;23:1552–1558.
46. Ejaz A, Wu D, Kwan P, Meydani M: Curcumin inhibits adipogenesis in 3T3-L1 adipocytes and angiogenesis and obesity in C57/BL mice. *J Nutr* 2009;139:919–925.

# Correlation of *HAMP* gene polymorphisms and expression with the susceptibility and length of hospital stays in Taiwanese children with Kawasaki disease

Ying-Hsien Huang<sup>1,\*</sup>, Kuender D. Yang<sup>2,\*</sup>, Yu-Wen Hsu<sup>3,4</sup>, Hsing-Fang Lu<sup>4,5</sup>, Henry Sung-Ching Wong<sup>4,6</sup>, Hong-Ren Yu<sup>1</sup>, Hsing-Chun Kuo<sup>7,8,9</sup>, Fu-Chen Huang<sup>1</sup>, Mao-Hung Lo<sup>1</sup>, Kai-Sheng Hsieh<sup>1</sup>, Su-Fen Chen<sup>11</sup>, Wei-Chiao Chang<sup>4,6,10</sup>, Ho-Chang Kuo<sup>1,6</sup>

<sup>1</sup>Department of Pediatrics and Kawasaki Disease Center, Kaohsiung Chang Gung Memorial Hospital and Chang Gung University College of Medicine, Kaohsiung, Taiwan

<sup>2</sup>Institute of Biomedical Sciences, Mackay Medical College, New Taipei City, Department of Pediatrics, Mackay Memorial Hospital, Taipei, and Institute of Clinical Medicine, National Yang Ming University, Taipei, Taiwan

<sup>3</sup>The Ph.D. Program for Translational Medicine, College of Medical Science and Technology, Taipei Medical University and Academia Sinica, Taipei, Taiwan

<sup>4</sup>Department of Clinical Pharmacy, Taipei Medical University, Taipei, Taiwan

<sup>5</sup>Department of Pharmacy, Taipei Medical University-Shuang Ho Hospital, Taipei, Taiwan

<sup>6</sup>Master's Program for Clinical Pharmacogenomics and Pharmacoproteomics, School of Pharmacy, Taipei Medical University, Taipei, Taiwan

<sup>7</sup>Department of Nursing, Chang Gung University of Science and Technology, Chiayi, Taiwan

<sup>8</sup>Research Center for Industry of Human Ecology and Research Center for Chinese Herbal Medicine, College of Human Ecology, Chang Gung University of Science and Technology, Taoyuan, Taiwan

<sup>9</sup>Chronic Diseases and Health Promotion Research Center, CGUST, Chiayi, Taiwan

<sup>10</sup>Center for Biomarkers and Biotech Drugs, Kaohsiung Medical University, Kaohsiung, Taiwan

<sup>11</sup>Department of Pharmacy, St Vincent Medical Center, Los Angeles, California, USA

\*These authors contributed equally to this work

**Correspondence to:** Ho-Chang Kuo, email: erickuo48@yahoo.com.tw  
Wei-Chiao Chang, email: wcc@tmu.edu.tw

**Keywords:** hepcidin, genetic polymorphism, kawasaki disease

**Received:** August 26, 2016

**Accepted:** March 27, 2017

**Published:** May 08, 2017

Copyright: Huang et al. This is an open-access article distributed under the terms of the Creative Commons Attribution License (CC-BY), which permits unrestricted use, distribution, and reproduction in any medium, provided the original author and source are credited.

## ABSTRACT

Kawasaki disease (KD) is a form of systemic vasculitis. Regarding its pathogenesis, *HAMP* gene encoding hepcidin, which is significant for iron metabolism, has a vital function. In this study, we recruited a total of 381 KD patients for genotyping. Data from 997 subjects (500 subjects from cohort 1; 497 subjects from cohort 2) were used for analysis. Using TaqMan allelic discrimination, we determined five tag SNPs (rs916145, rs10421768, rs3817623, rs7251432, and rs2293689). Treatment outcome data related to such clinical phenotypes as coronary artery lesions (CAL), coronary artery aneurysms (CAA), and intravenous immunoglobulin (IVIG) effects were also collected. Furthermore, we measured plasma hepcidin levels with an enzyme-linked immunosorbent assay. We found that *HAMP* gene polymorphism (rs7251432, and rs2293689) was significantly correlated with KD risk and that plasma hepcidin levels both before and after IVIG treatment had a significantly positive correlation with length of hospital stays ( $R = 0.217$ ,  $p = 0.046$  and  $R = 0.381$ ,  $p < 0.0001$ , respectively). In contrast, plasma hepcidin levels has a negative correlation with KD patients' albumin levels ( $R = -0.27$ ,  $p < 0.001$ ) prior to IVIG treatment. This study's findings indicate that *HAMP* might have a role in the disease susceptibility, as well as its expressions correlated length of hospital stays, and albumin levels in Taiwanese children with KD. Our results suggest that cytokine-activated endogenous or adoptively transferred NK cells might support conventional therapies improving the outcome of MM patients.

## INTRODUCTION

A form of acute vasculitis, KD (Kawasaki disease) affects various systems, most often in children under the age of five years old [1]. KD affects the vascular system in both small and medium-sized blood vessels and especially in coronary arteries [2]. As a result, nearly 20% of children who do not receive treatment suffer a coronary artery aneurysm [3]. The most serious complication of KD is the development of coronary artery lesions (CAL), including myocardial infarctions, coronary artery fistula formations [4], coronary artery dilatations, and coronary artery aneurysms (CAA) [5].

In addition to the diagnostic criteria by the American Heart Association and the American Academy of Pediatrics, such nonspecific clinical symptoms as uveitis, aseptic meningitis, gallbladder hydrops, urethritis, arthralgia, arthritis, hypoalbuminemia, liver function impairment anemia, and heart failure have also been found in KD sufferers [6], with anemia being the most commonly found [7–10]. Hepcidin, a protein for iron regulation, reduces iron level by inhibiting intestinal iron absorption and keeping iron storage in macrophages, leading to impaired hemoglobin synthesis [11]. It is essential not only for iron metabolism but also for the pathogenesis of inflammation anemia [11]. Unusually high levels of hepcidin have been found in anemia in various inflammatory disorders, including autoimmune diseases [12, 13], infections [14, 15], critical illnesses [16, 17], and obesity [18]. In our previous study, we also found that abnormally high levels of hepcidin could impair iron metabolism and subsequently correlate with reduced hemoglobin levels in KD patients [19, 20]. Furthermore, in that study, the changes in hepcidin levels after intravenous immunoglobulin (IVIG) treatment were correlated with CAL and IVIG resistance in KD patients [19]. An increasing amount of evidence has shown that iron levels are associated with coronary artery disease [21, 22] and vasculitis [23, 24]. Moreover, as KD occurs more commonly in Asian populations than European populations [2], we also reported that the C allele of rs916145 in the *HAMP* promoter area has a higher frequency of developing biliary atresia, which is consistent with the low incidence of biliary atresia in European populations [25]. However, no correlation studies between *HAMP* and KD have yet been reported. In this study, we aim to determine the role of *HAMP* in children's susceptibility to KD, CAL formation, and CAA, as well as IVIG treatment responses, lengths of hospital stays, and albumin levels.

## RESULTS

### Basal characteristics of KD patients

The KD patients' basal characteristics for genotyping and plasma hepcidin assay are summarized in Tables 1 and 2, respectively. This study was consisted of

381 KD patients and 997 controls (500 subjects data from cohort 1; 497 subjects data from cohort 2). Male subjects accounted for 66.8% of KD patients and 56% of healthy subjects. A total of 49 (12.9%) KD patients did not respond to their initial IVIG treatment, 64 (16.8%) KD patients developed CAL, and 16 (4.2%) patients developed CAA. The subjects' *HAMP* genotype distribution agreed with the Hardy-Weinberg equilibrium (Supplementary Table 1).

### Association study of *HAMP* gene polymorphisms for susceptibility to KD

We investigated the correlations between *HAMP* genetic polymorphisms and susceptibility for KD. As shown in Table 3, rs2293689 of *HAMP* significantly correlated with the risk of KD under the allelic models ( $p = 0.0410$ ). Application of second cohort, another polymorphism, rs7251432, was identified to associate with the susceptibility for KD under the recessive model ( $p = 0.0315$ ). (Table 3).

### Lack of correlation between *HAMP* polymorphisms and CAL formation, IVIG treatment, and aneurysm formation in KD patients

We also tested whether the *HAMP* polymorphisms correlated with the clinical phenotypes, but none of the polymorphisms had an association with CAL, CAA, or response to IVIG treatment (Tables 4, 5, and 6).

### Correlation between length of hospital stays and hepcidin levels in KD patients

In a prior study, we showed that the changes in hepcidin levels were related to the development of CAL and the response for IVIG treatment in KD patients [19]. In this study, we showed that longer hospital stays were observed in KD patients with CAL than in those without CAL ( $p = 0.005$ ) (Figure 1). Furthermore, we confirmed using linear regression modeling that plasma hepcidin levels both before and after receiving IVIG treatment were positively correlated with patients' length of hospital stays ( $R = 0.217$ ,  $p = 0.046$  and  $R = 0.381$ ,  $p < 0.0001$ , respectively), as shown in Figure 2.

### Correlation between AST, ALT, albumin, and hepcidin levels in KD patients

KD patients often present with hepatitis and jaundice [26], and since hepatocytes are the major producer of hepcidin, that could be directly related to the reason for modified hepcidin expression in KD patients. Furthermore, lower albumin levels were correlated with a resistance to intravenous immunoglobulin treatment and CAL formation [27–29]. We found that plasma hepcidin levels were



**Table 1: Basal characteristics of patients with Kawasaki disease**

Characteristics	Patients with KD
	<i>N</i> = 381
Male gender, No. (%)	247 (66.8%)
Mean (SD) age (years)	1.7 ± 0.08
Age range (years)	0–11
CAL formation	64 (16.8%)
Aneurysm formation	16 (4.2%)
IVIG resistance	49 (12.9%)

CAL: coronary artery lesions; IVIG: intravenous immunoglobulin; SD: standard deviation.

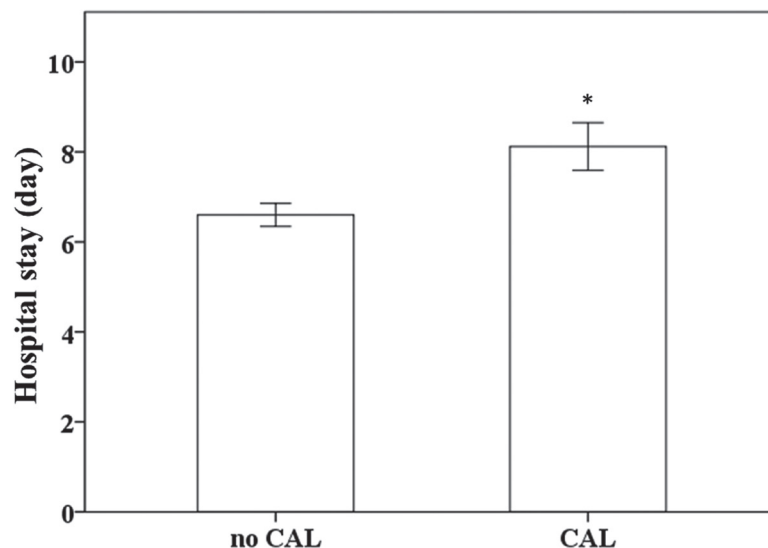


**Figure 1: Comparison of KD patients' length of hospital stays.** Data are presented as mean ± standard error. \* indicates  $p < 0.05$  between groups. KD indicates Kawasaki disease, CAL indicates coronary artery lesions.

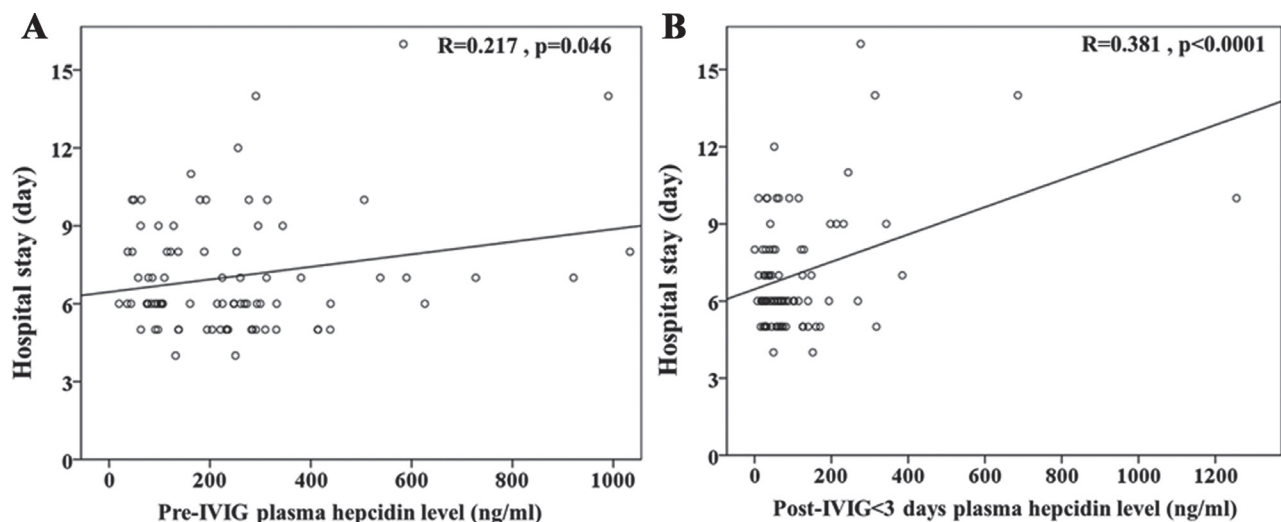


**Figure 2:** Univariate analysis illustrates that plasma hepcidin levels both (A) before and (B) after IVIG treatment were positively correlated with patients' length of hospital stays ( $R = 0.217, p = 0.046$ , and  $R = 0.381, p < 0.0001$ , respectively).

**Table 2: Basal characteristics of 85 Kawasaki disease patients for hepcidin assay**

Characteristics	pre-IVIG	post-IVIG < 3 days	p-value
	N = 85		
Mean (SEM), age (m)	21.6 ± 1.8		
Gender (male : female)	53:32		
CAL formation	25 (29%)		
IVIG resistance	7 (8%)		
WBC (1000/uL)	13.8 ± 0.5	10.6 ± 0.5	< 0.0001
CRP (mg/L)	87.2 ± 6.6	46.6 ± 6	< 0.0001
Albumin (g/dL)	3.1 ± 0.06	2.8 ± 0.01	0.007
GOT (U/L)	62.1 ± 7.3	43.4 ± 9.4	0.103
GPT (U/L)	77.1 ± 9.2	42.3 ± 9.4	0.007

CAL: coronary artery lesions; IVIG: intravenous immunoglobulin; CRP: C-reactive protein; GOT: Glutamic Oxaloacetic Transaminase; GPT: Glutamic Pyruvic Transaminase.

negatively correlated with albumin ( $R = -0.27$ ,  $p < 0.001$ ) prior to IVIG treatment in KD patients (Figure 3).

## DISCUSSION

We reported herein that *HAMP* correlated with KD patients' disease susceptibility and length of hospital stays. Furthermore, rs2293689 of *HAMP* is an important marker with a significant correlation with KD risk. Plasma hepcidin levels in the KD patients both before and after IVIG treatment were positively correlated with patients' length of hospital stays. In contrast, plasma hepcidin was negatively correlated with albumin before KD patients received IVIG treatment.

While there are many elevated inflammatory mediators in KD patients' peripheral blood, no particular biomarker can be used to successfully predict the susceptibility, morbidity, prognosis, and treatment response of KD. The susceptible gene(s) and mechanisms of immunopathogenesis for KD also need to be clarified. In our recently study, we uncovered KD patients showed remarkably hypomethylation at the gene promoters of toll like receptors (TLRs), especially TLR 1, 2, 4, 6, 8, and 9, and increased these TLR mRNA expressions [30]. Interestingly, TLR4 dependent macrophage signaling is associated with coronary arterial disease [31] and a TLR4 agonist has been shown to stimulate hepcidin expression [32]. Moreover, hepcidin not only controls iron metabolism

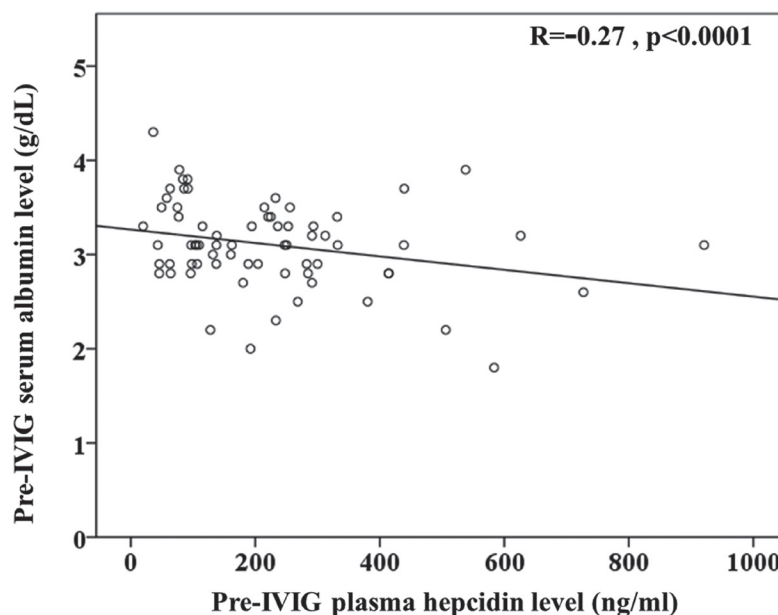


**Figure 3:** Univariate analysis illustrates that plasma hepcidin was negatively correlated with (c) albumin ( $R = -0.27$ ,  $p < 0.001$ ) prior to IVIG treatment in KD patients.

**Table 3: Genotype and allele frequencies of the *HAMP* gene in controls and patients with Kawasaki disease**

	Genotype	Case (%) (n = 381)	Control cohort 1 (%) (n = 497)	Control cohort 2 (%) (n = 500)	Cohort 1 Recessive P Value	Allelic P Value	Cohort 2 Recessive P Value	Allelic P Value
rs916145	CC	46 (13.1)	60 (12.2)	71 (14.2)	0.7108	0.6652	0.6481	0.4768
	CG	158 (45.0)	219 (44.7)	231 (46.2)				
	GG	147 (41.9)	211 (43.1)	198 (39.6)				
rs10421768	GG	0 (0.0)	0 (0.0)	0 (0.0)	1.0000	0.3270	1.000	0.4533
	AG	3 (0.8)	8 (1.6)	7 (1.4)				
	AA	354 (99.2)	489 (98.4)	493 (98.6)				
rs3817623	TT	2 (0.6)	2 (0.5)	1 (0.2)	0.8828	0.3129	0.3745	0.9983
	GT	30 (8.5)	45 (11.0)	46 (9.2)				
	GG	322 (90.9)	363 (88.5)	453 (90.6)				
rs7251432	GG	67 (18.8)	77 (16.1)	67 (13.4)	0.3120	0.1672	<b>0.0315*</b>	0.0939
	AG	163 (45.8)	212 (44.5)	243 (48.6)				
	AA	126 (35.4)	188 (39.4)	190 (38.0)				
rs2293689	TT	2 (0.6)	4 (1.3)	2 (0.4)	0.3333	<b>0.0410*</b>	0.7366	0.8016
	CT	44 (12.3)	54 (17.0)	60 (12.0)				
	CC	312 (87.1)	260 (81.7)	438 (87.6)				

\*Significant ( $P < 0.05$ ) values are in bold.

but also plays a role in the pathogenesis of inflammation anemia [11]. Since anemia is often found in KD patients [19], we also indicated that higher hepcidin levels cause iron deficiency in the serum, thus reducing the availability of iron for erythropoiesis [20]. Furthermore, hepcidin associated iron homeostasis influences the ability of the macrophage polarization program [33] and aberrant activation and infiltration of macrophages is thought to be involved in the formation of arteritis in KD [34]. Moreover, we have shown in a recent study that high-dose aspirin significantly hinders the decrease of hepcidin levels and may be associated with a decrease in hemoglobin during the acute phase of KD [35].

Hepatocytes are the major producer of hepcidin. Since KD patients often present with hepatitis and jaundice [26], that may be one of the main reasons for modified hepcidin expression in KD patients. In fact, various studies have shown that higher AST and ALT levels and lower albumin levels were correlated with IVIG treatment resistance and CAL formation [27–29]. We further demonstrated that changes in hepcidin levels after patients received IVIG treatment were correlated with IVIG resistance and CAL formation [19]. In this study, we uncovered that plasma hepcidin was positively correlated with AST and ALT and negatively correlated with albumin prior to IVIG treatment in KD patients. In a recent study, plasma hepcidin was observed to increase significantly in ICU patients when compared with controls and was the highest in septic patients [36]. Hepcidin-

induced low iron levels were also associated with both the short-term and long-term survival of critically ill patients [37]. Furthermore, Lin *et al.* identified hemoglobin as a useful marker for differentiating KD shock syndrome from toxic shock syndrome in a pediatric intensive care unit [38]. Therefore, the plasma hepcidin is greater in KD shock syndrome than in toxic shock syndrome. Therefore, the hepcidin and hemoglobin levels in KD can possibly be utilized clinically as a differential tool in the future. Based on the results in this study, we propose that hepcidin likely plays an important role in the pathogenesis and disease outcomes of KD patients. In the future, researcher should investigate the molecular machinery of hepcidin in KD and might unlock the mystery of KD.

However, this study still has limitations. The correlation coefficient between plasma hepcidin and several markers for KD severity were statistically significant but had values less than 0.4, thus potentially limiting the clinical application. Although *HAMP* demonstrated a borderline significance in the risk of KD in a Taiwanese population, clinical samples of a second population should be considered to confirm this significance.

In short, we reported herein that *HAMP* polymorphism might have a role in the disease susceptibility, as well as its expressions correlated with disease susceptibility, length of hospital stays, and albumin levels. This study provides a potential prognosis biomarker for Taiwanese children with KD.

**Table 4: Genotype and allele frequencies of *HAMP* gene in Kawasaki disease patients with or without coronary artery lesion formation**

	Genotype	CAL 2 (%) (n = 64)	Without (%) (n = 310)	Allele	CAL 2 (%) (n = 64)	Without (%) (n = 310)	Genotype <i>p</i> -value	Dominant <i>p</i> -value	Recessive <i>p</i> -value	Allelic <i>p</i> -value
rs916145	CC	10 (18.2)	36 (12.3)	C	47 (42.7)	202 (34.6)	0.2696	0.1501	0.2403	0.1026
	CG	27 (49.1)	130 (44.5)	G	64 (57.3)	382 (65.4)				
	GG	18 (32.7)	126 (43.2)							
rs10421768	GG	0 (0.0)	0 (0.0)	G	1 (0.9)	2 (0.3)	-	0.4275	-	0.4285
	AG	1 (1.7)	2 (0.7)	A	115 (99.1)	588 (99.7)				
	AA	57 (98.3)	293 (99.3)							
rs3817623	TT	0 (0.0)	2 (0.7)	T	5 (4.3)	28 (4.8)	0.8158	0.9447	0.5273	0.8222
	GT	5 (8.6)	24 (8.2)	G	111 (95.7)	556 (95.2)				
	GG	53 (91.4)	266 (91.1)							
rs7251432	GG	8 (13.6)	56 (19.1)	G	44 (37.3)	247 (42.2)	0.5787	0.5414	0.3130	0.3278
	AG	28 (47.4)	135 (46.1)	A	74 (62.7)	339 (57.8)				
	AA	23 (39.0)	102 (34.8)							
rs2293689	TT	0 (0.0)	2 (0.7)	T	4 (3.3)	43 (7.3)	0.2682	0.1127	0.5176	0.1013
	CT	4 (6.6)	39 (13.3)	C	118 (96.7)	543 (92.7)				
	CC	57 (93.4)	252 (86.0)							

**Table 5: Genotype and allele frequencies of the *HAMP* gene in Kawasaki disease patients with aneurysm or without aneurysm**

	Genotype	Aneurysm (%) (n = 16)	Without (%) (n = 362)	Allele	Aneurysm (%) (n = 16)	Without (%) (n = 362)	Genotype <i>p</i> -value	Dominant <i>p</i> -value	Recessive <i>p</i> -value	Allelic <i>p</i> -value
rs916145	CC	1 (7.1)	45 (13.4)	C	10 (35.7)	240 (35.6)	0.6052	0.6332	0.4999	0.9908
	CG	8 (57.1)	150 (44.5)	G	18 (64.3)	434 (64.4)				
	GG	5 (35.7)	142 (42.1)							
rs10421768	GG	0 (0.0)	0 (0.0)	G	0 (0.0)	3 (0.4)	-	0.7253	-	0.7258
	AG	0 (0.0)	3 (0.9)	A	28 (100.0)	683 (99.6)				
	AA	14 (100.0)	340 (99.1)							
rs3817623	TT	0 (0.0)	2 (0.6)	T	2 (6.7)	32 (4.7)	0.7571	0.5534	0.7655	0.6255
	GT	2 (13.3)	28 (8.3)	G	28 (93.3)	646 (95.3)				
	GG	13 (86.7)	309 (91.1)							
rs7251432	GG	3 (20.0)	64 (18.8)	G	14 (46.7)	283 (41.5)	0.7621	0.4702	0.9049	0.5740
	AG	8 (53.3)	155 (45.4)	A	16 (53.3)	399 (58.5)				
	AA	4 (26.7)	122 (35.8)							
rs2293689	TT	0 (0.0)	2 (0.6)	T	0 (0.0)	48 (7.0)	0.2909	0.1161	0.7590	0.1208
	CT	0 (0.0)	44 (12.9)	C	32 (100.0)	636 (93.0)				
	CC	16 (100.0)	296 (86.5)							

## PATIENTS AND METHODS

### Patients

The Institutional Review Board of Chang Gung Memorial Hospital approved our study, and we obtained written informed consent from the parents or guardians of all the participating children. We recruited 381 KD patients (Table 1) for this study, and all of them were first treated with one dose of intravenous immunoglobulin (IVIG) (2 g/kg)

over 12 h. We took two sets of blood samples: one within 24 h prior to IVIG treatment (pre-IVIG) and the other within 3 days following IVIG treatment (post-IVIG). We excluded any patients with symptoms that either did not correspond to the KD criteria or had experienced acute fever for less than 5 days. All patients were subjected to two-dimensional, pulse Doppler and color flow imaging at least three times within 8 weeks from the onset of the illness. If a patient was observed to have abnormal coronary arteries, an echocardiographic follow-up was

**Table 6: Genotype and allele frequencies of the *HAMP* gene in Kawasaki disease patients that respond or do not respond to intravenous immunoglobulin treatment**

	Genotype	Resistant (%) (n = 49)	Responsive (%) (n = 326)	Allele	Resistant (%) (n = 49)	Responsive (%) (n = 326)	Genotype <i>p</i> -value	Dominant <i>p</i> -value	Recessive <i>p</i> -value	Allelic <i>p</i> -value
rs916145	CC	5 (10.6)	40 (13.2)	C	36 (38.3)	212 (35.1)	0.3306	0.2444	0.6199	0.5467
	CG	26 (55.3)	132 (43.7)	G	58 (61.7)	392 (64.9)				
	GG	16 (34.0)	130 (43.1)							
rs10421768	GG	0 (0.0)	0 (0.0)	G	0 (0.0)	3 (0.5)	-	0.5068	-	0.5077
	AG	0 (0.0)	3 (1.0)	A	45 (100.0)	615 (99.5)				
	AA	45 (100.0)	306 (99.0)							
rs3817623	TT	0 (0.0)	2 (0.7)	T	6 (6.4)	28 (4.6)	0.4642	0.3464	0.5777	0.4504
	GT	6 (12.8)	24 (7.9)	G	88 (93.6)	582 (95.4)				
	GG	41 (87.2)	279 (91.5)							
rs7251432	GG	7 (15.2)	60 (19.5)	G	37 (40.2)	258 (41.9)	0.7292	0.9020	0.4911	0.7624
	AG	23 (50.0)	138 (44.8)	A	55 (59.8)	358 (58.1)				
	AA	16 (34.8)	110 (35.7)							
rs2293689	TT	0 (0.0)	2 (0.7)	T	7 (7.3)	41 (6.7)	0.7618	0.7184	0.5749	0.8236
	CT	7 (14.6)	37 (12.0)	C	89 (92.7)	573 (93.3)				
	CC	41 (85.4)	268 (87.3)							

scheduled every 3 to 6 months for one year and then once a year afterwards until the affected coronary arteries returned to normal, as reported in our previous studies [29, 39]. This current study carried out said the aforementioned echocardiography using a SONOS 5500 or 7500 cardiac scanner (Philips, Andover, MA, USA) and 5- to 8-MHz sector phased array transducers in order to visualize the diameters of both the right and left coronary arteries on the parasternal short-axis view of the aorta [4]. Pursuant to the guidelines of Japan's Ministry of Health, a CAL is considered a coronary artery if it has an internal diameter more than 3 mm (or 4 mm, if the patient was older than 5 years old) or if a segment has a diameter that is at least 1.5 times that of a contiguous segment, as observed on an echocardiogram. KD patients with coronary artery ectasia or dilatation that disappeared within the first 8 weeks after the onset of the illness were considered as having transient ectasia instead of CAL [40, 41]. We further classified coronary arteries based on whether aneurysms were present using the criteria published by the JCS Joint Working Group. A CAA (including medium and large aneurysms) was defined as a coronary artery with an internal diameter of at least 4 mm or, in children older than 5 years old, a segment with an internal diameter at least 1.5 times that of a contiguous segment as observed through echocardiography [40, 41]. A patient was considered to have responded to IVIG treatment if his/her fever abated 48 h after completing IVIG treatment and they had no recurrence of fever (defined as a temperature > 38°C) for at least 7 days afterwards, as well as visible improvement or normalization of inflammation [10, 29]. We also examined the plasma hepcidin in 85 patients with KD (Table 2) before and after they were treated with IVIG. The blood samples

were immediately placed in tubes that already had heparin, while the other plasma aliquots were stored at -80°C until they were assayed.

## DNA extraction

We treated the obtained blood cells with a 0.5% SDS lysis buffer and then protease K (1 mg/ml) for 4 hours at 60°C to digest nuclear proteins. All DNA was extracted using a Gentra extraction kit, which was followed by 70% alcohol precipitation.

## Genotyping

We selected five tagging SNPs of *HAMP* (rs916145, rs10421768, rs3817623, rs7251432, and rs2293689) with a minimum allelic frequency of 1% in the Han Chinese population from the HapMap database (<http://hapmap.ncbi.nlm.nih.gov/>). All *HAMP* gene polymorphisms were found in the introns. We carried out genotyping using a TaqMan Allelic Discrimination Assay (Applied Biosystems, Foster City, CA, USA). PCR was performed quickly with a 96-well microplate in an ABI 9700 Thermal Cycler using the following thermal cycling conditions: denaturation at 95°C for 10 minutes, followed by 40 cycles of denaturation at 92°C for 15 seconds each, and then annealing and extension at 60°C for 1 min as previously described [42]. We used System SDS software version 1.2.3 to quantify and analyze fluorescence. The average genotyping success rate of our laboratory was 95.7%; therefore, the genotyping data of some subjects were unavailable. The genotype data of the 500 control subjects were obtained from Taiwan's Bio-Bank.



## Measurement of cytokines by enzyme-linked immunoassay (ELISA)

The ELISA kits that we used for plasma hepcidin-25 were commercially available competitive assays with synthetic hepcidin (Bachem Biosciences, St. Helens, United Kingdom, Catalog Number: S-1337), and we used the performance protocol described in one of our previous studies [19].

## Statistical analysis

All data in this study are presented as mean  $\pm$  standard error. The genotypes and allele frequencies that correlated with KD susceptibility and disease outcomes (CAL formation, IVIG treatment response, and aneurysm) were analyzed using the Chi-square test, which was then used with 1 degree of freedom to carry out the Hardy-Weinberg equilibrium. Changes between the values before and after IVIG treatment were evaluated with a paired-sample *t*-test. Two-sided *p*-values  $< 0.05$  were considered statistically significant. All statistical analyses were performed using SPSS version 22.0 for Windows (SPSS software, Inc., Chicago, IL, USA) and JMP 9.0 for Windows.

## Abbreviations

CAA = coronary artery aneurysms, CAL = coronary artery lesions, IVIG = intravenous immunoglobulin, KD = Kawasaki disease, SNP = single nucleotide polymorphism.

## CONFLICTS OF INTEREST

The authors hereby state that they have no financial interests to disclose in relation to this article.

## GRANT SUPPORT

This study was partly supported by a grant from the Ministry of Science and Technology (MOST: 105-2314-B-182-050-MY3), the Ministry of Health and Welfare (PMRPG8E0011), and Chang Gung Memorial Hospital CMRPG8F1911, CMRPG8F1921, CMRPG8F1931, CMRPG8F1941 and in Taiwan. The funders had no role in study design, data collection and analysis, decision to publish, or preparation of the manuscript.

## REFERENCES

1. Kawasaki T, Kosaki F, Okawa S, Shigematsu I, Yanagawa H. A new infantile acute febrile mucocutaneous lymph node syndrome (MLNS) prevailing in Japan. *Pediatrics*. 1974; 54:271–276.

2. Wang CL, Wu YT, Liu CA, Kuo HC, Yang KD. Kawasaki disease: infection, immunity and genetics. *Pediatr Infect Dis J*. 2005; 24:998–1004.
3. Newburger JW, Takahashi M, Burns JC, Beiser AS, Chung KJ, Duffy CE, Glode MP, Mason WH, Reddy V, Sanders SP and et al. The treatment of Kawasaki syndrome with intravenous gamma globulin. *N Engl J Med*. 1986; 315:341–347.
4. Liang CD, Kuo HC, Yang KD, Wang CL, Ko SF. Coronary artery fistula associated with Kawasaki disease. *American heart journal*. 2009; 157:584–588.
5. Newburger JW, Takahashi M, Gerber MA, Gewitz MH, Tani LY, Burns JC, Shulman ST, Bolger AF, Ferrieri P, Baltimore RS, Wilson WR, Baddour LM, Levison ME, et al. Diagnosis, treatment, and long-term management of Kawasaki disease: a statement for health professionals from the Committee on Rheumatic Fever, Endocarditis, and Kawasaki Disease, Council on Cardiovascular Disease in the Young, American Heart Association. *Pediatrics*. 2004; 114:1708–1733.
6. Newburger JW, Takahashi M, Gerber MA, Gewitz MH, Tani LY, Burns JC, Shulman ST, Bolger AF, Ferrieri P, Baltimore RS, Wilson WR, Baddour LM, Levison ME, et al. Diagnosis, treatment, and long-term management of Kawasaki disease: a statement for health professionals from the Committee on Rheumatic Fever, Endocarditis and Kawasaki Disease, Council on Cardiovascular Disease in the Young, American Heart Association. *Circulation*. 2004; 110:2747–2771.
7. Alves NR, Magalhaes CM, Almeida Rde F, Santos RC, Gandolfi L, Pratesi R. Prospective study of Kawasaki disease complications: review of 115 cases. *Rev Assoc Med Bras*. 2011; 57:295–300.
8. Fukushima J, Takahashi N, Ueda Y, Ueda K. Incidence and clinical features of incomplete Kawasaki disease. *Acta Paediatr*. 1994; 83:1057–1060.
9. Kuo HC, Wang CL, Liang CD, Yu HR, Chen HH, Wang L, Yang KD. Persistent monocytosis after intravenous immunoglobulin therapy correlated with the development of coronary artery lesions in patients with Kawasaki disease. *J Microbiol Immunol Infect*. 2007; 40:395–400.
10. Kuo HC, Yang KD, Liang CD, Bong CN, Yu HR, Wang L, Wang CL. The relationship of eosinophilia to intravenous immunoglobulin treatment failure in Kawasaki disease. *Pediatr Allergy Immunol*. 2007; 18:354–359.
11. Fleming RE, Bacon BR. Orchestration of iron homeostasis. *The New England journal of medicine*. 2005; 352:1741–1744.
12. Abdel-Khalek MA, El-Barbary AM, Essa SA, Ghobashi AS. Serum hepcidin: a direct link between anemia of inflammation and coronary artery atherosclerosis in patients with rheumatoid arthritis. *J Rheumatol*. 2011; 38:2153–2159.
13. Demirag MD, Haznedaroglu S, Sancak B, Konca C, Gulbahar O, Ozturk MA, Goker B. Circulating hepcidin in

the crossroads of anemia and inflammation associated with rheumatoid arthritis. *Intern Med.* 2009; 48:421–426.

14. Armitage AE, Eddowes LA, Gileadi U, Cole S, Spottiswoode N, Selvakumar TA, Ho LP, Townsend AR, Drakesmith H. Hecpudin regulation by innate immune and infectious stimuli. *Blood.* 2011; 118:4129–4139.
15. de Mast Q, Nadjm B, Reyburn H, Kemna EH, Amos B, Laarakkers CM, Silalye S, Verhoef H, Sauerwein RW, Swinkels DW and van der Ven AJ. Assessment of urinary concentrations of hepcidin provides novel insight into disturbances in iron homeostasis during malarial infection. *J Infect Dis.* 2009; 199:253–262.
16. Isoda M, Hanawa H, Watanabe R, Yoshida T, Toba K, Yoshida K, Kojima M, Otaki K, Hao K, Ding L, Tanaka K, Takayama T, Kato K, et al. Expression of the peptide hormone hepcidin increases in cardiomyocytes under myocarditis and myocardial infarction. *J Nutr Biochem.* 2010; 21:749–756.
17. Sihler KC, Raghavendran K, Westerman M, Ye W, Napolitano LM. Hecpudin in trauma: linking injury, inflammation, and anemia. *J Trauma.* 2010; 69:831–837.
18. del Giudice EM, Santoro N, Amato A, Brienza C, Calabro P, Wiegierinck ET, Cirillo G, Tartaglione N, Grandone A, Swinkels DW, Perrone L. Hecpudin in obese children as a potential mediator of the association between obesity and iron deficiency. *J Clin Endocrinol Metab.* 2009; 94:5102–5107.
19. Kuo HC, Yang YL, Chuang JH, Tiao MM, Yu HR, Huang LT, Yang KD, Chang WC, Lee CP, Huang YH. Inflammation-induced hepcidin is associated with the development of anemia and coronary artery lesions in Kawasaki disease. *J Clin Immunol.* 2012; 32:746–752.
20. Huang YH, Kuo HC, Huang FC, Yu HR, Hsieh KS, Yang YL, Sheen JM, Li SC, Kuo HC. Hecpudin-Induced Iron Deficiency Is Related to Transient Anemia and Hypoferremia in Kawasaki Disease Patients. *International journal of molecular sciences.* 2016; 17.
21. Kaluza J, Larsson SC, Hakansson N, Wolk A. Heme iron intake and acute myocardial infarction: A prospective study of men. *International journal of cardiology.* 2014; 172:155–160.
22. Hunnicutt J, He K, Xun P. Dietary iron intake and body iron stores are associated with risk of coronary heart disease in a meta-analysis of prospective cohort studies. *The Journal of nutrition.* 2014; 144:359–366.
23. Oliveira R, Napoleao P, Banha J, Paixao E, Bettencourt A, da Silva BM, Pereira D, Barcelos F, Teixeira A, Patto JV, Viegas-Crespo AM, Costa L. Crosstalk between inflammation, iron metabolism and endothelial function in Behcet's disease. *Clinical hemorheology and microcirculation.* 2014; 56:175–185.
24. Mascitelli L, Goldstein MR. Hereditary hemochromatosis, iron, hepcidin, and coronary heart disease. *Medical hypotheses.* 2014; 82:402–403.
25. Huang YH, Huang CC, Chuang JH, Hsieh CS, Lee SY, Chen CL. Upstream stimulatory factor 2 is implicated in the progression of biliary atresia by regulation of hepcidin expression. *J Pediatr Surg.* 2008; 43:2016–2023.
26. Chen CJ, Huang FC, Tiao MM, Huang YH, Lin LY, Yu HR, Yang KD, Huang YC, Chen CC, Chang WC, Kuo HC. Sonographic gallbladder abnormality is associated with intravenous immunoglobulin resistance in Kawasaki disease. *ScientificWorldJournal.* 2012; 2012:485758.
27. Baek JY, Song MS. Meta-analysis of factors predicting resistance to intravenous immunoglobulin treatment in patients with Kawasaki disease. *Korean journal of pediatrics.* 2016; 59:80–90.
28. Yilmazer MM, Oner T, Gokalp S, Doksoz O, Guven B, Vupa Cilengiroglu O, Mese T, Tavli V. Risk factors for persistence of coronary artery abnormalities in Turkish children with Kawasaki disease. *The Turkish journal of pediatrics.* 2015; 57:248–253.
29. Kuo HC, Liang CD, Wang CL, Yu HR, Hwang KP, Yang KD. Serum albumin level predicts initial intravenous immunoglobulin treatment failure in Kawasaki disease. *Acta Paediatr.* 2010; 99:1578–1583.
30. Huang YH, Li SC, Huang LH, Chen PC, Lin YY, Lin CC, Kuo HC. Identifying genetic hypomethylation and upregulation of toll-like receptors in Kawasaki disease. *Oncotarget.* 2017.
31. Habib A, Polavarapu R, Karmali V, Guo L, Van Dam R, Cheng Q, Akahori H, Saeed O, Nakano M, Pachura K, Hong CC, Shin E, Kolodgie F, et al. Hecpudin-ferroportin axis controls toll-like receptor 4 dependent macrophage inflammatory responses in human atherosclerotic plaques. *Atherosclerosis.* 2015; 241:692–700.
32. Pietrangelo A, Dierssen U, Valli L, Garuti C, Rump A, Corradini E, Ernst M, Klein C, Trautwein C. STAT3 is required for IL-6-gp130-dependent activation of hepcidin *in vivo*. *Gastroenterology.* 2007; 132:294–300.
33. Agoro R, Mura C. Inflammation-induced up-regulation of hepcidin and down-regulation of ferroportin transcription are dependent on macrophage polarization. *Blood Cells Mol Dis.* 2016; 61:16–25.
34. Takahashi K, Oharaseki T, Yokouchi Y. Pathogenesis of Kawasaki disease. *Clin Exp Immunol.* 2011; 164:20–22.
35. Kuo HC, Lo MH, Hsieh KS, Guo MM, Huang YH. High-Dose Aspirin Is Associated with Anemia and Does Not Confer Benefit to Disease Outcomes in Kawasaki Disease. *PLoS One.* 2015; 10:e0144603.
36. Tacke F, Nuraldeen R, Koch A, Strathmann K, Hutschenreuter G, Trautwein C, Strnad P. Iron Parameters Determine the Prognosis of Critically Ill Patients. *Critical care medicine.* 2016; 44:1049–1058.
37. Lasocki S, Gaillard T, Rineau E. Iron is essential for living! *Crit Care.* 2014; 18:678.
38. Lin YJ, Cheng MC, Lo MH, Chien SJ. Early Differentiation of Kawasaki Disease Shock Syndrome and Toxic Shock

- Syndrome in a Pediatric Intensive Care Unit. *Pediatr Infect Dis J*. 2015; 34:1163–1167.
39. Kuo HC, Onouchi Y, Hsu YW, Chen WC, Huang JD, Huang YH, Yang YL, Chao MC, Yu HR, Juan YS, Kuo CM, Yang KD, Huang JS, et al. Polymorphisms of transforming growth factor-beta signaling pathway and Kawasaki disease in the Taiwanese population. *J Hum Genet*. 2011; 56:840–845.
40. Shulman ST, De Inocencio J, Hirsch R. Kawasaki disease. *Pediatr Clin North Am*. 1995; 42:1205–1222.
41. Kuo HC, Yu HR, Juo SH, Yang KD, Wang YS, Liang CD, Chen WC, Chang WP, Huang CF, Lee CP, Lin LY, Liu YC, Guo YC, et al. CASP3 gene single-nucleotide polymorphism (rs72689236) and Kawasaki disease in Taiwanese children. *J Hum Genet*. 2011; 56:161–165.
42. Huang YH, Hsu YW, Lu HF, Wong HS, Yu HR, Kuo HC, Huang FC, Chang WC, Kuo HC. Interferon-gamma Genetic Polymorphism and Expression in Kawasaki Disease. *Medicine*. 2016; 95:e3501.



# Phloretin Attenuates Allergic Airway Inflammation and Oxidative Stress in Asthmatic Mice

Wen-Chung Huang<sup>1,2†</sup>, Li-Wen Fang<sup>3†</sup> and Chian-Jiun Liou<sup>2,4\*</sup>

<sup>1</sup>Graduate Institute of Health Industry Technology, Research Center for Industry of Human Ecology, Research Center for Chinese Herbal Medicine, College of Human Ecology, Chang Gung University of Science and Technology, Taoyuan, Taiwan, <sup>2</sup>Division of Allergy, Asthma, and Rheumatology, Department of Pediatrics, Chang Gung Memorial Hospital, Taoyuan, Taiwan, <sup>3</sup>Department of Nutrition, I-Shou University, Kaohsiung, Taiwan, <sup>4</sup>Department of Nursing, Research Center for Chinese Herbal Medicine, Chang Gung University of Science and Technology, Taoyuan, Taiwan

## OPEN ACCESS

### Edited by:

Kottarappat N. Dileepan,  
University of Kansas Medical Center,  
USA

### Reviewed by:

David Dombrowicz,  
Institut national de la santé et de la  
recherche médicale, France  
Verica Paunovic,  
University of Belgrade, Serbia

### \*Correspondence:

Chian-Jiun Liou  
ccliu@mail.cgu.edu.tw

<sup>†</sup>These authors have contributed  
equally to this work.

### Specialty section:

This article was submitted to  
Inflammation,  
a section of the journal  
Frontiers in Immunology

Received: 14 September 2016

Accepted: 26 January 2017

Published: 13 February 2017

### Citation:

Huang W-C, Fang L-W and Liou C-J  
(2017) Phloretin Attenuates Allergic  
Airway Inflammation and Oxidative  
Stress in Asthmatic Mice.  
Front. Immunol. 8:134.  
doi: 10.3389/fimmu.2017.00134

Phloretin (PT), isolated from the apple tree, was previously demonstrated to have antioxidative and anti-inflammatory effects in macrophages and anti-adiposity effects in adipocytes. Inflammatory immune cells generate high levels of reactive oxygen species (ROS) for stimulated severe airway hyperresponsiveness (AHR) and airway inflammation. In this study, we investigated whether PT could reduce oxidative stress, airway inflammation, and eosinophil infiltration in asthmatic mice, and ameliorate oxidative and inflammatory responses in tracheal epithelial cells. BALB/c mice were sensitized with ovalbumin (OVA) to induce asthma symptoms. Mice were randomly assigned to the five experimental groups: normal controls; OVA-induced asthmatic mice; and OVA-induced mice injected intraperitoneally with one of the three PT doses (5, 10, or 20 mg/kg). In addition, we treated inflammatory human tracheal epithelial cells (BEAS-2B cells) with PT to assess oxidative responses and the levels of proinflammatory cytokines and chemokines. We found that PT significantly reduced goblet cell hyperplasia and eosinophil infiltration, which decreased AHR, inflammation, and oxidative responses in the lungs of OVA-sensitized mice. PT also decreased malondialdehyde levels in the lung and reduced Th2 cytokine production in bronchoalveolar lavage fluids. Furthermore, PT reduced ROS, proinflammatory cytokines, and eotaxin production in BEAS-2B cells. PT also suppressed monocyte cell adherence to inflammatory BEAS-2B cells. These findings suggested that PT alleviated pathological changes, inflammation, and oxidative stress by inhibiting Th2 cytokine production in asthmatic mice. PT showed therapeutic potential for ameliorating asthma symptoms in the future.

**Keywords:** asthma, cytokine, eosinophil, oxidative stress, phloretin

## INTRODUCTION

Allergic asthma is a complex, chronic inflammatory airway disease. Patients with sudden, acute asthma attacks exhibit shortness of breath, dry coughing, chest tightness, paroxysmal wheezing due to airway obstruction, troubled breathing, and even death (1). In recent years, public health surveys found that the mortality due to acute asthma was increasing in developing countries (2). Asthma progression involves pathology in the respiratory system, characterized by airway smooth muscle

proliferation, the airway narrowing, and goblet cell hyperplasia, accompanied by mucus hypersecretion, pulmonary eosinophilia, and airway hyperresponsiveness (AHR) (3, 4).

Recent studies have shown that the bronchial asthma is an inappropriate anaphylactic immune response to chronic lung inflammatory disease. Several immune cells, including Th2 cells, mast cells, eosinophils, and airway epithelial cells, secrete cytokines, chemokines, and inflammatory mediators that damage lung tissue and lead to the restricted breathing (4). Importantly, activated Th2 cells release additional cytokines, including IL-4, IL-5, and IL-13, to stimulate IgE production, which then causes mast cell activation, goblet cell hyperplasia, with excessive mucus secretion, eosinophil infiltration, and AHR (5). Furthermore, inflammatory immune cells, including eosinophils, neutrophils, monocytes, and epithelial cells, generate high levels of reactive oxygen species (ROS) to damage lung tissue (6, 7). Hence, asthma progression may be ameliorated by regulating the activity of Th2 cells and reducing the infiltration of inflammatory immune cells.

Phloretin (PT), a flavonoid of the chalcone class, is found in the fruit, leaves, and bark of apple trees (8). PT has many biological functions; it was shown to regulate glucose transporters, promote apoptosis in tumor cells, and enhance lipid metabolism to defend against obesity (9, 10). PT was also found to have anti-oxidase activity, which reduced oxidative damage in a rat model of cerebral ischemia (11).

Our earlier studies demonstrated that PT reduced the inflammatory and oxidative stress in LPS-induced acute lung injury mice (12). PT also suppressed inflammatory mediator expression in IL-1 $\beta$ -stimulated lung epithelial cells (10). Therefore, we reasoned that PT might improve asthma by blocking inflammatory responses and oxidative stress. In the current study, we treated asthmatic mice with intraperitoneal injections of PT to investigate whether PT could ameliorate the pathogenesis of asthma. We evaluated inflammation, oxidative stress, and immune function in asthmatic mice.

## ANIMALS AND METHODS

### Animals

Female BALB/c mice (6–8 weeks old) were obtained from the National Laboratory Animal Center in Taiwan. All mice were housed in air-conventional animal housing with food and water *ad libitum*. Animal care and experimental procedures were performed in accordance with the guidelines of the Laboratory Animal Care Committee of Chang Gung University of Science and Technology (IACUC approval number: 2014-023).

### Sensitization, Airway Challenge, and Drug Treatment

Phloretin (extracted from apple wood;  $\geq 99\%$  purity by HPLC; purchased from Sigma-Aldrich, St. Louis, MO, USA) was dissolved in DMSO. Mice were sensitized with intraperitoneal injections (200  $\mu$ l) that contained 50  $\mu$ g ovalbumin (OVA; Sigma, St. Louis, MO, USA) mixed with 2 mg aluminum hydroxide (Thermo, Rockford, IL, USA) in normal saline. Injections were performed on days 1–3 and 14, as described previously (13). On

days 14, 17, 20, 23, and 27, mice were challenged with inhalations of 2% OVA for 30 min, delivered with an ultrasonic nebulizer (DeVilbiss Pulmo-Aide 5650D, USA). One hour before the OVA inhalation challenge, mice were treated with or without intraperitoneal injections of PT. Then, the OVA challenge was followed by an AHR assay. Mice were randomly divided into five groups (12 mice each), as follows: healthy mice sensitized with normal saline and were given equal volume of DMSO by intraperitoneal injection (N group) (2); mice sensitized with OVA and were given equal volume of DMSO by intraperitoneal injection (OVA group); OVA-sensitized mice treated with 5, 10, or 20 mg/kg PT (PT5, PT10, and PT20 groups, respectively).

### Measurement of AHR

Airway hyperresponsiveness was measured to assess airway function after inhaling aerosolized methacholine, as described previously (14). All mice inhaled 0–40 mg/ml methacholine for 3 min; then, mice were placed in a single-chamber, whole-body plethysmograph (Buxco Electronics, Troy, NY, USA) to record the enhanced pause (Penh), a variable for estimating the AHR.

### Splenocyte Cultures and Serum Collection

Splenocytes ( $5 \times 10^6$  cells/ml) were isolated and cultured in RPMI 1640 medium containing 10% FBS (Biological Industries, Haemek, Israel), 100 U/ml penicillin and streptomycin, and 100  $\mu$ g/ml OVA for five continuous days. The supernatants were collected, and cytokine concentrations were measured, as previously described (13).

Blood collected from the orbital vascular plexus and centrifuged at 6,000 rpm for 5 min. The serum collected and stored at  $-80^\circ\text{C}$  as previously described. Serum was measured OVA-specific antibodies with an enzyme-linked immunosorbent assay (ELISA).

### Histological Analysis of Lung Tissue

Lung tissues were fixed in 10% formalin, embedded in paraffin, and cut into sections 6  $\mu$ m thick. Sections were stained with hematoxylin and eosin (HE), to examine eosinophil infiltration. Inflammatory index calculated and evaluated score using five-point scoring system as described previously (15). The score were considered by the inflammatory cell infiltration on perivascular regions and peribronchial of lungs. Furthermore, tracheal sections were stained with the periodic acid-Schiff (PAS) staining system (Sigma), to measure goblet cell hyperplasia, as described previously (14).

### Malondialdehyde (MDA) Activity

We measured MDA activity in lung tissues with the lipid peroxidation assay kit, according to the manufacturer's instructions (Sigma). MDA activity was measured as nanomolars of MDA in milligram weight of wet tissue with a Multi-Mode Microplate Reader (BioTek SynergyHT, Bedfordshire, UK).

### Glutathione (GSH) Assay

To detect glutathione levels in lung tissues, we employed a glutathione assay kit, according to the manufacturer's instructions



(Sigma). The kit measured total glutathione, glutathione disulfide, and reduced glutathione. The glutathione reaction was measured spectrophotometrically at 412 nm with a microplate reader (Multiskan FC, Thermo, Waltham, MA, USA). Glutathione expressed as nanomolars of MDA in milligram weight of wet tissue.

## Bronchoalveolar Lavage Fluid (BALF) and Cell Counting

Mice were anesthetized and sacrificed to collect BALF, as described previously (16). Mouse tracheas were intubated with an indwelling needle to wash the lungs with normal saline. The supernatants would assay cytokine and chemokine levels. We used Liu stain solution (Polysciences, Inc., Taipei, Taiwan) to differentiate cell morphology and determine cells counts.

## Enzyme-Linked Immunosorbent Assay

Serum OVA-specific antibodies, including IgE and IgG1, were measured with a specific ELISA kit (BD Biosciences). Serum of OVA-sensitized mice makes OVA-IgG1 standard curves for determining the concentrations of IgG1. Serum was diluted fivefold to detect the absorbance of OVA-IgE at an optical density of 450 nm, as previously described (14). Furthermore, the cell culture supernatants and BALF were used to measure with specific ELISA kits to detect the concentrations of CCL5, CCL11, CCL24, CCL26, intercellular adhesion molecule 1 (ICAM-1), IL-4, IL-5, IL-6, IL-8, IL-13, MCP-1, and tumor necrosis factor- $\alpha$  (TNF- $\alpha$ ), according to the manufacturer's instructions (R&D Systems, Minneapolis, MN, USA), as previously described (16).

## RNA Isolation and Real-time PCR

Lung tissues were homogenized, and RNA was extracted with TRIzol reagent (Life Technologies, Carlsbad, CA, USA); complementary DNA (cDNA) was generated from 1  $\mu$ g total RNA using cDNA synthesis kit (Life Technologies). cDNA gene expression assayed by real-time PCR performed with the SYBR Green system (Fermentas, Thermo, Waltham, MA, USA) and specific primers (Table 1) for the genes by the spectrofluorometric thermal cycler (iCycler; Bio-Rad Laboratories, Hercules, CA, USA). The average of gene cycle threshold ( $C_t$ ) was measured for each experiment.

Relative cDNA expressions ( $2^{-\Delta\Delta C_t}$ ) for the specific genes were determined by the compared  $C_t$  method, which generates  $\Delta\Delta C_t$  as the discrepancy between the housekeeping genes  $\beta$ -actin and the specific gene for each sample.

## BEAS-2B Cell Culture and PT Treatment

Phloretin was dissolved in DMSO at a concentration of 100 mM to produce a stock solution. After dilution, the DMSO component was  $\leq 0.1\%$  of the experimental culture medium. We seeded immortalized human bronchial epithelial cells (BEAS-2B) into 24-well plates with DMEM/F12 medium. Cell cultures were pretreated with PT (3–30  $\mu$ M) for 1 h, then treated with 10 ng/ml TNF- $\alpha$  for 24 h, or 10 ng/ml TNF- $\alpha$  and 20 ng/ml IL-4 for 24 h. The supernatants were collected, and the levels of cytokines or chemokines were determined with specific ELISA kits.

## Cell-Cell Adhesion Assay

BEAS-2B cells were treated with PT and stimulated with TNF- $\alpha$  for 24 h. The human monocytic cell line, THP-1, was cultured and stained with calcein-AM solution (Sigma) for 0.5 h, then cocultured with BEAS-2B cells for 1 h. Adherent cells were observed and evaluated with fluorescence microscopy (Olympus, Tokyo, Japan).

## Determination of ROS Production

TNF- $\alpha$ -stimulated BEAS-2B cells treated with PT were seeded in 96-well plates for 24 h. Next, cells were stained with 20  $\mu$ M 2',7'-dichlorofluorescein diacetate (DCFH-DA) for 30 min. Then, cells were lysed and analyzed with a Multi-Mode Microplate Reader (BioTek synergy HT); fluorescence was evaluated by exciting at 485 nm and measuring emission at 528 nm. Furthermore, intracellular ROS was visualized with a fluorescence microscope (Olympus).

## Western Immunoblot Analysis

Lung tissue proteins were quantified and separated on 10% SDS polyacrylamide gels. The proteins were transferred to polyvinylidene fluoride (PVDF) membranes (Millipore, Billerica, MA, USA) and incubated with primary antibodies overnight at 4°C. Then, membranes were washed and incubated with secondary

**TABLE 1 | Primers used in real-time PCR analyses of cytokine and chemokine mRNA expression levels.**

Gene	Primer forward	Primer reverse
CCL11	GGCTTCATGTAGTTCAGAT	CCATTGTGTTCTCAATAATCC
CCL24	AGGCAGTGAGAACCAAGT	GCGTCAATACCTATGTCCAA
COX-2	ACCAGCAGTTCAGTATCAGA	CAGGAGGATGGAGTTGTTGTAG
Gob5	AATGGATGAATGGCTCAGTGAT	TATTGTAGGAGGATGCGTTGTGTC
Intercellular adhesion molecule 1	AACAGAATGGTAGACAGCAT	TCCACCGAGTCTCTCTTAG
IFN- $\gamma$	CAGCAACAACATAAGCGTCATT	ACCTCAAACCTTGGCAATACTCA
IL-4	TCCGTGCTTGAAGAAGAACTC	GTGATGTGGACTTGGACTCATT
IL-5	ATCCTCCTGCCTCTCTTCC	GGTTCCATCTCCAGCACTTCA
IL-13	GCTCCAGCATTGAAGCAGTG	CGTGGCAGACAGGAGTGTT
iNOS	TTCCACAACCACTCAAGCA	TTAAGGCATCACAGTCCGAGTC
MUC5AC	AATGCTGGTGCCTGTGTCT	CCTCTATGCCATCTGTTGTG
$\beta$ -Actin	AAGACCTCTATGCCAACACAGT	AGCCAGAGCAGTAATCTCCTTC

antibodies. Finally, PVDF membranes were treated with Luminol/Enhancer Solution (Millipore) to detect antibody signals with the BioSpectrum 600 system (UVP, Upland, CA, USA). Primary antibodies included anti-HO-1, anti-Nrf2, and anti-Lamin B1 (Santa Cruz, CA, USA);  $\beta$ -actin expression was evaluated as a loading control (Sigma).

## Statistical Analysis

Data were assessed with one-way analysis of variance, followed by the Tukey–Kramer *post hoc* test for multiple comparisons. All values represent the mean  $\pm$  SEM. Values of  $p < 0.05$  were considered significant.

## RESULTS

### Effect of PT on Allergen-Induced AHR in Mice

We evaluated whether PT could improve shortness of breath and abnormal airflow in the airways of asthmatic mice. Airway function was evaluated as the AHR, and the Penh value was calculated

to determine the AHR. Mice were placed into the single-chamber whole-body plethysmograph to record the Penh, during inhalation of various methacholine doses (0–40 mg/ml). We found that, upon inhaling methacholine, the Penh value increased in a dose-dependent manner. The Penh values were greater in OVA-sensitized mice compared to normal mice (**Figure 1A**). At 40 mg/ml of inhaled methacholine, PT-treated asthmatic mice showed significantly lower Penh values (PT5,  $5.9 \pm 0.66$ ,  $p = 0.32$ ; PT10,  $4.41 \pm 0.58$ ,  $p < 0.05$ ; PT20,  $3.94 \pm 0.48$ ,  $p < 0.01$ ) compared to asthmatic mice in the OVA-sensitized group (OVA,  $6.96 \pm 0.78$ ). Hence, PT could significantly diminish AHR in asthmatic mice.

### PT Effect on Inflammatory Cells in BALF

We counted various types of inflammatory cells to assess whether PT decreased the inflammatory response in asthmatic mice by reducing the numbers of inflammatory cells in BALF (**Figure 1B**). Asthmatic mice treated with PT had significantly reduced numbers of eosinophils and total cells compared to the OVA group (eosinophils: PT5:  $6.2 \times 10^5 \pm 6.9 \times 10^4$ ,  $p = 0.57$ ;

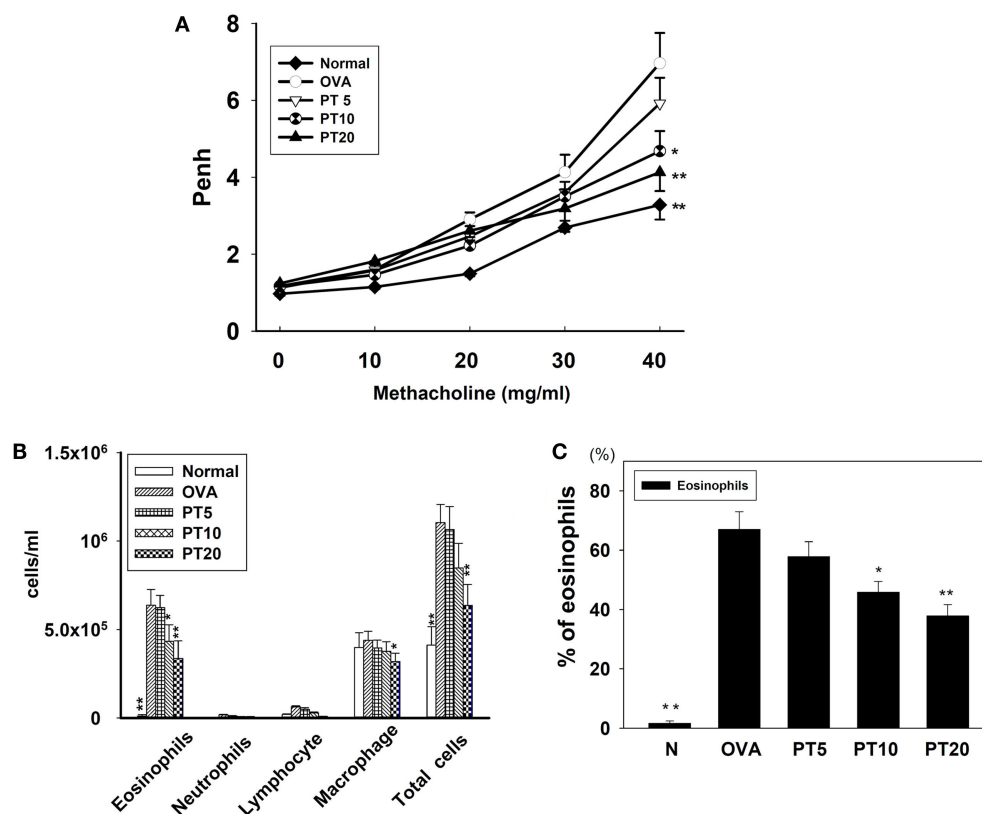


**FIGURE 1 | The effect of phloretin (PT) on airway hyperresponsiveness (AHR) and cell counts in bronchoalveolar lavage fluid (BALF) of asthmatic mice. (A)** Changes in AHR (Penh values) with inhalation of increasing methacholine doses (10–40 mg/ml) in normal (N) and OVA-stimulated (OVA) mice, without or with PT (PT5–20) treatment ( $n = 12$  mice/group, measured in three independent experiments). **(B)** Numbers of inflammatory cells and total cells in BALF with increasing PT doses; **(C)** percentage of eosinophils in BALFs from OVA-sensitive mice, treated or untreated with PT. All data are presented as means  $\pm$  SEM. \* $p < 0.05$  compared to OVA control group. \*\* $p < 0.01$  compared to the OVA control group. Three independent experiments were analyzed and compared with the OVA-sensitive mice.

PT10:  $4.3 \times 10^5 \pm 9.3 \times 10^3$ ,  $p < 0.05$ ; PT20:  $3.3 \times 10^5 \pm 1.1 \times 10^4$ ,  $p < 0.01$  vs. OVA:  $6.4 \times 10^5 \pm 8.9 \times 10^4$ ) (total cells: PT5:  $1.0 \times 10^6 \pm 1.3 \times 10^5$ ,  $p = 0.84$ ; PT10:  $8.4 \times 10^5 \pm 1.3 \times 10^4$ ,  $p = 0.24$ ; PT20:  $6.3 \times 10^5 \pm 1.2 \times 10^4$ ,  $p < 0.01$  vs. OVA:  $1.1 \times 10^6 \pm 1.0 \times 10^5$ ). Furthermore, the proportion of eosinophils in BALF derived from the P10 or the P20 group was significantly reduced compared to the proportion in the OVA group (Figure 1C).

## PT Modulated Chemokine and Cytokine Levels in BALF and Lung Tissue

The levels of cytokines and chemokines in BALF were determined by ELISA (Figure 2). Our results showed that PT could significantly suppress IL-4 levels compared to OVA-sensitization alone (PT5:  $32.4 \pm 6.2$  pg/ml,  $p = 0.33$ ; PT10:  $24.3 \pm 5.2$  pg/ml,  $p < 0.05$ ; PT20:  $18.5 \pm 4.8$  pg/ml,  $p < 0.05$  vs. OVA:  $41.3 \pm 3.8$  pg/ml). In addition, the PT groups had significantly decreased the levels of CCL11, CCL24, TNF- $\alpha$ , IL-6, IL-5, and IL-13 compared to the OVA group. A real-time PCR analysis of the expression of genes in lung tissue showed that PT could significantly decrease the levels of CCL11, CCL24, and ICAM-1 expression compared to the levels in OVA-sensitized asthmatic mice. PT also inhibited IL-4, IL-5, IL-13, MUC5AC, Gob5, iNOS, and COX-2 gene expression.

Furthermore, PT increased the expression of IFN- $\gamma$  compared to the expression in asthmatic mice (Figure 3).

## Effect of PT on Eosinophil Infiltration and Goblet Cell Hyperplasia in Lungs

Eosinophil infiltration in the lungs was evaluated with HE staining. Compared to normal mice, OVA-sensitized mice exhibited more infiltrating eosinophils between the bronchus and blood vessels (Figures 4A,B). PT reduced eosinophil infiltration in the lungs of asthmatic mice. We evaluated tracheal goblet cell hyperplasia with PAS staining. We found that PT could inhibit goblet cell hyperplasia compared to untreated, OVA-sensitized asthmatic mice (Figures 4C,D).

## Effects of PT on GSH and MDA Activity in the Lung

Acute asthma attacks can also cause oxidative stress. Previous studies showed that the expression of antioxidant HO-1 could protect and decrease lung damage during oxidative stress (17). We found that the lungs in PT-treated mice had increased HO-1 expression of lung compared to asthmatic mice. Nrf2, is a transcription factor, could translocate into the nucleus to

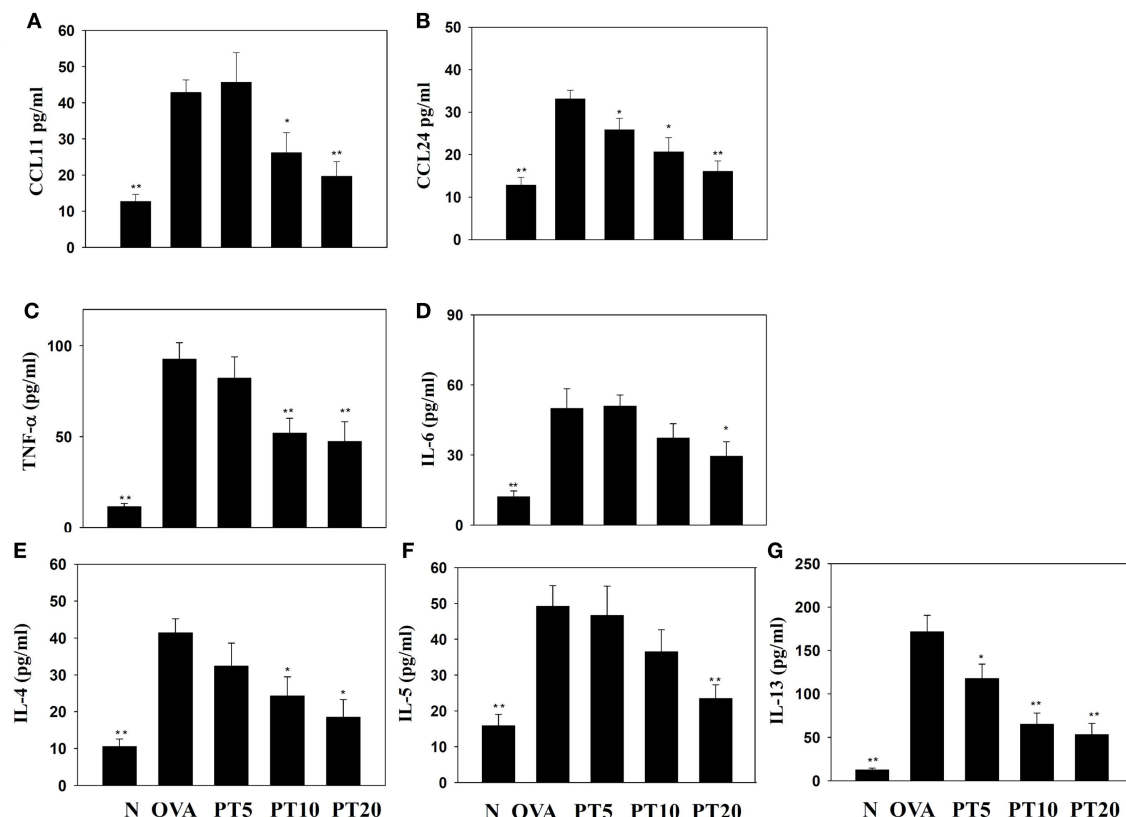


**FIGURE 2 | Effects of phloretin (PT) on the levels of cytokines and chemokines in bronchoalveolar lavage fluid (BALF).** The concentrations of (A) CCL11, (B) CCL24, (C) tumor necrosis factor- $\alpha$  (TNF- $\alpha$ ), (D) IL-6, (E) IL-4, (F) IL-5, and (G) IL-13 were measured by enzyme-linked immunosorbent assay in BALF from normal (N) and OVA-stimulated (OVA) mice, without or with PT (PT5-20) treatment. All data are presented as the means  $\pm$  SEM. \* $p < 0.05$  compared to the OVA control group. \*\* $p < 0.01$  compared to the OVA control group. Three independent experiments were analyzed and compared with the OVA-sensitive mice.

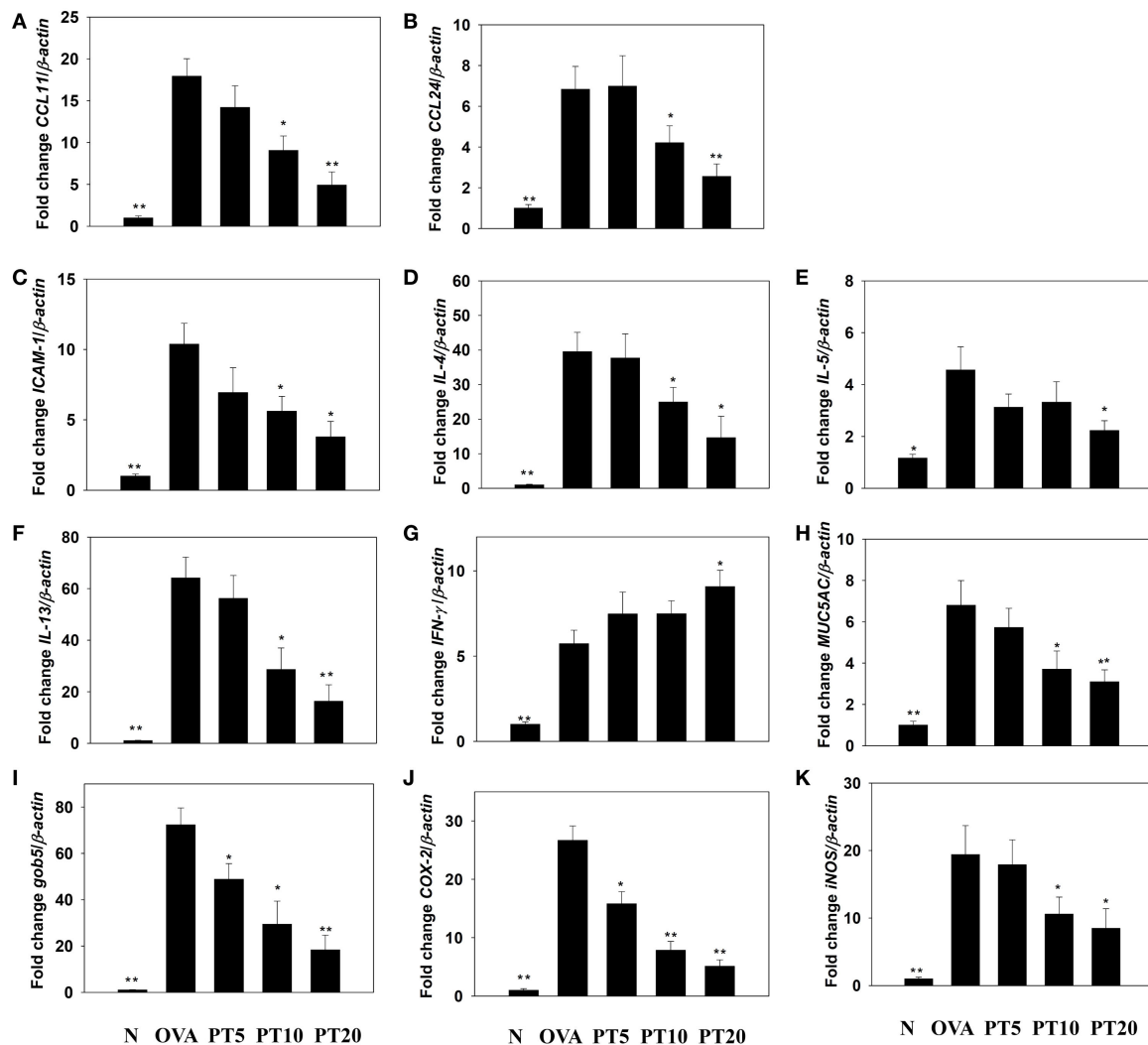


**FIGURE 3 | Phloretin (PT) effects on cytokine, chemokine, and inflammatory mediator mRNA expression in the lungs.** Gene expression levels of (A) CCL11, (B) CCL24, (C) ICAM-1, (D) IL-4, (E) IL-5, (F) IL-13, (G) IFN- $\gamma$ , (H) MUC5AC, (I) Gob5, (J) COX-2, and (K) iNOS were determined by real-time RT-PCR of RNA extracted from lung tissues of normal (N) and OVA-stimulated (OVA) mice, without or with PT (PT5-20) treatment. Fold changes in expression were measured relative to the  $\beta$ -actin expression (internal control). Data are presented as the mean  $\pm$  SEM. \* $p$  < 0.05 compared to OVA control mice. \*\* $p$  < 0.01 compared to OVA control mice. Three independent experiments were analyzed and compared with the OVA-sensitive mice.

promote HO-1 expression for antioxidant response. PT could increase nuclear Nrf2 expression of lung cells compared to OVA-sensitized asthmatic mice (Figure 5A). We also found that the OVA-sensitized asthmatic mice had significantly increased MDA activity and decreased GSH levels in lung tissues compared to the levels in normal mice (Figures 5B,C). However, PT significantly reduced MDA activity and promoted GSH production in lung tissues, compared to the levels in OVA-sensitized asthmatic mice.

### PT Modulated Splenocyte Cytokine Levels and Serum OVA-Specific Antibody

Splenocyte culture supernatant analyses showed that PT significantly attenuated the levels of IL-4, IL-5, and IL-13, compared to untreated OVA-sensitized cells. PT also significantly decreased

the levels of OVA-IgE and OVA-IgG1 in the serum of OVA-sensitized asthmatic mice (Figure 6).

### PT Suppressed Inflammatory Mediators in Activated BEAS-2B Cells

Phloretin could decrease IL-6, IL-8, CCL5, and MCP-1 levels in TNF- $\alpha$ -activated BEAS-2B cells. When BEAS-2B cells were stimulated with TNF- $\alpha$  and IL-4, PT also significantly inhibited CCL11, CCL24, and CCL26 production (Figure 7).

### PT Reduced Monocytic Cell Adhesion to BEAS-2B Cells

Phloretin significantly decreased ICAM-1 expression in TNF- $\alpha$ -activated BEAS-2B cells (Figure 8A). We also evaluated whether

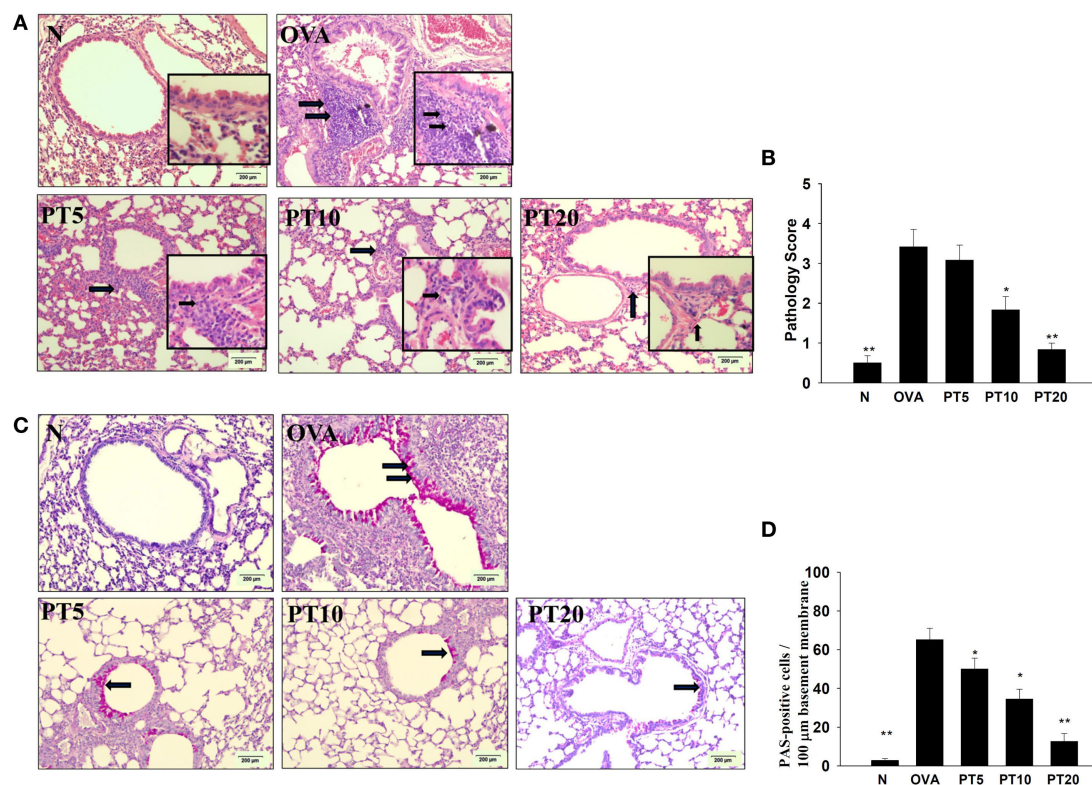


**FIGURE 4 | Phloretin (PT) effects on asthmatic lung tissue.** Histological sections of lung tissues from normal (N) and OVA-stimulated (OVA) mice, without or with PT (PT5–20) treatment. **(A)** PT reduced eosinophil infiltration; eosinophils are indicated with arrows (hematoxylin and eosin stain; 200× magnification). Amplification sections (400× magnification) were shown for the indicated areas. **(B)** Scoring of inflammation via pathological evaluation of inflammatory cell infiltration in lung sections. **(C)** Periodic acid-Schiff (PAS)-stained lung sections show goblet cell hyperplasia; goblet cells are indicated with arrows (200× magnification). **(D)** Results were expressed as the number of PAS-positive cells per 100 μm of basement membrane. All data are presented as the means ± SEM. \* $p < 0.05$  compared to the OVA control group. \*\* $p < 0.01$  compared to the OVA control group. Three independent experiments were analyzed and compared with the OVA-sensitive mice.

PT could inhibit the attachment of THP-1 monocyte cells to inflammatory BEAS-2B cells. TNF- $\alpha$ -stimulated BEAS-2B cells were cocultured with THP-1 cells (stained with calcein AM). PT treatment significantly reduced THP-1 cell adherence to TNF- $\alpha$ -activated BEAS-2B cells (Figures 8B,C).

### Effect of PT on ROS Production

BEAS-2B cells were stained with DCFH-DA, the cells were lysed, and ROS production was quantified with a Multi-Mode Microplate Reader. We found that PT reduced ROS production in TNF- $\alpha$ -activated BEAS-2B cells (Figure 9A). Furthermore, we examined intracellular ROS in intact cells with a fluorescence microscope. We observed that PT attenuated intracellular ROS expression in TNF- $\alpha$ -activated BEAS-2B cells (Figures 9B,C).

## DISCUSSION

Phloretin is a bioactive flavonoid derived from the apple tree. It has anti-inflammatory effects in inflammatory macrophages and human lung epithelial cells (4). Previous studies have shown that PT could regulate glucose transporters and increase lipolysis in

3T3-L1 adipocytes (10, 18). Our previous study found that PT improved the inflammatory and oxidative stress in LPS-induced acute lung injury mice (12). In the present study, we evaluated the hypothesis that PT might ameliorate the pathological manifestations of asthma in an asthmatic mouse model. These results suggested that PT could ameliorate local asthma symptoms in the lung by attenuating Th2 cell activity in the immune system of this experimental asthmatic model. PT acted by blocking the inflammatory response and alleviating oxidative stress.

Oxidative stress plays an important role in the development of several chronic diseases, including cardiovascular disorders, cancer, diabetes, and asthma (19). Asthma is a disorder involving pulmonary inflammation and allergic reaction; thus, excessive oxidative stress would exacerbate airway inflammation and cause aggravated bronchospasms that could worsen lung tissue damage (20). In several animal studies, excess ROS was reported to increase inflammatory cell infiltration into the lungs, stimulate extracellular matrix protein production, and stimulate proinflammatory cytokine production in airway epithelial cells (21, 22). It was previously shown that natural antioxidants could improve the pathological manifestations of asthma by blocking oxidative



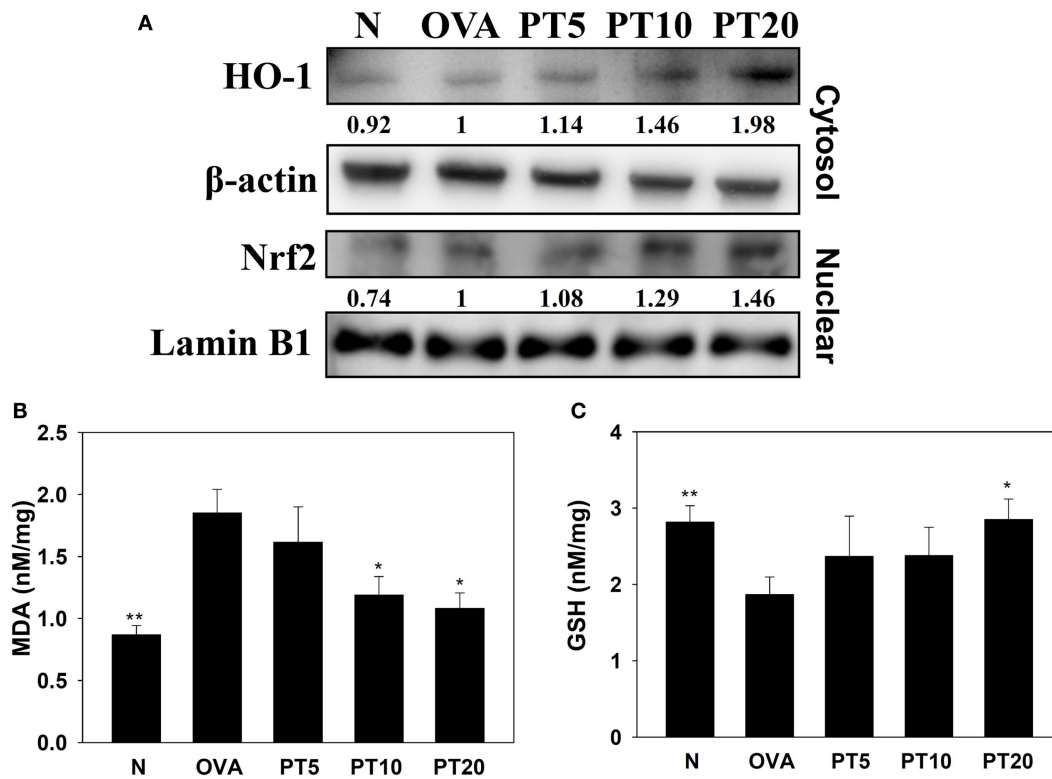


**FIGURE 5 | Phloretin (PT) effects on oxidative stress factors. (A)** Western blot shows PT modulation of HO-1 and Nrf2 expression in lung tissue of normal (N) and OVA-stimulated (OVA) mice, without or with PT (PT5-20) treatment. **(B)** Malondialdehyde (MDA) activity and **(C)** GSH activity in lung tissues of mice. Data are presented as the mean  $\pm$  SEM. \* $p < 0.05$  compared to OVA control mice. \*\* $p < 0.01$  compared to OVA control mice. Three independent experiments were analyzed and compared with the OVA-sensitive mice.

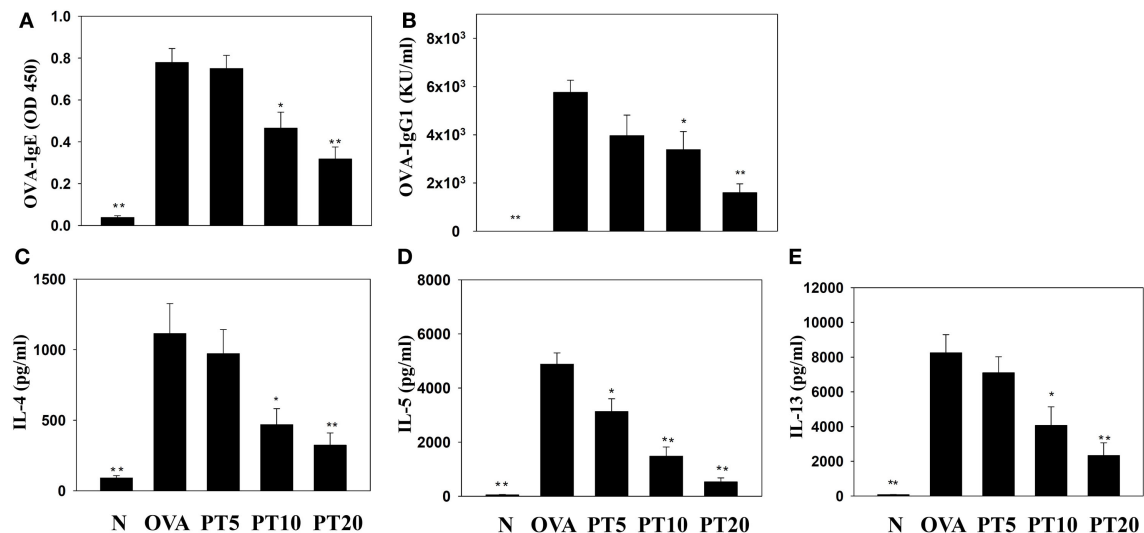


**FIGURE 6 | Phloretin (PT) effects on OVA-specific antibodies in serum.** Serum levels of **(A)** OVA-IgE and **(B)** OVA-IgG1 are shown from normal (N) and OVA-stimulated (OVA) mice, without or with PT (PT5-20) treatment. PT also changed the cytokine levels produced by OVA-activated splenocytes, including **(C)** IL-4, **(D)** IL-5, and **(E)** IL-13. All data are presented as the means  $\pm$  SEM. \* $p < 0.05$  compared to the OVA control group. \*\* $p < 0.01$  compared to the OVA control group. Three independent experiments were analyzed and compared with the OVA-sensitive mice.

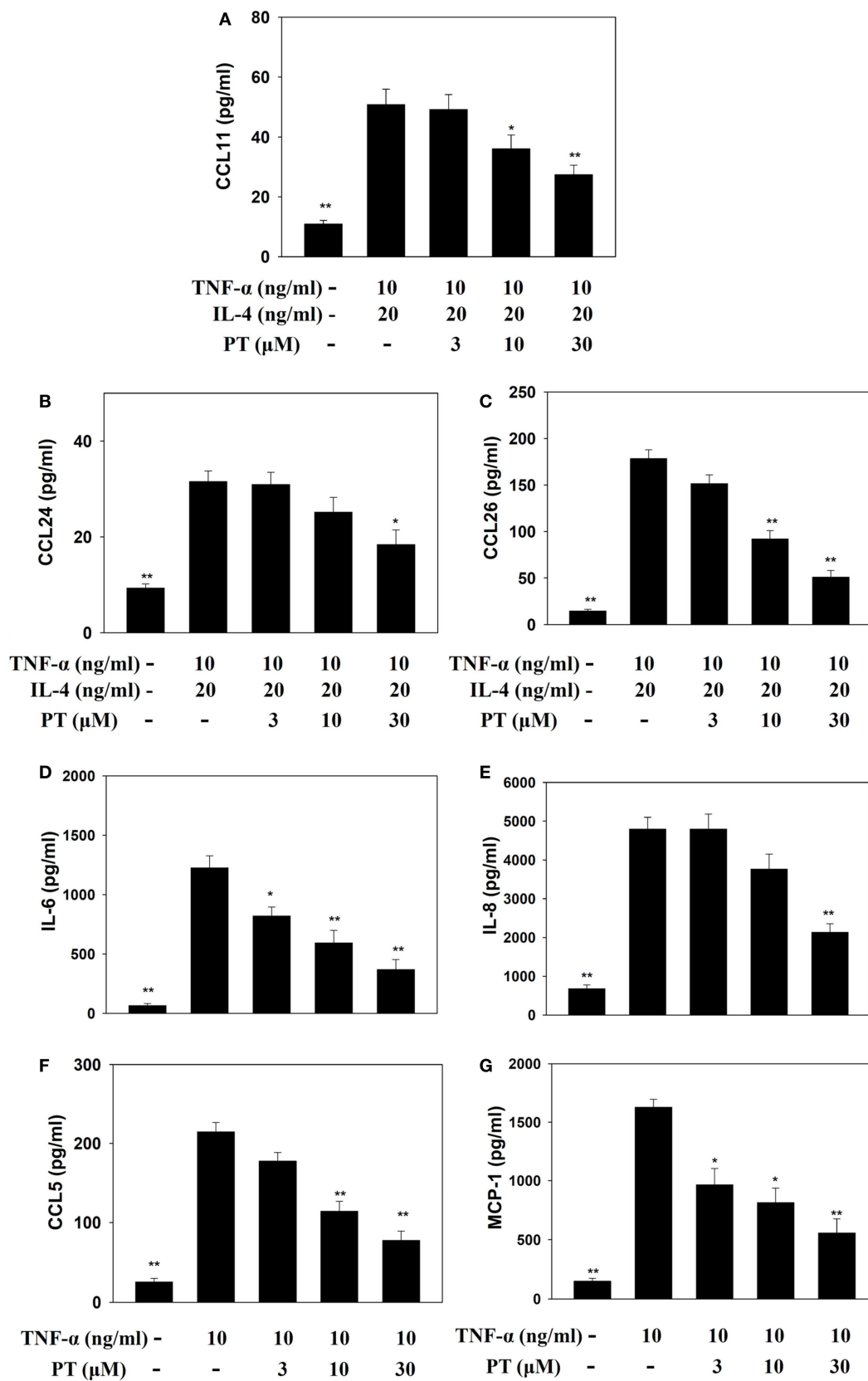
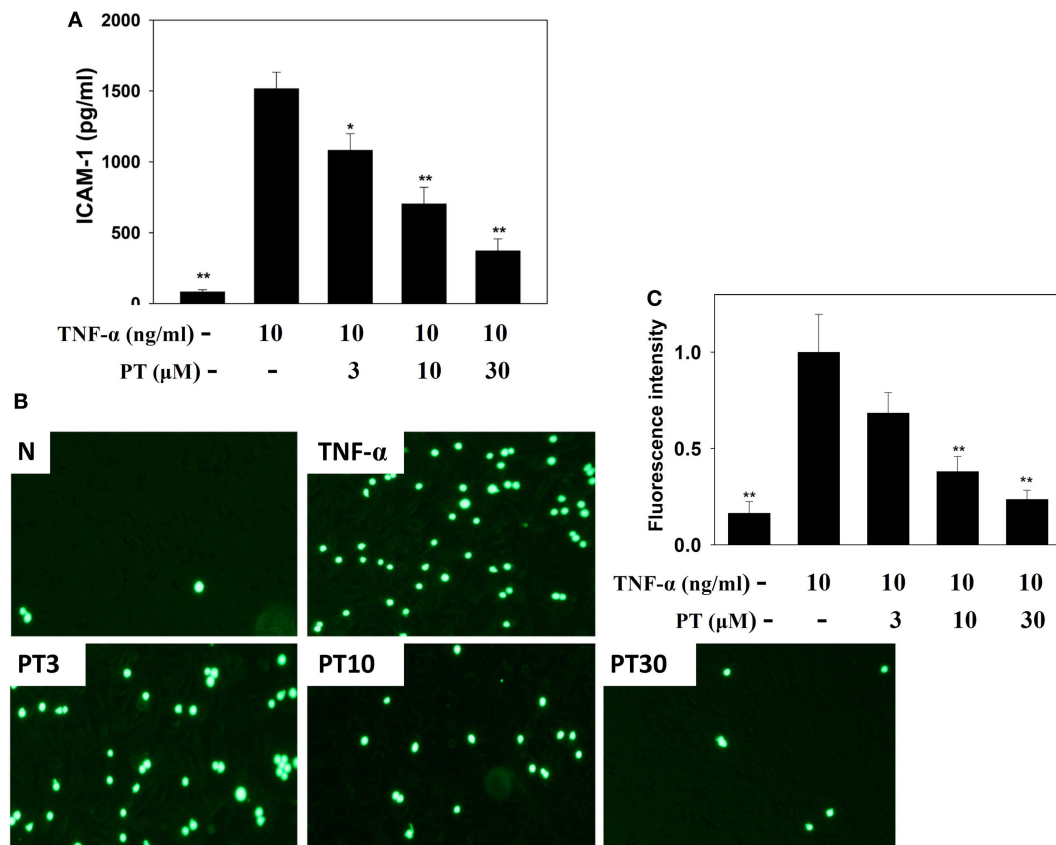


FIGURE 7 | Continued

**FIGURE 7 | Continued**

**Phloretin (PT) effects on cytokine and chemokine production in BEAS-2B cells.** Enzyme-linked immunosorbent assay results show (A) CCL11, (B) CCL24, (C) CCL26, (D) IL-6, (E) IL-8, (F) CCL5, and (G) MCP-1 levels in BEAS-2B cells treated with tumor necrosis factor- $\alpha$  (TNF- $\alpha$ ), IL-4, and/or PT. The data represent the mean  $\pm$  SEM; \* $p$  < 0.05, \*\* $p$  < 0.01, compared to BEAS-2B cells stimulated with TNF- $\alpha$  alone or TNF- $\alpha$  and IL-4. Three independent experiments were analyzed and compared with TNF- $\alpha$  alone or TNF- $\alpha$  and IL-4.



**FIGURE 8 | Phloretin (PT) inhibited THP-1 cell adherence to the activated BEAS-2B cells. (A)** PT decreased the levels of intercellular adhesion molecule 1 (ICAM-1) in BEAS-2B cells activated with tumor necrosis factor- $\alpha$  (TNF- $\alpha$ ). The data represent the mean  $\pm$  SEM; \* $p$  < 0.05, \*\* $p$  < 0.01, compared to BEAS-2B cells stimulated with TNF- $\alpha$ . **(B)** Fluorescence microscopy images of THP-1 cells labeled with calcein AM and mixed with normal (N) and TNF- $\alpha$ -activated BEAS-2B cells, in the absence or presence of PT. **(C)** Fluorescence intensity of monocytic cell adherence to BEAS-2B cells. The data represent the mean  $\pm$  SEM; \* $p$  < 0.05, \*\* $p$  < 0.01, compared to BEAS-2B cells stimulated with TNF- $\alpha$  alone or TNF- $\alpha$  and IL-4. Three independent experiments were analyzed and compared with TNF- $\alpha$  alone or TNF- $\alpha$  and IL-4.

stress in asthmatic mice (4, 23). Other studies showed that PT had antioxidative effects on inflammatory colorectal epithelial cells and attenuated oxidative reactions in rats that underwent cecal ligation and puncture-induced sepsis (24, 25). PT also improved oxidative injury in a rat model of cerebral ischemia (24).

Malondialdehyde is a lipid peroxidation marker. It is derived from prostaglandin biosynthesis in cells during oxidative stress (20). Antioxidant enzymes, such as GSH, catalase, and superoxide dismutase, offer protection from oxidation by suppressing the chronic inflammatory response and preventing the deterioration of lung tissue in allergic asthma (20, 22). In the current study, we demonstrated that PT significantly decreased MDA and

increased GSH, which ameliorated oxidative stress in lung tissues of asthmatic mice. We also found that PT could increase nuclear Nrf2 expression, which contributed to increasing HO-1 expression, and provided protection from oxidation in asthmatic lungs. Furthermore, our findings demonstrated that PT could suppress ROS production in TNF- $\alpha$ -activated human tracheal epithelial cells. Hence, we showed that PT could provide antioxidative effects to ameliorate lung injury in asthma.

Airway hyperresponsiveness is an important feature of asthma. Allergens might induce an acute asthma attack, which presents as bronchoconstriction and severe shortness of breath (1). Clinically, asthma is diagnosed in both children and adults by measuring the

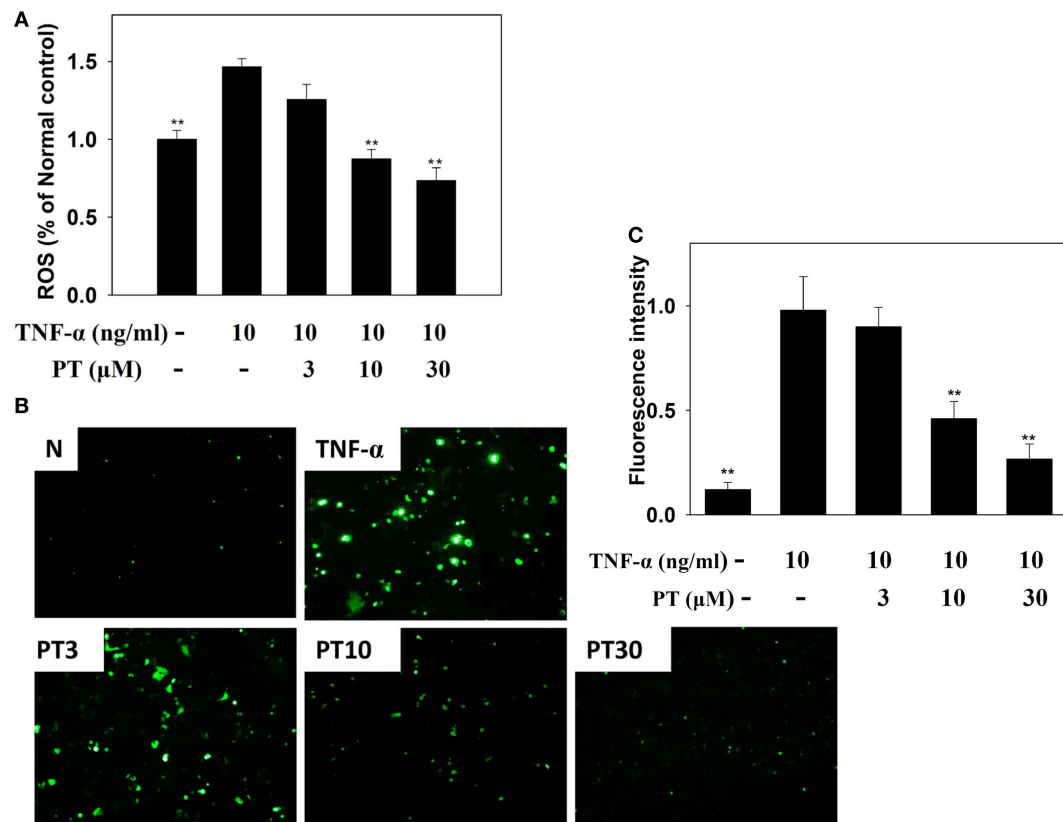


**FIGURE 9 | Phloretin (PT) effects on reactive oxygen species (ROS) production in activated BEAS-2B cells. (A)** Percentages of ROS detected in tumor necrosis factor- $\alpha$  (TNF- $\alpha$ )-activated BEAS-2B cells in the absence or presence of PT, compared to untreated cells (N); **(B)** fluorescence microscopy images of intracellular ROS. **(C)** Fluorescence intensity of intracellular ROS. Data represent the mean  $\pm$  SEM; \*\* $p$  < 0.01, compared to BEAS-2B cells stimulated with TNF- $\alpha$  alone. Three independent experiments were analyzed and compared with TNF- $\alpha$  alone or TNF- $\alpha$  and IL-4.

AHR, evaluating the airflow, and investigating the pathological features of asthma (22, 26). In patients with asthma, oxidative stress enhances the production of proinflammatory mediators, increases the AHR, and stimulates mucin secretion in the airways (27). PT significantly reduced elevations in inflammatory mediators in BALF and lung tissue of OVA-induced asthmatic mice and decreased proinflammatory cytokines and chemokines in human tracheal epithelial cells; thus, PT could ameliorate lung damage in asthma. Previous studies suggested that IL-13, which is a Th2-associated cytokine, could aggravate AHR in patients with asthma (28). In patients with asthma, where airway function is deteriorated and inflammatory responses are induced, high IL-13 levels have been observed in BALF and lung (29). We found that PT treatment reduced the IL-13 levels in BALF and suppressed IL-13 gene expression in the lungs of asthmatic mice, which may have contributed to AHR attenuation.

Excessive secretion of Th2 cytokines exacerbates the severity of an allergic response by increasing inflammatory cell infiltration and inducing goblet cell hyperplasia, which in turn, causes excess mucus secretion in asthmatic lungs (4, 30). In patients with asthma, Th2 cells release elevated IL-5 levels, which increase eosinophil differentiation in bone marrow cells (6). Eotaxins

(CCL11, CCL24, and CCL26) are thought to attract eosinophil migration into inflamed lung tissues, and the release of more inflammatory mediators by activated eosinophils increases lung tissue injury (5, 29). Previous study demonstrated that eosinophil would secrete major basic protein for induced mast cell degranulation to exacerbate allergy response (6). Eosinophil also released eosinophil cationic protein and eosinophil peroxidase to create the transmembrane channels for cytotoxic molecules into the cell (29). Hence, eosinophils accumulation in lung tissue would cause serious asthmatic allergy and inflammatory response. Eosinophils also induced the development of airway remodeling (5). Our results demonstrated that PT could inhibit IL-5, CCL11, and CCL24 expression in the lungs and BALF of asthmatic mice. PT also decreased the levels of CCL11, CCL24, and CCL26 in inflamed tracheal epithelial cells. Additionally, PT also reduced ICAM-1 in inflamed tracheal epithelial cells, which reduced their ability to adhere to inflammatory cells in lung tissues. Thus, PT could reduce eosinophil infiltration into lung tissue by blocking IL-5 and eotaxin production. Furthermore, activated macrophage also released more inflammatory cytokines to destroy the function of lung cell (31). In our murine asthma model, we found that asthma mice did not significantly increase

macrophage infiltration in BALF compared to normal mice. Asthmatic mice only treated with 20 mg/kg PT had significantly reduced numbers of macrophage compared to the OVA group. However, eosinophil activation and proliferation would induce the development of asthma disease (4). Hence, macrophages did not significantly affect asthma symptoms in PT-treated asthmatic mice.

Moreover, IL-4 can activate B cells to secrete IgE and bind to mast cells; this binding activates the complex of allergic responsive IgE and mast cells, and they release leukotrienes and histamine; these factors cause acute allergic and inflammatory reactions in patients with asthma (28). Importantly, PT can decrease Th2 cell production of IL-4 to reduce the pathological characteristics of asthma.

In patients with asthma, allergens stimulate airways and induce smooth muscle cell proliferation, which causes airway narrowing and tracheal goblet cell proliferation, which aggravates mucus secretion (32). These effects cause shortness of breath and difficulty in breathing. Furthermore, IL-4 and IL-13 can activate and stimulate goblet cell hyperplasia in the trachea (29). Our observations in asthmatic mice showed that PT reduced goblet cell hyperplasia and suppressed excessive mucus secretion, which improved mucus congestion and airway asphyxia by blocking the expression of IL-4 and IL-13 in BALF and lung tissue.

Glucose transporter 2 (GLUT2) plays an important role for sensing the levels intestinal glucose (33). In adipocyte and hepatocyte, more glucose accumulate could convert to lipid. Obesity could increase the developing asthma in obese adults and children (34). PT (an inhibitor of GLUT2 transporter) could decrease glucose into intestinal serosal fluid (35). However, we did not evidence whether PT modulated glucose levels to improve asthma symptom in this experimental asthma model.

Collectively, we demonstrated that PT significantly reduced eosinophil infiltration and mucus hypersecretion by suppressing eotaxin and Th2 cytokine production in asthmatic mice. These results suggested that PT has the potential to attenuate oxidative stress and inflammation in asthma.

## ETHICS STATEMENT

Animal care and experimental procedures were performed in accordance with the guidelines of the Laboratory Animal Care Committee of Chang Gung University of Science and Technology (IACUC approval number: 2014-023). Female BALB/c mice were obtained from the National Laboratory Animal Center in Taiwan. Mice were kept and maintained in air-conventional animal housing on a 12 h light/dark cycle. Before the experiment, the mice adapt the experimental environment of at least 1 week. The care and housing of experimental animals were approved in accordance with the guidelines of the Laboratory Animal Care Committee of Chang Gung University of Science.

## AUTHOR CONTRIBUTIONS

Designed and performed the experiments: C-JL, L-WF, and W-CH; analysis and interpretation of data: L-WF and W-CH; drafting the manuscript: C-JL and W-CH.

## FUNDING

This study was supported, in part, by grants from the Ministry of Science and Technology in Taiwan (104-2320-B-255-001) and from Chang Gung University of Science and Technology (EZRPF3F0241 and EZRPF3F0251).

## REFERENCES

- Ray A, Raundhal M, Oriss TB, Ray P, Wenzel SE. Current concepts of severe asthma. *J Clin Invest* (2016) 126:2394–403. doi:10.1172/jci84144
- Leinaar E, Alamian A, Wang L. A systematic review of the relationship between asthma, overweight, and the effects of physical activity in youth. *Ann Epidemiol* (2016) 26:504–510.e6. doi:10.1016/j.annepidem.2016.06.002
- Wesolowska-Andersen A, Seibold MA. Airway molecular endotypes of asthma: dissecting the heterogeneity. *Curr Opin Allergy Clin Immunol* (2015) 15:163–8. doi:10.1097/aci.0000000000000148
- Fahy JV. Type 2 inflammation in asthma – present in most, absent in many. *Nat Rev Immunol* (2015) 15:57–65. doi:10.1038/nri3786
- Kleinjan A. Airway inflammation in asthma: key players beyond the Th2 pathway. *Curr Opin Pulm Med* (2016) 22:46–52. doi:10.1097/mcp.0000000000000224
- Saglani S, Lloyd CM. Eosinophils in the pathogenesis of paediatric severe asthma. *Curr Opin Allergy Clin Immunol* (2014) 14:143–8. doi:10.1097/aci.0000000000000045
- Nakagome K, Matsushita S, Nagata M. Neutrophilic inflammation in severe asthma. *Int Arch Allergy Immunol* (2012) 158(Suppl 1):96–102. doi:10.1159/000337801
- Lin CC, Chu CL, Ng CS, Lin CY, Chen DY, Pan IH, et al. Immunomodulation of phloretin by impairing dendritic cell activation and function. *Food Funct* (2014) 5:997–1006. doi:10.1039/c3fo60548e
- Huang WC, Dai YW, Peng HL, Kang CW, Kuo CY, Liou CJ. Phloretin ameliorates chemokines and ICAM-1 expression via blocking of the NF-kappaB pathway in the TNF-alpha-induced HaCaT human keratinocytes. *Int Immunopharmacol* (2015) 27:32–7. doi:10.1016/j.intimp.2015.04.024
- Huang WC, Chang WT, Wu SJ, Xu PY, Ting NC, Liou CJ. Phloretin and phloretin promote lipolysis and inhibit inflammation in mouse 3T3-L1 cells and in macrophage-adipocyte co-cultures. *Mol Nutr Food Res* (2013) 57:1803–13. doi:10.1002/mnfr.201300001
- Fordham JB, Naqvi AR, Nares S. Leukocyte production of inflammatory mediators is inhibited by the antioxidants phloretin, silibinin, hesperetin, and resveratrol. *Mediators Inflamm* (2014) 2014:938712. doi:10.1155/2014/938712
- Huang WC, Lai CL, Liang YT, Hung HC, Liu HC, Liou CJ. Phloretin attenuates LPS-induced acute lung injury in mice via modulation of the NF-kappaB and MAPK pathways. *Int Immunopharmacol* (2016) 40:98–105. doi:10.1016/j.intimp.2016.08.035
- Huang WC, Liou CJ. Dietary acacetin reduces airway hyperresponsiveness and eosinophil infiltration by modulating eotaxin-1 and th2 cytokines in a mouse model of asthma. *Evid Based Complement Alternat Med* (2012) 2012:910520. doi:10.1155/2012/910520
- Huang WC, Chan CC, Wu SJ, Chen LC, Shen JJ, Kuo ML, et al. Matrine attenuates allergic airway inflammation and eosinophil infiltration by suppressing eotaxin and Th2 cytokine production in asthmatic mice. *J Ethnopharmacol* (2014) 151:470–7. doi:10.1016/j.jep.2013.10.065
- Myou S, Leff AR, Myo S, Boetticher E, Tong J, Meliton AY, et al. Blockade of inflammation and airway hyperresponsiveness in immune-sensitized mice by dominant-negative phosphoinositide 3-kinase-TAT. *J Exp Med* (2003) 198:1573–82. doi:10.1084/jem.20030298



16. Liou CJ, Lai YR, Chen YL, Chang YH, Li ZY, Huang WC. Matrine attenuates COX-2 and ICAM-1 expressions in human lung epithelial cells and prevents acute lung injury in LPS-induced mice. *Mediators Inflamm* (2016) 2016:3630485. doi:10.1155/2016/3630485
17. Paine A, Eiz-Vesper B, Blasczyk R, Immenschuh S. Signaling to heme oxygenase-1 and its anti-inflammatory therapeutic potential. *Biochem Pharmacol* (2010) 80:1895–903. doi:10.1016/j.bcp.2010.07.014
18. Shu G, Lu NS, Zhu XT, Xu Y, Du MQ, Xie QP, et al. Phloretin promotes adipocyte differentiation in vitro and improves glucose homeostasis in vivo. *J Nutr Biochem* (2014) 25:1296–308. doi:10.1016/j.jnutbio.2014.07.007
19. Aldakheel FM, Thomas PS, Bourke JE, Matheson MC, Dharmage SC, Lowe AJ. Relationships between adult asthma and oxidative stress markers and pH in exhaled breath condensate: a systematic review. *Allergy* (2016) 71:741–57. doi:10.1111/all.12865
20. Antus B. Oxidative stress markers in sputum. *Oxid Med Cell Longev* (2016) 2016:2930434. doi:10.1155/2016/2930434
21. El-Sherbeen NA, Hassan ZA, Ateyya H. Tiron ameliorates oxidative stress and inflammation in a murine model of airway remodeling. *Int Immunopharmacol* (2016) 39:172–80. doi:10.1016/j.intimp.2016.07.025
22. Fatani SH. Biomarkers of oxidative stress in acute and chronic bronchial asthma. *J Asthma* (2014) 51:578–84. doi:10.3109/02770903.2014.892965
23. Ma Y, Ge A, Zhu W, Liu YN, Ji NF, Zha WJ, et al. Morin attenuates ovalbumin-induced airway inflammation by modulating oxidative stress-responsive MAPK signaling. *Oxid Med Cell Longev* (2016) 2016:5843672. doi:10.1155/2016/5843672
24. Liu Y, Zhang L, Liang J. Activation of the Nrf2 defense pathway contributes to neuroprotective effects of phloretin on oxidative stress injury after cerebral ischemia/reperfusion in rats. *J Neurol Sci* (2015) 351:88–92. doi:10.1016/j.jns.2015.02.045
25. Aliomrani M, Sepand MR, Mirzaei HR, Kazemi AR, Nekoum S, Sabzevari O. Effects of phloretin on oxidative and inflammatory reaction in rat model of cecal ligation and puncture induced sepsis. *Daru* (2016) 24:15. doi:10.1186/s40199-016-0154-9
26. Tong X, Guo T, Liu S, Peng S, Yan Z, Yang X, et al. Macrolide antibiotics for treatment of asthma in adults: a meta-analysis of 18 randomized controlled clinical studies. *Pulm Pharmacol Ther* (2015) 31:99–108. doi:10.1016/j.pupt.2014.09.005
27. Li YJ, Kawada T, Azuma A. Nrf2 is a protective factor against oxidative stresses induced by diesel exhaust particle in allergic asthma. *Oxid Med Cell Longev* (2013) 2013:323607. doi:10.1155/2013/323607
28. Steinke JW, Lawrence MG. T-cell biology in immunotherapy. *Ann Allergy Asthma Immunol* (2014) 112:195–9. doi:10.1016/j.anai.2013.12.020
29. Parulekar AD, Diamant Z, Hanania NA. Role of T2 inflammation biomarkers in severe asthma. *Curr Opin Pulm Med* (2016) 22:59–68. doi:10.1097/mcp.0000000000000231
30. Hirahara K, Nakayama T. CD4+ T-cell subsets in inflammatory diseases: beyond the Th1/Th2 paradigm. *Int Immunol* (2016) 28:163–71. doi:10.1093/intimm/dxw006
31. Girodet PO, Nguyen D, Mancini JD, Hundal M, Zhou X, Israel E, et al. Alternative macrophage activation is increased in asthma. *Am J Respir Cell Mol Biol* (2016) 55:467–75. doi:10.1165/rcmb.2015-0295OC
32. Hall S, Agrawal DK. Key mediators in the immunopathogenesis of allergic asthma. *Int Immunopharmacol* (2014) 23:316–29. doi:10.1016/j.intimp.2014.05.034
33. Song MY, Wang J, Ka SO, Bae EJ, Park BH. Insulin secretion impairment in Sirt6 knockout pancreatic beta cells is mediated by suppression of the FoxO1-Pdx1-Glut2 pathway. *Sci Rep* (2016) 6:30321. doi:10.1038/srep30321
34. Rasmussen F, Hancox RJ. Mechanisms of obesity in asthma. *Curr Opin Allergy Clin Immunol* (2014) 14:35–43. doi:10.1097/ACI.0000000000000024
35. Kuhre RE, Bechmann LE, Wewer Albrechtsen NJ, Hartmann B, Holst JJ. Glucose stimulates neurotensin secretion from the rat small intestine by mechanisms involving SGLT1 and GLUT2, leading to cell depolarization and calcium influx. *Am J Physiol Endocrinol Metab* (2015) 308:E1123–30. doi:10.1152/ajpendo.00012.2015

**Conflict of Interest Statement:** The authors declare that the research was conducted in the absence of any commercial or financial relationships that could be construed as a potential conflict of interest.

Copyright © 2017 Huang, Fang and Liou. This is an open-access article distributed under the terms of the Creative Commons Attribution License (CC BY). The use, distribution or reproduction in other forums is permitted, provided the original author(s) or licensor are credited and that the original publication in this journal is cited, in accordance with accepted academic practice. No use, distribution or reproduction is permitted which does not comply with these terms.

## Article

# Briarenols C–E, New Polyoxygenated Briaranes from the Octocoral *Briareum excavatum*

Nan-Fu Chen <sup>1,2</sup>, Yin-Di Su <sup>3</sup>, Tsong-Long Hwang <sup>4,5,6</sup>, Zuo-Jian Liao <sup>3,7</sup>, Kuan-Hao Tsui <sup>8,9,10,11</sup>, Zhi-Hong Wen <sup>7,12</sup>, Yang-Chang Wu <sup>13,14,15,\*</sup> and Ping-Jyun Sung <sup>3,12,13,16,17,\*</sup>

- <sup>1</sup> Division of Neurosurgery, Department of Surgery, Kaohsiung Armed Forces General Hospital, Kaohsiung 802, Taiwan; chen06688@gmail.com
- <sup>2</sup> Department of Neurological Surgery, Tri-Service General Hospital, National Defense Medical Center, Taipei 114, Taiwan
- <sup>3</sup> National Museum of Marine Biology and Aquarium, Pingtung 944, Taiwan; gobetter04@gmail.tw (Y.-D.S.); liao771107@gmail.com (Z.-J.L.)
- <sup>4</sup> Graduate Institute of Natural Products, College of Medicine and Chinese Herbal Medicine Research Team, Healthy Aging Research Center, Chang Gung University, Taoyuan 333, Taiwan; htl@mail.cgu.edu.tw
- <sup>5</sup> Research Center for Chinese Herbal Medicine, Research Center for Food and Cosmetic Safety and Graduate Institute of Health Industry Technology, College of Human Ecology, Chang Gung University of Science and Technology, Taoyuan 333, Taiwan
- <sup>6</sup> Department of Anesthesiology, Chang Gung Memorial Hospital, Taoyuan 333, Taiwan
- <sup>7</sup> Doctoral Degree Program in Marine Biotechnology, National Sun Yat-Sen University and Academia Sinica, Kaohsiung 804, Taiwan; wzh@mail.nsysu.edu.tw
- <sup>8</sup> Department of Obstetrics and Gynecology, Kaohsiung Veterans General Hospital, Kaohsiung 813, Taiwan; khtsui60@gmail.com
- <sup>9</sup> Department of Obstetrics and Gynecology and Institute of Clinical Medicine, National Yang-Ming University, Taipei 112, Taiwan
- <sup>10</sup> Department of Biological Science, National Sun Yat-Sen University, Kaohsiung 804, Taiwan
- <sup>11</sup> Department of Pharmacy and Master Program, College of Pharmacy and Health Care, Tajen University, Pingtung 907, Taiwan
- <sup>12</sup> Department of Marine Biotechnology and Resources, National Sun Yat-Sen University, Kaohsiung 804, Taiwan
- <sup>13</sup> Graduate Institute of Natural Products, Kaohsiung Medical University, Kaohsiung 807, Taiwan
- <sup>14</sup> Research Center for Natural Products and Drug Development, Kaohsiung Medical University, Kaohsiung 807, Taiwan
- <sup>15</sup> Department of Medical Research, Kaohsiung Medical University Hospital, Kaohsiung 807, Taiwan
- <sup>16</sup> Graduate Institute of Marine Biology, National Dong Hwa University, Pingtung 944, Taiwan
- <sup>17</sup> Chinese Medicine Research and Development Center, China Medical University Hospital, Taichung 404, Taiwan
- \* Correspondence: yachwu@kmu.edu.tw (Y.-C.W.); pjsung@nmmmba.gov.tw (P.-J.S.); Tel.: +886-7-312-1101 (ext. 2197) (Y.-C.W.); +886-8-882-5037 (P.-J.S.); Fax: +886-7-311-4773 (Y.-C.W.); +886-8-882-5087 (P.-J.S.)

Academic Editor: Thomas J. Schmidt

Received: 16 February 2017; Accepted: 15 March 2017; Published: 17 March 2017

**Abstract:** Three new polyoxygenated briarane diterpenoids, briarenols C–E (1–3), were isolated from the octocoral *Briareum excavatum*. The structures of briaranes 1–3 were elucidated by interpretation of spectroscopic data, and the methylenecyclohexane ring in 1 was found to exist in a twisted boat conformation. Briarenol D (2) displayed an inhibitory effect on the release of elastase by human neutrophils with an IC<sub>50</sub> value of 4.65 μM. Briarenol E (3) was found to inhibit the protein expression of pro-inflammatory inducible nitric oxide synthase (iNOS) in a murine macrophage-like cell line, RAW 264.7, stimulated with lipopolysaccharides (LPS).

**Keywords:** *Briareum excavatum*; octocoral; briarane; briarenol; anti-inflammatory; elastase; iNOS

## 1. Introduction

Over the past 40 years, over 600 diterpenoids possessing the briarane carbon skeleton, most of which were found to contain a  $\gamma$ -lactone moiety in a bicyclo[8.4.0] system, have been isolated from marine coelenterates, mainly from the octocorals [1–6]. Increasing interest is being paid to these briaranes, not only due to their complex structures, but also owing to their interesting diverse bioactivities, such as anti-inflammatory activity [7–9]. In a continuing survey of Taiwanese marine invertebrates with promising novel briaranes, the octocoral *Briareum excavatum* (family Briareidae) was investigated. In this paper, we report the isolation, structure determination, and bioactivity of three new polyoxygenated briaranes, briarenols C–E (1–3), following further study of *B. excavatum* (Figure 1 and Supplementary Figures S1–S21).

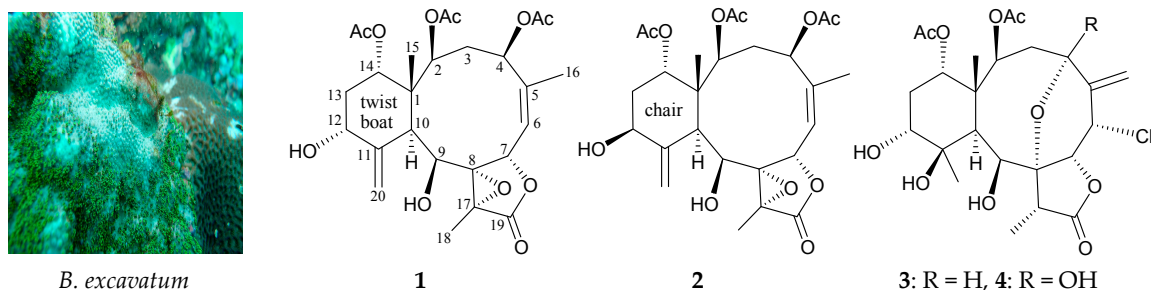


**Figure 1.** The octocoral *Briareum excavatum* and the structures of briarenols C–E (1–3) and briarenolide ZI (4).

## 2. Results and Discussion

Briarenol C (1) was obtained as a white amorphous powder. The high-resolution electrospray ionization mass spectrum (HRESIMS) showed a signal at  $m/z$  545.19930 (calcd. for  $C_{26}H_{34}O_{11} + Na$ , 545.19933), and therefore the molecular formula of 1 was determined to be  $C_{26}H_{34}O_{11}$  (10° of unsaturation degrees). Analysis of the IR spectra of 1 showed absorptions at 3428, 1772, and 1734  $cm^{-1}$ , indicating that the structure of 1 consisted of hydroxy,  $\gamma$ -lactone, and ester groups. Based on the results of the  $^{13}C$ -NMR and distortionless enhancement by polar transfer (DEPT) spectra (Table 1), the presence of a trisubstituted olefin and an exocyclic carbon-carbon double bond was deduced from the signals of four carbons at  $\delta_C$  150.6 (C-11), 144.8 (C-5), 123.4 (CH-6), and 109.3 (CH<sub>2</sub>-20); this was further supported by three olefin proton signals at  $\delta_H$  5.59 (1H, d,  $J$  = 10.0 Hz, H-6), 5.13 (1H, d,  $J$  = 1.2 Hz, H-20a), and 5.03 (1H, s, H-20b) in the  $^1H$ -NMR spectrum of 1 (Table 1). Four carbonyl resonances at  $\delta_C$  171.9 (C-19), 170.6 (an ester carbonyl), and 170.3 (2  $\times$  ester carbonyls) confirmed the presence of a  $\gamma$ -lactone and three esters in 1; three acetyl methyls ( $\delta_H$  2.04, 2.01, 1.91, each 3H  $\times$  s) were also observed. According to the overall unsaturation data, 1 was concluded to be a diterpenoid molecule possessing four rings. The presence of a tetrasubstituted epoxide that contained a methyl substituent was revealed by the signals of two oxygenated quaternary carbons at  $\delta_C$  71.4 (C-8) and 60.6 (C-17), and was further confirmed by the proton signal of a methyl singlet resonating at  $\delta_H$  1.53 (3H, s, H<sub>3</sub>-18).

The  $^1H$ -NMR coupling information obtained from the  $^1H$ - $^1H$  correlation spectroscopy (COSY) spectrum of 1 indicated the existence of H-2/H<sub>2</sub>-3/H-4, H-6/H-7, H-9/H-10, H-12/H<sub>2</sub>-13/H-14, and H-6/H<sub>3</sub>-16 (by allylic coupling) units (Table 1), which were established with the assistance of a heteronuclear multiple bond coherence (HMBC) experiment. The HMBC correlations between protons and quaternary carbons of 1, such as H-2, H-3 $\beta$ , H-10, H-13 $\alpha$ , H-14, H<sub>3</sub>-15/C-1; H-3 $\alpha$ , H-7, H<sub>3</sub>-16/C-5;

H-6, H<sub>3</sub>-18/C-8; H-10, H-13 $\beta$ /C-11; H-9, H<sub>3</sub>-18/C-17; and H<sub>3</sub>-18/C-19, allowed clarification of the carbon skeleton (Table 1). An exocyclic double bond at C-11 was confirmed by the HMBC correlations between H<sub>2</sub>-20/C-10, -12. The presence of a methyl group at C-5 was concluded based on the results of allylic coupling between H-6/H<sub>3</sub>-16 in the <sup>1</sup>H-<sup>1</sup>H COSY spectrum and by HMBC correlations between H<sub>3</sub>-16/C-4, -5, -6 and H-4/C-16. The junction C-15 methyl group was positioned at C-1, as HMBC correlations were found between H-2/C-15; H-10/C-15; and H<sub>3</sub>-15/C-1, -2, -10, -14. Two acetoxy groups were found to be attached at C-2 and C-14, respectively, based on the presence of HMBC correlations between H-2 ( $\delta_H$  4.80), H-14 ( $\delta_H$  4.74) and the acetate carbonyls at  $\delta_C$  170.6 and 170.3. Therefore, the remaining acetoxy and two hydroxy groups were inferred to be located at C-4, C-9, and C-12, respectively, as suggested by analysis of <sup>1</sup>H-<sup>1</sup>H COSY correlations and characteristic NMR signals, even though no HMBC correlation was observed between H-4 ( $\delta_H$  5.19) and the acetate carbonyl.

**Table 1.** <sup>1</sup>H (400 MHz, CDCl<sub>3</sub>) and <sup>13</sup>C (100 MHz, CDCl<sub>3</sub>) NMR data and <sup>1</sup>H-<sup>1</sup>H COSY and HMBC correlations for briarane 1.

Position	$\delta_H$ (J in Hz)	$\delta_C$ , Multiple	<sup>1</sup> H- <sup>1</sup> H COSY	HMBC
1		47.1, C		
2	4.80 d (4.4)	72.0, CH	H <sub>2</sub> -3	C-1, -4, -15, acetate carbonyl
3 $\alpha$ / $\beta$	1.96 m; 3.15 dd (12.8, 11.6)	37.7, CH <sub>2</sub>	H-2, H-4	C-1, -2, -4, -5
4	5.19 dd (12.8, 6.0)	73.0, CH	H <sub>2</sub> -3	C-3, -6, -16
5		144.8, C		
6	5.59 d (10.0)	123.4, CH	H-7, H <sub>3</sub> -16	C-8
7	5.94 d (10.0)	73.2, CH	H-6	C-5
8		71.4, C		
9	3.95 br s	72.3, CH	H-10	C-17
10	3.39 d (5.2)	44.4, CH	H-9	C-1, -2, -9, -11, -12, -15, -20
11		150.6, C		
12	4.51 dd (8.8, 7.6)	65.5, CH	H <sub>2</sub> -13	n.o. <sup>a</sup>
13 $\alpha$ / $\beta$	1.55 m; 2.62 ddd (16.0, 8.8, 4.4)	37.2, CH <sub>2</sub>	H-12, H-14	C-1, -11, -12, -14
14	4.74 d (4.4)	74.1, CH	H <sub>2</sub> -13	C-1, -10, -12, acetate carbonyl
15	1.34 s	16.4, CH <sub>3</sub>		C-1, -2, -10, -14
16	2.20 d (1.2)	25.6, CH <sub>3</sub>	H-6	C-4, -5, -6
17		60.6, C		
18	1.53 s	9.5, CH <sub>3</sub>		C-8, -17, -19
19		171.9, C		
20a	5.13 d (1.2)	109.3, CH <sub>2</sub>	H-20b	C-10, -12
b	5.03 s		H-20a	C-10, -12
OAc-2	2.01 s	170.6, C		Acetate carbonyl
		20.9, CH <sub>3</sub>		
OAc-4	1.91 s	170.3, C		Acetate carbonyl
		21.1, CH <sub>3</sub>		
OAc-14	2.04 s	170.3, C		Acetate carbonyl
		21.0, CH <sub>3</sub>		

<sup>a</sup> n.o. = not observed.

The proton chemical shifts of the briarane derivatives contained an 11,20-exocyclic carbon-carbon double bond. The difference between the two olefin protons (H-20a/b) was smaller than 0.2 ppm, whereas the cyclohexane rings exhibited a twisted boat conformation [10]. Owing to the chemical shifts of the C-20 methylene protons ( $\delta_H$  5.13 and 5.03), the configuration of the methylenecyclohexane ring in 1 was concluded to exist in a twisted boat conformation. The configuration of 1 was elucidated from the interactions observed in a nuclear Overhauser effect spectroscopy (NOESY) experiment (Figure 2) and from vicinal proton coupling constant analysis. In the NOESY experiment, the correlations of H-10 with H-2 and H-9, but not with H<sub>3</sub>-15, demonstrated that these protons (H-2, H-9, and H-10) were located on the same face of the molecule, and could be assigned as  $\alpha$  protons, as Me-15 was a  $\beta$ -substituent at C-1. H-14 was found to exhibit a correlation with H<sub>3</sub>-15, but not with H-10, indicating that this proton was of a  $\beta$ -orientation at C-14. H-12 was found to be correlated with H<sub>3</sub>-15, but not with H-10; one proton of the C-20 methylene ( $\delta_H$  5.03, H-20b) was correlated with H-9 and H-10, suggesting that the C-12 hydroxy group was  $\alpha$ -oriented. This was further supported by the fact that the methylenecyclohexane ring in 1 existed in a twisted boat conformation. The Z-configuration of the C-5/6 double bond was elucidated from the correlation between the C-6 olefin proton ( $\delta_H$  5.59) and the C-16 vinyl methyl ( $\delta_H$  2.20). One proton of the C-3 methylene ( $\delta_H$  3.15) was correlated with H<sub>3</sub>-15, but not with H-2, and it was therefore assigned as an H-3 $\beta$  proton. H-7 showed a correlation with H-3 $\beta$ , but

not with H-6, and a large coupling constant was detected between H-7 and H-6 ( $J = 10.0$  Hz), indicating that the dihedral angle between H-6 and H-7 was approximately  $180^\circ$ , and H-7 was  $\beta$ -oriented. Due to H-4 exhibiting a NOE interaction with H<sub>3</sub>-16, and a doublet coupling having been identified between H-4 and the C-3 methylene protons ( $J = 12.8, 6.0$  Hz), the acetoxy group at C-4 was identified as being  $\beta$ -oriented. H-9 was found to be correlated with H-10, H<sub>3</sub>-18, and H-20b, and from consideration of molecular models, H-9 was found to be reasonably close to H-10, H<sub>3</sub>-18, and H-20b; therefore, H-9 could be placed on the  $\alpha$  face in **1**, and H<sub>3</sub>-18 was  $\beta$ -oriented in the  $\gamma$ -lactone moiety.

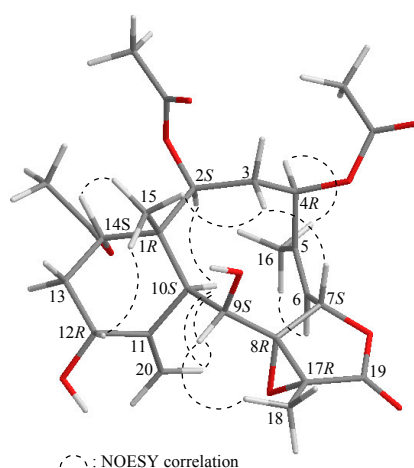


**Figure 2.** Selected protons with key NOESY correlations of **1**.

Since 1977, when the first briarane-type diterpenoid, briarein A, was isolated from the Caribbean octocoral *Briareum asbestinum* [11], all naturally derived briarane-based diterpenoids prepared from octocorals belonging to the genus *Briareum* have been found to possess a C-15 methyl group at C-1 trans to H-10, and these two groups were proven to be  $\beta$ - and  $\alpha$ -oriented, respectively. Based on biosynthetic derivation, the absolute configurations of the chiral carbons of **1** were assigned as 1R, 2S, 4R, 7S, 8R, 9S, 10S, 12R, 14S, and 17R.

Briarenol D (**2**) had the same molecular formula as **1**, C<sub>26</sub>H<sub>34</sub>O<sub>11</sub>, as determined by HRESIMS at  $m/z$  545.19950 (calcd. for C<sub>26</sub>H<sub>34</sub>O<sub>11</sub> + Na, 545.19933) with 10 degrees of unsaturation, indicating that compounds **1** and **2** were isomers. By detailed <sup>1</sup>H, <sup>13</sup>C, and 2D NMR spectroscopic analysis (Tables 1 and 2), compound **2** was found to have the same substituents as **1** (three acetoxy and two hydroxy groups). On the basis of the <sup>1</sup>H-<sup>1</sup>H COSY spectrum of **2** (Table 2), it was possible to establish the sequences of the protons attached to the carbon skeleton of **2**. Furthermore, a hydroxy proton signal at  $\delta_H$  3.00 (1H, d,  $J = 4.8$  Hz) was correlated in the <sup>1</sup>H-<sup>1</sup>H COSY spectrum with H-9 ( $\delta_H$  4.35, 1H, br s), indicating that this hydroxy group was positioned at C-9. The results of the HMBC correlation analysis of **2** confirmed the positions of the acetoxy groups at C-2 and C-4 by the connectivities between the oxymethine protons at  $\delta_H$  5.01 (H-2), 5.08 (H-4) and  $\delta_C$  170.4, 170.3 (2  $\times$  acetate carbonyls), respectively. Therefore, the remaining hydroxy and acetoxy groups were positioned at C-12 and C-14, respectively, as indicated by analysis of <sup>1</sup>H-<sup>1</sup>H COSY correlations and characteristic NMR signals analysis, even though no HMBC correlation was observed between H-14 ( $\delta_H$  4.76) and the acetate carbonyl. The stereochemistry of the stereogenic centers in the 10-membered ring (C-1, C-2, C-4, C-7, C-8, C-9, and C-10) and the  $\gamma$ -lactone moiety (C-17) of **2** was confirmed to be the same as that of **1** by comparison of the proton shifts, coupling constants, and NOESY correlations. The hydroxy and acetoxy groups at C-12 and C-14 were assigned  $\beta$ - and  $\alpha$ -configurations, primarily due to NOESY correlations between H-10/H-12 and H-14/H<sub>3</sub>-15, respectively. Thus, the methylenecyclohexane ring in **2** existed in a chair conformation, and the stereogenic centers of **2** were assigned as 1R, 2S, 4R, 7S, 8R, 9S, 10S, 12S, 14S, and 17R.



**Table 2.**  $^1\text{H}$  (400 MHz,  $\text{CDCl}_3$ ) and  $^{13}\text{C}$  (100 MHz,  $\text{CDCl}_3$ ) NMR data and  $^1\text{H}$ - $^1\text{H}$  COSY and HMBC correlations for briarane **2**.

Position	$\delta_{\text{H}}$ (J in Hz)	$\delta_{\text{C}}$ , Multiple	$^1\text{H}$ - $^1\text{H}$ COSY	HMBC
1		48.0, C		
2	5.01 d (7.2)	72.5, CH	H <sub>2</sub> -3	C-1, -3, -4, -10, -15, acetate carbonyl
3 $\alpha$ / $\beta$	2.00 m; 3.07 dd (15.2, 12.4)	37.6, CH <sub>2</sub>	H-2, H-4	C-1, -2, -4, -5
4	5.08 dd (12.4, 5.6)	72.8, CH	H <sub>2</sub> -3	C-3, -5, -6, -16, acetate carbonyl
5		143.6, C		
6	5.47 ddd (9.6, 1.2, 1.2)	123.4, CH	H-7, H <sub>3</sub> -16	C-4, -16
7	5.91 d (9.6)	74.2, CH	H-6	C-5, -6, -19
8		71.2, C		
9	4.35 br s	73.4, CH	H-10, OH-9	C-8, -10, -11
10	2.96 d (2.8)	44.1, CH	H-9	C-1, -2, -8, -9, -11, -12, -14, -15, -20
11		151.5, C		
12	4.31 dd (6.8, 6.8)	69.7, CH	H <sub>2</sub> -13	C-10, -11, -13, -14, -20
13 $\alpha$ / $\beta$	2.19 ddd (15.2, 6.8, 3.2); 1.81 ddd (15.2, 6.8, 3.6)	36.6, CH <sub>2</sub>	H-12, H-14	C-1, -11, -12, -14
14	4.76 dd (3.6, 3.2)	73.8, CH	H <sub>2</sub> -13	C-10, -12
15	1.30 s	14.7, CH <sub>3</sub>		C-1, -2, -10, -14
16	2.11 d (1.2)	25.4, CH <sub>3</sub>	H-6	C-4, -5, -6
17		62.2, C		
18	1.52 s	10.0, CH <sub>3</sub>		C-8, -17, -19
19		172.0, C		
20a	5.29 s	110.9, CH <sub>2</sub>	H-20b	C-10, -11, -12
b	5.07 s		H-20a	C-10, -11, -12
OAc-2		170.4, C		
	2.01 s	21.0, CH <sub>3</sub>		Acetate carbonyl
OAc-4		170.3, C		
	2.04 s	21.0, CH <sub>3</sub>		Acetate carbonyl
OAc-14		170.6, C		
	1.96 s	21.3, CH <sub>3</sub>		Acetate carbonyl
OH-9	3.00 d (4.8)		H-9	

Briarane **3** (briarenol E), with a molecular formula of  $\text{C}_{24}\text{H}_{33}\text{ClO}_{10}$  (on the basis of HRESIMS;  $m/z$  539.16555, calcd. for  $\text{C}_{24}\text{H}_{33}\text{ClO}_{10} + \text{Na}$ , 539.16545), was recognized as a 6-chlorinated briarane diterpenoid closely related to a known briarane, briarenolide **4** [12] (Figure 1), based on data obtained by 1D and 2D NMR analysis (Table 3). Briaranes **3** and **4** had identical substituents: secondary acetoxy groups at C-2 and C-14; an exocyclic methylene at C-5; a chloride atom at C-6; secondary hydroxy groups at C-9 and C-12; and a tertiary hydroxy group at C-11. In addition, they also had an ether bridge between C-4/8 in common. While briarane **4** was found to contain a tertiary hydroxy group at C-4 of the pyran ring, **3** had a hydrogen atom at that position. The  $^1\text{H}$ - and  $^{13}\text{C}$ -NMR data assignments of **3** were made in comparison with those of **4**. The  $^1\text{H}$ - $^1\text{H}$  COSY and HMBC correlations observed fully supported the derived locations of the functional groups. Briarane **3** was assigned as having a structure with the same stereochemistry as that of **4**, because for the stereogenic centers that **3** has in common with **4**, the  $^1\text{H}$ - and  $^{13}\text{C}$ -NMR chemical shifts and proton coupling constants matched well. Based on the above findings, the stereogenic centers of **4** were assigned as 1*R*, 2*S*, 4*S*, 6*S*, 7*R*, 8*R*, 9*S*, 10*S*, 11*R*, 12*R*, 14*S* and 17*R*. Thus, this compound was found to be the 4-dehydroxy derivative of briarenolide **4** [12].

In *in vitro* anti-inflammatory activity assays, it was found that briarane **2** showed a selective inhibitory effect on the release of elastase with an  $\text{IC}_{50}$  value of 4.65  $\mu\text{M}$ , by human neutrophils (Table 4). Briarane **1** was found to be inactive on the above two anti-inflammatory activity tests, indicating that the configuration of the methylenecyclohexane ring could significantly influence the anti-inflammatory activity. These results suggest that structural variations could influence the biological activities of the compounds of this type and may warrant further studies in the future.

Furthermore, Western blotting was used to assess the changes in the protein expression levels of pro-inflammatory inducible nitric oxide synthase (iNOS) and cyclooxygenase 2 (COX-2) in a murine macrophage-like cell line, RAW264.7, stimulated with lipopolysaccharides (LPS). In the treatment of cells with 10  $\mu\text{M}$ , briarenol E (**3**) reduced the levels of iNOS to 66.9%, in comparison with control cells stimulated with LPS only (Table 5 and Supplementary Figure S22). The results of the trypan blue exclusion test for cell viability showed that briaranes **1–3** did not induce significant cytotoxicity in RAW264.7 cells.

**Table 3.**  $^1\text{H}$  (400 MHz,  $\text{CDCl}_3$ ) and  $^{13}\text{C}$  (100 MHz,  $\text{CDCl}_3$ ) NMR data and  $^1\text{H}$ - $^1\text{H}$  COSY and HMBC correlations for briarane **3**.

Position	$\delta_{\text{H}}$ (J in Hz)	$\delta_{\text{C}}$ , Multiple	$^1\text{H}$ - $^1\text{H}$ COSY	HMBC
1		45.3, C		
2	4.99 d (6.4)	73.9, CH	H <sub>2</sub> -3	C-1, -3, -10, -14, -15, acetate carbonyl
3 $\alpha$ / $\beta$	1.34 dd (15.6, 4.8); 3.37 ddd (15.6, 12.8, 6.4)	35.8, CH <sub>2</sub>	H-2, H-4	C-1, -2, -4, -5
4	4.80 dd (12.8, 4.8)	76.3, CH	H <sub>2</sub> -3	C-2, -3, -6, -8, -16
5		138.0, C		
6	5.51 ddd (2.8, 2.4, 2.4)	55.1, CH	H-7, H <sub>2</sub> -16	C-5, -16
7	4.74 d (2.8)	80.5, CH	H-6	C-5, -6
8		82.0, C		
9	4.87 d (3.6)	76.3, CH	OH-9	C-1, -8, -10, -11, -17
10	2.16 s	40.4, CH	n.o. <sup>a</sup>	C-1, -2, -8, -9, -11, -12, -14, -15
11		78.4, C		
12	3.49 m	76.2, CH	H <sub>2</sub> -13, OH-12	n.o.
13 $\alpha$ / $\beta$	1.96 ddd (15.6, 3.6, 2.8); 2.43 ddd (15.6, 4.0, 2.8)	28.0, CH <sub>2</sub>	H-12, H-14	C-1, -12, -14
14	5.18 dd (2.8, 2.8)	76.4, CH	H <sub>2</sub> -13	C-2, -10, -12, acetate carbonyl
15	1.53 s	16.6, CH <sub>3</sub>		C-1, -2, -10, -14
16a	5.29 d (2.4)	115.7, CH <sub>2</sub>	H-6, H-16b	C-4, -6
b	5.46 d (2.4)		H-6, H-16a	C-4, -5, -6
17	2.59 q (7.2)	50.2, CH	H <sub>3</sub> -18	C-8, -9, -18, -19
18	1.29 d (7.2)	8.2, CH <sub>3</sub>	H-17	C-8, -17, -19
19		175.9, C		
20	1.54 s	29.5, CH <sub>3</sub>		C-10, -11, -12
OAc-2		170.8, C		
	1.99 s	21.2, CH <sub>3</sub>		Acetate carbonyl
OAc-14		169.2, C		
	2.04 s	21.1, CH <sub>3</sub>		Acetate carbonyl
OH-9	2.78 d (3.6)		H-9	
OH-12	2.71 d (9.2)		H-12	C-8, -9

<sup>a</sup> n.o. = not observed.**Table 4.** Inhibitory effects of briaranes **1–3** on superoxide anion generation and elastase release by human neutrophils in response to fMet-Leu-Phe/Cytochalasin B.

Compound	Superoxide Anions	Elastase Release
	IC <sub>50</sub> ( $\mu\text{M}$ ) <sup>a</sup>	IC <sub>50</sub> ( $\mu\text{M}$ )
<b>1</b>	>10	>10
<b>2</b>	>10	4.65 $\pm$ 1.50
<b>3</b>	>10	>10
LY294002 <sup>b</sup>	1.39 $\pm$ 0.32	3.30 $\pm$ 0.11

<sup>a</sup> Concentration necessary for 50% inhibition (IC<sub>50</sub>); results are presented as mean  $\pm$  S. E. M. ( $n$  = 3). <sup>b</sup> LY294002 (2-morpholin-4-yl-8-phenylchromen-4-one) was used as reference compound.**Table 5.** Effects of briaranes **1–3** on LPS-induced iNOS and COX-2 protein expression in macrophages.

Compound	iNOS	COX-2
	Expression (% of LPS Group)	Expression (% of LPS Group)
Control	0.79 $\pm$ 0.01	1.00 $\pm$ 0.02
LPS	100.00 $\pm$ 7.48	100.00 $\pm$ 18.39
<b>1</b>	93.22 $\pm$ 22.59	100.41 $\pm$ 1.08
<b>2</b>	78.35 $\pm$ 0.73	94.28 $\pm$ 21.35
<b>3</b>	66.86 $\pm$ 3.86	119.42 $\pm$ 1.33
DEX <sup>a</sup>	56.18 $\pm$ 4.53	17.42 $\pm$ 2.53

<sup>a</sup> Dexamethasone (DEX, 10  $\mu\text{M}$ ) was used as a positive control.

### 3. Experimental Section

#### 3.1. General Experimental Procedures

Melting points of the natural products were determined using Fargo apparatus (Panchum Scientific, Kaohsiung, Taiwan), and the values were uncorrected. Optical rotation values were

measured using a digital polarimeter (Jasco P-1010, Japan Spectroscopic Corp., Tokyo, Japan). IR spectra were obtained with a spectrophotometer (iS5 FT-IR, Thermo Scientific Nicolet, Waltham, MA, USA). NMR spectra were recorded on a NMR spectrometer (400 MHz Varian Mercury Plus, Varian, Palo Alto, CA, USA) using the residual  $\text{CHCl}_3$  signal ( $\delta_{\text{H}}$  7.26 ppm) and  $\text{CDCl}_3$  ( $\delta_{\text{C}}$  77.1 ppm) as the internal standard for  $^1\text{H}$ -NMR and  $^{13}\text{C}$ -NMR, respectively. Coupling constants ( $J$ ) are presented in Hz. ESIMS and HRESIMS were recorded using a mass spectrometer (Bruker 7 Tesla solariX FTMS system, Bruker, Bremen, Germany). Column chromatography was carried out with 230–400 mesh silica gel (Merck, Darmstadt, Germany). TLC was performed on plates precoated with 0.25-mm-thick Kieselgel 60 F<sub>254</sub> (Merck, Darmstadt, Germany); the plates were sprayed with 10%  $\text{H}_2\text{SO}_4$  solution followed by heating to visualize the spots. Normal-phase HPLC (NP-HPLC) was performed using a HPLC system equipped with a pump (L-7110, Hitachi, Tokyo, Japan) and an injection port (7725, Rheodyne, Rohnert Park, CA, USA). A semi-preparative normal-phase LiChrospher 250 mm  $\times$  10 mm column (Hibar, Si 60, 5  $\mu\text{m}$ ; Merck Darmstadt, Germany) was used for HPLC. Reverse-phase HPLC (RP-HPLC) was performed using a system equipped with a pump (L-7100, Hitachi, Tokyo, Japan), a photodiode array detector (L-2455 Hitachi, Tokyo, Japan), an injection port (Rheodyne 7725) and a 250 mm  $\times$  21.2 mm column (Luna RP-18e, 5  $\mu\text{m}$ , Torrance, CA, USA).

### 3.2. Animal Material

Specimens of *Briareum excavatum* were hand-picked by scuba divers in an area off the coast of Southern Taiwan in July 2011. The specimens were then stored in freezer immediately. A voucher specimen was deposited in the specimen bank of the National Museum of Marine Biology and Aquarium (NMMBA-TW-SC-2011-77) [13].

### 3.3. Extraction and Isolation

*B. excavatum* (wet weight, 6.32 kg; dry weight, 2.78 kg) samples were sliced and then extracted with a solvent mixture (methanol (MeOH):dichloromethane (DCM) = 1:1). The extract was partitioned between ethyl acetate (EtOAc) and  $\text{H}_2\text{O}$ . The EtOAc layer was separated on silica gel followed by elution chromatography with a mixture of *n*-hexane/EtOAc (stepwise, 100:1, pure EtOAc) to yield 26 subfractions, A–Z. Fractions M, N, O, and P were combined and further separated on silica gel and eluted using *n*-hexane/EtOAc (stepwise, 4:1, pure EtOAc) to afford 30 subfractions, M1–M30. Fractions M8–M11 were combined and separated on silica gel followed by elution chromatography with a mixture of DCM/EtOAc (stepwise, 20:1, pure EtOAc) to yield 24 subfractions, M8A–M8X. Fraction M8K was separated on silica gel followed by elution chromatography with a solvent mixture (*n*-hexane:acetone = 3:1) to yield 11 subfractions, M8K1–M8K11. Fraction M8K5 was repurified by NP-HPLC, using a solvent mixture (*n*-hexane:acetone = 2:1) to afford **2** (2.3 mg). Fraction V was chromatographed on silica gel and eluted using a mixture of DCM/EtOAc (stepwise, 20:1, pure EtOAc) into 14 subfractions, V1–V14. Fraction V8 was separated by NP-HPLC using a mixture of DCM/EtOAc (1:1) as the mobile phase to afford **1** (2.0 mg). Fraction V7 was separated by NP-HPLC using a mixture of *n*-hexane/acetone (2:1) as the mobile phase to afford **3** (5.5 mg).

Briarenol C (**1**): white powder; m.p. 167–168 °C;  $[\alpha]_{\text{D}}^{24}$   $-5$  (c 0.1,  $\text{CHCl}_3$ ); IR (neat)  $\nu_{\text{max}}$  3428, 1772, 1734  $\text{cm}^{-1}$ ;  $^1\text{H}$  (400 MHz,  $\text{CDCl}_3$ ) and  $^{13}\text{C}$  (100 MHz,  $\text{CDCl}_3$ ) NMR data (see Table 1); ESIMS:  $m/z$  545  $[\text{M} + \text{Na}]^+$ ; HRESIMS:  $m/z$  545.19930 (calcd. for  $\text{C}_{26}\text{H}_{34}\text{O}_{11} + \text{Na}$ , 545.19933).

Briarenol D (**2**): white powder; m.p. 158–159 °C;  $[\alpha]_{\text{D}}^{24}$   $+76$  (c 0.1,  $\text{CHCl}_3$ ); IR (neat)  $\nu_{\text{max}}$  3445, 1777, 1733  $\text{cm}^{-1}$ ;  $^1\text{H}$  (400 MHz,  $\text{CDCl}_3$ ) and  $^{13}\text{C}$  (100 MHz,  $\text{CDCl}_3$ ) NMR data (see Table 2); ESIMS:  $m/z$  545  $[\text{M} + \text{Na}]^+$ ; HRESIMS:  $m/z$  545.19950 (calcd. for  $\text{C}_{26}\text{H}_{34}\text{O}_{11} + \text{Na}$ , 545.19933).

Briarenol E (**3**): white powder; m.p. 193–194 °C;  $[\alpha]_{\text{D}}^{24}$   $-32$  (c 0.3,  $\text{CHCl}_3$ ); IR (neat)  $\nu_{\text{max}}$  3445, 1775, 1731  $\text{cm}^{-1}$ ;  $^1\text{H}$  (400 MHz,  $\text{CDCl}_3$ ) and  $^{13}\text{C}$  (100 MHz,  $\text{CDCl}_3$ ) NMR data (see Table 3); ESIMS:  $m/z$  539  $[\text{M} + \text{Na}]^+$ , 541  $[\text{M} + 2 + \text{Na}]^+$ ; HRESIMS:  $m/z$  539.16555 (calcd. for  $\text{C}_{24}\text{H}_{33}\text{ClO}_{10} + \text{Na}$ , 539.16545).

### 3.4. Generation of Superoxide Anions and Release of Elastase by Human Neutrophils

Human neutrophils were obtained by means of dextran sedimentation and Ficoll centrifugation. Measurements of superoxide anion generation and elastase release were carried out according to previously described procedures [14,15]. Briefly, superoxide anion production was assayed by monitoring the superoxide dismutase-inhabitable reduction of ferricytochrome c. Elastase release experiments were performed using MeO-Suc-Ala-Ala-Pro-Valp-nitroanilide as the elastase substrate.

### 3.5. In Vitro Anti-Inflammatory Assay

Murine macrophage-like cell line RAW264.7 was purchased from the American Type Culture Collection (ATCC, No TIB-71) (Manassas, VA, USA). The in vitro anti-inflammatory activities of compounds 1–3 were measured by investigating their inhibition effects on LPS-induced pro-inflammatory iNOS and COX-2 protein expressions in the macrophage cell line using western blot analysis [16–18]. Briefly, an inflammation response in RAW264.7 cells was induced by incubating cells in medium containing only LPS (10 ng/mL) without test compounds for 16 h. For the anti-inflammatory activity assay, Compounds 1–3 or dexamethasone (10  $\mu$ M) were added to the cells 10 min before LPS treatment. After incubation, the cells were lysed and the protein lysates analyzed by Western blotting. The protein expression levels were determined based on the immunoreactivity of proteins to antibodies, and were calculated with respect to the average optical density of the corresponding LPS-stimulated cells. Moreover, the effects of Compounds 1–3 on the viability of RAW 264.7 cells were also evaluated by the trypan blue exclusion test [17,18]. For statistical analysis, the data were analyzed by one-way analysis of variance (ANOVA), followed by the Student–Newman–Keuls *post hoc* test for multiple comparisons. A significant difference was defined as a *p*-value of <0.05.

## 4. Conclusions

The octocoral *Briareum excavatum* has proven to be a rich source of interesting briarane-related natural products with complex structures and extensive bioactivities. It is interesting to note that briarane-related natural products isolated from *B. excavatum* possessing a twisted boat conformation are rarely found. Briarenol D (2) is a compound potentially suitable for future development. This interesting species has been transplanted to culture tanks located in the National Museum of Marine Biology and Aquarium. A large quantity of cultured *B. excavatum* is being cultivated for extraction of natural material in order to establish a stable supply of bioactive substances.

**Supplementary Materials:** HRESIMS, 1D, 2D NMR spectra, and figure of Western blot of new compounds 1–3 are available online.

**Acknowledgments:** This research was supported by grants from the National Museum of Marine Biology & Aquarium; the National Dong Hwa University; the National Sun Yat-sen University; the Ministry of Science and Technology (Grant Nos. MOST 105-2325-B-291-001, 105-2811-B-291-001, 105-2811-B-291-002, 104-2320-B-291-001-MY3, and 104-2325-B-291-001), Taiwan, awarded to Yang-Chang Wu and Ping-Jyun Sung.

**Author Contributions:** Yang-Chang Wu and Ping-Jyun Sung designed the whole experiment and contributed to manuscript preparation; Nan-Fu Chen and Yin-Di Su researched the data; Tsong-Long Hwang, Zuo-Jian Liao, Kuan-Hao Tsui, and Zhi-Hong Wen analyzed the data and performed data acquisition.

**Conflicts of Interest:** The authors declare no conflict of interest.

## References

1. Sung, P.-J.; Sheu, J.-H.; Xu, J.-P. Survey of briarane-type diterpenoids of marine origin. *Heterocycles* **2002**, *57*, 535–579. [[CrossRef](#)]
2. Sung, P.-J.; Chang, P.-C.; Fang, L.-S.; Sheu, J.-H.; Chen, W.-C.; Chen, Y.-P.; Lin, M.-R. Survey of briarane-related diterpenoids: Part II. *Heterocycles* **2005**, *65*, 195–204. [[CrossRef](#)]
3. Sung, P.-J.; Sheu, J.-H.; Wang, W.-H.; Fang, L.-S.; Chung, H.-M.; Pai, C.-H.; Su, Y.-D.; Tsai, W.-T.; Chen, B.-Y.; Lin, M.-R. Survey of briarane-related diterpenoids: Part III. *Heterocycles* **2008**, *75*, 2627–2648. [[CrossRef](#)]

4. Sung, P.-J.; Su, J.-H.; Wang, W.-H.; Sheu, J.-H.; Fang, L.-S.; Wu, Y.-C.; Chen, Y.-H.; Chung, H.-M.; Su, Y.-D.; Chang, Y.-C. Survey of briarane-related diterpenoids: Part IV. *Heterocycles* **2011**, *83*, 1241–1258. [[CrossRef](#)]
5. Sheu, J.-H.; Chen, Y.-H.; Chen, Y.-H.; Su, Y.-D.; Chang, Y.-C.; Su, J.-H.; Weng, C.-F.; Lee, C.-H.; Fang, L.-S.; Wang, W.-H. Briarane diterpenoids isolated from gorgonian corals between 2011 and 2013. *Mar. Drugs* **2014**, *12*, 2164–2181. [[CrossRef](#)] [[PubMed](#)]
6. Su, Y.-D.; Su, J.-H.; Hwang, T.-L.; Wen, Z.-H.; Sheu, J.-H.; Wu, Y.-C.; Sung, P.-J. Briarane diterpenoids isolated from octocorals between 2014 and 2016. *Mar. Drugs* **2017**, *15*, 44. [[CrossRef](#)] [[PubMed](#)]
7. González, Y.; Torres-Mendoza, D.; Jones, G.E.; Fernandez, P.L. Marine diterpenoids as potential anti-inflammatory agents. *Mediat. Inflamm.* **2015**, *2015*, 263543. [[CrossRef](#)] [[PubMed](#)]
8. Wei, W.-C.; Sung, P.-J.; Duh, C.-Y.; Chen, B.-W.; Sheu, J.-H.; Yang, N.-S. Anti-inflammatory activities of natural products isolated from soft corals of Taiwan between 2008 and 2012. *Mar. Drugs* **2013**, *11*, 4083–4126. [[CrossRef](#)] [[PubMed](#)]
9. Senthilkumar, K.; Kim, S.-K. Marine invertebrate natural products for anti-inflammatory and chronic disease. *Evid. Based Complement. Altern. Med.* **2013**, *2013*, 572859. [[CrossRef](#)] [[PubMed](#)]
10. Sung, P.-J.; Wang, S.-H.; Chiang, M.-Y.; Su, Y.-D.; Chang, Y.-C.; Hu, W.-P.; Tai, C.-Y.; Liu, C.-Y. Discovery of new dhlorinated briaranes from *Junceella fragilis*. *Bull. Chem. Soc. Jpn.* **2009**, *82*, 1426–1432. [[CrossRef](#)]
11. Burks, J.E.; van der Helm, D.; Chang, C.Y.; Ciereszko, L.S. The crystal and molecular structure of briarein A, a diterpenoid from the gorgonian *Briareum asbestinum*. *Acta Cryst.* **1977**, *B33*, 704–709. [[CrossRef](#)]
12. Su, Y.-D.; Sung, C.-S.; Wen, Z.-H.; Chen, Y.-H.; Chang, Y.-C.; Chen, J.-J.; Fang, L.-S.; Wu, Y.-C.; Sheu, J.-H.; Sung, P.-J. New 9-hydroxybriarane diterpenoids from a gorgonian coral *Briareum* sp. *Int. J. Mol. Sci.* **2016**, *17*, 79. [[CrossRef](#)] [[PubMed](#)]
13. Samimi-Namin, K.; van Ofwegen, L.P. Overview of the genus *Briareum* (Cnidaria, Octocorallia, Briareidae) in the Indo-Pacific, with the description of a new species. *ZooKeys* **2016**, *557*, 1–44. [[CrossRef](#)] [[PubMed](#)]
14. Yang, S.-C.; Chung, P.-J.; Ho, C.-M.; Kuo, C.-Y.; Hung, M.-F.; Huang, Y.-T.; Chang, W.-Y.; Chang, Y.-W.; Chan, K.-H.; Hwang, T.-L. Propofol inhibits superoxide production, elastase release, and chemotaxis in formyl peptide-activated human neutrophils by blocking formyl peptide receptor 1. *J. Immunol.* **2013**, *190*, 6511–6519. [[CrossRef](#)] [[PubMed](#)]
15. Yu, H.-P.; Hsieh, P.-W.; Chang, Y.-J.; Chung, P.-J.; Kuo, L.-M.; Hwang, T.-L. 2-(2-Fluorobenzamido) benzoate ethyl ester (EFB-1) inhibits superoxide production by human neutrophils and attenuates hemorrhagic shock-induced organ dysfunction in rats. *Free Radic. Biol. Med.* **2011**, *50*, 1737–1748. [[CrossRef](#)] [[PubMed](#)]
16. Huang, S.-Y.; Chen, N.-F.; Chen, W.-F.; Hung, H.-C.; Lee, H.-P.; Lin, Y.-Y.; Wang, H.-M.; Sung, P.-J.; Sheu, J.-H.; Wen, Z.-H. Sinularin from indigenous soft coral attenuates nociceptive responses and spinal neuroinflammation in carrageenan-induced inflammatory rat model. *Mar. Drugs* **2012**, *10*, 1899–1919. [[CrossRef](#)] [[PubMed](#)]
17. Jean, Y.-H.; Chen, W.-F.; Sung, C.-S.; Duh, C.-Y.; Huang, S.-Y.; Lin, C.-S.; Tai, M.-H.; Tzeng, S.-F.; Wen, Z.-H. Capnellene, a natural marine compound derived from soft coral, attenuates chronic constriction injury-induced neuropathic pain in rats. *Br. J. Pharmacol.* **2009**, *158*, 713–725. [[CrossRef](#)] [[PubMed](#)]
18. Jean, Y.-H.; Chen, W.-F.; Duh, C.-Y.; Huang, S.-Y.; Hsu, C.-H.; Lin, C.-S.; Sung, C.-S.; Chen, I.-M.; Wen, Z.-H. Inducible nitric oxide synthase and cyclooxygenase-2 participate in anti-inflammatory and analgesic effects of the natural marine compound lemnalol from Formosan soft coral *Lemnalia cervicorni*. *Eur. J. Pharmacol.* **2008**, *578*, 323–331. [[CrossRef](#)] [[PubMed](#)]

**Sample Availability:** Samples of the compounds 1–3 are not available from the authors.



© 2017 by the authors. Licensee MDPI, Basel, Switzerland. This article is an open access article distributed under the terms and conditions of the Creative Commons Attribution (CC BY) license (<http://creativecommons.org/licenses/by/4.0/>).





## Full paper

## Amiodarone reduces depolarization-evoked glutamate release from hippocampal synaptosomes

Chia Yu Chang<sup>a</sup>, Chi Feng Hung<sup>b, d</sup>, Shu Kuei Huang<sup>e</sup>, Jinn Rung Kuo<sup>a</sup>, Su Jane Wang<sup>b, c, \*</sup><sup>a</sup> Department of Neurology, Chi Mei Medical Center, Tainan, Taiwan<sup>b</sup> School of Medicine, Fu Jen Catholic University, New Taipei City, Taiwan<sup>c</sup> Research Center for Chinese Herbal Medicine, College of Human Ecology, Chang Gung University of Science and Technology, Taoyuan City, Taiwan<sup>d</sup> Department of Fragrance and Cosmetic Science, Kaohsiung Medical University, Kaohsiung, Taiwan<sup>e</sup> Department of Anesthesiology, Far-Eastern Memorial Hospital, New Taipei City, Taiwan

## ARTICLE INFO

## Article history:

Received 23 November 2016

Received in revised form

26 January 2017

Accepted 22 February 2017

Available online 8 March 2017

## Keywords:

Amiodarone

Glutamate release

Ca<sup>2+</sup> channels

Synaptosomes

Hippocampus

## ABSTRACT

Decreased brain glutamate level has emerged as a new therapeutic approach for epilepsy. This study investigated the effect and mechanism of amiodarone, an anti-arrhythmic drug with antiepileptic activity, on glutamate release in the rat hippocampus. In a synaptosomal preparation, amiodarone reduced 4-aminopyridine-evoked Ca<sup>2+</sup>-dependent glutamate release and cytosolic Ca<sup>2+</sup> concentration elevation. Amiodarone did not affect the 4-aminopyridine-evoked depolarization of the synaptosomal membrane potential or the Na<sup>+</sup> channel activator veratridine-evoked glutamate release, indicating that the amiodarone-mediated inhibition of glutamate release is not caused by a decrease in synaptosomal excitability. The inhibitory effect of amiodarone on 4-aminopyridine-evoked glutamate release was markedly decreased in synaptosomes pretreated with the Ca<sub>v</sub>2.2 (N-type) and Ca<sub>v</sub>2.1 (P/Q-type) channel blocker ω-conotoxin MVIIC, the calmodulin antagonists W7 and calmidazolium, or the protein kinase A inhibitors H89 and KT5720. However, the intracellular Ca<sup>2+</sup>-release inhibitors dantrolene and CGP37157 had no effect on the amiodarone-mediated inhibition of glutamate release. Furthermore, amiodarone reduced the frequency of miniature excitatory postsynaptic currents without affecting their amplitude in hippocampal slices. Our data suggest that amiodarone reduces Ca<sup>2+</sup> influx through N- and P/Q-type Ca<sup>2+</sup> channels, subsequently reducing the Ca<sup>2+</sup>-calmodulin/protein kinase A cascade to inhibit the evoked glutamate release from rat hippocampal nerve terminals.

© 2017 The Authors. Production and hosting by Elsevier B.V. on behalf of Japanese Pharmacological Society. This is an open access article under the CC BY-NC-ND license (<http://creativecommons.org/licenses/by-nc-nd/4.0/>).

**Abbreviations:** [Ca<sup>2+</sup>]<sub>c</sub>, cytosolic free Ca<sup>2+</sup> concentration; DiSC<sub>3</sub>(5), 3',3',3'-dipropylthiadicarbocyanine iodide; DL-TBOA, DL-threo-beta-benzyl-oxy aspartate; Fura-2-AM, fura-2-acetoxymethyl ester; GDH, glutamate dehydrogenase; HBM, HEPES buffer medium; BSA, bovine serum albumin; CGP37157, 7-chloro-5-(2-chlorophenyl)-1,5-dihydro-4,1-benzothiazepin-2(3H)-one; H89, N-[2-(p-bromocinnamylamino)-ethyl]-5-isoquinolinesulfonamide dihydrochloride; KT5720, hexahydro-10-hydroxy-9-methyl-1-oxo-9,12-epoxy-1H-diindolo-benzodiazocine-10-carboxylic acid; GF109203X, bisindolylmaleimide I; mEPSCs, miniature excitatory postsynaptic currents; CNQX, 6-cyano-7-nitroquinoxaline-2,3-dione; D-AP5, D(-)-2-amino-5-phosphonopentanoic acid; CNS, central nervous system.

\* Corresponding author. School of Medicine, Fu Jen Catholic University, No. 510, Zhongzheng Rd., Xinzhuang Dist., New Taipei City 24205, Taiwan. Fax: +886 2 29052096.

E-mail address: [med0003@mail.fju.edu.tw](mailto:med0003@mail.fju.edu.tw) (S.J. Wang).

Peer review under responsibility of Japanese Pharmacological Society.

## 1. Introduction

Glutamate is the main excitatory neurotransmitter in the central nervous system (CNS) of mammals, in which it acts through ionotropic and metabotropic glutamate receptors to regulate many physiological functions including cognition, learning, and memory (1,2). However, excessive glutamate release and activation of glutamate receptors eventually lead to calcium overload and subsequent cell death, and this glutamate neurotoxicity has been implicated in the pathogenesis of numerous brain disorders including epilepsy (3–5). A significant increase in the glutamate level has been observed in patients with epilepsy as well as in experimental models of epilepsy (6–8). Thus, reducing glutamate release may be a potentially crucial mechanism for antiepileptic effects. Several clinically used antiepileptic drugs, such as carbamazepine, phenytoin, lamotrigine, and gabapentin, have been reported to exhibit such a mechanism (9–11).

<http://dx.doi.org/10.1016/j.jphs.2017.02.014>

1347-8613/© 2017 The Authors. Production and hosting by Elsevier B.V. on behalf of Japanese Pharmacological Society. This is an open access article under the CC BY-NC-ND license (<http://creativecommons.org/licenses/by-nc-nd/4.0/>).

Amiodarone is an anti-arrhythmic drug that is commonly prescribed to patients with atrial fibrillation and ventricular arrhythmias (12,13). The pharmacologic profile of this drug in the heart is complex, involving inhibition of sodium and calcium channels, modulation of potassium outward current, and antagonistic effects on adrenergic receptors (14–16). In addition to its anti-arrhythmic effects, amiodarone has been shown to pass into the brain (17) and to increase the concentrations of inhibitory neurotransmitters in the rat medulla oblongata (18). Furthermore, amiodarone attenuates pentylenetetrazole- and caffeine-induced seizures in mice (19). Thus, amiodarone may have antiepileptic effects, but the underlying mechanism is unclear.

Considering the involvement of excessive glutamate release in the pathogenesis of epilepsy, the antiepileptic effect of amiodarone in experimental models may be associated with a decrease in glutamate release. However, according to our review of the literature, no information is available regarding the possible effect of amiodarone on glutamate release at the presynaptic level. Therefore, the present study investigated the effect and mechanism of amiodarone on glutamate release from rat hippocampal nerve terminals (synaptosomes), a system particularly suited for studying presynaptic events (20). We also used intact neurons in hippocampal slices to examine the effect of amiodarone on spontaneous-release events; miniature excitatory postsynaptic currents (mEPSCs) (21). In this study, the hippocampus was chosen because of it plays a crucial role in the pathogenesis of epilepsy (22), and neurodegeneration of this brain region has been attributable to glutamate (23).

## 2. Material and methods

### 2.1. Chemicals

Amiodarone, 4-aminopyridine, veratridine, bafilomycin A1, DL-threo- $\beta$ -benzyloxyaspartate (DL-TBOA),  $\omega$ -conotoxin MVIIc, dantrolene, 7-chloro-5-(2-chlorophenyl)-1,5-dihydro-4,1-benzothiazepin-2(3H)-one (CGP37157), D(-)-2-amino-5-phosphonopentanoic acid (D-AP5), bisindolylmaleimide I (GF109203X), N-[2-(p-bromocinnamylamino)-ethyl]-5-isoquinolinesulfonamide dihydrochloride (H89), and hexahydro-10-hydroxy-9-methyl-1-oxo-9,12-epoxy-1H-diindolo-benzodiazocine-10-carboxylic acid (KT5720) were purchased from Tocris Cookson (Bristol, UK). 3',3',3'-dipropylthiadicarbocyanine iodide [DiSC<sub>3</sub>(5)], and fura-2-acetoxymethyl ester (Fura-2-AM) were purchased from Invitrogen (Carlsbad, CA, USA). Ethylene glycol bis ( $\beta$ -aminoethyl ether)-N,N,N',N'-tetraacetic acid (EGTA), tetrodotoxin and all other reagents were purchased from Sigma–Aldrich (St. Louis, MO, USA). DiSC<sub>3</sub>(5), and Fura-2 were dissolved in dimethylsulfoxide, with a final concentration in the medium was  $\leq 0.1\%$  (v/v).

### 2.2. Animals

Adult (150–200 g) and 8- to 23-day-old male Sprague–Dawley rats were purchased from BioLASCO (Taiwan Co., Ltd, Taipei, Taiwan). Animals were housed under constant conditions of temperature ( $22 \pm 1^\circ\text{C}$ ) and relative humidity (50–70%) with a regular light–dark schedule (lights on from 7 am to 7 pm) and free access to food and water. Animal experiments were in accordance with the National Institutes of Health Guide for the Care and Use of Laboratory, and were approved by the Institutional Animal Care and Use Committee at the Fu Jen Catholic University. All efforts were made to minimize animal suffering and to use a minimum number of animals necessary to produce reliable results.

### 2.3. Preparation of synaptosomes

Rats were decapitated, brains were quickly removed and the hippocampus dissected out at  $4^\circ\text{C}$ . As previously described (24), synaptosomes were prepared from the hippocampus of adult rats. The final synaptosomal pellets were resuspended in HEPES buffer medium (HBM) with the following composition (mM): NaCl, 140; KCl, 5; NaHCO<sub>3</sub>, 5; MgCl<sub>2</sub>·6H<sub>2</sub>O, 1; Na<sub>2</sub>HPO<sub>4</sub>, 1.2; glucose, 10; HEPES, 10; pH 7.4. Protein concentration was then determined using the Bradford assay. Synaptosomes were centrifuged in the final wash to obtain synaptosomal pellets with 0.5 mg protein. Synaptosomal pellets were stored on ice and used within 4–6 h.

### 2.4. Synaptosomal glutamate release

Glutamate release was assayed by on-line fluorimetry as described previously (24). Synaptosomal pellets were resuspended in HBM (0.5 mg/mL) and preincubated at  $37^\circ\text{C}$  for 1 h in the presence of  $16\ \mu\text{M}$  bovine serum albumin (BSA) to bind any free fatty acids released from synaptosomes during the preincubation. A 1 ml aliquot was transferred to a stirred and thermostated cuvette containing 2 mM NADP<sup>+</sup>, 50 units of glutamate dehydrogenase (GDH), and 1.2 mM CaCl<sub>2</sub>, and the fluorescence of NADPH was followed in a Perkin-Elmer LS-55 spectrofluorimeter (PerkinElmer Life and Analytical Sciences, Waltham, MA, USA) at excitation and emission wavelengths of 340 and 460 nm, respectively. A standard of exogenous glutamate (5 nmol) was added at the end of each experiment and the fluorescence change produced by the standard addition was used to calculate the released glutamate as nanomoles glutamate per milligram synaptosomal protein (nmol/mg). Release values quoted in the text and depicted in bar graphs represent the levels of glutamate cumulatively released after 5 min of depolarization, and are expressed as nmol/mg/5 min. Data were accumulated at 2-s intervals and cumulative data were analyzed using Lotus 1-2-3.

### 2.5. Synaptosomal cytosolic Ca<sup>2+</sup> concentration ([Ca<sup>2+</sup>]<sub>c</sub>)

[Ca<sup>2+</sup>]<sub>c</sub> was measured with fura-2. Synaptosomes were resuspended (2 mg/mL) in HBM containing  $16\ \mu\text{M}$  BSA in the presence of  $5\ \mu\text{M}$  fura-2 and 0.1 mM CaCl<sub>2</sub>, and incubated at  $37^\circ\text{C}$  for 30 min. After fura-2 loading, the synaptosomes were pelleted and resuspended in HBM containing bovine serum albumin. A 1 ml aliquot was stirred in a thermostated cuvette containing 1.2 mM CaCl<sub>2</sub> and the fluorescence was monitored at excitation wavelengths of 340 and 380 nm (emission wavelength 505 nm). Data was collected at 2-s intervals and [Ca<sup>2+</sup>]<sub>c</sub> (nM) was calculated using the equations described previously (25).

### 2.6. Synaptosomal plasma membrane potential

The plasma membrane potential was determined using a membrane-potential-sensitive dye, DiSC<sub>3</sub>(5) (26). Synaptosomes were resuspended in HBM and incubated in a stirred and thermostated cuvette at  $37^\circ\text{C}$  in a Perkin-Elmer LS-55 spectrofluorimeter. After 3 min of incubation,  $5\ \mu\text{M}$  DiSC<sub>3</sub>(5) was added and allowed to equilibrate before the addition of 1 mM CaCl<sub>2</sub> after 4 min of incubation. 4-aminopyridine was then added to depolarize the synaptosomes for 10 min, and DiSC<sub>3</sub>(5) fluorescence was monitored at excitation and emission wavelengths of 646 and 674 nm, respectively. Cumulative data were analyzed using Lotus 1-2-3 and expressed in fluorescence units.

### 2.7. Slice preparation and electrophysiological recording

Hippocampal slices (300  $\mu\text{m}$ ) were prepared from 8- to 23-day-old male rats ( $n = 5$ ), as described in detail previously (27, 28). The

slices were maintained in the artificial cerebrospinal fluid continuously oxygenated with 95% O<sub>2</sub>–5% CO<sub>2</sub> at room temperature for at least 1 h before use. Artificial cerebrospinal fluid comprised (in mM): 117 NaCl, 4.7 KCl, 2.5 CaCl<sub>2</sub>, 1.2 MgCl<sub>2</sub>, 25 NaHCO<sub>3</sub>, 1.2 NaH<sub>2</sub>PO<sub>4</sub>, 11 glucose (pH 7.4, 300 mOsm).

Slices were moved to a recording chamber mounted on a BX51W1 upright microscope (Olympus) equipped with infra-red differential interference contrast (IR-DIC). The chamber was continuously perfused with oxygenated artificial cerebrospinal fluid. Neurons were visualized with an Olympus Optical 40 × water immersion objective. Tight-seal (>1 GΩ) Whole-cell recordings were obtained from the cell body of neurons situated in the CA3 pyramidal layer. Patch electrodes were fabricated from borosilicate glass and had a 2–5 MΩ resistance after files with internal solution containing (in mM): 0.3 Na<sub>3</sub>GTP, 135 K-gluconate, 20 KCl, 0.1 EGTA, 2 CMgCl<sub>2</sub>, 4 Na<sub>2</sub>ATP, and 10 HEPES (pH 7.3, 280 mOsm). Neurons were voltage clamped at –70 mV using an Axopatch 200B amplifier (Axon Instruments, Foster City, CA, USA). Access resistance (8–30 MΩ) was regularly monitored during recordings and cells were rejected if it changed more than 15% during the experiments. Membrane currents were filtered at 2 kHz, digitized and stored on a computer using pCLAMP (Axon Instruments, Foster City, CA, USA). Data were analyzed offline using commercially available software.

## 2.8. Data and statistical analysis

Data are expressed as mean ± SEM. Statistical analysis was carried out by the two-tailed Student's *t* test when comparing two groups and by one-way ANOVA with Tukey's multiple comparisons *post hoc* tests when comparing more than two groups. Analysis was completed using SPSS software (Version 17.0; SPSS Inc., Chicago, IL, USA). Data were considered significant if *P* < 0.05.

## 3. Results

### 3.1. Amiodarone decreases 4-aminopyridine-evoked glutamate release from hippocampal synaptosomes

To examine whether amiodarone affects glutamate release, synaptosomes were incubated with amiodarone (0.5–10 μM), followed by the addition of the K<sup>+</sup> channel blocker 4-aminopyridine,

which depolarizes nerve terminals *in vitro*, in a manner corresponding to *in vivo* depolarization (29). Under control conditions, 4-aminopyridine (1 mM) evoked a glutamate release of  $6.8 \pm 0.3$  nmol/mg/5 min from synaptosomes incubated with 1.2 mM CaCl<sub>2</sub>. Preincubation with amiodarone (5 μM) for 10 min before 4-aminopyridine addition caused an inhibition of the 4-aminopyridine-evoked glutamate release by approximately 54% [ $3.1 \pm 0.2$  nmol/mg/5 min; *t*(12) = 15.6, *P* = 0.000; Fig. 1A]. The effect of amiodarone was dose-dependent, with an IC<sub>50</sub> of approximately 1 μM (Fig. 1B). Amiodarone did not affect the basal, prepolarization glutamate level.

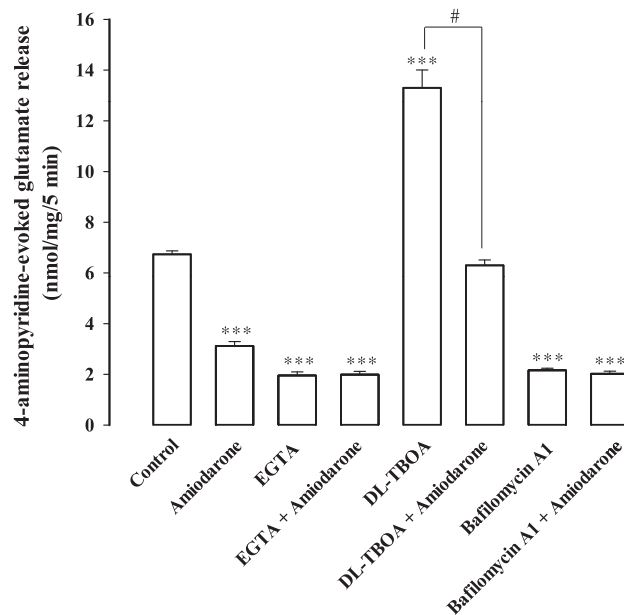


**Fig. 2.** Effect of external calcium omission, the glutamate transporter blocker DL-TBOA, and the vesicular transporter inhibitor bafilomycin A1 on the amiodarone-mediated inhibition of 4-aminopyridine-evoked glutamate release. Amiodarone (5 μM) was added 10 min before the addition of 4-aminopyridine and, whereas the other drugs were added 20 min prior to this. Each column is mean ± S.E.M. values of independent experiments, using synaptosomal preparations from 5 to 6 animals. \*\*\*, *P* < 0.001 versus control group. #, *P* < 0.05 versus the DL-TBOA-treated group.

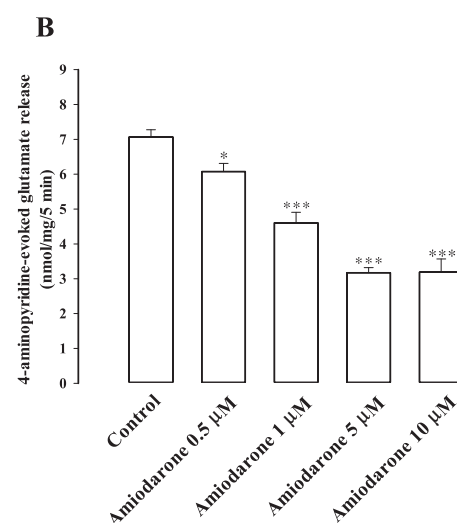
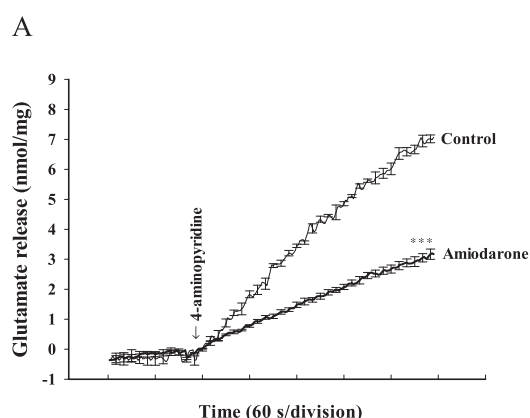


**Fig. 1.** Amiodarone inhibits the release of glutamate evoked by 4-aminopyridine in rat hippocampal synaptosomes. (A) Glutamate release was evoked by 4-aminopyridine (1 mM) in the absence (control) or presence of amiodarone (5 μM), added 10 min before the addition of 4-aminopyridine. (B) Concentration-dependent depression of glutamate release by amiodarone. Data represent mean ± S.E.M. values of independent experiments, using synaptosomal preparations from 5 animals. \*, *P* < 0.05, \*\*\*, *P* < 0.001 versus control group.

### 3.2. Effect of external calcium omission, the glutamate transporter blocker DL-TBOA, and the vesicular transporter inhibitor bafilomycin A1 on the capsaicin-mediated inhibition of 4-AP-evoked glutamate release

Fig. 2 shows that the glutamate release evoked by 4-aminopyridine (1 mM) in an extracellular  $\text{Ca}^{2+}$ -free solution containing EGTA (300  $\mu\text{M}$ ) was  $1.9 \pm 0.1$  nmol/mg/5 min [ $F(2,13) = 427.7$ ;  $P = 0.000$ ]. This  $\text{Ca}^{2+}$ -independent component of the 4-aminopyridine-evoked glutamate release was unaffected by 5  $\mu\text{M}$  of amiodarone ( $2.0 \pm 0.1$  nmol/mg/5 min;  $P = 0.98$ ; Fig. 2). DL-TBOA (10  $\mu\text{M}$ ), a non-selective inhibitor of all excitatory amino acid transporter subtypes, increased the 4-aminopyridine-evoked glutamate release [ $13.1 \pm 0.7$  nmol/mg/5 min;  $t(10) = 10.1$ ;  $P = 0.000$ ]. In the presence of DL-TBOA, amiodarone (5  $\mu\text{M}$ ) induced a 52% decrease in glutamate release evoked by 4-aminopyridine [ $6.3 \pm 0.2$  nmol/mg/5 min;  $F(2,13) = 89.5$ ;  $P = 0.000$ ; Fig. 2]. By contrast, bafilomycin A1 (0.1  $\mu\text{M}$ ), a vesicular transporter inhibitor, inhibited the 4-aminopyridine-evoked glutamate release by 69% [ $2.1 \pm 0.2$  nmol/mg/5 min;  $F(2,15) = 574.8$ ;  $P = 0.000$ ]. The subsequent application of 5  $\mu\text{M}$  amiodarone inhibited this release by 5% ( $2.0 \pm 0.1$  nmol/mg/5 min) versus the 54% inhibition obtained without bafilomycin A1 ( $P < 0.05$ ). These results indicate that amiodarone influences the evoked glutamate release by a decrease in vesicular exocytosis.

### 3.3. Effect of amiodarone on the synaptosomal $[\text{Ca}^{2+}]_c$ and membrane potential

Fig. 3A shows the  $[\text{Ca}^{2+}]_c$  levels determined in synaptosomes pretreated with fura-2. The stimulation of synaptosomes with 1 mM 4-aminopyridine caused an increase in  $[\text{Ca}^{2+}]_c$  levels to a plateau level ( $P = 0.000$ ). Preincubation with amiodarone (5  $\mu\text{M}$ ) for 10 min before 4-aminopyridine addition did not significantly affect basal  $\text{Ca}$  levels but reduced the 4-aminopyridine-evoked  $[\text{Ca}^{2+}]_c$  increase by 34% ( $t(10) = 6.7$ ,  $P = 0.003$ ). Fig. 3B shows the effect of amiodarone on the synaptosomal plasma membrane potential. The synaptosomal membrane potential can be monitored by positively charged membrane potential-sensitive cationic cyanide dye DiSC<sub>3</sub>(5). 4-aminopyridine (1 mM) application caused an increase in DiSC<sub>3</sub>(5) fluorescence. Preincubation with amiodarone (5  $\mu\text{M}$ ) for 10 min before 4-aminopyridine addition did not alter the resting membrane potential, and had no significant effect on the 4-aminopyridine-mediated increase in DiSC<sub>3</sub>(5) fluorescence ( $t(8) = -0.16$ ;  $P = 0.87$ ; Fig. 3B). Additionally, raising external potassium concentration (15 mM KCl) causes clamped depolarization of synaptosomes, leading to voltage-dependent calcium influx and the release of  $6.3 \pm 0.2$  nmol/mg/5 min. Addition of amiodarone (5  $\mu\text{M}$ ) caused an inhibition of KCl-evoked release of about 46% to  $3.4 \pm 0.2$  nmol/mg/5 min ( $t(8) = 5.3$ ;  $P = 0.000$ ; Fig. 3C). Furthermore, the release triggered by the  $\text{Na}^+$  channel activator veratridine

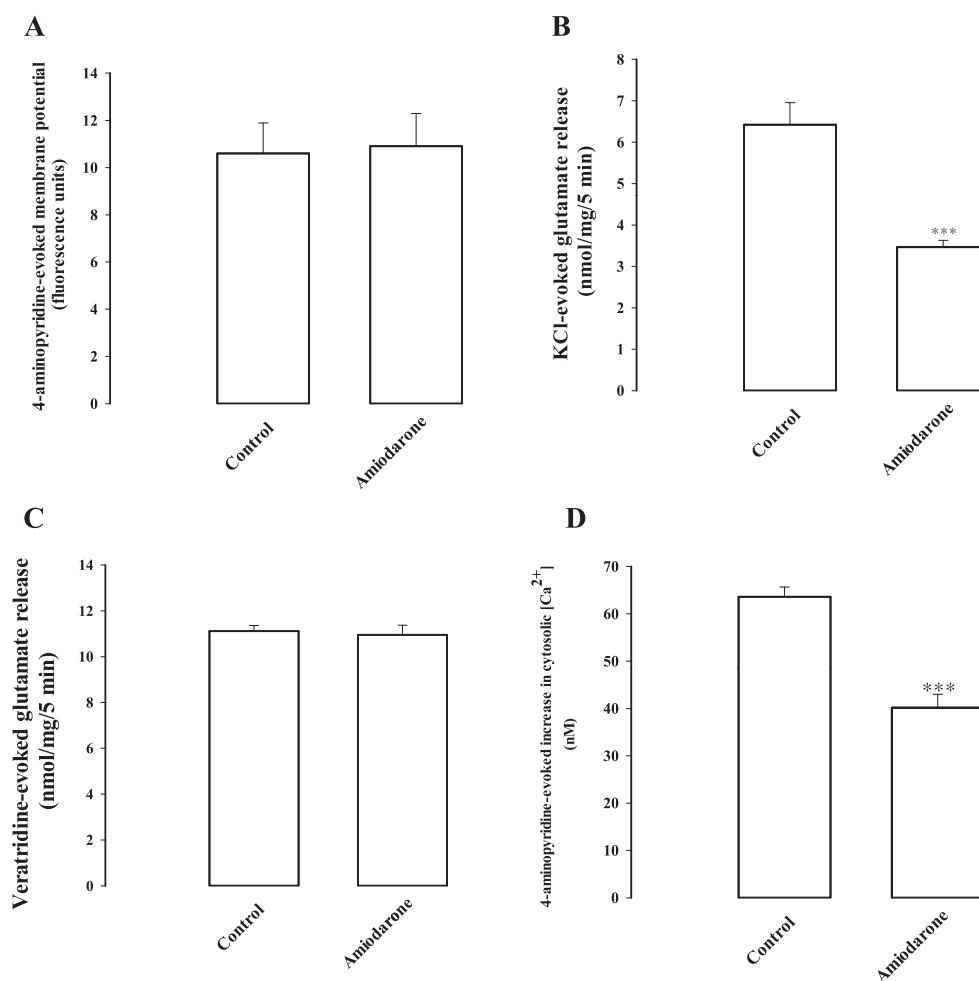


**Fig. 3.** Amiodarone effects on 4-aminopyridine-evoked change in synaptosomal cytosolic  $\text{Ca}^{2+}$  concentration ( $[\text{Ca}^{2+}]_c$ ) and membrane potential.  $[\text{Ca}^{2+}]_c$ . Synaptosomal membrane potential (A), glutamate release evoked by 15 mM KCl (B) or 50  $\mu\text{M}$  veratridine (C), and cytosolic  $[\text{Ca}^{2+}]$  induced by 4-aminopyridine (D) was examined in the absence (control) or presence of 5  $\mu\text{M}$  amiodarone, added 10 min before the addition of 4-aminopyridine. Each column is mean  $\pm$  S.E.M. values of independent experiments, using synaptosomal preparations from 5 animals. \*\*\*,  $P < 0.001$  versus control group.

(50  $\mu$ M;  $11.1 \pm 0.2$  nmol/mg/5 min) was unaffected by amiodarone (5  $\mu$ M;  $10.9 \pm 0.4$  nmol/mg/5 min;  $P = 0.75$ ; Fig. 3D).

### 3.4. Effect of a $\text{Ca}^{2+}$ channel blocker and intracellular $\text{Ca}^{2+}$ release inhibitors on the amiodarone-mediated inhibition of 4-AP-evoked glutamate release

Fig. 4 shows that  $\omega$ -conotoxin MVIIC (2  $\mu$ M), a wide-spectrum blocker of  $\text{Ca}_v2.2$  (N-type) and  $\text{Ca}_v2.1$  (P/Q-type) channels, reduced the 4-aminopyridine-evoked glutamate release by 66%, from  $6.9 \pm 0.2$  under control conditions to  $2.1 \pm 0.2$  nmol/mg/5 min [ $F(2,13) = 263.4$ ;  $P = 0.000$ ]. In the presence of  $\omega$ -conotoxin MVIIC, amiodarone (5  $\mu$ M) reduced the 4-aminopyridine-evoked glutamate release by only 10% ( $1.9 \pm 0.2$  nmol/mg/5 min), which was significantly less than the inhibition induced by amiodarone alone (55%,  $P < 0.05$ ). Dantrolene (100  $\mu$ M), a blocker of  $\text{Ca}^{2+}$  release from endoplasmic reticulum ryanodine receptors, and CGP37157, a membrane-permeant blocker of the mitochondrial  $\text{Na}^+/\text{Ca}^{2+}$  exchanger, reduced the 4-aminopyridine (1 mM)-evoked glutamate release by 32% ( $4.7 \pm 0.2$  nmol/mg/5 min;  $t(9) = 7.9$ ;  $P = 0.000$ ) and 28% ( $5.0 \pm 0.2$  nmol/mg/5 min;  $t(10) = 4.2$ ;  $P = 0.000$ ), respectively. In the presence of dantrolene or CGP37157, amiodarone (5  $\mu$ M) was still able to reduce glutamate release by 55% [ $F(2,13) = 176.7$ ;  $P = 0.000$ ] or 48% [ $F(2,15) = 45.3$ ;  $P = 0.000$ ], respectively (Fig. 4), which was not significantly different from the inhibition produced by amiodarone alone (55%;  $P > 0.05$ ).

### 3.5. Effect of the protein kinase A inhibitors H89 and KT5720 or the protein kinase C inhibitor GF109203X on the amiodarone-mediated inhibition of 4-aminopyridine-evoked glutamate release

Fig. 5 shows that the protein kinase A (PKA) inhibitor H89 (100  $\mu$ M) reduced the 4-aminopyridine (1 mM)-evoked glutamate release and prevented the inhibition of glutamate release by amiodarone (5  $\mu$ M) [ $F(2,19) = 104.6$ ;  $P = 0.000$ ]. In the seven tested

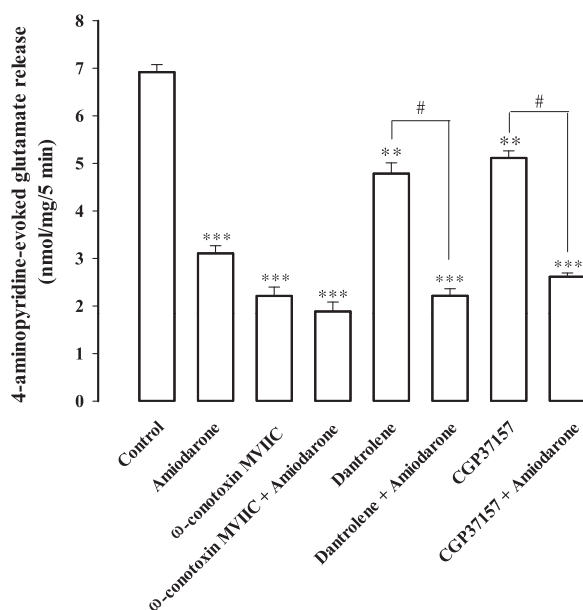


**Fig. 4.** Effect of  $\text{Ca}^{2+}$  channel blocker  $\omega$ -conotoxin MVIIC and intracellular  $\text{Ca}^{2+}$  release inhibitors dantrolene and CGP37157 on the amiodarone-mediated inhibition of 4-aminopyridine-evoked glutamate release. Amiodarone (5  $\mu$ M) was added 10 min before the addition of 4-aminopyridine, whereas the other drugs were added 30 min prior to this. Each column is mean  $\pm$  S.E.M. values of independent experiments, using synaptosomal preparations from 5 to 6 animals. \*\*,  $P < 0.01$ , \*\*\*,  $P < 0.001$  versus the control group; #,  $P < 0.05$  versus the dantrolene- or CGP37157-treated group.

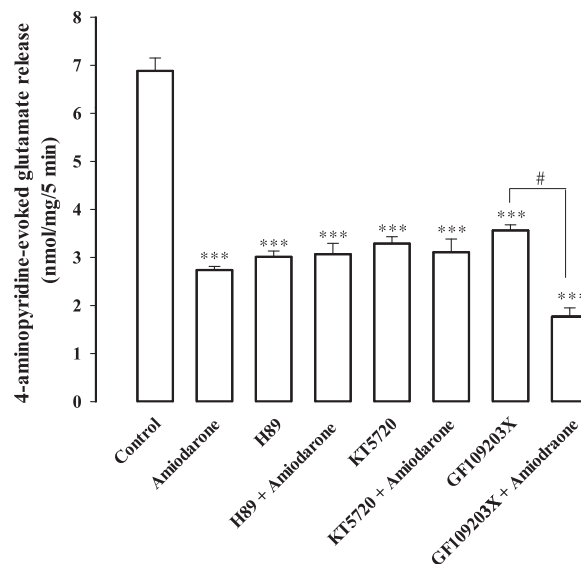


**Fig. 5.** The inhibitory action of amiodarone on glutamate release from synaptosomes is prevented by the protein kinase A inhibitor H89 and KT5720 not by the protein kinase C inhibitor GF109203X. Amiodarone (5  $\mu$ M) was added 10 min before the addition of 4-aminopyridine, whereas the other drugs were added 30 min prior to this. Each column is mean  $\pm$  S.E.M. values of independent experiments, using synaptosomal preparations from 5 to 6 animals. \*\*\*,  $P < 0.001$  versus the control group; #,  $P < 0.05$  versus the GF109203X-treated group.

synaptosomes, no statistical difference was observed between the release after H89 alone and after the H89 and amiodarone treatment ( $P = 0.98$ ). A similar result was also obtained with another PKA inhibitor KT5720 (10  $\mu$ M) [ $F(2,19) = 81.1$ ;  $P = 0.000$ ; Fig. 5]. In the presence of H89 or KT5720, therefore, amiodarone induced a statistically insignificant inhibition of glutamate release of 3% compared with the 55% inhibition produced by amiodarone alone. In contrast to the effect of H89 or KT5720, PKC inhibitor GF109203X (10  $\mu$ M) failed to influence the ability of amiodarone to inhibit 4-aminopyridine-evoked release of glutamate. In the presence of GF109203X (10  $\mu$ M) and amiodarone (5  $\mu$ M), the inhibition of glutamate release following 4-aminopyridine depolarization was significantly different from the effect of GF109203X alone [ $F(2,23) = 158.2$ ;  $P = 0.000$ ; Fig. 5].

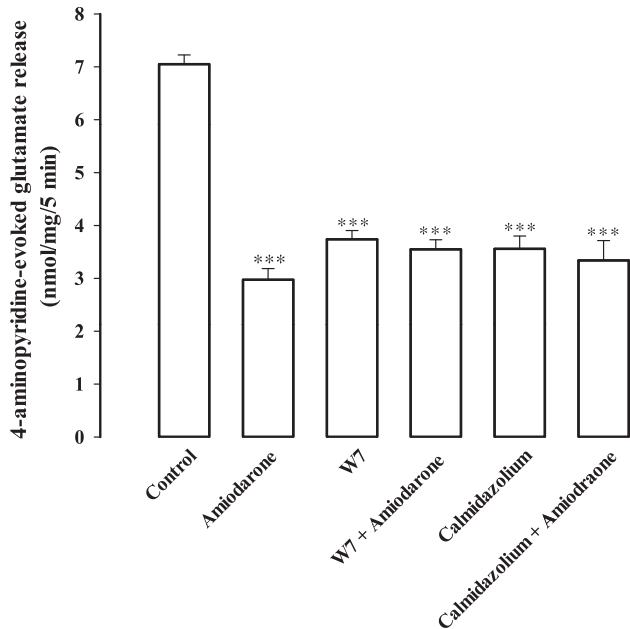
### 3.6. Effect of the calmodulin antagonists W7 and calmidazolium on the amiodarone-mediated inhibition of 4-aminopyridine-evoked glutamate release

Fig. 6 shows that W7 (25  $\mu$ M) reduced 4-aminopyridine-evoked glutamate release [ $F(2,12) = 118.9$ ;  $P = 0.000$ ]. In the presence of W7, amiodarone (5  $\mu$ M) produced a 5% decrease in the 4-aminopyridine-evoked glutamate release, which was significantly different from the inhibition produced by amiodarone alone (55%;  $P < 0.05$ ; Fig. 6). As with W7, in synaptosomes treated calmidazolium, an alternative calmodulin antagonist, amiodarone-mediated inhibition of 4-aminopyridine-evoked glutamate release was abolished [ $F(2,12) = 48.75$ ;  $P = 0.000$ ; Fig. 6].

### 3.7. Effect of amiodarone on miniature excitatory postsynaptic currents (mEPSCs) in hippocampal slices

Fig. 7 shows the effects of amiodarone on mEPSC frequency and amplitude in hippocampal slices; mEPSCs were recorded at a holding potential of  $-70$  mV and in the presence of the  $\text{Na}^+$  channel blocker tetrodotoxin (1  $\mu$ M) and GABA<sub>A</sub> receptor antagonist bicuculline





**Fig. 6.** Amiodarone-mediated inhibition of 4-aminopyridine-evoked glutamate release is prevented by the calmodulin antagonists W7 and calmidazolium. Amiodarone (5  $\mu$ M) was added 10 min before the addition of 4-aminopyridine, whereas the other drugs were added 30 min prior to this. Each column is mean  $\pm$  S.E.M. values of independent experiments, using synaptosomal preparations from 5 animals. \*\*\*,  $P < 0.001$  versus the control group.

(20  $\mu$ M). Fig. 7A shows a typical example of traces recorded from a signal cell, and amiodarone (5  $\mu$ M) reduced the occurrence of mEPSCs. In the five tested neurons, amiodarone reduced the frequency of mEPSCs by  $61.3\% \pm 2.6\%$  ( $t(10) = 5.2$ ;  $P = 0.000$ ), but the amplitude was unaffected ( $t(10) = -0.11$ ;  $P = 0.96$ ; Fig. 7B).

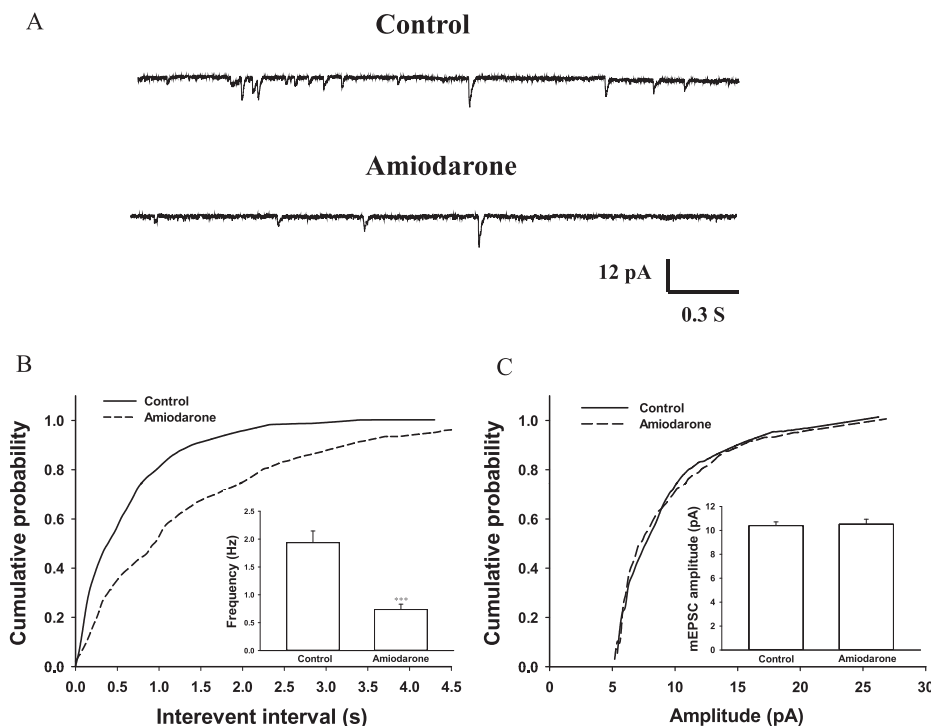


**Fig. 7.** Amiodarone decreases the frequency but not the amplitude of mEPSCs in the hippocampal brain slices. (A) Sample trace of mEPSCs in the absence (control) or presence of 5  $\mu$ M amiodarone. (B) Cumulative plot of interevent interval of mEPSCs. (C) Cumulative plot of amplitude of mEPSCs. Inset: The average amplitude and frequency of mEPSCs in the control and amiodarone treated groups. Each column is mean  $\pm$  S.E.M. values of 5 independent experiments. \*\*\*,  $P < 0.001$  versus the control group.

#### 4. Discussion

An abundant evidence suggests the relevance of glutamate to epilepsy and antiepileptic mechanisms. Therefore, in the present study, we focused on the effect of amiodarone, an anti-arrhythmic drug with antiepileptic effects (19), on glutamate release from rat hippocampal nerve terminals (synaptosomes) and slices. We found that amiodarone depressed the  $\text{Ca}^{2+}$ -dependent, exocytosis-like release of glutamate evoked by depolarizing stimuli in synaptosomes. Furthermore, we observed that amiodarone reduced the frequency, but not the amplitude, of mEPSCs in slice preparations, suggesting a reduction in the release probability and definitively evidencing a presynaptic component in synaptic transmission and regulation. This study is the first to present the effect of amiodarone on presynaptic glutamate release.

In synaptic terminals,  $\text{Na}^+$  channel inhibition or  $\text{K}^+$  channel activation stabilizes membrane excitability, which causes a decrease in voltage-dependent  $\text{Ca}^{2+}$  entry and a consequent decrease in glutamate release (29,30). Using fura-2, we demonstrated that amiodarone significantly reduced the evoked increase in intrasynaptosomal  $\text{Ca}^{2+}$  levels. Furthermore, the inhibitory effect of amiodarone on the 4-aminopyridine-evoked glutamate release from synaptosomes was prevented by blocking the  $\text{Ca}_v2.2$  (N-type) and  $\text{Ca}_v2.1$  (P/Q-type) channels, but it was not altered by blocking intracellular  $\text{Ca}^{2+}$  release. Therefore, these data demonstrate that a  $\text{Ca}_v2.2$  (N-type) and  $\text{Ca}_v2.1$  (P/Q-type) channel-mediated decrease in synaptosomal  $\text{Ca}^{2+}$  is instrumental for the amiodarone-mediated inhibition of glutamate release. In experimental cardiac preparations, amiodarone has been shown to inhibit  $\text{Ca}^{2+}$  currents (15). Regarding the possible mechanism of amiodarone-mediated presynaptic inhibition, a direct interaction between amiodarone and presynaptic voltage-dependent  $\text{Ca}^{2+}$  channels should be considered.

Our observations also demonstrate that the amiodarone-mediated inhibition of glutamate release is not due to a reduction

in synaptosomal excitability caused by the modulation of  $\text{Na}^+$  or  $\text{K}^+$  ion channels. First, amiodarone significantly inhibited 4-aminopyridine- and 15 mM external KCl-evoked glutamate release. This indicates that  $\text{Na}^+$  channels are not involved in the effect of amiodarone on the evoked glutamate release, because 4-aminopyridine-evoked glutamate release involves the action of  $\text{Na}^+$  and  $\text{Ca}^{2+}$  channels and 15 mM KCl-evoked glutamate release involves only  $\text{Ca}^{2+}$  channels (29,31). This suggestion is supported by the observation that amiodarone did not affect veratridine-induced glutamate release in synaptosomes. Veratridine directly activates the  $\text{Na}^+$  channel and thereby leads to plasma membrane depolarization,  $\text{Ca}^{2+}$  entry, and neurotransmitter release (20). Second, we observed no effect of amiodarone on the synaptosomal plasma membrane potential, indicating that amiodarone does not affect  $\text{K}^+$  conductance. Third, amiodarone did not affect the 4-aminopyridine-evoked  $\text{Ca}^{2+}$ -independent glutamate release, a component of glutamate release that is exclusively dependent on the membrane potential (32,33). Our finding is inconsistent with those of previous electrophysiological studies, which have reported that amiodarone inhibits  $\text{Na}^+$  and  $\text{K}^+$  currents in several experimental cardiac preparations (15,16,34). The reason for this discrepancy is presently unclear but may be related to the different experimental models applied.

We investigated how amiodarone inhibits presynaptic  $\text{Ca}^{2+}$  channels and glutamate release from hippocampal nerve terminals. In synaptic terminals, an increase in cytosolic  $\text{Ca}^{2+}$  affects a  $\text{Ca}^{2+}$ /calmodulin-dependent activation of adenylate cyclase (AC), including AC1 and AC8. The activation of these ACs increases cyclic adenosine monophosphate (cAMP) levels and activates PKA, which facilitates glutamate release (35–37). In the present study, we found that the inhibitory effect of amiodarone on the 4-aminopyridine-evoked glutamate release was prevented by the PKA inhibitors and the calmodulin antagonists. Thus, the inhibitory effect of amiodarone on the intrasynaptosomal  $\text{Ca}^{2+}$  levels observed here may cause a reduction of the  $\text{Ca}^{2+}$ -calmodulin/AC/cAMP/PKA cascade, thereby reducing glutamate release.

Amiodarone is a Class III anti-arrhythmic medication, commonly used to treat patients with refractory ventricular tachycardia and paroxysmal atrial fibrillation (12,38). In addition to its anti-arrhythmic effect, amiodarone has been shown to pass into the rat brain and reach the highest concentration 20–30 min after intravenous administration (17). Regarding its possible role in the central nervous system, amiodarone has been reported to exhibit a crucial antiepileptic effect in various animal models (19); however, its precise mechanism remains unclear. The present study provides evidence that amiodarone can inhibit glutamate release from hippocampal nerve terminals. This finding is in consistent with those of previous studies showing the similar effects of numerous antiepileptic drugs on glutamatergic transmission (9–11). Thus, amiodarone may attenuate seizures by reducing glutamate release from nerve terminals. Although we did not measure amiodarone concentrations in the brain, the concentration of amiodarone used in this study (5  $\mu\text{M}$ ) is close to those in the plasma of patients treated with amiodarone (0.7–3.7  $\mu\text{M}$ ) (39) and is nontoxic (40), suggesting that our finding has some clinical relevance.

In conclusion, our data show that amiodarone exerts an inhibitory effect on the evoked glutamate release from hippocampal nerve terminals by a mechanism that involves the suppressing voltage-dependent  $\text{Ca}^{2+}$  channels and  $\text{Ca}^{2+}$ -calmodulin/PKA cascade. This observation represents a crucial mechanism of action of amiodarone that might contribute to its antiepileptic activity as well as the prevention of calcium overload associated with neuronal injury in the brain. Further studies are needed to investigate these clinical applications.

## Conflicts of interest

None declared.

## Acknowledgments

This work was supported by the grant from the Chi-Mei Medical Center (103-CM-FJU-01).

## References

- Collingridge GL, Lester RA. Excitatory amino acid receptors in the vertebrate central nervous system. *Pharmacol Rev*. 1989;41:143–210.
- Greenamyre JT, Porter RH. Anatomy and physiology of glutamate in the CNS. *Neurology*. 1994;44:S7–S13.
- Gardoni F, Di Luca M. New targets for pharmacological intervention in the glutamatergic synapse. *Eur J Pharmacol*. 2006;545:2–10.
- Sundaram RS, Gowtham L, Nayak BS. The role of excitatory neurotransmitter glutamate in brain physiology and pathology. *Asian J Pharm Clin Res*. 2012;5:1–5.
- Kritis AA, Stamoula EG, Paniskaki KA, Vavilis TD. Researching glutamate – induced cytotoxicity in different cell lines: a comparative/collective analysis/study. *Front Cell Neurosci*. 2015;9:91.
- During MJ, Spencer DD. Extracellular hippocampal glutamate and spontaneous seizure in the conscious human brain. *Lancet*. 1993;341:1607–1610.
- Millan MH, Chapman AG, Meldrum BS. Extracellular amino acid levels in hippocampus during pilocarpine-induced seizures. *Epilepsy Res*. 1993;14:139–148.
- Wilson CL, Maidment NT, Shomer MH, Behnke EJ, Ackerson L, Fried I, et al. Comparison of seizure related amino acid release in human epileptic hippocampus versus a chronic, kainate rat model of hippocampal epilepsy. *Epilepsy Res*. 1996;26:245–254.
- Kammerer M, Brawek B, Freiman TM, Jackisch R, Feuerstein TJ. Effects of antiepileptic drugs on glutamate release from rat and human neocortical synaptosomes. *Naunyn Schmiedeberg Arch Pharmacol*. 2011;383:531–542.
- Quintero JE, Dooley DJ, Pomerleau F, Huettl P, Gerhardt GA. Amperometric measurement of glutamate release modulation by gabapentin and pregabalin in rat neocortical slices: role of voltage-sensitive  $\text{Ca}^{2+}$   $\alpha 2\delta$ -1 subunit. *J Pharmacol Exp Ther*. 2011;338:240–245.
- Sitges M, Guarneros A, Nekrasov V. Effects of carbamazepine, phenytoin, valproic acid, oxcarbazepine, lamotrigine, topiramate and vinpocetine on the presynaptic  $\text{Ca}^{2+}$  channel-mediated release of  $[^3\text{H}]$ glutamate: comparison with the  $\text{Na}^+$  channel-mediated release. *Neuropharmacology*. 2007;53:854–862.
- Manios EG, Mavrikakis HE, Kanoupakis EM, Kallergis EM, Dermizaki DN, Kambouraki DC, et al. Effects of amiodarone and diltiazem on persistent atrial fibrillation conversion and recurrence rates: a randomized controlled study. *Cardiovasc Drugs Ther*. 2003;17:31–39.
- Singh BN, Singh SN, Reda DJ, Tang XC, Lopez B, Harris CL. Amiodarone versus sotalol for atrial fibrillation. *N Engl J Med*. 2005;352:1861–1872.
- Polster P, Broekhuysen J. The adrenergic antagonism of amiodarone. *Biochem Pharmacol*. 1976;25:131–134.
- Varró A, Virág L, Papp JG. Comparison of the chronic and acute effects of amiodarone on the calcium and potassium currents in rabbit isolated cardiac myocytes. *Br J Pharmacol*. 1996;117:1181–1186.
- Kodama I, Kamiya K, Toyama J. Amiodarone: ionic and cellular mechanisms of action of the most promising class III agent. *Am J Cardiol*. 1999;84:20R–28R.
- Wyss PA, Moor MJ, Bickel MH. Single-dose kinetics of tissue distribution, excretion and metabolism of amiodarone in rats. *J Pharmacol Exp Ther*. 1990;254:502–507.
- Turovaya AY, Galenko-Yaroshevskii PA, Kade AKh, Uvarov AE, Kiguradze MI, Khvitiya NG, et al. Effects of verapamil and amiodarone on sympathoadrenal system and balance of excitatory and inhibitory amino acids in rat medulla oblongata. *Bull Exp Biol Med*. 2005;139:665–667.
- Ozbakis-Dengiz G, Bakirci A. Anticonvulsant and hypnotic effects of amiodarone. *J Zhejiang Univ Sci B*. 2009;10:317–322.
- Nicholls DG. The glutamatergic nerve terminal. *Eur J Biochem*. 1993;212:613–631.
- Bouron A. Modulation of spontaneous quantal release of neurotransmitters in the hippocampus. *Prog Neurobiol*. 2001;63:613–635.
- Spencer SS, Berg AT, Vickrey BG, Sperling MR, Bazil CW, Shinnar S, et al. Predicting long-term seizure outcome after resective epilepsy surgery: the multicenter study. *Neurology*. 2005;65:912–918.
- Cavus I, Pan JW, Hetherington HP, Abi-Saab W, Zaveri HP, Vives KP, et al. Decreased hippocampal volume on MRI is associated with increased extracellular glutamate in epilepsy patients. *Epilepsia*. 2008;49:1358–1366.
- Nicholls DG, Sihra TS. Synaptosomes possess an exocytotic pool of glutamate. *Nature*. 1986;321:772–773.
- Gryniewicz G, Poenie M, Tsien RY. A new generation of  $\text{Ca}^{2+}$  indicators with greatly improved fluorescence properties. *J Biol Chem*. 1985;260:3440–3450.

- (26) Akerman KE, Scott IG, Heikkilä JE, Heinonen E. Ionic dependence of membrane potential and glutamate receptor-linked responses in synaptoneurosomes as measured with a cyanine dye, DiSC3(5). *J Neurochem*. 1987;48:552–559.
- (27) Chang CY, Lin TY, Lu CW, Huang SK, Wang YC, Chou SS, et al. Hesperidin inhibits glutamate release and exerts neuroprotection against excitotoxicity induced by kainic acid in the hippocampus of rats. *Neurotoxicology*. 2015;50:157–169.
- (28) Chang Y, Lin TY, Lu CW, Huang SK, Wang YC, Wang SJ. Xanthohumol-induced presynaptic reduction of glutamate release in the rat hippocampus. *Food Funct*. 2016;7:212–226.
- (29) Nicholls DG. Presynaptic modulation of glutamate release. *Prog Brain Res*. 1998;116:15–22.
- (30) Wu LG, Saggau P. Presynaptic inhibition of elicited neurotransmitter release. *Trends Neurosci*. 1997;20:204–212.
- (31) Barrie AP, Nicholls DG, Sanchez-Prieto J, Sihra TS. An ion channel locus for the protein kinase C potentiation of transmitter glutamate release from guinea pig cerebrocortical synaptosomes. *J Neurochem*. 1991;57:1398–1404.
- (32) Attwell D, Barbour B, Szatkowski M. Nonvesicular release of neurotransmitter. *Neuron*. 1993;11:401–407.
- (33) Nicholls DG, Sihra TS, Sanchez-Prieto J. Calcium-dependent and -independent release of glutamate from synaptosomes monitored by continuous fluorimetry. *J Neurochem*. 1987;49:50–57.
- (34) Maltsev VA, Sabbah HN, Undrovinas AI. Late sodium current is a novel target for amiodarone: studies in failing human myocardium. *J Mol Cell Cardiol*. 2001;33:923–932.
- (35) Cooper DM. Molecular and cellular requirements for the regulation of adenylate cyclases by calcium. *Biochem Soc Trans*. 2003;31:912–915.
- (36) Andrade-Talavera Y, Duque-Feria P, Negrete-Díaz JV, Sihra TS, Flores G, Rodríguez-Moreno A. Presynaptic kainate receptor-mediated facilitation of glutamate release involves  $\text{Ca}^{2+}$ -calmodulin at mossy fiber-CA3 synapses. *J Neurochem*. 2012;122:891–899.
- (37) Rodríguez-Moreno A, Sihra TS. Presynaptic kainate receptor-mediated facilitation of glutamate release involves  $\text{Ca}^{2+}$ -calmodulin and PKA in cerebrocortical synaptosomes. *FEBS Lett*. 2013;587:788–792.
- (38) Chiba T, Kondo N, Takahara A. Influences of rapid pacing-induced electrical remodeling on pharmacological manipulation of the atrial refractoriness in rabbits. *J Pharmacol Sci*. 2016;130:170–176.
- (39) Vassallo P, Trohman RG. Prescribing amiodarone: an evidence-based review of clinical indications. *JAMA*. 2007;298:1312–1322.
- (40) Fabulas-Da CA, Aijjou R, Hachani J, Landry C, Cecchlli R, Culot M. In vitro blood-brain barrier model adapted to repeated-dose toxicological screening. *Toxicol In Vitro*. 2013;27:1944–1953.

## Article

# New Marine Sterols from a Gorgonian *Pinnigorgia* sp.

Yu-Chia Chang <sup>1,2,3</sup>, Tsong-Long Hwang <sup>4,5,6</sup>, Chih-Hua Chao <sup>7,8</sup> and Ping-Jyun Sung <sup>1,8,9,10,11,\*</sup>

<sup>1</sup> National Museum of Marine Biology & Aquarium, Pingtung 944, Taiwan; jay0404@gmail.com

<sup>2</sup> Doctoral Degree Program in Marine Biotechnology, National Sun Yat-sen University & Academia Sinica, Kaohsiung 804, Taiwan

<sup>3</sup> Greenhouse Systems Technology Center, Central Region Campus, Industrial Technology Research Institute, Nantou 540, Taiwan

<sup>4</sup> Graduate Institute of Natural Products, College of Medicine and Chinese Herbal Medicine Research Team, Healthy Aging Research Center, Chang Gung University, Taoyuan 333, Taiwan; htl@mail.cgu.edu.tw

<sup>5</sup> Research Center for Chinese Herbal Medicine, Research Center for Food and Cosmetic Safety, and Graduate Institute of Health Industry Technology, College of Human Ecology, Chang Gung University of Science and Technology, Taoyuan 333, Taiwan

<sup>6</sup> Department of Anesthesiology, Chang Gung Memorial Hospital, Taoyuan 333, Taiwan

<sup>7</sup> School of Pharmacy, China Medical University, Taichung 404, Taiwan; chchao@mail.cmu.edu.tw

<sup>8</sup> Chinese Medicine Research and Development Center, China Medical University Hospital, Taichung 404, Taiwan

<sup>9</sup> Graduate Institute of Marine Biology, National Dong Hwa University, Pingtung 944, Taiwan

<sup>10</sup> Graduate Institute of Natural Products, Kaohsiung Medical University, Kaohsiung 807, Taiwan

<sup>11</sup> Department of Marine Biotechnology and Resources, National Sun Yat-sen University, Kaohsiung 804, Taiwan

\* Correspondence: pjsung@nmmmba.gov.tw; Tel.: +886-8-882-5037; Fax: +886-8-882-5087

Academic Editor: Derek J. McPhee

Received: 19 January 2017; Accepted: 28 February 2017; Published: 3 March 2017

**Abstract:** Continuous chemical investigation of the gorgonian coral *Pinnigorgia* sp. resulted in the isolation of two new sterols, 5 $\alpha$ ,6 $\alpha$ -epoxy-(22*E*,24*R*)-3 $\beta$ ,11-dihydroxy-9,11-secoergosta-7-en-9-one (**1**) and (22*R*)-acetoxyl-(24 $\zeta$ )-ergosta-5-en-3 $\beta$ ,25-diol (**2**). The structures of sterols **1** and **2** were elucidated using spectroscopic methods. Sterol **1** displayed inhibitory effects on the generation of superoxide anions and the release of elastase by human neutrophils with IC<sub>50</sub> values of 8.65 and 5.86  $\mu$ M, respectively. The structure of a known metabolite, pubinernoid A (**3**), is revised as (+)-loliolide (**4**).

**Keywords:** gorgonian; *Pinnigorgia*; anti-inflammatory; superoxide anion; elastase; pubinernoid A; loliolide

## 1. Introduction

Gorgonian corals belonging to the genus *Pinnigorgia* have proven to be a rich source of sterols with unusual structural features [1–6]. In continuation of our effort to discover new natural products of this organism, its ethyl acetate extract exhibited anti-inflammatory activities by inhibiting the expression of superoxide anions and elastase by human neutrophils with IC<sub>50</sub> values of 1.89 and 1.57  $\mu$ g/mL, respectively. Two new sterols, 5 $\alpha$ ,6 $\alpha$ -epoxy-(22*E*,24*R*)-3 $\beta$ ,11-dihydroxy-9,11-secoergosta-7-en-9-one (**1**) and (22*R*)-acetoxyl-(24 $\zeta$ )-ergosta-5-en-3 $\beta$ ,25-diol (**2**) (Figure 1 and Supplementary Figures S1–S14), were isolated. The structures of these two sterols were established by spectroscopic analyses and sterol **1** was found to display anti-inflammatory activity.

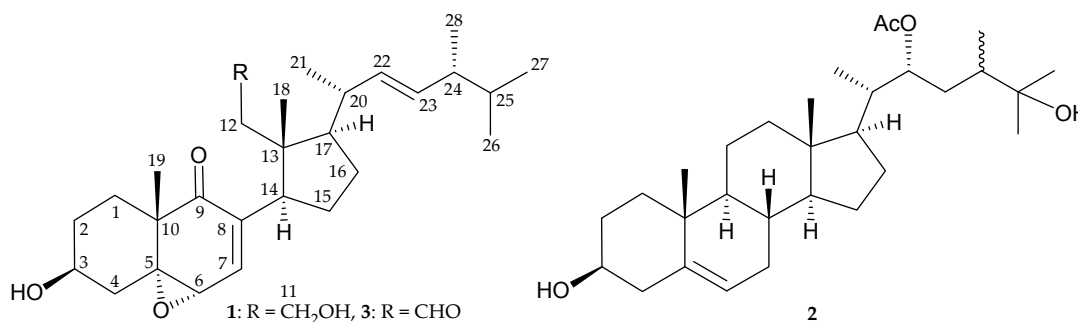


**Figure 1.** Chemical structures of 5 $\alpha$ ,6 $\alpha$ -epoxy-(22*E*,24*R*)-3 $\beta$ ,11-dihydroxy-9,11-secoergosta-7-en-9-one (1), (22*R*)-acetoxyl-(24*E*)-ergosta-5-en-3 $\beta$ ,25-diol (2), and 3-*O*-deacetyl-luffasterol B (3) [7].

## 2. Results and Discussion

The new sterol, 5 $\alpha$ ,6 $\alpha$ -epoxy-(22*E*,24*R*)-3 $\beta$ ,11-dihydroxy-9,11-secoergosta-7-en-9-one (1), was isolated as colorless oil. The high-resolution electrospray ionization mass spectrum (HRESIMS) showed a signal at  $m/z$  467.31308 (calcd. for C<sub>28</sub>H<sub>44</sub>O<sub>4</sub> + Na, 467.31373), and therefore the molecular formula of 1 was determined to be C<sub>28</sub>H<sub>44</sub>O<sub>4</sub> (7° of unsaturation degrees). The <sup>13</sup>C and distortionless enhancement polarization transfer (DEPT) spectrum of 1 showed that this compound has 28 carbons including six methyls, seven sp<sup>3</sup> methylenes, seven sp<sup>3</sup> methines, an sp<sup>3</sup> oxygenated tertiary carbon, two sp<sup>3</sup> quaternary carbons, three sp<sup>2</sup> methines, an sp<sup>2</sup> tertiary carbon and a ketonic carbonyl (Table 1). The IR spectrum of 1 revealed the presence of hydroxy ( $\nu_{\max}$  3398 cm<sup>-1</sup>) and  $\alpha,\beta$ -unsaturated ketonic carbonyl ( $\nu_{\max}$  1682 cm<sup>-1</sup>) groups. The latter structural feature was confirmed by the presence of signals at  $\delta_C$  201.9 (C-9), 141.4 (C-8) and 139.3 (CH-7) in the <sup>13</sup>C-NMR spectrum. A disubstituted olefin was identified from the signals of carbons at  $\delta_C$  134.4 (CH-22) and 133.0 (CH-23) and was confirmed by two olefin proton signals at  $\delta_H$  5.21 (1H, dd,  $J$  = 15.2, 6.4 Hz, H-23) and 5.24 (1H, dd,  $J$  = 15.2, 6.8 Hz, H-22) (Table 1). Four doublets at  $\delta_H$  1.03 (3H,  $J$  = 6.8 Hz), 0.91 (3H,  $J$  = 6.8 Hz), 0.83 (3H,  $J$  = 7.2 Hz) and 0.82 (3H,  $J$  = 6.8 Hz) were due to the Me-21, Me-28, Me-26 and Me-27 groups, respectively. Two sharp singlets for H<sub>3</sub>-18 and H<sub>3</sub>-19 appeared at  $\delta_H$  0.68 and 1.25, respectively. A trisubstituted epoxide was elucidated from the signals of an oxygenated tertiary carbon at  $\delta_C$  63.2 (C-5) and an oxymethine at  $\delta_C$  53.5 (CH-6); and further confirmed by the proton signal of a methine doublet at  $\delta_H$  3.39 (1H, d,  $J$  = 4.8 Hz, H-6). On the basis of the unsaturation data overall, 1 was concluded to be a secosterol molecule possessing four rings.

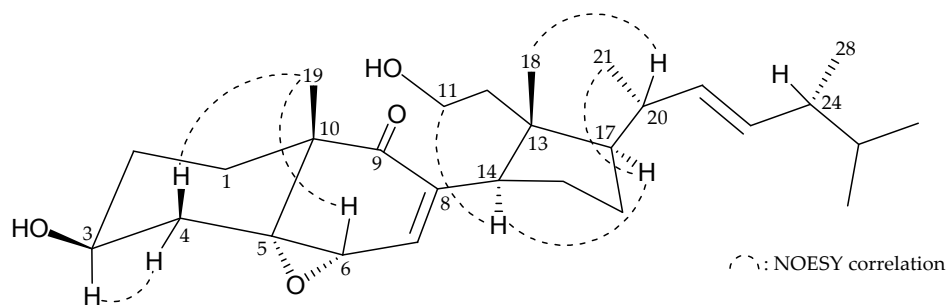
From the <sup>1</sup>H-NMR coupling information and <sup>1</sup>H-<sup>1</sup>H correlation spectroscopy (COSY) of 1 (Table 1), the following correlations were revealed: H<sub>2</sub>-1/H<sub>2</sub>-2/H-3/H<sub>2</sub>-4, H-6/H-7, H<sub>2</sub>-11/H<sub>2</sub>-12, H-14/H<sub>2</sub>-15/H<sub>2</sub>-16/H-17/H-20/H-22/H-23/H-24/H-25/H<sub>3</sub>-26, H-20/H<sub>3</sub>-21, H-24/H<sub>3</sub>-28 and H-25/H<sub>3</sub>-27. These data, together with the key heteronuclear multiple bond coherence (HMBC) correlations between H<sub>2</sub>-1, H<sub>2</sub>-4, H<sub>3</sub>-19/C-5; H-6/C-8; H-7, H<sub>3</sub>-19/C-9; H<sub>2</sub>-2, H<sub>3</sub>-19/C-10; and H<sub>2</sub>-12, H<sub>2</sub>-15, H<sub>3</sub>-18/C-13 (Table 1), all the information allowed determination of the carbon skeleton of 1. The stereochemistry of 1 was elucidated by analysis of the results of a nuclear Overhauser effect spectroscopy (NOESY) experiment. Assuming the  $\beta$ -orientation of H<sub>3</sub>-18 and H<sub>3</sub>-19, H-14 was found to exhibit correlations with H-11a ( $\delta_H$  3.81) and H-17, but not with H<sub>3</sub>-18, indicating that this proton was of an  $\alpha$ -orientation at C-14. In addition, the main NOESY correlation for 1 were interactions between H-3/H-4 $\alpha$ , H-4 $\beta$ /H<sub>3</sub>-19, H-6/H<sub>3</sub>-19, H-17/H<sub>3</sub>-21 and H<sub>3</sub>-18/H-20; thus, the 3-hydroxy and 5,6-epoxy groups in 1 should be positioned on the  $\beta$ - and  $\alpha$ -face, respectively (Figure 2).



**Table 1.**  $^1\text{H}$ - and  $^{13}\text{C}$ -NMR data,  $^1\text{H}$ - $^1\text{H}$  COSY, and HMBC correlations for secoesterol 1 and the  $^1\text{H}$ - and  $^{13}\text{C}$ -NMR data for 3-*O*-deacetylfluffasterol B (3).

Position	1				3	
	$\delta_{\text{H}}$ ( <i>J</i> in Hz) <sup>a</sup>	$\delta_{\text{C}}$ <sup>b</sup>	$^1\text{H}$ - $^1\text{H}$	HMBC	$\delta_{\text{H}}$ ( <i>J</i> in Hz) <sup>c</sup>	$\delta_{\text{C}}$ <sup>c</sup>
1a/b	2.09 m; 1.72 m	27.8, CH <sub>2</sub>	H <sub>2</sub> -2	C-5		27.8, CH <sub>2</sub>
2a/b	2.09 m; 1.65 m	30.5, CH <sub>2</sub>	H <sub>2</sub> -1, H-3	C-10	2.09 m; 1.68 m	30.5, CH <sub>2</sub>
3	3.98 m	68.3, CH	H <sub>2</sub> -2, H <sub>2</sub> -4	n. o. <sup>d</sup>	3.98 m	68.3, CH
4 $\alpha$	1.57 m	37.4, CH <sub>2</sub>	H-3, H-4 $\beta$	C-2, -3, -5	1.56 m	37.5, CH <sub>2</sub>
$\beta$	2.18 dd (12.8, 11.6)		H-3, H-4 $\alpha$	C-3	2.18 m	
5		63.2, C				63.5, C
6	3.39 d (4.8)	53.5, CH	H-7	C-7, -8	3.40 d (4.6)	53.5, CH
7	6.81 d (4.8)	139.3, CH	H-6	C-5, -6, -9, -14	6.84 dd (4.6, 1.0)	139.7, CH
8		141.4, C				140.5, C
9		201.9, C				200.6, C
10		45.6, C				45.4, C
11a	3.81 ddd (10.4, 10.4, 6.0)	59.1, CH <sub>2</sub>	H-11b, H <sub>2</sub> -12	n. o.	9.88 dd (3.8, 1.7)	203.4, CH
b	3.68 ddd (10.4, 8.8, 6.0)		H-11a, H <sub>2</sub> -12	n. o.		
12a	1.61 m	40.4, CH <sub>2</sub>	H <sub>2</sub> -11, H-12b	n. o.	2.27 dd (15.9, 3.8)	50.8, CH <sub>2</sub>
b	1.12 m		H <sub>2</sub> -11, H-12a	C-11, -13, -17	2.00 dd (15.9, 1.7)	
13		46.1, C				46.3, C
14	3.37 dd (10.8, 8.0)	43.8, CH	H <sub>2</sub> -15	n. o.	3.51 dd (10.3, 9.2)	45.0, CH
15a/b	1.69–1.56 m	26.9, CH <sub>2</sub>	H-14, H <sub>2</sub> -16	C-13, -14	1.78 m; 1.71 m	26.7, CH <sub>2</sub>
16a/b	1.69 m; 1.44 m	25.4, CH <sub>2</sub>	H <sub>2</sub> -15, H-17	n. o.		25.8, CH <sub>2</sub>
17	1.74 m	49.6, CH	H <sub>2</sub> -16, H-20	n. o.		51.9, CH
18	0.68 s	17.8, CH <sub>3</sub>		C-12, -13, -14, -17	0.76 s	17.1, CH <sub>3</sub>
19	1.25 s	21.4, CH <sub>3</sub>		C-1, -5, -9, -10	1.21 s	20.0, CH <sub>3</sub>
20	2.15 m	38.8, CH	H-17, H <sub>3</sub> -21, H-22	n. o.	2.18 m	43.0, CH
21	1.03 d (6.8)	21.4, CH <sub>3</sub>	H-20	C-17, -20, -22	1.00 d (6.8)	19.7, CH <sub>3</sub>
22	5.24 dd (15.2, 6.8)	134.4, CH	H-20, H-23	C-20, -24	5.20 dd (17.6, 7.4)	133.4, CH
23	5.21 dd (15.2, 6.4)	133.0, CH	H-22, H-24	C-20, -24	5.24 dd (17.6, 7.4)	134.0, CH
24	1.86 m	43.0, CH	H-23, H-25, H <sub>3</sub> -28	C-22, -23, -25	1.87 m	38.8, CH
25	1.47 m	33.1, CH	H-24, H <sub>3</sub> -26, H <sub>3</sub> -27	C-23, -24, -28	1.47 m	33.2, CH
26	0.83 d (7.2)	20.0, CH <sub>3</sub>	H-25	C-24, -25, -27	0.82 d (6.8)	21.9, CH <sub>3</sub>
27	0.82 d (6.8)	19.7, CH <sub>3</sub>	H-25	C-24, -25, -26	0.83 d (6.8)	21.1, CH <sub>3</sub>
28	0.91 d (6.8)	17.5, CH <sub>3</sub>	H-24	C-23, -24, -25	0.91 d (7.0)	17.8, CH <sub>3</sub>

<sup>a</sup> Spectra recorded at 400 MHz in CDCl<sub>3</sub>. <sup>b</sup> Spectra recorded at 100 MHz in CDCl<sub>3</sub>. <sup>c</sup> Selected  $^1\text{H}$ -NMR and  $^{13}\text{C}$ -NMR data were reported by Rueda et al. (see ref. [7]). These data were recorded at 400 MHz for  $^1\text{H}$  and 100 MHz for  $^{13}\text{C}$  in CDCl<sub>3</sub>. <sup>d</sup> n. o. = not observed.

**Figure 2.** Selected NOESY correlations observed for 1.

A large coupling constant observed between H-22 and H-23 ( $J = 15.2$  Hz) supported a *trans* relationship between H-22 and H-23. The configuration of C-24 was suggested to be *R* on the basis of the  $^{13}\text{C}$ -NMR chemical shift of C-28 ( $\delta_{\text{C}}$  17.5). It was reported that the  $^{13}\text{C}$ -NMR value of C-28 resonates at  $\delta_{\text{C}}$  17.68 ppm in the 24*R* epimer of a known sterol, (22*E*,24*R*)-24-methylcholesta-5,22-dien-3 $\beta$ -ol, with the same chain, and the 24*S* epimer, (22*E*,24*S*)-24-methylcholesta-5,22-dien-3 $\beta$ -ol, has a relative 0.4 ppm downfield chemical shift (Figure 3) [8].

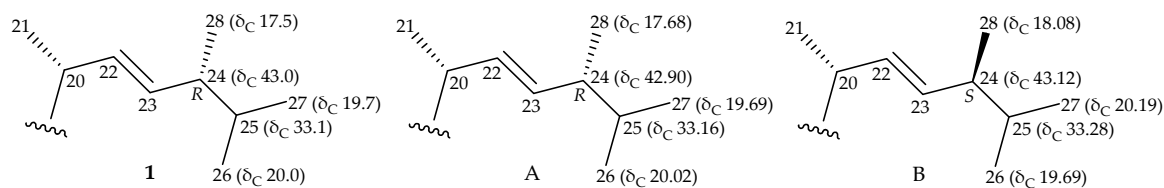


**Figure 3.** The  $^{13}\text{C}$ -NMR chemical shifts of the side-chain of secosterol **1**, (22*E*,24*R*)-24-methylcholesta-5,22-dien-3 $\beta$ -ol (**A**) and (22*E*,24*S*)-24-methylcholesta-5,22-dien-3 $\beta$ -ol (**B**) [8].

It was found that the NMR data of **1** were similar to those of a known 9,11-secosterol derivative, 3-*O*-deacetylfluffasterol **3** (**Figure 1**), isolated from the sponge *Spongia agaricina* [7], except that the signals corresponding to the 11-hydroxy group in **1** were replaced by signals for an aldehyde group in **3** [7] (Table 1). Furthermore, by comparison of the NMR data of **1** with those of **3**, we found that the  $^{13}\text{C}$  NMR chemical shifts of methines C-20 and C-24 for **3** ( $\delta_{\text{C}}$  43.0 and 38.8, respectively) should be interchangeable by comparison with those of **1** ( $\delta_{\text{C}}$  38.8 and 43.0, respectively) (Table 1), which was further confirmed by 2D NMR experiments. In a previous study, the structure of **1** as presented in this paper had been reported [9]. However, by comparison of the NMR data of **1** with those of reported data, we found that the NMR data ( $^1\text{H}$  and  $^{13}\text{C}$ ) for this compound differ significantly from those of **1** that reported herein (Table 1), because the structure of **1** has been established by extensive spectroscopic analysis, particularly with 2D NMR experiments. The authors suggested that the compound which was reported to possess the same structure as that of **1** in Reference [9] should be re-examined.

(22*R*)-Acetoxy-(24 $\xi$ )-ergosta-5-en-3 $\beta$ ,25-diol (**2**) was isolated as a colorless needles and its molecular formula was established as  $\text{C}_{30}\text{H}_{50}\text{O}_4$  (6 $^\circ$  of unsaturation) by HRESIMS at  $m/z$  497.36015 (calcd. for  $\text{C}_{30}\text{H}_{50}\text{O}_4 + \text{Na}$ , 497.36193). The IR spectrum of **2** indicated the presence of hydroxy ( $\nu_{\text{max}}$  3414  $\text{cm}^{-1}$ ) and ester carbonyl ( $\nu_{\text{max}}$  1730  $\text{cm}^{-1}$ ) groups. The whole series of spectroscopic data obtained from 1D and 2D NMR experiments (Table 2) clearly indicated that sterol **2** had the same core rings A–D and side chain as those of known sterols, 22(*R*),28-oxido-24 $\xi$ -methylcholest-5-en-3 $\beta$ ,25,28-triol (lobophytosterol) and (22*R*)-5 $\beta$ ,6 $\beta$ -epoxy-24 $\xi$ -methylcholestan-3 $\beta$ ,22(*R*),25-triol diacetate, respectively [10]. The  $^1\text{H}$ - $^1\text{H}$  COSY and HMBC correlations observed fully supported the locations of the functional groups, and, hence, (22*R*)-acetoxy-(24 $\xi$ )-ergosta-5-ene-3 $\beta$ ,25-diol (**2**) was assigned as structure **2**, with the same relative configurations as 22(*R*),28-oxido-24 $\xi$ -methylcholest-5-en-3 $\beta$ ,25,28-triol in the core rings A–D. The configuration of the C-22 stereogenic center was assigned as *R* on the basis of the NMR chemical shifts of C-22 oxymethine ( $\delta_{\text{H}}$  5.02, 1H, ddd,  $J$  = 10.8, 2.8, 2.4 Hz, H-22;  $\delta_{\text{C}}$  78.3, CH-22). It was reported that the  $^1\text{H}$ - and  $^{13}\text{C}$ -NMR values of C-22 oxymethine ( $\delta_{\text{H}}$  4.99, 1H, dt,  $J$  = 10.2, 2.5 Hz, H-22;  $\delta_{\text{C}}$  78.3, CH-22) in a 22*R* epimer of a known sterol, 5 $\beta$ ,6 $\beta$ -epoxy-24 $\xi$ -methylcholestan-3 $\beta$ ,22(*R*),25-triol diacetate [10], was found to possess the same side chain as that of **2**. The proton coupling constants and NMR chemical shift data also further supported these findings, though the configuration of C-24 was not determined at this stage.

The sterol analogues isolated from *Pinnigorgia* sp. were found to display interesting anti-inflammatory activities [1–3,5,6]. Based on these findings, the anti-inflammatory testing of sterols **1** and **2** were assayed and **1** showed inhibitory effects on the generation of superoxide anions and the release of elastase, respectively, by human neutrophils (Table 3).

**Table 2.**  $^1\text{H}$  (400 MHz,  $\text{CDCl}_3$ ) and  $^{13}\text{C}$  (100 MHz,  $\text{CDCl}_3$ ) NMR data and  $^1\text{H}$ - $^1\text{H}$  COSY and HMBC correlations for sterol **2**.

Position	$\delta_{\text{H}}$ (J in Hz)	$\delta_{\text{C}}$ , Multiple	$^1\text{H}$ - $^1\text{H}$ COSY	HMBC
1a/b	1.84 m; 1.06 m	37.2, $\text{CH}_2$	$\text{H}_2$ -2	C-2, -5
2a/b	1.84 m; 1.51 m	31.6, $\text{CH}_2$	$\text{H}_2$ -1, H-3	n. o. <sup>a</sup>
3	3.52 m	71.8, CH	$\text{H}_2$ -2, $\text{H}_2$ -4	n. o.
4a/b	2.30 m; 2.24 m	42.3, $\text{CH}_2$	H-3	C-2, -3, -5, -6, -10
5		140.7, C		
6	5.35 d (5.2)	121.6, CH	$\text{H}_2$ -7	C-4, -7, -8, -10
7a/b	1.97 m; 1.53 m	31.8, $\text{CH}_2$	H-6, H-8	C-6, -14
8	1.46 m	31.9, CH	$\text{H}_2$ -7, H-9, H-14	C-14
9	0.92 m	50.1, CH	H-8, $\text{H}_2$ -11	C-7, -8
10		36.5, C		
11a/b	1.50–1.40 m	21.1, $\text{CH}_2$	H-9, $\text{H}_2$ -12	C-9
12a/b	1.97 m; 1.17 m	39.7, $\text{CH}_2$	$\text{H}_2$ -11	n. o.
13		42.7, C		
14	0.98 m	56.3, CH	H-8, $\text{H}_2$ -15	n. o.
15a/b	1.56 m; 1.07 m	24.3, $\text{CH}_2$	H-14, $\text{H}_2$ -16	C-14
16a/b	1.81 m; 1.53 m	27.2, $\text{CH}_2$	$\text{H}_2$ -15, H-17	n. o.
17	1.15 m	53.1, CH	$\text{H}_2$ -16, H-20	C-12, -20
18	0.67 s	11.9, $\text{CH}_3$		C-12, -13, -14, -17
19	1.00 s	19.4, $\text{CH}_3$		C-1, -5, -9
20	1.75 m	39.8, CH	H-17, $\text{H}_3$ -21, H-22	n. o.
21	0.93 d (7.2)	13.0, $\text{CH}_3$	H-20	C-17, -20, -22
22	5.02 ddd (10.8, 2.8, 2.4)	78.3, CH	H-20, $\text{H}_2$ -23	n. o.
23a/b	1.84 m; 1.15 m	29.3, $\text{CH}_2$	H-22, H-24	C-20, -22
24	1.43 m	43.1, CH	$\text{H}_2$ -23, $\text{H}_3$ -28	n. o.
25		73.6, C		
26	1.13 s	25.0, $\text{CH}_3$		C-24, -25, -27
27	1.20 s	28.4, $\text{CH}_3$		C-24, -25, -26
28	0.91 d (7.2)	16.9, $\text{CH}_3$	H-24	C-23, -24, -25
22-OAc		171.0, C		
	2.04, s	21.6, $\text{CH}_3$		Acetate carbonyl

<sup>a</sup> n. o. = not observed.**Table 3.** Inhibitory effects of sterols **1** and **2** on superoxide anion generation and elastase release by human neutrophils in response to fMet-Leu-Phe/Cytochalasin B.

Compound	Superoxide Anions	Elastase Release
	$\text{IC}_{50}$ ( $\mu\text{M}$ ) <sup>a</sup>	$\text{IC}_{50}$ ( $\mu\text{M}$ )
<b>1</b>	$8.65 \pm 0.19$	$5.86 \pm 0.95$
<b>2</b>	> 10	> 10
<b>LY294002</b> <sup>b</sup>	$1.06 \pm 0.06$	$3.85 \pm 1.25$

<sup>a</sup> Concentration necessary for 50% inhibition ( $\text{IC}_{50}$ ); results are presented as mean  $\pm$  S.E.M. ( $n = 3$ ). <sup>b</sup> LY294002 (2-morpholin-4-yl-8-phenylchromen-4-one) was used as a reference compound.

In a previous study, we reported the isolation and structure elucidation of a natural product, pubinernoid A (**3**), from *Pinnigorgia* sp. [11] and this compound which has been previously isolated from a traditional Chinese medicinal plant *Schisandra pubescens* var. *pubinervis* [12]. Based on the detailed spectroscopic analysis and by comparing the  $^1\text{H}$ - and  $^{13}\text{C}$ -NMR chemical shifts in **3** with those of known carotenoid metabolites, ( $\pm$ )-loliolide, [13–19], the structure of pubinernoid A (**3**) should be revised as (+)-loliolide as presented in **4** (Figure 4). Because ( $\pm$ )-loliolide were synthesized by chemical methods [18] and the structure of (–)-loliolide was established by X-ray diffraction analysis [19], the structure of pubinernoid A (**3**) should be revised as (+)-loliolide (**4**).

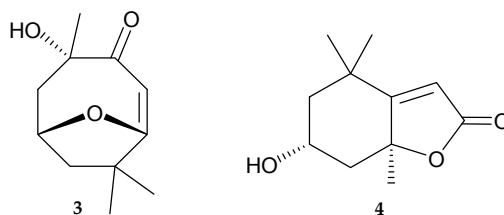


Figure 4. Chemical structures of pubinernoid A (3) and (+)-loliolide (4).

### 3. Experimental Section

#### 3.1. General Experimental Procedures

Optical rotations were measured on a Jasco P-1010 digital polarimeter (Japan Spectroscopic Corporation, Tokyo, Japan). Infrared spectra were recorded on a Jasco FT/IR-4100 spectrometer (Japan Spectroscopic Corporation); peaks are reported in  $\text{cm}^{-1}$ . The NMR spectra were recorded on a 400 MHz Varian Mercury Plus NMR spectrometer (Varian Inc., Palo Alto, CA, USA), using the residual  $\text{CHCl}_3$  signal ( $\delta_{\text{H}}$  7.26 ppm) as an internal standard for  $^1\text{H}$ -NMR and  $\text{CDCl}_3$  ( $\delta_{\text{C}}$  77.1 ppm) for  $^{13}\text{C}$ -NMR; coupling constants (J) are given in Hz. ESIMS and HRESIMS were recorded using a Bruker 7 Tesla solarix FTMS system (Bruker, Bremen, Germany). Column chromatography was performed on silica gel (230–400 mesh, Merck, Darmstadt, Germany). TLC was carried out on precoated Kieselgel 60 F<sub>254</sub> (0.25 mm, Merck); spots were visualized by spraying with 10%  $\text{H}_2\text{SO}_4$  solution followed by heating. Normal-phase HPLC (NP-HPLC) was performed using a system comprised of a Hitachi L-7110 pump (Hitachi Ltd., Tokyo, Japan) and a Rheodyne 7725 injection port (Rheodyne LLC, Rohnert Park, CA, USA). A semi-preparative normal-phase column (Supelco Ascentis Si Cat #:581515-U, 25 cm  $\times$  21.2 mm, 5  $\mu\text{m}$ , Sigma-Aldrich, St. Louis, MO, USA) was used for NP-HPLC. Reversed-phase HPLC (RP-HPLC) was performed using a system comprised of a Hitachi L-2130 pump (Hitachi Ltd., Tokyo, Japan), a Hitachi L-2455 photodiode array detector (Hitachi Ltd., Tokyo, Japan) and a Rheodyne 7725 injection port (Rheodyne LLC, Rohnert Park, CA, USA). A reverse phase column (Luna 5  $\mu\text{m}$  C18(2) 100 Å, AXIA Packed, 25 cm  $\times$  21.2 mm, Phenomenex Inc., Torrance, CA, USA) was used for RP-HPLC.

#### 3.2. Animal Material

Specimens of the gorgonian corals *Pinnigorgia* sp. were collected by hand using scuba off the coast of Green Island, Taiwan in August 2012 and stored in a freezer until extraction. A voucher specimen (NMMBA-TW-GC-2012-130) was deposited in the National Museum of Marine Biology & Aquarium, Taiwan. This organism was identified by comparison with previous descriptions [20].

#### 3.3. Extraction and Separation

Sliced bodies of *Pinnigorgia* sp. (wet weight 1.98 kg; dry weight 0.86 kg) were extracted with ethyl acetate (EtOAc) at room temperature. The EtOAc extract (84.9 g) was partitioned between methanol (MeOH) and *n*-hexane. The MeOH layer (12.6 g) was separated on Sephadex LH-20 and eluted using a mixture of dichloromethane (DCM) and MeOH (1:1) to yield 7 subfractions A–G. Fraction F was separated by silica gel column chromatography and eluted using *n*-hexane/acetone (stepwise, 1:1–pure acetone) to afford 8 subfractions F1–F8. Fraction F2 was purified by silica gel column chromatography and eluted using *n*-hexane/acetone (stepwise, 9:1–pure acetone) to yield 13 subfractions F2A–F2M. Fraction F2H was purified by NP-HPLC using a mixture of *n*-hexane/EtOAc (1:1) to afford 14 subfractions F2H1–F2H14. Fraction F2H12 was re-purified by RP-HPLC using a mixture of MeOH/ $\text{H}_2\text{O}$  (90:10, 4.0 mL/min flow rate) to yield 1 (2.8 mg). Fraction F2D was purified by NP-HPLC using a mixture of *n*-hexane/EtOAc (3:1) to afford 17 subfractions F2D1–F2D17. Fraction F2D12 was re-purified by RP-HPLC using MeOH (1.5 mL/min flow rate) to yield 2 (2.6 mg).

5 $\alpha$ ,6 $\alpha$ -Epoxy-(22E,24R)-3 $\beta$ ,11-dihydroxy-9,11-secoergosta-7-en-9-one (**1**): colorless oil;  $[\alpha]_D^{25}$   $-35$  (c 0.9, CHCl<sub>3</sub>); IR (neat)  $\nu_{\max}$  3398, 1682 cm<sup>-1</sup>; <sup>1</sup>H (400 MHz, CDCl<sub>3</sub>) and <sup>13</sup>C (100 MHz, CDCl<sub>3</sub>) NMR data (see Table 1); ESIMS  $m/z$  467 [M + Na]<sup>+</sup>; HRESIMS  $m/z$  467.31308 (calcd. for C<sub>28</sub>H<sub>44</sub>O<sub>4</sub> + Na, 467.31373).

(22R)-Acetoxy-(24 $\xi$ )-ergosta-5-en-3 $\beta$ ,25-diol (**2**): colorless needles; mp. 130–132 °C;  $[\alpha]_D^{27}$   $-111$  (c 0.7, CHCl<sub>3</sub>); IR (neat)  $\nu_{\max}$  3414, 1730 cm<sup>-1</sup>; <sup>1</sup>H (400 MHz, CDCl<sub>3</sub>) and <sup>13</sup>C (100 MHz, CDCl<sub>3</sub>) NMR data (see Table 2); ESIMS  $m/z$  497 [M + Na]<sup>+</sup>; HRESIMS  $m/z$  497.36015 (calcd. for C<sub>30</sub>H<sub>50</sub>O<sub>4</sub> + Na, 497.36193).

### 3.4. Generation of Superoxide Anions and Release of Elastase by Human Neutrophils

Human neutrophils were obtained by means of dextran sedimentation and Ficoll centrifugation. Measurements of superoxide anion generation and elastase release were carried out according to previously described procedures [21,22]. Briefly, superoxide anion production was assayed by monitoring the superoxide dismutase-inhabitable reduction of ferricytochrome *c*. Elastase release experiments were performed using MeO-Suc-Ala-Ala-Pro-Valp-nitroanilide as the elastase substrate.

## 4. Conclusions

Our further studies on *Pinnigorgia* sp. for the extraction of natural substances have led to the isolation of two new marine sterols, 5 $\alpha$ ,6 $\alpha$ -epoxy-(22E,24R)-3 $\beta$ ,11-dihydroxy-9,11-secoergosta-7-en-9-one (**1**) and (22R)-acetoxy-(24 $\xi$ )-ergosta-5-en-3 $\beta$ ,25-diol (**2**), and **1** showed potentially anti-inflammatory activity. These results suggested that continuing investigation of new secondary metabolites together with the potentially useful bioactive substances from *Pinnigorgia* sp. are worthwhile for future drug development.

**Supplementary Materials:** Supplementary materials Figure S1–S14 are available online.

**Acknowledgments:** This research was supported by grants from the National Museum of Marine Biology & Aquarium; the National Dong Hwa University; the National Sun Yat-sen University; and the National Research Program for Biopharmaceuticals, Ministry of Science and Technology (Grant No. MOST 105-2325-B-291-001, 105-2811-B-291-003, 104-2325-B-291-001, 103-2325-B-291-001, and 104-2320-B-291-001-MY3), awarded to P.-J. S.

**Author Contributions:** Ping-Jyun Sung designed the whole experiment and contributed to manuscript preparation. Yu-Chia Chang researched data. Tsong-Long Hwang and Chih-Hua Chao analyzed the data and performed data acquisition.

**Conflicts of Interest:** The authors declare no conflicts of interest.

## References and Notes

1. Chang, Y.-C.; Kuo, L.-M.; Su, J.-H.; Hwang, T.-L.; Kuo, Y.-H.; Lin, C.-S.; Wu, Y.-C.; Sheu, J.-H.; Sung, P.-J. Pinnigorgiols A–C, 9,11-secoosterols with a rare ring arrangement from a gorgonian coral *Pinnigorgia* sp. *Tetrahedron* **2016**, *72*, 999–1004. [[CrossRef](#)]
2. Chang, Y.-C.; Kuo, L.-M.; Hwang, T.-L.; Yeh, J.; Wen, Z.-H.; Fang, L.-S.; Wu, Y.-C.; Lin, C.-S.; Sheu, J.-H.; Sung, P.-J. Pinnisterols A–C, new 9,11-secoosterols from a gorgonian *Pinnigorgia* sp. *Mar. Drugs* **2016**, *14*, 12. [[CrossRef](#)] [[PubMed](#)]
3. Su, Y.-D.; Cheng, C.-H.; Wen, Z.-H.; Wu, Y.-C.; Sung, P.-J. New anti-inflammatory sterols from a gorgonian *Pinnigorgia* sp. *Bioorg. Med. Chem. Lett.* **2016**, *26*, 3060–3063. [[CrossRef](#)] [[PubMed](#)]
4. Chang, Y.-C.; Chen, N.-F.; Hwang, T.-L.; Tseng, C.-C.; Wu, T.-Y.; Peng, B.-R.; Wen, Z.-H.; Fang, L.-S.; Wu, Y.-C.; Sheu, J.-H.; Sung, P.-J. New marine sterols from an algal-bearing gorgonian coral *Pinnigorgia* sp. *Steroids* **2016**, *115*, 123–129. [[CrossRef](#)] [[PubMed](#)]
5. Chang, Y.-C.; Hwang, T.-L.; Sheu, J.-H.; Wu, Y.-C.; Sung, P.-J. New anti-inflammatory 9,11-secoosterols with a rare tricyclo[5,2,1]decane ring from a Formosan gorgonian *Pinnigorgia* sp. *Mar. Drugs* **2016**, *14*, 218. [[CrossRef](#)] [[PubMed](#)]



6. Chang, Y.-C.; Hwang, T.-L.; Kuo, L.-M.; Sung, P.-J. Pinnisterols D–J, new 11-acetoxy-9,11-secoosterols with a 1,4-quinone moiety from Formosan gorgonian coral *Pinnigorgia* sp. (Gorgoniidae). *Mar. Drugs* **2017**, *15*, 11. [CrossRef] [PubMed]
7. Rueda, A.; Zubía, E.; Ortega, M.J.; Carballo, J.L.; Salvá, J. New metabolites from the sponge *Spongia agaricina*. *J. Nat. Prod.* **1998**, *61*, 258–261. [CrossRef] [PubMed]
8. Wright, J.L.C.; McInnes, A.G.; Shimizu, S.; Smith, D.G.; Walter, J.A.; Idler, D.; Khalil, W. Identification of C-24 alkyl epimers of marine sterols by  $^{13}\text{C}$  nuclear magnetic resonances spectroscopy. *Can. J. Chem.* **1978**, *56*, 1898–1903.
9. Aiello, A.; Fattorusso, E.; Menna, M.; Carnuccio, R.; Iuvone, T. New cytotoxic steroids from the marine sponge *Dysidea fragilis* coming from the lagoon of Venice. *Steroids* **1995**, *60*, 666–673, The compound that was reported to possess the same structure as that of 1 was listed as compound 7 in this article. [CrossRef]
10. Carmely, S.; Kashman, Y. Isolation and structure elucidation of lobophytosterol, depresosterol and three other closely related sterols. *Tetrahedron* **1981**, *37*, 2397–2403. [CrossRef]
11. Chang, H.-H.; Chang, Y.-C.; Chen, W.-F.; Hwang, T.-L.; Fang, L.-S.; Wen, Z.-H.; Chen, Y.-H.; Wu, Y.-C.; Sung, P.-J. Pubinernoid A and apo-9'-fucoxanthinone, secondary metabolites from a gorgonian coral *Pinnigorgia* sp. *Nat. Prod. Commun.* **2016**, *11*, 707–708. [PubMed]
12. Huang, S.-X.; Yang, J.; Xiao, W.-L.; Zhu, Y.-L.; Li, R.-T.; Li, L.-M.; Pu, J.-X.; Li, X.; Li, S.-H.; Sun, H.-D. Three novel terpenoids from *Schisandra pubescens* var. *pubinervis*. *Helv. Chim. Acta* **2006**, *89*, 1169–1175. [CrossRef]
13. Hodges, R.; Porte, A.L. The structure of loliolide, a terpene from *Lolium perenne*. *Tetrahedron* **1964**, *20*, 1463–1467. [CrossRef]
14. Isoe, S.; Hyeon, S.B.; Katsumura, S.; Sakan, T. Photo-oxygenation of carotenoids. II. The absolute configuration of loliolide and dihydroactinidiolide. *Tetrahedron Lett.* **1972**, *13*, 2517–2520. [CrossRef]
15. Pettit, G.R.; Herald, C.L.; Ode, R.H.; Brown, P.; Gust, D.J.; Michel, C. The isolation of loliolide from an Indian Ocean opisthobranch mollusc. *J. Nat. Prod.* **1980**, *43*, 752–755. [CrossRef] [PubMed]
16. Ravi, B.N.; Murphy, P.T.; Lidgard, R.O.; Warren, R.G.; Wells, R.J.  $\text{C}_{18}$  terpenoid metabolites of the brown alga *Cystophora moniliformis*. *Aust. J. Chem.* **1982**, *35*, 171–182. [CrossRef]
17. Valdes, L.J., III. Loliolide from *Salvia divinorum*. *J. Nat. Prod.* **1986**, *49*, 171. [CrossRef]
18. Mori, K.; Khlebnikov, V. Synthesis of (+)-dihydroactinidiolide, (+)- and (–)-actinidiolide, (+)- and (–)-loliolide as well as (+)- and (–)-epilololide. *Liebigs Ann. Chem.* **1993**, 77–82. [CrossRef]
19. Sung, P.-J.; Chen, B.-Y.; Chen, Y.-H.; Chiang, M.-Y.; Lin, M.-R. Loliolide: Occurrence of a carotenoid metabolite in the octocoral *Briareum excavatum* (Briareidae). *Biochem. Syst. Ecol.* **2010**, *38*, 116–118. [CrossRef]
20. Fabricius, K.; Alderslade, P. *Soft Corals and Sea Fans—A Comprehensive Guide to the Tropical Shallow-Water Genera of the Central-West Pacific, the Indian Ocean and the Red Sea*, 1st ed.; Australian Institute of Marine Science: Queensland, Australia, 2001; pp. 218–219.
21. Yang, S.-C.; Chung, P.-J.; Ho, C.-M.; Kuo, C.-Y.; Hung, M.-F.; Huang, Y.-T.; Chang, W.-Y.; Chang, Y.-W.; Chan, K.-H.; Hwang, T.-L. Propofol inhibits superoxide production, elastase release, and chemotaxis in formyl peptide-activated human neutrophils by blocking formyl peptide receptor 1. *J. Immunol.* **2013**, *190*, 6511–6519. [CrossRef] [PubMed]
22. Yu, H.-P.; Hsieh, P.-W.; Chang, Y.-J.; Chung, P.-J.; Kuo, L.-M.; Hwang, T.-L. 2-(2-Fluorobenzamido) benzoate ethyl ester (EFB-1) inhibits superoxide production by human neutrophils and attenuates hemorrhagic shock-induced organ dysfunction in rats. *Free Radic. Biol. Med.* **2011**, *50*, 1737–1748. [CrossRef] [PubMed]

**Sample Availability:** Samples of the compounds 1 and 2 are not available from the authors.



© 2017 by the authors. Licensee MDPI, Basel, Switzerland. This article is an open access article distributed under the terms and conditions of the Creative Commons Attribution (CC BY) license (<http://creativecommons.org/licenses/by/4.0/>).

Contents lists available at [ScienceDirect](http://www.sciencedirect.com)

## Food and Bioproducts Processing

journal homepage: [www.elsevier.com/locate/fbp](http://www.elsevier.com/locate/fbp)

IChemE ADVANCING CHEMICAL ENGINEERING WORLDWIDE



# Facile synthesis of magnetic iron oxide nanoparticles for nattokinase isolation

Chi-Hsien Liu<sup>a,b,c,d,\*</sup>, Hsuan-Yu Lai<sup>a</sup>, Wei-Chi Wu<sup>d,e</sup><sup>a</sup> Graduate Institute of Biochemical and Biomedical Engineering, Chang Gung University, 259, Wen-Hwa First Road, Kwei-Shan, Tao-Yuan 333, Taiwan<sup>b</sup> Research Center for Chinese Herbal Medicine and Research Center for Food and Cosmetic Safety, College of Human Ecology, Chang Gung University of Science and Technology, 261, Wen-Hwa First Road, Taoyuan, Taiwan<sup>c</sup> Department of Chemical Engineering, Ming Chi University of Technology, 84, Gung-Juan Road, New Taipei City, Taiwan<sup>d</sup> Department of Ophthalmology, Chang Gung Memorial Hospital, 5, Fu-Hsing Street, Taoyuan, Taiwan<sup>e</sup> College of Medicine, Chang Gung University, 259, Wen-Hwa First Road, Taoyuan, Taiwan

## ARTICLE INFO

## Article history:

Received 11 November 2016

Received in revised form 6 January 2017

Accepted 10 January 2017

Available online 19 January 2017

## Keywords:

Nattokinase

Magnetic nanoparticles

Arginine

Adsorption

Conjugation

Isotherm

## ABSTRACT

Nattokinase, derived from a traditional Japanese food, has been considered a promising supplement for use in thrombosis prevention. The development of nano-technologies has resulted in new approaches for its bioseparation. A facile synthesis of the magnetic nanoparticles (MNPs) for nattokinase isolation has been developed in this study. The arginine-modified MNPs showed four-fold increase of nattokinase adsorption compared with the carboxylated MNPs. The content of arginine on the modified MNPs was 9.6–30  $\mu\text{mol/mg}$  by using the ninhydrin assay. A dose-dependent relationship between the nattokinase adsorption and the amount of arginine conjugated on MNPs was observed. The Langmuir isotherm model further confirmed the monolayer adsorption of nattokinase onto the surfaces of nanoparticles. The bare and arginine-modified MNPs were characterized by transmission electron microscopy and Fourier transform infrared spectroscopy. The arginine-modified nanoparticles could efficiently separate nattokinase from natto solution. Purified nattokinase will make further contributions in various biological and clinical fields. The conjugation process developed in the present study can be applied to modification of nanoparticle surfaces.

© 2017 Published by Elsevier B.V. on behalf of Institution of Chemical Engineers.

## 1. Introduction

Nattokinase (EC 3.4.21.62), derived from Japanese natto beans, is considered a promising agent in thrombosis therapy (Kurosawa et al., 2015). Like plasmin, nattokinase can efficiently degrade fibrin in blood clots and can increase the production of plasmin from plasminogen, due to its effect on the plasminogen activator. Immobilized nattokinase can allow treatment to be focused on the exact location of a clot, thus reducing the amount of enzyme required and, in turn, reducing the risk of eliciting an immune response (Ren et al., 2010). In patients with

proliferative vitreoretinal disorders, a high incidence of vitreous hemorrhage, retinal detachment, and resultant visual loss is found after vitreous surgeries (Wu et al., 2009). Nattokinase is reported to be a useful enzyme for the complete removal of the vitreous and associated proliferative tissues in proliferative vitreoretinal disorders (Takano et al., 2006). Amyloid fibrils formed *in vivo* are associated with various diseases, such as Alzheimer's disease, prion disease, and systematic amyloidosis, and enhancement of amyloid clearance is a therapeutic target for these amyloid-related diseases, and it has recently been

\* Corresponding author at: Graduate Institute of Biochemical and Biomedical Engineering, Chang Gung University, 259, Wen-Hwa First Road, Kwei-Shan, Tao-Yuan 333, Taiwan. Fax: +886 3 211 8800x3140.

E-mail address: [chl@mail.cgu.edu.tw](mailto:chl@mail.cgu.edu.tw) (C.-H. Liu).

<http://dx.doi.org/10.1016/j.fbp.2017.01.006>

0960-3085/© 2017 Published by Elsevier B.V. on behalf of Institution of Chemical Engineers.

shown that nattokinase is capable of degrading amyloid *in vitro* (Hsu et al., 2009).

Improvement of separation processing provides a key opportunity for the reduction of separation cost and time. Magnetic nanoparticles (MNPs) have received considerable attention as a result of several important properties they possess: large surface/volume ratios, high efficacy, and low toxicity (Chen et al., 2016). Pretreatment of complex mixtures with sedimentation and filtration can be eliminated using magnetic technologies (Makarchuk et al., 2016). Conventional adsorbents have diameters in the sub-micron to micron range, and have huge internal porosities to ensure an adequate surface area for adsorption. The diffusion limitation within the porous particles leads to a decrease in the adsorption rate and the available protein capacity (Lai et al., 2012). Therefore, an adsorbent with a high capacity and small diffusion resistance for the adsorption of biomolecules would be desirable. When using nanoparticles, the adsorptive process may be performed in a stirred suspension system instead of a conventional packed bed, since the nano-scaled size of nanoparticles results in high-pressure drops. Functionalized MNPs can bind to selected targets in the presence of other suspended solids, and specific labeling of the surfaces of the magnetic particles allows simple and rapid purification, with reduced costs and high efficacy. Compared with conventional isolation, the advantages of magnetic separation are attributed to its speed, accuracy, and simplicity. In addition, MNPs can be easily recovered and regenerated, even in the presence of colloidal contaminants, and the problems of membrane fouling in microfiltration and pressure drops in chromatography can be reduced by using magnetic separation. Specific interactions, such as enzyme-substrate, enzyme-inhibitor, and antibody-antigen, have been utilized for enzyme separation (Pascoal et al., 2011). For example, recent studies on functionalized nanomaterials for immobilization relied on microbial nucleator immobilization on magnetic nanoparticles (Zhou et al., 2014), immobilization of lipase on a novel functionalized nanocomposite membrane (Aghababae et al., 2016), and adsorption of lipase on multi-walled carbon nanotubes (Che Marzuki et al., 2015). Several crosslinking agents successfully conjugate the ligands and functionalize the MNPs. For example, carbonyldiimidazole can immobilize decarboxylase on the nanoparticle surface, using a zero-length amide bond (Qian et al., 2015).

Efficient purification of nattokinase from fermentation broth is essential for further applications of this enzyme. The multi-step process means that a long recovery time is required for purification of nattokinase, and it may result in a significant loss of enzyme activity (Kapoor et al., 2015). The summary of the literature on nattokinase purification is shown in Table 1. Traditional processes, including liquid chromatography and two phase extraction have been applied in enzyme isolation, as indicated in Table 1. Advances in nanotechnology provide new opportunities to establish new paradigms, and the development of a simple and low-cost method to purify nattokinase from fermentation broth is a fresh challenge. Further, few previous studies have examined the use of amino acid-modified magnetite to purify nattokinase. In the present study, potential ligands for nattokinase adsorption were conjugated on the surfaces of magnetic particles using carbonyldiimidazole as the coupling method. The morphology of the MNP was characterized using transition electron microscopy, and the surface modification of nanoparticles and adsorption mechanism of nattokinase were systematically investigated.

## 2. Materials and methods

### 2.1. Chemicals

The natto powder was kindly provided by Geneferm Biotech (Taipei, Taiwan). Coomassie blue G-250, carbonyldiimidazole, KBr, ethanol, phosphate-buffered saline (PBS), bovine serum albumin (BSA), dimethyl sulfoxide (DMSO), ninhydrin, acetic acid, arginine, and lysine were obtained from Sigma (St. Louis, USA). Iron oxide nanoparticles (carboxyl modification on the surface) were supplied from Taiwan Advance Nanotech

(Taoyuan, Taiwan). D-Valyl-L-leucyl-L-arginine-p-nitroaniline dihydrochloride (S-2251) for the analysis of nattokinase activity was obtained from Chromogenix (Lexington, USA). All materials and chemicals are of analytic grade and used without further purification.

### 2.2. Preparation and characterization of arginine MNPs

Ligands such as arginine and lysine have been used to modify the magnetic particles in order to evaluate their nattokinase adsorption according to our previous protocol (Liu et al., 2013). Arginine or lysine was conjugated on the nanoparticle surface using the carbonyldiimidazole and DMSO as the crosslinker and solvent, respectively. The particles were then washed three times with PBS and recovered using a magnetic separator (Millipore). The morphology of the magnetic nanoparticles was observed using transition electron microscopy (JEOL JEM 2000 EXII, Tokyo, Japan). Samples were diluted 1:25 with Milli-Q water and dried on a carbon film (CF200-Cu, Electron Microscopy Science, Washington DC, USA) for 12 h and then analyzed. Fourier transform infrared spectroscopy (Alpha, Bruker, Ettlingen, Germany) was used to characterize the presence of specific chemical groups in the modified magnetic nanoparticles. Powder samples (0.8 mg) were mixed with KBr (IR grade, Sigma) powder (80 mg) and compressed into a thin membrane using a desktop pellet press (ICL, Garfield, USA). The spectra of the analyses were characterized by Bruker OPUS software. The arginine immobilized on the magnetic nanoparticles was determined according to the amount of arginine consumed after the conjugation reaction. The reaction solution 10  $\mu$ L and ninhydrin solution 0.5 mL were sequentially placed in a test tube and heated in a boiling-water bath for 10 min. The tubes were immediately cooled in an ice-bath for 5 min after the heating reaction. 500  $\mu$ L of 50% ethanol was added to each tube and thoroughly mixed. The absorbance at 570 nm of the reaction mixture was measured.

### 2.3. Nattokinase assay

The protein content and the specific nattokinase activity in the natto powder were about 10% (w/w) and 1.29 U/mg, respectively. The natto solutions prepared by mixing 200 mg crude powder (258 U nattokinase) in 1 mL PBS were used for the adsorption experiments. Equilibrium experiments of adsorption and desorption were performed in the following manner. The MNPs (1.25 mg) were washed twice using the 100 mM pH 7.0 PBS. The nanoparticles were transferred to microcentrifuge tubes and incubated with a natto solution 0.1 mL on a vortex-mixer. The adsorbed nattokinase activity on the nanoparticles was calculated according to the mass-balance equation. The protein concentration was measured using a colorimetric reagent (Coomassie blue G-250) at 595 nm using BSA as the standard. The pH effects on the adsorption of the MNPs were investigated in 100 mM PBS in a pH range of 5–7 at 30 °C. Saturated adsorption was determined using the following procedure. The MNPs (1.25 mg) were added to 0.1 mL of a natto solution containing different nattokinase concentrations. The tested nattokinase concentrations ranged from 64.5 to 516 U/mL. The magnetic nanoparticles were magnetically separated from the solution after the vortex-mixing for 30 min. The activity of nattokinase adsorbed onto the magnetic adsorbents was measured using a chromogenic activity assay. The chromogenic protease substrate (D-val-leu-lys-p-

**Table 1 – Summary of previous methods for nattokinase purification.**

Method	Materials	Purification fold	Recovery Yield (%)	Pretreat/process time	Refs.
Liquid chromatography	CM-methacrylate column	74	7	Pretreat/slow	Deepak et al. (2009)
Liquid chromatography	Sephacryl S200/Q-sepharose column	39/86	52/24	Pretreat/slow	Jaouadi et al. (2010)
Liquid chromatography	Sephadex G-75/phenyl-sepharose column	23/56	48/43	Pretreat/slow	Wang et al. (2009a)
Reverse micelles extraction	AOT micelles	4	80	One step/fast	Liu et al. (2006)
Expanded bed process	Aminobenzamidine modified poly methyl methacrylate beads	9	85	One step/fast	Yang et al. (2006)
Expanded bed process	Fastline PRO beads	12	47	One step/fast	Lu et al. (2005)
Suspended magnetic adsorption	Arginine modified MNPs	8	15	One step/fast	This study

nitroaniline) was used to analyze the amidolytic ability of nattokinase. 10  $\mu$ L of the chromophoric substrate was added to 1 mL PBS solution containing 1.25 mg of magnetic nanoparticles for 1 min at 37 °C. Then, 0.25 mL of 20% acetic acid was added to stop the reaction. Finally, the absorbance at 405 nm was measured using the spectrophotometer (Unicam UV 500, Thermo, Cambridge, UK). One unit of nattokinase activity was defined as the amount of nattokinase that released 1 nmol of nitroaniline/min under the reaction condition. The results are an average of three separate experiments. The adsorption capacity of magnetic nanoparticles is determined in terms of nattokinase activity (U/mg). The protein concentration was measured using a colorimetric reagent (Coomassie brilliant blue G-250) at 595 nm with BSA as the standard.

#### 2.4. Nattokinase adsorption by arginine modified MNPs

Two isotherm models (Langmuir and Freundlich models) were used to analyze the nattokinase adsorption data. The parameters of the two models were fitted to the experimental data employing the hyperbola fitting method of Sigmaplot (Dundas, Germany).

$$Q^* = \frac{Q_m C^*}{K_d + C^*} \quad (1)$$

In Eq. (1),  $Q^*$  represents the equilibrium adsorption amount of the nattokinase (U/mg),  $C^*$  is the equilibrium nattokinase concentration in the solution (U/mL),  $Q_m$  is the maximum adsorption amount of the nattokinase per mg of nanoparticles (U/mg), and  $K_d$  is the Langmuir adsorption equilibrium constant (mL/U). Freundlich empirical Eq. (2) takes the form:

$$Q^* = K_f \times (C^*)^{1/n} \quad (2)$$

where  $K_f$  and  $n$  were the physical constants of Freundlich adsorption isotherm.

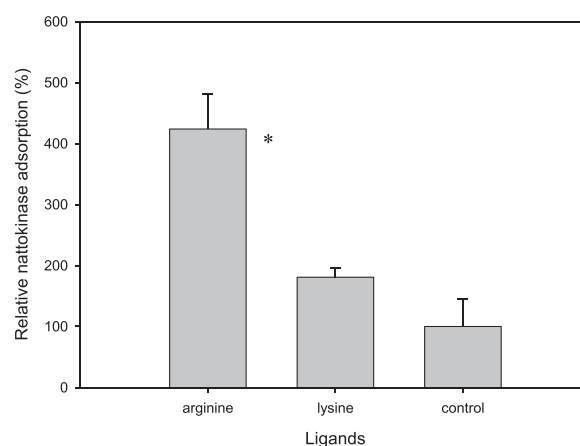


**Fig. 1 – Effects of immobilized ligands on nattokinase adsorption. The nattokinase activity (0.63 U/mg) adsorbed on the original nanoparticles was used as a 100% control. \* $p < 0.05$  as compared with the control. \*\* $< 0.01$  as compared with the lysine modified MNPs.**

#### 2.5. Statistical analysis

Data are reported as means  $\pm$  standard deviations ( $n = 3$ ). Two-tailed t-test inbuilt in MS Excel was used for evaluating the differences between the means of results for control groups and the experimental groups. The statistic test that P value is less than 0.05 will be considered significant.

### 3. Results and discussion

#### 3.1. Ligand effect on nattokinase adsorption

In order to functionalize nanoparticles that have carboxylate groups on their surfaces, cationic amino acids were immobilized onto magnetic particles to evaluate their capability of capturing nattokinase from solution. Arginine and lysine were used to modify the magnetic particles in order to evaluate their nattokinase adsorption. A ligand concentration (10 mg/mL) was used for the conjugation reaction by using the carbonyldiimidazole to covalently crosslink the arginine and carboxylated MNPs. Of the two amino acids,



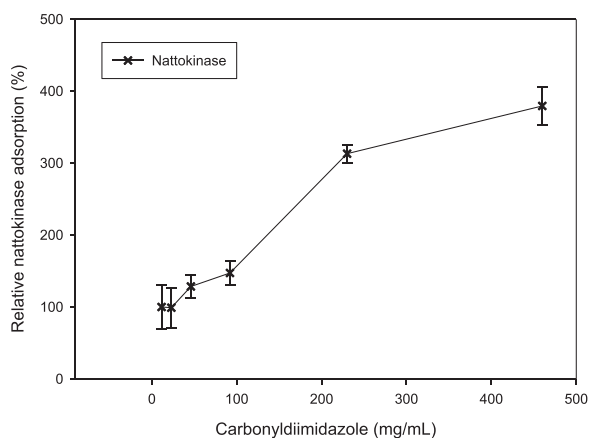


**Fig. 2 – The carbonyldiimidazole concentration in the modification process affected nattokinase adsorption. The nattokinase activity (0.63 U/mg) adsorbed on the original nanoparticles was used as a 100% control.**

arginine-modified MNPs had superior nattokinase adsorption (Fig. 1). Lysine modification also enhanced nattokinase adsorption by 1.8-fold compared with that of carboxylated MNPs (control). Interestingly, arginine modification enhanced nattokinase adsorption by 4.2-fold compared with control. Arginine–enzyme interaction can be applied to purify various proteases as reported by many studies. For example, trypsin recovery using sepharose coupled with peptides containing arginine has been carried out via the specific adsorption between trypsin and arginine (Kasai and Ishii, 1972). Urokinase can be purified by immobilizing arginine, or its methyl ester, as a ligand on the adsorbents (Huber et al., 1982; Sueishi et al., 1982). The specific interaction between arginine and various proteases, such as streptokinase (Dawson et al., 1994), urokinase (Kettner and Shaw, 1979), and nattokinase (the present study), might explain the adsorption enhancement effect. The adsorption of nattokinase on the lysine might be due to electrostatic interaction between surface ligands and nattokinase. Arginine is a cationic amino acid, having a basic side chain with two pK values—9.09 and 13.2. Previous studies have shown that arginine-modified dendrimers exhibit enhanced transfection efficiency and can be used as gene-delivery carriers (Luo et al., 2012). Polyarginine-modified nanoparticles can be successfully used for the selective extraction and enrichment of phosphorylated peptides and lactalbumin (Lai et al., 2012). However, very few studies have reported the use of arginine-modified magnetite to purify protease to our best knowledge. Arginine-modified MNPs could have the best nattokinase adsorption among the tested nanoparticles. The dose effect of the crosslinking agent and arginine on arginine modification on the MNP surface is evaluated sequentially in order to illustrate their specific interaction.

### 3.2. Functionalization of magnetic nanoparticles

Modification condition and ligand concentration have a great impact on surface functionalization. Various concentrations of the crosslinking carbonyldiimidazole were found to significantly affect nattokinase adsorption, as indicated in Fig. 2. Carbonyldiimidazole can activate carboxylic acids to conjugate with amino groups, creating zero-length amide bonds between the crosslinked molecules. However, the formation of activated species by carbonyldiimidazole must occur in a

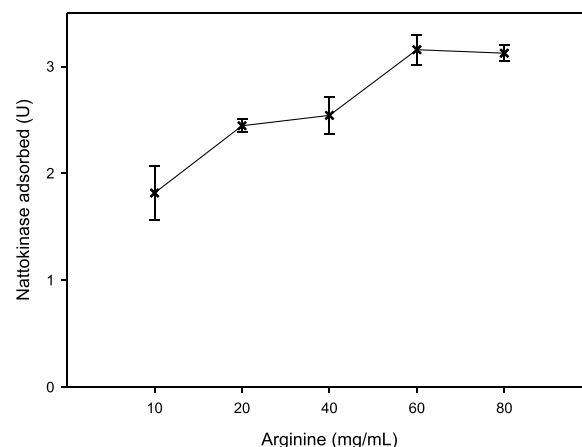


**Fig. 3 – Effects of arginine in the modification process on nattokinase adsorption. The adsorption solution contained 200 mg/mL natto powder and the adsorption was performed at 30 °C for 30 min. The concentration of nanoparticles used in this experiment was 1.25 mg.**

non-aqueous environment, due to the rapid breakdown of carbonyldiimidazole by hydrolysis. Herein, carbonyldiimidazole could activate hydroxyl or carboxyl groups on the magnetic nanoparticles and was then conjugated with amino groups on the ligands. The tested carbonyldiimidazole concentrations ranged from 11.5 to 460 mg/mL. When the carbonyldiimidazole concentration was increased from 11.5 to 230 mg/mL, the dose-dependent nattokinase adsorption was observed. The enzyme adsorption was enhanced 3-fold by increasing carbonyldiimidazole concentration compared with the control. When the carbonyldiimidazole was further increased to 460 mg/mL, the binding of nattokinase was saturated. The saturated adsorption might be due to the available carboxyl groups on the particle surfaces. In order to maximize arginine on these surfaces, the effects of the arginine concentration on nattokinase adsorption were evaluated by fixing the carbonyldiimidazole concentration at 230 mg/mL. A dose-dependent relationship between arginine in solution and arginine conjugated on the surface was observed when the concentration was increased from 10 to 80 mg/mL (Fig. 3). The conjugated arginine on the nanoparticles was 9.6–30  $\mu\text{mol}/\text{mg}$  particles in the tested arginine range, using the ninhydrin method. Only 10% of free arginine was immobilized on the particle surfaces. Wang et al. developed a green process for preparing arginine-modified iron nanoparticles by simply mixing  $\text{FeCl}_2$  with arginine. Similarly, the surface amine densities were calculated as approximately 5.6–7.8  $\mu\text{mol}/\text{mg}$  of nanoparticles (Wang et al., 2009b). The adsorption of nattokinase by the MNPs reached a plateau (3.16 U/mg) when the arginine concentration was increased to 60 mg/mL. This phenomenon of saturated adsorption could be explained by the steric hindrance of the adsorbed nattokinase on the particle surfaces, preventing further adsorption of free nattokinase from the solution. In the present study, the adsorption capacity of MNPs was determined in terms of nattokinase activity rather than nattokinase mass. The morphology of the MNPs was sequentially characterized by transition electron microscopy, and their microstructure is shown in Fig. 4. The size distributions of both magnetic particles (original and modified) were uniform, with an average size of 16 nm. In addition, some aggregation of MNPs was observed after arginine modification. The formation of par-



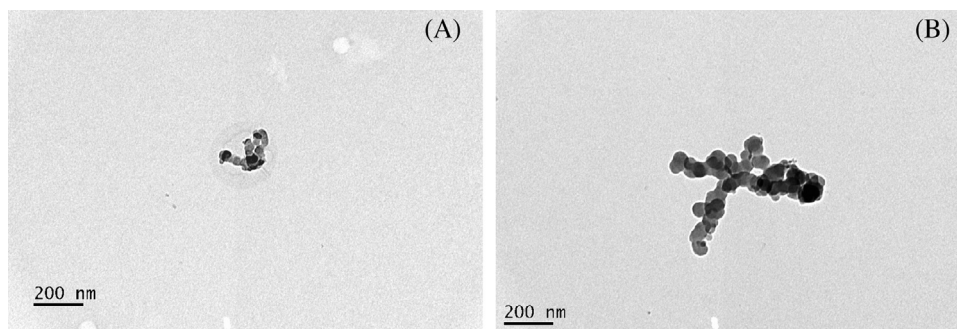


Fig. 4 – The TEM morphologies of the COOH MNPs (A) and arginine-modified MNPs (B).

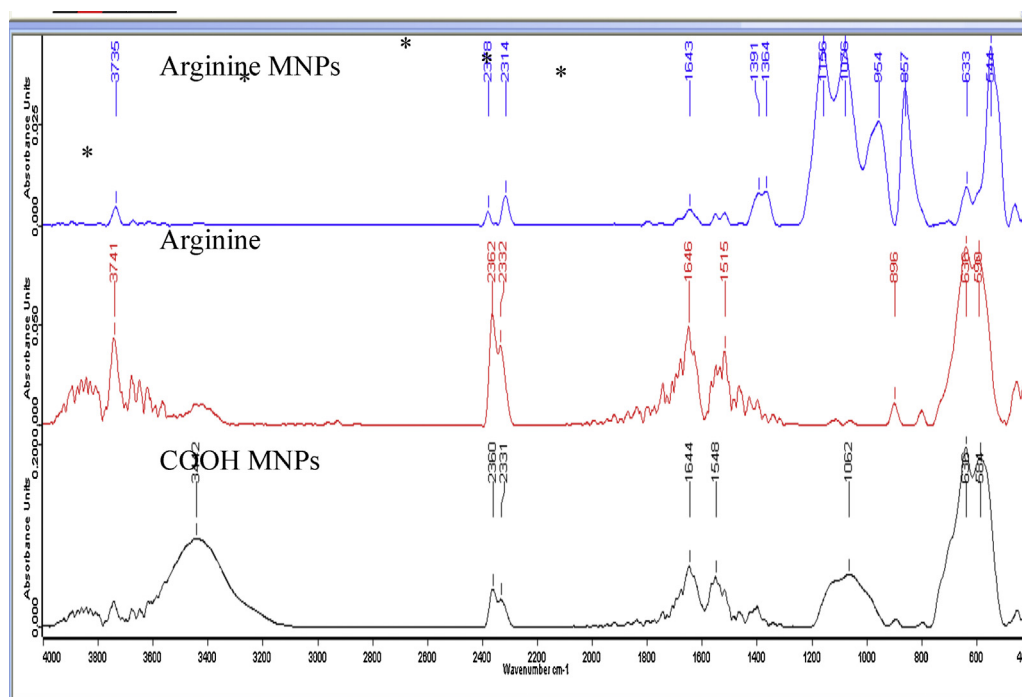


Fig. 5 – The spectra of Fourier transform infrared spectroscopy for two kinds of MNPs and arginine.

particle aggregation might be due to the crosslink between the arginine groups on the surfaces of two or several nanoparticles. This nano-scaled structure provides several advantages for biotechnological application, including low diffusion limitations, a high surface area, and high loading (Ma et al., 2006). Mass transfer effects in the nano-adsorbents will be reduced, since the nanoparticles have a large specific surface area and small diffusion resistance. Under ideal conditions, these nanoparticles are not hindered by the diffusional limitations that are associated with commercial porous adsorbents, for which the internal pores also provide diffusional resistance to the rate of protein adsorption (Bucak et al., 2003). The lysine modification and particle morphology were also characterized by infrared spectroscopy. The spectrum of Fourier transform infrared spectroscopy is widely used to investigate the characteristics of stretching vibrations of functional groups in materials. The infrared spectra of arginine, and the original (containing carboxyl groups) and arginine-modified magnetic particles are presented in Fig. 5. The COOH magnetic particles showed distinct absorption peaks at 3442 cm<sup>-1</sup>, and these have been reportedly attributed to the stretching of the C=O group; C–N stretch and C–H bend on the surface. Both modified and original MNPs showed a distinctive FeO peak at 1062 cm<sup>-1</sup>. The absorption peak of the modified particles and arginine at around 3700 cm<sup>-1</sup> was due to N–H

stretching vibrations of amide. The existence of arginine on the modified MNPs was confirmed in the present study.

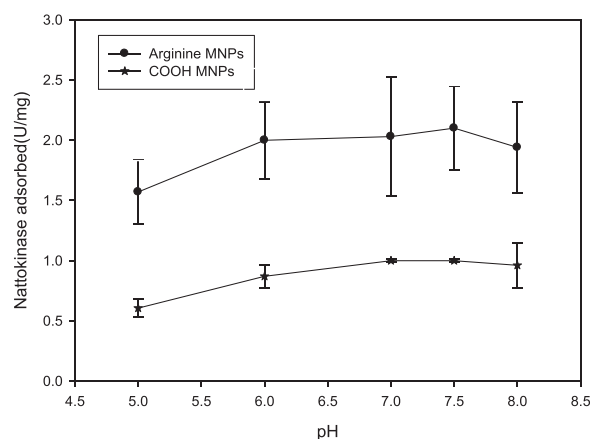
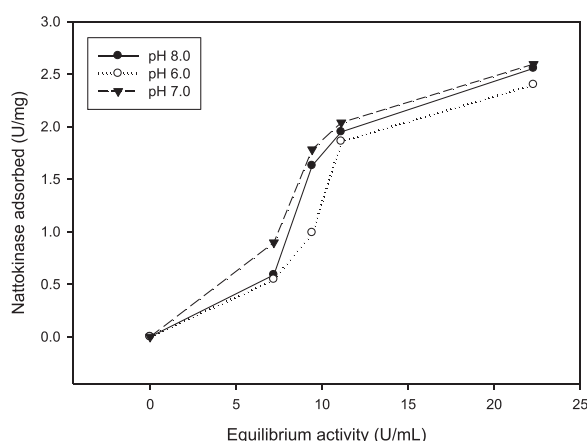


Fig. 6 – Effects of pH conditions on nattokinase adsorption by arginine modified MNPs and COOH MNPs. The concentration of nanoparticles used in this experiment was 1.25 mg. \*p < 0.05 as compared with the COOH MNPs.



**Fig. 7 – Effects of initial nattokinase dose on nattokinase adsorbed on arginine modified MNPs. The coefficients of variance for these data points are around 8%.**

**Table 2 – Isotherm parameters for the nattokinase adsorption by arginine-modified nanoparticles at various pH conditions.**

	Langmuir			Freundlich		
	$K_d$ (mL/U)	$Q_m$ (U/mg)	$r^2$	$K_f$	$n$	$r^2$
pH 6	0.0080	15.625	0.980	0.116	0.978	0.877
pH 7	0.0452	5.334	0.918	0.385	1.594	0.914
pH 8	0.0259	7.220	0.973	0.297	1.490	0.842

### 3.3. Effects of pH on nattokinase adsorption

Because buffer's pH influences protein surface charge, hydrophilicity, and conformational structure, the pH effect on the adsorption of nattokinase was investigated in the PBS. Fig. 6 shows the results of nattokinase adsorbed onto carboxylated and arginine-modified MNPs under different pH conditions. The activities of nattokinase on the arginine-modified nanoparticles were superior to those of the carboxylated nanoparticles under the tested pH condition. The results indicated that arginine modification could enhance nattokinase adsorption as compared with bare nanoparticles. The isoelectric point of nattokinase has been reported to be 8.7 (Fujita et al., 1993). This fact indicates the slightly positive charge of nattokinase under the neutral condition. The surface charge on the arginine-modified MNPs was around  $-20$  mV at pH 7. The electrostatic interaction between the modified MNPs and nattokinase might contribute the adsorption. In order to study the effects of natto concentration on nattokinase adsorption, equilibrium nattokinase were evaluated by increasing the natto powder from 50 to 400 mg/mL. Buffer pH slightly affected the adsorption of nattokinase on arginine-modified MNPs as shown in Fig. 7. Nattokinase binding to the surface was saturated when the activity of nattokinase in the solution reached 11 U. The adsorption of nattokinase was slightly lower under a basic condition (pH 8), as compared with a neutral condition.

The adsorption behavior between protein and adsorbents can be frequently analyzed using Langmuir and Freundlich equations (Sun et al., 2011). The parameters of the Langmuir and Freundlich isotherms for nattokinase onto arginine-modified nanoparticles are shown in Table 2. The Langmuir isotherm could better explain the adsorption of nattokinase than the Freundlich isotherm, as indicated by their

regression coefficients. The fact that the regression coefficients of the Langmuir mode ranged from 0.918 to 0.980 indicated the fitness of the experimental data. In contrast, the regression coefficients of the Freundlich equation under the three pH conditions were fair, with values of around 0.842–0.914. The Langmuir model is based on the assumption of surface homogeneity, such as equally available adsorption sites, monolayer surface coverage, and no interaction between adsorbed species, while the Freundlich equation assumes that the adsorption energy of a protein binding to a site on an adsorbent depends on whether or not the adjacent sites are already occupied. The Freundlich isotherm is not restricted to the formation of the monolayer. The fact that the modified MNPs had the minimal dissociation constant (0.008 mL/U) under the pH 6.0 condition indicated that its affinity was the strongest among the tested pH values. Besides, MNPs under the pH 6.0 condition had the maximum adsorption capacity ( $Q_m$ ) 15.6 U/mg, which was much higher than the experimental results (2.5 U/mg). The  $Q_m$  values under pH 7.0 and 8.0 conditions were 5.3 and 7.2 U/mg, respectively. The reason for the poor prediction might be due to that the natto solution is a complex fermentation mixture. The various proteins in the natto solution may compete with nattokinase to adsorb on the surfaces of nanoparticles. The molecular weight of nattokinase was approximately 28 kDa (Yang et al., 2006), which was equivalent to a 5 nm hydrodynamic diameter. This large protein size will decrease the diffusion rate in high protein feedstock (Bucak et al., 2003). The steric constraints of proteins and intermolecular interactions also affect the transfer of protein to nanoparticles. Yang et al. recently reported a method of purifying nattokinase from fermentation broth using magnetic beads immobilized with *p*-aminobenzamidine, a protease inhibitor (Yang et al., 2006). Several interactions between the enzyme and the arginine-modified surface might contribute to the adsorption phenomenon. Protonated amine groups of arginine on MNPs interact with anionic groups of nattokinase. The electrostatic interaction also contributes to the affinity between the nanoparticle surface and nattokinase. The pH effect on nattokinase adsorption in the present study showed a decreasing affinity of nattokinase above pH 7. The adsorption characteristics of arginine nanoparticles are comparable with the results of several previous studies. For example, magnetic PMMA beads functionalized with *p*-aminobenzamidine have been used to purify nattokinase (Yang et al., 2006). The maximum adsorption capacities for nattokinase and protein on magnetic PMMA beads were 309 U/mg and 2.9  $\mu$ g/mg, respectively. In contrast, the nattokinase activity and protein adsorbed on arginine-modified nanoparticles were 2.5 U/mg (2500 U/g) and 159  $\mu$ g/mg in this study. The conventional steps for nattokinase purification included acetone precipitation and CM-methacrylate chromatography (Deepak et al., 2009). The commercial Fastline-Pro adsorbent has been used for the capture of nattokinase from highly ionic fermentation broth in the expanded bed process, and the purification factor and recovery yield reached 12.3 and 47.3%, respectively (Lu et al., 2005). In the present study, our purification factor and recovery yield for the arginine-modified nanoparticles were 8.0 and 15%, respectively, in a 30-min suspended adsorption process. The nanoparticle adsorption was faster than in conventional strategies. However, the recovery yield of nattokinase using MNPs was lower than that obtained by chromatography or the expanded bed process (Table 1). Possessing high capacities, large surfaces, and small diffusion resistance, nano-scaled

nanoparticles can simplify the adsorption process for nattokinase as compared with the traditional techniques.

#### 4. Conclusion

We successfully synthesized novel MNPs by proper coating the arginine on the surfaces of nanoparticles. Arginine-modified MNPs can significantly enhance nattokinase adsorption compared with the bare MNPs. A dose-dependent relationship between the nattokinase adsorption and the amount of arginine conjugated on MNPs was observed. The Langmuir isotherm model further confirmed the mechanism of nattokinase adsorption onto nanoparticles from the natto solution. Our results indicate that arginine-modified MNPs could efficiently separate nattokinase from natto solution in the presence of other suspended solids. Pretreatment of complex mixtures with the sedimentation, centrifugation, and filtration processes can be eliminated using MNPs. Purified nattokinase will make further contributions in the prevention of several diseases, including thrombosis, amyloidosis, hypertension, and vitreous hemorrhage. Moreover, the conjugation process developed in the present study can be applied to modification of nanoparticle surfaces.

#### Conflict of interest

The authors have declared no conflict of interest.

#### Acknowledgements

The study is supported by the Chang Gung Memorial Hospital (CMRPD 1E0351, 1E0352), Taiwan. We express gratitude to Ministry of Science and Technology (MOST 105-2221-E-182-070) and Chang Gung University (BMRP 758) for funding and supporting the members of Liu's laboratory.

#### References

- Aghababaei, M., Beheshti, M., Razmjou, A., Bordbar, A.K., 2016. Covalent immobilization of *Candida rugosa* lipase on a novel functionalized Fe<sub>3</sub>O<sub>4</sub>@SiO<sub>2</sub> dip-coated nanocomposite membrane. *Food Bioprod. Process.* 100, 351–360.
- Bucak, S., Jones, D.A., Laibinis, P.E., Hatton, T.A., 2003. Protein separations using colloidal magnetic nanoparticles. *Biotechnol. Prog.* 19 (2), 477–484.
- Che Marzuki, N.H., Mahat, N.A., Huyop, F., Aboul-Enein, H.Y., Wahab, R.A., 2015. Sustainable production of the emulsifier methyl oleate by *Candida rugosa* lipase nanoconjugates. *Food Bioprod. Process.* 96, 211–220.
- Chen, S., Zhang, J., Jiang, S., Lin, G., Luo, B., Yao, H., Lin, Y., He, C., Liu, G., Lin, Z., 2016. Self-assembled superparamagnetic iron oxide nanoclusters for universal cell labeling and MRI. *Nanoscale Res. Lett.* 11 (1).
- Dawson, K.M., Marshall, J.M., Raper, R.H., Gilbert, R.J., Ponting, C.P., 1994. Substitution of arginine 719 for glutamic acid in human plasminogen substantially reduces its affinity for streptokinase. *Biochemistry* 33 (40), 12042–12047.
- Deepak, V., Ram Kumar Pandian, S.b., Kalishwaralal, K., Gurunathan, S., 2009. Purification, immobilization, and characterization of nattokinase on PHB nanoparticles. *Bioresour. Technol.* 100 (24), 6644–6646.
- Fujita, M., Nomura, K., Hong, K., Ito, Y., Asada, A., Nishimuro, S., 1993. Purification and characterization of a strong fibrinolytic enzyme (nattokinase) in the vegetable cheese natto, a popular soybean fermented food in Japan. *Biochem. Biophys. Res. Commun.* 197 (3), 1340–1347.
- Hsu, R.L., Lee, K.T., Wang, J.H., Lee, L.Y.L., Chen, R.P.Y., 2009. Amyloid-degrading ability of nattokinase from *Bacillus subtilis* natto. *J. Agric. Food Chem.* 57 (2), 503–508.
- Huber, K., Kirchheimer, J., Binder, B.R., 1982. Rapid isolation of high molecular weight urokinase from native human urine. *Thromb. Haemost.* 47 (3), 197–202.
- Jaouadi, B., Abdelmalek, B., Fodil, D., Ferradji, F.Z., Rekik, H., Zarai, N., Bejar, S., 2010. Purification and characterization of a thermostable keratinolytic serine alkaline proteinase from *Streptomyces* sp. strain AB1 with high stability in organic solvents. *Bioresour. Technol.* 101 (21), 8361–8369.
- Kapoor, R., Harde, H., Jain, S., Panda, A.K., Panda, B.P., 2015. Downstream processing, formulation development and antithrombotic evaluation of microbial nattokinase. *J. Biomed. Nanotechnol.* 11 (7), 1213–1224.
- Kasai, K.I., Ishii, S.I., 1972. Affinity chromatography of trypsin using a sepharose derivative coupled with peptides containing L-arginine in carboxyl termini. *J. Biochem.* 71 (2), 363–366.
- Kettner, C., Shaw, E., 1979. The susceptibility of urokinase to affinity labeling by peptides of arginine chloromethyl ketone. *BBA: Enzymology* 569 (1), 31–40.
- Kurosawa, Y., Nirengi, S., Homma, T., Esaki, K., Ohta, M., Clark, J.F., Hamaoka, T., 2015. A single-dose of oral nattokinase potentiates thrombolysis and anti-coagulation profiles. *Sci. Rep.* 5.
- Lai, B.H., Yeh, C.C., Chen, D.H., 2012. Surface modification of iron oxide nanoparticles with polyarginine as a highly positively charged magnetic nano-adsorbent for fast and effective recovery of acid proteins. *Process Biochem.* 47 (5), 799–805.
- Liu, J.G., Xing, J.M., Chang, T.S., Liu, H.Z., 2006. Purification of nattokinase by reverse micelles extraction from fermentation broth: effect of temperature and phase volume ratio. *Bioprocess Biosyst. Eng.* 28 (4), 267–273.
- Liu, C.H., Wu, W.C., Lai, H.Y., 2013. Adsorption of nattokinase by amino acid-conjugated magnetic nanoadsorbents. *Sep. Sci. Technol.* 48 (6), 923–930.
- Lu, M.H., Lin, D.Q., Wu, Y.C., Yun, J.X., Mei, L.H., Yao, S.J., 2005. Separation of nattokinase from *Bacillus subtilis* fermentation broth by expanded bed adsorption with mixed-mode adsorbent. *Biotechnol. Bioproc. Eng.* 10 (2), 128–135.
- Luo, K., Li, C., Li, L., She, W., Wang, G., Gu, Z., 2012. Arginine functionalized peptide dendrimers as potential gene delivery vehicles. *Biomaterials* 33 (19), 4917–4927.
- Ma, Z., Guan, Y., Liu, H., 2006. Superparamagnetic silica nanoparticles with immobilized metal affinity ligands for protein adsorption. *J. Magn. Magn. Mater.* 301 (2), 469–477.
- Makarchuk, O.V., Dontsova, T.A., Astrelin, I.M., 2016. Magnetic nanocomposites as efficient sorption materials for removing dyes from aqueous solutions. *Nanoscale Res. Lett.* 11 (1).
- Pascoal, A.M., Mitidieri, S., Fernandes, K.F., 2011. Immobilisation of beta-amylase from *Aspergillus niger* onto polyaniline. *Food Bioprod. Process.* 89 (4), 300–306.
- Qian, S., Wang, C., Wang, H., Yu, F., Zhang, C., Yu, H., 2015. Synthesis and characterization of surface-functionalized paramagnetic nanoparticles and their application to immobilization of  $\alpha$ -acetolactate decarboxylase. *Process Biochem.* 50 (9), 1388–1393.
- Ren, L., Wang, X., Wu, H., Shang, B., Wang, J., 2010. Conjugation of nattokinase and lumbricinase with magnetic nanoparticles for the assay of their thrombolytic activities. *J. Mol. Catal. B: Enzym.* 62 (2), 190–196.
- Sueishi, K., Nanno, S., Okamura, T., 1982. Purification and characterization of human kidney plasminogen activator dissimilar to urokinase. *Biochim. Biophys. Acta* 717 (2), 327–336.
- Sun, J., Rao, S., Su, Y., Xu, R., Yang, Y., 2011. Magnetic carboxymethyl chitosan nanoparticles with immobilized metal ions for lysozyme adsorption? *Colloid Surf. A: Physicochem. Eng. Asp.* 389 (1–3), 97–103.
- Takano, A., Hirata, A., Ogasawara, K., Sagara, N., Inomata, Y., Kawaji, T., Tanihara, H., 2006. Posterior vitreous detachment induced by nattokinase (subtilisin NAT): a novel enzyme for

- pharmacologic vitreolysis. *Invest. Ophthalmol. Vis. Sci.* 47 (5), 2075–2079.
- Wang, C., Ming, D.U., Zheng, D., Kong, F., Zu, G., Feng, Y., 2009a. Purification and characterization of nattokinase from *Bacillus subtilis* natto B-12. *J. Agric. Food Chem.* 57 (20), 9722–9729.
- Wang, Z., Zhu, H., Wang, X., Yang, F., Yang, X., 2009b. One-pot green synthesis of biocompatible arginine-stabilized magnetic nanoparticles. *Nanotechnology* 20 (46).
- Wu, W.C., Drenser, K.A., Lai, M., Capone, A., Trese, M.T., 2009. Plasmin enzyme-assisted vitrectomy for primary and reoperated eyes with stage 5 retinopathy of prematurity. *Retina* 29 (1), 127.
- Yang, C., Xing, J., Guan, Y., Liu, H., 2006. Superparamagnetic poly(methyl methacrylate) beads for nattokinase purification from fermentation broth. *Appl. Microbiol. Biotechnol.* 72 (3), 616–622.
- Zhou, Z., Jin, J., Yue, T., Lee, T.C., 2014. Optimization of covalent immobilization of extracellular ice nucleators from *Erwinia herbicola* on magnetic Fe<sub>3</sub>O<sub>4</sub>/chitosan nanoparticles for potential application in freeze concentration. *Food Bioprocess Technol.* 7 (11), 3259–3268.





# Water extract of *Helminthostachys zeylanica* attenuates LPS-induced acute lung injury in mice by modulating NF- $\kappa$ B and MAPK pathways



Chian-Jiun Liou<sup>a,b,1</sup>, Yu-Ling Huang<sup>c,1</sup>, Wen-Chung Huang<sup>b,d</sup>, Kuo-Wei Yeh<sup>b</sup>, Tzu-Yi Huang<sup>e</sup>, Chwan-Fwu Lin<sup>f,g,\*</sup>

<sup>a</sup> Department of Nursing, Research Center for Chinese Herbal Medicine, Chang Gung University of Science and Technology, No. 261, Wenhua 1st Rd., Guishan Dist., Taoyuan City 33303, Taiwan

<sup>b</sup> Division of Allergy, Asthma, and Rheumatology, Department of Pediatrics, Chang Gung Memorial Hospital, Guishan Dist., Taoyuan City 33303, Taiwan

<sup>c</sup> National Research Institute of Chinese Medicine, Ministry of Health and Welfare, No. 155-1, Sec. 2, Li-Nung St., Peitou, Taipei, Taiwan

<sup>d</sup> Graduate Institute of Health Industry Technology, Research Center for Industry of Human Ecology, Research Center for Chinese Herbal Medicine, College of Human Ecology, Chang Gung University of Science and Technology, No. 261, Wenhua 1st Rd., Guishan Dist., Taoyuan City 33303, Taiwan

<sup>e</sup> Department of Nursing, Tzu Chi University of Science and Technology, No. 880, Section 2, Chienkuo Rd., Hualien City 970, Taiwan

<sup>f</sup> Department of Cosmetic Science, Research Center for Chinese Herbal Medicine, Chang Gung University of Science and Technology, No. 261, Wenhua 1st Rd., Guishan Dist., Taoyuan City 33303, Taiwan

<sup>g</sup> Department of Anesthesiology, Chang Gung Memorial Hospital, Guishan Dist., Taoyuan City 33303, Taiwan

## ARTICLE INFO

### Keywords:

Acute lung injury

Cytokine

Lipopolysaccharide

*Helminthostachys zeylanica*

NF- $\kappa$ B

## ABSTRACT

**Ethnopharmacological relevance:** Previous studies showed that *Helminthostachys zeylanica* (L.) Hook. could reduce inflammatory responses in macrophage and brain astrocytes.

**Aim of the study:** In the present study, we evaluated whether an ethyl acetate extract (HZE) or a water extract (HZW) of *H. zeylanica* could reduce inflammatory responses in lung epithelial cells and ameliorate lipopolysaccharide (LPS)-induced acute lung injury in mice.

**Methods:** Human lung epithelial A549 cells were pre-treated with HZE or HZW (1–10  $\mu$ g/mL), then stimulated with LPS. BALB/c mice received oral HZW for 7 consecutive days, then an intratracheal instillation of LPS to induce lung injury.

**Results:** HZW reduced chemokine and proinflammatory cytokine production in LPS-activated A549 cells. HZW also suppressed ICAM-1 expression and reduced the adherence of acute monocytic leukemia cells to inflammatory A549 cells. HZE had less efficacy than HZW in suppressing inflammatory responses in A549 cells. In vivo, HZW significantly suppressed neutrophil infiltration and reduced the TNF- $\alpha$  and IL-6 levels in bronchoalveolar lavage fluid and serum from LPS-treated mice. HZW also modulated superoxide dismutase activity, glutathione, and myeloperoxidase activity in lung tissues from LPS-treated mice. HZW decreased the phosphorylation of mitogen-activated protein kinase and nuclear factor kappa B, and promoted heme oxygenase-1 expression in inflamed lung tissue from LPS-treated mice.

**Conclusion:** Our findings suggested that HZW reduced lung injury in mice by reducing oxidative stress and inflammatory responses. HZW also reduced inflammatory responses in human lung epithelial cells.

## 1. Introduction

Acute lung injury (ALI) and acute respiratory distress syndrome are characterized by neutrophil accumulations in the lung. This accumulation leads to severe pulmonary inflammation, reduced lung capacity, and increased pulmonary edema (Butt et al., 2016). ALI also causes fluid accumulation in alveoli, which leads to difficulty breathing, rapid

breathing, shortness of breath, and asphyxia, which increases the risk of mortality (Ghidoni et al., 2015). ALI can also develop into a respiratory disease with devastating complications, such as chronic obstructive pulmonary disease, ischemia/reperfusion injury, cystic fibrosis, asthma, and severe sepsis (Mokra and Kosutova, 2015).

Bacterial lipopolysaccharide (LPS), an important cell wall component of pathogenic gram-negative bacteria, can activate macrophages

\* Corresponding author at: Department of Cosmetic Science, Chang Gung University of Science and Technology, No. 261, Wenhua 1st Rd., Guishan Dist., Taoyuan City 33303, Taiwan.

E-mail address: [cfliu@mail.cgu.edu.tw](mailto:cfliu@mail.cgu.edu.tw) (C.-F. Lin).

<sup>1</sup> Chian-Jiun Liou and Yu-Ling Huang made equal contributions to this paper.

<http://dx.doi.org/10.1016/j.jep.2017.01.043>

Received 8 November 2016; Received in revised form 20 January 2017; Accepted 20 January 2017

Available online 21 January 2017

0378-8741/© 2017 Elsevier B.V. All rights reserved.



and neutrophils to defend against bacterial invasion. The airways of patients with ALI are infected with gram-negative bacteria, and their lung tissues secrete proinflammatory cytokines and chemokines, which aggravate immune inflammatory responses and cause pulmonary oxidative damage (Gong et al., 2014). In experimental animal models of ALI (ALI mice), delivery of LPS with an intratracheal or tail vein injection induced pulmonary inflammation and fever (Butt et al., 2016; Niu et al., 2015). Previous studies demonstrated that LPS could bind to toll-like receptor-4 expressed on immune cell membranes. This binding activated inflammatory signaling pathways (Rossol et al., 2011), including nuclear factor kappa B (NF- $\kappa$ B), an important transcription factor that induces the expression of inflammatory cytokines and mediators (Peri et al., 2010). LPS also contributed to the production of reactive oxygen species (ROS), which worsened cellular and lung tissue injuries in ALI mice (Mokra and Kosutova, 2015; Wang, 2014). Furthermore, mitogen-activated protein kinase (MAPK) pathways were activated, which also stimulated inflammatory gene expression in LPS-induced ALI mice (Chen et al., 2012). Therefore, we reasoned that suppressing both the NF- $\kappa$ B and MAPK pathways might ameliorate inflammatory responses and oxidative damage in ALI.

*Helminthostachys zeylanica* (L.) Hook. (Ophioglossaceae) is a common herb used to relieve fever symptoms and inflammatory diseases in Taiwan (Su et al., 2016). Previous studies found that the flavonoid, ugonin K, isolated from *H. zeylanica*, could reduce proinflammatory cytokine production in LPS-induced macrophages (Lee et al., 2011). An extract from *H. zeylanica* also reduced inflammatory responses and MMP-9 expression in bradykinin-activated brain astrocytes (Hsieh et al., 2015). In the present study, we evaluated whether a water extract (HZW) or an ethyl acetate extract (HZE) of *H. zeylanica* could protect ALI mice from LPS-induced lung injury. We evaluated the inflammatory response and oxidative stress in this animal model.

## 2. Materials and methods

### 2.1. *H. zeylanica* collection and extraction

The root of *H. zeylanica* was purchased in Wanhua, Taiwan. The herb was identified by Mr. Jun-Chih Ou. The roots of *H. zeylanica* (1.0 kg) were extracted with ethanol at 50 °C for 4 h. Then, the concentrated ethanol extract (38.0 g) was partitioned between the ethyl acetate extract (HZE, 14.2 g, yield 1.42%) and a water extract (HZW, 23.8 g, yield 2.38%).

### 2.2. HPLC analysis of *H. zeylanica*

The HPLC fingerprint of *H. zeylanica* was examined with the Hitachi HPLC system (L-2000 series, Tokyo, Japan). We injected 20  $\mu$ L of extract (4 mg/mL) into a reverse-phase column (Cosmosil 5C18-AR-II, 5 $\mu$ m, 25 cm $\times$ 4.6 mm I.D.), and the UV detection wavelength was set at 260 nm.

### 2.3. HZW and HZE treatment of A549 cells

A549, a human lung epithelial cell line, was obtained from the Bioresource Collection and Research Center in Taiwan. Cells were cultured in F-12 nutrient mixture medium (Life Technologies, Carlsbad, CA, USA), which contained 10% fetal bovine serum (Biological Industries, Haemek, Israel), penicillin (100 units/mL), and streptomycin (100  $\mu$ g/mL). HZE was dissolved in DMSO, and HZW was dissolved in PBS, to obtain stock solutions of 10 mg/mL. In all cell experiments, the DMSO concentration in the culture medium was  $\leq$ 0.1%.

A549 cells were pretreated with (1–10  $\mu$ g/mL) HZE or HZW for 1 h, then stimulated with 1  $\mu$ g/mL LPS for 24 h. The supernatants were collected and assayed with ELISA kits for the specific detection of selected chemokines or cytokines. Moreover, A549 cell viability was

tested with the MTT reagent; results were assayed at 570 nm on a microplate reader (Multiskan FC, Thermo, Waltham, MA, USA).

### 2.4. Cell-cell adhesion assay

A549 cells were treated with various doses of HZW or HZE and stimulated with LPS for 24 h, as previously described (Liou et al., 2016). Next, a calcein-AM solution (Sigma) was used to stain acute monocytic leukemia cells (THP-1 cells). THP-1 cells were co-cultured with the A549 cells to observe THP-1 adhesion. Adherent cells were detected (green fluorescence) with fluorescence microscopy (Olympus, Tokyo, Japan).

### 2.5. Animals

Female BALB/c mice (20–25 g, 6–8 weeks old) were purchased from the National Laboratory Animal Center in Taiwan. Mice were given a standard chow diet and clear water, and they were maintained in central air-conditioned animal housing. All experimental procedures were approved by the Laboratory Animal Care Committee of the Chang Gung University of Science and Technology (IACUC approval number: 2013-001).

### 2.6. HZW treatment and LPS-induced acute lung injury in mice

Mice were randomly assigned to five groups, with 8 mice in each group. The N group comprised normal control mice; the LPS group comprised mice challenged with LPS administered intratracheally; and three HZW groups comprised LPS-treated mice that were pretreated with 1 mg/kg HZW (HZW1), 5 mg/kg HZW (HZW5), or 10 mg/kg HZW (HZW10). On days 1–7, experimental mice received oral administrations of normal saline or the designated dose of HZW. On day 8, mice were anesthetized and treated with 50  $\mu$ L LPS (1  $\mu$ g/mL) or normal saline, administered intratracheally. Then, 4 h later, mice sacrificed, and the bronchoalveolar lavage fluid (BALF), lung tissue, and serum were harvested for the experiments.

### 2.7. BALF collection and cell count

BALF was collected as described previously (Huang et al., 2016). Briefly, mice were sacrificed, tracheae were intubated, and the lungs were flushed with normal saline. Isolated BALF cells were stained with Liu stain (Polysciences, Inc., Taipei, Taiwan). Neutrophils were counted with an optical microscope (Olympus, Tokyo, Japan). BALF supernatant was collected to evaluate secreted cytokines and chemokines.

### 2.8. Histological analyses of lung tissue

Lung tissues were fixed in formalin and embedded in paraffin. Lung sections were stained with hematoxylin and eosin (HE). Neutrophils were observed with an optical microscope (Olympus).

### 2.9. Wet-to-dry (W/D) weight ratio of lung tissue

Mice were sacrificed, and the right lung was excised to obtain its wet weight (W). Next, the lung was dried in an oven at 80 °C for 48 h, then weighed to obtain the dry weight (D). The W/D ratio was calculated to assess lung edema.

### 2.10. Myeloperoxidase and malondialdehyde activity

Lung tissues were homogenized in cool normal saline. Myeloperoxidase (MPO) activity was measured with a MPO fluorometric activity assay kit (Sigma). We used a lipid peroxidation assay kit (Sigma) to evaluate malondialdehyde (MDA) activity in the lungs,

according to the manufacturer's instructions. MPO and MDA activities were measured and calculated on a multi-mode microplate reader (BioTek SynergyHT, Bedfordshire, United Kingdom).

### 2.11. Glutathione and superoxide dismutase assay

Lung tissue was homogenized and glutathione (GSH) levels were evaluated with a glutathione assay kit (Sigma). Superoxide dismutase (SOD) activity was assayed with a SOD determination kit (Sigma), according to the manufacturer's instructions. Results were measured on a microplate reader (Multiskan FC, Thermo).

### 2.12. Western immunoblot analyses

Lung tissues were homogenized, and total proteins and nuclear proteins were extracted as described previously. Proteins were separated on a 10% SDS-PAGE, then transferred onto polyvinylidene fluoride (PVDF) membranes (Millipore, Billerica, MA, USA). Membranes were incubated with specific primary antibodies against ERK1/2, JNK, p38 (Millipore), phosphorylated-IkB- $\alpha$ , phosphorylated-ERK 1/2, phosphorylated-JNK, phosphorylated-p38 (Cell Signaling Technology, Boston, MA USA), p65, phosphorylated-p65, IkB- $\alpha$ , nuclear factor erythroid 2-related factor 2 (Nrf2), heme oxygenase (HO)-1, lamin B1 (Santa Cruz, CA, USA), and  $\beta$ -actin (Sigma). Then, membranes were washed and incubated with HRP-conjugated secondary antibody for 1 h. Luminol/Enhancer Solution (Millipore) was added, and protein signals were detected with the BioSpectrum 600 system (UVP, Upland, CA, USA).

### 2.13. Serum collection

Mice were anesthetized with isoflurane, and blood was collected from the orbital vascular plexus. Samples were centrifuged at 6000 rpm for 5 min, as previously described (Huang et al., 2014). Serum was stored at  $-80^{\circ}\text{C}$ , before assaying cytokines.

### 2.14. Cytokine assay

We analyzed serum, BALF, and cell culture medium samples with specific ELISA kits (R & D Systems, Minneapolis, MN, USA) to quantify IL-6, IL-8, MCP-1, CCL5, ICAM-1, and TNF- $\alpha$  production. Results were expressed in terms of optical density (OD) measured at 450 nm with a microplate reader (Thermo).

### 2.15. Real-time PCR

RNA was extracted from lung tissue with the TRIzol reagent (Life Technologies, Carlsbad, CA, USA). Next, cDNA was synthesized with a cDNA synthesis kit (Life Technologies). To detect specific gene expression, the cDNA was used as template in a real-time PCR kit (Bio-Rad Laboratories, Hercules, CA, USA) and amplified on a spectrofluorometric thermal cycler (iCycler; Bio-Rad). In this experiment, we used the specific primers shown in Table 1.

### 2.16. Statistical analyses

Experimental data were examined with a one-way analysis of variance (ANOVA), followed by Tukey–Kramer multiple comparisons. Results were expressed as the mean  $\pm$  SEM, and a  $p$ -value  $< 0.05$  was considered statistically significant.

## 3. Results

### 3.1. Comparison of HZW and HZE effects on activated A549 cells

HZW and HZE were analyzed with HPLC. We found that the HZE

**Table 1**

Primers used in real-time PCR analyses of the expression of proinflammatory mRNAs.

Gene	Primer Forward	Primer Reverse
IL-1 $\beta$	CACTACAGGCTCCGAGATGA	CGTTGCTTGGTTCTCCTTGT
IL-6	AGGACCAAGACCATCCAATTCA	GCTTAGGCATAACGCACACTAGG
TNF- $\alpha$	GCACCACCATCAAGGACTC	AGGCAACCTGACCACTCTC
iNOS	TTCCACAACCACTCAAGCA	TTAAGGCATCACAGTCCGAGTC
COX-2	ACCAGCAGTTCAGTATCAGA	CAGGAGGATGGAGTTGTTGTAG
ICAM-1	AACAGAATGGTAGACAGCAT	TCCACCGAGTCTCTTAG
CCL5	CGAAGGAACCGCAAGTGT	AGGACTAGAGCAAGCAATGAC
CCL11	GGCTTCATGTAGTTCCAGAT	CCATTGTGTTCTCAATAATCC
MCP-1	TTCCACAACCACTCAAGCA	TTAAGGCATCACAGTCCGAGTC
$\beta$ -actin	AAGACCTCTATGCCAACACAGT	AGCCAGAGCAGTAATCTCTTC

comprised mainly flavonoids (ugonin J and ugonin K) (Fig. 1). Next, we found that doses  $\leq 10$   $\mu\text{g/mL}$  of HZW or HZE did not significantly affect the viability of A549 cells (data not shown). Therefore, we used 1–10  $\mu\text{g/mL}$  HZW and HZE to evaluate their anti-inflammatory effects. First, we assayed whether HZW or HZE influenced the secretion of chemokines and cytokines in LPS-stimulated A549 cells (Fig. 2). Our results demonstrated that HZW pretreatment significantly reduced IL-6 and IL-8 levels compared to LPS-stimulation alone (IL-6; HZW 1  $\mu\text{g/mL}$ :  $154.9 \pm 4.9$  pg/mL,  $p < 0.01$ ; HZW 5  $\mu\text{g/mL}$ :  $101.8 \pm 5.8$  pg/mL,  $p < 0.01$ ; HZW 10  $\mu\text{g/mL}$ :  $59.3 \pm 4.7$  pg/mL,  $p < 0.01$ ; vs. LPS-treated control:  $207.1 \pm 6.7$  pg/mL) (IL-8; HZW 1  $\mu\text{g/mL}$ :  $4.25 \pm 0.21$  ng/mL,  $p < 0.05$ ; HZW 5  $\mu\text{g/mL}$ :  $3.59 \pm 0.13$  ng/mL,  $p < 0.01$ ; HZW 10  $\mu\text{g/mL}$ :  $1.63 \pm 0.11$  ng/mL,  $p < 0.01$ ; vs. LPS-treated control:  $5.31 \pm 0.23$  ng/mL). HZW also significantly, dose-dependently reduced the levels of MCP-1 and CCL5 in LPS-stimulated A549 cells. Surprisingly, HZE did not significantly reduce the levels of IL-6, IL-8, MCP-1, or CCL5. Only the highest dose (10  $\mu\text{g/mL}$ ), of HZE could significantly reduce the levels of IL-6 and IL-8. This showed that HZW could reduce the inflammatory response more effectively than HZE, in LPS-stimulated A549 cells.

### 3.2. Effects of HZW and HZE on LPS-induced ICAM-1 expression

A549 cells were pretreated with HZW or HZE, then stimulated with LPS for 24 h. The results showed that HZW significantly reduced ICAM-1 expression compared to LPS-stimulation alone in A549 cells (ICAM-1; HZW 1  $\mu\text{g/mL}$ :  $184.9 \pm 7.3$  pg/mL,  $p < 0.01$ ; HZW 5  $\mu\text{g/mL}$ :  $147.8 \pm 4.2$  pg/mL,  $p < 0.01$ ; HZW 10  $\mu\text{g/mL}$ :  $92.7 \pm 8.7$  pg/mL,  $p < 0.01$ ; vs. LPS-treated control:  $322.3 \pm 8.5$  pg/mL; Fig. 3A). We also found that HZW inhibited adherence of THP-1 cells to LPS-stimulated A549 cells (Fig. 3B). However, compared to HZW, HZE did not significantly reduce ICAM-1 levels or THP-1 cell adherence. Therefore, only HZW was investigated further to determine its effects on inflammation and oxidation in ALI mice.

### 3.3. Effects of HZW on neutrophil infiltration in LPS-induced lung injury

Mice treated with LPS alone showed more neutrophil infiltration in lung biopsies compared to untreated mice (N group). The HZW groups showed reduced neutrophil infiltration (Fig. 4). HZW also significantly inhibited the neutrophil count compared to the LPS-treated group (neutrophil counts: HZW1:  $5.2 \times 10^5 \pm 1.7 \times 10^4/\text{mL}$ ,  $p = 0.20$ ; HZW5:  $3.5 \times 10^5 \pm 1.5 \times 10^4/\text{mL}$ ,  $p < 0.05$ ; HZW10:  $2.4 \times 10^5 \pm 1.1 \times 10^4/\text{mL}$ ,  $p < 0.01$  vs. LPS:  $6.4 \times 10^5 \pm 2.2 \times 10^4/\text{mL}$ ; Fig. 5A).

### 3.4. Effects of HZW on cytokine and chemokine levels in BALF and lung tissue

Among ALI mice, HZW treatment significantly suppressed IL-6 and TNF- $\alpha$  levels in BALF compared to LPS alone (IL-6: HZW1,  $333.2 \pm$

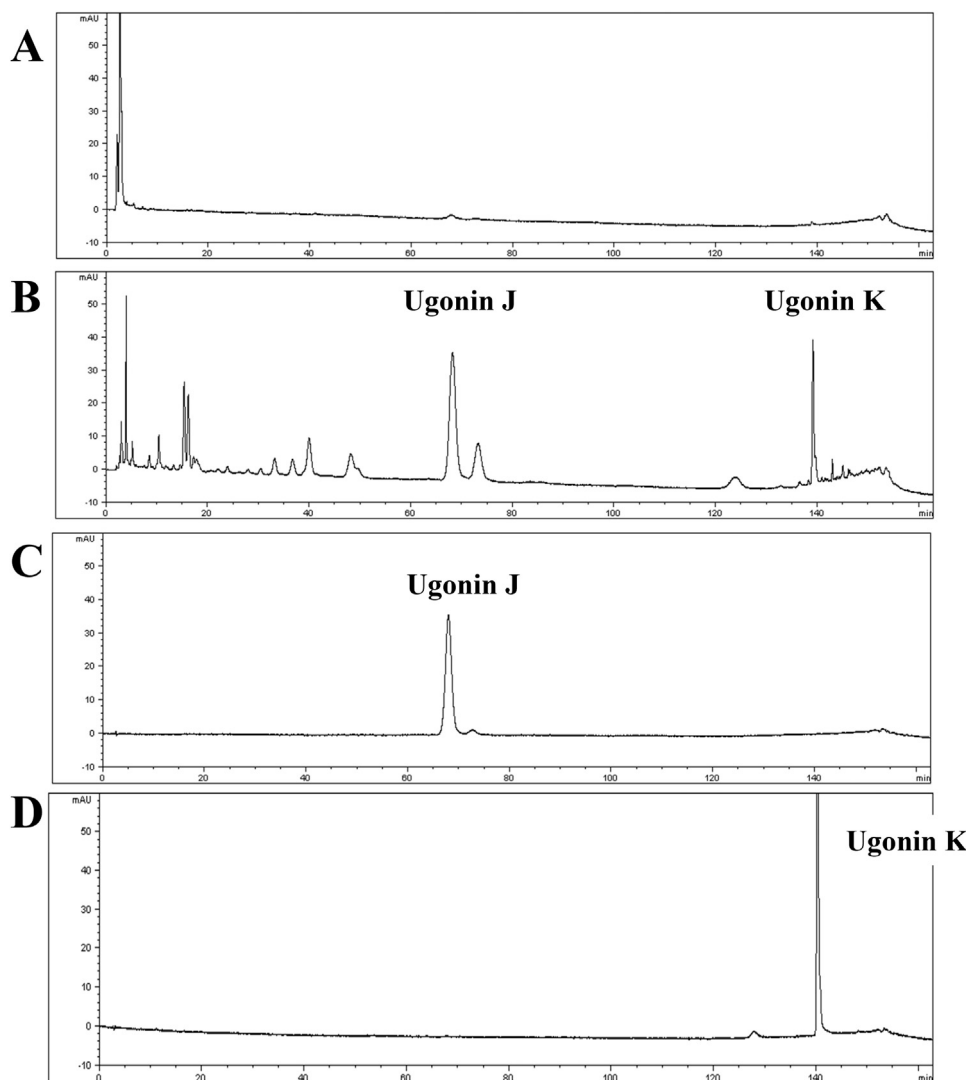


**Fig. 1.** HPLC profiles of *H. zeylanica* extracts. (A) The water extract (HZW) and (B) the ethyl acetate extract (HZE) were evaluated at 260 nm. The two major peaks on the HZE profile were identified as standard (C) ugonin J and (D) ugonin K compounds.

14.5 pg/mL,  $p=0.052$ ; HZW5,  $226.6 \pm 19.6$  pg/mL,  $p < 0.05$ ; HZW10,  $72.1 \pm 15.2$  pg/mL,  $p < 0.01$  vs. LPS:  $367.1 \pm 36.0$  pg/mL) (TNF- $\alpha$ : HZW1,  $439.4 \pm 58.4$  pg/mL,  $p=0.31$ ; HZW5,  $305.1 \pm 52.5$  pg/mL,  $p < 0.05$ ; HZW10,  $113.0 \pm 21.9$  pg/mL,  $p < 0.01$  vs. LPS:  $528.6 \pm 57.3$  pg/mL; Fig. 5B–C).

Gene expression assays in lung tissues showed that HZW significantly reduced *iNOS*, *COX-2*, *IL-1 $\beta$* , *IL-6*, *TNF- $\alpha$* , *CCL5*, *MCP-1*, and *ICAM-1* expression compared to expression levels observed with LPS-treatment alone (Fig. 6). However, HZW did not significantly inhibit *CCL11* gene expression. Furthermore, we found that HZW also significantly reduced protein levels in BALF compared to LPS alone (Fig. 7A).

### 3.5. Effects of HZW on lung W/D ratios in LPS-treated mice

The W/D ratios reflect the levels of lung edema. We found that LPS significantly increased the W/D ratio compared to no treatment (N group). Interestingly, HZW significantly reduced the W/D ratio compared to LPS alone (Fig. 7B).

### 3.6. The effects of HZW on MOP, MOD, GSH, and SOD activities in lung

We found that LPS significantly promoted MOP and MDA activities,

and repressed GSH and SOD activities, compared to no treatment (N group; Fig. 7C–F). Conversely, HZW significantly decreased LPS-induced MOP and MDA activity, and increased GSH and SOD production.

### 3.7. Effects of HZW on serum cytokine levels

Serum analyses demonstrated that HZW treatment suppressed IL-6 and TNF- $\alpha$  production, compared to LPS treatment alone (Fig. 8).

### 3.8. Effects of HZW on the phosphorylation of NF- $\kappa$ B and MAPK in lung tissue

HZW treatment reduced the phosphorylation of NF- $\kappa$ B subunits, I $\kappa$ B- $\alpha$  and p65, compared to LPS alone (Fig. 9A). HZW also decreased the phosphorylation of MAPK pathway proteins, ERK1/2, p38, and JNK, in LPS-stimulated lung tissues (Fig. 9B).

### 3.9. Effects of HZW on HO-1 and Nrf2 expression in lung tissue

LPS treatment induced HO-1 expression in lung tissue compared to no treatment (N group). HZW further increased HO-1 expression and increased Nrf2 expression compared to LPS treatment alone (Fig. 9C).

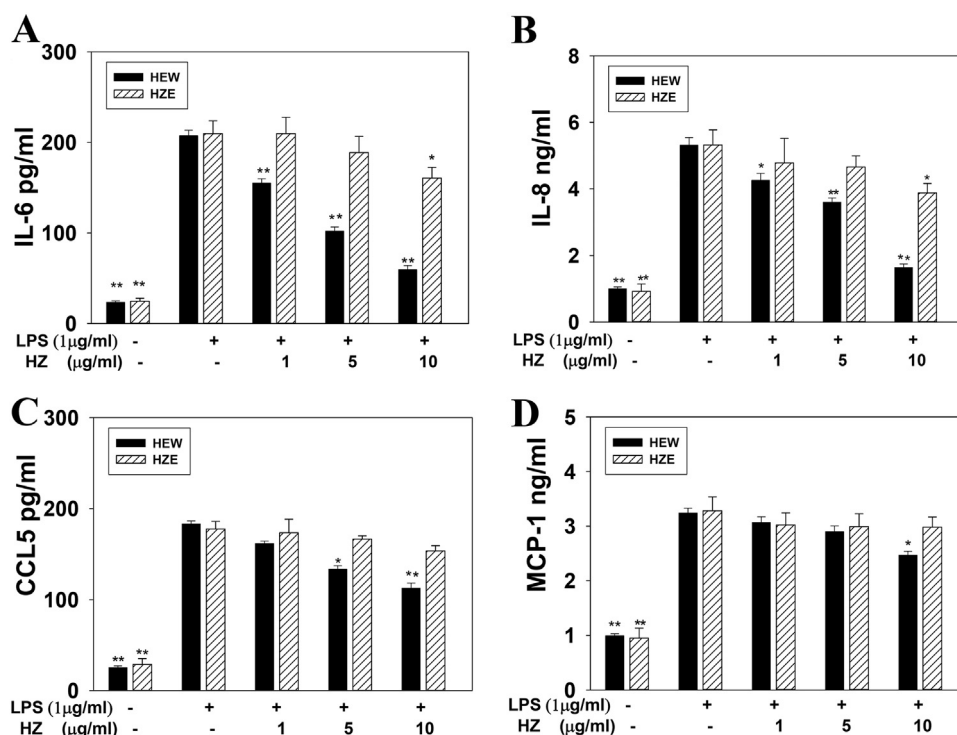


**Fig. 2.** Effects of HZW and HZE on cytokine and chemokine production in A549 cells. ELISA results show the levels of (A) IL-6, (B) IL-8, (C) CCL5, and (D) MCP-1. All data are presented as the mean  $\pm$  SEM. \* $p$  < 0.05 compared to the LPS-treated control group. \*\* $p$  < 0.01 compared to the LPS-treated control group. HZ: *Helminthostachys zeylanica*.

#### 4. Discussion

Previous studies confirmed that *H. zeylanica* extract had anti-inflammatory effects on LPS-stimulated macrophages (Su et al., 2016). It was also shown that neogonin A, a flavonoid isolated from *H. zeylanica*, could suppress inflammatory responses in RAW 264.7 macrophages by blocking the NF- $\kappa$ B pathway (Cao et al., 2016). Another study showed that *H. zeylanica* extract could improve liver damage and modulate serum enzymes in Wistar rats (Suja et al., 2004).

Moreover, ugonin U was shown to activate phospholipase C, which improved the inflammatory, oxidative, and immune effects of neutrophils (Chen et al., 2014). Ethyl acetate could isolate lipophilic alkaloids and flavonoids; while, water extract could isolate hydrophilic flavonoids, polysaccharides, or alkaloids. In the present study, we investigated HZE and HZW to determine whether they could suppress inflammation in lung epithelial cells, and ameliorate the lung inflammation and oxidative stress associated with ALI in mice. Our results showed that HZW significantly reduced the production of IL-6, IL-8,

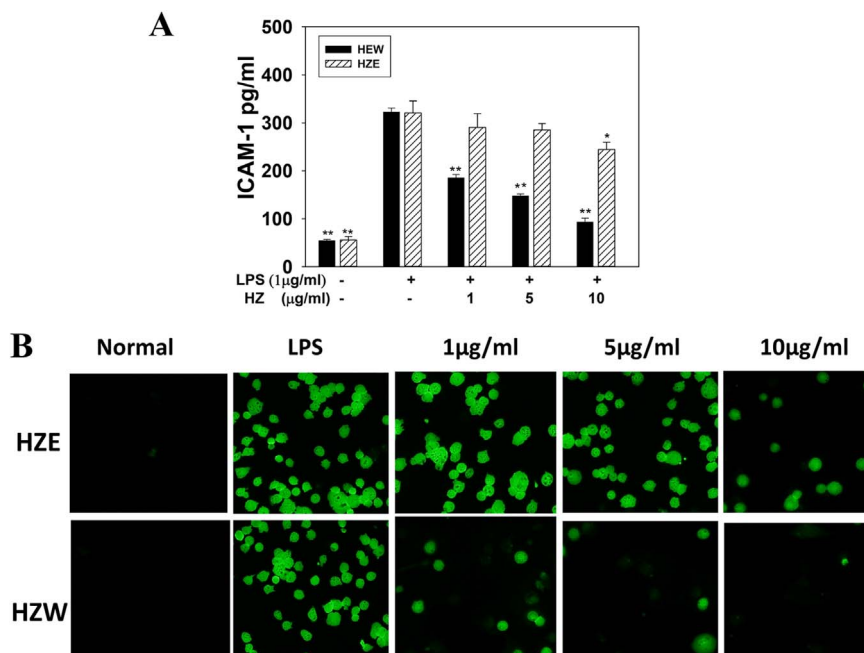


**Fig. 3.** HZW and HZE inhibited ICAM-1 levels and THP-1 cell adherence to activated A549 cells. (A) The levels of ICAM-1 detected by ELISA in LPS-activated A549 cells. The data represent the mean  $\pm$  SEM; \* $p$  < 0.05, \*\* $p$  < 0.01, compared to A549 cells stimulated with LPS alone. (B) Fluorescence microscopy images show THP-1 cells labeled with calcein-AM, mixed with normal or LPS-activated A549 cells, in the absence or presence of HZW or HZE, at the indicated doses. HZ: *Helminthostachys zeylanica*.



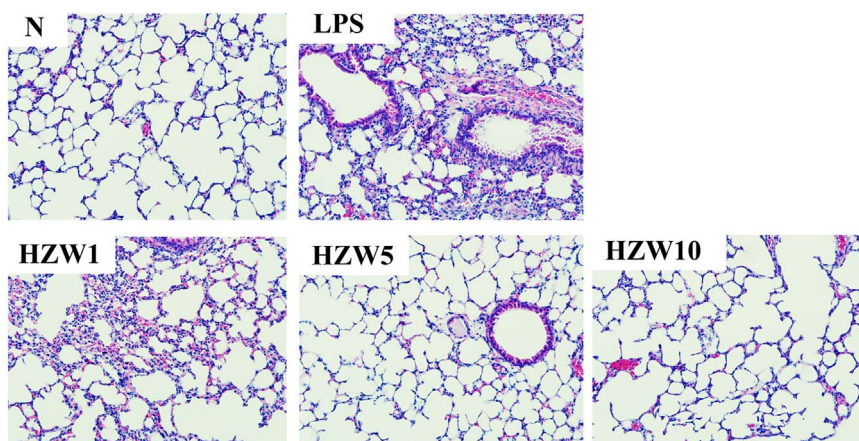


**Fig. 4.** HZW suppressed neutrophil infiltration into the lungs of ALI mice. HE stained sections show lung tissue (magnification  $\times 200$ ) for the following groups: N group: untreated control mice; LPS group: LPS treatment only; HZW1 group: 1 mg/kg HZW plus LPS; HZW5 group: 5 mg/kg HZW plus LPS; HZW10 group: 10 mg/kg HZW plus LPS.

CCL5, and MCP-1 in LPS-stimulated A549 cells. HZW also repressed ICAM-1 expression and reduced THP-1 cell adherence to LPS-stimulated A549 cells. Furthermore, we found that HZW could effectively inhibit neutrophil infiltration in the lungs and BALF, which led to diminished inflammatory and oxidative responses.

The HPLC profiles showed that HZE contained two major known compounds (ugonin J and ugonin K). However, HZE could not reduce the inflammatory response or decrease ROS levels as well as HZW, in LPS-stimulated A549 cells. HZW fraction contained the main compound that could reduce the oxidative stress and inflammatory response in ALI mice. Therefore, in the future, we plan to identify, isolate, and purify the bioactive compounds from HZW that ameliorated the damage induced by LPS in ALI mice.

ALI is a severe clinical illness characterized by neutrophil infiltration into pulmonary parenchyma. This infiltration accelerates disease progression. It induces alveolar barrier disruption and edema, increases microvascular permeability, decreases tidal volume, induces hypoxemia, and can even lead to pulmonary function disorder and

death (Butt et al., 2016). When gram-negative bacteria infect the airway, they release LPS, which causes lung inflammation and edema (Rossol et al., 2011). Neutrophils and macrophages are recruited to defend against infective microbes; they release inflammatory mediator enzymes to kill the bacteria (Konrad and Reutershan, 2012; Mokra and Kosutova, 2015). Unfortunately, neutrophils secrete mediators that can cause more serious inflammation and oxidative damage to infected lung tissue. Our findings showed that HZW effectively suppressed neutrophil infiltration in BALF and lung tissues, which might diminish the inflammatory response in ALI mice. HZW also reduced the W:D lung weight ratio, which indicated that it might reduce the edema caused by alveolar rupture and fluid accumulation.

In the current study, mice were orally administered HZW for 7 days. Then, mice were given intratracheal LPS to induce lung injury. Four hours later, the mice were sacrificed. Hence, we did not induce death from ALI in this experimental mouse model. However, we did observe significant increases in the levels of proinflammatory cytokines and chemokines in lung tissue. Oral administration of HZW decreased

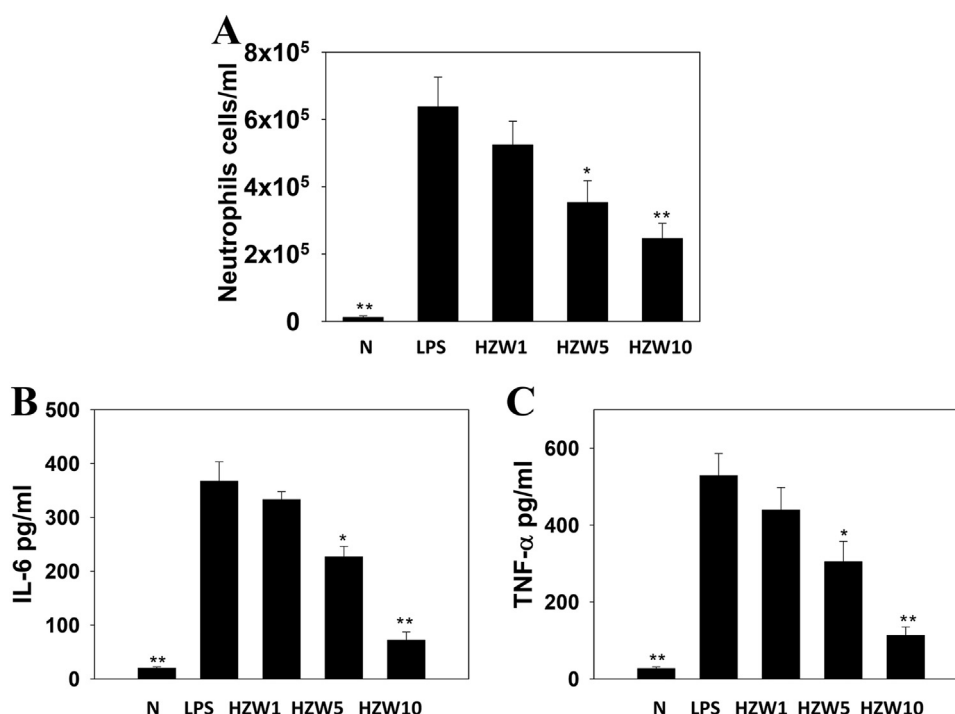


**Fig. 5.** HZW affects neutrophil counts and the levels of cytokines and chemokines in BALF. (A) Neutrophils were counted with microscopy; (B) the levels of IL-6 and (C) TNF-α were determined with ELISAs. All data are presented as the mean  $\pm$  SEM. \* $p < 0.05$  compared to the LPS-treated group. \*\* $p < 0.01$  compared to the LPS-treated group.



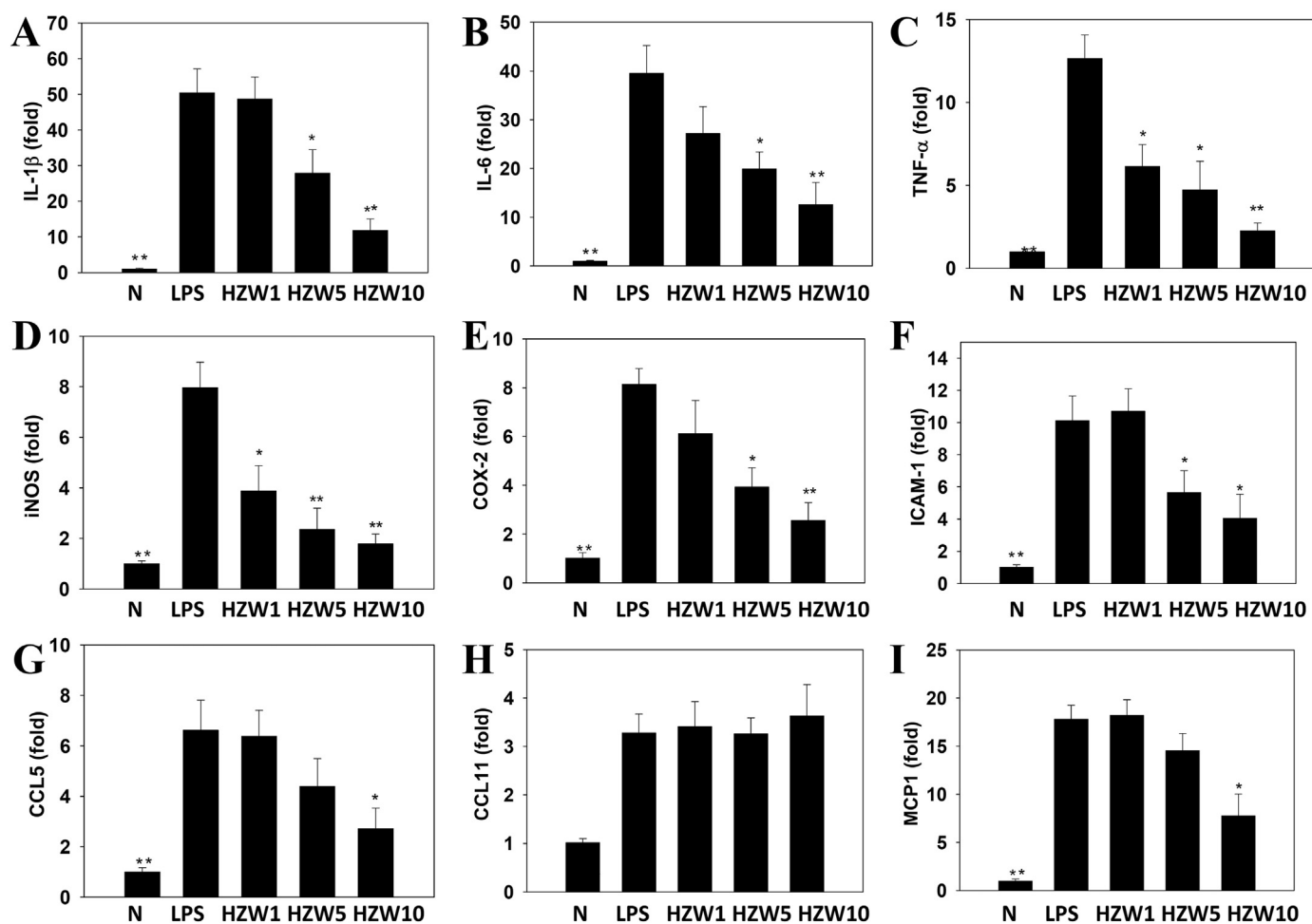


**Fig. 6.** Effects of HZW on gene expression of cytokines, chemokines, and inflammatory mediators in the lung. Fold-changes in gene expression are shown for (A) IL-1 $\beta$ , (B) IL-6, (C) TNF- $\alpha$ , (D) iNOS, (E) COX-2, (F) ICAM-1, (G) CCL5, (H) CCL11, and (I) MCP-1. Expression was measured with real-time PCR analysis of RNA extracted from lung tissues. Fold-changes in expression were evaluated relative to  $\beta$ -actin expression (internal control). Data are presented as the mean  $\pm$  SEM. \* $p$  < 0.05 compared to LPS-treated mice. \*\* $p$  < 0.01 compared to LPS-treated mice.

the levels of IL-6 and TNF- $\alpha$  in the serum and BALF of ALI mice. We also found that HZW significantly decreased the expression of proinflammatory cytokines, mediators, and chemokines in lung tissues compared to LPS alone.

Interestingly, HZW did not decrease the levels of CCL11, a chemokine that induces eosinophilic infiltration. Therefore, HZW might operate primarily by preventing neutrophil infiltration, and this might be sufficient to block LPS-induced lung disease. Moreover, we found that HZW diminished ICAM-1 expression and decreased THP-1 adherence to LPS-activated A549 cells in vitro. HZW also reduced ICAM-1 expression in lungs, which blocked neutrophil infiltration in vivo. Hence, oral administration of HZW appeared to have beneficial effects in ALI mice; it reduced neutrophil infiltration into the lungs, which reduced oxidative damage and the inflammatory response.

Other studies have shown that LPS could activate proinflammatory signaling pathways to increase the expression of genes that encoded proinflammatory cytokines and mediators (Guha and Mackman, 2001). Triptolide, an NF- $\kappa$ B inhibitor, had anti-inflammatory effects in LPS-induced ALI mice (Wei and Huang, 2014). Additionally, a MAPK inhibitor attenuated inflammatory and oxidative damage in the lungs of ALI mice (Qiu et al., 2016). In the present study, we demonstrated that HZW significantly reduced the phosphorylation of MAPK and NF- $\kappa$ B pathway proteins in lung tissues of ALI mice. That result suggested that HZW had the potential to diminish ALI by modulating both NF- $\kappa$ B and MAPK pathways in ALI mice.

Inflammatory tissue is often accompanied by oxidative stress, which exacerbates tissue damage (Antus, 2016). Oxidative metabolism releases free radicals and superoxide anions, which cause DNA breaks and cellular damage (Suzuki et al., 2015). Furthermore, neutrophils release oxidant enzymes to defend against invasive bacteria in the lungs of ALI mice (Konrad and Reutershan, 2012; Porto and Stein, 2016). In particular, myeloperoxidase (MPO) is produced in the granulocytes of neutrophils. When MPO is released, it produces hypohalous acids to kill pulmonary bacteria (Colgan, 2015; Ferrari and Andrade, 2015). However, MPO activity can also cause oxidative damage to the host tissue, during its attack against the bacterial invasion. Here, we found that HZW significantly reduced neutrophil infiltration and suppressed MPO activity, which ameliorated the lung injury in ALI mice. Other antioxidant flavonoids were previously shown to protect from oxidative damage and attenuate inflammatory responses in the lungs of ALI mice (Ferrari and Andrade, 2015). Our results demonstrated that HZW also increased SOD and GSH production to defend against oxidative damage in lung tissue. In addition, HZW effectively reduced ROS levels in inflammatory tracheal epithelial cells, and it reduced the expression of MDA, a lipid peroxidation marker, in lung tissues of ALI mice. Furthermore, HZW increased Nrf2 and HO-1 expression, which defend against oxidative damage. Hence, our results suggested that HZW could effectively reduce lung injury by decreasing oxidative stress in LPS-induced ALI mice.

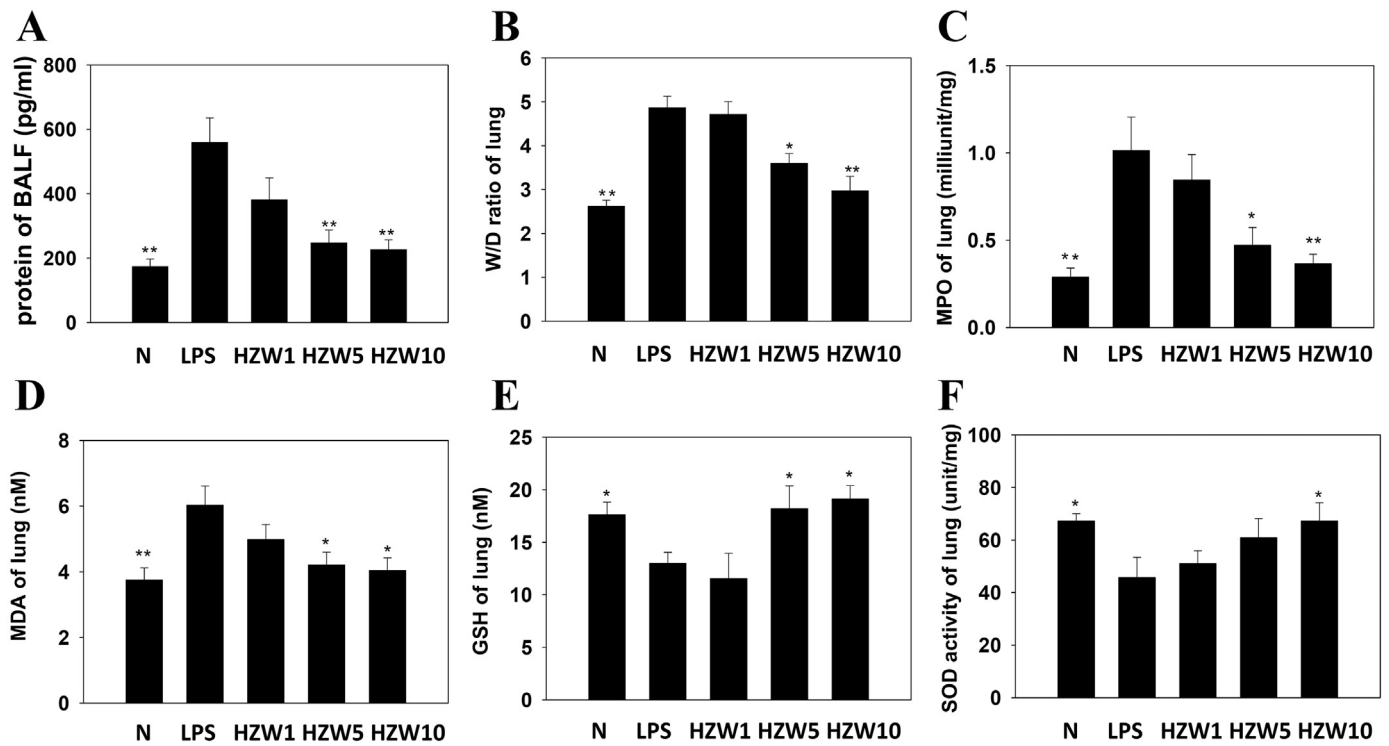


**Fig. 7.** HZW effects in the lung tissues of LPS-induced ALI mice. Graphs show effects on (A) the levels of protein, (B) W/D ratio, (C) MPO activity, (D) MDA activity, (E) GSH activity, (F) and SOD activity. Data are presented as the mean ± SEM. \* $p < 0.05$  compared to LPS-treated mice. \*\* $p < 0.01$  compared to LPS-treated mice.

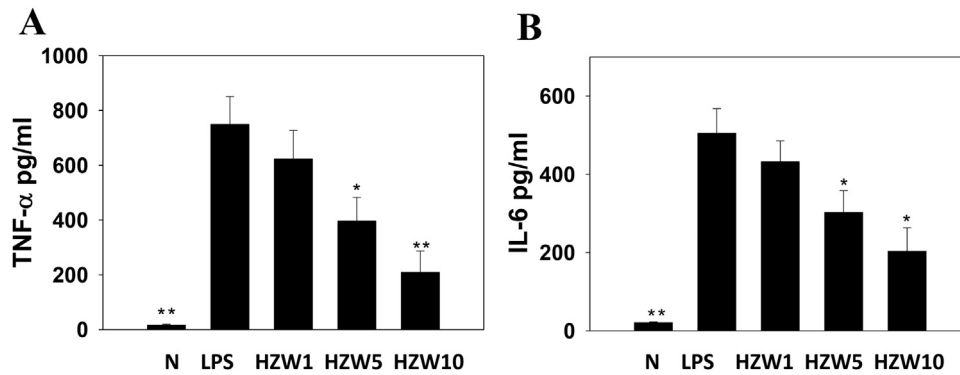


**Fig. 8.** HZW decreased serum levels of proinflammatory cytokines. ELISA results show changes in serum (A) IL-6 and (B) TNF-α levels. All data are presented as the mean ± SEM. \* $p < 0.05$  compared to LPS-treated mice. \*\* $p < 0.01$  compared to LPS-treated mice.

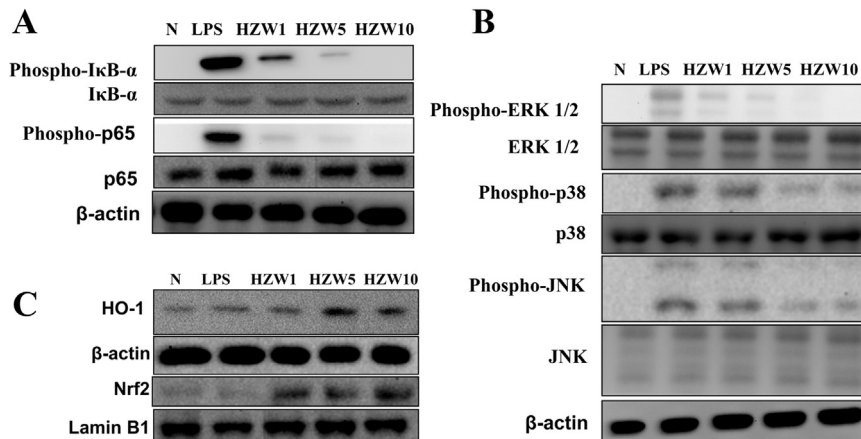


**Fig. 9.** HZW inhibits phosphorylation and expression of proinflammatory proteins. HZW inhibited LPS-induced phosphorylation of (A) the IκB-α and p65 subunits, in the NF-κB pathway; and (B) proteins in the MAPK pathway. (C) HZW increased HO-1 and Nrf2 protein expression in lung tissues from mice treated with LPS.

## 5. Conclusions

Our results showed that HZW, but not HZE, could reduce neutrophil infiltration and ameliorate inflammatory responses in ALI mice by blocking NF- $\kappa$ B and MAPK pathways and reducing oxidative stress. Thus, HZW showed potential as an anti-inflammatory and anti-oxidative therapeutic for maintaining lung function in ALI.

## Conflict of interest statement

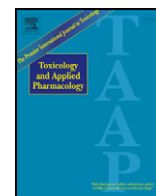
The authors have no conflicts of interest to declare.

## Acknowledgments

This study was supported, in part, by grants from the Chang Gung Memorial Hospital (CMRPF1C0201-3 and CMRPF1F0081) and by a grant from the Ministry of Science and Technology, Taiwan (MOST 104-2320-B-255-001).

## References

- Antus, B., 2016. Oxidative stress markers in sputum. *Oxid. Med. Cell Longev.* 2016, 2930434.
- Butt, Y., Kurdowska, A., Allen, T.C., 2016. Acute lung injury: a clinical and molecular review. *Arch. Pathol. Lab. Med.* 140, 345–350.
- Cao, L., Li, R., Chen, X., Xue, Y., Liu, D., 2016. Neougongin A inhibits lipopolysaccharide-induced inflammatory responses via downregulation of the NF- $\kappa$ B signaling pathway in RAW 264.7 macrophages. *Inflammation*. <http://dx.doi.org/10.1007/s10753-016-0429-9>.
- Chen, C.Y., Liaw, C.C., Chen, Y.H., Chang, W.Y., Chung, P.J., Hwang, T.L., 2014. A novel immunomodulatory effect of ugonin U in human neutrophils via stimulation of phospholipase C. *Free Radic. Biol. Med.* 72, 222–231.
- Chen, X., Yang, X., Liu, T., Guan, M., Feng, X., Dong, W., Chu, X., Liu, J., Tian, X., Ci, X., Li, H., Wei, J., Deng, Y., Deng, X., Chi, G., Sun, Z., 2012. Kaempferol regulates MAPKs and NF- $\kappa$ B signaling pathways to attenuate LPS-induced acute lung injury in mice. *Int. Immunopharmacol.* 14, 209–216.
- Colgan, S.P., 2015. Neutrophils and inflammatory resolution in the mucosa. *Semin. Immunol.* 27, 177–183.
- Ferrari, R.S., Andrade, C.F., 2015. Oxidative stress and lung ischemia-reperfusion injury. *Oxid. Med. Cell Longev.* 2015, 590987.
- Ghidoni, R., Caretti, A., Signorelli, P., 2015. Role of sphingolipids in the pathobiology of lung inflammation. *Mediat. Inflamm.* 2015, 487508.
- Gong, J., Wu, Z.Y., Qi, H., Chen, L., Li, H.B., Li, B., Yao, C.Y., Wang, Y.X., Wu, J., Yuan, S.Y., Yao, S.L., Shang, Y., 2014. Maresin 1 mitigates LPS-induced acute lung injury in mice. *Br. J. Pharmacol.* 171, 3539–3550.
- Guha, M., Mackman, N., 2001. LPS induction of gene expression in human monocytes. *Cell Signal* 13, 85–94.
- Hsieh, H.L., Yang, S.H., Lee, T.H., Fang, J.Y., Lin, C.F., 2015. Evaluation of anti-inflammatory effects of *Helminthostachys zeylanica* extracts via inhibiting bradykinin-induced MMP-9 expression in brain astrocytes. *Mol. Neurobiol.* <http://dx.doi.org/10.1007/s12035-015-9511-9>.
- Huang, W.C., Chan, C.C., Wu, S.J., Chen, L.C., Shen, J.J., Kuo, M.L., Chen, M.C., Liou, C.J., 2014. Matrine attenuates allergic airway inflammation and eosinophil infiltration by suppressing eotaxin and Th2 cytokine production in asthmatic mice. *J. Ethnopharmacol.* 151, 470–477.
- Huang, W.C., Lai, C.L., Liang, Y.T., Hung, H.C., Liu, H.C., Liou, C.J., 2016. Phloretin attenuates LPS-induced acute lung injury in mice via modulation of the NF- $\kappa$ B and MAPK pathways. *Int. Immunopharmacol.* 40, 98–105.
- Konrad, F.M., Reutershan, J., 2012. CXCR2 in acute lung injury. *Mediat. Inflamm.* 2012, 740987.
- Lee, C.H., Huang, Y.L., Liao, J.F., Chiou, W.F., 2011. Ugonin K promotes osteoblastic differentiation and mineralization by activation of p38 MAPK- and ERK-mediated expression of Runx2 and osterix. *Eur. J. Pharmacol.* 668, 383–389.
- Liou, C.J., Lai, Y.R., Chen, Y.L., Chang, Y.H., Li, Z.Y., Huang, W.C., 2016. Matrine attenuates COX-2 and ICAM-1 expressions in human lung epithelial cells and prevents acute lung injury in LPS-induced mice. *Mediat. Inflamm.* 2016, 3630485.
- Mokra, D., Kosutova, P., 2015. Biomarkers in acute lung injury. *Front. Pediatr.* 209, 52–58.
- Niu, X., Wang, Y., Li, W., Mu, Q., Li, H., Yao, H., Zhang, H., 2015. Protective effects of Isofraxidin against lipopolysaccharide-induced acute lung injury in mice. *Int. Immunopharmacol.* 24, 432–439.
- Peri, F., Piazza, M., Calabrese, V., Damore, G., Cighetti, R., 2010. Exploring the LPS/TLR4 signal pathway with small molecules. *Biochem. Soc. Trans.* 38, 1390–1395.
- Porto, B.N., Stein, R.T., 2016. Neutrophil extracellular traps in pulmonary diseases: too much of a good thing? *Front. Immunol.* 7, 311.
- Qiu, J., Chi, G., Wu, Q., Ren, Y., Chen, C., Feng, H., 2016. Pretreatment with the compound asperuloside decreases acute lung injury via inhibiting MAPK and NF- $\kappa$ B signaling in a murine model. *Int. Immunopharmacol.* 31, 109–115.
- Rossol, M., Heine, H., Meusch, U., Quandt, D., Klein, C., Sweet, M.J., Hauschildt, S., 2011. LPS-induced cytokine production in human monocytes and macrophages. *Crit. Rev. Immunol.* 31, 379–446.
- Su, L.H., Li, Y.P., Li, H.M., Dai, W.F., Liu, D., Cao, L., Li, R.T., 2016. Anti-inflammatory prenylated flavonoids from *Helminthostachys zeylanica*. *Chem. Pharm. Bull.* 64, 497–501.
- Suja, S.R., Latha, P.G., Pushpangadan, P., Rajasekharan, S., 2004. Evaluation of hepatoprotective effects of *Helminthostachys zeylanica* (L.) Hook against carbon tetrachloride-induced liver damage in Wistar rats. *J. Ethnopharmacol.* 92, 61–66.
- Suzuki, M., Bandoski, C., Bartlett, J.D., 2015. Fluoride induces oxidative damage and SIRT1/autophagy through ROS-mediated JNK signaling. *Free Radic. Biol. Med.* 89, 369–378.
- Wang, C., 2014. Obesity, inflammation, and lung injury (oili): the good. *Mediat. Inflamm.* 2014, 978463.
- Wei, D., Huang, Z., 2014. Anti-inflammatory effects of triptolide in LPS-induced acute lung injury in mice. *Inflammation* 37, 1307–1316.



# Ciproxifan, a histamine H<sub>3</sub> receptor antagonist and inverse agonist, presynaptically inhibits glutamate release in rat hippocampus

Cheng-Wei Lu<sup>a,b</sup>, Tzu-Yu Lin<sup>a,b</sup>, Chia-Ying Chang<sup>a,c</sup>, Shu-Kuei Huang<sup>a</sup>, Su-Jane Wang<sup>d,e,\*</sup>

<sup>a</sup> Department of Anesthesiology, Far-Eastern Memorial Hospital, Pan-Chiao District, New Taipei City 22060, Taiwan

<sup>b</sup> Department of Mechanical Engineering, Yuan Ze University, Taoyuan 320, Taiwan

<sup>c</sup> Department of Chemistry, Fu Jen Catholic University, No. 510, Chung-Cheng Road, Hsin-Chuang District, New Taipei City 24205, Taiwan

<sup>d</sup> School of Medicine, Fu Jen Catholic University, No. 510, Chung-Cheng Rd., Hsin-Chuang, New Taipei 24205, Taiwan

<sup>e</sup> Research Center for Chinese Herbal Medicine, College of Human Ecology, Chang Gung University of Science and Technology, Taoyuan City, Taiwan

## ARTICLE INFO

### Article history:

Received 11 November 2016

Revised 18 January 2017

Accepted 25 January 2017

Available online 27 January 2017

### Keywords:

Ciproxifan

H<sub>3</sub> receptor

Glutamate release

Gi/Go-protein/PLA<sub>2</sub>/PGE<sub>2</sub>/EP<sub>2</sub> pathway

Voltage-dependent Ca<sup>2+</sup> channels

Hippocampus

## ABSTRACT

Ciproxifan is an H<sub>3</sub> receptor antagonist and inverse agonist with antipsychotic effects in several preclinical models; its effect on glutamate release has been investigated in the rat hippocampus. In a synaptosomal preparation, ciproxifan reduced 4-aminopyridine (4-AP)-evoked Ca<sup>2+</sup>-dependent glutamate release and cytosolic Ca<sup>2+</sup> concentration elevation but did not affect the membrane potential. The inhibitory effect of ciproxifan on 4-AP-evoked glutamate release was prevented by the Gi/Go-protein inhibitor pertussis toxin and Ca<sub>v</sub>2.2 (N-type) and Ca<sub>v</sub>2.1 (P/Q-type) channel blocker ω-conotoxin MVIIC, but was not affected by the intracellular Ca<sup>2+</sup>-release inhibitors dantrolene and CGP37157. Furthermore, the phospholipase A<sub>2</sub> (PLA<sub>2</sub>) inhibitor OBAA, prostaglandin E<sub>2</sub> (PGE<sub>2</sub>), PGE<sub>2</sub> subtype 2 (EP<sub>2</sub>) receptor antagonist PF04418948, and extracellular signal-regulated kinase (ERK) inhibitor FR180204 eliminated the inhibitory effect of ciproxifan on glutamate release. Ciproxifan reduced the 4-AP-evoked phosphorylation of ERK and synapsin I, a presynaptic target of ERK. The ciproxifan-mediated inhibition of glutamate release was prevented in synaptosomes from synapsin I-deficient mice. Moreover, ciproxifan reduced the frequency of miniature excitatory postsynaptic currents without affecting their amplitude in hippocampal slices. Our data suggest that ciproxifan, acting through the blockade of Gi/Go protein-coupled H<sub>3</sub> receptors present on hippocampal nerve terminals, reduces voltage-dependent Ca<sup>2+</sup> entry by diminishing PLA<sub>2</sub>/PGE<sub>2</sub>/EP<sub>2</sub> receptor pathway, which subsequently suppresses the ERK/synapsin I cascade to decrease the evoked glutamate release.

© 2017 Elsevier Inc. All rights reserved.

**Abbreviations:** 4-AP, 4-aminopyridine; GPCR, G protein-coupled receptor; [Ca<sup>2+</sup>]<sub>i</sub>, cytosolic free Ca<sup>2+</sup> concentration; DISC<sub>3</sub>(5), 3',3',3'-dipropylthiadicarbocyanine iodide; DL-TBOA, DL-threo-beta-benzyl-oxy aspartate; Fura-2-AM, fura-2-acetoxymethyl ester; GDH, glutamate dehydrogenase; HBM, HEPES buffer medium; BSA, bovine serum albumin; TTX, tetrodotoxins; ω-CgTx MVIIC, ω-conotoxin MVIIC; PTX, pertussis toxin; PLA<sub>2</sub>, phospholipase A<sub>2</sub>; AA, arachidonic acid; PGE<sub>2</sub>, prostaglandin E<sub>2</sub>; EP<sub>2</sub>, PGE<sub>2</sub> subtype 2 receptor; PF04418948, 1-(4-fluorobenzoyl)-3-[[6-methoxy-2-naphthalenyl)methyl]-3-azetidinecarboxylic acid; FR180204, 5-(2-Phenyl-pyrazolo[1,5-a]pyridin-3-yl)-1H-pyrazolo[3,4-c]pyridazin-3-ylamine; OBAA, 4-(4-Octadecyl phenyl)-4-oxobutenoic acid; MAPK, mitogen-activated protein kinase; ERK, extracellular signal-regulated kinase; CGP37157, 7-chloro-5-(2-chlorophenyl)-1,5-dihydro-4,1-benzothiazepin-2(3H)-one; PD98059, 2-(2-amino-3-methoxyphenyl)-4H-1-benzopyran-4-one; H89, N-[2-(p-bromocinnamylamino)-ethyl]-5-isoquinolinesulfonamide dihydrochloride; VDCC, voltage-dependent Ca<sup>2+</sup> channel; Ca<sub>v</sub>2.2 and Ca<sub>v</sub>2.1 channel, Ca<sub>v</sub>2.2 (N-type) and Ca<sub>v</sub>2.1 (P/Q-type) channel; mEPSCs, miniature excitatory postsynaptic currents; CNQX, 6-cyano-7-nitroquinoxaline-2,3-dione; D-AP5, D(-)-2-amino-5-phosphonopentanoic acid; CNS, central nervous system.

\* Corresponding author at: School of Medicine, Fu Jen Catholic University, 510, Chung-Cheng Rd., Hsin-Chuang, New Taipei 24205, Taiwan.

E-mail address: [med0003@mail.fju.edu.tw](mailto:med0003@mail.fju.edu.tw) (S.-J. Wang).

## 1. Introduction

Schizophrenia, a debilitating psychiatric illness, affects approximately 1% of the population worldwide (Sullivan et al., 2003; Weiser et al., 2005). Current antipsychotic drugs mainly antagonize dopamine receptors. However, these drugs show considerable side effects, and 20%–35% of patients do not respond to these drugs (Suzuki et al., 2011). Therefore, discovering and developing novel therapeutics in treating schizophrenia is an urgent clinical need. The role of the glutamatergic system in the etiology of schizophrenia has received increased interest in addition to the existing dopaminergic theory (Coyle, 2006). Glutamate is the most abundant excitatory neurotransmitter in the brain and plays a crucial role in learning, memory, emotional regulation, and motivational behavior (Fonnum, 1984). Recent studies have reported that glutamate levels are elevated in patients with schizophrenia and decreased in those taking antipsychotic medications (de la Fuente-Sandoval et al., 2013; Kegeles et al., 2012; Marsman et al., 2013; Poels et al., 2014). Thus, increased brain glutamate level may be involved in the pathophysiology of schizophrenia, and decreased brain

glutamate level may represent a novel approach to the treatment of this disorder.

The histamine H<sub>3</sub> receptor, a G protein-coupled receptor (GPCR), is widely distributed in brain regions implicated in attention, learning, and memory such as the cerebral cortex and hippocampus (Bhowmik et al., 2012). Most H<sub>3</sub> receptors are located within the presynaptic active zone, where they act as autoreceptors or heteroreceptors regulating the release of various neurotransmitters such as histamine, dopamine, serotonin, acetylcholine, and noradrenaline (Feuerstein, 2008; Passani et al., 2007). Moreover, H<sub>3</sub> receptors have received distinct attention from the pharmaceutical and clinical research community because these receptors have been implicated in the pathogenesis and treatment of schizophrenia (Nuutinen and Panula, 2010; Passani and Blandina, 2011; Schwartz, 2011). Growing evidence has shown that several H<sub>3</sub> receptor antagonists exhibit antipsychotic activity in numerous experimental animal models of schizophrenia (Fox et al., 2005; Ligneau et al., 2007; Mahmood et al., 2012; Southam et al., 2009) and potentiate neurochemical and behavioral effects of the antipsychotic drug haloperidol (Pillot et al., 2002).

The hippocampus plays a crucial role in the pathogenesis of schizophrenia, and neurodegeneration of this brain region has been attributable to glutamate (Gallinat et al., 2016; Ota et al., 2017). Considering that glutamate is involved in the actions of antipsychotic drugs; therefore, in this study, we investigated the effect and mechanism of ciproxifan, an H<sub>3</sub> receptor antagonist with antipsychotic effects (Ligneau et al., 1998), on glutamate release from rat hippocampal nerve terminals (synaptosomes) stimulated using the K<sup>+</sup> channel blocker 4-aminopyridine (4-AP). 4-AP opens voltage-gated Ca<sup>2+</sup> channels and induces release of vesicular glutamate; the process simulates physiological stimulation and, therefore, is used in synaptosomal studies as a depolarizing agent (Nicholls, 1998). The synaptosome preparation provides a useful system to study directly the specific presynaptic regulation of neurotransmitter release given that this preparation is capable of accumulating, storing, and releasing neurotransmitters, and is devoid of functional glial and nerve cell body elements that might obscure interpretation because of modulatory loci at non-neuronal, post-synaptic, or network levels (Nicholls and Sihra, 1986). In addition, we used intact neurons in hippocampal slices to examine the effect of ciproxifan on the frequency and amplitude of miniature excitatory post-synaptic currents (mEPSCs). Analysis of the frequency and amplitude of mEPSC can provide useful indications of changes in the presynaptic release process and sensitivity of postsynaptic receptors, respectively (Margaroli and Tsien, 1992; Manabe et al., 1992).

## 2. Materials and methods

### 2.1. Chemicals

Ciproxifan, immepip, DL-threo-beta-benzyl-oxy aspartate (DL-TBOA), bafilomycin A1,  $\omega$ -conotoxin MVIIC ( $\omega$ -CgTX MVIIC), dantrolene, 7-chloro-5-(2-chlorophenyl)-1,5-dihydro-4,1-benzothiazepin-2(3H)-one (CGP37157), 2-(2-amino-3-methoxyphenyl)-4H-1-benzopyran-4-one (PD98059), 5-(2-Phenyl-pyrazolo[1,5-a]pyridin-3-yl)-1H-pyrazolo[3,4-c]pyridazin-3-ylamine (FR180204), 4-(4-Octadecyl phenyl)-4-oxobutenoic acid (OBAA), 1-(4-fluorobenzoyl)-3-[[6-methoxy-2-naphthalenyl)methyl]-3-azetidinedicarboxylic acid (PF04418948), 6-cyano-7-nitroquinoxaline-2,3-dione (CNQX), and D(-)-2-amino-5-phosphonopentanoic acid (D-AP5) were purchased from Tocris Cookson (Bristol, UK). Fura-2-acetoxymethyl ester (Fura-2-AM), and 3',3',3'-dipropylthiadicarbocyanine iodide [DiSC<sub>3</sub>(5)] were purchased from Invitrogen (Carlsbad, CA, USA). PGE<sub>2</sub> was purchased from Cayman Chemical (Ann Arbor, Michigan, USA). Ethylene glycol bis ( $\beta$ -aminoethyl ether)-N,N,N',N'-tetraacetic acid (EGTA), tetrodotoxin (TTX), pertussis toxin (PTX) and all other reagents were purchased from Sigma-Aldrich (St. Louis, MO, USA).

### 2.2. Preparation of synaptosomes

The handling and all procedures to sacrifice the animals used in this study were conducted in accordance with the National Institutes of Health Guide for the Care and Use of Laboratory Animals and were approved by the Institutional Animal Care and Use Committee at the Far-Eastern Memorial Hospital. Percoll gradient-purified synaptosomes were prepared from the whole hippocampus of adult male Sprague-Dawley rats (150–200 g; n = 35) or from six-week old male wild-type mice (129/C57B1/6 strain; n = 5) or synapsin I-deficient mutant mice (n = 6) generated as described (Lin et al., 2012). Briefly, animals were sacrificed by decapitation and the brains were removed at 4 °C. The hippocampus was rapidly dissected and homogenized in medium containing 0.32 M sucrose (pH 7.4). The homogenate was centrifuged for 10 min at 3000g (5000 rpm in a JA 25.5 rotor; Beckman Coulter, Inc., USA) and 4 °C, and the supernatant spun again at 14500g (11,000 rpm in a JA 25.5 rotor) for 12 min. The pellet was gently resuspended in 8 ml of 0.32 M sucrose (pH 7.4). An aliquot of this synaptosomal suspension (2 ml) was placed onto a 3 ml Percoll discontinuous gradient containing: 0.32 M sucrose, 1 mM EDTA, 0.25 mM DL-dithiothreitol, and 3%, 10%, or 23% Percoll (pH 7.4). After centrifugation at 32,500g (16,500 rpm in a JA 20.5 rotor) for 7 min at 4 °C, the synaptosomes were recovered from the 10% and 23% Percoll bands, and they were diluted in a final volume of 30 mL of HEPES buffer medium (HBM): 140 mM NaCl, 5 mM KCl, 5 mM NaHCO<sub>3</sub>, 1 mM MgCl<sub>2</sub>·6H<sub>2</sub>O, 1.2 mM Na<sub>2</sub>HPO<sub>4</sub>, 10 mM glucose, and 10 mM HEPES (pH 7.4). Protein concentration was then determined using the Bradford assay. Synaptosomes were centrifuged in the final wash to obtain synaptosomal pellets with 0.5 mg protein. Synaptosomal pellets were stored on ice and used within 4–6 h.

### 2.3. Immunocytochemistry

The synaptosomes were allowed to attach to polylysine coated coverslips for 60 min and then fixed for 30 min in 4% paraformaldehyde in 0.1 M phosphate buffer (pH 7.4). Following several washes with phosphate buffer, the synaptosomes were preincubated for 60 min in 3% normal goat serum diluted in 50 mM Tris buffer (pH 7.4) containing 0.9% NaCl (TBS) and 0.2% Triton X-100. Subsequently, they were then incubated for 90 min with the appropriate primary antibody diluted in TBS with 1% normal goat serum and 0.2% Triton X-100 as follows: synaptophysin (1:200; Abcam, Cambridge, UK) and H<sub>3</sub> receptor (1:100; Cell Signaling Technology, Beverly, MA, USA). After washing with TBS, the synaptosomes were incubated for 2 h in goat anti-mouse DyLight 549- and goat anti-rabbit fluorescein isothiocyanate (FITC)-conjugated secondary antibodies (1:200; Jackson Immuno-Research Inc., West Grove, PA, USA). After several washes in TBS, the synaptosomes were coverslipped with fluorescence mounting medium (DAKO North America, Inc., CA, USA). The synaptosomes were viewed with a upright fluorescence microscopy (Leica DM2000 LED, Wetzlar, Germany) using a mercury lamp as a source of light and equipped with a 100 $\times$  objective and images were captured using a CCD camera (SPOT RT3, Diagnostic Instruments, Sterling Heights, MI, USA).

### 2.4. Glutamate release

Glutamate release was assayed by on-line fluorimetry as described previously (Nicholls and Sihra, 1986). Synaptosomal pellets were resuspended in HBM (0.5 mg/mL) and preincubated at 37 °C for 1 h in the presence of 16  $\mu$ M bovine serum albumin (BSA) to bind any free fatty acids released from synaptosomes during the preincubation. A 1 mL aliquot was transferred to a stirred and thermostated cuvette containing 2 mM NADP<sup>+</sup>, 50 units of glutamate dehydrogenase (GDH), and 1.2 mM CaCl<sub>2</sub>, and the fluorescence of NADPH was followed in a Perkin-Elmer LS-55 spectrofluorimeter (PerkinElmer Life and Analytical Sciences, Waltham, MA, USA) at excitation and emission wavelengths of



340 and 460 nm, respectively. A standard of exogenous glutamate (5 nmol) was added at the end of each experiment and the fluorescence change produced by the standard addition was used to calculate the released glutamate as nanomoles glutamate per milligram synaptosomal protein (nmol/mg). Release values quoted in the text and depicted in bar graphs represent the levels of glutamate cumulatively released after 5 min of depolarization, and are expressed as nmol/mg/5 min. Data were accumulated at 2-s intervals and cumulative data were analyzed using Lotus 1-2-3.

### 2.5. Membrane potential

The synaptosomal membrane potential was estimated with a membrane potential-sensitive dye, DiSC<sub>3</sub>(5) (Akerman et al., 1987). Synaptosomes were resuspended in HBM and incubated in a stirred cuvette containing 5  $\mu$ M DiSC<sub>3</sub>(5) and 1.2 mM CaCl<sub>2</sub> at 37 °C in a Perkin-Elmer LS-55 spectrofluorimeter. After 3 min to allow for equilibration, the fluorescence was monitored at excitation and emission wavelengths of 646 and 674 nm, respectively. Data was collected at 2-s intervals. Cumulative data were analyzed using Lotus 1-2-3 and results are expressed in fluorescence units.

### 2.6. Cytosolic free Ca<sup>2+</sup> concentration ([Ca<sup>2+</sup>]<sub>c</sub>)

[Ca<sup>2+</sup>]<sub>c</sub> was measured with fura-2. Synaptosomes were resuspended (2 mg/mL) in HBM containing 16  $\mu$ M BSA in the presence of 5  $\mu$ M fura-2-AM and 0.1 mM CaCl<sub>2</sub> and incubated at 37 °C for 30 min in a stirred test tube. After fura-2 loading, synaptosomes were pelleted and resuspended in HBM containing BSA. The synaptosomal suspension was stirred in a thermostatted cuvette containing 1.2 mM CaCl<sub>2</sub> in a Perkin-Elmer LS-55 spectrofluorimeter, and the fluorescence was monitored at excitation wavelengths of 340 and 380 nm (emission wavelength 505 nm). Data was collected at 2-s intervals and cumulative data were analyzed using Lotus 1-2-3. [Ca<sup>2+</sup>]<sub>c</sub> (nM) was calculated using the equations described previously (Gryniewicz et al., 1985).

### 2.7. Western blotting

Synaptosomes were homogenized in a lysis buffer (10 mM HEPES buffer, pH 7.4), 1% Triton X-100, and protease inhibitor mixture. Lysates were clarified by centrifugation, and protein concentration was determined using a protein assay kit (Bio-Rad Laboratories, Hercules, CA, USA). Equal amounts of proteins were separated by SDS-PAGE and transferred to nitrocellulose membrane. The membranes were blocked with Tris-buffered saline that contained 5% low-fat milk and incubated with appropriate primary antibodies (anti-H<sub>3</sub> receptor, 1:1000; anti-phospho-ERK1/2, 1:2000; anti-ERK1/2, 1:1000; anti-phospho-synapsin-I (Ser<sup>62</sup>/Ser<sup>67</sup>), 1:1000;  $\beta$ -actin, 1:500; Cell Signaling Technology, Beverly, MA, USA) overnight at 4 °C. After three washes in Tris-buffered saline, the membrane was then treated with the secondary horseradish peroxidase-conjugated antibody (1:3000; BioRad, Milan, Italy) for 1 h at room temperature. The membranes were then washed at least three times with Tris-buffered saline and visualized using the enhanced chemiluminescence system (Amersham, Buckinghamshire, UK). The level of expression or phosphorylation was assessed by band density, which was quantified by densitometry. Densitometric quantification of bands was analyzed using Syngene software (SynGene, Cambridge, UK).

### 2.8. Slice preparation and electrophysiological recordings

Hippocampal slices were prepared from 8- to 23-day-old male rats (n = 5), as described in detail previously (Chang et al., 2015; Chang et al., 2016). Briefly, after decapitation, the hippocampus was positioned on the stage of a vibratome slicer (VT1000S, Leica, Germany) and cut to obtain 300  $\mu$ m thick transverse brain slices. The slices were

maintained in the artificial cerebrospinal fluid continuously oxygenated with 95% O<sub>2</sub>–5% CO<sub>2</sub> at room temperature for at least 1 h before use. Artificial cerebrospinal fluid comprised (in mM): 117 NaCl, 4.7 KCl, 2.5 CaCl<sub>2</sub>, 1.2 MgCl<sub>2</sub>, 25 NaHCO<sub>3</sub>, 1.2 NaH<sub>2</sub>PO<sub>4</sub>, 11 glucose (pH 7.4, 300 mOsm).

Slices were moved to a recording chamber mounted on a BX51W1 upright microscope (Olympus) equipped with infra-red differential interference contrast (IR-DIC). The chamber was continuously perfused with oxygenated artificial cerebrospinal fluid. Neurons were visualized with an Olympus Optical 40 $\times$  water immersion objective. Whole-cell voltage clamp recordings in hippocampal CA3 neurons were performed using pipettes of 2–5 M $\Omega$  resistance after files with an internal solution containing 0.3 mM Na<sub>3</sub>GTP, 135 mM K-gluconate, 20 mM KCl, 0.1 mM EGTA, 2 mM MgCl<sub>2</sub>, 4 mM Na<sub>2</sub>ATP, and 10 mM HEPES (pH 7.3, 280 mOsm). Pipettes were fabricated from borosilicate glass (outer diameter, 1.5 mm; internal diameter, 0.86 mm) by using a micropipette puller (P87, Sutter Instruments, USA). Positive pressure was applied to the recording pipette as it was lowered into the medium and approached the cell membrane. A constant negative pressure was applied to form the seal (>1 G $\Omega$ ) when the recording pipette was attached to the membrane, and the cell membrane was then drawn up quickly to rupture it and access the whole-cell configuration. Neurons were voltage clamped at –70 mV using an Axopatch 200B amplifier (Axon Instruments, Foster City, CA, USA). Access resistance (8–30 M $\Omega$ ) was regularly monitored during recordings and cells were rejected if it changed >15% during the experiments. Membrane currents were filtered at 2 kHz, digitized and stored on a computer using pCLAMP (Axon Instruments, Foster City, CA, USA). Data were analyzed using a commercially available software (Synaptosoft Inc., Fort Lee, NJ, USA).

### 2.9. Statistics

Statistical analysis was carried out by the two-tailed Student's *t*-test when comparing two groups and by one-way ANOVA with Tukey's multiple comparisons post hoc tests when comparing more than two groups. Analysis was completed using SPSS software (Version 17.0; SPSS Inc., Chicago, IL, USA). Data are expressed as mean  $\pm$  SEM. A value of *P* < 0.05 was considered significant.

## 3. Results

### 3.1. H<sub>3</sub> receptors are expressed in rat hippocampal nerve terminals

To analyze the distribution of H<sub>3</sub> receptors in hippocampal nerve terminals, synaptosomes were co-labeled with antibodies against the vesicle marker protein synaptophysin and H<sub>3</sub> receptors. H<sub>3</sub> receptor was detected in 63.3  $\pm$  3.9% (Fig. 1A and C) of the synaptophysin-containing particles (1108 particles from 10 fields; Fig. 1B). In addition, synaptophysin or H<sub>3</sub> receptor immunoreactivity was also observed by western blot analysis (Fig. 1D). This is the first direct anatomical evidence for H<sub>3</sub> receptors and synaptophysin co-localization in identical neuronal compartments.

### 3.2. Ciproxifan reduces glutamate release from synaptosomes

To examine whether H<sub>3</sub> receptor blockade affects glutamate release, synaptosomes were incubated with ciproxifan (5–50  $\mu$ M), followed by the addition of 1 mM 4-AP to trigger release. Under control conditions, 4-AP (1 mM) evoked a glutamate release of 7.1  $\pm$  0.1 nmol/mg/5 min from synaptosomes incubated with 1.2 mM CaCl<sub>2</sub>. Preincubation with ciproxifan (30  $\mu$ M) for 10 min before 4-AP addition caused an inhibition of the 4-AP-evoked glutamate release by approximately 38% [4.4  $\pm$  0.2 nmol/mg/5 min; *t*(12) = 11.3, *P* = 0.000; Fig. 2A]. The effect of ciproxifan was dose-dependent, with an IC<sub>50</sub> of approximately 21  $\mu$ M (Fig. 2B). Ciproxifan did not affect the basal, prepolarization glutamate level. By contrast, the 4-AP-evoked glutamate release was

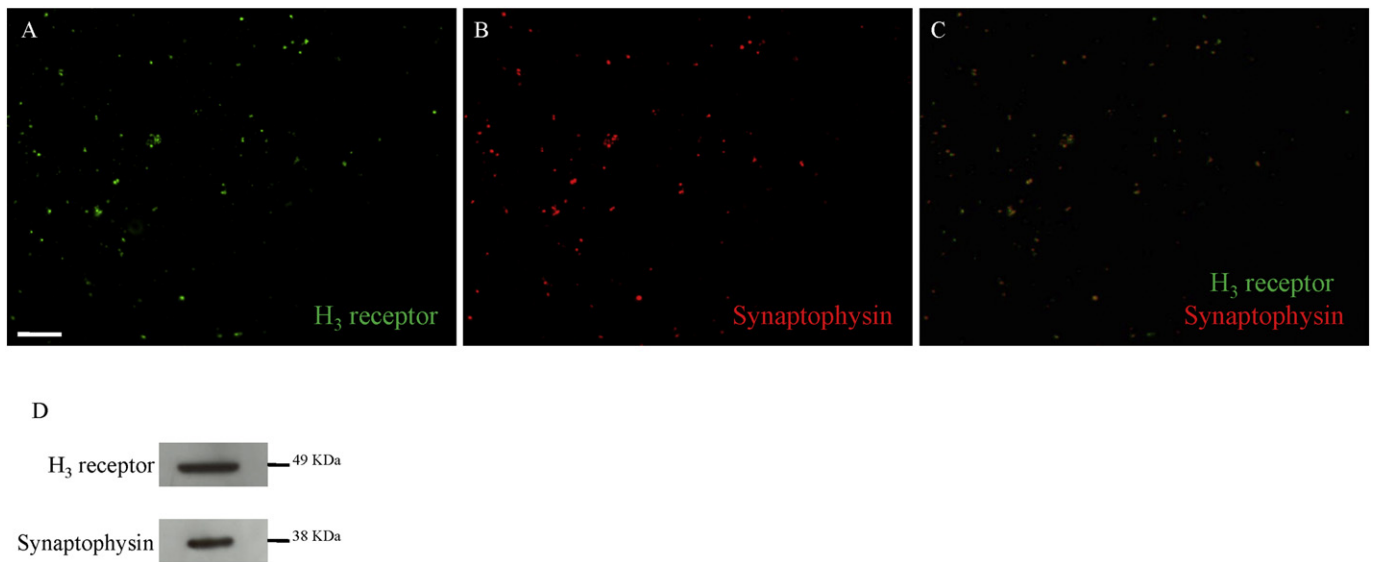


**Fig. 1.** H<sub>3</sub> receptors are present in rat hippocampal synaptosomes. Synaptosomes were fixed onto polylysine-coated coverslips and doublestained for immunocytochemistry with antisera against H<sub>3</sub> receptors and the vesicular marker synaptophysin (A–C). Scale bar, 30  $\mu$ m. (D) Western blot analysis of the expression of H<sub>3</sub> receptors and synaptophysin in synaptosomes.

increased by the H<sub>3</sub> receptor agonist imiprep 30  $\mu$ M in the presence of 1.2 mM CaCl<sub>2</sub> [ $10.6 \pm 0.3$  nmol/mg/5 min;  $t(8) = -7.47$ ,  $P = 0.000$ ; Fig. 2C]. Importantly, the facilitatory effect of imiprep on 4-AP-evoked glutamate release was completely blocked by ciproxifan 30  $\mu$ M [ $3.9 \pm 0.1$  nmol/mg/5 min;  $F(2,12) = 181.8$ ;  $P = 0.000$ ; Fig. 2C]. On the other hand, calcium-free medium containing 300  $\mu$ M EGTA reduced the 4-AP-evoked glutamate release to 25% of that of the control [ $1.8 \pm 0.1$  nmol/mg/5 min;  $F(2,12) = 383.72$ ;  $P = 0.000$ ]. This Ca<sup>2+</sup>-independent component of the 4-AP-evoked glutamate release was unaffected by 30  $\mu$ M of ciproxifan ( $1.7 \pm 0.1$  nmol/mg/5 min;  $P = 0.96$ ; Tukey's post hoc test; Table 1). DL-TBOA (10  $\mu$ M), a non-selective inhibitor of all excitatory amino acid transporter subtypes, increased the 4-AP-evoked glutamate release (because of inhibition of reuptake of released glutamate) [ $10.1 \pm 0.6$  nmol/mg/5 min;  $t(8) = -4.51$ ;  $P = 0.001$ ]. In the presence of DL-TBOA, ciproxifan (30  $\mu$ M) induced a 32% decrease in glutamate release evoked by 4-AP [ $6.9 \pm 0.5$  nmol/mg/5 min;  $F(2,11) = 13.7$ ;  $P = 0.001$ ; Table 1]. By contrast, bafilomycin A1 (0.1  $\mu$ M), a vesicular transporter inhibitor, inhibited the 4-AP-evoked glutamate release by 72% [ $2.0 \pm 0.2$  nmol/mg/5 min;  $F(2,14) = 129.4$ ;  $P = 0.000$ ]. The subsequent application of 30  $\mu$ M ciproxifan inhibited this release by 5% [ $1.9 \pm 0.2$  nmol/mg/5 min; Table 1] versus the 38% inhibition obtained without bafilomycin A1 ( $t(9) = 3.4$ ;  $P < 0.05$ ). These results indicate that ciproxifan influences the release of glutamate induced by a decrease in vesicular exocytosis.

### 3.3. Ciproxifan reduces the 4-AP-evoked increase in [Ca<sup>2+</sup>]<sub>i</sub> but fails to alter the synaptosomal membrane potential

Table 2 shows the [Ca<sup>2+</sup>]<sub>i</sub> levels determined in synaptosomes pretreated with fura-2. The stimulation of synaptosomes with 1 mM 4-AP caused an increase in [Ca<sup>2+</sup>]<sub>i</sub> levels to a plateau level ( $t(8) = -69.8$ ;  $P = 0.000$ ). Preincubation with ciproxifan (30  $\mu$ M) for 10 min before 4-AP addition did not significantly affect basal Ca levels but reduced the 4-AP-evoked [Ca<sup>2+</sup>]<sub>i</sub> increase by 20% [ $t(8) = 11.1$ ,  $P = 0.000$ ]. Table 2 also shows the effect of ciproxifan on the synaptosomal plasma membrane potential. The synaptosomal membrane potential can be monitored by positively charged membrane potential-sensitive cationic cyanide dye DiSC<sub>3</sub>(5). 4-AP (1 mM) application caused an increase in DiSC<sub>3</sub>(5) fluorescence. Preincubation with ciproxifan (30  $\mu$ M) for 10 min before 4-AP addition did not alter the resting membrane potential, and had no significant effect on the 4-AP-

mediated increase in DiSC<sub>3</sub>(5) fluorescence [ $t(8) = 0.21$ ,  $P = 0.84$ ; Table 2].

### 3.4. Decrease in voltage-dependent Ca<sup>2+</sup> influx appears to be associated with the observed ciproxifan-mediated inhibition of glutamate release

Table 3 shows that  $\omega$ -conotoxin MVIIC ( $\omega$ -CgTX MVIIC; 2  $\mu$ M), a wide-spectrum blocker of Ca<sub>v</sub>2.2 (N-type) and Ca<sub>v</sub>2.1 (P/Q-type) channels, reduced the 4-AP-evoked glutamate release by 66%, from  $7.1 \pm 0.1$  under control conditions to  $2.4 \pm 0.1$  nmol/mg/5 min [ $F(2,15) = 560.1$ ;  $P = 0.000$ ]. In the presence of  $\omega$ -CgTX MVIIC, ciproxifan (30  $\mu$ M) reduced the 4-AP-evoked glutamate release by only 4% ( $2.3 \pm 0.1$  nmol/mg/5 min), which was significantly less than the inhibition induced by ciproxifan alone (34%,  $t(10) = -4.88$ ,  $P < 0.05$ ). Dantrolene (100  $\mu$ M), a blocker of Ca<sup>2+</sup> release from endoplasmic reticulum ryanodine receptors, and CGP37157, a membrane-permeant blocker of the mitochondrial Na<sup>+</sup>/Ca<sup>2+</sup> exchanger, reduced the 4-AP (1 mM)-evoked glutamate release by 32% [ $4.8 \pm 0.2$  nmol/mg/5 min;  $F(2,13) = 120.55$ ;  $P = 0.000$ ] and 34% [ $4.7 \pm 0.2$  nmol/mg/5 min;  $F(2,18) = 228.5$ ;  $P = 0.000$ ], respectively. In the presence of dantrolene or CGP37157, ciproxifan (30  $\mu$ M) was still able to reduce glutamate release by 34% or 35%, respectively ( $P = 0.000$ ; Table 3), which was not significantly different from the inhibition produced by ciproxifan alone (38%; dantrolene,  $t(9) = -1.61$ ,  $P > 0.05$ ; CGP37157,  $t(11) = -1.96$ ,  $P > 0.05$ ).

### 3.5. The ciproxifan-mediated inhibition of 4-AP-evoked glutamate release is mediated by pertussis toxin-sensitive G protein and suppression of the PLA<sub>2</sub>/AA/PGE<sub>2</sub>/EP<sub>2</sub> signaling cascade

The H<sub>3</sub> receptor is a GPCR; therefore, we examined the signal transduction mechanism underlying the ciproxifan-mediated inhibition of glutamate release through H<sub>3</sub> receptor blockade. As shown in Table 4, synaptosomes were incubated for 4 h with pertussis toxin (PTX; 2  $\mu$ g/mL), a Gi/Go-protein inhibitor, which did not significantly alter the 4-AP (1 mM)-evoked glutamate release [ $F(2,12) = 1.99$ ;  $P = 0.18$ ]. In the PTX-treated synaptosomes, ciproxifan (30  $\mu$ M) resulted in a 5% inhibition of the 4-AP-evoked glutamate release, which was significantly different from the inhibition produced by ciproxifan alone (38%;  $t(10) = -11.2$ ,  $P < 0.05$ ). Interestingly, the phospholipase A<sub>2</sub> (PLA<sub>2</sub>) inhibitor OBAA (50  $\mu$ M) reduced 4-AP (1 mM)-evoked glutamate release and prevented the ciproxifan-mediated inhibition of

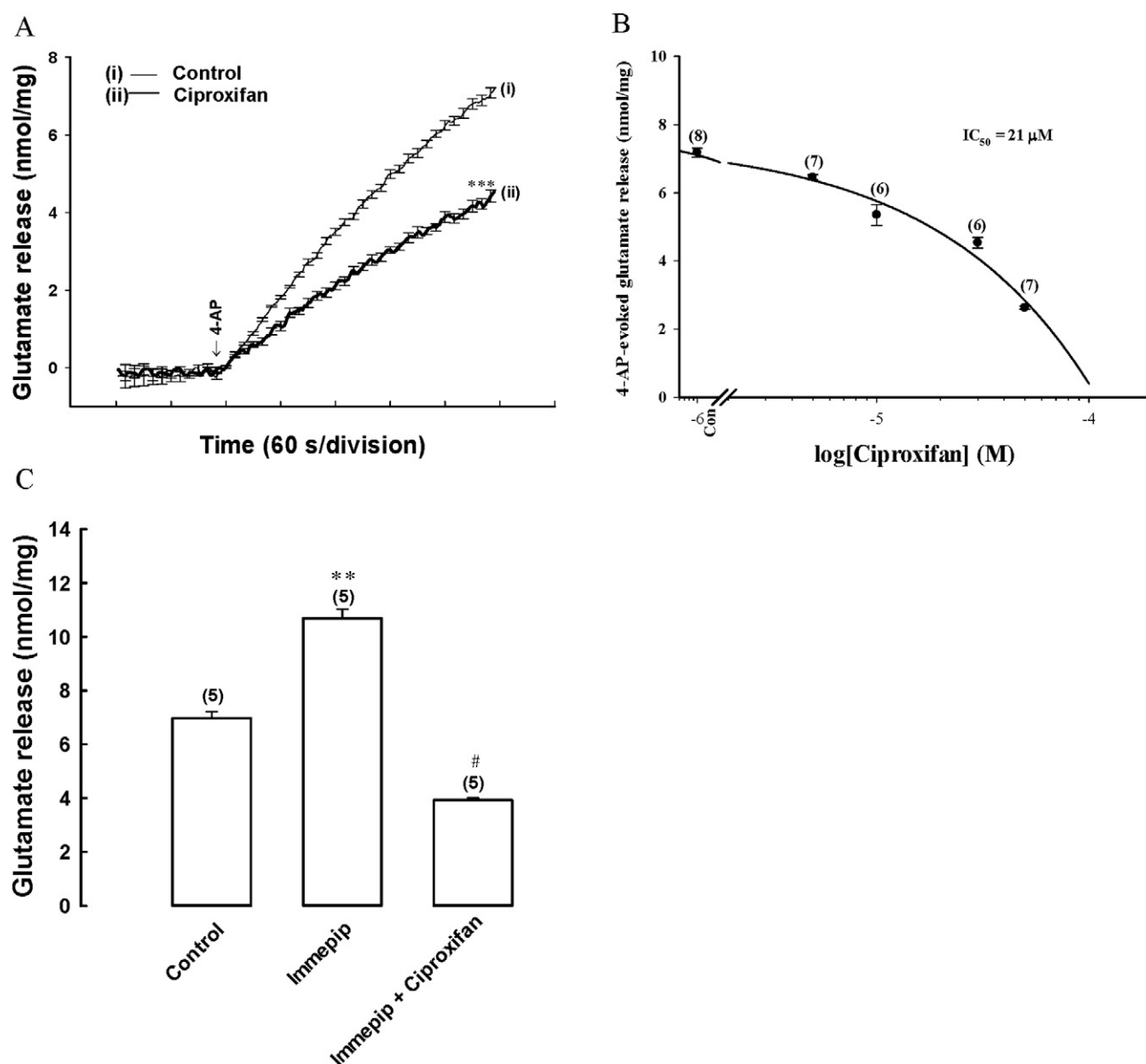


**Fig. 2.** Blockade of  $H_3$  receptors by ciproxifan inhibits the 4-AP-evoked glutamate release from hippocampal synaptosomes. (A) Glutamate release was evoked by 4-AP (1 mM) in the absence (control) or presence of 30  $\mu$ M ciproxifan, added 10 min before stimulation. (B) The log dose–response curve for ciproxifan inhibition of 4-AP-evoked glutamate release. (C) The facilitatory effect of  $H_3$  receptor agonist imnepip (30  $\mu$ M) on 4-AP-evoked glutamate release was completely blocked by ciproxifan (30  $\mu$ M). Data represent mean  $\pm$  SEM of independent experiments carried out with individual synaptosomal preparations from the indicated number of animals (n). \*\*\*  $P < 0.001$  versus control (two-tailed Student's  $t$ -test).

**Table 1**  
Effect of  $Ca^{2+}$  chelation, DL-TBOA, and bafilomycin A1 on the inhibition of 4-AP-evoked glutamate release by ciproxifan.

	4-AP-evoked glutamate release (nmol/mg/5 min)	n
Control	6.8 $\pm$ 0.2	5
Ciproxifan	3.9 $\pm$ 0.3***	5
$Ca^{2+}$ -free medium + EGTA	1.8 $\pm$ 0.1***	5
$Ca^{2+}$ -free medium + EGTA + Ciproxifan	1.8 $\pm$ 0.1***	5
DL-TBOA	10.1 $\pm$ 0.6***	5
DL-TBOA + Ciproxifan	6.9 $\pm$ 0.5*	5
Bafilomycin A1	2.0 $\pm$ 0.2***	6
Bafilomycin A1 + Ciproxifan	2.3 $\pm$ 0.3***	6

Data represent mean  $\pm$  SEM of independent experiments carried out with individual synaptosomal preparations from the indicated number of animals (n).

\*\*\*  $P < 0.001$  versus control (two-tailed Student's  $t$ -test).

#  $P < 0.05$  versus the DL-TBOA-treated group (one-way ANOVA).

glutamate release [ $F(2,14) = 4.23$ ;  $P = 0.03$ ; Table 4]. In the six tested synaptosomal preparations, no statistical difference was observed between the glutamate release after OBAA alone and after the OBAA and ciproxifan treatment ( $P = 0.89$ ; Tukey's post hoc test). In addition,

**Table 2**  
Effect of ciproxifan on synaptosomal membrane potential and cytosolic  $Ca^{2+}$  levels from rat cortical synaptosomes.

	Membrane potential (fluorescence units)			Cytosolic [ $Ca^{2+}$ ] (nM)		
	Basal	4-AP (1 mM)	n	Basal	4-AP (1 mM)	n
Control	5.9 $\pm$ 0.5	14.1 $\pm$ 1.0	5	178.4 $\pm$ 4.2	250.2 $\pm$ 4.1	5
Ciproxifan	5.7 $\pm$ 0.5	13.8 $\pm$ 1.0	5	182.1 $\pm$ 2.5	199.4 $\pm$ 4.2***	5

Data represent mean  $\pm$  SEM of independent experiments carried out with individual synaptosomal preparations from the indicated number of animals (n).

\*\*\*  $P < 0.001$  versus control (two-tailed Student's  $t$ -test).

**Table 3**

Effect of  $\omega$ -CgTX MVIIC, dantrolene, and CGP37157 on the ciproxifan-mediated inhibition of 4-AP-evoked glutamate release.

	4-AP-evoked glutamate release (nmol/mg/5 min)	n
Control	7.1 $\pm$ 0.1	6
Ciproxifan	3.9 $\pm$ 0.3***	6
$\omega$ -CgTX MVIIC	2.4 $\pm$ 0.1***	6
$\omega$ -CgTX MVIIC + ciproxifan	2.3 $\pm$ 0.1***	6
Dantrolene	4.8 $\pm$ 0.2***	5
Dantrolene + ciproxifan	3.4 $\pm$ 0.1***,#	5
CGP3715	4.7 $\pm$ 0.1***	6
CGP3715 + ciproxifan	3.0 $\pm$ 0.1***,#	7

Data represent mean  $\pm$  SEM of independent experiments carried out with individual synaptosomal preparations from the indicated number of animals (n).

\*\*\*  $P < 0.001$  versus control (two-tailed Student's *t*-test).

#  $P < 0.05$  versus the dantrolene- or CGP37157-treated group (one-way ANOVA).

arachidonic acid (AA, 50  $\mu$ M) and prostaglandin E<sub>2</sub> (PGE<sub>2</sub>, 5  $\mu$ M) enhanced the 4-AP-evoked glutamate release [AA,  $F(2,14) = 50.6$ ,  $P = 0.000$ ; PGE<sub>2</sub>,  $F(2,14) = 32.2$ ;  $P = 0.000$ ]. However, in the AA- or PGE<sub>2</sub>-treated synaptosomes, ciproxifan (30  $\mu$ M) failed to produce a significant inhibition of the 4-AP-evoked glutamate release (AA,  $P = 0.16$ ; PGE<sub>2</sub>,  $P = 0.86$ ; Tukey's post hoc test; Table 4). Furthermore, the PGE<sub>2</sub> subtype 2 receptor (EP2) antagonist PF04418948 (100  $\mu$ M) reduced the 4-AP-evoked glutamate release and completely prevented the effect of ciproxifan [ $F(2,14) = 89.1$ ,  $P = 0.000$ ; Table 4]. No statistical difference was observed between the glutamate release after PF04418948 alone and after the PF04418948 and ciproxifan treatment ( $P = 0.68$ ; Tukey's post hoc test).

### 3.6. Decreased extracellular signal-regulated kinase and synapsin I activity is involved in the ciproxifan-mediated inhibition of 4-AP-evoked glutamate release

Table 5 shows that the mitogen-activated protein kinase (MAPK) inhibitor PD98059 (50  $\mu$ M) reduced the 4-AP (1 mM)-evoked glutamate release and prevented the inhibition of glutamate release by ciproxifan [ $F(2,12) = 142.78$ ;  $P = 0.000$ ]. In the five tested synaptosomes, no statistical difference was observed between the release after PD98059 alone and after the PD98059 and ciproxifan treatment ( $P = 0.61$ ; Tukey's post hoc test). A similar result was also obtained using FR180204 (10  $\mu$ M), a selective extracellular signal-regulated kinase (ERK) inhibitor [ $F(2,16) = 37.21$ ;  $P = 0.000$ ; Table 5]. Fig. 3A shows the effect of ciproxifan on ERK1/2 phosphorylation in hippocampal synaptosomes. The depolarization of synaptosomes with 1 mM 4-AP in the presence of 1.2 mM CaCl<sub>2</sub> increased the phosphorylation of ERK1/2

**Table 4**

Effect of PTX, OBAA, AA, PGE<sub>2</sub>, and PF04418948 on the inhibition of 4-AP-evoked glutamate release by ciproxifan.

	4-AP-evoked glutamate release (nmol/mg/5 min)	n
Control	6.7 $\pm$ 0.2	5
Ciproxifan	4.2 $\pm$ 0.1***	5
PTX	6.5 $\pm$ 0.2	5
PTX + ciproxifan	6.2 $\pm$ 0.1	5
OBAA	5.9 $\pm$ 0.2**	6
OBAA + ciproxifan	5.8 $\pm$ 0.2**	6
AA	10.1 $\pm$ 0.2***	6
AA + ciproxifan	9.4 $\pm$ 0.2***	6
PGE <sub>2</sub>	9.5 $\pm$ 0.2***	6
PGE <sub>2</sub> + ciproxifan	9.3 $\pm$ 0.3***	6
PF04418948	3.1 $\pm$ 0.2***	6
PF04418948 + ciproxifan	2.8 $\pm$ 0.3***	6

Data represent mean  $\pm$  SEM of independent experiments carried out with individual synaptosomal preparations from the indicated number of animals (n).

\*\*\*  $P < 0.001$ .

\*\*  $P < 0.01$  versus control (two-tailed Student's *t*-test).

**Table 5**

Effect of PD98059 and FR180204 on the inhibition of 4-AP-evoked glutamate release by ciproxifan.

	4-AP-evoked glutamate release (nmol/mg/5 min)	n
Control	6.7 $\pm$ 0.2	5
Ciproxifan	4.2 $\pm$ 0.1***	6
PD98059	2.6 $\pm$ 0.3***	5
PD98059 + ciproxifan	2.3 $\pm$ 0.2***	5
FR180204	2.5 $\pm$ 0.4***	5
FR180204 + ciproxifan	2.3 $\pm$ 0.4***	5

Data represent mean  $\pm$  SEM of independent experiments carried out with individual synaptosomal preparations from the indicated number of animals (n).

\*\*\*  $P < 0.001$  versus control (two-tailed Student's *t*-test).

( $t(6) = -7.3$ ;  $P = 0.000$ ). Preincubation with ciproxifan (30  $\mu$ M) for 10 min before 4-AP addition reduced the 4-AP-evoked ERK1/2 phosphorylation [ $F(2,9) = 42.26$ ;  $P = 0.000$ ]. We also determined the effect of ciproxifan on the phosphorylation of synaptic vesicle-associated protein synapsin I, which is the major presynaptic substrate for MAPK/ERK (Jovanovic et al., 1996). Similar to ERK1/2 phosphorylation, 4-AP (1 mM) increased synapsin I phosphorylation ( $t(6) = -20.6$ ;  $P = 0.000$ ), and ciproxifan pretreatment blocked the response [ $F(2,9) = 23.2$ ;  $P = 0.000$ ; Fig. 3B].

### 3.7. Ciproxifan-mediated inhibition of 4-AP-evoked glutamate release is attenuated in synaptosomes from synapsin I-deficient mice

Fig. 4 shows the effect of ciproxifan on the 4-AP-evoked glutamate release in synaptosomes derived from wild-type and synapsin I-deficient mice. In the absence of ciproxifan (30  $\mu$ M), 4-AP (1 mM)-evoked glutamate release was decreased in the synapsin I-deficient mutant mice ( $2.8 \pm 0.2$  nmol/mg/5 min) compared with that in wild-type mice [ $5.2 \pm 0.3$  nmol/mg/5 min;  $t(9) = 6.86$ ;  $P = 0.000$ ]. In wild-type mice, ciproxifan (30  $\mu$ M) caused an inhibition of the 4-AP-evoked glutamate release [ $2.6 \pm 0.3$  nmol/mg/5 min; 50%;  $t(8) = 8.1$ ;  $P = 0.000$ ]. By contrast, ciproxifan did not significantly inhibit the 4-AP-evoked glutamate release in synapsin I-deficient mice ( $2.7 \pm 0.1$  nmol/mg/5 min;  $t(10) = 0.2$ ;  $P = 0.84$ ).

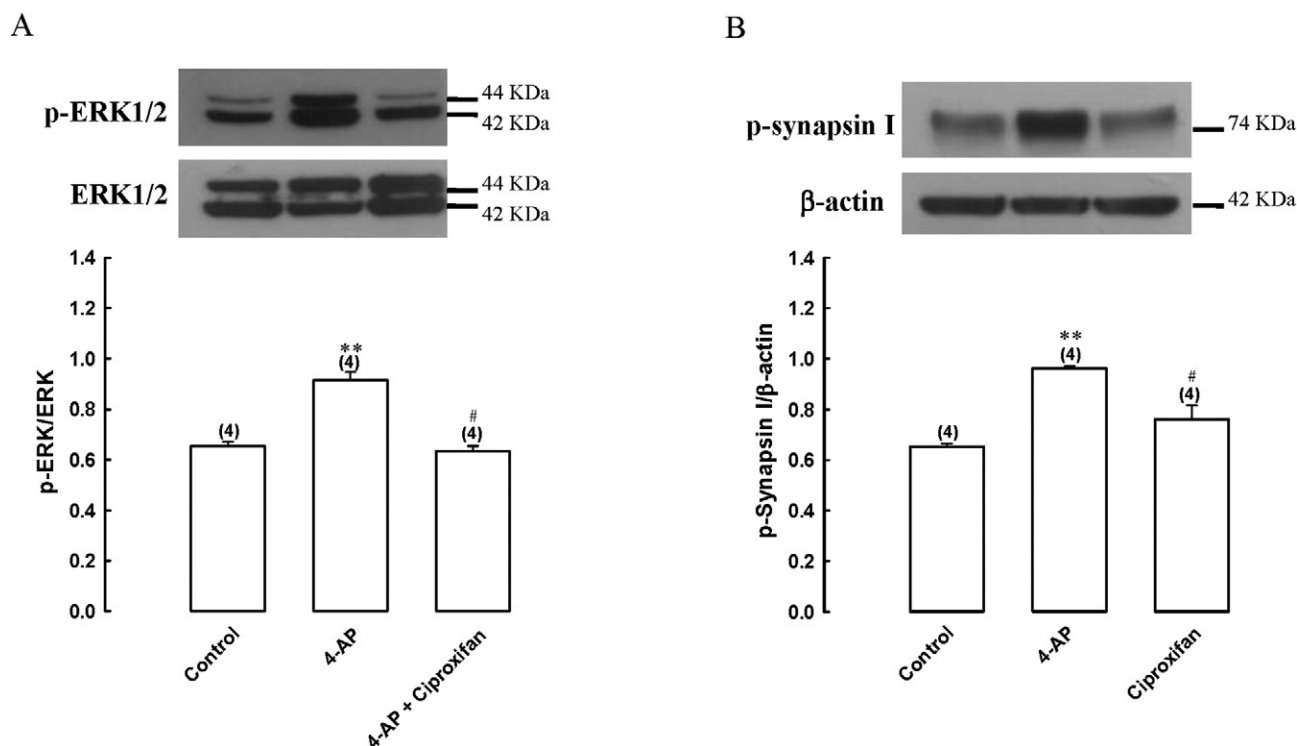
### 3.8. Ciproxifan reduces the frequency but not the amplitude of miniature excitatory postsynaptic currents (mEPSCs) in hippocampal slices

Fig. 5 shows the effects of ciproxifan on mEPSC frequency and amplitude in hippocampal slices; mEPSCs were recorded at a holding potential of  $-70$  mV and in the presence of the Na<sup>+</sup> channel blocker tetrodotoxin (TTX, 1  $\mu$ M) and GABA<sub>A</sub> receptor antagonist bicuculline (20  $\mu$ M). Fig. 5A shows a typical example of traces recorded from a signal cell, and ciproxifan (30  $\mu$ M) reduced the occurrence of mEPSCs. In the five tested neurons, ciproxifan reduced the frequency of mEPSCs by  $60.5\% \pm 5.8\%$  [ $t(8) = 3.68$ ;  $P = 0.006$ ; Fig. 5B], but the amplitude was unaffected [ $t(8) = 1.34$ ;  $P = 0.22$ ; Fig. 5C].

## 4. Discussion

The involvement of H<sub>3</sub> receptors in the modulation of neurotransmitter release has been demonstrated in neurons from several regions of the central nervous system (CNS) by using different experimental approaches involving brain slices (Arias-Montaña et al., 2001) and synaptosomes (Aquino-Miranda et al., 2016). The major finding of this study is that H<sub>3</sub> receptors are present in isolated hippocampal nerve terminals because they are colocalized with the presynaptic marker synaptophysin. The blockade of these receptors by ciproxifan causes the inhibition of the Ca<sup>2+</sup>-dependent, depolarization-evoked, exocytotic-like release of glutamate. Therefore, our data suggest the existence of presynaptic H<sub>3</sub> receptors functioning to facilitate glutamate release from hippocampal nerve terminals. This finding is supported by the





**Fig. 3.** Ciproxifan decreases the 4-AP-evoked phosphorylation of ERK and synapsin I, a presynaptic target of ERK, in synaptosomes. Phosphorylation of ERK (A) and synapsin I at MAPK-specific sites 4, 5 (P-SYN I site 4, 5) (B) was detected in the absence (control) or presence of 1 mM 4-AP, or 1 mM 4-AP and 30  $\mu$ M ciproxifan. Each column is mean  $\pm$  SEM of independent experiments carried out with individual synaptosomal preparations from the indicated number of animals (n). \*\*\*  $P < 0.001$  versus control (two-tailed Student's *t*-test). #,  $P < 0.05$  versus the 4AP-treated group (one-way ANOVA).

observation that the activation of  $H_3$  receptor by immpip increased the 4-AP-evoked glutamate release from synaptosomes. However, this observation is inconsistent with previous studies, which have reported that  $H_3$  receptor activation reduces depolarization-evoked dopamine release in mouse striatal slices and rat olfactory bulb slices (Aquino-Miranda et al., 2012; Schlicker et al., 1993). The reason for these discrepant results regarding the effects of  $H_3$  receptors on neurotransmitter levels is presently unclear. Nevertheless, this study is the

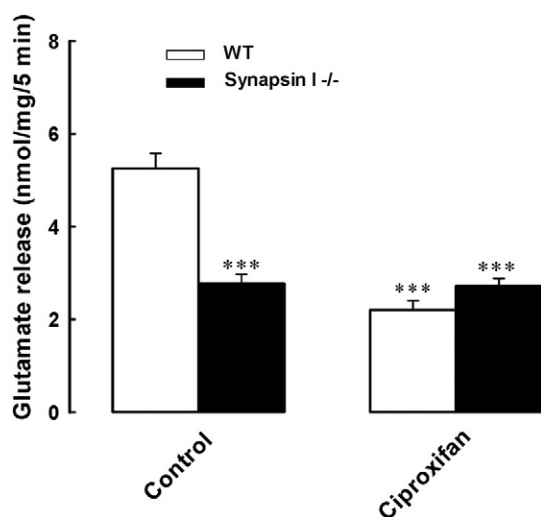


**Fig. 4.** Ciproxifan-mediated inhibition of glutamate release is attenuated in synaptosomes from synapsin I-deficient mice. Glutamate release was evoked by 4-AP (1 mM) in the absence (control) or presence of 30  $\mu$ M ciproxifan in synaptosomes from wild-type (WT) and synapsin I-deficient (SYN I<sup>-/-</sup>) mice. Each column is mean  $\pm$  SEM of independent experiments carried out with individual synaptosomal preparations from the indicated number of animals (n). \*\*\*  $P < 0.001$  versus WT control (two-tailed Student's *t*-test).

first to present the effect of  $H_3$  receptor blockade on presynaptic glutamate release.

Glutamate exocytosis from mammalian CNS nerve terminals is dependent on localized  $Ca^{2+}$  influx, chiefly through the  $Ca_v2.2$  (N-type) and  $Ca_v2.1$  (P/Q-type)  $Ca^{2+}$  channels (Millan and Sanchez-Prieto, 2002; Vazquez and Sanchez-Prieto, 1997). In synaptic terminals,  $Na^+$  channel inhibition or  $K^+$  channel activation stabilizes membrane excitability, which causes a subsequent decrease in the voltage-dependent  $Ca^{2+}$  entry and a consequent reduction in glutamate release (Nicholls, 1998; Wu and Saggau, 1997). We used fura-2 and demonstrated that ciproxifan significantly reduced the evoked increase in intrasynaptosomal  $Ca^{2+}$  levels. The inhibitory effect of ciproxifan on 4-AP-evoked glutamate release from synaptosomes was prevented by  $\omega$ -CgTX MVIIC but was not altered by dantrolene and CGP37157. Therefore, these data demonstrate that a  $Ca_v2.2$  (N-type) and  $Ca_v2.1$  (P/Q-type) channel-mediated decrease of synaptosomal  $Ca^{2+}$  is instrumental for the ciproxifan-mediated inhibition of glutamate release, whereas decreased intracellular  $Ca^{2+}$  release appears not be involved. In addition, our findings demonstrate that the inhibition of voltage-dependent  $Ca^{2+}$  channels and glutamate release by ciproxifan is not caused by a change in synaptosomal excitability because the synaptosomal plasma membrane potential, measured with a DiSC<sub>3</sub>(5) dye, was unaffected by ciproxifan. Moreover, ciproxifan did not significantly inhibit the 4-AP-evoked  $Ca^{2+}$ -independent glutamate release, a component of glutamate release that is exclusively dependent on membrane potential (Attwell et al., 1993; Nicholls et al., 1987).

It was unclear how the blockade of  $H_3$  receptors by ciproxifan inhibits presynaptic  $Ca^{2+}$  channels and glutamate release from hippocampal nerve terminals. Presynaptic  $H_3$  receptors are GPCRs with diverse intracellular signaling, which including the inhibition of adenylate cyclase, activation of  $PLA_2$  and MAPK, and mobilization of intracellular  $Ca^{2+}$  levels (Bhowmik et al., 2012). In the present study, ciproxifan, acting through a PTX-sensitive G protein-coupled  $H_3$  receptor, inhibits glutamate release from nerve terminals by reducing voltage-dependent  $Ca^{2+}$  entry via a signaling cascade involving the  $PLA_2/AA/PGE_2/EP_2$



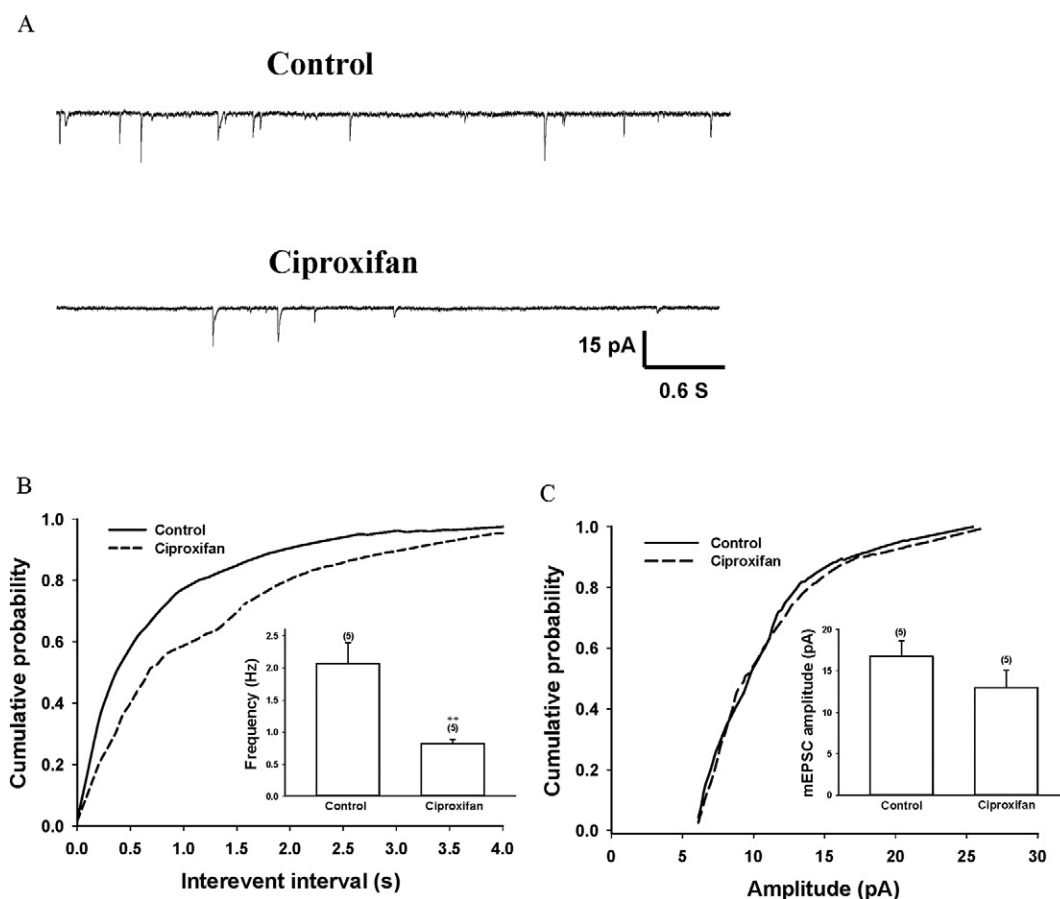


**Fig. 5.** Ciproxifan decreases the frequency but not the amplitude of mEPSCs in the hippocampal brain slices. (A) Sample trace of mEPSCs in the absence (control) or presence of 30  $\mu$ M ciproxifan. (B) Cumulative plot of interevent interval of mEPSCs. (C) Cumulative plot of amplitude of mEPSCs. Inset: The average amplitude and frequency of mEPSCs in the control and ciproxifan treated groups. Each column is mean  $\pm$  SEM of independent experiments carried out with individual synaptosomal preparations from the indicated number of animals (n). \*\*\*  $P < 0.001$  versus control (two-tailed Student's *t*-test).

receptor. Several lines of evidence support this notion. First, the inhibition of Gi/Go-protein by PTX completely blocked the ciproxifan-mediated inhibition of 4-AP-evoked glutamate release. Second, ciproxifan fails to inhibit the release of glutamate evoked by 4-AP in the presence of the PLA<sub>2</sub> inhibitor. Third, AA and PGE<sub>2</sub> increase 4-AP-evoked glutamate release and abrogate the ciproxifan-mediated inhibition of glutamate release. Finally, the inhibitory effect of ciproxifan on 4-AP-evoked glutamate release is antagonized by the EP<sub>2</sub> receptor antagonist PF04418948. In fact, PLA<sub>2</sub> activation, AA and PGE<sub>2</sub> production, and EP<sub>2</sub> receptor activation have been reported to enhance glutamate release from hippocampal nerve terminals (Damron and Dorman, 1993; Nishihara et al., 1995; Sang et al., 2005; Wang, 2006). Considering that H<sub>3</sub> receptor activation results in PLA<sub>2</sub> activation (Bhowmik et al., 2012), the blockade of H<sub>3</sub> receptor by ciproxifan may inhibit the PLA<sub>2</sub> activity, causing a decrease in AA and PGE<sub>2</sub> levels, which, by attenuating EP<sub>2</sub> receptor activation, may subsequently reduce Ca<sup>2+</sup> influx and glutamate release.

GPCR activation and depolarization-stimulated Ca<sup>2+</sup> entry can induce ERK activation (Copik et al., 2015; Eishindrolo and Kongsamut, 2013). ERK is capable to phosphorylating the synaptic vesicle protein synapsin I, thereby promoting the dissociation of synaptic vesicles from the actin cytoskeleton. This subsequently increases the availability of vesicles at the active zone for neurotransmitter exocytosis, resulting in increased glutamate release (Jovanovic et al., 1996; Schenk et al., 2005; Yamagata et al., 2002). Therefore, we assumed that the reduction of ciproxifan on Ca<sup>2+</sup> entry observed here suppresses ERK-dependent synapsin I phosphorylation and the consequent decreased availability of synaptic vesicles and, subsequently, glutamate release. Indeed, we found that ciproxifan decreased the 4-AP-evoked phosphorylation of

ERK and synapsin I, and the inhibitory effect of ciproxifan on the 4-AP-evoked glutamate release was prevented by the MAPK inhibitor PD98059 and ERK inhibitor FR180204. Moreover, a crucial finding is that the ciproxifan-mediated inhibition of the 4-AP-evoked glutamate release was attenuated by the genetic deletion of synapsin I. Therefore, the present results suggest that antagonism of H<sub>3</sub> receptors by ciproxifan reduces the Ca<sup>2+</sup> influx through N- and P/Q-type Ca<sup>2+</sup> channels by suppressing the Gi/Go-protein/PLA<sub>2</sub>/PGE<sub>2</sub>/EP<sub>2</sub> pathway, which subsequently reduces the ERK/SYN I phosphorylation to inhibit the evoked glutamate release from rat hippocampal nerve terminals (Fig. 6).

We used a whole-cell voltage clamp recording to examine the effect of ciproxifan on mEPSCs in rat hippocampal slices. The data demonstrated that ciproxifan significantly decreased the frequency of mEPSCs but did not affect the amplitude of mEPSCs. A decrease in the frequency of mEPSCs is typically interpreted to be due to a presynaptic action (e.g., a reduction in the probability of neurotransmitter release or number of quanta available for release), whereas a decrease in the amplitude of mEPSCs typically indicates a reduction in the postsynaptic sensitivity to the transmitter (Malgoli and Tsien, 1992; Manabe et al., 1992). Accordingly, the results suggest that ciproxifan presynaptically acted to inhibit glutamate release without changing the postsynaptic sensitivity to glutamate, which supports our synaptosomal findings.

H<sub>3</sub> receptor antagonists have been investigated considering several dimensions of animal behaviors for antipsychotic-like activities; pre-clinical studies have reported antipsychotic effects of H<sub>3</sub> receptor antagonists, suggesting these antagonists to be a novel class of antipsychotic agents (Fox et al., 2005; Ligneau et al., 2007; Mahmood et al., 2012; Southam et al., 2009). High glutamate levels have been reported in patients with schizophrenia (de la Fuente-Sandoval et al.,

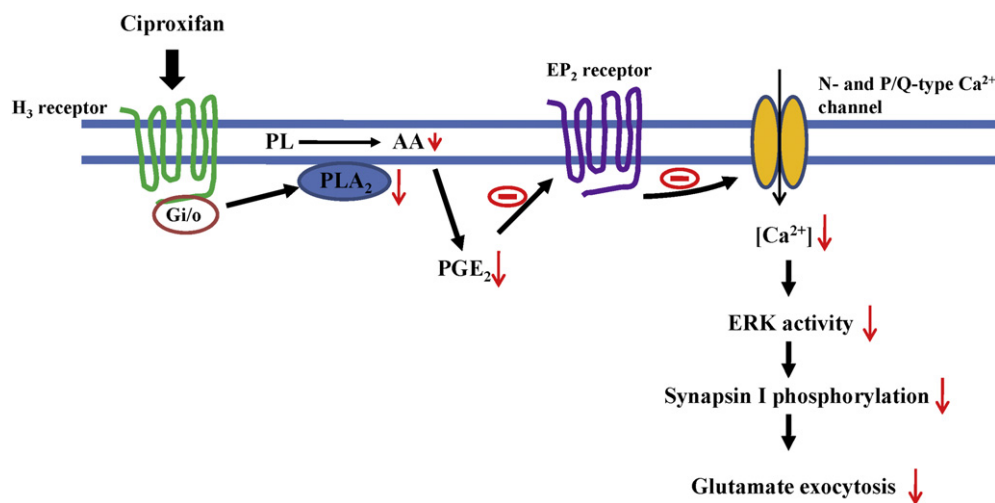


**Fig. 6.** Schematic representation of the pathway involved in the ciproxifan-mediated inhibition of evoked glutamate release from rat hippocampal nerve terminals. Ciproxifan, acting through a PTX-sensitive G protein-coupled  $H_3$  receptor, suppresses the  $PLA_2$  activity, causing a decrease in AA and  $PGE_2$  production. This, in turn, reduces the  $EP_2$  receptor activation and  $Ca^{2+}$  influx through N- and P/Q-type  $Ca^{2+}$  channels, which subsequently suppresses the ERK/synapsin I cascade to decrease the evoked glutamate release.

2013; Kegeles et al., 2012; Marsman et al., 2013). Abnormally high levels of glutamate are associated with neuronal death and neurobehavioural impairments in patients with schizophrenia (de Bartolomeis et al., 2012; Plitman et al., 2014). Drugs targeting the glutamate system have the potential to alleviate schizophrenia. The present study demonstrates that the  $H_3$  receptor antagonist ciproxifan reduces depolarization-evoked glutamate release from hippocampal synaptosomes. This result is in concordance with previous studies showing similar effects on the glutamatergic transmission of numerous antipsychotic drugs (Carli et al., 2011; Yamamura et al., 2009; Yang and Wang, 2008). On the basis of the aforementioned findings, we suggest that reduced glutamate release from nerve terminals is at least partially involved in the antipsychotic activity of ciproxifan. Notably, in the current study, ciproxifan produced a blockade of glutamate release in the absence of any added agonist. Therefore, this may indicate the effective use of  $H_3$  receptor antagonists as inverse agonists to inhibit the activated states of  $H_3$  receptors in nerve terminals. Supporting this hypothesis, native  $H_3$  receptors in the brain display a high constitutive activity that is abrogated by ciproxifan acting as an inverse agonist (Morisset et al., 2000; Rouleau et al., 2002).

In conclusion, our results show that ciproxifan reduces endogenous glutamate release from hippocampal nerve terminals, thus contributing to knowledge on the presynaptic  $H_3$  receptor modulation of excitatory transmission in the hippocampus and providing the rationale for using selective  $H_3$  receptor antagonists to treat schizophrenia and other pathological conditions associated with excessive glutamatergic neurotransmission.

#### Transparency document

The Transparency document associated with this article can be found, in online version.

#### Authorship contributions

Tzu-Yu Lin and Su-Jane Wang conceived and designed the experiments; Cheng-Wei Lu and Chia-Ying Chang performed the experiments; Cheng-Wei Lu and Shu-Kuei Huang analyzed the data; Su-Jane Wang wrote the manuscript.

#### Conflicts of interest

The authors declare there are no conflicts of interest.

#### Acknowledgements

This work was supported by the Ministry of Science and Technology [MOST 103-2314-B-418-006].

#### References

- Akerman, K.E., Scott, I.G., Heikkilä, J.E., Heinonen, E., 1987. Ionic dependence of membrane potential and glutamate receptor-linked responses in synaptosomes as measured with a cyanine dye, DiSC<sub>2</sub>(5). *J. Neurochem.* 48, 552–559.
- Aquino-Miranda, G., Osorio-Espinoza, A., Escamilla-Sánchez, J., González-Pantoja, R., Ortiz, J., Arias-Montaña, J.A., 2012. Histamine  $H_3$  receptors modulate depolarization-evoked [ $^3H$ ]-noradrenaline release from rat olfactory bulb slices. *Neuropharmacology* 62, 1127–1133.
- Aquino-Miranda, G., Escamilla-Sánchez, J., González-Pantoja, R., Bueno-Nava, A., Arias-Montaña, J.A., 2016. Histamine  $H_3$  receptor activation inhibits dopamine synthesis but not release or uptake in rat nucleus accumbens. *Neuropharmacology* 106, 91–101.
- Arias-Montaña, J.A., Floran, B., García, M., Aceves, J., Young, J.M., 2001. Histamine  $H_3$  receptor-mediated inhibition of depolarization-induced, dopamine  $D_1$  receptor-dependent release of [ $^3H$ ]-gamma-aminobutyric acid from rat striatal slices. *Br. J. Pharmacol.* 133, 165–171.
- Attwell, D., Barbour, B., Szatkowski, M., 1993. Nonvesicular release of neurotransmitter. *Neuron* 375, 645–653.
- Bhowmik, M., Khanam, R., Vohora, D., 2012. Histamine  $H_3$  receptor antagonists in relation to epilepsy and neurodegeneration: a systemic consideration of recent progress and perspectives. *Br. J. Pharmacol.* 167, 1398–1414.
- Carli, M., Calcagno, E., Mainolfi, P., Mainini, E., Invernizzi, R.W., 2011. Effects of aripiprazole, olanzapine, and haloperidol in a model of cognitive deficit of schizophrenia in rats: relationship with glutamate release in the medial prefrontal cortex. *Psychopharmacology* 214, 639–652.
- Chang, C.Y., Lin, T.Y., Lu, C.W., Wang, C.C., Wang, Y.C., Chou, S.S., Wang, S.J., 2015. Apigenin, a natural flavonoid, inhibits glutamate release in the rat hippocampus. *Eur. J. Pharmacol.* 762, 72–81.
- Chang, Y., Lin, T.Y., Lu, C.W., Huang, S.K., Wang, Y.C., Wang, S.J., 2016. Xanthohumol-induced presynaptic reduction of glutamate release in the rat hippocampus. *Food Funct.* 7, 212–226.
- Copik, A.J., Baldys, A., Nguyen, K., Sahdeo, S., Ho, H., Kosaka, A., Dietrich, P.J., Fitch, B., Raymond, J.R., Ford, A.P., et al., 2015. Isoproterenol acts as a biased agonist of the  $\alpha_1A$ -adrenoceptor that selectively activates the MAPK/ERK pathway. *PLoS One* 10, e0115701.
- Coyle, J.T., 2006. Glutamate and schizophrenia: beyond the dopamine hypothesis. *Cell. Mol. Neurobiol.* 26, 365–384.
- Damron, D.S., Dorman, R.V., 1993. Involvement of phospholipase A2 and arachidonic acid in the depolarization-evoked accumulation of  $Ca^{2+}$  in hippocampal mossy fiber nerve endings. *Neurochem. Res.* 18, 1231–1237.
- de Bartolomeis, A., Sarappa, C., Magara, S., Iasevoli, F., 2012. Targeting glutamate system for novel antipsychotic approaches: relevance for residual psychotic symptoms and treatment resistant schizophrenia. *Eur. J. Pharmacol.* 682, 1–11.
- de la Fuente-Sandoval, C., León-Ortiz, P., Azcárraga, M., Stephano, S., Favila, R., Díaz-Galvis, L., Alvarado-Alanis, P., Ramírez-Bermúdez, J., Graff-Guerrero, A., 2013. Glutamate levels in the associative striatum before and after 4 weeks of antipsychotic treatment in first-episode psychosis: a longitudinal proton magnetic resonance spectroscopy study. *JAMA Psychiat.* 70, 1057–1066.
- Eishengdrelo, H., Kongsamut, S., 2013. Minireview: targeting GPCR activated ERK pathways for drug discovery. *Curr Chem Genomics Transl. Med.* 7, 9–15.

- Feuerstein, T.J., 2008. Presynaptic receptors for dopamine, histamine, and serotonin. *Handb. Exp. Pharmacol.* 184, 289–338.
- Fonnum, F., 1984. Glutamate: a neurotransmitter in mammalian brain. *J. Neurochem.* 42, 1–11.
- Fox, G.B., Esbenshade, T.A., Pan, J.B., Radek, R.J., Krueger, K.M., Yao, B.B., Browman, K.E., Buckley, M.J., Ballard, M.E., Komater, V.A., et al., 2005. Pharmacological properties of ABT-239 [4-(2-{2-[(2R)-2-Methylpyrrolidinyl]ethyl}-benzofuran-5-yl)benzonitrile]: II. Neurophysiological characterization and broad preclinical efficacy in cognition and schizophrenia of a potent and selective histamine H3 receptor antagonist. *J. Pharmacol. Exp. Ther.* 313, 176–190.
- Gallinat, J., McMahon, K., Kühn, S., Schubert, F., Schaefer, M., 2016. Cross-sectional study of glutamate in the anterior cingulate and hippocampus in schizophrenia. *Schizophr. Bull.* 42, 425–433.
- Gryniewicz, G., Poenie, M., Tsien, R.Y., 1985. A new generation of  $\text{Ca}^{2+}$  indicators with greatly improved fluorescence properties. *J. Biol. Chem.* 260, 3440–3450.
- Jovanovic, J.N., Benfenati, F., Siow, Y.L., Sihra, T.S., Sanghera, J.S., Pelech, S.L., Greengard, P., Czernik, A.J., 1996. Neurotrophins stimulate phosphorylation of synapsin I by MAP kinase and regulate synapsin I-actin interactions. *Proc. Natl. Acad. Sci. U. S. A.* 93, 3679–3683.
- Kegeles, L.S., Mao, X., Stanford, A.D., Girgis, R., Ojeil, N., Xu, X., Gil, R., Slifstein, M., Abi-Dargham, A., Lisanby, S.H., et al., 2012. Elevated prefrontal cortex  $\gamma$ -aminobutyric acid and glutamate-glutamine levels in schizophrenia measured in vivo with proton magnetic resonance spectroscopy. *Arch. Gen. Psychiatry* 69, 449–459.
- Ligneau, X., Lin, J., Vanni-Mercier, G., Jouvett, M., Muir, J.L., Ganellin, C.R., Stark, H., Elz, S., Schunack, W., Schwartz, J., 1998. Neurochemical and behavioral effects of ciproxifan, a potent histamine H3-receptor antagonist. *J. Pharmacol. Exp. Ther.* 287, 658–666.
- Ligneau, X., Perrin, D., Landais, L., Camelin, J.C., Calmels, T.P., Berrebi-Bertrand, I., Lecomte, J.M., Parmentier, R., Anaclet, C., Lin, J.S., et al., 2007. BF2.649 [1-[3-{4-(4-Chlorophenyl)propoxy}propyl]piperidine, hydrochloride], a nonimidazole inverse agonist/antagonist at the human histamine H3 receptor: preclinical pharmacology. *J. Pharmacol. Exp. Ther.* 320, 365–375.
- Lin, T.Y., Lu, C.W., Wang, C.C., Lu, J.F., Wang, S.J., 2012. Hispidulin inhibits the release of glutamate in rat cerebrocortical nerve terminals. *Toxicol. Appl. Pharmacol.* 263, 233–243.
- Mahmood, D., Khanam, R., Pillai, K.K., Akhtar, M., 2012. Protective effects of histamine H3-receptor ligands in schizophrenic behaviors in experimental models. *Pharmacol. Rep.* 64, 191–204.
- Malgarioli, A., Tsien, R.W., 1992. Glutamate-induced long-term potentiation of the frequency of miniature synaptic currents in cultured hippocampal neurons. *Nature* 357, 134–139.
- Manabe, T., Renner, P., Nicoll, R.A., 1992. Postsynaptic contribution to long-term potentiation revealed by the analysis of miniature synaptic currents. *Nature* 355, 50–55.
- Marsman, A., van den Heuvel, M.P., Klomp, D.W., Kahn, R.S., Luijten, P.R., Hulshoff Pol, H.E., 2013. Glutamate in schizophrenia: a focused review and meta-analysis of  $^1\text{H}$ -MRS studies. *Schizophr. Bull.* 39, 120–129.
- Millan, C., Sanchez-Prieto, J., 2002. Differential coupling of N and P/Q-type calcium channels to glutamate exocytosis in the rat cerebral cortex. *Neurosci. Lett.* 330, 29–32.
- Morisset, S., Rouleau, A., Ligneau, X., Gbahou, F., Tardivel-Lacombe, J., Stark, H., Schunack, W., Ganellin, C.R., Schwartz, J.C., Arrang, J.M., 2000. High constitutive activity of native H3 receptors regulates histamine neurons in brain. *Nature* 408, 860–864.
- Nicholls, D.G., 1998. Presynaptic modulation of glutamate release. *Prog. Brain Res.* 116, 15–22.
- Nicholls, D.G., Sihra, T.S., 1986. Synaptosomes possess an exocytotic pool of glutamate. *Nature* 321, 772–773.
- Nicholls, D.G., Sihra, T.S., Sanchez-Prieto, J., 1987. Calcium-dependent and -independent release of glutamate from synaptosomes monitored by continuous fluorometry. *J. Neurochem.* 49, 50–57.
- Nishihara, I., Minami, T., Watanabe, Y., Ito, S., Hayaishi, O., 1995. Prostaglandin E2 stimulates glutamate release from synaptosomes of rat spinal cord. *Neurosci. Lett.* 96, 57–60.
- Nuutinen, S., Panula, P., 2010. Histamine in neurotransmission and brain diseases. *Adv. Exp. Med. Biol.* 709, 95–107.
- Ota, M., Sato, N., Hidese, S., Teraishi, T., Maikusa, N., Matsuda, H., Hattori, K., Kunugi, H., 2017. Structural differences in hippocampal subfields among schizophrenia patients, major depressive disorder patients, and healthy subjects. *Psychiatry Res.* 259, 54–59.
- Passani, M.B., Blandina, P., 2011. Histamine receptors in the CNS as targets for therapeutic intervention. *Trends Pharmacol. Sci.* 32, 242–249.
- Passani, M.B., Giannoni, P., Bucherelli, C., Baldi, E., Blandina, P., 2007. Histamine in the brain: beyond sleep and memory. *Biochem. Pharmacol.* 73, 1113–1122.
- Pillot, C., Ortiz, J., Héron, A., Ridray, S., Schwartz, J.C., Arrang, J.M., 2002. Ciproxifan, a histamine H3-receptor antagonist/inverse agonist, potentiates neurochemical and behavioral effects of haloperidol in the rat. *J. Neurosci.* 22, 7272–7280.
- Plitman, E., Nakajima, S., de la Fuente-Sandoval, C., Gerretsen, P., Chakravarty, M.M., Kobylanski, J., Chung, J.K., Caravaggio, F., Iwata, Y., Remington, G., et al., 2014. Glutamate-mediated excitotoxicity in schizophrenia: a review. *Eur. Neuropsychopharmacol.* 24, 1591–1605.
- Poels, E.M., Kegeles, L.S., Kantrowitz, J.T., Slifstein, M., Javitt, D.C., Lieberman, J.A., Abi-Dargham, A., Girgis, R.R., 2014. Imaging glutamate in schizophrenia: review of findings and implications for drug discovery. *Mol. Psychiatry* 19, 20–29.
- Rouleau, A., Ligneau, X., Tardivel-Lacombe, J., Morisset, S., Gbahou, F., Schwartz, J.C., Arrang, J.M., 2002. Histamine H3-receptor-mediated  $[35\text{S}]\text{GTP } \gamma\text{[S]}$  binding: evidence for constitutive activity of the recombinant and native rat and human H3 receptors. *Br. J. Pharmacol.* 135, 383–392.
- Sang, N., Zhang, J., Marcheselli, V., Bazan, N.G., Chen, C., 2005. Postsynaptically synthesized prostaglandin E2 (PGE2) modulates hippocampal synaptic transmission via a presynaptic PGE2 EP2 receptor. *J. Neurosci.* 25, 9858–9870.
- Schenk, U., Menna, E., Kim, T., Passafaro, M., Chang, S., De Camilli, P., Matteoli, M., 2005. A novel pathway for presynaptic mitogen-activated kinase activation via AMPA receptors. *J. Neurosci.* 25, 1654–1663.
- Schlicker, E., Fink, K., Detzner, M., Göthert, M., 1993. Histamine inhibits dopamine release in the mouse striatum via presynaptic H3 receptors. *J. Neural Transm. Gen. Sect.* 93, 1–10.
- Schwartz, J.C., 2011. The histamine H3 receptor: from discovery to clinical trials with pitolisant. *Br. J. Pharmacol.* 163, 713–721.
- Southam, E., Cilia, J., Gartlon, J.E., Woolley, M.L., Lacroix, L.P., Jennings, C.A., Cluderay, J.E., Reavill, C., Rourke, C., Wilson, D.M., et al., 2009. Preclinical investigations into the antipsychotic potential of the novel histamine H3 receptor antagonist GSK207040. *Psychopharmacology* 201, 483–494.
- Sullivan, P.F., Kendler, K.S., Neale, M.C., 2003. Schizophrenia as a complex trait: evidence from a meta-analysis of twin studies. *Arch. Gen. Psychiatry* 60, 1187–1192.
- Suzuki, T., Remington, G., Mulsant, B.H., Rajji, T.K., Uchida, H., Graff-Guerrero, A., Mamo, D.C., 2011. Treatment resistant schizophrenia and response to antipsychotics: a review. *Schizophr. Res.* 133, 54–62.
- Vazquez, E., Sanchez-Prieto, J., 1997. Presynaptic modulation of glutamate release targets different calcium channels in rat cerebrocortical nerve terminals. *Eur. J. Neurosci.* 9, 2009–2018.
- Wang, S.J., 2006. Facilitatory effect of aspirin on glutamate release from rat hippocampal nerve terminals: involvement of protein kinase C pathway. *Neurochem. Int.* 48, 181–190.
- Weiser, M., Davidson, M., Noy, S., 2005. Comments on risk for schizophrenia. *Schizophr. Res.* 79, 15–21.
- Wu, L., Saggau, P., 1997. Presynaptic inhibition of elicited neurotransmitter release. *Trends Neurosci.* 20, 204–212.
- Yamagata, Y., Jovanovic, J.N., Czernik, A.J., Greengard, P., Obata, K., 2002. Bidirectional changes in synapsin I phosphorylation at MAP kinase-dependent sites by acute neuronal excitation in vivo. *J. Neurochem.* 80, 835–842.
- Yamamura, S., Ohoyama, K., Hamaguchi, T., Nakagawa, M., Suzuki, D., Matsumoto, T., Motomura, E., Tanii, H., Shiroyama, T., Okada, M., 2009. Effects of zotepine on extracellular levels of monoamine, GABA and glutamate in rat prefrontal cortex. *Br. J. Pharmacol.* 157, 656–665.
- Yang, T.T., Wang, S.J., 2008. Aripiprazole and its human metabolite OPC14857 reduce, through a presynaptic mechanism, glutamate release in rat prefrontal cortex: possible relevance to neuroprotective interventions in schizophrenia. *Synapse* 62, 804–818.

Available online at [www.sciencedirect.com](http://www.sciencedirect.com)

ScienceDirect

journal homepage: [www.jfda-online.com](http://www.jfda-online.com)

## Review Article

# Recent advances in oral delivery of drugs and bioactive natural products using solid lipid nanoparticles as the carriers

Chih-Hung Lin<sup>a</sup>, Chun-Han Chen<sup>b,c</sup>, Zih-Chan Lin<sup>d</sup>, Jia-You Fang<sup>e,f,g,h,\*</sup><sup>a</sup> Center for General Education, Chang Gung University of Science and Technology, Kweishan, Taoyuan, Taiwan<sup>b</sup> Division of General Surgery, Department of Surgery, Chang Gung Memorial Hospital at Chiayi, Chiayi, Taiwan<sup>c</sup> Graduate Institute of Clinical Medical Sciences, College of Medicine, Chang Gung University, Kweishan, Taoyuan, Taiwan<sup>d</sup> Graduate Institute of Biomedical Sciences, Chang Gung University, Kweishan, Taoyuan, Taiwan<sup>e</sup> Pharmaceuticals Laboratory, Graduate Institute of Natural Products, Chang Gung University, Kweishan, Taoyuan, Taiwan<sup>f</sup> Chinese Herbal Medicine Research Team, Healthy Aging Research Center, Chang Gung University, Kweishan, Taoyuan, Taiwan<sup>g</sup> Research Center for Food and Cosmetic Safety and Research Center for Chinese Herbal Medicine, Chang Gung University of Science and Technology, Kweishan, Taoyuan, Taiwan<sup>h</sup> Department of Anesthesiology, Chang Gung Memorial Hospital, Kweishan, Taoyuan, Taiwan

## ARTICLE INFO

## Article history:

Received 20 January 2017

Accepted 21 February 2017

Available online 14 March 2017

## Keywords:

drug

gastrointestinal tract

natural compound

oral delivery

solid lipid nanoparticles

## ABSTRACT

Chemical and enzymatic barriers in the gastrointestinal (GI) tract hamper the oral delivery of many labile drugs. The GI epithelium also contributes to poor permeability for numerous drugs. Drugs with poor aqueous solubility have difficulty dissolving in the GI tract, resulting in low bioavailability. Nanomedicine provides an opportunity to improve the delivery efficiency of orally administered drugs. Solid lipid nanoparticles (SLNs) are categorized as a new generation of lipid nanoparticles consisting of a complete solid lipid matrix. SLNs used for oral administration offer several benefits over conventional formulations, including increased solubility, enhanced stability, improved epithelium permeability and bioavailability, prolonged half-life, tissue targeting, and minimal side effects. The nontoxic excipients and sophisticated material engineering of SLNs tailor the controllable physicochemical properties of the nanoparticles for GI penetration via mucosal or lymphatic transport. In this review, we highlight the recent progress in the development of SLNs for disease treatment. Recent application of oral SLNs includes therapies for cancers, central nervous system-related disorders, cardiovascular-related diseases, infection, diabetes, and osteoporosis. In addition to drugs that may be active cargos in SLNs, some natural compounds with pharmacological activity are also suitable for SLN encapsulation to enhance oral bioavailability. In this article, we systematically

\* Corresponding author. Pharmaceuticals Laboratory, Graduate Institute of Natural Products, Chang Gung University, 259 Wen-Hwa 1st Road, Kweishan, Taoyuan 333, Taiwan.

E-mail address: [fajy@mail.cgu.edu.tw](mailto:fajy@mail.cgu.edu.tw) (J.-Y. Fang).

<http://dx.doi.org/10.1016/j.jfda.2017.02.001>

1021-9498/Copyright © 2017, Food and Drug Administration, Taiwan. Published by Elsevier Taiwan LLC. This is an open access article under the CC BY-NC-ND license (<http://creativecommons.org/licenses/by-nc-nd/4.0/>).



introduce the concepts and amelioration mechanisms of the nanomedical techniques for drug- and natural compound-loaded SLNs.

Copyright © 2017, Food and Drug Administration, Taiwan. Published by Elsevier Taiwan LLC. This is an open access article under the CC BY-NC-ND license (<http://creativecommons.org/licenses/by-nc-nd/4.0/>).

## 1. Introduction

Oral delivery is the most accepted drug administration route among the various delivery pathways because of its advantages: painlessness, easy self-administration, high patient compliance, and feasibility for outpatients [1]. Nevertheless, chemical and enzymatic barriers in the gastrointestinal (GI) tract hinder the effectiveness of oral drug delivery. The epithelial cell monolayer in the GI membrane also contributes to poor permeability for numerous drugs [2]. Some poorly soluble drug molecules are difficult to dissolve in the GI tract, resulting in low bioavailability. Novel and sophisticated drug delivery systems are necessary to conquer these limitations. By optimizing the formulations, the delivery efficiency and bioavailability can be ameliorated to promote the therapeutic potency with reduced side effects. The oral delivery improvement using nanocarrier systems has gained more attention recently [3]. Nanoparticles are defined as particles ranging in size from 1 nm to several hundred nanometers that can load drugs for efficient delivery. The drugs or actives can either be integrated in the core or matrix or attached to the surface of nanoparticles that have a high surface/volume ratio [4]. With respect to pharmacokinetics, the drugs in nanocarriers generally revealed prolonged circulation time, increased half-life, reduced clearance, and increased mean residence time (MRT) [5].

Among the different types of nanocarriers, solid lipid nanoparticles (SLNs) are at the forefront of the potential application in oral drug delivery systems [6]. SLNs are nanocolloids developed at the beginning of the 1990s by Schwarz et al [7]. They are used as alternative carriers to conventional colloids such as emulsions, liposomes, and polymeric micelles. Basically, SLNs are made of a solid lipid core with a monolayer phospholipid shell. The lipophilic moiety of phospholipids is embedded in the lipid matrix (Figure 1). Many drugs or diagnostics can be entrapped by SLNs, especially lipophilic ingredients [8]. The use of SLNs for oral administration is a promising approach for enhancing and controlling drug delivery. The solid state of the nanoparticulate matrix provides protection to chemically labile drugs and prolongation of drug release. SLNs show low cytotoxicity to mammalian cells, demonstrating an acceptable tolerance to the body. SLNs can be orally administered as aqueous dispersions or in the dosage forms of capsules, tablets, and pellets [9]. With the evolution of nanomedicine, the application of SLNs is expected to change the landscape of oral delivery. In this review, we highlight recent advances in the application of SLNs for oral delivery of drugs and bioactive natural compounds. We focus on the reports of SLN development during the past 5 years of orally administered drugs for therapy against cancers, central nervous system (CNS) diseases, cardiovascular (CV)

diseases, bacterial/viral infection, and inflammation. The promising perspective in this emerging application is also discussed.

## 2. Nanocarriers for the oral route

The drugs should go through the stomach, intestinal lumen, the mucus membrane coating the intestinal epithelium, and finally the epithelium itself after oral administration. The inside of the stomach is composed of four layers; from the innermost layer to the outermost layer, these are the mucosa, submucosa, muscularis externa, and the serosa. The stomach is lined by a mucous membrane that contains glands (with chief cells) that secrete gastric fluid. The intestinal epithelium is made up of villi that vastly increase the surface region available for drug absorption [10]. Absorptive enterocyte cells and mucus-secreting goblet cells cover the villi, which are interspersed with the follicle-associated epithelium. The physiology of the GI tract can lead to poor absorption and availability of the drugs or actives because of the low mucosa permeability and drug degradation prior to absorption [11]. The multidrug efflux proteins such as P-glycoprotein rich in the epithelial cell membrane are another barrier for orally administered drugs. Some drugs or active ingredients show low aqueous solubility, and a high hepatic first-pass effect also limits GI absorption. The additional oral permeation challenges are chemical instability, a short half-life, and the effect of food [12]. Figure 2 summarizes the barriers and challenges for efficient oral delivery for administering drugs.

Nanomedicine offers improvement of oral delivery by bioavailability enhancement, adverse-effect minimization, and food-effect mitigation [13]. The nanocarriers can increase the dissolution rate of poorly soluble molecules in the GI tract. The poor stability in the GI tract can be overcome by

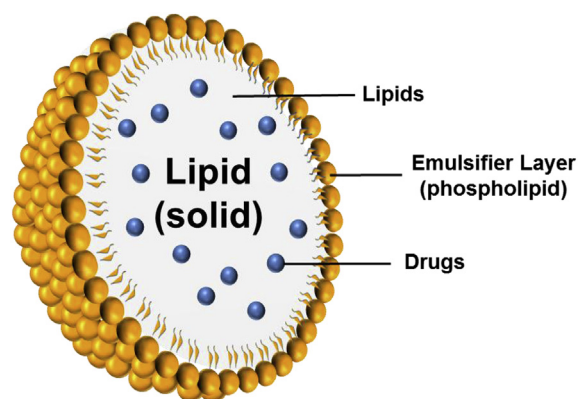


Figure 1 – Structures of solid lipid nanoparticles (SLNs).



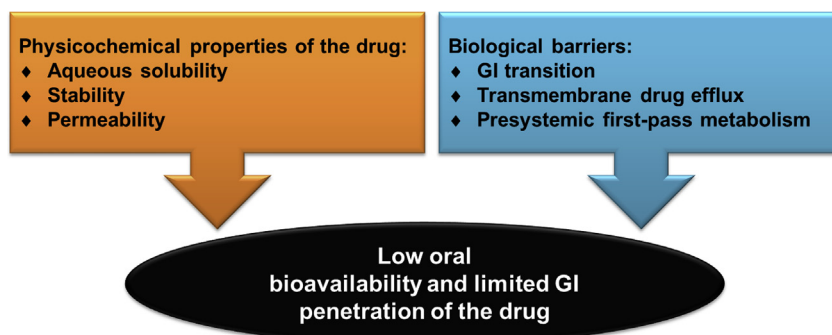


Figure 2 – Schematic diagram of the challenges for oral drug delivery. GI = gastrointestinal.

encapsulating the drugs in nanocarriers, thus rendering a protective impact toward chemical and enzymatic attacks in the tract. The designed nanocarrier systems provide intimate contact with the GI epithelium, prolonging residence time and revealing permeation enhancement for drug delivery [14]. The nanoparticles can at least to some extent transport into the mucus layer, releasing the payload. A presystemic metabolism functioning between the delivery system and the absorption membrane can thus be excluded. The nanocarriers are designed to modulate dimension, size, surface charge, surface property, and relative lipophilicity for preferentially penetrating across the GI membrane. Figure 3 illustrates nanocarrier strategies for ameliorating drug absorption across the GI tract.

Lymphatic drug delivery in the intestine is an alternative approach to bypassing first-pass metabolism. The lymphatic system forms a channel network throughout the body similar to blood circulation, but it is a one-way passage. The

predominant categories of conduits in the lymphatic system are the capillaries, collecting vessels, lymph nodes, and ducts [15]. The total lymph flow amount is about 120 mL/h. The lymphoid system is found to be an efficient route for oral administration of lipids across the intestinal membrane. The lipid-based nanoparticles are considered to favorably transfer into the lymph [16]. The nanoparticles reach the lymphatic system via microfold cells (M cells). The enhanced lymphatic delivery decreases the first-pass effect and improves oral bioavailability owing to the lymph vessels draining directly into the thoracic duct and farther into the venous blood [17].

### 3. Structure of SLNs

SLNs are colloidal systems made up of a solid lipid core matrix, which is stabilized in aqueous solution by emulsifiers.

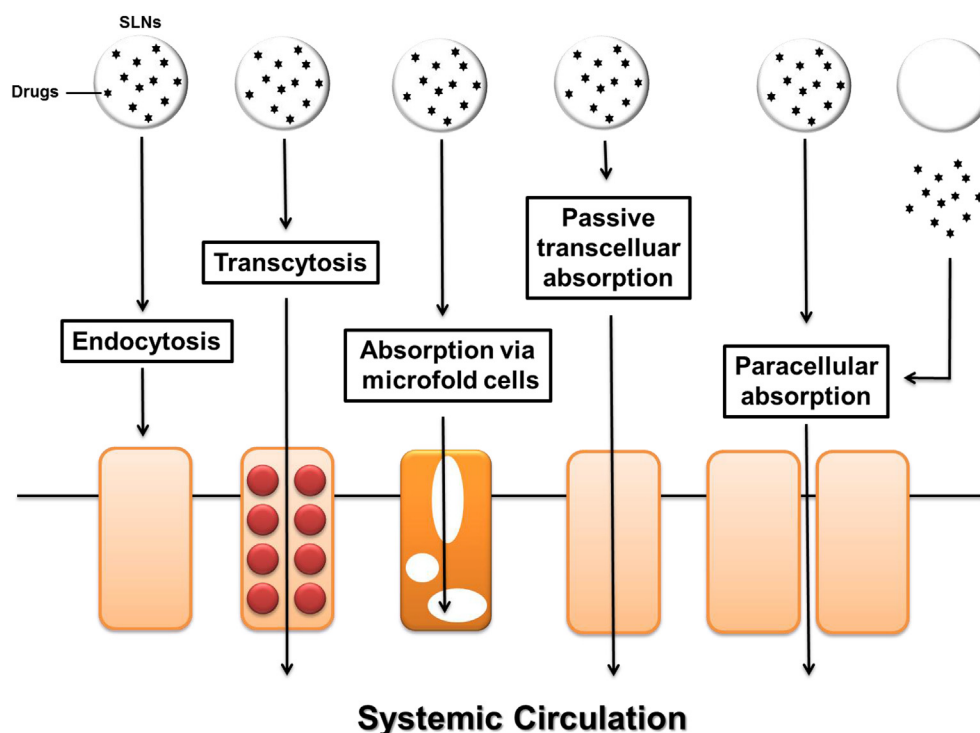


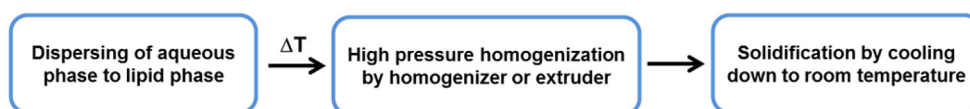
Figure 3 – Schematic diagram of various routes for oral delivery of solid lipid nanoparticles (SLNs).

This nanosystem provides advantages as a drug-delivery carrier, including stability, controlled release kinetics, tolerability, and protection of labile drugs [18]. The solid lipids commonly used in SLNs are glyceride mixtures, highly purified glycerides, or waxes that do not melt at body temperature. The safety of oral nanoformulations is a serious concern for their application [19,20]. A prerequisite for a new drug or formulation discovery is the confirmation of its safety when administered to the body. A balanced efficacy and safety is necessary when developing the nanomedicine for therapeutic application. The SLNs are developed by solid lipids and emulsifiers generally recognized as safe with respect to biocompatibility and nontoxicity. The lipid matrices are the natural or synthetic lipids that can be degraded, including triglycerides (trimyristin, tripalmitin, and tristearin), glyceryl monostearate (Imwitor), glyceryl behenate (Compritol 888 ATO), glyceryl palmitostearate (Precirol ATO 5), hard fat types (Witepsol), fatty acids (decanoic acid, palmitic acid, and stearic acid), waxes (cetyl palmitate, beeswax, and carnauba wax), and steroids (cholesterol) [8,21]. The drugs can be embedded in the voids of solid lipid matrix crystals. SLNs can encapsulate both lipophilic and hydrophilic drugs. Drug

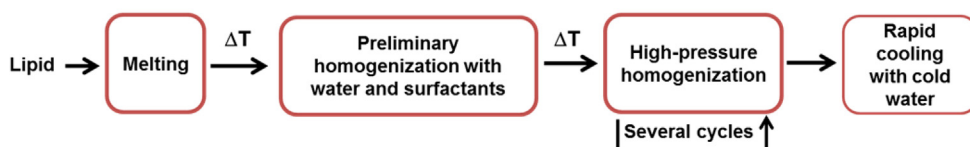
entrapment in the matrix depends on the types of solid lipids, drug solubility in the lipids, processing techniques, and polymorphic change in lipid crystals [22]. The emulsifiers or surfactants usually used for stabilizing the interface between the SLN shell and the aqueous medium are phospholipids (egg lecithin and soy lecithin), nonionic surfactants (Poloxamer, Pluronic, Brij, Tween, and Span), ionic surfactants (sodium cholate, sodium lauryl sulfate, stearylamine and trimethylammonium bromide), polyethylene glycol (PEG), and polyvinyl alcohol [23,24]. The lipids and surfactants are the two main materials used in SLNs. The materials cited in this section are basically safe for application.

Most of the materials for preparing SLNs are low cost with ease of scale-up for industrial production [25]. The solid lipid should be melted during the preparation process and then recrystallized at room temperature. There are several preparation methods for SLN production from the laboratory scale to the industrial scale. These include hot homogenization, high-pressure homogenization, ultrasonication, solvent evaporation, solvent emulsification–diffusion, microemulsion, double emulsion, supercritical fluid technique, and spray drying [26]. Figure 4 shows the preparation procedures

#### Hot homogenization



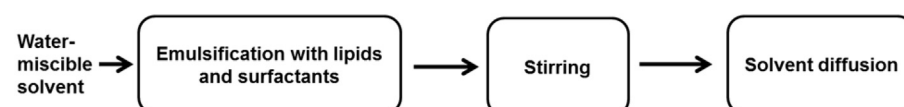
#### High-pressure homogenization



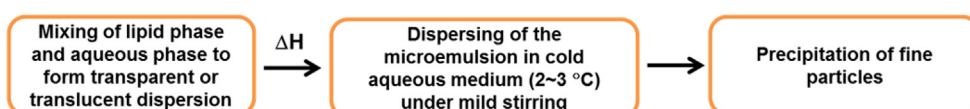
#### Solvent evaporation



#### Solvent emulsification-diffusion



#### Microemulsion



#### Double emulsion



Figure 4 – The general methods for preparation of solid lipid nano particles (SLNs).

of some methods. The physicochemical characterization of SLNs after preparation is a critical step for quality control and prediction of stability, drug release, and therapeutic efficacy. Photon correlation spectroscopy can be used to determine the particulate diameter, polydispersity, and zeta potential of SLNs [27]. The imaging systems such as scanning electron microscopy (SEM), transmission electron microscopy, and atomic force microscopy are the tools used for observing the particulate size, surface morphology, and particle shape. The crystalline confirmation of the lipids inside SLNs significantly affects the drug loading and stability. The polymorphism of the lipids is detected by X-ray diffraction, wide-angle X-ray scattering, and X-ray photoelectron spectroscopy [28]. Differential scanning calorimetry and Fourier transform infrared spectroscopy are used to identify the drug–matrix interaction.

#### 4. Application of SLNs as oral delivery systems

The drugs or actives should be solubilized to be absorbed by the GI system. In the lipid-based SLNs, the drugs are absorbed from the nanoformulations in the solid state [18]. Digestion of oral nanoparticles containing glycerides starts in the stomach by gastric lipase. The mechanical mixing of gastric fluid with amphiphilic products of lipid digestion results in the formation of crude emulsion. The SLNs are further digested in the intestinal fluid. The degradation products of lipids such as monoglycerides and fatty acids are able to promote intestinal drug transport by the production of mixed micelles with bile acids and subsequent uptake into the enterocytes [29]. The enormous effective surface area by virtue of the nano-sized SLNs can lead to an increased absorption rate. The tiny size of SLNs permits them to adhere to the GI mucus and also to enter the intervillar space, thus increasing the residence period for improved bioavailability. The surface-active capability of the emulsifiers can augment the drug absorption via the GI tract because of the altered GI membrane fluidity [30]. Cationic SLNs composed of cationic surfactants or lipids can be designed to ameliorate bioadhesion mediated by electrostatic interaction between the positively charged nanoparticles and the negatively charged mucosal surface [31]. SLNs have unique characteristics that make them promising candidates for lymphatic delivery of orally administered drugs [32]. The effect of emulsifiers on the preferential uptake of SLNs by Peyer's patch also improves the bioavailability of the oral drugs because of avoidance of first-pass metabolism.

SLNs can be digested in the GI tract. Thus, no translocation of intact nanoparticles to the circulation and other organs can be detected. Cai et al [32] demonstrated that no evidence supports absorption of integral SLNs via oral delivery. Contrary to this result, the *in vitro* experiment of SLN transcytosis into Caco-2 cell monolayers had suggested the transport of intact SLNs to the basolateral membrane side [33]. The internalization of SLNs is mediated via macropinocytosis, clathrin, and caveolae pathways. Li et al [34] reported that oral SLNs can be absorbed as intact nanoparticles through Peyer's patch and M cells in lymphoid follicles, especially in the ileum and colon.

#### 5. Oral delivery of SLNs for treating various diseases

Recent applications of oral SLNs include therapies for cancers, CNS-related disorders, CV-related diseases, infection, diabetes, and osteoporosis. The use of SLNs provides enhanced bioavailability and controlled drug release. Such ubiquitous properties arise from the specific features of surface modification, increased GI permeation, and resistance to degradation [35]. The following describes the different therapeutic approaches of oral SLNs for drug and pharmacologically active ingredient therapy. The pharmacokinetics, tissue distribution, and pharmacodynamics of the nanoparticles are the main evaluation platforms used to define the therapeutic effect for our description.

##### 5.1. Cancers

Nanomedicine is an efficient approach to promote the therapeutic benefit of anticancer drugs [36]. Intravenous drug administration for cancer therapy is inconvenient and painful for patients, leading to the requirement of regular hospital visits and low patient compliance. Oral chemotherapy would be preferable to intravenous delivery because it offers the benefits of improved compliance, low cost, and increased quality of life. Unfortunately, most anticancer drugs are not readily bioavailable via the oral route because of the harsh environment and permeation barrier of the GI tract [37]. For example, the oral bioavailability of paclitaxel has been found to be <1% [38]. Paclitaxel shows effective activity against ovarian, breast, and lung cancers as well as Kaposi's sarcoma. The oral availability of this drug is limited by cytochrome P450 activity and P-glycoprotein in the gut wall and liver [39]. SLNs as oral drug delivery systems are promising to solve the problems of oral anticancer drugs such as poor stability, healthy tissue toxicity, and high incidence of drug-resistant tumors [21].

Materials to improve the therapeutic advantages after oral administration can be applied to the surface of SLNs. Baek et al [40] had developed the surface-modified paclitaxel-loaded SLNs with hydroxypropyl- $\beta$ -cyclodextrin (HPCD). This dextrin is known to solubilize the drugs and prevent oxidation of lipids [41]. The HPCD-coated SLNs showed a paclitaxel encapsulation percentage of 71% with a mean size of 251 nm. The Caco-2 cell uptake of paclitaxel from SLNs was 5.3-fold greater than the Taxol formulation. The  $C_{\max}$  and lymph node concentrations of SLNs (1.44  $\mu\text{g/mL}$  and 11.12 ng/mg, respectively) were higher than those of the control solution (0.73  $\mu\text{g/mL}$  and 0.89 ng/mg, respectively) after oral paclitaxel application at 25 mg/kg. Pooja et al [42] prepared wheat germ agglutinin (WGA)-coated SLNs to improve oral paclitaxel delivery. WGA can bind to N-acetyl-D-glucosamine and sialic acid presenting on the cell surface throughout the intestine, leading to prolonged residence time [43]. The *in vitro* anti-cancer activity against A549 lung cancer cells showed a half-maximal inhibitory concentration ( $\text{IC}_{50}$ ) of 41 ng/mL and 165 ng/mL for WGA-coated SLNs and free paclitaxel, respectively. After oral administration at 25 mg/kg in rats, the area under the curve (AUC) of plasma concentration–time profiles

was higher for WGA-coated SLNs (30  $\mu\text{g h/mL}$ ) than conventional SLNs (16  $\mu\text{g h/mL}$ ) and the free control (8  $\mu\text{g h/mL}$ ). The inclusion of paclitaxel into WGA-coated SLNs led to doubling of MRT in contrast to the control solution.

Docetaxel is a second-generation taxane extensively used to treat breast, lung, prostate, and head/neck cancers. The development of an oral docetaxel formulation is hindered because of poor bioavailability. SLNs coated with Tween 80 or D- $\alpha$ -tocopheryl poly(ethylene glycol) succinate (TPGS) were prepared to improve the oral delivery of this drug [44]. The SLNs exhibited a sustained docetaxel release compared with Taxotere. The AUC of Tween 80 SLNs, TPGS SLNs, and Taxotere after oral administration (20 mg/kg) was 7.0  $\mu\text{g min/mL}$ , 12.9  $\mu\text{g min/mL}$ , and 3.9  $\mu\text{g min/mL}$ , respectively. The superior bioavailability of TPGS compared to Tween 80 nanocarriers is attributable to the better inhibition of drug efflux by TPGS along with lymphatic uptake. No evidence of intestinal damage was visualized after SLN administration. Doxorubicin is an anthracycline antibiotic that can inhibit various malignant tumors. The major limitations of doxorubicin are its serious cardiotoxicity and hepatotoxicity [45]. Patro et al [46] investigated the oral bioavailability and toxicity of doxorubicin-loaded SLNs with an emulsifier system of soy lecithin and poloxamer 188. The SLNs exhibited increased the  $C_{\text{max}}$  (6.7  $\mu\text{g/mL}$  vs. 2.4  $\mu\text{g/mL}$ ) and reduced clearance (36 mL/h kg vs. 619 mL/h kg) when compared to free doxorubicin. The mean survival time of breast cancer-bearing rats increased from 34 days (positive control) to 47 days and 88 days in the free doxorubicin and SLN groups. Cardiac toxicity measured by the lactic dehydrogenase level was less in the SLN-treated group compared to the free control. Doxorubicin was included in PEGylated SLNs as mucus-penetrating nanoparticles for oral delivery across the GI mucus [47]. Modification of nanoparticles by PEG–stearic acid increased the hydrophilicity of nanoparticles with a rapid mucus-penetrating transport property [48]. The permeation ability of SLNs across the Caco-2/HT29 coculture cell monolayer increased after coating with PEG–stearic acid. The *in vitro* everted rat gut sac technique demonstrated that PEGylated SLNs could facilitate penetrate mucus secretions. The pharmacokinetic data showed that the oral bioavailability of PEGylated nanosystems was 2.0- and 7.5-fold greater than conventional SLNs and free doxorubicin, respectively.

Vorinostat is a histone deacetylase inhibitor that efficiently induces cell cycle arrest and apoptosis for the treatment of cutaneous T cell lymphoma [49]. Tran et al [50] examined whether SLNs containing vorinostat could enhance multidrug-resistant cancer cells and oral delivery. The nanocarriers were spherical with a narrowly distributed size of about 100 nm, and were physically stable for at least 3 months. The SLNs were more cytotoxic than the free vorinostat in both sensitive (MCF-7 and A549) and resistant (MDA-MB-231) cells. The  $C_{\text{max}}$  and AUC values of SLNs were 1.6- and 2.5-fold higher than those of the free drug by oral delivery at 30 mg/kg in rats. Hashem et al [51] evaluated the cytotoxicity and oral bioavailability of SLNs encapsulating tamoxifen, the drug for breast cancer management. The SLNs prepared using glyceryl monostearate and stabilized with poloxamer 188 showed an entrapment percentage of 90% for tamoxifen. The *in vitro* release profiles revealed an initial burst effect followed by a

sustained drug release. The tamoxifen bioavailability could be increased to 1.6-fold by SLN administration.

Recent research indicates the usefulness of the compounds from natural resources for cancer prevention and treatment [52]. The antioxidant, anti-inflammatory, anti-apoptotic, vasodilating, and antimicrobial potentials of natural products are responsible for their anticancer effects [53].  $\gamma$ -Tocotrienol is a natural form of vitamin E with a potential anticancer effect in breast malignancy. However, the effective oral delivery of  $\gamma$ -tocotrienol is very low (9%) [54]. SLNs were used as the formulations for  $\gamma$ -tocotrienol to improve the intestinal permeation [55]. The *in situ* rat intestine perfusion study demonstrated a 10-fold increase of  $\gamma$ -tocotrienol permeation compared to the control. The cellular endocytosis is the major contribution of  $\gamma$ -tocotrienol uptake from SLNs. Following the oral administration of 10 mg/kg  $\gamma$ -tocotrienol, SLNs increased bioavailability by 3-fold compared to the control group. Cantharidin is an anticancer active present in mylabris. It can inhibit tumor growth by interfering with the metabolism of nucleic acids and proteins. Cantharidin is shown to be poorly water soluble with low oral bioavailability in the beagle dog breed [56]. Dang and Zhu [57] used SLNs as the vehicles for oral cantharidin delivery. The mean diameter of the nanoparticles was 121 nm with a high cantharidin encapsulation of 94%. After a single oral dose of cantharidin at 0.1 mg/kg in rats, the relative bioavailability of SLNs to the free compound was 251%.

Ferulic acid is one of the most abundant antioxidants found in wheat bran. It shows anticancer potential in breast, skin, colon, and liver cancers [58]. The poor aqueous solubility of ferulic acid has led to unsatisfactory oral bioavailability. The limited bioavailability of ferulic acid can be overcome by SLNs. Zhang et al [59] prepared ferulic acid-loaded SLNs made with glyceryl behenate. The pharmacokinetic parameters showed a higher  $C_{\text{max}}$  and half-life of SLNs (18.7  $\mu\text{g/mL}$  and 4.6 hours, respectively) compared with those of aqueous dispersion (10.0  $\mu\text{g/mL}$  and 2.1 hours, respectively), suggesting a sustained release from the lipid matrix. The *in vivo* imaging system also revealed a longer retention of SLNs in the small intestine than in the free control. Thakkar et al [60] combined ferulic acid and aspirin to be loaded in chitosan-coated SLNs for pancreatic cancer therapy. Chitosan-coated SLNs exhibited good stability in an acidic environment with the formation of a thick layer around the lipid core. This biopolymer coating also improved the mucoadhesion of SLNs [61]. The combination of low doses of free ferulic acid (200  $\mu\text{M}$ ) and aspirin (1 mM) inhibited pancreatic cancer cells MIA PaCa-2 and Panc-1 by 45% and 60%, respectively. A 5- and 40-fold dose decrease of ferulic acid (40  $\mu\text{M}$ ) and aspirin (25  $\mu\text{M}$ ) was found to show comparable cytotoxicity after SLN entrapment. In the *in vivo* pancreatic tumor xenograft mouse study, oral application of combined ferulic acid (75 mg/kg) and aspirin (25 mg/kg) in SLNs significantly suppressed tumor growth by 45% as compared to the control. Table 1 summarizes the profiles for anticancer therapy assisted by oral SLNs.

## 5.2. CNS-related disorders

CNS-related illnesses are a leading cause of disability and morbidity worldwide. However, the orally dosed drug



**Table 1 – Formulations of orally administered SLNs loaded with drugs or natural compounds against cancers and their benefits.**

Active ingredient	Lipid type	Surface decoration	Average size (nm)	Outcomes offered by SLNs	Reference
Paclitaxel	Stearic acid	HPCD	251	Improved AUC in plasma and lymph node	Back et al [40]
Paclitaxel	Monoglycerides, triglycerides, and stearic acid	WGA	150–198	Increased AUC and MRT	Pooja et al [42]
Docetaxel	Tristearin	Tween 80 and TPGS	189–215	Improved sustained release and AUC	Cho et al [44]
Doxorubicin	Precirol ATO 5	soy lecithin and poloxamer 188	217	Increased AUC and reduced cardiotoxicity	Patro et al [46]
Doxorubicin	Monostearin	PEG-stearic acid	153–160	Improved bioavailability and prolonged circulation time	Yuan et al [47]
Vorinostat	Compritol 888 ATO	None	~100	Enhanced $C_{max}$ and AUC	Tran et al [50]
Tamoxifen	Monostearin and stearic acid	Tween 80 and poloxamer 188	130–244	Improved bioavailability	Hashem et al [51]
$\gamma$ -Tocotrienol	Compritol 888 ATO	None	105	Increased intestine permeation and AUC	Abusal et al [55]
Cantharidin	Monostearin	None	121	Improved bioavailability	Dang and Zhu [57]
Ferulic acid	Compritol 888 ATO	None	86	Increased $C_{max}$ and half-life	Zhang et al [59]
Ferulic acid	Stearic acid	Chitosan	183–229	Tumor growth suppression	Thakkar et al [60]

AUC = area under the curve; HPCD = hydroxypropyl- $\beta$ -cyclodextrin; MRT = mean residence time; PEG = polyethylene glycol; TPGS = D- $\alpha$ -tocopheryl poly(ethylene glycol) succinate; WGA = wheat germ agglutinin.

treatments for depression, anxiety, and schizophrenia are usually limited by low aqueous solubility, food effect, first-pass effect, and a short half-life [62]. Medication for psychotic diseases often needs repeated daily dose administration. This can lead to less patient compliance, the need for hospitalization, and high cost [63]. As such, the application of nanomedicine to CNS-related diseases is a viable option for maximizing treatment efficacy. Apomorphine is a mixed dopamine  $D_1/D_2$  agonist for the treatment of Parkinson's disease approved by the U.S. Food and Drug Administration. The rapid degradation of apomorphine in the GI tract and the first-pass effect have resulted in a bioavailability of only 1.7% [64]. Tsai et al [65] developed SLNs for improving oral bioavailability and brain distribution of apomorphine. SLNs showed a bioavailability 13-fold higher than the reference solution at an oral dose of 26 mg/kg. Apomorphine distribution in the striatum, the major site of therapeutic action, also increased when using SLNs. In the rat model of Parkinson's disease induced by 6-hydroxydopamine, the contralateral rotation number increased from 20 to 115 after oral SLN administration.

Migraines are a debilitating headache disorder with symptoms of nausea, photophobia, and cognitive function impairment. Sumatriptan is the first drug approved by the U.S. Food and Drug Administration for acute migraine treatment. This drug undergoes incomplete absorption and first-pass metabolism, leading to a low oral bioavailability of 15% [66]. Chitosan-coated SLNs were used to encapsulate sumatriptan by using a solvent injection technique [67]. The nanoformulations showed a brain sumatriptan deposition of 5.28  $\mu\text{g/g}$  in the pharmacokinetic study. The  $\text{AUC}_{\text{brain}}/\text{AUC}_{\text{plasma}}$  of the drug was 4.5, indicating a targeting to the brain rather than plasma. The mouse model of photophobia demonstrated that the time spent in the lit chamber of a light/dark box was significantly increased by SLNs when compared to the free control. Rizatriptan is the second-generation antimigraine drug exerting selective vasoconstriction of the intracranial and extracerebral vessels. Girotra and Singh [68] investigated the brain targeting of SLNs for rizatriptan delivery. The *in vivo* study in rats exhibited an 18-fold increase of brain rizatriptan uptake after SLN delivery compared to the free drug at a dose of 5 mg/kg. The light/dark box study showed the improvement of photophobia by loading rizatriptan into SLNs.

Sulpiride is a selective antagonist of the central dopamine receptor used as an antipsychotic agent. In order to ameliorate the limited intestinal permeation, SLNs composed of stearic acid and Dynasan 118 were prepared for sulpiride delivery [69]. The drug permeability across the everted rat gut sac was 6.6  $\mu\text{g}/\text{cm}^2$  after 2 hours. The permeability was enhanced to 11.7  $\mu\text{g}/\text{cm}^2$  by SLNs. This can be attributed to the enhancement of the surface area, leading to a higher rate of dissolution and diffusion. Quetiapine is an antipsychotic drug with poor oral bioavailability (9%) because of the extensive first-pass effect [70]. An attempt to improve the oral bioavailability of quetiapine was performed by using SLNs [71]. The stable SLNs with a mean diameter of 175 nm and an encapsulation capacity of 92% were developed. The  $C_{max}$  was 1.9  $\mu\text{g}/\text{mL}$  for SLNs, whereas the  $C_{max}$  for the aqueous suspension was 0.1  $\mu\text{g}/\text{mL}$ . The oral bioavailability of SLNs increased 3.7 times



compared with the suspension. Venlafaxine is the first-line antidepressant for the treatment of major depressive disorders and anxiety. This drug is a substrate of P-glycoprotein that reduces penetration across the GI and blood–brain barrier [72]. Zhou et al [73] explored whether the venlafaxine efflux of P-glycoprotein could be reversed by SLN application. Mice were orally administered with SLNs containing venlafaxine (22 mg/kg) or free venlafaxine with verapamil. Verapamil is a P-glycoprotein inhibitor. The AUC of venlafaxine from the SLNs and verapamil-containing solution was 1.5- and 1.2-fold greater than that of venlafaxine alone, respectively. The AUC in the brain from SLNs was 1.5-fold higher compared to that in the venlafaxine solution.

Alzheimer's disease is a devastating and progressive neurodegenerative disorder characterized by amyloid- $\beta$  (A $\beta$ ) accumulation and intraneuronal neurofibrillary tangles. Numerous natural compounds and plant extracts are effective against chronic inflammation in Alzheimer's disease [74,75]. Chrysin is one of the natural compounds inhibiting the neuroinflammation caused by Alzheimer's disease [76]. The therapeutic efficiency of chrysin is limited because of its compromised oral delivery. The lipid peroxidation and increased acetylcholinesterase in A $\beta$ -injected rats could be restored by chrysin-loaded SLNs (5 mg/kg and 10 mg/kg) and the free compound (50 mg/kg and 100 mg/kg) [77]. The poor memory retention examined by radial arm maze training was recovered by treatment using SLNs at the lower dose compared to the free control.

Grape skins, mulberries, and peanuts are rich in resveratrol, a polyphenol reported to possess a wide variety of health benefits. Resveratrol is especially effective in the treatment of neurodegenerative illnesses such as Alzheimer's disease, Parkinson's disease, and brain ischemia [78]. As with most of the polyphenols, low aqueous solubility and poor GI absorption have limited resveratrol's therapeutic application. Pandita et al [79] entrapped resveratrol into SLNs to improve the oral bioavailability. SLNs prolonged resveratrol release up to 120 hours and followed Higuchi kinetics. Resveratrol is sensitive when exposed to light. Resveratrol content in SLNs (86%) was higher than that in solution (36%) after a 6-hour ultraviolet light irradiation. The lipid formulation produced an 8-fold increase in oral resveratrol bioavailability in rats. The half-life was found to be 2.4 hours and 11.5 hours for resveratrol suspension and SLNs, respectively. N-Trimethyl chitosan was coated on the surface of SLNs to increase the retention and penetration of SLNs in the GI tract [80]. The *in vitro* release study of chitosan-coated SLNs revealed negligible resveratrol release in simulated gastric fluid and sustained release in simulated intestinal fluid. After oral dosing at 25 mg/kg, the bioavailability of resveratrol increased 3.8-fold compared to that in the aqueous suspension.

Curcumin is a lipophilic polyphenol derived from the spice turmeric from the ground rhizome of *Curcuma longa*. It has been reported that curcumin exhibits antioxidant, anti-inflammatory, antimicrobial, anti-amyloid, and anticancer effects [81]. Of significant interest is curcumin's role in treating neurodegenerative diseases, including Alzheimer's disease and Parkinson's disease, and malignancy [82]. The oral bioavailability of curcumin is less than 1% because this compound has poor aqueous solubility and rapid metabolism [83].

Kakkar and Kaur [84] evaluated the effect of curcumin-loaded SLNs on Alzheimer's disease using the mouse model with treatment using AlCl<sub>3</sub>, a neurotoxicant. Oral treatment of free curcumin (50 mg/kg) showed 15% recovery in lipid peroxidation and 22% recovery in acetylcholinesterase with respect to the AlCl<sub>3</sub> treatment group. The SLNs demonstrated better results (97% and 73% recovery in lipid peroxidation and acetylcholinesterase) at a dose of 50 mg/kg. Improvement in learning ability in the Morris water maze test was achieved by free curcumin and SLNs at the oral dose of 50 mg/kg and 1 mg/kg, respectively. Kakkar et al [85] further examined the brain distribution of curcumin with oral delivery of SLNs. Confocal microscopy was used to visualize the yellow fluorescence of curcumin. The presence of fluorescent nanoparticles in the plasma and brain indicated effective penetration of oral SLNs across the gut wall and the blood–brain barrier. The AUC for SLNs was 8.1 times higher than that of free curcumin. A 30-fold increase in brain curcumin accumulation was detected for SLNs compared to the free control. Ji et al [86] decorated curcumin-loaded SLNs with Brij 78 and TPGS to inhibit the P-glycoprotein efflux pump. In the *in situ* single-pass intestinal perfusion test, the effective permeability coefficient of SLNs + Brij and SLNs + Brij + TPGS was 1.3 times and 1.4 times greater than conventional SLNs in the jejunum. The *in vivo* pharmacokinetic experiment in rats showed the AUC for SLNs as 12.3-fold higher than in suspension.

Chitosan as a mucoadhesive polymer was coated on the surface of SLNs to improve oral intake [87]. The oral absorption of curcumin suspension (50 mg/kg) showed a  $C_{max}$  of 0.28  $\mu$ g/mL. This value could be increased to 1.04  $\mu$ g/mL by SLN administration. The bioavailability of curcumin was increased by a factor of 6.9 after SLN delivery compared to suspension. Methylation of chitosan to N-trimethyl chitosan increases acid resistance and the mucoadhesive property [88]. N-Trimethyl chitosan-coated SLNs were developed to further ameliorate oral absorption [89]. Curcumin in chitosan-coated SLNs resulted in the release of 81% and 48% in simulated gastric fluid and simulated intestinal fluid, respectively. Release of curcumin from quarternized chitosan-coated SLNs was negligible (9%) in simulated gastric fluid and moderate (42%) in simulated intestinal fluid. The oral AUC of N-trimethyl chitosan-coated SLNs was 12.8  $\mu$ g h/mL, which was significantly higher than free curcumin (0.3  $\mu$ g h/mL), non-coated SLNs (6.0  $\mu$ g h/mL), and chitosan-coated SLNs (6.9  $\mu$ g h/mL). Another activity of curcumin on CNS-related disorders is the inhibition of cerebral ischemia [90]. Kakkar et al [91] assessed the effect of curcumin-loaded SLNs on the experimental platform of cerebral ischemic reperfusion injury in rats.  $\gamma$ -Scintigraphic study exhibited a 16-fold increase in brain AUC upon oral delivery of SLNs compared to the control solution. There was an improvement of 90% in cognition and 52% inhibition of acetylcholinesterase versus the nontreatment group. Table 2 depicts the oral delivery assisted by SLNs with the aim of CNS-related disorder treatment.

### 5.3. CV-related diseases

SLNs have been used orally, aiming at enhancing drug plasma concentration and prolonging circulation duration. These features are especially important for accomplishing better

**Table 2 – Formulations of orally administered SLNs loaded with drugs or natural compounds against CNS-related disorders and their benefits.**

Active ingredient	Indication	Lipid type	Average size (nm)	Outcomes offered by SLNs	Reference
Apomorphine	Parkinson's disease	Tripalmitin	63–155	Increased bioavailability and brain distribution	Tsai et al [65]
Sumatriptan	Migraine	Tripalmitin	192–301	Improved AUC <sub>0-12h</sub> /AUC <sub>0-12h</sub> ratio and photophobia	Hansraj et al [67]
Rizatriptan	Migraine	Precirol ATO 5	220	Improved brain uptake and photophobia	Girotra and Singh [68]
Sulpiride	Psychosis	Stearic acid and Dynasan 118	256	Increased gut permeability	Ibrahim et al [69]
Quetiapine	Psychosis	Dynasan 118	175	Enhanced C <sub>max</sub> and bioavailability	Narala and Veerabrahma [71]
Venlafaxine	Major depressive disorder and anxiety	Monostearin	186	Increased AUC in both plasma and brain	Zhou et al [73]
Chrysin	Alzheimer's disease	Stearic acid	240	Improved memory loss	Vedagiri and Thangarajan [77]
Resveratrol	Neurodegenerative disorders	Stearic acid	134	Increased bioavailability and half-life	Pandita et al [79]
Resveratrol	Neurodegenerative disorders	Precirol ATO 5	258	Increased C <sub>max</sub> and AUC	Ramalingam and Ko [80]
Curcumin	Alzheimer's disease	Compritol 888 ATO	135	Reduced neuroinflammation	Kakkar and Kaur [84]
Curcumin	Alzheimer's disease	Compritol 888 ATO	135	Improved AUC and brain distribution	Kakkar et al [85]
Curcumin	Alzheimer's disease	Monostearin	135	Improved jejunum permeability and bioavailability	Ji et al [86]
Curcumin	Alzheimer's disease	Monostearin	452	Increased C <sub>max</sub> and AUC	Ramalingam et al [87]
Curcumin	Alzheimer's disease	Palmitic acid	412	Increased AUC and half-life	Ramalingam and Ko [89]
Curcumin	Cerebral ischemia	Compritol 888 ATO	135	Increased AUC in brain and cognition	Kakkar et al [91]

AUC = area under the curve; CNS = central nervous system; SLN = solid lipid nanoparticle.

therapeutic benefits in treating CV-related diseases. Nimodipine is a calcium channel blocker used in the treatment of hypertension and stroke. Clinical studies demonstrate a low bioavailability of 4–13% for oral nimodipine [92]. Nimodipine-loaded SLNs were prepared with palmitic acid, poloxamer 188, and soy lecithin [93]. An accelerated stability test showed no significant change in size and polydispersity of the SLNs for 3 months. The bioavailability of oral SLNs containing nimodipine (8 mg/kg) was 2-fold greater than that of the solution in rats. Nisoldipine is another antihypertensive drug with low oral bioavailability. Dudhipala and Veerabrahma [94] developed optimal formulations of nisoldipine-loaded SLNs for improved delivery. The optimized SLNs were stable under refrigeration and at room temperature for 3 months. The pharmacokinetic study displayed a 2.2-fold increase in oral bioavailability by SLNs as compared with nisoldipine suspension. The pharmacodynamic study showed that SLNs could significantly reduce systolic blood pressure for a sustained period of 36 hours.

Candesartan cilexetil is a prodrug of candesartan, an angiotensin II type 1 receptor antagonist, used for hypertension and heart failure remission. This prodrug has poor aqueous solubility and low oral absorption. After inclusion of candesartan cilexetil (10 mg/kg) into SLNs using Dynasan as the solid lipid, oral bioavailability was enhanced more than 2.8-fold compared to the free control [95]. An extension of systolic blood pressure reduction was observed after SLN administration in hypertensive rats for 48 hours, whereas the period of blood pressure reduction was only 2 hours for the drug suspension. Zhang et al [96] elucidated the absorption mechanisms of candesartan cilexetil from SLNs. The pharmacokinetic study in rats indicated that the oral bioavailability and C<sub>max</sub> increased more than 12- and 27-fold after SLN incorporation, respectively. In the Caco-2 cell monolayer uptake, SLNs were distributed in the lysosomes and endoplasmic reticulum after internalization. The authors had suggested that SLNs could be internalized into the enterocytes and then diffused into the circulation via portal circulation and the lymphatic pathway. Carvedilol is an antihypertensive drug with a low oral bioavailability of 20% because of the first-pass effect. To improve the drug's oral delivery, SLNs were developed with N-carboxymethyl chitosan coating for protecting carvedilol in an acidic environment [97]. The polymer-coated SLNs had shown 5.2% of drug release in simulated gastric fluid for 24 hours. In simulated intestinal fluid (pH 7.4), the N-carboxymethyl chitosan on the SLN surface dissolved and the controlled release of carvedilol was detected. In the *in vivo* pharmacokinetics, the MRT was found to be 13.9 hours and 9.6 hours for polymer-coated SLNs and aqueous suspension, respectively. The AUC of polymer-coated SLNs was 6.3 µg h/mL, which was significantly higher than that of noncoated SLNs (2.9 µg h/mL) and the free control (2.0 µg h/mL).

Use of an iron supplement is an efficient way to treat the iron deficiency in anemia. However, the commercially available iron tablets often cause adverse effects on the GI system, resulting in constipation and blood in the stool [98]. Another concern is the high intersubject variability in iron absorption. This has led to the application of SLNs for oral iron delivery. Zariwala et al [99] prepared chitosan-coated SLNs for ferrous sulfate loading to test the Caco-2 absorption. The cell viability

after SLN treatment was >80% of the control cells. The Caco-2 iron absorption from chitosan-coated SLNs (643 ng/mg cell protein) was significantly higher than from noncoated SLNs (584 ng/mg cell protein) and the reference control (515 ng/mg cell protein). Hosny et al [100] assessed the *in vivo* pharmacokinetics of ferrous sulfate in SLNs. The iron-loaded SLNs exerted a biphasic release behavior, with a burst release within 30 minutes followed by sustained release. A 4-fold increase in oral iron bioavailability was achieved after oral administration of SLNs (10 mg/kg) in rabbits.

#### 5.4. Infection

Infection can cause host tissues to react to organisms and the toxins they produce. Nanocarriers can be effective drug delivery systems for treating infections [101]. Among the different types of nanosystems, SLNs were widely applicable for carrying anti-infection drugs to treat bacterial, fungal, viral, and parasitic infection. Isoniazid is an antitubercular drug recommended by the World Health Organization for management of all forms of tuberculosis. A short half-life of 1–4 hours suggests the need for repetitive dosing that may result in hepatotoxicity and neurotoxicity [102]. Isoniazid-incorporated SLNs were developed to attain prolonged circulation retention and improved bioavailability [103]. The *in vitro* isoniazid release displayed a triphasic pattern comprising an initial fast release, followed by a hump and finally a delayed release. A significant amelioration of bioavailability in rat plasma (6 times) and the brain (4 times) was found after oral SLN administration compared to free isoniazid (25 mg/kg). The SLNs showed a 3-fold higher median lethal dose (LD<sub>50</sub>) compared to the free drug in an acute toxicity study. Miconazole is a broad-spectrum antifungal drug with a low aqueous solubility of <1 µg/mL. Encapsulation of miconazole in SLNs showed a biphasic drug release with an initial burst and a following delayed release [104]. The SLNs showed better *Candida albicans* killing in the diffusion disk test, with the maximum inhibition diameter of 22 mm that was longer than the marketed capsule (14 mm). The *in vivo* pharmacokinetics in rabbits exhibited a 2.5-fold enhancement of oral bioavailability.

Lopinavir is a human immunodeficiency virus (HIV) protease inhibitor used in antiretroviral therapy. SLNs can act as a feasible carrier for lopinavir because of P-glycoprotein efflux and first-pass metabolism. The lopinavir-loaded SLNs composed of stearic acid were stable at 4°C for 4 months based on particulate size and the release profile [105]. Higher oral bioavailability was obtained for SLNs (2.5-fold) in comparison with lopinavir solution because of higher lymphatic delivery. In another study, Compritol 888 ATO was used as the solid lipid for preparing lopinavir-loaded SLNs [106]. The drug release showed a delayed pattern both in 0.1N HCl (pH 1.2) and phosphate buffer (pH 6.8). The SLNs could bypass P-glycoprotein efflux to reach systemic circulation, leading to a 3.6- and 4.9-fold increase in bioavailability and C<sub>max</sub> compared to solution. Efavirenz is a nonnucleoside reverse transcriptase inhibitor as the first-line antiretroviral drug to eradicate HIV infection. Gaur et al [107] investigated the enhanced oral bioavailability of efavirenz by SLNs. The optimized nanoformulations had shown good stability at 40°C for

about 6 months. SLNs revealed a 5.3-fold increase in C<sub>max</sub> and an 11.0-fold increase in AUC compared to drug suspension after oral administration in rats. Makwana et al [108] further explored the absorption pathways of SLNs for delivering efavirenz. The profiles of lymphatic absorption and tissue biodistribution in rats indicated that a large amount of nanoparticulate efavirenz had bypassed the portal system and recovered in the lymph via chylomicron uptake. Reduction of hepatic uptake by SLNs (44.7%) demonstrated liver bypass and thereby the oral bioavailability enhancement. A great amount of efavirenz was observed in the spleen, a principal lymphatic organ.

Malaria continues to be a vast health and economic problem in tropical regions. Primaquine is the only available drug for combating the relapsing form of malaria. The oral absorption of this drug is low because of first-pass metabolism and excretion. The high-dose use of primaquine usually produces hematological- and GI-related toxicity [109]. Primaquine entrapment in SLNs exhibited a sustained drug release over 72 hours [110]. When the *Plasmodium berghei*-infected mouse was orally administered with SLNs at a drug dose of 2 mg/kg/d for 4 days, the suppression of 94% was achieved by SLNs, whereas only 72% suppression was found for the free control. Arteether is an artemisinin analog for treatment of multidrug-resistant malaria. SLNs were used to resolve the low stability in the gastric environment and the short half-life of arteether [111]. The cell viability remained >90% for SLNs against macrophages, indicating the safety of their application. The half-life of arteether SLNs was found to be 4.5 hours, whereas arteether in ground nut oil and water as the vehicles showed a half-life of 3.3 hours and 2.0 hours. SLNs could increase oral bioavailability compared to ground nut oil by 1.7-fold. Praziquantel is currently used to treat schistosomiasis, a parasitic disease caused by *Schistosoma*. Because of its limited effect on schistosomiasis, de Souza et al [112] incorporated praziquantel into SLNs to check the possible promotion of its therapeutic activity. In the experiment focused on *Schistosoma mansoni* inhibition, SLNs were more effective than the free drug, leading to parasite killing in less time. Contrary to the cases of enhanced intestinal permeation by SLNs, the designed SLNs for praziquantel revealed less permeation across the duodenal segment than the free drug in the everted gut sac transport study. This may be attributed to a reduced availability of SLNs in mucosal bulk. This suggested a reservoir role of SLNs for praziquantel to kill the parasites located in the mesenteric vein of the intestine. The parasite *Trypanosoma cruzi* causes Chagas disease, which remains a serious health problem. Carneiro et al [113] evaluated the *in vitro* and *in vivo* activity of 5-hydroxy-3-methyl-5-phenylpyrazoline-1-(S-benzyl dithiocarbamate) (H2bdtc) as a free active or incorporated into SLNs. H2bdtc-loaded SLNs efficiently reduced parasitemia in mice at a concentration 100 times lower than benznidazole, the currently available drug for treating Chagas disease. In the *in vivo* study, oral administration of H2bdtc (4 µmol/kg) in SLNs eradicated 70% of the parasites in circulation, whereas free H2bdtc and benznidazole killed only 48% and 15% of the parasites. SLNs also diminished inflammation and lesions produced by the free drug in the liver and heart (Table 3).



**Table 3 – Formulations of orally administered SLNs loaded with drugs or natural compounds against infection and their benefits.**

Active ingredient	Indication	Lipid type	Average size (nm)	Outcomes offered by SLNs	Reference
Isoniazid	Tuberculosis	Compritol 888 ATO	48	Increased bioavailability and less acute toxicity	Bhandari and Kaur [103]
Miconazole	Fungi	Precirol ATO 5	23	Enhanced antifungal activity and bioavailability	Aljaeid and Hosny [104]
Lopinavir	Retrovirus	Stearic acid	181	Increased bioavailability	Negi et al [105]
Lopinavir	Retrovirus	Compritol 888 ATO	215	Increased $C_{max}$ and bioavailability	Negi et al [106]
Efavirenz	Retrovirus	Monosteatin	125	Increased $C_{max}$ and AUC	Gaur et al [107]
Efavirenz	Retrovirus	Compritol 888 ATO	168	Increased lymphatic uptake and bioavailability	Makwana et al [108]
Primaquine	Malaria	Stearic acid	236	Enhanced antimalarial efficacy	Omwoyo et al [110]
Arteether	Multidrug-resistant malaria	Monosteatin	100	Increased bioavailability and half-life	Dwivedi et al [111]
Praziquantel	Schistosomiasis	Stearic acid	506	Enhanced parasite killing	de Souza et al [112]
H2bdc	Chagas disease	Stearic acid	127	Enhanced parasite killing and diminished toxicity	Carneiro et al [113]

AUC = area under the curve; H2bdc = 5-hydroxy-3-methyl-5-phenyl-pyrazoline-1-(S-benzyl dithiocarbazate); SLNs = solid lipid nanoparticles.

## 5.5. Diabetes

Diabetes mellitus is one of the most common metabolic diseases worldwide. Hyperglycemia caused by diabetes is a serious pathologic condition producing neurological and CV damage. Diabetes is divided into two types: type 1 diabetes and type 2 diabetes. Type 1 diabetes occurs when the pancreas fails to produce sufficient insulin, giving rise to hyperglycemia. The patient requires a routine administration of insulin. Insulin absorption via the oral route is difficult because of acidic gastric pH, digestive enzymes, and the epithelial cells of the GI tract [114]. Researchers focus considerable attention on SLNs as the carriers to protect peptides and proteins known for their sensitivity to various environmental factors such as pH, temperature, and ionic strength [115]. Zhang et al [116] designed SLNs coated with stearic acid-octaarginine as carriers for insulin. Octaarginine is a cell-penetrating peptide that can facilitate cellular uptake of some drugs [117]. The size and insulin encapsulation of the octaarginine-coated SLNs were 162 nm and 77%, respectively. Octaarginine-coated and noncoated SLNs increased Caco-2 cell uptake by 2.3 times and 18.4 times, respectively. The SLNs containing octaarginine showed a significantly higher hypoglycemic effect (3-fold) in rats compared to noncoated SLNs. Ansari et al [118] developed SLNs composed of Dynasan 114 as the solid lipid matrix for oral insulin delivery. The permeability of insulin measured by the everted sac method showed a higher level of SLNs (14.8  $\mu\text{g}/\text{cm}^2$ ) than the insulin solution (8.0  $\mu\text{g}/\text{cm}^2$ ). SLNs provided better insulin protection from the GI environment as evident in the 5-fold higher bioavailability compared to the solution.

About 90% of diabetic patients are affected by noninsulin-dependent type 2. Glibenclamide is a second-generation sulfonylurea for type 2 diabetes treatment. The very low aqueous solubility is responsible for its limited oral bioavailability [119]. Gonçalves et al [120] developed SLNs coated with PEG to increase glibenclamide stability in gastric solution. The insulin release from SLNs obeyed a typical biphasic kinetic, where a complete release was achieved after 24 hours. The oral administration of free glibenclamide (5 mg/kg) in diabetic rats reduced the blood glucose concentration after 4 hours, and it then climbed quickly to the initially high level. Oral SLNs not only created a rapid onset of glucose lowering but also maintained the reduction for 8 hours after administration. Berberine is an isoquinoline alkaloid derived from *Coptis chinensis*. It is reported that berberine has the capability to treat diabetes by glycolysis stimulation and insulin secretion promotion [121]. Xue et al [122] encapsulated berberine by SLNs with a particulate size and entrapment efficiency of 77 nm and 58%, respectively. A single oral dose (50 mg/kg) in rats achieved a significant improvement of AUC by SLNs (179  $\mu\text{g h/L}$ ) compared to solution (86  $\mu\text{g h/L}$ ). Morphological analysis of the db/db mice indicated that SLNs potentially enhanced islet function and protected the islet from regeneration. *Andrographis paniculata* and its bioactive compound andrographolide have been reported to have antidiabetic and hypolipidemic activities [123]. Andrographolide is rapidly metabolized in the duodenum and jejunum to form sulfate conjugates [124]. The SLNs were prepared to load andrographolide with a high encapsulation percentage of 91% [125]. The oral bioavailability

and hypolipidemic activity of andrographolide was improved by SLNs because of the increase of solubility and stability in the intestine and the change of transport mode in Caco-2 cells. The bioavailability was increased 2.4-fold after andrographolide inclusion in SLNs.

### 5.6. Osteoporosis

Osteoporosis is a disease in which decreased bone strength increases the risk of a broken bone. It is the most common reason for a broken bone among the elderly and postmenopausal women. Oral raloxifene is approved for prevention and treatment of postmenopausal osteoporosis. Although 60% of raloxifene is absorbed orally, the absolute bioavailability is only 2% because of poor aqueous solubility and glucuronide conjugation [126]. SLNs for raloxifene delivery were prepared using Compritol 888 ATO as the lipid and poloxamer 188 as the emulsifier [127]. The release of free raloxifene was complete within 4 hours, whereas SLNs prolonged drug release up to 24 hours. The rats were orally administered raloxifene at a dose of 30 mg/kg. The bioavailability of SLNs was nearly 5 times that of free raloxifene. Tran et al [128] also prepared raloxifen-loaded SLNs to examine oral bioavailability and safety. The optimized SLNs showed an average size of 140 nm with ease of transport into the lymphatic system.  $C_{max}$  and AUC were increased by 3.1- and 2.7-fold by SLN formulation compared to the free drug. The cytotoxicity against NIH-3T3 cells exhibited nontoxicity of the SLNs. Alendronate is a nitrogen-containing bisphosphonate used for osteoporosis management. The challenge associated with oral alendronate is its low bioavailability (0.6 %) because of the difficulty of crossing the GI membrane [129]. The enteric-coated SLNs were designed to conquer this challenge to prevent alendronate contact with gastric mucosa [130]. The alendronate release percentage in 0.1N HCl was 5% and 85% for SLNs and commercial tablets, demonstrating the gastric resistance of the enteric-coated carrier. The drug release from SLNs occurred only at an alkaline pH. The pharmacokinetic determination of oral SLNs revealed that alendronate bioavailability increased 7.4-fold in rabbits.

Salmon calcitonin is a calcium-regulating peptide hormone secreted from the ultimobranchial gland of salmon. It is widely used in the treatment of postmenopausal osteoporosis. The oral bioavailability of calcitonin is <0.1% in rats and dogs [131]. SLNs encapsulating salmon calcitonin could increase Caco-2 cell uptake by 4 times compared to the free control [132]. The *in vivo* hypocalcemic effect in rats was better with prepared SLNs than with free calcitonin (17.4% vs. 2.0% reduction). The SLNs prepared with stearic acid and tripalmitin increased oral calcitonin bioavailability from 2% to 13%. Fan et al [133] prepared salmon calcitonin-loaded SLNs by coupling with peptide ligand CSKSSDYQC, which shows affinity with goblet cells on the epithelium, or IRQRRRR, which is a cell-penetrating peptide. The protective efficacy of SLNs on calcitonin against pancreatin was examined. Most of the free calcitonin was degraded within 15 minutes. A much slower degradation rate was found for SLNs. The permeability across the Caco-2 cell monolayer for nonconjugated, CSKSSDYQC and IRQRRRR SLNs was 2.1-, 5.9-, and 4.7-fold higher than that of the free control. The absolute

bioavailability of CSKSSDYQC (12.4%) and IRQRRRR SLNs (10.1%) was greater than that of unmodified SLNs (5.1%), suggesting the effectiveness of peptide conjugation for the enhancement of oral protein delivery.

## 6. Conclusions and perspectives

SLNs are the colloidal systems for the delivery of labile drugs with controlled release kinetics. SLN-based carriers are compatible with the oral administration route because of nontoxic excipients and increased bioavailability. This review represents the research advancements that had been undertaken to establish the oral SLNs with respect to their unique properties. In the past 5 years, the oral SLNs have gained some advances in the therapy of cancers and CNS-related diseases, which are the increasing health threats around the world. For instance, SLNs could enhance the bioavailability of docetaxel by a 3-fold compared to the commercially available Taxotere. The PEGylated SLNs provided a 7.5-fold increase of oral bioavailability than free doxorubicin. With respect to the treatment of Parkinson's disease, a 13-fold increase of oral apomorphine bioavailability was achieved by SLNs compared with the free drug. The introduction of SLNs for improved oral delivery also promotes the possibility of natural compound application for disease management because the oral bioavailability and half-life of natural products are always low in the body.

Despite the advantages of oral SLNs for drug delivery, several challenges remain to be resolved for better application in the future. The particle growing and unpredictable gelation tendency are the storage problems in some cases. The burst drug release for some oral SLNs may cause toxicity concerns. However, the very slow drug release can lead to inefficient activity in treating the diseases. The development of the formulation design of novel SLNs to provide a feasible release profile is important. This depends on the cargo drugs selected in SLNs, because different drugs show different physicochemical characters, and on the interaction with the nanoparticles. Prolonged drug circulation is a common phenomenon for oral delivery of SLNs. However, the negative side of prolonged circulation is the slow tissue accumulation of the nanoparticles, including the targeted tissue. Again, the optimization of SLN formulations is necessary.

The SLNs as drug nanocarriers have the potential to achieve the broad objectives for treating various diseases. A wider collection of the lipid materials may be illustrated for SLNs in the future. The lipids from natural sources can be a major origin of the SLN lipid matrix. More patented dosage forms of SLNs can be expected in the near future. SLNs based on the optimized formulations should have a place in modern pharmaceutical products because of the capability of enhancing drug therapy. An innovative formulation of a drug can extend the life of patients. A novel delivery system for old actives would result in the reduction of side effects and more-effective treatment achievement. Although many oral SLNs have been developed for testing in cell-based and animal studies, clinical trials for drug delivery application are still limited. This may be because of the high cost of clinical trials and the unknown side effects that should be identified and



explored first. At least a 5-fold-improved oral bioavailability needs to be achieved in most cases to justify the use of nanocarriers from the commercial point of view, unless other convincing benefits can be gained. A better understanding of the full potential of SLNs and the progress from laboratory bench to large-scale commercialization is required. The introduction and description of the SLNs for oral delivery outlined in this review may give relevant information to investigators involved in designing feasible and efficient delivery systems for the treatment of various diseases.

## Conflicts of interest

The authors declare no conflicts of interest.

## Acknowledgments

The authors are grateful to the financial support by Chang Gung Memorial Hospital (CMRPD1B0332) and Chang Gung University of Science and Technology (EZRP3G0171 and EZRP3G0181).

## REFERENCES

- [1] Choonara BF, Choonara YE, Kumar P, Bijukumar D, du Toit LC, Pillay V. A review of advanced oral drug delivery technologies facilitating the protection and absorption of protein and peptide molecules. *Biotechnol Adv* 2014;32:1269–82.
- [2] Ensign LM, Cone R, Hanes J. Oral drug delivery with polymeric nanoparticles: the gastrointestinal mucus barriers. *Adv Drug Deliv Rev* 2012;64:557–70.
- [3] Alai MS, Lin WJ, Pingale SS. Application of polymeric nanoparticles and micelles in insulin oral delivery. *J Food Drug Anal* 2015;23:351–8.
- [4] Jabir NR, Tabrez S, Ashraf GM, Shakil S, Damanhour GA, Kamal MA. Nanotechnology-based approaches in anticancer research. *Int J Nanomed* 2012;7:4391–408.
- [5] Li SD, Huang L. Pharmacokinetics and biodistribution of nanoparticles. *Mol Pharm* 2008;5:496–504.
- [6] Rostami E, Kashanian S, Azandaryani AH, Faramarzi H, Dolatabadi JE, Omidfar K. Drug targeting using solid lipid nanoparticles. *Chem Phys Lipids* 2014;181:56–61.
- [7] Schwarz C, Mehnert M, Lucks JS, Müller RH. Solid lipid nanoparticles (SLN) for controlled drug delivery: I. Production, characterization and sterilization. *J Control Rel* 1994;30:83–96.
- [8] Geszke-Moritz M, Moritz M. Solid lipid nanoparticles as attractive drug vehicles: composition, properties and therapeutic strategies. *Mater Sci Eng C Mater Biol Appl* 2016;68:982–94.
- [9] Ezzati Nazhad Dolatabadi J, Valizadeh H, Hamishehkar H. Solid lipid nanoparticles as efficient drug and gene delivery systems: recent breakthroughs. *Adv Pharm Bull* 2015;5:151–9.
- [10] Schenk M, Mueller C. The mucosal immune system at the gastrointestinal barrier. *Best Pract Res Clin Gastroenterol* 2008;22:391–409.
- [11] Sant S, Tao SL, Fisher OZ, Xu Q, Peppas NA, Khademhosseini A. Microfabrication technologies for oral drug delivery. *Adv Drug Deliv Rev* 2012;64:496–507.
- [12] Bak A, Leung D, Barrett SE, Forster S, Minnihan EC, Leithead AW, Cunningham J, Toussaint N, Crocker LS. Physicochemical and formulation developability assessment for therapeutic peptide delivery—a primer. *AAPS J* 2015;17:144–55.
- [13] Hu B, Liu X, Zhang C, Zeng X. Food macromolecule based nanodelivery systems for enhancing the bioavailability of polyphenols. *J Food Drug Anal* 2017;25:3–15.
- [14] Bernkop-Schnürch A. Nanocarrier systems for oral drug delivery: do we really need them? *Eur J Pharm Sci* 2013;49:272–7.
- [15] Saraf S, Ghosh A, Kaur CD, Saraf S. Novel modified nanosystem based lymphatic targeting. *Res J Nanosci Nanotechnol* 2011;1:60–74.
- [16] Chaudhary S, Garg T, Murthy RS, Rath G, Goyal AK. Recent approaches of lipid-based delivery system for lymphatic targeting via oral route. *J Drug Target* 2014;22:871–82.
- [17] Ali Khan A, Mudassir J, Mohtar N, Darwis Y. Advanced drug delivery to the lymphatic system: lipid-based nanoformulations. *Int J Nanomed* 2013;8:2733–44.
- [18] Kumar S, Randhawa JK. High melting lipid based approach for drug delivery: solid lipid nanoparticles. *Mater Sci Eng C Mater Biol Appl* 2013;33:1842–52.
- [19] Hunter AC, Elsom J, Wibroe PP, Moghimi SM. Polymeric particulate technologies for oral drug delivery and targeting: a pathophysiological perspective. *Nanomed Nanotechnol Biol Med* 2012;8(Suppl. 1):S5–20.
- [20] Fu PP, Xia Q, Hwang HM, Ray PC, Yu H. Mechanisms of nanotoxicity: generation of reactive oxygen species. *J Food Drug Anal* 2014;22:64–75.
- [21] Yadav P, Soni G, Mahor A, Alok S, Singh PP, Verma A. Solid lipid nanoparticles: an effective and promising drug delivery system—a review. *Int J Pharm Sci Res* 2014;5:1152–62.
- [22] Üner M, Yener G. Importance of solid lipid nanoparticles (SLN) in various administration routes and future perspectives. *Int J Nanomed* 2007;2:289–300.
- [23] Helgason T, Awad TS, Kristbergsson K, McClements DJ, Weiss J. Effect of surfactant surface coverage on formation of solid lipid nanoparticles (SLN). *J Colloid Interface Sci* 2009;334:75–81.
- [24] Botto C, Mauro N, Amore E, Martorana E, Giammona G, Bondi ML. Surfactant effect on the physicochemical characteristics of cationic solid lipid nanoparticles. *Int J Pharm* 2016;516:334–41.
- [25] Harde H, Das M, Jain S. Solid lipid nanoparticles: an oral bioavailability enhancer vehicle. *Expert Opin Drug Deliv* 2011;8:1407–24.
- [26] Battaglia L, Gallarate M. Lipid nanoparticles: state of the art, new preparation methods and challenges in drug delivery. *Expert Opin Drug Deliv* 2012;9:497–508.
- [27] Hwang TL, Aljuffali IA, Hung CF, Chen CH, Fang JY. The impact of cationic solid lipid nanoparticles on human neutrophil activation and formation of neutrophil extracellular traps (NETs). *Chem Biol Interact* 2015;235:106–14.
- [28] Ingham B. X-ray scattering characterization of nanoparticles. *Crystallogr Rev* 2015;21:229–303.
- [29] Muchow M, Maincent P, Müller RH. Lipid nanoparticles with a solid matrix (SLN, NLC, LDC) for oral drug delivery. *Drug Dev Ind Pharm* 2008;34:1394–405.
- [30] Dahan A, Hoffman A. Rationalizing the selection of oral lipid based drug delivery systems by an in vitro dynamic lipolysis model for improved oral bioavailability of poorly water soluble drugs. *J Control Release* 2008;129:1–10.
- [31] Doktorová S, Santos DL, Costa I, Andreani T, Souto EB, Silva AM. Cationic solid lipid nanoparticles interfere with the activity of antioxidant enzymes in hepatocellular carcinoma cells. *Int J Pharm* 2014;471:18–27.

- [32] Cai S, Yang Q, Bagby TR, Forrest ML. Lymphatic drug delivery using engineered liposomes and solid lipid nanoparticles. *Adv Drug Deliv Rev* 2011;63:901–8.
- [33] Chai GH, Xu Y, Chen SQ, Cheng B, Hu FQ, You J, Du YZ, Yuan H. Transport mechanisms of solid lipid nanoparticles across Caco-2 cell monolayers and their related cytotoxicology. *ACS Appl Mater Interfaces* 2016;8:5929–40.
- [34] Li H, Zhao X, Ma Y, Zhai G, Li L, Lou H. Enhancement of gastrointestinal absorption of quercetin by solid lipid nanoparticles. *J Control Release* 2009;133:238–44.
- [35] Ahmad J, Amin S, Rahman M, Rub RA, Singhal M, Ahmad MZ, Rahman Z, Addo RT, Ahmad FJ, Mushtaq G, Kamal MA, Akhter S. Solid matrix based lipidic nanoparticles in oral cancer chemotherapy: applications and pharmacokinetics. *Curr Drug Metab* 2015;16:633–44.
- [36] Fan Z, Fu PP, Yu H, Ray PC. Theranostic nanomedicine for cancer detection and treatment. *J Food Drug Anal* 2014;22:3–17.
- [37] Mei L, Zhang Z, Zhao L, Huang L, Yang XL, Tang J, Feng SS. Pharmaceutical nanotechnology for oral delivery of anticancer drugs. *Adv Drug Deliv Rev* 2013;65:880–90.
- [38] ten Tije AJ, Verweij J, Loos WJ, Sparreboom A. Pharmacological effects of formulation vehicles: implications for cancer chemotherapy. *Clin Pharmacokinet* 2003;42:665–85.
- [39] Hendriks JJ, Lagas JS, Rosing H, Schellens JH, Beijnen JH, Schinkel AH. P-glycoprotein and cytochrome P450 3A act together in restricting the oral bioavailability of paclitaxel. *Int J Cancer* 2013;132:2439–47.
- [40] Baek JS, So JW, Shin SC, Cho CW. Solid lipid nanoparticles of paclitaxel strengthened by hydroxypropyl- $\beta$ -cyclodextrin as an oral delivery system. *Int J Mol Med* 2012;30:953–9.
- [41] Zafar N, Fessi H, Elaissari A. Cyclodextrin containing biodegradable particles: from preparation to drug delivery applications. *Int J Pharm* 2014;461:351–66.
- [42] Pooja D, Kulhari H, Kuncha M, Rachamalla SS, Adams DJ, Bansal V, Sistla R. Improving efficacy, oral bioavailability, and delivery of paclitaxel using protein-grafted solid lipid nanoparticles. *Mol Pharm* 2016;13:3903–12.
- [43] Liu Y, Wang P, Sun C, Zhao J, Du Y, Shi F, Feng N. Bioadhesion and enhanced bioavailability by wheat germ agglutinin-grafted lipid nanoparticles for oral delivery of poorly water-soluble drug bufalin. *Int J Pharm* 2011;419:260–5.
- [44] Cho HJ, Park JW, Yoon IS, Kim DD. Surface-modified solid lipid nanoparticles for oral delivery of docetaxel: enhanced intestinal absorption and lymphatic uptake. *Int J Nanomed* 2014;9:495–504.
- [45] Zhang YW, Shi J, Li YJ, Wei L. Cardiomyocyte death in doxorubicin-induced cardiotoxicity. *Arch Immunol Ther Exp* 2009;57:435–45.
- [46] Patro NM, Devi K, Pai RS, Suresh S. Evaluation of bioavailability, efficacy, and safety profile of doxorubicin-loaded solid lipid nanoparticles. *J Nanopart Res* 2013;15:2124.
- [47] Yuan H, Chen CY, Chai GH, Du YZ, Hu FQ. Improved transport and absorption through gastrointestinal tract by PEGylated solid lipid nanoparticles. *Mol Pharm* 2013;10:1865–73.
- [48] Wang YY, Lai SK, Suk JS, Pace A, Cone R, Hanes J. Addressing the PEG mucoadhesivity paradox to engineer nanoparticles that “slip” through the human mucus barrier. *Angew Chem Int Ed Engl* 2008;47:9726–9.
- [49] Ozaki K, Kishikawa F, Tanaka M, Sakamoto T, Tanimura S, Kohno M. Histone deacetylase inhibitors enhance the chemosensitivity of tumor cells with cross-resistance to a wide range of DNA-damaging drugs. *Cancer Sci* 2008;99:376–84.
- [50] Tran TH, Ramasamy T, Truong DH, Shin BS, Choi HG, Yong CS, Kim JO. Development of vorinostat-loaded solid lipid nanoparticles to enhance pharmacokinetics and efficacy against multidrug-resistant cancer cells. *Pharm Res* 2014;31:1978–88.
- [51] Hashem FM, Nasr M, Khairy A. In vitro cytotoxicity and bioavailability of solid lipid nanoparticles containing tamoxifen citrate. *Pharm Dev Technol* 2014;19:824–32.
- [52] Aljuffali IA, Fang CL, Chen CH, Fang JY. Nanomedicine as a strategy for natural compound delivery to prevent and treat cancers. *Curr Pharm Design* 2016;22:4219–31.
- [53] Iriti M, Faoro F. Bioactivity of grape chemicals for human health. *Nat Prod Commun* 2009;4:611–34.
- [54] Yap SP, Yuen KH, Lim AB. Influence of route of administration on the absorption and disposition of alpha-, gamma- and delta-tocotrienols in rats. *J Pharm Pharmacol* 2003;55:53–8.
- [55] Abuasal BS, Lucas C, Peyton B, Alayoubi A, Nazzal S, Sylvester PW, Kaddoumi A. Enhancement of intestinal permeability utilizing solid lipid nanoparticles increases  $\gamma$ -tocotrienol oral bioavailability. *Lipids* 2012;47:461–9.
- [56] Dang YJ, Zhu CY. Determination of trace cantharidin in plasma and pharmacokinetic study in beagle dogs using gas chromatography-mass spectrometry. *J Anal Toxicol* 2009;33:384–8.
- [57] Dang YJ, Zhu CY. Oral bioavailability of cantharidin-loaded solid lipid nanoparticles. *Chin Med* 2013;8:1.
- [58] Henderson AJ, Ollila CA, Kumar A, Borresen EC, Raina K, Agarwal R, Ryan EP. Chemopreventive properties of dietary rice bran: current status and future prospects. *Adv Nutr* 2012;3:643–53.
- [59] Zhang Y, Li Z, Zhang K, Yang G, Wang Z, Zhao J, Hu R, Feng N. Ethyl oleate-containing nanostructured lipid carriers improve oral bioavailability of trans-ferulic acid as compared with conventional solid lipid nanoparticles. *Int J Pharm* 2016;511:57–64.
- [60] Thakkar A, Chenreddy S, Wang J, Prabhu S. Ferulic acid combined with aspirin demonstrates chemopreventive potential towards pancreatic cancer when delivered using chitosan-coated solid-lipid nanoparticles. *Cell Biosci* 2015;5:46.
- [61] Luo Y, Teng Z, Li Y, Wang Q. Solid lipid nanoparticles for oral drug delivery: chitosan coating improves stability, controlled delivery, mucoadhesion and cellular uptake. *Carbohydr Polym* 2015;122:221–9.
- [62] Dening TJ, Rao S, Thomas N, Prestidge CA. Oral nanomedicine approaches for the treatment of psychiatric illnesses. *J Control Rel* 2016;223:137–56.
- [63] Silva AC, Kumar A, Wild W, Ferreira D, Santos D, Forbes B. Long-term stability, biocompatibility and oral delivery potential of risperidone-loaded solid lipid nanoparticles. *Int J Pharm* 2012;436:798–805.
- [64] Subramony JA. Apomorphine in dopaminergic therapy. *Mol Pharm* 2006;3:380–5.
- [65] Tsai MJ, Huang YB, Wu PC, Fu YS, Kao YR, Fang JY, Tsai YH. Oral apomorphine delivery from solid lipid nanoparticles with different monostearate emulsifiers: pharmacokinetic and behavioral evaluations. *J Pharm Sci* 2011;100:547–57.
- [66] Jagdale SC, Pawar CR. Application of design of experiment for polyox and xanthan gum coated floating pulsatile delivery of sumatriptan succinate in migraine treatment. *Biomed Res Int* 2014;2014:547212.
- [67] Hansraj GP, Singh SK, Kumar P. Sumatriptan succinate loaded chitosan solid lipid nanoparticles for enhanced anti-migraine potential. *Int J Biol Macromol* 2015;81:467–76.
- [68] Girotra P, Singh SK. Multivariate optimization of rizatriptan benzoate-loaded solid lipid nanoparticles for brain targeting

- and migraine management. *AAPS PharmSciTech* 2016. <http://dx.doi.org/10.1208/s12249-016-0532-0>.
- [69] Ibrahim WM, AlOmran AH, Yassin AE. Novel sulpiride-loaded solid lipid nanoparticles with enhanced intestinal permeability. *Int J Nanomed* 2014;9:129–44.
  - [70] Raggi MA, Mandrioli R, Sabbioni C, Pucci V. Atypical antipsychotics: pharmacokinetics, therapeutic drug monitoring and pharmacological interactions. *Curr Med Chem* 2004;11:279–96.
  - [71] Narala A, Veerabrahma K. Preparation, characterization and evaluation of quetiapine fumarate solid lipid nanoparticles to improve the oral bioavailability. *J Pharm* 2013;2013:265741.
  - [72] Uhr M, Grauer MT, Holsboer F. Differential enhancement of antidepressant penetration into the brain in mice with *abcb1ab* (*mdr1ab*) P-glycoprotein gene disruption. *Biol Psychiatry* 2003;54:840–6.
  - [73] Zhou Y, Zhang G, Rao Z, Yang Y, Zhou Q, Qin H, Wei Y, Wu X. Increased brain uptake of venlafaxine loaded solid lipid nanoparticles by overcoming the efflux function and expression of P-gp. *Arch Pharm Res* 2015;38:1325–35.
  - [74] Apetz N, Munch G, Govindaraghavan S, Gyengesi E. Natural compounds and plant extracts as therapeutics against chronic inflammation in Alzheimer's disease—a translational perspective. *CNS Neurol Disord Drug Targets* 2014;13:1175–91.
  - [75] Tsai CH, Yen YH, Yang JPW. Finding of polysaccharide–peptide complexes in *Cordyceps militaris* and evaluation of its acetylcholinesterase inhibition activity. *J Food Drug Anal* 2014;23:63–70.
  - [76] Spilsbury A, Vauzour D, Spencer JP, Rattray M. Regulation of NF- $\kappa$ B activity in astrocytes: effects of flavonoids at dietary-relevant concentrations. *Biochem Biophys Res Commun* 2012;418:578–83.
  - [77] Vedagiri A, Thangarajan S. Mitigating effect of chrysin loaded solid lipid nanoparticles against amyloid  $\beta$ 25–35 induced oxidative stress in rat hippocampal region: an efficient formulation approach for Alzheimer's disease. *Neuropeptides* 2016;58:111–25.
  - [78] Diaz-Gerevini GT, Repossi G, Dain A, Tarres MC, Das UN, Eynard AR. Beneficial action of resveratrol: how and why? *Nutrition* 2016;32:174–8.
  - [79] Pandita D, Kumar S, Poonia N, Lather V. Solid lipid nanoparticles enhance oral bioavailability of resveratrol, a natural polyphenol. *Food Res Int* 2014;62:1165–74.
  - [80] Ramalingam P, Ko YT. Improved oral delivery of resveratrol from N-trimethyl chitosan-g-palmitic acid surface-modified solid lipid nanoparticles. *Colloids Surf B Biointerfaces* 2016;139:52–61.
  - [81] Minassi A, Sánchez-Duffhues G, Collado JA, Muñoz E, Appendino G. Dissecting the pharmacophore of curcumin. Which structural element is critical for which action? *J Nat Prod* 2013;76:1105–12.
  - [82] Lee WH, Loo CY, Bebawy M, Luk F, Mason RS, Rohanizadeh R. Curcumin and its derivatives: their application in neuropharmacology and neuroscience in the 21st century. *Curr Neuropharmacol* 2013;11:338–78.
  - [83] Prasad S, Tyagi AK, Aggarwal BB. Recent developments in delivery, bioavailability, absorption and metabolism of curcumin: the golden pigment from golden spice. *Cancer Res Treat* 2014;46:2–18.
  - [84] Kakkar V, Kaur IP. Evaluating potential of curcumin loaded solid lipid nanoparticles in aluminium induced behavioural, biochemical and histopathological alterations in mice brain. *Food Chem Toxicol* 2011;49:2906–13.
  - [85] Kakkar V, Mishra AK, Chuttani K, Kaur IP. Proof of concept studies to confirm the delivery of curcumin loaded solid lipid nanoparticles (C-SLNs) to brain. *Int J Pharm* 2013;448:354–9.
  - [86] Ji H, Tang J, Li M, Ren J, Zheng N, Wu L. Curcumin-loaded solid lipid nanoparticles with Brij78 and TPGS improved in vivo oral bioavailability and in situ intestinal absorption of curcumin. *Drug Deliv* 2016;23:459–70.
  - [87] Ramalingam P, Yoo SW, Ko YT. Nanodelivery systems based on mucoadhesive polymer coated solid lipid nanoparticles to improve the oral intake of food curcumin. *Food Res Int* 2016;84:113–9.
  - [88] Mansourpour M, Mahjub R, Amini M, Ostad SN, Shamsa ES, Rafiee-Tehrani M, Dorkoosh FA. Development of acid-resistant alginate/trimethyl chitosan nanoparticles containing cationic  $\beta$ -cyclodextrin polymers for insulin oral delivery. *AAPS PharmSciTech* 2015;16:952–62.
  - [89] Ramalingam P, Ko YT. Enhanced oral delivery of curcumin from N-trimethyl chitosan surface-modified solid lipid nanoparticles: pharmacokinetic and brain distribution evaluations. *Pharm Res* 2015;32:389–402.
  - [90] Shah FA, Gim SA, Sung JH, Jeon SJ, Kim MO, Koh PO. Identification of proteins regulated by curcumin in cerebral ischemia. *J Surg Res* 2016;201:141–8.
  - [91] Kakkar V, Muppu SK, Chopra K, Kaur IP. Curcumin loaded solid lipid nanoparticles: an efficient formulation approach for cerebral ischemic reperfusion injury in rats. *Eur J Pharm Biopharm* 2013;85:339–45.
  - [92] Hernández-Hernández R, Coll T, Rachitzky P, Armas-Hernández MJ, Armas-Padilla MC, Velasco M, Rizzo A. Comparison of two nimodipine formulations in healthy volunteers. *J Hum Hypertens* 2002;16:S142–4.
  - [93] Chalikwar SS, Belgamwar VS, Talele VR, Surana SJ, Patil MU. Formulation and evaluation of Nimodipine-loaded solid lipid nanoparticles delivered via lymphatic transport system. *Colloids Surf B Biointerfaces* 2012;97:109–16.
  - [94] Dudhipala N, Veerabrahma K. Pharmacokinetic and pharmacodynamic studies of nisoldipine-loaded solid lipid nanoparticles developed by central composite design. *Drug Dev Ind Pharm* 2015;41:1968–77.
  - [95] Dudhipala N, Veerabrahma K. Candesartan cilexetil loaded solid lipid nanoparticles for oral delivery: characterization, pharmacokinetic and pharmacodynamic evaluation. *Drug Deliv* 2016;23:395–404.
  - [96] Zhang Z, Gao F, Bu H, Xiao J, Li Y. Solid lipid nanoparticles loading candesartan cilexetil enhance oral bioavailability: in vitro characteristics and absorption mechanism in rats. *Nanomed Nanotechnol Biol Med* 2012;8:740–7.
  - [97] Venishetty VK, Chede R, Komuravelli R, Adepu L, Sistla R, Diwan PV. Design and evaluation of polymer coated carvedilol loaded solid lipid nanoparticles to improve the oral bioavailability: a novel strategy to avoid intraduodenal administration. *Colloids Surf B Biointerfaces* 2012;95:1–9.
  - [98] Muñoz M, García-Erce JA, Remacha ÁF. Disorders of iron metabolism: Part II. Iron deficiency and iron overload. *J Clin Pathol* 2011;64:287–96.
  - [99] Zariwala MG, Elsaid N, Jackson TL, Corral López F, Farnaud S, Somavarapu S, Renshaw D. A novel approach to oral iron delivery using ferrous sulphate loaded solid lipid nanoparticles. *Int J Pharm* 2013;456:400–7.
  - [100] Hosny KM, Banjar ZM, Hariri AH, Hassan AH. Solid lipid nanoparticles loaded with iron to overcome barriers for treatment of iron deficiency anemia. *Drug Des Devel Ther* 2015;9:313–20.
  - [101] Aljuffali IA, Huang CH, Fang JY. Nanomedical strategies for targeting skin microbiomes. *Curr Drug Metab* 2015;16:255–71.
  - [102] Preziosi P. Isoniazid: metabolic aspects and toxicological correlates. *Curr Drug Metab* 2007;8:839–51.



- [103] Bhandari R, Kaur IP. Pharmacokinetics, tissue distribution and relative bioavailability of isoniazid-solid lipid nanoparticles. *Int J Pharm* 2013;441:202–12.
- [104] Aljaeid BM, Hosny KM. Miconazole-loaded solid lipid nanoparticles: formulation and evaluation of a novel formula with high bioavailability and antifungal activity. *Int J Nanomed* 2016;11:441–7.
- [105] Negi JS, Chattopadhyay P, Sharma AK, Ram V. Development of solid lipid nanoparticles (SLNs) of lopinavir using hot self nano-emulsification (SNE) technique. *Eur J Pharm Sci* 2013;48:231–9.
- [106] Negi JS, Chattopadhyay P, Sharma AK, Ram V. Development and evaluation of glyceryl behenate based solid lipid nanoparticles (SLNs) using hot self-nanoemulsification (SNE) technique. *Arch Pharm Res* 2014;37:361–70.
- [107] Gaur PK, Mishra S, Bajpai M, Mishra A. Enhanced oral bioavailability of efavirenz by solid lipid nanoparticles: in vitro drug release and pharmacokinetics studies. *Biomed Res Int* 2014;2014:363404.
- [108] Makwana V, Jain R, Patel K, Nivsarkar M, Joshi A. Solid lipid nanoparticles (SLN) of efavirenz as lymph targeting drug delivery system: elucidation of mechanism of uptake using chylomicron flow blocking approach. *Int J Pharm* 2015;495:439–46.
- [109] Baird JK. Primaquine toxicity forestalls effective therapeutic management of the endemic malaras. *Int J Parasitol* 2012;42:1049–54.
- [110] Omwoyo WN, Ogutu B, Oloo F, Swai H, Kalombo L, Melariri P, Mahanga GM, Gathirwa JW. Preparation, characterization, and optimization of primaquine-loaded solid lipid nanoparticles. *Int J Nanomed* 2014;9:3865–74.
- [111] Dwivedi P, Khatik R, Khandelwal K, Taneja I, Raju KS, Wahajuddin, Paliwal SK, Dwivedi AK, Mishra PR. Pharmacokinetics study of arteether loaded solid lipid nanoparticles: an improved oral bioavailability in rats. *Int J Pharm* 2014;466:321–7.
- [112] de Souza AL, Andreani T, de Oliveira RN, Kiill CP, dos Santos FK, Allegratti SM, Chaud MV, Souto EB, Silva AM, Gremião MP. In vitro evaluation of permeation, toxicity and effect of praziquantel-loaded solid lipid nanoparticles against *Schistosoma mansoni* as a strategy to improve efficacy of the schistosomiasis treatment. *Int J Pharm* 2014;463:31–7.
- [113] Carneiro ZA, Maia PI, Sesti-Costa R, Lopes CD, Pereira TA, Milanezi CM, da Silva MA, Lopez RF, Silva JS, Deflon VM. In vitro and in vivo trypanocidal activity of H2bdtc-loaded solid lipid nanoparticles. *PLoS Negl Trop Dis* 2014;8:e2847.
- [114] Gundogdu E, Yurdasiper A. Drug transport mechanism of oral antidiabetic nanomedicines. *Int J Endocrinol Metab* 2014;12:e8984.
- [115] Almeida AJ, Souto E. Solid lipid nanoparticles as a drug delivery system for peptides and proteins. *Adv Drug Deliv Rev* 2007;59:478–90.
- [116] Zhang ZH, Zhang YL, Zhou JP, Lv HX. Solid lipid nanoparticles modified with stearic acid-octaarginine for oral administration of insulin. *Int J Nanomed* 2012;7:3333–9.
- [117] Golan M, Feinshtein V, David A. Conjugates of HA2 with octaarginine-grafted HPMA copolymer offer effective siRNA delivery and gene silencing in cancer cells. *Eur J Pharm Biopharm* 2016;109:103–12.
- [118] Ansari MJ, Anwer MK, Jamil S, Al-Shdefat R, Ali BE, Ahmad MM, Ansari MN. Enhanced oral bioavailability of insulin-loaded solid lipid nanoparticles: pharmacokinetic bioavailability of insulin-loaded solid lipid nanoparticles in diabetic rats. *Drug Deliv* 2016;23:1972–9.
- [119] Neugebauer G, Betzien G, Hrsta V, Kaufmann B, von Möllendorff E, Abshagen U. Absolute bioavailability and bioequivalence of glibenclamide (Semi-Euglucon N). *Int J Clin Pharmacol Ther Toxicol* 1985;23:453–60.
- [120] Gonçalves LM, Maestrelli F, Di Cesare Mannelli L, Ghelardini C, Almeida AJ, Mura P. Development of solid lipid nanoparticles as carriers for improving oral bioavailability of glibenclamide. *Eur J Pharm Biopharm* 2016;102:41–50.
- [121] Pirillo A, Catapano AL. Berberine, a plant alkaloid with lipid- and glucose-lowering properties: From in vitro evidence to clinical studies. *Atherosclerosis* 2015;243:449–61.
- [122] Xue M, Yang MX, Zhang W, Li XM, Gao DH, Ou ZM, Li ZP, Liu SH, Li XJ, Yang SY. Characterization, pharmacokinetics, and hypoglycemic effect of berberine loaded solid lipid nanoparticles. *Int J Nanomed* 2013;8:4677–87.
- [123] Yang T, Shi HX, Wang ZT, Wang CH. Hypolipidemic effects of andrographolide and neoandrographolide in mice and rats. *Phytother Res* 2013;27:618–23.
- [124] Ye L, Wang T, Tang L, Liu W, Yang Z, Zhou J, Zheng Z, Cai Z, Hu M, Liu Z. Poor oral bioavailability of a promising anticancer agent andrographolide is due to extensive metabolism and efflux by P-glycoprotein. *J Pharm Sci* 2011;100:5007–17.
- [125] Yang T, Sheng HH, Feng NP, Wei H, Wang ZT, Wang CH. Preparation of andrographolide-loaded solid lipid nanoparticles and their in vitro and in vivo evaluations: characteristics, release, absorption, transports, pharmacokinetics, and antihyperlipidemic activity. *J Pharm Sci* 2013;102:4414–25.
- [126] Gluck O, Maricic M. Skeletal and nonskeletal effects of raloxifene. *Curr Osteoporos Rep* 2003;1:123–8.
- [127] Kushwaha AK, Vuddanda PR, Karunanidhi P, Singh SK, Singh S. Development and evaluation of solid lipid nanoparticles of raloxifene hydrochloride for enhanced bioavailability. *Biomed Res Int* 2013;2013:584549.
- [128] Tran TH, Ramasamy T, Cho HJ, Kim YI, Poudel BK, Choi HG, Yong CS, Kim JO. Formulation and optimization of raloxifene-loaded solid lipid nanoparticles to enhance oral bioavailability. *J Nanosci Nanotechnol* 2014;14:4820–31.
- [129] Schnitzer T, Bone HG, Crepaldi G, Adami S, McClung M, Kiel D, Felsenberg D, Recker RR, Tonino RP, Roux C, Pinchera A, Foldes AJ, Greenspan SL, Levine MA, Emkey R, Santora 2nd AC, Kaur A, Thompson DE, Yates J, Orloff JJ. Therapeutic equivalence of alendronate 70 mg once-weekly and alendronate 10 mg daily in the treatment of osteoporosis. *Alendronate Once-Weekly Study Group. Aging* 2000;12:1–12.
- [130] Hosny KM. Alendronate sodium as enteric coated solid lipid nanoparticles; preparation, optimization, and in vivo evaluation to enhance its oral bioavailability. *PLoS One* 2016;11:e0154926.
- [131] Lee YH, Sinko PJ. Oral delivery of salmon calcitonin. *Adv Drug Deliv Rev* 2000;42:225–38.
- [132] Chen C, Fan T, Jin Y, Zhou Z, Yang Y, Zhu X, Zhang ZR, Zhang Q, Huang Y. Orally delivered salmon calcitonin-loaded solid lipid nanoparticles prepared by micelle-double emulsion method via the combined use of different solid lipids. *Nanomedicine* 2013;8:1085–100.
- [133] Fan T, Chen C, Guo H, Xu J, Zhang J, Zhu X, Yang Y, Zhou Z, Li L, Huang Y. Design and evaluation of solid lipid nanoparticles modified with peptide ligand for oral delivery of protein drugs. *Eur J Pharm Biopharm* 2014;88:518–28.



## Research Paper

# Ugonin U stimulates NLRP3 inflammasome activation and enhances inflammasome-mediated pathogen clearance



Chun-Yu Chen<sup>a,b,c</sup>, Chuan-Hui Yang<sup>a</sup>, Yung-Fong Tsai<sup>a,b,c</sup>, Chih-Chuang Liaw<sup>d</sup>, Wen-Yi Chang<sup>a,e</sup>,  
Tsong-Long Hwang<sup>a,c,e,f,\*</sup>

<sup>a</sup> Graduate Institute of Natural Products, College of Medicine, Chang Gung University, Taoyuan 333, Taiwan

<sup>b</sup> Graduate Institute of Clinical Medical Sciences, College of Medicine, Chang Gung University, Taoyuan 333, Taiwan

<sup>c</sup> Department of Anesthesiology, Chang Gung Memorial Hospital, Taoyuan 333, Taiwan

<sup>d</sup> Department of Marine Biotechnology and Resources, National Sun Yat-sen University, Kaohsiung 804, Taiwan

<sup>e</sup> Chinese Herbal Medicine Research Team, Healthy Aging Research Center, Chang Gung University, Taoyuan 333, Taiwan

<sup>f</sup> Research Center for Industry of Human Ecology, Research Center for Chinese Herbal Medicine, and Graduate Institute of Health Industry Technology, College of Human Ecology, Chang Gung University of Science and Technology, Taoyuan 333, Taiwan

## ARTICLE INFO

## Keywords:

Inflammasome  
Innate immunity  
Monocyte  
NLRP3  
Ugonin U

## ABSTRACT

The NOD-like receptor pyrin domain 3 (NLRP3) inflammasome contains Nod-like receptors, a subclass of pattern recognition receptors, suggesting that this complex has a prominent role in host defenses. Various structurally diverse stimulators activate the NLRP3 inflammasome through different signaling pathways. We previously reported that ugonin U (UgU), a natural flavonoid isolated from *Helminthostachys zeylanica* (L) Hook, directly stimulates phospholipase C (PLC) and triggers superoxide release in human neutrophils. In the present study, we showed that UgU induced NLRP3 inflammasome assembly and subsequent caspase-1 and interleukin (IL)-1 $\beta$  processing in lipopolysaccharide-primed human monocytes. Moreover, UgU elicited mitochondrial superoxide generation in a dose-dependent manner, and a specific scavenger of mitochondrial reactive oxygen species (ROS) diminished UgU-induced IL-1 $\beta$  and caspase-1 activation. UgU induced Ca<sup>2+</sup> mobilization, which was inhibited by treatment with inhibitors of PLC or inositol triphosphate receptor (IP<sub>3</sub>R). Blocking Ca<sup>2+</sup> mobilization, PLC, or IP<sub>3</sub>R diminished UgU-induced IL-1 $\beta$  release, caspase-1 activation, and mitochondrial ROS generation. These data demonstrated that UgU activated the NLRP3 inflammasome activation through Ca<sup>2+</sup> mobilization and the production of mitochondrial ROS. We also demonstrated that UgU-dependent NLRP3 inflammasome activation enhanced the bactericidal function of human monocytes. The ability of UgU to stimulate human neutrophils and monocytes, both of which are professional phagocytes, and its capacity to activate the NLRP3 inflammasome, which is a promising molecular target for developing anti-infective medicine, indicate that UgU treatment should be considered as a possible novel therapy for treating infectious diseases.

## 1. Introduction

Recognition of pathogenic microbes is the first and critical step of the host defense system, initiating a series of responses that are required for clearance of pathogens. The innate immune system utilizes various pattern recognition receptors (PRR), including Toll-like receptors, nucleotide-binding oligomerization domain-like receptors (NOD-

like receptors, NLRs), and RIG-like receptors, to identify pathogens or other danger signals [1]. The inflammasome contains NLRs, which are key cytosolic sensors, suggesting that the inflammasome plays a prominent role in intracellular sensing of various pathogen-associated molecular patterns (PAMPs) or host-derived signals of cell stress (danger-associated molecular patterns, DAMPs) [2,3]. Indeed, in response to PAMPs or DAMPs, the inflammasome is activated and

**Abbreviations:** ASC, apoptosis-associated speck-like protein containing a caspase recruitment domain; [Ca<sup>2+</sup>]<sub>i</sub>, intracellular calcium concentration; DAMPs, danger-associated molecular patterns; IP<sub>3</sub>, inositol triphosphate; IP<sub>3</sub>R, inositol triphosphate receptor; LPS, lipopolysaccharide; NADPH, the reduced form of nicotinamide adenine dinucleotide phosphate; NLRs, nucleotide-binding oligomerization domain-like receptors; PBMCs, peripheral blood mononuclear cells; PLC, phospholipase C; PBS, phosphate buffered saline; PRP, pattern recognition receptors; PAMP, pathogen-associated molecular patterns; ROS, reactive oxygen species; PMA, phorbol-12-myristate-13-acetate; UgU, ugonin U, 4''a,5'',6'',7'',8''a-hexahydro-5,3',4'-trihydroxy-5'',5'',8''a-trimethyl-4H-chromeno [2'',3'':7,6]flavone; UP-LPS, ultrapure lipopolysaccharide

\* Correspondence to: Graduate Institute of Natural Products, College of Medicine, Chang Gung University, 259 Wen-Hwa 1st Road, Kweishan, Taoyuan 333, Taiwan.

E-mail address: [htl@mail.cgu.edu.tw](mailto:htl@mail.cgu.edu.tw) (T.-L. Hwang).

<http://dx.doi.org/10.1016/j.redox.2016.12.018>

Received 21 November 2016; Received in revised form 10 December 2016; Accepted 17 December 2016

Available online 18 December 2016

2213-2317/ © 2016 The Authors. Published by Elsevier B.V.

This is an open access article under the CC BY-NC-ND license (<http://creativecommons.org/licenses/by-nc-nd/4.0/>).



induces immune responses that restrict pathogen replication [2,4,5].

As a cytoplasmic multi-molecular complex, the inflammasome serves as a platform for activation of caspase-1, which subsequently converts cytokine precursors into their mature forms [6]. The most characterized inflammasome is the NLRP3 inflammasome, which is composed of a sensing apparatus (NOD-like receptor pyrin domain 3, NLRP3), an adaptor (apoptosis-associated speck-like protein containing a caspase recruitment domain, ASC) and the pro-form of cytokine converting enzyme (pro-caspase-1) [7]. Numerous structurally diverse stimulators activate the NLRP3 inflammasome through different signaling pathways, including  $K^+$  efflux [7–11], reactive oxygen species (ROS) production [12–15],  $Ca^{2+}$  mobilization [11,16–19], mitochondrial destabilization [17,20–23], and lysosome rupture [24,25]. Therefore, it is critical that the molecular mechanisms by which novel stimulators activate the NLRP3 inflammasome are delineated in a context-specific manner.

The NLRP3 inflammasome plays a key role in host defenses against pathogenic bacteria and viruses [4,26]. This has stimulated research aimed at identifying chemical agents or natural products that can activate the complex and therefore modulate innate immunity and host defense [27–30]. We previously reported that ugonin U (UgU, 4''a,5'',6'',7'',8'',8''a-hexahydro-5,3',4'-trihydroxy-5'',5'',8''a-trimethyl-4H-chromeno [2'',3'':7,6]flavone, Fig. 1A) is the first identified natural flavonoid that directly stimulates phospholipase C (PLC) and induces a respiratory burst in human neutrophils [31]. UgU is isolated from *Helminthostachys zeylanica* (L) Hook, a pteridophyte with several medicinal properties including pain relief, detoxification, germ killing, and wound healing [32,33]. Moreover, UgU-induced PLC hydrolyzes phosphatidylinositol 4,5-bisphosphate ( $PIP_2$ ) into diacylglycerol (DAG) and inositol 1,4,5-triphosphate ( $IP_3$ ), which then promotes  $Ca^{2+}$  release from the endoplasmic reticulum. UgU can evoke  $Ca^{2+}$  mobilization and ROS production, both of which are signaling mediators involved in NLRP3 inflammasome activation. In this article, we evaluate the immuno-modulatory effects of UgU in human monocytes, which constitute another phagocyte subtype. We found that UgU induces  $Ca^{2+}$  mobilization, further promoting a series of signaling cascades that eventually activate the NLRP3 inflammasome in human monocytes. Furthermore, we show that UgU facilitates the bactericidal function of human monocytes to kill intracellular bacteria via activation of the NLRP3 inflammasome.

## 2. Materials and methods

### 2.1. Extraction of UgU

UgU (Fig. 1A) was extracted from rhizomes of *H. zeylanica* (L) Hook as previously described in detail [31]. In brief, the dried rhizomes of *H. zeylanica* (L) Hook were extracted with methanol (MeOH). The concentrated MeOH extract was consecutively partitioned with n-hexane,  $CHCl_3$ , and ethanol acetate (EtOAc). The EtOAc-soluble fraction was subjected to Sephadex LH-20 column chromatography. After loading the sample, it was eluted with MeOH to yield three fractions (Et1–Et3). Fraction Et2 was repeatedly separated by LH-20 column chromatography and reverse-phase high-performance liquid chromatography (MeOH: H<sub>2</sub>O (0.05% TFA): MeCN, 70:20:10; flow rate, 2 ml/min; UV detector, 300 nm) to yield UgU (4.5 mg; retention time, 44.42 min). The molecular formula was confirmed to be  $C_{25}H_{26}O_6$  by high-resolution fast-atom bombardment mass spectrometry.

### 2.2. Reagents

UgU was provided by Dr. Chih-Chuang Liaw, Department of Marine Biotechnology and Resources, National Sun Yat-sen University, Taiwan. Ficoll-Paque was purchased from GE Healthcare (Little Chalfont, Buckinghamshire, UK). Anti-NLRP3, anti-ASC, anti-pro-IL-

$1\beta$ , and anti- $\alpha$ -tubulin antibodies were purchased from Cell Signaling Technology (Beverly, MA, USA). Hank's balanced salt solution (HBSS) was obtained from Gibco (Grand Island, NY, USA). Fura-2-acetoxymethyl ester (Fura-2/AM) was purchased from Molecular Probes (Eugene, OR, USA). Nitrocellulose membranes were purchased from PerkinElmer Life Sciences (Boston, MA, USA). Immobilon Western chemiluminescence HRP substrate was purchased from Millipore Corporation (Billerica, MA, USA). BAPTA-AM, Bay 11-7082, gentamicin, RO 31-8220, and U73122 were purchased from Sigma-Aldrich (St. Louis, MO, USA). Xestospongin C (XeC) and Z-YVAD-FMK were purchased from Abcam (Cambridge, MA, USA). MitoSOX Red was purchased from Invitrogen (Waltham, MA, USA).

### 2.3. Cell preparation

This study was approved by the Institutional Review Board at Chang Gung Memorial Hospital, and written informed consent was acquired from every volunteer. Human monocytes were purified from peripheral blood mononuclear cells (PBMCs) using a modified cell culture flask adherence method [34,35]. Briefly, human whole blood was drawn from healthy donors (aged 20–30 years) who did not have any infection and did not take medicine within the week before sample collection. We then isolated PMBCs from whole blood using Ficoll-Paque density gradient centrifugation. PMBCs ( $2 \times 10^7$  cells/ml) were suspended in serum-free DMEM (10 ml) and seeded into 10-cm<sup>2</sup> culture disks for 3 h (37 °C, 5% CO<sub>2</sub>). The non-adherent cells were discarded by washing three times with warm phosphate buffered saline (PBS). The remaining adherent cells were incubated in cold 0.02% EDTA/PBS solution for 10 min and then detached by repeated aspiration and gentle expulsion of cold PBS. Isolated monocytes ( $1 \times 10^6$  cells/ml) were then suspended in DMEM. Cellular viability was determined by trypan blue exclusion.

The human monocytic cell line THP-1 (ATCC) and THP-1 with reduced NLRP3 activity (THP-1-NLRP3def; InvivoGen; San Diego, CA, USA) were maintained in RPMI-1640 medium containing 2 mM L-glutamine, 10 mM HEPES, 4500 mg/L glucose, 1 mM sodium pyruvate, and 1500 mg/l sodium bicarbonate, complemented with 10% fetal calf serum, 50 mM 2-mercaptoethanol, and 1% penicillin-streptomycin at 37 °C and 5% CO<sub>2</sub>. For experiments, THP-1 and THP-1-NLRP3def were differentiated with phorbol-12-myristate-13-acetate (PMA, 100 nM) for 3 h and then rest for 21 h before cell stimulation [6].

### 2.4. Cell stimulation

Activation of the NLRP3 inflammasome occurs via a two-step process. To upregulate NLRP3 inflammasome activity and enhance transcription of the pro-IL- $1\beta$  gene (signal 1), differentiated THP-1 cells (dTHP-1), differentiated THP-1-NLRP3def (dTHP-1-NLRP3def), and human monocytes were primed with ultrapure lipopolysaccharide (UP-LPS, 0.1  $\mu$ g/ml) for 3 h. In some experiments, different treatments using Z-YVAD-FMK (10  $\mu$ M), U73122 (1  $\mu$ M), XeC (5  $\mu$ M), BAPTA-AM (10  $\mu$ M), diphenyleneiodonium (DPI, 10  $\mu$ M), MitoTEMPO (10  $\mu$ M), Bay 11-7082 (10  $\mu$ M), or RO 31-8220 (1  $\mu$ M) were added for various times (XeC, 30 min; other inhibitors, 15 min). UgU (1–10  $\mu$ M) or nigericin (2.5  $\mu$ M), which offer signal 2 (secretion of IL- $1\beta$ ) in our experiments, were added and incubated for 60 min (UgU) or 15 min (nigericin) for ELISA and western blot analyses, and for 30 min (UgU) or 15 min (nigericin) in other experiments.

### 2.5. ELISA

Cells were cultured and treated as described above. Supernatants were harvested and frozen for human IL- $1\beta$  quantification using an ELISA assay kit (BD Biosciences) according to the manufacturer's instructions [36].

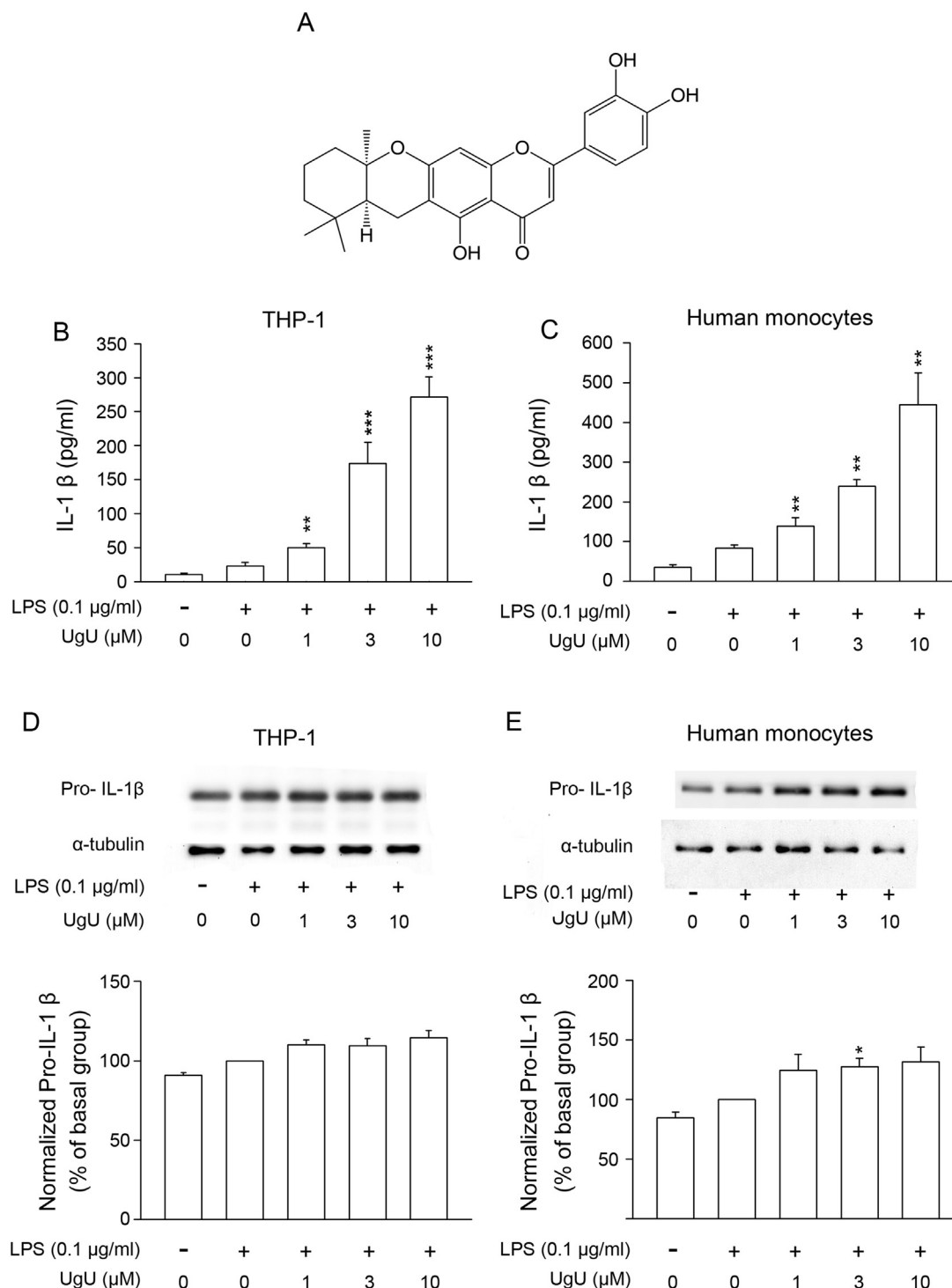


**Fig. 1. Ugonin U (UgU) induces IL-1 $\beta$  secretion in THP-1 and human monocytes.** (A) Chemical structure of UgU. (B, C) Concentration-dependent effects of UgU on IL-1 $\beta$  secretion. THP-1 ( $5 \times 10^5$  cells/ml) were differentiated with phorbol-12-myristate-13-acetate (PMA, 100 nM) for 3 h and then rested for 21 h. Differentiated THP-1 cells (dTHP-1,  $5 \times 10^5$  cells/ml) (B) and human monocytes ( $5 \times 10^5$  cells/ml) (C) were primed with ultrapure LPS (UP-LPS, 0.1  $\mu$ g/ml) for 3 h. Various concentrations of UgU (1, 3, and 10  $\mu$ M) were added and incubated for 60 min. Supernatants were collected for human IL-1 $\beta$  quantification using an ELISA assay. All data are expressed as the means  $\pm$  SEM (n=4). \*\* $p$  < 0.01, \*\*\* $p$  < 0.001 compared to the basal value. (D, E) UgU induced a slight increase in pro-IL-1 $\beta$ . LPS-primed dTHP-1 (D) and human monocytes (E) were treated with various concentrations of UgU for 60 min. Cells were lysed and pro-IL-1 $\beta$  was assayed by western blotting. Blots are representative of four independent experiments. All data are expressed as the means  $\pm$  SEM (n=4). \* $p$  < 0.05, compared to the basal value (UgU=0  $\mu$ M).

## 2.6. Western blot and immunoprecipitation

The treated cells were lysed with a buffer containing 50 mM Hepes (pH 7.4), 100 mM NaCl, 1 mM EDTA, 2 mM  $\text{Na}_3\text{VO}_4$ , 10 mM p-nitrophenyl phosphate, 5%  $\beta$ -mercaptoethanol, 1 mM phenylmethane-sulfonyl fluoride, 1% protease inhibitor cocktail (Sigma-Aldrich, St.

Louis, MO, USA), and 1% Triton X-100. After sonication, cell lysates were centrifuged at 14,000 rpm at 4  $^{\circ}\text{C}$  for 20 min. The supernatants were boiled for 5 min and then electrophoresed on SDS-acrylamide gels. Proteins were transferred to nitrocellulose membranes. After being blocked with 5% nonfat milk in a mixture of tris-buffered saline and Tween 20 (TBS-T), the membranes were incubated with diluted

primary antibodies, including anti-pro-IL-1 $\beta$  and anti- $\alpha$ -tubulin, at 4 °C overnight. The membranes were washed with 0.05% TBS-T and incubated with diluted horseradish peroxidase-conjugated secondary antibodies for 1 h. After being washed, the labeled protein was measured using an enhanced chemiluminescence system (Amersham Biosciences; Buckinghamshire, U.K.). Protein bands were analyzed using a BioSpectrum Imaging System (UVP; Upland, CA, USA) [31].

The lysates from LPS-primed dTHP-1 cells treated with UgU (10  $\mu$ M) were incubated with diluted anti-ASC antibodies (sc-22514, Santa Cruz Biotechnology) for 8 h at 4 °C under gentle rotation. Protein A/G PLUS-agarose beads (sc-2003, Santa Cruz Biotechnology) were added, and the immune complexes were pulled down over 1 h at 4 °C. Unbound proteins were removed by washing the beads with SDS-buffer. The bead-bound proteins were then boiled for 5 min, fractionated by SDS-PAGE, and analyzed by western blot using NLRP3 or ASC antibodies [37]. The procedures for analysis of protein bands were the same as those for western blots.

## 2.7. Determination of active caspase-1

An active caspase-1-specific fluorescent detection reagent, FLICA (FAM-YVAD-FMK, Immunochemistry Technologies, Bloomington, MN, USA), was used to analyze caspase-1 processing [38]. FLICA reagent specifically binds to the active form of caspase-1 and inhibits further activation once added. LPS-primed dTHP-1 cells and human monocytes were pretreated with or without inhibitors including U73122 (1  $\mu$ M), BAPTA-AM (10  $\mu$ M), or RO 31-8220 (1  $\mu$ M) for 15 min; or XcC (5  $\mu$ M) for 30 min before UgU stimulation. Cells were then washed and media were replaced with medium containing FLICA reagent and then incubated for 1 h. Next, the cells were washed three times to rinse away unbound FLICA. The green fluorescent signal, which is a marker of caspase-1 activity, was analyzed by flow cytometry (BD Accuri C6; BD Biosciences, San Jose, CA, USA).

## 2.8. Measurement of cytosolic Ca<sup>2+</sup> concentrations ([Ca<sup>2+</sup>])

LPS-primed human monocytes (5 $\times$ 10<sup>5</sup> cells/ml) were incubated with the Ca<sup>2+</sup>-sensitive dye Fura-2/AM (2  $\mu$ M) at 37 °C for 30 min, followed by centrifugation and resuspension in HBSS solution without CaCl<sub>2</sub>. The Fura-2/AM-labeled cells were treated with U73122 (1  $\mu$ M, 15 min), XcC (5  $\mu$ M, 30 min), or DMSO, followed by addition of UgU (10  $\mu$ M). We then used a fluorospectrophotometer (F-4500; Hitachi, Tokyo, Japan) with a dual-wavelength program to measure [Ca<sup>2+</sup>] (excitation wavelength, 340/380 nm; emission wavelength, 505 nm). At the end of each assay, we sequentially added Triton X-100 (0.05%) and ethylene glycol tetraacetic acid (20 mM) to get maximum and minimum values of fluorescence [39].

## 2.9. Assessment of mitochondrial superoxide

LPS-primed dTHP-1 cells (5 $\times$ 10<sup>5</sup> cells/ml) and human monocytes (5 $\times$ 10<sup>5</sup> cells/ml) were incubated in phenol red-free RPMI-1640 medium containing a mitochondrial superoxide specific indicator (MitoSOX Red reagent, 2.5  $\mu$ M) at 37 °C for 30 min [40]. Cells were washed and suspended in warm HBSS. The labeled cells were then treated as described above. MitoSOX fluorescence intensity was then measured by flow cytometry (BD Accuri™ C6) [41].

## 2.10. Determination of cAMP concentrations

The concentration of cAMP was measured using an enzyme immunoassay kit (GE Healthcare, Little Halfont, Buckinghamshire, UK). Cells were incubated with different concentrations of UgU, DMSO, or prostaglandin (3  $\mu$ M, as positive control) for 5 min. Dodecyltrimethylammonium bromide (0.5%) was used to hydrolyze cell membranes and release intra-cellular cAMP. Samples were cen-

trifuged at 3000 $\times$ g for 5 min at 4 °C to acquire cleared supernatants, which were then used to determine cAMP levels according to the manufacturer's instructions [42,43].

## 2.11. Gentamicin protection assay

A gentamicin protection assay was performed to assess intracellular bacteria survival in human monocytes [38]. One day before the experiment, isolated human monocytes were cultured in 24-well plates (5 $\times$ 10<sup>5</sup> cells/ml/well), and bacteria were prepared by growing *Staphylococcus aureus* in Luria-Bertani (LB) broth at 37 °C with shaking. On the day of the experiment, bacteria were centrifuged at 10,000 $\times$ g for 5 min and washed three times with PBS. Bacterial density was determined by measuring the optical density of a 3-ml aliquot of the suspensions in cuvettes at 670 nm. Human monocytes were primed with UP-LPS (0.1  $\mu$ g/ml) for 3 h and then infected with *S. aureus* at a multiplicity of infection (MOI) of 10. To increase the infection rate, plates were centrifuged for 15 min at 100 $\times$ g and incubated at 37 °C in 5% CO<sub>2</sub> for 20 min. Infected human monocytes were washed three times with warm HBSS to eliminate non-adherent bacteria. To kill extracellular bacteria, cells were then cultured in DMEM medium containing gentamicin (200  $\mu$ g/ml) for 30 min. After that, medium was replaced with fresh DMEM with or without UgU (1–10  $\mu$ M). The treated monocytes were incubated for 3 or 20 h, followed by washing once with HBSS and lysis with 1% Triton X-100. The survival of intracellular bacteria was quantified by spreading the serially-diluted lysate on LB agar plates and counting the colony forming units (CFUs) 24 h later.

## 2.12. Statistical analysis

To obtain results suitable for statistical analysis, 4–5 samples were used for each independent experiment. All results are expressed as mean  $\pm$  standard error of the mean (SEM). Statistical comparisons were made between two groups using Student's *t*-test. Values of *p* less than 0.05 were considered statistically significant.

# 3. Results

## 3.1. UgU induces IL-1 $\beta$ secretion in LPS-primed human monocytes

To investigate the role of UgU in NLRP3 inflammasome activation, we first examined whether UgU induces IL-1 $\beta$  as a downstream target of the complex. Secreted IL-1 $\beta$  increased induced by UgU (1–10  $\mu$ M, 60 min) in a dose-dependent manner in LPS-primed dTHP-1 and human monocytes (Fig. 1B, C). Western blotting analysis revealed that UgU induced a slight increase in pro-IL-1 $\beta$  (Fig. 1D, E); however, the increase in pro-IL-1 $\beta$  was much lower than that in mature IL-1 $\beta$  (Fig. 1), suggesting that UgU promotes IL-1 $\beta$  processing.

## 3.2. UgU stimulates caspase-1 and NLRP3 inflammasome activation

Next, our experiments utilizing a specific active caspase-1 fluorescent indicator, YVAD-FLICA, revealed that UgU dose-dependently induces caspase-1 activation in LPS-primed dTHP-1 and human monocytes (Fig. 2A, B, and C). Moreover, the caspase-1 specific inhibitor, Z-YVAD-FMK, reduced IL-1 $\beta$  secretion in both cells types, confirming that active caspase-1 is required for IL-1 $\beta$  secretion following UgU stimulation (Fig. 2D). In addition, we used THP-1-NLRP3def to verify which inflammasome was induced in response to UgU. We found that UgU-dependent IL-1 $\beta$  secretion and caspase-1 activation were abolished in these cells (Fig. 3A, B and Supplementary Fig. 1). Consistent with this, IL-1 $\beta$  secretion and caspase-1 activation in THP-1 were also inhibited by Bay 11-7082, a compound that reportedly inhibits NLRP3 inflammasome activation (Fig. 3C, D and Supplementary Fig. 1) [44,45]. Moreover, an immunoprecipitation

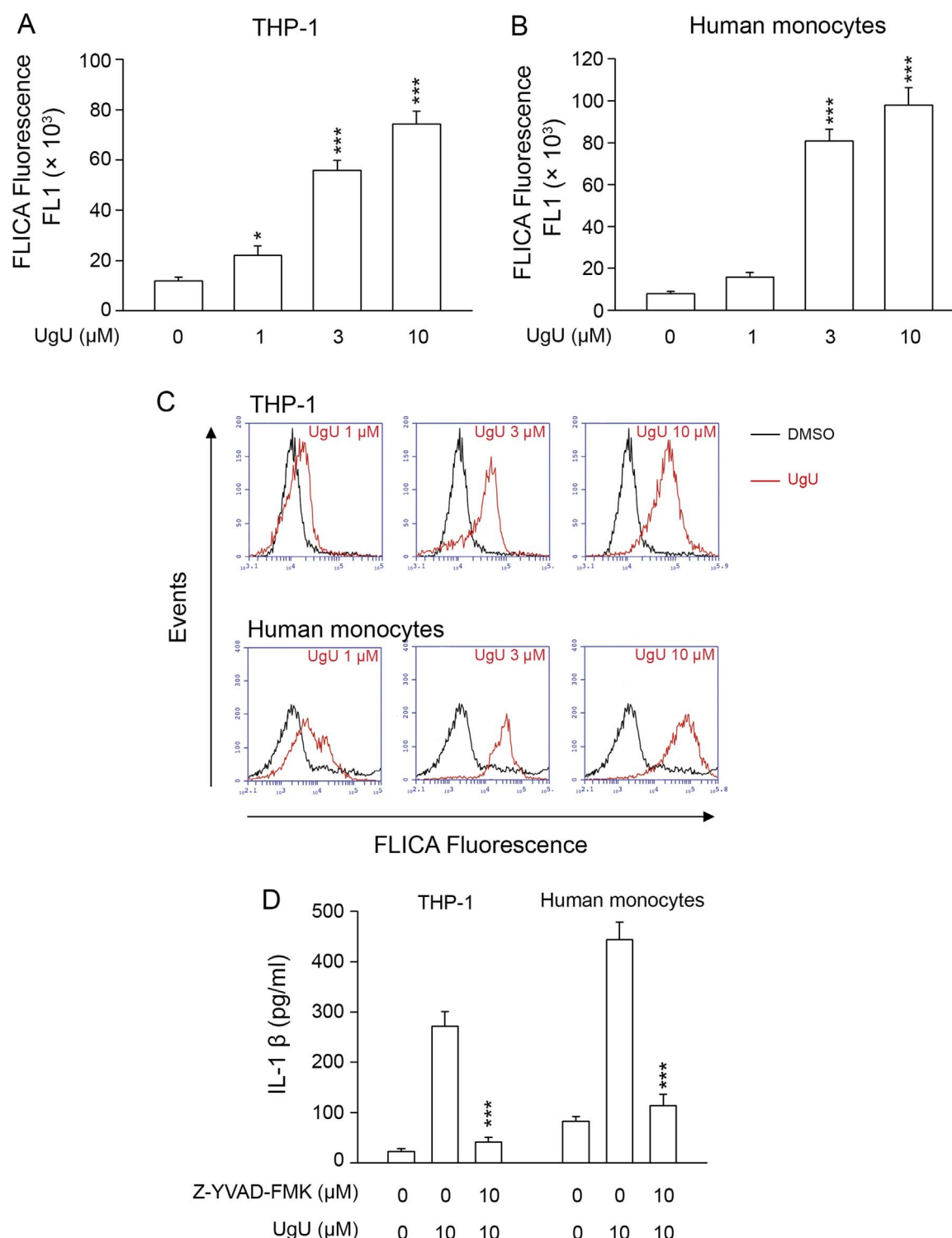


**Fig. 2. UgU activates caspase-1 in THP-1 and human monocytes, which is essential for IL-1 $\beta$  secretion.** (A) LPS-primed dTHP-1 ( $5 \times 10^5$  cells/ml) and (B) LPS-primed human monocytes ( $5 \times 10^5$  cells/ml) were incubated with the indicated concentrations of UgU for 30 min. Cells were stained with a fluorescent detection reagent specific for activated caspase-1 (FLICA reagent, FAM-YVAD-FMK). Fluorescence was monitored by flow cytometry. All data are expressed as the means  $\pm$  SEM ( $n=4$ ). \* $p < 0.05$ , \*\*\* $p < 0.001$  compared to the basal value (UgU=0  $\mu$ M). (C) Representative images from one of four independent experiments are shown. (D) The caspase-1 specific inhibitor, Z-YVAD-FMK (10  $\mu$ M), was added 15 min before LPS-primed dTHP-1 ( $5 \times 10^5$  cells/ml, left) and human monocytes ( $5 \times 10^5$  cells/ml, right) were stimulated with UgU (10  $\mu$ M). IL-1 $\beta$  secretion decreased in the presence of a caspase-1-specific inhibitor in both cells. All data are expressed as the means  $\pm$  SEM ( $n=4$ ). \*\*\* $p < 0.001$  compared to the control (UgU=10  $\mu$ M).

assay demonstrated that UgU enhanced the ASC-NLRP3 interaction in LPS-primed dTHP-1 cells (Fig. 3E). These assays prove that the NLRP3 inflammasome, but not other inflammasomes, is responsible for UgU-induced IL-1 $\beta$  secretion.

### 3.3. UgU elicits mitochondrial ROS production

A mitochondrial superoxide-specific fluorescent probe (MitoSOX Red) was used to evaluate whether UgU induces mitochondrial super-

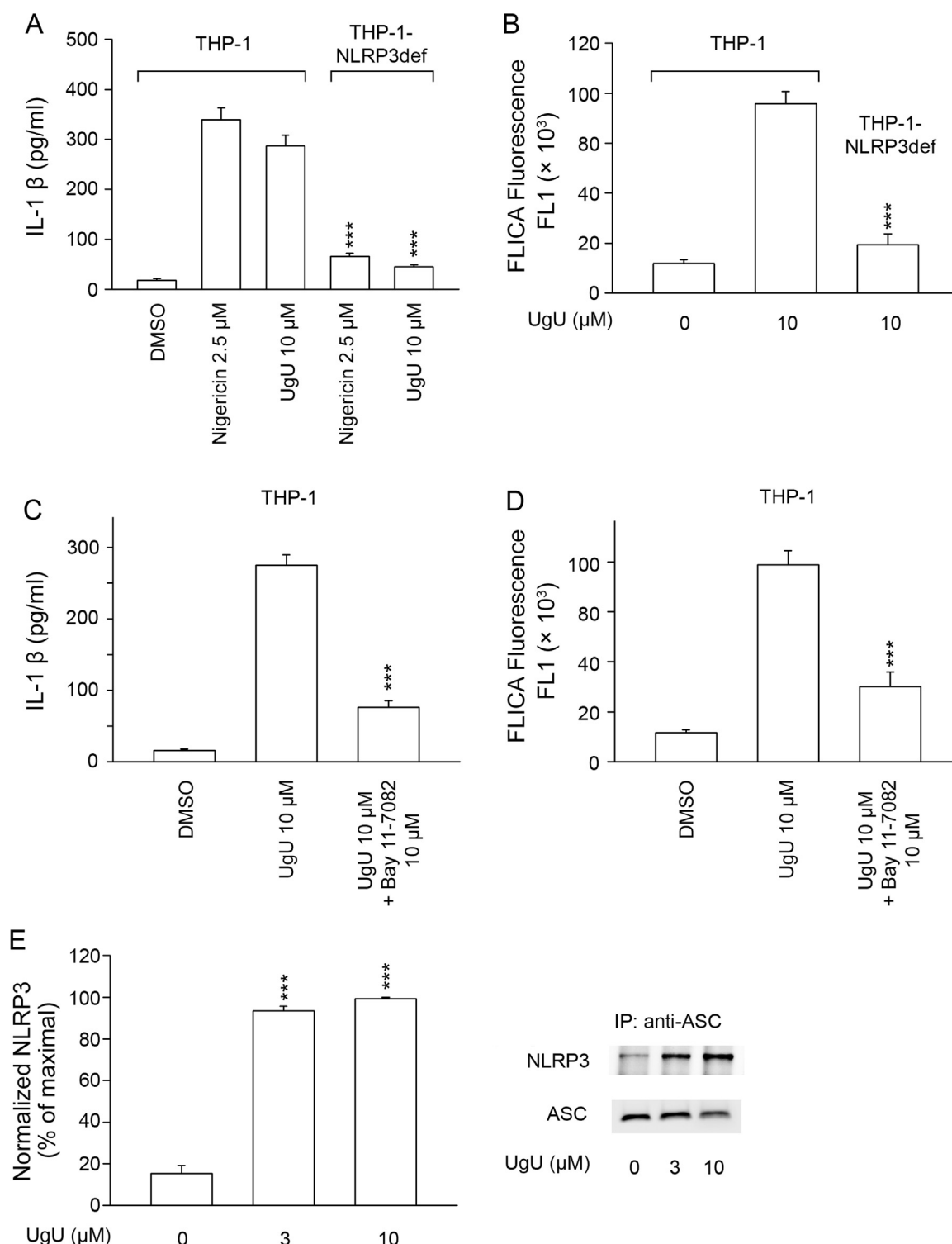


**Fig. 3. NLRP3 inflammasome is responsible for UgU-induced caspase-1 activation and IL-1 $\beta$  secretion.** (A, B) IL-1 $\beta$  secretion and caspase-1 activation were abolished in NLRP3-deficient THP-1 cells or (C, D) THP-1 treated with an NLRP3 inhibitor (Bay 11-7082). In IL-1 $\beta$  analyses, LPS-primed dTHP-1 and LPS-primed dTHP-1-NLRP3def were incubated with UgU (10  $\mu$ M, 60 min) or nigericin (2.5  $\mu$ M, 15 min), respectively. In activated caspase assays, LPS-primed dTHP-1 and LPS-primed dTHP-1-NLRP3def were incubated with UgU (10  $\mu$ M, 30 min) or nigericin (2.5  $\mu$ M, 15 min), respectively. Bay 11-7082 (10  $\mu$ M) were added 15 min before cell stimulation. Data are expressed as the mean  $\pm$  SEM (n=4). \*\*\* $p$  < 0.001 compared to the control. (E) An immunoprecipitation assay demonstrated the ASC-NLRP3 interaction. LPS-primed dTHP-1 ( $5 \times 10^5$  cells/ml) were stimulated with UgU (10  $\mu$ M). Cell lysates were immunoprecipitated with anti-ASC antibodies, followed by incubation with protein A/G agarose beads for 1 h at 4  $^{\circ}$ C. The bead-bound proteins were eluted and analyzed by western blot for NLRP3 or ASC. Data are expressed as the mean  $\pm$  SEM (n=4). \*\*\* $p$  < 0.001 compared to the basal value (UgU=0  $\mu$ M). Blots are representative of four independent experiments.

oxide. This experiment revealed that UgU elicited mitochondrial superoxide generation in a dose-dependent manner in LPS-primed dTHP-1 cells and human monocytes (Fig. 4A, B, and C). To further verify the origin of ROS during UgU-induced NLRP3 inflammasome

activation, we used a mitochondrial-target antioxidant (MitoTEMPO) and a NADPH oxidase (NOX) ROS inhibitor (DPI) in the following experiments. The results showed that MitoTEMPO, but not DPI, diminished IL-1 $\beta$  and caspase-1 activation (Fig. 4D, E, and



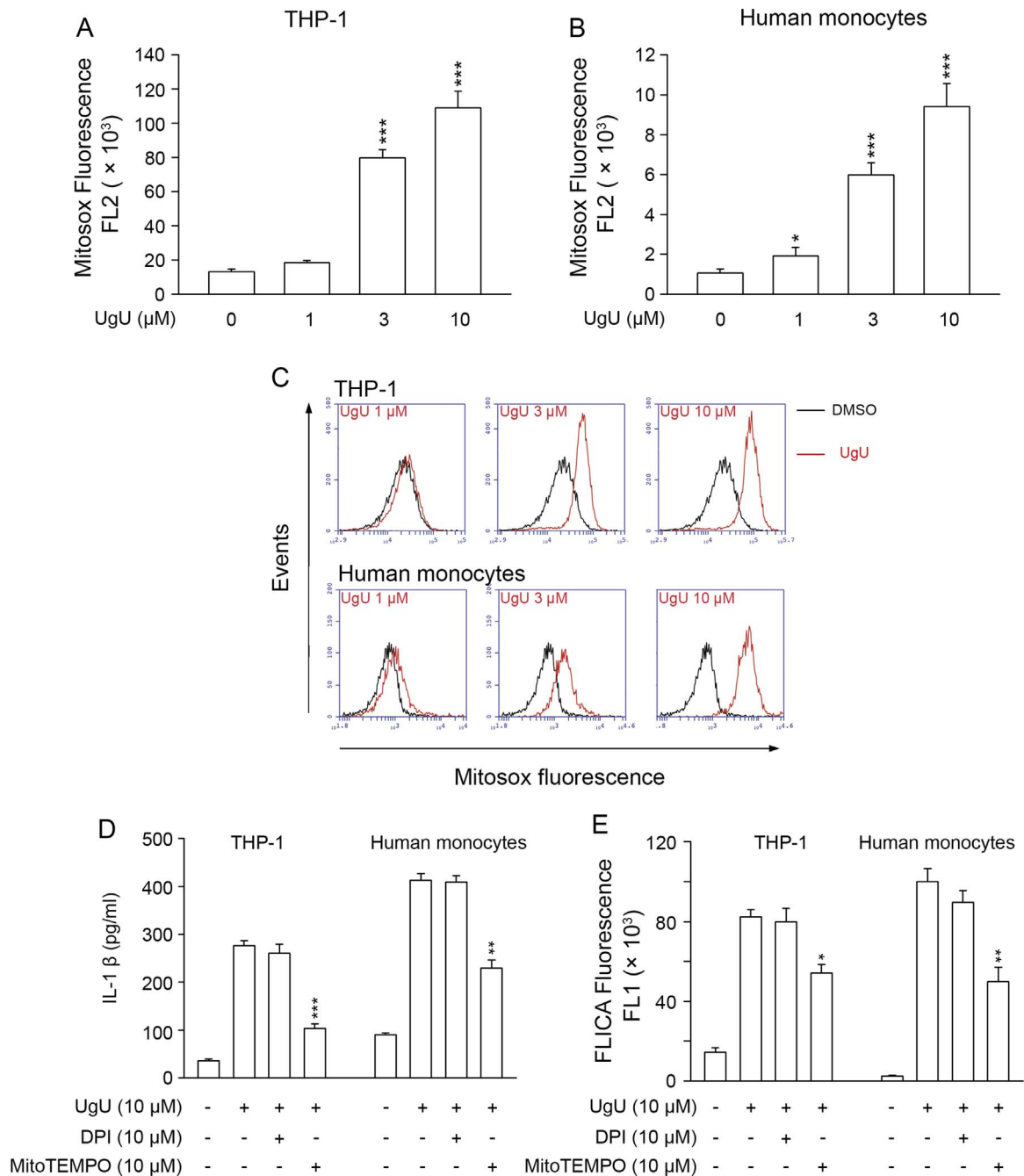


**Fig. 4.** UgU elicits mitochondrial superoxide generation in a dose-dependent manner in LPS-primed dTHP-1 cells and human monocytes. (A) LPS-primed dTHP-1 cells ( $5 \times 10^5$  cells/ml, upper pane) and (B) LPS-primed human monocytes ( $5 \times 10^5$  cells/ml, lower panel) were incubated in medium containing mitochondrial superoxide specific indicator (MitoSOX Red reagent, 2.5  $\mu$ M) at 37  $^{\circ}$ C for 30 min. The labeled cells were then stimulated with UgU (1, 3, and 10  $\mu$ M) for 30 min. MitoSOX fluorescent intensity was measured by flow cytometry. Data are expressed as the means  $\pm$  SEM ( $n=4$ ). \* $p < 0.05$ , \*\*\* $p < 0.001$  compared to the basal value (UgU=0  $\mu$ M). (C) Representative images from one of four independent experiments are shown. (D) IL-1 $\beta$  secretion and (E) caspase-1 activation was inhibited by a mitochondrial-specific antioxidant (MitoTEMPO), but not a NADPH oxidase (NOX) ROS inhibitor (DPI), in LPS-primed dTHP-1 cells (left) and human monocytes (right). Data are expressed as the means  $\pm$  SEM ( $n=4$ ). \*\* $p < 0.01$ , \*\*\* $p < 0.001$  compared to the control (UgU=10  $\mu$ M).

Supplementary Fig. 2).

**3.4. UgU-induced NLRP3 inflammasome activation is dependent on  $[Ca^{2+}]$  mobilization**

$Ca^{2+}$  mobilization plays a critical role in NLRP3 inflammasome activation [17,18]. In this study, we demonstrated that UgU induced intracellular  $[Ca^{2+}]$ , (Black line, Fig. 5A, B). We previously reported that UgU stimulated respiratory burst in human neutrophils via the PLC/inositol triphosphate ( $IP_3$ )/ $Ca^{2+}$  pathway [31]. We observed that

in the human monocytes, UgU-induced  $Ca^{2+}$  mobilization was inhibited by treatment with inhibitors of PLC (U73122, 1  $\mu$ M, 15 min) or the  $IP_3$  receptor ( $IP_3$ R, XeC, 5  $\mu$ M, 30 min).

Furthermore, UgU-induced IL-1 $\beta$  release, caspase-1 activation, and mitochondrial ROS production were inhibited by the PLC inhibitor (U73122),  $IP_3$ R inhibitors (XeC), or the  $Ca^{2+}$  chelator (BAPTA-AM), but not by a PKC inhibitor (RO 31-8220) (Figs. 6, 7, and Supplementary Fig. 3). These data suggest that UgU-induced NLRP3 inflammasome activation is  $Ca^{2+}$ -dependent, and that the  $Ca^{2+}$  release induced by UgU is mediated through a PLC/ $IP_3$  pathway. In contrast,

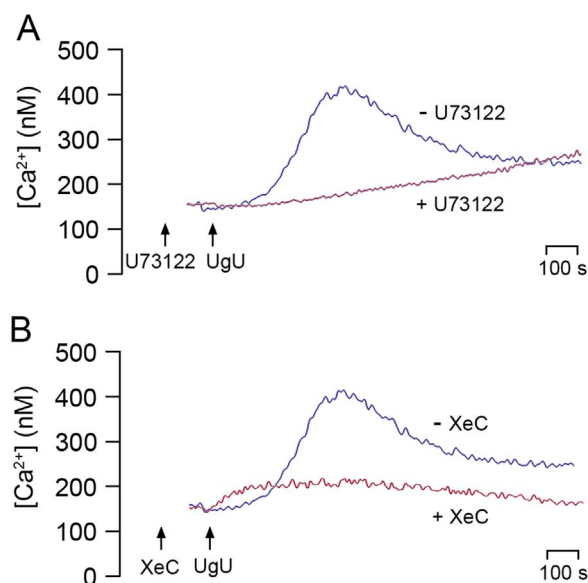


**Fig. 5.** UgU induces an increase in intracellular calcium ( $\text{Ca}^{2+}$ ). (A, B) Representative traces (black) of the effects of UgU on intracellular  $\text{Ca}^{2+}$  mobilization in human monocytes are shown. LPS-primed human monocytes ( $5 \times 10^5$  cells/ml) were labeled with Fura-2/AM and then stimulated with UgU ( $10 \mu\text{M}$ ) in  $\text{Ca}^{2+}$ -free HBSS. Fluorescence was monitored at  $37^\circ\text{C}$ . A phospholipase C (PLC) inhibitor (U73122,  $10 \mu\text{M}$ , 15 min) (A, red) or inositol triphosphate receptor ( $\text{IP}_3\text{R}$ ) inhibitor (Xestospongin C, XeC,  $5 \mu\text{M}$ , 30 min) (B, red) was added before human monocytes were stimulated with UgU. Representative images from one of five independent experiments are shown.

PKC did not play a role in UgU-associated inflammasome activation. Additionally, UgU did not affect cAMP levels in LPS-primed dTHP-1 compared with the positive control  $\text{PGE}_1$  (data not shown).

### 3.5. UgU augments intracellular bacteria clearance activity of human monocytes

A gentamicin protection test was employed to evaluate whether UgU affects the intracellular survival of *S. aureus* within human monocytes. *S. aureus* CFUs were higher at 20 h after infection than at 3 h after infection (data not shown), indicating that *S. aureus* had

replicated within the cell. The CFU number was lower in the group of LPS-primed human monocytes that were treated with UgU. Moreover, the decrease in intracellular *S. aureus* caused by UgU was partially reversed by an NLRP3 inflammasome inhibitor (Bay 11-7082) and caspase-1 inhibitor (Y-VZAD-FMK) (Fig. 8). These studies illustrate that UgU-enhanced germicidal activity of human monocytes against intracellular bacteria is mediated by NLRP3 inflammasome activation. Fig. 9.

## 4. Discussion

The NLRP3 inflammasome, which contains the evolutionarily ancient immunity receptor, NLR, is a key player in the host defense system [4]. Various structurally distinct stimulators activate the NLRP3 inflammasome, and employ diverse activation mechanisms to do so. In response to insults that cause cell stress, the inflammasome signaling cascade elicits the production of inflammatory cytokines and antimicrobial factors. There is a significant interest in chemical compounds or natural products that can activate the NLRP3 inflammasome, attributable to its significant role in protection against invading pathogens. In the current study, we demonstrate that UgU, a flavonoid extracted from *H. zeylanica* (L) Hook, provokes IL-1 $\beta$  secretion by activating the NLRP3 inflammasome.

Many pathways that lead to the NLRP3 inflammasome converge on ROS production [12,46]. Mitochondria and NOX are two major sources of intracellular ROS [47,48], and mitochondrial-derived ROS contribute to NLRP3 inflammasome activation [17,20,49]. However, the role of NOX-derived ROS in the process is still controversial [46,50–52]. In our study, a mitochondrial-target antioxidant (MitoTEMPO) abolished IL-1 $\beta$  release and caspase-1 activation induced by UgU, while a NOX inhibitor (DPI) had no effect. These results indicate that stimulation of the NLRP3 inflammasome by UgU is dependent upon mitochondrial ROS, but independent of NOX-derived ROS. Moreover, our data showed that UgU induced a slight increase in pro-IL-1 $\beta$ . Previous studies have shown that IL-1 $\beta$  induces pro-IL-1 $\beta$  production in an autocrine fashion [53]. ROS also play a role in NF- $\kappa\text{B}$  activation, which further increases pro-IL-1 $\beta$  production [54]. These data provide possible mechanisms by which UgU promotes a small increase in pro-IL-1 $\beta$  production. Furthermore, we previously reported that UgU is the first identified natural flavonoid as a PLC activator [31].

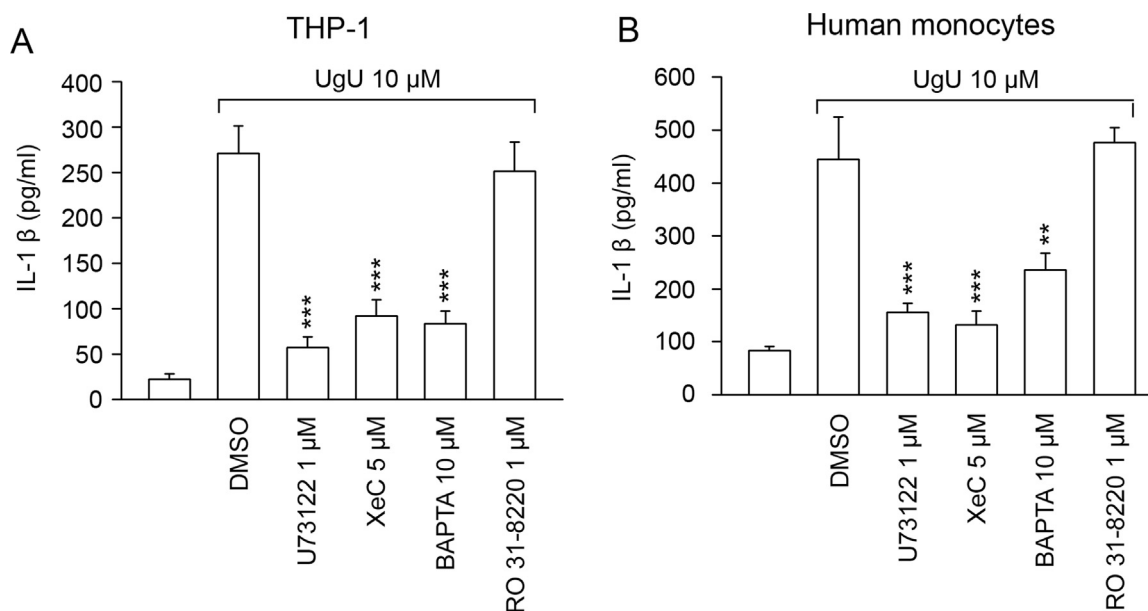


**Fig. 6.** UgU-induced IL-1 $\beta$  secretion is  $\text{Ca}^{2+}$ -dependent, and the source of  $\text{Ca}^{2+}$  is through PLC/ $\text{IP}_3$  pathway. IL-1 $\beta$  release induced with UgU in (A) LPS-primed dTHP-1 cells and (B) human monocytes was inhibited by a PLC inhibitor (U73122,  $1 \mu\text{M}$ ), an  $\text{IP}_3\text{R}$  inhibitor (XeC,  $5 \mu\text{M}$ ), or a calcium chelator (BAPTA-AM,  $10 \mu\text{M}$ ), but not a protein kinase C (PKC) inhibitor (RO 31-8220,  $1 \mu\text{M}$ ). All data are expressed as the means  $\pm$  SEM ( $n=4$ ). \*\*\* $p < 0.001$  compared to the control (UgU= $10 \mu\text{M}$ ).

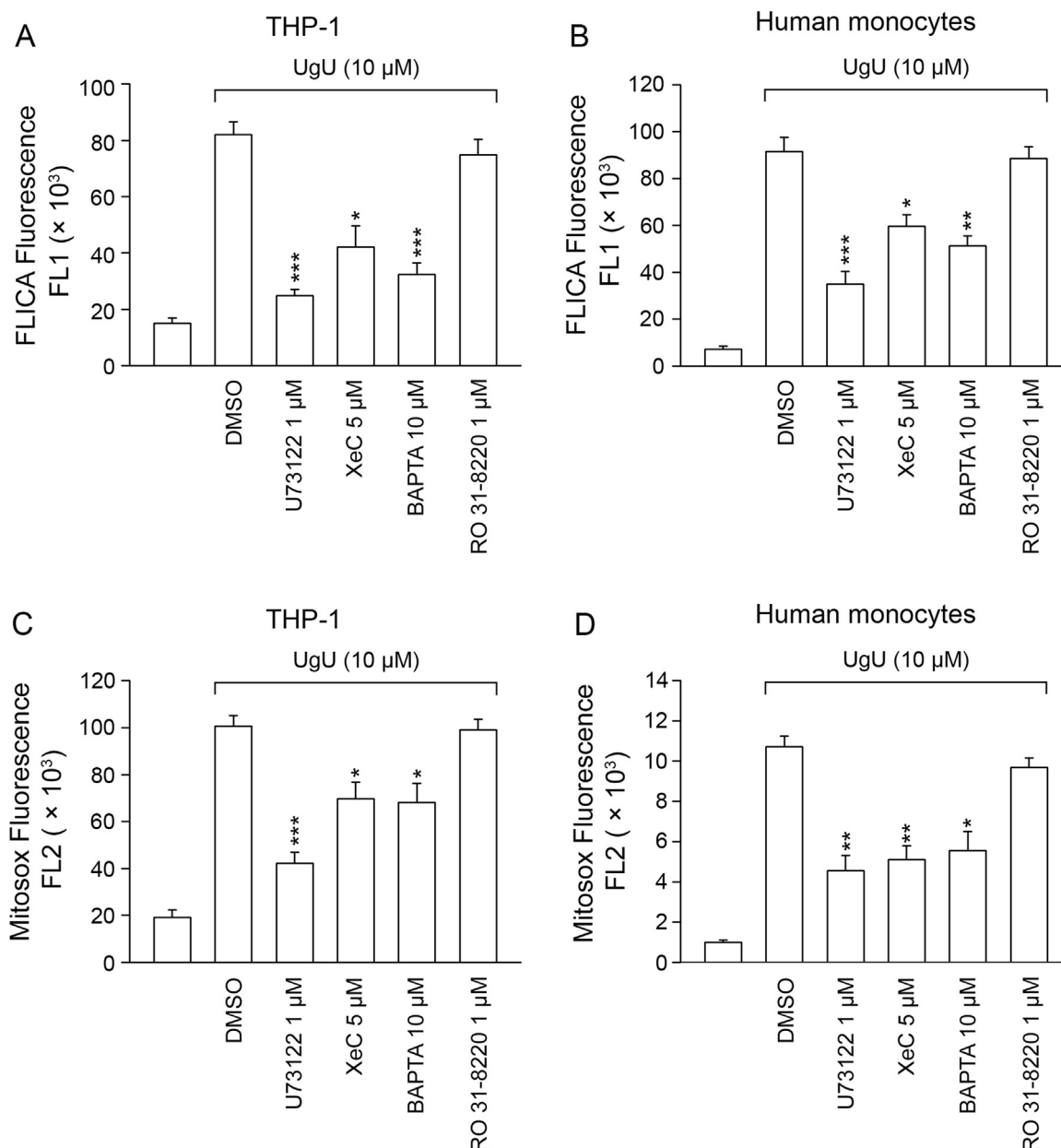


**Fig. 7. UgU-induced caspase-1 activation and mitochondria ROS production are inhibited when PLC, IP<sub>3</sub>R, or Ca<sup>2+</sup> mobilization is blocked.** (A, B) Caspase-1 activation and (C, D) mitochondria ROS production induced with UgU in LPS-primed dTHP-1 cells (A, C) and LPS-primed human monocytes (B, D) were inhibited by a PLC inhibitor (U73122, 1  $\mu$ M), an IP<sub>3</sub>R inhibitor (XeC, 5  $\mu$ M), or a calcium chelator (BAPTA-AM, 10  $\mu$ M), but not a PKC inhibitor (RO 31-8220, 1  $\mu$ M). Data are expressed as the means  $\pm$  SEM (n=5). \* $p$  < 0.05, \*\* $p$  < 0.01, \*\*\* $p$  < 0.001 compared to the control (UgU = 10  $\mu$ M).

Activation of PLC is an important pathway for intracellular Ca<sup>2+</sup> mobilization [55]. PLC metabolizes membrane phosphoinositides and produces IP<sub>3</sub>, which then binds with IP<sub>3</sub>R on the endoplasmic reticulum and releases Ca<sup>2+</sup> into the cytoplasm. Our study illustrates that UgU induces Ca<sup>2+</sup> mobilization in human monocytes. Blocking Ca<sup>2+</sup> mobilization inhibits UgU-induced mitochondrial ROS production. Consistent with other studies [17], our results provide evidence that Ca<sup>2+</sup> mobilization induces the production of mitochondrial ROS, which are important intermediaries of the NLRP3 inflammasome activation. In addition, our experiments showed that the Ca<sup>2+</sup> chelator, BAPTA-AM, did not completely inhibit caspase-1 activation and mitochondrial ROS production. Ca<sup>2+</sup> may have a direct activating effect on NLRP3 inflammasome [11,16–19]. Therefore, a parallel pathway of Ca<sup>2+</sup> activation of the NLRP3 inflammasome cannot be ruled out.

Antibiotics, one of the most important therapeutic agents in the

history of human medicine, have significantly reduced infection-associated morbidity and mortality. However, with the emergence of multiple antibiotic-resistant microbes, severe infectious diseases caused by these bacteria pose a serious problem to medical caregivers and academics in clinical research fields. As such, there is intense research into the molecular mechanisms by which bacteria develop antibiotic resistance and into the delineation of novel strategies to kill such pathogens. The inflammasome is an evolutionarily conserved cytosolic sensor that plays a critical role in host defenses against bacteria and viruses [5,26,30,56]. In response to pathogens, inflammasomes are activated and can induce immune responses that restrict pathogen replication. Therefore, the inflammasome is a potential molecular target for developing novel anti-bacteria agents [29,30]. In the current study, we show that UgU promotes the NLRP3 inflammasome-mediated innate immune response and enhances clearance of engulfed bacterial pathogens. Moreover, UgU-enhanced bactericidal

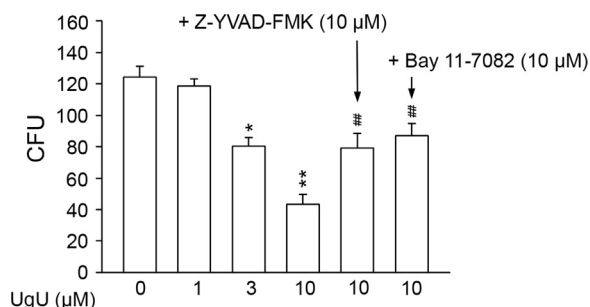


**Fig. 8. UgU augments the intracellular bacteria clearance activity of human monocytes.** UgU-induced dose-dependent reductions in colony forming units (CFUs) are shown. The decrease in CFUs caused by UgU was partially reversed by an NLRP3 inflammasome inhibitor (Bay 11-7082) and caspase-1 inhibitor (Y-VZAD-FMK). Cells were cultured in DMEM containing gentamicin (200 μg/ml) for 30 min. After that, medium was replaced with fresh DMEM with or without UgU (1, 3, and 10 μM). The treated monocytes were incubated for 20 h, followed by washing once with HBSS and then lysis with 1% Triton X-100. The survival of intracellular bacteria was determined by counting CFUs, which were formed 24 h after spreading the serially-diluted lysate on LB agar plates. Data are expressed as the means ± SEM (n = 3). \**p* < 0.05, \*\**p* < 0.01, compared to the basal value (UgU=0 μM). ##*p* < 0.01, compared to the UgU=10 μM group.

activity was reduced by NLRP3 inflammasome or caspase-1 inhibition, suggesting that UgU-induced NLRP3 inflammasome activation contributes to the antibacterial effects.

To date, however, specific molecular mechanisms linking inflammasome activation and intracellular bacteria clearance have remained unclear. A previous study reported that NLRP3 inflammasome and caspase-1 activation contribute to phagosome acidification and maturation, which are critically important for the clearance of engulfed bacteria [38]. Caspase-1 is activated and recruited to bacteria-containing phagosomes by the activated NLRP3 inflammasome [38]. Various studies show that microbes or their subcellular components negatively regulate the inflammasome in order to evade host defenses [5,38,57,58]. For instance, live bacteria can actively neutralize the acidity of phagosomes to escape inflammasome-associated bactericidal activities [38,59]. Accordingly, we infer that UgU augments the

bactericidal function of human monocytes by activating the NLRP3 inflammasome. In some respects, this is similar to the activity of nigericin, a potent NLRP3 inflammasome activator that attenuates viral infection in elderly mice with impaired NLRP3 inflammasome activity [30]. Moreover, we have reported that UgU activates human neutrophils and induces generation of ROS, which are toxic products that help eliminate intracellular pathogens. Taken together, these data suggest that UgU has the potential to be developed as a novel anti-infective drug, since it can activate the bactericidal activity of human neutrophils and monocytes. However, to clarify the effectiveness of UgU in treating microbial infections, more rigorous animal studies should be performed.

To conclude, we demonstrate that UgU activates the NLRP3 inflammasome and mature IL-1β secretion through a PLC/Ca<sup>2+</sup>/mitochondrial ROS cascade, whereas NADPH ROS were not involved. The activation facilitates the killing of engulfed bacteria by human monocytes. Thus, to the best of our knowledge, UgU is the first described natural flavonoid that activates human neutrophils and monocytes; both these cell types are expert microbial killers and are essential for the resolution of infections. Since the NLRP3 Inflammasome is a target for development of anti-infective medicines [29,30,60], we expect that further investigation of UgU will facilitate the development of novel anti-infective agents. Studies of UgU will also enhance our understanding of the pharmacology of flavonoids.

## Acknowledgements and funding

This work was supported by grants from Chang Gung Memorial Hospital, Taiwan (CMRPD1B0281~3, CMRPF1D0442~3, CMRPF1F0011~3, CMRPF1F0061~3 and BMRP450) and the National Science Council, Taiwan (NSC 102-2628-B-182-002-MY3, MOST 102-2628-B-255-003-MY3 and MOST 104-2320-B-255-004-MY3) awarded to Tsong-Long Hwang; Chang Gung Memorial Hospital, Taiwan (CMRPG3D1571) awarded to Chun-Yu Chen. The funders had no role in the study design, data collection and analysis, decision to publish, or preparation of the manuscript.

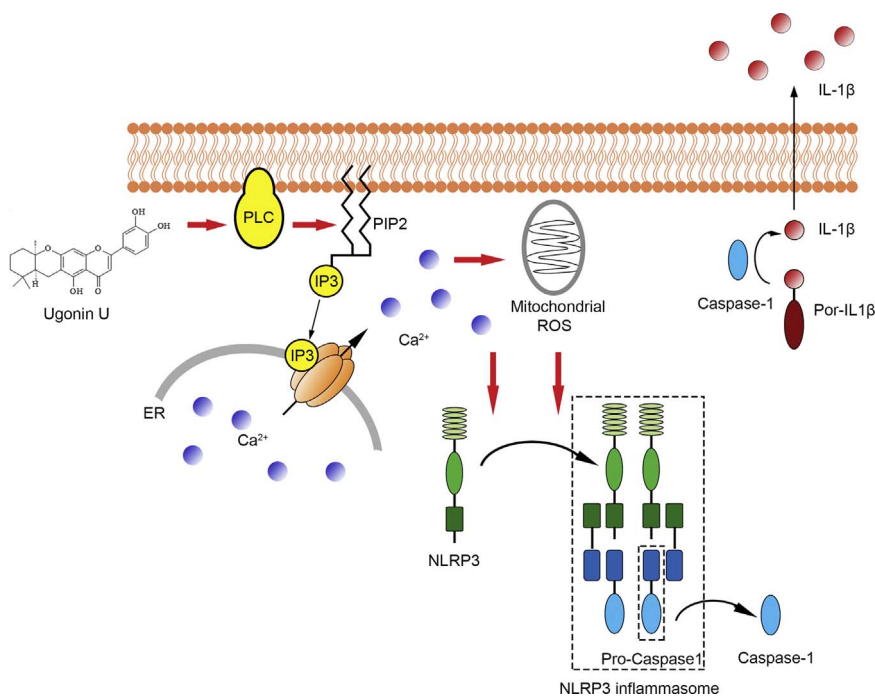


**Fig. 9. Schematic diagram illustrating the proposed signaling pathway involved in UgU-induced NLRP3 inflammasome assembly and the following molecular events in human monocytes.** UgU induces IL-1β release via the PLC/IP<sub>3</sub>/Ca<sup>2+</sup>/mitochondrial ROS pathway in human monocytes. UgU-induced Ca<sup>2+</sup> may have a direct activating effect on NLRP3 inflammasome. PKC, cAMP, and NOX-derived ROS are not involved.



## Appendix A. Supporting information

Supplementary data associated with this article can be found in the online version at doi:10.1016/j.redox.2016.12.018.

## References

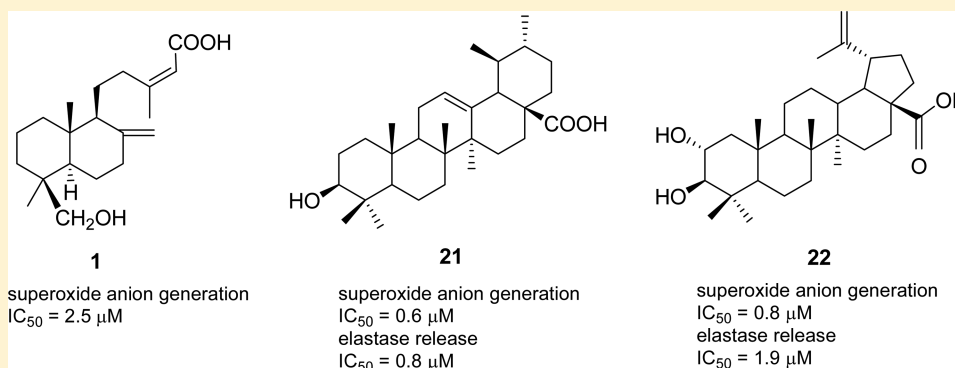
- [1] X. Cao, Self-regulation and cross-regulation of pattern-recognition receptor signalling in health and disease, *Nat. Rev. Immunol.* 16 (2016) 35–50.
- [2] E. Latz, T.S. Xiao, A. Stutz, Activation and regulation of the inflammasomes, *Nat. Rev. Immunol.* 13 (2013) 397–411.
- [3] J. Henao-Mejia, E. Elinav, T. Strowig, R.A. Flavell, Inflammasomes: far beyond inflammation, *Nat. Immunol.* 13 (2012) 321–324.
- [4] V.I. Maltez, E.A. Miao, Reassessing the evolutionary importance of inflammasomes, *J. Immunol.* 196 (2016) 956–962.
- [5] S. Shin, I.E. Brodsky, The inflammasome: learning from bacterial evasion strategies, *Semin. Immunol.* 27 (2015) 102–110.
- [6] F. Martinon, K. Burns, J. Tschopp, The inflammasome: a molecular platform triggering activation of inflammatory caspases and processing of proIL-beta, *Mol. Cell* 10 (2002) 417–426.
- [7] S.M. Man, T.D. Kanneganti, Regulation of inflammasome activation, *Immunol. Rev.* 265 (2015) 6–21.
- [8] J.M. Kahlenberg, G.R. Dubyak, Mechanisms of caspase-1 activation by P2X7 receptor-mediated K<sup>+</sup> release, *Am. J. Physiol. Cell Physiol.* 286 (2004) C1100–1108.
- [9] V. Petrilili, S. Papin, C. Dostert, A. Mayor, F. Martinon, J. Tschopp, Activation of the NALP3 inflammasome is triggered by low intracellular potassium concentration, *Cell Death Differ.* 14 (2007) 1583–1589.
- [10] J. Rivers-Auty, D. Brough, potassium efflux fires the canon: potassium efflux as a common trigger for canonical and noncanonical NLRP3 pathways, *Eur. J. Immunol.* 45 (2015) 2758–2761.
- [11] J.R. Yaron, S. Gangaraju, M.Y. Rao, X. Kong, L. Zhang, F. Su, Y. Tian, H.L. Glenn, D.R. Meldrum, K(+) regulates Ca(2+) to drive inflammasome signaling: dynamic visualization of ion flux in live cells, *Cell Death Dis.* 6 (2015) e1954.
- [12] J. Tschopp, K. Schroder, NLRP3 inflammasome activation: the convergence of multiple signalling pathways on ROS production?, *Nat. Rev. Immunol.* 10 (2010) 210–215.
- [13] R. Zhou, A. Tardivel, B. Thorens, I. Choi, J. Tschopp, Thioredoxin-interacting protein links oxidative stress to inflammasome activation, *Nat. Immunol.* 11 (2010) 136–140.
- [14] C. Adam, J. Wohlfarth, M. Haussmann, H. Sennefelder, A. Rodin, M. Maler, S.F. Martin, M. Goebeler, M. Schmidt, Allergy-inducing chromium compounds trigger potent innate immune stimulation via ROS-dependent inflammasome activation, *J. Invest. Dermatol.* (2016) (Epub ahead of print).
- [15] L. Minutoli, D. Puzzolo, M. Rinaldi, N. Irrera, H. Marini, V. Arcoraci, A. Bitto, G. Crea, A. Pisani, F. Squadrito, V. Trichilo, D. Bruschetta, A. Micali, D. Altavilla, ROS-mediated NLRP3 inflammasome activation in brain, heart, kidney, and testis, *Oxid. Med. Cell. Longev.* 2016 (2016) 2183026.
- [16] B. Rada, J.J. Park, P. Sil, M. Geiszt, T.L. Leto, NLRP3 inflammasome activation and interleukin-1beta release in macrophages require calcium but are independent of calcium-activated NADPH oxidases, *Inflamm. Res.* 63 (2014) 821–830.
- [17] T. Horng, Calcium signaling and mitochondrial destabilization in the triggering of the NLRP3 inflammasome, *Trends Immunol.* 35 (2014) 253–261.
- [18] T. Murakami, J. Ockinger, J. Yu, V. Byles, A. McColl, A.M. Hofer, T. Horng, Critical role for calcium mobilization in activation of the NLRP3 inflammasome, *Proc. Natl. Acad. Sci. USA* 109 (2012) 11282–11287.
- [19] M. Karmakar, M.A. Katsnelson, G.R. Dubyak, E. Pearlman, Neutrophil P2X7 receptors mediate NLRP3 inflammasome-dependent IL-1beta secretion in response to ATP, *Nat. Commun.* 7 (2016) 10555.
- [20] R. Zhou, A.S. Yazdi, P. Menu, J. Tschopp, A role for mitochondria in NLRP3 inflammasome activation, *Nature* 469 (2011) 221–225.
- [21] K. Shimada, T.R. Crother, J. Karlin, J. Dagvadorj, N. Chiba, S. Chen, V.K. Ramanujan, A.J. Wolf, L. Vergnes, D.M. Ojcius, A. Rentsendorj, M. Vargas, C. Guerrero, Y. Wang, K.A. Fitzgerald, D.M. Underhill, T. Town, M. Arditi, Oxidized mitochondrial DNA activates the NLRP3 inflammasome during apoptosis, *Immunity* 36 (2012) 401–414.
- [22] T. Misawa, M. Takahama, T. Kozaki, H. Lee, J. Zou, T. Saitoh, S. Akira, Microtubule-driven spatial arrangement of mitochondria promotes activation of the NLRP3 inflammasome, *Nat. Immunol.* 14 (2013) 454–460.
- [23] J. Dan Dunn, L.A. Alvarez, X. Zhang, T. Soldati, Reactive oxygen species and mitochondria: a nexus of cellular homeostasis, *Redox Biol.* 6 (2015) 472–485.
- [24] H. Lima Jr., L.S. Jacobson, M.F. Goldberg, K. Chandran, F. Diaz-Griffero, M.P. Lisanti, J. Brojatsch, Role of lysosome rupture in controlling Nlrp3 signaling and necrotic cell death, *Cell Cycle* 12 (2013) 1868–1878.
- [25] D.H. Abdelaziz, H. Khalil, E. Cormet-Boyaka, A.O. Amer, The cooperation between the autophagy machinery and the inflammasome to implement an appropriate innate immune response: do they regulate each other?, *Immunol. Rev.* 265 (2015) 194–204.
- [26] T.D. Kanneganti, Central roles of NLRs and inflammasomes in viral infection, *Nat. Rev. Immunol.* 10 (2010) 688–698.
- [27] R. Marty-Roix, G.I. Vladimer, K. Pouliot, D. Weng, R. Buglione-Corbett, K. West, J.D. MacMicking, J.D. Chee, S. Wang, S. Lu, E. Lien, Identification of QS-21 as an inflammasome-activating molecular component of saponin adjuvants, *J. Biol. Chem.* 291 (2016) 11233–11236.
- [28] Y. Yang, C. Inatsuka, E. Gad, M.L. Disis, L.J. Standish, N. Pugh, D.S. Pasco, H. Lu, Protein-bound polysaccharide-K induces IL-1beta via TLR2 and NLRP3 inflammasome activation, *Innate Immun.* 20 (2014) 857–866.
- [29] J.D. Thacker, B.J. Balin, D.M. Appelt, S. Sassi-Gaha, M. Purohit, R.F. Rest, C.M. Artlett, NLRP3 inflammasome is a target for development of broad-spectrum anti-infective drugs, *Antimicrob. Agents Chemother.* 56 (2012) 1921–1930.
- [30] H.W. Stout-Delgado, S.E. Vaughan, A.C. Shirali, R.J. Jaramillo, K.S. Harrod, Impaired NLRP3 inflammasome function in elderly mice during influenza infection is rescued by treatment with nigericin, *J. Immunol.* 188 (2012) 2815–2824.
- [31] C.Y. Chen, C.C. Liaw, Y.H. Chen, W.Y. Chang, P.J. Chung, T.L. Hwang, A novel immunomodulatory effect of ugonin U in human neutrophils via stimulation of phospholipase C, *Free Radic. Biol. Med.* 72 (2014) 222–231.
- [32] S.R. Suja, P.G. Latha, P. Pushpangadan, S. Rajasekharan, Evaluation of hepatoprotective effects of *Helminthostachys zeylanica* (L.) Hook against carbon tetrachloride-induced liver damage in Wistar rats, *J. Ethnopharmacol.* 92 (2004) 61–66.
- [33] Y.C. Huang, T.L. Hwang, C.S. Chang, Y.L. Yang, C.N. Shen, W.Y. Liao, S.C. Chen, C.C. Liaw, Anti-inflammatory flavonoids from the rhizomes of *Helminthostachys zeylanica*, *J. Nat. Prod.* 72 (2009) 1273–1278.
- [34] B. Freundlich, N. Avdalovic, Use of gelatin/plasma coated flasks for isolating human peripheral blood monocytes, *J. Immunol. Methods* 62 (1983) 31–37.
- [35] S. Bennett, S.N. Breit, Variables in the isolation and culture of human monocytes that are of particular relevance to studies of HIV, *J. Leukoc. Biol.* 56 (1994) 236–240.
- [36] H.M. Lee, J.M. Yuk, K.H. Kim, J. Jang, G. Kang, J.B. Park, J.W. Son, E.K. Jo, Mycobacterium abscessus activates the NLRP3 inflammasome via Dectin-1-Syk and p62/SQSTM1, *Immunol. Cell Biol.* 90 (2012) 601–610.
- [37] H. Kim, Y. Oh, K. Kim, S. Jeong, S. Chon, D. Kim, M.H. Jung, Y.K. Pak, J. Ha, I. Kang, W. Choe, Cyclophilin A regulates JNK/p38-MAPK signaling through its physical interaction with ASK1, *Biochem. Biophys. Res. Commun.* 464 (2015) 112–117.
- [38] A. Sokolovska, C.E. Becker, W.K. Ip, V.A. Rathinam, M. Brudner, N. Paquette, A. Tanne, S.K. Vanaja, K.J. Moore, K.A. Fitzgerald, A. Lacy-Hulbert, L.M. Stuart, Activation of caspase-1 by the NLRP3 inflammasome regulates the NADPH oxidase NOX2 to control phagosome function, *Nat. Immunol.* 14 (2013) 543–553.
- [39] M. Wan, X. Hua, J. Su, D. Thiagarajan, A.G. Frostegard, J.Z. Haegstrom, J. Frostegard, Oxidized but not native cardiolipin has pro-inflammatory effects, which are inhibited by Annexin A5, *Atherosclerosis* 235 (2014) 592–598.
- [40] D. Julian, K.L. April, S. Patel, J.R. Stein, S.E. Wohlgemuth, Mitochondrial depolarization following hydrogen sulfide exposure in erythrocytes from a sulfide-tolerant marine invertebrate, *J. Exp. Biol.* 208 (2005) 4109–4122.
- [41] C. Rogers, B. Davis, P.D. Neuffer, M.P. Murphy, E.J. Anderson, J. Robidoux, A transient increase in lipid peroxidation primes preadipocytes for delayed mitochondrial inner membrane permeabilization and ATP depletion during prolonged exposure to fatty acids, *Free Radic. Biol. Med.* 67 (2014) 330–341.
- [42] C. Balsalobre, J. Johansson, B.E. Uhlén, Cyclic AMP-dependent osmoregulation of crp gene expression in *Escherichia coli*, *J. Bacteriol.* 188 (2006) 5935–5944.
- [43] Y.F. Tsai, H.P. Yu, P.J. Chung, Y.L. Leu, L.M. Kuo, C.Y. Chen, T.L. Hwang, Osthol attenuates neutrophil oxidative stress and hemorrhagic shock-induced lung injury via inhibition of phosphodiesterase 4, *Free Radic. Biol. Med.* 89 (2015) 387–400.
- [44] C. Juliana, T. Fernandes-Alnemri, J. Wu, P. Datta, L. Solorzano, J.W. Yu, R. Meng, A.A. Qiong, E. Latz, C.P. Scott, E.S. Alnemri, Anti-inflammatory compounds parthenolide and Bay 11-7082 are direct inhibitors of the inflammasome, *J. Biol. Chem.* 285 (2010) 9792–9802.
- [45] M. Lamkanfi, J.L. Mueller, A.C. Vitari, S. Misaghi, A. Fedorova, K. Deshayes, W.P. Lee, H.M. Hoffman, V.M. Dixit, Glyburide inhibits the Cryopyrin/Nalp3 inflammasome, *J. Cell Biol.* 187 (2009) 61–70.
- [46] J.M. Abais, M. Xia, Y. Zhang, K.M. Boini, P.L. Li, Redox regulation of NLRP3 inflammasomes: ROS as trigger or effector?, *Antioxid. Redox Signal* 22 (2015) 1111–1129.
- [47] S. Dikalov, Cross talk between mitochondria and NADPH oxidases, *Free Radic. Biol. Med.* 51 (2011) 1289–1301.
- [48] Y. Teshima, N. Takahashi, S. Nishio, S. Saito, H. Kondo, A. Fukui, K. Aoki, K. Yufu, M. Nakagawa, T. Saikawa, Production of reactive oxygen species in the diabetic heart. Roles of mitochondria and NADPH oxidase, *Circ. J.* 78 (2014) 300–306.
- [49] K. Nakahira, J.A. Haspel, V.A. Rathinam, S.J. Lee, T. Dolinay, H.C. Lam, J.A. Englert, M. Rabinovitch, M. Cernadas, H.P. Kim, K.A. Fitzgerald, S.W. Ryter, A.M. Choi, Autophagy proteins regulate innate immune responses by inhibiting the release of mitochondrial DNA mediated by the NALP3 inflammasome, *Nat. Immunol.* 12 (2011) 222–230.
- [50] R. van Bruggen, M.Y. Koker, M. Jansen, M. van Houdt, D. Roos, T.W. Kuijpers, T.K. van den Berg, Human NLRP3 inflammasome activation is Nox1-4 independent, *Blood* 115 (2010) 5398–5400.
- [51] E.A. Bordt, B.M. Polster, NADPH oxidase- and mitochondria-derived reactive oxygen species in proinflammatory microglial activation: a bipartisan affair?, *Free Radic. Biol. Med.* 76 (2014) 34–46.
- [52] F.L. van de Veerdonk, S.P. Smeekens, L.A. Joosten, B.J. Kullberg, C.A. Dinarello, J.W. van der Meer, M.G. Netea, Reactive oxygen species-independent activation of the IL-1beta inflammasome in cells from patients with chronic granulomatous disease, *Proc. Natl. Acad. Sci. USA* 107 (2010) 3030–3033.
- [53] M. Clauzure, A.G. Valdivieso, M.M. Massip Copiz, G. Schulman, M.L. Teiber, T.A. Santa-Coloma, Disruption of interleukin-1beta autocrine signaling rescues complex I activity and improves ROS levels in immortalized epithelial cells with impaired cystic fibrosis transmembrane conductance regulator (CFTR) function, *PLoS One* 9 (2014) e99257.
- [54] M.J. Morgan, Z.G. Liu, Crosstalk of reactive oxygen species and NF-kappaB



- signaling, *Cell Res.* 21 (2011) 103–115.
- [55] S.G. Rhee, Regulation of phosphoinositide-specific phospholipase C, *Annu. Rev. Biochem.* 70 (2001) 281–312.
- [56] K. Shimada, T.R. Crother, J. Karlin, S. Chen, N. Chiba, V.K. Ramanujan, L. Vergnes, D.M. Ojcius, M. Ardit, Caspase-1 dependent IL-1 $\beta$  secretion is critical for host defense in a mouse model of *Chlamydia pneumoniae* lung infection, *PLoS One* 6 (2011) e21477.
- [57] M. Fraunholz, B. Sinha, Intracellular *Staphylococcus aureus*: live-in and let die, *Front. Cell. Infect. Microbiol.* 2 (2012) 43.
- [58] L. Munzenmayer, T. Geiger, E. Daiber, B. Schulte, S.E. Autenrieth, M. Fraunholz, C. Wolz, Influence of Sae-regulated and Agr-regulated factors on the escape of *Staphylococcus aureus* from human macrophages, *Cell. Microbiol.* 18 (2016) 1172–1183.
- [59] D.J. Hackam, O.D. Rotstein, W.J. Zhang, N. Demareux, M. Woodside, O. Tsai, S. Grinstein, Regulation of phagosomal acidification. Differential targeting of Na<sup>+</sup>/H<sup>+</sup> exchangers, Na<sup>+</sup>/K<sup>+</sup>-ATPases, and vacuolar-type H<sup>+</sup>-atpases, *J. Biol. Chem.* 272 (1997) 29810–29820.
- [60] B. Wegiel, R. Larsen, D. Gallo, B.Y. Chin, C. Harris, P. Mannam, E. Kaczmarek, P.J. Lee, B.S. Zuckerbraun, R. Flavell, M.P. Soares, L.E. Otterbein, Macrophages sense and kill bacteria through carbon monoxide-dependent inflammasome activation, *J. Clin. Invest.* 124 (2014) 4926–4940.

Chemical Constituents and Anti-inflammatory Principles from the Fruits of *Forsythia suspensa*Ping-Chung Kuo,<sup>†</sup> Hsin-Yi Hung,<sup>†</sup> Chi-Wei Nian,<sup>‡</sup> Tsong-Long Hwang,<sup>§</sup> Ju-Chien Cheng,<sup>⊥</sup> Daih-Huang Kuo,<sup>||</sup> E-Jian Lee,<sup>#</sup> Shih-Huang Tai,<sup>#</sup> and Tian-Shung Wu<sup>\*,†,||,⊥</sup><sup>†</sup>School of Pharmacy, National Cheng Kung University Hospital, College of Medicine, National Cheng Kung University, Tainan 701, Taiwan<sup>‡</sup>Department of Chemistry, National Cheng Kung University, Tainan 701, Taiwan<sup>§</sup>Graduate Institute of Natural Products, College of Medicine, Chang Gung University; Research Center for Industry of Human Ecology, Research Center for Chinese Herbal Medicine, and Graduate Institute of Health Industry Technology, College of Human Ecology, Chang Gung University of Science and Technology; and Department of Anesthesiology, Chang Gung Memorial Hospital, Taoyuan 333, Taiwan<sup>⊥</sup>Department of Medical Laboratory Science and Biotechnology, China Medical University, Taichung 404, Taiwan<sup>||</sup>Department of Pharmacy, College of Pharmacy and Health Care, Tajen University, Pingtung 907, Taiwan<sup>#</sup>Department of Surgery and Anesthesiology and Institute of Biomedical Engineering, National Cheng Kung University, Medical Center and Medical School, Tainan 701, Taiwan

## S Supporting Information



**ABSTRACT:** Fifty compounds were isolated from the fruits of *Forsythia suspensa*, including 13 new compounds characterized as eight new diterpenoids (1–8), three new lignans (9–11), a new iridoid (12), and a new triterpenoid (13). Their structures were established on the basis of spectroscopic and spectrometric analysis. Most of the isolated compounds were examined for their anti-inflammatory activity in vitro. The results showed that several compounds displayed significant inhibition of fMLP/CB-induced superoxide anion generation and elastase release, with IC<sub>50</sub> values ranging from 0.6 ± 0.1 to 8.6 ± 0.8 μg/mL and from 0.8 ± 0.3 to 7.3 ± 1.1 μg/mL, respectively.

Various autoimmune diseases, including rheumatoid arthritis, ischemia, reperfusion injury, chronic obstructive pulmonary disease, and asthma, are linked to neutrophil overexpression, according to recent study results.<sup>1–5</sup> Activated neutrophils secrete a series of cytotoxins, such as superoxide anions and elastase, in response to diverse stimuli.<sup>6,7</sup> Consequently, the concentrations of superoxide anions and elastase in infected tissues and organs will increase under physiological conditions. As a part of a continuing program aimed at discovering novel anti-inflammatory drugs, *Forsythia suspensa* (Thunb.) Vahl (Oleaceae) was selected for study due to previous reports related to anti-inflammatory, diuretic, drainage, and antimicrobial effects in Oriental medicine, in the removal of heat and toxins.<sup>8,9</sup> Previous investigations of species in the genus *Forsythia*

have afforded several sterols, triterpenoids, lignans, and phenylethanoid glycosides.<sup>10–21</sup> Therefore, the methanol extract of the fruits of *F. suspensa* was subjected to preliminary anti-inflammatory bioactivity screening. At the test concentration (10 μg/mL), this extract displayed inhibition of both superoxide anion generation and elastase release (91 ± 1.0% and 88 ± 4.0%, respectively). Thus, in the present investigation, fractionation procedures were applied and bioassay-guided purification afforded eight new diterpenoids (1–8), three new lignans (9–11), a new iridoid (12), and a new triterpenoid (13) (Figure 1), along with 37 known compounds. The chemical

Received: December 11, 2016

Published: February 20, 2017

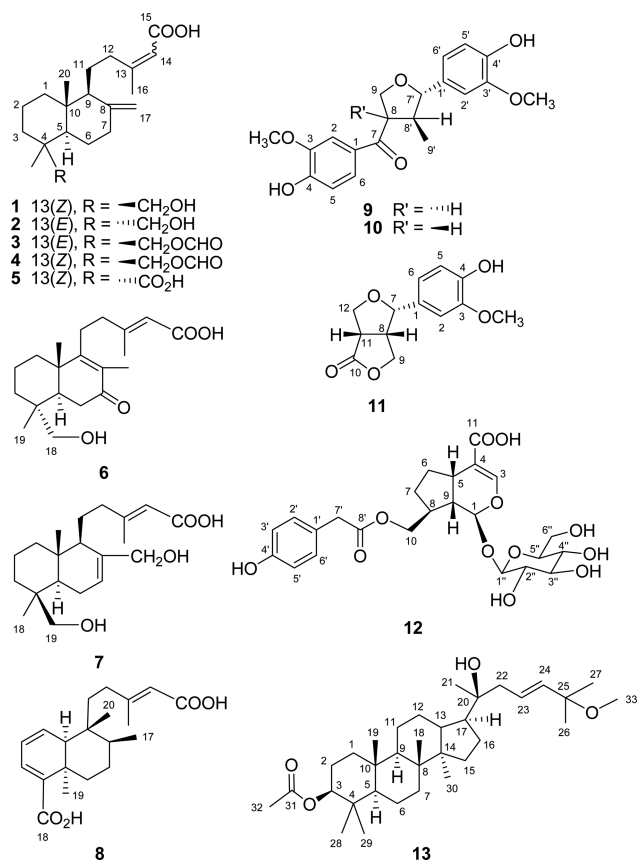


Figure 1. Structures of compounds 1–13.

structures of the new constituents were established on the basis of 1D and 2D NMR and mass spectrometric analysis.

The purified principles were examined for inhibition of superoxide anion generation and elastase release, thereby evaluating their in vitro anti-inflammatory potential.

## RESULTS AND DISCUSSION

The dried fruits of *F. suspensa* were refluxed with 95% aqueous ethanol solution, and the obtained extract was purified directly by reversed-phase Diaion HP-20 column chromatography without liquid–liquid partition, to avoid the absorption and degradation of low-polarity compounds. A sequential combination of conventional chromatographic techniques was utilized to isolate the constituents described below.

Compounds 1–7 exhibited similar UV and IR absorption characteristics. Combined mass spectrometric and NMR spectroscopic data analysis suggested these compounds to be diterpenoids. The HRESIMS of compounds 1 and 2 afforded similar sodium adduct ion peaks corresponding to the same molecular formula,  $\text{C}_{20}\text{H}_{32}\text{O}_3$ . On comparison of the  $^1\text{H}$  and  $^{13}\text{C}$  NMR spectra of 1 and 2 with those of agatholic acid (14) (Figure 2),<sup>22</sup> only minor differences were revealed among these compounds. Compound 1 displayed almost the same  $^1\text{H}$  and  $^{13}\text{C}$  NMR signals as those of 14 except that its NOESY spectrum exhibited a NOE correlation between H-14 ( $\delta$  5.67) and  $\text{CH}_3$ -16 ( $\delta$  1.93). Therefore, the geometry of the C-13/C-14 double bond was assigned as Z, different from that of 14. Accordingly, the structure of 1 was established as 19-hydroxylabda-8(17),13(Z)-dien-15-oic acid. In turn, in the NOESY spectrum of 2, there was a NOE correlation between H-14 ( $\delta$  5.67) and  $\text{CH}_2$ -12 ( $\delta$  1.99), suggesting the same E configuration of 2 as in 14. In addition, the NOESY correlations of H-5 ( $\delta$  1.43)/H-18 ( $\delta$  3.11, 3.42),  $\text{CH}_3$ -19 ( $\delta$  0.75)/ $\text{CH}_3$ -20 ( $\delta$  0.73), and  $\text{CH}_3$ -20 ( $\delta$  0.65)/H-11 ( $\delta$  1.51, 1.69) indicated a different C-4 configuration between 2 and 14.

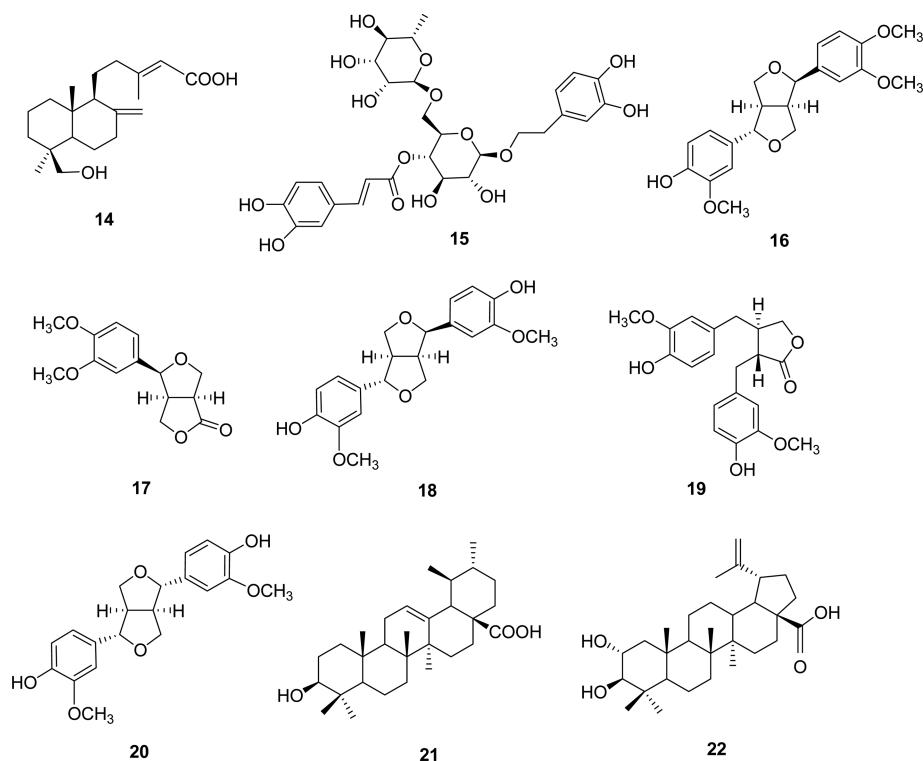


Figure 2. Structures of compounds 14–22.

Table 1.  $^1\text{H}$  NMR Spectroscopic Data of Compounds 1–8 [ $\delta_{\text{H}}$  mult. ( $J$  in Hz)]

position	1 <sup>a</sup>	2 <sup>a</sup>	3 <sup>b</sup>	4 <sup>b</sup>	5 <sup>a</sup>	6 <sup>a</sup>	7 <sup>b</sup>	8 <sup>a</sup>
1	1.78 m	1.76 m; 1.03 td (13.0, 4.4)	1.80 m; 1.11 m	1.79 m; 1.05 m	1.69 m; 1.19 m	1.92 m; 1.39 td		
(13.1, 3.7)								
2	1.89 m; 1.00 m	6.06 dd (9.7, 6.6)						
	1.51 m	1.58 m	1.52 m	1.51 m	1.57 m	1.71 m	1.49 m	6.25 dd (9.7, 5.3)
3	1.83 m; 0.99 m	1.44 m; 1.29 m	1.74 m; 1.05 m	1.74 m; 1.04 m	1.86 m; 1.62 m	1.55 td (13.3, 4.2); 1.35 m	1.88 m; 0.96 m	6.90 d (5.3)
5	1.30 m	1.43 m	1.30 m	1.29 m	2.09 dd (12.6, 2.9)	2.10 dd (14.2, 3.6)	1.39 m	
6	1.83 m; 1.33 m	1.64 m; 1.34 dd (13.0, 4.3)	1.84 m; 1.32 m	1.85 m; 1.35 dd (12.8, 4.1)	1.49 m; 1.35 m	2.45 dd (17.7, 3.6); 2.38 m	2.14 m; 1.94 m	2.89 dt (14.0, 3.2); 1.08 dd (14.0, 3.6)
7	2.40 dt (13.2, 2.8); 1.95 m	2.39 ddd (12.5, 4.3, 2.3); 2.00 m	2.40 dt (12.0, 3.2); 1.96 m	2.39 ddd (12.8, 3.7, 2.2); 1.95 m	2.36 m; 2.13 m		5.76 m	1.36 m; 1.19 m
8								1.45 m
9	1.66 m	1.64 m	1.67 m	1.59 m	1.95 m		1.89 m	
10								1.96 d (6.3)
11	1.63 m; 1.51 m	1.69 m; 1.52 m	1.65 m; 1.53 m	1.69 m; 1.51 m	1.63 m; 1.51 m	2.38 m	1.63 m; 1.41 m	1.41 m; 1.28 m
12	2.57 m	2.32 m; 2.00 m	2.57 m	2.30 ddd (14.3, 10.6, 4.2); 1.98 m	2.82 dt (10.5, 3.8); 2.27 m	2.29 td (11.9, 5.4)	2.52 m; 2.19 m	2.17 m
14	5.67 s	5.68 d (1.0)	5.69 s	5.67 br s	5.67 br s	5.75 s	5.74 d (1.2)	5.74 d (1.0)
16	1.93 s	2.17 d (1.0)	1.93 s	2.15 s	1.95 d (1.4)	2.23 s	2.19 d (1.2)	2.21 d (1.0)
17	4.85 s; 4.65 s	4.86 s; 4.51 s	4.87 s; 4.68 s	4.86 s; 4.51 s	4.86 s; 4.59 s	1.78 s	4.14 d (12.0); 3.98 d (12.0)	0.79 d (7.0)
18	0.98 s	3.42 d (11.0); 3.11 d (11.0)	0.98 s	0.98 s		3.41 d (11.0); 3.12 d (11.0)	0.98 s	
19	3.75 d (10.8); 3.38 d (10.8)		4.35 d (11.0); 3.92 d (11.0)	4.34 d (11.0); 3.92 d (11.0)	1.13 s	0.86 s	3.84 d (10.7); 3.50 d (10.7)	1.10 s
20	0.65 s	0.73 s	0.69 s	0.69 s	0.70 s	1.13 s	0.74 s	0.69 s
21			8.07 s	8.07 s				

<sup>a</sup> $^1\text{H}$  NMR data measured in  $\text{CDCl}_3$  at 700 MHz. <sup>b</sup> $^1\text{H}$  NMR data measured in  $\text{CDCl}_3$  at 400 MHz.

Table 2.  $^{13}\text{C}$  NMR Spectroscopic Data of Compounds 1–8

position	1 <sup>a</sup>	2 <sup>a</sup>	3 <sup>b</sup>	4 <sup>b</sup>	5 <sup>a</sup>	6 <sup>a</sup>	7 <sup>b</sup>	8 <sup>a</sup>
1	38.8	38.6	38.6	38.7	37.7	35.5	39.0	133.7
2	19.0	18.7	18.8	18.8	18.5	17.9	18.3	125.2
3	35.4	35.4	36.0	35.9	37.2	34.6	35.2	135.3
4	38.9	38.0	37.3	37.2	47.6	37.5	37.9	135.5
5	56.3	48.5	56.1	56.0	49.3	43.3	50.7	36.9
6	24.5	24.2	24.4	24.4	26.9	34.9	23.2	34.6
7	38.6	38.0	38.4	38.3	37.7	199.7	126.3	28.7
8	147.9	148.0	147.5	147.3	147.9	130.7	138.8	36.2
9	57.2	56.1	57.1	56.1	58.1	166.2	51.3	41.0
10	39.7	39.6	39.6	39.5	38.9	40.7	36.6	48.3
11	22.5	21.5	22.5	21.5	23.2	27.7	25.0	34.9
12	32.9	40.0	32.8	39.9	33.1	39.7	42.4	35.0
13	164.2	164.0	164.0	163.2	166.3	161.5	163.4	163.8
14	115.0	114.1	114.8	115.1	114.5	115.0	114.6	114.3
15	170.0	169.2	168.6	171.7	170.9	170.1	169.7	169.3
16	25.7	19.2	25.7	19.1	26.3	19.1	19.3	19.4
17	106.7	106.6	106.9	107.0	106.8	11.4	66.1	15.9
18	27.1	72.1	27.5	27.5	184.6	70.6	26.5	170.1
19	65.1	17.6	65.3	66.2	16.2	17.3	64.9	29.6
20	15.3	14.9	15.2	15.2	14.7	18.7	14.6	16.1
OCHO			161.4	161.4				

<sup>a</sup> $^{13}\text{C}$  NMR data measured in  $\text{CDCl}_3$  at 175 MHz. <sup>b</sup> $^{13}\text{C}$  NMR data measured in  $\text{CDCl}_3$  at 100 MHz.

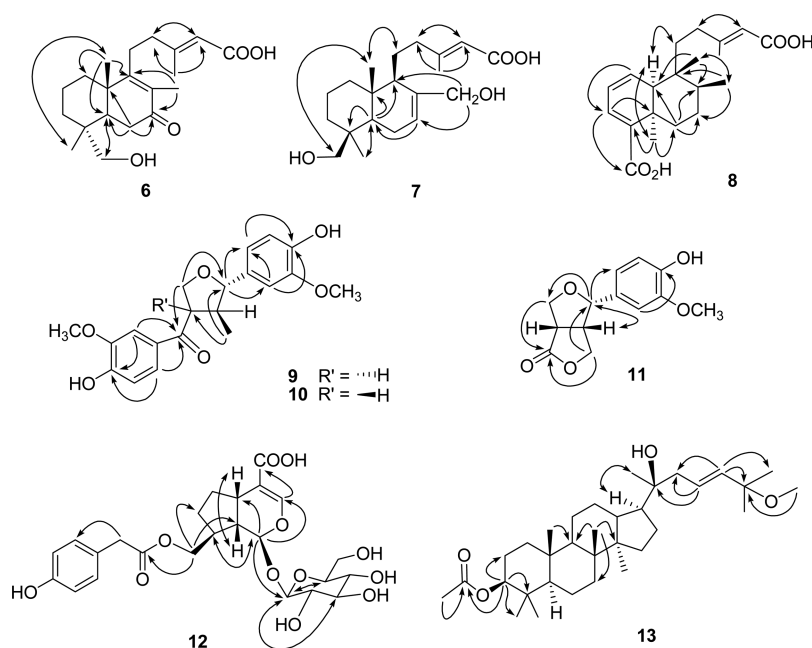


Figure 3. Diagnostic HMBC (→)/NOESY (↔) correlations of compounds 6–13.

Consequently, **2** was determined as 18-hydroxylabda-8(17),13(*E*)-dien-15-oic acid. All the proton and carbon signal assignments of **1** and **2** (Tables 1 and 2) were accomplished by a combination of 2D NMR experiments.

Compounds **3** and **4** revealed the same molecular formula of  $\text{C}_{21}\text{H}_{32}\text{O}_4$  through HRESIMS analysis. The difference between this molecular formula and that of **14** suggested the presence of a formate group in both **3** and **4**. This assumption was supported by the  $^1\text{H}$  and  $^{13}\text{C}$  NMR spectra, which showed signals at  $\delta_{\text{H}}$  8.07 and  $\delta_{\text{C}}$  161.4, and the connection of formate was confirmed to be at C-19 in each case by the  $^3\text{J}$ -HMBC correlation between H-19 and C-21. The only difference between **3**

and **4** was the configuration of the C-13/C-14 double bond, which was assigned as *E* in **3** and *Z* in **4**, respectively, according to the NOESY correlations of H-14/ $\text{CH}_2$ -12 in **3** and H-14/ $\text{CH}_3$ -16 in **4**. The other proton and carbon assignments of **3** and **4** (Tables 1 and 2) were completed with the assistance of 2D spectroscopic analyses. Consequently, the structures of **3** and **4** were established as 19-formyllabda-8(17),13(*E*)-dien-15-oic acid and 19-formyllabda-8(17),13(*Z*)-dien-15-oic acid, respectively (Figure 1).

The HRESIMS of **5** showed a sodium adduct ion peak at  $m/z$  357.2035 corresponding to the elemental formula,  $\text{C}_{20}\text{H}_{30}\text{O}_4$ . Comparison of the UV, IR, and  $^1\text{H}$  and  $^{13}\text{C}$  NMR data of **5**



with **1** indicated that the C-18 hydroxymethyl group in **1** was oxidized to a carboxylic acid in **5**. The NOESY spectrum of **5** displayed a NOE correlation between H-14 and CH<sub>3</sub>-16, suggesting a *Z* configuration of the C-13/C-14 double bond. The C-4 relative configuration was determined from the NOESY correlation between CH<sub>3</sub>-19 and CH<sub>3</sub>-20 and comparison with the reported data of pinifolic acid.<sup>23</sup> Thus, **5** was determined as labda-8(17),13(*Z*)-dien-15,18-dioic acid (Figure 1).

The molecular formula of **6** was also assigned as C<sub>20</sub>H<sub>30</sub>O<sub>4</sub> according to the HRESIMS analytical data. In its <sup>1</sup>H NMR spectrum, characteristic peaks appeared for an olefinic proton at δ 5.75 (1H, s, H-14) and a hydroxymethyl group at δ 3.41 (1H, d, *J* = 11.0, H-18a) and 3.12 (1H, d, *J* = 11.0, H-18b), respectively. However, in addition to the typical three methyl singlets at δ 0.86 (CH<sub>3</sub>-19), 1.13 (CH<sub>3</sub>-20), and 2.23 (CH<sub>3</sub>-16), the terminal vinyl group commonly found in the labdane compound class was replaced by a methyl singlet at δ 1.78 (CH<sub>3</sub>-17). In the downfield portion of the <sup>13</sup>C NMR spectrum, signals appeared for two sets of carbon–carbon double bonds (δ 115.0, 130.7, 161.5, 166.2), a carboxylic acidic carbon (δ 170.1), and a carbonyl carbon (δ 199.7), suggesting the presence of two α,β-unsaturated carbonyl functionalities. The locations of these two fragments were characterized as shown by the HMBC spectrum, which displayed <sup>2</sup>J, <sup>3</sup>J-HMBC couplings from H-6 to C-5, C-7, C-10; from H-14 to C-12, C-15, C-16; from CH<sub>3</sub>-16 to C-12, C-13, C-14; from CH<sub>3</sub>-17 to C-7, C-8, C-9; and from CH<sub>3</sub>-20 to C-1, C-5, C-9, C-10, respectively (Figure 3). In the NOESY spectrum of **6**, NOE correlations were observed between H-14/CH<sub>2</sub>-12, H-5/CH<sub>2</sub>-18, and CH<sub>3</sub>-19/CH<sub>3</sub>-20 (Figure 3), to confirm the C-4 configuration and the *E* geometry of the C-13/C-14 double bond. Consequently, the chemical structure of **6** was elucidated as 18-hydroxy-7-oxolabda-8(9),13(*E*)-dien-15-oic acid (Figure 1).

The HRESIMS of **7** exhibited a sodium adduct ion peak at *m/z* 359.2195, suggesting a molecular formula of C<sub>20</sub>H<sub>32</sub>O<sub>4</sub>. Comparison with **6** indicated one less index of hydrogen deficiency (IHD) in **7**, which was confirmed by the reduction of a carbonyl carbon in its <sup>13</sup>C NMR spectrum. Only three methyl groups at δ 0.74 (CH<sub>3</sub>-20), 0.98 (CH<sub>3</sub>-18), and 2.19 (CH<sub>3</sub>-16) were found in its <sup>1</sup>H NMR spectrum. In addition, there were resonances for two hydroxymethyl groups at δ 4.14 (1H, d, *J* = 12.0 Hz, H-17a), 3.98 (1H, d, *J* = 12.0 Hz, H-17b), 3.84 (1H, d, *J* = 10.7 Hz, H-19a), and 3.50 (1H, d, *J* = 10.7 Hz, H-19b). HMBC correlations of H-5/C-4, C-9, C-10, C-18, C-20; H-7/C-5; H-14/C-12, C-16; H-17/C-7, C-8, C-9; CH<sub>3</sub>-16/C-12, C-13, C-14, C-15; CH<sub>3</sub>-18/C-3, C-4, C-5, C-19; and CH<sub>3</sub>-20/C-1, C-5, C-9, C-10 were observed (Figure 3). In addition, the NOESY spectrum displayed NOE correlations between H-14/CH<sub>2</sub>-12, H-5/CH<sub>3</sub>-18, CH<sub>2</sub>-11/CH<sub>3</sub>-20, and CH<sub>2</sub>-19/CH<sub>3</sub>-20 (Figure 3), aiding in the assignment of the C-4 relative configuration and the *E* geometry of the C-13/C-14 double bond. This evidence supported the assignment of the structure of **7** as 17,19-dihydroxylabda-7(8),13(*E*)-dien-15-oic acid (Figure 1).

The molecular formula of **8** was assigned as C<sub>20</sub>H<sub>28</sub>O<sub>4</sub> according to the HRESIMS data. The UV spectrum exhibited two absorption maxima at 289 and 219 nm, and the IR absorption band at 1691 cm<sup>−1</sup> suggested the presence of a conjugated carboxylic acid group. The <sup>1</sup>H and <sup>13</sup>C NMR spectroscopic characteristics indicated **8** to be a diterpenoid. In its <sup>1</sup>H NMR spectrum, there were signals for four methyl groups at δ 0.69 (s, CH<sub>3</sub>-20), 0.80 (d, *J* = 7.0 Hz, CH<sub>3</sub>-17), 1.10 (s, CH<sub>3</sub>-19), and 2.21 (3H, d, *J* = 1.0 Hz, CH<sub>3</sub>-16) and four olefinic protons at δ 5.74 (1H, d, *J* = 1.0 Hz), 6.06 (1H, dd, *J* = 9.7, 6.6 Hz), 6.25

(1H, dd, *J* = 9.7, 5.3 Hz), and 6.90 (1H, d, *J* = 5.3 Hz), respectively. HMBC correlations were observed from H-1 to C-3, C-5, C-10; H-3 to C-5, C-18; H-6 to C-7, C-8, C-10; H-10 to C-1, C-2, C-4, C-9; H-14 to C-12, C-15, C-16; CH<sub>3</sub>-16 to C-12, C-13, C-14; CH<sub>3</sub>-17 to C-7, C-8, C-9; CH<sub>3</sub>-19 to C-4, C-5, C-6, C-10; and CH<sub>3</sub>-20 to C-8, C-9, C-10, C-11, respectively (Figure 3). These observations supported the locations of CO<sub>2</sub>H-18 at C-4, CH<sub>3</sub>-19 at C-5, CH<sub>3</sub>-17 at C-8, and CH<sub>3</sub>-20 at C-9. The relative configuration was determined by NOE correlations of CH<sub>3</sub>-17/CH<sub>3</sub>-20, CH<sub>3</sub>-19/H-10, and H-10/CH<sub>2</sub>-11 in its NOESY spectroscopy (Figure 3). Accordingly, the structure of **8** was established as shown in Figure 1, and this compound was accorded the trivial name forsythidin A.

Compounds **9** and **10** showed similar sodium adduct ion peaks and were both assigned a molecular formula of C<sub>20</sub>H<sub>22</sub>O<sub>6</sub>. Their UV, IR, and <sup>1</sup>H NMR spectroscopic characteristics indicated **9** and **10** to be lignan derivatives. The <sup>1</sup>H NMR data of **9** displayed two sets of ABX mutually coupled aromatic protons at δ 7.57 (1H, d, *J* = 2.0 Hz), 7.50 (1H, dd, *J* = 8.3, 2.0 Hz), and 6.95 (1H, d, *J* = 8.3 Hz) and δ 6.92 (1H, d, *J* = 2.0 Hz), 6.90 (1H, d, *J* = 8.3 Hz), and 6.84 (1H, dd, *J* = 8.3, 2.0 Hz), respectively. There were also typical proton signals at δ 4.38 (1H, dd, *J* = 8.7, 7.1 Hz, H-9a), 4.31 (1H, dd, *J* = 8.7, 7.1 Hz, H-9b), 4.51 (1H, d, *J* = 7.5 Hz, H-7'), 4.24 (1H, dt, *J* = 8.0, 7.1 Hz, H-8), and 2.50 (1H, m) that accounted for an oxygenated methylene, an oxygenated methine, and two aliphatic methines. In addition, a methyl group signal at δ 0.85 (3H, d, *J* = 7.0 Hz) and two methoxy group singlets at δ 3.92 and 3.97 were used to construct the 4,4'-dihydroxy-3,3'-dimethoxy-7,9'-epoxylignan-7'-one basic unit, which was verified by HMBC correlations from H-2 to C-4, C-6, C-7; from H-6 to C-2, C-4, C-7; from H-2' to C-4', C-6'; from H-6' to C-2', C-4'; from H-7' to C-2', C-6'; from H-9a to C-7, C-7', C-8; and from CH<sub>3</sub>-9' to C-7', C-8, C-8', respectively (Figure 3). The configurations of C-7', C-8, and C-8' were determined as *rel*-(7*R*, 8*R*, 8*S*) by the <sup>1</sup>H NMR coupling constants, the Cotton effects in the electronic circular dichroism (ECD) spectrum (Supporting Information), and NOE cross-peaks of H-7'/CH<sub>3</sub>-9' and H-8'/H-8' in the NOESY spectroscopic analysis.<sup>24–26</sup> Therefore, **9** was established as shown in Figure 1 and given the trivial name *rel*-(7*R*,8'*R*,8*S*)-forsythialan C following the previous convention.<sup>27</sup>

Compound **10** displayed closely related 1D and 2D NMR spectroscopic characteristics and the same planar structure as **9**. However, the proton coupling constants, the Cotton effects in the ECD spectrum (Supporting Information), and NOE cross-peaks of H-7'/CH<sub>3</sub>-9' and H-8/CH<sub>3</sub>-9' revealed a different configuration between compounds **9** and **10**. Compound **10** was established as *rel*-(7*R*,8'*R*,8*R*)-forsythialan C (Figure 1) according to the analytical results obtained.<sup>24–26</sup>

The molecular formula of **11** was assigned as C<sub>13</sub>H<sub>14</sub>O<sub>5</sub> according to the HRESIMS sodium adduct ion peak at *m/z* 273.0735 (calcd for C<sub>13</sub>H<sub>14</sub>O<sub>5</sub>Na, 273.0733). The UV and IR absorptions suggested **11** to be a lignan. However, in its <sup>1</sup>H NMR spectrum only one set of ABX mutually coupled aromatic protons was observed at δ 6.91 (1H, d, *J* = 8.0 Hz), 6.88 (1H, d, *J* = 1.4 Hz), and 6.71 (1H, dd, *J* = 8.0, 1.4 Hz). In addition, the typical signals characteristic for a 7,9-epoxylignan-10-one substructure at δ 4.97 (1H, d, *J* = 5.3 Hz, H-7), 4.51 (1H, d, *J* = 9.4 Hz, H-9a), 4.07 (1H, dd, *J* = 9.9, 8.2 Hz, H-12a), 3.97 (1H, dd, *J* = 9.4, 6.6 Hz, H-9b), 3.83 (1H, dd, *J* = 9.9, 3.2 Hz, H-12b), and 3.37–3.34 (2H, m, H-8 and -11) indicated a furofuran lignan basic structure, and its 2D structure was verified by

an HMBC experiment (Figure 3). The ECD spectral analysis of **11** revealed the same Cotton effects as those of forsythenin (Figure S47, Supporting Information),<sup>28</sup> and therefore the structure of **11** was established as 4-*O*-demethylforsythenin (Figure 1).

Compound **12** was purified as an optically active colorless syrup, and its HRESIMS revealed a sodium adduct ion peak at  $m/z$  533.1627 ( $[M + Na]^+$ ) indicating a molecular formula of  $C_{24}H_{30}O_{12}$ . The UV spectrum exhibited absorption maxima at 276, 237, and 218 nm, and the IR absorption bands at 3384 and 1691  $cm^{-1}$  were characteristic for the hydroxy and carbonyl groups, respectively. In its  $^1H$  NMR spectrum, there were typical signals present for an iridoid basic skeleton at  $\delta$  7.48 (1H, s, H-3), 5.16 (1H, d,  $J = 6.8$  Hz, H-1), 4.09 (2H, m, H-10), 2.79 (1H, m,  $J = 14.8, 7.2$  Hz, H-5), 2.31 (1H, m, H-8), 2.15 (1H, m, H-6a), 1.92 (1H, dd,  $J = 13.2, 7.1$  Hz, H-9), 1.79 (1H, m, H-7a), 1.42 (1H, m, H-6b), and 1.33 (1H, m, H-7b). In addition, there were also proton signals present for a set of sugar protons and those for a *p*-hydroxyphenylacetic acid moiety [ $\delta$  7.10 (2H, d,  $J = 8.5$  Hz, H-2' and -6'), 6.73 (2H, d,  $J = 8.5$  Hz, H-3' and -5'), 3.55 (2H, s, H-7')]. The saccharide substituent was identified as a glucose unit according to its chemical shifts in the  $^{13}C$  NMR spectrum. The configuration of the sugar moiety was inferred from the  $^1H$  NMR coupling constants and the NOESY spectrum. The connection locations of glucose and *p*-hydroxyphenylacetic acid were determined at C-1 and C-10, respectively, through HMBC analysis, in which were observed HMBC correlations from H-1 to C-1''/C-3/C-5/C-8/C-9 and from H-10 to C-8'/C-7/C-8/C-9 (Figure 3). Therefore, **12** was assigned as a 10-*p*-hydroxyphenylacetate derivative of adoxosidic acid, and its relative configuration was established by the NOESY correlations of H-1/H-8 and H-5/H-9 as being the same as adoxosidic acid.<sup>19</sup> No NOE interactions occurred between H-5 and H-1 and between H-5 and H-8. Conclusively, **12** was characterized as adoxosidic acid 10-*p*-hydroxyphenylacetate (Figure 1).

The molecular formula of **13** was established as  $C_{33}H_{56}O_4$  through HRESIMS analysis, in which six IHDs were evident. In its  $^1H$  NMR spectrum, there were proton signals characteristic of a triterpenoid basic skeleton for the eight methyl groups at  $\delta$  1.26 (6H, s,  $CH_3$ -26, 27), 1.12 (3H, s,  $CH_3$ -21), 0.95 (3H, s,  $CH_3$ -18), 0.86 (3H, s,  $CH_3$ -19), 0.85 (3H, s,  $CH_3$ -30), and 0.84 (6H, s,  $CH_3$ -28, 29). In addition, two downfield methyl groups were assigned for an acetyl methyl group at  $\delta$  2.04 (3H, s,  $CH_3$ -32) and a methoxy group at  $\delta$  3.15 (3H, s,  $CH_3$ -33). A mutually coupled doublet at  $\delta$  5.63 (1H, dt,  $J = 15.9, 7.3$  Hz, H-23) and 5.48 (1H, d,  $J = 15.9$  Hz, H-24) was indicative of a *trans* double bond. In the downfield region, an oxygenated proton at  $\delta$  4.47 (1H, dd,  $J = 10.3, 5.7$  Hz, H-3) suggested acetylation at C-3, which was supported by the HMBC correlations of H-3/C-31 and  $CH_3$ -32/C-31. The C-3 acetoxy group was established as  $\beta$  (equatorial) due to the large coupling constants of H-3 ( $J = 10.3, 5.7$  Hz), indicating its axial orientation. Other HMBC correlations (Figure 3) from H-23 to C-22/C-20/C-24/C-25, H-24 to C-22/C-23/C-25/C-26/C-27,  $CH_3$ -21 to C-17/C-20/C-22,  $CH_3$ -33 to C-25, H-3 to C-2/C-4/C-28/C-29,  $CH_3$ -18 to C-7/C-8/C-9/C-14,  $CH_3$ -19 to C-9/C-10, and  $CH_3$ -26 to C-24/C-25 were used to establish the planar structure of **13**. The configuration of OH-20 could be further determined as  $\beta$  by an NOE correlation between  $CH_3$ -21 and H-17 and by comparison of the  $^1H$  NMR spectrum of **13** with that for the 3-acetylsofouquierol.<sup>29</sup> According to the above evidence, the structure of **13** was proposed as 3 $\beta$ -acetoxy-25-methoxydammar-23-en-20 $\beta$ -ol (Figure 1).

In addition to the above-mentioned new compounds (**1**–**13**), 37 known compounds were also isolated and identified (Figure 2), including a phenylethanoid glycoside, forsythoside A (**15**),<sup>12</sup> 12 lignans and lignan glycosides, phillygenin (**16**),<sup>30</sup> forsythenin (**17**),<sup>28</sup> (+)-pinoresinol monomethyl ether,<sup>16</sup> (+)-epipinoresinol (**18**),<sup>31</sup> (–)-matairesinol (**19**),<sup>16</sup> (+)-pinoresinol (**20**),<sup>16</sup> salicifolol,<sup>32</sup> (–)-arctigenin,<sup>16</sup> (+)-pinoresinol mono- $\beta$ -D-glucopyranoside,<sup>33</sup> forsythialan A,<sup>27</sup> (+)-8-hydroxypinoresinol,<sup>34</sup> and isolaricresinol,<sup>35</sup> eight triterpenoids, dammar-24-en-3 $\beta$ -acetoxy-20-ol,<sup>36</sup> 3 $\beta$ -acetyl-20,25-epoxydammaran-24-ol,<sup>19</sup> 3 $\beta$ -acetoxyolean-12-en-28-oic acid,<sup>19</sup> cabralealactone 3-acetate,<sup>37</sup> cabralealactone 3-acetate 24-methyl ether,<sup>37</sup> garcinielliptone Q,<sup>38</sup> ursolic acid (**21**),<sup>39</sup> and alphitollic acid (**22**),<sup>40</sup> a sterol,  $\beta$ -sitosteryl-3-*O*- $\beta$ -D-glucopyranoside,<sup>41</sup> four benzenoids, 3,4-dimethoxybenzoic acid,<sup>19</sup> *p*-hydroxyphenylacetic acid,<sup>19</sup> *p*-hydroxyphenylacetic acid methyl ester,<sup>19</sup> and caffeic acid,<sup>19</sup> a monoterpenoid, 1-oxo-4-hydroxy-2(3)-en-4-ethylcyclohexa-5,8-olide,<sup>42</sup> nine diterpenoids, agatholic acid (**14**),<sup>22</sup> 3-oxoanticopalic acid,<sup>43</sup> labda-8(17),13(*Z*)-diene-15,19-dioic acid,<sup>44</sup> labda-8(17),13(*E*)-diene-15,19-dioic acid,<sup>44</sup> 19-hydroxy-8(17),*E*-13-labdadien-15-oate,<sup>45</sup> 3 $\beta$ -hydroxy-12,13*E*-biformene,<sup>46</sup> 3 $\beta$ -hydroxy-12,13*Z*-biformene,<sup>47</sup> dehydro-pinifolic acid,<sup>23</sup> and haplopappic acid,<sup>48</sup> and an iridoid, adoxosidic acid.<sup>19</sup>

Most of the purified compounds were examined for their inhibition of superoxide anion generation and elastase release by human neutrophils in response to *N*-formyl-L-methionylphenylalanine/cytochalasin B (fMLP/CB) (Table 3).<sup>49,50</sup> Several compounds displayed inhibition percentages greater than 50% at the test concentration of 10  $\mu g/mL$ , and in the concentration range used these compounds displayed inhibitory effects in a dose-dependent manner. Among these, **1**, **7**, and **14**–**22** displayed inhibition of superoxide anion generation with  $IC_{50}$  values ranging from  $0.6 \pm 0.1$  to  $8.6 \pm 0.8$   $\mu g/mL$ . In comparison, reference compound sorafenib<sup>49</sup> showed  $IC_{50}$  values of  $1.5 \pm 0.2$   $\mu g/mL$  in this assay (Table 3). In addition, compounds **19**, **21**, and **22** also exhibited inhibitory effects on elastase release, with  $IC_{50}$  values ranging from  $0.8 \pm 0.3$  to  $7.3 \pm 1.1$   $\mu g/mL$  (Table 3).

The conventional use of *F. suspensa* in traditional Chinese medicine is for eliminating heat from blood, and the mechanism of action may be related to anti-inflammatory bioactivity. The present experimental data not only suggest that the extracts and purified compounds of the fruits of *F. suspensa* have the potential to be developed as novel anti-inflammatory lead compounds or health foods but also merit further investigation of their anti-inflammatory mechanism.

## ■ EXPERIMENTAL SECTION

**General Experimental Procedures.** Optical rotations were measured using a JASCO DIP-370 digital polarimeter. UV spectra were recorded at room temperature on a Hitachi UV-3210 spectrophotometer. IR spectra were obtained with a Shimadzu FT-IR DR-8011 spectrophotometer.  $^1H$  and  $^{13}C$  NMR spectra were recorded on Bruker Avance III HD 700 and Avance III 400 NMR spectrometers. Chemical shifts are shown in  $\delta$  values (ppm) with tetramethylsilane as an internal standard. The ESIMS and HRESIMS were taken on a Bruker Daltonics APEX II 30e spectrometer (positive-ion mode). Column chromatography (CC) was performed on silica (70–230 mesh and 230–400 mesh, Merck), Diaion HP-20 (Mitsubishi), and  $C_{18}$  (Sigma-Aldrich) gels, respectively, and preparative TLC (thin-layer chromatography) was conducted on Merck precoated silica gel 60 F254 plates, using UV light to visualize the spots. High-performance liquid chromatography (HPLC) was

**Table 3. Inhibitory Effects of Isolated Compounds on Superoxide Anion Generation and Elastase Release by Human Neutrophils in Response to fMLP/CB**

compound	superoxide anion generation	elastase release
	IC <sub>50</sub> (μg/mL) <sup>a</sup>	IC <sub>50</sub> (μg/mL) <sup>a</sup>
1	2.5 ± 0.7 <sup>b</sup>	>10
2	>10	>10
4	>10	>10
5	>10	>10
6	>10	>10
7	8.3 ± 0.8 <sup>b</sup>	>10
8	>10	>10
12	>10	>10
13	>10	>10
14	7.4 ± 0.8 <sup>b</sup>	>10
15	1.4 ± 0.2 <sup>b</sup>	>10
16	6.4 ± 0.5 <sup>b</sup>	>10
17	5.6 ± 1.5 <sup>b</sup>	>10
18	3.4 ± 0.5 <sup>b</sup>	>10
19	4.3 ± 0.4 <sup>b</sup>	7.3 ± 1.1 <sup>b</sup>
20	1.3 ± 0.2 <sup>b</sup>	>10
21	0.6 ± 0.1 <sup>b</sup>	0.8 ± 0.3 <sup>b</sup>
22	0.8 ± 0.1 <sup>b</sup>	1.9 ± 0.7 <sup>b</sup>
3β-acetyl-20,25-epoxydammaran-24α-ol	>10	>10
dammar-24-en-3β-acetoxy-20-ol	>10	>10
3β-acetoxyolean-12-en-28-oic acid	>10	>10
cabralealactone 3-acetate	>10	>10
cabralealactone 3-acetate-24-methyl ether	>10	>10
garcinielliptone Q	>10	>10
1-oxo-4-hydroxy-2(3)-en-4-ethylcyclohexa-5,8-olide	>10	>10
3-oxoantipalic acid	>10	>10
dehydropinifolic acid	>10	>10
haplopappic acid	>10	>10
sorafenib <sup>c</sup>	1.5 ± 0.2	0.9 ± 0.1

<sup>a</sup>Concentration necessary for 50% inhibition (IC<sub>50</sub>). Results are presented as means ± SD (*n* = 3). <sup>b</sup>*p* < 0.001 compared with the control value. <sup>c</sup>Sorafenib, a tyrosine kinase inhibitor, was used as a positive control.

performed on a Shimadzu LC-20AT series pumping system equipped with a Shimadzu SPD-20A UV-vis detector and a SIL-10AF auto-sampling system at ambient temperature.

**Plant Material.** The fruits of *Forsythia suspensa* were provided and authenticated taxonomically by Gene Farm Biotechnology Co., Ltd., Shanhua, Tainan, Taiwan, in February 2013. A voucher specimen (Wu 2013FS) has been deposited in the Herbarium of National Cheng Kung University, Tainan, Taiwan.

**Extraction and Isolation.** The dried fruits of *F. suspensa* (10 kg) was refluxed with 95% ethanol (600 L × 3 × 2 h), and the extract was then filtered and concentrated under reduced pressure to obtain an ethanol extract (2650 g). Part of the ethanol extract (1000 g) was further dissolved in water and subjected to Diaion HP-20 CC eluted with H<sub>2</sub>O and a step gradient of MeOH to afford six fractions, i.e., F1 (pure H<sub>2</sub>O), F2 (H<sub>2</sub>O–MeOH = 9:1), F3 (H<sub>2</sub>O–MeOH = 4:1), F4 (H<sub>2</sub>O–MeOH = 2:1), F5 (H<sub>2</sub>O–MeOH = 1:1), and F6 (pure MeOH). These fractions were examined for their anti-inflammatory activity, with fractions F5 and F6 found to display significant inhibition of superoxide anion generation, with IC<sub>50</sub> values of 3.9 ± 1.4 and 2.5 ± 0.6 μg/mL, respectively. Therefore, these fractions were further chromatographed to isolate the bioactive compounds present. In addition, fraction F2 was also subjected to CC purification.

Fraction F2 was isolated by CC on C<sub>18</sub> silica gel with a step gradient with H<sub>2</sub>O and MeOH mixtures (1:0, 9:1, 5:1, 2:1, 1:1, 0:1) to afford three subfractions (Frs. 2-1–2-3). Fr. 2-1 was further purified by C<sub>18</sub> gel CC with H<sub>2</sub>O and MeOH (2:1) to obtain *p*-hydroxyphenylacetic acid (14.0 mg), caffeic acid (9.3 mg), adoxosidic acid (40.5 mg), and 1-oxo-4-hydroxy-2(3)-en-4-ethylcyclohexa-5,8-olide (10.8 mg), respectively. Fr. 2-3 was isolated by HPLC with an Agilent preparative RP-18 column (30 mm × 250 mm), eluted with H<sub>2</sub>O and MeOH (65:35), to afford **12** (22.0 mg) and *p*-hydroxyphenylacetic acid methyl ester (15.1 mg).

Fraction F5 was purified using C<sub>18</sub> gel CC eluted with gradient mixtures of H<sub>2</sub>O and MeOH (1:0, 9:1, 5:1, 2:1, 1:1, 0:1) to afford five subfractions (Frs. 5-1 to 5-5). Fr. 5-2 was subjected to HPLC with an Agilent semipreparative RP-18 column (21.2 mm × 250 mm) eluted with H<sub>2</sub>O and MeOH (60:40) to furnish **15** (520 mg). Fr. 5-3 was subjected to CC on C<sub>18</sub> silica gel with gradient mixtures of H<sub>2</sub>O and MeOH (1:0, 9:1, 5:1, 2:1, 1:1, 0:1) to afford several additional fractions. One of these, Fr. 5-3-5, was purified by HPLC on an Agilent analytical RP-18 column (4.6 mm × 250 mm), eluted with H<sub>2</sub>O and MeOH (70:30), to yield (+)-pinoresinol mono-β-D-glucopyranoside (2.3 mg), (+)-8-hydroxypinoresinol (2.0 mg), forsythalian A (2.0 mg), and isolariciresinol (1.8 mg), respectively.

Fraction F6 was subjected to silica gel CC with gradient mixtures of *n*-hexane and acetone to produce 19 subfractions (Frs. 6-1 to 6-19). Fr. 6-5 was purified by silica gel CC eluted by gradient elution with *n*-hexane and ethyl acetate to afford several additional fractions. Further purification by TLC using *n*-hexane–ethyl acetate (9:1) and recrystallization yielded 3β-acetyl-20,25-epoxydammaran-24α-ol (15.8 mg) and cabralealactone 3-acetate-24-methyl ether (8.3 mg). Recrystallization of Fr. 6-6 produced dammar-24-en-3β-acetoxy-20-ol (1.5 g). Fr. 6-8 was subjected to silica gel CC eluted with a gradient mixture of dichloromethane and isopropyl ether to afford three subfractions (Frs. 6-8-1–6-8-3). Fr. 6-8-2 was further isolated by silica gel CC, eluted with *n*-hexane–isopropyl ether (2:1), and subsequent preparative TLC using *n*-hexane–acetone (9:1) or recrystallization to afford **13** (2.7 mg), 3β-Acetoxyolean-12-en-28-oic acid (40.0 mg), cabralealactone 3-acetate (15.8 mg), garcinielliptone Q (1.2 g), and 19-hydroxy-8(17),*E*-13-labdadien-15-oate (2.6 mg), respectively.

Fr. 6-14 was isolated by silica gel CC by gradient elution with mixture of *n*-hexane and acetone to result in three fractions (Frs. 6-14-1–6-14-3). Fr. 6-14-1 was further purified by silica gel CC eluted with *n*-hexane–acetone (9:1) to produce several subfractions, and further purification by preparative TLC using *n*-hexane–ethyl acetate (9:1) and recrystallization yielded **1** (6.7 mg), **21** (11.0 mg), and 3-oxoantipalic acid (8.3 mg). Fr. 6-14-2 was subjected to silica gel CC eluted by *n*-hexane–ethyl acetate gradient mixtures, to yield several subfractions. One of these, Fr. 6-14-2-5, was isolated by silica gel CC using *n*-hexane–isopropyl ether–formic acid (1.3:1:0.01) and further purified by preparative TLC using *n*-hexane–ethyl acetate (9:1) to afford **2** (1.5 mg), **3** (7.9 mg), **4** (0.5 mg), **14** (630.0 mg), **22** (90.0 mg), 3β-hydroxy-12,13(*E*)-biformene (1.8 mg), labda-8(17),13(*Z*)-diene-15,19-dioic acid (2.0 mg), labda-8(17),13(*E*)-diene-15,19-dioic acid (4.6 mg), and 3β-hydroxy-12,13(*Z*)-biformene (1.5 mg), respectively. Fr. 6-16 was purified by silica gel CC eluted by *n*-hexane and ethyl acetate gradient mixtures to afford several fractions. Recrystallization of Fr. 6-16-3 resulted in **17** (19.0 mg).

Fr. 6-17 was subjected to silica gel CC with dichloromethane and isopropyl ether gradient mixtures to afford four subfractions (Frs. 6-17-1–6-17-4). Recrystallization of Fr. 6-17-1 produced **16** (320.0 mg). Fr. 6-17-2 was purified by preparative TLC and HPLC on an Agilent semipreparative RP-18 column (21.2 mm × 250 mm), by elution with H<sub>2</sub>O and MeOH (50:50), to yield **5** (21.3 mg), **8** (23.4 mg), **9** (6.0 mg), **10** (6.0 mg), **11** (0.7 mg), **18** (25.1 mg), **19** (8.6 mg), **20** (44.6 mg), (+)-pinoresinol monomethyl ether (1.8 mg), (–)-arctigenin (14.0 mg), salicifoliol (1.6 mg), dehydropinifolic acid (21.2 mg), and haplopappic acid (24.9 mg), sequentially. Frs. 6-18 and 6-19 were purified by silica gel CC with a mixture of CHCl<sub>3</sub> and MeOH (19:1), and final separation by preparative TLC and recrystallization afforded **6** (6.1 mg) and β-sitosterol-3-*O*-β-D-glucopyranoside (38.0 mg) from



Fr. 6-18 and 7 (19.7 mg) and 3,4-dimethoxybenzoic acid (18.2 mg) from Fr. 6-19.

**19-Hydroxylabda-8(17),13(Z)-dien-15-oic acid (1):** colorless powder (CHCl<sub>3</sub>); [ $\alpha$ ]<sub>D</sub><sup>25</sup> +3 (c 0.3, MeOH); UV (MeOH)  $\lambda_{\max}$  (log  $\epsilon$ ) 231 (3.03), 218 (3.05) nm; IR (neat)  $\nu_{\max}$  3446, 2942, 1715, 1452, 1376, 1248, 1029 cm<sup>-1</sup>; <sup>1</sup>H NMR (700 MHz, CDCl<sub>3</sub>) and <sup>13</sup>C NMR (175 MHz, CDCl<sub>3</sub>), see Tables 1 and 2; ESIMS *m/z* 343 ([M + Na]<sup>+</sup>, 100); HRESIMS *m/z* 343.2244 ([M + Na]<sup>+</sup>, calcd for C<sub>20</sub>H<sub>32</sub>O<sub>3</sub>Na, 343.2249).

**18-Hydroxylabda-8(17),13(E)-dien-15-oic acid (2):** colorless syrup; [ $\alpha$ ]<sub>D</sub><sup>25</sup> +23 (c 0.1, MeOH); UV (MeOH)  $\lambda_{\max}$  (log  $\epsilon$ ) 233 (2.76), 218 (2.89) nm; IR (neat)  $\nu_{\max}$  3428, 2927, 1694, 1444, 1259, 1158, 1040 cm<sup>-1</sup>; <sup>1</sup>H NMR (700 MHz, CDCl<sub>3</sub>) and <sup>13</sup>C NMR (175 MHz, CDCl<sub>3</sub>), see Tables 1 and 2; ESIMS *m/z* 343 ([M + Na]<sup>+</sup>, 100); HRESIMS *m/z* 343.2242 ([M + Na]<sup>+</sup>, calcd for C<sub>20</sub>H<sub>32</sub>O<sub>3</sub>Na, 343.2249).

**19-Formyllabda-8(17),13(E)-dien-15-oic acid (3):** colorless powder (CHCl<sub>3</sub>); [ $\alpha$ ]<sub>D</sub><sup>25</sup> +25 (c 0.1, MeOH); UV (MeOH)  $\lambda_{\max}$  (log  $\epsilon$ ) 235 (3.39), 218 (3.40) nm; IR (neat)  $\nu_{\max}$  3375, 2924, 1721, 1691, 1638, 1443, 1379, 1241, 1022 cm<sup>-1</sup>; <sup>1</sup>H NMR (400 MHz, CDCl<sub>3</sub>) and <sup>13</sup>C NMR (100 MHz, CDCl<sub>3</sub>), see Tables 1 and 2; HRESIMS *m/z* 371.2195 ([M + Na]<sup>+</sup>, calcd for C<sub>21</sub>H<sub>32</sub>O<sub>4</sub>Na, 371.2193).

**19-Formyllabda-8(17),13(Z)-dien-15-oic acid (4):** colorless powder (CHCl<sub>3</sub>); [ $\alpha$ ]<sub>D</sub><sup>25</sup> +20 (c 0.4, MeOH); UV (MeOH)  $\lambda_{\max}$  (log  $\epsilon$ ) 234 (2.96), 218 (2.98) nm; IR (neat)  $\nu_{\max}$  3375, 2930, 1721, 1693, 1442, 1252, 1173, 1020 cm<sup>-1</sup>; <sup>1</sup>H NMR (400 MHz, CDCl<sub>3</sub>) and <sup>13</sup>C NMR (100 MHz, CDCl<sub>3</sub>), see Tables 1 and 2; HRESIMS *m/z* 371.2195 ([M + Na]<sup>+</sup>, calcd for C<sub>21</sub>H<sub>32</sub>O<sub>4</sub>Na, 371.2193).

**Labda-8(17),13(Z)-diene-15,18-dioic acid (5):** colorless syrup; [ $\alpha$ ]<sub>D</sub><sup>25</sup> +1 (c 1.1, MeOH); UV (MeOH)  $\lambda_{\max}$  (log  $\epsilon$ ) 232 (2.43), 217 (2.51) nm; IR (neat)  $\nu_{\max}$  3400, 2927, 1690, 1644, 1449, 1265, 1186 cm<sup>-1</sup>; <sup>1</sup>H NMR (700 MHz, CDCl<sub>3</sub>) and <sup>13</sup>C NMR (175 MHz, CDCl<sub>3</sub>), see Tables 1 and 2; HRESIMS *m/z* 357.2035 ([M + Na]<sup>+</sup>, calcd for C<sub>20</sub>H<sub>30</sub>O<sub>4</sub>Na, 357.2036).

**18-Hydroxy-7-oxolabda-8(9),13(E)-dien-15-oic acid (6):** colorless powder (CHCl<sub>3</sub>); [ $\alpha$ ]<sub>D</sub><sup>25</sup> +27 (c 0.3, MeOH); UV (MeOH)  $\lambda_{\max}$  (log  $\epsilon$ ) 259 (3.21), 237 (3.24), 218 (3.22) nm; IR (neat)  $\nu_{\max}$  3402, 2932, 1697, 1649, 1452, 1239, 1147 cm<sup>-1</sup>; <sup>1</sup>H NMR (700 MHz, CDCl<sub>3</sub>) and <sup>13</sup>C NMR (175 MHz, CDCl<sub>3</sub>), see Tables 1 and 2; HRESIMS *m/z* 334.2039 ([M]<sup>+</sup>, calcd for C<sub>20</sub>H<sub>30</sub>O<sub>4</sub>, 334.2036).

**17,19-Dihydroxylabda-7(8),13(E)-dien-15-oic acid (7):** colorless powder (CHCl<sub>3</sub>); [ $\alpha$ ]<sub>D</sub><sup>25</sup> +2 (c 0.5, MeOH); UV (MeOH)  $\lambda_{\max}$  (log  $\epsilon$ ) 233 (2.49), 218 (2.57) nm; IR (neat)  $\nu_{\max}$  3389, 2928, 1695, 1649, 1447, 1375, 1241, 1156, 1024 cm<sup>-1</sup>; <sup>1</sup>H NMR (400 MHz, CDCl<sub>3</sub>) and <sup>13</sup>C NMR (100 MHz, CDCl<sub>3</sub>), see Tables 1 and 2; HRESIMS *m/z* 359.2195 ([M + Na]<sup>+</sup>, calcd for C<sub>20</sub>H<sub>32</sub>O<sub>4</sub>Na, 359.2193).

**Forsythidin A (8):** colorless syrup; [ $\alpha$ ]<sub>D</sub><sup>25</sup> +10 (c 0.5, MeOH); UV (MeOH)  $\lambda_{\max}$  (log  $\epsilon$ ) 289 (2.24), 219 (2.61) nm; IR (neat)  $\nu_{\max}$  3400, 2930, 2857, 1691, 1642, 1447, 1266 cm<sup>-1</sup>; <sup>1</sup>H NMR (700 MHz, CDCl<sub>3</sub>) and <sup>13</sup>C NMR (175 MHz, CDCl<sub>3</sub>), see Tables 1 and 2; HRESIMS *m/z* 355.1881 ([M + Na]<sup>+</sup>, calcd for C<sub>20</sub>H<sub>28</sub>O<sub>4</sub>Na, 355.1880).

**rel-(7R,8'R,8S)-Forsythialan C (9):** colorless syrup; [ $\alpha$ ]<sub>D</sub><sup>25</sup> +30 (c 0.3, MeOH); UV (MeOH)  $\lambda_{\max}$  (log  $\epsilon$ ) 301 (3.20), 273 (3.33), 244 (2.97) nm; ECD (MeOH) 285 ( $\Delta\epsilon$  +1.09), 254 ( $\Delta\epsilon$  +0.78), 236 ( $\Delta\epsilon$  +1.15), 207 ( $\Delta\epsilon$  +1.37) nm; IR (neat)  $\nu_{\max}$  3407, 2921, 1660, 1592, 1515, 1456, 1271, 1193 cm<sup>-1</sup>; <sup>1</sup>H NMR (400 MHz, CDCl<sub>3</sub>)  $\delta$  7.57 (1H, d, *J* = 2.0 Hz, H-2), 7.50 (1H, dd, *J* = 8.3, 2.0 Hz, H-6), 6.95 (1H, d, *J* = 8.2 Hz, H-5), 6.92 (1H, d, *J* = 1.8 Hz, H-2'), 6.90 (1H, d, *J* = 8.3 Hz, H-5'), 6.84 (1H, dd, *J* = 8.3, 2.0 Hz, H-6'), 4.51 (1H, d, *J* = 7.5 Hz, H-7'), 4.38 (1H, dd, *J* = 8.7, 7.1 Hz, H-9a), 4.31 (1H, dd, *J* = 8.7, 7.1 Hz, H-9b), 4.24 (1H, dt, *J* = 8.0, 7.1 Hz, H-8), 3.97 (3H, s, OCH<sub>3</sub>-3), 3.92 (3H, s, OCH<sub>3</sub>-3'), 2.50 (1H, m, H-8'), 0.85 (3H, d, *J* = 7.0 Hz, CH<sub>3</sub>-9'); <sup>13</sup>C NMR (100 MHz, CDCl<sub>3</sub>)  $\delta$  198.6 (C-7), 150.6 (C-4), 146.8 (C-3), 146.6 (C-3'), 145.2 (C-4'), 133.0 (C-1'), 130.6 (C-1), 123.6 (C-6), 119.2 (C-6'), 114.2 (C-5'), 113.8 (C-5), 109.7 (C-2), 108.5 (C-2'), 87.6 (C-7'), 69.6 (C-9), 56.1 (OCH<sub>3</sub>-3), 56.0 (OCH<sub>3</sub>-3'), 48.5 (C-8'), 46.1 (C-8), 13.2 (C-9'); HRESIMS *m/z* 381.1310 ([M + Na]<sup>+</sup>, calcd for C<sub>20</sub>H<sub>22</sub>O<sub>6</sub>Na, 381.1309).

**rel-(7R,8'R,8R)-Forsythialan C (10):** colorless syrup; [ $\alpha$ ]<sub>D</sub><sup>25</sup> +2.2 (c 0.1, MeOH); UV (MeOH)  $\lambda_{\max}$  (log  $\epsilon$ ) 301 (2.93), 275 (3.09), 244 (2.69) nm; ECD (MeOH) 287 ( $\Delta\epsilon$  +0.11), 257 ( $\Delta\epsilon$  +0.13), 207 ( $\Delta\epsilon$  +0.88) nm; IR (neat)  $\nu_{\max}$  3402, 2931, 1664, 1592, 1515, 1272, 1031 cm<sup>-1</sup>; <sup>1</sup>H NMR (400 MHz, CDCl<sub>3</sub>)  $\delta$  7.58 (1H, d, *J* = 1.9 Hz, H-2), 7.53 (1H, dd, *J* = 8.0, 1.9 Hz, H-6), 6.99 (1H, d, *J* = 8.2 Hz, H-5), 6.98 (1H, d, *J* = 1.5 Hz, H-2'), 6.88 (1H, d, *J* = 8.1 Hz, H-5'), 6.85 (1H, dd, *J* = 8.1, 1.7 Hz, H-6'), 4.38 (1H, d, *J* = 9.6 Hz, H-7'), 4.29 (1H, dd, *J* = 8.8, 8.6 Hz, H-9a), 4.16 (1H, dd, *J* = 8.6, 7.4 Hz, H-9b), 3.97 (3H, s, OCH<sub>3</sub>-3), 3.93 (3H, s, OCH<sub>3</sub>-3'), 3.82 (1H, dt, *J* = 9.1, 7.4 Hz, H-8), 2.59 (1H, m, H-8'), 1.03 (3H, d, *J* = 6.6 Hz, CH<sub>3</sub>-9'); <sup>13</sup>C NMR (100 MHz, CDCl<sub>3</sub>)  $\delta$  197.6 (C-7), 150.8 (C-4), 146.8 (C-3), 146.8 (C-3'), 145.5 (C-4'), 132.0 (C-1'), 130.0 (C-1), 123.7 (C-6), 120.2 (C-6'), 113.9 (C-5 and -5'), 110.1 (C-2), 108.7 (C-2'), 89.0 (C-7'), 70.6 (C-9), 56.1 (OCH<sub>3</sub>-3), 56.0 (OCH<sub>3</sub>-3'), 54.2 (C-8), 45.9 (C-8'), 15.0 (C-9'); HRESIMS *m/z* 381.1310 ([M + Na]<sup>+</sup>, calcd for C<sub>20</sub>H<sub>22</sub>O<sub>6</sub>Na, 381.1309).

**4-O-Demethylforsythenin (11):** colorless syrup; [ $\alpha$ ]<sub>D</sub><sup>25</sup> +11 (c 0.3, MeOH); UV (MeOH)  $\lambda_{\max}$  (log  $\epsilon$ ) 277 (2.51), 245 (2.53) nm; ECD (MeOH) 284 ( $\Delta\epsilon$  +0.06), 233 ( $\Delta\epsilon$  +0.11) nm; IR (neat)  $\nu_{\max}$  3428, 2924, 1744, 1517, 1460, 1274, 1186, 1090 cm<sup>-1</sup>; <sup>1</sup>H NMR (700 MHz, CDCl<sub>3</sub>)  $\delta$  6.91 (1H, d, *J* = 8.0 Hz, H-5), 6.88 (1H, d, *J* = 1.4 Hz, H-2), 6.71 (1H, dd, *J* = 8.0, 1.5 Hz, H-6), 4.97 (1H, d, *J* = 5.3 Hz, H-7), 4.51 (1H, d, *J* = 9.4, H-9a), 4.36 (1H, t, *J* = 9.0 Hz, H-12a), 4.07 (1H, dd, *J* = 9.9, 8.2 Hz, H-12a), 3.97 (1H, dd, *J* = 9.4, 6.6 Hz, H-9b), 3.90 (3H, s, OCH<sub>3</sub>-3), 3.83 (1H, dd, *J* = 9.9, 3.2 Hz, H-12b), 3.35 (2H, m, H-8 and -11); <sup>13</sup>C NMR (175 MHz, CDCl<sub>3</sub>)  $\delta$  178.7 (C-10), 146.8 (C-3), 145.3 (C-4), 128.4 (C-1), 118.8 (C-6), 114.5 (C-5), 108.4 (C-2), 84.1 (C-7), 70.9 (C-9), 68.4 (C-12), 56.0 (OCH<sub>3</sub>-3), 46.0 (C-11), 43.6 (C-8); HRESIMS *m/z* 273.0735 ([M + Na]<sup>+</sup>, calcd for C<sub>13</sub>H<sub>14</sub>O<sub>5</sub>Na, 273.0733).

**Adoxosidic Acid 10-p-Hydroxyphenylacetate (12):** colorless syrup; [ $\alpha$ ]<sub>D</sub><sup>25</sup> -55 (c 1.0, MeOH); UV (MeOH)  $\lambda_{\max}$  (log  $\epsilon$ ) 276 (3.51), 237 (3.83), 218 (3.81) nm; IR (neat)  $\nu_{\max}$  3384, 2943, 1708, 1629, 1516, 1238, 1159, 1075 cm<sup>-1</sup>; <sup>1</sup>H NMR (400 MHz, CD<sub>3</sub>OD)  $\delta$  7.48 (1H, s, H-3), 7.10 (2H, d, *J* = 8.5 Hz, H-2' and -6'), 6.73 (2H, d, *J* = 8.5 Hz, H-3' and -5'), 5.16 (1H, d, *J* = 6.8 Hz, H-1), 4.68 (1H, d, *J* = 7.9 Hz, H-1'), 4.09 (2H, m, H-10), 3.88 (1H, d, *J* = 12.0 Hz, H-6'a), 3.66 (1H, d, *J* = 12.0 Hz, H-6'b), 3.55 (2H, s, H-7'), 3.38 (1H, m, H-3''), 3.30 (2H, m, H-4'' and -5''), 3.23 (1H, t, *J* = 8.6 Hz, H-2''), 2.79 (1H, dd, *J* = 14.8, 7.2 Hz, H-5), 2.31 (1H, m, H-8), 2.15 (1H, m, H-6a), 1.92 (1H, dd, *J* = 13.2, 7.1 Hz, H-9), 1.79 (1H, m, H-7a), 1.42 (1H, m, H-6b), 1.33 (1H, m, H-7b); <sup>13</sup>C NMR (100 MHz, CD<sub>3</sub>OD)  $\delta$  174.4 (C-8'), 171.0 (C-11), 157.7 (C-4'), 153.6 (C-3), 131.5 (C-2' and -6'), 126.5 (C-1'), 116.4 (C-3' and -5'), 112.1 (C-4), 100.7 (C-1''), 98.5 (C-1), 78.4 (C-5''), 78.1 (C-3''), 74.8 (C-2''), 71.6 (C-4''), 68.8 (C-10), 62.9 (C-6''), 44.4 (C-9), 41.5 (C-7'), 41.2 (C-8), 36.7 (C-5), 33.6 (C-6), 28.7 (C-7); HRESIMS *m/z* 533.1627 ([M + Na]<sup>+</sup>, calcd for C<sub>24</sub>H<sub>30</sub>O<sub>12</sub>Na, 533.1630).

**3 $\beta$ -Acetoxy-25-methoxydammar-23-en-20 $\beta$ -ol (13):** colorless powder (CHCl<sub>3</sub>); [ $\alpha$ ]<sub>D</sub><sup>25</sup> +27 (c 0.13, MeOH); IR (neat)  $\nu_{\max}$  3459, 2945, 1730, 1456, 1373, 1248, 1075 cm<sup>-1</sup>; <sup>1</sup>H NMR (400 MHz, CDCl<sub>3</sub>)  $\delta$  5.63 (1H, dt, *J* = 15.9, 7.3 Hz, H-23), 5.48 (1H, t, *J* = 15.9 Hz, H-24), 4.47 (1H, dd, *J* = 10.3, 5.7 Hz, H-3), 3.15 (3H, s, CH<sub>3</sub>-33), 2.22 (2H, m, H-22), 2.04 (3H, s, CH<sub>3</sub>-32), 1.84 (2H, m, H-12), 1.71 (1H, m, H-16), 1.71 (1H, m, H-17), 1.70 (1H, m, H-13), 1.68 (2H, m, H-1), 1.63 (2H, m, H-2), 1.50 (1H, m, H-7), 1.49 (2H, m, H-6), 1.49 (1H, m, H-11), 1.44 (2H, m, H-16 and -15), 1.32 (1H, m, H-9), 1.27 (1H, m, H-7), 1.26 (6H, s, CH<sub>3</sub>-26, 27), 1.23 (1H, m, H-11), 1.12 (3H, s, CH<sub>3</sub>-21), 1.07 (1H, m, H-15), 0.95 (3H, s, CH<sub>3</sub>-18), 0.86 (3H, s, CH<sub>3</sub>-19), 0.85 (3H, s, CH<sub>3</sub>-30), 0.84 (6H, s, CH<sub>3</sub>-28 and -29), 0.82 (1H, m, H-5); <sup>13</sup>C NMR (100 MHz, CDCl<sub>3</sub>)  $\delta$  171.0 (C-31), 139.3 (C-24), 126.0 (C-23), 80.9 (C-3), 75.0 (C-20), 74.9 (C-25), 55.9 (C-5), 50.5 (C-9), 50.3 (C-14 and -33), 49.9 (C-17), 43.7 (C-22), 42.3 (C-13), 40.4 (C-8), 38.7 (C-1), 37.9 (C-4), 37.0 (C-10), 35.1 (C-7), 31.1 (C-15), 27.9 (C-28), 27.5 (C-12), 26.0 (C-27), 25.8 (C-21 and -26), 24.8 (C-16), 23.7 (C-2), 21.5 (C-11), 21.3 (C-32), 18.1 (C-6), 16.5 (C-29), 16.4 (C-19), 16.3 (C-30), 15.5 (C-18); HRESIMS *m/z* 539.4069 ([M + Na]<sup>+</sup>, calcd for C<sub>34</sub>H<sub>56</sub>O<sub>4</sub>Na, 539.4071).

**Preparation of Human Neutrophils.** A study involving human neutrophils was approved by the Institutional Review Board at Chang Gung Memorial Hospital, Taoyuan, Taiwan, and was conducted according to the Declaration of Helsinki (2013). The written informed consent was obtained from each healthy donor before blood was drawn. Blood was drawn from healthy human donors (20–30 years old) by venipuncture into heparin-coated Vacutainer tubes, using a protocol approved by the Institutional Review Board at Chang Gung Memorial Hospital. Blood samples were mixed gently with an equal volume of 3% dextran solution. Neutrophils were isolated with a standard method of dextran sedimentation prior to centrifugation in a Ficoll Hypaque gradient and hypotonic lysis of erythrocytes. The leukocyte-rich plasma was collected after sedimentation of the red cells for 30 min at room temperature, transferred to 20 mL of Ficoll solution (1.077 g/mL), and spun down at 400g for 40 min at 20 °C. The granulocyte/erythrocyte pellets were resuspended in ice-cold 0.2% NaCl to lyse erythrocytes. After 30 s, the same volume of 1.6% NaCl solution was added to reconstitute the isotonic condition. Purified neutrophils were pelleted and then resuspended in a calcium ( $\text{Ca}^{2+}$ )-free Hank's balanced salt solution buffer at pH 7.4 and were maintained at 4 °C before use.

**Measurement of Superoxide Anion Generation.** The assay of the generation of superoxide anion was based on the superoxide dismutase (SOD)-inhibitable reduction of ferricytochrome *c*.<sup>49,50</sup> In brief, after supplementation with 0.5 mg/mL ferricytochrome *c* and 1 mM  $\text{Ca}^{2+}$ , neutrophils ( $6 \times 10^5$  cells/mL) were equilibrated at 37 °C for 2 min and incubated with drugs or an equal volume of vehicle (0.1% DMSO, negative control) for 5 min. Cells were activated with 100 nM fMLP during the preincubation of 1  $\mu\text{g/mL}$  cytochalasin B (fMLP/CB) for 3 min. Changes in the absorbance with a reduction in ferricytochrome *c* at 550 nm were continuously monitored in a double-beam, six-cell positioner spectrophotometer with constant stirring (Hitachi U-3010, Tokyo, Japan). Calculations were based on differences in the reactions with and without SOD (100 U/mL) divided by the extinction coefficient for the reduction of ferricytochrome *c* ( $\epsilon = 21.1/\text{mM}/10 \text{ mm}$ ).

**Measurement of Elastase Release.** Degranulation of azurophilic granules was determined by elastase release as described previously.<sup>49,50</sup> Experiments were performed using MeO-Suc-Ala-Ala-Pro-Val-p-nitroanilide as the elastase substrate. Briefly, after supplementation with MeO-Suc-Ala-Ala-Pro-Val-p-nitroanilide (100  $\mu\text{M}$ ), neutrophils ( $6 \times 10^5$  cells/mL) were equilibrated at 37 °C for 2 min and incubated with test compounds or an equal volume of vehicle (0.1% DMSO, negative control) for 5 min. Cells were activated by 100 nM fMLP and 0.5  $\mu\text{g/mL}$  cytochalasin B, and changes in absorbance at 405 nm were continuously monitored to assay elastase release. The results were expressed as the percent of elastase release in the fMLP/CB-activated, drug-free control system.

**Statistical Analysis.** Results were expressed as means  $\pm$  SD. Calculations of 50% inhibitory concentrations ( $\text{IC}_{50}$ ) were computer-assisted (PHARM/PCS v.4.2). Statistical comparisons were made between groups using Student's *t* test. Values of *p* less than 0.05 were considered to be statistically significant.

## ■ ASSOCIATED CONTENT

### ● Supporting Information

The Supporting Information is available free of charge on the ACS Publications website at DOI: 10.1021/acs.jnatprod.6b01141.

Spectroscopic data (PDF)

## ■ AUTHOR INFORMATION

### Corresponding Author

\*Tel: +886-6-2747538. Fax: +886-6-2740552. E-mail: [tswu@mail.ncku.edu.tw](mailto:tswu@mail.ncku.edu.tw) (T.-S. Wu).

### ORCID

Tian-Shung Wu: 0000-0002-2117-0266

## Notes

The authors declare no competing financial interest.

## ■ ACKNOWLEDGMENTS

This study was sponsored by the Ministry of Science and Technology, Taiwan, granted to T.-S.W. The authors are also thankful for partial financial support from Chang Gung Memorial Hospital (CMRPD1B0281-3, CMRPF1D0442-3, CMRPF1F0011-3, CMRPF1F0061-3, and BMRP450 granted to H.-L.H.).

## ■ REFERENCES

- (1) Malech, H. L.; Gallin, J. I. *N. Engl. J. Med.* **1987**, *317*, 687–694.
- (2) Witko-Sarsat, V.; Rieu, P.; Descamps-Latscha, B.; Lesavre, P.; Halbwachs-Mecarelli, L. *Lab. Invest.* **2000**, *80*, 617–653.
- (3) Okajima, K.; Harada, N.; Uchiba, M. *J. Pharmacol. Exp. Ther.* **2002**, *301*, 1157–1165.
- (4) Ennis, M. *Curr. Allergy Asthma Rep.* **2003**, *3*, 159–165.
- (5) Vinten-Johansen, J. *Cardiovasc. Res.* **2004**, *61*, 481–497.
- (6) Hwang, T. L.; Li, G. L.; Lan, Y. H.; Chia, Y. C.; Hsieh, P. W.; Wu, Y. H.; Wu, Y. C. *Free Radical Biol. Med.* **2009**, *46*, 520–528.
- (7) Zarbock, A.; Ley, K. *Arch. Biochem. Biophys.* **2011**, *510*, 112–119.
- (8) Endo, K.; Takahashi, K.; Abe, T.; Hikino, H. *Heterocycles* **1981**, *16*, 1311–1314.
- (9) Endo, K.; Hikino, H. *Heterocycles* **1982**, *19*, 2033–2036.
- (10) Yui, C. L. *Yaoxue Xuebao* **1960**, *8*, 241–244.
- (11) Nishibe, S.; Okabe, K.; Tsukamoto, H. *Chem. Pharm. Bull.* **1982**, *30*, 4548–4553.
- (12) Kitagawa, S.; Nishibe, S.; Baba, H. *Yakugaku Zasshi* **1987**, *107*, 274–278.
- (13) Kitagawa, S.; Nishibe, S.; Benecke, R.; Thieme, H. *Chem. Pharm. Bull.* **1988**, *36*, 3667–3670.
- (14) Kuang, H. X.; Zhang, N.; Lu, Z. B. *Zhongyao Tongbao* **1988**, *13*, 32–63.
- (15) Rahman, M. M. A.; Dewick, P. M.; Jackson, D. E.; Lucas, J. A. *Phytochemistry* **1990**, *29*, 1971–1980.
- (16) Rouf, A. S. S.; Ozaki, Y.; Rashid, M. A.; Rui, J. *Phytochemistry* **2001**, *56*, 815–818.
- (17) Qu, H.; Zhang, Y.; Wang, Y.; Li, B.; Sun, W. *J. Pharm. Pharmacol.* **2008**, *60*, 261–266.
- (18) Qu, H.; Zhang, Y.; Chai, X.; Sun, W. *Bioorg. Chem.* **2012**, *40*, 87–91.
- (19) Kuo, P. C.; Chen, G. F.; Yang, M. L.; Lin, Y. H.; Peng, C. C. *BioMed Res. Int.* **2014**, *2014*, 110.1155/2014/304830.
- (20) Li, C.; Dai, Y.; Zhang, S. X.; Duan, Y. H.; Liu, M. L.; Chen, L. Y.; Yao, X. S. *Phytochemistry* **2014**, *104*, 105–113.
- (21) Zhang, F.; Yang, Y. N.; Song, X. Y.; Shao, S. Y.; Feng, Z. M.; Jiang, J. S.; Li, L.; Chen, N. H.; Zhang, P. C. *J. Nat. Prod.* **2015**, *78*, 2390–2397.
- (22) de Paiva Campello, J.; Fonseca, S. F. *Phytochemistry* **1975**, *14*, 2299–2300.
- (23) Teng, J.; Zhang, Y. W.; Duan, H. Q.; Takaishi, Y. *Nat. Prod. Res.* **2010**, *24*, 1587–1591.
- (24) Inoue, K.; Inouye, H.; Chen, C. C. *Phytochemistry* **1981**, *20*, 2271–2276.
- (25) Yamauchi, S.; Kumamoto, M.; Ochi, Y.; Nishiwaki, H.; Shuto, Y. *J. Agric. Food Chem.* **2013**, *61*, 12297–12306.
- (26) Zhuang, L. G.; Seligmann, O.; Lotter, H.; Wagner, H. *Phytochemistry* **1983**, *22*, 265–267.
- (27) Piao, X. L.; Jang, M. H.; Cui, J.; Piao, X. *Bioorg. Med. Chem. Lett.* **2008**, *18*, 1980–1984.
- (28) Ming, D. S.; Yu, D. Q.; Yu, S. S.; Liu, J.; He, C. H. *J. Asian Nat. Prod. Res.* **1999**, *1*, 221–226.
- (29) Xue, J.; Xie, L.; Liu, B. R.; Yu, L. X. *Zhongguo Tianran Yaowu* **2010**, *8*, 414–418.
- (30) Lim, H.; Lee, J. G.; Lee, S. H.; Kim, Y. S.; Kim, H. P. *J. Ethnopharmacol.* **2008**, *118*, 113–117.

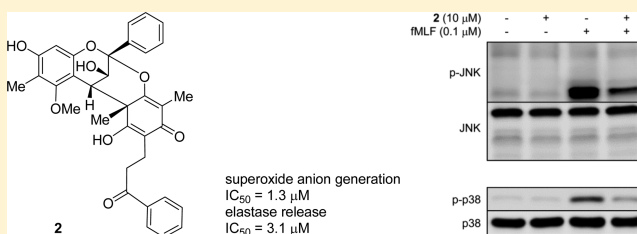


- (31) Nishibe, S.; Sakushima, A.; Kitagawa, S.; Klimek, B.; Benecke, R.; Thieme, H. *Shoyakugaku Zasshi* **1988**, *42*, 324–328.
- (32) González, A. G.; Estévez-Reyes, R.; Mato, C. *J. Nat. Prod.* **1989**, *52*, 1139–1142.
- (33) Klimek, B.; Tokar, M. *Acta Polym. Pharm.* **1998**, *55*, 499–504.
- (34) Chang, M. J.; Min, B. S.; Woo, M. H.; Hung, T. M.; Lee, H. K.; Kim, J. C.; Choi, J. S.; Bae, K. *Biosci., Biotechnol., Biochem.* **2008**, *72*, 2750–2755.
- (35) Kuang, H. X.; Xia, Y. G.; Yang, B. Y.; Liang, J.; Zhang, Q. B.; Li, G. Y. *Zhongguo Tianran Yaowu* **2009**, *7*, 278–282.
- (36) Bianchini, J. P.; Gaydou, E. M.; Rafarahitsimba, G.; Waegell, B.; Zahra, J. P. *Phytochemistry* **1988**, *27*, 2301–2304.
- (37) Hawas, U. W.; Gamal-Eldeen, A. M.; El-Desouky, S. K.; Kim, Y. K.; Huefner, A.; Saf, R. Z. *Naturforsch., C: J. Biosci.* **2013**, *68*, 29–38.
- (38) Lin, K. W.; Huang, A. M.; Yang, S. C.; Weng, J. R.; Hour, T. C.; Pu, Y. S.; Lin, C. N. *Food Chem.* **2012**, *135*, 851–859.
- (39) Jang, D. S.; Su, B. N.; Pawlus, A. D.; Kang, Y. H.; Kardono, L. B. S.; Riswan, S.; Afriastini, J. J.; Fong, H. H. S.; Pezzuto, J. M.; Kinghorn, A. D. *Phytochemistry* **2006**, *67*, 1832–1837.
- (40) Zhang, Q.; Lu, Z.; Li, X.; Zheng, Y.; Yao, D.; Gu, Y.; Huo, C.; Cong, B. *Chem. Nat. Compd.* **2015**, *51*, 178–180.
- (41) Qin, Y.; Zhang, W. L.; Lin, Y. Y.; Yang, M. Y. *Chin. J. Exp. Tradit. Med. Form.* **2013**, *19*, 149–152.
- (42) Alibés, R.; Cantó, M.; de March, P.; Figueredo, M.; Font, J. *Arkivoc* **2007**, 120–131.
- (43) Zinkel, D. F.; Magee, T. V. *Phytochemistry* **1987**, *26*, 769–774.
- (44) Lin, S. J.; Short, R. E.; Ford, S. P.; Grings, E. E.; Rosazza, J. P. N. *J. Nat. Prod.* **1998**, *61*, 51–56.
- (45) Zdero, C.; Bohlmann, F.; Niemeyer, H. M. *Phytochemistry* **1991**, *30*, 3669–3677.
- (46) Kagawa, K.; Tokura, K.; Uchida, K.; Kakushi, H.; Shike, T.; Kikuchi, J.; Nakai, H.; Dorji, P.; Subedi, L. *Chem. Pharm. Bull.* **1993**, *41*, 1604–1607.
- (47) Bohlmann, F.; Knoll, K. H.; King, R. M.; Robinson, H. *Phytochemistry* **1979**, *18*, 1997–2002.
- (48) Norin, T.; Sundin, S.; Theander, O. *Acta Chem. Scand.* **1971**, *25*, 607–610.
- (49) Yang, S. C.; Chung, P. J.; Ho, C. M.; Kuo, C. Y.; Hung, M. F.; Huang, Y. T.; Chang, W. Y.; Chang, Y. W.; Chan, K. H.; Hwang, T. L. *J. Immunol.* **2013**, *190*, 6511–6519.
- (50) Yu, H. P.; Hsieh, P. W.; Chang, Y. J.; Chung, P. J.; Kuo, L. M.; Hwang, T. L. *Free Radical Biol. Med.* **2011**, *50*, 1737–1748.

Anti-inflammatory Flavan-3-ol-dihydroretrochalcones from  
*Daemonorops draco*Ping-Chung Kuo,<sup>†,‡</sup> Hsin-Yi Hung,<sup>†,‡</sup> Tsong-Long Hwang,<sup>‡</sup> Wen-Ke Du,<sup>†</sup> Hsiang-Chih Ku,<sup>‡</sup> E-Jian Lee,<sup>§</sup> Shih-Huang Tai,<sup>§</sup> Fu-An Chen,<sup>⊥</sup> and Tian-Shung Wu<sup>\*,†,⊥,§</sup><sup>†</sup>School of Pharmacy, National Cheng Kung University Hospital, College of Medicine, National Cheng Kung University, Tainan 701, Taiwan<sup>‡</sup>Graduate Institute of Natural Products, College of Medicine, Chang Gung University; Research Center for Chinese Herbal Medicine, Research Center for Food and Cosmetic Safety, and Graduate Institute of Health Industry Technology, College of Human Ecology, Chang Gung University of Science and Technology; Department of Anesthesiology, Chang Gung Memorial Hospital, Taoyuan 333, Taiwan<sup>§</sup>Department of Surgery and Anesthesiology, and Institute of Biomedical Engineering, National Cheng Kung University, Medical Center and Medical School, Tainan 701, Taiwan<sup>⊥</sup>Department of Pharmacy, College of Pharmacy and Health Care, Tajen University, Pingtung 907, Taiwan

## S Supporting Information

**ABSTRACT:** Four A-type flavan-3-ol-dihydroretrochalcone dimers, dragonins A–D (1–4), were characterized from the traditional Chinese medicine Sanguis Draconis. The structures of 1–4 were elucidated by spectroscopic and spectrometric analyses. Compounds 1 and 2 exhibited significant inhibition of fMLP/CB-induced superoxide anion and elastase. The signaling pathways accounting for the inhibitory effects of compound 2 were also elucidated. These purified A-type flavan-3-ol-dihydroretrochalcones are new potential leads for the development of anti-inflammatory drugs.



Dragon's blood, usually produced from several plant genera including *Croton*, *Daemonorops*, *Dracaena*, and *Pterocarpus*, is a bright red resin that has been in continuous use as a dye, varnish, incense, and medicine since ancient times.<sup>1,2</sup> Only the East Asian resin collected from some *Daemonorops* species (*Sanguis Draconis*) is currently commercially available.<sup>3,4</sup> The characteristic flavonoid constituents from this species are flavan analogues containing A- and C-ring hydroxy groups.<sup>4</sup> Currently, *Daemonorops draco* (Willd.) Blume from Indonesia is the most commonly available species for Chinese medicinal formulas.<sup>2</sup> Pharmacological studies indicate that *D. draco*-derived constituents exhibit anticoagulation,<sup>5–8</sup> antiviral,<sup>2</sup> antibacterial,<sup>9</sup> anticancer,<sup>10–15</sup> anti-inflammatory,<sup>4</sup> and osteogenic bioactivities.<sup>16</sup> Previous investigations of the chemical composition of *D. draco* indicated the presences of flavans, chalcones, and bisflavans.<sup>10,17–22</sup> However, in recent decades, little progress had been made in the characterization of the compounds from *Sanguis Draconis*, which may be attributed to difficulties and limitations regarding the purification of the constituents. In addition, decomposition of some isolated compounds may be a serious problem, and solving this issue is a challenging task.<sup>9</sup> In the previous report, several deoxyproanthocyanidins were characterized and deduced as the oxidation products of the two simple units found in the resin, i.e., 7-hydroxy-5-methoxyflavan and 7-hydroxy-5-methoxy-6-

methylflavan.<sup>4</sup> Some purified constituents were identified as the products of the coupling reactions between 7-hydroxy-5-methoxyflavan and the quinone methide that resulted from the oxidation of 7-hydroxy-5-methoxy-6-methylflavan.<sup>4,23</sup> Therefore, in the present study, dragonins A–D (1–4) (Figure 1), four flavan-3-ol-dihydroretrochalcones with unprecedented carbon skeletons that are produced by the coupling reaction of 7-hydroxy-5-methoxy-6-methylflavan and different quinone methides, were characterized from *D. draco* by conventional column chromatographic techniques. Their presence in the crude extracts was identified by LC/MS/MS (Figures S34–S39, Supporting Information), and their structures were determined by spectroscopic and spectrometric techniques. The absolute configurations were established by electronic circular dichroism (ECD) analysis.

Dragonin A (1) was obtained as a colorless powder, and its molecular formula was established as C<sub>34</sub>H<sub>32</sub>O<sub>8</sub> from HRESIMS data analysis (*m/z* 591.1992 [M + Na]<sup>+</sup>, calcd. 591.1989). The UV absorption maxima (λ<sub>max</sub>) at 280, 242, and 209 nm indicated the presence of a benzene chromophore.<sup>24</sup> The IR absorption bands at 3310, 1671, and 1607 cm<sup>−1</sup> confirmed the presence of hydroxy, α,β-unsaturated carbonyl,

Received: January 14, 2017

Published: April 11, 2017

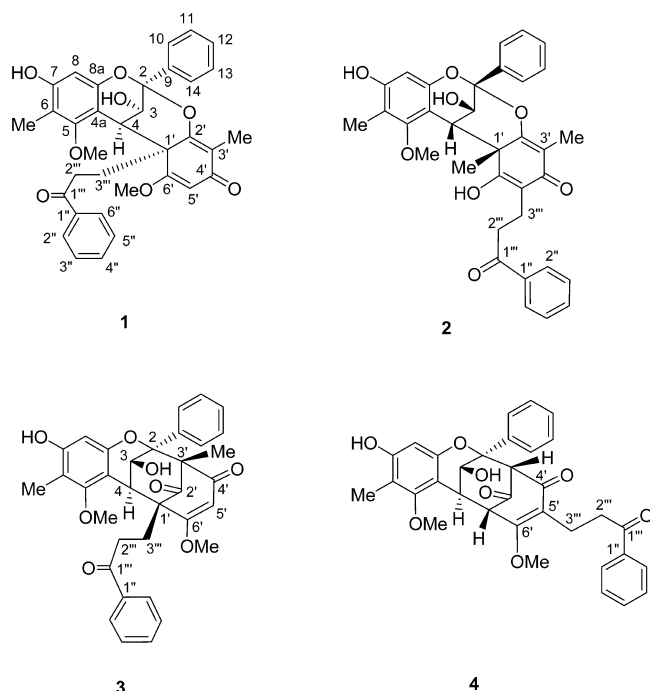


Figure 1. Structures of 1–4.

and C–C double bond functionalities. In the  $^1\text{H}$  NMR spectrum, there were typical signals at  $\delta$  8.28 (1H, s, OH-7), 7.92–7.42 (10 H, H-10–H-14, H-2''–H-6''), and 6.23 (1H, s, H-8), which were characteristic of the aromatic moieties of the flavan-3-ol and dihydroretrochalcone constituent units. The mutually coupled oxygenated methines including  $\delta$  4.90 (1H, dd,  $J$  = 5.6, 3.2 Hz, H-3), 4.45 (1H, d,  $J$  = 5.6 Hz, OH-3), and 3.87 (1H, d,  $J$  = 3.2 Hz, H-4) constructed the partial structure of the flavan-3-ol moiety. Two methylene groups at  $\delta$  2.94 (1H, m, H-3''), 2.87 (2H, m, H-2''), and 2.50 (1H, m, H-3'') and the  $\text{sp}^2$  carbon singlet of an  $\alpha,\beta$ -unsaturated carbonyl moiety at  $\delta$  5.40 (1H, s, H-5') suggested the presence of a chalcone unit. In addition, there were two methoxy groups at  $\delta$  3.81 (3H, s,  $\text{CH}_3\text{O}-6'$ ) and 3.67 (3H, s,  $\text{CH}_3\text{O}-5$ ) and two methyls attached to unsaturated functionalities at  $\delta$  2.00 (3H, s,  $\text{CH}_3-6$ ) and 1.60 (3H, s,  $\text{CH}_3-3'$ ). In the  $^{13}\text{C}$  NMR spectrum, two carbonyl carbons at  $\delta$  199.2 (C-1'') and 187.2 (C-4') and one hemiacetal carbon at  $\delta$  104.2 (C-2) could be characterized. Thus, compound 1 was composed of a flavan-3-ol and a dihydroretrochalcone unit, and these two units were attached via C-2 and C-4 of the flavan-3-ol moiety. Further HMBC analysis (Figure 2) indicated  $^2J$  and  $^3J$  correlations from H-4 to C-1'; from H-5' to C-1' and C-3'; and from  $\text{CH}_3-3'$  to C-2', C-3', and C-4', confirming the linkage between C-1' and C-4, the same as reported in the dracoflavans.<sup>4</sup> The major differences between 1 and the dracoflavans included replacement of the flavan moiety by a dihydroretrochalcone unit in 1. In addition, the B-ring of the dihydroretrochalcone moiety in 1 was changed to a 4,4-disubstituted 5-methoxy-2-methyl-3-oxocyclohexa-2,5-dien-1-one unit; therefore, an unprecedented carbon skeleton was revealed. The relative configuration of 1 was defined via NOESY data, in which correlations of H-3/H-10, H-3/H-2'', H-3/H-3'', and H-4/H-3'' indicated the 2*R*, 3*S*, 4*S*, 1'*S* or 2*S*, 3*R*, 4*R*, 1'*R* configurations (Figure 3). The ECD spectrum of 1 exhibited positive Cotton effects at 284, 246, and 217 nm, and according to the time-dependent density functional theory (TDDFT) calculations, the absolute config-

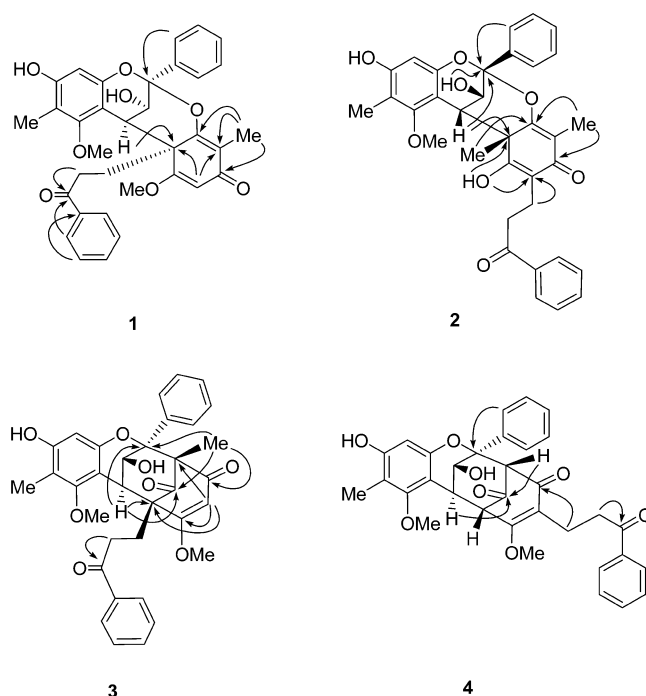


Figure 2. Significant HMBC correlations of 1–4.

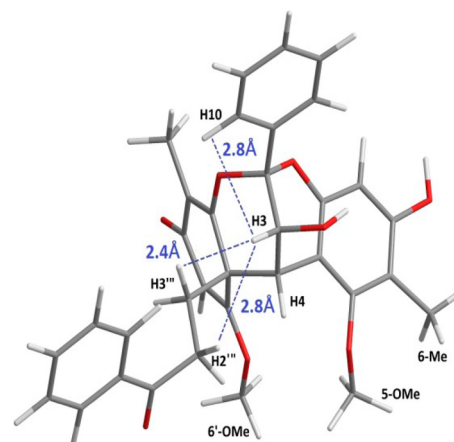


Figure 3. 3D structure of 1.

uration of 1 was determined as 2*S*, 3*R*, 4*R*, 1'*R* (Figures S8 and S9, Supporting Information). Based on the spectroscopic evidence, the structure of 1 was assigned as shown in Figure 1. The  $^1\text{H}$  and  $^{13}\text{C}$  NMR signals were assigned as listed in Table 1.

The molecular formula of compound 2 was determined as identical to that of 1, and its structure should also be similar to 1 according to the spectroscopic data. The difference between the spectra of 1 and 2 included the absence of the  $\text{sp}^2$  singlet of the  $\alpha,\beta$ -unsaturated carbonyl moiety ( $\delta$  5.40 in 1), replacement of the methoxy group ( $\delta$  3.81 in 1) by a hydroxy group in 2, and the presence of a methyl group ( $\delta$  1.69 in 2). The HMBC analysis revealed the  $^2J$ ,  $^3J$  correlations from H-4 to C-2, C-1'; from  $\text{CH}_3-1'$  to C-1', C-2'; from  $\text{CH}_3-3'$  to C-2', C-4'; and from OH-6' to C-1', C-5'. In the dihydroretrochalcone moiety, the phenylpropanone fragment was attached to C-5' rather than C-1', and a methyl group was present at C-1' to form the new carbon skeleton. The relative configuration of 2 was the same as 1 according to the NOESY correlations from H-3 to H-

Table 1.  $^1\text{H}$  and  $^{13}\text{C}$  NMR Spectroscopic Data of Compounds 1–4

position	1 <sup>a</sup>		2 <sup>b</sup>		3 <sup>a</sup>		4 <sup>a</sup>	
	H <sup>c</sup>	C	H	C	H	C	H	C
2		104.2		102.8		85.8		83.4
3	4.90 dd (5.6, 3.2)	65.3	4.57 dd (5.6, 3.2)	63.3	5.52 dd (7.4, 5.4)	65.9	5.44 dd (5.6, 4.0)	62.1
4	3.87 d (3.2)	43.4	3.73 d (3.2)	41.3	3.69 d (7.4)	42.2	3.88 dd (4.0, 4.0)	37.7
4a		104.9		103.8		103.7		105.7
5		159.6		158.3		160.1		158.7
6		111.2		109.2		110.9		111.5
7		156.6		155.4		157.2		157.4
8	6.23 s	98.0	6.10 s	96.8	6.32 s	99.1	6.31 s	99.4
8a		153.1		151.5		152.1		151.9
9		139.6		138.6		137.6		139.2
10, 14	7.76 d (7.6)	127.5	7.69 d (7.6)	126.5	7.31 m	128.1	7.57 m	127.4
11, 13	7.43 m	128.6	7.47 m	128.7	7.31 m	128.1	7.55 m	128.5
12	7.43 m	129.5	7.47 m	127.9	7.51 m	127.1	7.53 m	128.4
OH-3	4.45 d (5.6)		5.45 d (5.6)		3.86 d (5.4)		4.16 d (5.6)	
OH-7	8.28 s		9.33 s		8.41 s		8.50 s	
OH-6'			10.04 s					
1'		52.2		46.3		62.3	4.00 dd (4.0, 2.4)	56.1
2'		161.1		161.6		204.6		199.1
3'		124.9		120.4		72.3	3.43 d (2.4)	77.3
4'		187.2		186.1		191.8		188.9
5'	5.40 s	103.8		111.8	6.15 s	108.3		121.9
6'		173.1		169.6		176.4		170.2
1''		137.7		136.5		138.0		137.7
2'',6''	7.92 d (7.6)	128.8	7.96 d (7.6)	127.9	7.93 d (7.6)	128.7	8.05 d (7.6)	128.9
3'',5''	7.50 t (7.6)	129.4	7.55 t (7.6)	128.7	7.46 t (7.6)	129.4	7.30 m	129.5
4''	7.61 t (7.6)	133.8	7.66 t (7.6)	133.2	7.57 t (7.6)	133.6	7.64 t (7.6)	133.8
1'''		199.2		200.4		199.6		200.2
2'''	2.87 m	34.5	2.70 m	37.0	2.96 ddd (16.8, 11.2, 4.4)	34.5	3.19 m	36.1
			2.55 m		2.70 ddd (16.8, 11.2, 4.4)		3.11 m	
3'''	2.94 m	30.2	2.46 m	17.4	2.47 ddd (14.8, 11.2, 4.4)	25.1	2.74 m	19.3
	2.50 m				2.17 m		2.65 m	
Me-6	2.00 s	8.9	1.84 s	8.8	2.06 s	9.3	2.10 s	9.2
Me-1'			1.69 s	22.5				
Me-3'	1.60 s	8.3	1.51 s	8.4	0.99 s	11.0		
OMe-5	3.67 s	60.9	3.55 s	60.7	3.67 s	61.0	3.85 s	61.4
OMe-6'	3.81 s	56.1			4.09 s	58.1	4.20 s	57.0

<sup>a</sup> $^1\text{H}$  NMR data measured in acetone- $d_6$  at 400 MHz, and  $^{13}\text{C}$  NMR data measured in acetone- $d_6$  at 100 MHz. <sup>b</sup> $^1\text{H}$  NMR data measured in DMSO- $d_6$  at 400 MHz, and  $^{13}\text{C}$  NMR data measured in DMSO- $d_6$  at 100 MHz. <sup>c</sup> $\delta_{\text{H}}$  mult (J in Hz).

10 and from OH-3 to H-14. The ECD data (Figure S16, Supporting Information) confirmed the absolute configuration as 2R, 3S, 4S, 1'S. Thus, the structure of dragonin B (2) was established as shown in Figure 1.

Dragonin C (3) was also an isomer of 1 according to the HRESIMS data. The  $^1\text{H}$  and  $^{13}\text{C}$  NMR spectra displayed one extra carbonyl at  $\delta$  204.6 (C-2') and reduction of one C–C double bond. These suggested that the 4,4-disubstituted 5-methoxy-2-methyl-3-oxocyclohexa-2,5-dien-1-one moiety of 1 was changed to a 6-methoxy-3-methyl-5-ene-2,4-dione unit in 3. Correspondingly, the connectivities between the flavan-3-ol and dihydroretrochalcone moieties were from C-1' to C-4 and from C-3' to C-2, as was confirmed by the  $^2J$ ,  $^3J$ -HMBC cross-peaks from H-4 to C-2, C-1', C-2'; from  $\text{CH}_3$ -3' to C-2, C-2', C-4'; and from H-5' to C-1', C-3', C-6'. Although the phenylpropanone fragment of the dihydroretrochalcone moiety was attached to C-1' as in 1, the union between the flavan-3-ol and dihydroretrochalcone moieties was changed from a pyrane ring to a cyclohexanone unit. The relative configuration of 3 was determined by the NOESY cross-peaks of H-3/H-10, H-3/

OMe-6', H-4/H-3'', Me-3'/H-14, and H-2'''/OMe-6'. The absolute configuration of 3 was established as 2S, 3R, 4R, 1'S, 3'R according to its ECD spectrum and TDDFT-computed results (Figures S24 and S25, Supporting Information), and the structure of 3 was assigned as shown in Figure 1.

The molecular formula of dragonin D (4) was determined as  $\text{C}_{33}\text{H}_{30}\text{O}_8$  from its HRESIMS data, which suggested that one methyl group was replaced by a hydrogen compared to 3. Most of its NMR spectroscopic characteristics were similar to those of 3; however, the absence of the  $\text{sp}^2$  singlet of the  $\alpha,\beta$ -unsaturated carbonyl fragment was similar to that of 2. The HMBC data showed that the phenylpropanone moiety was attached to C-5' (correlation of H-3'''/C-4'), and the replacement of  $\text{CH}_3$ -3' (correlation of H-3'/C-2') by a hydrogen in 4 provided evidence for the unprecedented carbon skeleton. Thus, the 2D structure of 4 was determined as shown, and the absolute configuration was further established as 2R, 3R, 4S, 1'S, 3'S (Figure 1) according to its NOESY and ECD spectra (Figures S31 and S33, Supporting Information).

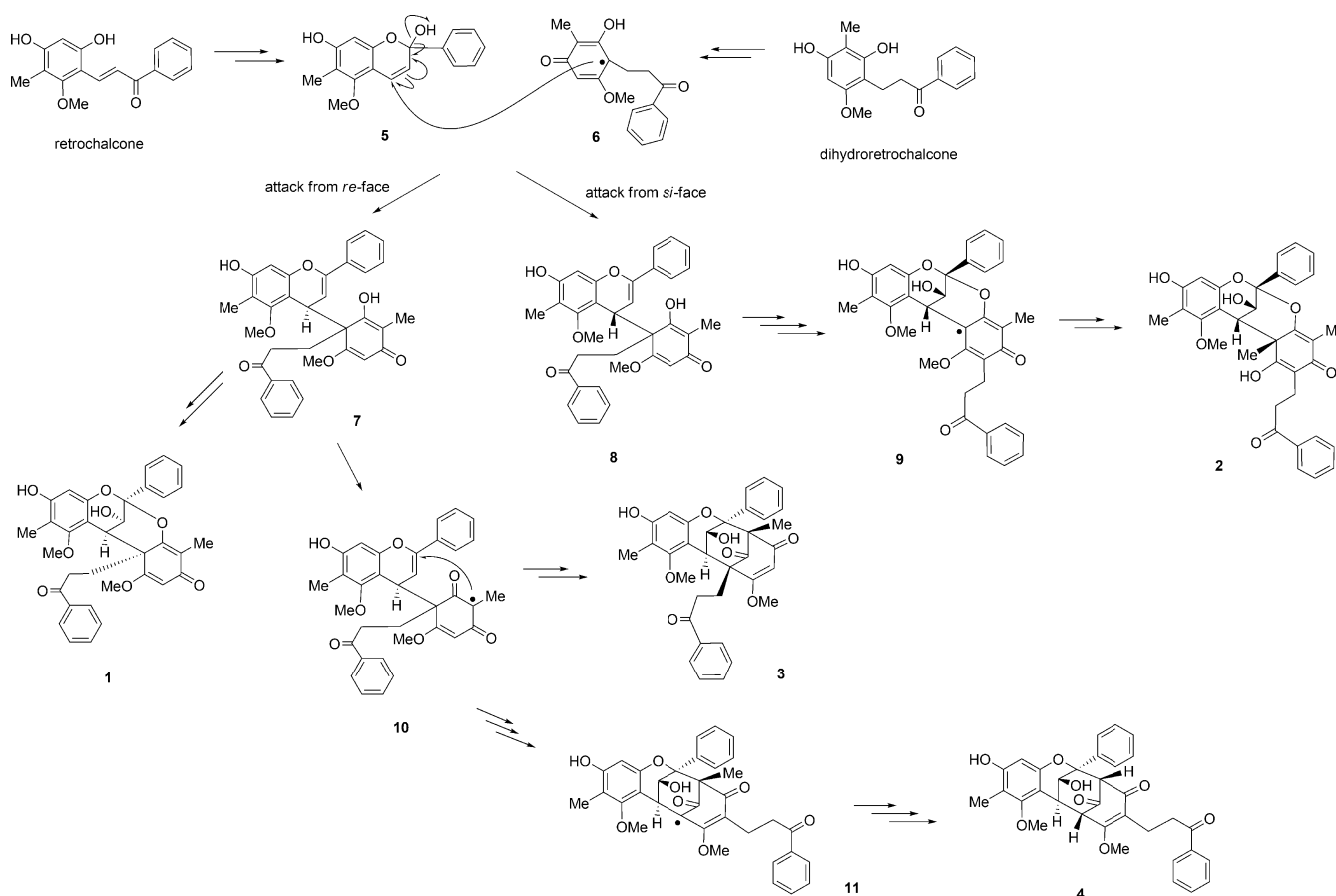


**Figure 4.** Plausible biosynthetic pathway toward 1–4.

The biosynthesis for 1–4 is proposed as shown in Figure 4. Cyclization and tautomerization of the retrochalcone resulted in the flav-3-ene 5. Radical-induced oxidation of the phenolic moiety in the dihydroretrochalcone produced the quinone radical 6. The radical attack of 6 on the double bond of 5 from the *re*-face produced 7 and, following ring cyclization, afforded the flavan-3-ol-dihydroretrochalcone 1. The *si*-face radical attack of 6 to 5 produced stereoisomer 8, and phenylpropanoyl rearrangement resulted in quinone radical 9. The methyl group shift from the neighboring methoxy group afforded compound 2. Formation of quinone radical 10 via 7 and subsequent cyclization between the flav-3-ene moiety and the quinone radical would give 3. If cyclization is accompanied by phenylpropanoyl rearrangement to produce radical 11, subsequent demethylation would yield 4.<sup>25</sup>

The anti-inflammatory activity of the isolates was evaluated by the cellular model in human neutrophils. Compounds 1–4 were tested for their inhibition on the production of superoxide anion and elastase by human neutrophils in response to formyl-L-methionyl-L-leucyl-L-phenylalanine/cytochalasin B (fMLP/CB).<sup>26,27</sup> Compounds 1 and 2 exhibited inhibition with IC<sub>50</sub> values in the range of 1.3 ± 0.5 and 4.5 ± 0.8 μM (Table 2). According to the above data, the purified flavan-3-ol-dihydroretrochalcones are new potential leads for the development of anti-inflammatory drugs. To test whether fMLF-mediated downstream signals, calcium and mitogen-activated protein kinases (MAPKs), are related to the inhibitory effects of compound 2, intracellular calcium ion concentration ([Ca<sup>2+</sup>]<sub>i</sub>) and ERK, p38 MAPK, and JNK phosphorylation were assayed. The duration and magnitude of the [Ca<sup>2+</sup>]<sub>i</sub> signal response to

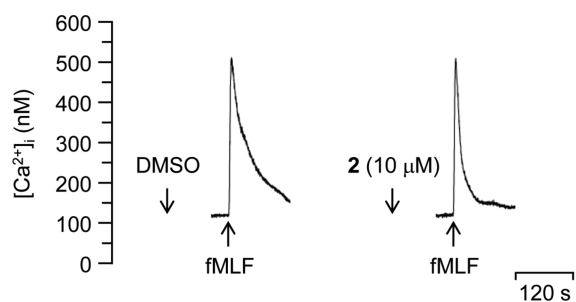
**Table 2.** Inhibitory Effects of Compounds 1–4 on Superoxide Anion Generation and Elastase Release by Human Neutrophils in Response to fMLP/CB

compound	IC <sub>50</sub> (μM) <sup>a</sup>	
	superoxide anion generation	elastase release
1	3.1 ± 0.9 <sup>b</sup>	4.5 ± 0.8 <sup>b</sup>
2	1.3 ± 0.5 <sup>b</sup>	3.1 ± 0.5 <sup>b</sup>
3	>10	>10
4	>10	>10
LY294002 <sup>c</sup>	0.4 ± 0.02 <sup>b</sup>	1.5 ± 0.3 <sup>b</sup>

<sup>a</sup>Concentration necessary for 50% inhibition. The results are presented as the means ± SEM (*n* = 3–5). <sup>b</sup>*p* < 0.001 compared to the control value. <sup>c</sup>A phosphatidylinositol-3-kinase inhibitor was used as a positive control.

fMLF are important for neutrophil superoxide anion generation and elastase release.<sup>28,29</sup> Compound 2 failed to affect the fMLF-induced peak [Ca<sup>2+</sup>]<sub>i</sub> values, but half of the peak value (*t*<sub>1/2</sub>) was considerably reduced by compound 2 (Figure 5). In addition, human neutrophils stimulated with fMLF afforded the rapid phosphorylation of ERK, p38 MAPK, and JNK.<sup>26</sup> Compound 2 inhibited the phosphorylation of JNK and p38 but not ERK (Figure 6). The results suggested that the inhibitory effects of compound 2 in fMLF-induced activation of human neutrophils are partially mediated by the reduction of JNK and p38 activation as well as calcium mobilization.





Compound	Peak $[Ca^{2+}]_i$ (nM)	$t_{1/2}$ (s)
Control	$389.51 \pm 15.85$	$24.75 \pm 2.81$
2 (10 $\mu$ M)	$370.61 \pm 7.66$	$7.17 \pm 0.90$ **

**Figure 5.** Compound 2 inhibited  $Ca^{2+}$  mobilization in fMLF-activated neutrophils. Fluo-3/AM-labeled human neutrophils were incubated with DMSO (as control) or 2 (10  $\mu$ M) for 5 min before stimulation of fMLF (0.1  $\mu$ M).  $Ca^{2+}$  mobilization was recorded in a spectrofluorometer in real time. The intracellular calcium concentration ( $[Ca^{2+}]_i$ ) peak and reduction of the time taken to decrease to half of its peak values ( $t_{1/2}$ ) are shown as the mean  $\pm$  SEM ( $n = 3$ ). \*\* $p < 0.01$ .

## EXPERIMENTAL SECTION

**General Experimental Procedures.** Optical rotations were measured with a JASCO P-2000 polarimeter with a 589 nm filter. UV spectra were recorded on a Hitachi U-0080-D spectrophotometer with a 0.1 dm length cell. IR spectra data were collected on a PerkinElmer FT-IR Spectrum RX I spectrometer using KBr pellets. ECD spectra were obtained using a JASCO J-720 spectropolarimeter.  $^1H$ ,  $^{13}C$ , and 2D NMR spectra were measured on the Bruker AVIII

400 spectrometer. HRESIMS spectra were acquired from Varian ProStar LC/Varian 901 FT-ICR and Bruker APEX II FT mass spectrometers. TLC and preparative TLC (pTLC) analyses were carried out with silica gel 60  $F_{254}$  (Merck KGaA, Darmstadt, Germany). Column chromatography (CC) was performed on Geduran Si 60 (40–63  $\mu$ m, Merck) and Sephadex LH-20 (25–100  $\mu$ m, Sigma-Aldrich, St. Louis, MO, USA). All solvents used in column chromatography were of pesticide residue analysis grade (Fluka, Munich, Germany; Sigma-Aldrich), analytical grade (J. T. Baker, Avantor, Center Valley, PA, USA), and chromatographic grade (Merck).

**Plant Material.** The resin of *Daemonorops draco* was bought from Chuang Song Zong Pharmaceutical Co. Ltd., Taiwan, in 2010 and identified by Prof. Chang-Sheng Kuoh, Department of Life Science, National Cheng Kung University (NCKU), Tainan, Taiwan. A voucher specimen (Wu-2010002) was stored in the School of Pharmacy, NCKU.

**Extraction and Isolation.** The resin of *D. draco* (3.0 kg) was dissolved in  $CHCl_3$  (12.0 L). The insoluble materials were filtered, and the filtrate was partitioned with  $H_2O$  (6.0 L) to yield a  $CHCl_3$ -soluble fraction (approximately 3.0 kg) and a water-soluble fraction (70 g). Part of the  $CHCl_3$ -soluble extract (0.5 kg) was purified on a silica gel column with a step gradient (*n*-hexane–acetone, 4:1, 2:1, 1:1, and 0:1) to give 10 fractions. Fraction 8 (31.2 g) was chromatographed on Sephadex LH-20 with an eluent mixture of  $H_2O$  and MeOH to produce nine subfractions (Fr. 8.1–8.9). Further purification of Fr. 8.5 yielded dragonin B (2) (50.6 mg). Fraction 9 (42.3 g) was separated by silica gel CC with a step gradient ( $CHCl_3$ –acetone, 20:1, 15:1, 10:1, 5:1, 2:1, 1:1, and 0:1) to produce eight subfractions (Fr. 9.1–9.8). Fr. 9.3 was purified by silica gel CC with a step gradient ( $CHCl_3$ –MeOH, 80:1, 40:1, 10:1, 5:1, 1:1, and 0:1) to provide four minor fractions (Fr. 9.3.1–9.3.4). Fr. 9.3.4 was chromatographed on Sephadex LH-20 with an eluent mixture of  $H_2O$  and MeOH, and

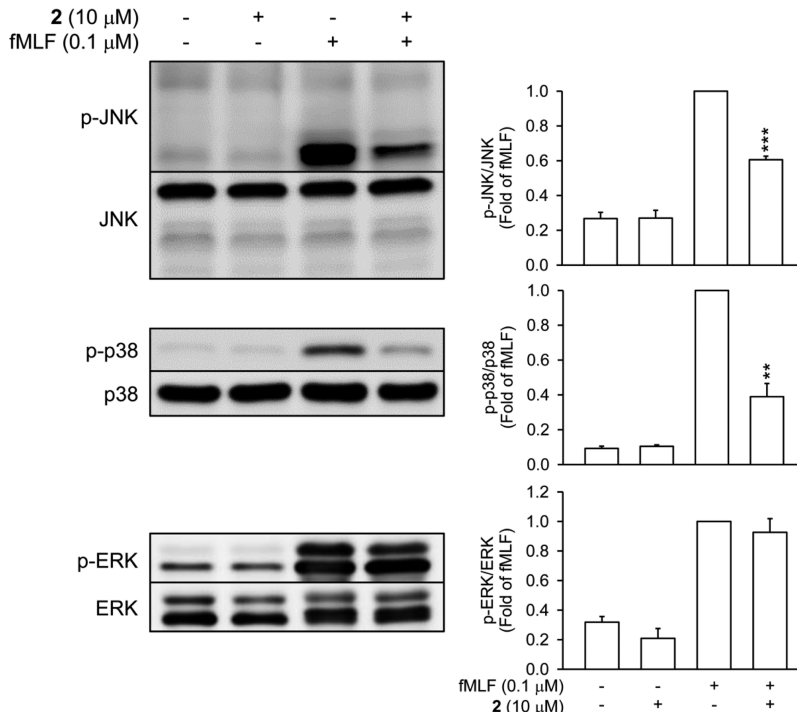


**Figure 6.** Compound 2 inhibited the phosphorylation of JNK and p38 but not ERK in fMLF-activated human neutrophils. Human neutrophils were preincubated with DMSO or 2 (10  $\mu$ M) before stimulation with fMLF (0.1  $\mu$ M). The Western blotting was performed under the same condition. After transferring the blots onto nitrocellulose membranes, we immediately cropped the targeted blots according to reference indicating markers, and then the targeted protein was immunoblotted with its specific antibody. Representative images from one of three independent experiments of Western blotting using antiphospho antibodies directed against JNK, p38, and ERK are shown. Bands on the blots were analyzed using a densitometer, and the quantitative ratios for all samples were normalized to the corresponding total protein. Data are shown as the mean  $\pm$  SEM ( $n = 3$ ). \*\* $p < 0.01$ ; \*\*\* $p < 0.001$ .

further purification was achieved using pTLC to give dragonin A (1) (2.2 mg), C (3) (2.6 mg), and D (4) (1.0 mg).

**Dragonin A (1):** colorless powder (CHCl<sub>3</sub>); [ $\alpha$ ]<sub>D</sub><sup>26</sup> +9 (c 0.07, MeOH); UV (MeOH)  $\lambda_{\max}$  (log  $\epsilon$ ) 280 (3.50), 242 (4.14), 209 (4.42) nm; ECD (MeOH) 284 ( $\Delta\epsilon$  +0.9), 246 ( $\Delta\epsilon$  +1.0), 217 ( $\Delta\epsilon$  +2.8) nm; IR (neat)  $\nu_{\max}$  3310, 2928, 2854, 1671, 1607, 1451, 1231, 1097, 960, 696 cm<sup>-1</sup>; <sup>1</sup>H NMR (400 MHz, acetone-*d*<sub>6</sub>) and <sup>13</sup>C NMR (100 MHz, acetone-*d*<sub>6</sub>), see Table 1; HRESIMS *m/z* 591.1992 ([M + Na]<sup>+</sup>, calcd for C<sub>34</sub>H<sub>32</sub>O<sub>8</sub>Na, 591.1989).

**Dragonin B (2):** colorless powder (CHCl<sub>3</sub>); [ $\alpha$ ]<sub>D</sub><sup>26</sup> -2 (c 0.05, MeOH); UV (MeOH)  $\lambda_{\max}$  (log  $\epsilon$ ) 283 (3.70), 247 (4.30), 209 (4.58) nm; ECD (MeOH) 281 ( $\Delta\epsilon$  -0.5), 234 ( $\Delta\epsilon$  -1.5), 209 ( $\Delta\epsilon$  -1.9) nm; IR (neat)  $\nu_{\max}$  3397, 2931, 1668, 1594, 1445, 1365, 1107, 953, 694 cm<sup>-1</sup>; <sup>1</sup>H NMR (400 MHz, DMSO-*d*<sub>6</sub>) and <sup>13</sup>C NMR (100 MHz, DMSO-*d*<sub>6</sub>), see Table 1; HRESIMS *m/z* 591.1991 ([M + Na]<sup>+</sup>, calcd for C<sub>34</sub>H<sub>32</sub>O<sub>8</sub>Na, 591.1989).

**Dragonin C (3):** colorless powder (CHCl<sub>3</sub>); [ $\alpha$ ]<sub>D</sub><sup>26</sup> +1 (c 0.09, MeOH); UV (MeOH)  $\lambda_{\max}$  (log  $\epsilon$ ) 281 (3.69), 247 (4.07), 210 (4.42) nm; ECD (MeOH) 295 ( $\Delta\epsilon$  -0.5), 206 ( $\Delta\epsilon$  -1.7) nm; IR (neat)  $\nu_{\max}$  3410, 2945, 1733, 1708, 1660, 1597, 1355, 1231, 1125, 697 cm<sup>-1</sup>; <sup>1</sup>H NMR (400 MHz, acetone-*d*<sub>6</sub>) and <sup>13</sup>C NMR (100 MHz, acetone-*d*<sub>6</sub>), see Table 1; HRESIMS *m/z* 591.1991 ([M + Na]<sup>+</sup>, calcd for C<sub>34</sub>H<sub>32</sub>O<sub>8</sub>Na, 591.1989).

**Dragonin D (4):** colorless powder (CHCl<sub>3</sub>); [ $\alpha$ ]<sub>D</sub><sup>26</sup> +3 (c 0.03, MeOH); UV (MeOH)  $\lambda_{\max}$  (log  $\epsilon$ ) 284 (3.72), 249 (3.90), 210 (4.35) nm; ECD (MeOH) 297 ( $\Delta\epsilon$  -1.1), 211 ( $\Delta\epsilon$  -1.3) nm; IR (neat)  $\nu_{\max}$  3405, 2926, 2855, 1737, 1663, 1594, 1357, 1224, 1115, 696 cm<sup>-1</sup>; <sup>1</sup>H NMR (400 MHz, acetone-*d*<sub>6</sub>) and <sup>13</sup>C NMR (100 MHz, acetone-*d*<sub>6</sub>), see Table 1; HRESIMS *m/z* 577.1834 ([M + Na]<sup>+</sup>, calcd for C<sub>33</sub>H<sub>30</sub>O<sub>8</sub>Na, 577.1833).

**Quantum Chemical Calculations.** The compound structure models were constructed according to the NOE analysis. The ECD calculations were performed with the Gaussian 09 software as described previously.<sup>30</sup>

**Preparation of Human Neutrophils.** A study involving human neutrophils was approved by the Institutional Review Board at Chang Gung Memorial Hospital, Taoyuan, Taiwan, and was conducted following the Declaration of Helsinki (2013). Neutrophils were purified as described previously.<sup>26,27</sup>

**Superoxide Anion Generation Measurement.** The assay of the generation of superoxide anion was based on the SOD-inhibited reduction of ferricytochrome *c*.<sup>26,27</sup>

**Elastase Release Measurement.** Degranulation of azurophilic granules was determined by elastase release as described previously.<sup>26,27</sup>

**Examination of ([Ca<sup>2+</sup>]).** Human neutrophils (6 × 10<sup>5</sup> cells/mL) were treated with Fluo-3/AM (2  $\mu$ M) for 30 min at 37 °C, followed by centrifugation and resuspension in HBSS solution containing CaCl<sub>2</sub> (1 mM). The Fluo-3/AM-labeled human neutrophils were treated with DMSO (0.1%, as control) or compound 2 (10  $\mu$ M) for 5 min. The [Ca<sup>2+</sup>]<sub>i</sub> in response to fMLF (0.1  $\mu$ M) was measured under continuous stirring using a spectrophotometer with an excitation wavelength of 488 nm and an emission wavelength of 520 nm.<sup>26</sup>

**Western Blot of Whole-Cell Lysates.** Human neutrophils were incubated with DMSO (0.1%, as control) or compound 2 (10  $\mu$ M) for 5 min and then activated by fMLF (0.1  $\mu$ M) for 30 s in the pretreatment of CB (1  $\mu$ g/mL). The reaction was stopped by heating at 100 °C for 15 min with sample buffer (62.5 mM pH 6.8 Tris-HCl, 4% sodium dodecyl sulfate, 5%  $\beta$ -mercaptoethanol, 2.5 mM Na<sub>3</sub>VO<sub>4</sub>, 0.00125% bromophenol blue, 10 mM *p*-nitrophenyl phosphate di(tris) salt, and 8.75% glycerol). Samples were centrifuged at 14000g for 20 min, and the supernatant was subjected to the immunoblotting assay. The target protein was characterized by immunoblotting with the corresponding antibody overnight at 4 °C, followed by incubation with horseradish peroxidase-conjugated, secondary anti-rabbit antibody (Cell Signaling Technology, Beverly, MA, USA) at room temperature for 1 h. The enhanced chemiluminescence solution was added to the membranes, and protein bands were detected using the BioSpectrum Imaging System (UVP; Upland, CA, USA).

**Statistical Analysis.** Experimental results were illustrated as the mean  $\pm$  SEM. The half-maximal inhibitory concentration (IC<sub>50</sub>) was computer-assisted calculated (PHARM/PCS v.4.2). Statistical comparisons between groups were performed through Student's *t* test. *p*-Values less than 0.05 were considered to be significant statistically.

## ■ ASSOCIATED CONTENT

### § Supporting Information

The Supporting Information is available free of charge on the ACS Publications website at DOI: 10.1021/acs.jnatprod.7b00039.

Supplementary spectroscopic data (PDF)

## ■ AUTHOR INFORMATION

### Corresponding Author

\*Tel: 886-6-2747538. Fax: 886-6-2740552. E-mail: [tswu@mail.ncku.edu.tw](mailto:tswu@mail.ncku.edu.tw) (T.-S. Wu).

### ORCID

Tian-Shung Wu: 0000-0002-2117-0266

### Author Contributions

\*P. C. Kuo and H. Y. Hung contributed equally to this work.

### Notes

The authors declare no competing financial interest.

## ■ ACKNOWLEDGMENTS

This study was sponsored by the Ministry of Science and Technology, Taiwan, granted to T.-S.W. and P.-C.K. The authors are also thankful to Chang Gung Memorial Hospital (CMRPD1B0281-3, CMRPF1D0442-3, CMRPF 1F0011-3, CMRPF1F0061-3, and BMRP450 granted to H.-L.H.) for partial financial support of the present research.

## ■ REFERENCES

- (1) *Chinese Herbal Medicine: Materia Medica*, 3rd ed.; Bensky, D. G. K., Ed.; Eastland Press: Seattle, 1993.
- (2) Gupta, D.; Bleakley, B.; Gupta, R. K. *J. Ethnopharmacol.* **2008**, *115*, 361–380.
- (3) Burkill, H. In *A Dictionary of Economic Products of Malay Peninsula*; Ministry of Agriculture: Kuala Lumpur, 1966; p 758.
- (4) Arnone, A.; Nasini, G.; Vajna de Pava, O.; Merlini, L. *J. Nat. Prod.* **1997**, *60*, 971–975.
- (5) Gibbs, A.; Green, C.; Doctor, V. M. *Thromb. Res.* **1983**, *32*, 97–108.
- (6) Tsai, W. J.; Hsieh, H. T.; Chen, C. C.; Chen, C. F. *J. Chin. Med.* **1995**, *6*, 59–73.
- (7) Tsai, W. J.; Hsieh, H. T.; Chen, C. C.; Kuo, Y. C.; Chen, C. F. *Eur. J. Pharmacol.* **1998**, *346*, 103–110.
- (8) Yi, T.; Chen, H. B.; Zhao, Z. Z.; Yu, Z. L.; Jiang, Z. H. *J. Ethnopharmacol.* **2011**, *133*, 796–802.
- (9) Rao, G. S. R.; Gerhart, M. A.; Lee, R. T.; Mitscher, L. A.; Drake, S. J. *Nat. Prod.* **1982**, *45*, 646–648.
- (10) Xia, M.; Wang, D.; Wang, M.; Tashiro, S. I.; Onodera, S.; Minami, M.; Ikejima, T. *J. Pharmacol. Sci.* **2004**, *95*, 273–283.
- (11) Xia, M.; Wang, M.; Tashiro, S. I.; Onodera, S.; Minami, M.; Ikejima, T. *Biol. Pharm. Bull.* **2005**, *28*, 226–232.
- (12) Xia, M.; Wang, M.; Cui, Z.; Tashiro, S. I.; Onodera, S.; Minami, M.; Ikejima, T. *J. Asian Nat. Prod. Res.* **2006**, *8*, 335–343.
- (13) He, Y.; Ju, W.; Hao, H.; Liu, Q.; Lv, L.; Zeng, F. *J. Huazhong Univ. Sci. Technol., Med. Sci.* **2011**, *31*, 215–219.
- (14) Rasul, A.; Ding, C.; Li, X.; Khan, M.; Yi, F.; Ali, M.; Ma, T. *Apoptosis* **2012**, *17*, 1104–1119.
- (15) Yu, J. H.; Zheng, G. B.; Liu, C. Y.; Zhang, L. Y.; Gao, H. M.; Zhang, Y. H.; Dai, C. Y.; Huang, L.; Meng, X. Y.; Zhang, W. Y.; Yu, X. F. *Int. J. Med. Sci.* **2013**, *10*, 1149–1156.

- (16) Wang, W.; Olson, D.; Cheng, B.; Guo, X.; Wang, K. J. *Ethnopharmacol.* **2012**, *142*, 168–174.
- (17) Robertson, A.; Whalley, W. B. *J. Chem. Soc.* **1950**, *0*, 1882–1884.
- (18) Nasini, G.; Piozzi, F. *Phytochemistry* **1981**, *20*, 514–516.
- (19) Arnone, A.; Nasini, G.; Merlini, L. *Heterocycles* **1989**, *29*, 1119–1125.
- (20) Arnone, A.; Nasini, G.; Merlini, L. *J. Chem. Soc., Perkin Trans. 1* **1990**, 2637–2640.
- (21) Shen, C. C.; Tsai, S. Y.; Wei, S. L.; Wang, S. T.; Shieh, B. J.; Chen, C. C. *Nat. Prod. Res.* **2007**, *21*, 377–380.
- (22) Nakashima, K. I.; Abe, N.; Kamiya, F.; Ito, T.; Oyama, M.; Iinuma, M. *Helv. Chim. Acta* **2009**, *92*, 1999–2008.
- (23) Camarda, L.; Merlini, L.; Nasini, G. In *Flavonoids and Bioflavonoids*; Farkas, L.; Kallay, F.; Gabor, M.; Wagner, H., Eds.; Akadémiai Kiadó: Budapest, 1982; pp 311–320.
- (24) Scott, A. I. In *Interpretation Ultraviolet Spectra of Natural Products*, 2nd ed.; Pergamon Press: New York, 1964.
- (25) Verma, A. K.; Pratap, R. *Tetrahedron* **2012**, *68*, 8523–8538.
- (26) Yang, S. C.; Chung, P. J.; Ho, C. M.; Kuo, C. Y.; Hung, M. F.; Huang, Y. T.; Chang, W. Y.; Chang, Y. W.; Chan, K. H.; Hwang, T. L. *J. Immunol.* **2013**, *190*, 6511–6519.
- (27) Yu, H. P.; Hsieh, P. W.; Chang, Y. J.; Chung, P. J.; Kuo, L. M.; Hwang, T. L. *Free Radical Biol. Med.* **2011**, *50*, 1737–1748.
- (28) Hwang, T. L.; Su, Y. C.; Chang, H. L.; Leu, Y. L.; Chung, P. J.; Kuo, L. M.; Chang, Y. J. *J. Lipid Res.* **2009**, *50*, 1395–1408.
- (29) Chang, H. L.; Chang, F. R.; Chen, J. S.; Wang, H. P.; Wu, Y. H.; Wang, C. C.; Wu, Y. C.; Hwang, T. L. *Eur. J. Pharmacol.* **2008**, *586*, 332–339.
- (30) Shih, H. C.; Kuo, P. C.; Wu, S. J.; Hwang, T. L.; Hung, H. Y.; Shen, D. Y.; Shieh, P. C.; Liao, Y. R.; Lee, E. J.; Gu, Q.; Lee, K. H.; Wu, T. S. *Bioorg. Med. Chem.* **2016**, *24*, 1439–1445.



Contents lists available at ScienceDirect

# Bioorganic & Medicinal Chemistry Letters

journal homepage: [www.elsevier.com/locate/bmcl](http://www.elsevier.com/locate/bmcl)

## Novel 11-norbetaenone isolated from an entomopathogenic fungus *Lecanicillium antillanum*



Chi-Ying Li<sup>a,1</sup>, I-Wen Lo<sup>a,1</sup>, Shih-Wei Wang<sup>b</sup>, Tsong-Long Hwang<sup>c,d,e</sup>, Yu-Ming Chung<sup>a</sup>, Yuan-Bin Cheng<sup>a,f,g</sup>, Sung-Pin Tseng<sup>h</sup>, Yi-Hung Liu<sup>i</sup>, Yu-Ming Hsu<sup>a</sup>, Shu-Rong Chen<sup>a</sup>, Hao-Chun Hu<sup>a</sup>, Fang-Rong Chang<sup>a,f,j,k,l,\*</sup>, Yang-Chang Wu<sup>a,m,n,o,p,\*</sup>

<sup>a</sup> Graduate Institute of Natural Products, College of Pharmacy, Kaohsiung Medical University, Kaohsiung 807, Taiwan

<sup>b</sup> Department of Medicine, Mackay Medical College, New Taipei City 252, Taiwan

<sup>c</sup> Graduate Institute of Natural Products, College of Medicine and Chinese Herbal Medicine Research Team, Healthy Aging Research Center, Chang Gung University, Taoyuan 333, Taiwan

<sup>d</sup> Research Center for Industry of Human Ecology, Research Center for Chinese Herbal Medicine, and Graduate Institute of Health Industry Technology, College of Human Ecology, Chang Gung University of Science and Technology, Taoyuan 333, Taiwan

<sup>e</sup> Department of Anesthesiology, Chang Gung Memorial Hospital, Taoyuan 333, Taiwan

<sup>f</sup> Center for Infectious Disease and Cancer Research, Kaohsiung Medical University, Kaohsiung 807, Taiwan

<sup>g</sup> Research Center for Natural Products & Drug Development, Kaohsiung Medical University, Kaohsiung 807, Taiwan

<sup>h</sup> Department of Medical Laboratory Science and Biotechnology, College of Health Sciences, Kaohsiung Medical University, Kaohsiung 807, Taiwan

<sup>i</sup> Instrumentation Center, National Taiwan University, Taipei 106, Taiwan

<sup>j</sup> Department of Marine Biotechnology and Resources, National Sun Yat-Sen University, Kaohsiung 804, Taiwan

<sup>k</sup> Cancer Center, Kaohsiung Medical University Hospital, Kaohsiung 807, Taiwan

<sup>l</sup> Research Center for Environmental Medicine, Kaohsiung Medical University, Kaohsiung 807, Taiwan

<sup>m</sup> School of Pharmacy, College of Pharmacy, China Medical University, Taichung 404, Taiwan

<sup>n</sup> Chinese Medicine Research and Development Center, China Medical University Hospital, Taichung 404, Taiwan

<sup>o</sup> Center for Molecular Medicine, China Medical University Hospital, Taichung 404, Taiwan

<sup>p</sup> Research Center for Chinese Herbal Medicine, China Medical University, Taichung 404, Taiwan

### ARTICLE INFO

#### Article history:

Received 10 January 2017

Revised 23 February 2017

Accepted 9 March 2017

Available online 11 March 2017

#### Keywords:

*Lecanicillium antillanum*

Betaenone

Secondary metabolite

Polyketide synthase

Anti-angiogenic effect

### ABSTRACT

A novel nor-betaenone compound, 11-norbetaenone (**1**), was isolated from the culture broth of an entomopathogenic fungus *Lecanicillium antillanum*. The structure was determined on the basis of 1D and 2D NMR spectroscopic data. The absolute stereochemistry of **1** was further confirmed by X-ray single crystallography analysis. It is the first secondary metabolite reported from the species *Lecanicillium antillanum*. And it is also the first time that a betaenone-type compound was isolated from the genus *Lecanicillium*. Furthermore, 11-norbetaenone (**1**) displayed significant anti-angiogenic effect by suppressing tube formation.

© 2017 Elsevier Ltd. All rights reserved.

Since 1983, the first polyketide containing a decalin motif was isolated from the plant-pathogenic fungus *Stemphylium botryosum*,<sup>1,2</sup> the polyketide decalins from microorganism were published in succession. Among these secondary metabolites, betaenones, the congeners with a 3-oxopropanol side chain, were also found in fungi *Phoma betae* (the causal fungus of beet leaf spot disease),<sup>3</sup> *Penicillium citrinum*,<sup>4</sup> three marine-associated fungi,

*Aspergillus* sp.,<sup>5</sup> *Microsphaeropsis* sp.,<sup>6</sup> and *Trichoderma harzianum*,<sup>7</sup> as well as a soil bacterium *Streptomyces* sp.<sup>8–10</sup> In addition to the phytotoxic characteristic,<sup>1–3</sup> these compounds showed the neurite outgrowth advance,<sup>5</sup> the antimicrobial activity against methicillin-resistant *Staphylococcus aureus* (MRSA),<sup>5</sup> and were potent inhibitors of protein kinase C (PKC), cyclin-dependent kinase 4 (CDK 4), and epidermal growth factor receptor (EGF-R) tyrosine kinases related to anti-cancer *in vitro*.<sup>8</sup>

Continuing our effort on discovery of bioactive natural products, the chemical investigation was applied to the *Lecanicillium antillanum*. Its chemical components and bioactivity have never been revealed yet.

\* Corresponding authors at: Graduate Institute of Natural Products, College of Pharmacy, Kaohsiung Medical University, Kaohsiung 807, Taiwan.  
E-mail addresses: [aaronfrf@kmu.edu.tw](mailto:aaronfrf@kmu.edu.tw) (F.-R. Chang), [yachwu@mail.cmu.edu.tw](mailto:yachwu@mail.cmu.edu.tw) (Y.-C. Wu).

<sup>1</sup> These two authors contributed equally to this work.

<http://dx.doi.org/10.1016/j.bmcl.2017.03.019>

0960-894X/© 2017 Elsevier Ltd. All rights reserved.



*Lecanicillium antillanum* was isolated from the sand sample from the seashore in Kaohsiung, Taiwan, and the fungus was identified based on morphology and the internal transcribed spacer (ITS1-5.8S-ITS2) rDNA analysis using universal fungal primers. It was cultivated by using 100 Erlenmeyer flasks (500 mL), each flask containing 150 mL and marine media (potato dextrose broth with 2% NaCl). The flasks were incubated on the rotator shaker at 150 rpm at 25 °C. After 14 days cultivation, 15 L of the whole broth was filtered to separate the filtrate from the mycelia. The filtrate was extracted with Ethyl Acetate (EtOAc) and concentrated under reduced pressure to obtain the crude extract (1.3 g). This extract was subjected to Sephadex LH-20 column chromatography and eluted with MeOH to yield six fractions (F1–F6). After inspection by NMR, Fraction F3 showed distinctly different and characteristic signals from signals for lipids (F1–F2) and signals for aromatic compounds in a small quantity (F5 and F6). And no distinguished signals could be recognized for the spectrum of F4. Fraction F3 (432.4 mg) was selected and separated by silica gel column chromatography with MeOH:CH<sub>2</sub>Cl<sub>2</sub> (1:24) to afford six subfractions (F3-1–F3-6). Subfraction F3-4 (61.4 mg) was further purified by silica gel column chromatography eluted with EtOAc:CH<sub>2</sub>Cl<sub>2</sub> (1:1) to give compound **1** (56.4 mg).

11-Norbetaenone (**1**), isolated as acicular crystals,  $[\alpha]_D^{23}$  98 (c 0.05, MeOH), possessed a molecular formula C<sub>20</sub>H<sub>34</sub>O<sub>4</sub> and four degrees of unsaturation deduced from HRESIMS data ( $m/z$  361.2346 [M+Na]<sup>+</sup>). The IR absorption bands at 3359, 1697, cm<sup>-1</sup> revealed the hydroxy and carbonyl functionalities of **1**, respectively (Fig. 1).

The <sup>1</sup>H NMR data Table 1 showed the presence of one primary methyl at  $\delta_H$  0.76 (t,  $J$  = 5.4 Hz), two secondary methyl at  $\delta_H$  0.61 (d,  $J$  = 6.8 Hz) and 0.93 (d,  $J$  = 6.8 Hz), and one tertiary methyl at  $\delta_H$  1.24 (s), as well as five protons ( $\delta_H$  3.37, 3.68, 3.76, 3.82, 3.88) on oxygen-bearing carbons and two olefinic protons at  $\delta_H$  5.69 (dt,  $J$  = 12.0, 6.0 Hz) and 6.07 (dt,  $J$  = 12.0, 6.0 Hz). The <sup>13</sup>C NMR (Table 1) and DEPT spectra of **1** indicated that 20 carbons can be categorized into four methyls, five methylenes (containing two oxygenated carbons and three aliphatic carbons), nine methines (consisting of two olefinic carbons, one oxygen-bearing carbon, and six aliphatic carbons), and two quaternary carbons (including one ketone carbonyl carbon and one aliphatic carbon). These data suggested that **1** has two rings apart from two hydrogen deficiency indexes contributed by a ketone group and a double bond.

Interpretation of the COSY spectrum, four partial structures of [H-1 ( $\delta_H$  6.07)/H-2 ( $\delta_H$  5.69)/H-3 ( $\delta_H$  1.93)], [H-9 ( $\delta_H$  3.37)/H-10 ( $\delta_H$  1.80)/H-5 ( $\delta_H$  1.95)/H-6 ( $\delta_H$  1.44)/H-7 ( $\delta_H$  1.01 and 1.55)/H-8 ( $\delta_H$  1.83), and outward to H<sub>3</sub>-20 ( $\delta_H$  0.61) and H<sub>2</sub>-21 ( $\delta_H$  3.68 and 3.76)], [H-12 ( $\delta_H$  1.12)/H<sub>3</sub>-15 ( $\delta_H$  0.93)], and [H<sub>2</sub>-17 ( $\delta_H$  2.66 and 2.85)/H<sub>2</sub>-18 ( $\delta_H$  3.82 and 3.88)] were observed. COSY data combined the HMBC correlations of H-2/C-4 ( $\delta_C$  52.6), C-10 ( $\delta_C$  45.6), H-3/C-4, C-5 ( $\delta_C$  42.5), H-5/C-4, H-8/C-9 ( $\delta_C$  78.9), H-9/C-1

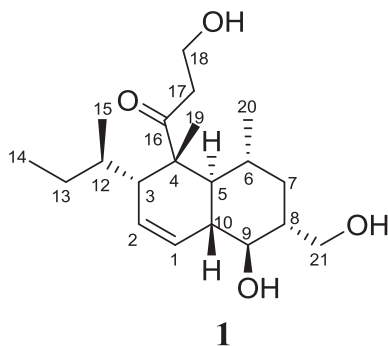


Fig. 1. Structure of **1**.

**Table 1**  
<sup>1</sup>H and <sup>13</sup>C NMR Data of **1** in CDCl<sub>3</sub>.<sup>a</sup>

No	$\delta_H$ (mult, $J$ values)	$\delta_C$ , type
1	6.07 (dt, 12.0, 6.0)	123.7, CH
2	5.69 (dt, 12.0, 6.0)	125.5, CH
3	1.93 (m)	52.4, CH
4		52.6, C
5	1.95 (d, 9.8)	42.5, CH
6	1.44 (m)	36.4, CH
7	1.01 (dt, 13.1, 11.5)	36.9, CH <sub>2</sub>
	1.55 (ddd, 13.1, 4.7, 2.9)	
8	1.83 (m)	46.5, CH
9	3.37 (t, 9.6)	78.9, CH
10	1.80 (m)	45.6, CH
11	—	—
12	1.12 (m)	37.2, CH
13	0.74 (m)	24.4, CH <sub>2</sub>
	1.46 (m)	
14	0.76 (d, 5.4)	12.5, CH <sub>3</sub>
15	0.93 (d, 6.8)	19.3, CH <sub>3</sub>
16		215.7, C
17	2.66 (ddd, 18.8, 6.1, 3.5)	41.1, CH <sub>2</sub>
	2.85 (ddd, 18.8, 7.4, 3.8)	
18	3.82 (m)	58.0, CH <sub>2</sub>
	3.88 (m)	
19	1.24 (s)	19.3, CH <sub>3</sub>
20	0.61 (d, 6.8)	22.7, CH <sub>3</sub>
21	3.68 (dd, 12.0, 9.0)	68.6, CH <sub>2</sub>
	3.76 (dd, 12.0, 6.0)	
OH-18	2.75 (t, 6.9)	

<sup>a</sup> <sup>1</sup>H and <sup>13</sup>C NMR data ( $\delta$ ) were measured at 400 and 100 MHz, respectively; Chemical shifts are presented in ppm;  $J$  values in Hz are in parentheses.

( $\delta_C$  123.7), C-21 ( $\delta_C$  68.6), and H<sub>2</sub>-21/C-7 ( $\delta_C$  36.9), C-9 established a 6/6-bicyclic fused ring system.

Moreover, the HMBC correlations of H-12/C-3 ( $\delta_C$  52.4), C-13 ( $\delta_C$  24.4), H<sub>3</sub>-14 ( $\delta_H$  0.76)/C-12 ( $\delta_C$  37.2), C-13, and H<sub>3</sub>-15 ( $\delta_H$  0.93)/C-3, C-13 as well as the COSY fragment of H-12/H<sub>3</sub>-15 connected a sec-butyl side chain at C-3. Similarly, the HMBC correlations of H<sub>2</sub>-17, H<sub>2</sub>-18, H-5 with the ketone C-16 ( $\delta_C$  215.7), and H<sub>3</sub>-19 ( $\delta_H$  1.24) with C-4, C-5, C-16, together with the H<sub>2</sub>-17/H<sub>2</sub>-18 sequence allowed the connection of 3-hydroxypropanoyl at C-4 and indicated the germinal relationship between this side chain and Me-19. The planar structure of **1** was therefore completed and the new 11-norbetaenone (Fig. 1) was illustrated in Fig. 2.

In terms of the stereochemistry of **1**, the configuration was determined by NOESY correlations mainly and by chemical shift comparison with published betaenone-type analogues.<sup>3,11</sup> Due to the absence of the NOESY correlation between H-5 and H-10 and the existence of endocyclic double bond (C<sub>1</sub>=C<sub>2</sub>), the decalin ring system was implied to possess a *trans*-junction and a pseudo-chair/chair conformation (Fig. 3).

In the light of the stereochemistry of betaenone B,<sup>3,11</sup> H-5 and H-10 were postulated to be at  $\alpha$  and  $\beta$  orientation, respectively.

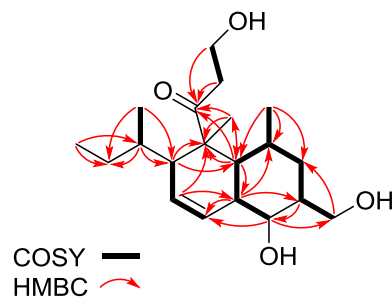


Fig. 2. Selected COSY and HMBC correlations of **1**.



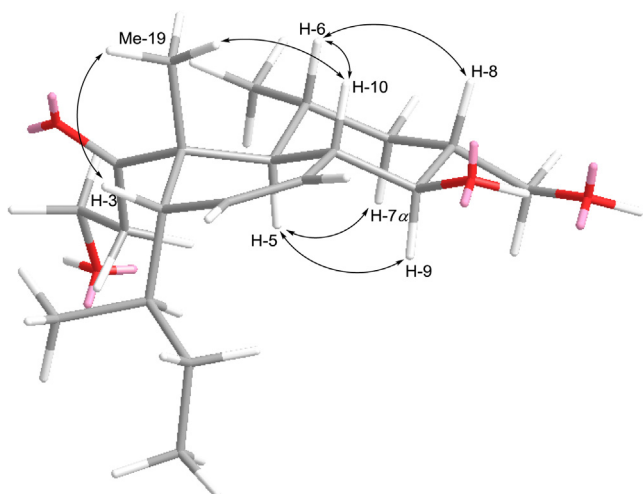


Fig. 3. Key NOESY (double headed arrow) correlations of **1**.

The NOESY correlations of H-5/H-7 $\alpha$ /H-9 indicated that these protons are  $\alpha$ -directed, while the NOESY correlations of H-6/H-8/H-10/H<sub>3</sub>-19 assigned that H-6, H-8, H-10, and Me-19 are all on the opposite site,  $\beta$  face. Additionally, the *R* configuration of the chiral center C-12 at *sec*-butyl side chain was decided by X-ray single crystallographic analysis (Fig. 4).

The proposed stereochemistry of **1** was corresponding to the X-ray crystal data, and **1** was named 11-norbetaenone. Crystallographic data for **1** have been deposited at the Cambridge Crystallographic Data Centre with the deposition number CCDC 1523586. It is the first natural product isolated from the species *Lecanicillium antillanum*, and it is also the first betaenone-type compound isolated from the genus *Lecanicillium*.

11-Norbetaenone (**1**) was evaluated for its biological activities. For anti-cancer assay,<sup>12</sup> it showed no activity against three human cancer cell lines (HepG2, MDA-MB231, and A549) at a concentration of 20  $\mu$ g/mL. In an anti-inflammatory activity assay,<sup>13,14</sup> **1** exhibited no significant activity in superoxide generation and elastase release assay at a concentration of 30  $\mu$ g/mL. In an antimicro-

bial activity assay,<sup>15</sup> test for methicillin-resistant *Staphylococcus aureus* (MRSA), it was inactive against bacteria growth at 2 mg/mL.

In addition, the anti-angiogenic effect of 11-norbetaenone (**1**) was evaluated in human endothelial progenitor cells (EPCs) using tube formation assay.<sup>16</sup> EPCs, mobilizing from the bone marrow to the bloodstream and inducing neovascularization during tissue ischemia, play important roles in maintaining vascular integrity and facilitating tissue repair,<sup>17,18</sup> and have the ability to self-renew, circulate, home to tumor sites as well as differentiate into mature endothelial cells that contribute to angiogenesis and vasculogenesis during the growth and metastatic spread of tumors.<sup>16,19,20</sup>

The process of angiogenesis mainly involves endothelial cells proliferation, migration and tube formation to form new blood vessels.<sup>21</sup> The function of tube formation is the most important step during angiogenesis. Assays that simulate the formation of capillary-like tubules are regarded as representative stage of angiogenesis and are used extensively to evaluate the potential compounds for anti-angiogenic effects.<sup>22</sup>

As shown in Fig. 5A, 11-norbetaenone (**1**) inhibited tube formation of EPCs in a concentration dependent manner, with an IC<sub>50</sub> value of  $34.1 \pm 1.7$   $\mu$ g/mL. Sorafenib, a well-known angiogenesis inhibitor, was used as a positive control for *in vitro* anti-angiogenesis assay. We next investigated whether the effect of 11-norbetaenone (**1**) was caused by its cytotoxicity, and therefore lactate dehydrogenase (LDH) assay to EPCs was performed. The results showed that 11-norbetaenone (**1**) did not induce lactate dehydrogenase (LDH) release in EPCs (Fig. 5B). On the basis of these findings, we suggest that 11-norbetaenone (**1**) exhibits a promising anti-angiogenic activity without acting in a cytotoxic fashion.

In summary, the investigation of the entomopathogenic fungus, *Lecanicillium antillanum*, led to the novel nor-betaenone compound, 11-norbetaenone (**1**), which is the first time a natural product were isolated from this genus. Except for the assay in anti-angiogenic activity, it is inactive in assays for cytotoxicity, anti-inflammatory activity and antimicrobial activity. It is also the first report that a betaenone-skeleton compound possesses anti-angiogenic activity. Our findings suggest that 11-norbetaenone (**1**) may serve as a lead for discovery of novel angiogenetic inhibitors in the treatment of angiogenesis-related diseases.

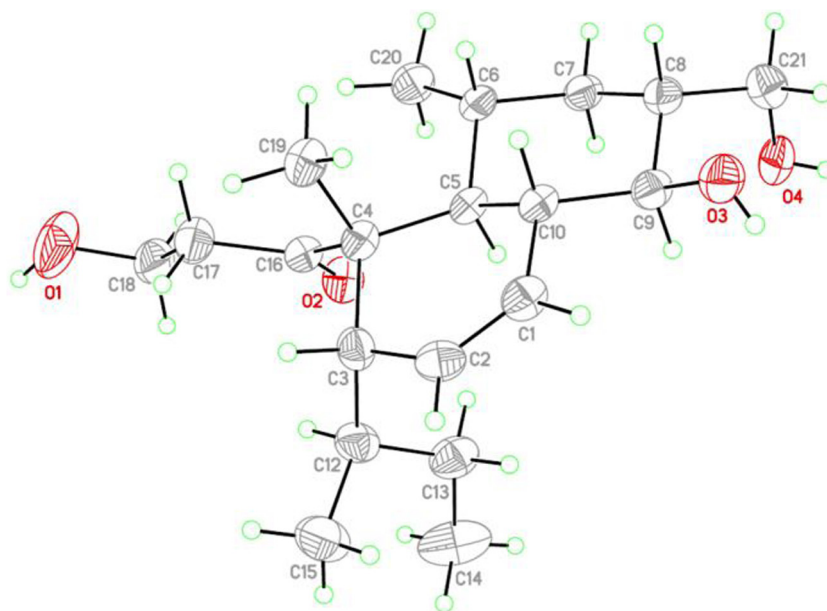
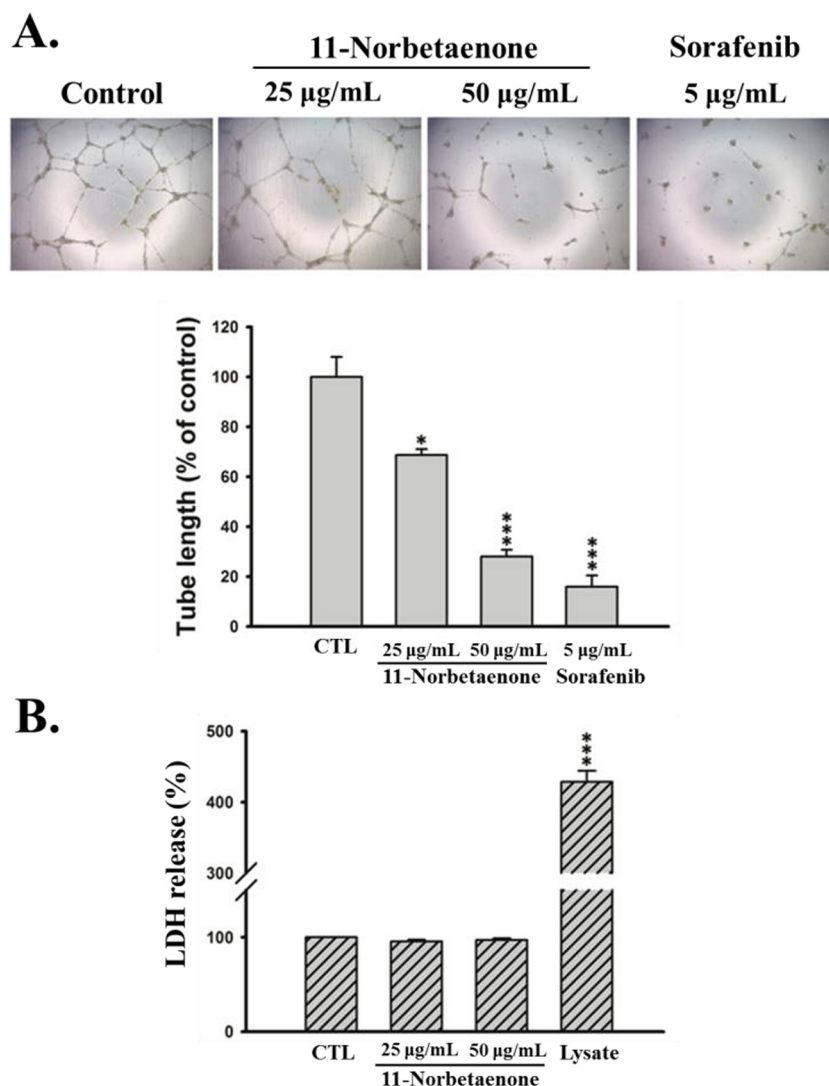


Fig. 4. X-ray crystallographic of **1**.



**Fig. 5.** Effect of 11-norbetaenone (**1**) on tube formation and cytotoxicity of human EPCs. (A) Cells were plated on Matrigel-coated plates in the indicated concentrations of 11-norbetaenone (**1**) and sorafenib for 24 h, and tubular morphogenesis was recorded by the inverted phase contrast microscope. Images were representative of results from seven separate experiments. Tube formation was quantified by measuring the length of tubes with the use of Image-J. (B) Cells were treated with 11-norbetaenone (**1**) for 24 h, then the cytotoxicity was determined using LDH assay. Data are expressed as mean  $\pm$  SEM of three to seven independent experiments. \* $P < 0.05$ , \*\*\* $P < 0.001$  compared with the control group.

## Acknowledgments

This work is supported by grants from Ministry of Science and Technology of Taiwan (MOST 103-2628-B-037-003-MY3 award to F.-R. Chang), National Health Research Institutes (NHRI-EX103-10241BI), and in part by the grant from Chinese Medicine Research Center, China Medical University (the Ministry of Education, the Aim for the Top University Plan). This study is also supported partially by Kaohsiung Medical University (Aim for the Top Universities Grant, grant No. KMU-TP104E39, KMU-TP104A26), Ministry of Health and Welfare of Taiwan (MOHW105-TDU-B-212-134007), and Health and welfare surcharge of tobacco products. X-ray single crystallography analysis is supported by Instrumentation Center, National Taiwan University. HRESI-MS is supported by the Joint Center for High Valued Instrument, National Sun Yat-sen University; 400 MHz NMR as well as ESI-MS are supported by Center for Research Resources and Development, Kaohsiung Medical University.

## Supplementary data

Supplementary data (General experimental procedures, fungal material, species identification, fermentation, extraction and isolation, X-ray single crystallographic analysis, mass and 1D and 2D NMR spectroscopic data of compounds **1**) associated with this article can be found, in the online version, at <http://dx.doi.org/10.1016/j.bmcl.2017.03.019>.

## References

- Barash I, Manulis S, Kashman Y, et al. *Science*. 1983;220:1605–1606.
- Manulis S, Kashman Y, Netzer D, Barash I. *Phytochemistry*. 1984;23:2913–2918.
- Ichihara A, Oikawa H, Hayashi K, Sakamura S. *J Am Chem Soc*. 1983;105:2907–2908.
- Kuramoto M, Yamada K, Shikano M, et al. *Chem Lett*. 1997;26:885–886.
- Tsukamoto S, Miura S, Yamashita Y, Ohta T. *Bioorg Med Chem Lett*. 2004;14:417–420.
- Brauers G, Edrada RA, Ebel R, et al. *J Nat Prod*. 2000;63:739–745.

7. Kobayashi M, Uehara H, Matsunami K, Aoki S, Kitagawa I. *Tetrahedron Lett.* 1993;34:7925–7928.
8. Sawa R, Takahashi Y, Itoh S, et al. *J Antibiot.* 1994;47:1266–1272.
9. Sawa R, Takahashi Y, Itoh S, et al. *J Antibiot.* 1992;45:136–139.
10. Sawa R, Takahashi Y, Sawa T, Naganawa H, Takeuchi T. *J Antibiot.* 1994;47:1273–1279.
11. Oikawa H, Ichihara A, Sakamura S. *Agric Biol Chem.* 1983;48:2603–2605.
12. Lai W-C, Tsui Y-T, Singab ANB, et al. *Int J Mol Sci.* 2013;14:15578–15598.
13. Yang S-C, Chung P-J, Ho C-M, et al. *J Immunol.* 2013;190:6511–6519.
14. Yu H-P, Hsieh P-W, Chang Y-J, Chung P-J, Kuo L-M, Hwang T-L. *Free Radic Biol Med.* 2011;50:1737–1748.
15. Zaidan MRS, Noor Rain A, Badrul AR, Adlin A, Norazah A, Zakiah I. *Trop Biomed.* 2005;22:165–170.
16. Su C-M, Hsu C-J, Tsai C-H, Huang C-Y, Wang S-W, Tang C-H. *Stem Cells.* 2015;2243–2245.
17. Urbich C, Dimmeler S. *Circ Res.* 2004;95:343–353.
18. Takayuki Asahara TM, Sullivan Alison, Silver Marcy, et al. *Science.* 1997;275:964–966.
19. Peters Jr BA, Diaz LA, Polyak K, et al. *Nat Med.* 2005;11:261–262.
20. Chung C-H, Chang C-H, Chen S-S, et al. *Evid Based Complement Alternat Med.* 2013;2013:1–10.
21. Folkman J. *Nat Rev Drug Discovery.* 2007;6:273–286.
22. Staton CA, Reed MWR, Brown NJ. *Int J Exp Pathol.* 2009;90:195–221.



Cite this: *Food Funct.*, 2017, **8**, 1859

# Capsaicin presynaptically inhibits glutamate release through the activation of TRPV1 and calcineurin in the hippocampus of rats

Cheng Wei Lu,<sup>a,d</sup> Tzu Yu Lin,<sup>a,d</sup> Ting Yang Hsie,<sup>c</sup> Shu Kuei Huang<sup>a</sup> and Su Jane Wang<sup>ib</sup> \*<sup>b,e</sup>

Capsaicin is the major ingredient in hot peppers of the plant *Capsicum genus* with neuroprotective effects in several preclinical models; its effect on glutamate release has been investigated in the rat hippocampus using isolated nerve terminals (synaptosomes) and brain slices. In a synaptosomal preparation, capsaicin dose-dependently reduced 4-aminopyridine-evoked  $\text{Ca}^{2+}$ -dependent glutamate release, with an  $\text{IC}_{50}$  of approximately 11  $\mu\text{M}$ . This inhibition was blocked by capsazepine, an antagonist of TRPV1, which was found to be colocalized with the vesicle marker protein synaptophysin in synaptosomes using double immunostaining. Capsaicin decreased 4-aminopyridine-evoked intrasynaptosomal  $\text{Ca}^{2+}$  concentration elevation and the capsaicin-mediated inhibition of glutamate release was prevented by the  $\text{Ca}_v2.2$  (N-type) and  $\text{Ca}_v2.1$  (P/Q-type) channel blocker  $\omega$ -conotoxin MVIIC, but was not affected by the intracellular  $\text{Ca}^{2+}$ -release inhibitors dantrolene and CGP37157. Furthermore, capsaicin increased the 4-aminopyridine-induced phosphorylation of protein phosphatase calcineurin and the calcineurin inhibitor cyclosporine A eliminated the inhibitory effect of capsaicin on evoked glutamate release. Additionally, capsaicin also reduced the frequency of miniature excitatory postsynaptic currents without affecting their amplitude in slice preparations. Together, these results suggest that capsaicin acts at TRPV1 present on hippocampal nerve terminals to increase calcineurin activation, which subsequently attenuates voltage-dependent  $\text{Ca}^{2+}$  entry to cause a decrease in evoked glutamate release.

Received 3rd January 2017,

Accepted 27th March 2017

DOI: 10.1039/c7fo00011a

[rsc.li/food-function](http://rsc.li/food-function)

## Introduction

Glutamate, the most prominent excitatory neurotransmitter in the central nervous system, acts through ionotropic and metabotropic receptors to regulate a variety of normal brain functions.<sup>1</sup> However, numerous neurological and psychiatric disorders, including epilepsy, pain states, schizophrenia, depression, and neurodegenerative disorders have been linked to the hyperactivity of the glutamate system.<sup>2,3</sup> One rational strategy to inhibit overall glutamatergic neurotransmission is to reduce glutamate release from nerve terminals. Indeed, such an approach has been proved by several clinically used drugs such as carbamazepine (an antiepileptic

drug), fluoxetine (an antidepressant), and riluzole (a neuroprotectant).<sup>4–7</sup>

Capsaicin (*trans*-8-methyl-*N*-vanillyl-6-nonenamide) is the major ingredient in hot peppers of the plant *Capsicum genus* and has wide applications in food, medicine, and pharmacy.<sup>8</sup> Capsaicin possesses anticancer, antioxidant, anti-inflammatory and analgesic properties,<sup>9–11</sup> and its neuroprotective activity has been reported in several *in vitro* and *in vivo* studies. For example, capsaicin protects against glutamate- or hypoxia-reoxygenation-induced neuronal death in cultured cortical and hippocampal neurons of rats,<sup>12,13</sup> attenuates brain damage in different ischemic models in rats and gerbils,<sup>14,15</sup> and prevents kainic acid-induced seizures in mice.<sup>16</sup> Although the mechanism by which capsaicin exhibits its neuroprotective effect is still unclear, desensitization of the transient receptor potential vanilloid 1 (TRPV1) receptor has been reported.<sup>15,17</sup> TRPV1, a nonselective cation channel with high  $\text{Ca}^{2+}$  permeability, is present in brain regions including hippocampus<sup>18,19</sup> and involved in synaptic plasticity such as long-term depression (LTD).<sup>20,21</sup> Electrophysiological studies have shown that capsaicin activates TRPV1 and increases  $\text{Ca}^{2+}$  influx, which would induce calcineurin (protein phosphatase 2B) activation and

<sup>a</sup>Department of Anesthesiology, Far-Eastern Memorial Hospital, New Taipei, Taiwan

<sup>b</sup>School of Medicine, Fu Jen Catholic University, New Taipei, Taiwan.

E-mail: [med0003@mail.fju.edu.tw](mailto:med0003@mail.fju.edu.tw); Fax: +886-2-29052096; Tel: +886-2-29053465

<sup>c</sup>P.H.D. Program in Nutrition & Food Science, Fu Jen Catholic University, New Taipei, Taiwan

<sup>d</sup>Department of Mechanical Engineering, Yuan Ze University, New Taipei, Taiwan

<sup>e</sup>Research Center for Chinese Herbal Medicine, College of Human Ecology, Chang Gung University of Science and Technology, Taoyuan City, Taiwan

subsequently down-regulate TRPV1 or voltage-dependent  $\text{Ca}^{2+}$  channels, and that may, in turn, depress excitatory synaptic transmission in hippocampal and dorsal root ganglion neurons.<sup>22–24</sup> However, capsaicin effects on glutamate release have not been examined directly at the presynaptic level.

In the current study, biochemical and electrophysiological approaches have been used to investigate the effect of capsaicin on glutamate release from rat hippocampal nerve terminals (synaptosomes) and slices. We found that capsaicin presynaptically inhibits glutamate release in the hippocampus. This inhibitory effect of capsaicin is mediated by the TRPV1 receptor, and appears to be related to the activation of protein phosphatase calcineurin, which subsequently reduces voltage-dependent  $\text{Ca}^{2+}$  entry. These effects may be crucial for understanding the neuroprotective effect of capsaicin in the brain.

## Materials and methods

### Chemicals

Capsaicin, capsazepine, bafilomycin A1, DL-threo- $\beta$ -benzyloxyaspartate (DL-TBOA), dantrolene, 7-chloro-5-(2-chlorophenyl)-1,5-dihydro-4,1-benzothiazepin-2(3H)-one (CGP37157),  $\omega$ -conotoxin MVIIC, 6-cyano-7-nitroquinoxaline-2,3-dione (CNQX), and D(-)-2-amino-5-phosphonopentanoic acid (D-AP5), bicuculline, and cyclosporin A were purchased from Tocris Cookson (Bristol, UK). Fura-2-acetoxymethyl ester (Fura-2-AM) was bought from Invitrogen (Carlsbad, CA, USA). 4-Aminopyridine, ethylene glycol bis ( $\beta$ -aminoethyl ether)-N,N,N',N'-tetraacetic acid (EGTA), tetrodotoxin, and all other reagents were purchased from Sigma-Aldrich Co. (St Louis, MO, USA). Capsaicin,  $\text{DiSC}_3(5)$ , and Fura-2 were dissolved in dimethylsulfoxide, with a final concentration of 0.1% (v/v) in the medium.

### Animals

Adult (150–200 g) and 8- to 23-day-old male Sprague-Dawley rats were purchased from BioLASCO (Taiwan Co., Ltd, Taipei, Taiwan). Animals were housed under constant conditions of temperature ( $22 \pm 1^\circ\text{C}$ ) and relative humidity (50–70%) with a regular light–dark schedule (lights on from 7 am to 7 pm) and free access to food and water. Animal experiments were in accordance with the National Institutes of Health Guide for the Care and Use of Laboratory (NIH Publication no. 85-23, revised 1996), and were approved by the Institutional Animal Care and Use Committee at the Far-Eastern Memorial Hospital. Special care was taken to minimize the number of animals used and their suffering.

### Synaptosome preparation

Rats were decapitated, brains were quickly removed and the whole hippocampus was dissected out at  $4^\circ\text{C}$ . As previously described,<sup>25</sup> the hippocampus was homogenized in a medium containing 0.32 M sucrose (pH 7.4) using a glass/Teflon tissue grinder; the homogenate was centrifuged at 3000g (5000 rpm in a JA 25.5 rotor; Beckman Coulter, Inc., USA) for 10 min to

remove nuclei and debris and the supernatant was gently stratified on discontinuous Percoll gradients (3%, 10%, and 23% v/v in 0.32 M sucrose) and centrifuged at 32 500g (16 500 rpm in a JA 20.5 rotor) for 7 min. The layer between 10 and 23% Percoll (synaptosomal fraction) was collected and washed by centrifugation. The synaptosomal pellets were resuspended in HEPES buffer medium with the following composition (mM): NaCl, 140; KCl, 5;  $\text{NaHCO}_3$ , 5;  $\text{MgCl}_2 \cdot 6\text{H}_2\text{O}$ , 1;  $\text{Na}_2\text{HPO}_4$ , 1.2; glucose, 10; HEPES, 10; pH 7.4. Protein concentration was then determined using the Bradford assay. Synaptosomes were centrifuged in the final wash to obtain synaptosomal pellets with 0.5 mg protein. Synaptosomal pellets were stored on ice and used within 4–6 h.

### Synaptosomal glutamate release

Glutamate release was assayed by on-line fluorimetry as described previously.<sup>26</sup> Synaptosomal pellets were resuspended in HEPES buffer medium ( $0.5 \text{ mg mL}^{-1}$ ) and preincubated at  $37^\circ\text{C}$  for 1 h in the presence of  $16 \mu\text{M}$  bovine serum albumin to bind any free fatty acids released from synaptosomes during the preincubation. A 1 mL aliquot was transferred to a stirred and thermostated cuvette containing 2 mM  $\text{NADP}^+$ , 50 units of glutamate dehydrogenase, and 1.2 mM  $\text{CaCl}_2$ , and the fluorescence of NADPH was followed in a PerkinElmer LS-55 spectrofluorimeter (PerkinElmer Life and Analytical Sciences, Waltham, MA, USA) at excitation and emission wavelengths of 340 and 460 nm, respectively. A standard of exogenous glutamate (5 nmol) was added at the end of each experiment and the fluorescence change produced by the standard addition was used to calculate the released glutamate as nanomoles of glutamate per milligram of synaptosomal protein ( $\text{nmol mg}^{-1}$ ). Release values quoted in the text and depicted in bar graphs represent the levels of glutamate cumulatively released after 5 min of depolarization, and are expressed as  $\text{nmol mg}^{-1}$  per 5 min. Data were accumulated at 2 s intervals. Cumulative data were analyzed using Lotus 1-2-3 spreadsheets and MicroCal Origin.

### Immunocytochemistry

The synaptosomes were allowed to attach to polylysine coated coverslips for 60 min and then fixed for 30 min in 4% paraformaldehyde in 0.1 M phosphate buffer (pH 7.4). Following several washes with phosphate buffer, the synaptosomes were preincubated for 60 min in 3% normal goat serum diluted in 50 mM Tris buffer (pH 7.4) containing 0.9% NaCl (Tris buffered saline) and 0.2% Triton X-100. Subsequently, they were then incubated for 90 min with the appropriate primary antibody diluted in Tris buffered saline with 1% normal goat serum and 0.2% Triton X-100 as follows: synaptophysin (1:200; Abcam, Cambridge, UK) and TRPV1 receptor (1:50; Cell Signaling Technology, Beverly, MA, USA). After washing with Tris buffered saline, the synaptosomes were incubated for 2 h in goat anti-mouse DyLight 549- and goat anti-rabbit fluorescein isothiocyanate (FITC)-conjugated secondary antibodies (1:200; Jackson ImmunoResearch Inc., West Grove, PA, USA). After several washes in Tris buffered saline, the synaptosomes



were coverslipped with fluorescence mounting medium (DAKO North America, Inc., CA, USA). The synaptosomes were viewed with a upright fluorescence microscope (Leica DM2000 LED, Wetzlar, Germany) using a mercury lamp as a source of light and equipped with a 100× objective and images were captured using a CCD camera (SPOT RT3, Diagnostic Instruments, Sterling Heights, MI, USA).

### Western blotting

Synaptosomes were homogenized in a lysis buffer (10 mM HEPES buffer, pH 7.4), 1% Triton X-100, and a protease inhibitor mixture. Lysates were clarified by centrifugation, and protein concentration was determined using a protein assay kit (Bio-Rad Laboratories, Hercules, CA, USA). Equal amounts of proteins were separated by SDS-PAGE and transferred to a nitrocellulose membrane. The membranes were blocked with Tris-buffered saline that contained 5% low-fat milk and incubated with appropriate primary antibodies (anti-TRPV1 receptor, 1:1000; anti-synaptophysin, 1:500; Cell Signaling Technology, Beverly, MA, USA) overnight at 4 °C. After three washes in Tris-buffered saline, the membrane was then treated with the secondary horseradish peroxidase-conjugated antibody (1:3000; BioRad, Milan, Italy) for 1 h at room temperature. The membranes were then washed at least three times with Tris-buffered saline and visualized using the enhanced chemiluminescence system (Amersham, Buckinghamshire, UK).

### Synaptosomal cytosolic $\text{Ca}^{2+}$ concentration ( $[\text{Ca}^{2+}]_c$ )

$[\text{Ca}^{2+}]_c$  was measured with fura-2. Synaptosomes were resuspended (2 mg  $\text{mL}^{-1}$ ) in HEPES buffer medium containing 16  $\mu\text{M}$  bovine serum albumin in the presence of 5  $\mu\text{M}$  fura-2 and 0.1 mM  $\text{CaCl}_2$  and incubated at 37 °C for 30 min in a stirred test tube. After fura-2 loading, synaptosomes were pelleted and resuspended in HEPES buffer medium containing bovine serum albumin. The synaptosomal suspension was stirred in a thermostated cuvette containing 1.2 mM  $\text{CaCl}_2$  in a PerkinElmer LS-55 spectrofluorimeter, and the fluorescence was monitored at excitation wavelengths of 340 and 380 nm (emission wavelength 505 nm). Data were collected at 2 s intervals.  $[\text{Ca}^{2+}]_c$  (nM) was calculated using the equations described by Grynkiewicz *et al.* (1985).<sup>27</sup> Cumulative data were analyzed using Lotus 1-2-3.

### Slice preparation and electrophysiological recordings

Hippocampal slices were prepared from 8- to 23-day-old male rats ( $n = 5$ ), as described in detail previously.<sup>28,29</sup> The hippocampus was positioned on the stage of a vibratome slicer (VT1000S, Leica, Germany) and cut to obtain 300  $\mu\text{M}$  thick transverse brain slices. The slices were maintained in the artificial cerebrospinal fluid continuously oxygenated with 95%  $\text{O}_2$ -5%  $\text{CO}_2$  at room temperature for at least 1 h before use. Artificial cerebrospinal fluid comprised (in mM): 117 NaCl, 4.7 KCl, 2.5  $\text{CaCl}_2$ , 1.2  $\text{MgCl}_2$ , 25  $\text{NaHCO}_3$ , 1.2  $\text{NaH}_2\text{PO}_4$ , 11 glucose (pH 7.4, 300 mOsm).

Slices were moved to a recording chamber mounted on a BX51 W1 upright microscope (Olympus) equipped with infra-red differential interference contrast (IR-DIC). The chamber was continuously perfused with oxygenated artificial cerebrospinal fluid. Neurons were visualized with an Olympus Optical 40× water immersion objective. Tight-seal ( $>1 \text{ G}\Omega$ ) whole-cell recordings were obtained from the cell body of neurons situated in the CA3 pyramidal layer. Patch electrodes had a 2–5  $\text{M}\Omega$  resistance after filling with internal solution containing (in mM): 0.3  $\text{Na}_3\text{GTP}$ , 135 K-gluconate, 20 KCl, 0.1 EGTA, 2  $\text{CaMgCl}_2$ , 4  $\text{Na}_2\text{ATP}$ , and 10 HEPES (pH 7.3, 280 mOsm). Neurons were voltage clamped at  $-70 \text{ mV}$  using an Axopatch 200B amplifier (Axon Instruments, Foster City, CA, USA). Access resistance (8–30  $\text{M}\Omega$ ) was regularly monitored during recordings and cells were rejected if it changed more than 15% during the experiments. Membrane currents were filtered at 2 kHz, digitized and stored on a computer using pCLAMP (Axon Instruments, Foster City, CA, USA). Data were analyzed offline using commercially available software.

### Data and statistical analysis

Data are expressed as mean  $\pm$  SEM. Statistical analysis was carried out by the two-tailed Student's *t* test when comparing two groups and by one-way ANOVA with Tukey's multiple comparisons *post hoc* tests when comparing more than two groups. Analysis was completed using SPSS software (Version 17.0; SPSS Inc., Chicago, IL, USA). Data were considered significant if  $P < 0.05$ .

## Results

### Effect of capsaicin on 4-aminopyridine-evoked glutamate release in rat hippocampal nerve terminals

Synaptosomes were purified from the hippocampus of rats, and exposed to the  $\text{K}^+$  channel blocker 4-aminopyridine, an agent whose action most closely mimics physiological stimulation,<sup>30</sup> to assess glutamate release. Under controlled conditions, 4-aminopyridine (1 mM) evoked a glutamate release of  $7.3 \pm 0.2 \text{ nmol mg}^{-1}$  per 5 min from synaptosomes incubated with 1.2 mM  $\text{CaCl}_2$  (Fig. 1A). Preincubation with capsaicin (30  $\mu\text{M}$ ) for 10 min before 4-aminopyridine addition caused an inhibition of the 4-aminopyridine-evoked glutamate release by approximately 51% [ $3.6 \pm 0.1 \text{ nmol mg}^{-1}$  per 5 min;  $t(10) = 13.2$ ,  $P < 0.001$ ; Fig. 1A]. Capsaicin did not affect the basal, pre-depolarization glutamate level. The effect of capsaicin was concentration-dependent; the maximal inhibition was observed when the compound was applied at 30  $\mu\text{M}$ , and the  $\text{IC}_{50}$  value was 11  $\mu\text{M}$  (Fig. 1B).

### Effect of the TRPV1 receptor antagonist capsazepine on the capsaicin-mediated inhibition of 4-aminopyridine-evoked glutamate release

Since capsaicin is known to exert its biological effects *via* activation of TRPV1 receptors, we examined the effect of capsaze-

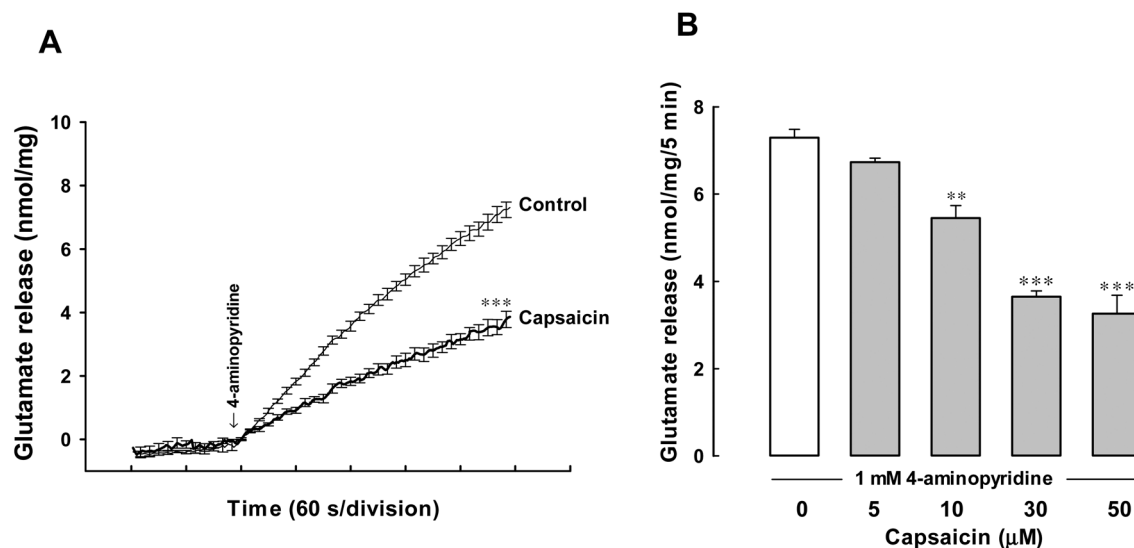


**Fig. 1** Capsaicin inhibits the 4-aminopyridine-evoked glutamate release in hippocampal synaptosomes. (A, B) Glutamate release was evoked by 4-aminopyridine (1 mM) in the absence (control) or presence of capsaicin (5, 10, 30, and 50  $\mu$ M). Capsaicin was added 10 min before the addition of 4-aminopyridine. Each column is mean  $\pm$  SEM values of independent experiments, using synaptosomal preparations from 5 to 6 animals. \*\*,  $P < 0.01$ , \*\*\*,  $P < 0.001$  versus the control group.

pine, an antagonist of the TRPV1 receptor, on the action of capsaicin on 4-aminopyridine-evoked glutamate release. Fig. 2A shows that capsazepine (30  $\mu$ M) did not affect 4-aminopyridine (1 mM)-evoked glutamate release [ $F(2,13) = 2.61$ ;  $P > 0.05$ ] but prevented the inhibitory effect of capsaicin (30  $\mu$ M) on 4-aminopyridine-evoked glutamate release. In the five tested synaptosomal preparations, no statistical difference was observed between the glutamate release after capsazepine alone and after the capsazepine and capsaicin treatment ( $P > 0.05$ ; Fig. 2A). Thus, the data favor the activation of TRPV1 receptors in the capsaicin-mediated inhibition of glutamate release. To confirm the presence of TRPV1 receptors in hippocampal nerve terminals, synaptosomes were co-labeled with antibodies against the vesicle marker protein synaptophysin and TRPV1 receptors (Fig. 2B and C). Among the nerve terminals that contained synaptophysin (3324 synaptic boutons from 25 fields),  $76.5 \pm 1.9\%$  also contained the TRPV1 receptor (Fig. 2D). In addition, synaptophysin or TRPV1 receptor immunoreactivity was also observed by western blot analysis (Fig. 2E).

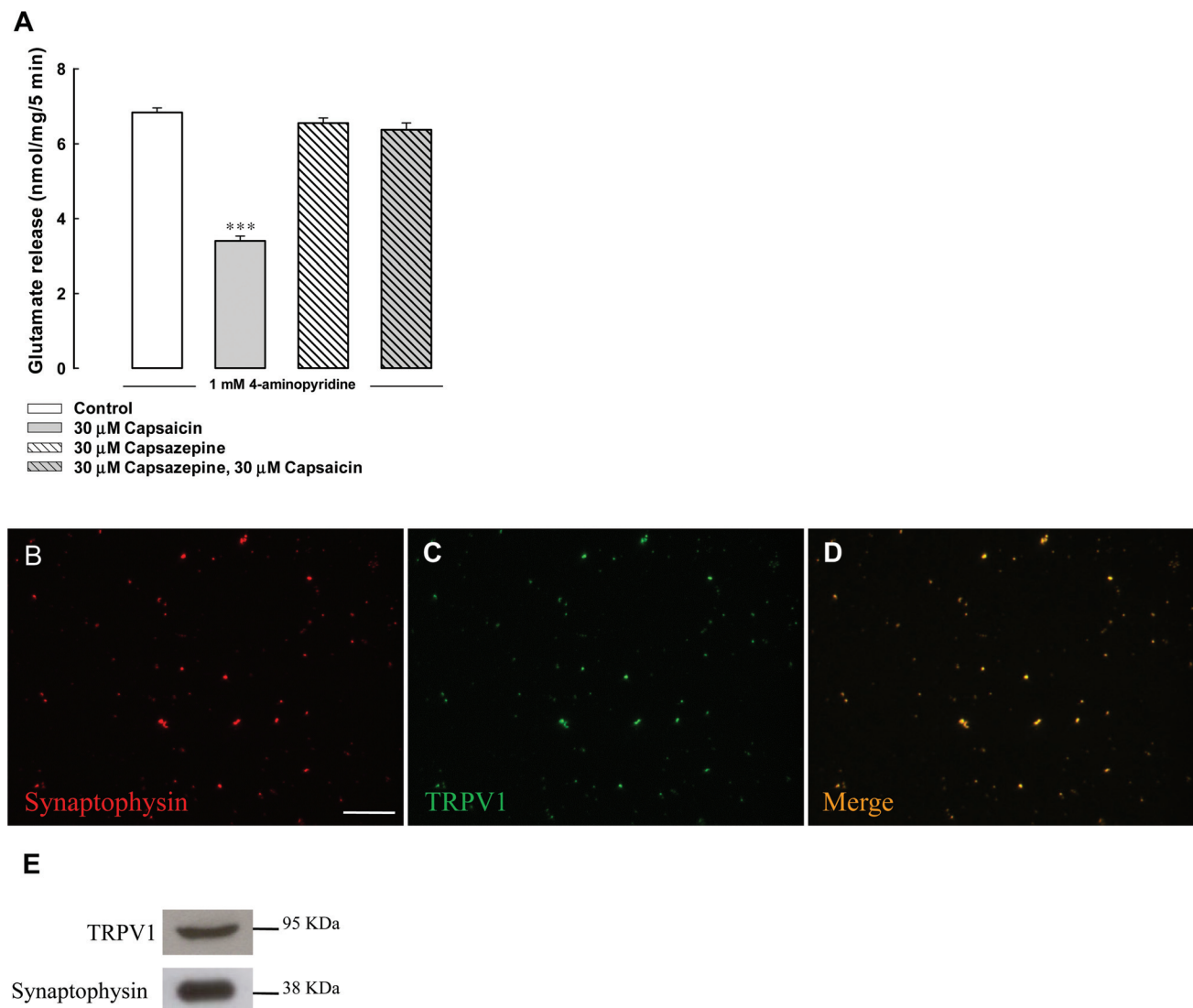
#### Effect of external calcium omission, the glutamate transporter blocker DL-TBOA, and the vesicular transporter inhibitor bafilomycin A1 on the capsaicin-mediated inhibition of 4-aminopyridine-evoked glutamate release

Fig. 3 shows that calcium-free medium containing 300  $\mu$ M EGTA reduced the 4-aminopyridine-evoked glutamate release [ $F(2,12) = 44.5$ ;  $P < 0.001$ ]. This  $\text{Ca}^{2+}$ -independent component of the 4-aminopyridine-evoked glutamate release was unaffected by 30  $\mu$ M of capsaicin ( $P = 1.00$ ). DL-TBOA (10  $\mu$ M), a non-selective inhibitor of all excitatory amino acid transporter

subtypes, increased the 4-aminopyridine-evoked glutamate release ( $P < 0.01$ ). In the presence of DL-TBOA, capsaicin (30  $\mu$ M) still significantly reduced the 4-aminopyridine-induced release of glutamate [ $F(2,12) = 8.4$ ;  $P < 0.05$ ; Fig. 3]. By contrast, bafilomycin A1 (0.1  $\mu$ M), a vesicular transporter inhibitor, inhibited the 4-aminopyridine-evoked glutamate release and prevented the inhibitory effect of capsaicin (30  $\mu$ M) on 4-aminopyridine-evoked glutamate release [ $F(2,13) = 91.8$ ;  $P < 0.001$ ]. In the five tested synaptosomal preparations, no statistical difference was observed between the release after bafilomycin A1 alone and after the bafilomycin A1 and capsaicin treatment ( $P > 0.05$ ; Fig. 3). These results indicate that capsaicin influences the release of glutamate induced by a decrease in vesicular exocytosis.

#### Effect of capsaicin on the 4-aminopyridine-evoked increase in $[\text{Ca}^{2+}]_c$

Fig. 4 shows the  $[\text{Ca}^{2+}]_c$  levels determined in synaptosomes pretreated with fura-2. The stimulation of synaptosomes with 1 mM 4-aminopyridine caused an increase in  $[\text{Ca}^{2+}]_c$  levels to a plateau level ( $P < 0.001$ ). Preincubation with capsaicin (30  $\mu$ M) for 10 min before 4-aminopyridine addition did not significantly affect basal Ca levels but reduced the 4-aminopyridine-evoked  $[\text{Ca}^{2+}]_c$  increase by 20% [ $t(8) = 11.1$ ,  $P < 0.001$ ]. In addition, 30  $\mu$ M capsazepine alone had no effect on the 4-aminopyridine-evoked increase of  $[\text{Ca}^{2+}]_c$  ( $P > 0.05$ ) and completely abolished the effect of capsaicin (Fig. 4). This indicates that capsaicin reduces evoked changes in  $[\text{Ca}^{2+}]_c$  with a pharmacological profile similar to that observed for the reduction of release (Fig. 2A).



**Fig. 2** Effect of capsazepine, an antagonist of the TRPV1 receptor, on capsaicin-mediated inhibition of 4-aminopyridine-evoked glutamate release. (A) Glutamate release was evoked by 4-aminopyridine (1 mM) in the absence (control) or presence of 30  $\mu$ M capsaicin, 30  $\mu$ M capsazepine, or 30  $\mu$ M capsazepine and 30  $\mu$ M capsaicin. Each column is mean  $\pm$  SEM values of independent experiments, using synaptosomal preparations from 5 animals. \*\*\*,  $P < 0.001$  versus the control group. (B–D) Synaptosomes were fixed onto polylysine-coated coverslips and double-stained for immunocytochemistry with antisera against TRPV1 receptors and the vesicular marker synaptophysin. Scale bar, 30  $\mu$ m. (E) Western blot analysis of the expression of TRPV1 receptors and synaptophysin in synaptosomes.

### Effect of $\text{Ca}^{2+}$ channel blockers and intracellular $\text{Ca}^{2+}$ release inhibitors on the capsaicin-mediated inhibition of 4-aminopyridine-evoked glutamate release

Fig. 5 shows that glutamate release evoked by 1 mM 4-aminopyridine was significantly decreased in the presence of 2  $\mu$ M  $\omega$ -conotoxin GVIA or 500 nM  $\omega$ -agatoxin IVA, which selectively blocks  $\text{Ca}_v2.2$  (N-type) and  $\text{Ca}_v2.1$  channels (P/Q-type), respectively ( $P < 0.001$ ).<sup>31,32</sup> In the presence of either  $\omega$ -conotoxin GVIA or  $\omega$ -agatoxin IVA alone, however, application of 30  $\mu$ M capsaicin was still able to reduce 4-aminopyridine-evoked glutamate release ( $P < 0.05$ ).  $\omega$ -Conotoxin MVIIC (2  $\mu$ M), a wide-spectrum blocker of  $\text{Ca}_v2.2$  (N-type) and  $\text{Ca}_v2.1$  (P/Q-type)

channels, reduced the 4-aminopyridine-evoked glutamate release [ $F(2,15) = 267.7$ ;  $P < 0.001$ ], and prevented the inhibition of glutamate release by capsaicin (30  $\mu$ M). The release measured in the presence of  $\omega$ -conotoxin MVIIC and capsaicin was similar to that obtained in the presence of  $\omega$ -conotoxin MVIIC alone ( $P > 0.05$ ). Dantrolene (100  $\mu$ M), a blocker of  $\text{Ca}^{2+}$  release from endoplasmic reticulum ryanodine receptors, reduced the 4-aminopyridine (1 mM)-evoked glutamate release ( $P < 0.001$ ). In the presence of dantrolene (100  $\mu$ M), the application of capsaicin (30  $\mu$ M) still effectively inhibited 4-aminopyridine-evoked glutamate release [ $F(2,15) = 134.9$ ;  $P < 0.05$ ; Fig. 5]. Similarly, CGP37157 (100  $\mu$ M), a membrane-permeant blocker of the mitochondrial  $\text{Na}^+/\text{Ca}^{2+}$  exchanger, reduced the

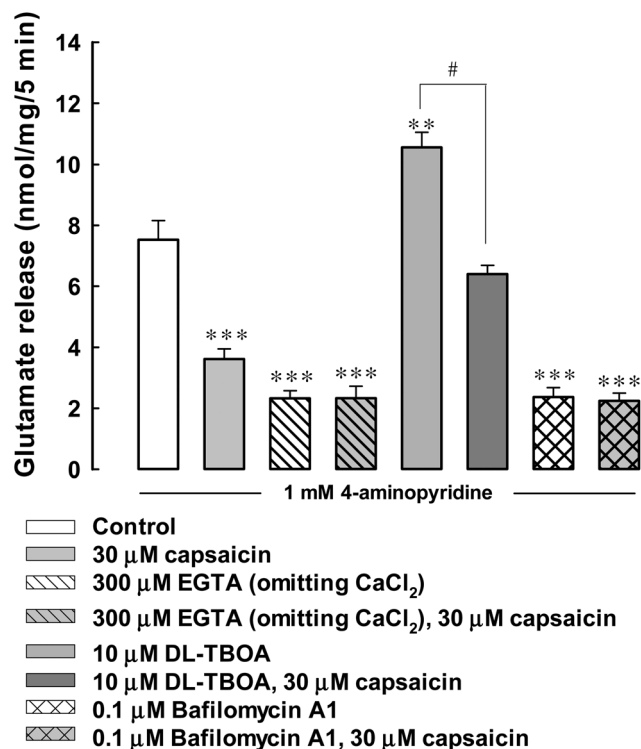


**Fig. 3** Effect of external calcium omission, the glutamate transporter blocker DL-TBOA, and the vesicular transporter inhibitor bafilomycin A1 on the capsaicin-mediated inhibition of 4-aminopyridine-evoked glutamate release. Glutamate release was evoked by 4-aminopyridine (1 mM) in the absence (control) or presence of 30 μM capsaicin, 300 μM EGTA (omitting CaCl<sub>2</sub>), 300 μM EGTA (omitting CaCl<sub>2</sub>) and 30 μM capsaicin, 10 μM DL-TBOA, 10 μM DL-TBOA and 30 μM capsaicin, 0.1 μM bafilomycin A1, or 0.1 μM bafilomycin A1 and 30 μM capsaicin. Capsaicin was added 10 min before depolarization and, EGTA, DL-TBOA or bafilomycin A1, 20 min prior to this. Each column is mean ± SEM values of independent experiments, using synaptosomal preparations from 5 animals. \*\*,  $P < 0.01$ , \*\*\*,  $P < 0.001$  versus the control group. #,  $P < 0.05$  versus the DL-TBOA-treated group.

release of glutamate evoked by 4-aminopyridine ( $P < 0.001$ ). In the presence of CGP37157 (100 μM) and capsaicin (30 μM), the inhibition of glutamate release following 4-aminopyridine-depolarization was significantly different from the effect of CGP37157 alone [ $F(2,14) = 128.7$ ;  $P < 0.05$ ; Fig. 5]. Thus, a decrease in Ca<sup>2+</sup> influx mediated by Ca<sub>v</sub>2.1 (P/Q-type) channels appears to be associated with the observed capsaicin-mediated inhibition of glutamate release.

#### Effect of the phosphatase 2B inhibitor cyclosporin A on the capsaicin-mediated inhibition of 4-aminopyridine-evoked glutamate release

The inhibitory effect of capsaicin on glutamate release may be due to the influence of protein phosphatase 2B calcineurin, as capsaicin has been shown to activate calcineurin and depress excitatory synaptic transmission.<sup>22–24</sup> To test this possibility, the effect of capsaicin was determined in the presence of cyclosporin A, a protein phosphatase 2B inhibitor. Fig. 6 shows that cyclosporin A (1 μM) facilitated the 4-aminopyri-

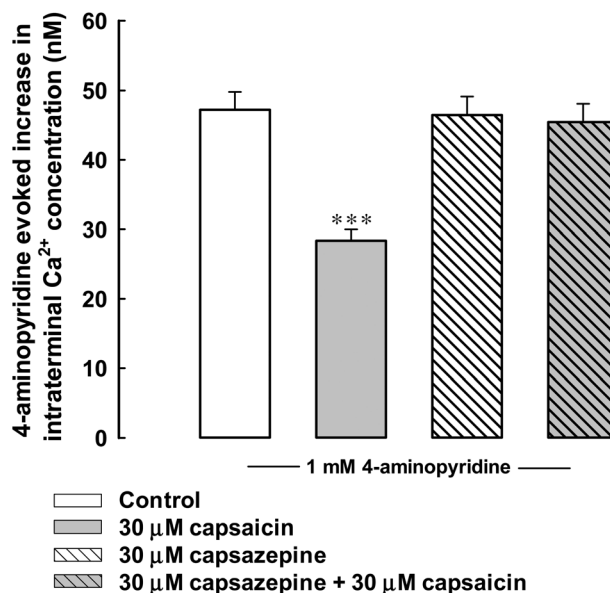


**Fig. 4** Capsaicin reduces 4-aminopyridine-evoked change in intraterminal Ca<sup>2+</sup> concentration, and this effect is prevented by capsazepine. Synaptosomes were stimulated with 1 mM 4-aminopyridine in the absence (control) or presence of 30 μM capsaicin, 30 μM capsazepine, or 30 μM capsazepine and 30 μM capsaicin added 10 min before stimulation. Each column is mean ± SEM values of independent experiments, using synaptosomal preparations from 5 animals. \*\*\*,  $P < 0.001$  versus the control group.

dine (1 mM)-evoked glutamate release [ $F(2,12) = 142.78$ ;  $P < 0.01$ ]. Capsaicin (30 μM) alone reduced the release of glutamate evoked by 4-aminopyridine, but this inhibition was significantly suppressed by the pretreatment with cyclosporin A, there being no statistical difference between the release after cyclosporin A alone and after cyclosporin A + capsaicin treatment ( $P > 0.05$ ; Fig. 6). Since calcineurin acts in a Ca<sup>2+</sup>- and calmodulin-dependent manner,<sup>33</sup> we test the effect of W7, a specific calmodulin antagonist, on the action of capsaicin. In the presence of W7 (25 μM), capsaicin (30 μM) still produced a large inhibition on 4-aminopyridine-evoked glutamate release, which was not significantly different from the effect of capsaicin alone [ $F(2,15) = 78.69$ ;  $P < 0.05$ ; Fig. 6]. W7 (25 μM) alone reduced 4-aminopyridine-evoked glutamate release ( $P < 0.001$ ; Fig. 6).

#### Effect of capsaicin on the miniature excitatory postsynaptic currents (mEPSCs) in the CA3 pyramidal neurons

Fig. 7 shows the effects of capsaicin on mEPSC frequency and amplitude in the CA3 pyramidal neurons; mEPSCs were recorded at a holding potential of −70 mV and in the presence of the Na<sup>+</sup> channel blocker tetrodotoxin (1 μM) and GABA<sub>A</sub> receptor antagonist bicuculline (20 μM). Fig. 7A shows a typical example of traces recorded from a single cell, and capsaicin (30 μM) reduced the occurrence of mEPSCs. In the five tested neurons, capsaicin reduced the frequency of mEPSCs by  $54.3\% \pm 4.8\%$  [ $t(8) = 3.3$ ;  $P < 0.01$ ; Fig. 7B], but the amplitude was unaffected [ $t(8) = 0.03$ ;  $P > 0.05$ ; Fig. 7C].



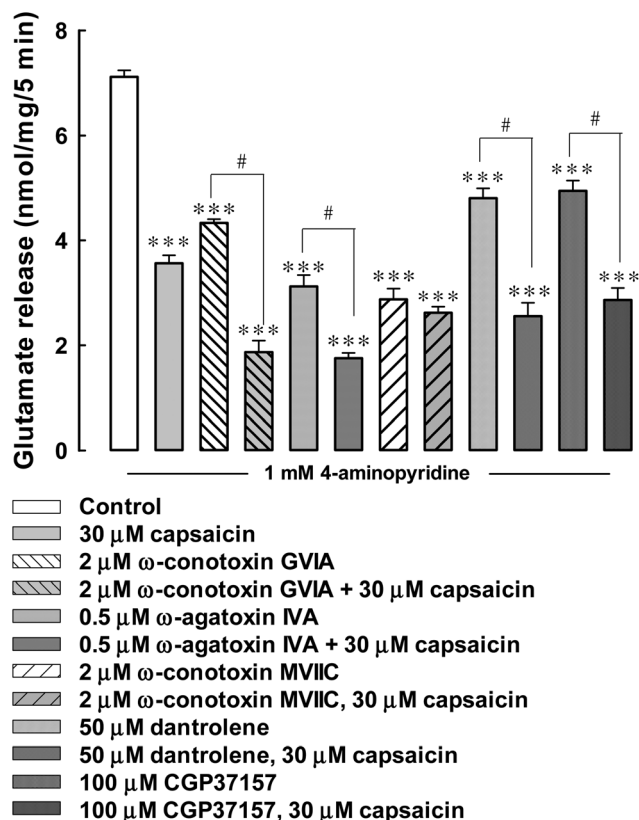


**Fig. 5** Effect of  $\text{Ca}^{2+}$  channel blockers and intracellular  $\text{Ca}^{2+}$  release inhibitors on the capsaicin-mediated inhibition of 4-aminopyridine-evoked glutamate release. Glutamate release was evoked by 4-aminopyridine (1 mM) in the absence (control) or presence of 30  $\mu$ M capsaicin, 2  $\mu$ M  $\omega$ -conotoxin GVIA, 2  $\mu$ M  $\omega$ -conotoxin GVIA and 30  $\mu$ M capsaicin, 0.5  $\mu$ M  $\omega$ -agatoxin IVA, 0.5  $\mu$ M  $\omega$ -agatoxin IVA and 30  $\mu$ M capsaicin, 2  $\mu$ M  $\omega$ -conotoxin MVIIC, 2  $\mu$ M  $\omega$ -conotoxin MVIIC and 30  $\mu$ M capsaicin, 50  $\mu$ M dantrolene, 50  $\mu$ M dantrolene and 30  $\mu$ M capsaicin, 100  $\mu$ M CGP37157, or 100  $\mu$ M CGP37157 and 30  $\mu$ M capsaicin. Capsaicin was added 10 min before depolarization, whereas the other drugs were added 30 min before depolarization. Each column is mean  $\pm$  SEM values of independent experiments, using synaptosomal preparations from 5 to 6 animals. \*\*\*,  $P < 0.001$  versus the control group; #,  $P < 0.05$  versus the  $\omega$ -conotoxin GVIA-,  $\omega$ -agatoxin IVA-, dantrolene- or CGP37157-treated group.

## Discussion

Capsaicin is a compound found in chili peppers and utilized as a traditional medicine for the treatment of various disorders.<sup>34</sup> The depression of capsaicin on excitatory synaptic transmission has been demonstrated in different experimental preparations,<sup>22,23,35</sup> however, no study has investigated whether capsaicin directly influences glutamate release at the presynaptic level. The present study focused on the effect of capsaicin on glutamate release from isolated hippocampal nerve terminals (synaptosomes), a preparation retaining the morphological and functional characteristics of nerve endings *in vivo*,<sup>36</sup> and found that capsaicin inhibited the  $\text{Ca}^{2+}$ -dependent, exocytosis-like release of glutamate evoked by depolarizing stimuli. In addition, using intact neurons in hippocam-

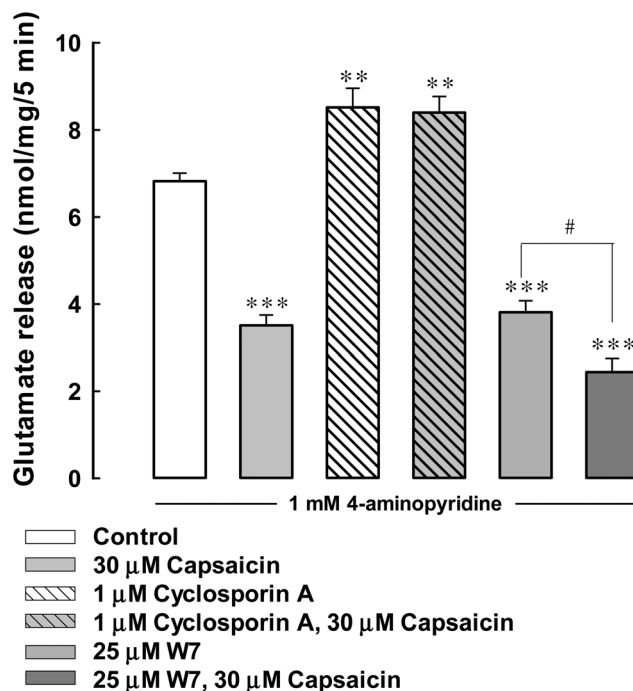


**Fig. 6** Effect of cyclosporin A, an inhibitor of protein phosphatase calcineurin, and W7, a calmodulin antagonist, on capsaicin-mediated inhibition of 4-aminopyridine-evoked glutamate release. Glutamate release was evoked by 4-aminopyridine (1 mM) in the absence (control) or presence of 30  $\mu$ M capsaicin, 1  $\mu$ M cyclosporin A, 1  $\mu$ M cyclosporin A and 30  $\mu$ M capsaicin, 25  $\mu$ M W7, or 25  $\mu$ M W7 and 30  $\mu$ M capsaicin. Capsaicin was added 10 min before depolarization, whereas the other drugs were added 30 min before depolarization. Each column is mean  $\pm$  SEM values of independent experiments, using synaptosomal preparations from 6 animals. \*\*,  $P < 0.01$ , \*\*\*,  $P < 0.001$  versus the control group; #,  $P < 0.05$  versus the W7-treated group.

pal slices, capsaicin reduced the frequency but not the amplitude of mEPSCs, suggesting a reduction in the release probability and definitively evidencing a presynaptic component in synaptic transmission and regulation.

Previous studies have reported that capsaicin exerts its biological effects through activating TRPV1 receptors; however, a TRPV1-independent action of capsaicin was also proposed.<sup>37</sup> TRPV1 receptor is a nonselective cation channel with high  $\text{Ca}^{2+}$  permeability and is present in numerous regions of the brain, including the hippocampus.<sup>18,19</sup> In the present study, through western blotting and immunocytochemistry we confirm the existence of TRPV1 receptors in hippocampal nerve terminals. Furthermore, the decrease in glutamate release produced by capsaicin was eliminated when synaptosomes were incubated with the TRPV1 antagonist capsazepine. On the basis of these results, we propose that capsaicin acts at TRPV1 receptors present on hippocampal nerve terminals, decreasing the evoked glutamate release. This suggestion is consistent with a previous study demonstrating that activation of TRPV1 by capsaicin inhibits acetylcholine release in mouse motor nerve terminals.<sup>38</sup>



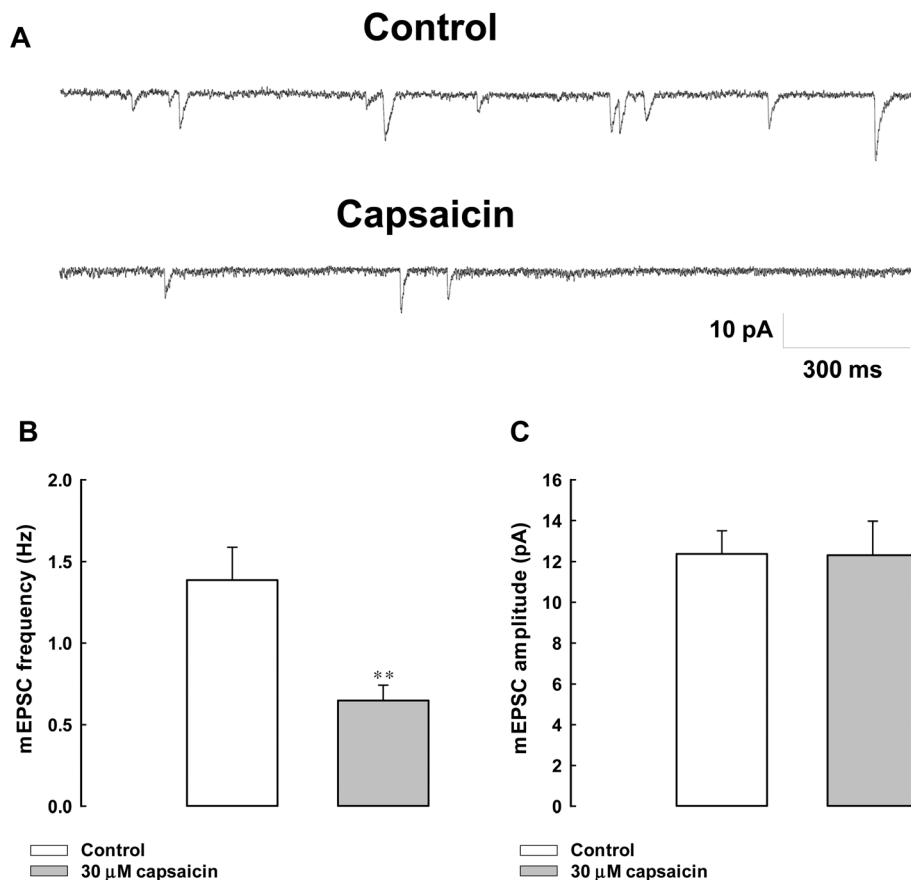


**Fig. 7** Capsaicin decreases the frequency but not the amplitude of mEPSCs in the hippocampal brain slices. (A) Sample trace of mEPSCs in the absence (control) or presence of 30 μM capsaicin. (B) The average amplitude and frequency of mEPSCs in the control and capsaicin treated groups. Each column is mean ± SEM values of independent experiments, using synaptosomal preparations from 5 animals. \*\*,  $P < 0.01$  versus the control group.

Capsaicin has been shown previously to activate TRPV1 and increase  $\text{Ca}^{2+}$  influx, which would induce protein phosphatase 2B calcineurin activation and subsequently down-regulate TRPV1 or voltage-dependent  $\text{Ca}^{2+}$  channels, and that may, in turn, depress excitatory synaptic transmission in hippocampal and dorsal root ganglion neurons.<sup>22–24</sup> We used fura-2 and demonstrated that capsaicin significantly reduced the evoked increase in intrasynaptosomal  $\text{Ca}^{2+}$  levels. Furthermore, the inhibitory effect of capsaicin on the 4-aminopyridine-evoked glutamate release from synaptosomes was prevented by blocking the  $\text{Ca}_v2.2$  (N-type) and  $\text{Ca}_v2.1$  (P/Q-type) channels but was not altered by blocking intracellular  $\text{Ca}^{2+}$  release. These results suggest that a reduction in synaptosomal  $\text{Ca}^{2+}$  mediated by  $\text{Ca}_v2.2$  (N-type) and  $\text{Ca}_v2.1$  (P/Q-type) channels is associated with the capsaicin-mediated inhibition of glutamate release. Our finding is supported by previous electrophysiological studies, which have shown that capsaicin inhibits high voltage-activated  $\text{Ca}^{2+}$  channels in several experimental preparations.<sup>23,39,40</sup>

Another intriguing finding of our study was that calcineurin plays a pivotal role in the inhibitory effect of glutamate release by capsaicin in hippocampal nerve terminals. Calcineurin is a

$\text{Ca}^{2+}$ /calmodulin-dependent protein phosphatase that is found in high concentrations in the presynaptic terminals, where it down-regulates voltage-dependent  $\text{Ca}^{2+}$  channels and limits glutamate release.<sup>41,42</sup> We found that inhibition of calcineurin with cyclosporine A abolished the inhibitory effect of capsaicin on evoked glutamate release. However, the calmodulin antagonist W7 failed to affect the inhibitory effect of capsaicin on glutamate release, which is consistent with previous studies<sup>22,23</sup> and suggests that calmodulin is not involved. Collectively, capsaicin, acting through the activation of TRPV1 present on hippocampal nerve terminals, causes the activation of calcineurin, which subsequently suppresses voltage-dependent  $\text{Ca}^{2+}$  channels to decrease the evoked glutamate release. A similar mechanism has also been reported in neurons from several regions of the central nervous system by using different experimental approaches involving cultured dorsal root ganglion neurons and hippocampal slices.<sup>23,24,43</sup> In addition to calcineurin, the protein kinase A (PKA) pathway has been shown to be involved in the action of capsaicin.<sup>44,45</sup> However, we observed that the capsaicin-mediated inhibition of 4-aminopyridine-evoked glutamate release persisted after treatment with the PKA inhibitor H89 (100 μM) [(nmol mg<sup>-1</sup> per

5 min) control 4-aminopyridine,  $6.7 \pm 0.1$ ; 4-aminopyridine + capsaicin,  $3.3 \pm 0.1$ ; 4-aminopyridine + H89,  $4.1 \pm 0.3$ ; 4-aminopyridine + H89 + capsaicin,  $2.5 \pm 0.2$ ], which excludes the involvement of PKA in inhibiting hippocampal glutamate release. The reason for the difference between the current and previous studies is unclear, but it might be attributable to the distinct experimental models used; previous studies have employed a cell culture model, whereas we used a nerve terminal (synaptosomal) model. In addition, several actions of capsaicin such as pain and hyperalgesia are reported to be associated with the activation of kainate receptors and Group II metabotropic glutamate receptors.<sup>46,47</sup> These receptors are present at the presynaptic level and play a crucial role in glutamate exocytosis.<sup>48,49</sup> Thus, the relationship between the capsaicin-mediated inhibition of glutamate release and these presynaptic receptors should be considered.

Capsaicin has been shown to possess neuroprotective activity both in animal and cell culture models of neurotoxicity such as ischemia and epilepsy.<sup>12,14–16</sup> Although the mechanism by which capsaicin exhibits its protective effect remains to be fully elucidated, decreased reactive oxygen species generation, antioxidant activity, inhibited inflammatory processes, TRPV1 desensitization, and endocannabinoid biosynthesis stimulation have been reported.<sup>13,15,16,50</sup> The present study demonstrates that capsaicin inhibits evoked  $\text{Ca}^{2+}$  influx and glutamate release. However, capsaicin did not affect the basal calcium levels and glutamate release from the nerve terminals, suggesting that capsaicin might reduce the release of glutamate when it is triggered by neuronal activation. Because the excitotoxicity caused by excessive glutamate has been proposed as an important contributing factor in many brain diseases, and decreased glutamate release is considered to be a therapeutic strategy,<sup>2,3</sup> we suggested that reduced glutamate release from nerve terminals is at least partially involved in the neuroprotective activity of capsaicin. In fact, several neuroprotectants (e.g. acacetin, luteolin, hesperidin) have been shown to dampen endogenous glutamate release from rat hippocampal synaptic terminals and to prevent the marked increase of glutamate overflow induced by glutamate analogs in the hippocampus.<sup>29,51,52</sup>

In conclusion, our data have shown that the activation of presynaptic TRPV1 by capsaicin in hippocampal nerve terminals results in the inhibition of glutamate release by a mechanism that involves the calcineurin activation and down-regulation of voltage-dependent  $\text{Ca}^{2+}$  channels. This investigation may be helpful in understanding the action of capsaicin in the brain and provides the rationale for using this compound to treat brain disorders such as ischemia, epilepsy, and neurodegenerative disorders, all characterized by excessive glutamate release.

## Conflict of interest

The authors declare no competing financial interest.

## Abbreviations

$[\text{Ca}^{2+}]_c$	Cytosolic free $\text{Ca}^{2+}$ concentration
Fura-2-AM	Fura-2-acetoxymethyl ester
CGP37157	7-Chloro-5-(2-chlorophenyl)-1,5-dihydro-4,1-benzothiazepin-2(3H)-one
H89	N-[2-(p-Bromocinnamylamino)-ethyl]-5-isoquinolinesulfonamide dihydrochloride
$\text{Ca}_v2.2$ and $\text{Ca}_v2.1$ channels	$\text{Ca}_v2.2$ (N-type) and $\text{Ca}_v2.1$ (P/Q-type) channels
VDCC	Voltage-dependent $\text{Ca}^{2+}$ channel
W7	N-(6-Aminoethyl)-5-chloro-1-naphthalene-sulphonamide
TRPV1	Transient receptor potential vanilloid 1
CNQX	6-Cyano-7-nitroquinoxaline-2,3-dione
D-AP5	D(-)-2-Amino-5-phosphonopentanoic acid
EGTA	Ethylene glycol bis ( $\beta$ -aminoethyl ether)-N,N,N',N'-tetraacetic acid
mEPSCs	Miniature excitatory postsynaptic currents.

## Acknowledgements

This work was supported by the research grants from the Far-Eastern Memorial Hospital (FEMH-2015-D-026; FEMH – 2016 – C – 022).

## References

- 1 P. M. Headley and S. Grillner, *Trends Pharmacol. Sci.*, 1990, **11**, 205–211.
- 2 D. W. Choi and S. M. Rothman, *Annu. Rev. Neurosci.*, 1990, **13**, 171–182.
- 3 B. Meldrum and J. Garthwaite, *Trends Pharmacol. Sci.*, 1990, **11**, 379–387.
- 4 S. J. Wang, C. F. Su and Y. H. Kuo, *Synapses*, 2003, **48**, 170–177.
- 5 S. J. Wang, K. Y. Wang and W. C. Wang, *Neuroscience*, 2004, **125**, 191–201.
- 6 G. Bonanno, R. Giambelli, L. Raiteri, E. Tiraboschi, S. Zappettini, L. Musazzi, M. Raiteri, G. Racagni and M. Popoli, *J. Neurosci.*, 2005, **25**, 3270–3279.
- 7 M. Kammerer, B. Brawek, T. M. Freiman, R. Jackisch and T. J. Feuerstein, *Naunyn-Schmiedeberg's Arch. Pharmacol.*, 2011, **383**, 531–542.
- 8 V. Fattori, M. S. Hohmann, A. C. Rossaneis, F. A. Pinho-Ribeiro and W. A. Verri, *Molecules*, 2016, **21**(pii), E844.
- 9 B. Joe and B. R. Lokesh, *Biochim. Biophys. Acta*, 1994, **1224**, 255–263.
- 10 C. S. Kim, T. Kawada, B. S. Kim, I. S. Han, S. Y. Choe, T. Kurata and R. Yu, *Cell. Signalling*, 2003, **15**, 299–306.
- 11 X. L. Ma, F. X. Zhang, F. Dong, L. Bao and X. Zhang, *Mol. Pain*, 2015, **11**, 22.
- 12 J. G. Lee, J. M. Yon, C. Lin, A. Y. Jung, K. Y. Jung and S. Y. Nam, *Food Chem. Toxicol.*, 2012, **50**, 3877–3885.

- 13 S. Y. Guo, G. P. Yang, D. J. Jiang, F. Wang, T. Song, X. H. Tan and Z. Q. Sun, *Can. J. Physiol. Pharmacol.*, 2008, **86**, 785–792.
- 14 N. H. Khatibi, V. Jadhav, S. Charles, J. Chiu, J. Buchholz, J. Tang and J. H. Zhang, *Acta Neurochir.*, 2011, **111**, 225–230.
- 15 S. Pegorini, D. Braidà, C. Verzoni, C. Guerini-Rocco, G. G. Consalez, L. Croci and M. Sala, *Br. J. Pharmacol.*, 2005, **144**, 727–735.
- 16 T. H. Lee, J. G. Lee, J. M. Yon, K. W. Oh, I. J. Baek, S. S. Nahm, B. J. Lee, Y. W. Yun and S. Y. Nam, *Neurochem. Int.*, 2011, **58**, 634–640.
- 17 W. B. Veldhuis, M. van der Stelt, M. W. Wadman, G. van Zadelhoff, M. Maccarrone, F. Fezza, G. A. Veldink, J. F. Vliegthart, P. R. Bär, K. Nicolay and V. Di Marzo, *J. Neurosci.*, 2003, **23**, 4127–4133.
- 18 E. Mezey, Z. E. Tóth, D. N. Cortright, M. K. Arzubi, J. E. Krause, R. Elde, A. Guo, P. M. Blumberg and A. Szallasi, *Proc. Natl. Acad. Sci. U. S. A.*, 2000, **97**, 3655–3660.
- 19 A. Tóth, J. Boczán, N. Kedei, E. Lizanecz, Z. Bagi, Z. Papp, I. Edes, L. Csiba and P. M. Blumberg, *Brain Res. Mol. Brain Res.*, 2005, **135**, 162–168.
- 20 H. E. Gibson, J. G. Edwards, R. S. Page, M. J. Van Hook and J. A. Kauer, *Neuron*, 2008, **57**, 746–759.
- 21 A. E. Chávez, C. Q. Chiu and P. E. Castillo, *Nat. Neurosci.*, 2010, **13**, 1511–1518.
- 22 D. P. Mohapatra and C. Nau, *J. Biol. Chem.*, 2005, **280**, 13424–13432.
- 23 Z. Z. Wu, S. R. Chen and H. L. Pan, *J. Biol. Chem.*, 2005, **280**, 18142–18151.
- 24 T. Jensen and J. G. Edwards, *Neurosci. Lett.*, 2012, **510**, 82–87.
- 25 P. R. Dunkley, P. E. Jarvie, J. W. Heath, G. J. Kidd and J. A. Rostas, *Brain Res.*, 1986, **372**, 115–129.
- 26 D. G. Nicholls and T. S. Sihra, *Nature*, 1986, **321**, 772–773.
- 27 G. Gryniewicz, M. Poenie and R. Y. Tsien, *J. Biol. Chem.*, 1985, **260**, 3440–3450.
- 28 Y. Chang, C. W. Lu, T. Y. Lin, S. K. Huang and S. J. Wang, *Am. J. Chin. Med.*, 2016, **44**, 943–962.
- 29 C. Y. Chang, T. Y. Lin, C. W. Lu, S. K. Huang, Y. C. Wang, S. S. Chou and S. J. Wang, *Neurotoxicology*, 2015, **50**, 157–169.
- 30 D. G. Nicholls, *Prog. Brain Res.*, 1998, **116**, 15–22.
- 31 E. Vazquez and J. Sanchez-Prieto, *Eur. J. Neurosci.*, 1997, **9**, 2009–2018.
- 32 C. Millan and J. Sanchez-Prieto, *Neurosci. Lett.*, 2002, **330**, 29–32.
- 33 M. Høy, K. Bokvist, W. Xiao-Gang, J. Hansen, K. Juhl, P. O. Berggren, K. Buschard and J. Gromada, *J. Biol. Chem.*, 2001, **276**, 924–930.
- 34 T. W. Corson and C. M. Crews, *Cell*, 2007, **130**, 769–774.
- 35 K. Yang, E. Kumamoto, H. Furue, Y. Q. Li and M. Yoshimura, *Brain Res.*, 1999, **830**, 268–273.
- 36 M. Martire, V. Barrese, M. D'Amico, F. A. Iannotti, R. Pizzarelli, I. Samengo, D. Viggiano, P. Ruth, E. Cherubini and M. Tagliatela, *J. Neurochem.*, 2010, **115**, 411–422.
- 37 Y. S. Lee, J. A. Lee, J. Jung, U. Oh and B. K. Kaang, *Neurosci. Lett.*, 2000, **288**, 57–60.
- 38 B. Thyagarajan, J. G. Potian, P. Baskaran and J. J. McArdle, *Eur. J. Pharmacol.*, 2014, **744**, 211–219.
- 39 Z. Z. Wu, S. R. Chen and H. L. Pan, *Neuroscience*, 2006, **141**, 407–419.
- 40 V. Comunanza, E. Carbone, A. Marcantoni, E. Sher and D. Ursu, *Pflugers Arch.*, 2011, **462**, 709–722.
- 41 T. L. Anthony and D. L. Kreulen, *Proc. West. Pharmacol. Soc.*, 1988, **31**, 5–8.
- 42 R. A. Nichols, G. R. Suplick and J. M. Brown, *J. Biol. Chem.*, 1994, **269**, 23817–23823.
- 43 J. G. Edwards, H. E. Gibson, T. Jensen, F. Nugent, C. Walther, J. Blickenstaff and J. A. Kauer, *Hippocampus*, 2012, **22**, 209–221.
- 44 R. Yang, Z. Xiong, C. Liu and L. Liu, *Cell Mol. Neurobiol.*, 2014, **34**, 56576.
- 45 I. Vetter, B. D. Wyse, G. R. Monteith, S. J. Roberts-Thomson and P. J. Cabot, *Mol. Pain*, 2006, **2**, 22.
- 46 M. S. Wallace, V. Lam and J. Schettler, *Pain Med.*, 2012, **13**, 1601–1610.
- 47 S. M. Carlton, J. Du and S. Zhou, *Brain Res.*, 2009, **1248**, 86–95.
- 48 J. V. Negrete-Díaz, T. S. Sihra, J. M. Delgado-García and A. Rodríguez-Moreno, *J. Neurophysiol.*, 2006, **96**, 1829–1837.
- 49 J. V. Negrete-Díaz, T. S. Sihra, J. M. Delgado-García and A. Rodríguez-Moreno, *J. Neural. Transm.*, 2007, **114**, 1425–1431.
- 50 V. Di Marzo, T. Bisogno, L. De Petrocellis, I. Brandi, R. G. Jefferson, R. L. Winckler, J. B. Davis, O. Dasse, A. Mahadevan, R. K. Razdan and B. R. Martin, *Biochem. Biophys. Res. Commun.*, 2001, **281**, 444–451.
- 51 T. Y. Lin, W. J. Huang, C. C. Wu, C. W. Lu and S. J. Wang, *PLoS One*, 2014, **9**, e88644.
- 52 T. Y. Lin, C. W. Lu, C. C. Chang, S. K. Huang and S. J. Wang, *J. Agric. Food Chem.*, 2011, **59**, 8458–8466.



## 6-Hydroxy-5,7-dimethoxy-flavone suppresses the neutrophil respiratory burst via selective PDE4 inhibition to ameliorate acute lung injury

Yung-Fong Tsai<sup>a,b,c</sup>, Tzu-Chi Chu<sup>a</sup>, Wen-Yi Chang<sup>a,d</sup>, Yang-Chang Wu<sup>e,f</sup>, Fang-Rong Chang<sup>g,h</sup>, Shun-Chin Yang<sup>a,i,j</sup>, Tung-Ying Wu<sup>f</sup>, Yu-Ming Hsu<sup>g</sup>, Chun-Yu Chen<sup>a,b,c</sup>, Shih-Hsin Chang<sup>a,k</sup>, Tsong-Long Hwang<sup>a,c,d,k,\*</sup>

<sup>a</sup> Graduate Institute of Natural Products, College of Medicine, Chang Gung University, Taoyuan 333, Taiwan

<sup>b</sup> Graduate Institute of Clinical Medical Sciences, College of Medicine, Chang Gung University, Taoyuan 333, Taiwan

<sup>c</sup> Department of Anesthesiology, Chang Gung Memorial Hospital, Taoyuan 333, Taiwan

<sup>d</sup> Chinese Herbal Medicine Research Team, Healthy Aging Research Center, Chang Gung University, Taoyuan 333, Taiwan

<sup>e</sup> School of Pharmacy, College of Pharmacy, China Medical University, Taichung 404, Taiwan

<sup>f</sup> Chinese Medicine Research and Development Center and Center for Molecular Medicine, China Medical University Hospital, Taichung 404, Taiwan

<sup>g</sup> Graduate Institute of Natural Products, College of Pharmacy, Kaohsiung Medical University, Kaohsiung 807, Taiwan

<sup>h</sup> Cancer Center, Kaohsiung Medical University Hospital, Kaohsiung, 807 Taiwan

<sup>i</sup> Graduate Institute of Biomedical Sciences, College of Medicine, Chang Gung University, Taoyuan 333, Taiwan

<sup>j</sup> Department of Anesthesiology, Taipei Veterans General Hospital and National Yang-Ming University, Taipei 112, Taiwan

<sup>k</sup> Research Center for Food and Cosmetic Safety, Research Center for Chinese Herbal Medicine, and Graduate Institute of Health Industry Technology, College of Human Ecology, Chang Gung University of Science and Technology, Taoyuan 333, Taiwan

### ARTICLE INFO

#### Keywords:

Acute lung injury

6-Hydroxy-5,7-dimethoxy-flavone

Neutrophil

Oxidative stress

Phosphodiesterases 4

### ABSTRACT

Over-activated neutrophils produce enormous oxidative stress and play a key role in the development of acute and chronic inflammatory diseases. 6-Hydroxy-5,7-dimethoxy-flavone (UFM24), a flavone isolated from the Annonaceae *Uvaria flexuosa*, showed inhibitory effects on human neutrophil activation and salutary effects on lipopolysaccharide (LPS)-induced acute lung injury (ALI) in mice. UFM24 potentially inhibited superoxide anion ( $O_2^{\cdot-}$ ) generation, reactive oxidants, and CD11b expression, but not elastase release, in *N*-formyl-L-methionyl-L-leucyl-L-phenylalanine (fMLF)-activated human neutrophils. However, UFM24 failed to scavenge  $O_2^{\cdot-}$  and inhibit the activity of subcellular NADPH oxidase. fMLF-induced phosphorylation of protein kinase B (Akt) was inhibited by UFM24. Noticeably, UFM24 increased cyclic adenosine monophosphate (cAMP) concentration and protein kinase (PK) A activity in activated human neutrophils. PKA inhibitors significantly reversed the inhibitory effects of UFM24, suggesting that the effects of UFM24 were through cAMP/PKA-dependent inhibition of Akt activation. Additionally, activity of cAMP-related phosphodiesterase (PDE)4, but not PDE3 or PDE7, was significantly reduced by UFM24. Furthermore, UFM24 attenuated neutrophil infiltration, myeloperoxidase activity, and pulmonary edema in LPS-induced ALI in mice. In conclusion, our data demonstrated that UFM24 inhibits oxidative burst in human neutrophils through inhibition of PDE4 activity. UFM24 also exhibited significant protection against endotoxin-induced ALI in mice. UFM24 has potential as an anti-inflammatory agent for treating neutrophilic lung damage.

### 1. Introduction

Bacterial endotoxemia in patients with sepsis may contribute to the development of acute lung injury (ALI) and acute respiratory distress syndrome (ARDS). ARDS features high morbidity and mortality [1,2].

ALI and ARDS are manifested by massive neutrophil activation and infiltration into lungs to disrupt the alveolar capillary barrier and to impair gas exchange in the respiratory tract [3]. Superoxide anion ( $O_2^{\cdot-}$ ) and reactive oxidants generated from activated neutrophils have been proposed to cause acute and chronic lung injury [4].

**Abbreviations:** AC, adenylate cyclase; ALI, acute lung injury; Akt, protein kinase B; ARDS, acute respiratory distress syndrome; cAMP, cyclic adenosine monophosphate; CB, cytochalasin B; COPD, chronic obstructive pulmonary disease; fMLF, *N*-formyl-L-methionyl-L-leucyl-L-phenylalanine; FPR, formyl peptide receptor; GPCR, G protein-coupled receptor; MPO, myeloperoxidase; NADPH, nicotinamide adenosine dinucleotide phosphate;  $O_2^{\cdot-}$ , superoxide anion; PDE, phosphodiesterase; PGE, prostaglandin E; PKA, protein kinase A; LDH, lactate dehydrogenase; PMA, phorbol myristate acetate; UFM24, 6-Hydroxy-5,7-dimethoxy-flavone

\* Corresponding author at: Graduate Institute of Natural Products, Chang Gung University, 259 Wen-Hwa 1st Road, Kweishan, Taoyuan 333, Taiwan.

E-mail address: [htl@mail.cgu.edu.tw](mailto:htl@mail.cgu.edu.tw) (T.-L. Hwang).

<http://dx.doi.org/10.1016/j.freeradbiomed.2017.03.002>

Received 23 September 2016; Received in revised form 26 January 2017; Accepted 1 March 2017

Available online 03 March 2017

0891-5849/© 2017 Elsevier Inc. All rights reserved.



Cyclic adenosine monophosphate (cAMP) is the essential secondary messenger of neutrophils and other inflammatory cells, and it down-regulates several biological functions of immune or inflammatory cells [5]. An increase in intracellular cAMP concentration reduced the lung damage caused by over-activated neutrophils in animal studies [6,7]. Cyclic nucleotide phosphodiesterase (PDE) is responsible for catalyzing the hydrolysis of cAMP to regulate its intracellular level. In the immune or inflammatory cells, cAMP-specific PDE4 is a major subtype of PDEs. Theophylline, a nonselective PDE inhibitor, has been used to treat pulmonary diseases for more than 70 years. However, its application is usually limited because of concerns about its safety, narrow therapeutic margin, and complex interactions with other drugs [8]. Selective PDE4 inhibitors have drawn a great deal of attention to their anti-inflammatory effects in neutrophils and airway smooth muscle cells as promising therapeutic target for treating lung diseases [9]. Gamble et al. [10] proposed that cilomilast, an oral PDE4 selective inhibitor, reduced cell counts of neutrophils by 37% in subepithelial tissues of the bronchus in patients with chronic obstructive pulmonary disease (COPD). The salutary effects of PDE4 inhibitors have been validated in various models of acute and chronic disease, such as asthma, COPD [11], septic shock [12], rheumatoid arthritis [13], type II diabetes [14], autoimmune diseases [15], psoriasis, and atopic dermatitis [16]. The clinical use of PDE4 inhibitor in patients is restricted because of safety concerns, the discovery of new PDE4 inhibitors has been in the spotlight of pharmaceutical research.

6-Hydroxy-5,7-dimethoxy-flavone ( $C_{17}H_{14}O_5$ , UFM24) was extracted and purified (Fig. 1A) from the leaves of an endemic traditional medicine, *Uvaria flexuosa* [17]. *U. flexuosa* is found in Vietnam and Cambodia. Available literature regarding *U. flexuosa* has primarily centered on the description of its phylogeny and morphological features. UFM24 was found in many plants and had anti-inflammatory, anti-oxidant, anti-cancer activities *in vitro* [18,19]. However, the effects of UFM24 in neutrophilic inflammation and its molecular mechanism of action remain elusive. Our study sought to investigate the salutary effects of UFM24 on human neutrophil activation *in vitro* and on lipopolysaccharide (LPS)-induced ALI in male C57BL/6 mice, as well as to determine the anti-inflammatory mechanism of UFM24. Together, the present results suggest that UFM24 inhibits  $O_2^{\cdot-}$  generation, reactive oxidant production, and CD11b expression in activated human neutrophils by selectively inhibiting PDE4 activity. Inhibition of PDE4 by UFM24 led to significant increases in cAMP accumulation and PKA activation in activated human neutrophils. To our knowledge, this is the first time that UFM24 has been proven as a PDE4 inhibitor. Notably, administration of UFM24 protected against endotoxin-induced ALI in a mouse model, and has emerging potential for clinical application in therapies for pulmonary inflammation.

## 2. Materials and methods

### 2.1. Reagents

UFM24 (6-hydroxy-5,7-dimethoxy-flavone,  $C_{17}H_{14}O_5$ , molecular weight 298) was purified from *U. flexuosa*. The purity of UFM24 exceeded 98%, and it was dissolved in dimethylsulfoxide (DMSO). 2-(4-Iodophenyl)-3-(4-nitrophenyl)-5-(2,4-disulfophenyl)-2H-tetrazolium monosodium salt (WST-1) was purchased from Dojindo (Kurnamoto, Japan). Methoxysuccinyl-Ala-Ala-Pro-Val-p-nitroanilide, rolipram, and Ro 318220 (3-(1-(3-(amidinothio)propyl-1H-indol-3-yl))-3-(1-methyl-1H-indol-3-yl) maleimide) were purchased from Calbiochem (La Jolla, CA, USA). CytoTox 96 Non-Radioactive Cytotoxicity Assay was purchased from Promega (Maddison, WI, USA). cAMP enzyme immunoassay kits, glycerol and Ficoll-Paque were from GE Healthcare (Little Chalfont, Buckinghamshire, UK). Dihydrorhodamine 123 (DHR123), Fluo-3 acetoxymethylester (Fluo-3/AM), and N-formyl-Nle-Leu-Phe-Nle-Tyr-Lys (FNLFNLYK) were purchased from Molecular Probes (Eugene, OR, USA). FITC-labeled anti-CD11b was purchased from

eBioscience (San Diego, CA, USA). PKA activity kits were purchased from Arbor Assays (Ann Arbor, MI, USA). PDE enzyme subtypes including 3B, 4A1A, 4B2, 4C1, 4D2, and 7A, were purchased from BPS Bioscience (Cornerstone Court West, CA, USA). PDE cAMP enzyme assays were purchased from Cisbio (Bedford, MA, USA). Antibodies to phospho-protein kinase B (Akt) (pan) and phospho-Akt (Ser 473) were purchased from Cell Signaling (Beverly, MA, USA). The other agents were all purchased from Sigma-Aldrich (St. Louis, MO, USA). In cell studies, the final concentration of DMSO was not allowed to exceed 0.4% to prevent bias of results.

### 2.2. Extraction and isolation

UFM24 was extracted from the fresh leaves of *U. flexuosa*. The structure of UFM24 was elucidated and confirmed by comparing the obtained spectroscopic data to those reported in the literature (Fig. 1A) [20]. UFM24 was a yellow powder and its molecular formula,  $C_{17}H_{14}O_5$ , was determined by the ESI-MS peak at  $m/z$  299  $[M+H]^+$ .  $^1H$  NMR (200 MHz,  $CDCl_3$ ):  $\delta$  3.96 (3H, s, 7-OCH<sub>3</sub>), 4.18 (3H, s, 5-OCH<sub>3</sub>), 6.99 (1H, s, 8-H), 7.12 (1H, s, 3-H), 7.45–7.48 (3H, m, H-3', 4', 5'), 7.91–7.96 (2H, dd,  $J=8.0$ , 2.0 Hz, H-2', 6');  $^{13}C$  NMR (50 MHz,  $CDCl_3$ ):  $\delta$  56.3 (q, 7-OCH<sub>3</sub>), 61.7 (q, 5-OCH<sub>3</sub>), 96.9 (d, C-8), 108.4 (d, C-3), 113.4 (s, C-10), 126.2 (2 $\times$ d, C-2', 6'), 129.2 (2 $\times$ d, C-3', 5'), 132.2 (d, C-4'), 131.2 (s, C-1'), 139.5 (s, C-6), 145.5 (s, C-9), 151.7 (s, C-5), 154.3 (s, C-7), 160.7 (s, C-2), 176.8 (s, C-4). The purity of UFM24 at 99% was assessed using a three-point peak purity method and determined by Shimadzu "Class VP" software.

### 2.3. Protocol of human neutrophil isolation

The study was designed following the principles of the contemporary revision of the Declaration of Helsinki 1975 and approved by the ethics committee of our hospital (Registration number: IRB 99-3848B). Blood samples were donated by healthy volunteers aged from 20 to 30 years after their written informed consent. Human neutrophils were isolated following standardized procedures as sedimentation in dextran solution, gradient centrifugation in Ficoll-Paque, and hypotonic lysis of erythrocytes [7,21]. The separated neutrophils contained more than 98% viable cells, and then were resuspended in no  $Ca^{2+}$  HBSS buffer at 4 °C before experiments.

### 2.4. Analysis of $O_2^{\cdot-}$ generation

The analysis of  $O_2^{\cdot-}$  generation from stimulated neutrophils was measured indirectly by the reduction of ferricytochrome c. After  $6 \times 10^5$  cells/ml neutrophils were added with ferricytochrome c (0.5 mg/ml), they were incubated for 2 min at 37 °C. Cells were then treated with DMSO or UFM24 for another 5 min, and were activated with fMLF (0.1  $\mu$ M) for 10 min or stimulated with phorbol myristate acetate (PMA, 5 nM) for 15 min. Cytochalasin B (CB, 1  $\mu$ g/ml) was added 3 min before fMLF induction. The change in absorbance was monitored continuously at 550 nm with a spectrophotometer (U-3010; Hitachi, Tokyo, Japan) [22].

### 2.5. Evaluation of intracellular reactive oxidant production

Human neutrophils ( $2.5 \times 10^6$  cells/ml) were incubated at 37 °C for 10 min with DHR123 (2  $\mu$ M). These cells were treated with UFM24 for 5 min, and then stimulated with 0.1  $\mu$ M fMLF for another 15 min. HBSS (at 4 °C) was poured into the sample solution to stop the reaction. Then, a flow cytometry was used to detect the intracellular reactive oxidant contents represented by the conversion of nonfluorescent DHR123 to fluorescent rhodamine 123.



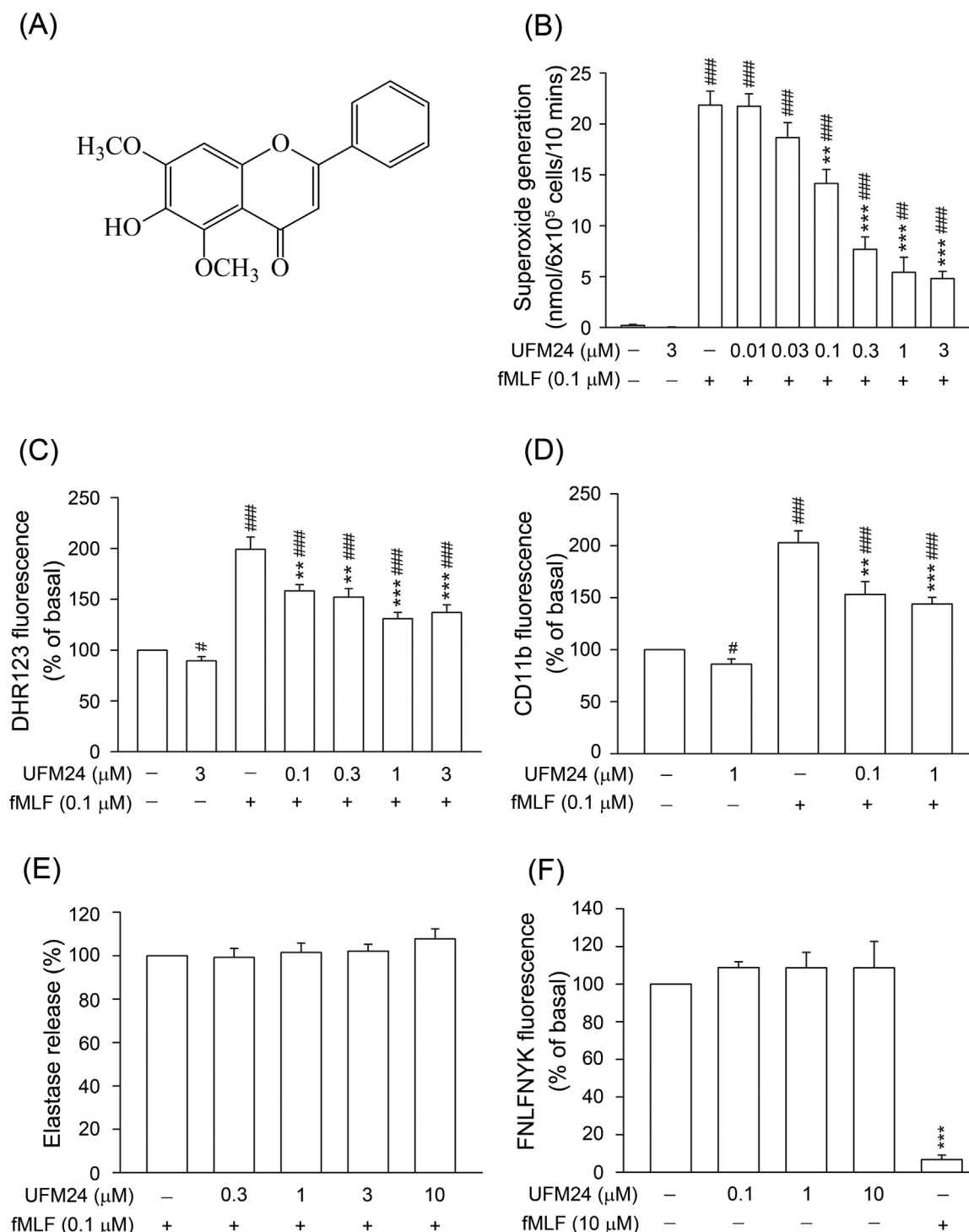


**Fig. 1.** UFM24 significantly inhibits  $O_2^{\bullet-}$  release, intracellular reactive oxidant formation, and integrin expression by fMLF-stimulated neutrophils. (A) Chemical structure of UFM24. Human neutrophils were pretreated with DMSO (as a control) or UFM24 (0.01–10 μM) for 5 min before cell stimulation. (B) Extracellular  $O_2^{\bullet-}$  release was induced by treating the neutrophils with fMLF/CB for 10 min and measured using a SOD-inhibitable cytochrome c reduction method ( $n=7$ ). (C) Cells stained with DHR123-dye were activated with fMLF/CB for 5 min. Intracellular  $O_2^{\bullet-}$  generation was expressed as fluorescence intensity analyzed by flow cytometry ( $n=10$ ). (D) Integrin expression is indicated as CD11b level after neutrophil activation was induced by fMLF/CB for 5 min. The expression was determined by monitoring the fluorescence intensity of FITC-labeled-anti-CD11b using flow cytometry ( $n=6$ ). (E) Elastase release was induced by fMLF/CB for 10 min and detected at 405 nm using a spectrophotometer ( $n=5$ ). (F) FPR1 receptor binding ability was measured after neutrophils were labeled with FNLFNK for 30 min. Receptor binding was detected using fluorescence-activated cell sorting flow cytometry ( $n=3$ ). All data are presented as means  $\pm$  SEM.  $**p < 0.01$ ;  $***p < 0.001$  compared with fMLF only.  $^{\#}p < 0.05$ ;  $^{##}p < 0.01$ ;  $^{###}p < 0.001$  compared with the basal group of non-stimulated cells.

## 2.6. Determination of CD11b expression

Neutrophils ( $2.5 \times 10^6/\text{ml}$ ) were equilibrated for 2 min at 37 °C and treated with UFM24 for 5 min. Then the cells were stimulated by fMLF (0.1 μM) for 5 min in the presence of CB (0.5 μg/ml). The activation of

cells was stopped by placing the cell samples on ice, and then samples were centrifuged at 4 °C. After removing the supernatants, neutrophils were resuspended in 80 μl HBSS (containing 0.5% bovine serum albumin) for FITC-labeled anti-CD11b (1.5 μg). After incubation for 90 min on ice in the dark, the immunofluorescently stained neutrophils

were immediately assayed for CD11b immunoreactivity by fluorescence-activated cell sorting (FACS) [7,23].

## 2.7. Determination of elastase release

Elastase is released from azurophilic granules when neutrophils are activated. Methoxysuccinyl-Ala-Ala-Pro-Val-p-nitroanilide was used as a substrate for neutrophil elastase [23]. After incubation with substrate (100  $\mu$ M) at 37 °C for 2 min, human neutrophils ( $6 \times 10^5$ /ml) were treated with DMSO or UFM24 for 5 min, and were activated with fMLF (0.1  $\mu$ M) after pretreatment with CB (0.5  $\mu$ g/ml) for 3 min before the activation. The change in absorbance of the mixture was monitored continuously for 10 min at 405 nm using a spectrophotometer [21].

## 2.8. FPR1 receptor binding analysis

A fluorescent analogue of fMLF, FNLFNKY, was used for this assay [24]. Neutrophils were incubated with DMSO or UFM24 for 5 min and then labeled with FNLFNKY (4 nM) for 30 min at 4 °C. Receptor binding was assayed by flow cytometry with FACS [25].

## 2.9. Measurement of lactate dehydrogenase (LDH) activity

To exclude the possible cytotoxicity of UFM24, LDH activity was measured using a commercial kit (Promega, Madison, WI, USA). Neutrophils were treated with UFM24 for 15 min following the protocol specified by the manufacturer and were then centrifuged at 200g at 4 °C for 10 min. Total LDH content was represented as 100% by lysing cells with 0.1% Triton X-100 at 37 °C for 30 min. The supernatant was mixed with LDH assay reagents for 30 min, and fluorescent intensity was measured at 492 nm. Cytotoxicity was determined as LDH release in the UFM24-treated group compared with cells incubated with DMSO alone [7,23].

## 2.10. Free radical-scavenging activity

The  $O_2^{\cdot-}$ -scavenging ability of UFM24 was determined using a cell-free xanthine/xanthine oxidase (XO) system. The assay buffer, which comprised 50 mM Tris (pH 7.4), 0.3 mM WST-1, and 0.02 U/ml XO was incubated at 30 °C and then incubated with or without UFM24 or superoxide dismutase (SOD) for 3 min. After 3 min incubation, xanthine (0.1 mM) was added and the mixture incubated for a further 10 min. Scavenging ability was determined as  $O_2^{\cdot-}$ -induced WST-1 reduction by absorbance changes measured at 450 nm [23]. Alternatively, a cell-free diphenyl-p-picrylhydrazyl (DPPH) system was adopted to test the ability of UFM24 to scavenge reactive radical species [26]. UFM24 was incubated in DPPH buffer for 15 min at room temperature, and the absorbance change was measured at 517 nm.  $\alpha$ -Tocopherol was used as a positive control.

## 2.11. Assay of NADPH oxidase activity

Neutrophils were incubated with 1 mM phenylmethylsulfonyl fluoride (PMSF) for 30 min at 4 °C, and disrupted by sonication in relaxation buffer (10 mM PIPES, 100 mM KCl, 3 mM NaCl, 3.5 mM  $MgCl_2$ , 1 mM EGTA, and 1 mM  $ATP(Na)_2$ ; pH 7.3). Unbroken neutrophils were discarded by centrifuging at 300g for 5 min. Then the supernatant was separated into cytosol and membrane fractions by centrifuging at 100,000g for 30 min at 4 °C. The membrane and cytosol fractions were mixed in Pi2M buffer (10 mM  $NaH_2PO_4/Na_2HPO_4 \cdot 12H_2O$ , 2.7 mM KCl, 138 mM NaCl and 2 mM  $MgCl_2$ ; pH 7.4) with 2  $\mu$ M GTP $\gamma$ S and 0.5 mg/ml ferricytochrome c at 30 °C, and 100  $\mu$ M sodium dodecyl sulfate (SDS) was added for 2 min. Then UFM24 was added for 1 min before treatment with 0.16 mM NADPH for a further 10 min. To determine the NADPH oxidase activity, the change in absorbance of the mixture was monitored continuously at 550 nm using a spectrophotometer [7,22].

## 2.12. Measurement of intracellular cAMP concentration

A commercial enzyme immunoassay kit (GE Healthcare, Little Chalfont, Buckinghamshire, UK) was used to assay cAMP concentrations. Neutrophils were incubated with UFM24 at 37 °C for 5 min before activation with fMLF for another 1 min. The mixtures were put on ice and neutrophils lysed by adding 0.5% dodecyltrimethylammonium bromide to terminate the reaction. The cAMP levels in the supernatants were assayed after centrifuging the mixtures at 3000g for 5 min at 4 °C [7].

## 2.13. Assay of PKA activity

Neutrophils ( $10^7$ /ml) were incubated with UFM24 for 5 min at 37 °C before activation with fMLF for another 0.5 min. Then the mixtures were placed on ice to stop the reaction. After centrifuging the mixtures at 4 °C, the supernatants were removed, and the pellet was lysed in Omnia cell extraction buffer (50 mM Tris, pH 7.4, 10 mM  $Na_4O_7P_2$ , 0.1 mM  $Na_3VO_4$ , 150 mM NaCl, 2 mM EGTA, 50 mM  $\beta$ -glycerophosphate, 30 mM NaF, 1 mM dithiothreitol, and 1% Triton X-100). The pellet samples were then sonicated and centrifuged at 14,000g for 30 min at 4 °C. The cytosolic fraction was obtained and used as sources for the PKA enzymes. PKA phosphorylated the immobilized PKA substrate on the 96-well microtiter plate in the presence of ATP. The specific antibody of phospho-PKA substrate bound to the immobilized phosphorylated substrate and was detected by peroxidase-conjugated anti-rabbit IgG. After incubation, the intensity of the developed color is proportional to the PKA activity. The PKA activity was measured using a PKA Colorimetric Activity Kit (Arbor Assays Headquarters, Ann Arbor, MI) [7,27].

## 2.14. Assay of PDE and adenylyl cyclase (AC) activities

Neutrophils ( $2 \times 10^8$  cells/ml) were sonicated at 4 °C in lysis buffer (25 mM Tris-HCl, pH 7.4, 0.25 M sucrose, 2 mM EDTA, 5 mM  $MgCl_2$ , 100  $\mu$ M PMSF, 1/100 Sigma protease inhibitor cocktail, and 1/100 Sigma phosphatase inhibitor cocktail). After centrifuging at 300g for 5 min at 4 °C to remove unbroken cells, the supernatant was centrifuged further at 20,000g for 15 min at 4 °C. The cytosolic fraction was obtained and used as sources for the PDE enzymes. The cytosolic fraction was incubated with UFM24 in PDE assay buffer (50 mM Tris-HCl, pH 7.4, and 5 mM  $MgCl_2$ ) in 96-well microtiter plates at 37 °C for 10 min. cAMP (60 nM) was added to the assay buffer to start the PDE reaction at 37 °C for 45 min, and then cAMP-d2 and anti-cAMP-criptate were added for 1 h. The cAMP concentration was detected using a homogeneous time resolved fluorescence (HTRF) reader following the instructions of HTRF assay kit (Cisbio, Bedford, MA, USA). The cAMP-specific PDE activity is directly proportional to the cAMP concentration [7,28,29].

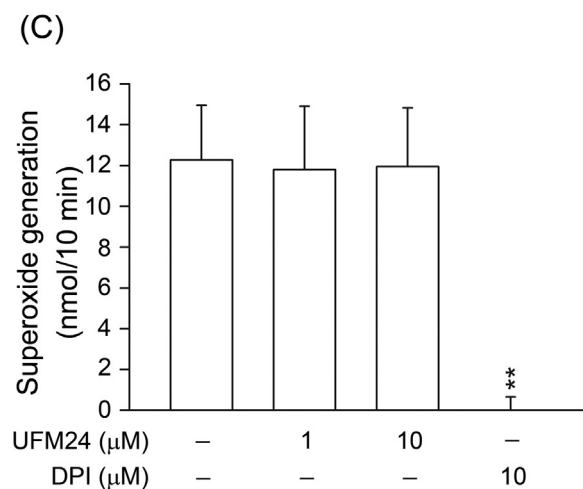
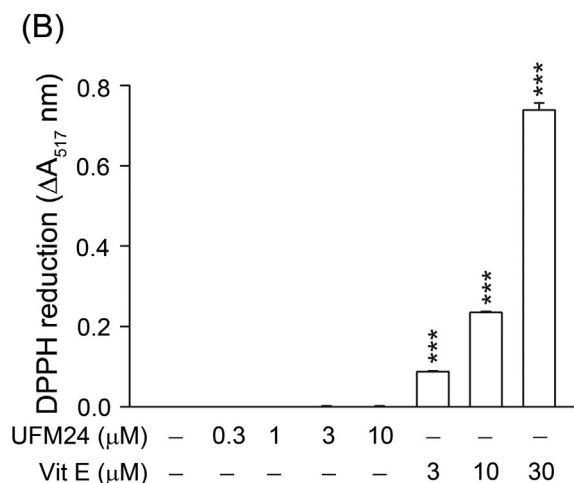
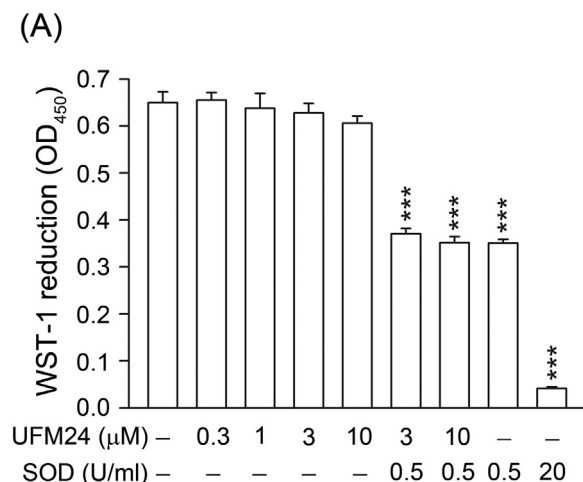
Additionally, HTRF assay kits were also used to assay the inhibitory effects of UFM24 on activities of PDE subtypes. PDE4A1A (0.04 ng/ $\mu$ l), PDE4B2 (0.01 ng/ $\mu$ l), PDE4C1 (0.04 ng/ $\mu$ l), PDE4D2 (0.008 ng/ $\mu$ l), PDE3B (0.05 ng/ $\mu$ l), and PDE7A (0.67 ng/ $\mu$ l) were incubated with UFM24 or a corresponding positive control for 10 min, and then 60 nM cAMP was added to the reaction mixture at 37 °C for 45 min.

To assay AC activity, cells ( $1.5 \times 10^7$  cells/ml) were sonicated in 4 °C lysis buffer (25 mM Tris-HCl, pH 7.4, 0.25 M sucrose, 2 mM EDTA, 5 mM  $MgCl_2$ , 100  $\mu$ M PMSF, 1/100 Sigma protease inhibitor cocktail, and 1/100 Sigma phosphatase inhibitor cocktail). After centrifuging at 300g for 5 min at 4 °C to remove unbroken cells, the supernatant was centrifuged further at 20,000g for 15 min at 4 °C. The pellet was used as sources for the AC enzymes and suspended in buffer (25 mM Tris-HCl, pH 7.4, 15 mM  $MgCl_2$ , and 1 mM DTT). The pellet fraction and UFM24 were added in the AC reaction mixture (25 mM Tris-HCl (pH 7.5), 1 mM ATP, 15 mM  $MgCl_2$ , 1 mM 3-isobutyl-1-methylxanthine (IBMX), 7.5 mM creatine phosphate, 0.5 mM dithiothreitol, and 3 units creatine

phosphokinase) at 30 °C for 20 min, and then placed in boiling water to stop the reactions. AC activity was expressed as cAMP levels, which were assayed by using a cAMP enzyme immunoassay kit (GE Healthcare, Little Chalfont, Buckinghamshire, UK) [29].

### 2.15. Measurement of intracellular calcium concentration ( $[Ca^{2+}]_i$ )

To measure  $[Ca^{2+}]_i$  assessment, neutrophils were labeled with



(caption on next column)

**Fig. 2.** UFM24 does not possess  $O_2^{\cdot-}$  or reactive radical species-scavenging ability and fails to affect the activity of NADPH oxidase. (A) A cell-free xanthine/XO system was used to assay the  $O_2^{\cdot-}$ -scavenging effect of UFM24 (0.3–10 μM). Reduction of WST-1 was monitored at 450 nm using a spectrophotometer, and SOD (0.5 and 20 U/ml) was used as the positive control. (B) To determine its antioxidant effect, UFM24 (0.3–10 μM) was incubated in DPPH buffer for 15 min, and the absorbance change was monitored spectrophotometrically at 517 nm in a cell-free DPPH assay. α-Tocopherol (Vit E, 3, 10, and 30 μM) was used as a positive control. (C) A SDS-reconstituted system was used to assay subcellular NADPH oxidase activity of neutrophils. The reaction mixture of cytosolic and membrane fractions was induced by the addition of 100 μM SDS at 30 °C before incubation with DMSO or UFM24 (1 and 10 μM) for 1 min. The changes in absorbance at 550 nm were determined when the reaction was initiated by the addition of 160 μM NADPH. Positive control was achieved by treatment with diphenyleneiodonium (DPI, 10 μM). All data are expressed as means ± SEM (n = 3–4). \*\*p < 0.01; \*\*\*p < 0.001 compared with control.

Fluo-3/AM (2 μM) at 37 °C for 45 min and were then washed and resuspended in HBSS solution. Fluo-3/AM-loaded cells were incubated with UFM24 for 5 min and were stimulated with fMLF (0.1 μM). The  $[Ca^{2+}]_i$  was detected using a spectrofluorometer (Hitachi F-4500) with excitation set at 488 nm and emission measured at 520 nm. The maximum ( $F_{max}$ ) and minimum ( $F_{min}$ ) fluorescence values were defined by administering Triton X-100 (0.05%) and ethylene glycol tetraacetic acid to the cell mixtures in sequence.  $[Ca^{2+}]_i$  was calculated as  $[Ca^{2+}]_i$  (nM) =  $K_d \times (F - F_{min}) / (F_{max} - F)$ .  $F$  is the peak value of fluorescence signal induced by fMLF, and the dissociation constant  $K_d$  is 400 nM [7,21].

### 2.16. Western blotting of whole-cell lysates

To prepare samples, human neutrophils were treated with UFM24 at 37 °C for 5 min, and activated with 0.1 μM fMLF for another 1 min. The reaction was terminated adding lysis buffer into mixtures and incubating them on ice for 30 min. Protein content was measured with a BCA protein assay kit (Pierce Biotechnology, Rockford, IL, USA) and was used to normalize the results. Electrophoresis on a 12% SDS-polyacrylamide gel (PAGE) was used to separate proteins in the sample mixtures, and then transferred onto nitrocellulose membranes by blotting. Akt blots were indicated with its corresponding rabbit primary antibody (1:1000), and detected by a horseradish peroxidase-conjugated secondary anti-rabbit antibody (1:3000, Cell Signaling Technology, Beverly, MA, USA). The expression of total Akt and phosphor-Akt (Ser 473) was assayed using an enhanced chemiluminescence system (Amersham Biosciences) with detection using a UVP Biospectrum Imaging System (UVP, Upland, CA, USA) [7,21]. The quantitative ratios for all samples were normalized to the total Akt protein.

### 2.17. LPS-induced model of ALI in mice

Protocols for animal studies were approved by the Institutional Animal Care and Use Committee of Chang Gung Memorial Hospital. All C57BL/6 mice were supplied by CD IGS, BioLasco, Ilan, Taiwan. Animals were housed in an air-conditioned room under an alternating 12 h light–dark cycle and adapted to this environment for one week before the experiment. All mice were fasted overnight except for water available ad libitum to prepare them for surgery.

A mouse model of ALI was adopted in this study. We administered vehicle (10% DMSO) or UFM24 (50 or 100 mg/kg body weight) intraperitoneally to male mice (20–25 g, 8 weeks old). All mice were randomly divided into four groups as follows: (I) sham-operated mice treated with vehicle, (II) sham-operated mice treated with UFM24, (III) ALI animals treated with vehicle, (IV) ALI animals treated with UFM24. One hour after administration of vehicle or UFM24, all mice received a tracheostomy under general anesthesia with Zoletil 50 (30 mg/kg) and xylazine (6 mg/kg). ALI was induced by slowly injecting 50 μl LPS (10 mg/kg body weight, *Escherichia coli* serotype 055:B5) or 0.9% saline (sham operation) via the tracheostomy. At 6 h after induction, the mouse lungs were resected for assays after opening the chest. The left

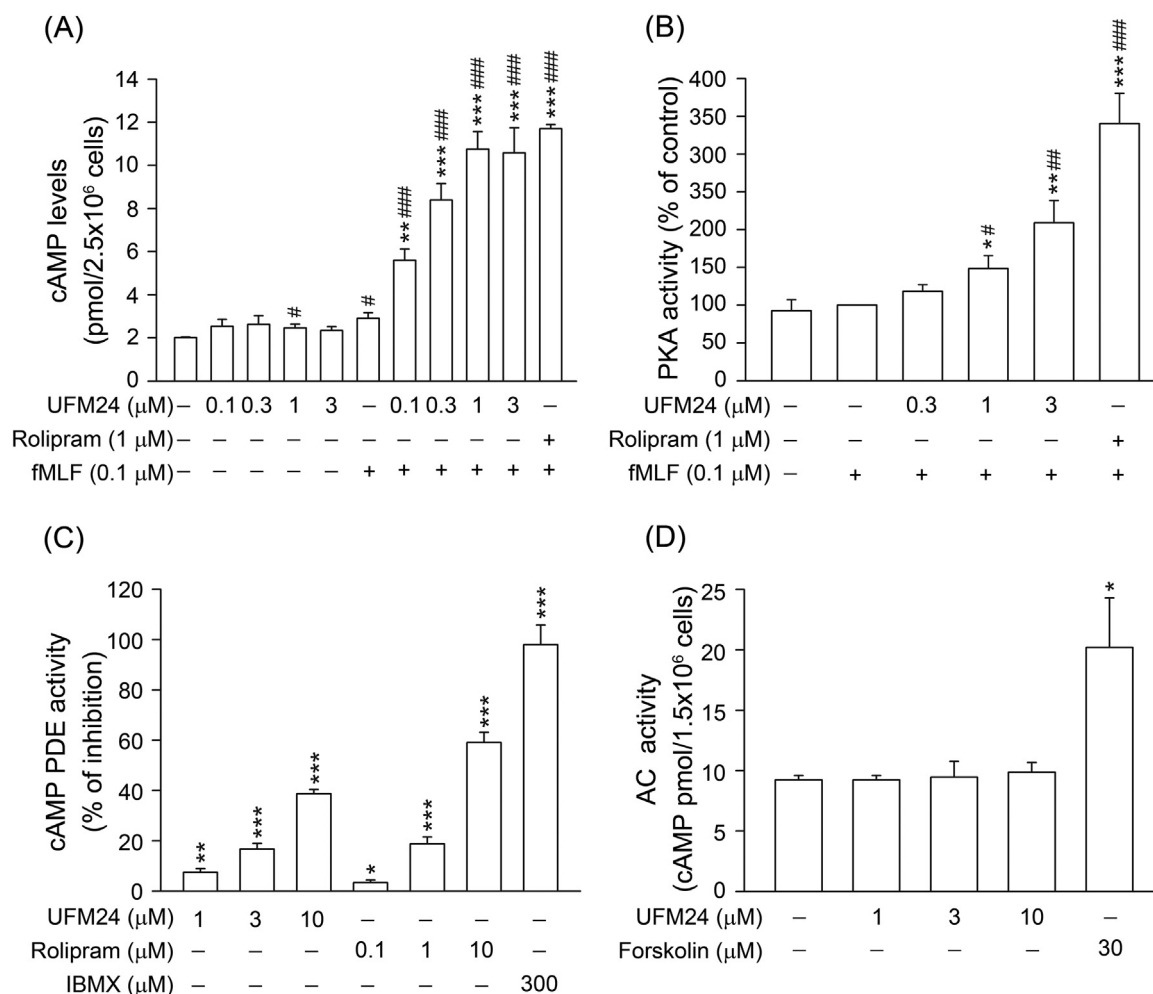


**Fig. 3.** UFM24 increases cAMP levels and PKA activities as well as inhibits cAMP-specific PDE activities in neutrophils. Human neutrophils were pretreated with DMSO (as control), UFM24 (0.1–3 μM), or rolipram (1 μM) for 5 min before activation with fMLF (0.1 μM) for 1 min. (A) cAMP concentrations and (B) PKA activities were assayed using commercial immunoassay kits. (C) Neutrophil homogenates were incubated with UFM24 (1, 3, and 10 μM), rolipram (0.1, 1, and 10 μM), or IBMX (300 μM), and then 60 nM cAMP was added to the reaction mixture for 20 min. Activity of cAMP-specific PDE was detected using an HTRF reader. (D) Neutrophil membrane fractions were preincubated with UFM24 (1, 3, and 10 μM) or forskolin (30 μM) for 20 min. AC activity was determined by measurement of cAMP levels using ELISA kits. All data are expressed as means ± SEM (n = 3–5). \**p* < 0.05; \*\**p* < 0.01; \*\*\**p* < 0.001 compared with the fMLF only (A and B) or the control (C and D). #*p* < 0.05; ##*p* < 0.01; ###*p* < 0.001 compared with the basal group of non-stimulated cells.

upper lung was assayed for tissue water content, and two pieces of right middle lung were kept for histological examination. All the others were used for the assay of MPO activity. The severity of pulmonary edema was determined by lung water content assay, and was shown as a wet-to-dry weight ratio referenced to sham-treated outcomes [21].

## 2.18. Lung water content assay

Left upper lung was cut into two pieces and weighed. After being dried at 70 °C for 3 days, tissues were reweighed. The water content of lung tissue was calculated as a wet-to-dry weight ratio.

## 2.19. Assays of myeloperoxidase (MPO) and cytokines in lung tissue

Lung tissues from each mouse was suspended in 1 ml, pH 6.0 buffer (0.5% hexadecyltrimethylammonium bromide in a 50 mM phosphate buffer), and then homogenized by sonication twice. After centrifuging at 2000g at 4 °C, the supernatants of homogenates were obtained for assays. To assay MPO activity, lung homogenates were incubated with *o*-dianisidine dihydrochloride and hydrogen peroxide in pH 6.0 phosphate buffer. MPO activity was measured by monitoring absorbance of the mixtures at 460 nm for 5 min using spectrophotometry. MPO activity was calculated by reference to a standard curve derived from human MPO (Sigma-Aldrich). Lung MPO activity was represented as

units per gram of tissue [30]. The expression levels of TNF-α and IL-6 in the supernatants of homogenates were assayed using ELISA MAX Deluxe Set (BioLegend, CA, USA) [31].

## 2.20. Immunohistochemistry stain for histological study

Immunohistochemistry staining was performed as previously described [32,33]. Ly-6G (Lymphocyte antigen 6 complex locus G6D), a marker for neutrophils, was detected immunohistochemically on formalin-fixed, paraffin-embedded sections (5 μm thick) using a bond polymer detection system and bond automated machine with a polymer refining kit. The rat anti-mouse-Ly-6G (Gr-1) monoclonal primary antibody (eBioscience, San Diego, CA, USA) was used at 1:200. After deparaffinization, antigens were retrieved using ER1 buffer. Sections were incubated with primary antibodies at room temperature for 60 min, followed with a poly-horseradish peroxidase anti-rat IgG reagent to localize the primary antibody, and diaminobenzidine was used as a chromogen to visualize the complex. Then the sections were counterstained with hematoxylin, dehydrated, cleared, and mounted. The morphology of pathological damage was evaluated using a microscope (Nikon Eclipse TS100).

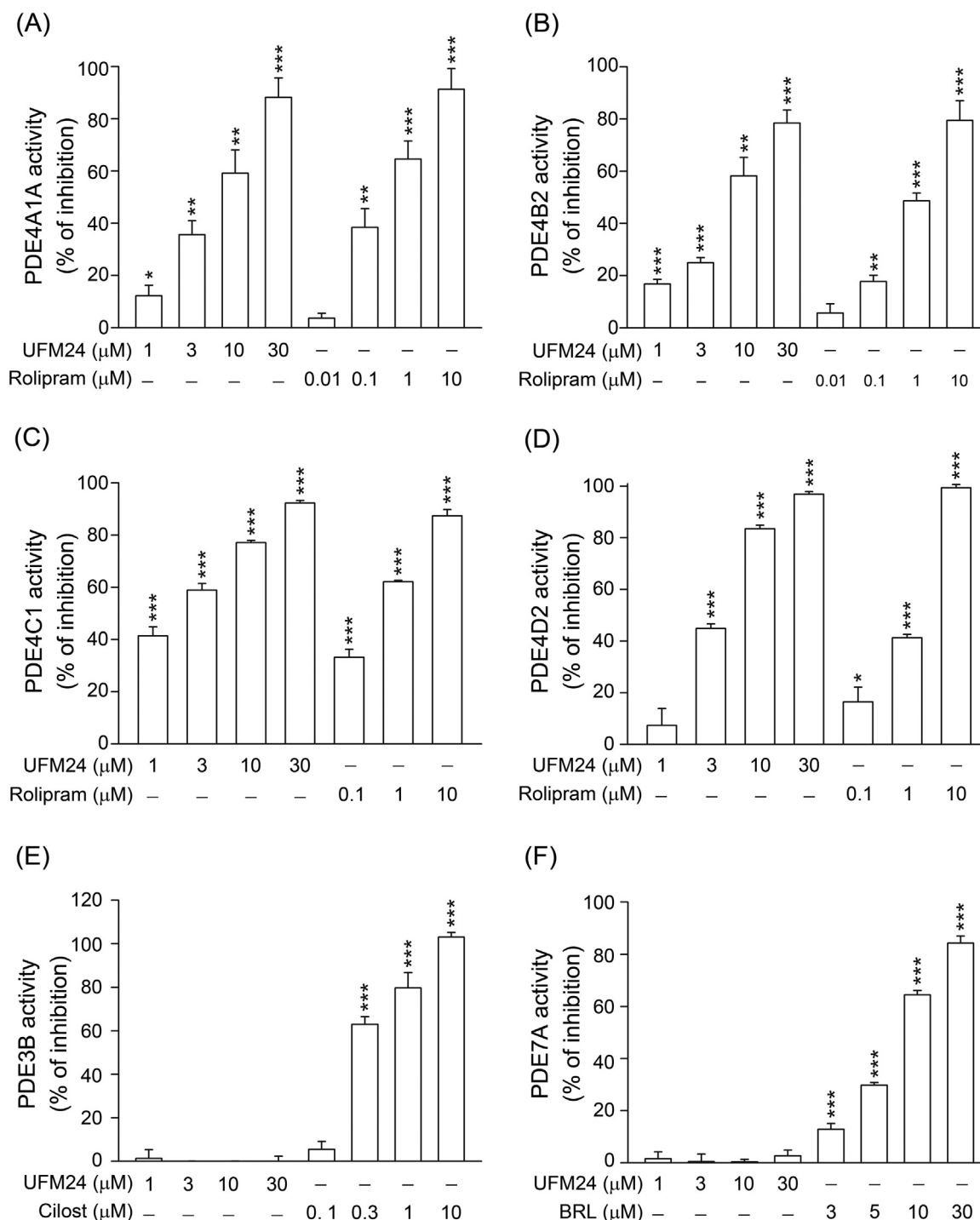


**Fig. 4.** UFM24 selectively inhibits the enzymatic activities of PDE4 in a survey of neutrophilic cAMP-specific PDE subtypes. PDE subtype enzymes, (A) PDE4A1A (0.04 ng/μl), (B) PDE4B2 (0.01 ng/μl), (C) PDE4C1 (0.04 ng/μl), (D) PDE4D2 (0.008 ng/μl), (E) PDE3B (0.05 ng/μl), and (F) PDE7A (0.67 ng/μl), and cAMP (60 nM) were incubated with DMSO (as control) or UFM24 (1–30 μM) at 37 °C for 10 min, followed by addition of each of the HTRF reagents (cAMP-d2 and anti-cAMP-cryptate). Enzymatic activities of PDE subtypes were assayed using an HTRF reader. Corresponding inhibitors, rolipram (0.01–10 μM), cilostamide (Cilost, 0.1–10 μM), or BRL50481 (BRL, 3–30 μM), were used as positive controls. All data are expressed as means ± SEM (n=3–5). \**p* < 0.05; \*\**p* < 0.01; \*\*\**p* < 0.001 compared with control.

## 2.21. Statistical analysis

All results are expressed as means ± SEM and were analyzed using Sigma Plot software (Systat Software, San Jose, CA, USA). Statistical analysis was performed using Student's *t*-test and one- or two-way analysis of variance followed by Bonferroni's multiple comparison test. A *p* < 0.05 was considered significant.

## 3. Results

### 3.1. UFM24 reduces $O_2^{\cdot-}$ release, intracellular reactive oxidant generation, and CD11b expression in fMLF-activated human neutrophils

Neutrophil respiratory burst, degranulation, and adhesion molecular expression are important in inflammation reactions. UFM24 (0.01–3 μM) significantly inhibited  $O_2^{\cdot-}$  generation in fMLF/CB-induced human neutrophils in a concentration-dependent manner, and the



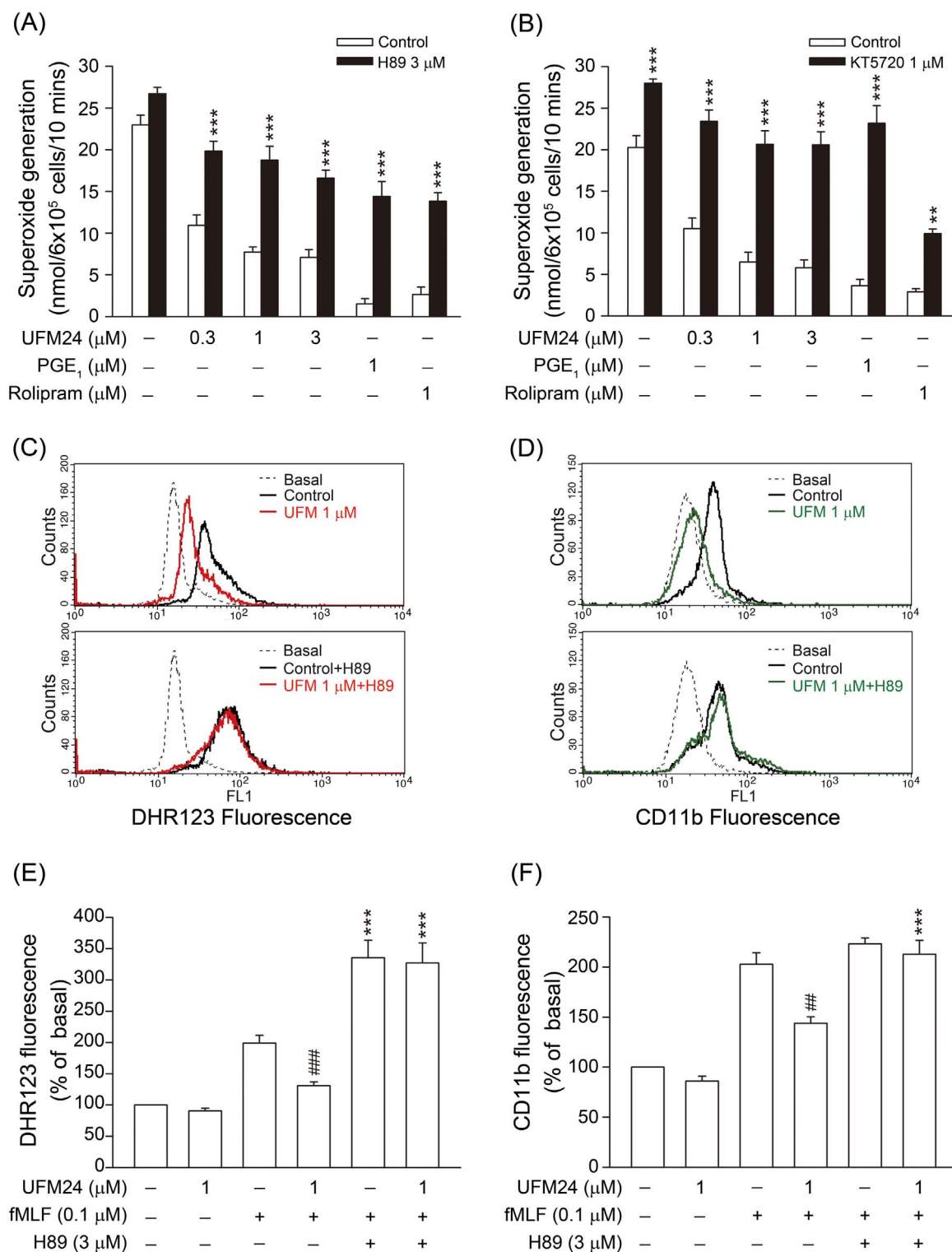


**Fig. 5.** PKA signal regulates the inhibitory effects caused by UFM24. PKA inhibitors were used to investigate the inhibitory effects of UFM24, PGE<sub>1</sub>, and rolipram. Neutrophils were treated with H89 (3 μM) or KT5720 (1 μM) for 5 min before the addition of UFM24 (0.3, 1, or 3 μM), PGE<sub>1</sub> (1 μM), or rolipram (1 μM), and then activated with fMLF. (A, B) Extracellular O<sub>2</sub><sup>•−</sup> (n=4 and 5), (C, E) intracellular reactive oxidants (n=10), and (D, F) CD11b (n=6) were measured. All data are expressed as means ± SEM. \*\*p < 0.01; \*\*\*p < 0.001 compared with the corresponding control. ##p < 0.01; ###p < 0.001 compared with fMLF only in (E) and (F).

IC<sub>50</sub> value was 0.22 ± 0.17 μM (Fig. 1B). An LDH release assay showed that incubating with UFM24 (up to 30 μM) did not affect neutrophil viability (data not shown). In addition, UFM24 suppressed intracellular reactive oxidant increase and integrin expression, as assayed by flow cytometry (Fig. 1C and D). In contrast, even treating cells with high concentration of UFM24 (10 μM) failed to show any inhibition on fMLF/CB-induced elastase release (Fig. 1E). Additionally, UFM24 did

not inhibit FPR1-specific ligand FNLNFK binding to FPR1 in human neutrophils (Fig. 1F).

To examine the ability of UFM24 on direct scavenging O<sub>2</sub><sup>•−</sup>, a cell-free xanthine/XO system was investigated. UFM24 did not change WST-1 reduction at concentrations of 0.3–10 μM, and SOD was used as a positive control. Also, UFM24 did not affect the removal of O<sub>2</sub><sup>•−</sup> by SOD at 0.5 U/ml (Fig. 2A). Furthermore, UFM24 also showed no

antioxidant ability by assaying with a DPPH free radical scavenging method (Fig. 2B), and  $\alpha$ -tocopherol (vitamin E) was a positive indicator. Taken together, the results confirmed that the inhibitory effects of UFM24 on  $O_2^{\cdot-}$  production were not mediated through the scavenging of free radicals. The generation of  $O_2^{\cdot-}$  was mediated through the activation of a multicomponent enzyme complex, NADPH oxidase [34]. Isolated neutrophil fractionations were used to assay SDS-reconstituted NADPH oxidase activities. As demonstrated in Fig. 2C, UFM24 (1 and 10  $\mu$ M) failed to affect  $O_2^{\cdot-}$  generation in activated subcellular NADPH oxidase. Diphenyleneiodonium (DPI, 10  $\mu$ M), an NADPH oxidase inhibitor, was indicated as a positive control. These data suggested that UFM24 does not block the respiratory burst by directly inhibiting NADPH oxidase activity.

### 3.2. Effect of UFM24 on cAMP/PKA signaling

An increase in cAMP levels leads to activation of the cAMP-dependent PKA signal and modulates neutrophil functions. To examine whether PKA mediates the inhibitory effect of UFM24, the concentrations of cAMP and activities of PKA were determined. When incubating human neutrophils with UFM24 (0.1–3  $\mu$ M) alone, only a slight, but insignificant increase in the cAMP concentrations was induced (Fig. 3A). Notably, UFM24 (0.1–3  $\mu$ M) induced a synergistic increase in cAMP levels in fMLF-activated neutrophils. In the measurement of PKA activity, UFM24 greatly enhanced PKA activity in a dose-dependent fashion in fMLF-activated neutrophils (Fig. 3B). These data suggest that the cAMP/PKA pathway mediates the inhibitory effects of UFM24.

### 3.3. UFM24 suppresses the activity of cAMP-specific PDEs in human neutrophils

An increase of intracellular cAMP concentration is attributed to inhibition of cAMP-specific PDEs activity or enhancement of AC activity. cAMP-specific PDEs can hydrolyze cAMP to inactive 5'-AMP. UFM24 (1, 3, and 10  $\mu$ M) significantly inhibited cAMP-specific PDE activity in neutrophil homogenates in a concentration-dependent manner (Fig. 3C). A specific PDE4 inhibitor (rolipram) and a non-specific PDE inhibitor (3-isobutyl-1-methylxanthine, IBMX) were indicated as positive controls. In addition, UFM24 did not show any effect on AC activity of neutrophil membrane fractions. Forskolin (30  $\mu$ M) was used as a positive control (Fig. 3D).

### 3.4. UFM24 selectively inhibits PDE4 activity

Three cAMP-specific PDEs, PDE3, PDE4, and PDE7, are found in human neutrophils [35–38]. The selectivity of inhibitory effects of UFM24 on these neutrophilic PDE subtypes was analyzed. Rolipram, cilostamide, and BRL50481 were used as positive controls for PDE4, PDE3, and PDE7 inhibition. UFM24 selectively inhibited the activities of PDE4 subtypes PDE4A1A, PDE4B2, PDE4C1, and PDE4D2, but not PDE3B and PDE7A (Fig. 4). The  $IC_{50}$  values of UFM24 for PDE4A1A, PDE4B2, PDE4C1 and PDE4D2 were  $7.51 \pm 2.09$ ,  $8.58 \pm 2.04$ ,  $1.75 \pm 0.34$ , and  $3.53 \pm 0.18$   $\mu$ M, respectively.

### 3.5. The inhibitory effects on cell functions by UFM24 are mediated through the PKA pathway

To confirm whether UFM24 inhibited cell functions, including  $O_2^{\cdot-}$  release, intracellular reactive oxidant generation, and CD11b expression, which were directly through the PKA pathway, two specific PKA inhibitors, H89 and KT5720, were used to test the hypothesis. Notably, H89 (3  $\mu$ M) and KT5720 (1  $\mu$ M) produced a profound reversal of the inhibitory effects of  $O_2^{\cdot-}$  production by UFM24 (0.3, 1, and 3  $\mu$ M), PGE<sub>1</sub> (1  $\mu$ M) and rolipram (1  $\mu$ M) (Fig. 5A and B). Besides, inhibition of intracellular reactive oxidant generation and CD11b expression

mediated by UFM24 were also markedly reversed by H89 (Fig. 5C–F). These evidences confirmed that PKA is involved in the inhibitory effects of UFM24 on neutrophil functions. Similarly, cilomilast (0.01–0.3  $\mu$ M), a second generation oral PDE4 inhibitor, significantly inhibited  $O_2^{\cdot-}$  generation, but not elastase release, in fMLF-stimulated human neutrophils. Also, the inhibitory effect of cilomilast on  $O_2^{\cdot-}$  generation was also reduced by H89 (Supplementary Fig. S1).

### 3.6. UFM24 attenuates Akt phosphorylation mediated through PKA pathway in fMLF-activated human neutrophils

The phosphorylation of Akt is related to the respiratory burst in activated neutrophils [39]. Stimulation of neutrophils with fMLF resulted in rapid phosphorylation of Akt. UFM24 (1 and 10  $\mu$ M) significantly inhibited fMLF-induced phosphorylation of Akt in a concentration-dependent manner, and the inhibitory effects can be reversed by the PKA inhibitor, H89 (Fig. 6).

### 3.7. Effect of UFM24 on $Ca^{2+}$ mobilization caused by fMLF activation

When human neutrophils are activated by fMLF, the intracellular  $Ca^{2+}$  concentration ( $[Ca^{2+}]_i$ ) increases rapidly and transiently via a G protein-coupled receptor (GPCR). This elevation of  $[Ca^{2+}]_i$  induces neutrophil activation. Any suppression in  $[Ca^{2+}]_i$  magnitude or duration is able to affect cell activation [40]. In our study, UFM24 (1, 3, and 10  $\mu$ M) failed to alter the peak concentration of cytosolic  $Ca^{2+}$  or to reduce the time taken for it to decline to half of its peak values ( $t_{1/2}$ ) in

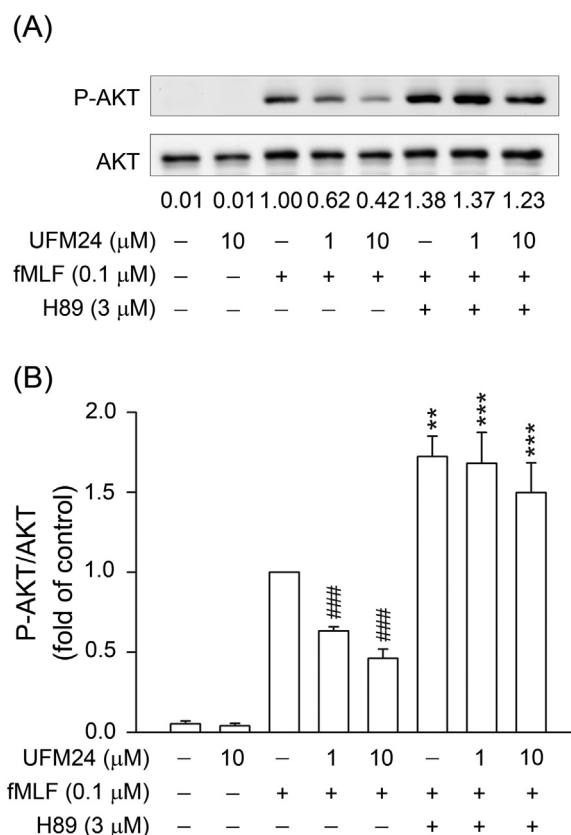
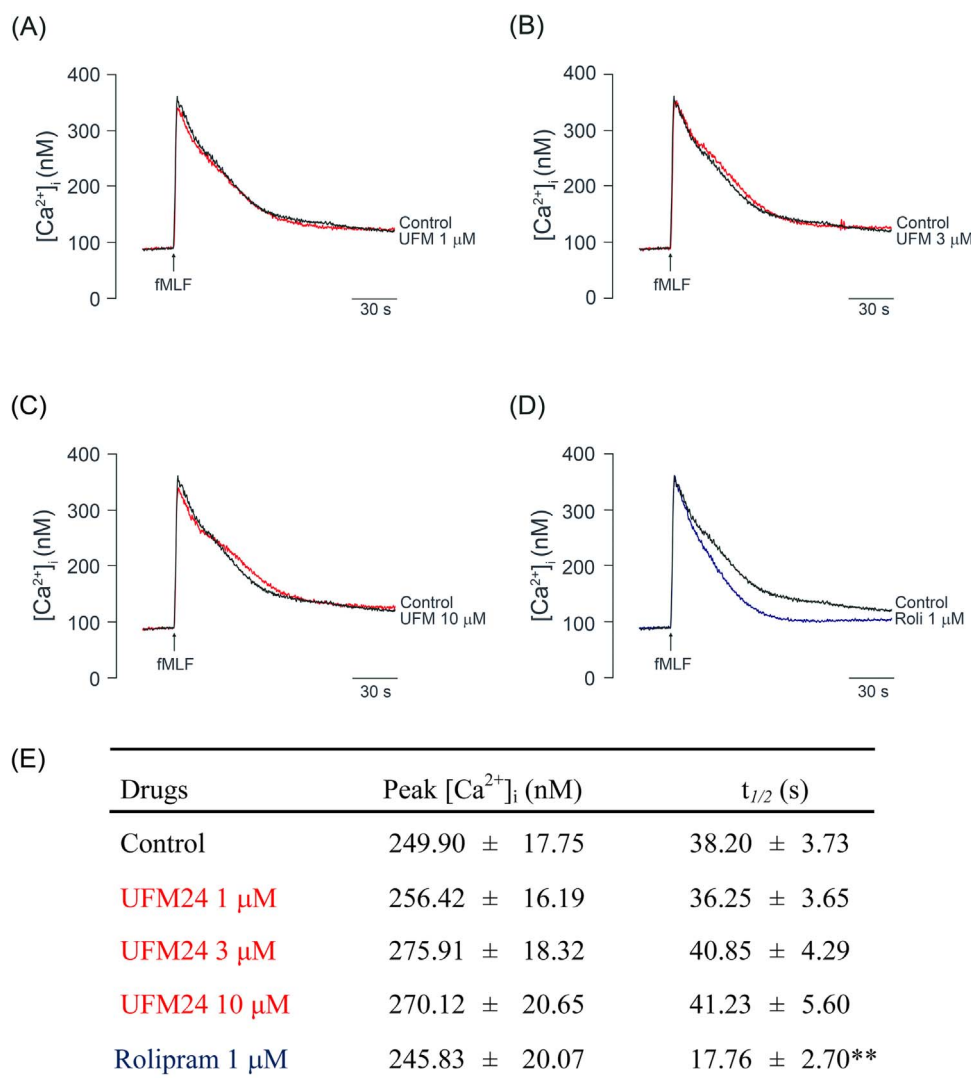


Fig. 6. UFM24 inhibits the phosphorylation of Akt in fMLF-activated human neutrophils. Neutrophils were incubated with UFM24 (1 and 10  $\mu$ M) for 5 min before activation with fMLF (0.1  $\mu$ M) for 1 min. (A) Phosphorylation of Akt was determined by Western blotting using antibodies against the phosphorylated form and the total protein. Cells were preincubated with H89 (3  $\mu$ M) for 5 min before adding UFM24. (B) Targeted blotted bands were assessed using a densitometer. The quantitative ratio of Akt expression of all samples was normalized to its corresponding total protein. All data are expressed as means  $\pm$  SEM (n=5). \*\* $p$  < 0.01; \*\*\* $p$  < 0.001 compared with the corresponding control. ### $p$  < 0.001 compared with fMLF only.



**Fig. 7.** UFM24 fails to affect intracellular  $Ca^{2+}$  mobilization in fMLF activated human neutrophils. Human neutrophils labeled with Fluo-3/AM dye were incubated with DMSO (as controls), (A, B, C) UFM24 (UFM, 1, 3, and 10 μM), and (D) rolipram (1 μM) for 5 min. Cells were stimulated with fMLF (0.1 μM), and  $Ca^{2+}$  mobilization was measured using a spectrofluorometer. (E) Data from (A–D) are expressed as means ± SEM (n=6). \*\*  $p < 0.01$  compared with control.

fMLF-activated neutrophils. However, rolipram (1 μM) showed a decrease effect in  $t_{1/2}$  value in fMLF-activated neutrophils (Fig. 7).

### 3.8. Effects of UFM24 on LPS-induced ALI in C57BL/6 mice

The results of lung damage are presented as sham-operated mice treated with vehicle (I) or UFM24 (II), and mice with LPS-resulted ALI treated with DMSO (III) or UFM24 (IV, V). LPS instilled into the lungs of mice resulted in an obvious increase in neutrophil infiltration, which was expressed as the increases in tissue MPO activity and immunohistochemical Ly-6G expression when compared with that in sham-operated mice. Intraperitoneal administration of UFM24 effectively inhibited the increase in pulmonary neutrophil infiltration in LPS-induced ALI (Fig. 8A and C III). The severity of lung edema was measured by analyzing the wet-to-dry-weight ratios of mouse lungs before and after LPS-induced injury. In the control LPS-induced group, the ratios were higher than for sham-operated animals (Fig. 8B). LPS caused obvious alveolar wall disruption and edematous change as well as hemorrhage (Fig. 8C and D). UFM24 significantly inhibited the ALI caused by LPS (Fig. 8). Additionally, cilomilast (10 mg/kg body weight) showed inhibitory effects on neutrophil accumulation and lung damage in LPS-induced ALI mice (Supplementary Fig. S2).

## 4. Discussion

Overwhelming bacterial infection leads to the development of sepsis, septic shock, organ damage, and mortality as uncontrollable immune responses in the host [41]. Bacterial endotoxin activates immune cells and their subsequent release of inflammatory mediators resulting in potentially lethal ALI or ARDS. At present, there are no effective therapeutics for bacterial endotoxin-induced clinical pathogenesis [42]. Neutrophils are chemotactically attracted into inflamed lung tissues by components of bacterial membranes, such as LPS or fMLF, and play a critical role in the progression of pathogenesis. Neutrophils contribute to the early innate defense by rapidly infiltrating inflamed tissues, where they produce and release  $O_2^{\cdot-}$  to regulate inflammatory reactions.  $O_2^{\cdot-}$  generation in neutrophils is called the respiratory burst. However,  $O_2^{\cdot-}$  function as a double-edged sword. Not only do they kill pathogens, but their cytotoxic properties also harm the extracellular environment, especially when they are over-produced [43]. Based on this consideration, it is important to develop therapeutics to restrain or regulate over-activated neutrophils. Flavone compounds have been reported to possess anti-inflammatory activity [44]. We sought to investigate the anti-inflammatory effects of a natural flavone UFM24 and the mediated signal transduction in human neutrophils. In our present findings, UFM24 specifically inhibited

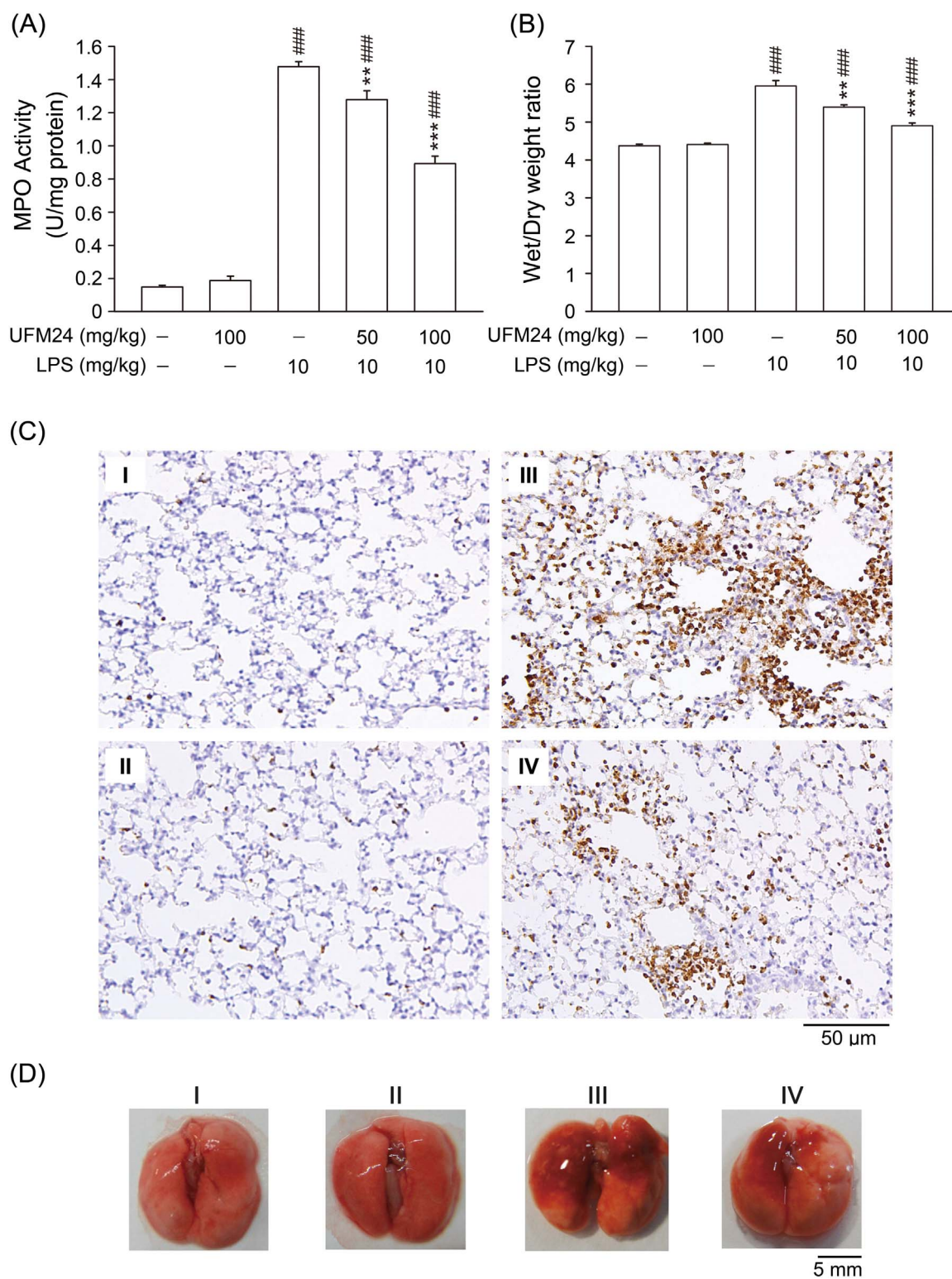


**Fig. 8.** Effects of UFM24 on MPO activities, wet-to-dry-weight ratios, and histopathologic examination of mouse lungs in LPS-induced acute lung injury (ALI). Mice were pretreated with 50  $\mu$ l UFM24 (50 or 100 mg/kg body weight) or vehicle (Veh; 10% DMSO) intraperitoneally. At 6 h after instilling LPS or 0.9% saline into the trachea, mouse lungs were resected to determine (A) MPO activities, (B) wet-to-dry-weight ratios, and (C) immunohistochemical detection for neutrophilic Ly-6G proteins in the lung tissues from (I) sham-operated mice treated with vehicle, (II) sham-operated mice treated with UFM24, (III) ALI animals treated with vehicle, (IV) ALI animals treated with UFM24. UFM24 clearly protected against lung damage at 6 h after LPS-induced ALI. Representative sections of lung are stained immunohistochemically using diaminobenzidine as a chromogen for the horseradish peroxidase-conjugated secondary antibody, and were observed at an original magnification of  $\times 200$ . (D) Representative photographs of mouse lungs were shown. All data are expressed as means  $\pm$  SEM for eight mice in each group. \*\*\* $p < 0.001$  compared with the ALI + Veh group (III). ### $p < 0.001$  compared with the sham-operated group (I).



PDE4 activity via the cAMP/PKA pathway, and clearly suppresses  $O_2^{\cdot-}$  generation, reactive oxidant production, and integrin CD11b expression in fMLF-induced neutrophils in a concentration-dependent manner. The present study suggests that UFM24 has potential as a therapeutic adjuvant to treat neutrophil-dominated inflammation.

In our study, UFM24 demonstrated inhibitory effects on  $O_2^{\cdot-}$  production, but failed to inhibit elastase release, in fMLF-activated neutrophils. UFM24 not only reduced extracellular  $O_2^{\cdot-}$  release, but also intracellular  $O_2^{\cdot-}$  generation. These inhibitory effects are not attributed to drug cytotoxicity or direct free radical-scavenging ability in cell-free assays. Neutrophil migration contributes to the progression of inflammation, and it is related to the expression of CD11b integrin on the cell membrane [45]. UFM24 clearly inhibited CD11b expression in a concentration-dependent manner. All of these inhibitory effects can be blocked abruptly by PKA inhibitors, and this finding suggested that the inhibitory effects of UFM24 are probably mediated through the PKA signal. FPR1 is a  $G_i$  protein-coupled receptor, and it was identified to have a high affinity for its ligand, fMLF. FPR1 can be activated by *N*-formyl peptides derived from parts of mitochondria released during apoptosis or from bacterial membrane components [46,47]. FPR1 binding initiates neutrophil activation in both septic and sterile inflammation. However, an FPR1 receptor binding assay using FNLFNYK suggested that the inhibitory effect of UFM24 was not mediated by reducing the FPR1 binding that activates neutrophils.

Increased oxidative stress in the respiratory burst reaction is mediated through the NADPH oxidase in human neutrophils. NADPH oxidase is composed of cytosolic  $p40^{phox}$ ,  $p47^{phox}$ ,  $p67^{phox}$ , and small GTPase rac2 with the membrane-bound flavocytochrome b558 complex [34,48]. Our data revealed that UFM24 was unable to inhibit NADPH oxidase activity in an SDS-reconstitution assay. The data suggest that UFM24 inhibits neutrophil cellular functions by modulating upstream signal transduction pathways.

An increase of intracellular cAMP levels activates PKA signal to inhibit neutrophil activation [49]. In our present study, UFM24 significantly increased the intracellular cAMP level and PKA activity in fMLF-activated neutrophils in a concentration-dependent manner. We conclude that UFM24 suppressed the neutrophil activation through the cAMP/PKA pathway. The level of intracellular cAMP increases after neutrophils are stimulated by fMLF [50]. The concentration of intracellular cAMP is regulated either by being degraded by PDEs or being synthesized by AC. We confirmed that UFM24 inhibited the activity of cAMP-specific PDEs, but not AC.

PDE4 inhibitors have been explored pharmacologically to treat acute or chronic lung diseases [51,52]. Notably, PDE4 inhibitors, cilomilast and roflumilast, have been used to treat COPD patients clinically [53]. The cAMP-specific PDE subtypes existing in human neutrophils include PDE3 (A, B), PDE4 (A, B, D), and PDE7 (A2) [35–38]. PDE3 is able to hydrolyze both cAMP and cGMP, and its affinity for cAMP is higher than that for cGMP. PDE4 and PDE7 are absolutely specific for cAMP. UFM24 effectively reduced the activities of the PDE4 family composed of four subtypes, 4A, 4B, 4C, and 4D, but failed to inhibit PDE3B and PDE7A. The present data suggest that UFM24 has promising potential as a new specific inhibitor of PDE4.

The downstream signaling pathway of GPCR was examined further to explore the mechanisms of the anti-inflammatory effects of UFM24 in neutrophils. The PI3K/Akt pathway and intracellular  $Ca^{2+}$  mobilization play crucial roles in neutrophil activation after agonists trigger GPCRs [54]. Akt can phosphorylate the  $p47^{phox}$  component of the NADPH oxidase complex to induce  $O_2^{\cdot-}$  production in neutrophils [55]. In immunoblotting assays, UFM24 inhibited Akt phosphorylation in a concentration-dependent manner, and this inhibition was notably reversed by a PKA inhibitor. However, UFM24 failed to inhibit  $Ca^{2+}$  mobilization in fMLF-stimulated neutrophils. These data suggest that the inhibitory effects of UFM24 on fMLF-activated  $O_2^{\cdot-}$  generation, reactive oxidant production, and CD11b expression in human neutrophils are regulated by inhibiting the PI3K/Akt pathway.

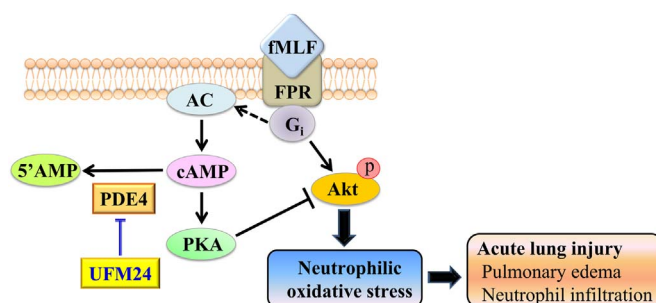


Fig. 9. A diagram showing that UFM24 inhibits  $O_2^{\cdot-}$  generation, reactive oxidant formation, and integrin expression in fMLF-activated neutrophils and protects against LPS-induced acute lung injury. UFM24 is a specific inhibitor of PDE4. The anti-inflammatory effects of UFM24 are mediated by inhibiting PDE4 and then enhancing cAMP/PKA-dependent inhibition of Akt activation. UFM24 ameliorates LPS-induced acute lung injury in mice.

To verify these anti-inflammatory effects of UFM24 *in vivo*, a mouse model of ALI induced by LPS was used to investigate the therapeutic value of UFM24. LPS can induce profound immune reactions, and is considered a potent toxin causing the development of vital organ damage or endotoxic shock with a high mortality [56]. Neutrophil infiltration into the lung is correlated with the severity of LPS-induced lung injury [57]. The present study found that UFM24 reduces pulmonary infiltration by neutrophils, pulmonary edema, alveolar wall disruption, and pulmonary hemorrhage in a mouse model of ALI induced by LPS. UFM24 also reduced the LPS-induced elevation of pro-inflammatory cytokines, TNF- $\alpha$  and IL-6, in inflamed lungs (Supplementary Fig. S3). These data suggest that UFM24 has potential as a new adjunct for the treatment of pulmonary injury related to over-activated neutrophils.

## 5. Conclusions

In summary, this present study is the first to our knowledge to demonstrate UFM24 as a selective inhibitor of PDE4. UFM24 significantly suppresses  $O_2^{\cdot-}$  production, reactive oxidant generation, and CD11b expression by fMLF-activated human neutrophils. The inhibitory effects of UFM24 are mediated by reducing the activity of the PDE4 and enhancing cAMP/PKA-dependent inhibition of Akt activation (Fig. 9). ALI and ARDS remain at a high risk for mortality and morbidity. The present results suggest that UFM24 has potential as an alternative treatment for ALI.

## Acknowledgements

This research was financial supported by the grants from the Ministry of Science Technology (NSC 102-2628-B-182-002-MY3, MOST 102-2628-B-255-003-MY3 and MOST 104-2320-B-255-004-MY3), Ministry of Education (EMRPD1F0311), and Chang Gung Memorial Hospital (CMRPD1B0281~3, CMRPF1D0442~3, CMRPF1F0011~3, CMRPF1F0061~3, CMRPG3E0101 and BMRP450), Taiwan. The funders had no role in study design, data collection and analysis, decision to publish, or preparation of the manuscript. We thank the Pathology core lab at Chang Gung University, Prof. Dr. Chuen Hsueh and M.S. Ya-Ping Liu for helping immunohistochemistry study.

## Appendix A. Supporting information

Supplementary data associated with this article can be found in the online version at doi:10.1016/j.freeradbiomed.2017.03.002.

## References

- [1] C. Pierrakos, J.L. Vincent, The changing pattern of acute respiratory distress syndrome over time: a comparison of two periods, *Eur. Respir. J.* 40 (2012)



- 589–595.
- [2] C.R. Raetz, C. Whitfield, Lipopolysaccharide endotoxins, *Annu. Rev. Biochem.* 71 (2002) 635–700.
  - [3] A. Davey, D.F. McAuley, C.M. O’Kane, Matrix metalloproteinases in acute lung injury: mediators of injury and drivers of repair, *Eur. Respir. J.* 38 (2011) 959–970.
  - [4] J. Bai, L. Tang, J. Lomas-Neira, Y. Chen, K.R. McLeish, S.M. Uriarte, C.S. Chung, A. Ayala, TAT-SNAP-23 treatment inhibits the priming of neutrophil functions contributing to shock and/or sepsis-induced extra-pulmonary acute lung injury, *Innate Immun.* 21 (2015) 42–54.
  - [5] T.L. Hwang, Y.L. Leu, S.H. Kao, M.C. Tang, H.L. Chang, Viscolin, a new chalcone from *Viscum coloratum*, inhibits human neutrophil superoxide anion and elastase release via a cAMP-dependent pathway, *Free Radic. Biol. Med.* 41 (2006) 1433–1441.
  - [6] H.P. Yu, P.W. Hsieh, Y.J. Chang, P.J. Chung, L.M. Kuo, T.L. Hwang, DSM-RX78, a new phosphodiesterase inhibitor, suppresses superoxide anion production in activated human neutrophils and attenuates hemorrhagic shock-induced lung injury in rats, *Biochem. Pharmacol.* 78 (2009) 983–992.
  - [7] Y.F. Tsai, H.P. Yu, P.J. Chung, Y.L. Leu, L.M. Kuo, C.Y. Chen, T.L. Hwang, Osthol attenuates neutrophilic oxidative stress and hemorrhagic shock-induced lung injury via inhibition of phosphodiesterase 4, *Free Radic. Biol. Med.* 89 (2015) 387–400.
  - [8] N.J. Gross, M.A. Giembycz, S.I. Rennard, Treatment of chronic obstructive pulmonary disease with roflumilast, a new phosphodiesterase 4 inhibitor, *Chron. Obstr. Pulm. Dis.* 7 (2010) 141–153.
  - [9] K.H. Abbott-Banner, C.P. Page, Dual PDE3/4 and PDE4 inhibitors: novel treatments for COPD and other inflammatory airway diseases, *Basic Clin. Pharmacol. Toxicol.* 114 (2014) 365–376.
  - [10] E. Gamble, D.C. Grootendorst, C.E. Brightling, S. Troy, Y. Qiu, J. Zhu, D. Parker, D. Matin, S. Majumdar, A.M. Vignola, C. Kroegel, T.T. Hansel, S.I. Rennard, C. Compton, O. Amit, T. Tat, J. Edelson, I.D. Pavord, K.F. Rabe, N.C. Barnes, P.K. Jeffery, Antiinflammatory effects of the phosphodiesterase-4 inhibitor cilomilast (Ariflo) in chronic obstructive pulmonary disease, *Am. J. Respir. Crit. Care Med.* 168 (2003) 976–982.
  - [11] B.J. Lipworth, Phosphodiesterase-4 inhibitors for asthma and chronic obstructive pulmonary disease, *Lancet* 365 (2005) 167–175.
  - [12] A. Link, S. Selezan, C. Maack, M. Lenz, M. Bohm, Phosphodiesterase 4 inhibition but not beta-adrenergic stimulation suppresses tumor necrosis factor- $\alpha$  release in peripheral blood mononuclear cells in septic shock, *Crit. Care* 12 (2008) R159.
  - [13] F.E. McCann, A.C. Palfreeman, M. Andrews, D.P. Perocheau, J.J. Inglis, P. Schafer, M. Feldmann, R.O. Williams, F.M. Brennan, Apremilast, a novel PDE4 inhibitor, inhibits spontaneous production of tumour necrosis factor- $\alpha$  from human rheumatoid synovial cells and ameliorates experimental arthritis, *Arthritis Res. Ther.* 12 (2010) R107.
  - [14] S. Vollert, N. Kaessner, A. Heuser, G. Hanauer, A. Dieckmann, D. Knaack, H.P. Kley, R. Beume, C. Weiss-Haliti, The glucose-lowering effects of the PDE4 inhibitors roflumilast and roflumilast-N-oxide in db/db mice, *Diabetologia* 55 (2012) 2779–2788.
  - [15] A.S. Paintlia, M.K. Paintlia, I. Singh, R.B. Skoff, A.K. Singh, Combination therapy of lovastatin and rolipram provides neuroprotection and promotes neurorepair in inflammatory demyelination model of multiple sclerosis, *Glia* 57 (2009) 182–193.
  - [16] T. Akama, S.J. Baker, Y.K. Zhang, V. Hernandez, H. Zhou, V. Sanders, Y. Freund, R. Kimura, K.R. Maples, J.J. Plattner, Discovery and structure-activity study of a novel benzoxaborole anti-inflammatory agent (AN2728) for the potential topical treatment of psoriasis and atopic dermatitis, *Bioorg. Med. Chem. Lett.* 19 (2009) 2129–2132.
  - [17] Y.M. Hsu, T.Y. Wu, Y.C. Du, M. El-Shazly, L. Beerhues, T.D. Thang, H. Van Luu, T.L. Hwang, F.R. Chang, Y.C. Wu, 3-Methyl-4,5-dihydro-oxepine, polyoxygenated seco-cyclohexenes and cyclohexenes from *Uvaria flexuosa* and their anti-inflammatory activity, *Phytochemistry* 122 (2016) 184–192.
  - [18] L.N. Seito, A.L. Ruiz, D. Vendramini-Costa, S.V. Tinti, J.E. de Carvalho, J.K. Bastos, L.C. Di Stasi, Antiproliferative activity of three methoxylated flavonoids isolated from *Zeyheria montana* Mart. (Bignoniaceae) leaves, *Phytother. Res.* 25 (2011) 1447–1450.
  - [19] L.N. Seito, J.M. Sforzin, J.K. Bastos, L.C. Di Stasi, *Zeyheria montana* Mart. (Bignoniaceae) as source of antioxidant and immunomodulatory compounds with beneficial effects on intestinal inflammation, *J. Pharm. Pharmacol.* 67 (2015) 597–604.
  - [20] B.J. Compton, L. Larsen, R.T. Weavers, Use of acyl substituents to favour 2,3-epoxidation of 5,7-dioxygenated flavones with dimethyldioxirane, *Tetrahedron* 67 (2011) 718–726.
  - [21] Y.F. Tsai, H.P. Yu, W.Y. Chang, F.C. Liu, Z.C. Huang, T.L. Hwang, Sirtinol inhibits neutrophil elastase activity and attenuates lipopolysaccharide-mediated acute lung injury in mice, *Sci. Rep.* 5 (2015) 8347.
  - [22] T.L. Hwang, H.W. Hung, S.H. Kao, C.M. Teng, C.C. Wu, S.J. Cheng, Soluble guanylyl cyclase activator YC-1 inhibits human neutrophil functions through a cGMP-independent but cAMP-dependent pathway, *Mol. Pharm.* 64 (2003) 1419–1427.
  - [23] H.P. Yu, P.W. Hsieh, Y.J. Chang, P.J. Chung, L.M. Kuo, T.L. Hwang, 2-(2-Fluorobenzamido)benzoate ethyl ester (EFB-1) inhibits superoxide production by human neutrophils and attenuates hemorrhagic shock-induced organ dysfunction in rats, *Free Radic. Biol. Med.* 50 (2011) 1737–1748.
  - [24] A.L. Stenfeldt, J. Karlsson, C. Wenneras, J. Bylund, H. Fu, C. Dahlgren, The non-steroidal anti-inflammatory drug piroxicam blocks ligand binding to the formyl peptide receptor but not the formyl peptide receptor like 1, *Biochem. Pharmacol.* 74 (2007) 1050–1056.
  - [25] S.C. Yang, P.J. Chung, C.M. Ho, C.Y. Kuo, M.F. Hung, Y.T. Huang, W.Y. Chang, Y.W. Chang, K.H. Chan, T.L. Hwang, Propofol inhibits superoxide production, elastase release, and chemotaxis in formyl peptide-activated human neutrophils by blocking formyl peptide receptor 1, *J. Immunol.* 190 (2013) 6511–6519.
  - [26] Z.J. Cheng, S.C. Kuo, S.C. Chan, F.N. Ko, C.M. Teng, Antioxidant properties of butein isolated from *Dalbergia odorifera*, *Biochim. Biophys. Acta* 1392 (1998) 291–299.
  - [27] A. Tetzner, K. Gebolis, C. Meinert, S. Klein, A. Uhlich, J. Trebicka, O. Villacanas, T. Walther, G-protein-coupled receptor MrgD is a receptor for angiotensin-(1-7) involving adenylyl cyclase, cAMP, and phosphokinase A, *Hypertension* 68 (2016) 185–194.
  - [28] M.S. Eapen, R. Sodhi, G. Balakrishnan, S. Dastidar, A. Ray, L. Vijayakrishnan, Evaluation of nonradioactive cell-free cAMP assays for measuring in vitro phosphodiesterase activity, *Pharmacology* 85 (2010) 280–285.
  - [29] T.L. Hwang, G.L. Li, Y.H. Lan, Y.C. Chia, P.W. Hsieh, Y.H. Wu, Y.C. Wu, Potent inhibition of superoxide anion production in activated human neutrophils by isopedicin, a bioactive component of the Chinese medicinal herb *Fissistigma oldhamii*, *Free Radic. Biol. Med.* 46 (2009) 520–528.
  - [30] H.P. Yu, Y.C. Hsieh, T. Suzuki, T. Shimizu, M.A. Choudhry, M.G. Schwacha, I.H. Chaudry, Salutary effects of estrogen receptor-beta agonist on lung injury after trauma-hemorrhage, *Am. J. Physiol. Lung Cell. Mol. Physiol.* 290 (2006) L1004–L1009.
  - [31] T. Ito, I.P. Fraser, Y. Yeo, C.B. Highley, E. Bellas, D.S. Kohane, Anti-inflammatory function of an in situ cross-linkable conjugate hydrogel of hyaluronic acid and dexamethasone, *Biomaterials* 28 (2007) 1778–1786.
  - [32] W.Y. Chuang, Y.S. Chang, Y.K. Chao, C.J. Yeh, S.H. Ueng, C.Y. Chang, Y.H. Liu, C.K. Tseng, H.K. Chang, Y.L. Wan, C. Hsueh, Phosphorylated mTOR expression correlates with podoplanin expression and high tumor grade in esophageal squamous cell carcinoma, *Int. J. Clin. Exp. Pathol.* 8 (2015) 12757–12765.
  - [33] W.Y. Chuang, H. Chang, L.Y. Shih, P.N. Wang, Y.S. Chang, T.L. Lin, Y.S. Hung, C.J. Yeh, S.H. Ueng, T.C. Tang, M.C. Kuo, P. Dunn, J.H. Wu, H.W. Kao, C.W. Ou, Y.L. Wan, C. Hsueh, CD5 positivity is an independent adverse prognostic factor in elderly patients with diffuse large B cell lymphoma, *Virchows Arch.* 467 (2015) 571–582.
  - [34] R. Takeya, H. Sumimoto, Regulation of novel superoxide-producing NAD(P)H oxidases, *Antioxid. Redox Signal.* 8 (2006) 1523–1532.
  - [35] K. Fan Chung, Phosphodiesterase inhibitors in airways disease, *Eur. J. Pharmacol.* 533 (2006) 110–117.
  - [36] M.J. Sanz, J. Cortijo, E.J. Morcillo, PDE4 inhibitors as new anti-inflammatory drugs: effects on cell trafficking and cell adhesion molecules expression, *Pharm. Ther.* 106 (2005) 269–297.
  - [37] S.J. Smith, S. Brookes-Fazakerley, L.E. Donnelly, P.J. Barnes, M.S. Barnette, M.A. Giembycz, Ubiquitous expression of phosphodiesterase 7A in human proinflammatory and immune cells, *Am. J. Physiol. Lung Cell. Mol. Physiol.* 284 (2003) L279–L289.
  - [38] B.E. VanOffelen, B.M. de Koster, J.G. Elferink, Interaction of cyclic GMP and cyclic AMP during neutrophil migration: involvement of phosphodiesterase type III, *Biochem. Pharmacol.* 56 (1998) 1061–1063.
  - [39] Q. Chen, D.W. Powell, M.J. Rane, S. Singh, W. Butt, J.B. Klein, K.R. McLeish, Akt phosphorylates p47phox and mediates respiratory burst activity in human neutrophils, *J. Immunol.* 170 (2003) 5302–5308.
  - [40] S. Brechard, E.J. Tschirhart, Regulation of superoxide production in neutrophils: role of calcium influx, *J. Leukoc. Biol.* 84 (2008) 1223–1237.
  - [41] E.S. Van Amersfoort, T.J. Van Berkel, J. Kuiper, Receptors, mediators, and mechanisms involved in bacterial sepsis and septic shock, *Clin. Microbiol. Rev.* 16 (2003) 379–414.
  - [42] R. Nijland, T. Hofland, J.A. van Strijp, Recognition of LPS by TLR4: potential for anti-inflammatory therapies, *Mar. Drugs* 12 (2014) 4260–4273.
  - [43] J. El-Benna, M. Hurtado-Nedelec, V. Marzaoui, J.C. Marie, M.A. Gougerot-Pocidalo, P.M. Dang, Priming of the neutrophil respiratory burst: role in host defense and inflammation, *Immunol. Rev.* 273 (2016) 180–193.
  - [44] E.S. Suyenaga, E.L. Konrath, R.R. Dresch, M.A. Apel, J.A. Zuanazzi, C.G. Chaves, A.T. Henriques, Appraisal of the antichemotactic activity of flavonoids on polymorphonuclear neutrophils, *Planta Med.* 77 (2011) 698–704.
  - [45] A. Zarbock, K. Ley, Protein tyrosine kinases in neutrophil activation and recruitment, *Arch. Biochem. Biophys.* 510 (2011) 112–119.
  - [46] H. Carp, Mitochondrial N-formylmethionyl proteins as chemoattractants for neutrophils, *J. Exp. Med.* 155 (1982) 264–275.
  - [47] W.A. Marasco, S.H. Phan, H. Krutzsch, H.J. Showell, D.E. Feltner, R. Nairn, E.L. Becker, P.A. Ward, Purification and identification of formyl-methionyl-leucyl-phenylalanine as the major peptide neutrophil chemotactic factor produced by *Escherichia coli*, *J. Biol. Chem.* 259 (1984) 5430–5439.
  - [48] L. Fialkow, Y. Wang, G.P. Downey, Reactive oxygen and nitrogen species as signaling molecules regulating neutrophil function, *Free Radic. Biol. Med.* 42 (2007) 153–164.
  - [49] T.L. Hwang, S.H. Yeh, Y.L. Leu, C.Y. Chern, H.C. Hsu, Inhibition of superoxide anion and elastase release in human neutrophils by 3'-isopropoxychalcone via a cAMP-dependent pathwaysynthesis and protects hepatocytes against reactive oxygen species during hyperglycemia: involvement of a cAMP-PKA-dependent signaling pathway, *Br. J. Pharmacol.* 48 (2006) 78–87.
  - [50] S. Spisani, M.C. Pareschi, M. Buzzi, M.L. Colamussi, C. Biondi, S. Traniello, G. Pagani Zecchini, M. Pagliarola Paradisi, I. Torrini, M.E. Ferretti, Effect of cyclic AMP level reduction on human neutrophil responses to formylated peptides, *Cell Signal.* 8 (1996) 269–277.
  - [51] A. Hatzelmann, E.J. Morcillo, G. Lungarella, S. Adnot, S. Sanjar, R. Beume, C. Schudt, H. Tenor, The preclinical pharmacology of roflumilast – a selective, oral phosphodiesterase 4 inhibitor in development for chronic obstructive pulmonary disease, *Pulm. Pharmacol. Ther.* 23 (2010) 235–256.
  - [52] Y. Wang, Y. Jiang, H. Tang, X. Wang, C. Zhao, J. Chen, Phosphodiesterases

- inhibition by Bacilli Calmette-Guerin contributes to decrease asthma in allergic rats, *Iran. J. Allergy Asthma Immunol.* 10 (2011) 207–220.
- [53] S.A. Antoniu, New therapeutic options in the management of COPD – focus on roflumilast, *Int. J. Chron. Obstr. Pulm. Dis.* 6 (2011) 147–155.
- [54] S. Korkmaz, I. Erturan, M. Naziroglu, A.C. Uguz, B. Cig, I.S. Ovey, Colchicine modulates oxidative stress in serum and neutrophil of patients with Behcet disease through regulation of  $\text{Ca}^{2+}$  release and antioxidant system, *J. Membr. Biol.* 244 (2011) 113–120.
- [55] C.R. Hoyal, A. Gutierrez, B.M. Young, S.D. Catz, J.H. Lin, P.N. Tsichlis, B.M. Babior, Modulation of p47PHOX activity by site-specific phosphorylation: akt-dependent activation of the NADPH oxidase, *Proc. Natl. Acad. Sci. USA* 100 (2003) 5130–5135.
- [56] H.R. Michie, K.R. Manogue, D.R. Spriggs, A. Revhaug, S. O'Dwyer, C.A. Dinarello, A. Cerami, S.M. Wolff, D.W. Wilmore, Detection of circulating tumor necrosis factor after endotoxin administration, *N. Engl. J. Med.* 318 (1988) 1481–1486.
- [57] T. Yoshikawa, H. Takano, S. Takahashi, H. Ichikawa, M. Kondo, Changes in tissue antioxidant enzyme activities and lipid peroxides in endotoxin-induced multiple organ failure, *Circ. Shock* 42 (1994) 53–58.

# Inhibition of glutamate release by cilnidipine in rat cerebrocortical nerve terminals (synaptosomes)

Cheng Wei Lu<sup>a,b</sup>, Tzu Yu Lin<sup>a,b</sup>, Shu Kuei Huang<sup>a</sup> and Su Jane Wang<sup>c,d</sup>

Cilnidipine is an antihypertensive drug that was reported to have a neuroprotective profile. The present study aimed to investigate the effect of cilnidipine on the 4-aminopyridine (4-AP)-induced glutamate release in the rat cerebral cortex using isolated nerve terminals (synaptosomes). Cilnidipine reduced the release of glutamate release induced by 4-AP in a concentration-dependent manner. This inhibitory effect was associated with a reduction in the 4-AP-induced intrasynaptosomal  $\text{Ca}^{2+}$  concentration elevation and was not because of an alteration of the synaptosomal membrane potential. The inhibition of glutamate release by cilnidipine was markedly reduced or eliminated in the presence of the  $\text{Ca}_v2.2$  (N-type) and  $\text{Ca}_v2.1$  (P/Q-type) channel blocker  $\omega$ -conotoxin MVIIC and the protein kinase A inhibitor H89. The intracellular  $\text{Ca}^{2+}$ -release inhibitors dantrolene and CGP37157, the mitogen-activated protein kinase inhibitor PD98059 or the protein kinase C inhibitor GF109203X failed to affect the action of cilnidipine. These

results suggest that cilnidipine inhibits glutamate release from rat cortical synaptosomes through the suppression of presynaptic voltage-dependent  $\text{Ca}^{2+}$  entry and protein kinase A activity. *NeuroReport* 28:527–532 Copyright © 2017 Wolters Kluwer Health, Inc. All rights reserved.

*NeuroReport* 2017, 28:527–532

**Keywords:** cerebrocortical nerve terminals, cilnidipine, glutamate release, protein kinase A, voltage-dependent  $\text{Ca}^{2+}$  channels

<sup>a</sup>Department of Anesthesiology, Far Eastern Memorial Hospital, <sup>b</sup>Department of Mechanical Engineering, Yuan Ze University, <sup>c</sup>School of Medicine, Fu Jen Catholic University, New Taipei City and <sup>d</sup>Research Center for Chinese Herbal Medicine, College of Human Ecology, Chang Gung University of Science and Technology, Taoyuan City, Taiwan

Correspondence to Su Jane Wang, PhD, School of Medicine, Fu Jen Catholic University, No. 510, Zhongzheng Road, Xinzhuang District, New Taipei City 24205, Taiwan  
Tel: +886 2 2905 3465; fax: +886 2 2905 2096;  
e-mail: med0003@mail.fju.edu.tw

Received 16 March 2017 accepted 6 April 2017

## Introduction

Excessive glutamatergic transmission has been implicated in the pathology of epilepsy and neuronal damage following ischaemia [1]. In favour of this hypothesis, considerable evidence indicates that excitatory amino acid antagonists show anticonvulsant and neuroprotective properties in various models of epilepsy and ischaemia [2,3]. Inhibition of glutamate release by antagonizing presynaptic  $\text{Ca}^{2+}$  channels, thereby preventing the spread of neuronal excitation, may be an alternative strategy for therapeutic intervention in epilepsy and cerebral ischaemia.

Cilnidipine is a slow-onset, long-acting second-generation 1,4-dihydropyridine inhibitor of both L-type and N-type  $\text{Ca}^{2+}$  channels, and it is used as an antihypertensive drug [4,5]. Cilnidipine has been reported to penetrate the blood–brain barrier [6] and attenuate ischaemia-induced brain damage [7,8]. This neuroprotective effect is shown to be associated with reduced extracellular glutamate levels [9,10]; however, no study has reported the effects of cilnidipine on glutamate release directly in nerve terminals.

To examine the presynaptic action of cilnidipine specifically, we used the isolated nerve terminals (synaptosomes) model to assess the characteristics and mechanism of action of cilnidipine involved in the regulation of glutamate release in the rat cerebral cortex. The isolated nerve terminal preparation is a well-established model for studying the presynaptic regulation of neurotransmitter

release by drugs in the absence of any postsynaptic effects [11].

## Materials and methods

### Animals

Male Sprague-Dawley rats (150–200 g) were purchased from BioLASCO (Taiwan Co. Ltd, Taipei, Taiwan). Animals were housed in a room maintained at 25°C with a 12 h light/dark cycle. Food and water were available *ad libitum*. Animal experiments were conducted in accordance with the National Institutes of Health Guide for the Care and Use of Laboratory and were approved by the Institutional Animal Care and Use Committee at the Fu Jen Catholic University (A10414).

### Chemicals

4-aminopyridine (4-AP), bafilomycin A1, DL-threo- $\beta$ -benzyl-oxyaspartate (DL-TBOA),  $\omega$ -conotoxin MVIIC ( $\omega$ -CgTX MVIIC), dantrolene, 7-chloro-5-(2-chlorophenyl)-1,5-dihydro-4,1-benzothiazepin-2(3H)-one (CGP37157), bisindolylmaleimide I (GF109203X), 2-(2-amino-3-methoxyphenyl)-4H-1-benzopyran-4-one (PD98059) and N-[2-(p-bromocinnamyl-amino)-ethyl]-5-isoquinolinesulphonamide dihydrochloride (H89) were purchased from Tocris Cookson (Bristol, UK). 3',3',3'-dipropylthiadicarbocyanine iodide [ $\text{DiSC}_3(5)$ ] and fura-2-acetoxymethyl ester were purchased from Invitrogen (Carlsbad, California, USA). Ethylene glycol bis ( $\beta$ -amino-ethyl ether)-N,N,N',N'-tetraacetic acid and all other reagents

were purchased from Sigma-Aldrich (St Louis, Missouri, USA).

### Preparation of synaptosomes

Rats were decapitated, and their cerebral cortex was removed and homogenized in 0.32 M sucrose solution. Homogenates were then subjected to low-speed centrifugation (16 500 rpm, 7 min) and synaptosomes were purified from the supernatant by discontinuous Percoll-density gradient centrifugation as described previously [12]. The final synaptosomal pellets were resuspended in HEPES buffer medium (HBM) with the following composition (mM): NaCl, 140; KCl, 5; NaHCO<sub>3</sub>, 5; MgCl<sub>2</sub>·6H<sub>2</sub>O, 1; Na<sub>2</sub>HPO<sub>4</sub>, 1.2; glucose, 10; HEPES, 10; and pH 7.4. Protein concentration was then determined using the Bradford assay. Synaptosomes were centrifuged in the final wash to obtain synaptosomal pellets with 0.5 mg protein. Synaptosomal pellets were stored on ice and used within 4–6 h.

### Glutamate release assay

Glutamate release was assayed by on-line fluorometry [13]. Pelleted synaptosomes were resuspended in HBM containing 16  $\mu$ M BSA and incubated in a stirred and thermostated cuvette at 37°C in a Perkin-Elmer LS-55 spectrofluorimeter (PerkinElmer Life and Analytical Sciences, Waltham, Massachusetts, USA). NADP<sup>+</sup> (2 mM), glutamate dehydrogenase (50 U/ml) and CaCl<sub>2</sub> (1.2 mM) were added after 3 min. 4-AP (1 mM) was applied to induce glutamate release. The oxidative deamination of released glutamate, leading to the reduction of NADP<sup>+</sup>, was monitored by measuring NADPH fluorescence at excitation and emission wavelengths of 340 and 460 nm, respectively. A standard of exogenous glutamate (5 nmol) was added at the end of each experiment and the change in fluorescence produced by the standard addition was used to calculate the released glutamate as nanomoles glutamate per milligram synaptosomal protein. Release values quoted in the text and shown in bar graphs represent the levels of glutamate cumulatively released after 5 min of depolarization, and are expressed as nmol/mg/5 min. Data were accumulated at 2 s intervals and cumulative data were analysed using Lotus 1–2–3.

### Synaptosomal cytosolic Ca<sup>2+</sup> concentration

Ca<sup>2+</sup> concentration [Ca<sup>2+</sup>]<sub>C</sub> was measured with fura-2. Synaptosomes were resuspended (2 mg/ml) in HBM containing 16  $\mu$ M BSA in the presence of 5  $\mu$ M fura-2 and 0.1 mM CaCl<sub>2</sub> and incubated at 37°C for 30 min in a stirred test tube. After fura-2 loading, synaptosomes were pelleted and resuspended in HBM containing BSA. The synaptosomal suspension was stirred in a thermostatted cuvette containing 1.2 mM CaCl<sub>2</sub> in a Perkin-Elmer LS-55 spectrofluorimeter and the fluorescence was monitored at excitation wavelengths of 340 and 380 nm (emission wavelength 505 nm). [Ca<sup>2+</sup>]<sub>C</sub> (nM) was

calculated using the equations described by Grynkiewicz *et al.* [14].

### Synaptosomal plasma membrane potential

The synaptosomal membrane potential can be determined by positively charged membrane potential-sensitive carbocyanine dyes such as DiSC<sub>3</sub>(5) [15]. Synaptosomes were resuspended in HBM and incubated in a stirred and thermostated cuvette at 37°C in a Perkin-Elmer LS-55 spectrofluorimeter. After 3 min of incubation, 5  $\mu$ M DiSC<sub>3</sub>(5) was added and allowed to equilibrate before the addition of 1.2 mM CaCl<sub>2</sub> or cilnidipine (5  $\mu$ M). 4-AP (1 mM) was added to depolarize the synaptosomes at 10 min and DiSC<sub>3</sub>(5) fluorescence was measured at excitation and emission wavelengths of 646 and 674 nm, respectively. Results are expressed in fluorescence units.

### Data analysis

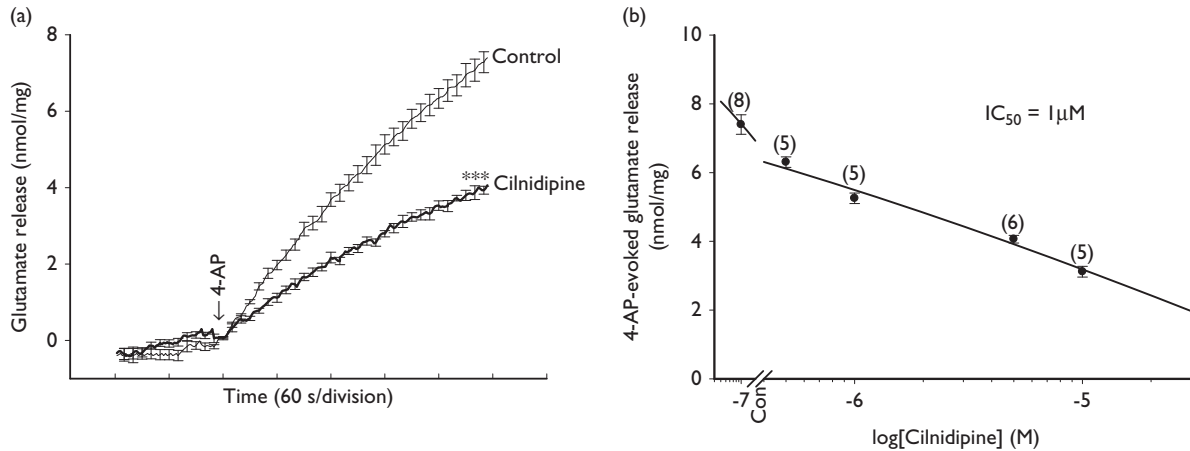
Data are presented as the mean  $\pm$  SEM. Statistical analysis was carried out using a two-tailed Student's *t*-test when comparing two groups and by one-way analysis of variance with Tukey's multiple comparisons post-hoc tests when comparing more than two groups. Analysis was completed using the SPSS software (version 17.0; SPSS Inc., Chicago, Illinois, USA). *P* value of less than 0.05 was considered statistically significant.

### Results

Synaptosomes were depolarized with the K<sup>+</sup> channel blocker 4-AP, which opens voltage-dependent Ca<sup>2+</sup> channels and induces the release of glutamate [16]. Figure 1a shows that 4-AP (1 mM) induced a glutamate release of  $7.3 \pm 0.3$  nmol/mg/5 min from synaptosomes incubated in the presence of 1.2 mM CaCl<sub>2</sub>. Preincubation of synaptosomes with cilnidipine (5  $\mu$ M) for 10 min inhibited the release of glutamate induced by 4-AP to  $3.9 \pm 0.1$  nmol/mg/5 min [ $t(12) = 9.7$ ,  $P < 0.001$ ; Fig. 1a]. The effect of cilnidipine was dose dependent, with an IC<sub>50</sub> of  $\sim 1$   $\mu$ M (Fig. 1b).

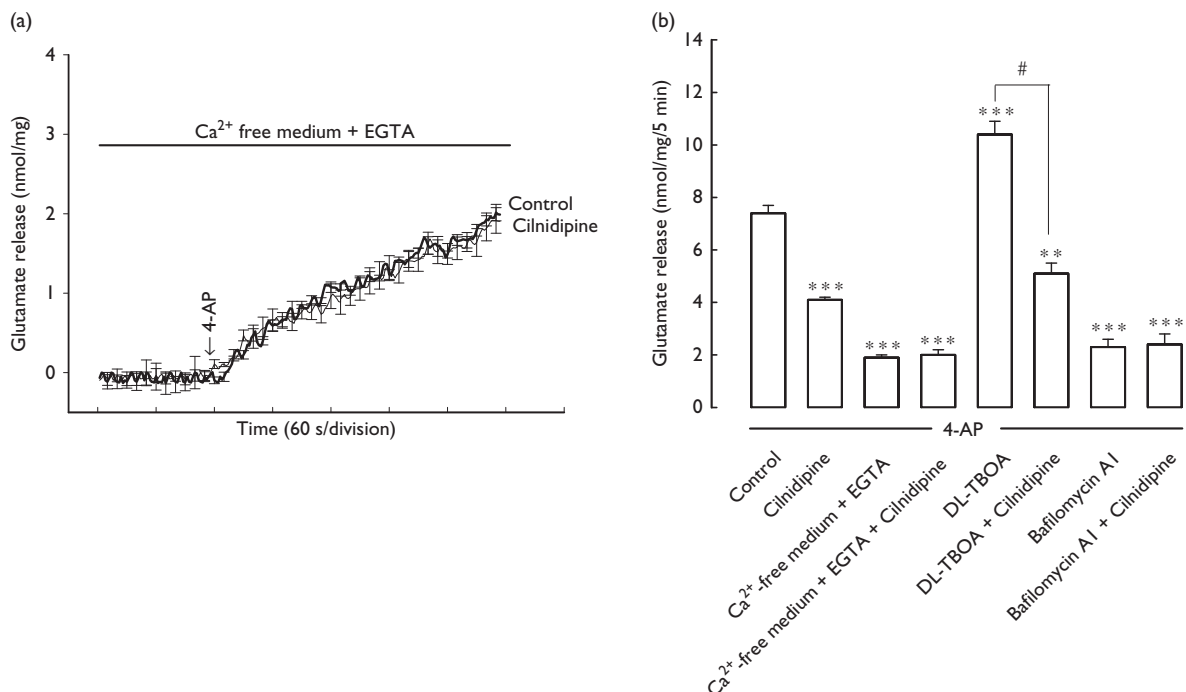
Figure 2 shows that the glutamate release induced by 4-AP (1 mM) in an extracellular Ca<sup>2+</sup>-free solution containing ethylene glycol bis ( $\beta$ -aminoethyl ether)-N,N,N',N'-tetraacetic acid (300  $\mu$ M) was  $1.9 \pm 0.1$  nmol/mg/5 min [ $F(2, 15) = 189.4$ ;  $P < 0.001$ ]. This Ca<sup>2+</sup>-independent component of the 4-AP-induced glutamate release was unaffected by cilnidipine 5  $\mu$ M ( $2.0 \pm 0.2$  nmol/mg/5 min;  $P = 0.97$ ). DL-TBOA (10  $\mu$ M), a nonselective inhibitor of all excitatory amino acid transporter subtypes, increased the 4-AP-induced glutamate release ( $P < 0.001$ ). In the presence of DL-TBOA, cilnidipine (5  $\mu$ M) still significantly reduced the 4-AP-induced release of glutamate [ $F(2, 15) = 46.1$ ;  $P < 0.001$ ; Fig. 2]. By contrast, bafilomycin A1 (0.1  $\mu$ M), a vesicular transporter inhibitor, inhibited the 4-AP-induced glutamate release and prevented the inhibitory effect of cilnidipine on 4-AP-induced glutamate release [ $F(2, 17) = 82.5$ ;  $P < 0.001$ ].

Fig. 1



Cilnidipine inhibits the 4-AP-induced glutamate release in rat cerebrocortical synaptosomes. (a) Glutamate release was induced by 4-AP (1 mM) in the absence (control) or the presence of cilnidipine (5  $\mu M$ ), added 10 min before the addition of 4-AP. (b) Concentration-dependent depression of glutamate release by cilnidipine. Data represent mean  $\pm$  SEM values of independent experiments using synaptosomal preparations from 5 to 6 animals. \*\*\* $P < 0.001$  versus the control group. 4-AP, 4-aminopyridine.

Fig. 2



Effect of external calcium omission, the glutamate transporter blocker DL-TBOA and the vesicular transporter inhibitor bafilomycin A1 on the cilnidipine-mediated inhibition of 4-AP-induced glutamate release. (a) Glutamate release was induced by 1 mM 4-AP in the absence (control) or the presence of 5  $\mu M$  cilnidipine under 300  $\mu M$  EGTA (without  $CaCl_2$ ). (b) Each column shows the mean  $\pm$  SEM values of independent experiments using synaptosomal preparations from 5 to 6 animals. \*\* $P < 0.01$ , \*\*\* $P < 0.001$  versus the control group. # $P < 0.05$  versus the DL-TBOA-treated group. 4-AP, 4-aminopyridine; DL-TBOA, DL-threo- $\beta$ -benzyloxyaspartate; EGTA, ethylene glycol bis ( $\beta$ -aminoethyl ether)-N,N,N',N'-tetraacetic acid.

In the five synaptosomal preparations tested, no statistical difference was observed between the release after bafilomycin A1 alone and after the bafilomycin A1 and

cilnidipine treatment ( $P > 0.05$ ; Fig. 2). These results indicate that cilnidipine influences the induced glutamate release by a decrease in vesicular exocytosis.



Table 1 shows the  $[Ca^{2+}]_C$  levels determined in synaptosomes pretreated with fura-2. The stimulation of synaptosomes with 1 mM 4-AP caused an increase in  $[Ca^{2+}]_C$  levels to a plateau level ( $P < 0.001$ ). Preincubation with cilnidipine (5  $\mu$ M) did not affect basal  $Ca^{2+}$  levels, but reduced the 4-AP-induced increase in  $[Ca^{2+}]_C$  [ $t(8) = 5.1$ ,  $P < 0.001$ ]. In addition, the effect of cilnidipine on the synaptosomal plasma membrane potential was examined using membrane potential-sensitive dye DiSC<sub>3</sub>(5). As shown in Table 1, 4-AP (1 mM) caused an increase in DiSC<sub>3</sub>(5) fluorescence. Preincubation of synaptosomes with cilnidipine (5  $\mu$ M) did not alter the resting membrane potential and produced no significant change in the 4-AP-mediated increase in DiSC<sub>3</sub>(5) fluorescence ( $P > 0.05$ ).

Figure 3 shows that glutamate release induced by 1 mM 4-AP was significantly decreased in the presence of 2  $\mu$ M  $\omega$ -CgTX MVIIC, a wide-spectrum blocker of  $Ca_v2.2$  (N-type) and  $Ca_v2.1$  (P/Q-type) channels, and prevented the inhibition of glutamate release by cilnidipine (5  $\mu$ M) [ $F(2, 12) = 210.9$ ;  $P < 0.001$ ]. The release measured in the presence of  $\omega$ -CgTX MVIIC and cilnidipine was similar to that obtained in the presence of  $\omega$ -CgTX MVIIC alone ( $P > 0.05$ ). Dantrolene (100  $\mu$ M), a blocker of  $Ca^{2+}$  release from endoplasmic reticulum ryanodine receptors, reduced the 4-AP (1 mM)-induced glutamate release ( $P < 0.001$ ). In the presence of dantrolene (100  $\mu$ M), the application of cilnidipine (5  $\mu$ M) still effectively inhibited 4-AP-induced glutamate release [ $F(2, 16) = 148.7$ ;  $P < 0.001$ ; Fig. 3]. Similarly, CGP37157 (100  $\mu$ M), a membrane-permeant blocker of the mitochondrial  $Na^+/Ca^{2+}$  exchanger, reduced the release of glutamate induced by 4-AP ( $P < 0.001$ ). In the presence of CGP37157 (100  $\mu$ M) and cilnidipine (5  $\mu$ M), the inhibition of glutamate release following 4-AP-depolarization was significantly different from the effect of CGP37157 alone [ $F(2, 16) = 118.2$ ;  $P < 0.001$ ; Fig. 3]. Thus, decrease in  $Ca^{2+}$  influx mediated by  $Ca_v2.2$  (N-type) and  $Ca_v2.1$  (P/Q-type) channels appears to be associated with the observed cilnidipine-mediated inhibition of glutamate release.

Figure 4 shows that H89 (100  $\mu$ M), a protein kinase A (PKA) inhibitor, reduced the 4-AP (1 mM)-induced glutamate release ( $P < 0.001$ ). In synaptosomes pretreated with H89, the inhibitory effect of cilnidipine (5  $\mu$ M) on 4-AP-induced glutamate release was prevented [ $F(2, 12) = 74.3$ ;  $P < 0.001$ ]. No statistical difference was observed between the release after H89 alone and after the H89 and cilnidipine treatment ( $P > 0.05$ ; Fig. 4). PD98059 (50  $\mu$ M), a

mitogen-activated/extracellular signal-regulated kinase inhibitor, reduced 4-AP (1 mM)-induced glutamate release ( $P < 0.001$ ). In synaptosomes pretreated with PD98059, cilnidipine (5  $\mu$ M) could still reduce 4-AP-induced glutamate release [ $F(2, 12) = 71.6$ ;  $P < 0.001$ ]. A statistical difference was observed between the release after PD98059 alone and after the PD98059 and cilnidipine treatment ( $P < 0.05$ ; Fig. 4). Similar results were also observed using 10  $\mu$ M GF109203X, a protein kinase C inhibitor [ $F(2, 12) = 256.1$ ;  $P < 0.001$ ; Fig. 4].

## Discussion

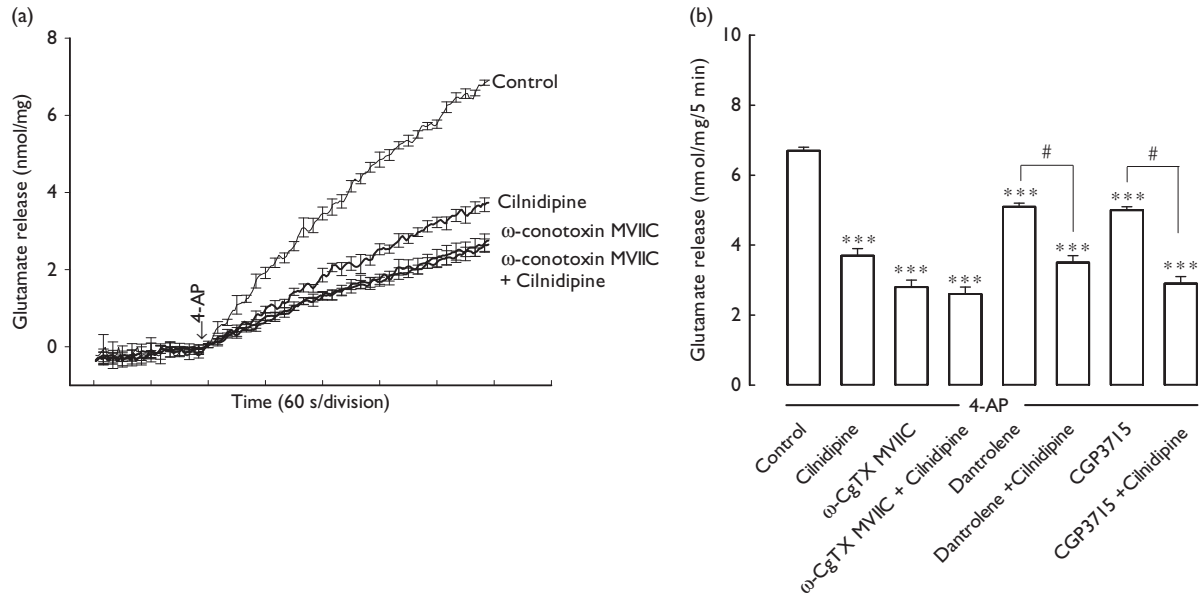
This study is the first to show that cilnidipine, a  $Ca^{2+}$  channel blocker that is used as an antihypertensive drug [4,5], inhibits glutamate release from cerebrocortical nerve terminals (synaptosomes) in rats. The release of neurotransmitter from presynaptic sites is a possible target for drug regulation of excitability and synaptic transmission in central neurons. In principle, neurotransmitter release is a complex phenomenon and can be modulated at several putative sites in the nerve terminal, including the  $Na^+$  channels,  $K^+$  channels,  $Ca^{2+}$  channels, as well as the release process itself. Activation of  $Na^+$  channels or inhibition of  $K^+$  channels is known to regulate membrane excitability and consequently the amount of transmitter release [17,18]. The results obtained in the present study indicate that cilnidipine inhibits the 4-AP-induced  $Ca^{2+}$ -dependent glutamate exocytosis primarily by reducing  $Ca^{2+}$  entry through  $Ca_v2.2$  (N-type) and  $Ca_v2.1$  (P/Q-type) channels, in the absence of any effect on synaptosomal excitability. First, cilnidipine significantly reduced the induced increase in  $[Ca^{2+}]_C$ . Second, when  $Ca_v2.2$  (N-type) and  $Ca_v2.1$  (P/Q-type) channels were blocked by  $\omega$ -CgTX MVIIC, the inhibitory effect of cilnidipine was markedly reduced compared with that without  $\omega$ -CgTX MVIIC preapplication. Third, cilnidipine-mediated inhibition of glutamate release was unchanged with or without the intracellular  $Ca^{2+}$ -release inhibitors dantrolene and CGP37157 preapplication. Finally, cilnidipine did not affect the synaptosomal membrane potential. Our finding is in agreement with previous electrophysiological data showing that cilnidipine inhibits high-voltage-activated  $Ca^{2+}$  currents in rat hippocampal neurons [19] and dorsal root ganglion neurons [20]. However, the blockade of  $Ca_v2.2$  (N-type) and  $Ca_v2.1$  (P/Q-type) channel activity could not fully block the action of cilnidipine on 4-AP-induced glutamate release (about 4% of inhibition remained); thus, we cannot rule out the possibility that other unidentified types of  $Ca^{2+}$  channels or other presynaptic pathways might be involved in the action of cilnidipine.

PKA is an important intracellular signalling system that is known to be present at the presynaptic level and plays a crucial role in neurotransmitter release [21,22]. In the present study, we found that PKA inhibitor H89 could successfully antagonize the inhibitory effect of

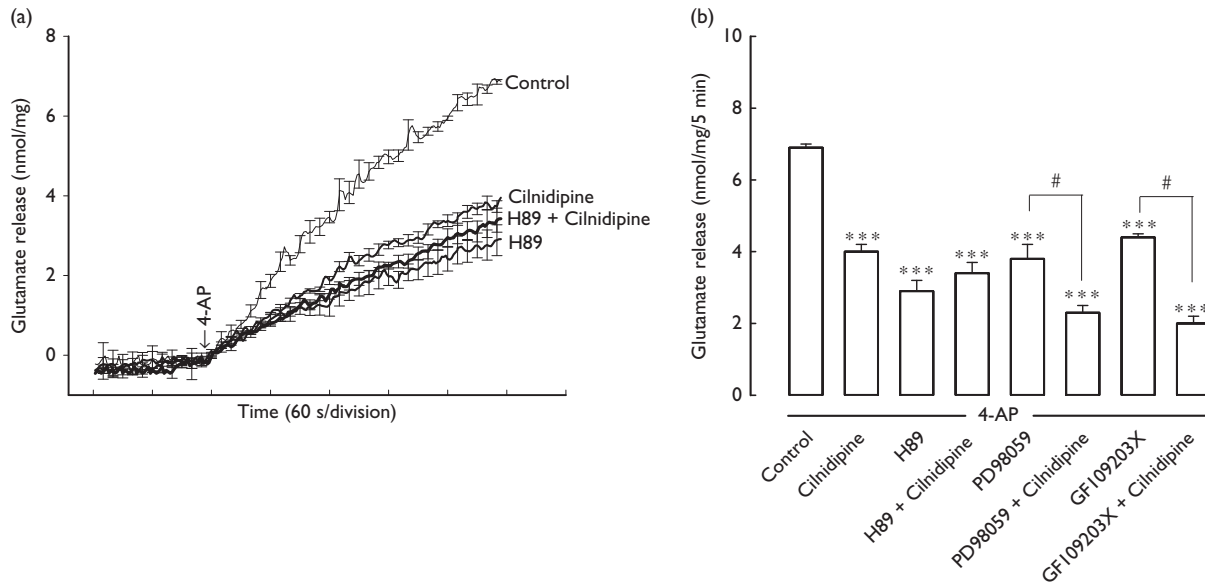
**Table 1 Effect of cilnidipine on synaptosomal membrane potential and cytosolic  $Ca^{2+}$  levels from rat cortical synaptosomes**

	Membrane potential (fluorescence units)			Cytosolic $[Ca^{2+}]$ (nM)		
	Basal	4-AP (1 mM)	n	Basal	4-AP (1 mM)	n
Control	1.4 $\pm$ 1.0	9.1 $\pm$ 0.5	5	137.1 $\pm$ 2.3	196.3 $\pm$ 4.6	5
Cilnidipine	0.7 $\pm$ 0.1	9.7 $\pm$ 1.1	5	135.4 $\pm$ 2.8	164.0 $\pm$ 4.4***	5

\*\*\* $P < 0.001$  versus the control group.

**Fig. 3**

Effect of  $\text{Ca}_v2.2$  (N-type) and  $\text{Ca}_v2.1$  (P/Q-type) channel blocker  $\omega$ -CgTX MVIIC or intracellular  $\text{Ca}^{2+}$  release inhibitors dantrolene and CGP37157 on the cilnidipine-mediated inhibition of 4-AP-induced glutamate release. (a) Glutamate release was induced by 1 mM 4-AP in the absence (control) or the presence of 5  $\mu\text{M}$  cilnidipine, 2  $\mu\text{M}$   $\omega$ -CgTX MVIIC, 2  $\mu\text{M}$   $\omega$ -CgTX MVIIC and 5  $\mu\text{M}$  cilnidipine. (b) Each column shows the mean  $\pm$  SEM values of independent experiments using synaptosomal preparations from 5 to 7 animals. \*\*\* $P < 0.001$  versus the control group; # $P < 0.05$  versus the dantrolene-treated or the CGP37157-treated group. 4-AP, 4-aminopyridine.

**Fig. 4**

Effect of the PKA inhibitor H89, MAPK inhibitor PD9805 and GF109203X, a PKC inhibitor on cilnidipine-mediated inhibition of 4-AP-induced glutamate release. (a) Glutamate release was induced by 1 mM 4-AP in the absence (control) or the presence of 5  $\mu\text{M}$  cilnidipine, 100  $\mu\text{M}$  H89 or 100  $\mu\text{M}$  H89 and 5  $\mu\text{M}$  cilnidipine. (b) Each column shows the mean  $\pm$  SEM values of independent experiments using synaptosomal preparations from five animals. 4-AP, 4-aminopyridine; MARK, mitogen-activated protein kinase; PKA, protein kinase A; PKC, protein kinase C. \*\*\* $P < 0.001$  versus the control group; # $P < 0.05$  versus the PD98059-treated or the GF109203X-treated group.

cilnidipine on 4-AP-induced glutamate release, whereas the protein kinase C inhibitor GF109203X or mitogen-activated protein kinase inhibitor PD98059 did not exert any effect. Thus, these observations from the present study point to the fact that suppression of PKA is linked to the inhibition of 4-AP-induced glutamate release by cilnidipine. In fact, depolarization-stimulated  $\text{Ca}^{2+}$  entry has been shown to enhance  $\text{Ca}^{2+}$ /calmodulin-dependent PKA cascade and glutamate release [23,24]. Thus, the inhibitory effect of cilnidipine on  $\text{Ca}^{2+}$  entry observed here may decrease the  $\text{Ca}^{2+}$ -calmodulin/PKA cascade and, in turn, glutamate release. In addition, several synaptic proteins involved in the synaptic vesicle trafficking/recruitment and exocytosis have been found to be phosphorylated by PKA [22]. It remains to be determined whether the suppression of PKA-dependent regulation of synaptic proteins is also involved in the inhibitory effect of cilnidipine on glutamate release.

## Conclusion

A role of cilnidipine in reducing ischaemic brain injury has been studied previously [7,8]; however, its precise mechanism remains unclear. Considering the fact that excitotoxicity caused by excessive glutamate has been proposed as an important contributing factor in many brain diseases [25], we suggested that reduced glutamate release from nerve terminals is at least partially involved in the neuroprotective activity of cilnidipine.

## Acknowledgements

This work was supported by a grant (104-FEMH-FJU-01) from the Far Eastern Memorial Hospital, Taiwan, Republic of China.

## Conflicts of interest

There are no conflicts of interest.

## References

- Choi DW. Glutamate neurotoxicity and diseases of the nervous system. *Neuron* 1998; **1**:623–634.
- Gigler G, Móricz K, Agoston M, Simó A, Albert M, Benedek A, *et al.* Neuroprotective and anticonvulsant effects of EGIS-8332, a non-competitive AMPA receptor antagonist, in a range of animal models. *Br J Pharmacol* 2007; **152**:151–160.
- Luján-Miras R. Metabotropic glutamate receptors: new molecular targets in the treatment of neurological and psychiatric diseases. *Rev Neurol* 2005; **40**:43–53.
- Takeda K, Yamagishi R, Masumiya H, Tanaka H, Shigenobu K. Effect of cilnidipine on L- and T-type calcium currents in guinea pig ventricle and action potential in rabbit sinoatrial node. *J Pharmacol Sci* 2004; **95**:398–401.
- Yoshimoto R, Dohmoto H, Yamada K, Goto A. Prolonged inhibition of vascular contraction and calcium influx by the novel 1,4-dihydropyridine calcium antagonist cinaldipine (FRC-8653). *Jpn J Pharmacol* 1991; **56**:225–229.
- Yano K, Takimoto S, Motegi T, Tomono T, Hagiwara M, Idota Y, *et al.* Role of P-glycoprotein in regulating cilnidipine distribution to intact and ischemic brain. *Drug Metab Pharmacokinet* 2014; **29**:254–258.
- Takahara A, Konda T, Enomoto A, Kondo N. Neuroprotective effects of a dual L/N-type  $\text{Ca}^{2+}$  channel blocker cilnidipine in the rat focal brain ischemia model. *Biol Pharm Bull* 2004; **27**:1388–1391.
- Son JW, Choi H, Yoo A, Park HH, Kim YS, Lee KY, *et al.* Activation of the phosphatidylinositol 3-kinase pathway plays important roles in reduction of cerebral infarction by cilnidipine. *J Neurochem* 2015; **135**:186–193.
- Takizawa S, Matsushima K, Fujita H, Nanri K, Ogawa S, Shinohara Y. A selective N-type calcium channel antagonist reduces extracellular glutamate release and infarct volume in focal cerebral ischemia. *J Cereb Blood Flow Metab* 1995; **15**:611–618.
- Valentino K, Newcomb R, Gadbois T, Singh T, Bowersox S, Bitner S, *et al.* A selective N-type calcium channel antagonist protects against neuronal loss after global cerebral ischemia. *Proc Natl Acad Sci USA* 1993; **90**:7894–7897.
- Perkinton MS, Sihra TS. A high-affinity presynaptic kainate-type glutamate receptor facilitates glutamate exocytosis from cerebral cortex nerve terminals (synaptosomes). *Neuroscience* 1999; **90**:1281–1292.
- Nicholls DG, Sihra TS. Synaptosomes possess an exocytotic pool of glutamate. *Nature* 1986; **321**:772–773.
- Wang SJ, Wu WM, Yang FL, Hsu GS, Huang CY. Vitamin B<sub>2</sub> inhibits glutamate release from rat cerebrocortical nerve terminals. *Neuroreport* 2008; **19**:1335–1338.
- Gryniewicz G, Poenie M, Tsien RY. A new generation of  $\text{Ca}^{2+}$  indicators with greatly improved fluorescence properties. *J Biol Chem* 1985; **260**:34403–34405.
- Akerman KE, Scott IG, Heikkilä JE, Heinonen E. Ionic dependence of membrane potential and glutamate receptor-linked responses in synaptoneuroosomes as measured with a cyanine dye, DiS-C<sub>2</sub>(5). *J Neurochem* 1987; **48**:552–559.
- Nicholls DG. Presynaptic modulation of glutamate release. *Prog Brain Res* 1998; **116**:15–22.
- Sihra TS, Nichols RA. Mechanisms in the regulation of neurotransmitter release from brain nerve terminals: current hypotheses. *Neurochem Res* 1993; **18**:47–58.
- Wu LG, Saggau P. Presynaptic inhibition of elicited neurotransmitter release. *Trends Neurosci* 1997; **20**:204–212.
- Murai Y, Uneyama H, Ishibashi H, Takahama K, Akaike N. Preferential inhibition of L- and N-type calcium channels in the rat hippocampal neurons by cilnidipine. *Brain Res* 2000; **854**:6–10.
- Fujii S, Kameyama K, Hosono M, Hayashi Y, Kitamura K. Effect of cilnidipine, a novel dihydropyridine  $\text{Ca}^{2+}$ -channel antagonist, on N-type  $\text{Ca}^{2+}$  channel in rat dorsal root ganglion neurons. *J Pharmacol Exp Ther* 1997; **280**:1184–1191.
- Millán C, Torres M, Sánchez-Prieto J. Co-activation of PKA and PKC in cerebrocortical nerve terminals synergistically facilitates glutamate release. *J Neurochem* 2003; **87**:1101–1111.
- Ferrero JJ, Alvarez AM, Ramírez-Franco J, Godino MC, Bartolomé-Martin D, Aguado C, *et al.*  $\beta$ -Adrenergic receptors activate exchange protein directly activated by cAMP (Epac), translocate Munc13-1, and enhance the Rab3A-RIM1 $\alpha$  interaction to potentiate glutamate release at cerebrocortical nerve terminals. *J Biol Chem* 2013; **288**:31370–31385.
- Rodríguez-Moreno A, Sihra TS. Presynaptic kainate receptor-mediated facilitation of glutamate release involves  $\text{Ca}^{2+}$ -calmodulin and PKA in cerebrocortical synaptosomes. *FEBS Lett* 2013; **587**:788–792.
- Andrade-Talavera Y, Duque-Feria P, Negrete-Díaz JV, Sihra TS, Flores G, Rodríguez-Moreno A. Presynaptic kainate receptor-mediated facilitation of glutamate release involves  $\text{Ca}^{2+}$ -calmodulin at mossy fiber-CA3 synapses. *J Neurochem* 2012; **122**:891–899.
- Beal MF. Mechanisms of excitotoxicity in neurologic diseases. *FASEB J* 1992; **6**:3338–3344.



## Research paper

## Anti-melasma codrug of retinoic acid assists cutaneous absorption with attenuated skin irritation

Pei-Wen Hsieh<sup>a,b,c</sup>, Chi-Feng Hung<sup>d</sup>, Chih-Hung Lin<sup>e</sup>, Chang-Wei Huang<sup>f</sup>, Jia-You Fang<sup>b,c,f,g,\*</sup><sup>a</sup> Medicinal Chemistry Laboratory, Graduate Institute of Natural Products, Chang Gung University, Kweishan, Taoyuan, Taiwan<sup>b</sup> Research Center for Food and Cosmetic Safety and Research Center for Chinese Herbal Medicine, Chang Gung University of Science and Technology, Kweishan, Taoyuan, Taiwan<sup>c</sup> Department of Anesthesiology, Chang Gung Memorial Hospital, Kweishan, Taoyuan, Taiwan<sup>d</sup> School of Medicine, Fu Jen Catholic University, Hsinchuang, New Taipei City, Taiwan<sup>e</sup> Center for General Education, Chang Gung University of Science and Technology, Kweishan, Taoyuan, Taiwan<sup>f</sup> Pharmaceutics Laboratory, Graduate Institute of Natural Products, Chang Gung University, Kweishan, Taoyuan, Taiwan<sup>g</sup> Chinese Herbal Medicine Research Team, Healthy Aging Research Center, Chang Gung University, Kweishan, Taoyuan, Taiwan

## ARTICLE INFO

## Article history:

Received 7 November 2016

Revised 16 December 2016

Accepted in revised form 12 January 2017

Available online 1 February 2017

## Keywords:

Codrug

Retinoic acid

Hydroquinone

Cutaneous absorption

Melasma

## ABSTRACT

Melasma treatment with combined retinoic acid (RA) and hydroquinone (HQ) usually causes unsatisfactory outcomes and safety concerns. This study attempted to evaluate the cutaneous absorption and skin tolerance of the codrug conjugated with RA and HQ via ester linkage. The codrug's permeation of the pig skin was estimated using Franz diffusion cell. The codrug and parent drugs were comparatively examined for anti-inflammatory activity and tyrosinase inhibition. In vivo cutaneous irritation was assessed on nude mouse skin. Chemical conjugation of RA with HQ increased the lipophilicity and thus the skin absorption. The codrug absorption produced a 5.5- and a 60.8-fold increment compared to RA skin deposition at an equimolar (1.2 mM) and saturated solubility dose, respectively. The cumulative amount of HQ derived from the codrug in the receptor was comparable to or less than that of topically applied HQ. The RA-HQ codrug was partly hydrolyzed on penetrating the skin. The hydrolysis rate in intact skin was significantly lower than that in esterase medium and skin homogenates. The codrug showed an interleukin (IL)-6 inhibition activity comparable to RA. A therapeutic index 6-fold greater than RA was obtained with the topical codrug. The tyrosinase inhibition percentage of the codrug and HQ was 13% and 21%, respectively. The skin tolerance test determined by transepidermal water loss (TEWL), redness, and histopathology had exhibited minor skin irritation caused by the codrug compared to the physical mixture of RA and HQ at an equivalent dose. Topical codrug delivery not only promoted RA absorption, but also diminished the adverse effects of the parent agents.

© 2017 Elsevier B.V. All rights reserved.

## 1. Introduction

Melasma is a facial hypermelanosis characterized by irregular melanin accumulation in the skin. It can be caused by ultraviolet (UV) light exposure, pregnancy, oral contraceptive consumption, and endocrine dysfunction [1]. Melasma is found in 41% of females between the period of pregnancy and menopause [2]. The condition often develops slowly and continues for 9–12 years [3]. The use of topically applied hydroquinone (HQ) is the standard management of melasma due to the inhibitory ability of melanin synthesis. Topical retinoic acid (RA) therapy is also standard for

melasma treatment owing to the bioactivity of cell-turnover regulation and its antioxidant property. The cutaneous photoaging and inflammation induced by UV can be reduced by RA [4]. Combined therapy using HQ plus RA is usually used in the treatment of melasma [5]. However, melasma is still recalcitrant to the dual drug treatment because it is prone to relapse with rebound hyperpigmentation. Subsequently, a prolonged treatment duration is necessary. This leads to a high incidence of adverse events (40%) in patients receiving combination therapy [6]. The undesired occurrence of skin itching, burning, and allergic dermatitis has led to the issue of patient compliance.

The simultaneous administration of two drugs in a physical mixture may not be an efficient method to achieve absorption to the target site and therefore may result in a poor response to the disease [7]. Structural manipulation of the drugs is a valid approach to enhance skin permeation. It is possible to covalently

\* Corresponding author at: Pharmaceutics Laboratory, Graduate Institute of Natural Products, Chang Gung University, 259 Wen-Hwa 1st Road, Kweishan, Taoyuan 333, Taiwan.

E-mail address: [fajy@mail.cgu.edu.tw](mailto:fajy@mail.cgu.edu.tw) (J.-Y. Fang).

conjugate two drug molecules to form codrugs to ameliorate cutaneous delivery. Like the prodrug strategy, the codrugs can improve the biomembrane passage, extend the therapeutic period, increase the therapeutic outcome, and minimize the toxicity as compared to the parent drugs [8]. The production of unwanted promoiety by prodrug hydrolysis is absent in the case of codrugs [9]. RA possesses a carboxylic acid moiety, while HQ contains the hydroxyl groups, recognizing a possible formation of the esterified codrug for treating melasma. We aimed to synthesize the RA-HQ codrug to evaluate skin absorption and irritation via topical application. It was hypothesized that the codrug would increase the lipophilicity and thus enhance the cutaneous penetration relative to the parent drugs. Improved melasma therapy with attenuated irritation was anticipated.

The physicochemical properties of the codrug such as the melting point, lipophilicity, and solubility in aqueous solution and oil were characterized in the present study. The codrug hydrolysis was examined in esterases and skin homogenates to confirm the cleavage after entering the skin. The skin absorption was assessed by Franz diffusion cell with pig skin as the permeation barrier. The parent agent alone and the physical mixture of RA and HQ were included for comparison. The therapeutic effect of the codrug itself could be inactive, less active, or more active than the parent drugs [10]. The pharmacological activity of the RA-HQ conjugate could not be neglected. The anti-cytokine action and tyrosinase inhibition of the codrug were tested to elucidate this plausibility. Finally, the *in vivo* skin irritation elicited by the codrug and parent actives was analyzed based on the cutaneous physiology and histopathology.

## 2. Materials and methods

### 2.1. Synthesis of the codrug

Retinoic acid (1 mmol) and hydroquinone (1.2 mmol) dissolved in dry dichloromethane tetrahydrofuran with a ratio of 2:1, *N,N*-dicyclohexylcarbodiimide (DCC, 1.3 mmol) and 4-(*N,N*-dimethylamino)-pyridine (DMAP, 0.8 mmol) were added to react under nitrogen. The reaction mixture was stirred for 48 h at room temperature. The solution was filtered and washed with an excess of dichloromethane. The filtrate was washed with water and dried over anhydrous magnesium sulfate. After removal of the solvent by evaporation under reduced pressure, the residue was purified by column chromatography on silica gel using ethyl acetate: *n*-hexane (44:5:6) as eluent. The scheme of synthesis is shown in

**Fig. 1.** The structure of the codrug was verified by nuclear magnetic resonance (NMR, Avance 400, Bruker) and Fourier transform infrared spectroscopy (FTIR, FT/IR-4100, Jasco). IR (KBr)  $\nu_{\max}$  3429, 2926, 2862, 1700, 1603, 1577, 1510, 1444, 1354, 1134, 955  $\text{cm}^{-1}$ ;  $^1\text{H}$  NMR (400 MHz,  $\text{CDCl}_3$ )  $\delta$  7.08 (1H, dd,  $J = 15.8, 11.6$  Hz), 6.96 (2H, d,  $J = 8.4$  Hz), 6.77 (2H, d,  $J = 8.4$  Hz), 6.37 (1H, d,  $J = 15.8$ ), 6.31 (1H, d,  $J = 15.8$  Hz), 6.18 (1H, d,  $J = 11.6$  Hz), 6.16 (1H, d,  $J = 15.8$  Hz), 5.98 (1H, s), 2.40 (3H, s), 2.02 (2H, m), 2.02 (3H, s), 1.76 (3H, m), 1.62 (2H, m), 1.47 (2H, m), 1.03 (6H, s).  $^{13}\text{C}$  NMR (100 MHz,  $\text{CDCl}_3$ )  $\delta$  166.6 (s), 155.6 (s), 153.2 (s), 144.1 (s), 140.4 (s), 137.6 (s), 137.2 (d), 134.7 (d), 132.0 (d), 130.2 (s), 129.4 (d), 129.1 (d), 122.6 (2C, d), 117.1 (d), 115.9 (2C, d), 40.0 (t), 33.5 (t), 29.4 (2C, q), 22.2 (q), 19.6 (t), 14.5 (q), 13.4 (q). **Figs. S1 and S2** show the spectra of RA, HQ, and RA-HQ codrug determined by NMR and FTIR, respectively.

### 2.2. Melting point

The melting points of the parent drugs and the codrug were measured by a differential scanning calorimeter (Q2000, TA Instruments).

### 2.3. *N*-octanol/water partitioning ( $\log P$ )

A methanolic solution (1 ml) of RA, HQ, or codrug (0.5 mg) was prepared in a glass tube. Methanol was evaporated by a vacuum. The *n*-octanol and deionized water, 1 ml of each, were added to the tube. After being shaken for 24 h at 37 °C, the phases were separated by centrifugation at 10000g for 10 min. The compound concentration in organic solvent and water was detected by high-performance liquid chromatography (HPLC). The *n*-octanol/water partition coefficient was calculated as  $\log P$ . The stationary phase of HPLC was a 25-cm-long, 4-mm inner diameter reverse-phase C18 column (Merck). The mobile phase for RA and the codrug consisted of methanol and pH 4.5 phosphate buffer (95:5) at a flow rate of 1 ml/min. The UV wavelength of the detector was set at 343 nm. The mobile phase for HQ consisted of methanol and pH 2 phosphate buffer (10:90). The flow rate and wavelength for HQ were 1 ml/min and 288 nm, respectively.

### 2.4. Saturated solubility

An excess amount of RA, HQ, or codrug was added to 1 ml of 50% propylene glycol (PG)/pH 7.4 buffer or mineral oil. The mixture in the test tube was shaken reciprocally at 37 °C for 24 h. After the

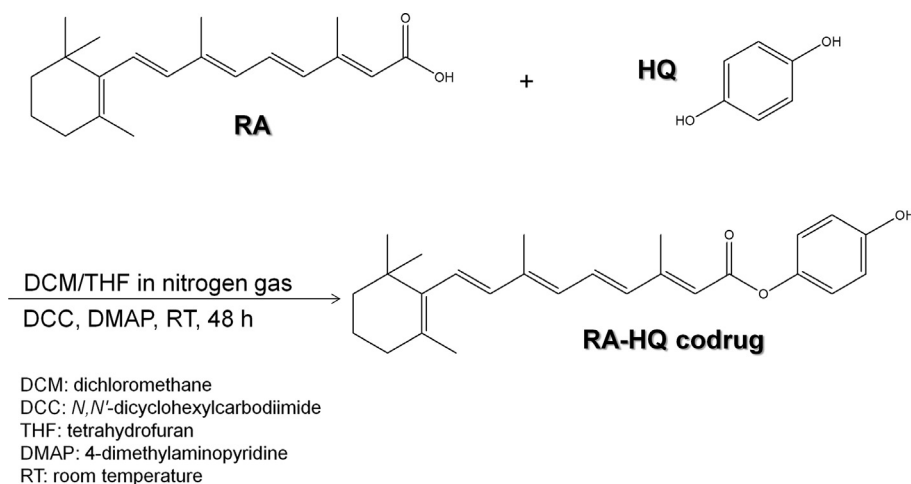


**Fig. 1.** Chemical reaction scheme for synthesizing retinoic acid (RA)-hydroquinone (HQ) codrug.



centrifugation at 10000g for 10 min, the supernatant was filtered through a PVDF membrane with a pore size of 0.45  $\mu\text{m}$ . The concentration of the compounds was quantified by HPLC.

## 2.5. Animals

The specific pathogen-free, 1-week-old pigs were purchased from Animal Technology Institute Taiwan (Miaoli, Taiwan). The 8-week-old female nude mice were obtained from National Laboratory Animal Center (Taipei, Taiwan). All animal studies were performed according to the institutional guidelines and were approved by the Animal Care and Use Committee of Chang Gung University.

## 2.6. Enzymatic hydrolysis of the codrug

The codrug hydrolysis was evaluated in the presence of esterases, pig skin homogenate, and nude mouse skin homogenate. The preparation procedures of esterase medium and skin homogenates were described previously [11]. The RA-HQ codrug at 0.5 mg/ml was pipetted into the esterase medium and skin homogenates (2 ml) and shaken at 37 °C for 200 min. The reaction mixture (200  $\mu\text{l}$ ) was withdrawn at predetermined intervals. Acetonitrile (400  $\mu\text{l}$ ) was added into the mixture to terminate the enzymatic reaction. The mixture was filtered through the PVDF membrane and then analyzed by HPLC to measure the codrug level remaining in the mixture.

## 2.7. In vitro cutaneous absorption

The cutaneous absorption of the permeants was analyzed using Franz diffusion cell. The excised skin was mounted on the Franz cell receptor with the stratum corneum (SC) side facing upward into the donor. The delipid, SC-stripped, and desebum skin were prepared according to our previous study [12,13]. The cell receptor was 5.5 ml of 30% ethanol in pH 7.4 buffer. The permeants in 50% PG/pH 7.4 buffer or mineral oil were loaded in the donor (0.5 ml). The permeant concentration in the donor was either the equimolar dose (1.2 mM) or the saturated solubility. The stirring rate and temperature of the receptor were set at 600 rpm and 37 °C, respectively. The skin and the receptor medium were taken at the end of the experiment (24 h). The permeant amount in the skin and receptor was analyzed by HPLC. The method to extract the permeants from the skin was the same as in our previous work [14].

## 2.8. Interleukin (IL)-6 expression in activated keratinocytes

The condition for culturing human immortalized keratinocytes (HaCaT) was described previously [15]. The cell viability after RA, HQ, or codrug treatment was evaluated by the method of 3-(4,5)-dimethylthiazol-2-yl)-2,5-diphenyltetrazolium bromide (MTT) [16]. The HaCaT cells starved in DMEM were treated with the compounds (5  $\mu\text{M}$ ) for 24 h to determine the IL-6 protein level. Imiquimod (20  $\mu\text{g}/\text{ml}$ ) was then treated for 4 h to activate the keratinocyte inflammation. The IL-6 protein was quantified by ELISA kit, based on the manufacturer's guidelines [17].

## 2.9. Tyrosinase inhibition

A tyrosinase solution (2 unit/ $\mu\text{l}$ ) in PBS was prepared to test the inhibitory ability of RA, HQ, or the codrug on tyrosinase activity. The reaction mixture consisted of 1  $\mu\text{l}$  tyrosinase solution and 5  $\mu\text{l}$  compound (0.2 mg/ml) in 94  $\mu\text{l}$  PBS in a 96-well plate. The mixture was incubated at 37 °C for 5 min. Subsequently, a 5-mM L-3,4-dihydroxyphenylalanine (L-DOPA) with a volume of 100  $\mu\text{l}$  was added to the plates for a 20-min incubation. The amount of

dopachrome in the mixture was analyzed by a spectrophotometer at 475 nm. The tyrosinase inhibition (%) was calculated [18]. The structures of the compounds were estimated for the ability to bind to tyrosinase by using the software from Discovery Studio 3.1 (Accelrys). The detailed process for this molecular docking was demonstrated in the previous investigation [19].

## 2.10. In vivo skin tolerance test

To examine whether the permeants induced skin irritation, a 0.3-ml aliquot of 50% PG/pH 7.4 buffer containing RA, HQ, or the codrug (1.2 mM) was spread over a nonwoven polyethylene cloth ( $1 \times 1 \text{ cm}^2$ ) for topical application on the nude mouse back. The cloth was fixed with Tegaderm® (3 M) and Fixomull® stretch adhesive tape (Beiersdorf AG). The cloth was removed and replaced with a new one each day for 5 days. The treated skin site was measured by transepidermal water loss (TEWL, TM300, Courage and Khazaka) and erythema (a\*, CD100, Yokogawa) every day after removing the cloth. At the end of the experiment, the skin surface's appearance was photographed using a handheld digital microscope (Mini Scope-V, M&T Optics). Then the mice were sacrificed to excise the dorsal skin for histopathological examination stained by hematoxylin and eosin (H&E). The skin slices were imaged under a light microscope (IX81, Olympus).

## 2.11. Data analysis

In the in vitro cutaneous absorption, the skin deposition and cumulative amount in the receptor ( $\text{nmol}/\text{cm}^2$ ) after a 24-h application were calculated as the representative data of skin permeability. In the case of the absorption from the saturated solution, the calibrated skin deposition (CSD) or calibrated cumulative amount (CCA) was computed from the skin deposition or cumulative amount divided by the applied dose (saturated solubility) in the donor. This allowed a fair comparison of cutaneous absorption among the permeants. The therapeutic index of the topically applied RA, HQ, or codrug was estimated from the result of the skin deposition or the cumulative amount multiplied by the bioactivity such as the IL-6 inhibition percentage and the tyrosinase inhibition percentage.

The experimental data were presented as mean and standard deviation (S.D.). The difference in the data of the different groups was compared using the Kruskal-Wallis test. The post hoc test for checking individual differences was the Dunn's test. A 0.05 level of probability ( $p < 0.05$ ) was recognized as the level of significance.

# 3. Results

## 3.1. Physicochemical properties of RA, HQ, and the codrug

The physicochemical characters of the RA-HQ codrug were measured and compared to those of the parent drugs as summarized in Table 1. The melting point revealed a lower value of the codrug (179 °C) as compared to RA (185 °C), suggesting the reduction of intermolecular cohesion and crystallinity. However, the melting point of the codrug was higher than that of HQ (174 °C). HQ exhibited a log *P* level of 0.48. The log *P* of RA and the codrug was not determined since almost all molecules were present in the organic phase but the concentration in the aqueous phase was below the limit of detection. A predicted log *P* (Alog *P*) was measured by Discovery Studio molecular modeling. The codrug showed an extremely lipophilic characteristic with an Alog *P* of 7.11, followed by RA and HQ. The Alog *P* of HQ (1.35) was found to be higher than the experimental log *P*. Table 1 shows an extremely high HQ solubility in aqueous solution. This medium could

**Table 1**

Physicochemical properties of retinoic acid (RA), hydroquinone (HQ), and RA-HQ codrug.

Compound	Molecular weight (g/mol)	Melting point (°C)	log $P^a$	Alog $P^{b,c}$	Solubility in 50% PG (nmol/ml)	Solubility in mineral oil (nmol/ml)
RA	300.44	185.20	– <sup>c</sup>	5.55	1116.03 ± 10.45	591.33 ± 3.03
HQ	110.11	173.66	0.48 ± 0.004	1.35	>5000	20.50 ± 0.35
Codrug	392.53	178.83	–	7.11	2.44 ± 0.63	132.71 ± 2.60

<sup>a</sup> log  $P$ , logarithm of compound amount in *n*-octanol/compound amount in water.<sup>b</sup> Alog  $P$ , the partition coefficient predicted by molecular modeling software.<sup>c</sup> –, Not determined.

dissolve HQ at an amount of >5000 nmol/ml. The aqueous solubility of RA was 1116 nmol/ml. The RA-HQ codrug demonstrated a very low solubility in aqueous medium due to its high lipophilicity. The mineral oil solubility of the codrug (133 nmol/ml) was higher compared to the aqueous solubility (2 nmol/ml). Contrary to this result, HQ and RA had lower oil solubility as compared to aqueous solubility. RA was 4.5 times more soluble in mineral oil than the codrug.

### 3.2. Enzymatic hydrolysis of the codrug

Fig. 2 depicts the percentage-time profiles for the disappearance of the codrug after hydrolysis. The codrug hydrolysis increased following the increase of incubation time up to 200 min. The sensitivity to hydrolysis in esterase medium and pig skin homogenate was approximate. The codrug percentage incubated in esterases and pig skin homogenate fell to 18% and 21% over 200 min, respectively. The codrug was more susceptible to nude mouse skin homogenate hydrolysis. The RA-HQ conjugate was almost cleaved in the mouse skin homogenate within 200 min, with 87% hydrolysis in the first 5 min.

### 3.3. In vitro cutaneous absorption

In the in vitro skin permeation, the donor concentration of the permeants was first fixed at an equimolar dose (1.2 mM). This dose was above the saturated solubility of RA and the codrug in 50% PG. On the other hand, HQ could be completely dissolved in the aqueous vehicle. Both the skin deposition and the cumulative amount in the receptor were determined. The permeant absorption by the skin can be predicted by skin deposition, while the cumulative amount measures the delivery into the deeper skin strata or systemic circulation. Table 2 lists the permeation parameters of the

permeants at molar equivalent. RA in 50% PG exhibited a deposition of 0.04 nmol/mg, whereas it could not be detected in the receptor at 24 h. When HQ was applied to the pig skin, the permeant was detectable in the receptor (49 nmol/cm<sup>2</sup>) but not in the skin reservoir. In addition to the codrug molecules, the parent drugs were present in the skin and the receptor after topical codrug delivery. This suggests the hydrolysis of the conjugate in the skin. However, only a limited codrug hydrolysis had occurred in the in vitro permeation study. The codrug deposition was 5-fold greater as compared to the skin deposition of topically applied RA. The codrug and RA in the receptor released from the codrug application were below the limit of quantification. The HQ amount in the receptor released from the codrug was relatively lower than the amount of topically applied HQ. The physical mixture of RA and HQ at an equivalent dose was also examined for its cutaneous absorption. The difference between the absorption parameters of the physical mixture and the single permeant was not statistically significant. As shown in Table 2, the absorption of RA and HQ from mineral oil was comparable to that from aqueous dispersion. The skin deposition of the codrug from mineral oil was 7 times lower than that released from 50% PG.

The permeants in the donor were also dosed with saturated solutions to keep a constant driving force with maximum thermodynamic activity. Table 3 shows CSD and CCA of the saturated permeant 50% PG solution. HQ was not examined in this study because of the extremely high solubility in the aqueous vehicle. The codrug gave a 61-fold greater skin deposition than RA. The parent RA could be released in the skin after topical codrug application. These compounds were not found in the receptor. The codrug could release HQ to the receptor with a CCA value of 16.4. In the case of mineral oil as the vehicle, the skin deposition of topically applied RA approximated the level of the codrug. The number of HQ molecules diffused to the receptor after codrug hydrolysis was significantly lower than that with topically applied HQ (0.4 versus 1.9).

### 3.4. Bioactivities of the codrug

The anti-inflammatory potency and tyrosinase inhibition were evaluated to estimate the possible bioactivities of the conjugate. The influence of the compounds on keratinocyte viability was first rated. As illustrated in Fig. 3A, the concentrations of ≤5 μM of all compounds were beneficial to maintain the life of the culture without cytotoxicity. The test compounds demonstrated a moderate cytotoxicity at 10 μM, with the codrug showing the least viability (45%). The keratinocytes were treated by imiquimod, a toll-like receptor agonist, to produce a cell-based model of skin inflammation. As depicted in Fig. 3B, imiquimod significantly increased the level of IL-6 protein, a cytokine involved in inflammation. RA at 5 μM revealed a 2-fold downregulation of IL-6 compared to the control. A similar result was detected for codrug treatment. HQ could not significantly reduce the IL-6 elevation by imiquimod. The therapeutic index was computed based on multiplying the skin deposition and IL-6 inhibition as demonstrated in Fig. 3C. This index can be used to assess the therapeutic potential of the

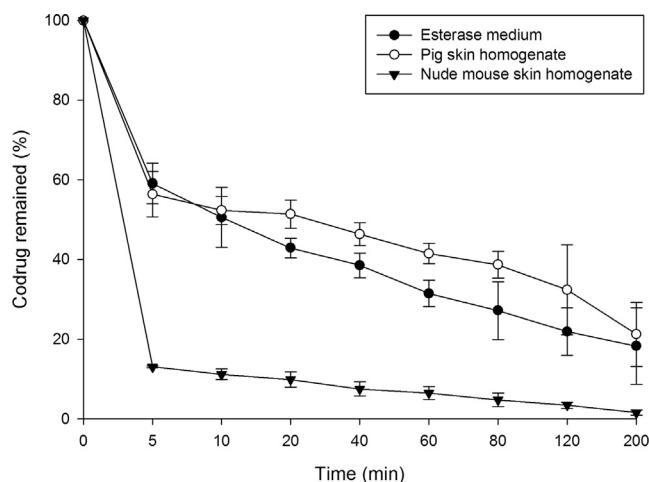


**Fig. 2.** Hydrolytic kinetics of retinoic acid (RA)-hydroquinone (HQ) codrug in esterases and skin homogenates at 37 °C. All data are presented as the mean ± S.D. of six experiments.

**Table 2**  
In vitro skin deposition (nmol/mg) and cumulative amount (nmol/cm<sup>2</sup>) of retinoic acid (RA), hydroquinone (HQ), RA-HQ codrug, and physical mixture at a dose of 1.2 mM from 50% PG/pH 7.4 buffer or mineral oil via pig skin at 24 h.

Donor medium	Permeant	Compound determined	Skin deposition (nmol/mg)	Cumulative amount (nmol/cm <sup>2</sup> )
50% PG	RA	RA	0.04 ± 0.02	–
	HQ	HQ	– <sup>a</sup>	49.29 ± 13.96
	Codrug	Codrug	0.21 ± 0.02	–
		RA	0.01 ± 0.002	–
		HQ	–	29.91 ± 11.32
	Physical mixture	RA	0.03 ± 0.01	–
		HQ	–	60.77 ± 25.42
Mineral oil	RA	RA	0.04 ± 0.01	–
	HQ	HQ	–	69.51 ± 19.48
	Codrug	Codrug	0.03 ± 0.01	–
		RA	0.003 ± 0.002	–
		HQ	–	56.24 ± 9.23

Each value represents the mean ± S.D. (n = 4).

<sup>a</sup> –, Not determined.

**Table 3**  
In vitro calibrated skin deposition (CSD) and calibrated cumulative amount (CCA) of retinoic acid (RA), hydroquinone (HQ), and RA-HQ codrug at a dose of saturated solubility from 50% PG/pH 7.4 buffer or mineral oil via pig skin at 24 h.

Donor medium	Permeant	Compound determined	CSD × 10 <sup>4a</sup>	CCA <sup>b</sup>
50% PG	RA	RA	1.80 ± 0.32	–
	Codrug	Codrug	100.67 ± 1.64	– <sup>c</sup>
		RA	8.68 ± 3.25	–
		HQ	–	16.40 ± 5.36
Mineral oil	RA	RA	0.55 ± 0.16	–
	HQ	HQ	–	1.91 ± 0.38
	Codrug	Codrug	0.55 ± 0.17	–
		RA	–	–
		HQ	–	0.37 ± 0.07

Each value represents the mean ± S.D. (n = 4).

<sup>a</sup> CSD, calibrated skin accumulation = skin deposition (nmol/mg) at 24 h/saturated solubility (nmol/ml).

<sup>b</sup> CCA, calibrated cumulative amount = cumulative amount (nmol/cm<sup>2</sup>) at 24 h/saturated solubility (nmol/ml).

<sup>c</sup> –, Not determined.

topically applied drug. No therapeutic index was obtained for HQ due to the negligible skin deposition. The codrug provided a therapeutic index 6-fold higher than that of RA.

HQ is a tyrosinase inhibitor blocking the biosynthesis of melanin for skin lightening. The effect of the compounds on tyrosinase suppression was examined as shown in Fig. 4A. No inhibition was revealed for RA treatment. HQ and the codrug inhibited tyrosinase activity by 21% and 13%, respectively. The therapeutic index for the tyrosinase inhibition was calculated as shown in Fig. 4B. The index was 2.6-fold greater for HQ than for the synthetic conjugate.

### 3.5. Cutaneous absorption via different skin types

The transport pathways of the permeants were elucidated by using different skin barriers, including delipid, SC-stripped, and desebum skins. The permeant dose was set at a molar equivalent (1.2 mM) in this study. The fold change of the skin deposition of the codrug was compared with that of RA in Fig. 5A. The codrug absorption in different skin types was estimated by summing the deposition of the codrug and the released RA within the skin. A significant 13-fold enhancement in RA deposition was obtained via the delipid skin compared to the intact skin. RA deposition was further enhanced 27-fold by using the SC-stripped skin over normal skin. Both delipidization and stripping resulted in a 2-fold increase of codrug absorption, which was much lower than that of RA. A 3-fold RA deposition enhancement was acquired by using desebum skin over intact skin. The sebum-removal process even slightly reduced codrug permeation compared to untreated skin (fold change = 0.9), though this level did not achieve a statistical significance.

The permeation of HQ and codrug via different skin modes was compared by calculating the cumulative HQ amount in the receptor. HQ penetration was about 5 times higher with delipidization and SC stripping than with intact skin. This suggests that the lipid domain in the SC was the predominant barrier for HQ transport. The cumulative amount enhancement by delipidization and stripping was much lower for the codrug than for HQ. The fold change by sebum removal was 1.1 and 0.8 for HQ and codrug delivery, respectively.

### 3.6. In vivo skin tolerance test

The nude mouse skin was challenged by the compounds for a consecutive 5 days. Fig. 6A illustrates the gross appearance of the dorsal skin. At day 5 after RA treatment, the skin ulceration with focal necrotic debris was coated on the skin surface. Edema and erythema were visualized in the RA-treated area. HQ and codrug administration led to a scaly skin surface without significant erosion. The severity for the topically applied codrug was less than that for RA exposure. Topical treatment with the RA and HQ mixture induced erosion and scaling as observed on the skin surface. Fig. 6B shows the close-up imaging of the cutaneous surface. The appearance of the HQ-treated skin was nearly normal. Skin exposure by RA, codrug, and the physical mixture showed ulceration and roughness. The order of degree of ulceration and roughness was RA > mixture > codrug. We assessed TEWL as an indicator of SC-barrier function. As shown in Fig. 6C, the TEWL resulting from RA was the greatest, followed by the mixture, codrug, and HQ. A similar trend was observed for the erythema parameter (a\*) as

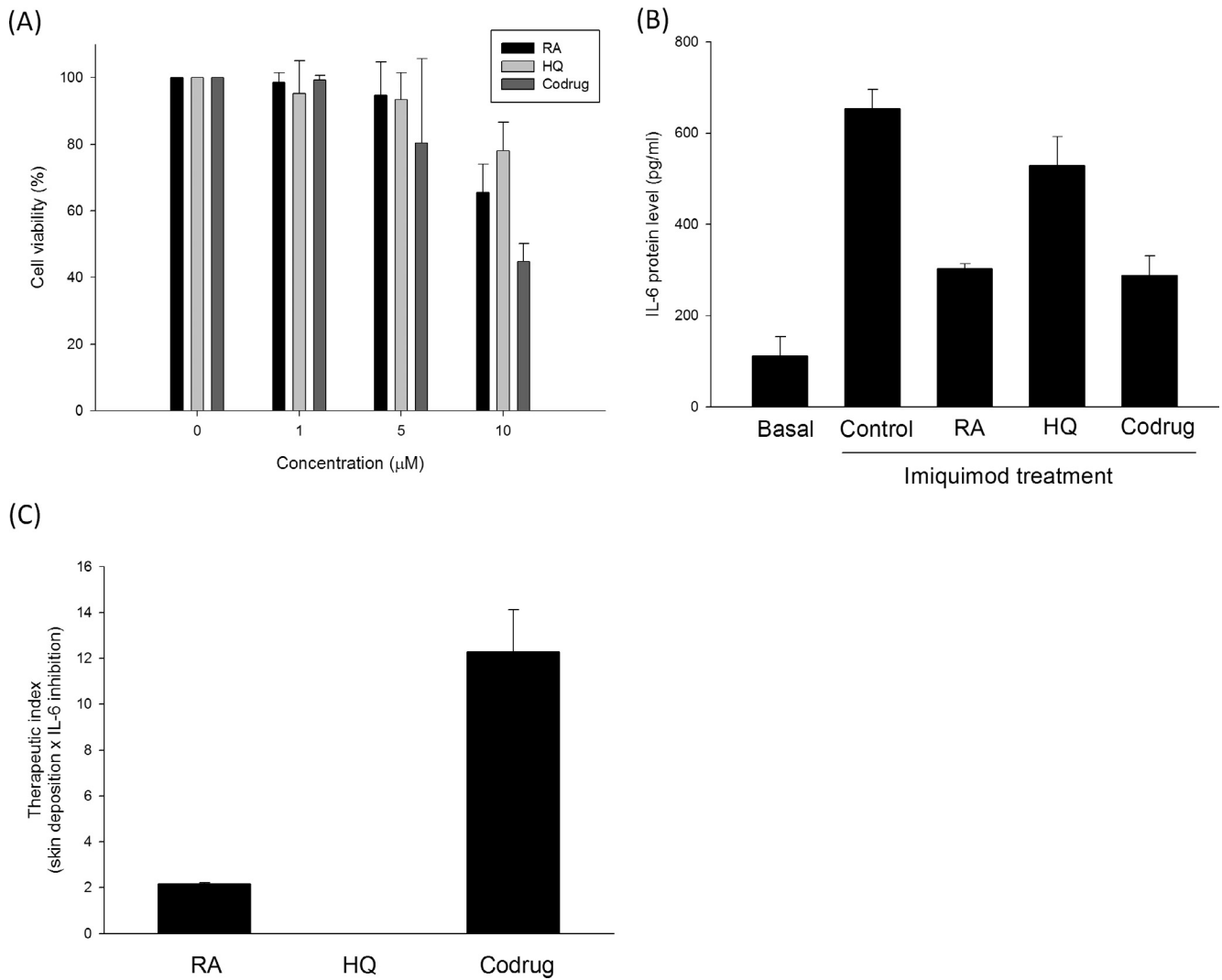


**Fig. 3.** Comparison of the therapeutic index of retinoic acid (RA)-hydroquinone (HQ) codrug and the parent drugs: (A) keratinocyte viability (%) treated by the compounds at the concentrations from 0 to 10 μM; (B) IL-6 inhibition in imiquimod-stimulated keratinocytes; and (C) therapeutic index of the compounds calculated as skin deposition multiplied by IL-6 inhibition percentage. All data are presented as the mean of three experiments ± S.D.

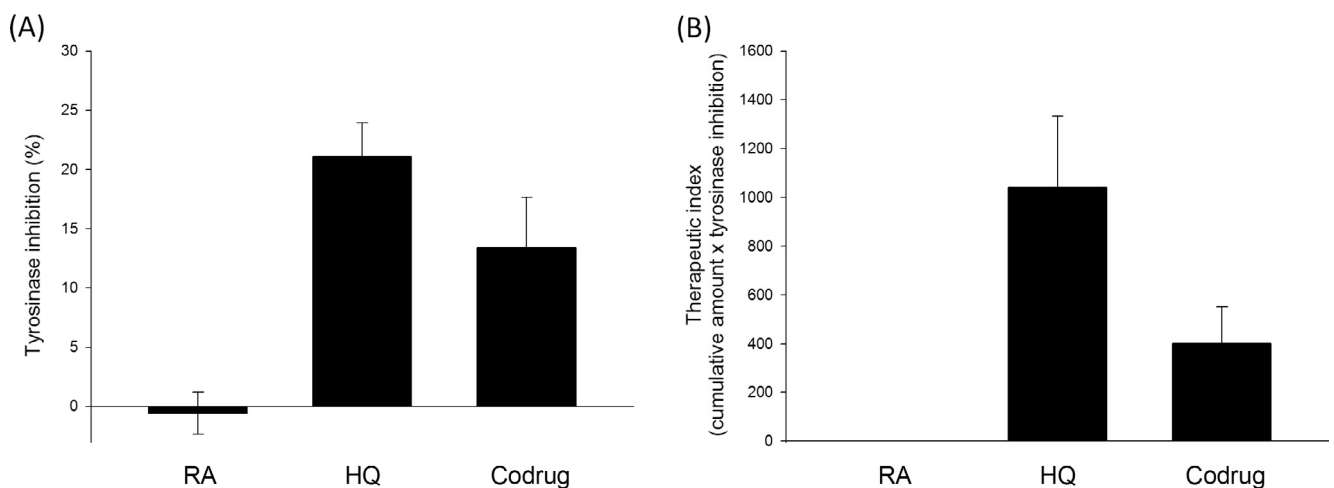


**Fig. 4.** Tyrosinase inhibition profiles of retinoic acid (RA)-hydroquinone (HQ) codrug and the parent drugs: (A) The tyrosinase inhibition (%) treated by the compounds; and (B) therapeutic index of the compounds calculated as skin deposition multiplied by tyrosinase inhibition percentage.

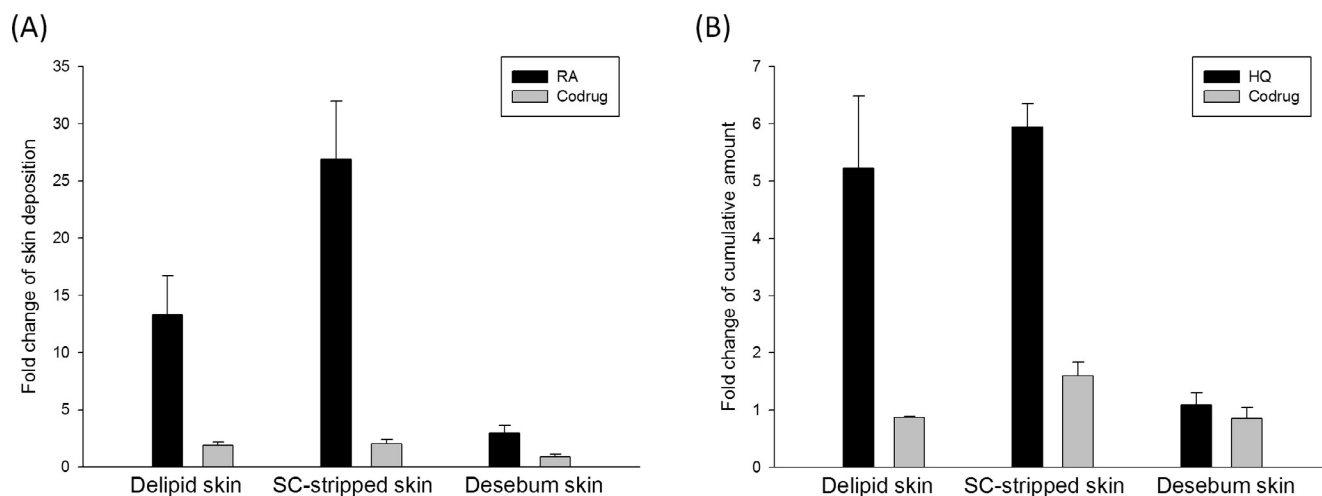


**Fig. 5.** Comparison of the fold change of in vitro skin permeation levels of retinoic acid (RA)-hydroquinone (HQ) codrug and the parent drugs via delipidized, stratum corneum (SC)-stripped, and desebum skins as compared to the permeation via intact skin: (A) skin deposition for comparison between RA and codrug; and (B) cumulative amount in receptor for comparison between HQ and codrug. All data are presented as the mean  $\pm$  S.D. of four experiments.

depicted in Fig. 6D. The redness detection taken before and after the completion of a 4-day treatment by the codrug did not show any significant change. The redness reached a significant increase on day 5 after codrug administration.

Fig. 6E reveals the H&E-stained histopathology of the skin. In the case of RA, ulceration and erosion in the epidermis were coated by necrotic tissue. Some granulation tissues were found in the dermis of the ulcer base. There were infiltrated immune cells and blood vessel proliferation in the dermal layer for the RA-treated skin. HQ treatment generally showed no morphological change, except congestion in the lower dermis. The codrug challenge had produced infiltrated inflammatory cells in the dermis. No epidermal damage was visible for codrug-treated skin. The skin histology of the physical mixture was similar to that of RA alone. For instance, epidermal abrasion and erosion could be seen with severe inflammation and congestion in the lower dermis.

#### 4. Discussion

Combination therapy is common in the management of melasma. However, the therapeutic outcomes of the combined drugs are still unsatisfactory because of the poor absorption and irritant potential. We are attempting to develop a codrug approach for RA and HQ to overcome these problems. The experimental data suggested that the RA-HQ codrug was more efficacious and better tolerated than the parent drugs.

RA-HQ codrug conversion into the parent actives in esterases and skin homogenates had suggested the hydrolysis of the ester bond. The codrug amount of >80% was cleaved in the enzyme dispersions within 200 min. Different from the hydrolysis test, the codrug showed a low cleavage to the parent compounds in the in vitro cutaneous absorption. Homogenization of skin tissue can expose some enzymes that are not readily available during transport through the skin with a rigid structure [11,20]. The enzymes and substrates should be in the same phase. The codrug with a steric structure may have obstacles to establishing contact with esterases.

RA is known to be poor at penetrating the skin [21]. The cutaneous absorption result demonstrated that the RA-HQ codrug was more extensively contained in the skin compared to RA in 50% PG. The codrug is regarded as a new chemical entity demanding full assessment of its pharmacological activity. Although the

RA-HQ codrug revealed a restrained hydrolysis in the skin, the conjugate itself showed bioactivity comparable to RA. RA and the codrug were not found in the receptor after topical application. Considering the maintenance of the sink condition in the receptor for all permeants, it is practical to suggest that the permeant diffusion across the skin was not restricted by the solubility in the receptor medium. Contrary to this result, HQ was found in the receptor but not in the skin reservoir. This consequence was quite different from the previous study [22], which demonstrated a detectable HQ skin deposition. This could be due to the relatively high HQ dose (20 mM) used in the previous study. The viable epidermis/dermis presents a more aqueous environment for permeant transport than the SC. Upon traversing the SC to the viable tissue, the hydrophilic permeant such as HQ readily diffuses through the skin to the receptor phase. This has suggested a low tissue binding affinity of HQ to the skin.

The initial stage of a permeant to penetrate the skin is the partitioning from the vehicle into the SC. The log *P* of the RA-HQ codrug was higher than that of RA, ensuring better absorption because of the enhanced lipophilicity for partitioning to the SC [23]. Unlike the absorption from aqueous dispersion, the codrug delivery was significantly decreased after incorporation in mineral oil. The increased codrug solubility in mineral oil compared to 50% PG impeded codrug partitioning into the SC because of the decreased tendency of the codrug release from the lipid vehicle. The HQ derived from topically applied codrug exhibited lower permeation than topically applied HQ. The impact of permeant solubility on the diffusion via the skin is well established [24]. HQ transfer across the aqueous epidermis/dermis met less resistance due to the high aqueous solubility. The codrug might form a reservoir in the lipophilic portion of the skin reservoir, but the subsequent release into the aqueous environment was limited. An insufficient codrug hydrolysis in the skin also resulted in the finite HQ in the receptor. This suggests the importance of an adequate lipophilicity-hydrophilicity balance for drug candidate absorption. The lessened receptor accumulation of HQ by codrug delivery was not totally unfavorable since the cumulative amount partially indicated the diffusion into the circulation. Topically administered HQ is able to enter into the vascular system, causing nephropathy, carcinogenesis, and bone marrow toxicity [25].

The most significant barrier for drug penetration is the SC. The SC layers include two fundamental domains, intercellular lipid and



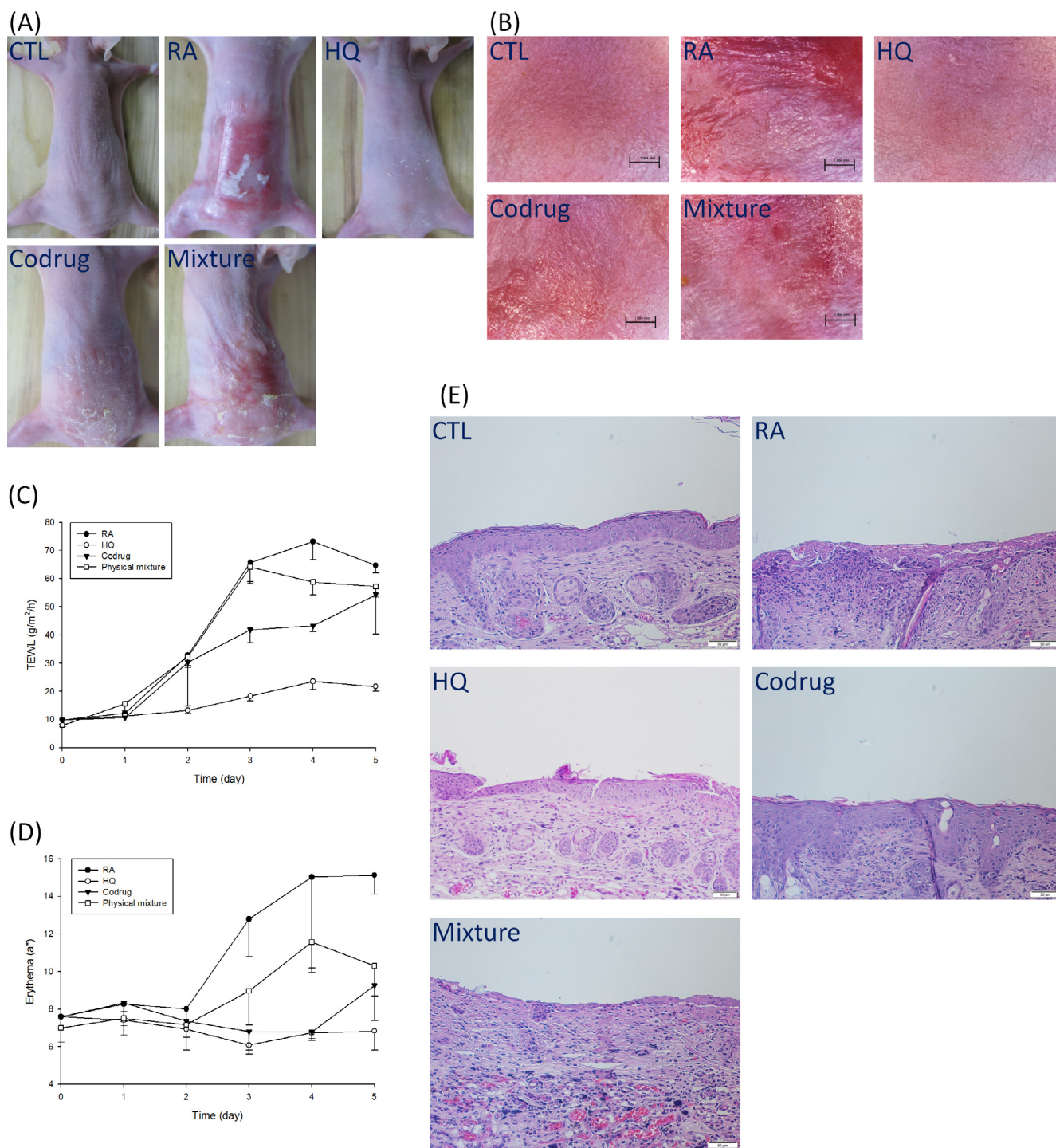


**Fig. 6.** In vivo skin tolerance of retinoic acid (RA)-hydroquinone (HQ) codrug and the parent drugs: (A) The skin surface of nude mouse after treatment of RA, HQ, codrug, and physical mixture; (B) the magnified images of nude mouse skin surface; (C) transepidermal water loss (TEWL) of nude mouse skin treated after treatment of RA, HQ, codrug, and physical mixture; (D) skin erythema ( $a^*$ ) of nude mouse skin treated after treatment of RA, HQ, codrug, and physical mixture; and (E) histological observation of nude mouse skin biopsy after treatment of RA, HQ, codrug, and physical mixture. All data in TEWL and skin erythema are presented as the mean  $\pm$  S.D. of four experiments.

proteinaceous phase, where the permeant must cross through [26]. The binding to keratin, the proteinaceous route, can be analyzed using delipid and SC-stripped skins. Both delipidization and SC stripping greatly enhanced RA absorption, with the stripping showing a higher skin deposition. This demonstrated RA binding to the proteinaceous domains. Although RA had a substantial affinity to protein, the lipid phase around the proteinaceous domains prevents the permeant from interactivity with keratin [27]. This

may contribute to the low absorption of RA into intact skin. The data represented that the delipid and SC-stripped skins had a cumulative amount at least 5 times higher than the intact skin for HQ absorption. The transport of HQ via delipid and SC-stripped skins was comparable, indicating that the SC lipids but not viable skin were the major barrier to topical HQ delivery.

Expulsion of lipids or the SC did not significantly affect the skin absorption of the RA-HQ codrug. This suggests that the codrug

design could overcome the SC barrier. The lipid domains were the main pathways for codrug passage. Sebum is a lipid film on superficial SC produced by pilosebaceous units. Sebum illustrates an important determinant on the drug partitioning to the SC [28]. Sebum removal significantly increased RA deposition compared to the untreated skin, suggesting a barrier effect of sebum for RA partitioning. No sebum partitioning was observed for HQ since there was no significant difference between the cumulative amount of sebum and the intact skin. It was evident that the codrug was readily available in the skin via facile partitioning because of the poorer absorption after sebum removal.

Both the codrug itself and the parent actives may display bioactivity. The greater activity for the codrugs than for the corresponding parent drugs is also conceivable [10]. RA is proposed as a cell division regulator to lower UV-induced production of free radicals and inflammation [29]. Our results had exhibited that the codrug could inhibit imiquimod-induced IL-6 expression in keratinocytes. The RA-HQ codrug was acknowledged as an agent with a therapeutic effect. The RA-HQ conjugate showed an inhibitory activity against tyrosinase, though this effect was more minor than that of HQ. The steric hindrance of the chemical structure raises the obstruction of contacting the copper in tyrosinase [30]. The codrug structure may meet this constraint.

The calculation of the therapeutic index based on in vitro data is an easy way to predict the therapeutic benefit of the topical drug delivery. The codrug revealed a higher index than RA, according to the anti-inflammatory activity. A high degree of codrug skin absorption contributed to the impressive index. On the other hand, the therapeutic index of tyrosinase inhibition of the codrug did not surpass that of HQ. The reasons for this were the insufficient HQ derived from the cutaneous hydrolysis of the codrug and the low melanogenic inhibition.

The recurrent nature of melasma signifies the requirement of a long-term treatment regimen. This can lead to a risk of adverse events by topically applied managements. Topical RA irritates the skin, causing peeling, desquamation, swelling, and erythema [31]. These adverse effects were also observed in our skin tolerance study. The desquamation was induced by keratolytic action, a mechanism of the RA effect on depigmentation. The consecutive RA-related challenges to the skin had exacerbated this effect, leading to severe cutaneous damage. The erosion in the epidermis caused barrier function deficiency, thus resulting in TEWL elevation and dry skin. RA-induced damage relates well to skin barrier disruption, which is quite different from the irritation caused by HQ [32]. HQ showed almost no irritation on the skin in the present study. This was because of the very low dose used in this work. An HQ concentration of >4% generated allergic dermatitis and amelanosis [31]. Our previous study [33] also reported a skin redness induced by topical HQ delivery at a dose of 8 mM. A mild irritation was observed on the skin following codrug treatment. Although the codrug was facily delivered into the skin depot, the irritation was inferior to that caused by RA. The physical mixture showed an irritation level higher than that of the codrug. This suggests that the masking of the carboxylic group of RA could lower the cutaneous impairment.

The codrug strategy for RA potentially proved a superior therapeutic index with less toxicity as compared to the parent drug. RA-HQ codrug is an active resembling the concept of an antedrug. The term antedrug is introduced to define a synthetic derivative that is bioconverted to less active metabolites [34]. A more potent and safer active can be obtained by designing an antedrug [35]. As melasma is prone to relapse, a more efficient and safer alternative is necessary for long-term management. The codrug may fulfill this criterion. The conjugate provided high skin absorption; thus, administration at a lower dose to avoid the adverse effects is attainable.

## 5. Conclusions

Conjugation of RA with HQ increased the lipophilicity, which was responsible for better skin absorption and increased availability for melasma treatment. A more significant interaction of the codrug with the skin structure compared to the parent actives was detected. The selection of a feasible vehicle is important for the effective partitioning to the SC. The codrug was stable in the vehicles while the codrug hydrolysis occurred after entering the skin. The RA-HQ codrug revealed bioactivities related to both RA and HQ, indicating different anti-melasma mechanisms in a single molecule. The measurement of the therapeutic index had anticipated a superior therapeutic benefit of the conjugate compared to topical RA permeation. Although the release of HQ from the codrug did not surpass the skin transport of topically applied HQ, the codrug strategy may lessen the risk of HQ penetration into the circulation. The experimental outcomes demonstrated less skin irritation elicited by the codrug compared to RA, assuring the practical use of the codrug for safer therapy. The results obtained in this study merit further investigation of the topically applied codrug for clinical application.

## Acknowledgement

The authors are grateful for the financial support from Chang Gung Memorial Hospital (BMRP428 and CMRPD1F0331-3).

## Appendix A. Supplementary material

Supplementary data associated with this article can be found, in the online version, at <http://dx.doi.org/10.1016/j.ejpb.2017.01.016>.

## References

- [1] A.K. Gupta, M.D. Gover, K. Nouri, S. Taylor, The treatment of melasma: a review of clinical trials, *J. Am. Acad. Dermatol.* 55 (2006) 1048–1065.
- [2] Z. Gong, W. Lai, G. Zhao, X. Wang, M. Zheng, L. Li, Q. Yang, Y. Dang, L. Liu, Y. Zou, Efficacy and safety of fluocinolone acetonide, hydroquinone, and tretinoin cream in Chinese patients with melasma: a randomized, double-blind, placebo-controlled, multicenter, parallel-group study, *Clin. Drug Invest.* 35 (2015) 385–395.
- [3] P.E. Grimes, J. Bhawan, I.L. Guevara, L.E. Colón, L.A. Johnson, R.W. Gottschalk, A. G. Pandya, Continuous therapy followed by a maintenance therapy regimen with a triple combination cream for melasma, *J. Am. Acad. Dermatol.* 62 (2010) 962–967.
- [4] R.R. Riahi, A.E. Bush, P.R. Cohen, Topical retinoids: therapeutic mechanisms in the treatment of photodamaged skin, *Am. J. Clin. Dermatol.* 17 (2016) 265–276.
- [5] M. Gold, M. Rendon, B. Dibernardo, S. Bruce, C. Lucas-Anthony, J. Watson, Open-label treatment of moderate or marked melasma with a 4% hydroquinone skin care system plus 0.05% tretinoin cream, *J. Clin. Aesthet. Dermatol.* 6 (2013) 32–38.
- [6] S. Rivas, A.G. Pandya, Treatment of melasma with topical agents, peels and lasers: an evidence-based review, *Am. J. Clin. Dermatol.* 14 (2013) 359–376.
- [7] N. Das, M. Dhanawat, B. Dash, R.C. Nagarwal, S.K. Shrivastava, Codrug: an efficient approach for drug optimization, *Eur. J. Pharm. Sci.* 41 (2010) 571–588.
- [8] P. Ghosh, D.M. Lee, K.B. Kim, A.L. Stinchcomb, Optimization of naltrexone diclofenac codrugs for sustained drug delivery across microneedle-treated skin, *Pharm. Res.* 31 (2014) 148–159.
- [9] S. Thomas, C.S. Vieira, M.A. Hass, L.B. Lopes, Stability, cutaneous delivery, and antioxidant potential of a lipoic acid and  $\alpha$ -tocopherol codrug incorporated in microemulsions, *J. Pharm. Sci.* 103 (2014) 2530–2538.
- [10] I.A. Aljuffali, C.F. Lin, C.H. Chen, J.Y. Fang, The codrug approach for facilitating drug delivery and bioactivity, *Expert Opin. Drug Deliv.* 13 (2016) 1311–1325.
- [11] K.S. Liu, K.C. Sung, S.A. Al-Suwayeh, M.C. Ku, C.C. Chu, J.J. Wang, J.Y. Fang, Enhancement of transdermal apomorphine delivery with a diester prodrug strategy, *Eur. J. Pharm. Biopharm.* 78 (2011) 422–431.
- [12] L.W. Zhang, S.A. Al-Suwayeh, P.W. Hsieh, J.Y. Fang, A comparison of skin delivery of ferulic acid and its derivatives: evaluation of their efficacy and safety, *Int. J. Pharm.* 399 (2010) 44–51.
- [13] C.F. Lin, C.F. Hung, I.A. Aljuffali, Y.L. Huang, W.C. Liao, J.Y. Fang, Methylation and esterification of magnolol for ameliorating cutaneous targeting and therapeutic index by topical application, *Pharm. Res.* 33 (2016) 2152–2167.

- [14] C.F. Hung, W.Y. Chen, I.A. Aljuffali, Y.K. Lin, H.C. Shih, J.Y. Fang, Skin aging modulates percutaneous drug absorption: the impact of ultraviolet irradiation and ovariectomy, *Age* 37 (2015) 21.
- [15] W.B. Wu, H.S. Chiang, J.Y. Fang, S.K. Chen, C.C. Huang, C.F. Hung, (+)-Catechin prevents ultraviolet B-induced human keratinocyte death via inhibition of JNK phosphorylation, *Life Sci.* 79 (2006) 801–807.
- [16] N.L. Wu, Y.C. Chiang, C.C. Huang, J.Y. Fang, D.F. Chen, C.F. Hung, Zeaxanthin inhibits PDGF-BB-induced migration in human dermal fibroblasts, *Exp. Dermatol.* 19 (2010) 173–181.
- [17] Y.K. Lin, S.H. Yang, C.C. Chen, H.C. Kao, J.Y. Fang, Using imiquimod-induced psoriasis-like skin as a model to measure the skin penetration of anti-psoriatic drugs, *PLoS ONE* 10 (2015) e0137890.
- [18] M. Miyazawa, T. Oshima, K. Koshio, Y. Itsuzaki, J. Anzai, Tyrosinase inhibitor from black rice bran, *J. Agric. Food Chem.* 51 (2003) 6953–6956.
- [19] P.W. Hsieh, I.A. Aljuffali, C.L. Fang, S.H. Chang, J.Y. Fang, Hydroquinone-salicylic acid conjugates as novel anti-melasma actives show superior skin targeting compared to the parent drugs, *J. Dermatol. Sci.* 76 (2014) 120–131.
- [20] A.P. Morris, K.R. Brain, C.M. Heard, Skin permeation and ex vivo skin metabolism of O-acyl haloperidol ester prodrugs, *Int. J. Pharm.* 367 (2009) 44–50.
- [21] K. Abdulmajed, C.M. Heard, Topical delivery of retinyl ascorbate co-drug 1. Synthesis, penetration into and permeation across human skin, *Int. J. Pharm.* 280 (2004) 113–124.
- [22] P.W. Hsieh, S.A. Al-Suwayeh, C.L. Fang, C.F. Lin, C.C. Chen, J.Y. Fang, The co-drug of conjugated hydroquinone and azelaic acid to enhance topical skin targeting and decrease penetration through the skin, *Eur. J. Pharm. Biopharm.* 81 (2012) 369–378.
- [23] P.K. Kiptoo, K.S. Paudel, D.C. Hammell, M.O. Hamad, P.A. Crooks, A.L. Stinchcomb, In vivo evaluation of a transdermal codrug of 6- $\beta$ -naltrexol linked to hydroxybupropion in hairless guinea pigs, *Eur. J. Pharm. Sci.* 33 (2008) 371–379.
- [24] Y.D. Yan, J.H. Sung, D.W. Lee, J.S. Kim, E.M. Jeon, D.D. Kim, D.W. Kim, J.O. Kim, M.G. Piao, D.X. Li, C.S. Yong, H.G. Choi, Evaluation of physicochemical properties, skin permeation and accumulation profiles of salicylic acid amide prodrugs as sunscreen agent, *Int. J. Pharm.* 419 (2011) 154–160.
- [25] J.M. Gillbro, M.J. Olsson, The melanogenesis and mechanisms of skin-lightening agents—existing and new approaches, *Int. J. Cosmet. Sci.* 33 (2011) 210–221.
- [26] K.B. Ita, Prodrugs for transdermal drug delivery—trends and challenges, *J. Drug Target.* 24 (2016) 671–678.
- [27] K. Abdulmajed, C.M. Heard, C. McGuigan, W.J. Pugh, Topical delivery of retinyl ascorbate co-drug 2. Comparative skin tissue and keratin binding studies, *Skin Pharmacol. Physiol.* 17 (2004) 274–282.
- [28] D. Schneider, K. Dennerlein, T. Göen, K.H. Schaller, H. Drexler, G. Korinth, Influence of artificial sebum on the dermal absorption of chemicals in excised human skin: a proof-of-concept study, *Toxicol. In Vitro* 33 (2016) 23–28.
- [29] E. Bagatin, L.R. Guadhim, M.M. Enokihara, A. Sanudo, S. Talarico, H.A. Miot, L. Gibson, Low-dose oral isotretinoin versus topical retinoic acid for photoaging: a randomized, comparative study, *Int. J. Dermatol.* 53 (2014) 114–122.
- [30] S.Y. Kwak, J.K. Yang, H.R. Choi, K.C. Park, Y.B. Kim, Y.S. Lee, Synthesis and dual biological effects of hydroxycinnamoyl phenylalanyl/prolyl hydroxamic acid derivatives as tyrosinase inhibitor and antioxidant, *Bioorg. Med. Chem. Lett.* 23 (2013) 1136–1142.
- [31] C.M.S. de Mendonça, I.P. de Barros Lima, D.F.S. Aragão, A.P.B. Gomes, Thermal compatibility between hydroquinone and retinoic acid in pharmaceutical formulations, *J. Therm. Anal. Calorim.* 115 (2014) 2277–2285.
- [32] K.A. Cheong, H.J. Kim, J.Y. Kim, C.H. Kim, W.S. Lim, M. Noh, A.Y. Lee, Retinoic acid and hydroquinone induce inverse expression patterns on cornified envelop-associated proteins: implication in skin irritation, *J. Dermatol. Sci.* 76 (2014) 112–119.
- [33] P.W. Hsieh, W.Y. Chen, I.A. Aljuffali, C.C. Chen, J.Y. Fang, Co-drug strategy for promoting skin targeting and minimizing transdermal diffusion of hydroquinone and tranexamic acid, *Curr. Med. Chem.* 20 (2013) 4080–4092.
- [34] M.O. Khan, K.K. Park, H.J. Lee, Antedugs: an approach to safer drugs, *Curr. Med. Chem.* 12 (2005) 2227–2239.
- [35] T. Matsufuji, K. Shimada, S. Kobayashi, M. Ichikawa, A. Kawamura, T. Fujimoto, T. Arita, T. Hara, M. Konishi, T. Abe-Ohya, M. Izumi, Y. Sogawa, Y. Nagai, K. Yoshida, Y. Abe, T. Kimura, H. Takahashi, Synthesis and biological evaluation of novel chiral diazepine derivatives as bombesin receptor subtype-3 (BRS-3) agonists incorporating an antedrug approach, *Bioorg. Med. Chem.* 23 (2015) 89–104.





## Original article

## Dipeptide HCH6-1 inhibits neutrophil activation and protects against acute lung injury by blocking FPR1

Shun-Chin Yang<sup>a,b,c,1</sup>, Shih-Hsin Chang<sup>a,d,1</sup>, Pei-Wen Hsieh<sup>a,c,d,e,f</sup>, Yin-Ting Huang<sup>a</sup>, Chiu-Ming Ho<sup>b</sup>, Yung-Fong Tsai<sup>f</sup>, Tsong-Long Hwang<sup>a,c,d,e,f,\*</sup><sup>a</sup> Graduate Institute of Natural Products, College of Medicine, Chang Gung University, Taoyuan 333, Taiwan<sup>b</sup> Department of Anesthesiology, Taipei Veterans General Hospital and National Yang-Ming University, Taipei 112, Taiwan<sup>c</sup> Division of Natural Products, Graduate Institute of Biomedical Sciences, College of Medicine, Chang Gung University, Taoyuan 333, Taiwan<sup>d</sup> Research Center for Industry of Human Ecology, Research Center for Chinese Herbal Medicine, and Graduate Institute of Health Industry Technology, Chang Gung University of Science and Technology, Taoyuan 333, Taiwan<sup>e</sup> Chinese Herbal Medicine Research Team, Healthy Aging Research Center, Chang Gung University, Taoyuan 333, Taiwan<sup>f</sup> Department of Anesthesiology, Chang Gung Memorial Hospital, Taoyuan 333, Taiwan

## ARTICLE INFO

## Keywords:

Chemotaxis

Elastase

Formyl peptide receptor 1

HCH6-1

Neutrophil

Superoxide anion

## ABSTRACT

Formyl peptide receptor 1 (FPR1) is an emerging therapeutic target for the discovery of drugs to treat neutrophilic inflammatory diseases. However, development of FPR1 antagonists for clinical use is still inadequate. The purpose of this study was to identify a synthetic dipeptide *N*-(*N*-benzoyl-L-tryptophanyl)-*D*-phenylalanine methyl ester (HCH6-1) as a FPR1 inhibitor and to investigate its protective effects against acute lung injury (ALI). HCH6-1 inhibited superoxide anion generation, elastase release, and chemotaxis in human neutrophils specifically activated by formyl-L-methionyl-L-leucyl-L-phenylalanine (fMLF), an FPR1 agonist. HCH6-1 produced right shifts in the concentration-response curves of fMLF, suggesting that HCH6-1 was a competitive antagonist of FPR1. Indeed, HCH6-1 bound to FPR1 in human neutrophils and neutrophil-like THP-1 as well as hFPR1-transfected HEK293 cells. Also, the FPR1 downstream signaling pathways were competitively inhibited by HCH6-1. Furthermore, HCH6-1 prevented pulmonary neutrophil infiltration and edema along with alveolar damage in LPS-induced ALI in mice. Our findings suggest that HCH6-1, a FPR1 antagonist, may have potential as a new therapeutic agent for treating FPR1-involved inflammatory lung diseases.

## 1. Introduction

During the inflammatory process, neutrophils are recruited into inflammatory areas to eliminate invasive pathogens [1]. However, excessive recruitment and activation of neutrophils are harmful to human health and are involved in the progression of acute and chronic inflammatory diseases, including acute lung injury (ALI), rheumatoid arthritis, and sepsis [2–4]. Superoxide anion and proteolytic enzymes released from activated neutrophils have been proposed to facilitate tissue injury [5,6]. The recruitment of activated neutrophils into the lung can cause endothelial damage and further enhance permeability of the alveolar-capillary barrier in ALI or acute respiratory distress

syndrome [7,8]. Mortality in ALI patients remains high despite several treatment strategies [9,10].

Formyl peptide receptor 1 (FPR1) mediates neutrophil activation in response to bacterial or mitochondrial formyl peptides stimulation [11–14]. FPR1 typically facilitates neutrophil immune responses in the presence of *N*-formyl peptides derived from bacteria in vitro [12,15,16]. Recent data suggested that *N*-formyl peptides are also considered damage-associated molecular patterns that trigger sterile inflammatory responses through FPR1-mediated responses [2,17–19]. Mitochondrial lysates from trauma-damaged tissue recruit neutrophils to induce severe inflammatory response syndrome via activation of FPR1 [20]. In addition, hepatocyte death is amplified by liver neu-

**Abbreviations:**  $[Ca^{2+}]_i$ , intracellular calcium concentration; ALI, acute lung injury; CB, cytochalasin B; CsH, cyclosporine H; FBS, fetal bovine serum; FNLNYK, *N*-formyl-Nle-Leu-Phe-Nle-Tyr-Lys-fluorescein; FPR1, formyl peptide receptor 1; HE, Hydroethidine; H89, *N*-[2-(*p*-bromocinnamylamino)ethyl]-5-isoquinolinesulfonamide; HCH6-1, *N*-(*N*-benzoyl-L-tryptophanyl)-*D*-phenylalanine methyl ester; LDH, lactate dehydrogenase; LTB4, leukotriene B4; MMK1, Leu-Glu-Ser-Ile-Phe-Arg-Ser-Leu-Leu-Phe-Arg-Val-Met; NMR, nuclear magnetic resonance; PKA, protein kinase A; THP-1 cells, human monocytic leukemia cells; WKYMVm, Trp-Lys-Tyr-Met-Val-D-Met; WST-1, 2-(4-iodophenyl)-3-(4-nitrophenyl)-5-(2,4-disulfophenyl)-2H-tetrazolium monosodium salt; WRW4, Trp-Arg-Trp-Trp-Trp-Trp-CONH2

\* Corresponding author at: Graduate Institute of Natural Products, College of Medicine, Chang Gung University, 259 Wen-Hwa 1st Road, Kweishan, Taoyuan 333, Taiwan.

E-mail address: [htl@mail.cgu.edu.tw](mailto:htl@mail.cgu.edu.tw) (T.-L. Hwang).

<sup>1</sup> These authors contributed equally to this work

<http://dx.doi.org/10.1016/j.freeradbiomed.2017.02.038>

Received 23 September 2016; Received in revised form 24 January 2017; Accepted 17 February 2017

Available online 21 February 2017

0891-5849/© 2017 Elsevier Inc. All rights reserved.

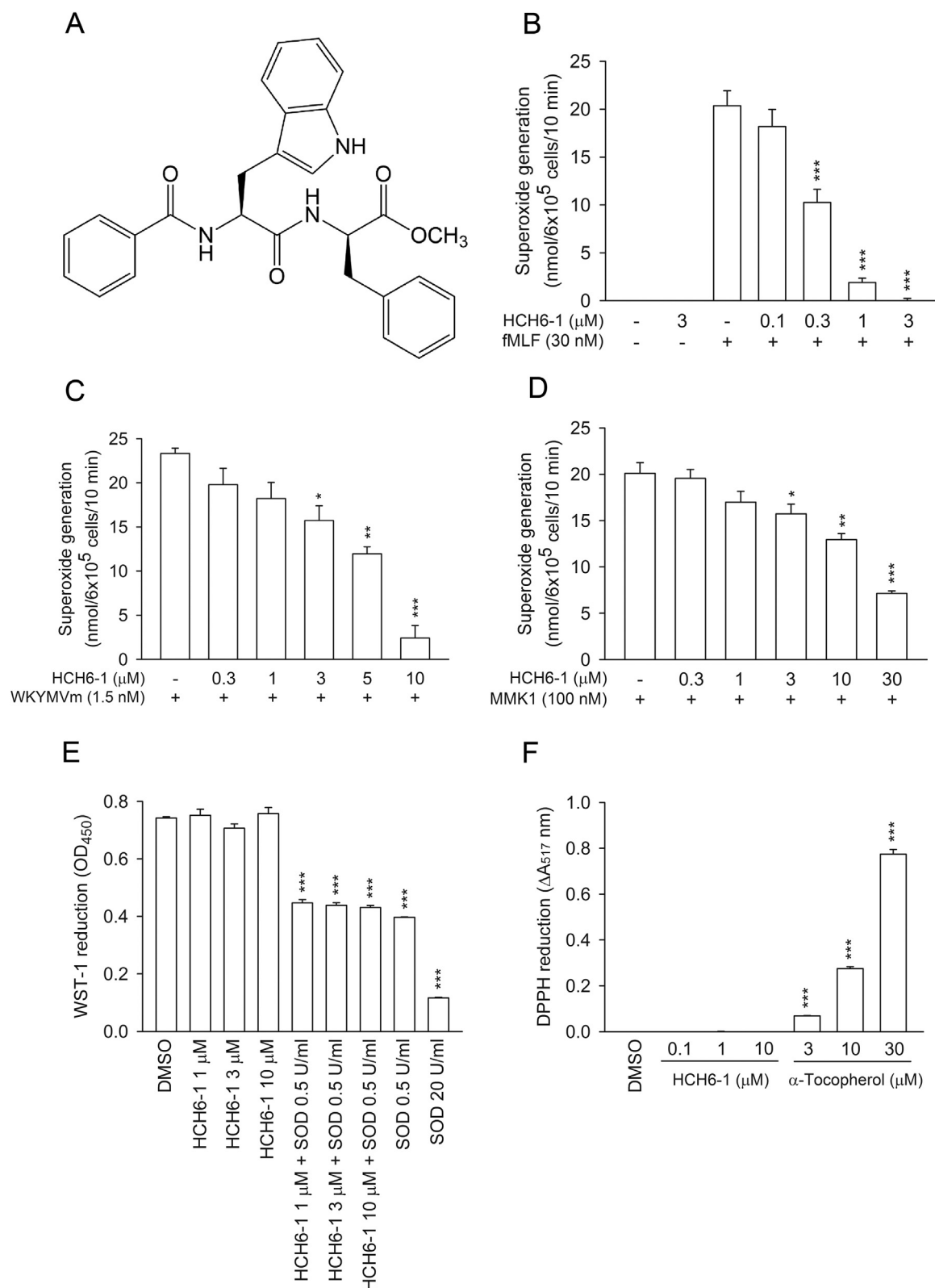


**Fig. 1.** HCH6-1 selectively inhibits extracellular superoxide anion generation in FPR1-agonist stimulated human neutrophils. (A) The chemical structure of HCH6-1. Human neutrophils were incubated with DMSO (as the control) or HCH6-1 for 5 min, and then activated by (B) fMLF, (C) WKYMVm or (D) MMK1 in the presence of CB for another 10 min. Superoxide anion generation was measured by cytochrome *c* reduction by spectrophotography. Reduction of (E) WST-1 and (F) DPPH level was measured at 450 nm and 517 nm, respectively. Data are mean  $\pm$  SEM. (n=4 for B and C, n=8 for D, n=3 for E and F). \**p* < 0.05; \*\**p* < 0.01; \*\*\**p* < 0.001 compared with the control.

trophil infiltration, and the release of mitochondrial products into the circulation may induce a systemic inflammatory response and further trigger lung injury [21]. Therefore, determining how to modulate FPR1 functions on immune responses is crucial.

Aurantiamide acetate and its analogs from *Polygonum chinensis* Linn have various biological activities. A series of dipeptide analogs of aurantiamide acetate exhibited inhibitory effects on superoxide anion generation and elastase release in formyl-L-methionyl-L-leucyl-L-phenyl-



lalanine (fMLF, FPR1 agonist)-activated human neutrophils [22,23]. *N*-(*N*-Benzoyl-L-tryptophanyl)-*D*-phenylalanine methyl ester (HCH6-1) (Fig. 1A), a dipeptide small molecule, was recently designed and synthesized from aurantiamide acetate. HCH6-1 showed a more potent inhibitory effect on FPR1-agonist-activated human neutrophils [24]. However, the exact pharmacological mechanism of HCH6-1 remains elusive, and its therapeutic potential *in vitro* and *in vivo* needs to be further explored.

We showed that HCH6-1 bound to FPR1 specifically inhibited chemotaxis, superoxide anion generation, and elastase release induced by *N*-formyl peptides in human neutrophils. In addition, HCH6-1 exhibited protective effects in lipopolysaccharide (LPS)-induced acute lung injury (ALI) in mice. We further explored the underlying signaling pathways of these anti-inflammatory effects of HCH6-1 and discussed the significance of these findings for developing an effective approach to treat neutrophilic inflammation.

## 2. Materials and methods

### 2.1. Reagents

HCH6-1 was synthesized from aurantiamide acetate by our group [24]. The purity of HCH6-1 was higher than 96% as determined by HPLC. We purchased Fluo-3/AM from Molecular Probes (Eugene, OR, USA). We obtained Methoxysuccinyl-ala-ala-pro-val-nitroanilide and *N*-[2-(*p*-bromocinnamylamino)ethyl] – 5-isoquinolinesulfonamide (H89) from Calbiochem (La Jolla, CA, USA). Leu-Glu-Ser-Ile-Phe-Arg-Ser-Leu-Leu-Phe-Arg-Val-Met (MMK1), Trp-Lys-Tyr-Met-Val-Met-NH<sub>2</sub> (WKYMVm), and Trp-Arg-Trp-Trp-Trp-Trp-CONH<sub>2</sub> (WRW4) were obtained from Tocris Bioscience (Ellisville, MO, USA). The antibody against p38 MAP kinase was obtained from Santa Cruz Biotechnology (Santa Cruz, CA, USA). Other antibodies were purchased from Cell Signaling (Beverly, MA, USA). 2-(4-Iodophenyl) – 3-(4-nitrophenyl) – 5-(2,4-disulfophenyl) – 2H-tetrazolium monosodium salt (WST-1) was obtained from Dojindo Laboratories (Kumamoto, Japan). All other pharmacologic agents were purchased from Sigma-Aldrich (St. Louis, MO, USA).

### 2.2. Isolation of human neutrophils

We collected venous blood from healthy volunteers who had not taken any drugs within at least 2 weeks. Briefly, neutrophils were extracted from the buffy coats of peripheral blood by the standard dextran sedimentation method and centrifuged in a Ficoll Hypaque gradient followed by hypotonic lysis of the erythrocytes. Purified neutrophils contained > 98% viable cells, determined by trypan blue exclusion. Neutrophils were stored at 4 °C and suspended in Hank's balanced salt solution (HBSS) without calcium. The Chang Gung Medical Foundation Institutional Review Board approved all human study protocols. Written informed consent was obtained from each volunteer before this study.

### 2.3. Differentiation of human monocytic leukemia (THP-1) cells

THP-1 cells were cultured in RPMI 1640 medium supplemented with 2 mM glutamine, 10% fetal bovine serum (FBS), and antibiotics (100 U/ml penicillin, 100 µg/ml streptomycin, and 2.5 µg/ml amphotericin B). THP-1 cells were treated with 300 µM dibutyryl cAMP for 48 h to induce cell differentiation [25].

### 2.4. Expression of FPR1 in HEK293 cells transfected with human FPR1 (hFPR1)

HEK293 cells were maintained in Dulbecco's modified Eagle's medium supplemented with 10% FBS, 2 mM glutamine, and antibiotics, then stably transfected with the pCMV6-AC vector containing the

human FPR1 gene (NM\_002029, OriGene, Rockville, MD, USA) for 72 h using X-tremeGENE Hp DNA Transfection reagent (Roche, Mannheim, Germany) according to the manufacturer's instructions. Transfected HEK293 cells were cultured in medium with G418 (2 mg/ml). G418-resistant clones were used for further studies [26].

### 2.5. Detection of superoxide anion production

Oxidative stress is involved in the pathogenesis of acute and chronic inflammatory disease. We used spectrophotography to measure the formation of extracellular superoxide anion. Briefly, superoxide anion generation was measured by superoxide dismutase-inhibitable ferricytochrome *c* reduction in activated human neutrophils. Human neutrophils were preincubated with 0.5 mg/ml ferricytochrome *c* and 1 mM Ca<sup>2+</sup> at 37 °C, and then treated with DMSO, HCH6-1, cyclosporine H (CsH), and WRW4 for 5 min before being activated by chemoattractants, including fMLF (FPR1 agonist), WKYMVm (dual FPR1/FPR2 agonist), MMK1 (FPR2 agonist), NaF (direct G protein activator), and phorbol 12-myristate 13-acetate (PMA, protein kinase C activator). Neutrophils were primed with or without cytochalasin B (CB) for 3 min before the addition of chemoattractants. The change in absorbance was continuously monitored at 550 nm by spectrophotometry (U-3010, Hitachi, Tokyo) [27].

Hydroethidine (HE), which was oxidized to ethidium, was used as a probe to detect intracellular superoxide anion production [28,29]. Neutrophils were labeled with HE (10 µM) for 15 min and incubated with testing drugs for 5 min before adding stimulants at 37 °C. The fluorescence intensity of oxidized products was assayed by flow cytometry (FACSCalibur™; BD Bioscience, San Jose, CA, USA). Diphenyleneiodonium (10 µM) and apocynin (0.5 µM), NADPH oxidase inhibitors, abolished the fMLF-induced fluorescence intensity, indicating that the effect is dependent on NADPH oxidase activation.

### 2.6. Measurement of elastase release

We used elastase release as evidence of degranulation of the activated neutrophils. Elastase release was measured by using methoxysuccinyl-Ala-Ala-Pro-Val-p-nitroanilide as the substrate and monitoring by spectrophotography at 405 nm. Briefly, the mixture of neutrophils (6 × 10<sup>5</sup> cells/ml) and 100 µM substrate and 1 mM CaCl<sub>2</sub> at 37 °C was treated with DMSO (control), HCH6-1, CsH, and WRW4 for 5 min, then activated by fMLF, WKYMVm, MMK1, NaF (direct G protein activator), leukotriene (LT) B<sub>4</sub> (BLT1 receptor agonist), and interleukin (IL) – 8 with CB pretreatment. The change in absorbance was monitored continuously by spectrophotometry. The results are shown as a percentage of elastase release in the control group.

### 2.7. Superoxide anion and 1,1-diphenyl-2-picrylhydrazyl (DPPH) scavenging assay

A cell-free xanthine/xanthine oxidase system was used to evaluate superoxide anion-scavenging. The reaction was carried out in a mixture of assay buffer containing 50 mM Tris (pH 7.4), 0.3 mM 2-(4-Iodophenyl) – 3-(4-nitrophenyl) – 5-(2,4-disulfophenyl) – 2H-tetrazolium monosodium salt (WST-1), testing samples, and 0.02 U/ml xanthine oxidase. After adding 0.1 mM xanthine to the assay buffer at 30 °C, WST-1 was reduced by superoxide anion and the change of absorbance was measured at 450 nm.

Antioxidant ability was determined by DPPH assay. The reaction was performed with the ethanol solution of DPPH (100 µM) incubated with testing drugs at 30 °C. The absorbance was measured at 517 nm and the effects were relative to those of the control.

### 2.8. Lactate dehydrogenase (LDH) release

LDH activity was detected in neutrophils, treated or not, by using a

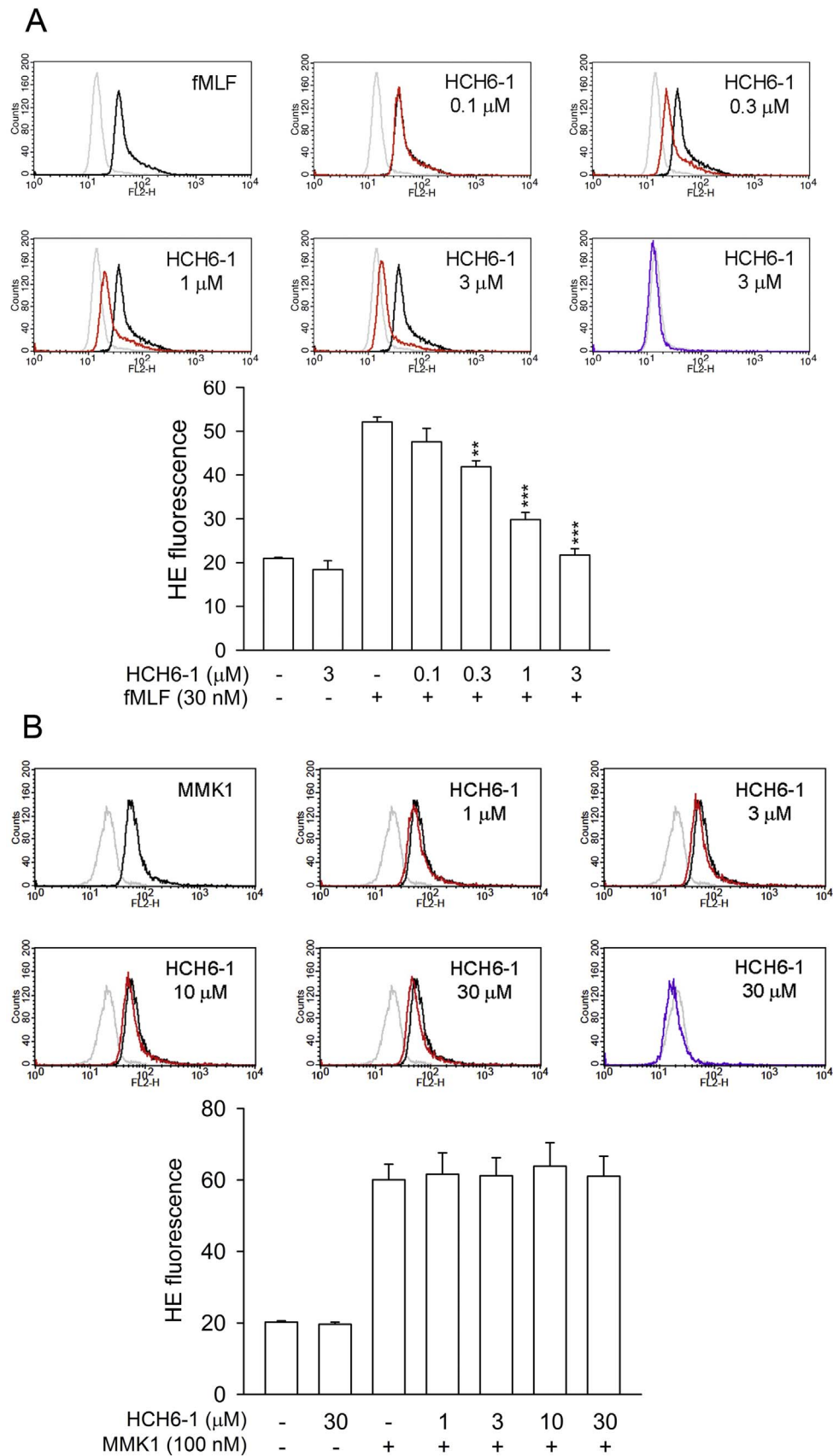


**Fig. 2.** HCH6-1 significantly suppresses intracellular superoxide anion generation from FPR1 agonist-activated human neutrophils. Human neutrophils were preincubated with DMSO (as the control) or HCH6-1 for 5 min and then activated by (A) fMLF or (B) MMK1 in the presence of CB for another 20 min. Representative histograms of typical fluorescence-activated cell sorting profiles for hydroethidine (HE) staining in unstimulated cells and cells stimulated with fMLF with or without HCH6-1 at the concentrations indicated. Mean fluorescence intensity (MFI) data are shown as mean  $\pm$  SEM ( $n=3$  or 4). \*\* $p < 0.01$ ; \*\*\* $p < 0.001$  compared with the fMLF.

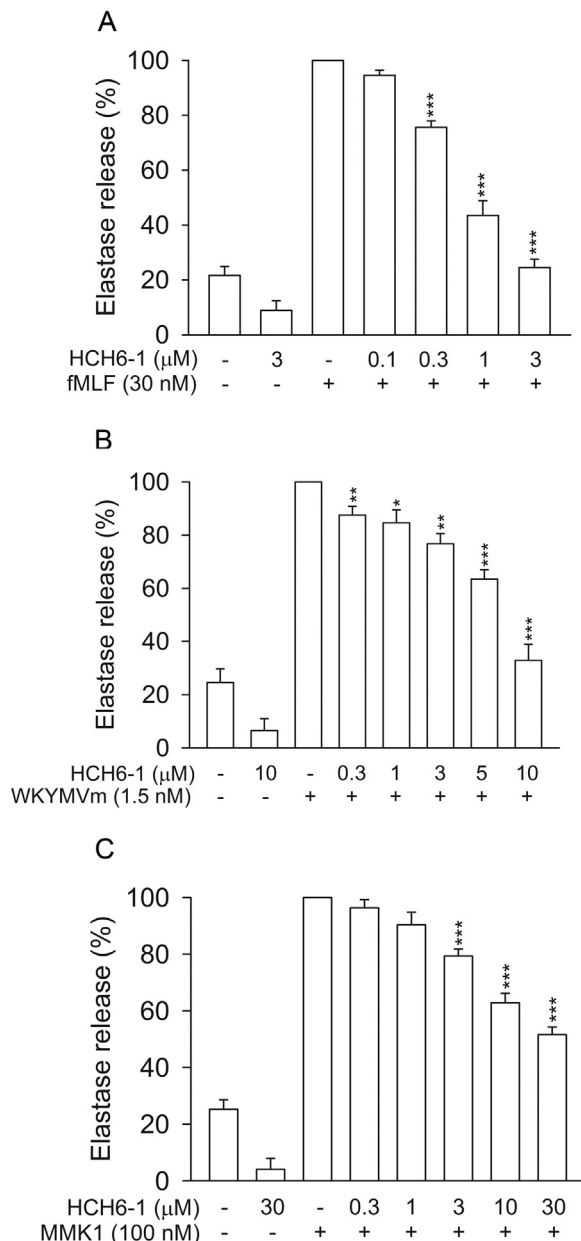


Fig. 3. HCH6-1 selectively inhibits elastase release in human neutrophils activated by fMLF. Human neutrophils were incubated with DMSO (as the control) or HCH6-1 for 5 min, and then activated by (A) fMLF, (B) WKYMVm, or (C) MMK1 in the presence of CB for another 10 min. Elastase release was measured spectrophotometrically at 405 nm. Data are expressed as mean  $\pm$  SEM ( $n=4$  or 6). \* $p < 0.05$ ; \*\* $p < 0.01$ ; \*\*\* $p < 0.001$  compared with the control.

commercially available method (Promega, Madison, WI, USA). LDH activity was expressed as a percentage of total LDH activity normalized by lysing the neutrophils with 0.1% Triton X-100 at 37 °C.

## 2.9. Chemotaxis assay

A 24-well microchemotaxis chamber was used for measuring cell migration (pore size 3 μm; Millipore, Darmstadt, Germany). Neutrophils were suspended at a final concentration of  $5 \times 10^6$  cells/ml and pretreated with testing drugs for 5 min at 37 °C in the top chamber. Chemoattractants were placed in the bottom chamber, and the number of migrated neutrophils was counted by using a Coulter counter (Beckman Coulter Inc., Fullerton, CA, USA).

## 2.10. Receptor binding assay

N-formyl-Nle-Leu-Phe-Nle-Tyr-Lys-fluorescein (FNLFNKYK), a fluorescent analog of fMLF, was used for receptor binding under flow cytometry monitoring [30]. Briefly, neutrophils were incubated with the test drugs for 5 min at 4 °C and labeled with FNLFNKYK for 30 min before flow cytometry. We used fMLF as a positive control.

## 2.11. Nuclear magnetic resonance (NMR)

HCH6-1 or fMLF, or both, was mixed with DMSO- $d_6$ . All mixed solutions were vortexed and transferred to 5-mm NMR tubes for NMR acquisition. The  $^1\text{H}$  NMR spectra from the mixture were acquired by using a Bruker AVANCE-400 MHz FT NMR spectrometer (BrukerBioSpin GmbH, Rheinstetten, Germany).

## 2.12. Determination of cAMP concentration

Neutrophils were incubated with HCH6-1 (1–10 μM) or DMSO (control) for 5 min and stimulated with fMLF for another 1 min. The reaction was then terminated by the addition of 0.5% dodecyltrimethylammonium bromide. After centrifugation at 3000g for 5 min at 4 °C, the supernatant was assayed for cAMP with an enzyme immunoassay kit (Amersham Biosciences, Buckinghamshire, UK).

## 2.13. Analysis of intracellular calcium level

Calcium influx was measured in response to chemoattractants by using human neutrophils labeled with Fluo-3/AM (2 μM) for 30 min at 37 °C. The neutrophils were excited sufficiently at 488 nm to assess the cytoplasmic calcium level by using a thermostat in a quartz cuvette after continuous stirring with a Hitachi F-4500 spectrofluorometer. The fluorescence ratio of the emission wavelength at 520 nm was recorded. After treatment with testing drugs for 5 min, stimulants were added to induce the peak intracellular calcium concentration ( $[\text{Ca}^{2+}]_i$ ). The  $[\text{Ca}^{2+}]_i$  level was then calculated according to fluorescence intensity as  $[\text{Ca}^{2+}]_i = K_d \times [(F - F_{\min}) / (F_{\max} - F)]$ , where  $F$  is the observed fluorescence intensity;  $F_{\max}$  and  $F_{\min}$  were obtained by adding 0.05% Triton X-100 and 20 mM EGTA, respectively, to the neutrophils; and  $K_d$  was 400 nM [31].

## 2.14. Immunoblotting analysis

Fresh neutrophils preincubated with testing drugs for 5 min were stimulated with fMLF for 30 s, and were then mixed with sample buffer for 15 min at 100 °C to stop the reaction. Supernatants were collected after centrifugation at 14,000g for 20 min at 4 °C. To separate the proteins, 12% SDS-PAGE was used. The samples were then blotted onto nitrocellulose membranes and incubated with primary antibodies and horseradish peroxidase-conjugated secondary anti-rabbit antibodies (Cell Signaling Technology, Beverly, MA, USA). The immunoreactive bands were visualized by using an enhanced chemiluminescence system (Amersham Biosciences, Piscataway Corp., NJ, USA). The intensity of the bands was analyzed by using UVP Biospectrum (UVP, LLC Upland, CA, USA).

## 2.15. LPS-induced acute lung injury model

C57BL/6 mice were purchased from BioLASCO Taiwan Co. (Taipei) and housed with a 12 h light and dark cycle. All animal experiments were performed according to the guidelines of the *Animal Welfare Act* and *The Guide for Care and Use of Laboratory Animals* from the National Institutes of Health. All experimental procedures followed the recommendations of the Institutional Animal Care and Use Committee of Chang Gung University. For inducing ALI, male mice were anesthetized in a chamber containing 2.5% isoflurane in oxygen, then challenged

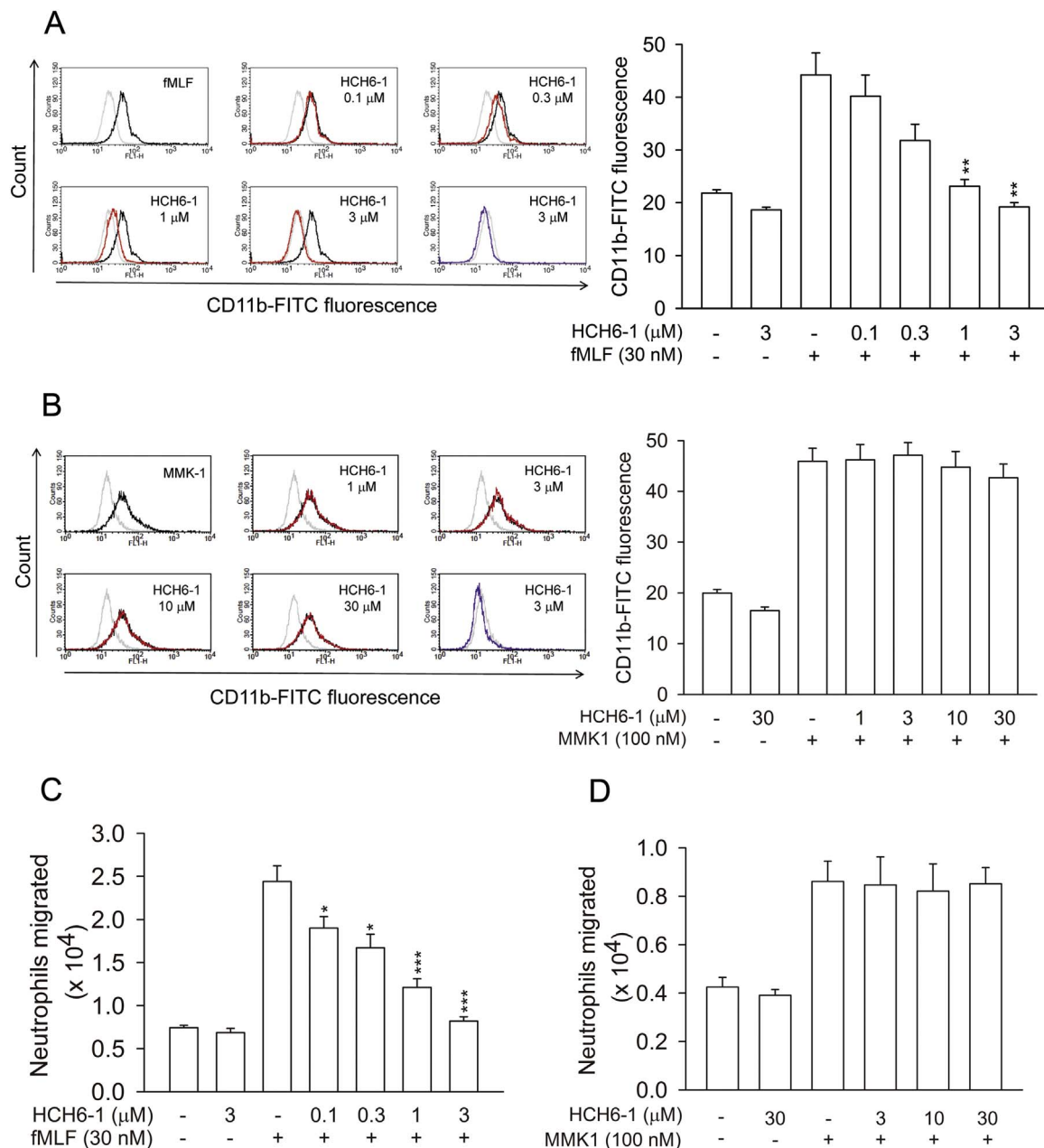


**Fig. 4.** HCH6-1 impairs CD11b expression and migration in human neutrophils induced by fMLF. Cells were preincubated with DMSO or HCH6-1 for 5 min, then activated by (A) fMLF or (B) MMK1 in the presence of CB for another 10 min. The fluorescence intensity of FITC-labeled anti-CD11b was monitored by flow cytometry. MFI data are shown as mean  $\pm$  SEM (n = 4). (C) fMLF or (D) MMK1 were added in the lower compartments and neutrophils preincubated with DMSO and HCH6-1 were placed in the upper compartments of chemotaxis wells. Migration of neutrophils is presented as the mean number of neutrophils migrated  $\pm$  SEM (n = 4). \* $p$  < 0.05; \*\* $p$  < 0.01; \*\*\* $p$  < 0.001 compared to the fMLF.

with an intra-tracheal spray of 50  $\mu$ g of LPS (*Escherichia coli* 0111:B4; Sigma-Aldrich, MO, USA) dissolved in 40  $\mu$ l normal saline. Mice without LPS spray were injected with saline as the controls. HCH6-1 (50 mg/kg) were injected intraperitoneally in mice (20–25 g, 7–8 weeks old) either 1 h before LPS spray or 30 min after LPS spray to yield the following experimental groups: sham, HCH6-1 only, LPS only, LPS + HCH6-1. Mice were euthanized by cervical dislocation under anesthesia and the lungs were removed 6 h after LPS application. The left lung lobe was fixed by 10% neutral buffered formalin for histological examination and the right 4 lobes were assayed for myeloperoxidase (MPO) activity [32].

## 2.16. MPO activity and total protein assay

Lung tissues were homogenized in 50 mM phosphate buffered saline

(PBS; pH 6.0) with 0.5% hexadecyltrimethylammonium bromide (HET AB) (Sigma-Aldrich, MO, USA) by using the MagNA Lyser Instrument (Roche, Mannheim, Germany) and centrifuged at 12,000g for 20 min at 4  $^{\circ}$ C to remove insoluble material. Peroxidase activity was measured as the oxidation of *o*-dianisidine dihydrochloride (Sigma-Aldrich, MO, USA). Briefly, the homogenate was added to 0.2 mg/ml *o*-dianisidine dihydrochloride containing 0.001%  $H_2O_2$  and incubated at room temperature for 10 min. The absorption was determined spectrophotometrically at 405 nm. MPO activity was normalized to protein concentration. Total protein concentration in lung was determined by the Bradford method (Bio-Rad, CA, USA) [27].

## 2.17. Histopathology and immunohistochemistry

Lung tissues were fixed in 10% neutral buffered formalin for 24 h,

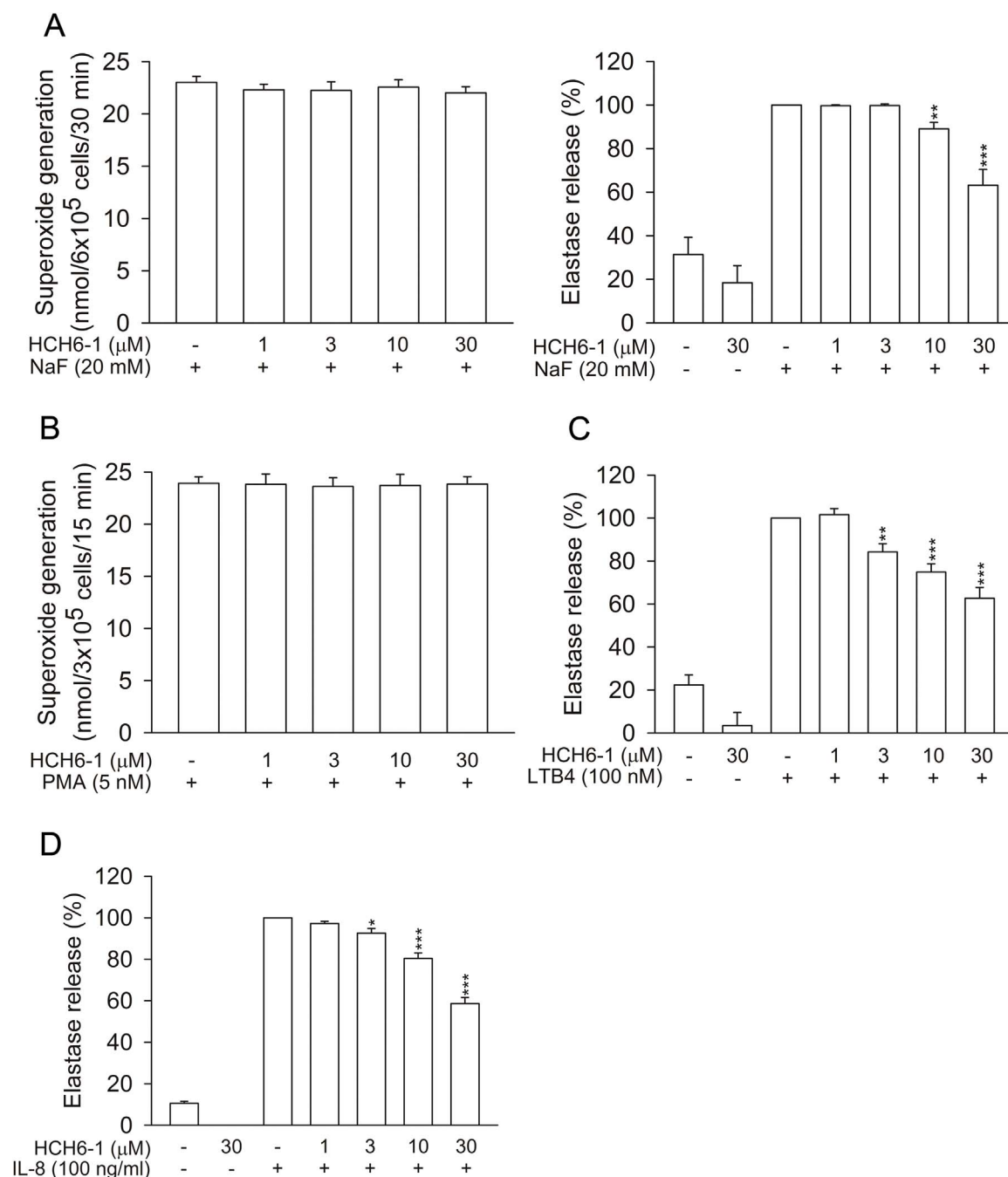


**Fig. 5.** HCH6-1 does not significantly inhibit superoxide anion generation and elastase release in non-FPR1 agonist-activated human neutrophils. Human neutrophils were incubated with DMSO (as the control) or HCH6-1 for 5 min, and then activated with (A) NaF, (B) PMA, (C) LTB4, or (D) IL-8 for another 10 min. Superoxide generation was measured by cytochrome *c* reduction. Elastase release was measured spectrophotometrically at 405 nm. All data are expressed as mean  $\pm$  SEM ( $n=4$ ). \*\* $p < 0.01$ ; \*\*\* $p < 0.001$  compared with the control.

then embedded in paraffin blocks and cut into 4- $\mu$ m-thick sections. Sections were stained with hematoxylin and eosin (H & E). Images were obtained under a light microscope. For immunofluorescence staining, Ly6G antibody (eBiosciences) was used as the primary antibody. The SuperPicture kit (Invitrogen) was used as the secondary antibody. Gray fluorescence in slides was examined under an Olympus fluorescence microscope.

## 2.18. Statistical analysis

All results are expressed as mean  $\pm$  SEM. One-way ANOVA analysis or Student *t*-test was used for analysis with use of SigmaPlot (Systat Software, San Jose, CA).  $P < 0.05$  was considered statistically

significant.

## 3. Results

### 3.1. HCH6-1 selectively reduces superoxide anion generation in FPR1 agonist-activated human neutrophils

Superoxide anion and reactive oxidants produced by neutrophils are biological programs involved in killing pathogens and are involved in many pathologic conditions [33]. To determine whether HCH6-1 alters the generation of extracellular superoxide anion in activated human neutrophils, we used the cell-impermeable cytochrome *c* reduction assay. HCH6-1 significantly inhibited superoxide anion generation in fMLF (FPR1 agonist)-



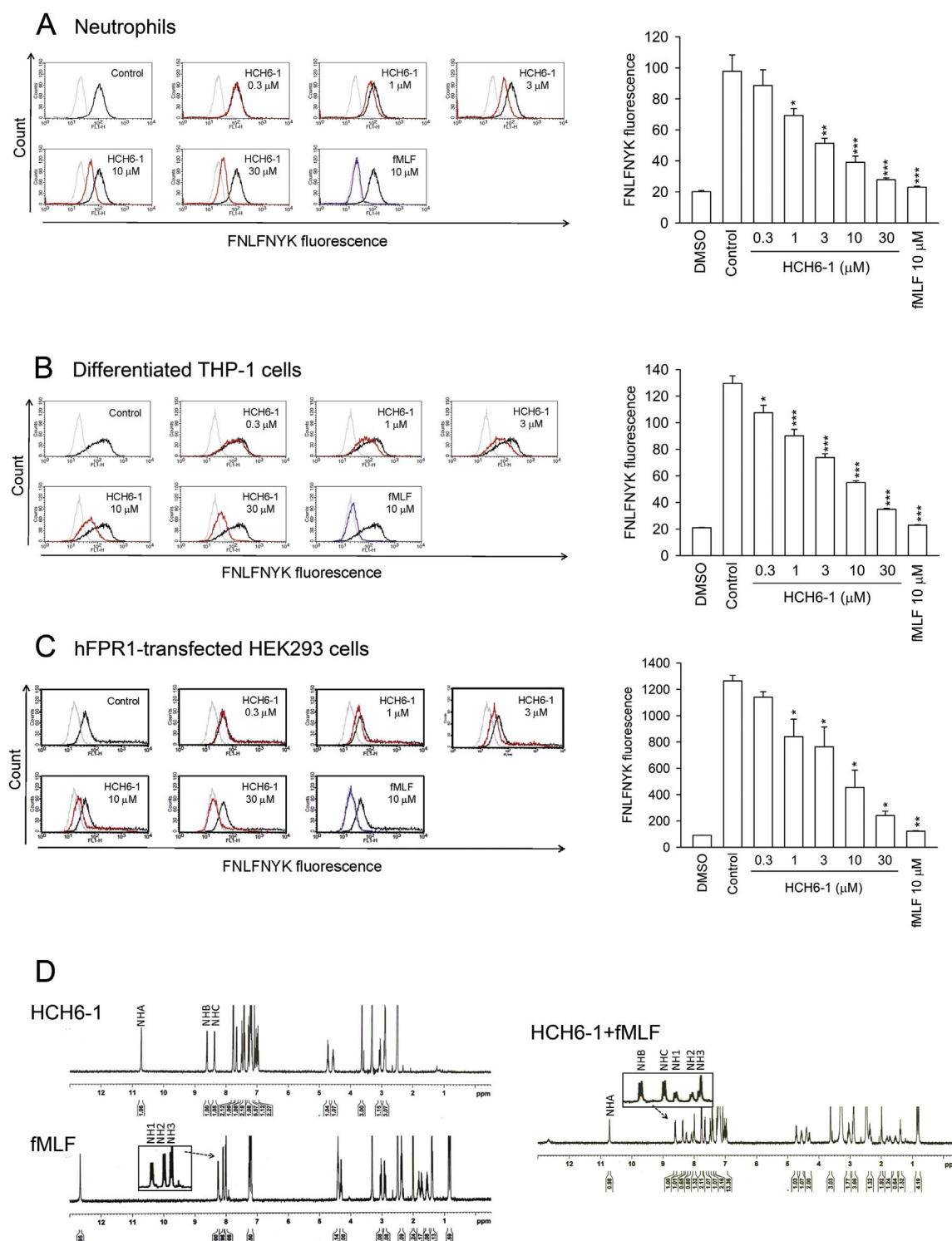


**Fig. 6.** HCH6-1 blocks FNLNFK binding to FPR1 in human neutrophils and neutrophil-like cells. Human neutrophils were preincubated with DMSO (as the control), fMLF (10  $\mu$ M), or (A) HCH6-1 for 5 min before labeling with the fluorescent peptide (FNLNFK) (4 nM) for 30 min. Representative histograms demonstrated typical fluorescence in the absence (gray line) or presence of FNLNFK control (black lines) or FNLNFK with inhibitors (color lines). (B) Differentiated THP-1 cells and (C) hFPR1-HEK293 cells were preincubated with DMSO (as the control), HCH6-1, or fMLF for 5 min before labeling with the fluorescence peptide (FNLNFK) (3 nM) for 30 min. Representative histograms demonstrate typical fluorescence in the absence (gray lines) or presence of FNLNFK control (black lines) or FNLNFK with inhibitors (red lines). MFI are shown as mean  $\pm$  SEM ( $n = 5$  for A,  $n = 6$  for B and C). \* $p < 0.05$ ; \*\* $p < 0.01$ ; \*\*\* $p < 0.001$  compared with the control. (D)  $^1\text{H}$  NMR spectra of HCH6-1 (3 mM), fMLF (3 mM), or combination of both. (For interpretation of the references to color in this figure legend, the reader is referred to the web version of this article.)

activated neutrophils, with  $\text{IC}_{50} 0.32 \pm 0.03 \mu\text{M}$  (Fig. 1B). HCH6-1 had fewer inhibitory effects in WKYMVm (dual FPR1/FPR2 agonist)- and MMK1 (FPR2 agonist)-activated neutrophils, with  $\text{IC}_{50} 4.98 \pm 0.27$  and  $17.68 \pm 2.77 \mu\text{M}$ , respectively (Fig. 1C and D).

CsH (FPR1 antagonist) and WRW4 (FPR2 antagonist) were used to verify the FPR1- and FPR2-induced neutrophil activities. CsH inhibited superoxide anion generation more in fMLF (FPR1 agonist)-activated neutrophils than in MMK1 (FPR2 agonist)-activated cells, with  $\text{IC}_{50}$

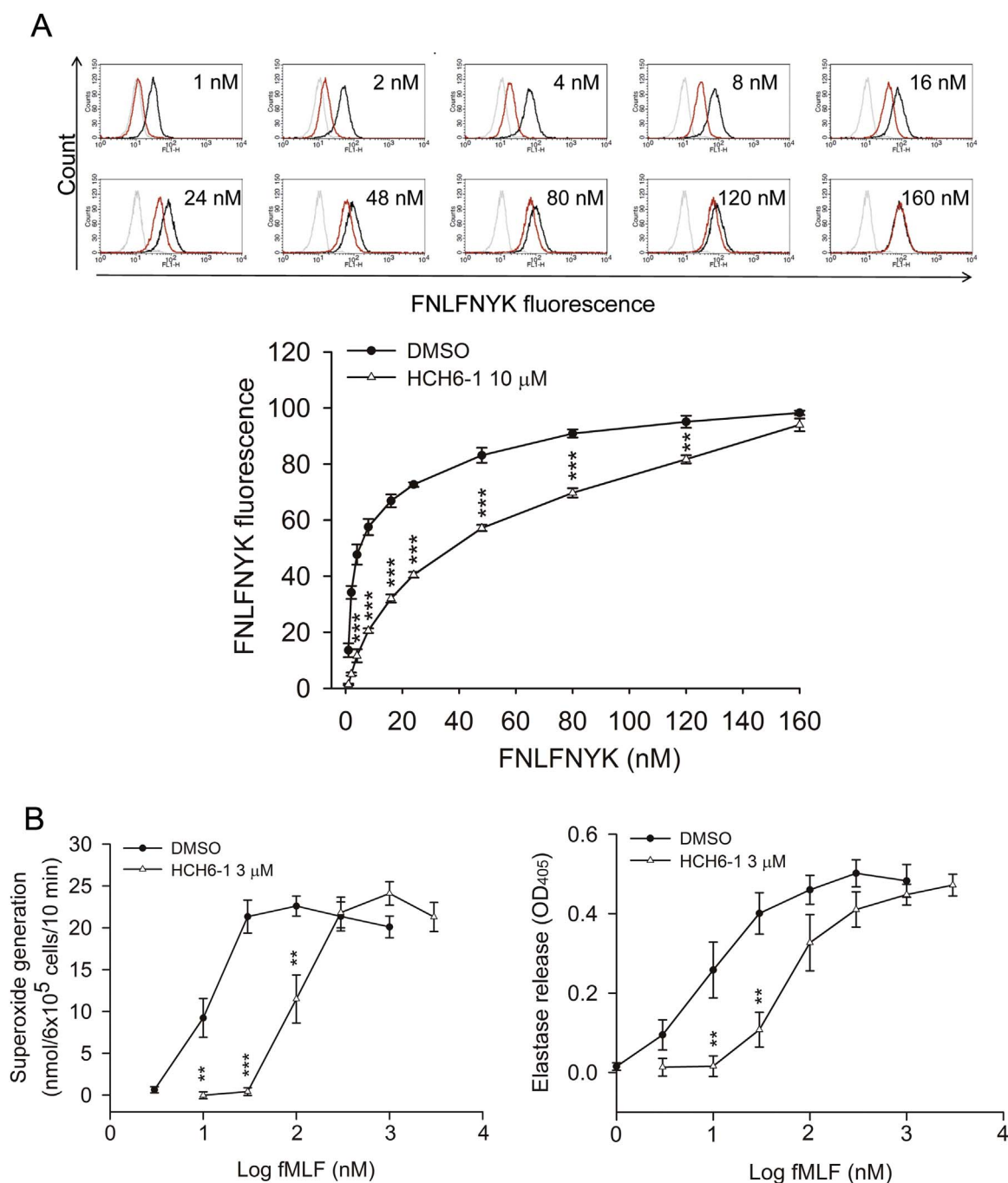


**Fig. 7.** HCH6-1 shows competitive inhibition on FPR1 in human neutrophils. (A) Human neutrophils were preincubated with DMSO (as the control) or HCH6-1 for 5 min before labeling with the fluorescent peptide (FNLFNKYK) (1–160 nM) for 30 min. Representative histograms of typical fluorescence in the absence (gray lines) or presence of FNLFNKYK control (black lines) or FNLFNKYK with inhibitors (red lines). MFI are mean  $\pm$  SEM (n = 6). Human neutrophils were incubated with DMSO (as the control) or HCH6-1 for 5 min, and then activated with different concentrations of fMLF in the presence of CB for 10 min (B) Extracellular superoxide anion and (C) elastase release were measured. All data are expressed as mean  $\pm$  SEM (n = 5). \*\* $p$  < 0.01; \*\*\* $p$  < 0.001 compared with the control. (For interpretation of the references to color in this figure legend, the reader is referred to the web version of this article.)

0.04  $\pm$  0.01 and 4.28  $\pm$  0.43  $\mu$ M, respectively (Supplementary Fig. 1A and B). In contrast, WRW4 dominantly suppressed superoxide anion generation in FPR2 agonist-activated neutrophils (Supplementary Fig. 1C and D).

HCH6-1 did not induce LDH release even at 30  $\mu$ M (data not shown), so it did not have cytotoxic effects in human neutrophils. To further exclude the antioxidant effects of HCH6-1 in cell-free systems, we used a reduction assay with WST-1 and DPPH. HCH6-1 did not alter the level of xanthine/xanthine oxidase superoxide anion and DPPH radical in cell-free systems (Fig. 1E and F). Superoxide dismutase and  $\alpha$ -tocopherol, respectively, were used as positive controls. Therefore, cell

cytotoxicity and free-radical scavenging effects did not account for the inhibitory activity of HCH6-1 in activated human neutrophils.

To examine the effect of HCH6-1 on intracellular superoxide anion generation in stimulated neutrophils, HE was used as the probe with flow cytometry. HCH6-1 significantly inhibited intracellular superoxide anion generation in fMLF-activated neutrophils, but not in MMK1-activated cells (Fig. 2A and B). These data suggested that HCH6-1 exhibited a selective inhibitory effect on FPR1-mediated superoxide anion generation in human neutrophils.

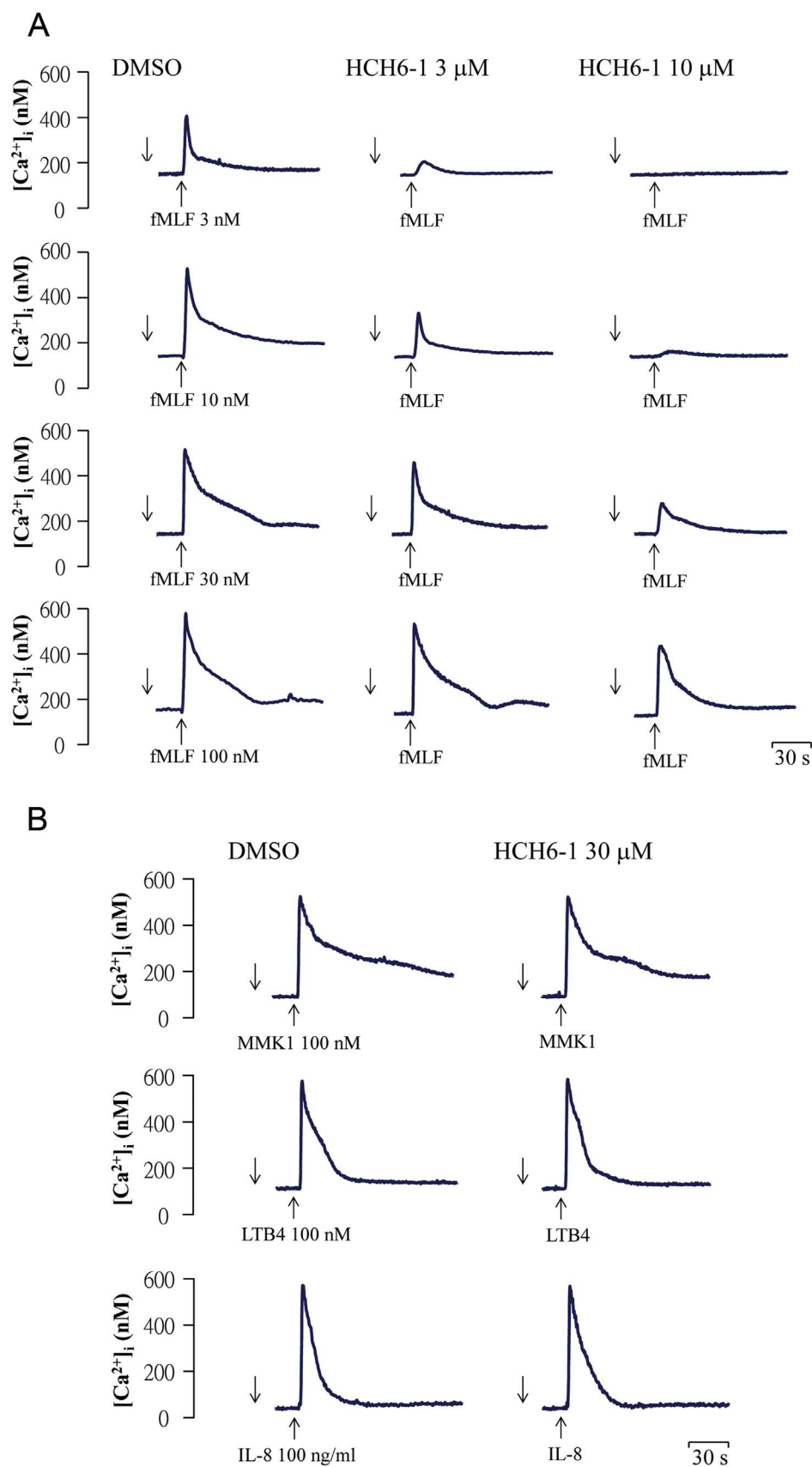


**Fig. 8.** HCH6-1 attenuates  $\text{Ca}^{2+}$  mobilization induced by FPR1 but not non-FPR1 in human neutrophils. Fluo-3/AM-labeled human neutrophils were incubated with DMSO (as the control) or HCH6-1 for 5 min. Cells were activated by (A) fMLF, (B) MMK1, LTB4, or IL-8. The mobilization of  $\text{Ca}^{2+}$  was determined in real time by spectrofluorometry ( $n=4$ ).

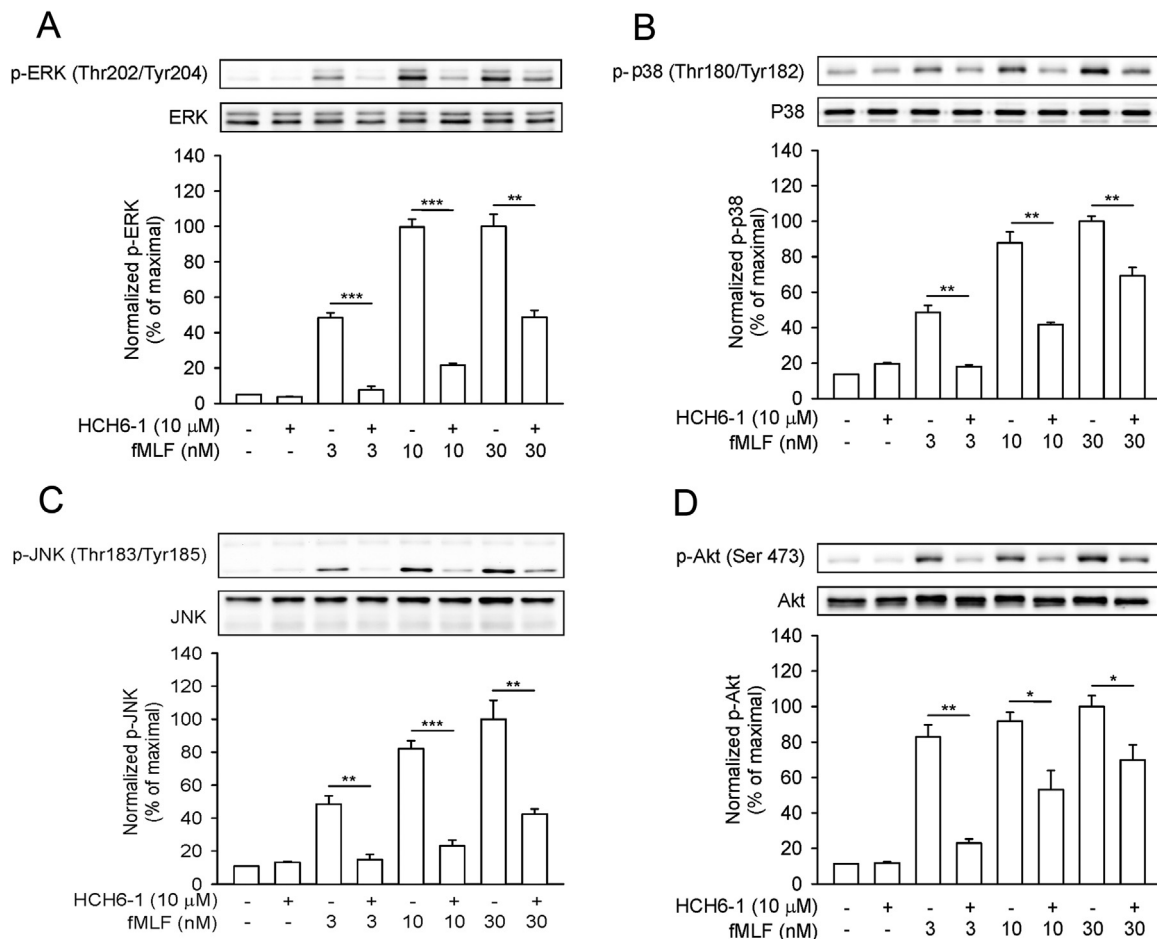


**Fig. 9.** HCH6-1 inhibits phosphorylation of MAPKs and Akt in fMLF-activated human neutrophils. Human neutrophils were incubated with DMSO (as the control) or HCH6-1 for 5 min before stimulation with or without fMLF for another 30 s. Phosphorylation of (A) ERK, (B) p38, (C) JNK and (D) Akt analyzed by immunoblotting with antibodies against the phosphorylated and total form of each protein. Data are normalized to the corresponding total protein level and expressed as mean  $\pm$  SEM relative to the mean maximal ratio. (n = 3 or 4). \* $p < 0.05$ ; \*\* $p < 0.01$ ; \*\*\* $p < 0.001$  compared with the corresponding control group.

### 3.2. HCH6-1 selectively inhibits elastase release in fMLF-activated neutrophils

In degranulation, neutrophils release proteolytic enzymes in response to an inflammatory stimulus [34]. To study whether HCH6-1 affected degranulation in activated neutrophils, elastase release was measured by spectrophotography. HCH6-1 significantly inhibited elastase release in fMLF-activated neutrophils, with  $IC_{50}$   $0.57 \pm 0.07$   $\mu$ M (Fig. 3A). However, in neutrophils triggered by WKYMVm or MMK1, HCH6-1 inhibited elastase release at higher concentrations, with  $IC_{50}$   $5.22 \pm 0.69$  and  $10.00 \pm 0.65$   $\mu$ M, respectively (Fig. 3B and C). CsH specifically suppressed elastase release in fMLF-activated neutrophils (Supplementary Fig. 2A and B), whereas WRW4 predominantly attenuated elastase release in FPR2 agonist-activated neutrophils (Supplementary Fig. 2C and D). Thus, HCH6-1 impaired the degranulation of FPR1-activated neutrophils.

### 3.3. HCH6-1 inhibits fMLF-induced neutrophil chemotaxis

We next evaluated chemotaxis, including expression of adhesion molecule CD11b and migration, in active neutrophils. HCH6-1 dose-dependently diminished CD11b expression up-regulated by fMLF in human neutrophils (Fig. 4A) but not MMK1 (Fig. 4B). Furthermore, HCH6-1 reduced the neutrophil migration induced by fMLF (Fig. 4C) but not MMK1 (Fig. 4D). These results suggested that HCH6-1 impaired chemotaxis only in FPR1-activated neutrophils. Similarly, CsH specifically inhibited neutrophil migration induced by fMLF but not MMK1

(Supplementary Fig. 3A and B).

### 3.4. HCH6-1 does not attenuate inflammatory responses in non-FPR agonist-stimulated neutrophils

To examine the effects of HCH6-1 in non-FPR agonist-stimulated neutrophil activations, we used NaF (20 mM, direct G protein activator), PMA (5 nM, protein kinase C activator), LTB4 (100 nM, BLT receptor agonist), and IL-8 to trigger neutrophil inflammatory responses. HCH6-1 failed to inhibit superoxide anion generation in NaF- and PMA-activated neutrophils (Fig. 5A and B). Furthermore, HCH6-1, only at higher concentrations, inhibited elastase release induced by NaF, LTB4, and IL-8 (Fig. 5A, C, and D). Because HCH6-1 did not suppress non-FPR1 agonist-induced inflammatory responses in human neutrophils, we hypothesized that HCH6-1 is a selective FPR1 inhibitor.

### 3.5. HCH6-1 binds to FPR1 in human neutrophils and neutrophil-like cells

To determine whether HCH6-1 binds to FPR1, we examined the binding of FNLFNKYK (fMLF fluorescent analog) to the surface of neutrophils by flow cytometry. We found that fMLF (10  $\mu$ M) completely inhibited the binding of FNLFNKYK (4 nM) to neutrophils (Fig. 6A). Compared with the controls, in treated neutrophils, HCH6-1 dose-dependently inhibited the binding of FNLFNKYK to FPR1. Similarly, CsH inhibited the binding of FNLFNKYK to FPR1 (Supplementary Fig. 3C). To further identify that HCH6-1 has a binding affinity for FPR1, we



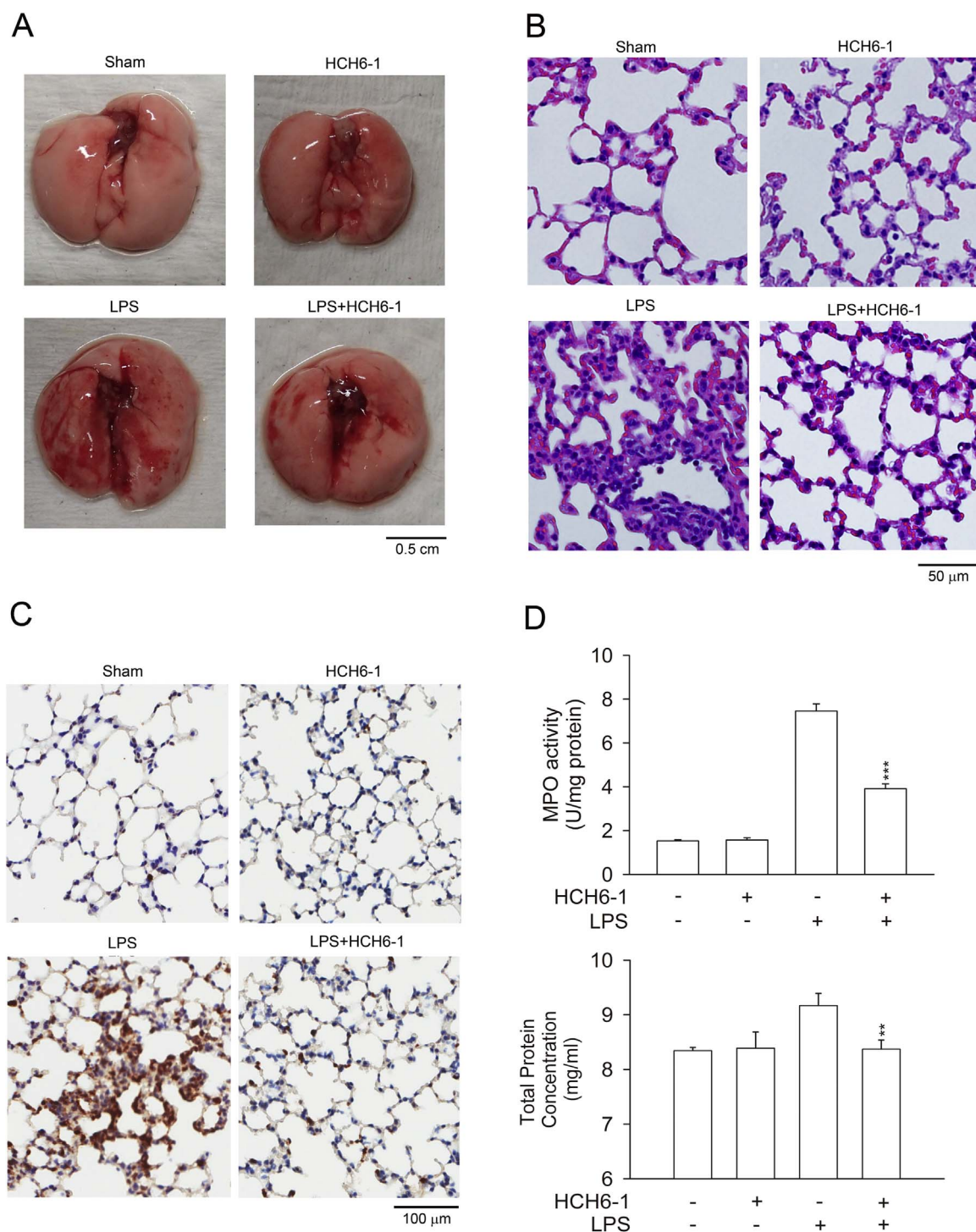


**Fig. 10.** HCH6-1 pretreatment ameliorates acute lung injury (ALI) induced by lipopolysaccharide (LPS) in mice. C57BL/6 mice were treated with DMSO or HCH6-1 (50 mg/kg) by intraperitoneal injection before LPS spray for 6 h to yield the following experimental groups: sham, HCH6-1 only, LPS only, LPS + HCH6-1. (A) Representative photos of lung. (B) Photomicrograph of hematoxylin–eosin stained lung sections by light microscopy with a 40 $\times$  objective. (C) Immunofluorescence staining of Ly6G (gray) in lung sections by fluorescence microscope with a 20 $\times$  objective. Representative images of lung sections from 6 experimental groups. (D) Myeloperoxidase (MPO) activity and total protein concentrations of lung tissues were assessed 6 h after LPS spray. (upper panel: MPO activity, lower panel: total lung protein concentration). Data are mean  $\pm$  SEM (n = 5–6). \*\* $p$  < 0.01; \*\*\* $p$  < 0.001 compared with the LPS group.

examined the binding of FNLFNK to neutrophil-like cells, including differentiated THP-1 cells and hFPR1-transfected HEK293 cells. We found that fMLF (10  $\mu$ M) completely inhibited the binding of FNLFNK (3 nM) to differentiated THP-1 cells and hFPR1-transfected HEK293 cells, respectively (Fig. 6B and C). In line with the result, HCH6-1 dose-dependently inhibited the binding of FNLFNK to FPR1 in both neutrophil-like cells.

The  $^1\text{H}$  NMR spectra of the HCH6-1 and fMLF mixture showed that these 2 compounds did not have structure-structure interaction (Fig. 6D). Thus, we ruled out the direct interaction of HCH6-1 with N-formyl peptide.

HCH6-1 is a stable dipeptide derivative of D-phenylalanine and L-tryptophan. However, D-phenylalanine and L-tryptophan did not alter superoxide anion production and elastase release in fMLF-activated



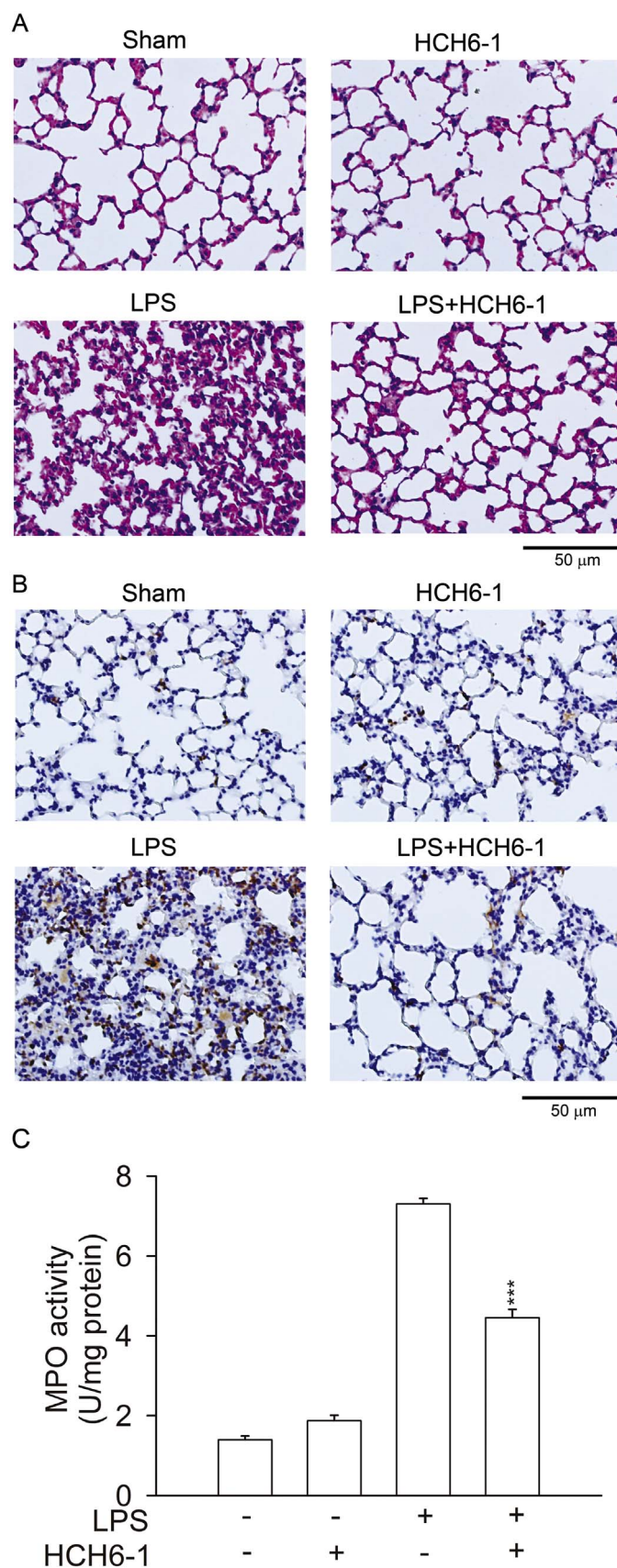


**Fig. 11.** HCH6-1 posttreatment diminishes acute lung injury (ALI) induced by lipopolysaccharide (LPS) in mice. ALI was induced by LPS spray for 6 h in C57BL/6 mice. DMSO or HCH6-1 (50 mg/kg) was injected intraperitoneally 30 min after LPS spray to yield the following experimental groups: sham, HCH6-1 only, LPS only, LPS + HCH6-1. (A) Photomicrograph of hematoxylin–eosin stained lung sections by light microscopy with a 40 $\times$  objective were examined 6 h after LPS spray. (B) Immunofluorescence staining of Ly6G (gray) in lung sections by fluorescence microscope with a 40 $\times$  objective were examined 6 h after LPS spray. Representative images of lung sections from 6 experimental groups. (C) MPO activity was assessed 6 h after LPS inhalation. Data are mean  $\pm$  SEM (n=6). \*\*\* $p$  < 0.001 compared with the LPS group.

human neutrophils (Supplementary Fig. 4A and B).

### 3.6. HCH6-1 has competitive inhibitory effects on FPR1-induced neutrophil responses

Receptor binding profiles of FNLFNYK revealed a rightward shift of the concentration response curve in the presence of HCH6-1 (Fig. 7A). Furthermore, HCH6-1 pretreatment produced right shifts in the concentration-response curves of fMLF for superoxide anion generation and elastase release (Fig. 7B and C). On the basis of these results, it is possible to postulate that HCH6-1 is a competitive inhibitor of FPR1.

### 3.7. Cyclic AMP (cAMP)/protein kinase A (PKA) does not mediate the inhibitory effects of HCH6-1

An elevated intracellular cAMP level is well known to diminish inflammatory mediator release by innate immune cells [35]. Our previous studies showed that cAMP-dependent PKA activation has a significant suppressive effect on neutrophil activation [36,37]. To determine whether the cAMP pathway is involved in the inhibitory effects of HCH6-1, cellular cAMP level was assayed. HCH6-1 did not increase cAMP levels in human neutrophils. It is notable that fMLF slightly increased the cAMP concentration, which was reduced by HCH6-1 (Supplementary Fig. 5A). The transient increase in cAMP caused by fMLF plays a negative feedback effect in neutrophil activation [27,38]. Intracellular cAMP level is regulated either by being synthesized by adenylate cyclases or by being degraded by phosphodiesterases. Rolipram, a phosphodiesterase 4 inhibitor, elevated cAMP concentration under resting condition and induced a significant increase in cAMP level in fMLF-activated human neutrophils (Supplementary Fig. 5A). In addition, H89 (3  $\mu$ M), a PKA inhibitor, reversed the inhibitory effects of PGE<sub>1</sub>, but not HCH6-1, on superoxide anion generation and elastase release in fMLF-activated human neutrophils (Supplementary Fig. 5B and C). The results suggested that cAMP/PKA pathway is not involved in HCH6-1-mediated inhibition of fMLF-induced neutrophil activation.

### 3.8. HCH6-1 inhibits transient increased intracellular calcium concentration ( $[Ca^{2+}]_i$ ) induced by fMLF but not non-FPR1 agonists

$Ca^{2+}$  signal plays an important role in regulating human neutrophil functions [39]. To determine whether HCH6-1 attenuates the  $Ca^{2+}$  signal in activated neutrophils, we assayed the  $[Ca^{2+}]_i$  level. Results showed that fMLF transiently increased the  $[Ca^{2+}]_i$  level in human neutrophils, and HCH6-1 dose-dependently and competitively inhibited the increase in peak  $[Ca^{2+}]_i$  in fMLF-activated neutrophils (Fig. 8A). In contrast, HCH6-1 had no effect on the peak  $[Ca^{2+}]_i$  level induced by MMK1, LTB<sub>4</sub>, and IL-8 (Fig. 8B). These results again support the hypothesis that HCH6-1 competitively and selectively binds to FPR1.

### 3.9. HCH6-1 attenuates phosphorylation of mitogen-activated protein kinases (MAPKs) and Akt protein in fMLF-activated human neutrophils

Activation of MAPKs and Akt signaling pathways is involved in regulation of neutrophil immune responses [40–43]. Significantly, we found that HCH6-1 competitively attenuated the fMLF-induced phosphorylation of ERK, p38 MAPK and JNK as well as Akt in human neutrophils (Fig. 9).

### 3.10. HCH6-1 ameliorates ALI in LPS-induced mice

The genetic ablation of *Fpr1* shows protective effects in ALI through reducing neutrophils recruitment [44]. The protective effect of HCH6-1 in LPS-induced ALI was tested. The morphology of mouse lung sections revealed more injury and congestion following LPS treatment (Fig. 10A). The histology of the mouse lung sections after LPS treatment

revealed inflammatory cell infiltration, inter-alveolar septal thickening, and interstitial edema. HCH6-1 pretreatment reduced inflammatory cell infiltration and distortion of pulmonary architecture in the presence of LPS. HCH6-1 alone did not induce airspace inflammation, which was similar to the sham group (Fig. 10B). Furthermore, LPS-induced elevation of MPO activity and total protein level was also diminished in the pretreatment of HCH6-1 (Fig. 10D). To confirm that infiltrated cells were neutrophils, we used immunofluorescence staining with antibodies for Ly6G (a neutrophil-specific marker). The non-LPS-challenged lung section showed no Ly6G staining. LPS treatment significantly increased Ly6G-positive cells, which were reduced by HCH6-1 (Fig. 10C). In addition, the protective effects of CsH were examined in LPS-induced ALI. CsH significantly reduced the MPO activity, neutrophils infiltration, and pulmonary edema in LPS-induced ALI mice (Supplementary Fig. 6).

To further test the therapeutic potential of HCH6-1, HCH6-1 was post-treated at 30 min after LPS spray. Similarly, HCH6-1 posttreatment showed inhibitory effects on neutrophil accumulation and lung damage in LPS-induced ALI mice (Fig. 11). Altogether, these results suggest that HCH6-1-mediated decreasing of neutrophil recruitment serves as a protective mechanism in ALI mice.

## 4. Discussion

Accumulating evidence underscores that neutrophil accumulation and activation are key actions in acute inflammatory processes such as ALI [4,8]. Sequestration and activation of human neutrophils may promote lung tissue damage by increasing inflammatory mediator release, thereby leading to endothelial dysfunction and airway space occupied by plasma protein [45]. A protective inflammatory response depends on the appropriate regulation of leukocytes in the acute phase. FPR receptors have major roles in inflammatory reactions, so significant effort has involved identifying receptor inhibitors/antagonists for members of this receptor family [46]. Our study adds to the current understanding of *N*-formyl peptide-mediated inflammation directly activating neutrophils, thereby contributing to the severity of lung injury. We found that a novel dipeptide, HCH6-1, inhibited chemotaxis, superoxide anion generation, and elastase release in human neutrophils specifically activated by *N*-formyl peptide. This dipeptide had protective effects on LPS-induced ALI in mice. The molecular mechanisms are competitively blocking FPR1 and related downstream signaling pathways, including calcium, MAPKs, and Akt signaling. Furthermore, HCH6-1 had inhibitory effects in neutrophil-like cells, including differentiated THP-1 cells and hFPR1-transfected HEK293 cells, so it can be used to treat neutrophilic inflammatory disease.

FPR1, which binds *N*-formyl peptides, is one of the G-protein coupled seven transmembrane receptors and is richly expressed on the surface of phagocytes [47,48]. *N*-formyl peptides are produced by bacteria and are also released from damaged mitochondria that can stimulate immune cells to induce inflammatory responses [49–52]. For instance, *N*-formyl peptides from the disrupted mitochondria of hepatic cells act on FPR1 to trigger a chemotactic response and induce an oxidative burst [53]. Mitochondrial *N*-formyl peptides in bony fractures can activate neutrophils to release matrix metalloproteinase 9 and IL-8 through calcium and ERK and induce an inflammatory response in lung tissue [54]. Moreover, fMLF is a traditional *N*-formyl peptide used to assay FPR1-related neutrophilic inflammation. Our data showed that HCH6-1 significantly inhibited chemotaxis, superoxide anion generation, and elastase release in fMLF-activated human neutrophils, so it had anti-inflammatory effects.

The formyl peptide receptors FPR1 and FPR2 have a similar sequence. Previous study demonstrated that the hexapeptide WKYMVm dually activates neutrophils via FPR1 and FPR2 [55]. Additionally, a synthetic peptide, MMK1, attracted neutrophil migration via more selective FPR2 activation [56]. We found HCH6-1 had fewer inhibitory effects in WKYMVm- or MMK1-treated cells and no

effect in other non-FPR agonist-stimulated cells. Consistent with our hypothesis, HCH6-1 had inhibitory effects specifically in FPR1 agonist-stimulated neutrophils. The NH group on fMLF and HCH6-1 did not interact on the NMR assay; thus the mechanisms of HCH6-1 were not via the interaction between the formyl peptide agonist and HCH6-1. We further investigated receptor binding with a fluorescent analog in the fMLF binding assay under flow cytometry. FNLFNKY is a fluorescent analog of fMLF and commonly used as a receptor binding assay [25,57]. Our data strongly suggested that HCH6-1 inhibited the fluorescent analog binding to FPR1 on the surface of activated neutrophils. Also, HCH6-1 bound to FPR1 in differentiated THP-1 and hFPR1-transfected HEK293 cells.

Previous research has demonstrated that activation of FPR1 led to a series of downstream signaling pathways, including cAMP, calcium, MAPKs, and Akt signaling [14]. Additionally, we and other researchers have shown that intracellular cAMP has a negative-feedback effect on superoxide anion generation and elastase release in FPR1 agonist-activated neutrophils [35,58]. In this study, HCH6-1 did not increase cAMP production in the presence or absence of fMLF. H89, a PKA inhibitor, did not reverse the inhibitory effects of HCH6-1 on superoxide anion generation and elastase release in fMLF-stimulated neutrophils. Accordingly, the suppressive effects of HCH6-1 were not through cAMP/PKA signaling pathways. Activated G<sub>i</sub> protein-coupled FPR1 can transiently and slightly elevate the intracellular cAMP level in human neutrophils [27]. This suggestion gains support from the results that fMLF slightly increased cAMP concentration, and that was greatly enhanced in the presence of rolipram. Interestingly, our results showed that HCH6-1 attenuated the fMLF-increased cAMP concentration, confirming that HCH6-1 inhibited FPR1 signaling. Furthermore, the binding of fMLF to FPR1 triggers a transient calcium influx and induces a number of immune responses in activated neutrophils [59]. In the present study, HCH6-1 dose-dependently attenuated the peak calcium influx induced by fMLF and exerted a competitive inhibitory profile, but it did not suppress calcium influx in non-FPR agonist-triggered cells. Moreover, activation of neutrophil by *N*-formyl peptides induces phosphorylation of the second messengers MAPKs and Akt [60,61]. We found that HCH6-1 competitively attenuated MAPKs and Akt protein phosphorylation. Taken together, these data provide evidence that the dipeptide HCH6-1 inhibits the downstream signaling pathways of FPR1.

CsH is a fungal peptide metabolite and acts as the competitive receptor-specific FPR1 antagonist [46]. Previous study demonstrated that CsH inhibited fMLF-induced superoxide anion generation and calcium influx [62]. Consistently, our data showed that CsH dominantly inhibited superoxide anion generation and elastase release as well as cell migration in fMLF-activated neutrophils. The same inhibitory profiles were shown in the presence of HCH6-1. On the receptor-binding assay, both CsH and HCH6-1 blocked the fluorescent analog binding to FPR1.

Sepsis is a life-threatening acute inflammatory disease associated with the presence of organ dysfunction. Acute respiratory distress syndrome caused by endotoxic shock is a leading cause of death in intensive care units [63,64]. The pathogenesis of lung injury is very complex. Neutrophil infiltration and activation are the most important features of ALI. *N*-formyl peptides have been shown to facilitate phagocyte chemotaxis and migration to the inflamed area to cause ALI [26,65]. Previous research has demonstrated that genetic ablation of *Fpr1* diminishes cigarette smoke-induced lung emphysema in mice. The *Fpr1* knockout mice display a noticeable decrease of neutrophils infiltration in the lung after cigarette smoke exposure [66]. Recent study shows that lack of FPR1 significantly reduces neutrophils infiltration in the lung in LPS-induced mice. Noticeably, CsH treatment has protective effects in LPS-induced ALI mice through inhibition of neutrophils recruitment [44]. Similarly, our data showed that CsH considerably decreased the MPO activity, neutrophils infiltration, and pulmonary edema in LPS-induced ALI mice. Therefore, FPR1 plays a

crucial role in LPS-induced ALI, and the FPR1 antagonist may have potential to treat ALI. The plasma level of mitochondrial *N*-formyl peptides, which is high in hemorrhagic shock patients, is associated with SIRS and lung injury [65]. Therefore, FPR1 is an emerging therapeutic target for the discovery of drugs to treat inflammatory lung diseases. Until now, however, no FPR1 antagonists are currently for clinical use. Our data showed that HCH6-1 inhibits infiltration of neutrophils and attenuates injury in LPS-induced ALI, revealing that HCH6-1 has a protective effect against neutrophil-mediated lung inflammation. In summary, our studies provide evidence that a dipeptide HCH6-1 is an FPR1 antagonist that inhibits *N*-formyl peptide-induced neutrophil activation. HCH6-1 has potential as a therapeutic agent to treat neutrophilic inflammatory diseases.

## Disclosures

The authors declare no competing financial interests.

## Acknowledgements

This research was supported by the Yen Tjing Ling Medical Foundation (CI-104-12), the Ministry of Science Technology (NSC 102-2628-B-182-002-MY3, MOST 102-2628-B-255-003-MY3 and MOST 104-2320-B-255-004-MY3), Ministry of Education (EMRPD1F0311), and Chang Gung Memorial Hospital (CMRPD1B0281~3, CMRPF1D0442~3, CMRPF1F0011~3, CMRPF1F0061~3 and BMRP450), Taiwan. The funders had no role in the study design, data collection and analysis, decision to publish, or preparation of the manuscript.

## Appendix A. Supporting information

Supplementary data associated with this article can be found in the online version at doi:10.1016/j.freeradbiomed.2017.02.038.

## References

- [1] A. Mantovani, M.A. Cassatella, C. Costantini, S. Jaillon, Neutrophils in the activation and regulation of innate and adaptive immunity, *Nat. Rev. Immunol.* 11 (2011) 519–531.
- [2] H. Shen, D. Kreisel, D.R. Goldstein, Processes of sterile inflammation, *J. Immunol.* 191 (2013) 2857–2863.
- [3] C.D. Sadik, N.D. Kim, A.D. Luster, Neutrophils cascading their way to inflammation, *Trends Immunol.* 32 (2011) 452–460.
- [4] Y.F. Tsai, T.L. Hwang, Neutrophil elastase inhibitors: a patent review and potential applications for inflammatory lung diseases (2010–2014), *Expert Opin. Ther. Pat.* 25 (2015) 1145–1158.
- [5] T. Yago, B.G. Petrich, N. Zhang, Z. Liu, B. Shao, M.H. Ginsberg, R.P. McEver, Blocking neutrophil integrin activation prevents ischemia-reperfusion injury, *J. Exp. Med.* 212 (2015) 1267–1281.
- [6] J. Grommes, S. Vijayan, M. Drechsler, H. Hartwig, M. Morgelin, R. Dembinski, M. Jacobs, T.A. Koepfel, M. Binnebosel, C. Weber, O. Soehnlein, Simvastatin reduces endotoxin-induced acute lung injury by decreasing neutrophil recruitment and radical formation, *PLoS One* 7 (2012) e38917.
- [7] J. Grommes, O. Soehnlein, Contribution of neutrophils to acute lung injury, *Mol. Med.* 17 (2011) 293–307.
- [8] R.L. Zemans, S.P. Colgan, G.P. Downey, Transendothelial migration of neutrophils: mechanisms and implications for acute lung injury, *Am. J. Respir. Cell Mol. Biol.* 40 (2009) 519–535.
- [9] R. Tiruvoipati, J. Botha, G. Peek, Effectiveness of extracorporeal membrane oxygenation when conventional ventilation fails: valuable option or vague remedy? *J. Crit. Care* 27 (2012) 192–198.
- [10] C.Y. Wang, C.S. Calfee, D.W. Paul, D.R. Janz, A.K. May, H. Zhuo, G.R. Bernard, M.A. Matthay, L.B. Ware, K.N. Kangelaris, One-year mortality and predictors of death among hospital survivors of acute respiratory distress syndrome, *Intensive Care Med.* 40 (2014) 388–396.
- [11] I. Migeotte, D. Communi, M. Parmentier, Formyl peptide receptors: a promiscuous subfamily of G protein-coupled receptors controlling immune responses, *Cytokine Growth Factor Rev.* 17 (2006) 501–519.
- [12] E. Schiffmann, H.V. Showell, B.A. Corcoran, P.A. Ward, E. Smith, E.L. Becker, The isolation and partial characterization of neutrophil chemotactic factors from *Escherichia coli*, *J. Immunol.* 114 (1975) 1831–1837.
- [13] H. Carp, Mitochondrial *N*-formylmethionyl proteins as chemoattractants for neutrophils, *J. Exp. Med.* 155 (1982) 264–275.
- [14] D.A. Dorward, C.D. Lucas, G.B. Chapman, C. Haslett, K. Dhaliwal, A.G. Rossi, The role of formylated peptides and formyl peptide receptor 1 in governing neutrophil function during acute inflammation, *Am. J. Pathol.* 185 (2015) 1172–1184.
- [15] E. Schiffmann, B.A. Corcoran, S.M. Wahl, *N*-formylmethionyl peptides as che-



- moattractants for leucocytes, in: *Proceedings of the Natl. Acad. Sci. USA* 72 1059–1062, 1975.
- [16] M.J. Rabiet, E. Huet, F. Boulay, Human mitochondria-derived N-formylated peptides are novel agonists equally active on FPR and FPR1, while *Listeria monocytogenes*-derived peptides preferentially activate FPR, *Eur. J. Immunol.* 35 (2005) 2486–2495.
  - [17] L. Galluzzi, O. Kepp, G. Kroemer, Mitochondria: master regulators of danger signaling, *Nat. Rev. Mol. Cell Biol.* 13 (2012) 780–788.
  - [18] D.V. Krysko, P. Agostinis, O. Krysko, A.D. Garg, C. Bachert, B.N. Lambrecht, P. Vandenabeele, Emerging role of damage-associated molecular patterns derived from mitochondria in inflammation, *Trends Immunol.* 32 (2011) 157–164.
  - [19] P. Kubes, W.Z. Mehal, Sterile inflammation in the liver, *Gastroenterology* 143 (2012) 1158–1172.
  - [20] Q. Zhang, M. Raouf, Y. Chen, Y. Sumi, T. Sursal, W. Junger, K. Brohi, K. Itagaki, C.J. Hauser, Circulating mitochondrial DAMPs cause inflammatory responses to injury, *Nature* 464 (2010) 104–107.
  - [21] P.E. Marques, S.S. Amaral, D.A. Pires, L.L. Nogueira, F.M. Soriani, B.H. Lima, G.A. Lopes, R.C. Russo, T.V. Avila, J.G. Melgaco, A.G. Oliveira, M.A. Pinto, C.X. Lima, A.M. De Paula, D.C. Cara, M.F. Leite, M.M. Teixeira, G.B. Menezes, Chemokines and mitochondrial products activate neutrophils to amplify organ injury during mouse acute liver failure, *Hepatology* 56 (2012) 1971–1982.
  - [22] C.T. Yen, T.L. Hwang, Y.C. Wu, P.W. Hsieh, Design and synthesis of new N-(fluorenyl-9-methoxycarbonyl) (Fmoc)-dipeptides as anti-inflammatory agents, *Eur. J. Med. Chem.* 44 (2009) 1933–1940.
  - [23] C.T. Yen, C.C. Wu, J.C. Lee, S.L. Chen, S.L. Morris-Natschke, P.W. Hsieh, Y.C. Wu, Cytotoxic N-(fluorenyl-9-methoxycarbonyl) (Fmoc)-dipeptides: structure-activity relationships and synergistic studies, *Eur. J. Med. Chem.* 45 (2010) 2494–2502.
  - [24] T.L. Hwang, C.H. Hung, C.Y. Hsu, Y.T. Huang, Y.C. Tsai, P.W. Hsieh, Design and synthesis of tryptophan containing dipeptide derivatives as formyl peptide receptor 1 antagonist, *Org. Biomol. Chem.* 11 (2013) 3742–3755.
  - [25] S.C. Yang, P.J. Chung, C.M. Ho, C.Y. Kuo, M.F. Hung, Y.T. Huang, W.Y. Chang, Y.W. Chang, K.H. Chan, T.L. Hwang, Propofol inhibits superoxide production, elastase release, and chemotaxis in formyl peptide-activated human neutrophils by blocking formyl peptide receptor 1, *J. Immunol.* 190 (2013) 6511–6519.
  - [26] S.C. Yang, C.F. Lin, W.Y. Chang, J. Kuo, Y.T. Huang, P.J. Chung, T.L. Hwang, Bioactive secondary metabolites of a marine *Bacillus* sp. inhibit superoxide generation and elastase release in human neutrophils by blocking formyl peptide receptor 1, *Molecules* 18 (2013) 6455–6468.
  - [27] Y.F. Tsai, H.P. Yu, P.J. Chung, Y.L. Leu, L.M. Kuo, C.Y. Chen, T.L. Hwang, Osthol attenuates neutrophilic oxidative stress and hemorrhagic shock-induced lung injury via inhibition of phosphodiesterase 4, *Free Radic. Biol. Med.* 89 (2015) 387–400.
  - [28] S.C. Yang, P.J. Sung, C.F. Lin, J. Kuo, C.Y. Chen, T.L. Hwang, Anti-inflammatory effects of secondary metabolites of marine *Pseudomonas* sp. in human neutrophils are through inhibiting P38 MAPK, JNK, and calcium pathways, *PLoS One* 9 (2014) e114761.
  - [29] Y.H. Kim, J.H. Hwang, J.R. Noh, G.T. Gang, S. Tadi, Y.H. Yim, N.H. Jeoung, T.H. Kwak, S.H. Lee, G.R. Kweon, J.M. Kim, M. Shong, I.K. Lee, C.H. Lee, Prevention of salt-induced renal injury by activation of NAD(P)H: quinone oxidoreductase 1, associated with NADPH oxidase, *Free Radic. Biol. Med.* 52 (2012) 880–888.
  - [30] M. Winther, M. Gabl, A. Welin, C. Dahlgren, H. Forsman, A neutrophil inhibitory peptiducin derived from FPR1 expected to target FPR1 signaling hijacks the closely related FPR2 instead, *FEBS Lett.* 589 (2015) 1832–1839.
  - [31] C.Y. Chen, Y.L. Leu, Y. Fang, C.F. Lin, L.M. Kuo, W.C. Sung, Y.F. Tsai, P.J. Chung, M.C. Lee, Y.T. Kuo, H.W. Yang, T.L. Hwang, Anti-inflammatory effects of *Perilla frutescens* in activated human neutrophils through two independent pathways: src family kinases and Calcium, *Sci. Rep.* 5 (2015) 18204.
  - [32] M. Maijo, L. Miro, J. Polo, J. Campbell, L. Russell, J. Crenshaw, E. Weaver, M. Moreto, A. Perez-Bosque, Dietary plasma proteins attenuate the innate immunity response in a mouse model of acute lung injury, *Br. J. Nutr.* 107 (2012) 867–875.
  - [33] P. Huebener, J.P. Pradere, C. Hernandez, G.Y. Gwak, J.M. Caviglia, X. Mu, J.D. Loike, R.E. Jenkins, D.J. Antoine, R.F. Schwabe, The HMGB1/RAGE axis triggers neutrophil-mediated injury amplification following necrosis, *J. Clin. Invest.* 125 (2015) 539–550.
  - [34] C.T. Pham, Neutrophil serine proteases: specific regulators of inflammation, *Net. Rev. Immunol.* 6 (2006) 541–550.
  - [35] C.H. Serezani, M.N. Ballinger, D.M. Aronoff, M. Peters-Golden, Cyclic AMP: master regulator of innate immune cell function, *Am. J. Respir. Cell Mol. Biol.* 39 (2008) 127–132.
  - [36] H.P. Yu, P.W. Hsieh, Y.J. Chang, P.J. Chung, L.M. Kuo, T.L. Hwang, 2-(2-Fluorobenzamido)benzoate ethyl ester (EFB-1) inhibits superoxide production by human neutrophils and attenuates hemorrhagic shock-induced organ dysfunction in rats, *Free Radic. Biol. Med.* 50 (2011) 1737–1748.
  - [37] T.L. Hwang, Y.L. Leu, S.H. Kao, M.C. Tang, H.L. Chang, Viscolin, a new chalcone from *Viscum coloratum*, inhibits human neutrophil superoxide anion and elastase release via a cAMP-dependent pathway, *Free Radic. Biol. Med.* 41 (2006) 1433–1441.
  - [38] S. Spisani, M.C. Pareschi, M. Buzzi, M.L. Colamussi, C. Biondi, S. Traniello, G. Pagani Zecchini, M. Pagliarunga Paradisi, I. Torrini, M.E. Ferretti, Effect of cyclic AMP level reduction on human neutrophil responses to formylated peptides, *Cell Signal* 8 (1996) 269–277.
  - [39] C.Y. Chen, C.C. Liaw, Y.H. Chen, W.Y. Chang, P.J. Chung, T.L. Hwang, A novel immunomodulatory effect of ugonin U in human neutrophils via stimulation of phospholipase C, *Free Radic. Biol. Med.* 72 (2014) 222–231.
  - [40] T.L. Hwang, C.C. Wang, Y.H. Kuo, H.C. Huang, Y.C. Wu, L.M. Kuo, Y.H. Wu, The hederagenin saponin SMG-1 is a natural FMLP receptor inhibitor that suppresses human neutrophil activation, *Biochem. Pharmacol.* 80 (2010) 1190–1200.
  - [41] A. Mocsai, Z. Jakus, T. Vantus, G. Berton, C.A. Lowell, E. Ligeti, Kinase pathways in chemoattractant-induced degranulation of neutrophils: the role of p38 mitogen-activated protein kinase activated by Src family kinases, *J. Immunol.* 164 (2000) 4321–4331.
  - [42] P.M. Dang, A. Stensballe, T. Boussetta, H. Raad, C. Dewas, Y. Kroviarski, G. Hayem, O.N. Jensen, M.A. Gougerot-Pocidalo, J. El-Benna, A specific p47phox -serine phosphorylated by convergent MAPKs mediates neutrophil NADPH oxidase priming at inflammatory sites, *J. Clin. Invest.* 116 (2006) 2033–2043.
  - [43] M. Hannigan, L. Zhan, Z. Li, Y. Ai, D. Wu, C.K. Huang, Neutrophils lacking phosphoinositide 3-kinase gamma show loss of directionality during N-formyl-Met-Leu-Phe-induced chemotaxis, in: *Proceedings of the Natl. Acad. Sci. USA* 99 3603–3608, 2002.
  - [44] J. Grommes, M. Drechsler, O. Soehnlein, CCR5 and FPR1 mediate neutrophil recruitment in endotoxin-induced lung injury, *J. Innate. Immun.* 6 (2014) 111–116.
  - [45] M.D. Tate, Y.M. Deng, J.E. Jones, G.P. Anderson, A.G. Brooks, P.C. Reading, Neutrophils ameliorate lung injury and the development of severe disease during influenza infection, *J. Immunol.* 183 (2009) 7441–7450.
  - [46] H. Cevik-Aras, C. Kalderen, A. Jenmalm Jensen, T. Oprea, C. Dahlgren, H. Forsman, A non-peptide receptor inhibitor with selectivity for one of the neutrophil formyl peptide receptors, FPR 1, *Biochem. Pharmacol.* 83 (2012) 1655–1662.
  - [47] M. Liu, K. Chen, T. Yoshimura, Y. Liu, W. Gong, A. Wang, J.L. Gao, P.M. Murphy, J.M. Wang, Formylpeptide receptors are critical for rapid neutrophil mobilization in host defense against *Listeria monocytogenes*, *Sci. Rep.* 2 (2012) 786.
  - [48] S.C. Yang, T.L. Hwang, The potential impacts of formyl peptide receptor 1 in inflammatory diseases, *Front. Biosci. (Elite Ed.)* 8 (2016) 436–449.
  - [49] B. McDonald, K. Pittman, G.B. Menezes, S.A. Hirota, I. Slaba, C.C. Waterhouse, P.L. Beck, D.A. Muruve, P. Kubes, Intravascular danger signals guide neutrophils to sites of sterile inflammation, *Science* 330 (2010) 362–366.
  - [50] G.B. Segel, M.W. Halterman, M.A. Lichtman, The paradox of the neutrophil's role in tissue injury, *J. Leukoc. Biol.* 89 (2011) 359–372.
  - [51] J. Hazeldine, P. Hampson, F.A. Opoku, M. Foster, J.M. Lord, N-Formyl peptides drive mitochondrial damage associated molecular pattern induced neutrophil activation through ERK1/2 and P38 MAP kinase signalling pathways, *Injury* 46 (2015) 975–984.
  - [52] E.D. Crouser, G. Shao, M.W. Julian, J.E. Macre, G.S. Shadel, S. Tridandapani, Q. Huang, M.D. Wewers, Monocyte activation by necrotic cells is promoted by mitochondrial proteins and formyl peptide receptors, *Crit. Care Med.* 37 (2009) 2000–2009.
  - [53] M. Raouf, Q. Zhang, K. Itagaki, C.J. Hauser, Mitochondrial peptides are potent immune activators that activate human neutrophils via FPR-1, *J. Trauma* 68 1328–1332; discussion 1332–1324, 2010.
  - [54] C.J. Hauser, T. Sursal, E.K. Rodriguez, P.T. Appleton, Q. Zhang, K. Itagaki, Mitochondrial damage associated molecular patterns from femoral reamings activate neutrophils through formyl peptide receptors and p44/42 MAP kinase, *J. Orthop. Trauma* 24 (2010) 534–538.
  - [55] T. Christophe, A. Karlsson, C. Dugave, M.J. Rabiet, F. Boulay, C. Dahlgren, The synthetic peptide Trp-Lys-Tyr-Met-Val-Met-NH<sub>2</sub> specifically activates neutrophils through FPR1/lipoxin A4 receptors and is an agonist for the orphan monocyte-expressed chemoattractant receptor FPR2, *J. Biol. Chem.* 276 (2001) 21585–21593.
  - [56] J.Y. Hu, Y. Le, W. Gong, N.M. Dunlop, J.L. Gao, P.M. Murphy, J.M. Wang, Synthetic peptide MMK-1 is a highly specific chemotactic agonist for leukocyte FPR1, *J. Leukoc. Biol.* 70 (2001) 155–161.
  - [57] M. Czapiga, J.L. Gao, A. Kirk, J. Lekstrom-Himes, Human platelets exhibit chemotaxis using functional N-formyl peptide receptors, *Exp. Hematol.* 33 (2005) 73–84.
  - [58] T.L. Hwang, G.L. Li, Y.H. Lan, Y.C. Chia, P.W. Hsieh, Y.H. Wu, Y.C. Wu, Potent inhibition of superoxide anion production in activated human neutrophils by isopedicin, a bioactive component of the Chinese medicinal herb *Fissistigma oldhamii*, *Free Radic. Biol. Med.* 46 (2009) 520–528.
  - [59] G. Tintinger, H.C. Steel, R. Anderson, Taming the neutrophil: calcium clearance and influx mechanisms as novel targets for pharmacological control, *Clin. Exp. Immunol.* 141 (2005) 191–200.
  - [60] J. Chen, H. Tang, N. Hay, J. Xu, R.D. Ye, Akt isoforms differentially regulate neutrophil functions, *Blood* 115 (2010) 4237–4246.
  - [61] L.W. Chen, M.W. Lin, C.M. Hsu, Different pathways leading to activation of extracellular signal-regulated kinase and p38 MAP kinase by formyl-methionyl-leucyl-phenylalanine or platelet activating factor in human neutrophils, *J. Biomed. Sci.* 12 (2005) 311–319.
  - [62] J. Karlsson, H. Fu, F. Boulay, J. Bylund, C. Dahlgren, The peptide Trp-Lys-Tyr-Met-Val-D-Met activates neutrophils through the formyl peptide receptor only when signaling through the formylpeptide receptor like 1 is blocked. A receptor switch with implications for signal transduction studies with inhibitors and receptor antagonists, *Biochem. Pharmacol.* 71 (2006) 1488–1496.
  - [63] C.E. Bryant, D.R. Spring, M. Gangloff, N.J. Gay, The molecular basis of the host response to lipopolysaccharide, *Nat. Rev. Microbiol.* 8 (2010) 8–14.
  - [64] L.B. Ware, M.A. Matthay, The acute respiratory distress syndrome, *N. Engl. J. Med.* 342 (2000) 1334–1349.
  - [65] C.F. Wenceslau, T. Szasz, C.G. McCarthy, B. Baban, E. NeSmith, R.C. Webb, Mitochondrial N-formyl peptides cause airway contraction and lung neutrophil infiltration via formyl peptide receptor activation, *Pulm. Pharmacol. Ther.* 37 (2016) 49–56.
  - [66] S.D. Shapiro, N.M. Goldstein, A.M. Houghton, D.K. Kobayashi, D. Kelley, A. Belaaouaj, Neutrophil elastase contributes to cigarette smoke-induced emphysema in mice, *Am. J. Pathol.* 163 (2003) 2329–2335.

# Arachidonic Acid Induces ARE/Nrf2-Dependent Heme Oxygenase-1 Transcription in Rat Brain Astrocytes

Chih-Chung Lin<sup>1</sup> · Chien-Chung Yang<sup>2,3</sup> · Yu-Wen Chen<sup>3</sup> · Li-Der Hsiao<sup>1</sup> · Chuen-Mao Yang<sup>1,3,4,5</sup>

Received: 22 March 2017 / Accepted: 28 April 2017  
© Springer Science+Business Media New York 2017

**Abstract** Arachidonic acid (AA) is a major product of phospholipid hydrolysis catalyzed by phospholipase A<sub>2</sub> during neurodegenerative diseases. AA exerts as a second messenger to regulate various signaling components which may be involved in different pathophysiological processes. Astrocytes are the main types of CNS resident cells which maintain and support the physiological function of brain. AA has been shown to induce ROS generation through activation of NADPH oxidases (Noxs) which may play a key role in the expression of heme oxygenase-1 (HO-1). Therefore, this study was designed to investigate the mechanisms underlying AA-induced HO-1 expression in rat brain astrocytes (RBA-1). We found that AA induced HO-1 protein and mRNA expression and promoter activity in RBA-1, which was mediated through the synthesis of 15-deoxy- $\Delta$ 12,14-prostaglandin

D<sub>2</sub>-activated peroxisome proliferator-activated receptor- $\gamma$  (PPAR $\gamma$ ) receptors. This note was confirmed by transfection with PPAR $\gamma$  small interfering RNAs (siRNA) which attenuated the AA-mediated responses. AA-induced HO-1 expression was mediated through Nox/ROS generation, which was inhibited by Nox inhibitors (diphenyleneiodonium and apocynin) and ROS scavengers (*N*-acetyl cysteine). Moreover, AA-induced HO-1 expression was mediated through phosphorylation of Src, Pyk2, platelet-derived growth factor, PI3K/Akt, and ERK1/2 which were inhibited by the pharmacological inhibitors including PP1, PF431396, AG1296, LY294002, and U0126 or by transfection with respective siRNAs. AA-enhanced Nrf2 expression and HO-1 promoter activity was inhibited by transfection with Nrf2 siRNA or by these pharmacological inhibitors. Furthermore, chromatin immunoprecipitation assay confirmed that Nrf2 and PPAR $\gamma$  were associated with the proximal antioxidant response element (ARE)-binding site on HO-1 promoter, suggesting that Nrf2/PPAR $\gamma$  are key transcription factors modulating HO-1 expression. AA-induced ARE promoter activity was also reduced by these pharmacological inhibitors. These findings suggested that AA increases formation of Nrf2 and PPAR $\gamma$  complex and binding with ARE1 binding site through Src, Pyk2, PI3K/Akt, and ERK1/2, which further induced HO-1 expression in RBA-1 cells.

Chih-Chung Lin and Chien-Chung Yang contributed equally to this work.

✉ Chuen-Mao Yang  
chuenmao@mail.cgu.edu.tw

- <sup>1</sup> Department of Anesthetics, Chang Gung Memorial Hospital at Linkou, and College of Medicine, Chang Gung University, Kwei-San, Tao-Yuan, Taiwan
- <sup>2</sup> Department of Traditional Chinese Medicine, Chang Gung Memorial Hospital, Linkou, Kwei-San, Tao-Yuan, Taiwan
- <sup>3</sup> Department of Physiology and Pharmacology and Health Aging Research Center, College of Medicine, Chang Gung University, Kwei-San, Tao-Yuan, Taiwan
- <sup>4</sup> Research Center for Industry of Human Ecology, Research Center for Chinese Herbal Medicine, and Graduate Institute of Health Industry Technology, Chang Gung University of Science and Technology, Tao-Yuan, Taiwan
- <sup>5</sup> Department of Physiology and Pharmacology, Chang Gung University, 259 Wen-Hwa 1st Road, Kwei-Shan, Tao-Yuan, Taiwan

**Keywords** AA · Heme oxygenase-1 · Nrf2 · PPAR $\gamma$

## Introduction

Acute and chronic inflammatory diseases are associated with sustained oxidative stress due to increased reactive oxygen species (ROS) that are known to trigger inflammation. Excessive production of ROS by two major sources,



mitochondria and NADPH oxidase (Nox), is responsible for a range of brain injury, inflammation, and degenerative diseases [1]. Noxs have been shown to be activated by several inflammatory factors including cytokines, endotoxins, and phospholipid metabolites such as arachidonic acid (AA) [2]. AA is one of polyunsaturated fatty acids, which is present in the highest levels in the mammalian neural tissues [3], and thus plays an important role in the maintenance of physiological functions of the CNS [4]. The elevated levels of AA have been demonstrated to initiate a wide array of cellular toxicities and diseases in various cell types in response to different stimuli [5, 6]. In contrast, AA was also found to be beneficial for human monocytes and macrophages to protect against apoptosis [7]. Moreover, AA provides a survival signaling which protects against apoptosis in astrocytes [8]. However, whether AA could exert as a protecting reagent in rat brain astrocyte (RBA-1) was still unknown.

HO-1 is an oxidative stress-inducible enzyme that mediates antioxidant and cytoprotective effects to maintain cellular redox homeostasis and protects cells from oxidative stress [9]. Several oxidative stress factors could activate Nox activity and produce intracellular ROS, leading to upregulation of HO-1 gene [10–12]. HO-1 also has immunomodulatory and anti-inflammatory effects in various cell types [13]. For example, HO-1-deficient mice exhibit a serious impairment of iron metabolism, leading to liver oxidative damage and inflammation [14]. Overexpression of HO-1 by adenovirus carried HO-1 plasmid attenuates rat brain damage after focal cerebral ischemia [15]. Thus, induction of HO-1 represents an adaptive response and increases cell resistance to oxidative injury. Although several studies have found that AA mediates neuroprotection in CNS, the signaling molecules involved in the AA-induced HO-1 expression are poorly understood.

AA could activate nonreceptor tyrosine kinases such as c-Src/Pyk2 through Nox/ROS and subsequently modulate transactivation of growth factor receptors and ERK1/2 activation in various cell types [2, 16]. In addition, accumulating evidence has shown that Nox/ROS-dependent HO-1 expression is mediated through the activation of c-Src and Pyk2 in various types of cells [11, 17, 18]. Transactivation of platelet-derived growth factor receptor (PDGFR) mediated through c-Src and Pyk2 has been shown to modulate several pathological processes in various cell types [2, 19]. Moreover, the family of mitogen-activated protein kinases (MAPKs), including Erk1/2, JNK1/2, and p38 MAPK, is activated by diverse stimuli and leading to HO-1 expression in various cell types [20, 21]. AA also potentiates hypoxia-induced IL-6 production through the MAPKs-dependent pathways in mouse embryonic stem cells [22]. In addition, the role of survival signalings PI3K/Akt also appears to be involved in the upregulation of HO-1 in different cell types [23, 24]. Thus, various compounds may induce HO-1 expression through different signaling molecules at different levels. For instance,

antioxidant phytochemical carnosol induces HO-1 expression by increasing nuclear factor-erythroid 2-related factor 2 (Nrf2) protein levels in a PI3K/Akt-dependent manner [23]. In PC12 cells, nerve growth factor (NGF) induces HO-1 expression via PI3K-cascade [24]. However, whether these signaling molecules also involved in AA induced the expression of HO-1 in RBA-1 is still unknown.

Moreover, HO-1 promoters are subjected to complex gene regulation that is tightly controlled by multiple transcription factors, including Nrf2 [9]. Much of this regulation occurs at sequences embedded in antioxidant response elements (AREs) located in the HO-1 promoter region [9]. Upon exposure to oxidative stress, Nrf2 dissociates from Keap1 and translocates to the nucleus wherein it oligomerizes with the proteins Maf binding to the ARE sites of target genes and leading to gene transcription [25]. Furthermore, AA can be converted into the various species of prostaglandins such as 15-deoxy- $\Delta^{12,14}$ -prostaglandin D<sub>2</sub> (15d-PGJ<sub>2</sub>) which also induced HO-1 expression through activation of proliferator-activated receptor- $\gamma$  (PPAR $\gamma$ ) in several types of cells [12, 26]. However, the detail mechanisms of Nrf2 and PPAR $\gamma$  that interacted with the AREs involved in transcriptional activation of HO-1 gene expression induced by AA are not well understood.

In this study, we made an attempt to investigate the molecular mechanisms by which AA induced HO-1 gene expression in RBA-1. Our results showed that AA-induced ARE/Nrf2 and PPAR $\gamma$ -dependent HO-1 expression is mediated through a Nox/ROS/c-Src/Pyk2/PDGFR/PI3K/Akt/Erk1/2 cascade in RBA-1 cells.

## Experimental Procedures

### Materials

AA, 15d-PGJ<sub>2</sub>, and PGE<sub>2</sub> were from Cayman Chemicals (Ann Arbor, MI). Dimethyl sulfoxide (DMSO), small interfering RNAs (siRNAs), PPAR $\gamma$  (SASI\_Rn01\_00077685), Pyk2 (SASI\_Rn01\_00044067), p110 (SASI\_Rn02\_00292737), and TRIZOL were from Sigma (St. Louis, MO). Lipofectamine 2000, OPTI-MEM, and siRNAs for c-Src (Csk-RSS321556), PDGFR $\alpha$  (Pdgfra-RSS351968), p85 (PiK3r1-RSS303756), Akt (Akt1-RSS301983), Erk2 (M64300\_Stealth\_490), and Nrf2 (nfe212-RSS343557) were from Invitrogen (Carlsbad, CA). BCA protein assay reagent was from Thermo Scientific (Philadelphia, PA). Anti-phospho-Pyk2 (Tyr<sup>402</sup>, no. 3291), anti-phospho-c-Src (Y<sup>416</sup>, no. 2101), anti-phospho-PDGFR (Tyr<sup>1018</sup>, no. 4547), anti-phospho-Akt (Ser<sup>473</sup>, no. 9271), and anti-phospho-Erk1/2 (Thr<sup>202</sup>/Tyr<sup>204</sup>, no. 9101) antibodies were from Cell Signaling (Danvers, MA). Anti-GAPDH (no. MCA-ID4) was from Encor (Gainesville, FL). Anti-PPAR $\gamma$  (sc-7273), anti-Pyk2 (sc-9019), anti-c-Src (sc-18), anti-PDGFR (sc-

338), anti-p85 (sc-423), anti-p110 (sc-7189), anti-Akt (sc-8312), anti-Erk2 (sc-154), anti-Nrf2 (sc-722), and anti-lamin A (sc-20680) antibodies were from Santa Cruz (Santa Cruz, CA). Anti-HO-1 antibody (ADI-SPA-895), 15d-PGJ<sub>2</sub> ELISA kit (ADI-900-023), apocynin (APO), diphenyleneiodonium (DPI), PF431396, PP1, AG1296, LY294002, and U0126 were from Enzo Life Sciences (Farmingdale, NY). SDS-PAGE reagents were from MDBio Inc. (Taipei, Taiwan).

### Cell Culture and Transfection

RBA-1 cells were originated from the primary cultured astrocytes of neonatal rat cerebrum and naturally developed through successive cell passages [27] and used throughout this study. The cells were cultured in DMEM/F-12 containing 5% FBS, and made quiescent at confluence by incubation in serum-free DMEM/F-12 for 24 h, and then incubated with AA at 37 °C for the indicated time intervals. When the inhibitors were used, cells were pretreated with the inhibitors for 1 h before exposure to AA. Treatment of RBA-1 with DMSO or the pharmacological inhibitors alone had no significant effect on cell viability determined by an XTT [2,3-bis-(2-methoxy-4-nitro-5-sulphophenyl)-2H-tetrazolium-5-carbox-anilide] assay (data not shown). Transient siRNA transfections were performed by using Lipofectamine 2000, 50 pmol of siRNA (2.5 µl of 20 µM siRNA stock solution), and 2.5 µl of Lipofectamine 2000 were diluted with 100 µl of OPTI-MEM, as suggested by the manufacturer.

### Preparation of Cell Extracts and Western Blot Analysis

The cells were washed with ice-cold PBS, scraped, and collected by centrifugation at 45,000×g for 1 h at 4 °C to yield the whole cell extract. Proteins were analyzed by SDS-PAGE and electrophoretically transferred onto a Hybond C membrane (Buckinghamshire, UK). Membranes were incubated overnight at 4 °C with their respective component antibodies or anti-GAPDH antibody used at a dilution of 1:2000 in Tween-Tris buffered saline. Membranes were washed with Tween-Tris buffered saline four times for 5 min each, incubated with a 1:1500 dilution of anti-mouse horseradish peroxidase antibody for 1 h. Following each incubation, the membrane was washed extensively with Tween-Tris buffered saline. The immunoreactive bands were detected by ECL reagents and captured by a UVP BioSpectrum 500 Imaging System (Upland, CA). The image densitometry analysis was quantified by an UN-SCAN-IT gel software (Orem, UT).

### Total RNA Extraction and Real-Time PCR Analysis

Quiescent RBA-1 cells were incubated with 30 µM AA for 4 h in the presence or absence of the indicated inhibitors. Total RNA was extracted by using TRIZOL according to the

protocol of manufacturer. Real-time PCR was performed with a TaqMan gene expression assay system, using primers and probe mixtures for

- HO-1
- sense: 5'-TTTCACCTTCCCGAGCAT-3'
- antisense: 5'-GCCTCTTCTGTCACCCTGT-3'
- probe: 5'-CATGAACACTCTGGAGATGACC-3'
- GAPDH
- sense: 5'-AACTTTGGCATCGTGGAAGG-3'
- anti-sense: 5'-GTGGATGCAGGGATGATGTTTC-3'
- probe: 5'-TGACCACAGTCCATGCCATC ACTGC-3'

obtained from Invitrogen (Carlsbad, CA). PCRs were performed using a 7500 Real-Time PCR System (Applied Biosystems, Foster City, CA). Relative gene expression was determined by the  $\Delta\Delta C_t$  method, where  $C_t$  meant threshold cycle. All experiments were performed in triplicate.

### Plasmid Construction, Transfection, and Luciferase Reporter Gene Assays

Quiescent RBA-1 cells were treated with 30 µM AA for 8 h in the presence or absence of the indicated inhibitors. The rat HO-1 promoter (accession no. J02722.1; -766 to +20) was constructed (sense primer: GGTACCCAGGAAGTCACAGT GTGGCC; antisense primer: CCCGAGCTCGTCTGA GCTGTGGGCGCTCCAT) and cloned into the pGL3-basic vector containing the luciferase reporter system. To obtain ARE-luciferase reporter construct, double-stranded oligonucleotides containing a single copy of the 41-bp pair murine GST-Ya ARE (5'-TAGCTTGGAATGACATTGCTAATGG TGACAAAGCAACTTT-3') were cloned into the pGL2 promoter vector [11]. RBA-1 cells were transfected with plasmid using the Lipofectamine 2000. Transfection with pGal encoding for  $\beta$ -galactosidase was used as a control of transfection efficiencies. To assess promoter activity, cells were collected and disrupted by sonication in a lysis buffer (25 mM Tris phosphate pH 7.8, 2 mM ethylenediaminetetraacetic acid, 1% Triton X-100, and 10% glycerol). After centrifugation, aliquots of the supernatants were tested for luciferase activity using a luciferase assay system (Promega, San Luis Obispo, CA). Firefly luciferase activities were standardized for  $\beta$ -galactosidase activity.

### Measurement of Intracellular ROS Generation

The peroxide-sensitive fluorescent probe 2',7'-dichloro fluorescein diacetate (H2DCF-DA) was used to assess the intracellular ROS generation [11] with minor modifications. Briefly, RBA-1 cells were incubated with 10 µM H2DCF-DA (in RPMI-1640) for 45 min at 37 °C. The medium was

removed and replaced with fresh RPMI-1640 media for AA treatments. The fluorescent intensity (relative fluorescence units) was measured at 485 nm excitation and 530 nm emission.

### Determination of NADPH Oxidase Activity by Chemiluminescence Assay

The Nox activity in intact cells was measured by using lucigenin chemiluminescence [11]. After incubation, the cells were gently scraped and centrifuged at 400×g for 10 min at 4 °C. The cell pellet was resuspended in a known volume (35 µl/well) of ice-cold RPMI 1640 medium, and the cell suspension was kept on ice. To a final 200 µl of prewarmed (37 °C) RPMI 1640 medium containing either NADPH (1 µM) or lucigenin (20 µM), 5 µl of cell suspension ( $2 \times 10^4$  cells) was added to initiate the reaction followed by immediate measurement of chemiluminescence using a luminometer (SynergyH1 Hybrid Reader, BioTek) in an out-of-coincidence mode. Appropriate blanks and controls were established, and chemiluminescence was recorded. Neither NADPH nor NADH enhanced the background chemiluminescence of lucigenin alone (30–40 cpm). Chemiluminescence was continuously measured for 12 min, and the activity of Nox was expressed as counts per million cells.

### Preparation and Analysis of Nuclear Extracts

Growth-arrested RBA-1 cells were incubated with 30 µM AA for the indicated time intervals. The nuclear fractions were prepared as previously described [28]. Nuclear extracts were analyzed by SDS-PAGE and subjected to immunoblot analysis using the respective antibodies.

### Chromatin Immunoprecipitation Assay

Quiescent RBA-1 cells were treated with 30 µM AA for 1 h in the presence or absence of the indicated inhibitors. After incubation, chromatin immunoprecipitation (ChIP) assay was performed as previously described [29]. Briefly, RBA-1 cells were cross-linked with 1% formaldehyde at room temperature and then lysed in 400 µl of cell lysis buffer. The resulting nuclear lysate was sonicated until cross-linked chromatin was sheared to an average length of 0.4–0.8 kb. Soluble chromatin was prepared using a ChIP Assay Kit (Merck KGaA, Darmstadt, Germany) according to the manufacturer's recommendations and immunoprecipitated without (input) or with anti-Nrf2 and anti-PPARγ antibodies. After reversion of the protein-DNA cross-links, DNA fragments in the eluate and input controls were purified using an EasyPure PCR Clean up kit from Bioman (Taipei, Taiwan) and then subjected to PCR amplification. A 328-bp DNA fragment containing the ARE1 sequence of the proximal HO-1 promoter region was amplified with the

primers forward, 5'-ACAGTGTGGCCCAGGTTCTA-3', and reverse, 5'-TTCTAGCTGTGAGATGCTGGT-3'. A negative control locus primers were used: forward, 5'-ACAA GGCTGCATCTTAAAGC-3', and reverse, 5'-TCTC TGCCTGGGTGTGCACC-3' (308 bp). The amount of DNA-bound Nrf2 or PPARγ was expressed as a PCR product analyzed on 2% agarose 1× TAE gel containing ethidium bromide.

### Statistical Analysis of Data

All the data were expressed as the mean or mean ± S.E.M of three individual experiments performed in duplicate or triplicate. The significance of difference between two groups was determined by paired two-tailed Student's *t* test for Western blot data. All other statistical analyses are comparison of multiple groups; a GraphPad Prism Program (GraphPad, San Diego, CA) by one-way analysis of variance (ANOVA) followed with Tukey's post-hoc test has been used. A *p* < 0.05 value was considered significant.

## Results

### AA Induces HO-1 Expression

To evaluate the effect of AA on HO-1 expression, RBA-1 cells were incubated with various concentrations of AA (5, 15, and 30 µM) for the indicated time intervals. The levels of HO-1 protein were determined by Western blot. We found that AA time and concentration dependently induced HO-1 expression (Fig. 1a). There was a significant increase within 4 h, reaching a maximal response within 16 h, and slightly declined within

**Fig. 1** AA induces HO-1 expression. **a** RBA-1 cells were incubated with different concentrations of AA for the indicated time intervals. The protein levels of HO-1 were determined by Western blot. **b, c** Cells were incubated with 30 µM AA for the indicated time intervals. HO-1 mRNA levels and promoter activity were determined by quantitative PCR and luciferase activity, respectively. **b** The relative quantity of mRNA was calculated by normalization to GAPDH. **c** The relative luciferase activity was normalized to β-gal expression. **d** Cells were incubated with 30 µM AA for the indicated time intervals. The media were saved to determine the levels of 15d-PGJ<sub>2</sub> by using an ELISA assay kit. **e** RBA-1 cells were incubated with 30 µM AA, 10 µM 15d-PGJ<sub>2</sub>, or 30 µM PGE<sub>2</sub> for the indicated time intervals. The protein levels of HO-1 and PPARγ were determined by Western blot. **f** RBA-1 cells were transfected with scrambled or PPARγ siRNA and then incubated with 30 µM AA for 6 h. The protein levels of HO-1 and PPARγ were determined by Western blot. **g** RBA-1 cells were transfected with scrambled or PPARγ siRNA and then incubated with 30 µM AA or 10 µM 15d-PGJ<sub>2</sub> for 4 h. The levels of HO-1 mRNA and promoter activity were determined by real-time PCR and luciferase activity, respectively. Results are representative of three independent experiments. **h** RBA-1 cells incubated with AA (10 or 30 µM) for various periods and the cell viability were determined by using XTT assay kit. Values are the mean ± SEM. \**p* < 0.05; #*p* < 0.01, as compared with the cells exposed to vehicle alone





24 h. To further examine whether the effect of AA on HO-1 expression mediated through a transcriptional level, HO-1 messenger RNA (mRNA) was determined by real-time PCR. AA (30  $\mu$ M) significantly induced HO-1 mRNA accumulation in a time-dependent manner with a maximal response within 4 h (Fig. 1b). In addition, we found that AA also enhanced HO-1 promoter activity in a time-dependent manner with a maximal response within 8 h (Fig. 1c).

AA could be further converted into PGs such as 15d-PGJ<sub>2</sub> which induced HO-1 expression in various cell types [12, 26]. First, RBA-1 cells were incubated with AA (30  $\mu$ M) for the indicated time intervals and the levels of 15d-PGJ<sub>2</sub> were determined by using an ELISA assay kit. We found that AA significantly stimulated an increase in the level of 15d-PGJ<sub>2</sub> within 2 h, reaching a maximal response within 6 h and declined by 45% within 16–24 h (Fig. 1d). As expected, 15d-PGJ<sub>2</sub> could induce HO-1 expression in RBA-1 cells, similar to those of AA, whereas PGE<sub>2</sub> failed to induce this response (Fig. 1e), suggesting the involvement of 15d-PGJ<sub>2</sub> in AA-induced HO-1 expression. PPAR $\gamma$  receptors have been shown to mediate 15d-PGJ<sub>2</sub>-induced HO-1 expression [30]. To test the role of PPAR $\gamma$  receptors in AA-induced HO-1 expression, RBA-1 cells were transfected with PPAR $\gamma$  siRNA which knocked down the level of PPAR $\gamma$  protein and also attenuated the AA-induced HO-1 protein and mRNA expression, and promoter activity (Fig. 1f, g). RBA-1 cells incubated with AA (10 or 30  $\mu$ M) for various periods had no significant effect on cell viability determined by using an XTT assay kit (Fig. 1h).

### AA-Induced HO-1 Expression is Mediated Through NADPH Oxidase Activation and ROS Generation

AA has been shown to produce ROS in various cell types [2, 31]. NADPH oxidase-derived ROS generation has been implicated in the upregulation of HO-1 [17, 32]. Thus, we evaluated the potential role of ROS in the AA-induced HO-1 expression. For this purpose, an ROS scavenger *N*-acetyl cysteine (NAC) was used. We found that pretreatment with NAC attenuated the AA-induced HO-1 protein (Fig. 2a, upper panel) and mRNA expression and promoter activity (Fig. 2b), suggesting the involvement of ROS in HO-1 expression.

NADPH oxidase complex plays a key role in the generation of ROS leading to several physiological and pathological processes [33, 34]. To further determine whether NADPH oxidase involved in ROS-dependent HO-1 expression induced by AA, the inhibitors of NADPH oxidase (DPI) and p47<sup>phox</sup> (APO) were used to test this hypothesis. The data in Fig. 2a, b showed that pretreatment with APO (1, 10, 100  $\mu$ M) or DPI (0.01, 0.1, 1  $\mu$ M) concentration dependently attenuated AA-induced HO-1 protein and mRNA expression, as well as promoter activity.

To further investigate whether AA stimulates Nox activity, as shown in Fig. 2c (gray bar), we found that AA stimulated Nox activity in a time-dependent manner and reached a maximal response within 60 min and slightly declined up to 120 min, which was blocked by pretreatment with DPI (1  $\mu$ M) or APO (100  $\mu$ M) (Fig. 2b, gray bar). In addition, AA time dependently induced ROS production (Fig. 2c, open bar), which was attenuated by pretreatment with either DPI or APO (Fig. 2d, open bar), suggesting that AA stimulated Nox-derived ROS generation resulting in HO-1 expression in RBA-1 cells.

### AA Induces HO-1 Expression via Pyk2 and c-Src

The focal adhesion tyrosine kinases such as Pyk2 have been shown to act as critical mediators for the activation of signaling pathways that regulate expression of several genes and cellular functions [35]. The involvement of Pyk2 in AA-induced HO-1 expression in RBA-1 cells was determined by using a Pyk2 inhibitor PF431396. Pretreatment with PF431396 (1, 3, 10  $\mu$ M) concentration dependently attenuated AA-induced HO-1 protein (Fig. 3a) and mRNA (Fig. 3b) expression. To further confirm the role of Pyk2 in AA-induced HO-1 expression, a Pyk2 siRNA was used. The results showed that transfection with Pyk2 siRNA significantly knocked down Pyk2 protein level and inhibited the AA-induced HO-1 expression (Fig. 3c). We further determined whether AA stimulated activation of Pyk2; the phosphorylation of Pyk2 was detected by Western blot. As shown in Fig. 3d, AA stimulated Pyk2 phosphorylation in a time-dependent manner, which was attenuated by pretreatment with PF431396 (10  $\mu$ M), PP1 (10  $\mu$ M), DPI (1  $\mu$ M), or APO (100  $\mu$ M), indicating that Pyk2 is a downstream component of c-Src and Nox/ROS in HO-1 expression.

Several studies have shown that nonreceptor tyrosine kinases (RTKs) such as c-Src may modulate many cellular functions and gene expressions [28, 29, 36]. To examine whether c-Src was required for AA-induced HO-1 expression, we found that pretreatment with the inhibitor of c-Src (PP1) concentration dependently attenuated the AA-induced HO-1 expression in RBA-1 cells (Fig. 3a). In addition, PP1 also reduced the AA-induced HO-1 mRNA levels and promoter activity (Fig. 3b). To confirm this note, transfection with c-Src siRNA also significantly reduced the c-Src protein level and then attenuated the AA-induced HO-1 expression (Fig. 3c). To further investigate whether AA-stimulated c-Src phosphorylation was necessary for HO-1 expression, as shown in Fig. 3d, AA time dependently stimulated c-Src phosphorylation which was attenuated by PP1 and DPI, but not by PF431396, suggesting that c-Src is an upstream component of Pyk2 and a downstream of Nox/ROS in the AA-induced HO-1 expression in RBA-1 cells.



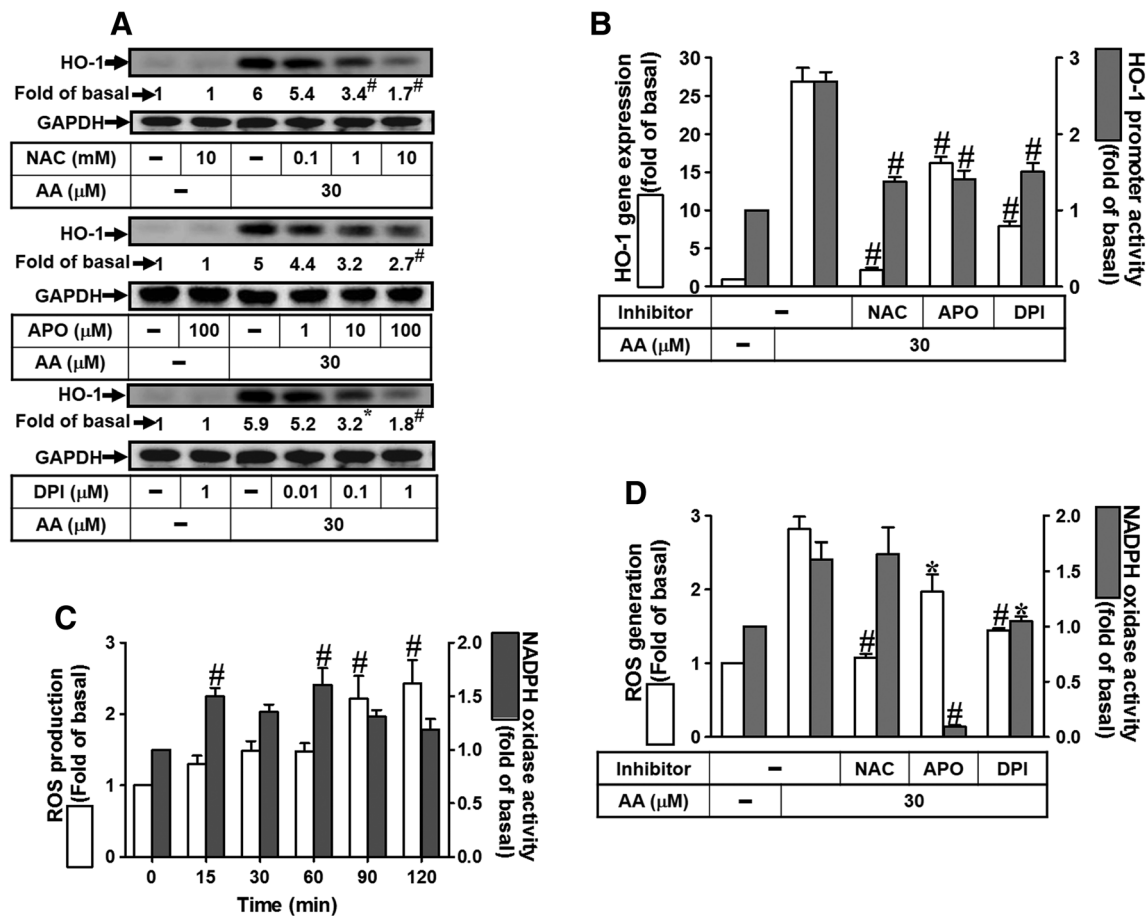


**Fig. 2** NADPH oxidase-dependent ROS generation contributes to AA-induced HO-1 expression. **a** RBA-1 cells were pretreated without or with NAC, apocynin (APO), or diphenyleneiodonium chloride (DPI) for 1 h before exposure to AA for 6 h. The protein levels of HO-1 and GAPDH (served as an internal control) were determined by Western blot. **b** Cells were pretreated with NAC (10 mM), APO (100 μM), or DPI (10 μM) for 1 h, and then incubated with AA for 4 h. The levels of HO-1 mRNA and promoter activity were determined by real-time PCR and luciferase

activity, respectively. **c** Cells were incubated with 30 μM AA for the indicated time intervals. **d** Cells were pretreated without or with NAC (10 mM), APO (100 μM), or DPI (10 μM) for 1 h and then incubated with AA for 1 h. **c, d** The Nox activity and ROS generation were analyzed. Data are expressed as mean ± SEM of three independent experiments. \* $p < 0.05$ ; # $p < 0.01$ , as compared with the cells exposed to vehicle (c) or AA alone (a, b, d)

### AA Induces HO-1 Expression via PDGFR

Accumulating evidence has indicated that activation of PDGFR upregulates HO-1 gene expression in various cell types [13, 37]. To investigate whether AA-induced HO-1 expression was mediated through PDGFR, the inhibitor of PDGFR (AG1296) was used. Pretreatment with AG1296 (0.1, 1, 10 μM) concentration dependently attenuated AA-induced HO-1 protein (Fig. 4a) and mRNA expression, as well as promoter activity (Fig. 4b). To further ensure the role of PDGFR in AA-induced HO-1 expression, a PDGFR siRNA was used. We found that transfection with PDGFR siRNA significantly knocked down PDGFR protein level and inhibited the AA-induced HO-1 expression (Fig. 4c). To further investigate whether AA-stimulated PDGFR phosphorylation was necessary for HO-1 expression, as shown in Fig. 4d, AA time dependently stimulated PDGFR phosphorylation which was attenuated by PP1 (10 μM), PF431396

(10 μM), DPI (1 μM), APO (100 μM), and AG1296 (10 μM), but not by LY294002 (30 μM), suggesting that PDGFR is a downstream component of Nox/ROS/c-Src/Pyk2 in HO-1 expression in RBA-1 cells. These data indicated that AA-induced HO-1 expression is mediated through a Nox/ROS/c-Src/Pyk2-dependent PDGFR pathway in RBA-1 cells.

### AA Induces HO-1 Expression via PI3K/Akt

Activation of PI3K/Akt has been shown to induce HO-1 gene expression in various cell types [13, 37]. To investigate whether AA-induced HO-1 expression was mediated through PI3K/Akt, the inhibitor of PI3K (LY294002) was used. As shown in Fig. 5a, b, pretreatment with LY294002 blocked HO-1 protein expression, mRNA levels, and HO-1 promoter activity induced by AA. To further confirm the role of PI3K/Akt in the AA-induced HO-1 expression,

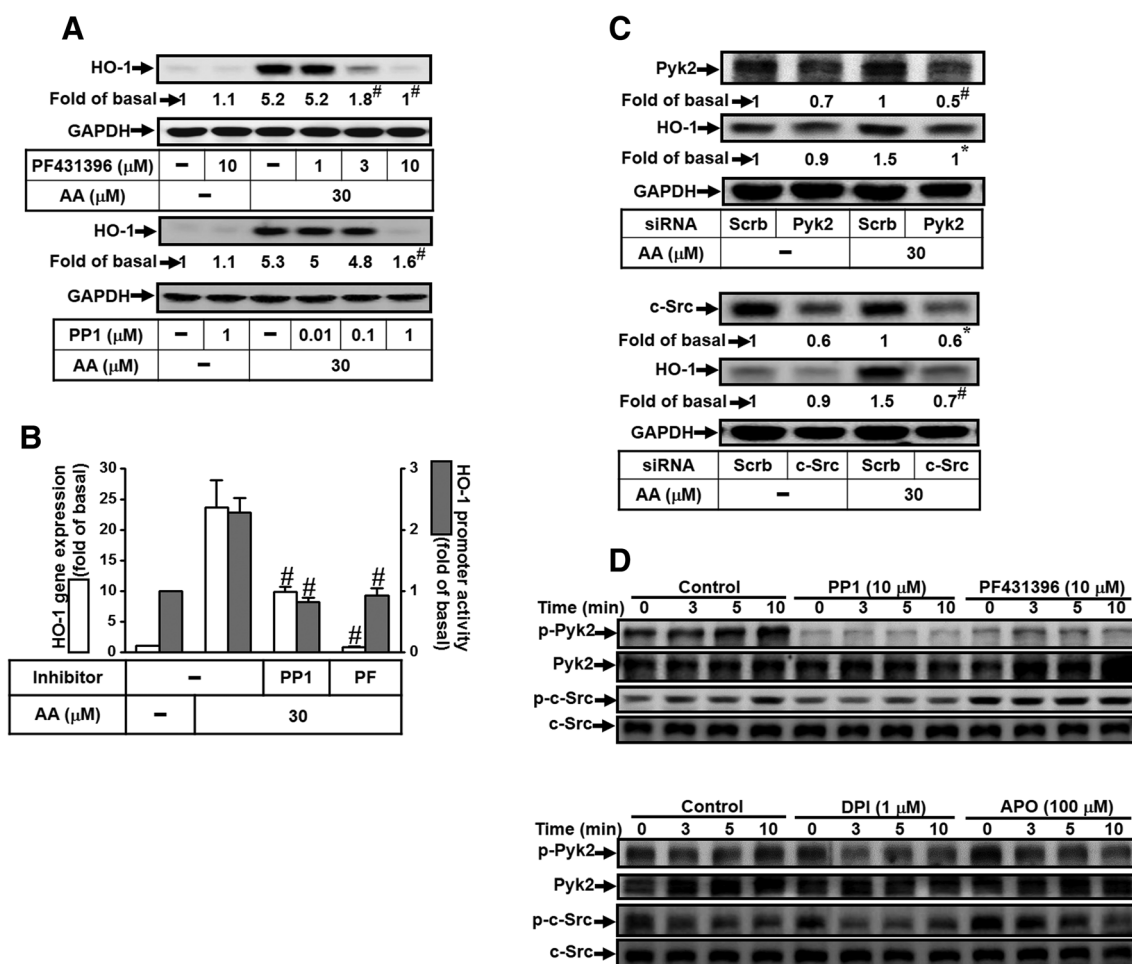


**Fig. 3** Pyk2 and c-Src are involved in AA-induced HO-1 expression. **a** RBA-1 cells were pretreated with PF431396 or PP1 for 1 h, and then incubated with AA for 6 h. The protein levels of HO-1 and GAPDH (served as an internal control) were determined by Western blot. **b** Cells were pretreated with PP1 (10 μM) or PF431396 (10 μM) for 1 h, and then incubated with AA for 4 h. The levels of HO-1 mRNA and promoter activity were determined by real-time PCR and luciferase activity, respectively. **c** Cells were transfected with scrambled, *Pyk2* or *c-Src* siRNA, and then incubated with AA for 6 h. The levels of *Pyk2*, *c-Src*,

*HO-1*, and *GAPDH* (served as an internal control) protein were determined by Western blot. **d** Cells were pretreated without or with *PP1* (10 μM), *PF431396* (10 μM), *DPI* (10 μM), or *APO* (100 μM) for 1 h, and then incubated with 30 μM AA for the indicated time intervals. The levels of phospho-Pyk2, phospho-c-Src, *Pyk2*, and *c-Src* were determined by Western blot. Data are expressed as mean ± SEM of three independent experiments. <sup>#</sup>*p* < 0.01, as compared with the cells exposed to AA alone

p110, p85, and Akt siRNA were used. The results showed that transfection with p110, p85, or Akt siRNA significantly knocked down p110, p85, or Akt protein levels, and subsequently attenuated the AA-induced HO-1 expression (Fig. 5c). Furthermore, to investigate whether AA-stimulated Akt phosphorylation was necessary for HO-1 expression, as shown in Fig. 5d, AA time dependently stimulated Akt phosphorylation which was attenuated by PP1 (10 μM), PF431396 (10 μM), DPI (1 μM), APO (100 μM), AG1296 (10 μM), and LY294002 (10 μM), suggesting that Akt is a downstream component of Nox/ROS/c-Src/Pyk2/PDGFR in HO-1 expression in RBA-1 cells. These results concluded that AA-induced HO-1 expression is mediated through a Nox/ROS/c-Src/Pyk2/PDGFR-dependent PI3K/Akt pathway in RBA-1 cells.

### AA Induces HO-1 Expression via p42/p44 MAPK

Nox-mediated ROS production could activate MAPKs which further induces the expression of several genes including HO-1 in many cell types [21, 38]. Thus, we determined the roles of MAPKs activated by ROS in the AA-induced HO-1 expression. As shown in Fig. 6a, AA-increased HO-1 expression was attenuated by the inhibitor of MEK1/2 (U0126) in a concentration-dependent manner. Furthermore, pretreatment with U0126 also attenuated AA-induced increase in HO-1 mRNA levels and promoter activity (Fig. 6b). Next, we examined whether AA-induced HO-1 expression via ROS-dependent signaling mediated through phosphorylation of p42/p44 MAPK. AA time dependently stimulated phosphorylation of p42/p44 MAPK which was inhibited by P1

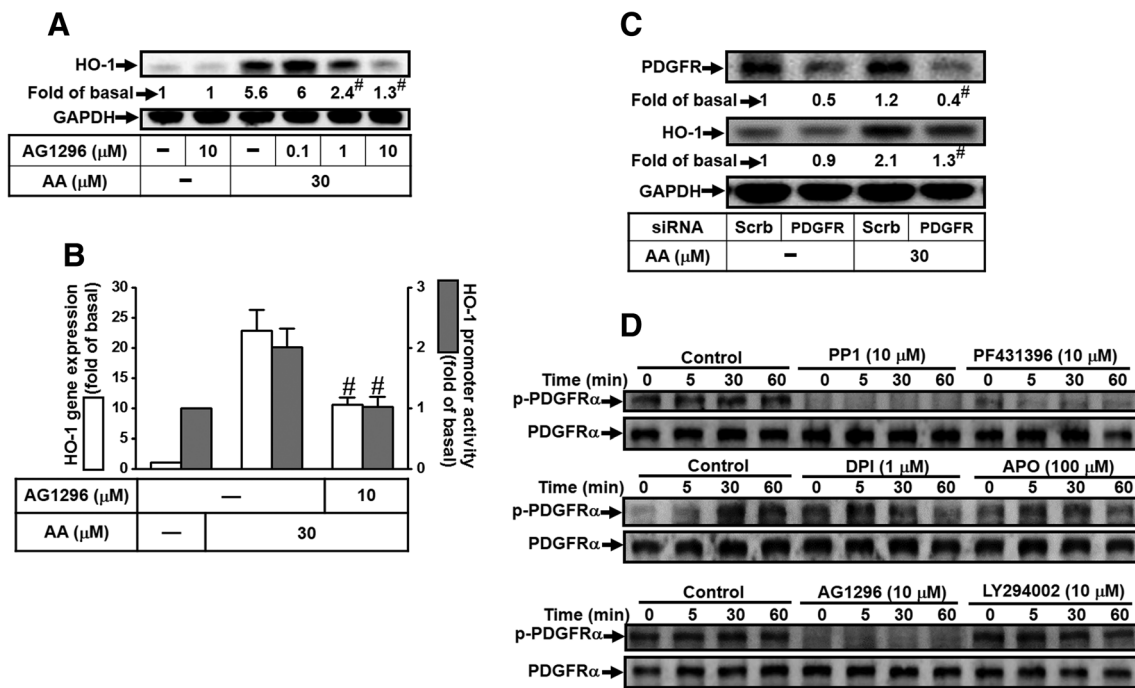


**Fig. 4** AA induces HO-1 expression via PDGFR. **a** RBA-1 cells were pretreated with various concentrations of AG1296 for 1 h and then incubated with AA for 6 h. The protein levels of HO-1 and GAPDH (served as an internal control) were determined by Western blot. **b** Cells were pretreated with AG1296 (10 μM) for 1 h, and then incubated with AA for 4 h. The levels of HO-1 mRNA and promoter activity were determined by real-time PCR and luciferase activity, respectively. **c** Cells were transfected with scrambled or PDGFR siRNA, and then incubated with AA for 6 h. The levels of PDGFR, HO-1, and GAPDH

(served as an internal control) proteins were determined by Western blot. **d** Cells were pretreated without or with PP1 (10 μM), PF431396 (10 μM), DPI (10 μM), APO (100 μM), AG1296 (10 μM), or LY294002 (30 μM) for 1 h, and then incubated with 30 μM AA for the indicated time intervals. The levels of phospho-PDGFR and PDGFR were determined by Western blot using the indicated antibodies. Results are representative of three independent experiments. Values are the mean ± SEM. <sup>#</sup>*p* < 0.01, as compared with the cells exposed to AA alone

(10 μM), PF431396 (10 μM), DPI (1 μM), APO (100 μM), AG1296 (10 μM), and LY294002 (10 μM) (Fig. 6c). These results suggested that AA-induced HO-1 expression is mediated through a Nox/ROS/c-Src/Pyk2/PDGFR/PI3K/Akt-dependent p42/p44 MAPK pathway in RBA-1 cells.

### AA Upregulates HO-1 Through Nrf2/ARE

HO-1 promoter contains putative AREs binding sites associated with Nrf2 that might represent potential targets tightly regulated by AA. Nrf2 is a key transcription factor to regulate the expression of antioxidant enzymes [9]. Thus, to determine whether AA stimulated Nrf2 translocation and phosphorylation leading to HO-1 expression, as shown in Fig. 7a, AA time dependently stimulated Nrf2 translocation into the nucleus with a maximal response within 60–120 min, which was inhibited by pretreatment with DPI, PP1, PF431396, AG1296, LY294002, and U0126 (Fig. 7b). To ensure the role of Nrf2 in AA-induced HO-1 expression, as shown in Fig. 7c, transfection with Nrf2 siRNA knocked down the Nrf2 protein levels and also attenuated the AA-induced HO-1 protein in RBA-1 cells. AA-induced mRNA expression and promoter activity were also attenuated by transfection with Nrf2 siRNA (Fig. 7d). Nrf2 has been reported to interact with

ARE leading to the expression of antioxidant enzymes [9]. To investigate whether Nrf2/ARE were responsible for AA-mediated HO-1 induction, AA-stimulated ARE promoter activity was determined in RBA-1 cells. We found that AA time dependently stimulated an increase in ARE transcriptional activity which was attenuated by pretreatment with DPI, APO, PP1, PF431396, AG1296, LY294002, and U0126 (Fig. 7e, f).

### Interaction Between PPARγ/Nrf2 and ARE Involved in AA-Induced HO-1 Expression

The 15d-PGJ<sub>2</sub> has been shown to regulate the translocation of Nrf2 into the nucleus leading to the expression of antioxidant enzymes such as HO-1 in macrophages [12, 26]. We also showed that AA-induced HO-1 was mediated through the biosynthesis of 15d-PGJ<sub>2</sub> via PPARγ receptors. Therefore, we investigated whether AA stimulated PPARγ promoter activity leading to HO-1 expression. We observed that AA time dependently stimulated an increase in PPARγ promoter activity with a maximal responses within 6 h, which was attenuated by pretreatment with T0070907 (T00, PPARγ antagonist), DPI, APO, PF431396, PP1, AG1296, LY294002, and U0126 (Fig. 8a, b).

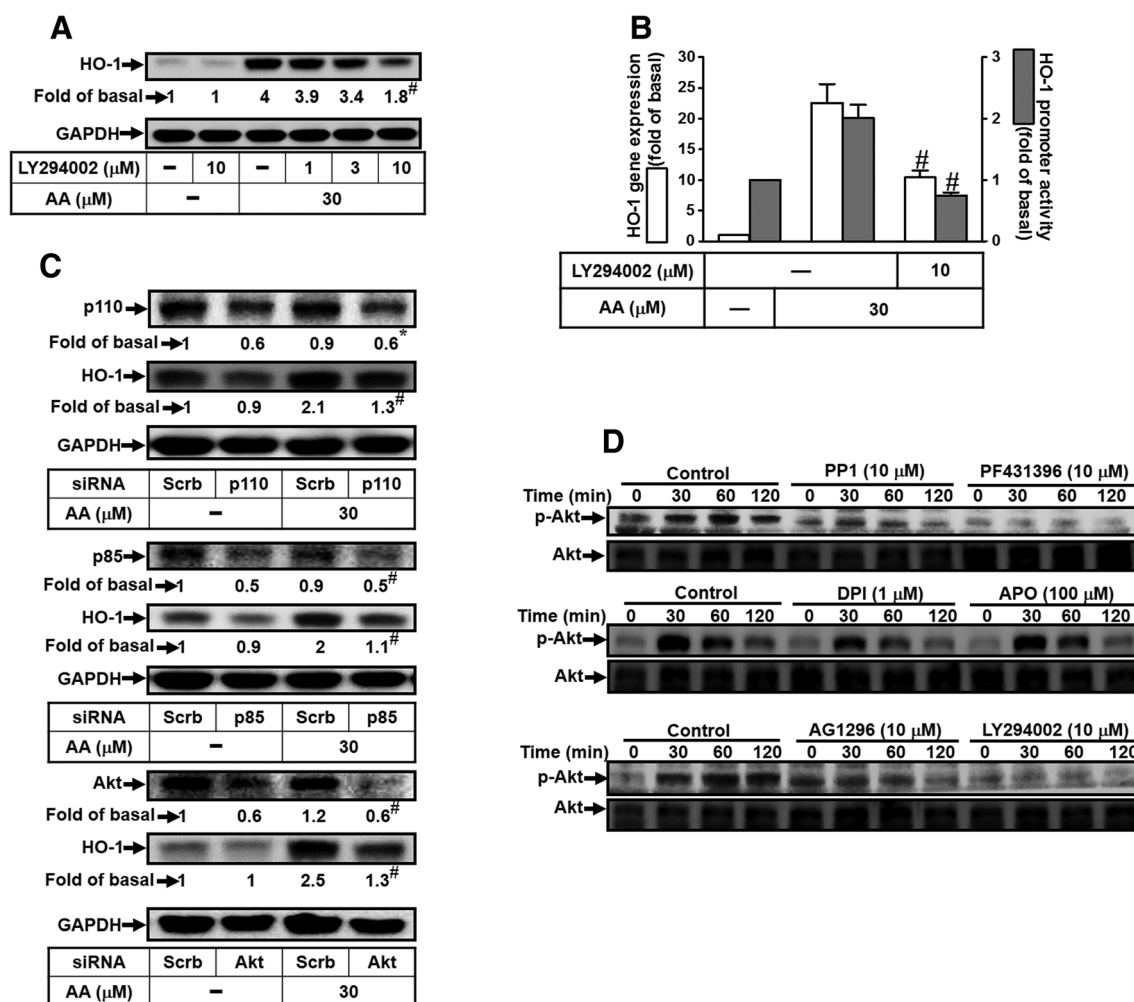


**Fig. 5** AA induces HO-1 expression via PI3K/Akt. **a** RBA-1 cells were pretreated with various concentrations of LY294002 for 1 h and then incubated with AA for 6 h. The protein levels of HO-1 and GAPDH (served as an internal control) were determined by Western blot. **b** Cells were pretreated with LY294002 (10  $\mu$ M) for 1 h, and then incubated with AA for 4 h. The levels of HO-1 mRNA and promoter activity were determined by real-time PCR and luciferase activity, respectively. **c** Cells were transfected with scrambled, p110, p85, or Akt siRNA, and then incubated with AA for 6 h. The levels of p110, p85, Akt, HO-1, and GAPDH (served as an internal control) protein were determined by Western blot. **d** Cells were pretreated without or with PP1 (10  $\mu$ M), PF431396 (10  $\mu$ M), DPI (10  $\mu$ M), APO (100  $\mu$ M), AG1296 (10  $\mu$ M), or LY294002 (30  $\mu$ M) for 1 h, and then incubated with 30  $\mu$ M AA for the indicated time intervals. The levels of phospho-Akt and Akt were determined by Western blot using the indicated antibodies. Results are representative of three independent experiments. Values are the mean  $\pm$  SEM. <sup>#</sup> $p < 0.01$ , as compared with the cells exposed to AA alone

Moreover, we investigated whether the AA stimulated the translocation of Nrf2 into the nucleus that was sufficient to promote binding of protein complexes containing this transcription factor to the ARE sequence corresponding to the rat HO-1 promoter. ChIP assays using an anti-Nrf2 or PPAR $\gamma$  antibody were performed with the primers specific to the ARE regions of HO-1. We found that AA time dependently stimulated the Nrf2 binding to the ARE sequence of rat HO-1 promoters, which was attenuated by DPI, APO, PP1, PF431396, AG1296, LY294002, and U0126 (Fig. 8c, d). These results suggested that AA stimulates nuclear Nrf2 and PPAR $\gamma$  accumulation, resulting in increased binding to the ARE sequences of HO-1 promoter and leading to HO-1 expression in RAB-1 cells.

and GAPDH (served as an internal control) protein were determined by Western blot. **d** Cells were pretreated without or with PP1 (10  $\mu$ M), PF431396 (10  $\mu$ M), DPI (10  $\mu$ M), APO (100  $\mu$ M), AG1296 (10  $\mu$ M), or LY294002 (30  $\mu$ M) for 1 h, and then incubated with 30  $\mu$ M AA for the indicated time intervals. The levels of phospho-Akt and Akt were determined by Western blot using the indicated antibodies. Results are representative of three independent experiments. Values are the mean  $\pm$  SEM. <sup>#</sup> $p < 0.01$ , as compared with the cells exposed to AA alone

## Discussion

AA, a potent activator of NADPH oxidase, can stimulate ROS generation [31], which could further induce the expression of antioxidant enzymes in various cell types [12]. The intracellular ROS can be accelerated under several stress conditions to induce HO-1 expression, an inducible and ubiquitous enzyme for the heme catabolism [10–12, 31]. Although several studies have found that HO-1 is expressed in the brain astrocytes exposed to various stimuli, little is known about the detail mechanisms of AA-induced HO-1 gene expression in RBA-1 cells. In the present study, we showed that Nox/ROS-dependent activation of c-Src/Pyk2/PDGFR/PI3K/Akt/Erk1/2 signaling cascade is involved in AA-induced HO-1



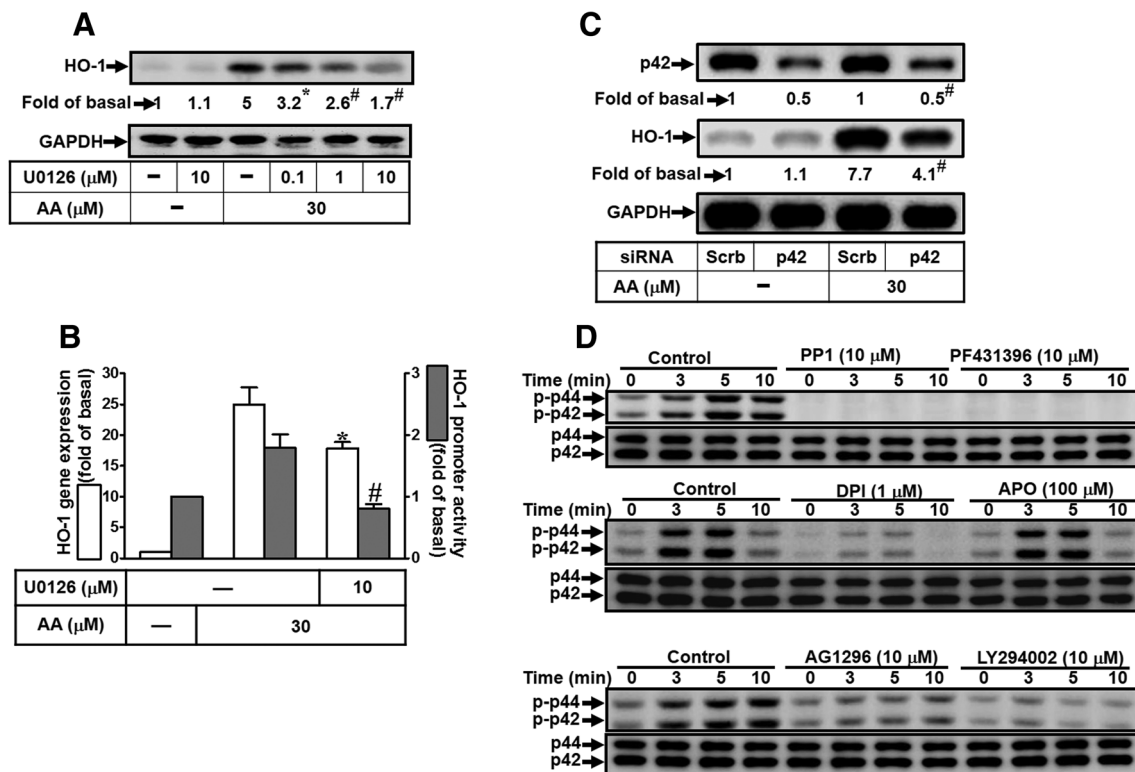


**Fig. 6** AA induces HO-1 expression via p42/p44 MAPK. **a** RBA-1 cells were pretreated with various concentrations of *U0126* for 1 h and then incubated with AA for 6 h. The protein levels of *HO-1* and *GAPDH* (served as an internal control) were determined by Western blot. **b** Cells were pretreated with *U0126* (10 μM) for 1 h, and then incubated with AA for 4 h. The levels of *HO-1* mRNA and promoter activity were determined by real-time PCR and luciferase activity, respectively. **c** Cells were transfected with scrambled, p42 siRNA, and then incubated with AA for 6 h. The levels of p42, *HO-1*, and *GAPDH* (served as an

internal control) proteins were determined by Western blot. **d** Cells were pretreated without or with *PP1* (10 μM), *PF431396* (10 μM), *DPI* (10 μM), *APO* (100 μM), *AG1296* (10 μM), or *LY294002* (30 μM) for 1 h, and then incubated with 30 μM AA for the indicated time intervals. The levels of phospho-p42/p44 MAPK and p42/p44 MAPK were determined by Western blot using the indicated antibodies. Results are representative of three independent experiments. Values are the mean ± SEM. #*p* < 0.01, as compared with the cells exposed to AA alone

expression (Fig. 8e). Activation of this signaling pathway resulted in the accumulation of nuclear Nrf2 and PPARγ binding to the ARE regions of rat *HO-1* promoter gene, and ultimately induces *HO-1* expression in RBA-1 cells.

AA is presented in the neural tissues to maintain physiological functions of the CNS [3, 4]. Different stimuli could induce the elevated levels of AA which initiate various diseases in different cell types [5, 6]. Moreover, AA has also been shown to be beneficial to protect against apoptosis in various cell types including astrocytes [7, 8]. In this study, we confirmed that AA may provide the beneficial effects via upregulation of *HO-1* protecting against inflammatory diseases under various pathological conditions. *HO-1* not only acts as an oxidative stress indicator but also exerts anti-inflammatory effects in various models [9, 39]. *HO-1* expression is upregulated within several hours under cellular stress exposure, such as oxidants, pathogens, chemokine mediators, growth factors, cellular injury, and diseases [10, 39–41]. The ROS-dependent *HO-1* induction could regulate the communication of intercellular and intracellular networks and relay the signals to tissues and organ systems, allowing them to appropriately respond to

adjust the stress or change in environmental insults. The *HO-1* gene is highly regulated by numerous stimulators at the transcriptional regulation in most cell types. The activated transcription factors interact with response elements on the *HO-1* promoter to regulate gene transcription [42].

ROS exerts as a messenger in the normal physiological functions and the inflammatory responses dependent on the cellular concentrations [43]. The excessive accumulation of ROS plays a causative role in numerous pathologies of inflammatory diseases [34, 44]. Rahman et al. indicate that activated phagocytes produce large amounts of ROS impairing cellular functions and accelerating inflammatory reactions [44]. The stimulated immune cells initiate Nox enzymatic activity to produce superoxide anion when encountering inhaled microorganisms or other mediators. It has been reported that upregulation of *HO-1* protein due to the Nox activity and intracellular ROS formation was induced by a range of stress stimuli such as LPS, cytokines or AA [10, 12, 31]. Therefore, to explore the relationship between Nox-dependent ROS generation and *HO-1* expression in RBA-1 cells challenged with AA, a thiol-containing compound (NAC) was used to



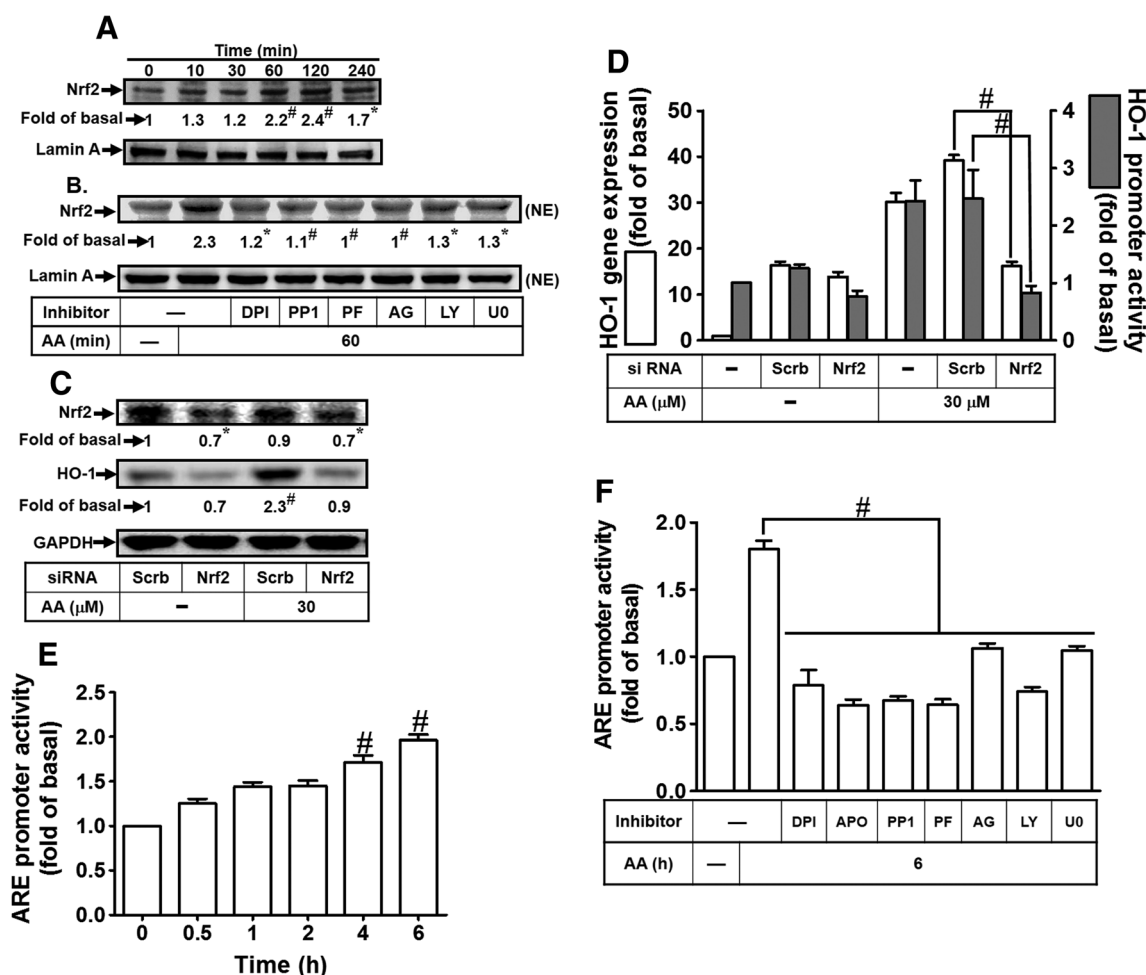


**Fig. 7** AA increases HO-1 expression through Nrf2 and ARE. **a, b** RBA-1 cells were pretreated without or with DPI (10 μM), PP1 (10 μM), PF431396 (10 μM), AG1296 (10 μM), LY294002 (30 μM), or U0126 (10 μM) for 1 h, and then incubated with 30 μM AA for the indicated time intervals. Nuclear extracts were prepared and analyzed by Western blot using anti-Nrf2 or anti-lamin A (served as a nuclear marker). **c** Cells were transfected with scrambled or Nrf2 siRNA, and then incubated with AA for 6 h. The levels of *Nrf2*, *HO-1*, and *GAPDH* (served as an internal control) protein were determined by Western blot. **d** Cells were transfected with scrambled or Nrf2 siRNA and then incubated with AA for 4 h. The levels of HO-1 mRNA and promoter activity were

determined by real-time PCR and promoter activity, respectively. **e, f** Cells were transfected with an ARE reporter gene together with a β-galactosidase plasmid, pretreated without or with DPI (10 μM), APO (100 μM), PP1 (10 μM), PF431396 (10 μM), AG1296 (10 μM), LY294002 (30 μM), or U0126 (10 μM) for 1 h, and then incubated with 30 μM AA for the indicated time intervals. ARE promoter activity was determined. Results are representative of three independent experiments. Values are the mean ± SEM. **a, e**  $p < 0.05$ ;  $^{\#}p < 0.01$ , as compared with the cells exposed vehicle alone. **b, c, d, f**  $p < 0.01$ , as compared with the cells exposed to AA alone

scavenge ROS with NAC significantly inhibited ROS generation and HO-1 induction by AA. These results are consistent with reports that NAC can reduce the injurious effects of hydrogen peroxide in human alveolar and bronchial epithelial cells [45] and the AA-mediated responses in rat glomerular mesangial cells [2]. These results confirmed that ROS play an important role in AA-induced HO-1 expression in RBA-1 cells. Moreover, two Nox-related inhibitors, DPI (a Nox inhibitor) and APO (a p47<sup>phox</sup> inhibitor), have been shown to prevent p47<sup>phox</sup> (a Nox subunit) translocation to the membrane and then inhibited Nox activation [46]. Our results confirmed that Nox plays an important role in AA-mediated responses which are attenuated by pretreatment with these Nox-

related inhibitors. This hypothesis is supported by previous reports showing that Nox-derived ROS generation is involved in HO-1 expression induced by various stimuli in different cell types [12, 47–49].

Our previous studies and others have also shown that Nox/ROS-dependent HO-1 expression is mediated through the activation of c-Src and Pyk2 in various types of cells [11, 17, 18, 32]. It is interesting to note that AA-induced HO-1 expression was attenuated by PP1 or PF431396 and by transfection with c-Src or Pyk2 siRNA. These results confirmed that c-Src and Pyk2 are involved in HO-1 expression, which may be due to the phosphorylation of c-Src and Pyk2 stimulated by AA. We also demonstrated that both c-Src and Pyk2 are downstream

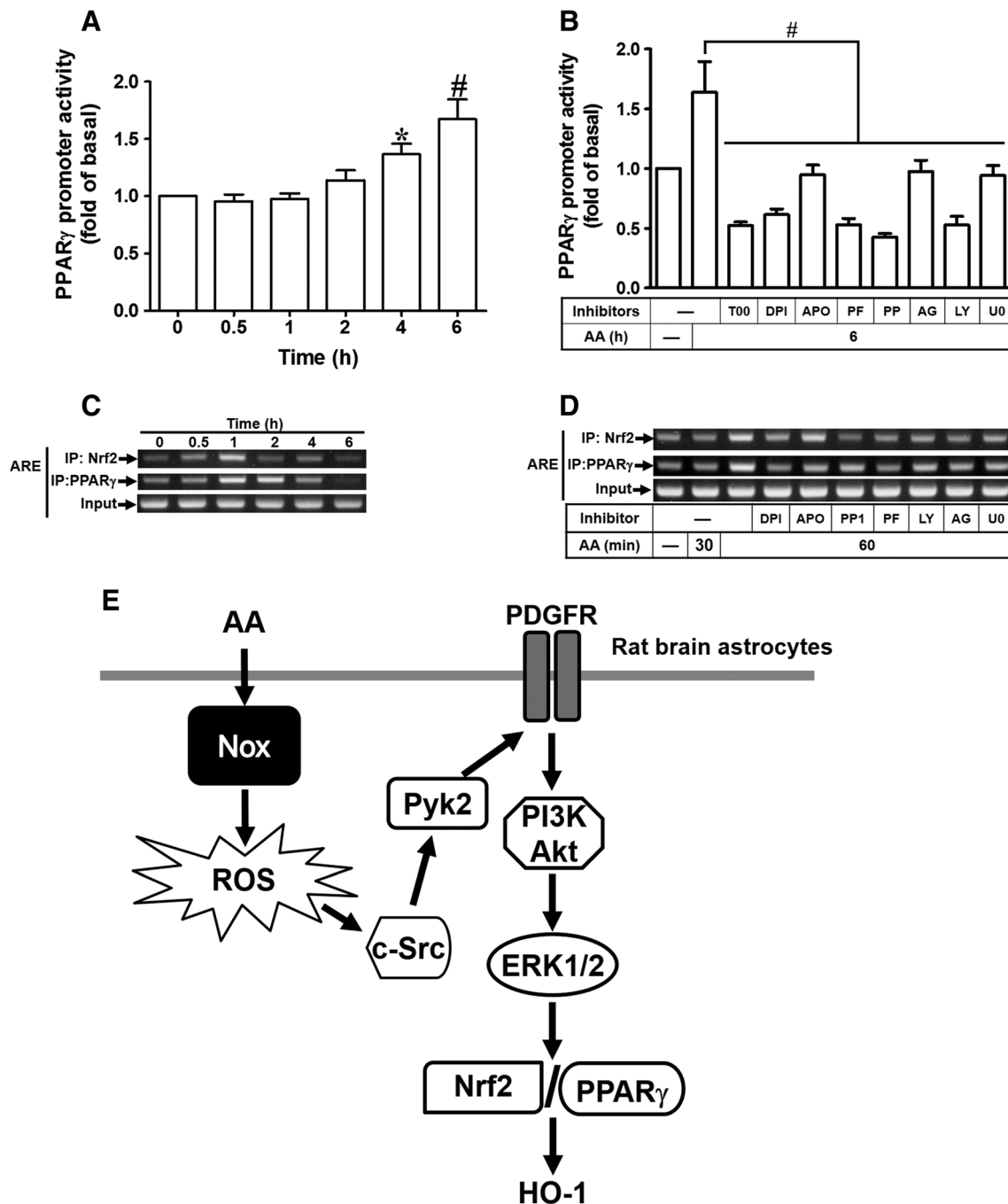


**Fig. 8** AA increases HO-1 expression through the association of Nrf2 and PPAR $\gamma$  with ARE. **a, b** RBA-1 cells were transfected with a PPAR $\gamma$  reporter gene together with a  $\beta$ -galactosidase plasmid, pretreated without or with T0070907 (10  $\mu$ M), DPI (10  $\mu$ M), APO (100  $\mu$ M), PF431396 (10  $\mu$ M), PP1 (10  $\mu$ M), AG1296 (10  $\mu$ M), LY294002 (30  $\mu$ M), or U0126 (10  $\mu$ M) for 1 h, and then incubated with 30  $\mu$ M AA for the indicated time intervals. PPAR $\gamma$  promoter activity was determined. **c, d** Cells were pretreated without or with DPI (10  $\mu$ M), APO (100  $\mu$ M), PP1 (10  $\mu$ M), PF431396 (10  $\mu$ M), LY294002 (30  $\mu$ M), AG1296 (10  $\mu$ M), or U0126 (10  $\mu$ M) for 1 h, and then incubated with 30  $\mu$ M AA for the indicated time

intervals. The ChIP assay was performed. ChIP assays were performed using an anti-Nrf2 or anti-PPAR $\gamma$  antibody, as described in the [Experimental Procedures](#). Results are representative of three independent experiments. Values are the mean  $\pm$  SEM. **a**  $p < 0.01$ , as compared with the cells exposed to vesicle alone. **b**  $p < 0.01$ , as compared with the cells exposed to AA alone. **e** The schematic signaling pathways involved in HO-1 expression in RBA-1 cells challenged with AA. AA activates Nox/ROS-dependent phosphorylation of c-Src/Pyk2/PDGFR/PI3K/Akt/p42/p44 MAPK cascade, which in turn triggers Nrf2 and PPAR $\gamma$  activation and ultimately induces HO-1 expression in RBA-1 cells

components of Nox/ROS, since AA-stimulated phosphorylation of c-Src and Pyk2 was attenuated by DPI and APO. The relationship between c-Src and Pyk2 in AA-mediated

responses was also differentiated by using respective inhibitors. Pretreatment with PP1 inhibited the AA-stimulated phosphorylation of c-Src and Pyk2; however, PF431396 only

attenuated phosphorylation of Pyk2, implying that Pyk2 was a downstream component of Nox/ROS/c-Src in AA-mediated responses. These data indicated that AA-induced HO-1 expression is mediated through a c-Src and ROS-dependent Pyk2 pathway in RBA-1 cells.

Transactivation of growth factor receptors such as PDGFR is mediated by nonreceptor tyrosine kinases including c-Src and Pyk2, which modulates several pathological processes in various cell types [2, 19]. In the present study, we confirmed that c-Src and Pyk2 transactivated PDGFR linking to PI3K/Akt/ERK1/2 and leading to HO-1 expression, revealed by using pharmacological inhibitors and transfection with respective siRNAs. Nonetheless, there is still controversial over the role of nonreceptor tyrosine kinases in the transactivation of growth factor receptors induced by various stimuli. In vascular smooth muscle cells, Pyk2 phosphorylation following the transactivation of EGFR contributed to the thrombin-stimulated Erk1/2 phosphorylation [19]. Conversely, wounding activated the EGFR through activation of Pyk2/c-Src complex in human corneal limbal epithelial cells [2]. Moreover, the roles of PI3K/Akt in the expression of HO-1 have also been documented in other cellular contexts, including the responses to carnosol [23] and nerve growth factor (NGF) [24]. In this study, we confirmed that PI3K/Akt activate the Erk1/2 signaling via c-Src/Pyk2-dependent transactivation of PDGFR, which is involved in AA-induced HO-1 expression in RBA-1 cells.

Abnormal MAPK activations trigger a variety of inflammatory responses and tissue injury [50]. Moreover, the MAPKs have been shown to act as an important regulatory molecule for induction of several inflammatory mediators in different cell types [51]. In the present study, we demonstrated that Erk1/2 are required for HO-1 induction by AA, since AA-mediated responses were attenuated by pretreatment with selective MEK1/2 pharmacological inhibitor U0126 or transfection with Erk1 or Erk2 siRNA. These kinases involved in AA-stimulated pathways were further supported by AA-mediated phosphorylation of Erk1/2. These results are consistent with the HO-1 expression mediated by Erk1/2 to activate ARE region, the Nrf2 binding site, in HepG2 cells [52] and heme-mediated neuronal injury [53]. Moreover, pretreatment with the inhibitor of c-Src (PP1), Pyk2 (PF431396), Nox (DPI and APO), ROS scavenger (NAC), PDGFR (AG1296), or PI3K (LY294002) significantly attenuated phosphorylation of Erk1/2 stimulated by AA, suggesting that Erk1/2 are downstream components of AA-stimulated Nox/ROS-dependent c-Src/Pyk2/PDGFR/PI3K/Akt cascade in RBA-1 cells. These results are also consistent with several reports that ROS-dependent MAPK pathways including Erk1/2 are involved in the regulation of cellular functions exposed to various stimuli in several cell types [54].

AREs play major functional roles for ROS-dependent induction of HO-1 [9]. ROS have been shown to activate

three major MAPKs (Erk1/2, p38 MAPK, and JNK1/2) and PI3K/Akt pathway followed by the activation of transcriptional factors including Nrf2 [55]. Activation of MAPKs leading to nuclear translocation of Nrf2 by the oxidized low-density lipoproteins was found to induce HO-1 expression in human vascular smooth muscle cells [56]. In PC12 cells, carnosol-induced HO-1 expression was mediated through PI3K/Akt-dependent Nrf2 upregulation [23], whereas peroxynitrite-induced HO-1 expression was mediated by activation of PI3K/Akt with subsequently increased nuclear translocation and ARE binding of Nrf2 [57], indicating the differently regulatory mechanisms in Nrf2/ARE activation in various cell types. Indeed, we found that AA induced nuclear Nrf2 accumulation and also enhanced ARE promoter activity in RBA-1 cells, which was mediated through Nox/ROS/c-Src/Pyk2/PI3K/Akt and Erk1/2. These results are consistent with previous reports showing that oxidant stress and antioxidant phytochemicals increase the translocation of Nrf2 protein into the nucleus for the induction of antioxidant genes through AREs in the promoters of HO-1 [9]. Although there are several reports linking the activation of MAPKs as well as PI3K/Akt signalings and Nrf2 that bind to ARE sequences for upregulation of HO-1 stimulated by various stimuli, little is known about the ARE transcriptional regulatory mechanisms of HO-1 induced by AA. In this study, ChIP assay showed that AA increased the levels of the Nrf2 in the nucleus and binding to ARE sequences in the promoter regions of HO-1 and regulated gene expression in RBA-1 cells.

In conclusion, as depicted in Fig. 8e, we found that AA stimulates NADPH oxidase-dependent ROS production and results in HO-1 expression. AA-stimulated Erk1/2 activation, which is involved in the regulation of HO-1 expression, is mediated through Nox/ROS/c-Src/Pyk2-dependent transactivation of PDGFR and downstream signaling to PI3K/Akt, resulting in the Nrf2 expression, which is associated with ARE binding site of rat HO-1 promoter region, which finally turns on the HO-1 gene expression.

**Acknowledgements** This work was supported by the Ministry of Science and Technology, Taiwan (Grant numbers MOST104-2320-B-182A-003-MY3, MOST104-2320-B-182-010, and MOST105-2320-B-182-005-MY3); Chang Gung Medical Research Foundation (Grant numbers CMRPD1F0022, CMRPD1F0023, CMRPD1F0511, CMRPD1F0512, CMRPG3E2232, CMRPG3F1531, CMRPG3F1532, CMRPG5F0201, and CMRPG5F0201); and the Ministry of Education, Taiwan (Grant numbers EMRPD1G0171 and EMRPD1G0281).

#### Compliance with Ethical Standards

**Conflict Interest** The authors declare that they have no conflict of interest

## References

- Halliwell B (2006) Oxidative stress and neurodegeneration: where are we now? *J Neurochem* 97(6):1634–1658. doi:10.1111/j.1471-4159.2006.03907.x
- Block K, Ricono JM, Lee DY, Bhandari B, Choudhury GG, Abboud HE, Gorin Y (2006) Arachidonic acid-dependent activation of a p22<sup>phox</sup>-based NAD(P)H oxidase mediates angiotensin II-induced mesangial cell protein synthesis and fibronectin expression via Akt/PKB. *Antioxid Redox Signal* 8(9–10):1497–1508. doi:10.1089/ars.2006.8.1497
- Diau GY, Hsieh AT, Sarkadi-Nagy EA, Wijendran V, Nathanielsz PW, Brenna JT (2005) The influence of long chain polyunsaturated supplementation on docosahexaenoic acid and arachidonic acid in baboon neonate central nervous system. *BMC Med* 3:11. doi:10.1186/1741-7015-3-11
- Uauy R, Dangour AD (2006) Nutrition in brain development and aging: role of essential fatty acids. *Nutr Rev* 64(5 Pt 2):S24–S33 discussion S72–91
- Martin C, Martinez R, Navarro R, Ruiz-Sanz JI, Lacort M, Ruiz-Larrea MB (2001) tert-Butyl hydroperoxide-induced lipid signaling in hepatocytes: involvement of glutathione and free radicals. *Biochem Pharmacol* 62(6):705–712
- Schnellmann RG, Yang X, Carrick JB (1994) Arachidonic acid release in renal proximal tubule cell injuries and death. *J Biochem Toxicol* 9(4):211–217
- Tommasini I, Guidarelli A, Cerioni L, Cantoni O (2004) The arachidonate-dependent cytoprotective signaling evoked by peroxynitrite is a general response of the monocyte/macrophage lineage. *Biochem Biophys Res Commun* 316(4):1191–1195. doi:10.1016/j.bbrc.2004.02.172
- Palomba L, Cerioni L, Cantoni O (2009) Arachidonic acid: a key molecule for astrocyte survival to peroxynitrite. *Glia* 57(15):1672–1679. doi:10.1002/glia.20879
- Ryter SW, Alam J, Choi AM (2006) Heme oxygenase-1/carbon monoxide: from basic science to therapeutic applications. *Physiol Rev* 86(2):583–650. doi:10.1152/physrev.00011.2005
- Jamal Uddin M, Joe Y, Kim SK, Oh Jeong S, Ryter SW, Pae HO, Chung HT (2016) IRG1 induced by heme oxygenase-1/carbon monoxide inhibits LPS-mediated sepsis and pro-inflammatory cytokine production. *Cell Mol Immunol* 13(2):170–179. doi:10.1038/cmi.2015.02
- Chi PL, Lin CC, Chen YW, Hsiao LD, Yang CM (2015) CO induces Nrf2-dependent heme oxygenase-1 transcription by cooperating with Sp1 and c-Jun in rat brain astrocytes. *Mol Neurobiol* 52(1):277–292. doi:10.1007/s12035-014-8869-4
- Itoh K, Mochizuki M, Ishii Y, Shibata T, Kawamoto Y, Kelly V, Sekizawa K et al (2004) Transcription factor Nrf2 regulates inflammation by mediating the effect of 15-deoxy- $\Delta^{12,14}$ -prostaglandin J<sub>2</sub>. *Mol Cell Biol* 24(1):36–45
- Paine A, Eiz-Vesper B, Blasczyk R, Immenschuh S (2010) Signaling to heme oxygenase-1 and its anti-inflammatory therapeutic potential. *Biochem Pharmacol* 80(12):1895–1903. doi:10.1016/j.bcp.2010.07.014
- Poss KD, Tonegawa S (1997) Reduced stress defense in heme oxygenase 1-deficient cells. *Proc Natl Acad Sci U S A* 94(20):10925–10930
- Chao XD, Ma YH, Luo P, Cao L, Lau WB, Zhao BC, Han F, Liu W et al (2013) Up-regulation of heme oxygenase-1 attenuates brain damage after cerebral ischemia via simultaneous inhibition of superoxide production and preservation of NO bioavailability. *Exp Neurol* 239:163–169. doi:10.1016/j.expneurol.2012.09.020
- Alexander LD, Ding Y, Alagarsamy S, Cui XL, Douglas JG (2006) Arachidonic acid induces ERK activation via Src SH2 domain association with the epidermal growth factor receptor. *Kidney Int* 69(10):1823–1832. doi:10.1038/sj.ki.5000363
- Han Z, Varadharaj S, Giedt RJ, Zweier JL, Szeto HH, Alevriadou BR (2009) Mitochondria-derived reactive oxygen species mediate heme oxygenase-1 expression in sheared endothelial cells. *J Pharmacol Exp Ther* 329(1):94–101. doi:10.1124/jpet.108.145557
- Yang CM, Lin CC, Lee IT, Hsu CK, Tai YC, Hsieh HL, Chi PL, Hsiao LD (2015) c-Src-dependent transactivation of EGFR mediates CORM-2-induced HO-1 expression in human tracheal smooth muscle cells. *J Cell Physiol* 230(10):2351–2361. doi:10.1002/jcp.24912
- Schauwienold D, Sastre AP, Genzel N, Schaefer M, Reusch HP (2008) The transactivated epidermal growth factor receptor recruits Pyk2 to regulate Src kinase activity. *J Biol Chem* 283(41):27748–27756. doi:10.1074/jbc.M801431200
- Elbirt KK, Whitmarsh AJ, Davis RJ, Bonkovsky HL (1998) Mechanism of sodium arsenite-mediated induction of heme oxygenase-1 in hepatoma cells. Role of mitogen-activated protein kinases. *J Biol Chem* 273(15):8922–8931
- Kietzmann T, Samoylenko A, Immenschuh S (2003) Transcriptional regulation of heme oxygenase-1 gene expression by MAP kinases of the JNK and p38 pathways in primary cultures of rat hepatocytes. *J Biol Chem* 278(20):17927–17936. doi:10.1074/jbc.M203929200
- Lee SH, Lee YJ, Han HJ (2010) Effect of arachidonic acid on hypoxia-induced IL-6 production in mouse ES cells: involvement of MAPKs, NF- $\kappa$ B, and HIF-1 $\alpha$ . *J Cell Physiol* 222(3):574–585. doi:10.1002/jcp.21973
- Martin D, Rojo AI, Salinas M, Diaz R, Gallardo G, Alam J, De Galarreta CM, Cuadrado A (2004) Regulation of heme oxygenase-1 expression through the phosphatidylinositol 3-kinase/Akt pathway and the Nrf2 transcription factor in response to the antioxidant phytochemical carnosol. *J Biol Chem* 279(10):8919–8929. doi:10.1074/jbc.M309660200
- Salinas M, Diaz R, Abraham NG, Ruiz de Galarreta CM, Cuadrado A (2003) Nerve growth factor protects against 6-hydroxydopamine-induced oxidative stress by increasing expression of heme oxygenase-1 in a phosphatidylinositol 3-kinase-dependent manner. *J Biol Chem* 278(16):13898–13904. doi:10.1074/jbc.M209164200
- Jaiswal AK (2004) Nrf2 signaling in coordinated activation of antioxidant gene expression. *Free Radic Biol Med* 36(10):1199–1207. doi:10.1016/j.freeradbiomed.2004.02.074
- Bianchi A, Moulin D, Hupont S, Koufany M, Netter P, Reboul P, Jouzeau JY (2014) Oxidative stress-induced expression of HSP70 contributes to the inhibitory effect of 15d-PGJ<sub>2</sub> on inducible prostaglandin pathway in chondrocytes. *Free Radic Biol Med* 76:114–126. doi:10.1016/j.freeradbiomed.2014.07.028
- Jou TC, Jou MJ, Chen JY, Lee SY (1985) Properties of rat brain astrocytes in long-term culture. *Taiwan Yi Xue Hui Za Zhi* 84(8):865–881
- Lin CC, Lee IT, Chi PL, Hsieh HL, Cheng SE, Hsiao LD, Liu CJ, Yang CM (2014) c-Src/Jak2/PDGFR/PKC $\delta$ -dependent MMP-9 induction is required for thrombin-stimulated rat brain astrocytes migration. *Mol Neurobiol* 49(2):658–672. doi:10.1007/s12035-013-8547-y
- Yang CM, Lin CC, Lee IT, Lin YH, Yang CM, Chen WJ, Jou MJ, Hsiao LD (2012) Japanese encephalitis virus induces matrix metalloproteinase-9 expression via a ROS/c-Src/PDGFR/PI3K/Akt/MAPKs-dependent AP-1 pathway in rat brain astrocytes. *J Neuroinflammation* 9:12. doi:10.1186/1742-2094-9-12
- Kitamura Y, Kakimura J, Matsuoka Y, Nomura Y, Gebicke-Haerter PJ, Taniguchi T (1999) Activators of peroxisome proliferator-activated receptor- $\gamma$  (PPAR $\gamma$ ) inhibit inducible nitric oxide synthase expression but increase heme oxygenase-1 expression in rat glial cells. *Neurosci Lett* 262(2):129–132



31. Matono R, Miyano K, Kiyohara T, Sumimoto H (2014) Arachidonic acid induces direct interaction of the p67<sup>phox</sup>-Rac complex with the phagocyte oxidase Nox2, leading to superoxide production. *J Biol Chem* 289(36):24874–24884. doi:[10.1074/jbc.M114.581785](https://doi.org/10.1074/jbc.M114.581785)
32. Choi AM, Alam J (1996) Heme oxygenase-1: function, regulation, and implication of a novel stress-inducible protein in oxidant-induced lung injury. *Am J Respir Cell Mol Biol* 15(1):9–19. doi:[10.1165/ajrcmb.15.1.8679227](https://doi.org/10.1165/ajrcmb.15.1.8679227)
33. Chrissobolis S, Faraci FM (2008) The role of oxidative stress and NADPH oxidase in cerebrovascular disease. *Trends Mol Med* 14(11):495–502. doi:[10.1016/j.molmed.2008.09.003](https://doi.org/10.1016/j.molmed.2008.09.003)
34. Lee IT, Yang CM (2012) Role of NADPH oxidase/ROS in pro-inflammatory mediators-induced airway and pulmonary diseases. *Biochem Pharmacol* 84(5):581–590. doi:[10.1016/j.bcp.2012.05.005](https://doi.org/10.1016/j.bcp.2012.05.005)
35. Lipinski CA, Loftus JC (2010) Targeting Pyk2 for therapeutic intervention. *Expert Opin Ther Targets* 14(1):95–108. doi:[10.1517/14728220903473194](https://doi.org/10.1517/14728220903473194)
36. Yeh PY, Li CY, Hsieh CW, Yang YC, Yang PM, Wung BS (2014) CO-releasing molecules and increased heme oxygenase-1 induce protein S-glutathionylation to modulate NF- $\kappa$ B activity in endothelial cells. *Free Radic Biol Med* 70:1–13. doi:[10.1016/j.freeradbiomed.2014.01.042](https://doi.org/10.1016/j.freeradbiomed.2014.01.042)
37. Shih RH, Lee IT, Hsieh HL, Kou YR, Yang CM (2010) Cigarette smoke extract induces HO-1 expression in mouse cerebral vascular endothelial cells: involvement of c-Src/NADPH oxidase/PDGFR/JAK2/STAT3 pathway. *J Cell Physiol* 225(3):741–750. doi:[10.1002/jcp.22270](https://doi.org/10.1002/jcp.22270)
38. McCubrey JA, Lahair MM, Franklin RA (2006) Reactive oxygen species-induced activation of the MAP kinase signaling pathways. *Antioxid Redox Signal* 8(9–10):1775–1789. doi:[10.1089/ars.2006.8.1775](https://doi.org/10.1089/ars.2006.8.1775)
39. Wagener FA, Volk HD, Willis D, Abraham NG, Soares MP, Adema GJ, Figdor CG (2003) Different faces of the heme-heme oxygenase system in inflammation. *Pharmacol Rev* 55(3):551–571. doi:[10.1124/pr.55.3.5](https://doi.org/10.1124/pr.55.3.5)
40. Magierowska K, Magierowski M, Hubalewska-Mazgaj M, Adamski J, Surmiak M, Sliwowski Z, Kwiecien S, Brzozowski T (2015) Carbon monoxide (CO) released from tricarbonyldichlororuthenium (II) dimer (CORM-2) in gastroprotection against experimental ethanol-induced gastric damage. *PLoS One* 10(10):e0140493. doi:[10.1371/journal.pone.0140493](https://doi.org/10.1371/journal.pone.0140493)
41. Wegiel B, Hanto DW, Otterbein LE (2013) The social network of carbon monoxide in medicine. *Trends Mol Med* 19(1):3–11. doi:[10.1016/j.molmed.2012.10.001](https://doi.org/10.1016/j.molmed.2012.10.001)
42. Rochette L, Cottin Y, Zeller M, Vergely C (2013) Carbon monoxide: mechanisms of action and potential clinical implications. *Pharmacol Ther* 137(2):133–152. doi:[10.1016/j.pharmthera.2012.09.007](https://doi.org/10.1016/j.pharmthera.2012.09.007)
43. Kamata H, Hirata H (1999) Redox regulation of cellular signalling. *Cell Signal* 11(1):1–14
44. Rahman I, Biswas SK, Kode A (2006) Oxidant and antioxidant balance in the airways and airway diseases. *Eur J Pharmacol* 533(1–3):222–239. doi:[10.1016/j.ejphar.2005.12.087](https://doi.org/10.1016/j.ejphar.2005.12.087)
45. Mulier B, Rahman I, Watchorn T, Donaldson K, MacNee W, Jeffery PK (1998) Hydrogen peroxide-induced epithelial injury: the protective role of intracellular nonprotein thiols (NPSH). *Eur Respir J* 11(2):384–391
46. Barbieri SS, Cavalca V, Eligini S, Brambilla M, Caiani A, Tremoli E, Colli S (2004) Apocynin prevents cyclooxygenase 2 expression in human monocytes through NADPH oxidase and glutathione redox-dependent mechanisms. *Free Radic Biol Med* 37(2):156–165. doi:[10.1016/j.freeradbiomed.2004.04.020](https://doi.org/10.1016/j.freeradbiomed.2004.04.020)
47. Yang CM, Lin CC, Hsieh HL (2017) High-glucose-derived oxidative stress-dependent heme oxygenase-1 expression from astrocytes contributes to the neuronal apoptosis. *Mol Neurobiol* 54(1):470–483. doi:[10.1007/s12035-015-9666-4](https://doi.org/10.1007/s12035-015-9666-4)
48. Cheng SE, Lee IT, Lin CC, Kou YR, Yang CM (2010) Cigarette smoke particle-phase extract induces HO-1 expression in human tracheal smooth muscle cells: role of the c-Src/NADPH oxidase/MAPK/Nrf2 signaling pathway. *Free Radic Biol Med* 48(10):1410–1422. doi:[10.1016/j.freeradbiomed.2010.02.026](https://doi.org/10.1016/j.freeradbiomed.2010.02.026)
49. Lee IT, Wang SW, Lee CW, Chang CC, Lin CC, Luo SF, Yang CM (2008) Lipoteichoic acid induces HO-1 expression via the TLR2/MyD88/c-Src/NADPH oxidase pathway and Nrf2 in human tracheal smooth muscle cells. *J Immunol* 181(7):5098–5110
50. Benvenisti-Zarom L, Chen-Roetling J, Regan RF (2006) Inhibition of the ERK/MAP kinase pathway attenuates heme oxygenase-1 expression and heme-mediated neuronal injury. *Neurosci Lett* 398(3):230–234. doi:[10.1016/j.neulet.2006.01.003](https://doi.org/10.1016/j.neulet.2006.01.003)
51. Lee IT, Yang CM (2013) Inflammatory signalings involved in airway and pulmonary diseases. *Mediat Inflamm* 2013:791231. doi:[10.1155/2013/791231](https://doi.org/10.1155/2013/791231)
52. Yuan X, Xu C, Pan Z, Keum YS, Kim JH, Shen G, Yu S, Oo KT et al (2006) Butylated hydroxyanisole regulates ARE-mediated gene expression via Nrf2 coupled with ERK and JNK signaling pathway in HepG2 cells. *Mol Carcinog* 45(11):841–850. doi:[10.1002/mc.20234](https://doi.org/10.1002/mc.20234)
53. Foresti R, Bani-Hani MG, Motterlini R (2008) Use of carbon monoxide as a therapeutic agent: promises and challenges. *Intensive Care Med* 34(4):649–658. doi:[10.1007/s00134-008-1011-1](https://doi.org/10.1007/s00134-008-1011-1)
54. Pawate S, Shen Q, Fan F, Bhat NR (2004) Redox regulation of glial inflammatory response to lipopolysaccharide and interferongamma. *Journal Neurosci Res* 77(4):540–551. doi:[10.1002/jnr.20180](https://doi.org/10.1002/jnr.20180)
55. Reuter S, Gupta SC, Chaturvedi MM, Aggarwal BB (2010) Oxidative stress, inflammation, and cancer: how are they linked? *Free Radic Biol Med* 49(11):1603–1616. doi:[10.1016/j.freeradbiomed.2010.09.006](https://doi.org/10.1016/j.freeradbiomed.2010.09.006)
56. Anwar AA, Li FY, Leake DS, Ishii T, Mann GE, Siow RC (2005) Induction of heme oxygenase 1 by moderately oxidized low-density lipoproteins in human vascular smooth muscle cells: role of mitogen-activated protein kinases and Nrf2. *Free Radic Biol Med* 39(2):227–236. doi:[10.1016/j.freeradbiomed.2005.03.012](https://doi.org/10.1016/j.freeradbiomed.2005.03.012)
57. Li MH, Cha YN, Surh YJ (2006) Peroxynitrite induces HO-1 expression via PI3K/Akt-dependent activation of NF-E2-related factor 2 in PC12 cells. *Free Radic Biol Med* 41(7):1079–1091. doi:[10.1016/j.freeradbiomed.2006.06.010](https://doi.org/10.1016/j.freeradbiomed.2006.06.010)





# Exploring the structure-permeation relationship of topical tricyclic antidepressants used for skin analgesia



Kuo-Sheng Liu<sup>a</sup>, Tse-Hung Huang<sup>b,c,d</sup>, Ibrahim A. Aljuffali<sup>e</sup>, En-Li Chen<sup>f</sup>,  
Jhi-Joung Wang<sup>g,\*</sup>, Jia-You Fang<sup>f,h,i,j,\*\*</sup>

<sup>a</sup> Department of Pharmacy, Chia Nan University of Pharmacy and Science, Tainan, Taiwan

<sup>b</sup> Department of Traditional Chinese Medicine, Chang Gung Memorial Hospital, Keelung, Taiwan

<sup>c</sup> School of Traditional Chinese Medicine, Chang Gung University, Taoyuan, Taiwan

<sup>d</sup> School of Nursing, National Taipei University of Nursing and Health Sciences, Taipei, Taiwan

<sup>e</sup> Department of Pharmaceutics, College of Pharmacy, King Saud University, Riyadh, Saudi Arabia

<sup>f</sup> Pharmaceutics Laboratory, Graduate Institute of Natural Products, Chang Gung University, Kweishan, Taoyuan, Taiwan

<sup>g</sup> Department of Medical Research, Chi Mei Medical Center, Tainan, Taiwan

<sup>h</sup> Chinese Herbal Medicine Research Team, Healthy Aging Research Center, Chang Gung University, Kweishan, Taoyuan, Taiwan

<sup>i</sup> Department of Anesthesiology, Chang Gung Memorial Hospital, Kweishan, Taoyuan, Taiwan

<sup>j</sup> Research Center for Industry of Human Ecology and Research Center for Chinese Herbal Medicine, Chang Gung University of Science and Technology, Kweishan, Taoyuan, Taiwan

## ARTICLE INFO

### Article history:

Received 10 November 2016

Received in revised form 6 March 2017

Accepted 19 March 2017

Available online 23 March 2017

### Keywords:

Tricyclic antidepressant

Propamine

Analgesia

Cutaneous absorption

Structure-permeation relationship

## ABSTRACT

The purpose of this study was to evaluate the skin permeation of tricyclic antidepressants (TCAs) with propamine moiety to select candidates for the development of topical analgesics to treat cutaneous pain. We sought to establish the structure-permeation relationship (SPR) of topical TCAs. The lipophilicity, melting point, and aqueous solubility were determined to develop the physicochemical characterization. The TCA permeation into pig and nude mouse skins was estimated using Franz diffusion cell. TCAs and lidocaine were comparatively examined for cutaneous analgesia by pinprick assay. Cutaneous tolerance to TCAs was assessed using nude mouse skin. The skin deposition increased following the increase of lipophilicity after excluding the effect of solubility, with clomipramine exhibiting the highest skin retention. A contrary result was observed for TCA penetration into the receptor. Of the permeants tested, clomipramine demonstrated the best skin-targeting ability. Nortriptyline and clomipramine demonstrated selective uptake into the hair follicles, exhibiting a 2.5-fold higher follicular accumulation than desipramine. Replacement of nitrogen with carbon in the seven-member ring increased skin absorption. The tertiary amine TCAs demonstrated higher absorption than the secondary amine TCAs. The position of the double bond also affected skin transport. Topical clomipramine had a longer duration of analgesic action than lidocaine (240 min versus 60 min). Exploring the SPR revealed that clomipramine could be an analgesic candidate drug for future development.

© 2017 Elsevier B.V. All rights reserved.

## 1. Introduction

Topical drug administration can be an efficient method for skin targeting and cutaneous disease management. The actives must

first be absorbed by the skin if the drugs are to provide therapeutic benefits. The drugs must diffuse across certain barriers, such as the stratum corneum (SC) and a tight junction, to achieve effective permeation. Various factors can influence this process, including the physicochemical characteristics of the drugs and the vehicles into which the drugs are loaded. An elucidation of how the physicochemical factors affect drug absorption is important for selecting and designing feasible drugs for topical application. The establishment of a structure-permeation relationship (SPR) attempts to link the delivery of the chemicals to their physicochemical properties and structures, thereby providing insights into the cutaneous absorption mechanisms (Riviere et al., 2014). The

\* Corresponding author at: Pharmaceutics Laboratory, Graduate Institute of Natural Products, Chang Gung University, 259 Wen-Hua 1st Road, Kweishan, Taoyuan 333, Taiwan.

\*\* Corresponding author at: Department of Medical Research, Chi Mei Medical Center, 901 Chung Hwa Road, Yungkuang, Tainan 710, Taiwan.

E-mail addresses: [400002@mail.chimei.org.tw](mailto:400002@mail.chimei.org.tw) (J.-J. Wang), [fajy@mail.cgu.edu.tw](mailto:fajy@mail.cgu.edu.tw) (J.-Y. Fang).

development of this relationship to predict the skin permeability of a series of drugs remains a challenge.

Numerous homologous series of tricyclic antidepressants (TCAs) are appropriate model permeants to organize SPR. TCAs are employed in the treatment of neuropathic skin pain. The mechanisms of TCA-related pain relief are the establishment of a blockade of the neuronal sodium channel and the *N*-methyl-D-aspartate receptor, activation of the  $\mu$ - and  $\delta$ -opioid receptors, and inhibition of norepinephrine reuptake (Kalso et al., 2013). Topically applied TCAs for analgesia exert peripheral effects approximating the administration region and reduce systemic adverse responses (Flores et al., 2012). TCAs can alleviate the pain associated with skin infection, malignant skin tumors, acute burns, postherpetic neuralgia, and radiation dermatitis (Jongen et al., 2014). Currently, only a few topical TCA options are commercially available. The clinical efficacy of the selected topical analgesics is often based on an empirical approach without wide studies on skin permeation (Peppin et al., 2015). The first objective of this study was to evaluate cutaneous absorption and the local anesthetic efficacy of a series of TCAs. We attempted to identify new candidates for peripheral pain treatment. Although some studies have been conducted for modeling SPR, the majority of the work focuses on the permeant transport across the skin (flux) but not on retention in the skin. Because the primary target of topical TCAs is the skin tissue, the second aim was to explore the relationship between cutaneous drug deposition and physicochemical properties. We endeavored to understand the mechanisms and pathways of TCA absorption as well as the permeant natures governing cutaneous delivery.

Most SPR databases employ heterogeneous permeants (Moss et al., 2002). The database involved in the homologous series is insufficient due to the limited physicochemical variety. As Fig. 1 illustrates, we chose the TCAs containing propamine moiety as the model permeants for investigating the SPR of these analogues. These structures are similar, although they do differ in some respects, including the presence of secondary amine (desipramine, protriptyline, and nortriptyline) or tertiary amine (imipramine and clomipramine), replacement of nitrogen (desipramine) with

carbon (nortriptyline), different positions of the double bond (protriptyline versus nortriptyline), and the absence or presence of chlorine (imipramine versus clomipramine). The physicochemical properties, including the melting point, the partition coefficient ( $\log P$ ), the capacity factor ( $\log K'$ ), and the aqueous solubility, were determined. The cutaneous absorption was evaluated by Franz diffusion cell with pig and nude mouse skins as the barriers. The in vivo analgesic activity of the topically applied TCAs was examined using the pinprick test. Finally, the in vivo skin tolerance of the topical TCAs was analyzed based on the profiles of cutaneous physiology and histology. The data collected in this study allowed us to discriminate the contributions of different drug properties to cutaneous transport.

## 2. Materials and methods

### 2.1. Conversion of TCA salts to base forms

All propamine TCAs were purchased from Sigma-Aldrich (St. Louis, MO, USA).  $\text{NH}_4\text{OH}$ /water solution at pH 9 was added by drops into methanol containing TCA salt to precipitate the base form. The precipitate was filtered and washed with double-distilled water for  $\text{NH}_4\text{OH}$  removal. The structures of the TCA base forms were validated by infrared spectrophotometry and nuclear magnetic resonance.

### 2.2. *N*-octanol/water partitioning ( $\log P$ ) and capacity factor ( $\log K'$ )

A methanolic solution (1 ml) of TCA base forms (0.5 mg) was prepared in a sample vial. Methanol was evaporated by a vacuum. *n*-octanol and double-distilled water, 1 ml of each, were added to the vial. After being shaken for 24 h at 37 °C, the *n*-octanol and water phases were divided by centrifugation at  $10,000 \times g$  for 10 min. The TCA concentration in *n*-octanol and water was quantified by high-performance liquid chromatography (HPLC). The partition coefficient was estimated as  $\log P$  ( $\log$  TCA concentration in *n*-octanol/TCA concentration in water). The stationary phase of HPLC was a 25-cm-long, 4-mm inner diameter

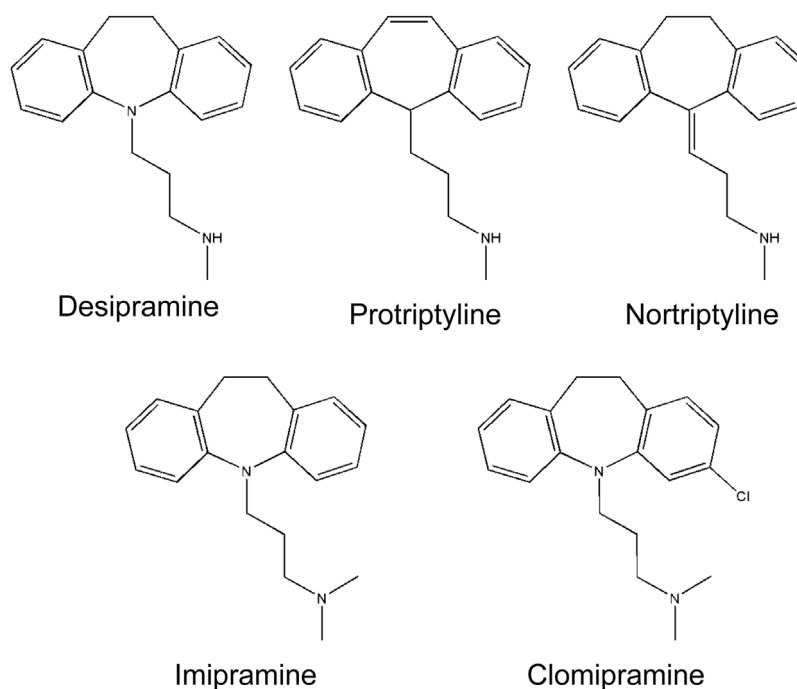


Fig. 1. The chemical structures of desipramine, protriptyline, nortriptyline, imipramine, and clomipramine.

reverse phase C18 column (Merck). The mobile phase consisted of acetonitrile and pH 2 water adjusted by phosphoric acid (45:55) at a flow rate of 1 ml/min. The wavelength of the UV/visible detector was 251 nm.

The log  $K'$  was measured using HPLC. The retention time of each TCA was detected, and the capacity factor was calculated by the equation  $\log K' = \log(t_r - t_0/t_0)$ . The  $t_r$  is the retention time of each TCA, whereas  $t_0$  is the retention time of the non-retained solvent peak.

### 2.3. Saturated solubility in 20% propylene glycol (PG)/water

An excess amount of propamine TCAs was incorporated in 20% PG/pH 7.4 buffer (1 ml). The test tube was shaken reciprocally for 24 h at 37 °C. After centrifugation at 10,000×g for 10 min, the supernatant was filtered through a PVDF membrane with a pore size of 0.45 µm. The solubility of the TCAs was detected using HPLC.

### 2.4. Animals

Specific-pathogen-free, 1-week-old pigs were obtained from the Animal Technology Institute Taiwan (Miaoli, Taiwan). The 8-week-old nude mice were supplied by the National Laboratory Animal Center (Taipei, Taiwan). All animal studies were conducted based on institutional guidelines and were approved by the Animal Care and Use Committee of Chang Gung University.

### 2.5. In vitro cutaneous absorption

The cutaneous absorption of five TCAs was analyzed using Franz diffusion cell. The excised dorsal skin or cellulose membrane (molecular weight cut-off of 6000–8000 Da, Membrane Filtration Products, Seguin, TX, USA) was mounted on the Franz cell receptor with the SC side facing upward into the donor. The subcutaneous fat was carefully removed for preparing the full-thickness skin. The SC-stripped and desebum skins were prepared according to the method used in previous studies (Zhang et al., 2010; Lin et al., 2016). The cell receptor was 5.5 ml of 30% ethanol in pH 7.4 buffer. The TCAs in 20% PG/pH 7.4 buffer were loaded into the donor compartment (0.5 ml). The permeant concentration in the donor was either the equimolar dose (15 mM) or the saturated solubility. The valid diffusion area was 0.785 cm<sup>2</sup>. The stirring rate and temperature of the receptor were maintained at 600 rpm and 37 °C, respectively. A 300-µl aliquot in the receptor was withdrawn at determined intervals after drug application, followed by an immediate replacement with fresh receptor medium. The skin was extracted at the end of the experiment (24 h). The TCA amount in the skin reservoir and receptor was measured by HPLC. The skin extraction procedure for determining TCA skin deposition was the same as that used in the previous work (Hung et al., 2015).

### 2.6. Hair follicle uptake

TCA accumulation in the hair follicles was determined using an in vitro cutaneous absorption experiment. The skin was stripped by applying adhesive tape 20 times to remove the SC. A drop of ethyl cyanoacrylate superglue (7004T, 3 M) was positioned on a glass slide, which was then pressed onto the surface of the SC-stripped skin. Subsequently, the slide was removed with one quick movement after a 5-min polymerization. The superglue remaining on the slide was scraped off. The casting was positioned in methanol (2 ml) and then shaken for 3 h. The final mixture was placed under a vacuum for methanol evaporation. The mobile phase of HPLC was added to dilute the samples for analysis of the drug amount in the follicles by HPLC.

### 2.7. In vivo pinprick test

The cutaneous analgesia of topical TCAs was assessed based on the cutaneous trunci muscle reflex (Gerner et al., 2006), defined as the reflex movement of the skin over the back produced by twitches of the lateral thoracic spinal muscle in response to a Von Frey filament. A 1.5 × 1.5 cm<sup>2</sup> area on the lumbar region of the nude mouse back was covered with gauze containing TCAs or lidocaine in 20% PG/pH 7.4 buffer at a dose of 15 mM (0.6 ml). After a 2-h administration, we applied six pinpricks at six points within each treatment area with a frequency of 0.5–1.0 Hz and recorded the number to which the mouse failed to respond. The number of times the pinprick failed to induce a reaction was used as the measurement of the analgesic activity of topical TCAs. The maximum value of % possible effect (% PE) was presented as the percentage of maximum possible effect (% MPE). The action duration was estimated as the time from drug removal to full recovery of muscle reflex (0% MPE recorded).

### 2.8. In vivo cutaneous tolerance test

To validate whether the TCAs elicited cutaneous irritation, a 0.3-ml aliquot of 20% PG containing TCAs (15 mM) was spread over a polyethylene cloth (1 × 1 cm<sup>2</sup>) for topical application on the dorsal region of the nude mouse. The cloth was covered with Tegaderm<sup>®</sup> (3 M) and Fixomull<sup>®</sup> adhesive tape (Beiersdorf AG). The TCA-loaded cloth was withdrawn and replaced with a new cloth daily for 7 consecutive days. The skin surface was assessed for transepidermal water loss (TEWL, TM300, Courage and Khazaka), skin redness (a\*, CD100, Yokogawa), and skin pH value (Skin-pH-Meter905, Courage and Khazaka) after removing the cloth. The appearance of the cutaneous surface was photographed using a handheld digital microscope (Mini Scope-V, M&T Optics). After the mouse was sacrificed, the dorsal skin was excised and stained by hematoxylin and eosin (H&E) for histopathological visualization. The skin slices were imaged under a light microscope (IX81, Olympus).

### 2.9. Molecular docking

The crystal structure of ceramide II and ceramide VI was used for molecular docking with TCAs by Discovery Studio<sup>®</sup> version 3.1 (Accelrys, San Diego, CA, USA). The superimposition of the compounds with ceramides was calculated to observe the conformation and ligand-binding activity. The negative CDOCKER energy was computed after conducting the molecular docking simulation of TCAs with ceramides. The pK<sub>a</sub>, hydrogen bond acceptor number, hydrogen bond donor number, and total polarity surface of the TCAs were also estimated by Discovery Studio<sup>®</sup>.

### 2.10. Data analysis

For the in vitro cutaneous absorption, the penetrated TCA amount across the skin into the receptor was plotted as a function of time. The flux (nmol/cm<sup>2</sup>/h) was calculated by the slope of penetrated amount-time curves. The drug-skin deposition was computed as the molar amount per mg of skin (nmol/mg). In the case of the absorption from the saturated solution, the calibrated skin deposition (CSD) and permeability coefficient were calculated from the skin deposition and flux divided by the applied saturated solubility in the donor. This allowed a fair comparison of cutaneous absorption among the TCAs. To evaluate the skin-targeting ability of the propamine TCAs, the dermal/transdermal selectivity index (S value) was measured by an equation of skin deposition/flux and CSD/permeability coefficient for the donor at an equivalent dose (15 mM) and saturated solubility, respectively.

The experimental data were presented as the mean and standard deviation (S.D.). The difference in the data of the different groups was compared using the Kruskal-Wallis test. The post hoc test for checking individual differences was the Dunn's test. A 0.05 level of probability ( $p < 0.05$ ) was recognized as the level of significance.

### 3. Results

#### 3.1. Physicochemical characteristics of the TCAs

The TCAs composing the propamine group were purchased as salt forms and converted into the free bases to examine their physicochemical properties and cutaneous absorption. Table 1 summarizes the molecular weight (MW), melting point, log  $P$ , log  $K'$ , and aqueous saturation solubility of the tested TCAs. The MW ranged between 263 and 315 g/mol, with clomipramine exhibiting the largest molecular size. Desipramine and nortriptyline had the highest melting point (214 °C and 213 °C), followed by clomipramine, imipramine, and protriptyline. The tertiary amine TCAs revealed a greater log  $P$  than the secondary amine TCAs. The presence of chlorine in the structure increased the partition coefficient (clomipramine versus imipramine). With respect to the secondary amine TCAs, the difference in the double bond positions caused a different log  $P$  (protriptyline versus nortriptyline). In addition to log  $P$ , the lipophilicity can be ranked by log  $K'$ . The trend of log  $K'$  was similar to that of log  $P$ . Desipramine has two nitrogen atoms, a higher number than were identified in the other secondary amine TCAs. The extra nitrogen contributed to a lower log  $K'$  of desipramine, although the log  $P$  of desipramine was slightly higher than that of protriptyline. This is because the molecular size also affects the partition coefficient of the homologous analogues, with higher MW presenting the greater log  $P$  (Geinoz et al., 2004). The saturated solubility of the compounds in PG/pH 7.4 buffer was determined after shaking for 24 h. Table 1 shows a higher aqueous solubility of secondary amine TCAs than tertiary amine TCAs. The compounds with higher lipophilicity demonstrated lower solubility. The predicted dissociation constant ( $pK_a$ ) shown in Table 1 demonstrates that desipramine, imipramine, and clomipramine have two values due to the two nitrogen atoms in the structure. The  $pK_a$  results indicated that the majority of the TCAs in the pH 7.4 environment would be positively ionized in the nitrogen in the alkyl chain. The ionization of nitrogen in the seven-member ring is difficult at pH 7.4 because of the secondary  $pK_a$  at 6.58.

#### 3.2. In vitro cutaneous absorption

Cutaneous absorption of the TCAs was compared by Franz cell assembly. Both the skin deposition and penetration across the skin were evaluated. The permeant absorption by the skin can be

measured by skin deposition whereas the cumulative amount in the receptor anticipates delivery into the systemic circulation. We confirmed that the receptor phase provided a sink condition. The donor TCA concentration was first fixed at an equivalent dose (15 mM). This dose was greater than the saturated solubility in 20% PG. Fig. 2A and B depicts the permeation parameters of TCAs at a molar equivalent using pig skin and nude mouse skin as the barrier, respectively. Pig and nude mouse skins were chosen as the permeation barriers because they have skin morphology and hair sparseness similar to human skin (Lin et al., 2013). As depicted in Fig. 2A, the pig skin deposition of secondary amine TCAs is greater than for tertiary amine drugs. A similar tendency was observed for flux. The flux calculated by the receptor amount fit a zero-order pattern.

The  $S$  value is an index specifying the selectivity between cutaneous targeting and transdermal delivery across the skin. A high  $S$  value represents drug targeting to the skin with less systemic effect. Of the TCAs tested, nortriptyline and clomipramine demonstrated the greatest  $S$  value in pig skin (Fig. 2A). The difference between the  $S$  value of nortriptyline and clomipramine was not statistically significant. As depicted in Fig. 2B, the nude mouse skin displayed less barrier function than pig skin. As with the pig skin, protriptyline (10.0 nmol/mg) and nortriptyline (10.7 nmol/mg) presented a higher mouse skin deposition than the other drugs. The flux across the mouse skin decreased following the increase of TCA lipophilicity. Clomipramine demonstrated a much higher  $S$  value than the other permeants. The  $S$  value of clomipramine was significantly greater than the  $S$  value of the other TCAs by approximately 6-fold.

The TCAs in the donor were also dosed with saturated solutions to maintain a constant driving force with maximum thermodynamic activity. Figs. 3A and B presents the CSD and permeability coefficient in pig skin and mouse skin, respectively. There were some differences in the tendency between the equimolar and saturated TCA doses. As illustrated in Fig. 3A and B, the increase in lipophilicity contributed to the increase of CSD. Imipramine and clomipramine, the permeants with tertiary amine moiety, generally displayed less of a permeability coefficient than the secondary amine TCAs. An exception was that protriptyline, one of the secondary amine compounds, exhibited a comparable permeability coefficient to the tertiary amine TCAs in the case of pig skin. The permeants with a lower permeability coefficient displayed a higher  $S$  value of pig skin, with clomipramine demonstrating the greatest  $S$  value (0.37). Clomipramine also manifested a high  $S$  value with mouse skin (1.30) relative to the other permeants.

#### 3.3. Permeation pathways of TCAs

The possible permeation pathways and mechanisms of TCAs were elucidated by examining the cutaneous absorption via SC-stripped and desebum pig skins. The role of appendageal routes for

**Table 1**  
Physicochemical properties of tricyclic antidepressants with propamine moiety.

Compound	MW <sup>a</sup> (g/mol)	M.P. <sup>b</sup> (°C)	log $P$ <sup>c</sup>	log $K'$ <sup>d</sup>	Solubility in 20% PG <sup>e</sup> (mM)	$pK_a$ <sup>f</sup>
Desipramine	266.4	214	1.33 ± 0.11	0.38	5.85 ± 0.37	6.58/10.65
Protriptyline	263.4	169	1.16 ± 0.04	0.39	5.55 ± 0.47	9.31
Nortriptyline	263.4	213	1.60 ± 0.06	0.43	5.39 ± 0.01	10.11
Imipramine	280.4	174	1.97 ± 0.06	0.43	2.67 ± 0.22	6.58/9.92
Clomipramine	314.9	192	2.20 ± 0.38	0.61	1.15 ± 0.09	6.58/10.45

<sup>a</sup> MW, molecular weight.

<sup>b</sup> M.P., melting point obtained from DrugBank Database ([www.drugbank.ca](http://www.drugbank.ca)).

<sup>c</sup> log  $P$ , n-octanol/water partition coefficient.

<sup>d</sup> log  $K'$ , logarithm of  $t_r - t_0/t_0$ ,  $t_r$  is the retention time of compound peak,  $t_0$  is the retention time of solvent peak.

<sup>e</sup> PG, propylene glycol.

<sup>f</sup>  $pK_a$  was calculated by Discovery Studio<sup>®</sup> 3.1.

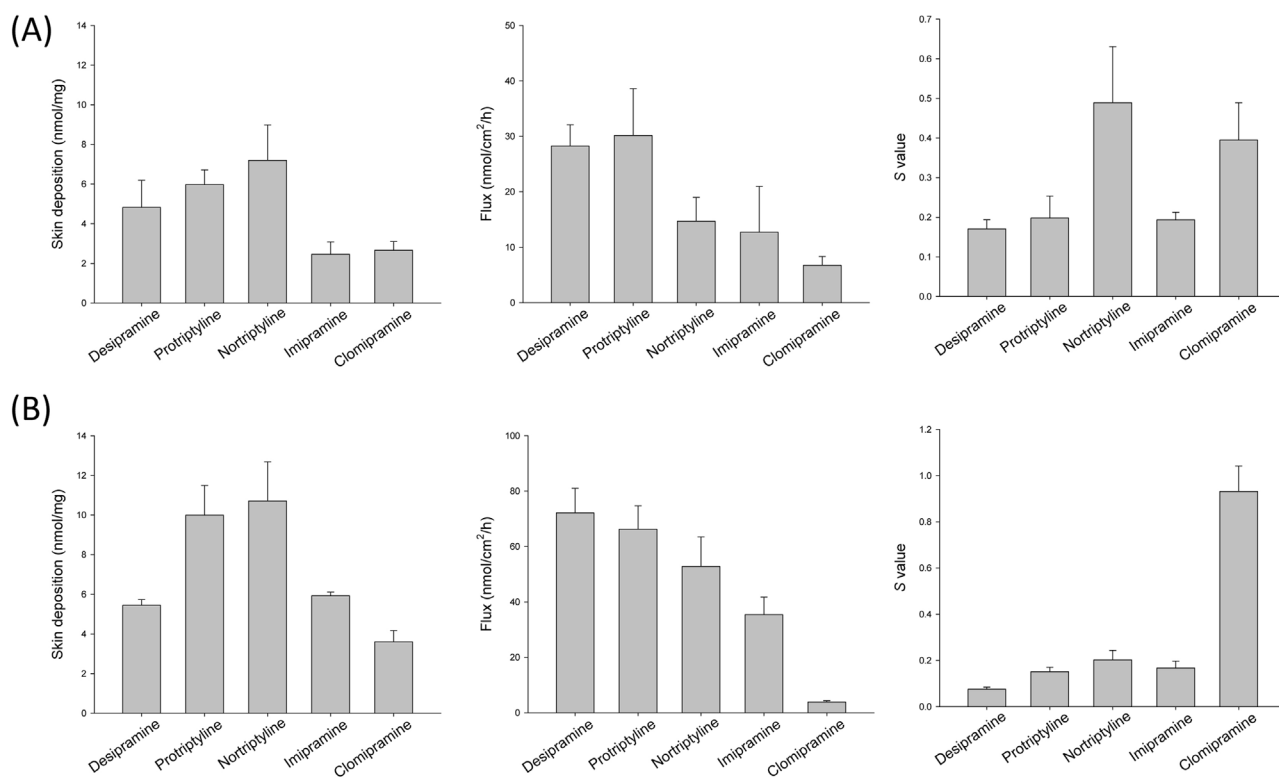


**Fig. 2.** Skin deposition, flux, and S value of tricyclic antidepressants at a dose of 15 mM after topical treatment on pig and nude mouse skins: (A) pig skin; and (B) nude mouse skin. The donor vehicle is 20% propylene glycol in pH 7.4 buffer. All data are presented as the mean of four experiments  $\pm$  S.D.

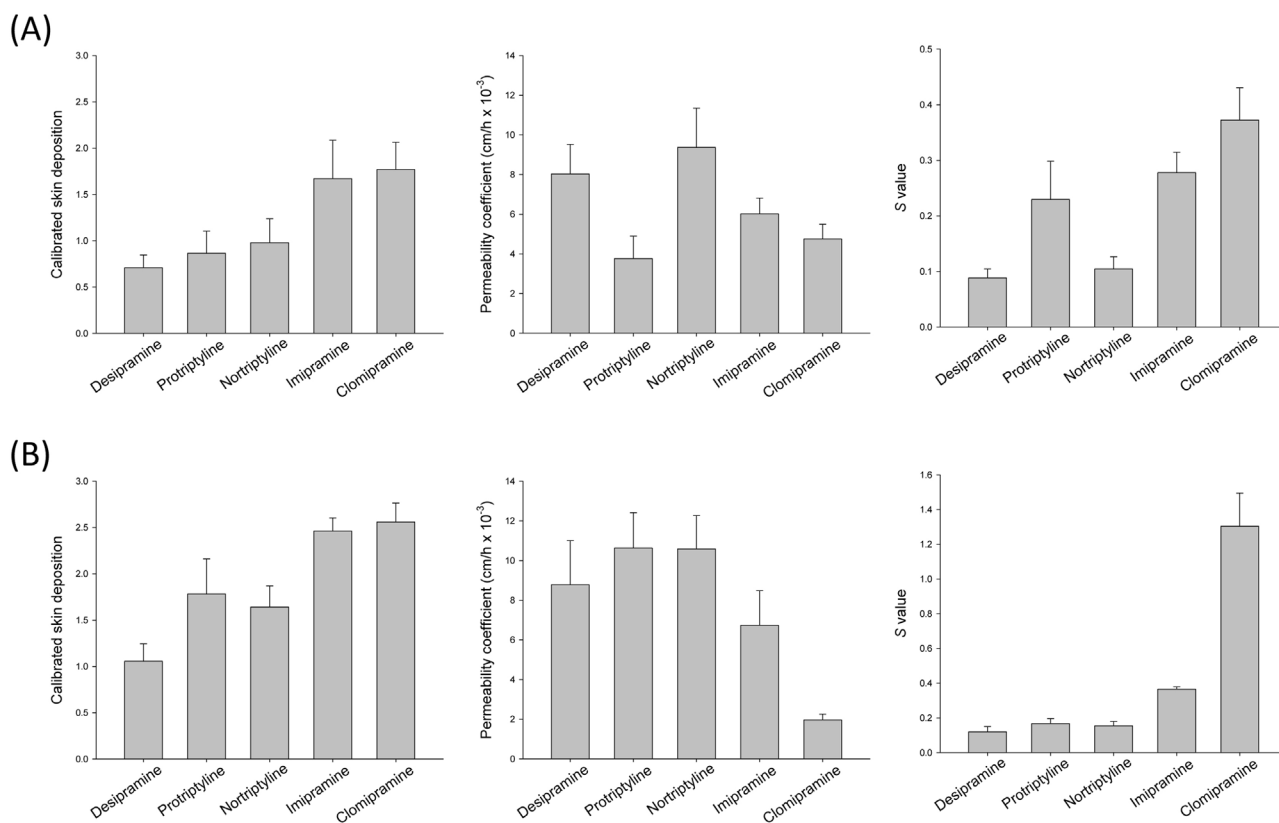


**Fig. 3.** Calibrated skin deposition (CSD), permeability coefficient, and S value of tricyclic antidepressants at a dose of saturated solubility after topical treatment on pig and nude mouse skins: (A) pig skin; and (B) nude mouse skin. The donor vehicle is 20% propylene glycol in pH 7.4 buffer. All data are presented as the mean of four experiments  $\pm$  S.D.



TCA absorption was assessed by determining drug uptake into the hair follicles. Desipramine, nortriptyline and clomipramine at the equimolar dose were selected as the donors in this experiment. Fig. 4A shows the released amount of TCAs in the receptor that penetrated the cellulose membrane. The transport through the cellulose membrane is an indicator of permeant release from the vehicle, which is a delivery stage before drug partitioning from the vehicle to the SC. The released amount increased following the increase in application time. The released TCAs represented a ceiling effect after an 8-h application. It can be observed that the more-lipophilic compounds demonstrated a lower release amount. The released amount at 24 h for desipramine, nortriptyline, and clomipramine was 2131, 1744, and 265 nmol/cm<sup>2</sup>, respectively. Fig. 4B illustrates the ratio of drug deposition in the SC-stripped and intact skin. Desipramine deposition in the SC-stripped skin was 1.5-fold higher than in the intact skin ( $p < 0.05$ ).

The extent of nortriptyline and clomipramine deposition in the SC-stripped skin did not substantially differ from the amount in the untreated skin.

Fig. 4C depicts the fold change of cutaneous deposition after sebum removal from the pig skin. The desebum process significantly assisted desipramine absorption into the skin reservoir ( $p < 0.05$ ). Sebum removal lowered the skin deposition of the more lipophilic TCAs such as nortriptyline and clomipramine ( $p < 0.05$ ). Table 2 summarizes the TCA uptake in the hair follicles. Nortriptyline, followed by clomipramine and desipramine, demonstrated the highest follicular uptake (8.6 nmol/cm<sup>2</sup>) in pig skin. There was no significant difference between the follicular accumulation of clomipramine and desipramine. As with pig skin, nortriptyline exhibited the highest uptake in the follicles of mouse skin (10.6 nmol/cm<sup>2</sup>). Clomipramine demonstrated a follicular uptake approximating the follicular desipramine stock.

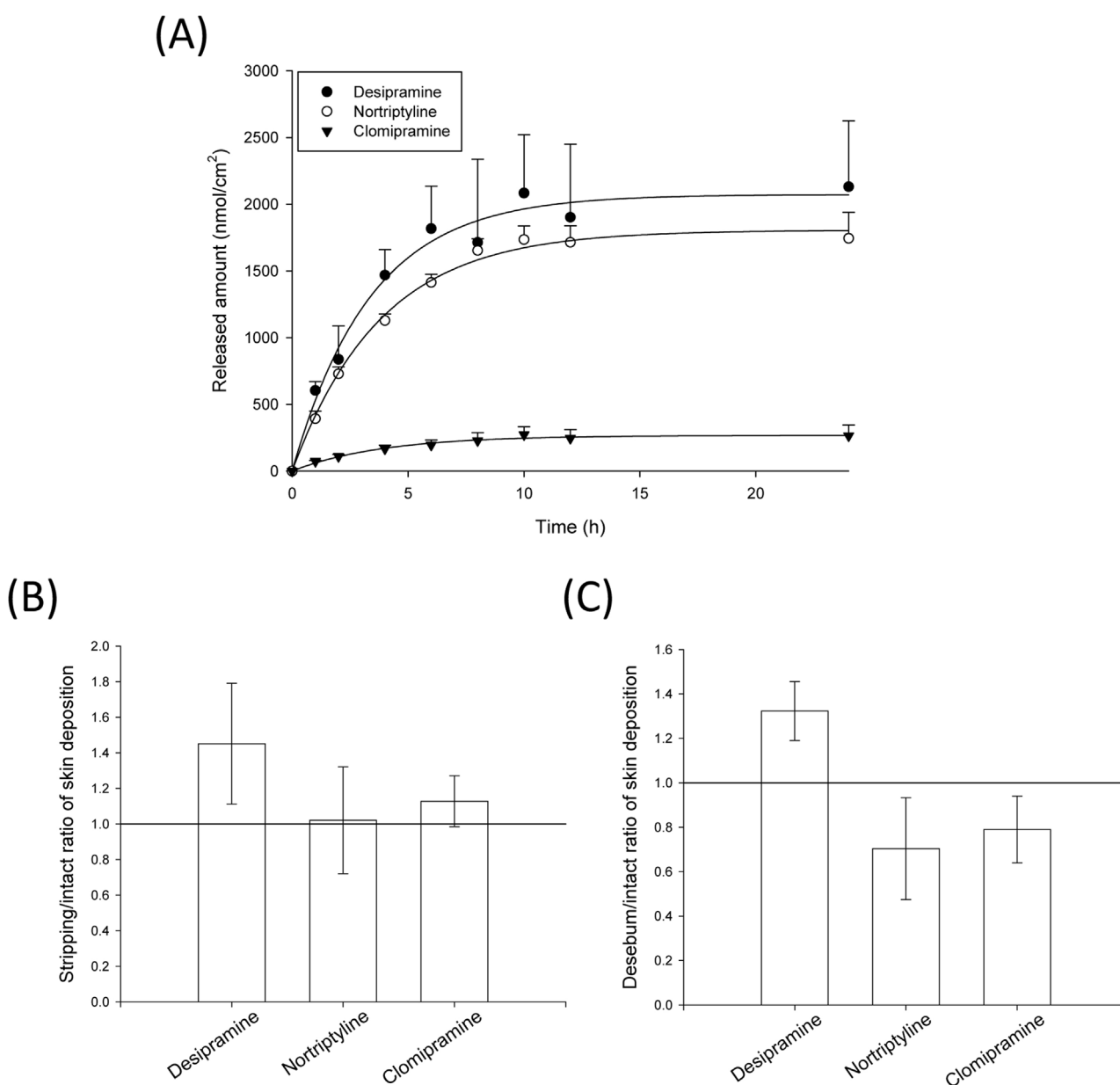


**Fig. 4.** The released amount and skin deposition of tricyclic antidepressants (15 mM) via cellulose membrane, stratum corneum (SC)-stripped skin, and desebum skin: (A) released amount-time profiles of cellulose membrane; (B) ratio of skin deposition between SC-stripped skin and intact skin; and (C) ratio of skin deposition between desebum skin and intact skin. All data are presented as the mean of four experiments  $\pm$  S.D.

**Table 2**

The follicular accumulation (nmol/cm<sup>2</sup>) of tricyclic antidepressants with propamine moiety after in vitro skin delivery at an infinite dose (15 mM).

Compound	Pig skin	Nude mouse skin
Desipramine	2.64 ± 0.13	3.64 ± 0.90
Nortriptyline	8.57 ± 3.26	10.58 ± 2.09
Clomipramine	3.63 ± 0.94	9.23 ± 1.85

The data represent the mean ± S.D. (n = 4).

### 3.4. In vivo pinprick test

The analgesic activity of desipramine, nortriptyline, and clomipramine was detected in nude mice by estimating pinprick scores. Fig. 5A presents the time course of cutaneous analgesia after topical administration of TCAs for 2 h. The local anesthetic, lidocaine, at a dose of 15 mM, was used as the positive control. The mice receiving topical lidocaine presented a high% MPE of approximately 90% at the initial stage (Fig. 5B). Clomipramine demonstrated a% MPE of approximately 30% at the beginning of the pinprick test. A large variation in analgesic response was observed for the desipramine and nortriptyline groups. Three of the six mice in the desipramine group demonstrated an analgesic response for 5 min. In the topical nortriptyline group, two of the six mice showed an analgesic response for only 2 min. Fig. 5C displays the time to full recovery for clomipramine and lidocaine. The antinociceptive effect of clomipramine lasted for 240 min. Lidocaine exposure showed an analgesic effect for only 60 min.

### 3.5. In vivo cutaneous tolerance test

Skin irritation hinders topical drug application although a successful therapy is nevertheless accomplished. The cutaneous tolerance of propamine TCAs was investigated in vivo based on the analysis of TEWL, skin redness, skin surface appearance, and histopathology. The nude mouse skin was challenged by the drugs for 7 consecutive days. We assessed TEWL as a measure of SC barrier integrity as shown in Fig. 6A. No TEWL increase was observed for TCA application compared to the control. The redness and skin pH value recorded after the completion of a 7-day treatment did not reveal any significant change. Fig. 6B shows the close-up images of the cutaneous surface. The appearance of nortriptyline-treated skin was nearly normal. Exposure to desipramine and clomipramine resulted in a rough and scaly surface, suggesting some detachment of skin components. The desipramine-treated skin exerted the most scaling on skin surface with some erythema. Although we could visualize the erythema in the desipramine-treated skin, the determination of skin redness by a\* might be interrupted by the white scaling in some regions of skin

surface. This led to the offset of higher a\* by scaling and a large error bar of a\* as shown in Fig. 6A.

Fig. 6C demonstrates the H&E-stained histology of nude mouse skin. The microscopic visualization showed an undamaged morphology of untreated skin. In cases of desipramine- and clomipramine-treated skins, desquamation was detected on the skin surface (arrows in Fig. 6C). This observation was consistent with the close-up pictures. Desipramine and clomipramine exhibited no morphological change in the viable epidermis/dermis. There was perivascular neutrophil infiltration in the upper dermis after nortriptyline exposure (rectangles in Fig. 6C), indicating an acute inflammation. This inflammation, however, could be classified as mild.

### 3.6. Molecular docking

A highly informative elucidation exploring the effect of lipophilicity on absorption is based on the hydrogen bond number and the total polarity surface measured by molecular modeling. Table 3 shows these parameters measured by Discovery Studio 3.1 (Accelrys). Desipramine, imipramine, and clomipramine possessed two hydrogen bond acceptors whereas the number for protriptyline and nortriptyline was only one. No hydrogen bond donor number was detected for tertiary amine drugs. The total polarity surface was increased following the decrease of lipophilicity. The TCA-ceramide interaction was further inspected by a computational study of best docking poses. Fig. 7A and B demonstrates the superimposition of TCAs with ceramide II and ceramide VI, respectively. All TCAs exhibited the ligand-binding activity to ceramides but in different conformations. The negative CDOCKER energy was compared after conducting the molecular docking simulation of TCAs with the lipids, as shown in Table 3. The more negative energy indicates a stronger binding interaction. There was a correlation between the CDOCKER and skin deposition of TCAs either for ceramide II or for ceramide VI.

## 4. Discussion

Patients with neuropathic pain always show an unsatisfactory response to pharmacological treatments. Only 40%–60% of patients achieve complete or partial pain relief (Gilron et al., 2015). Currently, the effect of topical drug administration for local analgesia is limited because of the drugs' short analgesic duration and poor absorption (Sandig et al., 2013). A search for new drug therapies is therefore urgent. We attempted to evaluate the skin absorption of propamine TCAs as the candidate analgesics. The use of skin retention data for analyzing SPR has been reported in some investigations; however, their use is limited. The present study was

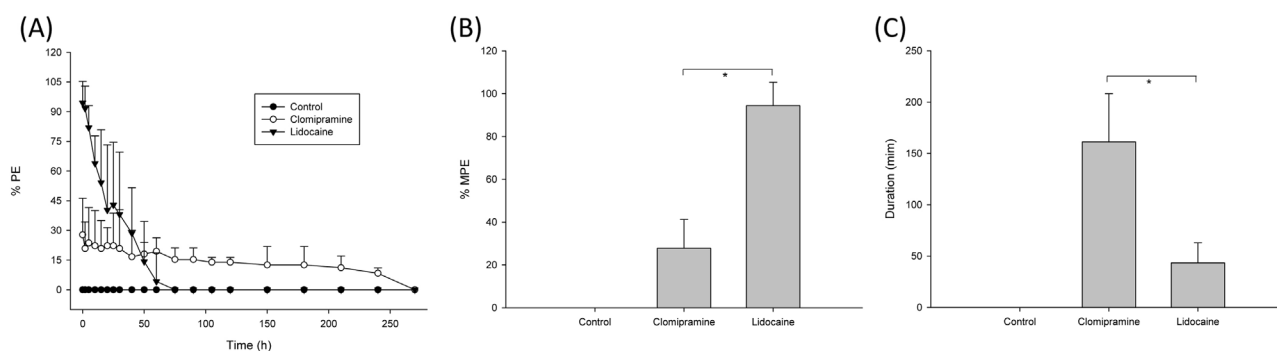


**Fig. 5.** In vivo cutaneous analgesia of clomipramine and lidocaine (15 mM) after topical application on nude mouse back for 2 h: (A) time-course of cutaneous analgesia (% PE); (B) percentage of the maximal possible effect (% MPE); and (C) time required for full recovery from cutaneous analgesia. \*,  $p < 0.05$ . All data are presented as the mean of six experiments ± S.D.

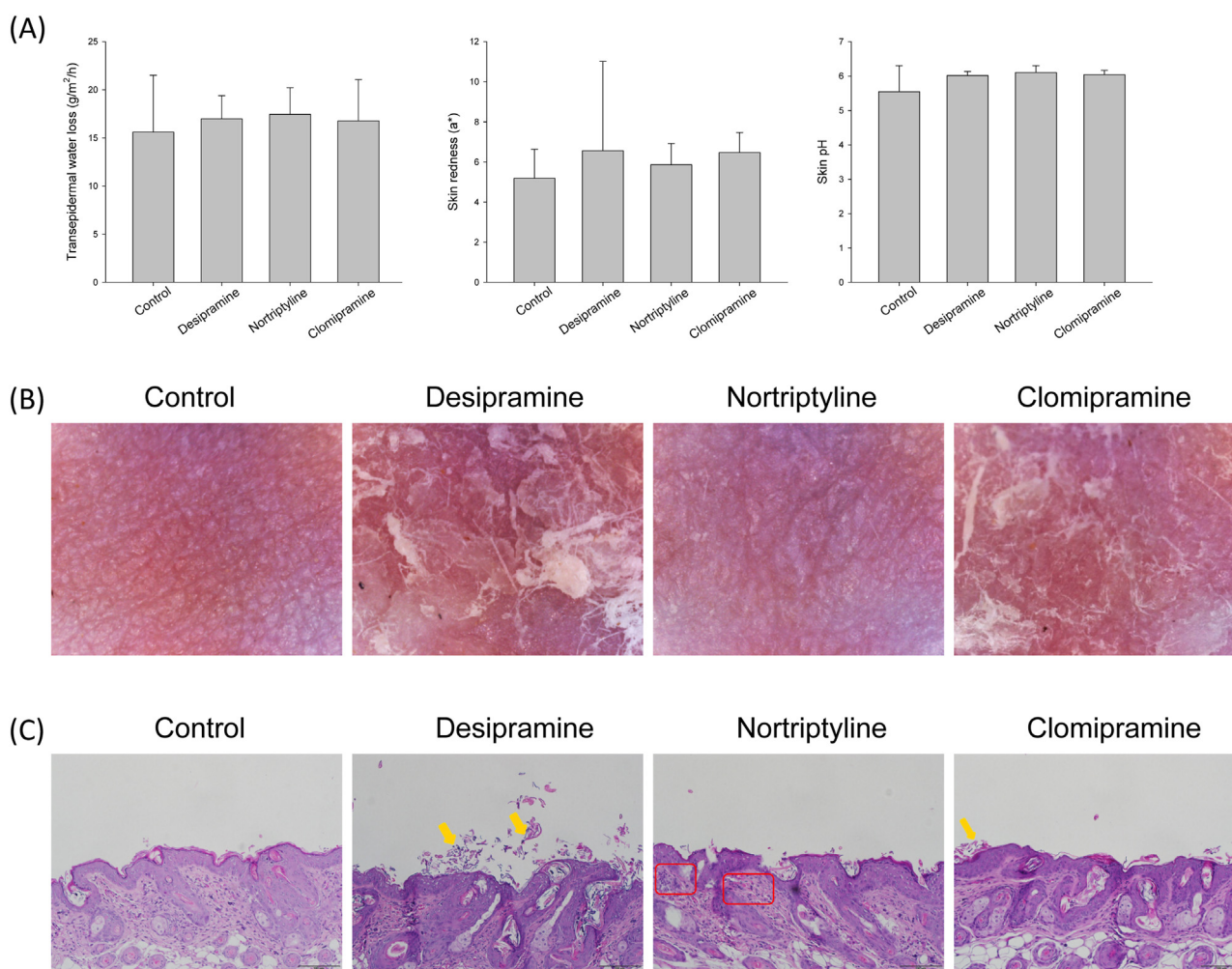


**Fig. 6.** In vivo nude mouse skin tolerance examination after a 7-day application of topically applied tricyclic antidepressants (15 mM): (A) transepidermal water loss (TEWL), skin redness ( $a^*$ ), and skin surface pH; (B) the close-up images; and (C) histopathology. The data in Fig. 6A are presented as the mean of six experiments  $\pm$  S.D.

**Table 3**

The hydrogen bond number, total polarity surface, and negative CDOCKER energy of tricyclic antidepressants with propamine moiety determined by molecular modeling.

Compound	Hydrogen bond accept number	Hydrogen bond donor number	Total polarity surface	–CDOCKER energy ceramide II	–CDOCKER energy ceramide VI
Desipramine	2	1	15.27	–13.59	–20.32
Protriptyline	1	1	12.03	–15.39	–23.65
Nortriptyline	1	1	12.03	–13.77	–17.54
Imipramine	2	0	6.48	–17.44	–24.70
Clomipramine	2	0	6.48	–19.46	–26.52

undertaken to change this insufficiency. The pH 7.4 buffer containing 20% PG was the donor vehicle for the tested TCAs because most attempts at modeling SPR have been based on the data of aqueous solution exposure (Riviere and Brooks, 2011). Our experimental results demonstrated that the structures of the TCAs greatly affected the cutaneous absorption, even though the structures were homologous. The physicochemical characteristics of the TCAs, including their lipophilicity, aqueous solubility, molecular size, and hydrogen bond number, could influence their skin delivery ability. Clomipramine was more efficacious with respect to targeting into the skin according to the  $S$  value. Clomipramine also caused a tolerable amount of skin irritation.

Desipramine and nortriptyline are the oral TCAs used for pain management in dermatology (Enamandram et al., 2015). The

administered dose for pain relief is equivalent for desipramine and nortriptyline. The tertiary amine TCAs, including imipramine and clomipramine, have been shown to reduce chronic pain via inducible nitric oxide synthase (iNOS) and serotonin release inhibition (Farghaly et al., 2012; Ferjan and Lipnik-Stangelj, 2013). The clinical trials also demonstrate the usefulness of nortriptyline for relieving neuropathic pain although this indication is not approved by USFDA (Gilron et al., 2009). To the best of our knowledge, no systemic examination of cutaneous absorption of the propamine TCAs has previously been presented. In the case of saturated solubility as the dose, the skin retention of TCAs increased following the increase of lipophilicity. The correlation coefficient between the skin deposition and log  $P$  for pig and mouse skin was 0.94 and 0.82, respectively. Clomipramine was the

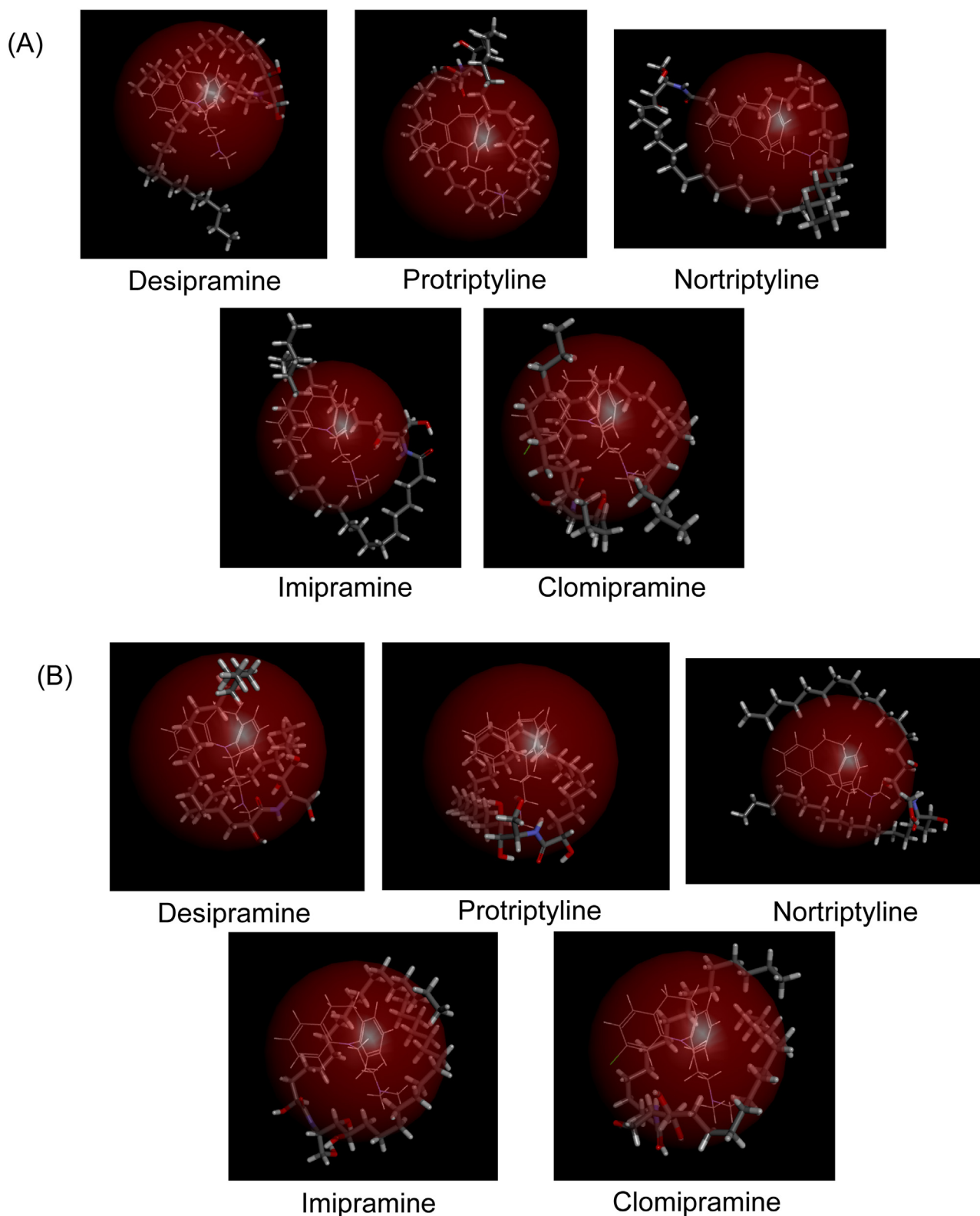


**Fig. 7.** Superimposition of the computed poses for the tricyclic antidepressants and ceramides: (A) tricyclic antidepressants and ceramide II; and (B) tricyclic antidepressants and ceramide VI.

permeant with the greatest deposition and cutaneous targeting. The SC is essentially a lipidic layer, which is regarded as the primary permeation barrier of the skin. A permeant's initial process to achieve skin permeation is the partitioning from the vehicle into the SC. Both  $\log P$  and  $\log K'$  can act as the factors

predicting permeant absorption from aqueous dispersion to the SC (Liu et al., 2011). The  $\log P$  and  $\log K'$  of the tertiary amine TCAs were higher than of the secondary amines, ensuring facile skin retention because of the enhanced lipophilicity for partitioning to the SC. The partitioning effect is more prominent when using PG as



a component of the vehicle because PG appears to demonstrate an enhancement mode for permeant partitioning (Diez-Sales et al., 2005).

Contrary to the case of a saturated solubility dose in the donor, a parabolic correlation was found between skin deposition and TCA lipophilicity for the dose that exceeded the saturated solubility (15 mM). This result suggests that the permeant concentration in the donor governed the pattern of skin retention. The data cannot be interpreted by considering only the lipophilicity. Aqueous solubility is a driving force for skin delivery (Kasting, 2013). The permeant should be in the solubilized state to cross the biomembrane. The tertiary amine TCAs of imipramine and clomipramine had a low solubility in the vehicle. The TCA transport across the cellulose membrane at the equivalent dose indicated drug release from the vehicle. Because of the absence of a skin barrier, the solubility in the vehicle is a critical factor for TCA release. The correlation coefficient between the released amount at 24 h and the solubility was 0.99 for the propamine TCAs. The results indicated a decreased release following the increase of  $\log P$ , which coincided with our inference. Another effect of low solubility is the creation of an extra barrier on the skin surface by the precipitate film of the non-dissolved permeants (Liu et al., 2016). Most models for investigating SPR are based on the permeation data obtained from the saturated solubility or a fraction of saturated solubility (Moss et al., 2002; Geinoz et al., 2004). Thus, the influence of solubility can be ignored in these cases. The permeation profiles after calibration by saturated solubility (CSD and permeability coefficient) imply the real absorption capability of the permeants.

The propamine TCAs with higher lipophilicity generally displayed a lower flux or permeability coefficient. For instance, the correlation coefficient between the flux and  $\log P$  was  $-0.96$  and  $-0.95$  for pig and mouse skin, indicating a reverse relationship between penetration into receptor and the lipophilicity. The penetration across the skin may have been minimized because the drug largely resided in the skin tissue. The more-lipophilic permeants easily partitioned into the SC but had difficulty partitioning from the SC to the viable skin because of the aqueous barrier function (Doan et al., 2010). This could have resulted in restricted penetration across the skin. Yamaguchi et al. (2008) demonstrated that the permeant diffusion from the SC to viable skin was reduced as the  $\log P$  increased for  $\log P > 1$ . According to the TCA deposition in the SC-stripped skin, desipramine skin retention significantly increased in the absence of SC. This suggests an easy partition and diffusion of this less-lipophilic TCA into the viable epidermis. However, SC stripping did not affect the cutaneous absorption of nortriptyline and clomipramine, demonstrating that the more-lipophilic TCAs overcome the SC barrier. The major resistance for more-lipophilic TCAs can be viable skin.

According to the Stokes-Einstein equation, the MW plays a distinct role in skin transport, particularly in the flux (Grice and Benson, 2013). The permeant diffusivity across the skin is size-dependent, with the large molecules displaying relatively slow diffusion to the receptor. Our results indicated less penetration into the receptor for the TCAs with larger molecular sizes although their molecular weight range was narrow. With respect to nude mouse skin delivery, the correlation coefficient was calculated as 0.94 and 0.98 between the penetration into receptor and MW for infinite and saturated dose, respectively. When a permeant traverses the skin from a liquid phase, it partially associates with the solvent cage from the applied dose. The detected penetration rate relates not only to the permeant itself but also to the overall solvated complex (Heard et al., 2003). Although the MW of tested TCAs fell into an appropriate range for cutaneous delivery ( $<500$  g/mol), the solvated complex may enlarge the molecular volume of the permeant. This possibility was unfavorable to a further degree to

the penetration across the skin as well as to the influence of lipophilicity. The MW appeared to affect permeant penetration across the skin rather than retention within the skin.

Lipophilicity and molecular size are the net results involving skin permeation. It should be noted that these factors may not completely reflect the permeation because the intermolecular forces between the permeants and the skin components associate with the permeant interaction with the skin. The SC includes two fundamental domains: the lipophilic lipid tails offer a nonpolar environment for transport, and the intercellular lipid polar head groups and corneocytes provide a polar environment. Ceramides are the predominant lipids in the SC. The head groups of ceramides can form dramatic hydrogen bonding to the permeants (Liu et al., 2011; Hsieh et al., 2012). The compounds' hydrogen bonding characters, including the hydrogen bond acceptor number and the hydrogen bond donor number, have been recognized as affecting skin delivery. Although the intermolecular hydrogen bonding between permeants and ceramides can increase retention in the SC, too high a hydrogen bond number in the permeants may hinder the diffusion because of the reduced permeant transport into the nonpolar region of the SC (Patel et al., 2002). The tertiary amine TCAs have two acceptor numbers of a hydrogen bond with no donor number. There is one donor number for the secondary amine TCAs. This indicates that the hydrogen bond acceptor was helpful in increasing polar interaction with ceramides, thus increasing skin deposition. Conversely, poor skin retention was observed in the presence of a hydrogen bond donor in the case of propamine TCA absorption. The parameter of the total polarity surface also indicates the unfavorable skin retention of the TCAs with higher polarity on their molecular surface. The values of correlation coefficient between CSD and total polarity surface of pig and mouse skin was  $-0.98$  and  $-0.99$ , respectively. The importance of the hydrogen bond acceptor number as the predictor of skin permeation was previously reported (Magnusson et al., 2004; Grice and Benson, 2013).

The ionized and nonionized forms of a permeant can affect the skin permeation. Generally, the nonionized molecules are easily absorbed by SC rather than ionic molecules because of the lipophilic affinity to SC lipids (Hadgraft and Valenta, 2000). However, the aqueous solubility of the ionized form is higher than the unionized form. The maximum skin delivery may occur at a pH with optimum vehicle environment. It is predicted that the majority of TCAs were ionized in the donor vehicle (pH 7.4) because of the  $pK_a$  at 9–10. Desipramine and clomipramine displayed higher  $pK_a$  than other TCAs. This result indicates that both compounds were more ionized at pH 7.4, which may contribute to the lower skin deposition of both compounds at the dose of 15 mM. However, the CSD of clomipramine was the highest among TCAs at the dose of saturated solubility. Protriptyline is the drug with the lowest  $pK_a$  value. The more unionized protriptyline at pH 7.4 led to the high skin absorption at the dose of 15 mM. This nonionized effect did not increase protriptyline absorption when compared with CSD. The ionized/nonionized proportion can be demonstrated to influence TCA delivery at high dose (suspension type) but not at low dose (solution type). Further study is required to explore the detailed mechanisms regarding the effect of  $pK_a$  on TCA absorption.

A more negative energy demonstrates a stable system for a likely binding interaction (Lee et al., 2014). We observed a correlation between the negative CDocker energy and TCA skin retention, with clomipramine demonstrating the highest energy and CSD. The correlation coefficient between CSD and negative CDocker energy of ceramide II was 0.93 for both pig and nude mouse skins. Moreover, the negative CDocker energy of tertiary amine TCAs was greater than the energy of secondary amine drugs, which was consistent with the trend of cutaneous absorption. This



result suggests that the docking approach can be exploited for anticipating the skin delivery of TCAs.

A balance of lipophilicity and hydrophilicity influences a permeant to achieve a maximum degree of skin transport. It is well known that a convex relationship exists between the permeation of chemicals and  $\log P$ , peaking at a  $\log P$  of 2–3 (Zhang et al., 2009; Riviere and Brooks, 2011). Our results were consistent with this rule because clomipramine, representing the TCAs with the greatest absorption, possessed a  $\log P$  of 2.2. The pilosebaceous glands secrete sebum, an oily substance that spreads on the SC surface and inside the hair follicles. Sebum was demonstrated to be an essential determinant in the drug partitioning to the SC (Schneider et al., 2016). Sebum removal significantly increased the desipramine deposition compared with the deposition in untreated skin, signifying a laborious partitioning of this drug into the sebum. Clomipramine exhibited poorer absorption after sebum removal, indicating the importance of sebum existence for clomipramine partitioning to the skin and subsequent diffusion. The higher CSD of clomipramine than other TCAs may be partially attributable to the easy partitioning to the sebum on the skin surface. The easy sebum partitioning of clomipramine also reflected its selectivity to the hair follicles, where the sebum resides. The experimental results showed a significant uptake of nortriptyline and clomipramine by the follicles, suggesting appendageal pathways for skin delivery. Although the follicles only occupy approximately 0.1% of the skin area, this pathway is nevertheless important for the selected permeation of hydrophilic molecules, macromolecules, and nanoparticles (Patzelt and Lademann, 2013). The follicular epithelium is much more permeable than the perifollicular epidermis. The high skin deposition of clomipramine may partially result from the entrance into the follicular infundibulum.

The difference in propamine TCA structures may affect their ability to enter the skin. The structural difference between nortriptyline and desipramine is the replacement of nitrogen with carbon in the seven-member ring. This replacement increased the CSD. Whether the double bond was in the propamine chain (nortriptyline) or in the seven-member ring (protriptyline) did not significantly influence cutaneous absorption. As expected, the additional carbon in the propamine chain (imipramine versus desipramine) promoted CSD but reduced the permeability coefficient. The incorporation of chlorine into the structure (clomipramine versus imipramine) did not alter the CSD. However, the halogenated TCA showed less penetration into the receptor than imipramine. This may be because of the higher MW and the more steric structure of clomipramine than imipramine. The melting point decrease of the homologous series of permeants can cause a weaker cohesiveness of the crystalline lattice structure, resulting in the ability to permeate the skin (Musazzi et al., 2015). This situation is not the case with propamine TCAs because there was no correlation between cutaneous absorption and the melting point. The influence of the melting point on cutaneous permeation is observed when the melting points of the drugs are inversely proportional to their lipophilicity and solubilization in skin lipids (Karande and Mitragotri, 2009). Because no relationship between the melting point and lipophilicity was detected, the cohesion and crystallinity of TCAs were not key determinants for their delivery.

The free nerve endings of pain are principally located within or beneath the epidermis. The rational strategy of choosing topical TCAs for skin analgesia should involve a drug with high retention in the epidermis and low penetration through the skin to diminish the adverse effects in systemic circulation. It is assumed that a high  $S$  value relates to a prolonged drug residence duration at the target area. The permeation profiles exhibited a superior  $S$  value of clomipramine compared with the other TCAs. This situation was particularly true for the nude mouse skin data. The thickness and

permeability of mouse skin are relatively low compared with human skin. The measurement of  $S$  value from nude mouse skin is specifically advantageous for selecting topical permeants because of the overestimation of the systemic levels (Lin et al., 2012). Amitriptyline is a topical TCA used for relief of skin pain and can induce systemic side effects such as drowsiness and cardiac toxicity (Scheinfield, 2014). Clomipramine may be an ideal candidate for achieving a satisfactory therapy with fewer systemic effects.

Patients who have neuropathic pain often do not respond to treatments with local anesthetics or analgesics due to inadequate dosage and duration (Jackson and Damm, 2011). The analgesic duration of a topical EMLA cream (lidocaine and prilocaine) is only 1–2 h. Our results in nude mice confirmed this short analgesic period with topical lidocaine. A mild and short-lasting analgesic effect was observed with topical amitriptyline (Dualé et al., 2008). To prolong local analgesia, improvement of topical antinociceptive treatment is crucial. Desipramine and nortriptyline manifested a deficient analgesia in the pinprick test. Clomipramine had a longer action duration than lidocaine although the % PE of topical clomipramine was incomplete. This result indicates that clomipramine may dissociate more slowly from its binding site of the sodium channel blockade than lidocaine. Because the skin deposition of clomipramine at the equivalent dose was lower than that for other TCAs, the superior analgesia of clomipramine may be a result of the more potent binding to the channel but not the cutaneous amount. Hair follicles contribute to a drug reservoir with long-term storage (Blume-Peytavi and Vogt, 2011). The high accumulation of clomipramine in the follicles further prolonged drug retention in the skin. The drug could diffuse from the follicles to the epidermis to produce pharmacological action.

No evidence of SC impairment was discovered after topical TCA application. The topical TCAs such as amitriptyline can induce some skin irritation, including erythema, burning, and itching (Thompson and Brooks, 2015). These symptoms were not noted in the TCAs tested, except for a scaly surface observed in the desipramine- and clomipramine-treated skins. The tolerance study conducted in this work required a consecutive-7-day treatment with the TCAs. The irritation incidence produced by the drugs would be low in practical use.

## 5. Conclusions

The present study investigated the skin permeation abilities of TCAs containing propamine moiety to select candidates with superior and prolonged skin analgesia for the development of topical agents to treat cutaneous pain. We explored the relationship between the physicochemical properties of TCAs and absorption. The lipophilicity, aqueous solubility, and molecular size affected TCA absorption. With respect to the TCA structures, the replacement of nitrogen with carbon and the presence of chlorine increased the permeation. Our data indicated a higher absorption of tertiary amine TCAs than secondary amine TCAs. Clomipramine generally demonstrated the greatest skin absorption and targeting after excluding the influence of solubility. Compared with lidocaine, clomipramine displayed a long-lasting analgesia in nude mice. This halogenated TCA is considered a powerful analgesic for topical dermal application. The design of appropriate formulations is the next step for further application. The results obtained in this study are beneficial to the development of topical agents for cutaneous pain relief.

## Acknowledgement

The authors are grateful for the financial support from Chang Gung Memorial Hospital, Keelung (CMRPG2F0291-2).

## References

- Blume-Peytavi, U., Vogt, A., 2011. Human hair follicle: reservoir function and selective targeting. *Br. J. Dermatol.* 165, 13–17.
- Díez-Sales, O., Garrigues, T.M., Herráez, J.V., Belda, R., Martín-Villodre, A., Herráez, M., 2005. In vitro percutaneous penetration of acyclovir from solvent systems and carbopol 971-P hydrogels: influence of propylene glycol. *J. Pharm. Sci.* 94, 1039–1047.
- Doan, K., Bronaugh, R.L., Yourick, J.J., 2010. In vivo and in vitro skin absorption of lipophilic compounds dibutyl phthalate, farnesol and geraniol in the hairless guinea pig. *Food Chem. Toxicol.* 48, 18–23.
- Dualé, C., Daveau, J., Cardot, J.M., Boyer-Grand, A., Schoeffler, P., Dubray, C., 2008. Cutaneous amitriptyline in human volunteers. *Anesthesiology* 108, 714–721.
- Enamandram, M., Rathmell, J.P., Kimball, A.B., 2015. Chronic pain management in dermatology: a guide to assessment and nonopioid pharmacotherapy. *J. Am. Acad. Dermatol.* 73, 563–573.
- Farghaly, H.S.M., Abdel-Zaher, A.O., Mostafa, M.G., Kotb, H.I., 2012. Comparative evaluation of the effect of tricyclic antidepressants on inducible nitric oxide synthase expression in neuropathic pain model. *Nitric Oxide* 27, 88–94.
- Ferjan, I., Lipnik-Štangelj, M., 2013. Chronic pain treatment: the influence of tricyclic antidepressants on serotonin release and uptake in mast cells. *Mediat. Inflamm.* 2013, 340473.
- Flores, M.P., de Castro, A.P.C.R., dos Santos Nascimento, J., 2012. Topical analgesics. *Rev. Bras. Anesthesiol.* 62, 244–252.
- Geinoz, S., Guy, R.H., Testa, B., Carrupt, P.A., 2004. Quantitative structure-permeation relationships (QSPeRs) to predict skin permeation: a critical evaluation. *Pharm. Res.* 21, 83–92.
- Gerner, P., Srinivasa, V., Zizza, A.M., Zhuang, Z.Y., Luo, S.H., Zurakowski, D., Eappen, S., Wang, G.K., 2006. Doxepin by topical application and intrathecal route in rats. *Anesth. Analg.* 102, 283–287.
- Gilron, I., Bailey, J.M., Tu, D., Holden, R.R., Jackson, A.C., Houlden, R.L., 2009. Nortriptyline and gabapentin, alone and in combination for neuropathic pain: a double-blind, randomized controlled crossover trial. *Lancet* 374, 1252–1261.
- Gilron, I., Baron, R., Jensen, T., 2015. Neuropathic pain: principles of diagnosis and treatment. *Mayo Clin. Proc.* 90, 532–545.
- Grice, J., Benson, H.A.E., 2013. Analyzing the skin barrier from down under. *Skin Pharmacol. Physiol.* 26, 254–262.
- Hadgraft, J., Valenta, C., 2000. pH, pK<sub>a</sub> and dermal delivery. *Int. J. Pharm.* 200, 243–247.
- Heard, C.M., Gallagher, S.J., Harwood, J., Maguire, P.B., 2003. The in vitro delivery of NSAIDs across skin was in proportion to the delivery of essential fatty acids in the vehicle: evidence that solutes permeate skin associated with their salvation cages? *Int. J. Pharm.* 261, 165–169.
- Hsieh, P.W., Al-Suwayeh, S.A., Fang, C.L., Lin, C.F., Chen, C.C., Fang, J.Y., 2012. The co-drug of conjugated hydroquinone and azelaic acid to enhance topical skin targeting and decrease penetration through the skin. *Eur. J. Pharm. Biopharm.* 81, 369–378.
- Hung, C.F., Chen, W.Y., Aljuffali, I.A., Lin, Y.K., Shih, H.C., Fang, J.Y., 2015. Skin aging modulates percutaneous drug absorption: the impact of ultraviolet irradiation and ovariectomy. *Age* 37, 21.
- Jackson, J.L., Damm, T.W., 2011. Barriers to the use of tricyclic antidepressants in the management of pain. *Pain Manage.* 1, 99–101.
- Jongen, J.L.M., Hans, G., Benzon, H.T., Huygen, F., Hartrick, C.T., 2014. Neuropathic pain and pharmacological treatment. *Pain Pract.* 14, 283–295.
- Kalso, E., Aldington, D.J., Moore, R.A., 2013. Drugs for neuropathic pain. *BMJ* 347, f7339.
- Karande, P., Mitragotri, S., 2009. Enhancement of transdermal drug delivery via synergistic action of chemicals. *Biochim. Biophys. Acta* 1788, 2362–2373.
- Kasting, G.B., 2013. Lipid solubility and molecular weight: whose idea was that? *Skin Pharmacol. Physiol.* 26, 295–301.
- Lee, Y., Kim, S., Kim, Y., Arooj, M., Kim, S., Hwang, S., Park, Kim, B.W., Lee, K.H., 2014. Binding mode analyses and pharmacophore model development for stilbene derivatives as a novel and competitive class of  $\alpha$ -glucosidase inhibitors. *PLoS One* 9, e85827.
- Lin, C.F., Leu, Y.L., Al-Suwayeh, S.A., Ku, M.C., Hwang, T.L., Fang, J.Y., 2012. Anti-inflammatory activity and percutaneous absorption of quercetin and its polymethoxylated compound and glycosides: the relationships to chemical structures. *Eur. J. Pharm. Sci.* 47, 857–864.
- Lin, C.F., Hwang, T.L., Al-Suwayeh, S.A., Huang, Y.L., Hung, Y.Y., Fang, J.Y., 2013. Maximizing dermal targeting and minimizing transdermal penetration by magnolol/honokiol methoxylation. *Int. J. Pharm.* 445, 153–162.
- Lin, C.F., Hung, C.F., Aljuffali, I.A., Huang, Y.L., Liao, W.C., Fang, J.Y., 2016. Methylation and esterification of magnolol for ameliorating cutaneous targeting and therapeutic index by topical application. *Pharm. Res.* 33, 2152–2167.
- Liu, X., Testa, B., Fahr, A., 2011. Lipophilicity and its relationship with passive drug permeation. *Pharm. Res.* 28, 962–977.
- Liu, K.S., Chen, Y.W., Aljuffali, I.A., Chang, C.W., Wang, J.J., Fang, J.Y., 2016. Topically applied mesoridazine exhibits the strongest cutaneous analgesia and minimized skin disruption among tricyclic antidepressants: the skin absorption assessment. *Eur. J. Pharm. Biopharm.* 105, 59–68.
- Magnusson, B.M., Anissimov, Y.G., Cross, S.E., Roberts, M.S., 2004. Molecular size as the main determinant of solute maximum flux across the skin. *J. Invest. Dermatol.* 122, 993–999.
- Moss, G.P., Dearden, J.C., Patel, H., Cronin, M.T.D., 2002. Quantitative structure-permeability relationships (QSPRs) for percutaneous absorption. *Toxicol. In Vitro* 16, 299–317.
- Musazzi, U.M., Matera, C., Dallanocce, C., Vacondio, F., De Amici, M., Vistoli, G., Cilurzo, F., Minghetti, P., 2015. On the selection of an opioid for local skin analgesia: structure-skin permeability relationships. *Int. J. Pharm.* 489, 177–185.
- Patel, H., ten Berge, W., Cronin, M.T.D., 2002. Quantitative structure-activity relationships (QSARs) for the prediction of skin permeation of exogenous chemicals. *Chemosphere* 48, 603–613.
- Patzelt, A., Lademann, J., 2013. Drug delivery to hair follicles. *Expert Opin. Drug Deliv.* 10, 787–797.
- Peppin, J.F., Albrecht, P.J., Argoff, C., Gustorff, B., Pappagallo, M., Rice, F.L., Wallace, M. S., 2015. Skin matters: a review of topical treatments for chronic pain: part two: treatments and applications. *Pain Ther.* 4, 33–50.
- Riviere, J.E., Brooks, J.D., 2011. Predicting skin permeability from complex chemical mixtures: dependency of quantitative structure permeation relationships on biology of skin model used. *Toxicol. Sci.* 119, 224–232.
- Riviere, J.E., Brooks, J.D., Collard, W.T., Deng, J., de Rose, G., Mahabir, S.P., Merritt, D. A., Marchiondo, A.A., 2014. Prediction of formulation effects on dermal absorption of topically applied ectoparasitocides dosed in vitro on canine and porcine skin using a mixture-adjusted quantitative structure permeability relationship. *J. Vet. Pharmacol. Ther.* 37, 435–444.
- Sandig, A.G., Campmany, A.C.C., Campos, F.F., Villena, M.J.M., Naveros, B.C., 2013. Transdermal delivery of imipramine and doxepin from newly oil-in-water nanoemulsions for an analgesic and anti-allodynic activity: development, characterization and in vivo evaluation. *Colloids Surf. B* 103, 558–565.
- Scheinfeld, N., 2014. Topical treatments of skin pain: a general review with a focus on hidradenitis suppurativa with topical agents. *Dermatol. Online J.* 20, 3.
- Schneider, D., Dennerlein, K., Göen, T., Schaller, K.H., Drexler, H., Korinth, G., 2016. Influence of artificial sebum on the dermal absorption of chemicals in excised human skin: a proof-of-concept study. *Toxicol. In Vitro* 33, 23–28.
- Thompson, D.F., Brooks, K.G., 2015. Systematic review of topical amitriptyline for the treatment of neuropathic pain. *J. Clin. Pharm. Ther.* 40, 496–503.
- Yamaguchi, K., Mitsui, T., Aso, Y., Sugibayashi, K., 2008. Structure-permeability relationship analysis of the permeation barrier properties of the stratum corneum and viable epidermis/dermis of rat skin. *J. Pharm. Sci.* 97, 4391–4403.
- Zhang, Q., Grice, J.E., Li, P., Jepps, O.G., Wang, G.J., Roberts, M.S., 2009. Skin solubility determines maximum transepidermal flux for similar size molecules. *Pharm. Res.* 26, 1974–1985.
- Zhang, L.W., Al-Suwayeh, S.A., Hsieh, P.W., Fang, J.Y., 2010. A comparison of skin delivery of ferulic acid and its derivatives: evaluation of their efficacy and safety. *Int. J. Pharm.* 399, 44–51.



# Resveratrol inhibits BK-induced COX-2 transcription by suppressing acetylation of AP-1 and NF- $\kappa$ B in human rheumatoid arthritis synovial fibroblasts

Chuen-Mao Yang<sup>a,b,c,\*</sup>, Yu-Wen Chen<sup>a</sup>, Pei-Ling Chi<sup>a</sup>, Chih-Chung Lin<sup>b</sup>, Li-Der Hsiao<sup>b</sup>

<sup>a</sup> Department of Physiology and Pharmacology and Health Aging Research Center, College of Medicine, Chang Gung University, Kwei-San, Tao-Yuan, Taiwan

<sup>b</sup> Department of Anesthetics, Chang Gung Memorial Hospital at Linkuo, and College of Medicine, Chang Gung University, Kwei-San, Tao-Yuan, Taiwan

<sup>c</sup> Research Center for Chinese Herbal Medicine and Research Center for Food and Cosmetic Safety, College of Human Ecology, Chang Gung University of Science and Technology, Tao-Yuan, Taiwan

## ARTICLE INFO

### Article history:

Received 23 January 2017

Accepted 7 March 2017

Available online 11 March 2017

### Keywords:

Bradykinin

Rheumatoid arthritis

PKC $\mu$

Cyclooxygenase-2

Resveratrol

## ABSTRACT

Bradykinin (BK) induces inflammation in rheumatoid arthritis (RA). Resveratrol is a potent activator of Sirt1 which could modulate inflammation through deacetylating histones of transcription factors. Here, we investigated the mechanisms underlying BK-induced COX-2 expression which is modulated by resveratrol/Sirt1 in human rheumatoid arthritis synovial fibroblasts (RASFs). We found that BK-induced COX-2 protein and mRNA expression associated with PGE<sub>2</sub> synthesis, and promoter activity was mediated through B2R receptors, which were attenuated by selective B2R antagonist Hoe140 or transfection with B2R siRNA. BK-induced responses were mediated through PKC $\mu$ , MAPKs, AP-1 and NF- $\kappa$ B which were inhibited by their respective inhibitors or siRNAs. Up-regulation of Sirt1 by resveratrol suppressed the BK-induced COX-2/PGE<sub>2</sub> production through inhibiting the interaction of AP-1 and NF- $\kappa$ B with COX-2 promoter in RASFs. BK-induced COX-2/PGE<sub>2</sub> expression is mediated through a B2R-PKC $\mu$ -dependent MAPKs, AP-1, and NF- $\kappa$ B cascade. Resveratrol inhibited the phosphorylation and acetylation of p65, c-Jun, and Fos and reduced the binding to the COX-2 promoter, thereby attenuated the COX-2 expression. Therefore, resveratrol may be a promising therapeutic intervention for treatment of inflammatory arthritis.

© 2017 Elsevier Inc. All rights reserved.

## 1. Introduction

The inflammatory milieu of the rheumatoid arthritis (RA) is a major consequence of immune responses, arising from the activation of RA synovial fibroblasts (RASFs) and complex interactions among kinin peptides and cytokines that lead to progressive destruction of joints [1–3]. Bradykinin (BK) has been recognized as a potent mediator of pain and swelling and initiates the release of cytokines from leukocytes in arthritis [4]. Elevated levels of BK have been reported in the patients with inflammatory joint diseases [5,6]. BK may interact with two types of G protein coupled receptors, termed as B1 and B2 [7]. B2 receptors (B2R) are most commonly found in various smooth muscles, whereas B1 receptors (B1R) are found in bone tissues [8]. Most of pathophysiological processes triggered by BK are mediated through activation of B2R which causes hydrolysis of phosphoinositide to generate inositol

trisphosphate (IP<sub>3</sub>) and diacylglycerol (DAG). IP<sub>3</sub> stimulates an increase in [Ca<sup>2+</sup>]<sub>i</sub> and DAG activates PKC isoforms in different cell types [9–11]. It has been reported that activation of B2R by BK induces COX-2 expression in human gingival fibroblasts and airway smooth muscle cells [12–14]. However, the detailed mechanisms of BK-mediated postreceptor signaling pathways leading to COX-2 expression are not completely understood in human RASFs.

Activation of PKC has been implicated in the development of RA [15]. It has been shown that BK stimulates translocation of PKC isoforms, such as PKC- $\alpha$ , - $\delta$ , and - $\zeta$ , in several cell systems [10,16], and involved in the regulation of cellular functions. In human RASFs, BK stimulates activation of protein kinase C $\delta$  leading to IL-6 secretion [10]. Activation of PKC $\epsilon$  involves in COX-2 expression induced by BK in tracheal smooth muscle cells [12]. BK activates MAPKs such as ERK1/2, p38 MAPK and JNK1/2 which are downstream of PKCs and leading to the expression of various inflammatory genes including COX-2 in different cell types [17,18]. In addition, COX-2 promoter consists of various binding sites for the transcription factors such as NF- $\kappa$ B and AP-1 which

\* Corresponding author at: Department of Physiology and Pharmacology, Chang Gung University, 259 Wen-Hwa 1st Road, Kwei-San, Tao-Yuan, Taiwan.

E-mail address: [chuenmao@mail.cgu.edu.tw](mailto:chuenmao@mail.cgu.edu.tw) (C.-M. Yang).

are activated by MAPKs and leading to the gene expression in various cell types [18,19]. However, the roles of PKC isozyme(s), MAPKs, NF- $\kappa$ B, and AP-1 involved in the BK-induced COX-2 expression in human RASFs remain unclear.

The most potent Sirtuin 1 (Sirt1) activator has been discovered on the basis of a screen for small molecule activators of Sirt1 [20]. Sirt1, a nuclear enzyme of the class III histone deacetylases (HDACs) modulating gene expression, involves in the regulation of pathophysiological processes [21–23]. Several studies have shown that Sirt1 exhibits anti-inflammatory properties in chronic inflammatory diseases [24–26]. However, the effects of Sirt1 on arthritis are controversial. Activation of Sirt1 by resveratrol suppresses the TNF- $\alpha$ -induced inflammation in human osteoarthritic chondrocytes [27] and protects cartilage against osteoarthritis progression in an experimental rabbit inflammatory arthritis model [28]. Whereas overexpression of Sirt1 in RA synovial cells increases production of pro-inflammatory cytokines [29], inhibition of Sirt1 activities in synovial macrophages of RA patients is found to reduce the expression of inflammatory mediators [30]. Therefore, we made an attempt to investigate the role of Sirt1 in BK-induced COX-2/PGE<sub>2</sub> production in human RASFs through overexpression of Sirt1 by resveratrol.

## 2. Materials and methods

### 2.1. Reagents and antibodies

Dulbecco's modified Eagle's medium (DMEM)/Ham's nutrient mixture F-12 (F-12) medium, fetal bovine serum (FBS), and siRNAs encoded p42 (MAPK1-HSS108536), JNK2 (MAPK9-HSS108551), p38 (MAPK14-HSS102352), c-Jun (JUN-HSS105641), c-Fos (FOS-HSS103799), and p65 (Rela-HSS184266) were purchased from Invitrogen (Carlsbad, CA). Hybond C membrane and enhanced chemiluminescence (ECL) Western blotting detection system were obtained from GE Healthcare Biosciences (Buckinghamshire, UK). Phospho-(Thr<sup>202</sup>/Tyr<sup>204</sup>)-ERK1/2 (#9101), phospho-(Thr<sup>180</sup>/Tyr<sup>182</sup>)-p38 MAPK (#9211), phospho-(Thr<sup>183</sup>/Tyr<sup>185</sup>)-JNK1/2 (#4668), phospho-PKC $\mu$  (Ser<sup>744/748</sup>) (#2054), phospho-I $\kappa$ B $\alpha$  (#2859), and phospho-p65 (#3031) antibodies were from Cell Signaling (Danvers, MA). B1R (sc-293196), B2R (sc-136216), COX-2 (sc-19999), p42 (sc-154), JNK2 (sc-827), p38 (sc-33688), phospho-c-Jun (sc-822), c-Jun (sc-1694), I $\kappa$ B $\alpha$  (sc-847), p65 (sc-7151),  $\beta$ -actin (sc-47778), G $\alpha$  (sc-823), Lamin A (sc-20680), Ac-Histone H3 (sc-8655-R) and c-Fos (sc-52) antibodies were from Santa Cruz (Santa Cruz, CA). GAPDH antibody was from Biogenesis (Bournemouth, UK). All primary antibodies were diluted at 1:1000 in phosphate-buffered saline (PBS) with 1% bovine serum albumin (BSA). Hoe 140, G66976, U0126, SB202190, SP600125, Bay11-7082, and tanshinone IIA (TSIIA) were from Biomol (Plymouth Meeting, PA). BI113823 was from Boehringer Ingelheim Pharma KG (Biberach, Germany). Bicinchnonic acid (BCA) protein assay reagent was from Pierce (Rockford, IL). PGE<sub>2</sub> enzyme immunoassay kit was from Cayman Chem. (Ann Arbor, MI). BK, enzymes, siRNAs encoded PKC $\mu$  (SASI\_Hs01\_00239143), B1R (SASI\_Hs01\_00012974) and B2R (SASI\_Hs01\_00174697\_AS), and other chemicals were from Sigma (St. Louis, MO). SDS-PAGE supplies were from MDBio Inc. (Taipei, Taiwan).

### 2.2. Isolation and culture of human synovial fibroblasts

This study was approved by the Institutional Review Board, Chang Gung Memorial Hospital. Human RASFs were isolated from synovial tissue obtained from patients with RA who underwent knee or hip surgery. Synovial strips were cut into small pieces and placed in 10-cm dishes. Osteoarthritis synovial fibroblasts

(OASFs) were isolated from synovial tissue obtained from patients with OA who underwent knee or hip joint surgery. Synovial fibroblasts were obtained from 26 patients with RA who underwent knee or hip surgery. RASFs were isolated, cultured, and characterized as previously described [30]. Experiments were performed using cells from passages 3 to 6.

### 2.3. Preparation of cell extracts and Western blot analysis

RASFs were incubated with BK for the indicated time intervals. Samples were analyzed by Western blot, as previously described [31]. The immunoreactive bands were detected by ECL reagents and captured by a UVP BioSpectrum 500 Imaging System (Upland, CA). The image densitometry analysis was quantified by an UN-SCAN-IT gel software (Orem, UT).

### 2.4. Plasmid construction, transfection, and luciferase reporter gene assays

The upstream region (−483 to +37) of the human COX-2 promoter was cloned into the pGL3-basic vector containing the luciferase reporter system [32]. The point mutations in the NF- $\kappa$ B and AP-1 binding sites of the COX-2 promoter were generated by site-directed mutagenesis that splices by overlap extension. Introduction of two double point-mutation into the AP-1-binding site (AP-1 domain; ACAGTCA to ACAACCA) and NF- $\kappa$ B-binding site (NF- $\kappa$ B domain; GGGACTACCC to GGGAGGACCC) to generate pGL3-COX-2 $\Delta$ AP-1 and pGL3-COX-2 $\Delta$ NF- $\kappa$ B, respectively, PCR was amplified from COX-2-luc as previously described [32]. The underlined nucleotides indicate the positions of substituted bases. All plasmids were prepared by using QIAGEN plasmid DNA preparation kits. These constructs were transfected into RASFs by using a Lipofectamine 2000 reagent according to the manufacturer's instructions. After incubation with BK, cells were collected and disrupted by sonication in a lysis buffer (25 mM Tris, pH 7.8, 2 mM EDTA, 1% Triton X-100, and 10% glycerol). After centrifugation, aliquots of the supernatants were used to test the promoter activity by using a luciferase assay system (Promega, Madison, WI). Firefly luciferase activities were standardized for  $\beta$ -galactosidase activity.

### 2.5. Cell fractions preparation and analysis

RASFs were shifted to serum-free DMEM/F-12 medium for 24 h and incubated with 1  $\mu$ M BK for the indicated time intervals. The membrane, cytosolic, and nuclear fractions were prepared as previously described [31]. Samples from these fractions were analyzed by Western blot using respective antibodies.

### 2.6. Transient transfection with siRNAs

RASFs (10<sup>6</sup> cells) were plated in 12-well culture plates for 24 h to about 80% confluence. Cells were washed once with PBS and 0.4 ml of serum-free DMEM/F-12 medium was added to each well. Transient transfection of siRNAs (100 nM) was performed by using Lipofectamine<sup>TM</sup> RNAiMAX reagent according to the manufacturer's instructions, as previously described [31].

### 2.7. Reverse transcription–polymerase chain reaction and qRT-PCR analyses

Total RNA was extracted from RASFs as previously described [31]. The cDNA obtained from 1  $\mu$ g total RNA was used as a template for polymerase chain reaction (PCR) amplification. Oligonucleotide primers were designed on the basis of Genbank entries



for human COX-2, B1R, B2R, c-Jun, c-Fos, and  $\beta$ -actin. The following primers were used for amplification reaction:

COX-2:

5'-TTCAAATGAGATTGTGGGAAAATTGCT-3' (sense),  
5'-AGATCATCTCTGCCTGAGTATCTT-3' (antisense);

B1R:

5'-TGGACCCAGTTTAACTGGCC-3' (sense),  
5'-ATGAAGTCCTCCCAAAGCA-3' (antisense);

B2R:

5'-TGGGGACGGTCC TGACGGTG-3' (sense),  
5'-GCCAGGATCAGGTCTGTG-3' (antisense);

c-Jun:

5'-GGATCAAGGCGGAGAGGAAG-3' (sense),  
5'-GCGTTAGCATGAGTTGGCAC-3' (antisense);

c-Fos:

5'-GGAGAATCCGAAGGGAAGG-3' (sense),  
5'-GCTTGGGCTCAGGGTCATTG-3' (antisense);

$\beta$ -actin:

5'-CTAGAAGCATTTGCGGTGGACGATGGAGGG-3' (sense),  
5'-TGACGGGGTCACCCACACTGTGCCATCTA-3' (antisense).

Moreover, the primers and probes used for real-time PCR of human COX-2, c-Fos, and GAPDH were obtained from Applied Biosystems (Foster City, CA). Each PCR was performed using 100 ng of cDNA, PCR Master Mix, and premade TaqMan gene expression assay components containing a FAM reporter dye at the 5' end of the TaqMan probe and a nonfluorescent quencher at the 3' end of the probe. Human GAPDH was used as a control to verify the quality of the cDNA template. Real-time PCR was performed and analyzed using a StepOnePlus quantitative PCR instrument (Applied Biosystems).

## 2.8. Chromatin immunoprecipitation (ChIP) assay

The ChIP assay was performed as previously described [31]. Soluble chromatin was immunoprecipitated using an anti-p65, anti-c-Jun or anti-c-Fos Ab. Following washing and elution, precipitates were heated overnight at 65 °C to reverse cross-linking of DNA and protein. DNA fragments were purified by phenol-chloroform extraction and ethanol precipitation. The purified DNA was subjected to PCR amplification using the primers specific for the region containing NF- $\kappa$ B and AP-1-binding sites present in the COX-2 promoter, sense primer (NF- $\kappa$ B): 5'-AAGACATCTGGCGGAAACC-3'; antisense primer: 5'-ACAATTGGTCGCTAACCGAG-3'; sense primer (AP-1): 5'-CACCGGGCTTACGCAATTTT-3'; antisense primer: 5'-ACGCTCACTGCAAGTCGTAT-3'. PCR fragments were analyzed on 2% agarose in 1X TAE gel containing ethidium bromide. The response elements of COX-2 promoter and locations of primers for ChIP assay are representation (Fig. 4E).

## 2.9. Measurement of PGE<sub>2</sub> release

Cells were treated with BK for the indicated time intervals. The media were collected, and PGE<sub>2</sub> was assayed using a PGE<sub>2</sub> enzyme

immunoassay kit according to the instructions of the manufacturer.

## 2.10. Statistical analysis

All the experiments were repeated at least five times with the similar results. The data were analyzed by using a GraphPad Prism Program (GraphPad, San Diego, CA) and expressed as the mean  $\pm$  SEM. The data statistical analyses were performed using Student's two-tailed paired *t*-test or one-way ANOVA (more than two groups of data, single factor) or two-way ANOVA (more than two groups of data, two factors), followed by Bonferroni's comparison post hoc test. Differences were considered statistically significant if the probability of the difference occurring by chance was less than 5 in 100 (*P* < 0.05).

## 3. Results

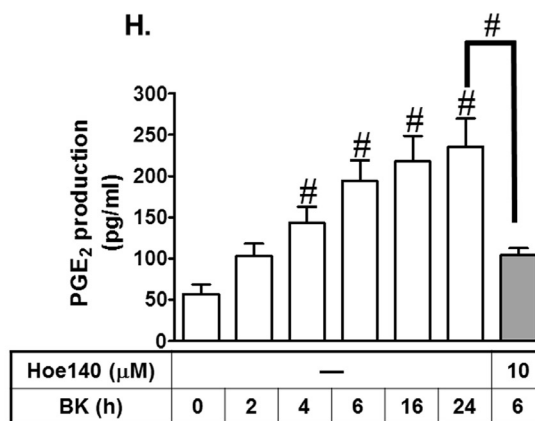
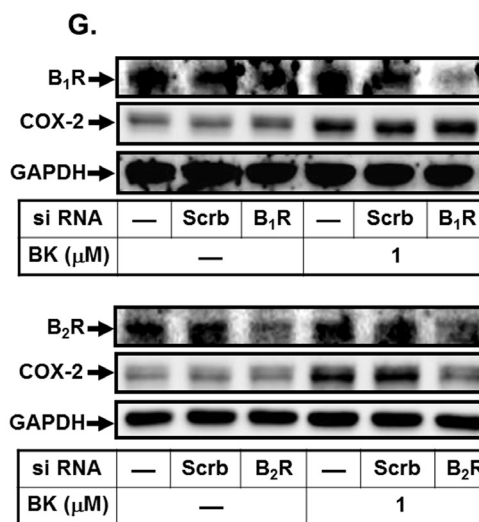
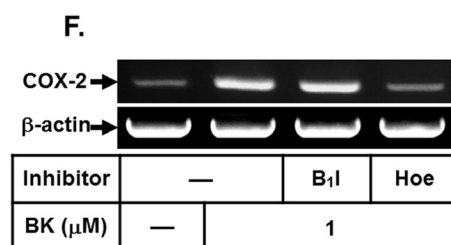
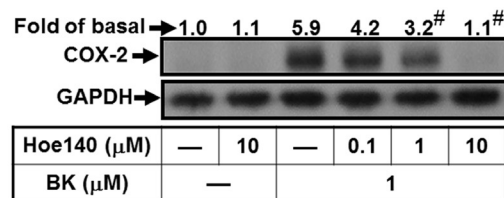
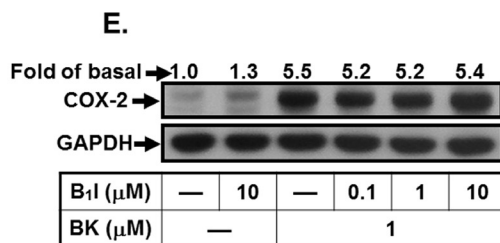
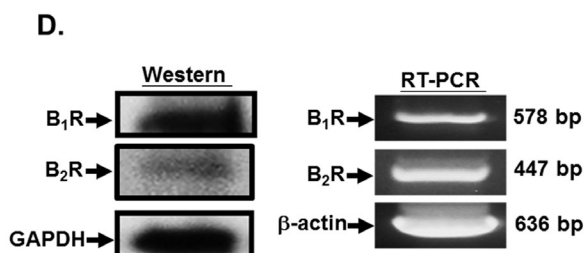
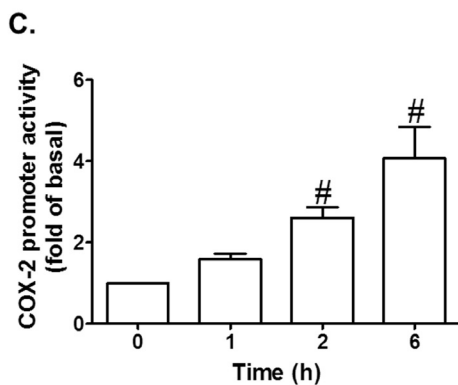
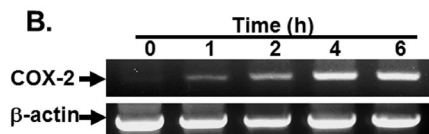
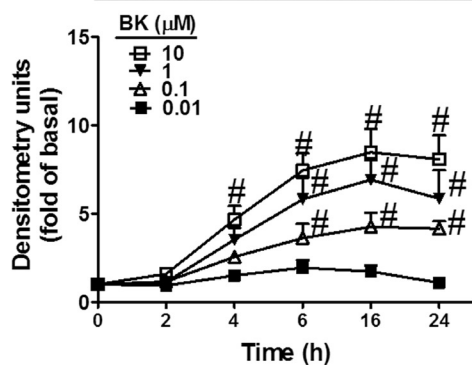
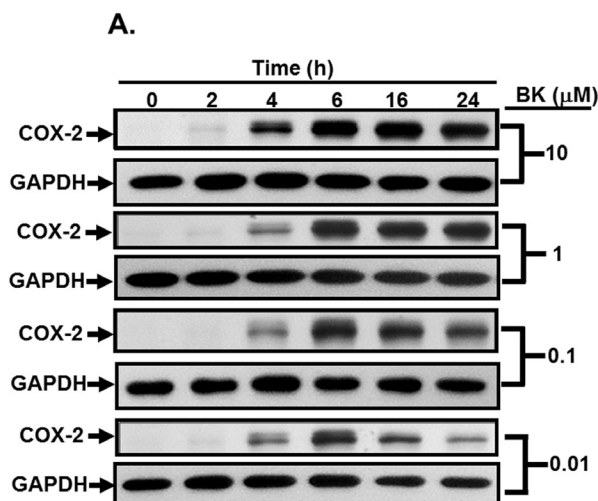
### 3.1. BK promotes the expression of COX-2 via B2R

BK induces the release of AA and PGs in various cell types [12,33]. COX-2 is known to regulate PG synthesis in various inflammatory diseases. Thus, we investigated whether BK could induce COX-2 expression and promote the synthesis of PGE<sub>2</sub> in human RASFs. We found that BK-induced COX-2 protein expression in a concentration- and time-dependent manner (Fig. 1A). To investigate the effect of BK on COX-2 expression at the transcriptional level, COX-2 mRNA expression and promoter luciferase activity were determined by RT-PCR and COX-2 promoter assay, respectively. As shown in Fig. 1B and C, BK stimulated COX-2 mRNA expression and promoter activity in a time-dependent manner with a maximal response within 6 h during the period of observation. B2Rs have been detected in the synovial fibroblasts from osteoarthritis patients [34], whereas no evidence supported the presence of the B1R subtype in this tissue. To investigate whether RASFs express BK receptor subtypes, as shown in Fig. 1D (right panel), RT-PCR products with the expected sizes of 578 bp for B1R and of 447 bp for B2R were detected in these cells. To confirm the expression of BK receptor proteins, the cell lysates were analyzed by Western blot using an anti-B1R or B2R antibody (left panel). Similar to the mRNA expression, both B1R and B2R proteins were identified in RASFs. Moreover, BK-induced COX-2 protein and mRNA expression were blocked by a selective B2R antagonist Hoe 140 but not by a selective B1R antagonist BI-113823 [35,36], as determined by Western blot and RT-PCR, respectively (Fig. 1E and F), suggesting the involvement of B2R in BK-induced responses in RASFs. This note was further supported by transfection with either B1R or B2R siRNA showing that BK-induced COX-2 expression was attenuated by transfection with B2R siRNA but not with B1R siRNA (Fig. 1G). In addition, we found that BK time-dependently induced an increase in PGE<sub>2</sub> synthesis, which was blocked by pretreatment with Hoe 140 (Fig. 1H). These results suggested that BK-induced COX-2 expression and PGE<sub>2</sub> production is mediated through B2R in human RASFs.

### 3.2. BK induces COX-2 expression via PKC $\mu$

In RA and OA patients, PKC $\mu$  is greater expressed than that of normal cells [37]. To determine whether PKC $\mu$  was involved in BK-triggered COX-2 induction, RASFs were pretreated with Gö6976, a potent inhibitor of PKC $\mu$  [38], for 1 h and then incubated with BK for 6 h and then the cell lysates were analyzed by Western blot. Pretreatment with Gö6976 caused a significant inhibition of BK-induced COX-2 protein expression in a concentration-dependent manner (Fig. 2A). BK-induced COX-2 protein expression





was also significantly inhibited by transfection of the cells with PKC $\mu$  siRNA (Fig. 2B). This down-regulation of COX-2 protein expression was confirmed by reduction of COX-2 mRNA and promoter activity in RASFs transfected with PKC $\mu$  siRNA (Fig. 2C), suggesting that PKC $\mu$  plays a potential role in BK-induced COX-2 expression in RASFs. Translocation of PKC isoforms to membranes is considered as a hallmark of PKC activation [39]. To further confirm the role of PKC $\mu$  in BK-induced COX-2 expression, we determined the effect of BK on translocation of PKC $\mu$  in RASFs, by Western blot using an anti-PKC $\mu$  antibody. We found that PKC $\mu$  was rapidly translocated from cytosol to plasma membrane as early as 3 min upon BK stimulation, and sustained over 60 min (Fig. 2D). BK-induced PKC $\mu$  membrane translocation was blocked by Hoe 140 and PKC $\mu$  siRNA (Fig. 2E). To determine whether BK stimulated COX-2 expression through activation of PKC $\mu$ , the phosphorylation of PKC $\mu$  was determined by Western blot using a specific phosphorylated PKC $\mu$  antibody. We found that BK stimulated a time-dependent phosphorylation of PKC $\mu$  (Ser<sup>744/748</sup>) with a maximal response within 10–30 min in RASFs. Pretreatment with Hoe 140 (10  $\mu$ M), Gö6976 (1  $\mu$ M), or transfection with PKC $\mu$  siRNA significantly blocked BK-stimulated PKC $\mu$  phosphorylation during the period of observation (Fig. 2F and G). In contrast, pretreatment with BI-113823 (a selective B1R antagonist) had no effect on BK-stimulated PKC $\mu$  phosphorylation, indicating that PKC $\mu$  activation was, at least in part, required for BK-induced COX-2 expression via B2Rs in RASFs.

### 3.3. BK induces COX-2 expression via MAPKs

BK has been shown to activate MAPKs which in turn regulates the expression of various genes including COX-2 in different cell types [17,18]. Thus, we further investigated whether BK-induced COX-2 expression was mediated through ERK1/2, p38 MAPK, and JNK1/2 in RASFs. As shown in Fig. 3A, BK-enhanced COX-2 protein expression was blocked by the inhibitor of MEK1/2 (U0126), p38 MAPK (SB202190), and JNK1/2 (SP600125) in a concentration-dependent manner. In addition, pretreatment with U0126 (10  $\mu$ M), SB202190 (10  $\mu$ M), and SP600125 (10  $\mu$ M) also significantly attenuated the BK-induced COX-2 mRNA expression and promoter activity (Fig. 3B). To further ensure that BK-induced COX-2 expression was mediated via these MAPKs, as shown in Fig. 3C, transfection with siRNA of ERK2, JNK2, or p38 down-regulated the expression of their respective proteins and subsequently attenuated BK-enhanced COX-2 expression. To determine whether BK stimulated COX-2 expression through activation of these MAPKs, the phosphorylation of ERK1/2, p38 MAPK, or JNK1/2 was determined by Western blot using their own specific phosphorylated forms of antibodies. We found that BK significantly stimulated ERK1/2, p38 MAPK, or JNK1/2 phosphorylation in a time-dependent manner, which was inhibited by their respective inhibitor U0126, SB202190, or SP600125, during the period of observation (Fig. 3D). To further investigate whether BK-stimulated MAPKs phosphorylation was mediated through B2R/PKC $\mu$ , RASFs were pretreated with Hoe 140 or transfected with PKC $\mu$  siRNA and the levels of MAPKs phosphorylation were determined by Western blot. We found that BK-stimulated

ERK1/2, p38 MAPK, and JNK1/2 phosphorylation was significantly attenuated by 10  $\mu$ M Hoe 140 or transfection with PKC $\mu$  siRNA. These results suggested that BK-induced COX-2 expression is mediated through B2R/PKC $\mu$ -dependent MAPKs in RASFs.

### 3.4. AP-1 is required for BK-induced COX-2 expression

AP-1 has been implicated in the regulation of COX-2 expression [40]. To determine whether BK-induced COX-2 expression was mediated through transcription factor AP-1, an AP-1 inhibitor tanshinone IIA was used. As shown in Fig. 4A, pretreatment with tanshinone IIA attenuated BK-induced COX-2 expression, suggesting that AP-1 is required for BK-induced COX-2 expression in RASFs. To confirm the role of AP-1 (containing immediate early gene c-Fos and c-Jun subunits) in BK-induced COX-2 expression, c-Jun and c-Fos siRNAs were used. We found that transfection with either c-Jun or c-Fos siRNA significantly reduced the protein expression of c-Jun or c-Fos, respectively, and then inhibited BK-induced COX-2 expression (Fig. 4B). Next, we examined whether activation of AP-1 is essential for BK-induced COX-2 gene up-regulation. The transcriptional activity of AP-1 was evaluated by transfection of RASFs with an AP-1 promoter plasmid. As shown in Fig. 4C and D, BK enhanced AP-1 transcriptional activity in a time-dependent manner, which was inhibited by U0126 or SP600125, but not by SB202190. On the other hand, we applied ChIP assay to determine whether BK stimulated the recruitment of c-Fos or c-Jun to the COX-2 promoter involved in COX-2 gene expression. Locations of primers used for ChIP assays (COX-2-NF- $\kappa$ B and COX-2-AP-1) and LPS-induced Ach3 associated region are indicated. Canonical putative binding sites in the COX-2 promoter region are also indicated: NF- $\kappa$ B (-221/-211, GGGGACT ACCC), AP-1 (-67/-58, GAAACAGTCA) and transcription initiation (+1) are also indicated (Fig. 4E). As shown in Fig. 4F, BK time-dependently stimulated the binding of c-Fos and c-Jun to the COX-2 promoter which was significantly attenuated by U0126, SP600125 and PKC $\mu$  siRNA, but not by SB202190. Finally, we used a point-mutated AP-1 within COX-2 promoter plasmid to confirm the role of AP-1 in BK-mediated COX-2 promoter induction. As shown in Fig. 4G, BK-stimulated COX-2 promoter activity was prominently attenuated in RASFs transfected with the point-mutated AP-1 COX-2 promoter plasmid. These data suggested that BK-induced COX-2 expression is mediated through a PKC $\mu$ /MAPKs-dependent AP-1 signaling in RASFs.

### 3.5. NF- $\kappa$ B is essential for BK-induced COX-2 expression

NF- $\kappa$ B-targeted genes are important in the expression of inflammatory proteins, including COX-2. To investigate whether activation of NF- $\kappa$ B is involved in the BK-induced COX-2 expression in RASFs, an inhibitor of I $\kappa$ B kinase Bay11-7082 was used. As shown in Fig. 5A, pretreatment of RASFs with Bay11-7082 concentration-dependently attenuated the BK-induced COX-2 expression. We found that activation of MAPKs and NF- $\kappa$ B is necessary for the BK-induced COX-2 protein expression in RASFs. It would be important to differentiate whether the phosphorylation of MAPKs is associated with NF- $\kappa$ B activation. Phosphorylation of

**Fig. 1.** BK-induced COX-2/PGE<sub>2</sub> production is mediated through B2R. (A) The cell lysates were analyzed by Western blot using an anti-COX-2 or anti-GAPDH (control) antibody. (B) The levels of COX-2 and  $\beta$ -actin (as an internal control) mRNA were analyzed by RT-PCR. (C) COX-2 promoter luciferase activity was analyzed. (D) Total RNA was extracted from RASFs and subjected to RT-PCR for B1 and B2 BK receptor mRNAs using the respective primers (right panel). B1 and B2 receptor protein were identified by Western blot (left panel). (E,F) RASFs were pretreated with BI-113823 or Hoe 140 for 1 h, and then incubated with BK for (E) 6 h or (F) 4 h. COX-2 protein and mRNA were determined by Western blot and RT-PCR, respectively. (G) RASFs were transfected with scrambled, B1R, or B2R siRNA and then incubated with BK for 6 h. The cell lysates were analyzed by Western blot using an anti-B1R, anti-B2R, anti-COX-2 or anti-GAPDH (control) antibody. The media were collected to determine the levels of PGE<sub>2</sub>. The basal level of PGE<sub>2</sub> in the medium was about 56  $\pm$  10 pg/ml (n = 5). Data are expressed as mean  $\pm$  S.E.M. of five independent experiments. \*P < 0.05, as compared with the cells exposed to vehicle alone (A,C,H). #P < 0.05, as compared with the cells exposed to BK alone (E,H).

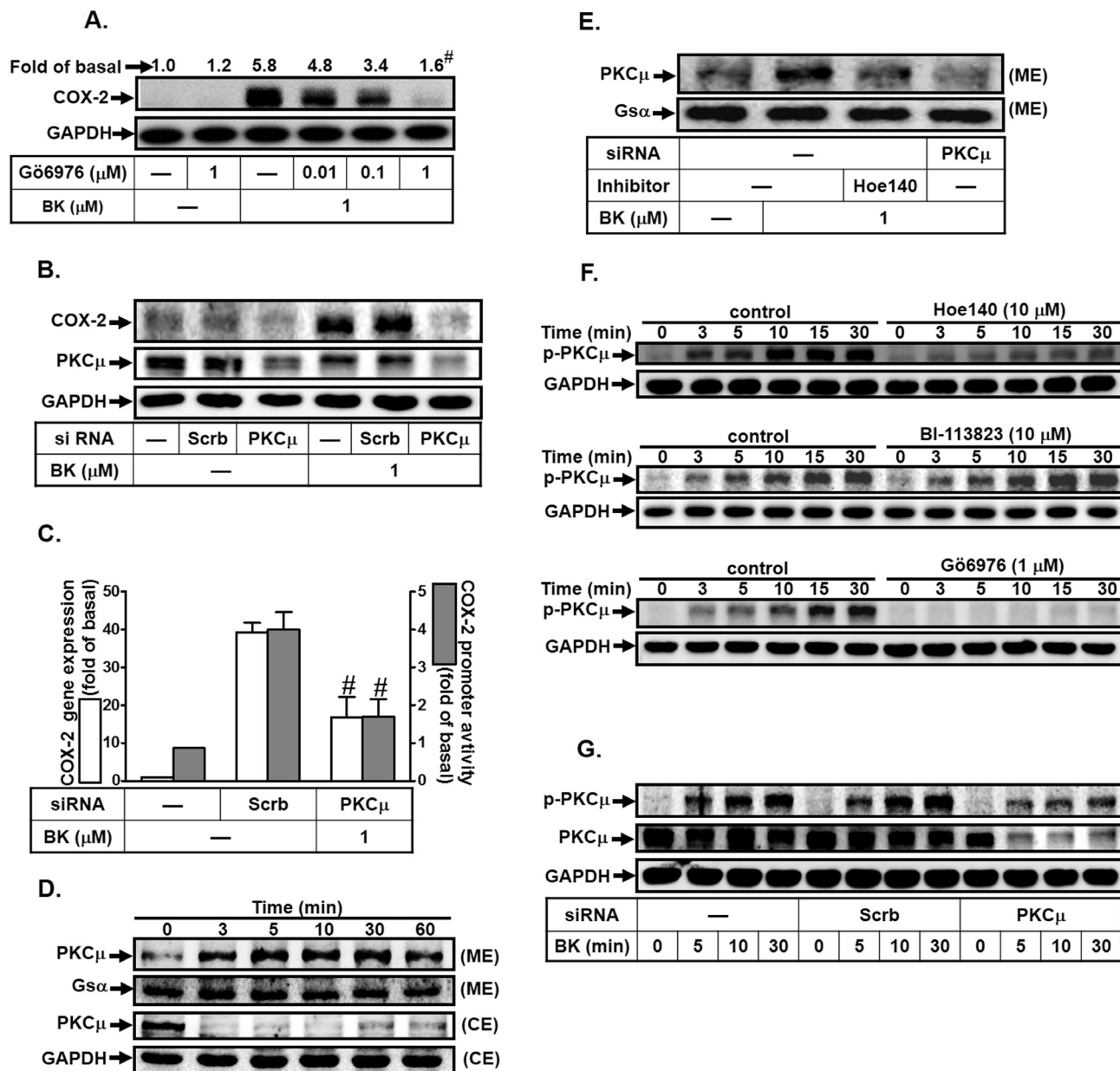


**Fig. 2.** BK-induced COX-2 expression requires B2R-dependent PKCμ activation. (A) RASFs were pretreated with Gö6976 for 1 h and then incubated with BK for 6 h. (B,C) RASFs were transfected with scrambled or PKCμ siRNA and then treated with BK for (B) 6 h or (C) 4 h. The protein levels of PKCμ and COX-2 were determined by Western blot. The mRNA levels and promoter activity of COX-2 were determined by real-time PCR and promoter assay, respectively. (D) RASFs were treated with BK for the indicated time intervals. Membrane and cytosolic fractions were prepared and subjected to western blot using an anti-PKCμ, anti-Gsα, or anti-GAPDH antibody. (E) RASFs were pretreated with Hoe140 (10 μM) or transfected with PKCμ siRNA and then incubated with BK for 10 min. Membrane fractions were prepared and subjected to western blot using an anti-PKCμ or anti-Gsα antibody. (F,G) Cells were pretreated with Hoe140, BI-113823, or Gö6976 for 1 h or transfected with PKCμ siRNA and then incubated with BK for the indicated time intervals. The cell lysates were analyzed by Western blot using an anti-phospho-PKCμ, anti-PKCμ, or anti-GAPDH. Data are expressed as mean ± S.E.M. of five independent experiments. <sup>#</sup>*P* < 0.05, as compared with the cells exposed to BK alone (A, C).

the NF-κB p65 has been recognized as a marker of NF-κB activation [41]. To investigate if p65 can be phosphorylated by BK, as shown in Fig. 5B, BK rapidly stimulated p65 phosphorylation on Ser<sup>536</sup> as early as 10 min and sustained over 30 min during the period of observation, which was inhibited by U0126, SB202190, SP600125, Gö6976, or transfection with PKCμ siRNA. To determine whether the involvement of NF-κB in the BK-induced responses is mediated through p65 (NF-κB subunit) translocation and phosphorylation/degradation of IκBα, the cytosolic and nuclear fractions were prepared and analyzed by Western blot. As shown in Fig. 5C, BK time-dependently stimulated phosphorylation and degradation of IκBα and translocation of p65 from the cytosolic

to the nuclear fractions. There was a significant phosphorylation and degradation of IκBα within 10–60 min, and following the nuclear translocation of p65 NF-κB within 30–90 min. We further found that BK-stimulated phosphorylation of IκBα and translocation of p65 were attenuated by pretreatment with the inhibitor of MEK1/2 (U0126), p38 MAPK (SB202190), JNK1/2 (SP600125), or NF-κB (Bay11-7082) (Fig. 5D). We also confirmed the p65 translocation by an immunofluorescence staining, which was inhibited by pretreatment with Bay11-7082 and these MAPKs inhibitors (Fig. 5E). To further verify that p65 is essential for BK-induced COX-2 expression, as shown in Fig. 5F, transfection with p65 siRNA significantly knocked down the p65 protein levels

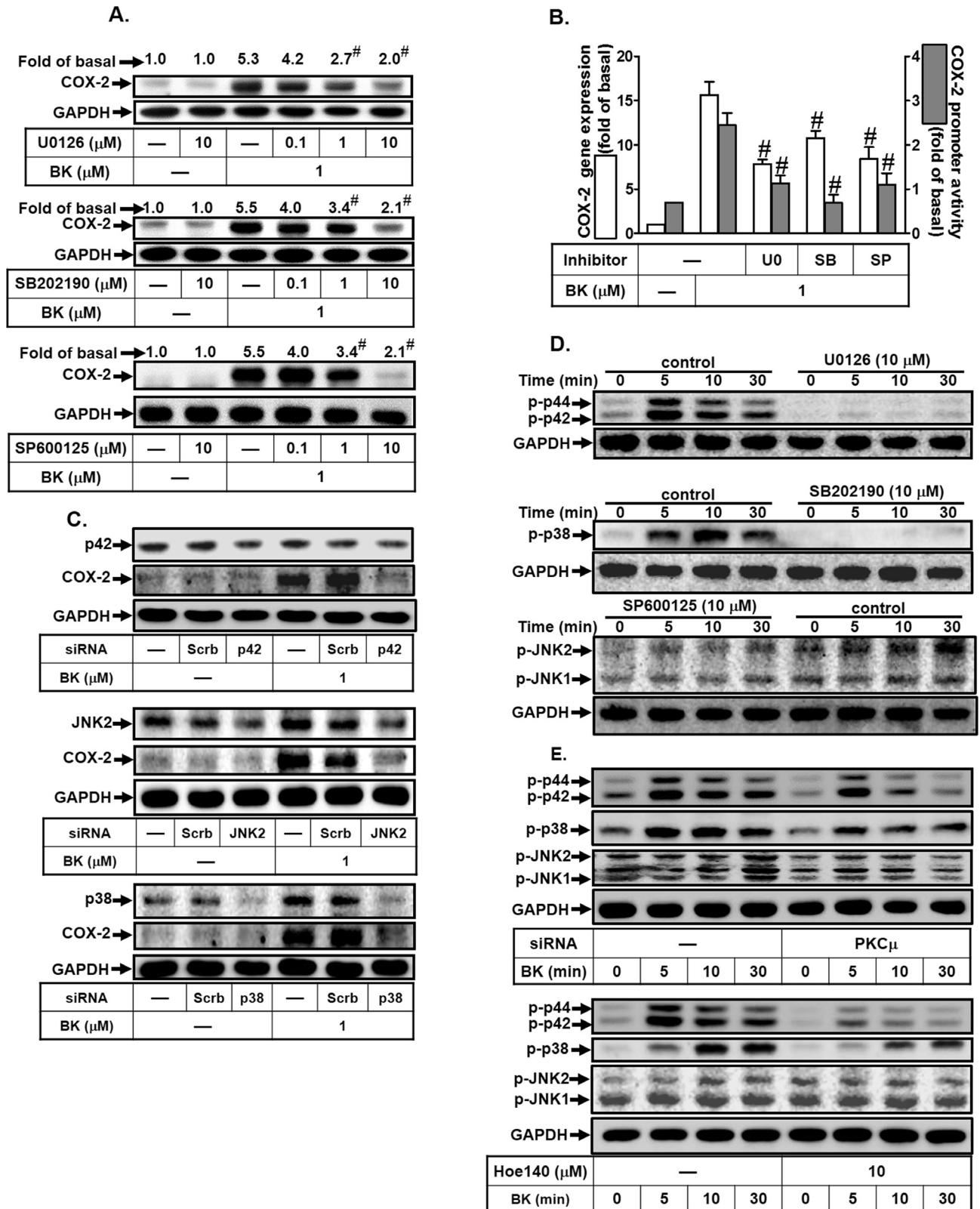


**Fig. 3.** PKC<sub>μ</sub>-dependent p38 MAPK, ERK1/2, and JNK-1/2 activation is required for BK-mediated COX-2 expression. RASFs were pretreated with U0126, SB202190, or SP600125 for 1 h, and then incubated with BK for (A) 6 h or (B) 4 h. The levels of COX-2 protein and mRNA, and promoter activity were determined by Western blot, real-time PCR, and promoter assay, respectively. (C) RASFs were transfected with scramble, p42, JNK2, or p38 siRNA and then incubated with BK for 6 h. Cell lysates were analyzed by Western blot using respective antibodies. (D,E) Cells were pretreated with U0126, SB202190, SP600125 and Hoe140 for 1 h, or transfected with PKC<sub>μ</sub> siRNA and then incubated with BK for the indicated time intervals. Cell lysates were analyzed by Western blot using respective antibodies. Data are expressed as mean ± S.E.M. of five independent experiments. <sup>#</sup>*P* < 0.05, as compared with the cells exposed to BK alone (A,B).

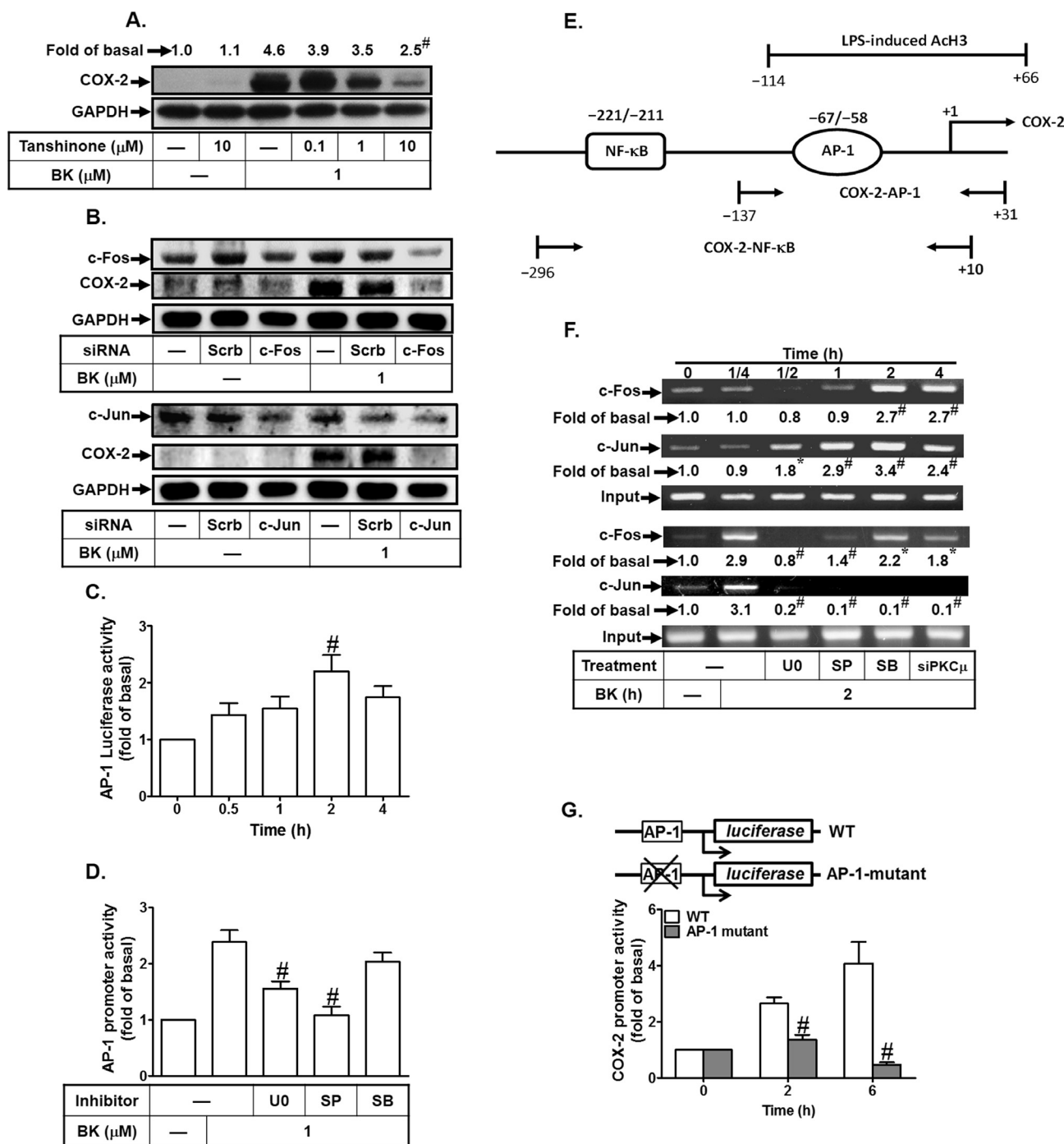


**Fig. 4.** Activation of AP-1 regulates BK-induced COX-2 expression. (A) RASFs were pretreated with Tanshinone IIA for 1 h and then incubated with BK for 6 h. (B) RASFs were transfected with siRNA of scrambled, c-Jun, or c-Fos and then incubated with BK for 6 h. (A,B) Protein levels of c-Fos, c-Jun, and COX-2 were determined by Western blot. (C) RASFs were transfected with an AP-1 promoter-luciferase reporter construct together with a  $\beta$ -galactosidase plasmid and then incubated with BK for the indicated time intervals or (D) pretreated with U0126, SP600125, or SB202190 for 1 h and then incubated with BK for 6 h. AP-1 promoter activity was determined and normalized to those of  $\beta$ -galactosidase. (E) Schematic representation of human COX-2 gene. Locations of primers used for ChIP assays (COX-2- NF- $\kappa$ B and COX-2-AP-1) and LPS-induced AcH3 associated region are indicated. Canonical putative binding sites in the COX-2 promoter region are also indicated: NF- $\kappa$ B (-221/-211, GGGGACTACCC), AP-1 (-67/-58, GAAACAGTCA) and transcription initiation (+1) are also indicated. The figure is not drawn to scale. (F) RASFs were pretreated without or with the indicated inhibitors for 1 h, or transfected with PKC $\mu$  siRNA and incubated with BK for the indicated time intervals (upper panel) or for 2 h (lower panel). The ChIP assay was performed. (G) RASFs were transfected with either wild-type COX-2 promoter (WT) or AP-1-mutated COX-2 promoter (AP-1-mutant) and then incubated with BK for the indicated time periods. COX-2 promoter activity was determined. Data are expressed as mean  $\pm$  S.E.M. of five independent experiments. <sup>#</sup> $P < 0.05$ , as compared with the cells exposed to BK alone (A,D,G). <sup>\*</sup> $P < 0.05$ , as compared with the cells exposed to vehicle alone (F).

and reduced the BK-induced COX-2 expression. The results suggested that BK-stimulated NF- $\kappa$ B translocation through ERK1/2, p38 MAPK, and JNK1/2 is required for COX-2 induction in RASFs.

Next, we examined whether transcriptional activation of NF- $\kappa$ B is essential for BK-induced COX-2 gene expression. The transcrip-

tional activity of NF- $\kappa$ B was evaluated by an NF- $\kappa$ B luciferase activity assay. As shown in Fig. 6A, BK enhanced NF- $\kappa$ B transcriptional activity in a time-dependent manner with a maximal response within 2–6 h. Moreover, pretreatment with Gö6976 (Go, 1  $\mu$ M), SP600125 (SP, 10  $\mu$ M), SB202190 (SB, 10  $\mu$ M), U0126



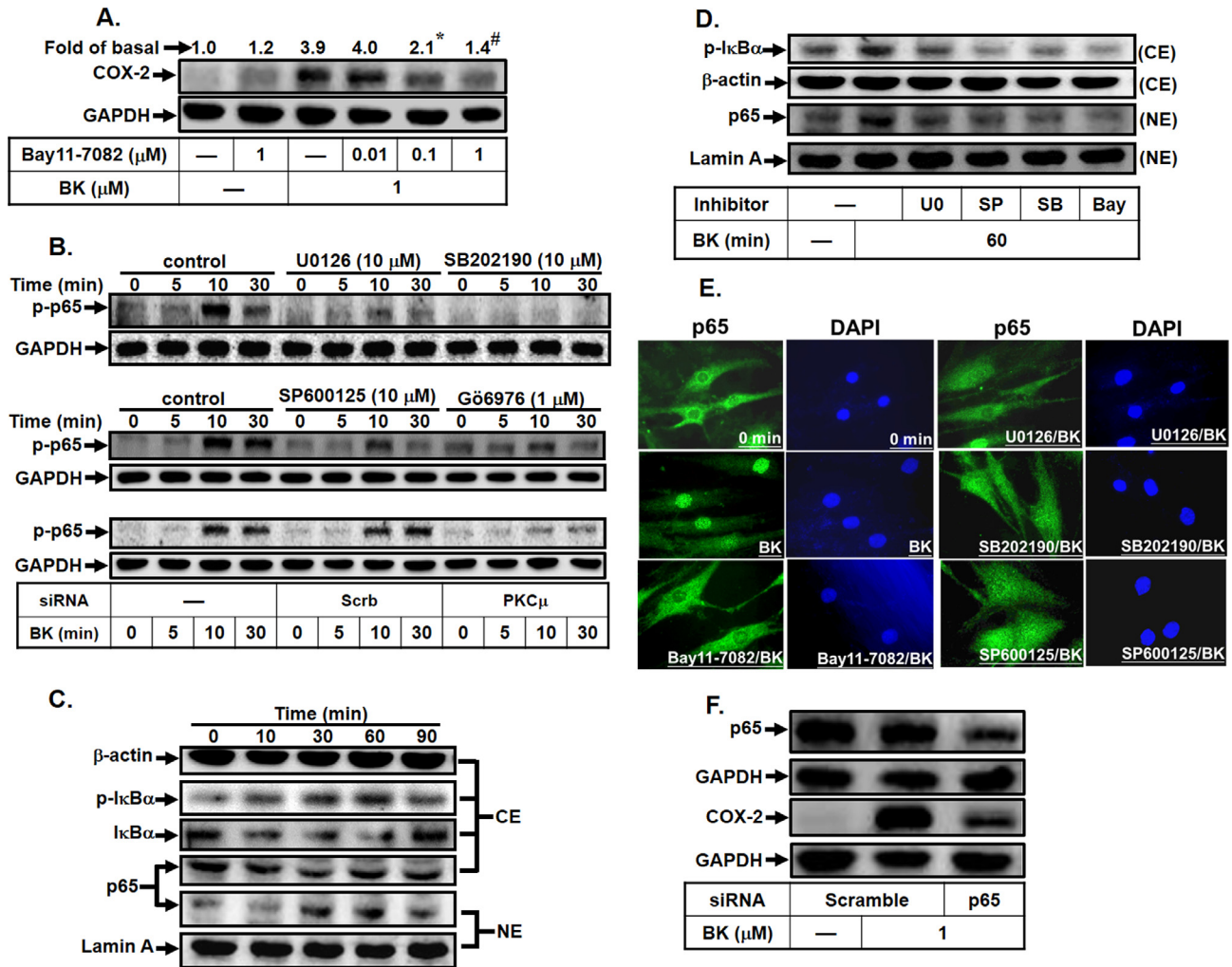


**Fig. 5.** NF-κB is essential for BK-induced COX-2 expression. (A) RASFs were pretreated with Bay 11-7082 for 1 h and incubated with BK for 6 h. (B) Cells were pretreated without (control) or with U0126, SB202190, SP600125, and Gö6976 for 1 h, or transfected with PKCμ siRNA and incubated with BK for the indicated time intervals. (C,D) RASFs were pretreated without or with the indicated inhibitors for 1 h and incubated with BK for (C) the indicated time intervals or (D) 1 h. The nuclear and cytosolic extracts were prepared and analyzed by Western blot. (E) RASFs were pretreated with the indicated inhibitors for 1 h and stimulated with BK for 1 h. NF-κB p65 translocation was observed by immunofluorescence double staining using an antibody specific for p65. DAPI was used to stain the nucleus (bottom left corner). (F) Cells were transfected with p65 or scrambled (scr) siRNA and then incubated with BK for 6 h. Cell lysates were analyzed by Western blot using respective antibodies. #*P* < 0.05, as compared with the cells exposed to BK alone (A).

(U0, 10 μM), or Bay11-7082 (Bay, 1 μM) attenuated NF-κB transcriptional activity stimulated by BK (Fig. 6B), demonstrating that BK enhances the NF-κB transcriptional activity through a PKCμ-dependent activation of MAPKs. Subsequently, we found that BK-stimulated NF-κB p65 binding activity in a time-dependent manner analyzed by a ChIP-PCR assay (Fig. 6C). BK-stimulated p65 binding activity to the COX-2 promoter was significantly inhibited by pretreatment with U0126, SB202190, SP600125, Bay11-7082, or transfection with PKCμ siRNA (Fig. 6D), suggesting that BK stimulates COX-2 promoter activity via a PKCμ/MAPKs-dependent NF-κB activation in human RASFs. To further ensure that NF-κB indeed mediates BK-induced COX-2 promoter activity through binding to its regulatory element within the COX-2 promoter region, the wild-type (WT) and mutated by a single-point mutation of the NF-κB binding site (mt-κB) COX-2 promoter plasmids were constructed (as illustrated in Fig. 6E, upper panel). BK-stimulated COX-2 promoter activity was significantly attenuated in RASFs transfected with an mt-κB-COX-2 plasmid (Fig. 6E, lower panel), indicating that NF-κB element is essential for BK-induced COX-2 promoter activity. These results

further confirmed that BK stimulates COX-2 promoter activity via enhancing NF-κB binding to the κB binding site within COX-2 promoter region in RASFs.

To determine whether PKCμ, MAPKs, AP-1 and NF-κB involved in COX-2 expression associated with PGE<sub>2</sub> production, as shown in Fig. 6F, BK enhanced a significant increase in PGE<sub>2</sub> production which was attenuated by the inhibitors of PKCμ (Gö6976), MEK1/2 (U0126), p38 MAPK (SB202190), JNK1/2 (SP600125), AP-1 (tanshinone II-A), or NF-κB (Bay11-7082), as determined by a PGE<sub>2</sub> ELISA kit. Taken together, these results demonstrated that in human RASFs, up-regulation of COX-2 expression associated with PGE<sub>2</sub> production by BK is mediated through activation of PKCμ, MAPKs, AP-1, and NF-κB.

### 3.6. Resveratrol reduces BK-mediated COX-2/PGE<sub>2</sub> production through Sirt1 upregulation

Resveratrol has been shown to be a potent activator of Sirt1 [21] which exerts anti-inflammatory and anti-oxidant effects on various cell types and animal models [22,23,25,26]. Thus, we investigate

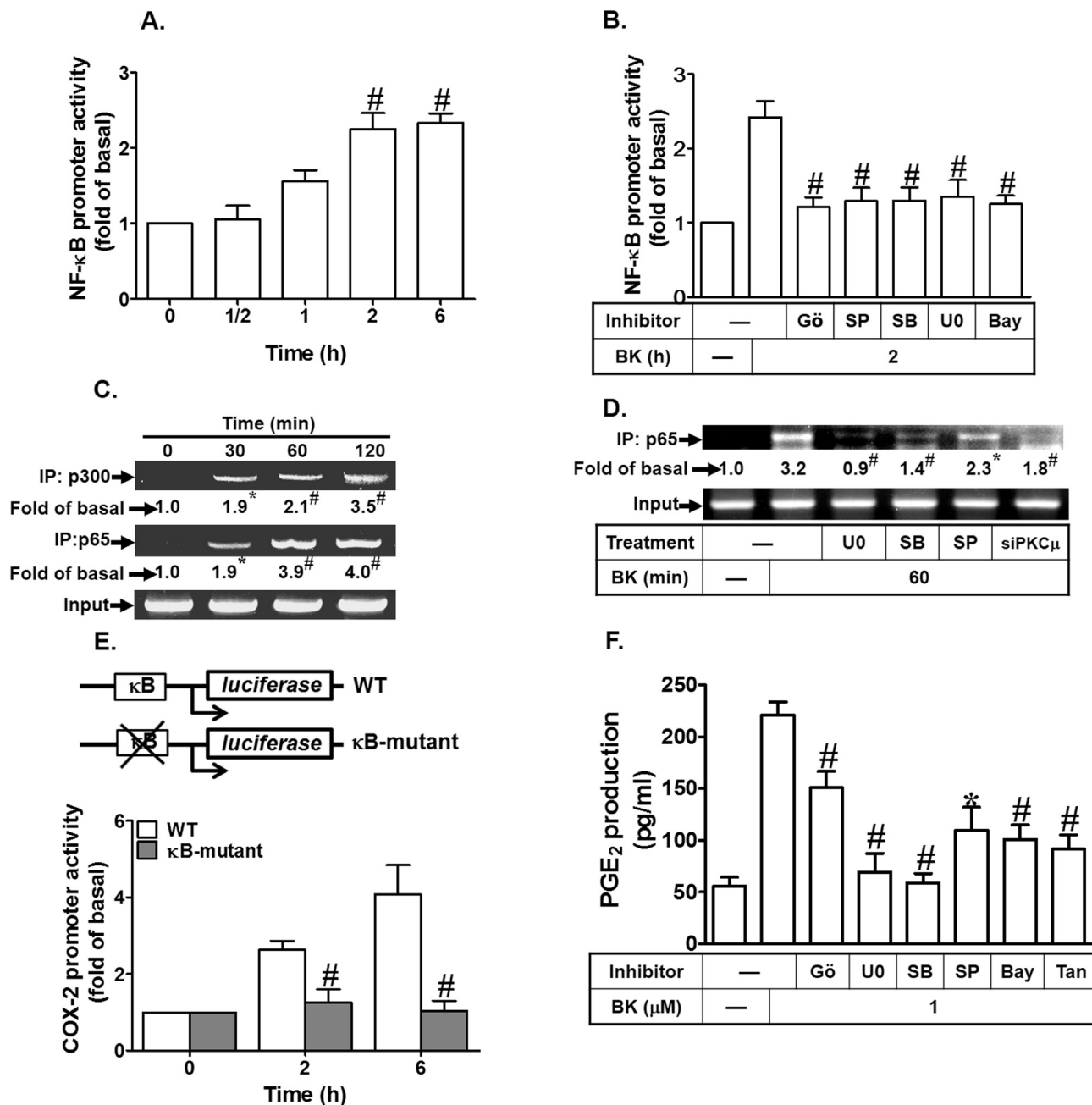
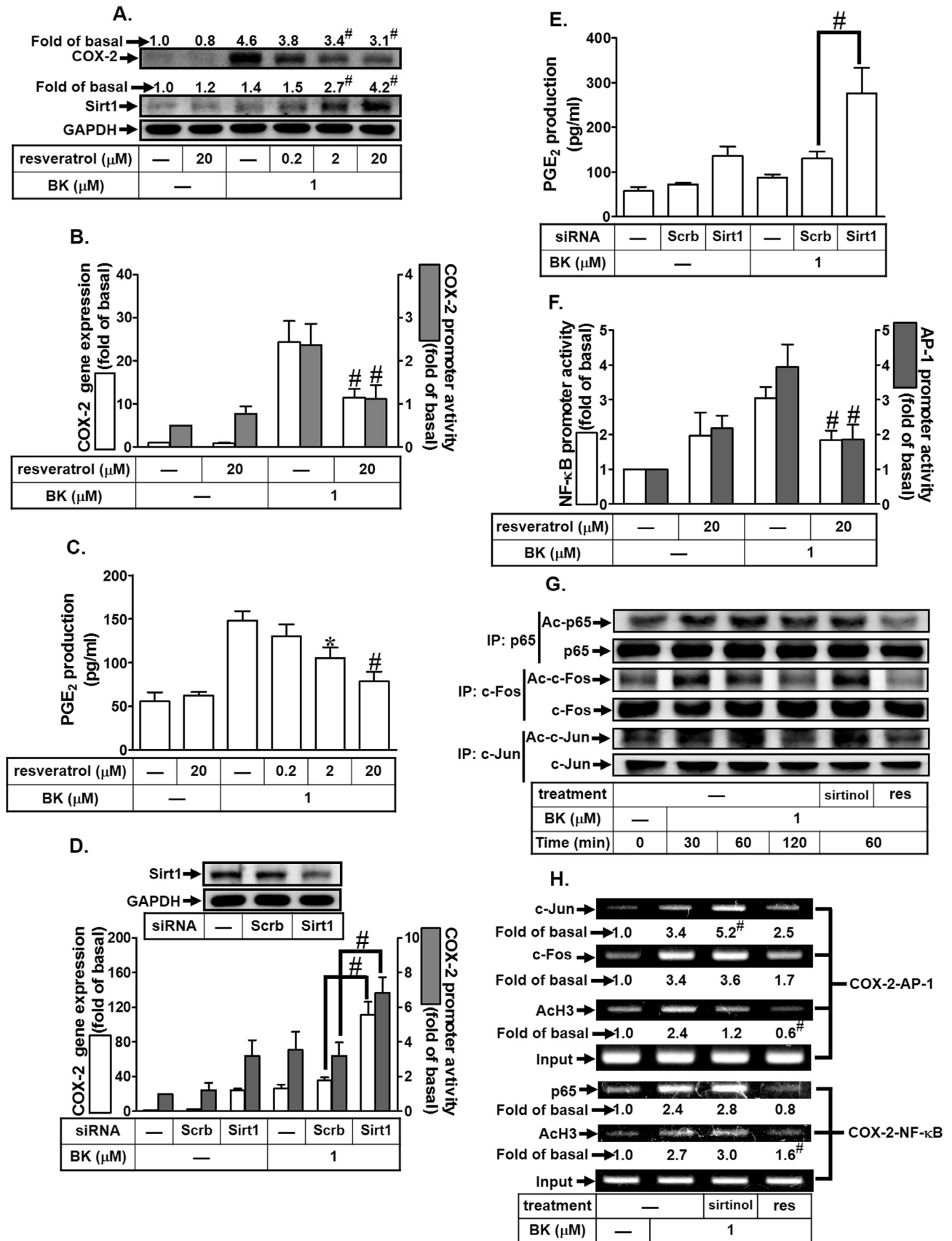


**Fig. 6.** BK augments NF-κB-dependent transcription of COX-2 promoter. RASFs were transfected with an NF-κB promoter gene, pretreated without (A) or with (B) G66976 (1 μM), U0126 (10 μM), SB202190 (10 μM), SP600125 (10 μM), or Bay 11-7082 (1 μM) for 1 h, and incubated with BK for (A) the indicated time intervals or for (B) 2 h. NF-κB promoter activity were determined. (C,D) RASFs were pretreated without or with the indicated inhibitors for 1 h, or transfected with PKCμ siRNA and incubated with BK for (C) the indicated time intervals or for (D) 30 min. The ChIP assay was performed. (E) Cells were transfected with either wild-type COX-2 promoter (WT) or NF-κB-mutated COX-2 promoter (κB-mutant) and then incubated with BK for the indicated time intervals. COX-2 promoter activity was determined. (F) RASFs were pretreated with the indicated inhibitors for 1 h, and incubated with BK for 6 h. The PGE<sub>2</sub> levels in the media were analyzed using a PGE<sub>2</sub> enzyme immunoassay kit. Data are expressed as mean ± S.E.M. of five independent experiments. <sup>#</sup>*P* < 0.05, as compared with the cells exposed to vehicle alone (A). <sup>\*</sup>*P* < 0.05, as compared with the cells exposed to BK alone (B, E, F).

whether the effect of resveratrol on the BK-induced COX-2/PGE<sub>2</sub> production is mediated through a Sirt1-dependent mechanism. RASFs were pretreated with resveratrol for 1 h and then challenged with BK. Resveratrol dose-dependently increased the expression of Sirt1 and accompanying with the down-regulation of the BK-induced COX-2 protein expression, mRNA levels, promoter activity, and PGE<sub>2</sub> production in RASFs (Fig. 7A–C). These results prompted us to recognize the potential role of Sirt1 in BK-mediated responses. To confirm this hypothesis, transfection of RASFs with Sirt1 siRNA knocked down the Sirt1 protein levels and enhanced the BK-induced COX-2 mRNA (by 66%) and promoter activity (by 120%)

and PGE<sub>2</sub> production (by 110%) (Fig. 7D and E). Since Sirt1 deacetylates a number of non-histone targets, including NF-κB and AP-1 [23], we further examined whether overexpression of Sirt1 by resveratrol could abolish NF-κB and AP-1 transcriptional activities stimulated by BK in RASFs. We found that BK-stimulated NF-κB and AP-1 promoter activities were decreased by pretreatment with resveratrol (Fig. 7F).

The acetylation of transcription factors triggers the transcription of several inflammatory genes induced by pro-inflammatory mediators [31,42]. To assess whether the acetylation levels of NF-κB p65, c-Jun, and c-Fos stimulated by BK, these transcriptional



factors were immunoprecipitated by using their own antibodies and the acetylated levels were determined by Western blot using respective anti-acetyl antibody. As shown in Fig. 7G, the levels of p65, c-Jun, and c-Fos acetylation were time-dependently increased in RASFs challenged with BK, which were attenuated by pretreatment with resveratrol, but not by a Sirt1 inhibitor (sirtinol). The transcription factors-triggered the expression of inflammatory genes may be mediated through the binding with their targeted gene promoters. To test this interaction, the binding of transcription factors to COX-2 gene promoter was determined by a ChIP assay. RASFs were pretreated with resveratrol or sirtinol for 1 h and then challenged with BK for another 1 h. Chromatin extracts from these cells were immunoprecipitated with an anti-p65, c-Jun, c-Fos or acetyl-histone 3 antibody and the DNA sequences encompassing the regions containing the NF- $\kappa$ B, c-Jun, or c-Fos binding sites in the COX-2 promoters were amplified by RT-PCR. We observed that BK stimulated the binding of p65, c-Jun, or c-Fos to the COX-2 promoter (Fig. 4E), which was reduced by resveratrol but not by sirtinol (Fig. 7H). Taken together, these results suggested that up-regulation of Sirt1 by resveratrol exerts a protective effect on BK-mediated inflammatory responses in human RASFs.

#### 4. Discussion

BK has been shown to enhance the expression of several inflammatory genes including COX-2 in RA and OA patients [10,43]. However, the detailed mechanisms of BK-induced the expression of COX-2 were still unclear in human RASFs. In the present study, we found that B2R-mediated PKC $\mu$ -dependent activation of MAPKs, NF- $\kappa$ B and AP-1 signaling cascades is essential for BK-induced COX-2/PGE<sub>2</sub> expression. Up-regulation of Sirt1 by resveratrol suppressed the BK-mediated NF- $\kappa$ B and AP-1 dependent responses in human RASFs.

COX-2 expression has been shown to be associated with synovial inflammation in arthritis [44]. Both B1R and B2R expressed on various cell types have been confirmed by immunohistochemical studies [45]. The roles of these BK receptors in different inflammatory conditions are controversial. B2R but not B1R is predominantly expressed in the synovial fibroblasts of OA patients [34] which contributes to the chronic inflammatory responses including the release of pro-inflammatory cytokines and the products of COX and lipoxygenase [46,47]. In contrast, BK activates both of B1R and B2R leading to bone resorption [48]. Moreover, activation of B1R also potentiates the effects of cytokines and PGs [49,50]. In this study, although both B1R and B2R were expressed on human RASFs, BK-induced COX-2/PGE<sub>2</sub> expression was mainly mediated through B2R, confirmed by using a selective B2R antagonist (Hoe140) or transfection with B2R siRNA. In contrast, pretreatment with selective B1R antagonist (BI-113823) or transfection with B1R siRNA failed to change the BK-mediated responses. The non-peptide B2R antagonist, fasitibant, is also effective in blocking the effect of BK in human synovial fibroblasts [51]. These results suggested that B2R might predominantly play a key role in the inflammatory responses in human RASFs, consistent

with the study showing that BK induces COX-2 expression via B2R in vascular smooth muscle cells [14].

PKC has been shown to mediate BK-induced COX-2 expression in airway smooth muscle cells and in astrocytes [11,12]. PKC $\mu$  has been detected in RA patients and is greater expressed than that of normal cells [37]. In this study, we further confirmed the role of PKC $\mu$  in the expression of inflammatory proteins such as COX-2 in human RASFs, by using the selective PKC $\mu$  inhibitor Gö6976 [38]. This note was further supported by transfection with PKC $\mu$  siRNA that inhibited BK-induced COX-2/PGE<sub>2</sub> expression. The involvement of PKC $\mu$  in BK-mediated responses was confirmed by enhancing the phosphorylation and translocation of PKC $\mu$  from the cytosol to the membrane fractions, which was antagonized by Hoe140 and Gö6976. These data suggested that BK-induced COX-2/PGE<sub>2</sub> expression is mediated through B2R-dependent PKC $\mu$  activation in RASFs.

The involvement of ERK1/2, p38 MAPK and JNK1/2 phosphorylation in BK-induced COX-2/PGE<sub>2</sub> expression was confirmed by using their respective inhibitors of U0126, SB202190, and SP600125 or transfection with siRNAs. These results are consistent with the reports that BK-induced COX-2/PGE<sub>2</sub> expression is mediated through activation of ERK1/2, p38 MAPK and JNK1/2 in different cell types [17,18]. MAPKs have been shown to be downstream components of PKCs. The relationship between B2R, PKC $\mu$  and MAPKs was differentiated by using Hoe 140, Gö6976 or transfection with PKC $\mu$  siRNA which antagonized the BK-stimulated phosphorylation of these MAPKs. These results suggested that BK-induced COX-2/PGE<sub>2</sub> expression is mediated through a B2R/PKC $\mu$ -dependent MAPKs cascade in RASFs.

BK has been shown to activate various intracellular signalings relayed to the nuclear transcription factors such as NF- $\kappa$ B [18] and AP-1 [19]. However, the upstream or downstream signaling components mediated BK responses that regulate COX-2 expression, are not completely defined in human RASFs. AP-1 comprises heterodimers of c-Fos and c-Jun or homodimers of c-Jun that regulates gene expression by binding to a consensus DNA motif in the promoter region of target genes [32,52]. In this study, we found the involvement of AP-1 in the BK-induced COX-2 expression was confirmed by using an AP-1 inhibitor tanshinone IIA or by transfection with c-Fos or c-Jun siRNA which attenuated the BK-induced COX-2 expression. Several studies have reported that activation of AP-1 is triggered by MAPKs [32,53] and PKC isoforms [54,55]. However, the roles of PKC $\mu$ , MAPKs and AP-1 in BK-induced COX-2/PGE<sub>2</sub> in RASFs are still unknown. In our study, BK time-dependently stimulated AP-1-luciferase promoter activity, which was inhibited by U0126 or SP600125, but not by SB202190. In response to BK, c-Fos and c-Jun time-dependently bound to the COX-2 promoter, indicating the pivotal roles of c-Fos and c-Jun of AP-1 subunits leading to COX-2 expression. The interaction between c-Jun and COX-2 promoter was inhibited by U0126, SP600125, SB202190 or PKC $\mu$  siRNA. However, pretreatment with U0126, SP600125, or PKC $\mu$  siRNA also inhibited the recruitment of c-Fos to the COX-2 promoter; SB202190 had no effect on this response. These results suggested that BK stimulates AP-1 transcriptional activity via PKC $\mu$ /MAPKs-dependent cascade and leading to COX-2/PGE<sub>2</sub>

**Fig. 7.** Resveratrol inhibits BK-induced NF- $\kappa$ B and AP-1 activation which binds with COX-2 promoter. (A–C) Cells were pretreated with resveratrol for 1 h, and then incubated with BK for (A) 6 h or (B) 4 h. (A) The protein levels of COX-2 and Sirt1 were determined by western blot. (B) The levels of COX-2 mRNA and promoter activity were determined by real-time PCR and luciferase activity assay. (C) The media were collected to determine the levels of PGE<sub>2</sub>. (D,E) RASFs were transfected with scrambled or Sirt1 siRNA and then incubated with BK for (D) 4 h or (E) 6 h. The levels of COX-2 mRNA and promoter activity and PGE<sub>2</sub> were determined. (F) RASFs were transfected with either NF- $\kappa$ B or AP-1 promoter, pretreated with resveratrol for 1 h, and then incubated with BK for 6 h. The levels of NF- $\kappa$ B and AP-1 promoter activities were determined. (G,H) RASFs were pretreated without or with resveratrol or sirtinol for 1 h and then incubated with BK for the indicated time intervals. The cell lysates were immunoprecipitated with an anti-NF- $\kappa$ B p65, anti-c-Fos, anti-c-Jun or anti-acetylated H<sub>3</sub> antibody and then analyzed by (G) western blot using an antibody as indicated or (H) the association of NF- $\kappa$ B or AP-1 (c-Fos and c-Jun) with COX-2 promoter DNA was amplified by PCR. Data are expressed as mean  $\pm$  S.E.M. of five independent experiments.  $^{\#}P < 0.05$ , as compared with the cells exposed to BK alone (B–F).



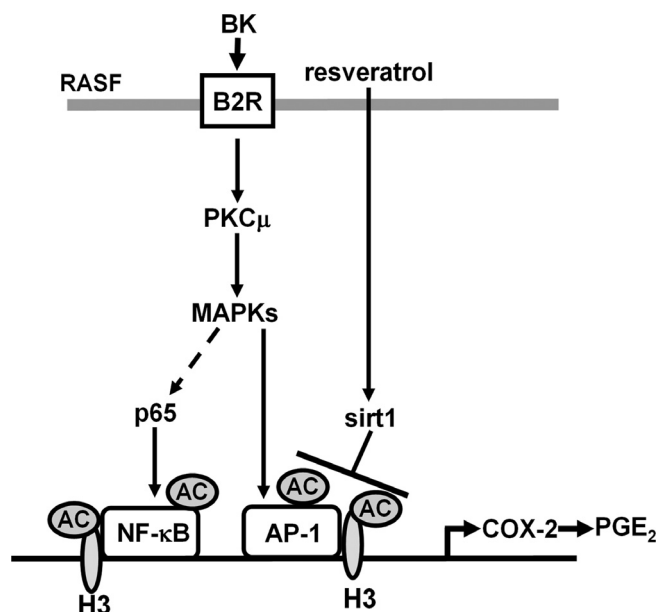


**Fig. 8.** Proposed model to illustrate the signaling pathways involved in COX-2 expression in human RASFs challenged with BK. In RASFs, BK activates B2R-dependent PKC $\mu$ -derived phosphorylation of MAPKs (ERK1/2, p38 MAPK, and JNK1/2), which in turn triggers AP-1 and NF- $\kappa$ B activation and ultimately induces COX-2 expression associated with PGE<sub>2</sub> production. Up-regulation and activation of sirt1 by resveratrol suppressed the BK-induced production of COX-2/PGE<sub>2</sub> through inhibiting the interaction of AP-1 and NF- $\kappa$ B with COX-2 promoter gene in RASFs.

expression in human RASFs. The different interaction between p38 MAPK and c-Fos or c-Jun was preserved further investigating.

NF- $\kappa$ B has been shown to be a major transcription factor mediated the expression of various inflammatory genes [41,56]. Several reports also indicate that MAPKs catalyze the phosphorylation of p65 in different cell types: (1) Hu et al. indicate that both of U0126 (20  $\mu$ M) treatment and DN-ERK2 transfection attenuate the TNF- $\alpha$ -stimulated p65 phosphorylation. Moreover, ERK1/2 also activate IKK $\beta$ -mediated p65 phosphorylation [57]; (2) Huang et al. also indicate that both of U0126 (10  $\mu$ M) and SP600125 (20  $\mu$ M) treatments, for ERK1/2 and JNK1/2 inhibition, reduce p65 phosphorylation [58]; and (3) Our previous report also indicates that the concentrations of SP600125 and SB202190 at 1  $\mu$ M, respectively, reduce p65 phosphorylation at S536 [59]. Our results showed the activation of NF- $\kappa$ B via a signaling cascade involving the B2R, PKC $\mu$ , MAPKs (ERK1/2, p38 MAPK, and JNK1/2) and ultimately contributing to COX-2 expression and PGE<sub>2</sub> production by BK. The common upstream regulatory step is activation of I $\kappa$ B kinase (IKK) complex [56]. As such, activation of NF- $\kappa$ B dimers is the result of IKK-mediated the phosphorylation-induced degradation of I $\kappa$ B, which enables the NF- $\kappa$ B to enter the nucleus and activates specific target gene expression [56]. In the present study, we found that pretreatment with Gö6976, U0126, SB202190, and SP600125 or transfection with PKC $\mu$  siRNA attenuated BK-induced the increase of p65 phosphorylation, p65 translocation from the cytosol to the nucleus, NF- $\kappa$ B-luciferase activity, and the binding of p65 to the element on the COX-2 promoter. Activation of NF- $\kappa$ B involved in the BK-induced responses was confirmed by using a selective NF- $\kappa$ B inhibitor Bay11-7082 or transfection with NF- $\kappa$ B p65 siRNA. These results are consistent with the reports that the involvement of MAPKs and NF- $\kappa$ B in the transcriptional regulation of many inflammatory genes and enzymes plays a pivotal role in the inflammatory responses in different cell types [11,31,48,60,61]. Based on these reports and our findings, we speculated that MAPKs may regulate IKK $\beta$ -mediated p65 phosphorylation directly or indirectly in

NF- $\kappa$ B pathway involved in BK-induced COX-2/PGE<sub>2</sub> expression in human RASFs.

The initiation of the gene transcription is triggered by untightening the DNA which is more easily binding with the transcription factors leading to the production of cytokines and inflammatory mediators [62]. Both AP-1 and NF- $\kappa$ B are the important transcription factors involved in the BK-induced the expression of several genes including COX-2 in various cell types [11,19,26,31]. Acetylation of AP-1 (c-Fos and c-Jun) and NF- $\kappa$ B p65 has been shown to be essential for the expression of inflammatory genes induced by various insults [31,42,53]. We noticed that both Ser276 and Ser536 are the targeted residues of activated p65. Especially, the correlation between phosphorylation at Ser276 and acetylated K310 has been shown to regulate the transcription of NF- $\kappa$ B target genes [63]. However, our results suggested that the phosphorylation at Ser536 and acetylation of p65 may be an important issue to further approach their roles in the regulation of gene expression.

To analyze the transcription factor association on promoter, previous report indicates that histone acetylation alters nucleosomal conformation to facilitate gene transcription [64]. Our results indicated that immunoprecipitated chromatin were analyzed with respective antibodies, such as c-Jun, c-Fos and AcH3 (with anti-acetyl-K9/14-histone H3 Ab), in ChIP assays. We noticed that LPS induces acetylation of H3 on the COX-2 promoter within 1 h and the replicon of ChIP (180 bp, from -114 to +66) containing the AP-1 binding site (-67 to -58, Fig. 4E) [65,66]. This region is similar to our AP-1 site primer design (-137 to +31). In addition, the  $\kappa$ B site (-221 to -210) [67] was also detected in the immunocomplex by using anti-p65 and AcH3 antibodies, respectively. All of these results showed the similar inductions (BK and sirtinol) pattern and reduced by Resveratrol.

Sirt1, a NAD<sup>+</sup> dependent histone deacetylase, causes various modifications of histone/protein acetylation status and ubiquitous expression in mammal cells. Previous reports indicate that at least 79 substrates or 136 associated proteins of Sirt1 are identified and regulate several biological functions such as metabolism and inflammation [68,69]. Sirt1 can deacetylate H4K16, H3K9 and H3K14. Moreover, Sirt1 mediates heterochromatin formation to silence gene expression [70,71]. We noticed that sirtinol treatment failed to affect the acetylated p65, c-Jun and c-Fos expression. However, sirtinol enhances the associations of p65, c-Jun and c-Fos with response elements, especially the AcH3 on  $\kappa$ B site, to activate COX-2 transcription. Sirt1 associates with c-Jun and c-Fos and mediates AP-1 deacetylation to repress gene transcription [26,72]. The results of Sirt1-KO mice show that the gene repression by resveratrol is a Sirt1-dependent manner in transcriptional regulation [72]. Sirt1 also associates with p65 and deacetylates K310Ac to regulate downstream gene transcription, cell survival and inflammatory responses [23,25]. In our study, we found that BK induced Sirt1 up-regulation about 40% and COX-2 expression about 4.6-fold (Fig. 7A). Importantly, resveratrol (20  $\mu$ M) induced Sirt1 to 4.2-fold which attenuated the BK-induced COX-2 induction by about 33%. We suggested that BK-induced the Sirt1 expression or activity is overcome by alternative pathways stimulated by BK in regulation of COX-2 transcription. As shown in Fig. 7B, the COX-2 mRNA expression exhibited the similar tendency in the BK-induced responses attenuated by resveratrol.

So far, resveratrol is the effective activator of Sirt1, which suppresses the expression of inflammatory genes mainly through deacetylation of AP-1 and NF- $\kappa$ B and leading to down regulation of inflammatory genes in different cell types and animals [22,23,25,26]. Moreover, pharmacological modulation of Sirt1 expression and activity are good approaches to regulate the cytokine response by inflammatory mediators [73]. We found that resveratrol significantly induced Sirt1 expression (Fig. 7A). The inductions of COX-2 and PGE<sub>2</sub>, the inflammatory markers, were



down-regulated by resveratrol through the Sirt1 induction or activity. To evaluate the transcriptional regulation, we also found that sirtinol enhances the associations of p65, c-Jun and c-Fos on response elements, especially the ACh3 on  $\kappa$ B site, to induce COX-2 expression. Our results are consistent with these reports that up-regulation of Sirt1 by resveratrol attenuated the acetylation of c-Jun and c-Fos (AP-1 subunits) and NF- $\kappa$ B and thereby suppressing COX-2 expression and PGE<sub>2</sub> synthesis induce by BK in human RASFs. This hypothesis was further confirmed by transfection with Sirt1 siRNA which knocking down Sirt1 protein markedly upregulated COX-2 and PGE<sub>2</sub> expression to attenuate the protective effect of resveratrol, supporting that these anti-inflammatory effects of resveratrol are mediated through a Sirt1-dependent manner. Resveratrol induced Sirt1 expression to reduce these BK-mediated responses and reflected its anti-inflammatory effect beneficial for inflammatory diseases.

In summary, as depicted in Fig. 8, our results demonstrated that in RASFs, activation of B2R-mediated PKC $\mu$ -dependent activation of MAPKs (ERK1/2, p38 MAPK, and JNK1/2), AP-1 and NF- $\kappa$ B is essential for BK-induced COX-2 gene expression and PGE<sub>2</sub> release. Involvement of PKC $\mu$ -dependent MAPKs and NF- $\kappa$ B/AP-1 activation in BK-induced COX-2/PGE<sub>2</sub> production was first demonstrated in RASFs and provided new insights into the mechanisms of BK-mediated inflammatory diseases. Agents with activity to block COX-2/PGE<sub>2</sub> via suppression of B2R activation have the potential to treat inflammatory arthritis, and deserve further development.

## Conflict of interest

The authors declare that there are no conflicts of interest.

## Acknowledgments

We greatly thank Ms. Hsiao-Wen Liu for her technical assistance during the preparation of this manuscript. This work was supported by the Ministry of Science and Technology, Taiwan; Grant number: MOST104-2320-B-182A-003-MY3, MOST104-2320-B-182-010 and MOST105-2320-B-182-005-MY3; Chang Gung Medical Research Foundation, Grant numbers: CMRPD1F0022, CMRPD1F0511, CMRPG3E2232, and CMRPG3F1531; and the Ministry of Education, Taiwan; Grant numbers: EMRPD1G0171 and EMRPD1G0281.

## References

- [1] A.K. Andersson, C. Li, F.M. Brennan, Recent developments in the immunobiology of rheumatoid arthritis, *Arthritis Res. Ther.* 10 (2008) 204.
- [2] S. Lefevre, A. Knedla, C. Tennie, A. Kampmann, C. Wunrau, R. Dinser, et al., Synovial fibroblasts spread rheumatoid arthritis to unaffected joints, *Nat. Med.* 15 (2009) 1414–1420.
- [3] U.H. Lerner, I.L. Jones, G.T. Gustafson, Bradykinin, a new potential mediator of inflammation-induced bone resorption. Studies of the effects on mouse calvarial bones and articular cartilage in vitro, *Arthritis Rheum.* 30 (1987) 530–540.
- [4] K.D. Bhoola, C.J. Elson, P.A. Dieppe, Kinins—key mediators in inflammatory arthritis? *Br. J. Rheumatol.* 31 (1992) 509–518.
- [5] K.M. Hargreaves, E.S. Troullos, R.A. Dionne, E.A. Schmidt, S.C. Schafer, J.L. Joris, Bradykinin is increased during acute and chronic inflammation: therapeutic implications, *Clin. Pharmacol. Ther.* 44 (1988) 613–621.
- [6] B.M. Selwyn, C.D. Figueroa, E. Fink, A. Swan, P.A. Dieppe, K.D. Bhoola, A tissue kallikrein in the synovial fluid of patients with rheumatoid arthritis, *Ann. Rheum. Dis.* 48 (1989) 128–133.
- [7] S.G. Farmer, R.M. Burch, Biochemical and molecular pharmacology of kinin receptors, *Ann. Rev. Pharmacol. Toxicol.* 32 (1992) 511–536.
- [8] J.N. Sharma, Basic and clinical aspects of bradykinin receptor antagonists, *Prog. Drug Res.* 69 (2014) 1–14.
- [9] C.M. Yang, S.F. Luo, W.B. Wu, S.L. Pan, Y.J. Tsai, C.T. Chiu, et al., Uncoupling of bradykinin-induced phosphoinositide hydrolysis and Ca<sup>2+</sup> mobilization by phorbol ester in canine cultured tracheal epithelial cells, *Br. J. Pharmacol.* 125 (1998) 627–636.
- [10] C.H. Lee, D.C. Shieh, C.Y. Tzeng, C.P. Chen, S.P. Wang, Y.C. Chiu, et al., Bradykinin-induced IL-6 expression through bradykinin B2 receptor, phospholipase C, protein kinase C $\delta$  and NF- $\kappa$ B pathway in human synovial fibroblasts, *Mol. Immunol.* 45 (2008) 3693–3702.
- [11] H.L. Hsieh, H.H. Wang, C.Y. Wu, M.J. Jou, M.H. Yen, P. Parker, et al., BK-induced COX-2 expression via PKC $\delta$ -dependent activation of p42/p44 MAPK and NF- $\kappa$ B in astrocytes, *Cell. Signal.* 19 (2007) 330–340.
- [12] L. Pang, M. Nie, L. Corbett, R. Donnelly, S. Gray, A.J. Knox, Protein kinase C- $\epsilon$  mediates bradykinin-induced cyclooxygenase-2 expression in human airway smooth muscle cells, *FASEB J.* 16 (2002) 1435–1437.
- [13] H.C. Rodgers, L. Pang, E. Holland, L. Corbett, S. Range, A.J. Knox, Bradykinin increases IL-8 generation in airway epithelial cells via COX-2-derived prostanoids, *Am. J. Physiol. Lung Cell. Mol. Physiol.* 283 (2002) L612–L618.
- [14] J.A. Rodriguez, P. De la Cerda, E. Collyer, V. Decap, C.P. Vio, V. Velarde, Cyclooxygenase-2 induction by bradykinin in aortic vascular smooth muscle cells, *Am. J. Physiol. Heart Circ. Physiol.* 290 (2006) H30–H36.
- [15] Z. Wei, F. Wang, J. Song, Q. Lu, P. Zhao, Y. Xia, et al., Norisoboldine inhibits the production of interleukin-6 in fibroblast-like synoviocytes from adjuvant arthritis rats through PKC/MAPK/NF- $\kappa$ B-p65/CREB pathways, *J. Cell. Biochem.* 113 (2012) 2785–2795.
- [16] C.C. Lin, H.L. Hsieh, R.H. Shih, P.L. Chi, S.E. Cheng, J.C. Chen, et al., NADPH oxidase 2-derived reactive oxygen species signal contributes to bradykinin-induced matrix metalloproteinase-9 expression and cell migration in brain astrocytes, *Cell Commun. Signal.* 10 (2012) 35.
- [17] A. Blaukat, A. Barac, M.J. Cross, S. Offermanns, I. Dikic, G protein-coupled receptor-mediated mitogen-activated protein kinase activation through cooperation of G $\alpha_q$  and G $\alpha_i$  signals, *Mol. Cell. Biol.* 20 (2000) 6837–6848.
- [18] P. Xie, D.D. Browning, N. Hay, N. Mackman, R.D. Ye, Activation of NF- $\kappa$ B by bradykinin through a G $\alpha_q$ - and G $\alpha_i$ -dependent pathway that involves phosphoinositide 3-kinase and Akt, *J. Biol. Chem.* 275 (2000) 24907–24914.
- [19] S.S. El-Dahr, S. Dipp, I.V. Yosipiv, W.H. Baricos, Bradykinin stimulates c-fos expression, AP-1-DNA binding activity and proliferation of rat glomerular mesangial cells, *Kidney Int.* 50 (1996) 1850–1855.
- [20] K.T. Howitz, K.J. Bitterman, H.Y. Cohen, D.W. Lamming, S. Lavu, J.G. Wood, et al., Small molecule activators of sirtuins extend *Saccharomyces cerevisiae* lifespan, *Nature* 425 (2003) 191–196.
- [21] M.T. Borra, B.C. Smith, J.M. Denu, Mechanism of human SIRT1 activation by resveratrol, *J. Biol. Chem.* 280 (2005) 17187–17195.
- [22] T. Wang, J. Gu, P.F. Wu, F. Wang, Z. Xiong, Y.J. Yang, et al., Protection by tetrahydroxystilbene glucoside against cerebral ischemia: involvement of JNK, SIRT1, and NF- $\kappa$ B pathways and inhibition of intracellular ROS/RNS generation, *Free Radical Biol. Med.* 47 (2009) 229–240.
- [23] F. Yeung, J.E. Hoberg, C.S. Ramsey, M.D. Keller, D.R. Jones, R.A. Frye, et al., Modulation of NF- $\kappa$ B-dependent transcription and cell survival by the SIRT1 deacetylase, *EMBO J.* 23 (2004) 2369–2380.
- [24] S. Rajendrasozhan, S.R. Yang, V.L. Kinnula, I. Rahman, SIRT1, an antiinflammatory and antiaging protein, is decreased in lungs of patients with chronic obstructive pulmonary disease, *Am. J. Respir. Crit. Care Med.* 177 (2008) 861–870.
- [25] H. Yang, W. Zhang, H. Pan, H.G. Feldser, E. Lainez, C. Miller, et al., SIRT1 activators suppress inflammatory responses through promotion of p65 deacetylation and inhibition of NF- $\kappa$ B activity, *PLoS ONE* 7 (2012) e46364.
- [26] R. Zhang, H.Z. Chen, J.J. Liu, Y.Y. Jia, Z.Q. Zhang, R.F. Yang, et al., SIRT1 suppresses activator protein-1 transcriptional activity and cyclooxygenase-2 expression in macrophages, *J. Biol. Chem.* 285 (2010) 7097–7110.
- [27] M.H. Moon, J.K. Jeong, Y.J. Lee, J.W. Seol, C.J. Jackson, S.Y. Park, SIRT1, a class III histone deacetylase, regulates TNF $\alpha$ -induced inflammation in human chondrocytes, *Osteoarthritis Cartilage* 21 (2013) 470–480.
- [28] N. Elmali, O. Baysal, A. Harma, I. Esenkaya, B. Mizrak, Effects of resveratrol in inflammatory arthritis, *Inflammation* 30 (2007) 1–6.
- [29] F. Niederer, C. Ospelt, F. Brentano, M.O. Hottiger, R.E. Gay, S. Gay, et al., SIRT1 overexpression in the rheumatoid arthritis synovium contributes to proinflammatory cytokine production and apoptosis resistance, *Ann. Rheum. Dis.* 70 (2011) 1866–1873.
- [30] A.M. Grabiec, S. Krausz, W. de Jager, T. Burakowski, D. Groot, M.E. Sanders, et al., Histone deacetylase inhibitors suppress inflammatory activation of rheumatoid arthritis patient synovial macrophages and tissue, *J. Immunol.* 184 (2010) 2718–2728.
- [31] P.L. Chi, S.F. Luo, H.L. Hsieh, I.T. Lee, L.D. Hsiao, Y.L. Chen, et al., Cytosolic phospholipase A<sub>2</sub> induction and prostaglandin E<sub>2</sub> release by interleukin-1 $\beta$  via the myeloid differentiation factor 88-dependent pathway and cooperation of p300, Akt, and NF- $\kappa$ B activity in human rheumatoid arthritis synovial fibroblasts, *Arthritis Rheum.* 63 (2011) 2905–2917.
- [32] W.H. Tung, H.L. Hsieh, C.M. Yang, Enterovirus 71 induces COX-2 expression via MAPKs, NF- $\kappa$ B, and AP-1 in SK-N-SH cells: Role of PGE<sub>2</sub> in viral replication, *Cell. Signal.* 22 (2010) 234–246.
- [33] J.V. Fahey, C.P. Ciosek Jr., D.S. Newcombe, Human synovial fibroblasts: the relationships between cyclic AMP, bradykinin, and prostaglandins, *Agents Actions* 7 (1977) 255–264.
- [34] B. Cassim, S. Naidoo, R. Ramsaroop, K.D. Bhoola, Immunolocalization of bradykinin receptors on human synovial tissue, *Immunopharmacology* 36 (1997) 121–125.
- [35] K. Wirth, F.J. Hock, U. Albus, W. Linz, H.G. Alpermann, H. Anagnostopoulos, et al., Hoe 140 a new potent and long acting bradykinin-antagonist: in vivo studies, *Br. J. Pharmacol.* 102 (1991) 774–777.
- [36] D. Wu, X. Lin, C. Bernloehr, T. Hildebrandt, H. Doods, Effects of a novel bradykinin B1 receptor antagonist and angiotensin II receptor blockade on experimental myocardial infarction in rats, *PLoS ONE* 7 (2012) e51151.

- [37] N. Zini, A. Bavelloni, G. Lisignoli, S. Ghisu, A. Valmori, A.M. Martelli, et al., PKC- $\zeta$  expression is lower in osteoblasts from arthritic patients: IL1- $\beta$  and TNF- $\alpha$  induce a similar decrease in non-arthritic human osteoblasts, *J. Cell. Biochem.* 103 (2008) 547–555.
- [38] M. Gschwendt, S. Dieterich, J. Rennecke, W. Kittstein, H.J. Mueller, F.J. Johannes, Inhibition of protein kinase C $\mu$  by various inhibitors. Differentiation from protein kinase c isoenzymes, *FEBS Lett.* 392 (1996) 77–80.
- [39] S.F. Steinberg, Distinctive activation mechanisms and functions for protein kinase C $\delta$ , *Biochem. J.* 384 (2004) 449–459.
- [40] Y.J. Kang, U.R. Mbonye, C.J. DeLong, M. Wada, W.L. Smith, Regulation of intracellular cyclooxygenase levels by gene transcription and protein degradation, *Prog. Lipid Res.* 46 (2007) 108–125.
- [41] S. Ghosh, D. Baltimore, Activation in vitro of NF- $\kappa$ B by phosphorylation of its inhibitor I $\kappa$ B, *Nature* 344 (1990) 678–682.
- [42] L. Chen, W. Fischle, E. Verdin, W.C. Greene, Duration of nuclear NF- $\kappa$ B action regulated by reversible acetylation, *Science* 293 (2001) 1653–1657.
- [43] S. Meini, C.A. Maggi, Knee osteoarthritis: a role for bradykinin? *Inflamm. Res.* 57 (2008) 351–361.
- [44] P.E. Lipsky, P.C. Isakson, Outcome of specific COX-2 inhibition in rheumatoid arthritis, *J. Rheumatol. Suppl.* 49 (1997) 9–14.
- [45] H. Shirasaki, E. Kanaizumi, T. Himi, Immunohistochemical localization of the bradykinin B1 and B2 receptors in human nasal mucosa, *Mediators Inflamm.* 2009 (2009) 102406.
- [46] M. Fujita, T. Andoh, K. Ohashi, A. Akira, I. Saiki, Y. Kuraishi, Roles of kinin B1 and B2 receptors in skin cancer pain produced by orthotopic melanoma inoculation in mice, *Eur. J. Pain* 14 (2010) 588–594.
- [47] F. Marceau, D.R. Bachvarov, Kinin receptors, *Clin. Rev. Allergy Immunol.* 16 (1998) 385–401.
- [48] S. Srivastava, K. Sharma, N. Kumar, P. Roy, Bradykinin regulates osteoblast differentiation by Akt/ERK/NF- $\kappa$ B signaling axis, *J. Cell. Physiol.* 229 (2014) 2088–2105.
- [49] H.P. Benton, T.R. Jackson, M.R. Hanley, Identification of a novel inflammatory stimulant of chondrocytes. Early events in cell activation by bradykinin receptors on pig articular chondrocytes, *Biochem. J.* 258 (1989) 861–867.
- [50] G.N. Kaufman, C. Zaouter, B. Valteau, P. Sirois, F. Moldovan, Nociceptive tolerance is improved by bradykinin receptor B1 antagonism and joint morphology is protected by both endothelin type A and bradykinin receptor B1 antagonism in a surgical model of osteoarthritis, *Arthritis Res. Ther.* 13 (2011) R76.
- [51] A. Gomis, S. Meini, A. Miralles, C. Valenti, S. Giuliani, C. Belmonte, et al., Blockade of nociceptive sensory afferent activity of the rat knee joint by the bradykinin B2 receptor antagonist fasilabant, *Osteoarthritis Cartilage* 21 (2013) 1346–1354.
- [52] R.C. Mifflin, J.I. Saada, J.F. Di Mari, P.A. Adegboyega, J.D. Valentich, D.W. Powell, Regulation of COX-2 expression in human intestinal myofibroblasts: mechanisms of IL-1-mediated induction, *Am. J. Physiol. Cell Physiol.* 282 (2002) C824–C834.
- [53] C.C. Lin, C.T. Kuo, C.Y. Cheng, C.Y. Wu, C.W. Lee, H.L. Hsieh, et al., IL-1 $\beta$  promotes A549 cell migration via MAPKs/AP-1- and NF- $\kappa$ B-dependent matrix metalloproteinase-9 expression, *Cell. Signal.* 21 (2009) 1652–1662.
- [54] B.Z. Simkhovich, K. Przyklenk, R.A. Kloner, Role of protein kinase C as a cellular mediator of ischemic preconditioning: a critical review, *Cardiovasc. Res.* 40 (1998) 9–22.
- [55] J.W. Soh, I.B. Weinstein, Roles of specific isoforms of protein kinase C in the transcriptional control of cyclin D1 and related genes, *J. Biol. Chem.* 278 (2003) 34709–34716.
- [56] T.D. Gilmore, Introduction to NF- $\kappa$ B: players, pathways, perspectives, *Oncogene* 25 (2006) 6680–6684.
- [57] J. Hu, H. Nakano, H. Sakurai, N.H. Colburn, Insufficient p65 phosphorylation at S536 specifically contributes to the lack of NF- $\kappa$ B activation and transformation in resistant JB6 cells, *Carcinogenesis* 25 (2004) 1991–2003.
- [58] J. Huang, H.M. Siragy, Regulation of (pro)renin receptor expression by glucose-induced mitogen-activated protein kinase, nuclear factor- $\kappa$ B, and activator protein-1 signaling pathways, *Endocrinology* 151 (2010) 3317–3325.
- [59] C.C. Yang, C.C. Lin, P.T. Chien, L.D. Hsiao, C.M. Yang, Thrombin/matrix metalloproteinase-9-dependent SK-N-SH cell migration is mediated through a PLC/PKC/MAPKs/NF- $\kappa$ B cascade, *Mol. Neurobiol.* 53 (2016) 5833–5846.
- [60] S.F. Luo, R.Y. Fang, H.L. Hsieh, P.L. Chi, C.C. Lin, L.D. Hsiao, et al., Involvement of MAPKs and NF- $\kappa$ B in tumor necrosis factor  $\alpha$ -induced vascular cell adhesion molecule 1 expression in human rheumatoid arthritis synovial fibroblasts, *Arthritis Rheum.* 62 (2010) 105–116.
- [61] S. Sacconi, S. Pantano, G. Natoli, P38-Dependent marking of inflammatory genes for increased NF- $\kappa$ B recruitment, *Nat. Immunol.* 3 (2002) 69–75.
- [62] K. Ito, Impact of post-translational modifications of proteins on the inflammatory process, *Biochem. Soc. Trans.* 35 (2007) 281–283.
- [63] L.F. Chen, S.A. Williams, Y. Mu, H. Nakano, J.M. Duerr, L. Buckbinder, et al., NF- $\kappa$ B RelA phosphorylation regulates RelA acetylation, *Mol. Cell Biol.* 25 (2005) 7966–7975.
- [64] K. Struhl, Histone acetylation and transcriptional regulatory mechanisms, *Genes Dev.* 12 (1998) 599–606.
- [65] T. Angrisano, R. Pero, M. Brancaccio, L. Coretti, E. Florio, A. Pezone, et al., Cyclical DNA methylation and histone changes are induced by LPS to activate COX-2 in human intestinal epithelial cells, *PLoS ONE* 11 (2016) e0156671.
- [66] Z.R. Healy, F. Zhu, J.D. Stull, K. Konstantopoulos, Elucidation of the signaling network of COX-2 induction in sheared chondrocytes: COX-2 is induced via a Rac/MEKK1/MKK7/JNK2/c-Jun-C/EBP $\beta$ -dependent pathway, *Am. J. Physiol.-Cell Physiol.* 294 (2008) C1146–C1157.
- [67] H. Inoue, T. Tanabe, Transcriptional role of the nuclear factor  $\kappa$  B site in the induction by lipopolysaccharide and suppression by dexamethasone of cyclooxygenase-2 in U937 cells, *Biochem. Biophys. Res. Commun.* 244 (1998) 143–148.
- [68] A. Sharma, V. Gautam, S. Costantini, A. Paladino, G. Colonna, Interactomic and pharmacological insights on human sirt-1, *Front. Pharmacol.* 3 (2012) 40.
- [69] M.W. McBurney, K.V. Clark-Knowles, A.Z. Caron, D.A. Gray, SIRT1 is a highly networked protein that mediates the adaptation to chronic physiological stress, *Genes Cancer* 4 (2013) 125–134.
- [70] A. Vaquero, M. Scher, D. Lee, H. Erdjument-Bromage, P. Tempst, D. Reinberg, Human Sirt1 interacts with histone H1 and promotes formation of facultative heterochromatin, *Mol. Cell* 16 (2004) 93–105.
- [71] T. Zhang, W.L. Kraus, SIRT1-dependent regulation of chromatin and transcription: linking NAD $^{+}$  metabolism and signaling to the control of cellular functions, *Biochim. Biophys. Acta* 1804 (2010) 1666–1675.
- [72] Z. Gao, J. Ye, Inhibition of transcriptional activity of c-Jun by SIRT1, *Biochem. Biophys. Res. Commun.* 376 (2008) 793–796.
- [73] Y. Alvarez, M. Rodriguez, C. Municio, E. Hugo, S. Alonso, N. Ibarrola, et al., Sirtuin 1 is a key regulator of the interleukin-12 p70/interleukin-23 balance in human dendritic cells, *J. Biol. Chem.* 287 (2012) 35689–35701.

Inflammation Modulatory Phorbol Esters from the Seeds of *Aquilaria malaccensis*

Vitthal D. Wagh,<sup>†,◇</sup> Michal Korinek,<sup>†,‡,◇</sup> I-Wen Lo,<sup>†</sup> Yu-Ming Hsu,<sup>†</sup> Shu-Li Chen,<sup>†</sup> Hsue-Yin Hsu,<sup>§</sup> Tsong-Long Hwang,<sup>⊥,||,▽</sup> Yang-Chang Wu,<sup>†,#</sup> Bing-Hung Chen,<sup>\*,‡,⊙,δ</sup> Yuan-Bin Cheng,<sup>\*,†,||,#</sup> and Fang-Rong Chang<sup>\*,†,||,□,△</sup>

<sup>†</sup>Graduate Institute of Natural Products, College of Pharmacy, <sup>‡</sup>Department of Biotechnology, College of Life Science, <sup>¶</sup>Center for Infectious Disease and Cancer Research, and <sup>#</sup>Research Center for Natural Products & Drug Development, Kaohsiung Medical University, Kaohsiung 807, Taiwan

<sup>§</sup>Department of Life Sciences, Tzu Chi University, Hualien 970, Taiwan

<sup>⊥</sup>Graduate Institute of Natural Products, College of Medicine, and Chinese Herbal Medicine Research Team, Healthy Aging Research Center, Chang Gung University, Taoyuan 333, Taiwan

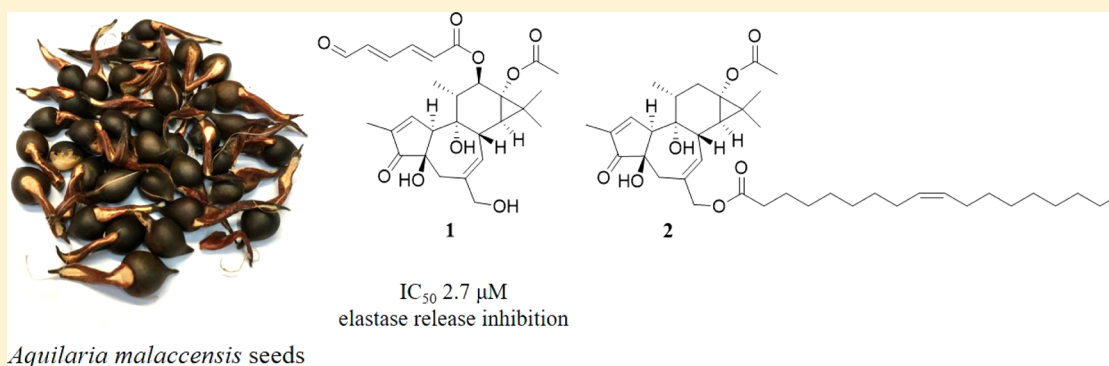
<sup>||</sup>Research Center for Chinese Herbal Medicine, Research Center for Food and Cosmetic Safety, and Graduate Institute of Health Industry Technology, College of Human Ecology, Chang Gung University of Science and Technology, Taoyuan 333, Taiwan

<sup>▽</sup>Department of Anesthesiology, Chang Gung Memorial Hospital, Taoyuan 333, Taiwan

<sup>⊙</sup>The Institute of Biomedical Sciences and <sup>△</sup>Department of Marine Biotechnology and Resources, National Sun Yat-sen University, Kaohsiung 804, Taiwan

<sup>□</sup>Cancer Center and <sup>δ</sup>Department of Medical Research, Kaohsiung Medical University Hospital, Kaohsiung 807, Taiwan

## S Supporting Information



**ABSTRACT:** The tree *Aquilaria malaccensis* is a valuable source of agarwood, which is used in herbal medicinal preparations. Phytochemical research on *A. malaccensis* seeds has led to the isolation of four new phorbol esters (1–4), two known phorbol esters (5, isolated from Nature for the first time, and 6), and two known glycerides (7 and 8). The structures of these isolates were elucidated by means of spectroscopic data interpretation. The inflammation-modulatory activities of the isolates on elastase release and superoxide anion generation in human neutrophils were evaluated. Interestingly, phorbol esters 1, 5, and 6 showed potent inhibitory activity on elastase release in human neutrophils, with IC<sub>50</sub> values of 2.7, 0.8, and 2.1 μM, respectively. All isolated phorbol esters exerted enhancing activity on superoxide anion generation. The results indicated that phorbol esters may play a bilateral modulatory role in the processes of inflammation. In addition, the compounds were evaluated for their cytotoxic properties against HepG2 (hepatoma), MDA-MB-231 (breast), and A549 (lung) cancer cells, but all compounds were inactive for all cell lines used (IC<sub>50</sub> > 10 μM).

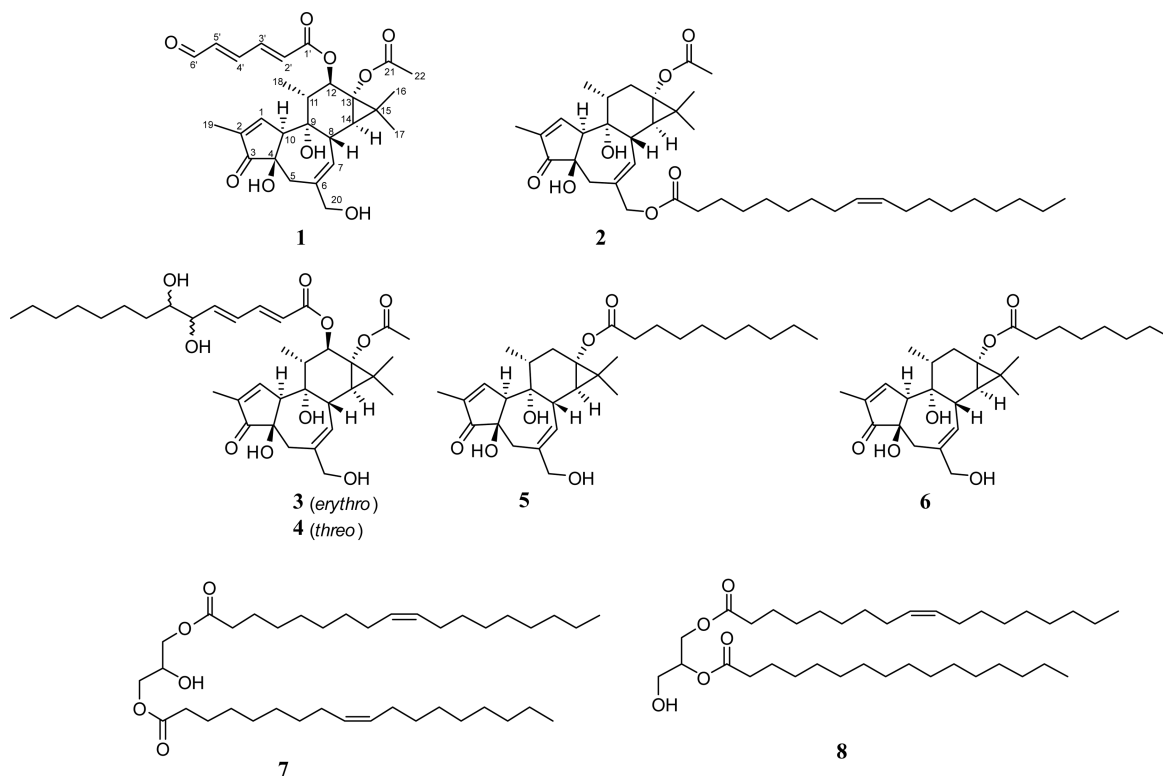
*Aquilaria malaccensis* Lam. (family Thymelaeaceae) is a tropical tree native to Malaysia, known locally as “Karas”. The tree is distributed also in the rainforests of Cambodia, India, Indonesia, Laos, the Philippines, Taiwan, and Thailand.<sup>1</sup> This species serves as the source of agarwood, a valuable fragrant resinous wood, which is used widely in religious ceremonies as well as in traditional medicinal preparations in Asia.<sup>2</sup> Agarwood oil has been used as antiasthmatic, aphrodisiac, astringent, cardiotonic,

and carminative agents and as a remedy for diarrhea, dysentery, gout, rheumatism, and paralysis.<sup>3</sup> Extracts of *A. malaccensis* have been investigated for their cardiotonic,<sup>4</sup> cytotoxic,<sup>5</sup> antitrypanosomal,<sup>6</sup> antibacterial,<sup>7</sup> and antiallergic<sup>8,9</sup> activities.

Received: November 25, 2016

Published: April 26, 2017

Chart 1



In a previously reported study, ferulyl glyceride and phorbol esters were isolated from the bark of *A. malaccensis*.<sup>6</sup> Gas chromatography–mass spectrometry analysis (GC-MS) of agarwood (*A. malaccensis*) revealed the presence of aromatic terpenes, with sesquiterpenes as the main components, and chromones, as well as benzenoids, sterols, and fatty acids.<sup>10</sup> GC-MS analysis of *A. malaccensis* seeds showed high amounts of unsaturated (oleic acid 68.5%) and saturated fatty acids.<sup>11</sup>

Currently, there is scarce information on the chemical composition as well as bioactivities of seeds of *A. malaccensis*. Previously, potent antiallergic and anti-inflammatory activities of a crude extract and chromatographic fractions were observed, and a promising antiallergic phorbol ester (aquimavitalin) with nanomolar IC<sub>50</sub> values was isolated.<sup>9</sup> In the current study, eight compounds were isolated, namely, four new phorbol esters (1–4), two known phorbol esters (5 and 6), and two known diglycerides (7 and 8), from the seeds of *A. malaccensis*. Their inflammation-modulatory and cytotoxic activities for cancer cell lines have been investigated.

## RESULTS AND DISCUSSION

Compound 1 was obtained as a colorless oil. The molecular formula was calculated as C<sub>28</sub>H<sub>34</sub>O<sub>9</sub> (12 degrees of unsaturation) from the analysis of its HRESIMS ( $m/z$  537.20959 [M + Na]<sup>+</sup>, calcd 537.20950). Its IR absorbance spectrum showed the presence of hydroxy (3413 cm<sup>−1</sup>), carbonyl (1713 cm<sup>−1</sup>), and olefinic (1597 cm<sup>−1</sup>) groups. The <sup>1</sup>H, <sup>13</sup>C, and HSQC NMR data of compound 1 (Tables 1 and 2) indicated the occurrence of two vinylic groups [ $\delta_H$  7.59 (s, H-1) and  $\delta_C$  160.5 (C-1),  $\delta_C$  133.0 (C-2);  $\delta_C$  140.6 (C-6),  $\delta_H$  5.69, (d,  $J$  = 4.2 Hz, H-7), 128.9 (C-7)], an oxygenated methine [ $\delta_H$  5.51 (d,  $J$  = 10.2 Hz, H-12),  $\delta_C$  78.2 (C-12)], an oxygenated methylene [ $\delta_H$  4.05 (d,  $J$  = 12.6 Hz, H-20a), 4.01 (d,  $J$  = 12.6 Hz, H-20b),  $\delta_C$  67.9 (C-20)], four methyls, a methylene, and four methines.<sup>13</sup> The <sup>1</sup>H–<sup>1</sup>H COSY spectrum

(Figure 1) showed correlations between H-10 ( $\delta$  3.27)/H-1 ( $\delta$  7.59)/Me-19 ( $\delta$  1.78), H<sub>2</sub>-5 ( $\delta$  2.49 and 2.55)/H-7 ( $\delta$  5.69)/H-8 ( $\delta$  3.27), H-14 ( $\delta$  1.12), and H-12 ( $\delta$  5.51)/H-11 ( $\delta$  2.23)/Me-18 ( $\delta$  0.92). The CH<sub>3</sub> proton at  $\delta_H$  1.78 (H-19) exhibited HMBC correlations to the vinylic carbon signal at  $\delta_C$  160.5 (C-1), quaternary carbon at  $\delta_C$  133.0 (C-2), and ketone at  $\delta_C$  208.7 (C-3), supporting an  $\alpha,\beta$ -unsaturated carbonyl moiety. The H-7 signal showed a HMBC correlation to the oxygenated methylene at  $\delta_C$  67.9 (C-20) and the methylene at  $\delta_C$  38.7 (C-5). The observation of two methyl singlets at  $\delta_H$  1.22 and  $\delta_H$  1.27 (H-16 and H-17) and a methine doublet at  $\delta_H$  1.12 ( $J$  = 5.4 Hz, H-14) together with HMBC correlations from the methyl signal [ $\delta_H$  1.27 (H-17)] to  $\delta_C$  25.9 (C-15) and  $\delta_C$  23.9 (C-16) were used to establish the presence of a dimethyl cyclopropane moiety. Furthermore, the connectivity of the H-12 ( $\delta$  5.51)/H-11 ( $\delta$  2.23)/Me-18 ( $\delta$  0.92) moiety with the dimethyl cyclopropane ring was established by means of HMBC correlations from the oxymethine proton signal at  $\delta_H$  5.51 (H-12) to  $\delta_C$  43.1 (C-11), 65.5 (C-13), 36.5 (C-14), 25.9 (C-15), and 14.5 (C-18) (Figure 1). Thus, compound 1 was deduced to possess a backbone of a phorbol-type diterpene.<sup>12,13</sup> Moreover, the NMR data of 1 were similar to those of the known phorbol esters 12-O-(2Z,4E,6E)-deca-2,4,6-trienylphorbol-13-acetate<sup>5</sup> and aquimavitalin,<sup>9</sup> except for the fatty acid moiety. There were two substituents detected in 1, namely, an acetyl group [ $\delta_C$  173.7 (C-21);  $\delta_H$  2.11 (s, H-22),  $\delta_C$  21.1 (C-22)] and a fatty acid moiety possessing four olefinic protons [ $\delta_H$  6.31 (d,  $J$  = 15.6 Hz, H-2'),  $\delta_C$  129.5 (C-2');  $\delta_H$  7.40 (dd,  $J$  = 15.6 and 11.4 Hz, H-3'),  $\delta_C$  140.8 (C-3');  $\delta_H$  7.17 (dd,  $J$  = 15.6 and 11.4 Hz, H-4'),  $\delta_C$  146.8 (C-4');  $\delta_H$  6.43 (dd,  $J$  = 15.6 and 7.8 Hz, H-5'),  $\delta_C$  137.2 (C-5')], and also a typical formyl group proton [ $\delta_H$  9.68 (d,  $J$  = 7.8 Hz, H-6'),  $\delta_C$  192.7 (C-6')] was evident. The structure of the long-chain fatty acid moiety was further assigned by COSY correlations between H-2' ( $\delta$  6.31)/H-3' ( $\delta$  7.40)/H-4' ( $\delta$  7.17)/H-5' ( $\delta$  6.43) and HMBC



Table 1.  $^1\text{H}$  NMR Data of Compounds 1–4 in  $\text{CDCl}_3$ <sup>a</sup>

position	1	2	3	4
1	7.59, s	7.60, s	7.60, s	7.60, s
5 $\alpha$	2.49, d (19.2)	2.38, d (18.8)	2.49, d (19.2)	2.49, d (19.2)
5 $\beta$	2.55, d (19.2)	2.50, d (18.8)	2.55, d (19.2)	2.55, d (19.2)
7	5.69, d (4.2)	5.70, d (4.4)	5.69, d (5.4)	5.69, d (4.8)
8	3.27, t (5.2)	2.99, t (5.2)	3.26, m	3.26, m
10	3.27, brs	3.28, brs	3.28, brs	3.28, brs
11	2.23, m	2.01, m	2.19, m	2.19, m
12 $\alpha$	5.51, d (10.2)	1.57, m	5.48, d (10.2)	5.47, d (10.2)
12 $\beta$		2.08, m		
14	1.12, d (5.4)	0.83, d (5.2)	1.10, d (5.4)	1.10, d (5.4)
16	1.22, s	1.06, s	1.21, s	1.21, s
17	1.27, s	1.19, s	1.26, s	1.26, s
18	0.92, d (6.6)	0.88, d (6.0)	0.91, d (6.6)	0.90, d (6.6)
19	1.78, brs	1.78, brs	1.78, brs	1.78, brs
20a	4.05, d (12.6)	4.48, d (12.4)	4.05, d (12.6)	4.05, d (13.2)
20b	4.01, d (12.6)	4.43, d (12.4)	3.95, d (12.6)	4.00, d (13.2)
22	2.11, s	2.06, s	2.10, s	2.10, s
2'	6.31, d (15.6)	2.29, t (7.6)	5.92, d (15.6)	5.92, d (15.6)
3'	7.40, dd (15.6, 11.4)	1.60, m	7.27, dd (14.4, 12.0)	7.27, dd (14.4, 12.0)
4'	7.17, dd (15.6, 11.4)	1.25–1.26, m	6.45, m	6.48, m
5'	6.43, dd (15.6, 7.8)	1.25–1.26, m	6.17, dd (15.6, 7.2)	6.12, dd (15.6, 6.0)
6'	9.68, d (7.8)	1.25–1.26, m	4.24, m	4.07, m
7'		1.25–1.26, m	3.74, m	3.52, m
8'		2.01, m	1.42, m	1.42, m
9'		5.33, m	1.27–1.29, m	1.26–1.30, m
10'		5.33, m	1.27–1.29, m	1.26–1.30, m
11'		2.01, m	1.27–1.29, m	1.26–1.30, m
12'		1.25–1.26, m	1.27–1.29, m	1.26–1.30, m
13'		1.25–1.26, m	1.27–1.29, m	1.26–1.30, m
14'		1.25–1.26, m	0.88, t (7.2)	0.88, t (7.2)
15'		1.25–1.26, m		
16'		1.25–1.26, m		
17'		1.25–1.26, m		
18'		0.88, t (6.8)		

<sup>a</sup> $^1\text{H}$  NMR spectra were measured at 600 MHz (1, 3, 4) and at 400 MHz (2) in  $\text{CDCl}_3$ .

correlations of H-2'/C-4' ( $\delta_{\text{C}}$  146.8) and H-3'/C-5' ( $\delta_{\text{C}}$  137.2). The  $^1\text{H}$  NMR coupling constants and NOESY correlations were used to identify the geometry of double bonds. Accordingly, the NMR data indicated that **1** possesses a (2*E*,4*E*)-6-oxohexa-2,4-dienoic acid moiety. The fatty acid moiety was attached to the phorbol backbone at C-12 according to the HMBC correlation of H-12 to C-1' ( $\delta_{\text{C}}$  165.4); so, therefore, the acetyl moiety was attached to C-13. The relative configuration of compound **1** was deduced by comparison of its NOESY correlation data (Figure 2) with literature values.<sup>13</sup> The NOESY correlations between H-11/H-17 and H-11/H-8 suggested that these protons are  $\beta$ -oriented. Further correlations between Me-18/H-12 $\alpha$  indicated that the fatty acid moiety is also  $\beta$ -oriented. On the basis of all of the above information, the structure of **1** was determined as 12-*O*-(2'*E*,4'*E*)-6-oxohexa-2',4'-dienoylphorbol-13-acetate.

Compound **2** was also obtained as a colorless oil. It was assigned with a molecular formula of  $\text{C}_{40}\text{H}_{62}\text{O}_7$  (10 degrees of unsaturation) on the basis of HRESIMS ( $m/z$  677.43884 [ $\text{M} + \text{Na}$ ]<sup>+</sup>, calcd 677.43878). The IR spectrum indicated the presence of hydroxy ( $3409\text{ cm}^{-1}$ ), carbonyl ( $1717\text{ cm}^{-1}$ ), and olefinic ( $1597\text{ cm}^{-1}$ ) groups. A comparison of the  $^1\text{H}$  and  $^{13}\text{C}$  NMR data (Tables 1 and 2) with **1** suggested that compound **2** possesses a 12-deoxyphorbol type of diterpenoid backbone. Moreover, the signals typical of a 12-deoxyphorbol derivative were detected [ $\delta_{\text{H}}$

2.99 (t,  $J = 5.2\text{ Hz}$ , H-8),  $\delta_{\text{C}}$  39.4 (C-8);  $\delta_{\text{H}}$  2.01 (m, H-11),  $\delta_{\text{C}}$  36.3 (C-11);  $\delta_{\text{H}}$  1.57 (m, H-12 $\alpha$ ),  $\delta_{\text{H}}$  2.08 (m, H-12 $\beta$ ),  $\delta_{\text{C}}$  31.9 (C-12)].<sup>14,15</sup> Furthermore, signals for acetyl [ $\delta_{\text{C}}$  173.2 (C-21);  $\delta_{\text{H}}$  2.06 (s, H-22),  $\delta_{\text{C}}$  21.2 (C-22)] and fatty acid moieties were observed in the NMR spectra. The COSY correlations of compound **2** (Figure 1) showed connectivities of the H-10 ( $\delta$  3.28)/H-1 ( $\delta$  7.60)/Me-19 ( $\delta$  1.78), H<sub>2</sub>-5 ( $\delta$  2.38 and 2.50)/H-7 ( $\delta$  5.70)/H-8 ( $\delta$  2.99)/H-14 ( $\delta$  0.83), and H<sub>2</sub>-12 ( $\delta$  1.57 and 2.08)/H-11 ( $\delta$  2.01)/Me-18 ( $\delta$  0.88) substituents for the skeleton, as well as H-2' ( $\delta$  2.29)/H-3' ( $\delta$  1.60)/H-4' ( $\delta$  1.25), and H-7' ( $\delta$  1.25)/H-8' ( $\delta$  2.01)/H-9' ( $\delta$  5.33)/H-10' ( $\delta$  5.33)/H-11' ( $\delta$  2.01)/H-12' ( $\delta$  1.25), for the long-chain fatty acid moiety.

To confirm the long-chain fatty acid moiety, compound **2** was subjected to methanolysis using a method reported by Ichihara et al.<sup>16</sup> Compound **2** was reacted with 1.2% HCl in methanol for 1.5 h at  $100\text{ }^\circ\text{C}$ , and the resulting fatty acid methyl ester was identified by GC-MS analysis as (9*Z*)-octadecenoic (oleic) acid methyl ester ( $t_{\text{R}}$  21.30,  $m/z$  296 [ $\text{M}$ ]<sup>+</sup>). Comparison of the spectra (Table 1) with the literature revealed that the data of compound **2** closely matched those of 12-deoxyphorbol-13-(9'*Z*)-octadecenoate-20-acetate.<sup>15</sup> However, the HMBC correlation from H-20 to C-1' ( $\delta_{\text{C}}$  173.6) indicated that the fatty acid moiety is linked to the backbone at C-20. Therefore, the acetyl



Table 2.  $^{13}\text{C}$  NMR Data of Compounds 1–4 in  $\text{CDCl}_3^a$ 

position	1	2	3	4
1	160.5, CH	161.3, CH	160.7, CH	160.7, CH
2	133.0, C	132.8, C	132.9, C	132.9, C
3	208.7, C	209.0, C	208.8, C	208.8, C
4	73.7, C	73.6, C	73.7, C	73.7, C
5	38.7, $\text{CH}_2$	39.0, $\text{CH}_2$	38.7, $\text{CH}_2$	38.7, $\text{CH}_2$
6	140.6, C	135.0, C	140.5, C	140.5, C
7	128.9, CH	133.7, CH	129.2, CH	129.2, CH
8	39.1, CH	39.4, CH	39.1, CH	39.1, CH
9	78.2, C	75.9, C	78.2, C	78.2, C
10	56.2, CH	55.7, CH	56.2, CH	56.2, CH
11	43.1, CH	36.3, CH	43.1, CH	43.1, CH
12	78.2, CH	31.9, $\text{CH}_2$	77.1, CH	77.2, CH
13	65.5, C	63.5, C	65.7, C	65.7, C
14	36.5, CH	32.3, CH	36.4, CH	36.4, CH
15	25.9, C	22.7, C	25.8, C	25.6, C
16	23.9, $\text{CH}_3$	23.2, $\text{CH}_3$	23.8, $\text{CH}_3$	23.8, $\text{CH}_3$
17	16.9, $\text{CH}_3$	15.3, $\text{CH}_3$	16.7, $\text{CH}_3$	16.8, $\text{CH}_3$
18	14.5, $\text{CH}_3$	18.5, $\text{CH}_3$	14.4, $\text{CH}_3$	14.4, $\text{CH}_3$
19	10.1, $\text{CH}_3$	10.1, $\text{CH}_3$	10.0, $\text{CH}_3$	10.1, $\text{CH}_3$
20	67.9, $\text{CH}_2$	69.5, $\text{CH}_2$	68.0, $\text{CH}_2$	68.0, $\text{CH}_2$
21	173.7, C	173.2, C	173.8, C	173.8, C
22	21.1, $\text{CH}_3$	21.1, $\text{CH}_3$	21.1, $\text{CH}_3$	21.1, $\text{CH}_3$
1'	165.4, C	173.6, C	165.4, C	165.4, C
2'	129.5, CH	34.2, $\text{CH}_2$	121.7, CH	121.9, CH
3'	140.8, CH	24.9, $\text{CH}_2$	143.9, CH	143.8, CH
4'	146.8, CH	29.1–29.7, $\text{CH}_2$	129.9, CH	129.7, CH
5'	137.2, CH	29.1–29.7, $\text{CH}_2$	140.0, CH	141.5, CH
6'	192.7, CH	29.1–29.7, $\text{CH}_2$	74.9, CH	75.0, CH
7'		29.1–29.7, $\text{CH}_2$	74.3, CH	74.3, CH
8'		27.2, $\text{CH}_2$	32.2, $\text{CH}_2$	33.1, $\text{CH}_2$
9'		129.8, CH	29.2, $\text{CH}_2$	29.2, $\text{CH}_2$
10'		130.0, CH	29.4, $\text{CH}_2$	29.5, $\text{CH}_2$
11'		27.2, CH	29.7, $\text{CH}_2$	29.7, $\text{CH}_2$
12'		29.1–29.7, $\text{CH}_2$	31.8, $\text{CH}_2$	31.8, $\text{CH}_2$
13'		29.1–29.7, $\text{CH}_2$	22.6, $\text{CH}_2$	22.6, $\text{CH}_2$
14'		29.1–29.7, $\text{CH}_2$	14.0, $\text{CH}_3$	14.1, $\text{CH}_3$
15'		29.1–29.7, $\text{CH}_2$		
16'		31.8, $\text{CH}_2$		
17'		22.7, $\text{CH}_2$		
18'		14.1, $\text{CH}_3$		

<sup>a</sup> $^{13}\text{C}$  NMR spectra were measured at 150 MHz (1, 3, 4) and at 100 MHz (2) in  $\text{CDCl}_3$ .

group was assigned to C-13. The relative configuration of 2 was assigned according to the ROESY spectrum (Figure 2). The correlations between H-11/H-8 and H-17/H-8 indicated that these protons are  $\beta$ -oriented. On the basis of the interpretation of the above spectroscopic data, compound 2 was assigned as 12-deoxy-13-O-acetylphorbol-20-(9'Z)-octadecenoate.

Compound 3 was isolated as another colorless oil. HRESIMS analysis indicated this compound to have a molecular formula of  $\text{C}_{36}\text{H}_{52}\text{O}_{10}$  ( $m/z$  667.34515  $[\text{M} + \text{Na}]^+$ ; calcd 667.34527), 10 degrees of unsaturation). The IR absorption bands of 3 showed hydroxy group ( $3392\text{ cm}^{-1}$ ), carbonyl ( $1710\text{ cm}^{-1}$ ), and olefinic ( $1632\text{ cm}^{-1}$ ) functionalities. The 1D (Tables 1 and 2) and 2D (Figure 1) NMR data of the skeleton of compound 3 closely matched those of compound 1, as a phorbol derivative, with there being two acyl substituents detected in 3. In addition to an acetyl group, the 1D NMR data indicated the presence of a long-chain fatty acid substituent possessing two double bonds along with two hydroxy groups. The  $^1\text{H}$  and  $^{13}\text{C}$  NMR data showed four vinylic protons at  $\delta_{\text{H}}$  5.92, 7.27, 6.45, and 6.17 with corresponding carbons at  $\delta_{\text{C}}$  121.7, 143.9, 129.9, and 140.0. The COSY cross-peaks between the vinylic protons suggested that the two double bonds are conjugated. The chemical shifts of H-2' to H-5' and C-2' to C-5' closely matched literature chemical shifts for methyl (2E,4E,8E)-6,13-dihydroxytetradeca-2,4,8-trienoate, indicating a 2',4'-diene moiety.<sup>17</sup> The positions of two hydroxy groups in the side chain were established according to 2D NMR data analysis (Figure 1). The COSY correlations of H-2' ( $\delta$  5.92)/H-3' ( $\delta$  7.27)/H-4' ( $\delta$  6.45)/H-5' ( $\delta$  6.17)/H-6' ( $\delta$  4.24)/H-7' ( $\delta$  3.74)/H-8' ( $\delta$  1.42) and HMBC correlations of H-2'/C-4' ( $\delta_{\text{C}}$  129.9), H-4'/C-6' ( $\delta_{\text{C}}$  74.9), and H-5'/C-6' ( $\delta_{\text{C}}$  74.9) revealed the connectivity of conjugated double bonds with a 6'-hydroxy methine proton [ $\delta_{\text{H}}$  4.24 (H-6'),  $\delta_{\text{C}}$  74.9, (C-6')] and a 7'-hydroxy proton [ $\delta_{\text{H}}$  3.74 (H-7'),  $\delta_{\text{C}}$  74.3, (C-7')]. By comparing the chemical shifts of the 6',7'-vicinal diol units of 3 and 4 (see below) with the reference compounds, methyl 9,10-(erythro)-dihydroxy-11(E)-octadecenoate and methyl 9,10-(threo)-dihydroxy-11(E)-octadecenoate,<sup>18</sup> two 6'- and 7'-hydroxymethine protons in 3,  $\delta_{\text{H}}$  4.24 (H-6') and 3.74 (H-7'), were downfield shifted when compared to those of compound 4,  $\delta_{\text{H}}$  4.07 (H-6') and 3.52 (H-7'). Thus, the structure of the fatty acid moiety was assigned in 3 as 12-O-(2E,4E)-6,7-(erythro)-dihydroxytetradeca-2,4-dienoic acid. The long-chain fatty acid was attached to the phorbol backbone at C-12 according to the HMBC correlation of H-12/C-1' ( $\delta_{\text{C}}$  165.4), and the acetyl moiety was attached to C-13. The NOESY correlations of 3 indicated the same relative configuration as in 1 (Figure 2). Therefore, the structure of 3 was proposed as 12-O-(2'E,4'E)-6',7'-(erythro)-dihydroxytetradeca-2',4'-dienoylphorbol-13-acetate.

Compound 4 was isolated as a further colorless oil. Its IR ( $3385\text{ cm}^{-1}$ ,  $1632\text{ cm}^{-1}$ ), HRESIMS ( $m/z$  667.34550  $[\text{M} + \text{Na}]^+$ , calcd 667.34527), and  $^{13}\text{C}$  NMR data were identical to those of compound 3. Therefore, the basic structure was assigned as a C-12 long-chain fatty acid and C-13 acetyl-disubstituted phorbol ester. However, in a comparison of the  $^1\text{H}$  NMR data with those of compound 3, the upfield chemical shifts of the 6',7'-vicinal diol were evident [ $\delta_{\text{H}}$  4.07 (m, H-6);  $\delta_{\text{H}}$  3.52 (m, H-7)],

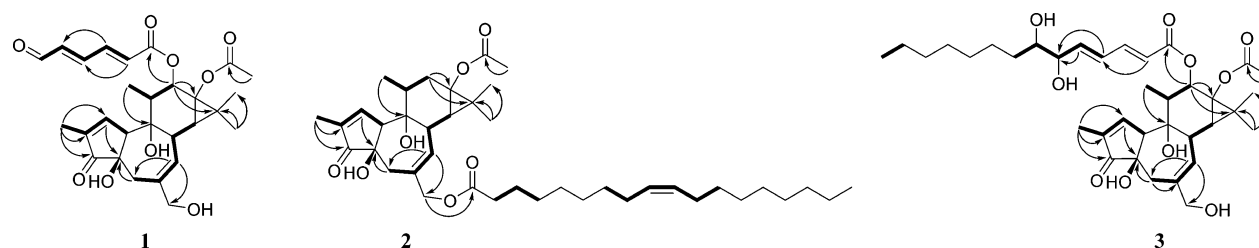


Figure 1. COSY (bold bonds) and selected HMBC (arrows) correlations of 1–3.

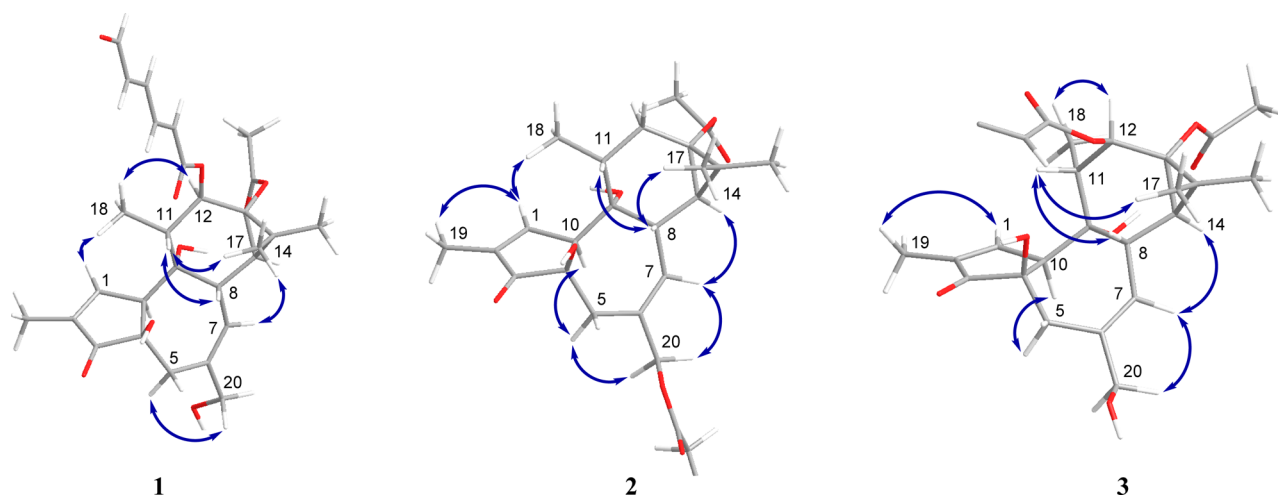


Figure 2. Key NOE (left right arrow) correlations of 1–3.

indicating a *threo* configuration. On the basis of the obtained data, compounds 3 and 4 were determined as stereoisomers, and compound 4 was assigned as 12-*O*-(2'*E*,4'*E*)-6',7'-(*threo*)-dihydroxytetradeca-2',4'-dienoylphorbol-13-acetate.

Compound 5, 12-*O*-deoxyphorbol 13-decanoate, was isolated as a natural product for the first time.<sup>19</sup> Compound 6 was identified as the phorbol ester, mellerin A.<sup>14</sup> In addition, known glycerides were purified, 1,3-dioleoyl glyceride, a major component of *A. malaccensis* seeds (7),<sup>20</sup> and 1-oleoyl-2-palmitoyl glyceride (8).<sup>21</sup> The NMR spectroscopic data of the known compounds were in agreement with the literature. To confirm the fatty acid moiety, compound 7 was subjected to methanolysis using the method reported by Ichihara et al.<sup>16</sup> The resulting fatty acid methyl ester was determined by GC-MS analysis as an oleic acid methyl ester. Using the same procedure, two long-chain substituents of compound 8 were identified by GC-MS analysis as oleic acid methyl ester and hexadecanoic (palmitic) acid methyl ester.

All isolated compounds were evaluated for their potential anti-inflammatory and cytotoxic activities. In the anti-inflammatory assay, 1 ( $IC_{50}$  2.7  $\mu$ M), 5 ( $IC_{50}$  0.8  $\mu$ M), and 6 ( $IC_{50}$  2.1  $\mu$ M) showed potent inhibitory activity on *N*-formyl-L-methionyl-L-leucyl-L-phenylalanine (fMLF)/cytochalasin B (CB)-induced elastase release by human neutrophils, comparable to a positive control, the PI3K inhibitor LY294002 ( $IC_{50}$  3.3  $\mu$ M) (Table 3). On the other hand, phorbol 12-myristate 13-acetate (PMA) showed an enhancing effect on elastase release. The conjugated aldehydic fatty acid substituent in 1 and saturated fatty acid substituents in 5 and 6 may play a role in their bioactivity. All phorbol esters (1–6 and PMA) showed enhancing activities on superoxide anion generation.

In general, phorbol esters trigger superoxide anion generation and cause pro-inflammatory effects. However, the extracts of the seeds of *A. malaccensis* exhibited an excellent superoxide anion generation inhibitory effect,<sup>9</sup> which could be due to a high content of free anti-inflammatory fatty acids in the seed oil of *A. malaccensis*.<sup>11,22</sup> Also, it may be suggested that the fatty acid substituents, which themselves show significant anti-inflammatory effects,<sup>22</sup> play an important role in mediating the effect of phorbol esters. In addition, for the first time, it was discovered in the present study that some of the phorbol esters inhibit elastase-releasing effects. These findings may provide insights for further research related to the inflammation-modulating activities of phorbol esters.

Table 3. Effects of Pure Compounds on Superoxide Anion Generation and Elastase Release in fMLF/CB-Induced Human Neutrophils

compound	superoxide anion	elastase release
	$IC_{50}$ ( $\mu$ M) <sup>a</sup>	$IC_{50}$ ( $\mu$ M) <sup>a</sup>
1	enhancing <sup>b</sup>	2.7 $\pm$ 0.6
2	enhancing <sup>b</sup>	>10
3	enhancing <sup>b</sup>	enhancing <sup>c</sup>
4	enhancing <sup>b</sup>	enhancing <sup>c</sup>
5	enhancing <sup>b</sup>	0.8 $\pm$ 0.3
6	enhancing <sup>b</sup>	2.1 $\pm$ 0.7
7	>10	>10
8	enhancing <sup>d</sup>	>10
PMA <sup>e</sup>	enhancing <sup>b</sup>	enhancing <sup>c</sup>
LY294002 <sup>f</sup>	1.8 $\pm$ 0.7	3.3 $\pm$ 0.7

<sup>a</sup> $IC_{50}$  values express the concentration of the sample required to inhibit superoxide anion generation or elastase release by 50%. Results are presented as means  $\pm$  SEM ( $n$  = 3–5). <sup>b</sup>The compounds showed enhancing effects on superoxide generation at 10  $\mu$ M (1 106.1%, 2 18.1%, 3 106.0%, 4 107.1%, 5 95.3%, 6 109.6%, PMA 102.7%) in the absence of fMLF/CB. Compared with fMLF/CB (as 100%). <sup>c</sup>The compounds showed enhancing effects on elastase release at 10  $\mu$ M (3 10.5%, 4 9.2%, PMA 44.2%) in the absence of fMLF/CB. Compared with fMLF/CB (as 100%). <sup>d</sup>The compound showed enhancing effects on superoxide generation at 10  $\mu$ M (8 74.5%) in the presence of CB. Compared with fMLF/CB (as 100%). <sup>e</sup>Phorbol 12-myristate 13-acetate (PMA), a PKC activator, was used as a positive control exerting enhancing effects. <sup>f</sup>LY294002, the PI3K inhibitor, was used as a positive control exerting suppressive effects.

## EXPERIMENTAL SECTION

**General Experimental Procedures.** Optical rotations were measured using a JASCO P-2000 digital polarimeter (JASCO Inc., Tokyo, Japan). A JASCO V-530 ultraviolet spectrophotometer (JASCO) was used to run UV spectra. IR spectra were obtained on an FT-IR-4100 JASCO spectrophotometer (JASCO). NMR spectra were obtained on a Varian VNMR-600 FT-NMR spectrometer (Varian Inc., Palo Alto, CA, USA) and on a JEOL JNM-ECS 400 NMR spectrometer (JEOL Ltd., Tokyo, Japan). Electrospray-ionization mass spectrometry (ESIMS) data were collected on a Waters micromass ZQ mass spectrometer (Waters Corporation, Milford, MA, USA). High-resolution ESIMS data were determined using a Bruker Daltonics APEX II mass spectrometer (FT-ICR/MS, FTMS) (Bruker Daltonics, Billerica, MA, USA). GC-MS data were collected using a DSQ II single quadrupole GC/MS (Thermo Fisher Scientific, Waltham, MA, USA).

equipped with an HP-SMS capillary column (0.25  $\mu$ m, 30 m  $\times$  0.25 mm, Agilent, Santa Clara, CA, USA). Sephadex LH-20 (GE Healthcare, Stockholm, Sweden) and silica gel (Kieselgel 60, 0.063–0.200 mm, Geduran Si 60, 0.040–0.063 mm, Merck KGaA) were used for column chromatography. Silica gel precoated (Kieselgel 60 F254 and RP-18 F254s, Merck KGaA) TLC plates were used. HPLC analyses were performed using a Shimadzu LC-10AT VP (Shimadzu Inc., Kyoto, Japan) pump interface equipped with a Shimadzu SPD-M10A VP diode array detector using a C<sub>18</sub> column (5  $\mu$ m, 250  $\times$  10 mm, Phenomenex Inc.). Dimethyl sulfoxide (DMSO), 3-(4,5-dimethylthiazol-2-yl)-2,5-diphenyltetrazolium bromide (MTT), phorbol 12-myristate 13-acetate (PMA), LY294002, and doxorubicin hydrochloride were purchased from Sigma-Aldrich (St. Louis, MO, USA).

**Plant Material.** The seeds of *A. malaccensis* were collected and identified by one of the authors (H.-Y.H.) in November 2014. A voucher specimen (no. KMU-AMS 1) has been deposited in the Graduate Institute of Natural Products, College of Pharmacy, Kaohsiung Medical University, Kaohsiung, Taiwan.

**Extraction and Isolation.** The dried and powdered seeds of *Aquilaria malaccensis* (462 g) were extracted with 90% EtOH (3  $\times$  5 L) to give an extract (27.7 g), which was suspended in water and further partitioned between ethyl acetate and H<sub>2</sub>O (1:1) to obtain an ethyl acetate layer. The ethyl acetate layer was then partitioned between 90% aqueous MeOH and *n*-hexane to afford a 90% MeOH layer (16.2 g) and an *n*-hexane partition (7.1 g). The water layer was partitioned with *n*-butanol to yield a water partition (1.6 g) and an *n*-butanol layer (0.4 g). The MeOH layer (16.2 g) was submitted to column chromatography (CC) over silica gel 60 (0.063–0.200 mm, Merck), eluted with *n*-hexane/CH<sub>2</sub>Cl<sub>2</sub>/MeOH (6:3:1 to 6:10:2), to afford six fractions: Fr.1 (2.9 g), Fr.2 (1.3 g), Fr.3 (6.8 g), Fr.4 (3.2 g), Fr.5 (1.7 g), and Fr.6 (97.9 mg). Fraction 4 was fractionated by Sephadex LH-20 CC with CH<sub>2</sub>Cl<sub>2</sub>/MeOH (1:1) as eluant, to yield eight further fractions (Fr.4-1 to Fr.4-8). Fraction 4-3 (762 mg) was purified using CC on silica gel (30 cm, 1.5 cm, Geduran Si 60, 0.040–0.063 mm, Merck) and eluted with a gradient of EtOAc/*n*-hexane (from 1:10 to 4:1) to obtain 15 subfractions (4-3-1 to 4-3-15), with compound 2 (39.5 mg) being purified from subfraction 4-3-6. Subfraction 4-3-3 was further fractionated over a Sephadex LH-20 column (CH<sub>2</sub>Cl<sub>2</sub>/MeOH, 8:2) to obtain five subfractions (4-3-3-1 to 4-3-3-5), and compound 7 (130.5 mg) was purified from subfraction 4-3-3-3. Subfraction 4-3-3-4 was subjected to silica gel CC and eluted with a gradient of *n*-hexane/CH<sub>2</sub>Cl<sub>2</sub>/MeOH (10:1:0 to 3:1:0.5), to yield compound 8 (4.6 mg). Subfraction 4-3-13 (23.5 mg) was separated by RP-HPLC (C<sub>18</sub> column, flow rate = 2.0 mL/min), with MeOH/H<sub>2</sub>O (60:40) used for elution, to afford compounds 1 (0.7 mg), 3 (0.9 mg), and 4 (1.0 mg).

Fraction 4-4 (174 mg) was further purified using column chromatography on silica gel (30 cm, 1.5 cm, Geduran Si 60, 0.040–0.063 mm, Merck), eluted with a gradient of EtOAc/*n*-hexane (from 1:15 to 4:1), to obtain 11 subfractions (4-4-1 to 4-4-11). Subfraction 4-4-7 (38 mg) was further purified by RP-HPLC (C<sub>18</sub> column flow rate = 2.0 mL/min), with MeOH/H<sub>2</sub>O (85:15), to yield compounds 5 (7.8 mg) and 6 (0.8 mg).

**12-O-(2'E,4'E)-6-Oxohepta-2',4'-dienoylphorbol-13-acetate (1):** colorless oil;  $[\alpha]_D^{25} +4.2$  (c 0.17, CHCl<sub>3</sub>); UV (MeOH)  $\lambda_{\max}$  (log  $\epsilon$ ) 295 (2.80), 249 (2.84) nm; IR (neat)  $\nu_{\max}$  3413, 2925, 2855, 2360, 2339, 1713, 1625, 1597, 1261, 1184, 755 cm<sup>-1</sup>; <sup>1</sup>H NMR (CDCl<sub>3</sub>, 600 MHz) and <sup>13</sup>C NMR (CDCl<sub>3</sub>, 150 MHz), see Tables 1 and 2; ESIMS found *m/z* 515 [M + H]<sup>+</sup>; HRESIMS *m/z* 537.20959 [M + Na]<sup>+</sup> (calcd for C<sub>28</sub>H<sub>34</sub>O<sub>9</sub>Na, 537.20950).

**12-Deoxy-13-O-acetylphorbol-20-(9'Z)-octadecenoate (2):** colorless oil;  $[\alpha]_D^{25} +2.9$  (c 0.3, CHCl<sub>3</sub>); UV (MeOH)  $\lambda_{\max}$  (log  $\epsilon$ ) 285 (2.78), 250 (2.83) nm; IR (neat)  $\nu_{\max}$  3409, 2922, 2855, 1717, 1375, 1332, 1152, 1021 cm<sup>-1</sup>; <sup>1</sup>H NMR (CDCl<sub>3</sub>, 400 MHz) and <sup>13</sup>C NMR (CDCl<sub>3</sub>, 100 MHz), see Tables 1 and 2; ESIMS *m/z* 655 [M + H]<sup>+</sup>; HRESIMS *m/z* 677.43884 [M + Na]<sup>+</sup> (calcd for C<sub>40</sub>H<sub>62</sub>O<sub>7</sub>Na, 677.43878); GC-MS analysis (*t*<sub>R</sub> 21.30, *m/z* 296 [M]<sup>+</sup>, fragmentation ions observed at *m/z* 264, 222, 137, 123, 110, 98, 83, 74, 69, oleic acid methyl ester).

**12-O-(2'E,4'E)-6',7'-(erythro)-Dihydroxytetradeca-2',4'-dienoylphorbol-13-acetate (3):** colorless oil;  $[\alpha]_D^{25} +10.4$  (c 0.17, CHCl<sub>3</sub>); UV (MeOH)  $\lambda_{\max}$  (log  $\epsilon$ ) 289 (2.79), 249 (2.83) nm; IR (neat)  $\nu_{\max}$  3392,

2925, 2851, 1710, 1632, 1455, 1375, 1261, 1024, 802, 755 cm<sup>-1</sup>; <sup>1</sup>H NMR (CDCl<sub>3</sub>, 600 MHz) and <sup>13</sup>C NMR (CDCl<sub>3</sub>, 150 MHz), see Tables 1 and 2; ESIMS *m/z* 645 [M + H]<sup>+</sup>; HRESIMS *m/z* 667.34515 [M + Na]<sup>+</sup> (calcd for C<sub>36</sub>H<sub>52</sub>O<sub>10</sub>Na, 667.34527).

**12-O-(2'E,4'E)-6',7'-(threo)-Dihydroxytetradeca-2',4'-dienoylphorbol-13-acetate (4):** colorless oil;  $[\alpha]_D^{25} +13.2$  (c 0.13, CHCl<sub>3</sub>); UV (MeOH)  $\lambda_{\max}$  (log  $\epsilon$ ) 289 (2.79), 249 (2.84) nm; IR (neat)  $\nu_{\max}$  3385, 2929, 2855, 1632, 1455, 1375, 1261, 1124, 802, 755 cm<sup>-1</sup>; <sup>1</sup>H NMR (CDCl<sub>3</sub>, 600 MHz) and <sup>13</sup>C NMR (CDCl<sub>3</sub>, 150 MHz), see Tables 1 and 2; ESIMS *m/z* 645 [M + H]<sup>+</sup>; HRESIMS *m/z* 667.34550 [M + Na]<sup>+</sup> (calcd for C<sub>36</sub>H<sub>52</sub>O<sub>10</sub>Na, 667.34527).

**1,3-Dioleoyl glyceride (7):** C<sub>37</sub>H<sub>72</sub>O<sub>5</sub>; ESIMS *m/z* 621 [M + H]<sup>+</sup>; GC-MS analysis (*t*<sub>R</sub> 21.30, *m/z* 296 [M]<sup>+</sup>, for oleic acid methyl ester, fragmentation ions observed at *m/z* 264, 222, 137, 123, 110, 98, 74, 69, 55).

**1-Oleoyl-2-palmitoyl glyceride (8):** C<sub>37</sub>H<sub>70</sub>O<sub>5</sub>; ESIMS *m/z* 595 [M + H]<sup>+</sup>; GC-MS analysis (*t*<sub>R</sub> 21.31, *m/z* 296 [M]<sup>+</sup>, fragmentation ions observed at *m/z* 264, 180, 137, 123, 110, 98, 74, 69, oleic acid methyl ester; *t*<sub>R</sub> 17.71, *m/z* 270 [M]<sup>+</sup>, fragmentation ions observed at *m/z* 227, 185, 143, 87, 74, palmitic acid methyl ester).

**Methylation of Samples for GC-MS Analysis.** The method of Ichihara et al. was utilized.<sup>16</sup> Lipid sample was placed in a screw-capped glass test tube and dissolved in 0.20 mL of toluene. To the lipid solution were added 1.50 mL of methanol (HPLC grade) and 0.30 mL of the 8.0% HCl solution, in order. The final HCl concentration was 1.2%. The reaction mixture was heated at 100 °C for 1 h. On cooling, the reaction was quenched by 1 mL of 6% aqueous K<sub>2</sub>CO<sub>3</sub> solution. Then, 1–2 mL of hexane (HPLC grade) was added, and the mixture was partitioned to yield a hexane layer (upper layer). The hexane layer was filtered through a 0.22  $\mu$ m filter (ChromTech, Apple Valley, MN, USA) into a GC-MS vial and then subjected to GC-MS analysis.

**GC-MS Analysis.** The methylated samples were analyzed by gas chromatography–mass spectrometry (DSQ II single quadrupole GC/MS, Thermo Fisher Scientific). Derivatized samples were vaporized at 250 °C in standard split mode (1:50) and separated on a 30 m  $\times$  0.25 mm HP-SMS capillary column with a 0.25  $\mu$ m coating (Agilent). The column oven temperature was set at 70 °C, held for 3 min, then increased to 180 °C at 20 °C/min, held for 5 min, then increased to 280 °C at 5 °C/min and held for 5 min. A helium gas carrier flow of 1 mL/min was used. The interface and ion source temperature were set to 250 °C. An electron-impact ionization of 30 eV was utilized, the injection volume was 1  $\mu$ L, and the mass range was *m/z* 38–600. Identification of the compounds was based on a comparison of mass spectra with the data from the Wiley/NBS Registry of Mass Spectral Data (version 5.0)/National Institute of Standards and Technology (NIST) MS Search (version 2.0).

**Superoxide Anion and Elastase Release Assays.** Blood was obtained from healthy human donors (20–30 years old), using a protocol approved by the Institutional Review Board at Chang Gung Memorial Hospital (protocol number 102-1595A3). Human neutrophils were isolated using a standard method of dextran sedimentation prior to centrifugation in a Ficoll-Hypaque gradient and hypotonic lysis of erythrocytes.<sup>23</sup> Purified neutrophils containing >98% viable cells were determined by the trypan-blue exclusion method.<sup>24</sup> The neutrophils were resuspended in a Ca<sup>2+</sup>-free Hank's buffered salt solution (HBSS) at pH 7.4 and were maintained at 4 °C prior to use.

**Superoxide Anion Generation Assay.** Neutrophil superoxide anion generation was determined using a superoxide dismutase (SOD)-inhibitory cytochrome reduction assay according to previously described procedures.<sup>25,26</sup> Briefly, after supplementation with 0.5 mg/mL ferricytochrome *c* and 1 mM Ca<sup>2+</sup>, neutrophils (3  $\times$  10<sup>5</sup> per mL) were equilibrated at 37 °C for 2 min and incubated with different concentrations of test compounds or DMSO (as control) for 5 min. Cells were incubated with cytochalasin B (1  $\mu$ g/mL) for 3 min prior to the activation with 100 nM *N*-formyl-L-methionyl-L-leucyl-L-phenylalanine for 10 min. Changes in absorbance with the reduction of ferricytochrome *c* at 550 nm were continuously monitored in a double-beam, six-cell positioner spectrophotometer with constant stirring (Hitachi U-3010, Tokyo, Japan). Calculations were based on the differences in the reactions with and without SOD (100 U/mL) divided



by the extinction coefficient for the reduction of ferricytochrome *c* ( $21.1 \text{ mM}^{-1} \text{ cm}^{-1}$ ). All experiments were repeated three times. LY294002 and PMA were used as positive controls.

**Elastase Release Inhibition Assay.** Degranulation of azurophilic granules was determined by measuring the elastase release, as described previously.<sup>26</sup> Experiments were performed using MeOSuc-Ala-Ala-Pro-Val-*p*-nitroanilide as the elastase substrate. After supplementation with MeOSuc-Ala-Ala-Pro-Val-*p*-nitroanilide ( $100 \mu\text{M}$ ), neutrophils ( $3 \times 10^5$  per mL) were equilibrated at  $37^\circ\text{C}$  for 2 min and incubated with each test compound for 5 min. Cells were stimulated with fMLF ( $100 \text{ nM}$ )/CB ( $0.5 \mu\text{g/mL}$ ), and changes in the absorbance at 405 nm were monitored continuously in order to measure the elastase release. The results were expressed as the percent of elastase release in the fMLF/CB-activated, drug-free control system. All experiments were repeated three times. LY294002 and PMA were used as positive controls.

**Cytotoxicity Assay.** The MTT viability assay was used according to a previously described method.<sup>27</sup> HepG2 ( $1 \times 10^4$  cells), A549 ( $5 \times 10^3$  cells), and MDA-MB-231 ( $1 \times 10^4$  cells) were seeded into 96-well plates. The cells were treated with the test compounds at a concentration of  $20 \mu\text{g/mL}$ . After 72 h, the medium was removed and  $100 \mu\text{L}$  of MTT solution ( $0.5 \text{ mg/mL}$ ) was added to each well. The plates were incubated at  $37^\circ\text{C}$  for 1 h to form formazan crystals, which were then dissolved by DMSO ( $100 \mu\text{L}$ ). Plates were gently shaken, and absorbance at 550 nm was measured using a microplate reader. The degree of cell viability of each sample was calculated as the percentage of control value (untreated cells). Doxorubicin hydrochloride was used as a positive control and exhibited  $\text{IC}_{50}$  values of 0.5, 0.3, and  $1.2 \mu\text{M}$  against A549, Hep-G2, and MDA-MB-231 cells, respectively.

## ■ ASSOCIATED CONTENT

### Supporting Information

The Supporting Information is available free of charge on the ACS Publications website at DOI: [10.1021/acs.jnatprod.6b01096](https://doi.org/10.1021/acs.jnatprod.6b01096).

$^1\text{H}$  NMR,  $^{13}\text{C}$  NMR, 2D NMR, and HRESIMS spectra of compounds 1–4 and GC-MS data of compounds 2, 7, and 8 (PDF)

## ■ AUTHOR INFORMATION

### Corresponding Authors

\*Tel: +886-7-3121101, ext. 2676. Fax: +886-7-3125339. E-mail: [bhchen@kmu.edu.tw](mailto:bhchen@kmu.edu.tw) (B.-H. Chen).

\*Tel: +886-7-3121101, ext. 2162. Fax: +886-7-3114773. E-mail: [jmb@kmu.edu.tw](mailto:jmb@kmu.edu.tw) (Y.-B. Cheng).

\*Tel: +886-7-3121101, ext. 2162. Fax: +886-7-3114773. E-mail: [aaronfrc@kmu.edu.tw](mailto:aaronfrc@kmu.edu.tw) (F. R. Chang).

### ORCID

Yuan-Bin Cheng: [0000-0001-6581-1320](https://orcid.org/0000-0001-6581-1320)

### Author Contributions

◇ V. D. Wagh and M. Korinek contributed equally to this work.

### Notes

The authors declare no competing financial interest.

## ■ ACKNOWLEDGMENTS

We thank the Center for Research Resources and Development at Kaohsiung Medical University for providing instrumentation support. This work was supported by grants from Ministry of Science and Technology, Taiwan (NSC 102-2628-B-037-003-MY3, MOST 103-2320-B-037-005-MY2, awarded to F.-R.C., MOST 103-2628-B-037-001-MY3 awarded to Y.-B.C.). This study was also supported by Kaohsiung Medical University, Taiwan (Aim for the Top Universities Grant, grant nos. KMUTP105E32, KMUTP104A26, KMUTP106009), and Ministry of

Health and Welfare, Taiwan (MOHW106-TDU-B-212-144007, Health and Welfare Surcharge of Tobacco Products).

## ■ REFERENCES

- (1) Jayaraman, S.; Daud, N.; Halis, R.; Mohamed, R. *J. For. Res.* **2014**, *25*, 535–540.
- (2) Zhang, Z.; Wei, J.; Han, X.; Liang, L.; Yang, Y.; Meng, H.; Xu, Y.; Gao, Z. *Int. J. Mol. Sci.* **2014**, *15*, 23589–23603.
- (3) Talukdar, A. *Int. J. Pharm. Pharm. Sci.* **2014**, *6*, 629–631.
- (4) Pant, P.; Rastogi, R. P. *Phytochemistry* **1980**, *19*, 1869–1870.
- (5) Gunasekera, S. P.; Kinghorn, A. D.; Cordell, G. A.; Farnsworth, N. R. *J. Nat. Prod.* **1981**, *44*, 569–572.
- (6) Dyary, H. O.; Arifah, A. K.; Sharma, R. S.; Rasedee, A.; Mohd-Aspollah, M. S.; Zakaria, Z. A.; Zuraini, A.; Somchit, M. N. *Trop. Biomed.* **2014**, *31*, 89–96.
- (7) Dash, M.; Patra, J. K.; Panda, P. P. *Afr. J. Biotechnol.* **2008**, *7*, 3531–3534.
- (8) Kim, Y. C.; Lee, E. H.; Lee, Y. M.; Kim, H. K.; Song, B. K.; Lee, E. J.; Kim, H. M. *J. Ethnopharmacol.* **1997**, *58*, 31–38.
- (9) Korinek, M.; Wagh, V. D.; Lo, I. W.; Hsu, Y. M.; Hsu, H. Y.; Hwang, T. L.; Wu, Y. C.; Cheng, Y. B.; Chen, B. H.; Chang, F. R. *Int. J. Mol. Sci.* **2016**, *17*, 398–410.
- (10) Jong, P. L.; Tsan, P.; Mohamed, R. *Int. J. Agric. Biol.* **2014**, *16*, 644–648.
- (11) Li, Y. J. *Anhui Agric. Sci.* **2008**, *36*, 2207–2208.
- (12) Wang, J. F.; Yang, S. H.; Liu, Y. Q.; Li, D. X.; He, W. J.; Zhang, X. X.; Liu, Y. F.; Zhou, X. *Bioorg. Med. Chem. Lett.* **2015**, *25*, 1986–1989.
- (13) Zhang, X. L.; Wang, L.; Li, F.; Yu, K.; Wang, M. K. *J. Nat. Prod.* **2013**, *76*, 858–864.
- (14) Zhao, W.; Wolfender, J. L.; Mavi, S.; Hostettmann, K. *Phytochemistry* **1998**, *48*, 1173–1177.
- (15) Wang, Y. B.; Huang, R.; Wang, H. B.; Jin, H. Z.; Lou, L. G.; Qin, G. W. *J. Nat. Prod.* **2006**, *69*, 967–970.
- (16) Ichihara, K.; Fukubayashi, Y. *J. Lipid Res.* **2010**, *51*, 635–640.
- (17) Arnone, A.; Nasini, G.; de Pava, O. V. *Phytochemistry* **1998**, *48*, 507–510.
- (18) Piazza, G. J.; Nunez, A.; Foglia, T. A. *Lipids* **2003**, *38*, 256–261.
- (19) Zayed, S.; Sorg, B.; Hecker, E. *Planta Med.* **1984**, *50*, 65–69.
- (20) Socha, A. M.; Kagan, G.; Li, W.; Hopson, R.; Sello, J. K.; Williard, P. G. *Energy Fuels* **2010**, *24*, 4518–4521.
- (21) Limb, J. K.; Kim, Y. H.; Han, S. Y.; Jhon, G. J. *J. Lipid Res.* **1999**, *40*, 2169–2176.
- (22) Hwang, T. L.; Su, Y. C.; Chang, H. L.; Leu, Y. L.; Chung, P. J.; Kuo, L. M.; Chang, Y. J. *J. Lipid Res.* **2009**, *50*, 1395–1408.
- (23) Boyum, A. J. *Clin. Lab. Invest.* **1968**, *97*, 77–89.
- (24) Jauregui, H. O.; Hayner, N. T.; Driscoll, J. L.; Williams-Holland, R.; Lipsky, M. H.; Galletti, P. M. *In Vitro* **1981**, *17*, 1100–1110.
- (25) Babior, B. M.; Kipnes, R. S.; Curnutte, J. T. *J. Clin. Invest.* **1973**, *52*, 741–744.
- (26) Hwang, T. L.; Leu, Y. L.; Kao, S. H.; Tang, M. C.; Chang, H. L. *Free Radical Biol. Med.* **2006**, *41*, 1433–1441.
- (27) Lai, W. C.; Tsui, Y. T.; Singab, A. N. B.; El-Shazly, M.; Du, Y. C.; Hwang, T. L.; Wu, C. C.; Yen, M. H.; Lee, C. K.; Hou, M. F. *Int. J. Mol. Sci.* **2013**, *14*, 15578–15594.



## Review article

# Protein-lipid nanohybrids as emerging platforms for drug and gene delivery: Challenges and outcomes



Mohamed Gaber<sup>a</sup>, Waseem Medhat<sup>a</sup>, Mark Hany<sup>a</sup>, Nourhan Saher<sup>a</sup>, Jia-You Fang<sup>b,c,d,\*</sup>,  
Ahmed Elzoghby<sup>a,e,\*\*</sup>

<sup>a</sup> Cancer Nanotechnology Research Laboratory (CNRL), Faculty of Pharmacy, Alexandria University, Alexandria 21521, Egypt

<sup>b</sup> Pharmaceutics Laboratory, Graduate Institute of Natural Products, Chang Gung University, Taoyuan 333, Taiwan

<sup>c</sup> Research Center for Industry of Human Ecology and Research Center for Chinese Herbal Medicine, Chang Gung University of Science and Technology, Kweishan, Taoyuan 333, Taiwan

<sup>d</sup> Department of Anesthesiology, Chang Gung Memorial Hospital, Kweishan, Taoyuan 333, Taiwan

<sup>e</sup> Department of Industrial Pharmacy, Faculty of Pharmacy, Alexandria University, Alexandria 21521, Egypt

## ARTICLE INFO

## Keywords:

Protein nanoparticles  
Lipid nanoparticles  
Liposomes  
Nanohybrids  
Drug delivery  
Gene delivery

## ABSTRACT

Nanoparticulate drug delivery systems have been long used to deliver a vast range of drugs and bioactives owing to their ability to demonstrate novel physical, chemical, and/or biological properties. An exponential growth has spurred in research and development of these nanocarriers which led to the evolution of a great number of diverse nanosystems including liposomes, nanoemulsions, solid lipid nanoparticles (SLNs), micelles, dendrimers, polymeric nanoparticles (NPs), metallic NPs, and carbon nanotubes. Among them, lipid-based nanocarriers have made the largest progress whether commercially or under development. Despite this progress, these lipid-based nanocarriers suffer from several limitations that led to the development of many protein-coated lipid nanocarriers. To less extent, protein-based nanocarriers suffer from limitations that led to the fabrication of some lipid bilayer enveloping protein nanocarriers. This review discusses in-depth some limitations associated with the lipid-based or protein-based nanocarriers and the fruitful outcomes brought by protein-lipid hybridization. Also discussed are the various hybridization techniques utilized to formulate these protein-lipid nanohybrids and the mechanisms involved in the drug loading process.

## 1. Introduction

Among the different types of clinically-used nano-formulations, lipid-based nanocarriers such as liposomes, lipid NPs, nanocapsules and nanoemulsions hold the biggest share. Many platforms exploit these lipid-based systems to deliver a variety of biologically active compounds due to the numerous benefits they confer such as being the least toxic for in-vivo applications [1–3]. These systems in general are biodegradable, biocompatible, non-immunogenic, and easy to prepare. They have been long used to alter drug properties and improve their therapeutic indices by modifying their absorption, reducing metabolism, decreasing toxicity, and increasing their biological half-lives. Liposomes can deliver both hydrophilic and hydrophobic drugs in their aqueous cores and hydrophobic bilayer coronas, respectively. Similarly, SLNs can incorporate both hydrophilic and hydrophobic drugs by means of high pressure homogenization (HPH) technique. Also, these systems have been a better alternative for gene delivery purposes

instead of viral vectors due to their non-antigenicity and ability to protect DNA from inactivation [4–6].

Despite the abovementioned advantages, all lipid-based nanocarriers seem to suffer from several disadvantages that hinder their promising progress. First, their colloidal and biological instabilities caused by their in vivo interactions with serum proteins and non-specific binding to cells such as lymphocytes, erythrocytes and endothelial cells. Second, in vivo, all lipid-based nanocarriers seem to suffer from increased reticuloendothelial system (RES) clearance [7–9]. This is caused by opsonization of lipid nanocarriers by complement proteins, fibronectin, and immunoglobulins which occurs mainly due to their hydrophobicity, rigidity, and/or their surface charges. As a result, this shortens their blood circulation times, and hence diminishes their efficacy. In addition, lipid nanoemulsions also suffer from rapid drug release due to the liquid state of their lipids. This in particular is not the case with SLNs which can offer a more sustained drug release due to their lipids' solid state. However, HPH commonly used to formulate

\* Corresponding author at: Pharmaceutics Laboratory, Graduate Institute of Natural Products, Chang Gung University, Taoyuan 333, Taiwan.

\*\* Corresponding author at: Cancer Nanotechnology Research Laboratory (CNRL), Faculty of Pharmacy, Alexandria University, Alexandria 21521, Egypt.  
E-mail addresses: [fajy@mail.cgu.edu.tw](mailto:fajy@mail.cgu.edu.tw) (J.-Y. Fang), [ahmed\\_elzoghby@alexu.edu.eg](mailto:ahmed_elzoghby@alexu.edu.eg) (A. Elzoghby).



SLNs may affect the stability of shear-sensitive drugs [10–12].

Numerous approaches were developed with the purpose of extending the circulation times of lipid carriers. PEGylation has been the most widely applied approach to reduce RES clearance due to the hydrophilicity, molecular flexibility, and neutrality of PEG. PEGylation decreases opsonization by providing a hydrated molecular corona around the nanocarrier, shielding surface charges, and becoming a steric barrier for opsonins to bind which extends blood circulation times of these PEGylated nanocarriers. However, PEG is not efficiently degraded by human enzymes leading to its accumulation *in vivo*, and hence subsequent toxicities could occur. Also, the reproducibility of PEGylated nanocarriers is relatively low and reports on its immunogenicity are not infrequent. As a result, a number of alternative approaches were developed. Coating the lipid nanocarriers with biodegradable proteins such as albumin, gelatin, silk fibroin (SF), and transferrin (Tf) that can carry the same functions as PEG seemed reasonable [13–15]. On one hand, these proteins can provide a hydrophilic corona, shield surface charges, and sterically hinder opsonin-binding in the same fashion as PEG, but on the other, their biodegradability and non-antigenicity have been well established. Also, these proteins can carry a lot of other different functions that PEG could not carry. For instance, some proteins can actively target particular tissues such as tumor cells by means of interaction with specific receptors overexpressed on these cells [16–19]. Moreover, the numerous functional groups available in protein structure can facilitate conjugation of drug or targeting ligand. In addition, proteins can enhance cellular uptake or gene transfection efficiency, enhance brain or ocular delivery of lipid-based nanocarriers, all of which PEG could not carry [20–24]. Through this review, we explain the limitations of lipid-based nanocarriers and the outcomes brought by their hybridization with different naturally-occurring proteins. In addition, we discuss the approaches that studied the consequences of encapsulation of protein nanocarriers within lipid bilayer coating. The various hybridization techniques and drug loading mechanisms utilized in the formulation of these protein-lipid nanohybrids are also discussed.

## 2. Hybridization techniques

In many studies, the surface of lipid nanocarriers including liposomes, SLNs, lipoplexes and lipid nanoemulsions was successfully functionalized with proteins via different mechanisms including covalent conjugation, desolvation, HPH, emulsification, or electrostatic coating. In few studies, protein nanocarriers were encapsulated within liposomes via film hydration, modified desolvation, and solvent injection methods.

### 2.1. Chemical conjugation

Several methods have been approached with the purpose of forming covalent bonds between proteins and lipid nanocarriers, however, the carbodiimide coupling method has been the most commonly applied one. This could be ascribed to it being a zero-length crosslinker, thus avoiding detrimental effects of intervening linkers or antibody formation against them. Also, of the two basic carbodiimide subtypes, the water soluble carbodiimide (1-ethyl-3-(3-dimethylaminopropyl) carbodiimide, EDC) is the most frequently utilized due to the hydrophilicity of most proteins and the hydrophilicity of its reaction by-products allowing easy purification. Carbodiimides are usually used in facilitating amide bond formation between carboxylic and amine groups which are both widely available on lipids and proteins. Furumoto et al. used *N*-glutarylphosphatidyl ethanolamine (NGPE) in the formulation of liposomes to provide a carboxylic functionality that could be exploited in amide bond formation with the amino groups of albumin. First, NGPE carboxylate was activated using EDC and the reactive intermediate formed was stabilized with *N*-hydroxysuccinimide (NHS). Then, the unreacted EDC was quenched with 2-mercaptoethanol to avoid activa-

tion of the carboxylic groups on albumin upon its addition thus avoiding self-polymerization [25]. Similarly, the carbodiimide method has been employed in forming gelatin-oleic acid (OA) conjugates [26], Tf-coated liposomes [27], and Tf-coated SLNs [28].

Activation of carboxylic functionalities of lipid components followed by conjugation to amino groups of the protein was found to yield lower sizes and higher conjugation efficiencies than the activation of protein carboxylic groups. The reason behind this is that proteins can self-polymerize upon activation owing to the existence of both, carboxylic and amino functionalities. In a study by Pooja et al., two different carbodiimide strategies were compared in the achievement of wheat germ agglutinin (WGA)-coated paclitaxel (PTX)-loaded SLNs. In the first one, stearyl amine was used to form SLNs to provide an amino group that could be coupled to the activated carboxylic group of WGA. Upon coupling, size increased from 149.8 nm to 239.2 nm and the conjugation efficiency was low, being just 11.45%. In the second strategy, stearic acid was used in the formation of SLNs to provide a carboxylic group that could be coupled to amino groups of WGA. Size increased to just 197.4 nm while the conjugation efficiency was significantly higher, being 74.1% [29].

On another avenue, the carbodiimide coupling method was not applicable for hybridization when the pH-remote loading method was utilized for encapsulation of doxorubicin (DOX) into liposomes. For efficient hybridization, the carbodiimide reaction has to be conducted under weakly acidic conditions thus making the efficient pH-remote loading of DOX unavailable. Alternatively, Yokoe et al. hybridized albumin with PEGylated liposomes containing dioleoylphosphatidyl ethanolamine (DOPE) via a hetero-bifunctional crosslinker, *N*-succinimidyl 3-(2-pyridyldithio)propionate (SPDP). The NHS ester end of SPDP forms an amide bond with amine-containing molecules while the pyridothiol group at the other end can form a disulfide bond with sulfhydryl residues. These sulfhydryl residues could be created on proteins with SPDP itself by reducing it with disulfide-reducing agents such as dithiothreitol (DTT) (Fig. 1a). First, an amide bond was formed between SPDP and DOPE to create a sulfhydryl-reactive DOPE. Then, sulfhydryl functionalities were created on albumin by coupling it first with SPDP then reducing it with DTT. Finally, a disulfide bond was formed upon the addition of albumin onto liposomes containing the sulfhydryl reactive-DOPE (Fig. 1b) [30].

Thiol-maleimide coupling technique has been widely exploited to form thioether linkages between maleimide-derivatized lipids and thiolated proteins. Thöle et al. prepared thiolated albumin using the hetero-bifunctional crosslinker, *N*-succinimidyl-*S*-acetyl-thioacetate (SATA). Then, PEGylated liposomes containing thiol-reactive maleimide were incubated with thiolated albumin leading to the formation of a thioether bond between maleimide and thiol functionalities [31]. In a similar way, Tf was thiolated using Traut's reagent and then it was added to maleimidebenzoyl-DOPE leading to the formation of Tf-conjugated lipids that were further used as a coating for PLGA NPs [32]. However, the thiol-maleimide coupling is faced with limited specificity for thiols and limited hydrolytic stability which led Xu et al. to exploit Staudinger ligation in conjugating Tf to DOPE. In Staudinger ligation, an azide-containing molecule reacts with a triphosphine derivative to form an aza-ylide intermediate. The triphosphine derivative contains an electrophilic trap, a methyl ester, which attacks the nucleophilic nitrogen of the intermediate. The result of such rearrangement is an amide bond between the azide-containing molecule and the triphosphine-containing molecule. DOPE was first activated with 2-(diphenylphosphino)terephthalic acid 1-methyl 4-penta-fluorophenyl-diester (DPPTPA) which provides a triphosphine for azide reaction and a methyl ester for the subsequent electrophilic trapping. Then, Tf was activated with *p*-azidophenyl isothiocyanate to react with liposomes containing the activated DOPE to form Tf-functionalized liposomes [33].

Using monoethanolamine (MEA) as a water soluble activator, an amphiphilic conjugate was fabricated from gelatin and OA by an

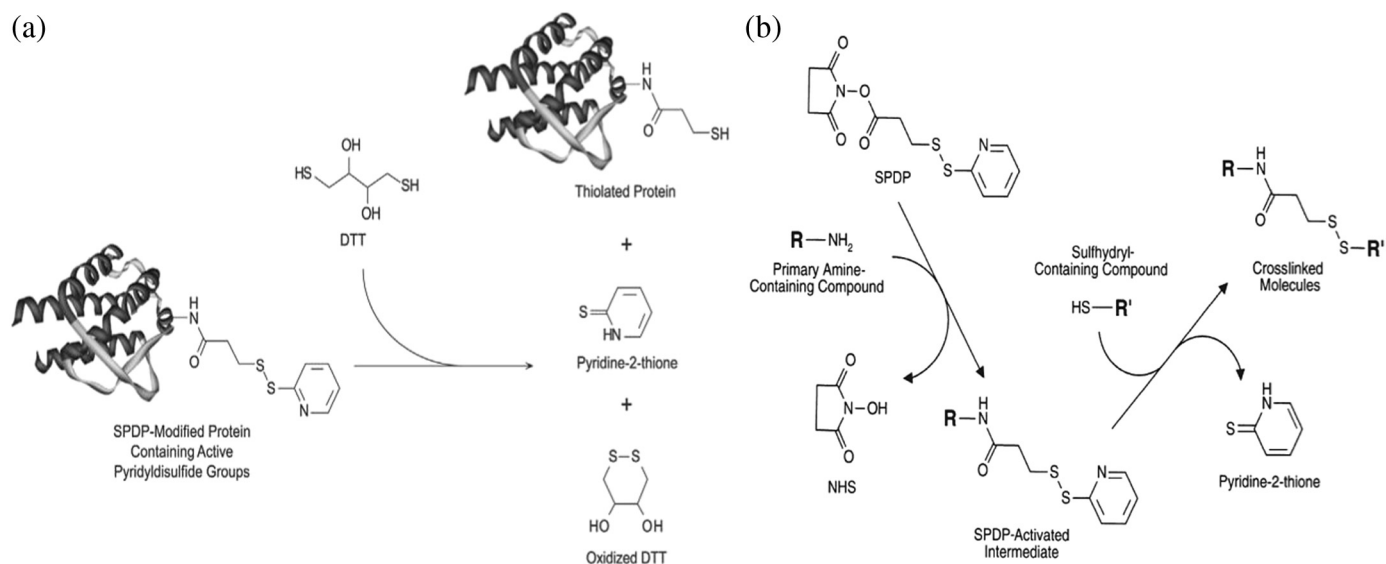


Fig. 1. (a) SPDP-modified protein yields a free sulfhydryl group upon reduction with DTT [34]. (b) SPDP can react with amine-containing molecules such as DOPE (R) through its NHS ester end. The pyridothiol group at the other end can then react with sulfhydryl-containing molecules such as that created on albumin (R') to form a cleavable disulfide bond [35].

aqueous method to overcome the opposing solubility between gelatin and OA without the necessity of using organic solvents. Because of the hydrophobicity of OA, it has to be first activated using MEA to facilitate its reaction with the hydrophilic gelatin in water. The aqueous gelatin solution was gradually added to OA/MEA colloidal aqueous solution while stirring till it became clear. The obtained solution was then spray-dried at a temperature of 130 °C for the evaporation of unreacted MEA and water allowing amide bond formation from the dehydration of the salts formed between gelatin amine groups and OA carboxylic groups. Self-assembled gelatin-OA NPs were obtained after dispersion in water with a size of 150–200 nm and a zeta potential ( $\zeta$ ) above  $-30$  mV [36].

## 2.2. High pressure homogenization

In this technique, protein-lipid mixed solution is subjected to intense turbulence and shear flow fields which disrupt the lipid phase into small droplets. Proteins get to stabilize these small droplets by forming a macromolecular layer around them thus decreasing the rate of coalescence [37]. HPH technique was successfully utilized to prepare albumin-coated teniposide-phospholipid complex. Briefly, aqueous albumin solution was added to teniposide-phospholipid complex solution in methylene chloride. Then, the dispersion was subjected to HPH for 5 to 10 cycles at a pressure of 5000 to 10,000 psi to yield nanohybrids with a size of 182.3 nm [38,39]. Similarly, whey protein isolate (WPI)-coated nanoemulsion and  $\beta$ -lactoglobulin ( $\beta$ LG)-coated lipid NPs were prepared by two-step homogenization technique. It was critical to cool the homogenizer during homogenization process to avoid solvent evaporation and protein thermal denaturation [40,41].

## 2.3. Electrostatic coating

Based on their isoelectric point (pI), proteins could be negatively or positively charged at pH values above or below their pI, respectively. Therefore, lipid nanocarriers could be electrostatically coated with oppositely charged proteins thus elaborating protein-lipid nanohybrids. Chen et al. electrostatically coupled indocyanine green-loaded liposomes with albumin to form albumin-coated liposomes. At pH 3, albumin (pI = 4.7) conferred a positive charge that was exploited to coat the negatively charged phosphatidyl ethanolamine-based liposomes. The albumin coating was concluded by the decrease in  $\zeta$  of liposomes from  $-43.5$  mV to  $-32.3$  mV and the increase in hydrodynamic diameter from 94.47 nm to 121.45 nm [42]. In our laboratory,

a negatively charged nanoemulsion ( $-35$  mV) was electrostatically coated with the cationic protein, lactoferrin (Lf, pI = 8.65) to form oily-core Lf nanocapsules which was concluded by the charge reversal to 16 mV. The nanocarriers successfully delivered quercetin and sorafenib to HepG2 liver cancer cells demonstrating a potential cytotoxicity. In contrast, benzalkonium chloride, a cationic surfactant, was incorporated into nanoemulsion to facilitate its coating with the anionic albumin forming nanocapsules that co-delivered exemestane and hesperetin to breast cancer cells. The coupling was concluded by the decrease in  $\zeta$  of the nanoemulsion from  $+38.8$  mV to  $+12.8$  mV and the size increase from 270.1 nm to 296.2 nm (Data to be published soon).

## 2.4. Double emulsification

In this technique, double nanocapsules with protein corona and lipid-polymer core were produced by double w/o/w emulsification. First, the internal aqueous phase containing biologically active proteins was dispersed into the oily component composed of linoleic acid and PLGA, and then emulsified to form the primary w/o emulsion. This emulsion was dispersed in an external aqueous phase containing fluorescently-labeled bovine serum albumin (BSA) solution to prepare double w/o/w emulsion. The unsaturated fatty acid, linoleic acid, was combined with PLGA to constitute the oily phase to; (a) facilitate the binding of BSA onto the nanocapsule surface thus overcoming the significant loss of the surface protein that previously occurred as a consequence of PLGA hydrolysis when used alone, and (b) to enhance the loading of the hydrophobic drug PTX in the oily phase [43].

## 2.5. Desolvation

Desolvation technique has been also exploited for the encapsulation of lipids within protein nanocarriers. Addition of a desolvating agent such as ethanol or acetone to an aqueous protein solution diminishes its water solubility thus inducing phase-separation and conformational change from the stretched to the coil form yielding NPs [20]. Gelatin-coated phospholipid nanohybrids were prepared by mixing aqueous gelatin solution with amphotericin B (AmB)/lecithin methanolic solution followed by addition of acetone. Gelatin was then precipitated onto lecithin to form gelatin-coated phospholipid nanohybrids (253 nm). Then, the NPs surface was hardened via glutaraldehyde cross-linking of the gelatin amino groups [44].

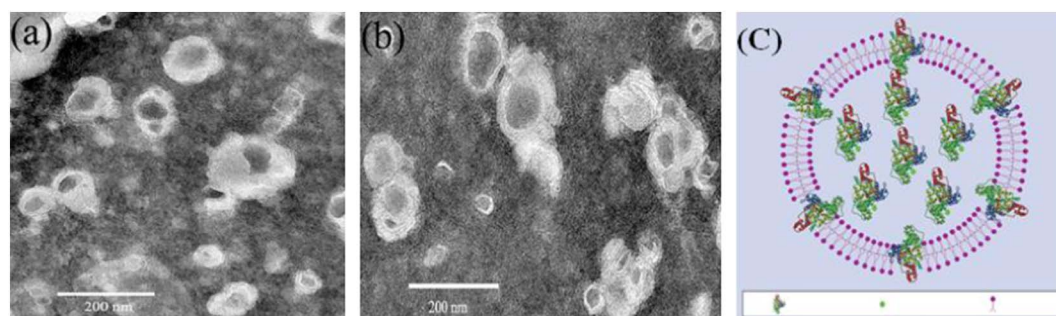


Fig. 2. TEM image of blank liposome (a) and PTX-liposome (b) [45], schematic illustration of lapatinib-phospholipid-albumin NPs (c) [47,48].

On the contrary, a desolvation-ultrasonication approach was exploited to develop lipid–protein nanocomplex (liposome). Upon dropping a PTX ethanolic solution to an aqueous BSA solution under stirring, the drug was precipitated and hydrophobically interacted with BSA forming a PTX-BSA conjugate. Phosphatidylcholine was then added to the PTX-BSA solution, followed by ultrasonication where the PTX-liposome was formed through the interaction of the PTX-BSA conjugate with phospholipid molecule. The liposomes appeared spherical with an aqueous inner phase enveloped by a multilayer configuration of lipid bilayers separated by interlayers of drug-BSA conjugate (Fig. 2a,b) [45,46]. In another investigation, without phospholipid, large unstable particles ( $> 1000$  nm) of lapatinib and albumin were formed, even after homogenization. However, incorporation of phospholipid enabled the formation of highly stable NPs with a small size of 66.8 nm without any need for high-pressure homogenization. Phospholipid molecules constituted most of the nanohybrid shell, whereas the albumin-lapatinib hydrophobic conjugate was in the core of the NPs. The authors suggested the anchoring of some albumin-lapatinib conjugate on the surface which might give the nanohybrid a cholesterol-like stabilizing effect (Fig. 2c) [47,48]. Albumin-phospholipid nanohybrids usually show a larger size and lower  $\zeta$  compared to phospholipid NPs due to the incorporation of albumin into the inner core of phospholipid NPs with some molecules anchored onto the NP inner surface [49].

## 2.6. Lipid film hydration

On the contrary to protein-functionalized lipid nanocarriers, liposomes could physically encapsulate protein NPs via lipid film hydration technique. Ruttala et al. encapsulated the desolvated albumin-PTX NPs (APNs) into PEGylated liposomal bilayer by thin-film hydration. First, PTX-loaded albumin NPs were developed by desolvation method. The phospholipids were dissolved in chloroform and evaporated under vacuum producing a lipid film which was hydrated with an aqueous solution of PTX-albumin NPs. The mixture was then extruded through  $0.2\ \mu\text{m}$  membrane thus producing uniform liposomes encapsulating albumin-PTX NPs (L-APNs) ( $\sim 210$  nm, PDI  $\sim 0.09$ , 4 mV). The nanohybrids exhibited larger size and smaller charge than that of blank liposomes, revealing incorporation of the APNs within the liposomal bilayer (Fig. 3) [50]. Furthermore, another hydrophobic drug curcumin was encapsulated in the liposomal bilayer to produce albumin-PTX NPs encapsulated in PEGylated curcumin liposomes [51].

## 2.7. Miscellaneous methods

Avidin-biotin interaction is one of the most popular and strongest non-covalent interactions used in bioconjugation. For the formation of Tf-coated lipoplexes, Tf was first biotinylated by the reaction with biotinamidocaproate-NHS and then mixed with streptavidin solution. Two novel cholesterol-based biotin derivatives were prepared by reacting biotin-NHS and biotinamidocaproate-NHS with cholesterolformyl hydrazide to yield biotinyl cholesterolformyl hydrazide (MSB1)

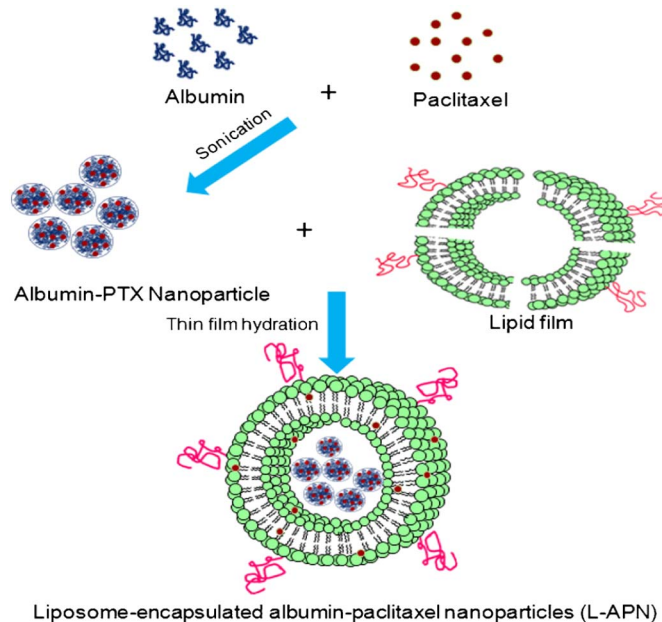


Fig. 3. Schematic representation of liposome-encapsulated albumin-PTX NPs [50].

and aminohexanoyl biotinyl cholesterolformyl hydrazide (MSB2), respectively. Liposomes prepared with the biotinylated cholesterol derivatives were then mixed with streptavidin-biotin-Tf to yield Tf-coated liposomes [52].

Another hybridization approach used fatty acid polymers for coating Rhodamine B-loaded gelatin NPs prepared by coacervation. The fatty acid myristoleic or OA was polymerized in situ on the surface of gelatin coacervates using a suitable initiator azobis 2-methylpropionamide dihydrochloride (AIBA) forming protective shells at the surface of gelatin NPs thereby retarding the release of the encapsulated dye [53].

## 3. Drug loading mechanisms

### 3.1. Covalent bonding

By virtue of the available functional groups in protein structure, drugs can be attached covalently to the protein shell of protein-lipid nanohybrids via carbodiimide or thiol-maleimide coupling techniques. The carboxylic functionalities of methotrexate were activated by carbodiimide and coupled to amines of albumin via amide bond. 31% of the free lysines in albumin were conjugated to methotrexate resulting in a methotrexate:albumin molar ratio of 11:1. Then, HPH technique was used for preparation of methotrexate-conjugated albumin-coated nanoemulsion [54]. An amide bond could also be formed from the reaction of anhydrides and amines of proteins. The  $\epsilon$ -amino groups of lysine on albumin were derivatized with cis-aconitic anhydride to form



a drug carrier complex with intrinsic anti-HIV activity. This complex was used afterwards to coat liposomes via thiol-maleimide coupling technique [55,56].

Vancomycin was covalently bonded to albumin via thiol-maleimide coupling. First, vancomycin has been made thiol-reactive through the addition of maleimide via the linker, 4-(*N*-maleimidomethyl) cyclohexane-1-carboxylic acid 3-sulfo-*N*-hydroxysuccinimide. Then, maleimide-derivatized vancomycin reacted with the only free thiol functionality found in Cys34 of albumin forming a thioether bond. The conjugation efficiency obtained was 36% with 0.28 mol of vancomycin per 1 mol of albumin. The formed conjugate was then used to form albumin-coated nanoemulsion via HPH technique [54].

### 3.2. Physical entrapment

#### 3.2.1. Desolvation

Using desolvation method, drugs could be physically encapsulated into protein NPs which are subsequently coated with lipids to form protein-lipid nanohybrids. PTX was physically encapsulated into albumin NPs using desolvation method where the drug was dissolved in ethanol that desolvated albumin upon its addition. The albumin-PTX NPs were then encapsulated within liposomes by lipid film hydration technique. The developed liposome-coated albumin NPs showed great encapsulation efficiency and PTX loading of approximately 99% and 6.5%, respectively [50]. Another alternative for solubilizing hydrophobic drugs using organic solvents is the inclusion within the hydrophobic cavity of cyclodextrin. The hydrophobic drug, zaltoprofen, was complexed with hydroxypropyl- $\beta$ -cyclodextrin to enable its incorporation into the aqueous gelatin solution prior to desolvation (Fig. 4). The desolvated gelatin NPs entrapped zaltoprofen with 76.21% efficiency which were then coated with OA [57].

#### 3.2.2. Hydrophobic interaction

Hydrophobic drugs could be efficiently encapsulated within the lipid fraction of nanohybrids by hydrophobic interaction which then gets coated with the protein shell. Docetaxel was efficiently loaded in olive oil of the organic phase of albumin-coated nanoemulsion with an entrapment efficiency of 99% [58]. In another approach, the hydrophobic core of self-assembled gelatin-OA conjugate NPs could be successfully utilized as a reservoir for encapsulation of PTX. This was facilitated by the hydrophobic interaction between PTX and OA that

significantly enhanced its solubility from 1.61  $\mu\text{g/ml}$  to 20.53  $\mu\text{g/ml}$  when compared with free PTX [36,59].

#### 3.2.3. Electrostatic interaction

Lipoplexes are based on the electrostatic interaction of cationic liposomes with negatively charged genetic material. The bcl-2 antisense oligodeoxynucleotide, G3139, has been electrostatically complexed with cationic liposomes containing dimethyldioctadecyl ammonium bromide (DDAB) forming lipoplexes with an encapsulation efficiency of 87.2%. Lipoplexes were further coated with human serum albumin (HSA) based on an electrostatic interaction [60]. In a study by Li et al., cationic albumin-pentaethylenehexamine (PEHA) conjugate was formed for the electrostatic complexation of RX-0047, an antisense oligonucleotide against the hypoxia inducible factor-1  $\alpha$  (HIF-1 $\alpha$ ). Albumin-PEHA solution was first mixed with an ethanolic solution of soy phosphatidylcholine, D- $\alpha$ -tocopheryl polyethylene glycol-1000 succinate and 2,3-dioleoyloxy-propyl-trimethylammonium chloride (DOTAP). Upon the addition of RX0047 solution, complexes were spontaneously formed showing full retardation of RX-0047 by albumin-PEHA conjugates at weight ratio of 1:10 on gel retardation assay [61].

Hydrophobic ion pairing is an interesting approach for increasing the encapsulation of hydrophilic ionizable drugs into lipid-protein nanohybrids. By virtue of its lipophilicity, OA was used for the electrostatic complexation of pirarubicin in order to reduce its hydrophilicity where the positively-charged amino groups of the drug interacted with the negatively charged carboxylates of OA resulting in an ion-pair complex with shielded charges. Thus, the drug lipophilicity was enhanced which improved its compatibility with OA and enhanced its encapsulation efficiency into the nanohybrids, being 91.63%. The pirarubicin-OA ion-pair was then dissolved with phospholipid in methylene chloride and further mixed with aqueous HSA solution using a high-pressure homogenizer to form nanohybrids [62].

#### 3.2.4. pH-remote loading

The pH-remote loading method has been applied in the entrapment of DOX into albumin-coated liposomes using an ammonium sulfate gradient with about 90% drug loading. Ammonium sulfate gradient method is favored since it neither needs the preparation of liposomes in acidic pH nor the alkalization of the extraliposomal aqueous phase. The main force driving the influx of DOX through the lipid bilayer is the

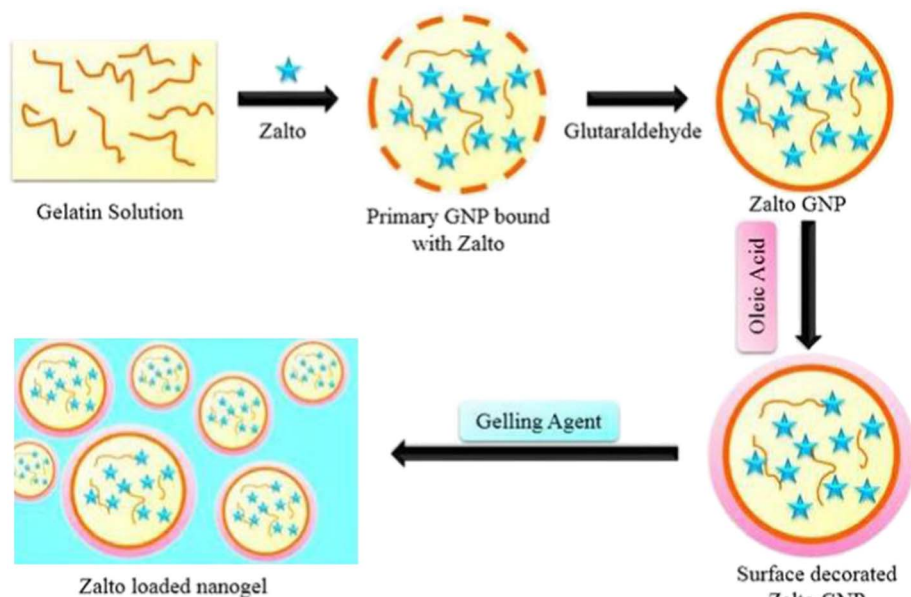


Fig. 4. Diagrammatic illustration of zaltoprofen-loaded gelatin nanogel [57].

**Table 1**  
Albumin-coated lipid nanocarriers.

Lipid system	Drug	Hybridization technique	Key outcomes	Ref.
Liposomes	CPT	Physical adsorption	Enhanced CPT in vitro and in vivo stability & 9.6-fold increase in CPT tumor accumulation	[63]
Liposomes	DOX	Electrostatic interaction	Decreased opsonization compared to Doxil®	[23]
Liposomes	Cis-aconitic anhydride	Chemical conjugation	Intrinsic anti-HIV activity with liver targeting capability	[55,56]
Liposomes	DOX	Chemical conjugation	Enhanced therapeutic index of DOX	[30]
Liposomes	Clodronate Zoledronate	Chemical conjugation	Enhanced targeting of macrophages	[64]
Liposomes	ICG	Electrostatic interaction	Improved serum stability of ICG & enhanced tumor imaging	[42]
Liposomes	PTX	Electrostatic interaction	1.9-fold increase in cellular uptake by MCF-7 due to dual targeting by BSA and FA	[65]
Lipoplexes	HSV-tk gene & IL-12 gene	Electrostatic interaction	Enhanced anti-tumor activity via synergistic combination of suicide gene therapy and vinblastine	[66,67]
Lipoplexes	G3139	Electrostatic interaction	Lipoplexes chemosensitized cancer cells to DOX	[60,68]
Lipoplexes	phrGFP siRNA	Electrostatic interaction	Enhanced serum stability with 11.6-fold increase in mean residence time	[69]
Nanoemulsion	Diclofenac	Chemical conjugation	Enhanced targeting of inflammatory sites	[7]
Nanoemulsion	CORM-2	High pressure homogenization	FA functionalization caused 7-fold increase in cellular uptake by lymphoma cells	[70]
Nanoemulsion	Docetaxel	Chemical conjugation	2.26-fold increase in tumor targeting with 80% tumor inhibition	[58]
Nanoemulsion	Methotrexate	High pressure homogenization	Enhanced tumor targeting of methotrexate	[54]
	Vancomycin		A significant decrease in MIC of vancomycin	
SLNs	Coumarin-6	Hydrophobic interaction	Dual targeting of enterohepatic tumors by UA and BSA	[71]
SLNs	Methotrexate	Chemical conjugation	15.2 times higher cellular uptake by brain capillaries	[10]
Phospholipid complex	Teniposide	High pressure homogenization	HSA enhanced the cellular uptake and anti-tumor activity of teniposide	[38]

CPT: Camptothecin, ICG: Indocyanine green, HSV-tk: Herpes Simplex Virus thymidine kinase, IL-12: Interleukin 12, G3139: Bcl-2 antisense oligodeoxyribonucleotide, phrGFPsiRNA: Humanized renilla green fluorescent protein siRNA, CORM-2: Carbon monoxide releasing molecule-2.

ammonia efflux which creates a  $[H^+]$  gradient. Unprotonated DOX gets protonated after crossing the liposomal membrane where it forms a gel-like precipitate with sulfate, thus trapped inside the liposomes [23].

#### 4. Implications of protein-lipid nanohybrids

##### 4.1. Reduced opsonization and prolonged circulation

Uncoated lipid nanocarriers can adsorb various opsonins such as serum proteins and cells which form a protein corona that surrounds the particles. The opsonization of these nanocarriers induces their clearance from blood by the RES resulting in a reduction of their circulation times. Several studies showed that pre-coating lipid nanocarriers with dysopsonic proteins (e.g. albumin) could significantly suppress the in vivo interactions with opsonins.

Indeed, albumin has been the most widely used protein to coat lipid-based nanocarriers; a summary of which is presented in Table 1. Yokoe et al. demonstrated the superiority of HSA-coated liposomes as delivery systems for DOX compared with their PEGylated counterparts in sarcoma-bearing rats. By virtue of its hydrophilicity, HSA-coated liposomes were less recognized by opsonins, and hence they had prolonged blood circulation times. This was indicated by the significantly higher area under the curve (AUC) for HSA-coated liposomes, being 89.7  $\mu\text{g h/ml}$ , compared to 33.8 and 4.52  $\mu\text{g h/ml}$  for their PEGylated counterparts and free DOX, respectively. Moreover, the clearance (CL) was significantly lower for HSA-coated liposomes, being 7 ml/h, compared to 17.9 and 131 ml/h for the PEGylated liposomes and free DOX, respectively [30]. In another investigation, the reduced opsonization and RES clearance of rat serum albumin (RSA)-coated PEGylated liposomes could be explained on the basis that binding of albumin: (a) changed the conformation of PEG molecules from the mushroom to brush-like conformation which reduced the interaction with phagocytes or other serum proteins, (b) blocked the binding sites for serum proteins onto the surface of PEGylated liposomes, and (c) increased the hydrophilicity of PEGylated liposomes (Fig. 5) [25].

Another approach used thermally-denatured BSA (dBSA) to coat the DOX-loaded liposomes which exhibited increased stability in plasma compared to their PEGylated counterparts. Thermal denaturation converted the tertiary and secondary structures of albumin into the primary one which showed to be more flexible and hydrophilic. This was ascribed to the breaking of the non-covalent linkages making up

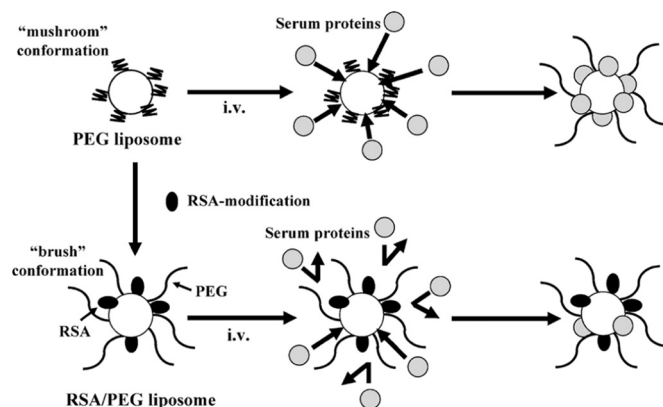


**Fig. 5.** Assumed mechanisms by which RSA-modification suppresses the association of serum proteins onto the surface of PEGylated liposome [25].

albumin's tertiary and secondary structures, and the appearance of new hydrogen bonding groups that can interact with the surrounding water molecules. This induced hydrophilicity to the liposomal surface resulted in a further reduction in opsonin binding which was indicated by the slight increase in particle size of BSA-coated liposomes from 110 to 125 nm after 48 h of incubation with blood plasma compared to a significant size increase from 108 to 247 nm showed by their PEGylated counterparts [23].

##### 4.2. Enhanced targeting efficacy

Certain proteins such as albumin, Tf, and Lf can enhance tumor targeting of anti-cancer drugs via interaction with specific receptors overexpressed on tumor cells. It was found that albumin can enhance drug accumulation in solid tumors via binding to gp60 (albumin), which is overexpressed on endothelial cells of tumor blood vessels, and SPARC (Secreted Protein, Acidic and Rich in Cysteine), an extracellular matrix glycoprotein overexpressed in a wide array of solid tumors. Coating of docetaxel-loaded stearylamine-based lipid nanoemulsion with albumin has enhanced its cytotoxicity to MCF-7 cells ( $IC_{50} = 14.52$  nM) compared to uncoated counterpart ( $IC_{50} = 22.97$  nM) or free drug ( $IC_{50} = 35.68$  nM). After injection into B16F10 melanoma-bearing mice, albumin-coated nanoemulsion showed a higher tumor growth inhibition of 80.01% compared to



54.27% for the uncoated nanoemulsion [58]. Like tumor tissues, protein functionalization of lipid nanocarriers can increase drug accumulation in inflammatory tissues. Coupling of albumin to diclofenac-loaded lipid nanoemulsion increased its anti-inflammatory efficacy upon injection into rats with granuloma air pouch-induced inflammation. The preferential accumulation of albumin-coated nanoemulsion into inflammatory sites could be attributed to: (1) The nanosize of the formulation which led to its passive accumulation into inflammatory sites through the enhanced permeation and retention (EPR) effect as a result of the physiological features of extravasation exhibited by inflammatory tissue. (2) Hypoalbuminemia which also contributed in the passive accumulation of albumin into inflammatory sites. (3) Albumin binding to albondin receptors overexpressed on the vascular endothelium of inflammatory sites. (4) Binding of albumin-coated nanoemulsion to SPARC receptors overexpressed on inflammatory cells which resulted in their subsequent endocytosis [7].

Tf, one of the human serum proteins, functions in vivo in the transport of ferric ions to tissues. Lipid nanocarriers have been mainly functionalized with Tf as a targeting ligand for cancer cells overexpressing Tf receptors (TfR); a summary of such systems is presented in Table 2. The high serum concentration of endogenous Tf may represent a strong limitation for targeting TfR by Tf-coated nanocarriers in vivo. However, the endogenous Tf is usually not iron-coupled and, thus, has a lower binding affinity for the TfR in comparison to the holo-Tf usually used in coating nanocarriers. Moreover, many Tf molecules are commonly attached to each nanocarrier thus facilitate multivalent binding with target cells in contrast with the monovalent circulating Tf. Therefore, Tf-lipid nanocarriers can overcome the availability of endogenous Tf in circulation [72]. Conjugation of Tf to curcumin-loaded SLNs significantly increased the intracellular retention of curcumin and enhanced its anti-proliferative action on MCF-7 breast cancer cells. This could be ascribed to the enhanced internalization of SLNs by TfR-mediated endocytosis and the bypass of membrane-associated efflux mechanisms since both, Tf and curcumin, inhibit P-glycoprotein efflux transporters [28].

Lf is an iron-binding 80 kDa glycoprotein of the Tf family with known antioxidant, antimicrobial, and antineoplastic effects. A variety of cells have shown to express receptors for Lf such as cells of the GIT, lymphocytes, macrophages, brain cells, breast cells, and hepatocytes. A number of lipid nanocarriers have been functionalized with Lf, a summary of which is included in Table 4. Two hepatocyte-associated Lf receptors (LfRs) namely, the asialoglycoprotein receptors and low-density lipoprotein receptor-related protein receptors were effectively targeted by Lf-coated PEGylated liposomes. Lf-PEGylated liposomes loaded with coumarin-6 showed 2.2-fold higher fluorescence intensity in HepG2 cells than uncoated liposomes. When compared to BSA as a ligand for hepatocytes, Lf-coated liposomes showed a higher cellular uptake that was inhibited by adding free Lf which was not the case for BSA. This indicated the receptor-mediated endocytosis of Lf by HepG2 cells unlike the non-specific one for BSA [73]. Overexpression of LfRs was also observed on lung cancer cells where targeting of bronchogenic carcinoma was achieved by Lf-coated PTX-loaded SLNs. The expression of LfRs on the apical side of the bronchial epithelial cells aided a higher cellular uptake for Lf-coated SLNs. This was manifested by the higher percentage of drug recovery in the lungs, being 20.5%, after 6 h of in vivo administration for the Lf-coated SLNs compared to 12.2% and 9.9% for the uncoated SLNs and free PTX, respectively [74].

In addition to albumin, Tf, and Lf, SF showed a promising targeting capacity, not by interaction with specific receptors, but by binding to the mucopolysaccharides overexpressed on tumor-like keloid fibroblasts. Therefore, SF was utilized for coating emodin-loaded liposomes for the targeting of such fibroblasts. SF-coated liposomes significantly decreased the survival rate of keloid fibroblasts to 57% after 24 h in comparison to 75% for the uncoated liposomes. When tested on the breast cancer cell line, MDA-MB-453, that overexpresses Her2/*neu*, SF-coated liposomes outdid uncoated ones in terms of cellular uptake of

emodin, inhibition of Her2/*neu* protein phosphorylation, and suppression of cancer cell growth. Beside its abovementioned targeting action, the adhesive properties of SF have put the liposomes in close proximity to the targeted cells thus increasing their binding chances and overcoming the shortcomings of Brownian motion [107,108].

Lectins, another group of proteins, bind specifically to the carbohydrate moiety of glycoproteins and glycolipids overexpressed in cancer cells. Coupling of a plant lectin, WGA, to PTX-loaded SLNs has enhanced their anticancer activity against A549 lung cancer cells via binding to NAG receptors overexpressed on these cells. The IC<sub>50</sub> values for PTX, untargeted SLNs and WGA-coated SLNs after 48 h of treatment were 164.56, 100.26 and 41.04 ng/ml, respectively. This could be attributed to the difference in uptake mechanisms where unconjugated SLNs were likely to enter cells through clathrin-mediated endocytosis whereas WGA-coated SLNs were internalized through lectin receptor-mediated endocytosis [29].

In addition to their intrinsic targeting action, proteins as the shell component of protein-lipid nanohybrids, contain multiple functional groups (e.g. amino, thiol and carboxylic) that enable conjugation with targeting ligands with the aim of dual-targeted drug delivery (Fig. 6). Loureiro et al. exploited the overexpression of folate receptors in many tumors to prepare a folic acid-tagged albumin-coated PEGylated nanoemulsion encapsulating CORM-2. Folate was efficiently conjugated to albumin with an amide bond using the carbodiimide method. The folic acid-tagged nanoemulsions showed a 7-fold increase in cellular uptake by A20 lymphoma cells in comparison to their untagged counterparts which was translated in vivo in a greater antitumor activity in lymphoma-bearing mice [70]. Another targeting ligand, ursodeoxycholic acid (UA), was covalently attached to the amino groups of BSA via carbodiimide coupling. The product of such conjugation, UA-modified BSA, was then used to coat SLNs. UA-modification caused 1.21 and 1.75 folds higher cellular uptake by hepatoma cells compared to their BSA-coated and uncoated counterparts. This was ascribed to dual targeting of liver tumor cells through UA which binds to bile acid receptors, and BSA which targets albondin and SPARC receptors [71].

In contrast to all the abovementioned studies which utilize the protein shell of the nanohybrids for site-specific targeting, some types of lipids have been explored as targeting moieties. An overview of all lipid-coated protein nanocarriers is presented in Table 3. The negatively charged lipid, 1,2-diacyl-sn-glycero-3-phospho-L-serine (PS), was found to be upregulated on the outer surface of many Leishmania species and appeared to be highly linked with its recognition by macrophages of the liver, spleen, lymph nodes, and bone marrow through several receptors such as scavenger receptors,  $\beta_2$  glycoprotein I, and gas-6. AmB-loaded gelatin NPs were coated with PS for targeted delivery of AmB to these macrophages. The PS-coated NPs showed a significantly higher localization in the liver and spleen than their uncoated counterparts or free AmB [109]. Surprisingly, a significantly higher uptake of liposome-coated PTX-loaded albumin NPs by human breast cancer (MCF-7) and mouse melanoma (B16F10) cells was achieved in comparison to Abraxane®, PTX-loaded albumin NPs. The authors attributed this behavior to the charge-based interaction between the positively charged DOTAP-containing liposomes and the cancer cells which are negatively charged. Moreover, the hydrophobic nature of the liposomes facilitated the internalization of the NPs through the cell membrane [50].

#### 4.3. Enhanced gene transfection efficiency

Cationic liposomal-DNA complexes, namely lipoplexes, are usually sought for gene delivery purposes to overcome the drawbacks of using their viral counterparts. However, lipoplexes themselves show poor gene transfection efficiency, as well as toxicity at higher concentrations. Moreover, the highly positive charge of lipoplexes leads to considerable reduction of their biological activity by interacting with the negatively

**Table 2**  
Transferrin-coated lipid nanocarriers.

Lipid system	Drug	Hybridization method	Key OUTCOMES	Ref.
Liposomes	DOX	Chemical conjugation Staudinger ligation	Enhanced uptake via dual Tf/folate targeting Enhanced uptake via dual Tf/TAT targeting Enhanced DOX cytotoxicity	[75,76] [77]
Liposomes	Cisplatin	Chemical conjugation	IC <sub>50</sub> of 26.66 µg/ml compared to 135.07 µg/ml for free cisplatin	[33] [78]
Liposomes	9-NC	Chemical conjugation	Enhanced lactone and liposomal stability	[79,80]
Liposomes	NCL-240 and Cobimetinib	Chemical conjugation	Synergism achieved with a combination index of 0.79	[81]
Liposomes	PTX	Chemical conjugation	8.6-fold increase in cellular uptake Dual bone targeting via Tf and alendronate	[82] [83]
Liposomes	Artemisinin	Chemical conjugation	Enhanced cytotoxicity compared to free drug or uncoated liposomes	[84]
Liposomes	NGF	Chemical conjugation	Enhanced BBB permeation by cereport and enhanced targeting by Tf	[85]
Liposomes	Citicoline	Chemical conjugation	Enhanced radioprotective effect of citicoline	[86]
Liposomes	Docetaxel	Chemical conjugation	7-fold increased uptake by SKOV3 cells	[87]
Liposomes	5-FU	Chemical conjugation	Enhanced brain uptake and sustained release	[88]
Liposomes	Docetaxel and QDs	Chemical conjugation	Targeted brain imaging and therapy	[89]
Liposomes	α-Mangostin	Chemical conjugation	Enhanced brain delivery of α-Mangostin	[90]
Liposomes	LSS670 and IP-10	Chemical conjugation	Enhanced tumor imaging and therapy	[91]
Liposome-coated MNPs	–	Physical mixing	Enhanced targeting via Tf/magnetofection	[92]
Lipid-coated MNPs	GFP	Electrostatic interaction	Magnetofection caused 300-fold increase in gene transfection by lipoplexes	[93]
Lipoplexes	LOR-1284 siRNA	Chemical conjugation	80% enhancement in gene silencing compared to 50% for free LOR-1284	[94,95]
Lipoplexes	G3139	Chemical conjugation	Sensitization of K562 cells to daunorubicin	[72,96]
Lipoplexes	p10	Chemical conjugation Streptavidin-biotin	Enhanced transfection through TfR targeting and lipid's fusogenicity	[97]
Lipoplexes	p53	Electrostatic interaction	2-fold increase in transfection of lipoplexes 60.7% tumor growth inhibition compared to 43.6% for uncoated lipoplexes	[52] [98]
Lipoplexes	IL-12	Electrostatic interaction	2-fold increase in IL-12 expression compared to uncoated lipoplexes	[99]
Lipoplexes	HSV-tk gene	Electrostatic interaction	Suicide gene therapy resulted in 100% cytotoxicity to oral cancer cells	[100,101]
Lipoplexes	anti-mCRP siRNA	Chemical conjugation	Enhanced antibody-based immunotherapy against cancer	[102]
Lipoplexes	Anti-luciferase or Anti-c-Jun siRNAs	Electrostatic interaction	40% gene silencing was achieved in vivo	[103]
SLNs	GFP	Chemical conjugation	Enhanced transfection through dual targeting by dexamethasone and Tf	[104]
SLNs	Curcumin	Chemical conjugation	Enhanced curcumin stability	[28]
NLCs	PTX and GFP	Electrostatic & hydrophobic interactions	Lower IC <sub>50</sub> compared to Taxol®	[105]
NLCs	DOX and pEGFP	Electrostatic interaction	66% tumor weight inhibition compared to 47% for their uncoated counterparts	[106]

RGD: cyclic arginine-glycine-aspartic acid peptide, LOR-1284 siRNA: siRNA targeting R2 subunit of ribonucleotide reductase, GFP: luciferase and green fluorescent protein reporter genes, 9-NC: 9-nitrocamptothecin, NCL-240: a novel small-molecule inhibitor of the PI3K/mTOR pathway, NGF: Neuron growth factor, BBB: Blood brain barrier, p10: firefly luciferase plasmid, TAT: Cationic cell-penetrating peptide derived from HIV-1 protein TAT, anti-mCRP: anti-membrane-bound complement regulatory proteins, 5-FU: 5-fluorouracil, QDs: Quantum dots, LSS670: X-SIGHT 670 Large Stokes Shift Dye, IP-10: IFN-γ-inducible protein-10 gene.

charged serum components and cell surfaces thus limiting their ability to reach target tissues. Coating cationic lipoplexes with albumin has shown significant enhancement of their in vivo transfection efficiency through overcoming the undesired interactions with serum components together with resistance to serum endonucleases. In addition, albumin can facilitate the binding of the lipoplexes to cellular surfaces and their internalization via endocytosis. It also can facilitate their escape from the endolysosomal compartment to get subsequently translocated into the nucleus. HSA-coated lipoplexes significantly increased the transfection of the suicide gene, HSV-tk and pCMVIL-12 encoding IL-12 gene in mammary adenocarcinoma TSA cells. Intratumoral injection of HSA-coated lipoplexes that contain the above plasmids followed by ganciclovir treatment showed a strong antitumor activity. This was established by the reduced tumor sizes and the more profound tumor necrotic and hemorrhagic areas when compared to those found in control animals. Coating the lipoplexes with HSA tripled their cellular uptake via binding to the albumin receptors overexpressed on tumor cells. However, their biological activity (i.e. transgene expression)

increased by 15 folds which is 5 folds higher than the increase in cellular uptake. This difference between uptake and biological activity indicated the facilitation of endolysosomal escape of the lipoplexes by HSA through its fusogenic properties. In addition, it was suggested that HSA could stimulate an immune response against the tumor which was indicated by the higher T-lymphocyte infiltration in animals treated with control HSA-coated lipoplexes compared to their non-treated counterparts [67]. Another useful approach is the use of the cationic peptides, protamines, for condensation of DNA to reduce the amount of exposed DNA. This, as a result, protects DNA from degradation and favors its cellular uptake and nuclear translocation; thus enhancing gene expression. Faneca et al. showed that co-coupling of HSA and protamine to lipoplexes resulted in a more enhanced transfection efficiency as well as a better resistance to serum inhibitory effect, even at a 60% concentration [115].

Two mechanisms may be involved in the enhanced gene expression by HSA-coated lipoplexes: (1) Promoting internalization of the lipoplexes via endocytosis. (2) Promoting intracellular delivery of DNA by

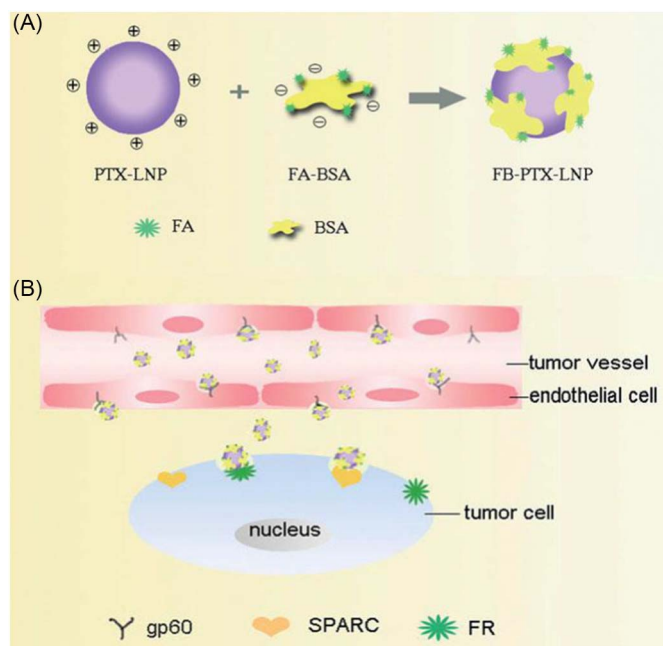


Fig. 6. Schematic illustration of the dual-targeting mechanism of the FB-PTX-LNP to tumor cell via binding to gp60 and SPARC by BSA and binding to folate receptors by folic acid [65].

facilitating its endosomal escape which could be elucidated according to the following hypotheses; (a) Albumin may have undergone partial protonation and conformational changes at the low endosomal pH thereby acquiring fusogenic properties that facilitate its interaction with the endosomal membrane and thus resulting in its destabilization or disruption, thereby improving intracellular gene delivery. The membrane destabilization may then favor a transbilayer/flip-flop movement of negatively charged lipids from the cytoplasmic leaflet of the endosomal membrane to the luminal one. A result of which is the dissociation of DNA from the lipoplexes and its subsequent entry into the cytoplasm. (b) The reversible expansion of albumin after its partial protonation at low pH and the subsequent exposure of its hydrophobic core domains might have been the factor that induced the flip-flop transbilayer movement and the dissociation of the lipoplexes [9].

Among the key factors that can affect the transfection efficiency of HSA-coated lipoplexes are the secondary structure and concentration of albumin. Relative to Oligofectamine-ODN complexes, HSA-coated liposomes exhibited a higher efficiency in delivering the antisense ODN, G3139, in human oral carcinoma, KB cells, resulting in a higher Bcl-2

downregulation and a more effective growth inhibition of cancer cells. Denaturation of albumin by heating at temperatures above 55 °C led to a significant reduction in Bcl-2 mRNA downregulation which could be attributed to the conformational change of its secondary structure from the  $\alpha$ -helical to the  $\beta$ -pleated one. A result of such change is an inability to interact with receptors which would diminish internalization as a result and a loss of its fusogenic properties. Moreover, the use of very high albumin concentrations did not enhance transfection which could be explained by the following mechanisms: (1) The competition between albumin and ODN, being both negatively charged, for association with the positively charged liposomes have led to an electrostatic destabilization of the ODN lipoplexes and thus inducing ODN release, (2) The increase of the negative charge of the lipoplexes by high albumin concentrations have led to an electrostatic repulsion with the negatively charged cellular surfaces, thus decreasing binding and uptake. (3) The aggregation of the carrier system caused by high amount of albumin [60].

Unlike albumin which can enhance lipoplexes uptake and induce a fusogenic escape from the endolysosomes, Tf can only enhance internalization of lipoplexes via TfR-mediated endocytosis. To overcome this challenge, Tf-coated fusogenic liposomes fabricated using a novel PEG derivative were coupled to p10-lipoplexes. PEG is well-known for its fusogenic properties as it could induce liposomal destabilization and subsequent endolysosomal fusion, resulting in drug release into the cytosol without degradation. However, to render such fusogenic properties pH-sensitive, carboxylic groups were incorporated to the PEG derivative, poly(glycidol), through the reaction with succinic anhydride. Incorporation of succinic anhydride increased the affinity of poly(glycidol) to the liposomes at low pH and hence induced the destabilization effect and fusogenicity due to the formation of hydrogen bonds between the unionized carboxylic groups of poly(glycidol) and liposomal phosphodiester groups along with the hydrophobic interaction of succinate groups with the liposomes. However, at higher pH of 7.4, such interactions could not take place due to the ionization of the carboxylic groups and the increased hydrophilicity of the polymer. Transfection efficiency seemed to be enhanced with increased association of these Tf-coated liposomes to p10-lipoplexes to a certain extent. Further increase was associated with detrimental effects on transfection. This was attributed to the appearance of unassociated Tf-coated liposomes which competitively inhibited the uptake of other Tf-coated liposomes coupled to p10-lipoplexes [97]. In another study, Tf-coupled lipid-coated magnetic NPs were utilized for enhancing GFP reporter gene expression. Applying static magnetic fields to improve gene delivery, magnetofection, has shown to enhance the cellular accumulation of gene delivery vectors. However, such enhancement did increase cellular uptake. Thus, Tf was coupled to these NPs to enhance their

Table 3  
Lipid-coated protein nanocarriers.

Lipid system	Protein	Drug	Hybridization technique	Key outcomes	Ref.
Liposomes	BSA	Coumarin-6	Hydrophobic interaction	Enhanced nanoparticle stability and sustained drug release were achieved	[49]
Liposomes	BSA	PTX	Lipid film hydration	Enhanced colloidal stability compared to Abraxane®	[50]
Liposomes	BSA	PTX and Curcumin	Lipid film hydration	Sustained and sequential release of curcumin first then PTX was achieved	[51]
Liposomes	HSA	RX-0047	Hydrophobic interaction	Gene downregulation was approximately twice as that of uncoupled liposomes	[61]
Liposomes	BSA	Borneol and PTX	Desolvation	Borneol increased the intracellular accumulation of PTX through P-gp inhibition	[45,46]
Liposomes	HSA	Pirarubicin	HPH	Reduction of pirarubicin toxicity was achieved	[62]
Liposomes	BSA	Lapatinib	Solvent injection	Better anti-tumor efficacy than the marketed product, Tykerb®	[47,48]
Lipid (PS)	Gelatin	AmB	Lipid film hydration	Enhanced macrophage targeting through PS coat	[109]
Fatty acid polymer	Gelatin	Rhodamine B	Coacervation/phase separation	OA imparted a slower drug release and a better loading efficiency than myristoleic acid	[53]
Solid lipids	Gelatin	bFGF	Emulsion/freeze drying	Enhanced nose-to-brain delivery of bFGF	[110,111]
OA	Gelatin	Zaltoprofen	Physical mixing	OA improved skin permeation of gelatin NPs	[57]
Liposomes	Gelatin	PTX	Lipid film hydration	Enhanced liposomal stability in lyophilization	[112,113]
Lipid (SPC)	Zein	Lutein	HPH	Enhanced lutein stability against photo- and thermal degradation	[114]

PS: 1,2-diacyl-sn-glycero-3-phospho-L-serine, bFGF: Basic fibroblast growth factor.

cellular uptake via TfR-mediated endocytosis. Up to 300-fold increase in cellular uptake was achieved by Tf-lipid-magnetic NPs compared to conventional liposomes [93].

Lf also showed a promising potential for enhancing the gene transfection efficiency of lipoplexes. A LF-derived peptide has been reported to enhance the nuclear translocation of liposomes along the induction of their subsequent fusion which led Weeke-Klimp et al. to couple Lf to stabilized plasmid lipid particles (SPLPs) with the purpose of enhancing hepatocyte transfection. After their systemic administration, a 5-fold increase in liver uptake was observed mainly by hepatocytes than that of un-modified SPLPs. But despite the capacity of LF-SPLPs to enhance the transfection in vitro in HepG2 and COS-7 cell lines, transfection was not attained in vivo. Such failure in vivo was attributed to the high stability of LF-SPLPs after their cellular uptake thus preventing dissociation and the subsequent release of plasmid from the endosome. In contrast to albumin, LF might not be a contributing factor in lipid destabilization in the endosome. Therefore, to enhance transfection in vivo, protein transduction domains (PTD), or nuclear localization peptides may be used to enhance plasmid release and/or to improve its nuclear translocation [116].

#### 4.4. Improved oral bioavailability

Protein-lipid nanohybrids could improve the oral bioavailability of drugs via different mechanisms such as protection from acidic pH and digestive enzymes, increasing the drug solubility, and/or intestinal permeability. WPI, composed mainly of  $\beta$ LG, is a safe and biocompatible protein commonly used for coating of many lipid nanocarriers, a summary of which is presented in Table 4 [130]. By virtue of its stable globular structure,  $\beta$ LG resists proteolytic degradation in the gastric acidity and was utilized as a pH-sensitive hydrogel former. The complexation of CLA with  $\beta$ LG improved its stability in the gastrointestinal pH range from 1.0 to 8.0. Moreover, the self-assembled nanocomplex conferred stability to digestive enzymes where slight hydrolysis occurred after treatment with both, pepsin and trypsin. The  $\beta$ LG-CLA complex also enhanced its intestinal absorption by Caco-2

cells as revealed by absorption of 85.9  $\mu$ M CLA compared to only 45.8  $\mu$ M by free CLA. This enhanced absorption could be attributed to the ability of  $\beta$ LG to cross the monolayer membrane of Caco-2 cells in addition to being transported by specific transcellular receptors such as human STRA6 and retinol-binding proteins [120]. The stabilizing effect of  $\beta$ LG was further exploited for coating quercetin-loaded liposomes for protection from acidity and gastric enzymes. Their size remained constant during simulated gastric digestion; whereas uncoated liposomes showed a rapid increase in size indicating their destabilization at low pH. This protective effect of WPI coat could be attributed to being indigestible by pepsin while dissociated from the liposomes in simulated intestinal fluid showing 200% size increase. Such dissociation is favored here since liposomes are known for their better cellular uptake which would, in turn, increase the bioavailability of their payloads [117].

Protein-lipid nanohybrids could also increase the solubility and/or intestinal permeability of poorly water soluble and low permeable drugs. Gelatin-coated phospholipid NPs showed an increase of 5.89 folds in the intestinal permeability and an increase of 4.69 folds in the oral bioavailability of the BCS class IV drug, AmB. In simulated gastric fluid, there was a significant reduction in particle size from 253 nm to 185 nm; however, a marginal reduction was observed in the drug entrapment from 50 to 38%. This indicated the preferential accumulation of AmB in the lecithin core that protected it from acid degradation. While in simulated intestinal fluid, there was no significant change in particle size which revealed the protection conferred by gelatin against pancreatic lipases [44]. In another investigation, amphiphilic gelatin-OA conjugates could improve the solubility of valsartan and aceclofenac (insoluble at pH 1.2), and telmisartan (insoluble at pH 6.8) which significantly enhanced their dissolution rates. The solubility was significantly enhanced for valsartan from 85.1 to 931.6  $\mu$ g/ml, for aceclofenac from 11.8 to 384.5  $\mu$ g/ml, and for telmisartan from 0.28 to 402.2  $\mu$ g/ml. Consequently, this led to complete dissolution of valsartan after 2 h while 70% enhancement in dissolution rate was observed for both, telmisartan and aceclofenac. Such enhancement was attributed to the hydrophobic interaction between the water-insoluble drugs

**Table 4**  
Milk protein-coated lipid nanocarriers.

Protein	Lipid system	Drug	Hybridization method	Key outcomes	Ref.
WPI	Liposomes	Quercetin	Electrostatic interaction	Enhancement of quercetin's oral bioavailability	[117]
WPI, SC, SPI	SLNs	$\beta$ -carotene	HPH	Increased stability and cellular uptake of $\beta$ -carotene	[118]
$\beta$ LG	Nanoemulsion	–	HPH	Reduced digestibility of the nanoemulsion	[41]
$\beta$ LG	Nanoemulsion	PTX	HPH	Endolysosomal system avoidance through a lipid raft-like pathway	[119]
$\beta$ LG	CLA	CLA	Hydrophobic interaction	62% inhibition of Caco-2 cells after 72 h compared to 17% by free CLA	[120]
$\alpha$ -LA	OA	$\alpha$ -tocopherol	Electrostatic and hydrophobic interactions	Liprotides enhanced the solubility and stability of $\alpha$ -tocopherol	[121]
Lf	SLNs	Carmustine	Chemical conjugation	Ten times increase in permeability coefficient of the BBB compared to uncoated SLNs	[122]
Lf	SLNs	Docetaxel	Chemical conjugation	52.75% apoptosis of U-87 MG cells compared to 25.80% for uncoated SLNs	[123]
Lf	SLNs	Rifampicin	Chemical conjugation	3.05 times increase in cellular uptake by the lungs compared to uncoated SLNs	[124]
Lf	SLNs	PTX	Chemical conjugation	IC <sub>50</sub> of 1.1 $\mu$ g/ml on bronchial epithelial cells compared to 4.6 $\mu$ g/ml for uncoated SLNs	[74]
Lf	NLCs	Curcumin	Electrostatic interaction	2.78-fold increase in brain accumulation ex vivo compared to uncoated NLCs	[125]
Lf	Liposomes	DOX	Electrostatic interaction	1.45-fold increase in cellular uptake of DOX by glioma cells compared to free DOX	[126,127]
Lf	Liposomes	Coumarin-6 and DiR	Chemical conjugation	2.7 times higher cellular uptake by HepG2 cells compared to uncoated liposomes	[73]
Lf	Liposomes	<sup>99m</sup> Tc-BMEDA	Chemical conjugation	2-fold increase in brain delivery in vivo compared to uncoated liposomes	[128]
Lf	Liposomes	Senktide	Chemical conjugation	Higher levels of dopamine in the nucleus accumbens were achieved	[129]
Lf	Lipoplexes	Luciferase gene	Chemical conjugation	Despite the significant increase in hepatocellular targeting, no gene transfection was achieved	[116]

SC: Sodium caseinate, SPI: Soy protein isolate,  $\alpha$ -LA:  $\alpha$ -lactalbumin, DiR: 1,10-dioctadecyltetramethyl indotricarbocyanine iodide (DiR), <sup>99m</sup>Tc-BMEDA: <sup>99m</sup>Tc labeled N,N-bis(2-mercaptoethyl)-N',N'-diethylethylenediamine.



and the hydrophobic OA core, the nano-size dispersion as well as drug amorphization [131].

Among various mechanisms to enhance the drug oral bioavailability is binding to the mucous layer of the small intestine “glyco-targeting”. The lectin WGA binds specifically to NAG and sialic acid available on cell surfaces within the whole intestine. Thus, the interaction between WGA-conjugated PTX-loaded SLNs and carbohydrate moieties along with the high bioadhesive capability of SLNs resulted in their longer residence in the intestine. Moreover, the ability of both lectins and SLN to bind M cells can also bypass the first pass hepatic metabolism resulting in greater oral bioavailability of PTX. After oral administration in Wistar rats, the AUC was significantly higher for WGA-SLNs (30.03 µg/ml/h) than uncoated SLNs (16.1 µg/ml/h) or free PTX (7.78 µg/ml/h) [29].

#### 4.5. Enhanced drug stability

Protein-lipid nanohybrids could also be utilized to provide greater stability to the loaded chemically unstable drugs. CPT is a cytotoxic alkaloid with a lactone ring that readily opens at physiological conditions yielding a biologically inactive carboxylate form. The chemical instability of CPT has been overcome by coating CPT-loaded liposomes with HSA. This prevented the interaction of serum albumin with the carboxylate form of CPT, thus inhibiting the equilibrium shift that led to the formation of more carboxylate resulting in a 2.5-fold increase in the plasma concentration of CPT compared to uncoated liposomes. Moreover, the use of the artificial lipid, 3,5-bis(dodecyloxy) benzoic acid (DB), led to a  $\pi$ - $\pi$  interaction between its phenyl groups and CPT which further enhanced the CPT stability showing an increase in its plasma concentration three times more than control liposomes without DB [63].

The naturally occurring antioxidant, lutein, was successfully protected from photo-degradation by the phospholipid/pluronic-coated zein NPs where 46.53% remained without degradation after 10 h of UV exposure compared to 15.91% and 1.42% for uncoated zein NPs and free drug, respectively. This protection was ascribed to the competitive absorption of UV photons by zein which was attributed to the abundance of aromatic amino acids in its sequence such as phenylalanine [114]. In an attempt to enhance the oxidative stability of  $\beta$ -carotene, vitamin A source,  $\beta$ -carotene-loaded SLNs were coated with three types of proteins: WPI, SC, and SPI. Generally, protein coating has enhanced the stability of SLNs to oxidation via the metal chelating and free radical scavenging properties of the amino acids; tyrosine, phenylalanine, tryptophan, cysteine, and histidine. However, SC showed the greatest stability enhancement followed by WPI and SPI. This was explained by the abundance of phosphoserine residues in SC that chelated the pro-oxidative ions, copper and iron as well as its ability to form thick interfacial layer (10–15 nm) around lipid droplets [118].

#### 4.6. Reduced toxicity

The systemic toxicity of some drugs was minimized by encapsulation into hybrid protein-lipid nano-formulations. The cardiac toxicity of DOX was reduced by coating PEGylated DOX-liposomes with HSA. In Yoshida sarcoma-bearing rats, the therapeutic index of DOX, ratio of tumor to heart tissue amount, was significantly higher for the HSA-coated PEGylated liposomes in comparison to either uncoated PEGylated liposomes (Doxil®) or free DOX (Fig. 7). This is ascribed to passive and active tumor-targeting of DOX by HSA-coated liposomes, unlike uncoated PEGylated liposomes which only confer passive targeting [30]. Similarly, encapsulation of pirarubicin in phospholipid-coated albumin NPs has been found to overcome various pirarubicin-associated toxicities including bone marrow suppression, cardiotoxicity, renal, liver and GIT toxicities. The lower toxicity in all these organs could be a result of the better biodistribution and the lower accumulation of the NPs in such organs [62].

In another investigation, the hemolytic and nephron-toxicities of AmB were reduced by incorporation into gelatin-coated phospholipid NPs. The aggregated form of AmB, rather than its native monomeric form, has been associated with these toxicities based on its inability to distinguish between ergosterol and cholesterol. AmB-loaded gelatin-lecithin NPs showed a lower ratio of aggregated to monomeric form than that of the marketed micellar product, Fungizone® and liposomal product, Fungisome® thus resulting in a lower hemolysis when incubated with RBCs. Moreover, the nephrotoxicity, indicated by BUN and creatinine levels, was significantly lower for the gelatin-lecithin NPs compared to Fungizone® [44].

#### 4.7. Intrinsic activity

A type of unique chemical complex can be formed from proteins and fatty acids that is cytotoxic to tumor cells. The first one was discovered through the conversion of unfolded  $\alpha$ -lactalbumin (apo  $\alpha$ -lactalbumin) in presence of OA, forming what was termed “HAMLET” (Human  $\alpha$ -lactalbumin made lethal to tumor cells) showing a core-shell structure composed of OA micellar core and apo  $\alpha$ -lactalbumin shell (Fig. 8) [132]. HAMLET was found to stimulate apoptosis in a targeted fashion in numerous types of cancer cells [133]. Further studying of the nature of apo  $\alpha$ -lactalbumin conversion has shown that the fatty acids required to yield cytotoxic and stable complexes were the C18 ones that have a double bond in cis conformation either at position 9 or 11. The cytotoxic characteristics of the complex were attributed to OA which is carried and protected by the protein component and then gets released in cell membranes rendering them more fluid. A general term, lipotides, was introduced for HAMLET and other similar complexes prepared from different proteins or fatty acids, such as complexes of OA with Lf [134], equine lysozyme [135], bovine  $\beta$ LG, and pike parvalbumin [136]. One of the methods used to prepare lipotides is to pass apo  $\alpha$ -lactalbumin through an ion exchange column conditioned with OA. Besides chromatography, other methods include alkaline unfolding and heating [137]. In addition to their innate cytotoxicity, lipotides may serve as carriers for hydrophobic drugs, such as vitamin E,  $\alpha$ -tocopherol (Toc). The lipotides were found to solubilize Toc, enhance its chemical stability, and transfer Toc into membranes in the same fashion as OA. These benefits, together with a high degree of biocompatibility, give lipotides a great potential as carriers for hydrophobic anticancer drugs [121].

Another protein-lipid complex with intrinsic activity was formed between cis-aconitic anhydride-derivatized HSA (Aco-HSA) and liposomes. Aco-HSA showed a very potent anti-HIV activity with an  $IC_{50}$  of 0.02 µg/ml. Unlike sulfated polysaccharides which showed a more potent anti-HIV activity, Aco-HSA didn't show any undesirable side effects such as the anticoagulant activity of dextran sulfate [138]. The mechanism of action of Aco-HSA appeared to be at the virus-cell binding step by preventing viral fusion with cell membranes. Aco-HSA is postulated to interact with the envelope glycoprotein, gp 41, or the V3 loop of gp 120. This interaction directly correlated with the Aco-HSA charge density. Increasing the degree of derivatization increased the negative charge and, as a result, strengthened the interaction and decreased the  $IC_{50}$ . Fully-derivatized HSA (Aco<sub>60</sub>-HSA) where all the 60 amino groups in lysine were conjugated to cis-aconitic anhydride showed a lower  $IC_{50}$  (0.02 µg/ml) than Aco<sub>39</sub>-HSA and Aco<sub>53</sub>-HSA which showed  $IC_{50}$  of 1.08 µg/ml and 0.04 µg/ml, respectively. Beside their intrinsic anti-HIV activity, these liposomal complexes have the capability to be loaded with other antiviral agents such as nucleoside analogues or other anti HIV-1 drugs (e.g. AZT) in order to possibly produce a synergistic anti-HIV activity [55].

#### 4.8. Theranostics

Protein-lipid nanohybrids could be utilized as theranostic carriers by the dual encapsulation of therapeutic drugs and diagnostic agents.



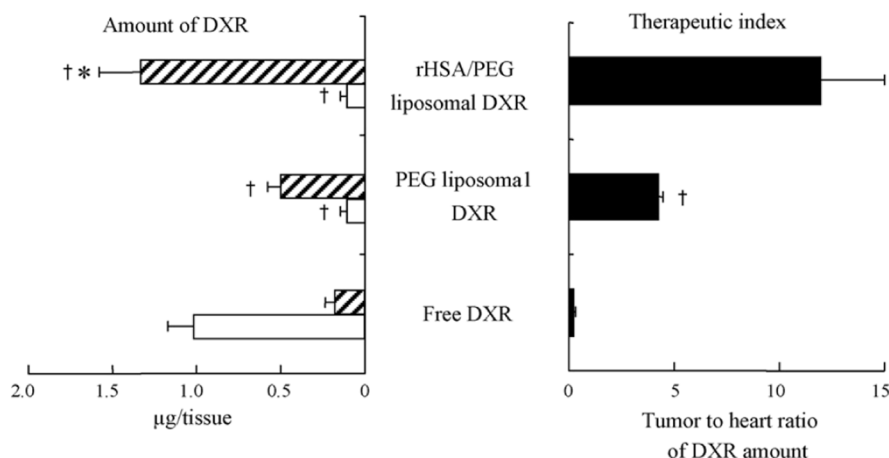


Fig. 7. DOX amount in tumor (black and white) and heart (white) after 3 h and therapeutic index (black) of HSA-coated PEGylated liposomes (rHSA/PEG liposomal DXR), uncoated PEGylated liposomes (PEG liposomal DXR), and free DOX (Free DXR) [30].

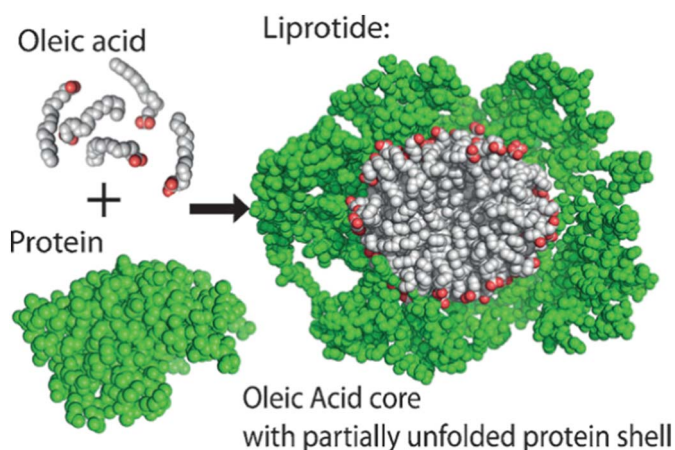


Fig. 8. Core-shell structure of lipitides [137].

Compared to organic fluorophores, QDs provide better photostability and enable multiplexing because of their narrow band emissions and broad absorption spectra [139]. For targeted imaging and therapy of brain cancer, Tf-functionalized TPGS liposomes were developed to co-encapsulate docetaxel and QDs. Their nanosize of 182.5 nm allowed the passive targeting of brain tumors via EPR effect and the overexpression of TfR on the BBB allowed their active targeting which translated in vivo in a 2.86-fold higher brain distribution of docetaxel than uncoated liposomes after 0.5 h of treatment. Tf-coated liposomes have also shown higher brain fluorescence intensity compared to uncoated liposomes [89].

#### 4.9. Miscellaneous

##### 4.9.1. Enhanced brain delivery

Cationized BSA (CBSA) as a ligand is known for its higher preferential accumulation in the brain tissues, which was attributed to its adsorptive-mediated transcytosis (AMT) in addition to its receptor-mediated endocytosis through binding to albumin and SPARC [140,141]. AMT is different from receptor-mediated transcytosis in involving no specific membrane receptors for uptake. AMT is mediated by the charge-based interaction between polycationic substances and the negative charge-bearing plasma membranes or glycoproteins. CBSA was exploited for its brain targeting capability to coat methotrexate-loaded SLNs. Transendothelial transport study on porcine brain capillary endothelial cells (BCECs) showed that the permeation coefficient of CBSA-coated SLNs was 15.2 times greater than that of uncoated SLNs. This transendothelial movement mediated by CBSA was

facilitated first by endocytosis followed by subsequent traffic of the SLNs to the other cell side. Moreover, cellular uptake studies on human neuroglial culture-1 tumor cells showed 18%, 50%, and 99% fluorescence after 8 h of incubation with the fluorescent dye (FITC), FITC-labeled SLNs and FITC-labeled CBSA-coated SLNs, respectively [10]. In another study investigating the uptake mechanism of CBSA-coated liposomes, it was found that caveolin-mediated endocytosis rather than clathrin-mediated one was responsible for the transendothelial movement of the liposomes through BCECs. This was confirmed by the marked inhibition of uptake via phenylarsineoxide, filipin, nocodazol, and free CBSA, however, no inhibition was observed after incubation with dansylcadaverin which inhibits the clathrin-mediated endocytosis process [31].

The expression of receptors of the milk protein, Lf (LfR), on the BBB and glioma cells has been well documented in several studies and so the exploitation of Lf as a ligand for brain delivery has been shown to be very effective, even more than Tf due to the very low endogenous Lf concentrations thus never saturating LfR. DOX-loaded liposomes were coated with Lf for combining both AMT and RMT for DOX transport. These procationic liposomes were prepared with a certain type of cholesterol that is neutral or anionic in physiological pH and is reversed cationic once in contact with the BBB. The cholesterol derivative, Cholest-5-en-3-ol-(3 $\beta$ )-[2-[[4-[(carboxymethyl)dithio]-1-iminobutyl] amino]ethyl] carbamate, used to form procationic liposomes contains two oppositely charged head groups connected via a disulfide linkage. With the aid Lf, the procationic liposomes were brought in contact with the BBB where the disulfide linkages were broken by reductases available on their intracellular membranes. This charge conversion of the procationic liposomes aided a charge-based interaction with the negatively-charged plasma membranes thus facilitating AMT. Moreover, the unidirectionality of Lf transport from the apical side of the BBB to the basolateral one led to its accumulation in neurons and the prevention of the backward transport of liposomes. As a result, the cellular uptake of the Lf-coated procationic liposomes in C6 glioma cells was 1.14, 1.19, and 1.45 times higher than procationic liposomes, conventional liposomes (prepared using normal cholesterol), and DOX, respectively [127].

Intranasal delivery of nanoparticles could effectively enhance drug penetration and absorption into the brain. The brain delivery of bFGF for the treatment of hemiparkinsonism was enhanced via intranasal administration of bFGF-loaded hybrid gelatin-nanostructured lipid carriers (GNLCs). Enhanced uptake by nasal epithelium was observed resulting in increased bFGF concentrations in both, the olfactory bulb and striatum. Being prepared with negatively charged lipids and surfactants, the NLCs showed a high negative  $\zeta$  of  $-27.6$  mV. This in turn have decreased their mucociliary clearance and increased

**Table 5**  
Gelatin and silk fibroin-coated lipid nanocarriers.

Protein	Lipid system	Drug	Hybridization technique	Key outcomes	Ref.
Gelatin	SLNs	AmB	Electrostatic and hydrophobic interactions	Enhanced oral bioavailability of AmB with lower associated hemolysis and nephrotoxicity	[44]
Gelatin	SLNs	IRT	Desolvation	IRT was successfully loaded with optimum physicochemical properties for tumor targeting	[26]
Gelatin	SLNs	PTX	Chemical conjugation	Enhanced antitumor activity compared to Taxol®	[36,145]
Gelatin	SLNs	Telmisartan, Valsartan, Aceclofenac	Chemical conjugation	Enhanced solubility of drugs in both acidic and alkaline conditions	[131]
Gelatin	PLA-DPPE NPs	DOX	Chemical conjugation	DOX release from NPs was pH-sensitive	[146]
SF	Liposomes	Emodin	Desolvation	Enhanced targeting of keloid fibroblasts	[108]
SF	Liposomes	Emodin	Desolvation	Enhanced cellular uptake by breast cancer cells	[107]
SF	Liposomes	Ibuprofen	Electrostatic and hydrophobic interactions	Enhanced ocular drug delivery due to the mucoadhesive properties of SF	[143]
SF	SLNs	Ceramide	Electrostatic interaction	Enhanced skin permeation with ceramide flux of 55 $\mu\text{g}/\text{cm}^2/\text{h}$	[142]

PLA: Poly(lactide), DPPE:1,2-dipalmitoyl-sn-glycero-3-phosphoethanolamine, IRT: Irinotecan.

their residence time, resulting in increased CNS bioavailability [110].

#### 4.9.2. Enhanced skin permeation

SF, a natural fibrous protein, is characterized by its high tensile strength and skin-adhesive properties [108]. Protein-lipid nanohybrids with SF as the protein component are included in Table 5. To enhance skin permeation of SLNs loaded with ceramide, SF coating was exploited to form a charge-based interaction between SLNs and the skin, both being negatively charged. To achieve this purpose, an acidified solution (pH 4.5) of SF was used below its pI of 5.3 giving it a positive charge. After 24 h, SF-coated SLNs demonstrated a skin-permeation ceramide flux of 55  $\mu\text{g}/\text{cm}^2/\text{h}$  compared to only 26  $\mu\text{g}/\text{cm}^2/\text{h}$  for uncoated SLNs [142]. In another approach, the gastrointestinal irritation and first pass metabolism of the anti-inflammatory agent, zaltoprofen, could be effectively overcome via topical nanogel containing OA-coated zaltoprofen-loaded gelatin NPs. While polymeric NPs like gelatin are usually unable to deliver drugs beyond the subcutaneous layer of the skin, the OA coat improved transdermal drug permeation due to its penetration enhancement properties. The ex vivo study using rat abdominal skin showed that cumulative drug release from the OA-coated NPs was 78.58% in comparison to 69.42% for the uncoated NPs [57].

#### 4.9.3. Improved ocular delivery

The critical environment of the eye makes ocular delivery of drugs a defying task. SF was exploited as a liposome-coating for the ocular delivery of the anti-inflammatory drug, ibuprofen, because its adhesive properties would overcome the multiple mechanisms that shorten drug residence time in the eye such as lacrimation, tear turnover, and tear dilution. Among different solvent concentrations, 50% methanol was used in the treatment of SF to convert its  $\alpha$ -helical structure into the  $\beta$ -pleated sheet which shows favorable characteristics such as water resistance, good tensile strength, and thermodynamic stability. The coated liposomes showed a slower prolonged release and better uptake by human corneal epithelial cells leading to an extended residence time in the eye. In comparison to ibuprofen solution and uncoated liposomes which almost reached platforms in 2 h, the in vitro corneal permeation of the SF-coated liposomes linearly increased after a lag time of 1 h (Fig. 9) [143].

#### 4.9.4. Enhanced pulmonary drug delivery

As an attempt to overcome the shortcomings of conventional lung cancer therapy, Tf-coated liposomes were investigated for delivery of DOX to an orthotopic lung cancer model via intracorporeal nebulization. Rats receiving aerosolized Tf-coated liposomes showed fewer and smaller tumor nodules compared to uncoated liposomes, free DOX or i.v. Tf-coated liposomes. The reason for such results could be the regional containment of DOX after aerosol delivery leading to higher

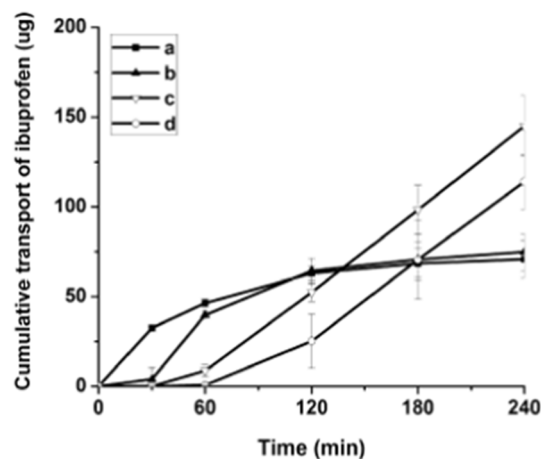


Fig. 9. In vitro corneal permeation of ibuprofen in solution (a), uncoated liposomes (b) and SF-coated liposomes prepared by 1.0% of SF at different dissolving time (c: 2 h; d: 8 h) [143].

local concentrations and lower systemic side effects [144].

## 5. Physicochemical properties of the nanohybrids

### 5.1. Particle size and structure

Protein-lipid hybridization has a variable impact on particle size due to the contribution of several factors such as the type of coating, its concentration, and the hybridization method. It seems that covalent protein conjugation onto the surface of lipid nanocarriers did not significantly increase the particle size. The size of SLNs did not change significantly after Tf conjugation to their surface (from 194 to 206 nm) [28]. On the contrary, electrostatic interaction between protein and lipid nanocarriers usually results in a remarkable size increase. Electrostatic coating of ibuprofen-loaded liposomes with SF increased their size from 180 nm to 230–290 nm due to gathering of vesicular liposomes to form multi-vesicular liposomes giving a higher particle size [143]. Hybridization affects not only the particle size but also the structural organization of the nanohybrids. TEM imaging of SF-coated liposomal emodin showed increased lamellar thickness from 26.2 nm in uncoated liposomes to 80.5 nm in coated ones despite the insignificant increase in the overall diameter. The thicker lamellae formed after coating contributed in 55% of nanohybrid diameter resulting in a more organized structure [108].

## 5.2. Surface charge

When preparing coated NPs, the coating material clearly becomes the main determinant of the surface charge. Both the formulation pH and protein concentration significantly affect the charge on the surface of protein-coated NPs. After coating of SLNs with SF (pI = 5.3),  $\zeta$  of the NPs changed according to pH changes (i.e., from +10 mV at pH 3 to –22 mV at pH 9). On the other hand,  $\zeta$  of uncoated SLNs remained negative and decreased from –23 mV at pH 3 to –77 mV at pH 9 due to ionization of carboxylic group of SA. Thus, the  $\zeta$  of SF-coated SLNs was close to that of SF at the same pH indicating that SF coat has the upper hand in controlling the overall surface charge [142]. Likewise,  $\zeta$  of SLNs prepared with TPGS was significantly decreased from –29.4 mV to –16.5 mV after conjugation of the cationic WGA (pI = 9) at physiological pH [29]. Using low concentration (0.25% w/v) of the cationic WPI to coat liposomes did not affect their  $\zeta$  (–30 mV). Whereas higher WPI concentration (0.5% w/v) resulted in negative charge neutralization thus reducing the  $\zeta$  close to zero leading to aggregate formation. Further increase in WPI concentration reversed the charge to a maximum of +27 mV at 3% w/v WPI with reduced aggregation [117].

## 5.3. Drug release

The protein coating of lipid nanocarriers may contribute efficiently in the modulation of drug release from such nanohybrids. Coating of emodin-loaded liposomes with SF has reduced the emodin release from 70% for uncoated liposomes to 50% for SF-coated ones after 6 days. Sustained emodin release was ascribed to the steric hindrance induced by the large SF coat. Protein-coating of the liposomes also modified the drug release mechanism from diffusion-swelling to solely diffusion-based release kinetics. SF demonstrated a tight packing of the liposomal lamellar structure thus inhibited the liposomal swelling that was responsible for the fast drug release thus allowing the retention of larger emodin amounts by cells [108].

On another avenue, phospholipids as nanocarriers suffer greatly from rapid drug release and short biological half-lives indicating their unsuitability for prolonged blood circulation purposes. To overcome this challenge, phospholipid-coated albumin NPs were developed that combined both, the phospholipid's anti-adhesive properties and the albumin's stabilization function. Phospholipid-coated albumin NPs showed a significantly slower release of coumarin-6 than phospholipid NPs containing no albumin. Albumin on the NPs' inner surface increased their rigidity, functioned as a barrier for metabolic enzymes, and hence sustained drug release [49]. In another investigation, coating of gelatin NPs with oleic and myristoleic acid polymers, significantly prolonged the release of rhodamine B. Approximately 45% of the dye was released from OA-coated NPs after 70 h compared to 60% and 80% from myristoleic-acid coated and uncoated gelatin NPs, respectively. This was ascribed to the longer chain of OA which imparted a better protection by blocking the surface pores of gelatin NPs [53]. Alternatively, the phospholipid coat may impart a pH-responsive drug release property to the nanohybrids. PTX release from Tf-conjugated copolymeric ( $\gamma$ -PGA-MAL-PLA-DPPE) NPs was found to be pH-sensitive with 62.1% of PTX was released from the nanohybrids at pH 7.4 after 72 h compared to 98% drug release at pH 5. This was attributed to the phospholipid component of the copolymer, DPPE, which, besides its high biocompatibility and flexibility, is known to be pH-sensitive thus targeting the tumor acidic microenvironment [147].

## 5.4. Colloidal stability

Protein pre-coating of lipid NPs may have additional advantages, which remain to be elucidated. In addition to protecting the payload inside NPs, and preferably, controlling its release, the protein coat may alter the physicochemical property of nanocarrier surface, thus circum-

venting the particle aggregation problem commonly encountered in formulating nanosized carriers. Higher stability of liposomes was achieved by WPI coating as shown by constant  $\zeta$  (+27 mV) and size (140 nm) during long-term storage, higher resistance to the osmotic effect of sugars and salts, and lower affectability towards low pH values during in vitro gastric digestion in addition to a higher resistance to lipase digestion. It is believed that the thick protein compact layer acts as a steric barrier against digestive enzymes or reduces van der Waals interactions [40,117].

One of the important factors influencing the colloidal stability of nanocarriers is the surface charge. It was found that WPI-coated nanoemulsions with a particle diameter of 66 nm tended to form aggregates (~10,000 nm) in pH values from 4.5 to 5.5 (close to pI of WPI) where the particle charge is almost zero. On the other hand, the nanohybrids remained stable in more acidic (pH 3–4) or basic (pH 6–8) conditions where they demonstrated high surface charge value inducing repulsive stabilization thus preventing aggregation [40].

On another avenue, one limitation of protein nanoparticles is their poor colloidal stability in vivo. Therefore, liposome-coated albumin NPs were prepared to overcome the hurdle of the colloidal instability of Abraxane®, an albumin-bound PTX, which was found to disassemble upon dilution. When compared to their uncoated counterparts, the liposome-coated albumin NPs were more stable maintaining their size of 210 nm, being unaffected by dilution up to 100 folds [50].

## 6. Challenges and limitations

Although current experimentations on protein-lipid nanohybrids show a great potential for reducing systemic toxicities of a myriad of drugs, very little is known about the toxicity of the nanohybrids themselves. Considering the materials being used, lipids and proteins are well-known for their safety and biodegradability which means that using them for nanohybrid fabrication is expected to be a safe approach [3,148]. However, some concerns about toxicity still exist. For example, the administration of nanohybrids that comprise an exogenous protein like BSA could trigger an immune response [47]. Similarly, the corn protein, zein was reported to resist digestion by pepsin and trigger an immunogenic response in corn protein-allergic piglets and patients [149]. Moreover, it has been established that NPs can show features that are significantly different from the constituting materials in bulk [150]. On top of that, the hybridization process could also lead to the development of new properties that were not evident in either component alone, or include other chemicals that exert certain toxicity (e.g. organic solvents or crosslinkers). This demonstrates the complexity of these systems, and that we cannot entirely predict the behavior of the nanohybrids in vivo based only on the characteristics of the constituting lipids and proteins used. In light of these facts, further toxicological studies are required in order to obtain a more clear vision about any side effects that could be caused by these nanohybrids [151].

## 7. Conclusions and future prospects

Many lipid-based and protein-based nano-formulations are already approved by FDA for the treatment of many diseases such as Abraxane®, AmBisome™, Doxil®, DepoCyt®, and DaunoXome®. Although the enhanced efficacy of these products compared to conventional drug therapies have been well established, they seem to suffer from many limitations as demonstrated by our review. Nanohybrids combining the benefits of both, lipids and proteins, overcame many of these limitations and enhanced their efficacy even more. MBP-426, a transferrin (Tf)-coated oxaliplatin-loaded liposomal formulation, is currently undergoing phase II clinical trials as a second-line treatment for esophageal, gastroesophageal or gastric adenocarcinomas. Preclinical studies of this formulation demonstrated an enhanced cytotoxicity to Colon 26 cell-line with an EC<sub>50</sub> of 8 µg/ml compared to 18 µg/ml for the uncoated liposomal formulation. Moreover, in mice bearing Colon 26



tumors, MBP-426 showed a 2.5 times enhancement in tumor accumulation compared to the uncoated formulation. Advancing with such promising results to phase I trials, 39 patients with advanced or metastatic solid tumors showed thrombocytopenia as the dose-limiting toxicity and a recommended dose of 226 mg/m<sup>2</sup> was chosen for further studies. Phase Ib trials in 9 patients were promising as well, where a dose of 170 mg/m<sup>2</sup> was recommended for phase II studies compared to 85 mg/m<sup>2</sup> for the uncoated liposomes. Moreover, a potential activity was observed for MBP-426 in two patients resistant to the uncoated formulation [152]. Another promising formulation, 2B3-101, is currently undergoing phase I/IIa clinical trials. 2B3-101 is a glutathione-coated DOX-loaded liposomal formulation that has shown great promise preclinically against brain and breast tumors. Although the toxicity profile is similar to the uncoated formulation, a significantly higher retention for 2B3-101 in rat brains was observed. Moreover, about 60% enhancement in survival was observed for the intracranial U87 xenograft-bearing mice compared to saline-treated controls. Currently, the safety and the pharmacokinetic profile of the formulation is being assessed solely or in combination with trastuzumab [153].

As shown in our review, extensive efforts have been made by researchers in developing protein-lipid nanohybrids on a laboratory scale. However, no scale up or industrial design has been considered which could hinder their market introduction. Indeed, few have reached early phases of clinical trials and none yet have been approved. Thus, it is imperative for future studies to focus on the fabrication strategies that allow large scale production in a reproducible manner. Albeit the lack of studies on their scalability, protein-lipid nanohybrids are very promising as a drug delivery platform to enhance the therapeutic efficacy of, not only conventional drugs, but also of nanoparticulate formulations already approved for clinical use.

## References

- [1] T.M. Allen, P.R. Cullis, Drug delivery systems: entering the mainstream, *Science* 303 (2004) 1818–1822.
- [2] M.L. Etheridge, S.A. Campbell, A.G. Erdman, C.L. Haynes, S.M. Wolf, J. McCullough, The big picture on nanomedicine: the state of investigational and approved nanomedicine products, *Nanomed. Nanotechnol. Biol. Med.* 9 (2013) 1–14.
- [3] A. Puri, K. Loomis, B. Smith, J.-H. Lee, A. Yavlovich, E. Heldman, et al., Lipid-based nanoparticles as pharmaceutical drug carriers: from concepts to clinic, *Crit. Rev. Ther. Drug Carrier Syst.* 26 (2009) 523–580.
- [4] A. Akbarzadeh, R. Rezaei-Sadabadi, S. Davaran, S.W. Joo, N. Zarghami, Y. Hanifepour, et al., Liposome: classification, preparation, and applications, *Nanoscale Res. Lett.* 8 (2013) 102.
- [5] M. Çağdaş, A.D. Sezer, S. Bucak, Liposomes as Potential Drug Carrier Systems for Drug Delivery, (2014).
- [6] A. Singhal, L. Huang, Gene transfer in mammalian cells using liposomes as carriers, in: J.A. Wolff (Ed.), *Gene Therapeutics: Methods and Applications of Direct Gene Transfer*, Birkhäuser Boston, Boston, MA, 1994, pp. 118–142.
- [7] P. Kandadi, M.A. Syed, S. Goparaboina, K. Veerabrahma, Albumin coupled lipid nanoemulsions of diclofenac for targeted delivery to inflammation, *Nanomed. Nanotechnol. Biol. Med.* 8 (2012) 1162–1171.
- [8] R.H. Müller, K. Mäder, S. Gohla, Solid lipid nanoparticles (SLN) for controlled drug delivery – a review of the state of the art, *Eur. J. Pharm. Biopharm.* 50 (2000) 161–177.
- [9] S. Simoes, V. Slepishkin, P. Pires, R. Gaspar, Pedroso de Lima MC, Duzgunes N. Human serum albumin enhances DNA transfection by lipoplexes and confers resistance to inhibition by serum, *Biochim. Biophys. Acta* 1463 (2000) 459–469.
- [10] A. Abhinav, M. Saikat, A. Himanshu, M. Subrata, P.A. Govind, Cationized albumin conjugated solid lipid nanoparticles as vectors for brain delivery of an anti-cancer drug, *Curr. Nanosci.* 7 (2011) 71–80.
- [11] K. Manjunath, J.S. Reddy, V. Venkateswarlu, Solid lipid nanoparticles as drug delivery systems, *Methods Find. Exp. Clin. Pharmacol.* 27 (2005) 127–144.
- [12] W. Mehnert, K. Mäder, Solid lipid nanoparticles: production, characterization and applications, *Adv. Drug Deliv. Rev.* 47 (2001) 165–196.
- [13] A.O. Elzoghby, M.W. Helmy, W.M. Samy, N.A. Elgindy, Novel ionically crosslinked casein nanoparticles for flutamide delivery: formulation, characterization, and in vivo pharmacokinetics, *Int. J. Nanomedicine* 8 (2013) 1721.
- [14] A.O. Elzoghby, N.I. Saad, M.W. Helmy, W.M. Samy, N.A. Elgindy, Ionically-crosslinked milk protein nanoparticles as flutamide carriers for effective anticancer activity in prostate cancer-bearing rats, *Eur. J. Pharm. Biopharm.* 85 (2013) 444–451.
- [15] A.O. Elzoghby, Gelatin-based nanoparticles as drug and gene delivery systems: reviewing three decades of research, *J. Control. Release* 172 (2013) 1075–1091.
- [16] A.O. Elzoghby, M.W. Helmy, W.M. Samy, N.A. Elgindy, Micellar delivery of flutamide via milk protein nanovehicles enhances its anti-tumor efficacy in androgen-dependent prostate cancer rat model, *Pharm. Res.* 30 (2013) 2654–2663.
- [17] A.O. Elzoghby, M.W. Helmy, W.M. Samy, N.A. Elgindy, Spray-dried casein-based micelles as a vehicle for solubilization and controlled delivery of flutamide: formulation, characterization, and in vivo pharmacokinetics, *Eur. J. Pharm. Biopharm.* 84 (2013) 487–496.
- [18] A.O. Elzoghby, W.M. Samy, N.A. Elgindy, Novel spray-dried genipin-crosslinked casein nanoparticles for prolonged release of alfuzosin hydrochloride, *Pharm. Res.* 30 (2013) 512–522.
- [19] A.O. Elzoghby, B.Z. Vranic, W.M. Samy, N.A. Elgindy, Swellable floating tablet based on spray-dried casein nanoparticles: near-infrared spectral characterization and floating matrix evaluation, *Int. J. Pharm.* 491 (2015) 113–122.
- [20] A.O. Elzoghby, W.M. Samy, N.A. Elgindy, Albumin-based nanoparticles as potential controlled release drug delivery systems, *J. Control. Release* 157 (2012) 168–182.
- [21] V. Gaberc-Porekar, I. Zore, B. Podobnik, V. Menart, Obstacles and pitfalls in the PEGylation of therapeutic proteins, *Curr. Opin. Drug Discov. Dev.* 11 (2008) 242–250.
- [22] M.D. Howard, M. Jay, T.D. Dziubla, X. Lu, PEGylation of nanocarrier drug delivery systems: state of the art, *J. Biomed. Nanotechnol.* 4 (2008) 133–148.
- [23] S.H. Jung, S.K. Kim, S.H. Jung, E.H. Kim, S.H. Cho, K.S. Jeong, et al., Increased stability in plasma and enhanced cellular uptake of thermally denatured albumin-coated liposomes, *Colloids Surf. B: Biointerfaces* 76 (2010) 434–440.
- [24] S.M. Moghimi, J. Szebeni, Stealth liposomes and long circulating nanoparticles: critical issues in pharmacokinetics, opsonization and protein-binding properties, *Prog. Lipid Res.* 42 (2003) 463–478.
- [25] K. Furumoto, J. Yokoe, K. Ogawara, S. Amano, M. Takaguchi, K. Higaki, et al., Effect of coupling of albumin onto surface of PEG liposome on its in vivo disposition, *Int. J. Pharm.* 329 (2007) 110–116.
- [26] C. Park, C.L. Vo, T. Kang, E. Oh, B.J. Lee, New method and characterization of self-assembled gelatin-oleic nanoparticles using a desolvation method via carbodiimide/N-hydroxysuccinimide (EDC/NHS) reaction, *Eur. J. Pharm. Biopharm.* 89 (2015) 365–373.
- [27] M. Voinea, E. Dragomir, I. Manduteanu, M. Simionescu, Binding and uptake of transferrin-bound liposomes targeted to transferrin receptors of endothelial cells, *Vasc. Pharmacol.* 39 (2002) 13–20.
- [28] R.S. Mulik, J. Monkkonen, R.O. Juvonen, K.R. Mahadik, A.R. Paradkar, Transferrin mediated solid lipid nanoparticles containing curcumin: enhanced in vitro anticancer activity by induction of apoptosis, *Int. J. Pharm.* 398 (2010) 190–203.
- [29] D. Pooja, H. Kulhari, M. Kuncha, S.S. Rachamalla, D.J. Adams, V. Bansal, et al., Improving efficacy, oral bioavailability, and delivery of paclitaxel using protein-grafted solid lipid nanoparticles, *Mol. Pharm.* 13 (2016) 3903–3912.
- [30] J. Yokoe, S. Sakuragi, K. Yamamoto, T. Teragaki, K. Ogawara, K. Higaki, et al., Albumin-conjugated PEG liposome enhances tumor distribution of liposomal doxorubicin in rats, *Int. J. Pharm.* 353 (2008) 28–34.
- [31] M. Thole, S. Nobmann, J. Huwyler, A. Bartmann, G. Fricker, Uptake of cationized albumin coupled liposomes by cultured porcine brain microvessel endothelial cells and intact brain capillaries, *J. Drug Target.* 10 (2002) 337–344.
- [32] Y. Zheng, B. Yu, W. Weecharangsan, L. Piao, M. Darby, Y. Mao, et al., Transferrin-conjugated lipid-coated PLGA nanoparticles for targeted delivery of aromatase inhibitor 7alpha-APTADD to breast cancer cells, *Int. J. Pharm.* 390 (2010) 234–241.
- [33] S. Xu, Y. Liu, H.C. Tai, J. Zhu, H. Ding, R.J. Lee, Synthesis of transferrin (Tf) conjugated liposomes via Staudinger ligation, *Int. J. Pharm.* 404 (2011) 205–210.
- [34] G.T. Hermanson, Chapter 2- Functional targets for bioconjugation, *Bioconjugate Techniques*, third ed., Academic Press, Boston, 2013, pp. 127–228.
- [35] G.T. Hermanson, Chapter 6- Heterobifunctional crosslinkers, *Bioconjugate Techniques*, third ed., Academic Press, Boston, 2013, pp. 299–339.
- [36] P.H.-L. Tran, T.T.-D. Tran, T.V. Vo, C.L.-N. Vo, B.-J. Lee, Novel multifunctional biocompatible gelatin-oleic acid conjugate: self-assembled nanoparticles for drug delivery, *J. Biomed. Nanotechnol.* 9 (2013) 1416–1431.
- [37] J. Floury, A. Desrumaux, J. Lardières, Effect of high-pressure homogenization on droplet size distributions and rheological properties of model oil-in-water emulsions, *Innovative Food Sci. Emerg. Technol.* 1 (2000) 127–134.
- [38] X. He, N. Xiang, J. Zhang, J. Zhou, Y. Fu, T. Gong, et al., Encapsulation of teniposide into albumin nanoparticles with greatly lowered toxicity and enhanced antitumor activity, *Int. J. Pharm.* 487 (2015) 250–259.
- [39] M.S. Freag, Y.S. Elnaggar, O.Y. Abdallah, Lyophilized phytosomal nanocarriers as platforms for enhanced diosmin delivery: optimization and ex vivo permeation, *Int. J. Nanomedicine* 8 (2013) 2385.
- [40] S.J. Lee, S.J. Choi, Y. Li, E.A. Decker, D.J. McClements, Protein-stabilized nanoemulsions and emulsions: comparison of physicochemical stability, lipid oxidation, and lipase digestibility, *J. Agric. Food Chem.* 59 (2011) 415–427.
- [41] E. Troncoso, J.M. Aguilera, D.J. McClements, Influence of particle size on the in vitro digestibility of protein-coated lipid nanoparticles, *J. Colloid Interface Sci.* 382 (2012) 110–116.
- [42] S. Chen, G. Yu, B. Zhang, Y. Wang, N. Zhang, Y. Chen, Human serum albumin (HSA) coated liposomal indocyanine green for in vivo tumor imaging, *RSC Adv.* 6 (2016) 15220–15225.
- [43] K. Qian, J. Wu, E. Zhang, Y. Zhang, A. Fu, Biodegradable double nanocapsule as a novel multifunctional carrier for drug delivery and cell imaging, *Int. J. Nanomedicine* 10 (2015) 4149–4157.
- [44] S. Jain, P.U. Valvi, N.K. Swarnakar, K. Thanki, Gelatin coated hybrid lipid

- nanoparticles for oral delivery of amphotericin B, *Mol. Pharm.* 9 (2012) 2542–2553.
- [45] B. Tang, G. Fang, Y. Gao, Y. Liu, J. Liu, M. Zou, et al., Liposomes loading paclitaxel for brain-targeting delivery by intravenous administration: in vitro characterization and in vivo evaluation, *Int. J. Pharm.* 475 (2014) 416–427.
- [46] B. Tang, G. Fang, Y. Gao, Y. Liu, J. Liu, M. Zou, et al., Lipid-albumin nanoassemblies co-loaded with borneol and paclitaxel for intracellular drug delivery to C6 glioma cells with P-gp inhibition and its tumor targeting, *Asian J. Pharm. Sci.* 10 (2015) 363–371.
- [47] H. Gao, S. Cao, C. Chen, S. Cao, Z. Yang, Z. Pang, et al., Incorporation of lapatinib into lipoprotein-like nanoparticles with enhanced water solubility and anti-tumor effect in breast cancer, *Nanomedicine (London, England)* 8 (2013) 1429–1442.
- [48] L. Zhang, S. Zhang, S.B. Ruan, Q.Y. Zhang, Q. He, H.L. Gao, Lapatinib-incorporated lipoprotein-like nanoparticles: preparation and a proposed breast cancer-targeting mechanism, *Acta Pharmacol. Sin.* 35 (2014) 846–852.
- [49] Q. Peng, X.Q. Wei, X.R. Shao, T. Zhang, S. Zhang, N. Fu, et al., Nanocomplex based on biocompatible phospholipids and albumin for long-circulation applications, *ACS Appl. Mater. Interfaces* 6 (2014) 13730–13737.
- [50] H.B. Ruttala, Y.T. Ko, Liposome encapsulated albumin-paclitaxel nanoparticle for enhanced antitumor efficacy, *Pharm. Res.* 32 (2015) 1002–1016.
- [51] H.B. Ruttala, Y.T. Ko, Liposomal co-delivery of curcumin and albumin/paclitaxel nanoparticle for enhanced synergistic antitumor efficacy, *Colloids Surf. B: Biointerfaces* 128 (2015) 419–426.
- [52] M. Singh, A. Hawtrey, M. Ariatti, Lipoplexes with biotinylated transferrin accessories: novel, targeted, serum-tolerant gene carriers, *Int. J. Pharm.* 321 (2006) 124–137.
- [53] D. Sarkar, Fabrication of an optimized fluorescer encapsulated polymer coated gelatin nanoparticle and study of its retarded release properties, *J. Photochem. Photobiol. A Chem.* 252 (2013) 194–202.
- [54] A. Loureiro, A.S. Abreu, M.P. Sárria, M.C.O. Figueiredo, L.M. Saraiva, G.J.L. Bernardes, et al., Functionalized protein nanoemulsions by incorporation of chemically modified BSA, *RSC Adv.* 5 (2015) 4976–4983.
- [55] J.A. Kamps, P.J. Swart, H.W. Morselt, R. Pauwels, M.P. De Bethune, E. De Clercq, et al., Preparation and characterization of conjugates of (modified) human serum albumin and liposomes: drug carriers with an intrinsic anti-HIV activity, *Biochim. Biophys. Acta* 1278 (1996) 183–190.
- [56] J.A.A.M. Kamps, H.W.M. Morselt, P.J. Swart, D.K.F. Meijer, G.L. Scherphof, Massive targeting of liposomes, surface-modified with anionized albumins, to hepatic endothelial cells, *Proc. Natl. Acad. Sci. U. S. A.* 94 (1997) 11681–11685.
- [57] S. Pawar, V. Pande, Oleic acid coated gelatin nanoparticles impregnated gel for sustained delivery of zaltoprofen: formulation and textural characterization, *Adv. Pharm. Bull.* 5 (2015) 537–548.
- [58] S. Muzammil Afzal, V.G. Naidu, N. Harishankar, V. Kishan, Albumin anchored docetaxel lipid nanoemulsion for improved targeting efficiency - preparation, characterization, cytotoxic, antitumor and in vivo imaging studies, *Drug Deliv.* 23 (2016) 1355–1363.
- [59] M.S. Freag, Y.S. Elnaggar, D.A. Abdelmonsif, O.Y. Abdallah, Layer-by-layer-coated lyotropic liquid crystalline nanoparticles for active tumor targeting of rapamycin, *Nanomedicine* 11 (2016) 2975–2996.
- [60] W. Weecharangsan, B. Yu, Y. Zheng, S. Liu, J.X. Pang, L.J. Lee, et al., Efficient delivery of antisense oligodeoxyribonucleotide g3139 by human serum albumin-coated liposomes, *Mol. Pharm.* 6 (2009) 1848–1855.
- [61] H. Li, J. Quan, M. Zhang, B.C. Yung, X. Cheng, Y. Liu, et al., Lipid-albumin nanoparticles (LAN) for therapeutic delivery of antisense oligonucleotide against HIF-1 $\alpha$ , *Mol. Pharm.* 13 (2016) 2555–2562.
- [62] J. Zhou, X. Zhang, M. Li, W. Wu, X. Sun, L. Zhang, et al., Novel lipid hybrid albumin nanoparticle greatly lowered toxicity of pirarubicin, *Mol. Pharm.* 10 (2013) 3832–3841.
- [63] M. Watanabe, K. Kawano, K. Toma, Y. Hattori, Y. Maitani, In vivo antitumor activity of camptothecin incorporated in liposomes formulated with an artificial lipid and human serum albumin, *J. Control. Release* 127 (2008) 231–238.
- [64] C. Vuarchey, S. Kumar, R. Schwendener, Albumin coated liposomes: a novel platform for macrophage specific drug delivery, *Nanotechnol. Dev.* 1 (2011) 2.
- [65] C. Chen, H. Hu, M. Qiao, X. Zhao, Y. Wang, K. Chen, et al., Anti-tumor activity of paclitaxel through dual-targeting lipoprotein-mimicking nanocarrier, *J. Drug Target.* 23 (2015) 311–322.
- [66] H. Faneca, A.S. Cabrita, S. Simoes, M.C. Pedroso de Lima, Evaluation of the antitumoral effect mediated by IL-12 and HSV-tk genes when delivered by a novel lipid-based system, *Biochim. Biophys. Acta* 1768 (2007) 1093–1102.
- [67] H. Faneca, A. Faustino, M.C. Pedroso de Lima, Synergistic antitumoral effect of vinblastine and HSV-Tk/GCV gene therapy mediated by albumin-associated cationic liposomes, *J. Control. Release* 126 (2008) 175–184.
- [68] W. Weecharangsan, R.J. Lee, Growth inhibition and chemosensitization of human carcinoma cells by human serum albumin-coated liposomal antisense oligodeoxyribonucleotide against bcl-2, *Drug Deliv.* 19 (2012) 292–297.
- [69] L. Piao, H. Li, L. Teng, B.C. Yung, Y. Sugimoto, R.W. Brueggemeier, et al., Human serum albumin-coated lipid nanoparticles for delivery of siRNA to breast cancer, *Nanomed. Nanotechnol. Biol. Med.* 9 (2013) 122–129.
- [70] A. Loureiro, G.J. Bernardes, U. Shimanovich, M.P. Sarria, E. Nogueira, A. Preto, et al., Folic acid-tagged protein nanoemulsions loaded with CORM-2 enhance the survival of mice bearing subcutaneous A20 lymphoma tumors, *Nanomed. Nanotechnol. Biol. Med.* 11 (2015) 1077–1083.
- [71] Y. Xu, X. Jin, Q. Ping, J. Cheng, M. Sun, F. Cao, et al., A novel lipoprotein-mimic nanocarrier composed of the modified protein and lipid for tumor cell targeting delivery, *J. Control. Release* 146 (2010) 299–308.
- [72] X. Yang, C.G. Koh, S. Liu, X. Pan, R. Santhanam, B. Yu, et al., Transferrin receptor-targeted lipid nanoparticles for delivery of an antisense oligodeoxyribonucleotide against Bcl-2, *Mol. Pharm.* 6 (2009) 221–230.
- [73] M. Wei, Y. Xu, Q. Zou, L. Tu, C. Tang, T. Xu, et al., Hepatocellular carcinoma targeting effect of PEGylated liposomes modified with lactoferrin, *Eur. J. Pharm. Sci.* 46 (2012) 131–141.
- [74] V. Pandey, K.R. Gajbhiye, V. Soni, Lactoferrin-appended solid lipid nanoparticles of paclitaxel for effective management of bronchogenic carcinoma, *Drug Deliv.* 22 (2015) 199–205.
- [75] J.Q. Gao, Q. Lv, L.M. Li, X.J. Tang, F.Z. Li, Y.L. Hu, et al., Glioma targeting and blood-brain barrier penetration by dual-targeting doxorubicin liposomes, *Biomaterials* 34 (2013) 5628–5639.
- [76] S.K. Sriraman, G. Salzano, C. Sarisozen, V. Torchilin, Anti-cancer activity of doxorubicin-loaded liposomes co-modified with transferrin and folic acid, *Eur. J. Pharm. Biopharm.* 105 (2016) 40–49.
- [77] C. Zheng, C. Ma, E. Bai, K. Yang, R. Xu, Transferrin and cell-penetrating peptide dual-functioned liposome for targeted drug delivery to glioma, *Int. J. Clin. Exp. Med.* 8 (2015) 1658–1668.
- [78] Q. Lv, L.M. Li, M. Han, X.J. Tang, J.N. Yao, X.Y. Ying, et al., Characteristics of sequential targeting of brain glioma for transferrin-modified cisplatin liposome, *Int. J. Pharm.* 444 (2013) 1–9.
- [79] J. Chen, S. Lu, W. Gu, P. Peng, J. Dong, F. Xu, et al., Characterization of 9-nitrocarnitoxin-in-cyclodextrin-in-liposomes modified with transferrin for the treating of tumor, *Int. J. Pharm.* 490 (2015) 219–228.
- [80] J. Chen, J. Yao, Z. Ma, P. Peng, S. Lu, Y. Hu, et al., Delivery of fluorescent-labeled cyclodextrin by liposomes: role of transferrin modification and phosphatidylcholine composition, *J. Lipid Res.* (2016) 1–11.
- [81] S.K. Sriraman, V. Geraldo, E. Luther, A. Degterev, V. Torchilin, Cytotoxicity of PEGylated liposomes co-loaded with novel pro-apoptotic drug NCL-240 and the MEK inhibitor cobimetinib against colon carcinoma in vitro, *J. Control. Release* 220 (2015) 160–168.
- [82] L. Qin, C.Z. Wang, H.J. Fan, C.J. Zhang, H.W. Zhang, M.H. Lv, et al., A dual-targeting liposome conjugated with transferrin and arginine-glycine-aspartic acid peptide for glioma-targeting therapy, *Oncol. Lett.* 8 (2014) 2000–2006.
- [83] Q. Chang, R. Geng, S. Wang, D. Qu, X. Kong, DOPA-based paclitaxel-loaded liposomes with modifications of transferrin and alendronate for bone and myeloma targeting, *Drug delivery* 23 (2016) 3629–3638.
- [84] I. Leto, M. Coronnello, C. Righeschi, M.C. Bergonzi, E. Mini, A.R. Bilia, Enhanced efficacy of artemisinin loaded in transferrin-conjugated liposomes versus stealth liposomes against HCT-8 Colon cancer cells, *ChemMedChem* 11 (2016) 1745–1751.
- [85] Y.C. Kuo, P.R. Chou, Neuroprotection against degeneration of sk-N-mc cells using neuron growth factor-encapsulated liposomes with surface cecropin and transferin, *J. Pharm. Sci.* 103 (2014) 2484–2497.
- [86] J. Suresh Reddy, V. Venkateswarlu, G.A. Koning, Radioprotective effect of transferrin targeted citocoline liposomes, *J. Drug Target.* 14 (2006) 13–19.
- [87] M.Q. Yuan, F. Zhu, J.Y. Lou, W.M. Yuan, L. Fu, S. Liu, et al., The anti-tumoral efficacy of a docetaxel-loaded liposomal drug delivery system modified with transferrin for ovarian cancer, *Drug Res.* 64 (2014) 195–202.
- [88] V. Soni, D.V. Kohli, S.K. Jain, Transferrin coupled liposomes as drug delivery carriers for brain targeting of 5-fluorouracil, *J. Drug Target.* 13 (2005) 245–250.
- [89] Singh R.P. Sonali, N. Singh, G. Sharma, M.R. Vijayakumar, B. Koch, et al., Transferrin liposomes of docetaxel for brain-targeted cancer applications: formulation and brain theranostics, *Drug delivery* 23 (2016) 1261–1271.
- [90] Z.L. Chen, M. Huang, X.R. Wang, J. Fu, M. Han, Y.Q. Shen, et al., Transferrin-modified liposome promotes alpha-mangostin to penetrate the blood-brain barrier, *Nanomed. Nanotechnol. Biol. Med.* 12 (2016) 421–430.
- [91] H. Zhuo, Y. Peng, Q. Yao, N. Zhou, S. Zhou, J. He, et al., Tumor imaging and interferon-gamma-inducible protein-10 gene transfer using a highly efficient transferrin-conjugated liposome system in mice, *Clin. Cancer Res.* 19 (2013) 4206–4217.
- [92] H. Ding, V. Sagar, M. Agudelo, S. Pilakka-Kanthikeel, V.S. Atluri, A. Raymond, et al., Enhanced blood-brain barrier transmigration using a novel transferrin embedded fluorescent magneto-liposome nanoformulation, *Nanotechnology* 25 (2014) 055101.
- [93] X. Pan, J. Guan, J.W. Yoo, A.J. Epstein, L.J. Lee, R.J. Lee, Cationic lipid-coated magnetic nanoparticles associated with transferrin for gene delivery, *Int. J. Pharm.* 358 (2008) 263–270.
- [94] Y. Li, R.J. Lee, X. Huang, Y. Li, B. Lv, T. Wang, et al., Single-step microfluidic synthesis of transferrin-conjugated lipid nanoparticles for siRNA delivery, *Nanomed. Nanotechnol. Biol. Med.* 13 (2017) 371–381.
- [95] Z. Yang, B. Yu, J. Zhu, X. Huang, J. Xie, S. Xu, et al., A microfluidic method to synthesize transferrin-lipid nanoparticles loaded with siRNA LOR-1284 for therapy of acute myeloid leukemia, *Nano* 6 (2014) 9742–9751.
- [96] S.J. Chiu, S. Liu, D. Perrotti, G. Marcucci, R.J. Lee, Efficient delivery of a Bcl-2-specific antisense oligodeoxyribonucleotide (G3139) via transferrin receptor-targeted liposomes, *J. Control. Release* 112 (2006) 199–207.
- [97] N. Sakaguchi, C. Kojima, A. Harada, K. Koivai, K. Shimizu, N. Emi, et al., Enhancement of transfection activity of lipoplexes by complexation with transferrin-bearing fusogenic polymer-modified liposomes, *Int. J. Pharm.* 325 (2006) 186–190.
- [98] M. Nakase, M. Inui, K. Okumura, T. Kamei, S. Nakamura, T. Tagawa, p53 gene therapy of human osteosarcoma using a transferrin-modified cationic liposome, *Mol. Cancer Ther.* 4 (2005) 625–631.
- [99] C. Tros De Ilarduya, M. Bunuales, C. Qian, N. Duzgunes, Antitumoral activity of transferrin-lipoplexes carrying the IL-12 gene in the treatment of colon cancer, *J. Drug Target.* 14 (2006) 527–535.



- [100] S.S. Neves, A.B. Sarmiento-Ribeiro, S.P. Simoes, M.C. Pedrosa de Lima, Transfection of oral cancer cells mediated by transferrin-associated lipoplexes: mechanisms of cell death induced by herpes simplex virus thymidine kinase/ganciclovir therapy, *Biochim. Biophys. Acta* 1758 (2006) 1703–1712.
- [101] Z.R. Zhong, Z.R. Zhang, Y. Deng, J. Liu, Q.G. Song, J. Liu, et al., Preparation of a TK/GCV administration system mediated by transferrin modified pro-cationic liposomes, *Pharmazie* 62 (2007) 522–527.
- [102] M. Cinci, S. Mamidi, W. Li, V. Fehring, M. Kirschfink, Targeted delivery of siRNA using transferrin-coupled lipoplexes specifically sensitizes CD71 high expressing malignant cells to antibody-mediated complement attack, *Target. Oncol.* 10 (2015) 405–413.
- [103] A.L. Cardoso, S. Simoes, L.P. de Almeida, N. Plesnila, M.C. Pedrosa de Lima, E. Wagner, et al., Tf-lipoplexes for neuronal siRNA delivery: a promising system to mediate gene silencing in the CNS, *J. Control. Release* 132 (2008) 113–123.
- [104] W. Wang, F. Zhou, L. Ge, X. Liu, F. Kong, Transferrin-PEG-PE modified dexamethasone conjugated cationic lipid carrier mediated gene delivery system for tumor-targeted transfection, *Int. J. Nanomedicine* 7 (2012) 2513–2522.
- [105] Z. Shao, J. Shao, B. Tan, S. Guan, Z. Liu, Z. Zhao, et al., Targeted lung cancer therapy: preparation and optimization of transferrin-decorated nanostructured lipid carriers as novel nanomedicine for co-delivery of anticancer drugs and DNA, *Int. J. Nanomedicine* 10 (2015) 1223–1233.
- [106] Y. Han, Y. Zhang, D. Li, Y. Chen, J. Sun, F. Kong, Transferrin-modified nanostructured lipid carriers as multifunctional nanomedicine for codelivery of DNA and doxorubicin, *Int. J. Nanomedicine* 9 (2014) 4107–4116.
- [107] S.K. Cheema, A.S. Gobin, R. Rhea, G. Lopez-Berestein, R.A. Newman, A.B. Mathur, Silk fibroin mediated delivery of liposomal emodin to breast cancer cells, *Int. J. Pharm.* 341 (2007) 221–229.
- [108] A.S. Gobin, R. Rhea, R.A. Newman, A.B. Mathur, Silk-fibroin-coated liposomes for long-term and targeted drug delivery, *Int. J. Nanomedicine* 1 (2006) 81–87.
- [109] R. Khatik, P. Dwivedi, P. Khare, S. Kansal, A. Dube, P.R. Mishra, et al., Development of targeted 1,2-diacyl-sn-glycero-3-phospho-l-serine-coated gelatin nanoparticles loaded with amphotericin B for improved in vitro and in vivo effect in leishmaniasis, *Expert Opin. Drug Deliv.* 11 (2014) 633–646.
- [110] Y.Z. Zhao, X. Li, C.T. Lu, M. Lin, L.J. Chen, Q. Xiang, et al., Gelatin nanostructured lipid carriers-mediated intranasal delivery of basic fibroblast growth factor enhances functional recovery in hemiparkinsonian rats, *Nanomed. Nanotechnol. Biol. Med.* 10 (2014) 755–764.
- [111] N. Elgindy, K. Elkhodairy, A. Molokhia, A. Elzoghby, Lyophilization monophase solution technique for preparation of amorphous flutamide dispersions, *Drug Dev. Ind. Pharm.* 37 (2011) 754–764.
- [112] P. Guan, Y. Lu, J. Qi, M. Niu, R. Lian, W. Wu, Solidification of liposomes by freeze-drying: the importance of incorporating gelatin as interior support on enhanced physical stability, *Int. J. Pharm.* 478 (2015) 655–664.
- [113] N. Elgindy, K. Elkhodairy, A. Molokhia, A. Elzoghby, Lyophilized flutamide dispersions with polyols and amino acids: preparation and in vitro evaluation, *Drug Dev. Ind. Pharm.* 37 (2011) 446–455.
- [114] T. Chuacharoen, C.M. Sabliov, Stability and controlled release of lutein loaded in zein nanoparticles with and without lecithin and pluronic F127 surfactants, *Colloids Surf. A Physicochem. Eng. Asp.* 503 (2016) 11–18.
- [115] H. Faneca, S. Simoes, Pedrosa de Lima MC. Association of albumin or protamine to lipoplexes: enhancement of transfection and resistance to serum, *J. Gene med.* 6 (2004) 681–692.
- [116] A.H. Weeke-Klimp, M. Bartsch, H.W. Morselt, I. Van Veen-Hof, D.K. Meijer, G.L. Scherphof, et al., Targeting of stabilized plasmid lipid particles to hepatocytes in vivo by means of coupled lactoferrin, *J. Drug Target.* 15 (2007) 585–594.
- [117] M. Frenzel, A. Steffen-Heins, Whey protein coating increases bilayer rigidity and stability of liposomes in food-like matrices, *Food Chem.* 173 (2015) 1090–1099.
- [118] J. Yi, T.I. Lam, W. Yokoyama, W.Y. Cheng, F. Zhong, Cellular uptake of beta-carotene from protein stabilized solid lipid nanoparticles prepared by homogenization-evaporation method, *J. Agric. Food Chem.* 62 (2014) 1096–1104.
- [119] W. He, Z. Jin, Y. Lv, H. Cao, J. Yao, J. Zhou, et al., Shell-crosslinked hybrid nanoparticles for direct cytosolic delivery for tumor therapy, *Int. J. Pharm.* 478 (2015) 762–772.
- [120] H.R. Jiang, N. Liu, Self-assembled beta-lactoglobulin-conjugated linoleic acid complex for colon cancer-targeted substance, *J. Dairy Sci.* 93 (2010) 3931–3939.
- [121] J.N. Pedersen, J.S. Pedersen, D.E. Otzen, The use of lipotides to stabilize and transport hydrophobic molecules, *Biochemistry* 54 (2015) 4815–4823.
- [122] Y.C. Kuo, S.J. Cheng, Brain targeted delivery of carmustine using solid lipid nanoparticles modified with tamoxifen and lactoferrin for antitumor proliferation, *Int. J. Pharm.* 499 (2016) 10–19.
- [123] I. Singh, R. Swami, D. Pooja, M.K. Jeengar, W. Khan, R. Sistla, Lactoferrin bioconjugated solid lipid nanoparticles: a new drug delivery system for potential brain targeting, *J. Drug Target.* 24 (2016) 212–223.
- [124] S. Shilpi, V.D. Vimal, V. Soni, Assessment of lactoferrin-conjugated solid lipid nanoparticles for efficient targeting to the lung, *Prog. Biomater.* 4 (2015) 55–63.
- [125] F. Meng, S. Asghar, S. Gao, Z. Su, J. Song, M. Huo, et al., A novel LDL-mimic nanocarrier for the targeted delivery of curcumin into the brain to treat Alzheimer's disease, *Colloids Surf. B: Biointerfaces* 134 (2015) 88–97.
- [126] H. Chen, Y. Qin, Q. Zhang, W. Jiang, L. Tang, J. Liu, et al., Lactoferrin modified doxorubicin-loaded procatonic liposomes for the treatment of gliomas, *Eur. J. Pharm. Sci.* 44 (2011) 164–173.
- [127] H. Chen, L. Tang, Y. Qin, Y. Yin, J. Tang, W. Tang, et al., Lactoferrin-modified procatonic liposomes as a novel drug carrier for brain delivery, *Eur. J. Pharm. Sci.* 40 (2010) 94–102.
- [128] F.Y. Huang, W.J. Chen, W.Y. Lee, S.T. Lo, T.W. Lee, J.M. Lo, In vitro and in vivo evaluation of lactoferrin-conjugated liposomes as a novel carrier to improve the brain delivery, *Int. J. Mol. Sci.* 14 (2013) 2862–2874.
- [129] M.A. De Luca, F. Lai, F. Corrias, P. Caboni, Z. Bimpisidis, E. Maccioni, et al., Lactoferrin- and antitransferrin-modified liposomes for brain targeting of the NK3 receptor agonist senktide: preparation and in vivo evaluation, *Int. J. Pharm.* 479 (2015) 129–137.
- [130] A.O. Elzoghby, W.M. Samy, N.A. Elgindy, Protein-based nanocarriers as promising drug and gene delivery systems, *J. Control. Release* 161 (2012) 38–49.
- [131] P.H. Tran, T.T. Tran, B.J. Lee, Enhanced solubility and modified release of poorly water-soluble drugs via self-assembled gelatin-oleic acid nanoparticles, *Int. J. Pharm.* 455 (2013) 235–240.
- [132] M. Svensson, A.K. Mossberg, J. Pettersson, S. Linse, C. Svanborg, Lipids as cofactors in protein folding: stereo-specific lipid-protein interactions are required to form HAMLET (human alpha-lactalbumin made lethal to tumor cells). *Protein science: a publication of the protein, Society* 12 (2003) 2805–2814.
- [133] C. Svanborg, H. Agerstam, A. Aronson, R. Bjerkvig, C. Düringer, W. Fischer, et al., HAMLET kills tumor cells by an apoptosis-like mechanism – cellular, molecular, and therapeutic aspects, *Adv. Cancer Res.* 88 (2003) 1–29.
- [134] B. Fang, M. Zhang, M. Tian, L. Jiang, H.Y. Guo, F.Z. Ren, Bovine lactoferrin binds oleic acid to form an anti-tumor complex similar to HAMLET, *Biochim. Biophys. Acta* 2014 (1841) 535–543.
- [135] S.B. Nielsen, K. Wilhelm, B. Vad, J. Schleucher, L.A. Morozova-Roche, D. Otzen, The interaction of equine lysozyme:oleic acid complexes with lipid membranes suggests a cargo off-loading mechanism, *J. Mol. Biol.* 398 (2010) 351–361.
- [136] S.E. Permyakov, E.L. Knyazeva, L.M. Khasanova, R.S. Fadeev, A.P. Zhadan, H. Roche-Hakansson, et al., Oleic acid is a key cytotoxic component of HAMLET-like complexes, *Biol. Chem.* 393 (2012) 85–92.
- [137] J.D. Kaspersen, J.N. Pedersen, J.G. Hansted, S.B. Nielsen, S. Sakthivel, K. Wilhelm, et al., Generic structures of cytotoxic lipotides: nano-sized complexes with oleic acid cores and shells of disordered proteins, *ChemBioChem* 15 (2014) 2693–2702.
- [138] N. Elgindy, K. Elkhodairy, A. Molokhia, A. Elzoghby, Biopolymeric nanoparticles for oral protein delivery: design and in vitro evaluation, *J. Nanomed. Nanotechnol.* 2011 (2012).
- [139] A.O. Elzoghby, A.L. Hemasa, M.S. Freag, Hybrid protein-inorganic nanoparticles: from tumor-targeted drug delivery to cancer imaging, *J. Control. Release* (2016).
- [140] A.O. Elzoghby, M.M. Elgohary, N.M. Kamel, Chapter six-implications of protein- and peptide-based nanoparticles as potential vehicles for anticancer drugs, *Adv. Protein Chem. Struct. Biol.* 98 (2015) 169–221.
- [141] A.O. Elzoghby, M.M. Abd-Elwakil, K. Abd-Elaslam, M.T. Elsayed, Y. Hashem, O. Mohamed, Natural polymeric nanoparticles for brain-targeting: implications on drug and gene delivery, *Curr. Pharm. Des.* 22 (2016) 3305–3323.
- [142] T.K. Kwon, K.B. Lim, J.-C. Kim, Solid lipid nanoparticles coated with silk fibroin, *J. Ind. Eng. Chem.* 17 (2011) 10–13.
- [143] Y. Dong, P. Dong, D. Huang, L. Mei, Y. Xia, Z. Wang, et al., Fabrication and characterization of silk fibroin-coated liposomes for ocular drug delivery, *Eur. J. Pharm. Biopharm.* 91 (2015) 82–90.
- [144] M.M. Gaspar, A. Radomska, O.L. Gobbo, U. Bakowsky, M.W. Radomski, C. Ehrhardt, Targeted delivery of transferrin-conjugated liposomes to an orthotopic model of lung cancer in nude rats, *J. Aerosol Med. Pulm. Drug Deliv.* 25 (2012) 310–318.
- [145] P.H. Tran, T.T. Tran, B.J. Lee, Biodistribution and pharmacokinetics in rats and antitumor effect in various types of tumor-bearing mice of novel self-assembled gelatin-oleic acid nanoparticles containing paclitaxel, *J. Biomed. Nanotechnol.* 10 (2014) 154–165.
- [146] S. Han, M. Li, X. Liu, H. Gao, Y. Wu, Construction of amphiphilic copolymer nanoparticles based on gelatin as drug carriers for doxorubicin delivery, *Colloids Surf. B: Biointerfaces* 102 (2013) 833–841.
- [147] C. Zhao, X. Liu, J. Liu, Z. Yang, X. Rong, M. Li, et al., Transferrin conjugated poly (gamma-glutamic acid-maleimide-co-L-lactide)-1,2-dipalmitoyl-sn-glycero-3-phosphoethanolamine copolymer nanoparticles for targeting drug delivery, *Colloids Surf. B: Biointerfaces* 123 (2014) 787–796.
- [148] M.S. Alqahtani, M.S. Islam, S. Podaralla, R.S. Kaushik, J. Reineke, T. Woyengo, O. Perumal, Food protein based core-shell nanocarriers for oral drug delivery: effect of shell composition on in vitro and in vivo functional performance of zein nanocarriers, *Mol. Pharm.* 14 (2017) 757–769.
- [149] P. Hurtado-López, S. Murdan, An investigation into the adjuvant activity and immunogenicity of zein microspheres being researched as drug and vaccine carriers, *J. Pharm. Pharmacol.* 58 (2006) 769–774.
- [150] A. Nel, T. Xia, L. Mädler, N. Li, Toxic potential of materials at the nanolevel, *Science* 311 (2006) 622–627.
- [151] I. Linkov, F.K. Satterstrom, L.M. Corey, Nanotoxicology and nanomedicine: making hard decisions, *Nanomed. Nanotechnol. Biol. Med.* 4 (2008) 167–171.
- [152] J.D. Heidel, M.E. Davis, Clinical developments in nanotechnology for cancer therapy, *Pharm. Res.* 28 (2011) 187–199.
- [153] R. van der Meel, L.J. Vehmeijer, R.J. Kok, G. Storm, E.V. van Gaal, Ligand-targeted particulate nanomedicines undergoing clinical evaluation: current status, *Adv. Drug Deliv. Rev.* 65 (2013) 1284–1298.

## Article

# Discovery of Indeno[1,2-*c*]quinoline Derivatives as Potent Dual Antituberculosis and Anti-Inflammatory Agents

Chih-Hua Tseng<sup>1,2,3,4,5</sup>, Chun-Wei Tung<sup>1,5,6</sup>, Chen-Hsin Wu<sup>7</sup>, Cherng-Chyi Tzeng<sup>3,5,7</sup>, Yen-Hsu Chen<sup>8,9,10,11,\*</sup>, Tsong-Long Hwang<sup>12,13,14,\*</sup> and Yeh-Long Chen<sup>4,5,7,\*</sup>

<sup>1</sup> School of Pharmacy, College of Pharmacy, Kaohsiung Medical University, Kaohsiung 807, Taiwan; chihhua@kmu.edu.tw (C.-H.T.); cwtung@kmu.edu.tw (C.-W.T.)

<sup>2</sup> Department of Fragrance and Cosmetic Science, College of Pharmacy, Kaohsiung Medical University, Kaohsiung 807, Taiwan

<sup>3</sup> Research Center for Natural Products and Drug Development, Kaohsiung Medical University, Kaohsiung 807, Taiwan; tzengch@kmu.edu.tw

<sup>4</sup> Center for Infectious Disease and Cancer Research, Kaohsiung Medical University, Kaohsiung 807, Taiwan

<sup>5</sup> Department of Medical Research, Kaohsiung Medical University-Hospital, Kaohsiung 807, Taiwan

<sup>6</sup> Ph.D. Program in Toxicology, Kaohsiung Medical University, Kaohsiung City 807, Taiwan

<sup>7</sup> Department of Medicinal and Applied Chemistry, College of Life Science, Kaohsiung Medical University, Kaohsiung 807, Taiwan; creator770326@hotmail.com

<sup>8</sup> Division of Infectious Diseases, Department of Internal Medicine, Kaohsiung Medical University-Hospital, Kaohsiung Medical University, Kaohsiung 807, Taiwan

<sup>9</sup> School of Medicine, College of Medicine, Kaohsiung Medical University, Kaohsiung 807, Taiwan

<sup>10</sup> Department of Laboratory Medicine, Kaohsiung Medical University-Hospital, Kaohsiung Medical University, Kaohsiung 807, Taiwan

<sup>11</sup> Center for Dengue Fever Control and Research, Kaohsiung Medical University, Kaohsiung 807, Taiwan

<sup>12</sup> Graduate Institute of Natural Products, College of Medicine, and Chinese Herbal Medicine Research Team, Healthy Aging Research Center, Chang Gung University, Taoyuan 333, Taiwan

<sup>13</sup> Research Center for Chinese Herbal Medicine, Research Center for Food and Cosmetic Safety, and Graduate Institute of Health Industry Technology, College of Human Ecology, Chang Gung University of Science and Technology, Taoyuan 333, Taiwan

<sup>14</sup> Department of Anesthesiology, Chang Gung Memorial Hospital, Taoyuan 333, Taiwan

\* Correspondence: infchen@gmail.com (Y.-H.C.); htl@mail.cgu.edu.tw (T.-L.H.); yeloch@kmu.edu.tw (Y.-L.C.); Tel.: +886-7-312-1101 (ext. 5677) (Y.-H.C.); +886-3-211-8506 (T.-L.H.); +886-7-312-1101 (ext. 2684) (Y.-L.C.); Fax: +886-7-322-8547 (Y.-H.C.); +886-3-211-8506 (T.-L.H.); +886-7-312-5339 (Y.-L.C.)

Academic Editors: Daniela Barlocco and Fiorella Meneghetti

Received: 17 May 2017; Accepted: 12 June 2017; Published: 16 June 2017

**Abstract:** A series of indeno[1,2-*c*]quinoline derivatives were designed, synthesized and evaluated for their anti-tuberculosis (anti-TB) and anti-inflammatory activities. The minimum inhibitory concentration (MIC) of the newly synthesized compound was tested against *Mycobacterium tuberculosis* H<sub>37</sub>R<sub>V</sub>. Among the tested compounds, (*E*)-*N'*-[6-(4-hydroxypiperidin-1-yl)-11H-indeno[1,2-*c*]quinolin-11-ylidene]isonicotino-hydrazide (**12**), exhibited significant activities against the growth of *M. tuberculosis* (MIC values of 0.96 µg/mL) with a potency approximately equal to that of isoniazid (INH), an anti-TB drug. Important structure features were analyzed by quantitative structure–activity relationship (QSAR) analysis to give better insights into the structure determinants for predicting the anti-TB activity. The anti-inflammatory activity was induced by superoxide anion generation and neutrophil elastase (NE) release using the formyl-L-methionyl-L-leucyl-L-phenylalanine (fMLF)-activated human neutrophils method. Results indicated that compound **12** demonstrated a potent dual inhibitory effect on NE release and superoxide anion generation with IC<sub>50</sub> values of 1.76 and 1.72 µM, respectively. Our results indicated that compound **12** is a potential lead compound for the discovery of dual anti-TB and anti-inflammatory drug candidates.

In addition, 6-[3-(hydroxymethyl)piperidin-1-yl]-9-methoxy-11*H*-indeno[1,2-*c*]quinolin-11-one (**4g**) showed a potent dual inhibitory effect on NE release and superoxide anion generation with IC<sub>50</sub> values of 0.46 and 0.68 µM, respectively, and is a potential lead compound for the discovery of anti-inflammatory drug candidates.

**Keywords:** indeno[1,2-*c*]quinoline; antimycobacterial activity; anti-inflammatory activity

## 1. Introduction

Tuberculosis (TB) is an infectious disease caused by *Mycobacterium tuberculosis* which primarily affects the lungs, causing an intense local inflammatory response that is critical to the pathogenesis of tuberculosis [1,2]. Therefore, TB is a chronic inflammatory condition in which regulatory and pro-inflammatory processes occur that contribute to severe lung pathology, leading to lung tissue necrosis and the promotion of mycobacterial dissemination and transmission [3]. Anti-inflammatory drugs, especially corticosteroids, are currently used for adjunctive therapy in most severe life-threatening forms of tuberculosis, such as meningitis and pericarditis [4]. The importance of developing new drugs with dual anti-inflammatory and antimycobacterial activities is amplified by the emergence of multi-drug resistant (MDR) strains and the global human immunodeficiency virus (HIV) pandemic [5–7]. The anti-leprosy drug clofazimine [8] exhibited dual anti-inflammatory and antimycobacterial activities. However, its potency is not sufficient, motivating the design and search for novel agents.

Quinoline-based anti-TB compound bedaquiline is a highly potent anti-TB agent, has a novel mode of action and was recently approved for the treatment of multidrug-resistant tuberculosis (MDR-TB) [9]. Currently there is considerable interest in the synthesis of indeno[2,1-*c*]quinoline derivatives, because of their antimycobacterial activities [10–12]. However, the isomeric indeno[1,2-*c*]quinoline derivatives have attracted only limited attention. Over the past few years, we have been particularly interested in the synthesis of fluoroquinolone and benzofuroquinoline derivatives for anti-TB evaluations [13–17]. We have also synthesized certain polycyclic heterocycles such as 9-anilinoacridine, 9-phenoxyacridine, 4-phenoxyfuro[2,3-*b*]quinoline, quinolin-2(1*H*)-one, furo[3,2:3,4]naphtha[1,2-*d*]imidazole and benzo[*f*]indole-4,9-dione derivatives for the evaluation of their anti-inflammatory activities [18–28]. In continuation of our efforts to identify potential anti-TB agents with novel types of structures which are distinct from those of existing drugs, we herein describe the synthesis of certain indeno[1,2-*c*]quinoline derivatives for anti-inflammatory and anti-TB evaluations. The aim of our current study is to identify novel skeletons that exhibit dual anti-inflammatory and antimycobacterial activities with low cytotoxicities.

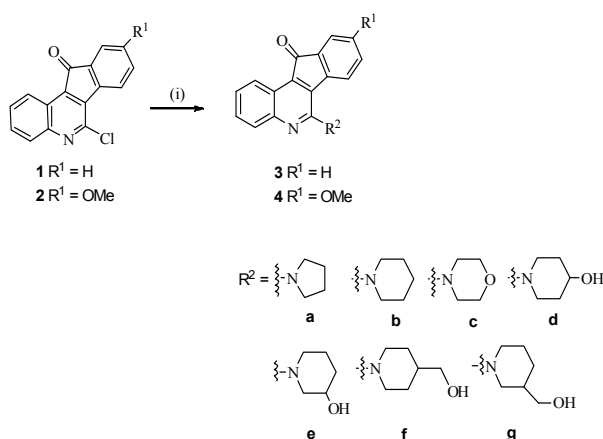
## 2. Results and Discussion

### 2.1. Chemistry

According to our previously reported procedures [29], 2-hydroxy-3-phenylquinoline-4-carboxylic acid was treated with POCl<sub>3</sub> to afford 6-chloro-11*H*-indeno[1,2-*c*]quinolin-11-one (**1**), which was then reacted with cyclic amines to give 6-cycloamino-11*H*-indeno[1,2-*c*]quinolin-11-ones (**3a–3g**). Accordingly, compounds **4a–4g** were prepared from the known 6-chloro-9-methoxy-11*H*-indeno[1,2-*c*]quinolin-11-one (**2**) [29] under similar reaction conditions as outlined in Scheme 1.

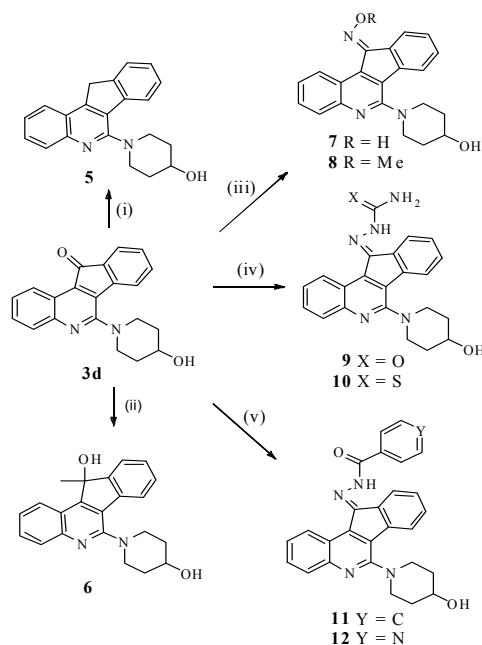
Among these compounds, 6-(4-hydroxypiperidin-1-yl)-11*H*-indeno[1,2-*c*]quinolin-11-one (**3d**) exhibited the most potent activity against the growth of *Mycobacterium tuberculosis* (minimum inhibitory concentration (MIC) value of 2.09 µg/mL), and therefore, we decided to select **3d** as a lead compound for structural optimization as described in Scheme 2. The Wolff–Kishner reduction of **3d** with hydrazine afforded 1-(11*H*-indeno[1,2-*c*]quinolin-6-yl)piperidin-4-ol (**5**)

in 43% yield. Treatment of **3d** with methyl magnesium bromide (Grignard reagent) afforded 6-(4-hydroxypiperidin-1-yl)-11-methyl-11*H*-indeno[1,2-*c*]quinolin-11-ol (**6**) in 71% yield. (*E*)-6-(4-hydroxypiperidin-1-yl)-11*H*-indeno[1,2-*c*]quinolin-11-one oxime (**7**) and (*E*)-6-(4-hydroxypiperidin-1-yl)-11*H*-indeno[1,2-*c*]quinolin-11-one *O*-methyl oxime (**8**) were obtained from **3d** by the treatment with  $\text{NH}_2\text{OH}$  and  $\text{NH}_2\text{OMe}$ , respectively. (*E*)-2-[6-(4-hydroxypiperidin-1-yl)-11*H*-indeno[1,2-*c*]quinolin-11-ylidene]hydrazinecarboxamide (**9**) and (*E*)-2-(6-(4-hydroxypiperidin-1-yl)-11*H*-indeno[1,2-*c*]quinolin-11-ylidene)hydrazinecarbothioamide (**10**) were obtained from **3d** by the treatment with semicarbazide and thiosemicarbazide, respectively. (*E*)-*N'*-[6-(4-hydroxypiperidin-1-yl)-11*H*-indeno[1,2-*c*]quinolin-11-ylidene]benzohydrazide (**11**) and (*E*)-*N'*-(6-(4-hydroxypiperidin-1-yl)-11*H*-indeno[1,2-*c*]quinolin-11-ylidene)isonicotinohydrazide (**12**) were obtained from **3d** by the treatment with benzhydrazide and isonicotinic acid hydrazide, respectively.



Reagents and conditions: (i) cyclic amines in ethoxyethanol, reflux (48–72%).

**Scheme 1.** Synthesis of indeno[1,2-*c*]quinoline derivatives **3a–4g**.



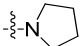
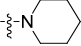
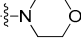
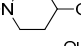
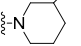
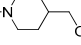
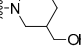
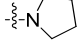
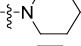
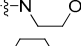
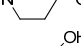
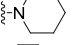
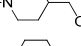
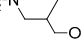
Reagents and conditions: (i)  $\text{NH}_2\text{NH}_2$ , 2-EtOEtOH, reflux, 4h (43%); (ii)  $\text{MeMgBr}$ , dry THF,  $0^\circ\text{C}$ , 12h (71%); (iii)  $\text{NH}_2\text{OR}$ ,  $\text{K}_2\text{CO}_3$ , 2-EtOEtOH, reflux, 3h (78% for **7**; 74% for **8**); (iv) semicarbazide or thiosemicarbazide, 2-EtOEtOH, reflux, 3h (68% for **9**; 54% for **10**); (v) benzhydrazide or Isonicotinic acid hydrazide, 2-EtOEtOH, reflux, 24h (61% for **11**; 65% for **12**)

**Scheme 2.** Synthesis of indeno[1,2-*c*]quinoline derivatives **5–12**.

## 2.2. Results and Discussion

The anti-TB activities of indeno[1,2-*c*]quinoline derivatives are summarized in Table 1. The 6-Cycloamino-11*H*-indeno[1,2-*c*]quinolin-11-ones (**3a–3g**) were found to be significantly inhibit the growth of *M. tuberculosis*, with MICs ranging from 2.09 to 4.97 µg/mL with >87% survival rate of Vero cells at a concentration of 20 µg/mL. Among them, 6-(4-hydroxypiperidin-1-yl)-11*H*-indeno[1,2-*c*]quinolin-11-one (**3d**) was the most active, with MIC of 2.09 µg/mL. However, their respective 9-methoxy counterparts **4a–4g** were inactive (MIC > 17 µg/mL) with an exception of 9-methoxy-6-(4-hydroxypiperidin-1-yl)-11*H*-indeno[1,2-*c*]quinolin-11-one (**4d**) which exhibited the MIC of 7.74 µg/mL. Further structural derivatization of **3d** resulted in two potential anti-TB agents, (*E*)-*N'*-[6-(4-hydroxypiperidin-1-yl)-11*H*-indeno[1,2-*c*]quinolin-11-ylidene]benzohydrazide (**11**) and (*E*)-*N'*-(6-(4-hydroxypiperidin-1-yl)-11*H*-indeno[1,2-*c*]quinolin-11-ylidene)isonicotinohydrazide (**12**) with MIC of 1.98 and 0.96 µg/mL. The anti-TB activity of **12** is equally active to the positive isoniazid (INH) with less cytotoxicity to the Vero cell. In addition, our results indicated that it is a feasible approach for the discovery of potential anti-TB agents through condensation of INH with an appropriate ketone.

**Table 1.** Anti-*Mycobacterium tuberculosis* H<sub>37</sub>Rv activities of indeno[1,2-*c*]quinoline derivatives. Results expressed as minimum inhibitory concentration (MIC) compared to isoniazid (INH).

Compounds	R <sup>1</sup>	R <sup>2</sup>	MIC (µg/ mL)	Survival Rate of Vero Cells @ 20 µg/mL (%)
<b>3a</b>	H		4.56	88.61
<b>3b</b>	H		4.93	96.18
<b>3c</b>	H		3.12	91.19
<b>3d</b>	H		2.09	91.23
<b>3e</b>	H		4.97	87.78
<b>3f</b>	H		3.98	91.11
<b>3g</b>	H		3.07	92.25
<b>4a</b>	OMe		17	89.62
<b>4b</b>	OMe		>20	99.55
<b>4c</b>	OMe		>20	94.47
<b>4d</b>	OMe		7.74	84.72
<b>4e</b>	OMe		19.10	87.59
<b>4f</b>	OMe		>20	90.26
<b>4g</b>	OMe		>20	87.60
	<b>5</b>		18.0	85.41
	<b>6</b>		>20	89.83
	<b>7</b>		>20	84.14
	<b>8</b>		>20	91.48
	<b>9</b>		>20	81.20
	<b>10</b>		>20	80.28
	<b>11</b>		1.98	89.55
	<b>12</b>		0.96	94.25
	<b>INH</b>		0.8–1.2	84.80



These indeno[1,2-*c*]quinolin-11-one derivatives were also evaluated for their inhibitory effects on superoxide anion generation and neutrophil elastase (NE) release in formyl-L-methionyl-L-leucyl-L-phenylalanine (fMLF)-activated human neutrophils and results are shown in Table 2. Compounds **3a–3c** were inactive while **3d–3g** exhibited a potent dual inhibitory effect on neutrophil elastase (NE) release and superoxide anion generation with  $IC_{50}$  value in a range of 1.78 and 4.50  $\mu$ M. These results indicated that the hydroxyl group substituted at the C6-piperidine ring is crucial for anti-inflammatory activities. Among them, 6-(4-hydroxypiperidin-1-yl)-11*H*-indeno[1,2-*c*]quinolin-11-one (**3d**) was the most potent dual inhibitor on NE release and superoxide anion generation with  $IC_{50}$  values of 2.20 and 1.78  $\mu$ M, respectively.

The same structure–activity relationships were observed for C9-methoxy derivatives in which compounds **4a–4c** were inactive, while their respective C6-hydroxypiperidine derivative **4d–4g** exhibited a potent dual inhibitory effect on NE release and superoxide anion generation. Among them, 9-methoxy-6-(3-piperidinemethano-1-yl)-11*H*-indeno[1,2-*c*]quinolin-11-one (**4g**) was the most potent dual inhibitor of NE release and superoxide anion generation, with  $IC_{50}$  values of 0.46 and 0.68  $\mu$ M, respectively. Compound **5** was only weakly active, while compound **6** was inactive indicated the reduction of the keto group is unfavorable. The keto group of **3d** can be converted into its oxime derivatives, compounds **7** and **8**, and retain comparable anti-inflammatory activity. However, the semicarbazone derivatives, compounds **9** and **10**, selectively inhibit superoxide anion generation with  $IC_{50}$  values of 3.64 and 2.41  $\mu$ M, respectively. The benzohydrazide derivative **11** was capable of inhibiting superoxide anion generation with  $IC_{50}$  value of 1.67  $\mu$ M but was inactive in the inhibition of NE release. (*E*)-*N'*-(6-(4-hydroxypiperidin-1-yl)-11*H*-indeno[1,2-*c*]quinolin-11-ylidene)isonicotino hydrazide (**12**) was found to be a potent dual inhibitor of NE release and superoxide anion generation, with  $IC_{50}$  values of 1.76 and 1.72  $\mu$ M, respectively, approximately equal potent to the positive LY294002.

To provide a better understanding of the relationship between the structure descriptors and anti-TB activities, a quantitative structure–activity relationship (QSAR) model was constructed to analyze important features and evaluate prediction performance. First, a total of 13 chemicals with determined MIC values as shown in Table 1 were randomly divided into a training dataset for model construction and a test dataset for independent test of the constructed model. The training and test datasets consist of 9 (**12**, **11**, **3g**, **3c**, **3e**, **3a**, **4d**, **4a** and **5**) and 4 (**3d**, **3f**, **3b** and **4e**) chemicals, respectively. Subsequently, each chemical was transformed into a vector of 1648 descriptors representing its structure features. The sequential feature selection algorithms developed by our group [30,31] were applied to simultaneously select a minimum number of relevant descriptors maximizing the  $R^2$  performance and develop multiple regression models for QSAR analysis. Please note that only the three most important features were considered due to the small number of chemicals in the dataset. In the QSAR analysis, pMIC values were utilized in that the MIC values in  $\mu$ g/mL were converted to  $\mu$ M/mL and then converted to  $-\log$  MIC (pMIC). The model is expected to be useful for chemicals within the pMIC range from 1.24 to 2.67. The final QSAR model with high performance with  $R^2 = 0.96$ ,  $R^2_{adj} = 0.94$ , root-mean-squared error (RMSE) = 0.085, and  $Q^2 = 0.86$  could well explain the variation of pMIC values representing the anti-TB activity. The constructed QSAR model and three important descriptors are shown in Table 3. SCH-6 (simple chain, order 6) represents the Chi chain descriptor of order 6 [32] that directly correlates with pMIC values with a high correlation coefficient of 0.83 for the 13 chemicals. CrippenLogP is the Crippen's LogP descriptor [33]. The hmax (representing the maximum hydrogen E-State value in a molecule) belongs to the descriptors of atom type electrotopological state [34–36].

**Table 2.** Anti-inflammatory activities of indeno[1,2-*c*]quinoline derivatives in formyl-L-methionyl-L-leucyl-L-phenylalanine (fMLF)-activated human neutrophils (IC<sub>50</sub> in  $\mu$ M) <sup>a</sup>.

Compounds	Superoxide Anion	Elastase Release
3a	>10	>10
3b	>10	>10
3c	>10	>10
3d	1.78 $\pm$ 0.44	2.20 $\pm$ 0.69
3e	2.90 $\pm$ 0.11	2.80 $\pm$ 0.09
3f	3.37 $\pm$ 0.17	4.50 $\pm$ 1.32
3g	2.77 $\pm$ 0.47	2.12 $\pm$ 1.19
4a	>10	>10
4b	>10	>10
4c	>10	>10
4d	2.82 $\pm$ 0.30	2.05 $\pm$ 0.24
4e	1.89 $\pm$ 0.65	2.93 $\pm$ 0.70
4f	1.93 $\pm$ 0.92	0.88 $\pm$ 0.30
4g	0.68 $\pm$ 0.14	0.46 $\pm$ 0.08
5	4.02 $\pm$ 1.08	5.29 $\pm$ 0.48
6	>10	>10
7	0.83 $\pm$ 0.47	1.39 $\pm$ 0.64
8	2.68 $\pm$ 0.95	2.13 $\pm$ 0.92
9	3.64 $\pm$ 1.43	>10
10	2.41 $\pm$ 0.36	>10
11	1.67 $\pm$ 0.87	>10
12	1.72 $\pm$ 0.23	1.76 $\pm$ 0.49
LY294002 <sup>b</sup>	1.36 $\pm$ 0.33	2.21 $\pm$ 0.45

<sup>a</sup> Concentration necessary for 50% inhibition (IC<sub>50</sub>); Results are presented as mean  $\pm$  SEM ( $n = 3$ ). <sup>b</sup> LY294002 (a phosphatidylinositol-3-kinase inhibitor) was used as a positive control for superoxide anion generation and elastase release.

**Table 3.** The quantitative structure–activity relationship (QSAR) analysis result for pMIC values of anti-tuberculosis (TB) activity. hmax.

	Coefficient	Estimate Std. Error	t-Value	Pr (> t )	
(Intercept)	0.5035	1.1585	0.435	0.681929	
SCH-6	11.463	1.0533	10.883	0.000114	***
CrippenLogP	−0.5711	0.1296	−4.407	0.006977	**
hmax	−3.8978	1.4043	−2.776	0.039106	*

\*\*\*  $p < 0.001$ , \*\*  $p < 0.01$ , \*  $p < 0.05$

While CrippenLogP and hmax show only a mild negative correlation to pMIC values with correlation coefficient values of  $-0.13$  and  $-0.01$ , respectively, for the 13 chemicals, the combination of all three descriptors largely enhances the prediction performance of the QSAR model with a 15% improvement on  $R^2$ . The observed and predicted pMIC values on the training dataset are shown in Table 4. To further evaluate the prediction ability of the QSAR model, the model was applied to predict the 4 chemicals in the test dataset. As shown in Table 5, the predicted and observed values for chemicals with exact MIC values are well correlated with a high correlation coefficient of 0.98. Altogether, the good performance of the QSAR models shows the importance of the three descriptors for determining the anti-TB activity. The model could be further tested and improved when more data are available.

**Table 4.** The comparison of observed and predicted values for the training dataset.

Compound	Observed pMIC	Predicted pMIC	Error
<b>12</b>	2.67	2.64	0.03
<b>11</b>	2.35	2.37	−0.02
<b>3g</b>	2.05	1.86	0.19
<b>3c</b>	2.01	2.08	−0.08
<b>3e</b>	1.82	1.80	0.02
<b>3a</b>	1.82	1.88	−0.06
<b>4d</b>	1.67	1.73	−0.06
<b>4a</b>	1.29	1.38	−0.10
<b>5</b>	1.24	1.18	0.07

**Table 5.** The comparison of observed and predicted values for the test dataset.

Compound	Observed pMIC	Predicted pMIC	Error
<b>3d</b>	2.20	2.00	0.20
<b>3f</b>	1.94	1.95	−0.01
<b>3b</b>	1.80	1.87	−0.07
<b>4e</b>	1.28	1.58	−0.30

### 3. Experimental Section

#### 3.1. General

Melting points were determined on a Electrothermal IA9100 melting point apparatus and are uncorrected. Nuclear magnetic resonance ( $^1\text{H}$  and  $^{13}\text{C}$ ) spectra were recorded on a Varian Gemini 200 spectrometer or Varian-Unity-400 spectrometer. Chemical shifts were expressed in parts per million ( $\delta$ ) with tetramethylsilane (TMS) as an internal standard and coupling constant ( $J$ ) in hertz (Hz). Thin-layer chromatography was performed on silica gel 60 F-254 plates purchased from E. Merck and Co. IR spectra were measured using a FTIR Perkin-Elmer system-2000 spectrometer (Perkin-Elmer, Waltham, MA, USA). The elemental analyses were performed in the Instrument Center of National Science Council at National Cheng-Kung University using Heraeus CHN-O Rapid EA (Heraeus Co., Harau, Germany), and all values are within  $\pm 0.4\%$  of the theoretical compositions.

#### 3.2. General Procedure for the Preparation of 6-Substituted-11H-indeno[1,2-c]quinolin-11-one Compounds **3a–g**, **4a**, **4d–g**

A mixture of 6-chloro-11H-indeno[1,2-c]quinolin-11-one (**1**) or 6-chloro-9-methoxy-11H-indeno[1,2-c]quinolin-11-one (**2**), cyclic amine (3.0 mmol), and 2-ethoxyethanol (30 mL) was heated at reflux for 3–6 h (TLC monitoring). The solvent was removed in vacuo and the residue was suspended in  $\text{H}_2\text{O}$  (20 mL). The resulting precipitate that separated was collected, washed with  $\text{H}_2\text{O}$ , and dried to give a crude solid. The crude product was purified by crystallization from EtOH to afford compounds **3a–g**, **4a**, **4d–g**. Preparation of compounds **4b** and **4c** had been described in our previous report [29].

##### 3.2.1. 6-(Pyrrolidin-1-yl)-11H-indeno[1,2-c]quinolin-11-one (**3a**)

Yield: 78%. m.p.: 163–164 °C. IR (KBr,  $\text{cm}^{-1}$ ): 2956, 1710.  $^1\text{H}$ -NMR (400 MHz,  $\text{CDCl}_3$ )  $\delta$  1.98–2.01 (*m*, 4H, pyrrolidinyll-H), 3.58–3.62 (*m*, 4H, pyrrolidinyll-H), 7.23–7.27 (*m*, 1H, 9-H), 7.35–7.39 (*m*, 1H, 8-H), 7.44–7.50 (*m*, 2H, 3-, 10-H), 7.53–7.57 (*m*, 1H, 2-H), 7.64 (*d*, 1H,  $J = 7.6$  Hz, 7-H), 7.78 (*d*, 1H,  $J = 8.8$  Hz, 4-H), 8.71 (*dd*, 1H,  $J = 1.6, 8.8$  Hz, 1-H).  $^{13}\text{C}$ -NMR (100 MHz,  $\text{CDCl}_3$ )  $\delta$  24.93 (2C), 50.16 (2C), 120.10, 123.63, 123.97, 124.24, 125.66, 127.23, 128.29, 129.85, 130.60, 133.22, 134.52, 136.17, 143.95, 149.18, 155.44, 195.74. Anal. calcd. for  $\text{C}_{20}\text{H}_{16}\text{N}_2\text{O}$ : C 79.98, H 5.37, N 9.33; found: C 79.93, H 5.39, N 9.28.

### 3.2.2. 6-(Piperidin-1-yl)-11H-indeno[1,2-c]quinolin-11-one (3b)

Yield: 75%. m.p.: 165–166 °C. IR (KBr,  $\text{cm}^{-1}$ ): 2934, 1715.  $^1\text{H-NMR}$  (400 MHz,  $\text{CDCl}_3$ )  $\delta$  1.71 (*br s*, 2H, piperidiny-H), 1.83–1.88 (*m*, 4H, piperidiny-H), 3.34 (*br s*, 4H, piperidiny-H), 7.26–7.30 (*m*, 1H, 9-H), 7.42–7.46 (*m*, 1H, 8-H), 7.48–7.52 (*m*, 1H, 3-H), 7.56–7.60 (*m*, 1H, 2-H), 7.64 (*d*, 1H,  $J = 7.2$  Hz, 10-H), 7.72 (*d*, 1H,  $J = 7.2$  Hz, 7-H), 7.84 (*d*, 1H,  $J = 8.4$  Hz, 4-H), 8.74 (*dd*, 1H,  $J = 1.2, 8.0$  Hz, 1-H).  $^{13}\text{C-NMR}$  (100 MHz,  $\text{CDCl}_3$ )  $\delta$  24.23, 25.87 (2C), 51.10 (2C), 120.67, 123.22, 123.99, 124.19, 126.60, 127.84, 128.70, 129.77, 132.31, 133.07, 134.72, 136.16, 143.59, 149.27, 158.27, 195.64. Anal. calcd. for  $\text{C}_{21}\text{H}_{18}\text{N}_2\text{O} \cdot 0.1 \text{H}_2\text{O}$ : C 79.77, H 5.80, N 8.86; found: C 79.77, H 5.74, N 8.75.

### 3.2.3. 6-(Morpholino-1-yl)-11H-indeno[1,2-c]quinolin-11-one (3c)

Yield: 62%. m.p.: 171–173 °C. IR (KBr,  $\text{cm}^{-1}$ ): 2838, 1719.  $^1\text{H-NMR}$  (400 MHz,  $\text{CDCl}_3$ )  $\delta$  3.41–3.44 (*m*, 4H, morpholiny-H), 3.98–4.01 (*m*, 4H, morpholiny-H), 7.28–7.32 (*m*, 1H, 9-H), 7.45–7.52 (*m*, 2H, 3-, 8-H), 7.58–7.63 (*m*, 1H, 2-H), 7.65–7.68 (*m*, 2H, 7-, 10-H), 7.86 (*ddd*, 1H,  $J = 0.8, 1.2, 8.4$  Hz, 4-H), 8.75 (*ddd*, 1H,  $J = 0.8, 1.6, 8.4$  Hz, 1-H).  $^{13}\text{C-NMR}$  (100 MHz,  $\text{CDCl}_3$ )  $\delta$  50.24 (2C), 66.79 (2C), 120.89, 123.18, 124.03, 124.48, 127.04, 127.98, 128.92, 130.02, 131.67, 133.13, 134.80, 136.44, 143.06, 149.16, 157.04, 195.24. Anal. calcd. for  $\text{C}_{20}\text{H}_{16}\text{N}_2\text{O}_2$ : C 75.93, H 5.10, N, 8.86; found: C 76.33, H 5.15, N, 8.82.

### 3.2.4. 6-(4-Hydroxypiperidin-1-yl)-11H-indeno[1,2-c]quinolin-11-one (3d)

Yield: 68%. m.p.: 208–208 °C. IR (KBr,  $\text{cm}^{-1}$ ): 3542, 2919, 1710.  $^1\text{H-NMR}$  (400 MHz,  $\text{CDCl}_3$ )  $\delta$  1.83–1.92 (*m*, 2H, piperidiny-H), 2.13–2.17 (*m*, 2H, piperidiny-H), 3.16–3.18 (*m*, 2H, piperidiny-H), 3.70–3.75 (*m*, 2H, piperidiny-H), 3.93–4.02 (*m*, 1H, piperidiny-H), 7.27–7.31 (*m*, 1H, 9-H), 7.43–7.52 (*m*, 1H, 3-, 8-H), 7.57–7.61 (*m*, 1H, 2-H), 7.64–7.70 (*m*, 2H, 7-, 10-H), 7.86 (*d*, 1H,  $J = 8.4$  Hz, 4-H), 8.73 (*dd*, 1H,  $J = 0.8, 8.4$  Hz, 1-H).  $^{13}\text{C-NMR}$  (100 MHz,  $\text{CDCl}_3$ )  $\delta$  34.37 (2C), 47.81 (2C), 67.90, 120.76, 123.06, 124.01, 124.36, 126.85, 127.76, 128.87, 129.96, 132.08, 133.02, 134.82, 136.34, 143.32, 149.02, 157.35, 195.41. Anal. calcd. for  $\text{C}_{21}\text{H}_{18}\text{N}_2\text{O}_2$ : C 76.34, H 5.49, N 8.48; found: C 76.09, H 5.56, N 8.36.

### 3.2.5. 6-(3-Hydroxypiperidin-1-yl)-11H-indeno[1,2-c]quinolin-11-one (3e)

Yield: 62%. m.p.: 211–212 °C. IR (KBr,  $\text{cm}^{-1}$ ): 3383, 2932, 1717.  $^1\text{H-NMR}$  (400 MHz,  $\text{DMSO}-d_6$ )  $\delta$  1.37–1.44 (*m*, 1H, piperidiny-H), 1.71–1.80 (*m*, 1H, piperidiny-H), 1.88–1.92 (*m*, 1H, piperidiny-H), 1.99–2.01 (*m*, 1H, piperidiny-H), 2.80 (*br s*, 1H, piperidiny-H), 2.92 (*br s*, 1H, piperidiny-H), 3.48 (*d*, 1H,  $J = 12.8$  Hz, piperidiny-H), 3.66 (*d*, 1H,  $J = 12.4$  Hz, piperidiny-H), 3.85 (*br s*, 1H, piperidiny-H), 4.99 (*br s*, 1H, -OH), 7.37–7.41 (*m*, 1H, 9-H), 7.48–7.52 (*m*, 1H, 8-H), 7.61–7.70 (*m*, 4H, 2-, 3-, 7-, 10-H), 7.80 (*d*, 1H,  $J = 8.4$  Hz, 4-H), 8.58 (*dd*, 1H,  $J = 0.8, 8.0$  Hz, 1-H).  $^{13}\text{C-NMR}$  (100 MHz,  $\text{DMSO}-d_6$ )  $\delta$  22.65, 32.81, 49.87, 56.95, 65.55, 119.89, 123.24, 123.49, 124.13, 126.77, 127.58, 129.22, 130.12, 131.57, 132.31, 135.47, 135.54, 142.55, 148.44, 157.10, 194.83. Anal. calcd. for  $\text{C}_{21}\text{H}_{18}\text{N}_2\text{O}_2 \cdot 1.2\text{H}_2\text{O}$ : C 71.65, H 5.84, N 7.96; found: C 71.49, H 5.77, N 7.90.

### 3.2.6. 6-(4-Piperidinemethano-1-yl)-11H-indeno[1,2-c]quinolin-11-one (3f)

Yield: 64%. m.p.: 223–224 °C. IR (KBr,  $\text{cm}^{-1}$ ): 3394, 2928, 1712.  $^1\text{H-NMR}$  (400 MHz,  $\text{CDCl}_3$ )  $\delta$  1.58–1.62 (*m*, 4H, piperidiny-H), 1.80 (*br s*, 1H, OH), 1.97 (*d*, 2H,  $J = 11.2$  Hz, piperidiny-H), 2.99 (*m*, 2H, piperidiny-H), 3.66 (*d*, 2H,  $J = 6.4$  Hz, 4'- $\text{CH}_2\text{OH}$ ), 3.83 (*d*, 2H,  $J = 13.2$  Hz, piperidiny-H), 7.27–7.31 (*m*, 1H, 9-H), 7.43–7.52 (*m*, 2H, 3-, 8-H), 7.56–7.61 (*m*, 1H, 2-H), 7.64–7.69 (*m*, 2H, 7-, 10-H), 7.85 (*d*, 1H,  $J = 8.4$  Hz, 4-H), 8.74 (*dd*, 1H,  $J = 1.6, 8.0$  Hz, 1-H).  $^{13}\text{C-NMR}$  (100 MHz,  $\text{CDCl}_3$ )  $\delta$  28.72 (2C), 38.45, 50.09 (2C), 67.79, 120.72, 123.15, 124.00, 124.27, 126.71, 127.82, 128.78, 129.85, 132.20, 133.05, 134.76, 136.21, 143.46, 149.20, 157.10, 195.55. Anal. calcd. for  $\text{C}_{22}\text{H}_{20}\text{N}_2\text{O}_2 \cdot 0.2\text{H}_2\text{O}$ : C 75.93, H 5.91, N 8.05; found: C 76.13, H 5.91, N 7.86.



## 3.2.7. 6-(3-Piperidinemethano-1-yl)-11H-indeno[1,2-c]quinolin-11-one (3g)

Yield: 54%. m.p.: 220–221 °C. IR (KBr,  $\text{cm}^{-1}$ ): 3355, 2936, 1715.  $^1\text{H-NMR}$  (400 MHz,  $\text{CDCl}_3$ )  $\delta$  1.31–1.40 (*m*, 1H, piperidiny-H), 1.75–1.88 (*m*, 2H, piperidiny-H), 1.92–1.99 (*m*, 1H, piperidiny-H), 2.10–2.18 (*m*, 1H, piperidiny-H), 2.52 (*br s*, 1H, 3'- $\text{CH}_2\text{OH}$ ), 3.05–3.20 (*m*, 2H, piperidiny-H), 3.59–3.66 (*m*, 3H, piperidiny-H), 3.75–3.79 (*m*, 1H, piperidiny-H), 7.25–7.29 (*m*, 1H, 9-H), 7.40–7.44 (*m*, 1H, 8-H), 7.46–7.51 (*m*, 1H, 3-H), 7.55–7.59 (*m*, 1H, 2-H), 7.62–7.65 (*m*, 2H, 7-, 10-H), 7.81 (*d*, 1H,  $J = 8.4$  Hz, 4-H), 8.72 (*dd*, 1H,  $J = 1.2, 8.8$  Hz, 1-H).  $^{13}\text{C-NMR}$  (100 MHz,  $\text{CDCl}_3$ )  $\delta$  24.43, 26.73, 38.34, 51.58, 51.89, 65.23, 120.51, 123.18, 124.01, 124.28, 126.52, 127.38, 128.73, 129.97, 131.95, 132.97, 134.73, 136.46, 143.42, 149.03, 157.40, 195.46. Anal. calcd. for  $\text{C}_{22}\text{H}_{20}\text{N}_2\text{O}_2$ : C 76.72, H 5.85, N 8.13; found: C, 76.66, H 5.86, N 8.00.

## 3.2.8. 9-Methoxy-6-(pyrrolidin-1-yl)-11H-indeno[1,2-c]quinolin-11-one (4a)

Yield: 79%. m.p.: 155–156 °C. IR (KBr,  $\text{cm}^{-1}$ ): 2934, 1715.  $^1\text{H-NMR}$  (400 MHz,  $\text{CDCl}_3$ )  $\delta$  1.99 (*m*, 4H, pyrrolidiny-H), 3.57 (*m*, 4H, pyrrolidiny-H), 3.86 (*s*, 3H, 9-OMe), 6.92 (*dd*, 1H,  $J = 2.4, 8.4$  Hz, 8-H), 7.20 (*d*, 1H,  $J = 2.4$  Hz, 10-H), 7.34–7.39 (*m*, 2H, 2-, 7-H), 7.50–7.54 (*m*, 1H, 3-H), 7.76 (*d*, 1H,  $J = 8.4$  Hz, 4-H), 8.66 (*dd*, 1H,  $J = 1.6, 8.4$  Hz, 1-H).  $^{13}\text{C-NMR}$  (100 MHz,  $\text{CDCl}_3$ )  $\delta$  24.84 (2C), 49.98 (2C), 55.72, 110.71, 118.59, 120.28, 123.67, 124.60, 125.67, 127.23, 129.33, 131.68, 135.19, 135.75, 135.91, 148.56, 155.25, 160.28, 195.55. Anal. calcd. for  $\text{C}_{21}\text{H}_{18}\text{N}_2\text{O}_2$ : C 76.34, H 5.49, N 8.48; found: C 76.04, H 5.56, N 8.38.

## 3.2.9. 6-(4-Hydroxypiperidin-1-yl)-9-methoxy-11H-indeno[1,2-c]quinolin-11-one (4d)

Yield: 72%. m.p.: 197–198 °C. IR (KBr,  $\text{cm}^{-1}$ ): 3295, 2939, 1713.  $^1\text{H-NMR}$  (400 MHz,  $\text{CDCl}_3$ )  $\delta$  1.81–1.90 (*m*, 2H, piperidiny-H), 2.12–2.16 (*m*, 2H, piperidiny-H), 3.09–3.15 (*m*, 2H, piperidiny-H), 3.67–3.72 (*m*, 2H, piperidiny-H), 3.87 (*s*, 3H, 9-OMe), 3.95–3.99 (*m*, 1H, piperidiny-H), 6.94 (*dd*, 1H,  $J = 2.4, 8.4$  Hz, 8-H), 7.21 (*d*, 1H,  $J = 2.4$  Hz, 10-H), 7.41–7.45 (*m*, 1H, 2-H), 7.53–7.57 (*m*, 2H, 3-, 7-H), 7.81 (*d*, 1H,  $J = 8.0$  Hz, 4-H), 8.67–8.70 (*m*, 1H, 1-H).  $^{13}\text{C-NMR}$  (100 MHz,  $\text{CDCl}_3$ )  $\delta$  34.41 (2C), 47.62 (2C), 55.77, 67.94, 110.78, 118.84, 120.93, 123.70, 124.08, 126.78, 127.86, 129.38, 132.99, 135.04, 135.33, 135.86, 148.59, 157.14, 160.68, 195.30. Anal. calcd. for  $\text{C}_{22}\text{H}_{20}\text{N}_2\text{O}_3$ : C 73.32, H 5.59, N 7.77; found: C 73.18, H, 5.80, N 7.52.

## 3.2.10. 6-(3-Hydroxypiperidin-1-yl)-9-methoxy-11H-indeno[1,2-c]quinolin-11-one (4e)

Yield: 66%. m.p.: 191–192 °C. IR (KBr,  $\text{cm}^{-1}$ ): 3408, 2937, 1714.  $^1\text{H-NMR}$  (400 MHz,  $\text{CDCl}_3$ )  $\delta$  1.58 (*br s*, 1H, piperidiny-H), 1.83–1.85 (*m*, 3H, piperidiny-H), 3.36–3.52 (*m*, 3H, piperidiny-H), 3.83 (*s*, 3H, 9-OMe), 3.94–3.97 (*m*, 1H, piperidiny-H), 4.10 (*s*, 1H, piperidiny-H), 6.87–6.92 (*m*, 1H, 10-H), 7.14–7.17 (*m*, 1H, 8-H), 7.37–7.44 (*m*, 2H, 2-, 3-H), 7.51–7.54 (*m*, 1H, 7-H), 7.74–7.77 (*m*, 1H, 4-H), 8.61–8.65 (*m*, 1H, 1-H).  $^{13}\text{C-NMR}$  (100 MHz,  $\text{CDCl}_3$ )  $\delta$  20.26, 32.35, 51.75, 54.10, 55.70, 65.46, 110.69, 118.87, 120.85, 123.64, 124.29, 126.83, 127.93, 129.78, 133.39, 134.60, 134.80, 134.83, 147.44, 156.07, 160.67, 194.81. Anal. calcd. for  $\text{C}_{22}\text{H}_{20}\text{N}_2\text{O}_3 \cdot 1.5\text{H}_2\text{O}$ : C 68.20, H 5.99, N 7.23; found: C 68.23, H 5.77, N 7.11.

## 3.2.11. 6-[4-(Hydroxymethyl)piperidin-1-yl]-9-methoxy-11H-indeno[1,2-c]quinolin-11-one (4f)

Yield: 68%. m.p.: 218–219 °C. IR (KBr,  $\text{cm}^{-1}$ ): 3352, 2928, 1711.  $^1\text{H-NMR}$  (400 MHz,  $\text{DMSO}-d_6$ )  $\delta$  1.40–1.49 (*m*, 2H, piperidiny-H), 1.62 (*m*, 1H, piperidiny-H), 1.86 (*d*, 2H,  $J = 11.2$  Hz, piperidiny-H), 2.81–2.87 (*m*, 2H, piperidiny-H), 3.39–3.44 (*m*, 2H, piperidiny-H), 3.64 (*d*, 2H,  $J = 11.2$  Hz, piperidiny-H), 3.83 (*s*, 3H, 9-OMe), 4.59 (*t*, 1H,  $J = 5.2$  Hz, -OH), 7.10–7.13 (*m*, 2H, 3-, 8-H), 7.44–7.49 (*m*, 2H, 2-, 7-H), 7.57–7.61 (*m*, 1H, 10-H), 7.74 (*d*, 1H,  $J = 8.0$  Hz, 4-H), 8.50 (*dd*, 1H,  $J = 0.8, 8.4$  Hz, 1-H).  $^{13}\text{C-NMR}$  (100 MHz,  $\text{DMSO}-d_6$ )  $\delta$  28.49, 38.10, 49.68 (2C), 55.75 (2C), 65.84, 110.79, 118.93, 120.01, 122.92, 124.29, 126.70, 127.58, 129.50, 132.58, 134.31, 134.36, 134.91, 147.83, 157.18, 160.38, 194.52. Anal. calcd. for  $\text{C}_{23}\text{H}_{22}\text{N}_2\text{O}_3 \cdot 0.25\text{H}_2\text{O}$ : C 72.89, H 6.00, N 7.39; found: C 72.54, H 5.96, N 7.33.

3.2.12. 6-[3-(Hydroxymethyl)piperidin-1-yl]-9-methoxy-11*H*-indeno[1,2-*c*]quinolin-11-one (**4g**)

Yield: 67%. m.p.: 243–244 °C. IR (KBr,  $\text{cm}^{-1}$ ): 3401, 2929, 1714.  $^1\text{H}$ -NMR (400 MHz,  $\text{DMSO-}d_6$ )  $\delta$  1.11–1.17 (*m*, 1H, piperidinyll-H), 1.78–1.92 (*m*, 4H, piperidinyll-H), 2.58–2.63 (*m*, 1H, piperidinyll-H), 2.77–2.82 (*m*, 1H, piperidinyll-H), 3.28–3.32 (*m*, 2H, piperidinyll-H), 3.57 (*d*, 1H,  $J = 12.4$  Hz, piperidinyll-H), 3.75 (*d*, 1H,  $J = 11.2$  Hz, piperidinyll-H), 3.84 (*s*, 3H, 9-OMe), 4.58 (*t*, 1H,  $J = 4.8$  Hz, -OH), 7.10–7.14 (*m*, 2H, 3-, 8-H), 7.45–7.53 (*m*, 2H, 2-, 7-H), 7.58–7.62 (*m*, 1H, 10-H), 7.75–7.77 (*m*, 1H, 4-H), 8.51–8.54 (*m*, 1H, 1-H).  $^{13}\text{C}$ -NMR (100 MHz,  $\text{DMSO-}d_6$ )  $\delta$  24.44, 26.74, 50.61, 53.40, 55.78 (2C), 64.07, 110.79, 119.03, 120.03, 122.95, 124.54, 126.74, 127.60, 129.55, 132.67, 134.35 (2C), 134.97, 147.88, 157.34, 160.40, 194.59. Anal. calcd. for  $\text{C}_{23}\text{H}_{22}\text{N}_2\text{O}_3 \cdot 0.25\text{H}_2\text{O}$ : C 72.89, H 6.00, N 7.39; found: C 72.94, H 5.96, N 7.40.

3.2.13. 1-(11*H*-Indeno[1,2-*c*]quinolin-6-yl)piperidin-4-ol (**5**)

A mixture of **3d** (0.25 g, 1.0 mmol), and 80% hydrazine monohydrate (1 mL) in 2-ethoxyethanol (30 mL) was refluxed for 4 h (TLC monitoring). The solvent was removed in vacuo, and the residue was poured into  $\text{H}_2\text{O}$  (100 mL). The resulting precipitate that separated was collected and crystallized from EtOH to give **5** (0.26 g, 82%). m.p.: 211–212 °C. IR (KBr,  $\text{cm}^{-1}$ ): 3384, 2926, 2928, 1573.  $^1\text{H}$ -NMR (400 MHz,  $\text{CDCl}_3$ )  $\delta$  1.88–1.97 (*m*, 2H, piperidinyll-H), 2.14–2.19 (*m*, 2H, piperidinyll-H), 3.14 (*br s*, 2H, piperidinyll-H), 3.76–3.80 (*m*, 2H, piperidinyll-H), 3.97 (*br s*, 1H, piperidinyll-H), 4.18 (*s*, 2H, 11- $\text{CH}_2$ ), 7.32–7.36 (*m*, 1H, 9-H), 7.40–7.47 (*m*, 2H, 2-, 8-H), 7.57–7.64 (*m*, 2H, 3-, 10-H), 7.89–8.00 (*m*, 3H, 1-, 4-, 7-H).  $^{13}\text{C}$ -NMR (100 MHz,  $\text{CDCl}_3$ )  $\delta$  34.63 (2C), 35.96, 47.77 (2C), 68.41, 122.61, 123.58, 123.74, 124.51 (2C), 126.21, 126.96, 128.30, 128.39, 128.80, 140.65, 142.63, 146.07, 151.69, 157.95. Anal. calcd. for  $\text{C}_{21}\text{H}_{20}\text{N}_2\text{O} \cdot 0.1\text{H}_2\text{O}$ : C 79.27, H 6.40, N 8.80; found: C 79.24, H 6.48, N 8.89.

3.2.14. 6-(4-Hydroxypiperidin-1-yl)-11-methyl-11*H*-indeno[1,2-*c*]quinolin-11-ol (**6**)

A mixture of **3d** (0.25 g, 1.0 mmol), dry THF (20 mL) and 2 M methyl magnesium bromide (2 mL) was stirred at 0 °C for 12 h (TLC monitoring). The solvent was removed in vacuo, and the residue was poured into  $\text{H}_2\text{O}$  (100 mL). The resulting precipitate that separated was collected and crystallized from EtOH to give **6** (0.25 g, 71%). m.p.: 146–147 °C. IR (KBr,  $\text{cm}^{-1}$ ): 3351, 2926, 1372.  $^1\text{H}$ -NMR (400 MHz,  $\text{CDCl}_3$ )  $\delta$  1.76–1.99 (*m*, 2H, piperidinyll-H), 1.92 (*s*, 3H, 11- $\text{CH}_3$ ), 2.10–2.19 (*m*, 2H, piperidinyll-H), 3.04–3.27 (*m*, 2H, piperidinyll-H), 3.75–3.78 (*m*, 2H, piperidinyll-H), 3.96 (*m*, 1H, piperidinyll-H), 7.36–7.48 (*m*, 3H, 2-, 8-, 9-H), 7.61–7.67 (*m*, 2H, 3-, 10-H), 7.87 (*d*, 1H,  $J = 7.2$  Hz, 7-H), 7.98 (*br s*, 1H, 4-H), 8.35–8.37 (*d*, 1H,  $J = 8.0$  Hz, 1-H).  $^{13}\text{C}$ -NMR (100 MHz,  $\text{CDCl}_3$ )  $\delta$  26.83, 34.51 (2C), 47.58 (2C), 67.98, 81.34, 118.87, 122.48 (2C), 122.85 (2C), 124.34 (2C), 124.67, 127.59, 128.74, 128.99 (2C), 129.26, 150.83. Anal. calcd. for  $\text{C}_{22}\text{H}_{22}\text{N}_2\text{O}_2 \cdot 0.7\text{H}_2\text{O}$ : C 73.60, H 6.57, N 7.80; found: C 73.90, H 6.78, N 7.43.

3.2.15. (*E*)-6-(4-Hydroxypiperidin-1-yl)-11*H*-indeno[1,2-*c*]quinolin-11-one Oxime (**7**)

A mixture of **3d** (0.27 g, 1.0 mmol), potassium carbonate (0.56 g, 4.00 mmol) and  $\text{NH}_2\text{OH} \cdot \text{HCl}$  (0.14 g, 2.0 mmol) in 2-ethoxyethanol (30 mL) was refluxed for 3 h (TLC monitoring). The solvent was removed in vacuo, and the residue was poured into  $\text{H}_2\text{O}$  (100 mL). The resulting precipitate that separated was collected and crystallized from EtOH to give **11** (0.27 g, 78%). m.p.: 155–156 °C. IR (KBr,  $\text{cm}^{-1}$ ): 3329, 2942.  $^1\text{H}$ -NMR (400 MHz,  $\text{DMSO-}d_6$ )  $\delta$  1.68–1.76 (*m*, 2H, piperidinyll-H), 1.98–2.00 (*m*, 2H, piperidinyll-H), 2.99 (*br s*, 2H, piperidinyll-H), 3.55–3.58 (*m*, 2H, piperidinyll-H), 3.74 (*br s*, 1H, piperidinyll-H), 4.83 (*br s*, 1H, -OH), 7.40–7.49 (*m*, 2H, 8-, 9-H), 7.57–7.64 (*m*, 2H, 2-, 3-H), 7.80–7.90 (*m*, 2H, 7-, 10-H), 8.43 (*d*, 1H,  $J = 7.6$  Hz, 4-H), 8.79 (*dd*, 1H,  $J = 1.2, 8.4$  Hz, 1-H), 13.39 (*s*, 1H, NOH).  $^{13}\text{C}$ -NMR (100 MHz,  $\text{DMSO-}d_6$ )  $\delta$  34.17 (2C), 48.04 (2C), 67.98, 120.79, 122.37, 125.30, 125.56, 126.19, 128.09, 128.25, 128.41, 128.87, 129.17, 130.87, 138.25, 139.59, 146.94, 153.91, 157.40. Anal. calcd. for  $\text{C}_{21}\text{H}_{19}\text{N}_3\text{O}_2 \cdot 0.2\text{H}_2\text{O}$ : C 72.27, H 5.60, N 12.04; found: C 72.67, H 5.72, N 11.63.

3.2.16. (*E*)-6-(4-Hydroxypiperidin-1-yl)-11*H*-indeno[1,2-*c*]quinolin-11-one *O*-methyl Oxime (**8**)

Compound **8** was prepared from **3d** and  $\text{NH}_2\text{OMe}\cdot\text{HCl}$  by the same procedure as described for the preparation of **7**. Yield: 74%. m.p.: 183–184 °C. IR (KBr,  $\text{cm}^{-1}$ ): 3350, 2938, 1025.  $^1\text{H}$ -NMR (400 MHz,  $\text{DMSO}-d_6$ )  $\delta$  1.66–1.74 (*m*, 2H, piperidinyll-H), 1.96–1.99 (*m*, 2H, piperidinyll-H), 2.96 (*br s*, 2H, piperidinyll-H), 3.51–3.54 (*m*, 2H, piperidinyll-H), 3.72 (*br s*, 1H, piperidinyll-H), 4.32 (*s*, 3H, =NOCH<sub>3</sub>), 4.83 (*br s*, 1H, -OH), 7.35–7.48 (*m*, 2H, 8-, 9-H), 7.54–7.63 (*m*, 2H, 2-, 3-H), 7.77–7.81 (*m*, 2H, 7-, 10-H), 8.22 (*d*, 1H, *J* = 7.6 Hz, 4-H), 8.72 (*dd*, 1H, *J* = 0.8, 8.4 Hz, 1-H).  $^{13}\text{C}$ -NMR (100 MHz,  $\text{DMSO}-d_6$ )  $\delta$  34.19 (2C), 48.01 (2C), 64.39, 66.62, 120.60, 122.57, 125.21, 125.79, 126.62, 128.09, 128.34, 128.68, 129.33, 130.00, 131.54, 138.73, 138.77, 147.05, 153.78, 157.28. Anal. calcd. for  $\text{C}_{22}\text{H}_{21}\text{N}_3\text{O}_2$ : C 73.52, H 5.89, N 11.69; found: C 73.24, H 5.93, N 11.49.

3.2.17. (*E*)-2-[6-(4-Hydroxypiperidin-1-yl)-11*H*-indeno[1,2-*c*]quinolin-11-ylidene]hydrazine Carboxamide (**9**)

A mixture of **3d** (0.27 g, 1.0 mmol) and semicarbazide (0.15 g, 2.0 mmol) in 2-ethoxyethanol (30 mL) was refluxed for 3 h (TLC monitoring). The solvent was removed in vacuo, and the residue was poured into  $\text{H}_2\text{O}$  (100 mL). The resulting precipitate that separated was collected and crystallized from EtOH to give **9** (0.27 g, 68%). m.p.: 289–290 °C. IR (KBr,  $\text{cm}^{-1}$ ): 3468, 1725.  $^1\text{H}$ -NMR (400 MHz,  $\text{DMSO}-d_6$ )  $\delta$  1.69–1.78 (*m*, 2H, piperidinyll-H), 1.99–2.02 (*m*, 2H, piperidinyll-H), 3.03 (*br s*, 2H, piperidinyll-H), 3.59–3.61 (*m*, 2H, piperidinyll-H), 3.76 (*br s*, 1H, OH), 7.00 (*br s*, 2H, NH<sub>2</sub>), 7.45–7.51 (*m*, 2H, 8-, 9-H), 7.58–7.65 (*m*, 2H, 2-, 3-H), 7.82 (*d*, 1H, *J* = 8.8 Hz, 10-H), 7.94 (*d*, 1H, *J* = 7.6 Hz, 7-H), 8.30 (*d*, 1H, *J* = 7.6 Hz, 4-H), 9.15 (*d*, 1H, *J* = 8.4 Hz, 1-H), 10.45 (*br s*, 1H, NH).  $^{13}\text{C}$ -NMR (100 MHz,  $\text{DMSO}-d_6$ )  $\delta$  34.04 (2C), 47.79 (2C), 65.71, 120.65, 122.49, 124.98, 125.75, 125.87, 126.86, 127.80, 128.18, 129.44, 130.39, 138.37, 141.52, 143.90, 145.40, 155.74, 156.57, 181.34. Anal. calcd. for  $\text{C}_{22}\text{H}_{21}\text{N}_5\text{O}_2\cdot 0.5\text{H}_2\text{O}$ : C 66.65, H 5.59, N 17.67; found: C 66.69, H 5.70, N 17.31.

3.2.18. (*E*)-2-[6-(4-Hydroxypiperidin-1-yl)-11*H*-indeno[1,2-*c*]quinolin-11-ylidene]hydrazine Carbothioamide (**10**)

Compound **10** was prepared from **3d** and thiosemicarbazide by the same procedure as described for the preparation of **9**. Yield: 54%. m.p.: 304–305 °C. IR (KBr,  $\text{cm}^{-1}$ ): 3408, 1601.  $^1\text{H}$ -NMR (400 MHz,  $\text{DMSO}-d_6$ )  $\delta$  1.68–1.77 (*m*, 2H, piperidinyll-H), 1.99–2.01 (*m*, 2H, piperidinyll-H), 3.03 (*br s*, 2H, piperidinyll-H), 3.57–3.60 (*m*, 3H, OH, piperidinyll-H), 3.75 (*br s*, 1H, piperidinyll-H), 7.46–7.50 (*m*, 3H, 8-, 9-H), 7.59–7.65 (*m*, 2H, 2-, 3-H), 7.81 (*d*, 1H, *J* = 8.0 Hz, 10-H), 7.91 (*d*, 1H, *J* = 7.2 Hz, 7-H), 8.10 (*d*, 1H, *J* = 7.6 Hz, 4-H), 8.25 (*br s*, 1H, NH), 8.99 (*br s*, 1H, NH), 9.07 (*d*, 1H, *J* = 7.6 Hz, 1-H), 11.30 (*br s*, 1H, NH).  $^{13}\text{C}$ -NMR (100 MHz,  $\text{DMSO}-d_6$ )  $\delta$  34.45 (2C), 48.09 (2C), 65.56, 121.45, 121.91, 125.09, 125.50, 127.17, 127.64, 128.62, 130.25, 140.06, 156.12, 156.59, 157.61, 173.59. Anal. calcd. for  $\text{C}_{22}\text{H}_{21}\text{N}_5\text{OS}\cdot 0.6\text{H}_2\text{O}$ : C 63.78, H 5.40, N 16.90; found: C 63.90, H 5.35, N 16.50.

3.2.19. (*E*)-*N'*-[6-(4-Hydroxypiperidin-1-yl)-11*H*-indeno[1,2-*c*]quinolin-11-ylidene]benzohydrazide (**11**)

A mixture of **3d** (0.27 g, 1.0 mmol) and benzohydrazide (0.27 g, 2.0 mmol) in 2-ethoxyethanol (30 mL) was refluxed for 24 h (TLC monitoring). The solvent was removed in vacuo, and the residue was poured into  $\text{H}_2\text{O}$  (100 mL). The resulting precipitate that separated was collected and crystallized from EtOH to give **11** (0.28 g, 61%). m.p.: 258–259 °C. IR (KBr,  $\text{cm}^{-1}$ ): 3422, 2937, 1660.  $^1\text{H}$ -NMR (400 MHz,  $\text{DMSO}-d_6$ )  $\delta$  1.70–1.78 (*m*, 2H, piperidinyll-H), 1.99–2.02 (*m*, 2H, piperidinyll-H), 3.03 (*br s*, 2H, piperidinyll-H), 3.58–3.61 (*m*, 2H, piperidinyll-H), 3.76 (*br s*, 1H, piperidinyll-H), 4.83 (*br s*, 1H, -OH), 7.45–7.52 (*m*, 2H, NH, 9-H), 7.61–7.72 (*m*, 5H, Ar-H), 7.81 (*d*, 1H, *J* = 8.4 Hz, 10-H), 7.93 (*d*, 1H, *J* = 7.6 Hz, 7-H), 8.07 (*m*, 2H, Ar-H), 8.26 (*d*, 1H, *J* = 8.0 Hz, 4-H), 9.17 (*br s*, 1H, 1-H), 12.09 (*s*, 1H, NH).  $^{13}\text{C}$ -NMR (100 MHz,  $\text{DMSO}-d_6$ )  $\delta$  34.20 (2C), 48.00 (2C), 65.71, 120.88, 122.53, 125.39, 125.76, 126.52, 126.94, 127.45, 127.98, 128.11, 128.27 (2C), 128.55, 128.69 (2C), 129.34, 131.48, 132.25, 133.05, 139.60,

140.64, 147.26, 157.17. Anal. calcd. for  $C_{28}H_{24}N_4O_2 \cdot 0.6H_2O$ : C 73.22, H 5.53, N 12.20; found: C 73.09, H 5.43, N 12.21.

### 3.2.20. (*E*)-*N'*-[6-(4-Hydroxypiperidin-1-yl)-11*H*-indeno[1,2-*c*]quinolin-11-ylidene]isonicotino Hydrazide (**12**)

Compound **12** was prepared from **3d** and isonicotinic acid hydride by the same procedure as described for the preparation of **11**. Yield: 65%. m.p.: 282–283 °C. IR (KBr,  $cm^{-1}$ ): 3365, 2948, 1649.  $^1H$ -NMR (400 MHz,  $DMSO-d_6$ )  $\delta$  1.68–1.77 (*m*, 2H, piperidiny-H), 1.99–2.01 (*m*, 2H, piperidiny-H), 3.02 (*br s*, 2H, piperidiny-H), 3.57–3.59 (*m*, 2H, piperidiny-H), 3.75 (*br s*, 1H, piperidiny-H), 4.84 (*br s*, 1H, -OH), 7.47–7.51 (*m*, 2H, 8-, 9-H), 7.61–7.65 (*m*, 2H, 2-, 3-H), 7.80 (*d*, 1H,  $J = 8.4$  Hz, 10-H), 7.90–7.95 (*m*, 3H, Ar-H), 8.27 (*d*, 1H,  $J = 7.2$  Hz, 4-H), 8.86 (*d*, 2H,  $J = 5.6$  Hz, pyridiny-H), 9.21 (*br s*, 1H, 1-H), 12.30 (*s*, 1H, NH).  $^{13}C$ -NMR (100 MHz,  $DMSO-d_6$ )  $\delta$  34.17 (2C), 48.05 (2C), 65.54, 120.79, 122.00 (2C), 122.57, 125.18, 125.80, 126.75, 127.74, 128.00, 128.15, 128.41, 129.39, 131.77, 139.76, 140.47, 147.29, 150.39 (2C), 157.14. Anal. calcd. for  $C_{27}H_{23}N_5O_2 \cdot 1.8H_2O$ : C 67.29, H 5.56, N 14.53; found: C 67.14, H 5.57, N 14.40.

### 3.3. Anti-*Mycobacterium* Activity

Primary screening is conducted against *M. tuberculosis* H<sub>37</sub>Rv (ATCC 27294) in BACTEC 12B medium (BD Microbiology Systems, Franklin Lakes, NJ, USA) using a broth microdilution assay to determine the actual minimum inhibitory concentration (MIC) using the Microplate Alamar Blue Assay (MABA) [37]. The MIC is defined as the lowest concentration effecting a reduction in fluorescence of 90% relative to controls. Vero cell (normal cell) viability is assessed on the basis of cellular conversion of 3-(4,5-dimethylthiazol-2-yl)-2,5-diphenyltetrazolium bromide (MTT), into a formazan product using the Promega Cell Titer 96 Non-radioactive Cell Proliferation Assay (Promega, Madison, WI, USA).

### 3.4. Superoxide Generation and Elastase Release

Superoxide generation and elastase release were carried out according to the procedures described previously [38]. Neutrophils ( $6 \times 10^5/mL$ ) were equilibrated at 37 °C for 2 min and incubated with compounds for 5 min. Neutrophils were then activated by fMLF (100 nM) in the pretreatment of cytochalasin B (1  $\mu g/mL$  for superoxide generation and 0.5  $\mu g/mL$  for elastase release) for 10 min. Superoxide anion production was assayed by monitoring the superoxide dismutase-inhibitable reduction of ferricytochrome C. Elastase release was performed using MeO-Suc-Ala-Ala-Pro-Valp-nitroanilide as the elastase substrate.

### 3.5. Quantitative Structure–Activity Relationship (QSAR)

Structure features of 1648 1D and 2D descriptors and PubChem fingerprints for chemicals were firstly generated by using the PaDEL-Descriptor [39] software (<http://padel.nus.edu.sg/software/padeldescriptor>). The calculations are mainly based on the Chemistry Development Kit [40] with some additional descriptors and fingerprints including atom-type electrotopological state descriptors, McGowan volume, molecular linear free energy relation descriptors, ring counts, count of chemical substructures, binary fingerprints and count of chemical substructures. It has been extensively utilized in many QSAR studies such as non-genotoxic hepatotoxicity prediction [41] and inhibitor design [42]. Sequential feature selection algorithms developed by our group were subsequently applied to simultaneously identify important features and build multiple [30,31] regression models. For each run, the descriptor with highest  $R^2$  performance was iteratively appended into the multiple regression model. To avoid overfitting problems, only descriptors with a maximum correlation coefficient to selected descriptors ranging from −0.5 to 0.5 were considered. Due to the small number of chemicals, only the best three descriptors were considered. The descriptor set with the highest  $R^2$  performance is utilized to construct the final multiple regression model for QSAR analysis. The measurements of  $R^2$ ,

$R_{adj}^2$ , root-mean-squared error (RMSE), and leave-one-out cross-validated  $Q^2$  were applied to evaluate the performance of the QSAR model.

#### 4. Conclusions

We have synthesized certain indeno[1,2-*c*]quinoline derivatives for anti-TB and anti-inflammatory evaluations. Among them, (*E*)-*N'*-[6-(4-hydroxypiperidin-1-yl)-11*H*-indeno[1,2-*c*]quinolin-11-ylidene]-isonicotinohydrazide (**12**), exhibited significant activities against the growth of *M. tuberculosis* (MIC values of 0.96 µg/mL) with a potency approximately equal to that of INH. Compound **12** has also demonstrated a potent dual inhibitory effect on NE release and superoxide anion generation with IC<sub>50</sub> values of 1.76 and 1.72 µM, respectively. These results indicated that compound **12** is a potential lead compound for the discovery of dual anti-TB and anti-inflammatory drug candidates. In addition, 6-[3-(hydroxymethyl)piperidin-1-yl]-9-methoxy-11*H*-indeno[1,2-*c*]quinolin-11-one (**4g**) showed a potent dual inhibitory effect on NE release and superoxide anion generation with IC<sub>50</sub> value of 0.46 and 0.68 µM respectively, and is a potential lead compound for the discovery of anti-inflammatory drug candidates. Further studies on the structural optimization and the molecular pharmacological mechanism of compounds **12** and **4g** are ongoing.

**Acknowledgments:** Financial support of this work by the *Minister of Science and Technology of the Republic of China* (MOST 105-2320-B-037-007, MOST 105-2320-B-037-011, MOST 104-2320-B255-004-MY3, MOST 103-2320-B-037-011-MY3) and Kaohsiung Medical University (KMU-TP104E16, KMU-TP104E42, KMU-TP104H07, KMU-TP104H08, KMU-TP105E16, KMU-TP105E33, KMU-TP105H07, KMU-TP105H08, 105KMUOR02) are gratefully acknowledged. We also thank Center for Research Resources and Development at Kaohsiung Medical University for the instrumentation and equipment support.

**Author Contributions:** Chih-Hua Tseng participated in synthesis, purification and characterization of the chemical compounds; Chun-Wei Tung participated in quantitative structure-activity relationship (QSAR) analysis; Chen-Hsin Wu and Cherng-Chyi Tzeng participated in synthesis, the interpretation of the results and in manuscript writing; Yen-Hsu Chen and Tsong-Long Hwang participated in the biological activity, the interpretation of the results and in manuscript writing; Yeh-Long Chen suggested the research idea, participated in the interpretation of the results and in manuscript writing.

**Conflicts of Interest:** The authors declare no conflict of interest.

#### References

1. Scott, H.M.; Flynn, J.L. Mycobacterium tuberculosis in chemokine receptor 2-deficient mice: Influence of dose on disease progression. *Infect. Immun.* **2002**, *70*, 5946–5954. [[CrossRef](#)] [[PubMed](#)]
2. Peters, W.; Scott, H.M.; Chambers, H.F.; Flynn, J.L.; Charo, I.F.; Ernst, J.D. Chemokine receptor 2 serves an early and essential role in resistance to *Mycobacterium tuberculosis*. *Proc. Natl. Acad. Sci. USA* **2001**, *98*, 7958–7963. [[CrossRef](#)] [[PubMed](#)]
3. O'Garra, A.; Redford, P.S.; McNab, F.W.; Bloom, C.I.; Wilkinson, R.J.; Berry, M.P.R. The immune response in tuberculosis. *Annu. Rev. Immunol.* **2013**, *31*, 475–527. [[CrossRef](#)] [[PubMed](#)]
4. Dooley, D.P.; Carpenter, J.L.; Rademacher, S. Adjunctive corticosteroid therapy for tuberculosis: A critical reappraisal of the literature. *Clin. Infect. Dis.* **1997**, *25*, 872–887. [[CrossRef](#)] [[PubMed](#)]
5. Worthington, R.J.; Melander, C. Combination approaches to combat multi-drug-resistant bacteria. *Trends Biotechnol.* **2013**, *31*, 177–184. [[CrossRef](#)] [[PubMed](#)]
6. Wallis, R.S.; Maeurer, M.; Mwaba, P.; Chakaya, J.; Rustonjee, R.; Migliori, G.B.; Marais, B.; Schito, M.; Churchyard, G.; Swaminathan, S.; et al. Tuberculosis—Advances in development of new drugs, treatment regimens, host-directed therapies, and biomarkers. *Lancet Infect. Dis.* **2016**, *16*, e34–e46. [[CrossRef](#)]
7. Rayasam, G.V.; Balganes, T.S. Exploring the potential of adjunct therapy in tuberculosis. *Trends Pharmacol. Sci.* **2015**, *36*, 506–513. [[CrossRef](#)] [[PubMed](#)]
8. Cholo, M.C.; Steel, H.C.; Fourie, P.B.; Germishuizen, W.A.; Anderson, R. Clofazimine: Current status and future prospects. *J. Antimicrob. Chemother.* **2012**, *67*, 290–298. [[CrossRef](#)] [[PubMed](#)]
9. Van Heeswijk, R.P.G.; Dannemann, B.; Hoetelmans, R.M.W. Bedaquiline: A review of human pharmacokinetics and drug–drug interactions. *J. Antimicrob. Chemother.* **2014**, *69*, 2310–2318. [[CrossRef](#)] [[PubMed](#)]



10. Upadhayaya, R.S.; Shinde, P.D.; Sayyed, A.Y.; Kadam, S.A.; Bawane, A.N.; Poddar, A.; Plashkevych, O.; Földesi, A.; Chattopadhyaya, J. Synthesis and structure of azole-fused indeno[2,1-c]quinolines and their anti-mycobacterial properties. *Org. Biomol. Chem.* **2010**, *8*, 5661–5673. [[CrossRef](#)] [[PubMed](#)]
11. Upadhayaya, R.S.; Lahore, S.V.; Sayyed, A.Y.; Dixit, S.S.; Shinde, P.D.; Chattopadhyaya, J. Conformationally-constrained indeno[2,1-c]quinolones—A new class of anti-mycobacterial agents. *Org. Biomol. Chem.* **2010**, *8*, 2180–2197. [[CrossRef](#)] [[PubMed](#)]
12. Upadhayaya, R.S.; Shinde, P.D.; Kadam, S.A.; Bawane, A.N.; Sayyed, A.Y.; Kardile, R.A.; Gitay, P.N.; Lahore, S.V.; Dixit, S.S.; Földesi, A.; et al. Synthesis and antimycobacterial activity of prodrugs of indeno[2,1-c]quinoline derivatives. *Eur. J. Med. Chem.* **2011**, *46*, 1306–1324. [[CrossRef](#)] [[PubMed](#)]
13. Sheu, J.Y.; Chen, Y.L.; Fang, K.C.; Wang, T.C.; Tzeng, C.C.; Peng, C.F. Synthesis and antibacterial activity of 1-(substituted-benzyl)-6-fluoro-1,4-dihydro-4-oxoquinoline-3-carboxylic acids and their 6,8-difluoro analogs. *J. Heterocycl. Chem.* **1998**, *35*, 955–964. [[CrossRef](#)]
14. Sheu, J.Y.; Chen, Y.L.; Tzeng, C.C.; Hsu, S.L.; Fang, K.C.; Wang, T.C. Synthesis, and antimycobacterial and cytotoxic evaluation of certain fluoroquinolone derivatives. *Helv. Chim. Acta* **2003**, *86*, 2481–2489. [[CrossRef](#)]
15. Zhao, Y.L.; Chen, Y.L.; Sheu, J.Y.; Chen, I.L.; Wang, T.C.; Tzeng, C.C. Synthesis and antimycobacterial evaluation of certain fluoroquinolone derivatives. *Bioorg. Med. Chem.* **2005**, *13*, 3921–3926. [[CrossRef](#)] [[PubMed](#)]
16. Chen, Y.L.; Huang, H.Y.; Chen, Y.W.; Huang, Z.Y.; Tzeng, C.C.; Liu, C.L.; Yao, C.W. Synthesis and antimycobacterial evaluation of metal-chelator bearing fluoroquinolones. *Chin. Pharm. J.* **2005**, *57*, 57–70.
17. Yang, C.L.; Tseng, C.H.; Chen, Y.L.; Lu, C.M.; Kao, C.L.; Tseng, H.Y.; Wu, M.H.; Tzeng, C.C. Identification of benzofuro[2,3-b]quinoline derivatives as a new class of antituberculosis agents. *Eur. J. Med. Chem.* **2010**, *45*, 602–607. [[CrossRef](#)] [[PubMed](#)]
18. Chen, Y.L.; Lu, C.M.; Chen, I.L.; Tsao, L.T.; Wang, J.P. Synthesis and antiinflammatory evaluation of 9-anilinoacridine and 9-phenoxyacridine derivatives. *J. Med. Chem.* **2002**, *45*, 4689–4694. [[CrossRef](#)] [[PubMed](#)]
19. Chen, Y.L.; Chen, I.L.; Lu, C.M.; Tzeng, C.C.; Tsao, L.T.; Wang, J.P. Synthesis and anti-inflammatory evaluation of 9-phenoxyacridine and 4-phenoxyfuro[2,3-b]quinoline derivatives. Part 2. *Bioorg. Med. Chem.* **2003**, *11*, 3921–3927. [[CrossRef](#)]
20. Chen, Y.L.; Chen, I.L.; Lu, C.M.; Tzeng, C.C.; Tsao, L.T.; Wang, J.P. Synthesis and anti-inflammatory evaluation of 4-anilino-furo[2,3-b]quinoline and 4-phenoxyfuro[2,3-b]quinoline derivatives. Part 3. *Bioorg. Med. Chem.* **2004**, *12*, 387–392. [[CrossRef](#)] [[PubMed](#)]
21. Kuan, Y.H.; Lin, R.H.; Chen, Y.L.; Tsao, L.T.; Tzeng, C.C.; Wang, J.P. Effective attenuation of acute lung injury in vivo and the formyl peptide-induced neutrophil activation in vitro by CYL-26z through the phosphoinositide 3-kinase gamma pathway. *Biochem. Pharmacol.* **2006**, *72*, 749–760. [[CrossRef](#)] [[PubMed](#)]
22. Chen, Y.L.; Zhao, Y.L.; Lu, C.M.; Tzeng, C.C.; Wang, J.P. Synthesis, cytotoxicity, and anti-inflammatory evaluation of 2-(furan-2-yl)-4-(phenoxy)quinoline derivatives, Part 4. *Bioorg. Med. Chem.* **2006**, *14*, 4373–4378. [[CrossRef](#)] [[PubMed](#)]
23. Lin, M.W.; Tsao, L.T.; Chang, L.C.; Chen, Y.L.; Huang, L.J.; Kuo, S.C.; Tzeng, C.C.; Lee, M.R.; Wang, J.P. Inhibition of lipopolysaccharide-stimulated NO production by a novel synthetic compound CYL-4d in RAW 264.7 macrophages involving the blockade of MEK4/JNK/AP-1 pathway. *Biochem. Pharmacol.* **2007**, *73*, 1796–1806. [[CrossRef](#)] [[PubMed](#)]
24. Tseng, C.H.; Lin, C.S.; Shih, P.K.; Tsao, L.T.; Wang, J.P.; Cheng, C.M.; Tzeng, C.C.; Chen, Y.L. Furo[3, 2:3,4]naphtho[1,2-d]imidazole derivatives as potential inhibitors of inflammatory factors in sepsis. *Bioorg. Med. Chem.* **2009**, *17*, 6773–6779. [[CrossRef](#)] [[PubMed](#)]
25. Tseng, C.H.; Tzeng, C.C.; Shih, P.K.; Yang, C.N.; Chuang, Y.C.; Peng, S.I.; Lin, C.S.; Wang, J.P.; Cheng, C.M.; Chen, Y.L. Identification of furo[3',2':3,4]naphtho[1,2-d]imidazole derivatives as orally active and selective inhibitors of microsomal prostaglandin E(2) synthase-1 (mPGES-1). *Mol. Divers.* **2012**, *16*, 215–229. [[CrossRef](#)] [[PubMed](#)]
26. Tsai, Y.R.; Huang, L.J.; Lee, M.R.; Chen, Y.L.; Kuo, S.C.; Tzeng, C.C.; Hsu, M.F.; Wang, J.P. The signaling mechanisms mediating the inhibitory effect of TCH-1116 on formyl peptide-stimulated superoxide anion generation in neutrophils. *Eur. J. Pharm.* **2012**, *682*, 171–180. [[CrossRef](#)] [[PubMed](#)]
27. Tseng, C.H.; Cheng, C.M.; Tzeng, C.C.; Peng, S.I.; Yang, C.L.; Chen, Y.L. Synthesis and anti-inflammatory evaluations of  $\alpha$ -lapachone derivatives. *Bioorg. Med. Chem.* **2013**, *21*, 523–531. [[CrossRef](#)] [[PubMed](#)]

28. Chen, Y.R.; Tseng, C.H.; Chen, Y.L.; Hwang, T.L.; Tzeng, C.C. Discovery of benzo[f]indole-4,9-dione derivatives as new type of anti-inflammatory agents. *Int. J. Mol. Sci.* **2015**, *16*, 6532–6544. [[CrossRef](#)] [[PubMed](#)]
29. Tseng, C.H.; Chen, Y.L.; Lu, P.J.; Yang, C.N.; Tzeng, C.C. Synthesis and antiproliferative evaluation of certain indeno[1,2-c]quinoline derivatives. *Bioorg. Med. Chem.* **2008**, *16*, 3153–3162. [[CrossRef](#)] [[PubMed](#)]
30. Tung, C.W. Prediction of pupylation sites using the composition of k-spaced amino acid pairs. *J. Theor. Biol.* **2013**, *336*, 11–17. [[CrossRef](#)] [[PubMed](#)]
31. Tung, C.W.; Wu, M.T.; Chen, Y.K.; Wu, C.C.; Chen, W.C.; Li, H.P.; Chou, S.H.; Wu, D.C.; Wu, I.C. Identification of biomarkers for esophageal squamous cell carcinoma using feature selection and decision tree methods. *Sci. World J.* **2013**, *2013*, 782031. [[CrossRef](#)] [[PubMed](#)]
32. Kier, L.B.; Hall, L.H. *Molecular Connectivity in Chemistry and Drug Research*; Academic Press: New York, NY, USA, 1976.
33. Wildman, S.A.; Crippen, G.M. Prediction of physicochemical parameters by atomic contributions. *J. Chem. Inf. Comput. Sci.* **1999**, *39*, 868–873. [[CrossRef](#)]
34. Gramatica, P.; Corradi, M.; Consonni, V. Modelling and prediction of soil sorption coefficients of non-ionic organic pesticides by molecular descriptors. *Chemosphere* **2000**, *41*, 763–777. [[CrossRef](#)]
35. Hall, L.H.; Kier, L.B. Electrotopological state indices for atom types: A novel combination of electronic, topological, and valence state information. *J. Chem. Inf. Comput. Sci.* **1995**, *35*, 1039–1045. [[CrossRef](#)]
36. Liu, R.; Sun, H.; So, S.S. Development of quantitative structure—Property relationship models for early ADME evaluation in drug discovery. 2. Blood-brain barrier penetration. *J. Chem. Inf. Comput. Sci.* **2001**, *41*, 1623–1632. [[CrossRef](#)] [[PubMed](#)]
37. Collins, L.; Franzblau, S.G. Microplate alamar blue assay versus BACTEC 460 system for high-throughput screening of compounds against *Mycobacterium tuberculosis* and *Mycobacterium avium*. *Antimicrob. Agents Chemother.* **1997**, *41*, 1004–1009. [[PubMed](#)]
38. Hwang, T.L.; Li, G.L.; Lan, Y.H.; Chia, Y.C.; Hsieh, P.W.; Wu, Y.H.; Wu, Y.C. Potent inhibition of superoxide anion production in activated human neutrophils by isopedicin, a bioactive component of the chinese medicinal herb *Fissistigma oldhamii*. *Free Radic. Biol. Med.* **2009**, *46*, 520–528. [[CrossRef](#)] [[PubMed](#)]
39. Yap, C.W. PaDEL-descriptor: An open source software to calculate molecular descriptors and fingerprints. *J. Comput. Chem.* **2011**, *32*, 1466–1474. [[CrossRef](#)] [[PubMed](#)]
40. Steinbeck, C.; Han, Y.; Kuhn, S.; Horlacher, O.; Luttmann, E.; Willighage, E. The Chemistry Development Kit (CDK): An open-source Java library for Chemo- and Bioinformatics. *J. Chem. Inf. Comput. Sci.* **2003**, *43*, 493–500. [[CrossRef](#)] [[PubMed](#)]
41. Tung, C.W.; Jheng, J.L. Interpretable prediction of non-genotoxic hepatocarcinogenic chemicals. *Neurocomputing* **2014**, *145*, 68–74. [[CrossRef](#)]
42. Chauhan, J.S.; Dhanda, S.K.; Singla, D.; The Open Source Drug Discovery; Agarwal, S.M.; Raghava, G.P.S. QSAR-based models for designing quinazoline/imidazothiazoles/pyrazolopyrimidines based inhibitors against wild and mutant EGFR. *PLoS ONE* **2014**, *9*, e101079. [[CrossRef](#)] [[PubMed](#)]

**Sample Availability:** Samples of the compounds reported herein are available from the authors.



© 2017 by the authors. Licensee MDPI, Basel, Switzerland. This article is an open access article distributed under the terms and conditions of the Creative Commons Attribution (CC BY) license (<http://creativecommons.org/licenses/by/4.0/>).

## Article

# Anti-Inflammatory and Neuroprotective Constituents from the Peels of *Citrus grandis*

Ping-Chung Kuo <sup>1,†</sup>, Yu-Ren Liao <sup>1,†</sup>, Hsin-Yi Hung <sup>1,†</sup>, Chia-Wei Chuang <sup>2</sup>,  
Tsong-Long Hwang <sup>3,4,5</sup>, Shiow-Chyn Huang <sup>6</sup>, Young-Ji Shiao <sup>7</sup>, Daih-Huang Kuo <sup>8</sup> and  
Tian-Shung Wu <sup>1,8,\*</sup>

<sup>1</sup> School of Pharmacy, College of Medicine, National Cheng Kung University, Tainan 701, Taiwan; z10502016@email.ncku.edu.tw (P.-C.K.); truthloveroy@yahoo.com.tw (Y.-R.L.); z10308005@email.ncku.edu.tw (H.-Y.H.)

<sup>2</sup> Department of Chemistry, National Cheng Kung University, Tainan 701, Taiwan; w96s062001@hotmail.com

<sup>3</sup> Graduate Institute of Natural Products, College of Medicine, Chang Gung University, Taoyuan 333, Taiwan; htl@mail.cgu.edu.tw

<sup>4</sup> Research Center for Chinese Herbal Medicine, Research Center for Food and Cosmetic Safety, and Graduate Institute of Health Industry Technology, College of Human Ecology, Chang Gung University of Science and Technology, Taoyuan 333, Taiwan

<sup>5</sup> Department of Anesthesiology, Chang Gung Memorial Hospital, Taoyuan 333, Taiwan

<sup>6</sup> Department of Pharmacy, Chia-Nan University of Pharmacy and Science, Tainan 717, Taiwan; schuang@mail.cnu.edu.tw

<sup>7</sup> Division of Basic Chinese Medicine, National Research Institute of Chinese Medicine, Ministry of Health and Welfare, Taipei 112, Taiwan; yshiao@nricm.edu.tw

<sup>8</sup> Department of Pharmacy, College of Pharmacy and Health Care, Tajen University, Pingtung 907, Taiwan; dhkou@tajen.edu.tw

\* Correspondence: tswu@mail.ncku.edu.tw; Tel.: +886-6274-7538

† These authors contributed equally to this work.

Academic Editor: Thomas J. Schmidt

Received: 19 April 2017; Accepted: 8 June 2017; Published: 9 June 2017

**Abstract:** A series of chromatographic separations performed on the ethanol extracts of the peels of *Citrus grandis* has led to the characterization of forty compounds, including seventeen coumarins, eight flavonoids, two triterpenoids, four benzenoids, two steroids, one lignan, one amide, and five other compounds, respectively. The chemical structures of the purified constituents were identified on the basis of spectroscopic elucidation, including 1D- and 2D-NMR, UV, IR, and mass spectrometric analysis. Most of the isolated compounds were examined for their inhibition of superoxide anion generation and elastase release by human neutrophils. Among the isolates, isomeranzin (**3**), 17,18-dihydroxybergamottin (**12**), epoxybergamottin (**13**), rhoifolin (**19**), vitexicarpin (**22**) and 4-hydroxybenzaldehyde (**29**) displayed the most significant inhibition of superoxide anion generation and elastase release with IC<sub>50</sub> values ranged from 0.54 to 7.57  $\mu$ M, and 0.43 to 4.33  $\mu$ M, respectively. In addition, 7-hydroxy-8-(2'-hydroxy-3'-methylbut-3'-enyl)coumarin (**8**) and 17,18-dihydroxybergamottin (**12**) also exhibited the protection of neurons against A $\beta$ -mediated neurotoxicity at 50  $\mu$ M.

**Keywords:** *Citrus grandis*; chromatographic method; spectroscopic elucidation; superoxide anion generation; elastase release; neuroprotective

## 1. Introduction

The genus *Citrus* is composed of various species grown all over the tropical and subtropical regions. Each species has its own characteristic aroma and some *Citrus* peel oils have been used

in a variety of products such as foods, beverages and perfumes [1]. A lot of scientific reports have been published regarding the compositions and significant bioactivity of the *Citrus* peels. *C. grandis* belongs to the family Rutaceae, which is cultivated throughout Taiwan, Indochina, and Southern China [2–11]. The peels of mature fruits of *C. grandis* have been used in traditional Chinese medicine for treating the common cold and cancer, and relieving exhaustion [12]. Many natural products such as flavonoids, coumarins, and terpenoids have been isolated from *C. grandis* [2–11]. Among these, various principles have been reported to exhibit antioxidant [13–16], anti-inflammatory [16–20], anti-microbial [21–24], and anti-cancer effects [25–28]. In addition, several compounds were subjected to the study related to the prevention of vascular diseases [29–32]. The constituents of the peels of *C. grandis* were found to be rich in coumarins and flavonoids. The substitution of multi-methoxyl group of flavonoids, polymethoxyflavones (PMFs) were found to be rich in *Citrus* which have been reported to exhibit antioxidant because of the delocalized electrons [33]. That is why the *Citrus* genus is an important food source for people, and it was also an important Chinese medicine from ancient times. In a previous study [34], *Citrus* flavonoids were reported to exhibit anti-inflammatory and neuroprotective bioactivities. Therefore, in the present study we wish to explore other bioactive principles of peels of *C. grandis*.

## 2. Results and Discussion

The dried peels of *C. grandis* were extracted with EtOH and the resulting extract was then filtered and concentrated. The EtOH extracts were suspended in distilled water and successively partitioned with EtOAc to afford EtOAc layer and water layer, respectively. A sequential combination of conventional chromatographic techniques was utilized to isolate the constituents described below. Totally 40 known compounds were isolated and identified, including seventeen coumarins (7-geranyloxy coumarin (1) [35], osthenol (2) [36], isomeranzin (3) [37], marmin (4) [37], epoxyaurapten (5) [38], meranzin hydrate (6) [39], hopeyhopin (7) [40], 7-hydroxy-8- (2'-hydroxy-3'-methylbut-3'-enyl) coumarin (8) [37], isoimperatorin (9) [41], bergamottin (10) [42], bergaptol (11) [43], 17,18-dihydroxybergamottin (12) [44], epoxybergamottin (13) [45], auraptenol (14) [39], columbianetin (15) [36], yuehgesin-C (16) [46], bergomottin (17) [47]); eight flavonoids (naringin (18) [48], rhoifolin (19) [49], naringenin 7-rutinoside (20) [50], melitidin (21) [51], vitexicarpin (22) [52], chrysosplins (23) [53], 5-hydroxy-3,6,7,3',4'-pentamethoxyflavone (24) [54], rubranonoside (25) [55]); two triterpenoids, friedelin (26) [56] and limonin (27) [48]; four benzenoids (eleutheroside B (28) [57], 4-hydroxy-benzaldehyde (29) [58], phlorin (30) [59], methyl 4-hydroxybenzoate (31) [58]); two steroids ( $\beta$ -sitosterol (32) [58], and  $\beta$ -sitosterol-3-O- $\beta$ -D-glucopyranoside (33) [58]); one lignan, syringaresinol (34) [60]; one amide, 2-hydroxybenzoic acid *N*-2-(4-hydroxyphenyl)ethylamide (35) [61]; and five others compounds (octadecatrienoic acid (36) [62], *myo*-inositol (37) [63], *scyllo*-inositol (38) [63], 1-methoxy- $\beta$ -carboline (39) [64], and adenosine (40) [65]), respectively. These compounds were subjected to spectroscopic elucidation, including UV, IR, 1D- and 2D-NMR data, along with the mass spectrometric analysis and their structures were identified by comparison of their physical and spectroscopic data with values reported in the literature.

Most of the purified compounds were examined for their inhibition of superoxide anion generation and elastase release by human neutrophils in response to *N*-formyl-L-methionyl-phenylalanine/cytochalasin B (fMLP/CB) [66,67]. Only compounds 3, 12, 13, 19, 22, and 29 (Figure 1) displayed inhibition percentages greater than 50% at the test concentration of 10  $\mu$ M and in the concentration range used these compounds displayed inhibitory effects in a dose-dependent manner. Compounds 3, 12, 13, 19, 22, and 29 all displayed inhibition of superoxide anion generation with IC<sub>50</sub> values ranging from  $0.54 \pm 0.24$  to  $7.57 \pm 3.19$   $\mu$ M, compared to the reference compound sorafenib [66] (IC<sub>50</sub> values of  $1.49 \pm 0.42$   $\mu$ M, Table 1). In addition, compounds 3, 13, and 29 also exhibited inhibitory effects on elastase release, with IC<sub>50</sub> values ranging from  $0.43 \pm 0.09$  to  $4.33 \pm 0.83$   $\mu$ M, compared to the reference compound sorafenib [66] (IC<sub>50</sub> values of  $0.93 \pm 0.10$   $\mu$ M, Table 1).

In the primary screening of the neuroprotective activity of the isolated compounds, 50  $\mu\text{M}$  of the compound was used. Alternatively, 10  $\mu\text{M}$  of the compound was used as this compound possessed neurotoxicity at 20  $\mu\text{M}$  (Figure 2A) [68]. The results showed that 7-hydroxy-8-(2'-hydroxy-3'-methylbut-3'-enyl)coumarin (**8**) and 17,18-dihydroxybergamottin (**12**) (Figure 1) protected neurons against  $\text{A}\beta$ -mediated neurotoxicity. The concentration dependency of neurons protection was further examined for compounds **8** and **12** and the experimental results displayed a dose-dependent manner as shown in Figure 2B,C.

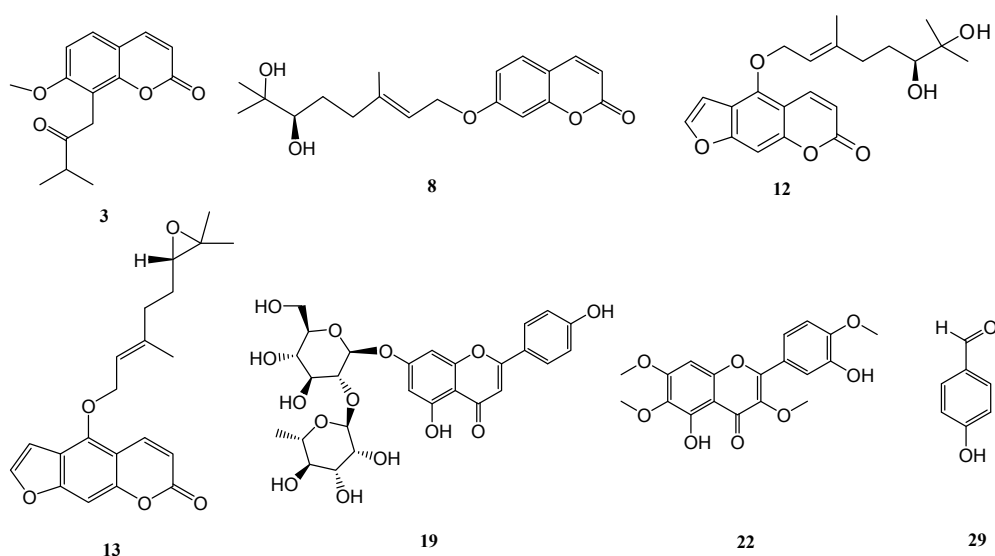


Figure 1. Structures of compounds **3**, **8**, **12**, **13**, **19**, **22**, and **29**.

Table 1. Inhibitory effects of isolated compounds on superoxide anion generation and elastase release by human neutrophils in response to fMLP/CB.

Compound	Superoxide Anion Generation	Elastase Release
	IC <sub>50</sub> ( $\mu\text{M}$ ) <sup>a</sup>	IC <sub>50</sub> ( $\mu\text{M}$ ) <sup>a</sup>
<b>3</b>	3.89 $\pm$ 0.45 ***	4.33 $\pm$ 0.83 ***
<b>12</b>	6.02 $\pm$ 2.46 ***	>10
<b>13</b>	7.57 $\pm$ 3.19 ***	3.58 $\pm$ 1.90 ***
<b>19</b>	3.79 $\pm$ 0.42 ***	>10
<b>22</b>	5.95 $\pm$ 1.56 ***	>10
<b>29</b>	0.54 $\pm$ 0.24 ***	0.43 $\pm$ 0.09 ***
Sorafenib <sup>b</sup>	1.49 $\pm$ 0.42	0.93 $\pm$ 0.10

<sup>a</sup> Concentration necessary for 50% inhibition (IC<sub>50</sub>). Results are presented as means  $\pm$  SD. ( $n = 3\sim 5$ ). \*\*\*  $p < 0.001$  compared with the control value. <sup>b</sup> Sorafenib, a tyrosine kinase inhibitor, was used as a positive control.

The present experimental data suggest that the extracts and purified compounds of the peel of *C. grandis* have the potential to be developed as novel anti-inflammatory lead drugs or health foods. In addition, some purified constituents also exhibited the protection of neurons against  $\text{A}\beta$ -mediated neurotoxicity. It merits further investigations of the anti-inflammatory and neuroprotective mechanism of these natural heterocyclic compounds.



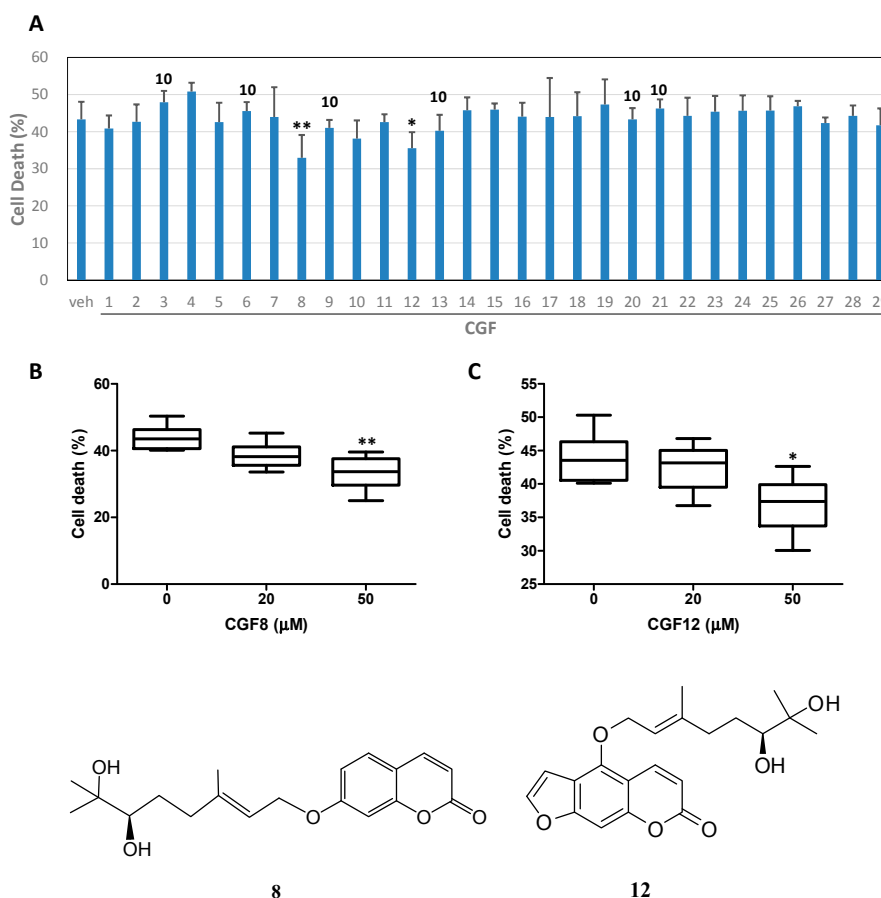


**Figure 2.** Compounds **8** and **12** protect cortical neurons against A $\beta$ -(25–35)-mediated neurotoxicity. Cortical neurons were pretreated with 50  $\mu$ M of compounds (or 10  $\mu$ M for those indicated as 10 above column). (A), or various concentration of compounds **8** (B) and **12** (C) for 2 h and then exposed to 10  $\mu$ M of A $\beta$ -(25–35) for 40 h. Cell viability was measured by MTT reduction assay. Results are means  $\pm$  S.D. from six independent experiments and expressed relative to control and plotted as box plot for showing the normal distribution. Significant differences between cells treated with A $\beta$ -(25–35) plus vehicle (veh) and A $\beta$ -(25–35) plus compounds are indicated by \*,  $p < 0.05$ ; \*\*,  $p < 0.01$ .

### 3. Materials and Methods

#### 3.1. General Information

Melting points were determined using an MP-S3 apparatus (Yanaco, Tokyo, Japan). UV spectra were recorded at room temperature on a U-0080-D spectrophotometer (Hitachi, Tokyo, Japan). IR spectra were obtained with a FT-IR Spectrum RX I spectrophotometer (PerkinElmer, Waltham, MA, USA). Optical rotations were measured using a P-2000 digital polarimeter (JASCO, Tokyo, Japan).  $^1\text{H}$ - and  $^{13}\text{C}$ -NMR spectra were recorded on Avance III HD 700 and Avance III 400 NMR spectrometers (Bruker, Billerica, MA, USA). Chemical shifts are shown in  $\delta$  values (ppm) with tetramethylsilane as an internal standard. The ESIMS and HRESIMS were taken on a Bruker Daltonics APEX II 30e spectrometer (positive-ion mode). Column chromatography (CC) was performed on silica (70–230 mesh and 230–400 mesh, Merck, Darmstadt, Germany), Diaion HP-20 (Mitsubishi, Tokyo, Japan), and C $_{18}$  (Sigma-Aldrich, St. Louis, MO, USA) gels, respectively, and preparative TLC (thin-layer chromatography) was conducted on Merck precoated silica gel 60 F254 plates, using UV light to visualize the spots. High-performance liquid chromatography (HPLC) was performed on an LC-20AT series pumping system (Shimadzu, Kyoto, Japan) equipped with a Shimadzu SPD-20A UV-vis detector, and a SIL-10AF auto-sampling system at ambient temperature.

### 3.2. Materials

The peels of *C. grandis* were bought from the market in Tainan, Taiwan in 2010 and identified by Prof. Chang-Sheng Kuoh, Department of Life Science, National Cheng Kung University (NCKU), Tainan, Taiwan. A voucher specimen (Wu-2010009) was stored in School of Pharmacy, NCKU.

### 3.3. Extraction and Isolation

The dried peels of *C. grandis* (1.0 kg) were pre-treated with EtOH for one day at room temperature and then extracted with 95% EtOH five times (10 L  $\times$  5 h) at room temperature. The resulting extract was then filtered and concentrated *in vacuo* to yield a crude extract. The EtOH extract (260 g) was suspended in distilled water and successively partitioned with EtOAc yielding an EtOAc layer (20 g) and water layer (240 g). The EtOAc-soluble fraction was subjected to silica gel CC using a gradient solvent system of *n*-hexane–acetone (8:1, 4:1, 1:1 and MeOH) to afford ten fractions (F1~F10) according to TLC monitoring. Recrystallization of water layer produced the solids *myo*-inositol (**37**) (10.3 mg) and *scyllo*-inositol (**38**) (8.2 mg). The mother liquid of water layer was applied to CC on Diaion HP-20 gel using a gradient of increasing MeOH in H<sub>2</sub>O to yield eight fractions (W1~W8).

Fractions F1 and F2 were combined and isolated by CC on silica gel with a step gradient with *n*-hexane and diisopropyl ether mixtures (11:1, 9:1, 5:1, 2:1, 1:1, 0:1) to afford three subfractions (F1-1~F1-3). F1-2 was further purified by silica gel CC and recrystallization to obtain friedelin (**26**) (10.3 mg). Fractions F3 and F4 were combined and performed silica gel CC with gradient mixtures of *n*-hexane and ethyl acetate to produce five subfractions (F3-1~F3-5). F3-2 was purified by silica gel CC by gradient elution of *n*-hexane and ethyl acetate to afford several additional fractions. Further purification by TLC using *n*-hexane-ethyl acetate (9:1) and recrystallization yielded isoimperatorin (**9**) (16.7 mg) and  $\beta$ -sitosterol (**32**) (265.7 mg). F3-4 was further purified by silica gel CC and recrystallization to obtain bergomottin (**17**) (2.5 mg) and octadecatrienoic acid (**36**) (10.4 mg).

Fraction F5 was subjected to silica gel CC with diisopropyl ether as eluent to afford six subfractions (F5-1~F5-6). F5-2 was purified by silica gel CC eluted by a gradient of *n*-hexane and diisopropyl ether to afford several minor fractions. Further purification by TLC using *n*-hexane and diisopropyl ether (3:1) and recrystallization yielded ostenol (**2**) (2.6 mg), isomeranzin (**3**) (3.2 mg), marmin (**4**) (1.1 mg), and 7-hydroxy-8-(2'-hydroxy-3'-methylbut-3'-enyl)coumarin (**8**) (2.5 mg). Recrystallization of minor fractions of F5-4 produced yuehgesin-C (**16**) (302.2 mg). F5-5 was subjected to silica gel CC eluted with a gradient of *n*-hexane and ethyl acetate to afford three subfractions (F5-5-1~F5-5-3). F5-5-2 was further isolated by silica gel CC, eluted with *n*-hexane-isopropyl ether (2:1) and subsequent preparative TLC using *n*-hexane-acetone (9:1) or recrystallization of the minor fractions to afford epoxybergamottin (**13**) (1.0 mg), columbianetin (**15**) (6.6 mg), and 5-hydroxy-3,6,7,3',4'-pentamethoxyflavone (**24**) (1.3 mg), respectively.

Fraction F7 was purified by silica gel CC eluted by a mixture of chloroform and acetone (9:1) to yield six subfractions (F7-1~F7-6). Recrystallization of subfractions F7-1 to F7-4 produced limonin (**27**) (98.3 mg), bergaptol (**11**) (7.0 mg), 17,18-dihydroxybergamottin (**12**) (22.2 mg), auraptanol (**14**) (13.5 mg), respectively. F7-5 was isolated on silica gel CC by gradient elution with *n*-hexane and acetone to afford several minor fractions. Further purification by TLC using chloroform and acetone (5:1) and recrystallization yielded vitexicarpin (**22**) (6.2 mg) and chrysosplins (**23**) (3.2 mg). Recrystallization of minor fractions of F7-6 produced *N*-[8'-(4'-hydroxyphenylethyl)]-2-hydroxy-benzoylamide (**35**) (4.0 mg).

Fractions F8 and F9 were combined and isolated by silica gel CC using a mixture of diisopropyl ether and ethyl acetate (1:1) to result in three subfractions (F8-1~F8-3). F8-2 was purified by silica gel CC with gradient elution using diisopropyl ether and ethyl acetate to afford several minor fractions. Further purification by TLC using diisopropyl ether and acetone (3:1) and recrystallization yielded meranzin hydrate (**6**) (2.8 mg), methyl 4-hydroxybenzoate (**31**) (2.1 mg), and syringaresinol (**34**) (1.9 mg).

Fractions W2 and W3 were combined and purified using C<sub>18</sub> gel CC eluted with a gradient of H<sub>2</sub>O and MeOH (1:0, 9:1, 5:1, 2:1, 1:1, 0:1) to afford three subfractions (W2-1~W2-3). W2-3 was isolated

by HPLC with an Agilent semi-preparative RP-18 column (21.2 mm × 250 mm) eluted with H<sub>2</sub>O and MeOH (60:40) to afford melitidin (**21**) (42.9 mg) and rubranonoside (**25**) (3.8 mg).

Fraction W4 was subjected to C<sub>18</sub> gel CC eluted with a gradient of H<sub>2</sub>O and MeOH to yield five subfractions (W4-1~W4-5). W4-2 was subjected to HPLC with an Agilent analytical RP-18 column (4.6 mm × 250 mm) eluted with H<sub>2</sub>O and MeOH (55:45) to furnish rhoifolin (**19**) (3.4 mg) and naringenin 7-rutinoside (**20**) (3.0 mg). W4-3 was isolated by C<sub>18</sub> gel CC with gradient mixtures of H<sub>2</sub>O and MeOH to afford several minor fractions. W4-3-2 was purified by HPLC on an Agilent analytical RP-18 column (4.6 mm × 250 mm) eluted with H<sub>2</sub>O and MeOH (70:30) to yield hopeyhopin (**7**) (3.8 mg) and eleutheroside B (**28**) (1.8 mg). Recrystallization of minor fractions of W4-4 resulted in adenosine (**40**) (13.9 mg).

Fractions W5 and W6 were combined and purified using C<sub>18</sub> gel CC eluted with mixtures of H<sub>2</sub>O and MeOH to afford four subfractions (W5-1~W5-4). Recrystallization of subfraction W5-1 produced naringin (**18**) (440.0 mg). W5-2 was isolated by C<sub>18</sub> gel CC with gradient mixtures of H<sub>2</sub>O and MeOH to afford phlorin (**30**) (26.3 mg). W5-3 was purified by HPLC on an Agilent analytical RP-18 column (4.6 mm × 250 mm) eluted with H<sub>2</sub>O and MeOH (65:35) to yield epoxyaurapten (**5**) (1.0 mg) and 1-methoxy- $\beta$ -carboline (**39**) (1.0 mg).

Fraction W7 was subjected to C<sub>18</sub> gel CC with gradient elution using H<sub>2</sub>O and MeOH to provide three subfractions (W7-1~W7-3). Recrystallization of subfractions W7-1 and W7-2 produced  $\beta$ -sitosterol-3-O- $\beta$ -D-glucopyranoside (**33**) (11.6 mg) and 7-geranyloxycoumarin (**1**) (4.0 mg), respectively. Further purification of W7-3 by preparative TLC using chloroform and acetone (5:1) and recrystallization yielded 4-hydroxybenzaldehyde (**29**) (1.9 mg).

### 3.4. Bioactivity Examination

#### 3.4.1. Preparation of Human Neutrophils

A study involving human neutrophils was approved by the Institutional Review Board at Chang Gung Memorial Hospital, Taoyuan, Taiwan, and was conducted according to the Declaration of Helsinki (2013). The written informed consent was obtained from each healthy donor before blood was drawn. Blood was drawn from healthy human donors (20–30 years old) by venipuncture into heparin-coated vacutainer tubes, using a protocol approved by the Institutional Review Board at Chang Gung Memorial Hospital. Blood samples were mixed gently with an equal volume of 3% dextran solution. Neutrophils were isolated with a standard method of dextran sedimentation prior to centrifugation in a Ficoll Hypaque gradient and hypotonic lysis of erythrocytes. The leukocyte-rich plasma was collected after sedimentation of the red cells for 30 min at room temperature, and was transferred to 20 mL Ficoll solution (1.077 g/mL) and spun down at 400 g for 40 min at 20 °C. The granulocyte/erythrocyte pellets were resuspended in ice-cold 0.2% NaCl to lyse erythrocytes. After 30 s, the same volume of 1.6% NaCl solution was added to reconstitute the isotonic condition. Purified neutrophils were pelleted and then resuspended in a calcium (Ca<sup>2+</sup>)-free Hank's balanced salt solution (HBSS) buffer at pH 7.4, and were maintained at 4 °C before use.

#### 3.4.2. Inhibition of Superoxide Anion Generation

The assay of the generation of superoxide anion was based on the SOD-inhibitable reduction of ferricytochrome c [65,66]. In brief, after supplementation with 0.5 mg/mL ferricytochrome c and 1 mM Ca<sup>2+</sup>, neutrophils ( $6 \times 10^5$  cells/mL) were equilibrated at 37 °C for 2 min and incubated with drugs or an equal volume of vehicle (0.1% DMSO, negative control) for 5 min. Cells were activated with 100 nM fMLP during the preincubation of 1  $\mu$ g/mL cytochalasin B (fMLP/CB) for 3 min. Changes in the absorbance with a reduction in ferricytochrome c at 550 nm were continuously monitored in a double-beam, six-cell positioner spectrophotometer with constant stirring (Hitachi U-3010). Calculations were based on differences in the reactions with and without SOD (100 U/mL)

divided by the extinction coefficient for the reduction of ferricytochrome c ( $\epsilon = 21.1/\text{mM}/10\text{ mm}$  at the concentration of 1 mM in cuvette with 1-cm optical path length).

### 3.4.3. Inhibition of Elastase Release

Degranulation of azurophilic granules was determined by elastase release as described previously [65,66]. Experiments were performed using MeO-Suc-Ala-Ala-Pro-Val-*p*-nitroanilide as the elastase substrate. Briefly, after supplementation with MeO-Suc-Ala-Ala-Pro-Val-*p*-nitroanilide (100  $\mu\text{M}$ ), neutrophils ( $6 \times 10^5/\text{mL}$ ) were equilibrated at 37 °C for 2 min and incubated with test compounds or an equal volume of vehicle (0.1% DMSO, negative control) for 5 min. Cells were activated by 100 nM fMLP and 0.5  $\mu\text{g}/\text{mL}$  cytochalasin B, and changes in absorbance at 405 nm were continuously monitored to assay elastase release. The results were expressed as the percent of elastase release in the fMLP/CB-activated, drug-free control system.

### 3.4.4. Statistical Analysis

Normal distribution with Shapiro-Wilk was performed. The results are expressed as the mean  $\pm$  SD. and were analyzed by analysis of variance (ANOVA) with post-hoc Bonferroni multiple comparisons tests. Calculations of 50% inhibitory concentrations ( $\text{IC}_{50}$ ) were computer-assisted (PHARM/PCS v.4.2). Statistical comparisons were made between groups using the Student's *t* test. Values of *p* less than 0.05 were considered to be statistically significant.

### 3.4.5. Neuroprotective Activity

Primary cultures of neonatal cortical neurons were prepared from the cerebral cortex of Harlan Sprague-Dawley rat pups at postnatal day 1 [67]. Briefly, each pup was decapitated and the cortex was digested in 0.5 mg/mL papain at 37 °C for 15 min. The tissue was dissociated in Hypertate A medium (containing B27 supplement) by aspirating trituration. Cells were plated ( $5 \times 10^4$  cells/cm<sup>2</sup>) onto poly-D-lysine-coated dishes and maintained in neurobasal medium containing B27 supplement, 10 units/mL penicillin, 10 mg/mL streptomycin, and 0.5 mg/mL glutamine (5% CO<sub>2</sub>/9% O<sub>2</sub>) for 3 days. Cells were then exposed to cytosine- $\beta$ -D-arabinofuranoside (5 mM) for 1 day to inhibit proliferation of non-neuronal cells. The cells were used for the experiment on the fifth day. The reduction of MTT was used to evaluate the cell viability. Cells were incubated with minimum essential medium containing 0.5 mg/mL MTT for 1 h. The medium was aspirated, and the formazan particle was dissolved with lysis buffer (10% sodium dodecyl sulfate, 3.3 mM HCl, 50% dimethylformamide). A 600 nm absorbance was measured by using enzyme-linked immunosorbent assay reader. The results are expressed as the mean  $\pm$  SD and were analyzed by analysis of variance (ANOVA) with post-hoc Bonferroni multiple comparisons tests.

**Acknowledgments:** This study is sponsored by the Ministry of Science and Technology, Taiwan, granted to T.-S.W. Authors are also thankful to Chang Gung Memorial Hospital (CMRPD1B0281~3, CMRPF1D0442~3, CMRPF1F0011~3, CMRPF1F0061~3 and BMRP450 granted to T.-L.H.) for the partial financial support for the present research.

**Author Contributions:** Ping-Chung Kuo, Yu-Ren Liao, Hsin-Yi Hung, and Chia-Wei Chuang performed the research and recorded the spectra. Tsong-Long Hwang had done most of the inhibition experiments on human neutrophils and Daih-Huang Kuo help to elucidate a part of the anti-inflammatory bioactivity. Young-Ji Shiao completed the neuroprotective bioactivity examination. Shiow-Chyn Huang and Yu-Ren Liao help to elucidate a part of the neuroprotective bioactivity. Tian-Shung Wu designed the research and provided the research outlines. Ping-Chung Kuo and Hsin-Yi Hung completed the manuscript draft. All authors read and approved the final manuscript.

**Conflicts of Interest:** The authors declare no conflict of interest.

## References

- Rendeiro, C.; Dong, H.; Saunders, C.; Harkness, L.; Blaze, M.; Hou, Y.; Belanger, R.L.; Corona, G.; Lovegrove, J.A.; Spencer, J.P. Flavanone-rich *Citrus* beverages counteract the transient decline in postprandial endothelial function in humans: A randomised, controlled, double-masked, cross-over intervention study. *Br. J. Nutr.* **2016**, *116*, 1999–2010. [[CrossRef](#)] [[PubMed](#)]
- Hattori, S.; Shimokoriyama, M.; Kanao, M. Studies on flavanone glycosides. IV. The glycosides of ripe fruit peel and flower petals of *Citrus aurantium* L. *J. Am. Chem. Soc.* **1952**, *74*, 3614–3615. [[CrossRef](#)]
- Wu, T.S.; Kuoh, C.S.; Furukawa, H. Acridone alkaloids and a coumarin from *Citrus grandis*. *Phytochemistry* **1983**, *22*, 1493–1497.
- McPhail, A.T.; Ju-ichi, M.; Fujitani, Y.; Inoue, M.; Wu, T.S.; Furukawa, H. Isolation and structures of citropone-A and -B from *Citrus* plants, first examples of naturally-occurring homoacridone alkaloids containing a tropone ring system. *Tetrahedron Lett.* **1985**, *26*, 3271–3272. [[CrossRef](#)]
- Wu, T.S.; Huang, S.C.; Jong, T.T.; Lai, J.S.; Furukawa, H. Honyumine, a new linear pyranoacridone alkaloids from *Citrus grandis* Osbeck. *Heterocycles* **1986**, *24*, 41–43. [[CrossRef](#)]
- Wu, T.S. Baiyumine-A and -B, two acridone alkaloids from *Citrus grandis*. *Phytochemistry* **1987**, *26*, 871–872. [[CrossRef](#)]
- Wu, T.S.; Huang, S.C.; Jong, T.T.; Lai, J.S.; Kuoh, C.S. Coumarins, acridone alkaloids and a flavone from *Citrus grandis*. *Phytochemistry* **1988**, *27*, 585–587. [[CrossRef](#)]
- Wu, T.S. Alkaloids and coumarins of *Citrus grandis*. *Phytochemistry* **1988**, *27*, 3717–3718. [[CrossRef](#)]
- Huang, S.C.; Chen, M.T.; Wu, T.S. Alkaloids and coumarins from stem bark of *Citrus grandis*. *Phytochemistry* **1989**, *28*, 3574–3576. [[CrossRef](#)]
- Wu, T.S.; Huang, S.C.; Lai, J.S. Stem bark coumarins of *Citrus grandis*. *Phytochemistry* **1994**, *36*, 217–219.
- Takemura, Y.; Ju-ichi, M.; Ito, C.; Furukawa, H.; Tokuda, H. Studies on the inhibitory effects of some acridone alkaloids on Epstein-Barr virus activation. *Planta Med.* **1995**, *61*, 366–368. [[CrossRef](#)] [[PubMed](#)]
- Zhang, T.; Peng, S. Introduction to the origin and evolution of Pomelo and its distribution in China. *Chin. J. Ecol.* **2000**, *19*, 58–61.
- Mokbel, M.S.; Hashinaga, F. Evaluation of the antioxidant activity of extracts from buntan (*Citrus grandis* Osbeck) fruit tissues. *Food Chem.* **2006**, *94*, 529–534. [[CrossRef](#)]
- Tsai, H.L.; Chang, S.K.; Chang, S.J. Antioxidant content and free radical scavenging ability of fresh red pummelo [*Citrus grandis* (L.) Osbeck] juice and freeze-dried products. *J. Agric. Food Chem.* **2007**, *55*, 2867–2872. [[CrossRef](#)] [[PubMed](#)]
- Kim, G.N.; Shin, J.G.; Jang, H.D. Antioxidant and antidiabetic activity of Dangyuja (*Citrus grandis* Osbeck) extract treated with *Aspergillus saitoi*. *Food Chem.* **2009**, *117*, 35–41. [[CrossRef](#)]
- Parhiz, H.; Roohbakhsh, A.; Soltani, F.; Rezaee, R.; Iranshahi, M. Antioxidant and anti-inflammatory properties of the *Citrus* flavonoids hesperidin and hesperetin: An updated review of their molecular mechanisms and experimental models. *Phytother. Res.* **2015**, *29*, 323–331. [[CrossRef](#)] [[PubMed](#)]
- La, V.D.; Zhao, L.; Epifano, F.; Genovese, S.; Grenier, D. Anti-inflammatory and wound healing potential of *Citrus auraptene*. *J. Med. Food* **2013**, *16*, 961–964. [[CrossRef](#)] [[PubMed](#)]
- Impellizzeri, D.; Bruschetta, G.; Di Paola, R.; Ahmad, A.; Campolo, M.; Cuzzocrea, S.; Esposito, E.; Navarra, M. The anti-inflammatory and antioxidant effects of bergamot juice extract (BJe) in an experimental model of inflammatory bowel disease. *Clin. Nutr.* **2014**, *33*, 749–753. [[CrossRef](#)] [[PubMed](#)]
- Mitoshi, M.; Kuriyama, I.; Nakayama, H.; Miyazato, H.; Sugimoto, K.; Kobayashi, Y.; Jippo, T.; Kuramochi, K.; Yoshida, H.; Mizushima, Y. Suppression of allergic and inflammatory responses by essential oils derived from herbal plants and *Citrus* fruits. *Int. J. Mol. Med.* **2014**, *33*, 1643–1651. [[CrossRef](#)] [[PubMed](#)]
- Noh, H.J.; Hwang, D.; Lee, E.S.; Hyun, J.W.; Yi, P.H.; Kim, G.S.; Lee, S.E.; Pang, C.; Park, Y.J.; Chung, K.H.; et al. Anti-inflammatory activity of a new cyclic peptide, citrusin XI, isolated from the fruits of *Citrus unshiu*. *J. Ethnopharmacol.* **2015**, *163*, 106–112. [[CrossRef](#)] [[PubMed](#)]
- Shende, S.; Ingle, A.P.; Gade, A.; Rai, M. Green synthesis of copper nanoparticles by *Citrus medica* Linn. (Idilimbu) juice and its antimicrobial activity. *World J. Microbiol. Biotechnol.* **2015**, *31*, 865–873. [[CrossRef](#)] [[PubMed](#)]



22. Chubukov, V.; Mingardon, F.; Schackwitz, W.; Baidoo, E.E.; Alonso-Gutierrez, J.; Hu, Q.; Lee, T.S.; Keasling, J.D.; Mukhopadhyay, A. Acute limonene toxicity in *Escherichia coli* is caused by limonene hydroperoxide and alleviated by a point mutation in alkyl hydroperoxidase AhpC. *Appl. Environ. Microbiol.* **2015**, *81*, 4690–4696. [[CrossRef](#)] [[PubMed](#)]
23. Wu, M.C.; Li, H.C.; Wu, P.H.; Huang, P.H.; Wang, Y.T. Assessment of oligogalacturonide from *Citrus* pectin as a potential antibacterial agent against foodborne pathogens. *J. Food Sci.* **2014**, *79*, 1541–1544. [[CrossRef](#)] [[PubMed](#)]
24. Vollmerhausen, T.L.; Ramos, N.L.; Dzung, D.T.; Brauner, A. Decoctions from *Citrus reticulata* Blanco seeds protect the uroepithelium against *Escherichia coli* invasion. *J. Ethnopharmacol.* **2013**, *150*, 770–774. [[CrossRef](#)] [[PubMed](#)]
25. Roohbakhsh, A.; Parhiz, H.; Soltani, F.; Rezaee, R.; Iranshahi, M. Molecular mechanisms behind the biological effects of hesperidin and hesperetin for the prevention of cancer and cardiovascular diseases. *Life Sci.* **2015**, *124*, 64–74. [[CrossRef](#)] [[PubMed](#)]
26. Murthy, K.N.; Jayaprakasha, G.K.; Patil, B.S. Cytotoxicity of obacunone and obacunone glucoside in human prostate cancer cells involves Akt-mediated programmed cell death. *Toxicology* **2015**, *329*, 88–97. [[CrossRef](#)] [[PubMed](#)]
27. Leclerc, L.; Fransolet, M.; Cote, F.; Cambier, P.; Arnould, T.; Van Cutsem, P.; Michiels, C. Heat-modified *Citrus* pectin induces apoptosis-like cell death and autophagy in HepG2 and A549 cancer cells. *PLoS ONE* **2015**, *10*, e0115831. [[CrossRef](#)] [[PubMed](#)]
28. Zeng, Z.Y.; Chen, Y.; Zou, L.; Zhang, Y.; Hu, F.; Feng, J.; Shen, J.; Wei, B. Naringin inhibits growth and induces apoptosis by a mechanism dependent on reduced activation of NF- $\kappa$ B/COX-2 caspase-1 pathway in HeLa cervical cancer cells. *Int. J. Oncol.* **2014**, *45*, 1929–1936. [[CrossRef](#)] [[PubMed](#)]
29. Razavi, B.M.; Arasteh, E.; Imenshahidi, M.; Iranshahi, M. Antihypertensive effect of auraptene, a monoterpene coumarin from the genus *Citrus*, upon chronic administration. *Iran. J. Basic Med. Sci.* **2015**, *18*, 153–158. [[PubMed](#)]
30. Orhan, I.E.; Nabavi, S.F.; Daglia, M.; Tenore, G.C.; Mansouri, K.; Nabavi, S.M. Naringenin and atherosclerosis: A review of literature. *Curr. Pharm. Biotechnol.* **2015**, *16*, 245–251. [[CrossRef](#)] [[PubMed](#)]
31. Liu, Y.; Niu, L.; Cui, L.; Hou, X.; Li, J.; Zhang, X.; Zhang, M. Hesperetin inhibits rat coronary constriction by inhibiting  $\text{Ca}^{2+}$  influx and enhancing voltage-gated  $\text{K}^{+}$  channel currents of the myocytes. *Eur. J. Pharmacol.* **2014**, *735*, 193–201. [[CrossRef](#)] [[PubMed](#)]
32. Chanut, A.; Claude, S.; Maier, J.A.; Kamran, K.M.; Rakotomanomana, N.; Shinkaruk, S.; Bérard, A.M.; Bennetau, P.C.; Mazur, A.; Morand, C. Flavanone metabolites decrease monocyte adhesion to TNF- $\alpha$ -activated endothelial cells by modulating expression of atherosclerosis-related genes. *Br. J. Nutr.* **2013**, *110*, 587–598. [[CrossRef](#)] [[PubMed](#)]
33. Wang, L.; Wang, J.; Fang, L.; Zheng, Z.; Zhi, D.; Wang, S.; Li, S.; Ho, C.T.; Zhao, H. Anticancer activities of citrus peel polymethoxyflavones related to angiogenesis and others. *Biol. Med. Res. Int.* **2014**, *30*, 453–463. [[CrossRef](#)] [[PubMed](#)]
34. Hwang, S.L.; Shih, P.H.; Yen, G.C. Neuroprotective effects of citrus flavonoids. *J. Agric. Food Chem.* **2012**, *60*, 877–885. [[CrossRef](#)] [[PubMed](#)]
35. Jun, M.; Bacay, A.F.; Moyer, J.; Webb, A.; Carrico-Moniz, D. Synthesis and biological evaluation of isoprenylated coumarins as potential anti-pancreatic cancer agents. *Bioorg. Med. Chem. Lett.* **2014**, *24*, 4654–4658. [[CrossRef](#)] [[PubMed](#)]
36. Beare, K.D.; McErlean, C.S.P. Accessing columbianetin-containing natural products via a domino on-water, in-water process. *Tetrahedron Lett.* **2013**, *54*, 1056–1058. [[CrossRef](#)]
37. Feger, W.; Brandauer, H.; Gabris, P.; Ziegler, H. Nonvolatiles of commercial lime and grapefruit oils separated by high-speed countercurrent chromatography. *J. Agric. Food Chem.* **2006**, *54*, 2242–2252. [[CrossRef](#)] [[PubMed](#)]
38. Francis Rouessac, M.A. Syntheses en serie racémique et en serie optiquement active d’une famille de dérivés oxygénés naturels de l’ombelliférone. Structure spatiale du (–) epoxy-3’6’ auraptène. *Tetrahedron* **1988**, *44*, 101–110.
39. Cai, J.N.; Basnet, P.; Wang, Z.T.; Komatsu, K.; Xu, L.S.; Tani, T. Coumarins from the fruits of *Cnidium monnieri*. *J. Nat. Prod.* **2000**, *63*, 485–488. [[CrossRef](#)] [[PubMed](#)]

40. Panthong, K.; Srisud, Y.; Rukachaisirikul, V.; Hutadilok-Towatana, N.; Voravuthikunchai, S.P.; Tewtrakul, S. Benzene, coumarin and quinolinone derivatives from roots of *Citrus hystrix*. *Phytochemistry* **2013**, *88*, 79–84. [[CrossRef](#)] [[PubMed](#)]
41. Znati, M.; Ben Jannet, H.; Cazaux, S.; Souchard, J.P.; Harzallah Skhiri, F.; Bouajila, J. Antioxidant, 5-lipoxygenase inhibitory and cytotoxic activities of compounds isolated from the *Ferula lutea* flowers. *Molecules* **2014**, *19*, 16959–16975. [[CrossRef](#)] [[PubMed](#)]
42. Marumoto, S.; Miyazawa, M. Structure-activity relationships for naturally occurring coumarins as beta-secretase inhibitor. *Bioorg. Med. Chem.* **2012**, *20*, 784–788. [[CrossRef](#)] [[PubMed](#)]
43. Esquivel-Ferrino, P.C.; Favela-Hernandez, J.M.; Garza-Gonzalez, E.; Waksman, N.; Rios, M.Y.; del Rayo Camacho-Corona, M. Antimycobacterial activity of constituents from *Foeniculum vulgare* var. *dulce* grown in Mexico. *Molecules* **2012**, *17*, 8471–8482. [[PubMed](#)]
44. Ohta, T.; Maruyama, T.; Nagahashi, M.; Miyamoti, Y.; Hosoi, S.; Kiuchi, F.; Yamazoe, Y.; Tsukamoto, S.; Paradisin, C. A new CYP3A4 inhibitor from grapefruit juice. *Tetrahedron* **2002**, *58*, 6631–6635. [[CrossRef](#)]
45. Abulrob, A.; Suller, M.T.E.; Gumbleton, M.; Simons, C.; Russell, A.D. Identification and biological evaluation of grapefruit oil components as potential novel efflux pump modulators in methicillin-resistant *Staphylococcus aureus* bacterial strains. *Phytochemistry* **2004**, *65*, 3021–3027. [[CrossRef](#)] [[PubMed](#)]
46. Lin, J.K.; Wu, T.S. Constituents of flowers of *Murraya paniculata*. *J. Chin. Chem. Soc.* **1994**, *41*, 213–216. [[CrossRef](#)]
47. Youkwan, J.; Sutthivaiyakit, S.; Sutthivaiyakit, P. Citrusosides A–D and furanocoumarins with cholinesterase inhibitory activity from the fruit peels of *Citrus hystrix*. *J. Nat. Prod.* **2010**, *73*, 1879–1883. [[CrossRef](#)] [[PubMed](#)]
48. Hamdan, D.; El-Readi, M.Z.; Tahrani, A.; Herrmann, F.; Kaufmann, D.; Farrag, N.; El-Shazly, A.; Wink, M. Chemical composition and biological activity of *Citrus jambhiri* Lush. *Food Chem.* **2011**, *127*, 394–403. [[CrossRef](#)] [[PubMed](#)]
49. Tan, X.Q.; Guo, L.J.; Chen, H.S.; Wu, L.S.; Kong, F.F. Study on the flavonoids constituents of *Trachelospermum jasminoides*. *J. Chin. Med. Mater.* **2010**, *33*, 58–60.
50. Matsubara, Y.; Kumamoto, H.; Iizuka, Y.; Murakami, T.; Okamoto, K.; Miyake, H.; Yokoi, K. Structure and hypertensive effect of flavonoid glycosides in *Citrus unshiu* peelings. *Agric. Biol. Chem.* **1985**, *49*, 909–914.
51. Donna, L.D.; Luca, G.D.; Mazzotti, F.; Napoli, A.; Salerno, R.; Taverna, D.; Sindona, G. Statin-like principles of bergamot fruit (*Citrus bergamia*): Isolation of 3-hydroxymethylglutaryl flavonoid glycosides. *J. Nat. Prod.* **2009**, *72*, 1352–1354. [[CrossRef](#)] [[PubMed](#)]
52. Lewin, G.; Maciuk, A.; Thoret, S.; Aubert, G.; Dubois, J.; Cresteil, T. Semisynthesis of natural flavones inhibiting tubulin polymerization, from hesperidin. *J. Nat. Prod.* **2010**, *73*, 702–706. [[CrossRef](#)] [[PubMed](#)]
53. Numonov, S.R.; Usmanova, S.K.; Aisa, H.A. A triterpenoid and flavonoids from *Dracocephalum heterophyllum*. *Chem. Nat. Compd.* **2013**, *48*, 1109–1110. [[CrossRef](#)]
54. Bowen, I.H.; Perera, K.P.W.C. Alkaloids, coumarins and flavonoids of *Micromelum zeylanicum*. *Phytochemistry* **1982**, *21*, 433–437. [[CrossRef](#)]
55. Akhtar, N.; Saleem, M.; Riaz, N.; Ali, M.S.; Yaqoob, A.; Nasim, F.; Jabbar, A. Isolation and characterization of the chemical constituents from *Plumeria rubra*. *Phytochem. Lett.* **2013**, *6*, 291–298. [[CrossRef](#)]
56. Ouyang, X.L.; Wei, L.X.; Fang, X.M.; Wang, H.S.; Pan, Y.M. Flavonoid constituents of *Euonymus fortunei*. *Chem. Nat. Compd.* **2013**, *49*, 428–431. [[CrossRef](#)]
57. Luyen, B.T.; Tai, B.H.; Thao, N.P.; Cha, J.Y.; Lee, H.Y.; Lee, Y.M.; Kim, Y.H. Anti-inflammatory components of *Chrysanthemum indicum* flowers. *Bioorg. Med. Chem. Lett.* **2015**, *25*, 266–269. [[CrossRef](#)] [[PubMed](#)]
58. Leu, Y.L.; Hwang, T.L.; Kuo, P.C.; Liou, K.P.; Huang, B.S.; Chen, G.F. Constituents from *Vigna vexillata* and their anti-inflammatory activity. *Int. J. Mol. Sci.* **2012**, *13*, 9754–9768. [[CrossRef](#)] [[PubMed](#)]
59. Louche, L.M.M.; Gaydou, E.M.; Lesage, J.C. Determination of phlorin as peel marker in orange (*Citrus sinensis*) fruits and juices. *J. Agric. Food Chem.* **1998**, *46*, 4193–4197. [[CrossRef](#)]
60. Sribuham, T.; Sriphana, U.; Thongsri, Y.; Yenjai, C. Chemical constituents from the stems of *Alyxia schlechteri*. *Phytochem. Lett.* **2015**, *11*, 80–84. [[CrossRef](#)]
61. Ley, J.P.; Blings, M.; Paetz, S.; Krammer, G.E.; Bertram, H.J. New bitter-masking compounds: Hydroxylated benzoic acid amides of aromatic amines as structural analogues of homoeriodictyol. *J. Agric. Food Chem.* **2006**, *54*, 8574–8579. [[CrossRef](#)] [[PubMed](#)]
62. Takaya, Y.; Kondo, Y.; Furukawa, T.; Niwa, M. Antioxidant constituents of radish sprout (Kaiware-daikon), *Raphanus sativus* L. *J. Agric. Food Chem.* **2003**, *51*, 8061–8066. [[CrossRef](#)] [[PubMed](#)]

63. Takahashi, H.; Kittaka, H.; Ikegami, S. Novel synthesis of enantiomerically pure natural inositols and their diastereoisomers. *J. Org. Chem.* **2001**, *66*, 2705–2716. [[CrossRef](#)] [[PubMed](#)]
64. Zhang, Q.; Shu, X.; Jing, F.; Wang, X.; Lin, C.; Luo, A. Preparative separation of alkaloids from *Picrasma quassioides* (D. Don) Benn. by conventional and pH-zone-refining countercurrent chromatography. *Molecules* **2014**, *19*, 8752–8761. [[CrossRef](#)] [[PubMed](#)]
65. Strehmel, N.; Böttcher, C.; Schmidt, S.; Scheel, D. Profiling of secondary metabolites in root exudates of *Arabidopsis thaliana*. *Phytochemistry* **2014**, *108*, 35–46. [[CrossRef](#)] [[PubMed](#)]
66. Yang, S.C.; Chung, P.J.; Ho, C.M.; Kuo, C.Y.; Hung, M.F.; Huang, Y.T.; Chang, W.Y.; Chang, Y.W.; Chan, K.H.; Hwang, T.L. Propofol inhibits superoxide production, elastase release, and chemotaxis in formyl peptide-activated human neutrophils by blocking formyl peptide receptor 1. *J. Immunol.* **2013**, *190*, 6511–6519. [[CrossRef](#)] [[PubMed](#)]
67. Yu, H.P.; Hsieh, P.W.; Chang, Y.J.; Chung, P.J.; Kuo, L.M.; Hwang, T.L. 2-(2-Fluorobenzamido) benzoate ethyl ester (EFB-1) inhibits superoxide production by human neutrophils and attenuates hemorrhagic shock-induced organ dysfunction in rats. *Free Radic. Biol. Med.* **2011**, *50*, 1737–1748. [[CrossRef](#)] [[PubMed](#)]
68. Wang, C.N.; Chi, C.W.; Lin, Y.L.; Chen, C.F.; Shiao, Y.J. The neuroprotective effects of phytoestrogens on amyloid  $\beta$  protein-induced toxicity are mediated by abrogating the activation of caspase cascade in rat cortical neurons. *J. Biol. Chem.* **2001**, *276*, 5287–5295. [[CrossRef](#)] [[PubMed](#)]

**Sample Availability:** Samples of the purified compounds are available from the authors.



© 2017 by the authors. Licensee MDPI, Basel, Switzerland. This article is an open access article distributed under the terms and conditions of the Creative Commons Attribution (CC BY) license (<http://creativecommons.org/licenses/by/4.0/>).

## A novel fine tuning scheme of miR-200c in modulating lung cell redox homeostasis

Yi-Hsuan Wu, Hsin-Ru Lin, Ying-Hsuan Lee, Pin-Hao Huang, Huei-Chung Wei, Arnold Stern & Daniel Tsun-Yee Chiu

To cite this article: Yi-Hsuan Wu, Hsin-Ru Lin, Ying-Hsuan Lee, Pin-Hao Huang, Huei-Chung Wei, Arnold Stern & Daniel Tsun-Yee Chiu (2017) A novel fine tuning scheme of miR-200c in modulating lung cell redox homeostasis, *Free Radical Research*, 51:6, 591-603, DOI: 10.1080/10715762.2017.1339871

To link to this article: <http://dx.doi.org/10.1080/10715762.2017.1339871>



Published online: 04 Jul 2017.



Submit your article to this journal 



Article views: 31



View related articles 



View Crossmark data 

ORIGINAL ARTICLE



## A novel fine tuning scheme of miR-200c in modulating lung cell redox homeostasis

Yi-Hsuan Wu<sup>a,b</sup>, Hsin-Ru Lin<sup>b,c</sup>, Ying-Hsuan Lee<sup>b</sup>, Pin-Hao Huang<sup>b</sup>, Huei-Chung Wei<sup>b</sup>, Arnold Stern<sup>d</sup> and Daniel Tsun-Yee Chiu<sup>a,b,e,f</sup>

<sup>a</sup>Research Center for Chinese Herbal Medicine, College of Human Ecology, Chang Gung University of Science and Technology, Taoyuan, Taiwan; <sup>b</sup>Department of Medical Biotechnology and Laboratory Sciences, College of Medicine, Chang Gung University, Taoyuan, Taiwan; <sup>c</sup>Molecular Medicine Research Center, Chang Gung University, Taoyuan, Taiwan; <sup>d</sup>New York University School of Medicine, New York, NY, USA; <sup>e</sup>Healthy Aging Research Center, Chang Gung University, Taoyuan, Taiwan; <sup>f</sup>Department of Pediatric Hematology/Oncology, Linkou Chang Gung Memorial Hospital, Taoyuan, Taiwan

### ABSTRACT

Oxidative stress induces miR-200c, the predominant microRNA (miRNA) in lung tissues; however, the antioxidant role and biochemistry of such induction have not been clearly defined. Therefore, a lung adenocarcinoma cell line (A549) and a normal lung fibroblast (MRC-5) were used as models to determine the effects of miR-200c expression on lung antioxidant response. Hydrogen peroxide (H<sub>2</sub>O<sub>2</sub>) upregulated miR-200c, whose overexpression exacerbated the decrease in cell proliferation, retarded the progression of cells in the G2/M-phase, and increased oxidative stress upon H<sub>2</sub>O<sub>2</sub> stimulation. The expression of three antioxidant proteins, superoxide dismutase (SOD)-2, haem oxygenase (HO)-1, and sirtuin (SIRT) 1, was reduced upon H<sub>2</sub>O<sub>2</sub> stimulation in miR-200c-overexpressed A549 cells. This phenomenon of increased oxidative stress and antioxidant protein downregulation also occurs simultaneously in miR-200c overexpressed MRC-5 cells. Molecular analysis revealed that miR-200c inhibited the gene expression of HO-1 by directly targeting its 3'-untranslated region. The downregulation of SOD2 and SIRT1 by miR-200c was mediated through zinc finger E-box-binding homeobox 2 (ZEB2) and extracellular signal-regulated kinase 5 (ERK5) pathways, respectively, where knockdown of ZEB2 or ERK5 decreased the expression of SOD2 or SIRT1 in A549 cells. LNA anti-miR-200c transfection in A549 cells inhibited the endogenous miR-200c expression, resulting in increased expressions of antioxidant proteins, reduced oxidative stress and recovered cell proliferation upon H<sub>2</sub>O<sub>2</sub> stimulation. These findings indicate that miR-200c fine-tuned the antioxidant response of the lung cells to oxidative stress through several pathways, and thus this study provides novel information concerning the role of miR-200c in modulating redox homeostasis of lung.

**Abbreviations:** ROS: reactive oxygen species; H<sub>2</sub>O<sub>2</sub>: hydrogen peroxide; HO-1: haem oxygenase-1; ERK5: extracellular-signal-regulated kinase-5; SIRT1: sirtuin-1; SOD2: superoxide dismutase 2; ZEB2: zinc finger E-box binding homeobox-2.

### ARTICLE HISTORY

Received 10 January 2017  
Accepted 5 June 2017

### KEYWORDS

H<sub>2</sub>O<sub>2</sub>; HO-1; ERK5; SIRT1; SOD2; antioxidant response

### Introduction

MiRNAs are small non-coding RNAs functioning as post-transcriptional regulators. The human genome encodes more than 1000 miRNAs that target most mammalian genes in many human cell types [1,2]. MiRNAs have diverse functions in embryogenesis, differentiation, developmental timing [3], organogenesis, growth control, and programmed cell death [4]. Some miRNAs are known as “redoximiRs” [5–11]. MiR-144 and -153 downregulate the nuclear factor E2-related factor 2 (Nrf2) pathway to maintain cellular redox homeostasis [6]. Cellular redox homeostasis is also regulated by miR-181a [7,8], miR-10a [9], and the miR-200 family [10,11], albeit through other mechanisms.

Despite the growing evidence of redoximiRs [5–11], their biological role and biochemistry have not yet been completely elucidated. MiR-200c, a member of redoximiRs, belongs to the miR-200 family and is easily induced by oxidative stress. MiRNA profiling data revealed an upregulation of miR-200c in hydrogen peroxide (H<sub>2</sub>O<sub>2</sub>)-treated human umbilical vein endothelial cells (HUVECs) [12], demonstrating the importance of miR-200c upregulation in the response of HUVECs to oxidative stress, which leads to apoptosis and senescence. Studies have reported a crosstalk between oxidative stress and miR-200c in different models, such as human fibroblasts [13], human cancer cells [14], and mouse models [15]. Few studies have illustrated the



role of and the mechanism underlying miR-200c induction in lung tissues to modulate the antioxidant capacity upon oxidant challenge.

Redox homeostasis occurs constantly in the lung. Abnormal redox homeostasis plays an important role in the progression of lung diseases, such as lung cancer, asthma, and chronic obstructive pulmonary disease [16–22]. The lung cells is at the interface between the environment and the rest of the body, making it particularly vulnerable to oxidative injury [23]. Therefore, it requires potent defence mechanisms for protecting against reactive oxygen species (ROS) [24], which initiate immune responses [25–27], and for participating in the killing of pathogens [25,27,28]. Antioxidant enzymes, including catalase, superoxide dismutase (SOD) [29], glutathione reductase and thioredoxin reductase [30–32], are present in the lung cells. MiR-200c is predominantly expressed in lung [33]; therefore, its role in modulating the antioxidant response in the lung must be elucidated.

The present study focussed on determining the regulatory functions of miR-200c in modulating the antioxidant response upon H<sub>2</sub>O<sub>2</sub> treatment in the lung epithelium A549 cells and fibroblast MRC-5 cells. MiR-200c overexpression in A549 cells reduced cellular proliferation, retarded cell cycle progression, and increased oxidative stress by reducing SOD2 production and haem oxygenase-1 (HO-1) expression as well as by inhibiting SIRT1 (sirtuin-1) expression upon H<sub>2</sub>O<sub>2</sub> stimulation. The same phenomena were observed in MRC-5 cells. MiR-200c downregulated SOD2, HO-1, and SIRT1 through distinct mechanisms, namely ZEB2 (zinc finger E-box binding homeobox-2) pathway, direct post-transcriptional modification and ERK5 (extracellular-signal-regulated kinase-5) signalling, respectively. These findings clarify the biological role and biochemistry of miR-200c in modulating H<sub>2</sub>O<sub>2</sub>-induced redox homeostasis in the lung cells.

## Material and methods

### Reagents

Antibodies against human HO-1 (sc-10789),  $\beta$ -actin (sc-1616), SIRT1 (sc-15404), ZEB2 (sc-271984), anti-horseradish peroxidase (HRP)-conjugated anti-mouse IgG and anti-rabbit IgG were purchased from Santa Cruz Biotechnology (Santa Cruz, CA). Human antibodies against SOD2 (#06-984) were from Millipore (Bedford, MA). Human antibodies against ERK5 (#3372) and ZEB1 (#3396) were from Cell Signaling Technology (Danvers, MA). All other chemicals were procured from Sigma-Aldrich (St. Louis, MO). miR-200c-LNA-inhibitor (4101122-001) and scramble control (199006-000) were purchased from Exiqon (Vedbaek, Denmark).

### Cell culture

A549 cells (a human alveolar epithelial cell carcinoma) and MRC-5 cells (a normal human lung fibroblasts) were purchased from the American Type Culture Collection (Manassas, VA) and cultured in Dulbecco modified Eagle media supplemented with 10% foetal bovine serum and antibiotics (100 U/ml penicillin and 100  $\mu$ g/ml streptomycin, Thermo Fisher Scientific, Haverhill, MA) at 37 °C in a humidified 5% CO<sub>2</sub> atmosphere.

### Expression cassette construction

The cassette for expressing miR-200c (pmiR-200c) and the miR-negative control (pmiR-Neg) were established following manual protocol by inserting mature miRNA or the negative control sequence (BLOCK-iT™ Pol II miR RNAi Expression Vector Kit; Thermo Fisher Scientific). The negative control sequence was shown below: 5'-GAAATGTACTGCGCTGGAGACGTTTTGGCCACTGACTGACGTCTCCACGCAGTACATTT-3'.

### Lentiviral particles preparation

HEK293FT were plated at  $3 \times 10^6$  per 100 mm Petri dish in 10 ml DMEM supplemented with 10% FBS. For miRNA lentiviral particles preparation, co-transfection was performed by Lipofectamine® 2000 (Thermo Fisher Scientific) using 3.5  $\mu$ g of pLP1, 2.5  $\mu$ g of pLP2, 3.5  $\mu$ g of pLP/VSVG together with 11  $\mu$ g of transgene expressing vectors (pmiR-200c or pmiR-Neg) following the manual protocol (ViraPower™ Lentiviral Bsd Support Kit; Thermo Fisher Scientific). For shRNA lentiviral particle preparation, co-transfection was performed by Lipofectamine® 2000 (Thermo Fisher Scientific) using 8  $\mu$ g of packing plasmid (pCMV- $\Delta$ R8.91), 8  $\mu$ g of pLKO.1 plasmids expressing shRNA, and 0.8  $\mu$ g of envelope plasmid (pMD.G) to produce shRNA lentivirus according to instructions (Academia Sinica, Taipei, Taiwan). The sequence of ZEB2 shRNA cassettes was (sense) 5'-CCGGGGAAGACAAGCTTCATATTCTCGAGAAATATGAA-G CTTGTCTTCCTTTTT-3'. The sequence of ERK5 shRNA cassettes was (sense) 5'-CCGGATTGTGGCTGAAATTGAGGACCTCGAGGTCTCAATTTTCAGCCACAATTTTT-3'. After 5 h incubation, media were replaced with 10 ml of complete media. The media containing lentivirus particles were harvested at 48 h and centrifuged at 4 °C, 1200 rpm, for 5 min. The supernatant was stored in aliquots at –80 °C until used.

### Transduction

A549 cells were transduced with miRNA expressing vector (pmiR-200c and pmiR-Neg) or with the shRNA

expression vector using lentivirus-mediated infection. Polybrene (8 µg/ml) was added into the media to enhance viral infection. A549 cells with stable expression of pmir-200c or pmir-Neg (A549-200c and A549-Neg) were selected by blasticidin.

### Exposure of cells to H<sub>2</sub>O<sub>2</sub>

A549 cells (in six-well plates,  $1 \times 10^5$  cells/well) were seeded and grown overnight in complete media. For H<sub>2</sub>O<sub>2</sub> treatment, cells were incubated with H<sub>2</sub>O<sub>2</sub> at the concentrations indicated in the figure legends for 1 h and replaced with fresh complete media (procedure is shown as Figure 1(A)). The experiments were incubated for different times as shown in the figure legends.

### RNA extraction and quantitative PCR

Total RNA was extracted using TRIzol<sup>TM</sup> reagent (Thermo Fisher Scientific). Reverse transcription was performed

with superscript III reverse transcriptase following the instructions of the manufacturer (Thermo Fisher Scientific). The quantitative PCR reaction was performed by Bio-Rad Lightcycler (Bio-Rad Laboratories, Hercules, CA). The primer sequences used in reverse transcription and quantitative PCR are shown in Table 1. The gene expression levels were normalised to the level of the housekeeping gene (*ACT-β*) and miRNA expression levels were normalised to the level of small nuclear RNA U6. Relative gene expression changes are reported as fold changes as described in indicated figure legends.

### Cellular proliferation assay in 12-well format

Cells ( $1 \times 10^4$ ) seeding in 12-well plates were treated with H<sub>2</sub>O<sub>2</sub> and further incubated for different times in culture. For determination of cell number, cells were fixed by 3.7% formaldehyde for 20 min then 50 µg/ml of DAPI in phosphate-buffered solution (PBS) was added

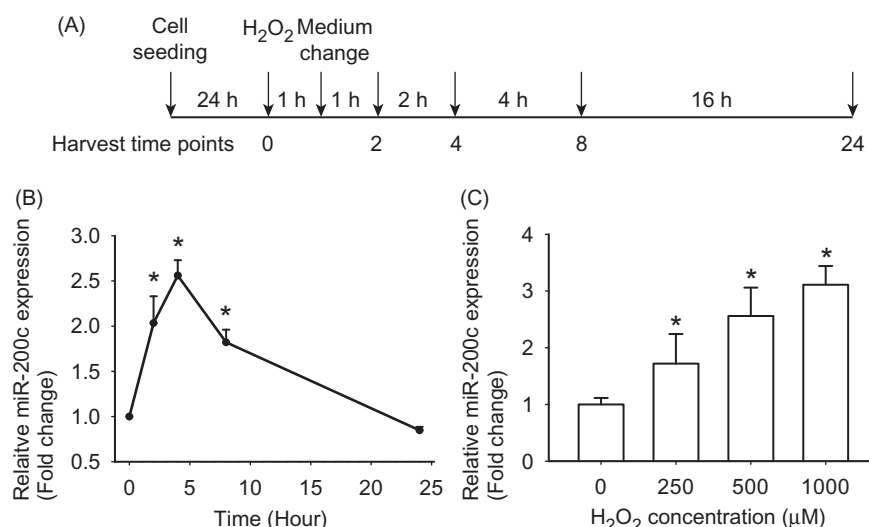


**Figure 1.** H<sub>2</sub>O<sub>2</sub> induces miR-200c expression in A549 cells. (A) Schematic presentation of H<sub>2</sub>O<sub>2</sub> treatment in A549 cells is shown. In brief, cells were treated with H<sub>2</sub>O<sub>2</sub> for 1 h and then cultured with fresh complete medium. RNA samples were harvested at indicated times; (B) A549 cells were exposed to 500 µM H<sub>2</sub>O<sub>2</sub> for 1 h and then changed with complete media for 24 h. The miR-200c level was expressed as fold change compared to that of the 0 h time point. Values present the average  $\pm$  SD of three experiments. \**p* < .05 versus 0 h time point; (C) A549 cells were exposed to 250, 500 and 1000 µM H<sub>2</sub>O<sub>2</sub>, and the induction level of miR-200c at 4 h was determined normalised to that of untreated cells. Values present the average  $\pm$  SD of three experiments. \**p* < .05 versus without H<sub>2</sub>O<sub>2</sub> treatment.

**Table 1.** Sequences of primers for the amplification of selected genes evaluated by quantitative PCR.

Gene	Functions	Sense (5'–3')	Antisense (5'–3')	Target size (bp)
<i>ACT-β</i> <sup>a</sup>	Q-PCR	TCCACCTTCAGCAGATG	GTGTAACGCACTAAGTCATAG	108
<i>ZEB1</i>	Q-PCR	GCCAATAAGCAAACGATTCTG	TTTGGCTGGATCACTTTCAAG	101
<i>HMOX1</i>	Q-PCR	CAGGAGCTGCTGACCCATGA	AGCAACTGTCGCCACCAGAA	195
<i>ZEB2</i>	Q-PCR	GGAGACGAGTCCAGCTAGTGT	CCACTCCACCTCCCTTATTTC	107
<i>SOD2</i>	Q-PCR	GCTCCGGTTTTGGGGTATCTG	GCGTTGATGTGAGGTTCCAG	92
<i>ERK5</i>	Q-PCR	TTTGCCTTACTCCACCTG	CCCATGTCGAAAGACTGGTT	225
<i>SIRT1</i>	Q-PCR	TAGCCTTGTCAGATAAGGAAGGA	ACAGCTTCACAGTCAACTTTGT	160
hsa-miR-200c RT primer	RT		CTCACTGGTGTGCTGGAGTCGGCAATTCAGTTGAGTCCATCAT	
Small nuclear RNA U6 RT primer	RT, Q-PCR	CTCGCTTCGGCAGCACA	AACGCTTCACGAATTGCGT	94
hsa-miR-200c	Q-PCR	CGGCGTAATACTGCCGGGTAA		66
Universal reverse	Q-PCR		CTGGTGTGCTGGAGTCGGCAATTC	

<sup>a</sup>Housekeeping gene transcript serving as the normalisation control for quantitative PCR. Q-PCR: quantitative PCR; RT: reverse transcription.

to each well at different time point and incubated for 1 h at room temperature. After washing with PBS, whole-well imaging acquisition was performed with the IN Cell Analyzer 2000 (GE Healthcare, Marlborough, MA) followed by nuclear counting with the IN Cell Investigator (GE Healthcare) software.

### ROS determination

The cellular oxidative stress level was monitored with CellROX Deep Red Reagents (Life Technologies). Briefly, cells ( $1 \times 10^5$ ) cultured in six-well plates were treated with  $H_2O_2$  for 1 h and then changed for fresh complete media for another 24 h. After stimulation, cells were washed then stained with medium containing  $5 \mu M$  Deep Red Reagents for 1 h at  $37^\circ C$  in dark. Finally, cells were detached by trypsinisation and re-suspended in PBS. Fluorescence was analysed by FACS flow cytometer (BD Biosciences, San Jose, CA).

### Cell cycle analysis

Cells were washed twice with PBS at room temperature then re-suspended at  $1 \times 10^6$  cells/ml in PBS. For propidium iodide (PI) staining, cells were fixed with ethanol at  $4^\circ C$  for 2 h and the rest of the steps were performed according to the manufacturer's procedure (Molecular Probes P3566, Thermo Fisher Scientific). Cells were washed twice with PBS, re-suspended in FACS buffer (PBS, 0.2% BSA and 1% sodium azide) and analysed using a FACS flow cytometer (BD Biosciences).

### Western blot analysis

After incubation, cells were washed with  $1 \times$  PBS and lysed in lysis buffer (0.5 M Tris-HCl, pH 6.8, 5% SDS, 25% glycerol and 12.5%  $\beta$ -mercaptoethanol). The prepared samples were resolved on 10 or 12% SDS-PAGE, electro-transferred onto a PVDF membrane (Millipore), and probed with indicated antibodies. Proteins of interest were detected with HRP-conjugated secondary antibodies and visualised using enhanced chemiluminescence (Pierce ECL, Thermo Fisher Scientific) on Fuji SuperFims.

### Luciferase activity assay

The human *ZEB2*, *HMOX1* and *ERK5* 3'-UTR target sequences containing potential target sites for miR-200c were cloned into the pMIR-REPORTER Luciferase vector (Thermo Fisher Scientific) following the manufacturer's protocol. The pMIR vectors containing *ZEB1* 3'-UTR sequences were used as controls. The primers for cloning 3'-UTR sequences of the target gene were shown as below: *ZEB1*: 5'-TGCCTGAACCTCAGACCTA

GTA-3' and 5'-TGTGAGATGGGAGTCTGGTAAA-3'; *ZEB2*: 5'-GAGCTCTAAAAGGTGCCCCGACTAC-3' and 5'-GCCG GCTTCGAGCATGGTCATTTTCA-3'; *HMOX1*: 5'-ATTCTCTTG GCTGGCTTCCT-3' and 5'-TTAAACACCTCCCTCCCCAC-3'; *ERK5*: 5'-GCCTTGCTGCCACAGTAGAC-3' and 5'-TTTCAGGTGCAGAAGGGAAC-3'. The miR-200c target sequences in the 3'-UTR of *HMOX1* and *ERK5* were deleted by site-directed mutagenesis and named as *HMOX1-D* and *ERK5-D*. The A549 cells cultured in 24-well plates were transfected with 175 ng of pMIR-*HMOX1* or pMIR-*ERK5* or pMIR-*ZEB1* together with 875 ng of the miR-200c overexpression vector (pmiR-200c) and 200 ng of pRL-TK vector by Lipofectamine<sup>®</sup> 2000 (Thermo Fisher Scientific). Forty-eight hours after transfection, the luciferase activity was measured by using the Dual Luciferase Assay (Promega, Wisconsin, MA) with a GLOMAX luminometer (Promega). Cellular extracts were assayed for luciferase activity and normalised to Renilla luciferase levels. Data were present relative to the pMIR levels (relative light unit; RLU).

### Statistical analysis

Statistical analyses employed a two-tailed Student's *t*-test. A *p* value  $< .05$  was considered statistically significant. The data are representative of at least three independent experiments, and values are given as the mean  $\pm$  standard deviation (SD).

## Results

### The induction of miR-200c in A549 cells upon $H_2O_2$ stimulation

Lung epithelial cells, A549 cells, were used as a model to determine whether  $H_2O_2$  induces the oxidant-sensitive miRNA miR-200c. Figure 1(A) shows the  $H_2O_2$  treatment procedure. A549 cells treated with  $500 \mu M$   $H_2O_2$  showed  $2.0 \pm 0.30$  (2 h)-,  $2.6 \pm 0.17$  (4 h)-,  $1.8 \pm 0.14$  (8 h)-, and  $0.8 \pm 0.04$  (24 h)-fold induction of miR-200c (Figure 1(B)); this induction increased with dose [ $1.7 \pm 0.52$  (250  $\mu M$ ),  $2.6 \pm 0.50$  (500  $\mu M$ ), and  $3.1 \pm 0.33$  (1000  $\mu M$ ) fold as compared with that of untreated cells, respectively; Figure 1(C)].

### Inhibition of cellular proliferation in miR-200c-overexpressed A549 cells upon $H_2O_2$ stimulation

The lentiviral transduction of miR-200c-overexpressed A549 cells (A549-200c) was performed to determine the role of miR-200c induction in cellular functions. MiR-200c expression in the A549-200c cells was  $4.9 \pm 0.98$ -fold relative to that in the A549-Neg cells (Figure 2(A)). The expression of *ZEB1*, the well-known target of

miR-200c [34], was analysed in these cells. The gene and protein expressions of ZEB1 were downregulated in the A549-200c cells compared with that in the A549-Neg cells ( $0.5 \pm 0.04$  fold and  $0.6 \pm 0.03$  fold in transcription and translational level, respectively,  $p < .05$ ; Figure 2(B)). The cellular proliferation assay revealed that the proliferation of the A549-200c cells upon  $H_2O_2$  stimulation was decreased as compared with that of the A549-Neg cells (Figure 2(C)). Cell proliferation did not clearly vary under basal culture conditions between A549-200c and A549-Neg cells, and acute  $H_2O_2$  stimulation inhibited the cell proliferation in both A549-Neg and A549-200c cells (data not shown).

### Increased cellular oxidative stress, decreased cell cycle progression and antioxidant downregulations by $H_2O_2$ in miR-200c-overexpressed A549 cells

$H_2O_2$  acute stimulation dose-dependently increased oxidative stress in the A549-Neg cells at 24 h post-treatment [ $1.3 \pm 0.04$  (500  $\mu M$ ) and  $1.8 \pm 0.27$  (1000  $\mu M$ ) fold]

compared with the A549-Neg cells without  $H_2O_2$  treatment as measured through CellROX Deep Red Reagents (Figure 3(A)). The fluorescence of the A549-200c cells was increased [ $1.6 \pm 0.17$  (500  $\mu M$ ) and  $2.9 \pm 0.36$  (1000  $\mu M$ ) fold] compared with that of the A549-Neg cells without  $H_2O_2$  treatment (Figure 3(A)). The A549-Neg and A549-200c cells were further evaluated through flow cytometry to investigate the effects of miR-200c on the cell cycle (Figure 3(B)). The acute  $H_2O_2$  treatment in the A549-200c cells reduced the fraction of cells in the G0/1 phase compared with that in the A549-Neg cells, with a concomitant increase in the fraction of cells in the G2/M phase (Figure 3(B)). The G0/1-phase cell fractions were  $40.5 \pm 0.67\%$  and  $34.6 \pm 0.21\%$  in the A549-Neg and A549-200c cells, and the G2/M-phase cell fractions were  $38.0 \pm 0.01\%$  and  $46.2 \pm 0.34\%$  in the A549-Neg cells and A549-200c cells, respectively (Figure 3(B)). These results suggest a decreased growth rate of the A549-200c cells upon  $H_2O_2$  treatment because of increased oxidative stress and a decrease of the progression in the G2/M-phase.

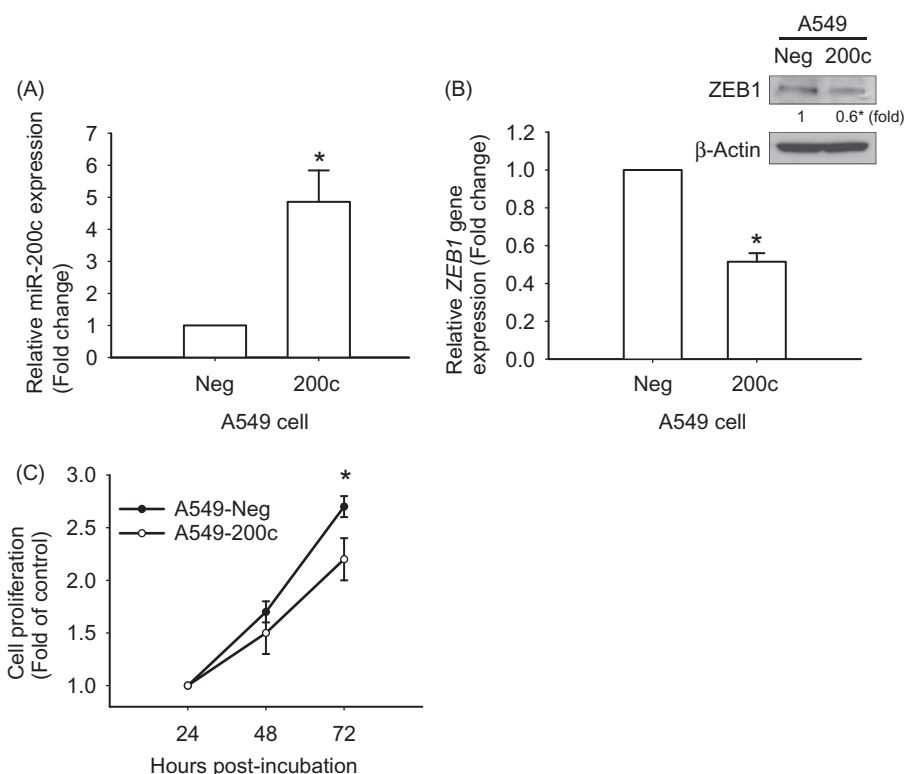


**Figure 2.** A549-200c cells displayed a decreased growth rate upon acute  $H_2O_2$  stimulation. (A) A549-200c and A549-Neg cells were established by lentiviral transduction. The expression level of miR-200c was determined by quantitative PCR normalised to the small RNA U6. Data were expressed relative to A549-Neg cells. Values present the average  $\pm$  SD of three experiments.  $*p < .05$  versus A549-Neg cells; (B) the gene expression level of ZEB1, the main targets of miR-200c, were determined by quantitative PCR normalised to  $ACT-\beta$ . Data were expressed relative to A549-Neg cells. Values present the average  $\pm$  SD of three experiments.  $*p < .05$  versus A549-Neg cells. The protein expressions of ZEB1 in A549-Neg and A549-200c cells were analysed by Western blot, and  $\beta$ -actin was used as loading control. The relative expression of the indicated protein was shown as the number normalised to A549-Neg cells by densitometer. The data were repeated for three times as independent experiments.  $*p < .05$  versus A549-Neg cells; (C) cell proliferation was measured by the 12-well format assay (as shown in "Material and methods" section) at 24, 48 and 72 h after acute  $H_2O_2$  treatment (500  $\mu M$ ) and converted to a fold of the A549-Neg cells at 24 h. Values present the average  $\pm$  SD of three experiments.  $*p < .05$  versus A549-Neg cells at indicated time point.

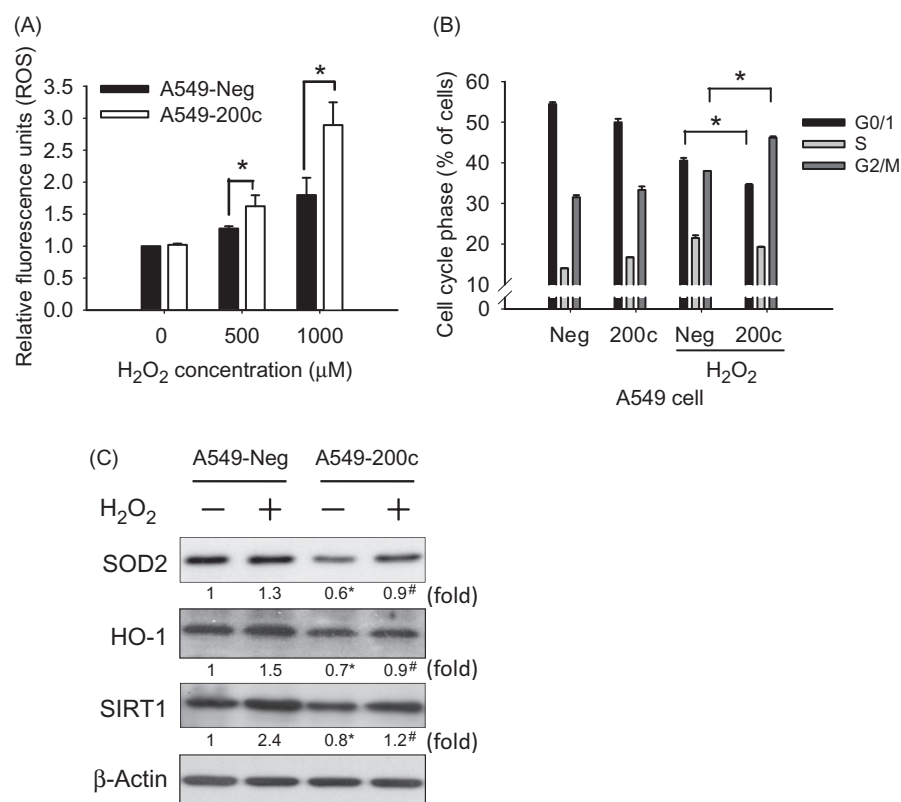


**Figure 3.** Overexpression of miR-200c in A549 cells increased cellular oxidative stress and slowed the progression through the G2/M phase upon H<sub>2</sub>O<sub>2</sub> treatment. (A) Oxidative stress was performed using CellROX<sup>®</sup> Deep Red Reagents. After H<sub>2</sub>O<sub>2</sub> treatment and culturing for 24 h, cells were stained with CellROX<sup>®</sup> Deep Red Reagents (1000 nM) for 60 min and then analysed by flow cytometry. Data were expressed as the fold change relative to A549-Neg cells without H<sub>2</sub>O<sub>2</sub> stimulation. Values present the average  $\pm$  SD of three experiments. \* $p < .05$ ; (B) A549-Neg and A549-200c cells were stimulated by H<sub>2</sub>O<sub>2</sub> (500  $\mu$ M) for 1 h and cultured for 24 h. Cells were fixed and DNA content was obtained by PI staining. The cell cycle was analysed by FACS analysis. The percentages of cells in each phase (G0/1–S–G2/M) were shown. Values present the average  $\pm$  SD of three experiments. \* $p < 0.05$ . (C) The protein expressions of SOD2, HO-1 and SIRT1 upon H<sub>2</sub>O<sub>2</sub> treatment in A549-Neg and A549-200c cells were analysed by Western blot. Cells were treated with H<sub>2</sub>O<sub>2</sub> (500  $\mu$ M) for 1 h, the media was replaced with fresh complete media and cultured for another 24 h. The cell lysate was harvested for Western blot analysis. The relative expression of the indicated protein was shown as the number normalised to A549-Neg cells without H<sub>2</sub>O<sub>2</sub> treatment by densitometer. The data were repeated for three times as independent experiments. \* $p < .05$  represent levels of significant difference when comparing A549-200c with A549-Neg in the condition of with or without H<sub>2</sub>O<sub>2</sub> treatment, respectively.

The protein expressions of SOD2, the highest expression in lung cells [35], HO-1, the predicted target gene of miR-200c, and SIRT1, a product capable of detoxifying mitochondrial ROS [36], were then examined. The expression of the three antioxidant proteins was inhibited in the A549-200c cells in basal and H<sub>2</sub>O<sub>2</sub> stimulation conditions, as assessed using Western blot analysis (Figure 3(C)). These results indicate that miR-200c overexpression downregulated the expression of the three antioxidant proteins.

#### **Same phenomena of increased cellular oxidative stress and antioxidant downregulation by H<sub>2</sub>O<sub>2</sub> stimulation in miR-200c-overexpressed MRC-5 cells**

In order to assess whether miR-200c downregulate the antioxidant capacity could be also investigated in other cells, the lentiviral transduction of miR-200c-overexpressed

MRC-5 cells (MRC5-200c) was performed. MiR-200c expression in the MRC5-200c cells was  $7.8 \pm 0.56$ -fold relative to that in the MRC5-Neg cells (Figure 4(A)). H<sub>2</sub>O<sub>2</sub> acute stimulation (500  $\mu$ M) increased oxidative stress in the MRC5-Neg and MRC5-200c cells at 24 h after treatment as compared with the MRC5-Neg cells without H<sub>2</sub>O<sub>2</sub> treatment evaluated by CellROX Deep Red assay (Figure 4(B)). The fluorescence of the A549-200c cells with H<sub>2</sub>O<sub>2</sub> stimulation was significantly increased [ $1.4 \pm 0.04$  (500  $\mu$ M)] compared with that of the A549-Neg cells [ $1.1 \pm 0.05$  (500  $\mu$ M)] with H<sub>2</sub>O<sub>2</sub> treatment (Figure 4(B)). The expression of three antioxidants, SOD2, HO-1 and SIRT1, was inhibited in the MRC5-200c cells in basal and H<sub>2</sub>O<sub>2</sub> stimulation conditions, as assessed using Western blot analysis (Figure 4(C)). These results indicate that miR-200c induction downregulated the antioxidant capacity of lung cells.



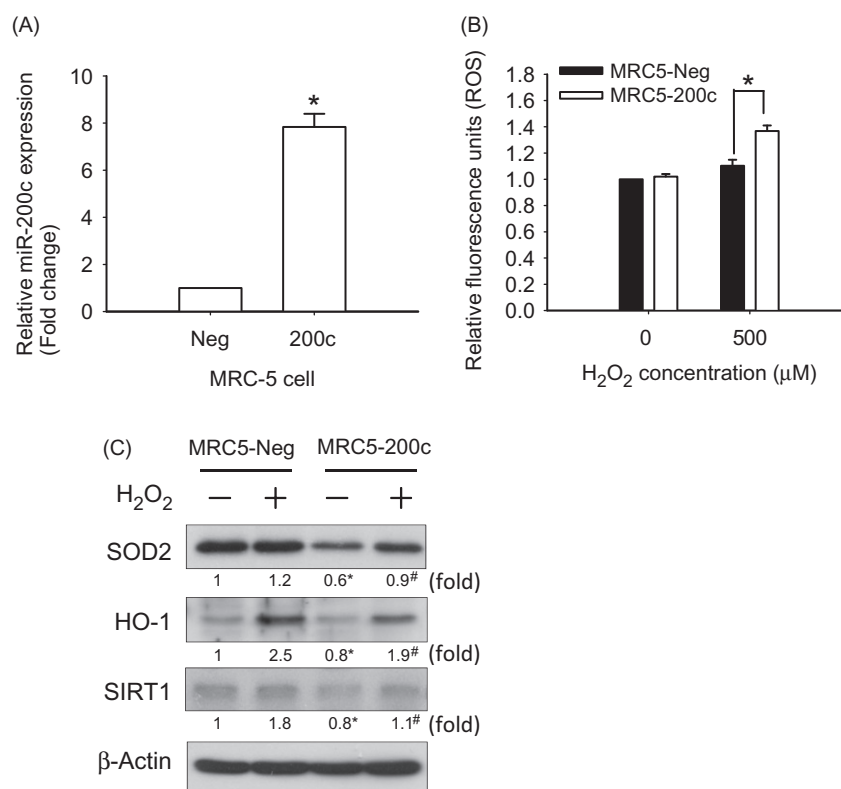


**Figure 4.** Overexpression of miR-200c increased oxidative stress and decreased antioxidant protein expressions in MRC-5 cells upon H<sub>2</sub>O<sub>2</sub> stimulation. (A) MRC5-200c and MRC5-Neg cells were established by lentiviral transduction. The expression level of miR-200c was determined by quantitative PCR normalised to the small RNA U6. Data were expressed relative to A549-Neg cells. Values present the average  $\pm$  SD of three experiments. \* $p$  < .05 versus MRC5-Neg cells; (B) oxidative stress determination was performed using CellROX<sup>®</sup> Deep Red Reagents. After H<sub>2</sub>O<sub>2</sub> treatment for 1 h and then culturing for 24 h, cells were stained with CellROX<sup>®</sup> Deep Red Reagents (1000 nM) for 60 min and then analysed by flow cytometry. Data were expressed as the fold change relative to MRC5-Neg cells without H<sub>2</sub>O<sub>2</sub> stimulation. Values present the average  $\pm$  SD of three experiments. \* $p$  < .05; (C) the protein expressions of SOD2, HO-1 and SIRT1 upon H<sub>2</sub>O<sub>2</sub> treatment in MRC5-Neg and MRC5-200c cells were analysed by Western blot. Cells were treated with H<sub>2</sub>O<sub>2</sub> (500  $\mu$ M) for 1 h, the media was replaced with fresh complete media and cultured for another 24 h. The cell lysate was harvested for Western blot analysis. The relative expression of the indicated protein was shown as the number normalised to MRC5-Neg cells without H<sub>2</sub>O<sub>2</sub> treatment by densitometer. The data were repeated for three times as independent experiments. \*,# $p$  < .05 represent levels of significant difference when comparing MRC5-200c with MRC5-Neg in the condition of with or without H<sub>2</sub>O<sub>2</sub> treatment, respectively.

### Fine tuning of three genes coding for different antioxidants by miR-200c via distinct pathways

In order to delineate the mechanism of antioxidant downregulation, the antioxidant gene expression was first evaluated. The expressions of *SOD2*, *HMOX1*, and *SIRT1* were significantly downregulated in the A549-200c cells relative to that in the A549-Neg cells under basal culture conditions (Figure 5(A)). The expressions of *ZEB2* and *ERK5*, the upstream regulator of *SOD2* and *SIRT1* [37], respectively, were also downregulated in the A549-200c cells relative to that in the A549-Neg cells under basal culture conditions (Figure 5(A)). The protein expression levels of *ZEB2* (left panel of Figure 5(B)) and *ERK5* (left panel of Figure 5(C)) were downregulated in A549-200c cells. *ZEB2* and *ERK5* small hairpin RNA were constructed to elucidate the mechanism underlying the miR-200c-induced downregulation of antioxidants. The knockdown of *ZEB2* or

*ERK5* in the A549 cells inhibited the protein expression of *SOD2* (right panel of Figure 5(B)) and *SIRT1* (right panel of Figure 5(C)), indicating that *SOD2* and *SIRT1* are downregulated by miR-200c, in part, by targeting *ZEB2* and *ERK5*, respectively. The luciferase reporter plasmid containing the 3'-untranslated region (UTR) sequence of *ZEB1* or *ZEB2* or *HMOX1* or *ERK5* or *HMOX1-D* or *ERK5-D* (miR-200c seed sequence deletion of *HMOX1* and *ERK5*) (constructs as Figure 5(D)), renilla plasmid, and miR-200c-overexpressed or negative control plasmid were cotransfected into A549 cells to delineate the mechanistic downregulation of antioxidant expression by miR-200c. The relative fluorescence after transfection for 24 h was decreased in the cells transfected with the *ZEB2* or *HMOX1* or *ERK5* or *ZEB1* reporter plasmid ( $72.2 \pm 5.32\%$ ,  $80.4 \pm 3.73\%$ ,  $80.3 \pm 4.32\%$  and  $61.7 \pm 7.87\%$ , respectively; Figure 5(E)) in miR-200c-overexpressed group compared with that in negative

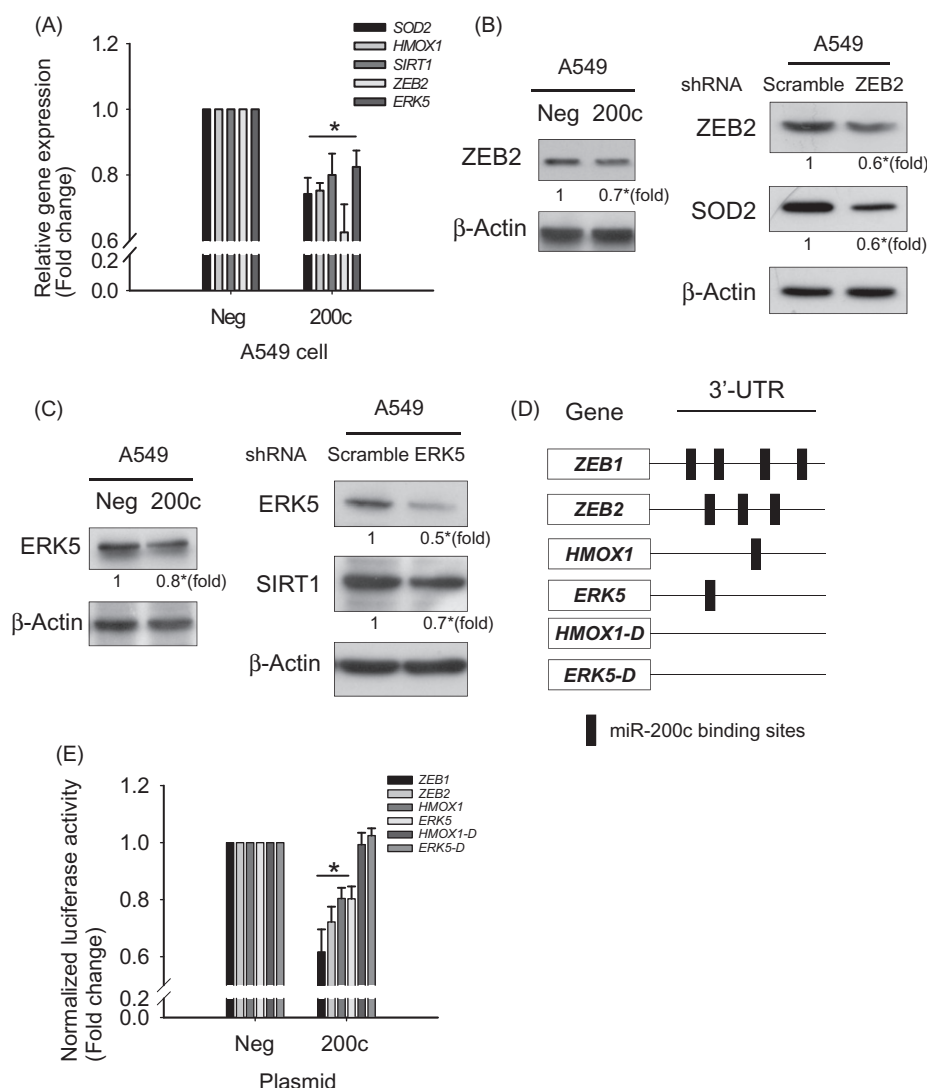


**Figure 5.** The mechanistic analyses about downregulation of SOD2, HO-1 and SIRT1 by miR-200c were through different pathways. (A) The gene expressions of *SOD2*, *HMOX1*, *SIRT1*, *ZEB2* and *ERK5* in A549-Neg and A549-200c cells were analysed by quantitative PCR normalised to *ACT-β*. Data were expressed relative to A549-Neg cells. Values present the average  $\pm$  SD of three experiments. \* $p < .05$  versus A549-Neg cells; (B) the ZEB2 protein expression level of A549-Neg and A549-200c cells were measured by Western blot, using  $\beta$ -actin as loading control (left panel). ZEB2 was knocked down in A549 cells using lentivirus transduction for 72 h and the cell lysate was harvested for determining ZEB2 and SOD2 protein expressions, where  $\beta$ -actin used as the loading control. The relative expression of the indicated protein was shown as the number normalised to A549-Neg cells or Scramble control cells by densitometer. The data were repeated for three times as independent experiments. \* $p < .05$  versus A549-Neg cells or Scramble control cells; (C) the ERK5 protein expression level of A549-Neg and A549-200c cells were measured by Western blot, using  $\beta$ -actin as loading control (left panel). ERK5 was knocked down in A549 cells using lentivirus transduction for 72 h and the cell lysate was harvested for determining ERK5 and SIRT1 protein expressions, where  $\beta$ -actin used as the loading control. The relative expression of the indicated protein was shown as the number normalised to A549-Neg cells or Scramble control cells by densitometer. The data were repeated for three times as independent experiments. \* $p < .05$  versus A549-Neg cells or Scramble control cells; (D) schematic presentation of the construction of reporter plasmid with 3'-UTR region of target gene are shown. The miR-200c binding sites are indicated by labelled boxes. Deletion (*HMOX1-D* and *ERK5-D*) forms of *HMOX1* and *ERK5* 3'-UTR region were established by site-directed mutagenesis (Stratagene, Amsterdam, Netherlands) targeting the miR-200c binding sites. (E) A549 cells were cotransfected with pmir-200c or pmir-Neg plasmid, Renilla plasmid and firefly luciferase reporter plasmids containing the 3'-UTR sequence of *ZEB1*, *ZEB2*, *HMOX1*, *ERK5*, *HMOX1-D* or *ERK5-D*. Luciferase activities were assayed at 24 h after transfection, and firefly luciferase activity was standardised by the Renilla luciferase activity. Values present the average  $\pm$  SD of three experiments. The values were expressed relative to the pmir-Neg plasmid. \* $p < .05$  versus pmir-Neg plasmid.

control group. However, the relative fluorescence value of transfection with *HMOX1-D* or *ERK5-D* was almost the same as the negative controls ( $99.3 \pm 4.15\%$  and  $102.5 \pm 2.56\%$ , respectively). These data indicate that the induction of miR-200c by  $H_2O_2$  inhibits *HMOX1* expression by directly targeting the 3'-UTR of *HMOX1* and ZEB2 and ERK5 signalling mediate the decreased induction of SOD2 and SIRT1 in the A549-200c cells.

### **MiR-200c inhibition by LNA increases antioxidant capacity and makes cell more resistant to oxidative damage**

In order to further assess that modulation of miR-200c status could affect antioxidant capacity, we used LNA to inhibit the endogenous miR-200c expression in A549 cells. MiR-200c expression in the miR-200c-LNA treated

A549 cells was  $38.4 \pm 2.46\%$  relative to that in the Scramble LNA treated cells (Figure 6(A)). The expression of the three antioxidants, SOD2, HO-1 and SIRT1, was increased in the miR-200c LNA treated cells, as assessed using Western blot analysis (Figure 6(B)). Through CellROX Deep Red Reagents to measure the oxidative stress, the fluorescence of the miR-200c LNA treated cells upon  $H_2O_2$  stimulation was significantly decreased [ $1.2 \pm 0.07$  (500  $\mu$ M)] compared with that of the scramble controls [ $1.4 \pm 0.03$  (500  $\mu$ M)] (Figure 6(C)) upon  $H_2O_2$  stimulation. From the cellular proliferation data, inhibition of endogenous miR-200c make cell more resistant to  $H_2O_2$  damage and increase cell growth as compared with control counterparts (Figure 6(D)). These results indicate that inhibition of miR-200c status by LNA can upregulated cellular antioxidant capacity.

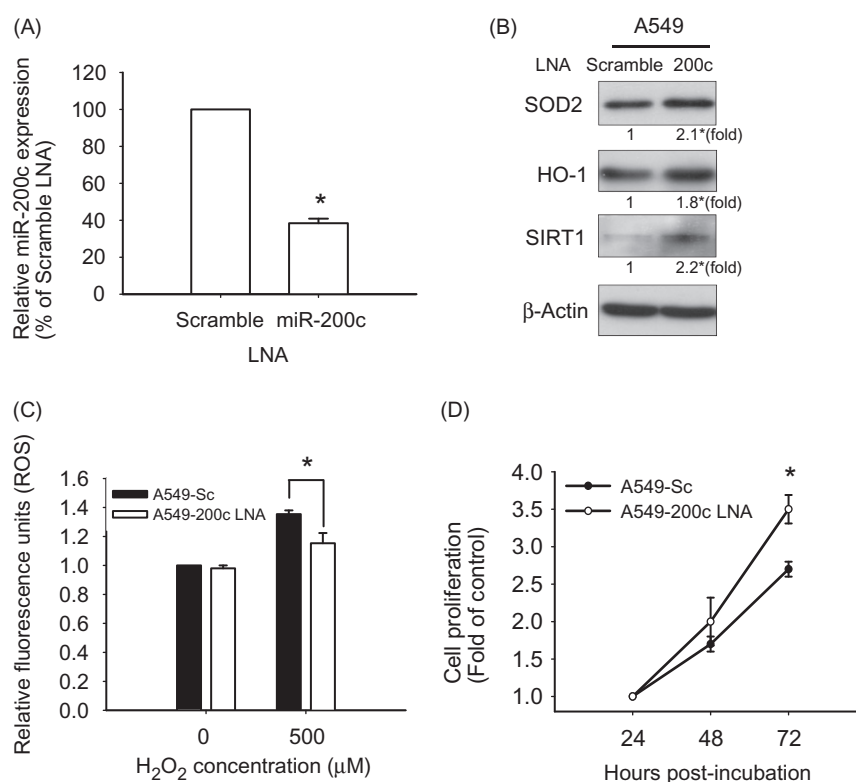


**Figure 6.** Inhibition of miR-200c increased the antioxidant capacity of A549 cells to reduce the ROS upon  $H_2O_2$  stimulation and increased cell proliferation. (A) Real-time PCR analysis of miR-200c expression was determined in miR-200c-LNA or Scramble-LNA transfected A549 cells. Total RNA were collected at 48 h after transfection, and small RNA U6 was used as normalised control. Relative miR-200c expression was shown compared to A549 cells transfected with Scramble-LNA. Values present the average  $\pm$  SD of three experiments. \* $p < .05$  versus Scramble-LNA; (B) Antioxidant-associated proteins, SOD2, HO-1 and SIRT1, of scramble- or miR-200c-LNA transfected A549 cells was analysed by Western blot, and  $\beta$ -actin was used as loading control. The relative expression of the indicated protein was shown as the number normalised to Scramble LNA treated cells by densitometer. The data were repeated for three times as independent experiments. \* $p < .05$  versus Scramble LNA treated cells; (C) oxidative stress was performed using CellROX<sup>®</sup> Deep Red Reagents. After  $H_2O_2$  treatment and culturing for 24 h, cells were stained with CellROX<sup>®</sup> Deep Red Reagents (1000 nM) for 60 min and then analysed by flow cytometry. Data were expressed as the fold change relative to A549-Sc cells without  $H_2O_2$  stimulation. Values present the average  $\pm$  SD of three experiments. \* $p < .05$ ; (D) cell proliferation was measured by the 12-well format assay (as shown in "Material and methods" section) at 24, 48 and 72 h after  $H_2O_2$  treatment (500  $\mu$ M) and converted to a fold of the A549-Sc cells at 24 h. Values present the average  $\pm$  SD of three experiments. \* $p < .05$  versus A549-Sc cells at indicated time point.

## Discussion

The current study clarifies the redox-modulating role and biochemistry of  $H_2O_2$ -induced miR-200c expression in lung cells. A549 and MRC-5 cells were used as a lung epithelial cell and fibroblasts model to determine the effects of miR-200c expression on the antioxidant response. The expression of three genes coding for the antioxidants SOD2, SIRT1, and HO-1 was decreased in the miR-200c-overexpression cells. This modulation of gene expression occurred through distinct mechanisms, the ZEB2 and ERK5 pathways and the direct post-transcriptional modification of the *HMOX1* target.

The regulatory role of miR-200c in the expression of SOD2 has not been completely elucidated. SOD2, a major antioxidant enzyme in the lung, transforms toxic superoxide from the mitochondrial electron transport chain into  $H_2O_2$  and oxygen. In oral and oesophageal cancers, the gene expression of SOD2 seems to be transcriptionally regulated by ZEB2 [38]. MiR-200c overexpression in A549 and MRC-5 cells inhibits SOD2 at the transcriptional and translational levels. The current study supports the notion that ZEB2 plays a major role in regulating SOD2 expression because ZEB2 knock-down in cells reduced SOD2 expression. Moreover, this observation documents, for the first time, the regulatory role of miR-200c in SOD2 expression in the lung.

Studies have reported the antioxidant role of HO-1 [39,40]; however, the miR-200c-induced decrease in HO-1 expression has not been completely delineated. HO-1 expression is mainly regulated at the transcriptional level through a network of signalling pathways that modulate the activities of Nrf2 and Bach1 in response to oxidative stress [41]. Multiple studies have provided evidence indicating that HO-1 expression is regulated by the post-transcriptional modifications of miRNAs in various cell types [42,43]. MiR-200c negatively regulates HO-1 in renal proximal tubular epithelial cells [44], according to the predicted miR-200c binding site in the 3'-UTR of *HMOX1*. In the current study, a luciferase reporter plasmid containing the *HMOX1* 3'-UTR and its control without miR-200c seed sequence *HMOX1D* were constructed, and miR-200c overexpression reduced luciferase expression in A549 cells but not affect the luciferase expression of *HMOX1D*. These findings provide mechanistic details regarding how miR-200c downregulates *HMOX1* expression.

The current study also clarifies mechanisms underlying the inhibition of SIRT1 induction by miR-200c upon oxidant challenge. A possible mechanism is that miR-200c regulates the antioxidant response in the lung, particularly through SIRT1 signalling by controlling its upstream signalling molecule, ERK5. SIRT1 plays a

protective role against oxidative stress-induced injury [45,46]. In the lung, the overexpression of SIRT1 promotes the stability of Nrf2 and increases its transcriptional activity, resulting in the activation of the Nrf2-antioxidant response element signalling pathway and the upregulation of the expression of Nrf2 downstream genes, including SOD2 and HO-1 [47,48]. Thus, the miR-200c-mediated regulation of the ERK5–SIRT1 axis provides a novel mechanism explaining how miRNAs regulate redox homeostasis in a rather complex but delicate manner.

The induction of miR-200c in lung cells leads to the inhibition of cellular antioxidant response and increased susceptibility to oxidative stress and subsequent oxidative damage. Oxidative damage is often accompanied by many deleterious cellular effects, such as decreased cell proliferation [49]. The decreased antioxidant

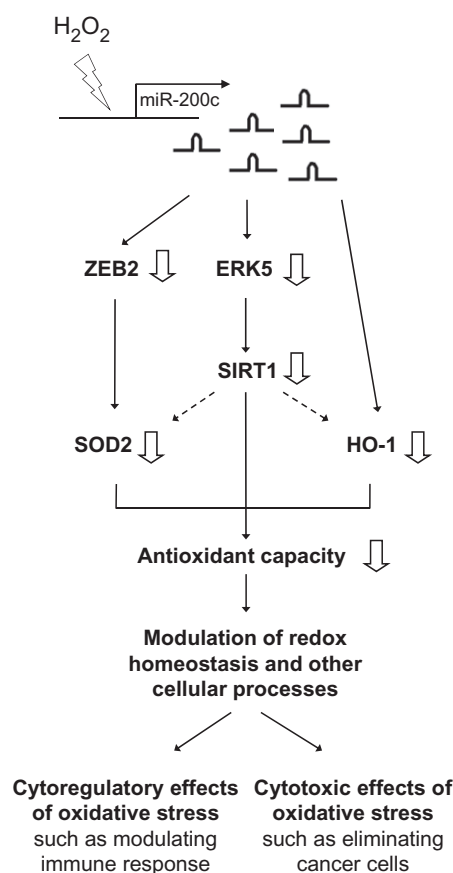


**Figure 7.** A schematic diagram shows how  $H_2O_2$ -induced miR-200c affects the antioxidant response and cellular function. Upon  $H_2O_2$  stimulation, miR-200c is transiently induced in lung, leading to inhibition of the expression of the cellular antioxidant proteins, SOD2, HO-1 and SIRT1 via distinct pathway. The decrease in antioxidant capacity can lead to an increase in oxidative stress, which has dual effects on cellular function. An upward arrow indicates increase in expression or response, while a downward arrow indicates decrease in expression or response.

response in the lung cells because of miR-200c induction can promote particular cellular responses, such as immune and inflammatory responses [49,50,51], as proposed in Figure 7. The scheme proposed in Figure 7 depicts how miR-200c modulates redox homeostasis, in concordance with the findings of previous studies [12,52,53]. MiR-200c regulated SOD2 expression through the ZEB2 pathway. The miR-200c-induced decrease in HO-1 expression was mediated by the direct transcriptional modification of the 3'-UTR of *HMOX1*. The expression of SIRT1 was controlled by regulating its upstream signal molecule, ERK5. Lung cells may be highly adaptable to variations in oxidative stress under various atmospheric conditions because of the concerted effort of these distinct mechanisms of miR-200c to modulate the cellular antioxidant capacity. Our observations also support the regulation of miR-200c in tumour suppression [54–58], which exemplifies the cytotoxic effects of oxidative stress. However, the role of miR-200c in tumorigenesis requires further elucidation. This study helps defining the biochemistry of miR-200c in modulating redox homeostasis and elucidating its possible physiological role in lung tissues.

The current study clearly demonstrates that miR-200c induction upon oxidative stress reduces the antioxidant response in the lung cells by mediating SOD2, HO-1, and SIRT1 expression through distinct mechanisms. MiR-200c potentially plays a major role in modulating redox homeostasis in the lung.

## Acknowledgements

Y.-H.W., H.-R.L., Y.-H.L., P.-H.H. and H.-C.W. were responsible for performing experiments. Y.-H.W., H.-R.L. and D.T.-Y.C. were responsible for planning experiments, analysing data and writing the manuscript. A.S. was responsible for writing the article and English editing.

## Disclosure statement

No potential conflict of interest was reported by the authors.

## Funding

The supports for the current study by grants from Chang Gung University (BMRP098, CMRPD1F0461, CMRPD1C0773, CMRPD3D0161, and CMRPD3D0162), the Ministry of Science and Technology of Taiwan (MOST103-2320-B-182-026-MY2 and MOST105-2320-B-182-031-MY2) and the Ministry of Education of Taiwan (EMRPD1G0181) are greatly appreciated.

## References

- Lewis BP, Burge CB, Bartel DP. Conserved seed pairing, often flanked by adenosines, indicates that thousands of human genes are microRNA targets. *Cell* 2005;120:15–20.
- Berezikov E. Evolution of microRNA diversity and regulation in animals. *Nat Rev Genet* 2011;12:846–860.
- Takahashi K, Yamanaka S. A developmental framework for induced pluripotency. *Development* 2015;142:3274–3285.
- Maltby S, Plank M, Tay HL, Collison A, Foster PS. Targeting microRNA function in respiratory diseases: mini-review. *Front Physiol* 2016;7:21.
- Zhang C, Shu L, Kong AT. MicroRNAs: new players in cancer prevention targeting Nrf2, oxidative stress and inflammatory pathways. *Curr Pharmacol Rep* 2015;1:21–30.
- Narasimhan M, Patel D, Vedpathak D, Rathinam M, Henderson G, Mahimainathan L. Identification of novel microRNAs in post-transcriptional control of Nrf2 expression and redox homeostasis in neuronal, SH-SY5Y cells. *PLoS One*. 2012;7:e51111.
- Wang L, Huang H, Fan Y, Kong B, Hu H, Hu K, et al. Effects of downregulation of microRNA-181a on H2O2-induced H9c2 cell apoptosis via the mitochondrial apoptotic pathway. *Oxid Med Cell Longev* 2014;2014:960362.
- Pizzimenti S, Ferracin M, Sabbioni S, Toaldo C, Pettazoni P, Dianzani MU, et al. MicroRNA expression changes during human leukemic HL-60 cell differentiation induced by 4-hydroxynonenal, a product of lipid peroxidation. *Free Radic Biol Med* 2009;46:282–288.
- Zhou L, Wang L, Song L, Liu R, Zhang H, Huang M, Chen H. The identification and characteristics of immune-related microRNAs in haemocytes of oyster *Crassostrea gigas*. *PLoS One* 2014;9:e88397.
- Magenta A, Greco S, Gaetano C, Martelli F. Oxidative stress and microRNAs in vascular diseases. *IJMS* 2013;14:17319–17346.
- Mateescu B, Batista L, Cardon M, Gruosso T, de Feraudy Y, Mariani O, et al. miR-141 and miR-200a act on ovarian tumorigenesis by controlling oxidative stress response. *Nat Med* 2011;17:1627–1635.
- Magenta A, Cencioni C, Fasanaro P, Zaccagnini G, Greco S, Sarra-Ferraris G, et al. miR-200c is upregulated by oxidative stress and induces endothelial cell apoptosis and senescence via ZEB1 inhibition. *Cell Death Differ* 2011;18:1628–1639.
- Li G, Luna C, Qiu J, Epstein DL, Gonzalez P. Alterations in microRNA expression in stress-induced cellular senescence. *Mech Ageing Dev* 2009;130:731–741.
- Schickel R, Park SM, Murmann AE, Peter ME. miR-200c regulates induction of apoptosis through CD95 by targeting FAP-1. *Mol Cell* 2010;38:908–915.
- Xu S, Zhang R, Niu J, Cui D, Xie B, Zhang B, et al. Oxidative stress mediated-alterations of the microRNA expression profile in mouse hippocampal neurons. *IJMS* 2012;13:16945–16960.
- Watson WH, Ritzenthaler JD, Roman J. Lung extracellular matrix and redox regulation. *Redox Biol* 2016;8:305–315.
- Aversa S, Marseglia L, Manti S, D'Angelo G, Cuppari C, David A, et al. Ventilation strategies for preventing oxidative stress-induced injury in preterm infants with



- respiratory disease: an update. *Paediatr Respir Rev* 2016;17:71–79.
18. Ni L, Chuang CC, Zuo L. Fine particulate matter in acute exacerbation of COPD. *Front Physiol* 2015;6:294.
  19. Ferrari RS, Andrade CF. Oxidative stress and lung ischemia-reperfusion injury. *Oxid Med Cell Longev* 2015;2015:590987.
  20. Mannam P, Srivastava A, Sugunaraj JP, Lee PJ, Sauler M. Oxidants in acute and chronic lung disease. *J Blood Lymph* 2014;4:pii:1000128.
  21. Antus B, Kardos Z. Oxidative stress in COPD: molecular background and clinical monitoring. *CMC* 2015;22: 627–650.
  22. Jiang L, Diaz PT, Best TM, Stimpfl JN, He F, Zuo L. Molecular characterization of redox mechanisms in allergic asthma. *Ann Allergy Asthma Immunol* 2014;113:137–142.
  23. Sundar IK, Yao H, Rahman I. Oxidative stress and chromatin remodeling in chronic obstructive pulmonary disease and smoking-related diseases. *Antioxid Redox Signal* 2013;18:1956–1971.
  24. Zhao Q, Mao A, Yan J, Sun C, Di C, Zhou X, et al. Downregulation of Nrf2 promotes radiation-induced apoptosis through Nrf2 mediated Notch signaling in non-small cell lung cancer cells. *Int J Oncol* 2016;48: 765–773.
  25. Wu YH, Chiu DT, Lin HR, Tang HY, Cheng ML, Ho HY. Glucose-6-phosphate dehydrogenase enhances antiviral response through downregulation of NADPH sensor HSCARG and upregulation of NF-kappaB signaling. *Viruses* 2015;7:6689–6706.
  26. Reddy SS, Chauhan P, Maurya P, Saini D, Yadav PP, Barthwal MK. Coagulin-L ameliorates TLR4 induced oxidative damage and immune response by regulating mitochondria and NOX-derived ROS. *Toxicol Appl Pharmacol* 2016;309:87–100.
  27. Lin HR, Wu YH, Yen WC, Yang CM, Chiu DT. Diminished COX-2/PGE2-mediated antiviral response due to impaired NOX/MAPK signaling in G6PD-knockdown lung epithelial cells. *PLoS One* 2016;11:e0153462.
  28. Al-Khafaji AB, Tohme S, Yazdani HO, Miller D, Huang H, Tsung A. Superoxide induces neutrophil extracellular trap formation in a TLR-4 and NOX-dependent mechanism. *Mol Med* 2016;22:621–631.
  29. Budinger GR, Mutlu GM, Urich D, Soberanes S, Buccellato LJ, Hawkins K, et al. Epithelial cell death is an important contributor to oxidant-mediated acute lung injury. *Am J Respir Crit Care Med* 2011;183: 1043–1054.
  30. Villegas L, Stidham T, Nozik-Grayck E. Oxidative stress and therapeutic development in lung diseases. *J Pulm Respir Med* 2014;4:194.
  31. Xu J, Li T, Wu H, Xu T. Role of thioredoxin in lung disease. *Pulm Pharmacol Ther* 2012;25:154–162.
  32. Rahman I, Biswas SK, Jimenez LA, Torres M, Forman HJ. Glutathione, stress responses, and redox signaling in lung inflammation. *Antioxid Redox Signal* 2005;7:42–59.
  33. Wang Y, Weng T, Gou D, Chen Z, Chintagari NR, Liu L. Identification of rat lung-specific microRNAs by microRNA microarray: valuable discoveries for the facilitation of lung research. *BMC Genomics* 2007;8:29.
  34. Zhou X, Wang Y, Shan B, Han J, Zhu H, Lv Y, et al. The downregulation of miR-200c/141 promotes ZEB1/2 expression and gastric cancer progression. *Med Oncol* 2015;32:428.
  35. Kinnula VL, Crapo JD. Superoxide dismutases in the lung and human lung diseases. *Am J Respir Crit Care Med* 2003;167:1600–1619.
  36. Yuan Y, Cruzat VF, Newsholme P, Cheng J, Chen Y, Lu Y. Regulation of SIRT1 in aging: roles in mitochondrial function and biogenesis. *Mech Ageing Dev* 2016;155: 10–21.
  37. Lopez-Royuela N, Rathore MG, Allende-Vega N, Annicotte JS, Fajas L, Ramachandran B, et al. Extracellular-signal-regulated kinase 5 modulates the antioxidant response by transcriptionally controlling Sirtuin 1 expression in leukemic cells. *Int J Biochem Cell Biol* 2014;53:253–261.
  38. Kinugasa H, Whelan KA, Tanaka K, Natsuzaka M, Long A, Guo A, et al. Mitochondrial SOD2 regulates epithelial-mesenchymal transition and cell populations defined by differential CD44 expression. *Oncogene* 2015;34:5229–5239.
  39. Ryter SW, Choi AM. Heme oxygenase-1: redox regulation of a stress protein in lung and cell culture models. *Antioxid Redox Signal* 2005;7:80–91.
  40. Shekhawat GS, Verma K. Haem oxygenase (HO): an overlooked enzyme of plant metabolism and defence. *J Exp Bot* 2010;61:2255–2270.
  41. Kozakowska M, Szade K, Dulak J, Jozkowicz A. Role of heme oxygenase-1 in postnatal differentiation of stem cells: a possible cross-talk with microRNAs. *Antioxid Redox Signal* 2014;20:1827–1850.
  42. Xiao S, Wang X, Ni H, Li N, Zhang A, Liu H, et al. MicroRNA miR-24-3p promotes porcine reproductive and respiratory syndrome virus replication through suppression of heme oxygenase-1 expression. *J Virol* 2015;89:4494–4503.
  43. Skrzypek K, Tertilt M, Golda S, Ciesla M, Weglarczyk K, Collet G, et al. Interplay between heme oxygenase-1 and miR-378 affects non-small cell lung carcinoma growth, vascularization, and metastasis. *Antioxid Redox Signal* 2013;19:644–660.
  44. Stachurska A, Ciesla M, Kozakowska M, Wolfram S, Boesch-Saadatmandi C, Rimbach G, et al. Cross-talk between microRNAs, nuclear factor E2-related factor 2, and heme oxygenase-1 in ochratoxin A-induced toxic effects in renal proximal tubular epithelial cells. *Mol Nutr Food Res* 2013;57:504–515.
  45. Alcendor RR, Gao S, Zhai P, Zablocki D, Holle E, Yu X, et al. Sirt1 regulates aging and resistance to oxidative stress in the heart. *Circ Res* 2007;100:1512–1521.
  46. Wang SJ, Zhao XH, Chen W, Bo N, Wang XJ, Chi ZF, Wu W. Sirtuin 1 activation enhances the PGC-1alpha/mitochondrial antioxidant system pathway in status epilepticus. *Mol Med Rep* 2015;11:521–526.
  47. Ding YW, Zhao GJ, Li XL, Hong GL, Li MF, Qiu QM, et al. SIRT1 exerts protective effects against paraquat-induced injury in mouse type II alveolar epithelial cells by deacetylating NRF2 in vitro. *Int J Mol Med* 2016;37:1049–1058.
  48. Miyashita H, Watanabe T, Hayashi H, Suzuki Y, Nakamura T, Ito S, et al. Angiogenesis inhibitor

- vasohibin-1 enhances stress resistance of endothelial cells via induction of SOD2 and SIRT1. *PLoS One* 2012;7:e46459.
49. Yang HC, Wu YH, Liu HY, Stern A, Chiu DT. What has passed is prolog: new cellular and physiological roles of G6PD. *Free Radic Res* 2016;50:1047–1064.
  50. Grasberger H, Gao J, Nagao-Kitamoto H, Kitamoto S, Zhang M, Kamada N, et al. Increased expression of DUOX2 is an epithelial response to mucosal dysbiosis required for immune homeostasis in mouse intestine. *Gastroenterology* 2015;149:1849–1859.
  51. Leoncini S, De Felice C, Signorini C, Zollo G, Cortelazzo A, Durand T, et al. Cytokine dysregulation in MECP2- and CDKL5-related Rett syndrome: relationships with aberrant redox homeostasis, inflammation, and omega-3 PUFAs. *Oxid Med Cell Longev* 2015;2015: 421624.
  52. Chuang TD, Ho M, Khorram O. The regulatory function of miR-200c on inflammatory and cell-cycle associated genes in SK-LMS-1, a leiomyosarcoma cell line. *Reprod Sci* 2015;22:563–571.
  53. Cortez MA, Valdecanas D, Zhang X, Zhan Y, Bhardwaj V, Calin GA, et al. Therapeutic delivery of miR-200c enhances radiosensitivity in lung cancer. *Mol Ther* 2014;22:1494–1503.
  54. Li J, Tan Q, Yan M, Liu L, Lin H, Zhao F, et al. miRNA-200c inhibits invasion and metastasis of human non-small cell lung cancer by directly targeting ubiquitin specific peptidase 25. *Mol Cancer* 2014;13:166.
  55. Bai T, Dong DS, Pei L. Synergistic antitumor activity of resveratrol and miR-200c in human lung cancer. *Oncol Rep* 2014;31:2293–2297.
  56. Zeng Z, Chen Z, Xu S, Zhang Q, Wang X, Gao Y, Zhao KS. Polydatin protecting kidneys against hemorrhagic shock-induced mitochondrial dysfunction via SIRT1 activation and p53 deacetylation. *Oxid Med Cell Longev* 2016;2016:1737185.
  57. Koutsaki M, Spandidos DA, Zaravinos A. Epithelial-mesenchymal transition-associated miRNAs in ovarian carcinoma, with highlight on the miR-200 family: prognostic value and prospective role in ovarian cancer therapeutics. *Cancer Lett* 2014;351:173–181.
  58. Nishijima N, Seike M, Soeno C, Chiba M, Miyanaga A, Noro R, et al. miR-200/ZEB axis regulates sensitivity to nintedanib in non-small cell lung cancer cells. *Int J Oncol* 2016;48:937–944.



# Pterostilbene, a Methoxylated Resveratrol Derivative, Efficiently Eradicates Planktonic, Biofilm, and Intracellular MRSA by Topical Application

Shih-Chun Yang<sup>1</sup>, Chih-Hua Tseng<sup>2,3,4,5</sup>, Pei-Wen Wang<sup>6</sup>, Po-Liang Lu<sup>7,8</sup>, Yi-Han Weng<sup>1</sup>, Feng-Lin Yen<sup>5,9\*</sup> and Jia-You Fang<sup>1,10,11\*</sup>

<sup>1</sup>Pharmaceutics Laboratory, Graduate Institute of Natural Products, Chang Gung University, Taoyuan, Taiwan, <sup>2</sup>School of Pharmacy, College of Pharmacy, Kaohsiung Medical University, Kaohsiung, Taiwan, <sup>3</sup>Research Center for Natural Products and Drug Development, Kaohsiung Medical University, Kaohsiung, Taiwan, <sup>4</sup>Center for Infectious Disease and Cancer Research, Kaohsiung Medical University, Kaohsiung, Taiwan, <sup>5</sup>Department of Fragrance and Cosmetic Science, College of Pharmacy, Kaohsiung Medical University, Kaohsiung, Taiwan, <sup>6</sup>Department of Medical Research, China Medical University Hospital, China Medical University, Taichung, Taiwan, <sup>7</sup>Department of Internal Medicine, Kaohsiung Medical University Hospital, Kaohsiung, Taiwan, <sup>8</sup>College of Medicine, Kaohsiung Medical University, Kaohsiung, Taiwan, <sup>9</sup>Institute of Biomedical Sciences, National Sun Yat-Sen University, Kaohsiung, Taiwan, <sup>10</sup>Research Center for Food and Cosmetic Safety and Research Center for Chinese Herbal Medicine, Chang Gung University of Science and Technology, Taoyuan, Taiwan, <sup>11</sup>Department of Anesthesiology, Chang Gung Memorial Hospital, Taoyuan, Taiwan

## OPEN ACCESS

### Edited by:

Patrick Rik Butaye,  
Ghent University, Belgium

### Reviewed by:

Tom Coenye,  
Ghent University, Belgium  
Osmar Nascimento Silva,  
Universidade Católica Dom Bosco,  
Brazil

### \*Correspondence:

Feng-Lin Yen  
flyen@kmu.edu.tw  
Jia-You Fang  
fajy@mail.cgu.edu.tw

### Specialty section:

This article was submitted to  
Antimicrobials, Resistance and  
Chemotherapy,  
a section of the journal  
Frontiers in Microbiology

**Received:** 02 March 2017

**Accepted:** 31 May 2017

**Published:** 13 June 2017

### Citation:

Yang S-C, Tseng C-H, Wang P-W,  
Lu P-L, Weng Y-H, Yen F-L and  
Fang J-Y (2017) Pterostilbene, a  
Methoxylated Resveratrol Derivative,  
Efficiently Eradicates Planktonic,  
Biofilm, and Intracellular MRSA by  
Topical Application.  
Front. Microbiol. 8:1103.  
doi: 10.3389/fmicb.2017.01103

Pterostilbene is a methoxylated derivative of resveratrol originated from natural sources. We investigated the antibacterial activity of pterostilbene against drug-resistant *Staphylococcus aureus* and the feasibility of using it to treat cutaneous bacteria. The antimicrobial effect was evaluated using an *in vitro* culture model and an *in vivo* mouse model of cutaneous infection. The minimum inhibitory concentration (MIC) assay demonstrated a superior biocidal activity of pterostilbene compared to resveratrol (8~16-fold) against methicillin-resistant *S. aureus* (MRSA) and clinically isolated vancomycin-intermediate *S. aureus* (VISA). Pterostilbene was found to reduce MRSA biofilm thickness from 18 to 10  $\mu\text{m}$  as detected by confocal microscopy. Pterostilbene showed minimal toxicity to THP-1 cells and was readily engulfed by the macrophages, facilitating the eradication of intracellular MRSA. Pterostilbene exhibited increased skin absorption over resveratrol by 6-fold. Topical pterostilbene application improved the abscess formation produced by MRSA by reducing the bacterial burden and ameliorating the skin architecture. The potent anti-MRSA capability of pterostilbene was related to bacterial membrane leakage, chaperone protein downregulation, and ribosomal protein upregulation. This mechanism of action was different from that of resveratrol according to proteomic analysis and molecular docking. Pterostilbene has the potential to serve as a novel class of topically applied agents for treating MRSA infection in the skin while demonstrating less toxicity to mammalian cells.

**Keywords:** pterostilbene, resveratrol, MRSA, skin infection, biofilm, proteomics

## INTRODUCTION

*Staphylococcus aureus* (*S. aureus*) is the main cause of bacterial infection in community settings and hospitals. The mortality produced by *S. aureus* is higher than the sum of viral hepatitis, human immunodeficiency virus, tuberculosis, and influenza in the United States (Hoyert and Xu, 2012). Conventional antibiotics have the ability to fight against *S. aureus* infection. Nevertheless, the multi-drug-resistant *S. aureus* strains such as methicillin-resistant *S. aureus* (MRSA) are an increasing health threat and economic burden. It is reported that there were 23,000 deaths due to MRSA in the United States in 2014 (Barman et al., 2016). *S. aureus* is frequently found in the skin where it may cause cellulitis, folliculitis, and abscess (Water et al., 2015). The management of cutaneous infection has been complicated by the emergence of MRSA. Moreover, the infections associated with biofilm and intracellular MRSA are difficult to cure because of their inherent resistance to antimicrobial drugs and host cells. Biofilm is the bacterial community enclosed by the self-secreted matrix and extracellular polymeric substance forming the barrier that prevents the penetration of antibiotics (Chung and Toh, 2014). The microorganisms become recalcitrant through intracellular persistence in mammalian cells. This urges the development of novel antibacterial agents to overcome the biocidal resistance.

Resveratrol is a natural compound derived from grapes, peanuts, cranberries, and other botanical sources (Figure 1). In addition to its wide bioactivities, resveratrol can inhibit the growth of some pathogenic bacteria and fungi (Chan, 2002; Paulo et al., 2010; Park et al., 2016). Pterostilbene is a methoxylated form of resveratrol that primarily exists in blueberries (Figure 1). It exhibits chemopreventive, anti-inflammatory, anti-atherosclerotic, and neuroprotective activities (Kosuru et al., 2016). Recently, clinical trials have been conducted to assess the prevention of cardiac diseases by pterostilbene (Riche et al., 2014). It has been reported that pterostilbene can assist anti-MRSA activity of oxacillin and may show potent eradication against *Candida albicans* biofilm (Li et al., 2014; Ishak et al., 2016). Some reports have been published to approve the possible candidacy of pterostilbene as an antibacterial agent; however, information about *in vivo* efficacy and the mechanism of action is still lacking. The aim of this study was to evaluate pterostilbene for biocidal activity against planktonic, biofilm, and intracellular bacteria as well as for its *in vivo* capability in skin-infection inhibition.

A panel of MRSA, *Pseudomonas aeruginosa* (*P. aeruginosa*), and drug-resistant clinical isolates was selected to test the antimicrobial activity of pterostilbene and resveratrol for comparison. The cutaneous targeting favors more drug retention in the skin for efficient bacterial eradication. We compared the cutaneous absorption of pterostilbene and resveratrol to evaluate the targeting ability. Whether the skin was tolerant to topically applied pterostilbene was investigated *in vitro* and *in vivo*. Finally, we explored the mechanisms of antibacterial activity of pterostilbene by proteomic analysis and molecular docking.

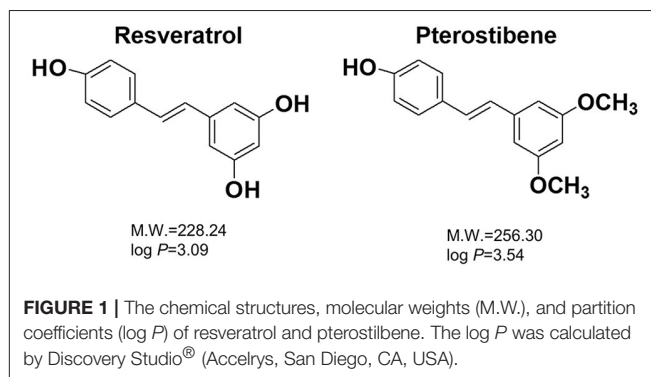


**TABLE 1 |** The MIC and MBC of MRSA, VISA, and *P. aeruginosa* after treatment of resveratrol and pterostilbene.

Bacteria	MIC (mM)		MBC (mM)	
	Resveratrol	Pterostilbene	Resveratrol	Pterostilbene
MRSA (ATCC 33591)	1.25	0.16~0.63	5.00~10.00	0.16~0.63
MRSA (KM-1)	1.25	0.078	5.00~10.00	0.078~0.156
MRSA (KM-2)	1.25	0.078	5.00~10.00	0.078
VISA (KV-1)	1.25	0.078	5.00~10.00	0.078~0.156
VISA (KV-5)	1.25	0.078	5.00~10.00	0.078~0.156
<i>P. aeruginosa</i>	5.00	5.00	10.00	5.00~10.00

KM-1, KM-2, KV-1, and KV-2 are the clinical isolates of bacteria.  
Each value represents the mean  $\pm$  S.D. ( $n = 3$ ).

## MATERIALS AND METHODS

### Bacterial Strains and Culture Conditions

Table 1 summarizes the strains employed in this report. We used the Gram-positive (MRSA, ATCC 33591) and Gram-negative (*P. aeruginosa*) bacteria. Four drug-resistant clinical isolates were used, two of which were MRSA (KM-1 and KM-2). The other two isolates were vancomycin-intermediate *S. aureus* (VISA, KV-1, and KV-5). All clinical strains were provided by Kaohsiung Medical University Hospital. The bacteria were grown in trypticase soy broth (TSB) at 37°C until achieving OD<sub>600</sub> = 3.0 under aerobic conditions.

### Minimum Inhibitory Concentration (MIC) and Minimum Bactericidal Concentration (MBC)

The antibacterial activity of resveratrol and pterostilbene (Sigma-Aldrich, St. Louis, MO, USA) was evaluated by MIC and MBC determination. A 2-fold broth-dilution method was utilized to assess MIC. The bacterial population was exposed to several dilutions of compounds ranging from 0.018 to 10 mM and incubated at 37°C for 16 h. An ELISA reader was used to detect MIC at 595 nm. MIC was measured as the highest dilution revealing no bacterial growth. For MBC assay, the bacteria were diluted in PBS and positioned on plates. The compounds with different dilutions were incubated with the microorganisms for



16 h. The colony-forming unit (CFU) was counted. The highest dilution, which resulted in a 99.9% reduction of cell numbers, was recognized as MBC.

## Bacterial Survival Detected by Confocal Microscopy

The viability of MRSA after resveratrol or pterostilbene treatment at 1.25 mM was examined using SYTO9 reagent (Molecular Probes, Eugene, OR, USA). The bacterial pellet was obtained by centrifugation at 12,000 rpm for 3 min. The pellet was resuspended in culture medium (1 ml) with the compounds. After treatment at 37°C for 4 h, the samples were stained with SYTO9 and incubated for 15 min. The samples were visualized under a confocal microscope (Leica TCS SP8, Wetzlar, Germany).

## Disk Diffusion Assay

The assay was performed by plating MRSA ( $OD_{600} = 0.8$ ) on the agar plate. The 6 mm-diameter disk was put on the agar medium, and the compounds (1.25 mM) with a volume of 10  $\mu$ l were pipetted into the disk. The plate was incubated at 37°C for 12 h. Subsequently, the diameter of the inhibition zone was measured.

## Total Protein Amount

MRSA was grown in TSB to  $OD_{600} = 1.0$  and then treated with the compounds at 2 mM at 37°C for 2 h. After centrifugation, the pellet was resuspended with water (0.5 ml). Following sonication for 20 min, MRSA was centrifuged at 4°C and 10,000 rpm for 15 min. The total protein amount of MRSA was estimated using a Bio-Rad protein assay kit (Hercules, CA, USA) in ELISA at 595 nm.

## Transmission Electron Microscopy (TEM)

MRSA at  $OD_{600} = 1.0$  was treated with pterostilbene (0.5 mM) in TSB at 37°C for 4 h. The bacteria were fixed with 4% glutaldehyde, followed by 1% osmium tetroxide fixation for 2 h. After dehydration in an ascending series of ethanol, the sample was embedded in Spurr's resin. The bacteria sample on the carbon grid was then observed under TEM (JEOL JEM-1200Ex, Tokyo, Japan).

## Biofilm Assay

The MRSA biofilm was grown in a Cellview® dish by incubating the bacteria ( $OD_{600} = 0.1$ ) in TSB containing 1% glucose at 37°C for 24 h. The biofilm was then treated with pterostilbene at a dose of 0.5 mM for 24 h. The biofilm was marked by a Live/Dead BacLight® kit (Molecular Probes) for 15 min. The biofilm was gently rinsed with PBS. The 3D biofilm structure and the biofilm thickness was determined by confocal microscopy.

## Intracellular MRSA Killing

The macrophages differentiated from THP-1 monocytes by phorbol myristate acetate (0.1  $\mu$ M) were used as the host cells to evaluate the activity of pterostilbene toward intracellular bacteria. THP-1 were infected by MRSA at different cell numbers ( $2 \times 10^5$ ,  $2 \times 10^6$ ,  $5 \times 10^6$ , and  $1 \times 10^7$  cells/ml) for 20 min. After being washed with PBS, the cells were incubated with pterostilbene at 0.1 mM. After a 4-h period, the samples were rinsed with PBS. Triton X-100 (1%) was incorporated into the medium for cell

lysis. The resultant solution was cultured on the agar plate for 20 h to count CFU.

## Animals

Female nude mice (8 weeks old) were obtained from National Laboratory Animal Center (Taipei, Taiwan). The experiments were performed in strict accordance with the recommendations set forth in the Guidelines for the Institutional Animal Care and Use Committee of Chang Gung University.

## Cutaneous Absorption Test

The *in vitro* cutaneous absorption of resveratrol and pterostilbene was conducted using Franz diffusion cell. The excised dorsal skin of the nude mouse was mounted between the donor and receptor with the stratum corneum (SC) facing upward from the donor. The donor and receptor were filled with 20% propylene glycol (PG)/pH 7.4 buffer (0.5 ml) and 30% ethanol/pH 7.4 buffer (5.5 ml), respectively. Either the supersaturated suspension (15 mM) or the saturated solution of the compounds was placed in the donor to examine permeability. The other processes and the permeant amount extracted from the skin were the same as in our previous study (Lin et al., 2016). Both the skin deposition (nmol/mg) and flux (nmol/cm<sup>2</sup>/h) were determined as the permeation capability for the supersaturated suspension. The flux was calculated by a linear regression from the slope of the penetrated amount-time curves. In the case of the saturated solution, the calibrated skin accumulation (CSA) and permeability coefficient ( $K_p$ ) were computed using the skin deposition and flux divided by the saturated solubility (applied permeant dose) in the donor, respectively.

## In vivo Cutaneous MRSA Infection

The nude mouse back was intradermally injected with MRSA ( $1 \times 10^7$  CFU) in PBS (150  $\mu$ l). Then 20% PG/pH 7.4 buffer (control group) or pterostilbene (15 mM) with a volume of 0.2 ml was topically applied above the injected site every 24 h for 7 consecutive days. The macroscopic appearance of the skin was monitored at day 1, 3, and 7. Transepidermal water loss (TEWL, TM300, Courage and Khazaka, Köln, Germany) and the yellow-green color (b\*) of the skin were analyzed from 0 to 7 days post-administration. At the end of the experiment (day 7), the mouse was sacrificed and the treated skin site was excised for histological examination and MRSA counting. The skin specimen was homogenized by MagNA Lyser (Roche, Indianapolis, IN, USA). The bacterial cell number was determined by plating serially diluted skin homogenate on TSB for 24 h. The CFU was estimated as the corresponding number of MRSA.

## Keratinocyte Cytotoxicity

The possible cytotoxicity of resveratrol and pterostilbene on keratinocytes (HaCaT cells) was evaluated by MTT assay as described previously (Pan et al., 2015). Briefly, HaCaT cells were seeded in a 96-well plate with  $1 \times 10^4$  cells/well at 37°C for 24 h. Each well was treated with resveratrol or pterostilbene at 0.01, 0.05, and 0.125 mM for 24 h. MTT (0.5 mg/ml) was pipetted into the well and then incubated for 3 h. The ELISA reader at 550 nm



was used to estimate the cell viability (%). All procedures were done in the dark.

Intracellular adenosine triphosphate (ATP) was also detected by a bioluminescence assay based on the ATP-dependent luciferin-luciferase reaction using a commercial kit as described previously (Hidalgo and Domínguez, 1998). To determine the viability by the ATP content, after 24 h of culture, 100  $\mu$ l of CellTiter-Glo<sup>®</sup> reagent (Promega, Madison, WI, USA) was added to the wells. The mixture was shaken for 5 min to elicit cell lysis. The plate was incubated at room temperature for 10 min to stabilize the luminescent signal. The luminescence was detected with a luminometer (Chameleon V, Hidex, Finland).

## Human Neutrophil Cytotoxicity

The human neutrophils were obtained from healthy volunteers, all between 20 and 30 years of age, using a protocol approved by the Institutional Review Board at Chang Gung Memorial Hospital. The neutrophil-purification procedure was performed according to our previous study (Yang et al., 2016). The neutrophils ( $6 \times 10^5$  cells/well) were incubated with the compounds (0.01, 0.05, and 0.125 mM) for 15 min at 37°C. Lactate dehydrogenase (LDH) leakage from the neutrophils was determined using a CytoTox 96<sup>®</sup> kit (Promega, Fitchburg, WI, USA). The cytotoxicity was calculated by LDH release in cell-free medium as a percentage of total LDH release. The complete LDH leakage was detected by 0.1% Triton X-100 exposure.

## In vivo Cutaneous Irritation

The 20% PG/pH 7.4 buffer with or without pterostilbene (15 mM) at a volume of 0.6 ml was applied daily on the nude mouse back for 7 consecutive days. The application area was  $1.5 \times 1.5$  cm<sup>2</sup>. The experimental protocol was the same as with the previous work (Pan et al., 2014). After a 7-day administration, the treated skin area was monitored by macroscopic and microscopic observations. Hematoxylin and eosin (H&E) were utilized to stain skin slices for histological observation under optical microscopy (Olympus IX81, Tokyo, Japan).

## Proteomic Analysis

The cultured MRSA was treated by resveratrol or pterostilbene at 2 mM for 2 h. The bacterial protein preparation protocol was the same as the method of total-protein-amount measurement. The SDS-PAGE was performed with a 5% stacking gel and a 10% separating gel followed by Coomassie blue staining. The stained bands were withdrawn and digested by trypsin at 37°C overnight. The digested proteins were acidified with 0.5% trichloroacetic acid and then loaded into an AnchorChip<sup>®</sup> 600/384. A Bruker Ultraflex<sup>®</sup> spectrometer (Bremen, Germany) was used to analyze the MALDI-TOF/TOF mass. The detailed procedures were shown in our previous study (Pan et al., 2010).

## Molecular Modeling for Compound-Protein Interaction

The crystal structure of the MRSA proteins was used for molecular docking with resveratrol and pterostilbene by Discovery Studio<sup>®</sup> (Accelrys, San Diego, CA, USA). The superimposition of the compounds with these proteins was

calculated to observe the conformation and ligand-binding activity. The dock score energy was also computed after conducting the molecular docking simulation of resveratrol or pterostilbene with the proteins.

## Statistical Analysis

The data presented as the mean and standard deviation (S.D.). The difference in the data of the different experimental groups was analyzed by the Kruskal-Wallis test. The *post-hoc* test for checking individual differences was Dunn's test. Significance was indicated as  $p < 0.05$ .

## RESULTS

### Comparison of Antibacterial Activity between Resveratrol and Pterostilbene

We assessed the antibacterial activity of resveratrol and pterostilbene against a panel of pathogens representing MRSA, clinical strains of MRSA and VISA, and *P. aeruginosa*. **Table 1** lists the MIC and MBC ranges for the compounds against six different species. In contrast to resveratrol, pterostilbene demonstrated potent inhibitory and biocidal activities against the Gram-positive bacteria. The MIC of pterostilbene for the drug-resistant *S. aureus* was 8~16-fold lower than resveratrol. A significant 128-fold reduction in the MBC of pterostilbene was observed when compared to resveratrol. To examine whether the compounds could suppress the growth of Gram-negative bacteria, the susceptibility of *P. aeruginosa* to the two agents was evaluated. Resveratrol and pterostilbene were basically equipotent to *P. aeruginosa* growth inhibition. The potency for killing *P. aeruginosa* could be regarded as low.

The live MRSA strain (ATCC 33591) was viewed under confocal microscopy as illustrated in **Figure 2A**. Resveratrol and pterostilbene did not affect MRSA viability at the concentration of 0.01 mM but significantly reduced the growth at the higher concentrations when compared with the control. Pterostilbene mediated less viable MRSA as compared to resveratrol exposure. The growth inhibition of MRSA by the natural compounds was also recognized using an agar diffusion assay. The inhibition zone with a diameter of 6.9 mm was measured for resveratrol and 10.3 mm for pterostilbene (**Figure 2B**). No significant difference in the inhibition zones between the two compounds was detected for *P. aeruginosa*. Protein reduction deals with the stress response in bacteria treated with antibiotics. The total protein amount in MRSA is estimated after the application of the compounds as shown in **Figure 2C**. Resveratrol and pterostilbene caused a 51 and 56% decrease in total protein compared to the control, respectively. The protein quantity of MRSA after resveratrol and pterostilbene treatments was comparable.

### Antibacterial Activity of Pterostilbene against Biofilm and Intracellular MRSA

**Figure 3A** depicts the TEM photographs of MRSA morphology with and without pterostilbene exposure for 4 h. The intact MRSA (control) displayed a smooth and bright appearance on the cellular surface. When the bacteria were treated with pterostilbene, the cell wall/membrane perturbation was

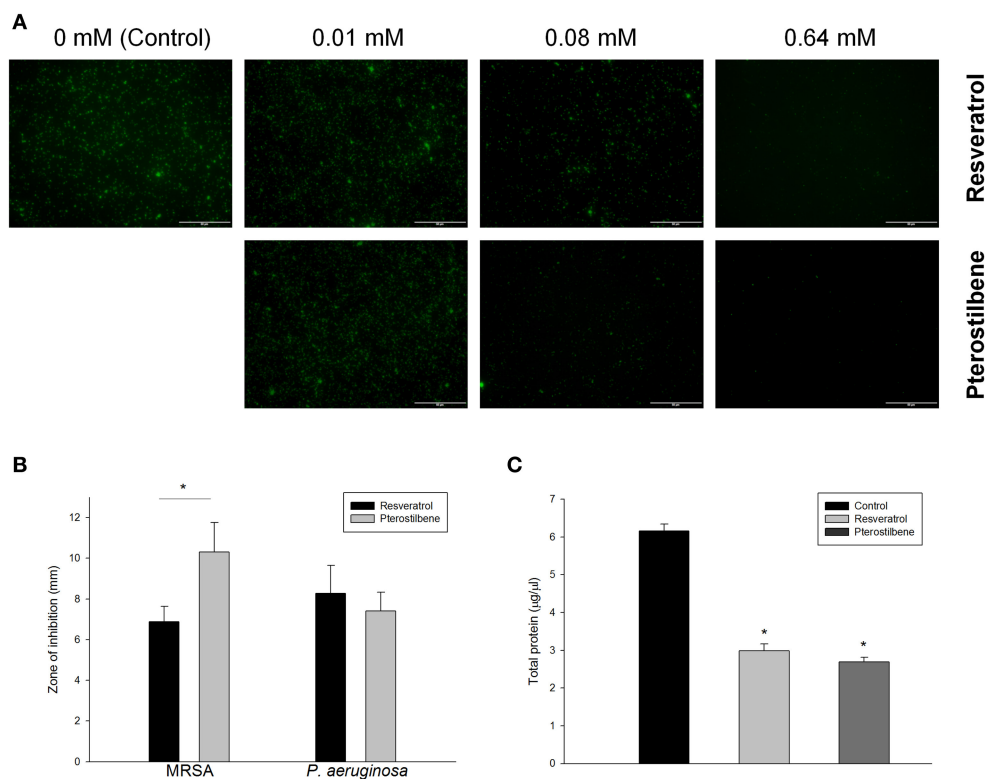


**FIGURE 2 |** Antibacterial activity of resveratrol and pterostilbene: **(A)** the live MRSA strain viewed under confocal microscopy, **(B)** zone of inhibition measured from disk diffusion assay, and **(C)** total protein amount in MRSA. Each value represents the mean and SD ( $n = 4$ ).

visualized (red arrow). The cytoplasm of pterostilbene-treated bacteria became amorphous and empty, suggesting the loss of cytoplasmic contents. The grainy appearance typical for intact cells was lost as a result of pterostilbene treatment. These observations may indicate that osmotic disturbance caused the MRSA damage.

**Figure 3B** presents the anti-biofilm effect of pterostilbene against MRSA observed by confocal microscopy. Biofilm formation is a predominant virulence factor of MRSA. We stained the viable and dead bacteria using SYTO9 and propidium iodide (PI), respectively. The viable fraction of intact biofilm (green color) showed a well-developed and dense morphology without significant bacterial death (red color). Pterostilbene was active against MRSA biofilm formation due to the decrement of biomass and thickness. As shown in **Figure 3C**, pterostilbene incubation reduced biofilm thickness from 18 to 10  $\mu\text{m}$ . The MRSA death rate in biofilm was significantly increased by pterostilbene. MRSA is difficult to eliminate with traditional antibiotics because of the intracellular persistence. Macrophages are the major immune cells present as the first line of defense against endocytosis bacteria. We evaluated whether pterostilbene could be endocytosed by macrophages for intracellular killing of MRSA. THP-1 cells were infected by different numbers of MRSA as shown in **Figure 3D**. The treatment of infected THP-1 with pterostilbene resulted in a dramatic reduction of live MRSA. This treatment did not cause any cytotoxic effect

on THP-1. A decrease of about 75% in intracellular MRSA survival was detected for pterostilbene treatment. There was no significant difference in the bacterial inhibition percentage among pterostilbene applications on different MRSA burdens.

## Cutaneous Absorption Test

Cutaneous absorption of resveratrol and pterostilbene was compared by Franz cell assembly. Both the skin deposition and penetration across the skin were estimated. The permeant absorption by the skin can be measured as skin deposition, while the cumulative amount in the receptor anticipates the delivery into the deeper skin strata or systemic circulation. The donor permeant concentration was first fixed at an equivalent dose (15 mM). This dose was higher than the saturated solubility of both compounds in a 20% PG vehicle. As summarized in **Table 2**, the skin deposition and flux of pterostilbene are much higher than those of resveratrol. The delivery of pterostilbene into the skin was 6-fold greater than the delivery of resveratrol. The permeants in the donor were also dosed with saturated solution to keep a constant driving force with maximum thermodynamic activity. **Table 2** demonstrates the CSA and  $K_p$  in nude mouse skin. With an equivalent dose, pterostilbene exhibited a higher skin delivery as compared to resveratrol. We showed a 5-fold rise in the deposition compared to resveratrol. To rate the possible anti-MRSA activity of the compounds after topical application, the therapeutic index (TI) was calculated based on

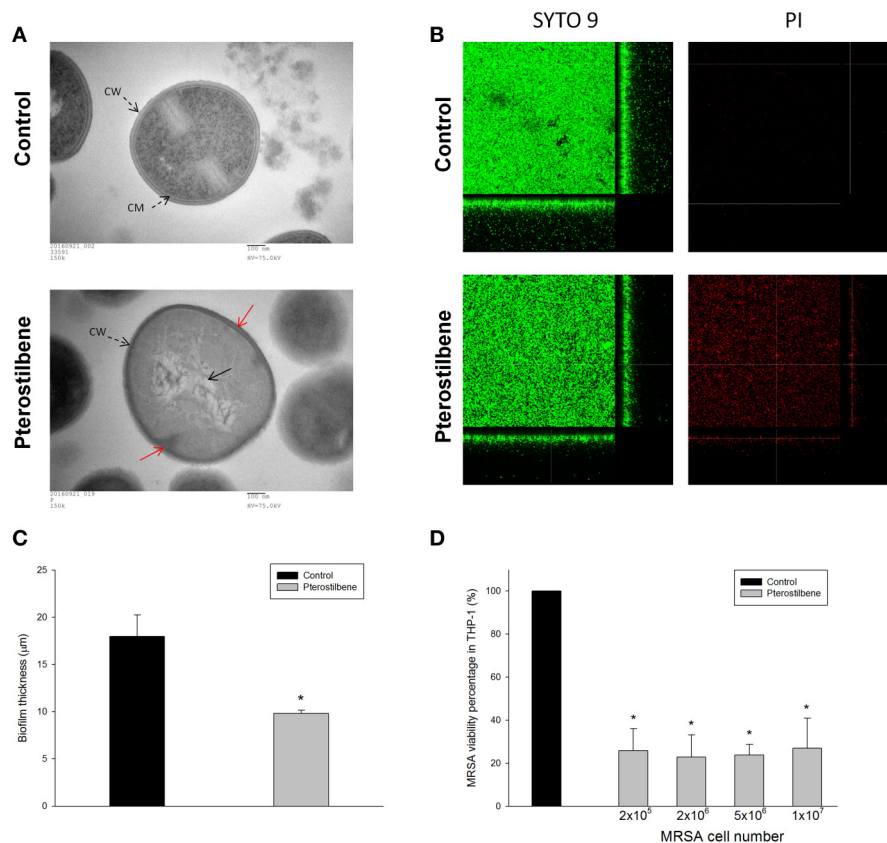


**FIGURE 3 |** Anti-MRSA activity of pterostilbene: **(A)** Morphological changes of MRSA viewed under TEM, **(B)** the three-dimensional images of biofilm, **(C)** the corresponding biofilm thickness, and **(D)** intracellular MRSA killing in macrophages (THP-1). Each value represents the mean and S.D. ( $n = 4$ ).

multiplying the skin deposition and the anti-MRSA inhibition zone as presented in **Figure 2B**. As shown in **Table 2**, the TI of pterostilbene is greater than that of resveratrol in both conditions of equivalent and saturated doses. Pterostilbene gave an 8~9-fold greater TI than resveratrol, with the expectation of an effective antimicrobial capability of topically applied pterostilbene.

### In vivo Cutaneous MRSA Infection

To further determine the therapeutic efficiency of pterostilbene, the nude mouse was challenged with MRSA followed by topical delivery of vehicle control or pterostilbene. The macroscopic observation in **Figure 4A** reveals the skin infection in the control group, which can be seen by the presence of abscess at the injection area (red arrow) after 1 day of injection. The abscess worsened following the increase of incubation time. Application of pterostilbene significantly restrained the size of eschar. There is only a phyma (red arrow) in the injection site after pterostilbene exposure. TEWL was monitored daily to evaluate the skin-barrier function as depicted in **Figure 4B**. Pterostilbene significantly ameliorated the disrupted skin barrier produced by MRSA invasion. The TEWL for pterostilbene application approximated the non-treatment control. The abscess-generated pus revealed a yellow-brown appearance. The yellow-brown color can be quantified by the  $b^*$  axis of colorimetry. As shown in **Figure 4C**,

the yellow-brown level of the injection site in the non-treated control increased following the increase of incubation time. This yellow-brown color could be inhibited by pterostilbene.

Seven days after infection, the mouse was sacrificed and the MRSA burden in the skin was determined. Pterostilbene was effective at inhibiting MRSA growth, resulting in about a 3-log CFU lessening compared to the control (**Figure 4D**). We next examined the skin architecture by H&E staining. As seen in **Figure 4E**, the skin section of MRSA infection (control) reveals total damage to the epidermis, degenerated dermis, and inflammatory cell infiltration. The MRSA burden was mixed with the immune cells in the dermis and subcutis, suggesting a deep inflammation. The infected skin exposed to pterostilbene showed nearly normal features. The immune cell infiltration was largely restricted in the pterostilbene-treated skin.

### Effect of Resveratrol and Pterostilbene on Cytotoxicity

The application of the antibacterial drugs can be limited because of the cytotoxic effect on mammalian cells. The prerequisite of antibacterial agent development is the assurance of safety. As shown in **Figure 5A**, resveratrol and pterostilbene at 0.01 mM were found to be non-toxic to keratinocytes, whereas a mild cytotoxicity at the higher concentrations was detected.

**TABLE 2 |** Nude mouse skin permeation parameters of resveratrol and pterostilbene after *in vitro* percutaneous absorption from 20% PG/pH 7.4 buffer suspension at a determined concentration (15 mM) and at a saturated concentration.

Compound	Suspension (mM)			Saturated solution		
	Skin deposition (nmol/mg)	Flux (nmol/cm <sup>2</sup> /h)	TI <sup>a</sup>	CSA <sup>b</sup> (nmol/mg/solubility)	K <sub>p</sub> <sup>c</sup> (cm/h × 10 <sup>-3</sup> )	TI <sup>a</sup>
Resveratrol	1.71 ± 0.62	5.98 ± 1.20	11.78	0.24 ± 0.05	2.70 ± 2.64	1.65
Pterostilbene	10.40 ± 1.03	41.38 ± 1.14	107.33	1.29 ± 0.21	13.00 ± 1.11	13.31

<sup>a</sup>TI, therapeutic index=skin deposition or CSA × antibacterial inhibition zone.

<sup>b</sup>CSA, calibrated skin accumulation=cumulative amount in the skin/saturated solubility.

<sup>c</sup>K<sub>p</sub>, permeability coefficient=flux/saturated solubility.

The data represent the mean ± S.D. (n = 4).

A higher level of cell viability was observed for pterostilbene (86%) over resveratrol (74%) at the dose of 0.05 mM. We also employed intracellular ATP analysis for evaluating HaCaT viability as shown in **Figure 5B**. The viability could be maintained to >80% after treatment of resveratrol or pterostilbene at the concentration range of 0.01~0.125 mM. Neutrophils were also examined for viability since there is neutrophil-rich infiltrate in the MRSA-infected skin wounds. The neutrophil cytotoxicity can be determined by LDH release associated with membrane damage. LDH assay indicates that resveratrol and pterostilbene at the concentrations of 0.01~0.125 mM can generally maintain neutrophil viability to >80% as shown in **Figure 5C**. There was no significant difference of LDH leakage between the control and the compound-treated groups.

### **In vivo Cutaneous Irritation**

The safety of topically applied pterostilbene was elucidated using a skin irritation test on nude mice. **Figure 6A** shows the macroscopic appearance of the dorsal skin after pterostilbene administration. A slight erythema (red arrow) visualized at the pterostilbene-treated site could be categorized as very mild. The possible irritation of the skin was further checked by microscopic examination as illustrated in **Figure 6B**. The vehicle control displayed an intact morphology without damage. The biopsied skin specimen after pterostilbene exposure showed a comparative structure vs. the control skin, suggesting a preferred biocompatibility to the skin.

### **Proteomic Analysis**

The 2D protein gel electrophoresis combined with MALDI-TOF/TOF mass was employed to analyze the protein profiles of MRSA after treatment with resveratrol and pterostilbene to elucidate the antibacterial mechanisms. **Figure 7A** shows the results of SDS-PAGE. The protein bands of resveratrol- and pterostilbene-treated MRSA were quite different from those of non-treated bacteria. Eleven protein bands differentially expressed in MRSA after compound exposure are labeled in **Figure 7A**. The significant change in the proteins elicited by resveratrol and pterostilbene was determined by mass spectra as demonstrated in **Table 3**. The band numbers in **Figure 7** refer to those in **Table 3**. With respect to resveratrol, seven proteins were upregulated. On the other hand, pterostilbene caused the increased expression of five proteins. Chaperone proteins and glyceraldehyde-3-phosphate dehydrogenase (GAPDH) were

upregulated in resveratrol-treated MRSA but downregulated in the pterostilbene-treated group. The expression of 30S and 50S ribosomal proteins was increased after compound treatment, with pterostilbene showing greater upregulation. A similar trend was observed for alkaline shock protein (ASP).

The possible interaction between the compounds and the selected proteins was examined by a computational study of best docking poses as shown in **Figure 7B**. Both compounds had exhibited the ligand-binding activity to chaperone ClpB but different conformations. The dock score was compared after conducting the molecular docking simulation of the compounds with the proteins as demonstrated in **Figure 7B**. A greater dock score indicates a stable system for a likely binding interaction. We found a stronger binding of chaperone to pterostilbene (dock score = 102) than to resveratrol (dock score = 94). Contrary to this result, a comparable interaction of GAPDH to resveratrol (dock score = 50) and pterostilbene (dock score = 45) was observed. The conformation orientation of resveratrol and pterostilbene to elongation factor G (EFG) was similar, with pterostilbene possessing more amino acid interactions. There was no interaction between ribosomes and the compounds after docking the conformation.

## **DISCUSSION**

The drug resistance of planktonic, biofilm, and intracellular bacteria highlights the need to develop new antibacterial agents. Here we report the discovery that pterostilbene, a natural product, demonstrated antimicrobial activity against MRSA and VISA. Pterostilbene offered superior antibacterial potency compared to resveratrol. The proteomic profiles suggested that the mode of action of pterostilbene was different from that of resveratrol. Pterostilbene was shown to induce cell membrane disruption. It was also observed that pterostilbene reached a therapeutic level to eradicate MRSA in biofilm and the infected host cells. The *in vitro* cytotoxicity of mammalian cells and an *in vivo* skin irritation test had confirmed the preliminary safety of this compound.

Most MRSA found in clinical settings is multidrug resistant (Cihlova et al., 2015). After its introduction in 1958, vancomycin served as the last line of defense for anti-MRSA therapy. However, the emergence of vancomycin-resistant bacteria was reported in the early 2000s (Chang et al., 2016). The findings



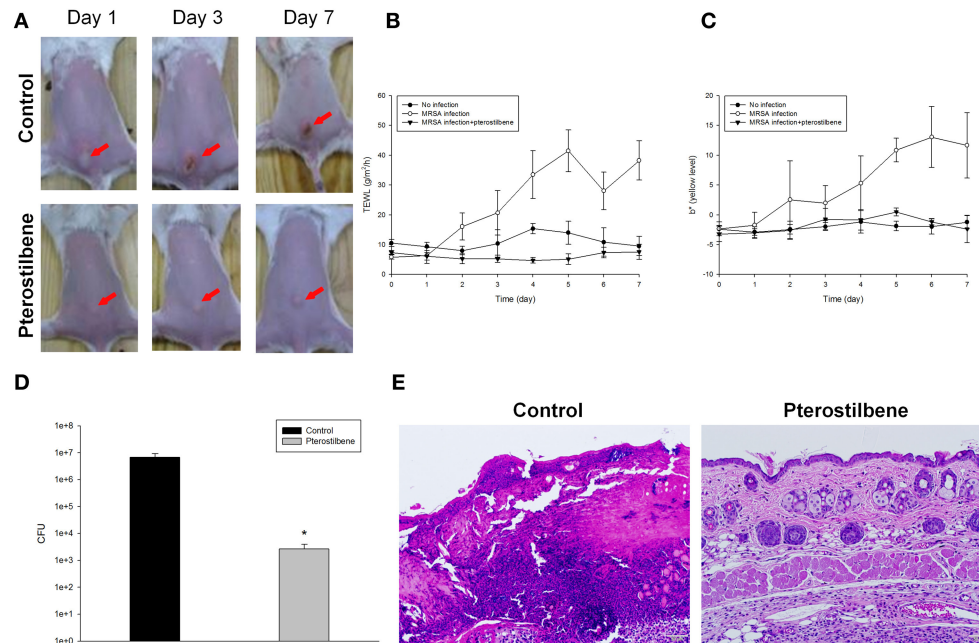


**FIGURE 4 |** *In vivo* topical application of pterostilbene against MRSA: **(A)** The skin surface of mice after treatment of MRSA at day 1, 3, and 7; **(B)** Transepidermal water loss (TEWL) of mice skin treated with MRSA; **(C)** Yellow/blue color ( $b^*$ ) of mice skin treated with MRSA; **(D)** Survival of MRSA in mice skin treated with MRSA. Seven days after infection, skin lesions were cut, homogenized, and bacterial count was determined by CFU assay, and **(E)** Histological observation of mice skin biopsy after treatment of MRSA. On day 7, biopsy specimens were taken immediately after the termination of the experiment and stained with hematoxylin and eosin (H&E). Scale bar = 50  $\mu$ m. Each value represents the mean and S.D. ( $n = 6$ ).

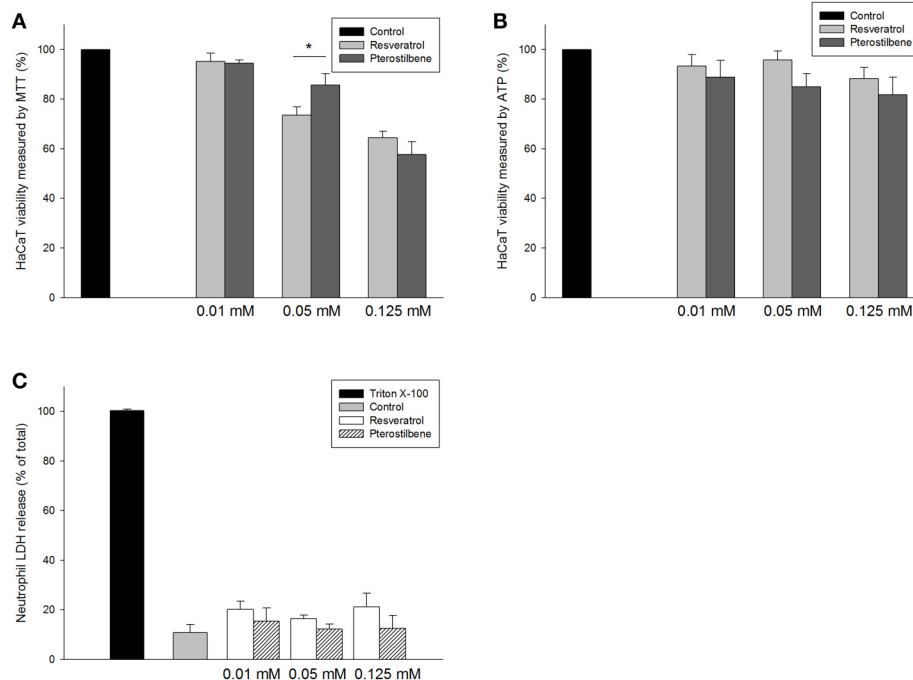


**FIGURE 5 |** *In vitro* cytotoxicity of resveratrol and pterostilbene to: **(A)** HaCaT keratinocyte cell viability measured by MTT assay; **(B)** HaCaT keratinocyte cell viability measured by ATP assay; and **(C)** human neutrophils determined by LDH release. Each value represents the mean  $\pm$  S.D. ( $n = 4$ ). \* $p < 0.05$ .



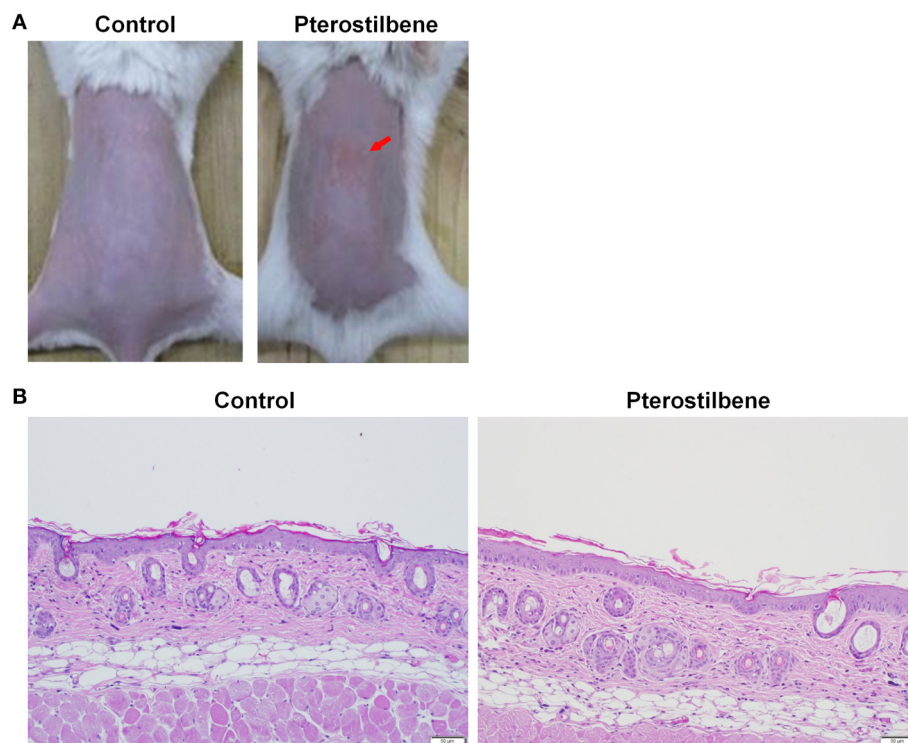


**FIGURE 6 |** Skin tolerance examination of mouse skin a 7-day treatment of topically applied pterostilbene: **(A)** Macroscopic appearance and **(B)** skin specimen stained with hematoxylin and eosin (H&E).

in the *in vitro* antibacterial test intensified the potential of pterostilbene for the treatment of infection caused by *S. aureus* bacteria that are resistant to methicillin and vancomycin. The antibacterial activity of pterostilbene against *P. aeruginosa* was not prominent. The previous study (Paulo et al., 2010) indicates a lesser antimicrobial effect of resveratrol against Gram-negative bacteria than Gram-positive bacteria. This could be because Gram-negative bacteria are structurally and chemically complex. The lack of inhibitory effect on Gram-negative bacteria led to the prediction that pterostilbene would be a drug candidate for specifically treating diseases involving staphylococci.

The phenotypic drug resistance of *S. aureus* has been attributed to multiple factors, including the biofilm activity as a permeation barrier and the intracellular retention in immune cells (Nair et al., 2016). MRSA is known to form biofilm composed of an extracellular polymeric substance matrix, which is tough to combat with conventional antibiotics and host defense. Biofilm fabrication is an essential factor contributing to *S. aureus* infection in the skin (Archer et al., 2011). An ideal anti-MRSA agent should be able to penetrate and destroy the biofilm matrix. Our results indicated that pterostilbene had the activity to eradicate biofilm. The reduction of biofilm formation by pterostilbene was related to the MRSA killing inside the biofilm according to the confocal imaging. The dead bacteria were visualized throughout the full thickness of the biofilm. The biofilm might not be a main barrier for pterostilbene delivery. Pterostilbene was inferred to

stick to the biofilm surface, penetrate the matrix, and then distribute all over the depth of the biofilm. Most antibacterial drugs have poor cellular permeation, resulting in restricted intracellular distribution and unsatisfactory antibacterial activity. For instance, vancomycin is unable to show a biocidal effect on MRSA residing in macrophages (Pumerantz et al., 2011). Antibiotics such as aminoglycosides and  $\beta$ -lactams possess limited cellular penetration owing to low lipophilicity (Mu et al., 2016). The lipophilicity of pterostilbene ( $\log P = 3.54$ ) is greater than that of resveratrol ( $\log P = 3.09$ ). The macrophages might tend to engulf pterostilbene, making this compound a suitable agent to kill MRSA inside the immune cells.

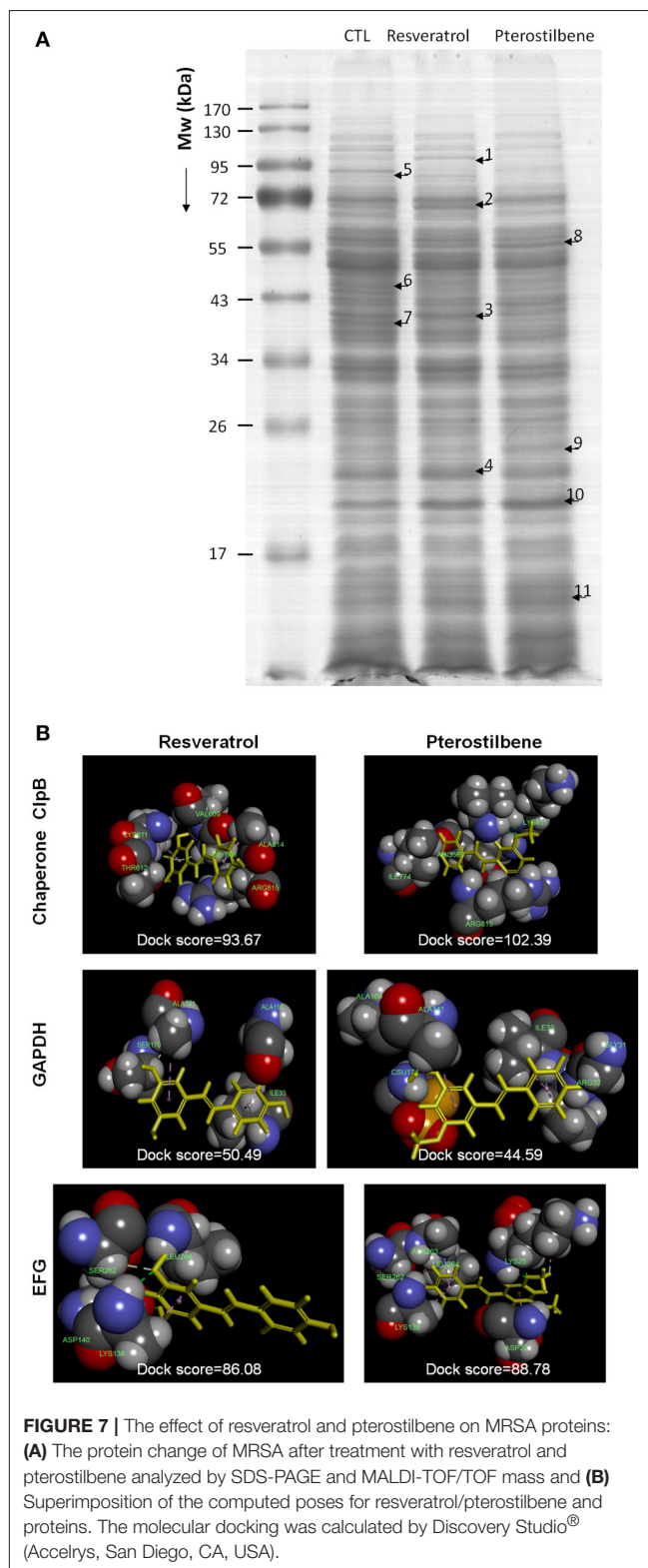
The cutaneous absorption of resveratrol and pterostilbene had demonstrated a similar trend either at the equivalent dose or at the dose of saturated solubility, with pterostilbene showing higher skin delivery than resveratrol. A topically applied drug in aqueous vehicle first partitions and accumulates into the SC, which is rich in lipids. The higher lipophilicity of pterostilbene contributed to the facile deposition in the skin. Previous studies (Lin et al., 2012, 2016) showed that the use of methoxylation was an efficient way to enhance permeant lipophilicity for increased entry into the SC lipid bilayers. Ceramides are the predominant lipids in the SC. The hydrogen bond donor number of the permeant has been recognized as impacting interaction with the head groups of ceramides (Patel et al., 2002; Liu et al., 2011). The hydrogen bond donor number of resveratrol and pterostilbene is 3 and 1, respectively, based on the measurement

by Discovery Studio®. Fewer hydrogen bond numbers in the permeants may accelerate the diffusion because of the increased permeant transport into the non-polar region of the SC. The greater absorption of pterostilbene than resveratrol was also approved in the case of oral delivery. Pterostilbene was reported to have an oral bioavailability of 80% compared to 20% for resveratrol due to the presence of two methoxyl moieties of pterostilbene (Kapetanovic et al., 2011). The assessment of TI based on *in vitro* results is an easy method with the use of the preliminary measurement of topically applied agents. A high skin deposition and antibacterial activity of pterostilbene had led to an impressive TI for therapeutic intervention. Topically applied pterostilbene created a cutaneous reservoir in the skin that could prolong the residence time to eliminate pathogenic microbes.

Approximately 75% of community-associated MRSA infection occurs in the skin (Kurosu et al., 2013). The bacterial abscess caused by MRSA is difficult to treat using conventional antibiotic therapy due to the biofilm-like nature (Han et al., 2009). We appraised the *in vivo* anti-MRSA efficacy of pterostilbene in the nude mouse abscess model, which resembled localized cutaneous infection. Topically applied pterostilbene readily diffused into the skin and abscess to form a reservoir. The depot of pterostilbene facilitated the efficient delivery to the targeted infection region. The MRSA burden, skin barrier function, and inflammation were significantly improved by pterostilbene.

A number of antimicrobial formulations can cause local reactions such as erythema, rash, burning sensation, and tenderness when applied topically (Verma and Pathak, 2012). We showed *in vitro* that pterostilbene had tolerable levels of toxicity toward cultured keratinocytes. The *in vivo* safety evaluation through topical administration exhibited minimal adverse events. MRSA-infected skin is often accompanied by neutrophil and macrophage migration and infiltration for host defense (Martinez et al., 2009). Pterostilbene revealed limited toxicity against neutrophils for maintaining the host's defense ability to constrain bacterial growth. A recent clinical trial reports that oral pterostilbene at doses of 100~250 mg did not produce any significantly adverse effects (Riche et al., 2013), suggesting the safety of pterostilbene administration in humans.

The generation of oxidative stress is one of the important bacterial killing mechanisms. The cellular membrane oxidation induced by resveratrol for bacterial lethality is proposed (Subramanian et al., 2014). The previous study (Li et al., 2014) suggested that pterostilbene altered the gene expression that functions in oxidative stress in *C. albicans*. Pterostilbene exposure to cancer cells has been shown to increase reactive oxidative species (ROS) production (Mannal et al., 2010). Thus, pterostilbene may exhibit the oxidative activity needed to kill MRSA bacteria. Recently, Liu et al. (2016) reported that *S. aureus* lethality induced by ciprofloxacin and daptomycin could be antagonized by resveratrol. This interference could be due to resveratrol's strong antioxidant effect. The limited anti-MRSA activity of resveratrol shown in the present study may also relate to this offset effect. We demonstrated through TEM that pterostilbene triggered bacterial membrane perturbation, resulting in increased cell permeability. The PI



staining inside the dead MRSA in the biofilm study had verified the compromised membrane integrity after pterostilbene exposure. The membrane disintegration tends to leach out the macromolecules such as DNA, RNA, and proteins. This led to

TABLE 3 | Differentially expressed proteins follow resveratrol and pterostilbene treatments.

Band No.	Protein	Accession no.	Mw (Da)	Matched-peptides	Sequence coverage % (SCORE)	Ratios to control <sup>a</sup>		Biological function
						Resveratrol	Pterostilbene	
1	Chaperone protein ClpB (CLPB)	Q6GAV1	87,165	27	45% (191)	3.85 ± 0.04	−1.26 ± 0.02	Part of a stress-induced multi-chaperone system, it is involved in the recovery of the cell from heat-induced damage, in cooperation with DnaK, DnaJ, and GrpE. Acts as a chaperone.
2	Chaperone protein DnaK (DNAK)	P64408	66,321	18	43% (123)	5.41 ± 0.07	−1.50 ± 0.04	0.038
3	Glyceraldehyde-3-phosphate dehydrogenase (GAPDH)	P0A038	36,382	12	48% (117)	1.50 ± 0.02	−3.82 ± 0.06	0.041
4	50S ribosomal protein L6 (RL6)	Q7A084	19,802	10	62% (96)	1.62 ± 0.11	2.27 ± 0.01	0.028
5	Elongation factor G (EFG)	P68791	76,877	29	45% (212)	−3.19 ± 0.07	−1.47 ± 0.13	0.036
6	Arginine deiminase (ARCA)	Q8NUK7	47,069	20	46% (145)	−2.57 ± 0.03	−1.50 ± 0.05	0.025
6	Glucose-6-phosphate isomerase (G6PI)	Q8NXF1	49,849	14	48% (93)	−2.26 ± 0.05	−1.42 ± 0.01	0.036
7	Citrate synthase 2 (CISY2)	P39120	40,614	10	31% (92)	−3.37 ± 0.02	−2.17 ± 0.02	0.048
8	Phosphoenolpyruvate carboxykinase [ATP] (PCKA)	P0C1S4	58,803	19	36% (102)	1.52 ± 0.04	2.83 ± 0.01	0.013
9	30S ribosomal protein S4 (RS4)	P66564	23,027	21	61% (159)	−1.40 ± 0.05	2.69 ± 0.01	0.032
10	Alkaline shock protein 23 (ASP)	P0A0P7	19,210	11	68% (124)	1.59 ± 0.01	2.93 ± 0.01	0.018
11	30S ribosomal protein S13 (RS13)	P66389	10,343	10	89% (92)	1.59 ± 0.01	2.03 ± 0.05	0.021

<sup>a</sup>Ratios to control indicated the fold changes in protein volume between resveratrol-, pterostilbene-treated samples vs. control samples, respectively. The higher ratios (> 1.0) mean the proteins whose expression levels were increased upon treatments of compounds, while lower ratios (< 1.0) indicate the proteins were downregulated under the exposure to compounds.

<sup>b</sup>p-values were generated by analyzing the gel images using Prodigy SameSpots<sup>TM</sup> software. Differences were considered significant at *p* < 0.05 after the comparison of the ratios to control between resveratrol and pterostilbene groups.

the reduction of the total protein amount in MRSA treated with pterostilbene.

Although pterostilbene disrupted the membrane integrity, this effect could be considered as mild, based on the bacterial morphology. The anti-MRSA activity of pterostilbene was not only mediated by membrane damage but also by the protein expression change. The antibacterial agents possibly interact with pathogens in different locations such as the wall, membrane, and cytoplasm. We had employed a proteomic approach to characterize the functional proteins of MRSA with resveratrol and pterostilbene treatments. Both compounds revealed quite different protein expressions in MRSA. Chaperones and GAPDH were upregulated by resveratrol but downregulated by pterostilbene. Chaperones are components of the *S. aureus* wall stress regulon. There is a link between chaperones and antibiotic resistance. Chaperone proteins in *S. aureus* contribute to the adaptation to antibiotics (Frees et al., 2014). Overproduced chaperones aid the survival of *S. aureus* in environmental stress. Resveratrol might be the source of stress to activate the chaperone regulon for an adaptive response. Disruption of chaperones leads to the dramatic decrease of MRSA resistance to antibiotics (Jousselin et al., 2012). Pterostilbene significantly decreased chaperone expression in MRSA, suggesting that this agent inhibited the action of chaperones and sustained the bacteria in a state of high stress for killing the bacteria. This could lead to the greater biocidal activity of pterostilbene compared to resveratrol. GAPDH is important during *S. aureus* infection and is necessary for virulence and pathogenesis (Purves et al., 2010). GAPDH induced by oxidative stress can protect *S. aureus* against oxidative damage. This resistance against ROS is the key to survival (Weber et al., 2004). The pterostilbene-elicited GAPDH inactivation could be one mechanism for MRSA growth arrest. The antibacterial mechanisms of pterostilbene are quite different from those of resveratrol with regard to MRSA susceptibility and resistance.

Ribosomes are the resistance proteins that work against antibiotics (Costerton et al., 1999). They play a critical role in substrate stability during protein synthesis. 30S ribosome S13 and 50S ribosome L6 were upregulated by both compounds for a resistant response. The ribosome expression was higher for pterostilbene than for resveratrol. The bacteria develop two main strategies to cope with stress, namely chaperones and proteolysis. The chaperone-protease complex contributes to the quality control of Gram-positive bacteria proteins, which is essential for survival when encountering stress (Molière and Turgay, 2009). The protease is responsible for *S. aureus* ribosome cleavage (Wall et al., 2015). The chaperone overexpression by resveratrol led to the chaperone-mediated proteolysis for ribosome inactivation. This might result in the lower expression of ribosomes by resveratrol than by pterostilbene, which downregulated chaperones. Resveratrol even reduced 30S ribosome S4 expression, while pterostilbene promoted the manifestation of this protein.

Chaperones and ribosomes are possible targets for some antibiotics such as peptides, macrolides, oxazolidinones, and tetracyclines to kill the bacteria (Poehlsgaard and Douthwaite, 2005; Frees et al., 2014). In order to understand the possible

interaction between the proteins and antibacterial agents, the molecular docking simulation of the compounds to the selected proteins was computed. A higher dock score demonstrates a stable system for binding interaction. Docking is a method that predicts the preferred orientation of one molecule to another molecule when bound to each other for forming a stable complex. It can be used to anticipate the strength of association or binding affinity between two molecules (Kitchen et al., 2004). Pterostilbene provided a stronger interaction with chaperone ClpB compared to resveratrol, indicating a probable target of chaperones for pterostilbene. A contrary result was shown in the case of GAPDH. There was no binding activity between the 30S and 50S ribosomes and the compounds, indicating that resveratrol and pterostilbene did not directly interact with ribosomes to evoke a bactericidal effect. The enhanced or suppressed ribosome expression by the compounds could be due to the regulation by DNA and other proteins such as chaperones and proteases.

Ribosomal protection protein (RPP) is derived from the EFG subfamily. The ribosomal protection mediated by RPP is important for drug-resistant bacteria against stress and antibiotics (Kobayashi et al., 2007). EFG enhances the translocation step in the protein synthesis of bacteria (Savelsbergh et al., 2009). The EFG downregulation by resveratrol and pterostilbene could result in the decrease of the total protein amount as shown in our results because of the synthetic disturbance. Borg et al. (2015) demonstrated that antibiotic fusidic acid is a ribosomal peptide elongation inhibitor that targets EFG to block protein synthesis. Resveratrol may be a strong elongation inhibitor since this molecule could downregulate EFG by 3.2-fold. The docking energy of EGF to resveratrol was comparable with that of pterostilbene, although pterostilbene reduced EFG expression by only 1.5-fold. The same as heat shock proteins, ASP is a stress-induced biomarker for *S. aureus* to adapt to the environment (Kuroda et al., 1995). Pterostilbene was more potent in upregulating ASP than resveratrol. This suggests that MRSA should produce more ASP for defending harsher intervention such as pterostilbene treatment. However, no docking was found between ASP and either compound.

The above data indicate that resveratrol and pterostilbene killed MRSA by disintegrating the cell surface and by changing the proteins, thereby making the bacteria susceptible to stress. The direct interaction of the compounds with the microbial membrane and key proteins could inhibit pathogen growth or cause cell death. We demonstrated that resveratrol and pterostilbene showed different mechanisms for anti-MRSA activity. The different targets might be involved in the mechanisms of the action of resveratrol and pterostilbene. It should be cautious to use proteomics and molecular docking for elucidating the anti-MRSA pathways since these techniques cannot fully explore the mechanisms or targets of the antibacterial agents. It is only a preliminary prediction of the possible targets. Further investigation is needed to explore the underlying and detailed mechanisms of action. Our aim is to offer an initial direction for the future study. More biochemical assays and genetic approaches are needed to confirm the



anti-MRSA hypothesis for resveratrol and pterostilbene raised in this study.

## CONCLUSIONS

We attempted to examine the possible application of pterostilbene for therapeutic intervention of drug-resistant bacteria. Resveratrol and pterostilbene exhibited antibacterial activity without exerting unacceptable cytotoxicity on mammalian cells. Pterostilbene was more efficient for bacterial eradication than resveratrol. Pterostilbene was able to reduce biofilm formation and kill the MRSA in immune cells by virtue of its strong antibacterial activity and facile delivery across biomembranes. This natural agent also showed a 6-fold higher cutaneous absorption compared to resveratrol. Pterostilbene had unique mechanisms of action different from resveratrol according to proteomic assay. Bacterial membrane disruption

and the change of stress-induced protein profiles were the biocidal mechanisms of pterostilbene. This compound is of interest as a feasible antimicrobial candidate for use against MRSA infection in skin tissues.

## AUTHOR CONTRIBUTIONS

Conceived and designed the experiments: FY and JF. Performed the experiments: SY, CT, and YW. Analyzed the data: PW. Contributed reagents/materials/analysis tools: PL. Wrote the paper: SY, FY, and JF.

## ACKNOWLEDGMENTS

The authors are grateful for the financial support from Chang Gung Memorial Hospital (CMRPD1B0332 and CMRPD1F0231-3).

## REFERENCES

- Archer, N. K., Mazaitis, M. J., Costerton, J. W., Leid, J. G., Powers, M. E., and Shirliff, M. E. (2011). *Staphylococcus aureus* biofilms: properties, regulation, and roles in human disease. *Virulence* 2, 445–459. doi: 10.4161/viru.2.5.17724
- Barman, T. K., Kumar, M., Mathur, T., Chaira, T., Ramkumar, G., Kalia, V., et al. (2016). *In vitro* and *in vivo* activities of a bi-aryl oxazolidinone, RBx 11760, against Gram-positive bacteria. *Antimicrob. Agents Chemother.* 60, 7134–7145. doi: 10.1128/AAC.00453-16
- Borg, A., Holm, M., Shiroyama, I., Haurlyuk, V., Pavlov, M., Sanyal, S., et al. (2015). Fusidic acid targets elongation factor G in several stages of translocation on the bacterial ribosome. *J. Biol. Chem.* 290, 3440–3454. doi: 10.1074/jbc.M114.611608
- Chan, M. M. (2002). Antimicrobial effect of resveratrol on dermatophytes and bacterial pathogens of the skin. *Biochem. Pharmacol.* 63, 99–104. doi: 10.1016/S0006-2952(01)00886-3
- Chang, H. C., Huang, Y. T., Chen, C. S., Chen, Y. W., Huang, Y. T., Su, J. C., et al. (2016). *In vitro* and *in vivo* activity of a novel sorafenib derivative SC5005 against MRSA. *J. Antimicrob. Chemother.* 71, 449–459. doi: 10.1093/jac/dkv367
- Chung, P. Y., and Toh, Y. S. (2014). Anti-biofilm agents: recent breakthrough against multi-drug resistant *Staphylococcus aureus*. *Pathog. Dis.* 70, 231–139. doi: 10.1111/2049-632X.12141
- Cihalova, K., Chudobova, D., Michalek, P., Moulick, A., Guran, R., Kopel, P., et al. (2015). *Staphylococcus aureus* nd MRSA growth and biofilm formation after treatment with antibiotics and SeNPs. *Int. J. Mol. Sci.* 16, 24656–24672. doi: 10.3390/ijms161024656
- Costerton, J. W., Stewart, P. S., and Greenberg, E. P. (1999). Bacterial biofilms: a common cause of persistent infections. *Science* 284, 1318–1322. doi: 10.1126/science.284.5418.1318
- Frees, D., Gerth, U., and Ingmer, H. (2014). Clp chaperones and proteases are central in stress survival, virulence and antibiotic resistance of *Staphylococcus aureus*. *Int. J. Med. Microbiol.* 304, 142–149. doi: 10.1016/j.ijmm.2013.11.009
- Han, G., Martinez, L. R., Mihu, M. R., Friedman, A. J., Friedman, J. M., and Nosanchuk, J. D. (2009). Nitric oxide releasing nanoparticles are therapeutic for *Staphylococcus aureus* abscesses in a murine model of infection. *PLoS ONE* 4:e7804. doi: 10.1371/journal.pone.0007804
- Hidalgo, E., and Dominguez, C. (1998). Study of cytotoxicity mechanisms of silver nitrate in human dermal fibroblasts. *Toxicol. Lett.* 98, 169–179. doi: 10.1016/S0378-4274(98)00114-3
- Hoyert, D. L., and Xu, J. (2012). Deaths: preliminary data for 2011. *Natl. Vital. Stat. Rep.* 61, 1–51.
- Ishak, S. F., Ghazoli, A. R., Zin, N. M., and Basri, D. F. (2016). Pterostilbene enhanced anti-methicillin resistant *Staphylococcus aureus* (MRSA) activity of oxacillin. *Am. J. Infect. Dis.* 12, 1–10. doi: 10.3844/ajidsp.2016.1.10
- Jousselin, A., Renzoni, A., Andrey, D. O., Monod, A., Lew, D. P., and Kelly, W. L. (2012). The posttranslational chaperone lipoprotein PrsA is involved in both glycopeptides and oxacillin resistance in *Staphylococcus aureus*. *Antimicrob. Agents Chemother.* 56, 3629–3640. doi: 10.1128/AAC.06264-11
- Kapetanovic, I. M., Muzzio, M., Huang, Z., Thompson, T. N., and McCormick, D. L. (2011). Pharmacokinetics, oral bioavailability, and metabolic profile of resveratrol and its dimethylether analog, pterostilbene, in rats. *Cancer Chemother. Pharmacol.* 68, 593–601. doi: 10.1007/s00280-010-1525-4
- Kitchen, D. B., Decornez, H., Furr, J. R., and Bajorath, J. (2004). Docking and scoring in virtual screening for drug discovery: methods and applications. *Nat. Rev. Drug Discov.* 3, 935–949. doi: 10.1038/nrd1549
- Kobayashi, T., Nonaka, L., Maruyama, F., and Suzuki, S. (2007). Molecular evidence for the ancient origin of the ribosomal protection protein that mediates tetracycline resistance in bacteria. *J. Mol. Evol.* 65, 228–235. doi: 10.1007/s00239-007-9006-z
- Kosuru, R., Rai, U., Prakash, S., Singh, A., and Singh, S. (2016). Promising therapeutic potential of pterostilbene and its mechanistic insight based on preclinical evidence. *Eur. J. Pharmacol.* 789, 229–243. doi: 10.1016/j.ejphar.2016.07.046
- Kuroda, M., Ohta, T., and Hayashi, H. (1995). Isolation and the gene cloning of an alkaline shock protein in methicillin resistant *Staphylococcus aureus*. *Biochem. Biophys. Res. Commun.* 207, 978–984. doi: 10.1006/bbrc.1995.1281
- Kurosu, M., Siricilla, S., and Mitachi, K. (2013). Advances in MRSA drug discovery: where are we and where do we need to be? *Expert Opin. Drug Discov.* 8, 1095–1116. doi: 10.1517/17460441.2013.807246
- Li, D. D., Zhao, L. X., Mylonakis, E., Hu, G. H., Zou, Y., Huang, T. K., et al. (2014). *In vitro* and *in vivo* activities of pterostilbene against *Candida albicans* biofilms. *Antimicrob. Agents Chemother.* 58, 2344–2355. doi: 10.1128/AAC.01583-13
- Lin, C. F., Hung, C. F., Aljuffali, I. A., Huang, Y. L., Liao, W. C., and Fang, J. Y. (2016). Methylation and esterification of magnolol for ameliorating cutaneous targeting and therapeutic index by topical application. *Pharm. Res.* 33, 2152–2167. doi: 10.1007/s11095-016-1953-x
- Lin, C. F., Leu, Y. L., Al-Suwayeh, S. A., Ku, M. C., Hwang, T. L., and Fang, J. Y. (2012). Anti-inflammatory activity and percutaneous absorption of quercetin and its polymethoxylated compound and glycosides: the relationships to chemical structures. *Eur. J. Pharm. Sci.* 47, 857–864. doi: 10.1016/j.ejps.2012.04.024
- Liu, X., Testa, B., and Fahr, A. (2011). Lipophilicity and its relationship with passive drug permeation. *Pharm. Res.* 28, 962–977. doi: 10.1007/s11095-010-0303-7
- Liu, Y., Zhou, J., Qu, Y., Yang, X., Shi, G., Wang, X., et al. (2016). Resveratrol antagonizes antimicrobial lethality and stimulates recovery of bacterial mutants. *PLoS ONE* 11:e0153023. doi: 10.1371/journal.pone.0153023



- Mannal, P., McDonald, D., and McFadden, D. (2010). Pterostilbene and tamoxifen show an additive effect against breast cancer *in vitro*. *Am. J. Surg.* 200, 577–580. doi: 10.1016/j.amjsurg.2010.07.022
- Martinez, L. R., Han, G., Chacko, M., Mihu, M. R., Jacobson, M., Gialanella, P., et al. (2009). Antimicrobial and healing efficacy of sustained release nitric oxide nanoparticles against *Staphylococcus aureus* skin infection. *J. Invest. Dermatol.* 129, 2463–2469. doi: 10.1038/jid.2009.95
- Molière, N., and Turgay, K. (2009). Chaperone-protease systems in regulation and protein quality control in *Bacillus subtilis*. *Res. Microbiol.* 160, 637–644. doi: 10.1016/j.resmic.2009.08.020
- Mu, H., Tang, J., Liu, Q., Sun, C., Wang, T., and Duan, J. (2016). Potent antibacterial nanoparticles against biofilm and intracellular bacteria. *Sci. Rep.* 6:18877. doi: 10.1038/srep18877
- Nair, S., Desai, S., Poonacha, N., Vipra, A., and Sharma, U. (2016). Antibiofilm activity and synergistic inhibition of *Staphylococcus aureus* biofilms by bactericidal protein P128 in combination with antibiotics. *Antimicrob. Agents Chemother.* 60, 7280–7289. doi: 10.1128/AAC.01118-16
- Pan, T. L., Wang, P. W., Aljuffali, I. A., Huang, C. T., Lee, C. W., and Fang, J. Y. (2015). The impact of urban particulate pollution on skin barrier function and the subsequent drug absorption. *J. Dermatol. Sci.* 78, 51–60. doi: 10.1016/j.jdermsci.2015.01.011
- Pan, T. L., Wang, P. W., Aljuffali, I. A., Leu, Y. L., Hung, Y. Y., and Fang, J. Y. (2014). Coumarin derivatives, but not coumarin itself, cause skin irritation via topical delivery. *Toxicol. Lett.* 226, 173–181. doi: 10.1016/j.toxlet.2014.02.009
- Pan, T. L., Wang, P. W., Al-Suwayeh, S. A., Chen, C. C., and Fang, J. Y. (2010). Skin toxicology of lead species evaluated by their permeability and proteomic profiles: a comparison of organic and inorganic lead. *Toxicol. Lett.* 197, 19–28. doi: 10.1016/j.toxlet.2010.04.019
- Park, S., Cha, S. H., Cho, I., Park, S., Park, Y., Cho, S., et al. (2016). Antibacterial nanocarriers of resveratrol with gold and silver nanoparticles. *Mater. Sci. Eng. C* 58, 1160–1169. doi: 10.1016/j.msec.2015.09.068
- Patel, H., ten Berge, W., and Cronin, M. T. D. (2002). Quantitative structure-activity relationships (QSARs) for the prediction of skin permeation of exogenous chemicals. *Chemosphere* 48, 603–613. doi: 10.1016/S0045-6535(02)00114-5
- Paulo, L., Ferreira, S., Gallardo, E., Queiroz, J. A., and Domingues, F. (2010). Antimicrobial activity and effects of resveratrol on human pathogenic bacteria. *World J. Microb. Biotechnol.* 26, 1533–1538. doi: 10.1007/s11274-010-0325-7
- Poehlsgaard, J., and Douthwaite, S. (2005). The bacterial ribosome as a target for antibiotics. *Nat. Rev. Microbiol.* 3, 870–881. doi: 10.1038/nrmicro1265
- Pumerantz, A., Muppidi, K., Agnihotri, S., Guerra, C., Venketaraman, V., Wang, J., et al. (2011). Preparation of liposomal vancomycin and intracellular killing of methicillin-resistant *Staphylococcus aureus* (MRSA). *Int. J. Antimicrob. Agents* 37, 140–144. doi: 10.1016/j.ijantimicag.2010.10.011
- Purves, J., Cockayne, A., Moody, P. C., and Morrissey, J. A. (2010). Comparison of the regulation, metabolic functions, and roles in virulence of the glyceraldehyde-3-phosphate dehydrogenase homologues gapA and gapB in *Staphylococcus aureus*. *Infect. Immun.* 78, 5223–5232. doi: 10.1128/IAI.00762-10
- Riche, D. M., McEwen, C. L., Riche, K. D., Sherman, J. J., Wofford, M. R., Deschamps, D., et al. (2013). Analysis of safety from a human clinical trial with pterostilbene. *J. Toxicol.* 2013:463595. doi: 10.1155/2013/463595
- Riche, D. M., Riche, K. D., Blackshear, C. T., McEwen, C. L., Sherman, J. J., Wofford, M. R., et al. (2014). Pterostilbene on metabolic parameters: a randomized, double-blind, and placebo-controlled trial. *Evid. Based Complement. Altern. Med.* 2014:459165. doi: 10.1155/2014/459165
- Savelsbergh, A., Rodnina, M. V., and Wintermeyer, W. (2009). Distinct functions of elongation factor G in ribosome recycling and translocation. *RNA* 15, 772–780. doi: 10.1261/rna.1592509
- Subramanian, M., Goswami, M., Chakraborty, S., and Jawali, N. (2014). Resveratrol induced inhibition of *Escherichia coli* proceeds via membrane oxidation and independent of diffusible reactive oxygen species generation. *Redox Biol.* 2, 865–872. doi: 10.1016/j.redox.2014.06.007
- Verma, P., and Pathak, K. (2012). Nanosized ethanolic vesicles loaded with econazole nitrate for the treatment of deep fungal infections through topical gel formulation. *Nanomed. Nanotechnol. Biol. Med.* 8, 489–496. doi: 10.1016/j.nano.2011.07.004
- Wall, E. A., Caulfield, J. H., Lyons, C. E., Manning, K. A., Dokland, T., and Christie, G. E. (2015). Specific N-terminal cleavage of ribosomal protein L27 in *Staphylococcus aureus* and related bacteria. *Mol. Microbiol.* 95, 258–269. doi: 10.1111/mmi.12862
- Water, J. J., Smart, S., Franzyk, H., Foged, C., and Nielsen, H. M. (2015). Nanoparticle-mediated delivery of the antimicrobial peptide plectasin against *Staphylococcus aureus* in infected epithelial cells. *Eur. J. Pharm. Biopharm.* 92, 65–73. doi: 10.1016/j.ejpb.2015.02.009
- Weber, H., Engelmann, S., Becher, D., and Hecker, M. (2004). Oxidative stress triggers thiol oxidation in the glyceraldehyde-3-phosphate dehydrogenase of *Staphylococcus aureus*. *Mol. Microbiol.* 52, 133–140. doi: 10.1111/j.1365-2958.2004.03971.x
- Yang, S. C., Aljuffali, I. A., Sung, C. T., Lin, C. F., and Fang, J. Y. (2016). Antimicrobial activity of topically-applied soyaethyl morpholinium ethosulfate micelles against *Staphylococcus* species. *Nanomedicine* 11, 657–671. doi: 10.2217/nnm.15.217

**Conflict of Interest Statement:** The authors declare that the research was conducted in the absence of any commercial or financial relationships that could be construed as a potential conflict of interest.

The reviewer TC and handling Editor declared their shared affiliation, and the handling Editor states that the process nevertheless met the standards of a fair and objective review.

Copyright © 2017 Yang, Tseng, Wang, Lu, Weng, Yen and Fang. This is an open-access article distributed under the terms of the Creative Commons Attribution License (CC BY). The use, distribution or reproduction in other forums is permitted, provided the original author(s) or licensor are credited and that the original publication in this journal is cited, in accordance with accepted academic practice. No use, distribution or reproduction is permitted which does not comply with these terms.

# Bioactive Triterpenoids from the Leaves and Twigs of *Lithocarpus litseifolius* and *L. corneus*

## Authors

Yuan-Bin Cheng<sup>1,2,3,4\*</sup>, Fan-Jin Liu<sup>1\*</sup>, Chih-Hsin Wang<sup>1</sup>, Tsong-Long Hwang<sup>5,6,7</sup>, Yung-Fong Tsai<sup>5,6,7</sup>, Chia-Hung Yen<sup>1,3</sup>, Hui-Chun Wang<sup>1</sup>, Yen-Hsueh Tseng<sup>8</sup>, Ching-Te Chien<sup>9</sup>, Yi-Ming Arthur Chen<sup>3,10</sup>, Fang-Rong Chang<sup>1,11</sup>, Yang-Chang Wu<sup>1,2,4</sup>

## Affiliations

- 1 Graduate Institute of Natural Products, College of Pharmacy, Kaohsiung Medical University, Kaohsiung, Taiwan
- 2 Research Center for Natural Products & Drug Development, Kaohsiung Medical University, Kaohsiung, Taiwan
- 3 Center for Infectious Disease and Cancer Research, Kaohsiung Medical University, Kaohsiung, Taiwan
- 4 Department of Medical Research, Kaohsiung Medical University Hospital, Kaohsiung, Taiwan
- 5 Graduate Institute of Natural Products, College of Medicine, Chang Gung University, Taoyuan, Taiwan
- 6 Research Center for Chinese Herbal Medicine, Research Center for Food and Cosmetic Safety, and Graduate Institute of Health Industry Technology, College of Human Ecology, Chang Gung University of Science and Technology, Taoyuan, Taiwan
- 7 Department of Anesthesiology, Chang Gung Memorial Hospital, Taoyuan, Taiwan
- 8 Department of Forestry, National Chung Hsing University, Taichung, Taiwan
- 9 Division of Silviculture, Taiwan Forestry Research Institute, Taipei, Taiwan
- 10 Department of Microbiology and Institute of Medical Research, College of Medicine, Kaohsiung Medical University, Kaohsiung, Taiwan
- 11 Cancer Center, Kaohsiung Medical University Hospital, Kaohsiung, Taiwan

## Key words

*Lithocarpus litseifolius*, *Lithocarpus corneus*, Fagaceae, triterpenoids, anti-inflammatory, anti-HIV

received November 24, 2016

revised May 23, 2017

accepted June 13, 2017

## Bibliography

DOI <https://doi.org/10.1055/s-0043-113826>


Published online | Planta Med © Georg Thieme Verlag KG  
Stuttgart · New York | ISSN 0032-0943

## Correspondence

Prof. Fang-Rong Chang  
Graduate Institute of Natural Products, College of Pharmacy,  
Kaohsiung Medical University  
100, Shih-Chuan 1st Road, 80708 Kaohsiung, Taiwan  
Phone: + 88 6 73 12 11 01 ext. 2162, Fax: + 88 6 73 11 47 73  
[aaronfrc@kmu.edu.tw](mailto:aaronfrc@kmu.edu.tw)

## Correspondence

Prof. Yang-Chang Wu  
Graduate Institute of Natural Products, College of Pharmacy,  
Kaohsiung Medical University  
100, Shih-Chuan 1st Road, 80708 Kaohsiung, Taiwan  
Phone: + 88 63 12 11 01 ext. 5347, Fax: + 88 6 73 11 47 73  
[yachwu@kmu.edu.tw](mailto:yachwu@kmu.edu.tw)

 Supporting information available online at  
<http://www.thieme-connect.de/products>

## ABSTRACT

Phytochemical investigation of the leaves and twigs of *Lithocarpus litseifolius* and *Lithocarpus corneus* resulted in the isolation of four new triterpenoids (1–4), three triterpenoids (5–7) isolated from a natural source for the first time, and six known compounds (8–13). In addition, four known triterpenoids (14–17) were isolated from *L. corneus*. Compound 1 is a 3,4-seco-lupane-type triterpenoid, and compounds 2–4 are lupane-type triterpenoids in different oxidation states. The structures of all isolated compounds were identified by spectroscopic methods, especially NMR and mass spectrometry data. The absolute configuration of 2 and 3 was confirmed by X-ray single crystallographic analysis. The anti-inflammatory activities of 1–17 and anti-HIV activities of 2–17 were evaluated. Among them, 3-*epi*-betulinic acid (8) showed a strong anti-HIV activity comparable to abacavir, a drug used for treating HIV/AIDS. 3,4-seco-4(23),20(29)-lupadiene-3,28-dioic acid (5) exhibited potent inhibition of superoxide-anion generation with  $86.9 \pm 2.8\%$  inhibition at  $1 \mu\text{M}$ .

\* These authors contributed equally to this work.

## Introduction

The genus *Lithocarpus* (Fagaceae) distributed in East Asia comprises more than 300 species, among which 15 species are found in Taiwan. In previous pharmacological studies, *Lithocarpus* plants were reported to have anti-tumor [1], anti-hyperglycemic [2], anti-hypertensive [3], anti-inflammatory [4], and anti-oxidant [5] activities. Triterpenes [6–9], steroids [7], chalcones [10], and various phenolic compounds [4] were found to be major constituents of *Lithocarpus* plants. *Lithocarpus litseifolius* (Hance) Schott (syn. *Lithocarpus synbalanos* [Hance] Chun [11]) is a dominant species that grows in the central mountainous areas of Taiwan. In a preliminary screening, the methanolic extracts (20 µg/mL) of *L. litseifolius* and *Lithocarpus corneus* (Lour.) Rehder demonstrated potent anti-inflammatory effects by inhibiting superoxide anion generation ( $94.7 \pm 1.3\%$  and  $92.8 \pm 0.4\%$ , respectively) and elastase release ( $103.6 \pm 1.0\%$  and  $90.5 \pm 6.9\%$ , respectively) from human neutrophils in response to *N*-formylmethionyl-leucyl-phenylalanine (fMLP). In addition, these two extracts showed no cytotoxic effect against HepG2, MDA-MB-231, and A549 cell lines, which suggests that they are non-toxic. Due to the promising bioactivity data and the absence of information on the constituents of those two species, phytochemical investigations of the leaves and twigs of *L. litseifolius* and *L. corneus* were carried out. The separation, structure elucidation, and anti-inflammatory and anti-HIV activities of the isolated compounds from the leaves and twigs of *L. litseifolius* and *L. corneus* are herein reported.

## Results and Discussion

Leaves and twigs of *L. litseifolius* were extracted by methanol. The crude extract was partitioned between water and ethyl acetate, and the ethyl acetate soluble fraction was separated by repeated column chromatography. As a result, four new triterpenoids (1–4), three triterpenoids [3,4-*seco*-4(23),20(29)-lupadiene-3,28-dioic acid (5), 3,4-*seco*-olean-4(23),12-diene-3,28-dioic acid (6), and 3,4-*seco*-ursan-4(23),12-diene-3,28-dioic acid (7)] were isolated for the first time from a natural source [12, 13] (► Fig. 1), and six known compounds [3-*epi*-betulinic acid (8), betulinic acid (9), betulonic acid (10), cyclicodiscic acid (11), lupeol (12), and 3-*epi*-glutanol (13)] were identified [14–19]. In addition, four known triterpenoids [alphitolic acid (14), 2 $\alpha$ ,3 $\beta$ ,28-lup-20(29)-en-triol (15), maslinic acid (16), and corosolic acid (17)] were isolated from the leaves and twigs of *L. corneus* [20–23].

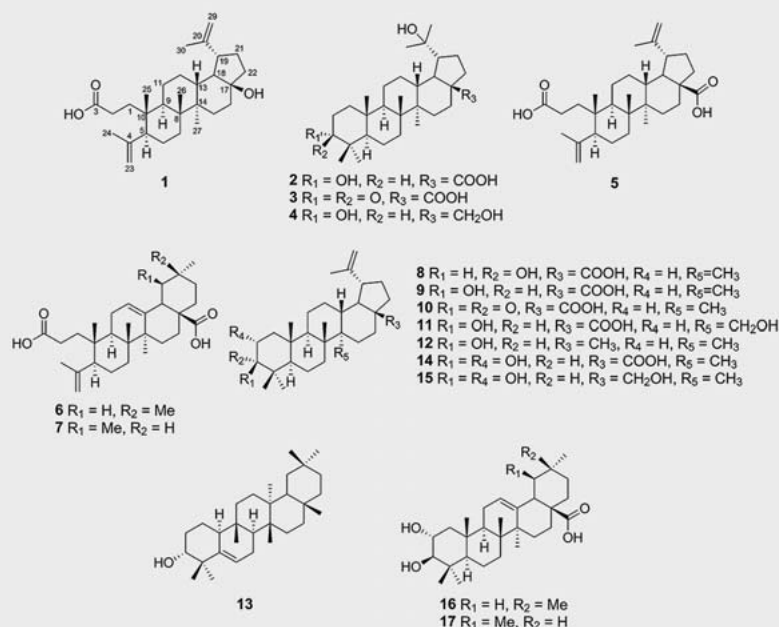
Synbalanic acid (1) was obtained as a yellowish amorphous powder. The HRESIMS data of 1 showed a sodiated pseudo-molecular ion peak at  $m/z$  465.3342, consistent with the molecular formula  $C_{29}H_{46}O_3$ . The infrared (IR) absorption bands of 1 indicated the presence of hydroxy ( $3450\text{ cm}^{-1}$ ) and carboxyl ( $1708\text{ cm}^{-1}$ ) functionalities. The  $^1\text{H}$  NMR data of 1 (► Table 1) demonstrated the presence of five methyls ( $\delta_{\text{H}}$  0.90, 1.03, 1.01, 1.83, and 2.03) and two terminal olefinic methylenes ( $\delta_{\text{H}}$  4.88, 4.92, 5.13, and 5.14). In the  $^{13}\text{C}$  NMR (► Table 1) and DEPT (distortionless enhancement by polarization transfer) spectra of 1, 29 carbon signals were observed. These signals included an acid carbonyl ( $\delta_{\text{C}}$  177.7), two olefinic quaternary carbons ( $\delta_{\text{C}}$  148.1 and 151.3), two terminal olefinic methylenes ( $\delta_{\text{C}}$  109.6 and 113.7), four qua-

ternary carbons ( $\delta_{\text{C}}$  39.6, 40.3, 41.4, and 79.2), five methines ( $\delta_{\text{C}}$  41.7, 45.6, 50.2, 52.9, and 55.0), 10 methylenes ( $\delta_{\text{C}}$  22.2, 24.9, 27.1, 29.0, 29.8, 30.0, 32.7, 34.0, 35.5, and 38.5), and five methyls ( $\delta_{\text{C}}$  14.7, 15.7, 20.8, 21.0, and 23.8). Comparison of the aforementioned NMR data with those of 3,4-*seco*-4(23),20(29)-lupadiene-3,28-dioic acid (5) suggested that 1 had a similar 3,4-*seco*-lupane skeleton. In contrast to compound 5, the carboxylic carbon C-28 in 5 was absent in 1, and a hydroxy group attached at C-17 ( $\delta_{\text{C}}$  79.2) was found instead.

The planar structure of 1 was elucidated by analysis of the COSY and HMBC correlations (► Fig. 2). In the COSY spectrum, correlations of H<sub>2</sub>-6 ( $\delta_{\text{H}}$  1.96 and 1.72)/H<sub>2</sub>-7 ( $\delta_{\text{H}}$  1.36) and H-9 ( $\delta_{\text{H}}$  1.67)/H<sub>2</sub>-11 ( $\delta_{\text{H}}$  1.54 and 1.20)/H<sub>2</sub>-12 ( $\delta_{\text{H}}$  1.27)/H-13 ( $\delta_{\text{H}}$  1.24) were found. These two proton sequences and the HMBC correlations of Me-25 ( $\delta_{\text{H}}$  0.90)/C-1 ( $\delta_{\text{C}}$  35.5), C-5 ( $\delta_{\text{C}}$  50.2), C-9 ( $\delta_{\text{C}}$  41.7), C-10 ( $\delta_{\text{C}}$  39.6), Me-26 ( $\delta_{\text{H}}$  1.01)/C-7 ( $\delta_{\text{C}}$  32.7), C-8 ( $\delta_{\text{C}}$  40.3), C-9, C-14 ( $\delta_{\text{C}}$  41.4), and Me-27 ( $\delta_{\text{H}}$  1.00)/C-8, C-13 ( $\delta_{\text{C}}$  45.6), C-14 indicated the existence of rings B and C and three methyl groups attached at C-8, C-10, and C-14. In addition, the proton spin system H-13 ( $\delta_{\text{H}}$  1.24)/H-18 ( $\delta_{\text{H}}$  1.80)/H-19 ( $\delta_{\text{H}}$  2.52)/H<sub>2</sub>-21 ( $\delta_{\text{H}}$  1.79 and 1.38)/H<sub>2</sub>-22 ( $\delta_{\text{H}}$  1.78 and 0.96) and H<sub>2</sub>-15 ( $\delta_{\text{H}}$  1.44 and 1.26)/H<sub>2</sub>-16 ( $\delta_{\text{H}}$  2.02) was also observed in COSY. These two partial structures and the HMBC correlations of Me-27/C-15 ( $\delta_{\text{C}}$  29.0), H<sub>2</sub>-21/C-17, and H<sub>2</sub>-16/C-17 were used to establish the structure of rings D and E. The COSY cross-peaks of H<sub>2</sub>-1 ( $\delta_{\text{H}}$  1.96)/H<sub>2</sub>-2 ( $\delta_{\text{H}}$  2.67 and 2.51) and the HMBC correlations of H-2/C-3 ( $\delta_{\text{C}}$  177.3) were used to link C-1 to C-3. The HMBC correlations of Me-24 ( $\delta_{\text{H}}$  1.83)/C-4 ( $\delta_{\text{C}}$  148.1), C-5, C-23 ( $\delta_{\text{C}}$  113.8), and Me-30 ( $\delta_{\text{H}}$  2.03)/C-19 ( $\delta_{\text{C}}$  55.0), C-20 ( $\delta_{\text{C}}$  151.3), C-29 (109.6) indicated the presence of two isopropenyl groups attached at C-5 and C-19, respectively. On the basis of the above two-dimensional NMR data, the planar structure of 1 was established.

The relative configuration of 1 was determined by NOESY correlations and is illustrated in ► Fig. 2. In the NOESY spectrum, correlations between H<sub>2</sub>-23/Me-25/Me-26/H-13/H-19 indicated that these protons were located on the same face of the molecule and they were assigned to be  $\beta$ -oriented. On the other hand, the NOESY cross-peaks between H-5/H-9/Me-27/H-18 suggested these protons to be  $\alpha$ -oriented. The  $S^*$ -configuration of C-17 was determined by comparing the  $^{13}\text{C}$  chemical shifts of C-17 and those carbons nearby with those of close analogues, 28-norlup-20(29)-ene-3 $\beta$ ,17 $\beta$ -diol and 4,7 $\beta$ ,17-trihydroxy-3,4-*seco*-28-norlup-20(29)-en-3-oic acid [24, 25]. Therefore, the configuration of 1 was determined to be 5 $S^*$ ,8 $R^*$ ,9 $R^*$ ,10 $S^*$ ,13 $R^*$ ,14 $R^*$ ,17 $S^*$ ,18 $R^*$ ,19 $R^*$  and the trivial name synbalanic acid was given.

3 $\alpha$ ,20-dihydroxy-28-lupanoic acid (2) exhibited the molecular formula  $C_{30}H_{50}O_4$ , as deduced from a pseudo-molecular ion peak at  $m/z$  497.3601 [ $M + Na$ ] $^+$  in HRESIMS. The IR spectrum of 2 revealed the presence of hydroxyl and carboxyl groups at  $3423\text{ cm}^{-1}$  and  $1699\text{ cm}^{-1}$ , respectively. The  $^1\text{H}$  NMR data of 2 (► Table 1) clearly revealed the presence of seven methyls and one oxymethine. The  $^{13}\text{C}$  and DEPT spectra of 2 showed 30 carbon signals, including seven quaternary carbons, six methines, ten methylenes, and seven methyls. The close similarity of the NMR data of 2 and 3 $\beta$ ,20-dihydroxylupane-28-oic acid [26] suggested that they were structurally related analogues.



► **Fig. 1** Isolated compounds 1–17 from *L. litseifolius* and *L. corneus*.

The obvious differences between them were the  $^1H$  and  $^{13}C$  NMR shifts of C-3 in  $\beta$ ,20-dihydroxylupane-28-oic acid ( $\delta_H$  3.55,  $t, J = 9.0$  and  $\delta_C$  78.3) slightly changed in **2** ( $\delta_H$  3.61,  $t, J = 4.0$  and  $\delta_C$  75.3), which suggested that **2** is a stereoisomer of  $\beta$ ,20-dihydroxylupane-28-oic acid. In the COSY spectrum, the three proton sequences  $H_2-1$  ( $\delta_H$  1.73 and 1.46)/ $H_2-2$  ( $\delta_H$  2.00 and 1.76)/ $H-3$ ,  $H-9$  ( $\delta_H$  1.59)/ $H_2-11$  ( $\delta_H$  1.66 and 1.36)/ $H_2-12$  ( $\delta_H$  2.33 and 1.85)/ $H-13$  ( $\delta_H$  2.90)/ $H-18$  ( $\delta_H$  1.93)/ $H-19$  ( $\delta_H$  2.73)/ $H_2-21$  ( $\delta_H$  2.22 and 1.66)/ $H_2-22$  ( $\delta_H$  2.13 and 1.70), and  $H_2-15$  ( $\delta_H$  2.00 and 1.28)/ $H_2-16$  ( $\delta_H$  2.70 and 1.58) were found. These findings and the HMBC correlations (► **Fig. 3**) of Me-24 ( $\delta_H$  0.87)/C-3, C-4 ( $\delta_C$  38.1), C-5 ( $\delta_C$  49.2), C-23 ( $\delta_C$  29.3), Me-25 ( $\delta_H$  0.85)/C-1 ( $\delta_C$  33.9), C-5, C-9 ( $\delta_C$  50.9), C-10 ( $\delta_C$  37.5), Me-26 ( $\delta_H$  1.13)/C-7 ( $\delta_C$  35.1), C-8 ( $\delta_C$  41.8), C-14 ( $\delta_C$  43.7), and Me-27 ( $\delta_H$  1.04)/C-8, C-13 ( $\delta_C$  38.8), C-14, C-15 ( $\delta_C$  30.7) were used to build a 6/6/6/6/5-fused pentacyclic ring system. In addition, HMBC correlations from Me-29 ( $\delta_H$  1.45) to C-19 ( $\delta_C$  50.2), C-20 ( $\delta_C$  72.3), and C-30 ( $\delta_C$  27.2) evidenced a dimethyl carbinol group attached at C-19. The carboxyl group was located at C-17 by the HMBC correlations from both  $H_2-16$  and  $H_2-22$  to C-28 ( $\delta_C$  179.4). According to these two-dimensional NMR data, the planar structure of **2** was established.

The relative configuration of **2** was determined by a NOESY experiment, and the key correlations are shown in ► **Fig. 3**. The NOESY spectrum of **2** exhibited correlations of  $H-3$ /Me-24 and Me-25/Me-26/ $H-13$ / $H-19$ , suggesting these protons to be  $\beta$ -oriented. On the other hand, NOESY correlations of  $H-5$  ( $\delta_H$  1.68)/Me-27,  $H-9$ /Me-27/ $H-18$  indicated that these protons were  $\alpha$ -oriented. Furthermore, compound **2** was successfully crystallized from MeOH/ $H_2O$  15:1 and analyzed by X-ray single crystal diffraction using mirror Cu-K $\alpha$  radiation (► **Fig. 4**). Therefore, the absolute configuration of **2** was determined to be 3*R*,5*R*,8*R*,9*R*,10*R*,

13*R*,14*R*,17*S*,18*S*,19*R*. From all these data, the structure of **2** was assigned to 3 $\alpha$ ,20-dihydroxy-28-lupanoic acid.

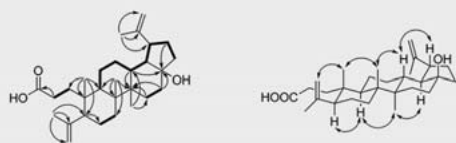
Compound **3** was obtained as colorless crystals and found to have the molecular formula  $C_{30}H_{48}O_4$  as inferred from its HRESIMS ( $m/z$  495.3443 [ $M + Na$ ] $^+$ ). The IR and one- and two-dimensional NMR spectroscopic data of **3** were similar to those of **2**, suggesting that these two compounds were structural analogues. The major difference between **3** and **2** was that the oxymethine signal of  $H-3$  in **2** was absent in **3**. In the  $^{13}C$  NMR spectra (► **Table 1**), **3** was found to have an additional carbonyl resonance at  $\delta$  216.6 and to lack an oxymethine signal, in comparison to **2**. The presence of a ketone group at C-3 ( $\delta_C$  216.6) was confirmed by the HMBC correlations of Me-24 ( $\delta_H$  1.11)/C-3 and  $H_2-2$  ( $\delta_H$  2.46)/C-3. The absolute configuration of **3** was also determined by X-ray single crystallographic analysis (► **Fig. 4**) and found to be 5*R*,8*R*,9*R*,10*R*,13*R*,14*R*,17*S*,18*S*,19*R*. Consequently, the structure of compound **3** was assigned as shown in ► **Fig. 1**. It was noted that a compound named “20-hydroxy-3-oxo-28-lupanoic acid” has been reported in two papers. In one report, the compound was in fact isolated as methyl ester derivative after treatment with  $CH_2N_2$  [27]. In the second reference, it is not clear whether the acid or the methyl ester had been obtained [28].

The HRESIMS provided the molecular formula  $C_{30}H_{52}O_3$  for compound **4**. The IR and  $^1H$  and  $^{13}C$  NMR data were quite similar to those of **2**, suggesting that **4** also belonged to lupane-type triterpenes. The major difference between them was that the acid carbonyl signal in **2** was missing in **4**, and an additional oxygenated methylene signal ( $\delta_C$  59.9) was found in the  $^{13}C$  spectrum of **4**. This oxygenated methylene was assigned to be C-28 by the HMBC correlations from  $H_2-28$  ( $\delta_H$  4.19 and 3.68) to C-16 ( $\delta_C$  34.2), C-17 ( $\delta_C$  49.8), C-22 ( $\delta_C$  30.6). The C-28 hydroxymethyl and the hydroxy group at C-3 were both found to be on the  $\beta$ -face,

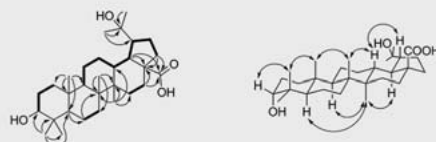
► **Table 1**  $^1\text{H}$  (400 MHz) and  $^{13}\text{C}$  NMR (100 MHz) data of 1–4 in  $\text{C}_5\text{D}_5\text{N}$  [ $\delta$  (ppm),  $J$  (Hz)].

	1			2			3			4		
Position	$\delta_{\text{C}}$		$\delta_{\text{H}}$ ( $J$ in Hz)	$\delta_{\text{C}}$		$\delta_{\text{H}}$ ( $J$ in Hz)	$\delta_{\text{C}}$		$\delta_{\text{H}}$ ( $J$ in Hz)	$\delta_{\text{C}}$		$\delta_{\text{H}}$ ( $J$ in Hz)
1	35.5	$\text{CH}_2$	1.96, m	33.9	$\text{CH}_2$	1.73, m 1.46, m	39.7	$\text{CH}_2$	1.74, m 1.28, m	33.9	$\text{CH}_2$	1.72, m 1.47, m
2	29.8	$\text{CH}_2$	2.67, m 2.51, m	26.6,	$\text{CH}_2$	2.00, m 1.76, m	34.3	$\text{CH}_2$	2.46, m	26.5	$\text{CH}_2$	2.02, m 1.76, m
3	177.3	qC		75.3	CH	3.61, br t, $J = 4.0$	216.6	qC		75.2	CH	3.60, br s
4	148.1	qC		38.1	qC		47.3	qC		38.0	qC	
5	50.2	CH	2.14, m	49.2	CH	1.68, m	54.8	CH	1.34, m	49.1	CH	1.66, m
6	38.5	$\text{CH}_2$	1.96, m 1.72, m	18.7	$\text{CH}_2$	1.50, m	19.9	$\text{CH}_2$	1.34, m	18.6	$\text{CH}_2$	1.47, m
7	32.7	$\text{CH}_2$	1.36, m	35.1	$\text{CH}_2$	1.44, m 1.52, m	34.3	$\text{CH}_2$	1.41, m	34.8	$\text{CH}_2$	1.38, m
8	40.3	qC		41.8	C		41.4	qC		42.0	C	
9	41.7	CH	1.67, m	50.9	CH	1.59, m	50.2	CH	1.40, m	50.6	CH	1.57, m
10	39.6	qC		37.5	qC		36.9	qC		37.5	qC	
11	22.2	$\text{CH}_2$	1.54, m 1.20, m	21.9	$\text{CH}_2$	1.66, m 1.36, m	22.4	$\text{CH}_2$	1.48, m 1.29, m	21.7	$\text{CH}_2$	1.65, m 1.30, m
12	30.1	$\text{CH}_2$	1.27, m	29.4	$\text{CH}_2$	2.33, m 1.85, m	29.5	$\text{CH}_2$	1.83, m	29.1	$\text{CH}_2$	2.40, m
13	45.6	CH	1.24, m	38.8	CH	2.90, dt, $J = 3.8, 13.1$	38.9	CH	2.91, dt, $J = 12.0, 3.5$	36.9	CH	1.85, m
14	41.4	qC		43.7	qC		43.6	qC		43.7	qC	
15	29	$\text{CH}_2$	1.44, m 1.26, m	30.7	$\text{CH}_2$	2.00, m 1.28, m	30.7	$\text{CH}_2$	1.97, m 1.30, m	27.8	$\text{CH}_2$	1.95, m 1.06, m
16	34	$\text{CH}_2$	2.02, m	33.1	$\text{CH}_2$	2.70, d, $J = 14.2$ 1.58, m	33.1	$\text{CH}_2$	2.71, m 1.62, m	34.2	$\text{CH}_2$	2.42, m 1.16, m
17	79.2	qC		59.2	qC		59.2	qC		49.8	qC	
18	52.9	CH	1.80, m	49.2	CH	1.93, m	49.1	CH	1.98, m	49.2	CH	1.79, m
19	55	CH	2.52, m	50.2	CH	2.73, d, $J = 8.3$	50.2	CH	2.75, m	50.7	CH	2.12, m
20	151.3	qC		72.3	qC		72.3	qC		72.3	qC	
21	24.9	$\text{CH}_2$	1.79, m 1.38, m	29.7	$\text{CH}_2$	2.22, m 1.66, m	29.6	$\text{CH}_2$	2.25, m 1.68, m	28.5	$\text{CH}_2$	2.12, m 1.64, m
22	27.1	$\text{CH}_2$	1.78, m 0.96, m	37.7	$\text{CH}_2$	2.13, m 1.70, m	37.4	$\text{CH}_2$	2.15, m 1.70, m	30.6	$\text{CH}_2$	2.41, m 1.57, m
23	113.7	$\text{CH}_2$	4.98, br s 4.92, br s	29.3	$\text{CH}_3$	1.21, s	21.2	$\text{CH}_3$	1.00, s	29.3	$\text{CH}_3$	1.20, s
24	23.8	$\text{CH}_3$	1.83, s	22.6	$\text{CH}_3$	0.87, s	26.8	$\text{CH}_3$	1.11, s	22.6	$\text{CH}_3$	0.89, s
25	21	$\text{CH}_3$	0.90, s	16.4	$\text{CH}_3$	0.85, s	16.1	$\text{CH}_3$	0.79, s	16.3	$\text{CH}_3$	0.89, s
26	15.7	$\text{CH}_3$	1.01, s	16.8	$\text{CH}_3$	1.13, s	16.5	$\text{CH}_3$	1.07, s	16.4	$\text{CH}_3$	1.07, s
27	14.7	$\text{CH}_3$	1.00, s	15.3	$\text{CH}_3$	1.04, s	15.2	$\text{CH}_3$	1.14, s	15.4	$\text{CH}_3$	1.00, s
28	109.6	$\text{CH}_2$	5.14, s 4.88, s	179.4	qC		179.3	qC		59.9	$\text{CH}_2$	4.19, d, $J = 10.7$ 3.68, d, $J = 10.7$
29	20.8	$\text{CH}_3$	2.03, s	31.6	$\text{CH}_3$	1.45, s	31.8	$\text{CH}_3$	1.48, s	32.2	$\text{CH}_3$	1.43, s
30				27.2	$\text{CH}_3$	1.37, s	26.7	$\text{CH}_3$	1.39, s	25.8	$\text{CH}_3$	1.32, s

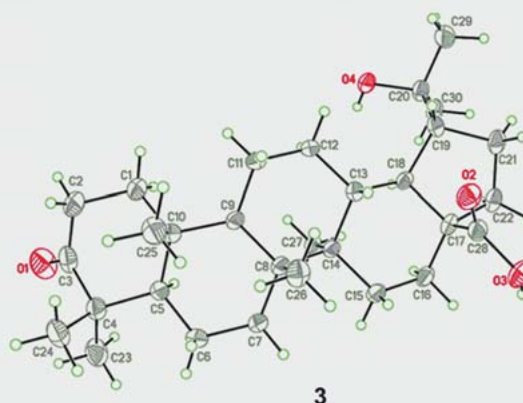
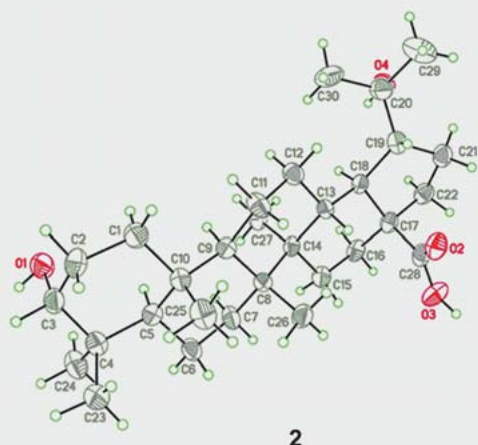




► **Fig. 2** COSY (bold bond), selected HMBC (arrow), and key ROESY (left right arrow) correlations of 1.



► **Fig. 3** COSY (bold bond), selected HMBC (arrow), and key ROESY (left right arrow) correlations of 2.



► **Fig. 4** Perspective drawing of the X-ray structures of 2 and 3.

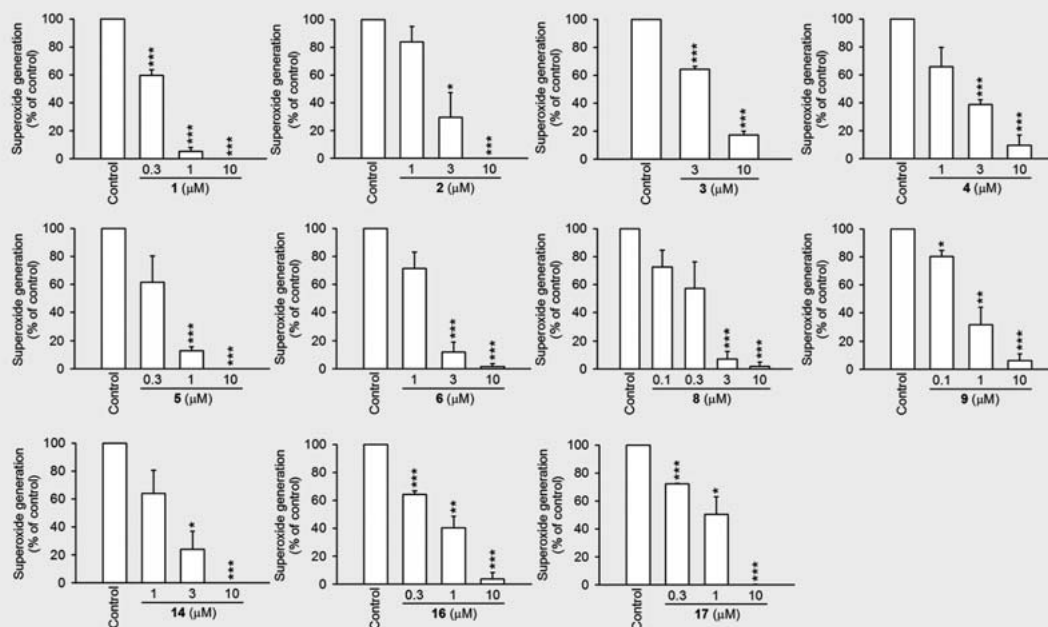
based on the NOESY correlations of H-28/H-13 ( $\delta_{\text{H}}$  1.85)/Me-26 ( $\delta_{\text{H}}$  1.07)/Me-25 ( $\delta_{\text{H}}$  0.89)/Me-24 ( $\delta_{\text{H}}$  0.89)/H-3 ( $\delta_{\text{H}}$  3.60) and H-28/H-19 ( $\delta_{\text{H}}$  2.12). From all of these data, the structure of 4 was assigned to 3 $\alpha$ ,20,28-trihydroxy-lupane.

Compounds 2–17 were evaluated for their anti-inflammatory activity by investigating their inhibitory effects on superoxide anion generation (► **Fig. 5**) and elastase release (► **Fig. 6**) from human neutrophils in response to fMLP. LY294002, a phosphatidylinositol-3-kinase inhibitor, was used as a positive control for inhibition of superoxide anion generation and elastase release. Among the tested samples, compound 5 showed the most potent anti-inflammatory activity on superoxide anion and elastase release, respectively. Moreover, compounds 2–17 were also assayed for *in vitro* inhibitory activity against HIV (► **Table 2**). The anti-retroviral drug abacavir was used as a positive control.

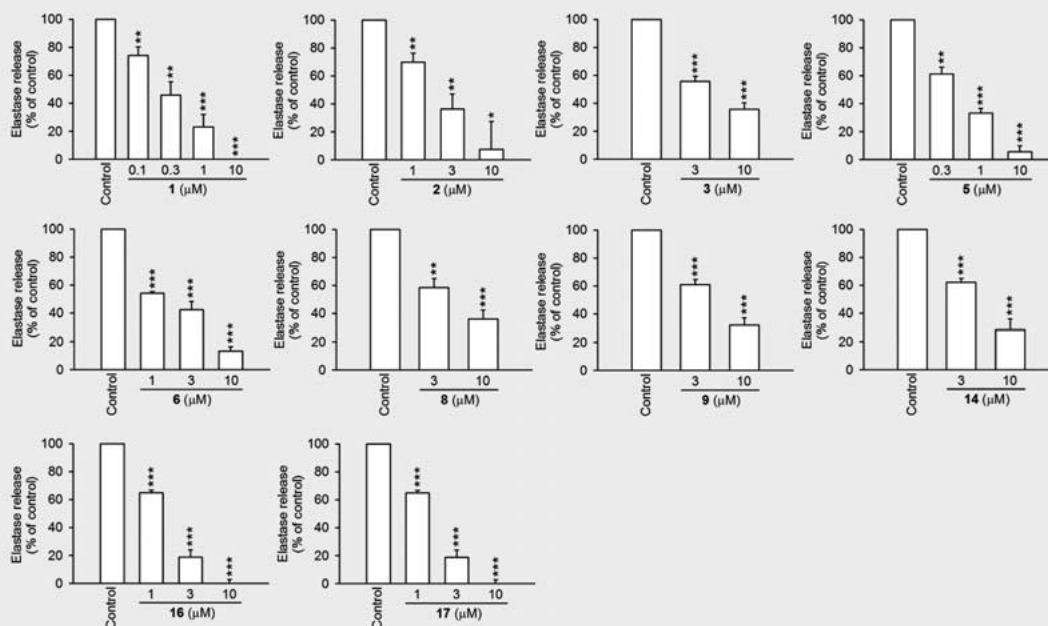
Compounds 8, 11, and 14 showed strong anti-HIV activity with ~60–70% inhibition at 10  $\mu\text{M}$ , which is comparable to abacavir, a common medication used for HIV/AIDS treatment. It is noteworthy that compound 11 had no notable cytotoxicity to normal cell and showed a larger selective index (SI) value than that of abacavir, and it might have some potential as a new anti-HIV lead compound. On the basis of our anti-HIV data, the following preliminary structure-activity relationships can be deduced as illustrated in ► **Fig. 7**. (1) The presence of an A-seco structure decreases anti-HIV activity (5 versus 8). (2) The  $\alpha$ -hydroxy at C-3 increases anti-

HIV activity (8 versus 9). (3) The presence of a hydroxy group at C-2 increases anti-HIV activity (14 versus 9). (4) The presence of a hydroxy group at C-27 increases anti-HIV activity (11 versus 9). (5) The presence of a carboxyl group at C-17 increases anti-HIV activity (14 versus 15). (6) Lupane-type triterpenes have stronger anti-HIV activity than oleanane-type triterpenes (14 versus 16). (7) The presence of a dimethyl carbinol group at C-17 increases anti-HIV activity (8 versus 2).

In recent years, lupane-type pentacyclic triterpenes have received much attention due to accumulating evidence of their anti-tumor, anti-viral, and anti-microbial effects [29–31]. In this study, the anti-inflammatory and anti-HIV activities of lupane and 3,4-seco-lupane-type triterpenoids were evaluated. Interestingly 3,4-seco-lupane-type triterpenoids showed stronger anti-inflammatory effects but lower anti-HIV activity than lupane-type triterpenoids. In addition, 3 $\alpha$ -hydroxy lupane-type triterpenoids had better anti-inflammatory and anti-HIV activities than the 3 $\beta$ -hydroxy analogues. Our findings may encourage synthetic efforts for the development of new anti-inflammatory and anti-HIV lupane derivatives.



► **Fig. 5** Effects of compounds on superoxide anion generation in fMLP/CB-induced (CB: cytochalasin B) human neutrophils in dose-dependent manners. Data are expressed as mean  $\pm$  SEM ( $n = 3$ ). \* $p < 0.05$ , \*\* $p < 0.01$ , \*\*\* $p < 0.001$  compared with the control.



► **Fig. 6** Effects of compounds on elastase release in fMLP/CB-induced human neutrophils. Data are expressed as mean  $\pm$  SEM ( $n = 3$  or  $n = 4$ ). \* $p < 0.05$ , \*\* $p < 0.01$ , \*\*\* $p < 0.001$  compared with the control.

► **Table 2** Effects of compounds 2–17 on HIV infection and cell viability.

Compound	HIV infection activity			Cell viability		
	Concentration ( $\mu\text{M}$ )			Concentration ( $\mu\text{M}$ )		
	1	10	100	1	10	100
2	97.9 $\pm$ 10.7	96.9 $\pm$ 11.0	23.3 $\pm$ 1.3	101.8 $\pm$ 7.1	98.7 $\pm$ 5.5	105.8 $\pm$ 5.4
3	89.4 $\pm$ 9.7	77.7 $\pm$ 5.1	56.2 $\pm$ 5.3	105.2 $\pm$ 4.6	108.8 $\pm$ 7.1	99.2 $\pm$ 4.5
4	83.2 $\pm$ 38.9	122.9 $\pm$ 48.6	14.0 $\pm$ 2.8	100.9 $\pm$ 0.3	99.5 $\pm$ 1.8	98.5 $\pm$ 2.2
5	103.0 $\pm$ 8.7	83.4 $\pm$ 12.8	29.9 $\pm$ 1.6	102.7 $\pm$ 3.7	108.0 $\pm$ 1.7	109.5 $\pm$ 2.0
6	102.1 $\pm$ 11.0	97.1 $\pm$ 9.4	42.4 $\pm$ 6.4	99.7 $\pm$ 2.1	103.6 $\pm$ 0.6	116.9 $\pm$ 0.8
7	112.3 $\pm$ 9.9	158.6 $\pm$ 11.1	39.4 $\pm$ 8.1	99.6 $\pm$ 0.8	103.2 $\pm$ 0.5	117.6 $\pm$ 1.8
8	70.0 $\pm$ 9.7	33.8 $\pm$ 2.7	2.3 $\pm$ 0.3	100.3 $\pm$ 3.3	69.2 $\pm$ 3.7	15.6 $\pm$ 0.8
9	95.8 $\pm$ 7.8	71.6 $\pm$ 6.9	13.2 $\pm$ 2.5	100.0 $\pm$ 0.7	99.1 $\pm$ 2.4	101.3 $\pm$ 0.6
10	84.9 $\pm$ 7.8	67.8 $\pm$ 8.4	16.8 $\pm$ 1.3	105.5 $\pm$ 2.7	108.5 $\pm$ 1.8	7.1 $\pm$ 0.3
11	61.5 $\pm$ 34.7	42.6 $\pm$ 23.5	30.6 $\pm$ 15.4	99.4 $\pm$ 0.9	99.0 $\pm$ 1.8	92.6 $\pm$ 0.5
12	110.3 $\pm$ 10.2	160.3 $\pm$ 14.9	384.8 $\pm$ 30.4	106.8 $\pm$ 6.4	105.6 $\pm$ 1.8	94.0 $\pm$ 8.7
13	100.2 $\pm$ 4.2	150.3 $\pm$ 18.1	202.9 $\pm$ 25.3	104.3 $\pm$ 0.9	104.0 $\pm$ 2.8	107.7 $\pm$ 4.7
14	86.3 $\pm$ 8.1	41.4 $\pm$ 3.9	2.4 $\pm$ 0.3	103.4 $\pm$ 1.8	105.3 $\pm$ 0.5	12.0 $\pm$ 1.6
15	100.3 $\pm$ 10.7	63.0 $\pm$ 7.4	3.3 $\pm$ 0.5	107.8 $\pm$ 1.7	108.4 $\pm$ 6.5	83.4 $\pm$ 4.5
16	93.4 $\pm$ 8.0	89.7 $\pm$ 5.8	2.4 $\pm$ 0.2	100.6 $\pm$ 1.2	101.3 $\pm$ 1.5	110.3 $\pm$ 1.4
17	97.0 $\pm$ 8.3	103.7 $\pm$ 13.3	1.9 $\pm$ 0.1	101.1 $\pm$ 1.4	103.4 $\pm$ 1.0	31.9 $\pm$ 4.3
Abacavir <sup>a</sup>	97.9 $\pm$ 10.9	30.6 $\pm$ 4.4	1.9 $\pm$ 0.8	99.7 $\pm$ 1.4	101.8 $\pm$ 0.9	99.3 $\pm$ 1.7

<sup>a</sup>Positive control in HIV infection assay.

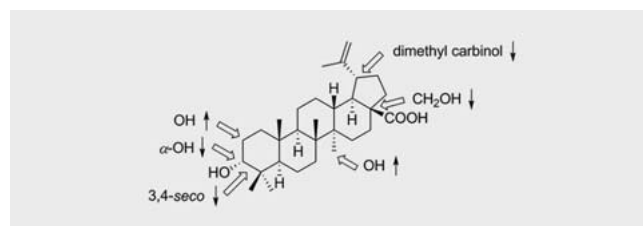
## Materials and Methods

### General experimental procedures

Merck Silicagel 60 and GE LH-20 gels were used for open column chromatography. HPLC was performed on Phenomenex Luna C<sub>18</sub> (5  $\mu\text{m}$ , 250  $\times$  10 mm) and Luna Si (5  $\mu\text{m}$ , 250  $\times$  4.6 mm) columns. The instrumentation for normal phase HPLC was composed of a Hitachi L-7100 pump and a Hitachi Bischoff refractive index detector. The instrumentation for reverse phase HPLC was composed of a Shimadzu LC-20AD pump and Shimadzu SPD-M10A diode array detector. IR spectra were measured with a Perkin Elmer 2000 FT-IR spectrophotometer. Optical rotations were obtained on a Jasco P-2000 polarimeter. NMR spectra were obtained on JEOL ECS 400 MHz, Varian Unity plus 400 MHz, and Varian Mercury plus 400 MHz NMR. ESI-MS data were measured on a Waters Micromass ZQ mass spectrometer. High-resolution ESI-MS data were collected on a Bruker Daltonics APEX II  $\alpha$ 30e mass spectrometer. Crystal data were obtained on a Bruker D8 VENTURE single-crystal XRD equipped with Oxford Cryostream 800+.

### Materials

Twigs and leaves of *L. litseifolius* were collected in Nantou County, Taiwan, in August 2014 and were identified by Prof. Yen-Hsueh Tseng. The specimens of *L. corneus* were collected in Pingtung County, Taiwan, in October 2014 and were identified by Prof. Ching-Te Chien. Voucher specimens (code no. KMU-LS and KMU-LC) were deposited in the Graduate Institute of Natural



► **Fig. 7** Structure-activity relationship studies for the anti-HIV effect of lupane-type triterpene. The structural modifications leading to activity changes are indicated by arrows (↓ or ↑). The bold white arrows indicated the specific position that functional group might change. The most active compound 8 was used for the SAR (structure activity relationship) description.

Products, College of Pharmacy, Kaohsiung Medical University, Kaohsiung, Taiwan.

### Extraction and isolation

The air-dried leaves and twigs of *L. litseifolius* (2.8 kg) were ground and extracted by MeOH at room temperature (15 L  $\times$  3). The crude extract (410.5 g) was partitioned between water and EtOAc (ethyl acetate). The EtOAc-soluble portion was further partitioned between hexanes and 75% MeOH (aq). After evaporation under reduced pressure, the 75% MeOH-soluble fraction (123.4 g) was separated by silica gel column chromatography with hexanes/EtOAc/MeOH mixtures of increasing polarity to give nine fractions

and **13** (126.0 mg). Fraction 5 (0.8 g) was subjected to a LH-20 column eluted with MeOH/CH<sub>2</sub>Cl<sub>2</sub> 1:1 to yield a subfraction 5A. Subfraction 5A (652.5 mg) was isolated by HPLC (SiO<sub>2</sub>, 2.0 mL/min, *n*-hexane/CH<sub>2</sub>Cl<sub>2</sub>/acetone 5:5:1) to give **12** (41.2 mg). Fraction 6 (2.1 g) was also separated by a LH-20 column eluted by MeOH/CH<sub>2</sub>Cl<sub>2</sub> 1:1 to give subfractions 6A and 6B. Subfraction 6A (796.5 mg) was further purified by a silica gel column eluted with *n*-hexane/CH<sub>2</sub>Cl<sub>2</sub>/acetone (100:5:1 to 0:0:1) to afford **9** (3.7 mg) and **10** (186.8 mg). Subfraction 6B (1.2 g) was chromatographed by a silica gel column (hexanes/CH<sub>2</sub>Cl<sub>2</sub>/acetone, gradient) to obtain **8** (31.8 mg). Fraction 7 (17.0 g) was dissolved in CH<sub>2</sub>Cl<sub>2</sub> to give a CH<sub>2</sub>Cl<sub>2</sub> soluble portion fraction 7A. This fraction (1.1 g) was subjected to a LH-20 column eluted with MeOH/CH<sub>2</sub>Cl<sub>2</sub> 1:1 to yield a subfraction 7A1 (360.7 mg). Subfraction 7A1 was isolated by HPLC (SiO<sub>2</sub>, 2.0 mL/min, *n*-hexane/CH<sub>2</sub>Cl<sub>2</sub>/acetone 5:5:1) to give **5** (59.8 mg). Fraction 8 (25.0 g) was dissolved in CH<sub>2</sub>Cl<sub>2</sub> to give a CH<sub>2</sub>Cl<sub>2</sub>-soluble fraction 8A. Fraction 8A (16.2 g) was separated on a silica gel column (hexanes/EtOAc/acetone/MeOH, gradient) to give subfraction 8A1. Subfraction 8A1 (1.9 g) was isolated by a LH-20 column eluted by MeOH/CH<sub>2</sub>Cl<sub>2</sub> 1:1 to give subfraction 8A1A. Subfraction 8A1A (964.1 mg) was purified by RP-HPLC (C<sub>18</sub>, 2.0 mL/min, 85% MeOH) to give **1** (4.0 mg), **2** (47.8 mg), **3** (194.1 mg), **4** (41.8 mg), **6** (13.9 mg), **7** (29.2 mg), and **11** (1.9 mg).

The air-dried leaves and twigs of *L. corneus* (7.9 kg) were ground and extracted by MeOH (20 L × 3) at room temperature to give a crude extract (383.0 g). The crude extract was partitioned as described above. The 75% MeOH layer (72.9 g) was fractionated on a silica gel column eluted with hexanes/CH<sub>2</sub>Cl<sub>2</sub>/acetone/MeOH mixtures of increasing polarity to furnish 12 fractions. Fraction 9 (0.8 g) was separated by a LH-20 column eluted with MeOH to yield a subfraction 9C. The subfraction 9C (0.3 g) was further separated by a silica gel column eluted with MeOH/CH<sub>2</sub>Cl<sub>2</sub> 1:40 to give subfractions 9C1–9C3. Subfraction 9C1 (55.1 mg) was purified by RP-HPLC (C<sub>18</sub>, 2.0 mL/min, 85% MeOH) to afford **15** (27.2 mg). Subfraction 9C2 (101.9 mg) was fractionated by RP-HPLC (C<sub>18</sub>, 2.0 mL/min, 85% MeOH with 0.05% CH<sub>3</sub>COOH) to give **14** (60.9 mg). Separation of subfraction 9C3 (84.5 mg) by RP-HPLC (C<sub>18</sub>, 2.0 mL/min, 85% MeOH) afforded **16** (8.7 mg) and **17** (6.2 mg).

## Isolates

Synbalanic acid (**1**): yellowish amorphous powder;  $[\alpha]_D^{25} + 435.1$  (c 0.2, CHCl<sub>3</sub>); IR (neat)  $\nu_{\max}$  3450, 2930, 2362, 1708, 1450, 888 cm<sup>-1</sup>; <sup>1</sup>H NMR (C<sub>5</sub>D<sub>5</sub>N, 400 MHz) and <sup>13</sup>C NMR (C<sub>5</sub>D<sub>5</sub>N, 100 MHz) spectroscopic data, see ▶ **Table 1**; HRESIMS  $m/z$  465.33416 ([M + Na]<sup>+</sup>, calcd. for C<sub>29</sub>H<sub>46</sub>NaO<sub>3</sub>, 465.33392).

3 $\alpha$ ,20-dihydroxy-28-lupanoic acid (**2**): white needles; M.p.: 296–297 °C;  $[\alpha]_D^{25} - 1.2$  (c 0.8, CHCl<sub>3</sub>); IR (neat)  $\nu_{\max}$  3428, 1643, 714, 430 cm<sup>-1</sup>; <sup>1</sup>H NMR (C<sub>5</sub>D<sub>5</sub>N, 400 MHz) and <sup>13</sup>C NMR (C<sub>5</sub>D<sub>5</sub>N, 100 MHz) spectroscopic data, see ▶ **Table 1**; HRESIMS  $m/z$  497.36012 ([M + Na]<sup>+</sup>, calcd. for C<sub>30</sub>H<sub>50</sub>NaO<sub>4</sub>, 497.36013).

20-hydroxy-3-oxo-28-lupanoic acid (**3**): white needles; M.p.: 298–299 °C;  $[\alpha]_D^{25} + 8.5$  (c 5.7, CHCl<sub>3</sub>); IR (neat)  $\nu_{\max}$  3333, 2920, 1696, 1463, 1385, 1181, 1028, 737, 571 cm<sup>-1</sup>; <sup>1</sup>H NMR (C<sub>5</sub>D<sub>5</sub>N, 400 MHz) and <sup>13</sup>C NMR (C<sub>5</sub>D<sub>5</sub>N, 100 MHz) spectroscopic data,

see ▶ **Table 1**; HRESIMS  $m/z$  495.34432 ([M + Na]<sup>+</sup>, calcd. for C<sub>30</sub>H<sub>48</sub>NaO<sub>4</sub>, 495.34448).

3 $\alpha$ ,20,28-trihydroxy-lupane (**4**): yellowish amorphous powder;  $[\alpha]_D^{25} + 12.7$  (c 2.1, CHCl<sub>3</sub>); IR (neat)  $\nu_{\max}$  3353, 2939, 2359, 1709, 1455, 1366, 1137, 1066, 1030, 990, 530 cm<sup>-1</sup>; <sup>1</sup>H NMR (C<sub>5</sub>D<sub>5</sub>N, 400 MHz) and <sup>13</sup>C NMR (C<sub>5</sub>D<sub>5</sub>N, 100 MHz) spectroscopic data, see ▶ **Table 1**; HRESIMS  $m/z$  483.38065 ([M + Na]<sup>+</sup>, calcd. for C<sub>30</sub>H<sub>52</sub>NaO<sub>3</sub>, 483.38087).

## Anti-inflammatory assay

Human neutrophils were obtained from healthy human donors by venipuncture (Chang Gung Medical Foundation, IRB: 104-8612C; date of the study approval: November 25, 2015) and were isolated by Ficoll centrifugation and dextran sedimentation. Purified neutrophils were re-suspended in a calcium (Ca<sup>2+</sup>)-free HBSS (Hank's balanced salt solution) buffer at pH 7.4 and were maintained at 4 °C before use.

For superoxide anion generation assay, neutrophils (6 × 10<sup>5</sup> cell/mL) were equilibrated in ferricytochrome c (0.5 mg/mL) and Ca<sup>2+</sup> (1 mM) at 37 °C for 5 min and incubated with DMSO (dimethyl sulfoxide) (0.1%) or test compounds for another 5 min. Cells were activated with fMLF (*N*-formyl-methionyl-leucyl-phenylalanine) (0.1  $\mu$ M) for 10 min after the priming with cytochalasin B (CB, 1  $\mu$ g/mL) for 3 min. The change in absorbance was monitored continuously at 550 nm with a spectrophotometer (U-3010, Hitachi). For elastase release assay, neutrophils (6 × 10<sup>5</sup> cell/mL) were equilibrated in MeO-Suc-Ala-Ala-Pro-Val-p-nitroanilide (100  $\mu$ M) and Ca<sup>2+</sup> (1 mM) at 37 °C for 5 min and incubated with DMSO (0.1%) or test compounds for another 5 min. Cells were activated with fMLF (0.1  $\mu$ M) for 10 min after the priming with CB (0.5  $\mu$ g/mL) for 3 min. The change in absorbance was monitored continuously at 405 nm with a spectrophotometer [32, 33]. The positive control LY294002 was purchased from Sigma-Aldrich, and its purity was ≥ 98% (HPLC). Results are expressed as means ± SEM (n = 3 or n = 4), and statistical analysis was performed with Sigma-Plot 8.0 (Systat Software).

## Anti-HIV assay

Cell lines: MAGI-CCR-5 (MAGIC-5) cells were obtained from the U.S. National Institutes of Health (NIH) AIDS Research and Reference Reagent Program. MAGIC-5, HacaT, and HEK293T cells were cultured in Dulbecco's Modified Eagle's Medium (Gibco BRL) supplemented with 10% heat-inactivated fetal bovine serum (HyClone), penicillin (100 U/mL), streptomycin (100 mg/mL), nonessential amino acids (0.1 mM), and L-glutamine (2 mM) (Gibco BRL).

Plasmids: The plasmid pNL-Luc-E-R-, which was obtained from the U.S. NIH AIDS Research and Reference Reagent Program, contains an envelope defective in the HIV-1 genome with a firefly luciferase reporter gene. Plasmids pCH119 containing envelope genomic segments of HIV-1 CRF07\_BC strain was generously provided by Dr. David C. Montefiori from the Duke University Medical Center in Durham, North Carolina.

HIV-1 pseudotyped virus preparation: Pseudotyped viruses expressing the HIV-1 CRF07\_BC Env protein were generated by co-transfecting HEK293T cells with plasmid DNAs from pNL-Luc-E-R- and pCH119. For transfection experiments, 1.2 × 10<sup>6</sup> HEK293T

cells were seeded 1 d before transfection in a 10 cm plate. Forty-eight hours after transfection, the culture supernatants were harvested and filtered through a 0.45 mm filter (Millipore).

**Assay for drug susceptibility:** The resultant pseudotyped virus was used to infect MAGIC-5 cells in the presence or absence of testing drugs for 24 h. The drug susceptibility of pseudotyped HIV-1 viruses in the MAGIC-5 cells was evaluated by measuring luciferase activity with a luciferase reporter assay kit (Promega, Catalog E1980) and a luminometer. HIV infection activity was calculated as following: (luciferase activity<sup>Drug</sup>/luciferase activity<sup>DMSO</sup>) × 100%. Each test was performed in duplicate. Data are mean ± SD of three independent experiments.

**Cytotoxicity assay:** HacaT cells were seeded in a 96-well plate (3000 cells per well) in at least six replicates for each experiment. Cells were treated with the indicated concentrations of testing compounds for 72 h. At the assay time point, alamarBlue® (10%, Thermo Fisher Scientific) was added and further incubated for 4 h at 37 °C. Fluorescence of the reduced alamarBlue® was measured by microplate reader (Synergy HT, BioTek Instruments). The amount of fluorescence for each group was normalized to the DMSO solvent control group and shown as viable percentage. All data are presented as mean ± SD of three independent experiments.

The positive control abacavir was obtained from the U.S. NIH AIDS Research and Reference Reagent Program and its purity was ≥ 95%.

## Supporting information

The one- and two-dimensional NMR spectra of new compounds 1–4 and the X-ray data of 2 and 3 are available and published on the journal homepage at <https://www.thieme-connect.de/products/ejournals/abstract/10.1055/s-0043-113826>.

## Acknowledgements

This work was supported by grants from the Ministry of Science and Technology of Taiwan (MOST103-2628-B-037-001-MY3 awarded to Y.-B. C.), the National Health Research Institute (NHRI-EX103-10241BI), and in part from a grant from Chinese Medicine Research Center, China Medical University (the Ministry of Education, the Aim for the Top University Plan). This study was supported partially by Kaohsiung Medical University (Aim for the Top Universities Plan, grant No. KMU-TP105E32), the Ministry of Health and Welfare of Taiwan (MOHW106-TDU-B-212-144007), and the Health and Welfare surcharge of tobacco products.

## Conflict of Interest

There is no conflict of interest.

## References

- [1] Lin CY, Wang L, Wang H, Fang ST, Zhang QB, Yang L, Guo H, Lin P, Zhang J, Wang XJ. *Lithocarpus polystachyus* Rehd leaf aqueous extract inhibits human breast cancer growth *in vitro* and *in vivo*. *Nutr Cancer* 2014; 66: 613–624
- [2] Hou SZ, Chen SX, Huang S, Jiang DX, Zhoua CJ, Chen CQ, Liang YM, Lai XP. The hypoglycemic activity of *Lithocarpus polystachyus* Rehd. leaves in the experimental hyperglycemic rats. *J Ethnopharmacol* 2011; 138: 142–149
- [3] Hou SZ, Xu SJ, Jiang DX, Chen SX, Wang LL, Huang S, Lai XP. Effect of the flavonoid fraction of *Lithocarpus polystachyus* Rehd. on spontaneously hypertensive and normotensive rats. *J Ethnopharmacol* 2012; 143: 441–447
- [4] Xie Y, Ma G, Wei H, Yuan JQ, Wu HF, Zhou XL, Yang JS, Xu XD. Three new phenolics and other constituents from the seeds of *Lithocarpus pachyphylloides*. *Molecules* 2013; 18: 10397–10403
- [5] Yang WM, Liua JK, Qin XD, Wu WL, Chen ZH. Antioxidant activities of three dihydrochalcone glucosides from leaves of *Lithocarpus pachyphyllus*. *Z Naturforsch C Biosci* 2004; 59: 481–484
- [6] Hui WH, Li MM. Acidic triterpenoids from *Lithocarpus attenuata*. *Phytochemistry* 1975; 14: 785–787
- [7] Hui WH, Li MM. Further triterpenoids from the stem of *Lithocarpus polystachya*. *Phytochemistry* 1977; 16: 111–112
- [8] Wang HM, Ning RN, Shen Y, Chen ZH, Li JL, Zhang RJ, Leng Y, Zhao WM. Lithocarpic acids A–N, 3,4-*seco*-cycloartane derivatives from the cupules of *Lithocarpus polystachyus*. *J Nat Prod* 2014; 77: 1910–1920
- [9] Ning RN, Wang HM, Yu S, Chen ZH, Zhang RJ, Leng Y, Zhao WM. Lithocarpic acids O–S, five homo-cycloartane derivatives from the cupules of *Lithocarpus polystachyus*. *Bioorg Med Chem Lett* 2014; 24: 5395–5398
- [10] Qin XD, Liu JK. A new sweet dihydrochalcone-glucoside from leaves of *Lithocarpus pachyphyllus* (Kurz) Rehd. (Fagaceae). *Z Naturforsch C Biosci* 2003; 58: 759–761
- [11] The Plant List. Available at <http://www.theplantlist.org>. Accessed January 1, 2013
- [12] Valterová I, Klinot J, Vystrčil A. Preparation and antibacterial activity of di-, tri and tetraoic acids derived from 3,4-secolupane. *Collect Czech Chem Commun* 1983; 48: 649–661
- [13] Finlay HJ, Honda T, Gribble GW, Danielpour D, Benoit NE, Suh N, Williams C, Michael BS. Novel A-ring cleaved analogs of oleanolic and ursolic acids, which affect growth regulation. *Bioorg Med Chem Lett* 1997; 7: 1769–1772
- [14] Ma Z, Hano Y, Qiu F, Chen Y, Nomura T. Determination of the absolute stereochemistry of lupine triterpenoids by fructofuranoside method and ORD spectrum. *Tetrahedron Lett* 2004; 45: 3261–3263
- [15] Peng C, Bodenhausen G, Qiu SX, Fong HHS, Farnsworth NR, Yuan SG, Zheng CZ. Computer-assisted structure elucidation: application of CISOC-SES to the resonance assignment and structure generation of betulinic acid. *Magn Reson Chem* 1998; 36: 267–278
- [16] Drag M, Surowiak P, Malgorzata DZ, Dietel M, Lage H, Oleksyszyn J. Comparison of the cytotoxic effects of birch bark extract, betulin and betulinic acid towards human gastric carcinoma and pancreatic carcinoma drug-sensitive and drug-resistant cell line. *Molecules* 2009; 14: 1639–1651
- [17] Tchivounda HP, Koudogbo B, Besace Y, Casadevall E. Cyclicodiscic acid, a dihydroxy pentacyclic triterpene carboxylic acid from *Cylicodiscus gabunensis*. *Phytochemistry* 1990; 29: 3255–3258
- [18] Shahlaei M, Ghanadian SM, Ayatollahi AM, Mesaik MA, Abdalla OM, Afsharypour S, Rabbani M. Molecular modeling, structure activity relationship and immunomodulatory properties of some lupeol derivatives. *Med Chem Res* 2013; 22: 1795–1803



- [19] Huynh NV, Nguyen THT, Nguyen KPP, Hansen PE. Structural studies of the chemical constituents of *Tithonia tagetiflora* Desv. (Asteraceae). *Magn Reson Chem* 2013; 51: 439–443
- [20] Lee SM, Park JG, Lee YH, Lee CG, Min BS, Kim JH, Lee HK. Anti-complementary activity of triterpenoids from fruits of *Zizyphus jujuba*. *Biol Pharm Bull* 2004; 27: 1883–1886
- [21] Hao J, Zhang X, Zhang P, Liu J, Zhang LY, Sun HB. Efficient access to isomeric 2,3-dihydroxy lupanes: first synthesis of alphetolic acid. *Tetrahedron* 2009; 65: 7975–7984
- [22] Sommerwerk S, Heller L, Serbian I, Csuk R. Straightforward partial synthesis of four diastereomeric 2,3-dihydroxy-olean-12-en-28-oic acids from oleanolic acid. *Tetrahedron* 2015; 71: 8528–8534
- [23] Abigail HP, Moustapha B, César IA, José Fausto RC, Alejandra RM, Isela RMJ, José Alejandro CL. Aortic relaxant activity of *Crataegus gracilior* Phipps and identification of some of its chemical constituents. *Molecules* 2014; 19: 20962–20974
- [24] Lee CK. A new norlupene from the leaves of *Melaleuca leucadendron*. *J Nat Prod* 1998; 61: 375–376
- [25] Akihisa TS, Takamine YS, Yoshizumi KZ, Tokuda HK, Kimura YK, Ukiya MT, Nakahara TR, Yokochi TS, Ichiishi EC, Nishino HY. Microbial transformations of two lupane-type triterpenes and anti-tumor-promoting effects of the transformation products. *J Nat Prod* 2002; 65: 278–282
- [26] Farimani MM, Moghaddam FM, Esmaeili MA, Amind G. A lupane triterpenoid and other constituents of *Salvia eremophila*. *Nat Prod Res* 2012; 26: 2045–2049
- [27] Gonzálezc AG, Amaroc J, Fragac BM, Luisc JG, Fayosa J, Peralesa A, Méndezb MP. Minor triterpenes from *Orthopterygium huancuy*. *Phytochemistry* 1984; 23: 2079–2080
- [28] Ali AE. Cytotoxic lupane-, secolupane-, and oleanane-type triterpenes from *Viburnum awabuki*. *Nat Prod Res* 2008; 22: 191–197
- [29] Hsu TI, Chen YJ, Hung CY, Wang YC, Lin SJ, Su WC, Lai MD, Kim SY, Wang Q, Qian K, Goto M, Zhao Y, Kashiwada YS, Lee KH, Chang WC, Hung JJ. A novel derivative of betulinic acid, SYK023, suppresses lung cancer growth and malignancy. *Oncotarget* 2015; 6: 13671–13687
- [30] Li J, Goto M, Yang X, Morris-Natschke SL, Huang L, Chen CH, Lee KH. Fluorinated betulinic acid derivatives and evaluation of their anti-HIV activity. *Bioorg & Med Chem Lett* 2016; 26: 68–71
- [31] Amoussa AMO, Lagnika L, Bourjot M, Vonthron-Senecheau C, Sann A. Triterpenoids from *Acacia ataxacantha* DC: antimicrobial and antioxidant activities. *BMC Complement Altern Med* 2016; 16: 284
- [32] Yu HP, Hsieh PW, Chang YJ, Chung PJ, Kuo LM, Hwang TL. 2-(2-Fluorobenzenamido)benzoate ethyl ester (EFB-1) inhibits superoxide production by human neutrophils and attenuates hemorrhagic shock-induced organ dysfunction in rats. *Free Radic Biol Med* 2011; 50: 1737–1748
- [33] Yang SC, Chung PJ, Ho CM, Kuo CY, Hung MF, Huang YT, Chang WY, Chang YW, Chan KH, Hwang TL. Propofol inhibits superoxide production, elastase release, and chemotaxis in formyl peptide – activated human neutrophils by blocking formyl peptide receptor 1. *J Immunol* 2013; 190: 6511–6519



Cite this: *Anal. Methods*, 2017, 9, 3329

# Development and validation of an LC-MS/MS method for simultaneous quantification of hesperidin and hesperetin in rat plasma for pharmacokinetic studies†

Jr-Ting Lee,<sup>a</sup> Li-Heng Pao,<sup>bc</sup> Chang-Da Hsieh,<sup>a</sup> Pei-Wei Huang<sup>c</sup>  
and Oliver Yoa-Pu Hu<sup>ib</sup>\*<sup>c</sup>

A simple and sensitive method for the determination of hesperidin and hesperetin was necessary for a pharmacokinetic (PK) study in Wistar rats. Polarity-switching mode was utilized to acquire positive ion electrospray data for hesperidin and neohesperidin dihydrochalcone- $d_3$ , and negative ionization data for hesperetin and *rac*-hesperetin- $d_3$ . The analytes were investigated in the multiple reaction monitoring mode as the precursor/product ion pair of  $m/z$  611.2  $\rightarrow$  303.1 for hesperidin,  $m/z$  616.3  $\rightarrow$  308.3 for neohesperidin dihydrochalcone- $d_3$ ,  $m/z$  301.3  $\rightarrow$  164.1 for hesperetin, and  $m/z$  304.3  $\rightarrow$  164.1 for *rac*-hesperetin- $d_3$ . Hesperidin and hesperetin in rat plasma were separated with solid-phase extraction using a HyperSep Retain PEP column and separated on a Hypersil GOLD Phenyl reversed-phase column using a gradient elution of 0.1% formic acid in water and acetonitrile. Hesperidin was validated over the concentration range of 1–1000 ng mL<sup>-1</sup>, and hesperetin was validated over the range of 0.2–100 ng mL<sup>-1</sup>, both with  $r > 0.999$ . The respective within- and between-run precisions were 2.06–9.54% and 2.11–7.76%, and the within- and between-run accuracies were –6.52% to 3.82% and –1.62% to 2.33%, respectively, for both analytes. Extraction recoveries of these analytes were >87%. The matrix effects were between 94.7% and 113.6%. All of the analytes were stable during the assay and storage in Wistar rat plasma. The lower limit of quantification of the active metabolite hesperetin is up to 200 pg mL<sup>-1</sup>, so complete plasma concentration–time profiles can be obtained by the LC-MS/MS method without the need for enzymatic hydrolysis of the serum sample.

Received 6th January 2017

Accepted 5th May 2017

DOI: 10.1039/c7ay00051k

rsc.li/methods

## 1. Introduction

Several studies have shown that following oral administration, hesperidin is hydrolyzed by  $\beta$ -glucosidases to hesperetin aglycon before absorption. Absorbed hesperetin is then immediately metabolized to glucuronide and sulfate conjugates in the intestinal epithelium and liver.<sup>1,2</sup> Hesperidin and hesperetin have a variety of pharmacological activities, such as reduction of capillary fragility associated with scurvy, antioxidant properties,<sup>3,4</sup> antiplatelet activities,<sup>5</sup> antihypertensive effects,<sup>6</sup> and

cholesterol reduction in the serum of rats fed a cholesterol-enriched diet.<sup>7,8</sup> The compounds show a wide array of biological activities that contribute to the protection of human health, and they are abundant in citrus fruits.

Despite their wide range of therapeutic activities, the compounds are barely soluble in water (<0.01%),<sup>9</sup> which restricts their use as potent phytochemicals. Further, citrus flavonoids are well known for their inhibition of selected cytochrome P450 isoenzymes, which may explain the altered bioavailability of certain orally administered drugs.<sup>1</sup> In oral administration studies, these flavonoids are usually dissolved in vehicles to enhance their absorption. To evaluate the bioavailability of hesperidin, one must understand the bioactive form, hesperetin, *in vivo*. Moreover, the short elimination half-life (3.17 h for hesperidin<sup>10</sup> and 2.2 h for hesperetin<sup>11</sup>) also restricts their use. Maintaining a steady plasma concentration of the active moieties is required to enable their therapeutic activity; this necessitates the development of a dosage form that can maintain the concentration of the actives in the blood for a longer period of time.

<sup>a</sup>Department of Pharmacy, Taipei Veterans General Hospital Yuli Branch, No. 91, Xinxing St., Yuli Township, Hualien County 981, Taiwan, Republic of China

<sup>b</sup>Research Center for Chinese Herbal Medicine and Research Center for Food and Cosmetic Safety, College of Human Ecology, Chang Gung University of Science and Technology, No. 261, Wen-hwa 1st Rd., Kwei-shan Township, Taoyuan County 333, Taiwan, Republic of China

<sup>c</sup>School of Pharmacy, National Defense Medical Center, 9F, No. 161 Minchuan East Road, Sec. 6, Neihu Dist., Taipei City 114, Taiwan, Republic of China. E-mail: yoaupu@aliyunmca.com; Fax: +886 2 8792 4859; Tel: +886 2 8792 3100 extn 18176

† Electronic supplementary information (ESI) available. See DOI: 10.1039/c7ay00051k

In order to meet these challenges, we chose hydroxypropyl methylcellulose (HPMC), which has been used frequently in the formulation of sustained-release matrix tablets because, among other useful properties, it is a well-known crystallization inhibitor.<sup>12,13</sup> This property helps generate and maintain an elevated concentration of free drug during the absorption phase *via* generation of a supersaturated state.<sup>14,15</sup> Drug formulation with HPMC improves the rate and extent of absorption of many drugs and enhances oral bioavailability. The aim of the present work was to develop and validate a method with appropriate sensitivity, selectivity, accuracy, and precision to evaluate a new HPMC-based formulation of hesperidin in rats by means of a pharmacokinetic (PK) study.

Until now, researchers have used a high-performance liquid chromatography (HPLC) method with ultraviolet (UV) detection to assay the hesperidin metabolite but have been unable to concurrently assay hesperidin and its metabolite hesperetin. Lack of specificity and low sensitivity limit effective detection. For example, Yamada *et al.* reported that the limits of detection of an assay in rat plasma were approximately 15 ng mL<sup>-1</sup> for hesperetin and 30 ng mL<sup>-1</sup> for hesperidin.<sup>9</sup> Unfortunately, these are not sufficiently sensitive to measure the plasma concentration of the drugs following oral administration. More effective methods for detecting low levels of hesperidin and hesperetin include: liquid chromatography (LC) with ultraviolet (UV) detection,<sup>11,16</sup> microbore HPLC,<sup>17</sup> liquid chromatography-tandem mass spectroscopy (LC-MS/MS),<sup>10,18–21</sup> and gas chromatography.<sup>22,23</sup> In 2012, Tong *et al.*<sup>10</sup> developed an LC-MS/MS method and acquired 5 major citrus flavanones, including hesperidin and hesperetin, from *Fructus aurantii*, which is used in traditional Chinese medicine. The calibration curves were linear over the range of 0.5–100 ng mL<sup>-1</sup> for hesperidin and 5–1000 ng mL<sup>-1</sup> for hesperetin. However, the ranges of Tong's methods may still cannot cover the whole plasma concentration–time profiles. A more sensitive method with appropriated specificity is still needed.

Therefore, this study aimed to develop and validate a simplified, rapid, sensitive, and selective LC-MS/MS method that could be used to simultaneously determine the concentration of the free form of hesperidin and its active metabolite, hesperetin, in rat plasma without the need for enzymatic hydrolysis. The goal was a new method that both minimized experimental errors and also permitted analysts to obtain the *in vivo* free concentration of hesperetin. We used Wistar rats in this study because they are a well studied model for *in vivo* pharmacokinetic studies.<sup>2</sup>

## 2. Experimental procedure

### 2.1. Chemicals and reagents

Hesperidin and hesperetin (both ≥98% purity) were purchased from Cayman Chemical (Ann Arbor, MI, USA). Methanol (MeOH) and dimethyl sulfoxide (DMSO) were purchased from Tedia Company (Fairfield, OH, USA) and Sigma-Aldrich (St. Louis, MO, USA), respectively. Analytical grades of formic acid and acetonitrile (ACN) were purchased from Merck (Darmstadt, Germany). Water was prepared using the Milli-Q water-

purification system (Millipore, Bedford, MA, USA). Sodium pentobarbital was purchased from SCI Pharmtech (Taoyuan, Taiwan). Heparin sodium was obtained from China Chemical & Pharmaceutical (Taipei, Taiwan). Standard hesperidin and hesperetin were purchased from Extrasynthese (Genay, France). Neohesperidin dihydrochalcone-d<sub>3</sub> and *rac*-hesperetin-d<sub>3</sub> were purchased from Toronto Research Chemicals (Toronto, ON, Canada). All these standard compounds possessed purity >98%. HPMC K15M was generously donated by the Dow Chemical (Midland, MI, USA). The HyperSep Retain PEP column was obtained from Thermo Fisher Scientific (Waltham, MA, USA).

### 2.2. Instruments

The LC-MS/MS system consisting of an Applied AB Sciex QTrap 5500 Triple Quadrupole mass spectrometer (Foster City, CA, USA) was coupled to an ekspert ultraLC 100-XL (Dublin, Ireland) Ultra High Performance Liquid Chromatography (UHPLC) system. Data acquisition was performed with Analyst 1.6.1 Applied Biosystems/MDS SCIEX software (Concord, ON, CANADA).

**2.2.1. Liquid chromatography.** The UHPLC system was equipped with an ekspert ultraLC 100-XL system controller, an ultraLC 100-XL HPLC pump, and autosampler (Dublin, Ireland). Samples (5 µL) were injected onto a Hypersil GOLD (2.1 × 100 mm, 3 µm) phenyl column (Thermo Scientific) maintained at 40 °C. The mobile phase consisted of solvent A (0.1% formic acid in water) and solvent B (0.1% formic acid in ACN). The 12 min gradient was as follows: 77% A (0–3 min), 40% A (3–3.5 min), 40% A (3.5–7 min), 77% A (7–7.1 min), and 77% A (7.1–12 min). The flow rate was set at 0.3 mL min<sup>-1</sup>. The autosampler was conditioned at 4 °C.

**2.2.2. Mass spectrometry.** The triple-quadrupole MS detector was operated in a positive ion electrospray ionization (ESI) method for hesperidin and neohesperidin dihydrochalcone-d<sub>3</sub> (internal standard [IS]) and in a negative ion ESI method for hesperetin and *rac*-hesperetin-d<sub>3</sub> (IS). A multiple reaction monitoring mode using polarity switching between the positive and negative ion mode was applied. The polarity was switched every 50 ms. The ESI was operated in either positive ion ESI mode (4650 V) or negative ion ESI mode (–4500 V), and the main working parameters were set as follows: high-purity nitrogen gas was used as collision-induced dissociation gas (medium), curtain gas (setting 20), and nebulizer gas (setting 40); the turboion spray temperature was set at 550 °C. The MS/MS transitions and fragmentation conditions selected for the individual analytes are shown in Table 1. The peak full width at half maximum was set at 0.7 Th for both Q1 and Q3. The scan time for each analyte was 0.1 s.

### 2.3. Standards and samples preparation

**2.3.1. Standard solutions.** Hesperidin (1 mg mL<sup>-1</sup>) and hesperetin (100 µg mL<sup>-1</sup>) were prepared in MeOH. All stock solutions were stored at –20 °C and protected from light. They were stable for at least 180 days. Equal volumes of hesperidin and hesperetin stock solution were mixed. Then, the working solution for the standard curve and quality control (QC) samples from the mixture were diluted with MeOH : H<sub>2</sub>O

Table 1 Multiple-reaction monitoring transitions and fragmentation parameters for hesperidin, hesperetin, and internal standards<sup>a</sup>

Optimized parameters drug	Molecular weight (Da)	Polarity	Precursor	Product	DP (V)	FP (V)	CEP (V)	CE (eV)	CXP (V)
Hesperidin	610.57	ES <sup>+</sup>	611.2	303.1	50	260	10	30	9
Hesperetin	302.28	ES <sup>−</sup>	301.3	164.1	−60	−200	−5	−35	−10
<b>Internal standard</b>									
Neohesperidin	615.59	ES <sup>+</sup>	616.3	308.3	50	260	10	30	9
dihydrochalcone-d <sub>3</sub>									
<i>rac</i> -Hesperetin-d <sub>3</sub>	305.3	ES <sup>−</sup>	304.3	164.1	−60	−200	−5	−35	−10

<sup>a</sup> DP: declustering potential; FP: focusing potential; CEP: cell entrance potential; CE: collision energy; CXP: cell exit potential.

(50 : 50, v/v). Neohesperidin dihydrochalcone-d<sub>3</sub> (1 µg mL<sup>−1</sup>) and *rac*-hesperetin-d<sub>3</sub> (200 ng mL<sup>−1</sup>) were mixed in MeOH : H<sub>2</sub>O (50 : 50, v/v) and used as an IS.

**2.3.2. Plasma standard and quality control samples.** Standard calibration samples were prepared by adding 50 µL of IS solution and 10 µL of working solution into 90 µL of rat blank plasma. Calibration curves were made for 6 different concentrations. Calibration standards of each analyte were fixed at concentrations of 1, 10, 50, 100, 500, and 1000 ng mL<sup>−1</sup> for hesperidin and 0.2, 1, 5, 10, 50, and 100 ng mL<sup>−1</sup> for hesperetin.

QC samples were prepared in a similar manner at 4 different concentrations. QC samples were prepared at the lower limit of quantification (LLOQ), low, middle, and high concentrations set at 1, 3, 450, and 900 ng mL<sup>−1</sup> for hesperidin and 0.2, 0.6, 45, and 90 ng mL<sup>−1</sup> for hesperetin.

**2.3.3. Sample preparation.** The plasma samples were thawed at room temperature before analysis. To a 100 µL aliquot of plasma sample, 50 µL of IS solution was added. Then these mixtures were acidified with 200 µL of 0.05% formic acid in H<sub>2</sub>O, and 100 µL of H<sub>2</sub>O was added. Solid-phase extraction (SPE) was conducted using a HyperSep Retain PEP column. The cartridges were conditioned sequentially with 1 mL of MeOH and 1 mL of H<sub>2</sub>O before use. The diluted plasma sample solutions were then loaded onto SPE cartridges, and the loaded cartridges were washed with 1 mL of H<sub>2</sub>O; subsequently, the analyte was eluted with 1 mL of MeOH. The eluate was then evaporated to dryness under an N<sub>2</sub> stream and reconstituted with 100 µL of MeOH : H<sub>2</sub>O (20 : 80, v/v) and vortexed for 30 s. Finally, the solvent was transferred to the autosampler vials, and 5 µL was injected into the LC-MS/MS system.

## 2.4. Method validation

The method validation assays were conducted based on the current US FDA Bioanalytical Method Validation Guidance.<sup>24</sup> The following parameters were determined for the validation of the analytical method developed for hesperidin and hesperetin in Wistar rat plasma: selectivity, linearity, LLOQ, precision, accuracy, extraction recovery, matrix effect, and stability.

Selectivity was evaluated by comparison of chromatograms of 6 different sources of blank plasma to ensure that there were no significant interfering peaks at the retention times at the LLOQ of the analytes. In each run, a blank plasma sample

(processed with or without IS) was analyzed to linearity, and LLOQ, a line  $Y = aX + b$ , was fitted through the standard curve consisting of a weighted linear regression (weight =  $1/x$ ) of the peak area ratio of hesperidin and hesperetin to the IS ( $Y$ ) versus the actual concentration of the analyte ( $X$ ). In the present study, LLOQ is defined as the lowest plasma concentration in the calibration curve, indicating that the analyte response at LLOQ was 5 times the baseline noise and could be determined with a precision of  $\leq 20\%$  and an accuracy of 80–120%.

To assess precision and accuracy, the within-run precision and accuracy were determined by analyzing QC samples ( $n = 6$ ). The between-run precision and accuracy were also verified by analyzing QC samples in 6 batches on different days. The precision was presented as a relative standard deviation (RSD), which was obtained by dividing the standard deviation by the average value, and the resulting value was then multiplied by 100 for expression as a percentage. The accuracy was shown as relative error (RE), which was evaluated as: (mean calculated concentration – concentration spiked)  $\times 100\%$ /concentration spiked. The acceptable within- and between-run precision and accuracy were set at  $\leq 15\%$ , except for LLOQ.

The evaluations for recovery and matrix effects were performed in triplicate at low, middle, and high QC concentrations. The extraction recoveries were determined by comparing the response ratios of extracted plasma standards with those of extracted blank plasma spiked with corresponding concentrations of analytes. The response was defined as the peak area of hesperidin and hesperetin divided by the peak area of the IS. Blank plasma from 6 rats was used to assess the matrix effect. The absolute and relative matrix effects were previously defined by Matuszewski *et al.*<sup>25</sup> The absolute matrix effect was evaluated by comparing the peak areas of hesperidin and hesperetin added to extracted blank plasma with those of the extracted water. The RSD of the mean peak areas of hesperidin and hesperetin in the extracted blank plasma indicated the relative matrix effect.

The results were evaluated by comparison of the calculated concentration with the initial values. The stability tests were performed in triplicate at low, middle, and high QC concentrations. The percentage of deviation in the concentrations was used as an indicator of stability. The analyte was considered stable when it remained within 15% of the initial value. Comparisons were made between stock solutions (stored at  $-20^\circ\text{C}$  for 180 days) and freshly made ones (stored at  $-80^\circ\text{C}$ ) at 250 ng mL<sup>−1</sup> ( $n$



= 3). Short-term temperature stability was evaluated to evaluate the analytes' stability in the matrix. During the examination, samples were stored at room temperature (25 °C) for at least 4 h prior to extraction. To assess the injector stability of the processed samples, the QC samples were extracted and placed in the autosampler at 4 °C for 24 h and then injected into the LC-MS/MS system for analysis. The freeze-thaw stability was determined after 3 freeze (−80 °C) and thaw (25 °C) cycles before analysis. The long-term stability was evaluated after storage: the QC samples stored in a freezer at −80 °C remained stable for a minimum of 60 days. All samples were subsequently thawed and analyzed together with freshly prepared calibration samples.

## 2.5. Application of the method

This analytical method was used to evaluate the performance of a new formulation of hesperidin in a 2.5% HPMC K15M dosage form, in Wistar rats, and the free-form plasma concentrations of hesperidin and its active metabolite, hesperetin, were measured.

**2.5.1. Experimental animals.** This study was approved by the Institutional Animal Care and Use Committee of the National Defense Medical Center, Taipei, Taiwan (10-082). And all experiments were performed in compliance with the article 15 to 17 in the Chapter 3 of Application of Animal Science of Taiwan Animal Protection Act. Male Wistar rats, each weighing between 300 g and 330 g at 9 weeks of age, were purchased from the National Applied Research Laboratories and National Laboratory Animal Center (Taiwan) and randomly divided to 2 groups ( $n = 6$  per group). They were placed in individual cages, and tap water (*ad libitum*) was available throughout the study period. The standard diet (Young Li Trading Co. LTD., Taiwan) was administered, and controlled temperature, humidity, and light/dark cycles (12 h/12 h) were maintained for a week.

**2.5.2. Pharmacokinetic study.** All rats ( $n = 6$ ) were anesthetized intraperitoneally with pentobarbital (50 mg kg<sup>−1</sup>). The right internal artery was cannulated with PE 50 tubing for collecting blood. Catheter insertion was performed using the cut-down technique. The distal end of the catheter was tunneled under the skin and externalized through an incision in the back of the neck. After the surgery, the rats were secured overnight (approximately 16 h) for recovery. The rats were administered a dose of 800 mg kg<sup>−1</sup> body weight hesperidin in 2.5% HPMC K15M : DMSO = 8.5 : 1.5 (v/v) *via* gastric gavage. Blood samples (300 µL) were obtained at 0.083, 0.167, 0.33, 0.67, 1, 2, 3, 4, 5, 6, 8, 10, 12, 16, 20, 24, and 48 h. The blood was drawn at each time point, and an equivalent volume of isotonic saline was infused to restore the amount of blood removed. Four hours after administration of the dose, the rats had free access to pellet chow and water *ad libitum* during the entire experiment. Plasma was obtained after centrifugation of the blood sample at 13 000 rpm for 5 min. All samples were stored at −80 °C until analysis.

## 3. Results and discussion

### 3.1. Method development

Hesperidin has been analyzed using both positive ion ESI<sup>18,19,26</sup> and negative ion ESI,<sup>10,27–30</sup> and hesperetin also has been

analyzed using positive ion ESI<sup>10,31</sup> and negative ion ESI<sup>20,27,30</sup> by LC-MS/MS. In terms of the intensity of the precursor/product ions, not only the negative ion ESI for hesperidin but also the positive ion ESI for hesperetin were found to be weak and resulted in relatively poor correlation coefficients of the calibration curves ( $r \leq 0.9$ ). The necessary changes have been made to improve the intense product ion. Positive ion ESI for hesperidin and negative ion ESI for hesperetin were used for the first time in this study, and better correlation coefficients were observed ( $r \geq 0.999$ ). The MS parameters were optimized as shown in Table 1. A full-scan mass spectrum of each analyte was acquired in both the positive and negative ion modes using ESI. The most intense product ion during positive ion ESI appeared at  $m/z$  303.1 for hesperidin, and at  $m/z$  308.3 for neohesperidin dihydrochalcone-d<sub>3</sub>. Furthermore, the most intensive product ion during negative ion ESI appeared at  $m/z$  164.1 for hesperetin and  $m/z$  164.1 for *rac*-hesperetin-d<sub>3</sub>. The MS/MS settings were adjusted to maximize the response of each precursor-product ion combination. According to the Official Journal of the European Communities, a stable-isotope-labeled analyte is preferable as the IS for the quantification of the analyte in complex matrices by LC-MS/MS analysis.<sup>32</sup> Therefore, neohesperidin dihydrochalcone-d<sub>3</sub> and *rac*-hesperetin-d<sub>3</sub> were chosen as the IS for positive and negative ion ESI, respectively.

During method development, the 2 different columns, Atlantis T3 (C<sub>18</sub> reversed-phase columns; Waters, Milford, MA, USA) and Hypersil GOLD phenyl for analyte separation, were assessed. The peak separation was performed with an Atlantis T3 column, and the mobile phase consisted of 0.1% formic acid in ACN and H<sub>2</sub>O (65 : 35, v/v). The flow rate was 0.2 mL min<sup>−1</sup>, and the run time was 4 min. A broad-peak chromatogram, poor resolution of analytes, and short retention times of hesperidin (1.67 min) and hesperetin (2.36 min) were observed in our laboratory. By changing to the Hypersil GOLD phenyl column and an ACN:H<sub>2</sub>O:formic acid gradient system, we achieved symmetrical, sharp, well-resolved peaks, possibly because the presence of the phenyl group in particular enhanced the separation of aromatic and moderately polar compounds by providing a second mode of interaction through the phenyl ring in the Hypersil GOLD phenyl column.<sup>33</sup> Hesperidin and hesperetin are also polyphenolic compounds that present a common benzo-γ-pyrone nucleus,<sup>34</sup> so a Hypersil GOLD phenyl column offers excellent separation.

Methods such as liquid-liquid extraction (LLE) or SPE have been used for flavanone extraction and purification. We examined the discrepancies between LLE and SPE recovery. Following one-step protein precipitation with ethyl acetate, results for hesperidin and hesperetin, respectively, were 61% ± 8% and 92% ± 9% at the low QC concentration, 69% ± 6% and 93% ± 3% at the middle QC concentration, and 66% ± 7% and 96% ± 6% at the high QC concentration. When SPE was applied, results were 113% ± 32% and 103% ± 10% at the low QC concentration, 93% ± 9% and 106% ± 11% at the middle QC concentration, and 87% ± 6% and 99% ± 25% at the high QC concentration for hesperidin and hesperetin, respectively. The recoveries by SPE were much closer to 100% for both



hesperidin and hesperetin, so we adopted the SPE method for sample preparation.

To ensure that hesperidin's active metabolite, hesperetin, was formed *in vivo* instead of *in vitro* during the analysis, blank plasma was spiked only with the parent drug, hesperidin, at 3 different QC concentrations, and hesperidin and hesperetin were quantified simultaneously. No hesperetin peak was found at the low QC concentration. Even at the middle QC and high QC concentrations, only 0.8% of hesperetin was formed from hesperidin during analytical procedures, indicating that hesperetin was stable during the experimental process.

### 3.2. Selectivity

Representative chromatograms of drug-free plasma are shown in Fig. 1a; positive and negative ion analytes of pure compound mixture are shown in Fig. 1b; and those of blank plasma samples spiked with hesperidin and hesperetin at LLOQ and neohesperidin dihydrochalcone- $d_3$  ( $1 \mu\text{g mL}^{-1}$ ) and *rac*-hesperetin- $d_3$  ( $200 \text{ ng mL}^{-1}$ ) are shown in Fig. 1c. The retention times were 2.38, 3.64, 4.76, and 4.75 min for hesperidin, neohesperidin dihydrochalcone- $d_3$ , hesperetin, and *rac*-hesperetin- $d_3$ , respectively. No significant interfering peaks caused by endogenous compounds or reagents appeared at the retention times of these analytes and the IS in the chromatogram of blank plasma. Note, however, that the hesperidin sample was 98% pure, Fig. 1b was obtained from a sample with a high concentration ( $1 \text{ mg mL}^{-1}$ ) of analyte, and that Fig. 1c was obtained from a sample with a low concentration ( $1 \text{ ng mL}^{-1}$ ) of analyte that had an associated large noise component; the second peak in Fig. 1c was a contaminant because the peak was not seen in the high-concentration sample (Fig. 1b).

### 3.3. Method validation

**3.3.1. Linearity and LLOQ.** The standard calibration curves of hesperidin and hesperetin were determined using the 6-point concentration curve. The best-fit line of the calibration curve for each analyte was obtained using a weighting factor of  $1/x$ . Linearity was obtained with correlation coefficients of  $r = 0.9992 \pm 0.0082$  for hesperidin and  $r = 0.9997 \pm 0.0015$  for hesperetin. With this method, the LLOQ of hesperidin was  $1 \text{ ng mL}^{-1}$  and that of hesperetin was  $0.2 \text{ ng mL}^{-1}$ .

**3.3.2. Precision and accuracy.** The data regarding precision and accuracy are shown in Table 2. The within- and between-run precision values for both analytes were 2.06–6.09% and 2.11–7.76%, respectively. The within- and between-run accuracy values for both analytes were –6.52% to 3.82% and –1.62% to 2.33%, respectively. Consequently, we concluded that the results for the QC standards were acceptable because the values did not deviate by more than  $\pm 15\%$  ( $\pm 20\%$  for LLOQ) from their nominal values, indicating that the method was precise and accurate.

**3.3.3. Extraction recovery and matrix effects.** The absolute and relative matrix effects are shown in Table 3. This study yielded a mean recovery  $>87\%$  for all analytes. No significant matrix effects were observed for the probe substrates. The matrix caused only relatively minor effects on the ionization efficiency of the analytes, and the suppression or enhancement of the ionization was between 94.7% and 113.6% for each analyte. The relative matrix effects were all  $<14.0\%$ .

**3.3.4. Stability.** All stock samples were divided into 2 or 3 storage tubes before use; 1 tube was used for the experiment, and the remaining tubes were frozen for use as backups and for

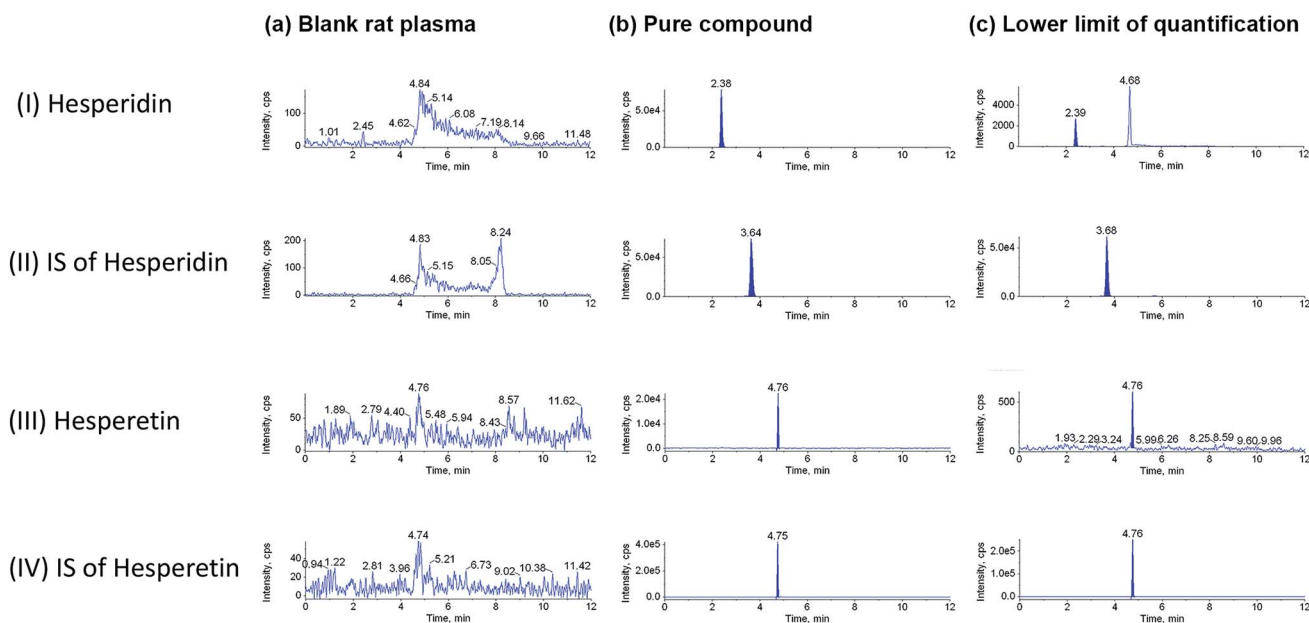


**Fig. 1** Multiple reaction monitoring ion chromatograms of (a) blank rat plasma sample; (b) positive and negative ion analytes of pure compound mixture; (c) blank rat plasma sample spiked with hesperidin and hesperetin at the lower limit of quantitation, neohesperidin dihydrochalcone- $d_3$  ( $1 \mu\text{g mL}^{-1}$ ) and *rac*-hesperetin- $d_3$  ( $200 \text{ ng mL}^{-1}$ ). The positive mode, peak I and peak II (internal standards, IS), represent hesperidin and neohesperidin dihydrochalcone- $d_3$ , respectively. The negative mode, peak III and peak IV (IS), indicate hesperetin and *rac*-hesperetin- $d_3$ , respectively.

Table 2 Intra- and interday precision and accuracy for determination of hesperidin and hesperetin in rat plasma<sup>a</sup>

	Added concentration (ng mL <sup>-1</sup> )	Within run ( <i>n</i> = 6)			Between run ( <i>n</i> = 6)		
		Calculated concentration (ng mL <sup>-1</sup> )	RSD (%)	RE (%)	Calculated concentration (ng mL <sup>-1</sup> )	RSD (%)	RE (%)
Hesperidin	1	1.02 ± 0.06	5.70	1.55	0.98 ± 0.07	7.06	-1.62
	3	2.92 ± 0.18	6.09	-2.72	3.02 ± 0.16	5.36	0.72
	450	467 ± 13.9	2.97	3.82	452 ± 12.1	2.67	0.36
	900	895 ± 33.6	3.76	-0.57	885 ± 19.9	2.25	-1.62
Hesperetin	0.2	0.19 ± 0.02	9.54	-6.52	0.20 ± 0.02	7.76	2.33
	0.6	0.57 ± 0.01	2.06	-4.57	0.60 ± 0.03	4.73	-0.41
	45	44.4 ± 0.93	2.10	-1.25	45.1 ± 1.13	2.52	0.11
	90	89.7 ± 2.43	2.71	-0.34	89.1 ± 1.88	2.11	-1.03

<sup>a</sup> Results are expressed as mean ± SD. RSD: relative standard deviation; RE: relative error.

Table 3 Extraction recoveries and absolute and relative matrix effects of the assay<sup>e</sup>

Analyte	Recovery <sup>c</sup> (%) <i>n</i> = 3			Absolute and relative matrix effect <sup>d</sup> (%) <i>n</i> = 6		
	LOQ	MOQ	HOQ	LOQ	MOQ	HOQ
Hesperidin <sup>a</sup>	113 ± 19	93 ± 9	87 ± 6	107.4 (14.0)	98.2 (4.4)	96.1 (10.0)
Hesperetin <sup>b</sup>	103 ± 10	106 ± 11	99 ± 25	94.7 (7.4)	98.8 (3.9)	100.1 (3.5)
Neohesperidin dihydrochalcone-d <sub>3</sub> (IS of positive ion ESI)				109.9 (12.1)	113.6 (12.7)	111.5 (11.8)
<i>rac</i> -Hesperetin-d <sub>3</sub> (IS of negative ion ESI)				111.3 (10.3)	101.3 (6.8)	104.2 (4.6)

<sup>a</sup> Neohesperidin dihydrochalcone-d<sub>3</sub> (1 µg mL<sup>-1</sup>) was added to solutions at 3 concentrations: hesperidin (3, 450, and 900 ng mL<sup>-1</sup>). <sup>b</sup> *rac*-Hesperetin-d<sub>3</sub> (200 ng mL<sup>-1</sup>) was added to solutions at 3 concentrations: hesperetin (0.6, 45, and 90 ng mL<sup>-1</sup>). <sup>c</sup> The results of recovery are expressed as mean ± SD. <sup>d</sup> The results are expressed as an absolute matrix effect percentage (relative matrix effect percentage). <sup>e</sup> LOQ: limit of quantitation; MOQ: middle of quantification concentrations; HOQ: high of quantification concentrations; IS: internal standard; ESI: electrospray ionization.

stability studies. As shown in Table 4, stability test values were all >85.0%. No significant degradation was found in the analyte concentrations when extracts were kept in stock solutions stored at -20 °C for 180 days. All experiments (except extractions and drying) were performed on ice in laboratories controlled to 25 °C room temperature, and were conducted in ≤3 h; thus we tested sample stability at 4 h to ensure that no significant degradation had taken place. Similarly, autosampler manipulations of the samples were conducted in ≤20 h, so we tested sample stabilities at 24 h and found no significant degradation. We limited plasma samples to ≤3 freeze-thaw cycles, tested plasma samples after 3 cycles, and found no significant degradation. Finally, plasma samples were stored at -80 °C for 180 days, and after testing we found no significant degradation. The results indicated that this analytical method can be applied for plasma-sample analysis.

### 3.4. *In vivo* pharmacokinetic study

In order to compensate for the short elimination half-life (*t*<sub>1/2</sub>) and to increase bioavailability, HPMC K15M was chosen as a vehicle in this study because of its well-known sustained-release properties. After a single oral administration of 800 mg kg<sup>-1</sup> hesperidin in HPMC K15M to 6 Wistar male rats, free plasma concentrations of hesperidin and hesperetin were determined by the LC-MS/MS method just discussed. The PK parameters of free hesperidin and hesperetin were calculated by WinNonlin using the noncompartmental model (Pharsight, Sunnyvale, CA, USA) and are summarized in Table 5. The mean plasma concentrations *versus* time profiles of free hesperidin and hesperetin in Wistar male rats are shown in Fig. 2. With the dosage form studied, a double peak in the plasma concentration-time profile was obtained. This is similar to the findings reported in previously published PK studies of hesperidin and

Table 4 Summary of hesperidin and hesperetin stability tests in rat plasma (results are expressed as percentages of controls)

Stability	Stock solutions (-20 °C for 180 days)	Short term (25 °C for 4 h)	Autosampler (4 °C for 24 h)	Plasma freeze-thaw cycles (3 cycles)	Long-term plasma storage (-80 °C for 180 days)
Hesperidin	93.3–101.3	97.2–103.3	101.6–102.4	99.8–112.4	96.9–101.6
Hesperetin	92.4–96.8	97.6–98.6	99.2–103.3	98.2–100.5	98.0–100.5

**Table 5** Pharmacokinetic parameters of hesperidin and hesperetin in 6 Wistar rats following oral administration of 800 mg kg<sup>-1</sup> using the noncompartmental method except as indicated (*n* = 6)<sup>a</sup>

Pharmacokinetic parameters	Hesperidin	Hesperetin
Peak concentration ( $C_{\max}$ ; ng mL <sup>-1</sup> )	313.06 ± 27.8	43.5 ± 16.0
Time to reach peak concentration ( $T_{\max}$ ; h)	9.3 ± 1.9	14 ± 3.1
Elimination half-life ( $t_{1/2}$ ; h)	9.6 ± 0.7	6.2 ± 1.1
Elimination rate constant ( $K_e$ ; 1/h)	0.07 ± 0.01	0.12 ± 0.02
Area under concentration–time curve ( $AUC_{0-t}$ ; ng h mL <sup>-1</sup> )	3170 ± 1031	468 ± 88
Area under concentration–time curve ( $AUC_{0-\infty}$ ; ng h mL <sup>-1</sup> )	3410 ± 1114	473 ± 88
Mean residence time (h)	15.9 ± 1.1	14.6 ± 1.7
Clearance (CL/F; L h <sup>-1</sup> kg <sup>-1</sup> )	264.3 ± 97.0	1762 ± 384

<sup>a</sup> Values are mean ± SD.

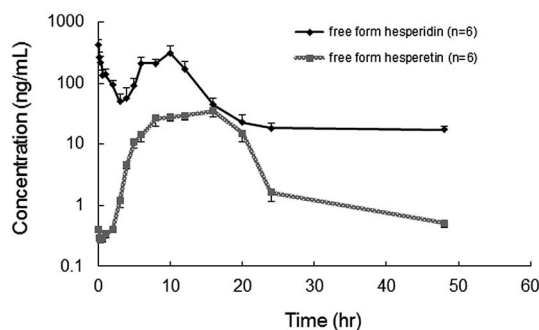


**Fig. 2** Mean plasma concentration–time profiles for hesperidin and hesperetin after a single oral dose of hesperidin (800 mg kg<sup>-1</sup> in HPMC K15M) to 6 Wistar male rats. Each point represents mean ± SE.

naringenin.<sup>9,10,18,31,35</sup> For example, Ma *et al.*<sup>18</sup> carried out a series of experiments and proved that enterohepatic circulation contributes to the double peak in the plasma concentration–time curve because of drug reabsorption. Another possible reason for the hesperidin double peak may be the effect of the HPMC polymer on the formulation: because hesperidin was dissolved in DMSO before HPMC K15M was added, the first peak could reflect the immediate release as hesperidin dissolves in DMSO, and the second peak could be the sustained release of hesperidin as it is released from the HPMC K15M matrix.<sup>12,13,36,37</sup>

After the Wistar rats were administered hesperidin in HPMC K15M, the plasma levels of free hesperidin rapidly reached  $C_{\max}$  within 5 min but dropped sharply afterwards. The second peak occurred between hour 5 and hour 12. The mean value of hesperidin  $C_{\max}$  (313.06 ng mL<sup>-1</sup>) appeared at 9.3 h with a  $t_{1/2}$  of 9.6 ± 0.7 h. In contrast, hesperetin was detected at hour 3, and the maximum (about 26.67–35.49 ng mL<sup>-1</sup>) was reached between hour 8 and hour 16. Hesperetin  $C_{\max}$  (43.5 ng mL<sup>-1</sup>) appeared at hour 14, and the  $t_{1/2}$  was 6.2 ± 1.1 h. The  $t_{1/2}$  values of hesperidin and hesperetin were larger than the values reported in previous studies.<sup>10,11</sup>

In this study, no enzymes were used to cleave conjugates of hesperetin, including glucuronic acids, sulfates, and sugars from the aglycone (hesperetin). Therefore, the results represent the free concentrations of hesperetin. Some of the methods in past studies were not sufficiently sensitive to detect the concentration

of unhydrolyzed hesperetin; hence, they relied on enzymatic hydrolysis to increase the concentration of conjugated hesperetin in the blood. However, the use of  $\beta$ -glucuronidase concentration and the length of the incubation time varied among studies.<sup>9,11,16,20,21,38,39</sup> This LC-MS/MS method we developed has a linear range from 0.2 to 100 ng mL<sup>-1</sup> for hesperetin. Therefore, it was unnecessary to hydrolyze the plasma sample enzymatically to cleave the glucuronic acid and sulfate conjugates of hesperetin. These tedious and time-consuming steps can be avoided, and the data obtained truly reflect the *in vivo* free concentration of hesperetin. The free concentration of hesperetin may indicate pharmacologic activities associated with healing effects and the change of unconjugated medicine in human bodies, because only the free form can conjugate with receptor and really has activities. ESI Fig. S1 and S2† show the structures and product ion mass spectra of hesperetin and hesperidin, respectively.

## 4. Conclusion

The LC-MS/MS method reported here is a simultaneous, simple, precise, sensitive, and selective assay for the determination of free hesperidin and hesperetin in Wistar rat plasma with a linear range from approximately 1 to 1000 ng mL<sup>-1</sup> for hesperidin and approximately 0.2 to 100 ng mL<sup>-1</sup> for hesperetin. This method is suitable for routine application because it requires only a small amount of plasma and a simple SPE for sample pretreatment with high extraction recovery. On the other hand, the LLOQ sensitivity of hesperetin is up to 200 pg mL<sup>-1</sup>, so complete plasma concentration–time profiles can be obtained with this LC-MS/MS method without enzymatic hydrolysis of the plasma sample. Not only can experimental error be avoided, but the *in vivo* free concentration of hesperetin can also be measured.

## Conflict of interest statement

The authors have no conflicts of interest to declare.

## Financial support

We are grateful to the Institute for the Biotechnology and Medicine Industry, and to the Department of Health, Taiwan, the Republic of China, for partially supporting this research.

## Abbreviations

AUC	Area under concentration–time curve
CL	Clearance
$C_{\max}$	Peak concentration
DMSO	Dimethyl sulfoxide
ESI	Electrospray ionization
HPLC	High-performance liquid chromatography
HPMC	Hydroxypropyl methylcellulose
IS	Internal standard
$K_e$	Elimination rate constant
LC-MS/MS	Liquid chromatography–tandem mass spectrometry
LLE	Liquid–liquid extraction
LLOQ	Lower limit of quantification
MRT	Mean residence time
QC	Quality control
RE	Relative error
RSD	Relative standard deviation
SD	Sprague–Dawley
SPE	Solid-phase extraction
$t_{1/2}$	Elimination half-life
$T_{\max}$	Time to reach peak concentration

## Acknowledgements

The authors would like to thank the following colleagues for their contributions and feedback for this paper: Daniel Steve Villarreal, I-Ching Yang, Hong-Jaan Wang, Hung-Ta Liu, Wen-Hao Lin, Shan-Chu He, Ping Yang, and Sin-Yu Yeh.

## References

- 1 B. Ameer, R. A. Weintraub, J. V. Johnson, R. A. Yost and R. L. Rouseff, *Clin. Pharmacol. Ther.*, 1996, **60**, 34–40.
- 2 H. Matsumoto, Y. Ikoma, M. Sugiura, M. Yano and Y. Hasegawa, *J. Agric. Food Chem.*, 2004, **52**, 6653–6659.
- 3 F. A. van Acker, O. Schouten, G. R. Haenen, W. J. van der Vijgh and A. Bast, *FEBS Lett.*, 2000, **473**, 145–148.
- 4 A. Garg, S. Garg, L. J. Zaneveld and A. K. Singla, *Phytother. Res.*, 2001, **15**, 655–669.
- 5 C. A. Rice-Evans, N. J. Miller and G. Paganga, *Free Radical Biol. Med.*, 1996, **20**, 933–956.
- 6 M. G. Hertog, E. J. Feskens, P. C. Hollman, M. B. Katan and D. Kromhout, *Lancet*, 1993, **342**, 1007–1011.
- 7 H. J. Kim, S. M. Jeon, M. K. Lee, Y. Y. Cho, E. Y. Kwon, J. H. Lee and M. S. Choi, *J. Med. Food*, 2010, **13**, 808–814.
- 8 E. M. Kurowska and J. A. Manthey, *J. Agric. Food Chem.*, 2004, **52**, 2879–2886.
- 9 M. Yamada, F. Tanabe, N. Arai, H. Mitsuzumi, Y. Miwa, M. Kubota, H. Chaen and M. Kibata, *Biosci., Biotechnol., Biochem.*, 2006, **70**, 1386–1394.
- 10 L. Tong, D. Zhou, J. Gao, Y. Zhu, H. Sun and K. Bi, *J. Pharm. Biomed. Anal.*, 2010, **58**, 58–64.
- 11 I. Erlund, E. Meririnne, G. Alftan and A. Aro, *J. Nutr.*, 2001, **131**, 235–241.
- 12 S. L. Raghavan, B. Kieper, A. F. Davis, S. G. Kazarian and J. Hadgraft, *Int. J. Pharm.*, 2001, **221**, 95–105.
- 13 J. J. Torres-Labandeira, P. Davignon and J. Pitha, *J. Pharm. Sci.*, 1991, **80**, 384–386.
- 14 P. Gao, A. Akrami, F. Alvarez, J. Hu, L. Li, C. Ma and S. Surapaneni, *J. Pharm. Sci.*, 2009, **98**, 516–528.
- 15 N. Kohri, Y. Yamayoshi, H. Xin, K. Iseki, N. Sato, S. Todo and K. Miyazaki, *J. Pharm. Pharmacol.*, 1999, **51**, 159–164.
- 16 F. I. Kanaze, E. Kokkalou, M. Georgarakis and I. Niopas, *J. Pharm. Biomed. Anal.*, 2004, **36**, 175–181.
- 17 T. H. Tsai and M. C. Liu, *J. Chromatogr. B: Anal. Technol. Biomed. Life Sci.*, 2004, **806**, 161–166.
- 18 Y. Ma, P. Li, D. Chen, T. Fang, H. Li and W. Su, *Int. J. Pharm.*, 2006, **307**, 292–299.
- 19 T. Fang, Y. Wang, Y. Ma, W. Su, Y. Bai and P. Zhao, *J. Pharm. Biomed. Anal.*, 2006, **40**, 454–459.
- 20 C. Gardana, S. Guarnieri, P. Riso, P. Simonetti and M. Porrini, *Br. J. Nutr.*, 2007, **98**, 165–172.
- 21 K. Maiti, K. Mukherjee, V. Murugan, B. P. Saha and P. K. Mukherjee, *AAPS PharmSciTech*, 2009, **10**, 943–950.
- 22 M. Spanakis, S. Kamas and I. Niopas, *Biomed. Chromatogr.*, 2009, **23**, 124–131.
- 23 Z. Füzfa and I. Molnár-Perl, *J. Chromatogr. A*, 2007, **1149**, 88–101.
- 24 Food and Drug Administration, *Guidance for Industry: Bioanalytical Method Validation*, US Department of Health and Human Services, FDA, Center for Drug Evaluation and Research, Rockville, MD, 2001.
- 25 B. K. Matuszewski, M. L. Constanzer and C. M. Chavez-Eng, *Anal. Chem.*, 2003, **75**, 3019–3030.
- 26 C. Ma, W. Gao, Y. Gao, S. Man, L. Huang and C. Liu, *Phytochem. Anal.*, 2011, **22**, 112–118.
- 27 J. A. Yáñez, C. M. Remsberg, N. D. Miranda, K. R. Vega-Villa, P. K. Andrews and N. M. Davies, *Biopharm. Drug Dispos.*, 2008, **29**, 63–82.
- 28 M. Careri, L. Elviri and A. Mangia, *Rapid Commun. Mass Spectrom.*, 1999, **13**, 2399–2405.
- 29 X. Li, H. Xiao, X. Liang, D. Shi and J. Liu, *J. Pharm. Biomed. Anal.*, 2004, **34**, 159–166.
- 30 A. Ćirić, H. Prosen, M. Jelikić-Stankov and P. Đurđević, *Talanta*, 2012, **99**, 780–790.
- 31 Y. Liu, F. Xu, Z. Zhang, R. Song and Y. Tian, *Biomed. Chromatogr.*, 2008, **22**, 736–745.
- 32 Commission of the European Communities, Implementing Council Directive 96/23/EC concerning the performance of analytical methods and the interpretation of results, available at: [http://eur1.craw.eu/img/page/Legislation/657\\_2002\\_EN.pdf](http://eur1.craw.eu/img/page/Legislation/657_2002_EN.pdf), accessed September 3, 2016.
- 33 Thermo Fisher, Hypersil GOLD Phenyl Columns, Product Specifications, available at: [http://www.biosseparacio.hu/\\_user/browser/File/Thermo/GOLDPhenyl.pdf](http://www.biosseparacio.hu/_user/browser/File/Thermo/GOLDPhenyl.pdf), accessed September 3, 2016.
- 34 K. E. Heim, A. R. Tagliaferro and D. J. Bobilya, *J. Nutr. Biochem.*, 2002, **13**, 572–584.
- 35 H. Sun, T. Dong, A. Zhang, J. Yang, G. Yan, T. Sakurai, X. Wu, Y. Han and X. Wang, *Phytother. Res.*, 2013, **27**, 1345–1351.

- 36 T. Ishikawa, Y. Watanabe, K. Takayama, H. Endo and M. Matsumoto, *Int. J. Pharm.*, 2000, **202**, 173–178.
- 37 G. Yan, H. Li, R. Zhang and D. Ding, *Drug Dev. Ind. Pharm.*, 2000, **26**, 681–686.
- 38 A. Lévêques, L. Actis-Goretti, M. J. Rein, G. Williamson, F. Dionisi and F. Giuffrida, *J. Pharm. Biomed. Anal.*, 2012, **57**, 1–6.
- 39 I. Baranowska and S. Magiera, *Anal. Bioanal. Chem.*, 2011, **399**, 3211–3219.





# dsRNA Binding Domain of PKR Is Proteolytically Released by Enterovirus A71 to Facilitate Viral Replication

Yu-Hsiu Chang<sup>1,2</sup>, Kean Seng Lau<sup>3</sup>, Rei-Lin Kuo<sup>4,5</sup> and Jim-Tong Horng<sup>1,3,4,5,6\*</sup>

<sup>1</sup> Graduate Institute of Biomedical Sciences, College of Medicine, Chang Gung University, Taoyuan, Taiwan, <sup>2</sup> National Defense Medical Center, Institute of Preventive Medicine, Taipei, Taiwan, <sup>3</sup> Department of Biochemistry and Molecular Biology, College of Medicine, Chang Gung University, Taoyuan, Taiwan, <sup>4</sup> Research Center for Emerging Viral Infections, College of Medicine, Chang Gung University, Taoyuan, Taiwan, <sup>5</sup> Molecular Infectious Disease Research Center, Chang Gung Memorial Hospital, Taoyuan, Taiwan, <sup>6</sup> Research Center for Chinese Herbal Medicine and Research Center for Food and Cosmetic Safety, College of Human Ecology, Chang Gung University of Science and Technology, Taoyuan, Taiwan

## OPEN ACCESS

### Edited by:

Chang H. Kim,  
Purdue University, United States

### Reviewed by:

Yihong Peng,  
Peking University Health Science  
Center, China  
Chih-Ho Lai,  
Chang Gung University, Taiwan  
Cheng-Wen Lin,  
China Medical University, Taiwan

### \*Correspondence:

Jim-Tong Horng  
jimtong@mail.cgu.edu.tw

**Received:** 19 March 2017

**Accepted:** 12 June 2017

**Published:** 28 June 2017

### Citation:

Chang Y-H, Lau KS, Kuo R-L and Horng J-T (2017) dsRNA Binding Domain of PKR Is Proteolytically Released by Enterovirus A71 to Facilitate Viral Replication. *Front. Cell. Infect. Microbiol.* 7:284. doi: 10.3389/fcimb.2017.00284

Enterovirus 71 (EV-A71) causes hand, foot and mouth disease in young children and infants, but can also cause severe neurological complications or even death. The double-stranded RNA (dsRNA)-dependent protein kinase R (PKR), an interferon-induced antiviral protein, phosphorylates the regulatory  $\alpha$ -subunit of the eukaryotic translation initiation factor 2 in response to viral infection, thereby blocking the translation of cellular and viral mRNA and promoting apoptosis. The cleavage of PKR after infection with poliovirus, a prototype enterovirus, has been reported by others, but the underlying mechanism of this cleavage and its role in viral replication remain unclear. In the present study, we show that viral 3C protease cleaves PKR at a site, Q188, which differs from the site cleaved during apoptosis, D251. In contrast to the conventional phosphorylation of PKR by dsRNA, EV-A71 3C physically interacts with PKR to mediate the phosphorylation of PKR; this effect is dependent on 3C protease activity. Overexpression of a catalytically inactive PKR mutant (K296H) accelerates viral protein accumulation and increases virus titer, whereas a K64E substitution in the dsRNA binding site abolishes this advantage. We also demonstrate that PKR cleavage mediated by EV-A71 3C protease produces a short N-terminal PKR fragment that can enhance EV-A71 replication, in terms of viral RNA, viral protein, and viral titers. We conclude that PKR is co-opted by EV-A71 via viral protease 3C-mediated proteolytic activation to facilitate viral replication.

**Keywords:** EV-A71, 3C protease, PKR, Enterovirus, interaction effects

## INTRODUCTION

Enterovirus A71 (EV-A71), which belongs to the *Enterovirus* genus of the *Picornaviridae* family, is the major pathogen of human hand, foot, and mouth disease (HFMD). Severe infection with EV-A71 may lead to various neurological complications and even death in some patients, especially children under 5 years old (Lin et al., 1998). EV-A71 is a small, non-enveloped, positive-sense, single-stranded RNA virus. The viral genome is ~7,500 nucleotides in length, with a single open reading frame that encodes a large precursor polypeptide. This precursor is proteolytically

processed into mature structural and non-structural proteins. The structural proteins (VP4, VP2, VP3, and VP1) constitute the capsid shell and the non-structural proteins (2A, 2B, 2C, 2BC, 3A, 3B, 3AB, 3C, 3D, and 3CD) are associated with viral replication (McMinn, 2002). In addition to its activity in viral protein processing, 3C protease is linked to a number of biological processes. When expressed in neuronal cells, 3C protease induces apoptosis through caspase activation (Li et al., 2002). In addition, the polyadenylation factor CstF-64 has been identified as a substrate for 3C protease. Cleavage of CstF-64 by 3C protease impairs host RNA processing and adenylation, thereby providing a suitable environment for viral replication (Weng et al., 2009). Moreover, 3C protease blocks type I interferon (IFN) responses by targeting innate immune factors: it inhibits interferon regulatory factor (IRF) 3 activation (Lei et al., 2010) and cleaves TIR-domain-containing adapter-inducing interferon- $\beta$  (TRIF; Lei et al., 2011), IRF7 (Lei et al., 2013), and IRF9 (Hung et al., 2011), which mediate antiviral and immunoregulatory activities. 3C protease also mediates the cleavage of the transforming growth factor  $\beta$ -activated kinase 1 (TAK1)/TAK1/MAP3K7 binding protein (TAB)1/TAB2/TAB3 complex to interfere with nuclear factor (NF)- $\kappa$ B activation (Lei et al., 2014). A recent report showed that 3C protease interacts with and cleaves NLR family pyrin domain containing 3 (NLRP3) to counteract the protective role of the NLRP3 inflammasome against EV-A71 infection (Wang et al., 2015).

IFN-induced double-stranded RNA (dsRNA)-activated protein kinase R (PKR) is an IFN-stimulated gene (Gale and Katze, 1998; Peters et al., 2001; Pindel and Sadler, 2011) and acts as a pathogen recognition receptor (Gilfooy and Mason, 2007) by recognizing dsRNA, a typical by-product of viral infection, for IFN induction. PKR consists of two functionally distinct domains: an N-terminal regulatory domain and a C-terminal catalytic kinase domain. The regulatory domain contains two dsRNA-binding motifs; binding of dsRNA induces PKR dimerization and allows the exposure of the catalytic site, autophosphorylation, and activation of the kinase (Wu and Kaufman, 1997; Nanduri et al., 2000; Dar et al., 2005; Dey et al., 2005). Activated PKR catalyzes the phosphorylation of the regulatory  $\alpha$ -subunit of the eukaryotic translation initiation factor 2 (eIF2 $\alpha$ ; Meurs et al., 1992; Clemens and Elia, 1997), consequently blocking the initiation of mRNA translation, which results in the global arrest of both cellular and viral protein synthesis and can lead to apoptosis in response to virus infection (Balachandran et al., 1998).

In addition to, its role in translational control through eIF2 $\alpha$  phosphorylation, PKR plays a role in regulating several signal transduction cascades in the cell. The transcription factor nuclear factor NF- $\kappa$ B can be activated indirectly by PKR, independent of its kinase function, via association with tumor necrosis factor receptor-associated factor (TRAF) and activation of the I $\kappa$ B kinase complex (Gil et al., 2004; Bonnet et al., 2006). PKR has also been shown to play a role in the activation of p38 mitogen-activated protein kinase (MAPK) and the stress-activated protein kinase (SAPK)/c-Jun amino-terminal kinase (JNK; Goh et al., 2000), which are also key components in the host innate immune response. Furthermore, recent studies

have revealed a kinase-independent role for PKR in apoptosis-associated speck-like protein assembly and caspase-1 activation during inflammasome formation (Hett et al., 2013).

Viruses have developed many mechanisms to counteract the antiviral function of PKR. Influenza virus NS1 (Chien et al., 2004), rotavirus NSP3 (Langland et al., 1994), and vaccinia E3L protein (Langland and Jacobs, 2004) bind to and sequester viral dsRNA, thus avoiding PKR activation. Adenovirus, Epstein-Barr virus, and hepatitis C virus produce RNA with secondary structures that bind directly to PKR but do not lead to the activation of the kinase (Langland et al., 2006). The Japanese encephalitis virus blocks PKR-mediated growth repression via NS2A (Tu et al., 2012). The interaction of hepatitis C virus NS5A and E2 with PKR directly inhibits PKR dimerization and activation (Gale et al., 1998; Taylor et al., 1999). PKR is rapidly degraded in poliovirus (PV)-infected cells (Black et al., 1989). PV is a prototype member of the *Picornaviridae* family, and studies have demonstrated that although PV infection induces PKR and eIF2 $\alpha$  phosphorylation, there is significant degradation of PKR after PV infection. It has been suggested that the destabilization of PKR in PV-infected cells is caused by cooperation between viral dsRNA and a cellular protease, representing an example of viral-counteraction strategies. However, the detailed mechanism of PKR degradation remains unclear. In this study, we observed the cleavage of PKR during EV-A71 infection. This effect required 3C protease, which mediated PKR cleavage independently of caspases. Furthermore, we demonstrate that the kinase activity of PKR plays a negative role in EV-A71 infection. Our results also indicate that the 3C protease-generated fragments of PKR facilitated viral replication.

## MATERIALS AND METHODS

### Cell Culture, Virus, and Infection

Human rhabdomyosarcoma (RD) and human embryonic kidney (HEK) 293T cells were cultured in Dulbecco's modified Eagle's medium (DMEM, Invitrogen, Carlsbad, CA, USA) that contained 10% heat-inactivated fetal bovine serum (Gibco BRL, San Francisco, CA, USA) at 37°C in humidified air with 5% CO<sub>2</sub>. The EV-A71 (TW/2331/98, genotype C) virus strain was produced from an infectious clone generously provided by Dr. Mei-Shang Ho (Academia Sinica, Taiwan). EV-A71 propagation and titer determination by plaque-forming assay using RD cells were performed essentially as described previously (Chang et al., 2012). Viral infection was carried out by preadsorbing EV-A71 at a multiplicity of infection (m.o.i.) of 10 for 1 h [1 to 0 h post-infection (p.i.)] at 37°C, and the unbound virus was removed and washed with phosphate-buffered saline (PBS). The cells were then cultured in DMEM supplemented with 2% fetal bovine serum and harvested at the indicated times p.i.

### Plasmids and Constructions

Full-length PKR was amplified by PCR from cDNA prepared from RD cells and the product was inserted into the *NheI* and *PstI* sites of pLKO\_AS3Wpuro-eGFP-C1, pLKO\_AS3Wpuro-nHAcFlag and pLKO\_AS3Wpuro vectors, which were obtained from the National RNAi Core Facility (Academia Sinica, Taiwan).

PKR variants K296H, D251N, K64E, A67E, Q138A, Q150A, Q154A, Q163A, Q188A, and PKR(1–188)K64E were constructed by site-directed mutagenesis using Pfu DNA polymerase (Stratagene, La Jolla, CA, USA). To construct plasmids P1 (encoding a precursor of viral capsid proteins VP4, VP2, VP3, and VP1), P2 (encoding a precursor of viral proteins 2A, 2B, and 2C), and P3 (encoding a precursor of viral proteins 3A, 3B, 3C, and 3D), fragments and viral proteases 2A and 3C of EV-A71 (TW/2331/98) cDNA were cloned into the *NheI* and *EcoRI* sites of the pLKO\_AS3Wpuro-cFlag vector. The H40D, C147S, and R84Q mutants of 3C were produced using a site-directed mutagenesis kit (Stratagene). All constructs were confirmed by subsequent sequencing. Plasmids were transfected into designated cells using Lipofectamine 2000 (Invitrogen) as described by the manufacturer.

## Antibodies and Reagents

Rabbit polyclonal antibody against EV-A71 3A was prepared as described (Tang et al., 2007). Mouse monoclonal antibodies against glyceraldehyde 3-phosphate dehydrogenase (GAPDH) (G8795) and Flag (F1804) were purchased from Sigma-Aldrich (St Louis, MO, USA). Rabbit monoclonal antibodies against phospho-eIF2 $\alpha$  (#3597) and PKR (Ab32052, against amino acids 50–150 of human PKR) were obtained from Cell Signaling (Beverly, MA, USA) and Abcam (Cambridge, UK), respectively. Mouse monoclonal antibody against green fluorescent protein (GFP) (SC-9996) and rabbit polyclonal antibodies against eIF2 $\alpha$  (SC-11386) and poly (ADP-ribose) polymerase (PARP) (SC-7150) were obtained from Santa Cruz Biotechnology (Santa Cruz, CA, USA). Mouse monoclonal antibody against EV-A71 3C and rabbit polyclonal antibody against phospho-PKR were obtained from GeneTex (Irvine, CA, USA). Poly(I:C) and 2-aminopurine (2-AP) was purchased from Invivogen (San Diego, CA, USA). Staurosporine was purchased from Sigma-Aldrich.

## Western Blot Analysis

The protein concentration was measured with a protein assay kit (Bio-Rad, Richmond, CA, USA). Equal amounts of whole-cell extracts were separated by 8–12% sodium dodecyl sulfate-polyacrylamide gel electrophoresis (SDS-PAGE). After electrophoresis, proteins were transferred to a polyvinylidene difluoride (PVDF) membrane (Millipore, Billerica, MA, USA). The membranes were blocked for 1 h at room temperature in 5% dried milk and then were probed with the indicated primary antibodies at an appropriate dilution overnight at 4°C. The following day, the membranes were incubated with horseradish peroxidase (HRP)-conjugated anti-mouse or HRP-conjugated anti-rabbit antibody. HRP was detected using Immobilon Western HRP Chemiluminescence Substrate (Millipore).

## Flow Cytometry for Apoptosis Detection

RD cells in 6-well plates were transfected with 3C and 3C H40D/C147S mutant and treated with 2-AP. Forty-eight hours later, apoptosis was measured by flow cytometry using an Annexin V Kit (SC-4252 AK, Santa Cruz Biotechnology) according to the manufacturer's protocol. Briefly, the cells were dissociated with trypsin, washed with PBS twice and then

stained with Annexin V-fluorescein isothiocyanate (FITC) and propidium iodide (PI) for 15 min. After staining, cells were analyzed using a CytoFLEX flow cytometer and Kaluza software (Beckman Coulter, Brea, CA, USA).

## Reverse Transcription-Quantitative PCR (RT-qPCR)

Total RNA extraction and reverse transcription were performed using an RNeasy Mini Kit (Qiagen, Venlo, Netherlands) and Superscript cDNA synthesis kit, respectively. Total RNA was converted into cDNA using random primers. The synthesized cDNA was measured by qPCR (Applied Biosystems® 7500 fast Real-Time PCR System) using a QuantiTect SYBR Green PCR kit (Qiagen) with the following gene-specific primers. EV71, CCC CTG AAT GCG GCT AAT C and GAT TGT CAC CAT AAG CAG C; GAPDH, ATC CTG GGC TAC ACT GAG CA; and GGT CCA GGG GTC TTA CT. Human GAPDH gene expression was used as an internal control. All qPCR experiments were performed in triplicate using samples with no template as a negative control.

## Immunoprecipitation

HEK-293T cells ( $7 \times 10^6$  cells/well, 6-well plate) were transfected with 2  $\mu$ g of various plasmids using Lipofectamine 2000, and were harvested 24 h post-transfection for further experiments. For the assay, transfected cells were washed twice with PBS and then scraped into a lysis buffer (150 mM NaCl, 1% Triton X-100, 0.5% sodium deoxycholate, 50 mM Tris-HCl, pH 7.5, and 2 mM EDTA) with freshly added protease inhibitors. Lysates of cells were incubated with anti-Flag antibody at 4°C overnight on a rotator in the presence of protein A/G agarose beads (Roche, Basel, Switzerland). After incubation, beads were washed three times, and the precipitated proteins were boiled at 95°C in SDS-PAGE sample buffer. Samples were resolved by SDS-PAGE and were transferred to a PVDF membrane for western blot analysis.

## Statistics

A student *t*-test was used for two-tailed comparisons. A *P* < 0.05 was considered significant. The symbols \* and \*\* were used to indicate *p* < 0.05 and < 0.01, respectively.

## RESULTS

### PKR Is Phosphorylated and Cleaved during EV-A71 Infection

We have shown previously that EV-A71 infection induces the phosphorylation of eIF2 $\alpha$  by PKR, resulting in a gradual shutoff of translation during infection (Jheng et al., 2010). It is worth noting that PKR is not only phosphorylated but also degraded by EV-A71, consistent with observations during PV infection (Black et al., 1989, 1993; **Figure 1A**). We determined the activation status of endogenous PKR over the time course of EV-A71 infection by immunoblotting with antibodies against phosphorylated PKR and its downstream substrate eIF2 $\alpha$  in human RD cells (**Figure 1A**). The phosphorylated PKR and eIF2 $\alpha$  became detectable at 5 h p.i., whereas viral 3C and 3CD proteins were detected as early as 3 h p.i., suggesting that EV-A71



triggers PKR activation at an early stage of infection. In addition, the PKR levels were decreased after viral infection, which was likely the result of the inhibition of translation mediated by eIF2 $\alpha$  phosphorylation, or apoptosis-induced PKR cleavage. Because the reduction in PKR occurred simultaneously with its phosphorylation, we ruled out the possibility of translation inhibition. We treated RD cells with staurosporine (STS) to induce apoptosis to determine the status of PKR (Belmokhtar et al., 2001; **Figure 1B**). As expected, STS treatment caused apoptosis, as indicated by the cleavage of PARP. This apoptosis caused a smaller decrease in the PKR level than that seen in the EV-A71-infected cells, and produced different cleavage patterns compared to those seen in viral infection. We detected a small cleavage product (about 20-kDa) of PKR at 8 h p.i. Therefore, the reduction in PKR might result from proteolysis induced by EV-A71 infection.

### Viral 3C Protease Cleaves PKR at a Site Distinct from That Cleaved during Apoptosis

We investigated which viral protein was responsible for the reduction in PKR by individually overexpressing the viral proteases 2A and 3C and the intermediate P1, P2, and P3 fragments in RD cells and then measuring the endogenous PKR levels at 24 and 48 h post-transfection (**Figure 2A**). Overexpression of viral 3C (lanes 4 and 5, **Figure 2A**) and the P3 fragment from which 3C is derived (lanes 10 and 11, **Figure 2A**) caused an increase in phosphorylation and a moderate decrease in PKR, suggesting the possibility that viral 3C protease itself could contribute to PKR degradation. Viral proteases process not only viral polypeptides but also a number of host innate immune proteins (Pathinayake et al., 2015). We hypothesized that the reduction in PKR was caused by viral protease cleavage. To confirm this hypothesis, we generated recombinant GFP-PKR-K296H (a kinase-dead mutant), which could be preferentially expressed in cells relative to wild-type GFP-PKR (**Figure 2B**). We then used GFP-PKR-K296H to monitor the cleavage pattern. We expressed GFP-PKR-K296H in 293T cells for 24 h and then transfected the cells with 2A-Flag or 3C-Flag for another 24 h. We were able to detect a cleavage product of 45 kDa when PKR was coexpressed with 3C but not when it was coexpressed with 2A or vector control (lane 6 compared with lanes 2 and 4, **Figure 2C**). These results demonstrate that viral 3C protease but not 2A protease was associated with cleavage of the recombinant PKR.

Because it has been demonstrated that PKR is cleaved by caspase at an early stage of apoptosis (Saelens et al., 2001), and because previous studies have also shown that 3C induces apoptosis when expressed in neuronal cells (Li et al., 2002), the cleavage we observed probably occurs as a result of 3C-induced apoptosis. We further compared the PKR cleavage patterns between 3C coexpression and STS-induced apoptosis, and used coexpression of the 3C catalytic site mutant C147S as a negative control (**Figure 2D**). The fragment resulting from 3C-induced cleavage of PKR was smaller than that produced by STS-induced cellular apoptosis (60 vs. 45 kDa, compare lanes

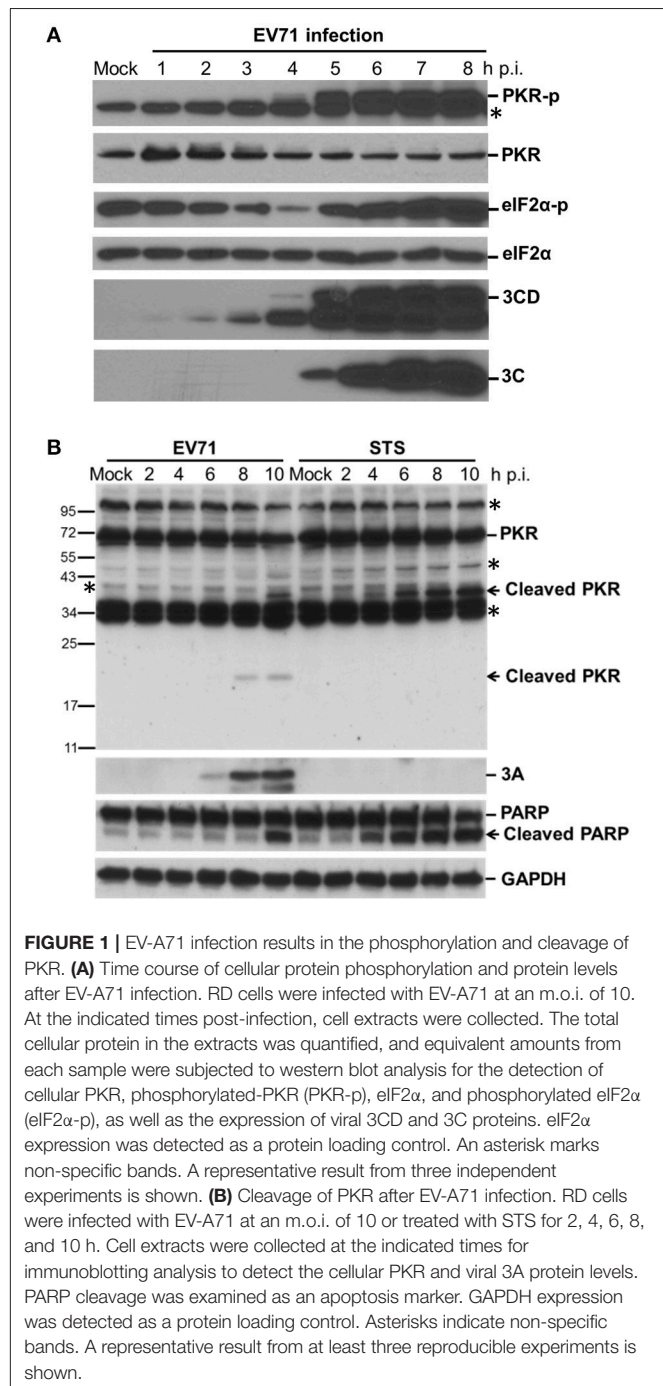


**FIGURE 1 |** EV-A71 infection results in the phosphorylation and cleavage of PKR. **(A)** Time course of cellular protein phosphorylation and protein levels after EV-A71 infection. RD cells were infected with EV-A71 at an m.o.i. of 10. At the indicated times post-infection, cell extracts were collected. The total cellular protein in the extracts was quantified, and equivalent amounts from each sample were subjected to western blot analysis for the detection of cellular PKR, phosphorylated-PKR (PKR-p), eIF2 $\alpha$ , and phosphorylated eIF2 $\alpha$  (eIF2 $\alpha$ -p), as well as the expression of viral 3CD and 3C proteins. eIF2 $\alpha$  expression was detected as a protein loading control. An asterisk marks non-specific bands. A representative result from three independent experiments is shown. **(B)** Cleavage of PKR after EV-A71 infection. RD cells were infected with EV-A71 at an m.o.i. of 10 or treated with STS for 2, 4, 6, 8, and 10 h. Cell extracts were collected at the indicated times for immunoblotting analysis to detect the cellular PKR and viral 3A protein levels. PARP cleavage was examined as an apoptosis marker. GAPDH expression was detected as a protein loading control. Asterisks indicate non-specific bands. A representative result from at least three reproducible experiments is shown.

6 and 8, **Figure 2D**), although the apoptosis marker PARP was still cleaved when 3C was expressed. To confirm this finding, we generated a GFP-PKR-K296H/D251N mutant; in which D251, a site known to be cleaved by caspases 3, 7, and 8 during cellular apoptosis, is mutated. The D251N mutation abolished the STS-induced PKR cleavage (lanes 8 and 9, **Figure 2E**), but not that induced by 3C (lanes 5 and 6, **Figure 2E**). These results suggest that 3C cleaves PKR at a site that differs from that cleaved during apoptosis.

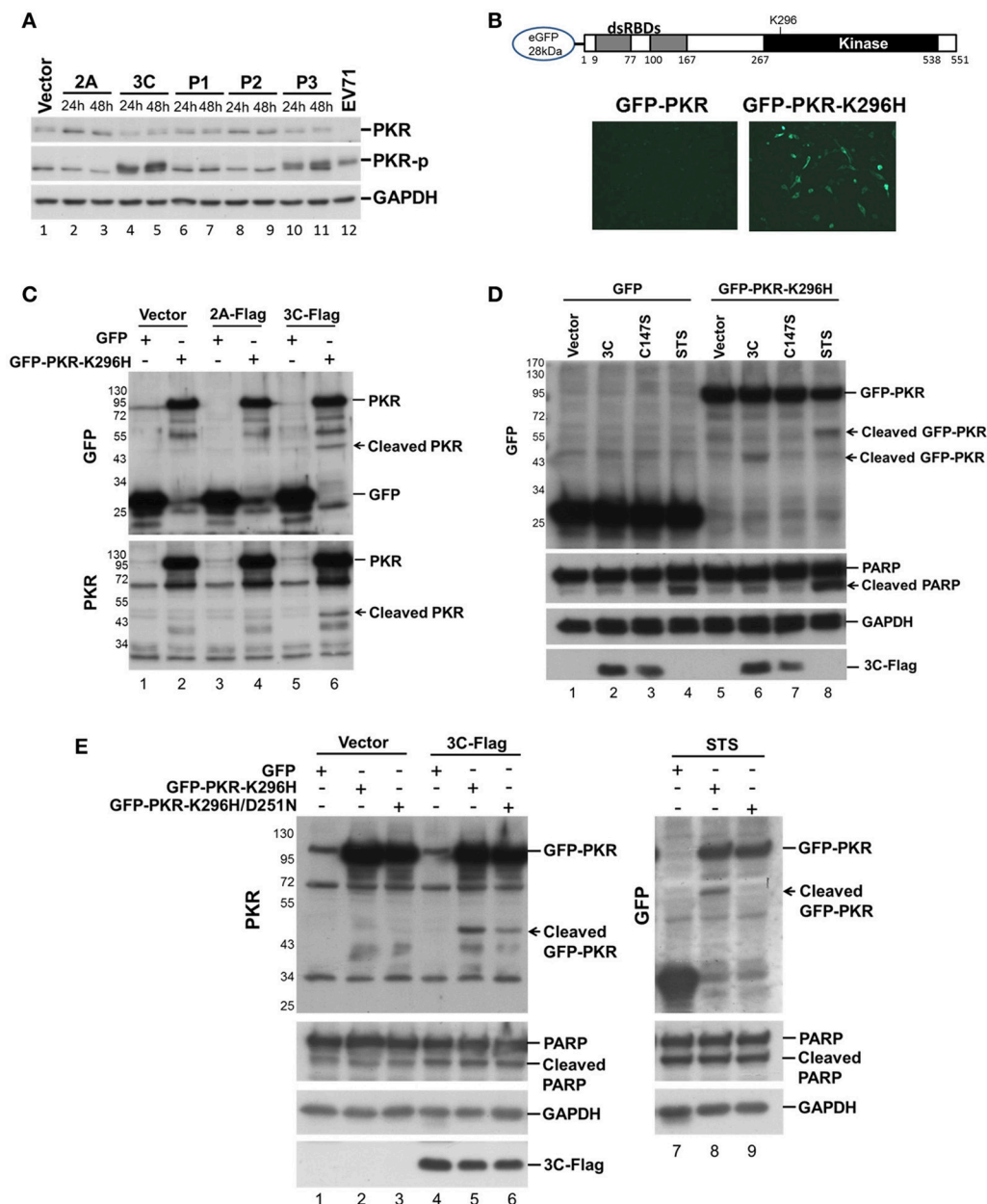
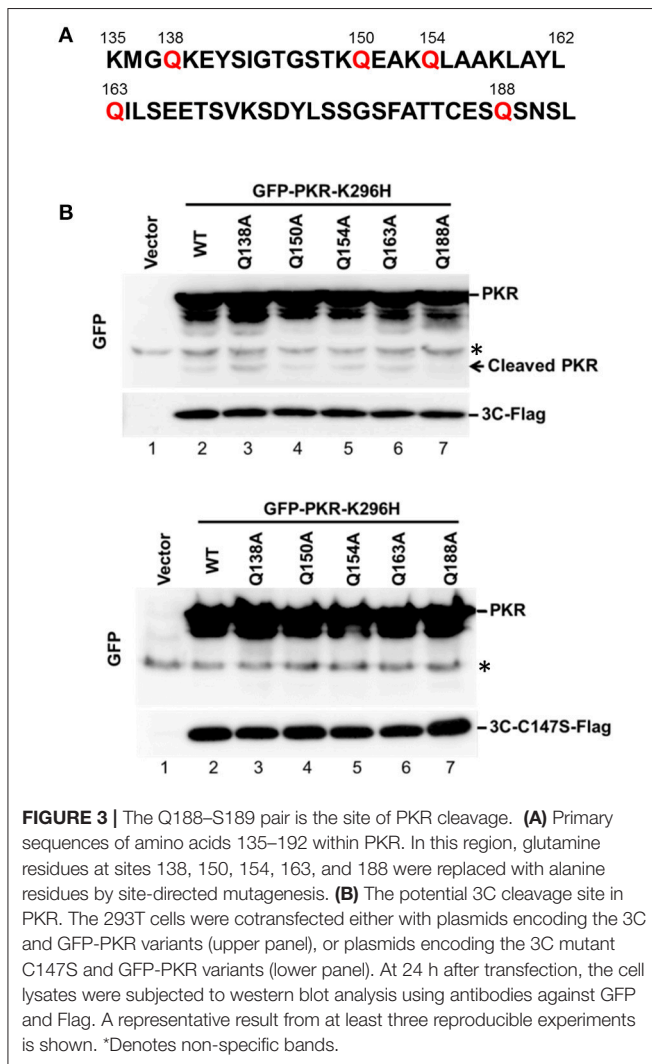


**FIGURE 2 |** Viral 3C protease is related to the cleavage of recombinant PKR. **(A)** Plasmids expressing viral 2A, 3C, P1, P2, and P3 were transfected into RD cells for 24 and 48 h. Equivalent amounts of protein from the cellular extracts were analyzed by immunoblotting using anti-PKR, PKR-p, and anti-GAPDH specific antibodies. An EV-A71-infected cellular extract served as a positive control. A representative result from three independent experiments is shown. **(B)** Schematic structure of the recombinant PKR, which has an N-terminal-linked GFP to allow monitoring of the cleavage product. RD cells were transfected with GFP-PKR or GFP-PKR-K296H for 24 h and the GFP expression was monitored using an EVOS fluorescence cell imaging system. **(C)** Plasmids expressing GFP-PKR-K296H were transfected into 293T cells for 24 h which were then transfected with the plasmid encoding 2A-Flag or 3C-Flag for another 24 h. Cell extracts were collected for immunoblotting using anti-GFP and anti-PKR antibodies. **(D)** A comparison of the cleavage patterns for 3C- and STS-induced PKR proteolysis. The 293T cells were transfected with GFP or GFP-PKR-K296H for 24 h and were then transfected with either empty vector, 3C-Flag, or C147S for another 24 h, or treated with STS for 8 h. Cell extracts were analyzed by immunoblotting using anti-GFP, anti-PARP, anti-GAPDH, and anti-Flag antibodies. A representative result from at least three reproducible experiments is shown. **(E)** Viral 3C cleaves PKR at a site that differs from that of apoptosis-induced PKR cleavage. The 293T cells were transfected with GFP, GFP-PKR-K296H, or GFP-PKR-K296H/D251N for 24 h, and were then transfected with either vector or 3C-Flag for another 24 h, or treated with STS for 8 h. The cell extracts were analyzed by immunoblotting using anti-PKR, anti-PARP, anti-GAPDH, and anti-Flag antibodies. A representative result from at least three reproducible experiments is shown.





## Amino Acid Residues Q188–S189 in PKR Are Necessary for 3C Protease-Mediated Cleavage

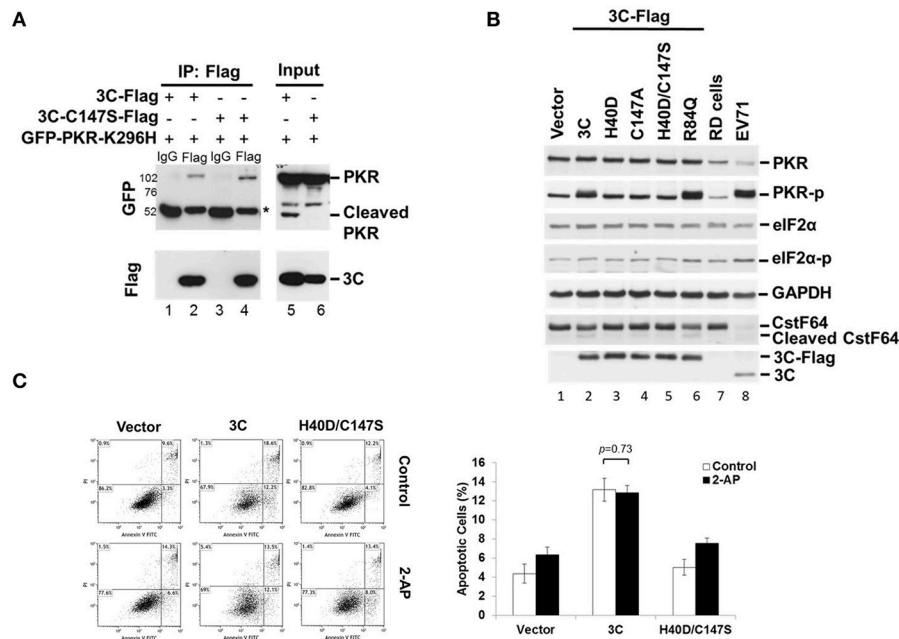
Because 3C protease-mediated PKR cleavage produces a 20-kDa N-terminal product, we inferred that a cleavage site may exist between amino acids 138 and 188 (Figure 3A). This region contains several glutamine residues and resembles the signature Q-G/Q-S sequence of cleavage sites for other enterovirus 3C proteins. To map the potential 3C-cleavage site of PKR, we constructed a series of mutants in which Q was replaced with A. These mutants were coexpressed with 3C or its mutant C147S in 293T cells, and cell lysates were subjected to western blot analysis. As shown in Figure 3B, Q188A was more refractory to cleavage by 3C than other mutants, suggesting that the Q188–S189 pair is a major cleavage site of 3C within PKR (lane 7, top, Figure 3B). No cleavage of PKR was detected by the 3C-C147S mutant (lower panel of Figure 3B).

## EV-A71 3C Physically Associates with PKR and Induces PKR Phosphorylation

When investigating which viral protein was responsible for PKR reduction, we observed an unexpected phosphorylation of PKR (Figure 2A). Overexpression of viral 3C and the P3 fragment from which 3C is derived strikingly induced PKR phosphorylation, suggesting the possibility that viral 3C protease interacts with PKR and contributes to its phosphorylation. To examine the nature of the 3C–PKR interaction, we carried out immunoprecipitation analysis in 293T cells coexpressing PKR-K296H and 3C or protease-inactive 3C mutant C147S (Figure 4A). The results revealed that both 3C and its C147S variant were specifically associated with PKR (lanes 2 and 4, top panel, Figure 4A), but only the wild-type 3C generated the cleavage product detected in the input (lane 5, top panel, Figure 4A); however, this product was not pulled down by 3C (lane 2 of Figure 4A). We further examined the role of 3C catalytic activity in PKR phosphorylation by examining 3C variants defective in protease activity (H40D, C147S, and double-mutant H40D/C147S; Figure 4B). We used CstF64 as a control for catalytic activity because only wild-type 3C protease could cleave this substrate, although not as robustly as the virus itself (lower panel of Figure 4B). Overexpression of wild-type 3C, the R84Q mutant (defective in RNA binding) of 3C, and EV-A71 infection (lanes 2, 6, and 8, Figure 4B) induced PKR phosphorylation, whereas this capacity was lost in the 3C catalytic-site mutants H40D, C147S, and H40D/C147S (lanes 3, 4, and 5, Figure 4B). These results demonstrated that the protease activity of 3C contributed to the phosphorylation of PKR. Despite this PKR phosphorylation, we noticed that there was no obvious activation of downstream eIF2 $\alpha$ . Previous studies have shown that 3C induces apoptosis when expressed in neuronal cells (Li et al., 2002) and that PKR mediates apoptosis (Balachandran et al., 1998). We investigated whether this 3C-induced apoptosis was caused by the activation of PKR. To this end, the PKR inhibitor 2-AP was added to 3C- or H40D/C147S-expressing 293T cells and the status of apoptosis was analyzed by Annexin V/PI staining (Figure 4C). The results showed that 3C, but not H40D/C147S, induced apoptosis in the 293T cells and that this was not abolished by 2-AP treatment. These data, therefore, suggest that although 3C induces PKR phosphorylation, 3C-induced apoptosis is not caused by PKR activation.

## Expression of a Catalytically Inactive PKR Mutant Results in Increases in Viral Proteins and Virus Titer

PKR is an IFN-induced, dsRNA-activated protein kinase that can function as a host antiviral factor. We used a chemical-induced GyrB-PKR model (Ung et al., 2001) to mimic PKR dimerization and activation in cells (Figure S1A). Coumermycin A1 (Cou A) induced dimerization and phosphorylation of wild-type GyrB-PKR, but not the kinase dead mutant GyrB-PKR-K296H (Figure S1B). Dimerization of GyrB-PKR suppressed viral protein synthesis when Cou A was added in the early stage of EV-A71 infection (compare lanes 5 and 6 with lanes 7 and 8, Figure S1B). The suppression effect of PKR dimerization on viral



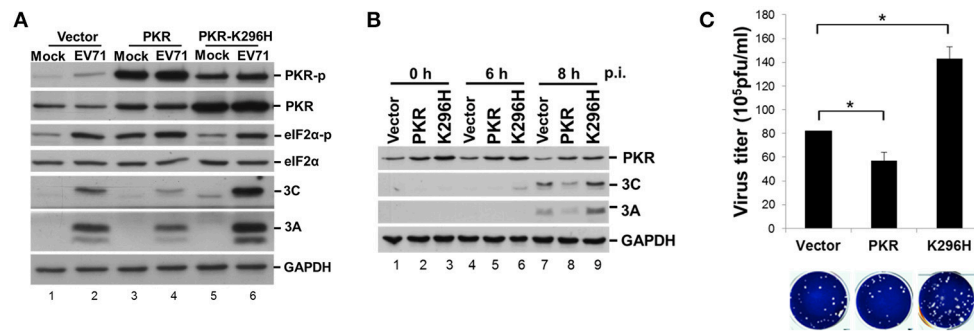


**FIGURE 5 |** Expression of a PKR kinase-dead mutant results in an increase of viral proteins and virus titer. **(A)** RD cells were transiently expressed with PKR or the K296H mutant for 24 h, and then infected with EV-A71 at an m.o.i. of 10. Immunoblot analysis was performed for detecting the presence and phosphorylation of PKR (anti-PKR, anti-PKR-p) and eIF2 $\alpha$  (anti-eIF2 $\alpha$ , anti-eIF2 $\alpha$ -p), and the expression of viral 3A and 3C proteins. GAPDH expression was used as a protein loading control. A representative result from three independent experiments is shown. **(B)** Stable RD cells expressing vector alone, PKR, or K296H were selected by addition of 3  $\mu$ g/mL puromycin. Cells were infected with EV-A71 at an m.o.i. of 10 and then the cellular extracts were harvested at 0, 6, and 8 h post-infection. Immunoblot analysis was performed to detect the presence of PKR and viral 3A and 3C proteins. A representative result based on three independent experiments is shown. **(C)** RD cells stably expressing PKR or the K296H mutant were infected with EV-A71 at an m.o.i. of 10 for 8 h. The RD cells and culture supernatant were harvested for virus titer determination by plaque assay. The results are expressed as the mean  $\pm$  SD ( $n = 3$ ). \* $p < 0.05$ .

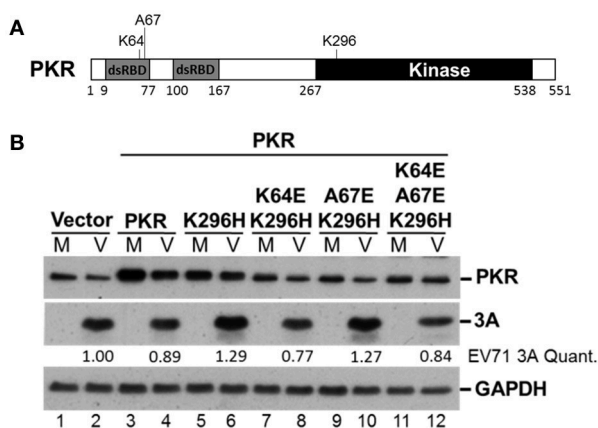


**FIGURE 6 |** The PKR mutant K296H increases the viral protein accumulation caused by the dsRNA binding domain. **(A)** Schematic representation of the PKR mutants. **(B)** Plasmids encoding vector alone, PKR, K296H, K64E/K296H, A67E/K296H, or K64E/A67E/K296H were transfected into RD cells, which were then selected by the addition of 3  $\mu$ g/mL puromycin. Stable expressing cells were infected with EV-A71 at an m.o.i. of 10 and the cellular extracts were harvested after 8 h. Immunoblot analysis was performed to detect PKR, viral 3A protein, and GAPDH. The relative amount of 3A protein was quantified by densitometry and was first normalized to GAPDH and then to that of the vector control. A representative result based on three independent experiments is shown.

contribute to EV-A71 replication. To determine the function of this small N-terminal PKR fragment, we constructed a plasmid expressing the first 188 amino acid residues of PKR, termed PKR(1–188), and examined its effect on EV-A71 replication (Figure 7). RD cells were transfected with increasing amounts of PKR(1–188) plasmid. Western blotting results showed that PKR(1–188) increased viral 3A protein expression in a dose-dependent manner (top panel, Figure 7A). In contrast, the increase in viral 3A protein expression was eliminated in cells

expressing the dsRNA binding mutant PKR(1–188)K64E (lower panel, Figure 7A). To confirm this enhancing effect of PKR(1–188), we analyzed the viral titer (Figure 7B) and viral RNA synthesis (Figure 7C) in a time-course experiment. Consistent with the increase in viral protein expression, viral titer and viral RNA synthesis were augmented in PKR(1–188)-expressing cells compared with vector-control cells. In conclusion, the EV-A71 3C protease cleaved PKR to generate an N-terminal fragment PKR(1–188) that enhanced virus replication.

## DISCUSSION

PKR was recognized as an antiviral protein because of its ability to control translation through phosphorylation of eIF2 $\alpha$ , and a number of viruses have strategies designed to counteract its action. PV is the prototype and most intensively studied enterovirus. Previous studies have reported that PKR is highly activated and rapidly degraded in PV-infected cells (Black et al., 1989, 1993). The degradation of PKR in infected cells requires PV gene expression but not PKR catalytic activity. However, PV-encoded proteases 2A, 3C, and 3CD are not directly responsible for the degradation of PKR. Therefore, it was proposed that a cellular protease activated after PV infection was responsible for PKR degradation and that the protease-sensitive site was located within the N-terminal dsRNA-binding domain of PKR. However, we observed PKR cleavage during EV-A71 infection that was not caused by viral infection-induced caspase activation during apoptosis, because it resulted in a different cleavage profile (Figure 1B). Our work demonstrated that in EV-A71, viral protease 3C directly interacts with and cleaves PKR at Q188, proximal to the dsRNA-binding domain of PKR. This difference might be because 3C of EV-A71 has a less strict cleavage specificity than that of PV (Sun et al., 2016). The 3C of PV preferentially cleaves polypeptides with QG junctions, whereas previous studies identified that the 3C of EV-A71 cleaves



at a QS site that has an aliphatic amino acid as the fourth amino acid residue preceding the cleavage site (also known as the P4 position) (Lei et al., 2011, 2013, 2014). Our results are consistent with this finding and show that the Q188–S189 pair in PKR, which has an aliphatic leucine residue at the P4 position, represents the signature of the EV-A71 3C cleavage site.

The formation of stress granules (SGs) is a typical response when cells are challenged by viral invasion. Phosphorylation of eIF2 $\alpha$  is the major pathway leading to SG formation (Anderson and Kedersha, 2002). PKR is one of the four known cellular eIF2 $\alpha$  kinases responsible for translation inhibition during cellular stress, and a recent report indicated that PKR is recruited to the SG complex (Reineke et al., 2015). We also showed that EV-A71 infection induced and modulated endoplasmic reticulum stress for viral replication by inducing PKR-dependent cytosolic accumulation of an endoplasmic reticulum chaperone protein, 78 kDa glucose-regulated protein/binding immunoglobulin protein (GRP78/BiP) (Jheng et al., 2010, 2016). Thus, PKR is a central molecule at the crossroads of innate immune and cellular stress responses because of its capacity to sense dsRNA in virus-infected cells. It has been reported that EV-A71 3C antagonizes the innate IFN response through cleavage of TRIF, IRF7, and IRF9 (Hung et al., 2011; Lei et al., 2011, 2013). The 3C proteins of encephalomyocarditis virus and PV cleave Ras GTPase-activating protein-binding protein 1, a component of SGs, to escape the antiviral responses of SG assembly (White et al., 2007; Ng et al., 2013). Our experiments demonstrate for the first time that PKR is a target of 3C in a strategy to counteract the host antiviral defense.

PKR is activated by dsRNA-mediated dimerization. Binding of dsRNA induces a conformational change that leads to the release of the dsRNA-binding domain from the kinase domain and induces dimerization of PKR via the kinase domain, subsequent PKR autophosphorylation and phosphorylation of eIF2 $\alpha$ , and results in the inhibition of protein synthesis followed by apoptosis (see graph in **Figure 8**). In addition to dsRNA, PKR can be activated by protein-protein interactions (Peters et al., 2001). The PKR activating protein (also known as PACT) can heterodimerize with PKR through its dsRNA-binding domain and activate it in the absence of dsRNA. In our study, we observed that 3C expression in cells induces PKR phosphorylation in the absence of dsRNA stimulation and that this induction requires protease activity. In addition, we have demonstrated that 3C directly interacts with PKR (**Figure 4A**). This suggests that binding to 3C triggers a conformational change in PKR that subsequently allows its phosphorylation. However, the phosphorylation of PKR induced by 3C did not correlate with subsequent phosphorylation of eIF2 $\alpha$  (**Figure 4B**). This result implies that 3C induces PKR phosphorylation but not dimerization, i.e., that 3C might block PKR dimerization. A previous study reported that the 3C protease activity of EV-A71 triggers caspase-dependent apoptosis in human glioblastoma cells (Li et al., 2002). It should be noted here that phosphorylation of eIF2 $\alpha$  represents one of the mechanisms by which PKR triggers apoptosis. Our results show that treatment with PKR inhibitor 2-AP was incapable of inhibiting 3C-induced apoptosis (**Figure 4C**), suggesting that 3C-induced apoptosis is not induced via PKR activation. This result is consistent with our finding that

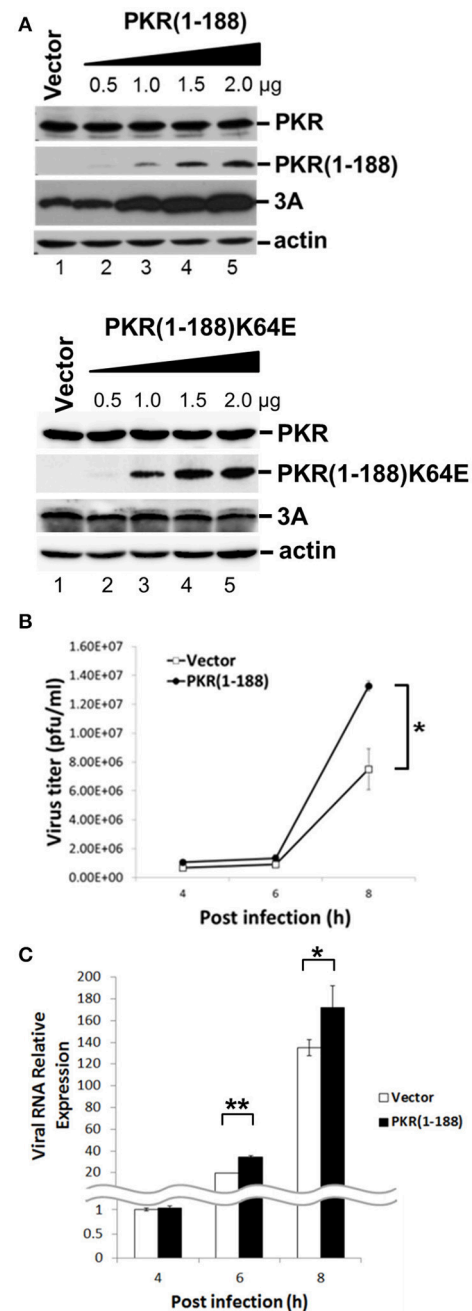
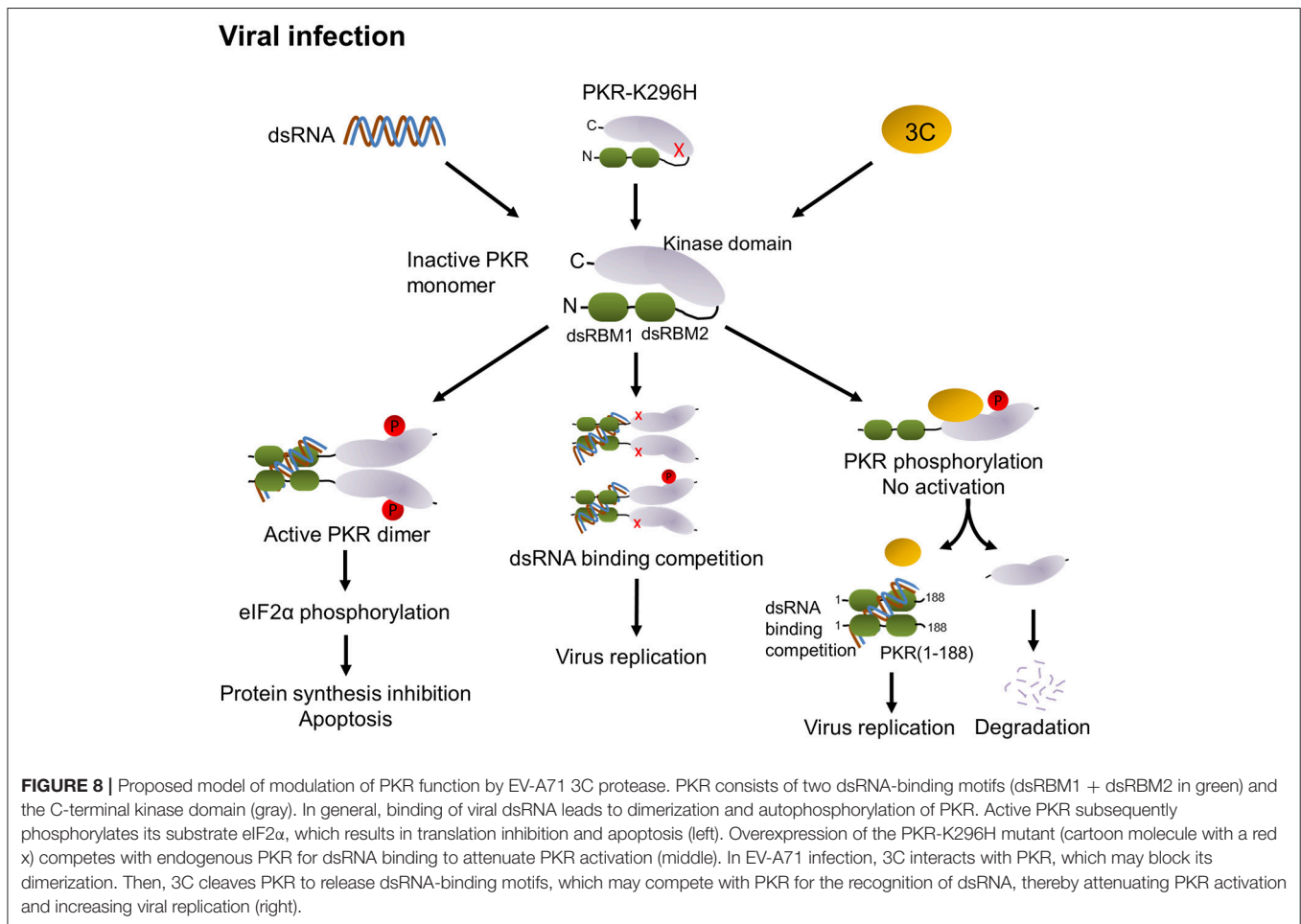


**FIGURE 7 |** The fragment amino acids 1–188 of PKR facilitates virus replication. **(A)** RD cells were transfected with the vector, increasing concentrations of plasmids encoding the PKR(1–188) or PKR(1–188)K64E fragment. At 48 h after transfection, the cells were infected with EV-A71 at an m.o.i. of 10 for another 8 h. The cell extracts were analyzed by immunoblotting using anti-PKR, anti-3A and anti-actin antibodies. PKR(1–188) was detected with anti-PKR antibody. Actin expression was used as a protein loading control. A representative result from at least three reproducible experiments is shown. **(B,C)** RD cells were transfected with the vector or of plasmids encoding the PKR (1–188) fragment. At 48 h after transfection, the cells were infected with EV-A71 at an m.o.i. of 10 and then the culture supernatant was harvested at 4, 6, and 8 h p.i. for virus titer determination by plaque assay **(B)**; and the total RNA was extracted for intracellular EV-A71 RNA quantification by RT-qPCR **(C)**. GAPDH mRNA quantification was used for normalization. The results are expressed as the mean  $\pm$  SD ( $n = 3$ ). \* $p < 0.05$ ; \*\* $p < 0.01$ .



3C-induced phosphorylation of PKR was independent of PKR activation. However, our data showed that an inactive 3C mutant still interacted with PKR but hardly induced phosphorylation of PKR. We cannot rule out the possibility that the proteolytic activity of 3C induces other unidentified mechanisms that cause the observed phosphorylation of PKR, or that the 3C mutant might induce a transient phosphorylation that we did not detect. Therefore, we propose that 3C negatively regulates the PKR-eIF2 $\alpha$  pathway through interacting with and cleaving PKR (Figure 8).

EV-A71 utilize internal ribosome entry sites (IRES) located in the 5' untranslated region to translate viral proteins in a cap-independent manner (McMinn, 2002). IRES-mediated translation initiation may require both canonical cellular translation factors and auxiliary factors known as IRES trans-acting factors. eIF2 has been identified as a canonical factor that must prebind the 40S ribosomal subunit. eIF2 $\alpha$  delivers an initiator tRNA<sup>Met</sup> to the small 40S ribosomal subunit in a guanosine-5'-triphosphate (GTP)-dependent manner. Activated PKR catalyzes the phosphorylation of eIF2 $\alpha$ , which blocks its capacity to recycle GTP (Holcik and Sonenberg, 2005). Without GTP recycling, eIF2 $\alpha$  becomes unavailable to form the eIF2-GTP-tRNA<sup>Met</sup> ternary complex, subsequently causing stalling of mRNA translation initiation, and resulting in

the global arrest of both cellular and IRES-dependent viral protein synthesis.

In the current study, overexpression of PKR led to increased eIF2 $\alpha$  phosphorylation and decreased viral replication (Figure 5), demonstrating the antiviral function of the PKR-eIF2 $\alpha$  pathway. In contrast, overexpression of a catalytically inactive PKR mutant led to increased viral protein accumulation and infectious virus yield. The addition of the PKR/K296H mutant decreased endogenous PKR phosphorylation and caused only a moderate decrease in eIF2 $\alpha$  phosphorylation during EV-A71 infection (Figure 5A). We postulated that this phenomenon may be the result of competition with endogenous PKR for either dimerization or dsRNA binding. To directly address this possibility, we generated K64E and A67E substitutions in the dsRNA binding site and dimerization site, respectively, within the inactive PKR K296H mutant (Figure 6). The upregulation of viral protein expression by the PKR K296 mutant was eliminated by the additional mutation K64E but not A67E, reflecting that competition for dsRNA binding, rather than for dimerization, was the major mechanism by which the catalytically inactive PKR mutant facilitated EV-A71 replication.

Interestingly, we also discovered that the PKR cleavage during EV-A71 infection generated a short PKR(1-188) product containing two dsRNA binding domains. Our data raised the



possibility that this cleavage product of PKR could have a positive effect on virus infection. Indeed, ectopic expression of PKR(1–188) enhanced viral protein accumulation and EV-A71 replication (Figure 7). We hypothesized that PKR(1–188) could have a protective function, similar to that of influenza NS1 protein (Chien et al., 2004), by binding to and sequestering viral dsRNA molecules. However, the cleavage at the Q188–S189 site appeared to be inefficient because the cleavage products were not easily detectable by western blotting. Nevertheless, our results suggested that small amounts of the cleavage products may be sufficient to facilitate EV-A71 replication.

A previous study showed that the N-terminal 1–265 amino acids of PKR are responsible for the activation of the NF- $\kappa$ B signaling pathway by interacting with the I $\kappa$ B kinase complex, whereas the 1–180 amino acids restricted to the two dsRNA binding domains were unable to stimulate an NF- $\kappa$ B response (Bonnet et al., 2006). The N-terminal cleavage product of PKR by 3C precisely eliminates the mechanism designed to stimulate NF- $\kappa$ B activation. Furthermore, the C-terminal 258–551 amino acid kinase domain of PKR generated by caspase cleavage cooperates to activate PKR (Kalai et al., 2007). This reminds us of the possibility that the C-terminal cleavage product of PKR by 3C may, in turn, activate the remaining PKR. However, when we generated PKR K296H-Flag plasmid carrying a C-terminal Flag tag and expressed this plasmid in RD cells, the C-terminal cleavage product of PKR was undetectable during viral infection (data not shown). These results suggested that the products of PKR cleavage by 3C are inactive in stimulating an antiviral response, supported by the fact that cleavage of PKR by 3C clearly attenuated PKR function.

In summary, our results identified a novel role for EV-A71 3C in suppressing the cellular antiviral molecule PKR. We propose

that 3C employs two mechanisms: (i) interacting with PKR to block its dimerization, and (ii) PKR cleavage, to counteract PKR activation (Figure 8). Overall, the fine-tuning of PKR activation in EV-A71-infected cells would dictate the outcomes of EV-A71 infection.

## AUTHOR CONTRIBUTIONS

Conceived and designed the experiments: YC, KL, RK, and JH. Performed the experiments: YC and KL. Analyzed the data: YC, KL, and JH. Wrote the paper and edited the manuscript: YC and JH.

## FUNDING

This work was supported by grants from Chang Gung Memorial Hospital (CMRPD1D0323, CMRPD1E0043, and BMRP416) and the Ministry of Science and Technology of Taiwan (MOST105-2632-B-182-002- and 105-2311-B-182-001-).

## ACKNOWLEDGMENTS

We thank Drs. Shin-Ru Shih (Research Center for Emerging Viral Infections, Chang Gung University, Taoyuan, Taiwan) and Mei-Shang Ho (Institute of Biomedical Sciences, Academia Sinica, Nankang, Taiwan) for the reagents.

## SUPPLEMENTARY MATERIAL

The Supplementary Material for this article can be found online at: <http://journal.frontiersin.org/article/10.3389/fcimb.2017.00284/full#supplementary-material>

## REFERENCES

- Anderson, P., and Kedersha, N. (2002). Visibly stressed: the role of eIF2, TIA-1, and stress granules in protein translation. *Cell Stress Chaperones* 7, 213–221. doi: 10.1379/1466-1268(2002)007<0213:VSTROE>2.0.CO;2
- Balachandran, S., Kim, C. N., Yeh, W. C., Mak, T. W., Bhalla, K., and Barber, G. N. (1998). Activation of the dsRNA-dependent protein kinase, PKR, induces apoptosis through FADD-mediated death signaling. *EMBO J.* 17, 6888–6902. doi: 10.1093/emboj/17.23.6888
- Belmokhtar, C. A., Hillion, J., and Segal-Bendirdjian, E. (2001). Staurosporine induces apoptosis through both caspase-dependent and caspase-independent mechanisms. *Oncogene* 20, 3354–3362. doi: 10.1038/sj.onc.1204436
- Black, T. L., Barber, G. N., and Katze, M. G. (1993). Degradation of the interferon-induced 68,000-Mr protein kinase by poliovirus requires RNA. *J. Virol.* 67, 791–800.
- Black, T. L., Safer, B., Hovanessian, A., and Katze, M. G. (1989). The cellular 68,000-Mr protein kinase is highly autophosphorylated and activated yet significantly degraded during poliovirus infection: implications for translational regulation. *J. Virol.* 63, 2244–2251.
- Bonnet, M. C., Daurat, C., Ottone, C., and Meurs, E. F. (2006). The N-terminus of PKR is responsible for the activation of the NF- $\kappa$ B signaling pathway by interacting with the IKK complex. *Cell. Signal.* 18, 1865–1875. doi: 10.1016/j.cellsig.2006.02.010
- Chang, C. W., Leu, Y. L., and Horng, J. T. (2012). Daphne Genkwa sieb. Et zucc. Water-soluble extracts act on enterovirus 71 by inhibiting viral entry. *Viruses* 4, 539–556. doi: 10.3390/v4040539
- Chien, C. Y., Xu, Y., Xiao, R., Aramini, J. M., Sahasrabudhe, P. V., Krug, R. M., et al. (2004). Biophysical characterization of the complex between double-stranded RNA and the N-terminal domain of the NS1 protein from influenza A virus: evidence for a novel RNA-binding mode. *Biochemistry* 43, 1950–1962. doi: 10.1021/bi030176o
- Clemens, M. J., and Elia, A. (1997). The double-stranded RNA-dependent protein kinase PKR: structure and function. *J. Interferon Cytokine Res.* 17, 503–524. doi: 10.1089/jir.1997.17.503
- Dar, A. C., Dever, T. E., and Sicheri, F. (2005). Higher-order substrate recognition of eIF2 $\alpha$  by the RNA-dependent protein kinase PKR. *Cell* 122, 887–900. doi: 10.1016/j.cell.2005.06.044
- Dey, M., Cao, C., Dar, A. C., Tamura, T., Ozato, K., Sicheri, F., et al. (2005). Mechanistic link between PKR dimerization, autophosphorylation, and eIF2 $\alpha$  substrate recognition. *Cell* 122, 901–913. doi: 10.1016/j.cell.2005.06.041
- Donnelly, N., Gorman, A. M., Gupta, S., and Samali, A. (2013). The eIF2 $\alpha$  kinases: their structures and functions. *Cell. Mol. Life Sci.* 70, 3493–3511. doi: 10.1007/s00018-012-1252-6
- Gale, M. J. Jr., Korth, M. J., and Katze, M. G. (1998). Repression of the PKR protein kinase by the hepatitis C virus NS5A protein: a potential mechanism of interferon resistance. *Clin. Diagn. Virol.* 10, 157–162. doi: 10.1016/S0928-0197(98)00034-8
- Gale, M. J. Jr., and Katze, M. G. (1998). Molecular mechanisms of interferon resistance mediated by viral-directed inhibition of PKR, the interferon-induced protein kinase. *Pharmacol. Ther.* 78, 29–46. doi: 10.1016/S0163-7258(97)00165-4

- Gil, J., Garcia, M. A., Gomez-Puertas, P., Guerra, S., Rullas, J., Nakano, H., et al. (2004). TRAF family proteins link PKR with NF- $\kappa$ B activation. *Mol. Cell. Biol.* 24, 4502–4512. doi: 10.1128/MCB.24.10.4502-4512.2004
- Gilfoy, F. D., and Mason, P. W. (2007). West Nile virus-induced interferon production is mediated by the double-stranded RNA-dependent protein kinase PKR. *J. Virol.* 81, 11148–11158. doi: 10.1128/JVI.00446-07
- Goh, K. C., deVeer, M. J., and Williams, B. R. (2000). The protein kinase PKR is required for p38 MAPK activation and the innate immune response to bacterial endotoxin. *EMBO J.* 19, 4292–4297. doi: 10.1093/emboj/19.16.4292
- Hett, E. C., Slater, L. H., Mark, K. G., Kawate, T., Monks, B. G., Stutz, A., et al. (2013). Chemical genetics reveals a kinase-independent role for protein kinase R in pyroptosis. *Nat. Chem. Biol.* 9, 398–405. doi: 10.1038/nchembio.1236
- Holcik, M., and Sonenberg, N. (2005). Translational control in stress and apoptosis. *Nat. Rev. Mol. Cell Biol.* 6, 318–327. doi: 10.1038/nrm1618
- Hung, H. C., Wang, H. C., Shih, S. R., Teng, I. F., Tseng, C. P., and Hsu, J. T. (2011). Synergistic inhibition of enterovirus 71 replication by interferon and rupintrivir. *J. Infect. Dis.* 203, 1784–1790. doi: 10.1093/infdis/jir174
- Jheng, J. R., Lau, K. S., Tang, W. F., Wu, M. S., and Horng, J. T. (2010). Endoplasmic reticulum stress is induced and modulated by enterovirus 71. *Cell. Microbiol.* 12, 796–813. doi: 10.1111/j.1462-5822.2010.01434.x
- Jheng, J. R., Wang, S. C., Jheng, C. R., and Horng, J. T. (2016). Enterovirus 71 induces dsRNA/PKR-dependent cytoplasmic redistribution of GRP78/BiP to promote viral replication. *Emerg. Microbes Infect.* 5:e23. doi: 10.1038/emi.2016.20
- Kalai, M., Suin, V., Festjens, N., Meeus, A., Bernis, A., Wang, X. M., et al. (2007). The caspase-generated fragments of PKR cooperate to activate full-length PKR and inhibit translation. *Cell Death Differ.* 14, 1050–1059. doi: 10.1038/sj.cdd.4402110
- Langland, J. O., and Jacobs, B. L. (2004). Inhibition of PKR by vaccinia virus: role of the N- and C-terminal domains of E3L. *Virology* 324, 419–429. doi: 10.1016/j.virol.2004.03.012
- Langland, J. O., Cameron, J. M., Heck, M. C., Jancovich, J. K., and Jacobs, B. L. (2006). Inhibition of PKR by RNA and DNA viruses. *Virus Res.* 119, 100–110. doi: 10.1016/j.virusres.2005.10.014
- Langland, J. O., Pettiford, S., Jiang, B., and Jacobs, B. L. (1994). Products of the porcine group C rotavirus NSP3 gene bind specifically to double-stranded RNA and inhibit activation of the interferon-induced protein kinase PKR. *J. Virol.* 68, 3821–3829.
- Lei, X., Han, N., Xiao, X., Jin, Q., He, B., and Wang, J. (2014). Enterovirus 71 3C inhibits cytokine expression through cleavage of the TAK1/TAB1/TAB2/TAB3 complex. *J. Virol.* 88, 9830–9841. doi: 10.1128/JVI.01425-14
- Lei, X., Liu, X., Ma, Y., Sun, Z., Yang, Y., Jin, Q., et al. (2010). The 3C protein of enterovirus 71 inhibits retinoid acid-inducible gene I-mediated interferon regulatory factor 3 activation and type I interferon responses. *J. Virol.* 84, 8051–8061. doi: 10.1128/JVI.02491-09
- Lei, X., Sun, Z., Liu, X., Jin, Q., He, B., and Wang, J. (2011). Cleavage of the adaptor protein TRIF by enterovirus 71 3C inhibits antiviral responses mediated by Toll-like receptor 3. *J. Virol.* 85, 8811–8818. doi: 10.1128/JVI.00447-11
- Lei, X., Xiao, X., Xue, Q., Jin, Q., He, B., and Wang, J. (2013). Cleavage of interferon regulatory factor 7 by enterovirus 71 3C suppresses cellular responses. *J. Virol.* 87, 1690–1698. doi: 10.1128/JVI.01855-12
- Li, M. L., Hsu, T. A., Chen, T. C., Chang, S. C., Lee, J. C., Chen, C. C., et al. (2002). The 3C protease activity of enterovirus 71 induces human neural cell apoptosis. *Virology* 293, 386–395. doi: 10.1006/viro.2001.1310
- Lin, T.-Y., Chang, L.-Y., and Huang, Y.-C. (1998). Fulminant neurogenic pulmonary oedema with hand, foot, and mouth disease. *Lancet* 352, 367–368. doi: 10.1016/S0140-6736(98)24031-1
- McMinn, P. C. (2002). An overview of the evolution of enterovirus 71 and its clinical and public health significance. *FEMS Microbiol. Rev.* 26, 91–107. doi: 10.1111/j.1574-6976.2002.tb00601.x
- Meurs, E. F., Watanabe, Y., Kadereit, S., Barber, G. N., Katze, M. G., Chong, K., et al. (1992). Constitutive expression of human double-stranded RNA-activated p68 kinase in murine cells mediates phosphorylation of eukaryotic initiation factor 2 and partial resistance to encephalomyocarditis virus growth. *J. Virol.* 66, 5805–5814.
- Nanduri, S., Rahman, F., Williams, B. R., and Qin, J. (2000). A dynamically tuned double-stranded RNA binding mechanism for the activation of antiviral kinase PKR. *EMBO J.* 19, 5567–5574. doi: 10.1093/emboj/19.20.5567
- Ng, C. S., Jogi, M., Yoo, J. S., Onomoto, K., Koike, S., Iwasaki, T., et al. (2013). Encephalomyocarditis virus disrupts stress granules, the critical platform for triggering antiviral innate immune responses. *J. Virol.* 87, 9511–9522. doi: 10.1128/JVI.03248-12
- Pathinayake, P. S., Hsu, A. C., and Wark, P. A. (2015). Innate immunity and immune evasion by enterovirus 71. *Viruses* 7, 6613–6630. doi: 10.3390/v7122961
- Peters, G. A., Hartmann, R., Qin, J., and Sen, G. C. (2001). Modular structure of PACT: distinct domains for binding and activating PKR. *Mol. Cell. Biol.* 21, 1908–1920. doi: 10.1128/MCB.21.6.1908-1920.2001
- Pindel, A., and Sadler, A. (2011). The role of protein kinase R in the interferon response. *J. Interferon Cytokine Res.* 31, 59–70. doi: 10.1089/jir.2010.0099
- Reineke, L. C., Kedersha, N., Langereis, M. A., van Kuppeveld, F. J., and Lloyd, R. E. (2015). Stress granules regulate double-stranded RNA-dependent protein kinase activation through a complex containing G3BP1 and Caprin1. *Mbio* 6:e02486. doi: 10.1128/mBio.02486-14
- Saelens, X., Kalai, M., and Vandenabeele, P. (2001). Translation inhibition in apoptosis: caspase-dependent PKR activation and eIF2- $\alpha$  phosphorylation. *J. Biol. Chem.* 276, 41620–41628. doi: 10.1074/jbc.M103674200
- Sun, D., Chen, S., Cheng, A., and Wang, M. (2016). Roles of the picornaviral 3C proteinase in the viral life cycle and host cells. *Viruses* 8:82. doi: 10.3390/v8030082
- Tang, W. F., Yang, S. Y., Wu, B. W., Jheng, J. R., Chen, Y. L., Shih, C. H., et al. (2007). Reticulon 3 binds the 2C protein of enterovirus 71 and is required for viral replication. *J. Biol. Chem.* 282, 5888–5898. doi: 10.1074/jbc.M611145200
- Taylor, D. R., Shi, S. T., Romano, P. R., Barber, G. N., and Lai, M. M. (1999). Inhibition of the interferon-inducible protein kinase PKR by HCV E2 protein. *Science* 285, 107–110. doi: 10.1126/science.285.5424.107
- Tu, Y. C., Yu, C. Y., Liang, J. J., Lin, E., Liao, C. L., and Lin, Y. L. (2012). Blocking double-stranded RNA-activated protein kinase PKR by Japanese encephalitis virus nonstructural protein 2A. *J. Virol.* 86, 10347–10358. doi: 10.1128/JVI.00525-12
- Ung, T. L., Cao, C., Lu, J., Ozato, K., and Dever, T. E. (2001). Heterologous dimerization domains functionally substitute for the double-stranded RNA binding domains of the kinase PKR. *EMBO J.* 20, 3728–3737. doi: 10.1093/emboj/20.14.3728
- Wang, H., Lei, X., Xiao, X., Yang, C., Lu, W., Huang, Z., et al. (2015). Reciprocal regulation between enterovirus 71 and the NLRP3 inflammasome. *Cell Rep.* 12, 42–48. doi: 10.1016/j.celrep.2015.05.047
- Weng, K. F., Li, M. L., Hung, C. T., and Shih, S. R. (2009). Enterovirus 71 3C protease cleaves a novel target CstF-64 and inhibits cellular polyadenylation. *PLoS Pathog.* 5:1000593. doi: 10.1371/journal.ppat.1000593
- White, J. P., Cardenas, A. M., Marissen, W. E., and Lloyd, R. E. (2007). Inhibition of cytoplasmic mRNA stress granule formation by a viral proteinase. *Cell Host Microbe* 2, 295–305. doi: 10.1016/j.chom.2007.08.006
- Wu, S., and Kaufman, R. J. (1997). A model for the double-stranded RNA (dsRNA)-dependent dimerization and activation of the dsRNA-activated protein kinase PKR. *J. Biol. Chem.* 272, 1291–1296. doi: 10.1074/jbc.272.2.1291

**Conflict of Interest Statement:** The authors declare that the research was conducted in the absence of any commercial or financial relationships that could be construed as a potential conflict of interest.

The reviewer C-HL declared a shared affiliation, though no other collaboration, with the authors to the handling Editor, who ensured that the process nevertheless met the standards of a fair and objective review.

Copyright © 2017 Chang, Lau, Kuo and Horng. This is an open-access article distributed under the terms of the Creative Commons Attribution License (CC BY). The use, distribution or reproduction in other forums is permitted, provided the original author(s) or licensor are credited and that the original publication in this journal is cited, in accordance with accepted academic practice. No use, distribution or reproduction is permitted which does not comply with these terms.

Article

# Sterols from the Octocoral *Nephthea columnaris*

Ta-Yuan Whuang <sup>1,2,†</sup>, Hong-Chieh Tsai <sup>3,4,†</sup>, Yin-Di Su <sup>2</sup>, Tsong-Long Hwang <sup>5,6,7,\*</sup> and Ping-Jyun Sung <sup>1,2,8,9,10,\*</sup>

<sup>1</sup> Graduate Institute of Marine Biology, National Dong Hwa University, Pingtung 944, Taiwan; xdanielzero@gmail.com

<sup>2</sup> National Museum of Marine Biology and Aquarium, Pingtung 944, Taiwan; gobetter04@gmail.com

<sup>3</sup> Graduate Institute of Clinical Medical Sciences, College of Medicine, Chang Gung University, Taoyuan 333, Taiwan; Newcomer9999@gmail.com

<sup>4</sup> Department of Neurosurgery, Chang Gung Memorial Hospital, Taoyuan 333, Taiwan

<sup>5</sup> Graduate Institute of Natural Products, College of Medicine and Chinese Herbal Medicine Research Team, Healthy Aging Research Center, Chang Gung University, Taoyuan 333, Taiwan

<sup>6</sup> Research Center for Chinese Herbal Medicine, Research Center for Food and Cosmetic Safety, and Graduate Institute of Health Industry Technology, College of Human Ecology, Chang Gung University of Science and Technology, Taoyuan 333, Taiwan

<sup>7</sup> Department of Anesthesiology, Chang Gung Memorial Hospital, Taoyuan 333, Taiwan

<sup>8</sup> Chinese Medicine Research and Development Center, China Medical University Hospital, Taichung 404, Taiwan

<sup>9</sup> Graduate Institute of Natural Products, Kaohsiung Medical University, Kaohsiung 807, Taiwan

<sup>10</sup> Department of Marine Biotechnology and Resources, National Sun Yat-sen University, Kaohsiung 804, Taiwan

\* Correspondence: htl@mail.cgu.edu.tw (T.-L.H.); pjsung@nmmmba.gov.tw (P.-J.S.); Tel.: +886-3-2118800 (ext. 5523) (T.-L.H.); +886-8-8825037 (P.-J.S.);

Fax: +886-3-2118506 (T.-L.H.); +886-8-8825087 (P.-J.S.)

† These authors contributed equally to this work.

Received: 23 May 2017; Accepted: 1 July 2017; Published: 4 July 2017

**Abstract:** Two new sterols, columnaristerols B (1) and C (2), along with two known analogues, 5,6-epoxylitosterol (3) and litosterol (4), were obtained from the octocoral *Nephthea columnaris*. The structures of new sterols 1 and 2 were elucidated by using spectroscopic methods and comparing the spectroscopic data with those of known related metabolites. Sterol 3 was found to suppress superoxide anion production and elastase secretion by human neutrophils.

**Keywords:** octocoral; *Nephthea columnaris*; columnaristerol; litosterol; superoxide anion; elastase

## 1. Introduction

The octocoral *Nephthea columnaris* (Studer, 1895) (family Nephtheidae, order Alcyonacea, class Anthozoa, phylum Cnidaria) comprises large quantities of terpenoid [1,2] and steroid [3,4] analogues, which often have complex structures and biological activities. In continuing studies of the constituents of *N. columnaris* collected from the southern waters off the coast of Taiwan, two new sterols, columnaristerols B (1) and C (2), and known analogues, 5,6-epoxylitosterol (3) and litosterol (4) [5] (Figure 1), were obtained. Sterol 3 was found to inhibit the production of superoxide anions and release of elastase by human neutrophils.

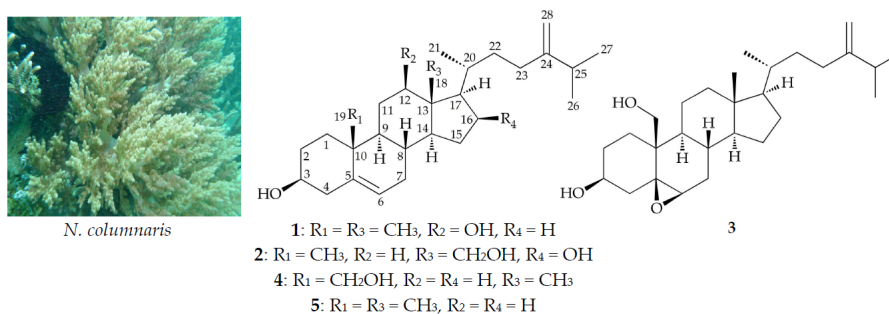


**Figure 1.** Octocoral *N. columnaris* and structures of columnaristerols B (1), C (2), 5,6-epoxylitosterol (3), litosterol (4), and 24-methylenecholesterol (5).

## 2. Results and Discussion

Columnaristerol B (1) was obtained as a non-crystalline powder, and high-resolution electrospray ionization mass spectrum (HRESIMS) analysis revealed that 1 had a pseudomolecular peak at  $m/z$  437.33918 (calcd. for C<sub>28</sub>H<sub>46</sub>O<sub>2</sub> + Na, 437.33900), which established the molecular formula C<sub>28</sub>H<sub>46</sub>O<sub>2</sub>, indicating six degrees of unsaturation. Data from <sup>1</sup>H NMR and distortionless enhancement of polarization transfer (DEPT) analyses and examination along with the molecular formula of the compound suggested that there were two exchangeable protons that required the presence of two hydroxyl groups. IR spectrum analysis showed a broad absorption at 3386 cm<sup>−1</sup>, which further confirmed that interpretation. Combined examination of the molecular formula, <sup>13</sup>C NMR and DEPT data revealed the presence of 28 carbons in 1 (Table 1), including five methyls, nine sp<sup>3</sup> methylenes, eight sp<sup>3</sup> methines (including two oxymethines, δ<sub>C</sub> 79.5 and 71.7), an exocyclic double bond (δ<sub>C</sub> 156.8 and 106.0), a trisubstituted double bond (δ<sub>C</sub> 140.6 and 121.6), and two sp<sup>3</sup> quaternary carbons.

**Table 1.** <sup>1</sup>H (400 MHz, CDCl<sub>3</sub>) and <sup>13</sup>C (100 MHz, CDCl<sub>3</sub>) NMR data and <sup>1</sup>H–<sup>1</sup>H COSY and HMBC correlations for sterol 1.

Position	δ <sub>H</sub> (J in Hz)	δ <sub>C</sub> , Multiple	<sup>1</sup> H– <sup>1</sup> H COSY	HMBC
1α/β	1.84 m; 1.09 m	37.2, CH <sub>2</sub>	H <sub>2</sub> -2	C-2, C-3, C-5, C-10, C-19
2α/β	1.84 m; 1.49 m	31.6, CH <sub>2</sub>	H <sub>2</sub> -1, H-3	C-3
3	3.51 m	71.7, CH	H <sub>2</sub> -2, H <sub>2</sub> -4	n. o. <sup>a</sup>
4a/b	2.31 ddd (12.8, 4.8, 2.0); 2.22 m	42.1, CH <sub>2</sub>	H-3	C-2, C-3, C-5, C-6, C-10
5	-	140.6, C	-	-
6	5.35 br d (5.2)	121.6, CH	H <sub>2</sub> -7	C-4, C-7, C-8, C-10
7a/b	1.99 m; 1.49 m	31.5, CH <sub>2</sub>	H-6, H-8	C-5, C-6, C-8, C-9
8	1.36 m	30.6, CH	H <sub>2</sub> -7, H-9, H-14	C-7, C-9, C-10, C-13, C-14
9	1.06 m	49.5, CH	H-8, H <sub>2</sub> -11	C-7, C-11
10	-	36.5, C	-	-
11a/b	1.71 m; 1.49 m	31.3, CH <sub>2</sub>	H-9, H-12	C-8, C-9, C-12, C-13
12	3.46 ddd (10.8, 5.2, 4.4)	79.5, CH	H <sub>2</sub> -11	C-18
13	-	47.6, C	-	-
14	0.92 m	54.7, CH	H-8, H <sub>2</sub> -15	C-8, C-12, C-13, C-15, C-18
15a/b	1.64 m; 1.21 m	23.8, CH <sub>2</sub>	H-14, H <sub>2</sub> -16	C-8, C-14, C-16, C-17
16a/b	1.76 m; 1.52 m	24.4, CH <sub>2</sub>	H <sub>2</sub> -15, H-17	n. o.
17	1.44 m	57.3, CH	H <sub>2</sub> -16, H-20	C-12, C-13, C-16, C-18, C-20, C-21, C-22
18	0.72 s	7.8, CH <sub>3</sub>	-	C-12, C-13, C-14, C-17
19	1.02 s	19.3, CH <sub>3</sub>	-	C-1, C-5, C-9, C-10
20	1.77 m	33.4, CH	H-17, H <sub>3</sub> -21, H <sub>2</sub> -22	C-16
21	1.04 d (6.4)	21.5, CH <sub>3</sub>	H-20	C-17
22a/b	1.64 m; 1.14 m	33.4, CH <sub>2</sub>	H-20, H <sub>2</sub> -23	C-21
23a/b	2.12 m; 1.92 m	32.5, CH <sub>2</sub>	H <sub>2</sub> -22	C-20, C-22, C-24, C-28
24	-	156.8, C	-	-
25	2.23 m	33.8, CH	H <sub>3</sub> -26, H <sub>3</sub> -27	C-23, C-24, C-26, C-27, C-28
26	1.02 d (6.8)	21.8, CH <sub>3</sub>	H-25	C-24, C-25, C-27
27	1.03 d (6.8)	22.0, CH <sub>3</sub>	H-25	C-24, C-25, C-26
28a/b	4.72 br s; 4.67 br s	106.0, CH <sub>2</sub>	-	C-23, C-24, C-25

<sup>a</sup> n. o. = not observed.

In addition, the  $^1\text{H}$  NMR spectrum (Table 1) exhibited five methyl signals at  $\delta_{\text{H}}$  1.04 (3H, d,  $J = 6.4$  Hz), 1.03 (3H, d,  $J = 6.8$  Hz), 1.02 (3H, d,  $J = 6.8$  Hz), 1.02 (3H, s), and 0.72 (3H, s). As the trisubstituted double bond and exocyclic double bond accounted for two of the six degrees of unsaturation, the remaining four degrees of unsaturation were ascribed to the presence of a tetracyclic compound.

By  $^1\text{H}$ - $^1\text{H}$  correlation spectroscopy (COSY) of **1**, proton signal correlations between  $\delta_{\text{H}}$  1.09/ $\delta_{\text{H}}$  1.84 and 1.49/ $\delta_{\text{H}}$  3.51/ $\delta_{\text{H}}$  2.31 and 2.22;  $\delta_{\text{H}}$  5.35/ $\delta_{\text{H}}$  1.99 and 1.49/ $\delta_{\text{H}}$  1.36/ $\delta_{\text{H}}$  1.06/ $\delta_{\text{H}}$  1.71 and 1.49/ $\delta_{\text{H}}$  3.46;  $\delta_{\text{H}}$  1.36/ $\delta_{\text{H}}$  0.92/ $\delta_{\text{H}}$  1.64 and 1.21/ $\delta_{\text{H}}$  1.76 and 1.52/ $\delta_{\text{H}}$  1.44/ $\delta_{\text{H}}$  1.77/ $\delta_{\text{H}}$  1.64 and 1.14/ $\delta_{\text{H}}$  2.12 and 1.92;  $\delta_{\text{H}}$  1.77/ $\delta_{\text{H}}$  1.04;  $\delta_{\text{H}}$  2.23/ $\delta_{\text{H}}$  1.02; and  $\delta_{\text{H}}$  2.23/ $\delta_{\text{H}}$  1.03 established the proton sequences  $\text{H}_2\text{-1}/\text{H}_2\text{-2}/\text{H-3}/\text{H}_2\text{-4}$ ,  $\text{H-6}/\text{H}_2\text{-7}/\text{H-8}/\text{H-9}/\text{H}_2\text{-11}/\text{H-12}$ ,  $\text{H-8}/\text{H-14}/\text{H}_2\text{-15}/\text{H}_2\text{-16}/\text{H-17}/\text{H-20}/\text{H}_2\text{-22}/\text{H}_2\text{-23}$ ,  $\text{H-20}/\text{H}_3\text{-21}$ ,  $\text{H-25}/\text{H}_3\text{-26}$ , and  $\text{H-25}/\text{H}_3\text{-27}$ , respectively (Table 1). These data, together with the key heteronuclear multiple bond coherence (HMBC) correlations from  $\text{H}_2\text{-4}$  to C-5, C-6, and C-10; from H-6 to C-4 and C-10; from  $\text{H}_2\text{-7}$  to C-5; from H-8 to C-10; from  $\text{H}_2\text{-11}$  to C-13; from H-12 to C-18; from H-14 to C-12, C-13, and C-18; from H-17 to C-12, C-13, and C-18; from  $\text{H}_3\text{-18}$  to C-12, C-13, C-14, and C-17; from  $\text{H}_3\text{-19}$  to C-1, C-5, C-9, and C-10; from  $\text{H}_2\text{-23}$  to C-24 and C-28; from H-25 to C-23, C-24, and C-28; from  $\text{H}_3\text{-26}$  to C-24; from  $\text{H}_3\text{-27}$  to C-24; and from  $\text{H}_2\text{-28}$  to C-24 enabled elucidation of the carbon skeleton of **1** (Table 1). Moreover, the planar structure of **1** was determined by comparison of the  $^{13}\text{C}$  NMR data with those of a known principal sterol, 24-methylenecholesterol (**5**) (Figure 1) [5,6].

The relative stereochemistry of **1** was established by comparison of NMR data with those of sterol **5** [5,6] and from the interactions observed in the nuclear Overhauser effect spectroscopy (NOESY) experiment, which were corroborated by MM2 force field calculations, suggesting the most stable conformation to be as shown in Figure 2 [7]. The configurations at C-3 ( $\delta_{\text{C}}$  71.7), C-8 ( $\delta_{\text{C}}$  30.6), C-9 ( $\delta_{\text{C}}$  49.5), C-10 ( $\delta_{\text{C}}$  36.5), C-13 ( $\delta_{\text{C}}$  47.6), C-14 ( $\delta_{\text{C}}$  54.7), C-17 ( $\delta_{\text{C}}$  57.3), and C-20 ( $\delta_{\text{C}}$  33.4) in **1** were found to be similar to those of **5** (C-3,  $\delta_{\text{C}}$  71.7; C-8,  $\delta_{\text{C}}$  31.9; C-9,  $\delta_{\text{C}}$  50.1; C-10,  $\delta_{\text{C}}$  36.5; C-13,  $\delta_{\text{C}}$  42.3; C-14,  $\delta_{\text{C}}$  56.7; C-17,  $\delta_{\text{C}}$  56.0; C-20,  $\delta_{\text{C}}$  35.7) [5], (C-3,  $\delta_{\text{C}}$  71.84; C-8,  $\delta_{\text{C}}$  31.94; C-9,  $\delta_{\text{C}}$  50.17; C-10,  $\delta_{\text{C}}$  36.52; C-13,  $\delta_{\text{C}}$  42.31; C-14,  $\delta_{\text{C}}$  56.80; C-17,  $\delta_{\text{C}}$  56.04; C-20,  $\delta_{\text{C}}$  35.79) [6]. A key correlation map obtained from the NOESY experiment for **1** showed interactions between  $\text{H-1}\alpha$  ( $\delta_{\text{H}}$  1.84)/ $\text{H-3}$  ( $\delta_{\text{H}}$  3.51),  $\text{H-1}\alpha/\text{H-9}$  ( $\delta_{\text{H}}$  1.06),  $\text{H-2}\alpha$  ( $\delta_{\text{H}}$  1.84)/ $\text{H-3}$ ,  $\text{H-8}$  ( $\delta_{\text{H}}$  1.36)/ $\text{H}_3\text{-18}$  ( $\delta_{\text{H}}$  0.72),  $\text{H-8}/\text{H}_3\text{-19}$  ( $\delta_{\text{H}}$  1.02),  $\text{H-9}/\text{H-12}$  ( $\delta_{\text{H}}$  3.46),  $\text{H-12}/\text{H-14}$  ( $\delta_{\text{H}}$  0.92),  $\text{H-14}/\text{H-17}$  ( $\delta_{\text{H}}$  1.44), and  $\text{H}_3\text{-18}/\text{H-20}$  ( $\delta_{\text{H}}$  1.77) (Figure 2). Thus, the hydroxyl groups at C-3 and C-12 should be positioned on the  $\beta$ -face according to modeling analysis [7]. The aforementioned findings clearly confirmed the structure of columnaristerol B (**1**).

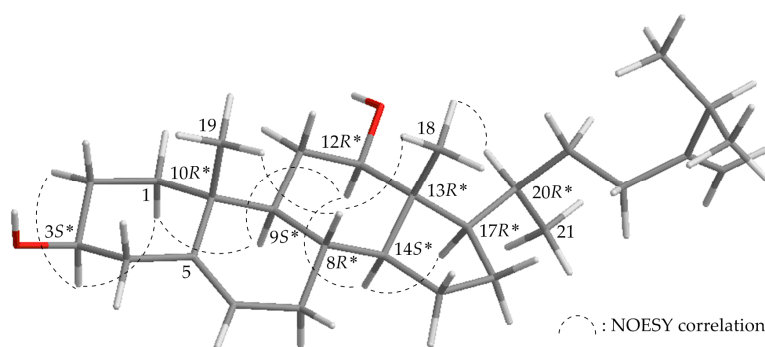


**Figure 2.** Computer-generated model of **1** using MM2 force field calculations and selected protons with key NOESY correlations. Red color: oxygen atom; gray color: hydrogen atom; black color: carbon atom; \*: relative configuration.

HRESIMS of new metabolite columnaristerol C (**2**) suggested a molecular formula of  $\text{C}_{28}\text{H}_{46}\text{O}_3$ , as analysis showed a signal at  $m/z$  453.33366 (calcd. for  $\text{C}_{28}\text{H}_{46}\text{O}_3 + \text{Na}$ , 453.33392); in addition, the presence of a hydroxyl group was determined, as the IR spectrum of **2** showed a band at  $\nu_{\text{max}}$  3331  $\text{cm}^{-1}$ . The existence of a tertiary methyl ( $\delta_{\text{H}}$  1.03), three secondary methyls ( $\delta_{\text{H}}$  1.04, 3H, d,  $J = 6.4$  Hz; 1.02,



6H, d,  $J = 6.8$  Hz), two oxymethines ( $\delta_{\text{H}}$  4.25, 1H, m; 3.53, 1H, m), and one oxymethylene ( $\delta_{\text{H}}$  4.00, 3.68,  $J_{\text{AB}} = 12.0$  Hz) were identified from the  $^1\text{H}$  NMR data, and the presence of a trisubstituted double bond was revealed by NMR data at  $\delta_{\text{H}}$  5.38 (1H, m), and  $\delta_{\text{C}}$  140.9 (C) and 121.2 (CH) (Table 2). Combined analysis of the molecular formula and the resonances of the  $^{13}\text{C}$  NMR and DEPT spectra revealed that **2** contained 4 methyls, 10  $\text{sp}^3$  methylenes (including 1 oxymethylene), 8  $\text{sp}^3$  methines (including 2 oxymethines), 2  $\text{sp}^3$  quaternary carbons, 1  $\text{sp}^2$  methylene, 1  $\text{sp}^2$  methine, and 2  $\text{sp}^2$  quaternary carbons. Comparison of the NMR chemical shift values of **2** with those of 24-methylenecholesterol (**5**) [5,6], as well as its HMBC cross-peaks from  $\text{H}_2$ -18 to C-12, C-13, C-14, and C-17, and  $^1\text{H}$ - $^1\text{H}$  COSY correlations between the oxymethine proton signal at  $\delta_{\text{H}}$  4.25 (H-16)/ $\delta_{\text{H}}$  2.42 and 1.52 ( $\text{H}_2$ -15) and  $\delta_{\text{H}}$  4.25 (H-16)/ $\delta_{\text{H}}$  1.20 (H-17), suggested that **2** may be a 16,18-dihydroxyl analogue of **5**. Finally, the structure of **2** was confirmed based on the NOESY correlations (Figure 3) observed between H-3/H-4 $\alpha$ , H-4 $\beta$ /H<sub>3</sub>-19, H-8/H<sub>2</sub>-18, H-8/H<sub>3</sub>-19, H-9/H-14, H-14/H-16, and H<sub>2</sub>-18/H-20.

**Table 2.**  $^1\text{H}$  (400 MHz,  $\text{CDCl}_3$ ) and  $^{13}\text{C}$  (100 MHz,  $\text{CDCl}_3$ ) NMR data and  $^1\text{H}$ - $^1\text{H}$  COSY and HMBC correlations for sterol **2**.

Position	$\delta_{\text{H}}$ ( $J$ in Hz)	$\delta_{\text{C}}$ , Multiple	$^1\text{H}$ - $^1\text{H}$ COSY	HMBC
1a/b	1.81 m, 1.01 m	37.2, $\text{CH}_2$	$\text{H}_2$ -2	C-5
2a/b	1.83 m, 1.48 m	31.6, $\text{CH}_2$	$\text{H}_2$ -1, H-3	n. o. <sup>a</sup>
3	3.53 m	71.7, CH	$\text{H}_2$ -2, $\text{H}_2$ -4	n. o.
4 $\alpha$ / $\beta$	2.32 m, 2.21 m	42.2, $\text{CH}_2$	H-3	C-3, C-5, C-6
5	-	140.9, C	-	-
6	5.38 m	121.2, CH	$\text{H}_2$ -7	C-4, C-7, C-8, C-10
7a/b	2.30 m, 1.69 m	31.0, $\text{CH}_2$	H-6, H-8	C-5, C-6
8	1.94 m	27.6, CH	$\text{H}_2$ -7, H-9, H-14	C-14
9	1.08 m	50.5, CH	H-8, $\text{H}_2$ -11	C-19
10	-	36.6, C	-	-
11	1.50 m	21.4, $\text{CH}_2$	H-9, $\text{H}_2$ -12	n. o.
12a/b	2.12 m, 1.17 m	38.9, $\text{CH}_2$	$\text{H}_2$ -11	C-18
13	-	46.4, C	-	-
14	1.14 m	60.4, CH	H-8, $\text{H}_2$ -15	C-8, C-9, C-12, C-13, C-16, C-17, C-18
15a/b	2.42 m, 1.50 m	41.8, $\text{CH}_2$	H-14, H-16	C-13, C-16, C-17
16	4.25 m	70.1, CH	$\text{H}_2$ -15, H-17	C-13, C-17
17	1.20 m	55.8, CH	H-16, H-20	C-13, C-15, C-18, C-20
18a/b	4.00 d (12.0), 3.68 d (12.0)	62.8, $\text{CH}_2$	-	C-12, C-13, C-14, C-17
19	1.03 s	19.4, $\text{CH}_3$	-	C-1, C-5, C-9, C-10
20	1.95 m	34.9, CH	H-17, H <sub>3</sub> -21, $\text{H}_2$ -22	C-22
21	1.04 d (6.4)	19.2, $\text{CH}_3$	H-20	C-17, C-20, C-22
22a/b	1.55 m, 1.17 m	34.9, $\text{CH}_2$	H-20, $\text{H}_2$ -23	n. o.
23a/b	2.10 m, 1.91 m	30.7, $\text{CH}_2$	$\text{H}_2$ -22	C-20, C-22, C-24, C-28
24	-	156.6, C	-	-
25	2.21 m	33.8, CH	H <sub>3</sub> -26, H <sub>3</sub> -27	C-23, C-24, C-26, C-27, C-28
26	1.02 d (6.8)	21.9, $\text{CH}_3$	H-25	C-24, C-27
27	1.02 d (6.8)	22.0, $\text{CH}_3$	H-25	C-24, C-26
28a/b	4.72 br s, 4.66 br s	106.0, $\text{CH}_2$	-	C-23, C-25

<sup>a</sup> n. o. = not observed.

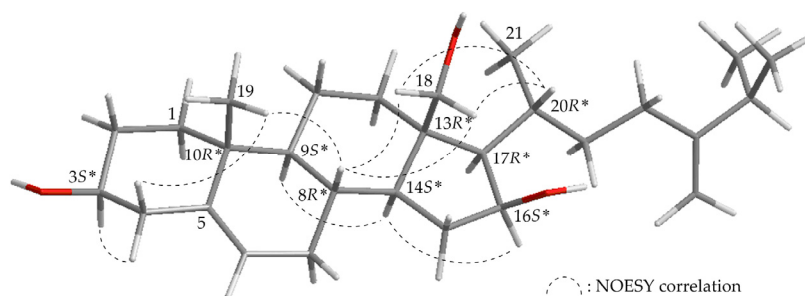


**Figure 3.** Computer-generated model of **2** using MM2 force field calculations and selected protons with key NOESY correlations. Red color: oxygen atom; gray color: hydrogen atom; black color: carbon atom; \*: relative configuration.

Sterols **3** and **4** were identified as 5,6-epoxylitosterol (5 $\beta$ ,6 $\beta$ -epoxyergost-24(28)-ene-3 $\beta$ ,19-diol) and litosterol (ergosta-5,24(28)-diene-3 $\beta$ ,19-diol), which had been previously isolated from the Okinawan soft coral *Litophyton viridis* [5]. To the best of our knowledge, this was the first time that these two marine-origin sterols had been obtained from *Nephthea columnaris*.

In vitro anti-inflammatory activity assays were performed using human neutrophils, and the results demonstrated that sterol **3** had inhibitory effects on the generation of superoxide anions and the release of elastase, with IC<sub>50</sub> values of 4.60 and 3.90  $\mu$ M, respectively, but sterol **4** displayed no anti-inflammatory effects (Table 3). Comparison with the structures and anti-inflammatory activities of sterols **3** and **4** implied that the presence of a 5 $\beta$ ,6 $\beta$ -epoxy group enhanced the activity.

**Table 3.** Inhibitory effects of sterols **1–4** on superoxide anion generation and elastase release by human neutrophils in response to fMet-Leu-Phe/Cytochalasin B.

Compound	Superoxide Anions	Elastase Release
	IC <sub>50</sub> ( $\mu$ M) <sup>a</sup>	IC <sub>50</sub> ( $\mu$ M)
<b>1</b>	>10	>10
<b>2</b>	>10	>10
<b>3</b>	4.60 $\pm$ 0.85	3.90 $\pm$ 0.88
<b>4</b>	>10	>10
LY294002 <sup>b</sup>	1.94 $\pm$ 0.81	4.44 $\pm$ 0.72

<sup>a</sup> Concentration necessary for 50% inhibition (IC<sub>50</sub>); results are presented as mean  $\pm$  SEM ( $n$  = 3). <sup>b</sup> LY294002 (2-morpholin-4-yl-8-phenylchromen-4-one) was used as the reference compound.

### 3. Experimental Section

#### 3.1. General Experimental Procedures

Column chromatography was carried out using silica gel (230–400 mesh size; Merck, Darmstadt, Germany). TLC was performed on plates precoated with Kieselgel 60 (with fluorescent indicator 254, 0.25-mm-thick; Merck), and the spots on the plates were visualized by spraying with 10% H<sub>2</sub>SO<sub>4</sub> solution followed by heating. Normal-phase HPLC (NP-HPLC) was performed using a HPLC system equipped with a Hitachi L-7110 pump (Hitachi, Tokyo, Japan) and an injection port (7725; Rheodyne, Rohnert Park, CA, USA). A semi-preparative normal-phase column (25 cm  $\times$  21.2 mm, 5  $\mu$ M, Ascentis Si, Cat.: 581515-U, Sigma-Aldrich, St. Louis, MO, USA) was employed. Reverse-phase HPLC (RP-HPLC) was performed using a system equipped with a Hitachi L-7100 pump, a photodiode array detector (Hitachi L-2455), an injection port (Rheodyne 7725) and a 250  $\times$  21.2 mm column (5  $\mu$ M, Luna RP-18e; Phenomenex Inc., Torrance, CA, USA) or a 250  $\times$  10.0 mm column (5  $\mu$ M; Ascentis C18 Cat.: 581343-U, Sigma-Aldrich). IR spectra were obtained using a spectrophotometer (Nicolet iS5 FT-IR; Thermo Scientific, Waltham, MA, USA). NMR spectra were recorded on a NMR spectrometer (Varian Mercury 400 MHz Plus system; Varian, Palo Alto, CA, USA) using the residual CHCl<sub>3</sub> signal ( $\delta$ <sub>H</sub> 7.26 ppm) and CDCl<sub>3</sub> signal ( $\delta$ <sub>C</sub> 77.1 ppm) as the internal standard for <sup>1</sup>H NMR and <sup>13</sup>C NMR, respectively. Coupling constants ( $J$ ) are presented in Hz. ESIMS and HRESIMS were recorded using a mass spectrometer (7 Tesla Solarix FTMS system; Bruker, Bremen, Germany). Melting points of the natural products were determined using a Fargo apparatus (Panchum Scientific, Kaohsiung, Taiwan), and the values were uncorrected. Optical rotation values were measured using a digital polarimeter (Jasco P-1010; Japan Spectroscopic, Tokyo, Japan).

#### 3.2. Animal Material

Specimens of the octocoral *N. columnaris* were collected by hand using scuba equipment off the coast of Southern Taiwan in February, 2012. The samples were stored in a –20 °C freezer immediately until extraction. A voucher specimen (NMMBA-TW-SC-12057) was deposited in the National Museum of Marine Biology and Aquarium, Taiwan [8].

### 3.3. Extraction and Isolation

Sliced bodies of *N. columnaris* (wet weight 800 g, dry weight 76.7 g) were extracted with a mixture of methanol (MeOH) and dichloromethane (DCM) (*v:v* = 1:1). The extract (25.1 g) was partitioned between ethyl acetate (EtOAc) and H<sub>2</sub>O. The EtOAc layer (7.35 g) was separated on silica gel and eluted with *n*-hexane/EtOAc (stepwise, *v:v* = 100:1 to 100% EtOAc) to yield 12 subfractions A–L. Fraction G was separated by silica gel column chromatography and then eluted with *n*-hexane/acetone (stepwise, *v:v* = 20:1 to 100% acetone) to afford 10 subfractions G1–G10. Fraction G5 was purified by NP-HPLC using a mixture of *n*-hexane/acetone (*v:v* = 3:1) to afford ten subfractions G5A–G5J. Fraction G5E was repurified by RP-HPLC using a mixture of acetonitrile/H<sub>2</sub>O (*v:v* = 80:20) to yield four subfractions G5E1–G5E4. Fraction G5E3 was repurified by RP-HPLC using a mixture of MeOH/H<sub>2</sub>O (*v:v* = 95:5 at a flow rate of 4.0 mL/min) to yield **1** (0.8 mg). Fraction I was separated by silica gel column chromatography and then eluted with *n*-hexane/EtOAc (stepwise, *v:v* = 100:1 to 100% EtOAc) to afford 15 subfractions I1–I15. Fraction I13 was purified by NP-HPLC using a mixture of *n*-hexane/acetone/DCM (*v:v:v* = 3:1:1) to afford 11 subfractions I13A–I13K. Fraction I13G was repurified by RP-HPLC using a mixture of MeOH/H<sub>2</sub>O/tetrahydrofuran (*v:v:v* = 90:9.5:0.5 at a flow rate of 2.0 mL/min) to yield **2** (0.7 mg). Fraction I13H was repurified by RP-HPLC using a mixture of MeOH/H<sub>2</sub>O (*v:v* = 80:20) to afford seven subfractions I13H1–I13H7. Fraction I13H7 was further separated by NP-HPLC using a mixture of *n*-hexane/EtOAc (*v:v* = 2:1) to afford three subfractions I13H7A–I13H7C. Fraction I13H7C was repurified by RP-HPLC using a mixture of MeOH/H<sub>2</sub>O (*v:v* = 95:5 at a flow rate of 4.0 mL/min) to yield **3** (1.3 mg) and **4** (5.1 mg), respectively.

Columnaristerol B (**1**): white powder; mp 143–144 °C;  $\alpha_D^{25}$  −200 (*c* 0.53, CHCl<sub>3</sub>); IR (neat)  $\nu_{\max}$  3386 cm<sup>−1</sup>, 1643 cm<sup>−1</sup>; <sup>1</sup>H (400 MHz, CDCl<sub>3</sub>) and <sup>13</sup>C (100 MHz, CDCl<sub>3</sub>) NMR data (see Table 1); ESIMS: *m/z* 437 [M + Na]<sup>+</sup>; HRESIMS: *m/z* 437.33918 (calcd. for C<sub>28</sub>H<sub>46</sub>O<sub>2</sub> + Na, 437.33900).

Columnaristerol C (**2**): white powder; mp 140 °C;  $\alpha_D^{25}$  +31 (*c* 0.22, CHCl<sub>3</sub>); IR (neat)  $\nu_{\max}$  3331 cm<sup>−1</sup>, 1640 cm<sup>−1</sup>; <sup>1</sup>H (400 MHz, CDCl<sub>3</sub>) and <sup>13</sup>C (100 MHz, CDCl<sub>3</sub>) NMR data (see Table 2); ESIMS: *m/z* 453 [M + Na]<sup>+</sup>; HRESIMS: *m/z* 453.33366 (calcd. for C<sub>28</sub>H<sub>46</sub>O<sub>3</sub> + Na, 453.33392).

5,6-Epoxytosterol (**3**): white powder; mp 160–161 °C (ref. [5], mp 179–183 °C);  $\alpha_D^{25}$  +17 (*c* 0.07, CHCl<sub>3</sub>) (ref. [5], [ $\alpha$ ] D +3.8 (*c* 0.26, CHCl<sub>3</sub>)); IR (neat)  $\nu_{\max}$  3386 cm<sup>−1</sup>, 1641 cm<sup>−1</sup>; <sup>1</sup>H (CDCl<sub>3</sub>, 400 MHz) and <sup>13</sup>C (CDCl<sub>3</sub>, 100 MHz) NMR data were found to be in complete agreement with previous reports [5]; ESIMS *m/z* 453 [M + Na]<sup>+</sup>.

Litosterol (**4**): white powder; mp 147–149 °C (ref. [5], mp 147.5–150 °C);  $\alpha_D^{25}$  −31 (*c* 0.26, CHCl<sub>3</sub>) (ref. [5], [ $\alpha$ ] D −25.8 (*c* 0.24, CHCl<sub>3</sub>)); IR (neat)  $\nu_{\max}$  3419 cm<sup>−1</sup>, 1635 cm<sup>−1</sup>; <sup>1</sup>H (CDCl<sub>3</sub>, 400 MHz) and <sup>13</sup>C (CDCl<sub>3</sub>, 100 MHz) NMR data were found to be in complete agreement with previous reports [5]; ESIMS *m/z* 437 [M + Na]<sup>+</sup>.

### 3.4. Molecular Mechanics Calculations

Implementation of the MM2 force field [7] in ChemBio 3D Ultra software from Cambridge Soft Corporation (ver. 12.0, Cambridge, MA, USA) was used to create molecular models.

### 3.5. Generation of Superoxide Anions and Release of Elastase by Human Neutrophils

Human neutrophils were obtained from whole blood using the method of dextran sedimentation and Ficoll centrifugation. Measurements of superoxide anion generation and the release of elastase by neutrophils were carried out according to previously described procedures [9,10]. Briefly, superoxide anion production was assayed by monitoring the superoxide dismutase-inhibitable reduction of ferricytochrome *c*. Elastase release experiments were performed using MeO–Suc–Ala–Ala–Pro–Valp–nitroanilide as the elastase substrate.

#### 4. Conclusions

In the present study, our further investigation of natural substances obtained by extraction of *N. columnaris* led to the isolation of two new sterols, columnaristerols B (1) and C (2), as well as two known sterols, 5,6-epoxylitosterol (3) and litosterol (4) [5]. Our results demonstrated that 3 possessed potential anti-inflammatory activity in a human neutrophil model. The findings suggested that continued investigation of interesting secondary metabolites together with potentially useful bioactive substances from *N. columnaris* is worthwhile to inform potential new drug development.

**Supplementary Materials:** HRESIMS, and 1D ( $^1\text{H}$  NMR,  $^{13}\text{C}$  NMR, and DEPT spectra) and 2D (HSQC,  $^1\text{H}$ – $^1\text{H}$  COSY, HMBC, and NOESY spectra) NMR spectra of new compounds 1 and 2 are available online at [www.mdpi.com/1660-3397/15/7/212/s1](http://www.mdpi.com/1660-3397/15/7/212/s1).

**Acknowledgments:** This research was supported by grants from the National Museum of Marine Biology and Aquarium; the National Dong Hwa University; the National Sun Yat-sen University; and the National Research Program for Biopharmaceuticals, Ministry of Science and Technology (Grant Nos: MOST 105-2325-B-291-001, 104-2325-B-291-001, 103-2325-B-291-001, and 104-2320-B-291-001-MY3) awarded to Ping-Jyun Sung.

**Author Contributions:** Tsong-Long Hwang and Ping-Jyun Sung designed the whole experiment and contributed to manuscript preparation. Ta-Yuan Whuang and Hong-Chieh Tsai researched data. Yin-Di Su analyzed the data and performed data acquisition.

**Conflicts of Interest:** The authors declare no conflicts of interest.

#### References

1. Hsiao, T.-H.; Sung, C.-S.; Lan, Y.-H.; Wang, Y.-C.; Lu, M.-C.; Wen, Z.-H.; Wu, Y.-C.; Sung, P.-J. New anti-inflammatory cembranes from the cultured soft coral *Nephthea columnaris*. *Mar. Drugs* **2015**, *13*, 3443–3453. [CrossRef] [PubMed]
2. Hsiao, T.-H.; Cheng, C.-H.; Wu, T.-Y.; Lu, M.-C.; Chen, W.-F.; Wen, Z.-H.; Dai, C.-F.; Wu, Y.-C.; Sung, P.-J. New cembranoid diterpenes from the cultured *Nephthea columnaris*. *Molecules* **2015**, *20*, 13205–13215. [CrossRef] [PubMed]
3. Whuang, T.-Y.; Tsai, W.-C.; Chen, N.-F.; Chen, Z.-C.; Tsui, K.-H.; Wen, Z.-H.; Su, Y.-D.; Chang, Y.-C.; Chen, Y.-H.; Lu, M.-C.; et al. Columnaristerol A, a novel 19-norsterol from the Formosan octocoral *Nephthea columnaris*. *Bioorg. Med. Chem. Lett.* **2016**, *26*, 4966–4969. [CrossRef] [PubMed]
4. Lin, C.-C.; Whuang, T.-Y.; Su, J.-H.; Hwang, T.-L.; Wu, Y.-C.; Sung, P.-J. 4 $\alpha$ -Methylergosta-22(E), 24(28)-dien-3 $\beta$ -ol, a new marine sterol from the octocoral *Nephthea columnaris*. *Nat. Prod. Commun.* **2017**, *12*, 345–346.
5. Iguchi, K.; Saitoh, S.; Yamada, Y. Novel 19-oxygenated sterols from the Okinawan soft coral *Litophyton viridis*. *Chem. Pharm. Bull.* **1989**, *37*, 2553–2554. [CrossRef]
6. McInnes, A.G.; Walter, J.A.; Wright, J.L.C.  $^{13}\text{C}$  NMR spectra of  $\Delta^{24(28)}$  phytosterols. *Org. Magn. Reson.* **1980**, *13*, 302–303. [CrossRef]
7. Allinger, N.L. Conformational analysis. 130. MM2. A hydrocarbon force field utilizing  $V_1$  and  $V_2$  torsional terms. *J. Am. Chem. Soc.* **1977**, *99*, 8127–8134. [CrossRef]
8. Van Ofwegen, L.P. Annotated check list of New Caledonian soft corals. In *Compendium of Marine Species of New Caledonia*, 2nd ed.; Payri, C.E., Richer de Forges, B., Eds.; Institut de Recherche Pour le Développement: Nouméa, New Caledonia, France, 2007; pp. 139–144.
9. Yang, S.-C.; Chung, P.-J.; Ho, C.-M.; Kuo, C.-Y.; Hung, M.-F.; Huang, Y.-T.; Chang, W.-Y.; Chang, Y.-W.; Chan, K.-H.; Hwang, T.-L. Propofol inhibits superoxide production, elastase release, and chemotaxis in formyl peptide-activated human neutrophils by blocking formyl peptide receptor 1. *J. Immunol.* **2013**, *190*, 6511–6519. [CrossRef] [PubMed]
10. Yu, H.-P.; Hsieh, P.-W.; Chang, Y.-J.; Chung, P.-J.; Kuo, L.-M.; Hwang, T.-L. 2-(2-Fluorobenzamido) benzoate ethyl ester (EFB-1) inhibits superoxide production by human neutrophils and attenuates hemorrhagic shock-induced organ dysfunction in rats. *Free Radic. Biol. Med.* **2011**, *50*, 1737–1748. [CrossRef] [PubMed]



© 2017 by the authors. Licensee MDPI, Basel, Switzerland. This article is an open access article distributed under the terms and conditions of the Creative Commons Attribution (CC BY) license (<http://creativecommons.org/licenses/by/4.0/>).



***Psychosomatic Medicine***

Author's Accepted Manuscript

**Article Title:** Risk of epilepsy in individuals with posttraumatic stress disorder: a nationwide longitudinal study

**Authors:** Yu-Hsiung Chen, Han-Ting Wei, Ya-Mei Bai, Ju-Wei Hsu, Kai-Lin Huang, Tung-Ping Su, Cheng-Ta Li, Wei-Chen Lin, Yi-Hui Wu, Tai-Long Pan, Tzeng-Ji Chen, Shih-Jen Tsai, Mu-Hong Chen

**DOI:** 10.1097/PSY.0000000000000463

**Received Date:** May 06, 2016

**Revised Date:** January 01, 2017

This manuscript has been accepted by the editors of *Psychosomatic Medicine*, but it has not yet been copy edited; information within these pages is therefore subject to change. During the copy-editing and production phases, language usage and any textual errors will be corrected, and pages will be composed into their final format.

Please visit the journal's website ([www.psychosomaticmedicine.org](http://www.psychosomaticmedicine.org)) to check for a final version of the article.

When citing this article, please use the following: *Psychosomatic Medicine* (in press) and include the article's digital object identifier (DOI).



# **Risk of Epilepsy in Individuals With Posttraumatic Stress Disorder: A Nationwide Longitudinal Study**

Yu-Hsiung Chen, M.D.<sup>a, #</sup>, Han-Ting Wei, M.D.<sup>a, j, #</sup>, Ya-Mei Bai, M.D., PH.D.<sup>a, b</sup>, Ju-Wei Hsu, M.D.<sup>a, b</sup>,  
Kai-Lin Huang, M.D.<sup>a, b</sup>, Tung-Ping Su, M.D.<sup>a, b</sup>, Cheng-Ta Li, M.D., Ph.D.<sup>a, b</sup>, Wei-Chen Lin, M.D.<sup>a, b</sup>,  
Yi-Hui Wu, M.D.<sup>e, f</sup>, Tai-Long Pan, PH.D.<sup>g, h, i</sup>, Tzeng-Ji Chen, M.D., PH.D.<sup>c, d</sup>, Shih-Jen Tsai, M.D.<sup>a, b, \*</sup>,  
Mu-Hong Chen, M.D.<sup>a, b, \*</sup>

<sup>a</sup>. Department of Psychiatry, Taipei Veterans General Hospital, Taipei, Taiwan

<sup>b</sup>. Division of Psychiatry, School of Medicine, National Yang-Ming University, Taipei, Taiwan

<sup>c</sup>. Department of Family Medicine, Taipei Veterans General Hospital, Taipei, Taiwan

<sup>d</sup>. Institute of Hospital and Health Care Administration, National Yang-Ming University, Taipei, Taiwan

<sup>e</sup>. Department of Neurology, Taipei Veterans General Hospital, Taipei, Taiwan

<sup>f</sup>. Center for Geriatrics and Gerontology, Taipei Veterans General Hospital, Taipei, Taiwan.

<sup>g</sup>. School of Traditional Chinese Medicine, Chang Gung University, Taoyuan, Taiwan

<sup>h</sup>. Research Center for Chinese Herbal Medicine and Research Center for Food and Cosmetic Safety, College

of Human Ecology, Chang Gung University of Science and Technology, Taoyuan, Taiwan

<sup>i</sup>. Liver Research Center, Chang Gung Memorial Hospital, Taoyuan, Taiwan.

<sup>j</sup>. Division of Psychiatry, Kunming Branch, Taipei City Hospital

#: Equally contributed

**Short title:** PTSD and Epilepsy.

### **Correspondence**

Mu-Hong Chen, M.D.

E-mail: kremer7119@gmail.com

Department of Psychiatry, Taipei Veterans General Hospital, No. 201, Shih-Pai Road, Sec. 2, 11217, Taipei, Taiwan.

Tel : 886 -2- 28344012. Fax : 886 -2- 28344012.

Shih-Jen Tsai, M.D.

Email: tsai610913@gmail.com

Department of Psychiatry, Taipei Veterans General Hospital, No. 201, Shih-Pai Road, Sec. 2, 11217, Taipei, Taiwan.

Tel : 886 -2- 28344012. Fax : 886 -2- 28344012.

**Conflict of Interest:** No conflict of interest.

**Funding Source:** The study was supported by grant from Taipei Veterans General Hospital (V103E10-001, V104E10-002, V105E10-001-MY2-1, V105A-049). The funding source had no role in any process of our study.

**Financial Disclosure:** All authors have no financial relationships relevant to this article to disclose.

## Abstract

**Objective:** Several cross-sectional studies reported a relationship between post-traumatic stress disorder (PTSD) and epilepsy. However, the temporal association between PTSD and epilepsy has rarely been investigated. We hypothesized that the risk of developing epilepsy later in life would be higher in patients with PTSD than in those without PTSD. **Methods:** Using the Taiwan National Health Insurance Research Database, 6425 individuals with PTSD and 24,980 age-/sex-matched controls were enrolled between 2002 and 2009 in our study, and followed up to the end of 2011. Those who developed epilepsy during the follow-up period were identified. **Results:** Individuals with PTSD had a higher incidence of developing epilepsy (2.65 vs. 0.33 per 1000 person-years,  $p < 0.001$ ), with an earlier onset of epilepsy ( $37.53 \pm 15.80$  vs.  $48.11 \pm 23.97$  years,  $p = 0.002$ ), than did the controls. Individuals with PTSD had an elevated risk of developing epilepsy (hazard ratio [HR]: 3.72, 95% confidence interval [CI]: 2.27–6.11) during the follow-up after adjustment for demographic data and medical and psychiatric comorbidities. Sensitivity analyses after excluding the observation in the first year (HR: 2.53, 95% CI: 1.44–4.47) and the first 3 years (HR: 2.14, 95% CI: 1.15–4.01) revealed consistent results. **Conclusions:** These results supported a temporal association between PTSD and the development of epilepsy. Further studies are warranted to investigate the underlying pathophysiological pathways that explain the longitudinal association of PTSD with subsequent epilepsy.

**Keywords:** PTSD; Epilepsy; Temporal association.

**Abbreviation:** PTSD: post-traumatic stress disorder; NHIRD: National Health Insurance Research Database; NCS-R: National Comorbidity Survey Replication; HR: hazard ratio; CI: confidence interval; IL: interleukin.

ACCEPTED

Posttraumatic stress disorder (PTSD) is a severe and disabling mental disorder that occurs in individuals who have experienced traumatic events such as combat, severe physical or sexual assault, serious accidents, torture, the sudden unexpected death of a loved one, or natural disasters (1, 2). The WHO World Mental Health surveys on the global burden of mental disorders in 28 countries throughout the world reported that the prevalence of PTSD varied by countries, and ranged between a low of 0.3% in China and 6.1% in New Zealand (3). In Taiwan, a 3-year follow-up study surveying residents who had experienced a severe earthquake reported that the prevalence of PTSD was 6.5% at 3 years after the earthquake (4). Patients with PTSD were at an increased risk of suicide, mental and physical comorbidities, physical illnesses, and inability to work (1, 2, 4, 5).

The association between psychiatric disorders and epilepsy has been proposed and studied in several decades (6). A review article concluded that the most common psychiatric disorders among patients with epilepsy included mood disorders (24%–75%), anxiety disorders (10%–25%), psychotic disorders (2%–7%), and personality disorders (1%–2%) (6). However, the association between PTSD and epilepsy has been investigated less frequently, and only a few studies have suggested that a comorbid relationship exists between psychological trauma and PTSD and epilepsy (7, 8). For instance, Kessler et al analyzed epilepsy-related mental and physical comorbidities in the National Comorbidity Survey Replication (NCS-R) and observed that the risk of comorbid PTSD was higher in patients with epilepsy than in those without epilepsy (odds ratio [OR]: 2.0, 95% confidence interval [CI]: 1.2–3.3) (7). Zeber et al assessed personal functioning in patients with epilepsy only and in patients with both epilepsy and psychiatric conditions and reported that PTSD caused the greatest decrease in self-reported health conditions (9). Sledjeski et al



examined the association among the number of lifetime traumas, PTSD, and self-reported chronic mental conditions and reported a graded relationship among trauma exposure, PTSD, and epilepsy; moreover, patients with PTSD had the highest risk of epilepsy (OR: 3.8, 95% CI: 1.1–13.8), whereas people without trauma experiences had the lowest risk of epilepsy (8). However, these studies have several limitations, such as the self-reported assessment of epilepsy instead of a physician-given diagnosis of epilepsy, and they used a cross-sectional study design instead of the longitudinal follow-up study design, which prevented them from clarifying the temporal association between PTSD and epilepsy. In addition, several neurobiological pathophysiologies were proposed to suggest a potential association between psychological trauma, PTSD, and epilepsy. The kindling phenomenon in PTSD with the processes of trauma-induced neural sensitization, repetitive stimulation of subconvulsive electrical pulses, and final full-blown epileptic attacks may contribute to the PTSD-related epileptogenesis (10-12).

In the current study, we included a large sample from the Taiwan National Health Insurance Research Database (NHIRD) and used a longitudinal study design to investigate the temporal association between PTSD and epilepsy. We hypothesized that the risk of developing epilepsy later in life would be higher in patients with PTSD than in those without PTSD.

## Methods

**Data source.** Taiwan's National Health Insurance is a mandatory universal health insurance program that was inaugurated in 1995 and covers up to 99% of the country's 23 million residents. The NHIRD is administered by the National Health Research Institute and provides comprehensive patient information, such as demographic data, clinical visit dates, and disease diagnoses. The National Health Insurance

Institute audits and releases the NHIRD for use in health service studies. All identities are encrypted to ensure patient privacy. The diagnostic codes used are based on the International Classification of Diseases, Ninth Revision, Clinical Modification (ICD-9-CM). The NHIRD has been used extensively in numerous epidemiologic studies in Taiwan (13-17).

**Inclusion criteria for patients with PTSD and the control group.** Individuals who had received a diagnosis of PTSD (ICD-9-CM code: 309.81) given by board-certificated psychiatrists on the basis of clinical judgment and psychiatric interview between January 1, 2002 and December 31, 2009 and who had no history of epilepsy (ICD-9-CM code: 345) before enrollment were included as the PTSD cohort. The time of PTSD diagnosis was defined as the time of enrollment. The age-, sex-, and time of enrollment-matched (1:4) control cohort was randomly identified after eliminating the study subjects, those who had been given a diagnosis of PTSD at any time, and those with epilepsy before enrollment. Diagnosis of epilepsy (ICD-9-CM code: 345) given by neurologists, emergency room physicians, internal medicine physicians, or pediatricians based on their clinical judgment or electroencephalography examination were identified during the follow-up (from enrollment to December 31, 2011, or to death). Epilepsy-related medical comorbidities were assessed, including cerebrovascular diseases, meningitis and encephalitis, and head injury (18-20). Depressive disorder was also identified as a confounding factor because of a high comorbidity of PTSD and depression (20). Level of urbanization (level 1 to level 5; level 1: most urbanized region; level 5: least urbanized region) was also assessed for our study. This study was approved by Institutional Review Board of Taipei Veterans General Hospital, Taiwan.

**Statistical analysis.** For between-group comparisons, the independent t test was used for continuous variables and Pearson's  $X^2$  test for nominal variables, where appropriate. The Cox regression model was used to investigate the hazard ratio (HR) with a 95% CI of epilepsy between patients with PTSD and control group after adjustment for demographic data (age, sex, level of urbanization, and income) and medical (cerebrovascular diseases, meningitis and encephalitis, and head injury) and psychiatric (depressive disorder) comorbidities. The log-minus-log plot was evaluated, supporting the appropriate and reasonable use of Cox regression models in our study. Sensitivity analyses were performed to investigate the above associations after excluding the first year and the first 3-years of observation. We also performed sub-analyses of the risk of epilepsy with PTSD stratified by age group: children (<18 years), adults (18–64 years), and the elderly ( $\geq 65$  years), because age was an index of brain development and degeneration so we can further investigate the PTSD condition in different age group (children, adults, and the elderly) with the subsequent risk of epilepsy. In addition, to reduce the potential confounding risks from medical illnesses, the analysis excluding head injury, cardiovascular diseases, and meningitis and encephalitis was performed. A two-tailed *P*-value of less than 0.05 was considered statistically significant. All data processing and statistical analyses were performed with Statistical Package for Social Science (SPSS) version 17 software (SPSS Inc.) and Statistical Analysis Software (SAS) version 9.1 (SAS Institute, Cary, NC).

## Results

In all, 6425 patients with PTSD and 24,980 age-/sex-matched controls were included in our study, with a mean age of  $34.89 \pm 15.06$  years; most participants (77%) were female. During the follow-up period, patients with PTSD had a higher incidence of developing epilepsy (2.65 vs. 0.33 per 1000 person-years,  $p <$

0.001), with an earlier onset of epilepsy ( $37.53 \pm 15.80$  vs.  $48.11 \pm 23.97$  years,  $p = 0.002$ ) and a shorter duration between enrollment and diagnosis of epilepsy ( $2.57 \pm 2.19$  vs.  $4.37 \pm 2.43$  years,  $p < 0.001$ ), than did the controls (Table 1). Regarding the types of epilepsy, 87% in the PTSD cohort and 76% in the control cohort were the generalized type, and 13% and 24% were the localized type (Table 1). Patients with PTSD had a higher prevalence of depressive disorder (67.0% vs. 4.1%,  $p < 0.001$ ), cerebrovascular diseases (5.5% vs. 2.6%,  $p < 0.001$ ) and head injury (6.8% vs. 1.0%,  $p < 0.001$ ) than did the controls (Table 1). In addition, patients with PTSD resided in more rural area ( $p < 0.001$ ) and had a lower income ( $p < 0.001$ ) (Table 1).

Kaplan-Meier survival analysis with a log-rank test revealed a significant association between PTSD and subsequent risk of epilepsy ( $p < 0.001$ ) (Fig.1). Cox regression model with an adjustment of demographic data and medical and psychiatric comorbidities found that patients with PTSD had an increased risk of developing epilepsy (HR: 3.72, 95% CI: 2.27–6.11) during the follow-up compared with those without PTSD (Table 2). Age was not significantly related to the risk of subsequent epilepsy (HR: 1.01, 95% CI: 0.99–1.02,  $p = 0.388$ ). Regarding the types of epilepsy, PTSD was associated with an increased risk of generalized type of epilepsy (HR: 4.11, 95% CI: 2.38–7.12) (Table 3). A trend association between PTSD and localized type of epilepsy (HR: 2.57, 95% CI: 0.80–8.20) was also noted (Table 3). Sensitivity analyses after excluding the observation in the first year (HR: 2.53, 95% CI: 1.44–4.47) and the first 3 years (HR: 2.14, 95% CI: 1.15–4.01) also revealed consistent results (Table 4). The analysis excluding head injury, cardiovascular diseases, and meningitis and encephalitis also confirmed the consistent finding that PTSD was an independent risk factor for the subsequent risk of epilepsy (HR: 4.83, 95% CI: 2.64–8.84). Furthermore, in analyses stratified by age group, children aged younger than 18 years (HR: 4.53, 95% CI:

1.28–16.03) and adults aged between 18 and 64 years (HR: 4.96, 95% CI: 2.75–8.93), but not the elderly aged 65 years and more (HR: 0.60, 95% CI: 0.15–2.34), with PTSD were more likely to develop epilepsy later in life (Table 2). In addition, depressive disorder (HR: 1.76, 95% CI: 1.11–2.79), cerebrovascular disease (HR: 2.44, 95% CI: 1.47–4.04), head injury (HR: 4.17, 95% CI: 2.67–6.52), and meningitis and encephalitis (HR: 5.81, 95% CI: 2.36–14.34) were associated with an increased risk of developing epilepsy (Table 2).

## Discussion

Our study is the first longitudinal study investigating the temporal association between PTSD and epilepsy, especially generalized type of epilepsy. Our results support our hypothesis that the risk of developing epilepsy later in life is higher in patients with PTSD, particularly children and adults, than in those without PTSD. In addition, the age of epilepsy onset was significantly younger in patients with PTSD than in the control group.

In the clinical aspect, several studies have suggested that a relationship exists between PTSD and epilepsy (7, 8, 21–23). Harriet et al. surveyed 35 patients with intractable epilepsy and reported that the lifetime prevalence of PTSD in those patients was significantly higher than the population prevalence of PTSD (51.4% vs. 6%) (22). Using the NCS-R data, two studies reported that the prevalence of PTSD was higher in patients with epilepsy than in those without epilepsy (16.0% vs. 6.7%,  $p < 0.001$ ) and that patients with PTSD were more prone to receiving an epilepsy diagnosis than those without PTSD were (4.4% vs. 0.8%,  $p < 0.001$ ) (7, 8). Furthermore, Sledjeski et al. suggested that a dose-dependent relationship exists



between trauma experience (OR: 2.0, 95% CI: 0.7–6.0) and PTSD (OR: 3.8, 95% CI: 1.1–13.8) and epilepsy risk; furthermore, they demonstrated that the relationship between PTSD and epilepsy can be explained by the number of lifetime trauma experiences when their analysis was performed using a subset of people with trauma experiences (8). Shibahara et al. assessed patients with newly diagnosed neurological diseases after the Great East Japan Earthquake in 2011 and reported that the number of patients with epilepsy was significantly higher during the 8-week period after the earthquake than during the same periods in 2008, 2009, and 2010 ( $p = 0.0062$ ) (24), indicating an increased risk of epilepsy following a life-threatening natural disaster (24). In our study, only children and adults, but not elderly people aged  $\geq 65$  years, with PTSD had an increased risk of epilepsy during the follow-up period in our study. The negative association of PTSD with epilepsy in this elderly population may be due to the small sample size and confounding effects of medical and psychiatric comorbidities, such as depression and head injury. In addition, previous studies have suggested that psychiatric comorbidities could exacerbate the epilepsy itself and also reported that anti-epileptic medications had some behavioral and cognitive influences (6, 25). Further studies would be necessary to elucidate whether adequate treatment for PTSD may reduce the risk of subsequent epilepsy and alleviate the clinical course of epilepsy, and how to choose appropriate anti-epileptic medications for the comorbid condition.

We proposed several mechanisms to explain the temporal association between PTSD and the subsequent risk of epilepsy. First, increasing evidence has suggested that PTSD-related anatomical and functional brain changes include multiple brain regions involved in emotion, fear processing, and memory, such as the hippocampus, amygdala, prefrontal cortex, anterior cingulate gyrus, orbitofrontal cortex, and

locus coeruleus (12, 26). Grillon et al. reported several pathophysiologies of PTSD, including the kindling-like process, fear conditioning, and sensitization (27). Regarding the kindling phenomenon in PTSD, the process is initiated by trauma-induced neural sensitization and followed by the repetitive stimulation of subconvulsive electrical pulses (10-12), which is subsequently accompanied by anatomical and functional changes in the limbic system and other related brain regions (10). The trauma causes anatomical and functional changes in the brain, followed by repetitive subthreshold stimulations, and full-blown seizures finally evolve (12, 28). In addition, Grillon et al. suggested that the repetitive activation of conditioned fear memories, a core symptom of PTSD, contributed to this kindling-like process (27). Our results may support the hypothesis that, during the follow-up period, the risk of epilepsy is higher in patients with PTSD than in those without PTSD, and that the average duration between PTSD and epilepsy development is approximately 2.5 years, indicating that the repetitive stimulation of subconvulsive electrical pulses took time to develop into a full-blown seizure attack after an initial severe trauma. Second, the altered neuroimmunological system and dysregulated proinflammatory cytokine secretions from PTSD may explain the temporal association between PTSD and epilepsy. Previous studies have reported that the levels of proinflammatory cytokines, including tumor necrosis factor- $\alpha$ , interleukin (IL)-6, and IL-1 $\beta$ , are higher in patients with PTSD than in controls and these levels correlated positively with the duration of PTSD symptoms (29, 30). Gill et al. reported that the higher level of IL-6 following a trauma was associated with the risk of PTSD and resulted in a subsequent vicious cycle of excessive neuroinflammation and injured neuron cells (31, 32). Vezzani et al. demonstrated that the overexpression of IL-6 in the brain of transgenic mice was related to the occurrence of sporadic spontaneous seizures (33). Collectively, this evidence suggests that PTSD-related chronic neuroinflammation and neuronal damage may increase the susceptibility

to epileptogenesis. In addition, Theoharides et al. suggested treating neuroinflammation to alleviate epilepsy (34). However, additional studies are required to investigate these mechanisms and elucidate the definite underlying mechanisms connecting PTSD or a broader spectrum of psychological trauma exposure to epilepsy.

In addition, compatible with the findings of previous studies, we observed that depressive disorder, cerebrovascular disease, head injury, and meningitis and encephalitis were associated with an increased risk of epilepsy. For instance, Kanner et al. reported that patients with depressive disorder had an increased risk of developing epilepsy, and further found that depression comorbidity would worsen the treatment response to anticonvulsants and epilepsy surgery (35). Camilo et al. reported that the overall rate of postischemic stroke epilepsy was approximately 2%–4% and that patients with early postischemic seizures were nearly 16 times (95% CI: 2.8–21.7) more likely to develop epilepsy than were those without early seizures (36, 37). Annegers et al. reported that moderate and severe traumatic head injury increased the risk of epilepsy by approximately 3-fold (HR: 2.9, 95% CI: 1.9–4.1) and 17-fold (HR: 17.0, 95% CI: 12.3–23.6), respectively (38). A population-based cohort study reported that the 20-year risk of seizures was higher in patients with bacterial meningitis or viral encephalitis (2.4%–22%) than in the general population (39).

Finally, we would like to discuss the sex composition of PTSD patients in our study. In the US, women were approximately twice as likely to be diagnosed with PTSD as men, but the female to male ratio of PTSD prevalence in our data was closer to 3 to 1. Previous studies investigating the PTSD prevalence among people after catastrophic typhoon (71.4% vs. 28.6%) or among people after severe earthquake (71.5% vs. 28.5%) in

Taiwan also supported this higher female to male ratio (40, 41). In the US, the war-related trauma may be related to the higher prevalence of PTSD in men, resulting in a lower female to male ratio of PTSD prevalence. However, the prevalence of PTSD indeed varied by races, countries, and sex. Further studies would be necessary to investigate the reason why the female to male ratio in Taiwan was slightly higher than that in US.

Our study has several limitations that should be addressed. First, the incidence of epilepsy may be underestimated because only patients who sought medical assistance were included in our study. Moreover, the possibility of non-neurological seizures may exist in clinical practice. However, the diagnosis of epilepsy was given by board-certified physicians, yielding improved diagnostic validity. Second, a significant association between PTSD and generalized type of epilepsy, but only a trend association between PTSD and localized type of epilepsy, was noted in our study. The results may prompt further investigation to clarify the definite association between PTSD and different types of epilepsy and to investigate the underlying mechanisms. Third, PTSD medications were not analyzed in our study because analyzing them during such a long follow-up period and adjusting for them in the regression model was difficult. It is possible that PTSD medications may have a role in the risk of subsequent epilepsy. Additional studies would be required to evaluate the role of PTSD medications in the development of epilepsy. Fourth, our study was a longitudinal follow-up study based on the registered database in Taiwan. We investigated the temporal associations after all data were collected for a defined period. A prospective study would be required to validate our finding in the future. Fifth, our study suggested a temporal association between PTSD and epilepsy in the Taiwanese population. This finding may be not directly generalized to other populations

worldwide. Further studies in other countries or in other ethnicities would be required to confirm our finding.

Sixth, certain information, including details of traumatic events, family history, personal lifestyle, PTSD severity, and environmental factors, is not available in the NIHRD. Without this information, we were unable to examine their influence.

In conclusion, the risk of developing epilepsy later in life is higher in patients with PTSD, than in those without PTSD after adjustment for demographic data and medical comorbidities. Additional studies are required to investigate the definite pathophysiological mechanisms underlying the association between PTSD and the subsequent risk of epilepsy, and to clarify whether prompt intervention for PTSD can decrease the risk of epilepsy.

### **Acknowledgement**

We thank Mr I-Fan Hu for his friendship and support.

### **Author Contributions**

Dr Mu-Hong Chen, Dr Yu-Hsiung Chen, Dr Han-Ting Wei and Dr Shih-Jen Tsai designed the study and wrote the protocol and manuscripts; Dr Ya-Mei Bai, Dr Ju-Wei Hsu, Dr Kai-Lin Huang, Dr Tung-Ping Su, Dr Cheng-Ta Li, Dr Yi-Hui Wu, Prof Tai-Long Pan, and Dr Wei-Chen Lin assisted with the preparation and proofreading of the manuscript; Dr Ya-Mei Bai, Dr Tzeng-Ji Chen, and Dr Mu-Hong Chen performed the statistical analysis and provided advice on statistical analysis.



## References

1. Stein DJ, Seedat S, Iversen A, Wessely S. Post-traumatic stress disorder: medicine and politics. *Lancet*. 2007;369(9556):139-44. Epub 2007/01/16. doi: 10.1016/S0140-6736(07)60075-0. PubMed PMID: 17223477.
2. Yehuda R. Post-traumatic stress disorder. *The New England journal of medicine*. 2002;346(2):108-14. Epub 2002/01/11. doi: 10.1056/NEJMra012941. PubMed PMID: 11784878.
3. Kessler RC, Aguilar-Gaxiola S, Alonso J, Chatterji S, Lee S, Ormel J, Ustun TB, Wang PS. The global burden of mental disorders: an update from the WHO World Mental Health (WMH) surveys. *Epidemiol Psychiatr Soc*. 2009;18(1):23-33. PubMed PMID: 19378696; PMCID: PMC3039289.
4. Chou FH, Wu HC, Chou P, Su CY, Tsai KY, Chao SS, Chen MC, Su TT, Sun WJ, Ou-Yang WC. Epidemiologic psychiatric studies on post-disaster impact among Chi-Chi earthquake survivors in Yu-Chi, Taiwan. *Psychiatry and clinical neurosciences*. 2007;61(4):370-8. Epub 2007/07/06. doi: 10.1111/j.1440-1819.2007.01688.x. PubMed PMID: 17610661.
5. Kessler RC, Sonnega A, Bromet E, Hughes M, Nelson CB. Posttraumatic stress disorder in the National Comorbidity Survey. *Archives of general psychiatry*. 1995;52(12):1048-60. Epub 1995/12/01. PubMed PMID: 7492257.
6. Jones R, Rickards H, Cavanna AE. The prevalence of psychiatric disorders in epilepsy: a critical review of the evidence. *Functional neurology*. 2010;25(4):191-4. Epub 2011/03/11. PubMed PMID: 21388578.
7. Kessler RC, Lane MC, Shahly V, Stang PE. Accounting for comorbidity in assessing the burden of epilepsy among US adults: results from the National Comorbidity Survey Replication (NCS-R). *Mol Psychiatry*. 2012;17(7):748-58. doi: 10.1038/mp.2011.56. PubMed PMID: 21577213; PMCID: 3165095.

8. Sledjeski EM, Speisman B, Dierker LC. Does number of lifetime traumas explain the relationship between PTSD and chronic medical conditions? Answers from the National Comorbidity Survey-Replication (NCS-R). *Journal of behavioral medicine*. 2008;31(4):341-9. doi: 10.1007/s10865-008-9158-3. PubMed PMID: 18553129; PMCID: 2659854.
9. Zeber JE, Copeland LA, Amuan M, Cramer JA, Pugh MJV. The role of comorbid psychiatric conditions in health status in epilepsy. *Epilepsy & Behavior*. 2007;10(4):539-46.
10. Adamec R. Transmitter systems involved in neural plasticity underlying increased anxiety and defense—Implications for understanding anxiety following traumatic stress. *Neuroscience & Biobehavioral Reviews*. 1997;21(6):755-65.
11. Friedman MJ. Neurobiological sensitization models of post-traumatic stress disorder: their possible relevance to multiple chemical sensitivity syndrome. *Toxicology and Industrial Health*. 1993;10(4-5):449-62.
12. Iancu I, Rosen Y, Moshe K. Antiepileptic drugs in posttraumatic stress disorder. *Clinical neuropharmacology*. 2002;25(4):225-9.
13. Chen MH, Pan TL, Li CT, Lin WC, Chen YS, Lee YC, Tsai SJ, Hsu JW, Huang KL, Tsai CF, Chang WH, Chen TJ, Su TP, Bai YM. Risk of stroke among patients with post-traumatic stress disorder: nationwide longitudinal study. *Br J Psychiatry*. 2015;206(4):302-7. doi: 10.1192/bjp.bp.113.143610. PubMed PMID: 25698764.
14. Li CT, Chen LF, Tu PC, Wang SJ, Chen MH, Su TP, Hsieh JC. Impaired prefronto-thalamic functional connectivity as a key feature of treatment-resistant depression: a combined MEG, PET and rTMS study. *PLoS One*. 2013;8(8):e70089. doi: 10.1371/journal.pone.0070089. PubMed PMID: 23936378; PMCID:

15. Cheng CM, Wu YH, Tsai SJ, Bai YM, Hsu JW, Huang KL, Su TP, Li CT, Tsai CF, Yang AC, Lin WC, Pan TL, Chang WH, Chen TJ, Chen MH. Risk of developing Parkinson's disease among patients with asthma: a nationwide longitudinal study. *Allergy*. 2015. Epub 2015/08/28. doi: 10.1111/all.12758. PubMed PMID: 26310430.
16. Li CT, Bai YM, Huang YL, Chen YS, Chen TJ, Cheng JY, Su TP. Association between antidepressant resistance in unipolar depression and subsequent bipolar disorder: cohort study. *The British journal of psychiatry : the journal of mental science*. 2012;200(1):45-51. Epub 2011/10/22. doi: 10.1192/bjp.bp.110.086983. PubMed PMID: 22016435.
17. Shen CC, Tsai SJ, Perng CL, Kuo BI, Yang AC. Risk of Parkinson disease after depression: a nationwide population-based study. *Neurology*. 2013;81(17):1538-44. Epub 2013/10/04. doi: 10.1212/WNL.0b013e3182a956ad. PubMed PMID: 24089392.
18. Lee JE, Garber B, Zamorski MA. Prospective Analysis of Premilitary Mental Health, Somatic Symptoms, and Postdeployment Postconcussive Symptoms. *Psychosom Med*. 2015;77(9):1006-17. doi: 10.1097/PSY.0000000000000250. PubMed PMID: 26458235.
19. Suls J, Green PA, Davidson KW. A Biobehavioral [corrected] Framework to Address the Emerging Challenge of Multimorbidity. *Psychosom Med*. 2016;78(3):281-9. doi: 10.1097/PSY.0000000000000294. PubMed PMID: 26867072; PMCID: PMC4889007.
20. Tegethoff M, Belardi A, Stalujanis E, Meinlschmidt G. Association between mental disorders and physical diseases in adolescents from a nationally representative cohort. *Psychosom Med*. 2015;77(3):319-32. doi: 10.1097/PSY.0000000000000151. PubMed PMID: 25851547.

21. D'Alessio L, Giagante B, Oddo S, Silva W, Solís P, Consalvo D, Kochen S. Psychiatric disorders in patients with psychogenic non-epileptic seizures, with and without comorbid epilepsy. *Seizure*. 2006;15(5):333-9.
22. Rosenberg HJ, Rosenberg SD, Williamson PD, Wolford GL. A comparative study of trauma and posttraumatic stress disorder prevalence in epilepsy patients and psychogenic nonepileptic seizure patients. *Epilepsia*. 2000;41(4):447-52.
23. Elghazouani F, Aarab C, Faiz F, Midaoui A, Barrimi M, Elrhazi K, Berraho A, Belahssen MF, Rammouz I, Aalouane R. [Psychiatric disorders and associated factors in patients with epilepsy in Fez, Morocco]. *L'Encephale*. 2015;41(6):493-8. doi: 10.1016/j.encep.2013.06.004. PubMed PMID: 26548617.
24. Shibahara I, Osawa S, Kon H, Morita T, Nakasato N, Tominaga T, Narita N. Increase in the number of patients with seizures following the Great East-Japan Earthquake. *Epilepsia*. 2013;54(4):e49-52. Epub 2013/01/09. doi: 10.1111/epi.12070. PubMed PMID: 23294222.
25. Cavanna AE, Ali F, Rickards HE, McCorry D. Behavioral and cognitive effects of anti-epileptic drugs. *Discovery medicine*. 2010;9(45):138-44. Epub 2010/03/03. PubMed PMID: 20193640.
26. Newport DJ, Nemeroff CB. Neurobiology of posttraumatic stress disorder. *Current opinion in neurobiology*. 2000;10(2):211-8.
27. Grillon C, Southwick S, Charney D. The psychobiological basis of posttraumatic stress disorder. *Molecular psychiatry*. 1996;1(4):278-97.
28. Post R, Weiss S. Kindling: implications for the course and treatment of affective disorders. *Anticonvulsants in Psychiatry Hampshire, UK, Wrightson Biomedical*. 1994:113-37.
29. Spivak B, Shohat B, Mester R, Avraham S, Gil-Ad I, Bleich A, Valevski A, Weizman A. Elevated levels

- of serum interleukin-1 beta in combat-related posttraumatic stress disorder. *Biological psychiatry*. 1997;42(5):345-8. Epub 1997/09/01. doi: 10.1016/S0006-3223(96)00375-7. PubMed PMID: 9276074.
30. Tucker P, Ruwe WD, Masters B, Parker DE, Hossain A, Trautman RP, Wyatt DB. Neuroimmune and cortisol changes in selective serotonin reuptake inhibitor and placebo treatment of chronic posttraumatic stress disorder. *Biological psychiatry*. 2004;56(2):121-8. Epub 2004/07/03. doi: 10.1016/j.biopsych.2004.03.009. PubMed PMID: 15231444.
31. Fries E, Hesse J, Hellhammer J, Hellhammer DH. A new view on hypocortisolism. *Psychoneuroendocrinology*. 2005;30(10):1010-6.
32. Gill JM, Saligan L, Woods S, Page G. PTSD is associated with an excess of inflammatory immune activities. *Perspectives in psychiatric care*. 2009;45(4):262-77.
33. Vezzani A, Granata T. Brain inflammation in epilepsy: experimental and clinical evidence. *Epilepsia*. 2005;46(11):1724-43.
34. Theoharides TC, Zhang B. Neuro-inflammation, blood-brain barrier, seizures and autism. *Journal of neuroinflammation*. 2011;8:168. Epub 2011/12/02. doi: 10.1186/1742-2094-8-168. PubMed PMID: 22129087; PMCID: 3293070.
35. Kanner AM. Is depression associated with an increased risk of treatment-resistant epilepsy? Research strategies to investigate this question. *Epilepsy Behav*. 2014;38:3-7. doi: 10.1016/j.yebeh.2014.06.027. PubMed PMID: 25260238.
36. Camilo O, Goldstein LB. Seizures and epilepsy after ischemic stroke. *Stroke*. 2004;35(7):1769-75.
37. So E, Annegers J, Hauser W, O'Brien P, Whisnant J. Population-based study of seizure disorders after cerebral infarction. *Neurology*. 1996;46(2):350-5.



38. Annegers JF, Hauser WA, Coan SP, Rocca WA. A population-based study of seizures after traumatic brain injuries. *New England Journal of Medicine*. 1998;338(1):20-4.
39. Annegers J, Hauser W, Beghi E, Nicolosi A, Kurland L. The risk of unprovoked seizures after encephalitis and meningitis. *Neurology*. 1988;38(9):1407-.
40. Chen CH, Tan HK, Liao LR, Chen HH, Chan CC, Cheng JJ, Chen CY, Wang TN, Lu ML. Long-term psychological outcome of 1999 Taiwan earthquake survivors: a survey of a high-risk sample with property damage. *Comprehensive psychiatry*. 2007;48(3):269-75. Epub 2007/04/21. doi: 10.1016/j.comppsy.2006.12.003. PubMed PMID: 17445522.
41. Chen YL, Hsu WY, Lai CS, Tang TC, Wang PW, Yeh YC, Huang MF, Yen CF, Chen CS. One-year follow up of PTSD and depression in elderly aboriginal people in Taiwan after Typhoon Morakot. *Psychiatry and clinical neurosciences*. 2015;69(1):12-21. Epub 2014/07/30. doi: 10.1111/pcn.12227. PubMed PMID: 25066670.

## FIGURE CAPTION

Figure 1. Survival curve of developing epilepsy in patients with PTSD and the control group.

PTSD: post-traumatic stress disorder.

ACCEPTED

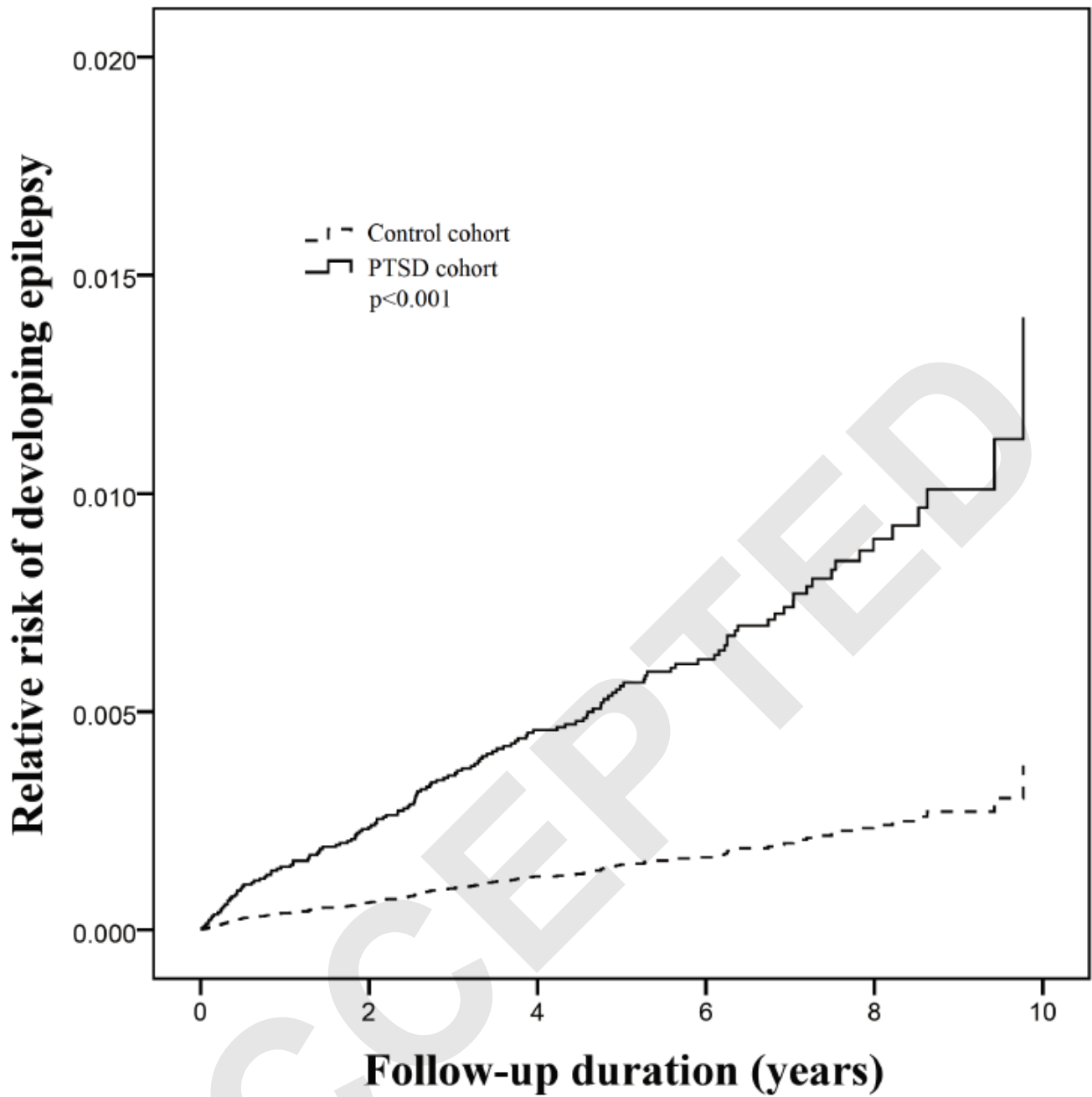


Table 1. Demographic data and incidence of epilepsy in patients with PTSD and the control group.

	Patients with PTSD (n=6245)	Controls (n=24980)	p-value
Age at enrollment (years, SD, n, %)	34.89 (15.06)	34.89 (15.06)	
Sex (M, %)	1435 (23)	5740 (23)	
Epilepsy (n, 1000 person-years, %)	92 (2.65)	46 (0.33)	<0.001
Generalized epilepsy	80 (87)	35 (76)	
Localized epilepsy	12 (13)	11 (24)	
Age at diagnosis (years, SD)	37.53 (15.80)	48.11 (23.97)	0.002
Duration between enrollment and diagnosis of epilepsy (years, SD)	2.57 (2.19)	4.37 (2.43)	<0.001
Comorbidities (n, %)			
Depression	4183 (67.0)	1017 (4.1)	<0.001
Cerebrovascular disease	346 (5.5)	660 (2.6)	<0.001
Head injury	423 (6.8)	243 (1.0)	<0.001
Meningitis and encephalitis	36 (0.6)	99 (0.4)	0.063
Level of urbanization (n, %)			<0.001
1 (most urbanized)	1524 (24.4)	8144 (32.6)	
2	2057 (32.9)	7785 (31.2)	
3	909 (14.6)	4118 (16.5)	
4	751 (12.0)	3164 (12.7)	
5 (most rural)	1004 (16.1)	1769 (7.1)	
Income-related insured amount			<0.001
≤ 15,840 NTD/month	2973 (47.6)	8961 (35.9)	
15,841~25,000NTD/month	2015 (32.3)	8738 (35.0)	
≥ 25,001NTD/month	1257 (20.1)	7281 (29.1)	

PTSD: post-traumatic stress disorder; SD: standard deviation; NTD: New Taiwan Dollar.

The independent t test was used for continuous variables and Pearson's  $\chi^2$  test for nominal variables, where appropriate.

Table 2. Risk of developing epilepsy in patients with PTSD and the control group.

	< 18 years	18~64 years	≥ 65 years	Total
	HR (95%CI)	HR (95%CI)	HR (95%CI)	HR (95%CI)
PTSD, presence vs. absence*	<b>4.53 (1.28~16.03)</b>	<b>4.96 (2.75~8.93)</b>	0.60 (0.15~2.34)	<b>3.72 (2.27~6.11)</b>
Comorbidities, presence vs. absence				
Depression	2.35 (0.56~9.95)	1.63 (0.95~2.78)	<b>3.93 (1.05~14.68)</b>	<b>1.76 (1.11~2.79)</b>
Cerebrovascular disease	6.83 (0.44~106.10)	<b>2.30 (1.26~4.21)</b>	2.27 (0.81~6.35)	<b>2.44 (1.47~4.04)</b>
Head injury	2.21 (0.22~22.33)	<b>4.05 (2.48~6.63)</b>	<b>6.84 (1.84~25.43)</b>	<b>4.17 (2.67~6.52)</b>
Meningitis and encephalitis	2.81 (0.56~9.94)	<b>5.39 (1.69~17.15)</b>	8.08 (0.81~80.92)	<b>5.81 (2.36~14.34)</b>

\*: Cox regression analyses adjusting for demographic data and medical and psychiatric comorbidities and PTSD as a binary variable.

PTSD: post-traumatic stress disorder; HR: hazard ratio; CI: confidence interval.

**Bold** type indicates the statistical significance.



Table 3. Risk of developing epilepsy in patients with PTSD and the control group, stratified by epilepsy type.

	Epilepsy	
	Generalized type	Localized type
	HR (95% CI)	HR (95% CI)
PTSD, presence vs. absence*	<b>4.11 (2.38~7.12)</b>	2.57 (0.80~8.20)
Comorbidities, presence vs. absence		
Depression	<b>1.86 (1.13~3.08)</b>	1.27 (0.40~4.01)
Cerebrovascular disease	1.78 (0.99~3.19)	<b>9.75 (3.33~28.57)</b>
Head injury	<b>4.26 (2.63~6.90)</b>	<b>3.64 (1.15~11.52)</b>
Meningitis and encephalitis	<b>7.20 (2.91~17.83)</b>	-

\*: Cox regression analyses adjusting for demographic data and medical and psychiatric comorbidities and PTSD as a binary variable.

PTSD: post-traumatic stress disorder; HR: hazard ratio; CI: confidence interval.

**Bold** type indicates the statistical significance.

Table 4. Sensitivity tests of developing epilepsy in patients with PTSD and the control group.

	Total*	$\geq 1$ year* <sup>+</sup>	$\geq 3$ years* <sup>++</sup>
	HR (95%CI)	HR (95%CI)	HR (95%CI)
PTSD			
Absence	1	1	1
Presence	<b>3.72 (2.27~6.11)</b>	<b>2.53 (1.44~4.47)</b>	<b>2.14 (1.15~4.01)</b>

\*: Cox regression analyses adjusting for demographic data and medical and psychiatric comorbidities and PTSD as a binary variable.

+: excluding the first year of observation.

++: excluding the first 3-years of observation.

PTSD: post-traumatic stress disorder; HR: hazard ratio; CI: confidence interval.

**Bold** type indicates the statistical significance.



Available online at  
**ScienceDirect**  
[www.sciencedirect.com](http://www.sciencedirect.com)

Elsevier Masson France  
**EM|consulte**  
[www.em-consulte.com/en](http://www.em-consulte.com/en)



## Original article

# Osthole attenuates lipid accumulation, regulates the expression of inflammatory mediators, and increases antioxidants in FL83B cells



Wen-Chung Huang<sup>a,b,1</sup>, Po-Chen Liao<sup>b,c,1</sup>, Chun-Hsun Huang<sup>d,e</sup>, Sindy Hu<sup>e</sup>,  
 Shih-Chun Huang<sup>b</sup>, Shu-Ju Wu<sup>b,e,\*</sup>

<sup>a</sup> Graduate Institute of Health Industry Technology, Research Center for Industry of Human Ecology, Research Center for Chinese Herbal Medicine, College of Human Ecology, Chang Gung University of Science and Technology, No.261, Wenhua 1st Rd., Guishan Dist., Taoyuan City 33303, Taiwan

<sup>b</sup> Department of Nutrition and Health Sciences, Research Center for Food and Cosmetic Safety, and Research Center for Chinese Herbal Medicine, College of Human Ecology, Chang Gung University of Science and Technology, No.261, Wenhua 1st Rd., Guishan Dist., Taoyuan City 33303, Taiwan

<sup>c</sup> Institute of Oral Biology, National Yang-Ming University, Taipei, Taiwan

<sup>d</sup> Department of Cosmetic Science, Chang Gung University of Science and Technology, No.261, Wenhua 1st Rd., Guishan Dist., Taoyuan City 33303, Taiwan

<sup>e</sup> Aesthetic Medical Center, Department of Dermatology, Chang Gung Memorial Hospital, Guishan Dist., Taoyuan 33303, Taiwan

## ARTICLE INFO

### Article history:

Received 6 January 2017

Received in revised form 12 April 2017

Accepted 13 April 2017

### Keywords:

Nonalcoholic fatty liver disease

p38 MAPK

NF-κB

Antioxidant

Osthole

## ABSTRACT

Osthole is found in *Cnidium monnieri* (L.) and has anti-inflammatory and anti-oxidative properties. It also inhibits the proliferation of hepatocellular carcinoma cells. This study aimed to evaluate the osthole suppressive nonalcoholic fatty liver disease effects in oleic acid (OA)-induced hepatic steatosis and if it can modulate inflammatory responses and oxidative stress. FL83B cells were pretreated with OA (250 μM) for 24 h, and then added different concentrations of osthole (3–100 μM) for 24 h. Subsequently, lipolysis and transcription factors of adipogenesis and phosphorylation of AMP-activated protein kinase proteins were measured. In addition, cells with OA-induced steatosis were H<sub>2</sub>O<sub>2</sub>-stimulated, and then incubated with osthole to evaluated if it could suppress its progression to steatohepatitis. Osthole significantly enhanced glycerol release and lipolysis protein expression. Osthole also promoted phosphorylation of AMP-activated protein kinases and increased the activity of triglyceride lipase and hormone-sensitive lipase. Osthole suppressed the nuclear transcription factor kappa-B and the p38 mitogen-activated protein kinase pathway, and decreased the malondialdehyde concentration in FL83B cells with OA-induced steatosis that were treated with H<sub>2</sub>O<sub>2</sub>. These results suggest that osthole might suppress nonalcoholic fatty liver disease by decreasing lipid accumulation, and through its anti-oxidative and anti-inflammatory effects via blocked NF-κB and MAPK signaling pathways.

© 2017 Elsevier Masson SAS. All rights reserved.

## 1. Introduction

Nonalcoholic fatty liver disease (NAFLD) is a serious and widespread metabolic disorder and encompasses a wide spectrum of liver conditions ranging from simple steatosis, to steatohepatitis and fibrosis, and end-stage liver diseases, including cirrhosis and hepatocellular carcinoma [1,2]. Many recent studies have found that NAFLD is associated with serious cardiometabolic

abnormalities, including type 2 diabetes mellitus, metabolic syndrome, obesity, and dysregulated insulin action in the liver [3].

The hallmark of NAFLD is excessive lipid accumulation in the liver, mainly triacylglycerol, in the absence of significant ethanol consumption. This accumulation interferes with the signaling pathways involved in the normal metabolism of hepatocytes, causes insulin resistance, and may even lead to metabolic syndrome abnormalities [4]. Hepatic lipid accumulation results from an imbalance between lipid availability and lipid disposal, and eventually triggers lipid peroxidative stress and hepatic injury [5]. Current treatments for patients with fatty liver disease include change of lifestyle and improvement of insulin sensitivity to alleviate the associated metabolic syndrome [6]. The AMP-activated protein kinase (AMPK) pathway is important in lipid metabolism. Studies indicated that phosphorylated acetyl-CoA carboxylase-1 (ACC-1) activated by phosphorylation of AMPK,

\* Corresponding author at: Department of Nutrition and Health Sciences, Chang Gung University of Science and Technology, No.261, Wenhua 1st Rd., Guishan Dist., Taoyuan City 33303, Taiwan.

E-mail address: [sjwu@gw.cgust.edu.tw](mailto:sjwu@gw.cgust.edu.tw) (S.-J. Wu).

<sup>1</sup> Wen-Chung Huang and Po-Chen Liao are equal contributors to the work.

which can suppress acetyl-CoA catalyze to malonyl-CoA during fatty acid (FA) and triglyceride synthesis [7–9].

Osthole, 7-methoxy-8-(3-methyl-2-butenyl) coumarin, is an active constituent of *Cnidium monnieri* (L.) that has been extracted from many medicinal plants. Osthole has long been used in traditional Chinese medicine for the treatment of eczema, cutaneous pruritus, *Trichomonas vaginalis* infection, and sexual dysfunction [10]. Recent studies have revealed that osthole may have anti-proliferative, vasorelaxant, anti-inflammatory, antimicrobial, anti-allergic, and prophylactic effects in hepatitis [11]. Furthermore, anti-cancer effects have been reported for osthole [12–14]. However, the effects of osthole on lipid metabolism and anti-oxidation remain unclear. A few experiments indicated that osthole treatment attenuated liver steatosis by decreasing triglyceride synthesis and had nominal effects on insulin resistance and liver inflammation in histological sections and an animal model [15–17]. The aims of the present study were to examine osthole-induced AMPK signaling, the potential mechanisms for controlling hepatocellular lipid metabolism, and to test the effects of osthole on intrahepatic fatty acid synthesis and inflammation.

## 2. Materials and methods

### 2.1. Materials

Osthole (Fig. 1A) purchased from the ChromaDex (Irvine, CA, USA). The purity was >97.9% as determined by HPLC. Stock solution (100 mM) prepared by dissolving osthole in DMSO and stored at  $-20^{\circ}\text{C}$ , as previously described [10]. The final concentration in culture medium of DMSO was  $\leq 0.1\%$ .

### 2.2. Cell line and treatment

FL83B cells purchased from the Bioresource Collection and Research Center (BCRC, Taiwan). Cells were cultured in F12 medium (Invitrogen-Gibco™, Paisley, Scotland) added with 10% FBS, 2 mM glutamine, 1% penicillin and streptomycin at  $37^{\circ}\text{C}$  in a humidified atmosphere containing 5%  $\text{CO}_2$ . Cells exposed to oleic acid (OA) 250  $\mu\text{M}$  for 24 h, then treated with osthole (3–100  $\mu\text{M}$ ) in OA microenvironment for 24 h.

### 2.3. Cell viability assay

Using MTT assay performed to evaluate the cytotoxicity of osthole. Cells were plated in 96-well plates cultured overnight and treated with osthole for 24 h. The MTT solution (5 mg/ml) was added to each well and incubated for 4 h at  $37^{\circ}\text{C}$ , followed by isopropanol dissolution of formazan crystals. The OD absorbance

was spectrophotometrically measured at 570 nm using a microplate reader (Gene5, Synergy HT, BioTek, USA).

### 2.4. Oil red O staining

FL83B cells treated drug in 6-well plates for 24 h and fixed using 10% formalin for 30 min. Cells stained with oil red O (Sigma Chemical, St. Louis, MO, USA) for 1 h at room temperature. To remove excess dye cells were washed three times with 1 mL of PBS and dipped in 100% isopropanol. The OD value was measured at 490 nm using a microplate reader (Gene5, Synergy HT, BioTek, USA) to quantify the lipid accumulation.

### 2.5. Measurement of glycerol production

FL83B cells treated with osthole in OA microenvironment for 24 h, and glycerol levels of culture medium quantified using glycerol quantification kit (GPO-Trinder) according to the manufacturer's instructions (Sigma-Aldrich). The results quantified at 570 nm using a microplate reader (Gene5, Synergy HT, BioTek, USA).

### 2.6. Antioxidant assay: malondialdehyde concentration and superoxide dismutase activity

FL83B cells treated with OA for 24 h and  $\text{H}_2\text{O}_2$  (500  $\mu\text{M}$ ) for 2 h; then, the cells treated with osthole for 24 h. Superoxide dismutase (SOD) and malondialdehyde (MDA) measured according to the commercial kit instructions (Sigma-Aldrich), and the absorbance at 450 and 532 nm with a spectrophotometer, respectively.

### 2.7. Preparation of total and nuclear proteins

FL83B cells treated with OA for 24 h and stimulated with  $\text{H}_2\text{O}_2$  for 2 h. Then, cells treated with osthole in 6 well plates. Cells were harvested with 300  $\mu\text{L}$  protein lysis buffer (150 mM NaCl, 1 mM EDTA, 1 mM DTT, 50 mM Tris-HCl, pH 7.4, 0.5% NP40, and 0.1% sodium dodecyl sulfate [SDS]) containing protease inhibitor cocktail and phosphatase inhibitors (Sigma). Cytoplasm and nuclear proteins were using the NE-PER® extraction reagent kits (Pierce, Rockford, IL, USA). Proteins quantitated using BCA assay kit (Pierce)[18].

### 2.8. Western blot analysis

An equal amount of protein was separated on polyacrylamide gels and transferred onto polyvinylidene fluoride membranes (Millipore, Billerica, MA, USA). Membranes were incubated with different primary antibodies for phosphorylated acetyl-CoA

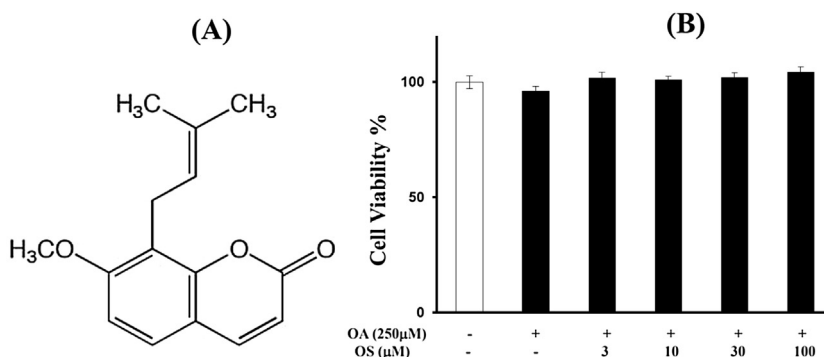
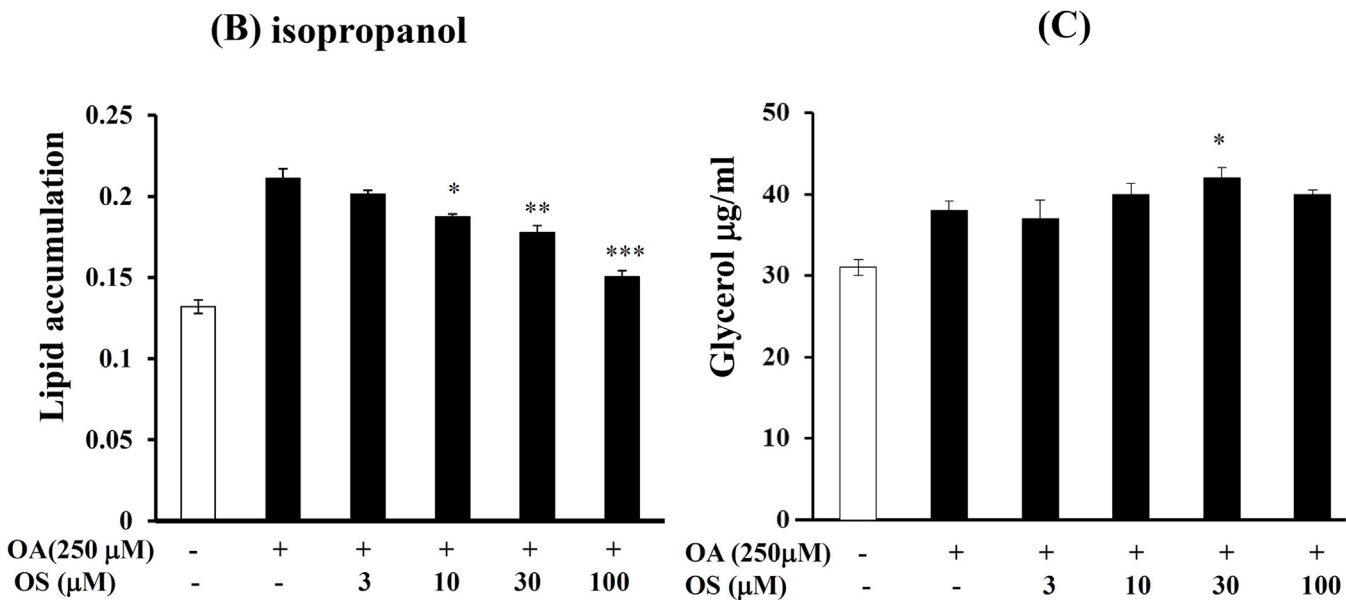
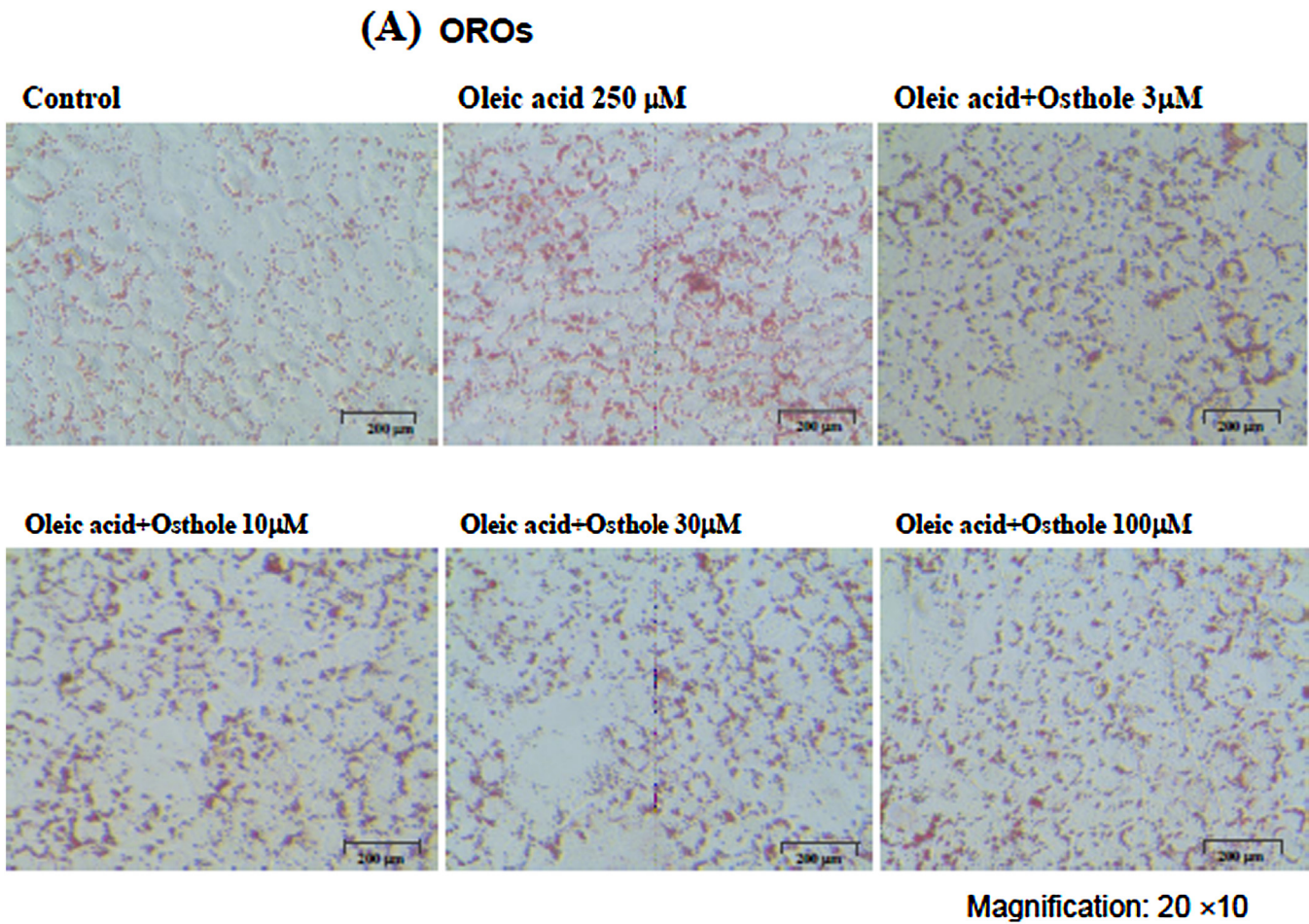


Fig. 1. Structures of osthole (A) and the cytotoxicity of osthole in FL83B cells (B).

carboxylase (ACC), fatty acid synthase (FAS), proliferator-activated receptor  $\gamma$  (PPAR- $\gamma$ ), CAAT/enhancer binding protein alpha (C/EBP $\alpha$ ), C/EBP $\beta$ , phosphorylated hormone-sensitive lipase (HSL), and adipose triglyceride lipase (ATGL) (Epitomics, Burlingame, CA

USA); sterol regulatory element-binding protein 1c (SREBP-1c), phosphorylated AMPK $\alpha$ , SIRT-1, cyclooxygenase-2 (COX-2), p65, and proliferating cell nuclear antigen (Santa Cruz, CA, USA); phosphorylated extracellular signal-regulated kinase 1/2 (ERK1/2),



**Fig. 2.** The effects of osthole on oil red O stain (A), 100% isopropanol release of a lipid droplet (B), and the glycerol assay (C) in FL83B cells. Cells were pretreated with OA and treated with osthole for 24 h. The cells were stained with oil red O to observe triglyceride content by OD at 490 nm, and the glycerol concentrations were measured in supernatants. Data are presented as the mean  $\pm$  standard deviation (SD),  $n=3$ ; \*\*\* $p < 0.005$ , \*\* $p < 0.01$ , \* $p < 0.05$ , compared with OA alone.



phosphorylated p38, phosphorylated c-Jun N-terminal kinase (JNK), phosphorylated I $\kappa$ B- $\alpha$ , ERK1/2, p38, JNK, and I kappa B alpha (I $\kappa$ B- $\alpha$ ) (Millipore); and  $\beta$ -actin (Sigma-Aldrich) overnight at 4 °C. Followed by incubation with horseradish peroxidase (HRP) conjugated secondary antibodies for 1 h at room temperature. The signals were incubated in ECL kit (Millipore) and detection image in BioSpectrum 600 system (UVP, Upland, CA, USA). Working concentration of primary antibodies are 1–2  $\mu$ g/ml.

### 2.9. RNA isolation and real-time PCR for gene expression

Total RNA was isolated with TRIzol (Invitrogen, Carlsbad, CA, USA) and PCR analyzed according to the manufacturer's instructions (Applied Biosystems, Foster City, CA, USA). The primer sequences (sense/antisense) used were: SIRT1, forward 5'-GAC GCT GTG GCA GAT TGT TA-3' and reverse 5'-GGA ATC CCA CAG AGA CAG A-3'; FAS, forward 5'-GGT CGT TTC TCC ATT AAA TTC TCA T-3' and reverse 5'-CTA GAA ACT TTC CCA GAA ATC TTC C-3'; HSL, forward 5'-GCT GGG CTG TCA AGC ACT GT-3' and reverse 5'-GTA ACT GGG TAG GCT GCC AT-3'; SREBP-1c, forward 5'-GGA GCC ATG GAT TGC ACA TT-3' and reverse 5'-GGC CCG GGA AGT CAC TGT-3'. Data were expressed as the signals of interest band to against  $\beta$ -actin mRNA expression.

### 2.10. Statistical analysis

All data were presented as the mean  $\pm$  standard deviation (SD). Statistical analysis was performed using one-way analysis of variance and post hoc analysis with Dunnett's test, with  $p < 0.05$  considered significant.

## 3. Results

### 3.1. Cytotoxicity of osthole in FL83B cells

The MTT assay was used to detect cytotoxicity in FL83B cells. At concentrations  $\leq 100 \mu$ M, osthole did not significantly affect cell viability (Fig. 1B). Therefore, 3–100  $\mu$ M osthole was used in all experiments.

### 3.2. The effect of osthole on lipid accumulation

Previous study demonstrated that OA-induced steatosis in hepatocytes [19]. Therefore, we endeavored to examine the effect of osthole on lipogenesis. FL83B cells were pretreated with OA

(250  $\mu$ M) for 24 h, then treated with or without various concentrations of osthole for 24 h. Lipid accumulation was measured by oil red O staining (Fig. 2A) and lipid accumulation (Fig. 2B). We found that 10–100  $\mu$ M osthole significantly decreased lipid accumulation compared with the OA group. In addition, treatment with 10–100  $\mu$ M osthole significantly increased glycerol release (osthole 3  $\mu$ M:  $36.6 \pm 3.8$ ,  $p = 0.38$ ; osthole 10  $\mu$ M:  $40 \pm 2.3$ ,  $p < 0.05$ ; osthole 30  $\mu$ M:  $42.5 \pm 2.1$ ,  $p < 0.05$ ; osthole 100  $\mu$ M:  $40.81 \pm 2.83$ ,  $p < 0.05$  versus OA:  $37.5 \pm 2.1$ ; Fig. 2C).

### 3.3. The effect of osthole on the expression of proteins involved in lipolysis

The two-hit hypothesis in the NAFLD pathogenesis considers extensive lipid accumulation is the first hit [20]. Hence, we analyzed the enzymes involved in triglyceride lipolysis. We found osthole can significantly increase the release of glycerol from hepatocytes with OA-induced lipid accumulation (Fig. 2) and treatment with osthole enhanced expression of ATGL and phosphorylated HSL (Fig. 3). Osthole concentrations  $\geq 3 \mu$ M significantly increased phosphorylated HSL expression in a dose-response manner, 10 and 100  $\mu$ M osthole enhanced ATGL expression compared with the OA group. This is important to induce the expression of lipolytic enzymes in hepatocytes lipid accumulation. Activated ATGL hydrolyzes triacylglycerol into diacylglycerol (DAG) and free FA, phosphorylated HSL hydrolyzes DAG into monoacylglycerol and (MAG) and one molecule of FA. Therefore, activating lipolysis and decreasing lipid accumulation may reduce the incidence of NAFLD.

### 3.4. The effect of osthole on FAS and transcription factors of adipogenesis

The transcription factors of adipogenesis including PPAR $\gamma$ , C/EBP $\alpha$ , C/EBP $\beta$  and SREBPs. SREBP1c closely mimics that of known C/EBP targets for lipid biosynthesis and plays a central role in the induction of PPAR $\gamma$  expression. Thus, up-regulated PPAR and SREBP-1c expression can activate lipid biosynthesis, leading to excessive lipid accumulation in hepatocytes [7]. To examine the effects of osthole on adipogenesis, OA-induced steatosis in FL83B hepatocytes were treated with osthole for 24 h. We found that Treatment with 100  $\mu$ M osthole decreased expression of FAS compared with the OA group. Osthole could directly regulate SREBP1c expression and at 100  $\mu$ M significantly inhibit PPAR $\gamma$ , C/

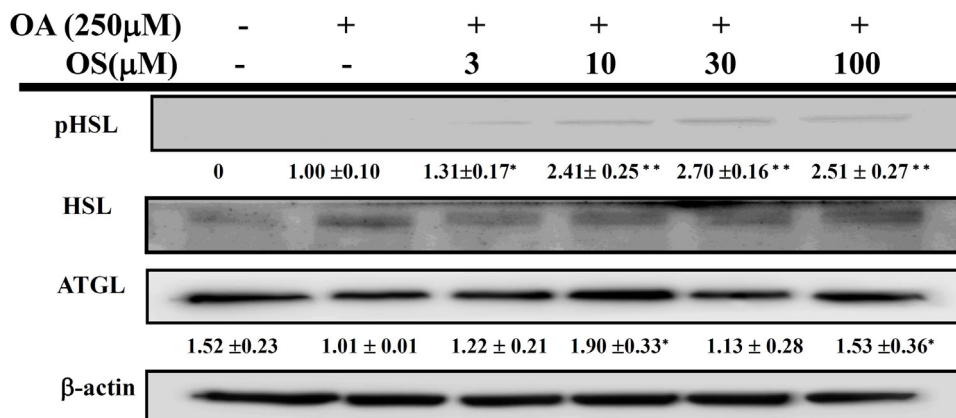


**Fig. 3.** Effects of osthole (OS) on lipolysis protein expression in hepatocytes. The FL83 B cells ( $10^6$  cells/mL) were pretreated with OA and then treated with OS for 24 h. The ATGL and phosphorylated HSL proteins were detected by Western blots ( $n = 3$  per group) in OS-treated cells. Expression of  $\beta$ -Actin was used as an internal control.

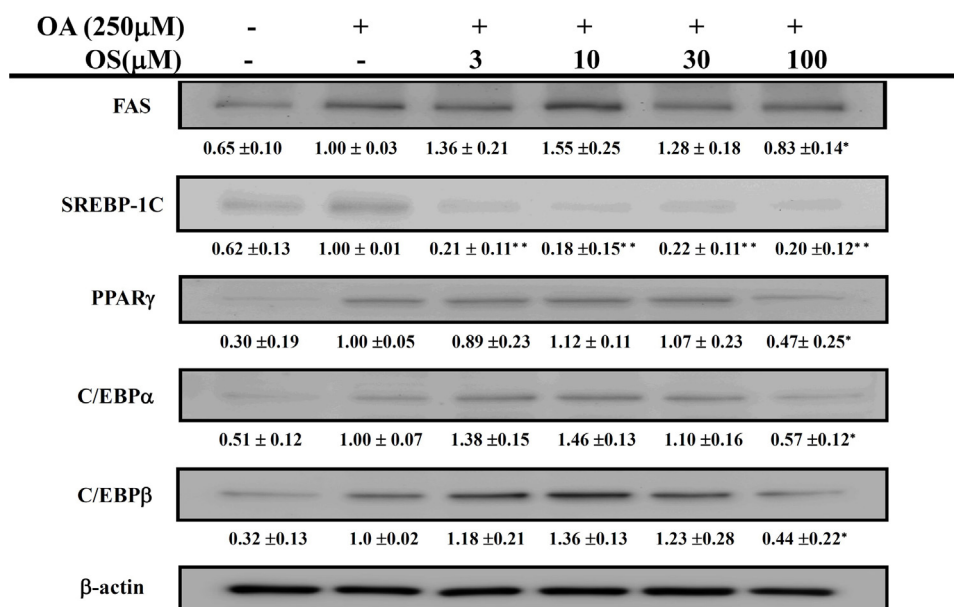


**Fig. 4.** Effects of osthole on transcription factors of adipogenesis in hepatocytes. The FL83B cells ( $10^6$  cells/mL) were pretreated with OA and treated with osthole (OS) for 24 h. The PPAR $\gamma$ , SREBP-1, C/EBP $\alpha$ , and C/EBP $\beta$  proteins were detected in OS-treated cells by Western blots ( $n = 3$  per group). Expression of  $\beta$ -Actin was used as an internal control.

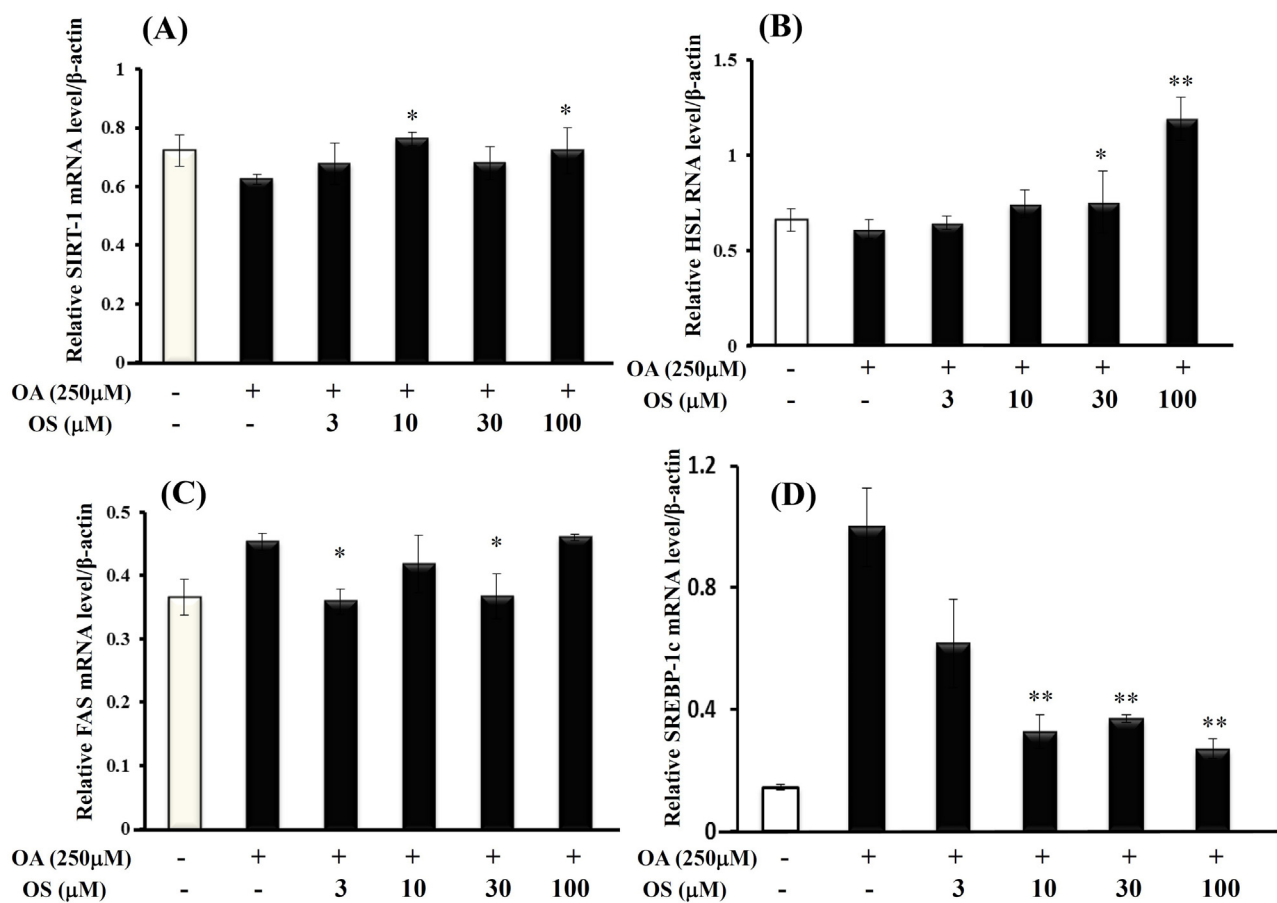


**Fig. 5.** The mRNA expression of lipolysis proteins SIRT-1 (A) and HSL (B) and the adipogenesis proteins FAS (C) and SREBP1c (D). Lipolysis and adipogenesis proteins were quantified in FL83B cells treated with different concentrations of osthole (3–100  $\mu$ M) for 24 h. Data are presented as the mean  $\pm$  standard deviation (SD); \* $p < 0.05$ , \*\* $p < 0.01$ , compared with OA alone.

EBP $\alpha$ , and C/EBP $\beta$  protein expression compared with the OA group (Fig. 4).

### 3.5. The effect of osthole on the gene expression of lipolysis and adipogenesis

The relative gene expression levels of lipolysis and adipogenesis were the ratio of different gene expression and  $\beta$ -actin. Compared with OA alone, osthole significantly enhanced the mRNA expression of SIRT-1 (3  $\mu$ M osthole:  $0.68 \pm 0.07$ ; 10  $\mu$ M osthole:  $0.76 \pm 0.02$ ,  $P < 0.05$ ; 30  $\mu$ M osthole:  $0.68 \pm 0.06$ ; 100  $\mu$ M osthole:  $0.72 \pm 0.08$ ,  $P < 0.05$  vs. OA alone:  $0.62 \pm 0.02$ ; Fig. 5A) and HSL (3  $\mu$ M osthole:  $0.61 \pm 0.01$ ; 10  $\mu$ M osthole:  $0.65 \pm 0.03$ ; 30  $\mu$ M osthole:  $0.74 \pm 0.05$ ,  $P < 0.05$ ; 100  $\mu$ M osthole:  $1.22 \pm 0.04$ ,  $P < 0.01$  vs. OA alone:  $0.66 \pm 0.02$ ; Fig. 5B). In addition, osthole significantly decreased the mRNA expression of FAS (3  $\mu$ M osthole:  $0.34 \pm 0.01$ ,  $P < 0.05$ ; 30  $\mu$ M osthole:  $0.36 \pm 0.06$ ,  $P < 0.05$  vs. OA alone:  $0.46 \pm 0.03$ ; Fig. 5C) and SREBP1c (3  $\mu$ M osthole:  $0.62 \pm 0.23$ ; 10  $\mu$ M osthole:  $0.33 \pm 0.09$ ,  $P < 0.01$ ; 30  $\mu$ M osthole:  $0.38 \pm 0.05$ ,  $P < 0.01$ ; 100  $\mu$ M osthole:  $0.27 \pm 0.06$ ,  $P < 0.01$  vs. OA alone:  $1.01 \pm 0.21$ ; Fig. 5D). These results suggest that osthole can suppress the OA-induced lipid accumulation in FL83B cells.

### 3.6. The effect of osthole on the AMPK pathway

The AMPK is a metabolic energy regulator as described previously [7]. AMPK phosphorylation stimulates ACC phosphorylation, which regulates enzymes during fatty acid synthesis for malonyl-CoA production. SIRT1 regulates hepatocyte lipid metabolism through activating AMPK [7–9]. Thus, up-regulated Sirt1 and AMPK are expected to improve lipid metabolism and decrease lipid accumulation. We also investigated whether osthole could modulate the Sirt1 and AMPK pathway in OA-induced steatosis. Osthole significantly increased SIRT1 deacetylase activity and phosphorylation of AMPK, and its downstream target ACC, in osthole concentration at 3–30  $\mu$ M (Fig. 6). Our results indicated that osthole may protect against free fatty acid-induced lipid

accumulation by activating SIRT1 and AMPK overexpression in hepatocytes.

### 3.7. Osthole increased the antioxidant capacity in $H_2O_2$ -induced hepatic steatosis cells

Oxidative stress plays a critical role in the “second hit” of the NAFLD pathogenesis, involving lipid peroxidation and inflammation, as the steatosis progresses to steatohepatitis [20]. This study to investigate osthole whether inhibited  $H_2O_2$ -induced lipid peroxidation and oxidative stress, MDA is a lipid peroxidation product and SOD is an antioxidant enzyme. Hence, we investigated whether osthole may decrease the MDA concentration and increase SOD activity. Compared with OA +  $H_2O_2$  group, osthole significantly decreased the MDA concentration (10  $\mu$ M osthole:  $3.6 \pm 0.8$ ,  $P < 0.05$ ; 30  $\mu$ M osthole:  $2.6 \pm 0.2$ ,  $P < 0.01$ ; 100  $\mu$ M osthole:  $1.3 \pm 0.4$ ,  $P < 0.01$  vs. OA alone:  $4.19 \pm 0.02$ ) (Fig. 7A) and enhanced the SOD activity (10  $\mu$ M osthole:  $60.2 \pm 2.8$ ,  $P < 0.05$ ; 30  $\mu$ M osthole:  $63.4 \pm 2.2$ ,  $P < 0.05$  vs. OA alone:  $56.2 \pm 7.1$ ) (Fig. 7B).

### 3.8. Effects of osthole on $H_2O_2$ -induced COX-2 protein expression and NF- $\kappa$ B activation in hepatic steatosis cells

The “second hit” is believed to result from an increase in oxidative stress and expression of inflammatory mediators [20]. Previously studies indicated that improved liver inflammation could alleviate hepatic steatosis in mouse models of NASH. The NF- $\kappa$ B pathway plays a critical role in the inflammatory response by regulating the expression of inflammatory cytokines, e.g., TNF- $\alpha$  [21]. Hence, we investigated whether osthole may suppress COX-2, the phosphorylation of I $\kappa$ B- $\alpha$ , and translocation of NF- $\kappa$ B (active subunit p65) into the nucleus. Osthole significantly suppressed COX-2 protein expression in a concentration-dependent manner compared with  $H_2O_2$ -stimulated cells (Fig. 8A). We observed that osthole significantly suppressed I $\kappa$ B- $\alpha$  phosphorylation and degradation compared with  $H_2O_2$ -induced FL83B cells (Fig. 8B), and p65 was mostly distributed in the cytoplasm and hardly

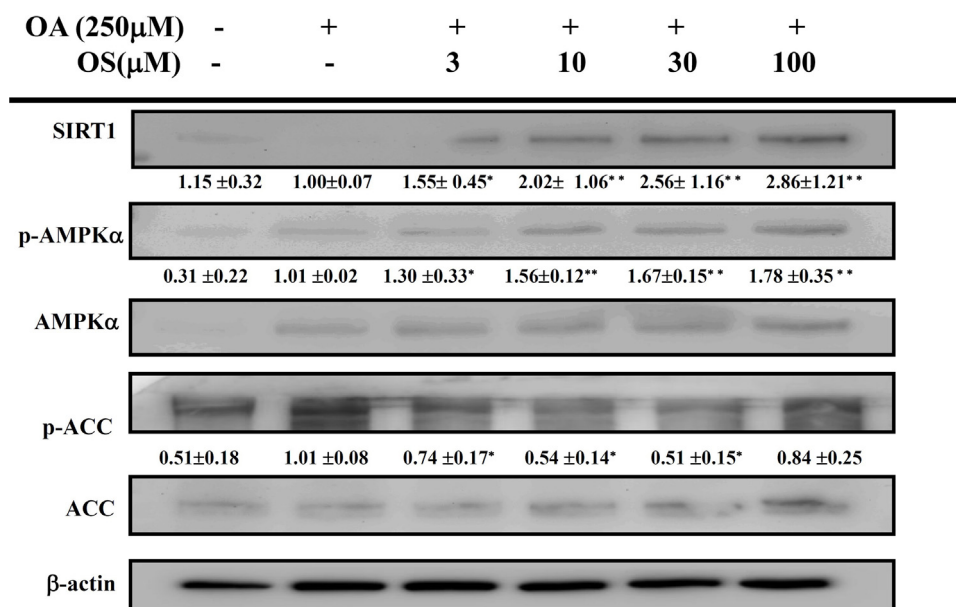


**Fig. 6.** Effects of osthole on the AMPK pathway in hepatocytes. The FL83B cells ( $10^6$  cells/mL) were pretreated with OA and treated with osthole for 24 h. Phosphorylated and unphosphorylated AMPK $\alpha$  and ACC, SIRT-1, and FAS proteins were detected by Western blots ( $n = 3$  per group) in OS-treated cells. Expression of  $\beta$ -Actin expression was used as an internal control.

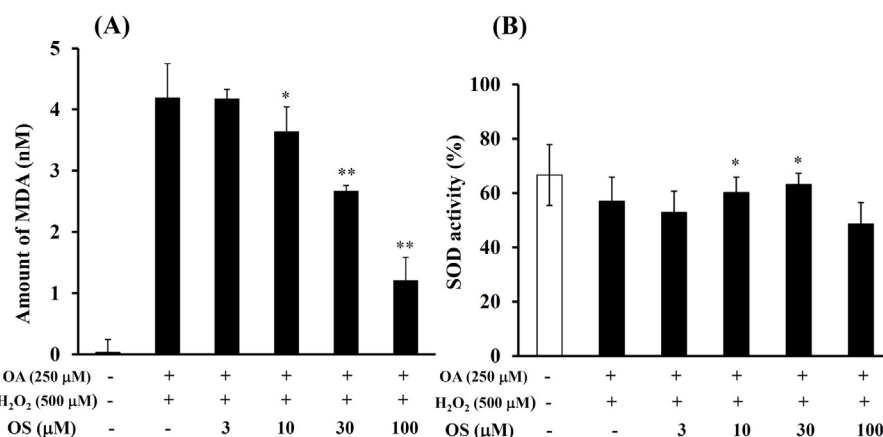


**Fig. 7.** Effects of osthole (OS) on the antioxidant activity in hepatocytes. The FL83B cells ( $10^6$  cells/mL) were pretreated with OA (250 μM) for 24 h, treated with H<sub>2</sub>O<sub>2</sub> (250 μM) for 2 h, and then with different concentrations of OS for 24 h. The MDA concentration (A) and SOD activity (B) were measured. Data are presented as the mean  $\pm$  standard deviation (SD); \* $p < 0.05$ , \*\* $p < 0.01$ , compared with OA alone.

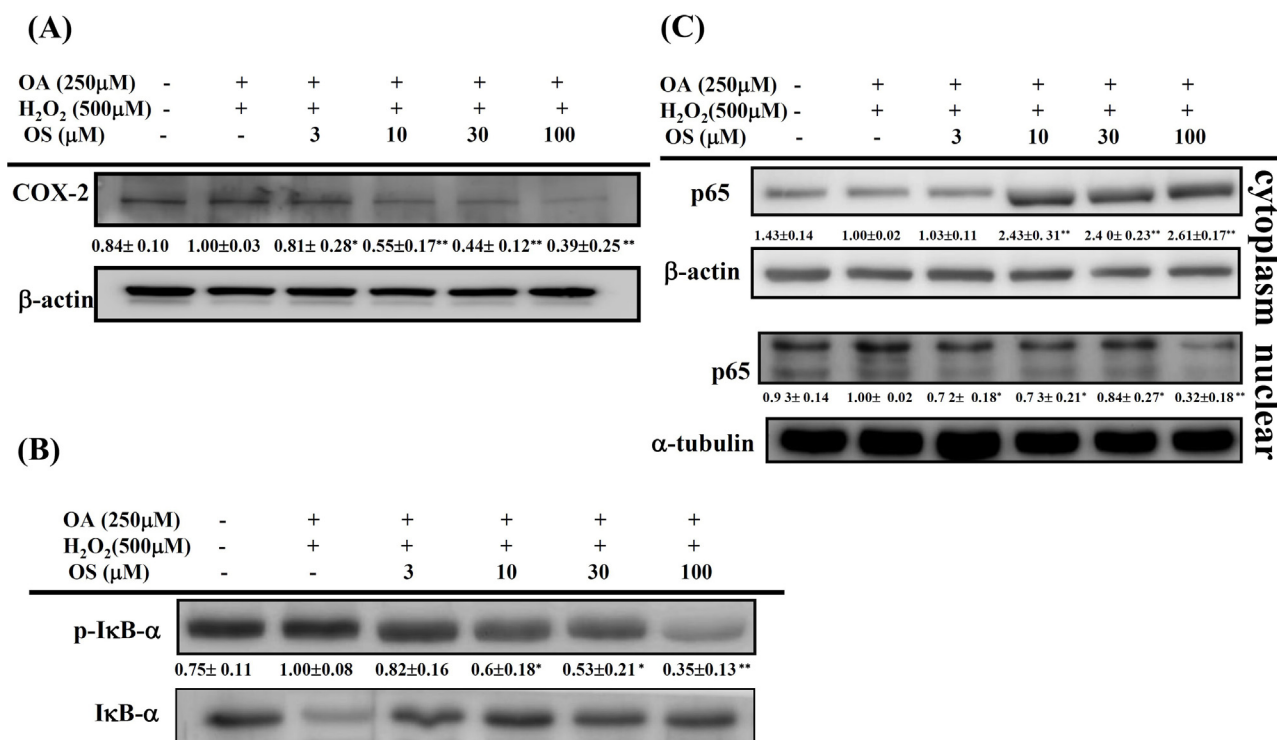


**Fig. 8.** Effects of osthole (OS) on H<sub>2</sub>O<sub>2</sub>-induced production of COX-2 (A), β-actin expression was used as an internal. Phosphorylation of the active subunit of IκB-α, p65 (B), with total IκB-α levels used as internal controls. For the nuclear translocation of NF-κB (p65) (C), cells were pretreated with OA (250 μM) for 24 h and then H<sub>2</sub>O<sub>2</sub> (250 μM) for 2 h. Then, cells were treated with different concentrations of OS for 24 h. The internal controls were α-tubulin in the nucleus and β-actin in the cytosol. The densitometry values from three independent experiments were analyzed and compared with the H<sub>2</sub>O<sub>2</sub>-treated group.

translocated into the nucleus in unstimulated cells (Fig. 8C). Interestingly, osthole suppressed the nuclear translocation of p65 in a concentration-dependent manner compared with H<sub>2</sub>O<sub>2</sub>-induced cells.

### 3.9. Effect of osthole on MAPK pathways in H<sub>2</sub>O<sub>2</sub>-activated hepatic steatosis cells

Previous studies have shown that the MAPK signaling pathways are closely related with mechanisms of inflammation and are involved in the pathological process of NAFLD [22]. Here, we investigated whether osthole affects the MAPK pathways in FL83B

cells with H<sub>2</sub>O<sub>2</sub>-activated hepatic steatosis. We found that osthole (100 μM) significantly decreased phosphorylation of p38 compared with H<sub>2</sub>O<sub>2</sub>-activated FL83B cells; however, osthole didn't suppress phosphorylation of ERK1/2 and JNK (Fig. 9).

## 4. Discussion

A “two-hit” hypothesis has been proposed in NAFLD for the progression to steatohepatitis. First, hepatic intracellular reversible deposition of triacylglycerols and development of hepatic steatosis (“first hit”) occurs; then, oxidative stress and cytokine-induced liver injury are responsible for the switch from steatosis to

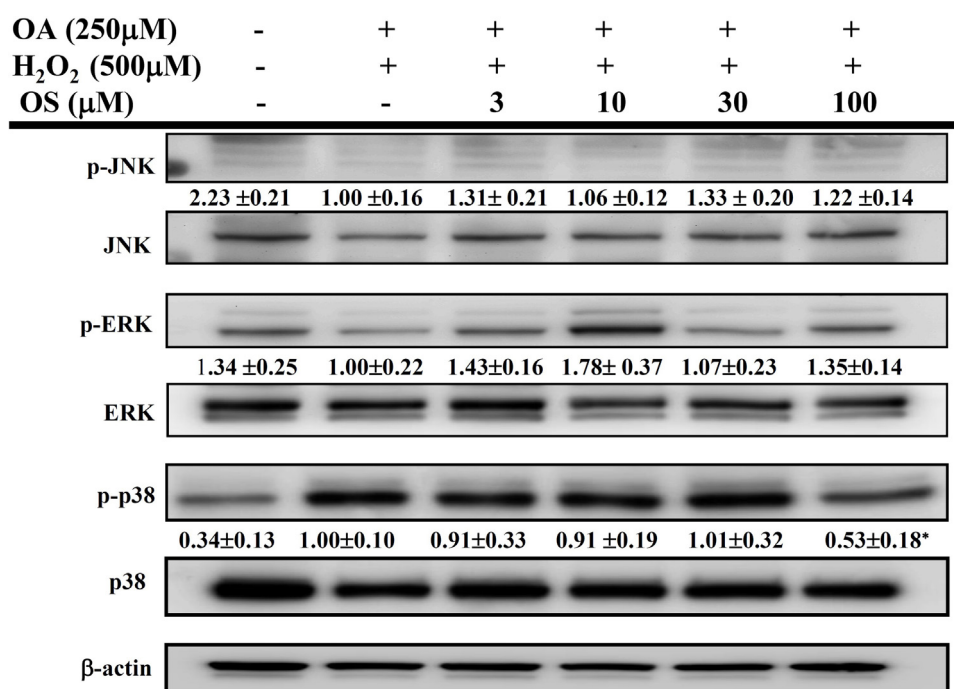


**Fig. 9.** Effect of osthole (OS) on H<sub>2</sub>O<sub>2</sub>-induced phosphorylation of MAPK. The FL83B cells were pretreated with OA (250 μM) for 24 h and then H<sub>2</sub>O<sub>2</sub> (250 μM) was added for 2 h. Cells were then treated with different concentrations of OS for 24 h. Total MAPK levels were used as internal controls. The densitometry values of three independent experiments were analyzed and compared with the H<sub>2</sub>O<sub>2</sub>-treated group.

steatohepatitis (“second hit”) [20]. There is evidence that the rate of de novo lipid synthesis is elevated because of unnecessary activation of lipogenic transcription factors, as an excess supply of dietary lipids was observed in insulin resistant patients with NAFLD, compared with healthy subjects [23]. Furthermore, liver lipid synthesis is positively modulated by increased activity of the transcription factors PPAR and SREBP-1c [24]. Overexpression of genes that activate lipogenic genes, such as SREBP-1, FAS, and ACC have been found in steatotic human livers and obese mice [25,26].

Osthole, a coumarin compound, was isolated from the dried fruits of *Cnidium monnieri* (Umbelliferae). A previous study indicated that osthole induced a significant acceleration of beta-oxidation of hepatic fatty acids, via an increase in acyl-CoA oxidase and carnitine palmitoyl transferase 1a mRNA expression, in stroke-prone spontaneously hypertensive rats, suggesting osthole suppressed hepatic lipid accumulation [27]. A recent study demonstrated that osthole is a dual agonist of PPAR α/γ, and decreases hepatic lipid accumulation and inflammatory cytokine production [28]. Thus, osthole may increase expression of the lipolysis proteins, pHSL and ATGL, and suppress the adipogenesis transcription factors SREBP1, PPARγ, and CEBPα/β, to decrease lipid accumulation. In addition, researchers indicated that AMPK activation by SIRT1 also protects against FAS induction and lipid accumulation caused by high free fatty acids in hepatocytes [29]. In this study, we found that osthole increased SIRT1-mediated AMPK activation in a dose-dependent manner and also enhanced the basal phosphorylation of AMPK and ACC, but suppressed expression of FAS in hepatocytes with accumulated lipids caused by high free fatty acids. The present study provided direct evidence of the beneficial effects of osthole on hepatocyte lipid metabolism.

It has been proposed that oxidative stress is the main instigator triggering the progression of steatosis to steatohepatitis. The “second hit” involves lipid peroxidation, pro-inflammatory cytokines, and mitochondrial dysfunction promoting hepatic injury, inflammation, and fibrosis and leading to the development and progression of NAFLD [30]. Many studies demonstrated the

association between the levels of lipid oxidation products and the pathogenesis of NAFLD and NASH. Previously studies showed that lipid accumulation was accompanied by increased generation of oxidative stress and cellular inflammatory responses [31]. Various antioxidants have been used to treat NAFLD, including radical scavenger vitamin E and β-carotene to prevent lipid peroxidation [32]. Clinical studies indicated that dietary supplementation with vitamin E significantly improved liver transaminase and serum TNF-α levels in patients with NASH [32], and recent studies demonstrated that osthole had good antioxidant activity [33]. This study found that osthole decreased the level of the lipid peroxidation product, MDA, and improved the activity of the antioxidant enzyme, SOD, which can metabolize H<sub>2</sub>O<sub>2</sub> to non-toxic H<sub>2</sub>O.

Inflammatory reactions and oxidative stress are implicated in the pathogenesis of steatosis to steatohepatitis. Studies had shown that lipid accumulation activated MAPKs and NF-κB [34]. Therefore, fatty acids are believed to agitate the progress of steatohepatitis by inducing cellular stress and organelle toxicity [35]. A study demonstrated that osthole inhibited PPAR α/γ and decreased inflammatory cytokine production [28]. The reduced activity of PPARγ by osthole may have advantageous effects on hepatic lipid storage and the inflammatory response; therefore, osthole may act as a PPAR agonist to reduce hepatic steatosis. Furthermore, activation of NF-κB seems to be a major determinant for disease progression from steatosis to steatohepatitis, and can trigger intercellular cascades to induce and maintain inflammation. NF-κB (is a hetero-dimer of p65 and p50) was suppressed by IκB (a hetero dimer containing IκB-α and IκB-β subunits) in the cytoplasm. The phosphorylation of IκBα leads to the activation of NF-κB, which is rapidly degraded through protease to release NF-κB from the cytoplasm into the nucleus to express proinflammatory cytokines and COX-2 [7,10]. Our results indicated osthole decrease the inflammatory mediator COX-2 expression via suppression of the NF-κB pathway. In addition, activation of MAPK-related signaling may be critical step in promoting



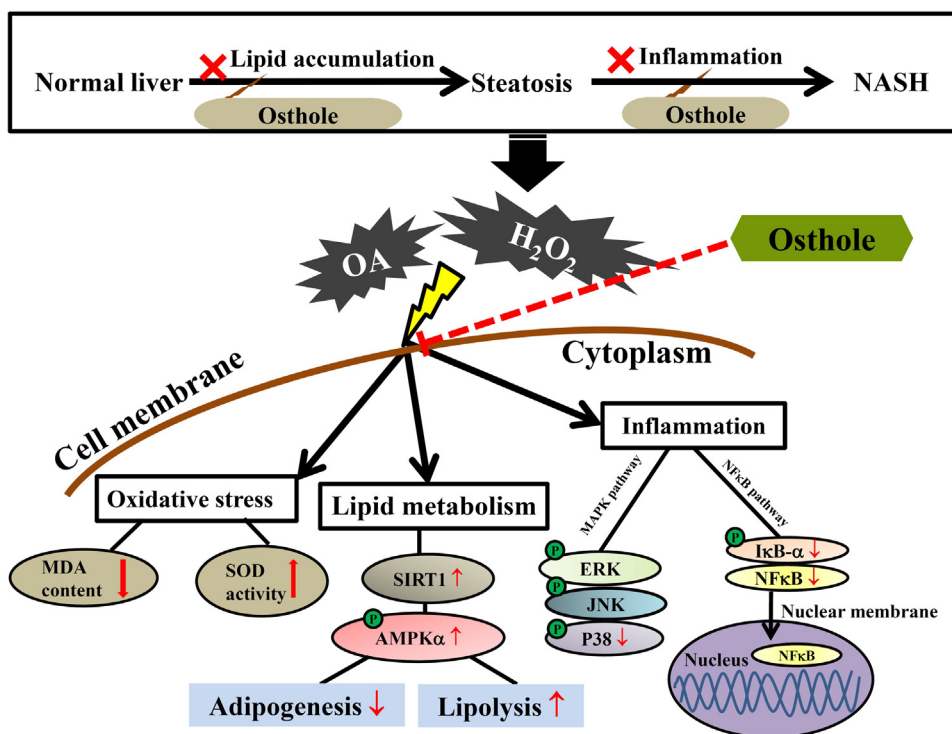


**Fig. 10.** Model explaining the mechanism of Osthole attenuates lipid accumulation, regulates the expression of inflammatory mediators, and increases antioxidant in FL83B Cells.

progression from lipid accumulation and steatosis to inflammation. We found that osthole may decrease inflammatory responses through suppression of NF- $\kappa$ B and the p38 MAPK pathway in hepatic steatosis stimulated by  $H_2O_2$ .

In this study, MTT assay showed that osthole at concentrations  $\leq 100 \mu\text{M}$  did not significantly affect cell viability. Previously studies indicated that treated with osthole ( $100 \mu\text{M}$ ) for 24 h, inhibited proliferation in lung cancer cells (A549) [36]. In addition, hepatocellular carcinoma (HCC) cell lines including human HCC cell line (SK-HP-1, SMMC-7721, HepG-2) and murine HCC cell line (Hepa1-6) were treated with osthole at different doses (0, 41.0, 84.0, 123.0, 164.0 and  $205.0 \mu\text{M}$ ) for 48 h. MTT assay was measured cell growth inhibition rate at 48 h after osthole treatment. Osthole inhibited the proliferation of all four HCC cell lines in a dose-dependent manner. There was no significant difference in drug sensitivity ( $IC_{50}$ :  $189.5 \mu\text{M}$ ,  $161.9 \mu\text{M}$ ,  $161.4 \mu\text{M}$  and  $137.0 \mu\text{M}$ , respectively) between the four HCC cell lines. And osthole was administered at the dose of  $123.0 \mu\text{M}$ , showed that SMMC-7721 and Hepa1-6 cells both exhibited increased cell percentages in G2 phase [37]. In contrast, this study we used normal hepatocytes (FL83B cells) and treated with osthole  $\leq 100 \mu\text{M}$  no longer than 24 h. Hence, we confirmed osthole  $\leq 100 \mu\text{M}$  have no inhibitory effect in FL83B cells growth.

To summarize, osthole suppressed hepatic lipid accumulation by increasing lipolysis and decreasing adipogenesis transcription factors. Osthole also increased SIRT1, which regulates hepatic lipid metabolism through activation of AMPK. During the steatosis, osthole significantly inhibited lipid peroxidation and COX-2 expression by suppressing activation of NF- $\kappa$ B and the p38 MAPK pathway in  $H_2O_2$ -stimulated FL83B cells (Fig. 10).

## 5. Conclusion

Osthole suppressed hepatic lipid accumulation through activated AMPK pathway improved lipolysis and suppressed adipogenesis transcription factors protein expression. Simultaneously,

osthole by intervening NF- $\kappa$ B and p38 MAPK pathways suppressed inflammation. We believe that osthole shows promise as a natural anti-NAFLD drug to attenuate liver inflammatory disease.

## Author's disclosure

The authors report no declarations of interest.

## Acknowledgements

This study was supported in part by grants from the Chang Gung Memorial Hospital (CMRPF1F0121) and Ministry of Science and Technology in Taiwan (MOST 105-2320-B-255-004-), and Chang Gung University of Science and Technology (EZRPF3F0141).

## References

- [1] R. Gupta, A. Bhangoo, N.A. Matthews, H. Anhalt, Y. Matta, B. Lamichhane, S. Narwal, G. Wetzler, S. Ten, The prevalence of non-alcoholic fatty liver disease and metabolic syndrome in obese children, *J. Pediatr. Endocrinol. Metab.* 24 (2011) 907–911.
- [2] Y.P. Hwang, H.G. Kim, J.H. Choi, M.T. Do, Y.C. Chung, T.C. Jeong, H.G. Jeong, S-allyl cysteine attenuates free fatty acid-induced lipogenesis in human HepG2 cells through activation of the AMP-activated protein kinase-dependent pathway, *J. Nutr. Biochem.* 24 (2013) 1469–1478.
- [3] V. Nobili, M. Manco, R. Devito, C.V. Di, D. Comparcola, M.R. Sartorelli, F. Piemonte, M. Marcellini, P. Angulo, Lifestyle intervention and antioxidant therapy in children with nonalcoholic fatty liver disease: a randomized controlled trial, *Hepatology* 48 (2008) 119–128.
- [4] G. Musso, R. Gambino, M. Cassader, Recent insights into hepatic lipid metabolism in non-alcoholic fatty liver disease (NAFLD), *Prog. Lipid Res.* 48 (2009) 1–26.
- [5] G.R. Romeo, J. Lee, S.E. Shoelson, Metabolic syndrome insulin resistance, and roles of inflammation-mechanisms and therapeutic targets, *Arterioscler. Thromb. Vasc. Biol.* 32 (2012) 1771–1776.
- [6] Q. Liu, S. Bengmark, S. Qu, The role of hepatic fat accumulation in pathogenesis of non-alcoholic fatty liver disease (NAFLD), *Lipids Health Dis.* 9 (2010) 42.
- [7] W.C. Huang, W.T. Chang, S.J. Wu, P.Y. Xu, N.C. Ting, C.J. Liou, Phloretin and phlorizin promote lipolysis and inhibit inflammation in mouse 3T3-L1 cells and in macrophage-adipocyte co-cultures, *Mol. Nutr. Food Res.* 57 (2013) 1803–1813.

- [8] R. Lage, C. Dieguez, A. Vidal-Puig, M. Lopez, AMPK: a metabolic gauge regulating whole-body energy homeostasis, *Trends Mol. Med.* 14 (2008) 539–549.
- [9] X. Hou, S. Xu, K.A. Maitland-Toolan, K. Sato, B. Jiang, Y. Ido, F. Lan, K. Walsh, M. Wierzbicki, T.J. Verbeuren, R.A. Cohen, M. Zang, SIRT1 regulates hepatocyte lipid metabolism through activating AMP-activated protein kinase, *J. Biol. Chem.* 29 (2008) 20015–20026.
- [10] S.J. Wu, Osthole attenuates inflammatory responses and regulates the expression of inflammatory mediators in HepG2Cells grown in differentiated medium from 3T3-L1 preadipocytes, *J. Med. Food* 18 (2015) 972–979.
- [11] M. Zimecki, J. Artym, W. Cisowski, I. Mazol, M. Włodarczyk, M. Glensk, Immunomodulatory and anti-inflammatory activity of selected osthole derivatives, *Z. Naturforsch. C* 64 (2009) 361–368.
- [12] S.Y. Chou, C.S. Hsu, K.T. Wang, M.C. Wang, C.C. Wang, Antitumor effects of Osthol from *Cnidium monnieri*: an in vitro and in vivo study, *Phytother. Res.* 21 (2007) 226–230.
- [13] D. Ding, S. Wei, Y. Song, L. Li, G. Du, H. Zhan, Y. Cao, Osthole exhibits anti-cancer property in rat glioma cells through inhibiting PI3K/Akt and MAPK signaling pathways, *Cell. Physiol. Biochem.* 32 (2013) 1751–1760.
- [14] X. Xu, Y. Zhang, D. Qu, T. Jiang, S. Li, Osthole induces G2/M arrest and apoptosis in lung cancer A549 cells by modulating PI3 K/Akt pathway, *J. Exp. Clin. Cancer Res.* 29 (2011) 33–30.
- [15] V.C. Lin, C.H. Chou, Y.C. Lin, J.N. Lin, C.C. Yu, C.H. Tang, H.Y. Lin, T.D. Way, Osthole suppresses fatty acid synthase expression in HER2-overexpressing breast cancer cells through modulating Akt/mTOR pathway, *J. Agric. Food Chem.* 58 (2010) 4786–4793.
- [16] H.H. Nam, D.W. Jun, H.J. Jeon, J.S. Lee, W.K. Saeed, E.K. Kim, Osthol attenuates hepatic steatosis via decreased triglyceride synthesis not by insulin resistance, *World J. Gastroenterol.* 20 (2014) 11753–11761.
- [17] F. Sun, M.L. Xie, L.J. Zhu, J. Xue, Z.L. Gu, Inhibitory effect of osthole on alcohol-induced fatty liver in mice, *Dig. Liver Dis.* 41 (2009) 127–133.
- [18] W.C. Huang, S.J. Wu, Y.L. Laic, C.J. Liou, Phloretin inhibits interleukin-1 $\beta$ -induced COX-2 and ICAM-1 expression through inhibition of MAPK, Akt, and NF- $\kappa$ B signaling in human lung epithelial cells, *Food Funct.* 10 (2015) 1960–1967.
- [19] Y.J. Hwang, H.R. Wi, H.R. Kim, K.W. Park, K.A. Hwang, *Pinus densiflora* Sieb. et Zucc. alleviates lipogenesis and oxidative stress during oleic acid-induced steatosis in HepG2 cells, *Nutrients* 23 (2014) 2956–2972.
- [20] Z. Lu, J.T. Wai, J.Y. Jin, J.Z. Bei, Signal transductions and nonalcoholic fatty liver: a mini-review, *Int. J. Clin. Exp. Med.* 7 (2014) 1624–1631.
- [21] S.M. Abd El-Kader, E.M. El-Den Ashmawy, Non-alcoholic fatty liver disease: the diagnosis and management, *World J. Hepatol.* 7 (2015) 846–858.
- [22] C. Garcia-Ruiz, J.C. Fernandez-Checa, Mitochondrial glutathione: hepatocellular survival-death switch, *J. Gastroenterol. Hepatol.* 21 (2006) S3–S6.
- [23] K.L. Donnelly, C.I. Smith, S.J. Schwarzenberg, J. Jessurun, M.D. Boldt, E.J. Parks, Sources of fatty acids stored in liver and secreted via lipoproteins in patients with nonalcoholic fatty liver disease, *J. Clin. Invest.* 115 (2005) 1343–1351.
- [24] G.Y. Lee, H. Jang, J.H. Lee, J.Y. Huh, S. Choi, J. Chung, J.B. Kim, PIASy-mediated sumoylation of SREBP1c regulates hepatic lipid metabolism upon fasting signaling, *Mol. Cell. Biol.* 34 (2014) 926–938.
- [25] M. Bell, H. Wang, H. Chen, J.C. McLenithan, D.W. Gong, R.Z. Yang, D. Yu, S.K. Fried, M.J. Quon, C. Londos, C. Sztalryd, Consequences of lipid droplet coat proteins downregulation in liver cells: abnormal lipid droplet metabolism and induction of insulin resistance, *Diabetes* 57 (2008) 2037–2045.
- [26] B.K. Straub, P. Stoeffel, H. Heid, R. Zimbelmann, P. Schirmacher, Differential pattern of lipid droplet-associated proteins and de novo perilipin expression in hepatocyte steatogenesis, *Hepatology* 47 (2008) 1936–1946.
- [27] H. Ogawa, N. Sasai, T. Kamisako, K. Baba, Effects of osthol on blood pressure and lipid metabolism in stroke-prone spontaneously hypertensive rats, *J. Ethnopharmacol.* 30 (2007) 26–31.
- [28] X. Zhao, J. Xue, X.L. Wang, Y. Zhang, M. Deng, M.L. Xie, Involvement of hepatic peroxisome proliferator-activated receptor  $\alpha/\gamma$  in the therapeutic effect of osthole on high-fat and high-sucrose-induced steatohepatitis in rats, *Int. Immunopharmacol.* 22 (2014) 176–181.
- [29] M. Boutant, C. Cantó, SIRT1 metabolic actions: integrating recent advances from mouse models, *Mol. Metab.* 3 (2014) 5–18.
- [30] S. Stojavljević, M. Gomerčić Palčić, L. Virović Jukić, L. Smirčić Duvnjak, M. Duvnjak, Adipokines and proinflammatory cytokines, the key mediators in the pathogenesis of nonalcoholic fatty liver disease, *World J. Gastroenterol.* 20 (2014) 18070–18091.
- [31] Y. Sumida, E. Niki, Y. Naito, T. Yoshikawa, Involvement of free radicals and oxidative stress in NAFLD/NASH, *Free Radic. Res.* 47 (2013) 869–880.
- [32] C.A. Loguercio, M. Federico, C. Trappoliere, S.I. de Tuccillo, L.A. Di, M. Niosi, M.V. D'Auria, R. Capasso, C. Del Vecchio Blanco, The effect of a silybin vitamin E-phospholipid complex on nonalcoholic fatty liver disease: a pilot study, *Dig. Dis. Sci.* 52 (2007) 2387–2395.
- [33] S.M. Yang, Y.L. Chan, K.F. Hua, J.M. Chang, H.L. Chen, Y.J. Tsai, Y.J. Hsu, L.K. Chao, F.L. Yang, Y.L. Tsai, S.H. Wu, Y.F. Wang, C.L. Tsai, A. Chen, S.M. Ka, Osthole improves an accelerated focal segmental glomerulosclerosis model in the early stage by activating the Nrf2 antioxidant pathway and subsequently inhibiting NF- $\kappa$ B-mediated COX-2 expression and apoptosis, *Free Radic. Biol. Med.* 73 (2014) 260–269.
- [34] J.K. Reddy, M.S. Rao, Lipid metabolism and liver inflammation. II. Fatty liver disease and fatty acid oxidation, *Am. J. Physiol. Gastrointest. Liver Physiol.* 290 (2006) G852–G858.
- [35] A.M. Diehl, Lessons from animal models of NASH, *Hepatol. Res.* 33 (2005) 138–144.
- [36] X.M. Xu, M.L. Zhang, Y. Zhang, L. Zhao, Osthole induces lung cancer cell apoptosis through inhibition of inhibitor of apoptosis family proteins, *Oncol. Lett.* 12 (2016) 3779–3784.
- [37] L. Zhang, G. Jiang, F. Yao, Y. He, G. Liang, Y. Zhang, B. Hu, Y. Wu, Y. Li, H. Liu, Growth inhibition and apoptosis induced by osthole, a natural coumarin, in hepatocellular carcinoma, *PLoS One* 7 (5) (2012) e37865.



## Cross-talk between bacterial two-component systems drives stepwise regulation of flagellar biosynthesis in swarming development



Chia-Fong Wei <sup>a,1</sup>, Yu-Huan Tsai <sup>a,1</sup>, Sheng-Hui Tsai <sup>a</sup>, Chuan-Sheng Lin <sup>a</sup>,  
Chih-Jung Chang <sup>a</sup>, Chia-Chen Lu <sup>b</sup>, Hsiou-Chen Huang <sup>c</sup>, Hsin-Chih Lai <sup>a,d,e,\*</sup>

<sup>a</sup> Department of Medical Biotechnology and Laboratory Science, Center for Molecular and Clinical Immunology, College of Medicine, Chang Gung University, Taoyuan, Taiwan

<sup>b</sup> Department of Respiratory Therapy, Fu Jen University, New Taipei City, Taiwan

<sup>c</sup> Graduate Institute of Biotechnology, National Chung Hsing University, Taichung, Taiwan

<sup>d</sup> Research Center for Chinese Herbal Medicine and Research Center for Food and Cosmetic Safety, College of Human Ecology, Chang Gung University of Science and Technology, Taoyuan, Taiwan

<sup>e</sup> Department of Laboratory Medicine and Chang Gung Immunology Consortium, Chang Gung Memorial Hospital, Taoyuan, Taiwan

### ARTICLE INFO

#### Article history:

Received 17 March 2017

Received in revised form

25 April 2017

Accepted 13 May 2017

Available online 15 May 2017

#### Keywords:

RssAB

QseBC

Swarming

Two-component system

### ABSTRACT

Swarming motility is a mode of bacterial movement over a solid surface driven by rotating flagella in a coordinated manner. Bacteria can use two-component system (TCS), which typically comprises a sensor kinase and a specific cognate response regulator, to properly react to environmental changes. We previously showed that the TCS RssAB suppresses flagellar biosynthesis master regulator *flhDC* specifically in swarming lag phase to control surface migration timing without affecting expansion rate in *Serratia marcescens* swarming development. Here we demonstrate that the TCS QseBC, which has been found in several human pathogens involved in flagellar and virulence regulation, has cross-talk with RssAB. We demonstrate that the phosphorylated QseB repressed *flhDC* expression, reducing swarming migration rate with modest effect on migration initiation. Unexpectedly, the QseC can dephosphorylate non-cognate response regulator RssB. Deletion of *qseC* prolonged RssAB signaling, reduced *flhDC* expression, and delayed migration initiation. Our data suggest that QseC is a flagellar biosynthesis activator by de-repressing RssB ~ P and QseB ~ P respectively in lag and migration phases in a stage-specific manner in swarming development.

© 2017 Elsevier Inc. All rights reserved.

### 1. Introduction

Swarming is a flagella-driven surface migration behavior that confers bacteria to rapidly colonize nutrient-rich environments, facilitating colony spread and accelerating biomass production [1]. Swarming has been found in many genera of Gram-negative and Gram-positive flagellated bacteria [2,3], characterized by a static lag phase and an active migration phase associated with striking metabolic and morphological changes [4,5].

*Serratia marcescens* is a Gram-negative bacterium and an opportunistic human pathogen capable of colonizing a wide variety

of ecological niches, such as soil, water, plants, insects, fishes, and humans [6]. We previously showed that the pigmented clinical isolate *S. marcescens* CH-1 displays swarming on 0.8% agar surface [7]. We further identified a two-component system (TCS) RssA-RssB (RssAB), which suppresses hemolysin and flagellar biosynthesis, regulating duration of swarming lag phase in response to environmental iron [7–11]. Upon binding of iron, the sensor kinase RssA phosphorylates its cognate response regulator RssB, conferring binding of downstream promoter DNAs to regulate gene expression [8,9,11]. The phosphorylated RssB (RssB ~ P) can bind the promoter region (−655+1) of *flhDC*, which encodes the master regulators of bacterial flagellar biosynthesis, thereby repressing *flhDC* gene expression and controlling the timing of migration initiation in swarming development [9,12].

QseBC is a TCS that has been demonstrated to regulate flagella-driven motility by controlling *flhDC* in *Escherichia coli* [13]. QseB is a response regulator and QseC is a sensor kinase. In

\* Corresponding author. Department of Medical Biotechnology and Laboratory Science, Center for Molecular and Clinical Immunology, College of Medicine, Chang Gung University, Taoyuan, Taiwan.

E-mail address: [hclai@mail.cgu.edu.tw](mailto:hclai@mail.cgu.edu.tw) (H.-C. Lai).

<sup>1</sup> These authors contributed equally to this work.

enterohaemorrhagic *E. coli* (EHEC), while the phosphorylated QseB (QseB ~ P) binds the promoter of *flhDC* *in vitro* and upregulates *flhDC* expression [14,15], the unphosphorylated QseB acts as a transcriptional repressor binding the middle region of *flhDC* promoter, thereby reducing bacterial motility [16]. In contrast, in uropathogenic *E. coli* (UPEC) QseC is a phosphatase of QseB ~ P, which can be phosphorylated by non-cognate sensor kinase PmrB, and only the phosphorylated form of QseB represses bacterial motility and *flhDC* gene expression [17–19]. These studies demonstrate that QseBC may evolve to use diverse molecular mechanisms in regulating bacterial flagellar biosynthesis.

Here we demonstrate that in *S. marcescens* QseBC is involved in *flhDC* regulation. While QseB ~ P modulates swarming migration rate by suppressing *flhDC* gene expression with modest effect on migration initiation timing, QseC can dephosphorylate RssB ~ P, thereby deactivating RssAB signaling and conferring bacterial surface migration initiation in swarming development. These findings identify a crosstalk between two TCSs, both of which cooperatively regulate flagellar biosynthesis in swarming development in a stage-specific manner.

## 2. Materials and methods

### 2.1. Bacterial strains and growth conditions

Bacterial strains and plasmids used in this study are listed in Table S1. *E. coli* and *S. marcescens* strains were grown in Luria-Broth (LB) media (Alpha Biosciences, USA) at 37 °C and 30 °C, respectively. Antibiotics were used at the following concentrations (μg/mL): ampicillin (Amp), 100; chloramphenicol, 50; gentamycin (Gm), 10; kanamycin (Km), 50; tetracycline (Tc), 12.

### 2.2. Motility assay

Swarming and swimming motility assays were performed on LB medium solidified with 0.8% (wt/vol) and 0.3% (wt/vol) Eiken agar, respectively. Overnight cultured bacteria (1 μL, 10<sup>9</sup> CFU/mL) were inoculated onto (swarming) or into (swimming) the centers of LB agar plates and incubated at 30 °C.

### 2.3. Quantitative RT-PCR

RNAs were extracted by using RNA isolation kit (Geneaid, Taiwan) according to the manufacturer's instruction. The total RNA was then reverse transcribed into cDNA using SuperScript III First-Strand Synthesis System kit (Invitrogen) according to the manufacturer's protocol. Quantitative PCR was performed with Light-Cycler 480 (Roche, Germany) and KAPA SYBR FAST master mix (2 × ) qPCR kit (Kapa Biosystems, USA). The primers were designed to amplify the coding sequences of these genes as follows: PJCG026/PJCG027 for 16S rRNA; PJCG048/PJCG049 for *flhDC*; PJCG054/PJCG055 for *qseB*. Data were analyzed by the 2<sup>−ΔΔCT</sup> method [20].

### 2.4. Protein purification

Purified proteins used in this study were purified as described [8,9]. Protein concentrations were determined by measuring absorbance at 595 nm using the Bradford protein assay kit (Bio-Rad).

### 2.5. Antibodies

Primary antibodies used in this study are listed below MONO-TOPE™ *Salmonella* flagellin monoclonal antibody (1:1000; ViroStat,

USA); GroEL polyclonal antibody (1:5000; Sigma-Aldrich); anti-His monoclonal antibody (1:5000; LTK BioLaboratories, Taiwan).

### 2.6. Electrophoretic mobility shift assay

To evaluate the binding of QseB to the *flhDC* promoter, a probe for *flhDC* promoter [12] was amplified by PCR using the template pHCL230 and digoxigenin-M13F/M13R primers. For competition assays, unlabeled DNA fragment of *flhDC* and *rssB* promoters [8] were PCR-amplified from genomic DNA of *S. marcescens* by primers PJCG039/PJCG043 and PJCG085/PJCG086, respectively. The protein-DNA interactions and gel electrophoresis analysis were performed as previously described [8,11].

### 2.7. Image of RssB localization by fluorescent microscopy

The assay was performed as previously described [9]. At indicated time point, wildtype and Δ*qseC* were harvested from swarming plates to determine the percentage of population showing EGFP-RssB localizing at the cell membrane (signal OFF) or in cytosol (signal ON). One hundred cells were counted for each sample.

### 2.8. In vitro GST pull-down assay

The GST pull-down assays were performed as described [9]. Briefly, purified GST or GST-tagged proteins were added in 1 mL interaction buffer [20 mM Tris-HCl (pH 7.5), 10 mM MgCl<sub>2</sub>, 100 mM KCl, 200 mg/mL BSA] supplemented with 30 μL 50% glutathione sepharose-4B beads and incubated at 4 °C for 1 h. After centrifugation at 3000 × g for 5 min and discarding the supernatants, the beads were incubated with indicated His-tagged proteins in 1 mL interaction buffer at 4 °C for another hour. The beads were then washed with aliquots of interaction buffer for four times and then resuspended in 15 μL sample buffer [50 mM Tris-HCl (pH 6.8), 10% SDS, 0.5% bromophenol blue, 30% glycerol, 5% β-mercaptoethanol] for SDS PAGE analysis and immunoblotting assays.

### 2.9. Phosphotransfer and phosphatase assays

For the phosphotransfer assay, 10 μM cQseC was autophosphorylated in a total volume of 100 μL TKMD buffer containing 20 μM ATP and 50 μCi of [γ-<sup>32</sup>P] ATP. After 30 min of incubation, RssB (20 μM) was added into the reaction mixture (*t* = 1). All phosphotransfer reactions were carried out at room temperature. For the phosphatase assay, 20 μM RssB was phosphorylated by His-tagged cRssA in TKMD buffer with 20 μM of 50 μCi [γ-<sup>32</sup>P] ATP for 1 h at room temperature [8]. cRssA was removed through pull-down by Ni-NTA beads and the fraction containing phosphorylated RssB was collected by a Micro Bio-Spin 6 chromatography column (Bio-Rad) to remove ATP. The RssB ~ P was then incubated with 10 μM cQseC in TKMD buffer at room temperature. A 10 μL aliquot was mixed with 2 μL of 6 × sample buffer to stop the reaction at indicated time points.

### 2.10. Accession numbers

RssA (AAN28325), RssB (AAN28326), QseB (AGH55580), QseC (AGH55581).



### 3. Results

#### 3.1. *qseB*, *qseC* and *qseBC* mutants show distinct swarming behaviors

Sequence analysis identified a putative *qseBC* locus on chromosome of *S. marcescens* CH-1. The amino acid sequences of QseB and QseC in *S. marcescens* CH-1 share 68.8% and 56.8% identities with those of EHEC O157H7, respectively (Genebank: AGH55580 and AGH55581). To understand whether the putative QseBC is implicated in bacterial motility, we constructed the markless mutants  $\Delta qseBC$ ,  $\Delta qseB$  and  $\Delta qseC$  (Fig. S1). We then tested the swarming motility of these mutants on LB medium solidified with 0.8% Eiken agar. Deletion of *qseC* reduced bacterial swarming motility (Fig. 1A) by reducing migration rate (Fig. 1B) and extension of lag phase for approximately 60 min (Fig. 1C), accompanied with reduced *flhDC* expression (Fig. 1D) and flagella production (Fig. 1E) in swarming development. Whereas  $\Delta qseB$  and  $\Delta qseBC$  showed accelerated migration rate (Fig. 1B) with modest effect on migration initiation timing (Fig. 1C), coupled with higher *flhDC* expression and flagella (Fig. 1D and E) during migration. Of note, while deletion of *qseC* resulted in reduced swimming motility ( $p < 0.05$ ),  $\Delta qseB$  and  $\Delta qseBC$  showed no significant differences in swimming motility compared to the wildtype strain CH-1 (Fig. 1F).

#### 3.2. Phosphorylated QseB directly binds *flhDC* promoter

QseB binds *flhDC* promoter and suppresses the gene expression in EHEC [16], while in UPEC only the phosphorylated QseB is capable of regulating downstream genes [18,19]. To investigate the impact of phosphorylation on QseB downstream gene regulation in *S. marcescens*, we determined the implication of QseB phosphorylation in its direct binding with the promoter (−655 to +1) of *flhDC* [12]. Neither GST nor GST-fused QseB bound *flhDC* promoter without prior phosphorylation treatment, whereas phosphorylated QseB after incubation with a phospho-donor acetyl-phosphate was able to bind *flhDC* promoter (Fig. 2A). Competition experiment demonstrated that excess of *flhDC* promoter DNA, instead of that of *rssB*, was able to compete the binding of QseB ~ P and release probe-labelled *flhDC* promoter, confirming the specific binding between QseB ~ P and *flhDC* promoter (Fig. 2B). Together, phosphorylation is required for QseB to bind *flhDC* promoter, thereby regulating migration rate in *S. marcescens* swarming development.

#### 3.3. QseC interacts with non-cognate response regulator RssB

As deletion of *qseC* resulted in delay of migration initiation (Fig. 1C) and RssB ~ P is responsible for suppressing migration initiation [9,19], we hypothesized that QseC acts as a phosphatase

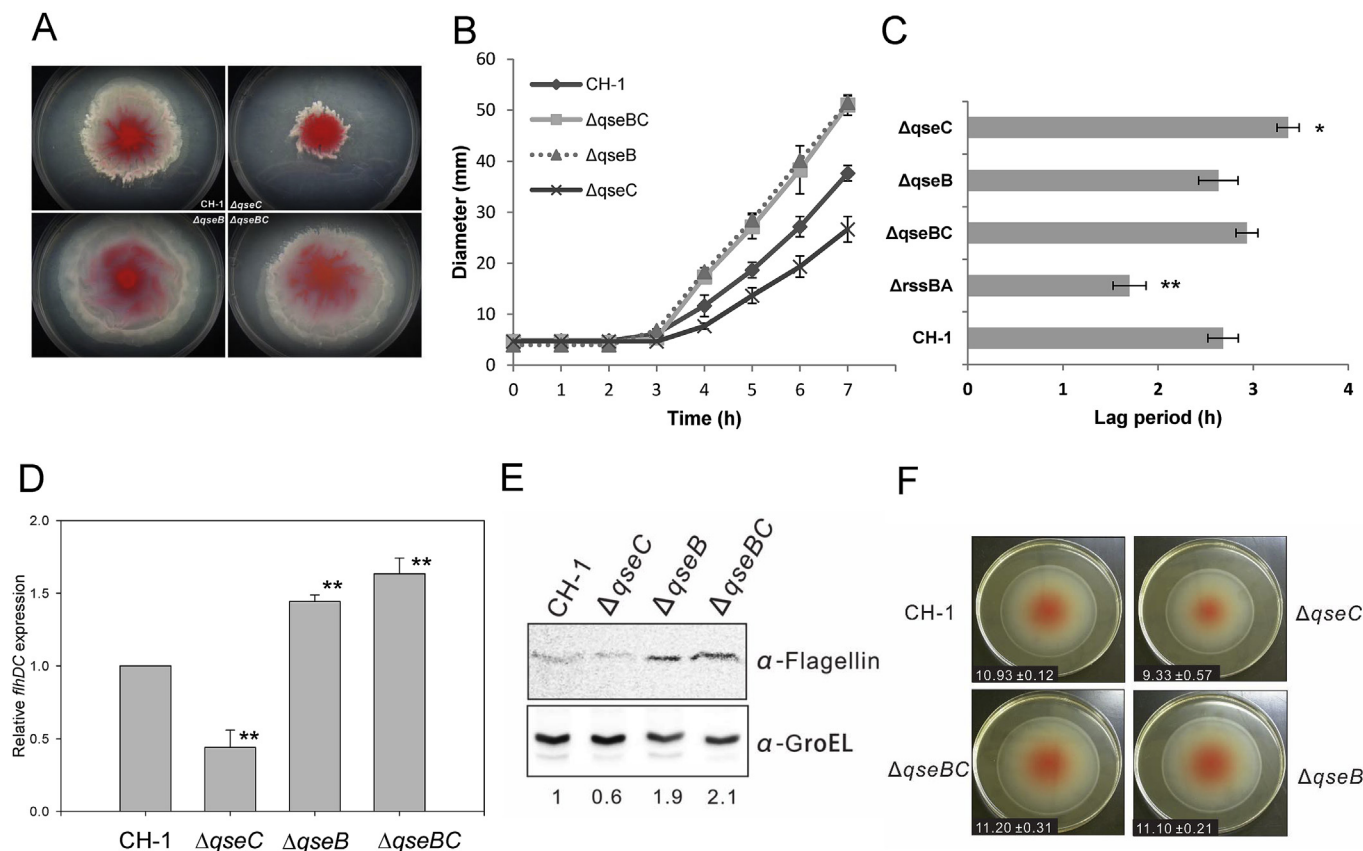


**Fig. 1. QseBC is involved in swarming motility regulation in *S. marcescens*.** The wildtype strain CH-1 and 3 different *qseBC* mutants,  $\Delta qseC$ ,  $\Delta qseB$ , and  $\Delta qseBC$  were applied for swarming motility assay. Overnight bacterial culture was inoculated onto 0.8% w/v agar LB plates. Representative swarming patterns at 8 h post inoculation (hpi) (A) and time-course swarming distances (colony diameter,  $n = 3$ ) (B) were shown. (C) The duration of lag period of each strain before the onset of surface migration was measured. At 4 hpi when migration had begun for all the 4 strains, cells on the plates were harvested for RNA and protein extraction. (D) The relative *flhDC* expression at 4 hpi was evaluated by qPCR. (E) Production of flagellin proteins at 4 hpi was analyzed by Western blot, where GroEL served as an internal control. Protein expression level (the bottom of the lower panel) was quantified by Multi Gauge software (Fujifilm) represented by the ratio of flagellin expression normalized to the amounts of GroEL for each strain compared to that of wildtype strain CH-1. The results shown are representative of 3 independent experiments. (F) Bacteria were inoculated into 0.3% w/v LB agar plates and representative images at 16 hpi were shown. The swimming distances (diameter in cm) were denoted as mean with SD.  $n = 3$ . The data in (B), (C) and (D) are shown as mean with SD. Statistical analyses in (C) and (D) were performed to compare with that of CH-1 using one-way ANOVA and Tukey's test for multiple comparisons. \*,  $p < 0.05$ . \*\*,  $p < 0.01$ .



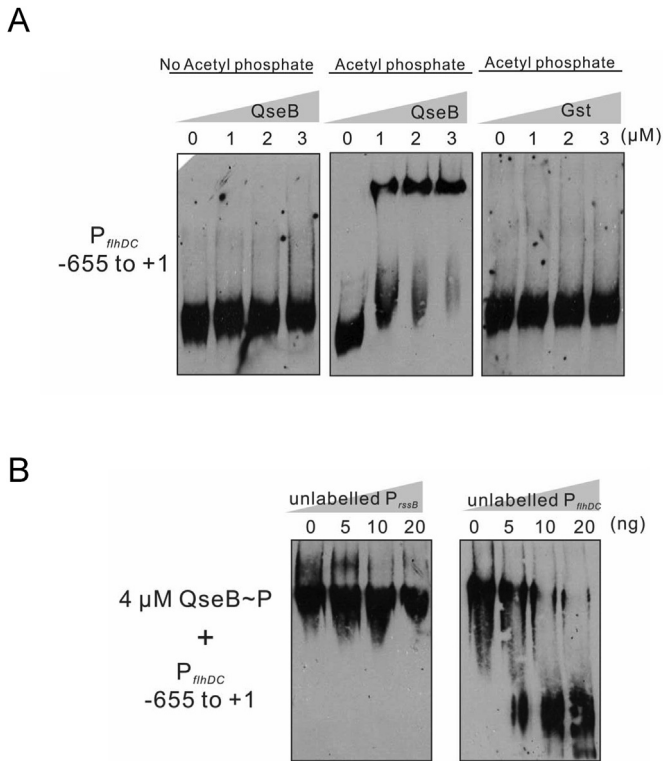


**Fig. 2. Phosphorylation is required for QseB to bind *flhDC* promoter.** (A) An electrophoretic mobility shift assay was performed using the DIG-labelled *flhDC* promoter fragment (–655 bp to +1 bp) with GST-tagged QseB or GST only as a negative control. Acetyl phosphate was used as a phosphor-donor to phosphorylate QseB. (B) Competition assays were performed using 8  $\mu$ M of phosphorylated GST-fused QseB with 0.5 ng of DIG-labelled *flhDC* promoter in the presence of increasing amounts of unlabelled promoter fragments (*rssB* and *flhDC*) as indicated.

of RssB ~ P to regulate migration initiation in swarming development. We performed an *in vitro* pull-down assay with purified proteins to address potential interaction between RssB and QseC. The His-tagged cytoplasmic regions of RssA (cRssA)/QseC (cQseC) and GST fused RssB/QseB were purified as previously described [9]. While GST did not pull down cRssA nor cQseC (Fig. 3A, lanes 1 and 2), GST-tagged RssB was able to pull down both cRssA and non-cognate kinase cQseC (Fig. 3A, lanes 4 and 5), and GST-tagged QseB interacted with cQseC (Fig. 3A, lane 6). In contrast, QseB did not pull down detectable cRssA, indicating the paucity of interaction between these two proteins (Fig. 3A, lane 3). We further performed a pull-down assay using either non-phosphorylated or phosphorylated response regulators RssB and QseB. In contrast to the interaction between RssA and RssB where phosphorylation of RssB decreases their interaction affinity [9], phosphorylated form of both RssB and QseB pulled down more cQseC compared to their non-phosphorylated ones (Fig. 3B). These data indicate that cQseC interacts with both RssB and QseB, especially the phosphorylated ones.

To determine whether QseC can act as a kinase or phosphatase of RssB, we performed a phosphor-transfer assay with purified proteins. cQseC was rapidly autophosphorylated after incubating with [ $\gamma$ - $^{32}$ P] ATP within 1 min, and phosphorylation of RssB was observed within 10 min of incubation with phosphorylated cQseC (Fig. 3C). We further addressed phosphatase activity of QseC against RssB ~ P. GST-tagged RssB was first phosphorylated by cognate sensor kinase cRssA as described previously [8]. After removing the His-tagged cRssA by Ni-NTA beads, RssB ~ P was either incubated alone or incubated with cQseC. We found that 75% of RssB ~ P was

dephosphorylated after 30 min incubation with cQseC, while only 30% of RssB ~ P was dephosphorylated when RssB ~ P was alone (Fig. 3D). Together with the observation that RssB ~ P has higher interaction affinity with cQseC, we postulated that QseC may facilitate RssB dephosphorylation and RssAB signaling deactivation.

#### 3.4. Deletion of *qseC* prolongs RssAB signaling and delays migration initiation in swarming development

Our previous studies have demonstrated that RssAB signaling is activated in response to environmental iron and RssB would be distributed in cytoplasm to bind downstream promoters during lag phase at 2 h in swarming development [9,11]. This signaling event would be deactivated at 3 h when surface migration is initiated where RssB relocates to cell membrane [9,11]. To understand whether QseC facilitates RssB dephosphorylation and RssAB signaling deactivation, we investigated RssAB signaling in swarming development in the absence of QseC (Fig. 4). While almost 80% of cells showed RssAB deactivation (RssB at cell membrane) at 3 h when migration had begun in wildtype strain CH-1 (Figs. 1C and 4B, CH-1), deletion of *qseC* resulted in prolonged RssAB signaling where approximately 80% of cells exhibited RssB distributed in cytosol at 3 h when  $\Delta$ qseC had not showed surface migration (Figs. 1C and 4B,  $\Delta$ qseC). At 4 h when  $\Delta$ qseC began to migrate, both CH-1 and  $\Delta$ qseC had approximately 80% of cell exhibiting membrane-localized RssB, indicative of the OFF state of RssAB signaling. Together with the *in vitro* data that QseC had higher affinity to RssB ~ P compared to RssB and QseC can dephosphorylate RssB ~ P (Fig. 3), and our previous studies showing that RssAB signaling downregulates *flhDC* expression [11,12,21], these suggest that QseC facilitates deactivation of RssAB signaling, thereby derepressing *flhDC* suppression by RssB ~ P and triggering surface migration initiation in swarming development.

#### 4. Discussion

As a predominant signal transduction system in bacteria, TCSs have been evolved to have specific interactions between sensor kinases and cognate response regulators, making cross-system interaction extremely rare [22]. Among the few examples, cross-interactions between QseBC and PmrAB have been investigated involving antibiotic resistance in UPEC [17,18]. PmrB is a kinase for both cognate response regulator PmrA and non-cognate response regulator QseB in response to extracellular iron [17]. In addition to phosphor-donor, sensor kinases can also display phosphatase activity toward their cognate phosphorylated regulators [23]. Here we report that QseC serves as a phosphatase in cross-talk between QseBC and RssAB. This cross-talk co-opts these two TCSs in regulating bacterial flagellar biosynthesis and motility on surfaces.

QseBC has been demonstrated to regulate swimming motility in various bacterial species such as *E. coli* [13,19]. The defective swarming was also observed in UPEC and *Aeromonas hydrophila* *qseC* deletion mutants [19,24]. Here we characterized QseBC in swarming development in *S. marcescens*. Accordingly, deletion of *qseC* in *S. marcescens* reduced both swimming and swarming motility. We further showed that QseB reduces *flhDC* expression, as in EHEC and UPEC [16,19]. In contrast to EHEC and UPEC, in which deletion of *qseB* does not significantly affect motility, we found that *qseB* deletion accelerated surface migration in swarming development with modest impact on swimming motility in *S. marcescens*. Moreover, in contrast to EHEC where QseB binds *flhDC* promoter without phosphorylation, phosphorylation is required for QseB to bind *flhDC* promoter in *S. marcescens* as in UPEC [16,19]. Together, the QseB-mediated *flhDC* regulation in *S. marcescens* is distinct from that in EHEC, further highlighting the diversity of QseBC regulation

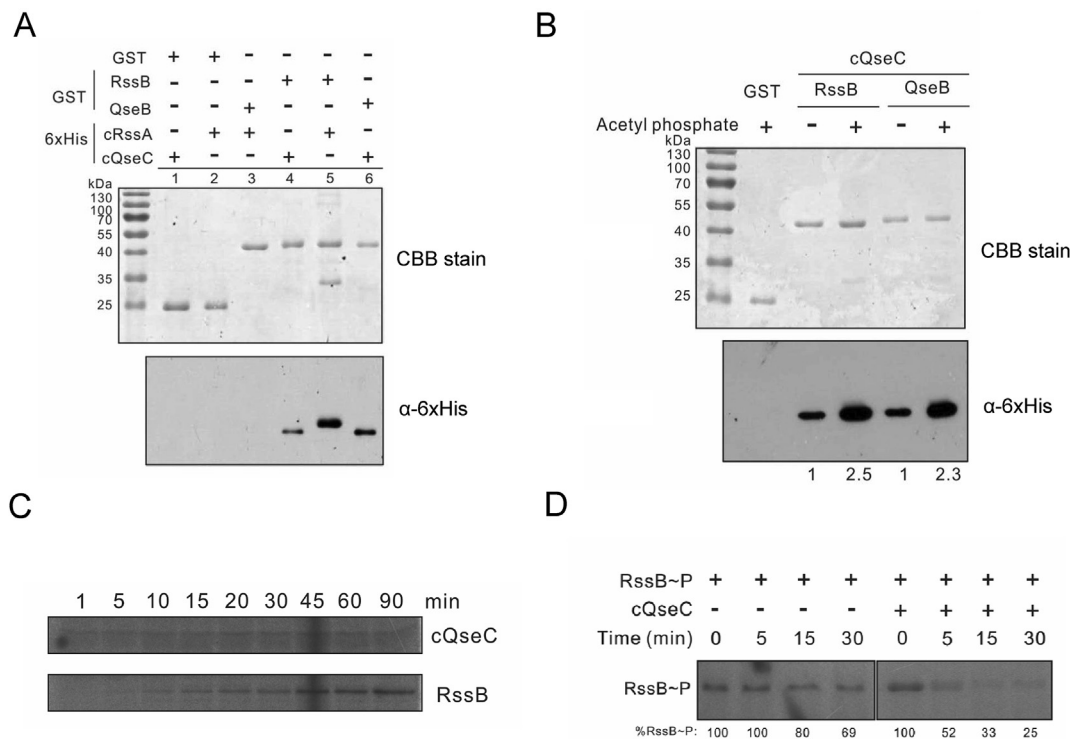


**Fig. 3. QseC acts as a kinase and phosphatase of RssB *in vitro*.** (A) Protein interactions were determined by *in vitro* pull-down assay using glutathione-sepharose beads that pull down GST-tagged proteins and corresponding interacting proteins. The response regulators RssB and QseB were fused to GST as baits, and the cytoplasmic part of sensor kinases RssA (cRssA) and QseC (cQseC) were 6 × His tagged for subsequent immuno-detection. Each reaction mixture was incubated as indicated, followed by SDS PAGE separation and analysis by Coomassie Brilliant Blue (CBB) staining or immuno-detection with anti-6 × His antibody. (B) The effect of response regulator phosphorylation on protein interaction was determined by *in vitro* pull-down assay. GST-tagged RssB or QseB was either pre-incubated with 50 mM acetyl phosphate (+) or without (-), and reacted with His-tagged cQseC followed by SDS PAGE separation and analysis by CBB staining or immuno-detection with anti-6 × His antibody. The relative amount of His-tagged cQseC shown below was quantified by the ImageJ software. (C) Phosphotransfer assay was performed with purified cQseC incubated with [ $\gamma$ - $^{32}$ P]-ATP and purified GST-tagged RssB. Samples were harvested at the time points indicated. (D) GST-fused RssB was phosphorylated by His-tagged cRssA with [ $\gamma$ - $^{32}$ P]-ATP followed by purification with glutathione-sepharose beads. The purified phosphorylated RssB was then incubated without or with cQseC. Samples were harvested at the time points indicated. The %RssB ~ P was calculated based on the peak intensity of each band determined by the ImageJ software and normalized to that at  $t = 0$ . The results shown are representative of 3 independent experiments.

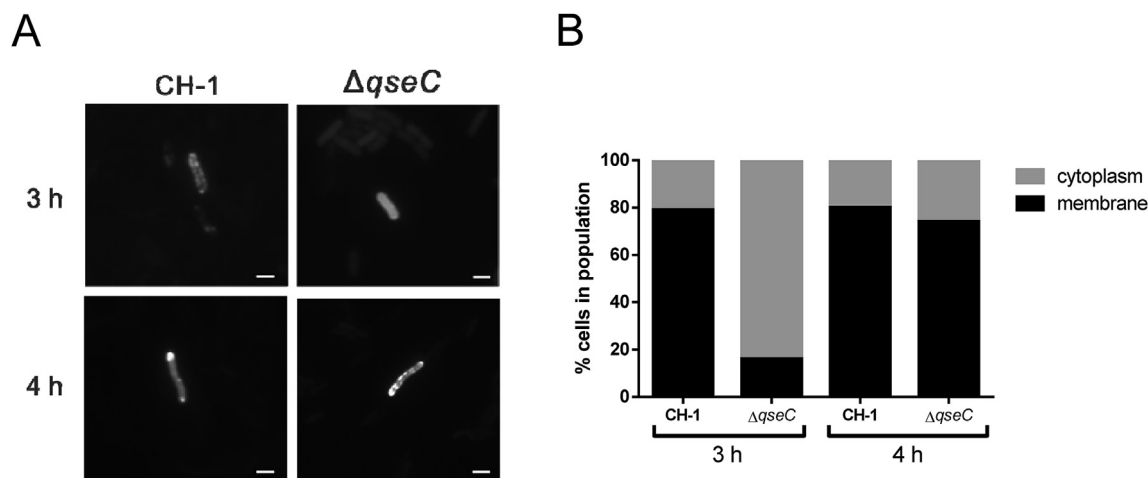


**Fig. 4.  $\Delta qseC$  exhibits prolonged RssAB signaling in swarming development.** Swarming motility assay was performed using CH-1 or  $\Delta qseC$  harboring pEGFP-RssB plasmid. Bacterial cells on swarming plates were harvested at 3 and 4 hpi, followed by examination under a fluorescent microscope. (A) Representative image of cytoplasmic localization of EGFP-tagged RssB for each condition was shown. Cytoplasmic and membrane location of EGFP-RssB indicates ON (activated) and OFF (inactivated) RssAB signaling states, respectively. Scale bars, 2  $\mu$ m. (B) The percentage of cells showing EGFP-RssB localizing at the cell membrane or in the cytoplasm was quantified for the wildtype strain CH-1 and  $\Delta qseC$  mutant at 3 and 4 hpi. At least 100 cells were counted for each condition. The results shown are representative of 4 independent experiments.

mode in bacteria.  
We previously identified environmental iron as a signal of RssAB in regulating surface migration initiation timing in swarming

development [11]. As a phosphatase of RssB ~ P, QseC also modulates migration timing in swarming. Moreover, QseC may regulate migration rate through modulating the phosphorylation state of its

cognate response regulator QseB. QseC in EHEC senses epinephrine, norepinephrine and autoinducer-3 followed by autophosphorylation [25]. It is not clear whether QseC phosphatase activity requires external signals. Investigating the signals modulating QseC kinase/phosphatase activity in *S. marcescens* may identify additional environmental cues that regulate swarming development at different stages.

QseBC in UPEC has been demonstrated to interact with the PmrAB where PmrB phosphorylates both PmrA and QseB in presence of iron [17,18]. As PmrB is an iron sensor, this suggests that environmental iron can modulate QseB target genes, such as *flhDC* and other virulence factors. Here we showed that QseBC in *S. marcescens* interacts with the iron-sensing RssAB. While QseC can target RssB as a kinase and a phosphatase (Fig. 3C and D), RssA cannot interact with QseB (Fig. 3A). Our previous work also showed that RssAB regulates environmental iron availability by controlling *pvcABC* expression and production of the iron chelator ICDH-Coumarin [11]. Our results thus suggest that QseC signals, such as epinephrine/norepinephrine/autoinducer-3, may control iron homeostasis through cross-system interaction between QseBC and RssAB. In addition, sequence analysis identifies PmrAB in the genome of *S. marcescens* CH-1 (data not shown). *S. marcescens* CH-1 may thus serve as a model organism to investigate cross-system interactions among three TCSs and its implication in bacterial multicellular behavior and virulence *in vivo* [21].

This work uncovers an interaction between QseBC and RssAB in regulating *flhDC* expression, where QseC plays a pivotal role in controlling migration initiation timing by affecting RssAB signaling, and regulates migration rate by modulating QseB phosphorylation. As deletion of *qseC* showed distinct phenotype in migration rate compared to that of *qseB* deletion mutant (Fig. 1B), we propose that there is another kinase that can phosphorylate QseB to counteract with phosphatase activity of QseC in regulating migration rate in swarming development. Understanding the QseB phospho-donor, which could be PmrB, and the signals modulating QseC property in *S. marcescens*, would help unraveling the regulation of bacterial swarming development.

## Acknowledgments

We thank Dr. Ching-Hsiu Tsai and Dr. I-Hsuan Chen at National Chung Hsing University (NCHU) for their assistance on radiation experiments. This work was supported by Ministry of Science and Technology (MOST101-2320-B-182-023-MY3, MOST103-2320-B-182-027-MY3, MOST105-2320-B-182-032-MY3) and Chang Gung Memorial hospital (BMRPA04, CMRPD1C0781-3, CORPD1F0011-2, QZRPD132).

## Appendix A. Supplementary data

Supplementary data related to this article can be found at <http://dx.doi.org/10.1016/j.bbrc.2017.05.077>.

## Transparency document

Transparency document related to this article can be found online at <http://dx.doi.org/10.1016/j.bbrc.2017.05.077>.

## References

- [1] G.M. Fraser, C. Hughes, Swarming motility, *Curr. Opin. Microbiol.* 2 (1999)

- 630–635.
- [2] N. Verstraeten, K. Braeken, B. Debkumari, M. Fauvart, J. Fransaer, J. Vermant, J. Michiels, Living on a surface: swarming and biofilm formation, *Trends Microbiol.* 16 (2008) 496–506.
- [3] D.B. Kearns, A field guide to bacterial swarming motility, *Nature reviews, Microbiology* 8 (2010) 634–644.
- [4] W. Kim, M.G. Surette, Metabolic differentiation in actively swarming *Salmonella*, *Mol. Microbiol.* 54 (2004) 702–714.
- [5] R.M. Harshey, Bacterial motility on a surface: many ways to a common goal, *Annu. Rev. Microbiol.* 57 (2003) 249–273.
- [6] A. Hejazi, F.R. Falkner, *Serratia marcescens*, *J. Med. Microbiol.* 46 (1997) 903–912.
- [7] H.C. Lai, P.C. Soo, J.R. Wei, W.C. Yi, S.J. Liaw, Y.T. Horng, S.M. Lin, S.W. Ho, S. Swift, P. Williams, The RssAB two-component signal transduction system in *Serratia marcescens* regulates swarming motility and cell envelope architecture in response to exogenous saturated fatty acids, *J. Bacteriol.* 187 (2005) 3407–3414.
- [8] J.R. Wei, Y.H. Tsai, P.C. Soo, Y.T. Horng, S.C. Hsieh, S.W. Ho, H.C. Lai, Biochemical characterization of RssA-RssB, a two-component signal transduction system regulating swarming behavior in *Serratia marcescens*, *J. Bacteriol.* 187 (2005) 5683–5690.
- [9] Y.H. Tsai, J.R. Wei, C.S. Lin, P.H. Chen, S. Huang, Y.C. Lin, C.F. Wei, C.C. Lu, H.C. Lai, RssAB signaling coordinates early development of surface multicellularity in *Serratia marcescens*, *PLoS one* 6 (2011) e24154.
- [10] P.C. Soo, Y.T. Horng, Y.L. Chang, W.W. Tsai, W.Y. Jeng, C.C. Lu, H.C. Lai, ManA is regulated by RssAB signaling and promotes motility in *Serratia marcescens*, *Res. Microbiol.* 165 (2014) 21–29.
- [11] C.S. Lin, Y.H. Tsai, C.J. Chang, S.F. Tseng, T.R. Wu, C.C. Lu, T.S. Wu, J.J. Lu, J.T. Horng, J. Martel, D.M. Ojcius, H.C. Lai, J.D. Young, An iron detection system determines bacterial swarming initiation and biofilm formation, *Sci. Rep.* 6 (2016) 36747.
- [12] P.C. Soo, Y.T. Horng, J.R. Wei, J.C. Shu, C.C. Lu, H.C. Lai, Regulation of swarming motility and *flhDC<sub>SM</sub>* expression by RssAB signaling in *Serratia marcescens*, *J. Bacteriol.* 190 (2008) 2496–2504.
- [13] V. Sperandio, A.G. Torres, J.B. Kaper, Quorum sensing *Escherichia coli* regulators B and C (QseBC): a novel two-component regulatory system involved in the regulation of flagella and motility by quorum sensing in *E. coli*, *Mol. Microbiol.* 43 (2002) 809–821.
- [14] M.B. Clarke, V. Sperandio, Transcriptional autoregulation by quorum sensing *Escherichia coli* regulators B and C (QseBC) in enterohaemorrhagic *E. coli* (EHEC), *Mol. Microbiol.* 58 (2005) 441–455.
- [15] M.B. Clarke, V. Sperandio, Transcriptional regulation of *flhDC* by QseBC and sigma (FlhA) in enterohaemorrhagic *Escherichia coli*, *Mol. Microbiol.* 57 (2005) 1734–1749.
- [16] D.T. Hughes, M.B. Clarke, K. Yamamoto, D.A. Rasko, V. Sperandio, The QseC adrenergic signaling cascade in Enterohaemorrhagic *E. coli* (EHEC), *PLoS Pathog.* 5 (2009) e1000553.
- [17] K.R. Guckes, E.J. Breland, E.W. Zhang, S.C. Hanks, N.K. Gill, H.M. Algood, J.E. Schmitz, C.W. Stratton, M. Hadjifrangiskou, Signaling by two-component system noncognate partners promotes intrinsic tolerance to polymyxin B in uropathogenic *Escherichia coli*, *Sci. Signal* 10 (2017).
- [18] K.R. Guckes, M. Kostakioti, E.J. Breland, A.P. Gu, C.L. Shaffer, C.R. Martinez 3rd, S.J. Hultgren, M. Hadjifrangiskou, Strong cross-system interactions drive the activation of the QseB response regulator in the absence of its cognate sensor, *Proc. Natl. Acad. Sci. U. S. A.* 110 (2013) 16592–16597.
- [19] M. Kostakioti, M. Hadjifrangiskou, J.S. Pinkner, S.J. Hultgren, QseC-mediated dephosphorylation of QseB is required for expression of genes associated with virulence in uropathogenic *Escherichia coli*, *Mol. Microbiol.* 73 (2009) 1020–1031.
- [20] K.J. Livak, T.D. Schmittgen, Analysis of relative gene expression data using real-time quantitative PCR and the 2(-Delta Delta C(T)) method, *Methods* 25 (2001) 402–408.
- [21] C.S. Lin, J.T. Horng, C.H. Yang, Y.H. Tsai, L.H. Su, C.F. Wei, C.C. Chen, S.C. Hsieh, C.C. Lu, H.C. Lai, RssAB-FlhDC-ShlBA as a major pathogenesis pathway in *Serratia marcescens*, *Infect. Immun.* 78 (2010) 4870–4881.
- [22] M.T. Laub, M. Goulian, Specificity in two-component signal transduction pathways, *Annu. Rev. Genet.* 41 (2007) 121–145.
- [23] A.Y. Mitrophanov, E.A. Groisman, Signal integration in bacterial two-component regulatory systems, *Genes Dev.* 22 (2008) 2601–2611.
- [24] B.K. Khajanchi, E.V. Kozlova, J. Sha, V.L. Popov, A.K. Chopra, The two-component QseBC signalling system regulates *in vitro* and *in vivo* virulence of *Aeromonas hydrophila*, *Microbiology* 158 (2012) 259–271.
- [25] V. Sperandio, A.G. Torres, B. Jarvis, J.P. Nataro, J.B. Kaper, Bacteria-host communication: the language of hormones, *Proc. Natl. Acad. Sci. U. S. A.* 100 (2003) 8951–8956.

# Post-traumatic Stress Disorder and Risk of Parkinson Disease: A Nationwide Longitudinal Study

Yee-Lam E. Chan, M.D., Ya-Mei Bai, M.D., Ph.D., Ju-Wei Hsu, M.D., Kai-Lin Huang, M.D., Tung-Ping Su, M.D., Cheng-Ta Li, M.D., Ph.D., Wei-Chen Lin, M.D., Tai-Long Pan, Ph.D., Tzeng-Ji Chen, M.D., Ph.D., Shih-Jen Tsai, M.D., Mu-Hong Chen, M.D.

---

**Objective:** Increasing evidence has suggested a relationship between post-traumatic stress disorder (PTSD) and neurodegenerative disorder, such as Alzheimer disease. The association between PTSD and Parkinson disease (PD), however, remains unclear. **Method:** Using the Taiwan National Health Insurance Research Database, 7,280 subjects (1,456 patients aged  $\geq 45$  years with PTSD and 5,824 age-/sex-matched individuals without PTSD) were enrolled between 2002 and 2009 and followed to the end of 2011. Subjects who developed PD during the follow-up period were identified. **Results:** An increased risk of developing PD was found in patients with PTSD (Wald  $\chi^2 = 12.061$ , hazard ratio [HR]: 3.46, 95% confidence interval [CI]: 1.72–6.96) compared with individuals without PTSD, after adjusting for demographic data and medical and psychiatric comorbidities. The sensitivity tests after excluding the first year observation (Wald  $\chi^2 = 7.948$ , HR: 3.01, 95% CI: 1.40–6.46) and the first 3-year observation (Wald  $\chi^2 = 5.099$ , HR: 3.07, 95% CI: 1.16–8.15) were consistent. **Conclusions:** Patients with PTSD had an elevated risk of developing PD in later life. Further studies would be required to clarify the exact pathophysiology between PTSD and PD and to investigate whether the prompt intervention for PTSD may reduce this risk. (Am J Geriatr Psychiatry 2017; 25:917–923)

**Key Words:** PTSD, psychological trauma, Parkinson disease, temporal association

---

Received December 19, 2016; revised March 8, 2017; accepted March 20, 2017. From the Department of Psychiatry (Y-LEC, Y-MB, J-WH, K-LH, T-PS, C-TL, W-CL, S-JT, M-HC); Department of Family Medicine (T-JC), Taipei Veterans General Hospital, Taipei, Taiwan; Division of Psychiatry (Y-MB, J-WH, K-LH, T-PS, C-TL, W-CL, S-JT, M-HC), School of Medicine; Institute of Hospital and Health Care Administration (T-JC), National Yang-Ming University, Taipei, Taiwan; School of Traditional Chinese Medicine (T-LP), Chang Gung University, Taoyuan, Taiwan; Liver Research Center (T-LP), Chang Gung Memorial Hospital, Taoyuan, Taiwan; and the Research Center for Chinese Herbal Medicine and Research Center for Food and Cosmetic Safety (T-LP), College of Human Ecology, Chang Gung University of Science and Technology, Taoyuan, Taiwan. Send correspondence and reprint requests to Kai-Lin Huang, M.D., Department of Psychiatry, Taipei Veterans General Hospital, No. 201, Shih-Pai Road, Sec. 2, 11217 Taipei, Taiwan. e-mail: [klh0503@gmail.com](mailto:klh0503@gmail.com); Mu-Hong Chen, M.D., Department of Psychiatry, Taipei Veterans General Hospital, No. 201, Shih-Pai Road, Sec. 2, 11217 Taipei, Taiwan. e-mail: [kremer7119@gmail.com](mailto:kremer7119@gmail.com)

© 2017 American Association for Geriatric Psychiatry. Published by Elsevier Inc. All rights reserved.

<http://dx.doi.org/10.1016/j.jagp.2017.03.012>



Parkinson disease (PD) is the second most common neurodegenerative disease, and patients with PD present with motor symptoms such as rest tremor, muscular rigidity, movement slowness, and postural instability and nonmotor symptoms such as olfactory dysfunction, cognitive impairment, psychiatric symptoms, sleep disorders, autonomic dysfunction, pain, and fatigue.<sup>1-3</sup> The worldwide prevalence of PD ranges from 41 per 100,000 people for those aged 40–49 years to 1903 per 100,000 people for those aged 80 years and older.<sup>1,4</sup> A complicated interplay of genetic and environmental factors affecting numerous fundamental cellular processes, including the formation and aggregation of Lewy bodies and loss of dopaminergic neurons in the substantia nigra, contributes to PD development.<sup>1,2</sup>

Accumulating evidence has suggested that stress and post-traumatic stress disorder (PTSD) are associated with an increased propensity for neurodegenerative disorders, particularly Alzheimer disease.<sup>5-7</sup> Yaffe et al. followed 181,093 midlife veterans without dementia (53,155 veterans with and 127,938 veterans without PTSD) for 10 years and reported that, compared with the patients without PTSD, those with PTSD were 2.31 times (95% confidence interval [CI]: 2.24–2.39) more likely to develop incident dementia.<sup>8</sup> The authors also reported that PTSD is associated with all dementia types, including Alzheimer disease (hazard ratio [HR]: 1.71, 95% CI: 1.58–1.85), vascular dementia (HR: 1.69, 95% CI: 1.54–1.85), frontotemporal dementia (HR: 2.19, 95% CI: 1.43–3.34), and Lewy body dementia (2.05, 95% CI: 1.59–2.62).<sup>8</sup> Moreover, extensive research has indicated that stress can directly induce neurotoxicity in some brain regions, such as the hippocampus, prefrontal cortex, striatum, and substantia nigra, and cause brain degeneration and pathological alterations.<sup>9</sup> Furthermore, several studies have hypothesized a relationship between psychological stress and PD development.<sup>10-12</sup> A recent 8-year follow-up study on 67,786 patients who experienced adjustment and mood symptoms after stressful life events reported that those with adjustment disorder had an increased PD risk (standardized incidence ratios: 1.84, 95% CI: 1.53–2.20).<sup>13</sup> The association between PTSD, a severe mental disorder resulting from a life-threatening trauma, and PD development has rarely been investigated, however. In addition, increasing evidence has reported that PTSD patients were more likely to have the risk of traumatic brain injury, which has been regarded as

an important risk of PD development.<sup>14,15</sup> Both traumatic brain injury and PTSD would lead to neurodegeneration, but the impact of PTSD on the association between traumatic brain injury and PD was rarely clarified.<sup>7</sup>

This study investigated the association of PTSD with PD development by using the Taiwan National Health Insurance Research Database (NHIRD), a large sample size, and a longitudinal follow-up study design. We hypothesized that, compared with patients without PTSD, patients with PTSD are more likely to develop PD in later life.

---

## METHODS

### Data Source

Taiwan's National Health Insurance is a mandatory universal health insurance program that was inaugurated in 1995 and covers up to 99% of the country's 23 million residents. The NHIRD is administered by the National Health Research Institute and provides comprehensive patient information, such as demographic data, clinical visit dates, and disease diagnoses. All identities are encrypted to ensure patient privacy. The diagnostic codes used are based on the *International Classification of Diseases, Ninth Revision, Clinical Modification* (ICD-9-CM). The NHIRD has been used extensively in numerous epidemiologic studies in Taiwan.

### Inclusion Criteria for Patients with PTSD and the Non-PTSD Group

Patients aged 45 years and older who were diagnosed with PTSD (ICD-9-CM code: 309.81) by board-certificated psychiatrists on the basis of clinical judgment and psychiatric interview between January 1, 2002, and December 31, 2009, and who had no history of PD (ICD-9-CM code: 332) before enrollment in the administrative data set were included as the PTSD cohort. The time of PTSD diagnosis was defined as the time of enrollment. The age-, sex-, and time of enrollment-matched (1:4) non-PTSD cohort was randomly identified after eliminating the study individuals, those who had been given a diagnosis of PTSD at any time, and those with Parkinson disease before enrollment. Cases of PD (ICD-9-CM code: 332.0)



diagnosed by board-certified neurologists were identified during the follow-up period and followed until December 31, 2011, or the date of death. Medical and psychiatric comorbidities during the whole follow-up period were also assessed as confounding factors; these included depressive disorder (ICD-9-CM codes: 296.2, 296.3, 300.4), hypertension (ICD-9-CM codes: 401–405), dyslipidemia (ICD-9-CM codes: 272.0–272.4), diabetes mellitus (ICD-9-CM codes: 250), cerebrovascular diseases (ICD-9-CM codes: 430–438), epilepsy (ICD-9-CM codes: 345), migraine (ICD-9-CM codes: 346), and traumatic brain injury (ICD-9-CM codes: 800–804, 850–854). The level of urbanization (1–5; level 1: most urbanized; level 5: least urbanized) was also assessed. The Taipei Veterans General Hospital institutional review board permitted this study.

### Statistical Analysis

For between-group comparisons, the F test was used for continuous variables and Pearson's  $\chi^2$  test was used for nominal variables, where appropriate. Proportional hazards assumption was met by the log minus log

plot evaluation. The Cox regression model was used to investigate the HRs with 95% CIs of developing PD after adjustment for demographic data (age, sex, level of urbanization, and income) and medical and psychiatric comorbidities. Sensitivity tests were performed to validate the findings after we excluded observations on the first year and the first 3 years. All data processing and statistical analyses were performed using the Statistical Package for Social Science (SPSS) Version 17 software (IBM, Armonk, NY) and Statistical Analysis Software (SAS) Version 9.1 (SAS Institute, Cary, NC).

## RESULTS

In all, 1,456 patients with PTSD and 5,824 age-/sex-matched individuals without PTSD were included in our study, with a female predominance (Table 1). During the follow-up period, patients with PTSD had a higher incidence of developing PD (2.0% versus 0.5%,  $\chi^2 = 30.390$ ,  $p < 0.001$ ) and a shorter duration between PTSD and PD development ( $3.18 \pm 2.07$  versus

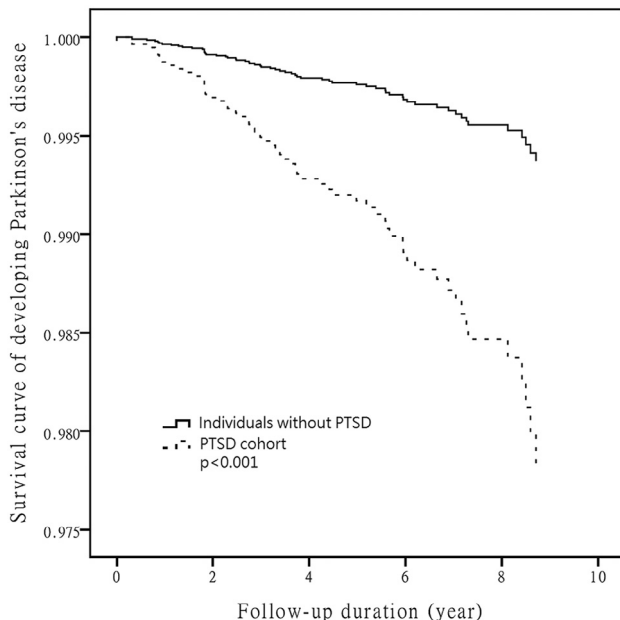
**TABLE 1. Demographic Data and Incidence of Parkinson Disease of Patients with PTSD and the Control Group**

	Patients with PTSD (N = 1,456)	Individuals without PTSD (N = 5,824)	$\chi^2/F$ test <sup>a</sup>	p
Age at diagnosis of PTSD/enrollment, years (SD)	55.69 (8.72)	55.68 (8.71)	0.001	0.978
Male sex, N (%)	350 (24.0)	1,400 (24.0)	0.001	1.000
Parkinson disease, N (%)	29 (2.0)	31 (0.5)	30.390	<0.001
Age at diagnosis (years, SD)	67.40 (10.90)	71.89 (9.64)	2.868	0.096
Duration between PTSD/enrollment and diagnosis, years (SD)	3.18 (2.07)	4.51 (2.58)	4.755	0.033
Medical comorbidities, N (%)				
Depressive disorder	1,016 (69.8)	297 (5.1)	3,298.637	<0.001
Hypertension	581 (39.9)	2,153 (36.9)	4.358	0.040
Dyslipidemia	420 (28.8)	1,481 (25.4)	7.124	0.008
Diabetes mellitus	289 (19.8)	1,018 (17.5)	4.487	0.036
Cerebrovascular diseases	227 (15.6)	524 (9.0)	54.870	<0.001
Traumatic brain injury	106 (7.3)	83 (1.4)	158.069	<0.001
Epilepsy	31 (2.1)	60 (1.0)	11.418	0.001
Migraine	114 (7.8)	218 (3.7)	44.778	<0.001
Level of urbanization, N (%)			125.560	<0.001
1 (most urbanized)	326 (22.4)	1815 (31.2)		
2	463 (31.8)	1811 (31.1)		
3	170 (11.7)	835 (14.3)		
4	231 (15.9)	826 (14.2)		
5 (most rural)	266 (18.3)	537 (9.2)		
Income-related insured amount, N (%)			20.279	<0.001
≤15,840 NTD/month	684 (47.0)	2,461 (42.2)		
15,841–25,000 NTD/month	435 (29.9)	1,684 (28.9)		
≥25,001 NTD/month	337 (23.1)	1,683 (28.9)		

Notes: PTSD: post-traumatic stress disorder; SD: standard deviation; NTD: New Taiwan Dollar.

<sup>a</sup>F test (df = 1, 7282) for continuous variables and Pearson's  $\chi^2$  test (df = 1) for nominal variables.

**FIGURE 1.** Survival curve of developing Parkinson disease among patients with PTSD and control group. Kaplan-Meier survival analysis with a log rank test ( $\chi^2 = 30.936$ ,  $df = 1$ ).



$4.51 \pm 2.58$  years,  $F = 0.001$ ,  $p = 0.033$ ) (Table 1). In addition, patients with PTSD had a higher prevalence of medical and psychiatric comorbidities, including depressive disorder (69.8% versus 5.1%,  $\chi^2 = 3298.637$ ,  $p < 0.001$ ), hypertension (39.9% versus 36.9%,  $\chi^2 = 4.358$ ,  $p = 0.04$ ), dyslipidemia (28.8% versus 25.4%,  $\chi^2 = 7.124$ ,  $p = 0.008$ ), diabetes mellitus (19.8% versus 17.5%,  $\chi^2 = 4.487$ ,  $p = 0.036$ ), cerebrovascular diseases (15.6% versus 9.0%,  $\chi^2 = 54.870$ ,  $p < 0.001$ ), traumatic brain injury (7.3% versus 1.4%,  $\chi^2 = 158.069$ ,  $p < 0.001$ ), epilepsy (2.1% versus 1.0%,  $\chi^2 = 11.418$ ,  $p = 0.001$ ), and migraine (7.8% versus 3.7%,  $\chi^2 = 44.778$ ,  $p < 0.001$ ), than did the individuals without PTSD (Table 1). Finally, we calculated the interclass correlation to confirm the level of dependence between two groups. The number of interclass correlation was 0, meaning there was no matching-related dependence.

Kaplan-Meier survival analysis with a log-rank test demonstrated that patients with PTSD had a higher likelihood of developing PD ( $\chi^2 = 30.936$ ,  $df = 1$ ,  $p < 0.001$ ) than the non-PTSD group (Figure 1). The Cox regression model showed that patients with PTSD had an increased risk (Wald  $\chi^2 = 12.061$ , HR: 3.46, 95% CI:

**TABLE 2.** Risk of Developing Parkinson Disease of Patients with PTSD and the Control Group

	Parkinson disease		
	Wald $\chi^2$	HR	95% CI
PTSD, presence versus absence	<b>12.061</b>	<b>3.46</b>	<b>1.72–6.96</b>
Comorbidities, presence versus absence			
Depressive disorder	0.024	1.06	0.52–2.17
Hypertension	0.006	1.02	0.57–1.85
Dyslipidemia	1.123	1.37	0.77–2.45
Diabetes mellitus	0.200	0.87	0.46–1.63
Cerebrovascular diseases	0.491	1.63	0.90–2.98
Traumatic brain injury	0.001	1.01	0.35–2.90
Epilepsy	<b>13.157</b>	<b>4.74</b>	<b>2.05–10.99</b>
Migraine	0.280	0.68	0.16–2.83

Notes: Cox regression model with the Wald  $\chi^2$  test ( $df = 1$ ) adjusting for demographic data and medical and psychiatric comorbidities and PTSD as a binary variable.

PTSD: post-traumatic stress disorder; HR: hazard ratio; CI: confidence interval.

**Bold type** indicates statistical significance.

1.72–6.96) of developing PD in later life after adjustment for demographic data and medical and psychiatric comorbidities compared with the non-PTSD group (Table 2). The sensitivity tests after excluding the first year observation (Wald  $\chi^2 = 7.948$ , HR: 3.01, 95% CI: 1.40–6.46) and the first 3-year observation (Wald  $\chi^2 = 5.099$ , HR: 3.07, 95% CI: 1.16–8.15) were consistent (Table 3). Furthermore, epilepsy was related to the risk of PD development (Wald  $\chi^2 = 13.157$ , HR: 4.74, 95% CI: 2.05–10.99) (Table 2). In addition, given that traumatic brain injury was an important PD risk factor, a univariate model was used and showed a trend significance between traumatic brain injury and PD (Wald  $\chi^2 = 3.729$ , HR: 2.72, 95% CI: 0.99–7.39). The significance disappeared, however, in the multivariate model with a full adjustment of demographic data and comorbidities.

## DISCUSSION

Accumulating evidence has suggested a relationship between psychological trauma and PD risk.<sup>11–13,16,17</sup> In 1980, Gibberd et al. followed a group of 4,684 ex-Far East prisoners of war released in 1945 and reported that PD often developed years after release, with a prevalence much higher than that in the normal population.<sup>18</sup> Vlajinac et al. investigated stressful life events experienced by 110 patients with newly

**TABLE 3. Sensitivity Test for the Risk of Developing Parkinson Disease of Patients with PTSD and the Control Group**

	Total		>1 year		>3 years	
	Wald $\chi^2$	HR (95% CI)	Wald $\chi^2$	HR (95% CI)	Wald $\chi^2$	HR (95% CI)
PTSD, presence vs. absence	<b>12.061</b>	<b>3.46 (1.72–6.96)</b>	<b>7.948</b>	<b>3.01 (1.40–6.46)</b>	<b>5.099</b>	<b>3.07 (1.16–8.15)</b>

Notes: Cox regression model with the Wald  $\chi^2$  test (df = 1) adjusting for demographic data and medical and psychiatric comorbidities and PTSD as a binary variable.

PTSD: post-traumatic stress disorder; HR: hazard ratio; CI: confidence interval.

**Bold type** indicates statistical significance.

diagnosed PD and reported that patients with PD had a higher risk of stressful life events, such as child death (odds ratio [OR]: 14.9, 95% CI: 1.8–121.9), spouse death (OR: 2.5, 95% CI: 1.2–5.3), and involvement in a war (OR: 4.3, 95% CI: 1.4–12.9) or an air raid (OR: 25.9, 95% CI: 13.4–49.7), than did those in the non-PTSD group.<sup>17</sup> Furthermore, they indicated that the risk of PD significantly increased with the number of stressful events.<sup>17</sup> Svensson et al. reported that patients who developed adjustment disorders because of incapability to cope with a particular stress were likely to develop PD in later life.<sup>13</sup> In our study, we first proposed the association of PTSD with PD risk. Compared with the individuals without PTSD, the patients with PTSD had an increased risk of PD in later life, after adjustment for medical and psychiatric comorbidities.

Some animal and molecular studies have supported the relationship between psychological stress or trauma and PD risk. Sugama et al. reported that the loss of dopaminergic neurons in the substantia nigra pars compacta was evident after 2 weeks of chronic restraint stress and progressed in a time-dependent manner, reaching up to 61% at 16 weeks.<sup>19</sup> Furthermore, the authors investigated whether chronic stress affects other major dopaminergic systems, including the ventral tegmental area (VTA) and tuberoinfundibular (TIDA) system and reported that tyrosine hydroxylase-immunoreactive neurons decreased by 9.8%, 19.2%, and up to 40% in the second, fourth, and 16th weeks in the VTA during chronic stress, respectively, and by 10.9%, 38.2%, and approximately 60% in the second, fourth, and 16th weeks in the TIDA system, respectively.<sup>20</sup> In addition, de Pablos et al. reported that chronic stress enhanced the activation of midbrain microglia and exacerbated the death of nigral dopaminergic neurons in stressed rats.<sup>21</sup> Furthermore, Corral-Frias et al. investigated the role of the VTA in a rodent model of PTSD with long-term

behavioral changes after a brief but intense foot shock followed by three brief reminders and reported that the firing rate of VTA dopaminergic cells significantly decreased 2 weeks after the trauma.<sup>22</sup> On the basis of all of the aforementioned results, we concluded that psychological stress and trauma can trigger dopaminergic neurodegeneration in the substantia nigra pars compacta and VTA and may increase the risk of PD in later life.

PTSD-related hypothalamic–pituitary–adrenal (HPA) axis dysfunction and altered immunological regulation may explain the relationship between PTSD and PD risk.<sup>21,23–27</sup> The patients with PTSD exhibited the paradoxical phenomenon of low plasma and urinary cortisol levels and high corticotropin-releasing hormone levels; this phenomenon, caused by the increased sensitivity of the HPA axis to negative feedback, may lead to a dysregulated immune state and altered brain function.<sup>28,29</sup> Moreover, de Pablos et al. examined the inflammatory process in stressed rats and reported that a glucocorticoid-dependent pathway is involved in the death of dopaminergic neurons in the substantia nigra through the activation of microglia and increased levels of several proinflammatory cytokines, including tumor necrosis factor (TNF)- $\alpha$  and interleukin (IL)-6.<sup>21</sup> Furthermore, Ros-Bernal et al. demonstrated that the overall level of the glucocorticoid receptor was decreased in the substantia nigra of patients with PD and that mice with selective inactivation of the glucocorticoid receptor gene in microglia had increased loss of dopaminergic neurons.<sup>25</sup> Studies have reported that the levels of TNF- $\alpha$ , IL-6, and IL-1 $\beta$  were higher in patients with PTSD than in individuals without PTSD, and the high levels positively correlated with the PTSD symptom duration.<sup>26,27</sup> In addition, Reale et al. demonstrated that the levels of IL-1 $\beta$  and TNF- $\alpha$  in the plasma were higher in patients with PD than in individuals without PTSD and that the levels of cytokines

were significantly correlated with the severity and stage of PD.<sup>24</sup> Pott Godoy et al. indicated that central and systemic IL-1 $\beta$  exacerbated the dopaminergic neurodegeneration in the substantia nigra and motor symptoms in a rat model of PD.<sup>30</sup> Acute severe psychological trauma can dysregulate the HPA axis and increase central and systemic inflammation, thus increasing the risk of PD.

Several studies have suggested a relationship between epilepsy and PD,<sup>31,32</sup> consistent with our findings. Gaitatzis et al. investigated the medical conditions in patients with epilepsy and reported that the risk of neurodegenerative disorders, including PD (rate ratio: 3.19, 95% CI: 2.44–4.18), was higher in the patients with epilepsy than in individuals without PTSD.<sup>32</sup> Feddersen et al. reported that approximately 2.6% of patients with PD had a diagnosis of epilepsy and a higher risk of status epilepticus than did those without PD.<sup>31</sup> The prevalence of epilepsy was only 2.1% in the PTSD cohort in our study, however, so it may be premature to regard epilepsy as a convincing risk factor of PD. The association between epilepsy and PD needs further investigation. In addition, traumatic brain injury was not a significant risk factor of PD after adjusting for medical and psychiatric comorbidities in our study, which may indicate that PTSD and related comorbidities confounded the relationship between traumatic brain injury and PD. Further studies would be necessary to elucidate the inter-relationships among PTSD, traumatic brain injury, and PD.

Our study has several limitations. First, the incidence of PD may have been underestimated because only those who sought medical help and consultation were included in our study. Nevertheless, PD was diagnosed by board-certified neurologists, yielding an improved diagnostic validity. Second, the potential bias

of misclassification may be existent because those who did not seek medical help and consultation for PTSD may be classified in the non-PTSD samples. The misclassification bias may underestimate our current finding. Further clinical follow-up study would be necessary to validate our results. Third, given that PTSD is a chronic mental disorder, PTSD patients may be more likely to contact with the medical system, and to incidentally get the PD diagnosis. Besides, it may be possible that PTSD medication-related extrapyramidal side effect was erroneously diagnosed as PD. Nevertheless, in our study, secondary parkinsonism was excluded in the main outcome, and the PD diagnosis was given by neurologists, having an improved diagnostic validity. Fourth, some information, such as trauma type, PTSD severity, traumatic brain injury severity, family history, personal lifestyle, and environmental factors, was unavailable in the NHIRD. Thus, we could not evaluate the effect of these factors on PD risk.

In conclusion, patients with PTSD have an increased risk of PD in later life. Additional studies are warranted to validate our findings and elucidate the pathophysiology underlying the relationship between PTSD and PD, and to investigate whether the prompt intervention for PTSD may reduce this risk.

We thank Mr. I-Fan Hu for his friendship and support.

MHC and YLC designed the study and wrote the protocol and manuscript. SJT, YMB, JWH, KLH, TPS, CTL, TLP, and WCL assisted with the preparation and proofreading of the manuscript. YMB, TJC, and MHC provided advice on statistical analysis.

The authors declare no conflict of interest.

The study was supported by grants from Taipei Veterans General Hospital (V103E10-001, V104E10-002, V105E10-001-MY2-1, V105A-049).

## References


1. Kalia LV, Lang AE: Parkinson's disease. *Lancet* 2015; 386:896–912
2. Nussbaum RL, Ellis CE: Alzheimer's disease and Parkinson's disease. *N Engl J Med* 2003; 348:1356–1364
3. Postuma RB, Berg D, Adler CH, et al: The new definition and diagnostic criteria of Parkinson's disease. *Lancet Neurol* 2016; 15:546–548
4. Pringsheim T, Jette N, Frolkis A, et al: The prevalence of Parkinson's disease: a systematic review and meta-analysis. *Mov Disord* 2014; 29:1583–1590
5. Greenberg MS, Tanev K, Marin MF, et al: Stress, PTSD, and dementia. *Alzheimers Dement* 2014; 10:S155–S165
6. Khachaturian AS, Khachaturian ZS: Military risk factors for Alzheimer's dementia and neurodegenerative disease. *Alzheimers Dement* 2014; 10:S90–S91
7. Weiner MW, Veitch DP, Hayes J, et al: Effects of traumatic brain injury and posttraumatic stress disorder on Alzheimer's disease in veterans, using the Alzheimer's Disease Neuroimaging Initiative. *Alzheimers Dement* 2014; 10:S226–S235
8. Yaffe K, Vittinghoff E, Lindquist K, et al: Posttraumatic stress disorder and risk of dementia among US veterans. *Arch Gen Psychiatry* 2010; 67:608–613

9. Lucassen PJ, Pruessner J, Sousa N, et al: Neuropathology of stress. *Acta Neuropathol* 2014; 127:109–135
10. Djamshidian A, Lees AJ: Can stress trigger Parkinson's disease? *J Neurol Neurosurg Psychiatry* 2014; 85:878–881
11. Hou G, Tian R, Li J, et al: Chronic stress and Parkinson's disease. *CNS Neurosci Ther* 2014; 20:1–2
12. Smith AD, Castro SL, Zigmond MJ: Stress-induced Parkinson's disease: a working hypothesis. *Physiol Behav* 2002; 77:527–531
13. Svensson E, Farkas DK, Gradus JL, et al: Adjustment disorder and risk of Parkinson's disease. *Eur J Neurol* 2016; 23:751–756
14. Ascherio A, Schwarzschild MA: The epidemiology of Parkinson's disease: risk factors and prevention. *Lancet Neurol* 2016; 15:1257–1272
15. Carlson K, Kehle S, Meis L, et al: The Assessment and Treatment of Individuals with History of Traumatic Brain Injury and Post-Traumatic Stress Disorder: A Systematic Review of the Evidence. Washington, DC: Department of Veterans Affairs, 2009. Available from: <https://www.ncbi.nlm.nih.gov/books/NBK49144/>
16. Hemmerle AM, Herman JP, Seroogy KB: Stress, depression and Parkinson's disease. *Exp Neurol* 2012; 233:79–86
17. Vlajinac H, Sipetic S, Marinkovic J, et al: The stressful life events and Parkinson's disease: a case-control study. *Stress Health* 2013; 29:50–55
18. Gibberd FB, Simmonds JP: Neurological disease in ex-Far-East prisoners of war. *Lancet* 1980; 2:135–137
19. Sugama S, Sekiyama K, Kodama T, et al: Chronic restraint stress triggers dopaminergic and noradrenergic neurodegeneration: possible role of chronic stress in the onset of Parkinson's disease. *Brain Behav Immun* 2016; 51:39–46
20. Sugama S, Kakinuma Y: Loss of dopaminergic neurons occurs in the ventral tegmental area and hypothalamus of rats following chronic stress: possible pathogenic loci for depression involved in Parkinson's disease. *Neurosci Res* 2016; 111:48–55
21. de Pablos RM, Herrera AJ, Espinosa-Oliva AM, et al: Chronic stress enhances microglia activation and exacerbates death of nigral dopaminergic neurons under conditions of inflammation. *J Neuroinflammation* 2014; 11:34
22. Corral-Frias NS, Lahood RP, Edelman-Vogelsang KE, et al: Involvement of the ventral tegmental area in a rodent model of post-traumatic stress disorder. *Neuropsychopharmacology* 2013; 38:350–363
23. Finsterwald C, Alberini CM: Stress and glucocorticoid receptor-dependent mechanisms in long-term memory: from adaptive responses to psychopathologies. *Neurobiol Learn Mem* 2014; 112:17–29
24. Reale M, Iarlori C, Thomas A, et al: Peripheral cytokines profile in Parkinson's disease. *Brain Behav Immun* 2009; 23:55–63
25. Ros-Bernal F, Hunot S, Herrero MT, et al: Microglial glucocorticoid receptors play a pivotal role in regulating dopaminergic neurodegeneration in parkinsonism. *Proc Natl Acad Sci U S A* 2011; 108:6632–6637
26. Spivak B, Shohat B, Mester R, et al: Elevated levels of serum interleukin-1 beta in combat-related posttraumatic stress disorder. *Biol Psychiatry* 1997; 42:345–348
27. Tucker P, Ruwe WD, Masters B, et al: Neuroimmune and cortisol changes in selective serotonin reuptake inhibitor and placebo treatment of chronic posttraumatic stress disorder. *Biol Psychiatry* 2004; 56:121–128
28. Bremner JD, Vythilingam M, Anderson G, et al: Assessment of the hypothalamic-pituitary-adrenal axis over a 24-hour diurnal period and in response to neuroendocrine challenges in women with and without childhood sexual abuse and posttraumatic stress disorder. *Biol Psychiatry* 2003; 54:710–718
29. Wentworth BA, Stein MB, Redwine LS, et al: Post-traumatic stress disorder: a fast track to premature cardiovascular disease? *Cardiol Rev* 2013; 21:16–22
30. Pott Godoy MC, Tarelli R, Ferrari CC, et al: Central and systemic IL-1 exacerbates neurodegeneration and motor symptoms in a model of Parkinson's disease. *Brain* 2008; 131:1880–1894
31. Feddersen B, Remi J, Einhellig M, et al: Parkinson's disease: less epileptic seizures, more status epilepticus. *Epilepsy Res* 2014; 108:349–354
32. Gaitatzis A, Carroll K, Majeed A, et al: The epidemiology of the comorbidity of epilepsy in the general population. *Epilepsia* 2004; 45:1613–1622



Article

# Response of Dermal Fibroblasts to Biochemical and Physical Cues in Aligned Polycaprolactone/Silk Fibroin Nanofiber Scaffolds for Application in Tendon Tissue Engineering

Chih-Hao Chen <sup>1,2</sup>, Shih-Hsien Chen <sup>1</sup>, Chang-Yi Kuo <sup>1</sup>, Meng-Lun Li <sup>1</sup> and Jyh-Ping Chen <sup>1,2,3,4,\*</sup> 

<sup>1</sup> Department of Chemical and Materials Engineering, Chang Gung University, Taoyuan 33302, Taiwan; chchen5027@gmail.com (C.-H.C.); e26449@hotmail.com (S.-H.C.); onesky1997@hotmail.com (C.-Y.K.); lujason45k13@hotmail.com (M.-L.L.)

<sup>2</sup> Department of Plastic and Reconstructive Surgery and Craniofacial Research Center, Chang Gung Memorial Hospital, Kwei-San, Taoyuan 33305, Taiwan

<sup>3</sup> Institute Research Center for Chinese Herbal Medicine and Research Center for Food and Cosmetic Safety, College of Human Ecology, Chang Gung University of Science and Technology, Kwei-San, Taoyuan 33302, Taiwan

<sup>4</sup> Department of Materials Engineering, Ming Chi University of Technology, Tai-Shan, New Taipei City 24301, Taiwan

\* Correspondence: jpchen@mail.cgu.edu.tw; Tel.: +886-3-211-8800 (ext. 5298)

Received: 6 July 2017; Accepted: 6 August 2017; Published: 11 August 2017

**Abstract:** Silk fibroin (SF) and fiber alignment were introduced into polycaprolactone (PCL)-based electrospun nanofibers as chemical and physical cues for tendon tissue engineering applications. The physicochemical properties of random PCL (RP) nanofibers, random PCL/SF (RPSF) nanofibers and aligned PCL/SF (APSF) nanofibers were characterized for fiber orientation and SF blending effects. An in vitro cell culture with rabbit dermal fibroblasts (RDFBs) on nanofibers indicated that SF promotes cell proliferation to a higher extent than fiber alignment. Cells aligned in the direction of fiber axes could be confirmed through scanning electron microscopy (SEM) observation and cytoskeleton staining. The quantitative real-time polymerase chain reaction (qRT-PCR) experiments indicated up-regulated gene expression of tendon marker proteins (type I collagen (Col I), fibronectin and biglycan) on APSF nanofibers and tendon reconstruction was confirmed from Col III gene expression. Animal experiments with Achilles tendon defect repairs in rabbits were carried out with RPSF and APSF scaffolds. The beneficial effects of fiber alignment were verified from histological and immunohistochemical staining, where cell migration and extracellular matrix protein deposition tend to stretch in a parallel direction along the axial direction of APSF nanofibers with enhanced Col I and tenascin C production. Biomechanical testing indicated the tensile stiffness and maximum load of cell-seeded APSF scaffolds were 60.2 and 81.3% of normal tendon values, respectively, which are significantly higher than cell-seeded RPSF or acellular APSF and RPSF scaffolds. These results suggest that APSF nanofiber scaffolds combined with RDFBs have the potential to repair the gap defects of Achilles tendons in vivo and to effectively restore the function and structure of tendons.

**Keywords:** silk fibroin; polycaprolactone; nanofibers; alignment; tendon; tissue engineering

## 1. Introduction

Due to the unique structure and functions of tendons, the repair of tendon defects remains a major challenge for clinicians. Ineffective treatments of patients frequently lead to the functional impairment

of tendons. In addition, hypocellularity and hypovascularity of tendons reduce the healing ability; thus, full recovery is relatively difficult [1]. Current tendon defect reconstruction or repair is based on artificial and autologous tendons or allografts. Since allografts have several limitations such as the risk of transmitting infectious diseases, a lack of durability and functionality, insufficient supply, a potential incompatibility with the recipient's body and immune system and the difficulty of their preservation during transportation, the autograft method is more widely used in clinical practices [2–4]. Although autografts may produce satisfactory long-term results and be compatible with the body's immune system, patients often experience donor site morbidities. Moreover, the grafts are unable to achieve the required biomechanical strength during the tendon reconstruction process due to poor graft efficiency [5,6]. On the other hand, tissue-engineered scaffolds of varying sizes and shapes can be combined with special physical and biochemical cues to provide a suitable environment for cells to attach and proliferate in order to facilitate matrix deposition in scaffolds, and thus to induce tendon regeneration and accelerate tendon repair [7–10].

Electrospinning can easily and directly process biocompatible polymers into nanofibers. The nanofibrous scaffold will have a high surface area and proper pore size that can be applied for various applications, such as drug delivery, wound dressing and tissue engineering [11,12]. However, typical nanofibers that have been fabricated via electrospinning were usually collected in a random orientation that exhibits isotropic mechanical properties. In order to further enhance the mechanical strength and possibly provide physical cues for attached cells, methods have been proposed to induce the aligned orientation of electrospun nanofibers [13]. The anisotropic structure of nanofibers will be suitable for tendons, ligament, muscle and nerve tissue engineering as an ideal scaffold [4]. Specifically, with the unique anisotropic structure and biomechanical property of tendon tissue, the ideal scaffold for tendon tissue engineering should have an analogous form and possess comparable physical properties that would enhance the quality of engineered tendon tissue. Aligned nanofibers thus represent a unique group of fibrous scaffolds that not only resemble the anisotropic structure but also induce a particular cell orientation response [4].

Polycaprolactone (PCL) is a semi-crystalline, biocompatible and biodegradable polymer with a melting point of 60 °C and a glass transition temperature of −60 °C. Several reports have demonstrated PCL as an ideal scaffold material for tendon tissue engineering due to its good mechanical properties [13]. However, the hydrophobic property and slow degradation of PCL may limit its application in tissue engineering. As one of the two proteins secreted by silk worms, silk fibroin (SF) could be used as for various biomedical applications [14]. Existing literature supports the notion that SF, as a matrix material, can promote cell growth [15,16]. With its minimal inflammatory response in vivo and high oxygen/water permeability, SF could be deemed one of the best biomaterials for skeletal tissue regeneration [17]. Scaffolds fabricated from SF were applied for different regenerative medicine applications to regenerate bone, eye, nerve, skin, tendon, ligament, and cartilage [18]. Together with its hydrophilic property, we postulated that SF, acting as biochemical cues, could be blended with PCL to fabricate nanofibers to improve the cellular response of nanofiber scaffolds.

Type I collagen (Col I) fiber bundles are major extracellular matrix components of tendons, in addition to a small amount of other types of collagens and matrix materials. Being oriented parallel to their long axes, Col I fiber bundles endow tendons with the ability to resist high tensile loads. Tendons also contain various types of cells (mainly fibroblasts) that are arranged in a parallel manner [19]. Therefore, aligned nanofibers that can support fibroblast attachment and guide cell proliferation along the co-axial orientation of nanofibers, combined with subsequent extracellular matrix (ECM) secretion with a controlled parallel spatial deposit of ECM proteins, will be a preferred scaffold for tendon tissue engineering [20].

Combining biochemical cues from SF and physical cues from fiber alignment, aligned PCL/SF nanofibers constitute a desirable nanofiber scaffold for tendon tissue engineering. By combining the favorable properties of PCL and SF through their use in the process of fabricating a new, blended, aligned nanofiber scaffold, we will demonstrate that the cells/scaffold construct from rabbit dermal

fibroblasts (RDFBs) and the aligned PCL/SF nanofiber scaffold are suitable for repairing Achilles tendon defects in rabbit/animal model.

In this study, SF and PCL were used as basal materials to fabricate random PCL (RP) nanofibers, random PCL/SF (RPSF) nanofibers and aligned PCL/SF (APSF) nanofibers through electrospinning. The physicochemical properties of nanofiber scaffolds were first characterized in detail, followed by in vitro cell culture with rabbit dermal fibroblasts (RDFBs) to compare the cellular response of RDFBs to nanofibers with biochemical and physical cues. The nanofiber scaffolds were lastly combined with RDFBs to examine the feasibility of Achilles tendon defect repair in rabbits.

## 2. Results and Discussion

### 2.1. Characterization of Nanofibers

#### 2.1.1. SEM Analysis

Figure 1A shows the SEM images of RP, RPSF and APSF nanofibers. The images confirm no bead formation on the surface of the nanofibers. By using static and rotating collectors, RP and RPSF nanofiber scaffolds are expected to be composed of random nanofibers, while the APSF nanofiber scaffold will contain aligned nanofibers. Indeed, significant fiber orientation differences between RP (RPSF) and APSF could be observed, with APSF displaying a uniform aligned nanofiber arrangement in one direction. It has been shown that cells were guided to align along the topographical alignment of aligned nanofibers and fiber alignment had a profound effect on cell proliferation, cell orientation and tendon strength [21]. The hydrophilicity of the nanofiber scaffold was determined by measuring the water contact angles, as shown in the inserts of Figure 1A. The RP showed a water contact angle of  $117.5^\circ$ . However, by adding SF, the water contact angle of the RPSF was significantly reduced to  $91.4^\circ$ , indicating the formation of a comparatively more hydrophilic surface. We hypothesized that the increased hydrophilic nature of RPSF is due to the blending with SF, which contained a significant number of hydrophilic functional groups and thus improved the hydrophilicity of RPSF. In comparison, the APSF exhibited a more significant drop in water contact angle to  $27.5^\circ$  when the fiber orientation was changed from random to alignment. According to the literature, the surface roughness of materials can create higher degrees of barrier effect, which would prevent the wider extension of water droplets on the substrate surface, and thereby increase the water contact angle [22]. Since APSF will have a smoother surface, a lower degree of roughness with an axial alignment of nanofibers, its water contact angle is much lower than that of the randomly oriented RPSF [23]. The physical effect (due to fiber orientation) on reducing the water contact angle could be seen to be much more pronounced than the biochemical effect (by blending PCL with SF).

The orientation of nanofibers is shown in Figure 1B with histograms showing the fiber orientation of RP, RPSF, and APSF nanofibers relative to a vertical line setting at  $0^\circ$ . The angular distribution of RP ( $41.2^\circ$ ), RPSF ( $43.6^\circ$ ), and APSF ( $14.2^\circ$ ) indicates APSF has a significant alignment compared to RP and RPSF. Figure 1C shows the diameter distribution of nanofibers. The average fiber diameter of RP (mean  $\pm$  standard deviation (SD)) is  $549.4 \pm 172.4$  nm, which is similar to that of RPSF at  $582.5 \pm 178.6$  nm. Although the fiber diameter of APSF appeared to shift to a lower value ( $363.7 \pm 116.0$  nm), there is no significant difference of the average fiber diameter among all nanofiber scaffolds. This might be due to the insufficient number of measurements of fiber diameters.

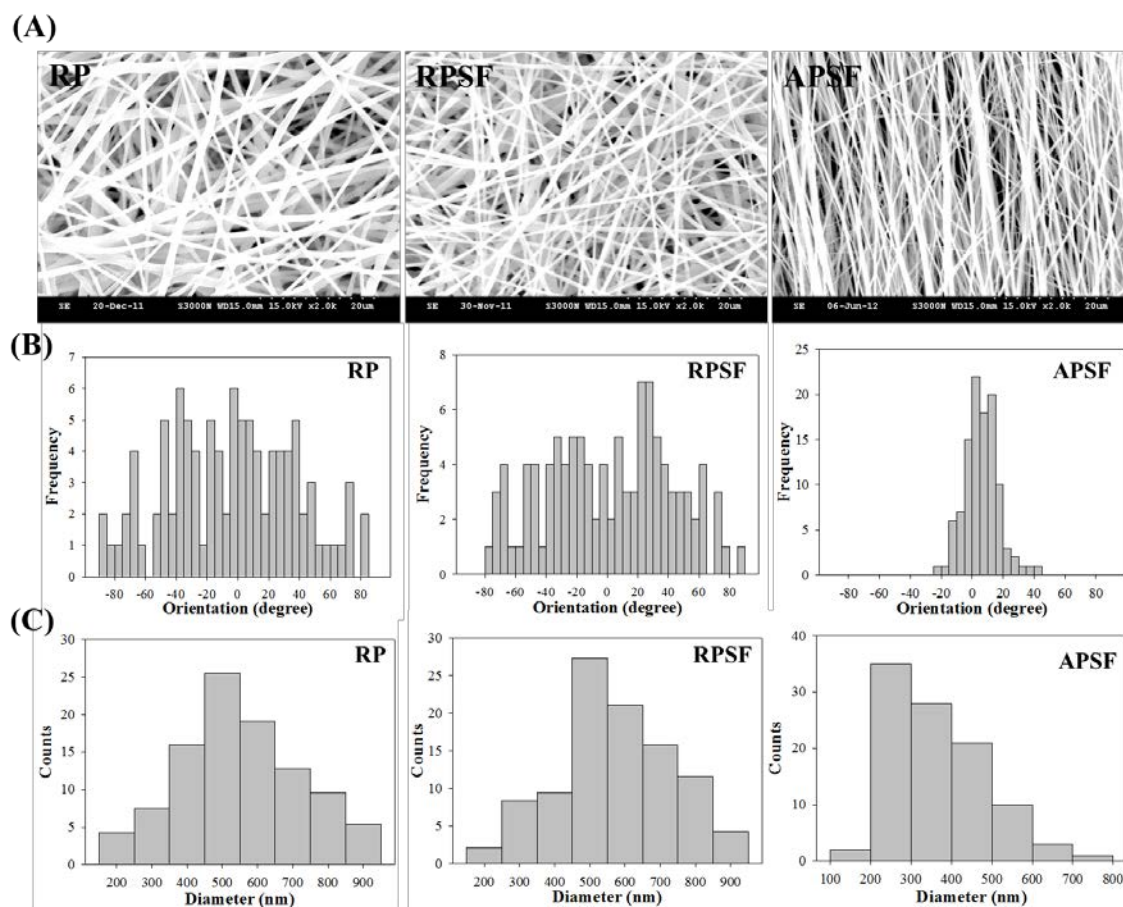


**Figure 1.** (A) Scanning electron microscope (SEM) analysis of random polycaprolactone (PCL) (RP) nanofibers, random PCL/silk fibroin (SF) (RPSF) nanofibers and aligned PCL/SF (APSF) nanofibers. From SEM analysis, the histograms representing fiber orientation (relative to a vertical line setting at 0°); (B) and fiber diameter distribution; (C) were calculated.

### 2.1.2. Thermogravimetric Analysis (TGA) and Derivative Thermogravimetric Analysis (DTA)

To determine the thermal properties, TGA was used to obtain the decomposition curves of RP and RPSF nanofiber scaffolds, and to compare these with that of SF sponge. Since the thermal decomposition curve of SF sponge is similar to that of SF nanofibers [24], SF sponge was used for comparison here. The TGA results in Figure 2A shows that the decomposition of RP started at ~350 °C due to PCL pyrolysis and the residual weight approached zero after 420 °C, as usually observed for a synthetic polymer [25]. From the DTA results in Figure 2B, RP exhibited a peak thermal decomposition temperature at 380 °C. In comparison, the SF sponge began to show a significant weight loss when the temperature reached 250 °C (Figure 2A) and the peak temperature was at 300 °C (Figure 2B). Since SF has a comparatively more complex protein structure, the pyrolysis process remained incomplete until 600 °C and the percentage of weight retained in SF at 600 °C was ~35% of the initial weight. This could be attributed to the slow thermal decomposition nature of natural polymers compared to synthetic ones [26]. The initiation decomposition of SF at ~100 °C was due to the presence of moisture. RPSF showed an intermediate residual weight at 600 °C (~14%) due to blending PCL with SF. Most importantly, the DTA curves of RPSF showed two peak temperatures corresponding to those of SF and RP at 300 and 380 °C, respectively, confirming the blending of PCL with SF, and each polymer in composite PCL/SF nanofibers did not influence the thermal properties of the other polymer.

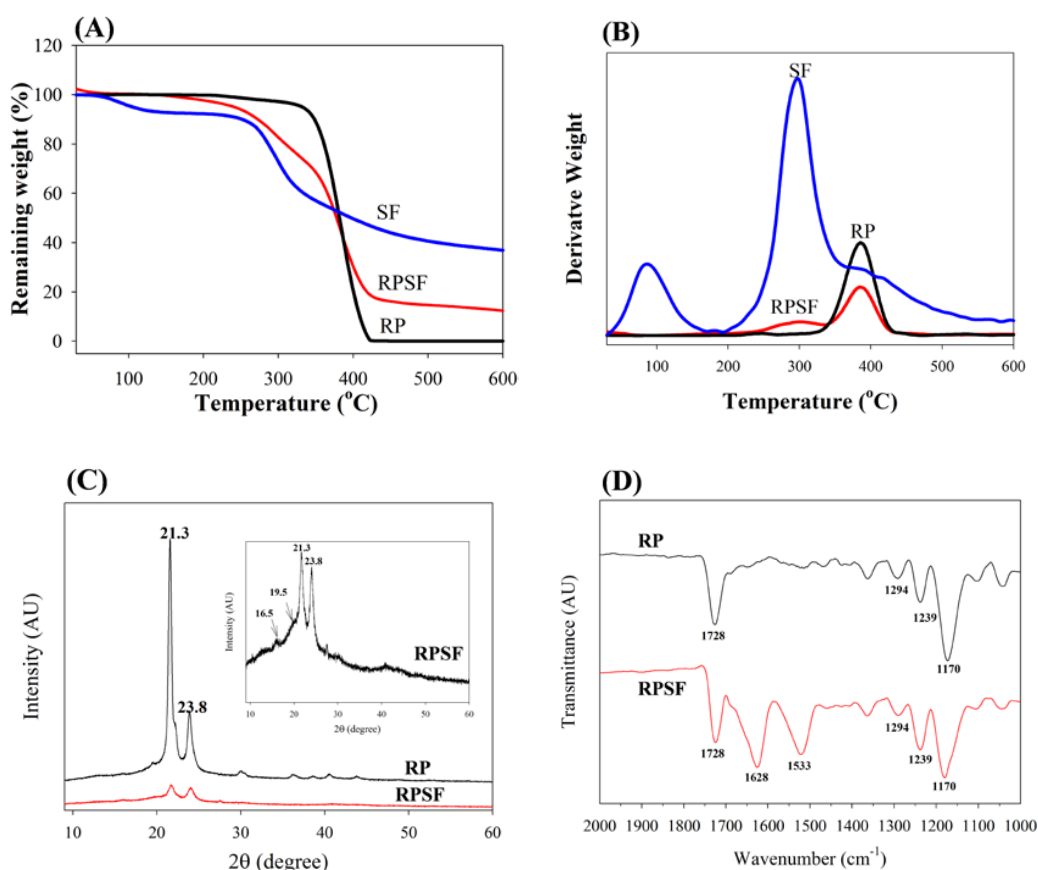


**Figure 2.** TGA (A) and DTA (B) of random PCL (RP) and random PCL/SF (RPSF) nanofiber scaffolds and SF sponges. XRD (C) and FTIR (D) analysis of random PCL (RP) and random PCL/SF (RPSF) nanofiber scaffolds.

### 2.1.3. XRD and FTIR Analysis

XRD was employed to investigate the crystal lattice in the electrospun nanofibers (Figure 2C). Both RP and RPSF nanofibers displayed (110) and (200) diffraction peaks of PCL at 21.3° and 23.7°. Two additional weak peaks could be identified in RPSF as methanol-treated SF would exhibit a major diffraction peak at 19.5° and two minor peaks at 16.5° and 22.5°, corresponding to the 4.55, 5.37, and 3.98 Å spacing, respectively, which are characteristics of the  $\beta$ -sheet crystalline structure [27]. The last SF peak at 22.5° was merged with the strong PCL peak at 21.3°. Therefore, RPSF shows diffraction peaks from PCL, with a domination of PCL over SF in determining the crystalline structure of nanofibers. However, the intensities of the (110) and (200) diffraction peaks of the RP were greater than those of RPSF, indicating that SF may interfere with the development of PCL crystals in RPSF [28]. The presence of SF in the PCL/SF blend will therefore influence the crystalline structure of PCL from XRD analysis.

The FTIR spectra confirmed the blending of SF with PCL (Figure 2D). Typical vibration peaks associated with PCL were observed in the spectra of RP. These include 1728 cm<sup>-1</sup> (carbonyl C=O stretching), 1294 cm<sup>-1</sup> (C–O and C–C stretching), 1239 cm<sup>-1</sup> (asymmetric C–O–C stretching) and 1170 cm<sup>-1</sup> (symmetric C–O–C stretching) [29]. The characteristic transmittance peaks of RPSF show both SF and PCL characteristic peaks. Additional transmittance peaks of SF in RPSF compared with RP can be identified at 1628 cm<sup>-1</sup> (amide I) and 1533 cm<sup>-1</sup> (amide II), with 1241 cm<sup>-1</sup> (amide III) merged with the C–O–C asymmetric stretching band of PCL in the composite. The shift of the transmittance peaks from 1650 cm<sup>-1</sup> (amide I) and 1538 cm<sup>-1</sup> (amide II), which represents a random



coil conformation [30], to 1628 and 1533  $\text{cm}^{-1}$  also indicates the ethanol post-treatment step successfully insolubilized SF with a transition of SF from the random coil to  $\beta$ -sheet conformation.

#### 2.1.4. Mechanical Test

The effect of fiber alignment and SF blending on the mechanical properties of nanofiber scaffolds was studied with random and aligned scaffolds of roughly the same thickness ( $\sim 100\ \mu\text{m}$ ). Table 1 and Figure 3 show the favorable mechanical strength and ductility of RP over RPSF scaffolds. A previous study indicated that PCL is subject to acidic hydrolysis by trifluoroacetic acid (TFA) over time, which might decrease the mechanical properties of RPSF vs. RP [31]. Comparing RPSF and APSF, although the ultimate strain is comparable, the Young's modulus and the ultimate stress were significantly higher for the aligned nanofiber than the random nanofiber scaffolds. The ultimate stress increased 16-fold and the modulus increased 18-fold when random fiber morphology was changed to aligned fiber morphology. The Young's modulus of APSF is also significant higher than that of RP (4.6-fold). Indeed, previous reports showed that the mechanical properties of nanofiber scaffolds are highly dependent on the orientation distribution and the components of electrospun nanofibers [32,33]. Nonetheless, the large increase in mechanical properties for the aligned scaffold may be also influenced by the higher packing factor of aligned fibers when compared to randomly-oriented fibers. Thus, we could not rule out the possibility that more fibers per unit scaffold volume may be the cause of the remarkable increase in the mechanical performance of APSF. As discussed before, the XRD analysis indicates SF may interfere with the development of PCL crystals in RPSF (Figure 2C), which may further influence the mechanical properties after blending PCL with SF in RPSF. Although SF does not result in improved mechanical properties, enhanced cellular response may be possible by introducing SF in RPSF (will be shown below). Nonetheless, we could verify that the aligned structural arrangement of nanofibers engendered a much higher mechanical strength than random nanofibers, which would contribute to the generation of a more robust scaffold for tendon tissue engineering.

**Table 1.** Mechanical properties of random PCL (RP), random PCL/SF (RPSF) and aligned PCL/SF (APSF) nanofiber scaffolds. Values are mean  $\pm$  SD of six independent measurements.

Scaffold	Ultimate Stress (MPa)	Ultimate Strain (%)	Young's Modulus (MPa)
RP	$1.48 \pm 0.21$	$39.75 \pm 6.61$	$15.28 \pm 5.31$
RPSF	$0.06 \pm 0.01^*$	$2.05 \pm 0.30^*$	$3.93 \pm 0.05^*$
APSF	$0.94 \pm 0.11^{*,\#}$	$1.72 \pm 0.19^*$	$70.52 \pm 2.83^{*,\#}$

Values are means  $\pm$  SD. \*  $p < 0.05$  compared with RP; #  $p < 0.05$  compared with RPSF. RP: random PCL nanofiber scaffolds. RPSF: random PCL/SF nanofiber scaffolds. APSF: aligned PCL/SF nanofiber scaffolds.

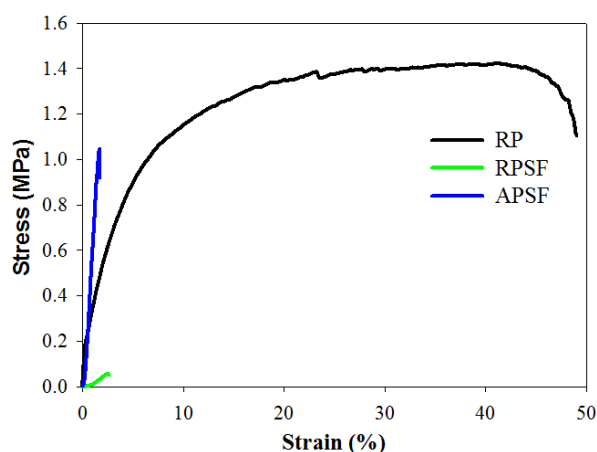


**Figure 3.** The tensile stress-strain curves of random PCL (RP), random PCL/SF (RPSF) and aligned PCL/SF (APSF) nanofiber scaffolds.

## 2.2. In Vitro Cell Culture

### 2.2.1. Cell Proliferation

Cell proliferation was compared by determining the viable cell number from 3-(4,5-dimethylthiazol-2-yl)-5-(3-carboxymethoxyphenyl)-2-(4-sulfophenyl)-2H-tetrazolium (MTS) assays at different time points (day 3, 5 and 7) and normalized to the cell number of each scaffold at day 0 (Figure 4). All scaffolds have a similar relative cell number on day 3, with no significant difference. Although RPSF and APSF have no significant difference in cell number on day 5, both groups have a significantly higher relative cell number compared with RP on day 5 and 7. SF in composite nanofiber scaffolds were shown to promote cell proliferation for chondrocytes, osteoblasts and mesenchymal stem cells [34,35]. Furthermore, an additional contribution from blending PCL with SF may be the enhancement of the hydrophilicity of the nanofiber scaffold, as a balance between the hydrophilicity and hydrophobicity of a scaffold was reported to exert positive effects on cell growth [36]. The introduction of biological functional groups, such as  $-NH_2$  and  $-COOH$ , via SF in RPSF and APSF may also enhance cell proliferation as they were shown to promote cell-scaffold recognition and subsequent proliferation [37]. Considering the effect of fiber alignment, APSF showed no significant difference in relative cell number from RPSF on day 5, but showed significantly higher relative cell number on day 7. Indeed, the physical cue from fiber alignment may further contribute to promote cell proliferation.

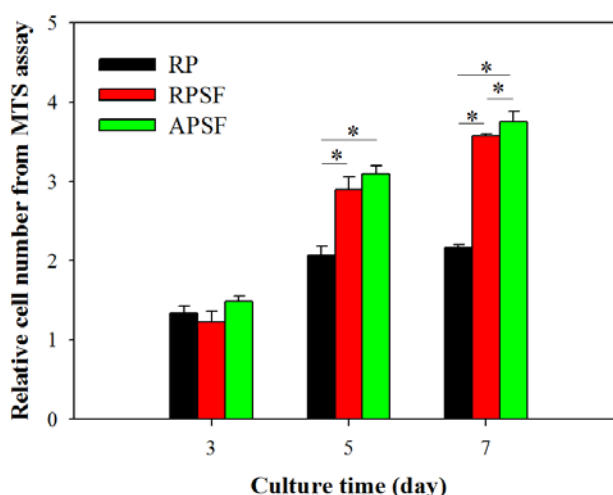


**Figure 4.** The proliferation of dermal fibroblasts in random PCL (RP), random PCL/SF (RPSF) and aligned PCL/SF (APSF) nanofiber scaffolds. The cell number in each group was normalized to its cell number at day 0. \*  $p < 0.05$ .

### 2.2.2. SEM Observation

Figure 5A shows the morphology of RDFBs adhered on RP, RPSF, and APSF after cultured for 3 and 7 days. The SEM micrographs on day 3 indicate that cells attached to RP scaffolds had a lower degree of spreading with hindered cytoskeletal extensions compared with RPSF, which is consistent with previous reports that electrospun SF nanofibers could promote keratinocytes and fibroblast adhesion and spreading [38,39]. However, the morphology of attached cells on APSF was significantly different, as the aligned structural arrangement of APSF induced cells to migrate and proliferate in the direction of the nanofiber. On day 7, in which the cells completely attached themselves to the nanofibers, the filopodial extensions were much more visible and higher compared to day 3, irrespective of the random or aligned fiber morphology. The cell distribution on RP and RPSF was more scattered, whereas that on APSF was more aligned with a higher cell density, which is consistent with the viable cell number assay from Figure 4. Based on SEM observation, we conclude that the

aligned structural arrangement of APSF aided the oriented growth of RDFBs and provided a favorable environment for cell attachment and proliferation.

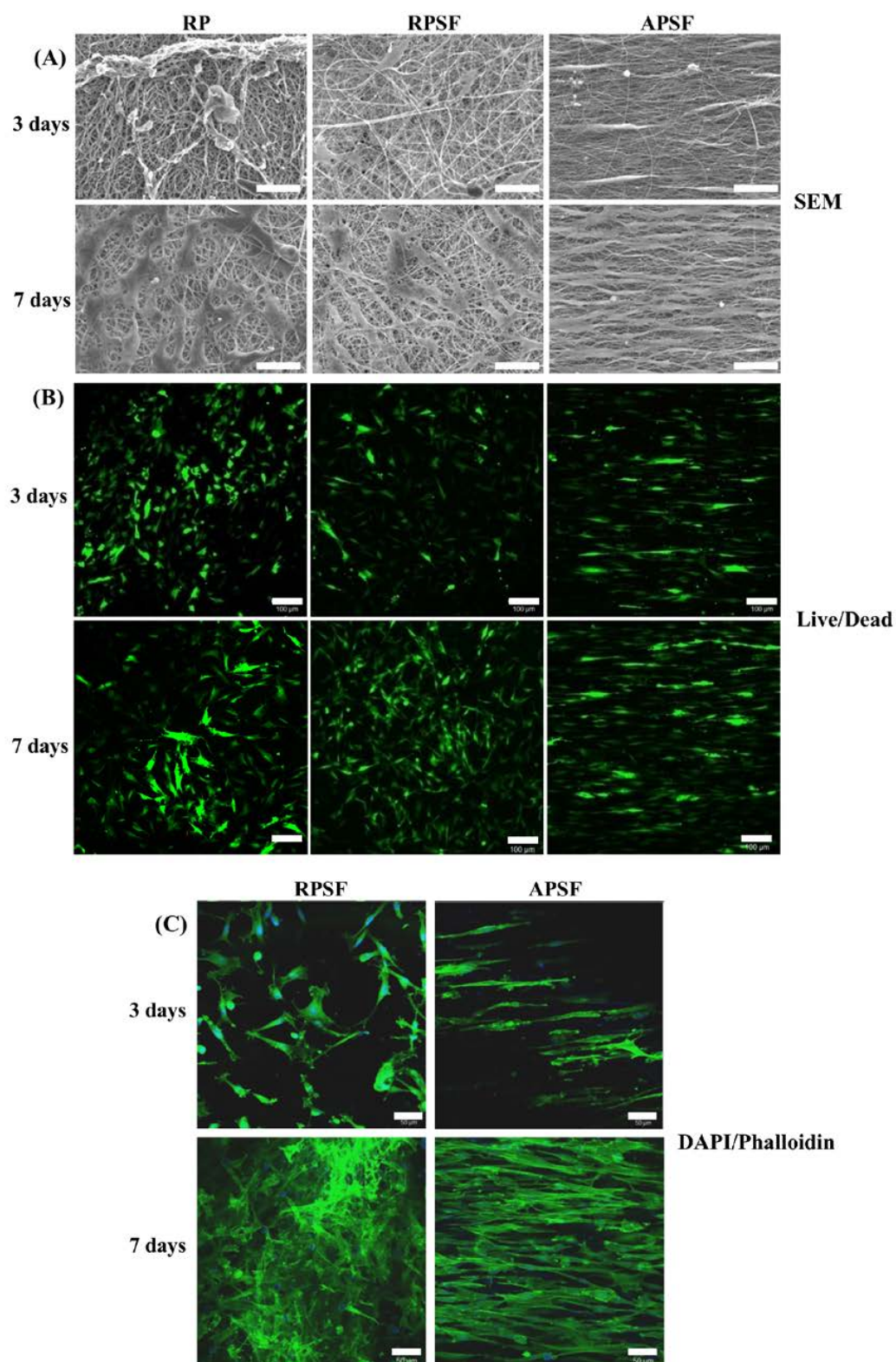


**Figure 5.** The SEM observation ((A), bar = 50  $\mu$ m), live/dead staining ((B), bar = 100  $\mu$ m) and 4',6-diamidino-2-phenylindole (DAPI)/phalloidin staining ((C), bar = 50  $\mu$ m) of dermal fibroblasts in random PCL/SF (RPSF) and aligned PCL/SF (APSF) nanofiber scaffolds.

### 2.2.3. Live/Dead Assay

The viability and morphology of cells seeded on random and aligned scaffolds were further examined through live/dead staining. Figure 5B shows the confocal fluorescent micrographs of RDFBs adhered on RP, RPSF, and APSF at day 3 and 7. The live cells (green color) seeded on RP and RPSF were randomly oriented with irregular shapes and minimum dead cells (red color) were found. In contrast, the cells seeded on APSF were oriented in the direction of fiber alignment with elongated shapes with no dead cells observed. At day 7, the cell morphology was similar to what was observed at day 3, but with a significantly higher cell density due to cell proliferation. For RP, a relatively high number of dead cells were observed on day 7, which was consistent with its lower cell proliferation rate compared to RPSF and APSF (Figure 4). Similar to day 3, the cells in APSF proliferated in the direction of fiber alignment, as observed from SEM images (Figure 5A).

### 2.2.4. 4',6-Diamidino-2-Phenylindole (DAPI)/Phalloidin Staining

In order to test the responses of RPSFs to nanofiber scaffolds, cells were cultured in the scaffolds and double stained with fluorescein isothiocyanate (FITC)-phalloidin and DAPI to elucidate the cytoskeletal arrangement of fibroblasts (Figure 5C). Since RP had comparatively less cell spreading, only RPSF and APSF were taken for cytoskeletal staining. On day 3, cells in RPSF exhibited a disorganized actin cytoskeleton in contrast to a cytoskeleton consisting of a large number of actin filaments aligned parallel to the axes of the nanofibers for cells in APSF. The difference in cell morphology was even more pronounced on day 7. Cells were randomly distributed in RPSF to form a thick cell layer, while cells in APSF exhibited a high degree organization of spindle-shaped cytoskeletons, supporting the results observed from SEM and live/dead assays [21]. Hence the results from the DAPI/phalloidin fluorescent staining cross-confirmed that the oriented cell proliferation was solely affected by the nature of the substrate structure originating from its fiber orientation.

### 2.2.5. Gene Expression

The gene expression of tendon marker proteins Col I, Col III, fibronectin and biglycan at three and seven days is shown in Figure 6. In accordance with the nature of early or late expressed genes, Col III and fibronectin showed earlier gene up-regulation (day 3) than Col I and biglycan (day 7). Col I is a crucial protein during the tendon reconstruction process. As collagen matures, the amount of Col I secretion increases to make it a late-stage gene marker for tendon. Higher amounts of Col I indicates an increased number of organized fibers. No significant difference in Col I gene expression was found between RP and RPSF; however, APSF showed significantly higher Col I gene expression than RP and RPSF. This suggests that fiber alignment is the most important factor in inducing the secretion of Col I. Col III is a crucial protein during the period of tendon inflammation and proliferation and is an early-stage gene marker for tendon, as well as the main component of collagen during the early stages of tendon maturation. It will be gradually replaced by longitudinally-aligned long Col I fibrils when the tendon remodels and matures during healing [40]. No significant differences in Col III gene expression were observed between RP and APSF on day 3; however, RPSF and APSF showed significant differences at the same time. This again endorses the advantage of aligned structural arrangement in the production of early marker Col III. Surprisingly, by day 7, RP showed a significantly higher level of Col III expression compared to APSF and RPSF. In other words, the amount of Col III production was higher for cells in RP but not different for cells in RPSF and APSF. Since Col III is produced during the collagen maturation process, we assume that this might be due to the slow collagen maturation process for RDFBs in RP. Moreover, the aligned morphology of APSF could lead to faster tendon reconstruction; thus, cells in APSF show the lowest Col III gene expression.

Fibronectin regulates initial cell attachment and survival and is a well-known marker for active connective tissue repair [41]. Hence, fibronectin is an early-stage marker with its maximum secretion during the cell proliferation stage, which diminishes during the cell maturation stage.

The down-regulation of fibronectin gene at day 7 is consistent with other studies, where cells synthesized fibronectin during proliferation and early differentiation. Once the cells reached maturation and accumulated collagens, the production of fibronectin sharply reduced [42]. Significant differences were observed in fibronectin gene expression between RP and APSF as well as APSF and RPSF at day 3. The drastic up-regulation of fibronectin gene expression in APSF could be due to the effect of aligned fiber morphology, which enhanced cell proliferation and increased the cell survival rate. However, at day 7, all scaffolds showed decreased fibronectin gene expression compared to day 3. This indicates cell maturation changes consistent with the trend observed for changes in Col I and Col III production at different times. Biglycan is a glycoprotein, its primary functions being the regulation of growth factor activity during the tendon repair and development process as well as the regulation of the organization, arrangement and the diameter of collagen fibrils in the ECM of the tendon [43]. Biglycan is over-expressed during the re-organization phase of tendon development and repair, coinciding with Col I over-expression. The results confirm that biglycan expression of cells in APSF was the highest among all scaffolds at both time points. This demonstrates the advantage of APSF in facilitating cell organization and arrangements to generate a neo-tendon tissue similar to a native tendon *in vitro*.

Overall, the qRT-PCR results demonstrated a gene expression profile associated with tendon differentiation *in vitro*. Furthermore, the up-regulation of tendon matrix protein genes (Col I, fibronectin and biglycan) in RDFS and tendon reconstruction (Col III) could be shown by combining cues from SF and fiber alignment. A significantly higher gene up-regulation was observed in the aligned composite scaffold (APSF), suggesting a synergistic effect of SF and fiber alignment on RDFS for tendon tissue engineering *in vivo*.

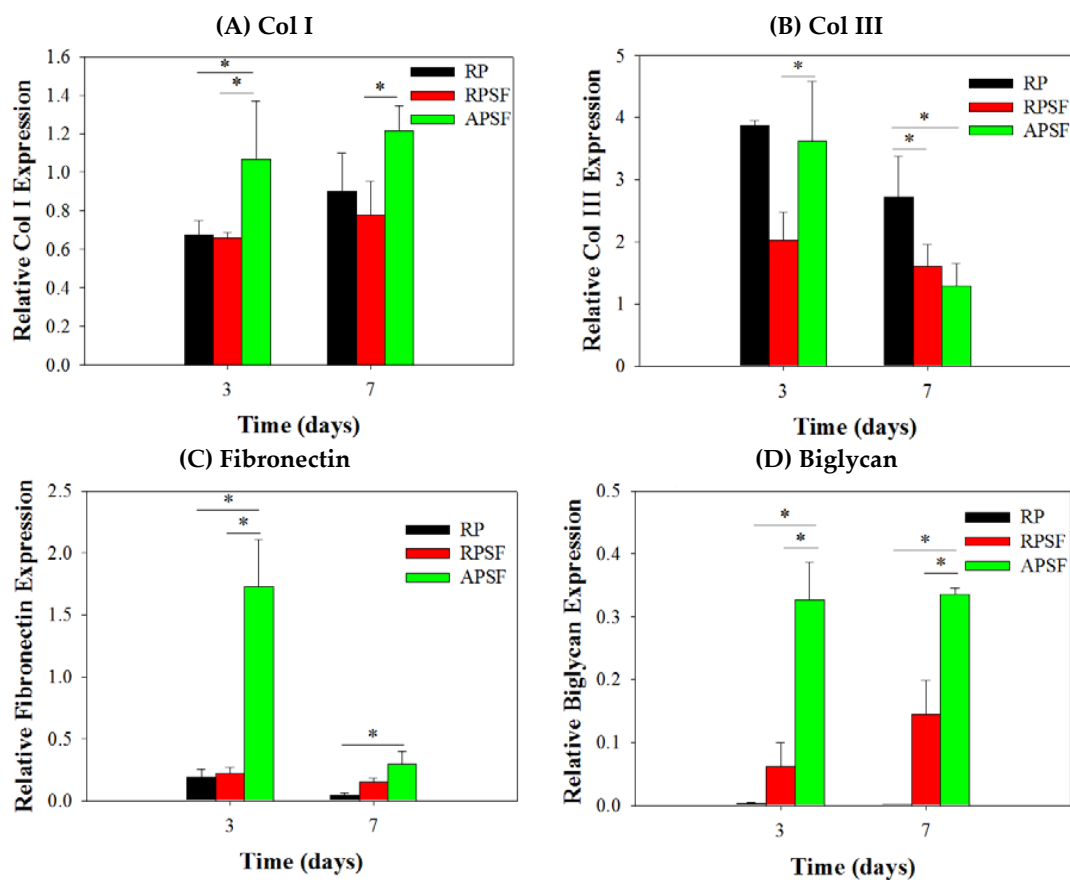


**Figure 6.** Gene expression of (A) type I collagen (Col I); (B) type III collagen (Col III); (C) fibronectin and (D) biglycan in random PCL (RP), random PCL/SF (RPSF) and aligned PCL/SF (APSF) nanofiber scaffolds by quantitative real-time polymerase chain reaction (qRT-PCR). \*  $p < 0.05$ .



## 2.3. Animal Study

### 2.3.1. Histological Staining

Figure 7 is the histological staining of explants after 6 and 12 weeks. No cells could be found for acellular scaffolds at week 6 but infiltrated cells from surrounding tissues could be identified at week 12. For cell-seeded scaffolds, both RPSF and APSF exhibited much higher cellular densities across the scaffolds than their acellular counterparts. Though the cell densities were similar, cell orientation was significantly different between the cell-seeded scaffolds. Cell alignment was observed at 6 and 12 weeks in APSF, suggesting that migration and proliferation of RDFBs on aligned nanofibers tend to stretch in a parallel direction along the alignment of the nanofibers. We were able to confirm that the aligned structural arrangement can easily mimic the natural tendon structure to guide RDFBs in vivo. Masson's trichrome staining was used to evaluate the collagen distribution in ECM of neo-tendon tissues. Since tendons are composed of collagen fibers, such staining methods can clearly depict the extent of collagen deposition and thereby can confirm the formation of neo-tendon tissues. From Masson's trichrome staining, no significant staining intensity was observed for the absence of collagen fibers in acellular RPSF group at both time points. A similar trend was also observed for the acellular APSF group. Significantly higher staining intensities were observed in cell-seeded implants with a slightly increasing dark blue color intensity of stained collagen. Collagen fibers were randomly oriented in the cells/RPSF group, whereas an oriented distribution was found in the cells/APSF group with more collagen deposition. Thus, Masson's trichrome staining confirms that the amount and the orientation of ECM deposition of RDFBs is also influenced by the alignment of nanofibers; an advantage offered by cells/APSF constructs in simulating natural tendon environment in vivo.

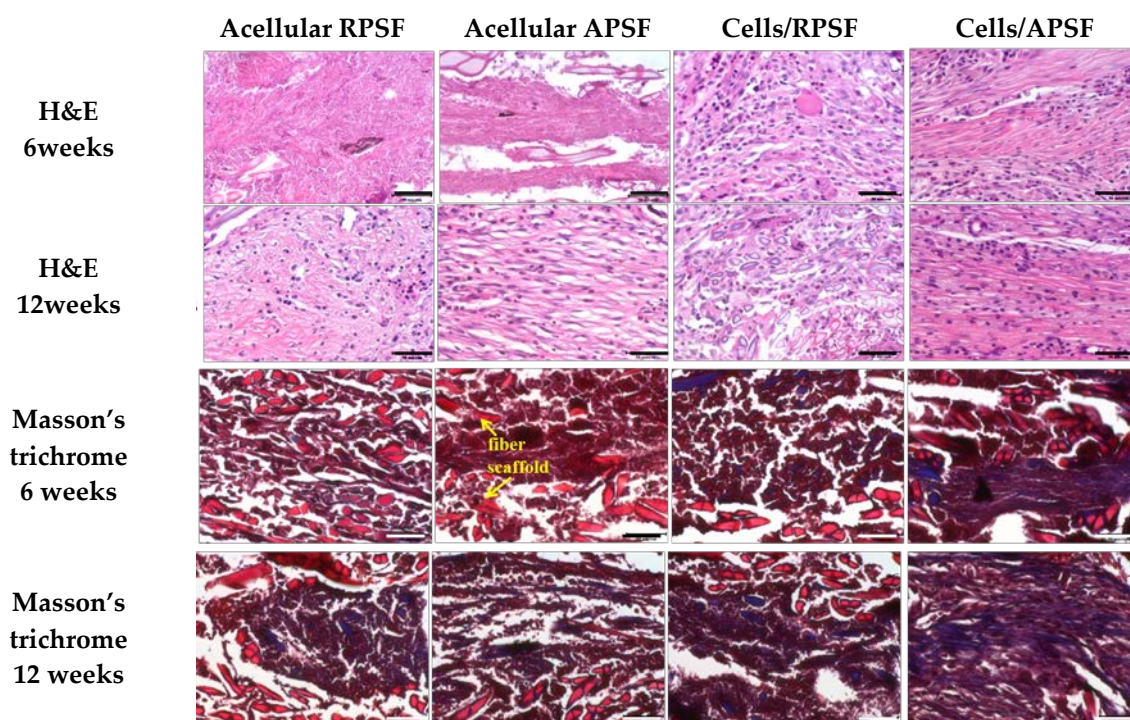


**Figure 7.** Tissue section staining using hematoxylin-eosin (H&E) and Masson's trichrome after 6 and 12 weeks. RPSF: random PCL/SF nanofiber scaffolds. APSF: aligned PCL/SF nanofiber scaffolds. Bar = 50  $\mu$ m.

### 2.3.2. Immunohistochemical (IHC) Staining

The presence of Col I, Col III and tenascin C were confirmed through IHC staining of cell-seeded scaffolds (Figure 8). A general observation of the IHC staining results confirmed Col I, Col III and tenascin C were organized along the direction of fiber alignment in APSF, mimicking native tendon tissue structure. The IHC staining revealed a denser deposition of Col I and Col III in the ECM on aligned nanofibers compared to those on random nanofibers six weeks post-implantation. Furthermore, a denser deposition of another tendon-specific ECM protein, tenascin C, was also evident in APSF.

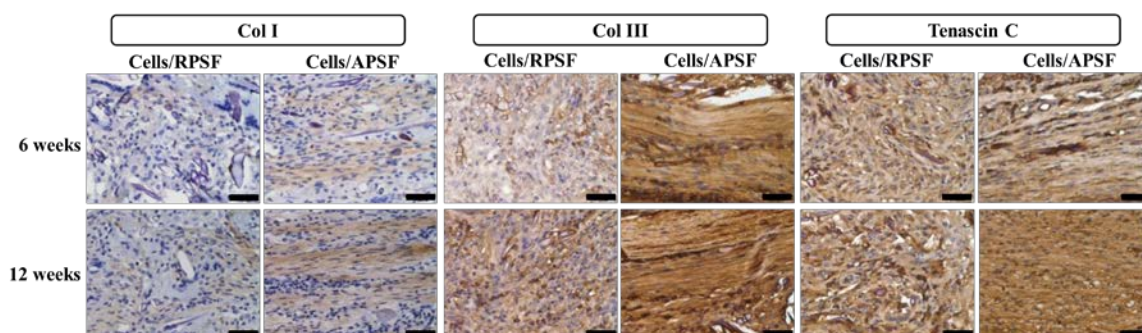


**Figure 8.** The immunohistochemical staining of type I collagen (Col I), type III collagen (Col III) and tenascin C after 6 and 12 weeks. RPSF: random PCL/SF nanofiber scaffolds. APSF: aligned PCL/SF nanofiber scaffolds. Bar = 50  $\mu$ m.

Col I is the predominant protein in tendon, making up 86% of the dry weight of the tissue [44]. It is secreted by cells at maturation and evaluation of its presence in implanted samples could confirm tissue reconstruction. At week 6, Col I secreted by cells in RPSF was minimal in contrast to higher Col I production in APSF. At week 12, the deposition of Col I in APSF increased and the distribution became more aligned along the direction of cell distribution. Although Col I also showed an increasing trend from 6 to 12 weeks in RPSF, its content was much lower in comparison with APSF. This result indicated that aligned nanofiber scaffolds promote Col I production *in vivo* and is in line with the *in vitro* gene expression results in Figure 6. The physical cues from electrospun nanofibers was suggested to affect cell behavior and fate, as aligned nanofibers induced ligament fibroblast alignment and Col I production [45].

Col III is typically over-expressed during the early inflammatory and proliferative stages of tendon healing. It is characterized by short, disorganized fibrils [7]. The production rate of Col III decreased with the maturation of cells and growth of collagen fibers. A similar relationship between the time-dependent increased deposition of Col I and Col III was observed. At week 6, APSF exhibits increased Col III deposition compared with RPSF. At week 12, the deposition of Col III increased from week 6 for RPSF, but no significant difference was observed for APSF. At this stage, cells in APSF had already entered the tendon reconstruction stage and stopped Col III secretion, which is again consistent with *in vitro* Col III gene expression (Figure 6). Overall, Col III staining confirms aligned scaffolds could promote tendon maturation and provides cues to lead neo-tendon tissues into the reconstruction phase during tendon regeneration. The aligned structural arrangement of Col III in APSF also re-confirms the effect of nanofiber alignment in the reconstruction of tendon tissue network.

Tenascin C is a tendon ECM protein secreted during the proliferation or reconstruction of tendons and modulates cell-ECM interactions such as cell adhesion and migration [46]. By week 6, the APSF group had a higher amount of tenascin C than RPSF. This demonstrates the priority of the aligned structure in inducing differentiation of RDFBs to tendon cells, which increased tenascin C secretion. By week 12, the amount of tenascin C in APSF increased significantly and the structural arrangement became more oriented. Conversely, RPSF exhibited no significant changes in tenascin C intensity from week 6. Although the lack of quantitative IHC data may be a limitation of this study, the qualitative IHC

results endorse the importance of APSF in inducing oriented arrangement of cells and differentiation of RDFBs to tenocytes. The IHC results thus confirmed the advantage of uni-axial fiber orientation in the reconstruction of tendon tissues in vivo.

### 2.3.3. Biomechanical Testing

Structural biomechanical properties (linear stiffness and maximum force) that depend on specimen dimensions were determined for normal tendon and explanted acellular and cell-seeded scaffolds 12 weeks post-operation (Table 2). By 12 weeks post-operation, the tensile stiffness of cells/RPSF and cells/APSF reached 28.4% and 60.2% of that of normal tendon, respectively. The mean tensile stiffness of the cells/RPSF group was significantly lower than that of the cells/APSF group, but both are significantly different from that of normal tendon. The mean tensile stiffness of acellular APSF and RPSF are also significantly less than those of their cell-seeded counterparts. For maximum load, a similar trend was observed for acellular and cell-seeded scaffolds. Hence, the ability of the scaffolds to reach a significant strength was clearly not a result of the acellular scaffold but rather from the regenerated tissue, while the aligned nanofiber scaffold APSF resulted in a significantly higher tensile stiffness or load compared with RPSF. Comparing the cell-seeded scaffolds, the mean ultimate load of cells/RPSF and cells/APSF are significantly different, and the values reached 43.8% and 81.3% of that of normal tendon, respectively. Most importantly, there is no significant difference in maximum load between cells/APSF and normal tendon ( $p > 0.05$ ).

Our biomechanical analysis results compare favorably with those from previous Achilles tendon repair studies. Bone marrow mesenchymal stem cell-collagen gel constructs were implanted in immature rabbits with a 1-cm long gap defect in the Achilles tendon. The acellular and cell-seeded scaffolds respectively gave 32% and 63% in stiffness and 30% and 69% in maximum force as percentages of normal Achilles tendon values [47]. A similar study employing a different cell-to-collagen ratio was used to repair 2-cm gap defects in rabbit Achilles tendons [48]. The best construct gave 53% maximum force and 64% tensile stiffness of normal tendon values at 12 weeks after surgery. For comparison, the cells/APSF group showed a substantially larger maximum load and similar stiffness in our study using the nanofiber scaffold. In a different study, the mean tensile stiffness was reported to be 56% and 87% of normal tendon values for acellular and bone marrow stromal cell-seeded knitted poly-lactide-co-glycolide scaffolds at 12 weeks post-operation in regeneration of rabbit Achilles tendon with 1-cm gap defect [8]. Interesting, although the mean stiffness of regenerated tendon is smaller in our study using RDFBs in APSF, the increase of stiffness from acellular to cell-seeded scaffolds is similar in both studies (31% vs. 32%).

**Table 2.** Biomechanical tests of normal tendon, regenerated tendons from acellular RPSF, acellular APSF, cells/RPSF and cells/APSF after 12 weeks. Values are mean  $\pm$  SD of six independent measurements.

Groups	Stiffness (N/mm)	Maximum Load (N)
Normal tendon	29.9 $\pm$ 5.8	382.3 $\pm$ 58.2
Acellular RPSF	4.5 $\pm$ 0.7	114.3 $\pm$ 11.6
Acellular APSF	10.1 $\pm$ 1.8	216.4 $\pm$ 33.0
Cells/RPSF	8.5 $\pm$ 1.1	167.3 $\pm$ 25.4
Cells/APSF	18.0 $\pm$ 3.8 *	310.9 $\pm$ 73.5 *,#

Values are means  $\pm$  SD. \*  $p < 0.05$  compared with cells/RPSF; #  $p > 0.05$  compared with normal tendon. RPSF: random PCL/SF nanofiber scaffolds. APSF: aligned PCL/SF nanofiber scaffolds.

## 3. Materials and Methods

### 3.1. Materials

Polycaprolactone (PCL, average molecular weight = 80,000 Da) was purchased from Sigma-Aldrich (St. Louis, MO, USA). *Bombyx mori* silk fiber was supplied by Shitan Chuanmin silkworm farm in



Miaoli County, Taiwan. Fetal bovine serum (FBS) and Dulbecco's Modified Eagle's medium (DMEM) were purchased from Thermo Fisher Scientific (Waltham, MA, USA). Dichloromethane (DCM) and dimethylformamide (DMF) were purchased from J.T. Baker (Philipsburg, NJ, USA). Trifluoroacetic acid (TFA) and hexafluoroisopropanol (HFIP) were purchased from Sigma-Aldrich (St. Louis, MO, USA). Dialysis membrane tubes (CelluSep H1) were purchased from Orange Scientific (Braine-l'Alleud, Belgium). Except *Bombyx mori* silk fiber, all chemicals were used as received.

### 3.2. Preparation of Nanofiber Scaffolds by Electrospinning

Silk fibroin (SF) was prepared from *B. mori* silk by a stepwise purification method [49]. Electrospinning was adopted for the preparation of random PCL (RP) nanofibers, random PCL/SF (RPSF) nanofibers and aligned PCL/SF (APSF) nanofibers. PCL was dissolved in a DCM/DMF (4:1, *v/v*) solvent mixture to prepare a 10% (*w/v*) PCL solution. SF and PCL were dissolved in a TFA/HFIP (1:3, *v/v*) solvent mixture to obtain a SF/PCL solution having a final concentration of 26% (*w/v*) (13% SF and 13% PCL). Five milliliters of pre-made electrospinning solution of PCL and SF/PCL was pumped from a syringe fitted with a 23-gauge needle at 1 mL/h and 30 kV. The fibers were collected by a grounded static collector kept 15 cm from the tip of the needle to obtain RP and RPSF nanofibers, respectively, with ~100  $\mu\text{m}$  thickness. The APSF nanofibers were prepared with the same thickness using the same electrospinning setup but at 16 kV voltage and using a rotating collector (10 cm diameter, rotate at 3500 rpm) and 10 cm tip-to-collector distance. The thickness of all scaffolds was measured with a dial thickness gauge (TECLOCK SM-1201, Nagano, Japan). All SF-containing nanofibers were immersed in a 7% (*v/v*) ammonia/75% (*v/v*) ethanol solution at room temperature for 30 min to remove residual TFA and to attain the water insolubility of SF [24]. Subsequently, the membrane was washed with copious phosphate buffered saline (PBS) to remove ammonia. The membranes were dried in an oven at 37 °C before use.

### 3.3. Characterization of Nanofiber Scaffolds

#### 3.3.1. SEM Analysis

The prepared fibrous membranes were cut into 0.5 cm  $\times$  0.5 cm square pieces and pasted onto a carbon tape fixed aluminum stub for conductive coating at 20 mA for 60 s. The morphology of nanofibers was examined with a scanning electron microscope (SEM) (S-3000N, Hitachi Ltd., Tokyo, Japan) and the average fiber diameter was determined using ImageJ software from at least 100 fibers from 10 images. The orientation of nanofibers was calculated from the frequency of fibers with fiber orientation (degree) ranging from  $-90^\circ$  to  $90^\circ$  relative to a defined vertical direction ( $0^\circ$ ) from 100 fibers. The fiber orientation was analyzed using circular statistics with the CircStat toolbox for MATLAB (MathWorks, Natick, MA, USA) to calculate the angular distribution value.

#### 3.3.2. TGA and DTA

A thermogravimetric analysis (TGA) and derivative thermogravimetric analysis (DTA) were performed to evaluate the thermal properties of RP and RPSF nanofibers in nitrogen atmosphere. Samples were allowed to undergo thermal decomposition at a controlled heating rate of 10 °C/min from 25 to 500 °C using TGA 2050 from TA instruments (New Castle, DE, USA). The decomposition behavior was monitored by plotting weight (%) and derivative weight (%/°C) vs. temperature (°C).

#### 3.3.3. XRD and FTIR Analysis

The X-ray diffraction (XRD) patterns were obtained from a D5005 X-ray diffractometer (Siemens AG, Munich, Germany) from  $5^\circ$  to  $60^\circ$  at a scanning speed of  $1.2^\circ \text{ min}^{-1}$ . Fourier-transform infrared (FTIR) spectroscopy was used for chemical analysis using a Horiba FT-730 spectrometer (Horiba, Ltd., Kyoto, Japan) in the attenuated total reflection configuration. The scanning wavenumber was from 600 to  $2000 \text{ cm}^{-1}$  with a resolution of  $2 \text{ cm}^{-1}$ .

### 3.3.4. Mechanical Testing

Tensile properties were evaluated using a H1KT tabletop mechanical testing machine (Tinius Olsen, Horsham, PA, USA) having a 10 N loading cell. Samples were cut into strips ( $10 \times 50 \text{ mm}^2$ ) and allowed to undergo tensile elongation at a crosshead speed of 5 mm/min and a gauge length of 30 mm. Young's modulus (MPa), ultimate stress (MPa) and ultimate strain (%) were calculated from the tensile stress-strain curves ( $n = 6$ ).

## 3.4. In Vitro Cell Culture

### 3.4.1. Isolation of Rabbit Dermal Fibroblasts (RDFBs)

Fresh skin harvested from the back of New Zealand white rabbits (2–3 kg weight) were collected under aseptic condition. After thorough washing in PBS and soaking in 0.25% chloramphenicol solution for 10 min, the harvested skins were minced into small pieces ( $2 \times 2 \times 2 \text{ mm}^3$ ) and subjected to digestion with 0.25% type I collagenase in DMEM high glucose at 37 °C in a rotation incubator for 8 h. The isolated cells were plated on T75 flask and cultured in DMEM containing 10% FBS, penicillin (100 U/mL), streptomycin (100 µg/mL), and ascorbic acid (50 µg/mL) at 37 °C in a CO<sub>2</sub> incubator with medium change every three days. Cells from the second and third passage were used for the in vitro studies.

### 3.4.2. Cell Proliferation

All nanofiber scaffolds were treated with 75% ethanol overnight and rinsed twice with PBS for 30 min before use. The membrane (15 mm diameter) was pre-conditioned by immersion in DMEM for 1 day and placed in a 24-well culture plate and each well was seeded with 100 µL of RDFBs cell suspension ( $5 \times 10^4$  cells) and incubated at 37 °C for 4 h to allow cell adhesion. The membrane was transferred to a new well and cultured in 1.5 mL cell culture medium (DMEM supplemented with 10% FBS and 1% antibiotic-antimycotic) in a CO<sub>2</sub> incubator at 37 °C with medium change every 2 days. The number of viable cells was determined at day 3, 5 and 7 using MTS assays with the CellTiter 96® AQueous One Solution from Promega (Madison, WI, USA). An ELISA plate reader (Synergy HT, BioTek, Winooski, VT, USA) was used for colorimetric measurements of the formazan product at 492 nm.

### 3.4.3. SEM Observation

For SEM observations, cell-seeded scaffolds at day 3 and 7 were fixed in 2.5% glutaraldehyde solution and dehydrated through a graded series of ethanol soaks, and finally dried using hexamethyldisilazane overnight. Completely dehydrated samples were sputter-coated with gold at 20 mA for 60 s. Samples were mounted on aluminum stubs, fixed with carbon tapes and observed under a SEM (Hitachi S-3000N, Hitachi Ltd., Tokyo, Japan, Hitachi S3000N) at an accelerating voltage of 10 kV.

### 3.4.4. Live/Dead Assay

Cell viability was assessed by using the live/dead viability/cytotoxicity assay kit from Thermal Fisher Scientific (Waltham, MA, USA), which allows the simultaneous fluorescence staining of viable and dead cells. RDFBs were cultured in nanofiber scaffolds for 3 and 7 days, followed by removal of the medium and PBS washing for three times. The solution for Live/Dead cell staining was prepared by mixing 3 µL of 4 mM calcein AM solution (for live cells) (excitation at 494 nm and emission at 517 nm) and 5 µL of 2 mM ethidium homodimer-1 (EthD-1) solution (for dead cells) (excitation at 528 nm and emission at 617 nm) in 10 mL cell culture medium [21]. One milliliter of staining solution was added to each cell-seeded scaffold placed in a well of a 24-well culture plate in dark. The scaffold



was incubated at 37 °C for 30 min, followed by observation under a confocal laser scanning microscope (Zeiss LSM 510 Meta, Oberkochen, Germany).

#### 3.4.5. DAPI/Phalloidin for Cytoskeletal Staining

The cytoskeleton arrangements of attached RDFBs on nanofiber scaffolds were determined from F-actin staining at day 3 and 7. The scaffolds were fixed in 4% paraformaldehyde for 10 min after washed with PBS. The scaffolds were further washed repeatedly in PBS and treated with 0.1% Triton X-100 in PBS for 10 min. After washing twice with PBS, the samples are stained with 20 µg/mL fluorescein isothiocyanate (FITC)-phalloidin for 30 min. After additional washing in PBS and staining cell nuclei were stained with 1 µg/mL (4',6-diamidino-2-phenylindole) (DAPI) for 5 min, the samples were observed under a confocal laser scanning microscope (Zeiss LSM 510 Meta, Oberkochen, Germany), The excitation and emission wavelengths for DAPI are 358 and 461 nm, respectively, and the corresponding wavelengths for FITC-phalloidin are 496 and 516 nm.

#### 3.4.6. RNA Extraction and cDNA Synthesis

The RNA isolation and cDNA synthesis steps were performed as per standard procedures by using TRIzol from Invitrogen (Carlsbad, CA, USA) to isolate RNA from RDFBs. Cell suspension was collected by rupturing the membranes and the solution obtained was placed in a 1.5 mL micro centrifuge tube.

After adding 200 µL chloroform, the solution was vortexed for 15~30 s, followed by incubation in an ice bath for 5 min and centrifuged at  $12,000\times g$  for 15 min. The supernatant RNA layer was isolated and reacted with an equal volume of isopropanol at  $-80\text{ }^{\circ}\text{C}$  for 30 min. The solution was further centrifuged at  $12,000\times g$  for 15 min at  $4\text{ }^{\circ}\text{C}$ . The supernatant was removed and 1 mL of 75% ice cold ethanol was added. The solution was mixed at  $4\text{ }^{\circ}\text{C}$  for 10 min and centrifuged at  $12,000\times g$  for 10 min. This step was repeated twice and the final supernatant solution was removed. The precipitate was dried at room temperature for 10 min and incubated with 20 µL of DEPC (Invitrogen, Carlsbad, CA, USA) treated water at  $55\text{--}60\text{ }^{\circ}\text{C}$  for 30 min for complete dissolution of RNA.

#### 3.4.7. Quantitative Real-Time Polymerase Chain Reaction (qRT-PCR)

SuperScript III reverse transcriptase (Invitrogen, Carlsbad, CA, USA) was used to reversely transcribe total RNA into cDNA. Glyceraldehyde 3-phosphate dehydrogenase (GAPDH) was used as the reference gene for internal control. A CFD-3120 Mini Option detection system (Bio-Rad, Hercules, CA, USA) together with SYBR Green RT-PCR kit (SYBR Green I SuperMix, Bio-Rad Laboratories Inc., Hercules, CA, USA) were used for the qRT-PCR measurements using the  $2^{-\Delta\Delta\text{CT}}$  relative quantification method. Gene expression of type I collagen (Col I), type III collagen (Col III), fibronectin and biglycan were analyzed with the primer sequences reported before ( $n = 6$ ) [7].

### 3.5. Animal Study

#### 3.5.1. Implant Preparation and Experimental Design

One hundred microliter of RDFBs cell suspension ( $2.5 \times 10^5$  cells) were seeded evenly onto sterilized RPSF or APSF nanofiber scaffolds ( $30\text{ mm} \times 30\text{ mm} \times 0.1\text{ mm}$ ) in culture dishes and cultured in a  $\text{CO}_2$  incubator for one week with medium change every 2 days to form cell-scaffold constructs. Forty-eight 6-month-old New Zealand white rabbits (National Laboratory Animal Breeding and Research Center, Taipei, Taiwan, China) were used in this study, as per the guidelines of the Institutional Animal Care and Use Committee of Chang Gung University (IACUC Approval No.: CGU14-139). Experimental animals were randomly divided into 4 groups, including acellular RPFS, acellular APFS, cells/RPSF and cells/APFS ( $n = 12$  in each group). Each group was then divided into two subgroups of 6 and 12 weeks post-operation ( $n = 6$ ). An Achilles tendon partial defect model of the posterior leg was designed and the rabbits were pre-anesthetized by the intramuscular injection

of ketamine (20 mg/kg). The posterior leg of rabbits was carefully shaved and general anesthesia was then induced by 4% isoflurane and was maintained with 2% isoflurane with O<sub>2</sub> at 2.5 L/min throughout the surgery. The rabbit was put in a prone position with full ankle extension and the surgical field of hind leg was sterilized. All surgical instruments were sterilized before the operation and were kept sterile during the whole procedure. Through a 5-cm longitudinal incision at the left posterior leg, a 2-cm lateral segment of the Achilles tendon with paratenon was excised and the medial half was left intact. For each of the experimental group, the cell-seeded scaffold was placed on top of a SF microfibrinous membrane of the same size (30 mm × 30 mm × 0.2 mm), wrapped and tied to form a cord-shape implant (3-mm diameter) that mimicked the tendon size. The implants were inserted into the defect and a modified Kessler core pattern suture was anchored at both ends of the remaining tendon by using a 4-0 polydioxanone suture (PDS) [50]. The implantation of acellular scaffolds without RDFBs was performed in the same way as a control. After surgery, the skins were closed by 4-0 Ethilon® sutures (Ethicon, Johnson & Johnson, New Brunswick, NJ, USA) and 3 mg/kg gentamicin was administered intramuscularly as prophylactic antibiotics. The wounds were dressed by gentamicin ointment to prevent infection and rabbits were kept in cages for their free activities. The detailed surgical procedure is provided in the Supplementary Materials.

### 3.5.2. Histological Observation

At 6 and 12 weeks, six rabbits from each group were euthanized with lethal doses of pentobarbital (0.5 g/kg bodyweight). The specimens were harvested and subject to histological examination of 4 µm slices of 10% formaldehyde-fixed and paraffin-embedded samples. Hematoxylin and eosin (H&E), Masson's trichrome and immunohistochemical (IHC) staining of Col I, Col III and tenascin C were performed following standard protocols [51].

### 3.5.3. Biomechanical Tests

The mechanical features of 12-week implanted samples were investigated through biomechanical testing within 6 h of explantation. A universal testing machine (UN-7001, Gotech Testing Machines Inc., Taichung City, Taiwan) with a 5000 N load cell was used by fixing each end of the harvested sample to a non-slip clamp (TA-2) and elongated axially at a speed of 2 mm/min until rupture. Structural properties were determined from the load-elongation curves, including the maximum load (N) at failure and the tensile stiffness (N/mm) that was calculated from the linear region of the force-displacement curve ( $n = 6$ ).

### 3.6. Statistical Analyses

All data were expressed as the mean ± standard deviation (SD). A one-way ANOVA LSD test was used for statistical analyses with a  $p$  value less than 0.05 considered statistically significant.

## 4. Conclusions

We have demonstrated the effects of SF and fiber alignment in PCL-based nanofibers on scaffold physicochemical properties, cell response in vitro and tendon tissue regeneration in vivo in this study. A well-dispersed blending of SF with PCL could be confirmed and electrospinning was able to produce nanofiber scaffolds with random and aligned nanofibers. The aligned composite APSF scaffold exhibited the highest Young's modulus and hydrophilicity. In vitro cell culture studies confirmed that the addition of SF favored cell proliferation. SEM and confocal microscopic analysis confirmed the effect of fiber alignment on the direction of cell migration and proliferation. Overall, the APSF scaffold facilitated cell proliferation, up-regulated gene expression of tendon-specific ECM proteins in vitro and increased the production and deposition of collagen and tenascin C in vivo, indicating its potential in tendon tissue engineering applications. The nanofiber scaffold developed in this study demonstrates the combined effect of biochemical and physical cues to ameliorate the biological and mechanical properties of the neo-tendon tissue for repair of Achilles tendon defects in rabbit/animal model.

**Supplementary Materials:** The following are available online at [www.mdpi.com/2079-4991/7/8/219/s1](http://www.mdpi.com/2079-4991/7/8/219/s1), Figure S1: Surgical procedure for repairing Achilles tendon defect repairs in rabbits with RPSF and APSF scaffolds. (A) The electrospun scaffold (right) seeded with dermal fibroblast cells was wrapped to itself with seal off two ends; (B) exploration of rabbit Achilles tendon; (C) isolation of the lateral segment of the Achilles tendon; (D) a 2-cm tendon defect was made completely; (E) the defect was repaired with the cells/scaffold construct using modified Kessler suture technique; (F) gross view immediate after tendon repair.

**Acknowledgments:** The financial assistance was provided by grants from the Ministry of Science and Technology (MOST104-2923-E-182-001-MY3, NMRPG3G0461), Chang Gung Memorial Hospital (BMRP249, CMRPG3A1431-2, CRRPD2D0013) and the Ministry of Health and Welfare (MOHW104-TDU-PB-212-12208).

**Author Contributions:** C.H. Chen, S.H. Chen, C.Y. Kuo and J.P. Chen conceived and designed the experiments; M.L. Li performed the experiments; C.H. Chen, S.H. Chen and M.L. Li analyzed the data; C.H. Chen, C.Y. Kuo and J.P. Chen wrote the paper.

**Conflicts of Interest:** The authors declare no conflict of interest.

## References

- Barber, J.G.; Handorf, A.M.; Allee, T.J.; Li, W.-J. Braided nanofibrous scaffold for tendon and ligament tissue engineering. *Tissue Eng. Part A* **2011**, *19*, 1265–1274. [[CrossRef](#)] [[PubMed](#)]
- Majima, T.; Funakosi, T.; Iwasaki, N.; Yamane, S.-T.; Harada, K.; Nonaka, S.; Minami, A.; Nishimura, S.-I. Alginate and chitosan polyion complex hybrid fibers for scaffolds in ligament and tendon tissue engineering. *J. Orthop. Sci.* **2005**, *10*, 302–307. [[CrossRef](#)] [[PubMed](#)]
- Sahoo, S.; Toh, S.L.; Goh, J.C. A bFGF-releasing silk/PLGA-based biohybrid scaffold for ligament/tendon tissue engineering using mesenchymal progenitor cells. *Biomaterials* **2010**, *31*, 2990–2998. [[CrossRef](#)] [[PubMed](#)]
- An, J.; Chua, C.K.; Leong, K.F.; Chen, C.-H.; Chen, J.-P. Solvent-free fabrication of three dimensionally aligned polycaprolactone microfibers for engineering of anisotropic tissues. *Biomed. Microdevices* **2012**, *14*, 863–872. [[CrossRef](#)] [[PubMed](#)]
- McNally, P.D.; Marcelli, E.A. Achilles allograft reconstruction of a chronic patellar tendon rupture. *Arthroscopy* **1998**, *14*, 340–344. [[CrossRef](#)]
- Chen, J.; Yu, Q.; Wu, B.; Lin, Z.; Pavlos, N.J.; Xu, J.; Ouyang, H.; Wang, A.; Zheng, M.H. Autologous tenocyte therapy for experimental achilles tendinopathy in a rabbit model. *Tissue Eng. Part A* **2011**, *17*, 2037–2048. [[CrossRef](#)] [[PubMed](#)]
- Sahoo, S.; Ang, L.-T.; Goh, J.C.-H.; Toh, S.-L. Bioactive nanofibers for fibroblastic differentiation of mesenchymal precursor cells for ligament/tendon tissue engineering applications. *Differentiation* **2010**, *79*, 102–110. [[CrossRef](#)] [[PubMed](#)]
- Ouyang, H.W.; Goh, J.C.; Thambyah, A.; Teoh, S.H.; Lee, E.H. Knitted poly-lactide-co-glycolide scaffold loaded with bone marrow stromal cells in repair and regeneration of rabbit achilles tendon. *Tissue Eng.* **2003**, *9*, 431–439. [[CrossRef](#)] [[PubMed](#)]
- Moffat, K.L.; Kwei, A.S.-P.; Spalazzi, J.P.; Doty, S.B.; Levine, W.N.; Lu, H.H. Novel nanofiber-based scaffold for rotator cuff repair and augmentation. *Tissue Eng. Part A* **2008**, *15*, 115–126. [[CrossRef](#)] [[PubMed](#)]
- Chieruzzi, M.; Pagano, S.; Moretti, S.; Pinna, R.; Milia, E.; Torre, L.; Eramo, S. Nanomaterials for tissue engineering in dentistry. *Nanomaterials* **2016**, *6*, 134. [[CrossRef](#)] [[PubMed](#)]
- Martins, A.; Reis, R.; Neves, N. Electrospinning: Processing technique for tissue engineering scaffolding. *Int. Mater. Rev.* **2008**, *53*, 257–274. [[CrossRef](#)]
- Zhang, W.; Ronca, S.; Mele, E. Electrospun nanofibres containing antimicrobial plant extracts. *Nanomaterials* **2017**, *7*, 42. [[CrossRef](#)] [[PubMed](#)]
- Yang, C.; Deng, G.; Chen, W.; Ye, X.; Mo, X. A novel electrospun-aligned nanoyarn-reinforced nanofibrous scaffold for tendon tissue engineering. *Colloids Surf. B* **2014**, *122*, 270–276. [[CrossRef](#)] [[PubMed](#)]
- Lu, G.; Liu, S.; Lin, S.; Kaplan, D.L.; Lu, Q. Silk porous scaffolds with nanofibrous microstructures and tunable properties. *Colloids Surf. B* **2014**, *120*, 28–37. [[CrossRef](#)] [[PubMed](#)]
- Kasoj, N.; Bora, U. Silk fibroin in tissue engineering. *Adv. Healthc. Mater.* **2012**, *1*, 393–412. [[CrossRef](#)] [[PubMed](#)]
- Altman, G.H.; Diaz, F.; Jakuba, C.; Calabro, T.; Horan, R.L.; Chen, J.; Lu, H.; Richmond, J.; Kaplan, D.L. Silk-based biomaterials. *Biomaterials* **2003**, *24*, 401–416. [[CrossRef](#)]

17. MacIntosh, A.C.; Kearns, V.R.; Crawford, A.; Hatton, P.V. Skeletal tissue engineering using silk biomaterials. *J. Tissue Eng. Regen. Med.* **2008**, *2*, 71–80. [[CrossRef](#)] [[PubMed](#)]
18. Jao, D.; Mou, X.; Hu, X. Tissue regeneration: A silk road. *J. Funct. Biomater.* **2016**, *7*, 22. [[CrossRef](#)] [[PubMed](#)]
19. Kannus, P. Structure of the tendon connective tissue. *Scand. J. Med. Sci. Sports* **2000**, *10*, 312–320. [[CrossRef](#)] [[PubMed](#)]
20. Leung, M.; Jana, S.; Tsao, C.-T.; Zhang, M. Tenogenic differentiation of human bone marrow stem cells via a combinatory effect of aligned chitosan-poly-caprolactone nanofibers and TGF- $\beta$ 3. *J. Mater. Chem. B* **2013**, *1*, 6516–6524. [[CrossRef](#)]
21. Teh, T.K.; Toh, S.-L.; Goh, J.C. Aligned hybrid silk scaffold for enhanced differentiation of mesenchymal stem cells into ligament fibroblasts. *Tissue Eng. Part C* **2011**, *17*, 687–703. [[CrossRef](#)] [[PubMed](#)]
22. Chung, J.Y.; Youngblood, J.P.; Stafford, C.M. Anisotropic wetting on tunable micro-wrinkled surfaces. *Soft Matter* **2007**, *3*, 1163–1169. [[CrossRef](#)]
23. Kai, D.; Prabhakaran, M.P.; Jin, G.; Ramakrishna, S. Guided orientation of cardiomyocytes on electrospun aligned nanofibers for cardiac tissue engineering. *J. Biomed. Mater. Res. Part B Appl. Biomater.* **2011**, *98*, 379–386. [[CrossRef](#)] [[PubMed](#)]
24. Chen, J.P.; Chen, S.H.; Lai, G.J. Preparation and characterization of biomimetic silk fibroin/chitosan composite nanofibers by electrospinning for osteoblasts culture. *Nanoscale Res. Lett.* **2012**, *7*, 170. [[CrossRef](#)] [[PubMed](#)]
25. Chen, J.P.; Chang, Y.S. Preparation and characterization of composite nanofibers of polycaprolactone and nanohydroxyapatite for osteogenic differentiation of mesenchymal stem cells. *Colloids Surf. B* **2011**, *86*, 169–175. [[CrossRef](#)] [[PubMed](#)]
26. Chen, C.H.; Chen, S.H.; Shalumon, K.T.; Chen, J.P. Dual functional core-sheath electrospun hyaluronic acid/polycaprolactone nanofibrous membranes embedded with silver nanoparticles for prevention of peritendinous adhesion. *Acta Biomater.* **2015**, *26*, 225–235. [[CrossRef](#)] [[PubMed](#)]
27. Kim, S.H.; Nam, Y.S.; Lee, T.S.; Park, W.H. Silk fibroin nanofiber. Electrospinning, properties, and structure. *Polym. J.* **2003**, *35*, 185–190. [[CrossRef](#)]
28. Lim, J.S.; Ki, C.S.; Kim, J.W.; Lee, K.G.; Kang, S.W.; Kweon, H.Y.; Park, Y.H. Fabrication and evaluation of poly(epsilon-caprolactone)/silk fibroin blend nanofibrous scaffold. *Biopolymers* **2012**, *97*, 265–275. [[CrossRef](#)] [[PubMed](#)]
29. Li, L.; Li, H.; Qian, Y.; Li, X.; Singh, G.K.; Zhong, L.; Liu, W.; Lv, Y.; Cai, K.; Yang, L. Electrospun poly(varepsilon-caprolactone)/silk fibroin core-sheath nanofibers and their potential applications in tissue engineering and drug release. *Int. J. Biol. Macromol.* **2011**, *49*, 223–232. [[CrossRef](#)] [[PubMed](#)]
30. Jeong, L.; Lee, K.Y.; Liu, J.W.; Park, W.H. Time-resolved structural investigation of regenerated silk fibroin nanofibers treated with solvent vapor. *Int. J. Biol. Macromol.* **2006**, *38*, 140–144. [[CrossRef](#)] [[PubMed](#)]
31. Bhattarai, N.; Li, Z.; Gunn, J.; Leung, M.; Cooper, A.; Edmondson, D.; Veis, O.; Chen, M.-H.; Zhang, Y.; Ellenbogen, R.G.; et al. Natural-synthetic polyblend nanofibers for biomedical applications. *Adv. Mater.* **2009**, *21*, 2792–2797. [[CrossRef](#)]
32. Zhang, D.; Ni, N.; Chen, J.; Yao, Q.; Shen, B.; Zhang, Y.; Zhu, M.; Wang, Z.; Ruan, J.; Wang, J.; et al. Electrospun SF/PLCL nanofibrous membrane: A potential scaffold for retinal progenitor cell proliferation and differentiation. *Sci. Rep.* **2015**, *5*, 14326. [[CrossRef](#)] [[PubMed](#)]
33. Xie, J.; Li, X.; Lipner, J.; Manning, C.N.; Schwartz, A.G.; Thomopoulos, S.; Xia, Y. “Aligned-to-random” nanofiber scaffolds for mimicking the structure of the tendon-to-bone insertion site. *Nanoscale* **2010**, *2*, 923–926. [[CrossRef](#)] [[PubMed](#)]
34. Zhang, X.; Reagan, M.R.; Kaplan, D.L. Electrospun silk biomaterial scaffolds for regenerative medicine. *Adv. Drug Deliv. Rev.* **2009**, *61*, 988–1006. [[CrossRef](#)] [[PubMed](#)]
35. Lai, G.J.; Shalumon, K.T.; Chen, S.H.; Chen, J.P. Composite chitosan/silk fibroin nanofibers for modulation of osteogenic differentiation and proliferation of human mesenchymal stem cells. *Carbohydr. Polym.* **2014**, *111*, 288–297. [[CrossRef](#)] [[PubMed](#)]
36. Lampin, M.; Warocquier, C.; Legris, C.; Degrange, M.; Sigot-Luizard, M.F. Correlation between substratum roughness and wettability, cell adhesion, and cell migration. *J. Biomed. Mater. Res.* **1997**, *36*, 99–108. [[CrossRef](#)]

37. Faucheux, N.; Schweiss, R.; Lutzow, K.; Werner, C.; Groth, T. Self-assembled monolayers with different terminating groups as model substrates for cell adhesion studies. *Biomaterials* **2004**, *25*, 2721–2730. [[CrossRef](#)] [[PubMed](#)]
38. Min, B.M.; Lee, G.; Kim, S.H.; Nam, Y.S.; Lee, T.S.; Park, W.H. Electrospinning of silk fibroin nanofibers and its effect on the adhesion and spreading of normal human keratinocytes and fibroblasts in vitro. *Biomaterials* **2004**, *25*, 1289–1297. [[CrossRef](#)] [[PubMed](#)]
39. Yen, K.-C.; Chen, C.-Y.; Huang, J.-Y.; Kuo, W.-T.; Lin, F.-H. Fabrication of keratin/fibroin membranes by electrospinning for vascular tissue engineering. *J. Mater. Chem. B* **2016**, *4*, 237–244. [[CrossRef](#)]
40. Lin, T.W.; Cardenas, L.; Soslowsky, L.J. Biomechanics of tendon injury and repair. *J. Biomech.* **2004**, *37*, 865–877. [[CrossRef](#)] [[PubMed](#)]
41. Venugopal, J.R.; Zhang, Y.; Ramakrishna, S. In vitro culture of human dermal fibroblasts on electrospun polycaprolactone collagen nanofibrous membrane. *Artif. Organs* **2006**, *30*, 440–446. [[CrossRef](#)] [[PubMed](#)]
42. Chen, J.; Horan, R.L.; Bramono, D.; Moreau, J.E.; Wang, Y.; Geuss, L.R.; Collette, A.L.; Volloch, V.; Altman, G.H. Monitoring mesenchymal stromal cell developmental stage to apply on-time mechanical stimulation for ligament tissue engineering. *Tissue Eng.* **2006**, *12*, 3085–3095. [[CrossRef](#)] [[PubMed](#)]
43. Berglund, M.; Reno, C.; Hart, D.A.; Wiig, M. Patterns of mrna expression for matrix molecules and growth factors in flexor tendon injury: Differences in the regulation between tendon and tendon sheath. *J. Hand Surg. Am.* **2006**, *31*, 1279–1287. [[CrossRef](#)] [[PubMed](#)]
44. Sharma, P.; Maffulli, N. Basic biology of tendon injury and healing. *Surgeon* **2005**, *3*, 309–316. [[CrossRef](#)]
45. Lee, C.H.; Shin, H.J.; Cho, I.H.; Kang, Y.M.; Kim, I.A.; Park, K.D.; Shin, J.W. Nanofiber alignment and direction of mechanical strain affect the ecm production of human acl fibroblast. *Biomaterials* **2005**, *26*, 1261–1270. [[CrossRef](#)] [[PubMed](#)]
46. Doroski, D.M.; Brink, K.S.; Temenoff, J.S. Techniques for biological characterization of tissue-engineered tendon and ligament. *Biomaterials* **2007**, *28*, 187–202. [[CrossRef](#)] [[PubMed](#)]
47. Young, R.G.; Butler, D.L.; Weber, W.; Caplan, A.I.; Gordon, S.L.; Fink, D.J. Use of mesenchymal stem cells in a collagen matrix for achilles tendon repair. *J. Orthop. Res.* **1998**, *16*, 406–413. [[CrossRef](#)] [[PubMed](#)]
48. Juncosa-Melvin, N.; Boivin, G.P.; Galloway, M.T.; Gooch, C.; West, J.R.; Butler, D.L. Effects of cell-to-collagen ratio in stem cell-seeded constructs for achilles tendon repair. *Tissue Eng.* **2006**, *12*, 681–689. [[CrossRef](#)] [[PubMed](#)]
49. Shalumon, K.T.; Lai, G.J.; Chen, C.H.; Chen, J.P. Modulation of bone-specific tissue regeneration by incorporating bone morphogenetic protein and controlling the shell thickness of silk fibroin/chitosan/nanohydroxyapatite core-shell nanofibrous membranes. *ACS Appl. Mater. Interfaces* **2015**, *7*, 21170–21181. [[CrossRef](#)] [[PubMed](#)]
50. Jordan, M.C.; Schmitt, V.; Jansen, H.; Meffert, R.H.; Hoelscher-Doht, S. Biomechanical analysis of the modified Kessler, Lahey, Adelaide, and Becker sutures for flexor tendon repair. *J. Hand Surg. Am.* **2015**, *40*, 1812–1817. [[CrossRef](#)] [[PubMed](#)]
51. Lai, G.J.; Shalumon, K.T.; Chen, J.P. Response of human mesenchymal stem cells to intrafibrillar nanohydroxyapatite content and extrafibrillar nanohydroxyapatite in biomimetic chitosan/silk fibroin/nanohydroxyapatite nanofibrous membrane scaffolds. *Int. J. Nanomed.* **2015**, *10*, 567–584.



© 2017 by the authors. Licensee MDPI, Basel, Switzerland. This article is an open access article distributed under the terms and conditions of the Creative Commons Attribution (CC BY) license (<http://creativecommons.org/licenses/by/4.0/>).





## Review

## Major achievements of evidence-based traditional Chinese medicine in treating major diseases



Jung Chao<sup>a,b,c,1</sup>, Yuntao Dai<sup>a,1</sup>, Robert Verpoorte<sup>d</sup>, Wing Lam<sup>e</sup>, Yung-Chi Cheng<sup>e</sup>, Li-Heng Pao<sup>b</sup>, Wei Zhang<sup>a</sup>, Shilin Chen<sup>a,\*</sup>

<sup>a</sup> Institute of Chinese Materia Medica, China Academy of Chinese Medical Sciences, Beijing

<sup>b</sup> Graduate Institute of Health-Industry Technology, Research Center for Food and Cosmetic Safety, and Research Center for Chinese Herbal Medicine, College of Human Ecology, Chang Gung University of Science and Technology, Taoyuan City

<sup>c</sup> Department of Chinese Pharmaceutical Sciences and Chinese Medicine Resources, China Medical University, Taichung

<sup>d</sup> Natural Products Laboratory, Institute of Biology, Leiden University, Leiden

<sup>e</sup> Department of Pharmacology, Yale University School of Medicine, New Haven, CT

## ARTICLE INFO

## Article history:

Received 28 February 2017

Accepted 15 June 2017

Available online 19 June 2017

## Keywords:

Traditional Chinese medicine

Western medicine

Artemisinin

Evidence-based traditional medicines

Drug development

Quality control

## ABSTRACT

A long history of use and extensive documentation of the clinical practices of traditional Chinese medicine resulted in a considerable number of classical preparations, which are still widely used. This heritage of our ancestors provides a unique resource for drug discovery. Already, a number of important drugs have been developed from traditional medicines, which in fact form the core of Western pharmacotherapy. Therefore, this article discusses the differences in drug development between traditional medicine and Western medicine. Moreover, the article uses the discovery of artemisinin as an example that illustrates the “bedside–bench–bedside” approach to drug discovery to explain that the middle way for drug development is to take advantage of the best features of these two distinct systems and compensate for certain weaknesses in each. This article also summarizes evidence-based traditional medicines and discusses quality control and quality assessment, the crucial steps in botanical drug development. Herbgonomics may provide effective tools to clarify the molecular mechanism of traditional medicines in the botanical drug development. The totality-of-the-evidence approach used by the U.S. Food and Drug Administration for botanical products provides the directions on how to perform quality control from the field throughout the entire production process.

© 2017 Elsevier Inc. All rights reserved.

## Contents

1. Introduction	95
2. Comparison of drug development in traditional medicine and Western medicine	95
3. Drugs derived from traditional medicines for treatment of chronic diseases	95
4. Development of artemisinin: learning from ancient healing practices	100
5. Quality control and quality assessment of botanical products: the stumbling block of traditional medicine development	100
6. Future directions	102
Acknowledgements	102
References	102

\* Corresponding author.

E-mail address: [slchen@icmm.ac.cn](mailto:slchen@icmm.ac.cn) (S. Chen).

<sup>1</sup> These authors contributed equally to this work.

## 1. Introduction

Nature is a major source of new therapeutic small molecules. About half the pharmaceuticals developed over the last three decades and approved by the U.S. Food and Drug Administration (FDA) are natural products, semisynthetic derivatives, or based on a prototype from nature [1–4]. In this period, a highly reductionist approach, based on the “single target–single compound” paradigm, or “cell-based screening” dominated the drug development in the Western pharmaceutical industry, an approach that is clearly different from those used by traditional medical systems. Thus, a more phenomenological, descriptive, and system-based (homeostasis) view is the basic concept in traditional Chinese medicine (TCM). Traditional medical doctors often apply a holistic approach in prescribing a personalized mixture of (herbal) components to a patient. In the past, the two philosophies, one adopted by Western medicine and the other adopted by TCM, did not match well. However, new insights into the complexity of human health and disease, particularly through the advent of the “omics” technologies and more systemic thinking in life sciences, have resulted in a rethinking of the importance of traditional medicine [5]. The 2015 Nobel Prize in Physiology or Medicine was recognition of the importance of traditional medicines by the Western medical world. Systemic approaches to studying health through observation-based systems biology are becoming more important now. At the same time, the need for evidence-based use of traditional medicines finds a foothold in the East. Combining traditional and Western medicine will result in important benefits for primary health care. Moreover, it opens new perspectives for drug discovery and development as the processes move from the “single target–single compound” approach to more systemic approaches to preventing and treating diseases.

This article reviews evidence-based traditional medicines for the treatment of some major diseases. In addition, we discuss differences between the development models of evidence-based traditional medicines and novel Western medicines using the discovery of artemisinin as an example. The “bedside–bench–bed side” approach to drug discovery seems to be a middle way for drug development, taking advantage of the best features of both systems and compensating for some of their weaknesses.

## 2. Comparison of drug development in traditional medicine and Western medicine

The major difference in drug development in ancient times and present days is that in the past, medicines were tested directly on humans, whereas the starting point of drug development today is screening at either the molecular or cellular level (Fig. 1A) [6–8]. In medicinal plant research, after proving the activity in bioassays at the level of molecules or cell lines, bioassay-guided fractionation is used to isolate and identify the active compound(s). Finally, the activity of the active compound(s) is further elucidated *in vivo* using whole organisms (Fig. 1A2). This illustrates the bottom-up reductionist approach practiced in Western biomedical sciences. In the past three decades, the search for novel drugs has relied on hypothesis-free and high-throughput screening (HTS) of a large number of pure compounds, combinatorial compound libraries, or extracts of various organisms, including plants, using enzyme- and receptor-binding assays related to the target disease [9]. However, this approach has not always been successful, which is best illustrated by a slowly decreasing number of novel small-molecule drugs entering the market. The problems encountered can be illustrated by the case of huperzine A, an alkaloid from *Huperzia serrata*, which showed multiple beneficial effects in preclinical models but failed in a phase 2 clinical study for Alzheimer’s disease [10]. More-

over, in complex mixtures of compounds present in herbal medicines, certain combinations of compounds may be needed to attain activity. A study of *Berberis fremontii* has shown that the antimicrobial effect of the bioactive compound berberine was enhanced more than 100-fold in combination with an inactive component, 5'-methoxyhydnocarpin, isolated from the same plant [11]. This further supports the idea that the resistance of plants against microorganisms is based on synergistic effects and explains why to date no antibiotic has been developed from plants [12]. Synergy thus may play an important role, as also shown in the example of St. John’s wort, in which no single active compound has been found that could explain the proven clinical activity of the plant [6]. These examples indicate the limitations of screening approaches using cell-based assays or HTS, which will not detect the synergy and prodrugs. In addition, testing of bioavailability, a major factor contributing to the effect of a medicine, requires *in vivo* studies [13,14].

Generally, treatment with traditional medicines is based on holistic characterization of the patient’s syndrome. Traditional prescriptions usually comprise a group of herbs specifically tailored to the syndrome [15]. In the past, these traditional medicine mixtures must have been tested directly on humans (Fig. 1A1). After their efficacy and safety was established in humans, traditional medicines were used to cure diseases, treat symptoms, and/or maintain homeostasis. Considering the original theory of mixing certain medicinal plants, one may expect some sort of synergism to be involved, such as acting on different targets, affecting bioavailability, suppressing adverse side effects, and altering drug metabolism and excretion [16]. Consequently, the reductionist approach, i.e., testing single active components against well-defined targets, does not lead to understanding the pharmacology of a multicomponent agent as it fails to integrate the results obtained using separate reductionist approaches. Such an approach does not result in a systemic understanding of the concerted pharmacological interventions of multicomponent mixtures [17]. In contrast, traditional medical systems are aimed at a holistic understanding of the whole organism and at applying this wisdom in a top-down manner in a search for knowledge.

Therefore, instead of using a reductionist approach, evidence of the activity of a traditional medicine should come from *in vivo* tests, preferably through clinical trials or animal experiments [6]. Wang et al. pointed out the importance of metabolomics as a tool in such a systemic approach to understanding Chinese medicine [18]. The importance of such an approach is confirmed by the analysis made by Swinney and Anthony who found that more than half of the first-in-class novel antitumor compounds in the years 1999–2008 were found through phenotypic screening [19], a general trend for all the 259 novel drugs that were approved by the FDA in the period mentioned. Moffat et al. further elaborated on this and gave a vision how such an approach can even be more effective in the future [20]. Classical pharmacology, wherein a traditional preparation is taken as a starting point, holds promise for studying the synergetic nature of herbal medicine [6], while clinical trials will show if there is an activity. The various “omics” technologies, applied in a systems biology approach, offer excellent tools to get an insight into possible modes of action [6,16,18]. Animal experiments, including novel model organisms such *Caenorhabditis elegans* and zebrafish, may be used to obtain a further insight into the activity.

## 3. Drugs derived from traditional medicines for treatment of chronic diseases

Chronic disease refers to a disease that has a long period of development and lasts for a long time. Common chronic diseases

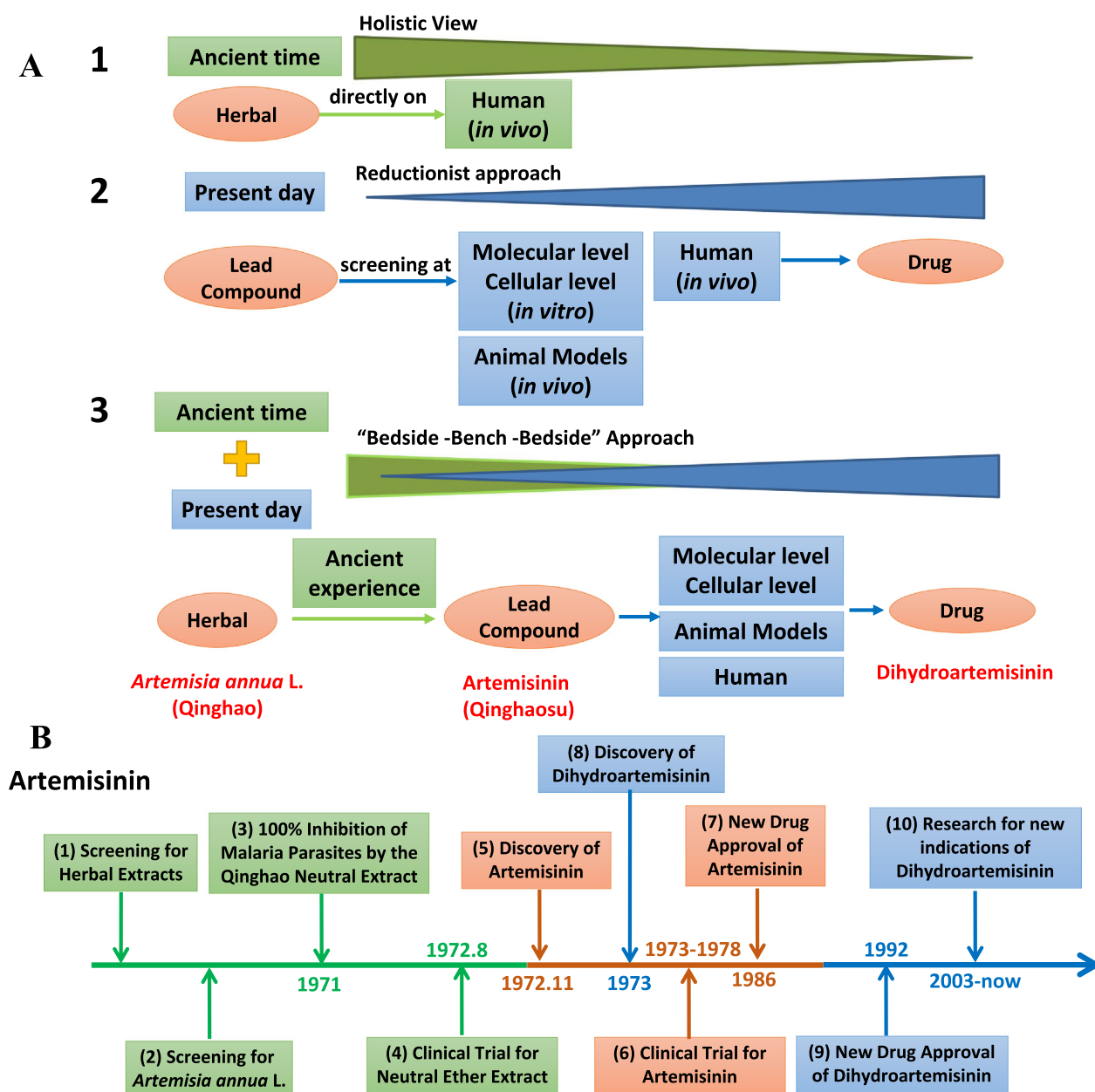


**Fig. 1.** Comparison between traditional medicine and Western medicine (A) and development of artemisinin (B). (A1) The development model of traditional medicine; (A2) the development model of Western medicine; (A3) the “bedside-bench-bedside” approach in traditional and Western medicine. (B) The development course of artemisinin: stage 1 (green), stage 2 (red), and stage 3 (blue).

include cardiovascular diseases, diabetes, cancer, chronic obstructive pulmonary disease, digestive system diseases, and mental disorders. Their complexity is the most prominent feature of chronic diseases, with often multifactorial pathogenesis. Western medicine mainly involves a symptomatic treatment, and the drugs applied are mainly single-target, single-factor treatments. Western medicine is characterized by a rapid effect but also results in side effects, and it is easy to produce dependence and drug-induced diseases. In TCM, where diagnosis and treatment are considered from the holistic perspective, the applied medicine includes multiple components and has multiple targets so as to play a comprehensive role in treatment.

Compared with Western medicine, TCM mainly shows advantages in the following aspects: (1) Western medicine has shown no success in treating some specific diseases that are treated in Chinese medicine; (2) Western medicine treatments have shown

a poor performance for specific diseases; (3) Although there is a treatment for a specific disease, adverse effects of a Western medicine have limited its application; (4) Some TCM treatments for specific diseases were recorded in ancient TCM documents, and today’s rigorous research and clinical practice have proven their effectiveness.

Development of evidence-based traditional medicines is the only valid argument to convince Western medical science to start using such medicines [16]. The many centuries old successful use of traditional medicines, in itself, is not accepted as evidence. Obviously, experimental clinical evidence can be further explored and may lead to novel insights into human diseases and pharmacology. In the course of development of the modern science, some drugs for certain indications have been developed from prescriptions used in TCM for the treatment of cardiovascular diseases, metabolic diseases, and cancer. Table 1 shows some selected important

**Table 1**  
Selected Chinese herbal medicines and Chinese patented medicines for treating major diseases.

Name	Description	Disease/indication	Reference
<i>Infectious disease</i>			
Artemisinin (qinghaosu)	Artemisinin is an antimalarial drug isolated from <i>Artemisia annua</i> L. It was first discovered by Youyou Tu, a Chinese scientist, who was awarded the 2015 Nobel Prize in Physiology or Medicine for her discovery	Malaria	[15,28]
Tetrandrine	Tetrandrine is a pure compound isolated from the roots of <i>Stephania tetrandra</i> S. Moore (Menispermaceae). Tetrandrine disrupts two-pore channel function, halts virus trafficking, and prevents infection	Ebola virus disease	[52]
Lianhua–Qingwen capsules	Lianhua–Qingwen capsules (LQCs) are a traditional Chinese patented medicine developed from two classical traditional Chinese medicine (TCM) formulae, Maxing–Shigan–Tang and Yinqiao–San, which have a long history of clinical application in the treatment of viral influenza. LQCs are composed of 13 herbs, including Lianqiao (the fruits of <i>Forsythia suspensa</i> (Thunb.) Vahl), Jinyinhua (The flowers or flower buds of <i>Lonicera japonica</i> Thunb.), Mahuang (the stems of <i>Ephedra sinica</i> Stapf or <i>E. intermedia</i> Schrenk et C. A. Mey. or <i>E. equisetina</i> Bge.), Kuxingren (the seeds of <i>Prunus armeniaca</i> L. var. <i>ansu</i> Maxim. or <i>P. sibirica</i> L. or <i>P. mandshurica</i> (Maxim.) Koehne or <i>P. armeniaca</i> L.), Banlangen (the roots of <i>Isatis indigotica</i> Fort.), Mianmaguanzhong (the rhizomes of <i>Dryopteris crassirhizoma</i> Nakai), Yuxingcao (the aerial parts of <i>Houttuynia cordata</i> Thunb.), Guanghuoxiang (The aerial parts of <i>Pogostemon cablin</i> (Blanco) Benth.), Dahuang (the roots and rhizomes of <i>Rheum palmatum</i> L. or <i>R. tanguticum</i> Maxim. ex Balf. or <i>R. officinale</i> Baill.), Hongjiingtian (the roots and rhizomes of <i>Rhodiola crenulata</i> (Hook. f. et Thoms.) H. Ohba), Gancao (the roots and rhizomes of <i>Glycyrrhiza uralensis</i> Fisch. or <i>G. inflata</i> Bat. or <i>G. glabra</i> L.), Bohe (the aerial parts of <i>Mentha haplocalyx</i> Briq.), and Shigao (gypsum)	Influenza A virus subtype H1N1, reduces time to fever resolution in patients with H1N1 influenza virus infection	[26,30,32,33]
Maxingshgan–Yinqiaosan	The TCM formula Maxingshgan–Yinqiaosan is composed of 12 herbs: Zhimahuang (honey-fried stems of <i>Ephedra sinica</i> Stapf or <i>E. intermedia</i> Schrenk et C. A. Mey. or <i>E. equisetina</i> Bge.), Zhimu (the rhizomes of <i>Anemarrhena asphodeloides</i> Bge.), Qinghao (the aerial parts of <i>A. annua</i> L.), Shigao (gypsum), Jinyinhua (The flowers or flower buds of <i>L. japonica</i> Thunb.), Huangqin (the roots of <i>Scutellaria baicalensis</i> Georgi), Chaoxingren (stir-baked seeds of <i>P. armeniaca</i> L. var. <i>ansu</i> Maxim. or <i>P. sibirica</i> L. or <i>P. mandshurica</i> (Maxim.) Koehne or <i>P. armeniaca</i> L.), Lianqiao (the fruits of <i>F. suspensa</i> (Thunb.) Vahl), Bohe (the aerial parts of <i>M. haplocalyx</i> Briq.), Zhebeimu (the bulbs of <i>Fritillaria thunbergii</i> Miq.), Niubangzi (the fruits of <i>Arctium lappa</i> L.), and Gancao (the roots and rhizomes of <i>G. uralensis</i> Fisch. or <i>G. inflata</i> Bat. or <i>G. glabra</i> L.)	Influenza A virus subtype H1N1, reduces time to fever resolution in patients with H1N1 influenza virus infection	[26,34]
Banlangen	Banlangen (the roots of <i>I. indigotica</i> Fort.) have long been used to treat seasonal influenza in China. Banlangen acts via multiple modes, which target not only the virus but also various components of the host's immune response	Seasonal influenza	[26,35–37]
<i>Cardiovascular disease</i>			
Compound Danshen dripping pills (Dantonic, T89)	Chinese patented drug, extracts of Danshen (the roots and rhizomes of <i>Salvia miltiorrhiza</i> Bge.) and Sanqi (the roots and rhizomes of <i>Panax notoginseng</i> (Burk.) F. H. Chen) with borneol in a capsule form. An application for Compound Danshen dripping pills has been filed with U.S. FDA, and a phase III clinical trial has been completed	Angina pectoris	[5–7]
Di'ao Xinxuekang capsules	Di'ao Xinxuekang capsules were successfully approved by the Dutch Medicines Evaluation Board and were the first TCM product used as a medicine in Europe. The active ingredient (dioscin) of Di'ao Xinxuekang capsules is extracted from Shanyao (the rhizomes of <i>Dioscorea opposita</i> Thunb.)	Angina pectoris	[53–55]
Qili Qiangxin capsules	Qili qiangxin capsules are a formulation based on several common medicinal herbs in TCM, which are well known to have cardiotonic and immunomodulatory effects. It is prepared from 11 Chinese herbs, including Huangqi (the roots of <i>Astragalus membranaceus</i> (Fisch.) Bge. var. <i>mongholicus</i> (Bge.) Hsiao or <i>A. membranaceus</i> (Fisch.) Bge.), Renshen (the roots and rhizomes of <i>Panax ginseng</i> C.A.Mey.), Fuzi (the roots of <i>Aconitum carmichaelii</i> Debx.), Danshen (the roots and rhizomes of <i>S. miltiorrhiza</i> Bge.), Tinglizi (the seeds of <i>Descurainia sophia</i> (L.) Webb. ex Prantl. or <i>Lepidium apetalum</i> Wild.), Zexie (the rhizomes of <i>Alisma orientale</i> (Sam.) Juzep.), Yuzhu (the rhizomes of <i>Polygonatum odoratum</i> (Mill.) Druce), Guizhi (the twigs of <i>Cinnamomum cassia</i> Presl), Honghua (the flowers of <i>Carthamus tinctorius</i> L.), Xiangjiapi (the cortex of <i>Periploca sepium</i> Bge.), and Chenpi (the pericarps of <i>Citrus reticulata</i> Blanco)	Chronic heart failure	[56–58]
Danhong injection	Injection of a Chinese patented compound, which is extracted from Danshen (the roots and rhizomes of <i>S. miltiorrhiza</i> Bge.) and Honghua (the flowers of <i>C. tinctorius</i> L.), is widely prescribed to patients with coronary heart disease	Chronic stable angina, acute myocardial infarction, ischemic stroke	[59–63]
Shenfu injection	Shenfu injection has been used in treating cardiac diseases for a long time in China. It is prepared from two Chinese herbs, renshe (the roots and rhizomes of <i>P. ginseng</i> C. A. Mey.), Fuzi (the roots of <i>A. carmichaelii</i> Debx.)	Chronic heart failure	[64–66]
Xuezhikang capsules	Hong Qu (100% Red yeast rice), obtained by fermentation with <i>Monascus</i> strains	Hyperlipidemia	[67–72]
<i>Metabolic disease</i>			
Berberine	Berberine is an isoquinoline derivative alkaloid isolated from Huanglian (the rhizomes of <i>Coptis chinensis</i> Franch. or <i>C. deltoidea</i> C. Y. Cheng et Hsiao or <i>C. teeta</i> Wall.), which has been widely used as a drug to treat gastrointestinal infections (e.g., bacterial diarrhea). Berberine is considered an antibiotic. In addition, it has been used as an antihyperglycemic agent by many physicians in China. Berberine appears to have an additional, cholesterol-lowering, effect in treating diabetes, which is frequently found in patients with hyperlipidemia	Hyperglycemia, hyperlipidemia, bacterial diarrhea	[11,73–75]

(continued on next page)

Table 1 (continued)

Name	Description	Disease/indication	Reference
Gegen–Qinlian decoction	Gegen–Qinlian decoction is a classical formula in TCM. It is widely used to treat diarrhea in clinical practice. Gegen–Qinlian decoction has been reported to show potentially beneficial effects in the treatment of diabetes in animal trials, as well as in some clinical observations. It is prepared from four Chinese herbs, including Gegen (the roots of <i>Pueraria lobata</i> (Willd.) Ohwi), Huangqin (the roots of <i>S. baicalensis</i> Georgi), Huanglian (the rhizomes of <i>C. chinensis</i> Franch. or <i>C. deltoidea</i> C. Y. Cheng et Hsiao or <i>C. teeta</i> Wall.), and Gancao (the roots and rhizomes of <i>G. uralensis</i> Fisch. or <i>G. inflata</i> Bat. or <i>G. glabra</i> L.)	Hyperglycemia, diarrhea	[76–78]
Cancer Arsenic trioxide (Pishuang)	An ancient remedy used in TCM, Pishuang has attracted worldwide interest because it shows substantial anticancer activity in patients with acute promyelocytic leukemia. The key molecular mechanism has been revealed to be related to the degradation of promyelocytic leukemia–retinoic acid receptor $\alpha$ (RAR $\alpha$ )	Acute promyelocytic leukemia	[79–81]
Realgar–Indigo naturalis	The Realgar–Indigo naturalis formula (RIF) is a TCM formula, and the main components are Xionghuang (realgar, mined ore), Qingdai (the leaves or stems of <i>Baphicacanthus cusia</i> (Nees) Bremek. or <i>Polygonum tinctorium</i> Ait. or <i>Isatis indigotica</i> Fort.), and Dansen (the roots and rhizomes of <i>S. miltiorrhiza</i> Bge.). The major active ingredients are tetraarsenic tetrasulfide, indirubin, and tanshinone IIA. A recent multicenter clinic trial showed that a complete remission rate of around 97% and a 5-year overall survival rate of 86% were achieved in acute promyelocytic leukemia patients receiving RIF, with moderate adverse effects such as gastrointestinal discomfort and rash	Acute promyelocytic leukemia	[82]
Lingzhi	Lingzhi (the fruiting bodies of <i>Ganoderma lucidum</i> (Leyss. ex Fr.) Karst. or <i>Ganoderma sinense</i> Zhao, Xu et Zhang) is a medicinal mushroom, which has potential anticancer and immunomodulatory properties. Cancer patients have been using <i>G. lucidum</i> -derived supplements more commonly as an alternative medicine. Triterpenes and polysaccharides isolated from <i>G. lucidum</i> are considered the active compounds. Scientific data have also shown that <i>G. lucidum</i> reduces obesity by modulating the composition of the gut microbiota	Complementary treatments for cancer	[83–85]
Liu Jun Zi Tang (Rikkunshito, TJ-43)	Liu Junzi Tang is a traditional herbal formula widely used for various gastrointestinal tract disorders such as chronic gastritis, gastric ulcer, and duodenal ulcer. It has been reported to have potentially beneficial effects in the treatment of chronic obstructive pulmonary disease in animal trials, showing anti-inflammatory and antioxidative properties through the inhibition of nuclear factor- $\kappa$ B activation. It is a hot-water extract of the mixture of eight crude medicinal herbs, including Renshen (the roots and rhizomes of <i>P. ginseng</i> C.A.Mey.), Baizhu (the rhizomes of <i>Atractylodes macrocephala</i> Koidz.), Fuling (the sclerotium of <i>Poria cocos</i> (Schw.) Wolf), Banxia (the rhizomes of <i>Pinellia ternata</i> (Thunb.) Breit.), Chenpi (the pericarps of <i>C. reticulata</i> Blanco), Gancao (the roots and rhizomes of <i>G. uralensis</i> Fisch. or <i>G. inflata</i> Bat. or <i>G. glabra</i> L.), Ganjiang (the rhizomes of <i>Zingiber officinale</i> Rosc.), and Dazao (the fruits of <i>Ziziphus jujube</i> Mill.)	Treatments for various gastrointestinal tract disorders	[86–90]

Note: The name of each medicine is listed in the following format: the Chinese pinyin (the medicinal part of the plant and the Latin name of the plants), wherein the “Chinese pinyin” refers to the pharmaceutical name in China and the “Latin name” of the plants are cited from Chinese pharmacopoeia.



**Table 2**  
Important botanical drugs and traditional Chinese medicine (TCM) products approved by the U.S. Food and Drug Administration (FDA) and those for which an application has been filed with U.S. FDA.

Name	Year of approval	Origin/ingredients	Clinical trials	Disease/indication	Reference
<i>Botanical drugs approved by U.S. FDA</i>					
Veregen™ (sinecatechins)	2006	The green tea-derived product contains 15% (w/w) sinecatechins, a partially purified fraction of a water extract of green tea leaves of <i>Camellia sinensis</i> (Theaceae)	Randomized, double-blinded, vehicle-controlled study	Topical use to treat external genital and perianal warts (condyloma acuminatum)	[42,43]
Fulyzaq® (crofelemer)	2012	A delayed-release tablet containing 125 mg of crofelemer, a botanical drug substance derived from the red latex of <i>Croton lechleri</i> (Euphorbiaceae)	Randomized, double-blinded, placebo-controlled and placebo-free study	Oral use for symptomatic relief of noninfectious diarrhea in patients with HIV/AIDS on antiretroviral therapy	[44,45]
<i>Selected TCM products for which an application has been filed with U.S. FDA</i>					
Name	Current state	Origin/ingredients	Disease/indication (ClinicalTrials.gov identifier)		Reference
Dantonic (T89, Compound Danshen dripping pills)	Phase III	Extracts of Danshen (the roots and rhizomes of <i>S. miltiorrhiza</i> Bge.) and Sanqi (the roots and rhizomes of <i>P. notoginseng</i> (Burk.) F.H. Chen) with borneol in a capsule form	Angina pectoris, cardiovascular disease (NCT01659580, completed)		[91–93]
Kanglaite injection	Phase III	Coix seed oil (with soybean phospholipids and glycerol as excipients)	Pancreatic cancer (NCT00733850, phase II) Stage IV non-small-cell lung carcinoma (NCT01640730, phase III, terminated)		[94]
HMPL-004	Phase III	An extract from a single herb, Chuanxinlian (the aerial parts of <i>Andrographis paniculata</i> (Burm. f.) Nees)	Ulcerative colitis, inflammatory bowel disease (NCT01882764, terminated)		[95–97]
PHY-906 (KD018) (Huangqin–Tang)	Phase II	An oral form of a spray-dried aqueous extract composed of four main herbs, Huangqin (the roots of <i>S. baicalensis</i> Georgi), Gancao (the roots and rhizomes of <i>G. uralensis</i> Fisch. or <i>G. inflata</i> Bat. or <i>G. glabra</i> L.), Baishao (the roots of <i>Paeonia lactiflora</i> Pall.), and Dazao (the fruits of <i>Z. jujube</i> Mill.)	Rectal cancer, reduces chemotherapy-induced toxicity (irinotecan), especially diarrhea (NCT00730158)		[98–100]
Fuzheng Huayu tablets	Phase II	A TCM formulation consisting of Danshen (the roots and rhizomes of <i>S. miltiorrhiza</i> Bge.), Taoren (the seeds of <i>Prunus persica</i> (L.) Batsch or <i>P. davidiana</i> (Carr.) Franch.), Songhuafen (the pollen of <i>Pinus massoniana</i> Lamb. or <i>P. tabulaeformis</i> Carr.), Jiaogulan (the aerial parts of <i>Gynostemma pentaphyllum</i> (Thunb.) Makino), Wuweizi (the fruits of <i>Schisandra chinensis</i> (Turcz.) Baill.), and Dongchongxiacao (the sub-seeds and larvae of <i>Cordyceps sinensis</i> (Berk.) Sacc.)	Chronic hepatitis C infection (liver fibrosis) (NCT00854087)		[101–103]
Xuezhikang capsules	Phase II	100% Red yeast rice (Hong Qu), obtained by fermentation with <i>Monascus</i> strains	Hyperlipidemia (NCT01327014)		[67–72]
KYG0395 (Guizhi Fuling capsules)	Phase II	A TCM formulation composed of five herbs, including Rougui (the cortex of <i>Cinnamomum cassia</i> Presl), Fuling (the sclerotium of <i>P. cocos</i> (Schw.) Wolf), Mudanpi (the cortex of <i>Paeonia suffruticosa</i> Andr.), Taoren (the seeds of <i>P. persica</i> (L.) Batsch or <i>P. davidiana</i> (Carr.) Franch.), and Shaoyao (the roots of <i>Paeonia lactiflora</i> Pall. or <i>P. veitchii</i> Lynch)	Primary dysmenorrhea (NCT01588236)		[104–106]
KT07 (Lianhua–Qingwen capsules)	Phase II	A TCM formulation composed of 11 herbs, including Lianqiao (the fruits of <i>F. suspensa</i> (Thunb.) Vahl), Jinyinhua (the flowers or flower buds of <i>L. japonica</i> Thunb.), Mahuang (the stems of <i>E. sinica</i> Stapf or <i>E. intermedia</i> Schrenk et C. A. Mey. or <i>E. equisetina</i> Bge.), Kuxingren (the seeds of <i>P. armeniaca</i> L. var. <i>ansu</i> Maxim. or <i>P. sibirica</i> L. or <i>P. mandshurica</i> (Maxim.) Koehne or <i>P. armeniaca</i> L.), Banlangen (the roots of <i>I. indigotica</i> Fort.), Mianmaguanzhong (the rhizomes of <i>D. crassirhizoma</i> Nakai), Yuxingcao (the aerial parts of <i>H. cordata</i> Thunb.), Guanghuoxiang (the aerial parts of <i>Pogostemon cablin</i> (Blanco) Benth.), Hongjingtian (the roots and rhizomes of <i>Rhodiola crenulata</i> (Hook. f. et Thoms.) H. Ohba), Gancao (the roots and rhizomes of <i>G. uralensis</i> Fisch. or <i>G. inflata</i> Bat. or <i>G. glabra</i> L.), Bohe (the aerial parts of <i>M. haplocalyx</i> Briq.), and Shigao (gypsum)	Influenza, human (NCT02867358)		[30,32,33]

Note: The name of each medicine is listed in the following format: the Chinese pinyin (the medicinal part of the plant and the Latin name of the plants), wherein the “Chinese pinyin” refers to the pharmaceutical name in China and the “Latin name” of the plants are cited from Chinese pharmacopoeia.

evidence-based Chinese herbal medicines and Chinese patented medicines for treating cancer, infectious, cardiovascular, and metabolic diseases. Table 2 shows the most important botanical drugs and TCM products approved by the U.S. FDA and those for which an application has been filed with the U.S. FDA. It is worth noting that the use of a single herb for the treatment of a specific disease is rare in TCM; instead, personalized mixtures of various (herbal) components are used. This is a major bottleneck in terms of drug development from traditional medicines because in clinical trials, the norm is to use the same treatment for all patients and compare the results with those of some control treatments.

#### 4. Development of artemisinin: learning from ancient healing practices

Development of artemisinin-based antimalarials represents one of the great victories in drug discovery, combining a holistic traditional approach and an evidence-based Western approach (a bedside-bench-bedside approach) (Fig. 1A3) [15,21–25]. It illustrates how healing traditions can point scientists in the direction to find new medicines and exemplifies how challenging the development of therapeutics from plants can be.

Humans have faced threat of diseases such as malaria throughout their existence. In China, the practice of diagnostic and treatment principles related to epidemic diseases was recorded in the classical Chinese medical book *Emperor Internal Medical Classic* [26]. This book describes the experience and prescriptions used to combat epidemics. It serves as an important source of inspiration for the development of new drugs [26,27].

The discovery of artemisinin was a complex team effort, initially led by the Chinese and later bringing in Western nonprofit and government entities and pharmaceutical companies [8,15]. The development process of artemisinin-based antimalarials can be divided into three stages: the discovery of a 100% effective extract from *Artemisia annua* L., the development of artemisinin, and, finally, the development of dihydroartemisinin (Fig. 1B).

The first stage, the discovery of ~100% effective extract from *A. annua*, was inspired by TCM. The breakthrough in finding an effective extract was a critical step in the entire process. The work started with collecting prescriptions that were associated with possible antimalarial activities by reviewing ancient traditional Chinese medical manuscripts and folk recipes and interviewing experienced Chinese medical practitioners [28]. The TCM experience laid a solid foundation for further studies. The scientists screened 380 extracts from approximately 200 Chinese herbs in a mouse model of malaria; however, no clearly significant results were obtained. By going back to the literature on traditional uses, a sentence relevant to the use of qinghao for alleviating malaria symptoms was noted in Ge Hong's *A Handbook of Prescriptions for Emergencies*: "A handful of qinghao immersed with 2 liters of water, wring out the juice and drink it all." This provided an idea for an effective extraction method. This information implied that the heating involved in the conventional extraction step may have destroyed the active compounds, and a lower temperature might be necessary to preserve the antimalarial activity. Finally, an extract with ~100% antimalarial effect was obtained. Thus, the old clinical experience described in traditional Chinese medical literature led to the discovery of artemisinin [15,28].

In the second stage, the development of artemisinin, classical activity-guided compound isolation was involved, and an evidence-based study was carried out, including characterization of active compounds, activity tests in animals, and clinical activity tests, leading to the development of pharmaceutical formulations. Of note, artemisinin is present in low concentrations in *Artemisia* plants from the Beijing region, and there were only few details

recorded on the species and the effective plant parts used. According to plant taxonomists, there are at least six different *Artemisia* species in China. Research on the herb qinghao was performed to find the right species for pharmaceutical production [15,28]. Only fresh leaves of the species *A. annua* were found to contain meaningful amounts of artemisinin.

The third stage included the development of dihydroartemisinin. The first artemisinin-based antimalarial drug had two major drawbacks [28]. One was its poor solubility in both water and oil, and the other was a relatively high recurrence rate of malaria. In the third stage, a classical approach of structure modification was applied to obtain new compounds with potentially better antimalarial activity. Artemisinin is a sesquiterpene with the formula  $C_{15}H_{22}O_5$ , featuring a very unusual peroxide bridge in the center. Through modification of different parts of the artemisinin molecule, it was confirmed that the peroxy group was the functional group for antimalarial activity. Various candidate compounds were synthesized, such as dihydroartemisinin, artesunate, and arteether, which remarkably improved the efficacy and usefulness of the drug. In addition, new indications for treating cancer were recently reported for artemisinin derivatives [29].

Nowadays, inspired by traditional Chinese prescriptions recommended for the treatment of other epidemic diseases, such as influenza, a number of products such as Lianhuaqingwen capsules [26,30–33], Maxingshgan–Yinqiaosan [34], and Banlangen (the root of *Isatis indigotica*) [35] have been developed and widely used in China for the treatment of influenza. Different mechanisms of actions seem to be involved. Lianhuaqingwen capsules inhibit virus shedding and shorten the duration of fever [26]. Maxingshgan–Yinqiaosan reduces the time to fever resolution in patients with H1N1 influenza virus infection [26,34]. Banlangen has been widely used to treat seasonal influenza [26] and plays a variety of roles in protecting against viral infection, such as by preventing viral infection, inhibiting viral replication [35], and exerting immune modulatory effects [36,37]. Therefore, Chinese herbal prescriptions often provide markedly different effects than those of marketed chemically synthesized drugs, i.e., the former act through multiple modes that target not only the virus but also various components of the host's immune response, creating a synergistic effect [26].

#### 5. Quality control and quality assessment of botanical products: the stumbling block of traditional medicine development

In terms of quality control (QC), there are two different approaches. One is the case of the Chinese materia medica, which is sold as such to the public. The other is the industrialized production of evidence-based herbal medicines. Here we discuss the latter case.

The consistent quality of drugs, especially traditional medicines, is a crucial issue in evidence-based traditional medicines. Many factors may affect their quality, starting from the origin of the plant [38], cultivation methods [39], postharvest methods and processing [40], and manufacturing [41] (Fig. 2). Developing a QC system for a botanical preparation is a critical and fundamental step for the manufacturing of a standardized product suitable for biological and clinical studies [37]. Two U.S. FDA-approved botanical new drug applications (NDAs), Veregen® (sinecatechins, 2006) and Fulyzaq® (crofelemer, 2012), are the first examples where QC was developed for the registration dossiers [42–45].

However, the developed QC procedures may not be sufficient for an industrial manufacturing process. The two examples clearly show the following challenges in QC of botanical products [46]: (1) The use of complex mixtures with not well-defined active components, including possible prodrugs and synergistic effects between compounds present; (2) The lack of data on the correlation of

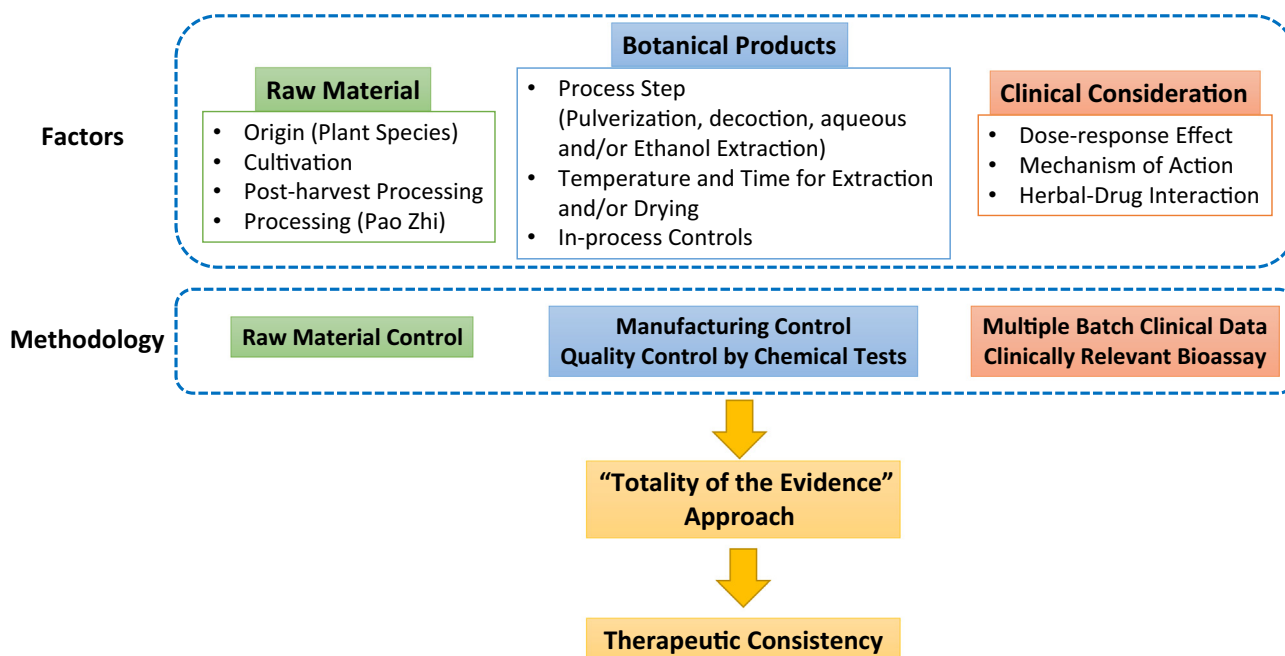


Fig. 2. Factors that may affect the quality of botanical drug products and the totality-of-the-evidence approach for quality control to ensure therapeutic consistency.

chemical properties with clinical effects. The clinical response results on the acceptance ranges for these components were primarily established based on the levels observed for multiple batches tested in clinical studies; (3) Although the majority of components can be adequately characterized and quantified, minor components in mixtures may be problematic, although they may be quite important for quality; and (4) Significant variations in chemical components were detected in herbal materials from different batches; correspondingly, the products might also have considerable batch-to-batch variability.

Taken together, the conventional chemistry, manufacturing, and controls (CMC) data (primarily from chemical testing) used to ensure the quality of small-molecule products may be insufficient for the manufacturing of evidence-based herbal medicines. In fact, instead of QC on the end product, one should establish a quality management system in which all critical steps in the chain, from seeds to the patient, are identified and thus can be monitored. This implies good practices in all steps of cultivation, harvesting, postharvest processing, extraction, and pharmaceutical production of the final formulations.

Given the heterogeneous nature of botanical drug products, chemical testing alone may not be sufficient for QC and, therefore, for ensuring therapeutic consistency. To overcome these issues, the U.S. FDA has developed a totality-of-the-evidence approach according to the knowledge and experience acquired from the review of botanical investigational new drug and NDA submissions and published in the *Guidance for Industry: Botanical Drug Development* (2016) [39]. The integrated approach considers the CMC data and other evidence, including raw material control, clinically relevant bioassay(s), and clinical data [38].

Raw material control is a key step toward improving the quality of a botanical product and ensuring the safety, efficacy, and consistent quality of the final products. Botanical raw material control, including the implementation of good agricultural and collection practices and restricted harvesting of botanical raw material in specific eco-geographical regions, reduces the variability at the plant and raw material levels [46]. In cases of complicated taxonomy and when identification issues related to the botanical raw material exist, DNA barcoding may be warranted [39]. DNA bar-

coding has been widely used for closely related species or cultivars that cannot be unambiguously distinguished by traditional identification methods (e.g., chemical identification, spectroscopic and chromatographic methods) [47]. Herbgonomics is now being applied to many areas of herb-related biological research to help understand the quality of traditional medicines and molecular herb identification through the establishment of herbal gene bank [39,48].

Clinically relevant (bio)assays are very important to ensure the quality and therapeutic consistency of evidence-based herbal medicines [49]. In the case of the QC method for crofelemer (Fulyzaq), knowledge of crofelemer's mechanism of action led to the important development of a clinically relevant bioassay, which enabled the establishment of clinically relevant specifications [46]. Clinical standardization based on the relevant bioassay developed on the basis of the mechanism of action of crofelemer (Fulyzaq) could potentially provide some more flexibility for the manufacturer to make post-approval changes such as the diversity of the raw material supply [46].

However, for traditional medicines with multiple indications and not well-defined modes of action and active compounds, a separate biological assay would be needed for each indication [49]. A typical example of a traditional medicine with multiple indications is *Uraria crinita* (UC) (Leguminosae), a traditional edible plant with a wide range of biological activities [40]. In the case of QC for UC, bioassays involving estrogen receptor alpha activity, nuclear factor erythroid 2-related factor 2 activity, antioxidant activity, and cyclooxygenase-2 inhibition have been applied. These activities of UC are relevant to its traditional uses such as detoxification, detumescence, and the treatment of traumatic injuries. The above examples indicate that clinically relevant bioassays, which reflect the drug's known or intended mechanism of action, are preferred. It is important for the evidence-based use to know whether activities correlate with different chemical profiles.

Clinical data include dose-response data and data for multiple batches [49]. Clinical data on the dose-response effect and multiple batch analyses are used to show whether the clinical response is sensitive to variations among different batches and doses of a botanical drug. If clinical effects are not sensitive to doses or

batches, it can reasonably be assumed that the variations within the established specifications will not probably affect the therapeutic consistency of drug products. Clinical studies that evaluated two doses of sin catechins (Veregen) (10% and 15%) indicated that small variations in any of the uncharacterized fractions might not have an impact on the therapeutic effect [46]. The dose-response data for crofelemer (Fulyzaq) (125–500 mg) showed that the drug effects were not related to the tested doses. The clinical data for multiple batches of crofelemer (Fulyzaq) did not reveal any noticeable differences among batches that were manufactured using different drug substance batches. These observations showed that in this case, the natural variation observed is unlikely to have a significant impact on the therapeutic effect [46]. Therefore, clinical data have important implications in the determination of QC methods for botanical products and the establishment of standards.

## 6. Future directions

The long history of use and extensive documentation of TCM clinical practices have accumulated a considerable number of classical preparations and theories on human health and diseases, which provide a unique resource for drug discovery and a better understanding of the human condition [26,50]. Systemic studies of these traditional medicines have two potential outcomes: evidence-based use of traditional medicines and new leads for drug development. The latter has the potential to not only contribute to the present-day “single target–single compound” approach used in the pharmaceutical industry but to also lead to new approaches to treating diseases by using synergism and antagonism, as well as prodrugs, to support and improve human health.

QC of traditional medicines is an urgent and challenging need, but well-defined methodologies for standardized assessment of the quality, efficacy, and safety of traditional medicines are lacking. The totality-of-the-evidence approach used by the U.S. FDA for botanical products shows the direction on how to control quality from the field throughout the entire production process [46,49]. In fact, it requires quality management by applying good practice protocols to all steps in the chain, from planting seeds to the patient. This includes identification of possible problems in the chain, e.g., the use of pesticides, fungal toxin formation, diseased plants, the time and season of harvesting, incorrect plant species, postharvest processing, and drying of raw materials, for which QC traceability systems have been developed in China. Standardization of agricultural and manufacturing processes is a key step for the consistent quality of products from different batches and producers.

Definition of a “standard decoction” (Biaozhuan Tangji) may result in consistent quality of products for clinics and research, although one should keep in mind that the extraction process of a mixture of herbs does not necessarily provide the same extract as the one obtained by mixing extracts of single herbs. Validation of such an approach is necessary for each preparation. In all cases, it is of great importance to rely on traditional preparation methods when developing a standard procedure, as can be learned from ancient TCM documents, particularly for the QC of individual raw ingredients.

A single-herb standard process guided by the theory of TCM can be used to ensure constant quality of the herbal material. However, it is preferable that the traditional method is followed by making a final preparation. Extraction of a mixture of herbs could provide different results from those obtained by mixing single-herb extracts. Any change in the traditional process needs to be validated, for which various metabolomics tools are important and should be applied in combination with validation of the biological

activity obtained by traditional and possible novel processing methods.

For the mechanism study of disease treatment with herbal medicines, herbgenomics will provide cutting-edge technologies. Herbgenomics has been proposed as a new discipline, and it includes herbal structural genomics, functional genomics, transcriptomics, proteomics, metabolomics, epigenomics, and metagenomics [48]. It will facilitate the understanding of the mechanism of herbs in the disease treatment and provide support for personalized precise medicine. It will accelerate the application of cutting-edge technologies in herbal research and provide an unprecedented opportunity to revolutionize the use and acceptance of traditional herbal medicines.

The study of the biosynthetic pathways of secondary metabolites will provide a chemical bank for the discovery of new drugs from nature. Research on *Ganoderma lucidum* (Lingzhi or “mushroom of immortality”), *Salvia miltiorrhiza*, and *Catharanthus roseus* has provided effective model systems for the study of biosynthetic pathways of some important secondary metabolites (pharmaceutically active components) in medicinal herbs [51].

Learning from nature and our ancestors should lead our research and development aimed at evidence-based, reliable traditional medicines. At the same time, it opens a way to discoveries for developing novel therapeutics for the treatment and prevention of diseases.

## Acknowledgements

We would like to thank Editage [[www.editage.cn](http://www.editage.cn)] for English language editing.

## References

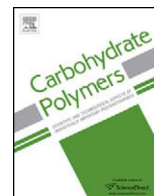
- [1] D.J. Newman, G.M. Cragg, Natural Products as Sources of New Drugs from 1981 to 2014, *J. Nat. Prod.* 79 (3) (2016) 629–661.
- [2] D.J. Newman, G.M. Cragg, Natural products as sources of new drugs over the 30 years from 1981 to 2010, *J. Nat. Prod.* 75 (3) (2012) 311–335.
- [3] D.J. Newman, G.M. Cragg, Natural products as sources of new drugs over the last 25 years, *J. Nat. Prod.* 70 (3) (2007) 461–477.
- [4] D.J. Newman, G.M. Cragg, K.M. Snader, Natural products as sources of new drugs over the period 1981–2002, *J. Nat. Prod.* 66 (7) (2003) 1022–1037.
- [5] Yan Schroën, Herman A. van Wietmarschen, Mei Wang, Eduard P. van Wijk, Thomas Hankemeier, Xu. Guowang, et al., East is East and West is West, and never the twain shall meet? *Science* 346 (6216 Suppl) (2015) S10–S12.
- [6] R. Verpoorte, Y.H. Choi, H.K. Kim, Ethnopharmacology and systems biology: a perfect holistic match, *J. Ethnopharmacol.* 100 (1–2) (2005) 53–56.
- [7] J. Chao, T.C. Lu, J.W. Liao, T.H. Huang, M.S. Lee, H.Y. Cheng, et al., Analgesic and anti-inflammatory activities of ethanol root extract of *Mahonia oiwakensis* in mice, *J. Ethnopharmacol.* 125 (2) (2009) 297–303.
- [8] J.P. Briggs, A global scientific challenge: Learning the right lessons from ancient healing practices, *Science* 346 (6216 Suppl) (2015) S7–S9.
- [9] A.L. Harvey, R. Edrada-Ebel, R.J. Quinn, The re-emergence of natural products for drug discovery in the genomics era, *Nat. Rev. Drug Discovery* 14 (2) (2015) 111–129.
- [10] M.S. Rafii, S. Walsh, J.T. Little, K. Behan, B. Reynolds, C. Ward, et al., Alzheimer's Disease Cooperative A phase II trial of huperzine A in mild to moderate Alzheimer disease, *Neurology* 76 (16) (2011) 1389–1394.
- [11] F.R. Stermitz, P. Lorenz, J.N. Tawara, L.A. Zenewicz, K. Lewis, Synergy in a medicinal plant: antimicrobial action of berberine potentiated by 5'-methoxyhydrnocarpin, a multidrug pump inhibitor, *Proc. Natl. Acad. Sci. U.S.A.* 97 (4) (2000) 1433–1437.
- [12] A.C. Abreu, A. Coqueiro, A. Sultan, N. Lemmens, H.K. Kim, R. Verpoorte, et al., Looking to nature for a new concept in antimicrobial treatments: isoflavonoids from *Cytisus striatus* as antibiotic adjuvants against MRSA, *Sci. Rep.* (2017).
- [13] Thomas Friedemann, Min Li, Jian Fei, Udo Schumacher, Juxian Song, S. Schröder, Hypothesis-driven screening of Chinese herbs for compounds that promote neuroprotection, *Science* 350 (6262) (2015) S69–S71.
- [14] J.L. Medina-Franco, M.A. Giulianotti, G.S. Welmaker, R.A. Houghten, Shifting from the single to the multitarget paradigm in drug discovery, *Drug Discovery Today* 18 (9–10) (2013) 495–501.
- [15] Y. Tu, The discovery of artemisinin (qinghaosu) and gifts from Chinese medicine, *Nat. Med.* 17 (10) (2011) 1217–1220.
- [16] R. Verpoorte, Good practices: the basis for evidence-based medicines, *J. Ethnopharmacol.* 140 (3) (2012) 455–457.



- [17] Wei Jia, Tai-ping Fan, Xiaoning Wang, G. Xie, The polypharmacokinetics of herbal medicines, *Science* 350(6262) (2015) S76–S79.
- [18] M. Wang, R.J. Lamers, H.A. Korthout, J.H. van Nesselrooij, R.F. Witkamp, R. van der Heijden, et al., Metabolomics in the context of systems biology: bridging traditional Chinese medicine and molecular pharmacology, *Phytother. Res: PTR* 19 (3) (2005) 173–182.
- [19] D.C. Swinney, J. Anthony, How were new medicines discovered? *Nat. Rev. Drug Discovery* 10 (7) (2011) 507–519.
- [20] J.G. Moffat, J. Rudolph, D. Bailey, Phenotypic screening in cancer drug discovery – past, present and future, *Nat. Rev. Drug Discovery* 13 (8) (2014) 588–602.
- [21] J. Han, J.G. Lee, S.S. Min, S.H. Park, C.K. Angerhofer, G.A. Cordell, et al., Synthesis of new artemisinin analogues from artemisinic acid modified at C-3 and C-13 and their antimalarial activity, *J. Nat. Prod.* 64 (9) (2001) 1201–1205.
- [22] D.L. Klayman, A.J. Lin, N. Acton, J.P. Scovill, J.M. Hoch, W.K. Milhous, et al., Isolation of artemisinin (qinghaosu) from *Artemisia annua* growing in the United States, *J. Nat. Prod.* 47 (4) (1984) 715–717.
- [23] L.N. Misra, A. Ahmad, R.S. Thakur, H. Lotter, H. Wagner, Crystal structure of artemisinic acid: a possible biogenetic precursor of antimalarial artemisinin from *Artemisia annua*, *J. Nat. Prod.* 56 (2) (1993) 215–219.
- [24] A. Ranasinghe, J.D. Sweatlock, R.G. Cooks, A rapid screening method for artemisinin and its congeners using ms/ms: search for new analogues in *Artemisia annua*, *J. Nat. Prod.* 56 (4) (1993) 552–563.
- [25] T.E. Wallaart, W. van Uden, H.G. Lubberink, H.J. Woerdenbag, N. Pras, W.J. Quax, Isolation and identification of dihydroartemisinic acid from *Artemisia annua* and its possible role in the biosynthesis of artemisinin, *J. Nat. Prod.* 62 (3) (1999) 430–433.
- [26] Zi-Feng Yang, Elaine Lai-Han Leung, Liang Liu, Zhi-Hong Jiang, N. Zhong, Developing influenza treatments using traditional Chinese medicine, *Science* 347(6219 Suppl) (2015) S35–S37.
- [27] L. Jiang, L. Deng, T. Wu, Chinese medicinal herbs for influenza, *The Cochrane database of systematic reviews* (3) (2013) CD004559.
- [28] Y. Tu, Artemisinin—a gift from traditional Chinese medicine to the world (Nobel Lecture), *Angew. Chem.* 55 (35) (2016) 10210–10226.
- [29] W.E. Ho, H.Y. Peh, T.K. Chan, W.S. Wong, Artemisinins: pharmacological actions beyond anti-malarial, *Pharmacol. Ther.* 142 (1) (2014) 126–139.
- [30] Z. Tao, Y. Yang, W. Shi, M. Xue, W. Yang, Z. Song, et al., Complementary and alternative medicine is expected to make greater contribution in controlling the prevalence of influenza, *Biosci. Trends* 7 (5) (2013) 253–256.
- [31] L. Dong, J.W. Xia, Y. Gong, Z. Chen, H.H. Yang, J. Zhang, et al., Effect of Lianhuaqingwen capsules on airway inflammation in patients with acute exacerbation of chronic obstructive pulmonary disease, Evidence-based complementary and alternative medicine: eCAM 2014 (2014) 637969.
- [32] P. Zhao, H.Z. Yang, H.Y. Lv, Z.M. Wei, Efficacy of Lianhuaqingwen capsule compared with oseltamivir for influenza A virus infection: a meta-analysis of randomized, controlled trials, *Altern. Ther. Health Med.* 20 (2) (2014) 25–30.
- [33] Z.P. Duan, Z.H. Jia, J. Zhang, S. Liu, Y. Chen, L.C. Liang, et al., Natural herbal medicine Lianhuaqingwen capsule anti-influenza A (H1N1) trial: a randomized, double blind, positive controlled clinical trial, *Chin. Med. J.* 124 (18) (2011) 2925–2933.
- [34] C. Wang, B. Cao, Q.Q. Liu, Z.Q. Zou, Z.A. Liang, L. Gu, et al., Oseltamivir compared with the Chinese traditional therapy maxingshigan-yinqiaosan in the treatment of H1N1 influenza: a randomized trial, *Ann. Internal Med.* 155 (4) (2011) 217–225.
- [35] Z. Yang, Y. Wang, Z. Zheng, S. Zhao, J. Zhao, Q. L et al., Antiviral activity of Isatis indigotica root-derived clemastin B against human and avian influenza A and B viruses in vitro, *Int. J. Mol. Med.* 31 (4) (2013) 867–873.
- [36] C.K. Mok, S.S. Kang, R.W. Chan, P.Y. Yue, N.K. Mak, L.L. Poon, et al., Anti-inflammatory and antiviral effects of indirubin derivatives in influenza A (H5N1) virus infected primary human peripheral blood-derived macrophages and alveolar epithelial cells, *Antiviral Res.* 106 (2014) 95–104.
- [37] N.K. Mak, C.Y. Leung, X.Y. Wei, X.L. Shen, R.N. Wong, K.N. Leung, et al., Inhibition of RANTES expression by indirubin in influenza virus-infected human bronchial epithelial cells, *Biochem. Pharmacol.* 67 (1) (2004) 167–174.
- [38] G.H. Lai, J. Chao, M.K. Lin, W.T. Chang, W.H. Peng, F.C. Sun, et al., Rapid and sensitive identification of the herbal tea ingredient *Taraxacum formosanum* using loop-mediated isothermal amplification, *Int. J. Mol. Sci.* 16 (1) (2015) 1562–1575.
- [39] Shilin Chen, Jingyuan Song, Chao Sun, Xu. Jiang, Yingjie Zhu, Rob Verpoorte, et al., Herbal genomics: examining the biology of traditional medicines, *Science* 347 (6219 Suppl) (2015) S27–S29.
- [40] J. Chao, Y. Dai, H.Y. Cheng, W. Lam, Y.C. Cheng, K. Li, et al., Improving the Concentrations of the Active Components in the Herbal Tea Ingredient *Uraria crinita*: The Effect of Post-harvest Oven-drying Processing, *Sci. Rep.* 7 (2017) 38763.
- [41] S. Yao, J. Zhang, D. Wang, J. Hou, W. Yang, J. Da, et al., Discriminatory components retracing strategy for monitoring the preparation procedure of Chinese patent medicines by fingerprint and chemometric analysis, *PloS One* 10 (3) (2015) e0121366.
- [42] Approved Labeling for Veregen (NDA 021902), [http://www.accessdata.fda.gov/drugsatfda\\_docs/nda/2006/021902s000\\_prntbl.pdf](http://www.accessdata.fda.gov/drugsatfda_docs/nda/2006/021902s000_prntbl.pdf).
- [43] Drug Approval Package, Drugs@FDA FDA: Veregen (NDA 021902), [http://www.accessdata.fda.gov/drugsatfda\\_docs/nda/2006/021902s000TOC.cfm](http://www.accessdata.fda.gov/drugsatfda_docs/nda/2006/021902s000TOC.cfm).
- [44] Approved Labeling for Fulyzaq (NDA 202292) [http://www.accessdata.fda.gov/drugsatfda\\_docs/nda/2012/202292Orig1s000Lbl.pdf](http://www.accessdata.fda.gov/drugsatfda_docs/nda/2012/202292Orig1s000Lbl.pdf).
- [45] Drug Approval Package, Drugs@FDA FDA: Fulyzaq Delayed-Release Tablets (NDA 202292) [http://www.accessdata.fda.gov/drugsatfda\\_docs/nda/2012/202292Orig1s000TOC.cfm](http://www.accessdata.fda.gov/drugsatfda_docs/nda/2012/202292Orig1s000TOC.cfm).
- [46] Sau L. Lee, Jinhui Dou, Rajiv Agarwal, Robert Temple, Julie Beitz, Charles Wu, et al., Evolution of traditional medicines to botanical drugs, *Science* 347 (6219 Suppl) (2015) S32–S34.
- [47] S. Chen, X. Pang, J. Song, L. Shi, H. Yao, J. Han, et al., A renaissance in herbal medicine identification: from morphology to DNA, *Biotechnol. Adv.* 32 (7) (2014) 1237–1244.
- [48] S.L. Chen, J.Y. Song, *Herbgenomics, China J. Chin. Mater. Med.* 41 (2016) 3881–3889.
- [49] Botanical Drug Development Guidance for Industry, <http://www.fda.gov/downloads/AboutFDA/CentersOffices/CDER/ucm106136.pdf>, 2016.
- [50] J. Chang, Medicinal herbs: drugs or dietary supplements? *Biochem. Pharmacol.* 59 (3) (2000) 211–219.
- [51] S. Chen, J. Xu, C. Liu, Y. Zhu, D.R. Nelson, S. Zhou, et al., Genome sequence of the model medicinal mushroom *Ganoderma lucidum*, *Nat. Commun.* 3 (2012) 913.
- [52] Y. Sakurai, A.A. Kolokoltsov, C.C. Chen, M.W. Tidwell, W.E. Bauta, N. Klugbauer, et al., Two-pore channels control Ebola virus host cell entry and are drug targets for disease treatment, *Science* 347 (6225) (2015) 995–998.
- [53] Y. Yu, S. Hu, G. Li, J. Xue, Z. Li, X. Liu, et al., Comparative effectiveness of Di'ao Xin Xue Kang capsule and Compound Danshen tablet in patients with symptomatic chronic stable angina, *Sci. Rep.* 4 (2014) 7058.
- [54] Y. Jia, C. Chen, C.S. Ng, S.W. Leung, Meta-analysis of randomized controlled trials on the efficacy of Di'ao xinxuekang capsule and isosorbide dinitrate in treating angina pectoris, Evidence-based complementary and alternative medicine: eCAM 2012 (2012) 904147.
- [55] L.Y. Wang, J.Y. Tang, J. Liu, W. Lu, Y.N. Yu, B.W. Chen, et al., Dynamic changes in phenotypic groups in patients with stable angina pectoris after treatment with xinxuekang capsule: a randomized controlled trial, *Curr. Vasc. Pharmacol.* 13 (4) (2015) 492–503.
- [56] J. Sun, K. Zhang, W.J. Xiong, G.Y. Yang, Y.J. Zhang, C.C. Wang, et al., Clinical effects of a standardized Chinese herbal remedy Qili Qiangxin, as an adjuvant treatment in heart failure: systematic review and meta-analysis, *BMC Complementary Altern. Med.* 16 (2016) 201.
- [57] W.H. Tang, Y. Huang, Cardiotoxic modulation in heart failure: insights from traditional Chinese medicine, *J. Am. Coll. Cardiol.* 62 (12) (2013) 1073–1074.
- [58] X. Li, J. Zhang, J. Huang, A. Ma, J. Yang, W. Li, G. Efficacy/Safety of Qili Qiangxin Capsules for Chronic Heart Failure Study, A multicenter, randomized, double-blind, parallel-group, placebo-controlled study of the effects of qili qiangxin capsules in patients with chronic heart failure, *J. Am. College Cardiol.* 62 (12) (2013) 1065–1072.
- [59] P. Liao, L. Wang, L. Guo, R. Zeng, J. Huang, M. Zhang, Danhong injection (a traditional Chinese patent medicine) for acute myocardial infarction: a systematic review and meta-analysis, Evidence-based complementary and alternative medicine: eCAM 2015 (2015) 646530.
- [60] P.Q. Wang, D.D. Li, W. Dong, J. Liu, Y.N. Yu, C.T. Shen, et al., Danhong injection in the treatment of chronic stable angina: study protocol for a randomized controlled trial, *Trials* 16 (2015) 474.
- [61] B. Li, Y. Wang, J. Lu, J. Liu, Y. Yuan, Y. Yu, et al., Evaluating the effects of Danhong injection in treatment of acute ischemic stroke: study protocol for a multicenter randomized controlled trial, *Trials* 16 (2015) 561.
- [62] X. Zhang, H. Wang, Y. Chang, Y. Wang, X. Lei, S. Fu, et al., An overview of meta-analyses of danhong injection for unstable angina, Evidence-based complementary and alternative medicine: eCAM 2015 (2015) 358028.
- [63] H. Wang, S. Ren, C. Liu, X. Zhang, An overview of systematic reviews of danhong injection for ischemic stroke, Evidence-based complementary and alternative medicine: eCAM 2016 (2016) 8949835.
- [64] N. Zhang, J. Liu, Z. Qiu, Y. Ye, J. Zhang, T. Lou, Shenfu injection for improving cellular immunity and clinical outcome in patients with sepsis or septic shock, *Am. J. Emergency Med.* (2016).
- [65] S. Wen-Ting, C. Fa-Feng, X. Li, L. Cheng-Ren, L. Jian-Xun, Chinese medicine shenfu injection for heart failure: a systematic review and meta-analysis, Evidence-based complementary and alternative medicine: eCAM 2012 (2012) 713149.
- [66] C. Liu, Y. Hou, X. Wang, Z. Zhao, Z. Liu, J. Zhai, J. Mao, H. Shang, Clinical assessment of Shenfu injection loading in the treatment of patients with exacerbation of chronic heart failure due to coronary heart disease: study protocol for a randomized controlled trial, *Trials* 16 (2015) 222.
- [67] M. Li, Q. He, Y. Chen, B. Li, B. Feng, Z. Zhang, J. Wang, Xuezhikang capsule for type 2 diabetes with hyperlipemia: a systematic review and meta-analysis of randomized clinical trials, Evidence-based complementary and alternative medicine: eCAM 2015 (2015) 468520.
- [68] P.M. Moriarty, E.M. Roth, A. Karns, P. Ye, S.P. Zhao, Y. Liao, et al., Effects of Xuezhikang in patients with dyslipidemia: a multicenter, randomized, placebo-controlled study, *J. Clin. Lipidol.* 8 (6) (2014) 568–575.
- [69] Y. Feng, H. Xu, K. Chen, Natural polypill Xuezhikang: its clinical benefit and potential multicomponent synergistic mechanisms of action in cardiovascular disease and other chronic conditions, *J. Altern. Complementary Med.* 18 (4) (2012) 318–328.
- [70] P. Ye, Z.L. Lu, B.M. Du, Z. Chen, Y.F. Wu, X.H. Yu, et al., Investigators Effect of xuezhikang on cardiovascular events and mortality in elderly patients with a history of myocardial infarction: a subgroup analysis of elderly subjects from



- the China Coronary Secondary Prevention Study, *J. Am. Geriatrics Soc.* 55 (7) (2007) 1015–1022.
- [71] J.J. Li, Z.L. Lu, W.R. Kou, Z. Chen, Y.F. Wu, X.H. Yu, et al., Chinese coronary secondary prevention study, impact of xuezhikang on coronary events in hypertensive patients with previous myocardial infarction from the china coronary secondary prevention study (CCSPS), *Ann. Med.* 42 (3) (2010) 231–240.
- [72] J.J. Li, Z.L. Lu, W.R. Kou, Z. Chen, Y.F. Wu, X.H. Yu, et al., Chinese coronary secondary prevention study, beneficial impact of xuezhikang on cardiovascular events and mortality in elderly hypertensive patients with previous myocardial infarction from the china coronary secondary prevention study (CCSPS), *J. Clin. Pharmacol.* 49 (8) (2009) 947–956.
- [73] H.H. Yu, K.J. Kim, J.D. Cha, H.K. Kim, Y.E. Lee, N.Y. Choi, et al., Antimicrobial activity of berberine alone and in combination with ampicillin or oxacillin against methicillin-resistant *Staphylococcus aureus*, *J. Med. Food* 8 (4) (2005) 454–461.
- [74] H. Dong, N. Wang, L. Zhao, F. Lu, Berberine in the treatment of type 2 diabetes mellitus: a systemic review and meta-analysis, *Evid Based Complement Alternat. Med.* 2012 (2012) 591654.
- [75] W. Kong, J. Wei, P. Abidi, M. Lin, S. Inaba, C. Li, et al., Berberine is a novel cholesterol-lowering drug working through a unique mechanism distinct from statins, *Nat. Med.* 10 (12) (2004) 1344–1351.
- [76] J. Xu, F. Lian, L. Zhao, Y. Zhao, X. Chen, X. Zhang, et al., Structural modulation of gut microbiota during alleviation of type 2 diabetes with a Chinese herbal formula, *ISME J* 9 (3) (2015) 552–562.
- [77] C.H. Zhang, G.L. Xu, Y.H. Liu, Y. Rao, R.Y. Yu, Z.W. Zhang, et al., Anti-diabetic activities of Gegen Qinlian Decoction in high-fat diet combined with streptozotocin-induced diabetic rats and in 3T3-L1 adipocytes, *Phytomedicine* 20 (3–4) (2013) 221–229.
- [78] X.L. Tong, L.H. Zhao, F.M. Lian, Q. Zhou, L. Xia, J.C. Zhang, et al., Clinical observations on the dose-effect relationship of gegen qin lian decoction on 54 out-patients with type 2 diabetes, *J. Tradit. Chin. Med.* 31 (1) (2011) 56–59.
- [79] X.W. Zhang, X.J. Yan, Z.R. Zhou, F.F. Yang, Z.Y. Wu, H.B. Sun, et al., Arsenic trioxide controls the fate of the PML-RARalpha oncoprotein by directly binding PML, *Science* 328 (5975) (2010) 240–243.
- [80] J. Hu, Y.F. Liu, C.F. Wu, F. Xu, Z.X. Shen, Y.M. Zhu, et al., Long-term efficacy and safety of all-trans retinoic acid/arsenic trioxide-based therapy in newly diagnosed acute promyelocytic leukemia, *Proc. Natl. Acad. Sci. U.S.A.* 106 (9) (2009) 3342–3347.
- [81] P.Z. Zheng, K.K. Wang, Q.Y. Zhang, Q.H. Huang, Y.Z. Du, Q.H. Zhang, et al., Systems analysis of transcriptome and proteome in retinoic acid/arsenic trioxide-induced cell differentiation/apoptosis of promyelocytic leukemia, *Proc. Natl. Acad. Sci. U.S.A.* 102 (21) (2005) 7653–7658.
- [82] L. Wang, G.B. Zhou, P. Liu, J.H. Song, Y. Liang, X.J. Yan, et al., Dissection of mechanisms of Chinese medicinal formula Realgar-Indigo naturalis as an effective treatment for promyelocytic leukemia, *Proc. Natl. Acad. Sci. U.S.A.* 105 (12) (2008) 4826–4831.
- [83] C.J. Chang, C.S. Lin, C.C. Lu, J. Martel, Y.F. Ko, D.M. Ojcius, et al., *Ganoderma lucidum* reduces obesity in mice by modulating the composition of the gut microbiota, *Nat. Commun.* 6 (2015) 7489.
- [84] K.S. Bishop, C.H. Kao, Y. Xu, M.P. Glucina, R.R. Paterson, L.R. Ferguson, From 2000years of *Ganoderma lucidum* to recent developments in nutraceuticals, *Phytochemistry* 114 (2015) 56–65.
- [85] X. Jin, J. Ruiz Beguerie, D.M. Sze, G.C. Chan, *Ganoderma lucidum* (Reishi mushroom) for cancer treatment, *Cochrane Database Syst. Rev.* 4 (2016) CD007731.
- [86] K. Tominaga, T. Arakawa, Clinical application of kampo medicine (rikkunshito) for common and/or intractable symptoms of the gastrointestinal tract, *Front. Pharmacol.* 6 (2015) 7.
- [87] N. Fujitsuka, A. Asakawa, A. Morinaga, M.S. Amitani, H. Amitani, G. Katsuura, et al., Increased ghrelin signaling promotes survival in mouse models of human aging through activation of sirtuin1, *Mol. Psychiatry* 21 (11) (2016) 1613–1623.
- [88] R. Zhou, F. Luo, H. Lei, K. Zhang, J. Liu, H. He, et al., Liujunzi Tang, a famous traditional Chinese medicine, ameliorates cigarette smoke-induced mouse model of COPD, *J. Ethnopharmacol.* 193 (2016) 643–651.
- [89] N. Fujitsuka, Y. Uezono, Rikkunshito, a ghrelin potentiator, ameliorates anorexia-cachexia syndrome, *Front. Pharmacol.* 5 (2014) 271.
- [90] H. Takeda, C. Sadakane, T. Hattori, T. Katsurada, T. Ohkawara, K. Nagai, et al., Rikkunshito, an herbal medicine, suppresses cisplatin-induced anorexia in rats via 5-HT<sub>2</sub> receptor antagonism, *Gastroenterology* 134 (7) (2008) 2004–2013.
- [91] Y. Jia, F. Huang, S. Zhang, S.W. Leung, Is danshen (*Salvia miltiorrhiza*) dripping pill more effective than isosorbide dinitrate in treating angina pectoris? A systematic review of randomized controlled trials, *Int. J. Cardiol.* 157 (3) (2012) 330–340.
- [92] Y. Yao, Y. Feng, W. Lin, Systematic review and meta-analysis of randomized controlled trials comparing compound danshen dripping pills and isosorbide dinitrate in treating angina pectoris, *Int. J. Cardiol.* 182 (2015) 46–47.
- [93] S. Ling, R.Z. Luo, L. Nheu, Z.X. Guo, H. Sun, P.A. Komesaroff, A phase I dose-escalation study to evaluate tolerability in a Western population to T89, a modern cardiovascular herbal medicine, *J. Cardiovasc. Pharmacol.* 60 (6) (2012) 513–519.
- [94] Y. Lu, C.S. Li, Q. Dong, Chinese herb related molecules of cancer-cell-apoptosis: a minireview of progress between Kanglaite injection and related genes, *J. Exp. Clin. Cancer Res.* CR 27 (2008) 31.
- [95] K.S. Michelsen, M.H. Wong, B. Ko, L.S. Thomas, D. Dhali, S.R. Targan, HMPL-004 (*Andrographis paniculata* extract) prevents development of murine colitis by inhibiting T-cell proliferation and TH1/TH17 responses, *Inflammatory Bowel Diseases* 19 (1) (2013) 151–164.
- [96] W.J. Sandborn, S.R. Targan, V.S. Byers, D.A. Rutty, H. Mu, X. Zhang, et al., *Andrographis paniculata* extract (HMPL-004) for active ulcerative colitis, *Am. J. Gastroenterol.* 108 (1) (2013) 90–98.
- [97] T. Tang, S.R. Targan, Z.S. Li, C. Xu, V.S. Byers, W.J. Sandborn, Randomised clinical trial: herbal extract HMPL-004 in active ulcerative colitis – a double-blind comparison with sustained release mesalazine, *Alimentary Pharmacol. Ther.* 33 (2) (2011) 194–202.
- [98] S.H. Liu, Y.C. Cheng, Old formula, new Rx: the journey of PHY906 as cancer adjuvant therapy, *J. Ethnopharmacol.* 140 (3) (2012) 614–623.
- [99] W. Lam, S. Bussom, F. Guan, Z. Jiang, W. Zhang, E.A. Gullen, et al., The four-herb Chinese medicine PHY906 reduces chemotherapy-induced gastrointestinal toxicity, *Sci. Transl. Med.* 2 (45) (2010) 45ra59.
- [100] Wing Lam, Shwu-Huey Liu, Z. Jiang, Y.-C. Cheng, Lessons from the development of the traditional Chinese medicine formula PHY906, *Science* 347 (6219 Suppl) (2015) S43–S44.
- [101] S. Dong, Q.L. Chen, S.B. Su, Curative effects of fuzheng huayu on liver fibrosis and cirrhosis: a meta-analysis, Evidence-based complementary and alternative medicine: eCAM 2015 (2015) 125659.
- [102] P. Liu, Fuzheng huayu capsule in the treatment of liver fibrosis: clinical evidence and mechanism of action, *Chin. J. Integr. Med.* 18 (5) (2012) 398–400.
- [103] C. Liu, Y. Hu, L. Xu, C. Liu, P. Liu, Effect of Fuzheng Huayu formula and its actions against liver fibrosis, *Chin. Med.* 4 (2009) 12.
- [104] Y.X. Zhong, X.L. Jin, S.Y. Gu, Y. Peng, K.R. Zhang, B.C. Ou-Yang, et al., Integrated identification, qualification and quantification strategy for pharmacokinetic profile study of Guizhi Fuling capsule in healthy volunteers, *Sci. Rep.* 6 (2016) 31364.
- [105] J.A. Lee, S. Park, J. Jung, J.H. Jun, J. Choi, M.S. Lee, Herbal medicine (Gyejibongneyong-hwan) for treating primary dysmenorrhoea: a protocol for a systematic review of randomised controlled trials, *BMJ Open* 6 (9) (2016) e011071.
- [106] N.N. Chen, M. Han, H. Yang, G.Y. Yang, Y.Y. Wang, X.K. Wu, et al., Chinese herbal medicine Guizhi Fuling Formula for treatment of uterine fibroids: a systematic review of randomised clinical trials, *BMC Complementary Altern. Med.* 14 (2014) 2.



# Injectable thermosensitive hydrogel containing hyaluronic acid and chitosan as a barrier for prevention of postoperative peritoneal adhesion

Chih-Hao Chen<sup>a,b</sup>, Shih-Hsien Chen<sup>a</sup>, Shih-Hsuan Mao<sup>b</sup>, Ming-Jin Tsai<sup>a</sup>, Pang-Yun Chou<sup>b</sup>, Chien-Hung Liao<sup>c</sup>, Jyh-Ping Chen<sup>a,b,d,e,\*</sup>

<sup>a</sup> Department of Chemical and Materials Engineering, Chang Gung University, Taoyuan 33302, Taiwan, ROC

<sup>b</sup> Department of Plastic and Reconstructive Surgery and Craniofacial Research Center, Chang Gung Memorial Hospital, Kwei-San, Taoyuan 33305, Taiwan, ROC

<sup>c</sup> Department of Trauma and Emergency Surgery, Chang Gung Memorial Hospital, Taoyuan 33305, Taiwan, ROC

<sup>d</sup> Research Center for Chinese Herbal Medicine and Research Center for Food and Cosmetic Safety, College of Human Ecology, Chang Gung University of Science and Technology, Kwei-San, Taoyuan 33302, Taiwan, ROC

<sup>e</sup> Department of Materials Engineering, Ming Chi University of Technology, Tai-Shan, New Taipei City 24301, Taiwan, ROC

## ARTICLE INFO

### Article history:

Received 10 February 2017

Received in revised form 16 May 2017

Accepted 5 June 2017

Available online 10 June 2017

### Keywords:

Hyaluronic acid

Chitosan

Peritoneal adhesion

Injectable

Thermosensitive

Hydrogel

## ABSTRACT

Peritoneal adhesion is one of the common complications after abdominal surgery. Injectable thermosensitive hydrogel could serve as an ideal barrier to prevent this postoperative tissue adhesion. In this study, poly(*N*-isopropylacrylamide) (PNIPAm) was grafted to chitosan (CS) and the polymer was further conjugated with hyaluronic acid (HA) to form thermosensitive HA-CS-PNIPAm hydrogel. Aqueous solutions of PNIPAm and HA-CS-PNIPAm at 10%(w/v) are both free-flowing and injectable at room temperature and exhibit sol-gel phase transition around 31 °C; however, HA-CS-PNIPAm shows less volume shrinkage after gelation and higher complex modulus than PNIPAm. Cell culture studies indicate both injectable hydrogel show barrier effects to reduce fibroblasts penetration while induce little cytotoxicity in vitro. From a sidewall defect-bowel abrasion model in rats, significant reduction of postoperative peritoneal adhesion was found for peritoneal defects treated with HA-CS-PNIPAm compared with those treated with PNIPAm and untreated controls from gross and histological evaluation. Furthermore, HA-CS-PNIPAm did not interfere with normal peritoneal tissue healing and did not elicit acute toxicity from blood analysis and tissue biopsy examination. By taking advantage of the easy handling and placement properties of HA-CS-PNIPAm during application, this copolymer hydrogel would be a potentially ideal injectable anti-adhesion barrier after abdominal surgeries.

© 2017 Elsevier Ltd. All rights reserved.

## 1. Introduction

Postoperative adhesion remains one of the common and serious complications after abdominal and gynecological surgeries with the incidence estimated to be over 80% postoperative (Yeo & Kohane, 2008). Although it could be asymptomatic, some patients eventually developed complications such as chronic abdominal pain (Mueller, Tschudi, Herrmann, & Klaiber, 1995), bowel obstruction (Fazio et al., 2006), abscess formation (Reijnen, Bleichrodt,

& Van Goor, 2003) and infertility (Boland & Weigel, 2006). Re-operation can be frustrated for both patients or surgeons, and adhesion will further raise difficulty and time in surgery and risk of iatrogenic bowel injury subsequently (Coleman, McLain, & Moran, 2000; Van Der Krabben et al., 2000). According to previous reports, adhesions are induced by prolonged inflammation of injured tissues, fibroblast in-growth and neovascularization (Ar'Rajab et al., 1996), which commonly develop within 72 h of surgery (Boland & Weigel, 2006). Peritoneal adhesion is likely to initiate when organs are handled during operations or temporarily shifted from their normal positions (diZerega & Campeau, 2001). Moreover, insoluble fibrin from blood coagulation becomes a temporary matrix that can form the initial bridging between tissue surfaces in the abdomen. This matrix provides a structure for fibroblasts to attach, which further reduce fibrinolysis of the viscous fibrin matrix on the peri-

\* Corresponding author at: 259 Wen-Hwa 1st Road, Kwei-San, Taoyuan 33302, Taiwan, ROC.

E-mail addresses: [jpchen@mail.cgu.edu.tw](mailto:jpchen@mail.cgu.edu.tw), [jpchen1125@hotmail.com](mailto:jpchen1125@hotmail.com) (J.-P. Chen).

toneal surface by plasmin and fibroblasts, followed by remodeling into dense fibrotic tissues (Boland & Weigel, 2006).

In order to diminish the incidence of the noxious complications, two major postoperative anti-adhesion approaches have been investigated widely, i.e. pharmacological treatments (Aysan, Bektas, Ersoz, Sari, & Huq, 2010; Segura, Schmokel, & Hubbell, 2007) and barrier-based devices (Chang, Lee, Wu, Yang, & Chien, 2012; Kumar, Wong, & Leaper, 2009; Menzies et al., 2006; Ohya, Sonoda, Nakayama, & Matsuda, 2005; Wallwiener et al., 2006; Yeo, Burdick et al., 2006; Yeo, Highley et al., 2006; Yeo et al., 2007). Among these modalities, barriers devices are currently recognized as the most effective ones in lessening adhesion (Wallwiener et al., 2006). Decreases in incidence and severity of adhesion have been validated since introduction of those barriers to prevent post-surgical adhesion (Fazio et al., 2006; Kumar et al., 2009). With the evolution of surgical procedures and the concept of minimal invasiveness, the laparoscopic surgery has gained its popularity and been proved to reduce the adhesion rate (Boland & Weigel, 2006; Schnüriger et al., 2011). However, the application of common adhesion barriers would be limited under the laparoscopic approach. For instance, the biodegradable barrier film Seprafilm™ is difficult to cover a complex geometry and aggressively adhere to moisture surface, which make the manipulation less convenient especially in laparoscopic surgery. In contrast, Adept™ is the only adhesion reduction solution approved by the U.S. Food and Drug Administration and is regarded as an effective anti-adhesion device in laparoscopic surgery (Menzies et al., 2006). Nevertheless, its fluidity causes leakage from the surgical site with limited adherence to designated regions. Peritoneal irritation due to lavage with large volume of fluids is also another concern.

To conquer this obstacle, much attention has been paid to the development of injectable hydrogels as anti-adhesion barriers recently (Zhang et al., 2014). Injectable hydrogel that are cross-linkable in situ were reported for postoperative anti-adhesion uses but were less favorable due to long gelling times or requirements of assistance from external devices (Lee, Tsai, Wen, & Huang, 2012; Yeo, Burdick et al., 2006; Yeo, Highley et al., 2006; Yeo et al., 2007). An alternative injectable hydrogel for anti-adhesion purpose would be an aqueous solution of a thermosensitive polymer, which will form a rigid gel at the physiological temperature with sol-gel phase transition above the polymer's lower critical solution temperature (LCST). In this circumstance, the barrier could be injected during minimal invasive surgery and conform to the complex geometry of the tissue surface. Poly(*N*-isopropylacrylamide) (PNIPAm) is one of the most well-studied thermosensitive polymers for biomedical applications with its LCST being 32 °C in water, and the polymer solution could transform into a gel in situ without external assistance under physiological conditions (Okano, Yamada, Sakai, & Sakurai, 1993). However, there are some limitations while applying PNIPAm alone. Therefore, modification of PNIPAm by grafting with other biocompatible carbohydrate polymers was shown to fortify the mechanical properties of the hydrogel and reduce its cytotoxicity (Chen & Cheng, 2006). Indeed, during the last decade, thermosensitive copolymer hydrogels based on PNIPAm have been applied in fields of tissue engineering, drug or gene delivery, and wound dressing (Yang & Lin, 2004), but not as anti-adhesion barriers.

Hyaluronic acid (HA) has a number of physicochemical properties that are desirable for preventing postoperative adhesions. For this reason, HA is one of the most widely explored biomaterials for this application (Chen, Chen, Shalumon, & Chen, 2014; Kiefer et al., 2016; Kuo, Chang, Wang, Tang, & Yang, 2014; Li et al., 2014). Chitosan is a natural polymer of D-glucosamine and *N*-acetylglucosamine derived from chitin and widely used in biomedical applications due to its unique characteristics such as biocompatibility, biodegradability, hemostatic and antimicro-

bial activities (Ong, Wu, Moochhala, Tan, & Lu, 2008), and free radical scavenging activities (Xie, Xu, & Liu, 2001). That chitosan membranes showed poor cell affinity and reduce fibroblast adhesions implicate its potential role in anti-adhesion application (Dash, Chiellini, Ottenbrite, & Chiellini, 2011). Recently, an electrospun polycaprolactone nanofibrous membrane grafted with chitosan was shown to enhance the anti-adhesion effect after tendon surgery (Chen, Chen, Fong, & Chen, 2014). A polysaccharide-based hydrogel containing carboxymethyl chitosan also showed potential application in the prevention of postoperative adhesion (Lou et al., 2012). Combining the demonstrated anti-adhesion effects offered by HA and chitosan and the phase transition behavior endowed by PNIPAm, we hypothesize a thermosensitive copolymer hydrogel containing those polymers (HA-CS-PNIPAm) will be an excellent candidate to be used as an injectable anti-adhesion barrier for prevention of postoperative peritoneal adhesion. Therefore, we first synthesized and confirmed the phase transition behavior of the polymers, followed by examining its cytotoxicity and barrier effect in vitro. Through the sidewall abrasion model in rats, the anti-adhesion efficacy of HA-CS-PNIPAm was verified in vivo for future clinical implications.

## 2. Materials and methods

### 2.1. Materials

*N*-isopropylacrylamide (NIPAm) and 2,2'-azobis(2-methylpropionitrile) (AIBN) were recrystallized from *n*-hexane and methanol, respectively. Mercaptoacetic acid (MAA) was used as a chain transfer agent. Chitosan (molecular weight =  $1 \times 10^5$  Da, degree of deacetylation = 98%), 2-(*N*-morpholino)ethanesulfonic acid (MES), 1-ethyl-3-(3-dimethylaminopropyl) carbodiimide hydrochloride (EDC), *N*-hydroxysuccinimide (NHS) and 2,4,6-trinitrobenzene sulfonic acid (TNBS) were purchased from Sigma-Aldrich. HA (sodium hyaluronate) with an average molecular weight of  $1.3 \times 10^6$  Da was purchased from Bloomage Freda Biopharm Co. Dulbecco's Modified Eagle's medium (DMEM, Sigma-Aldrich) and fetal bovine serum (FBS, HyClone) were used for cell culture.

### 2.2. Preparation of HA-CS-PNIPAm copolymer

Using AIBN as an initiator, PNIPAm with a carboxylic acid-ended group was prepared in benzene by free radical polymerization between NIPAm monomers and MAA (Chen & Cheng, 2006). To synthesize chitosan-grafted PNIPAm, 0.5 g chitosan and 5 g PNIPAm were dissolved in 50 ml MES buffer (0.1 M, pH 5) containing 0.458 g EDC and 1.375 g NHS. After reacting at 25 °C for 12 h at 180 rpm, the polymer was purified by thermally induced precipitation at 50 °C for 30 min (in the presence of 0.6 M NaCl) and centrifuged at  $15000 \times g$  for 20 min. The precipitate was dissolved in 50 ml MES buffer (0.1 M, pH 5) and purified three times as before to remove residual chitosan. For HA-CS-PNIPAm synthesis, chitosan-grafted PNIPAm prepared above and HA (0.25 g) was dissolved in 100 ml of 0.1 M MES buffer (pH 5) and the reaction was carried out in the presence of 0.458 g EDC and 1.375 g NHS. After the reaction at 25 °C for 12 h at 180 rpm, residual HA was removed by precipitation at 50 °C as described above. Purified HA-CS-PNIPAm could be obtained after dialysis (MWCO = 50,000) against distilled de-ionized (DDI) water at 4 °C for 4 days and lyophilization (Chen & Cheng, 2009).

### 2.3. Characterization of hydrogels

#### 2.3.1. Determination of LCST

To determine the LCST, 10% (w/v) polymer solutions were prepared in DDI water. The sol-gel phase transition of the polymer

solution was measured using an UV/Vis spectrophotometer (ThermoSpectronic Helios Alpha) equipped with a circulator bath for temperature control. The absorbance of the polymer solution at 470 nm ( $OD_{470}$ ) was recorded from 26 to 40 °C. The polymer solution was equilibrated for 30 min at each test temperature. From the thermos-precipitation curve by plotting  $OD_{470}$  vs. temperature, the LCST of the polymer was obtained as the temperature when the absorbance is half of the maximum value. For differential scanning calorimetry (DSC) analysis, 10  $\mu$ l of 10%(w/v) polymer solutions prepared in DDI water were placed in a 20  $\mu$ l DSC aluminum pan and analyzed with a Q20 DSC (TA Instruments). The scan rate was 1 °C/min from 10 to 40 °C under 30 ml/min nitrogen.

### 2.3.2. Rheological properties

The temperature effect on gelation was monitored by measuring the viscosity and complex shear modulus ( $G^*$ ) as a function of temperature using a Carri-Med CSL2 100 controlled stress rheometer (TA Instruments). A 60 mm diameter cone and plate with 2° cone angle was used. The storage modulus ( $G'$ ), loss modulus ( $G''$ ) and apparent dynamic viscosity were determined using Rheology Solutions software provided by TA Instruments. The combined viscous and elastic behavior is given by the absolute value of the complex shear modulus  $G^*$  with  $G^* = \sqrt{G'^2 + G''^2}$ . For viscosity measurement, the parameter settings were set at temperature ramp: gap = 52  $\mu$ m, temperature = 25–33 °C, shear stress = 2 Pa, ramp duration = 10 min. For modulus measurements, the parameter settings were set at oscillation step: gap = 52  $\mu$ m, temperature = 20–50 °C, shear stress = 1 Pa, frequency = 0.5 Hz.

### 2.3.3. Water content

To determine the water content of the hydrogel, 1 ml of 10%(w/v) polymer solution prepared in DDI water was placed in a 37 °C incubator for 1 h. Additional 1 ml DDI water was added to ensure hydrogel wettability after gelation. Two days after incubation at 37 °C, the residual water on hydrogel surface was removed and the weight of hydrogel was measured. The water content was defined as the weight of water per unit weight of polymer and determined with the following equation,

$$\text{Water content} = \frac{W_{\text{hydrogel}} - W_{\text{polymer}}}{W_{\text{polymer}}}$$

where  $W_{\text{polymer}}$  is the dry weight of the polymer, and  $W_{\text{hydrogel}}$  is the wet weight of the hydrogel after gelation at 37 °C.

### 2.3.4. Volume shrinkage

The volume change (%) of the hydrogel was defined as the percentage of volume decrease when a polymer solution at 25 °C gelled at 37 °C with the following equation,

$$\begin{aligned} \text{Volumeshrinkage (\%)} &= - \left( 1 - \frac{V_i - V_{H_2O}}{V_i} \right) \times 100\% \\ &= - \left( 1 - \frac{V_w}{V_i} \right) \times 100\% = - \frac{V_{H_2O}}{V_i} \times 100\% \end{aligned}$$

where  $V_i$  is the volume of initial polymer solution at 25 °C,  $V_{H_2O}$  is the volume of water squeezed out as polymer hydrogel formed, and  $V_w$  is the volume of water in polymer hydrogel after gelation at 37 °C.

## 2.4. In vitro evaluation of cytotoxicity and barrier effects

### 2.4.1. Cytotoxicity assay of hydrogels

Cytotoxicity of the polymer was examined by MTT assay of cell viability according to ISO 10993-5 using mouse fibroblastic NIH

3T3 cells. 0.2 ml of 10%(w/v) polymer solution was placed in a 24-well culture plate and incubated at 37 °C for 1 h for gel formation. The hydrogel was extracted with in Dulbecco's modified Eagle's medium (DMEM) supplemented with 10% fetal bovine serum (FBS) at 37 °C for 24 h to obtain the extraction medium. The extraction medium (2 ml) was used to culture  $1 \times 10^4$  cells in a CO<sub>2</sub> incubator at 37 °C under 5% CO<sub>2</sub>/95% air condition. The relative cell viability was determined at 24 and 48 h by MTT assays using 3-(4,5-dimethylthiazol-2-yl)-2,5-diphenyl tetrazolium bromide. The absorbance ( $OD_{540}$ ) of the formazan product was determined by an ELISA plate reader (BioTek Synergy HT) at 540 nm. The absorbance for cells cultured with fresh culture medium was used as the control.

### 2.4.2. Cells migration test

Cell migration assay in a double chamber dish separated by a cell culture insert with 8  $\mu$ m polycarbonate porous membrane (Transwell™, Corning, New York, USA) was used to evaluate the barrier effect of hydrogel in vitro. Mouse fibroblastic NIH 3T3 cells were inoculated at a density of  $1.0 \times 10^5$ /well in the upper chamber containing DMEM with 2% FBS with or without placing hydrogel (height = 3.0 mm) at the bottom of the insert. After 24 h of culture at 37 °C, cell migration was determined by the cells that moved into the lower chamber containing DMEM with 10% FBS as driven by difference in serum concentration. The cells in the lower chamber were observed by an inverted microscope and determined with a DNA Quantitation Kit (Sigma-Aldrich) using bisBenzimide H 33258 (Hoechst 33258).

## 2.5. In vivo evaluation for prevention of postoperative peritoneal adhesion

All animal procedures were approved by the Institutional Animal Care and Use Committee of Chang Gung University. The animals were purchased from National Laboratory Animal Breeding and Research Center, Taipei, Taiwan.

### 2.5.1. Sidewall defect-cecum abrasion model in rats

The anti-adhesion efficacy of PNIPAm and HA-CS-PNIPAm hydrogel was evaluated by using a rat model of sidewall defect-bowel abrasion (Ersoy, Ozturk, Yazgan, Ozdogan, & Gundogdu, 2008). Adult SD male rats weighted 200–250 g and aged 6–8 weeks were randomly divided into 3 groups ( $n = 8$  in each group). After general anesthesia by ketamine hydrochloride and xylazine hydrochloride (1:1 mixture, 1.0 ml/kg via muscle injection), peritoneal intestinal adhesion was induced by creating a  $2 \times 2$  cm<sup>2</sup> defect on the left lateral abdominal wall, including the peritoneum and part of the underlying muscle. The corresponding cecum was abraded by a surgical brush until spot bleeding. For the animals in experimental groups, 1 ml of PNIPAm or HA-CS-PNIPAm solution (10%(w/v) in normal saline) was injected to cover both defects, while gelation occurred rapidly in situ. The peritoneum and abdominal wall were closed with 4-0 Vicryl sutures, and the skin was closed with 4-0 Ethylon sutures. Animals with their defects untreated and rinsed with 1 ml of normal saline were set as the control group.

### 2.5.2. Gross observation

Two weeks after operation, rats were euthanized and underwent laparotomy to examine the severity and extension of peritoneal adhesions. The scores of tenacity of the adhesion were defined as described previously: 0, no adhesions; 1, gentle blunt dissection required to free adhesions; 2, aggressive blunt dissection required to free adhesions; 3, sharp dissection required to free adhesions (Hooker, Taylor, & Driman, 1999). Two surgeons were invited to determine the adhesion scores in a blinded manner.



### 2.5.3. Histological evaluation

Specimens were taken from the damaged cecum, damaged abdominal wall, and adhesion tissues contained in the abdominal wall and cecum. For histopathological examination, the obtained tissues were fixed immediately in 10% formaldehyde in phosphate buffered saline (PBS) (pH = 7.4) for 72 h and embedded in paraffin. The tissues were then serially sectioned, stained with hematoxylin and eosin (H&E) and Masson's trichrome. All slides were analyzed using light microscopy (Olympus BX 45) by two pathologists in a blinded manner. The scores from histology were defined as: 0, no adhesions; 1, minimal and loose; 2, moderate; 3: florid and dense (Hooker et al., 1999).

### 2.5.4. Scanning electron microscopy (SEM) observation of healed defect

To understand the morphological change of peritoneal defects after application of hydrogels, a peritoneal defect of  $2 \times 2 \text{ cm}^2$  was made including the peritoneum and part of the underlying muscle in SD male rats. The corresponding cecum haustra was kept intact. 1 ml of HA-CS-PNIPAm solution (10%(w/v) in normal saline) was injected to cover the peritoneal defect. The lateral abdominal walls including the defects were harvested 3, 7 and 14 days post-treatment. SEM was used to observe the tissue surface morphology change during the remesothelialization process. The harvested specimens were fixed with 2.5% glutaraldehyde, dehydrated in a critical point apparatus, and then examined by SEM (Philips XL-30, Japan) after gold sputter coating for 60 s.

### 2.6. Systemic toxicity test

To further evaluate the systemic toxicity of HA-CS-PNIPAm hydrogel, all rats were closely observed for their general condition, body weight, morbidity and mortality after operation. Blood samples from each rat one week after experiment were drawn to perform blood counts (white blood cell count, red blood cell count, hemoglobin and hematocrit) and biochemical analysis (aspartate aminotransferase, alanine aminotransferase, blood urea nitrogen and creatinine) of major organ functions before euthanasia. After sacrificing, the major organs of rats including heart, lung, liver and kidney were harvested and fixed in 10% formaldehyde in PBS. The tissues were then embedded and sectioned, followed by H&E staining, and analyzed by two pathologists.

### 2.7. Statistical analysis

Each of the experiments was repeated at least four times, and the values were expressed as means  $\pm$  standard deviations. For comparison between two groups of data, the Student's *t*-test was performed. Since adhesion scores did not always follow a normal distribution, statistical inferences were made using the Mann–Whitney *U* test using the SPSS 10.0 (SPSS Inc., Chicago, IL) software. Differences were considered to be statistically significant at  $p < 0.05$ .

## 3. Results

### 3.1. Synthesis and characterization of hydrogels

The relative compositions of CS, HA and PNIPAm in HA-CS-PNIPAm could be calculated to be 12.6%(w/w), 5.5%(w/w) and 81.9%(w/w), respectively (Chen & Cheng, 2009). The polymer PNIPAm and HA-CS-PNIPAm solutions are free-flowing at 25 °C and transform into gels at 37 °C (Chen & Cheng, 2006). Furthermore, the solid hydrogel remained stationary when the sample vial was inverted, verifying the high structural strength of the injectable

thermosensitive polymer hydrogel at the physiological temperature. The LCST was determined from the sol-gel phase transition by measuring the turbidity of a 10%(w/v) polymer solution. The relative absorbance of the polymer solution increased with temperature and the LCST could be calculated to be 29.5 and 31.4 °C for PNIPAm and HA-CS-PNIPAm, respectively, by defining the LCST being the temperature corresponding to half of the maximum change in the absorbance (Fig. 1A). The gelling processes of PNIPAm and HA-CS-PNIPAm are also thermoreversible as subsequent cooling cycle resulted in gel-sol transition and fully reversible gel melting (Chen & Cheng, 2009). The DSC thermogram shows a single endothermic peak for both polymers (Fig. 1B). The temperatures at the onsets of the DSC endotherms were 1.8–1.9 °C lower than the peak temperatures at 30.4 °C, which could be referred to as the LCST (Feil, Bae, Feijen, & Kim, 1993). Gel formation was also traced through the viscosity of the 10%(w/v) polymer solution as a function of temperature, which significantly increased after gelation (Fig. 1C). The viscosity of PNIPAm solution sharply increased and PNIPAm eventually became a non-flowing gel at 29.6 °C. A similar transition temperature was found for HA-CS-PNIPAm solution at 30.5 °C. To evaluate the temperature-responsive change of gel strength, the complex shear modulus of the hydrogel ( $G^*$ ) at different temperatures were determined. The  $G^*$  value dramatically increased around 30 °C during the heating process from 20 to 50 °C. It reached the maximum value at 40–45 °C followed by a decreasing trend due to the volume shrinkage of the hydrogel. The  $G^*$  value at of HA-CS-PNIPAm hydrogel is 3.1 times that of PNIPAm at 37 °C, indicating higher mechanical strength of this polymer solution after gel formation.

The water contents at 37 °C are  $1.25 \pm 0.06$  and  $7.08 \pm 0.11 \text{ g water/g polymer}$  for PNIPAm and HA-CS-PNIPAm hydrogels, respectively. The volume changes (shrinkage) of PNIPAm and HA-CS-PNIPAm hydrogels from 25 °C to 37 °C were  $87.6 \pm 2.8\%$  and  $20.7 \pm 0.49\%$ , respectively. The dramatic volume shrinkage of PNIPAm removes close to 90% of the water in the polymer solution, producing low water content hydrogel. In contrast, HA-CS-PNIPAm that contains chitosan and HA molecules can reduce the volume change by 76% and increase the water content in the hydrogel to 5.7-fold compared with PNIPAm.

### 3.2. Cytotoxicity and cell migration assay

To evaluate the in vitro cytotoxicity of PNIPAm and HA-CS-PNIPAm hydrogel, viability of cells cultured in the extraction medium of hydrogel was compared to the control where cells were cultured in fresh culture medium. The HA-CS-PNIPAm group showed no cytotoxicity (relative cell viability  $>80\%$ ) after 24 and 48 h of culture, which did not show significant difference from the PNIPAm group at both time points.

From cells migration assay, the number of fibroblasts that moved from the upper to the lower chamber dramatic decreased due to the barrier effect of PNIPAm and HA-CS-PNIPAm hydrogels (Fig. 2). The cells numbers in the lower chambers of PNIPAm and HA-CS-PNIPAm groups were significant reduced compared to the control group without placing hydrogel at the bottom of the cell insert ( $p < 0.05$ ), indicating both thermosensitive hydrogels can act as a barrier to prevent cell migration. The level of reduction in cell migration is also higher for HA-CS-PNIPAm compared with PNIPAm as significantly fewer cells were found in the lower chamber, implicating its improved effectiveness in anti-adhesion application in vivo.

### 3.3. Anti-peritoneal adhesion evaluation in rats

There were no signs of hemorrhage, infection or unexpected death of animals before sacrifice during the animal experiment.



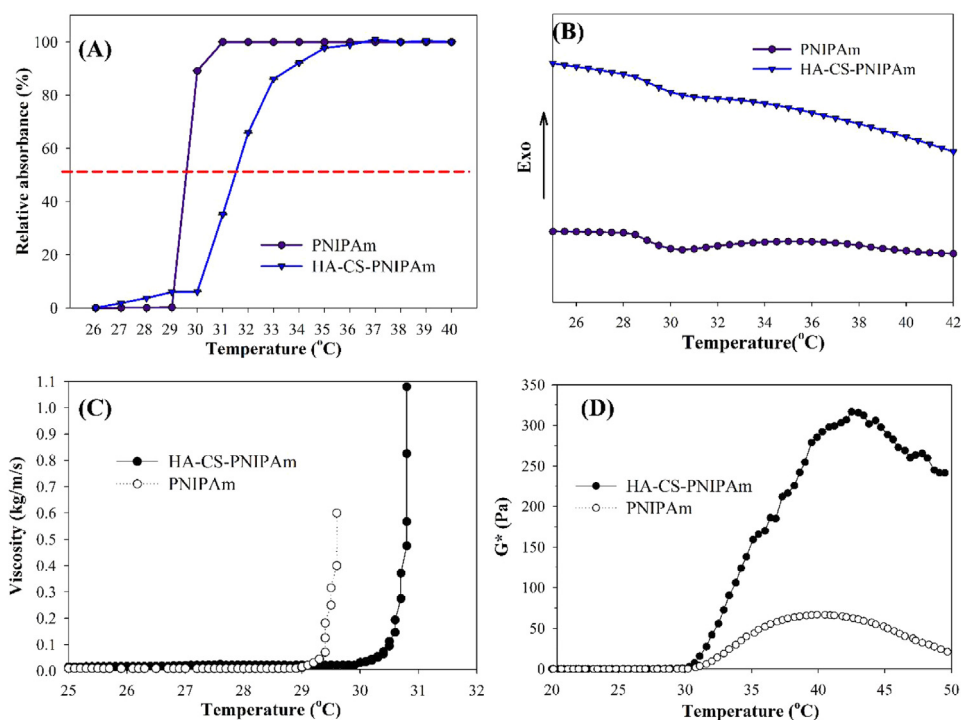


**Fig. 1.** The sol-gel phase transition behavior of 10%(w/v) PNIPAm and HA-CS-PNIPAm solutions by measuring solution absorbance with a spectrophotometer (A), thermal properties with a differential scanning calorimeter (B), and viscosity (C) and complex shear modulus (D) with a rheometer.

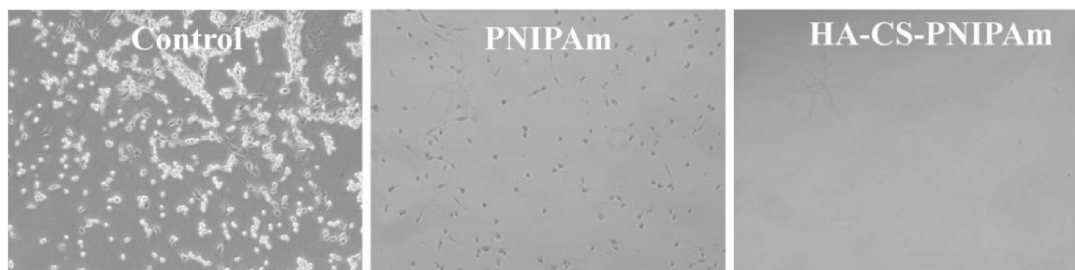


**Fig. 2.** Cell migration test was performed with fibroblastic NIH3T3 cells cultured in a double chamber dish separated by a cell culture insert. PNIPAm or HA-CS-PNIPAm hydrogel was placed at the bottom of the cell culture insert and compared with control without hydrogel. Fibroblast cells in the lower chamber were observed under an inverted microscope (A) and determined quantitatively from DNA assays (B). Data are showed as mean  $\pm$  SD from 6 measurements. \* $p < 0.05$  vs. control; # $p < 0.05$  vs. PNIPAm.

**Table 1**

Number of rats with different peritoneal adhesion scores and the median score from gross view and histology evaluations (n = 8 in each group).

Gross view	Control	PNIPAm	HA-CS-PNIPAm
Score 0	0	2	6
Score 1	0	4	2
Score 2	3	2	0
Score 3	5	0	0
Median score	3.0	1.0 <sup>*</sup>	0.0 <sup>*,#</sup>
Histology	Control	PNIPAm	HA-CS-PNIPAm
Score 0	0	2	7
Score 1	0	5	1
Score 2	2	1	0
Score 3	6	0	0
Median score	3.0	1.0 <sup>*</sup>	0.0 <sup>*,#</sup>

Scores from gross view: 0, no adhesions; 1, gentle blunt dissection required to free adhesions; 2, aggressive blunt dissection required to free adhesions; 3, sharp dissection required to free adhesions. Scores from histology: 0, no adhesions; 1, minimal and loose; 2, moderate; 3: florid and dense.

<sup>\*</sup> p < 0.05 vs. control.

<sup>#</sup> p < 0.005 vs. PNIPAm from Mann–Whitney U tests.

Peritoneal-intestinal adhesions were successfully induced using a sidewall defect and bowel abrasion model in rats. For the experiment group, 1 ml of PNIPAm or HA-CS-PNIPAm solution (10%(w/v)) was slowly injected onto the defect at room temperature with sufficient coverage, and gelation was observed in situ within 10–20 s with elevation in temperature to physiological condition. For the control group, abdominal walls were closed up without applying any barrier agent on the defect.

Two weeks after surgery, all rats were euthanized to determine the extent of intra-abdominal adhesion. The representative gross view of adhesion formation for control and experiment groups is shown in Fig. 3. The untreated control group showed heavy adhesion around the peritoneum and cecum and a sharp dissection was required to detach the large fibrous tissue bridging the surroundings of both. Considering the PNIPAm group, moderate adhesion with slight bridging between the cecum and the surrounding peritoneum was observed. In contrast, animals treated with HA-CS-PNIPAm did not suffer from adhesion and the defects were almost repaired within two weeks. Based on gross observation, the extent of tissue adhesion was further evaluated and compared among groups in Table 1. Most (6 out of 8) of the rats in the HA-CS-PNIPAm group did not suffer from adhesion, whereas animals treated with PNIPAm suffered from mild adhesions with only 2 out of 8 animals showing no adhesion. Severe adhesions were observed for animals in the control group with all animals showing adhesion scores higher than 2. There is significant reduction in the median adhesion score for HA-CS-PNIPAm compared with other groups.

From histological observations, the defects treated with HA-CS-PNIPAm hydrogel had been reperitonealized after two weeks of observation. Some of the animals treated with PNIPAm still suffered from mild to moderate tissue adhesion along the cecum and abdominal wall. The control group showed severe adhesion with penetration of adhesion into the abdominal wall (Fig. 4). The adhesion scores from histology also underline the consistency of HA-CS-PNIPAm in preventing peritoneal adhesion formation with a significantly lower median score compared with other groups (Table 1).

Further consideration of the healing dynamics from the surface morphology of the peritoneum under SEM indicates minimum healing defect after HA-CS-PNIPAm treatment (Fig. 5). The peritoneal SEM image at day 14 of HA-CS-PNIPAm application showed no observable difference from that of normal peritoneum. Both histology and SEM examinations indicated that HA-CS-PNIPAm

hydrogel did not interfere with wound healing, and was effective for prevention of postoperative peritoneal adhesion.

#### 3.4. Systemic toxicity test of the hydrogel as a barrier material

On blood sampling of animals one week after the experiment, the application of HA-CS-PNIPAm hydrogel did not significantly alter the level of blood counts and hepatic or renal functions from hematologic study compared to untreated control at acute stage (Table 2). When the animals were euthanized after two weeks, major organs were also harvested for assessment of the in vivo toxicity of the hydrogel. No gross abnormalities were observed in the treated rats. Histological examination of liver, heart, spleen, and kidney biopsy did not reveal any observable differences between the HA-CS-PNIPAm and the untreated control groups (Fig. 6). No apparent abnormalities were found in the mesothelial cells layers of other abdominal viscera for animals in the experiment group. There were also no significant inflammatory cells or tissue necrosis in the control or experiment groups.

## 4. Discussion

Postoperative adhesion and subsequent complications can be frustrating and inevitable in patients who underwent intra-abdominal or gynecologic surgery. To eliminate postoperative adhesion, current concepts of management include minimizing peritoneal trauma, preventing fibrin formation and employing physical barriers (Schnüriger et al., 2011), with employing physical barriers regarded as one of the most effective and promising approaches. The ideal barrier should be biocompatible, biodegradable, and prevent fibroblasts penetration or in-growth. Moreover, the material should attach to the tissues securely in the complex geometry of tissues, not be disturbed by the restricted space during application (e.g. abdomen), and, most importantly, not impair normal tissue healing. With increased popularity of laparoscopic approach, the application of membrane-typed anti-adhesion barriers, however, has been limited due to the difficulty in accessibility. In this study, we proposed to use HA-CS-PNIPAm thermosensitive hydrogel as an intra-abdominal anti-adhesion barrier. Increase of LCST is expected when combining hydrophilic carbohydrate polymers (HA and chitosan) with PNIPAm. Nonetheless, by controlling the percentages of carbohydrate moieties in HA-CS-PNIPAm, the copolymer could be verified to be still temperature-sensitive with a LCST below the physiological temperature (Fig. 1A–C), indicating the feasibility for clinical applications. It is conceivable that when linear chains of PNIPAm were grafted to chitosan and further conjugated with HA, HA-CS-PNIPAm would show enhanced mechanical strength compared to PNIPAm due to the increase in molecular weight and entanglement of polymer chains (Fig. 1D). This will be beneficial for HA-CS-PNIPAm to be applied as an injectable barrier to prevent postoperative peritoneal adhesion. Due to the higher water absorption and retention ability of HA and chitosan, HA-CS-PNIPAm also retains significantly more water than PNIPAm after gel formation. The lubrication effect from high water content of HA-CS-PNIPAm may also contribute to minimizing tissue adhesion formation.

The postoperative adhesion is initiated by the inflammation of injured tissues, followed by recruiting fibroblasts in-growth within the matrix constructed by fibrin mesh. Later in the process, the fibroblasts serve as chemo-attractant and secrete collagen to reinforce the formed adhesion tissues (Boland & Weigel, 2006). Fibroblasts, indeed, constituted an essential part in adhesion formation. Therefore, preventing invasion of fibroblasts should decrease adhesion formation. From in vitro experiments, the HA-CS-PNIPAm hydrogel inhibited the migration of fibroblasts, indicating less



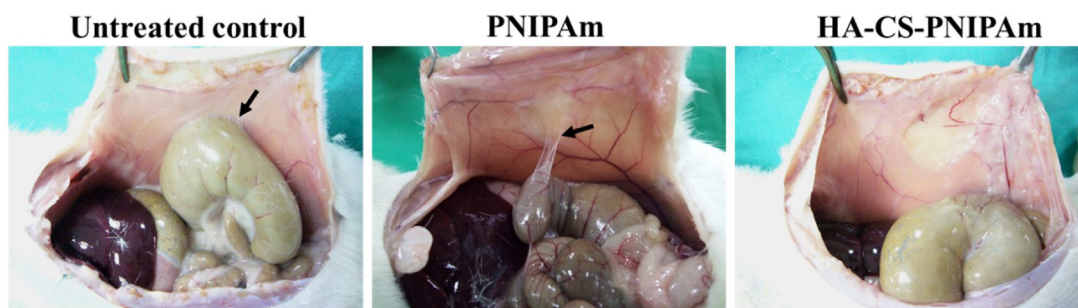


**Fig. 3.** Gross evaluation of postoperative peritoneal adhesions. Severe adhesion was found between peritoneum and cecum in untreated control group. Mild and focal adhesions with thin filaments were developed after application of PNIPAm hydrogel. No adhesion was identified in HA-CS-PNIPAm group and the healing of peritoneal defect was found with reperitonealization. Black arrows indicate the adhesions.

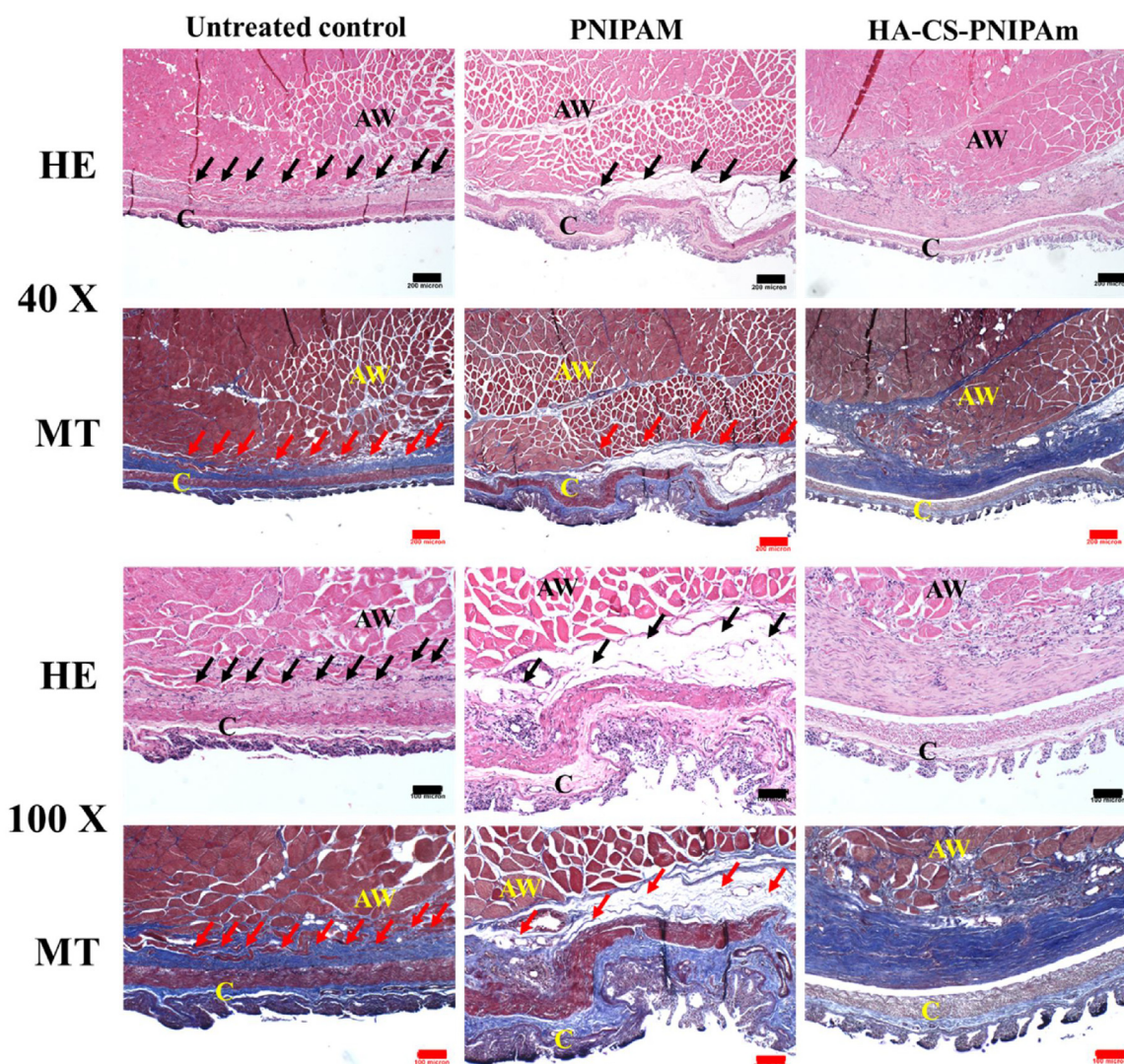


**Fig. 4.** The histological evaluation of injured peritoneal sites 2 weeks post-treatment. Severe peritoneal adhesion in untreated control group; mild to moderate adhesion between cecum and abdominal wall in animals treated with PNIPAm; no adhesion between cecum and abdominal wall in animals treated with HA-CS-PNIPAm. Hematoxylin and eosin (HE) and Masson's trichrome (MT) stains at 40 $\times$  (bar = 200  $\mu$ m) and 100 $\times$  (bar = 100  $\mu$ m) are shown. AW: abdominal wall; C: cecal mucosa; Black and red arrows indicate adhesions. (For interpretation of the references to colour in this figure legend, the reader is referred to the web version of this article.)

fibrotic tissue formation *in vivo* (Fig. 2). Through an animal model of rat sidewall defect-cecum abrasion, the HA-CS-PNIPAm hydrogel demonstrated superior anti-adhesion effects compared with PNIPAm or untreated control (Table 1; Figs. 3 and 4), without jeopardizing normal tissue healing (Fig. 5).

PNIPAm is a versatile thermosensitive polymer and has been applied in many fields. Only few articles have discussed its anti-adhesion properties. Ohya et al. (2005) demonstrated that PNIPAm-grafted HA and PNIPAm-grafted gelatin possess anti-adhesion and hemostatic aid properties, respectively. They



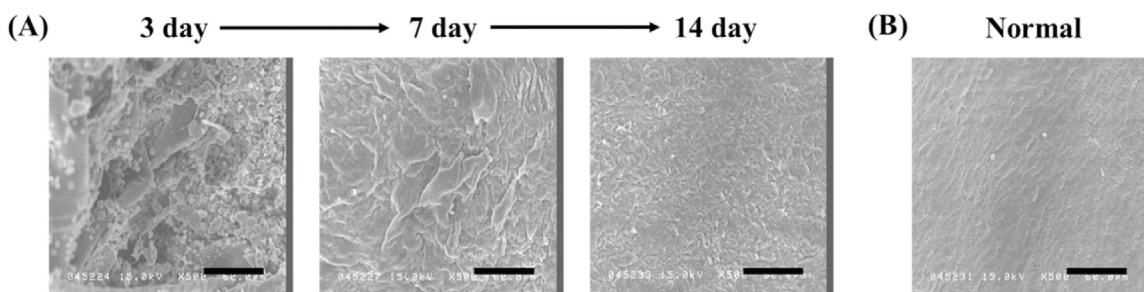


**Fig. 5.** SEM of the surface morphology of the peritoneum defect treated with HA-CS-PNIPAm hydrogel. (A) Disruption of peritoneum could be identified 3 days after application of HA-CS-PNIPAm. The defect area was covered by migrating mesothelial cells and the hydrogel covering the surface of the peritoneum reduced with time at day 7. Complete peritoneal recovery with hydrogel degradation was noted 14 days after application. The peritoneal SEM at day 14 of HA-CS-PNIPAm application showed no observable difference from that of normal peritoneum (B). Bar = 60  $\mu$ m.

**Table 2**

Blood analysis for evaluation of systemic toxicity.

Groups	WBC ( $10^3$ cells/ $\mu$ l)	RBC ( $10^6$ cells/ $\mu$ l)	HGB (g/dl)	HCT (%)	AST (U/L)	ALT (U/L)	BUN (U/L)	CRE (U/L)
Control	8.5 $\pm$ 0.7	2.6 $\pm$ 0.2	15.3 $\pm$ 0.6	47.5 $\pm$ 1.0	193.5 $\pm$ 88.5	61.5 $\pm$ 17.0	25.7 $\pm$ 5.6	0.16 $\pm$ 0.01
HA-CS-PNIPAm	7.4 $\pm$ 0.8*	2.7 $\pm$ 0.1*	14.4 $\pm$ 0.5*	45.6 $\pm$ 1.7*	146.3 $\pm$ 48.6*	59.3 $\pm$ 17.8*	26.3 $\pm$ 1.9*	0.17 $\pm$ 0.01*

WBC = white blood cell; RBC = red blood cell; HGB = hemoglobin; HCT = hematocrit; AST = aspartate aminotransferase; ALT = alanine aminotransferase; BUN = blood urea nitrogen; CRE = creatinine.

\*  $p > 0.05$  compared with control.

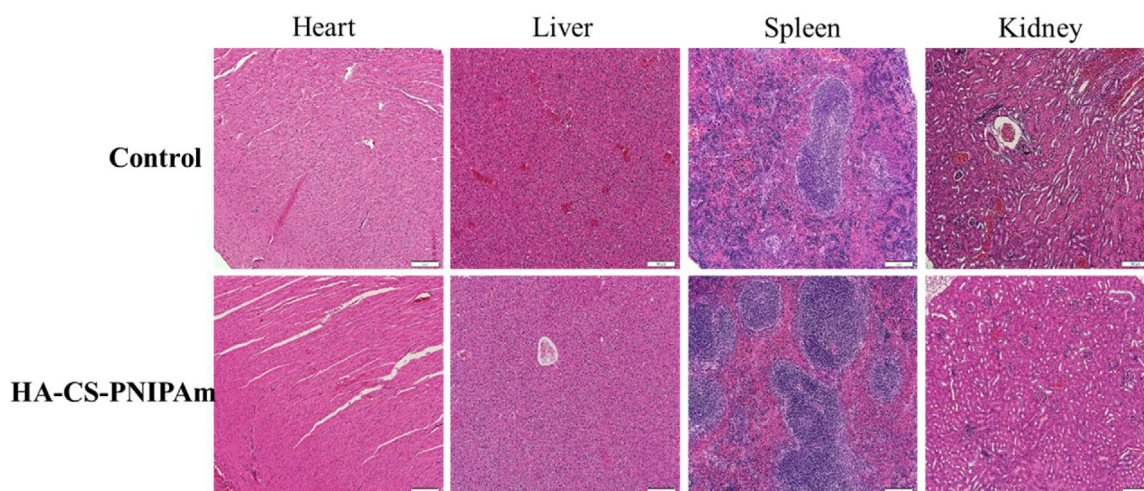


**Fig. 6.** Histological examination of heart, liver, spleen and kidney after euthanization at day 14. Tissue biopsy did not reveal any observable differences between the untreated control and the HA-CS-PNIPAm group. Bar = 100  $\mu$ m.

suggested that these PNIPAm-grafted copolymers could suppress cells spreading as a non-cell-adhesive matrix with superior sealing effect. In our study, the migration of fibroblasts was nearly blocked by HA-CS-PNIPAm hydrogels (Fig. 2), implicating that the hydrogel could prevent accumulation of fibrotic cells at wounded site and subsequent adhesion formation similar to prior PNIPAm-based copolymers. The beneficial effects of incorporating HA and chitosan in the hydrogel barrier could stem from various possible mechanisms. Initiation of coagulation cascade and deposition of fibrin matrix not only serve as an essential factor in hemostatic process but also lead to fibrotic tissues formation (Boland & Weigel, 2006). Chitosan and its products have been reported to have hemostatic effect and accelerated the coagulation process compared to conventional interventions (Ong et al., 2008). Continuous oozing or aggressive hemostatic interventions would aggravate adhesion formation owing to excessive formation of fibrin and inflammation, respectively. With hemostatic effect in concordance with sealing effect, we believed that chitosan-containing hydrogel has better ability to induce hemostasis and prevent subsequent

adhesion. Previous studies suggested that increase in biocompatibility of chitosan-grafted polymers corresponds to increase in hydrophilicity or positive charge (Vihola, Laukkanen, Valtola, Tenhu, & Hirvonen, 2005). Chitosan-grafted PNIPAm also improved water retention compared with PNIPAm alone (Fang, Chen, Leu, & Hu, 2008). Indeed, in vivo studies using rat models demonstrated barrier gels containing chitosan and its derivatives can be safely applied to the intraperitoneal cavity to reduce adhesion formation without adversely affecting wound healing (Diamond et al., 2003; Lauder, Garcea, Strickland, & Maddern, 2011; Yeo, Burdick et al., 2006; Yeo, Highley et al., 2006). The scientific rationale for HA in the prevention of adhesion formation is based on many biological effects, including non-coagulant activity, modulation of fibrous tissue formation, barrier effect to fibrinogen and inhibition of superoxide release from granulocytes (Chen, Chen, Shalumon, & Chen, 2015). HA has also been widely used as an ideal biomaterial to construct anti-adhesion barriers with its unique physicochemical properties, such as good lubricating capability, biocompatibility, and biodegradability, which make HA the major component in anti-

adhesion barriers after abdominal and pelvic surgeries (Zhao et al., 2010). Many previous reports have indicated that anti-adhesion materials made from HA can prevent tissue adhesions when used as physical barriers (Chen, Chen, Shalumon et al., 2014).

In this study, by taking advantages of the beneficial effects from both carbohydrate polymers toward anti-adhesion application, we grafted PNIPAm to chitosan followed by conjugating with HA to design anti-adhesion barriers with demonstrated efficacy toward prevention of peritoneal adhesion after abdominal surgery. HA and chitosan would improve biocompatibility of PNIPAm hydrogel. Nonetheless, there was no significant difference in biocompatibility between PNIPAm and HA-CS-PNIPAm from in vitro cytotoxicity tests. During animal experiments, HA-CS-PNIPAm was well tolerated with no evidence of severe inflammatory response, postoperative complications or systemic toxicity. The synergistic benefits endowed by HA and CS in HA-CS-PNIPAm could provide the molecular mechanism for the demonstrated superior anti-adhesion efficacy of HA-CS-PNIPAm over PNIPAm in vivo.

Although PNIPAm hydrogel could also function as an injectable anti-adhesion barrier with its cell blocking characteristics, insufficiency in mechanical strength and large volume contraction after gel formation have been its disadvantages. Such disadvantages could be facially circumvented by incorporating HA and chitosan into the polymer to substantially enhance mechanical strength and reduce volume shrinkage. Grafting natural polymers to PNIPAm was demonstrated to be an effective way to improve the mechanical strength of the hydrogel (Chen & Cheng, 2006; Kim, Lee, Kim, & Lee, 2002). During in vivo study, we created the same size of wounded area and treated with an equivalent amount of polymer solution (1 ml) to provide complete coverage of the wound. The results demonstrated that HA-CS-PNIPAm has superior anti-adhesion effect compared to PNIPAm and control groups (Fig. 3). Although the severity of adhesion formation was also reduced by application of PNIPAm hydrogel, the adhesion was persistently presented at the edge of the wounds, which was less frequently noticed for HA-CS-PNIPAm (Fig. 4). Substantial volume contraction of PNIPAm hydrogel could be responsible for this inferior performance as the wound area not fully covered by the formed gel, which could lead to subsequent adhesion formation in 2 weeks. Indeed, previous study suggested that HA-CS-PNIPAm has improved mechanical properties in terms of shrinkage-resistance with excellent repeatability (Chen & Cheng, 2006). For anti-adhesion application, maintenance of structure after sol-gel transition at the application site is crucial to avoid further invasion of fibrotic and inflammatory cells and contact of adjacent wounded tissues.

It is crucial to balance between reperitonealization and prevention of adhesion. The fibrinous exudate and fibrosis formation are designated as a healing platform in normal circumstance, and the adhesion may bridge surrounding structures with supplements during healing (Boland & Weigel, 2006). In our study, both visceral and parietal peritoneum was intact 2 weeks post-treatment as observed from H&E stain (Fig. 4) and under SEM (Fig. 5). It was suggested that the rate of reperitonealization is consistent and not limited by the cells migration from periphery (Boland & Weigel, 2006), indicating that adhesion is not mandatory as an element in peritoneal healing process. It was reported that the anti-adhesion material is unlikely to affect the reperitonealization process unless it is cytotoxic, non-biocompatible or interference with free-floating mesothelial cells attaching to the injured site (Foley-Comer et al., 2002). Several barriers have shown negative effects on reperitonealization due to prolonged stay (Yeo, Burdick et al., 2006; Yeo, Highley et al., 2006; Yeo et al., 2007). However, residual HA-CS-PNIPAm hydrogel could be observed 14 days post-treatment (Fig. 5). Longer degradation time might benefit the potency of anti-adhesion but could also elicit severe inflammatory response and, possibly, new lesions (Wallwiener et al.,

2006). There has no consensus about the ideal sustainability of anti-adhesion barriers. Despite reperitonealization by covering a sheet of mesothelium will complete in first 7–10 days (Boland & Weigel, 2006; Liakakos, Thomakos, Fine, Dervenis, & Young, 2001), the influence of matrix remodeling and cell-matrix interaction by barriers is still not fully understood. We suggest that the sustainability is not a major concern as long as no severe inflammatory response or impaired healing occurs as consequences.

Regarding the biodegradation for the different components of the HA-CS-PNIPAm polymer, the biodegradation of HA is a step-wise process that can occur via enzymatic (hyaluronidase,  $\beta$ -D-glucuronidase, and  $\beta$ -N-acetyl-hexosaminidase) or non-enzymatic reactions (Fakhari & Berkland, 2013). Chitosan is thought to be degraded in vertebrates predominantly by lysozyme and by bacterial enzymes in the colon (Kean & Thanou, 2010). For the non-biodegradable PNIPAm component in HA-CS-PNIPAm, although it is known that monomeric NIPAm is toxic, in vitro assays have shown PNIPAm of different molecular weights to be not cytotoxic against different cell lines at biomedical-relevant concentrations (up to 1 mg/ml) (Mortisen, Peroglio, Alini, & Eglin, 2010; Naha et al., 2010; Vihola et al., 2005; Wadajkar, Koppolu, Rahimi, & Nguyen, 2009; Xu et al., 2010). PNIPAm-based injectable thermosensitive hydrogels did not show detrimental effects to adjacent tissues in vivo (Cui, Lee, Pauken, & Vernon, 2011; Liao, Chen, & Chen, 2011). Indeed, although PNIPAm is not biodegradable, it has shown good biocompatibility in vivo (Ibusuki, Iwamoto, & Matsuda, 2003), as low molecular weight PNIPAm can undergo renal clearance (Kohori et al., 1998). Using PNIPAm polymers (22 kDa) with molecular weights below the renal cutoff, in vivo toxicity was not found for PNIPAm-based hydrogels (Campbell, Patenaude, & Hoare, 2013; Patenaude & Hoare, 2012). It should be emphasized that the molecular weight of the PNIPAm (21 kDa) used here is below the renal cutoff (~40 kDa) using the chain transfer agent (MAA) during the free radical polymerization step, which can allow for the potential clearance of this product from the body (Peroglio et al., 2012). This could be supported by a study reporting the fate of PNIPAm polymers in vivo after intravenous administration. It was found the elimination occurred mainly through urinary excretion, which was principally governed by molecular weight. Above a threshold of 32 kDa, the polymer chains avoided glomerular filtration and presented prolonged circulation times (Bertrand, Fleischer, Wasan, & Leroux, 2009).

Grafting with carbohydrate polymers have been shown to reduce the cytotoxicity of PNIPAm-based polymers due to increased hydrophilicity and charge density (Fang et al., 2008; Sofia, Premnath, & Merrill, 1998; Vihola et al., 2005). During the course of animal study, all animals remained healthy throughout the experimental period. There was also no evidence of organ damage and acute intoxication from histological (Fig. 6) and blood examinations (Table 2). Taken together, application of HA-CS-PNIPAm may be deemed relatively safe with controlled administration. However, long-term effects and metabolic profiles of HA-CS-PNIPAm in vivo require further investigations including monitor of metabolic pathways and metabolites.

Although anti-adhesion barriers have demonstrated their efficacy in clinical practice, there are still several concerns. A previous study showed that Seprafilm™ might increase the risk of anastomotic leakage (Fazio et al., 2006). The definite mechanism and solutions have yet been developed. In our study, the HA-CS-PNIPAm hydrogel has shown the great potency in averting postoperative adhesion. However, we could not validate the effect of postoperative leakage due to the design of the animal model. Previous studies demonstrated that PNIPAm-based material has a great potential for drug delivery, scaffolds for tissue engineering and wound healing (Chen & Cheng, 2006; Fang et al., 2008; Yang & Lin, 2004), but not for anti-adhesion application. This study demonstrates the applicabil-



ity of HA-CS-PNIPAm to prevent post-surgical peritoneal adhesion in vivo. It is conceivable HA-CS-PNIPAm could further combine with anti-inflammatory drugs to enhance the anti-adhesion efficacy. Further investigation is required to evaluate the adverse effects and future implications.

## 5. Conclusions

Anti-adhesion barriers have been widely accepted to eliminate postoperative adhesion and its sequel. However, suitable barriers are still limited to face the increasing trend of laparoscopic surgical approach. Injectable thermosensitive hydrogel that could be gelled in situ without the help from external factors is one of the promising barriers for such purposes. In this study, we successfully demonstrated the use of HA-CS-PNIPAm, which is synthesized by combining HA and chitosan with the sol-gel phase transition property of PNIPAm, to reduce postoperative peritoneal adhesion. The hydrogel showed the barrier effect that prevents migration of fibroblasts without significant cytotoxicity in vitro. With side-wall abrasion models in rats, HA-CS-PNIPAm hydrogel provided superior anti-adhesion effects compared with PNIPAm and untreated control. No disruption of reperitonealization was discovered via SEM observation two weeks post-treatment. Histological and blood examinations indicated no evidence of organ damage and acute toxicity. We conclude that HA-CS-PNIPAm hydrogel is an effective and safe anti-adhesion barrier for intra-abdominal application by injection. Along with its thermosensitive sol-gel phase transformation at the physiological temperature, it could be applied laparoscopically without additional manipulation. Versatility of this hydrogel would prompt more implications such as providing pharmacological supplements or prompting healing by acting as scaffolds for tissue regeneration.

## Acknowledgements

The financial assistance was provided by grants from the Ministry of Science and Technology (MOST103-2321-B-182-017), Chang Gung Memorial Hospital (BMRP249, CRPD2G0011) and the Ministry of Health and Welfare (MOHW105-TDU-PB-212-000009).

## References

- Ar'Rajab, A., Mileski, W., Sentementes, J. T., Sikes, P., Harris, R. B., & Dawidson, I. J. (1996). The role of neutrophils in peritoneal adhesion formation. *Journal of Surgical Research*, 61(1), 143–146.
- Aysan, E., Bektas, H., Ersoy, F., Sari, S., & Huq, G. (2010). Effects of contractubex on the prevention of postoperative peritoneal adhesion. *Journal of Surgical Research*, 164(2), 193–197.
- Bertrand, N., Fleischer, J. G., Wasan, K. M., & Leroux, J. C. (2009). Pharmacokinetics and biodistribution of N-isopropylacrylamide copolymers for the design of pH-sensitive liposomes. *Biomaterials*, 30(13), 2598–2605.
- Boland, G. M., & Weigel, R. J. (2006). Formation and prevention of postoperative abdominal adhesions. *Journal of Surgical Research*, 132(1), 3–12.
- Campbell, S. B., Patenaude, M., & Hoare, T. (2013). Injectable superparamagnets: Highly elastic and degradable poly(N-isopropylacrylamide)-superparamagnetic iron oxide nanoparticle (SPION) composite hydrogels. *Biomacromolecules*, 14(3), 644–653.
- Chang, J. J., Lee, Y. H., Wu, M. H., Yang, M. C., & Chien, C. T. (2012). Electrospun anti-adhesion barrier made of chitosan alginate for reducing peritoneal adhesions. *Carbohydrate Polymers*, 88(4), 1304–1312.
- Chen, J. P., & Cheng, T. H. (2006). Thermo-responsive chitosan-graft-poly(N-isopropylacrylamide) injectable hydrogel for cultivation of chondrocytes and meniscus cells. *Macromolecular Bioscience*, 6(12), 1026–1039.
- Chen, J. P., & Cheng, T. H. (2009). Preparation and evaluation of thermo-reversible copolymer hydrogels containing chitosan and hyaluronic acid as injectable cell carriers. *Polymer*, 50(1), 107–116.
- Chen, S. H., Chen, C. H., Shalumon, K., & Chen, J. P. (2014). Preparation and characterization of antiadhesion barrier film from hyaluronic acid-grafted electrospun poly (caprolactone) nanofibrous membranes for prevention of flexor tendon postoperative peritendinous adhesion. *International Journal of Nanomedicine*, 9, 4079.
- Chen, S. H., Chen, C. H., Fong, Y. T., & Chen, J. P. (2014). Prevention of peritendinous adhesions with electrospun chitosan-grafted polycaprolactone nanofibrous membranes. *Acta Biomaterialia*, 10(12), 4971–4982.
- Chen, C. H., Chen, S. H., Shalumon, K., & Chen, J. P. (2015). Dual functional core-sheath electrospun hyaluronic acid/polycaprolactone nanofibrous membranes embedded with silver nanoparticles for prevention of peritendinous adhesion. *Acta Biomaterialia*, 26, 225–235.
- Coleman, M. G., McLain, A. D., & Moran, B. J. (2000). Impact of previous surgery on time taken for incision and division of adhesions during laparotomy. *Diseases of the Colon & Rectum*, 43(9), 1297–1299.
- Cui, Z., Lee, B. H., Pauken, C., & Vernon, B. L. (2011). Degradation, cytotoxicity, and biocompatibility of NIPAAm-based thermosensitive, injectable, and bioresorbable polymer hydrogels. *Journal of Biomedical Materials Research A*, 98(2), 159–166.
- Dash, M., Chiellini, F., Ottenbrite, R. M., & Chiellini, E. (2011). Chitosan—A versatile semi-synthetic polymer in biomedical applications. *Progress in Polymer Science*, 36(8), 981–1014.
- Diamond, M. P., Luciano, A., Johns, D. A., Dunn, R., Young, P., & Bieber, E. (2003). Reduction of postoperative adhesions by N,O-carboxymethylchitosan: A pilot study. *Fertility and Sterility*, 80(3), 631–636.
- diZerega, G. S., & Campeau, J. D. (2001). Peritoneal repair and post-surgical adhesion formation. *Human Reproduction Update*, 7(6), 547–555.
- Ersoy, E., Ozturk, V., Yazgan, A., Ozdogan, M., & Gundogdu, H. (2008). Effect of polylactic acid film barrier on intra-abdominal adhesion formation. *Journal of Surgical Research*, 147(1), 148–152.
- Fakhari, A., & Berkland, C. (2013). Applications and emerging trends of hyaluronic acid in tissue engineering, as a dermal filler and in osteoarthritis treatment. *Acta Biomaterialia*, 9(7), 7081–7092.
- Fang, J. Y., Chen, J. P., Leu, Y. L., & Hu, J. W. (2008). Temperature-sensitive hydrogels composed of chitosan and hyaluronic acid as injectable carriers for drug delivery. *European Journal of Pharmaceutics and Biopharmaceutics*, 68(3), 626–636.
- Fazio, V. W., Cohen, Z., Fleschman, J. W., van Goor, H., Bauer, J. J., Wolff, B. G., et al. (2006). Reduction in adhesive small-bowel obstruction by Seprafilm® adhesion barrier after intestinal resection. *Diseases of the Colon & Rectum*, 49(1), 1–11.
- Feil, H., Bae, Y. H., Feijen, J., & Kim, S. W. (1993). Effect of comonomer hydrophilicity and ionization on the lower critical solution temperature of N-isopropylacrylamide copolymers. *Macromolecules*, 26(10), 2496–2500.
- Foley-Comer, A. J., Herrick, S. E., Al-Mishlab, T., Prele, C. M., Laurent, G. J., & Mutsaers, S. E. (2002). Evidence for incorporation of free-floating mesothelial cells as a mechanism of serosal healing. *Journal of Cell Science*, 115(Pt. 7), 1383–1389.
- Hooker, G. D., Taylor, B. M., & Driman, D. K. (1999). Prevention of adhesion formation with use of sodium hyaluronate-based bioresorbable membrane in a rat model of ventral hernia repair with polypropylene mesh—A randomized, controlled study. *Surgery*, 125(2), 211–216.
- Ibusuki, S., Iwamoto, Y., & Matsuda, T. (2003). System-engineered cartilage using poly(N-isopropylacrylamide)-grafted gelatin as in situ-formable scaffold: In vivo performance. *Tissue Engineering*, 9(6), 1133–1142.
- Kean, T., & Thanou, M. (2010). Biodegradation, biodistribution and toxicity of chitosan. *Advanced Drug Delivery Review*, 62(1), 3–11.
- Kiefer, D. G., Muscat, J. C., Santorelli, J., Chavez, M. R., Ananth, C. V., Smulian, J. C., et al. (2016). Effectiveness and short-term safety of modified sodium hyaluronic acid-carboxymethylcellulose at cesarean delivery: A randomized trial. *American Journal of Obstetrics and Gynecology*, 214(3), 373.e371–373.e312.
- Kim, J. H., Lee, S. B., Kim, S. J., & Lee, Y. M. (2002). Rapid temperature/pH response of porous alginate-g-poly(N-isopropylacrylamide) hydrogels. *Polymer*, 43(26), 7549–7558.
- Kohori, F., Sakai, K., Aoyagi, T., Yokoyama, M., Sakurai, Y., & Okano, T. (1998). Preparation and characterization of thermally responsive block copolymer micelles comprising poly(N-isopropylacrylamide-b-dl-lactide). *Journal of Controlled Release*, 55(1), 87–98.
- Kumar, S., Wong, P. F., & Leaper, D. J. (2009). Intra-peritoneal prophylactic agents for preventing adhesions and adhesive intestinal obstruction after non-gynaecological abdominal surgery. *Cochrane Database of Systematic Reviews*, (1). Cd005080.
- Kuo, S. M., Chang, S. J., Wang, H. Y., Tang, S. C., & Yang, S. W. (2014). Evaluation of the ability of xanthan gum/gellan gum/hyaluronan hydrogel membranes to prevent the adhesion of postrepaired tendons. *Carbohydrate Polymers*, 114, 230–237.
- Lauder, C. I. W., Garcea, G., Strickland, A., & Maddern, G. J. (2011). Use of a modified chitosan-dextran gel to prevent peritoneal adhesions in a rat model. *Journal of Surgical Research*, 171(2), 877–882.
- Lee, M. W., Tsai, H. F., Wen, S. M., & Huang, C. H. (2012). Photocrosslinkable gellan gum film as an anti-adhesion barrier. *Carbohydrate Polymers*, 90(2), 1132–1138.
- Li, L., Wang, N., Jin, X., Deng, R., Nie, S., Sun, L., et al. (2014). Biodegradable and injectable in situ cross-linking chitosan-hyaluronic acid based hydrogels for postoperative adhesion prevention. *Biomaterials*, 35(12), 3903–3917.
- Liakakos, T., Thomakos, N., Fine, P. M., Dervenis, C., & Young, R. L. (2001). Peritoneal adhesions: Etiology, pathophysiology, and clinical significance. Recent advances in prevention and management. *Digestive Surgery*, 18(4), 260–273.
- Liao, H. T., Chen, C. T., & Chen, J. P. (2011). Osteogenic differentiation and ectopic bone formation of canine bone marrow-derived mesenchymal stem cells in injectable thermo-responsive polymer hydrogel. *Tissue Engineering Part C Methods*, 17(11), 1139–1149.

- Lou, W., Zhang, H., Ma, J., Zhang, D., Liu, C., Wang, S., et al. (2012). *In vivo* evaluation of in situ polysaccharide based hydrogel for prevention of postoperative adhesion. *Carbohydrate Polymers*, 90(2), 1024–1031.
- Menzies, D., Pascual, M. H., Walz, M. K., Duron, J. J., Tonelli, F., Crowe, A., et al. (2006). Use of icodextrin 4% solution in the prevention of adhesion formation following general surgery: From the multicentre ARIEL Registry. *Annals of the Royal College of Surgeons of England*, 88(4), 375–382.
- Mortisen, D., Peroglio, M., Alini, M., & Eglin, D. (2010). Tailoring thermoreversible hyaluronan hydrogels by click chemistry and RAFT polymerization for cell and drug therapy. *Biomacromolecules*, 11(5), 1261–1272.
- Mueller, M. D., Tschudi, J., Herrmann, U., & Klaiber, C. H. (1995). An evaluation of laparoscopic adhesiolysis in patients with chronic abdominal pain. *Surgical Endoscopy*, 9(7), 802–804.
- Naha, P. C., Bhattacharya, K., Tenuta, T., Dawson, K. A., Lynch, I., Gracia, A., et al. (2010). Intracellular localisation, geno- and cytotoxic response of poly(*N*-isopropylacrylamide) (PNIPAM) nanoparticles to human keratinocyte (HaCaT) and colon cells (SW 480). *Toxicology Letters*, 198(2), 134–143.
- Ohya, S., Sonoda, H., Nakayama, Y., & Matsuda, T. (2005). The potential of poly(*N*-isopropylacrylamide)-grafted hyaluronan and PNIPAM-grafted gelatin in the control of post-surgical tissue adhesions. *Biomaterials*, 26(6), 655–659.
- Okano, T., Yamada, N., Sakai, H., & Sakurai, Y. (1993). A novel recovery system for cultured cells using plasma-treated polystyrene dishes grafted with poly(*N*-isopropylacrylamide). *Journal of Biomedical Materials Research*, 27(10), 1243–1251.
- Ong, S. Y., Wu, J., Mochhala, S. M., Tan, M. H., & Lu, J. (2008). Development of a chitosan-based wound dressing with improved hemostatic and antimicrobial properties. *Biomaterials*, 29(32), 4323–4332.
- Patenaude, M., & Hoare, T. (2012). Injectable, degradable thermoresponsive poly(*N*-isopropylacrylamide) hydrogels. *ACS Macro Letters*, 1(3), 409–413.
- Peroglio, M., Grad, S., Mortisen, D., Sprecher, C. M., Illien-Junger, S., Alini, M., et al. (2012). Injectable thermoreversible hyaluronan-based hydrogels for nucleus pulposus cell encapsulation. *European Spine Journal*, 21(Suppl. 6), S839–849.
- Reijnen, M., Bleichrodt, R. P., & Van Goor, H. (2003). Pathophysiology of intra-abdominal adhesion and abscess formation, and the effect of hyaluronan. *British Journal of Surgery*, 90(5), 533–541.
- Schnüriger, B., Barmparas, G., Branco, B. C., Lustenberger, T., Inaba, K., & Demetriades, D. (2011). Prevention of postoperative peritoneal adhesions: A review of the literature. *The American Journal of Surgery*, 201(1), 111–121.
- Segura, T., Schmokel, H., & Hubbell, J. A. (2007). RNA interference targeting hypoxia inducible factor 1 $\alpha$  reduces post-operative adhesions in rats. *Journal of Surgical Research*, 141(2), 162–170.
- Sofia, S. J., Premnath, V., & Merrill, E. W. (1998). Poly (ethylene oxide) grafted to silicon surfaces: Grafting density and protein adsorption. *Macromolecules*, 31(15), 5059–5070.
- Van Der Krabben, A. A., Dijkstra, F. R., Nieuwenhuijzen, M., Reijnen, M. M., Schaapveld, M., & Van Goor, H. (2000). Morbidity and mortality of inadvertent enterotomy during adhesiotomy. *British Journal of Surgery*, 87(4), 467–471.
- Vihola, H., Laukkanen, A., Valtola, L., Tenhu, H., & Hirvonen, J. (2005). Cytotoxicity of thermosensitive polymers poly(*N*-isopropylacrylamide), poly(*N*-vinylcaprolactam) and amphiphilically modified poly(*N*-vinylcaprolactam). *Biomaterials*, 26(16), 3055–3064.
- Wadajkar, A. S., Koppolu, B., Rahimi, M., & Nguyen, K. T. (2009). Cytotoxic evaluation of *N*-isopropylacrylamide monomers and temperature-sensitive poly(*N*-isopropylacrylamide) nanoparticles. *Journal of Nanoparticle Research*, 11(6), 1375–1382.
- Wallwiener, M., Brucker, S., Hierlemann, H., Brochhausen, C., Solomayer, E., & Wallwiener, C. (2006). Innovative barriers for peritoneal adhesion prevention: Liquid or solid? A rat uterine horn model. *Fertility and Sterility*, 86(Suppl. 4), 1266–1276.
- Xie, W., Xu, P., & Liu, Q. (2001). Antioxidant activity of water-soluble chitosan derivatives. *Inorganic & Medicinal Chemistry Letters*, 11(13), 1699–1701.
- Xu, F. J., Zhu, Y., Liu, F. S., Nie, J., Ma, J., & Yang, W. T. (2010). Comb-shaped conjugates comprising hydroxypropyl cellulose backbones and low-molecular-weight poly(*N*-isopropylacrylamide) side chains for smart hydrogels: Synthesis, characterization, and biomedical applications. *Bioconjugate Chemistry*, 21(3), 456–464.
- Yang, J. M., & Lin, H. T. (2004). Properties of chitosan containing PP-g-AA-g-NIPAAm bigraft nonwoven fabric for wound dressing. *Journal of Membrane Science*, 243(1), 1–7.
- Yeo, Y., & Kohane, D. S. (2008). Polymers in the prevention of peritoneal adhesions. *European Journal of Pharmaceutics and Biopharmaceutics*, 68(1), 57–66.
- Yeo, Y., Burdick, J. A., Highley, C. B., Marini, R., Langer, R., & Kohane, D. S. (2006). Peritoneal application of chitosan and UV-cross-linkable chitosan. *Journal of Biomedical Materials Research Part A*, 78A(4), 668–675.
- Yeo, Y., Highley, C. B., Bellas, E., Ito, T., Marini, R., Langer, R., et al. (2006). In situ cross-linkable hyaluronic acid hydrogels prevent post-operative abdominal adhesions in a rabbit model. *Biomaterials*, 27(27), 4698–4705.
- Yeo, Y., Ito, T., Bellas, E., Highley, C. B., Marini, R., & Kohane, D. S. (2007). In situ cross-linkable hyaluronan hydrogels containing polymeric nanoparticles for preventing postsurgical adhesions. *Annals of Surgery*, 245(5), 819–824.
- Zhang, Y., Gao, C., Li, X., Xu, C., Zhang, Y., Sun, Z., et al. (2014). Thermosensitive methyl cellulose-based injectable hydrogels for post-operation anti-adhesion. *Carbohydrate Polymers*, 101, 171–178.
- Zhao, C., Sun, Y. L., Kirk, R. L., Thoreson, A. R., Jay, G. D., Moran, S. L., et al. (2010). Effects of a lubricin-containing compound on the results of flexor tendon repair in a canine model in vivo. *The Journal of Bone and Joint Surgery*, 92(6), 1453–1461.



# Structural characterization of an immunostimulating polysaccharide from the stems of a new medicinal *Dendrobium* species: *Dendrobium Taiseed Tosnobile*

Li-Chan Yang<sup>a</sup>, Chang-Chi Hsieh<sup>b</sup>, Chi-Luan Wen<sup>c</sup>, Chun-Hui Chiu<sup>d</sup>, Wen-Chuan Lin<sup>a,\*</sup>

<sup>a</sup> Department of Pharmacy, China Medical University, Taichung, Taiwan

<sup>b</sup> Department of Animal Science and Biotechnology, Tunghai University, Taichung, Taiwan

<sup>c</sup> Taiwan Seed Improvement and Propagation Station, Council of Agriculture, Taichung, Taiwan

<sup>d</sup> Graduate Institute of Health-Industry Technology, Research Center for Food and Cosmetic Safety, and Research Center for Chinese Herbal Medicine, College of Human Ecology, Chang Gung University of Science and Technology, Taiwan

## ARTICLE INFO

### Article history:

Received 14 March 2017

Received in revised form 1 May 2017

Accepted 30 May 2017

Available online 2 June 2017

### Keywords:

Polysaccharide

Heteromannan

Immunostimulating

*Dendrobium Taiseed Tosnobile*

Cytotoxicity

Phagocytosis

## ABSTRACT

*Dendrobium Taiseed Tosnobile*, a new *Dendrobium* species developed by crossbreeding *Dendrobium tosaense* and *Dendrobium nobile*, exhibits the characteristics of high mass production and high polysaccharide content. This study investigated the structural characterization and immunostimulating effects of a polysaccharide isolated from *D. Taiseed Tosnobile* (DTTPS). DTTPS was fractionated using a DEAE-650 M column to obtain the major neutral polysaccharide (DTTPS-N). The structural characteristics of DTTPS-N were investigated through high-performance anion exchange chromatography, high-performance size exclusion chromatography, gas chromatography-mass spectrometry, and nuclear magnetic resonance spectroscopy. In the immunostimulating experiment, BALB/c mice were administered DTTPS (100 and 300 mg/kg) daily for 3 weeks. The results revealed that DTTPS-N comprised arabinose, galactose, glucose, mannose, and xylose at a ratio of 1:1.5:3.0:29.9:1.3. DTTPS-N comprised (1 → 3; 1 → 4)-Man as the backbone, and its average molecular weight was 281 kDa. Pharmacological experiments demonstrated that DTTPS substantially increased the population of splenic natural killer (NK) cells, NK cytotoxicity, macrophage phagocytosis, and cytokine induction. This is the first study to demonstrate the structural characteristics and immunopharmacological effects of an active polysaccharide derived from *D. Taiseed Tosnobile*.

© 2017 Elsevier B.V. All rights reserved.

## 1. Introduction

Herba *Dendrobii* is a high-grade Chinese medicine popularly used for antipyretic, ophthalmic, and tonic purposes [1]. Herba *Dendrobii* is highly valued in Asian countries and is prepared from several *Dendrobium* species such as *Dendrobium huoshanense*, *Dendrobium nobile*, and *Dendrobium tosaense*. Because Herba *Dendrobii* is highly valuable in the commercial market and its growth rate is slow, wild medicinal *Dendrobium* is rare and is protected. Recently, researchers have attempted to improve the large-scale cultivation of Herba *Dendrobii*. A solution is to develop a new giant-type species of Herba *Dendrobii* with a higher growth rate. The Taiwan Seed Improvement and Propagation Station developed *Dendrobium*

*Taiseed Tosnobile*, a new *Dendrobium* species, by crossbreeding *D. tosaense* and *D. nobile* as the seed parent and pollen parent, respectively. *D. Taiseed Tosnobile* exhibits the characteristics of high yield, easy cultivation, and no special pest control requirements.

Several studies on Herba *Dendrobii* have indicated that its polysaccharides are critical compounds that exhibit pharmacological activities [2]. Similarly, numerous studies have reported the structural characteristics of the polysaccharides of other *Dendrobium* species, and some of their pharmacological properties, including antitumor, antihyperglycemic, antioxidant, and immunomodulatory activities [3–5].

Although *D. Taiseed Tosnobile* was developed by crossbreeding two medicinal *Dendrobium* species, its pharmacological properties have not yet been confirmed. This paper reports several structural characteristics of aqueous extracts and purified polysaccharides isolated from the stem of *D. Taiseed Tosnobile*, and the immunomodulatory effects of *in vivo* oral administration of the *D. Taiseed Tosnobile* polysaccharide.

\* Corresponding author at: Department of Pharmacology, China Medical University, No. 91 Hsueh Shih Road, Taichung, Taiwan.

E-mail address: [wclin@mail.cmu.edu.tw](mailto:wclin@mail.cmu.edu.tw) (W.-C. Lin).



**Table 1**  
Primers used for ITS region amplification and sequencing.

Property	Primer	Primer sequence
Primer for ITS1-5.8S-ITS	5'-18S 3'-28S	5'-GAGGAATTCCTAGTAAGCGCGAGTC-3' 5'-CCCTTCATCTTCCCTCGCGGT-3'
Primer for DNA sequencing		5'-GAGGAATTCCTAGTAAGCGCGAGTC-3' 5'-CGACTCGCCGACAGCGCTCGTGGT-3'

The ITS region of the nuclear ribosomal DNA was amplified through PCR by using the primers of 5'-18S and 3'-28S, which were modified by Lin et al. [29] and Wu et al. [30]. This resulted in an approximately 1100-bp amplified fragment after electrophoresis in 1% agarose gel. The sequencing primers of the ITS amplification region were modified by Wu et al. [1]. The DNA sequencing data were verified through a comparison with the sequences of other species by using the BLAST of the NCBI nucleotide databank.

## 2. Materials and methods

### 2.1. DNA sequencing and sequence alignment

*D. Taiseed Tosnobile*, *D. tosaense*, and *D. nobile* plants were provided by the Taiwan Seed Improvement and Propagation Station (Taichung, Taiwan). DNA sequencing and sequence alignment of these *Dendrobium* species were performed according to a previously described method (Chiang et al., 2012). In brief, genomic DNA (gDNA) was extracted from fresh stems by using a commercial gDNA purification kit (Genemark, Taipei, Taiwan) and stored at  $-20^{\circ}\text{C}$  until use. Table 1 lists the universal primers used for the polymerase chain reaction (PCR) amplification and sequencing of the internal transcribed spacer (ITS) region. PCR was performed using 50 ng of the respective gDNA and a commercial PCR kit (MasterMix, Thermal, USA) on a thermal cycler (ABI, USA). PCR comprised an initial denaturation step at  $94^{\circ}\text{C}$  for 5 min, followed by 25 cycles at  $94^{\circ}\text{C}$  for 20 s,  $54.5^{\circ}\text{C}$  for 20 s, and  $68^{\circ}\text{C}$  for 20 s, and a final extension step at  $68^{\circ}\text{C}$  for 5 min. Approximately 10  $\mu\text{L}$  of the PCR products was electrophoresed on 1% agarose gel, stained with ethidium bromide, and visualized under UV light. The remaining PCR products were stored at  $4^{\circ}\text{C}$  until use. The ITS DNA sequencing of *D. Taiseed Tosnobile*, *D. nobile*, and *D. tosaense* was performed by Mission Biotech (Taipei, Taiwan), using their standard procedures. The ITS region of each individual PCR product was sequenced in both the 5' and 3' directions at least three times to define the ITS sequences. The DNA sequencing data were verified through a comparison with the sequences of other species by using the basic local alignment search tool (BLAST) at the website of the National Center for Biotechnology Information (NCBI; <http://www.ncbi.nlm.nih.gov/blast/blast.cgi>).

### 2.2. Polysaccharide preparation

#### 2.2.1. Polysaccharide isolation

The dry stem of *D. Taiseed Tosnobile* was provided by the Taiwan Seed Improvement and Propagation Station (Taichung, Taiwan). The plant materials were crushed and extracted in distilled water at  $95^{\circ}\text{C}$ . The aqueous extracts were then evaporated under reduced pressure to reduce the volume. The aqueous extracts of *D. Taiseed Tosnobile* (at a concentration of 100 mg/mL) were added to a 4-fold volume of 95% ethanol to precipitate the crude polysaccharides. The crude polysaccharides were then treated using a commercial total dietary fiber assay kit (K-TDFR, Megazyme, Ireland) to eliminate the protein and starch contents. After enzymatic treatment, a 4-fold volume of 95% ethanol was added to precipitate the polysaccharides (DTTPS).

#### 2.2.2. Purification and fractionation of polysaccharides

DTTPS was fractionated using anion-exchange chromatography on a diethylaminoethyl (DEAE) 650 M column (Toyoparl, Tokyo,

Japan). The DEAE column was eluted with 20 mM Tris-HCl (pH 7.8), followed by a sodium chloride gradient (0–0.2 M), to obtain the neutral polysaccharide fraction (DTTPS-N) and acidic polysaccharide fraction (DTTPS-A). The carbohydrate elution profile of the DTTPS was analyzed according to the phenol-sulfuric acid method, with glucose as the standard, and measured at 490 nm using a TRAID LT ELISA reader [6]. The relevant fractions were collected, concentrated, and precipitated by adding ethanol. For chemical analysis, the protein content of the pooled polysaccharide fractions was measured using a modified Bradford method assay, with bovine serum albumin as the standard [7]. In addition, the carbohydrate content of the polysaccharides was measured using the phenol-sulfuric acid method, as previously described. The contents of uronic acid were determined using the m-hydroxydiphenyl method, with galacturonic acid as the standard [8].

#### 2.2.3. Characterization of indigestible polysaccharides and the neutral polysaccharide fraction

For nuclear magnetic resonance (NMR) analysis, DTTPS-N (5 mg) was dissolved in deuterium oxide (0.5 mL), and the  $^1\text{H}$  NMR and  $^{13}\text{C}$  NMR spectra were recorded on a Varian VNMR-700 NMR spectrometer at 303 K, using 3-(trimethylsilyl)-propionic 2,2,3,3-d<sub>4</sub> acid sodium salt as an internal reference ( $\delta$  0.00 ppm). The relative molecular mass (Mr) was determined through high-performance size exclusion chromatography (HP-SEC), using a TSKgel guard column (75  $\times$  7.5 mm i.d.; TOSOH, Tokyo, Japan), TSKgel G4000PWXL, and G2500PWXL (300  $\times$  7.8 mm i.d., TOSOH) connected in series. The column was eluted with a 0.3 M sodium nitrate solution containing 0.02% sodium azide, with a flow rate of 0.8 mL/min at  $65^{\circ}\text{C}$ . The peaks were detected using an interferometric refractometer (Wyatt, CA, USA). The average Mr was estimated through a comparison with the retention time of a pullulan standard P-82 kit (molecular weights of standards: P-800, 708 kDa; P-400, 375 kDa; P-200, 200 kDa; P-100, 107 kDa; P-50, 47.1 kDa; P-20, 21.1 kDa; P-10, 9.6 kDa; and P-5, 5.9 kDa; Shodex, Kanagawa, Japan). For monosaccharide composition analysis, the samples were hydrolyzed at  $100^{\circ}\text{C}$  for 4 h with 2 M trifluoroacetic acid (Sigma-Aldrich, St. Louis, MO, USA), and the resulting samples were assessed using high-performance anion exchange chromatography with pulsed amperometric detection (HPAEC-PAD). The peaks were detected using an 817 Bioscan PAD detector (Metrohm, Zofingen, Switzerland) with a CarboPac PA1 column (Dionex, Sunnyvale, CA, USA). The eluent comprised 10 mM sodium hydroxide and 1 mM barium acetate (Sigma-Aldrich) at a flow rate of 1.0 mL/min. Linkage analysis was performed through methylation, as described by Liane et al. [9]. Methylation was performed with methyl iodide (Sigma-Aldrich) in dimethyl sulfoxide (Sigma-Aldrich) and sodium hydroxide (Wako, Osaka, Japan). Following methylation, DTTPS and DTTPS-N were hydrolyzed with 2 M trifluoroacetate and then reduced and acetylated using the alditol acetate method. Inositol was used as an internal control. Gas chromatography-mass spectrometry (GC-MS) of the partially methylated alditol acetates was performed on a DB-5 column (0.2  $\mu\text{m}$  i.d. 30 m, OV-1701, Agilent) using the following temperature program:  $100^{\circ}\text{C}$  for 2 min; the gradient was warmed to  $180^{\circ}\text{C}$  at  $8^{\circ}\text{C}/\text{min}$  (for 2 min); when  $180^{\circ}\text{C}$  was reached, the temperature was increased to  $240^{\circ}\text{C}$  at a rate of  $2^{\circ}\text{C}/\text{min}$  (for 5 min). Helium was used as the carrier gas (1.0 mL/min, constant flow). The mass spectrometry conditions were as follows: ionization potential, 70 eV; source temperature,  $300^{\circ}\text{C}$ .

### 2.3. Innate immunomodulation of DTTPS in BALB/c mice

#### 2.3.1. Animals

Eight-week-old male BALB/c mice were provided by the National Laboratory Animal Center (Taipei, Taiwan). The animal

experimental protocols complied with the institutional guidelines of China Medical University for the use of laboratory animals. The guidelines are corresponded to the National Institutes of Health guide for the care and use of Laboratory animals (NIH Publications No. 8023, revised 1978). The animals were housed in an air-conditioned room (21 °C–24 °C) with humane care and 12 h of light daily (8:00 a.m. to 8:00 p.m.) and were allowed free access to food pellets and water throughout the study period. The experiment was performed on 36 BALB/c mice with body weights ranging from 24 to 26 g. The mice were randomly divided into three groups, receiving oral administration of distilled water (control group) or DTTPS (100 or 300 mg/kg body weight) daily for 3 weeks. The body weights of the mice were measured once per week until the end of the experiment. At the end of the experiment, the animals were sacrificed using CO<sub>2</sub>. Their spleens were removed, weighed under sterile conditions, and then subjected to splenocyte preparation. Peritoneal cells were prepared according to the methods described by Zhang et al. [10] and used for additional phagocytosis assays.

### 2.3.2. Flow cytometry analyses

The splenocytes were isolated from the control and the DTTPS mice. In brief, the spleen was aseptically extracted and placed in cold Roswell Park Memorial Institute (RPMI) 1640 medium (Gibco, NY, USA). The spleen was teased apart and passed through a nylon mesh (BD Falcon, CA, USA). The spleen cell suspensions were hemolyzed with 0.1 and 2 M Hanks' balanced salt solution to lyse the red blood cells and then added to 5 mL of RPMI 1640 medium containing 10% fetal bovine serum (FBS), 2 mM L-glutamine (Gibco), 100 μM 2-mercaptoethanol (Gibco), 1.0 mM sodium pyruvate (Gibco), and 100 U/mL of penicillin (Gibco). Single spleen cell suspensions were centrifuged at 4 °C and 300 × g for 10 min. The cell viability of the splenocytes was determined using a FACSCalibur™ flow cytometer (Becton-Dickinson, CA, USA) with a propidium iodide/RNAase (Invitrogen) stain. All the antibodies used for flow cytometry were purchased from eBioscience (CA, USA). The splenocyte cells (5 × 10<sup>5</sup> cells/25 μL) were stained with 10 μL of fluorescein isothiocyanate (FITC)-labeled antimouse CD4, phycoerythrin (PE)-labeled CD8, PE-Cy5-labeled antimouse CD3, FITC-labeled antimouse CD19, PE-labeled CD3, PE-Cy5-labeled CD45, PE-labeled Tim3, PE-Cy5-labeled CD278, FITC-labeled antimouse Pan NK (CD49b), and PE-labeled NK-T (CD160) at 4 °C for 30 min in the dark. After incubation, the unlabeled antibodies were washed with 3 mL of phosphate-buffered saline (PBS) containing 0.05% sodium azide and then resuspended in 200 μL of a fluorescence-activated cell sorting buffer containing 2.0% FBS and 0.05% sodium azide (Sigma-Aldrich). Subsequently, the cells were analyzed using a flow cytometer, and the data were analyzed using CellQuest software (Becton-Dickinson). The flow cytometry results were obtained as percentages of positive fluorescent cells.

### 2.3.3. Splenocyte proliferation assays

The splenocytes were isolated from the control and DTTPS mice (100 and 300 mg/kg), then seeded into a 96-well plate at 5 × 10<sup>6</sup> cell/mL in 100 μL of RPMI 1640 medium (Gibco) and stimulated with Con A (5 μg/mL), lipopolysaccharide (LPS) (10 μg/mL), or RPMI 1640 medium to achieve a final volume of 200 μL. After 48 h of incubation, the splenocyte proliferation was measured using an MTS assay [11], and the plate was measured at 492 nm by using the TRAIID LT ELISA reader. The stimulation index was calculated as the absorbance value for stimulated cultures divided by the absorbance value for non-stimulated cultures.

### 2.3.4. Evaluation of cytotoxicity assays

YAC-1 lymphoma cells were obtained from the Food Industry Research and Development Institute (Hsinchu, Taiwan) and cultured in RPMI-1640 medium (Gibco) supplemented with 10% (v/v)

FBS (Gibco), 100 μg/mL of streptomycin, and 100 U/mL of penicillin (Gibco) at 37 °C in a humidified atmosphere containing 5% CO<sub>2</sub>. For the cytotoxicity assay, the YAC-1 cell line (as target (T) cells) was incubated with BCECF-AM (molecular probe) at 37 °C for 30 min with gentle agitation. The BCECF-AM-labeled YAC-1 cells were washed twice with the RPMI-1640 medium. The splenocytes (as effector (E) cells) were harvested from the mice in an innate immune experiment and an antitumor experiment. The cytotoxicity assays of splenocytes were performed using a modified method described previously [12]. The splenocytes and BCECF-AM-labeled YAC-1 cells were placed in V-bottom 96-well plates, and the E/T ratios were 5, 10, and 25, over a 4-h incubation period; subsequently, these cell mixtures were centrifuged at 410 × g for 10 min. The total fluorescence intensity of the BCECF-labeled YAC-1 cells (T) was determined after lysis with 1.0% Triton X-100. The fluorescence intensity of the supernatants was measured using the TRAIID LT ELISA reader at 485-nm excitation and 535-nm emission. The cytotoxicity activity of the splenocytes was determined as follows: percent specific cytotoxicity = (fluorescence intensity of target cells treated with splenocytes isolated from the experimental group - fluorescence intensity of spontaneously released target cells) / (total fluorescence intensity of target - fluorescence intensity of spontaneously released target cells) × 100.

### 2.3.5. Phagocytosis

The peritoneal cells of the mice from each treated group were isolated. The macrophage and neutrophil counts were determined through flow cytometry with the size (FCS-H) and granularity (SSC-H) coordinates. The isolated peritoneal cells (1 × 10<sup>5</sup> cells/well) and the commercial FITC-labeled *Escherichia coli* cells (BioParticles, OR, USA) were cocultured in round-bottom 96-well plates. The phagocytosis assays were performed at 37 °C and 150 rpm for 2 h, with a multiplicity of infection (MOI) of 1:1, 1:5, or 1:25. Following incubation, the peritoneal cells and bacteria were washed three times with PBS. The extracellular fluorescence was quenched with trypan blue (Gibco). The quenching prevented the interference of uningested bacteria in the fluorescence, which was determined using the TRAIID LT ELISA reader at 485-nm excitation and 535-nm emission.

### 2.3.6. Cytokine production analysis

The separated splenocytes were isolated from the BALB/c mice of both the control and DTTPS (100 and 300 mg/kg) groups. The splenocytes were seeded into 24-well plates at a density of 2 × 10<sup>6</sup>/mL; stimulated with Con A (5 μg/mL), LPS (10 μg/mL), or RPMI 1640 medium; and incubated for 24 and 48 h. After incubation, the supernatants were harvested and used for the cytokine assays (interleukin (IL)-2, IL-4, IL-6, and interferon (IFN)-γ), by using commercial ELISA kits (eBioscience, CA, USA).

### 2.3.7. Statistical analysis

The results are expressed as mean ± SD. All the experimental data were analyzed using one-way analysis of variance with the Dunnett test. All *P* values < 0.05 were considered statistically significant.

## 3. Results

### 3.1. DNA sequence analysis

The ITS sequences (ITS1, 5.8S, and ITS2) of *D. Taiseed Tosnobile*, *D. tosaense*, and *D. nobile* were 639, 661, and 663 bp, respectively. The lengths of 18S, ITS1, 5.8S, ITS2, and 28S of *D. Taiseed Tosnobile* were 217, 234, 162, 243, and 243 bp, respectively. The nucleotide identities of the ITS regions of *D. Taiseed Tosnobile* and *D. tosaense* exhibited a 99% similarity with variations in five nucleotides. By



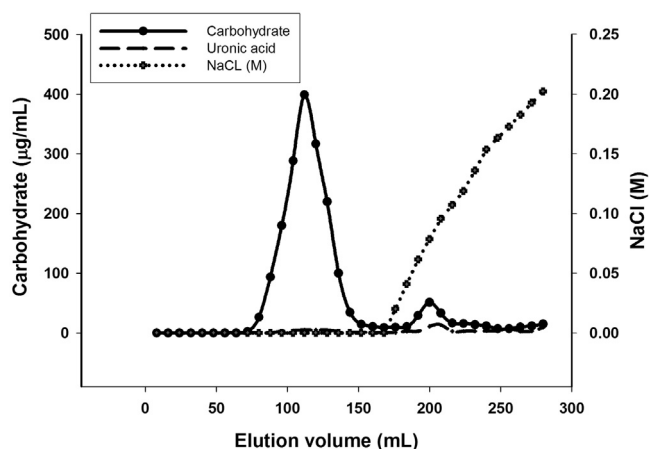


**Fig. 1.** Chromatographic fractionation of polysaccharides isolated from *Dendrobium Taiseed Tosnobile* (DTTPS). DTTPS were separated on DEAE-650 M and eluted with 20 mM tris buffer (pH 7.8), followed by a sodium chloride gradient (0–0.2 M); the carbohydrate and uronic acid contents were determined through a phenol–sulfuric acid method and m-hydroxydiphenyl method, respectively.

contrast, a 94% similarity was observed in the ITS regions between *D. Taiseed Tosnobile* and *D. nobile*, with variations in 37 nucleotides.

### 3.2. Preparation and characterization of *D. Taiseed Tosnobile* polysaccharides

The yield of aqueous extracts from the dry *D. Taiseed Tosnobile* stem was 20.3%. The yields of crude polysaccharides and DTTPS were 8.3% and 5.8%, respectively, for dry stems. The DTTPS comprised 98% carbohydrates and <1% protein. The uronic acid content in DTTPS was 2.9% on a carbohydrate basis. Protein and uronic acid were both undetectable in the neutral polysaccharide fraction (DTTPS-N). DTTPS was fractionated using the DEAE-650 M column to obtain one major (neutral polysaccharide, 95%) and one minor (acid polysaccharide) fraction, which were collected based on the total carbohydrate elution profile (Fig. 1). The uronic acid content was determined from the elution and was distributed only in the acid polysaccharide fractions.  $^1\text{H}$  and  $^{13}\text{C}$  NMR analysis (700 MHz) revealed the structural characteristics of the DTTPS-N (Fig. 2). Fig. 2A shows that the strong signal observed at 4.79 ppm corresponded to water, whereas the signals at 4.50–4.53 and 5.41–5.52 ppm were consistent with the presence of  $\beta$ - and  $\alpha$ -anomeric protons, respectively. The signal at 4.17 ppm corresponded to mannose [13]. The field signals at 3.31–4.08 ppm were attributed to H-2 to H-6. The signal at 2.155 ppm belonged to the methyl group of the *O*-acetyl groups in the  $^1\text{H}$  NMR spectrum. Fig. 2B shows that the signals for the methyl group and ketone of the *O*-acetyl groups were detected at 20.41–20.47 ppm and 172.87–173.31 ppm in the  $^{13}\text{C}$  NMR, respectively. The signals at 99.03–102.41 ppm belonged to the anomeric carbons (C-1), and the signals from 60.39 to 78.38 ppm were attributed to C-2 to C-6 of the residues in the  $^{13}\text{C}$  NMR spectrum.

Based on the calibration curves derived from the pullulan standards, the HP-SEC analysis results revealed that the molecular weight distribution of DTTPS-N ranged from 11 to 696 kDa (Fig. 3). The average molecular weight of the DTTPS-N was 281 kDa. The HPAEC-PAD analysis of the monosaccharide composition revealed that the DTTPS comprised arabinose, galactose, glucose, mannose, and xylose at a ratio of 1:1.6:2.6:23.3:1.41. The DTTPS-N comprised arabinose, galactose, glucose, mannose, and xylose at a ratio of 1:1.5:3.0:29.9:1.3. Moreover, the GC-MS analysis demonstrated the glycosidic linkage composition of the DTTPS-N (Table 2) and indicated that the DTTPS-N comprised 99.5% of nonbranch linkages.

**Table 2**

Glycosidic linkage types of the neutral polysaccharide (DTTPS-N).

	Terminal	Non-branch					
Mol%	T-Glc	2-Ara	6-Gal	2-Glc	3-Glc	3-Man	4-Man
	0.53	3.45	4.07	0.46	7.37	28.9	55.25
	0.53%	99.47%					

(Mol%, the mole percent).

The neutral polysaccharide (DTTPS-N) derived from *D. Taiseed Tosnobile* was determined through GC-MS for linkage analysis. The methylation of DTTPS-N was performed before analysis.

The predominant linkage component of the DTTPS-N was (1 → 4)-mannose at a 55.3% composition, and the other major component was (1 → 3)-mannose at a 28.9% composition. The other linkage types detected, such as (1 → 2)-Ara, (1 → 6)-Gal, and (1 → 2)-Glc, were relatively smaller.

### 3.3. Innate immunomodulation of DTTPS in BALB/c mice

Following a 6-week treatment, no significant differences were observed in the body and spleen weights of the mice among the groups. In the control group, the body and spleen weights of the mice were  $27.1 \pm 0.6$  g and  $0.123 \pm 0.003$  g, respectively.

#### 3.3.1. Flow cytometry assays of splenocytes

The flow cytometry analyses revealed the effects of DTTPS on the splenic T cells ( $\text{CD45}^+\text{CD3}^+$ ), B cells ( $\text{CD45}^+\text{CD19}^+$ ), T helper cells ( $\text{Th}$ ,  $\text{CD3}^+\text{CD4}^+$ ), cytotoxic T cells ( $\text{Tc}$ ,  $\text{CD3}^+\text{CD8}^+$ ), and natural killer (NK) cells ( $\text{CD49b}^+\text{CD3}^-$ ; Table 3). The results revealed that DTTPS exhibited no marked effects on the splenic T or B cells, or their ratio. Moreover, the Th and Tc cell populations exhibited no significant differences among the groups. However, the splenic NK cell population was substantially upregulated by DTTPS. Oral DTTPS administration led to 15.1% (100 mg/kg) and 17.2% (300 mg/kg) increases in the splenic NK cell population compared with that in the control group.

#### 3.3.2. Splenocyte proliferation assays

Fig. 4 illustrates the effects of DTTPS on splenocyte proliferation through mitogen (LPS or Con A) stimulation. Splenocyte proliferation was substantially enhanced through LPS stimulation in a dose-dependent manner in both the DTTPS-treated groups (100 and 300 mg/kg) compared with in the control group. In addition, the DTTPS treatments (100 and 300 mg/kg) significantly upregulated the splenocyte proliferation through Con A stimulation compared with that in the control group. In addition, compared with the control group, DTTPS resulted in 52.5% and 72.5% increases in splenocyte proliferation in both the DTTPS-treated (100 and 300 mg/kg) groups, respectively.

#### 3.3.3. Cytotoxic activity of DTTPS

Fig. 5A illustrates the cytotoxic activities of the splenocytes from mice receiving DTTPS treatment for 3 weeks. No marked differences were observed in the cytotoxicity of splenocytes among the groups at an E/T ratio of 5. The DTTPS-treated mice exhibited enhanced splenocyte cytotoxicity at an E/T ratio of 10. Moreover, DTTPS promoted the cytotoxic activity of splenocytes at an E/T ratio of 25. Furthermore, at an E/T ratio of either 10 or 25, DTTPS enhanced the cytotoxic activity of the splenocytes in a dose-dependent manner. However, significant differences were observed in the splenic NK cytotoxicity after high-dose DTTPS treatment (300 mg/kg) compared with that in the control groups at E/T ratios of 10 and 25 alone but not at an E/T ratio of 5.

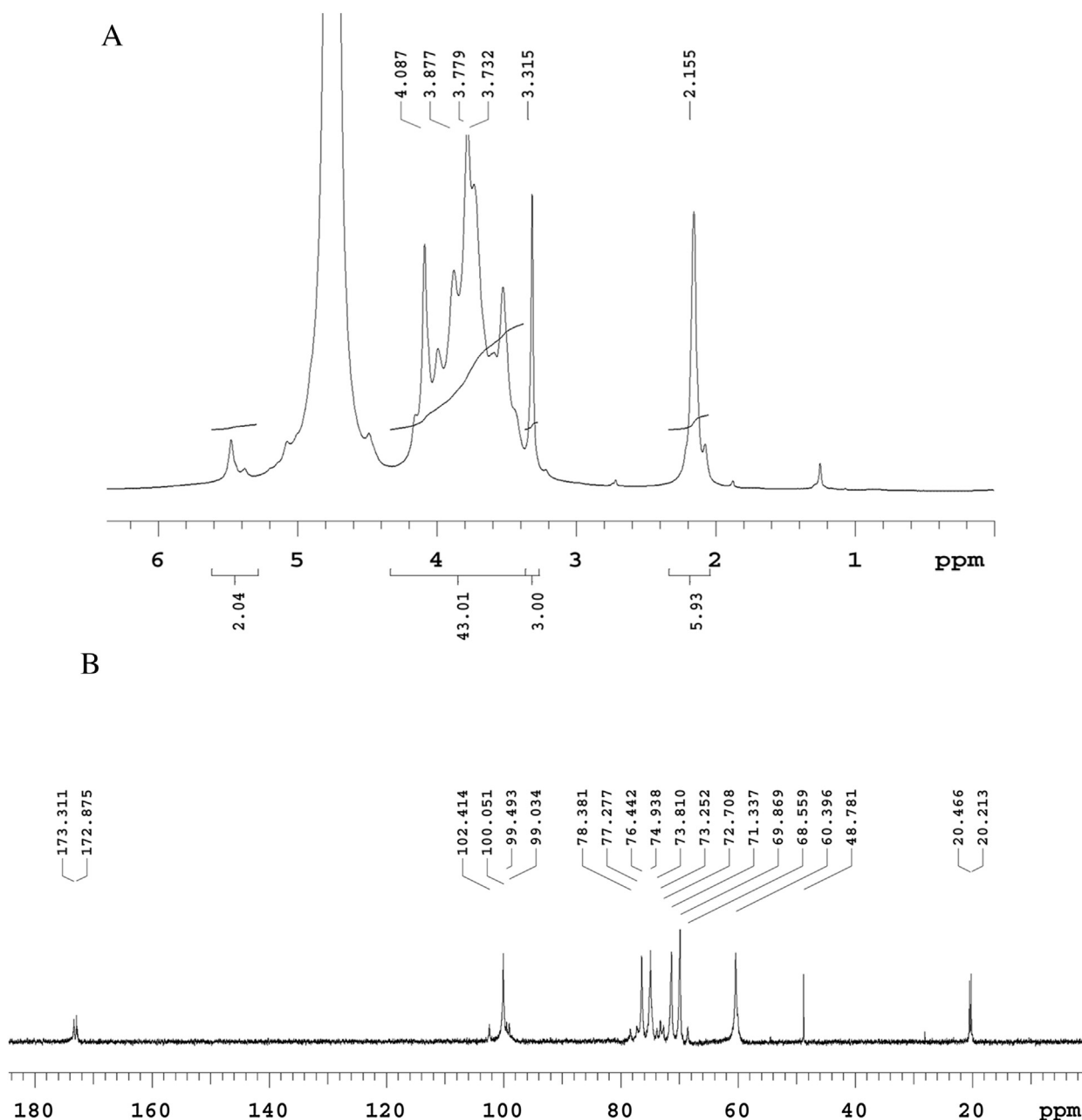


Fig. 2.  $^1\text{H}$  NMR (A) and  $^{13}\text{C}$  NMR (B) spectra of DTTPS-N.

Table 3

Immunomodulatory effects of DTTPS on the population of splenic lymphocytes in BALB/c mice.

Groups	Dose (mg/kg)	T cell (%)	B cell (%)	Helper T cell (%)	Cytotoxic T cell (%)	Natural Killer (%)
Control	–	37.1 ± 6.1	52.4 ± 6.2	23.1 ± 3.0	14.0 ± 1.8	10.5 ± 1.2
DTP	100	35.3 ± 4.2	52.6 ± 4.2	22.0 ± 3.1	13.3 ± 1.9	12.1 ± 1.0*
	300	35.6 ± 4.3	52.1 ± 2.8	21.5 ± 1.9	14.1 ± 2.2	12.3 ± 1.0*

All values are expressed as mean ± SD (n = 12). Values were significantly different compared with the control group, according to Dunnett's test: \*  $P < 0.05$ .

### 3.3.4. Effects of DTTPS on phagocytic activity

The phagocytosis of the extracellular FITC-labeled *E. coli* was investigated using the peritoneal neutrophils and macrophages isolated from the BALB/c mice receiving oral DTTPS treatment. The phagocytic activity of DTTPS was observed at various MOI ratios. Fig. 5B shows that DTTPS enhanced the phagocytic activity, with an increase in the swallowed pathogens. Moreover, at MOIs of 1, 5, and 25, the phagocytic activity was markedly improved in the

DTTPS-treated group compared with in the control group. These results demonstrated that both low- and high-dose DTTPS treatments (100 and 300 mg/kg) markedly upregulated the phagocytic activity compared with that in the control group. However, the marked phagocytic activities exhibited by DTTPS were not dose dependent.

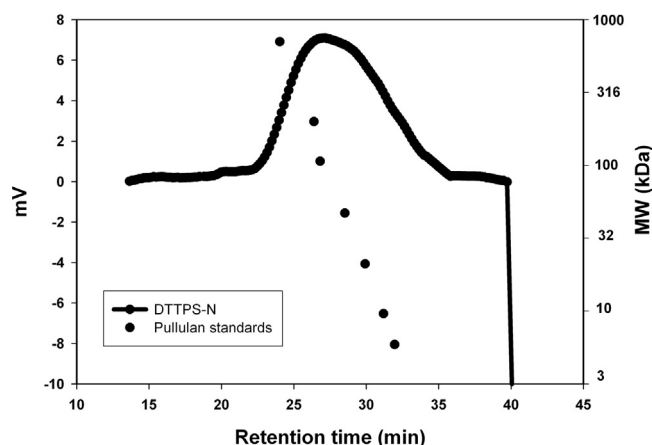


**Fig. 3.** High-performance size exclusion chromatography (HP-SEC) of DTPS-N for molecular weight analysis. HP-SEC was performed using an HPLC system equipped with an RI detector and a TSKgel guard column PWH (75 × 7.5 mm i.d.; TOSOH, Tokyo, Japan), TSKgel G4000PWXL, and G2500PWXL (300 × 7.8 mm i.d., TOSOH) connected in series. The molecular weights of the pullulan standards were 708 kDa, 375 kDa, 200 kDa, 107 kDa, 47.1 kDa, 21.1 kDa, 9.6 kDa, and 5.9 kDa. The standard curve axis is right off the figure.

### 3.3.5. Cytokine production

Fig. 6 illustrates the cytokines produced by the isolated splenocytes, which were incubated with or without mitogen (ConA and LPS) for 24–72 h. After 48 h of incubation, the concentrations of the IL-2 secreted in the supernatants were determined. The results revealed that the IL-2 concentrations in both the DTPS groups (100 and 300 mg/kg) were increased after Con A stimulation. IL-4 and IL-6 were collected from the supernatants after 72 and 24 h of incubation, respectively. However, the IL-4 and IL-6 concentrations exhibited no significant differences in both the groups, with and without mitogen stimulation. After 72 h of incubation, the IFN- $\gamma$  concentrations in the supernatants increased markedly only with ConA stimulation. In addition, the IFN- $\gamma$  secretion from the splenocytes isolated from the DTPS-treated group (300 mg/kg) was significantly higher than that from the control group.

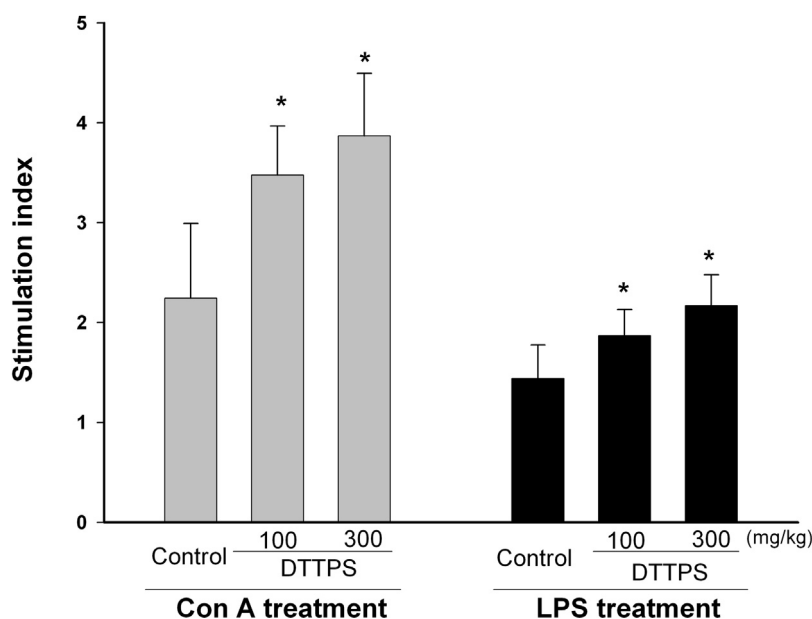


**Fig. 4.** Splenocyte proliferations assay of DTPS in BALB/c mice. The proliferation of splenocytes was induced by a mitogen, Con A or LPS. All values are expressed as mean  $\pm$  SD (n = 12). Values were significantly different compared with the control group, according to Dunnett's test: \*  $P < 0.05$ .

## 4. Discussion

Herba *Dendrobii* has been used as a long history of medicinal use in Asia. In this study, *D. Taiseed Tosnobile*, a new hybrid *Dendrobium* species, was investigated for its polysaccharide structural characteristics and polysaccharide-related immunomodulatory activities. The two medicinal *Dendrobium* species *D. tosaense* and *D. nobile* served as the seed parent and the pollen parent to *D. Taiseed Tosnobile*, respectively. DNA sequencing analysis confirmed a 99% and 94% similarity of the ITS regions of *D. Taiseed Tosnobile* to those of *D. tosaense* and *D. nobile*, respectively, thereby indicating that *D. Taiseed Tosnobile* exhibited a genotype closer to that of *D. tosaense* than to that of *D. nobile*. A critical problem in the medicinal herb market is that several medicinal plant species are protected and have small wild population; this is particularly the case for herbs in the Orchidaceae family. The development of *D. Taiseed Tosnobile* might solve this problem in the medicinal herb market.

Previous studies have identified that the polysaccharides of Herba *Dendrobii* from several species exhibit antioxidant, immunostimulating, and antitumor activities [4]. Hence, this study investigated the structural characteristics and immunomodulatory properties of *D. Taiseed Tosnobile* and suggested that these properties might contribute to the therapeutic potential of this plant.

In this study, the polysaccharides were isolated from the stem of *D. Taiseed Tosnobile* and subjected to primary structural characterization. DTPS fractioning, using the DEAE-650 M column, revealed that DTPS was primarily composed of DTPS-N (95%). Previous studies have reported that DTPS-N comprises 87% and 75% of the crude polysaccharides in *D. tosaense* and *D. nobile*, respectively [14,15]. Furthermore, Zha et al. [5] reported that the neutral polysaccharide fraction comprised 81% of the crude polysaccharides of *D. huoshanense*. This indicates that the neutral polysaccharide fraction represents a major portion of the DTPS; a similar finding is observed in other medicinal *Dendrobium*. The monosaccharide composition analyses revealed that DTPS and DTPS-N comprised arabinose, galactose, glucose, mannose, and xylose at distinct ratios. *D. nobile* and *D. tosaense* exhibited varying monosaccharide compositions: *D. nobile* comprised rhamnose, arabinose, xylose, mannose, glucose, and galactose at a molar ratio of 1.00:2.80:2.20:30.76:117.96:31.76 [16], and *D. tosaense* comprised

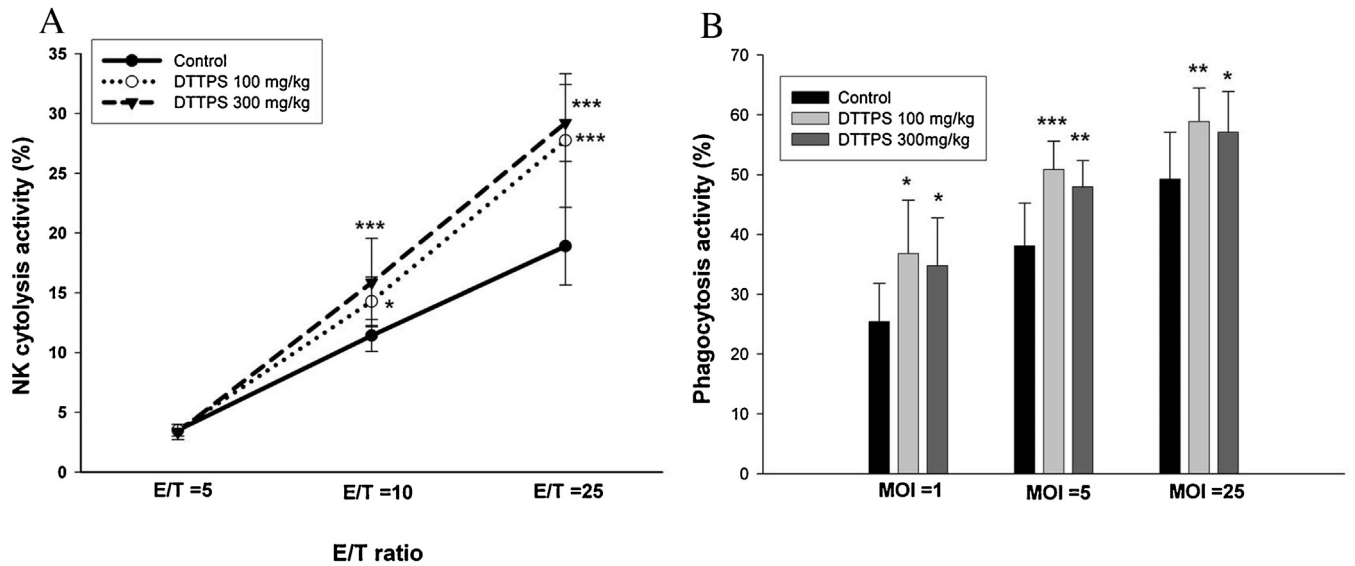


**Fig. 5.** Innate immune modulations of DTTPS in BALB/c mice. (A) Evaluation of splenic NK cytotoxicity against YAC-1 cells in control and DTTPS-treated mice; (B) phagocytic activity of peritoneal neutrophils and macrophages in control and DTTPS-treated mice. All values are expressed as mean  $\pm$  SD ( $n = 12$ ). Values were significantly different compared with the control group, according to Dunnett's test: \*  $P < 0.05$ , \*\*  $P < 0.01$  and \*\*\*  $P < 0.001$ .

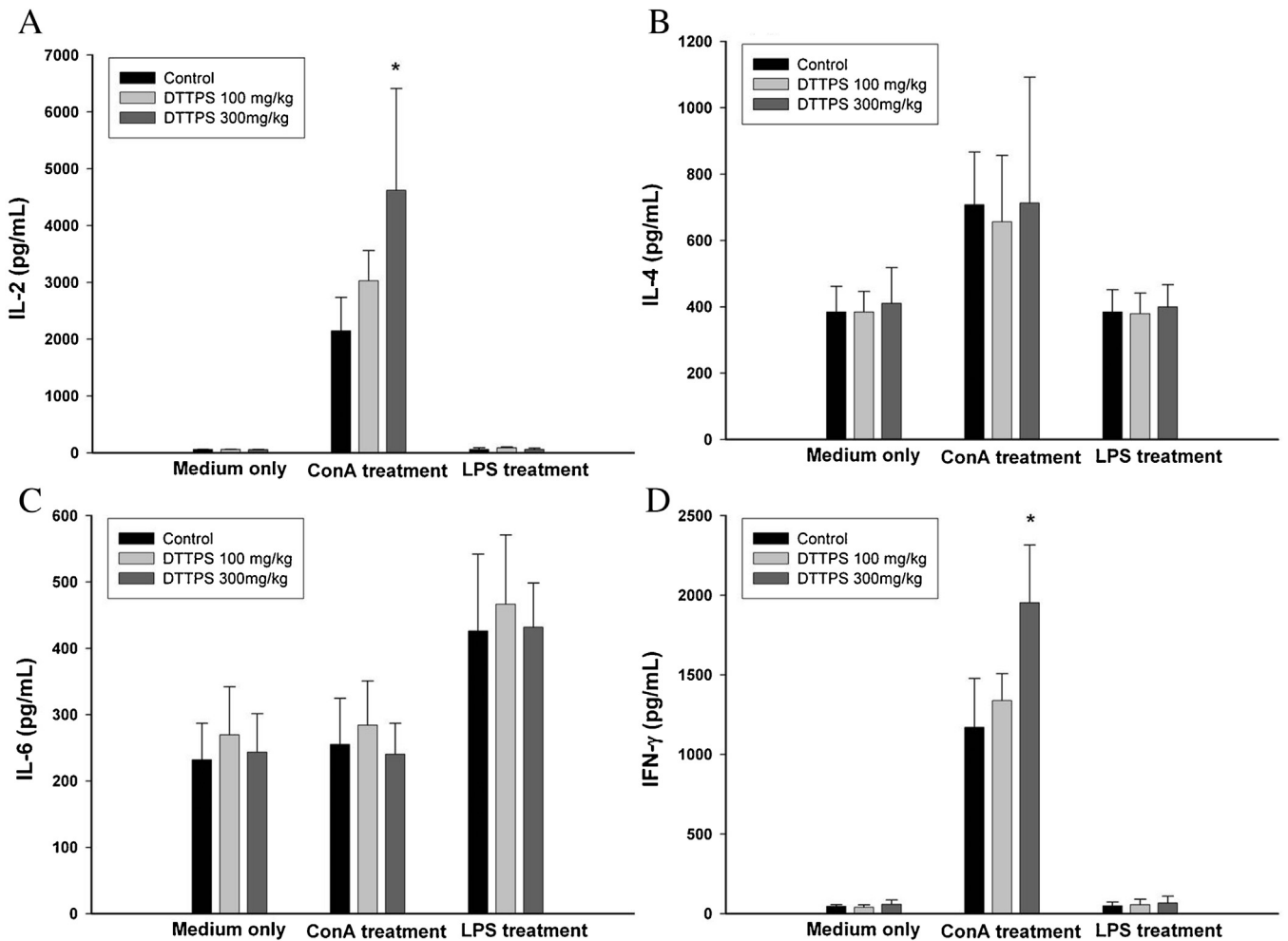


**Fig. 6.** Cytokine production assays for DTTPS in BALB/c mice; (A) IL-2, (B) IL-4, (C) IL-6, and (D) IFN- $\gamma$ . The cytokines were secreted by separated splenocytes from control and DTTPS-treated mice, and splenocyte proliferation was induced by the mitogen ConA or LPS. All values are expressed as means  $\pm$  SD ( $n = 12$ ). Values were significantly different compared with the control group, according to Dunnett's test: \*  $P < 0.05$ .

galactose, glucose, and mannose at a ratio of 1: 9.1:150.7 [14]. Although the monosaccharide composition of *D. Taiseed Tosnobile* was similar to that of *D. nobile*, the major component differed. Mannose was the major component of both *D. Taiseed Tosnobile* and *D. tosaense*. The linkage analysis indicated that nonbranched (1 → 4)-Man and (1 → 3)-Man linkages were the backbones of DTTPS-N. Hua et al. [17] reported that the molar ratio of (1 → 4)-Man (the major backbone of *D. officinale*) was 26.1%. In addition, Yang et al. [14] reported that nonbranched (1 → 4)-Man was the backbone of the neutral polysaccharide of *D. tosaense*, whereas Hsieh et al. [13] reported that the stem mucilage of *D. huoshanense* contains glucomannan in (1 → 4)-Glc and (1 → 4)-Manp linkages. This evidence suggests that (1 → 4)-Man linkages might be common in medicinal *Dendrobium* species. The signals at 20.41–20.47 ppm and 172.87–173.31 ppm were thought to belong to the O-acetyl groups of DTTPS-N in the  $^{13}\text{C}$  NMR spectrum, although the signals from the carboxyl carbon of uronic acids appear in the field of 170–180 ppm. However, DTTPS-N is a neutral polysaccharide fraction, and no uronic acid was detected in DTTPS-N. Therefore, the signals at 172.87–173.31 ppm were considered to belong to the acetyl groups and not uronic acids. The substitution of O-acetyl groups in polysaccharides derived from the *Dendrobium* species were reported to appear in *D. officinale* and *D. huoshanense* [5,13,18]. Xing et al. [18] named O-acetyl-glucomannan as Dendronan because it is common in medical *Dendrobium* species.

In traditional medicine, Herba *Dendrobii* is orally administered as an aqueous extract. Because polysaccharides are the primary ingredients of medicinal *Dendrobium*, the present study investigated the pharmacological effects of oral DTTPS administration in mice to elucidate its immunomodulatory effects. Oral DTTPS administration did not exert any effects on the spleen or body weight of the mice. In addition, this study demonstrated the effects of DTTPS on the splenic lymphocyte population; DTTPS boosted the splenic NK cell population but exerted no effects on the populations of T cells, B cells, cytotoxic T cells, or helper T cells. Contrary to the adaptive immunity of cytotoxic T cells, NK cells play a critical role in innate immunity and serve as the first line of defense against various invasions. These cells exhibit spontaneous cytotoxicity against pathogen-infected or malignant cells without antigen-specific recognition [19]. Our previous study reported that the anticancer activity of arabinogalactan results from the stimulation of NK cells [20].

Moreover, DTTPS not only enhanced the splenic NK cell population but also promoted their cytotoxic activities. In general, macromolecules such as polysaccharides cannot be absorbed in the gastrointestinal tract. However, oral DTTPS administration for 3 weeks affected the population and cytotoxicity of the splenic NK cells; a possible mechanism is that orally administered DTTPS may mediate intestinal interactions among the microfold (M)-cells [21]. M cells are epithelial cells specialized in transporting macromolecules in Peyer's patches, which are involved in the intestinal immune system. Volman et al. [22] suggested that orally administered polysaccharides directly affect immunity after being absorbed by intestinal macrophages and transported to the lymph nodes, spleen, and bone marrow.

In addition to the cytotoxicity of NK cells, the phagocytosis of macrophages is a critical barrier for the innate immunity of host defense. Macrophages are known as a crucial antigen-presenting cells [23]. During phagocytosis, macrophages digest pathogens and present the antigens of these pathogens to the T lymphocytes, thereby regulating adaptive immunity [23]. This study demonstrated that DTTPS promoted the phagocytic activity of macrophages isolated from mice. On the basis of the enhancement of the cytotoxicity of NK cells and phagocytosis of macrophages, DTTPS can be considered as a potent immunomodulator of innate immunity.

Although the flow cytometry analyses revealed that DTTPS did not influence the T or B cell population of the splenocytes, the splenocyte proliferation assays demonstrated that DTTPS acted as a mitogen for the splenocytes. We investigated the mitogenic effects on the splenocytes isolated from DTTPS-treated mice as well as the comitogenic effects of DTTPS on the ConA- or LPS-activated splenocytes. ConA and LPS serve as mitogens to T and B lymphocytes, respectively. Oral DTTPS administration promoted the proliferation of the separated splenocytes under the stimulation of mitogens. Moreover, oral DTTPS administration increased the reaction levels of the immune cells to mitogens. In the present study, DTTPS stimulated the T and B cell proliferation in the splenocytes. Both T and B cells are involved in cellular and humoral immunities, respectively, and thus play a critical role in host defense [22]. The development of effective T and B cell immunity might be stimulated by the lymphocyte proliferation response. Our previous study revealed that a distinct polysaccharide, arabinogalactan, stimulated only the LPS-activated splenocytes [20]. These results demonstrated that polysaccharides with varying structural characteristics might affect the immune system through various mechanisms or pathways.

Several polysaccharides derived from plants induce the production of cytokines such as tumor necrosis factor alpha, IL-1 h, IL-6, IL-8, IL-12, IFN- $\gamma$ , and IFN- $\beta$ 2 [23]. Cytokine secretion is considered a part of the immunomodulatory ability of polysaccharides. In the present study, the splenocytes isolated from the DTTPS-treated mice were activated by LPS and ConA to investigate the secretion of cytokines such as IL-2, IL-4, IL-6, and IFN- $\gamma$ . IL-2 and IFN- $\gamma$  secretions were significantly increased in the DTTPS group exhibiting ConA-activated splenocytes. IL-2 contributes to innate immunity, particularly against pathogen infections [24]. IL-2 is essential for the growth, proliferation, and differentiation of T cells and is typically produced by T cells during an immune response [24]. Reportedly, ConA triggers the activation and proliferation of T cells by interacting with their receptors [25]. The present study revealed that oral DTTPS administration promoted T cell activation in splenocytes. However, the mechanism of IL-2 induction by DTTPS remains unclear. IFN- $\gamma$ , also referred as type II interferon, is a crucial cytokine against pathogenic infections and tumors in both innate and adaptive immunities. IFN- $\gamma$  is primarily secreted by NK and T cells as part of innate and antigen-specific immunities, respectively [26]. A prominent characteristic of IFN- $\gamma$  is its ability to activate macrophages [27]. The induction of IFN- $\gamma$  in the DTTPS-treated splenocytes might explain the potent cytotoxic and phagocytic activities of DTTPS observed in the present study. A previous study reported that the polysaccharides and aqueous extracts of *D. officinale* markedly increased the IFN- $\gamma$  production by murine splenocytes [28]. Moreover, the polysaccharides of *D. huoshanense* significantly enhanced the IFN- $\gamma$  production [5,13]. The stimulation of IFN- $\gamma$  secretion might be a typical immunomodulatory characteristic of medicinal *Dendrobium* species.

In summary, the polysaccharides of *D. Taiseed Tosnobile* primarily comprise neutral polysaccharides. The major polysaccharide contained (1 → 4)Man as the backbone and exhibited potent immunomodulatory effects. This study also demonstrated the pharmacological effects of *D. Taiseed Tosnobile* in immunomodulation; however, the safety and toxicity of *D. Taiseed Tosnobile* remains unknown. Considering that this is a novel species of medicinal *Dendrobium*, the safety of *D. Taiseed Tosnobile* should be confirmed in future studies.

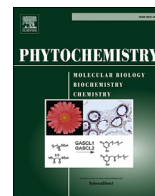
## Acknowledgements

This study was supported by grants from the Department of Health, Executive Yuan of the Republic of China (CCMP 100-RD-108) and China Medical University (CMU104-N-07).



## References

- [1] C.T. Wu, K.S. Huang, C.H. Yang, Y.C. Chen, J.W. Liao, C.L. Kuo, C.L. Chen, S.F. Lo, C.C. Hsieh, H.S. Tsay, Inhibitory effects of cultured *Dendrobium tosaense* on atopic dermatitis murine model, *Int. J. Pharm.* (2013).
- [2] T.B. Ng, J. Liu, J.H. Wong, X. Ye, S.C. Wing Sze, Y. Tong, K.Y. Zhang, Review of research on *Dendrobium*, a prized folk medicine, *Appl. Microbiol. Biotechnol.* 93 (5) (2012) 1795–1803.
- [3] J.H. Wang, J.P. Luo, X.Q. Zha, B.J. Feng, Comparison of antitumor activities of different polysaccharide fractions from the stems of *Dendrobium nobile* Lindl, *Carbohydr. Polym.* 79 (1) (2010) 114–118.
- [4] Y. Zhao, Y.O. Son, S.S. Kim, Y.S. Jang, J.C. Lee, Antioxidant and anti-hyperglycemic activity of polysaccharide isolated from *Dendrobium chrysotoxum* Lindl, *J. Biochem. Mol. Biol.* 40 (5) (2007) 670–677.
- [5] X.Q. Zha, J.P. Luo, S.Z. Luo, S.T. Jiang, Structure identification of a new immunostimulating polysaccharide from the stems of *Dendrobium huoshanense*, *Carbohydr. Polym.* 69 (1) (2007) 86–93.
- [6] M. Dubois, K. Gilles, J.K. Hamilton, P.A. Rebers, F. Smith, A colorimetric method for the determination of sugars, *Nature* 168 (4265) (1951) 167.
- [7] S.J. Compton, C.G. Jones, Mechanism of dye response and interference in the Bradford protein assay, *Anal. Biochem.* 151 (2) (1985) 369–374.
- [8] A.E. Castagne, Uronic acid determination, *Carbohydr. Res.* 42 (2) (1975) 382–386.
- [9] C. Laine, T. Tamminen, A. Vikkula, T. Vuorinen, Methylation analysis as a tool for structural analysis of wood polysaccharides, *Holzforschung* 56 (6) (2002) 607–614.
- [10] X. Zhang, R. Goncalves, D.M. Mosser, The isolation and characterization of murine macrophages, *Curr. Protoc. Immunol.* (2008), Chapter 14, Unit 14.1.
- [11] P. Wang, S.M. Henning, D. Heber, Limitations of MTT and MTS-based assays for measurement of antiproliferative activity of green tea polyphenols, *PLoS One* 5 (4) (2010) e10202.
- [12] Y. Kimura, M. Sumiyoshi, Effects of various *Eleutherococcus senticosus* cortex on swimming time, natural killer activity and corticosterone level in forced swimming stressed mice, *J. Ethnopharmacol.* 95 (2–3) (2004) 447–453.
- [13] Y.S. Hsieh, C. Chien, S.K. Liao, S.F. Liao, W.T. Hung, W.B. Yang, C.C. Lin, T.J. Cheng, C.C. Chang, J.M. Fang, C.H. Wong, Structure and bioactivity of the polysaccharides in medicinal plant *Dendrobium huoshanense*, *Bioorg. Med. Chem.* 16 (11) (2008) 6054–6068.
- [14] L.C. Yang, T.J. Lu, C.C. Hsieh, W.C. Lin, Characterization and immunomodulatory activity of polysaccharides derived from *Dendrobium tosaense*, *Carbohydr. Polym.* 111 (2014) 856–863.
- [15] J.H. Wang, X.Q. Zha, J.P. Luo, X.F. Yang, An acetylated galactomannoglucan from the stems of *Dendrobium nobile* Lindl, *Carbohydr. Res.* 345 (8) (2010) 1023–1027.
- [16] A. Luo, X. He, S. Zhou, Y. Fan, T. He, Z. Chun, In vitro antioxidant activities of a water-soluble polysaccharide derived from *Dendrobium nobile* Lindl. extracts, *Int. J. Biol. Macromol.* 45 (4) (2009) 359–363.
- [17] Y.F. Hua, M. Zhang, C.X. Fu, Z.H. Chen, G.Y. Chan, Structural characterization of a 2-O-acetylglucosaminan from *Dendrobium officinale* stem, *Carbohydr. Res.* 339 (13) (2004) 2219–2224.
- [18] X.H. Xing, S.W. Cui, S. Nie, G.O. Phillips, H.D. Goff, Q. Wang, Study on *dendrobium officinale* O-acetyl-glucosaminan (*Dendronan* (R)) part II. Fine structures of O-acetylated residues, *Carbohydr. Polym.* 117 (2015) 422–433.
- [19] F.L. Lai, Y.H. Wang, Y.W. Chung, S.M. Hwang, L.S. Huang, Cell docking, movement and cell–cell interactions of heterogeneous cell suspensions in a cell manipulation microdevice, *Sensors (Basel)* 11 (10) (2011) 9613–9627.
- [20] L.C. Yang, C.C. Hsieh, T.J. Lu, W.C. Lin, Structurally characterized arabinogalactan from *Anoectochilus formosanus* as an immuno-modulator against CT26 colon cancer in BALB/c mice, *Phytomedicine* 21 (5) (2014) 647–655.
- [21] I. Suzuki, H. Tanaka, A. Kinoshita, S. Oikawa, M. Osawa, T. Yadomae, Effect of orally administered beta-glucan on macrophage function in mice, *Int. J. Immunopharmacol.* 12 (6) (1990) 675–684.
- [22] J.J. Volman, J.D. Ramakers, J. Plat, Dietary modulation of immune function by beta-glucans, *Physiol. Behav.* 94 (2) (2008) 276–284.
- [23] I.A. Schepetkin, M.T. Quinn, Botanical polysaccharides: macrophage immunomodulation and therapeutic potential, *Int. Immunopharmacol.* 6 (3) (2006) 317–333.
- [24] T.R. Malek, The biology of interleukin-2, *Annu. Rev. Immunol.* 26 (2008) 453–479.
- [25] R. Palacios, Concanavalin A triggers T lymphocytes by directly interacting with their receptors for activation, *J. Immunol.* 128 (1) (1982) 337–342.
- [26] U. Boehm, T. Klamp, M. Groot, J.C. Howard, Cellular responses to interferon-gamma, *Annu. Rev. Immunol.* 15 (1997) 749–795.
- [27] S. Herbst, U.E. Schaible, B.E. Schneider, Interferon gamma activated macrophages kill mycobacteria by nitric oxide induced apoptosis, *PLoS One* 6 (5) (2011) e19105.
- [28] X.F. Liu, J. Zhu, S.Y. Ge, L.J. Xia, H.Y. Yang, Y.T. Qian, F.Z. Ren, Orally administered *Dendrobium officinale* and its polysaccharides enhance immune functions in BALB/c mice, *Nat. Prod. Commun.* 6 (6) (2011) 867–870.
- [29] T.C. Lin, C.C. Hsieh, D.C. Agrawal, C.L. Kuo, F.S. Chueh, H.S. Tasy, ITS sequence based phylogenetic relationship of dangshen radix, *J. Food Drug Anal.* 4 (2007) 428–432.
- [30] C.T. Wu, C.C. Hsieh, W.C. Lin, C.Y. Tang, Y.C. H. Y.C. Huang, Y.J.J.F.D.A. Ko, Internal transcribed spacer sequence-based identification and phylogenetic relationship of *I-Tiao-Gung* originating from *Flemingia* and *Glycine* (Leguminosae) in Taiwan, *J. Food. Drug Anal.* 21(4) (2013) 356–362.



# Isoflavones and anti-inflammatory constituents from the fruits of *Psoralea corylifolia*

Chiang-Hsiang Chen<sup>a, b, 1</sup>, Tsong-Long Hwang<sup>c, d, e</sup>, Li-Chai Chen<sup>b, f, 1</sup>,  
Tsung-Hsien Chang<sup>g</sup>, Chun-Sheng Wei<sup>f, 1</sup>, Jih-Jung Chen<sup>a, h, \*</sup>

<sup>a</sup> Faculty of Pharmacy, School of Pharmaceutical Sciences, National Yang-Ming University, Taipei, 112, Taiwan

<sup>b</sup> Department of Pharmacy, Tajen University, Pingtung, 907, Taiwan

<sup>c</sup> Graduate Institute of Natural Products, College of Medicine, Chang Gung University, Taoyuan, 333, Taiwan

<sup>d</sup> Research Center for Industry of Human Ecology, Research Center for Chinese Herbal Medicine, Graduate Institute of Health Industry Technology, College of Human Ecology, Chang Gung University of Science and Technology, Taoyuan, 333, Taiwan

<sup>e</sup> Department of Anesthesiology, Chang Gung Memorial Hospital, Taoyuan, 333, Taiwan

<sup>f</sup> Department of Pharmacy, Zuoying Branch of Kaohsiung Armed Forces General Hospital, Kaohsiung, 813, Taiwan

<sup>g</sup> Department of Medical Education and Research, Kaohsiung Veterans General Hospital, Kaohsiung, 813, Taiwan

<sup>h</sup> Department of Medical Research, China Medical University Hospital, China Medical University, Taichung, 404, Taiwan

## ARTICLE INFO

### Article history:

Received 11 April 2017

Received in revised form

2 August 2017

Accepted 7 August 2017

### Keywords:

*Psoralea corylifolia*

Leguminosae

Structure elucidation

Isoflavone

Anti-inflammatory activity

## ABSTRACT

The fruits of *Psoralea corylifolia*, known as *Psoraleae Fructus* (*Buguzhi* in Chinese), are traditionally used for the treatment of spermatorrhea, nephritis, asthma, pollakiuria, and various inflammatory diseases. Three previously undescribed isoflavone derivatives, 7-*O*-methylcorylifol A, 7-*O*-isoprenylcorylifol A, and 7-*O*-isoprenylneobavaisoflavone, have been isolated from the fruits of *P. corylifolia*, together with 9 known compounds. The structures of these compounds were determined through spectroscopic and MS analyses. Among the isolated compounds, 7-*O*-methylcorylifol A and psoralen exhibited potent inhibition ( $IC_{50}$  values  $\leq 10.89 \mu M$ ) of superoxide anion generation by human neutrophils in response to *N*-formyl-L-methionyl-L-leucyl-L-phenylalanine/cytochalasin B (fMLP/CB). 7-*O*-isoprenylcorylifol A, 7-*O*-isoprenylneobavaisoflavone, and 12,13-dihydro-12,13-epoxybakuchiol inhibited fMLP/CB-induced elastase release with  $IC_{50}$  values  $\leq 14.30 \mu M$ . In addition, 7-*O*-isoprenylcorylifol A, bakuchiol, 12,13-dihydro-12,13-epoxybakuchiol, and psoralidin showed potent inhibition with  $IC_{50}$  values  $\leq 36.65 \mu M$ , against lipopolysaccharide (LPS)-induced nitric oxide (NO) generation.

© 2017 Elsevier Ltd. All rights reserved.

## 1. Introduction

*Psoralea corylifolia* L. (Leguminosae) is an annual herb distributed in India, Malay peninsula, Indonesia, China, and Taiwan (Huang and Ohashi, 1993). Dry fruit of *P. corylifolia* Linn is one of the most popular Traditional Chinese Medicine (TCM) and officially listed in Chinese Pharmacopoeia (Pharmacopoeia of the People's Republic of China, 2005). This crude drug has been used for the treatment of spermatorrhea, nephritis, asthma, pollakiuria, and various inflammatory diseases (Chopra et al., 2013). Various flavonoids (Anand et al., 1978; Lee et al., 2005; Tsai et al., 1996; Xin et al.,

2010; Yin et al., 2004), coumarins (Xin et al., 2010), chalcones (Lee et al., 2005; Yin et al., 2004), isoflavones (Yin et al., 2004), meroterpenes (Xin et al., 2010; Yin et al., 2006), coumestans (Gupta et al., 1990), and their derivatives were isolated from this plant in previous studies. Many of these compounds exhibit anti-inflammatory (Anand et al., 1978), phytoestrogen (Xin et al., 2010), anti-nitric oxide synthase (iNOS) (Lee et al., 2005), anti-platelet aggregation (Tsai et al., 1996), antibacterial (Yin et al., 2004), and anti-*Helicobacter pylori* (Yin et al., 2006) activities.

Human neutrophils are known to play crucial roles in host defense against microorganisms and in pathogenesis of various diseases such as asthma, chronic obstructive pulmonary disease (COPD), ischemia-reperfusion injury, and rheumatoid arthritis (Witko-Sarsat et al., 2000). In response to different stimuli, activated neutrophils secrete a series of cytotoxins, such as the superoxide anion radical ( $O_2^{\bullet -}$ ), a precursor to other reactive oxygen

\* Corresponding author. Faculty of Pharmacy, National Yang-Ming University, Taipei, 11221, Taiwan.

E-mail address: [chenjj@ym.edu.tw](mailto:chenjj@ym.edu.tw) (J.-J. Chen).

<sup>1</sup> Authors have contributed equally in this manuscript.

species (ROS), granule proteases, bioactive lipids, and neutrophil elastase, a major contributor to destruction of tissue in chronic inflammatory disease (Borregaard, 1998; Witko-Sarsat et al., 2000; Faurschou and Borregaard, 2003; Roos et al., 2003). Nitric oxide (NO) is a mediator in the inflammatory response involved in host defense (Vane et al., 1994). Suppression of the extensive or inappropriate activation of neutrophils and/or macrophages by drugs has been proposed as a way to ameliorate inflammatory diseases. The effects on pro-inflammatory responses of isolates were evaluated by suppressing fMLP-induced  $O_2^{\bullet-}$  and elastase generation by human neutrophils and by inhibiting LPS-induced NO release by murine macrophages. In a screening program searching for anti-inflammatory compounds from medicinal plants, *P. corylifolia* has been found to be an active species. The MeOH extract of the fruits of *P. corylifolia* showed potent inhibitory effects on superoxide anion and elastase generation by human neutrophils in response to fMLP and on NO generation by murine macrophages in response to LPS. Fig. 1 illustrates the structures of three new isoflavone derivatives, 7-O-methylcorylifol A (**1**), 7-O-isoprenylcorylifol A (**2**), and 7-O-isoprenylneobavaisoflavone (**3**). Nine known compounds (**4–12**), have been isolated and identified from the fruits of *P. corylifolia* and their structures are depicted in Fig. 2.

## 2. Results and discussion

### 2.1. General

Chromatographic purification of the EtOAc-soluble fraction of a MeOH extract of fruits of *P. corylifolia* on a silica gel column and preparative thin-layer chromatography (TLC) afforded three previously undescribed (**1–3**) and nine known compounds (**4–12**) (Figs. 1 and 2).

### 2.2. Structure elucidation of the isoflavone derivatives

7-O-Methylcorylifol A (**1**) was isolated as a yellowish amorphous powder. Its molecular formula,  $C_{26}H_{28}O_4$ , was determined on

the basis of the *quasi*-molecular ion at  $m/z$  427.1882 ( $[M + Na]^+$ , calcd for  $C_{26}H_{28}O_4Na$ : 427.1885) in the HR-ESI-MS spectrum (positive-ion mode) and was supported by the  $^1H$ -,  $^{13}C$ -, and DEPT NMR data. The presence of a conjugated carbonyl group was revealed by the band at  $1626\text{ cm}^{-1}$  in the IR spectrum, which was confirmed by the resonance at  $\delta_C$  176.0 in the  $^{13}C$ -NMR spectrum. The IR of **1** also showed the OH absorption at  $3334\text{ cm}^{-1}$ . The  $^1H$ -NMR spectrum of **1** showed the resonances for seven aromatic protons [ $\delta_H$  6.85 (1H, d,  $J = 7.8\text{ Hz}$ , H-5'), 6.86 (1H, d,  $J = 2.4\text{ Hz}$ , H-8), 6.99 (1H, dd,  $J = 9.0, 2.4\text{ Hz}$ , H-6), 7.28 (1H, dd,  $J = 7.8, 2.0\text{ Hz}$ , H-6'), 7.31 (1H, d,  $J = 2.0\text{ Hz}$ , H-2'), 7.91 (1H, s, H-2), 8.21 (1H, d,  $J = 9.0\text{ Hz}$ , H-5)], a methoxy group [ $\delta_H$  3.92 (3H, s, OMe-7)], an OH group [ $\delta_H$  5.52 (1H, br s,  $D_2O$  exchangeable, OH)], and a geranyl group [ $\delta_H$  1.59 (3H, s, H-9''), 1.67 (3H, s, H-8''), 1.78 (3H, s, H-10''), 2.08 (2H, m, H-4''), 2.12 (2H, m, H-5''), 3.41 (1H, d,  $J = 7.2\text{ Hz}$ , H-1''), 5.07 (1H, br t,  $J = 7.2\text{ Hz}$ , H-6''), 5.36 (1H, br t,  $J = 7.2\text{ Hz}$ , H-2'')]. Comparison of the  $^1H$  and  $^{13}C$ -NMR data of **1** with those of corylifol A [6] suggested that their structures are closely related, except that the 7-methoxy group ( $\delta_H$  3.92) of **1** replaced the 7-hydroxy group of corylifol A (Yin et al., 2004). This was supported by HMBC correlation between OMe-7 ( $\delta_H$  3.92) and C-7 ( $\delta_C$  163.9) and NOESY correlations between OMe-7 ( $\delta_H$  3.92) and both H-6 ( $\delta_H$  6.99) and H-8 ( $\delta_H$  6.86). The full assignment of  $^1H$  and  $^{13}C$ -NMR resonances was supported by  $^1H$ – $^1H$  COSY, DEPT, HSQC, NOESY (Fig. 3), and HMBC (Fig. 3) spectral analyses. On the basis of the above data, the structure of **1** was elucidated as 7-O-methylcorylifol A.

7-O-Isoprenylcorylifol A (**2**) was isolated as a yellowish amorphous powder. The ESI-MS afford the *quasi*-molecular ion  $[M + Na]^+$  at  $m/z$  481, implying a molecular formula of  $C_{30}H_{34}O_4Na$ , which was confirmed by the HR-ESI-MS ( $m/z$  481.2357  $[M + Na]^+$ , calcd 481.2355). The presence of a conjugated carbonyl group was revealed by the band at  $1625\text{ cm}^{-1}$  in the IR spectrum, which was confirmed by the resonance at  $\delta_C$  176.1 in the  $^{13}C$ -NMR spectrum. The  $^1H$  and  $^{13}C$ -NMR data of **2** were similar to those of 7-O-methylcorylifol A (**1**), except that the 7-O-isoprenyl group [ $\delta_H$  1.79 (3H, s, H-5'''), 1.83 (3H, s, H-4'''), 4.62 (1H, d,  $J = 6.8\text{ Hz}$ , H-1'''), 5.51 (1H, br t,  $J = 6.8\text{ Hz}$ , H-2''')] of **2** replaced the 7-methoxy group [ $\delta_H$  3.92 (3H,

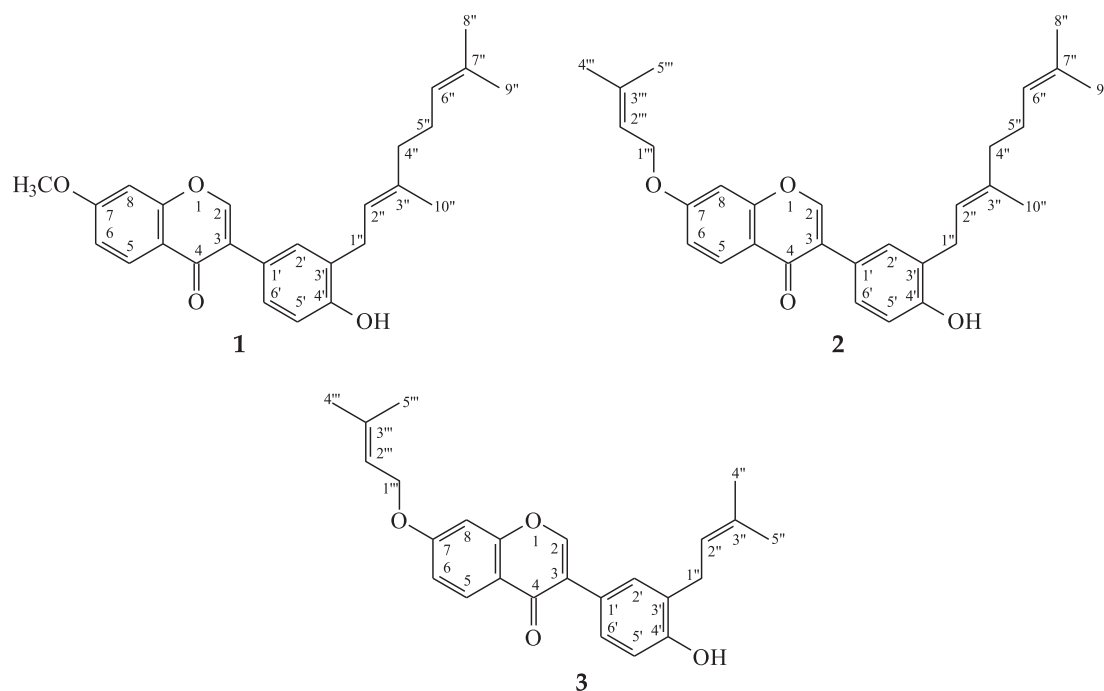


Fig. 1. The chemical structures of previously undescribed compounds **1–3** isolated from *P. corylifolia*.

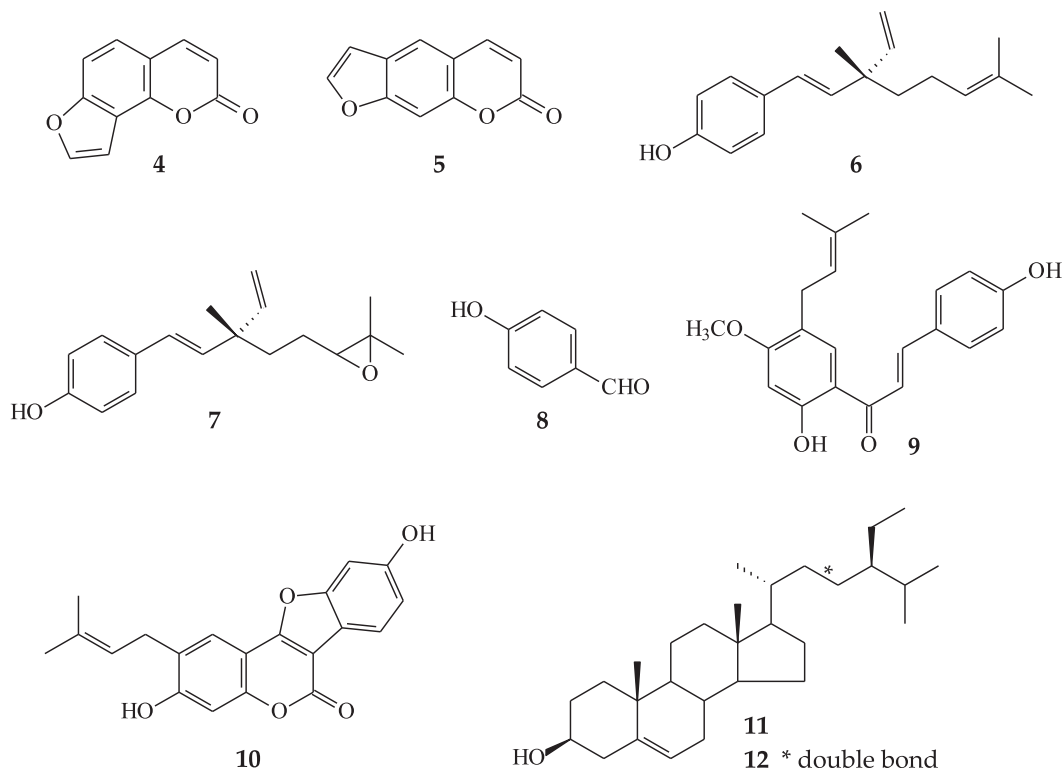


Fig. 2. The chemical structures of known compounds 4–12 isolated from *P. corylifolia*.

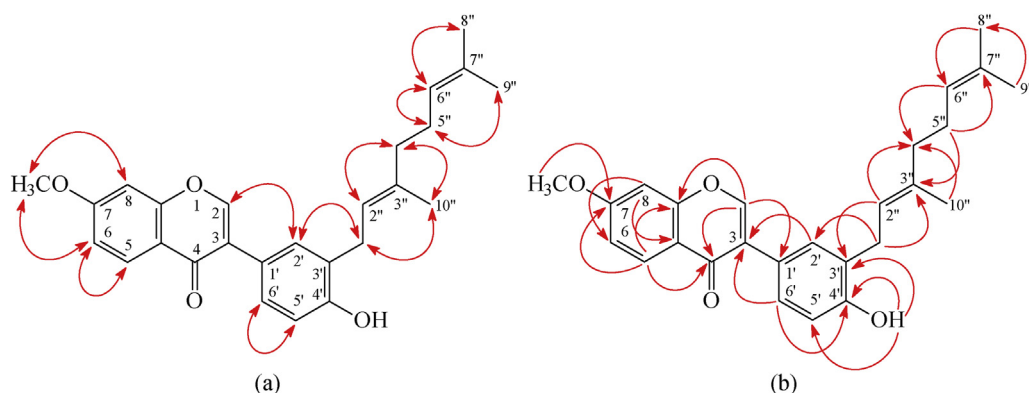


Fig. 3. Key NOESY (a) and HMBC (b) correlations of **1**.

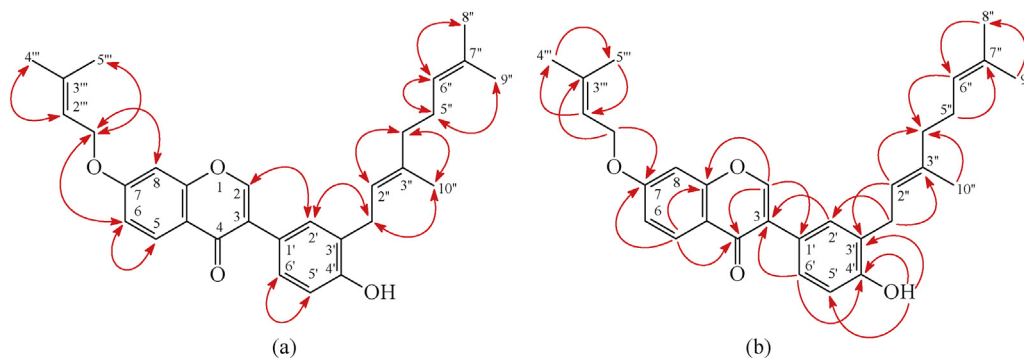
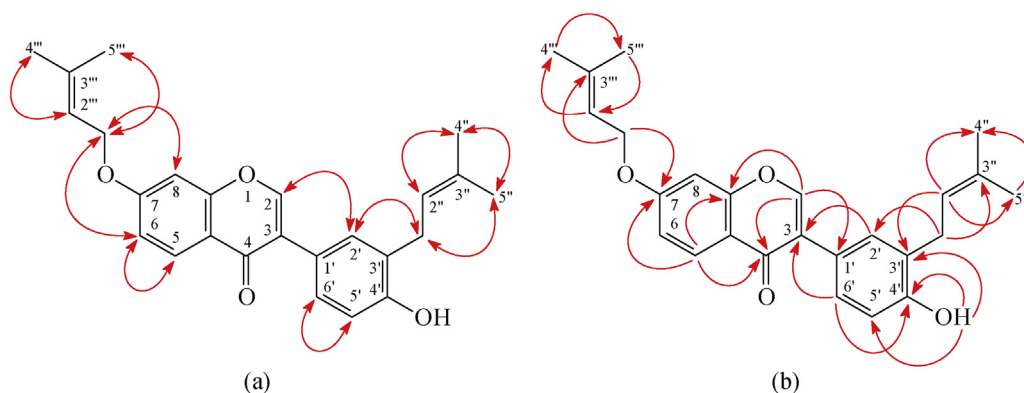
s, OMe-7)] of **1**. This was supported by HMBC correlations between H-1''' ( $\delta_{\text{H}}$  4.62) and C-7 ( $\delta_{\text{C}}$  163.2), C-2''' ( $\delta_{\text{C}}$  118.5), and C-3''' ( $\delta_{\text{C}}$  139.4) and NOESY correlations between H-1''' ( $\delta_{\text{H}}$  4.62) and H-6 ( $\delta_{\text{H}}$  6.99) and H-8 ( $\delta_{\text{H}}$  6.86). According to the above data, the structure of **2** was elucidated as 7-*O*-isoprenylcorylifol A. This was further confirmed by the  $^1\text{H}$ – $^1\text{H}$ -COSY, NOESY (Fig. 4), DEPT, HSQC, and HMBC (Fig. 4) techniques.

7-*O*-Isoprenylneobavaisoflavone (**3**) was isolated as yellowish amorphous powder. The molecular formula  $\text{C}_{25}\text{H}_{26}\text{O}_4$  was deduced from a sodium adduct ion at  $m/z$  413.1725 [ $\text{M} + \text{Na}]^+$  (calcd 413.1729) in the HRESI mass spectrum. The presence of a conjugated carbonyl group was revealed by the band at  $1624\text{ cm}^{-1}$  in the IR spectrum, which was confirmed by the resonance at  $\delta_{\text{C}}$  176.0 in the  $^{13}\text{C}$ -NMR spectrum. The  $^1\text{H}$  and  $^{13}\text{C}$ -NMR data of **3** were similar to those of 7-*O*-isoprenylcorylifol A (**2**), except that the isoprenyl group [ $\delta_{\text{H}}$  1.77 (3H, d,  $J = 1.2\text{ Hz}$ , H-5''), 1.79 (3H, s, H-4''), 3.39 (1H, d,

$J = 7.2\text{ Hz}$ , H-1''), 5.35 (1H, br t,  $J = 7.2\text{ Hz}$ , H-2'');  $\delta_{\text{C}}$  17.9 (C-5''), 25.8 (C-4''), 29.9 (C-1''), 121.7 (C-2''), 134.8 (C-3'')] at C-3' of **3** replaced the 3,7-dimethylocta-2,6-dienyl group at C-3' of 7-*O*-isoprenylcorylifol A (**2**). This was supported by (i) the HMBC correlations (Fig. 5) between H-1'' ( $\delta_{\text{H}}$  3.39) and C-2' ( $\delta_{\text{C}}$  130.7), C-3' ( $\delta_{\text{C}}$  126.9), and C-4' ( $\delta_{\text{C}}$  154.5); and (ii) the NOESY correlation (Fig. 5) between H-1'' ( $\delta_{\text{H}}$  3.39) and H-2' ( $\delta_{\text{H}}$  7.31). The structure elucidation of **3** was supported by  $^1\text{H}$ – $^1\text{H}$  COSY and NOESY (Fig. 5) experiments, and  $^{13}\text{C}$  NMR assignments were confirmed by DEPT, HSQC, and HMBC (Fig. 5) techniques.

### 2.3. Structure identification of the known isolates

The known isolates were readily identified by a comparison of physical and spectroscopic data (UV, IR,  $^1\text{H}$ -NMR,  $[\alpha]_{\text{D}}$ , and MS) with corresponding authentic samples or literature values, and this

Fig. 4. Key NOESY (a) and HMBC (b) correlations of **2**.Fig. 5. Key NOESY (a) and HMBC (b) correlations of **3**.

included two coumarins, isopsoralen (= angelicin) (**4**) (Mar et al., 2001; Wulff et al., 1988) and psoralen (**5**) (Lin et al., 2007; Mar et al., 2001), two meroterpenes, bakuchiol (**6**) (Chen et al., 2008a; Labbé et al., 1996; Lin et al., 2007) and 12,13-dihydro-12,13-epoxybakuchiol (**7**) (Labbé et al., 1996), a phenol derivative, *p*-hydroxybenzaldehyde (**8**) (Woodhead et al., 1982; Yasuhara et al., 1999), a chalcone, bavachalcone (**9**) (Sugamoto et al., 2011; Yin et al., 2004), a coumestan derivative, psoralidin (**10**) (Khastgir et al., 1961), and a steroid mixture of  $\beta$ -sitosterol (**11**) and stigmasterol (**12**) (Chen et al., 2008b).

#### 2.4. Biological studies

Reactive oxygen species (ROS) (e.g., superoxide anion ( $O_2^{\cdot-}$ ) and hydrogen peroxide) and granule proteases (e.g., elastase, cathepsin G, and proteinase-3) produced by human neutrophils are involved in the pathogenesis of a variety of inflammatory diseases. In this study, the effects on neutrophil pro-inflammatory responses of compounds isolated from the fruits of *P. corylifolia* were evaluated by suppressing fMLP/CB-induced superoxide radical anion ( $O_2^{\cdot-}$ ) generation and elastase release by human neutrophils. The inhibitory activity data on neutrophil pro-inflammatory responses are shown in Table 1. Diphenyleneiodonium and phenylmethylsulfonyl fluoride were used as positive controls for  $O_2^{\cdot-}$  generation and elastase release, respectively. From the results of our biological tests, the following conclusions can be drawn: (a) 7-*O*-Methylcorylifol A (**1**) and psoralen (**5**) exhibited inhibitory activities ( $IC_{50}$  values  $\leq 10.89 \mu M$ ) on human neutrophil  $O_2^{\cdot-}$  generation. (b) 7-*O*-Isoprenylcorylifol A (**2**), 7-*O*-isoprenylneobavaisoflavone (**3**), and 12,13-dihydro-12,13-epoxybakuchiol (**7**) inhibited fMLP/CB-induced elastase release with  $IC_{50}$  values  $\leq 14.30 \mu M$ . (c) The

meroterpene derivative **7** {with the (3,3-dimethyloxiran-2-yl) methyl moiety at C-11} exhibited more effective inhibition than its analogues **6** (with the 11-isoprenyl group) against fMLP-induced elastase release. (d) Psoralen (**5**) (with a furan moiety at C-6,7) exhibited more effective inhibition than its analogue, isopsoralen (**4**) (with a furan moiety at C-7,8) against fMLP-induced  $O_2^{\cdot-}$  generation. (e) Psoralen (**5**) and 7-*O*-isoprenylcorylifol A (**2**) were the most effective among the isolated compounds, with  $IC_{50}$  values of  $5.91 \pm 3.22$  and  $7.13 \pm 1.33 \mu M$ , respectively, against fMLP-induced superoxide anion generation and elastase release.

Nitric oxide (NO) is a mediator in the inflammatory response involved in host defense. The anti-inflammatory effects of the compounds isolated from the fruits of *P. corylifolia* were also evaluated by suppressing lipopolysaccharide (LPS)-induced NO generation in murine macrophage cell line RAW264.7. The popular murine macrophage cell line, RAW264.7, is often used to initially screen natural products for anti-inflammatory activity (Yang et al., 2016, 2017). The inhibitory activity data of the isolated compounds **1–12** on NO generation by macrophages are compiled in Table 2. Quercetin which was reported to inhibit NO production by LPS-stimulated macrophage (Motai and Kitanaka, 2005; Wang et al., 2005) was used as the positive control. From the results of our anti-inflammatory tests, the following conclusions could be drawn: (a) 7-*O*-Isoprenylcorylifol A (**2**), bakuchiol (**6**), 12,13-dihydro-12,13-epoxybakuchiol (**7**), and psoralidin (**10**) exhibited inhibition ( $IC_{50} \leq 36.65 \mu M$ ) of NO generation by murine macrophages in response to LPS. (b) Psoralen (**5**) (with a furan moiety at C-6,7) exhibited more effective inhibition than its analogue, isopsoralen (**4**) (with a furan moiety at C-7,8) against LPS-induced NO generation. (c) The meroterpene derivative **6** (with the 11-isoprenyl group) exhibited more effective inhibition than its analogues **6**



**Table 1**

Inhibitory effects of compounds **1–12** from the fruits of *P. corylifolia* on superoxide radical anion generation and elastase release by human neutrophils in response to fMet-Leu-Phe/cytochalasin B <sup>a</sup>.

Compounds	Superoxide anion	Elastase
	IC <sub>50</sub> [μM] <sup>b</sup> or (Inh %) <sup>c</sup>	
7-O-Methylcorylifol A ( <b>1</b> )	10.89 ± 1.41 <sup>g</sup>	26.82 ± 3.67 <sup>g</sup>
7-O-Isoprenylcorylifol A ( <b>2</b> )	(0.45 ± 3.04)	7.13 ± 1.33 <sup>f</sup>
7-O-Isoprenylneobavaisoflavone ( <b>3</b> )	(1.42 ± 1.48)	13.79 ± 3.00 <sup>g</sup>
Isopsoralen (= Angelicin) ( <b>4</b> )	(44.91 ± 6.46) <sup>e</sup>	(27.73 ± 4.22) <sup>f</sup>
Psoralen ( <b>5</b> )	5.91 ± 3.22 <sup>e</sup>	(24.70 ± 5.99)
Bakuchiol ( <b>6</b> )	alone induced superoxide anion generation and elastase release	
12,13-Dihydro-12,13-epoxybakuchiol ( <b>7</b> )	alone induced superoxide anion generation	14.30 ± 3.05 <sup>f</sup>
<i>p</i> -Hydroxybenzaldehyde ( <b>8</b> )	(38.72 ± 4.80)	(28.93 ± 5.14) <sup>e</sup>
Bavachalcone ( <b>9</b> )	alone induced superoxide anion generation and elastase release	
Psoralidin ( <b>10</b> )	(19.38 ± 6.88) <sup>e</sup>	(18.15 ± 5.53) <sup>e</sup>
Mixture of β-sitosterol ( <b>11</b> ) and stigmasterol ( <b>12</b> )	(2.75 ± 1.02)	(3.18 ± 1.15)
Diphenyleneiodonium <sup>d</sup>	1.78 ± 0.53 <sup>g</sup>	—
Phenylmethylsulfonyl fluoride <sup>d</sup>	—	198.2 ± 28.5 <sup>g</sup>

<sup>a</sup> Results are presented as averages ± SEM (*n* = 4).

<sup>b</sup> Concentration necessary for 50% inhibition (IC<sub>50</sub>). If IC<sub>50</sub> value of compound was <30 μM, it was displayed as IC<sub>50</sub> [μM].

<sup>c</sup> Percentage of inhibition (Inh %) at 30 μM. If IC<sub>50</sub> value of compound was ≥30 μM, it was shown as (Inh %) at 30 μM.

<sup>d</sup> Diphenyleneiodonium (a NADPH oxidase inhibitor) and phenylmethylsulfonyl fluoride (a serine protease inhibitor) were used as the positive controls in the generation of superoxide anion and release of elastase, respectively.

<sup>e</sup> *p* < 0.05 compared with the control.

<sup>f</sup> *p* < 0.01 compared with the control.

<sup>g</sup> *p* < 0.001 compared with the control.

**Table 2**

Inhibitory effects of compounds **1–12** from the fruits of *P. corylifolia* on nitric oxide (NO) generation by RAW264.7 murine macrophages in response to lipopolysaccharide (LPS).

Compounds	IC <sub>50</sub> (μM) <sup>a</sup>
7-O-Methylcorylifol A ( <b>1</b> )	45.33 ± 1.85*
7-O-Isoprenylcorylifol A ( <b>2</b> )	33.15 ± 2.34*
7-O-Isoprenylneobavaisoflavone ( <b>3</b> )	41.71 ± 3.28
Isopsoralen (= Angelicin) ( <b>4</b> )	56.82 ± 3.70*
Psoralen ( <b>5</b> )	40.15 ± 2.27*
Bakuchiol ( <b>6</b> )	21.57 ± 1.03**
12,13-Dihydro-12,13-epoxybakuchiol ( <b>7</b> )	36.65 ± 1.38**
<i>p</i> -Hydroxybenzaldehyde ( <b>8</b> )	>100
Bavachalcone ( <b>9</b> )	64.32 ± 4.13
Psoralidin ( <b>10</b> )	27.46 ± 2.75***
Mixture of β-sitosterol ( <b>11</b> ) and stigmasterol ( <b>12</b> )	>100
Quercetin <sup>b</sup>	33.08 ± 2.17*

<sup>a</sup> The IC<sub>50</sub> values were calculated from the slope of the dose-response curves (SigmaPlot). Values are expressed as average ± SEM (*n* = 4). \**P* < 0.05, \*\**P* < 0.01 compared with the control.

<sup>b</sup> Quercetin was used as a positive control.

(with the 11-isoprenyl group) against LPS-induced NO generation. (d) Bakuchiol (**6**) is the most effective among the isolated compounds, with IC<sub>50</sub> = 21.57 ± 1.03 μM, against LPS-induced NO generation. (e) Cytotoxic effects were determined using MTT assay. The high cell viability (>93%) indicated that the inhibitory activities of compounds **2**, **6**, **7**, and **10** on LPS-induced NO production did not result from their cytotoxicities.

The above findings indicated that the promising inhibitory activity against fMLP-induced O<sub>2</sub><sup>•−</sup> and elastase generation and LPS-induced NO release of *P. corylifolia* and its isolates could stimulate future development of new anti-inflammatory agents.

### 3. Concluding remarks

Twelve compounds, including three previously undescribed isoflavone derivatives, 7-O-methylcorylifol A (**1**), 7-O-isoprenylcorylifol A (**2**), and 7-O-isoprenylneobavaisoflavone (**3**), were isolated from the fruits of *P. corylifolia*. The structures of these compounds were established on the basis of spectroscopic data.

Reactive oxygen species (ROS) [e.g., superoxide anion (O<sub>2</sub><sup>•−</sup>), hydrogen peroxide] and granule proteases (e.g., elastase, cathepsin G) produced by human neutrophils contribute to the pathogenesis of inflammatory diseases. The effects on neutrophil pro-inflammatory responses of isolates were evaluated by suppressing fMLP/CB-induced O<sub>2</sub><sup>•−</sup> generation and elastase release by human neutrophils. The results of anti-inflammatory experiments indicate that compounds **1–3**, **5**, and **7** can significantly inhibit fMLP-induced O<sub>2</sub><sup>•−</sup> generation and/or elastase release. Psoralen (**5**) and 7-O-isoprenylcorylifol A (**2**) were the most effective among the isolated compounds, with IC<sub>50</sub> values of 5.91 ± 3.22 and 7.13 ± 1.33 μM, respectively, against fMLP-induced superoxide anion generation and elastase release. Furthermore, compounds **2**, **6**, **7**, and **10** showed potent inhibition with IC<sub>50</sub> values of 33.15 ± 2.34, 21.57 ± 1.03, 36.65 ± 1.38, and 27.46 ± 2.75 μM, respectively, against LPS-induced NO generation. Thus, our study suggests *P. corylifolia* and its isolates (especially **2**, **5–7**, and **10**) could be further developed as potential candidates for the treatment or prevention of various inflammatory diseases.

## 4. Experimental

### 4.1. General experimental procedures

Melting points were determined on a Yanaco micro-melting point apparatus and were uncorrected. Optical rotations were measured using a Jasco DIP-370 polarimeter (Japan Spectroscopic Corporation, Tokyo, Japan) in CHCl<sub>3</sub>. Ultraviolet (UV) spectra were obtained on a Jasco UV-240 spectrophotometer. Infrared (IR) spectra (neat or KBr) were recorded on a Perkin Elmer 2000 FT-IR spectrometer (Perkin Elmer Corporation, Norwalk, CT, USA). Nuclear magnetic resonance (NMR) spectra, including correlation spectroscopy (COSY), nuclear Overhauser effect spectrometry (NOESY), heteronuclear multiple-bond correlation (HMBC), and heteronuclear single-quantum coherence (HSQC) experiments, were acquired using a Varian Unity 400 or a Varian VNMR-600 spectrometer (Varian Inc., Palo Alto, CA, USA) operating at 400 or 600 MHz (<sup>1</sup>H) and 100 or 150 MHz (<sup>13</sup>C), respectively, with chemical shifts given in ppm (δ) using tetramethylsilane (TMS) as an internal standard. Electrospray ionization (ESI) and high-resolution

electrospray ionization (HRESI)-mass spectra were recorded on a Bruker APEX II (Bruker, Bremen, Germany) or a VG Platform Electrospray ESI/MS mass spectrometer (Fison, Villeurbanne, France). Silica gel (70–230, 230–400 mesh, Merck) was used for column chromatography (CC). Silica gel 60 F-254 (Merck, Darmstadt, Germany) was used for thin-layer chromatography (TLC) and preparative thin-layer chromatography (PTLC).

#### 4.2. Plant material

The fruits of *Psoralea corylifolia* L. (Leguminosae) were collected from Changjhih Township, Pingtung County, Taiwan, in September 2009 and identified by Prof. J.-J. Chen. A voucher specimen (PC-200909) was deposited in the Faculty of Pharmacy, National Yang-Ming University, Taipei, Taiwan.

#### 4.3. Extraction and isolation

The dried fruits (3.8 kg) of *P. corylifolia* were extracted three times with MeOH (15 L each) for 3 days. The extract was concentrated under reduced pressure at 35 °C, and the residue (395 g) was partitioned between EtOAc and H<sub>2</sub>O (1:1) to provide the EtOAc-soluble fraction (fraction A; 94 g). The H<sub>2</sub>O-soluble fraction was further extracted with BuOH, and the BuOH-soluble part (fraction B; 140 g) and the H<sub>2</sub>O-soluble one (fraction C; 152 g) were separated. Fraction A (94 g) was purified by CC (4.3 kg of SiO<sub>2</sub>, 70–230 mesh; *n*-hexane/EtOAc gradient) to afford 12 fractions: A1–A12. Fraction A2 (8.7 g) was subjected to CC (390 g of SiO<sub>2</sub>, 230–400 mesh; *n*-hexane/EtOAc 15:1–0:1, 750 mL-fractions) to give 10 subfractions: A2-1–A2-10. Fraction A2-3 (435 mg) was purified by CC (19.5 g of SiO<sub>2</sub>, 230–400 mesh, *n*-hexane/EtOAc (7:1–0:1), 200 mL-fractions) to give 9 subfractions: A2-3-1–A2-3-9. Fraction A2-3-4 (88 mg) was further purified by preparative TLC (SiO<sub>2</sub>; *n*-hexane/EtOAc 5:1) to obtain bakuchiol (**6**) (4.3 mg, 0.0000011%) (*R*<sub>f</sub> = 0.46). Fraction A2-3-5 (75 mg) was further purified by preparative TLC (SiO<sub>2</sub>; *n*-hexane/EtOAc 5:1) to afford *p*-hydroxybenzaldehyde (**8**) (3.8 mg, 0.000001%) (*R*<sub>f</sub> = 0.16). Part (86 mg) of fraction A2-4 was further purified by preparative TLC (SiO<sub>2</sub>; CHCl<sub>3</sub>/acetone 60:1) to yield 12,13-dihydro-12,13-epoxybakuchiol (**7**) (4.5 mg, 0.0000012%) (*R*<sub>f</sub> = 0.48). Fraction A3 (9.5 g) was subjected to CC (428 g of SiO<sub>2</sub>, 230–400 mesh; *n*-hexane/EtOAc 10:1–0:1, 850 mL-fractions) to give 10 subfractions: A3-1–A3-10. Part (78 mg) of fraction A3-1 was further purified by preparative TLC (SiO<sub>2</sub>; CHCl<sub>3</sub>/acetone, 60:1) to obtain bakuchiol (**6**) (3.8 mg, 0.000001%) (*R*<sub>f</sub> = 0.49). Fraction A3-5 (750 mg) was washed with MeOH and filtered to obtain mixture of β-sitosterol (**11**) and stigmasterol (**12**) (128 mg, 0.000034%) after recrystallization (MeOH). Fraction A3-6 (90 mg) was purified by preparative TLC (SiO<sub>2</sub>; *n*-hexane/acetone 5:1) to obtain isopsoralen (= angelicin) (**4**) (10.4 mg, 0.0000027%) (*R*<sub>f</sub> = 0.29). Fraction A4 (8.7 g) was subjected to CC (395 g of SiO<sub>2</sub>, 230–400 mesh; *n*-hexane/acetone 6:1–0:1, 700 mL-fractions) to afford 8 subfractions: A4-1–A4-8. Part (82 mg) of fraction A4-2 was further purified by preparative TLC (SiO<sub>2</sub>; CHCl<sub>3</sub>/EtOAc 80:1) to yield psoralen (**5**) (3.9 mg, 0.000001%) (*R*<sub>f</sub> = 0.53). Part (84 mg) of fraction A4-4 was further purified by preparative TLC (SiO<sub>2</sub>; CHCl<sub>3</sub>/MeOH 30:1) to afford 7-*O*-isoprenylneobavaisoflavone (**3**) (4.1 mg, 0.0000011%) (*R*<sub>f</sub> = 0.49). Part (75 mg) of fraction A4-5 was further purified by preparative TLC (SiO<sub>2</sub>; CHCl<sub>3</sub>/MeOH 60:1) to obtain 7-*O*-methylcorylifol A (**1**) (4.5 mg, 0.0000012%) (*R*<sub>f</sub> = 0.35). Fraction A6 (9.3 g) was subjected to CC (420 g of SiO<sub>2</sub>, 230–400 mesh; *n*-hexane/acetone 5:1–0:1, 600 mL-fractions) to afford 9 subfractions: A6-1–A6-9. Part (77 mg) of fraction A6-2 was purified by preparative TLC (SiO<sub>2</sub>; *n*-hexane/acetone, 3:1) to obtain 7-*O*-isoprenylcorylifol A (**2**) (4.5 mg, 0.0000012%) (*R*<sub>f</sub> = 0.31). Part (83 mg) of fraction A6-4 was further

purified by preparative TLC (SiO<sub>2</sub>; *n*-hexane/acetone 2:1) to afford bavachalcone (**9**) (3.6 mg, 0.00000095%) (*R*<sub>f</sub> = 0.65). Part (92 mg) of fraction A6-6 was further purified by preparative TLC (SiO<sub>2</sub>; *n*-hexane/acetone 2:1) to yield psoralidin (**10**) (4.5 mg, 0.0000012%) (*R*<sub>f</sub> = 0.51).

7-*O*-Methylcorylifol A (**1**): yellowish amorphous powder; UV (MeOH): λ<sub>max</sub> (log ε) = 220 (4.36), 239 (4.40), 248 (4.40), 294 (sh, 4.14) nm; IR (KBr): ν<sub>max</sub> = 3334 (OH), 1626 (C=O) cm<sup>-1</sup>; <sup>1</sup>H-NMR (CDCl<sub>3</sub>, 600 MHz): δ = 1.59 (3H, s, H-9''), 1.67 (3H, s, H-8''), 1.78 (3H, s, H-10''), 2.08 (2H, m, H-4''), 2.12 (2H, m, H-5''), 3.41 (2H, d, *J* = 7.2 Hz, H-1'), 3.92 (3H, s, OMe-7), 5.07 (1H, br t, *J* = 7.2 Hz, H-6''), 5.36 (1H, br t, *J* = 7.2 Hz, H-2''), 5.52 (1H, br s, D<sub>2</sub>O exchangeable, OH-4'), 6.85 (1H, d, *J* = 7.8 Hz, H-5'), 6.86 (1H, d, *J* = 2.4 Hz, H-8), 6.99 (1H, dd, *J* = 9.0, 2.4 Hz, H-6), 7.28 (1H, dd, *J* = 7.8, 2.0 Hz, H-6'), 7.31 (1H, d, *J* = 2.0 Hz, H-2'), 7.91 (1H, s, H-2), 8.21 (1H, d, *J* = 9.0 Hz, H-5); <sup>13</sup>C-NMR (CDCl<sub>3</sub>, 150 MHz): δ = 16.2 (C-10''), 17.7 (C-9''), 25.7 (C-8''), 26.4 (C-5''), 30.0 (C-1''), 39.7 (C-4''), 55.8 (OMe), 100.0 (C-8), 114.5 (C-6), 116.0 (C-5'), 118.4 (C-4a), 121.6 (C-2''), 123.8 (C-6''), 124.1 (C-1'), 125.1 (C-3), 126.9 (C-3'), 127.8 (C-5), 128.2 (C-6'), 130.7 (C-2'), 132.0 (C-7''), 138.6 (C-3''), 152.1 (C-2), 154.7 (C-4'), 157.9 (C-8a), 163.9 (C-7), 176.0 (C-4); ESI-MS: *m/z* = 427 [M + Na]<sup>+</sup>; HR-ESI-MS: *m/z* = 427.1882 [M + Na]<sup>+</sup> (calcd for C<sub>26</sub>H<sub>28</sub>O<sub>4</sub>Na, 427.1885).

7-*O*-Isoprenylcorylifol A (**2**): yellowish amorphous powder; UV (MeOH): λ<sub>max</sub> (log ε) = 217 (4.38), 240 (4.40), 248 (4.40), 297 (sh, 4.08) nm; IR (KBr): ν<sub>max</sub> = 3352 (OH), 1625 (C=O) cm<sup>-1</sup>; <sup>1</sup>H-NMR (CDCl<sub>3</sub>, 400 MHz): δ = 1.59 (3H, s, H-9''), 1.66 (3H, s, H-8''), 1.77 (3H, s, H-10''), 1.79 (3H, s, H-5'''), 1.83 (3H, s, H-4'''), 2.07 (2H, m, H-4''), 2.11 (2H, m, H-5''), 3.39 (2H, d, *J* = 7.2 Hz, H-1''), 4.62 (1H, d, *J* = 6.8 Hz, H-1'''), 5.07 (1H, br t, *J* = 7.2 Hz, H-6''), 5.36 (1H, br t, *J* = 7.2 Hz, H-2''), 5.51 (1H, br t, *J* = 6.8 Hz, H-2'''), 5.78 (1H, br s, D<sub>2</sub>O exchangeable, OH-4'), 6.83 (1H, d, *J* = 8.0 Hz, H-5'), 6.86 (1H, d, *J* = 2.4 Hz, H-8), 6.99 (1H, dd, *J* = 9.2, 2.4 Hz, H-6), 7.26 (1H, dd, *J* = 8.0, 2.0 Hz, H-6'), 7.29 (1H, d, *J* = 2.0 Hz, H-2'), 7.90 (1H, s, H-2), 8.20 (1H, d, *J* = 9.2 Hz, H-5); <sup>13</sup>C-NMR (CDCl<sub>3</sub>, 100 MHz): δ = 16.2 (C-10''), 17.7 (C-9''), 18.3 (C-5'''), 25.7 (C-8''), 25.8 (C-4'''), 26.4 (C-5''), 29.8 (C-1''), 39.7 (C-4''), 65.4 (C-1'''), 100.8 (C-8), 115.0 (C-6), 116.0 (C-5'), 118.2 (C-4a), 118.5 (C-2''), 121.7 (C-2''), 123.8 (C-6''), 123.9 (C-1'), 125.1 (C-3), 126.9 (C-3'), 127.7 (C-5), 128.2 (C-6'), 130.6 (C-2'), 131.9 (C-7''), 138.4 (C-3''), 139.4 (C-3'''), 152.1 (C-2), 154.7 (C-4'), 157.9 (C-8a), 163.2 (C-7), 176.1 (C-4); ESI-MS: *m/z* = 481 [M + Na]<sup>+</sup>; HR-ESI-MS: *m/z* = 481.2357 [M + Na]<sup>+</sup> (calcd for C<sub>30</sub>H<sub>34</sub>O<sub>4</sub>Na: 481.2355).

7-*O*-Isoprenylneobavaisoflavone (**3**): yellowish amorphous powder; UV (MeOH): λ<sub>max</sub> (log ε) = 219 (4.37), 240 (4.40), 248 (4.41), 296 (sh, 4.13) nm; IR (KBr): ν<sub>max</sub> = 3334 (OH), 1624 (C=O) cm<sup>-1</sup>; <sup>1</sup>H-NMR (CDCl<sub>3</sub>, 400 MHz): δ = 1.77 (3H, d, *J* = 1.2 Hz, H-5''), 1.79 (3H, s, H-4''), 1.79 (3H, s, H-5'''), 1.83 (3H, d, *J* = 0.8 Hz, H-4'''), 3.39 (2H, d, *J* = 7.2 Hz, H-1''), 4.62 (1H, d, *J* = 6.8 Hz, H-1'''), 5.35 (1H, br t, *J* = 7.2 Hz, H-2''), 5.51 (1H, br t, *J* = 6.8 Hz, H-2'''), 5.46 (1H, br s, D<sub>2</sub>O exchangeable, OH-4'), 6.84 (1H, d, *J* = 8.0 Hz, H-5'), 6.86 (1H, d, *J* = 2.4 Hz, H-8), 6.99 (1H, dd, *J* = 9.2, 2.4 Hz, H-6), 7.27 (1H, dd, *J* = 8.0, 2.0 Hz, H-6'), 7.31 (1H, d, *J* = 2.0 Hz, H-2'), 7.90 (1H, s, H-2), 8.20 (1H, d, *J* = 9.2 Hz, H-5); <sup>13</sup>C-NMR (CDCl<sub>3</sub>, 100 MHz): δ = 17.9 (C-5''), 18.3 (C-5'''), 25.8 (C-4''), 25.8 (C-4'''), 29.9 (C-1''), 65.4 (C-1'''), 100.8 (C-8), 115.0 (C-6), 115.9 (C-5'), 118.3 (C-4a), 118.5 (C-2'''), 121.7 (C-2''), 124.2 (C-1'), 125.1 (C-3), 126.9 (C-3'), 127.7 (C-5), 128.2 (C-6'), 130.7 (C-2'), 134.8 (C-3''), 139.4 (C-3'''), 152.1 (C-2), 154.5 (C-4'), 157.9 (C-8a), 163.2 (C-7), 176.0 (C-4); ESI-MS: *m/z* = 413 [M + Na]<sup>+</sup>; HR-ESI-MS: *m/z* = 413.1725 [M + Na]<sup>+</sup> (calcd for C<sub>25</sub>H<sub>26</sub>O<sub>4</sub>Na: 413.1729).

#### 4.4. Biological assay

The effect of the isolated compounds on neutrophil pro-inflammatory response was evaluated by monitoring the

inhibition of superoxide anion generation and elastase release in fMLP/CB-activated human neutrophils in a concentration-dependent manner. The purity of the tested compounds was >98% as identified by NMR and MS.

#### 4.4.1. Preparation of human neutrophils

Human neutrophils from venous blood of healthy, adult volunteers (20–28 years old) were isolated using a standard method of dextran sedimentation prior to centrifugation in a Ficoll Hypaque gradient and hypotonic lysis of erythrocytes (Boyum, 1968). Purified neutrophils containing >98% viable cells, as determined by the trypan blue exclusion method (Jauregui et al., 1981), were resuspended in a calcium ( $\text{Ca}^{2+}$ )-free HBSS buffer at pH 7.4 and were maintained at 4 °C prior to use.

#### 4.4.2. Measurement of superoxide anion generation

The assay for measurement of superoxide anion generation was based on the SOD-inhibitable reduction of ferricytochrome *c* (Babior et al., 1973; Hwang et al., 2006). In brief, after supplementation with 0.5 mg/mL ferricytochrome *c* and 1 mM  $\text{Ca}^{2+}$ , neutrophils ( $6 \times 10^5/\text{mL}$ ) were equilibrated at 37 °C for 2 min and incubated with different concentrations (30–0.01  $\mu\text{M}$ ) of compounds or DMSO (as control) for 5 min. Cells were incubated with cytochalasin B (1  $\mu\text{g}/\text{mL}$ ) for 3 min prior to the activation with 100 nM formyl-L-methionyl-L-leucyl-L-phenylalanine for 10 min. Changes in absorbance with the reduction of ferricytochrome *c* at 550 nm were continuously monitored in a double-beam, six-cell positioner spectrophotometer with constant stirring (Hitachi U-3010, Tokyo, Japan). Calculations were based on differences in the reactions with and without SOD (100 U/mL) divided by the extinction coefficient for the reduction of ferricytochrome *c* ( $\epsilon = 21.1/\text{mM}/10 \text{ mm}$ ).

#### 4.4.3. Measurement of elastase release

Degranulation of azurophilic granules was determined by measuring elastase release as described previously (Hwang et al., 2006). Experiments were performed using MeO-Suc-Ala-Ala-Pro-Val-*p*-nitroanilide as the elastase substrate. Briefly, after supplementation with MeO-Suc-Ala-Ala-Pro-Val-*p*-nitroanilide (100  $\mu\text{M}$ ), neutrophils ( $6 \times 10^5/\text{mL}$ ) were equilibrated at 37 °C for 2 min and incubated with compounds for 5 min. Cells were stimulated with fMLP (100 nM)/CB (0.5  $\mu\text{g}/\text{mL}$ ), and changes in absorbance at 405 nm were monitored continuously in order to assay elastase release. The results were expressed as the percent of elastase release in the fMLP/CB-activated, drug-free control system.

#### 4.4.4. Determination of NO production

The murine macrophage cell line RAW264.7 was cultured in Dulbecco's modified Eagle's medium (DMEM, Gibco BRL Life Technologies, Inc.) supplemented with 10% heat-inactivated fetal bovine serum (FBS) and incubated at 37 °C in a humidified 5%  $\text{CO}_2$  atmosphere with a 96-well flat-bottomed culture plate. After 24 h, the condition medium was replaced with fresh DMEM; and FBS. Then, compounds **1–12** (0, 3, 15, 30, and 60  $\mu\text{M}$ ) were added, respectively, in the presence of lipopolysaccharide (LPS; 1  $\mu\text{g}/\text{mL}$ ; Sigma, Cat No: L-2654) and incubated under the same condition for 24 h. The cultured cells were then centrifuged, and the supernatants were used for NO-production measurement. The supernatant was mixed with an equal volume of the Griess reagent (1% sulfanilamide, 0.1% *N*-(naphthalen-1-yl)ethylenediamine dihydrochloride in 2.5%  $\text{H}_2\text{PO}_4$  soln.) and incubated for 10 min at room temperature. Nitrite concentration was determined by measuring the absorbance at 540 nm using an ELISA plate reader ( $\mu$  Quant) (Johansson et al., 2002). The percentage of NO inhibition of the test compound was calculated as follows: inhibitory rate (%) =  $(1 - (\text{LPS}/\text{sample} -$

untreated))/(LPS – untreated)  $\times 100$ . All tests were run in quadruplicate and averaged. The data were expressed as a mean of four experiments. The software SigmaPlot was used for determining the  $\text{IC}_{50}$  values.

#### 4.4.5. Cell viability assay

A MTT colorimetric assay was used to determine cell viability. The assay was modified from that of Mosmann (1983). The test is based upon the selective ability of living cells to reduce the yellow soluble salt, MTT, to a purple-blue insoluble formazan. MTT (Merck; dissolved in phosphate-buffered saline at 5 mg/mL) soln. was added onto the attached cells mentioned above (10  $\mu\text{L}$  per 100  $\mu\text{L}$  culture) and incubated at 37 °C for 4 h. Then, DMSO was added, and amount of colored formazan metabolite formed was determined by absorbance at 550 nm. The optical density of formazan formed in control (untreated) cells was taken as 100% viability.

#### 4.4.6. Statistical analysis

Results are expressed as the mean  $\pm$  SEM, and comparisons were made using Tukey's HSD test. A probability of 0.05 or less was considered significant. The software SigmaPlot was used for the statistical analysis.

### Acknowledgments

This research was supported by grants from the Ministry of Science and Technology, Taiwan (No. NSC 101-2320-B-127-001-MY3 and MOST 105-2320-B-010-040), awarded to Prof. J.-J. Chen.

### Appendix A. Supplementary data

Supplementary data related to this article can be found at <http://dx.doi.org/10.1016/j.phytochem.2017.08.004>.

### References

- Anand, K.K., Sharma, M.L., Singh, B., Ghatak, B.J., 1978. Antiinflammatory, antipyretic & analgesic properties of bavachinin—a flavanone isolated from seeds of *Psoralea corylifolia* Linn. (Babchi). Indian J. Exp. Biol. 16, 1216–1217.
- Babior, B.M., Kipnes, R.S., Curnutte, J.T., 1973. Biological defense mechanisms. The production by leukocytes of superoxide, a potential bactericidal agent. J. Clin. Invest. 52, 741–744.
- Borreagaard, N., 1998. The human neutrophil. Function and dysfunction. Eur. J. Haematol. 41, 401–413.
- Boyum, A., 1968. Isolation of mononuclear cells and granulocytes from human blood. Isolation of mononuclear cells by one centrifugation, and of granulocytes by combining centrifugation and sedimentation at 1 g. Scand. J. Clin. Lab. Invest. 97, 77–89.
- Chen, H., Du, X., Tang, W., Zhou, Y., Zuo, J., Feng, H., Li, Y., 2008a. Synthesis and structure-immunosuppressive activity relationships of bakuchiol and its derivatives. Bioorg. Med. Chem. 16, 2403–2411.
- Chen, J.J., Luo, Y.T., Hwang, T.L., Sung, P.J., Wang, T.C., Chen, I.S., 2008b. A new indole alkaloid and anti-inflammatory constituents from *Strychnos cathayensis*. Chem. Biodivers. 5, 1345–1352.
- Chopra, B., Dhinra, A.K., Dhar, K.L., 2013. *Psoralea corylifolia* L. (Buguchi) — folklore to modern evidence: review. Fitoterapia 90, 44–56.
- Faurschou, M., Borregaard, N., 2003. Neutrophil granules and secretory vesicles in inflammation. Microbes Infect. 5, 1317–1327.
- Gupta, S., Jha, B.N., Gupta, G.K., Gupta, B.K., Dhar, K.L., 1990. Coumestans from seeds of *Psoralea corylifolia*. Phytochemistry 29, 2371–2373.
- Huang, T.C., Ohashi, H., 1993. Leguminosae In: Flora of Taiwan, second ed., vol. 3. Editorial Committee of the Flora of Taiwan, Taipei, Taiwan, pp. 160–396.
- Hwang, T.L., Leu, Y.L., Kao, S.H., Tang, M.C., Chang, H.L., 2006. Viscolin, a new chalcone from *Viscum coloratum*, inhibits human neutrophil superoxide anion and elastase release via a cAMP-dependent pathway. Free Radic. Biol. Med. 41, 1433–1441.
- Jauregui, H.O., Hayner, N.T., Driscoll, J.L., Williams-Holland, R., Lipsky, M.H., Galletti, P.M., 1981. Trypan blue dye uptake and lactate dehydrogenase in adult rat hepatocytes-freshly isolated cells, cell suspensions, and primary monolayer cultures. In Vitro 17, 1100–1110.
- Johansson, M., Köpcke, B., Anke, H., Sterner, O., 2002. Biologically active secondary metabolites from the ascomycete A111-95. 2. Structure elucidation. J. Antibiot. 55, 104–106.
- Khastgir, H.N., Duttgupta, P.C., Sengupta, P., 1961. The structure of psoralidin.

- Tetrahedron 14, 275–283.
- Labbé, C., Faini, F., Coll, J., Connolly, J.D., 1996. Bakuchiol derivatives from the leaves of *Psoralea glandulosa*. *Phytochemistry* 42, 1299–1303.
- Lee, M.H., Kim, J.Y., Ryu, J.H., 2005. Prenylflavones from *Psoralea corylifolia* inhibit nitric oxide synthase expression through the inhibition of I- $\kappa$ B- $\alpha$  degradation in activated microglial cells. *Biol. Pharm. Bull.* 28, 2253–2257.
- Lin, C.F., Huang, Y.L., Chien, M.Y., Sheu, S.J., Chen, C.C., 2007. Analysis of bakuchiol, psoralen and angelicin in crude drugs and commercial concentrated products of *Fructus Psoraleae*. *J. Food Drug Anal.* 15, 433–437.
- Mar, W.C., Je, K.H., Seo, E.K., 2001. Cytotoxic constituents of *Psoralea corylifolia*. *Arch. Pharm. Res.* 24, 211–213.
- Mosmann, T., 1983. Rapid colorimetric assay for cellular growth and survival: application to proliferation and cytotoxicity assays. *J. Immunol. Methods* 65, 55–63.
- Motai, T., Kitanaka, S., 2005. Sesquiterpene chromones from *Ferula fukanensis* and their nitric oxide production inhibitory effects. *J. Nat. Prod.* 68, 1732–1735.
- Pharmacopoeia of the People's Republic of China, 2005. Chemical Industry Publications, Beijing, Vol. I, pp. 129–130.
- Roos, D., van Bruggen, R., Meischl, C., 2003. Oxidative killing of microbes by neutrophils. *Microbes. Infect.* 5, 1307–1315.
- Sugamoto, K., Matsusita, Y., Matsui, K., Kurogi, C., Matsui, T., 2011. Synthesis and antibacterial activity of chalcones bearing prenyl or geranyl groups from *Angelica keiskei*. *Tetrahedron* 67, 5346–5359.
- Tsai, W.J., Hsin, W.C., Chen, C.C., 1996. Antiplatelet flavonoids from seeds of *Psoralea corylifolia*. *J. Nat. Prod.* 59, 671–672.
- Vane, J.R., Mitchell, J.A., Appleton, I., Tomlinson, A., Bishop-Bailey, D., Croxtall, J., Willoughby, D.A., 1994. Inducible isoforms of cyclooxygenase and nitric-oxide synthase in inflammation. *Proc. Nat. Acad. Sci. U. S. A.* 91, 2046–2050.
- Wang, L.Y., Unehara, T., Kitanaka, S., 2005. Anti-inflammatory activity of new guaiane type sesquiterpene from *Wikstroemia indica*. *Chem. Pharm. Bull.* 53, 137–139.
- Witko-Sarsat, V., Rieu, P., Descamps-Latscha, B., Lesavre, P., Halbwachs-Mecarelli, L., 2000. Neutrophils: molecules, functions and pathophysiological aspects. *Lab. Invest. Investig.* 80, 617–653.
- Woodhead, S., Galeffi, C., Bettolo, G.B.M., 1982. *p*-Hydroxybenzaldehyde as a major constituent of the epicuticular wax of seedling *Sorghum bicolor*. *Phytochemistry* 21, 455–456.
- Wulff, W.D., McCallum, J.S., Kunng, F.A., 1988. Two regiocomplementary approaches to angular furanocoumarins with chromium carbene complexes: synthesis of sphondin, thiosphondin, heratomin, and angelicin. *J. Am. Chem. Soc.* 110, 7419–7434.
- Xin, D., Wang, H., Yang, J., Su, Y.F., Fan, G.W., Wang, Y.F., Zhu, Y., Gao, X.M., 2010. Phytoestrogens from *Psoralea corylifolia* reveal estrogen receptor-subtype selectivity. *Phytomedicine* 17, 126–131.
- Yang, C.S., Chen, J.J., Huang, H.C., Huang, G.J., Wang, S.Y., Sung, P.J., Cheng, M.J., Wu, M.D., Kuo, Y.H., 2017. New benzenoid derivatives and other constituents from *Lawsonia inermis* with inhibitory activity against NO production. *Molecules* 22, 936.
- Yang, C.S., Huang, H.C., Wang, S.Y., Sung, P.J., Huang, G.J., Chen, J.J., Kuo, Y.H., 2016. New diphenol and isocoumarins from the aerial part of *Lawsonia inermis* and their inhibitory activities against NO production. *Molecules* 21, 1299.
- Yasuhara, A., Kasano, A., Sakamoto, T., 1999. An efficient method for the deallylation of allyl aryl ethers using electrochemically generated nickel. *J. Org. Chem.* 64, 4211–4213.
- Yin, S., Fan, C.Q., Dong, L., Yue, J.M., 2006. Psoracorylifols A–E, five novel compounds with activity against *Helicobacter pylori* from seeds of *Psoralea corylifolia*. *Tetrahedron* 62, 2569–2575.
- Yin, S., Fan, C.Q., Wang, Y., Dong, L., Yue, J.M., 2004. Antibacterial prenylflavone derivatives from *Psoralea corylifolia*, and their structure–activity relationship study. *Bioorg. Med. Chem.* 12, 4387–4392.

# SCIENTIFIC REPORTS

OPEN

## The long non-coding RNA LOC441204 enhances cell growth in human glioma

Tzu-Kang Lin<sup>1</sup>, Chang-Nen Chang<sup>1</sup>, Cheng-Shian Tsai<sup>1</sup>, Yin-Cheng Huang<sup>1</sup>, Yu-Jen Lu<sup>1</sup>, Wei-Jan Chen<sup>2</sup>, Yang-Hsiang Lin<sup>3</sup>, I.-Hsiao Chung<sup>3</sup> & Kwang-Huei Lin<sup>3,4,5</sup>

Glioma is the most common and aggressive type of brain tumor. While long non-coding RNAs (lncRNAs) are clearly more abundant in human brain than protein-coding genes, the specific roles of lncRNAs and mechanisms underlying their dysregulation in glioma remain unclear. Here, we focused on lncRNAs that are differentially expressed in brain tumor and their potential biological functions. LOC441204, a novel non-coding RNA gene displaying high expression in clinical specimens of brain tumor and significant upregulation in glioma cell lines in microarray analyses, was selected for further study. Notably, knockdown of LOC441204 suppressed tumor cell proliferation in two glioma cell lines. Moreover, LOC441204-induced tumor cell growth was mediated the stabilization of  $\beta$ -catenin pathway. Briefly, LOC441204 bound to  $\beta$ -catenin preventing its degradation, resulting in downstream p21 repression and cdk4 activation to enhance glioma cell proliferation. Collectively, our findings indicate a pro-oncogenic role of LOC441204 in tumor cell growth through activation of the  $\beta$ -catenin/p21/cdk4 cascade to act as a potential diagnostic marker or therapeutic target in brain tumor.

Glioma is the major malignant brain tumor type in adults, accounting for 30% of all brain tumors and 80% of malignant brain tumors<sup>1</sup>. Despite the relatively high frequency of gliomas, the etiology of these tumors remains largely unknown. Diffuse gliomas, including astrocytomas and oligodendrogliomas, belong to a single pathologic class but have different histologies and molecular etiologies<sup>2</sup>. For each type of glioma, there are neoplasms that span a broad spectrum of biological aggressiveness<sup>3</sup>. Gliomas are rarely curable. Without treatment, the average life expectancy for patients is only 4–5 months<sup>4</sup>. Therefore, development of effective strategies and identification of novel pathways remain an urgent need for the early diagnosis and treatment of glioma.

Recent reports have revealed an important role of the non-protein coding part of the human genome in cancer formation and progression<sup>5</sup>. Among the different types of non protein-coding RNAs, long non-coding RNAs (lncRNAs) play a pivotal role in cancer biology<sup>6</sup>. LncRNAs are aberrantly expressed in different cancer types, and levels of specific lncRNAs have been shown to be associated with clinical parameters, prognosis, potential therapeutic targets and diagnosis of cancer. Over the past few decades, molecular expression profiles have provided additional information to help distinguish between glioma subtypes<sup>7,8</sup>. Aberrantly expressed molecular markers have additionally been employed to elucidate the mechanisms of glioma progression and malignant transformation<sup>9</sup>.

Despite significant progress in research on lncRNAs in human cancers, limited data are available for brain tumors. Further understanding of brain tumor biology is necessary to clarify the pathogenic mechanisms mediated by lncRNAs. While several lncRNAs have been reported in association with brain tumors to date, these earlier studies lack clinical significance or mechanistic information. Here we investigated the lncRNAs associated with proliferative activity and molecular mechanisms underlying the pathogenesis of brain tumors. Several lncRNA genes displayed higher or lower expression than normal in clinical specimens of brain tumors, suggesting a potential role in glioma progression. Microarray analysis revealed that LOC441204, a novel lncRNA that has not

<sup>1</sup>Department of Neurosurgery, Chang Gung Memorial Hospital, Linko, Chang Gung University, Taoyuan, Taiwan, R.O.C. <sup>2</sup>Cardiovascular Division, Chang Gung Memorial Hospital, Chang Gung University College of Medicine, Taoyuan, Taiwan, R.O.C. <sup>3</sup>Department of Biochemistry, College of Medicine, Chang Gung University, Taoyuan, Taiwan, R.O.C. <sup>4</sup>Liver Research Center, Chang Gung Memorial Hospital, Linko, Taoyuan, Taiwan, R.O.C. <sup>5</sup>Research Center for Chinese Herbal Medicine, College of Human Ecology, Chang Gung University of Science and Technology, Taoyuan, Taiwan, R.O.C. Correspondence and requests for materials should be addressed to K.-H.L. (email: [khlin@mail.cgu.edu.tw](mailto:khlin@mail.cgu.edu.tw)) or I.-H.C. (email: [isiou2007@yahoo.com.tw](mailto:isiou2007@yahoo.com.tw))



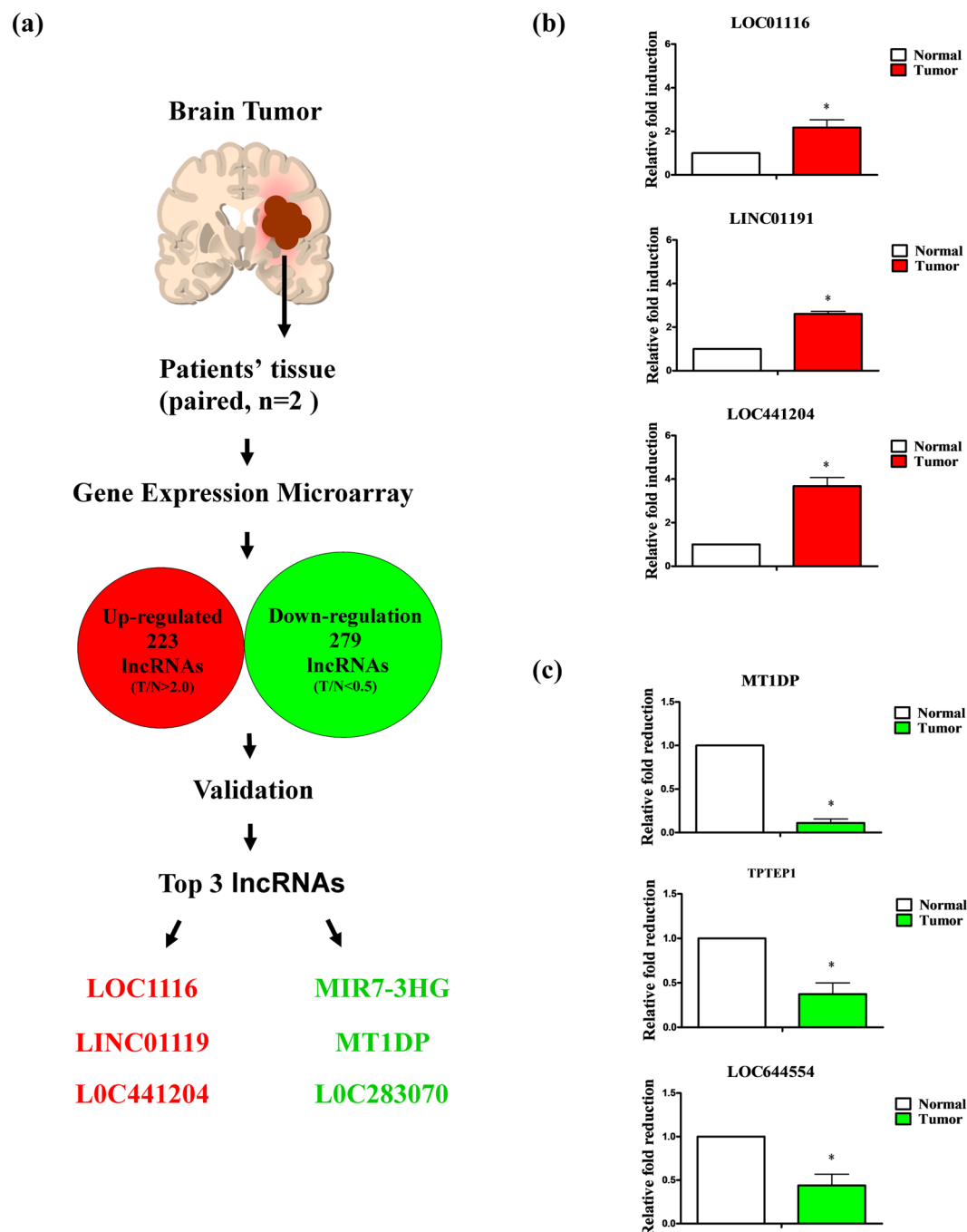


**Figure 1.** Analysis and validation of lncRNAs in brain tumor specimens. (a) Schematic diagram showing application of gene expression microarrays to lncRNA analysis. (b) Upregulation and (c) downregulation of lncRNAs in brain tumor specimens measured using q-RT-PCR. Differences were analyzed using Kruskal-Wallis test (\* $P < 0.05$ ).

been reported in association with human cancer to date, is overexpressed in clinical specimens of brain tumor. We further characterized this aberrantly expressed lncRNA to determine its efficacy as a novel biomarker and/or therapeutic target in brain tumor.

## Results

**Expression of lncRNA in brain tumor.** To identify aberrantly expressed lncRNAs, we characterized lncRNA expression patterns in brain tumor specimens using oligonucleotide arrays (paired patient samples,  $N = 2$ ). Overall, 502 lncRNAs with altered expression were identified, among which 223 were upregulated and 279 were downregulated (Fig. 1a). The potential functions of these lncRNAs in brain tumor progression were examined, focusing on the top three upregulated non-coding genes (fold change  $> 2$ ), *LOC01116*, *LINC01191* and *LOC441204* (Table 1). Higher expression of these genes was validated in clinical specimens of brain tumors

Up-regulated lncRNAs <sup>a</sup>	
Gene symbol	Fold change (T/N > 2.0)
LOC01116	10.154
LINC01191	8.865
LOC441204	5.634
EGFEM1P	5.042
PVT1	4.971
CD99P1	4.547
LOC285370	4.296
LOC284576	3.375
LINC00467	3.118
ZNF788	2.966
Down-regulated lncRNAs <sup>a</sup>	
Gene symbol	Fold change (T/N < 0.5)
TPTEP1	0.050
MT1DP	0.102
LOC644554	0.125
FLJ42875	0.128
LINC00323	0.147
ANKRD19P	0.159
LOC729178	0.161
PART1	0.192
LMF1	0.201
LOC100131289	0.215

**Table 1.** Dys-regulated lncRNAs in brain tumor. <sup>a</sup>Top 10 ranking of up- and down-regulated lncRNAs in clinical specimens were listed. (T/N fold change >2.0 or <0.5).

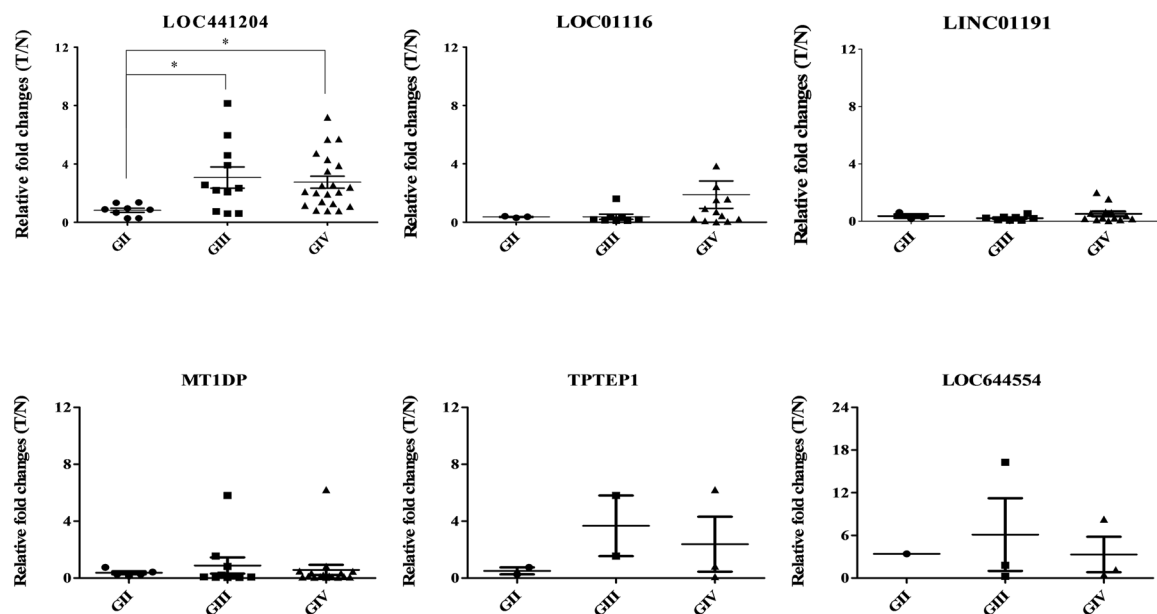
	No. <sup>a</sup>	LOC441204 (T/N) <sup>b</sup>	P
Age (years)			
<60	29	2.31 ± 0.40	0.18
>60	11	3.54 ± 0.95	
Gender			
Male	26	2.28 ± 0.39	0.34
Female	14	3.33 ± 0.86	
Location of brain			
Right	22	2.26 ± 0.57	0.21
Left	18	2.96 ± 0.55	
Grade			
Grade II	9	0.99 ± 0.21	0.04*
Grade III	9	3.61 ± 0.77	
Grade IV	22	3.17 ± 0.57	
Tumor size (cm)			
<4	11	1.31 ± 0.36	0.02*
>4	29	2.69 ± 0.47	

**Table 2.** Clinical parameters of LOC441204 in brain tumor patients. <sup>a</sup>No: Case numbers. <sup>b</sup>LOC441204 (T/N): Fold change of LOC441204 expression in clinical specimens.

(n = 3), with increases of 2- to 4-fold (Fig. 1b). Analysis of downregulated non-coding genes (fold change < 0.5) revealed that expression was decreased 8- to 20-fold (Fig. 1c). These results confirmed aberrant expression of lncRNAs in brain tumor.

**High expression of LOC441204 is correlated with brain tumor progression.** qRT-PCR analysis of LOC441204 expression was performed in 40 consecutive patients to determine its clinicopathological significance and function in brain tumors (Table 2). Notably, LOC441204 increased expression significantly in malignant (GIII + GIV) compared to the begin stage (GII) (Fig. 2a) and size (Fig. 2b). However, the other dys-regulated lncRNAs do not have such correlations (Fig. 2). Thus, we focused on *LOC441204*, in view of the association between its high expression in tumors and clinical stage. Together, the results indicate that LOC441204 expression

(a)



(b)

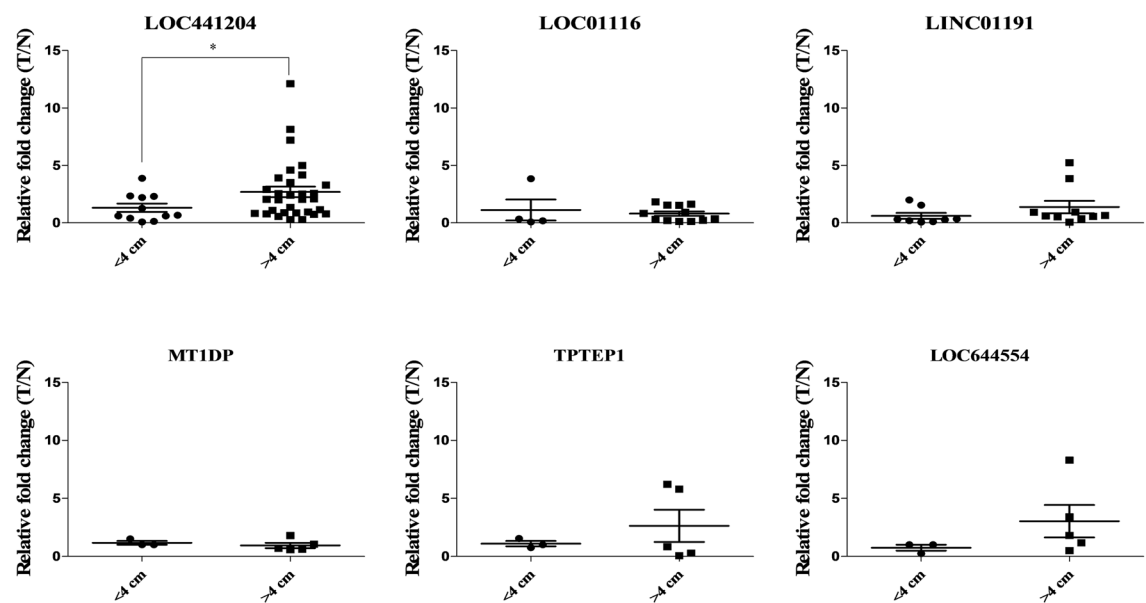


**Figure 2.** Clinical correlations of lncRNAs with associated parameters in brain tumor. Q-RT-PCR analysis of dys-regulated lncRNAs expression in 40 paired brain tumor specimens. (a) Tumor grade, (b) Tumor size. T/N ratios of lncRNAs. Differences were analyzed using one-way ANOVA, \* $P < 0.05$ .

is associated with tumor malignant phenotype and may therefore serve as an effective diagnostic or therapeutic marker for brain tumor.

**LOC441204 is associated with brain tumor cell proliferation.** To determine the effects of LOC441204 on cell proliferation, we established LOC441204 knockdown U87MG and control cell lines. Notably, LOC441204-depleted U87MG cells displayed significantly decreased proliferation, compared with control cells (Fig. 3a,b). Levels of proliferation-associated molecules,  $\beta$ -catenin and cdk4, were additionally decreased in LOC441204-depleted cells, relative to control cells (Fig. 3c). p21, a growth inhibitor associated with cancer

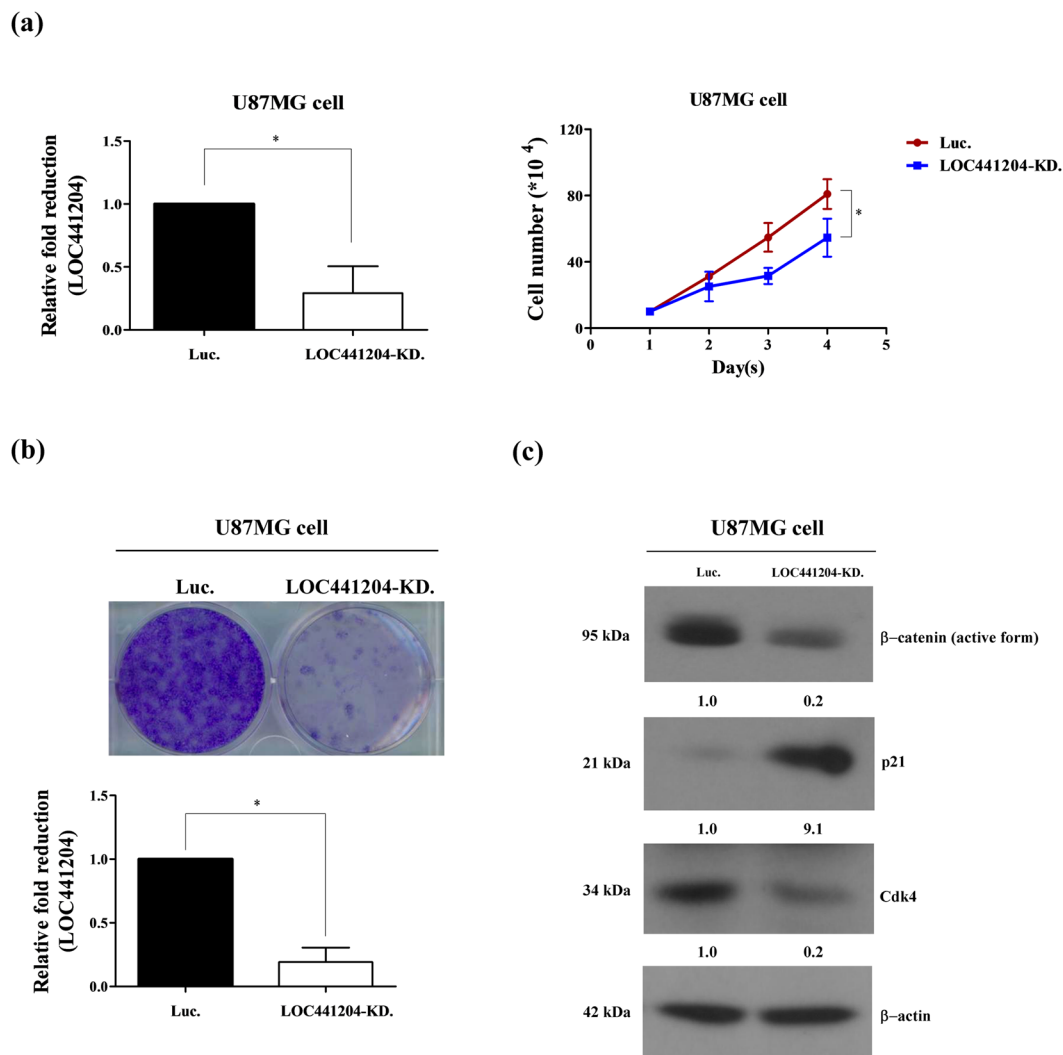


**Figure 3.** LOC441204 depletion suppresses U87MG cell proliferation. (a) *Right panel:* The cell growth ability of U87MG was analyzed under LOC441204-depleted (LOC441204 KD) and control (Luc) conditions. *Left panel:* Quantification of LOC441204 expression. (b) Colony assay of U87MG under similar conditions. (c) Western blot analysis of  $\beta$ -catenin, p21 and cdk4 expression levels in cell lines. Differences were analyzed using the Kruskal–Wallis test (\* $P < 0.05$ ).

proliferation and downregulated by  $\beta$ -catenin, was significantly increased in LOC441204-depleted cells, implicating a role of LOC441204 in accelerating tumor cell proliferation.

**LOC441204 depletion suppresses brain tumor cell proliferation.** To confirm the promotory effect of LOC441204 on cell growth, we established another LOC441204 knockdown cell line, T98. Consistently, depletion of LOC441204 in T98 cells led to a significant decrease in proliferative ability, compared with that of control cells (Fig. 4a,b). Additionally, levels of  $\beta$ -catenin and cdk4 were downregulated and p21 was upregulated in LOC441204 knockdown cells (Fig. 4c).

**LOC441204 depletion promotes  $\beta$ -catenin degradation.** To further identify the effects of LOC441204 on  $\beta$ -catenin, LOC441204 knockdown cell lines in U87MG and T98 were established and analyzed. Depletion of LOC441204 in these cells led to a significant increase in  $\beta$ -catenin degradation by ubiquitylation compared to the control cells (Fig. 5a,b). Together, LOC441204 may protect  $\beta$ -catenin from ubiquitin-mediated protein degradation.

**LOC441204 interacts with  $\beta$ -catenin in brain tumor cell.** To identify the mechanism that LOC441204 protects  $\beta$ -catenin from degradation, RNA immunoprecipitation (RIP) assay was performed. Notably, LOC441204 bound to  $\beta$ -catenin in control cells, and this interaction was decreased in LOC441204 knockdown cell lines (Fig. 5c,d). Collectively, these results support LOC441204 promotes cell proliferation in brain tumors through stabilization of  $\beta$ -catenin to activate the  $\beta$ -catenin/p21/cdk4 pathway (Fig. 5e).

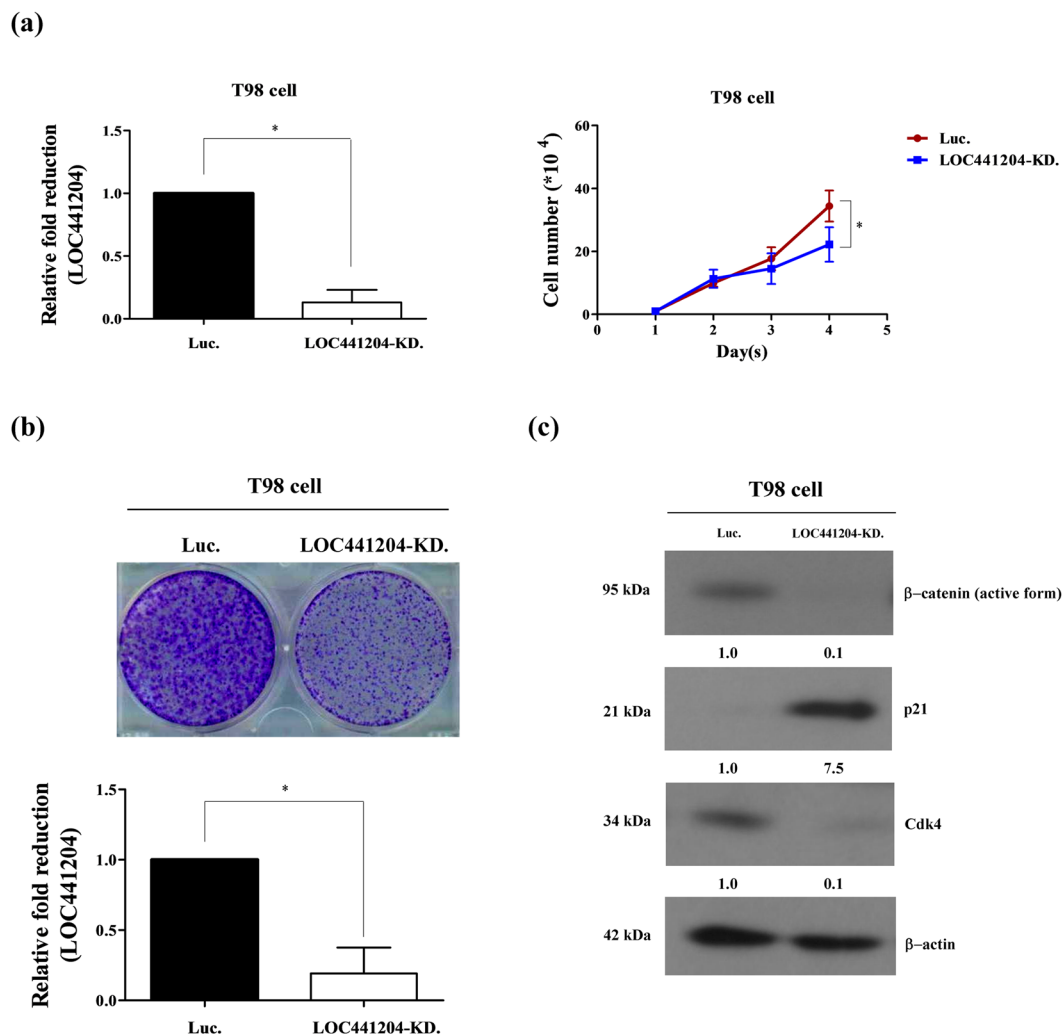


**Figure 4.** LOC441204 depletion suppresses T98 cell proliferation. (a) *Right panel:* The proliferation ability of T98 was analyzed under LOC441204-depleted (LOC441204-KD.) and control (Luc.) conditions. *Left panel:* Quantification of LOC441204 expression. (b) Colony assay of the T98 cell line under similar conditions. (c) Western blot analysis of  $\beta$ -catenin, p21 and cdk4 expression levels in cell lines. Differences were analyzed using the Kruskal–Wallis test (\* $P < 0.05$ ).

## Discussion

We used oligonucleotide microarray analysis to detect lncRNAs differentially expressed in brain tumor, with a view to establishing their specific roles in carcinogenesis. Clinical specimens were further evaluated for aberrant expression of lncRNAs to identify potential biomarkers of glioma proliferation. Our data showed high expression of a novel lncRNA, LOC441204, in brain tumor specimens that was positively correlated with tumor grade and size. Loss-of-function studies clearly demonstrated that LOC441204 promotes cell proliferation. These results provide strong evidence that LOC441204 is a novel oncogene that may serve as a cell growth marker for brain tumor progression.

lncRNAs are important regulators of gene expression proposed to exert multiple effects through distinct mechanisms, including regulation of gene transcription in basal transcription machinery, posttranscriptional regulation of RNA splicing, and epigenetic regulation<sup>10–12</sup>. Studies to date have shown that about 18% of the non-protein coding genes that produce lncRNAs are associated with cancer, compared to only 9% of all human protein-coding genes<sup>13</sup>. Aberrantly expressed lncRNAs have been distinguished as potential biomarkers and therapeutic targets in a variety of cancer types<sup>14–16</sup>. In this study, we identified and validated sets of lncRNA genes in brain tumors. Our findings suggest that specific lncRNAs play important roles in the progression of human glioma.

Several lncRNAs have been reported in association with brain tumor. MEG3, a non-coding RNA, may serve as a tumor suppressor gene at chromosome 14q32 involved in meningioma progression<sup>17,18</sup>. H19 is reported to regulate glioma development by driving miR-675 expression, providing important clues for understanding the key roles of the lncRNA-miRNA functional network in glioma<sup>19</sup>. ASLNC22381 and ASLNC20819 play critical roles via their target IGF-1 in the malignant glioblastomas (GBM) that arise from astrocytes<sup>20</sup>. Knockdown



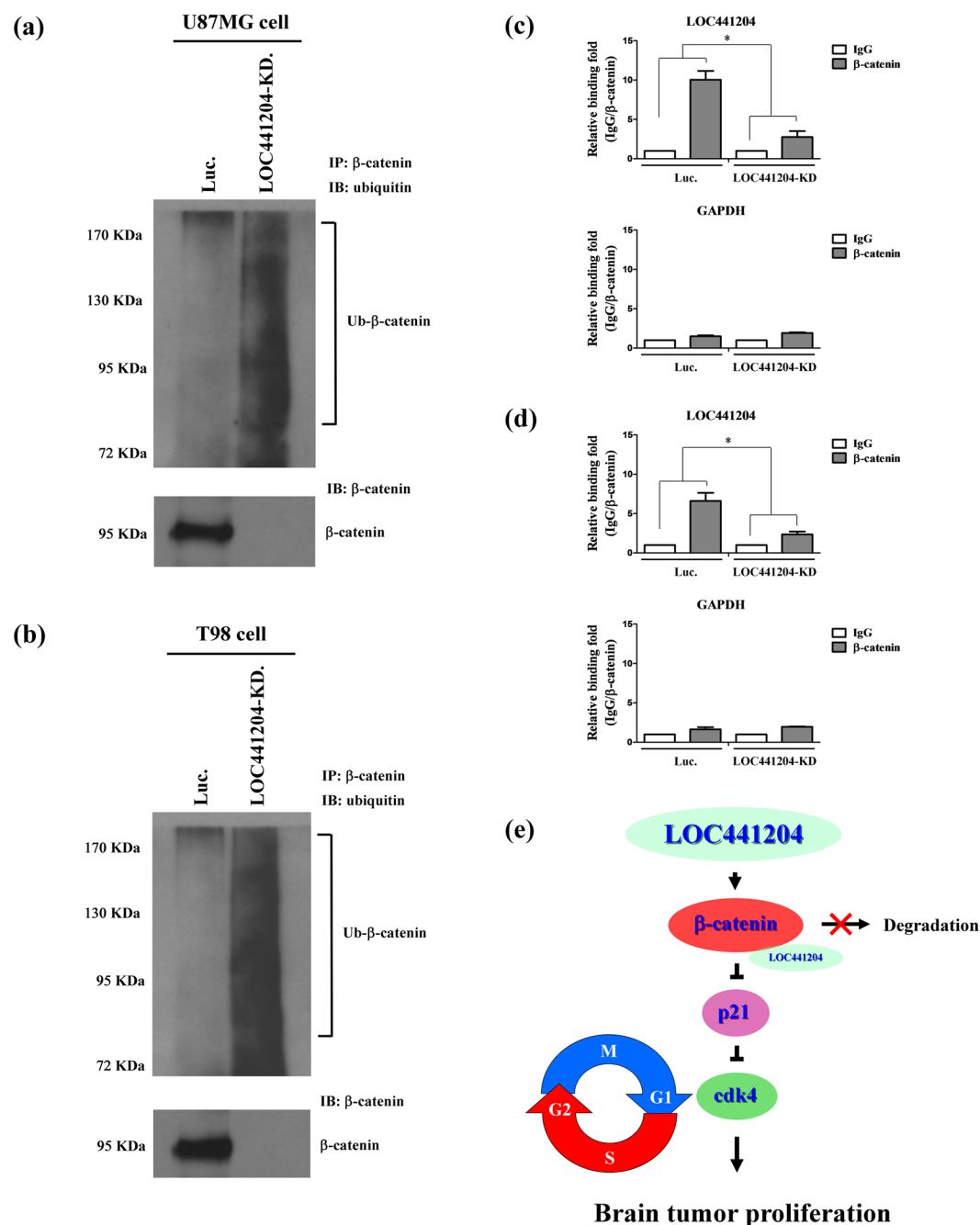


**Figure 5.**  $\beta$ -catenin degraded by ubiquitylation in LOC441204 depleted cells. The immunoprecipitation assays of (a) U87MG and (b) T98 cell lines were analyzed under LOC441204-depleted (LOC441204-KD.) and control (Luc.) conditions. Ubiquitinated  $\beta$ -catenin was analyzed by Western blot. The RIP assays were performed in (c) U87MG and (d) T98 cell lines under similar conditions. GAPDH is a negative binding control. (e) Schematic diagram of LOC441204-mediated enhancing of brain tumor proliferation through the  $\beta$ -catenin/p21/cdk4 cascade. Differences were analyzed using the Kruskal–Wallis test (\* $P < 0.05$ ).

of TUG1 increases blood-tumor barrier (BTB) permeability via binding to miR-144 and reducing tight junction protein expression in endothelial cells through targeting HSF2. TUG1 represents a potentially useful therapeutic target for enhancing BTB permeability<sup>21</sup>. LncRNA expression patterns are distinct between genotoxic stress-induced apoptosis and necrosis in human glioma cells. Thus, the sets of lncRNA expressed during genotoxic stress-induced apoptosis are specifically responsive to DNA damage agents. To our knowledge, no studies to date have reported an association between LOC441204 and brain tumor progression or involvement of a LOC441204-mediated pathway in brain tumor proliferation.

$\beta$ -Catenin is a core factor in tumor cell growth that inhibits expression of its downstream target gene encoding p21 to enhance cancer proliferation<sup>22,23</sup>. p21 is a key cell cycle regulator that arrests cells in the G1 and G2

phases<sup>24, 25</sup>. Additionally, p21 is reported as an inhibitor of cdk4, a well-known G1 phase regulator in the cell cycle<sup>26, 27</sup>. No reports have linked the regulation of lncRNA with  $\beta$ -catenin/p21 in brain tumors. Experiments from the current study showed that LOC441204 enhances the growth ability of glioma cell lines and stimulates proliferation through protection and activation of  $\beta$ -catenin/p21/cdk4 components.

In conclusion, this is the first report to demonstrate involvement of the lncRNA LOC441204 in glioma cell proliferation via a mechanism involving the  $\beta$ -catenin/p21/cdk4 cascade. Our data collectively provide insights into the role of LOC441204 in brain tumor progression and strongly support its potential utility as a therapeutic target in glioma.

## Materials and Methods

**Ethics statement.** All experiments were performed in accordance with the approved guidelines of the Chang Gung Memorial Hospital Institutions Review Board (IRB: 103–3212B and 103–4688B). Informed consent was obtained from all patients involved in the study.

**Tissue specimens.** Brain tumor tissue and adjacent noncancerous mucosa were obtained from Department of Neurosurgery, Chang Gung Memorial Hospital.

**RNA extraction and gene expression microarrays.** Total RNA from paired brain tumor tissue and adjacent noncancerous mucosa samples (N = 2) was extracted using TRIzol reagent (Life Technologies, Rockville, MD, USA) as described previously<sup>28, 29</sup>. Total RNA (20  $\mu$ g) was used for labeling and hybridization with the SurePrint G3 Human Gene Expression array (Agilent, Welgene Biotech, Taiwan) containing 7419 lncRNAs and 27958 human genes. Slides were scanned and intensities measured using GenePix Pro 4.1 software (Axon Instruments Inc. Foster City, CA, USA).

**Cell culture.** U87MG and T98 human glioma cell lines were routinely cultured at 37 °C in a humidified atmosphere of 95% air and 5% CO<sub>2</sub> in Minimum Essential Medium (MEM) supplemented with 10% or 15% fetal bovine serum (FBS).

**Immunoblot analysis.** Total cell lysates and conditioned media were prepared and protein concentrations determined using the Bradford assay kit (Pierce Biotechnology, Rockford, IL, USA). Equivalent amounts of protein were fractionated via sodium dodecyl sulfate–polyacrylamide gel electrophoresis (SDS–PAGE) on a 10% gel. Separated proteins were transferred to nitrocellulose membrane (pH 7.9; Amersham Biosciences Inc., Piscataway, NJ, USA), followed by blocking with 5% non-fat powdered milk and incubation with specific primary antibodies, including anti-active  $\beta$ -catenin (Millipore, Merck Life Science business, Germany; 05–665), anti-p21 (Thermo, Thermo Fisher Scientific, USA; #MS-891) and anti-cdk4 (Santa Cruz Biotechnology, Santa Cruz, CA, USA; sc-260), at 4 °C overnight. After washing, membranes were incubated with horseradish peroxidase (HRP)-conjugated anti-mouse, anti-rabbit or anti-goat IgG secondary antibody, as appropriate, for 1 h at room temperature. Immune complexes were visualized using an enhanced chemiluminescence (ECL) detection kit (Amersham) and Fuji X-ray film.

**Lentivirus infection and shRNA-mediated stable cell lines.** Short hairpin RNA (shRNA) sequences targeting *LOC441204* were purchased from the National RNAi Core Facility (Institute of Molecular Biology, Academia Sinica, Taiwan). Lentivirus was packaged control vector and shRNA targeting *LOC441204* into 293 T cells, and collected from the supernatant. Lentiviral particles were infected into U87MG or T98 cells, and stable cell lines were established using puromycin as a selection marker.

**Proliferation and colony formation assays.** The influence of LOC441204 on cell proliferation ability was determined using U87MG-LOC441204-depleted and T98-LOC441204-depleted cells. Briefly, cell density was adjusted to 10<sup>4</sup> or 10<sup>6</sup> cells/ml, and 100  $\mu$ l suspension seeded on a 24-well plate. The medium used was MEM containing 10% fetal bovine serum (FBS). After incubation for 1–4 days or 1–2 weeks at 37 °C, harvested cells were subjected to cell counting or crystal violet staining. Experiments were performed at least three times.

**RIP assay.** LOC441204-depleted and control cells were washed twice with ice-cold 1X PBS and removed from the culture plate using a cell scraper in 1 ml ice-cold polysomal lysis buffer (100 mM KCl, 5 mM MgCl<sub>2</sub>, 10 mM HEPES (pH 7.0), 0.5% NP40, 1 mM DTT, 50 U RNase inhibitor (SUPERase-in; Ambion, Austin, TX, USA), protease inhibitor cocktail (Roche) per 10 cm dish. Subsequently, suspension was passed through a 27.5-G needle eight times to promote cell lysis. Whole-cell extracts were collected by centrifugation (16000 g, 15 min) and pre-cleared with magnetic protein-G beads (Invitrogen) at 4 °C for 1 h. Immunoprecipitation was performed by adding the  $\beta$ -catenin antibody to the precleared extracts and incubating at 4 °C overnight. Magnetic protein-G beads were then added to each IP sample and rotated for 1 h at 4 °C. The beads were pelleted and washed with polysomal lysis buffer. After several washes, 20 U of DNase I (Roche) and 10X reaction buffer was added and incubated at 37 °C for 15 min to remove all contaminating DNA. Then, 1 ml Trizol reagent was added to the beads and the RNA was extracted and analyzed by q-RT-PCR.

**Ubiquitylation assay.** LOC441204-depleted and control cells were treated with MG132 (10 mM) for an additional 4 h and extracted by lysis buffer containing protease inhibitors. Cell lysate was incubated with protein A/G (Santa Cruz) for 1 h to prevent non-specific binding. Products were incubated overnight at 4 °C with  $\beta$ -catenin antibody (Thermo Fisher Scientific), precipitated with protein A/G (Santa Cruz) for 1 h at 4 °C. The ubiquitinated  $\beta$ -catenin signal was detected by Ubiquitin antibody (Epitomics Inc., Burlingame, CA, USA).

**Statistical analysis.** Data are expressed as mean values  $\pm$  SEM of at least three experiments. Statistical analyses were performed using Student's *t* test and one-way analysis of variance (ANOVA). Where appropriate, Mann–Whitney *U* or Fisher's exact test was used to compare two groups, and Kruskal–Wallis test or Pearson's  $\chi^2$  test used if more than two groups were compared. Spearman's correlation test was employed to assess the relationship between data obtained from two different examinations. *P*-values  $< 0.05$  were considered statistically significant.

## References

- Goodenberger, M. L. & Jenkins, R. B. Genetics of adult glioma. *Cancer Genet* **205**, 613–621, doi:10.1016/j.cancergen.2012.10.009 (2012).
- Wu, W. *et al.* Joint NCCTG and NABTC prognostic factors analysis for high-grade recurrent glioma. *Neuro Oncol* **12**, 164–172, doi:10.1093/neuonc/nop019 (2010).
- Scott, J. G. *et al.* Aggressive treatment is appropriate for glioblastoma multiforme patients 70 years old or older: a retrospective review of 206 cases. *Neuro Oncol* **13**, 428–436, doi:10.1093/neuonc/nor005 (2011).
- Farina, P., Lombardi, G., Bergo, E., Roma, A. & Zagonel, V. Treatment of malignant gliomas in elderly patients: a concise overview of the literature. *Biomed Res Int* **2014**, 734281, doi:10.1155/2014/734281 (2014).
- Schmitt, A. M. & Chang, H. Y. Long Noncoding RNAs in Cancer Pathways. *Cancer Cell* **29**, 452–463, doi:10.1016/j.ccell.2016.03.010 (2016).
- Huarte, M. The emerging role of lncRNAs in cancer. *Nat Med* **21**, 1253–1261, doi:10.1038/nm.3981 (2015).
- Huang, H. *et al.* Gene expression profiling and subgroup identification of oligodendrogliomas. *Oncogene* **23**, 6012–6022, doi:10.1038/sj.onc.1207781 (2004).
- Ji, P. *et al.* MALAT-1, a novel noncoding RNA, and thymosin beta4 predict metastasis and survival in early-stage non-small cell lung cancer. *Oncogene* **22**, 8031–8041, doi:10.1038/sj.onc.1206928 (2003).
- Zhang, X. *et al.* Long non-coding RNA expression profiles predict clinical phenotypes in glioma. *Neurobiol Dis* **48**, 1–8, doi:10.1016/j.nbd.2012.06.004 (2012).
- Cui, M. *et al.* Long noncoding RNA HULC modulates abnormal lipid metabolism in hepatoma cells through an miR-9-mediated RXRA signaling pathway. *Cancer Res* **75**, 846–857, doi:10.1158/0008-5472.CAN-14-1192 (2015).
- Gutschner, T. *et al.* The noncoding RNA MALAT1 is a critical regulator of the metastasis phenotype of lung cancer cells. *Cancer Res* **73**, 1180–1189, doi:10.1158/0008-5472.CAN-12-2850 (2013).
- Medrzycki, M. *et al.* Histone h1.3 suppresses h19 noncoding RNA expression and cell growth of ovarian cancer cells. *Cancer Res* **74**, 6463–6473, doi:10.1158/0008-5472.CAN-13-2922 (2014).
- Yang, Z. *et al.* Long noncoding RNAs in the progression, metastasis, and prognosis of osteosarcoma. *Cell Death Dis* **7**, e2389, doi:10.1038/cddis.2016.272 (2016).
- Fatima, R., Akhade, V. S., Pal, D. & Rao, S. M. Long noncoding RNAs in development and cancer: potential biomarkers and therapeutic targets. *Mol Cell Ther* **3**, 5, doi:10.1186/s40591-015-0042-6 (2015).
- Li, Y. *et al.* Genome-wide DNA methylome analysis reveals epigenetically dysregulated non-coding RNAs in human breast cancer. *Sci Rep* **5**, 8790, doi:10.1038/srep08790 (2015).
- Mohankumar, S. & Patel, T. Extracellular vesicle long noncoding RNA as potential biomarkers of liver cancer. *Brief Funct Genomics* **15**, 249–256, doi:10.1093/bfpg/elt058 (2016).
- Balik, V. *et al.* MEG3: a novel long noncoding potentially tumour-suppressing RNA in meningiomas. *J Neurooncol* **112**, 1–8, doi:10.1007/s11060-012-1038-6 (2013).
- Zhang, X. *et al.* Maternally expressed gene 3, an imprinted noncoding RNA gene, is associated with meningioma pathogenesis and progression. *Cancer Res* **70**, 2350–2358, doi:10.1158/0008-5472.CAN-09-3885 (2010).
- Shi, Y. *et al.* Long non-coding RNA H19 promotes glioma cell invasion by deriving miR-675. *PLoS One* **9**, e86295, doi:10.1371/journal.pone.0086295 (2014).
- Han, L. *et al.* LncRNA profile of glioblastoma reveals the potential role of lncRNAs in contributing to glioblastoma pathogenesis. *Int J Oncol* **40**, 2004–2012, doi:10.3892/ijo.2012.1413 (2012).
- Cai, H. *et al.* The long noncoding RNA TUG1 regulates blood-tumor barrier permeability by targeting miR-144. *Oncotarget* **6**, 19759–19779, doi:10.18632/oncotarget.4331 (2015).
- Kamei, J., Toyofuku, T. & Hori, M. Negative regulation of p21 by beta-catenin/TCF signaling: a novel mechanism by which cell adhesion molecules regulate cell proliferation. *Biochem Biophys Res Commun* **312**, 380–387, doi:S0006291X03022265 [pii] (2003).
- van de Wetering, M. *et al.* The beta-catenin/TCF-4 complex imposes a crypt progenitor phenotype on colorectal cancer cells. *Cell* **111**, 241–250, doi:S0092867402010140 (2002).
- Abbas, T. & Dutta, A. p21 in cancer: intricate networks and multiple activities. *Nat Rev Cancer* **9**, 400–414, doi:10.1038/nrc2657 (2009).
- Karimian, A., Ahmadi, Y. & Yousefi, B. Multiple functions of p21 in cell cycle, apoptosis and transcriptional regulation after DNA damage. *DNA Repair (Amst)* **42**, 63–71, doi:10.1016/j.dnarep.2016.04.008 (2016).
- He, G. *et al.* Induction of p21 by p53 following DNA damage inhibits both Cdk4 and Cdk2 activities. *Oncogene* **24**, 2929–2943, doi:10.1038/sj.onc.1208474 (2005).
- Leontieva, O. V. & Blagosklonny, M. V. CDK4/6-inhibiting drug substitutes for p21 and p16 in senescence: duration of cell cycle arrest and MTOR activity determine geroconversion. *Cell Cycle* **12**, 3063–3069, doi:10.4161/cc.26130 (2013).
- Chung, I. H. *et al.* ChIP-on-chip analysis of thyroid hormone-regulated genes and their physiological significance. *Oncotarget* **7**, 22448–22459, doi:10.18632/oncotarget.7988 (2016).
- Chung, I. H. *et al.* Overexpression of lipocalin 2 in human cervical cancer enhances tumor invasion. *Oncotarget* **7**, 11113–11126, doi:10.18632/oncotarget.7096 (2016).

## Acknowledgements

This work is supported by grants from the Chang Gung Memorial Hospital (CMRPG3E0711, CMRPG3F0401, CMRPG3G0381 to T.K.L. and CMRPD1D0381, CMRPD1D0382, CMRPD1D0383, NMRPD1D1011, NMRPD1D1012, NMRPD1D1013, MOST-103- 2320-B-182-017-MY3 to K.H.L.).

## Author Contributions

T.K.L. and I.H.C. were responsible for conceptualization of the study. Y.H.L., Y.J.L. and C.S.T. contributed to the methodology. I.H.C. and K.H.L. performed the investigations. I.H.C. and T.K.L. wrote the manuscript. W.J.C., C.N.C. and Y.C.H. were responsible for visualization of figure legends. I.H.C., T.K.L. and K.H.L. supervised activity planning and execution.

## Additional Information

**Supplementary information** accompanies this paper at doi:[10.1038/s41598-017-05688-0](https://doi.org/10.1038/s41598-017-05688-0)

**Competing Interests:** The authors declare that they have no competing interests.

**Publisher's note:** Springer Nature remains neutral with regard to jurisdictional claims in published maps and institutional affiliations.



**Open Access** This article is licensed under a Creative Commons Attribution 4.0 International License, which permits use, sharing, adaptation, distribution and reproduction in any medium or format, as long as you give appropriate credit to the original author(s) and the source, provide a link to the Creative Commons license, and indicate if changes were made. The images or other third party material in this article are included in the article's Creative Commons license, unless indicated otherwise in a credit line to the material. If material is not included in the article's Creative Commons license and your intended use is not permitted by statutory regulation or exceeds the permitted use, you will need to obtain permission directly from the copyright holder. To view a copy of this license, visit <http://creativecommons.org/licenses/by/4.0/>.

© The Author(s) 2017

# SCIENTIFIC REPORTS

OPEN

## High-intensity Interval Training Improves Mitochondrial Function and Suppresses Thrombin Generation in Platelets undergoing Hypoxic Stress

Li-Hua Wu<sup>1,2</sup>, Shao-Chiang Chang<sup>1</sup>, Tieh-Cheng Fu<sup>2</sup>, Ching-Hui Huang<sup>1</sup> & Jong-Shyan Wang<sup>1,2,3</sup>

This study elucidates how high-intensity interval training (HIT) and moderate-intensity continuous training (MCT) affect mitochondrial functionality and thrombin generation (TG) in platelets following hypoxic exercise (HE, 100W under 12% O<sub>2</sub> for 30 min). Forty-five healthy sedentary males were randomized to engage either HIT (3-minute intervals at 40% and 80%VO<sub>2max</sub>, n = 15) or MCT (sustained 60%VO<sub>2max</sub>, n = 15) for 30 minutes/day, 5 days/week for 6 weeks, or to a control group (CTL, n = 15) that did not received exercise intervention. Before the intervention, HE (i) reduced the ATP-linked O<sub>2</sub> consumption rate (OCR), the reserve capacity of OCR, and the activities of citrate synthase (CS) and succinate dehydrogenase (SDH), (ii) lowered mitochondrial membrane potential (MP) and elevated matrix oxidant burden (MOB) in platelets, and (iii) enhanced dynamic TG in platelet-rich plasma (PRP), which responses were attenuated by pretreating PRP with oligomycin or rotenone/antimycin A. However, 6-week HIT (i) increased mitochondrial OCR capacity with enhancing the CS and SDH activities and (ii) heightened mitochondrial MP with depressing MOB in platelets following HE, compared to those of MCT and CTL. Moreover, the HIT suppressed the HE-promoted dynamic TG in PRP. Hence, we conclude that the HIT simultaneously improves mitochondrial bioenergetics and suppresses dynamic TG in platelets undergoing hypoxia.

Regular exercise may reduce the risk of major vascular thrombotic events and protect people against cardiovascular diseases<sup>1,2</sup>. Moreover, high-intensity exercise elicits a greater central hemodynamic adaptation than low and moderate levels of exercise<sup>3</sup>. However physical exercise imposes, paradoxically, both enhancing and suppressing effects on platelet reactivity and coagulation, depending on the type and intensity of exercise<sup>1</sup>. Systemic hypoxia has detrimental effects on the haemostatic system, such as accelerating prothrombinase complex assembly and facilitating thrombin generation (TG)<sup>4,5</sup>. Pathological investigations have also demonstrated that a hypercoagulable state contributes to increased risks of vascular thrombotic events in patients with episodic hypoxia, such as obstructive sleep apnea<sup>6</sup> and chronic obstructive pulmonary disease<sup>7</sup>. To the best of our knowledge, what kind of exercise strategy improves aerobic capacity and simultaneously increases the resistance to thrombotic risk provoked by hypoxia has not yet been established.

Increased thrombin activity is an essential pathogenic process of cardiovascular diseases<sup>8</sup>. Functional mitochondria in platelet has demonstrated the direct involvements of the cellular ATP production, redox balance, and thrombogenesis<sup>9,10</sup>. Platelet activation results in its mitochondrial membrane potential collapse and reactive oxygen species (ROS) production, consequently facilitating the exposure of phosphatidylserine (PS)<sup>10</sup>. The negatively charged PS on platelets can bind coagulant factors VIII (FVIII), Va, and Xa, providing a strongly

<sup>1</sup>Healthy Aging Research Center, Graduate Institute of Rehabilitation Science, Medical College, Chang Gung University, Tao-Yuan, Taiwan. <sup>2</sup>Heart Failure Center, Department of Physical Medicine and Rehabilitation, Chang Gung Memorial Hospital, Keelung, Taiwan. <sup>3</sup>Research Center for Chinese Herbal Medicine, College of Human Ecology, Chang Gung University of Science and Technology, Tao-Yuan, Taiwan. Correspondence and requests for materials should be addressed to J.-S.W. (email: [s5492@mail.cgu.edu.tw](mailto:s5492@mail.cgu.edu.tw))



	HIT		MCT		CTL	
	Pre	Post	Pre	Post	Pre	Post
<b>Anthropometric parameters</b>						
Age (year)	22.2 ± 0.4	—	22.1 ± 0.5	—	21.9 ± 0.7	—
Height (cm)	171.0 ± 1.0	—	172.1 ± 1.2	—	172.2 ± 1.3	—
Weight (kg)	69.7 ± 1.1	70.3 ± 2.1	67.3 ± 1.9	67.0 ± 1.8	67.8 ± 3.1	67.8 ± 3.1
BMI (kg/m <sup>2</sup> )	23.8 ± 0.5	23.4 ± 0.6	22.0 ± 0.5	21.9 ± 0.5	22.3 ± 0.8	22.3 ± 0.8
HR (beats/min)	72 ± 1	68 ± 2 <sup>+</sup>	71 ± 2	67 ± 2 <sup>+</sup>	73 ± 2	72 ± 3
SBP (mmHg)	120 ± 2	115 ± 2 <sup>+</sup>	121 ± 3	116 ± 3 <sup>+</sup>	123 ± 2	122 ± 3
DBP (mmHg)	74 ± 2	72 ± 2	74 ± 3	72 ± 2	75 ± 3	74 ± 3
<b>Ventilation threshold</b>						
Work-rate (watt)	100 ± 5	156.5 ± 7.5* <sup>+</sup>	99.4 ± 5.7	131.8 ± 6.0*	104.0 ± 6.2	108.1 ± 6.2
HR (beats/min)	133 ± 2	154 ± 2.8* <sup>+</sup>	134 ± 3	146 ± 4.0*	132 ± 4	134 ± 5
$\dot{V}_E$ (l/min)	36.2 ± 1.8	53.5 ± 3.0* <sup>+</sup>	36.5 ± 2.1	47.0 ± 2.6*	35.2 ± 4.2	36.5 ± 2.6
$\dot{V}O_2$ (ml/min/kg)	16.4 ± 0.7	23.8 ± 1.0* <sup>+</sup>	17.5 ± 0.7	21.2 ± 0.9*	16.9 ± 0.9	17.0 ± 0.8
$\dot{V}CO_2$ (ml/min/kg)	16.5 ± 0.7	23.8 ± 1.0* <sup>+</sup>	17.5 ± 0.7	21.4 ± 1.1*	17.0 ± 0.9	17.2 ± 0.9
<b>Peak performance</b>						
Work-rate (watt)	184.7 ± 6.3	237.6 ± 7.0* <sup>+</sup>	182.4 ± 5.4	213.5 ± 5.5*	180 ± 7	182 ± 9
HR (beats/min)	194 ± 2	195 ± 2	193 ± 2	194 ± 2	195 ± 3	194 ± 2
$\dot{V}_E$ (l/min)	103.3 ± 3.0	133.6 ± 4.2* <sup>+</sup>	98.7 ± 3.5	114.1 ± 3.2*	105.1 ± 4.1	104.2 ± 5.1
$\dot{V}O_2$ (ml/min/kg)	31.7 ± 0.5	39.7 ± 0.6* <sup>+</sup>	32.2 ± 0.6	36.2 ± 0.6*	31.4 ± 0.6	31.4 ± 0.6
$\dot{V}CO_2$ (ml/min/kg)	38.0 ± 0.6	47.4 ± 0.7* <sup>+</sup>	38.6 ± 0.8	43.4 ± 0.8*	37.7 ± 0.7	37.5 ± 0.6

**Table 1.** The effects of interval and continuous exercise regimens on exercise performance. Values were mean ± SEM. HIT, high-intensity interval training group; MCT, moderate-intensity continuous training group; CTL, control group; Pre, pre-intervention; Post, post-intervention; BMI, body mass index;  $\dot{V}_E$ , minute ventilation;  $\dot{V}O_2$ , oxygen consumption;  $\dot{V}CO_2$ , carbon dioxide production. \* $P < 0.05$ , Pre vs. Post; <sup>+</sup> $P < 0.05$ , HIT vs. MCT.

catalytic surface for the assembly of prothrombinase and tenase, thus triggering TG in blood<sup>10</sup>. Our early study further demonstrated that severe hypoxic exposure (12% O<sub>2</sub>) promoted FVIII-dependent TG by elevating oxidative stress; this hypoxic effect was ameliorated by pretreatment with antioxidant vitamin E<sup>5</sup>. However, a previous study has indicated that exercise training decreased the coagulant factor expression and PS exposure of platelets and the shedding of procoagulant microparticles from platelets, thereby depressing dynamic TG in platelets<sup>11</sup>.

Warm-up exercise (40%VO<sub>2max</sub>) has been shown to reduce high-intensity exercise (80%VO<sub>2max</sub>)-induced risks of inflammatory thrombosis associated with leukocytes and platelets, which is a form of preconditioning<sup>12</sup>. Recently, our investigation revealed that high-intensity interval exercise training (HIT) that consists of alternating mild-(40%VO<sub>2max</sub>) and high-(80%VO<sub>2max</sub>) intensity exercise significantly suppressed neutrophil-promoted blood coagulation by down-regulating expression of procoagulant factors under hypoxic condition<sup>13</sup>. Accordingly, we further hypothesize that HIT effectively reduces platelet-induced TG undergoing hypoxic stress, which is associated with alleviating platelet mitochondrial dysfunction cause by hypoxia.

To answer the abovementioned questions, this study evaluated how two isovolumic exercise regimens [*i.e.*, HIT (3-minute intervals at 40% and 80%VO<sub>2max</sub>) and moderate-intensity continuous exercise training (MCT, sustained 60%VO<sub>2max</sub>)] for 6 weeks affected (i) mitochondrial oxidative phosphorylation (OXPHOS) and oxidative stress, (ii) mitochondrial biogenesis, and (iii) dynamic TG in platelets following hypoxic exercise (HE, 100 W under 12% O<sub>2</sub> for 30 min). The aim of the present study is to establish an effective exercise strategy for improving individual aerobic capacity and simultaneously ameliorating the risk of platelet mitochondrial dysfunction and subsequent TG evoked by hypoxic stress.

## Results

**Aerobic fitness.** Anthropometric variables did not significantly differ among the three groups at the beginning of the study (Table 1). Both HIT and MCT for 6 weeks lowered HR and systolic blood pressure at rest, as well as, increased work-rate, minute ventilation ( $\dot{V}_E$ ), O<sub>2</sub> consumption ( $\dot{V}O_2$ ), and CO<sub>2</sub> production ( $\dot{V}CO_2$ ) at the ventilation threshold and peak performance (Table 1,  $P < 0.05$ ). Moreover, the HIT group exhibited a greater improvement in pulmonary ventilation and aerobic capacity than did the MCT group (Table 1,  $P < 0.05$ ). However, control subjects that did not receive exercise intervention (CTL) for 6 weeks showed no changes in these cardiopulmonary responses to a graded exercise test (GXT) (Table 1).

**Mitochondrial membrane potential (MP), matrix oxidant burden (MOB), and biogenesis in platelets.** Acute bout of 12% O<sub>2</sub> exercise significantly increased platelet counts in blood ( $P < 0.05$ , Table 2). However, blood platelet counts before or after the HE test remained unchanged following the 6-week intervention with HIT, MCT or CTL (Table 2). Figure 1 shows the analysis of platelet mitochondrial count (Fig. 1e–h),

		HIT		MCT		CTL	
		Pre	Post	Pre	Post	Pre	Post
Platelet count (x10 <sup>3</sup> cells/ $\mu$ l)							
	R	224 $\pm$ 11	216 $\pm$ 12	232 $\pm$ 10	226 $\pm$ 18	234 $\pm$ 12	237 $\pm$ 9
	HE	264 $\pm$ 21*	252 $\pm$ 23*	272 $\pm$ 16*	266 $\pm$ 12*	284 $\pm$ 20*	287 $\pm$ 17*
Platelet mitochondrial biogenesis (mean fluorescence intensity)							
Complex II	R	21.7 $\pm$ 2.8	22.1 $\pm$ 2.4	22.6 $\pm$ 1.9	22.5 $\pm$ 2.6	23.5 $\pm$ 1.9	23.4 $\pm$ 2.5
	HE	21.6 $\pm$ 2.3	23.1 $\pm$ 2.8	23.0 $\pm$ 1.6	23.9 $\pm$ 2.5	23.7 $\pm$ 2.1	24.3 $\pm$ 1.7
Complex IV	R	16.9 $\pm$ 2.8	17.0 $\pm$ 2.5	16.3 $\pm$ 1.7	16.9 $\pm$ 2.1	17.4 $\pm$ 1.3	16.9 $\pm$ 1.5
	HE	16.0 $\pm$ 2.7	17.1 $\pm$ 1.9	16.7 $\pm$ 1.1	16.8 $\pm$ 1.4	16.9 $\pm$ 1.7	17.0 $\pm$ 0.8
Ratio of Complex IV to Complex II							
	R	0.78 $\pm$ 0.04	0.77 $\pm$ 0.03	0.72 $\pm$ 0.05	0.71 $\pm$ 0.04	0.74 $\pm$ 0.04	0.72 $\pm$ 0.03
	HE	0.74 $\pm$ 0.06	0.73 $\pm$ 0.04	0.73 $\pm$ 0.04	0.72 $\pm$ 0.05	0.71 $\pm$ 0.03	0.70 $\pm$ 0.04

**Table 2.** The effects of interval and continuous exercise regimens on platelet count and mitochondrial biogenesis. Values were mean  $\pm$  SEM. HIT, high-intensity interval training group; MCT, moderate-intensity continuous training group; CTL, control group; Pre, pre-intervention; Post, post-intervention; R, resting; HE, hypoxic exercise test. \* $P < 0.05$ , R vs. HE.

MP (Fig. 1i–l), and MOB (Fig. 1m–p) using a FACScan flow cytometer. Although no changes were observed in the mitochondrial count (Fig. 2a–c), the HE decreased the mitochondrial MP (Fig. 2d–f,  $P < 0.05$ ) and elevated the MOB (Fig. 2g–i,  $P < 0.05$ ) in platelets. After 6 weeks of the intervention, HIT, rather than MCT, inhibited the HE-induced decrease of mitochondrial MP (Fig. 2d,  $P < 0.05$ ) and increase of MOB (Fig. 2g,  $P < 0.05$ ) in platelets. However, no significant changes in the mitochondrial count, MP, and MOB of platelets were observed after CTL for 6 weeks (Fig. 2c,f,i).

In mitochondrial biogenesis, acute HE did not change the levels of Complex IV and II, as well as, the ratio of Complex IV to II in platelets (Table 2). Furthermore, no significant changes in these mitochondrial biogenetic variables of platelets occurred after 6-week interventions with HIT, MCT, or CTL (Table 2).

**Mitochondrial respiration of platelets.** Figures 3a–h show the analysis of  $O_2$  consumption rate (OCR) in the intact (3a–3d) and permeabilized (3e–3h) platelets using high-resolution respirometry (Oroboros O2K). An acute bout of 12%  $O_2$  exercise significantly decreased ATP-linked OCR (Fig. 4a–c,  $P < 0.05$ ) and the reserve capacity of OCR (Fig. 4g–i,  $P < 0.05$ ) in intact platelets. The HE also suppressed the fatty acid oxidation (FAO)- (Fig. 5d–f,  $P < 0.05$ ), Complex I- (Fig. 5g–i,  $P < 0.05$ ), and Complex II- (Fig. 5j–l,  $P < 0.05$ ) mediated OCRs in permeabilized platelets. After 6 weeks, both HIT and MCT significantly elevated the reserve capacity of OCR in intact platelets at rest (Fig. 4g and h,  $P < 0.05$ ), whereas only HIT alleviated the suppression of the OCR reserve capacity caused by HE (Fig. 4g,  $P < 0.05$ ). Moreover, the two exercise regimens enhanced the Complex II-mediated OCR at rest (Fig. 5j and k,  $P < 0.05$ ), while only HIT diminished the depression of FAO- (Fig. 5d), Complex I- (Fig. 5g), and Complex II- (Fig. 5j) mediated OCRs and the capacity for electron transport system (ETS) (Fig. 5p) in platelets caused by HE. However, there were no significant changes in the HE-mediated mitochondrial respiration of platelets after 6 weeks of CTL (Figs 4 and 5).

Before various interventions, the HE test also suppressed the bioenergetics health index (BHI) value in platelets (Fig. 6a–c,  $P < 0.05$ ). After 6 weeks, both HIT (Fig. 6a,  $P < 0.05$ ) and MCT (Fig. 6b,  $P < 0.05$ ) significantly elevated the BHI value in platelets at rest, whereas only HIT attenuated the suppression of BHI caused by HE (Fig. 6a,  $P < 0.05$ ). However, the activities of Complex IV in platelet mitochondria at rest or after HE remained unchanged following 6 weeks of HIT, MCT, or CTL (Fig. 6d–f).

**Enzyme activities of glycolysis and the Krebs cycle in platelets.** Acute HE increased the activity of lactate dehydrogenase (LDH) and decreased the activities of citrate synthase (CS) and succinate dehydrogenase (SDH) in platelets (Table 3,  $P < 0.05$ ). After 6 weeks of the intervention, HIT, but not MCT, attenuated the extents of the HE-enhanced LDH activity and the HE-depressed CS and SDH activities in platelets (Table 3). However, the two exercise regimens did not influence the activities of hexokinase (HK) and pyruvate dehydrogenase (PDH) in platelets at rest and after HE (Table 3). Additionally, various enzyme activities of glycolysis and Krebs cycle in platelets at rest or after HE remained unchanged after 6 weeks of CTL (Table 3).

**Dynamic TG in platelet-rich plasma (PRP).** Figure 7a–g show the samples of the HE-mediated dynamic TG in pretreating PRP with various mitochondrial modulators following 6 weeks of HIT. With respect to the analytic parameters of dynamic TG, acute HE increased the ETP (Table 3,  $P < 0.05$ ), peak height (Table 4,  $P < 0.05$ ), and rate (Fig. 8a–c,  $P < 0.05$ ) of TG but not changed the lag time of TG (Table 4) in PRP before the intervention. Moreover, the changes of parameters of dynamic TG caused by HE were attenuated by pretreating PRP with oligomycin (Table 4 and Fig. 8d–f) or rotenone plus antimycin A (Table 4 and Fig. 8j–l). Six weeks of HIT (Fig. 7a–d) and MCT (Fig. 7e–h) significantly decreased the extents of HE-promoted ETP (Table 4,  $P < 0.05$ ) and peak height (Table 4,  $P < 0.05$ ) and rate (Fig. 8a,  $P < 0.05$ ) of TG in PRP. However, pretreating PRP with oligomycin (Table 4, Fig. 8d–f), rather than rotenone plus antimycin A (Table 4 and Fig. 8j–l), inhibited the training effects of HIT and MCT on the dynamic TG in PRP. Additionally, CTL did not significantly change the values of resting

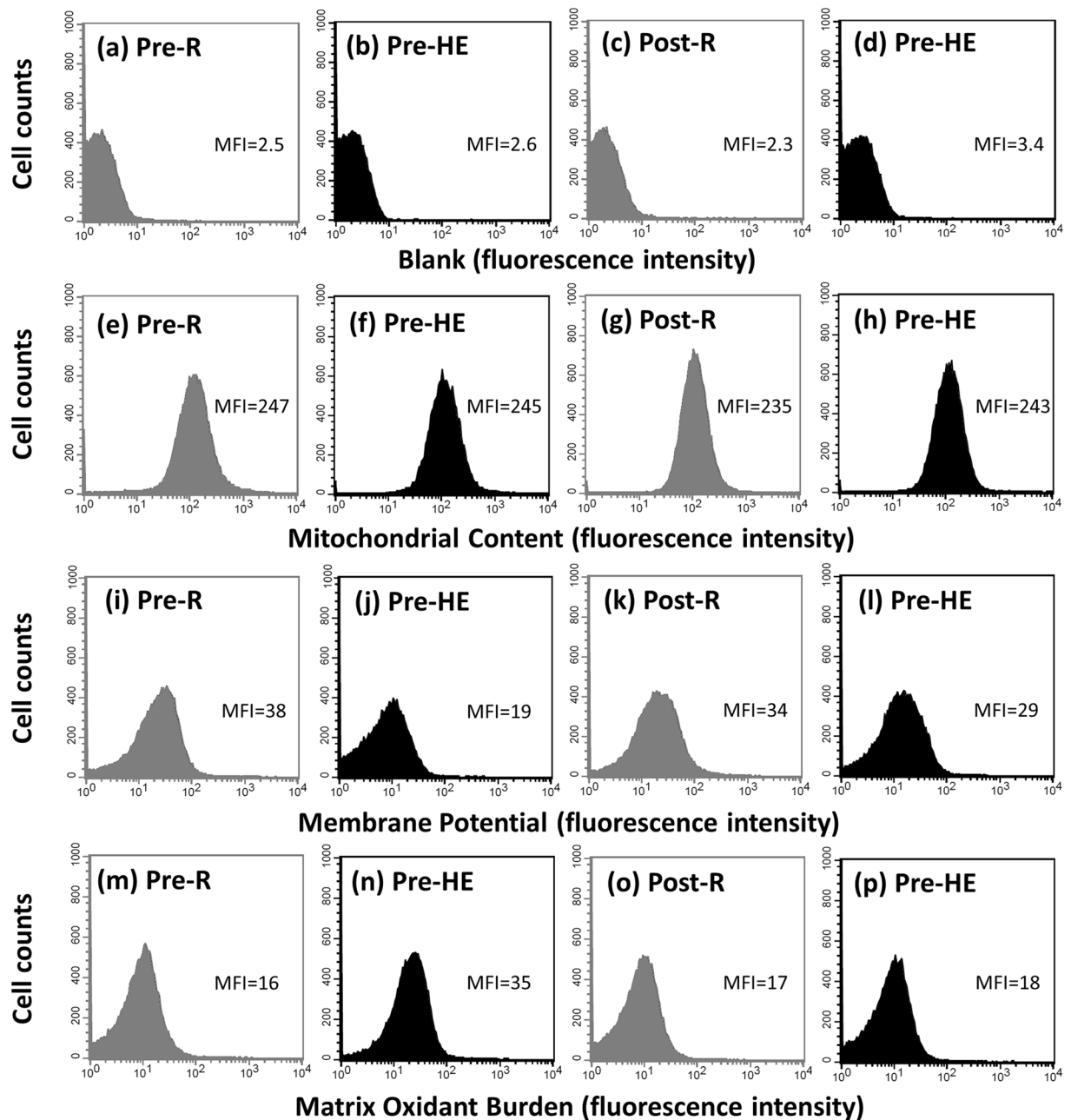


**Figure 1.** Graph showing the effect of high-intensity interval training (HIT) on mitochondrial content, mitochondrial membrane potential, and matrix oxidant burden in platelets using a FACScan flow cytometer. **Pre**, before HIT; **Post**, after HIT; **R**, resting; **HE**, hypoxic (12%O<sub>2</sub>) exercise test. **Blank (a–d)**, platelets without treating fluorescent dye; **Mitochondrial content (e–h)**, platelets stained with MitoTracker Green FM; **Mitochondrial membrane potential (i–l)**, platelet stained with tetramethylrhodamine ethyl ester; **Matrix oxidant burden (m–p)**, platelet stained with MitoSOX Red; **MFI**, mean fluorescence intensity.

and HE-mediated dynamic TG parameters in untreated and oligomycin- or rotenone plus antimycin A-treated PRP (Table 4 and Fig. 8).

## Discussion

Mitochondrial dysfunction is associated with oxidative stress and thought to be a common underlying mechanism of metabolic and cardiovascular diseases<sup>14–16</sup>. This study is the first to demonstrate that acute bout of 12% O<sub>2</sub> exercise elevates mitochondrial oxidative stress and subsequently suppresses the CS and SDH activities and the ETS efficiency in platelets, which responses are accompanied by accelerating TG in PRP. Notably, the HIT regimen effectively ameliorates the HE-induced mitochondrial dysfunction of platelets by depressing the cellular oxidative stress, which may reduce the risk of platelet-mediated TG evoked by hypoxia.

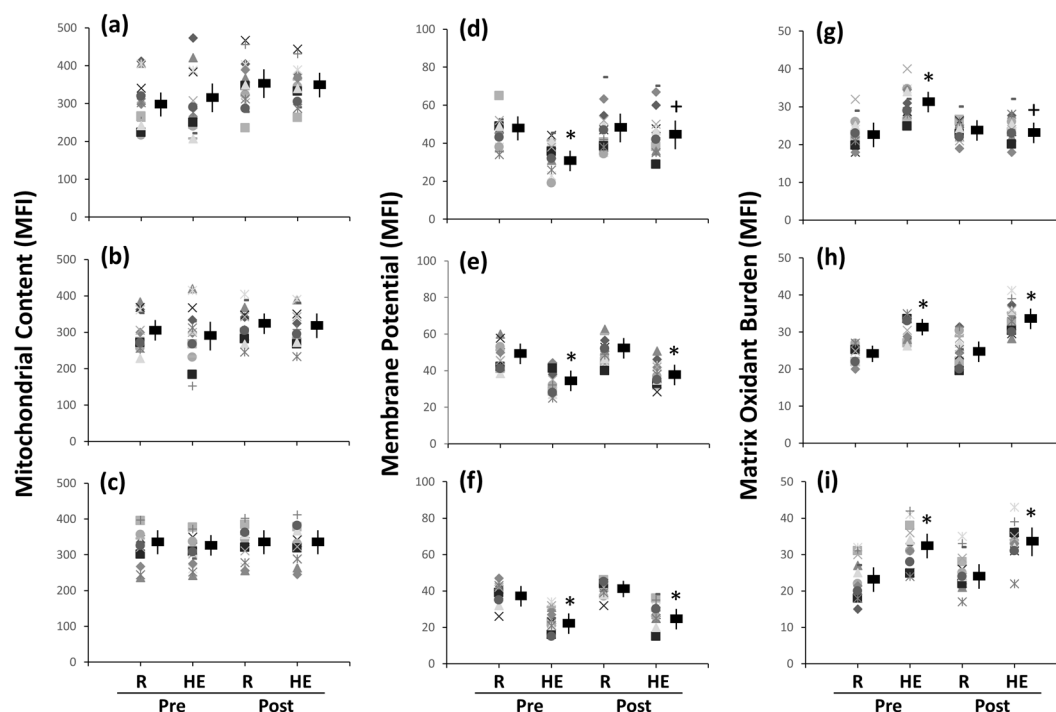


**Figure 2.** Effects of interval and continuous exercise regimens on (a–c) mitochondrial content, (d–f) mitochondrial membrane potential, and (g–i) matrix oxidant burden in platelets. **HIT**, high-intensity interval training group (a,d,g); **MCT**, moderate-intensity continuous training (b,e,h); **CTL**, control group (c,f,i); **Pre**, pre-intervention; **Post**, post-intervention; **R**, resting; **HE**, hypoxic (12%O<sub>2</sub>) exercise test; **MFI**, mean fluorescence intensity. \* $P < 0.05$ , R vs. HE; + $P < 0.05$ , Pre vs. Post. Values were mean  $\pm$  SEM.

**Mitochondrial oxidative phosphorylation in platelets.** Mitochondria are highly sensitive to hypoxic stress and respond dynamically to changes in their cellular microenvironment<sup>17</sup>. The present study showed that acute HE decreased mitochondrial MP and increased MOB in platelets, which may reflect mitochondrial oxidative damage of platelets caused by HE. Additionally, the HE-induced decrease in ATP-linked OCR and reserve capacity of OCR may be associated with modified activities of mitochondrial enzymes and/or an impeded the flow of electrons, thereby decreasing the ETS efficiency after HE. Acute HE also significantly decreased the CS and SDH activities and was accompanied by increased the LDH activity, suggesting that the HE shifts platelet metabolic pathways from mitochondrial respiration to glycolysis<sup>18,19</sup>. Furthermore, the HE substantially depressed the capacity of Complex I- and II-related respirations and the efficiency of ETS in platelets in a substrate-rich environment. Summarily, acute HE globally decreases mitochondrial substrate availability and impairs mitochondrial bioenergetics and/or integrity in platelets.

In this investigation, the HIT regimen significantly enhanced platelet CS and SDH activities, as well as, Complex I- and II-related respirations following HE. The enhanced OCR of platelets by HIT may indicate a greater capacity of mitochondrial OXPHOS in platelets due to increased Complex protein activities of the ETS, elevated ATP production rate, or heightened levels of NADH and FADH<sub>2</sub>. Moreover, increased resistance to the HE-depressed platelet mitochondrial OCR after HIT may improve the flexibility of platelet activation caused by HE. A recent study has indicated that hypoxia or ischemia results in accumulation of intracellular succinate levels, thus leading to elevated mitochondrial ROS production<sup>20</sup>. The elevation of oxidative stress may also induce succinate accumulation by decreasing SDH activity<sup>21</sup>. Therefore, the increased SDH activity and Complex II respiration of platelets in the HIT groups may quickly eliminate succinate, thereby further retarding the ROS production from platelet mitochondria following HE.

**Mitochondrial biogenesis in platelets.** Early studies on exercise intervention predominantly focused on mitochondrial functionality in skeletal muscles<sup>22</sup>. An acute bout of exercise promotes transcriptional or post-translational regulation of peroxisome proliferator-activated receptor gamma coactivator-1 $\alpha$ , whereas chronic exercise increases the rates of muscular mtDNA gene expression by upregulating Tfam in skeletal muscles<sup>22</sup>. In the present study, no significant changes in resting and HE-related platelet biogenetic parameters, such as the Complex IV/II ratio, were observed after 6 weeks of HIT or MCT. Accordingly, we propose that platelet metabolic adaptation induced by HIT may be associated with improved ETS efficiency rather than modulated mitochondrial biogenesis in platelets.

**Dynamic TG in PRP.** Extremely hypoxic environments are associated with increased incidence of vascular thromboembolic events<sup>23,24</sup>. Blood is subjected to oxidative stress during extremely hypoxic exposure<sup>4</sup>; elevated oxidative stress may contribute to coagulation system<sup>4</sup> and platelet activation<sup>11</sup>. In the present study, acute HE

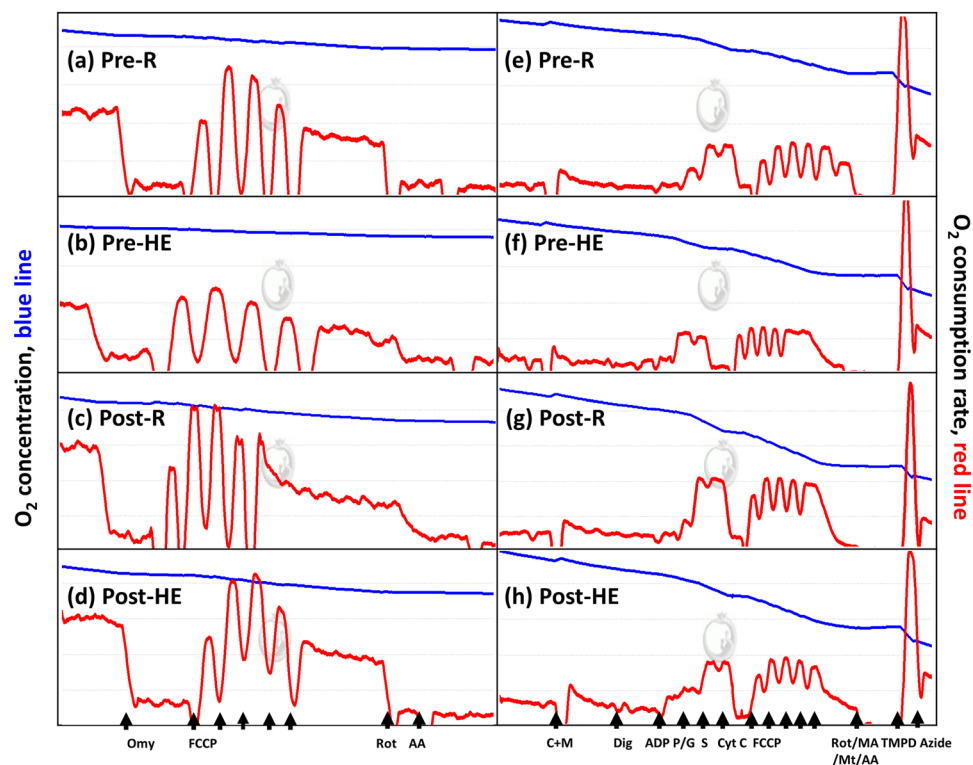


**Figure 3.** Graph showing measurement of mitochondrial  $O_2$  consumption rate (OCR) in platelets using a high-resolution respirometry (Oroboros O2K). (a–d), the OCR protocol in intact platelets; (e–h), the OCR [substrate, uncoupler, inhibitor titration (SUIT)] protocol in permeabilized platelets. **Omy**, oligomycin; **FCCP**, carbonyl cyanide-p-trifluoromethoxyphenylhydrazone; **Rot**, rotenone; **AA**, antimycin A; **M**, malate; **C**, palmitoyl-DL carnitine-HCl; **Dig**, digitonin; **ADP**, adenosine diphosphate; **P**, pyruvate; **G**, glutamate; **S**, succinate; **Cyst C**, cytochrome c; **MA**, malonic acid; **Mt**, myxothiazol. **Pre**, before high-intensity interval training (HIT); **Post**, after HIT; **R**, resting; **HE**, hypoxic ( $12\%O_2$ ) exercise test.

facilitated TG in PRP and was accompanied by lost mitochondrial MP and increased MOB in platelets. Hence, increased ROS level by changed coupling of mitochondrial ETS may participate in platelet-mediated TG undergoing hypoxic stress. However, HIT for 6 week markedly depresses the HE-induced oxidative damage of platelet mitochondria and consequently attenuates the platelet-mediated TG caused by HE.

**Limitations of study.** Our small size in each group ( $n = 15$ ) is a major limitation of this study. However, the results of aerobic capacity and mitochondrial bioenergetics and dynamic TG in platelets obtained from this investigation have high values of statistical power from 0.853 to 1.000. Additionally, the subjects used tended to be young, males, and healthy, thus further clinical evidence was required to extrapolate the present results to the elderly, females or patients with platelet or thrombotic disorders.

In this study, acute bout of HE promoted dynamic TG in PRP, whereas pretreating PRP with mitochondrial ETS inhibitors attenuated acute exercise effects. Moreover, 6 weeks of HIT also suppressed the extent of HE-promoted dynamic TG in PRP. Whether the suppression of HE-induced TG in PRP caused by HIT involves (i) change of plasma composition or/and (ii) down-regulation of procoagulant factors on platelets to diminish the enhancement of plasma TG by HE remains unresolved. Hence, the potential confounding effects of the different plasma compositions at various experimental conditions need further study.

Aim of this study mainly focus on examining the effects of exercise on platelet-induced TG rather than platelet reactivity (adhesion and aggregation). Our previous studies have investigated the effect of exercise training on platelet adhesiveness and aggregability and their underlying mechanisms<sup>25</sup>. However, the role of platelet mitochondrial function on exercise-mediated platelet reactivity requires further explored.

**Conclusions.** Acute  $12\% O_2$  exercise elevated oxidative stress and decreased the ETS efficiency in platelet mitochondria. Although no changes were found in mitochondrial biogenesis, 6 week of HIT enhanced mitochondrial OXPHOS capacity and attenuated the HE-depressed mitochondrial ETS efficiency in platelets. Therefore, the HIT regimen effectively improve platelet bioenergetics, possibly by enhancing mitochondrial quality rather than quantity in platelets. Moreover, HIT also markedly reduces the enhancement of platelet-mediated TG by HE, which response is associated with alleviating the HE-induced mitochondrial dysfunction of platelets. These experimental findings may facilitate the identification of effective exercise training regimens to increase aerobic capacity and minimize platelet mitochondrial dysfunction and subsequent thrombus formation evoked by hypoxic stress.



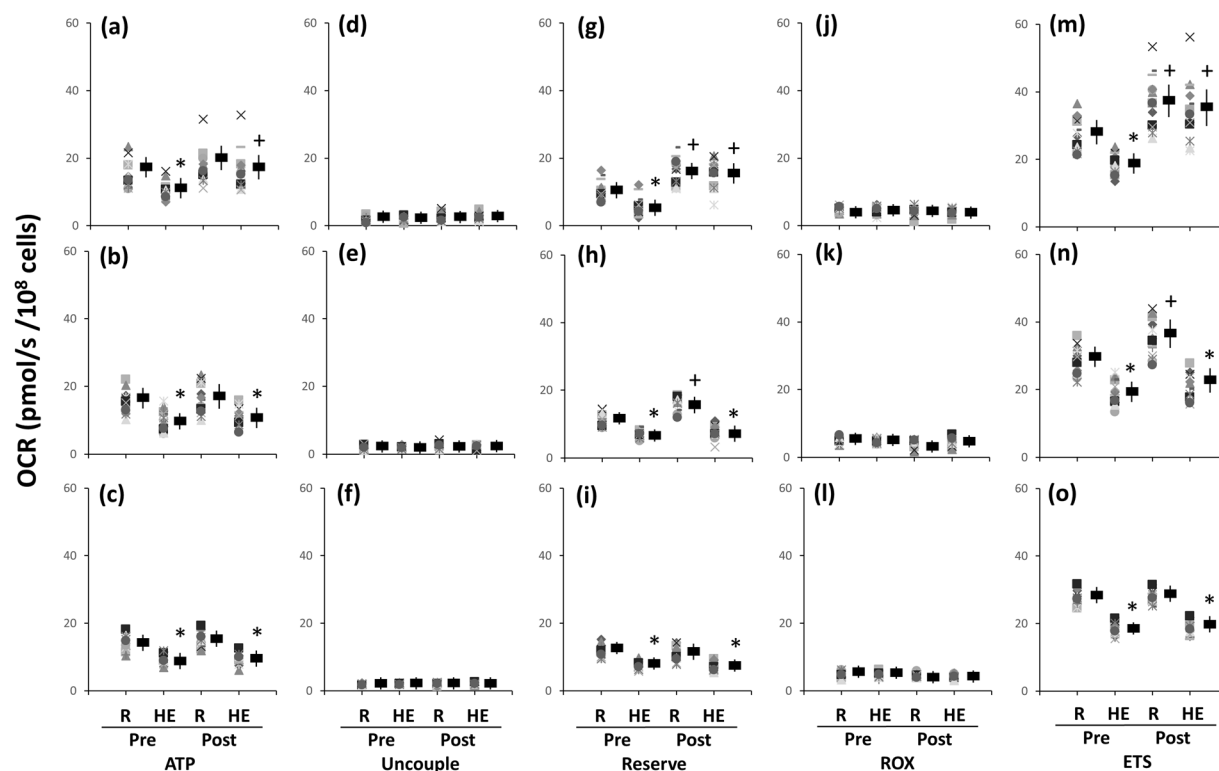


**Figure 4.** Effects of interval and continuous exercise regimens on mitochondrial  $O_2$  consumption rate (OCR) in the intact platelets. HIT (a,d,g,j,m), high-intensity interval training group; MCT (b,e,h,k,n), moderate-intensity continuous training; CTL (c,f,i,l,o), control group; Pre, pre-intervention; Post, post-intervention; R, resting; HE, hypoxic (12% $O_2$ ) exercise test; ATP, ATP-linked OCR; Uncouple, uncouple OCR; RESERVE, the reserve capacity of OCR; ROX, residual  $O_2$  consumption. \* $P < 0.05$ , R vs. HE; + $P < 0.05$ , Pre vs. Post. Values were mean  $\pm$  SEM.

## Materials and Methods

**Subjects.** The study was in accordance with the Declaration of Helsinki and approved by the Chang Gung Memorial Hospital Institutional Review Board, Taiwan. All experiments were performed in accordance with relevant guidelines and regulations. A total of 45 sedentary males who were non-smokers, did not use medications or vitamins, and were free of any cardiopulmonary/hematological risks were recruited from Chang Gung University, Taiwan. According to our previous studies, the menstrual phases of women influence activity of cardiac autonomic nervous system<sup>26</sup> and platelet reactivity<sup>27</sup>. Hence, this study excluded female subjects to avoid the effects of gender and the menstrual phase on cardiovascular<sup>26</sup> and hematological<sup>27</sup> functions. No subjects had engaged in any regular physical activity (exercise frequency  $\leq$  once weekly, duration  $< 20$  min) or had been exposed to high altitudes ( $\geq$  altitude of 3000 m) for at least 1 year before the experiment. All subjects provided informed consent after the experimental procedures were explained. These subjects were randomly divided into three groups: the HIT ( $n = 15$ ), MCT ( $n = 15$ ), and CTL ( $n = 15$ ) groups. Moreover, all subjects arrived at the testing center at 9:00 AM to eliminate any possible circadian effects. The experimental environment was maintained at a temperature of  $22 \pm 0.5^\circ C$  with a relative humidity of  $60 \pm 5\%$ . Participants were instructed to fast for at least 8 hours and to refrain from strenuous physical exercise for at least 48 hours before sampling.

**Training protocols.** Both the HIT and MCT groups performed exercise regimens on a stationary bicycle ergometer 5 times a week for 6 weeks. For comparison, CTL participants did not undergo any exercise but were carefully monitored, and we recorded information on their physical activity and nutritional intake for 6 weeks. HIT subjects warmed up for 3 min at 30% of  $VO_{2max}$  before starting five exercise cycles, each lasting 3 min at 80% of  $VO_{2max}$  interspersed with a 3 min active recovery period at 40% of  $VO_{2max}$ . The exercise session was terminated with a 3 min cool-down period at 30% of  $VO_{2max}$ . The MCT group had the same warm-up and cool-down protocols as the HIT group, except that the training period was 30 min at 60% of  $VO_{2max}$ <sup>13, 28</sup>. The two exercise protocols were isovolumic with the same exercise duration [i.e., HIT exercise volume: 6 min ( $40\%VO_{2max} + 80\%VO_{2max}$ )  $\times 5$  cycles = MCT exercise volume: 30 min ( $60\%VO_{2max}$ )]. Each subject used a heart rate (HR) monitor (Tango, SunTech Medical) to obtain the assigned intensity of exercise. The work-rate of the bicycle ergometer was adjusted continuously to ensure that the intensity of exercise matched the target HR throughout the training period. The percentage of HR reserve (%HRR) is widely considered to be equivalent to the percentage of  $VO_2$  reserve for exercise prescription purposes<sup>29</sup>. Accordingly, the target HRs of HIT and MCT were calculated using the following equations<sup>29</sup>:

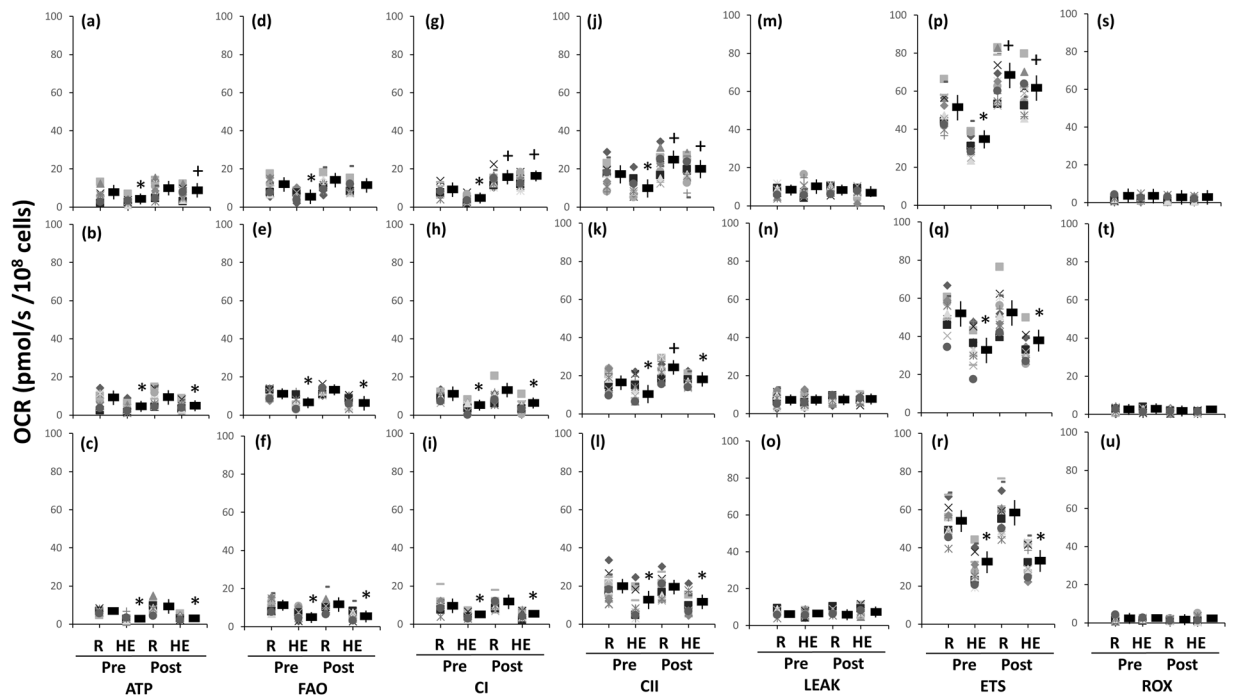


**Figure 5.** Effects of interval and continuous exercise regimens on mitochondrial O<sub>2</sub> consumption rate (OCR) in the permeabilized platelets. **HIT** (a,d,g,j,m,p,s), high-intensity interval training group; **MCT** (b,e,h,k,n,q,t), moderate-intensity continuous training; **CTL** (c,f,i,l,o,r,u), control group; **Pre**, pre-intervention; **Post**, post-intervention; **R**, resting; **HE**, hypoxic (12%O<sub>2</sub>) exercise test; **ATP**, ATP-linked OCR; **FAO**, fatty acid oxidation; **ETS**, electron transport system; **CI**, Complex I respiration; **CII**, Complex I respiration; **ROX**, Residual O<sub>2</sub> consumption. \**P* < 0.05, *Rt* vs. *HE*; +*P* < 0.05, *Pre* vs. *Post*. Values were mean ± SEM.

$$\text{Peak HR} = 220 - \text{age} \quad (1)$$

$$\% \text{HHR} = \%(\text{peak HR} - \text{resting HR}) + \text{resting HR} \quad (2)$$

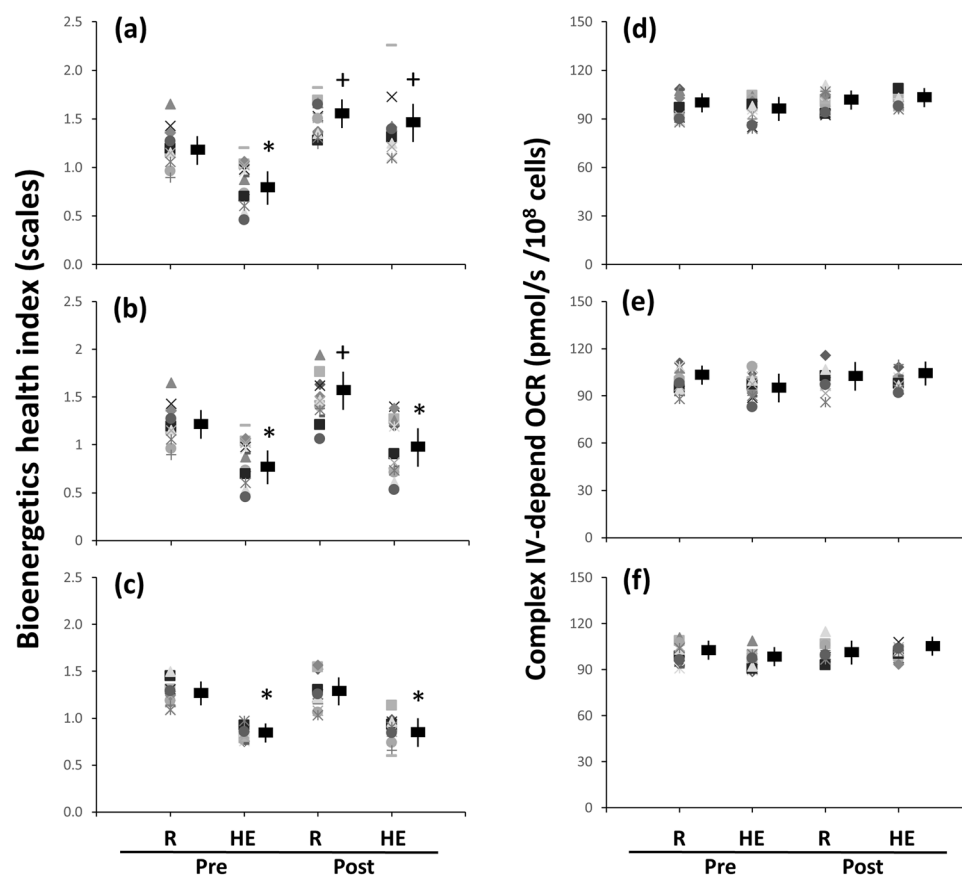
$$\text{Target HR of HIT} = 3 - \text{minute intervals at 40\% HHR and 80\% HRR} \quad (3)$$

$$\text{Target HR of MCT} = \text{sustained 60\% HRR} \quad (4)$$

All subjects recorded their daily activities and nutritional intake throughout the experiment using the International Physical Activity Questionnaire Short Form<sup>30</sup> and the Written Diet Record<sup>31</sup>, respectively. The participants were instructed to refrain from extra regular exercise until the end of the study. Moreover, the participant compliance rates for the three interventions were 100%. All subjects completed the exercise intervention and/or tests at the beginning of the present study and after 6 weeks in the three groups.

**GXT.** Subjects performed a GXT on a bicycle ergometer (Corival 400, Lode) to assess their aerobic capacity 4 days before and 4 days after the 6 week interventions<sup>18,28</sup>. The GXT was composed of 2 min of unloaded pedaling followed by a continuous increase in work-rate of 30 W per 3 min until exhaustion (*i.e.*, VO<sub>2max</sub>). The V<sub>E</sub>, VO<sub>2</sub>, and VCO<sub>2</sub> were measured breath by breath with a computer-based system (MasterScreen CPX, Cardinal-health Germany). The defined VO<sub>2max</sub> was required to achieve the following 3 of 4 criteria: (i) the level of VO<sub>2</sub> increased less than 2 mL/kg/min over at least 2 min; (ii) HR exceeded its predicted maximum; (iii) the respiratory exchange ratio exceeded 1.2, and (iv) the venous lactate concentration exceeded 8 mM, consistently with the guidelines of the American College of Sports Medicine for exercise testing<sup>32</sup>. The value of ventilatory threshold was determined by applying the following ventilatory criteria: (i) the V<sub>E</sub>/VO<sub>2</sub> ratio increased without a corresponding increase in the V<sub>E</sub>/VCO<sub>2</sub> ratio; (ii) PETO<sub>2</sub> increased without a decrease in the PETCO<sub>2</sub>, and (iii) a departure from linearity for V<sub>E</sub><sup>32</sup>.

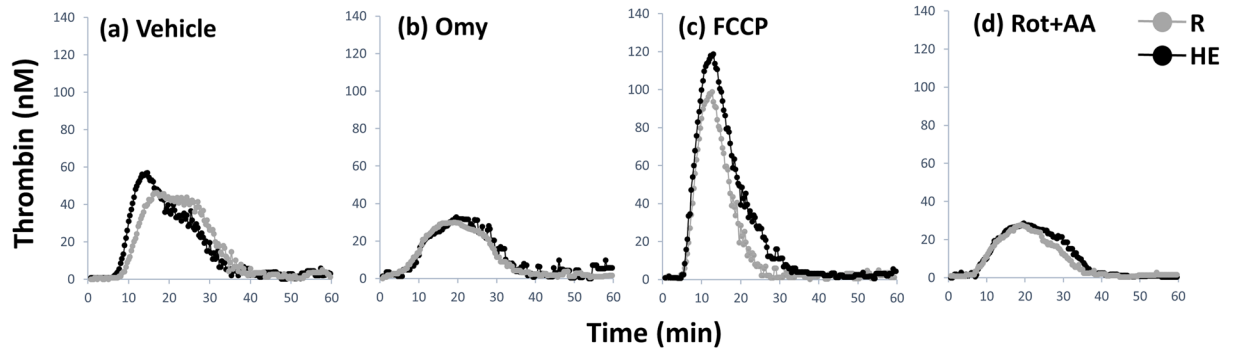
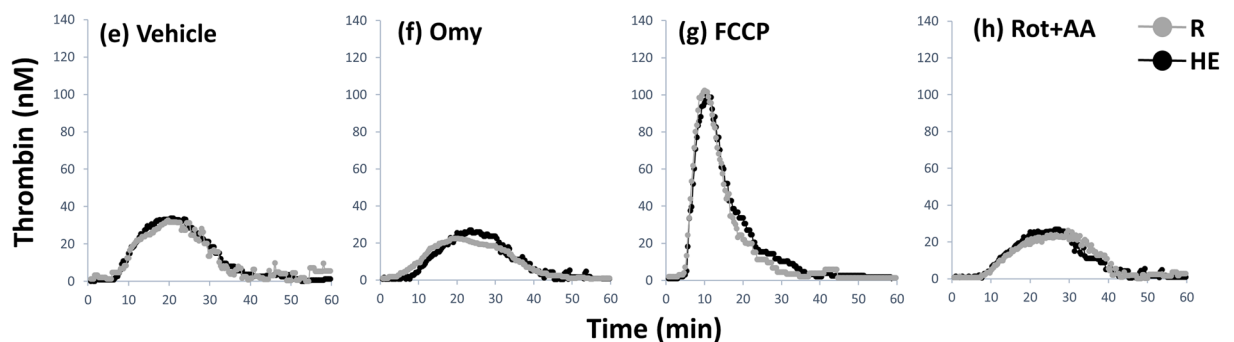
**The HE test and blood collection.** Each subject performed the HE test on the 2<sup>nd</sup> day before the intervention and on the 2<sup>nd</sup> day after the intervention in an air-conditioned normobaric hypoxia chamber (Colorado Mountain Room, Boulder, CO) as described in our previous studies<sup>18,28</sup>. The hypoxia chamber was maintained at a temperature of 22 ± 0.5 °C with a relative humidity of 60 ± 5%; a CO<sub>2</sub> scrubber eliminated CO<sub>2</sub> in the air (<3,500 ppm). The HE test on the bicycle ergometer required 50 W of warm-up for 3 min, an increase in the



**Figure 6.** Effects of interval and continuous exercise regimens on (a–c) bioenergetics health index (BHI) and (d–f) Complex IV activity in platelets. HIT, high-intensity interval training group (a,d); MCT, moderate-intensity continuous training (b,e); CTL, control group (c,f); Pre, pre-intervention; Post, post-intervention; R, resting; HE, hypoxic (12%O<sub>2</sub>) exercise test. \* $P < 0.05$ , R vs. HE; + $P < 0.05$ , Pre vs. Post. Values were mean  $\pm$  SEM.

	HIT		MCT		CTL	
	Pre	Post	Pre	Post	Pre	Post
<b>Glycolysis</b>						
Hexokinase activity (nmol/min/10 <sup>8</sup> cells)						
R	27.9 $\pm$ 1.9	26.7 $\pm$ 1.7	24.7 $\pm$ 2.4	25.9 $\pm$ 1.1	24.4 $\pm$ 1.4	23.3 $\pm$ 1.3
HE	27.5 $\pm$ 1.7	27.3 $\pm$ 1.1	24.8 $\pm$ 2.7	26.6 $\pm$ 1.5	25.7 $\pm$ 1.2	23.8 $\pm$ 1.1
Pyruvate dehydrogenase activity (nmol/min/10 <sup>8</sup> cells)						
R	1.18 $\pm$ 0.03	1.13 $\pm$ 0.03	1.16 $\pm$ 0.03	1.04 $\pm$ 0.03	1.26 $\pm$ 0.05	1.18 $\pm$ 0.04
HE	1.30 $\pm$ 0.04	1.17 $\pm$ 0.03	1.27 $\pm$ 0.04	1.12 $\pm$ 0.03	1.26 $\pm$ 0.06	1.26 $\pm$ 0.05
Lactate dehydrogenase activity (nmol/min/10 <sup>8</sup> cells)						
R	32.2 $\pm$ 4.5	30.1 $\pm$ 1.6	31.6 $\pm$ 2.5	31.8 $\pm$ 2.5	35.6 $\pm$ 2.4	33.5 $\pm$ 2.6
HE	40.1 $\pm$ 4.6*	33.6 $\pm$ 1.5 <sup>+</sup>	41.2 $\pm$ 2.4*	37.9 $\pm$ 2.5*	42.5 $\pm$ 2.2*	41.6 $\pm$ 2.8*
<b>Krebs cycle</b>						
Citrate synthase activity (nmol/min/10 <sup>8</sup> cells)						
R	5.50 $\pm$ 0.22	5.83 $\pm$ 0.25	5.63 $\pm$ 0.17	5.74 $\pm$ 0.21	5.54 $\pm$ 0.17	5.68 $\pm$ 0.34
HE	4.45 $\pm$ 0.32*	5.88 $\pm$ 0.43 <sup>+</sup>	4.61 $\pm$ 0.24*	4.61 $\pm$ 0.32*	4.52 $\pm$ 0.24*	4.55 $\pm$ 0.29*
Succinate dehydrogenase activity (nmol/min/10 <sup>8</sup> cells)						
R	9.46 $\pm$ 0.82	9.59 $\pm$ 1.32	9.37 $\pm$ 0.91	9.62 $\pm$ 0.83	9.12 $\pm$ 0.42	9.41 $\pm$ 0.45
HE	6.77 $\pm$ 0.91*	8.82 $\pm$ 0.81 <sup>+</sup>	6.39 $\pm$ 0.92*	6.83 $\pm$ 0.72*	6.47 $\pm$ 0.61*	6.57 $\pm$ 0.60*

**Table 3.** The effects of interval and continuous exercise regimens on enzyme activities of glycolysis and Krebs cycle in platelets. Values were mean  $\pm$  SEM. HIT, high-intensity interval training group; MCT, moderate-intensity continuous training group; CTL, control group; Pre, pre-intervention; Post, post-intervention; R, resting; HE, hypoxic exercise test. \* $P < 0.05$ , R vs. HE; + $P < 0.05$ , Pre vs. Post.

**Pre-HIT****Post-HIT**

**Figure 7.** The calibrated, automatic thrombinographic analysis of high-intensity interval training (HIT) effect on dynamic thrombin generation in platelet-rich plasma (PRP). **Pre-HIT**, before HIT; **Post-HIT**, after HIT; **R**, resting; **HE**, hypoxic (12%O<sub>2</sub>) exercise test; **Omy**, oligomycin; **FCCP**, carbonyl cyanide-p-trifluoromethoxyphenylhydrazone; **Rot**, rotenone; **AA**, antimycin A.

work-rate to 100 W with continuous exercise for 30 min, and then recovery to 50 W of a cool-down period for 3 min. During the test, the O<sub>2</sub> concentration was set to 12%, which corresponds to an altitude of 4,460 m<sup>19,29</sup>. For safety reasons, the HE test was terminated immediately when the level of O<sub>2</sub> saturation dropped to <70% or the subject complained of discomfort. All subjects were free of acute mountain sickness symptoms during the experimental period.

At rest and immediately after the HE test, 40 ml blood samples were collected from an antecubital vein using a clean venipuncture (20 gauge needle). The first 2 ml of blood was discarded, and the remaining blood was used to measure hematological parameters. Blood cells were counted using a Sysmax SF-3000 cell counter (GMI, Inc., Ramsey, MN).

**Platelet isolation.** Blood samples were collected in polypropylene tubes that contained sodium citrate (3.8 g/dl, 1–9 vol. blood). PRP was prepared by centrifugation at 300 g for 10 min at room temperature (20 °C). Platelets were pelleted by centrifugation of the PRP at 1,500 g for 10 min and then washed once with phosphate buffered saline containing ethylenediaminetetraacetic acid (final concentration, 4 mM) (Sigma) to prohibit platelet activation. The number of platelets was adjusted to  $2 \times 10^8$  cells/ml with RPMI medium (Sigma). The tests of blood samples were repeated to ensure reproducibility. The analysis of platelet functions was completed within 2 hours after cell purification.

**Mitochondrial content, MP, and MOB in platelets.** The relative quantification of platelet mitochondrial-localized dyes using the single-color flow cytometric analysis allows for the sensitive measurement of a variety of mitochondrial parameters, including mitochondrial content, MP, and MOB, as described in previous studies<sup>18,33</sup>. The platelet suspensions ( $2 \times 10^8$  cells/ml) were incubated with MitoTracker Green FM (a green-fluorescent mitochondrial stain, 200 nM) (Invitrogen), tetramethylrhodamine ethyl ester (TMRE, a mitochondrial potential-sensitive probe, 20 nM) (Invitrogen), or MitoSOX Red (a mitochondrial superoxide indicator, 6.6 μM) (Invitrogen) in the dark for 30 min at 4 °C. Then, the platelets were gated separately from other particles on the basis of forward/sideways scatter, and the mean fluorescence intensity from 100,000 events representing the platelets was calculated using a FACScan flow cytometer (Becton Dickinson).

**Mitochondrial respiration and BHI in intact platelets.** The mitochondrial O<sub>2</sub> consumption of platelets ( $2 \times 10^8$  cells/ml) in RPMI 1460 medium was measured using high-resolution respirometry (Oroboros O2K). Mitochondrial respiration coupled towards ATP production (ATP-linked OCR) was measured by the fall in O<sub>2</sub> consumption following the addition of oligomycin (0.2 μg/ml), an inhibitor of ATP synthase. The remaining rate of mitochondrial respiration represents a proton leak that uncouples OXPHOS from the ETS. The total

	HIT		MCT		CTL	
	Pre	Post	Pre	Post	Pre	Post
<b>Vehicle</b>						
Lag time (min)						
R	9.1 ± 0.1	9.0 ± 0.1	9.1 ± 0.2	8.9 ± 0.1	9.1 ± 0.2	9.1 ± 0.2
HE	9.1 ± 0.1	9.0 ± 0.1	9.2 ± 0.1	8.9 ± 0.1	9.2 ± 0.2	9.3 ± 0.2
ETP (mM × min)						
R	879 ± 25	876 ± 24	873 ± 14	871 ± 15	855 ± 25	885 ± 25
HE	1105 ± 34*	845 ± 6 <sup>+</sup>	1101 ± 35*	870 ± 14 <sup>+</sup>	1103 ± 42*	1139 ± 48*
Peak height (mM)						
R	50.7 ± 1.7	45.5 ± 1.2	52.2 ± 1.3	49.6 ± 1.4	50.3 ± 3.7	51.0 ± 1.2
HE	70.1 ± 3.2*	45.0 ± 1.3 <sup>+</sup>	67.6 ± 2.5*	49.1 ± 1.7 <sup>+</sup>	71.6 ± 5.1*	76.3 ± 2.9*
<b>Oligomycin</b>						
Lag time (min)						
R	8.9 ± 0.1	9.0 ± 0.1	8.9 ± 0.1	8.8 ± 0.1	8.8 ± 0.2	8.7 ± 0.2
HE	8.8 ± 0.1	8.9 ± 0.1	8.8 ± 0.1	8.7 ± 0.1	8.8 ± 0.2	8.9 ± 0.2
ETP (mM × min)						
R	779 ± 31	795 ± 17	791 ± 17	791 ± 14	795 ± 25	782 ± 20
HE	825 ± 32	788 ± 29	845 ± 18	803 ± 17	846 ± 25	834 ± 41
Peak height (mM)						
R	45.0 ± 1.2	44.7 ± 1.6	45.3 ± 1.2	44.3 ± 1.6	44.2 ± 3.0	43.7 ± 1.2
HE	47.0 ± 1.3	44.0 ± 1.5	46.8 ± 1.2	44.0 ± 1.4	46.2 ± 3.0	44.9 ± 1.0
<b>Carbonyl cyanide-p-trifluoromethoxyphenylhydrazone</b>						
Lag time (min)						
R	6.9 ± 0.2	7.0 ± 0.1	6.9 ± 0.2	7.0 ± 0.1	7.0 ± 0.3	6.9 ± 0.2
HE	6.7 ± 0.2	7.0 ± 0.1	6.9 ± 0.2	6.9 ± 0.1	6.9 ± 0.2	7.1 ± 0.2
ETP (mM × min)						
R	1005 ± 23	955 ± 22	1027 ± 25	1032 ± 21	1069 ± 28	1040 ± 26
HE	1222 ± 28*	951 ± 20 <sup>+</sup>	1215 ± 32*	1025 ± 18 <sup>+</sup>	1252 ± 30*	1243 ± 33*
Peak height (mM)						
R	78.1 ± 3.4	79.2 ± 2.9	82.6 ± 2.8	76.8 ± 2.9	83.6 ± 6.1	87.3 ± 2.1
HE	108.1 ± 3.4*	78.6 ± 1.7 <sup>+</sup>	106.5 ± 2.7*	79.4 ± 2.62 <sup>+</sup>	111.7 ± 7.2*	112.5 ± 4.8*
<b>Rotenone plus Antimycin A</b>						
Lag time (min)						
R	9.0 ± 0.2	9.0 ± 0.1	9.1 ± 0.2	8.8 ± 0.1	9.0 ± 0.2	8.7 ± 0.2
HE	8.9 ± 0.2	8.9 ± 0.1	9.0 ± 0.1	8.8 ± 0.1	9.0 ± 0.2	8.8 ± 0.3
ETP (mM × min)						
R	833 ± 22	723 ± 21 <sup>+</sup>	840 ± 31	749 ± 16 <sup>+</sup>	833 ± 20	829 ± 26
HE	847 ± 20	735 ± 21 <sup>+</sup>	879 ± 27	754 ± 13 <sup>+</sup>	859 ± 24	841 ± 24
Peak height (mM)						
Rest	49.0 ± 2.1	33.3 ± 0.9 <sup>+</sup>	45.3 ± 1.8	34.7 ± 1.3 <sup>+</sup>	46.4 ± 3.0	47.0 ± 1.3
HE	50.4 ± 1.7	32.6 ± 1.0 <sup>+</sup>	48.1 ± 1.5	37.0 ± 1.8 <sup>+</sup>	49.8 ± 3.1	47.8 ± 1.5

**Table 4.** The effects of interval and continuous exercise regimens on dynamic thrombin generation in platelet-rich plasma. Values were mean ± SEM. HIT, high-intensity interval training group; MCT, moderate-intensity continuous training group; CTL, control group; Pre, pre-intervention; Post, post-intervention; R, resting; HE, hypoxic exercise test; ETP, endogenous thrombin potential. \* $P < 0.05$ , R vs. HE; <sup>+</sup> $P < 0.05$ , Pre vs. Post.

O<sub>2</sub> consumption of platelets was measured at baseline and after the addition of the uncoupling agent carbonyl cyanide-p-trifluoromethoxyphenylhydrazone (FCCP; 2 μM) to induce maximal O<sub>2</sub> consumption. The difference between the basal and maximal respiration is called the reserve capacity of OCR. Non-mitochondrial respiration (non-mito OCR) was quantified by inhibiting mitochondrial respiration through the addition of rotenone (a mitochondrial Complex I inhibitor, 1 μM) and antimycin A (a mitochondrial Complex III inhibitor, 1 μM)<sup>18,34</sup>.

The BHI was calculating from the result of coupling control protocol to quantify platelet mitochondrial function using the following equations<sup>35</sup>:

$$\text{Log}[(\text{ATP-linked OCR}) \times (\text{Reserved capacity of OCR}) / (\text{Proton leak}) \times (\text{Non-mito OCR})] \quad (1)$$

$$\text{ATP-linked OCR} = \text{Routine state} - \text{Leak state} \quad (2)$$



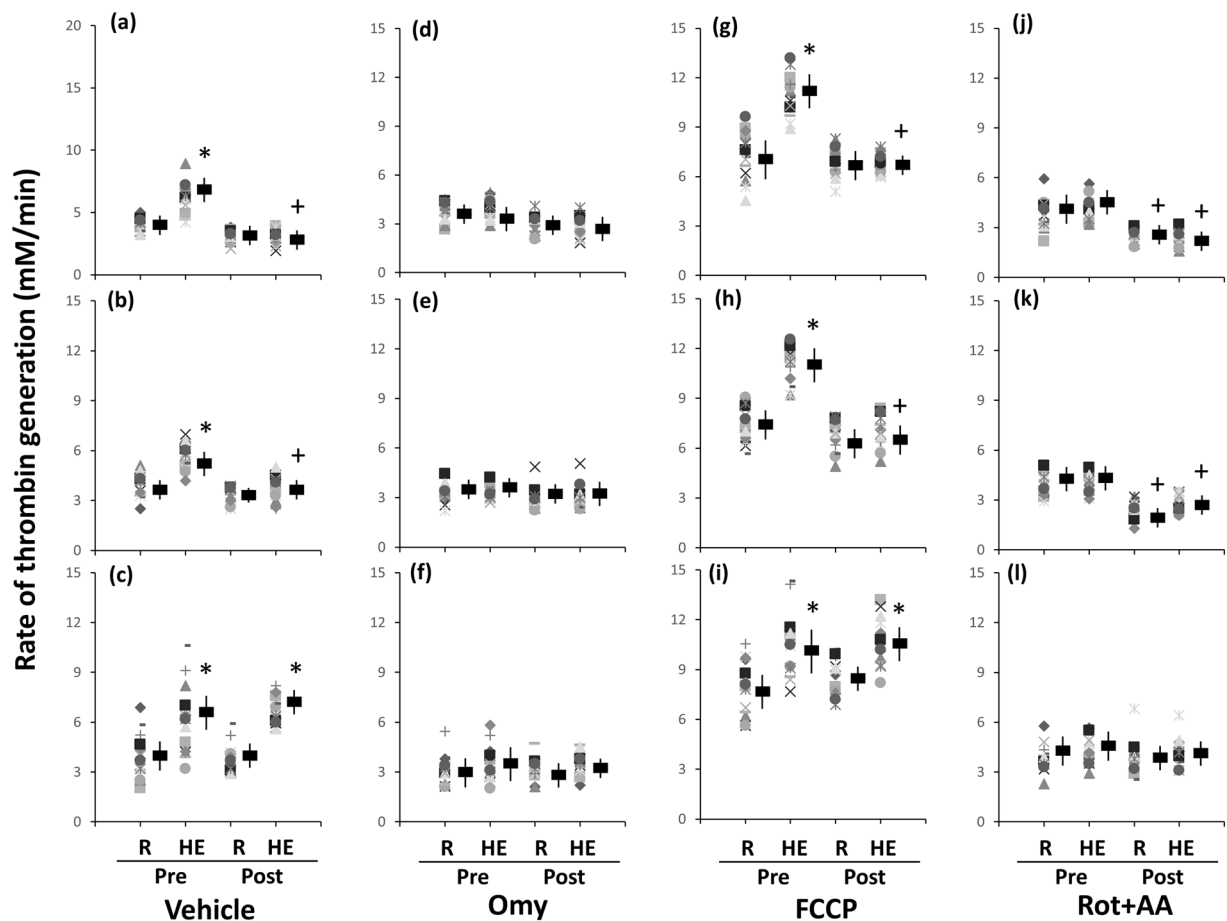


**Figure 8.** Effects of interval and continuous exercise regimens on the rate of thrombin generation in platelet-rich plasma. HIT (a,d,g,j), high-intensity interval training group; MCT (b,e,h,k), moderate-intensity continuous training; CTL (c,f,i,l), control group; Pre, pre-intervention; Post, post-intervention; R, resting; HE, hypoxic (12%O<sub>2</sub>) exercise test; ETP, endogenous thrombin potential; Omy, oligomycin; FCCP, carbonyl cyanide-p-trifluoromethoxyphenylhydrazone; Rot, rotenone; AA, antimycin A. \**P* < 0.05, R vs. HE; +*P* < 0.05, Pre vs. Post. Values were mean ± SEM.

$$\text{Reserved capacity} = \text{ETS state} - \text{Routine state} \quad (3)$$

$$\text{Non-mito OCR} = \text{Residual O}_2\text{consumption (ROX)state} \quad (4)$$

$$\text{Proton leak} = \text{Leak state} - \text{ROX state} \quad (5)$$

**Mitochondrial respiration in permeabilized platelets.** A substrate, uncoupler, inhibitor titration (SUIT) protocol was applied to permeabilized platelets preparation and analyzed the respiration capacity of platelet mitochondria. By multiple substrate titration, electron flow from FAO and mitochondrial Complex I and II were well controlled, and the mitochondrial OCR of each state was measured by a high-resolution respirometry (Oroboros O2K)<sup>18,34</sup>.

Intact platelets ( $2 \times 10^8$  cells/ml) were incubate at 37 °C in the O2K chamber of mitochondria respiratory medium MiR05 (EGTA 0.5 mM, MgCl<sub>2</sub> · 6H<sub>2</sub>O 3 mM, lactobionic acid 60 mM, taurine 20 mM, KH<sub>2</sub>PO<sub>4</sub> 10 mM, HEPES 20 mM, D-sucrose 110 mM, and bovine serum albumin 1 g/l, pH = 7.1). Data acquisition was started after the oxygen flux stabilized. The O<sub>2</sub> consumption in this state was the routine respiration from endogenous substrates in cells. Then the plasma membrane was permeabilized by digitonin (0.1 mg) titration after a concomitant addition of malate (2 mM) and palmitoyl-DL-carnitine-HCl (20 μM). Since the absence of adenylate in the chamber, the respiration in this state was caused by mitochondrial proton leakage (LEAK). The O<sub>2</sub> consumption by FAO was evaluated by addition of 1 mM ADP (Calbiochem). Oxidative phosphorylation capacity of mitochondrial Complex I and II were acquired through the addition of NADH resources pyruvate (5 mM) and glutamate (10 mM) and SDH resource succinate (10 mM). A cytochrome c (10 μM) test was applied to evaluate whether the outer mitochondrial membrane was intact. The maximal convergent capacity of the ETS was subsequently obtained by FCCP titration (0.5 μM/steps).

Finally, the inhibitors for Complex I, II and III (0.1  $\mu\text{M}$  rotenone, 5 mM malonic acid, and 0.5  $\mu\text{M}$  myxothiazol/2.5  $\mu\text{M}$  antimycin A) were progressively added to suppress the  $\text{O}_2$  consumption of platelets mitochondria. At last, tetramethyl-p-phenylenediamine (TMPD, 0.5 mM) applied as an artificial substrate for reducing cytochrome c, was added for cytochrome c oxidase activity measurement and then blocked by mitochondrial Complex IV inhibitor sodium azide (200 mM). All chemicals were purchased from Sigma-Aldrich (St Louis, MO, USA) if not stated otherwise.

**Enzyme activities of glycolysis and the Krebs cycle in platelets.** The activities of HK (Sigma), PDH (BioVision), and LDH (Sigma) in glycolysis and the activities of CS (BioVision) and SDH (BioVision) in the Krebs cycle of platelets ( $1 \times 10^8$  cells/ml) were measured with commercially available colorimetric kits according to the manufacturer's instructions<sup>18</sup>.

**Dynamic TG assay.** The dynamic TG in PRP was measured by calibrated, automatic thrombinography (Synapse/Thromboscope BV, Maastricht, the Netherlands), as described in our earlier works<sup>4,13</sup>. Oligomycin (2  $\mu\text{g/ml}$ ), FCCP (3.75  $\mu\text{M}$ ), or rotenone (0.1  $\mu\text{M}$ ) plus antimycin A, (2.5  $\mu\text{M}$ ) were added to the PRP ( $2 \times 10^8$  cells/ml), which was then warmed to 37°C for 10 min. Following incubation, eighty microliters of the PRP samples were allocated into the wells of round bottom 96-well microtiter plates (Nunc). Twenty microliters of reagent containing tissue factor (TF) was mixed with the plasma samples to obtain a final concentration of 0.5 pM TF. Coagulation was started by adding 0.1 M  $\text{CaCl}_2$  (20  $\mu\text{L}$ ) in a fresh mixture of flubuffer (containing 20 mM HEPES and 60 mg/mL bovine serum albumin in pH 7.35) containing 2.5 mM Z-Gly-Gly-Arg-AMC (the fluorogenic substrate) (Synapse/Thromboscope BV, Maastricht, the Netherlands). Upon cleaving by thrombin, the fluorescent AMC (7-amino-4-methylcoumarin) is released and measured with a 390-nm-excitation and a 460-nm-emission filter set in an Ascent Fluoroskan (Thermo Fisher Scientific Inc., the Netherlands). All reagents were warmed to 37°C before the experiment began. Fluorescence was recorded for 60 min. The fluorescence signal was corrected for substrate consumption, plasma colour variability and inner filter fluorescence effect by running in parallel calibrating wells where 80 microliters plasma samples were mixed with 20 microliters Thrombin Calibrator from Thromboscope BV.

The calculated data using analytic software from Synapse/Thromboscope BV were plotted and expressed in terms of lag time (time until initial thrombin formation, min), endogenous thrombin potential (ETP, area under the thrombin curve,  $\text{nM} \times \text{min}$ ), the peak height of thrombin (nM), and the rate of TG (mean slope = peak height/[time to peak-lag time],  $\text{nM/min}$ )<sup>4,13</sup>.

**Statistical analysis.** The results are expressed as the mean  $\pm$  SEM. The statistical software package StatView was used for data analysis. Experimental results in each group were analyzed by the repeated measures ANOVA and Bonferroni's post-hoc test to compare the count, mitochondrial OXPHOS, oxidative stress and biogenesis of platelets, as well as, the dynamic TG in PRP before and immediately after HE at the beginning of the present study and after 6 weeks. In addition, the comparison of cardiopulmonary fitness during GXT at the beginning of the present study and 6 weeks later in various groups was analyzed by the repeated measures ANOVA and Bonferroni's post-hoc test. The criterion for statistical significance was  $P < 0.05$ .

## References

- Lee, K. W. & Lip, G. Y. Effects of lifestyle on hemostasis, fibrinolysis, and platelet reactivity: a systematic review. *Arch Intern Med* **163**, 2368–2392 (2003).
- Lee, K. W. & Lip, G. Y. Acute versus habitual exercise, thrombogenesis and exercise intensity. *Thromb Haemost* **91**, 416–419 (2004).
- Kesaniemi, Y. K. *et al.* Dose-response issues concerning physical activity and health: an evidence-based symposium. *Med Sci Sports Exerc* **33**, S351–S358 (2001).
- Wang, J. S., Cheng, M. L., Yen, H. C., Lou, B. S. & Liu, H. C. Vitamin E suppresses the enhancement of factor VIII-dependent thrombin generation by systemic hypoxia. *Stroke* **40**, 656–659 (2009).
- Monteiro, R. Q. *et al.* Hypoxia regulates the expression of tissue factor pathway signaling elements in a rat glioma model. *Oncol Lett* **12**, 315–322 (2016).
- von Kanel, R. & Dimsdale, J. E. Hemostatic alterations in patients with obstructive sleep apnea and the implications for cardiovascular disease. *Chest* **124**, 1956–196 (2003).
- Ashtiani, J., Mukae, H., Arimura, Y. & Matsukura, S. Elevated plasma procoagulant and fibrinolytic markers in patients with chronic obstructive pulmonary disease. *Intern Med* **41**, 181–185 (2002).
- Kalz, J., ten Cate, H. & Spronk, H. M. Thrombin generation and atherosclerosis. *J Thromb Thrombolysis* **37**, 45–55 (2014).
- Zharikov, S. & Shiva, S. Platelet mitochondrial function: from regulation of thrombosis to biomarker of disease. *Biochem Soc Trans* **41**, 118–123 (2013).
- Obydeny, S. I., Sveshnikova, A. N., Ataulakhov, F. I. & Pantelev, M. A. Dynamics of calcium spiking, mitochondrial collapse and phosphatidylserine exposure in platelet subpopulations during activation. *J Thromb Haemost* **14**, 1867–1881 (2016).
- Chen, Y. W., Chen, Y. C. & Wang, J. S. Absolute hypoxic exercise training enhances *in vitro* thrombin generation by increasing procoagulant platelet-derived microparticles under high shear stress in sedentary men. *Clin Sci (Lond)* **124**, 639–649 (2013).
- Wang, J. S., Yen, H. L. & Yang, C. M. Warm-up exercise suppresses platelet-eosinophil aggregation and platelet-promoted release of eosinophil oxidant products enhanced by severe exercise under shear flow and inflammation in men. *Thromb Haemost* **207**, 174–186 (2006).
- Chen, Y. C., Ho, C. W., Tsai, H. H. & Wang, J. S. Interval and continuous exercise regimens suppress neutrophil-derived microparticle formation and neutrophil-promoted thrombin generation under hypoxic stress. *Clin Sci (Lond)* **128**, 425–436 (2015).
- Martín-Fernández, B. & Gredilla, R. Mitochondria and oxidative stress in heart aging. *Age (Dordr)* **38**, 225–238 (2016).
- Walters, J. W., Amos, D., Ray, K. & Santanam, N. Mitochondrial redox status as a target for cardiovascular disease. *Curr Opin Pharmacol* **27**, 50–55 (2016).
- Rocha, M. *et al.* Mitochondrial dysfunction and oxidative stress in insulin resistance. *Curr Pharm Des* **19**, 5730–5741 (2013).
- Mazure, N. M., Brahimi-Horn, M. C. & Pouyssegur, J. Hypoxic mitochondria: accomplices in resistance. *Bull Cancer* **98**, 40–46 (2011).
- Tsai, H. H. *et al.* Exercise training alleviates hypoxia-induced mitochondrial dysfunction in the lymphocytes of sedentary males. *Sci Rep* **6**, 35170 (2016).

19. Schönerberger, M. J. & Kovacs, W. J. Hypoxia signaling pathways: modulators of oxygen-related organelles. *Front Cell Dev Biol* **3**, 42 (2015).
20. Chouchani, E. T. *et al.* Ischaemic accumulation of succinate controls reperfusion injury through mitochondrial ROS. *Nature* **515**, 431–435 (2014).
21. Mills, E. & O'Neill, L. A. Succinate: a metabolic signal in inflammation. *Trends Cell Biol* **24**, 313–320 (2014).
22. Carter, H. N., Chen, C. C. & Hood, D. A. Mitochondria, muscle health, and exercise with advancing age. *Physiology (Bethesda)* **30**, 208–223 (2015).
23. Kotwal, J., Apte, C. V., Kotwal, A., Mukherjee, B. & Jayaram, J. High altitude: a hypercoagulable state: results of a prospective cohort study. *Thromb Res* **120**, 391–397 (2007).
24. Gupta, N. & Ashraf, M. Z. Exposure to high altitude: a risk factor for venous thromboembolism? *Semin Thromb Hemost* **38**, 156–163 (2012).
25. Wang, J. S. Exercise prescription and thrombogenesis. *J Biomed Sci* **13**, 753–761 (2006).
26. Huang, S. C. *et al.* Comparison of cardiac autonomic nervous system disturbed by sleep deprivation in sex and menstrual phase. *Chin J Physiol* **58**, 114–123 (2015).
27. Wang, J. S., Jen, C. J., Lee, H. & Chen, H. I. Effects of short-term exercise on female platelet function during different phases of the menstrual cycle. *Arteriosclero Thromb Vasc Biol* **17**, 1682–1686 (1997).
28. Weng, T. P., Huang, S. C., Chuang, Y. F. & Wang, J. S. Effects of interval and continuous exercise training on CD4 lymphocyte apoptotic and autophagic responses to hypoxic stress in sedentary men. *PLoS One* **8**, e80248 (2013).
29. Swain, D. P., Leutholtz, B. C., King, M. E., Haas, L. A. & Branch, J. D. Relationship between % heart rate reserve and %VO<sub>2</sub> reserve in treadmill exercise. *Med Sci Sports Exerc* **30**, 318–321 (1988).
30. Lee, P. H., Macfarlane, D. J., Lam, T. H. & Stewart, S. M. Validity of the International Physical Activity Questionnaire Short Form (IPAQ-SF): a systematic review. *Int J Behav Nutr Phys Act* **8**, 115 (2011).
31. Ortega, R. M., Pérez-Rodrigo, C. & López-Sobaler, A. M. Dietary assessment methods: dietary records. *Nutr Hosp* **31**, S38–S45 (2015).
32. American College of Sports Medicine, General principle of exercise prescription. In ACSM's Guidelines for Exercise Testing and Prescription (Thompson, W. R., Gordon, N. F. & Pescatello, L. S., eds), Lippincott Williams & Wilkins, Philadelphia. pp. 152–182, (2010).
33. Pendergrass, W., Wolf, N. & Poot, M. Efficacy of MitoTracker Green and CMXRosamine to measure changes in mitochondrial membrane potentials in living cells and tissues. *Cytometry A* **61**, 162–169 (2004).
34. Sjövall, F. *et al.* Mitochondrial respiration in human viable platelets—methodology and influence of gender, age and storage. *Mitochondrion* **13**, 7–14 (2013).
35. Chacko, B. K. *et al.* The Bioenergetic Health Index: a new concept in mitochondrial translational research. *Clin Sci (Lond)* **127**, 367–373 (2014).

## Acknowledgements

The authors would like to thank the volunteers for their enthusiastic participation in the present study. This work was supported by the National Science Council of Taiwan (grant number NSC 105-2314-B-182-013-MY3, 103-2314-B-182-005-MY3), Chang Gung Medical Research Program (grant number CMRPD3D0133, CMRPD1E0262), and Healthy Aging Research Center, Chang Gung University (grant number EMRPD1A0841).

## Author Contributions

Jong-Shyan Wang was involved in conception and design of research; Li-Hua Wu and Shao-Chiang Chang performed experiments; Jong-Shyan Wang and Li-Hua Wu analyzed data, interpreted results of experiments, prepared the Figures, and drafted the paper; Jong-Shyan Wang, Tieh-Cheng Fu, and Ching-Hui Huang edited and revised the paper; Li-Hua Wu, Shao-Chiang Chang, Tieh-Cheng Fu, Ching-Hui Huang, and Jong-Shyan Wang approved the final version of paper.

## Additional Information

**Competing Interests:** The authors declare that they have no competing interests.

**Publisher's note:** Springer Nature remains neutral with regard to jurisdictional claims in published maps and institutional affiliations.



**Open Access** This article is licensed under a Creative Commons Attribution 4.0 International License, which permits use, sharing, adaptation, distribution and reproduction in any medium or format, as long as you give appropriate credit to the original author(s) and the source, provide a link to the Creative Commons license, and indicate if changes were made. The images or other third party material in this article are included in the article's Creative Commons license, unless indicated otherwise in a credit line to the material. If material is not included in the article's Creative Commons license and your intended use is not permitted by statutory regulation or exceeds the permitted use, you will need to obtain permission directly from the copyright holder. To view a copy of this license, visit <http://creativecommons.org/licenses/by/4.0/>.

© The Author(s) 2017